2007

Proceedings of the 29th Monitoring Research Review: Ground-Based Nuclear Explosion Monitoring Technol

Proceedings of the 29th Monitoring Research Review: Ground-Based Nuclear Explosion Monitoring Technologies

September 25–27, 2007

Denver, Colorado

Volume I

Seismic Regional Characterizationand Wave Propagation
Seismic Event Detection and Location
Seismic Identification and Source Characterization

Approved for Public Release; further dissemination unlimited.

National Nuclear Security Administration

AIR FORCE RESEARCH LABORATORY

LA-UR-07-5613

To view these Proceedings online, visit
https://www.nemre.nnsa.doe.gov/review2007

Vol. I

ACKNOWLEDGEMENTS

The National Nuclear Security Administration (NNSA) and the Air Force Research Laboratory (AFRL) gratefully acknowledge the important contributions of the following people for their work to produce the ***Proceedings of the 29th Monitoring Research Review: Ground-Based Nuclear Explosion Monitoring Technologies.***

Authors of papers for excellent research, technical documentation, and cooperation with electronic submission processes.

Dr. Anton M. Dainty, Mr. Robert J. Raistrick, Dr. Frederick R. Schult, AFRL/VSBYE, and ***Ms. Doris Richards***, ESC/PAM, for review and clearance of abstracts and papers related to AFRL contracts.

Dr. Mark T. Woods, Air Force Technical Applications Center (AFTAC)/TTR, for review and clearance of abstracts and papers related to AFTAC contracts.

Dr. Leigh S. House, NNSA/LANL, for technical consultation on papers related to NNSA contracts.

Dr. Stanley D. Ruppert, Lawrence Livermore National Laboratory (LLNL), for assistance in ensuring that the CDs could be read on a variety of platforms and for burning the CDs.

Mr. Marvin A. Wetovsky, Los Alamos National Laboratory (LANL), for overall coordination of the Proceedings development and for technical editing and formatting of abstracts and papers.

Ms. Deidré A. Plumlee, LANL, for composition and format of the electronic submissions of the Proceedings covers.

Ms. Jody Benson and ***Ms. Eileen F. Patterson***, LANL, for supplementary technical editing of papers.

Ms. AnnMarie Cutler, LANL, for design and artwork of the CD label.

Ms. Sandra Valdez, LANL, for labeling the CDs.

Mr. Geoff Miller, Ms. Karen LaRue, Ms. Diana Hollis, Mr. Leo Beckstead, Ms. Sandra Bonchin, Mr. Burton Krohn, and ***Mr. Randy Drake***, LANL, for classification review of compiled papers.

IRM-RMMSO, LANL, for color printing and binding of the hard copies.

Ms. Leslie A. Casey, NNSA, for review and clearance of abstracts and papers related to NNSA contracts and for NNSA overall support of the Proceedings.

Dr. Sam J. Dahdouh, NNSA/NREI, for review of abstracts and papers related to NNSA contracts.

Mr. Steven T. Eacret and ***Mr. David C. Bissell***, Space and Missile Defense Command (SMDC), for review and clearance of abstracts and papers related to SMDC contracts. Additional thanks to ***Dr. Mark S. Pickens***, SMDC Lead, and ***Ms. Charlotte Green***, SMDC Administrative Support.

Ms. Mary L. Girven, Sandia National Laboratories (SNL), for making everyone's job easier with web-based technology for abstract and paper submission, on-line review and approval tools, and creation of the master files for the hardcopy, CD, and website versions of the Proceedings.

Ms. Guadalupe (Lupe) Massoth, SNL, for providing assistance to Mary Girven on website development and help in creating the master files.

Dr. David B. Harris, LLNL; ***Mr. Phillip E. Harben***, LLNL; ***Dr. W. Scott Phillips***, LANL, ***Mr. Ward L. Hawkins***, LANL; ***Dr. Dale N. Anderson***, Pacific Northwest National Laboratory (PNNL); ***Dr. Harry S. Miley***, PNNL; ***Dr. Ted W. Bowyer***, PNNL; ***Mr. J. Mark Harris***, SNL; and ***Dr. Christopher J. Young***, SNL, for a myriad of internal management and technical reviews of NNSA abstracts and papers.

Table of Contents - Volume I

1. Seismic Regional Characterization and Wave Propagation 1

1-01 **Fatehi, A. and K. Koper**
Modeling P Wave Multipathing in Southeast Asia 3

1-02 **Ferris, A. and D. Reiter**
Using Small-Aperture Arrays to Identify Far-Regional P-Wave Arrivals 14

1-03 **Fisk, M. and S. Taylor**
Robust Magnitude and Path Corrections for Regional Seismic Phases in Eurasia by Constrained Inversion and Enhanced Kriging Techniques 24

1-04 **Ford, S., D. Dreger, K. Mayeda, W. Walter, L. Malagnini, and W. Phillips**
Regional Analysis of Lg Attenuation: Comparison of 1-D Methods in Northern California and Application to the Yellow Sea/Korean Peninsula 34

1-05 **Gerstoft, P., W. Kuperman, K. Sabra, M. Fehler, S. Taylor, and T. Tanimoto**
Extracting Short-Period Surface Waveforms from Seismic Noise for the Purpose of Estimating Local and Near-Regional Velocity and Attenuation Structure 44

1-06 **Ghalib, H., M. Sibol, Y. Chen, R. Herrmann, G. Aleqabi, H. Tkalcic, B. Ali, B. Saleh, D. Mahmood, R. Wagner, P. Shore, O. Shaswar, A. Mahmood, S. Abdullah, F. Ibrahim, R. Zand, B. Ali, L. Omar, N. Aziz, N. Ahmed, T. Al-Nasiri, A. Ali, A. Taqi, and S. Khalaf**
Seismic Velocity Modeling of North and Northeast Iraq Using Receiver Functions 54

1-07 **Gritto, R., J. Siegel, and W. Chan**
Structure of the Moho Discontinuity Beneath South Korea from Travel-Time Waveform Analysis 62

1-08 **Harris, D., J. Zucca, D. McCallen, M. Pasyanos, M. Flanagan, S. Myers, W. Walter, A. Rodgers, and P. Harben**
Considerations of the Use of 3-D Geophysical Models to Predict Test Ban Monitoring Observables 70

1-09 **Helmberger, D., J. Tromp, and A. Rodgers**
Advanced Waveform Simulation for Seismic Monitoring Events 80

1-10 **Kim, W., H. Patton, G. Randall, and P. Richards**
Improvements to a Major Digital Archive of Seismic Waveforms from Nuclear Explosions: Borovoye Seismogram Archive 91

1-11 **Lay, T., X. Xie, X. Yang, and M. Arrowsmith**
Development of Regional Phase Tomographic Attenuation Models for Eurasia 100

1-12 **Levshin, A., M. Barmin, X. Yang, M. Ritzwoller, and G. Randall**
Toward a Rayleigh Wave Attenuation Model for Central Asia and Surrounding Regions 111

1-13 **Mackey, K., H. Hartse, L. Steck, R. Stead, C. Rowe, K. Fujita, and L. Gutirrez**
Seismic Characterization of Northeast Asia 123

1-14 **Martin, R., M. Krasovec, S. Romer, L. Hutchings, W. Foxall, E. Vergino, L. Gülen, and M. Toksöz**
Extension of the Caucasus Seismic Information Network Study into Central Asia 133

1-15 **Mellors, R., R. Gok, and E. Sandvol**
High-Resolution Seismic Velocity and Attenuation Models of the Caucasus-Caspian Region 143

1-16 **Morozov, I., C. Zhang, and E. Morozova**
Frequency-Dependent Short-Period Explosion Coda Amplitudes in Northern Eurasia 152

1-17 **Morozov, I., E. Morozova, and S. Smithson**
Digital Database of Deep Seismic Sounding Profiles in Northern Eurasia 164

1-18 **Myers, S., J. Wagoner, and S. Larsen**
Numerical Experiments Investigating the Source of Explosion S-Waves 175

1-19 **Nyblade, A., W. Walter, R. Gok, L. Linzer, and R. Durrheim**
Developing and Exploiting a Unique Seismic Data Set from South African Gold Mines for Source Characterization and Wave Propagation 185

1-20 **Pasyanos, M., W. Walter, M. Flanagan, R. Gok, S. Myers, and K. Dyer**
Enhancements of Geophysical Models for Monitoring 195

1-21 **Pitarka, A., D. Helmberger, and S. Ni**
Analysis and Simulation of Three-Dimensional Scattering Due to Heterogeneous Crustal Structure and Surface Topography on Regional Phases; Magnitude and Discrimination 205

1-22 **Pulliam, J., M. Sen, and A. Gangopadhyay**
Waveform Modeling of Teleseismic S, Sp, SsPmP, and Shear-Coupled PL Waves for Crust and Upper Mantle Velocity Structure 214

1-23 **Ritzwoller, M., Y. Yang, R. Richmond, M. Pasyanos, A. Villasenor, V. Levin, A. Hofstetter, V. Pinsky, N. Kraeva, and A. Lerner-Lam**
Short Period Surface Wave Dispersion Across the Mediterranean Region: Improvements Using Regional Seismic Networks 226

1-24 **Rodi, W. and D. Reiter**
SAsia3D: A 3-D Crust and Upper-Mantle Velocity Model of South Asia Derived from Joint Inversion of P-Wave Travel Times and Surface-Wave Dispersion Data 236

1-25 **Romanowicz, B., A. Cao, A. Kim, M. Panning, M. Pasyanos, and D. Dreger**
Calibration of Three-Dimensional Upper Mantle Structure in Eurasia Using Regional and Teleseismic Full Waveform Seismic Data 247

1-26 **Rowe, C., W. Phillips, M. Maceira, M. Begnaud, L. Steck, X. Yang, C. Lucero, H. Hartse, R. Stead, K. Mackey, K. Fujita, and C. Ammon**
Geophysical Imaging of Asia and Siberia: Tomograhy for Seismic Velocity, Upper Mantle Gradient, Lg Attenuation, and Joint Inversion of Surface Wave Dispersion, Receiver Functions and Satellite Gravity Data 256

1-27 **Sandvol, E., B. Xueyang, E. Zor, J. Xie, B. Mitchell, and D. Schaff**
Lg and Pg Attenuation in the Middle East 266

1-28 **Shearer, P. and J. Lawrence**
Transition Zone Wave Propagation: Characterizing Travel-Time and Amplitude Information 274

1-29 **Stevens, J., J. Given, H. Xu, and G. Baker**
Development of Surface Wave Dispersion and Attenuation Maps and Improved Methods for Measuring Surface Waves 282

1-30 **Toksöz, M., R. Van der Hilst, M. Benoit, L. Gülen, D. Kalafat, H. Kuleli, C. Li, and Y. Sun**
Seismic Tomography of the Arabian-Eurasian Collision Zone and Surrounding Areas 292

1-31 **Toksöz, M., R. Van der Hilst, Y. Sun, C. Li, and H. Yao**
P- and S-Wave Velocity Structure of the Crust and Upper Mantle Under China and Surrounding Areas from Body and Surface Wave Tomography 302

1-32 **van der Lee, S., S. Chang, M. Flanagan, H. Bedle, F. Marone, E. Matzel, M. Pasyanos, A. Rodgers, B. Romanowicz, and C. Schmid**
Joint Inversion for 3-Dimensional S-Velocity Mantle Structure Along the Tethyan Margin 312

1-33 **Xie, X., T. Lay, R. Wu, and Y. He**
Near Source Energy Partitioning for Regional Waves in 2D and 3D Models: Effects from Random Free Surface Scattering 322

1-34 **Zhang, H., K. Mackey, K. Fujita, L. Steck, C. Rowe, C. Thurber, and S. Roecker**
High-Resolution Three-Dimensional Seismic Imaging of Baikal and Amur Regions of Eastern Russia 333

1-35 **Zhang, Z., Y. Shen, L. Zhao, P. Chen, and X. Yang**
Refined Local and Regional Seismic Velocity and Attenuation Models from Finite-Frequency Waveforms 343

1-36 **Zhou, R., B. Stump, Z. Yang, Y. Chen, R. Herrmann, R. Burlacu, C. Hayward, and K. Pankow**
Broadband Network Operation and Shear Velocity Structure Beneath the Xiuyan Area, NE China 353

2. Seismic Event Detection and Location 363

2-01 **Begnaud, M., C. Rowe, L. Steck, and W. Kim**
Improving Location/Detection Methods for Monitoring Research Using Large-Scale Correction Surfaces, Cross-Correlation Techniques and Genetic Algorithms 365

2-02 **Bondár, I., B. Kohl, E. Bergman, K. McLaughlin, Y. Kung, and E. Engdahl**
Global Ground Truth Data Set with Waveform and Improved Arrival Data 375

2-03 **Bondár, I., K. McLaughlin, and H. Israelsson**
Improved Event Location Uncertainty Estimates 385

2-04 **Engdahl, E., E. Bergman, S. Myers, and F. Ryall**
Improved Ground Truth in Southern Asia Using In-Country Data, Analyst Waveform Review, and Advanced Algorithms 395

2-05 **Ichinose, G., H. Thio, and D. Helmberger**
Ground Truth Locations Using Synergy Between Remote Sensing and Seismic Methods 406

2-06 **Myers, S., S. Ballard, C. Rowe, G. Wagner, M. Antolik, W. Phillips, A. Ramirez, M. Begnaud, M. Pasyanos, D. Dodge, M. Flanagan, K. Hutchenson, G. Barker, J. Dwyer, and D. Russell**
Tomography and Methods of Travel-Time Calculation for Regional Seismic Location 414

2-07 **Nyblade, A., R. Brazier, A. Adams, Y. Park, A. Rodgers, and A. Al-Amri**
Ground Truth, Magnitude Calibration and Regional Phase Propagation and Detection in the Middle East and Horn of Africa 424

2-08 **Ren, Y., T. Yang, W. Zhang, Y. Shen, B. Covellone, and X. Yang**
Crustal and Mantle Structure Beneath Eastern Eurasia from Inversions of Finite-Frequency Body and Surface Waves 434

2-09 **Ringdal, F., S. Gibbons, and D. Harris**
Adaptive Waveform Correlation Detectors for Arrays: Algorithms for Autonomous Calibration 444

2-10 **Rodi, W.**
Error Analysis in the Joint Event Location/Seismic Calibration Inverse Problem 454

2-11 **Rodi, W. and S. Myers**
Modeling Travel-Time Correlations Based on Sensitivity Kernels and Correlated Velocity Anomalies 463

2-12 **Salzberg, D. and M. Marshall**
Seismic Source Locations and Parameters for Sparse Networks by Matching Observed Seismograms to Semi-Empirical Synthetic Seismograms: Applications to Lop Nor and North Korea 472

2-13 **Schaff, D. and F. Waldhauser**
Improving Magnitude Detection Thresholds Using Multi-Station, Multi-Event, and Multi-Phase Methods 482

2-14 **Standley, I. and W. Pike**
Progress in the Development of Rugged Low Power Compact Silicon MEMS Sensors for Use in Nuclear Explosion Monitoring 491

2-15 **Stroujkova, A., D. Reiter, and R. Shumway**
Regional Seismic Focal Depth Estimation in Complex Tectonic Environments 501

3. Seismic Identification and Source Characterization 513

3-01 **Abercrombie, R., K. Mayeda, W. Walter, G. Viegas, and K. Murphy**
Seismic Source Scaling and Discrimination in Diverse Tectonic Environments 515

3-02 **Anderson, D., D. Fagan, M. Tinker, G. Kraft, and K. Hutchenson**
A Mathematical Statistics Formulation of the Teleseismic Explosion Identification Problem with Multiple Discriminants 526

3-03 **Arrowsmith, M., S. Arrowsmith, B. Stump, and M. Hedlin**
Discrimination Capability for Mining Events in the Altai-Sayan Region of Russia and the Western United States 531

3-04 **Bonner, J., M. Pasyanos, M. Johnson, and D. Harkrider**
Calibration of the Ms(VMAX) Technique in Eurasia 541

3-05 **Fisk, M., S. Taylor, H. Patton, and W. Walter**
Next-Generation MDAC Discrimination Procedure Using Multi-Dimensional Spectral Analyses 551

3-06 **Ford, S., D. Dreger, and W. Walter**
Identifying Isotropic Events Using an Improved Regional Moment Tensor Inversion Technique 561

3-07 **Gitterman, Y., A. Hofstetter, and V. Pinsky**
Depth-of-Burial and Decoupling Explosion Experiments in Israel: Near-Source and Near-Regional Seismic Energy Generation 571

3-08 **Hartse, H., G. Randall, X. Yang, and C. Rowe**
Regional Event Identification Research in Asia 582

3-09 **Herrmann, R., W. Walter, and M. Pasyanos**
Seismic Source and Path Calibration in the Korean Peninsula, Yellow Sea, and Northeast China 592

3-10 **Le Bras, R. and T. Hampton**
Inclusion of a Body Wave Seismic Moment Tensor Estimator in the CTBTO/IDC Processing Suite 602

3-11 **Leidig, M., J. Bonner, R. Martin, S. Dougherty, and K. Murphy**
Effects of Frozen Rock on Explosive Coupling 612

3-12 **Mayeda, K. and J. Bonner**
Regional P Coda for Stable Estimates of Body Wave Magnitude: Extending the Ms:mb Discriminant to Smaller Events 622

3-13 **Mayeda, K. and W. Phillips**
Small-Event Yield and Source Characterization Using Local P- and S-Wave Coda Source Spectra 627

3-14 **Phillips, W., H. Patton, R. Stead, G. Randall, and H. Hartse**
Regional Magnitude Research Supporting Broad-Area Monitoring of Small Seismic Events 635

3-15 **Pitarka, A., K. Mayeda, and N. Collins**
Developing Multiple-Frequency Discriminants for Use with Regional Coda-Amplitude Measurements 644

3-16 **Sammis, C.**
Characterizing Fracture Damage at Frozen and Unfrozen Sites in the Alaska Frozen Rock Experiment and its Effect on Seismic Radiation 650

3-17 **Shearer, P. and B. Allmann**
Spectral Studies of Shallow Earthquakes and Explosions in Southern California 656

3-18 **Stevens, J., H. Xu, and G. Baker**
Analysis of Shear Wave Generation by Decoupled and Partially Coupled Explosions 664

3-19 **Stump, B., R. Burlacu, C. Hayward, J. Bonner, K. Pankow, A. Fisher, and S. Nava**
Seismic and Infrasound Energy Generation and Propagation at Local and Regional Distances: Phase 1 - Divine Strake Experiment 674

3-20 **Walter, W., E. Matzel, M. Pasyanos, D. Harris, R. Gok, and S. Ford**
Empirical Observations of Earthquake-Explosion Discrimination Using P/S Ratios and Implications for the Sources of Explosion S-Waves 684

Seismic Regional Characterization and Wave Propagation

MODELING P WAVE MULTIPATHING IN SOUTHEAST ASIA

Ali Fatehi and Keith D. Koper

Saint Louis University

Sponsored by the Air Force Research Laboratory

Contract No. FA8718-06-C-0003

ABSTRACT

We have used data from the small aperture Chiang Mai seismic array (CMAR) in Thailand to characterize P-wave propagation in the mantle transition zone beneath south Asia. Our data consist of nearly 1700 events, which occurred at regional distances from CMAR with continental ray paths. We used time domain beam-forming techniques to estimate the 2D slowness vectors of all the first arriving energy and found only mild anomalies in back azimuth from what is predicted for the U.S. Geological Survey (USGS) epicenters. We also found that later arriving energy, appearing either as discrete secondary phases or as part of the coda, arrives along the great circle paths as well. This justified the use of slant-stack techniques that assume great circle propagation but retain high resolution in time. We designed an algorithm that generates smoothed slant-stacks and automatically picks local maxima in time-ray parameter space for a user-defined level of significance. The resulting values were averaged into time-distance bins in order to generate an image of P wave propagation across the region. We find that when large numbers of data are combined, the resulting images tend to be smeared and lack clear signals from triplications associated with the 410-km and 660-km discontinuities. This is true for a variety of frequency bands, beam formation techniques, binning parameters, and alignment techniques. In general, differences among source properties and lateral variation in Earth structure are significant enough to defocus the images. However, we find that triplicated arrivals are often visible for individual events and small geographical clusters of events.

We have implemented a modeling technique that uses a niching genetic algorithm to globally search the model space and find groups of acceptable models. The models are described by 10–12 parameters that represent P velocities at nodes in the upper mantle, as well as the depths for discontinuities near 410 km and 660 km. We have experimented with objective functions defined using the curvature of the first arriving travel time curve, differential travel times at various distances, and combinations of the two. Estimates of differential ray parameters for multiple arrivals are not included in the objective function because the predicted differences are generally too small to be observed robustly at CMAR. Tests with noise-free synthetic data indicate good recovery of the input model in the upper mantle, with discontinuity depths usually within ±5 km, and velocity jumps within 20%. We are currently working on developing 1D models for the individual events and event groupings in which triplicated arrivals are confidently observed.

OBJECTIVES

Detection and location of small magnitude seismic events is one the current challenges of verification seismology. Local and regional analysis of small magnitude data is of great importance since these data do not produce sufficient teleseismic data. Locally recorded phases such as Pn, Pg, and Lg, show considerable variability in travel time and waveform character from region to region, since they travel in the lithosphere, which is the most heterogeneous layer of the Earth. Regional P waveforms are also complicated since they turn in the mantle transition zone (MTZ). The two global discontinuities at 410 and 660 km depth that bound the MTZ, cause the multipathing of P waves in which several distinctive P waves arrive in a short time window. Although the MTZ is less heterogeneous than the lithosphere, it has significant lateral variations, which makes the situation even more complicated. Two other seismic discontinuities are also thought to exist at least in specific regions at depths near 220 km (Gu et al., 2001) and 520 km (Shearer, 1996; Ryberg et al., 1997).

It is important to understand regional distance P-wave propagation in verification studies. Multipathing can reduce the amplitude of the first arriving P wave by partitioning energy into later arriving phases. This effect should be recognized and accounted for to avoid underestimating the magnitude of the seismic event. Multipathing can also bias the observation of depth phases. Depth phases from the crustal events can arrive in the same time window as later arriving waves from the MTZ. Due to the importance of event depth as a discrimination factor, it is crucial to distinguish between wave types.

The goals of this study are to document and model P wave multipathing owing to discontinuities and velocity gradients in the upper mantle beneath south Asia. We use data from the CMAR array in Thailand, which occurred between 1/1/1995 and 12/31/2005. The events have epicentral distances of 13°–30° with primarily continental paths. We use array-processing techniques to determine the subtle differences in arrival time and slowness of multipathed P waves. First arrival and differential time (later-arriving relative to first arrival) data are used to generate 1D velocity models for specific geographic corridors.

RESEARCH ACCOMPLISHED

Development of the CMAR Database

The relevant CMAR data used in this study consist of about 1700 events with magnitude of at least 4.0 mb, that occurred in South Asia at distances of 13^{o}–30^{o} from the CMAR. At these distances waves turn in the upper mantle and have potentially complicated interactions with discontinuities and velocity gradients in the transition zone. We selected events that provided continental paths to the CMAR and for which P-wave arrival times had been reported to the USGS. The seismicity covers a wide range of distances and azimuths yielding ray paths that preferentially sample the complicated tectonics of the India-Eurasia collision zone (Figure 1). Nearly all of the events are at shallow depths, though a significant group of intermediate depth events occur in the Hindu-Kush region at distances of 25^{o}–30^{o} from CMAR.

Array Processing of CMAR Data

The Chiang Mai Array (CMAR) is deployed in northern Thailand and consists of 18 short-period, vertical-component seismometers deployed with an effective aperture of about 10 km. The station geometry leads to an array response function that is roughly symmetrical but also relatively broad. At 1 Hz the side lobes of the array response function are outside of the relevant slowness domain; however the main peak has a half-width of about 4 s/deg. The relatively low precision of the array makes it challenging to discriminate among triplicated arrivals based on ray parameter, since multiply arriving waves are often predicted to have differential slownesses on the order of 0.5–2.0 s/deg.

Using seismic array techniques has two primary advantages: an increase in signal-to-noise ratio and the ability to robustly determine the direction from which seismic energy arrives. We used the Generic Array Processing (GAP) software package (Koper, 2005) for the array processing of CMAR data. In GAP slowness analysis is done in the time domain by repeated beam formation over a grid of potential slowness vectors. A variety of beam-forming techniques are available such as simple delay and sum, nth root stacking, and phase-weighted stacking (PSW) (Rost and Thomas, 2002). The non-linear beamforming techniques (i.e., PSW) often lead to a much higher increase in signal-to-noise compared to the $\sqrt{N}$ enhancement expected from linear approaches.

Within GAP Cartesian or polar components of the 2D horizontal slowness vector can be obtained simultaneously. Ray parameter and back azimuth can be inferred while one of them is held constant. There is also the capability of inferring the relative slowness between two phases or time windows. In all cases uncertainties for slowness parameters are determined with a stochastic bootstrap-type error estimation algorithm (i.e., Tichelaar and Ruff, 1989). For example, when estimating uncertainties associated with the estimate of a horizontal slowness vector, a pseudo-array is generated by randomly resampling the *N* array traces with replacement until *N* traces have been selected. A grid search is then carried out on the pseudo-array to determine the optimal slowness vector. This process is repeated M times to generate a population of optimal slowness vectors. This population is then used to calculate the model covariance matrix, from which a 95% confidence ellipse can be determined. Alternatively, error bounds on either the ray parameter or back azimuth can be estimated from the population of bootstrap solutions.

Figure 2 shows the PSW slant-stack (bottom left) and the optimal 2D slowness vector search (bottom right) for a mb = 6.1 event at a distance of 24.7° from the CMAR. This event was a nuclear test that occurred at Lop Nor, China on May 15, 1995. Beam amplitude is calculated using a 3rd-order phase-weighted stack (PSW) that significantly amplifies coherent energy while providing less waveform distortion than N-th root stacking (Schimmel and Paulssen, 1997). A record section of the waveforms for this event is also shown in the figure (top left). The slant-stack has been obtained using a fixed back azimuth of 335°. At this distance transition zone multipathing can be expected. The result of slant-stack shows a few later arrivals from which the first one arrives about 10 s after the primary P wave. For this later arriving phase, a grid search could be carried out to obtain the optimal differential ray parameter.

Slowness Residuals and Slowness-Azimuth Station Corrections (SASC)

We have obtained slowness residuals of the first P wave arrivals for all the events with quality data. For each event, the reported depth and distance in the USGS preliminary determination of epicenters (PDE) catalog have been used to compute the theoretical 2D slownesses, assuming propagation in IASPEI91. We used these slowness residuals to obtain SASC corrections for the CMAR. The SASC map (Figure 3, left) is produced using the method explained by Bondar et al. (1999). Events with mb $\geq$ 4.7 and bins with the minimum of two observations were used in computing the corrections. When data permits, it is ideal to set the number of minimum observations to higher values. Figure 3 (right) shows the same corrections obtained by Bondar et al. (1999) for the CMAR using a different data set. Our residuals show a consistent azimuthal bias, which is likely due to heterogeneous structure beneath the CMAR, such as a dipping Moho. The mean of the back azimuth residuals however, is small enough to justify using a fixed back azimuth, slant-stack (or vespagram) approach.

Vespagram Stacking

To obtain a coherent picture of later-arriving phases we stacked the vespagrams of the events and binned the results in time and distance. This gives the hit count, or a 2D histogram of number of arrivals in time and distance. To identify the later arrivals in slant-stacks, we used an automated algorithm to pick the arrival time and ray parameter of all local maxima whose beam amplitude is above a given threshold. The threshold value is a fraction of the global maximum value of the beam amplitude for each event. Due to the presence of other arrivals (depth phases and scattered energy) we did not get a coherent travel time curve from the stacking of the vespagrams. To eliminate some of the spurious arrivals, we smoothed the slant-stacks prior to arrival picking. Smoothing reduces some of the noise by averaging the data and eliminating some of the local minima in slant-stacks.

Figure 4 (top) shows the smoothed version of a slant-stack for an event (mb = 4.6, Δ = 26.38°) in which the black circles show the arrivals, which were picked automatically using a fraction value of 0.5. Arrival picking from the smoothed slant-stacks provides better results but the problem of unwanted arrivals still exists. For instance, unless we are able to identify the depth phases, the automatic picker will pick them, if they have higher amplitude than the threshold value. Figure 4 (bottom left) shows the 2D histogram (hit counts) of the arrivals (picked from the smoothed slant-stacks using a fraction value of 0.5) for all events using a bin size of 1° × 1 s. The bottom right figure shows the binned results for ray parameter vectors of the same arrivals. Vectors shown in the figure are the average of the vectors in each bin. In both figures the preliminary reference Earth model (PREM) travel time curve is shown for comparison.

Incoherent Stacking of Array Beams

We produced an event stack of receiver beams to reduce some of the noise in the beams of closely located events. This method works better if one is able to stack events in smaller distance bins. We binned the events in 1° bins and produced the stack of the beams in each bin. Stacks were computed relative to the theoretical first arrival and to the manually picked first arrival of each beam. While some of the beam stacks showed a little improvement in noise reduction, we did not observe a consistent pattern of later arriving phases in our final stacks. Since our data covers a wide range of back azimuths (Figure 1), we formed 2D bins of data (1° distance and 10° back azimuth) and computed the stack of the beams in each bin. Stacks in some bins show later arrivals consistent with those predicted by PREM or IASPEI91. In general the two methods of imaging later arrivals (vespagram and beam tacking) show effectiveness in certain geographic corridors but not over the entire region.

Modeling Observed First Arrivals

First P-wave arrival times, which have been manually picked for 2D slowness analysis, were used for modeling the Earth structure (including MTZ) in our study region. Among the 1700 events, 1562 events had a readable first arrival. We binned the data in distance and used the mean and standard deviation of each bin in modeling. To reduce the effect of depth on first arrivals we shifted the binned data by their mean: each mean (in a specific bin) is considered a data point. We took the mean of all data points and subtracted it from each data point. The results are our final observed first arrivals to be modeled. In this way we do not model the absolute travel times but mostly the shape of the travel time curve (Figure 5, left).

Uppermost mantle and MTZ structure affect the shape of the travel time curve at regional distances. Figure 5 (right) shows the effect of a change in MTZ alone on travel time curve. We modeled the first arrival data allowing the variation only in MTZ structure. We then extended our method to include crust and upper mantle structures in the modeling using a niching genetic algorithm (NGA) (Koper et al., 1999). Several tests were done using synthetic data to fine-tune the NGA input parameters, which helps to decide on appropriate model parameters. Observed first arrivals were binned (0.4° bin size) and both observed and theoretical data were shifted as explained earlier. A least-squares approach was used in defining the misfit between the observed and theoretical data and the standard deviations of the observed data in each bin were used as weighting factors. The set of acceptable Earth models broadly spans the search bounds, as the first arrivals provide a relatively soft constraint on structure; however this constraint can be valuable when combined with observations of later arrivals.

Modeling Later Arriving and Differential Times

Figures 4 (bottom left) shows the results of stacking smoothed versions of vespagrams. Because of the presence of other arrivals it is not easy to model the stacks. It is also not feasible to identify other phases and eliminate them from the stacks. Besides these problems, location errors also introduce bias in the stacking results when we compare them to the theoretical data. For these reasons we computed differential times for each event from the individual slant-stacks and then stacked the results in time and distance. Differential time stacks are also contaminated by other arrivals and may not be easy to model. Because of this decoherence in the stacks we intend to model individual beams, and small groups of beams, in which triplicated phases can be confidently observed. So far we have performed synthetic tests that indicate recovery of test models is feasible if enough observations are used (Figure 6).

CONCLUSIONS AND RECOMMENDATIONS

The small aperture of the CMAR makes it challenging to identify triplicated P waves on the basis of differential ray parameters. We have tried a variety of binning, stacking, and beam-forming techniques, but it is difficult to produce coherent images of upper mantle triplications when combining beams from many different events. In general, the differences in source properties and lateral variations in Earth structure are large enough to trump the expected signal from waves interacting with transition zone discontinuities. However, for many individual events and small groups of events, it is possible to detect the expected signal. For these cases we have a developed a non-linear global search technique that finds groups of acceptable radial Earth models. Tests with synthetic data indicate that features such as the depths and velocity changes associated with transition zone discontinuities are reasonably well-resolved when a large enough number of later-arriving phases are included. We are currently applying this modeling technique to the data in which we the have the most confidence in the coherence of later arriving phases.

REFERENCES

Bondar, I., R. G. North, and G. Beall (1999). Teleseismic slowness-azimuth station corrections for the International Monitoring System seismic network, *Bull. Seism. Soc. Am*. 89: 989–1003.

Gu, Yu. J., A. M. Dziewonski, and G. Ekstrom (2001). Preferential detection of the Lehman discontinuity beneath continents, *Geophys. Res. Lett*. 28: 4655–658.

Koper, K .D. (2005). The Generic Array Processing (GAP) software package, Annual SSA Meeting, Lake Tahoe, NV.

Koper, K. D., M. E. Wysession, and D. A. Wiens (1999). Multimodal function optimization with a niching genetic algorithm: A seismological example, *Bull. Seism. Soc. Am*. 89: 978–988.

Rost, S. and Ch. Thomas (2002). Array seismology: Methods and applications, *Rev. of Geophys*. 40: 1008, doi:10.1029/2000RG000100.

Ryberg, T., F. Wenzel, A. V. Egorkin, and L. Solodilov (1997). Short-period observation of the 520 km discontinuity in northern Eurasia, *J. Geophys. Res.* 102: 5413–5422.

Schimmel, M. and H. Paulssen (1997). Noise reduction and detection of weak, coherent signals through phase weighted stacks, *Geophys. J. Int*. 130: 497–505.

Shearer, P. M. (1996). Transition zone velocity gradients and the 520-km discontinuity, *J. Geophys. Res*. 101: 3053–3066.

Tichelaar, B. W. and L. J. Ruff (1989). How good are our best models? Jacknifing, bootstrapping, and earthquake depth, *Eos Trans. AGU*, 70.

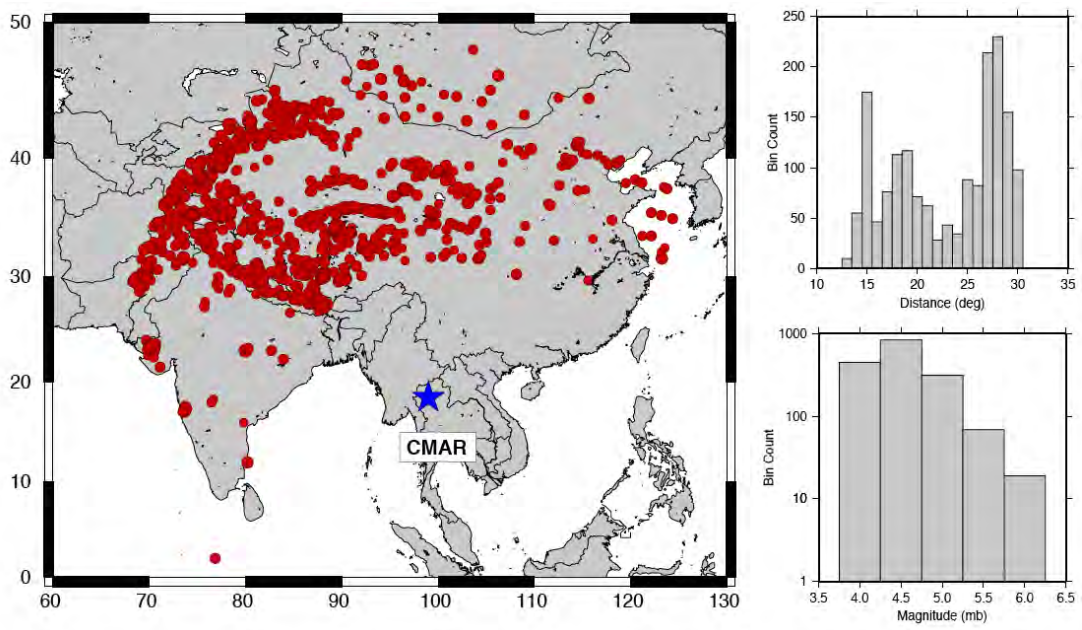

Figure 1. (Left) Epicenters for nearly 1700 seismic events that occurred at distances of 13°–30° from the CMAR from Jan. 1995 through Oct. 2005. Only events with primarily continental paths to the CMAR and mb ≥ 4.0 were selected. (Right) histograms of epicentral distance (top) and magnitude of the events.

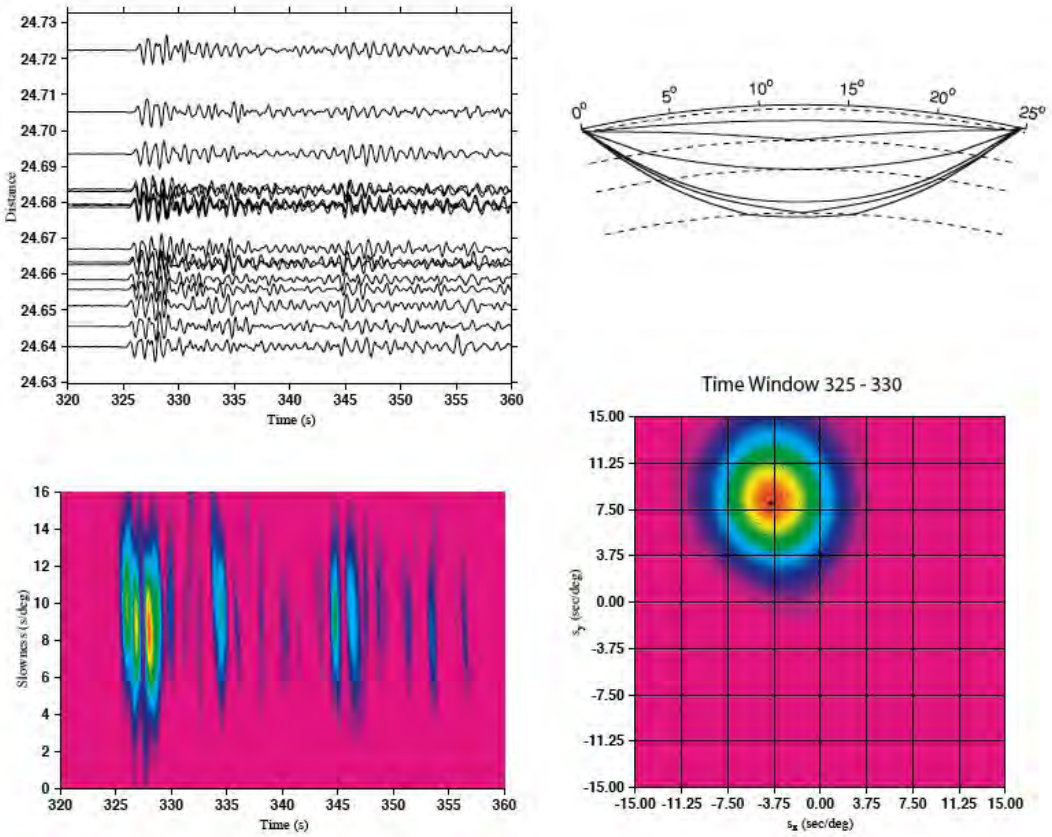

Figure 2. (Top left) Record section of waveforms for a mb = 5.0 event with a epicentral distance of 27.7°. (Top right) PSW slant-stack of the event assuming a fixed back azimuth of 311°. (Bottom) Grid search results for the optimal 2D slowness vector in the time window of the first P wave.

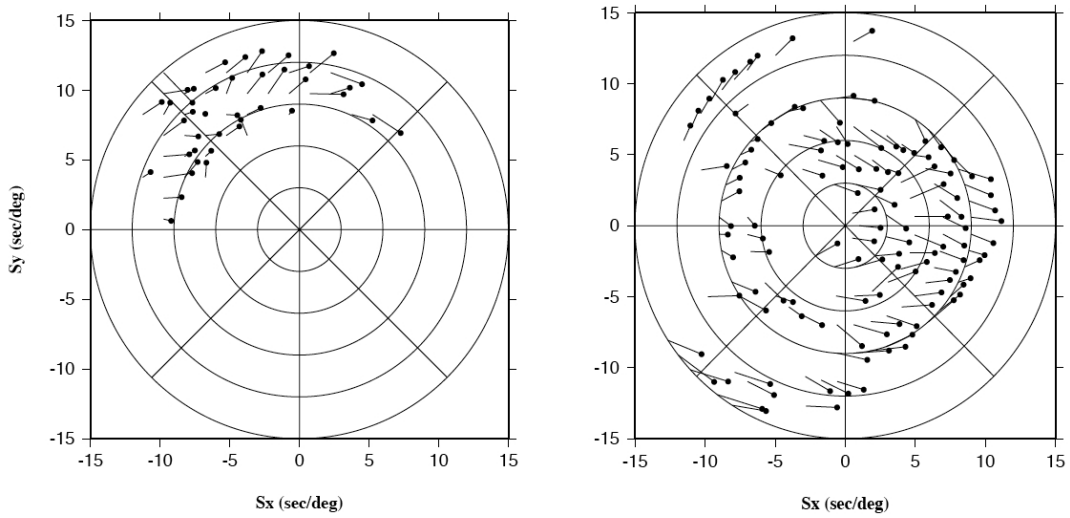

Figure 3. (Left) Slowness-azimuth station correction for CMAR obtained from the binned slowness residuals of first arrivals. The average residuals in each bin are shown as vectors in which the base of the vectors are the observed values and the circles are the theoretical values. Only events with mb ≥ 4.7 and bins with at least 2 observations are used. (Right) Same corrections for CMAR obtained by Bondar et al. (1999) using a different data set.

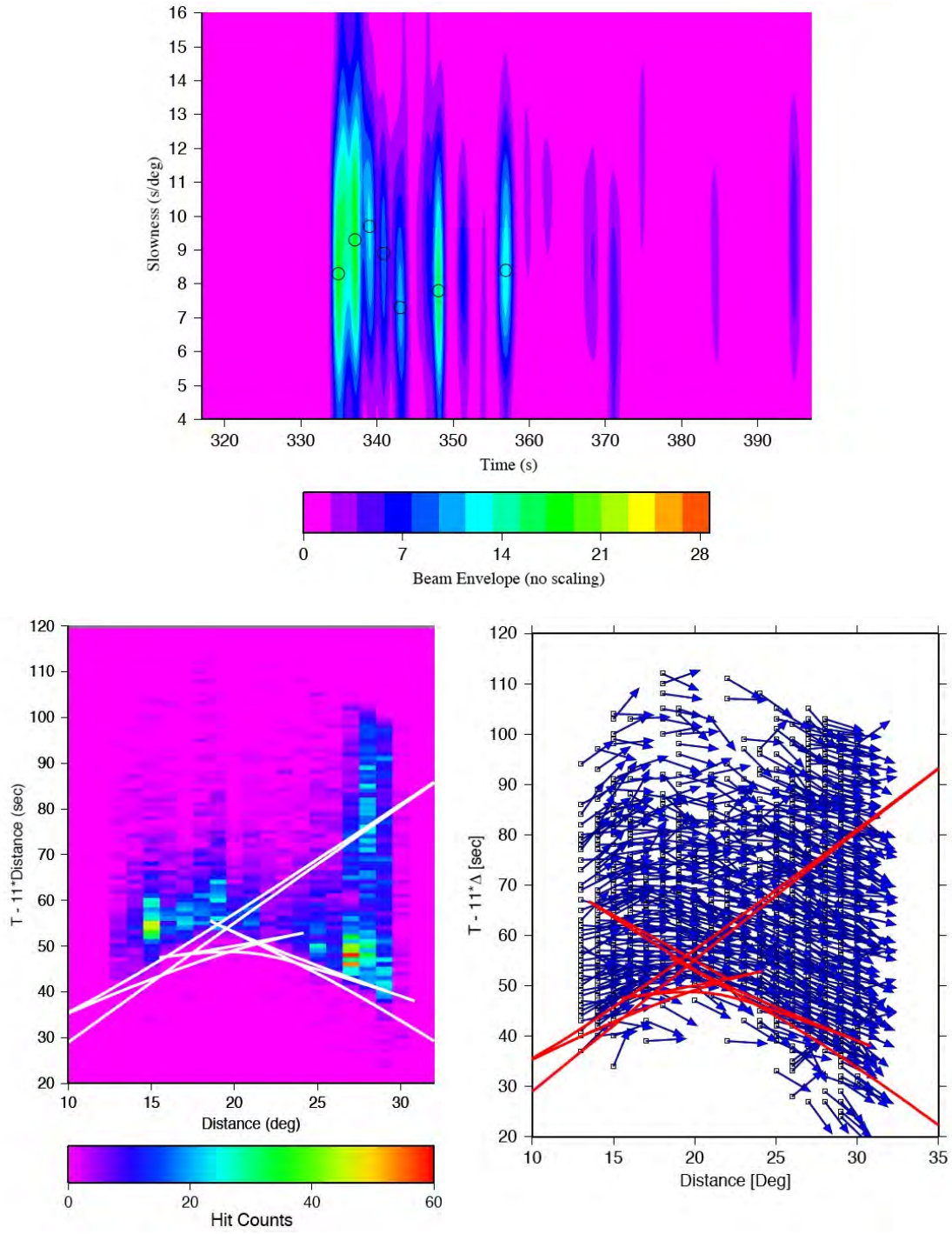

Figure 4. (Top) Smoothed version of the slant-stack for an event with mb = 4 .6 and Δ = 2 6.38°. Black circles show the arrivals picked by an automatic picker using a fraction value of 0.5. (Bottom left) 2D histogram of the arrivals for all events with quality data (picked as shown in top figure) binned by 1° × 1 s. (Right) binned results for the (bin average) ray parameter vectors obtained from the smoothed slant-stacks of the events. PREM travel time curve is shown in both (bottom) figures for comparison.

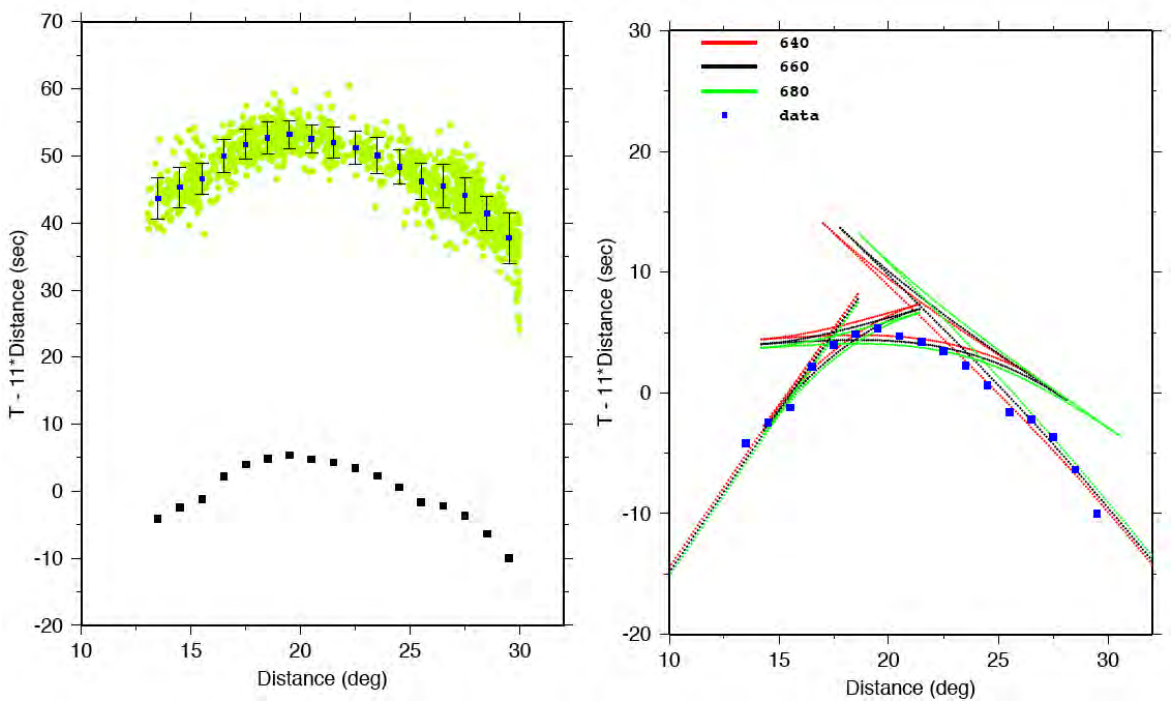

Figure 5. (Left) Manually picked arrival times (green circles) for 1562 events are binned using a bin size of 1°. Blue squares and error bars represent the mean and standard deviation in each bin. Black squares show the shifted data to be used in modeling (see text for explanation). (Right) Changes in travel time shape for different models. Data (binned in 1° bins) and models are shown after shifting. Only the 660 depth has been changed in the models.

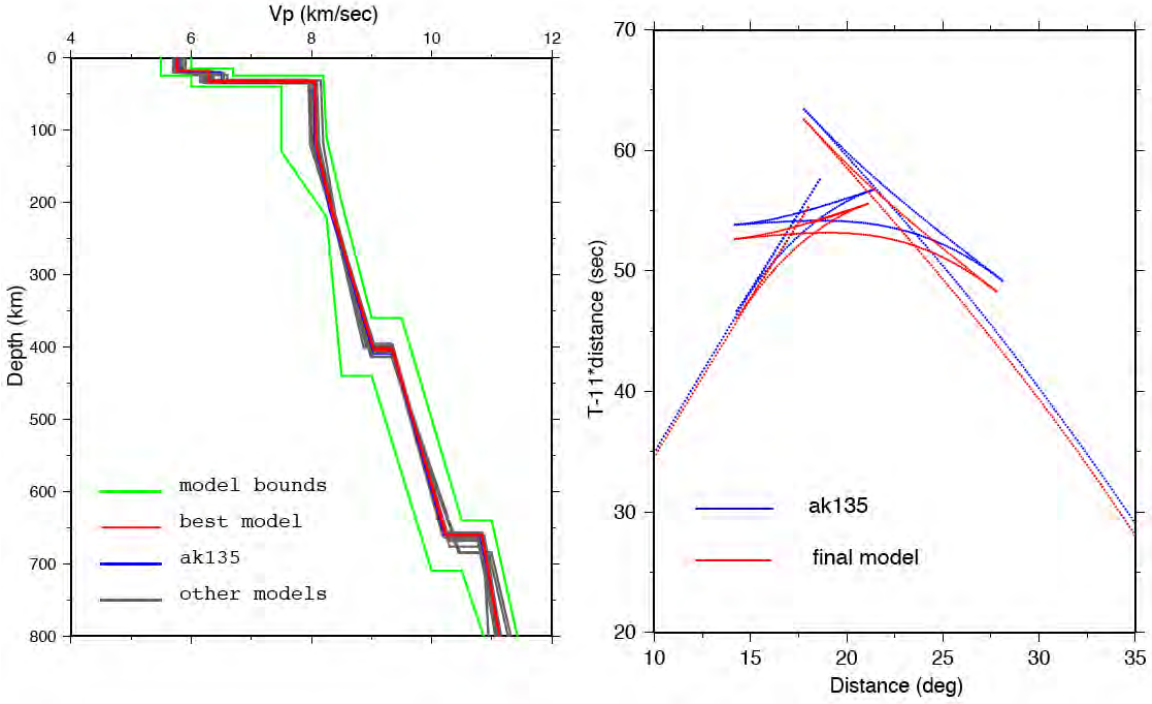

Figure 6. (Left) Velocity models obtained from the modeling of synthetic differential times (later arriving relative to first arrival) using NGA. The 410 discontinuity depth in the best model was 405 km. Except for crustal structure and 410 depth all other parts of the velocity model (by which the synthetics were created) were obtained from the modeling with insignificant differences.

USING SMALL-APERTURE ARRAYS TO IDENTIFY FAR-REGIONAL P-WAVE ARRIVALS

Aaron Ferris[1] and Delaine Reiter[1]

Weston Geophysical Corp.[1]

Sponsored by Air Force Research Laboratory

Contract No. FA8718-06-C-0002

ABSTRACT

Seismic observations recorded at far-regional distances contain information that could potentially be highly useful to monitoring seismologists. However, that information is currently under-utilized, because of propagation complexities that cause significant difficulties in the interpretation of seismograms. At far-regional distances (~ 14°–18°) seismic waves sample upper-mantle heterogeneities and the discontinuities at approximately 410 and 660 km depth, and this interaction results in triplications and interference phenomena in the observed data. In central Asia, these complications along the propagation path produce travel-time bulletins that exhibit large residuals (1–8 s) for the direct *P* arrival from far-regional events.

The regional seismic arrays that have been built in the last fifteen years should be rich sources of data for the study of far-regional wave phenomena. Unfortunately, the aperture of many modern regional arrays is so small (~ 2–3 km) that any study of phase characteristics beyond accurate picks of primary phase onset times is quite difficult. The goal of our project is to develop methods that can increase the accuracy of primary and early coda phase identification at currently deployed small-aperture regional arrays. These methods include modifications to two well-known τ-p filtering (or velocity spectra analysis) methods: Nth-root and phase-weighted stacking. We have applied our methods to vertical-component data recorded at distances between 14°–18° by small-aperture arrays in central Asia. Our results indicate that in many cases we can identify closely spaced arrivals by their slowness values in a time window that includes the direct *P* arrival, depth phases and arrivals from upper-mantle discontinuities.

OBJECTIVE

The major upper-mantle discontinuities at approximately 410- and 660-km depth have a strong effect on the patterns of body-wave arrivals observed between epicentral distances of 15°–27°. At far-regional distances (14°–18°), there are typically several *P* arrivals occurring within the first 15–25 s of the seismogram, with horizontal slowness values ranging from 8–11 s/deg. In a 1-D reference model such as IASPEI91 (Kennett and Engdahl, 1991), these arrivals include the direct *P* arrival, a refracted arrival from 165 km depth, and refracted arrivals from the 410-km and 660-km discontinuities. The triplications from the main *P* phases are also complicated by possible depth phases, which have equivalent travel-time curves at a positive time offset that depends on earthquake depth and the velocity structure above the source. The seismograms may be further complicated by upper-mantle heterogeneities encountered along the source-to-receiver path.

For example, in central Asia the travel-time bulletins of far-regional events exhibit large travel-time residuals (1–8 s) for the direct *P* arrival. These residuals are likely due to a combination of phase identification errors and inadequate upper-mantle models in the region. The goal of our research is to improve phase characterization in the early body-wave coda observed at far-regional distances. An important component of our research is the development and application of accurate array-processing techniques to the triplicated arrivals observed at small-aperture arrays installed in central Asia.

RESEARCH ACCOMPLISHED

To address our research objective we are using array-based methods that can differentiate between closely spaced arrivals in array seismograms. Numerous array-processing techniques have been developed to lower the detection threshold for small events by suppressing noise and enhancing coherent signal. Techniques such as frequency-wavenumber (*f-k*) or travel-time slowness (τ-*p*) analysis are commonly used for array-based signal characterization. In the case of *f-k* analysis, the apparent slowness and back azimuth of a signal can be determined from the 2-D Fourier transform of an array signal. In τ-*p* processing, the array seismograms are mapped into travel-time slowness (or back-azimuth) space by employing slant-stack summation or Velocity-Spectra Analysis (known as *vespa* processing). Both of these methods can be successfully used to identify a secondary arrival via its slowness value.

However, the small aperture (~2–3 km) of many of the newer arrays installed for nuclear monitoring purposes presents a serious problem for *f-k* and τ-*p* methods at far-regional distances. For an array slant stack to resolve the slowness of secondary arrivals, array elements must have an inter-element spacing that produces time shifts of at least several samples over a reasonable range of slowness values. Figure 1 illustrates this effect using synthetic seismograms and two six-element arrays of 3- and 25-km apertures. We modeled the response of the arrays for a 5-km deep event at 16° epicentral distance using a reflectivity method and the AK135 reference model (Kennett et al., 1995), adding Gaussian noise at a 3 dB level to the resulting waveforms. Then we calculated a 4th-root slant stack of the synthetics over the initial wavetrain for a slowness range from 0.5–0.25 s/km. The red circles in the vespagrams (bottom panels) of Figure 1 mark the slowness-time peaks averaged for regions containing energy within 15% of the maximum; the circles' diameters illustrate the standard errors in the peak measurement.

Phase arrivals from this distance take ~0.2 s to cross the 3-km aperture array and ~2.5 seconds to cross the 25-km aperture array. For the closely spaced elements of the 3-km aperture array, small slowness values (high horizontal phase velocity) result in time shifts of only a few samples (1–6) between array elements, producing poorly resolved apparent arrival slowness. This is clearly apparent in the comparison between the bottom subpanels in Figure 1, in which the vespagram of the 3-km aperture array is heavily smeared along the slowness axis compared to the vespagram of the 25-km aperture array.

This smearing effect in slowness space for small-aperture arrays is the primary obstacle to the development of robust array-processing techniques at far-regional and near-teleseismic distances. To address the problem we have adapted some familiar processing techniques, such as the Nth-root and phase-weighted stacking, to our specific problem.

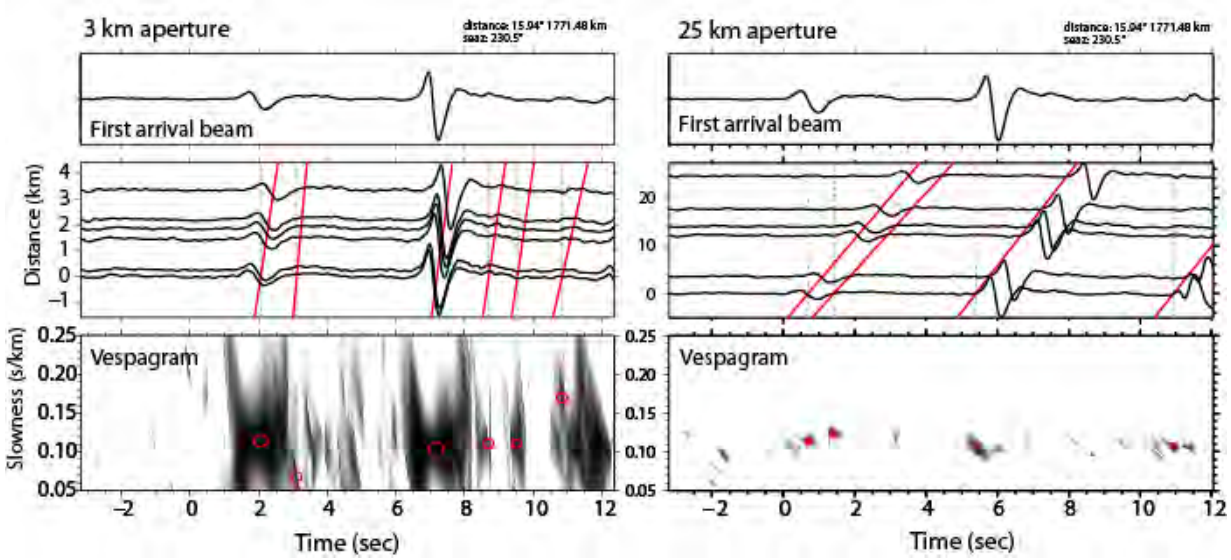

Figure 1. A synthetic example of the slant-stack process for a far-regional event recorded at a 3-km aperture array (left) and a 25-km aperture array (right). Top panels show the array beam computed using the first-arrival slowness value. Middle panels show the array elements sorted by distance. Red lines show the travel-time curves for the slowness values determined from the 4th-root vespagrams (bottom panels). The slowness vespagrams for both arrays are plotted at the same color scale, and red circles mark the time-slowness peaks, averaged for vespa regions containing energy within 15% of the maximum.

Array Processing Methods for Small-Aperture Regional Arrays

We analyze the early *P*-wave coda of far-regional observations on small-aperture arrays using two τ-p processing methods that are commonly used in phase identification (for a general survey of techniques, see Rost and Thomas, 2002). The first method is known as Nth-root stacking (Muirhead and Datt, 1976) and the second as phase-weighted stacking (Schimmel and Paulssen, 1997). Both techniques are variations on the slant-stack method, in which waveforms are beamed for a range of slowness values and a known back azimuth. The beam power is then displayed as a function of travel time and slowness; these images are commonly referred to as vespagrams or vespas (Velocity Spectral Analysis). The two vespa techniques differ in the mechanism employed to enhance weak arrivals and suppress incoherent signal, as we explain below.

Nth-root stacking analysis

To form an Nth-root stack, the signed Nth-root (N) of each array trace (s_j) is taken before beam summation over the M array traces, for a given slowness value (u) and time sample (t), i.e.,

$$v'_{u,N} = \frac{1}{M}\sum_{j=1}^{M}\left|s_j\left(t-t_{u,j}\right)\right|^{1/N}\frac{s_j(t)}{\left|s_j(t)\right|} \quad . \qquad (1)$$

After summation across the array, the beam is raised to the Nth-power and the saved sign is applied:

$$v_{u,N} = \left|v'_{u,N}\right|^{N}\frac{v'_{u,N}}{\left|v'_{u,N}\right|} \quad . \qquad (2)$$

Increasing the value of N decreases the amplitude variation in a trace; this boosts the amplitudes of coherent, small amplitude arrivals and decreases the dominance of large amplitude arrivals. In our application at small-aperture arrays it is necessary to accentuate very small differences in potential slowness maxima across the smeared slowness

axis. Therefore, we have selected a root value of $N = 15$ to enhance coherent arrivals and allow us to more easily pick a slowness peak in the Nth-root vespagram. Figure 2 illustrates how smaller values of N produce broader peaks in the vespa image, making slowness determination less precise. In addition, to further enhance coherent, small-amplitude arrivals, we perform the 15th-root stacking in sliding window segments of 1.5 to 3.0 s along the entire signal window of interest.

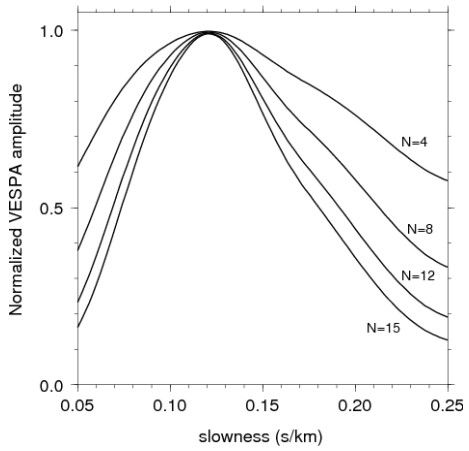

Figure 2. Time slice (t = 2.0 s) through the 3-km aperture vespagram shown on the left in Figure 1 for increasing values of the Nth root. Larger Nth root values sharpen the peaks in the vespagram, improving slowness resolvability at small-aperture arrays.

Phase-weighted stacking analysis

In phase-weighted stacking, a coherency measure based on the instantaneous phase provides a weight for each sample of the beam. The instantaneous phase is determined for each array trace using complex trace analysis (Schimmel and Paulsen, 1997). For each array trace $s(t)$, a analytic signal $S(t)$ is constructed with $s(t)$ as the real part and the Hilbert transform $H[s(t)]$ as the imaginary part:

$$S(t) = s(t) + i\mathrm{H}[s(t)] \ , \tag{3}$$

which can also be expressed as

$$S(t) = s(t) + i\mathrm{H}[s(t)] = A(t)\exp(i\phi(t)). \tag{4}$$

Here, $A(t)$ is the envelope of the trace and $\varphi(t)$ is the instantaneous phase (Bracewell, 1965). Schimmel and Paulssen (1997) showed that the sum of two analytic signals $C(\tau) = S_1(\tau) + S_2(\tau)$ is maximal at fixed time $t = \tau$ when the two instantaneous phases are equal. In order to deal with the amplitude variation between the analytic signals, amplitudes are normalized on a sample by sample basis before summation. This leads to the phase stack $c(t)$, obtained independent of the amplitude,

$$c(t) = \frac{1}{M}\sum_{j=1}^{M}\exp(i\varphi_j(t)), \tag{5}$$

where M is the number of traces. The phase stack is a measure of coherency as a function of time that varies between 0 and 1. If two signals have the same phase, $c(t)$ will have a value of 1. In phase-weighted stacking, this coherency value weights the samples of a normal linear stack, such that

$$PWS(t) = \frac{1}{M}\sum s_j(t)c(t)^{\gamma}. \tag{6}$$

In essence, the phase stack applies a filter that depends on the similarity or dissimilarity of the signals. The sharpness of the filter can be controlled by the power factor γ.

In contrast to the Nth-root stacking process, sliding sub-windows are not used in phase-weighted stacking, because the amplitude is normalized on a sample-by-sample basis prior to coherency weighting. Coherent small-amplitude arrivals consequently have the same weight as coherent large-amplitude arrivals, and thus have the same amplitude in the final vespagram.

Following Nth-root or phase-weighted stacking analysis, we run an arrival detector over the final vespagram image that triggers on peaks over a certain amplitude threshold. The triggered arrival detections can then be compared to predictions from a given velocity model. We have applied both 15th-root and phase-weighted stacking methods to far-regional data recorded on small-aperture arrays in central Asia and show examples of the results in the next section.

Application of Methods to Regional Arrays in Kazakhstan

The Makanchi (MKAR) and Karatau (KKAR) arrays in Kazakhstan record the abundant seismicity that occurs across central and southern Asia. Our current event database is comprised of far-regional distance (14°–18°) seismograms for earthquakes occurring from 2002 to 2006. In Figure 3 we show the configurations of the arrays as well as database events from 2002–04 recorded at each (or both) of the arrays. The MKAR and KKAR arrays have similar configurations: a central sensor surrounded by 3 sensors in an inner ring, and 5 sensors in an outer ring. The aperture of the outer ring is ~ 2 km at KKAR and ~3 km at MKAR. The main instruments at both arrays are vertical-component borehole seismometers (GS-21) recording continuous data at 20 Hz. At KKAR the borehole seismometers are at 50 m depth, and at MKAR they are at 30 m depth. Each array also houses 3-component broadband seismometers; those stations are labeled KK31 and MK31 in Figure 3. In the current study we are only concerned with the vertical channel borehole data.

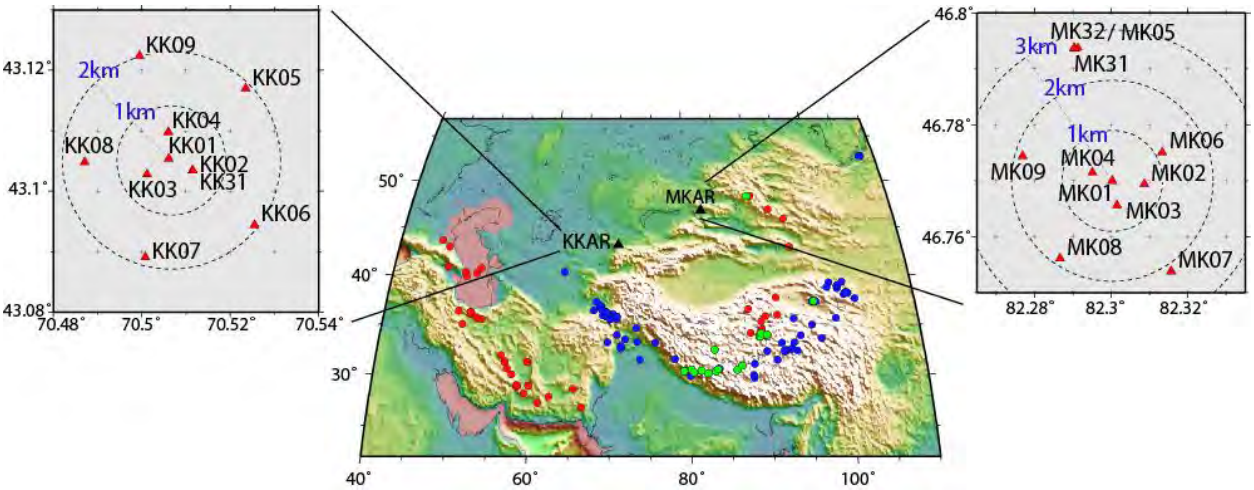

Figure 3. Location map of the KKAR and MKAR arrays and study events. Inset maps show the details of the array configurations. The main map shows the earthquakes (2002–2004) in our study database. Red circles are earthquakes occurring at far-regional distances from KKAR, and blue circles are at far-regional distance from MKAR. Green circles are earthquakes recorded by both arrays at far-regional distances.

To ensure the validity of the hypocenter estimates (particularly the depths), we relocated the events in the database using a grid-search event location algorithm (Rodi, 2006), the AK135 velocity model, and the time-defined phases in the Engdahl, van der Hilst and Buland (EHB) bulletins (Engdahl et al., 1998). We retained those events for which the relocation hypocenters produced small errors in both epicenter and depth. The resulting database contains 72 events observed at KKAR and 97 observed at MKAR. International Seismic Centre (ISC) body-wave magnitudes in our database range from 4.5–6.2 with a mean of 4.9. As shown in Figure 3, most of the events occur southwest to southeast of the arrays, with only a few to the north. This reflects the predominant seismicity patterns in the region, which are associated with interaction between the Indian, Eurasian, and Arabian plates. In general, the arrays have low noise levels, and the earthquakes are well-recorded across the arrays.

Most events in our current database display an emergent first arrival (Figure 4), and we observe few events with obvious impulsive first arrivals, for both KKAR and MKAR events. Since the emergent signal is observed for most events, independent of source location, it's likely that the emergent signal is a consequence of interaction with the upper mantle discontinuity at 410 km, rather than of source effects, such as array orientation along a nodal-plane or a double-couple source mechanism.

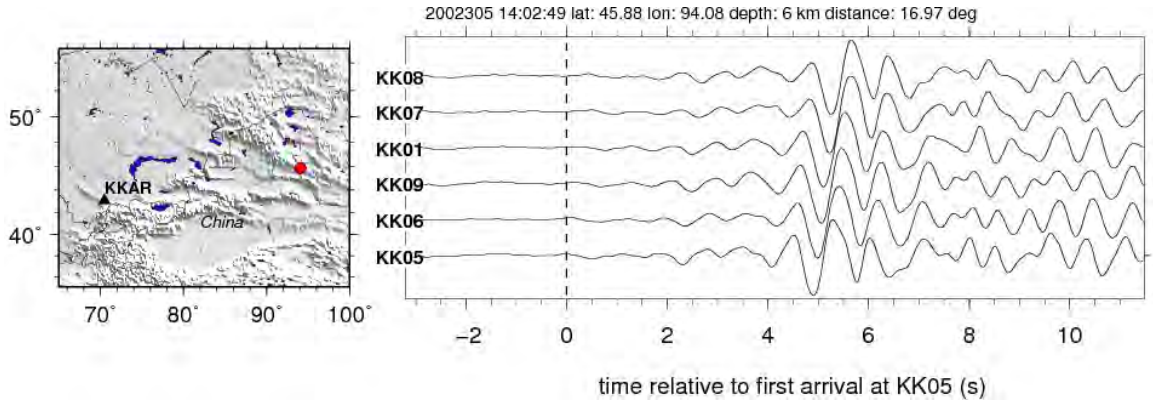

Figure 4. Left: Map showing the event (red circle) and array (triangle) locations. Right: Array gather from the far-regional earthquake recorded at KKAR. Note the emergent first arrivals and the large amplitude energy between 4–7 s. Zero offset corresponds to the first arrival at station KK05.

As we demonstrated earlier with synthetics, the limited aperture of arrays such as MKAR and KKAR creates slowness and arrival-time uncertainties in secondary phase identification. For example, far-regional *P* waves with horizontal slownesses between 8–11 s/deg traverse a 2–3 km aperture array in 0.2–0.3 s. This very small move-out results in an over-weighting of small slowness values in the beaming process, which causes smearing and reduced resolution in the slowness domain. We have found that eliminating some of the array elements in the secondary phase processing improves slowness and arrival-time estimation. At both KKAR and MKAR, there are four center elements within several 100 m of each other, so we omit those and include only the outer ring of elements and one center element in our stacking procedures.

Another uncertainty in our calculations is in the back azimuth computed for the array-to-event orientation, which is used in our τ-p processing to rotate the array. This back azimuth is computed using assumptions that the event is well-located and that the great-circle path is followed between the event and station (i.e., there is little velocity heterogeneity along the source-to-receiver path). These are significant assumptions, which affect the accuracy and precision of our results if they are incorrect. At far-regional distances a poor event location is less problematic than path heterogeneity in back-azimuth computations. For example, at far-regional distances an event mislocated by as much as 50 km changes the computed back azimuth by less than 0.5°, which has a minimal effect on a slant-stack process. On the other hand, significant path deviations from the assumed great circle can cause problems in the slant-stack computation. For the MKAR and KKAR small-aperture arrays, even a relatively small back-azimuth uncertainty (on the order of 2°–5°) can change the arrays' distance ordering by ~0.6 km for the outer array elements, which is equivalent to a 1–2 sample time shift.

To determine back-azimuth corrections for KKAR and MKAR, we average the back-azimuth residuals observed for our dataset, similar to Mykkeltveit et al. (1990). We use phase-weighted stacking to calculate the coherence values for fixed arrival slowness and varied back azimuth. The maximum coherence above 0.85 is then mapped and the average deviation of the back-azimuth residual is found over the processing window of interest. Figure 5 shows an example of this processing for an event observed at a distance of 14.7° from MKAR. The middle panel of Figure 5 shows the phase-weighted coherence image at all azimuths, and the top panel of Figure 5a shows a zoomed view of the maximum coherence values at each time sample in the processing window, from which the average back-azimuth residual is calculated. The back-azimuth residual for this particular event is –9.2°.

In Figure 6 we show histograms of the percent frequency versus back-azimuth residual for our MKAR and KKAR database For the complete MKAR dataset we find an average back-azimuth deviation of –10° ± 5° (observed– predicted) for far-regional arrivals; at KKAR the average back-azimuth deviation is –4° ± 8°. The average back-azimuth residual at both arrays is fairly high, and it is not clear what the source of these large negative residuals is. However, most of the events in our far-regional databases are located in the most heterogeneous lithosphere on Earth. This makes it more likely that lateral heterogeneity along the far-regional path between the earthquake sources and arrays is the primary cause of high back-azimuth residuals, rather than near-receiver structure.

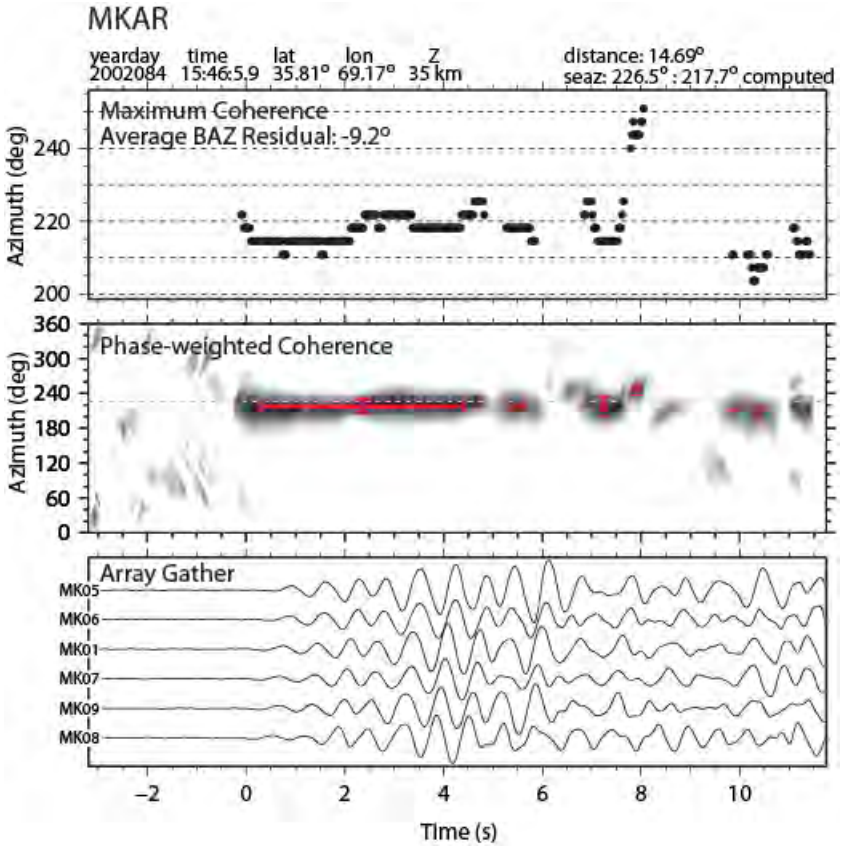

Figure 5. Example of a back-azimuth uncertainty calculation found using phase-weighted stacking. Bottom panel shows the MKAR array waveforms. The middle panels show the results of phase-weighted stacking for the back-azimuth value, and the top panel is a zoom in on the high-value coherence values. This particular example has a back-azimuth residual of –9.2°.

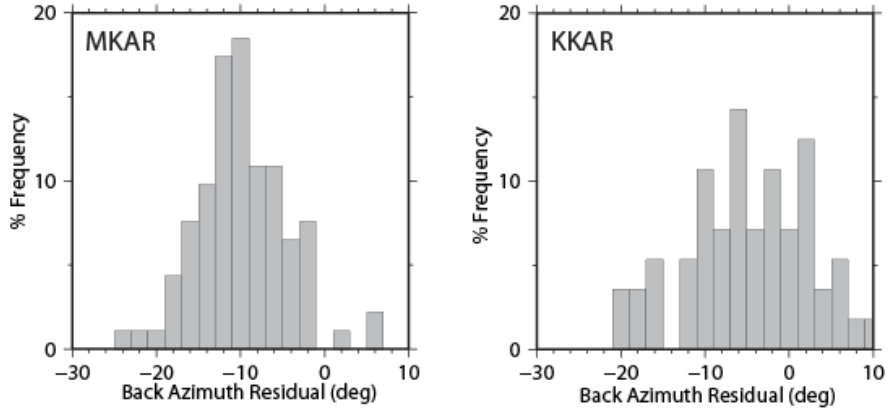

Figure 6. The percent occurrence of particular back-azimuth residuals for the MKAR and KKAR event databases.

Comparison between Nth-Root and Phase-Weighted Stacking

Following the back-azimuth calibration of the MKAR and KKAR arrays, we processed the KKAR and MKAR array data in our event database using 15th-root and phase-weighted stacking methods. As mentioned earlier, we dropped several of the inner array elements in the stacking procedures to further enhance slowness resolution at the small-aperture arrays. For each event, we analyzed a 13-s window of signal, which included the direct *P* arrival, possible depth phases and arrivals from the 410-km discontinuity. After we applied the two stacking methods, we ran our arrival detection algorithm on the resulting vespa images.

In Figure 7 we illustrate the application of our methods on two events from the database. The left side of Figure 7 shows the analysis of an event in the Himalayas observed at KKAR; the right side of the figure shows the results from an event from the northeastern edge of the Tibetan Plateau observed at MKAR. The top two subpanels in Figure 7 show the best beam computed from the distance-sorted array gather, based on the first-arriving *P* slowness from the phase-weighted stacking. The bottom two subpanels show the results of applying the 15th-root and phase-weighted stacking analysis to the two event observations. On each of these results we plotted the IASPEI91 predictions for the transition-zone *P* and *pP* arrivals (red squares), found using the TauP Toolkit (Crotwell et al., 1999). The IASPEI91 arrival times are relative to the zero-time offset of the closest array element; in other words, we always plot the IASPEI91 first arrival at zero time, regardless of whether it matches the observed first arrival. The presence of more than one red square for a given arrival is an effect of upper-mantle triplication that creates multiple arrivals. We also plotted red crosses at the phase arrivals found by our arrival detection algorithm. The differences between the red crosses and the yellow squares reflect misfit between the reference and actual velocity models along the propagation path, as well as potential differences in the published and actual earthquake depths.

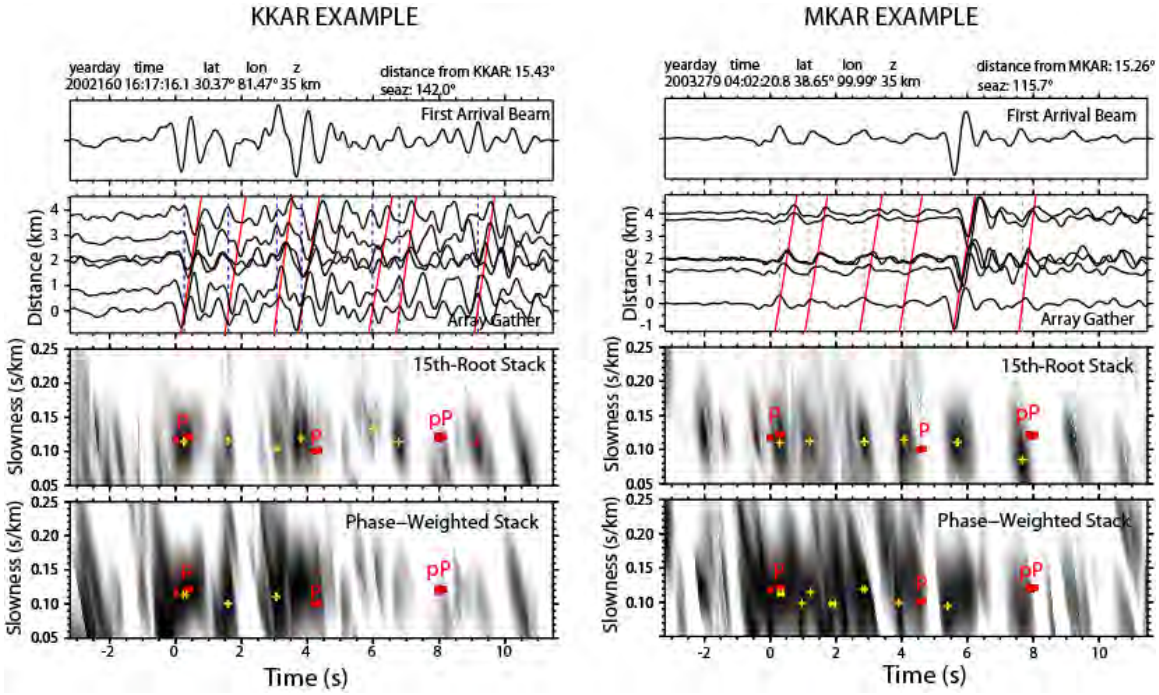

Figure 7. Examples comparing the Nth-root and phase-weighted stacking procedures for far-regional observations at KKAR (left) and MKAR (right). The top two panels show the array best beams and gathers ordered by distance. Red lines are the arrival-time curves based on slowness values computed in the 15th-root results. The bottom two panels are the 15th-root stack and phase-weighted stack vespagrams. Red squares are the IASPEI91-predicted arrival times and slowness; yellow crosses are the arrivals determined from vespa processing.

In general, we find that both methods detect the primary coherent arrivals. In many cases, events with lower levels of noise exhibit sharper arrivals in the 15th-root stacking results. This may be related to the nature of the Nth-root coherency weighting, which appears more effective at suppressing noise. In other words, in the absence of

significant noise, more of the seismogram is weighted similarly, broadening peaks in the vespagram with respect to time. This is evident from a visual comparison between the 15th-root and phase-weighted stacking results of the MKAR example shown in Figure 7.

We also have found that, for the same event, 15th-root and phase-weighted stacking do not always detect the same arrivals. Large amplitude arrivals are almost always detected by both processing methods, but the same does not hold true for weaker arrivals. The differences for weaker arrivals may be caused by the particular implementation of our post-processing arrival detector, which has a tunable threshold that favors larger amplitude arrivals. This is an issue we will continue to address in future work.

Figure 7 also demonstrates that a comparison of the stacking-derived arrival times and slowness to IASPEI91 predictions do not always coincide. The first arrival is usually the best-matched in slowness—within ±0.02 s/km. Subsequent arrivals are more difficult to pair up by arrival time, but generally have slowness values within ±0.04 s/km of nearby predicted arrivals, albeit with significant scatter.

CONCLUSIONS AND RECOMMENDATIONS

The small aperture (~2–3 km) of many of the recent regional arrays installed for nuclear monitoring purposes restricts their usefulness at far-regional distances, where triplicated arrivals from the upper-mantle discontinuities make phase identification more difficult. Our research is focused on developing methods to accurately determine the slowness and arrival time of primary and secondary arrivals at these distances, with the final goal of incorporating the results in computations for event location and magnitude determination. We have found that we can adapt familiar array-processing techniques to the far-regional phase detection problem. Specifically, we are successfully applying15th-root and phase-weighted stacking to emphasize small, coherent arrivals that occur in a 15–25 s window following the initial P-wave arrival. The processing adaptations that we have employed reduce the strong smearing effects that occur in slowness space at small-aperture arrays.

We have applied our techniques to a large database of moderate-sized earthquakes occurring at far-regional distances from two arrays in central Asia. Our results indicate that we can differentiate between closely spaced arrivals in the early body-wave coda. However, it is also apparent that in many cases a simple global reference model cannot capture the phase succession and arrival-time behavior in the complex tectonic regions of central and southern Asia. In our continuing work under this project we will focus on developing ~~t~~emplates" of typical events and associated phase behavior. These templates will be supported by accurate 1-D velocity models and full-waveform modeling, in specific regions such as Iran, Turkmenistan, Pakistan, northern India, and western China.

REFERENCES

Bracewell, R. N. (1965). *The Fourier transform and its applications*. New York: McGraw-Hill.

Crotwell, H. P., T. J. Owens, and J. Ritsema (1999). The TauP Toolkit: Flexible seismic travel-time and ray path utilities, *Seism. Res. Ltrs*. 70: 154–160.

Engdahl, E. R., R. van der Hilst and R. Buland (1998). Global teleseismic earthquake relocation with improved travel times and procedures for depth determination, *Bull. Seis. Soc. Am.* 88: 722–743.

Kennett, B. L. N. and E. R. Engdahl (1991). Travel times for global earthquake location and phase identification, *Geophys. J. Int.* 105: 429–465.

Kennett, B. L. N., E. R. Engdahl, and R. P. Buland (1995). Constraints on seismic velocities in the earth from traveltimes, *Geophys. J. Int.* 122: 108–124.

Muirhead, K. J. and R. Datt (1976). The Nth root process applied to seismic array data, *Geophys. J. R. Astron. Soc.* 47: 197–210.

Mykkeltveit, S., F. Ringdal, T. Kvaerna, and R. W. Alewine (1990). Application of regional arrays in seismic verification research, *Bull. Seis. Soc. Am.* 80: 1777–1800.

Rodi, W. (2006). Grid-search event location with non-Gaussian errors, *Phys. Earth & Planet. Int.* 158: 55–66.

Rost, S. and C. Thomas (2002). Array seismology: methods and applications, *Rev. Geophys.* 40: 1008, doi:10.1029/2000RG000100.

Schimmel, N. and H. Paulssen (1997). Noise reduction and detection of weak, coherent signals through phase weighted stacking, *Geophys. J. Int.* 130: 497–505.

ROBUST MAGNITUDE AND PATH CORRECTIONS FOR REGIONAL SEISMIC PHASES IN EURASIA BY CONSTRAINED INVERSION AND ENHANCED KRIGING TECHNIQUES

Mark D. Fisk[1] and Steven R. Taylor[2]

ATK Mission Research[1] and Rocky Mountain Geophysics, LLC[2]

Sponsored by National Nuclear Security Administration
Office of Nonproliferation Research and Development
Office of Defense Nuclear Nonproliferation

Contract No. DE-AC52-06NA27321

ABSTRACT

This project is to develop and test two methods to improve magnitude and path corrections for regional seismic phase amplitudes. Objectives of the first method, a constrained inversion approach, are to improve estimates of geometrical spreading and Q for Pn, Pg, Sn, Lg in Eurasia, by eliminating trade-offs with source corner-frequency estimates, and to improve source parametrizations, in terms of grids of stress drop and corner frequency scaling. Using waveform cross-correlations from Dr. Schaff of Lamont-Doherty Earth Observatory for 4,236 events prior to 2000 in Eurasia, (1) data were obtained for event pairs or clusters in a data set from Los Alamos National Laboratory (LANL); (2) additional seismograms from IRIS were incorporated; (3) regional phase picks were added; (4) network-averaged relative spectra (for large-over-small event pairs) were processed for Pn, Pg, Sn and/or Lg; and (5) relative spectra of a Brune model were fit to the empirical relative spectra. Cases were considered with the apparent stress-drop scaling parameter, ψ (as defined by Walter and Taylor, 2002), as a free parameter or fixed at 0.0 or 0.25. Preliminary kriged grids of stress drop have been computed for Eurasia, based on relative spectra for individual phases and combining the results for the various phases. The results thus far seem to show that the scaling of corner frequency with seismic moment for earthquakes is very consistent among the various regional phases. An interesting observation is that the estimated P- and S-wave corner frequencies for a given event are very similar for a majority of earthquake pairs throughout many diverse areas of Eurasia, comparable to findings by Walter and Taylor (2002) for western U.S. earthquakes. Important implications of this result are discussed. These analyses have been automated and are being applied to almost 3600 earthquake pairs in Eurasia from 2000 to 2007.

The objective of the second method, an extension to Bayesian kriging, is to provide robust path corrections and uncertainties for regional seismic phase amplitudes that properly treat localized calibration events which may have anomalous, correlated amplitudes. To first demonstrate the problem, a Bayesian kriging approach is applied to explosions and clusters of earthquakes with distinct focal mechanisms at the Nevada Test Site (NTS), including a cluster of Rock Valley earthquakes with anomalously high P/Lg values. The results indicate that explosions can be mis-categorized as earthquakes when using such earthquake clusters for kriging because the localized reference data is weighted too high in estimating the corrections and the posterior calibration variance becomes too small. To address this issue, a fundamental improvement to the kriging methodology, incorporating an additional correlation length to treat correlated focal mechanisms, is presented and tested on the NTS data sets and on large samples of explosions and earthquakes worldwide. Application to the worldwide data sets indicates that the power of the hypothesis test to reject earthquakes as explosions is marginally reduced, without mis-categorizing any known explosions and providing a robust treatment of clustered reference data.

OBJECTIVES

We are developing and testing two methods to improve magnitude and path corrections for regional seismic phase amplitudes. Objectives of the first method, a constrained inversion approach, are to improve estimates of geometrical spreading and Q models for Pn, Pg, Sn, Lg in Eurasia, by eliminating trade-offs with source corner frequencies, and to improve source parametrizations in Eurasia, in terms of grids of stress drop and corner frequency scaling. The objective of the second method, an extension to Bayesian kriging, is to provide robust path-specific corrections and uncertainties for regional phase amplitudes, that properly treats localized calibration events that may have anomalous, correlated amplitudes. This project has three main tasks: (Task 1) Assemble multiple data sets of regional seismic recordings of earthquakes throughout broad areas of Eurasia. Apply waveform cross-correlation techniques to determine nearby pairs/clusters of events. Assemble spectral amplitude measurements of Pn, Pg, Sn, Lg for the events. (Task 2) Implement a technique to estimate corner frequencies and scaling parameters for Pn, Pg, Sn, Lg, by fitting relative spectra of a Brune model to data for pairs of nearby earthquakes of different moments. Compute grids of stress drop and earthquake corner-frequency scaling with moment for Eurasia. Use spectral amplitude data for regional phases and constrained source parametrizations to perform a robust inversion for geometrical spreading and Q model parameters. Test and evaluate resulting magnitude and distance corrections on events in Eurasia, using cross-validation methods. (Task 3) Investigate clusters of earthquakes at NTS and regions in Eurasia, and assess the potential for events with anomalous, correlated mechanisms to bias kriged amplitude correction grids beyond existing uncertainty estimates. Develop a technique to quantify the correlation of regional phase amplitudes within clusters. Extend a Bayesian kriging method to incorporate these correlation measures in the computation of amplitude correction and uncertainty grids. Test and evaluate the methods on events in Eurasia, using cross-validation techniques. We plan to deliver the techniques, parametrizations of stress drop, corner frequency scaling, geometrical spreading and Q models, and kriged amplitude correction and uncertainty grids for stations in Eurasia.

RESEARCH ACCOMPLISHED

Constrained Inversion Technique

Following Taylor et al. (2002), the amplitude spectrum for a given phase and station, for event i, may be expressed as

$$A_i(f) = S_i(f, f_c) G(r_i, r_0) \exp\left(-\frac{\pi f}{Q(f)\nu} r_i\right) P(f) \quad , \tag{1}$$

where f is the frequency, $S_i(f, f_c)$ is the source spectrum with corner frequency f_c, r_i is the epicentral distance, ν is the group velocity, $P(f)$ is a unitless station term, $Q(f) = Q_0 f^{\gamma}$ is the frequency-dependent attenuation, and $G(r, r_0)$ is the frequency-independent geometrical spreading, assumed to be inversely proportional to distance to a power η, beyond a reference distance r_0. Taylor et al. (2002) and others have used the logarithm of Equation (1) in a grid-search procedure to simultaneously estimate all of the parameters. However, significant trade-offs between Q and corner frequencies are known to exist and are difficult to constrain by standard techniques and available data (e.g., Taylor and Hartse, 1998). This can lead to improperly correcting regional amplitudes for distance and magnitude.

Instead of performing a grid search for all parameters simultaneously, we use relative spectra for event pairs with similar locations and mechanisms, but different moments, to factor out path and station effects and estimate the source parameters. We then constrain the source parameters and invert for values of η, Q_0, and γ. That is, for a pair of nearby earthquakes with similar radiation patterns, the model relative spectra for a given phase type is given by

$$\frac{A_1(f)}{A_2(f)} = \frac{S_1(f)}{S_2(f)} = \frac{M_0^{(1)}[1 + (f/f_c^{(2)})^2]}{M_0^{(2)}[1 + (f/f_c^{(1)})^2]} \quad . \tag{2}$$

For a Brune (1970) dislocation source, the corner frequency for seismic phase type ξ is given by

$$f_c(\xi) = c_\xi v_s(\xi)\left(\frac{\sigma_b}{M_0}\right)^{1/3}, \quad (3)$$

where σ_b is the stress drop, $v_s(\xi)$ is the source medium velocity for P or S waves, and c_ξ is a constant that can depend on phase type. Walter and Taylor (2002) allow for non-constant stress drop by defining the apparent stress drop for a given moment, M_0, as

$$\sigma_b = \sigma_b^{(0)}\left(\frac{M_0}{M_0^{(0)}}\right)^{\psi}, \quad (4)$$

where $\sigma_b^{(0)}$ is the stress drop at reference moment $M_0^{(0)}$. Setting $\log M_0^{(0)} = 15.05$ (in MKS units; M_W 4.0), and using pairs of localized earthquakes, we fit $\sigma_b^{(0)}$ and ψ to empirical relative spectra of regional phases. Figure 1 illustrates the relative spectra and model fits for an event pair in 1997. The relative spectra are quite similar for the various phases, although over different frequency ranges because of phase-dependent signal-to-noise limitations. Hence, the model fits and estimated corner frequencies are very similar. This appears to be a fairly common and important phenomenon for the earthquakes analyzed.

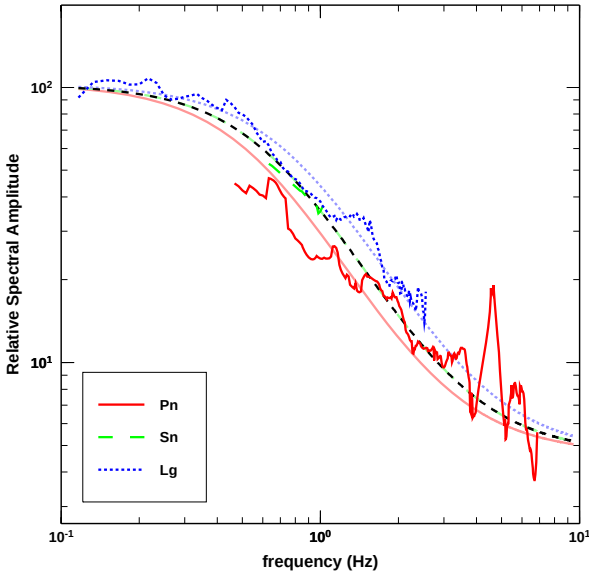

Figure 1. Example of relative spectra for a pair of M_W 6.0 and 4.7 earthquakes in Kyrgyzstan. Model fits for each phase are represented by similar line types. The black dashed curve shows the model fit using relative spectra for all available phases.

Using waveform cross-correlations for 4,236 events in Eurasia prior to 2000 (*cf.* Schaff and Richards, 2004) to find pairs or clusters of events in the LANL database, we acquired additional seismograms from IRIS to augment the LANL data set, added and refined the regional phase picks, processed the spectra, averaged relative spectra over stations, and fit the model for each phase and using all available phases simultaneously, as in Figure 1. We allow the relative moments to be estimated directly from the relative spectra or to use moment magnitudes (M_W) from LANL. We performed three types of fits in which the apparent stress-drop scaling parameter, ψ, is a free parameter or fixed at 0.0 or 0.25. The latter two cases correspond, respectively, to corner frequency scaling as $M_0^{-1/3}$ (Brune, 1970) or as $M_0^{-1/4}$ (Nuttli, 1983; Cong et al., 1996; Walter and Taylor, 2002). We computed kriged grids of stress drop for these cases.

Figure 2 shows corner frequency estimates versus log moment for Pn, Sn, and Lg for events in Eurasia, fixing $\psi = 0$ in this case. Linear fits are shown with (dashed) and without (solid) the slopes fixed at –1/3. Given the scatter, the fits are remarkably consistent and the slope estimates are all close to –0.33 for all phases. Fixing $\psi = 0.25$, the slope estimates are about –0.27. For ψ as a free parameter, the average value of ψ is 0.14 and the slope estimates are about –0.29. Clearly, the value of ψ affects the slope estimates of corner-frequency scaling with moment. Further work is needed to assess whether these differences are statistically significant.

Figure 3 shows that Pn and Lg corner frequencies are fairly similar for most of the earthquakes in diverse areas of Eurasia, comparable to findings by Walter and Taylor (2002) for western U.S. earthquakes. This is important for two reasons. First, it may help explain why P/S ratios discriminate effectively at higher frequencies, in most areas examined (provided path and station effects are properly treated). That is, as shown by Fisk (2006, 2007) the frequency dependence of P/S discrimination performance depends on the ratio of P- and S-wave corner frequencies squared, which is significantly larger for explosions than earthquakes at all sites examined. Thus, P/S ratios exhibit less frequency dependence for earthquakes than explosions. Second, this result may allow a more robust fitting of Brune source model parameters, using a broader range of frequencies, by

combining relative spectra of regional P and S phases for earthquakes (e.g., black dashed curve in Figure 1).

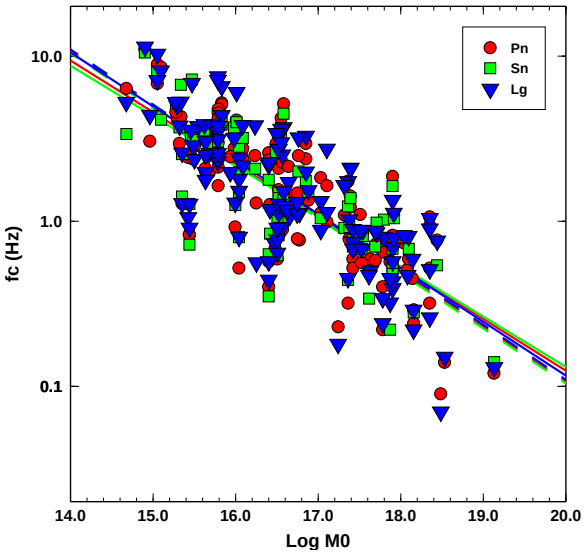

Figure 2. Corner frequency estimates versus log moment for Pn, Sn, and Lg for events in Eurasia. Linear fits are shown with (dashed) and without (solid) the slopes fixed at –1/3.

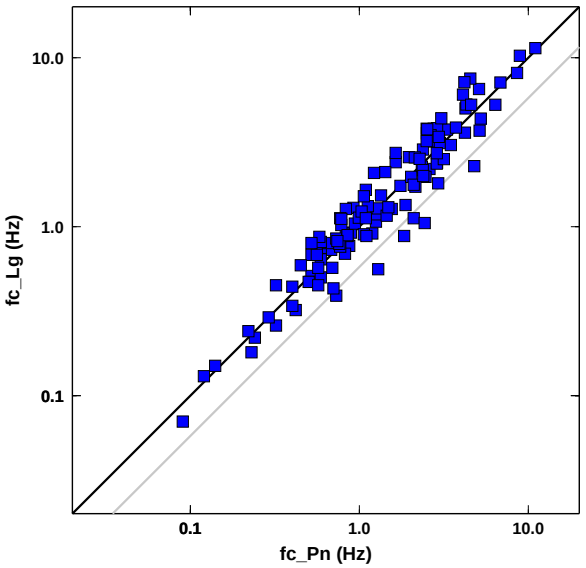

Figure 3. Estimated Lg versus Pn corner frequencies, indicating similar values for most of the earthquakes. Black and gray lines represent ratios of 1.0 and 1.73 (*cf.* Madariaga, 1976; Choy and Boatwright, 1995).

Figure 4 shows preliminary stress-drop grids, based on Lg and Pn data. Both grids exhibit remarkable similarity. There is concern that some stress-drop grids might be biased, at least in certain areas, because of trade-offs with Q. Such a bias is not present in our analysis because we are using relative spectra, which factor out effects of Q. Further work is needed to incorporate much more data and interpret these stress-drop grids.

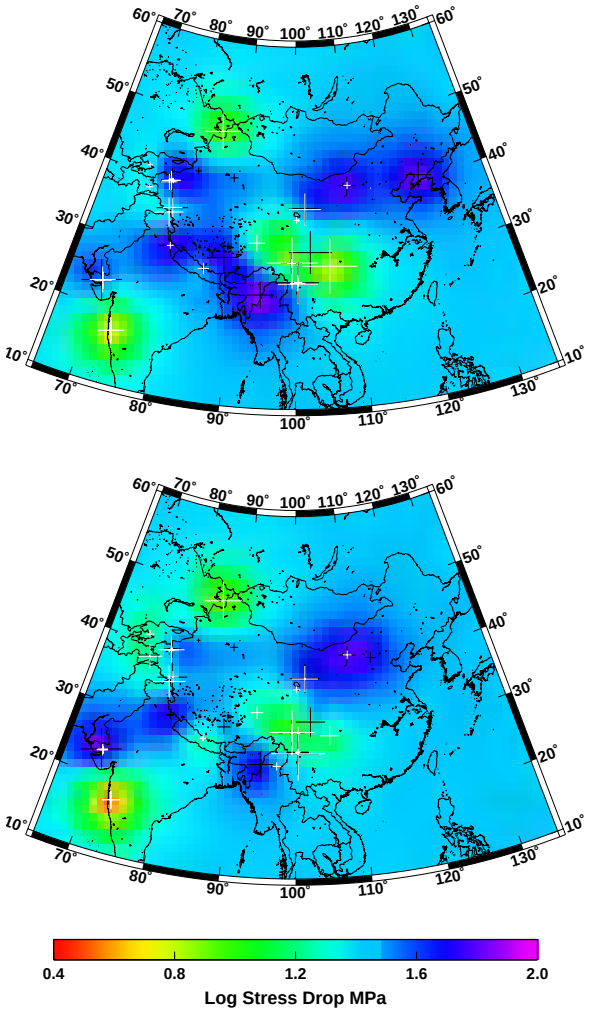

Figure 4. Kriged grids of stress drop using Lg (top) and Pn (bottom) data.

Further work is also needed to quantify the various uncertainties and the calibration and residual variances used for kriging. For some earthquake clusters, the estimated stress drops are all within about a factor of 2. For other clusters, the stress drops can vary by up to a factor of almost 60. We are examining the implications of this result on the variability and kriging of stress drop.

Treatment of Correlation for Clustered Reference Data in Kriging Regional Seismic Discriminants

Despite demonstrations that kriging regional amplitudes or P/S ratios improves discrimination performance (Phillips et al., 1998; Phillips, 1999; Rodgers et al., 1998, 1999; Fisk et al., 2001; Taylor et al., 2002, Bottone et al., 2002; Fan et al., 2002), there are concerns that calibration data from events with anomalous mechanisms, depths, and/or paths could significantly bias the correction grids. The Bayesian kriging method of Bottone et al. (2002) will properly account for such situations, including computation of the uncertainties, provided the residual variance (see below) is uncorrelated. The method uses the fact that the amplitude ratios are spatially correlated, with a typical correlation length of about 600 km, corresponding largely to path variations of P/S discriminants on regional distance scales. Estimating the local corrections in this way removes about half the variance in the data. The remaining (residual) variance is treated as uncorrelated. However, for clusters of events with similar mechanisms that treatment is incorrect – there is correlation in the residual variance, although at a much shorter length scale (e.g., of faulting zones) than the variance associated with path effects. We show that ignoring this correlation can lead to serious discrimination errors, while treating it provides a robust solution at very little cost in terms of discrimination power. We first examine this issue using explosions and two aftershock sequences at NTS, including one near Little Skull Mountain (LSM) and the unusually shallow (1-3 km) Rock Valley (RV) sequence. Walter et al. (1995) showed that Pn/Lg for the RV events are considerably higher than those for the LSM events, especially at KNB. We then extend the kriging methodology by incorporating an additional correlation length to treat similar mechanisms over relatively short distance scales. We test the extended method on NTS and worldwide data sets of explosions and earthquakes and discuss implications of this study for monitoring UNEs using regional seismic P/S data.

Case Studies for NTS Using the Old Methodology

We consider four cases in which only one station, either MNV or KNB, is used to monitor this area (more realistic of monitoring with a sparse global network) and either the LSM or RV events are used for kriging. For all cases, we use the distance corrections and Bayesian kriging technique, including the parameters, from Bottone et al. (2002). Figure 5 shows the grids of the corrections (left) and calibration standard deviations (right) for log[Pn/Lg(6-8 Hz)] at MNV using 30 LSM (top) or 10 RV (bottom) earthquakes as reference events. In both cases, the corrections near NTS are fairly close to zero, the distance-corrected average for earthquakes worldwide. The calibration standard deviation near NTS for MNV, using the 30 LSM events for calibration (upper right plot), is as low as about 0.08, compared to the *a priori* value of $\sigma_c = 0.25$ far from calibration data. Figure 6 is similar, but for station KNB using 54 LSM (top) or 11 RV (bottom) earthquakes as reference events. The most significant difference from Figure 5 is that the corrections near NTS for KNB using the 11 RV events is nearly 0.6 units higher than the corrected worldwide average for earthquakes of zero, which is 2.4 times higher than the *a priori* calibration standard deviation of 0.25.

Figure 7 shows discrimination results for the four cases, using the same procedure for all cases, except for the various correction and uncertainty grids of Figures 5 and 6. For case #1, 76 of 78 explosions (97.4%) are categorized as *explosion-like* and 26 of 40 earthquakes (65.0%) are categorized as *earthquake-like*. For case #2, 66 of 78 explosions (84.6%) are categorized as *explosion-like* and 33 of 40 earthquakes (82.5%) are categorized as *earthquake-like.* For case #3, 19 of 88 explosions (21.6%) are categorized as *explosion-like* and 39 of 65 earthquakes (60.0%) are categorized as *earthquake-like*. For these three cases, all other events are *undetermined*. These results are appropriate, given the calibration data. More importantly, no events were categorized as the incorrect event type for these three cases. However, for case #4 (lower right plot of Figure 7), although 93% of the earthquakes are categorized properly, 11 of 88 explosions (12.5%) are mis-categorized as *earthquake-like* (green stars). The problem is that the RV events have anomalously high Pn/Lg values at KNB – more than two-sigma above the worldwide average – and the posterior calibration uncertainty computed by the old algorithm is relatively small, given 11 RV reference events. The kriging calculation would be valid, if Pn/Lg data for these events were uncorrelated. However, since the RV mechanisms are correlated (Smith and Brune, 1993), the Pn/Lg data are not independent and this intrinsic correlation should be treated.

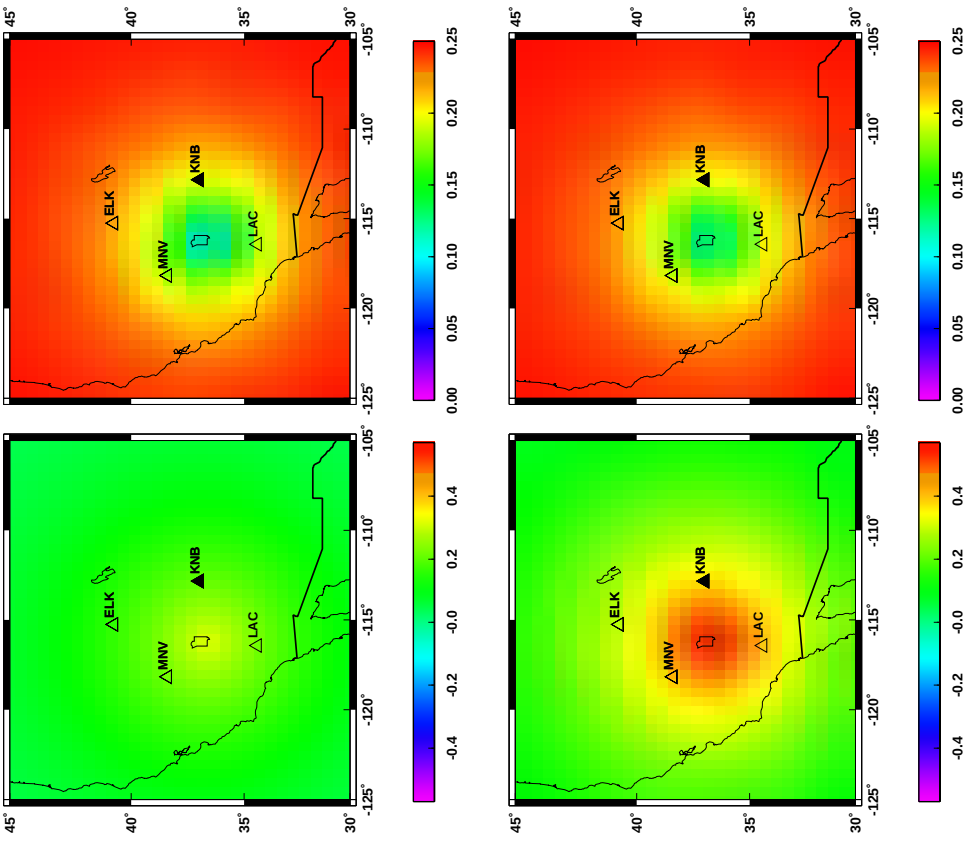

Figure 6. Similar to Figure 5, but for station KNB, using 54 LSM (upper) and 11 RV (lower) earthquakes as reference events for the Bayesian calibration technique.

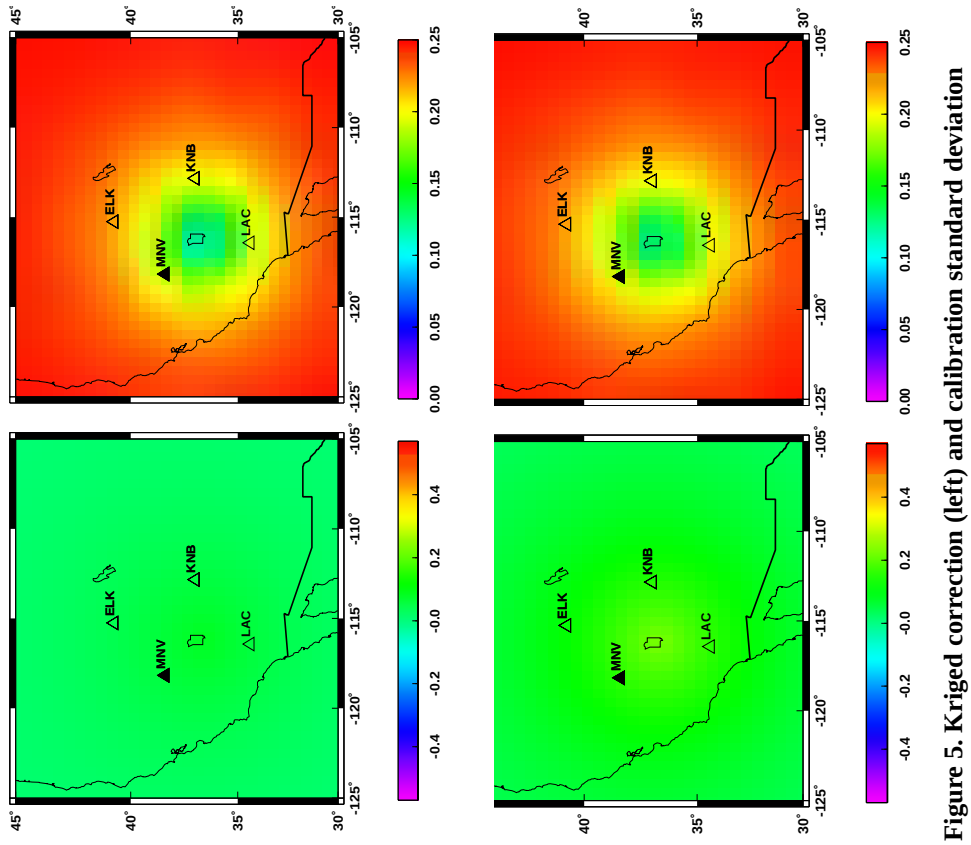

Figure 5. Kriged correction (left) and calibration standard deviation (right) grids for log[Pn/Lg(6-8 Hz)] at station MNV, using 30 LSM (upper) and 10 RV (lower) earthquakes as reference events for the Bayesian calibration technique. The station for which the correction and uncertainty grids apply are represented by a solid triangle in each plot.

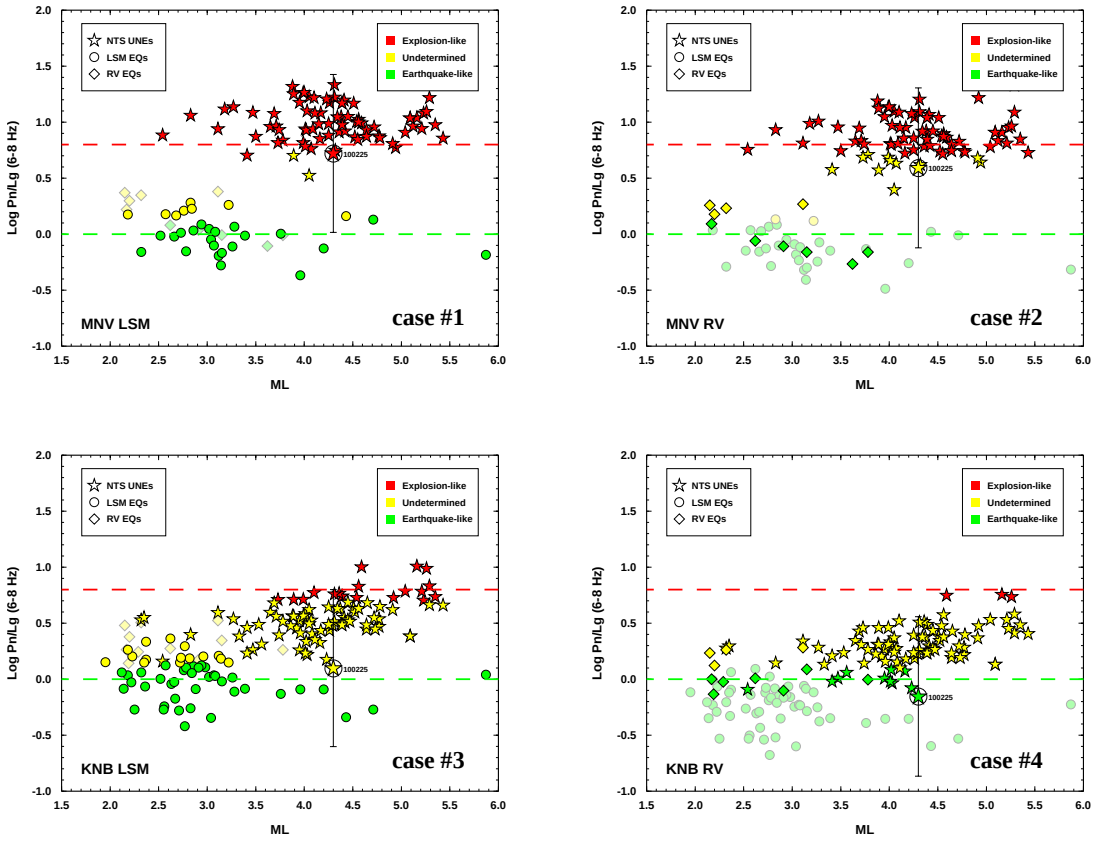

Figure 7. Discrimination results for NTS explosions and earthquakes at MNV (top) and KNB (bottom), based on the correction and uncertainty grids shown in Figures 5 and 6, using LSM (left) and RV (right) events for calibration. Faint markers correspond to events that were not used for kriging, but were tested by the discrimination criteria. Dashed lines in each plot are global means for earthquakes and explosions and the error bar represents the 99.5% confidence interval for an explosion, VILLITA.

Application of the New Methodology to NTS Events

Bottone et al. (2002) show that the covariance, Σ, computed from N reference events is an N-by-N-dimensional matrix with two terms, $\Sigma^{-1} = A^{-1} + B^{-1}$, which is used in the computation of the corrections and the posterior variance. Elements of the calibration covariance are $B_{ij} = \sigma_c^2 \exp(-\Delta(\mathbf{s}_i,\mathbf{s}_j)/\alpha_c)$, $i, j = 1, 2, \ldots, N$, where $\Delta(\mathbf{s}_i,\mathbf{s}_j)$ is the distance between locations $\mathbf{s}_i$ and $\mathbf{s}_j$. Assuming there is no correlation in the residual variance, then $A = \sigma_r^2 I_N$, where I_N is the identity matrix in N dimensions. If there is correlation in the residual variance, then A becomes

$$A_{ij} = \sigma_r^2 g(\Delta(\mathbf{s}_i,\mathbf{s}_j)) = \sigma_r^2 \exp(-\Delta(\mathbf{s}_i,\mathbf{s}_j)/\alpha_r) , \quad (5)$$

where g is a correlation function that we have chosen to be exponential. In the limit α_r goes to zero, the new formula reduces to the old one. We refer to the use of Equation (5), with nonzero α_r, as the new or extended method. Physically, the original correlation length, α_c, treats the effects of regional path variations on the spatial correlation of regional P/S discriminants and is estimated to be about 5 to 6 degrees for Pn/Lg and Pn/Sn in various region types (Bottone et al., 2002). The new correlation length, α_r, treats correlated data for localized events, e.g., with similar focal mechanisms that typically occur on much shorter distance scales of faulting zones. Since further work is needed to estimate α_r, we explore the effect of using various values in a reasonable range. It will be seen that there is little overall sensitivity to the precise value.

We now test whether the new method provides a remedy to the case of using KNB data for RV events to calibrate NTS. Even using values of α_r as small as 5–6 km is sufficient so that no NTS explosions are mis-categorized as *earthquake-like*. This corresponds to inter-spatial correlation values of 0.64 to 0.96 for the RV events, with a median of 0.84. The kriged grids, computed by the new method are shown in Figure 8. The corrections and uncertainties near NTS are not affected nearly as much by the 11 RV events, relative to the worldwide prior, as before in Figure 6, since the RV data are no longer treated as independent. Now 5 of 88 NTS explosions (5.7%) are categorized as *explosion-like* and 83 are *undetermined*. Of the 65 earthquakes, 28 (43.1%) are categorized as *earthquake-like* and the remaining, including all 11 RV events, are *undetermined*. Clearly, the power of the discrimination test is quite low for this case, but note that no events are mis-categorized and this RV case is very anomalous and rare (i.e., $2.4\sigma_c$) compared to earthquakes worldwide. Below we examine the performance of the test for worldwide sets of earthquakes and explosions. Before considering that case, we also replicated the set of 11 RV earthquakes to examine whether the problem recurs if the sample of anomalous reference events becomes large. Even replicating the RV training set 20 times (i.e., 220 training samples), none of the explosions are mis-categorized and the results for the earthquakes are qualitatively the same. Thus, the improved method seems to be very robust to even large samples of anomalous reference events.

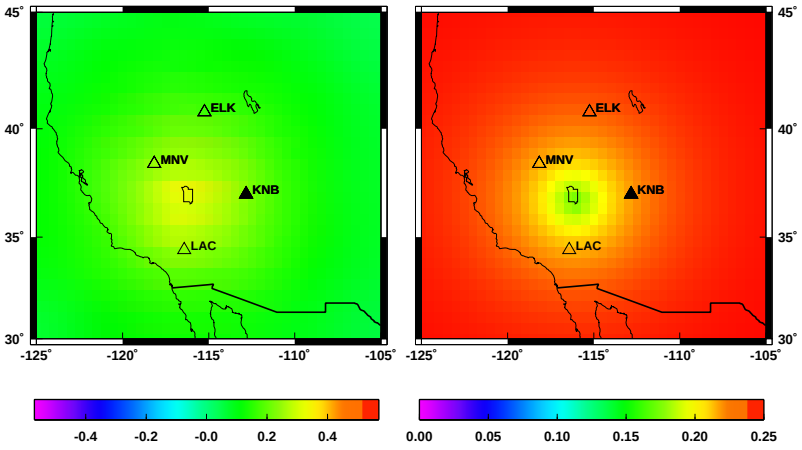

Figure 8. Similar to Figure 6, but applying the extended kriging methodology to station KNB, using the 11 RV earthquakes as calibration events. Near NTS the correction grid does not have such high values and the uncertainty grid does not have such low values, as in the corresponding lower two plots of Figure 6.

Application to Worldwide Data Sets

While the previous section demonstrates a remedy to guard against mis-categorizing explosions, it remains to be seen whether the discrimination test has sufficient power to be useful in the general case, in light of the reduced power for events near NTS when the anomalous RV earthquakes are used for calibration. We now examine how the new correlation function, g, affects the performance of the event-screening procedure of Bottone et al. (2002) that was applied to worldwide sets of 4173 earthquakes and 140 explosions. For this analysis, we use the same data sets that were considered by Bottone et al. (2002). Since the specific value of the correlation length, α_r, requires much more work to estimate, we apply the extended method using various values of α_r. As a conservative approach, one could use a fairly large correlation length; i.e., assume that all localized sets of events might be highly correlated.

Figure 9 shows the percentage of earthquakes that are rejected as being explosions at the 0.005 significance level versus various values of the correlation length, α_r, ranging from 0 to 4 degrees. The baseline case of $\alpha_r = 0$ corresponds to the original analysis performed by Bottone et al. (2002). As expected, the power typically decreases with increasing α_r because the posterior variance generally increases. However, for $\alpha_r = 0.5$ the power of the test increases slightly as compared to the baseline case. The can occur because the posterior means at some locations also change somewhat. For a correlation length of 1.0 degree, the power decreases by only about 2%. This is quite remarkable because it suggests that a rather conservative value of α_r may be used to protect against such cases as at NTS, without much degradation to the overall power of the discrimination test for broad-area monitoring.

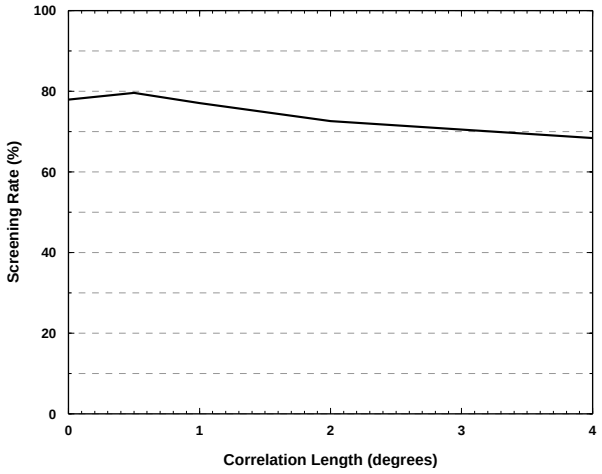

Figure 9. Percentage of earthquakes worldwide that are rejected as being *explosion-like* at the 0.005 significance level as a function of α_r.

CONCLUSIONS AND RECOMMENDATIONS

We acquired and processed spectra for earthquake pairs and/or clusters prior to 2000, based on waveform cross-correlation results from Schaff. Preliminary results indicate that estimated corner frequencies for regional P and S waves from earthquakes are very similar for a majority of the events. In conjunction with results by Fisk (2006, 2007), this may explain the frequency dependence of P/S discriminants. It may also allow more robust fitting of Brune source model parameters, using a broader range of frequencies, by combining relative spectra of regional P and S phases for earthquakes.

We are extending this analysis to event pairs in Eurasia since 2000. Using the Preliminary Determination of Epicenters (PDE) catalog, we formed a list of candidate pairs, based on proximity, and acquired regional data from IRIS for the events. We then computed waveform cross-correlations to find pairs with similar waveforms. We processed and fit network-averaged relative spectra for almost 3600 pairs of events. We have automated all of these processing steps. We are performing quality control of the results, which we plan to merge with our previous results to obtain more extensive estimates of corner frequencies and stress-drop parameters for Eurasia. We also plan to examine uncertainties in these estimates and begin estimating Q and geometrical spreading parameters with source terms fixed.

We also studied the impact of using event clusters with anomalous P/S data for kriging. In the worst scenario, using only RV events to calibrate NTS for KNB, 11 of 88 UNEs were mis-categorized as *earthquake-like* because the RV events have very high Pn/Lg values (2.4σ above the global earthquake average) at KNB and the posterior calibration variance computed by the old method is small, treating the RV events as independent. Since the RV earthquakes had similar mechanisms, mainly left lateral strike-slip faulting on northeast-striking high-angle structures (Smith and Brune, 1993), it is invalid to treat them as independent. Although the procedure of Bottone et al. (2002) was used for this study, the problem is inherent to any kriging method that does not treat intrinsic correlations of clustered calibration data.

We showed that the new kriging method, that introduces a second correlation length, limits the effective number of reference samples for clustered events. This extension keeps the corrections from weighting local clusters too highly and the posterior calibration variance from being too small. We showed that the new method did not mis-categorize any NTS UNEs, even when replicating the set of RV events 20 times. Thus, the extended method seems very robust. Although many events were *undetermined* for this case, this is the appropriate result, based on the reference data. Fortunately, such cases are rare (<1% for 2.4σ). In fact, application to global data sets shows that the power of the test to reject earthquakes as explosions did not degrade much, even for conservatively large values of α_r. Thus, a practical solution to this problem is available (e.g., using a conservative value of $\alpha_r = 1.0$) and it provides useful monitoring performance. Further work is needed to estimate α_r. Although this does not seem necessary for the global case, application to specific sites may improve significantly by using site-specific values. We plan to analyze relevant data for earthquake clusters in Eurasia to examine this issue.

ACKNOWLEDGMENTS

We thank Gary McCartor and Steve Bottone for many useful discussions, Bill Walter of LLNL for regional seismic amplitudes for NTS events, Ward Hawkins of LANL for seismic data for events in Eurasia, and David Schaff for waveform cross-correlation values. We also acknowledge the IRIS DMC for data used in this study.

REFERENCES

Bottone, S., M. D. Fisk and G. D. McCartor (2002). Regional seismic event characterization using a Bayesian formulation of simple kriging, *Bull. Seism. Soc. Am.* 92: 2277–2296.

Brune, J. N. (1970). Tectonic stress and the spectra of seismic shear waves from earthquakes, *J. Geophys. Res.* 75: 4997–5009.

Choy and Boatwright (1995). Global patterns of radiated seismic energy and apparent stress, *J. Geophys. Res.* 100: 18,205–18,228.

Cong, L., J. Xie and B. J. Mitchell (1996). Excitation and propagation of Lg from earthquakes in central Asia with implications for explosion/earthquake discrimination, *J. Geophys. Res.* 101: 27,779–27,789.

Fan G.-W., T. Lay and S. Bottone (2002). Path corrections for source discriminants: a case study at two international seismic monitoring stations, *Pure and Appl. Geophys., Special Edition on Monitoring the Comprehensive Nuclear-Test-Ban Treaty: Seismic Event Discrimination and Identification* 159: 651–678.

Fisk, M. D. (2007). Corner Frequency Scaling of Regional Seismic Phases for Underground Nuclear Explosions at the Nevada Test Site, *Bull. Seism. Soc. Am.*: 97: 977–988.

Fisk, M. D. (2006). Source spectral modeling of regional P/S discriminants at nuclear test sites in China and the Former Soviet Union, *Bull. Seism. Soc. Am.* 96: 2348–2367.

Fisk, M. D., S. Bottone, and G. D. McCartor (2001). Regional Seismic Event Characterization Using Bayesian Calibration, MRC-R-1621, Mission Research Corp., Santa Barbara, CA.

Madariaga, R. (1976). Dynamics of an expanding circular fault, *Bull. Seism. Soc. Am.* 66: 639–667.

Nuttli, O. W. (1983). Average seismic source-parameter relations for mid-plate earthquakes, *Bull. Seism. Soc. Am.* 73: 519–535.

Phillips, W. S. (1999). Empirical path corrections for regional seismic phases, *Bull. Seism. Soc. Am.* 89: 384–393.

Phillips, W. S., G. E. Randall and S. R. Taylor (1998). Path correction using interpolated amplitude residuals: An example from central China, *Geophys. Res. Lett.* 25: 2729–2732.

Rodgers, A. J., T. Lay, G. Fan and W. R. Walter (1998). Calibration of distance and path effects on regional P/S discriminants at station ABKT (Alibek, Turkmenistan): statistical analysis of crustal waveguide effects, UCRL-JC-129165, Lawrence Livermore National Laboratory.

Rodgers, A. J., W. R. Walter, C. A. Schultz, S. C. Myers, and T. Lay (1999). A comparison of methodologies for representing path effects on regional P/S discriminants, *Bull. Seism. Soc. Am.* 89: 394–408.

Schaff, D. P. and P. G. Richards (2004). Repeating seismic events in China, *Science* 303: 1176–1178.

Smith, K. D. and J. N. Brune (1993). A sequence of very shallow earthquakes in the Rock Valley fault zone; southern Nevada test site, *EOS Suppl.* 74: 417.

Taylor, S. R., and H. E. Hartse (1998). A procedure for estimation of source and propagation amplitude corrections for regional seismic discriminants, *J. Geophys. Res.* 103: 2781–2789.

Taylor, S. R., A. A. Velasco, H. E. Hartse, W. S. Phillips, W. R. Walter, and A. J. Rodgers (2002). Amplitude corrections for regional seismic discriminants, *Pure and Appl. Geophys., Special Edition on Monitoring the Comprehensive Nuclear-Test-Ban Treaty: Seismic Event Discrimination and Identification* 159: 623–650.

Walter, W. R., K. M. Mayeda, and H. J. Patton (1995). Phase and spectral ratio discrimination between NTS earthquakes and explosions. Part I: Empirical observations, *Bull. Seism. Soc. Am.*, 85, 1050–1067.

Walter, W. R. and S. R. Taylor (2002). A Revised Magnitude and Distance Amplitude Correction (MDAC2) Procedure for Regional Seismic Discriminants: Theory and Testing at NTS, *UCRL-ID-146882*, LA-UR-02-1008.

REGIONAL ANALYSIS OF LG ATTENUATION: COMPARISON OF 1-D METHODS IN NORTHERN CALIFORNIA AND APPLICATION TO THE YELLOW SEA/KOREAN PENINSULA

Sean R. Ford[1], Douglas S. Dreger[1], Kevin M. Mayeda[2], William R. Walter[3], Luca Malagnini[4], and W. Scott Phillips[5]

University of California, Berkeley[1], Weston Geophysical[2], Lawrence Livermore National Laboratory[3], Istituto Nazionale di Geofisca e Vulcanologia[4], and Los Alamos National Laboratory[5]

Sponsored by National Nuclear Security Administration
Office of Nonproliferation Research and Development
Office of Defense Nuclear Nonproliferation

Contract No. DE-FC52-05NA26605/BAA05-22

ABSTRACT

The measurement of regional attenuation Q^{-1} can produce method dependent results. The discrepancies among methods are due to differing parameterizations (e.g., geometrical spreading rates), employed data sets (e.g., choice of path lengths and sources), and methodologies themselves (e.g., measurement in the frequency or time domain). We apply the coda normalization (CN), two-station (TS), reverse two-station (RTS), source-pair/receiver-pair (SPRP), and the new coda-source normalization (CS) methods to measure Q of the regional phase, Lg (Q_{Lg}), and its power-law dependence on frequency of the form $Q_0 f^{\eta}$ with controlled parameterization in the well-studied region of northern California using a high-quality data set from the Berkeley Digital Seismic Network. We test the sensitivity of each method to changes in geometrical spreading, Lg frequency bandwidth, the distance range of data, and the Lg measurement window. For a given method, there are significant differences in the power-law parameters, Q_0 and η, due to perturbations in the parameterization when evaluated using a conservative pairwise comparison. The CN method is affected most by changes in the distance range, which is most probably due to its fixed coda measurement window. Since, the CS method is best used to calculate the total path attenuation, it is very sensitive to the geometrical spreading assumption. The TS method is most sensitive to the frequency bandwidth, which may be due to its incomplete extraction of the site term. The RTS method is insensitive to parameterization choice, whereas the SPRP method as implemented here in the time-domain for a single path has great error in the power-law model parameters and η is greatly affected by changes in the method parameterization. When presenting results for a given method it is best to calculate $Q_0 f^{\eta}$ for multiple parameterizations using some a priori distribution. We also investigate the difference in power-law Q calculated among the methods by considering only an approximately homogeneous subset of our data. All methods return similar power-law parameters, though the 95% confidence region is large. We adapt the CS method to calculate Q_{Lg} tomography in northern California. Preliminary results show that by correcting for the source, tomography with the CS method may produce better resolved attenuation structure.

OBJECTIVES

Understanding of regional attenuation Q^{-1} can help with structure and tectonic interpretation (Aleqabi and Wysession, 2006; Benz et al., 1997; Frankel, 1990), and correcting for the effects of attenuation can lead to better discrimination of small nuclear tests (e.g. Baker et al., 2004; Mayeda et al., 2003; Taylor et al., 2002). Present threshold algorithms for event identification rely on *Q* models that are derived differently, and the models can vary greatly for the same region. For example, recent one-dimensional (1-D) Q studies in South Korea find frequency-dependent Q_{Lg} that at 1 Hz range from 450 to 900 (Chung and Lee 2003; Chung et al., 2005). Another example is the case of Tibet where a wide variety of *Q* values have been reported (e.g. Fan and Lay, 2003; Xie et al. 2004). In order to reliably use reported *Q* estimates for either monitoring applications, or for tectonic interpretation it is essential to know the uncertainty in the estimate. Commonly, individual studies will present aleatoric (random) uncertainty, however epistemic (bias) uncertainty is not possible to assess, when only a single method and parameterization is considered. In order to better understand the effects of different methods and parameterizations on *Q* models, we implement four popular methods and one new method to measure *Q* of the regional seismic phase, *Lg* (Q_{Lg}), using a high-quality data set from the Berkeley Digital Seismic Network (BDSN). The CN method is implemented in the time domain for paths leading to a common station and it returns a stable *Q* measurement when the region near a station is homogenous. The CS method uses previously calculated coda-derived source spectra to remove the source term in the frequency domain and is best suited to calculate an effective *Q* for a given path. The TS and RTS methods are implemented in the frequency domain and the calculated *Q* is more stable due to the extraction of the source term. The RTS method produces a power-law *Q* with less error than the TS method due to its additional extraction of the site terms, though it is more restrictive in its data requirements. The SPRP method is the RTS method with a relaxation of the data requirements and is implemented in the time domain here.

Through this approach we identify both aleatoric and epistemic uncertainty. With a more complete knowledge of uncertainty it will be possible to better assess the results of published attenuation studies and the presented multi-method analysis procedure employed in future efforts can lead to improved estimates of regional *Q*.

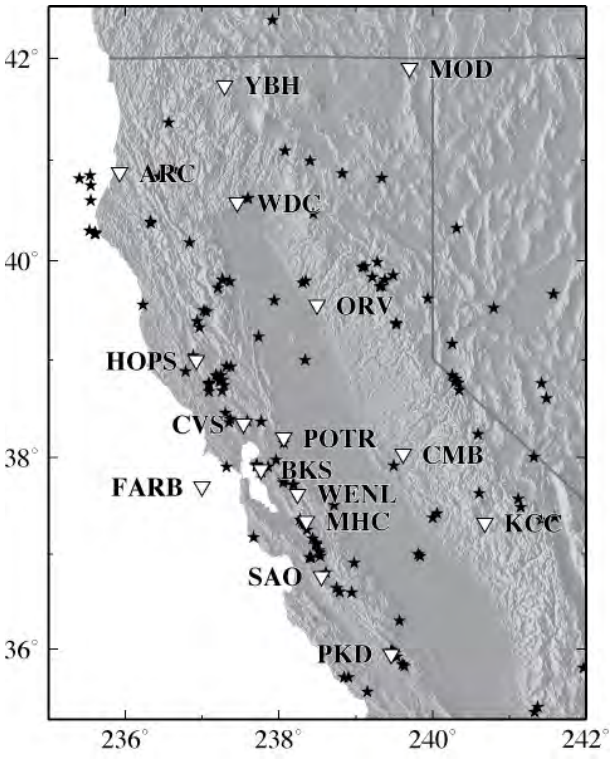

Figure 1. Events (stars), stations (inverted triangles), used in the study.

RESEARCH ACCOMPLISHED

The data set consists of 158 earthquakes recorded at 16 broadband (20 sps) three-component stations of the BDSN between 1992 and 2004 (Figure 1). The wide distribution of data parameters allows for sensitivity testing. We calculate Q_{Lg} by fitting the power-law model, $Q_0 f^{\eta}$ using five different methods. The first two methods use the seismic coda to correct for the source effect. The last three methods use a spectral ratio technique to correct for source, and possibly site effects. In the following we summarize the methods and point out significant differences. Our philosophy in presenting each of the methods is to maintain the approach and style of the popular version of each method as close as possible. Later, we will attempt to normalize each of the methods for comparison and sensitivity testing.

Coda Normalization (CN)

The CN method uses the local shear-wave coda as a proxy for the source and site effects, thus amplitude ratios remove these two effects from the *S*-wave spectrum (Aki, 1980; Yoshimoto et al., 1993). In his original application, Aki (1980) assumed that the local shear-wave coda was homogeneously distributed in space and time. For the current study region, Figure 1 of Mayeda et al. (2005) shows that the coda at ~1 Hz is

in fact homogeneous, at least up to ~240 km. This method assumes the *Lg* amplitude A_{Lg} at a given distance *r* and frequency *f* can be estimated by

$$A_{Lg}(f,r) = S(f)R(\theta)I(f)P(f)G(r)\exp\left(\frac{-r\pi f}{QU}\right), \quad (1)$$

where $S(f)$ is the source spectrum and $R(\theta)$ is the source radiation in the source-receiver direction θ. $P(f)$ is the site term, $I(f)$ is the instrument term, and $G(r)$ is the geometrical spreading term, approximated here as an inverse power-law where γ is the spreading rate and is given in Table 1. The final term is an apparent attenuation, where U is the *Lg* group velocity, which is fixed at 3.5 km/s for this and all other methods. The CN method also assumes that the coda spectrum $C(f)$ is approximately equal to the source spectrum at a given critical propagation time t_C. The coda excitation term is assumed to be constant at all distances for a given t_C. If the source radiation is smoothed by considering several sources at many source-receiver directions we can take the ratio of A_{Lg} to C, measured at t_C, which effectively removes instrument, site, and source contributions resulting in only the geometrical spreading and attenuation terms. The natural log of this spectral ratio taken at discrete frequency bands (between 0.25, 0.5, 1, 2, 4, and 8 Hz) results in the equation of a line as a function of distance and the slope is related to Q^{-1}. Q^{-1} at the center frequency of each band then reveals a power-law model for each station.

A_{Lg} is the maximum envelope amplitude in each bandpassed (8-pole acausal Butterworth filter), windowed (according to the window parameter in Table 1) and tapered raw vertical trace. C is the root-mean-square (rms) amplitude in each bandpassed 10 second window centered on a t_C of 150 sec. Data were excluded if either A_{Lg} or C had a SNR less than two, where noise is measured as the maximum amplitude in a window the same length as A_{Lg} prior to the event. This method is similar to that of Chung and Lee (2003), whereas Frankel (1990) used a weighted average of the smoothed coda to measure C. We calculate Q^{-1} with all records at a given station, where the slope is calculated with an iteratively weighted least-squares method. The resulting Q^{-1} are then fit in the log domain as a function of midpoint frequency with a weighted (the squared inverse of the standard error in each Q^{-1} measurement) least-squares line to calculate the power-law parameters.

Coda-Source Normalization (CS)

The CS method uses the stable, coda-derived source spectra to isolate the path attenuation component of the *Lg* spectrum (Walter et al., 2007). This method assumes A_{Lg} is represented as in equation (1) with $S(f)$ described as in Aki and Richards (2002), $G(r)$ is a critical distance formulation (Street et al., 1975). We assume a site term $P(f)$ of unity and thus any site effect is projected into the path attenuation term.

The windowed (according to the window parameter in Table 1) and tapered transverse component is transferred to velocity and its Fourier amplitude is calculated. A_{Lg} is then the mean of the Fourier amplitude for fixed discrete frequency bands (between 0.2, 0.3, 0.5, 0.7, 1, 1.5, 2, 3, 4, 6, and 8 Hz). Path attenuation can then be extracted with the log transform where the same frequency bands are used to calculate the source spectra, $S(f)$, and $P(f)$ is fixed to unity. Source spectra derived from the coda are calculated via the methodology of Mayeda et al. (2003) and from the northern California study of Mayeda et al. (2005). $Q(f)$ is only calculated for records where A_{Lg} is two times the amplitude of the pre-event signal (SNR > 2). Q at the center frequency of each band then reveals a power-law model for each event-station path. We fit a least-squares line in the log domain (a robust regression gave similar results) and the intercept term is then the log transform of Q_0 and the slope is η.

Table 1. Method parameterization.

Group	Spreading exponent [γ]	Measurement band (Hz)	Epicentral distance [*r*] (km)	*Lg* Velocity window (km/s)
Control	0.50	0.50–8	100 - 400	2.6–3.5
Test 1 (γ)	**0.83**			
Test 2 (Bandwidth)		**0.25–4**		
Test 3 (Distance)			**100 - 700**	
Test 4 (Window)				**3.0–3.6**

Two-Station (TS)

The TS method takes the ratio of *Lg* recorded at two different stations along the same narrow path from the same event in order to remove the common source term (e.g., Chavez and Priestley, 1986; Xie and Mitchell, 1990). We implement this method in the frequency domain and take the ratio of two terms with the form of equation (1), which can then be transformed to the log-domain and a linear regression is possible to calculate the power-law parameters. However, random error due to propagation can produce a negative argument in the exponential term of equation (1) at some frequencies (Xie, 1998), which prohibits analysis in the log-domain. Therefore, we perform a non-linear regression on the argument that minimizes the sum of squares error on the power-law function in the least-squares sense (Bates and Watts, 1988).

Reverse Two-Station (RTS)

The RTS method uses two TS setups, where a source is on either side of the station pair in a narrow azimuthal window (Chun et al., 1987). The two ratios are combined to remove the common source and site terms.

Source-Pair/Receiver-Pair (SPRP)

The SPRP method is the RTS method with a relaxation on the narrow azimuthal window requirement (Shih et al., 1994). We implement this method in the time-domain. Unlike the RTS method, data are no longer restricted by a given azimuth but by a distance formulation. A_{Lg} is the maximum zero-to-peak amplitude in each bandpassed (8-pole acausal Butterworth filter), windowed (according to the window parameter in Table 1) and tapered vertical component record that has been transferred to velocity. The equation is least-squares fit as a function of the effective interstation distance for the same discrete frequency bands as in the CN method, where f is the midpoint of these frequency bands. The slope of the fit is a function of Q^{-1} in the band that was measured. The resulting Q^{-1} are then fit in the log domain as a function of midpoint frequency with a weighted (the squared inverse of the standard error in each Q^{-1} measurement) least-squares line to calculate the power-law parameters.

Method Comparison

Since each method has a different data requirement it is improper to compare the methods with the full data set. For example, the CN method will sample geology at all back-azimuths relative to a station, whereas the RTS method is restricted to a narrow azimuthal window aligned roughly along a pair of stations and events.

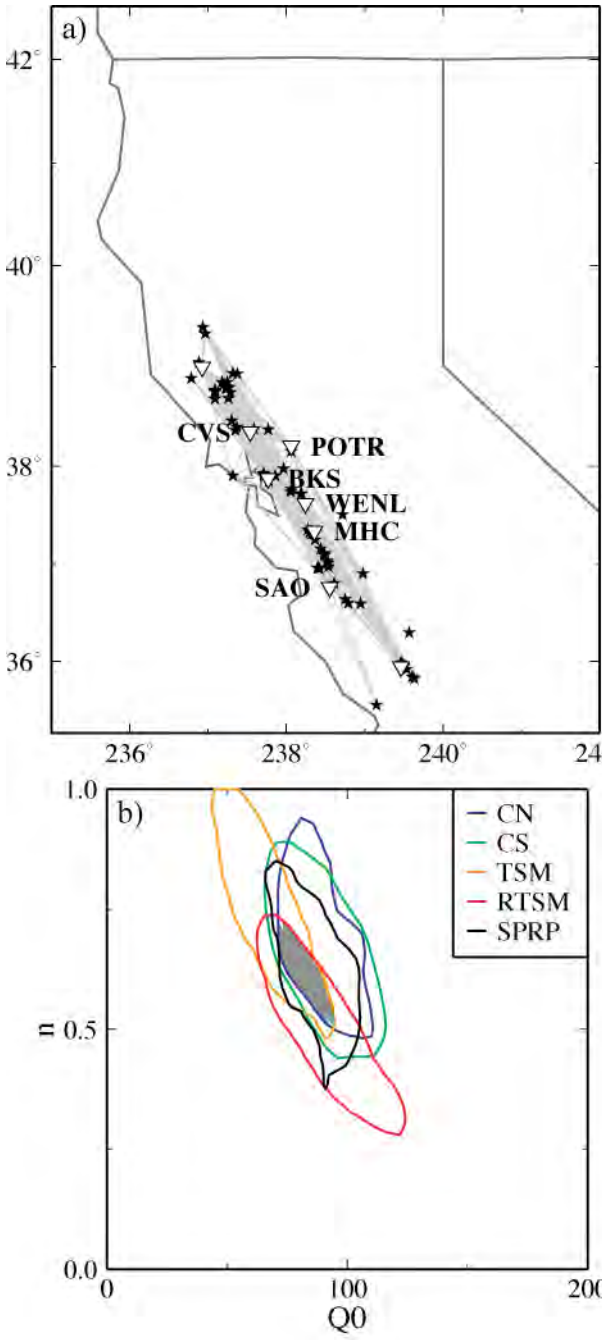

Figure 2. Method comparison. (a) Map (same region as Figure 1) of the subset used in the comparison analysis. Data are in a small region near the San Francisco Bay Area, primarily along the Franciscan block. (b) Power-law parameters and their empirical 95% confidence regions are given. The intersecting region is shaded grey.

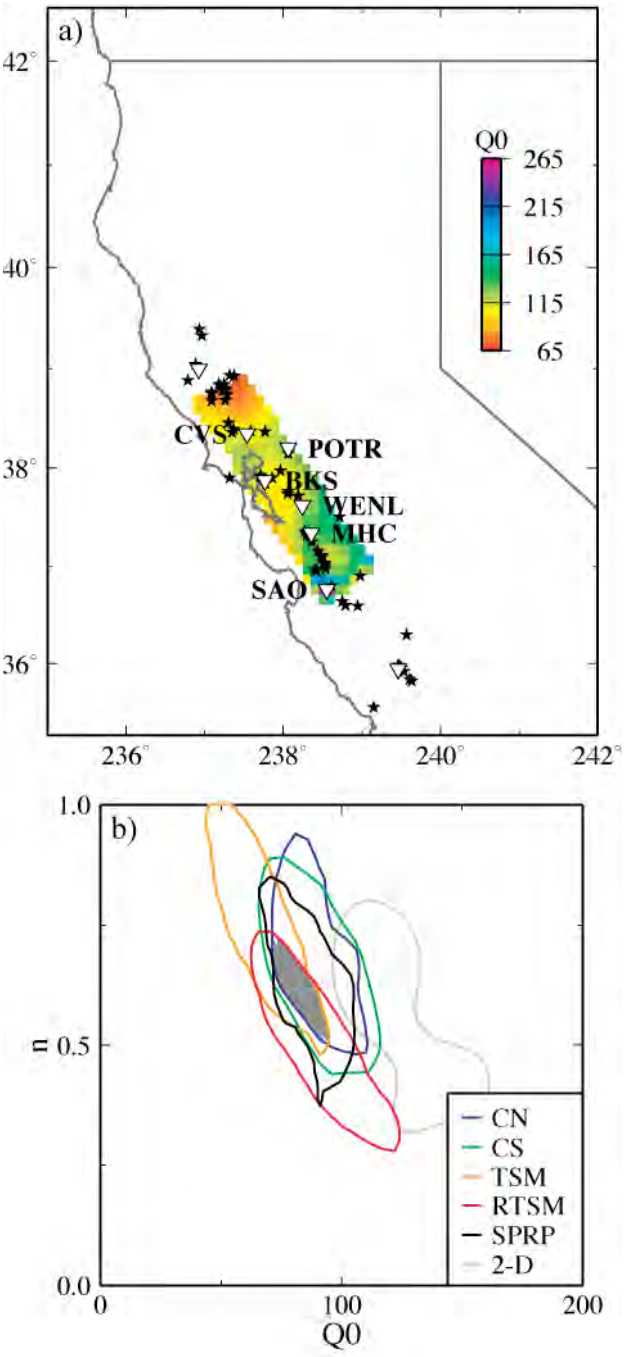

Figure 3. Method comparison with tomographic results of (Mayeda et al. 2005). (a) Region where 2-D direct wave attenuation coefficients are used, which covers the same area as the paths and stations in Figure 2a. (b) Comparison of tomographic results where empirical distribution (light grey) is from data at each node with 1-D results.

In an attempt to normalize the data set used for each method, we restrict the data to lie in a small region along the Franciscan block (Figure 2a). We implement all five methods to calculate $Q_0 f^{\eta}$ in the region (Figure 2b). The populations are then smoothed with a two-dimensional gaussian kernel (Venables and Ripley, 2002) to produce an empirical distribution so that the 95% confidence region can be estimated. The grey region in Figure 2b represents a parameter space that fits all studies. Mayeda et al. (2005) present Q tomography for Northern California in order to compare 1-D and 2-D methods to calculate both coda and direct wave (*S*, *Lg*, or surface wave) attenuation. We extend the analysis for comparison with the results from the 1-D analysis of the sub-region. Power law parameters from the Mayeda et al. (2005) study are calculated by fitting a least-squares line to the Q estimated for each frequency band at the midpoint of the band in the log domain. We extract the power-law parameters at points within the sub-region (Figure 3a) and, as above, we produce an empirical distribution (Figure 3b). The range in η and variance of Q_0 are similar between the 1-D and 2-D results, but the mean of the Q_0 distribution is shifted by about 30. This may be due to some regularization effects. This analysis shows that some of the variability in the 1-D analysis is due to 2-D structure.

Sensitivity Tests

Using the complete data set, we investigated how the choice of parameterization affects the results. In each test, only one parameter was varied, and $Q_0 f^{\eta}$ was calculated with each of the methods. The varied parameters are geometrical spreading rate, measurement bandwidth, epicentral distance, and the *Lg* window. The values of the varied parameters are listed in Table 1, where the range was chosen based on the values used in previous studies.

For the CN method, standard error regions were constructed from the covariance of the power-law model parameters estimated by bootstrapping the residuals of the weighted least-squares fit 1000 times (Aster et al., 1996). Figure 4a shows the standard error regions for each test at station PKD. All tests cluster around the control parameters except the distance test (Test 3). To assess the significance of model parameterization differences we perform an analysis of covariance (ANCOVA) for the weighted least-squares regression with Tukey's honest significant difference pairwise comparison tests (Faraway, 2004). A difference in the model parameters is only significant if the 95% confidence region of the mean difference in the model parameters between two tests does not include zero. We group all significant differences between a

given test and the control parameterization and plot the median, 25th and 75th percentile values of that group (Figure 4b). In this way, we can try and separate aleatoric uncertainty due to poorly constrained power-law model parameters and epistemic uncertainty due to the choice of parameterization for each method, and one can think of the confidence regions in panel a) of Figures 4 as the aleatoric uncertainty, and the values in panel b) as epistemic uncertainty. There is a significant difference for almost all CN method comparisons in η, and the greatest difference for both model parameters is when the epicentral distance of the data set is changed (Test 3). This is due to the fixed time t_C at which the coda is measured, where for greater distances it is more appropriate to increase t_C.

Standard error regions and pairwise comparisons are calculated for the CS method as described above, though the residuals and ANCOVA are for a direct linear regression. For most tests only a small fraction of the comparisons are significant. However, when γ is changed in Test 1, there is a significant difference in Q_0 for 39% of the path comparisons, where the median difference is almost 50. This effect highlights the difficulty in extracting an intrinsic Q from the full path attenuation when examining a single path. The CS method is best for evaluating the total path term.

Since the TS and RTS methods require nonlinear regressions, we estimate covariance matrices from the bootstrapped power-law model parameter populations. ANCOVA is performed with this estimated covariance and the pairwise comparisons are made with the results. A change in epicentral distance does not significantly affect the power-law parameters for both the TS and RTS methods, but a change in bandwidth (Test 2) produces an interquartile range of 0.05 to 0.22 for the difference in η using the TS method. The TS method is sensitive to site effects and this difference may be due to site effects that are different below 1 Hz than they are above it. For several stations in the BDSN this seems to be the case (Malagnini et al., 2007). The RTS method doesn't suffer from this same dependency and its median significant differences are low for all tests.

As previously stated, the SPRP method implemented in the time domain requires a distribution of effective interstation distances that can best be given when several interstation paths are considered. However, it should be able to constrain $Q_0 f^{\eta}$ for a single interstation path, and in order to allow for comparison with the implementation of the other interstation methods, TS and RTS, we carry out the method on an interstation basis. Due to such large standard error regions only around half of the pairwise comparisons give a significant difference in Q_0. However, the same comparisons reveal a large difference in η for all but the γ test (Test 1).

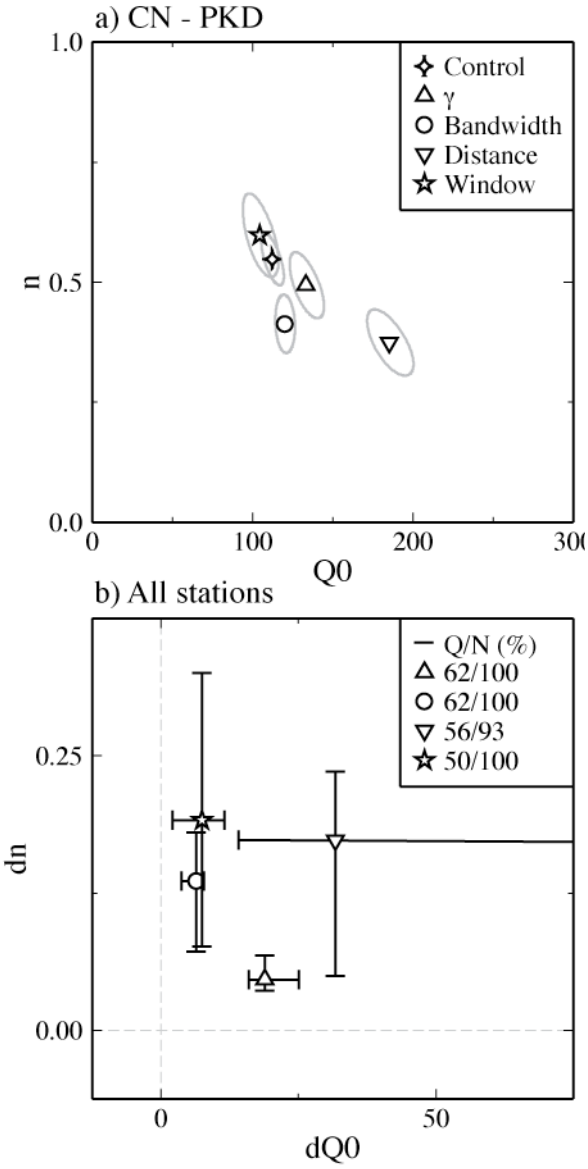

Figure 4. Parameterization effects of the coda-normalization method. a) Power-law parameters (Q_0, η) for each choice of parameterization and the standard error region. b) Results of significant difference in pairwise comparisons between the Control parameterization and its deviations (similar symbol as a) for all measurements in the method. The upper right box gives percentage of measurements that had a significant difference and the symbols are at the median difference (δQ_0, $\delta\eta$) with upper (3rd quartile) and lower (1st quartile) bounds given by the bars.

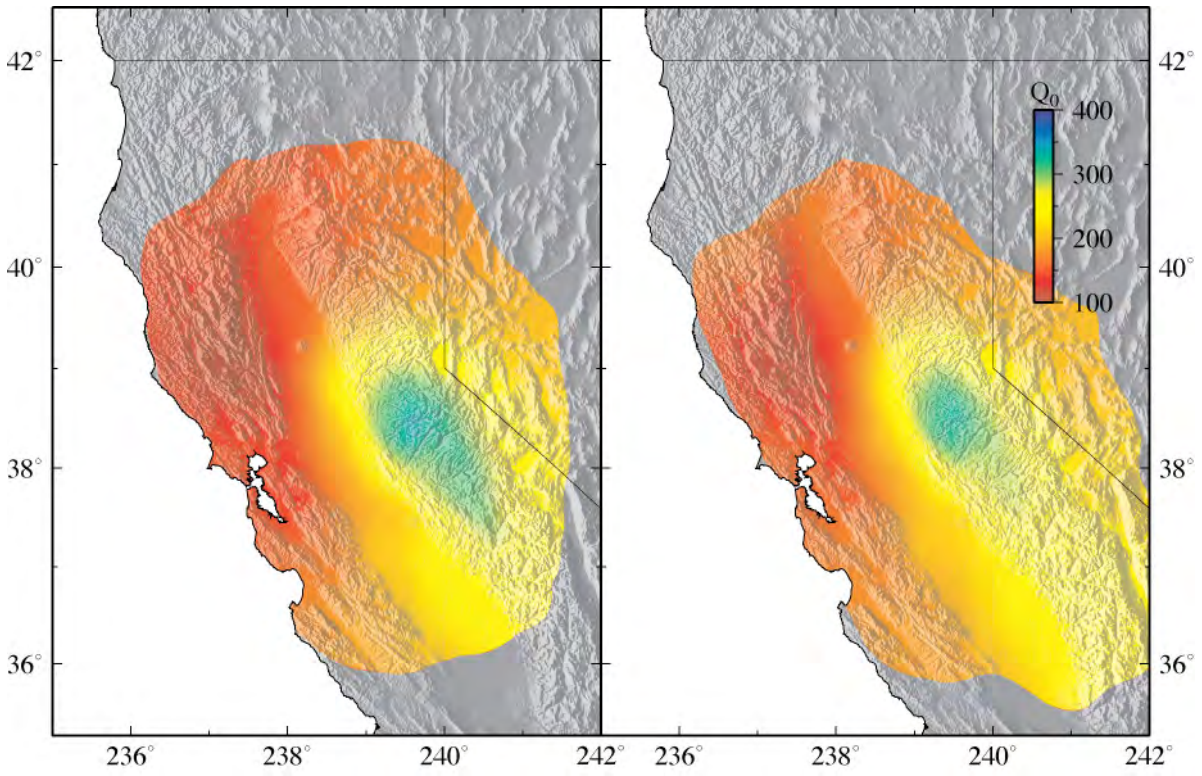

Figure 5. Attenuation tomography using amplitudes (a) where the source and site term is solved for in the inversion and (b) where the source term is removed from the amplitudes using a coda-derived moment rate.

Discussion

Each method analyzed here is employed for different types of investigation. Each method has different advantages, disadvantages and assumptions. The CN method returns a stable *Q* measurement when the region near a station is homogenous. The CS method is best suited to calculate an effective *Q* for a given path, where the site term is mapped into the path attenuation. Also, since it measures the path directly from the event to station, there is a trade-off between geometrical spreading and effective *Q*. If the uncertainties in the type of geometrical spreading are large, then it may be best to test several forms of spreading, or to fold the spreading term into the entire path effect if this is appropriate for the application. The CS method can be used to calculate corrected amplitudes for use in a tomographic inversion. We have created such a scheme by adapting the method of Phillips et al. (2005) and preliminary results show that this method may resolve structure more tightly (Figure 5).

The TS and RTS methods are more stable due to the extraction of the source term. The RTS method produces the least error due to its additional extraction of the site terms, though it is more restrictive in its data requirements. Xie (2002) calculates the bias due to the site term assumption in the TS method and finds that it is small. In order to test this assumption we compare the average power-law parameters for paths calculated by both the TS and RTS methods (Figure 6a). The values of the parameters are approximately the same for both methods, though there is scatter. A more direct test is to compare the power-law parameters calculated for paths to station BKS and new data from a nearly co-located BRK (Figure 6b). Malagnini et al. (2007) find a significant difference in the site term between BKS and BRK and this difference is evident in Figure 6b. Stacking ratios with common interstation paths could reduce the variance, but this is only appropriate for tectonically stable areas. Aster et al. (1996) calculates spectral ratios with the multi-taper method and is able to produce more stable spectra and a more realistic variance in the spectral measurement.

The SPRP method is the RTS method with a relaxation of the data requirements and is appropriate for very laterally homogeneous *Q*. The SPRP method is implemented in the frequency domain by Fan and Lay (2003), and in the time domain by Shih et al. (1994) and Chung et al. (2005), where they find clusters in small regions that are very different from the overall 1-D *Q* model. The SPRP method in the time domain is much better suited for a large homogeneous region, where several interstation regions can be grouped together. In the implementation here, we calculate $Q_0 f^{\eta}$ for each interstation path that fits the above criteria (<41% of the available paths), which results in pooling of data points near the true interstation distance. This can greatly effect the linear regression and produce large error in the model parameters.

CONCLUSIONS AND RECOMMENDATIONS

We apply the coda normalization (CN), two-station (TS), reverse two-station (RTS), source-pair/ receiver-pair (SPRP), and the new coda-source normalization (CS) methods to measure Q_{Lg} and its power-law dependence ($Q_0 f^{\eta}$) in northern California in order to understand the variability due to parameterization choice and method. We investigate the reliability of the methods by comparing them with each other for an approximately homogeneous region in the Franciscan block near the San Francisco Bay Area. All methods return similar power-law parameters, especially in their 95% confidence regions. If we consider the joint distributions of each method $Q_0 = 85 \pm 40$ and $\eta = 0.65 \pm 0.35$ (both ~95% CI), where η is not as well constrained. We test the sensitivity of each method to changes in geometrical spreading, *Lg* frequency bandwidth, the distance range of data, and the *Lg* measurement window. For a given method, there are significant differences in the power-law parameters, Q_0 and η, due to perturbations in the parameterization when evaluated using a conservative pairwise comparison. The CN method is affected most by changes in the distance range, which is most probably due to its fixed coda measurement window or the fact that at larger distances the coda is not homogeneously distributed. Since, the CS method is best used to calculate the total path attenuation, it is very sensitive to the geometrical spreading assumption. The TS method is most sensitive to the frequency bandwidth, which may be due to its incomplete extraction of the site term. The RTS method is insensitive to parameterization choice, whereas the SPRP method as implemented here in the time-domain for a single path has great error in the power-law model parameters and η is greatly affected by changes in the method parameterization. When presenting results for a given method it is best to calculate $Q_0 f^{\eta}$ for multiple parameterizations using some a priori distribution. We plan to implement the methods introduced here to find 1-D and 2-D attenuation in the Yellow Sea / Korean Peninsula region.

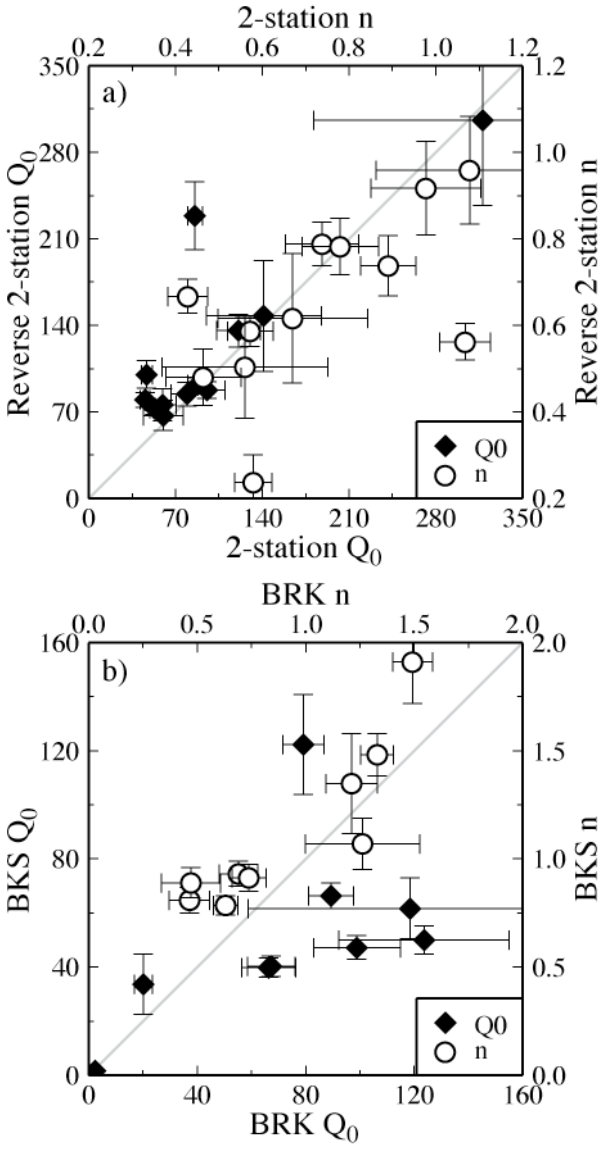

Figure 6. An investigation into site effects. (a) Power-law parameters for paths measured by both the RTS and TS methods. (b) Power-law parameters measured at nearly co-located stations BKS and BRK using the TS method.

ACKNOWLEDGEMENTS

Figures were made with Generic Mapping Tools (Wessel and Smith, 1998).

REFERENCES

Aki, K. and P. G. Richards (2002). *Quantitative Seismology*. Sausalito, Calififormia: University Science Books.

Aki, K. (1980). Attenuation of shear-waves in the lithosphere for frequencies from 0.05 to 25 Hz, *Phys. Earth Planet. Inter.* 21: 50–60.

Aleqabi, G. I. and M. E. Wysession (2006). Q(Lg) distribution in the basin and range province of the western United States, *Bull. Seism. Soc. Amer.* 96: 348–354.

Aster, R. C., G. Slad, J. Henton, and M. Antolik (1996). Differential analysis of coda Q using similar microearthquakes in seismic gaps. Part 1: Techniques and application to seismograms recorded in the Anza seismic gap, *Bull. Seis. Soc. Amer.* 86: 868–889.

Baker, G. E., J. Stevens, and H. M. Xu (2004). Lg group velocity: A depth discriminant revisited, *Bull. Seism. Soc. Amer*. 94: 722–739.

Bates, D. M. and D. Watts (1988). *Nonlinear Regression Analysis and Its Applications*. New York: Wiley.

Benz, H. M., A. Frankel, and D. M. Boore (1997). Regional Lg attenuation for the continental United States, *Bull. Seism. Soc. Amer*. 87: 606–619.

Chavez, D. E. and K. F. Priestley (1986). Measurement of frequency dependent Lg attenuation in the Great Basin, *Geophys. Res. Lett.* 13: 551–554.

Chun, K., G. F. West, R. J. Kokoski, and C. Samson (1987). A novel technique for measuring Lg attenuation: Results from Eastern Canada between 1 to 10 Hz, *Bull. Seism. Soc. Amer.* 77: 398–419.

Chung, T. W., Y. K. Park, I. B. Kang, and K. Lee (2005). Crustal Q_{Lg}^{-1} in South Korea using the source pair/receiver pair method, *Bull. Seis. Soc. Amer*. 95: 512–520.

Chung, T. and K. Lee (2003). A study of high-frequency Q_{Lg}^{-1} in the crust of South Korea, *Bull. Seism. Soc. Amer*. 93: 1401–1406.

Fan, G. and T. Lay (2003). Strong Lg wave attenuation in the northern and eastern Tibetan Plateau measured by a two-station/two-event stacking method, *Geophys. Res. Lett.* 30.

Faraway, J. J. (2004). *Linear Models with R*. Boca Raton, Florida: Chapman & Hall/CRC Press.

Frankel, A. (1990). Attenuation of high-frequency shear waves in the crust: measurements from New York State, South Africa, and Southern California, *J. Geophys. Res.* 95: 17441–17457.

Malagnini, L., K. Mayeda, R. Uhrhammer, A. Akinci, and R. B. Herrmann (2007). A regional ground-motion excitation/attenuation model for the San Francisco region, *Bull. Seism. Soc. Amer.* 97: 843–862.

Mayeda, K., L. Malagnini, W. S. Phillips, W. R. Walter, and D. Dreger (2005). 2-D or not 2-D, that is the question: A northern California test, *Geophys. Res. Lett.* 32: L12301.

Mayeda, K., A. Hofstetter, J. L. O'Boyle, and W. R. Walter (2003). Stable and transportable regional magnitudes based on coda-derived moment-rate spectra, *Bull. Seis. Soc. Amer*. 93: 224–239.

Phillips, W. S., H. E. Hartse, and J. T. Rutledge (2005). Amplitude ratio tomography for regional phase *Q*, *Geophys.Res.Lett.* 32: L21301.

Shih, X. R., K. Y. Chun, and T. Zhu (1994). Attenuation of 1–6 s L_g waves in Eurasia, *J. Geophys. Res.* 99: 23,859–23,875.

Street, R. L., R. B. Herrmann, and O. W. Nuttli (1975). Spectral characteristics of the L_g wave generated by central United States earthquakes, *Geophys. J. R. Astron. Soc.* 41: 51–63.

Taylor, S., A. Velasco, H. Hartse, W. S. Philips, W. R. Walter, and A. Rodgers (2002). Amplitude corrections for regional discrimination, *Pure. App. Geophys.* 159: 623–650.

Venables, W. N. and B. D. Ripley (2002). *Modern Applied Statistics with S*. New York: Springer.

Walter, W. R., K. Mayeda, L. Malagnini, and L. Scognamiglio (2007). Regional body-wave attenuation using a coda source normalization method: Application to MEDNET records of earthquakes in Italy, *Geophys. Res. Lett.* 34: L10308.

Xie, J., R. Gok, J. Ni, and Y. Aoki, (2004). Lateral variations of crustal seismic attenuation along the INDEPTH profiles in Tibet from Lg Q inversion, *J. Geophys. Res.* 109: B10308.

Xie, J. and B. J. Mitchell (1990). Attenuation of multiphase surface waves in the Basin and Range Province. Part I: Lg and Lg coda, *Geophys. J. Int.* 102: 121–137.

Xie, J. (2002). Lg Q in the eastern Tibetan Plateau, *Bull. Seis. Soc. Amer*. 92: 871–876.

Xie, J. (1998). Spectral inversion of Lg from earthquakes: A modified method with applications to the 1995, western Texas earthquake sequence, *Bull. Seis. Soc. Amer.* 88: 1525–1537.

Yoshimoto, K., H. Sato, and M. Ohtake (1993). Frequency-dependent attenuation of P and S waves in the Kanto area, Japan, based on the coda-normalization method, *Geophys. J. Int.* 114: 165–174.

EXTRACTING SHORT-PERIOD SURFACE WAVEFORMS FROM SEISMIC NOISE FOR THE PURPOSE OF ESTIMATING LOCAL AND NEAR-REGIONAL VELOCITY AND ATTENUATION STRUCTURE

Peter Gerstoft[1], William A Kuperman[1], Karim G. Sabra[1], Michael C Fehler[2], Steven R Taylor[3], and Toshiro Tanimoto[4]

University of California, San Diego[1], Los Alamos National Laboratory[2], Rocky Mountain Geophysics, LLC[3], and University of California, Santa Barbara[4]

Sponsored by Air Force Research Laboratory

Contract No. FA8718-07-C-0005[1–4]

ABSTRACT

This paper investigates the utility of computing Time-Domain Green's Functions (TDGF) to be used for estimating velocity and attenuation structure for the purposes of nuclear explosion monitoring over local and near-regional distances. Our objective is to extend and apply the methodology of deriving TDGF for propagation between two receivers by cross correlation of seismic noise and/or coda of earthquakes observed at the receivers. We have previously shown that it is possible to obtain travel-time information for short-period surface waves (around 6 s) by cross correlating seismic noise at local and regional scales. The noise source exploited for this was the ever-present microseisms. In the present report, we focus on characterizing the spatiotemporal variation in microseisms from the Southern California seismic array.

OBJECTIVES

Our objective is to extend and apply the methodology of deriving TDGF for propagation between two receivers by cross-correlation of seismic noise and/or coda of earthquakes observed at the receivers. We have previously shown that it is possible to obtain travel-time information for short-period surface waves (around 6 s) by cross-correlating seismic noise at local and regional scales. We propose to add the following improvements the TDGF method: 1) modifications to better handle cases having non-isotropic noise; 2) implementing a system identification approach for obtaining reliable amplitude information for the TDGF, allowing for the estimation of attenuation along paths between receivers, and 3) extracting TDGF from Lg or Sn coda.

In the present report, we focus on characterizing the azimuthal variation in microseisms form the Southern California seismic array. A non-uniform azimuthal distribution of energy might cause bias in travel times. The next objective will then be to demonstrate how much bias this will cause the extracted Greens functions and then use advanced beamforming approaches to correct for this bias.

RESEARCH ACCOMPLISHED

Introduction

Cross-correlation of noise recordings has been demonstrated to be a way to infer the impulse response between receivers. Extensive work has been performed on this topic in the last few years in various fields of wave physics such as ultrasonics, underwater acoustics, and geophysics, with early demonstrations by Weaver and Lobkis, 2001, and Larose et al., 2004. Despite the very different scales involved in ultrasonics (wavelength ~ mm) compared to geophysics (wavelength ~ km), the basic physics of the process is the same. The impulse response between two receivers is the part of the noise that is coherent between the two points, even if, at first sight, it is deeply buried in local incoherent noise. After cross-correlating over a long time (for example, one month in Sabra et al., 2005b; Shapiro et al., 2005), the time derivative of the noise cross-correlation function (DCF) converges to the impulse response between the two receivers filtered in the bandwidth of the noise spectrum.

A main issue in the convergence of the correlation process resides in the temporal and spatial distribution of the noise sources. From the temporal point of view, the noise spectrum defines the bandwidth frequency in which the impulse response will be retrieved. When receivers are far away from each other, the amplitude sensitivity of the receivers has to be such that the coherent propagating noise can be recorded on both receivers despite geometrical spreading and attenuation. This explains why only the slowly attenuated Rayleigh waves have dominated the results obtained so far from correlation of seismic noise. Using data recorded on a dense seismic network in Parkfield, California, we have successfully demonstrated that body waves can be retrieved (Roux et al., 2005b). The spatial distribution of seismic noise is also of importance. When noise sources are uniformly distributed on both sides of the receivers, the correlation function is symmetric in time, showing both the impulse response and its time-reversed signal (Snieder, 2004; Roux et al., 2005a; Sabra et al., 2005a). However, recent investigations using noise data recorded in Southern California did not result in a symmetric noise correlation function (NCF) because the noise was dominated by microseism originating from the ocean (Sabra et al., 2005a; Shapiro et al., 2005; Gerstoft et al., 2006b).

Noise Cross-Correlation and the TGDF

The cross-correlation C_{ij} is computed from the observed fields $v_i(\mathbf{r}_1,t)$ located at $\mathbf{r}_1$ recording component *i* and $v_j(\mathbf{r}_2,t)$ located at $\mathbf{r}_2$ recording component *j* by integration over the observation period *T*

$$C_{ij}(1,2,t) = \int_0^T v_i(\mathbf{r}_1,\tau) v_i(\mathbf{r}_1,t-\tau)\mathrm{d}\tau \qquad (1)$$

In practice, the cross-correlation is computed for each day and then ensemble averaged over all observed days.

Analytic derivations for specific propagation models (Snieder, 2004; Roux et al., 2005a; Sabra et al., 2005a) and discussions in (Weaver and Lobkis, 2001; Weaver and Lobkis, 2004) give the following relationship between the

time-derivative of the noise cross-correlation $C_{ij}(1,2,t)$ between two seismic stations 1 (located at $\mathbf{r}_1$ recording component *i*) and 2 (located at $\mathbf{r}_2$ recording component *j*) for the TDGF $G_{ij}(\mathbf{r}_1;\mathbf{r}_2,t)$

$$\frac{dC}{dt} \approx -G_{ij}(\mathbf{r}_1;\mathbf{r}_2,t) + G_{ij}(\mathbf{r}_1;\mathbf{r}_2,-t) \tag{2}$$

The TDGF $G_{ij}(\mathbf{r}_1;\mathbf{r}_2,t)$ relates a unit force in direction *i* at $\mathbf{r}_1$ to the displacement response in direction *j* at $\mathbf{r}_2$.

In Equation (1), the terms on the right-hand side are respectively: (1) the TDGF that comes from noise events that propagate from station 1 to 2 and yields a positive-correlation time-delay *t* and (2) the time-reversed TDGF which comes from noise events that propagate from station 2 to 1 and yields a negative correlation time-delay *–t*. Thus, for a uniform noise source distribution surrounding the two stations, the derivative of the DCF will be a symmetric function with respect to the arrival time because seismic noise sources are distributed on both sides of the station pair. However, in the case of a predominant directional noise source (e.g., noise originating from ocean microseisms, see next section), the DCF will likely be one-sided.

The DCF depends on the noise-spatial distribution and previous theoretical formulations assume an isotropic distribution. However, it can be argued qualitatively that if the noise field were dominated by a one-sided noise distribution, the DCF would have a shape as suggested in trace "B" of Figure 1b. This might represent the case of seismic noise dominated by microseisms (Sabra et al., 2005b*;* Shapiro et al., 2005). Another important case is a noise field that has two uncorrelated propagating components, e.g., seismic noise propagating as surface waves and body waves. The DCF would then have a shape as shown in trace "A" in Figure 1b.

Removal/Reduction of Noise Directionality

The seismic noise field is typically not isotropic and is dominated by noise sources having some preferred direction from a region, such as ocean microseisms (Bromirsky and Duennebier, 2002). Then, the station pair orientation will influence the quality of the TDGF that can be obtained from noise correlation. This yields one-sided arrival-time structure for the DCF. It can also cause a bias in travel-time estimation between the station pairs if the waves are not incoming near the station-pair axis (Gerstoft et al., 2006a). For example, if the noise source signal propagates mainly at an angle of 45 deg with respect to station pair axis, the resulting arrival DCF would overestimate the actual wave velocity by a factor of sqrt(2).

To first order for a weakly scattering medium (e.g., the Earth's crust but not a random cavity), the regions of constructive interference for the noise sources contributing to the time-averaged DCF are roughly located in the two broad end-fire beams (Snieder, 2004; Roux et al., 2004; Sabra et al., 2005a). Noise sources located outside of these end-fire beams typically have a weaker contribution to the DCF. Thus, for a weakly scattering medium and anisotropic noise source distribution, coherent waveforms may not emerge easily from the DCF if the station pair is oriented roughly perpendicular to the main propagation path of the noise sources.

In order to obtain unbiased TDGF, it is preferable to have noise coming from all directions (Wapenaar, 2004). In practice, the noise is strongly directional, but even then, it is still possible to obtain reasonable estimates of the arrival time. These will likely be biased, and we expect that the amplitude of the arrival is more sensitive to a nonuniform distribution of the noise. In principle, by beamforming it should be possible to eliminate certain directions and/or enhance arrivals from other directions. The approach would then be transforming the noise to the two-dimensional (2-D) slowness domain, filtering, and then transforming the slowness spectrum back to the time domain. As long as the propagating noise level is above the nonpropagating noise level, we expect such a transformation to be feasible. Three related filtering approaches are a) removal of noise propagating in certain directions, b) enhancing certain directions, and c) equalizing the directional noise arrival spectrum so that the noise arrives uniformly from all directions. Instead of forming a beam in the direction towards the noise source (Rost and Thomas, 2002), we will null steer on these sources, which actually is the complement of beamforming and a standard goal of adaptive array processing (e.g., Johnson and Dudgeon, 1993). The purpose of this is to eliminate signals from certain directions. Ideally, this would lead to spatial prewhitening of the signals. The spatial prewhitening should give good results as long as noise is propagating in all directions (it should not be a problem

that some directions have more energy). Spatially prewhitening the propagating noise field should result in more stable TDGF and unbiased travel times.

Seismic Noise Beamforming

Using continuous data recorded in the year 2006 on all the 155 seismic stations (vertical component with sampling rate 1 per second) in Southern California, we formed beams and determined the azimuth and slowness of the waves crossing the array as a function of frequency (Johnson and Dudgeon, 1993; Rost and Thomas, 2002). A similar processing was used for detecting Katrina in California (Gerstoft et al., 2006a) and proceeds as follows:

First, in the monthly time series, unwanted events (e.g., earthquakes) are removed by truncating signal amplitude above one standard deviation, calculated for the monthly time series. The data is split into 512-s time series, Fourier transformed, and corrected for instrument response. For each frequency, we only keep the phase of the signal. Amplitude information is lost here, but this will remove undesirable signals caused by local site amplification effects and local large noise event. This is also consistent with the simple plane wave model used in the processing. However, all frequencies will then have equal power, meaning that the typical microseism spectrum will not be retrieved if the resulting power spectrum is extracted. At each frequency, we have a complex-valued vector $\mathbf{v}(\omega, t_i)$ containing the response from the 155 stations, where t_i refers to the time of the Fourier transform. The cross-spectral density matrix is then formed by ensemble averaging ($\dagger$ denotes the transpose complex conjugate)

$$\mathbf{C}(\omega, t) = \sum_{n=1}^{N} \mathbf{v}(\omega, t + t_n)^{\dagger} \mathbf{v}(\omega, t + t_n) \qquad (3)$$

The *i*th row and jth column of $\mathbf{C}$ contains the average phase delay between the *i*th and *j*th seismometer at frequency ω. In the time domain, this would correspond to the cross-correlation between the two seismometers. For this study, we used N=10. This corresponds to an averaging time of 10*512 s or 1.5 hour, agreeing well with the minimum resolution time of weather systems. For a given frequency ω, phase slowness s, and azimuth θ, the plane wave response for the array of geophones is

$$\mathbf{p}(\omega, s, \theta, \mathbf{r}) = \exp(i\omega s \mathbf{re}) \qquad (4)$$

where $\mathbf{e} = (\sin\theta, \cos\theta)$ is the directional cosines and $\mathbf{r}$ is the coordinates of the geophones with respect to their mean. The beamforming output is then given by

$$b(\omega, s, \theta, t) = \mathbf{p}^{\dagger}(\omega, s, \theta, \mathbf{r}) \mathbf{C}(\omega, t) \mathbf{p}(\omega, s, \theta, \mathbf{r}) \qquad (5)$$

Processing a whole year of data gives a four-dimensional (4-D) matrix containing the beamformer output as a function of time, frequency, angle, and slowness. There is no averaging across frequency giving a frequency resolution of 1/512= 0.002 Hz. Based on a plane wave simulation, for a 0.1-Hz frequency and phase speed of 3 km/s, the array 3-dB beamwidth was 4º. Inhomogeneous velocity structure and array bias may cause a further smearing out of the peaks.

For each frequency analyzed, we searched for the combination of phase slowness and azimuth that gave the best fit to the data. Based on these phase slownesses, it was observed that they are independent of both time and azimuth and showed the Rayleigh wave dispersion with frequency $s = s(\omega)$, similar to the results in Gerstoft et al., 2006a. The dispersion can be determined by averaging over time and azimuth. Thus, the beamformer output only depends on $b(\omega, s, \theta, t)$.

Beamformer Output

The beamformer output is shown in Figure 2 at three frequencies 0.07 Hz (primary microseisms), 0.12, and 0.14 Hz (secondary microseism) for the whole month of January and July 2006.

In January, a string of storms (Bancroft, 2006) hit the Vancouver Island/Oregon area. The seismic noise from most of these storms was detected by the Southern California array. An example of such a storm is shown in Figure 3 for 2100 UTC Jan 8, both for the significant wave height and the dominant peak frequency (Tolman, 2005). In the beamformer output (Figures 2a and 2b) the primary microseisms (0.07 Hz) can clearly be seen for azimuths from 310–340º consistent with a source region in the costal areas of the N Pacific. After the ocean waves hit the Northern Pacific Coast, ocean waves for the same storm arrives in Southern California/Baja California area about a day later (excellent hindcast videos demonstrate this [Tolman, 2005]). This can be seen in Figure 2a as striations from about 300º to 160º for all three frequencies. For most of the storms the primary microseisms give a strong response at 160º corresponding to a source region near the coast of Baja California.

Strong microseisms can be seen from azimuth 40–60º corresponding to a source region in the Northwest Atlantic. The microseisms also correlate well with the storm activity in the Labrador Sea/Northwest Atlantic (Bancroft, 2006). Most of these storms are not easily identifiable in the secondary microseism bands (Figure 3a), although later discussion shows primary and secondary microseisms.

For the secondary microseisms (0.12 and 0.14 Hz in Figure 2a), a broad azimuth range from about 160-320º is fairly uniformly activated. This indicates a different source mechanism for the secondary microseisms, as has been advocated by interaction of opposing wave trains. A weak response can also be seen at azimuth 140º. This corresponds to microseisms from the Gulf of California. One reason that the primary microseisms are stronger in azimuth 300-340º and the secondary microseisms are weaker in that azimuth may be because of higher attenuation for high-frequency waves including both scattering and intrinsic attenuation.

In July, the North Pacific is relatively calm, and the primary microseisms mainly come from a constant azimuth about 210º. This constant direction does not mean that all storms come from this direction as these waves have been refracted near the coast and propagate perpendicular to the coast. The secondary microseisms are seen from a wider azimuth from 170–270º, again indicating a difference in excitation mechanism.

Whole Year

A good overview of the microseisms activity can be obtained by examining the azimuth corresponding to the maximum beamformer output. Figure 4 shows variations in azimuth for the whole year in the frequency interval 0.04-0.18 Hz. The main feature is that in the winter months most peak azimuths come from NW (hereafter we use abbreviations for azimuth, N, S, E, and W), whereas in the summer months they come from SSW.

The signature for each storm emerges in this figure as striations, as higher frequencies arrive later. This feature can be explained from the dispersion of the ocean waves (Haubrich et al., 1963) and gives us a clue on distance to the storms. In deep water, the ocean-wave group speed at frequency *f* is given by

$$c_g = \frac{g}{4\pi f} \tag{6}$$

Since propagation of ocean waves in the frequency range 0.04-0.18 Hz can be regarded as those of deep-water waves, if the distance from a storm is *R*, the arrival time is given as $T = R / c_g = 4\pi f R / g$. From the arrival azimuth versus frequency and time, we can measure the slope $\frac{dT}{df}$, and this gives the distance to the storm

$$R = \frac{dT}{df}\frac{g}{4\pi} \tag{7}$$

This can be used to determine the distance to the storm if all waves are recorded at the same point. The storms in January (Figure 4) have a slope of 40 days/Hz typically, giving a distance to the storm of 4000 km. This corresponds to the storms originating in the NE Pacific. This can be confirmed by watching the hindcasts (Tolman, 2005). In November and December, the N Pacific storms originate in the NW Pacific and thus the distance to the coast is

considerably less, resulting in a small slope. In the winter (November–February), it is observed that peak azimuth of the primary microseisms comes from NW, but the secondary comes from about W, thus the generation of the microseisms is not at the same point. This will cause a bias in the estimated distances above but the above formula can still be used for a rough estimate.

A few storms in June-September have a steeper slope of 80 days/Hz, giving a distance to the storm of 8000 km. This corresponds to storms in the South Pacific and is in agreement with the hindcasts (see videos [Tolman, 2005]) and previous observations (Haubrich et al., 1963). The fact that we can observe the striations of most storms indicates that the ocean waves have propagated a long distance before coupling into seismic energy. This implies that a major part of the microseisms has been generated along the Pacific Coast. The linear signature of the storms can be observed in the secondary microseisms band in Figure 4. This is due to the dispersive nature of the ocean waves, and thus a part of the energy in the secondary microseism band is generated by direct interaction with the ocean wave. In general, the secondary microseism is distributed over a large azimuth, 90-180º (Figure 4).

Spectral low amplitudes are seen between the primary and secondary microseisms (typically, 0.08-0.1 Hz), and it is often possible to observe distant events. In September, signals for tropical storm Ernesto (1–3 Sep) and Hurricanes Florence (11–13 Sep) and Helene (25–29 Sep), can be observed. Tropical storm Ernesto was the weakest and made landfall at 4 am UTC 1 September in North Carolina. Microseisms can first be observed a day later from the coast of Georgia (dashed lines in Figure 5a). About 1–1.5 days after landfall, microseisms from the coast of Virginia are observed (solid lines in Figure 5a).

In the summer and fall, noise from NE occurs mostly in the 0.1 Hz spectral low where there is not much power from the Pacific Ocean waves. The origin of this noise is not clear since it do not correlate with major storms (Bancroft, 2006). Several storms from the Lawrence Sea can be observed in February and March in the primary and secondary microseism bands. According to the Mariners Weather Log (Bancroft, 2006), the western North Atlantic storm of February 22 to March 1 developed hurricane force winds. It can be observed with azimuths from 36–50º corresponding to the extent of the northeast coast of the Labrador Peninsula; see Figure 5b. Schulte-Pelkum et al. (2004) also observed microseisms in California from the Labrador Sea. Note, that land fast sea ice covers the NE coast of Labrador Peninsula in the winter. Other storms described in the Mariners Weather Log can also be observed: the North Atlantic storm of February 10–14 and the western Atlantic storm of March 26–28. Note, that the two western Atlantic storms generate strongly localized secondary microseisms.

CONCLUSIONS AND RECOMMENDATIONS

Microseisms are often the propagating background noise exploited when extracting the impulse response from noise. Thus, it is important to understand their origin and spatiotemporal distribution. When extracting the impulse response from noise, azimuthal variations can cause biases in the extracted impulse response, and this will also cause an unknown bias in the tomographic surface velocity. If the azimuthal variation in the microseisms is known, we might potentially be able to correct for this bias in the resulting estimate of the impulse response. In the present report, we are mainly concerned with describing the variation. Frequency domain beamforming using distributed arrays provides a powerful tool to monitor microseisms.

Microseisms were examined for a whole year with their daily and seasonal variations. From this it is clear that most of the microseisms are generated near the coasts. Distance to the storms can be estimated approximately, using the gradient of striation in the azimuth vs. frequency plot. In winter, the primary microseisms are dominated by excitation in northwest direction, thus, the North Pacific, but some significant excitation is occurring also in the North Atlantic. Much smaller excitations are also seen off the coast of Southern California. In summer, the azimuth of excitation is about 210º suggesting excitation near the coastal area of Southern California and mainly by ocean waves shoaling in the perpendicular direction to the coast. Excitation of the secondary microseisms occurs over wider azimuth from about 180–320º throughout the year, although the azimuth range is wider in winter. Differences in excitation mechanisms between the primary and secondary microseisms are thus obvious from beamforming results.

REFERENCES

Bancroft, G. P, Mariners Weather Log, National Weather Service (NWS), http://www.vos.noaa.gov/mwl.shtml.

Bromirsky, P. D., and F. K. Duennebier (2002). The near-coastal microseism spectrum: spatial and temporal wave climate relationships, *J. Geophys. Res*. 107: (B8), 2166, doi:10.1029/2001JB000265.

Gerstoft, P., MC Fehler, and KG Sabra (2006a). When Katrina hit California, *Geophys. Res. Lett*. 33: L17308, doi:10.1029/2006GL027270.

Gerstoft, P., K. G. Sabra, P. Roux, W. A. Kuperman, and M. C. Fehler (2006b). Green's functions extraction and surface-wave tomography from microseisms in southern California, *Geophysics* 71: S123–S131.

Johnson, D. H. and D. E. Dudgeon (1993). *Array Signal Processing: Concepts and Techniques*, Prentice-Hall.

Larose E., A. Derode, M. Campillo, and M. Fink (2004). Imaging from one-bit correlations of wideband diffuse wavefields, *J. Appl. Phys* 95: 8393–8399.

Rost, S., and C. Thomas (2002). Array seismology: methods and applications, *Reviews of geophysics* 40: doi:20.1029/200RG000100.

Roux, P., K.G. Sabra, W.A. Kuperman and A. Roux (2005a). Ambient noise cross-correlation in free space: theoretical approach, *J. Acoust. Soc. Am.* 117: 79–84.

Roux, P., K. G. Sabra, P. Gerstoft, W.A. Kuperman, and M. Fehler (2005b). P-waves from cross-correlation of seismic noise, *Geophys. Res. Lett*. 32: L19303, doi:10.1029/2005GL023803.

Sabra, K. G., P. Gerstoft, P. Roux, W.A. Kuperman, and M. C. Fehler (2005a). Extracting time-domain Greens function estimates from ambient seismic noise, *Geophys. Res. Lett*. 32: L03310.

Sabra, K., P. Gerstoft, P Roux, W.A. Kuperman, M. Fehler (2005b). Surface wave tomography from microseisms in Southern California, AGU *Geophys. Res. Lett*. 32: L14311, doi:10.1029/2005GL023155.

Shapiro, N. M., M. Campillo, L. Stehly and M.H. Ritzwoller (2005). High-resolution surface-wave tomography from ambient seismic noise, *Science* 29: 1615–1617.

Schulte-Pelkum, V., P. S. Earle, F. L. Vernon (2004). strong directivity of ocean-generated seismic noise, *Geochem. Geophys. Geosyst*. 5: 10.1029/2003GC000520.

Snieder, R. (2004). Extracting the Green s function from the correlation of coda waves: A derivation based on stationary phase, *Physical Review E* 69: 046610.

Tolman, H. L. (2005). Manual and Wave User system documentation of WAVEWATCH-III version 2.22, US Depart. of Commerce. Hindcast files available from http://polar.ncep.noaa.gov.

Wapenaar, K. (2004). Retrieving the Elastodynamic Green's Function of an Arbitrary Inhomogeneous Medium by Cross Correlation, Phys. *Rev. Lett* 93: 254301.

Weaver, R. L., and O.I. Lobkis (2001). Ultrasonics without a source: thermal fluctuation correlations at MHz Frequencies, *Phys. Rev. Lett.* 87: 134301.

Weaver, R. L., and O. I. Lobkis (2004). Diffuse fields in open systems and the emergence of the Green's function, *J. Acoust. Soc. Am*. 116: 2731–2734.

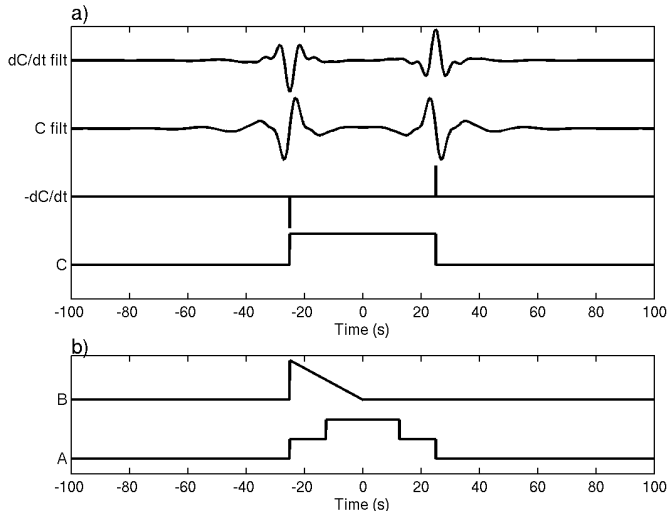

Figure 1. a) Schematic of the measured cross-correlation function and its time-derivative for an isotropic distribution of random impulse sources for infinite bandwidth or for a finite bandwidth (0.05–0.2 Hz). b) Influence of the noise source spatial distribution and origin. Trace B: A single-sided noise source distribution yields a one-sided noise cross-correlation function. Trace A: Cross-correlation function of a noise field having two propagating components with different velocities and amplitudes.

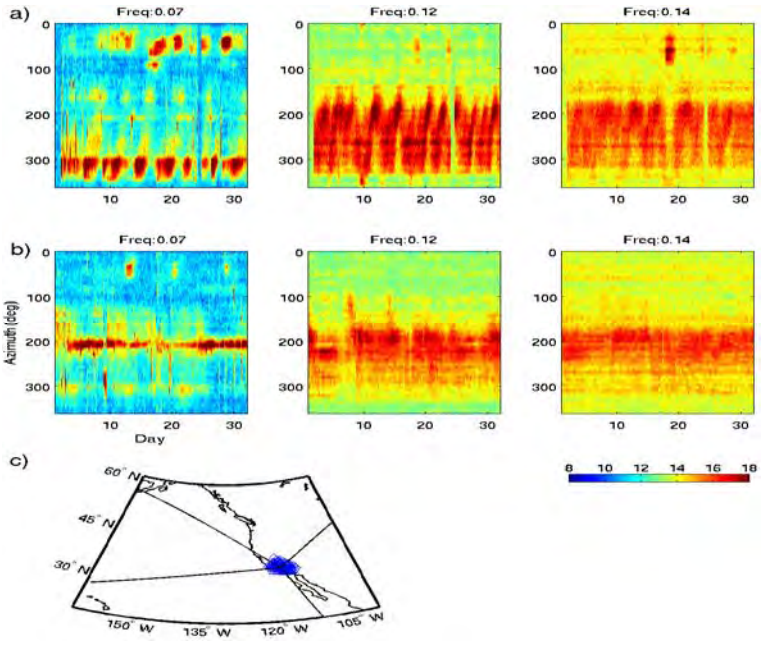

Figure 2. Beamformer output versus azimuth and days in month for frequencies 0.7, 0.12, and 0.14 Hz during a) January and b) July 2006. c) Map of region, showing stations in Southern California and important azimuths from the array: 45º, 150º, 270º, and 320º.

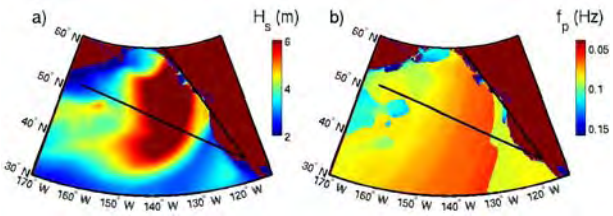

Figure 3. January storm in the North Pacific. In January a string of storms originating from the NE Pacific hit the Pacific coast, here shown for 8 January 21:00 UTC, showing a) significant wave height and b) peak frequency. Azimuths 310^o and 340^o are indicated.

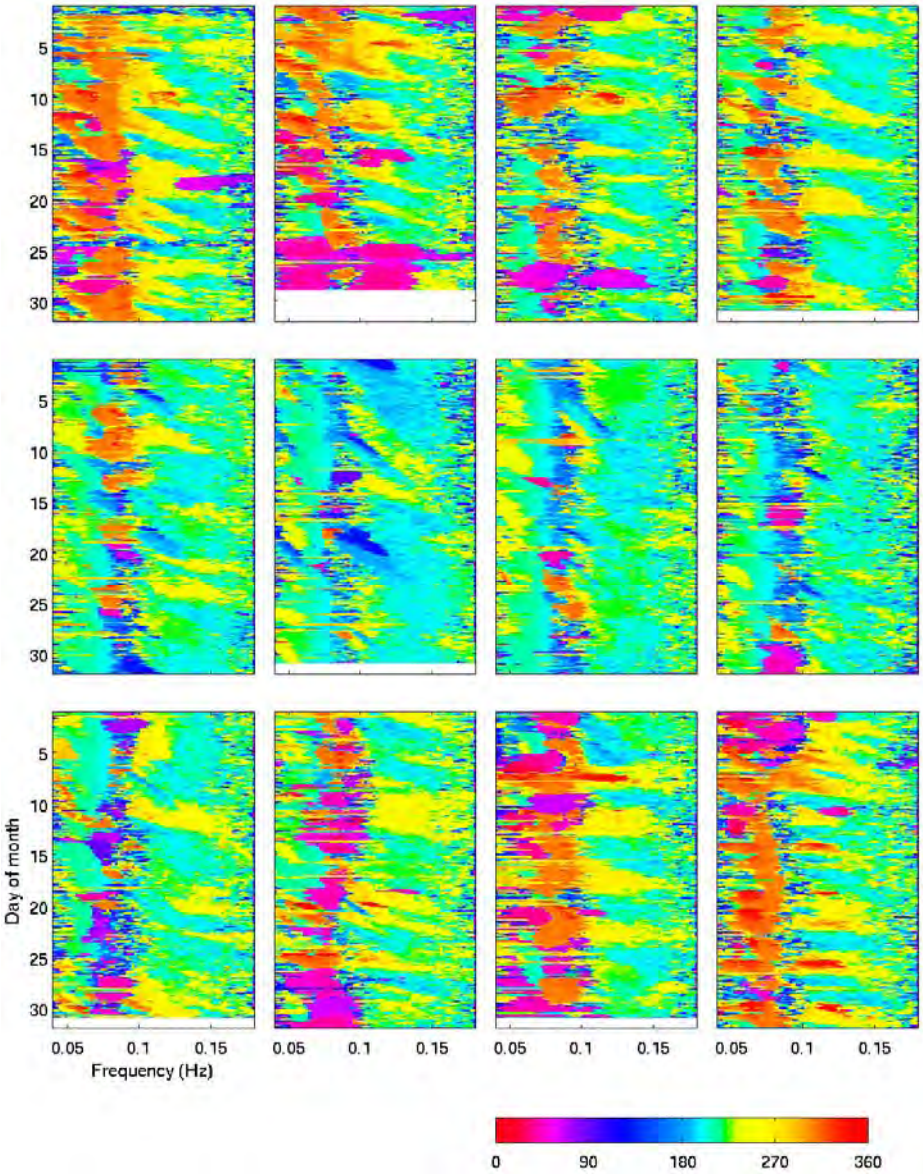

Figure 4. Azimuth (deg) from whole array for each month of 2006. Each subplot corresponds to one month.

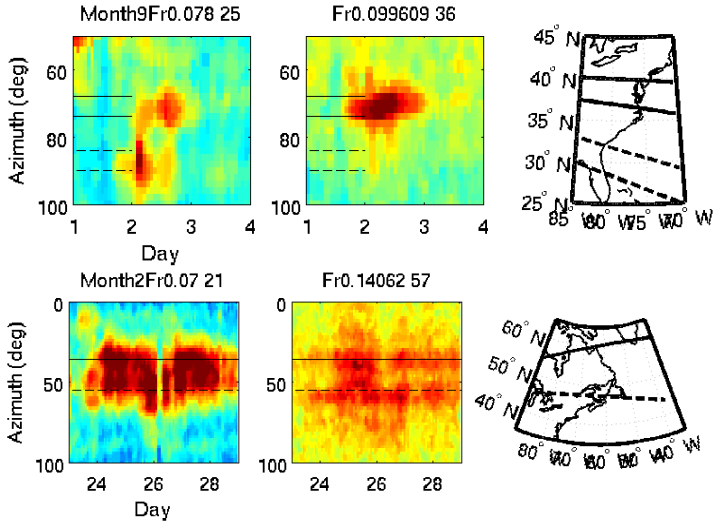

Figure 5. Beamformer output for two storms in the Atlantic. a) Tropical storm Ernesto 1–3 September at frequency 0.08 and 0.1 Hz and corresponding map. b) North Atlantic storm of 24 February to 1 March at frequency 0.7 and 1.4 Hz. The azimuths corresponding to the NE of the Newfoundland/ Labrador Peninsula is shown in the map.

SEISMIC VELOCITY MODELING OF NORTH AND NORTHEAST IRAQ USING RECEIVER FUNCTIONS

Hafidh A. A. Ghalib[1], Matthew S. Sibol[1], Youlin Chen[1], Robert B. Herrmann[2], Ghassan I. Aleqabi[3], Hrvoje Tkalcic[1, 4], Bakir S. Ali[5], Borhan I. Saleh[5], Dawood S. Mahmood[6, 7], Robert A. Wagner[1], Patrick J. Shore[3], Omar K. Shaswar[9, 10], Aras Mahmood[5], Shaho Abdullah[5], Fadhil Ibrahim[8], Rashid Zand[8], Basoz Ali[5], Layla Omar[5], Nokhsha I. Aziz[5], Nian H. Ahmed[5], Talal Al-Nasiri[10], Ali A. Ali[7], Abdul-Karem A. Taqi[7], and Samira R. Khalaf[7]

Harris Corporation[1], Saint Louis University[2], Washington University in Saint Louis[3], Australian National University[4], Sulaimaniyah Seismological Observatory[5], Iraq Meteorological Organization[6], Baghdad Seismological Observatory[7], Erbil Seismological Observatory[8], Sulaimaniyah University[9], and University of Baghdad[10]

Sponsored by Air Force Research Laboratories

Contract No. FA8718-04-C-0016

ABSTRACT

A primary objective of this project is to estimate the local and regional seismic velocity structures of north and northeastern Iraq, including the northern extension of the Zagros collision zone, using well-established seismological techniques. This is a region where global seismic network coverage is poor and where extrapolated velocity models found in the literature lack sufficient accuracy to permit events to be located with significant precision. Installed in late 2005, ten broadband three-component stations composing the North Iraq Seismographic Network (NISN) provided the unique data that made this phase of the study possible. The results of teleseismic P-wave receiver functions (RF) analysis and velocity structure estimation are presented herein. RF is a time series computed from three-component seismograms that show the relative response of earth structure near a receiver. To date, over 4500 waveforms from about 150 events recorded by NISN stations during the period 30 November 2005 to 31 August 2006 have been scrutinized. Based on the USGS Preliminary Determination of Epicenters (PDE) bulletins, the epicenteral distances of these teleseismic events to NISN stations range from 30º to 90º, and their magnitudes equal or exceed 5.5. Additional data recorded from September 2006 through March 2007 will also be examined. It is anticipated that this will nearly double the amount of data available for reliably estimating the velocity structure of the region. Preliminary results indicate that the depth of the Moho varies considerably beneath NISN. It is relatively shallow (35–45 km) to the northwest and deeper (50–60 km) under the southeastern portion of the network area. Although these initial results correspond well with the tectonic and physiographic framework of the Arabian plate, the values will be further revised and constrained when surface wave dispersion analysis is added to the process.

OBJECTIVE

Estimating the seismic velocity structure beneath stations of the North Iraq Seismographic Network (NISN) is the focus of this paper. To fulfill this objective, the well-known RF inversion technique is first applied to the data. Other inversion and waveform modeling approaches to better constrain or improve the velocity models will follow. In other words, this is a preliminary outcome of the ongoing research to improve our understanding of the study area. In progress is the simultaneous inversion of the RF and surface wave dispersion. The latter provides valuable constraint on the RF computational process and the estimated seismic velocity structures. Evaluation of the resulting models will be performed through relocation of recorded events, synthetic waveform analysis, and correlation with available geophysical and geological information.

In August 2005 and in cooperation with the Sulaimaniyah, Erbil, Baghdad, and Mosul seismological observatories (SSO, ESO, BSO and MSO, respectively), the first two temporary stations (KSLY and ERBL) were deployed. The existing NISN was deployed in November of the same year. Stations BHD in Baghdad and MSL in Mosul, however, were installed in April 2006. The names, geographical coordinates, and elevation of the stations are given in Table 1. To date, more than 100 gigabytes of unprecedentedly high-quality, continuous, three-component broadband seismic data have been collected at a rate of 100 sps.

Table 1. Parameters of the North Iraq Seismological Network (NISN)

North Iraq Seismological Network (NISN)						
No.	**Station Name**	**Latitude (degrees)**	**Longitude (degrees)**	**Elevation (meters)**	**Installation Date**	**Removal Date**
1	KSBB	35.0415	45.7092	550	11/25/2005	
2	KSSS	35.7696	46.2362	1515	11/26/2005	
3	KSWW	36.1493	45.2624	1310	11/28/2005	
4	KSJS	35.4965	45.3452	825	11/27/2005	
5	KEHH	36.6764	45.0470	1725	11/30/2005	
6	KESM	36.9846	44.1981	1000	12/01/2005	
7	KDDA	37.2125	42.8207	750	12/02/2005	
8	KEKZ	35.9893	44.0970	450	12/03/2005	
9	MSL	36.3817	43.1483	242	04/06/2006	
10	BHD	33.2744	44.3858	32	04/11/2006	
11	KSLY	35.5559	45.4534	912	08/23/2005	04/04/2006
12	ERBL	36.3772	44.2086		08/21/2005	11/29/2005

Except for BHD all the other stations are located in the foothills and folded belts to the southwest and south of the Zagros and Taurus (Bitlis) zones, respectively. Figure 1 shows a generalized diagram of the seismotectonic framework of the Arabian plate. NISN stations (white triangles) are located along the northeast boundary of the plate where the Zagros thrust zone and the Bitlis suture zone converge. This region is characterized by a high level of seismic activity, as evidenced by the large number of local and regional events recorded by NISN (Ghalib et al., 2006) and by the teleseismically located earthquakes reported by the United Stated Geological Survey (USGS) bulletins (Figure 1).

Until the deployment of the NISN, most research efforts concerning the study area were conducted using distant stations. More recently Pasyanos et al. (2004) produced a generalized velocity model for the Zagros fold and thrust zones. Prior to that, Ghalib (1992) produced average velocity models derived from the dispersion of Rayleigh waves recorded at station TAB in near by northwestern Iran.

RESEARCH ACCOMPLISHED

RF is a time series computed from three-component seismograms that show the relative response of earth structure near a receiver (Ammon, 2006). The RF methodology has been extensively used by seismologists. While the overall method is straightforward to define, the computation of reliable receiver functions can be problematic due to the non-uniqueness of RF inversions and has been the subject of many papers, including Burdick and Langston (1977), Langston (1977), Ammon (1991), Cassidy (1992), Ligorría and Ammon (1999), Park and Levin (2000), and

Helffrich (2006). With these efforts, many techniques have been developed to overcome difficulties stemming from instabilities in the deconvolution process. At this early stage of research, the Ammon (2006) and Herrmann (2006) approach and computational software are used to determine the RF and invert for the seismic velocity models but without the benefit of utilizing surface waves (an invaluable step being considered next).

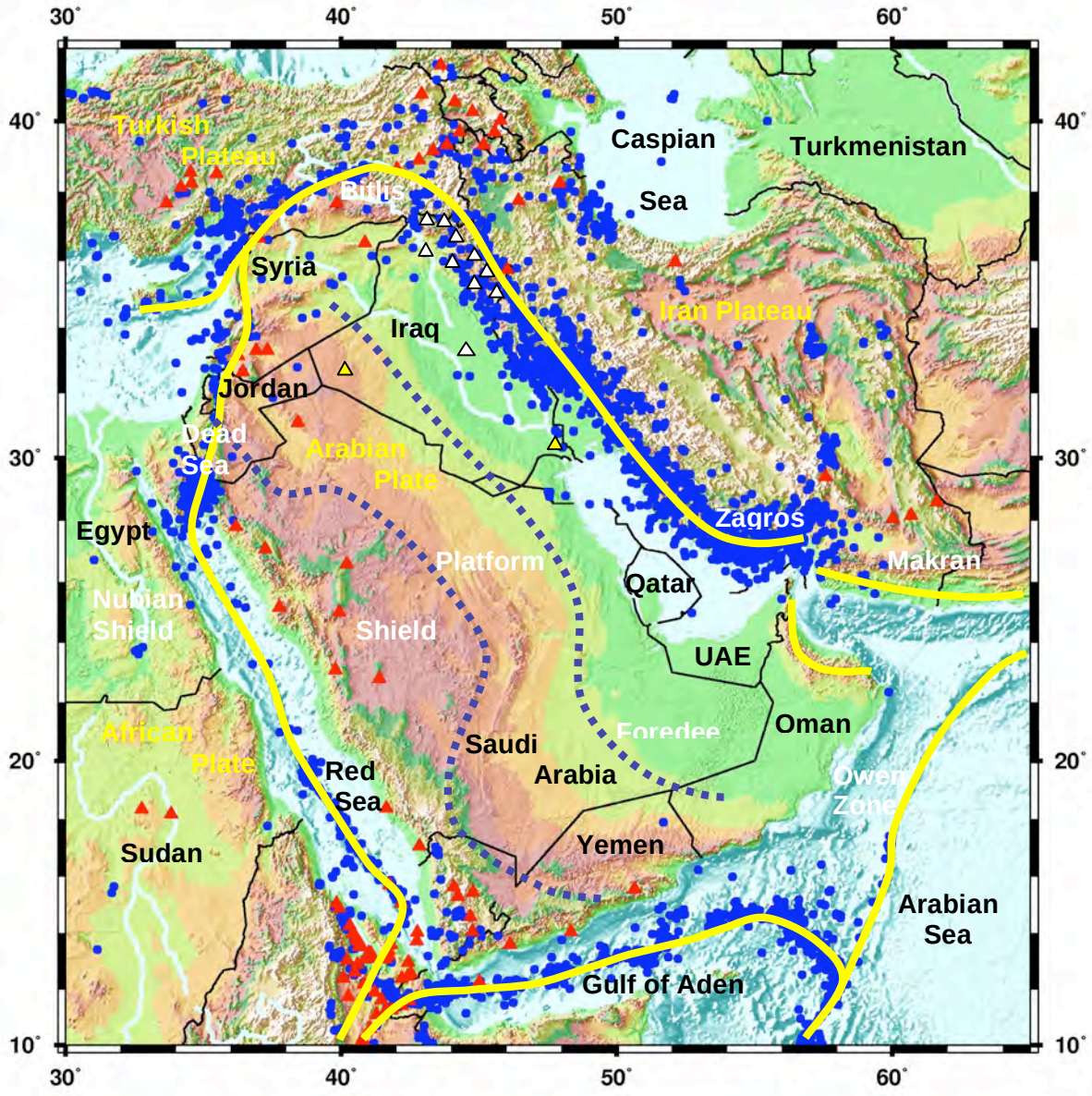

Figure 1. Map of the Arabian Peninsula and surrounding regions. The major geographic, tectonic, and geologic features (Arabian Shield, Platform, and Foredeep) are labeled. The plate boundaries (Gulf of Aden, the Red Sea, the transform fault along the Dead Sea and East Anatolia of the Turkish plateau, the Bitlis Suture in eastern Turkey, the northwest-southeast trending Zagros thrust zone, the Makran east-west trending continental margin and subduction zone, and the Owen fracture zone in the Arabian Sea) are marked with yellow lines. Earthquakes and volcanoes are shown as blue circles and red triangles, respectively. White triangles represent the 10 stations that compose the NISN. The yellow triangles reflect the location of some of Iraq Seismological Network (ISN), but those are currently not operational.

A search of the PDE bulletins for the period from 30 November 2005 to 31 August 2006 resulted in a long list of teleseismic events at various azimuths and epicenteral distances in the range of 30–90 degrees from NISN. Corresponding searches of NISN records resulted in about 150 events with magnitudes equal to or exceedng 5.5 and over 4500 waveforms available for scrutiny and analysis. Figure 2 is an example of well-recorded teleseismic P waveforms at stations KSBB, KSSS, and KSWW. The event occurred in the Kuril Islands on 22 June 2006, and its magnitude (Mw) was 6.0. The quality of observed P waves was assigned a subjective grading scale (A, good, through D, poor) to reflect the quality of recorded signal-to-noise levels (i.e., acceptable level of signal-to-noise ratio to produce stable and reliable receiver functions). This exercise helped with the waveform selection process and with understanding of the impact of lower-grade signals on the RF and resulting models. In the final data processing, only good-quality waveforms (grade A and B) were used.

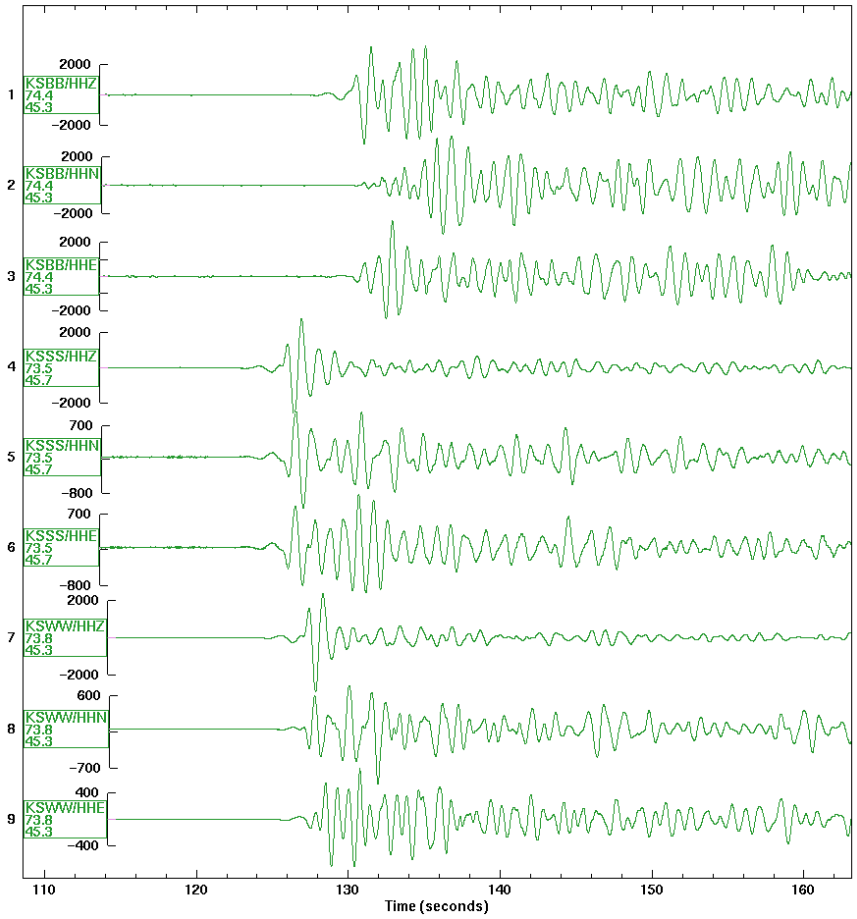

Figure 2. Sample teleseismic P waveforms of a Kuril Islands event recorded at three of NISN stations (KSBB, KSSS, and KSWW) and used in the RF inversion. The event occurred on 22 June 2006, and according to the USGS PDE, its magnitude (Mw) was 6.0.

After the data were reformatted to include the required event location (latitude, longitude, and depth) and P-wave arrival time in the SAC header, the receiver functions were estimated for each high-quality station seismogram. Also in preparation for the inversion process, a simple multi-layered initial shear velocity model was created to follow the general characteristics of the models derived by Ghalib (1992), using the group velocity dispersion curves of observed Rayleigh waves traversing the study area. The S-velocity of the crustal layers was set to 4.0 km/s and the upper mantle layers (below 90 km) to 4.5 km/s to reflect the lower-than-average velocity structure previously observed throughout the region. The thicknesses of the layers vary from 0.5 km at the top and to a maximum of 10 km at the bottom of the crust (a gradual increase with depth). In the upper mantle, the layer thicknesses range from 10 to 100 km.

The RF inversion process is iterative and requires a certain measure of damping administration to control the problem of finding a reasonable model. Figure 3 is an example of the observed (blue) and estimated (red) RF for 39 events recorded at station KSWW. The best fit of these receiver functions ranges from 60% to 93%, and the back-azimuth to these events ranges from 20 to 120 degrees.

The resulting preliminary one-dimensional seismic velocity models for stations KESM, KEHH, KSWW, KSSS, KDDA, KEKZ, KSJS, and KSBB are presented in Figure 4. No models were estimated for stations MSL and BHD due to the scarcity of data available at the time and to the generally low signal-to-noise ratios that disqualified most of the available waveforms recorded at these two stations. Common among the eight models is the relatively

lower-than-average shear velocities of the layers when compared with other regions of the Earth and the presence of a significant discontinuity at about 15 km depth. The depth of the Moho seems to vary from about 45 to 55 km. These results may not be final, but they are certainly consistent with previous observations made by, among others, Aleqabi et al. (2007), Pasyanos et al. (2004) and Ghalib (1992). Also noticeable is the diminishing data resolution at depths exceeding about 80 km. The observed change in shear velocity values below that depth is simply a perturbation in response to the better-estimated velocities of the crustal layers where the data resolution is highest.

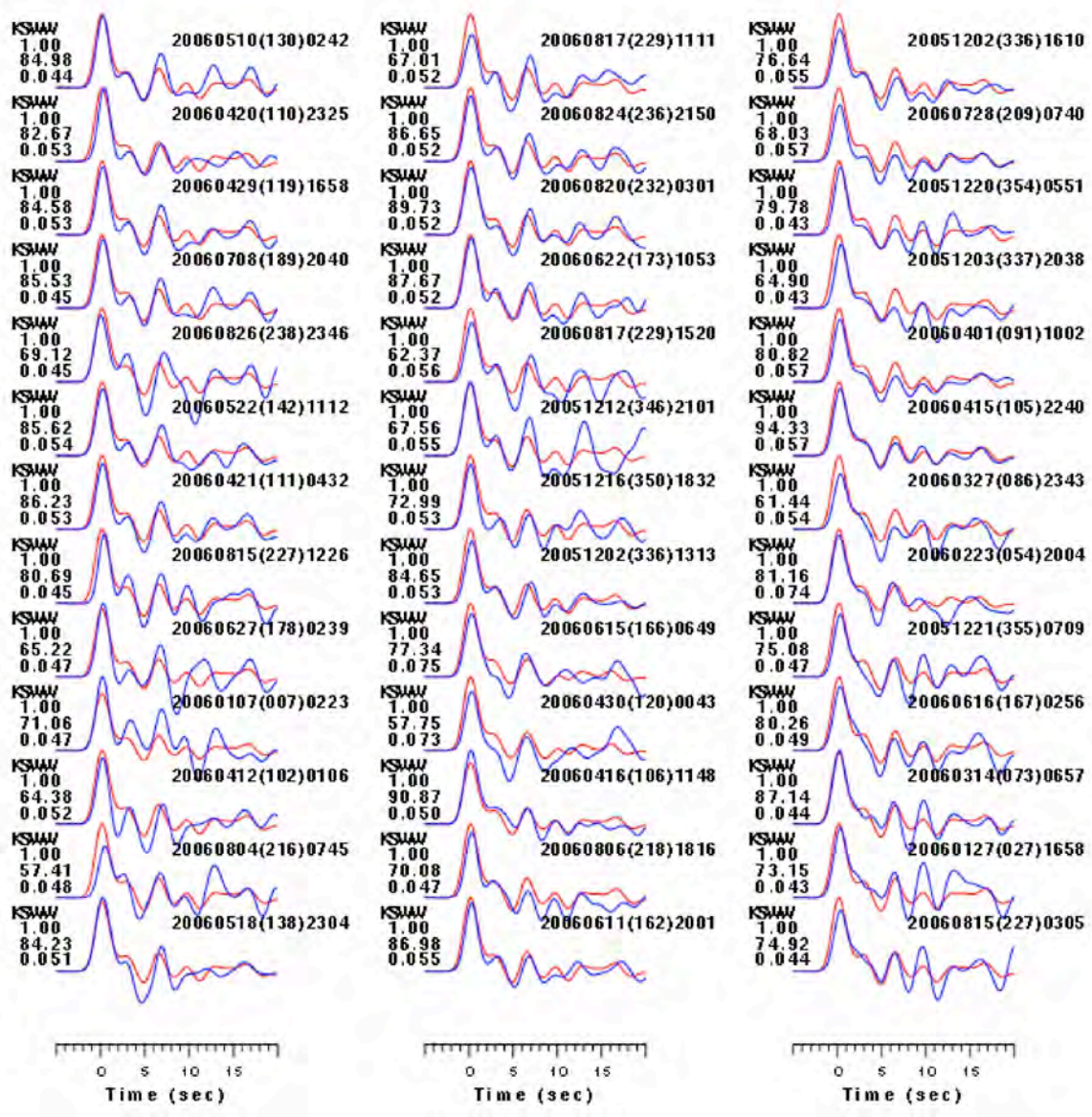

Figure 3. Sample receiver functions for 29 teleseismic events recorded at station KSWW. The observed RF are shown in blue and estimated from the inversion process in red. The best fit for these RF range from 60% to 95%.

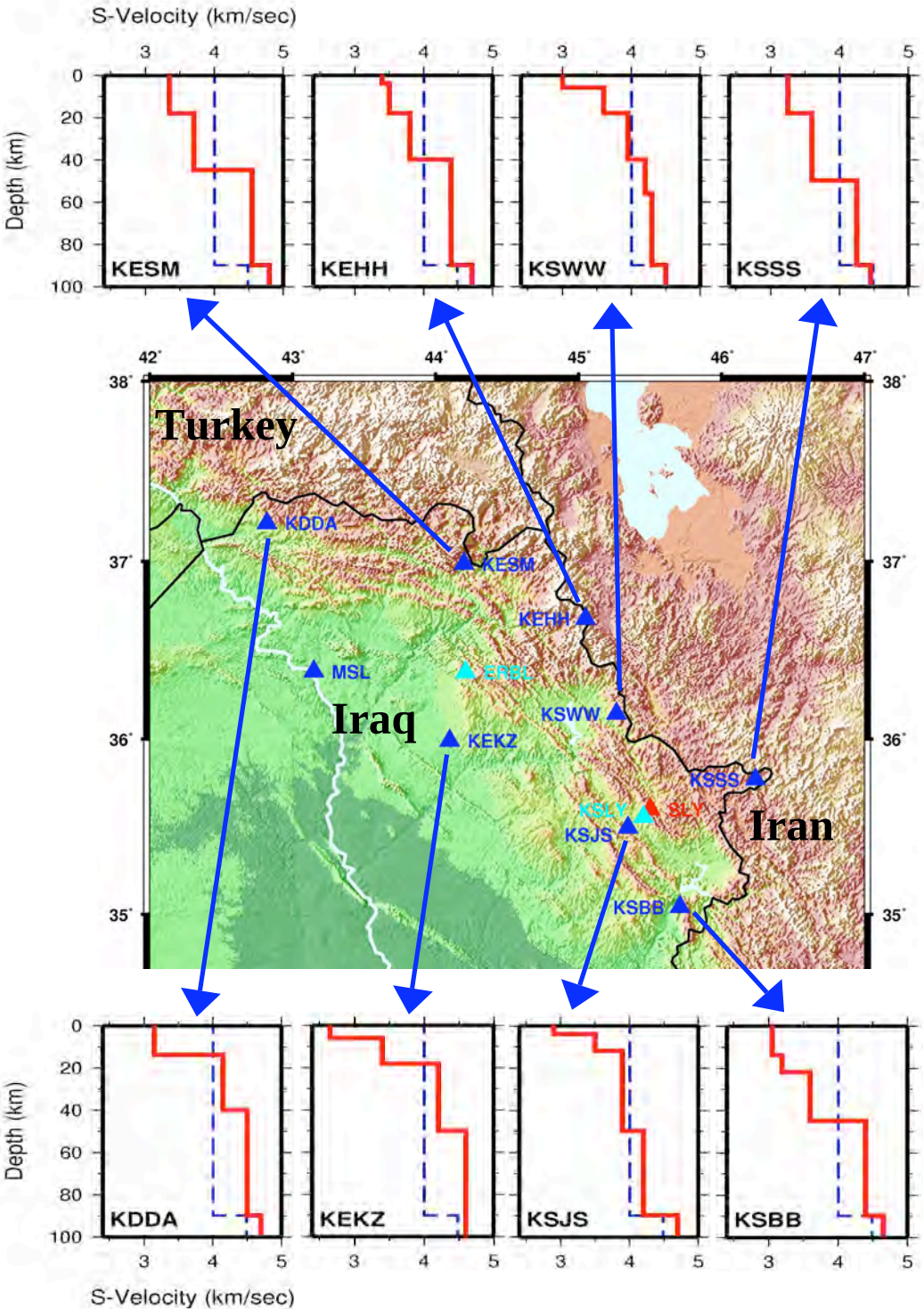

Figure 4. **A map showing the location of NISN (marked with blue triangles) and the preliminary shear-velocity models obtained from RF inversion. Station ERBL and KSLY (aqua triangles) are the temporary stations. Station SLY (red triangle) belongs to the ISN.**

CONCLUSIONS AND RECOMMENDATIONS

This report signifies the initial outcome of an ongoing effort to estimate the seismic velocity structure beneath eight of the NISN three-component broadband stations. At this early stage of the research, the models are exclusively estimated from the inversion of the receiver functions of teleseismic P wave seismograms. Most significant about these models is that they consistently reflect lower-than-average velocities, as has been previously observed, and seem to characterize the seismic structure of this region.

Evaluation of the presented models is premature since more teleseismic P- and surface-wave data are being scrutinized for processing and simultaneous inversion. The amount of available data is expected to double, and more than one RF inversion approach is being considered. These data will help generate more-reliable models that can withstand the test of relocating events with higher precision and synthetic waveform modeling that matches well with the observed seismograms.

ACKNOWLEDGEMENTS

All maps were generated using the Generic Mapping Tools (GMT) by Wessel and Smith (1998). Thanks to David Kallus for setting up the computational software.

REFERENCE

Aleqabi, G., M. Wysession, H. A. A. Ghalib, M. Sibol, B. Saeed Ali, B. Saleh, A. Mahmood, S. Abdullah, L. Omar, N. Aziz, N. Ahmed, D. Mahmood, N. Alridaha, T. Alnasiry, O. Shaswar, A. Ali, A. Taqi, S. Khalaf, and F. Ibrahim (2007). Seismic velocity structure of Iraq and surrounding regions from surface-waves waveform inversion, (Abstract) *Seism. Res. Lett.* 78: 310.

Ammon, C. J. (1991). The isolation of receiver effects from teleseismic P waveforms, *Bull. Seism. Soc. Am.* 81: 2504–2510.

Ammon, C. J. (2006). Receiver-Function Analysis, Pennsylvania State University, Web page: http://eqseis.geosc.psu.edu/~cammon/HTML/RftnDocs/rftn01.html

Burdick, L. J. and C. A. Langston, (1977). Modeling crustal structure through the use of converted phases in teleseismic body-wave forms, *Bull. Seism. Soc. Am.* 67: 677–691.

Cassidy, J. F. (1992). Numerical experiments in broadband receiver function analysis, *Bull. Seism. Soc. Am.* 82: 1453–1474.

Ghalib, H. A. A., G. I. Aleqabi, B. S. Ali, B. I. Saleh, D. S. Mahmood, I. N. Gupta. R. A. Wagner, P. J. Shore, A. Mahmood, S. Abdullah, O. K. Shaswar, F. Ibrahim, B. Ali, L. Omar, N. I. Aziz, N. H. Ahmed, A. A. Ali, A.-K. A. Taqi, and S. R. Khalaf (2006). Seismic characteristics of northern Iraq and surrounding regions, in *Proceedings of the 28th Seismic Research Review: Ground-Based Nuclear Explosion Monitoring Technologies*, LA-UR-06-5471, Vol. 1, pp. 40–48.

Ghalib, H. A. A. (1992). Seismic velocity and attenuation of the Arabian plate, Ph.D. dissertation, Saint Louis University, p. 314.

Helffrich, G. (2006). Extended-time multitaper frequency domain cross-correlation receiver-function estimation, *Bull. Seism. Soc. Am.* 96: 344–34.

Herrmann, R. B. (2006). Surface waves, receiver functions and crustal structure, in *Computer Programs in Seismology*, Version. 3.30, Saint Louis University, St. Louis, MO. Web page: http://www.eas.slu.edu/People/RBHerrmann/CPS330.html.

Langston, C. A. (1977). The effect of planar dipping structure on source and receiver responses for constant ray parameter, *Bull. Seism. Soc. Am.* 67: 1029–1050.

Ligorría, J. P. and C. J. Ammon (1999). Iterative deconvolution and receiver-function estimation, *Bull. Seism. Soc. Am.* 89: 1395–1400.

Park, J. and V. Levin (2000). Receiver functions from multiple-taper spectral correlation estimates, *Bull. Seism. Soc. Am*. 90: 1507–1520.

Pasyanos, M. E., W. R. Walter, M. Flanagan, P. Goldstein, and J. Bhattacharyya (2004). Building and testing a priori geophysical model for western Eurasia and North Africa, *Pure Appl. Geophys*. 166: 47.

Wessel, P. and W. H. F. Smith (1998). New, improved version of Generic Mapping Tools released, *EOS, Trans. AGU* 79: 579.

STRUCTURE OF THE MOHO DISCONTINUITY BENEATH SOUTH KOREA FROM TRAVEL-TIME WAVEFORM ANALYSIS

Roland Gritto, Jacob E. Siegel, and Winston C. Chan

Harris Corporation

Sponsored by Air Force Research Laboratory

Contract No. FA8718-06-C-0006

ABSTRACT

The current study is intended to collect and process seismic waveform data, perform comprehensive 3-D tomographic inversions, and produce high-resolution 3-D crustal P- and S-wave velocity models for the South Korean peninsula. The current phase of our study is concerned with the analysis and archival of Korean Meteorological Administration (KMA) waveform data from 2001 through 2006 and the mapping of the Moho discontinuity beneath the South Korean Peninsula. Phase arrival information from both, velocity and accelerometer sensors were collected. The analysis included 226 events throughout the region producing a total of 6,275 phase picks including Pg, Pn, Sg/Lg, and Sn phases. A total of 3,550 P-wave and 2,725 S-wave phases were identified. Using the combination of all available velocity and accelerometer data it was possible to estimate depth locations for 198 KMA events. The hypocenters were subsequently used to derive travel-time distance curves to appraise the quality of the travel-time picks. Static corrections were calculated for each seismic station within the KMA network to remove the effects of local inhomogeneities in the vicinity of each station. After applying static corrections to the observed travel-times, refracted P-wave phases along the Moho boundary were selected from the dataset to estimate the depth and topography of the Moho discontinuity. In total, 526 Pn phases were collected from the KMA data with hypocentral distances from 130 km to over 650 km. The resulting Moho topography reveals a slightly undulating interface with a large-scale dip from north (31 km) to south (38 km) and a depth range from 32 km in the east to 39 km in the south-west. On a smaller scale, a more pronounced depression is evident in the south-central part of the mapped area, which opens to the south. The presented results are corroborated by other studies which mapped the Moho interface using surface-wave dispersion and receiver-function analysis. The present study is complementary to these earlier works, in that a different method and a different dataset generated comparable results.

OBJECTIVES

The primary objective of this research is to produce high-resolution 3-dimensional crustal P- and S-wave velocity models of the South Korean Peninsula. The structure of the crustal model will be supplemented by the derivation of a 3-D Moho interface below the peninsula. The resulting velocity and structural models will provide valuable information for regionalization and relocation studies.

RESEARCH ACCOMPLISHED

During the first part of the research, phase waveform data from the KMA were analyzed for the years 2001 through 2006. The KMA operates a dense seismic network consisting of over 80 stations with velocity and accelerometer sensors. The analyzed data consist of triggered waveforms recorded for local and regional events throughout the Korean Peninsula. Phase arrival information of these data was subsequently used to delineate the structure of the Moho interface between crust and mantle.

Korean Meteorological Administration (KMA) Waveform Data

The KMA of the Republic of Korea (ROK) operates a dense network of seismic stations throughout the country. The network consists of 85 stations comprised of velocity and accelerometer sensors. Station configurations include combinations of velocity and accelerometer sensors as well as single sensor sites. The analyzed data included triggered waveforms of local and regional events from 2001 through 2006. For stations with single sensor configuration, the analyzed data were obtained from either velocity or accelerometer data, while both velocity and accelerometer data were obtained for those stations with dual sensor configuration. The intention is to improve the significance of data for stations where travel-time data from more than one instrument are available.

Travel Time Analysis of KMA Waveform Data

The analysis of the KMA waveform data produced a total of 6,275 phase picks from 226 events located throughout the Korean Peninsula. The number of located events amounts to a seismicity rate of approximately 38 events per year and confirms previous estimates for this region. Identified phases included Pg, Pn, Sg/Lg, and Sn. The number of individual identified phases amounted to 3,550 P-wave and 2,725 S-wave phases. Because the accelerometer data contain higher frequency information, epicentral distances from the events to the accelerometer stations were generally shorter than those associated with velocity stations, which helped to constrain the depth of the events. Furthermore, this approach decreased the uncertainty of the hypocenter location. Using the combination of velocity and accelerometer data, it was possible to estimate depth locations for 198 of the KMA events.

Quality control of the data was performed using travel-time-distance curves. The phase picks of the KMA data from 2001-2006 are shown in Figure 1. The travel-time of P- and S-wave phases is plotted as a function of hypocentral distance to assess the quality of the selected phase picks. The diamond-shaped symbols represent the P- and S-wave phases determined from the waveform data. The short black horizontal lines at each data point represent the relative location error for each hypocenter estimate associated with that phase pick. For each hypocenter, a relative error is calculated separately for the x-, y- and z-direction. In order to facilitate the presentation of this uncertainty, we take the relative errors for the three directions and calculate a single resulting vector, which represents the radius of a sphere around each hypocenter estimate indicating the uncertainty in its location. Therefore, the short black horizontal lines in Figure 1 represent the length of the radius of the error sphere for each hypocenter estimate. In contrast, the short black vertical lines at each data point represent the relative timing error for the event time associated with that phase pick. Considering all phase picks from velocity and accelerometer data, the average hypocentral error was reduced by 17% relative to the original hypocenters published by the KMA. The colored solid lines in Figure 1 represent the best linear fit, in a least-squares sense, through the cloud of travel-time picks. It can be seen that the fit is very good for hypocentral distances below 400 km. Although the number of events decreases for hypocentral distances beyond 400 km, the linear fit is still good at greater distances. The velocities values listed in Figure 1 are averaged P- and S-wave velocities of the crust and upper mantel as determined from the slope of the travel-time distance curves. These values are in good agreement with typical published estimates for the Korean Peninsula (Chang and Baag, 2006). If the model of a single-layered crust is employed to determine average crustal thickness from the travel-time curves in Figure 1, a value of

32 km is obtained. In comparison, Chang and Baag (2006) conducted receiver function studies based on teleseismic body wave data. They report a distribution of crustal thicknesses from 28 km in the eastern part to 35 km in the south-western part of South Korea. Therefore, the average value of 32 km, determined from the phase picks of the KMA data, appears to be a good estimate for crustal thickness, giving confidence in the obtained arrival times. A separate method to estimate Moho topography is presented in the next section.

Estimation of 3-D Moho Structure from Refracted P-waves

Two important parameters that define crustal structure are the depth and topography of the Moho boundary between crust and mantle. The topography of this interface can help to explain crustal tectonics and consequently the kinematics of wave propagation through the crust. Refracted P-wave phases along the Moho boundary can be used to estimate the depth of this interface. As can be seen in Figure 1, refracted Pn phases were observed between hypocentral distances from 130 km to over 650 km. In total, 637 Pn phases were collected from the KMA data from 2001-2006.

Before the depth and topography of the Moho could be estimated, near-station effects due to inhomogeneities in the near subsurface had to be removed from the Pn travel times. These static corrections prevent travel-time anomalies from near surface inhomogeneities to be mapped into anomalies of Moho elevation at depth. The static corrections were estimated using a least-squares approach minimizing the misfit between observed and calculated Pg travel times. The least-squares approach jointly inverted for a homogenous crustal velocity model and static correction terms at each recording station. These static corrections were subsequently subtracted from the Pn travel times before they were used to estimate Moho topography.

Several approximations have to be considered when estimating depth from travel times of refracted waves. The most important is that of a one-dimensional velocity model of a layer over a half space. In the current case, the velocity estimates for the crust and upper mantle derived from the linear fits in Figure 1 are utilized. Furthermore, it is assumed that the Moho interface is piece-wise flat over the propagation distance of each refracted phase along this boundary. With these approximations, ray theory and the principles of refraction seismology were applied to determine Moho depth and topography. For each refracted ray path, two depth-estimates for the Moho interface below the hypocenter and recording station were calculated together with the dip of the Moho interface between these two points. A maximum-likelihood approach was applied to the results of a grid search over a two dimensional depth-and-dip space to minimize the misfit between observed and calculated Pn travel times. Once the depth and dip of the Moho interface was determined below each hypocenter and recording station, the data were interpolated using an adjustable-tension continuous-curvature surface-gridding approach (Wessel and Smith, 1995). The result of the gridding is shown in Figure 2, which displays a 3-D surface plot of the Moho interface below South Korea. The emerging pattern reveals a slightly undulating interface with a large-scale dip from north (31 km) to south (38 km). On a smaller scale, a more pronounced depression is evident in the south-central part of the mapped area, which opens to the south. This low in topography reaches depth of 37-38 km. In order to place the Moho interface in spatial relation to the peninsula and its seismicity, Figure 3 shows a 3-dimensional composite plot of the Korean peninsula with the location of the KMA network at the surface (red triangles), the seismicity from 2001-2006 (green dots), the ray coverage for all P-wave phases analyzed for this time interval, and the Moho topography at depth. It should be noted that all rays are simplified as straight rays and that refracted rays have been omitted to not obscure the view of the Moho interface at depth. It can be seen that the seismicity is confined to the upper 20 km of the crust. However, for the tomography study during the second phase of this project, the rays associated with Pn phases that are refracted across the Moho interface will cover the region in the lower half of the crust.

To help associate Moho topography with the geography of South Korea, a contour plot of the Moho was generated and projected onto a map of the Korean Peninsula. The result is presented in Figure 4. In addition to the large-scale dip from north to south discussed in Figure 2, it can now be seen that the depth of the interface ranges from 32 km in the east to 39 km in the southwest. It should be noted that contours near the edges of the map are more uncertain due to the lack of ray coverage in these regions. The contour plot reinforces the previous interpretation that the main depression of the Moho is located below the south-central part of the country.

Appraisal of Moho Depth Estimates

Although the current analysis is based on the assumptions of a piece-wise flat Moho and a single crustal layer with homogeneous velocity, the obtained results are robust nevertheless. The largest error resulting from the violation of a piece-wise flat horizon might occur in the southeast corner of the map, where the Moho reaches a maximum dip of 3.1^{o} over a short distance, which is likely to produce some curvature of the interface. The assumption of a piece-wise flat horizon would lead to a maximum depth error of 1.1 km, which is less than the estimated elevation change in that area. The error caused by a heterogeneous velocity distribution in the crust cannot be assessed, because the magnitude and complexity of velocity heterogeneity cannot be determined accurately enough at this stage of the project. However, it is possible to appraise the uncertainty in Moho depth based on the uncertainty in the velocity estimates given by the travel-time curves in Figure 1. If the largest deviations in crustal and mantle velocity are applied to the region with the steepest dip (3.1^{o} in the south-east corner of the map), the maximum resulting depth error of the Moho interface would be 1.8 km. Again, this error is less than the estimated elevation change in this area. Therefore, the derived pattern of Moho elevation appears to be a robust estimate compared to the maximum errors based on the assumption made in this approximation.

Interpretation of Moho Topography

To interpret the Moho topography, it is necessary to incorporate the crustal tectonics of the Korean Peninsula. While the pattern of Moho topography does not mimic the general northeast/southwest trend of the major geologic terrains of the Korean Peninsula, it coincides to a certain degree with the surface topography. The central depression of the Moho interface is co-located with the Yeongnam Massif, which may indicate isostatic compensation for this mountain range (Kwon and Yang, 1985; Choi and Shin, 1996). In contrast, the Gyeonggi Massif in the northeast is located over a shallow section of the crust, requiring a different mechanism to compensate for the uplift. The observed thinning of the crust could result in stronger influences of mantle dynamics on crustal structures in this region. However, to determine the mechanism most plausible for the uplift of the Gyeonggi Massif requires a detailed tomographic study, which will be performed in the second phase of this project.

CONCLUSIONS AND RECOMMENDATIONS

The presented results are corroborated by the studies of Chang and Baag (2006), Herrmann et al. (2006) and Yoo et al. (2007), who mapped the Moho interface using surface-wave dispersion and receiver-function analysis. In both studies, a pattern of the Moho interface, similar to the one displayed in Figures 2 and 4, was found. The present study is complementary to the earlier works, in that a different method and a different dataset generated comparable results.

ACKNOWLEDGEMENTS

The figures and maps throughout this document were created using the Generic Mapping Tools by Wessel and Smith (1995).

REFERENCES

Chang, S. J. and C. E. Baag (2006). Crustal Structure in South Korea from Joint Analysis of Broadband Waveforms and Travel Times, *Bull. Seis. Soc. Am*. 96: 856–870, doi:10.1785/0120040165.

Choi, K. S. and Y. H. Shin (1996). Isostasy in and around the Korean Peninsula by analyzing gravity and topography data, *J. Geol. Soc. Korea* 32: 407–420.

Herrmann R. B., Y. S. Jeon, H. J. Yoo, K. H. Cho, W. R. Walter, and M. Pasyanos (2006). Seismic source and path calibration in the Korean Peninsula, Yellow Sea, and Northeast China, in *Proceedings of the 28th Seismic Research Review on Ground Based Nuclear Explosion Monitoring Technologies*, LA-UR-06-5471, Vol. 1, pp. 60–70.

Kwon, B. D. and S. Y. Yang (1985). A study on the crustal structure of the southern Korean Peninsula through gravity analysis, *J. Korean Inst. Mining Geol*. 18: 309–320.

Wessel, P. and Smith, W. (1995). New version of the generic mapping tools released. *EOS Trans. AGU* 76: 329.

Yoo, H. J., R. B. Herrmann, K. H. Cho, and K. Lee (2006). Imaging the three-dimensional crust of the Korean Peninsula by joint inversion of surface-wave dispersion and teleseismic receiver functions, *Bull. Seism. Soc. Am*. 97: 1001–1011.

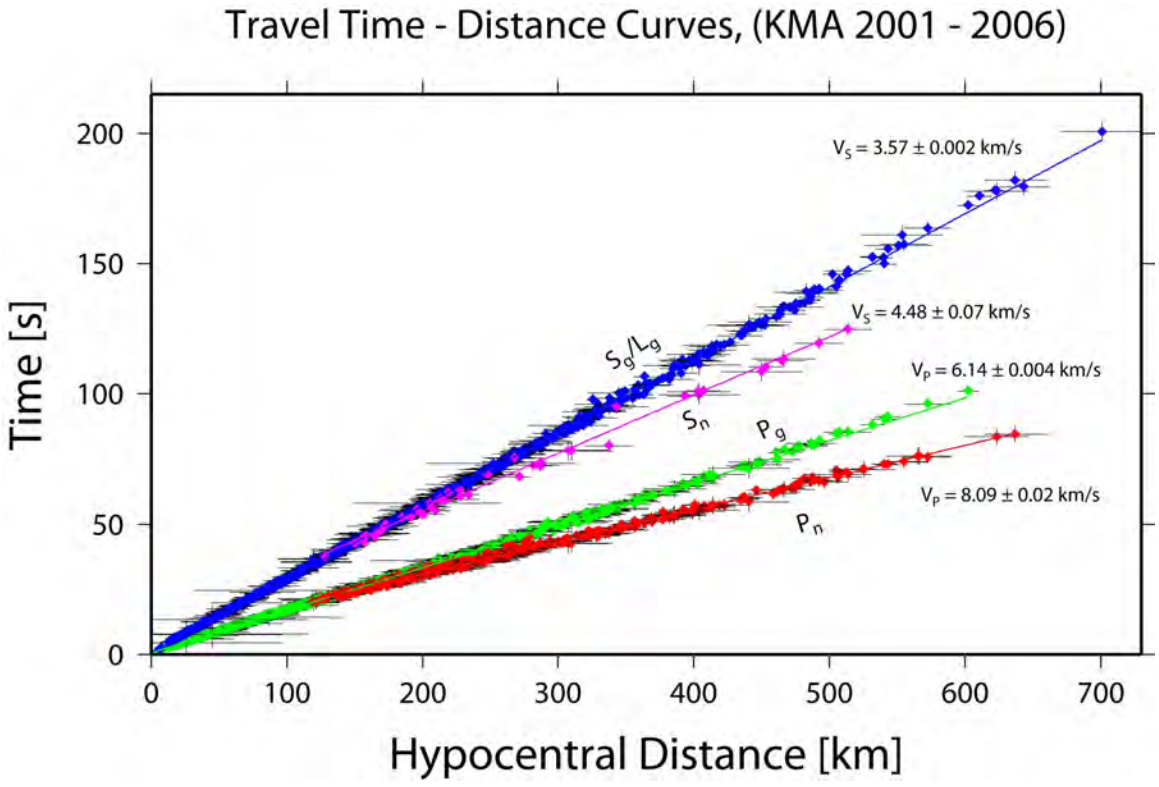

Figure 1. Travel-time as a function of hypocentral distance for the P- and S-wave phase picks as determined from KMA waveform data for the period 2001-2006. The phase picks are indicated by colored diamonds, while the solid colored lines represent their best least-squares fit resulting in the velocity values as noted. The short black horizontal lines at each data point represent the relative location error for each hypocenter estimate associated with that phase pick. The short black vertical lines at each data point represent the relative timing error for event time associated with that phase pick.

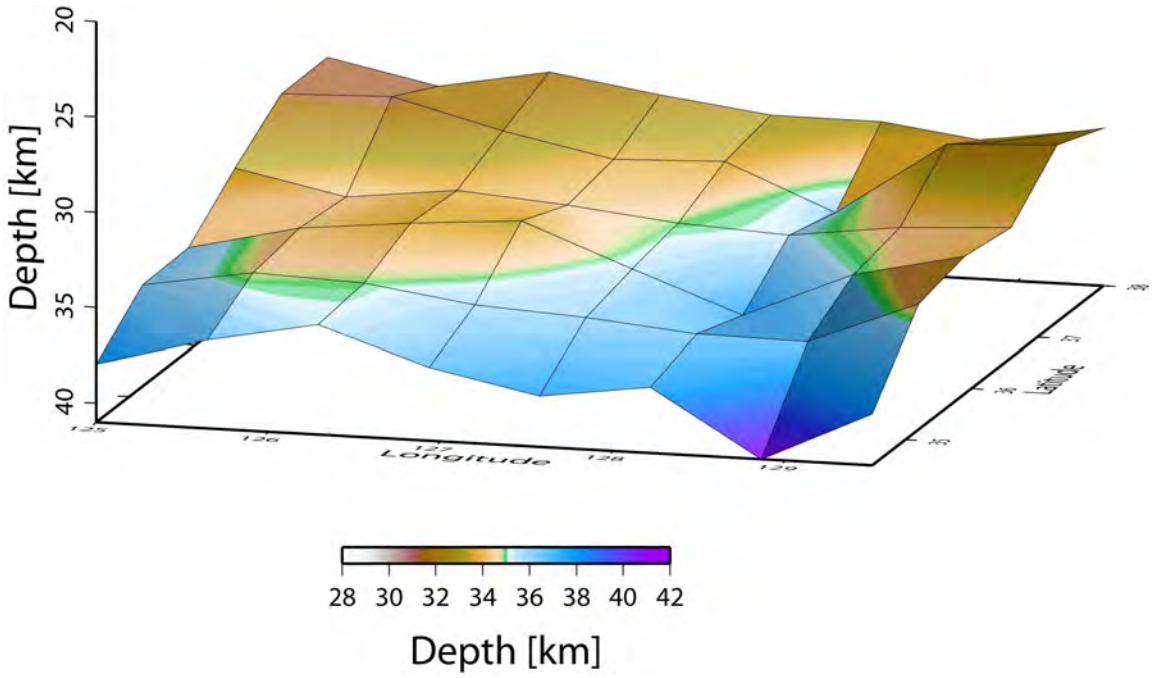

Figure 2. Three-dimensional surface plot of the Moho discontinuity below South Korea. The mapped surface is based on P-wave refraction data recorded by the KMA from 2001 to 2006.

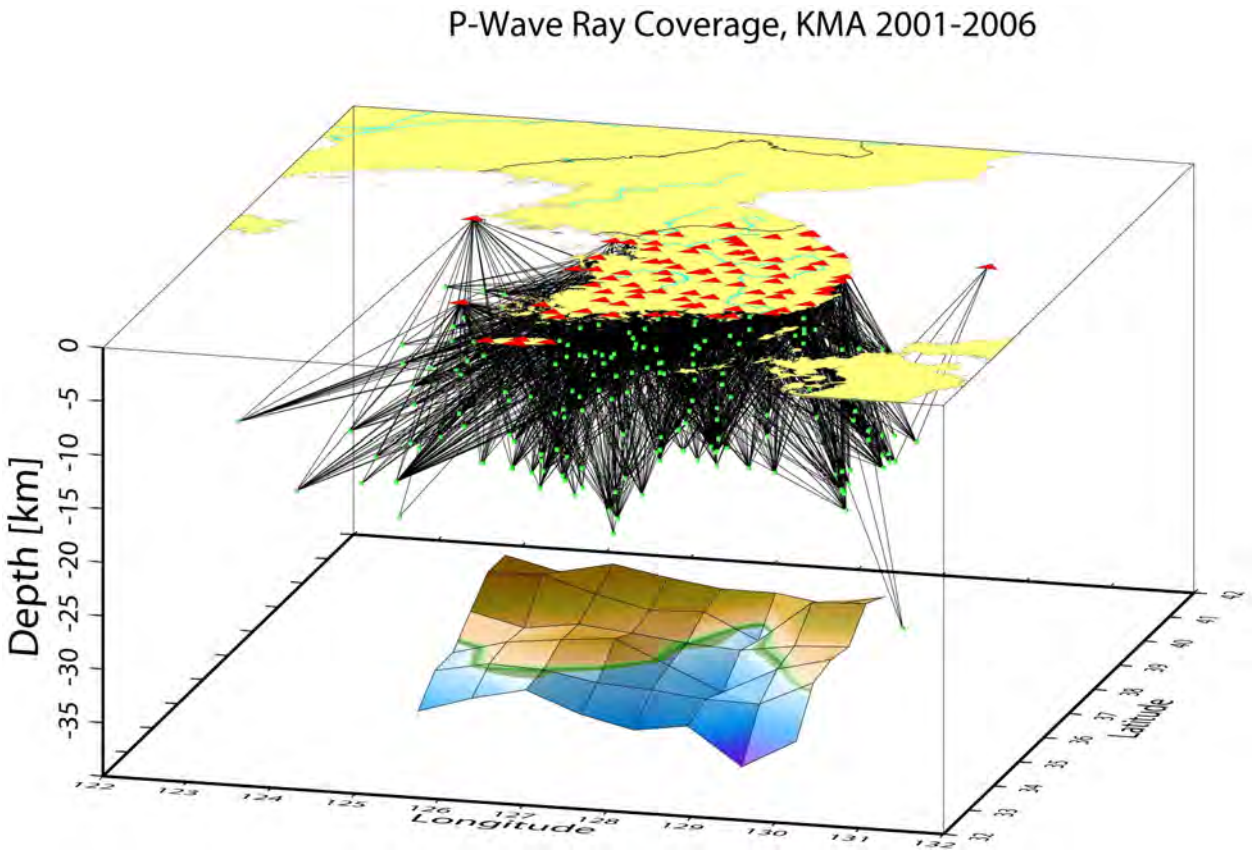

Figure 3. Three-dimensional image of the Moho topography and seismicity below South Korea from the analysis of KMA data for the period 2001-2006. Epicenters are indicated by green circles, seismic stations by red triangles along the surface, and the 3-d P-wave ray coverage by black lines. Vertical exaggeration is greater than 23:1.

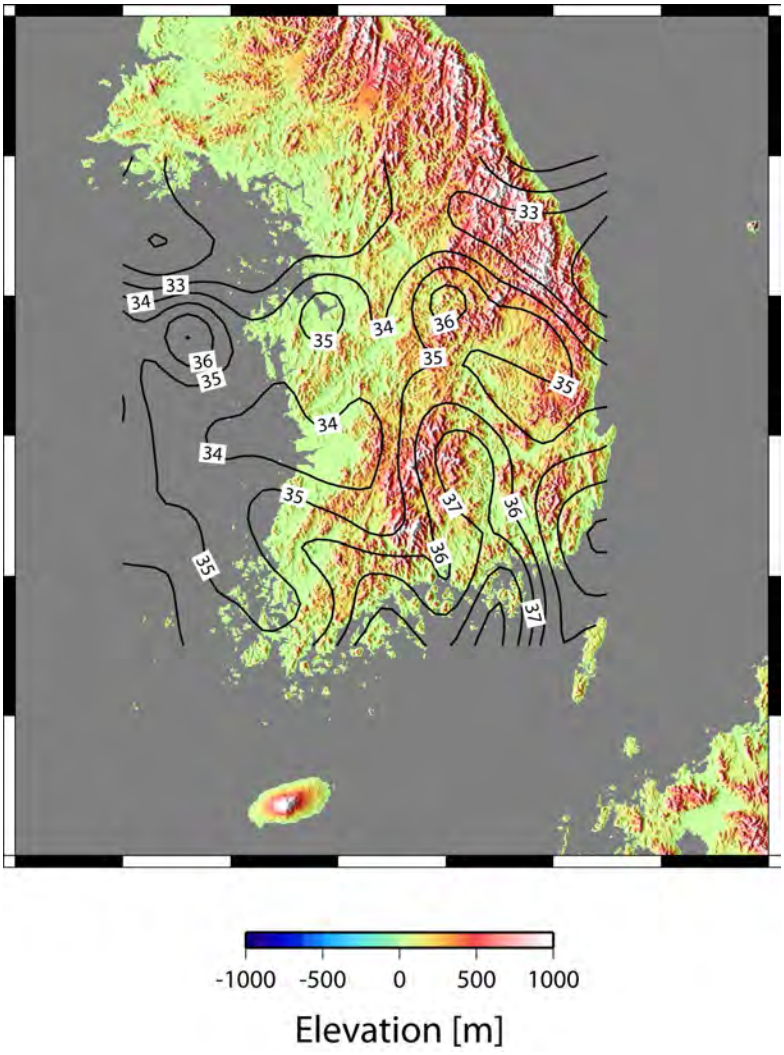

Figure 4. Contour map of the Moho interface below South Korea superimposed on a topography map of the Korean Peninsula. Contour intervals are in kilometers. The contoured surface is based on P-wave refraction data recorded by the KMA from 2001 to 2006.

CONSIDERATIONS ON THE USE OF 3-D GEOPHYSICAL MODELS TO PREDICT TEST BAN MONITORING OBSERVABLES

David B. Harris, John J. Zucca, David McCallen, Michael E. Pasyanos, Megan P. Flanagan, Stephen C. Myers, William R. Walter, Arthur J. Rodgers, Phil E. Harben

Lawrence Livermore National Laboratory

Sponsored by National Nuclear Security Administration
Office of Nonproliferation Research and Development
Office of Defense Nuclear Nonproliferation

Contract No. W-7405-ENG-48

ABSTRACT

The use of 3-D geophysical models to predict nuclear test ban monitoring observables (phase travel times, amplitudes, dispersion, etc.) is widely anticipated to provide improvements in the basic seismic monitoring functions of detection, association, location, discrimination and yield estimation. A number of questions arise when contemplating a transition from 1-D, 2-D and 2.5-D models to constructing and using 3-D models, among them:

1) Can a 3-D geophysical model or a collection of 3-D models provide measurably improved predictions of seismic monitoring observables over existing 1-D models, or 2-D and 2½-D models currently under development?

2) Is a single model that can predict all observables achievable, or must separate models be devised for each observable? How should joint inversion of disparate observable data be performed, if required?

3) What are the options for model representation? Are multi-resolution models essential? How does representation affect the accuracy and speed of observable predictions?

4) How should model uncertainty be estimated, represented, and how should it be used? Are stochastic models desirable?

5) What data types should be used to construct the models? What quality control regime should be established?

6) How will 3-D models be used in operations? Will significant improvements in the basic monitoring functions result from the use of 3-D models? Will the calculation of observables through 3-D models be fast enough for real-time use or must a strategy of pre-computation be employed?

7) What are the theoretical limits to 3-D model development (resolution, uncertainty) and performance in predicting monitoring observables? How closely can those limits be approached with projected data availability, station distribution and inverse methods?

8) What priorities should be placed on the acquisition of event ground truth information, deployment of new stations, development of new inverse techniques, exploitation of large-scale computing, and other activities in the pursuit of 3-D model development and use?

In this paper, we examine what technical issues must be addressed to answer these questions. Although convened for a somewhat broader purpose, the June 2007 Workshop on Multi-resolution 3D Earth Models held in Berkeley, CA also touched on this topic. Results from the workshop are summarized briefly at the end of this paper.

OBJECTIVES

The objective of this paper is to lay out technical considerations in the development and use of three-dimensional (3D) geophysical models for predicting the seismic observables used to monitor compliance with nuclear test ban treaties. These considerations could inform the structure of a program designed to develop a 3D model or models intended for operational use.

RESEARCH ACCOMPLISHED

Monitoring Observables

For purposes of this discussion, the basic seismic monitoring functions consist of phase detection, phase association, event location, discrimination, and characterization (i.e. magnitude and yield estimation). The potential seismic observables useful for these basic functions range from parametric data such as phase amplitudes, arrival times and surface wave dispersion characteristics (e.g., group delay) to derived waveform characteristics such as the coda envelope, to, in some cases, the full seismic waveform. Treaty monitoring is carried out at local (< ~200 km), regional (< ~2000 km) and teleseismic (> ~2000 km) distances. The principal phases are P, S, and surface waves (Rg) at local distances, and Pn, Pg, Sn, Lg, and the surface waves (Rayleigh, Love) at regional distances (Figure 1). A very large number of phases are available for monitoring purposes at teleseismic ranges, though the principal phases that are intensively calibrated are the first arriving P and S, and surface waves.

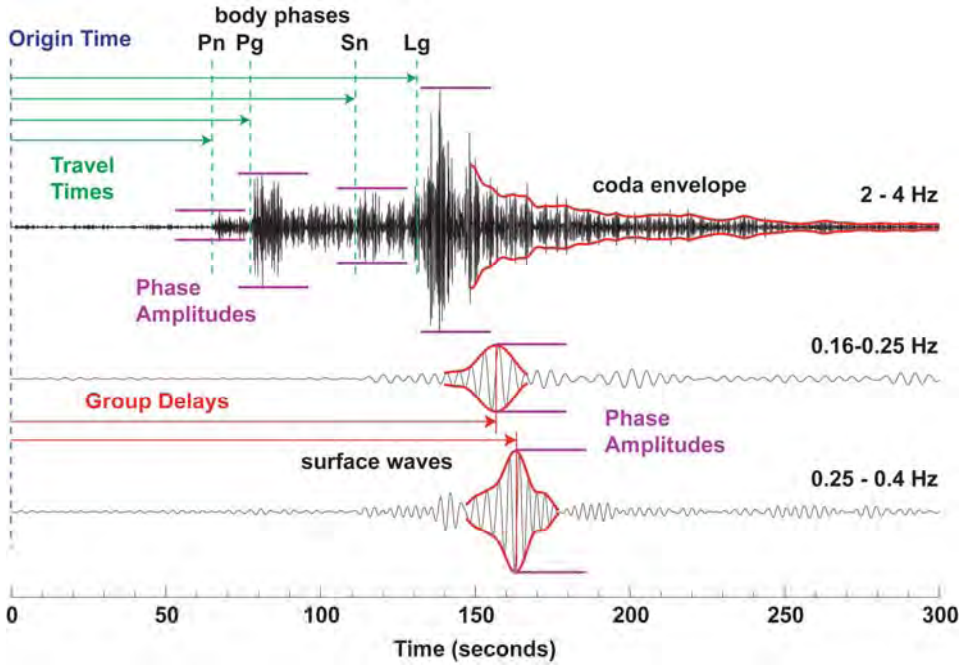

Figure 1. Principal parametric observables at regional distances consist of arrival times and amplitudes of the 4 major phases (top trace) Pn, Pg, Sn, Lg, and dispersion characteristics of long and short period surface waves (bottom traces).

One of the most important factors affecting the development and use of 3D models (principally through the required resolution of the models) is the frequency band in which monitoring observables are measured. The nuclear test monitoring band extends from 20 seconds (for Ms, magnitude measurements from surface wave amplitudes) to 10 Hz or even higher (for body wave amplitude measurements used in discrimination and arrival time picks used in location). Generally data are not available to constrain 3D models sufficiently to make accurate predictions of waveforms at the high-frequency end of the spectrum. However, it may be possible to develop stochastic models that predict bulk characteristics of seismic waves, such as amplitude and coda shape.

Modeling Objectives: Accuracy, Operational Considerations

Seismic events are detected and interpreted by a process of matching observed signal characteristics with characteristics predicted by a model from trial values of the principal event parameters: location, origin time, magnitude, mechanism and source time history. Often the process is iterative, as indicated in Figure 2. The process drives the residuals (differences) between predicted and measured values as close to zero as possible. Usually station corrections for each predicted observable are developed from observations of ground truth events. Station corrections can be appreciable where models (whose geophysical parameters vary relatively smoothly compared to the Earth) fail to predict observables closely enough. Station corrections typically take the form of maps of residual bias (variation from zero) as a function of latitude, longitude, and sometimes depth of the sources observed by the station.

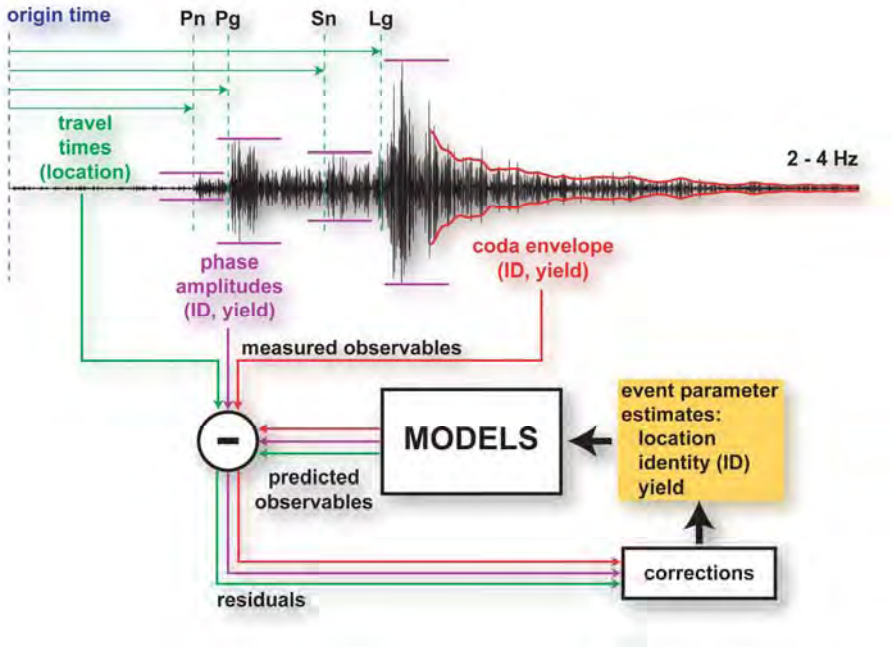

Figure 2. Models form the core of an iterative process of predicting observed signal characteristics (parameters, envelopes, waveforms) in order to detect, locate, identify and characterize seismic events.

The physical parameters comprising the models include compressional (P) and shear (S) velocities, intrinsic attenuation for both P and S, and medium density. In a 3D model, these parameters would be mapped as a function of latitude, longitude, and depth from the surface. Additional, higher-order physical parameters such as anisotropy may need to be considered as well.

It is desirable to concentrate as much as possible of the predictive capability of this system in the model, since the model will provide predictions for stations that do not have empirical corrections either because the stations are newly deployed or because they observe relatively aseismic regions. Clearly, one of the principal objectives in building a model is to make predictions derived from it as accurate as possible.

However, accuracy is not the only objective. The models of interest to the monitoring community are intended to be embedded in pipelines detecting and interpreting events from real-time data streams. Consequently, calculations of observables from the models must be fast enough to keep pace with a real-time system. Often, as is the case with location, predictions of observables must be made repeatedly when interpreting a single event as the estimation algorithm iterates to a solution from a starting estimate. Hundreds or thousands of evaluations of observed parameters may be required to interpret a single event. This requirement implies, for example, that travel-time estimates be calculated in just milliseconds.

Geographical coverage is another issue; global capability is required, but especially good predictions are desirable in Eurasia and Africa.

In addition, the predictions made by models must be seamless. Heretofore, highly accurate local and regional observable (e.g., travel-time) models have been spliced together to form a single model spanning a large (global or continental) region. This practice sometimes has led to boundaries between regions with offsets in the predicted observables. These offsets have been somewhat artificially or arbitrarily smoothed together to avoid presenting discontinuities to estimation algorithms. A desire to avoid such discontinuities is driving the monitoring community toward development of increasingly geographically comprehensive models, ideally embedding high-resolution regional geophysical models seamlessly in global models. There is a spreading consensus that any blending or splicing that needs to be done, should occur in the geophysical models and not in the derived predictions of observables. Because of the heterogeneity of regions, comprehensive geophysical models are necessarily going to be at least 2D and more generally 3D.

There is a question as to whether 3D models will provide sufficiently improved accuracy to justify the added cost of developing them and the pipeline support to use them. It is clear that a patchwork quilt of 1D models is not sufficiently accurate, particularly around boundaries among regions described by distinct 1D models where discontinuities are an issue, and by defaulting to iasp91 in regions where no data are available. They also are complex to implement and maintain. Currently the National Nuclear Security Administration (NNSA) labs are engaged in building 2.5D approximations to 3D models for predicting regional phase travel times. These are planned to be tomographic models, which should be seamless and provide greater predictive accuracy than 1D models everywhere, including in aseismic regions.

One Model or Many?

Previous seismological practice in model building was to construct separate models for each observable to be predicted, and generally to use data of the intended observable to invert for the model. Hence, body wave travel-time observations were used to construct predominantly P velocity models and surface wave dispersion data to construct shear wave models. These models often had their best resolutions at different depths due to the fact that body phases sample the earth (travel) deeper than surface waves. Measurements made from disparate wave types represent different averages of often distinct geophysical parameters.

Current practice, especially in global tomography, is to perform joint inversions of several or even many data types to estimate one or often several geophysical parameters. The use of multiple data types improves coverage by providing constraints at different depths and observations over a larger number of (great circle) paths.

While the desirability of inverting many data types simultaneously to produce models is generally accepted, a question remains about whether to strive for a single model to predict all observables or individual models to predict each observable separately. A single model is desirable for operational and maintenance simplicity, but it may be that dedicated models will have greater prediction accuracy, especially if they employ specialized representations for the observable in question (such as dispersion maps for surface wave group delay predictions instead of P and S velocity models).

Model Representation Uncertainty

There are a number of separate issues to be resolved that fall under the general heading of model representation. While not necessarily unique to 3D models, these issues are exacerbated by “the curse of dimensionality,” the rapid increase in complexity, and storage and computational requirements in the transition to 3D representations.

The first issue is the mathematical form of representation for any particular geophysical quantity. Options include sampling the quantity on a regular geographic grid of points or cells, sampling on a tessellated mesh, and representation in terms of the coefficients in any basis function expansion. Often models are described most simply as a stack of layers in depth in latitude-longitude cells; the parameters are layer thicknesses, P and S velocities, intrinsic Q for P and S waves, and medium density.

One consideration for the choice of representation is the fidelity of the model to the Earth it represents. Model fidelity is influenced by the resolution of the representation and the accuracy of suitable interpolation schemes.

Generally, the greater the resolution, the more accurate the representation (especially of boundaries) and the larger the space required to store the model. The accuracy of the model, however, is most fundamentally limited by the coverage of the data used to construct it.

A solution, almost sure to be employed in development of large 3D models, is the use of multiple resolutions. The model may be very dense in the shallow regions of the crust and lithosphere, where heterogeneity is greatest, and more accurate predictions of rapidly-varying observables is desired. The model may be sparse in the deeper, more homogeneous mantle and core. In the nuclear test ban application, some geographic regions will be more accurately and finely represented than others of lesser importance.

A second consideration is the accuracy of the waveform or parameter observable generated by forward calculation through the model. Computed observable accuracies may require resolutions that exceed those required for model fidelity. Numerical requirements may dictate sampling densities as high as ten times per wavelength, often much more finely sampled than justified by available constraints on the model implied by available data. The choice of model representation often significantly influences numerical accuracy, as can happen with the superior definition of reflecting boundaries finite or spectral element methods.

A third and related consideration is the speed with which observables can be calculated through the model. Many algorithms required extraction of Earth model quantities along great circle paths or along more arbitrary paths (as with full ray tracing). Such algorithms place a premium on fast interpolation methods, since they require geophysical parameter values at points generally not coincident with mesh or grid sample locations. Tesselation meshes have to be “walked” to find the specific tetrahedra where model values are required. Efficiency of model interrogation and interpolation, accuracy, and model storage requirements may trade against each other.

The second major issue is the estimation and representation of model uncertainty. In current practice, the majority of models, even the vast majority, are deterministic. Where uncertainties in model parameters are estimated and reported at all, usually Gaussian statistics are assumed and model parameters are described as the mean of the distribution. The variance may be estimated from *a priori* considerations of normal geophysical variation, or more robustly through a statistical procedure such as the jackknife or bootstrap during inversion. Although variations among different model parameters are almost certainly correlated, covariance estimates are not commonly reported.

Stochastic geophysical models [e.g. Pasyanos et al., 2006] are an attractive though computationally- and storage-intensive alternative (particularly in 3D) to deterministic models. Stochastic models represent uncertainty with a collection of thousands of realizations that provide a posterior distribution on sample models that are consistent with available data (see e.g., Figure 3). The density of sample models in the model parameter space constitutes an approximate probability distribution on the model that can be used to extract moments (mean model, variance) that characterize uncertainty. This representation easily embraces non-Gaussian, and even multi-modal, statistics. Relatively efficient grid-search methods exist to produce the collection of realizations that constitute a 3-D stochastic model by fitting simultaneously a variety of observation data. However, large-scale computing is required to check the thousands of representative sample 3-D models against available data by predicting a variety of observables (surface wave dispersion, body-wave travel times, receiver functions, etc.). Stochastic models of this sort readily allow the estimation of uncertainty in predicted observables, since multiple estimates of the observables can be obtained by forward calculation through the suite of sample realizations. The result is a distribution on the observables, as shown in Figure 3.

A Priori Model Development

Geophysical models can be developed in several ways, including the compilation of existing information from diverse sources such as maps, general physical constraints on earth structure and specific geologic descriptions from prior studies into *a priori* geophysical models. Figure 4 below, shows various aspects of a unified 3D geophysical model of Eurasia and North Africa developed by the NNSA labs. Lawrence Livermore National Laboratory (LLNL) constructed the western half of the model, which is designated the WENA (Western Eurasia, North Africa) model. The WENA model is compiled from a large number of literature sources [Pasyanos et al, 2004]. *A priori* models are useful in themselves, but also may serve as the starting point for the other major class of models, tomographic models, often as Bayesian priors. Tomographic models are obtained by inverting mathematically observations of phase travel times, amplitudes, dispersion and other characteristics over many crossing paths to constrain the 3D velocity structure and other model parameters.

Model Validation

Model validation is an essential component of all model development and acceptance as it tests the predictive capabilities of a model. The fundamental steps of validation are the same as in model estimation from data: (1) collection of ground truth information on events for which seismic observables can be measured, (2) development of procedures to predict those observables through the model, (3) collection of waveform or other data from which to measure observables, (4) making the measurements and (5) comparing the measurements with the model predictions. The additional step in model construction not performed in validation is adjusting the model parameters in an iterative process to better match the measurements.

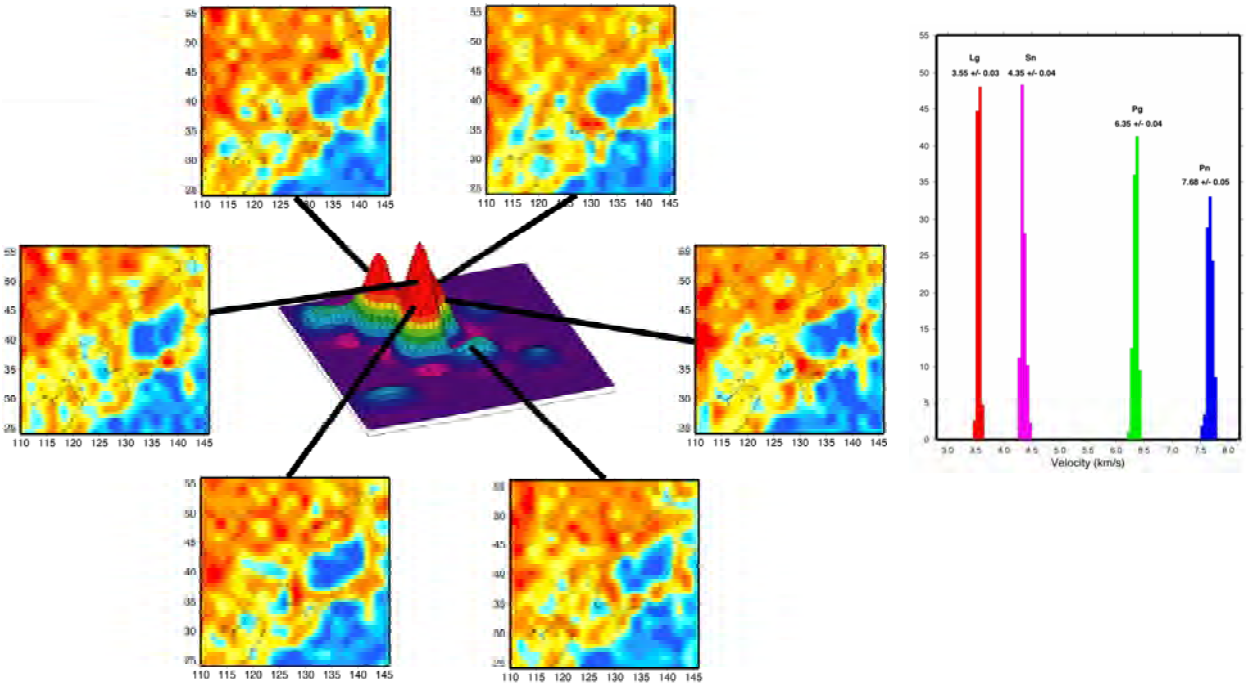

Figure 3. Six realizations from a 3D stochastic geophysical model surrounding the Korean peninsula demonstrate the concept that the uncertainty for the model is captured by a probability distribution represented by the density of realizations in model space. At upper right, distributions for predicted travel-time observables along a specific path show the ability of this type of model to predict uncertainties in monitoring observables.

An example of travel-time model validation is shown in Figure 5 for the WENA model [Flanagan et al., 2007]. In this case, the model is used to predict first P arrival times. Since this is a 3-D model, the travel times are predicted with a 3-D finite-difference code solving the eikonal equations. This assessment shows that even an *a priori* 3-D geophysical model improves travel time predictions compared to a standard (iasp91) 1-D Earth model.

Validation of tomographic (data-driven) models presents a dilemma: how much of the available ground truth information and measurements should be used to develop the model and how much should be held out to perform validation? To prevent circularity problems, the same data cannot be used for both functions. Cross validation and similar statistical sampling techniques can obviate this problem at added computational cost. The problem becomes particularly acute in the development of 3D models, because the added dimension of such models means that many more model parameters must be estimated, and more and more data are required to constrain the estimates.

Data Types Required for the Inverse Problem

In this paper, we use the term "inverse problem" to mean the problem of estimating geophysical model parameters from seismic and other observables. By contrast, the forward problem is that of predicting the observables from an extant model. The data types required or available to solve the inverse problem are many and varied. They include measurements of the observable types that the models are intended to predict: P and S absolute and differential travel times, P and S wave amplitudes, and surface wave dispersion. They also include other types of data that provide additional, often complementary constraints: receiver functions, structural constraints from refraction and reflection seismology, gravity anomaly data from satellite orbital perturbations, heat flow, normal mode peak splitting, and constraints from geologic or tectonic interpretations, to name some of the more important types.

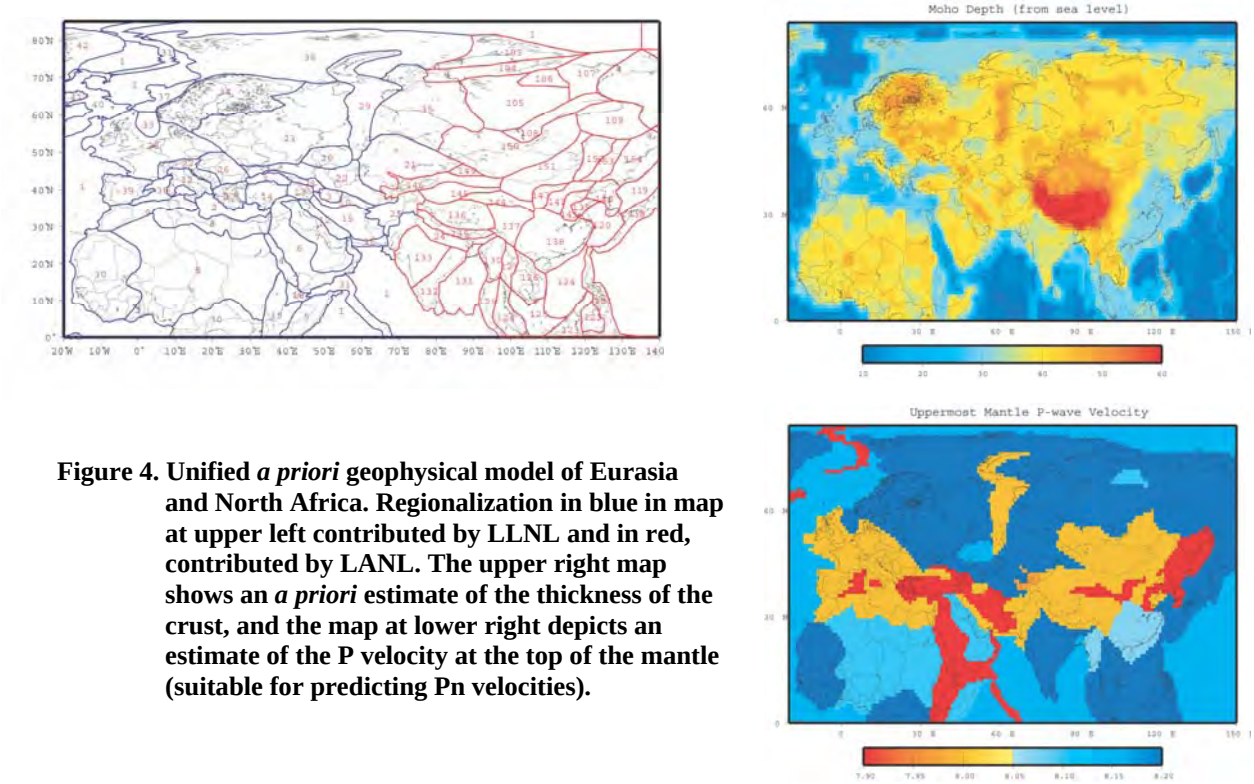

Figure 4. Unified *a priori* geophysical model of Eurasia and North Africa. Regionalization in blue in map at upper left contributed by LLNL and in red, contributed by LANL. The upper right map shows an *a priori* estimate of the thickness of the crust, and the map at lower right depicts an estimate of the P velocity at the top of the mantle (suitable for predicting Pn velocities).

As mentioned earlier, different data types result from waves or fields that sample different portions of the earth and do so with different weighting or averaging over the regions to be model (expressed as different resolution kernels in inverse methods). The issue for developing large-scale 3D models is again the curse of dimensionality—3D models have many more parameters to estimate than 2D or 1D models. The larger and more varied the volume of data brought to bear on the problem, the more certain will be the result and the better the resolution (within limits set by the distribution of stations and sources).

Path Coverage and Data Quality

Data coverage and quality issues are among the most important practical considerations when contemplating the construction of 3D models. For those data types that are seismic observables, the distribution of paths sampling the volume of the Earth is not under our control. Events are not uniformly distributed, but highly concentrated along plate boundaries. Stations are not uniformly distributed either, because of the fact that land mass constitutes only 30% of the earth's surface, and many regions are inaccessible for political or logistical reasons.

The number of events available to provide data for model building is further constrained by quality requirements. Especially for constraining the velocities of models from seismic wave travel-time observations, the locations,

depths, and origin times of events have to be known accurately. This has led to requirements on ground truth information, generally designated as GTx, where "x" specifies the uncertainty in the location of the event, e.g., 1 km, 5 km, or 25 km. A significant issue for the development of 3D models is that the number of events with the most desirable ground truth levels (GT5 or better) is in the low thousands, whereas the total number of events reported in major bulletins is in the many hundreds of thousands. The development of high quality ground truth information remains a priority for model development.

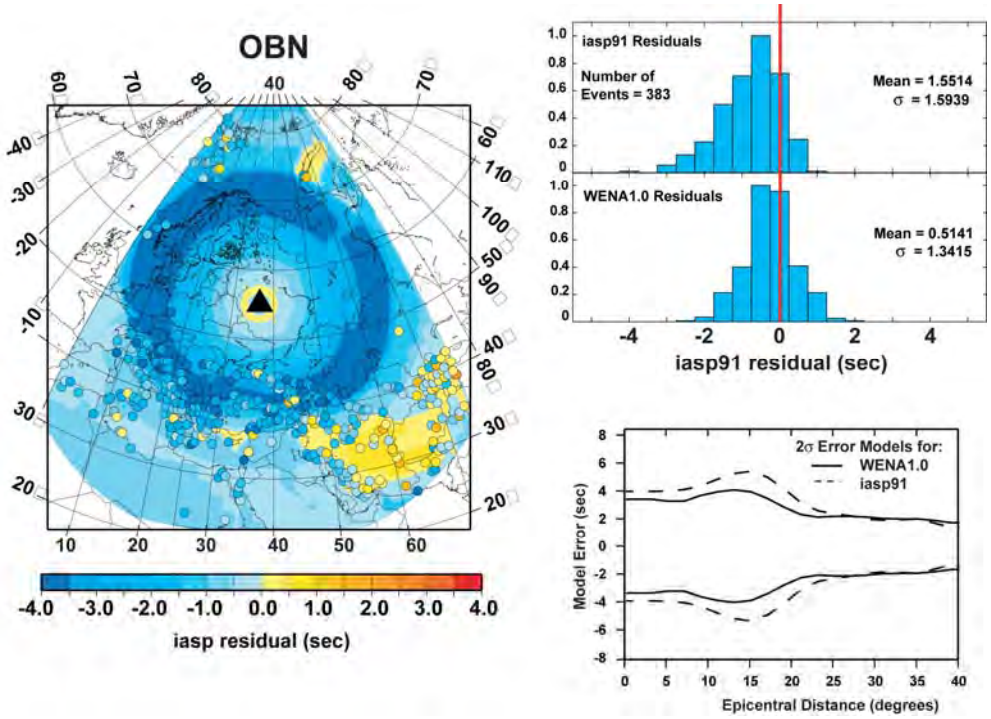

Figure 5. Observed travel-time residuals at station OBN (Obninsk, Russia) against predictions from the 1-D iasp91 model. At left, the measured (color coded) residuals against iasp91 predictions are plotted as points, superimposed on a surface representing the difference between the 3-D WENA model prediction and the iasp91 prediction. Note that the *a priori* WENA prediction correlates well with the measured residuals. Summary statistics at right show that the WENA residuals are closer to zero mean and have smaller variance than the iasp91 residuals.

The Inverse Problem: Objective Functions and Inversion Methods

From what we have discussed so far, we see that the 3D models of interest to the monitoring community ultimately are likely to be global, multi-resolution models with considerable detail at shallow depths in certain continental regions and less detail under the oceans and in the deeper mantle and core. Development of such models will make extensive use of *a priori* constraints to offset, to the degree possible, the relatively insufficient (though still very large) quantity of data available to estimate model parameters. To minimize pipeline complexity and maximize software maintainability, there will be pressure to consolidate predictive capability into as few separate models as possible, ideally into a single model. The model or models that emerge will be multifaceted, representing simultaneously many or all geophysical parameters of interest and predicting many or all monitoring observables. Correspondingly, many disparate data types will have to be inverted simultaneously to estimate the model parameters.

This inversion problem represents a significant challenge. A number of factors will have to be addressed simultaneously in deciding a suitable inversion technique: the mathematical objective functions used as figures of model merit (including the related statistical descriptions of prediction residuals), whether parametric or waveform data will be fit, the resolution of the model, the computational and storage requirements.

The statistics of the residuals (Figure 2) between model predictions and data will largely drive the objective functions. If Gaussian statistics are adequate, then least-squares objectives may be indicated. If correlated residuals are likely, then an objective function with suitable covariance structure will be required. If non-Gaussian or multimodal statistics are likely, then a grid-search approach might be required, such as a Markov-Chain Monte Carlo (MCMC) method. A multiple objective approach (next section) might be superior when several disparate observables are predicted by the same model. *A priori* constraints on the models may suggest Bayesian objective functions.

The choice of inversion engine also may be driven by the desirability of performing constrained optimization. Physical constraints (realistic ranges of velocities and densities, or rheological conditions, for example) may required penalty function, barrier function, interior point, or other constrained optimization techniques.

If stochastic models are desired, as may happen if a realistic exploration is required of model tradeoffs and parameter correlations, then a sophisticated grid search (MCMC, simulated annealing) will be necessary. These options almost surely will require large-scale computing to construct 3D models.

Development of even deterministic 3D models with global coverage will require large amounts of computer storage and speed. A typical model might be hundreds of megabytes or even larger. If fitting full waveforms, or some functionals of waveforms (e.g., envelopes) in the higher frequency bands of monitoring interests becomes important, then model prediction of observables (waveforms) will require computers with hundreds or thousands of processors. If stochastic sampling approaches are employed, then storage for thousands of models will be required. The inversion problem then would be in the terascale or petascale range.

June 2007 3D Model Workshop

On June 6 and 7, 2007, LLNL hosted a workshop on the future of 3D models in seismic monitoring and hazard applications. The objective of the workshop was to bring together government, industry, and academic leaders in the seismic monitoring and hazard communities to explore issues surrounding the transition to 3D models. Several trends favoring 3D models are converging: the continued proliferation of digital seismic stations globally, the increasing availability of data from these stations, the decreasing cost of computer storage and processing power, and the increasing sophistication of modeling techniques.

While it is not yet certain that the use of 3D models can provide significantly better monitoring performance than that obtained with 2D and 2.5D models, there are indications that this is the case, especially where full waveform predictions are required. For example, the influence of basins on phase amplification and attenuation at the local and regional scales is significant in event discrimination and estimation of mechanism and explosion yields. Examples of significant off-azimuth and multipath wave propagation effects have been noted in complex regions, which can, for example, bias location and surface wave magnitude estimates. The partition of energy between Sn and Lg phases, crucial to discrimination, is strongly affected by propagation along paths that contain some leg of oceanic crust. Accurate numerical predictions of these effects remain elusive, but almost surely will involve the use of 3D structure. All of these effects are likely to become more important as smaller events are observed at ever higher frequencies and closer range.

Whether good 3D models can be developed is an issue, especially at resolutions required to support accurate high-frequency (above e.g. 1 Hz) numerical waveform predictions. The prospects for developing models with increased resolution are improving with the availability of data from more stations, and innovative techniques for exploiting those data, particularly ambient noise tomography. Improvement in the number and distribution of stations and availability of data is still the single most important factor in constraining 3D models.

However, significant improvements in the large-scale exploitation of available data with joint inversion of multiple data types, multiple-objective optimization to implement joint inversion, and sophisticated adjoint methods also play a major role. New adjoint methods allow much more accurate computation of the sensitivity of waveforms to complex 3D structure. Spherical finite-difference solvers for the eikonal wave equation should provide more accurate predictions of travel-time from 3D models. These techniques and others are being demonstrated on the local and regional scales with models of the San Francisco Bay Area, southern California and the entire state with unprecedented resolution.

One key to widespread adoption of these techniques is the availability of relatively inexpensive high-performance computing. Development of strategic computing to petascale levels is being driven by the Department of Energy through its stockpile stewardship program. Commercial high-performance computing is not far behind with terascale computing now becoming available at universities and in the private sector. Large-scale computing also is a requirement for accurate nonlinear simulations of the explosion source that will use the best available 3D geophysical models to predict regional seismic observables using a domain decomposition approach. Realistic first-principles calculations of shock and material damage around the source are a promising means for predicting explosion signatures in regions where no historic nuclear test data are available.

The prospect of building 3D models as a community project similar to the SCEC Community Modeling Environment [SCEC, 2007] was raised and a specific proposal was presented to construct two models (one P, one S) linked through a common crust and lithosphere discontinuity structure. The intent of the P model would be to predict teleseismic and regional P travel times in order to improve event location estimates. The S model would be constructed from surface-wave dispersion measurements with periods of 20 seconds and greater. It's purpose would be to predict Rayleigh and possibly Love wave phase and group velocities at regional and teleseismic ranges for the purpose of estimating Ms and moment tensors. The models both were proposed to be hierarchical and multi-resolution to provide increased resolution where justified by data coverage. A common format and shared structure would allow the models to be merged into a single model at some point.

The overriding consideration in development of such a model pair was to pick a practical goal as a starting point for a collaborative effort with sufficient flexibility to be extended to more complex models, if warranted. There also was a strong requirement to develop models immediately useful for monitoring objectives.

CONCLUSIONS AND RECOMMENDATIONS

The proposal for a community 3D model came at the very end of the June workshop. We recommend conducting a follow-on workshop dedicated to completing specifications for a 3D model for monitoring applications and to examining practical means for building such a model. The June workshop made clear that there is significant possible synergy in techniques for constructing models among the diverse test ban, hazard and global earth structure communities, even though the objectives, scales and geographic boundaries of the models they develop individually might differ substantially. The notion of constructing a multiresolution community model should be examined to determine whether a common set of modeling objectives can be found to provide incentives for all to collaborate on data, techniques and computing resources.

ACKNOWLEDGEMENTS

The authors would like to thank the attendees of the June 3D Model workshop for their participation, and particularly the participants who prepared presentations: Dr. David Russell, Dr. Thomas Brocher, Dr. William Menke, Dr. Jeroen Tromp, Dr. Cliff Thurber, Dr. Michael Ritzwoller, Dr. Charles Ammon, Dr. Peter Shearer, Dr. Dmitri Kuznezov, Dr. Norm Abrahamson, Dr. Jacobo Bielak, Dr. Tarabay Antoun, Dr. Donald Helmberger, Dr. Thorne Lay, and Dr. Paul Richards.

REFERENCES

Flanagan, M. P., S. C. Myers, and K. D. Koper, (2007) "Regional Travel-Time Uncertainty and Seismic Location Improvement Using a Three Dimensional *a priori* Velocity Model," *Bull. Seis. Soc. Am.*, **97**(2), in press 2007.

Pasyanos, M. E., W. R. Walter, M. P. Flanagan, P. Goldstein and J. Bhattacharyya, (2004) "Building and Testing an *a priori* Geophysical Model for Western Eurasia and North Africa," *Pure Appl. Geophys*., **161**, 235-281.

Pasyanos, M.E., G.A. Franz, and A.L. Ramirez (2006), "Reconciling data using Markov Chain Monte Carlo: An application to the Yellow Sea - Korean Peninsula region," *J. Geophys. Res.*, **111**, B03313, doi:10.1029/2005JB003851.

SCEC Community Modeling Environment (2007), http://epicenter.usc.edu/cmeportal/index.html.

ADVANCED WAVEFORM SIMULATION FOR SEISMIC MONITORING EVENTS

Don V. Helmberger[1], Jeroen Tromp[1], and Arthur J. Rodgers[2]

California Institute of Technology[1] and Lawrence Livermore National Laboratory[2]

Sponsored by National Nuclear Security Administration
Office of Nonproliferation Research and Development
Office of Defense Nuclear Nonproliferation

Contract No. DE-FC52-06NA27319[1,2]

ABSTRACT

Comprehensive nuclear-test-ban monitoring in terms of location and discrimination has progressed significantly in recent years. However, the characterization of sources and the estimation of low yields remains a particular challenge. As the recent Korean shot demonstrated, we can probably expect to have a small set of teleseismic, far-regional and high-frequency regional data to analyze in estimating the yield of an event. Since stacking helps to bring signals out of the noise, it becomes useful to conduct comparable analyses on neighboring events, earthquakes in this case. If these auxiliary events have accurate moments and source descriptions, we have a means of directly comparing effective source strengths. Although we will rely on modeling codes, 1D, 2D, and 3D, we will also apply a broadband calibration procedure to use longer periods (P >5 s) of waveform data to calibrate short-period (P between 0.5 to 2 Hz) and high-frequency (P between 2 to 10 Hz) as path-specific station corrections from well-known regional sources. We have expanded our basic cut-and-paste (CAP) methodology to include not only timing shifts but also amplitude (f) corrections at recording sites. The name of this method was derived from source inversions that allow timing shifts between "waveform segments" (or cutting the seismogram up and re-assembling) to correct for crustal variation. For convenience, we will refer to these f-dependent refinements as CAP+ for (short period, SP) and CAP++ for still higher frequency. These methods allow the retrieval of source parameters using only P-waveforms where radiation patterns are obvious as demonstrated in this report and are well suited for explosion P-wave data. The method is easily extended to all distances because it uses Green's function although there may be some changes required in t* to adjust for offsets between local vs. teleseismic distances. In short, we use a mixture of model-dependent and empirical corrections to tackle the path effects. Although we rely on the large TriNet array as a testbed for refining methods, we will present some preliminary results on Korea and Iran.

OBJECTIVE

Our main objective is to develop methods for locating and identifying seismic events, focusing primarily on earthquakes but including mining blasts and explosions. To advance methodologies, we want to use our computational resources to address both deterministic approaches as well as to develop a better physical understanding of scattering where frequency-dependent coda magnitudes prove so effective. While the latter is apparently source-reduction pattern free (above some cut-off frequency), the direct phases are not and thus the combination should be even more effective in discrimination. In this report, we concentrate on the direct phases and produce a very well recorded set of events ($2 < M < 5$) which can be used for calibration and scattering models.

RESEARCH ACCOMPLISHED

The primary objective of this research is to use earthquake data to model and calibrate paths so that more accurate estimates of explosion strengths can be established for regions of interest. The basic idea of using events ($M_w > 4$) to calibrate paths has been introduced earlier, i.e., Song and Helmberger (1998). They attempted to build on the empirical Green's function method, Hartzell (1978), by generating pseudo Green's functions that are less dependent on source excitation. The method uses the perturbation of individual generalized ray responses calculated from a 1D model where each layer is divided into blocks and allowed to vary in velocity. The small shifts produced by these tomographic changes are assembled to force 1D Green's functions to fit data better using a simulated annealing algorithm. Application to a set of the Landers' earthquake aftershocks is given in Helmberger et al. (2001) where the most variable velocities occur along the surface or just above the Moho.

Several automated waveform modeling techniques are currently available for estimating source parameters based on fitting long-period (LP) data (periods > 5 s). Most methods rely on a library of 1D Green's functions which are compared against observed records to deduce moment, mechanism, and depth for $M > 3.5$. A method we prefer uses a cut-and-paste procedure (CAP) which allows P-waves to be fit independent of the stronger surface waves, where timing shifts are allowed between phases. This approach is somewhat simpler than those discussed above. These shifts can be used to derive a new 3D model as demonstrated in this report or stored as a tomographic-type map to be used in extracting parameters for smaller events. An example of the CAP analysis is given in Figures 1 and 2 for a moderate magnitude event occurring in Iran. Note that the Pnl portions of the vertical and radial segments have been enhanced on the left and fit separately. The numbers below each trace indicates the cross-correlations (top) and shifts (lower). The header line states the model, the strike (59°), the dip (80°), and the slip direction (40°). The depth is estimated to be 4 km, and has a magnitude M_w of 5.2. The number after the station name indicates the distance in km. This event is well-recorded globally and becomes a natural starting place for using a combination of regional and teleseismic data to study events.

A collection of this type of data is being assembled (Rodgers et al., 1999). However, we concentrate on the technique development using the Southern California Seismic Network as a testbed. We address *five issues*: (1) refining models and CAP validation, (2) two-station solutions, (3) extension of CAP to contain amplitude corrections, (4) directivity and cluster analysis, and (5) site characterization.

1. Refining Velocity Models and Validation

Using the CAP method, we have avoided propagational complexities by allowing shifts in record segments. Here we will use these shifts to refine crustal structure. The procedure for refining the upper crust is displayed in Figure 3. We have obtained the shift required to align the 1D synthetics with the observed waveforms for about 200 events. The delays are given in terms of a spider diagram where the model produces early synthetics in general (red). The cross-correlations are displayed in similar fashion where most of the fits are good (blue). The delays for all of the events can be assembled and used to generate a tomography image (block-type) and slightly smoothed as displayed for Love waves. Earlier sensitivity studies indicate that the seismogenic layer containing the source controls the timing, Song et al. (1996).

Synthetics (upper right) can then be generated with a fast (2D) FD routine assuming the mechanisms obtained from the CAP solutions, Helmberger and Vidale (1988). The bottom seismogram was generated with FK-1D, Saikia (1994). Comparisons for the 1D and 2D FD synthetics are also included for comparison with the data trace (top). These records are filtered to 5s which is the normal filter (LP) used in the CAP inversion. The spider diagram at the bottom (2D) indicates the improvement in timing of the new model although the fits remain unchanged. These calculations are fast, taking about 5 minutes per event on a desktop computer. Similar results are obtained for the other events and will be presented at the annual meeting.

2. Locating and Modeling Regional Earthquakes with Two Stations

We have introduced a new technique to retrieve source parameters including location by using established shifts, either from measurements or 3D models, Tan et al. (2006). The method conducts a grid search in a cube centered over the source target comparing synthetics with shifts to observed records to determine location, depth, origin time, and mechanism that best fits the 3-component seismograms. The method was tested on 28 events beneath the Tibetan Plateau against a Program for the Array Seismic Studies of the Continental Lithosphere (PASSCAL) array solutions. Here we test over 160 events against a large station distribution, with a sample of the average fits and one of the poorest (Figure 4).

3. Extension of CAP to Shorter Periods

The changeover from LP (> 5 s) to SP (< 0.5 s) waveform modeling is facing the inherent trade-offs between source complexity and structural heterogeneity. Under such circumstances, analyzing clustered events provides a practical way to "separate" the source from the structural effect. The feasibility is displayed in Figure 5, where we compare the records at the same station GSC from three clustered events of different sizes. The two smaller events are overwhelmed by noise in long-period (0.05-0.2 Hz) frequency band; however, they produce decent signals at higher frequencies, such as 0.5–2 Hz, or 2–8 Hz. In particular, at 0.5–2 Hz, the discrepancies between the records from the magnitude 4 (13938812) and magnitude 2 (13937632) events are mainly caused by their differences in size and focal mechanism, while the effects from the detailed rupture processes are considerably smaller. This suggests that short-period P-waves can be used for determining focal mechanisms of magnitude 2 events if we could calibrate the path effect using magnitude 4 events with known source mechanisms. The same is true when it comes to the magnitude 2 (13937632) and magnitude 1 (13939108) events at higher frequency (2–8 Hz). On the other hand, the smaller events can provide excellent empirical Green's functions for studying the detailed rupture process of the magnitude 4 event. Such a "two way" calibration process is what we have demonstrated in our recent papers (Tan and Helmberger, 2007a and 2007b).

The discrepancies between the observed P-waves and the synthetics are mainly manifested as amplitude differences. For a quantification purpose, we define the function of "amplitude amplification factor" (AAF) as

$$AAF = \sqrt{\frac{\int u^2(t)\,dt}{\int s^2(t)\,dt}}, \qquad (1)$$

where u(t) and s(t) are the data and synthetics, respectively. The integration is over a 2 s window centered on the onset of the P-wave. It appears that the most anomalous AAFs occur for the stations in the basins. In particular, these stations are consistently characterized by large AAFs (> 1) on the vertical component, but small AAFs (< 1) on the radial component. This discrepancy between the vertical and radial components has been noted by many previous investigators (e.g., Savage and Helmberger, 2004) and is addressed later in this proposal. By comparing the AAFs derived from all the calibration events, particularly, the thrust and the strike-slip events, we found a large number (~70) of stations display stable and mechanism-independent AAFs, which suggests the amplitude discrepancy of the synthetic P-waves could be corrected to model the observations, hence determine the earthquake source parameters.

We invert the short-period P waves with a similar grid-search approach as in the long-period inversion, where we minimize the L2 norm of the misfit between the data and synthetics:

$$e = \left\| u(t) - AAF \,.\, s(t) \right\|. \tag{2}$$

The AAFs in equation (2) are taken as the averages of the AAFs derived from all the calibration events to account for the structural effect. The few stations that display rapid variations of the AAFs among the calibration events are discarded. The validation test with respect to the calibration events shows remarkable agreement between the results from short-period P-wave inversions and their LP solutions. The same strategy can be carried to higher-frequency bands, e.g., 2–8 Hz, and hence be applied to smaller events. To examine the AAFs at higher frequencies and their usefulness in determining smaller events' focal mechanisms, we conducted an AAF calibration process at 2–8 Hz with 21 $M_w \sim 2.5$ events from the Big Bear cluster. Although the site deviations are generally larger, the AAFs still appear stable and mechanism-independent. More importantly, when we conducted *P* wave inversions with these AAF corrections for the calibration events, their resulted mechanisms agree with those determined at 0.5–2 Hz solutions. A few examples of the resultant waveform fits are given in Figure 6. Note the nodal behavior of the few stations, such as NBS, HEC, BEL, BLA, RVR, and SVD. This preliminary study suggests that the P-wave radiation pattern is still preserved for a large number of stations at 2–8 Hz. As the AAFs for these stations are calibrated, they can be used for studying source mechanisms of magnitude 1 events. Thus, these small events can be used to study the directivity of events $2.5 < M_w < 3.5$ using the same procedure given by Eq. (4). Note at these frequencies, we can study small explosions.

4. Rupture Directivity and Cluster Analysis

Most large events (M > 3.5) show considerable rupture directivity in terms of source duration variation with azimuth. Here we will take the magnitude 2 events as empirical Green's functions (EGFs) to investigate the rupture processes of the 7 larger strike-slip events ($M_w > 3.5$) from the Big Bear sequence. Rather than deconvolution (e.g., McGuire, 2004) or estimating finite-moment tensors (FMTs), we propose an alternative approach of forward modeling to retrieve the relative source-time function (RSTFs). Let d(t) and g(t) be the records from a large event ($M_w > 3.5$) and the associated EGF event at the same station, which can be related by the relative source time function, RSTF(t) of the large event as:

$$d(t) = g(t) * RSTF(t). \tag{3}$$

Assuming a simple trapezoidal shape of RSTF(t) according to the 1D Haskell model (Haskell, 1964), where a RSTF(t) can be parameterized as the convolution of two boxcars, featuring the rise time τ_1 and the rupture time τ_2, we can solve for the *RSTF*(*t*) in a grid search manner by minimizing the misfit defined as

$$\begin{aligned} &e = \left\| d(t) - \Delta M_0 g(t) * RSTF(t) \right\|, \\ &where\ RSTF(t) = \tau_1(t) * \tau_2(t). \end{aligned} \tag{4}$$

Here the parallels denote the L_2 norm. ΔM_0 is an amplitude scaling factor to account for the two events' known difference in size and radiation patterns. We first use the event 13937492 to illustrate the whole process, which is also the smallest ($M_w \sim 3.5$) among our analyzed events (Figure 7).

5. Site Characterization

Thus, it appears that the greatest barrier to modeling at short periods (< 2 s) or wavelengths less than 10 km is simply the scattering produced by the surface. This is no surprise to those researchers working with down-hole arrays, but it is surprising how well simple calibration works to correct for some of these complicated features. Although not discussed here, one of the greatest advantages of working with wavelengths less than a few km is that directivity effects are relatively obvious as displayed earlier. While the AAFs themselves are back-azimuth and distance-dependent, their ratios between the vertical and radial components appear constant and are possibly simple functions of site conditions

(Figure 8). Note the clustering of the *AAF(v)/AAF(r)* ratios at the various stations from events at different locations. There is also good correlation between the *AAF(v)/AAF(r)* ratios and the surface geology; the relationship between this ratio and the site condition will be pursued as more measurements are made.

RECOMMENDATIONS

In summary, we are adjusting our research efforts to address one of the primary issues facing the Air Force Technical Applications Center (AFTAC)monitoring community, namely, discrimination at high frequency (HF) and yield estimation of small explosions. Since these events are P-wave rich, we have extended our regional modeling efforts to 8 Hz where the surface conditions at the recording station play a key role. To achieve this, we rely on empirical corrections of 1D Green's functions stepping downward in magnitudes as the fault-dimensions become shorter and shorter, avoiding rupture properties, i.e., 4's are used to study 3's, 3's to study 2's, etc. This hybrid approach now appears to work for CAP (shifts only), CAP+ (corrected for amplitude, 2 to 0.5 Hz), and CAP++ (corrected for 2 to 8 Hz). These corrections are path-dependent and rely on earthquakes for calibration although the shifts can probably be obtained from tomography and site conditions from topography images. The next step is to apply these methods to explosions, including Nevada Test Site explosions, and compare with other methods, Coda magnitudes, etc.

REFERENCES

Hartzell, S. H. (1978). Earthquake aftershocks as Green's functions, *Geophys Res. Lett.* 5: 1–4.

Haskell, N. A. (1964). Total energy and energy spectra density of elastic waves from propagating faults, *Bull. Seismol. Soc. Am.* 54: 1811–1841.

Helmberger, D. V. and J. E. Vidale (1988). Modeling strong motions produced by earthquakes with 2D numerical codes, *Seismol. Soc. Am. Bull.* 78: 109–121.

Helmberger, D. V., X. J. Song, and L. Zhu (2001). Crustal complexity from regional waveform tomography: Aftershocks of the 1992 Landers earthquake, California, *J. Geophys. Res.* 106: 609–620.

Lin, G. and Peter Shearer (2007). Estimating local V_p/V_s ratios within similar earthquake clusters, *Bull. Seismol. Soc. Am*. 97: 379–388.

McGuire, J. J. (2004). Estimating finite source properties of small earthquake ruptures, *Bull. Seismol. Soc. Am*. 94: 377–393.

Rodgers, A. J., W. Walter, R. Mellors, A. M. S. Al-Amri, and Y.-S.Zhang (1999). Lithospheric structure of the Arabian Shield and Platform from complete regional waveform modeling and surface wave group velocities, *Geophys. J. Int.* 138: 871–78.

Saikia, C. K. (1994). Modified frequency-wavenumber algorithm for regional seismograms using Filon's quadrature-modeling of Lg waves in North America, *Geophys. J. Int*. 118: 142–158.

Savage, B. and D. V. Helmberger (2004). Site response from incident *Pnl* waves, *Bull. Seismol. Soc. Am.* 94: 357–362.

Song, Xi J., D. V. Helmberger, and L. Zhao (1996). Broad-band modeling of regional seismograms: The basin and range crustal structure, *Geophys. J. Int.* 125: 15–19.

Song, Xi J. and D. V. Helmberger (1998). Pseudo Green's functions and waveform tomography, *Bull. Seismol. Soc. Am.* 88: 304–312.

Tan, Ying (2006). Broadband waveform modeling over a dense seismic network, Ph.D. thesis, California Institute of Technology, Pasadena, California.

Tan, Ying, L. Zhu, D. V. Helmberger, and C. Saikia (2006). Locating and modeling regional earthquakes with two stations, *J. Geophys. Res.* 111: 306–320.

Tan, Ying and D. V. Helmberger (2007). A new method for determining small earthquake source parameters using short-period P waves, *Bull. Seismol. Soc. Am.* (in press).

Tan, Ying and D. V. Helmberger (2007). Rupture directivity of the 2003 Big Bear aftershocks, *Bull. Seismol. Soc. Am.* (in press).

Zhu, Lupei and D. V. Helmberger (1996). Advancement in Source Estimation Techniques Using Broadband Regional Seismograms, *Bull. Seismol. Soc. Am.* 86**:** 1634–1641.

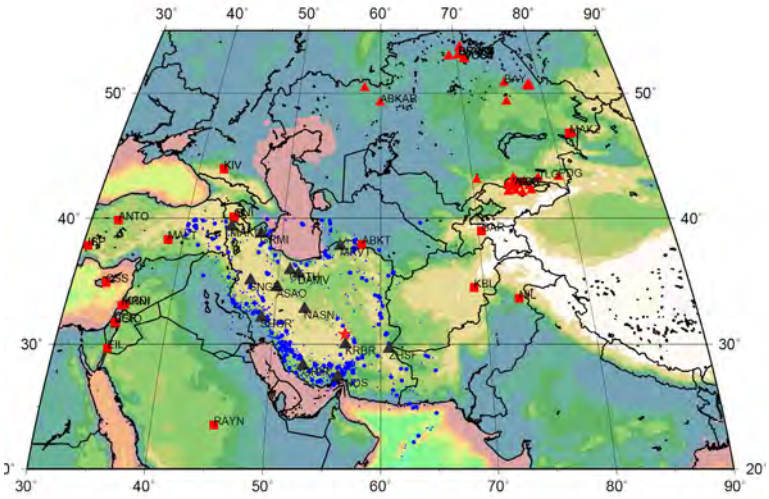

Figure 1. GSN (red square), KZ and KN (red triangles) and IIEES (black triangles) stations in and around Iran. Blue dots indicate earthquakes from the National earthquake Information Center (NEIC) catalog (big dots: earthquake > M5, small dots: < M5). The red star is the 060507 event modeled with the CAP algorithm for IIEES stations.

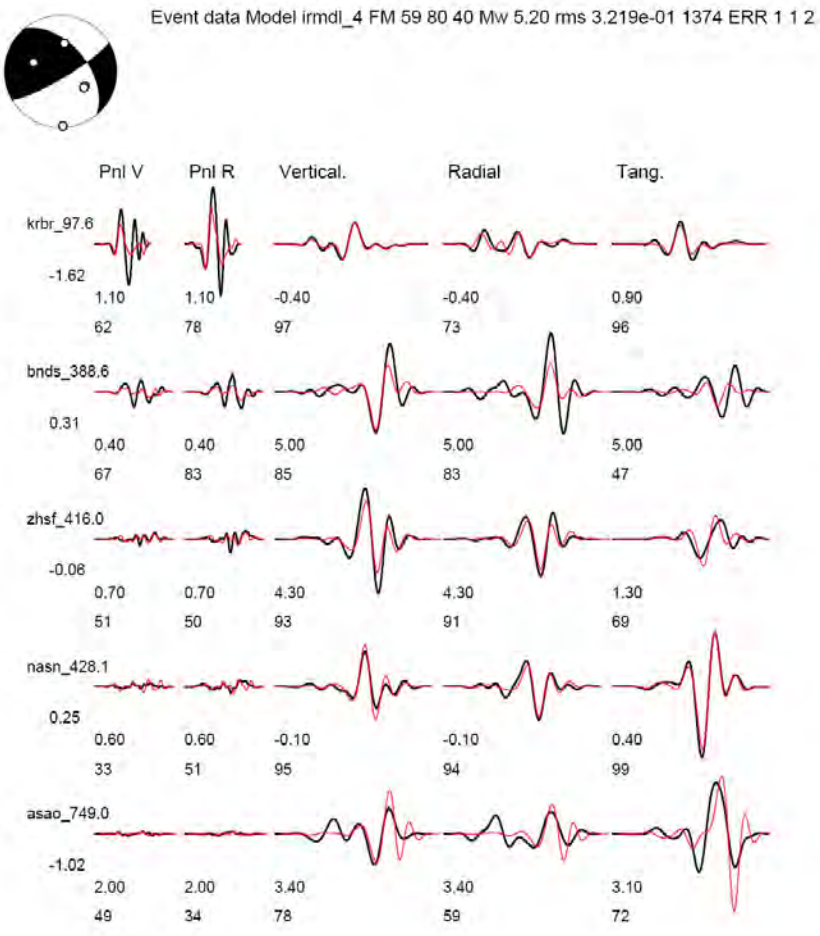

Figure 2. Application of CAP to the modeling of the 060507 event. This earthquake features a mostly strike-slip mechanism with some normal component. The focal depth is estimated to be around 4 km, as compared to 14 km from the IIEES catalog. The closest station is 90 km away, so depth ca not be well resolved just from first arrivals.

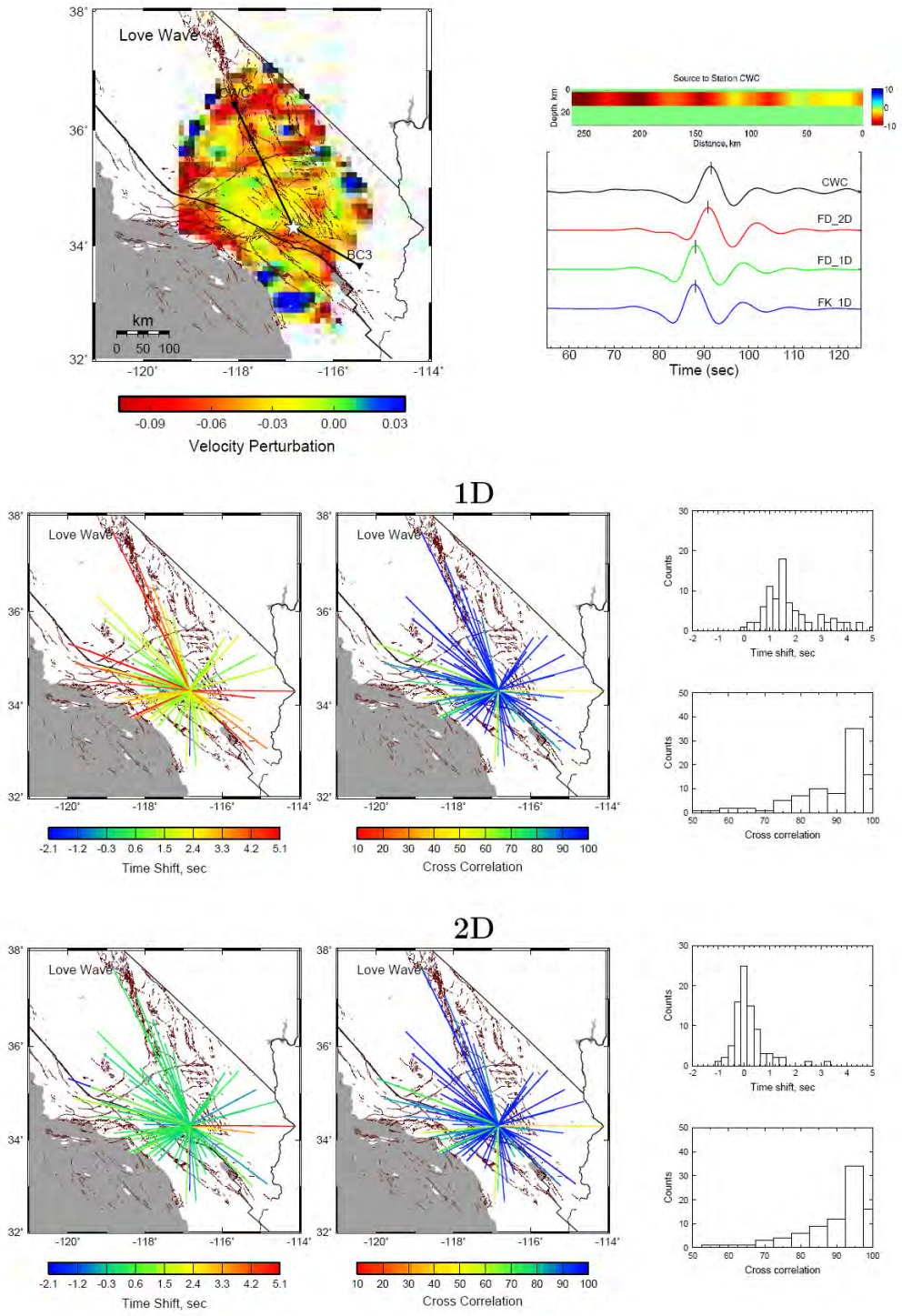

Figure 3. The top panel displays the Love wave phase velocity perturbation in southern California with a selected source (star)-receiver (triangle) path, along which the 2D cross section is shown and the synthetics are compared against the data on the right. The lower panel summarizes the comparison between 1D and 2D synthetics against the observed Love waves for a Big Bear event.

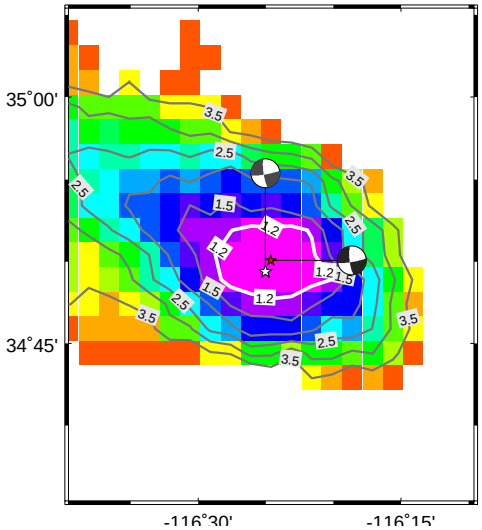

Figure 4. Grid-search results of source parameters for two southern California events using the two stations GSC and PAS. The top panel displays the source-receiver geometry, and the lower panel displays the results. The white stars denote the best solution with the 1.2 contour for the location uncertainty estimates. Also included for comparison are the locations from Lin and Shearer (2007) (red stars) and the mechanisms from the whole TriNet array (Tan, 2006).

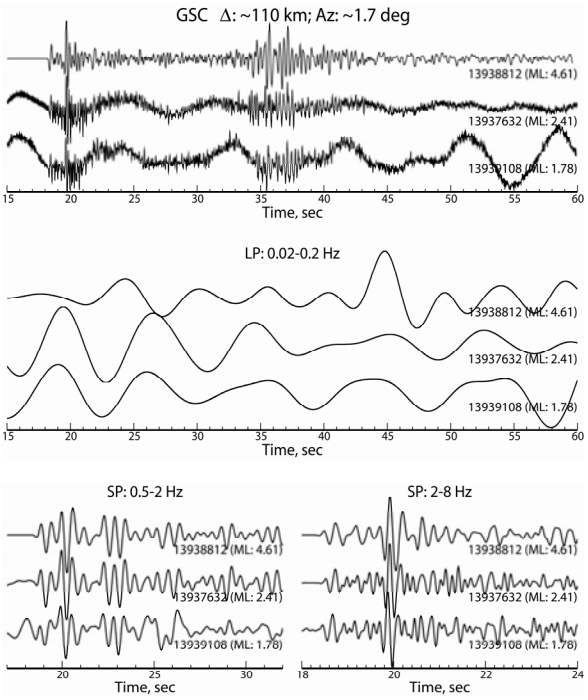

Figure 5. Comparison of the GSC records of three clustered, but different-sized events from the 2003 Big Bear sequences. The original broadband and filtered records of different frequency bands (0.02–0.2 Hz, 0.5–2 Hz, 2–8 Hz) are displayed from top to bottom. The short period comparisons are concentrated on the P-wave trains.

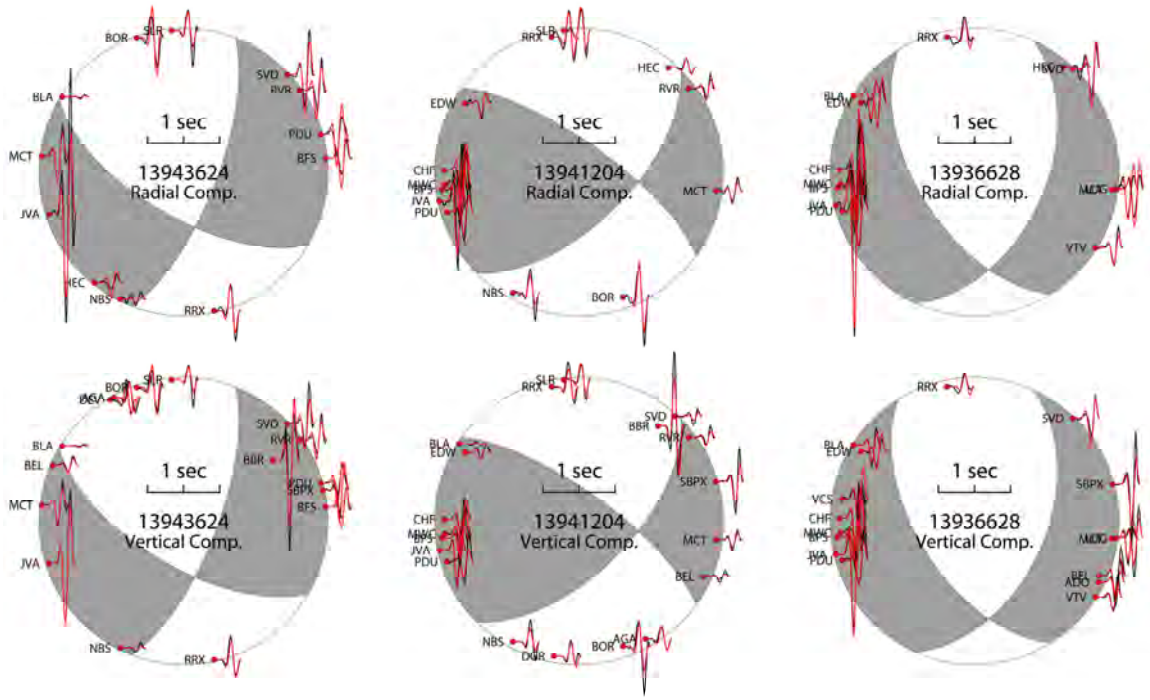

Figure 6. Comparison of the P-wave waveform fits from the 2–8 Hz short-period inversions for three events with different mechanisms.

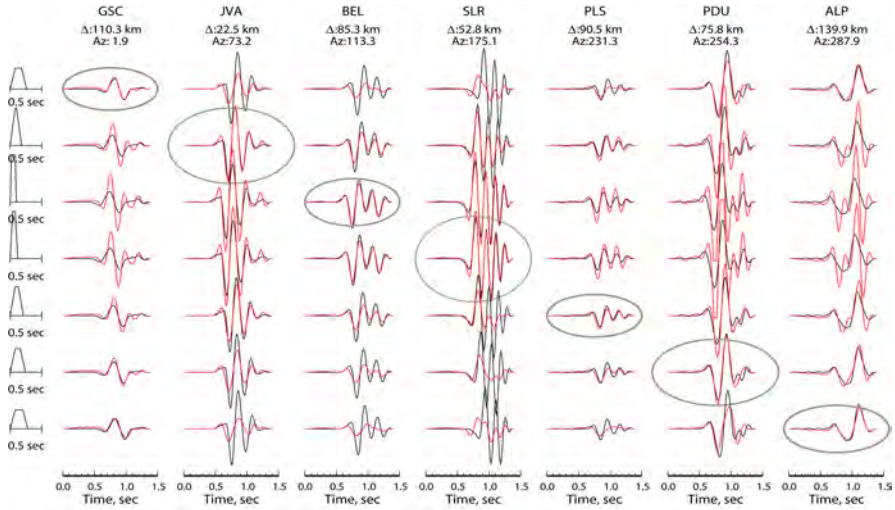

Figure 7a

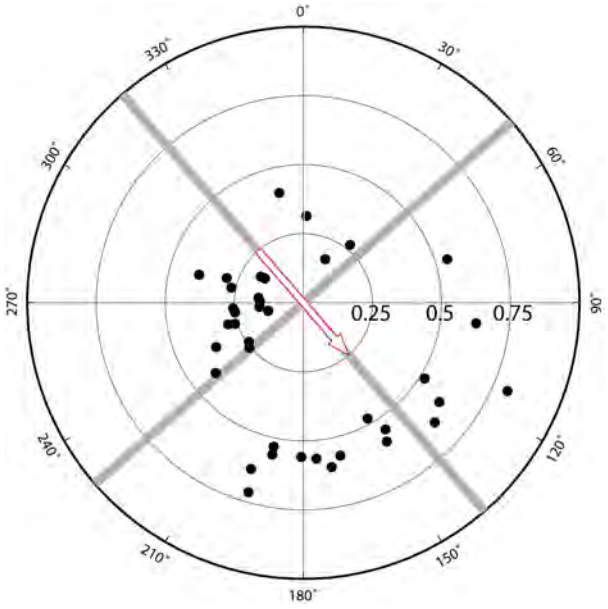

Figure 7b

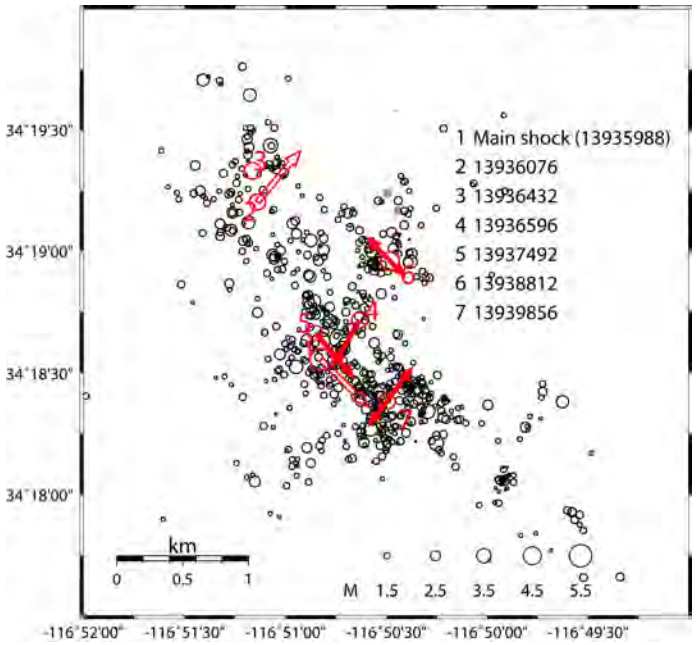

Figure 7c

Figure 7. (a) The selected waveform fits (vertical P-waves) between the records from event 13937492 (black) and the "synthetics"(red) constructed with EGFs from event 13937632. The RSTFs are given to the left. Plotted are the absolute amplitudes, except that a scaling factor of 1/4, 1/2 and 2 has been applied to the stations JVA, PDU, and PLS, respectively, for the display purposes. The obtained best RSTFs for the stations are circled. Note the apparent azimuthal pattern of the RSTFs.
(b).The vertical *P* wave amplitude ratios between the event 13937492 (*M* ~ 3.5) and 13937632 (*M* ~ 2.5). The two events have similar strike slip focal mechanisms. The two gray lines display the strikes of their fault planes. Note the amplitude ratios for the southeastern stations are consistently larger than those for the northwestern stations, due to the rupture directivity effect of the bigger event.
(c) The inferred rupture directivities from the Big Bear cluster. The arrows point to the rupture directions, while their lengths (for the solid ones) indicate the fault lengths. Note that the ruptured planes correlate well with the seismicity lineations, suggesting cross-over faults at depth.

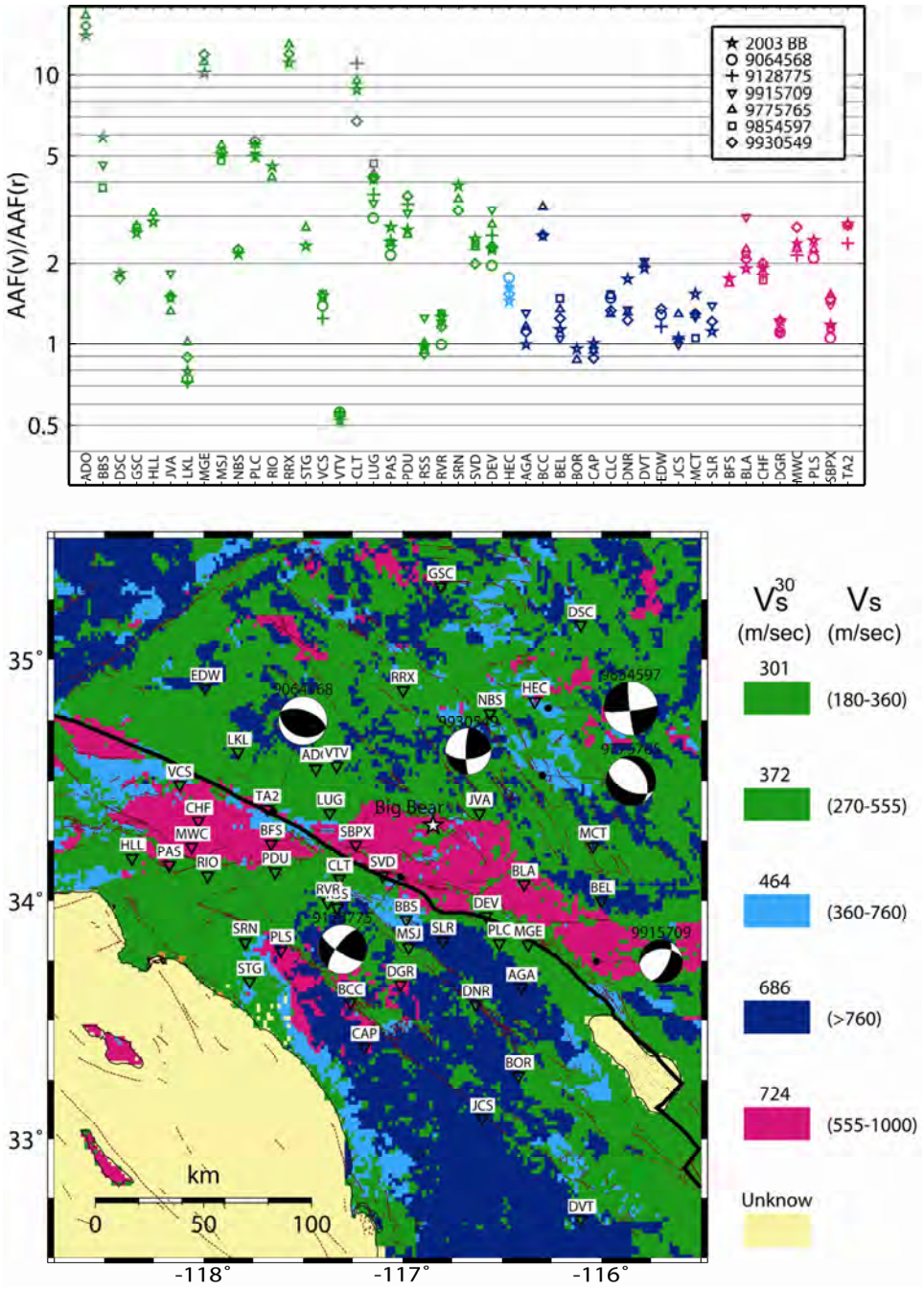

Figure 8. (top) The comparison of the ratios between the AAFs for the vertical and radial components from six events vs. those from the 2003 Big Bear sequence. The stations are grouped and color-coded according to their site-conditions as shown in the bottom. (bottom) The source parameters of the events for comparison (from Tan (2006)) and the station locations are displayed on a geologically-determined site-condition map from Wills et al. (2000). Labeled is the representative V_s^{30} of the top 30 m for each category, and the expected range of V_s.

IMPROVEMENTS TO A MAJOR DIGITAL ARCHIVE OF SEISMIC WAVEFORMS FROM NUCLEAR EXPLOSIONS: BOROVOYE SEISMOGRAM ARCHIVE

Won-Young Kim[1], Howard J. Patton[2], George E. Randall[2], and Paul G. Richards[1]

Lamont-Doherty Earth Observatory of Columbia University[1] and Los Alamos National Laboratory[2]

Sponsored by Air Force Research Laboratory

Contract No. FA8718-07-C-0004

ABSTRACT

We have just started a three-year project to generate in modern form an easily usable archive of digital seismograms derived from regional waveforms recorded at the Borovoye Observatory (BRV), northern Kazakhstan, over a 30-year period going back to 1966 and spanning the time when state-of-the-art sensors and dataloggers were introduced at this site by several different western groups. The BRV seismograms, which include multi-channel regional signals from more than 300 underground nuclear explosions carried out in Eurasia, were made generally available to western scientists in 2001, but only as copies of the bits in the original digital waveforms. These copies contain large numbers of glitches and did not include instrument responses for approximately two-thirds of the events.

Since 2001, scientists at Los Alamos National laboratory (LANL) have processed the BRV regional signals for approximately one third of the events, mainly those for which instrument responses were available. Because many different and important uses of the Borovoye archive have been made in recent years, we are completing the work of improving the archive to modern standards, as well as this may be achieved. Our project is a joint effort by scientists at Lamont-Doherty Earth Observatory of Columbia University (LDEO) and LANL.

The LANL team has deglitched waveform data recorded by the STsR-TSG system, because it was the best system, and a preliminary instrument response for this system has been available. There appear to be at least two sources of glitches, the most easily explained and corrected for being time marks. More difficult and time consuming are glitches representing bit failures either in the original data stream or in the long term deterioration of the archive. A script-driven SAC macro featuring semi-automatic glitch removal coupled with visualization for quality control was developed at LANL by Dr. W. Scott Phillips. The automatic glitch recognition and removal utilizes seismogram differentiation and localized polynomial fitting with L1 linear programming to remove the glitch and interpolate through it with high fidelity on either side of the glitch. This phase of the processing is activated on successive passes with the user specifying an amplitude threshold for the glitch recognition software on each pass. This allows each successive pass to uncover glitches with smaller and smaller amplitudes. This de-glitcher is robust and has been successfully run on even heavily contaminated signals.

The instrument response of the 24-channel STsR-TSG system may further be calibrated by using waveform data from both the STsR-TSG system and modern broadband seismographs deployed during 1994–1996. The BRV archive contains waveform data from the STsR-TSG system up to 1996, which include four French underground nuclear explosions (UNE) from Mururoa and Fangataufa conducted in 1995–1996, and two UNEs from the Lop Nor Chinese test site (10/07/1994 and 05/15/1995. In July 1994, Won-Young Kim (LDEO) deployed a modern broadband seismometer (STS-2 with T_0 = 120 sec) and a 24-bit A/D datalogger at the same seismic pier with the STsR-TSG system, for the purpose of calibrating waveform data from those systems at a later date.

The earlier STsR-SS system consists of a 3-component short-period seismometer SKM (T_0 = 2 s) and 3-component long-period seismometer SKD (T_0 = 25 s). The STsR-SS system formally operated during 02/14/1973 - 03/29/1991 and produced on-scale seismic records from many strong earthquakes and large UNEs from the Semipalatinsk test site, because the STsR-SS system long- and short-period channels are recorded with very low gain (0.5 - 5 counts/μm for SKD; 200 to 2000 counts/μm for SKM)). We have begun to determine accurate STsR-SS system responses and we are calibrating the instrument gains for each event, because many events during 1973–1991 have waveform data recorded both on STsR-TSG and STsR-SS systems.

OBJECTIVES

We propose to generate in modern form an easily usable archive of digital seismograms derived from regional waveforms recorded at the BRV, northern Kazakstan, over a 30-year period going back to 1966 and spanning the time when state-of-the-art sensors and dataloggers were introduced at this site in the summer of 1994. Specifically, we propose to process 1200 to 1400 digital waveforms from the Borovoye archive, for more than 200 underground nuclear explosions in Eurasia for which digital records are available but not yet in useful form due to problems with glitches and instrument calibration that have not yet been taken into account.

RESEARCH ACCOMPLISHED

Preliminary Work at LANL on Deglitching the Borovoye Archive

The extensive glitching of waveforms in the Borovoye Archive makes it impossible to fully utilize this data resource. Time-domain filtering, three-component processing, spectral analysis, etc., are all seriously impacted by the presence of glitches occurring throughout the time series. Researchers at LANL recognized the limitations these glitches posed for most data analysis a few years ago, and began a project to deglitch a portion of the Archive that was deemed of highest immediate value to the research programs at LANL: the data recorded on the STsR-TSG system for which instrument responses had been determined (Kim and Ekström, 1996).

Raw waveforms of the Borovoye Archive are contaminated with glitches on all seismometer channels and their different gain levels, for the entire time period that data are available. Figure 1 shows examples from the KSVM, low-gain system in the 1984–1985 time frame. The extent of visible glitching can be seen to vary greatly in these examples. Many glitches are not visible to the naked eye on the vertical scale of these plots, so the problem is more extensive than it may appear from just plotting the seismogram trace.

There appear to be at least two sources of glitches. The most easily corrected and explained are time marks characterized by a distinct period and the largest amplitude glitches. There are some waveforms for which the time-mark glitch is the primary problem.

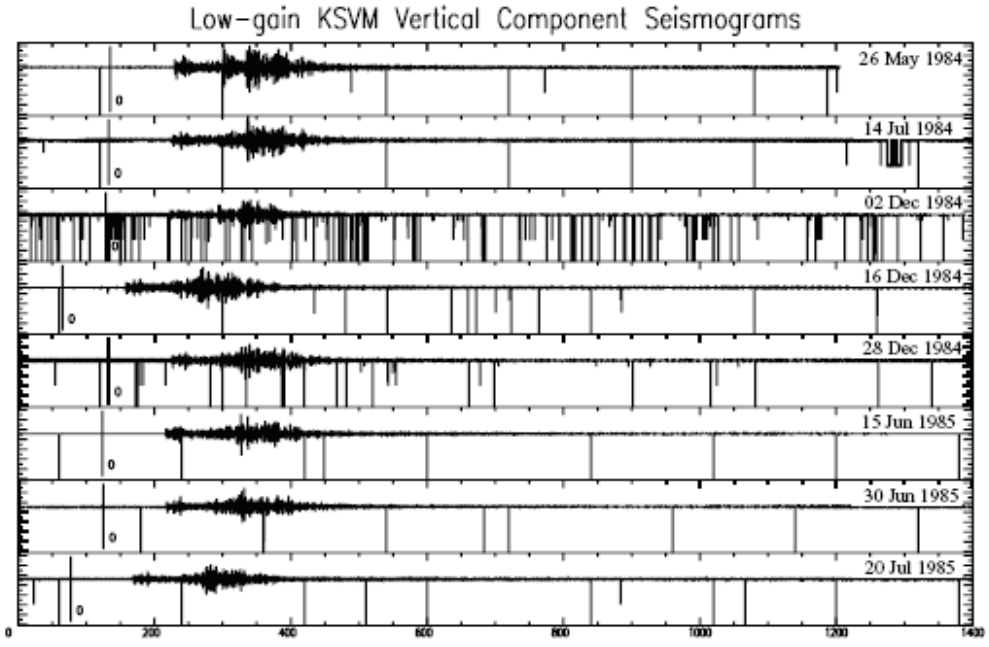

Figure 1. Example BRV archive seismograms (KSVM channel – low-gain) with various levels of glitches.

The more difficult and time consuming glitches appear in some cases to be bit errors. During interactive passes over problematic waveforms, we have found many glitches where the difference between the glitch and the apparent waveform is either a power of 2 (e.g., 16, 32, 64, 128 ...) or a sum of powers of 2 (e.g., 48 = 16 + 32, 96 = 32 + 64, 80 = 16 + 64, ...) which represent bit failures either in the original data stream or in the long-term deterioration of the archive. Many of these small bit errors are readily found by the deglitcher that will be discussed below. While the repair process is at best semi-automatic, the opportunity for restoring this unique historical digital waveform archive of Soviet-era and Chinese tests is now at hand with the availability of reliable deglitching software, albeit the labor to do so is tedious and time consuming.

The deglitching project at LANL led to the development of a processing code by Dr. W. Scott Phillips for removing glitches on successive passes over the seismogram. This code is a script-driven seismic analysis code (SAC) macro featuring semi-automatic glitch removal capabilities coupled with visualization of the deglitching for quality control purposes. This macro and attending Fortran codes are far more sophisticated than the glitch-removal command in SAC. The automatic glitch recognition and removal phase utilizes a process of seismogram differentiation and localized polynomial fitting with L1 linear programming software to remove the glitch, interpolate through it, and return the seismogram with high fidelity on either side of the glitch. This phase of the processing is activated on successive passes with the user specifying an amplitude threshold for the glitch recognition software on each pass. This allows each successive pass to uncover glitches with smaller and smaller amplitudes. An example where this deglitching software was applied to the most seriously contaminated seismogram in Figure 1 is shown in Figure 2.

LANL's emphasis has been to deglitch the STsR–TSG data with available response information. Far less deglitching of the older KOD and STsR-SS data has been carried out due to its limited utility without sensor response information to correct the data to reflect accurate ground motion. Scott Phillips developed the deglitching process and codes for his work on regional coda wave magnitudes. George Randall has applied the deglitcher to data for a regional discrimination study and Howard Patton to data for a regional *Ms* study. Multiple gain channels were processed in many cases to extend the dynamic range of the recovered data. High-gain channels are frequently

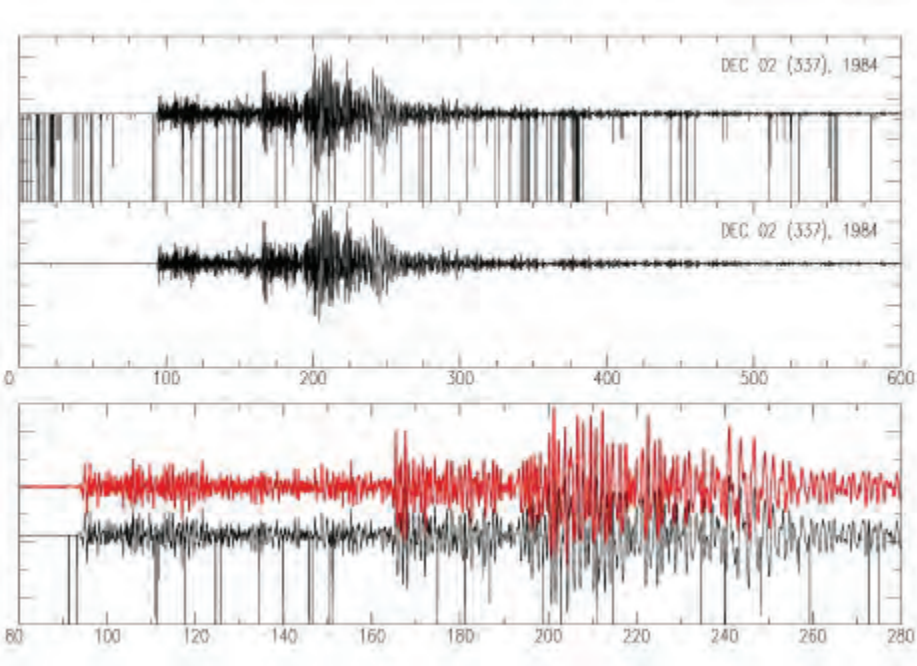

Figure 2. Plots show the raw time series, and after deglitching, for 10 minutes of data, including a long segment of coda waves. The lower plot is an enlargement of 200 s of data, centered on the main signal. The deglitched waveform is plotted in red.

clipped, but provide useful coda information and can be picked for the first arriving *P* phase. Low-gain channels frequently provide useful data when high-gain channels are clipped but are composed of largely quantization noise in lower amplitude segments of the seismograms. The deglitched waveforms have been entered into the LANL Research database, and delivered to the NNSA Knowledge Base along with the research results for discrimination, regional *Ms*, and regional coda wave magnitude studies.

Simulation of Broadband Spectra

LANL researchers have also experimented with constructing broadband Rayleigh wave amplitude spectra using waveforms off the low-gain KSVM channel and the longer period DS channel. An example of the corrected records is shown in Figure 3. Low-frequency (~0.3 Hz) *Rg* waves are commonly recorded on the vertical component KSVM channel for many Balapan explosions, and this Figure shows an example for the last nuclear test conducted at the Semipalatinsk test site on 19 October 1989. Surface waves are well recorded on the DS channel for this event. The lower plot shows spectra obtained for the time windows indicated on the seismograms, where the amplitudes have been corrected in the frequency domain for the instrument responses of the KSVM and DS systems. The shapes of these responses are plotted with the data, a step made possible because the instrument responses for the TSG system have been worked out and these responses are included with the current CSS3.0 formatted data. The instrument-corrected KSVM spectrum for Rayleigh waves (red) shows good agreement with the corrected DS spectrum (black) out to almost 0.2 Hz. The DS spectrum is suspect for frequencies above 0.5 Hz due to unusual response behavior. In any case, the broadband spectrum (green) was constructed by suturing the two channels in the 0.4-0.6 Hz range. This procedure has been carried out on most Balapan explosions occurring in the 1987–89 time frame, and all show extremely rapid amplitude fall-off for frequencies above 0.5 Hz. A goal of this proposed work is to construct broadband waveforms using better instrument response information to combine data channels.

Table 1. Characteristics of STsR-SS System in Borovoye Waveform Archive

System name	Seismometer	Channel type	Ts[(1)] (sec)	Ds[(2)]	Sm[(3)] (ct/μm)	fn[(4)] (Hz)	dt[(5)] (msec)	Channel number
STsR-SS 02/14/73-03/29/91[(7)]	SKM-3 (76-80)	HG[(6)]	2	0.5	2000	1.8	24	7,8, 9
					1000	1.8	32	7,8,9
		LG(Z)			200	1.8	32	1
	SKD	HG	25	0.71	5	0.14	192	2,3,4
		LG			0.5	0.14	192	1,5,10

[(1)] Ts = Seismometer natural period in seconds. [(2)] Ds = Seismometer damping constant, critical damping= 0.71. [(3)] Sm = Nominal sensitivity (gain) in counts/micron [ct/μm] for ground displacement. [(4)] fn = Normalization frequency where nominal sensitivity is measured. [(5)] dt = Sampling interval in milliseconds. [(6)] HG is actually the base channel and not necessarily a high-gain; LG =low-gain channels and (Z) indicates that it is only vertical component. [(7)] These date are the formal period of operation of the systems by Russian Institute for the Dynamics of the Geospheres, Moscow, Russia. However, notice that the BRV waveform archive contains waveform data from TSG system up to 1996.

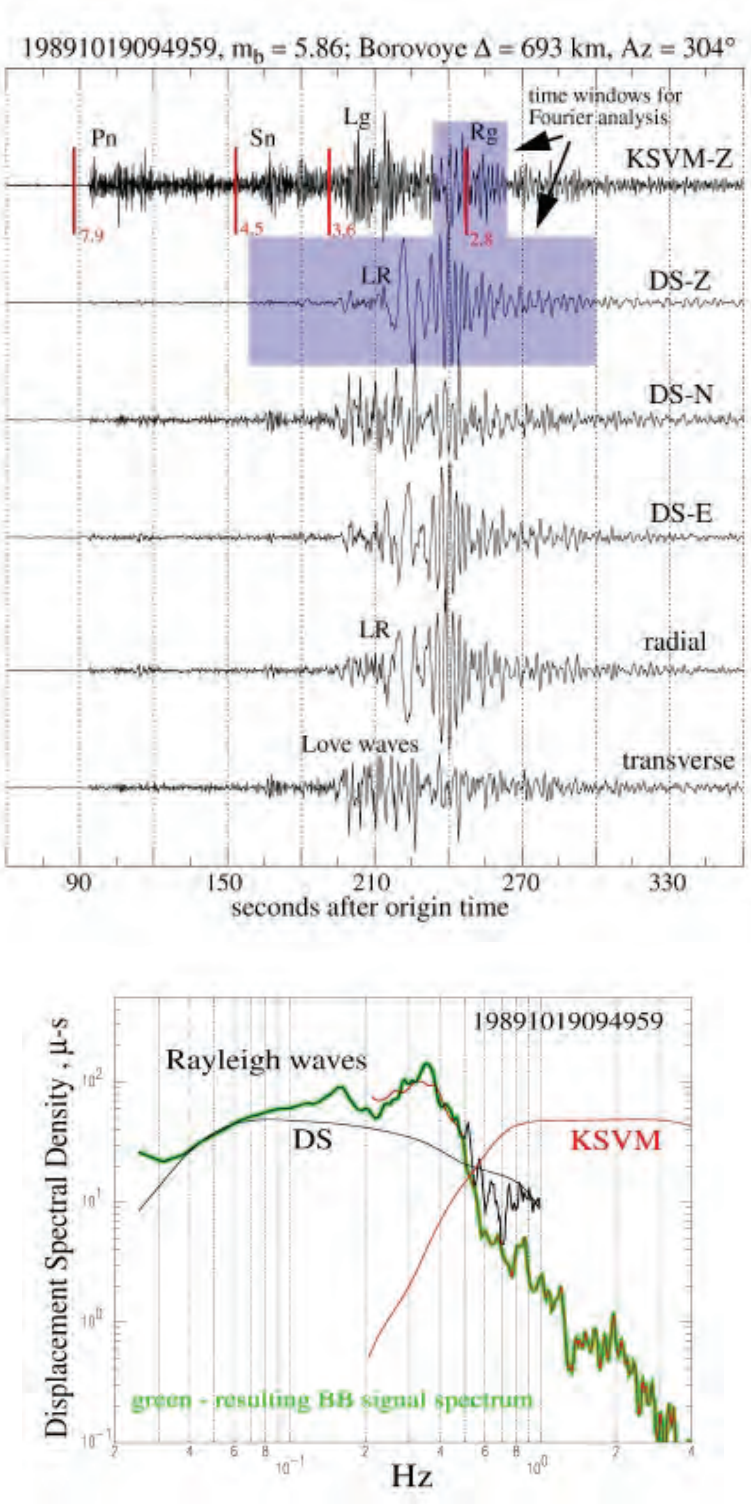

Figure 3. Top: BRV seismograms, after processing. Bottom: corresponding spectra.

Preliminary Determination of STsR–SS System Response

The STsR-SS system consists of 3-component short-period seismometer SKM (T_0=2 s) and 3-component long-period seismometer SKD (T_0 = 25 s)(see Figure 4). The SS system formally operated during the period 14 February 1973 to 29 March 1991, and UNE data in the BRV explosion archive covers the period from 6 June 1973 (an NTS explosion) to 16 August 1990 (Lop Nor test site). The SS system produced 10 channel digital seismogram data with 3-component short- and long-period waveform data, and a low-gain short-period vertical-component, plus an additional combination of long- and short-period channels to fill the sequential digitization process. Hence, the sampling intervals are designed as integer multiples of each channel. Short-period channels are sampled at 32 milliseconds (msec), and long–period channels are sampled with 192 msec intervals. Although the SS system has been operated together with STsR–TSG system, the accurate instrument response of short- and long-period seismographs of the SS system have not yet been determined, mainly due to lack of reliable calibration pulses. Hence, we will determine accurate instrument responses of the SS system by comparing the waveform data from SS system that are also recorded on TSG system. As indicated by the characteristics shown in Table 1, the SS system has produced many on–scale waveforms due to its low gain channels.

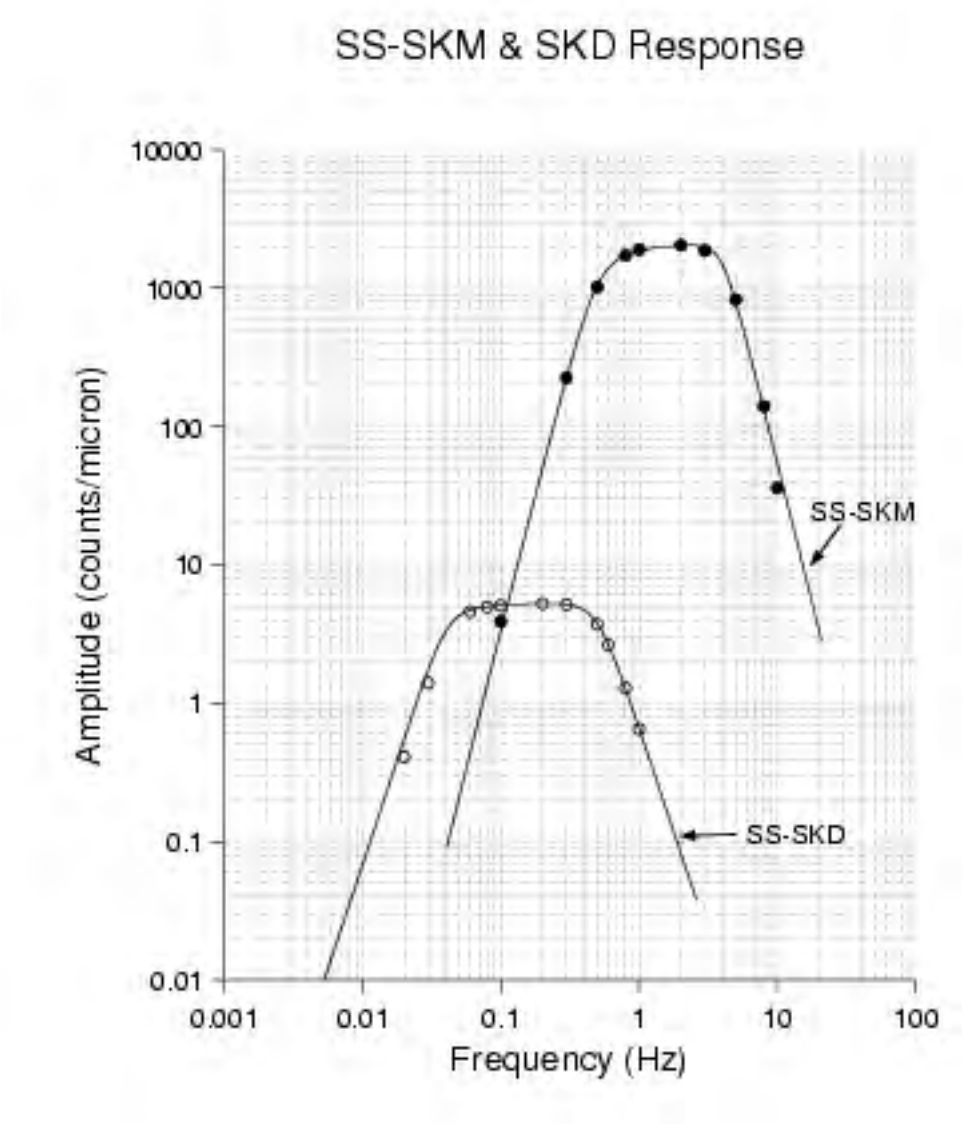

Figure 4. A preliminary, nominal displacement spectral amplitude response of the STsR–SS short–period (SKM) and long–period seismographs (SKD).

Regional Spectra and Spectral Ratios for the Lop Nor Test Site

China carried out nuclear tests at the Lop Nor test site in western China beginning in 1964. From 1969 to 1996, 22 underground nuclear tests (UNTs) are known to have been conducted at this site. The Borovoye archive has waveform data from 11 UNTs as listed in Table 2. Three additional Lop Nor UNTs were recorded by a modern broadband seismographic system deployed in Kazakstan by Won-Young Kim from Lamont in the summer of 1994. Kim encouraged the Borovoye staff to continue operating the ailing TSG system so that we would have seismic data from the TSG system that can be calibrated against the modern, high-dynamic range broadband system. Hence, we have two latest Lop Nor UNTs recorded both by the TSG and the modern (STS–2 seismometer and datalogger with a 24-bit A/D) broadband system, as well as the three UNTs with only broadband recording, providing a unique data set. UNTs at Lop Nor are clustered into two groups; according to the topography and geology, UNTs in subregion A are in vertical shafts, while UNTs in subregion B are detonated in horizontal tunnels (Waldhauser et al., 2004).

The BRV archive include the first known underground nuclear test at Lop Nor on Sept. 22, 1969. This archive provides the greatest number of seismographic records available at a single site at regional distances (see Table 2). The magnitude of these events ranges from $m_b(P)$ 4.9 to 6.2 and vertical-component records from 12 UNTs are shown in Figure 5. The epicentral distance from the Lop Nor Chinese Test Site to BRV is about 1840-1895 km and records show clear *Sn* and *Lg* waves (Fig. 5), but note that *Sn* and *Lg* waves are less well excited by the smallest event on July 29, 1996 ($m_b(P)$= 4.9). Such observation would be important to verify if the magnitude dependence of *P/S* spectral amplitude ratios reported by Ringdal (1997) applies to events at Lop Nor. We are studying this size-dependence of spectral ratios for Lop Nor explosions.

Table 2. Borovoye data for Chinese Nuclear Tests at Lop Nor Test Site, 1969–1995[(1)]

N	Date Year-Mo-Da	Time (hr:mn:sec)	Lat. (°N)	Long. (°E)	$m_b(P)$	Instrument type[(2)]	Comments
01	1969-09-22	16:15:01.57	41.373	88.352	5.2	KODB	**tunnel**/*P* wave only
02	1976-10-17	05:00:00.82	41.7086	88.3897	4.9	SS	**tunnel**
03	1978-10-14	01:00:00.17	41.5413	88.7545	4.9	SS/TSG	shaft
04	1983-10-06	10:00:00.14	41.5409	88.7283	5.5	SS/TSG	shaft
05	1984-10-03	06:00:00.08	41.5799	88.7246	5.4	SS	shaft
06	1984-12-19	05:59:59.82	41.7081	88.3862	4.7	SS/TSG	**tunnel**
07	1987-06-05	05:00:00.48	41.5558	88.7431	6.2	SS/TSG	shaft
08	1990-08-16	05:00:00.05	41.5274	88.7358	6.2	SS/TSG	shaft
09	1993-10-05	01:59:59.69	41.5957	88.7060	5.9	TSG	shaft
10	1994-10-07	03:26:00.18	41.5735	88.7191	5.9	TSG/BB	shaft
11	1995-05-15	04:06:00.20	41.5513	88.7496	6.1	TSG/BB	shaft
12	1995-08-17	01:00:00.14	41.5412	88.7522	6.1	BB	shaft
13	1996-06-08	02:56:00.06	41.5804	88.6893	5.9	BB	shaft
14	1996-07-29	01:49:00.17	41.7163	88.3748	4.9	BB	**tunnel**

(1) location and origin time from Waldhauser et al. (2004), except the first UNT on Sept. 22, 1969; body–wave magnitude from PDE.

(2) Instrument type= instrument used, KODB= KOD low-gain system; SS=STsR–SS system; TSG=STsR–TSG system; BB = broadband sensor (STS-2 with T_0=120 s) and 24-bit A/D datalogger.

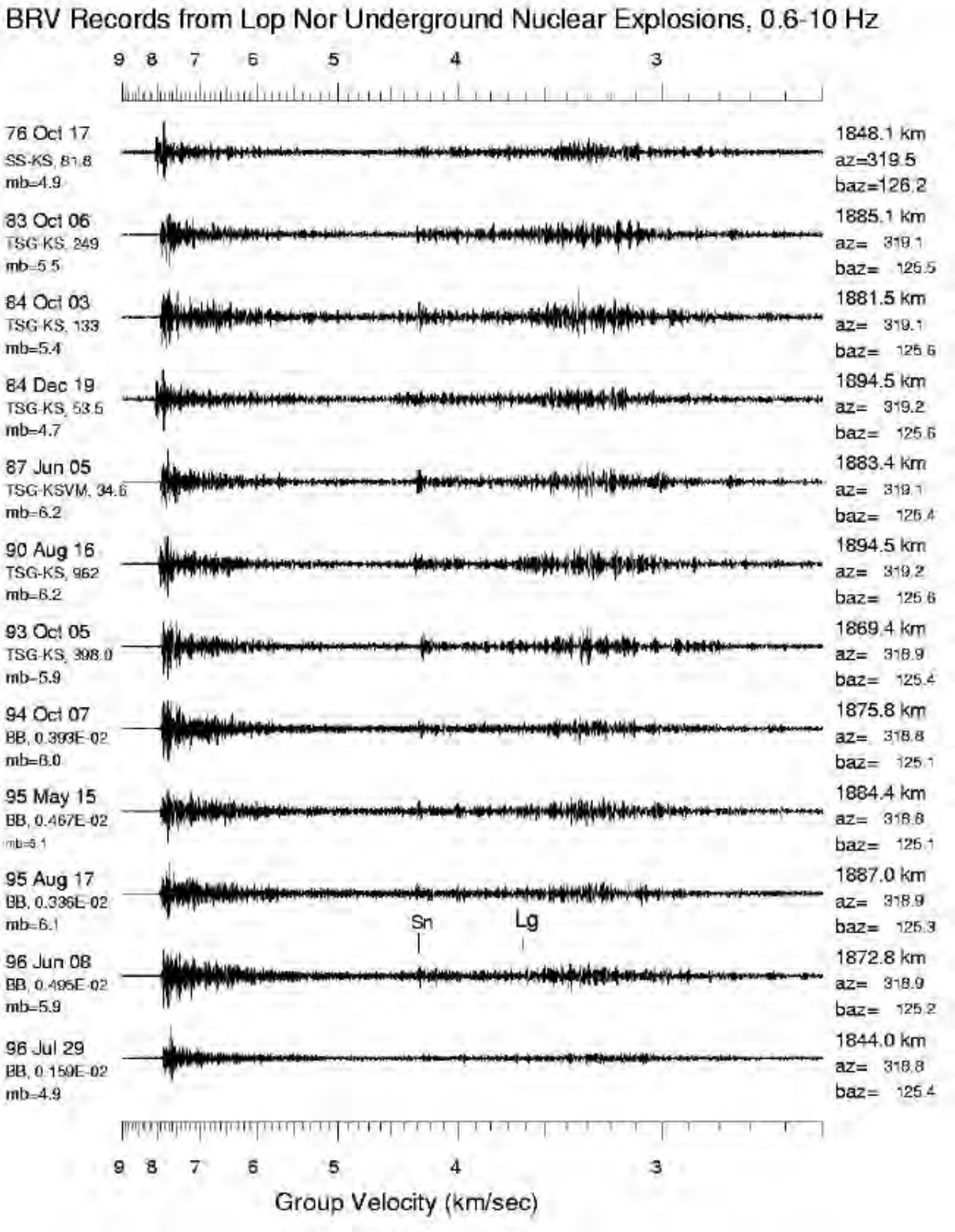

Figure 5. Vertical component records at BRV from 12 underground nuclear tests from Lop Nor. Records are plotted with group velocity in km/sec and event date, instrument used and magnitude are indicated at the beginning of each trace. SS–KS=SS system KS channel, TSG–KS=TSG system KS channel, and BB=new broadband system.

CONCLUSIONS AND RECOMMENDATIONS

Since our project has just begun, we list a number of studies, some of them ongoing within the monitoring community, which are likely to benefit from our project, i.e., an improved BRV waveform archive. The candidate studies are presented as the following questions:

- Can the traditional *mb: Ms* discriminant, long applied to teleseismic signals in which *Ms* is measured from amplitudes of surface waves with period around 20 s, be applied successfully to small seismic events recorded at regional distances, for which the *Ms* measurement is made at a period significantly shorter than 20 s? Practical answers to this question are needed for underground nuclear explosions conducted in (for example) Eurasia, in regions having characteristics very different from the western U.S. where most U.S. testing experience was acquired. Studies of this nature can benefit from the improved BRV archive because for many events it contains short-period and long-period channels.
- How consistently do the regional seismic signals of nuclear explosions exhibit features that are consistently different from the regional signals generated by shallow earthquakes (within the crust), by sub-crustal earthquakes, and by deeper earthquakes? (Note that many earthquake signals are being routinely acquired today by the well-instrumented modem BRVK station.)
- How consistently do the regional seismic signals of nuclear explosions exhibit features that are consistently different from regional signals from mining blasts of various types? (Note that mining blast signals are being routinely acquired today by the well-instrumented modem BRVK station.)

ACKNOWLEDGEMENTS

We thank staff at the Institute for Dynamics of Geosphere, Moscow, Russia led by Drs. Vitaly Adushkin and Vladimir Ovtchinnikov, who copied BRV waveform archive from old 35 mm tapes into modern medium and performed extensive data reformatting work. We also like to thank staff at the Institute of Geophysical Research, National Nuclear Center, Republic of Kazakstan led by Drs. Nadezhda Belyashova and Natalia Mihailova who provided us with ground-truth data on shot hole locations of Semipalatinsk test site.

REFERENCES

Kim, W- Y. and G. Ekström (1996). Instrument responses of digital seismographs at Borovoye, Kazakstan, by inversion of transient calibration pulses. *Bull. Seism. Soc. Am*. 86: 191–203.

Ringdal, F. (1997). Study of low-magnitude seismic events near the Novaya Zemlya nuclear test site, *Bull. Seism. Soc. Am.* 87: 1563–1575.

Waldhauser, F., D. Schaff, P. G. Richards, and W.-Y. Kim (2004). Lop Nor revisited: Underground nuclear explosion locations, 1976-1996, from double-difference analysis of regional and teleseismic data, *Bull. Seism. Soc. Am.* 94: 1879–1889.

DEVELOPMENT OF REGIONAL PHASE TOMOGRAPHIC ATTENUATION MODELS FOR EURASIA

Thorne Lay[1], Xiao-Bi Xie[1], Xiaoning (David) Yang[2], and Marie D. Arrowsmith[2]

University of California, Santa Cruz[1] and Los Alamos National Laboratory[2]

Sponsored by National Nuclear Security Administration
Office of Nonproliferation Research and Development
Office of Defense Nuclear Nonproliferation

Contract No. DE-FC52-05NA26606[1]and DE-AC52-06NA25396[2]

ABSTRACT

We are developing regional-phase (Pn, Pg, Sn, Lg) tomographic attenuation models for Eurasia. The models will be integrated into the National Nuclear Security Administration (NNSA) Knowledge Base and used in the Magnitude and Distance Amplitude Correction (MDAC) station calibration for the development of regional seismic discriminants. Our current focus is on Pn, an extremely important phase in seismic event identification.

Accurately accounting for regional-phase geometric spreading is critical for the development of useful attenuation models. It is particularly important for Pn and Sn waves because the propagation mode of these waves makes them more susceptible to upper mantle velocity structures and the Earth's sphericity, which in turn causes the geometric spreading of Pn (and Sn) to be dependent on frequency as well as on range in a complicated way. We conduct numerical simulations to quantify P_n and S_n geometric spreading in a spherical Earth model with constant mantle velocities. Based on our simulation results, we present new P_n and S_n geometric spreading models in the forms $G(r,f) = [10^{n_3(f)}/r_0](r_0/r)^{n_1(f)\log(r_0/r)+n_2(f)}$ and $n_i(f) = n_{i1}\left[\log(f/f_0)\right]^2 + n_{i2}\log(f/f_0) + n_{i3}$,

where i = 1, 2 or 3. r is epicentral distance; f is frequency; r_0 = 1 km and f_0 = 1 Hz. We derive values of coefficients n_{ij} by fitting the model to computed P_n and S_n amplitudes for a spherical Earth model having a 40-km-thick crust, generic values of P and S velocities and a constant-velocity uppermost mantle.

We apply the new spreading model to observed data in Eurasia to estimate average P_n attenuation, obtaining more reasonable results compared to using the standard power-law model. Our new P_n and S_n geometric-spreading models provide generally applicable reference behavior for spherical Earth models with constant uppermost-mantle velocities. Since our region of interest encompasses most of Eurasia from the Equator to the North Pole, simple regular gridding methods such as dividing the region with latitude and longitude lines would result in cells with drastically different cell sizes for the tomographic inversion. To avoid this problem and to optimize the resolution of the tomographic model based on data distribution, we have implemented several gridding schemes. They include equal-cell-size gridding and variable-cell-size gridding based on certain criteria such as the number of path hits. These gridding schemes will be tested in future tomographic inversions to find an optimum gridding method.

To prepare for the attenuation tomographic inversion, we have been collecting and measuring regional-phase amplitude data from the Incorporated Research Institute for Seismology Data Management Center and from the Los Alamos National Laboratory Ground-Based Nuclear Explosion Monitoring Research and Engineering program database. Initial Pn amplitude measurements exhibit similar decay behavior as what we see in the synthetic data. To improve our data coverage, we are conducting further data collection, phase picking and amplitude measurement.

OBJECTIVE

The objective of this project is to develop 1-Hz, two-dimensional, regional-phase (*Pn*, *Pg*, *Sn* and *Lg*) tomographic attenuation models for Eurasia. The models will be used in MDAC for improved event identification.

RESEARCH ACCOMPLISHED

Pn geometric spreading

Accurately accounting for geometric spreading is critical for the development of meaningful regional-phase attenuation models. This is particularly true for *Pn* and *Sn* waves because the nature of their wave propagation renders them acutely sensitive to upper mantle velocity structure and the Earth's sphericity. Even simple one-dimensional (1D) velocity models can produce geometric spreading of *Pn* and *Sn* that is strongly dependent on frequency and range (e.g., Sereno and Given, 1990). If frequency dependence of the geometric spreading actually occurs and is neglected, the attenuation model will acquire incorrect frequency dependence. Similar arrival times of *Pg* and *Pn* phases and *Pn* and *P* phases at their respective crossover distances result in rapidly changing *P*-wave amplitudes, difficulty in phase isolation and identification, and uncertainty in appropriate specification of the propagation path and geometric spreading at these distances. Lateral variation of Moho topography and upper-mantle lid velocity and fine scale heterogeneity of the lower crust and/or mantle lid further introduce 2D and 3D complexities into *Pn* and *Sn* spreading.

We conduct most of our simulations using the reflectivity method. Results from reflectivity calculations are compared with results calculated with a 2D finite-difference code (Xie and Lay, 1994) and a 2.5D axisymmetric spherical finite-difference code, SHaxi, to confirm that the earth flattening transform (EFT) and layer discretization required by the reflectivity method do not produce numerical artifacts. The reflectivity method generates complete synthetic seismograms within a specified slowness range for 1D, plane-layered velocity models. In order to use the reflectivity method for a spherically symmetric Earth model, we apply the EFT to transform the spherical Earth model to a plane Earth model. Transformations of velocity v and depth z are (Chapman, 1973; Müller, 1977)

$$v_f = \frac{R}{R - z_r} v_r \quad \text{and} \quad z_f = R \ln\left(\frac{R}{R - z_r}\right), \tag{1}$$

where R is the radius of the Earth. Subscript r designates values in the spherical (radially symmetric) model and subscript f designates values in the plane (flat) model. The density ρ transformation is

$$\rho_f = \left(\frac{R}{R - z_r}\right)^m \rho_r, \tag{2}$$

which is not unique since m can take any value between -5 and 1. For regional body-waves, the choice of m is not critical (Müller, 1977). We choose m = -1 for *P*/*SV* simulations (Müller, 1977) and m = -5 for *SH* simulations (Chapman, 1973). We experimented with different values of m and the results were basically unchanged. Finally the transformation of amplitudes calculated from plane-model simulations back to corresponding amplitudes in the spherical model is

$$A_r = \left(\frac{\Delta}{\sin\Delta}\right)^{1/2} \left(\frac{R}{R - Z_r}\right)^{\frac{m+5}{2}} A_f, \tag{3}$$

where Z_r is the depth of the source in the spherical model and Δ is epicentral distance in radians.

We approximate the velocity gradient resulting from the EFT (Equations 1 and 2) with homogeneous layers in the plane Earth model, as is required by the reflectivity method. The thickness of these layers affects the accuracy of the approximation, with thinner layers yielding more accurate results. We set the thickness of these layers to be about 0.4 of the minimum wavelength of the waves to be modeled, which appears to be more than adequate. Further reducing the ratio (e.g., from 0.4 to 0.2 of the minimum wavelength) does not alter the results appreciably. The total thickness of the gradient zone is set to be more than 100 km larger than the maximum penetration depth of the direct wave in a homogeneous spherical model recorded at the longest epicentral distance considered. This thickness guarantees that no P_n or S_n waves observed within the distance range of interest are affected by the lower boundary of the gradient zone. Below the gradient zone, the velocity is constant.

We use the same generic spherical Earth model considered by Sereno and Given (1990) as the base model for our simulations and use the synthetics from the simulation to derive parameters of the P_n and S_n geometric-spreading models that we develop. The reference Earth model consists of a 40-km-thick outer layer, representative of an average continental crust, with a constant-velocity mantle underneath (Figure 1). The model has no anelastic attenuation. The simplicity of this model allows us to isolate the effects of the sphericity on P_n and S_n geometric spreading. We use an isotropic point source for P_n simulations. The source for S_n(*SH*) simulations is a fundamental fault vertical strike-slip source and the source for S_n(*SV*) simulations is a dip-slip source. For all source types in our main calculations, a delta function is used as the source time function; source depth is 15 km and source strength is 10^{15} N m. Three-component synthetic ground displacements are computed at 33 locations distributed log-evenly along a linear profile from 200 km (1.8°) to 2500 km (22.5°). The Nyquist frequency of the seismograms is 20 Hz.

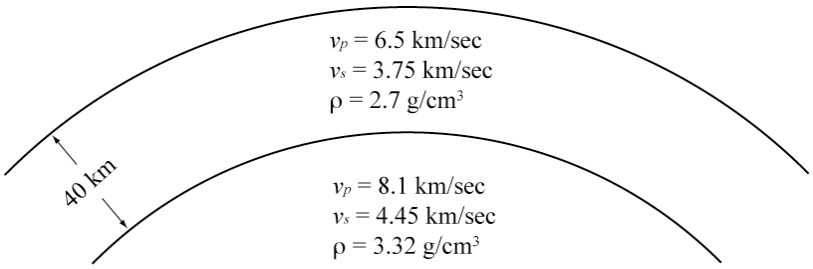

Figure 1. Base Earth model used for P_n and S_n simulations and the development of new P_n and S_n geometric-spreading models. Quality factor Q is infinite throughout the model.

We cut P_n and S_n portions of the synthetic seismograms using fixed-velocity windows. The velocities that we use to define the widths of P_n windows are 7.6 km/sec and 8.2 km/sec and those for S_n windows are 4.0 km/sec and 4.7 km/sec (Hartse, et al., 1997). The windows are centered at the peaks of the phases. We also tested a fixed-window-width method and the results remained essentially the same. We window P_n and S_n(*SV*) from vertical-component seismograms and S_n(*SH*) from transverse-component seismograms. After P_n and S_n seismograms are windowed, we taper the seismograms with small tapers (between 2% to 20% depending on the length of the signal relative to the window length) and Fourier transform the seismograms to obtain the amplitude spectra. We make spectral-amplitude measurements at 100 frequencies log-evenly distributed between 0.75 and 13 Hz. Amplitude at each frequency f_i is calculated by taking the average of the amplitudes between frequencies $f_i/\sqrt{2}$ and $\sqrt{2}\, f_i$.

To accurately assess the geometric spreading of seismic phases, the propagation medium used for the simulation should have no attenuation. However, in order to avoid a computational singularity, the reflectivity method requires a nonzero amount of attenuation for the medium. We take an asymptotic approach similar to that used by Yang (2002) to derive P_n and S_n amplitudes for an elastic model without attenuation from amplitudes calculated for a group of anelastic models. We first make 20 calculations for models that have attenuation quality factor Q log-linearly increasing from 10,000 to 100,000. For each calculation, a single Q is used for both P and S waves and for all parts of the model. Amplitudes at each frequency and each epicentral distance from these calculations are then fit by a quadratic polynomial as a function of 1/Q. The limit of the polynomial as Q approaches infinity is taken as the amplitude at that frequency and distance for the elastic model.

P_n Modeling Results

Figure 2 plots the vertical synthetic P_n seismograms from the base-model simulation at selected epicentral distances. Q used in this simulation is 100,000. The seismograms are low-pass filtered below 10 Hz to suppress numerical noise near the Nyquist frequency. The figure reveals several interesting characteristics of P_n traveling in a spherical Earth model with constant mantle velocities. Due to the sphericity, the apparent P_n velocity is not constant, but varies with epicentral distance. As is predicted by theory (e.g., Červený and Ravindra, 1971), the pulse shape of P_n evolves from that of the impulse source at distances close to the critical distance (about 0.8° for the base model and a 15-km-deep source) to the shape of a far-field body wave, which is the time derivative of the source pulse, at farther distances. The amplitude of the phase changes in a complex manner, first decreasing and then increasing, within this distance range. At about 10° to 12°, the first pulse separates from the rest of the P_n wave packet and somewhere between 16° and 19°, a second pulse separates.

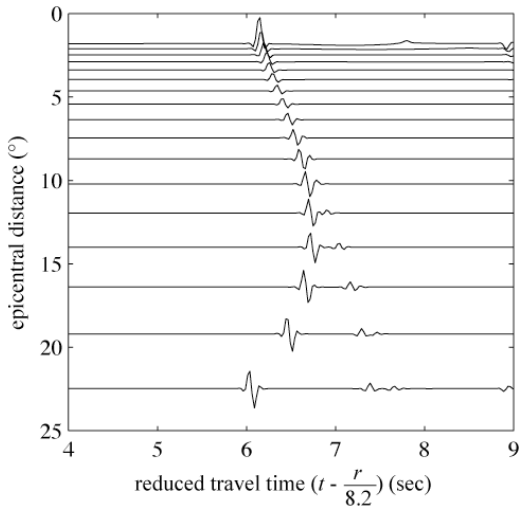

Figure 2. Synthetic P_n seismograms from base-model calculations. The seismograms are filtered below 10 Hz. Travel time is reduced by 8.2 km/sec. Only every other trace calculated is plotted to enhance clarity. *r* is epicentral distance in kilometers.

For high-frequency P_n at distances away from the critical distance, Červený and Ravindra (1971) offer a detailed decription of the signal behavior from ray theory. Although Červený and Ravindra (1971) describe the phenomenon for a plane-layered Earth model with positive and constant velocity gradient in the mantle, their description and conclusions are applicable to the spherical-Earth-model situation as well since the spherical model can be mapped, through the EFT, into a plane-layered model with an approximately constant velocity gradient in the uppermost mantle. Following Červený and Ravindra (1971), the P_n phase at distances between about 5° and 10° in Figure 2 can be thought of as the superposition of individual waves reflected n times (n = 0, 1, 2, …) from the underside of the Moho. The superposed wave is termed interference head waves by Červený and Ravindra (1971) and is likened to the "whispering gallery" phenomenon by Menke and Richards (1980). As distance increases, individual components of the interference head wave start to separate from the wave packet due to their increasingly shorter path lengths compared with path lengths of the remaining waves in the wave packet. The first wave to separate is the wave that has no reflection at the Moho (the direct or diving wave). This is evidenced as the separation of the first pulse in Figure 2. The second separated pulse in the figure is the wave that is reflected once from the Moho. From ray theory, the epicentral distance at which the k-time reflected wave separates from the interference head-wave packet is (Červený and Ravindra, 1971, Eq. 6.4)

$$r_k = (2H - d)\frac{v_c}{\sqrt{v_m^2 - v_c^2}} + \left[\frac{32 v_m^3 T (1+k)^2 \left(1+\frac{1}{2}k\right)^2}{g^2\left(1+\frac{2}{3}k\right)}\right]^{1/3}, \qquad (4)$$

where H is crustal thickness; d is source depth; v_c is P-wave velocity of the crust; v_m is P-wave velocity at the top of the mantle; T is pulse width of the wave and g is velocity gradient (dv/dz) at the top of the mantle resulting from the EFT. From Equation 4 and for the base model, a wave with a pulse width of about 0.1 second (10-Hz) that undergoes no reflection at the Moho will separate at about 9.8° and the wave that has one reflection will separate at about 16.6°. These predictions are consistent with the synthetics in Figure 2.

Figure 3 shows the amplitude spectra of synthetic P_n at the same epicentral distances as those in Figure 2 from the Q = 100,000 computation. The figure illustrates the evolution of P_n spectrum from proportional to the source spectrum to proportional to the time derivative of the source spectrum.

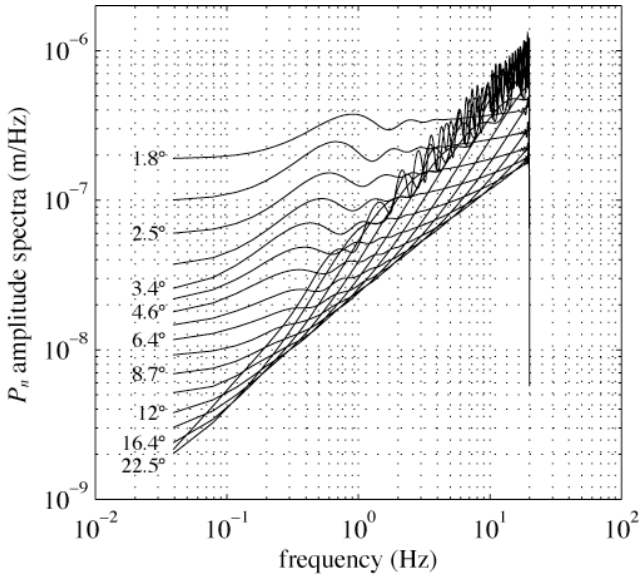

Figure 3. Amplitude spectra of P_n at the same distances as those in Figure 2. Some of the distances are marked on the left of the corresponding spectra.

As was described above, we use an asymptotic method to derive spectral amplitudes for an elastic model from amplitudes obtained using anelastic simulations. Figure 4 gives an illustration of the method. Plotted in the figure are P_n amplitudes at different frequencies measured from calculations using different quality factors. The amplitudes are computed at 22.5° epicentral distance and are normalized by the maximum amplitude in the figure. Quadratic polynomial fits of the amplitudes are plotted as solid lines. The polynomial fits are almost perfect, indicating that our approach is appropriate. Amplitudes at other distances are fit as well as those shown in Figure 4.

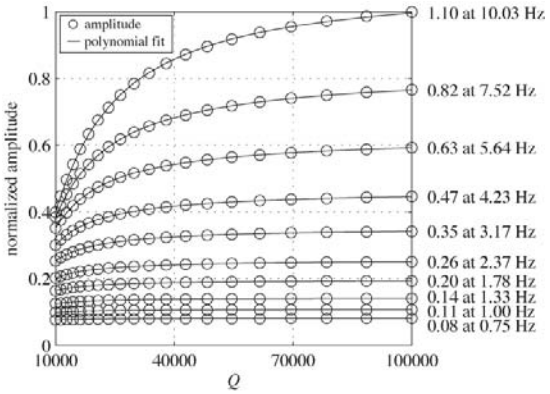

Figure 4. An illustration of how elastic results are obtained from anelastic calculations. Circles are amplitudes at 22.5° epicentral distance for different frequencies plotted against *Q* used in their calculations. The amplitudes are normalized by the maximum amplitude in the plot, which is the 10.03-Hz amplitude from the *Q* = 100,000 calculation. Solid lines are corresponding quadratic polynomial fits of the amplitudes. Numbers on the right are the limits of normalized amplitudes at corresponding frequencies as *Q* approaches infinity.

To visualize the P_n amplitude decay in a spherical Earth model, we plot 10-Hz P_n amplitudes for the base model in Figure 5. We extend the epicentral-distance range to between 135 km (1.2°) and 8000 km (71.9°) for this particular simulation in order to better depict the evolution of P_n waves. Amplitudes at distances beyond about 20° are measured from the direct wave that has been completely separated from the interference head waves. The

amplitudes are corrected for the free-surface effect, which is only important at teleseismic distances. Also plotted in the figure are the amplitude decay of a conical head wave in a plane one-layer-over-half-space model (Aki and Richards, 2002; Eq. 6.26) and the amplitude decay of infinite-frequency direct wave in a spherical Earth model from ray tracing. At distances close to the critical distance, P_n geometric spreading behaves like that of a conical head wave. As distance increases, P_n spreading starts to deviate from that of the head wave and at about 5°, P_n amplitudes begin to increase. As was mentioned before, 10-Hz direct-wave energy would separate from the rest of the interference head wave at about 10°. It seems from the figure that this separation is manifested in a change in the smoothness of the P_n amplitude variation followed by a reduced rate of amplitude increase. In the range beyond the critical distance and before the direct-wave separation, P_n evolves from a wave similar to a conical head wave to the interference head wave, which is a superposition of multiple waves reflected from the Moho. As the epicentral distance approaches teleseismic distances, the direct-wave spreading approaches that of the infinite-frequency wave from ray tracing results, as is expected. The direct wave dominates the whole P_n wave packet at long distances. We do not see significant difference between spectral amplitudes obtained by windowing the whole P_n wave packet and those obtained by just windowing the direct wave after its separation from the packet. This is consistent with theoretical predictions (Červený and Ravindra, 1971).

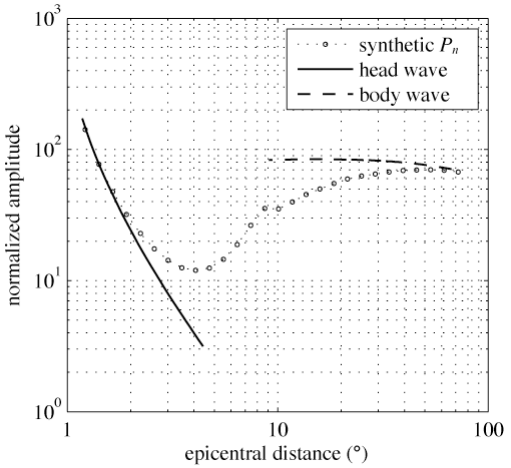

Figure 5. 10-Hz synthetic P_n amplitude decay in a spherical Earth model with constant mantle velocities. The solid line depicts the theoretical amplitude decay of a conical head wave in a plane one-layer-over-half-space Earth model. The dashed line is the amplitude decay of infinite-frequency direct wave in a spherical homogeneous Earth model from ray-tracing calculations.

P_n geometric spreading in a spherical Earth model is not only different from that of a head wave as is shown in Figure 5, but also frequency dependent. Figure 6 shows the P_n amplitude-variation surface as a function of distance and frequency for the base model. The strong frequency dependence of the amplitudes is apparent. Amplitudes at higher frequencies are affected more by the sphericity than are lower-frequency amplitudes. The separation distance of the direct wave from the interference head waves becomes shorter as frequency becomes higher (Equation 4).

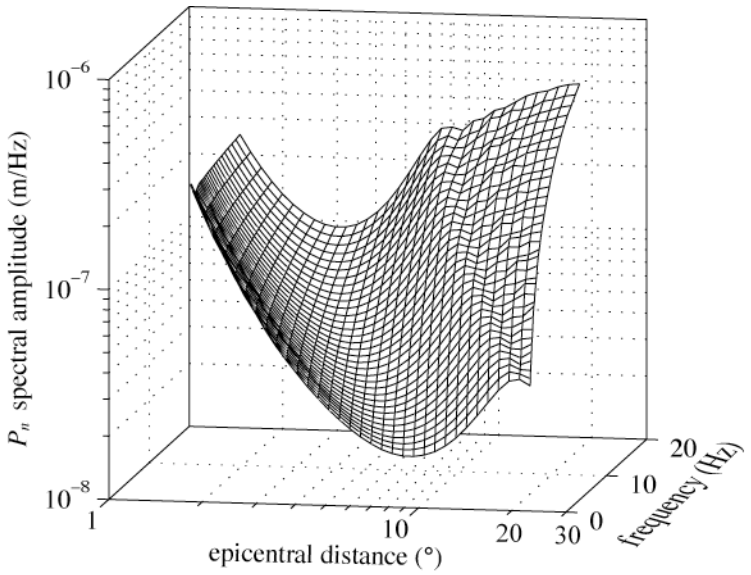

Figure 6. Synthetic P_n amplitudes as a function of epicentral distance and frequency.

A New P_n Geometric-Spreading Representation for a Spherical Earth Model

Figures 5 and 6 illustrate that a frequency-independent, power-law model cannot accurately represent P_n geometric spreading in a spherical Earth model. Such a representation would plot as a straight line in Figure 5, which is clearly inappropriate for modeling P_n geometric spreading over a wide distance range. In addition, a power-law model with constant exponent does not take into account the frequency dependence of P_n spreading shown in Figure 6. Based on the P_n amplitude-decay behavior shown in Figures 5 and 6, we propose a new empirical P_n geometric-spreading model that fits the synthetic data much better and that also results in more reasonable anelastic-attenuation estimates from observed data, as we will discuss in more detail in the next section.

The amplitude spectrum of P_n can be parameterized as

$$A(r,\theta,f) = K(f) M_0 R(\theta) G(r,f) \exp\left(-\frac{\pi f}{Q(f) v} r\right) S(f) \tag{5}$$

with the new geometric-spreading model expressed as

$$G(r,f) = \frac{10^{n_3(f)}}{r_0}\left(\frac{r_0}{r}\right)^{n_1(f)\log\left(\frac{r_0}{r}\right)+n_2(f)} \qquad (r_0 = 1 \text{ km}) \tag{6}$$

and

$$n_i(f) = n_{i1}\left[\log\left(\frac{f}{f_0}\right)\right]^2 + n_{i2}\log\left(\frac{f}{f_0}\right) + n_{i3} \qquad (i = 1, 2, 3;\ f_0 = 1 \text{ Hz}). \tag{7}$$

In Equation 5, K is a frequency-dependent scaling factor; M_0 is source moment; R is source radiation pattern; Q is P_n quality factor; v is P_n velocity; S is receiver site response; r is epicentral distance; θ is azimuth angle and f is frequency. r_0 and f_0 are included in Equations 6 and 7 in order for the new model to have the same dimension as standard power-law models (e.g., Street et al., 1975; Sereno et al., 1988). The main differences between the new geometric-spreading model (Equations 6 and 7) and the standard frequency-independent power-law model are the addition of the first term in the exponent and the frequency dependence of parameters n_i. In the logarithm domain, the new model is a quadratic function of log-distance, whereas the power-law model is linear. The reason for choosing a log-quadratic function is to keep the parameterization as simple as possible while providing a good fit to the synthetics. The adoption of a quadratic functional form for n_i (Equation 7) is based on the behavior of n_i versus frequency obtained by fitting Equation 6 to synthetic P_n amplitudes at individual frequencies.

If we take common logarithm of Equation 6, substitute Equation 7 into the result and let r_0 and f_0 equal one, we obtain

$$\begin{aligned}\log[G(r,f)] = {} & n_{11}(\log f)^2(\log r)^2 + n_{12}\log f(\log r)^2 + n_{13}(\log r)^2 \\ & -n_{21}(\log f)^2\log r - n_{22}\log f\log r - n_{23}\log r \\ & +n_{31}(\log f)^2 + n_{32}\log f + n_{33}\end{aligned}, \quad (8)$$

where r is in kilometers and f is in hertz. To derive coefficients n_{ij}, we fit Equation 8 to synthetic P_n amplitudes shown in Figure 6 in a least-squares sense. P_n amplitudes are corrected for M_0 used in the simulation (10^{15} N m) and K before the fitting. Since the source that we use in the simulation has a flat spectrum, K is frequency independent. We use $K = (4\pi\rho v^3)^{-1}$ (Denny and Johnson, 1991), where ρ is density and v is P-wave velocity of the source region. Source radiation and site response are unity. We use P_n amplitudes at epicentral distances beyond 300 km (2.7°) and before the start of the direct-wave separation to fit the model. We use 300 km as the lower distance limit because reliable P_n observations are typically made at some distances beyond the P_g crossover distance (~200 km). The choice of 300 km is also to avoid possible long-period numeric-noise contamination at short distances, as is indicated in Figure 6. The upper distance limits are based on the observation that within these distances, P_n is the result of the interference of all of its components including the direct wave. At larger distances, the direct wave separates from the rest of the wave packet and the characteristics of P_n become different. The P_n amplitude decay within the defined distance range also has a smooth pattern and thus is easier to fit by a simple mathematical model. The upper distance limits vary from 7.3° to 17.3° for the frequency range between 13 and 0.75 Hz. Within the specified distance limits, the new spreading model is applicable. Since at about 15°, P_n in the real Earth is overtaken by upper-mantle triplications resulting from reflections and refractions at 410-km and 660-km discontinuities and is no longer the first arrival, P_n is usually used within the distance range where the new spreading model is valid for frequencies below about 2 Hz. For higher frequencies, the range-of-applicability of the new model is shorter, but observationally high-frequency signals are generally only detectable above the noise level at shorter distances. Coefficients n_{ij} (i = 1, 2, 3; j = 1, 2, 3) from the fitting are listed in Table 1. The inclusion of r_0 and f_0 in the model also guarantees that even though the values of the coefficients are derived using Equation 8 with r in kilometers and f in hertz, they are valid for r and f in any units as long as r_0 and f_0 are converted accordingly.

Table 1 Coefficients of the new P_n geometric-spreading model

n_{11}	n_{12}	n_{13}	n_{21}	n_{22}	n_{23}	n_{31}	n_{32}	n_{33}
-0.217	1.79	3.16	-1.94	8.43	18.6	-3.39	9.94	20.7

Application to Observed Data

The key value of any mathematical model of the physical world is for the model to be able to provide physically reasonable descriptions of observed data. To test the validity and usefulness of the new P_n geometric-spreading model and the associated choice of a constant-velocity mantle lid structure, we correct a set of observed P_n spectral amplitudes for geometric spreading with the new model and estimate the average medium attenuation. We then compare the results with those published in the literature.

We represent observed P_n amplitudes by Equation 5. For the purpose of testing the new P_n geometric-spreading model, we simplify Equation 5 by assuming that site response is unity for all stations and source radiation patterns can be ignored. We presume that errors introduced by these simplifications are random and should not affect average-attenuation estimates systematically. With known or estimated source moments, an assumed scaling factor K and a P_n geometric-spreading model, we can estimate the average attenuation quality factor at each frequency by least-squares fitting the logarithm of source and geometric-spreading corrected spectral amplitudes as a function of epicentral distance.

The observed P_n amplitudes are measured on vertical-component ground-displacement data recorded by stations in and around China and in southern Europe for events in the same region. The same windowing method as the method we employ to measure the synthetic P_n amplitudes is used. Analyst picks reported in global catalogs (ISC, EDR, REB, EHB, etc.) are used to center the P_n windows. We derive source moments from body-wave magnitudes (m_b). We only use amplitudes from events with m_b equal to or smaller than 6 to avoid magnitude saturation. We use a

simplified version of the scaling factor K expressed as $K(f) = \{4\pi\rho v^3[1+(f/f_c)^2]\}^{-1}$ using crustal P-wave velocity and density of the base Earth model as v and ρ. Source corner frequency f_c is calculated from source moment using the relationship $\log M_0 = 17.08\text{-}3.24\log f_c$ derived by Xie and Patton (1999) from P_n amplitude data recorded in central Asia. For comparison, we use both the new P_n geometric-spreading model and the power-law model with two different exponents, -1.1 (Walter and Taylor, 2002) and -1.3, in the attenuation estimation. When the new spreading model is used, we limit the epicentral distances of the amplitudes used in the estimation to within the distance range where the model is valid. For power-law model corrections, we use amplitudes between 300 km (2.7°) and 1668 km (15°). Attenuation is estimated at 0.75, 1.0, 2.0, 4.0 and 6.0 Hz. The new spreading model is used in the correction. Although the amplitudes show a large scatter, a linear decay trend due to realistic values of medium attenuation is discernable.

Table 2 lists estimated average quality factors using different geometric-spreading corrections from observed P_n amplitudes. Using the power-law spreading model results in some negative values at low frequencies. At high frequencies, the power-law model yields estimates that range from over 1000 to over 5000. On the other hand, Q estimates using the new spreading model are positive and below 700 at all frequencies. These values can be compared with published P-wave quality factors in the mantle lid, as we discuss below.

Table 2 Average P_n quality factor estimated using different geometric-spreading models

	data frequency (Hz)				
	0.75	1.0	2.0	4.0	6.0
new model	440	338	312	557	678
power-law model 1*	-1669	9241	1206	2204	3450
power-law model 2**	-734	-2153	1850	3260	5246

* model with exponent of -1.1

** model with exponent of -1.3

Using theory, observed body-wave spectra and waveform modeling, Lundquist and Cormier (1980) derive generic absorption-band P-wave Q models for the mantle. The Q values of these models range from about 100 to 500 for frequencies between 0.7 Hz and 6.0 Hz in the depth range of 45 to 200 km. In their paper, Lundquist and Cormier (1980) also cites results of some other Q studies that use free-oscillation data, long-period surface waves and high-frequency (1-5 Hz) body waves. The frequency-independent P-wave Q models from these studies have values from about 100 to 250 for depths between 50 and 150 km. Der et al. (1986) construct a P-wave Q model for the Eurasian Shield using a large set of teleseismic body waves. Their model has values between about 350 and 900 for frequencies between 0.3 and 10 Hz at depths between 100 and 200 km. Above 100 km, Q values increase to between 600 and 1500 for the same frequency range.

More recently, some studies make direct P_n Q estimations. Sereno *et al.* (1988) and Sereno (1990) obtain P_n Q models for Scandinavia and eastern Kazakhstan respectively by inverting broadband P_n spectra. The 0.75- to 6-Hz P_n Q values that they estimated are between 283 and 768 for Scandinavia and between 260 and 735 for eastern Kazakhstan. Although Sereno et al. (1988) and Sereno (1990) assume a power-law P_n geometric-spreading model with an exponent of -1.3, their P_n Q estimates are more in line with the average P_n Q estimates that we obtain using the new P_n spreading model than with those from power-law model corrections (Table 2). A possible explanation for this observation is that the majority of their data are recorded within 1000-km epicentral distance. At short distances, the power-law spreading model has a gentler slope than the new spreading model does and therefore would yield smaller Q estimates from short-distance data. However, for a broader distance range such as the distance range that our dataset covers, the power-law model yields larger, sometimes negative, Q estimates because of the steeper slope of the model at long distances. The implication is that if a power-law P_n spreading model with a specific exponent is used, it will only be applicable as an approximation in a limited distance range and models with different exponents are needed for different distance ranges. Our parameterization remedies this failing.

Comparing Q values in Table 2 with those published in the literature, we conclude that the new P_n geometric-spreading model yields Q estimates that are generally consistent with published results over the broad region of Eurasia. The Q estimates with power-law model corrections, on the other hand, have values that are either negative or seem to be too large. It should be noted that Q values estimated in this fashion represent only the average P_n attenuation behavior over the broad region of Eurasia. They may not be accurate for any particular region due to the deviation of the uppermost-mantle velocity structure, including any non-zero mantle lid velocity gradient or lateral heterogeneity, from the constant-velocity structure that we use to develop the geometric-spreading model. The fact that we obtain reasonable Q values for data spanning a large distance range demonstrates that our reference model at least provides reasonable average behavior without any peculiarities such as negative Q values.

S_n Simulations

In addition to simulating P_n propagation in a spherical Earth model, we also simulate S_n propagation in the same base model. Except for different source types and different slowness integration limits, other modeling parameters in the S_n simulation are kept the same as those used in the P_n simulation. The behavior of S_n in a spherical Earth model is very similar to the behavior of P_n waves. The only difference is that the separation of individual waves from the interference wave packet occurs at shorter distances for S_n. This difference can be predicted using Equation 4, although the equation was originally derived only for P_n waves. $S_n(SH)$ spectral amplitudes also form a surface with a shape similar to that of the P_n amplitude surface shown in Figure 6.

Because of the similarities between P_n and S_n propagation in a spherical Earth model with constant mantle velocities, we propose an S_n geometric-spreading model that has the same functional form as that of the new P_n spreading model (Equations 6 and 7). We derive the values of the coefficients n_{ij} by fitting synthetic $S_n(SH)$ amplitudes. $S_n(SV)$ amplitudes are severely contaminated by P-wave energy up to 1000 km, and thus are not suitable for fitting. Beyond 1000 km, $S_n(SV)$ and $S_n(SH)$ amplitudes decay similarly. It suggests that the S_n spreading model developed by fitting $S_n(SH)$ amplitudes is also suitable for describing $S_n(SV)$ geometric spreading.

We correct synthetic $S_n(SH)$ amplitudes for source moment, source radiation pattern, and the scaling factor K before the fitting. We use $K = (4\pi\rho v^3)^{-1}$, but now v is S-wave velocity of the crust. We again set the lower-distance limit to 300 km (2.7°) for amplitudes used in the fitting. The upper distance limits are from 6.2° to 14.4° for frequencies from 13 Hz to 0.75 Hz. The limits set the distance range within which the S_n spreading model is valid. Table 3 lists the coefficients n_{ij} for the S_n geometric-spreading model from the fitting.

Table 3 Coefficients of the new $S_n(SH)$ geometric-spreading model

n_{11}	n_{12}	n_{13}	n_{21}	n_{22}	n_{23}	n_{31}	n_{32}	n_{33}
-0.347	2.16	3.54	-2.69	10.1	20.4	-4.38	11.7	23.1

CONCLUSIONS AND RECOMMENDATIONS

The new P_n and S_n geometric-spreading models are useful in common situations where only simple velocity models with uppermost-mantle structure represented as constant-velocity half space or a stack of constant velocity layers are available. If the mantle-lid velocity gradient is well resolved in a given region, which is sometimes the case, simulations for that gradient can be performed to obtain appropriate geometric-spreading corrections. Since the effect of sphericity is equivalent to the effect of a positive velocity gradient in a plane-layered model, we anticipate that the functional form of our geometric-spreading models will remain the same for Earth models in which an effective (physical plus effects of the sphericity) positive velocity gradient exists. Only the coefficients will differ. Of course, any Q determinations will trade-off directly with errors due to having the wrong velocity model, and if one can determine specific structural parameters they should be used to make specific geometric spreading terms.

Quantifying the effects of specific mantle-lid velocity gradients, Moho irregularity and lateral velocity heterogeneity in the uppermost mantle on P_n and S_n geometric spreading through 2D and 3D numerical modeling will be the subject of a separate study. It is reasonable to assume that except for the case of different lid velocity gradients, many effects will contribute primarily to scatter around the fundamental behavior of our geometric-spreading models.

REFERENCES

Aki, K., and P. G. Richards (2002). *Quantitative Seismology*, 2nd edition, University Science Books, Sausalito, California.

Červený, V., and R. Ravindra (1971). *Theory of Seismic Head Waves*, University of Toronto Press, Toronto.

Chapman, C. H. (1973). The Earth flattening transformation in body wave theory, *Geophys. J. R. astr. Soc.* 35: 55–70.

Denny, M. D., and L. R. Johnson (1991). The explosion seismic source function: models and scaling laws reviewed, in *Explosion Source Phenomenology*, S. R. Taylor, H. J. Patton, and P. G. Richards (Editors), American Geophysical Union, Washington, DC, 1–24.

Der, Z. A., A. C. Lees, and V. C. Cormier (1986). Frequency dependence of Q in the mantle underlying the shield areas of Eurasia. III. The Q model, *Geophys. J. Int.* 87: 1103–1112.

Hartse, H. E., S. R. Taylor, W. S. Phillips, and G. E. Randall (1997). A preliminary study of regional seismic discrimination in central Asia with emphasis on western China, *Bull. Seism. Soc. Am.* 87: 551–568.

Lundquist, G. M., and V. C. Cormier (1980). Constraints on the absorption band model of Q, *J. Geophys. Res.* 85: 5244–5256.

Menke, W. H., and P. G. Richards (1980). Crust-mantle whispering gallery phases: a deterministic model of teleseismic P_n wave propagation, *J. Geophys. Res.* 85: 5416–5422.

Müller, G. (1977). Earth-flattening approximation for body waves derived from geometric ray theory—improvements, corrections and range of applicability, *J. Geophys.* 42: 429–436.

Sereno, T. J., and J. W. Given (1990). P_n attenuation for a spherically symmetric Earth model, *Geophys. Res. Lett.* 17: 1141–1144.

Sereno, T. J., S. R. Bratt, and T. C. Bache (1988). Simultaneous inversion of regional wave spectra for attenuation and seismic moment in Scandinavia, *J. Geophys. Res.* 93: 2019–2035.

Sereno, T. J. (1990). Frequency-dependent attenuation in eastern Kazakhstan and implications for seismic detection threshold in the Soviet Union, *Bull. Seism. Soc. Am.* 80: 2089-2105.

Street, R. L., R. B. Herrmann and O. W. Nuttli (1975). Spectral characteristics of the L_g wave generated by central United States earthquakes, *Geophys. J. R. astr. Soc.* 41**:** 51–63.

Walter, W. R., and S. R. Taylor (2002). A revised magnitude and distance amplitude correction (MDAC2) procedure for regional seismic discriminants: theory and testing at NTS, Lawrence Livermore National Laboratory, UCRL-ID-146882, pp. 13.

Xie, X.-B., and T. Lay (1994). The excitation of Lg waves by explosions: A finite-difference investigation, *Bull. Seism. Soc. Am.* 84: 324–342.

Xie, J., and H. J. Patton (1999). Regional phase excitation and propagation in the Lop Nor region of central Asia and implications for *P*/*Lg* discriminants, *J. Geophys. Res.* 104: 941–954.

Yang, X. (2002). A numerical investigation of L_g geometric spreading, *Bull. Seism. Soc. Am.* 92: 3067–3079.

TOWARD A RAYLEIGH WAVE ATTENUATION MODEL FOR CENTRAL ASIA AND SURROUNDING REGIONS

Anatoli L. Levshin[1], Mikhail P. Barmin[1], Xiaoning (David) Yang[2], Michael H. Ritzwoller[1], and George E. Randall[2]

University of Colorado at Boulder[1] and Los Alamos National Laboratory[2]

Sponsored by National Nuclear Security Administration
Office of Nonproliferation Research and Development
Office of Defense Nuclear Nonproliferation

Contract Nos. DE-FC52-05NA26608[1] and DE-AC52-06NA25396[2]

ABSTRACT

We report on progress toward an attenuation model for short-period (10-20 s) Rayleigh waves in Central Asia and surrounding regions. This model will be defined by maps of attenuation across the region of study in the specified period band. The model is designed to calibrate the regional surface-wave magnitude scale and to extend the teleseismic 'surface-wave magnitude–body-wave magnitude' (*Ms-mb*) discriminant to regional distances (Marshall and Basham, 1971; Bonner et al., 2006; Russell, 2006). Work is progressing in three stages: (1) data accumulation and amplitude measurements, (2) estimation of attenuation coefficients, and (3) tomographic inversion of attenuation data.

The first stage in model construction was the measurement of Rayleigh wave spectral amplitudes. To overcome inherent difficulties due to multipathing and scattering of short-period surface waves we applied the Surface Wave Amplitude Measurement Tool (SWAMTOOL) designed at Los Alamos National Laboratory (LANL) (Yang et al., 2005), which incorporates dispersion analysis, phase-matched filtering, and additional means to estimate the quality and reliability of the measurements. We enhanced SWAMTOOL by providing different options for phase-matched filtering of surface wave signals (Levshin et al., 2006). We collected and processed waveform data for 200 earthquakes occurring throughout 2003-2006 inside and around Eurasia. The records of about 140 broadband permanent and temporary stations were used. The existing broadband station distribution and the pattern of seismicity provided sufficient number of spectral amplitude measurements between 12 and 20 s periods for the construction of the two–dimensional (2-D) tomographic maps of attenuation coefficients. Measurements at periods below about 12 s are too scarce for tomographic inversion.

At the second stage of the work, spectral attenuation coefficients were estimated using both inter-station measurements and single-station measurements corrected for source and receiver terms. The model-related part of corrections was based on a three-dimensional (3-D) global model of the crust and upper mantle CUB2 by Shapiro and Ritzwoller (2002). Information about source mechanisms of selected events was taken from the Harvard centroid moment tensor catalog CMT (Dziewonski et al., 1981) and the hypocenter information from the catalog EHB by Engdahl et al. (1998).

The third stage is now in progress. It includes the refining of source parameters (especially, the depth and the scalar moments), recalculation of attenuation coefficients after this refinement, grooming of resulting coefficients, and the multi-stage tomograhic inversion of data. Preliminary tomographic maps of attenuation for the set of periods from 12 to 20 s have been obtained.

OBJECTIVES

The objectives of the study are 1) to develop short-period (10 – 18s), two-dimensional (2-D) Rayleigh-wave attenuation models for Central Asia along with associated uncertainty statistics through a tomographic approach, and 2) to calibrate Russell's (2006) *Ms* formula with these models for the same region. This report describes the results of developing the attenuation model.

RESEARCH ACCOMPLISHED

Introduction

Knowledge of the losses of seismic energy during the propagation of the wave from the source to receivers is essential for the estimation of the surface wave magnitude *Ms* and the seismic moment of the source. This is especially important for monitoring of underground nuclear explosions, in which the estimation of *Ms* is used as a part of the most robust seismic discriminant, the *Ms*-*mb* discriminant. In order to apply this discriminant to regional-distance monitoring, a modified *Ms* formula using shorter-period (< 20 s) surface wave amplitudes is required (e.g., Marshall and Basham, 1970; Bonner et al., 2006; Russell, 2006). The purpose of this work is to construct short-period (10-20 s) two-dimensional (2-D) Rayleigh-wave attenuation models for Central Asia and to use them to calibrate the *Ms* formula of Russell (2006).

The first stage in model construction was the measurement of Rayleigh wave spectral amplitudes. To overcome inherent difficulties due to multipathing and scattering of short-period surface waves we applied the SWAMTOOL designed at the LANL (Yang et al., 2005). We enhanced SWAMTOOL by providing different options for phase-matched filtering of surface wave signals (Levshin et al., 2006). Waveform data for 200 earthquakes occurring throughout 2003-2006 inside and around Eurasia from about 140 broadband permanent and temporary stations have been collected and processed. This data set provided a sufficient number of spectral amplitude measurements between 12 and 18 s periods for the construction of the two–dimensional (2-D) tomographic maps of attenuation coefficients.

At the second stage of the work, spectral attenuation coefficients were estimated using both inter-station measurements and single-station measurements corrected for the source and receiver terms. The model-related part of corrections was based on a three-dimensional (3-D) global model of the crust and upper mantle CUB2 by Shapiro and Ritzwoller (2002). Information about source mechanisms of selected events was taken from the Harvard centroid moment tensor catalog CMT (Dziewonski et al., 1981) and the hypocenter information from the catalog EHB by Engdahl et al. (1998).

The third stage is now in progress. It includes the refining of source parameters (especially, the depth and the scalar moments), recalculation of attenuation coefficients after this refinement, grooming of resulting coefficients, and the multi-stage tomograhic inversion of data. Preliminary tomographic maps of attenuation for the set of periods from 12 to 20 s have been obtained.

Surface Wave Data Collection and Selection

We collected and processed surface-wave waveform data for 200 events that occurred in and around Eurasia through 2003-2006. Selected events are characterized by magnitudes *Ms* between 5 and 6 and source depths less than 70 km. Several global and regional broadband networks have existed in Eurasia during the considered time interval. These include Global Seismographic Network (GSN), International Monitoring System (IMS), GEOSCOPE, GEOFON, Mediterranean Seismic Network (MEDNET), China Digital Seismological Network (CDSN), Kyrgyz Seismic Network (KNET), Kazakhstan Seismic Network (KAZNET), and others. There have also been many temporary network deployments in the region including close to 10 projects of the Program for the Array Seismic Studies of the Continental Lithosphere (PASSCAL). Maps with the station and event distribution are shown in Figure 1. The original records were requested and provided by the Data Management Center (DMC) of Incorporated Research

Institutions for Seismology (IRIS). After standard preprocessing all records were corrected for the instrument responses and converted to displacements using the Seismic Analysis Code (SAC). Then we apply SWAMTOOL, and as an output we obtain the raw spectral amplitudes of Rayleigh waves in the period range defined by the magnitude of an earthquake, the epicentral distance and the level of a background noise. Altogether more than 9000 records were selected for measurements. The path coverage for the set of periods is shown in Figure 2 and 3, both for source-station paths and paths between pairs of stations. The conditions for selecting such pairs of stations are:(a) the difference in azimuths from epicenter to the stations is less than 1°; (b) the distance between stations is more than 300 km and less than 5000 km.

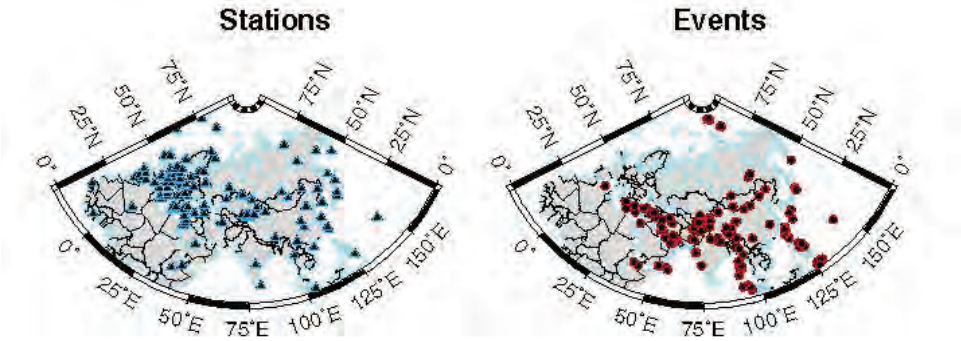

Figure 1. Stations and events selected for surface-wave data analysis.

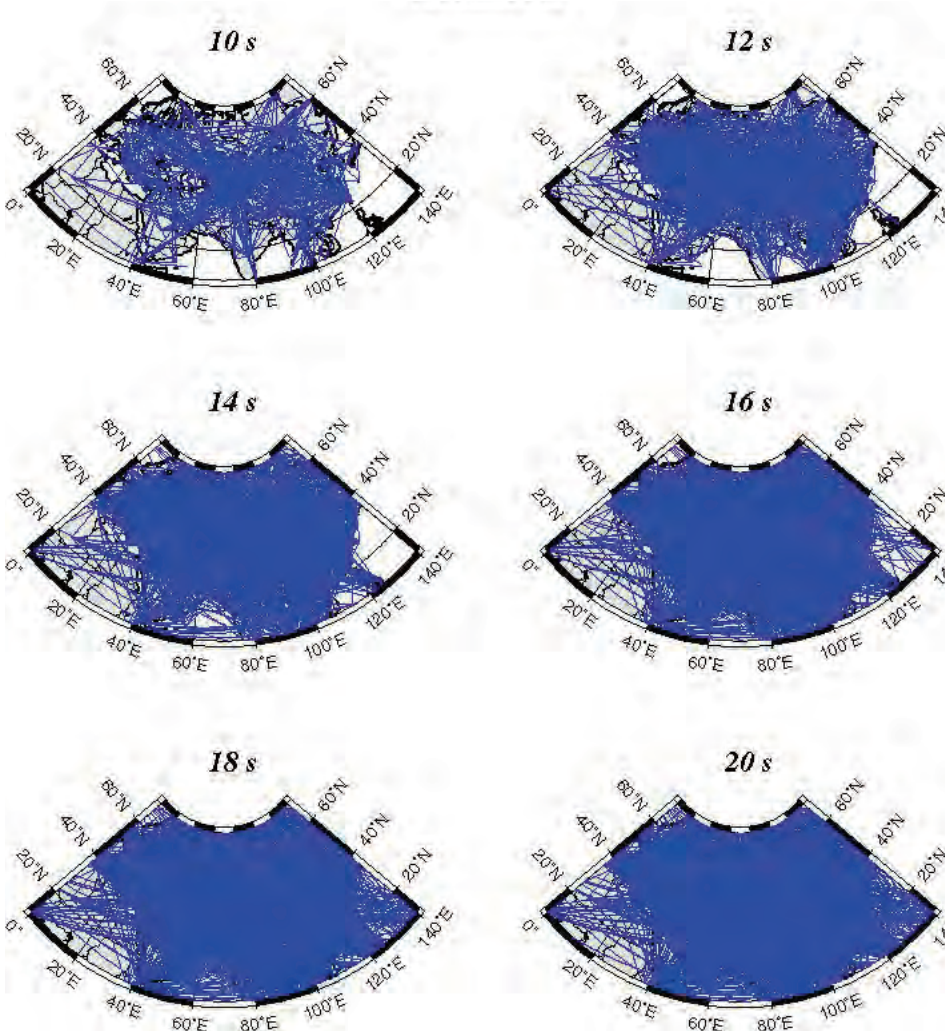

Figure 2. The single-station paths used for spectral amplitude measurements at indicated periods.

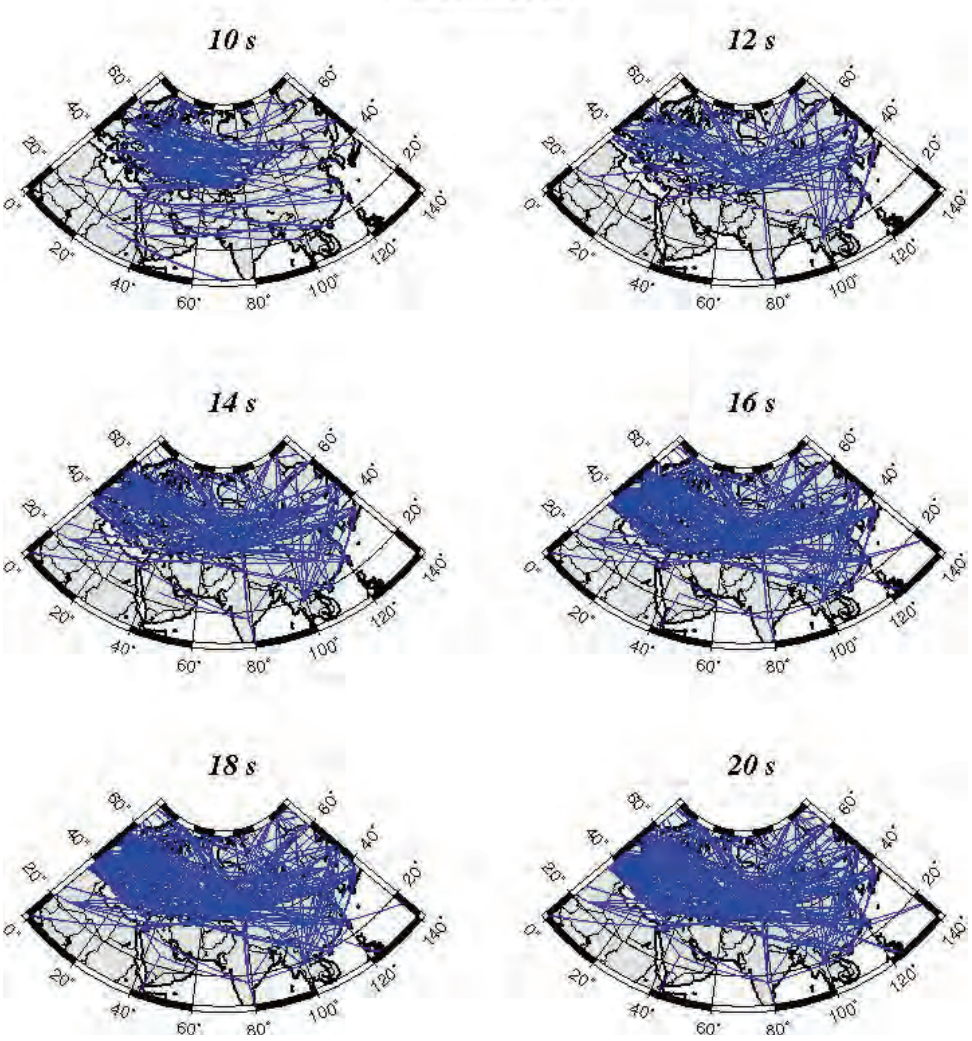

Figure 3. The inter-station paths used for spectral amplitude measurements at indicated periods

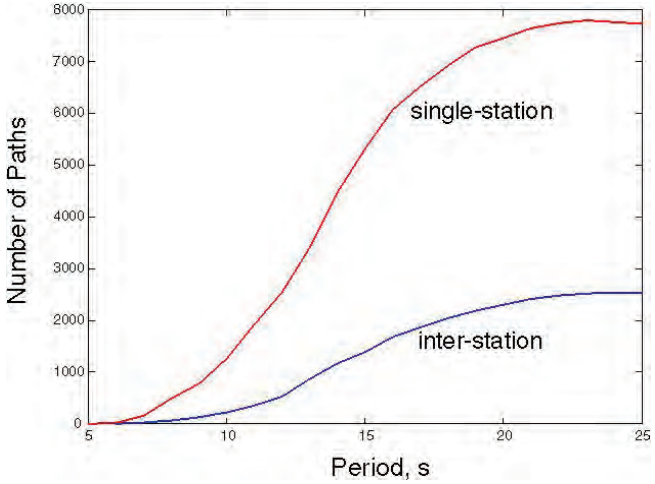

Figure 4. Number of paths for which the spectral amplitudes have been measured.

Figure 4 presents the numbers of obtained single-station and inter-station measurements as a function of period. For the measurements of attenuation we selected data with quality factors, which are assigned by the analyst, of 'fair' or better, and observed backazimuth differs from great-circle backazimuth by less than 30°. This selection significantly decreased the data scatter.

Observed and Predicted Spectral Amplitudes, and Attenuation Coefficients

To determine attenuation coefficients from observed spectral amplitudes we use theoretical predictions based on 3-D-model CUB2.0 of the crust and upper mantle (Shapiro & Ritzwoller, 2002) presented on 2°×2°grid. Following the asymptotic theory of surface wave propagation in a 3-D medium (Woodhouse, 1974; Levshin et al., 1989) we calculated the predicted spectral amplitude A_{th} for a given 'event-station' pair as

$$A_{th} = S(\omega, h, \varphi)\frac{\exp(-\overline{\alpha}(\omega)\Delta R_0)}{\sqrt{R_0 \sin(\Delta)}} B(\omega) \qquad (1)$$

Here ω is a circular frequency, h is the source depth, φ is an azimuth from epicenter to the station, and $S(\omega,h,\varphi,)$ is the source-dependent term.

$$S(\omega, h, \varphi) = M_0 \,|\, \mathbf{m} * \mathbf{E}(\omega, h, \varphi) \,| \qquad (2)$$

Here M_0 is a scalar moment, **m** is a moment tensor, and $\mathbf{E}(\omega,h,\varphi)$ is a strain tensor for the Rayleigh wave at given frequency and depth for the one-dimensional (1-D) structure at the grid point nearest to the epicenter. R_0 is the Earth radius, Δ is an epicentral distance in radians, $\overline{\alpha}$ is an attenuation coefficient at given ω for an average continental model. $B(\omega)$ is the station term:

$$B(\omega) = \left(I_0 U\right)^{-1/2} \qquad (3)$$

Here I_0 is a normalized kinetic energy of Rayleigh wave, and U is a corresponding group velocity at given frequency ω for the 1-D local model at the grid point nearest to the station. The values of station correction B normalized by the corresponding values for the average continental model vary in the range 0.45-1.6 for periods below 13 s and 0.75-1.35 for longer periods depending on the local structure near the station. Observed spectral amplitude A_{obs} should differ from predicted one by the exponential factor:

$$A_{obs} = A_{th} \exp[-(\alpha(\omega) - \overline{\alpha}(\omega))\Delta R_0] \qquad (4)$$

where α(ω) is the wanted attenuation coefficient along the path 'epicenter-station'. The inter-station attenuation coefficient α_{12} is determined from two observed spectral amplitudes A_{2obs} and A_{1obs} according to relation:

$$A_{2obs} = A_{1obs}\sqrt{\frac{\sin(\Delta_2)}{\sin(\Delta_1)}}\frac{B_1}{B_2}\exp[-\alpha_{12}(\omega)(\Delta_2 - \Delta_1)R_0] \qquad (5)$$

To avoid effects caused by the poor 'near-node' radiation we exclude records for which the theoretical value of $|\boldsymbol{m}*\boldsymbol{E}(\omega,h,\varphi)|$ for a given azimuth φ is less than 0.1 of its maximum value. Using formulas (1)-(5) to find the epicenter-station and inter-station attenuation coefficients for all selected paths we obtain a preliminary data set for the attenuation tomography. However, the behavior of corrected observed amplitudes as a function of distance (Figure 5a) shows that there are indications of a possible bias in source parameters which results in non-zero crossing by the least-square line at the zero distance.

Previous study (Levshin et al., 2006) demonstrated the significant dependence of measured epicenter-station attenuation coefficients on source mechanism and depth. Taking into account the accuracy of the CMT moment tensor solutions and possible uncertainties in the source depths both at the CMT and EHB catalogs we applied a Monte Carlo procedure to refine these solutions for each event by minimizing the differences between observed

attenuation coefficients and ones predicted by the average continental model. The scatter of data has been critically diminished (Figure 6); there is the zero crossing of the regression line at zero distance as it should be in a real Earth. The differences in source parameters before and after optimization are shown in Figure 7. The general tendency to decrease the scalar moments by optimization agrees with results by Yang at al. (2004) for the 20 s period. To evaluate the scatter quantitatively we apply the cluster analysis similar to one which was used for evaluation of velocity scattering in group velocity tomography (Ritzwoller & Levshin, 1998). We consider some paths belonging to a cluster if the end points of these paths belong to the same cell 50 km x 50 km size. The average attenuation coefficient for the region under study and corresponding error bars obtained by the cluster analysis are shown in Figure 8.

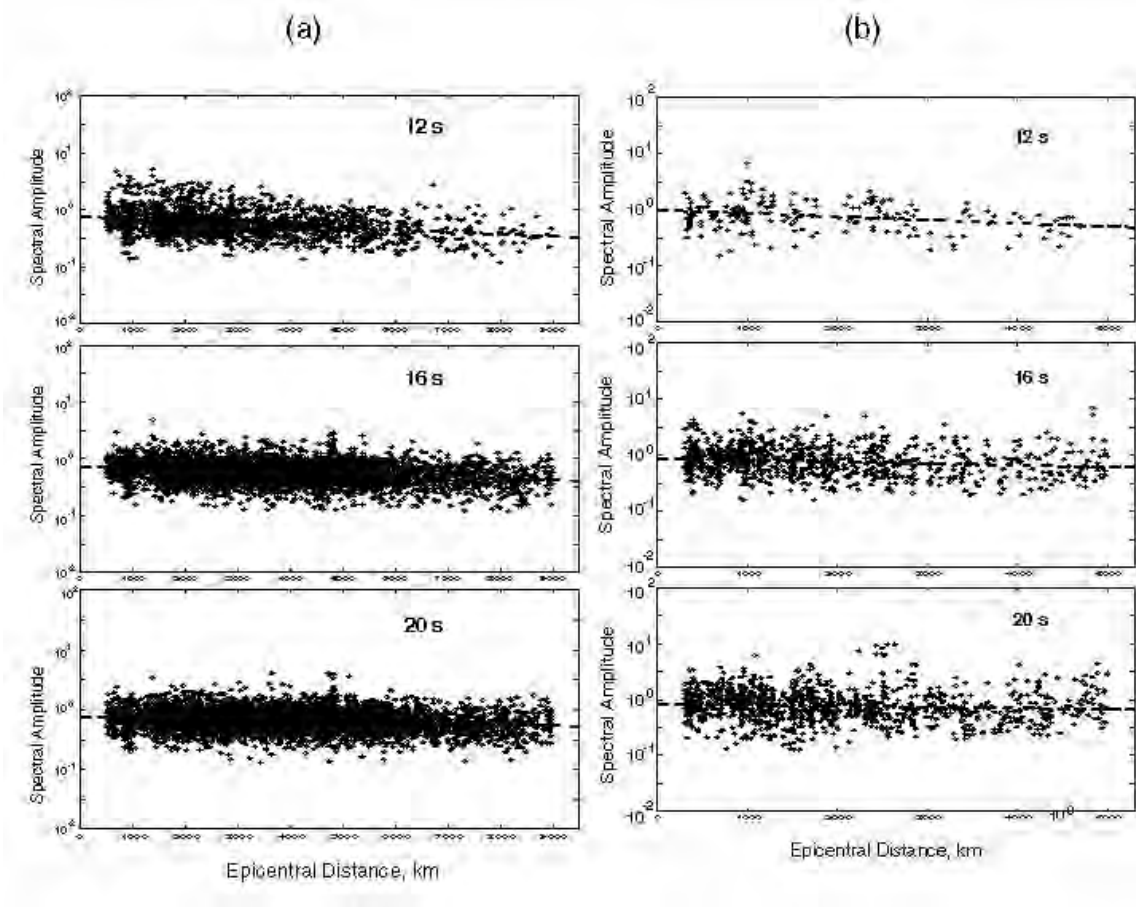

Figure 5. (a) Corrected single station amplitudes as a function of source-receiver distance. (b) Corrected two-station amplitude ratio as a function of inter-station distance. The dashed line is the least-square fit of the data.

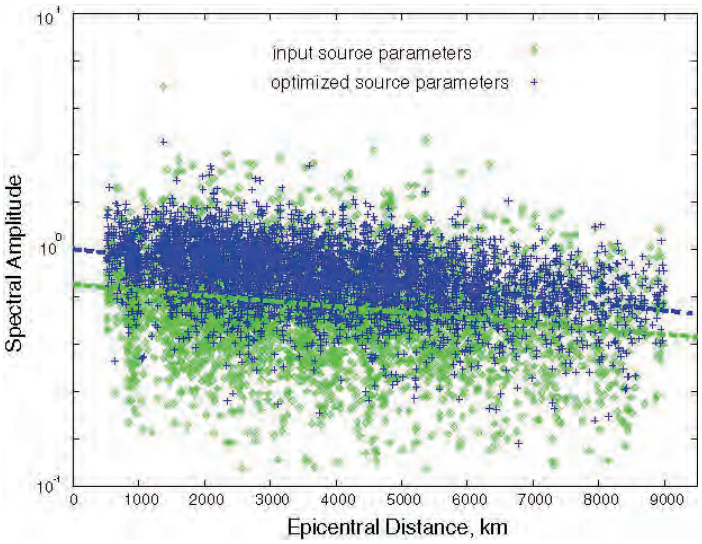

Figure 6. Effect of source parameters' optimization on data shown in Figure 5a at 16s period.

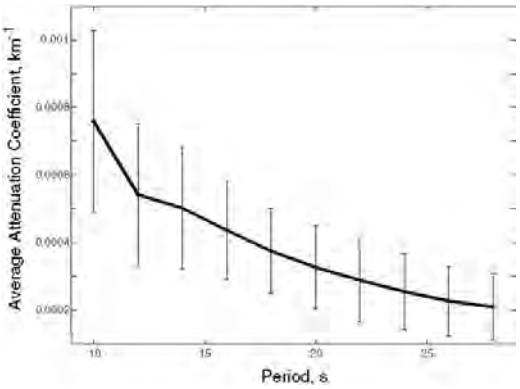

Figure 7. Average attenuation coefficients for a region under study for designated periods obtained using single-station data. Error bars for single-station data are also shown.

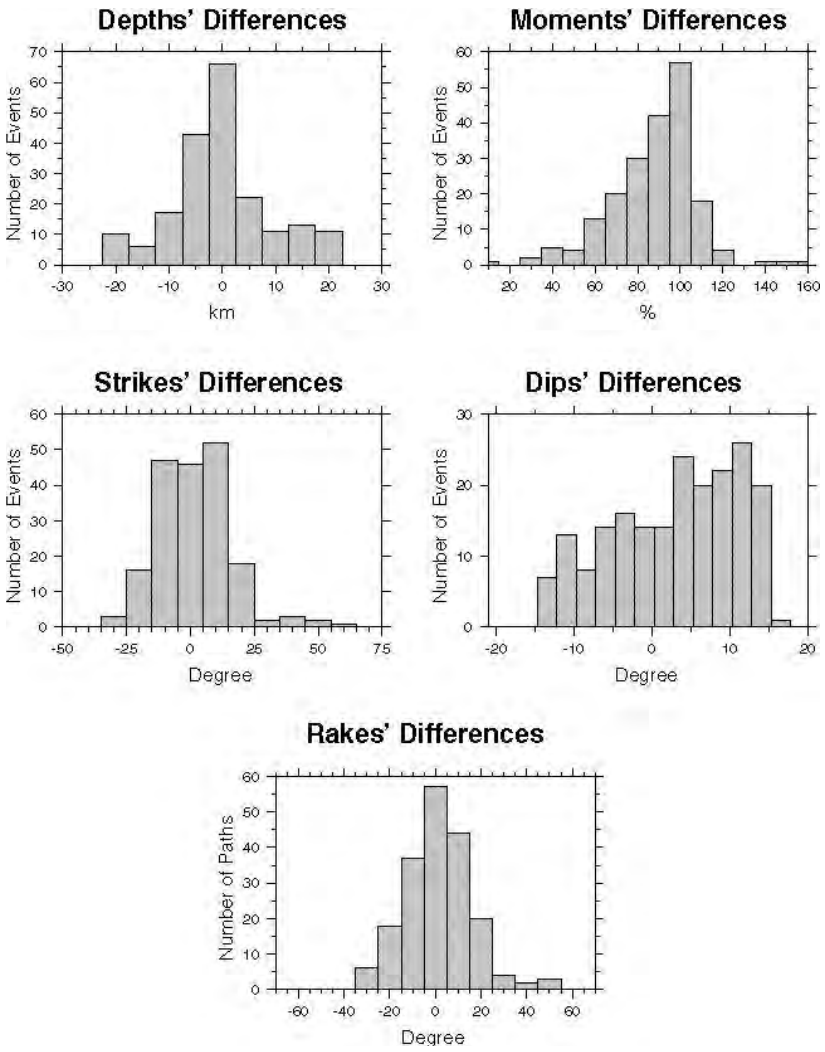

Figure 8. Histograms of differences in source parameters before and after optimization. Differences in scalar moments (top right) are presented as the ratios of moments after and before optimization.

Preliminary Tomographic Maps

Selected data were used for 2-D tomographic inversion using technique described by Barmin et al. (2001). The path density of selected paths for periods 12, 16, and 18 s is shown in Figure 9. We define path density as a number of paths crossing the equatorial cell of size 2°×2°. Figure 9 demonstrates the spatial resolution achieved with selected data. Resulting maps for periods 12, 14, 16, and 18 s are shown in Figure 10.

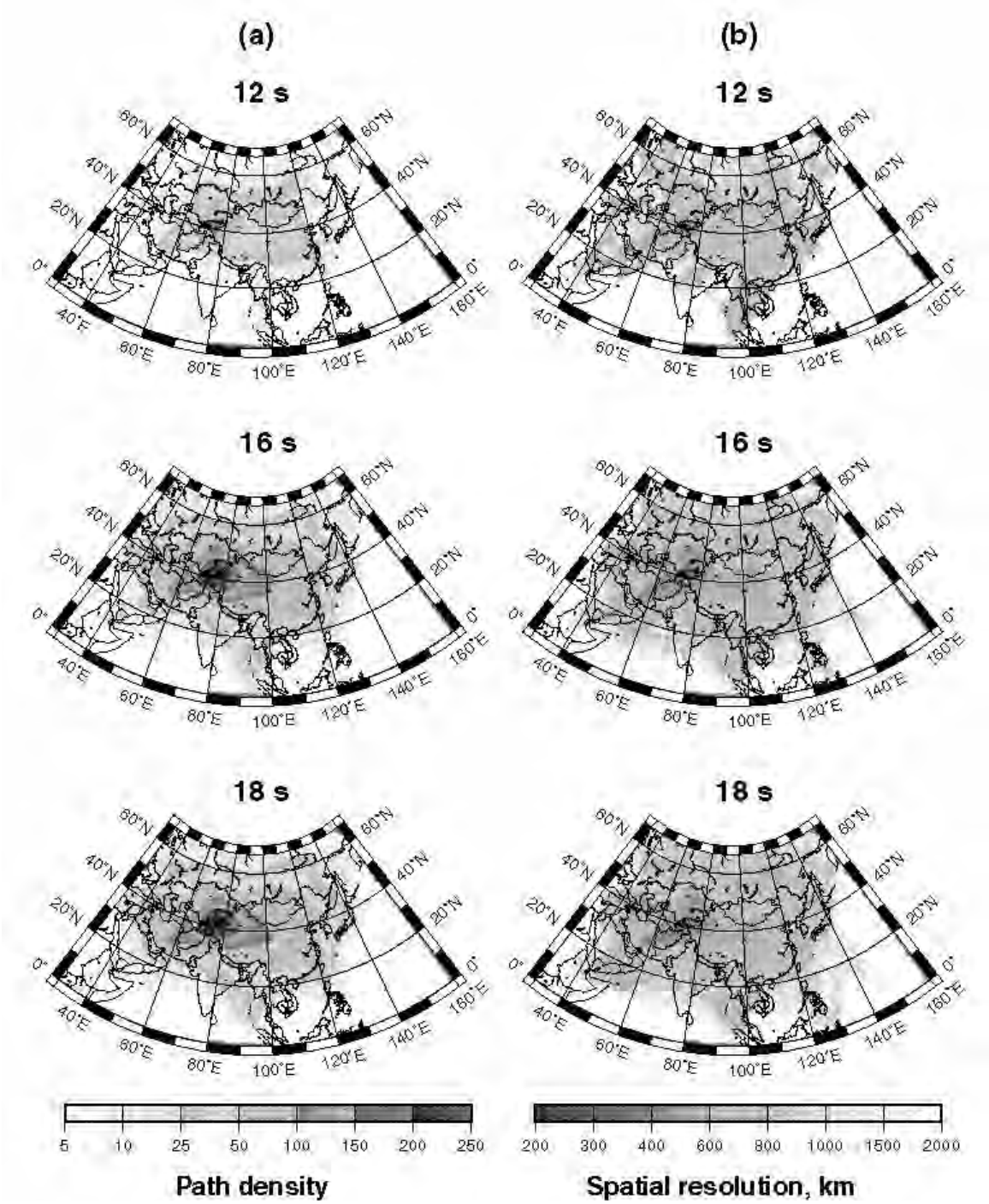

Figure 9. Maps of path density (a) and spatial resolution (b).

We compared these maps with maps obtained by correcting only the scalar moments for each event to minimize residuals of tomographic inversions without changing other source parameters. Comparison shows that the differences between two types of maps are relatively small. Both types of maps display many features that correlate well with geology and tectonics of the studied territory. Low attenuation is typical for stable cratonic regions and high attenuation is observed for tectonically active regions

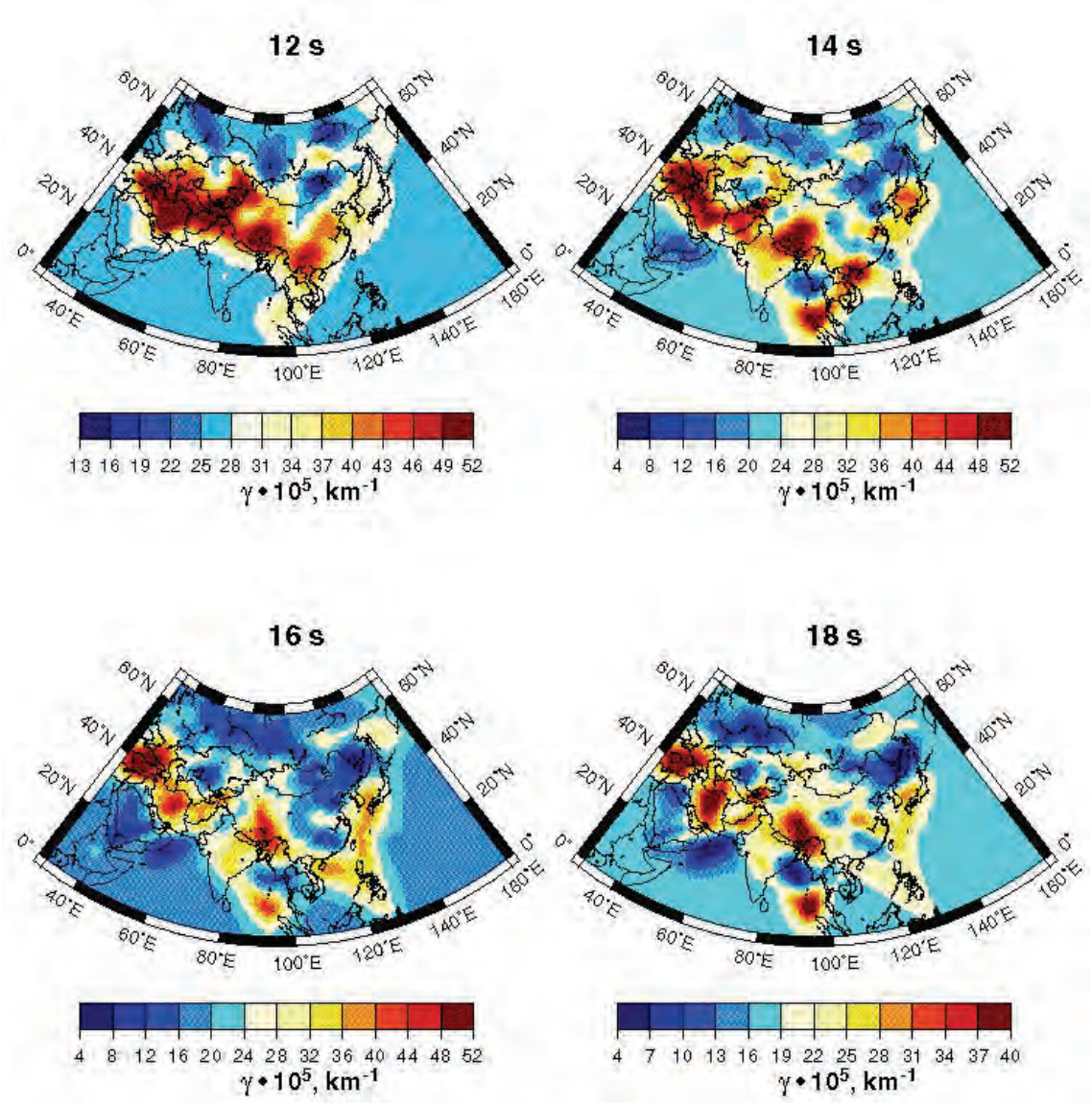

Figure 10. Maps of attenuation coefficients across Eurasia.

CONCLUSIONS AND RECOMMENDATIONS

The modified SWAMTOOL technique permits reliable measurement of surface wave amplitude spectra and evaluation of the quality of measurements. We found that the existing networks and the pattern of seismicity will provide a significant amount of data on spectral amplitudes for periods in the range 12-20 s, appropriate for 2-D tomographic inversion for attenuation coefficients. Data for shorter periods are too scarce for tomographic inversion.

The careful selection of data based on quality estimates by SWAMTOOL and refinement of the source parameters provides a reliable input for 2-D tomographic inversion for attenuation coefficients of Rayleigh waves at periods 12 – 20 s. The preliminary tomographic maps for this range of periods have been obtained which exhibit clear correlation with geology and tectonics of the territory under study. The evaluation of stability of inversion to

different schemes of source parameters' optimization are ongoing. We are also investigating a refined two-station amplitude-ratio measurement procedure to improve both the coverage and the measurement quality of amplitude ratios. Improved ratio measurements will be used in tomographic inversions to produce results that are to be compared with results from single-station amplitude tomographic inversions

ACKNOWLEDGEMENTS

The authors highly appreciate the opportunity to receive digital records from IRIS DMC, GEOSCOPE, and GEOFON. Most figures have been plotted using Generic Mapping Tool (Wessel & Smith 1995: GMT)

REFERENCES

Barmin, M. P., M. H. Ritzwoller, and A. L. Levshin (2001). A fast and reliable method for surface wave tomography, *Pure Appl. Geophys*. 158 (8): 1351–1375.

Basham, P. W. (1971). A new magnitude formula for short period continental Rayleigh waves, *Geophys. J. R. Ast . Soc.* 23: 255–260.

Bonner, J. L., D. R. Russel, D. G. Harkrider, D. T. Reiter, and R. B. Herrmann (2006). Development of a time- main, variable-period surface wave magnitude measurement procedure for application at regional and teleseismic distances, *Bull. Seism. Soc. Am*. 96: 678–696.

Dziewonski, A., Chou, T.-A. & Woodhouse, J. H. (1981). Determination of earthquake source parameters from waveform data for studies of global and regional seismicity, *J. Geophys. Res*. 86: 2825–2852

Engdahl, E. R., R. van der Hilst, and R. Buland (1998). Global teleseismic earthquake relocation with improved travel times and procedures for depth determination. *Bull. Seism. Soc. Am*. 88: 722–743.

Levshin, A. L., T. B. Yanovskaya, A. V. Lander, B. G. Bukchin, M. P. Barmin, L. I. Ratnikova, and E. N. Its (1989). *Seismic Surface Waves in Laterally Inhomogeneous Earth*. (Ed. V.I. Keilis-Borok), Kluwer Publ. House.

Levshin, A.L., X. Yang, M. H. Ritzwoller, M. P. Barmin, and A. R. Lowry (2006). Toward a Rayleigh wave attenuation model for Central Asia, in *Proceedings of the 28th Seismic Research Review: Ground-Based Nuclear Explosion Monitoring Technologies*, LA-UR-06-5741, Vol. 1, pp. 1–10.

Marshall, P. D. and P. W. Basham (1972). Discrimination between earthquakes and underground explosions employing an improved *Ms* scale, *Geophys. J. R. astr. Soc*. 28: pp. 431–458.

Russell, D. R. (2006). Development of a time-domain, variable-period surface wave magnitude measurement procedure for application at regional and teleseismic distances, Part I: Theory, *Bull. Seism. Soc. Am*. 96: pp. 665–677.

Shapiro, N. M. and M. H. Ritzwoller (2002). Monte-Carlo inversion for a global shear-velocity model of the crust and upper mantle, *Geophys. J. Int*. 151: pp. 88–105.

Wessel, P. A. and W. H. Smith (1995). New version of the generic mapping tools released, *EOS, Trans. Amer. Geophys. Un*. 76: Suppl., 329.

Woodhouse, J. H. (1974). Surface waves in a laterally varying layered structure, *Geophys. J. Roy. Astr. Soc*. 37, 461–490.

Yang, X., S. R. Taylor, and H. J. Patton (2004). The 20-s Rayleigh wave attenuation tomography for Central and Southeastern Asia, *J. Geophys. Res.* 108 : B12304, doi:10.1029/2004JB003193.

Yang, X.A., A. R. Lowry, A. L. Levshin, and M. H. Ritzwoller (2005). Toward a Rayleigh wave attenuation model for Eurasia and calibrating a new *Ms* formula, in *Proceedings of the 27th Seismic Research Review: Ground-Based Nuclear Explosion Monitoring Technologies,* LA-UR-05-6407, Vol. 1, pp. 259–265.

SEISMIC CHARACTERIZATION OF NORTHEAST ASIA

Kevin G. Mackey[1], Hans E. Hartse[2], Lee K, Steck[2], Richard J. Stead[2], Charlotte A. Rowe[2], Kazuya Fujita[1], and Luiza Gutirrez[1]

Michigan State University[1] and Los Alamos National Laboratory[2]

Sponsored by the National Nuclear Security Administration
Office of Nonproliferation Research and Development
Office of Defense Nuclear Nonproliferation

Contract Nos. DE-FC52-2004NA25540[1] and DE-AC52-06NA25396[2]

ABSTRACT

Our project of seismic characterization of northeast Asia continues on a multi-faceted approach concentrating on eastern Russia. The field work aspects of the project have included temporary station deployments, new permanent seismic station installations, and calibration of existing digital stations. Seismic station deployments include a 5 station temporary deployment in the Stanovoi Range in southern Yakutia/northern Amur region and two stations deployed in the vicinity of Yakutsk. The station deployments in the Stanovoi Range investigated the connection between a young volcanic field and a large cluster of poorly located historical seismicity and were the first ever seismic deployments in that region of eastern Russia. The volcanic field appears to be aseismic although surrounding areas were found to be very active, with more than 20 locatable local events per day recorded. We also mapped large scale active thrust faults in the region, which combined with observed seismicity will help us understand expected seismicity patterns, location quality, and tectonic models. We also are working on establishing 2 permanent stations in the Amur region and continue to work on station calibrations, with recent data acquired at Stekolnyi.

Our Siberia database enhancements for this past year include (1) addition of new earthquakes and explosions and associated phase data, amplitudes, etc., primarily from the Irkutsk, Yakutsk, and Magadan networks for the years 1999-2006; (2) additions of amplitude data primarily from the Chukotka and Amur regions to aid amplitude tomography efforts; and (3) general quality control efforts primarily targeting unmerged, multi-author origins, the resolution of duplicated arrival information, and the inclusion of United States Geological Survey Earthquake Data Reports (USGS EDR) and International Seismological Centre (ISC) magnitudes for larger events where Russian network operators did not report a K-class or a magnitude estimate.

We have been performing Pn and Pg tomography to obtain average crustal and upper mantle velocities in northeast Asia. Pn velocities are higher beneath the Siberian Platform and generally lower under the tectonically active regions in the central and eastern portions of our study area. Pg velocities show a similar geographic trend, and our results agree closely with Pg results from earlier studies. Pg velocities beneath Sakhalin Island are anomalously low, and we are working to understand this observation. Travel time correction surfaces will be developed from the tomographic maps, and these will be compared to correction surfaces currently being developed from the raw travel time data.

We are using catalog amplitude parameters to derive a two-dimensional (2-D) function that maps laterally varying attenuation features. We are using selected Pg and Sg amplitude readings from the Siberia database. We derive the 2-D attenuation mapping using tomographic methods and compare our results with known tectonic and seismic velocity perturbation features derived in previous work.

We have continued our explosion discrimination work with the current focus on data obtained by our deployed digital stations over the period 2000-2006. We have examined amplitude ratios and find similar results to those previously obtained using analog records. The best results are obtained using full vector ratios, which results in correct event identification as high as 82%.

OBJECTIVES

The main objective of our current research is to improve the overall seismic characterization of northeastern Asia. To accomplish this we seek to develop a complete seismicity database and use this database to discriminate industrial explosions, develop velocity models, and understand the relationship between the sizes and locations of events.

RESEARCH ACCOMPLISHED

Characterization of Seismicity in the Stanovoi Volcanic Field Region

The Stanovoi region of southern Yakutia is one of the most poorly understood seismically active regions in eastern Russia. Although a considerable number of earthquakes have been located in the region (Figures 1 and 2), the epicenters are poor as only regional stations located fairly far away were used in the locations. In addition, the active faults in the region and type of faulting are unknown. The levels of microseismicity are also unknown as no seismic stations have ever been deployed within several hundred kilometers. Within the Stanovoi region, a province of Cenozoic basaltic volcanism (0.5-1.0 ma) exists that is in the general vicinity of a cluster of previously located earthquakes. It has been previously unknown if the seismicity has any connection to the volcanic field or to apparent faults visible in the topography of the region. In addition, the proposed Russian extension of the Tanlu fault from China may terminate in the vicinity of the Stanovoi Range (Mackey et al., 2003). In this study we conducted a temporary deployment of 5 broadband seismic stations encircling the Stanovoi volcanic field in an attempt to characterize the area and gain insight into the many questions of the area.

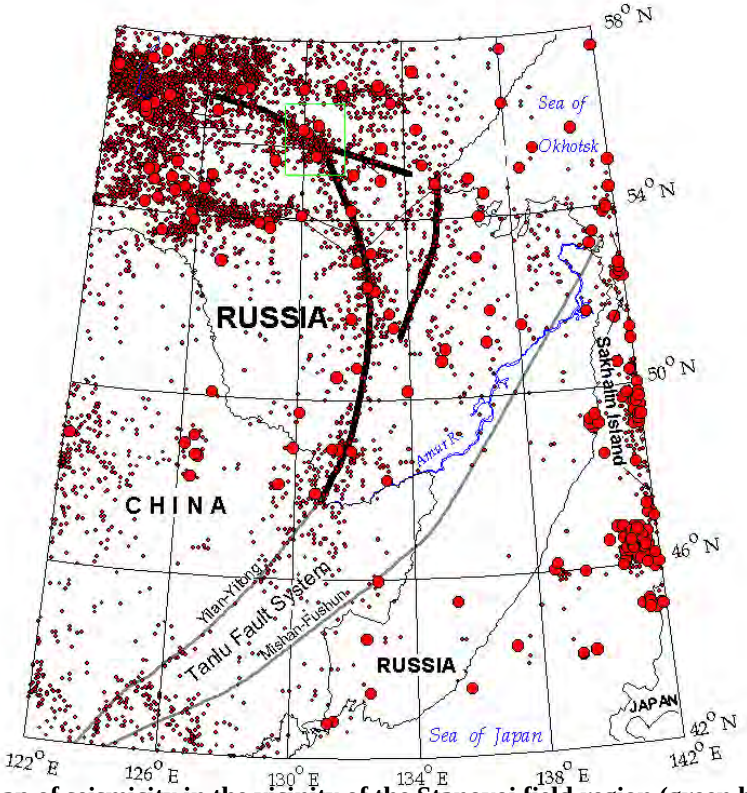

Figure 1. Index map of seismicity in the vicinity of the Stanovoi field region (green box). The heavy black line indicates possible extension of the Tanlu fault into Russia from China. In the vicinity of the Stanovoi region, it intersects a large generally east-west fault system (also heavy line) that is clearly visible on topographic maps and satellite images, but essentially unstudied. Figure modified from Mackey et al., 2003.

Station Deployments

Five broadband seismometers and digital recorders were deployed by helicopter on 12 August 2006 in the vicinity of the Stanovoi volcanic field (Figure 2). Typical station installation included digging a post hole for the instrument and burying it for thermal and wind isolation (Figure 3). Two stations were powered by batteries and solar panels, which were hampered by nearly continuous rain and poor weather starting August 13. These stations operated intermittently over about 20 days of the deployment portion of the experiment. One of these two stations was destroyed by a bear on about 23-24 August (Figure 3). Three stations were powered by large batteries. Two of these stations failed early (operating 5 and 12 days respectively) due to drained batteries. The third battery powered station was destroyed by a bear on 16 August.

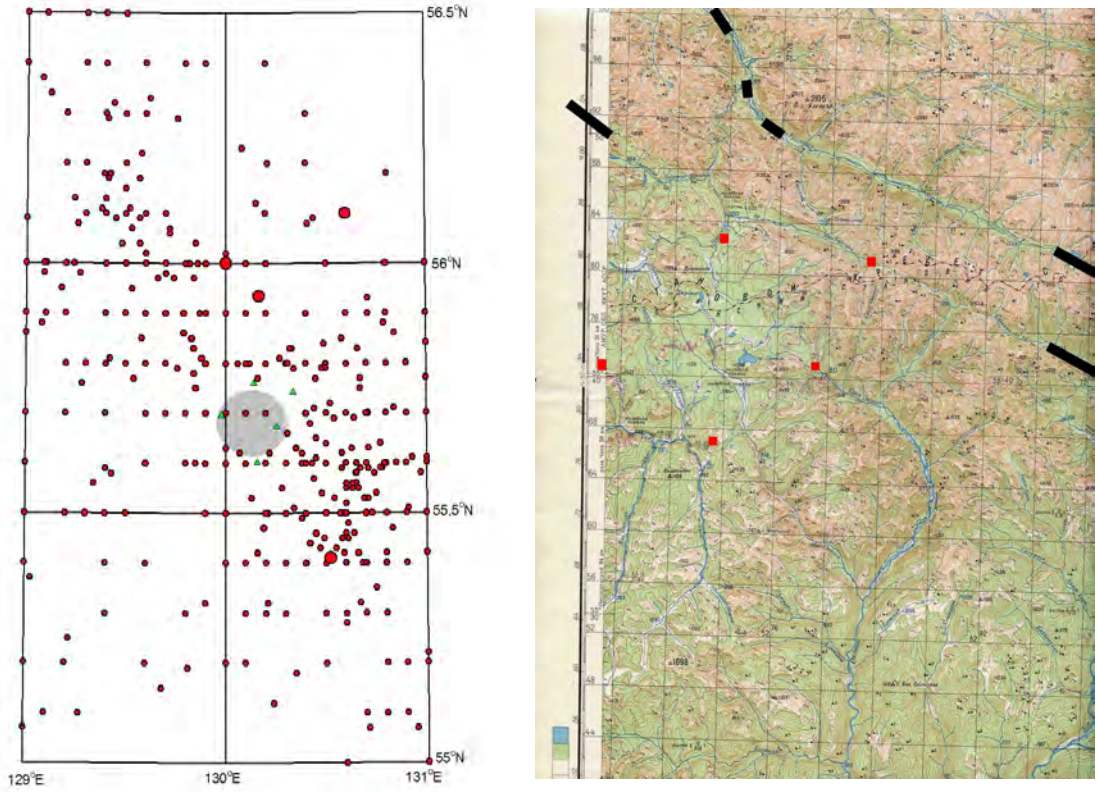

Figure 2. Left - Historic seismicity of the Stanovoi volcanic field region (approximately the grey circle). Events larger than magnitude 4.0 are shown as larger. Stations deployed as a part of this study are shown as green triangles. Note that the epicenters scatter nearly everywhere, with a slight concentration to the southeast of the volcanic field. Right - Topographic map of the Stanovoi deployment region. Stations are shown with red squares. The two eastern stations were destroyed by bears. Black bars indicate linear trends interpreted to be faults. Extensive thrust fault scarps were visible in the southern valley wall of the southern valley near the western edge of this map. The region of the Stanovoi volcanic field generally encompasses the region encircled by the seismic stations. Grid lines on this map are spaced at 4-km intervals.

Volcanic Field and Fault Lineations

Topographic maps of the Stanovoi volcanic field region indicate two large parallel linear features generally striking east-west immediately to the north of the volcanic field (Figure 2). These have previously been interpreted as strike-slip faults based on their linearity. However, in the process of deploying to the field area by helicopter, we traveled along the southern of the two valleys. In the southern side of the valley, approximately 20-40 km west of the deployed station sites, there are extensive young fault scarps on the side of the valley. The scarps are very well defined in places and are clearly southward dipping thrust faults (Figure 4). The scarps and thrust fault shown are poorly documented in the literature. There is also evidence of strike-slip faulting along the northern sides of both the northern and southern lineations. Collectively, this may indicate a region of complex tectonics.

Figure 3. Left - Typical station installation consisting of a Geotech Instruments KS-2000 broadband seismometer, Smart24 digitizer, and large battery. Right – A seismic station shown as found after destruction by a bear. The bear removed all station coverings and batteries and extracted the seismometer from its posthole.

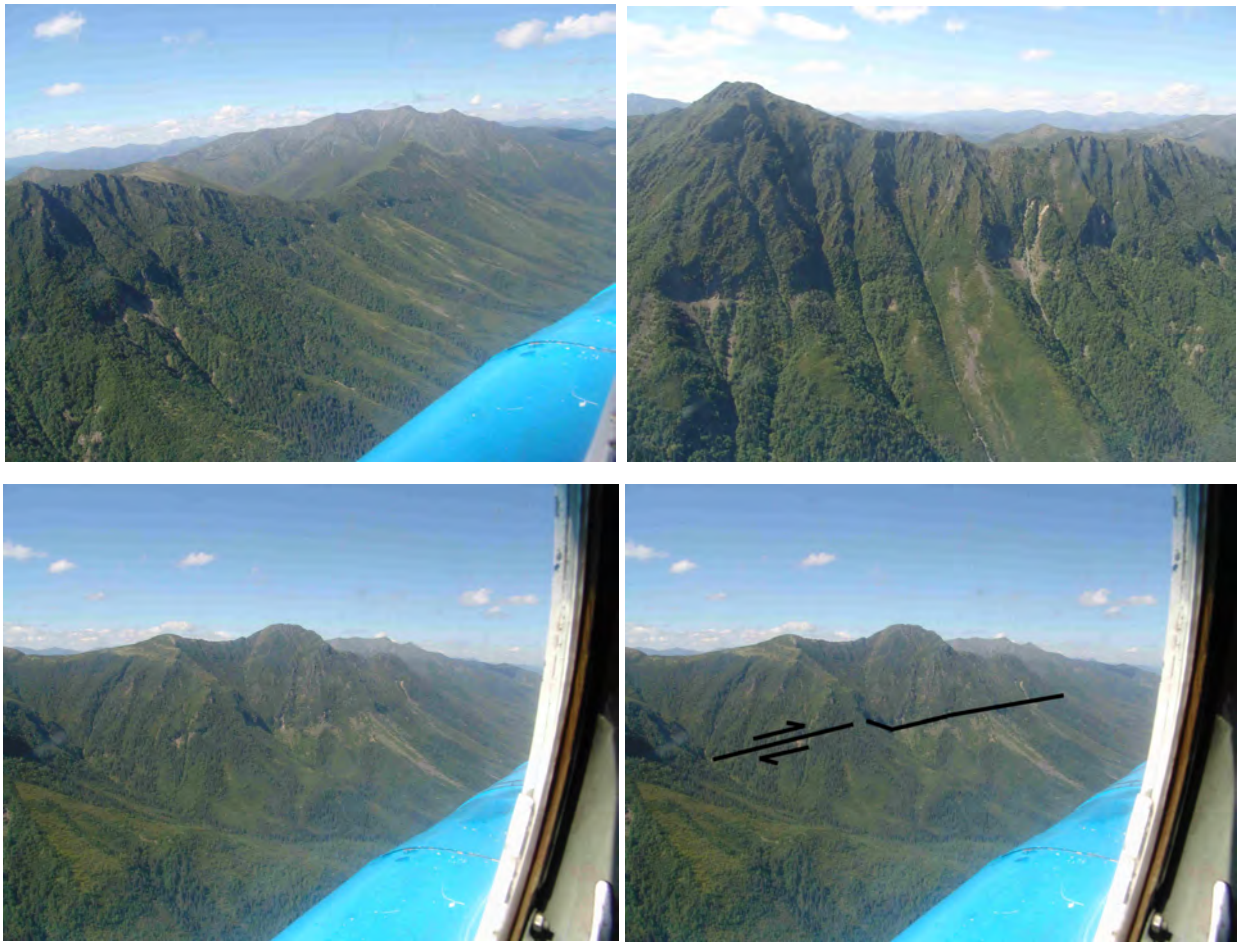

Figure 4. Upper—Photos of a well defined fault scarp visible along the southern wall of the southern linear valley (Figure 2, right) just west of the Stanovoi volcanic field. Lower—Interpretation of the same fault scarp as a thrust where the plunging dip is apparent in a side valley.

Seismicity

Although we experienced difficulty with some equipment and station destruction by bears, the situation was compensated for by higher levels of seismicity than was expected. Analysis of five days of seismic data revealed approximately 100 locatable earthquakes occurring within 50 km of the deployed stations (Figure 5) and many additional events at greater distances. A review of remaining data when only 1 or 2 stations were operating indicated many additional events. Most events are found to occur in localized clusters immediately to the southeast of the deployed network. The events located in the vicinity of the volcanic field range in magnitude from a maximum of about 2.7 down to less than 0.0. Note that there is no evidence of any type of aftershock sequence being recorded here. It is interesting to note that no events have yet been found that occur within the boundaries of the volcanic field, which thus far appears quiescent. With a couple exceptions, the events all occur to the south of the presumed strike-slip faults, consistent with the southern side being underlain by an active thrust. Depths of the locatable earthquakes are generally ranging between 9 and 15 km. An image of seismograms showing several events is in Figure 6.

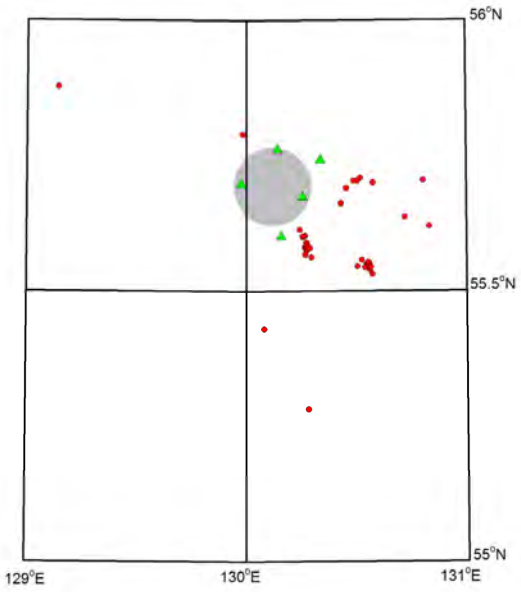

Figure 5. Locations of earthquakes recorded during the first four days of network deployment (red). Deployed stations shown as green triangles. Note that most events occur to the south and east of the stations, and no events are found that have occurred within the Stanovoi volcanic field (grey circle).

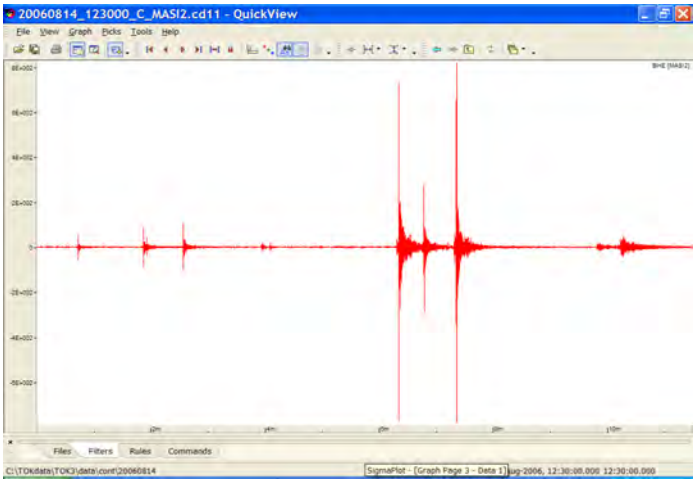

Figure 6. Image of multiple earthquakes of varying distances occurring within minutes of each other. These events occurred on September 14, 2006.

Stanovoi Study Conclusions

We have conducted the first targeted seismicity characterization study in the vicinity of the Stanovoi Range and the young Stanovoi volcanic field. Previously it was unknown if seismicity in the immediate vicinity was associated with the volcanic field. From the seismicity data and geological observations while in the field, we can make several basic conclusions for seismic characterization of the area: 1) The Stanovoi Range is more seismically active than was previously understood. 2) There appears to be no seismic activity associated with the Stanovoi volcanic field, thus explosive volcanic events are not to be expected. 3) The area may be dominated by north-south convergence and thrusting and, given the extent of visible scarps, the region may be expected to generate large earthquakes.

Database Expansion

We added about 17,000 new events to our database, with most additions coming from the Irkutsk, Yakutsk, and Magadan networks for the years 1999-2007 (Figure 7). Our total event count is now over 250,000, with over 342,000 distinct origins tied to the events. These new events also included about 100,000 new arrival times, bringing our total arrival count to about 1.44 million. Michigan State University (MSU) provided additional amplitude values from hardcopy bulletins for the Chukotka and Amur regions to provide improved ray coverage for ongoing tomography projects (see Rowe et al., these Proceedings, and Zhang et al., these Proceedings). Between new bulletins and the supplemental amplitude values we added about 60,000 new entries to our database, bringing the total amplitude count to near 690,000. For some larger events (about M > 6.0), Russian networks operators did not provide K-class or magnitude estimates. For these events, we are now obtaining magnitude values from the Los Alamos National Laboratory (LANL) global database, typically reported by the ISC or the USGS. Finally, we spent time merging some distinct origins into single events, and we corrected some origin time and arrival time data entry errors, which typically involved typos for hours, minutes, or seconds in our original bulletins.

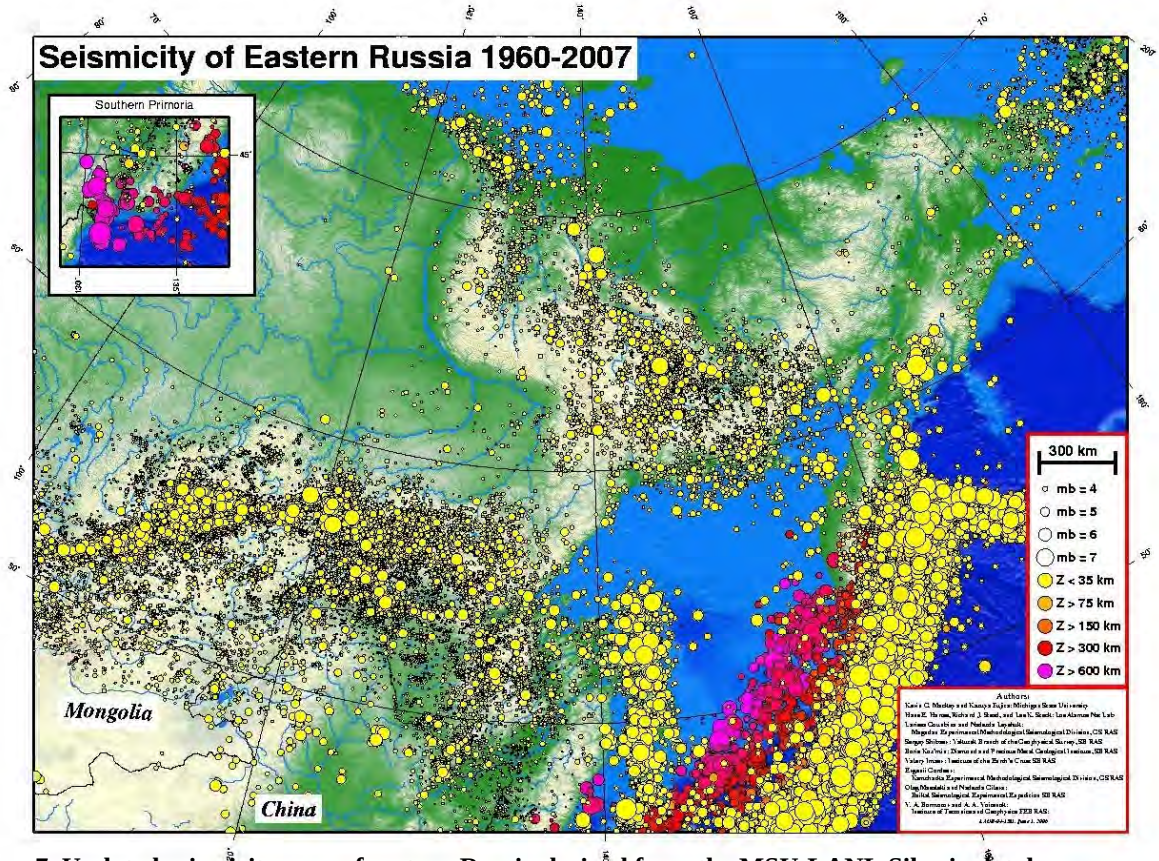

Figure 7. Updated seismicity map of eastern Russia derived from the MSU-LANL Siberia database.

Tomography

Results of crustal Pg phase velocity tomography and Lg attenuation tomography may be found in the paper by Rowe et al., these Proceedings. This work was conducted in part under this contract. Related work performed under a different contract is presented in Zhang et al., these Proceedings.

Digital Waveform Explosion Discrimination

Amplitude Discrimination

We have expanded our explosion discrimination research. Our previous work investigated explosion discrimination using amplitude data reported in the historic Russian seismic bulletins, which were derived from analog records. The methodology and results for the analog data discrimination are presented in Mackey et al. (2006) and Linkimer (2006). We apply the same methodology here to investigate Pg/Sg ratio discriminants using digital seismograms. We analyzed 34 explosion waveforms and 211 earthquake waveforms, picking amplitudes for all components of Pg and Sg waves. The digital waveforms analyzed were all within the Magadan region and recorded short period seismometers (3 components) stations, with the exception of data from Seimchan, recording broadband STS-1 instruments; thus it is possible to compare results of the analog and new digital studies. Following our previous methodology, we calculated 5 Pg/Sg ratios varying by component (Pg_z/Sg_z, Pg_h/Sg_h, Pg_z/Sg_h, Pg_h/Sg_z, and full vector Pg/Sg). We have not yet calculated network averaged ratios with the analog data, as additional stations need to be analyzed.

Comparing results of analog data discrimination (Mackey et al., 2006; Linkimer, 2006) with new digital data results, we find that we achieve better results using digital data, with generally a 10-12% improvement. In both cases, full vector Pg/Sg ratios discriminate best (Figure 8), and Pg_h/Sg_z are worst (Table 1). We also note that the critical values obtained for discriminating explosions are 2-3 times larger (depending on ratio) or higher for the digital data than the analog data (note that the critical value is the Pg/Sg ratio value that best discriminates explosions from earthquakes). It is unclear why the critical values differ between digital and analog data. Application of critical values derived from analog data is not transportable to digital data even though the seismometers used are identical (Table 1, column 4).

Table 1. Comparison of event discrimination results between analog and digital data for the Magadan region of eastern Russia.

Raw Phase Ratio	Analog Results (Mackey et al., 2006; Linkimer, 2006)		Digital Results		Results of Analog Critical Value Applied to Digital Data
Discriminant	% Events Correctly Classified	Critical Value	% Events Correctly Classified	Critical Value	% Events Correctly Classified
Pg_h/Sg_h	70.7%	0.23	80.7%	0.55	59.8%
Pg_z/Sg_z	63.8%	0.33	80.5%	0.88	65.5%
Pg_h/Sg_z	62.8%	0.48	73.9%	0.83	68.8%
Pg_z/Sg_h	67.0%	0.18	79.5%	0.62	58.3%
Full Vector	70.9%	0.27	82.4%	0.41	63.3%

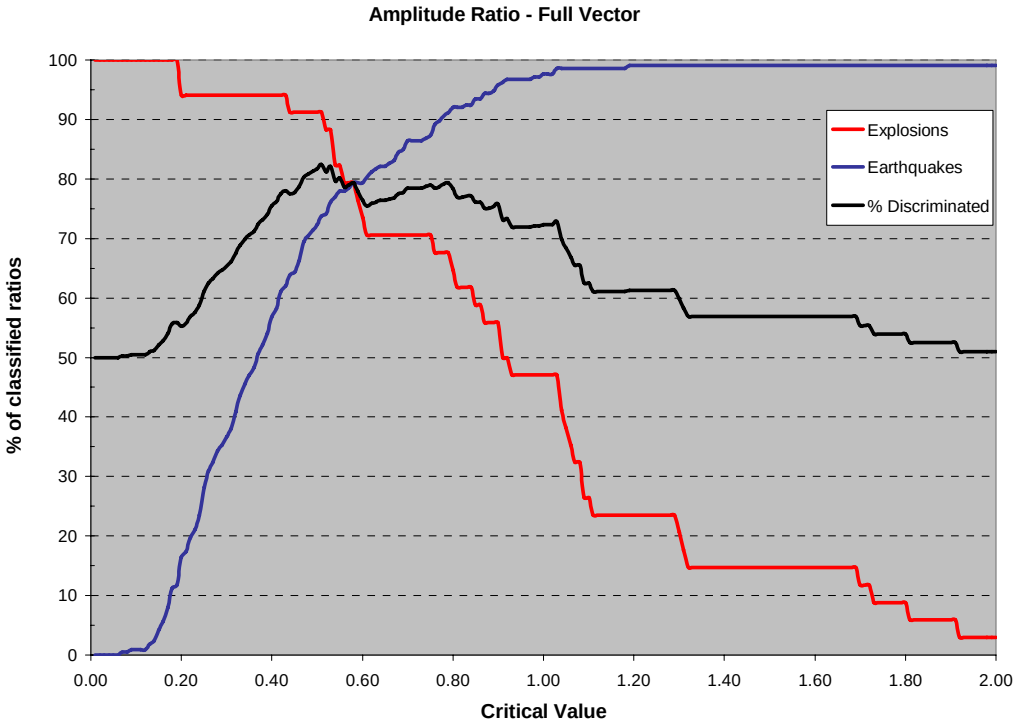

Figure 8. Full vector Pg/Sg ratio critical value determination for discriminating explosions from earthquakes using digital data from the Magadan region, eastern Russia.

Spectral Discrimination

Many of the mining explosions that take place in eastern Russia are ripple fire explosions in surface or open pit mines. Most mines in this area fire lines with a 50-ms delay. In effect, this generates a 20 Hz signal in the ground that appears to be characteristic of the regions mine explosions when the spectral amplitudes are compared to earthquakes. Figure 9 compares the typical spectral amplitude of a mine explosion to an earthquake of a similar size and distance. Note that the explosion has a spectral amplitude peak in the 18-20 Hz range, which is absent on the earthquake spectrum. It is unclear why the spectral amplitude peak of the explosions occurs slightly below the expected 20 Hz, though it may be a result of delays being slightly greater than the presumed 50 ms. The spectral peak is visible using just the P wave or S wave, or the entire waveform and is apparent on all components. Additional research is needed to develop a viable discrimination methodology using this technique.

CONCLUSIONS

The research performed here has significant implications for the interpretation of seismicity and tectonics in the Amur District, where there is significant contamination of the seismicity catalogs by industrial explosions and where the present-day tectonics are poorly understood. This will affect interpretation of tomographic models of the region (e.g., Zhang et al., this volume) and similar studies as they are extended into the even less well-known Magadan and northeastern Yakutian regions.

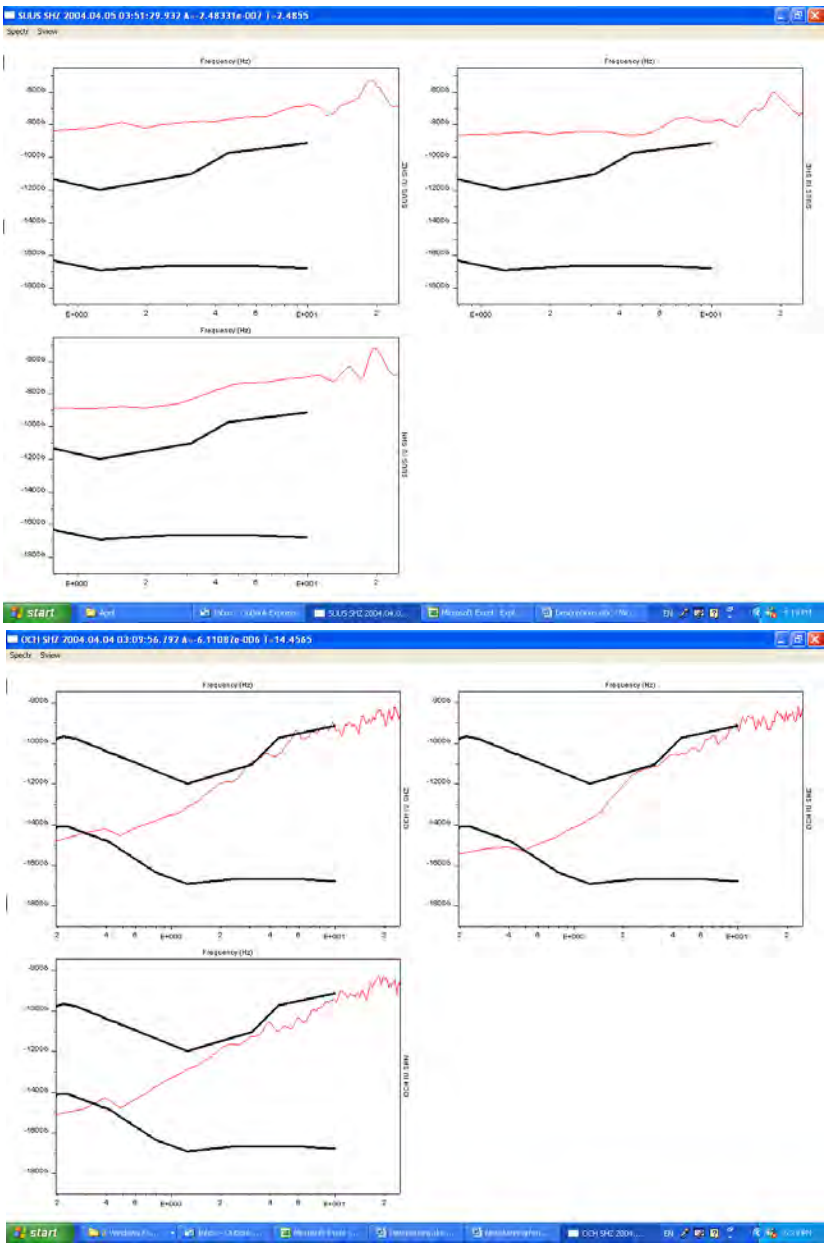

Figure 9. Top - Three component spectral amplitude plots for a mine explosion. Note that there is a dominant peak at 19-20 Hz that may result from a 50 ms delay between lines fired in the explosion. Bottom – a similar three-component spectral amplitude plot for a tectonic earthquake showing the absence of a 20 Hz peak.

REFERENCES

Linkimer, L. (2006). Discrimination of Earthquakes and Explosions in Eastern Russia by Amplitude Ratios Obtained from Analog Records. *MS Thesis*, Michigan State University, East Lansing, 180pp.

Mackey, K. G., H. Hartse, K. Fujita, L. Linkimer, L. Steck, R. Stead, and C. Rowe (2006). Seismic characterization of northeast Asia, in *Proceedings of the 28th Seismic Research Review: Ground-Based Nuclear Explosion Monitoring Technologies*, LA-UR-06-5471, Vol. 1, pp. 93–102.

Mackey, K. G., K. Fujita, L. V. Gounbina, B. M. Koz'min, V. S. Imaev, L. P. Imaeva, and B. M. Sedov, (2003). Explosion Contamination of the Northeast Siberian Seismicity Catalog: Implications for Natural Earthquake Distributions and the Location of the Tanlu Fault in Russia, *BSSA*, 93 (2): 737–746.

Rowe, C. A., W. S. Phillips, M. Maceira, M. L. Begnaud, L. K. Steck, X. Yang, C. L. Lucero, H. E. Hartse, R. J. Stead, K. Mackey, K. Fujita, and C. Ammon, (2007). Geophysical imaging of Asia and Siberia: Tomography for seismic velocity, upper mantle gradient, Lg attenuation, and joint inversion of surface wave dispersion, receiver functions and satellite gravity data, in current. Proceedings.

Zhang, H., K. G. Mackey, K. Fujita, L. Steck, C. Rowe, C. Thurber, and S. Roecker, (2007). High resolution three-dimensional seismic imaging of Baikal and Amur regions of eastern Russia, in current Proceedings.

EXTENSION OF THE CAUCASUS SEISMIC INFORMATION NETWORK STUDY INTO CENTRAL ASIA

Randolph J. Martin[1], Mary L. Krasovec[1], Spring A. Romer[1], Larry J. Hutchings[2], William Foxall[2], Eileen S. Vergino[2], Levent Gulen[3], and M. Nafi Toksöz[3]

New England Research[1], Lawrence Livermore National Laboratory[2], and Earth Resources Laboratory[3]

Sponsored by National Nuclear Security Administration
Office of Nonproliferation Research and Development
Office of Defense Nuclear Nonproliferation

Contract No. DE-AC52-04NA25612

ABSTRACT

The Central Asian Seismic Research Initiative (CASRI) is an extension of the Caucasus Seismic Information Network (CauSIN). Both projects seek to build knowledge bases of geological, geophysical, and seismic information in their respective regions and to use crustal modeling techniques to create a combined model of the regions to aid in seismic monitoring.

Catalog and phase arrival data from local networks in the CASRI region (Kazakhstan, Kyrgyzstan, Tajikistan, and Uzbekistan) have been collected. The historical catalog contains nearly 11,000 events from 500 AD through the present. The modern catalog of the region includes 469 events from 1991 to 2005.

Participants in the project are validating data quality and preparing phase arrival tables. Because these data have never before been shared with the world-wide seismic community, care is being taken to use consistent station naming and descriptions for each station. The phase arrival data from Kazakhstan includes 2,991 seismic phases for 71 events in Kazakhstan and 2,257 phases for events in other countries in the region. Kyrgyzstan's phase data include 2,500 arrivals picked from roughly half of the events in the country; local scientists are continuing to make picks from the rest of their data and will eventually expand to pick times from events in the other CASRI countries.

Other new acquisitions include newly released explosion data in paper print-out format, which provide ground truth and are invaluable to crustal tomography and validation of earth models. These data include 600 records from 177 events and 33 stations. Event-station separations range from 450 to 2,500 km. These data are in the process of being digitized.

This seismic travel time data, combined with the available geophysical and tectonic information, will be used for the tomographic modeling of the CASRI region.

OBJECTIVE

The primary goal of this project is to develop a database of geology and active tectonics in the Caucasus and Central Asian regions. With this new database, we will be able to improve earthquake locations and identify potential "ground truth" (GT) events. The dense network, calibration events (mining and quarry blasts), improved models, and better location algorithms (including multiple-event grid search, and double difference) will improve the event locations. Scientists at collaborating countries are very eager to assist with this task, since improved locations will aid in the identification of active faults.

With the GT events to serve as validation, we will obtain a detailed crust/upper mantle structure in Central Asia, using data from newly installed seismic stations as well as GSN and other stations operated as part of the national networks.

RESEARCH ACCOMPLISHED

Event Catalog

Figure 1 shows locations of events in the unified catalog from local networks in the CASRI region. It includes almost 11,000 events from historic times through 2005.

Phase Arrival Data

Phase arrival tables have been received from CASRI participants (Kazakhstan, Kyrgyzstan, Tajikistan, and Uzbekistan). Because these data have not previously been shared with the world-wide seismic community, care is being taken to use consistent station naming and descriptions for each station, and to ensure the quality of the phase picks. The data are still undergoing this processing.

The National Nuclear Center (NNC) in Kazakhstan operates a number of stations, (listed in Table 1 and shown in Figure 2) most of which are analog stations still operating from the Soviet era. Scientists at the NNC have put a great of effort into picking travel times from analog records and have contributed over 5,000 phase picks to the CASRI database; 2,991 of these picks are from 71 events in Kazakhstan, 2,257 are from events in other countries in the region.

Table 1. Coordinates of NNC station network, Kazakhstan. The coordinates of 3-component instruments are shown for the arrays.

Station name	Station code	Elevation, m	Latitude	Longitude
Borovoye (IRIS)	BRVK	315	53.0578	70.2828
Vostochnoye (array)	VOS	300	52.7232	70.9797
Zerenda (array)	ZRNK	384	52.9508	69.0043
Chkalovo (array)	CHKZ	123	53.6762	70.6152
Kurchatov (IRIS)	KURK	240	50.7149	78.6208
Makanchi (IRIS)	MAKZ	600	46.8075	81.9774
Talgar	TLG	1210	43.2487	77.2237
Podgornoye	PDG	1277	43.3274	79.4849
Karatau (array)	KKAR	475	43.1034	70.5115
Makanchi (array)	PS23	554	46.7937	82.2904
Borovoye (array)	AS057	361	53.0240	70.3880
Aktyubinsk	AKTK	360	50.4348	58.0167
Akbulak (array)	ABKAR	362	49.2558	59.9431

Kyrgyzstan operates the Kyrgyz broadband seismic network (KNET), shown in Figure 3. Phase data include 2,500 arrivals picked from roughly half of the events in the country; local scientists are continuing to make picks from the rest of their data and will eventually expand to pick times from events in the other CASRI countries.

Uzbekhistan's store of seismic records are still being analyzed by local scientists. There have been 75 analog stations operating at different times within the country from 1901 to the present. Uzbek scientists have identified 46 stations that have recorded for a consistent period (others were for special deployments), and currently have 19 analog seismic stations operating. Phase arrivals from 21 events have been identified in the Tashkent station, and records from the Ferghana station are being analyzed now. Phase-arrival data from these records will be added to the CASRI database as soon as they are available.

Tajikistan's seismic network includes only strong motion stations. These records are useful to the seismic hazards assessment carried out by project participants at Lawrence Livermore but do not contribute to the crustal tomography studies, which are the focus of this report.

GT Event Data

On October 9, 2006, at 01:35, North Korea carried out an underground nuclear test. This event was registered by nuclear monitoring seismic stations network of Kazakhstan's NNC; the clearest signals were recorded by Akbyulak stations, Borovoye large aperture array (Vostochnoye, Zerenda, Chkalovo stations)., shown in Figure 4. There stations are located 3,750–4,500 km away from the explosion epicenter.

Seismic event parameters: North Korea nuclear test
Origin time 01:35:28 41.311
Coordinates: latitude 41.311, longitude 129.114
Magnitude 3.6–4.2

Another GT event is the crash of the "Dnepr" carrier rocket, which fell to earth during a failed launch in June 26, 2006. Two seismic arrays in the National Nuclear Center monitoring network registered the seismic signature of the event. Akbulak is in Western Kazakhstan and Karatayu located in Southern Kazakhstan; these stations were 571 km and 625 km away from the event, respectively. Figure 5 shows the detected signals. The Center for Acquisition and Processing of the Special Seismic Information, Almaty, calculated the event energy to correspond to an earthquake with a magnitude of M = 3, energy class 6.

A third source of GT data is a series of underground nuclear explosions that were carried out in Kazakhstan. A total of 177 events were recorded on 33 stations in Central Asia at distances from 450 to 2500 km, resulting in approximately 600 photographic paper records, which are currently being processed.

Tomography: Expanding on the CauSIN Project

One of the main goals of this project is to use phase-arrival times to form tomographic images of the crust and upper mantle. The approach we are using is the same as that applied in the CauSIN region, which utilized data from local networks in the Central Caucasus countries of the Republic of Georgia, Armenia, and Azerbaijan, in combination with data from the International Seismological Centre (ISC) and the Army's Space Missile Defense Command (SMDC), to form images of unprecedented resolution.

During the CauSIN project, a 3-D P-wave velocity model was developed for the crust and uppermost mantle of the Caucasus and the surrounding area by applying the tomography method of Sun and Toksöz (2006); 300,000 high-quality P-wave first arrivals from 43,000 events between 1964 and 2005 were used. This tomographic method accommodated velocity discontinuities, such as the Moho, in addition to smooth velocity variations. The spatial resolution was 1° × 1° in the horizontal direction and 10 km in depth.

Figures 6 and 7 shows Pn and P wave imaging results from the CauSIN project. Strong P-wave velocity variations of more than 6% found in the study area indicate the existence of significant structural heterogeneities in the crust and uppermost mantle in this region. The Pn velocities shown in Figure 6 have similar features to those obtained by Al-Lazki et al. (2004). High Pn velocities are dominant under eastern Azerbaijan/southern Caspian and under the eastern Black Sea. The extent of the anomalies require further

confirmation; because of the distribution of earthquake epicenters and stations in the CauSIN database, rays traversing the area are mostly NW-SE, and likely have resulted in "smearing" along the dominant ray direction.

Repeating this imaging process with a joint dataset from the CauSIN and CASRI projects will extend our data coverage to the east, and should improve the image of the high velocity zones under the northern and southern Caspian Sea.

Events, stations, and ray paths in the current CASRI phase arrival time database are shown in Figure 8. This includes ISC data up until 2002 and is currently being updated to include more recent ISC data as well as the data discussed in the previous sections of this report.

CONCLUSION AND RECOMMENDATION

Efforts at improving communication and increasing the availability of seismic data among the countries of the Caucuses have met with success. Progress has been made in building a database that can be used toward the final goal of improving crustal models of the region.

REFERENCES

Al-Lazki, Ali I., E. Sandvol, D. Seber, M. Barazangi, N. Turkelli, and R. Mohamad (2004). Pn tomography imaging of mantle lid velocity and anisotrophy at the junction of the Arabian, Eurasian and African plates, *Geophy. J. Int*. 158: 1024–1040.

International Seismological Centre (2001). *Bull, Internatl. Seis. Cent*., on-line bulletin, http://www.isc.ac.uk/.

Sun, Y. and M. N. Toksöz (2006). Crustal structure of China and surrounding regions from P wave traveltime tomography. *J. Geophys. Res*. 111: B03310, doi:10.1029/2005JB003962.

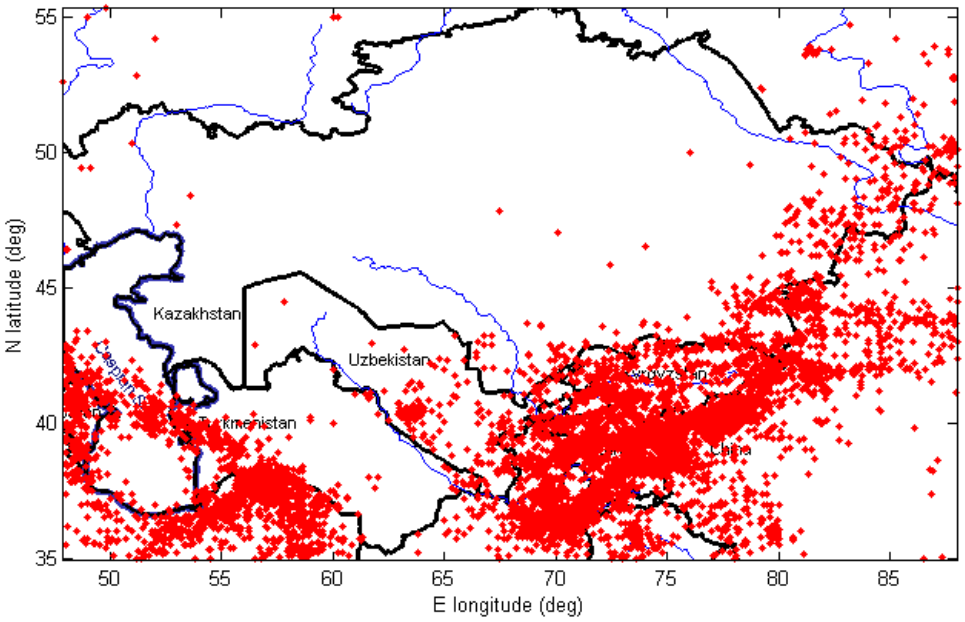

Figure 1. Events in the unified CASRI database, which includes nearly 11,000 events, both historical and from modern records.

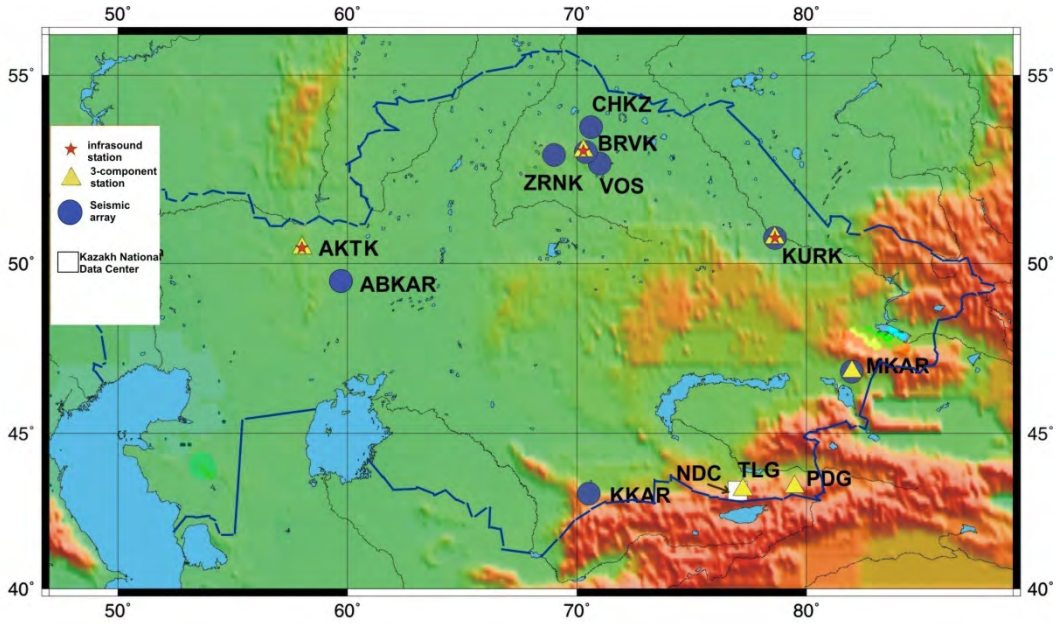

Figure 2. Kazakhstan's seismic array. More information about these stations is given in Table 1.

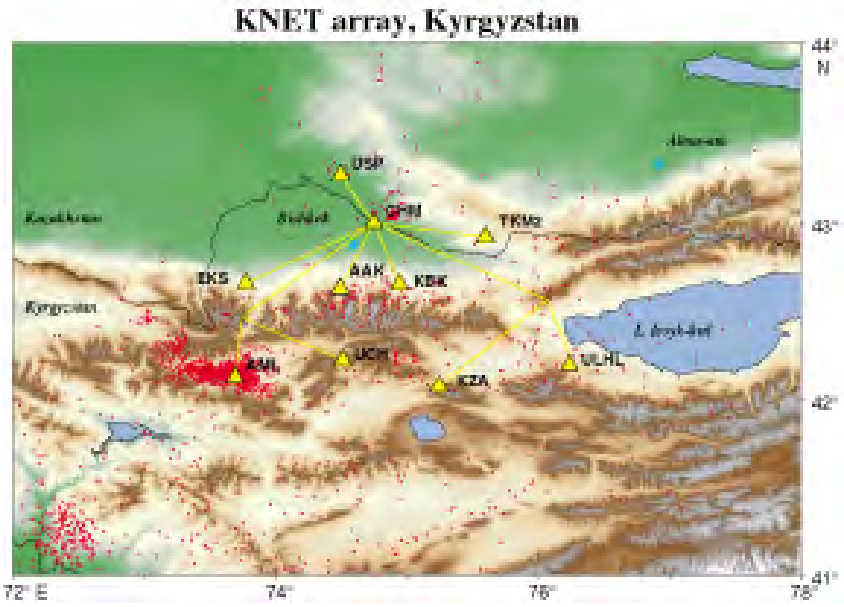

Figure 3. Kyrgyzstan's KNET seismic array.

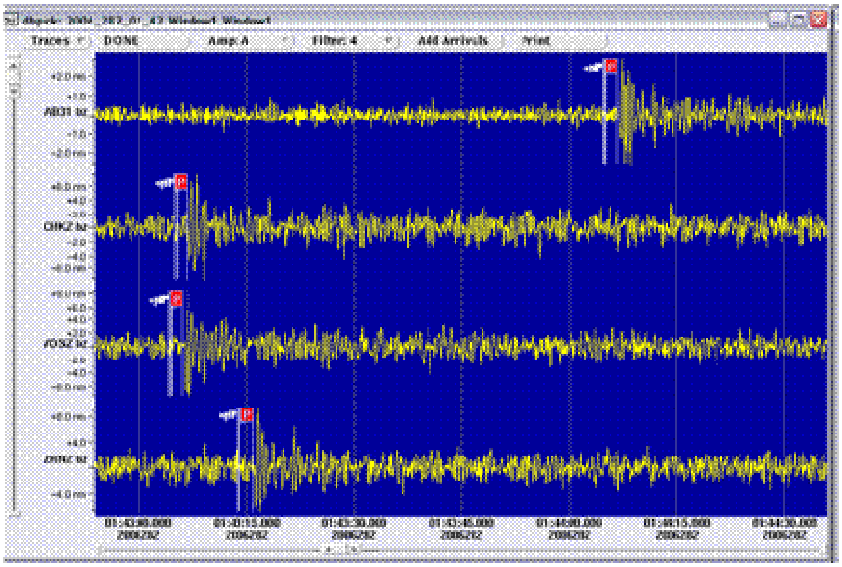

Figure 4: Records of the underground explosion carried out by North Korea on October 9, 2006. These are from Akbyulak stations, Borovoye large aperture array in Kazakhstan (Vostochnoye, Zerenda, Chkalovo stations.)

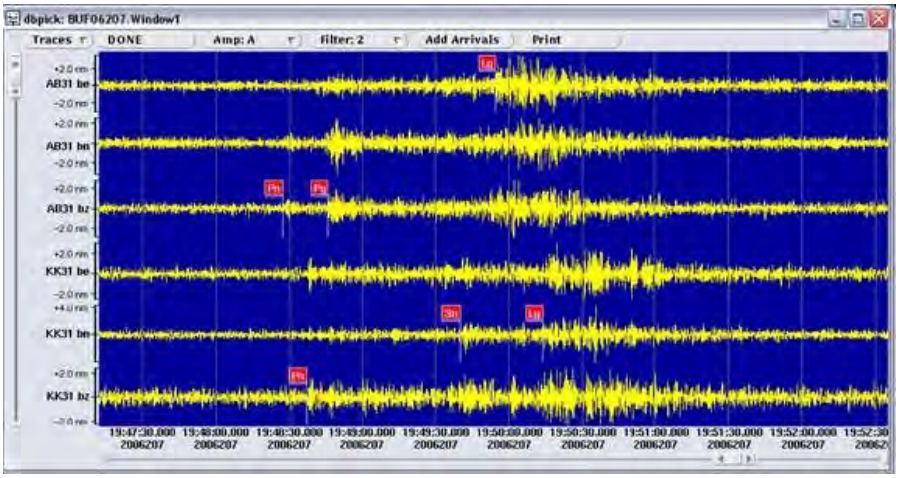

Figure 5. Records of the fall of the "Dnepr" carrier rocket on the territory of Kazakhstan. The upper three traces are recorded at the Akbulak station, and the lower three are at Karatayu. Both are in the Kazakhstan seismic array.

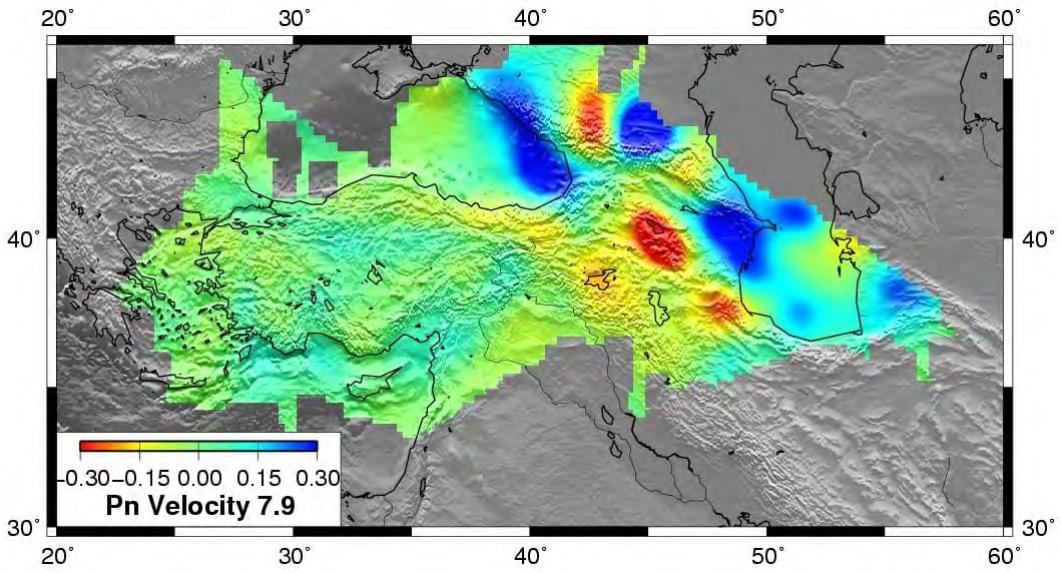

Figure 6. Imaged Pn velocity lateral variations in the CauSIN region. Average Pn velocity is 7.9 km/s, and variation corresponds with color. Red represents lower velocity than the average, and blue denotes higher velocity.

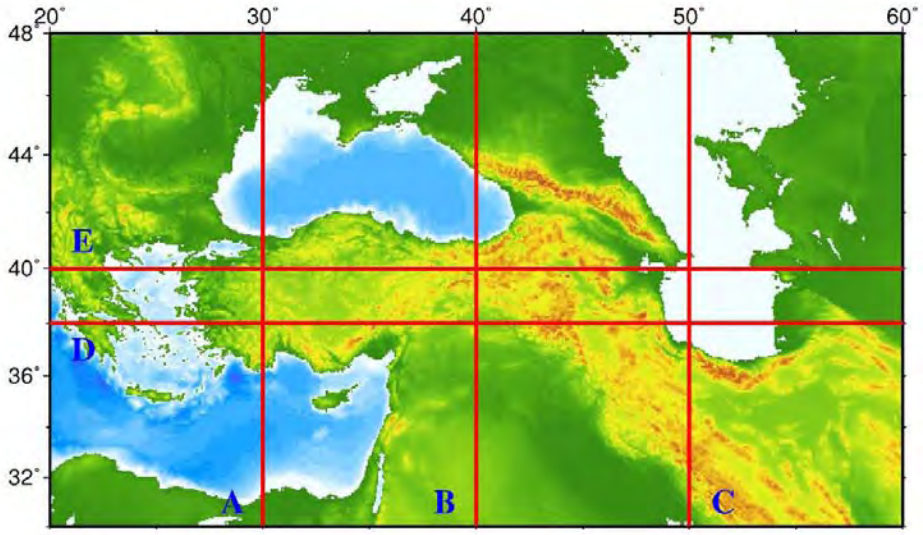

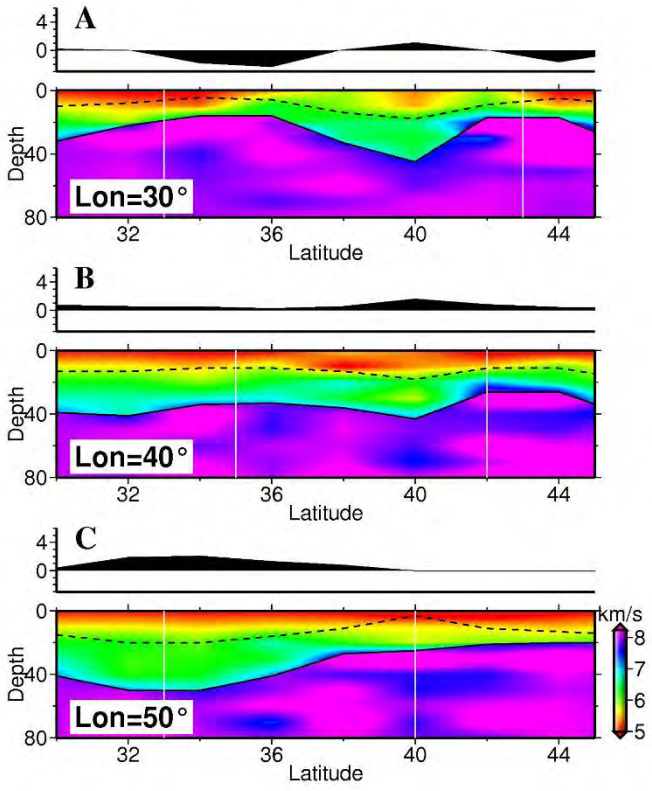

Figure 7: The tomography image produced during the CauSIN project. The top plot shows locations of vertical cross sections. Cross sections in the bottom plot are N-S slices at longitudes of 30°, 40°, and 50°. (The E-W slices D and E aren't shown here.) The surface topography along each profile is shown on the top of each cross section. The black curved lines show the Conrad (dashed) and Moho (solid) discontinuities. See text for discussion.

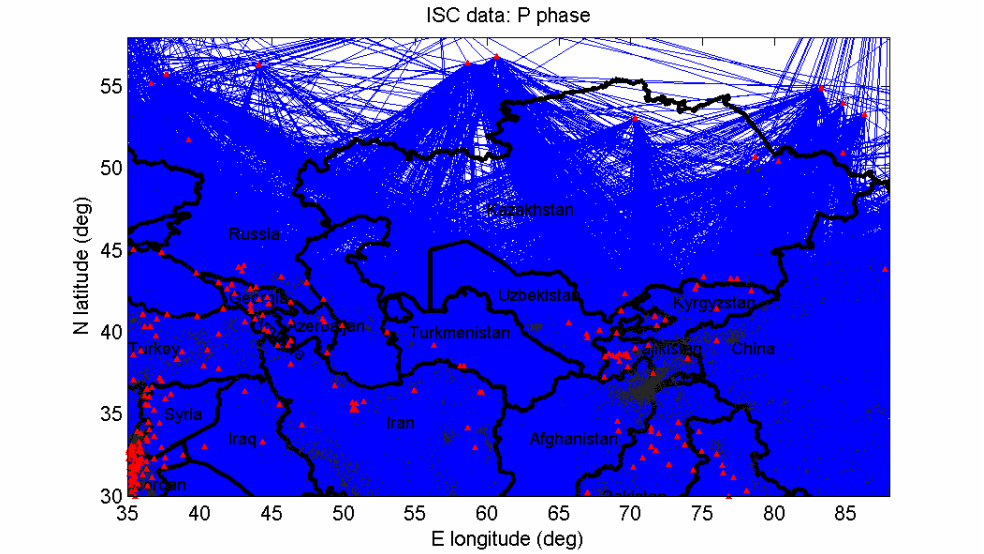

Figure 8: P raypaths in the CASRI region, from the ISC database for the years 1964–2002. This includes nearly 120,000 picks from over 14,000 events and 1200 stations but does not yet include data from local networks in the CASRI countries.

HIGH-RESOLUTION SEISMIC VELOCITY AND ATTENUATION MODELS OF THE CAUCASUS-CASPIAN REGION

Robert J. Mellors[1], Rengin Gök[2], and Eric A. Sandvol[3]

San Diego State University[1], Lawrence Livermore National Laboratory[2],
and University of Missouri-Columbia[3]

Sponsored by Air Force Research Laboratory

Contract No. FA8718-07-C-0007/BAA07-18

ABSTRACT

The southwest edge of Eurasia is a tectonically and structurally complex region that includes the Caspian and Black Sea basins, the Caucasus Mountains, and the high plateaus south of the Caucasus. Crustal and upper mantle velocities show great heterogeneity in this region and regional phases display variations in both amplitudes and travel time. Furthermore, due to a lack of quality data, the region has largely been unexplored in terms of the detailed lithospheric seismic structure. A unified high-resolution 3D velocity and attenuation model of the crust and upper mantle will be developed and calibrated. This model will use new data from 23 new broadband stations in the region analyzed with a comprehensive set of techniques. Velocity models of the crust and upper mantle will be developed using a joint inversion of receiver functions and surface waves. The surface wave modeling will use both event-based methods and ambient noise tomography. Regional phase (*Pg*, *Pn*, *Sn*, and *Lg*) Q model(s) will be constructed using the new data in combination with existing data sets. The results of the analysis (both attenuation and velocity modeling) will be validated using modeling of regional phases, calibration with selected events, and comparison with previous work. All results will be integrated into the Knowledge Base.

OBJECTIVES

The Caucasus-Caspian region is an area of complex structure accompanied by large variations in seismic wave velocities and attenuation (e.g,. Ritzwoller and Levshin, 1998; Murphy et al., 2005; Mitchell et al., 1997). In such areas, accurate geophysical models are fundamentally important to nuclear monitoring. In particular, the great thickness and irregular geometry of the low velocity and low density sediments in the Caspian and Black Sea basins (e.g. Laske and Masters, 1997) creates profound effects on seismic waveforms, especially on surface waves and regional phases. These effects are compounded by variations in crustal structure in the Caucasus and by high attenuation under the East Anatolian plateau (Al-Lazki et al., 2003; Sandvol et al., 2001). As regional models based on widely spaced stations they may suffer from insufficient spatial sampling; a comprehensive velocity and attenuation model is being developed using new broadband data that has become available in this area.

The primary focus is the Caucasus-Caspian region, which is roughly defined as lying between 40 and 55 E longitude and between 37 and 44 N latitude (Figure 1). A unified upper mantle/crustal velocity model will be developed using multiple techniques. In addition, the same data will be used to construct detailed maps of regional phase attenuation (*Lg*, *Pg*, *Pn*, and *Sn*). Finally, the results will be compared and validated using the various algorithms as well as independent data sets (local and regional events and active source studies).

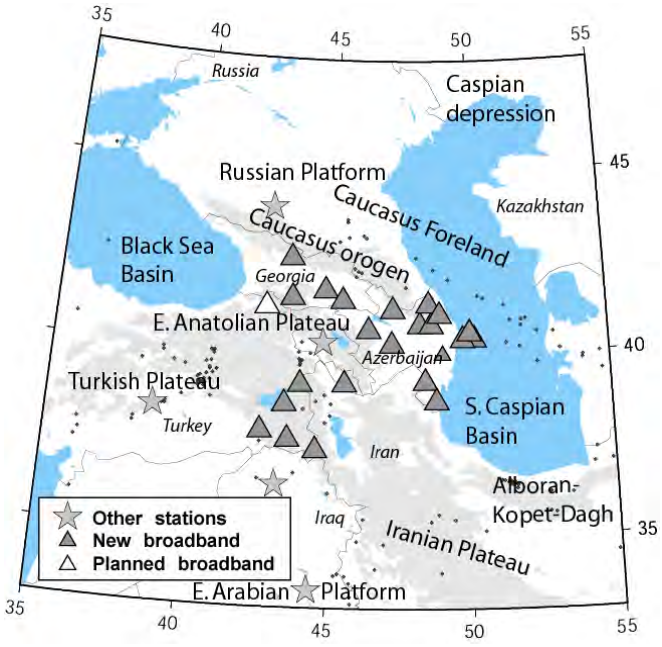

Figure 1 Regional map showing newly available broadband stations (triangles) and two years (2003–2004) of earthquakes from the Preliminary Determination of Epicenters (PDE) catalog (dots) to show distribution of regional events. Names and locations of geophysical regions from Sweeney and Walter (1998).

Previous Work

The region shows considerable spatial variability in travel times and phase propagation throughout the area (Table 1). Myers and Schultz (2000) noted errors of 42 km when locating events in the Caucasus Mountains with sparse regional stations and a standard model (prior to application of an empirical correction). They also noted that arrivals at regional distances are “strongly affected by upper-mantle-discontinuities.” Regional phase variations have been documented on a regional basis by a number of studies but reliable direct phase Q measurements are still lacking, mainly because of sparse station coverage and irregular distribution of earthquakes (e.g., Kadinsky-Cade et al., 1981; Rodgers et al., 1997a; Mitchell, 1997; Cong and Mitchell, 1998; Sarker and Abers, 1998; Baumgardt, 2001; Sandvol et al., 2001; McNamara and Walter, 2001; Gök et al., 2000; Gök et al, 2003). Here we summarize the regions and relevant seismic characteristics, where known.

The South Caspian and the Black Sea basins are thought to be underlain by oceanic crust although it is possible the South Caspian may simply be thinned continental crust overlain by thick sediments (Mangino and Priestly, 1998; Baumgardt, 2001). The great thickness (up to 20 km) of sediments in the South Caspian strongly affects surface waves as well, but efforts to resolve the situation by modeling higher frequency surface waves were inconclusive due to possible 3D effects (Priestley et al., 2001). Improved coverage and the use of ambient noise tomography should be useful in resolving this question. *Lg*, which is critical for discrimination purposes, is blocked by both the Black Sea and South Caspian basins. *Sn* does propagate through the South Caspian (Rodgers et al., 1997b; Sandvol et al., 2001). A large amount of active source data have been collected, which is useful for constraining the shallow velocity structure and depth of the sedimentary cover (Neprochnov et al., 1970; Belousov et al., 1992, Davies and Stewart, 2005; Knapp et al, 2004).

West of the Caspian in the Caucasus orogenic belt and foreland, events (Myers and Schultz, 2000) are subject to substantial travel-time anomalies at regional distances. It is unclear whether the *Lg* blockage observed in the South Caspian extends into the Greater Caucasus, as the available studies disagree. Rodgers et al. (1997b) and McNamara and Walter (2001) infer partial blockage of *Lg* in a belt extending from the Black Sea to the South Caspian. Alternatively, Sandvol et al. (2001) observe relatively efficient *Lg* propagation in the Caucasus and Central Caspian and attribute most of the attenuation to ray paths that cross the Anatolian plateau. Baumgardt (2001) reports unblocked *Lg* from Caucasus events to stations in Iran but blockage in the Caspian depression. The discrepancies among studies may reflect the poor station coverage with resulting poor resolution of ray paths. The crustal structure of this region still remains unclear given the lack of the data in the region. The boundary between the South Caspian and the Central Caspian is called the Absheron-Balkhan sill, an area of high seismicity and may be an area of incipient subduction (Jackson et al., 2002; Brunet et al., 2003).

The South Caspian blends into the southern Caucaus in the Kura depression, a sedimentary basin with uncertain structure (i.e. is it an onshore extension of the South Caspian or is it underlain by continental crust?). Poor *Sn* propagation is evident throughout the Anatolian Plateau. The southern Caucasus (or Lesser Caucasus) differs from the Greater Caucasus to the north due to extensive Quaternary volcanism. Near the South Caspian, the southern Caucasus merges into the Alborz Mountain belt, an area of clear *Lg* propagation as well as *Pg* and *Pn*.

Table 1. Summary of regional phase propagation among regions addressed in this report. Note the great variation across short distances. This table is adapted from Sweeney and Walters (1998).

Area	Regional phases	Seismicity	Other
Caucasus orogen	*Pn, Sn?*	High	
Caucasus foreland	*Pn,Pg,Lg?*	Mod deep?	Sediments Subduction?
Black Sea	*Pn,Sn*	Low	Sediments/oceanic crust
S. Caspian	*Pn,Sn*	Low	Thick sediments; oceanic crust?
E. Anatolian	*Pn*	High	Volcanic
Iranian Plateau	*Pn,Pg,Lg*	Mod.	

Little broadband data has been previously available for the region. Relevant global stations exist in the S. Caucasus (GNI), Eurasian platform (KIV), east of the Caspian (ABKT) and to the south (MSL and BHD). A broadband array was temporarily installed in 1992 at ABKT and a broadband network was installed in the Caucasus from 1991 to 1994. A limited amount of broadband data was collected from a temporary deployment of broadband stations at three sites (LNK, BAK, and SHE) occupied during the two-year Caspian Seismic Deployment. However, data return from these sites was limited and Mangino and Priestley (1998) presented receiver functions only from one station (LNK). Recently, permanent broadband stations have been deployed across the region as part of various national networks. Much of this data remains under the control of various institutes, and we are working with these institutes to analyze the data.

Methods and Data

The work consists of four basic tasks: data collection, regional phase analysis, velocity model development, and model validation. Data collection is ongoing and will include data from at least 23 new broadband stations in the region from several different adjoining countries and operated by different institutions. These stations will allow us to extend many of the high resolution models created in eastern Turkey into the Caucasus.

Regional phase analysis will define crustal and upper mantle propagation and attenuation within the region. By using the relatively dense coverage of broadband stations we intend to construct a detailed map of regional phase propagation in and around the region (*Pg*, *Pn*, *Lg*, and *Sn*). The primary questions are: What is the lateral extent of *Lg* blockage in the South Caspian and Black Sea? How far and to what degree does it extend into the Caucasus? What are the boundaries of *Sn* propagation? Do we see effects due to the Central, North, and Pre-Caspian basins on *Lg*? Two methods will be used to isolate the regional wave path: the two-station method for measuring inter-station Q and the reversed two-station, two-event spectral ratio method (Chun et al., 1987; Zor et al., 2007). This method has the advantage that we should be able to isolate the relative station response without having to assume that our response information is reliable. Once *Lg* Q has been measured, the results will be inverted to create *Lg* Q tomography maps, as is required for a regional phase Q model. The rapid changes in *Lg* in the region require dense station spacing. The two-station methods will also be used to measure *Pg*, *Pn*, and *Sn* Q. Laterally varying *Pn* Q models are more difficult to develop than *Lg* or *Pg* Q models because *Pn* is observed only in a limited distance range (between ~2°–14°), thus reducing the number of *Pn* paths available, and this will make inversion difficult. However, it is expected that the resulting blockage maps will be superior to existing maps. We will further refine our existing blockage maps for *Sn* (e.g., Sandvol et al., 2001) and then use to these to estimate a maximum allowable Q for those regions with *Sn* blockage.

In parallel with the attenuation work, crustal and upper mantle velocity structure will be determined using surface wave and receiver functions modeling. Results from the surface wave work and receiver functions will be jointly inverted for a unified model (Gök et al., 2006). Both phase and group velocities will be measured. The phase velocities will be event based (Forsyth et al., 1998). The ambient noise correlation will be measured using continuous data (Shapiro and Campillo, 2005). Pasyanos and Walter (2002) performed a study of surface wave group velocity dispersion across Western Eurasia and North Africa and a larger-scale across Eurasia, North Africa and surrounding regions (Pasyanos, 2005) using 30,000 Rayleigh and 20,000 Love wave paths. We will be adding group velocity measurements to existing Rayleigh and Love measurements. Receiver functions are a well-established technique (e.g., Langston, 1979; Ammon et al., 1990; Zhu and Kanamori, 2000) that use teleseismic P (or S) phases to estimate crustal and upper mantle velocity structure in the vicinity of the seismometer. Mangino and Priestley (1998) applied receiver function analysis to the Caspian Seismic Experiment station LNK (near the current broadband station LKR) and found "considerable variation over fairly short horizontal distances." Their results under LNK showed a thinner crust and approximately 13 km of sediment over a high velocity mid to lower crust. As receiver functions are effective at identifying discontinuities, combining receiver function analysis with surface wave data is a powerful technique. The joint inversion method of Julia et al. (2000) will be used.

Finally, the velocity and attenuation models will be validated using alternate data sources (such as reflection data), modeling, and ground truth data. The velocity model will be calibrated in two ways: by calculating source locations and mechanisms using our velocity models and by comparing with previous (especially seismic refraction and reflection) data sets.

RESEARCH ACCOMPLISHED

Data Collection

Station data availability from all stations in the region is being compiled for continuous data to achieve maximum coverage for ambient noise tomography, and data from all stations will be collected over the next few weeks. Some event data has been collected (Figure 2). Initial analysis of teleseismic data from the region has begun using receiver functions (Figure 3).

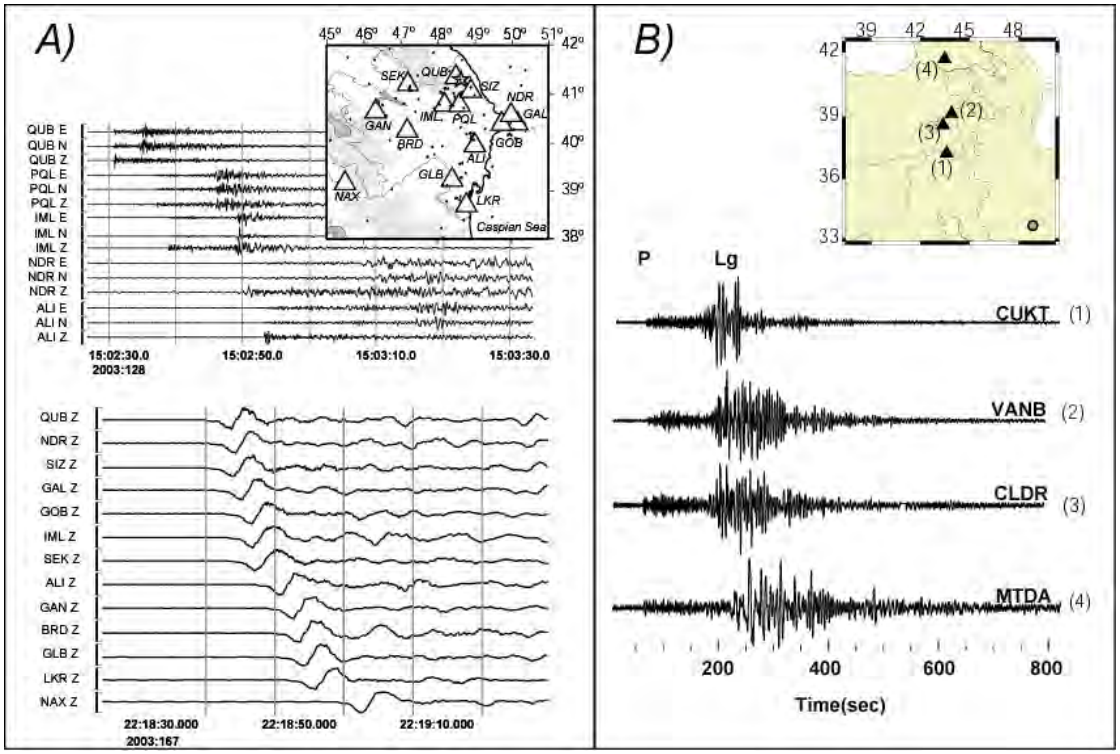

Figure 2. (A, top) Example of a local event recorded by the Azerbaijan network located near station QUB (no filter). Dots are local events recorded by the network in three months. (A, bottom) Example of 16 June 2003 teleseism approximately 67 degrees away recorded by the Azerbaijan network, low-pass filtered at 1 s. Traces are normalized. (B) Example of a regional event (small circle) recorded by stations in eastern Turkey and Georgia.

Receiver Functions

A preliminary set of events for receiver functions have been calculated for some of the stations using the data in hand (Figure 3). Both spectral division and time domain iterative deconvolution are being applied to telesismic events within 30º–90º. Receiver functions in Figure 3 were determined using deconvolution by spectral division with a water level of 0.01 and a Gaussian filter of 1.5. Noise levels vary greatly from station to station, which leads to differing numbers of events possessing high signal-to-noise at each station. In general, noise levels (likely due to water waves in Caspian) were highest near the coast. Coastal stations also lie on sedimentary bedrock and some of the variability is probably due to multiples and possibly structure within the crust. Modeling is ongoing to match the receiver functions.

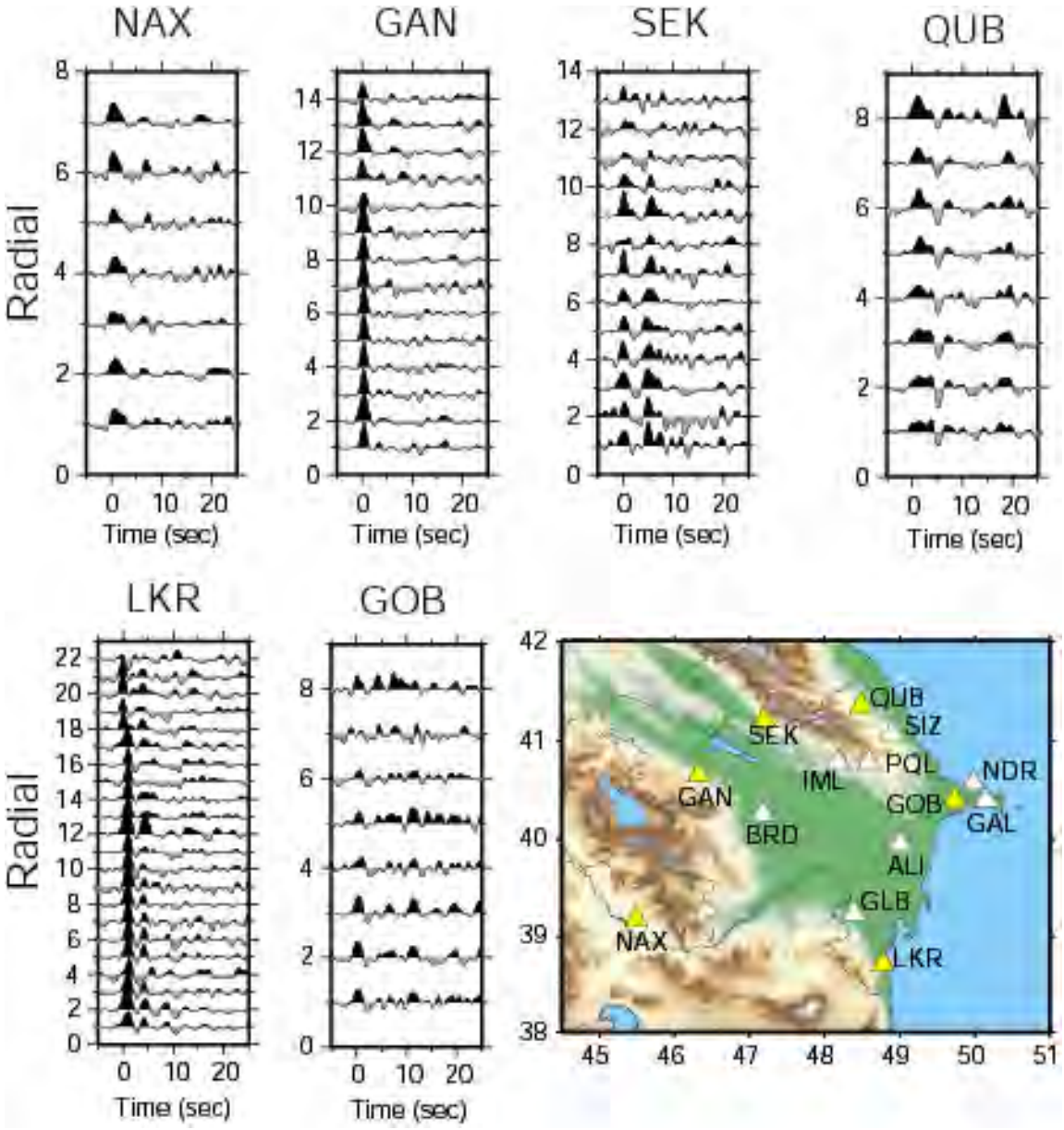

Figure 3. Preliminary P-receiver functions for stations colored in yellow. Data availability and noise levels vary from station to station, which results in varying numbers of events. Note the great variability in phases and hence crustal structure across the region.

CONCLUSIONS AND RECOMMENDATIONS

Preliminary analysis of receiver functions shows clear consistency between events and the outlook is promising for this technique despite the complex structure and basin sediments. Results for station LKR are similar to those from the Mangino and Priestley (1998) study, which was situated near the same site. Alternate methods of deconvolution will be tested to improve the results and the examples shown so far represent a fraction of the available data. We will be using higher Gaussian filter widths to be able to resolve the smaller scale variation within the crust. We will be calculating the S-receiver functions to be able to calculate the depth of the Lithospheric Asthenospheric Boundary. The Mohorovicic discontinuity (Moho) conversion can be seen on S-receiver functions where we will be using our P-receiver functions to fix the Moho depth. Once sufficient data has been collected, event-based and

noise-correlated surface wave analysis will begin. Similarly, the event data are being collected for regional phase attenuation maps.

ACKNOWLEDGEMENTS

Thanks to A. Gasanov and G. Yetirmishli for providing this initial set of data from the Azerbaijan network. C. Ammon and J. Julia provided software used in the analysis of that set of data.

REFERENCES

Al-Lazki, A. I., D. Seber, E. Sandvol, N. Turkelli, R. Mohamad, and M. Barazangi (2003). Tomographic Pn velocity and anisotropy structure beneath the Anatolian plateau (eastern Turkey) and the surrounding regions, *Geophys. Res. Lett*. 30.

Ammon, C. J., G. E. Randall, and G. Zandt (1990). On the nonuniqueness of receiver function inversions, *J. Geophys. Res*. 95: 15,303–15,318.

Baumgardt, D. R. (2001). Sedimentary basins and the blockage of Lg wave propagation in the continents, *Pure Appl. Geophys.* 158: 1207–1250.

Belousov, V. V., N. I. Pavlenkova, and G. N. Kvyatkovskaya (1992). Structure of the crust and upper mantle of the [former] USSR, *Int. Geol. Rev*. 34: 213–338.

Brunet, M. F., M. V. Korotaev, A. V. Ershov, and A. M. Nikishin (2003). The South Caspian Basin: A review of its evolution from subsidence modeling, *Sed. Geol*. 156: 1–4, 119–148.

Chun, K.-Y., G. F. West, R. J. Kokoski, and C. Samson (1987). A novel technique for measuring Lg attenuation: Results from eastern Canada between 1 and 10 Hz, *Bull. Seis. Soc. Am.* 77: 398–419.

Cong, L. and B. Mitchell (1998). Lg coda Q and its relation to the geology and tectonics of the Middle East. *Pure Appl. Geophys*. 153: 2–4, 563–585.

Davies, R. J. and S. A. Stewart (2005). Emplacement of giant mud volcanoes in the South Caspian Basin: 3D seismic reflection imaging of their root zones, *J. Geo. Soc*. 162: 1–4.

Forsyth, D. W., S. C. Webb, L. M. Dorman, and Y. Shen (1998). Phase velocities of Rayleigh waves in the MELT experiment on the East Pacific Rise. *Science* 280: 1235–1238.

Gök, R., N. Turkelli, E. Sandvol, D. Seber, and M. Barazangi (2000). Regional wave propagation in Turkey and surrounding regions, *Geophys. Res. Let*. 27: 429–432.

Gök R., E. Sandvol, N. Türkelli, D. Seber and M. Barazangi (2003). Sn attenuation in the Anatolian and Iranian plateau and surrounding regions, *Geophys. Res. Lett*. 30.

Gök, R., M. E. Pasyanos, and E. Zor (2006). Lithospheric Structure of the Continent-Continent Collision Zone: Eastern Turkey, *J. Geophys. Res*. (submitted).

Jackson, J., K. Priestley, M. Allen, and M. Berberian (2002). Active tectonics of the South Caspian Basin, *Geophys. J. Inter.*148: 214–245.

Julia, J., C. Ammon, R. Herrman, and A. Correig, (2000). Joint inversion of receiver function and surface wave dispersion observations, *Geophys. Jour. Int.,* 143: 99–112.

Kadinsky-Cade, K., M. Barazangi, J. Oliver, and B. Isacks (1981). Lateral variations of high-frequency seismic wave propagations at regional distances across the Turkish and Iranian plateaus, *J. Geophys. Res.* 86: 9377–9396.

Knapp, C., J. Knapp, and J. A. Connor (2004). Crust-scale structure of the South Caspian Basin revealed by deep seismic reflection profiling, *Marine Petro. Geol.* 21: 1073–1081.

Langston, C. A. (1979). Structure under Mount Rainier, Washington, inferred from teleseismic body waves. *J. Geophys. Res*. 84: 4749–4762.

Laske, G. and G. Masters (1997). A global digital map of sediment thickness, *EOS Trans. AGU* 78: F483.

Mangino, S and K. Priestley (1998). The crustal structure of the southern Caspian region, *Geophys. J. Inter.* 133: 630–648.

McNamara, D. and W. Walter (2001). Mapping crustal heterogeneity using Lg propagation efficiency throughout the Middle East, southern Europe, and northern Africa, *Pure Appl. Geophys*. 158: 1165–1188.

Mitchell, B. (1997). Lg coda variation across Eurasia and its relation to crustal evolution, *J. Geophys. Res.* 102: 22,767–22,779.

Murphy, J. R., W. Rodi, M. Johnson, D. Sultanov, T. Bennett, M. Toksoz, V. Ovtchinnikov, B. Barker, D. Reiter, A. Rosca, and Y. Shchukin (2005). Calibration of International Monitoring System (IMS) stations in central and eastern Asia for improved seismic event location. *Bull. Seismol. Soc. Am.* 95: 1535–1560.

Myers, S. C. and C. A. Schultz (2000). Improving sparse network seismic location with Bayesian kriging and teleseismically constrained calibration events, *Bull. Seismol. Soc. Am.* 90: 199–211.

Neprochnov, Y. P., I. P. Kosminskaya, and Y. P. Malovitsky (1970). Structure of the crust and upper mantle of the Black and Caspian seas, *Tectonophysics* 10: 517–538.

Pasyanos, M. E. and W. R. Walter (2002). Crust and upper mantle Structure of North Africa, Europe, and the Middle East from inversion of surface waves, *Geophys. J. Int.* 149: 462–480.

Pasyanos, M. E. (2005). A variable resolution surface wave dispersion study of Eurasia, North Africa, and surrounding regions, *J. Geophys. Res*. 110: B12301, doi: 10.1029/2005JB003749.

Priestley, K., H. Patton, and C. Schultz (2001). Modeling anomalous surface-wave propagation across the southern Caspian Basin, *Bull. Seismol. Soc. Am*. 91: 1924–1929.

Ritzwoller, M. H. and A .L. Levshin (1998). Eurasian surface wave tomography: Group velocities, *J. Geophys. Res.* 103: 4839–4878.

Rodgers, A. J., T. Lay, W. Walter, and K. M. Mayeda (1997a). A comparison of regional-phase amplitude ratio measurement techniques, *Bull. Seismol. Soc. Am*. 87: 613–621.

Rodgers, A. J., J. F. Ni, and T. M. Hearn (1997b). Propagation characteristics of short-period Sn and Lg in the Middle East, *Bull. Seismol. Soc. Am.* 87: 396–413.

Sandvol, E., K. Al-Damegh, A. Calvert, D. Seber, M. Barazangi, Mohamad, R, R. Gök, N. Turkelli, and C. Gurbuz (2001). Tomographic imaging of Lg and Sn propagation in the Middle East, *Pure Appl. Geophys*. 158: 1121–1163.

Sarker, G. and G. A. Abers (1998). Deep structures along the boundary of a collisional belt: Attenuation tomography of P and S waves in the Greater Caucasus. *Geophys. J. Inter*. 133: 326–340.

Shapiro, N. M., M. Campillo, L. Stehly, and M. H. Ritzwoller (2005). High resolution surface wave tomography from ambient seismic noise, *Science* 307: 1615–1618.

Sweeney, J. and W. R. Walter (1998). Preliminary definition of geophysical regions for the Middle East and North Africa, Lawrence Livermore National Laboratory report UCRL-ID-132899, 38 pp.

Sweeney, J. and W. R. Walter (1998). Preliminary definition of geophysical regions for the Middle East and North Africa, Lawrence Livermore National Laboratory report UCRL-ID-132899.

Zhu, L. and H. Kanamori (2000). Moho depth variation in Southern California from teleseismic receiver functions, *J. Geophys. Res.* 105: 2969–2980.

Zor, E., E. Sandvol, J. Xie, N. Türkelli, B. Mitchell, A. Gasanov, and G. Yetirmishli (2007). Crustal attenuation within the Turkish Plateau and surrounding regions, *Bull. Seismol. Soc. Am.* 97: 151–161.

FREQUENCY-DEPENDENT SHORT-PERIOD EXPLOSION CODA AMPLITUDES IN NORTHERN EURASIA

Igor B. Morozov, Chaoying Zhang, and Elena A. Morozova

University of Saskatchewan

Sponsored by the National Nuclear Security Administration
Office of Nonproliferation Research and Development
Office of Defense Nuclear Nonproliferation

Contract No. DE-FC52-05NA26609

ABSTRACT

Travel-time and magnitude-yield calibration of Northern Eurasia, which is largely aseismic, can be improved by using the large chemical and peaceful nuclear explosion (PNE) seismic data sets acquired by the Soviet deep seismic sounding (DSS) program. Eleven major data sets of this program have recently been digitized and have become available to nuclear test monitoring research. Although the PNEs have been already used in several monitoring studies, the chemical-explosions data sets are still incompletely explored. In the present study, we use inversion and numerical modeling to analyze the coda amplitude parameters and *P*-wave travel times from numerous DSS explosions, which could lead to a detailed empirical mapping of seismic properties within northern Eurasia.

For proper mapping of coda parameters, it is important to select a parameterization that reflects the fundamental physics and is stable in respect to unconstrained factors. We investigated two types of such parameterizations, namely the frequency-dependent coda attenuation $Q_{coda}(f)$ and frequency-independent attenuation with geometric spreading (γ,Q_{coda}). By utilizing a newly developed, parallelized version of the one-dimensional (1-D) *reflectivity* program, we were able to model within the 0.2 to 10 Hz frequency band and to 800 sec times, which nearly covers the complete DSS time-frequency range. Several complexly layered velocity models related to the study area were tested.

The numerical modeling showed that for a fixed intrinsic *S*-wave *Q* of the crust, the resulting $Q_{coda}(f)$ exhibited a strong positive frequency dependence. This spurious frequency dependence is due to a disregard of ray bending and other geometrical propagation effects and not related to model rheology. Notably, similar strong $Q_{coda}(f) \propto f^{0.8-1.0}$ dependencies were observed in many PNE coda records and also in other areas. By contrast, coda amplitude inversion using the geometric-spreading model results in a stable spreading parameter, $\gamma \approx -0.008$ and a frequency-independent Q_{coda} varying from ~2Q for Q = 300 to ~1.2Q when Q = 1000. The variations in $Q_{coda}(Q)$ as well as the fact that $Q_{coda} > Q$ are consistent with a part of seismic coda energy propagating through the mantle. Tests for variations of the crustal velocity structure suggest that the $Q_{coda}(Q)$ dependence is relatively stable, and therefore it can be used to invert for the intrinsic/scattering attenuation of the crust from coda measurements.

We have assembled a database of coda records from selected PNEs and chemical explosions and performed their inversion and preliminary interpretation based on the (γ,Q_{coda}) model. As in the modeling, parameter γ is relatively stable, whereas Q_{coda} shows variations that can be associated with tectonic structures. Crustal Q parameters are further mapped from the inverted modeled $Q_{coda}(Q)$ dependence.

In order to further expand the DSS database, we have obtained earthquake recordings from several DSS PNE profiles. In the ongoing work, we are utilizing these data for coda magnitude analysis and derivation of empirical magnitude (apparent coda source spectra) relationships. Additionally, we present an update of our first-arrival travel-time calibration model for Northern Eurasia using the PNE as well as selected chemical-explosion records. These efforts should ultimately lead to a unified three-dimensional/two-dimensional (3-D/2-D) calibration model of Northern Eurasia, including travel times, stable coda magnitudes, and magnitude-yield relations. This model will bridge the gap between Europe, central Asia, the European Arctic, and eastern Siberia and provide additional calibration information for further studies in these areas.

OBJECTIVES

Many seismic monitoring studies are based on properties of the seismic coda from earthquakes and explosions and, in particular, on its amplitude decay and attenuation. Short-period coda amplitude decays lead to the most stable estimates of source magnitudes (Phillips, 2004), and measured coda attenuation (Q) is often related to crustal properties that are difficult to measure otherwise (Aki and Chouet, 1975). High-frequency (>5 Hz) codas from PNEs in the east European platform also led several researchers (Ryberg et al., 1995; Enderle et al., 1997; Morozov et al., 1998a,b; Ryberg and Wenzel, 1999; Morozov, 2001) to propose sharply contrasting models of small-scale heterogeneity of the uppermost mantle.

Despite its broad use in seismological practice, the causes of variations of coda Q with frequency are still not well understood. In many studies, strong frequency dependencies of coda Q, as well as body- and surface-wave Q, were documented. This dependence is commonly presented in a power-law form:

$$Q(f) = Q_0\left(f \big/ f_0\right)^{\eta}, \tag{1}$$

where f_0 is some reference frequency often taken to equal 1 Hz (Aki and Chouet, 1975). Both Q_0 and exponent η are considered constant within the frequency band of interest. Note that Q typically increases with frequency ($\eta > 0$), and large values of $\eta \sim 0.5$-1 are not uncommon in *Lg* Q and *Lg* coda Q studies (e.g., Nuttli, 1973; Hasegawa, 1985; Der et al., 1986; Campillo, 1987, 1990; Benz et al., 1997; Frankel et al., 1990; Mitchell and Cong, 1998; Mitchell et al., 1997, 1998; McNamara et al., 1996; McNamara, 2000; and Erickson et al., 2004). Visco-elastic rheological models were proposed to explain observations of frequency-dependent Q in Earth materials (Liu et al., 1976). Correlation to tectonics in North America suggested that active tectonic regions are generally characterized by low Q_0 and high η, while stable cratons are generally characterized by higher Q_0 and lower η (Erickson et al., 2004). However, in our PNE studies in the Siberian Craton, extremely high values of $\eta \approx 1$ were found in combination with very high Q_0 (Morozov et al., 2006). For $\eta \approx 1$, the coda amplitude decay becomes in fact frequency-independent, and this suggests a hypothesis that high apparent η could in fact indicate low attenuation and significant geometric spreading. An argument in favor of such an interpretation will be given below.

In coda measurements, its $Q(f)$ value is derived from the following model of time-frequency dependent coda amplitudes:

$$A(t, f) = A_0(f)\exp\left(-\frac{\pi f}{Q(f)}t\right), \tag{2}$$

where t is the time after the primary arrival and $A_0(f)$ is the coda spectrum at t=0. Note that the key assumption of model (2) is that the geometrical spreading of coda waves ($\propto t^{-\zeta}$ in Aki and Chouet, 1975) is compensated by the scattering volume increasing as the time t increases. Similarly, note that in surface wave studies (e.g., Erickson et al., 2004), frequency-dependent Q can be measured only by time-domain techniques, which also rely on compensation of geometrical spreading (Nuttli, 1973).

In this report, we show that observations of frequency-dependent coda Q may be related not to crustal rheology but to the chosen parameterization Eq. (2). Compensation of geometrical spreading in Eq. (2) should be relatively complete for local earthquake codas involving straight scattered rays and uniform scattering volumes (Aki and Chouet, 1975). However, at crustal-scale and regional distances, scattering tends to concentrate near the surface, and scattered waves consist of complex assemblages of diving, refracted, reflected, guided, and surface modes. Based on various assumptions about these modes and stochastic properties of the crust, several coda models can be used (e.g., Aki and Chouet, 1975; Sato and Fehler, 1998). In practice, however, with virtually any coda model, additional *ad hoc* distance and spectral corrections are required (Mayeda and Walter, 1996; Phillips et al., 2004). Here, we introduce such a correction by noting that an uncompensated (most likely, undercompensated) geometrical spreading $G(t)$ should remain in the coda. Because it is only practical to seek a two-parameter coda description [similar to (Q_0, η) in Eq. (1)], we abandon the frequency dependence of Q_{coda} in relation (2) and approximate the geometrical spreading as $\exp(-\gamma t)$, yielding:

$$A(t, f) = A_0(f)\exp\left[-\left(\gamma + \frac{\pi f}{Q_{coda}}\right)t\right], \quad (3)$$

where the geometric spreading (relaxation) parameter γ is measured in units of 1/*time*. A similar expression for frequency dependence of surface wave attenuation was given by Dainty (1981). Note that the extreme case of $\eta = 1$ [$Q \propto f$ in Eq. (2)] simply corresponds to geometrical spreading with low attenuation ($Q_{coda}=\infty$) in relation (3).

Our objective below is to show that the (Q_0, η) description of frequency-dependent coda attenuation (and maybe also in other types of bulk crustal Q) can be effectively and usefully replaced with (γ, Q_{coda}). The principal advantages of such a replacement are three-fold: 1) formula (3) does not rely on assumptions about geometrical spreading but empirically parameterizes it instead; 2) geometrical spreading and Q are explicitly separated; and 3) Q_{coda} becomes frequency-independent, in agreement with simple Newtonian solid-state mechanics, at least within the presently available data resolution. The somewhat puzzling increase of Q with frequency suggesting depletion of scatterers at shorter scale lengths becomes explained by geometrical spreading due to diving (among other) scattered waves. In addition, as our analysis of PNE profiles shows (see example below and Part II of this paper), parameter γ appears to be relatively stable across large areas, whereas Q_{coda} shows strong variability between different tectonic structures.

Below, we analyze the (Q_0, η) and (γ, Q_{coda}) parameterizations of coda attenuation using numerical examples. We generate four finite-difference models of PNE coda wavefields resulting from realistic crustal and upper-mantle velocity models and test them for variations of crustal velocities and Q. As expected, the (Q_0, η) parameterization leads to strong spurious $Q_{coda}(f)$ dependencies. Inversion of this $Q_{coda}(f)$ for the true crustal Q could represent a non-trivial task. By contrast, in the (γ, Q_{coda}) model, the values of γ can be predicted from the crustal structure, and Q_{coda} can be uniquely related to Q of the crust. Repeated for several types of velocity structures and crustal velocities, this modeling allows us to construct "calibration" dependences $Q(Q_{coda})$ from numerical models and use them to invert the observed coda data for crustal properties in future research. In addition, we derive an approximate mapping of (γ, Q_{coda}) parameters into (Q_0, η) and discuss the potential causes of observing low or high values of η. It appears that rather than η or Q_0, as an attribute of the velocity structure, γ could be a better factor differentiating between stable (cold) and active (hot) tectonic zones.

Overall, it appears that parameterization (γ, Q_{coda}) is not only safer theoretically, but also provides the basis for inverting coda amplitudes for bulk crustal *S*-wave attenuation and for tying them to the tectonics. Because of its explicit separation of geometrical and attenuation effects, the approach is also likely to help in building more robust and transportable coda magnitudes and Q-based seismic regionalization.

RESEARCH ACCOMPLISHED

We examine the effective frequency dependence of coda attenuation by numerically modeling the teleseismic *P* wave coda resulting from scattering of seismic energy from near-surface crustal heterogeneities. The use of near-surface crustal scatterers simplifies our computations, and it is also justified by the increased heterogeneity of the shallow crust and supported by several array observations (e.g., Greenfield, 1971; Dainty, 1985 and 1990; Bannister et al., 1990; Gupta et al., 1991) and previous coda modeling (Dainty and Schultz, 1995). The choice of the *P*-wave coda is due to several reasons (Morozov and Smithson, 2000): 1) *S*- and L_g phases are less pronounced in the PNE records; 2) their codas lie on top of the *P*-wave coda, complicating the observation and requiring their decomposition; and 3) the L_g phase is significantly more difficult to model accurately. Similarly, the Rayleigh wave (R_g) decays quickly in near-surface sediments, and it is not viewed as a significant factor in coda formation (Dainty, 1985). R_g is not seen beyond ~200 km in PNE records and is also difficult to reproduce numerically; consequently it is not examined here. The use of *P*-wave coda of arrivals at ~2900 km from the source provides a sufficient coda time window before the onset of the *S*-wave phase.

Crustal and coda attenuation. It is important to differentiate between two different Q values used in this study. The intrinsic or elastic crustal attenuation describes the loss of seismic energy in the crust to internal friction, such as damping by fluids in cracks and pores or friction along grain boundaries. It is denoted by a Q value, where $Q = \frac{2\pi E}{\Delta E}$, with E being the energy and ΔE - the energy dissipation during one wave cycle (Aki and Richards,

2002). By contrast, Q_{coda} measures the coda amplitude decay rate, determined from the decay slope of amplitude A versus time t from a semi-log plot of the seismic trace envelope in Eq. (2). By taking the natural logarithm: $\ln A = \ln A_0 - \frac{\pi f}{Q_{coda}} t$, we obtain a straight line with slope $s = \frac{-\pi f}{Q_{coda}}$ in the (*time*,ln*A*) domain. Thus, the frequency-dependent $Q_{coda}(f)$ is defined as: $Q_{coda} = \frac{-\pi f}{s}$, where slope s is measured from the logarithm of the seismic trace envelope.

Numerical Coda Model. The scattering model represents crustal heterogeneities as scatterers distributed within Earth's crust. The resultant scattered coda intensity U recorded at a receiver at time t is an integral over volume V containing all scatterers (Figure 1):

$$U(\vec{r},t) = \int dt_s \iint_S d^2\vec{r}_s \Psi(\vec{r}_s) U_{source}(\vec{r}_s, t_s) G(\vec{r} - \vec{r}_s, t - t_s) . \quad (4)$$

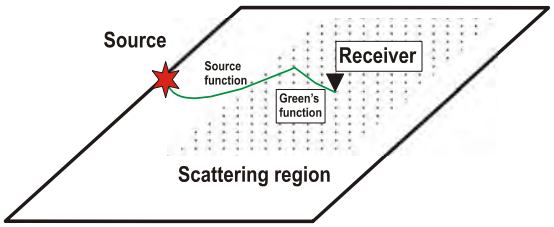

Figure 1. Surface scattering model (Eq. 4). Seismic energy originates at the source, scatters from randomly and uniformly distributed surface points, and is detected at receiver. The source and Green's functions are simulated by 1-D *reflectivity* modeling.

For a given coda time t and velocity of a particular scattered mode (e.g., v = 2.9 - 3.5 km/s for a scattered L_g), contributions of scattered energy originate from an elliptical ring surrounding the receiver (Morozov and Smithson 2000). The scattering area within the ring increases with time due to its increasing radius and partly compensates the energy decay from the geometrical spreading. For example, for a plane of constant scattering potential and no intrinsic attenuation, coda energy would not decay, provided only surface-wave modes contribute to the scattered Green's function.

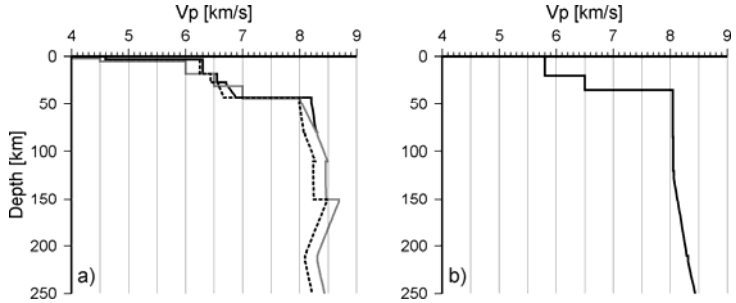

Figure 2. Upper 250 km of 1-D V_P velocity models used in creation of synthetic seismograms. a) Models based on PNE Quartz results by Morozova et al. (1999): Quartz (solid black line), Warm Quartz (dotted black), and Complex Crust (gray); b) iasp91 model.

Synthetic seismic sections created using the reflectivity method (Fuchs and Müller, 1971) were used as source and Green's functions in several 1-D crustal and upper mantle models (Figure 2). The original FORTRAN program by

K. J. Sandmeier was modified to handle larger computations, parallelized, and incorporated into our data processing system (SIA; Chubak and Morozov, 2006) allowing seamless filtering, inverting, saving, and plotting the results.

A detailed description of this tool can be obtained from the SIA web service: http://seisweb.usask.ca/SIA/ps.php?doc=reflect.

Computations were performed on a 66-processor 1.6-GHz Opteron cluster and produced 800-second, 3-component synthetic records sampled at 20-ms intervals and output at 10-km intervals from near-0 to 3500 km from the source. Modeling frequency band was 0.2–20 Hz using a "delta-function" source function suitable for spectral measurements. A sufficiently dense phase velocity spectrum was selected to avoid frequency aliasing during numerical mode summations. As with any implementations of the propagator matrix method (Aki and Richards, 2002), all *P*/*SV* mode conversions and multiples were accounted for in the modeling.

We used four different velocity models to compute the synthetics (Figure 2), including the global iasp91 model (Kennett and Engdahl, 1991), consisting of a simple three-layer crust and a mantle without strong gradients and low-velocity zones. However, the iasp91 model is too slow for platform areas of northern Eurasia, and the remaining three models were based on the detailed models derived from the NE profile Quartz and considered the best match for the study area (Mechie et al., 1993; Morozova et. al., 1999). The "Quartz" model contains a 3-gradient layer crust overlain by a 3-km-thick sediment layer and complex mantle with low velocity zones at 110- and 210-km depths (Figure 2). Another "Complex Crust" model has a high-contrast, 5-layer crust with a somewhat exaggerated attenuative layer (Q_S = 10) on its top and the Quartz mantle (Figure 2b). Model "Warm Quartz" (Figure 2a) was an attempt to simulate a high-heat flow regime in the Quartz model by applying a temperature-related negative velocity gradient within the crust (Christensen and Mooney, 1995). Note that all three Quartz-based models show more complex waveforms (including crustal L_g phases in addition to the *P* and *S* phases) compared with the iasp91 (Figure 2). In order to collect data on the sensitivity of the results to crustal velocities alone, we also repeated the Quartz simulations after applying ±5% perturbations of crustal velocities.

Multiple simulations were performed for each model, with *P*- and *S*-wave quality factors for layers in the crustal part of the model set equal—$Q_P = 2Q$ and $Q_S = Q$, respectively, with values of Q ranging from 100 to 1000 to encompass the expected Earth's whole-crust Q_S values. This range of Q_S corresponds to *Lg* Q values of ~300-1000 measured from 19 Russian PNEs by Li et al. (submitted to the Bulletin of the Seismological Society of America [BSSA]) and extended to low-Q values to investigate crustal effects. Mantle attenuation in each velocity model was fixed using the mantle Q_p values derived from *P*-wave Quartz PNE data (Morozov et al., 1998b). The teleseismic *P* coda was measured at 2900-km offsets to allow a significant time interval in which to perform the measurement before the onset of the P_g and *S* waves. Numerical evaluation of integral (4) was performed by using Monte-Carlo sampling in order to avoid spurious coherency that could be caused by spatial aliasing when using a regular integration grid. As above, the synthetic coda generation was implemented in an SIA tool sharing much of its libraries with other codes (http://seisweb.usask.ca/SIA/ps.php?doc=syncoda).

Using the resulting coda records, log-amplitude slope measurements were performed on coda envelopes in the manner of Morozov and Smithson (2000) (Figure 3). Both L_2- (root mean square [RMS]) and L_1-norm fitting (e.g., Aster et al., 2002) were tried, with uncertainties measured using 50% jack-knife resampling. Owing to large sampling volumes and stable coda envelopes, both the differences between the L_2 and L_1 norms and the corresponding slope uncertainties were negligible for the subsequent analysis.

Modeling Results. We performed measurements of the teleseismic *P*-wave codas for each of the four velocity models. Coda traces were band-pass filtered to center frequencies of 0.4, 0.79, 1.58, 3.16, 4.48, 6.32, 8.94, 12.6, and 17.8 Hz to examine the log-amplitude slopes as functions of frequency. Figure 4 shows the results for models Quartz and Complex Crust with $Q_S = Q = 500$.

In Figure 4, coda slope values show clear linear dependencies to about 7 to 10 Hz, after which the fidelity of modeling appears to drop, and the slopes flatten out (attenuation is replaced by frequency-independent

numerical noise of unclear nature). By fitting straight lines to the points within the 0 to 7 Hz range, we find that the intercepts at $f = 0$ Hz are non-zero, $\gamma \approx 0.8 \cdot 10^{-2}$, and $\gamma \approx 1.6 \cdot 10^{-2}$ for the two models and measure Q_{coda} from their slopes (see Eq. 3) as $Q_{coda} \approx 800$ and 600, respectively, Note that γ is clearly positive in all cases considered here, indicating that the geometrical spreading is only partly compensated by surface scattering. Also note the flattening of *slope*(*f*) dependencies at higher frequencies due to the reduction in the signal/noise ratio and outliers at lower frequencies, most likely associated with tuning effects within the crustal layers (Figure 4).

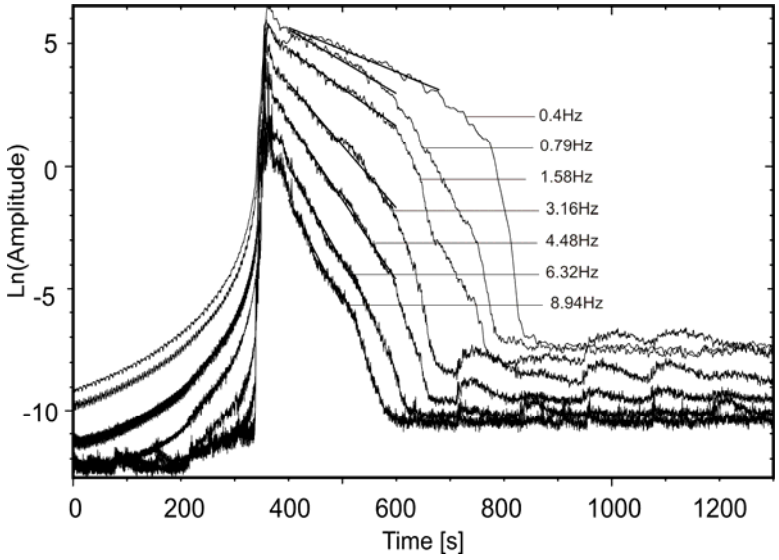

Figure 3. Log-amplitude synthetic coda for Quartz model at selected frequencies (labeled). Straight lines indicate the measured amplitude fits. Note the progressive change in coda shapes with increasing frequencies.

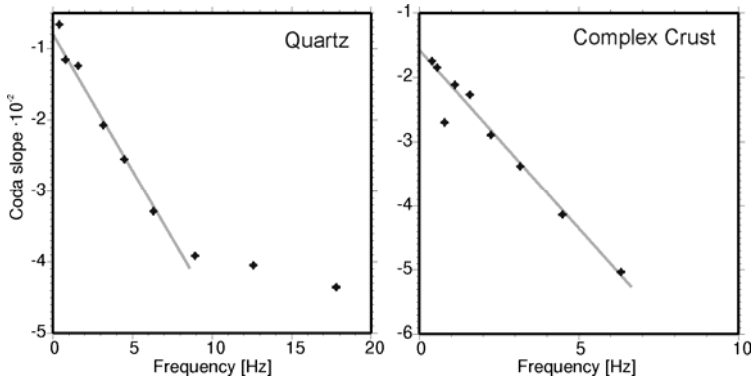

Figure 4. Measured log-amplitude coda slopes from models Quartz and Complex Crust with crustal Q_S = 500. Note the linearly decreasing (steepening) coda slopes with frequencies increasing to ~7-10 Hz. Solid gray lines indicate linear regressions using formula (3): $\gamma = 0.8 \cdot 10^{-2}$ and Q_{coda} = 800 for Quartz, and $\gamma = 1.6 \cdot 10^{-2}$ and Q_{coda} = 600 for Complex Crust models.

Alternatively, when converted to Q_{coda} by using Eq. (2), the values of slope result in frequency-dependent $Q_{coda}(f)$ (Figure 5), which one could also fit using a dependence of type (1) with $Q_0 \approx 250$ at 1 Hz and $\eta \approx 0.5$ [see the discussion of conversion to (η, Q_0) below]. Although this interpretation could be acceptable within the synthetic or real data uncertainties, our model contains no mechanisms to support an *in situ* frequency-dependent attenuation. Therefore the observed $Q_{coda}(f)$ (Figure 5) should be viewed as an "apparent" quantity or as an observational artifact.

By selecting linear ln($A(t)$) dependencies (3) for each frequency, we found that the values of γstayed approximately constant in all cases (values shown in labels in Figure 6). These observations were expected (see *Discussion*), as γ should principally depend on the crustal structure. By using these constant ã's and for any frequency (Figure 6), the observed coda slopes can be transformed into the following ratios:

$$\alpha(Q) = \frac{Q_{coda}}{Q} = \frac{\pi f}{-Q\left(\frac{d \ln A(t, f)}{dt} + \gamma\right)} \qquad (5)$$

Note that the resulting Q_{coda}/Q ratio is nearly frequency-independent, greater than 1, and approaches 1 for high Q. Because of these properties, $\alpha(Q)$ can be tabulated and approximated from numerical modeling (lines in Figure 6) and utilized as a "calibration curve" for inverting the Q_{coda} observations for crustal Q. Interestingly, functions are very close (within ~0.2 difference) for all three Quartz-based models, despite the strong difference in γ for the Complex Crust model (Figure 6). However, the $\alpha(Q)$ for iasp91 model is strongly different from those for Quartz in its shape, values, and stability in respect to frequency variations (Figure 6).

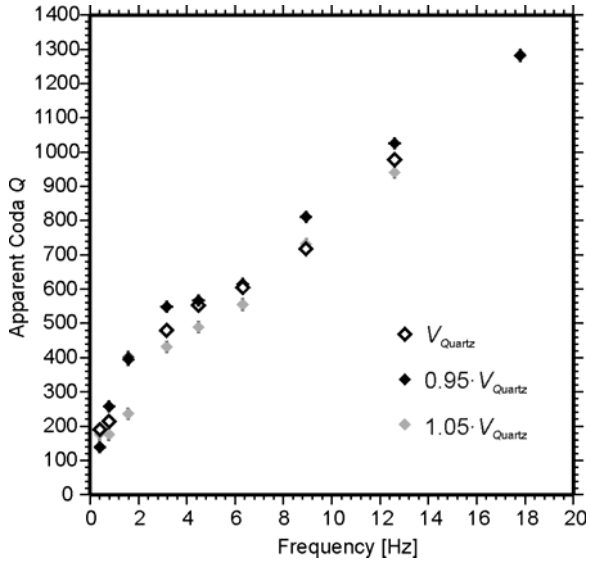

Figure 5. Measured log-amplitude coda slopes transformed to apparent coda $Q_{coda}(f)$ according to relation (2). Note the strong frequency dependence ($\eta \approx 0.5$) of $Q_{coda}(f)$ despite the constant-Q modeled crustal rheology.

Finally, both γ and the functional form of $\alpha(Q)$ should depend on the velocity and density structures of the models. We tested this dependence by using four different types of models (Figure 2) and also by adding velocity perturbations to Quartz model. The results suggest that γ and $\alpha(Q)$ indeed correlate with the structural model styles and crustal velocities, as will be further elaborated on in *Discussion*.

Mapping the (γ,Qcoda) parameterization to (Q_0, η). In most practical cases, the time-frequency amplitude decays $A(f, t)$ can be satisfactorily matched in either (γ, Q_{coda}) or (Q_0, η) forms, and approximate mapping between them can be developed. Consider an attenuation process (e.g., coda) governed by Eq. (3) but parameterized by Eqs. (2) and (1). Therefore, for the time-dependent part of $\ln A(f, t)$, we have

$$\gamma + \frac{\pi f}{Q_{coda}} \approx \frac{\pi f}{Q_o \left(f / f_0 \right)^{\eta}} = q f^{1-\eta}, \tag{6}$$

where q is a constant. For a specific range of frequencies and coda times, transformation (γ, Q_{coda}) $\rightarrow$ (Q_0, η) can be found numerically by least-squares fitting the logarithm of Eq. (6):

$$\ln q + (1-\eta) \ln f \approx \ln\left(\gamma + \frac{\pi f}{Q_{coda}} \right), \tag{7}$$

and solving it for $\ln q$ and $(1-\eta)$. The resulting (Q_0, η) parameters for our numerical experiments are shown in Figure 7. Note that η is principally controlled by the γQ_{coda} product, with $Q_0 = Q_{coda}$ when $\gamma = 0$ and decreasing with increasing γ (Figure 7). Thus, high $\eta \approx 1$ should be expected in areas of low attenuation, with high geometric spreading, or when measurements are carried out at lower frequencies. Therefore, stable platforms (such as the Siberian Craton in eastern Russia) could exhibit high apparent frequency dependence of Q_{coda} simply on account of their high Q. More detail on this can be found in Morozov et al. (submitted to BSSA).

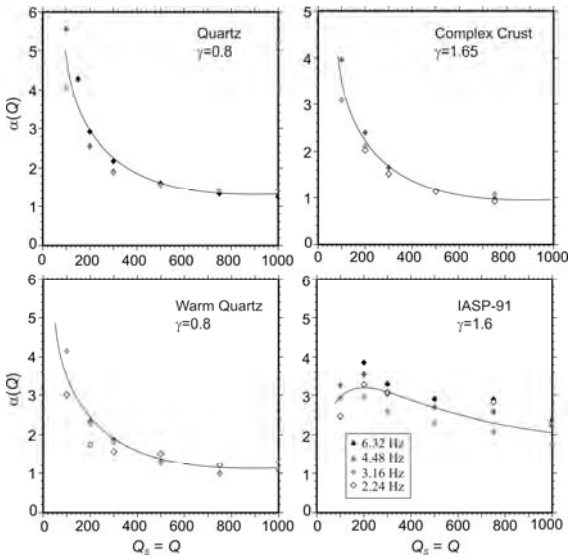

Figure 6. $\alpha(Q_S)$ from Eq. (5) for the four models of this study and different frequencies (labeled symbols), obtained directly from coda slopes by using γ values in Eq. (3) shown in the labels. The lines represent the suggested empirical $\alpha(Q_S)$ dependences for each velocity structure, picked by hand.

PNE data example. The use of (γ, Q_{coda}) description allows us to resolve the following, recent, and hitherto puzzling observation from the PNE profiles. Within the east European platform, measurements from Quartz profile resulted in Q_{coda}(~2 Hz) = 380 and Q_{coda}(~5 Hz) ≈ 430, which was interpreted in the power-law form (1) as $Q_{coda}(f) \approx 270 \cdot f^{0.3}$ (Morozov and Smithson, 2000). However, within the Siberian Craton (PNE Kimberlite-3), practically frequency-independent coda amplitude decays were observed, corresponding to $Q_{coda}(f) \approx 1050 \cdot f^{1.0}$ (Morozov et al., 2006). Although the attenuation was expected to be low within the Siberian Craton, its strong frequency dependence is vastly different from the east European platform and is surprisingly high even for tectonically active areas (Erickson et al., 2004).

The explanation of the above in the (γ, Q_{coda}) form is quite simple. From the Quartz-4 data, the logarithms of coda amplitudes can be interpreted by using $\gamma \approx 0.75 \cdot 10^{-2}$ s^{-1} and frequency-independent $Q_{coda} \approx 850$, with an estimated range of uncertainty of 780 to 960 (Figure 8). From Kimberlite-3 records, γ turns out to be nearly the same, and $Q_{coda} \approx 2500 \pm 300$ (Figure 8). Thus, the Siberian Craton should occupy a region in the upper parts of the diagrams in Figure 7, where $\eta \approx 1$. Note that both values of γ also agree remarkably well with the numerical simulations based on Quartz velocity model data above (Figure 4). The values of Q within the Siberian Craton are very high, in agreement with observations of short-period P_g waves propagating to over 1600 km from the PNEs (Morozov et al., 2006). These are likely the longest-propagating short-period *Pg* observed anywhere on Earth.

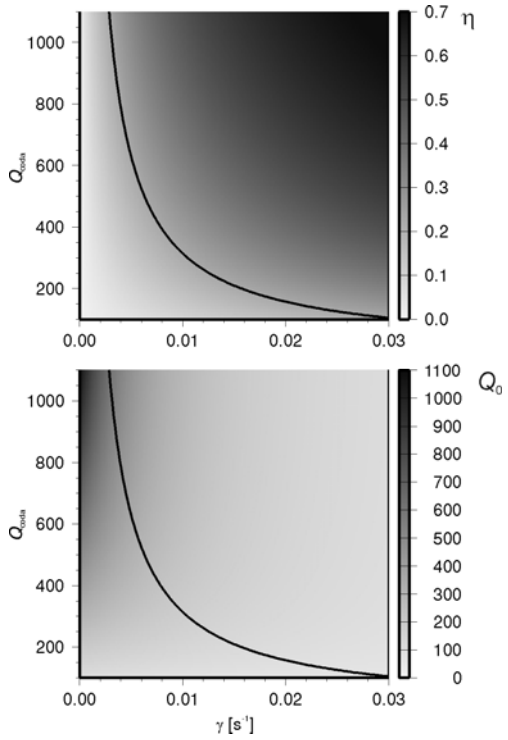

Figure 7. Mapping of (γ, Q_{coda}) to (Q_0, η) approximated for *f*requencies of 1 to 10 Hz. The hyperbolas drawn in both plots correspond to $Q_{coda}\gamma = \pi \cdot 1$Hz. Note that η increases with increasing $Q_{coda}\gamma$.

CONCLUSIONS AND RECOMMENDATIONS

Frequency-dependent attenuation often observed in regional coda measurements can be interpreted in two ways: by frequency-dependent coda $Q_{coda}(f)$ or by means of effective, uncompensated geometrical

spreading (γ) and frequency-independent coda attenuation (Q_{coda}). The second of these alternatives offers a number of practical advantages: 1) it is better justified theoretically and does not require unusual crustal rheologies or inverted scaling properties; 2) its parameters can be quantitatively related to the *in situ* velocity/density (γ) and attenuation (Q_{coda}) crustal structures; 3) the resulting Q_{coda} appears to correspond to crustal Q_S and can be directly correlated to the observed *Lg Q*; 4) the frequency-independent parameters allow easier comparisons between different areas and studies; and 5) as stable characteristics, these parameters are likely to improve coda magnitude analysis and coda *Q* regionalization.

Frequency-dependent inelasticity due to spectral variations of scatterer density is certainly possible and likely to be present in Earth's crust. However, the objective of this paper was to show that it may not be as pervasive as suggested by many frequency-dependent *Q* observations. Within the available data quality, observations of apparent *Q*(*f*) at short periods could often be successfully explained by combinations of geometrical spreading (or turbidity in elastic scattering—Dainty, 1981) and frequency-independent attenuation. Separation of these physical parameters of the crust provides several insights for interpretation and allows linking the seismic velocity, structure, coda, and *Lg Q* results. This conclusion is almost certainly the case with PNE data, and it may also apply to a variety of other seismic datasets (e.g., surface waves).

Numerical modeling of PNE coda wavefields argues strongly in favor of the new (γ, Q_{coda}) interpretation and illustrates the mechanisms leading to such an apparent *Q*(*f*). The inverted Q_{coda} values can be systematically mapped into the true *S*-wave attenuation factors within the crust. By contrast, when interpreted using the traditional approach, the synthetic coda shows strong spurious frequency-dependent Q_{coda}.

PNEs in Russia in two different areas were found to have similar γvalues, although strongly different Q_{coda}. We also suggest that parameter γcould provide a better, stable, and transportable discriminant for differentiating between tectonic types of the crust. From a limited preliminary example, this discriminant may relate to the presence of localized attenuative or scattering structures within the crust and be applicable to both North America and Northern Eurasia.

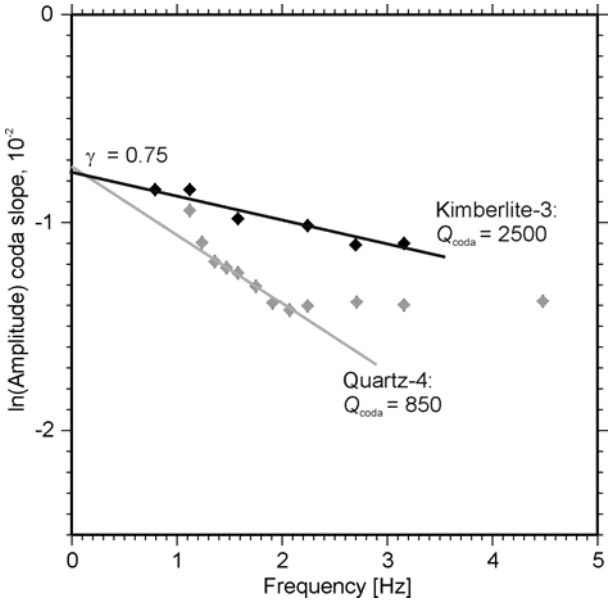

Figure 8. Log-amplitude coda slopes in real data from PNEs Quartz-4 (recorded within the east European platform, at ~2600-km source-receiver offset; same data as in Morozov et al.,

2002) and Kimberlite-3 (recording within the Siberian Craton at ~1100-km offsets). Note the different Q_{coda} values (lines and labels), whereas the γ values are similar and close to those modelled. Also note that because of lower-magnitude source and longer recording distance, the usable frequency band is narrower for Quartz PNE records.

REFERENCES

Aki, K. and B. Chouet (1975). Origin of coda waves: source, attenuation, and scattering effects, J. Geophys. Res. 80: 3,322–3,342.

Aki, K., and Richards, P. G. (2002). Quantitative Seismology, Second Edition, University Science Books, Sausalito, CA.

Aster, R., B. Borchers, and C. Thurber (2002). Parameter Estimation and Inverse Problems, preliminary edition.

Bannister, S. G., E. S. Husebye, and B. O. Ruud (1990). Teleseismic P coda analyzed by three-component and array techniques: deterministic location of topographic P-to-Rg scattering near the NORESS array, BSSA, 80: 1969–1986.

Benz, H., A. Frankel, and D. Boore (1997). Regional Lg attenuation in the continental United States, *Bull. Seism. Soc. Am*. 87: 600–619.

Campillo, M. (1987). Lg wave propagation in a laterally varying crust and the distribution of the apparent quality factor in central France, *J. Geophys. Res*., 92: 12604-12614.

Campillo, M. (1990). Propagation and attenuation characteristics of the crustal phase Lg, Pure Appl. Geoph., 132: 1–17.

Christensen, N. I., and W. D. Mooney (1995). Seismic velocity structure and composition of the continental crust: A global view, *J. Geophys. Res*. 100: B7, 9761–9788.

Chubak, G., and I. B. Morozov (2006). Integrated software framework for processing of geophysical data, *Computers & Geosciences* 32: 767–775.

Dainty, A. M. (1981). A scattering model to explain seismic Q observations in the lithosphere between 1 and 30 Hz, Geophys. Res. Lett. 8: 1126–1128.

Dainty, A. M. (1985). Air Force Geophysical Laboratory Report, AFGL-TF-86-0218.

Dainty, A. M. (1990). Studies of coda using array and three-component processing, PAGEOPH, 132: 221–244.

Dainty, A. M. and C. A. Schultz (1995). Crustal reflections and the nature of regional P coda, *Bull. Seismol. Soc. Am.*, 85: 851–858.

Der, Z. A., A. C. Lees, and V. F. Cormier (1986). Frequency dependence of Q in the mantle underlying the shield region of Eurasia, Part III: The Q-model, *Geophys. J. R. Astr. Soc*. 87: 1103–1112.

Enderle, U., M. Titgemeyer, M. Itzin, C. Prodehl, and K. Fuchs (1997). Scales of structure in the lithosphere - Images of processes, *Tectonophysics*, 275: 165–198.

Erickson, D., D. E. McNamara, and H. Benz (2005). Frequency-dependent Lg Q within the continental United States, *Bull. Seism. Soc. Am*. 94: 1630–1643.

Frankel, A., A. McGarr, J. Bicknell, J. Mori, L. Seeber, and E. Cranswick (1990). Attenuation of high-frequency shear waves in the crust: measurements from New York state, South Africa, and southern California, J. *Geophys. Res*. 95: 17441–17457.

Fuchs, K., and G. Müller (1971). Computation of synthetic seismograms with the reflectivity method and comparison with observations, *J. R. Astronom. Soc*. 23: 417–433.

Greenfield, R. J. (1971). Short-period P-wave generation by Rayleigh-wave scattering at Novaya Zemlya, *JGR* 76: 7988–8002.

Gupta, I.N., T. W. McElfresh, and R. A. Wagner (1991). Near-source scattering of Rayleigh to P in teleseismic arrivals from Pahute Mesa (NTS shots, in: Taylor, S. R., H. J. Patton, and P. G. Richards (Eds.), Explosion Source Phenomenology, *AGU Geophys. Monograph* 65: 151–160.

Hasegawa, H. S. (1985). Attenuation of Lg waves in the Canadian Shield, *Bull. Seism. Soc. Am*. 75: 1569–1582.

Kennett, B. L. N. and R. Engdahl (1991). Traveltimes for global earthquake location and phase identification, *Geophys. J. Int*. 105: 429–465.

Li, H., I. B. Morozov, and S. B. Smithson (submitted to *Bull. Seism. Soc. Am*.) Mapping Lg Q at 1-3 Hz in Northern Eurasia using nuclear-explosion profiles.

Liu, H. P., Anderson, D. L., Kanamori, H. (1976). Velocity dispersion due to anelasticity: implications for seismology and mantle composition, *Geophysical Journal of the Royal Astronomical Society* 47: 41–58.

Mayeda, K., and W. R. Walter (1996). Moment, energy, stress drop, and source spectra of western United States earthquakes from regional coda envelopes, *J. Geophys. Res*. 101: 11195–11208.

McNamara, D. E. (2000). Frequency-dependent Lg attenuation in south-central Alaska, *Geophys. Res. Lett*. 27: 3949–3952.

McNamara, D. E., T. J. Owens, and W. R. Walter (1996). Propagation characteristics of Lg across the Tibetian Plateau, *Bull. Seism. Soc. Am*. 86: 457–469.

Mechie, J., A. V. Egorkin, K. Fuchs, T. Ryberg, L. Solodilov, and F. Wenzel (1993). P-wave velocity structure beneath northern Eurasia from long-range recordings along the profile Quartz, Phys. *Earth Planet Inter*. 79: 269–286.

Mitchell, B. J. and L. Cong (1998). Lg coda Q and its relation to the structure and evolution of continents: a global Perspective, *Pure Appl. Geophys*. 153: 655–663.

Mitchell, B. J., Pan, Y., Xie, J., Cong, L. (1997). Lg coda Q variation across Eurasia and its relation to crustal evolution, *J. Geophys. Res*. 102: 22767–22779.

Morozov, I. B. (2001). Comment on "High-frequency wave propagation in the uppermost mantle" by T. Ryberg and F. Wenzel, *J. Geophys. Res*. 106: 30,715–30,718.

Morozov, I. B., and S. B. Smithson (2000).Coda of long-range arrivals from nuclear explosions, *Bull. Seism. Soc. Am*. 90: 929–939.

Morozov, I. B., E. A. Morozova, and S. B. Smithson (1998a). On the nature of the teleseismic Pn phase observed in the recordings from the ultra-long profile "Quartz", Russia, *Bull. Seism. Soc. Am*. 88: 62–73.

Morozov, I. B., E. A. Morozova, S. B. Smithson, and L. N. Solodilov (1998b). 2-D image of seismic attenuation beneath the Deep Seismic Sounding profile "Quartz", Russia, *Pure and Applied Geoph*. 153: 311–348.

Morozov, I., Morozova, E., Zhang, C. Chubak, G., Phillips, W. S. and Lipovetsky, I. (2006). Magnitude-yield and travel-time calibration of northern Eurasia using deep seismic sounding datasets, in *Proceedings of the* 28*th Seismic Research Review: Ground-Based Nuclear Explosion Monitoring Technologies*, LA-UR-06-5471, Vol. 1, pp. 130–140.

Morozov, I. B., C. Zhang, J. N. Duenow, E. A. Morozova, and S. B. Smithson (2007). Frequency dependence of regional coda Q: Part I. Numerical modelling and an example from Peaceful Nuclear Explosions," submitted to BSSA.

Morozova, E. A., I. B. Morozov, S. B. Smithson., and L. N. Solodilov (1999). Heterogeneity of the uppermost mantle beneath Russian Eurasia from the ultra-long range profile QUARTZ, *J. Geophys. Res*. 104: (B9), 20,329–20,348.

Nuttli, O. W. (1973). Seismic wave attenuation and magnitude relations for eastern North America, *J. Geophys. Res*., 78, 5212–5218.

Phillips, W. S., H. J. Patton, S. R. Taylor, H. E. Hartse, and R. E. Randall (2004). Calibration for coda based magnitude and yield, in *Proceedings of the 26th Seismic Research Review: Ground-Based Nuclear Explosion Monitoring Technologies*, LA-UR-06-5471, Vol. 1, pp. 449-456.

Ryberg, T., and F. Wenzel (1999). High-frequency wave propagation in the uppermost mantle, *J. Geophys. Res*., 104, 10,655–10,666.

Ryberg, T., K. Fuchs, A. V. Egorkin, and L. Solodilov (1995). Observations of high-frequency teleseismic Pn on the long-range Quartz profile across northern Eurasia, *J. Geophys. Res*. 100: 18151–18163.

Sato, H., and M. Fehler (1998). Seismic Wave Propagation and Scattering in the Heterogeneous Earth, Springer-Verlag, New York.

DIGITAL DATABASE OF DEEP SEISMIC SOUNDING PROFILES IN NORTHERN EURASIA

Igor B. Morozov[1,2], Elena A. Morozova[1,2], and Scott B. Smithson[2]

University of Saskatchewan[1] and University of Wyoming[2]

Sponsored by Air Force Research Laboratory

Contract No. DTRA01-01-C-0081

ABSTRACT

In several years of cooperation with the various successors of the Special Geophysical Expedition (Moscow, Russia) we produced a digital data set of seismic records from the unique program of ultra-long-range deep seismic sounding (DSS) profiling conducted in the former Soviet Union from the early 1970s through late 1980s. The program was unique in using peaceful nuclear explosions (PNEs) recorded along 3000-4000-km long, reversed, three-component seismic profiles. Each profile recorded one to four PNEs and several dozen chemical explosions at the same receiver locations. Long listening times of up to ~600 sec after the first arrivals allowed recording of the secondary phases (*S*, *Lg*, *Pg*, *Rg*) critical for nuclear test monitoring. The energies of the PNEs ($m_b \approx 5$) were sufficient for reliable recordings beyond 3000 km, which included consistent reflections from the mantle transition zone and several reflections from the core-mantle boundary. Chemical explosions of 5-12 tons yielded clear reflections from ~100-km depths and were recorded to 300-600-km distances.

The digitization efforts have resulted in 22 PNEs and several hundred chemical explosions now available through the Incorporated Research Institutions for Seismology (IRIS) data center. To date, complete sets of records from projects AGATE, BAZALT, BATHOLITH-1 and 2, CRATON, KIMBERLITE, RIFT, RUBY-1 and 2, and QUARTZ and SPAT were delivered in long-record Society for Exploration Geophysics (SEG-Y) standard format. For seamless data exchange with the test monitoring researchers, we have also incorporated the waveforms and ancillary data into the National Nuclear Security Administration (NNSA) database schema. Only three additional projects (BITUM, PRICASPIY, and PNE SPAT) recoverable from field magnetic tapes remain not included in the DSS PNE database.

Long-range DSS data sets provide nearly the only dense three-component recordings of regional phases in the aseismic regions of Northern Eurasia. PNE data sets cover the intermediate distance ranges (~0-3200 km) and bridge the gap between controlled-source and earthquake seismology. Dense, linear, and reversed systems of DSS observations lead to unusually detailed models of the crust and uppermost mantle over 4000-km long geotraverses. Our final objective is to combine these models in an unusually well-constrained, detailed, interactive three-dimensional (3-D) structural model of Northern Eurasia. The model can also be integrated with empirical phase calibration information, thereby leading to a unified calibration model of the region.

OBJECTIVES

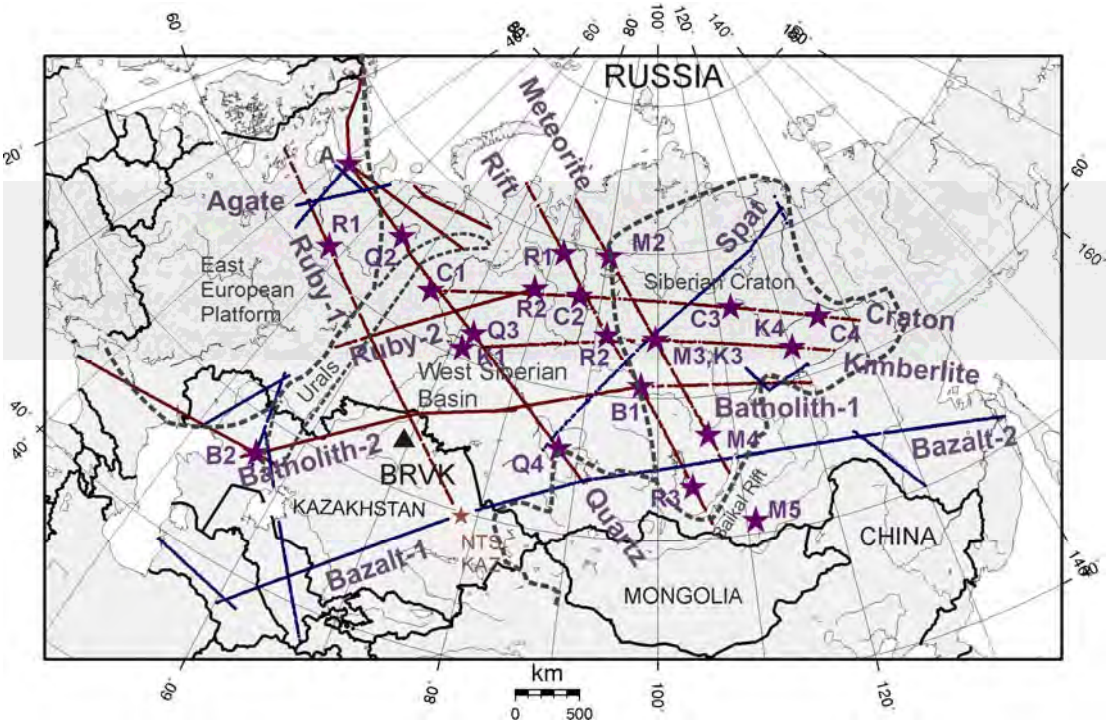

Figure 1. Twelve DSS PNE projects delivered to the public domain as a result of this project (blue labels). The PNEs (large stars) are labeled using the first letters of the corresponding profiles names and PNE number (for example, Q2 stands for PNE QUARTZ-2. PNE AGATE is shown without a number). Sultanov et al. (1999) reported the coordinates and other parameters of the PNEs used in these profiles. Colored triangles in the profiles represent the recording stations. Typically, 30-50 chemical explosions were also recorded in each profile. Major tectonic units are indicated. The Semipalatinsk nuclear test site is indicated (NTS KAZ), and the Borovoye IMS station is also shown (BRVK).

Note the extent of systematic, continuous profiling, with PNEs (labeled stars) detonated at the intersections of a two-dimensional (2-D) grid and recorded in two, and often in four, directions.

The objective of this research was to create digital copies of seismic records from most of DSS data sets preserved to date and to make them available for monitoring and broader seismological studies. This task was approached through long-term cooperation between the University of Wyoming (UW) seismology group and Center for Regional Geophysical and Geoecological Studies (GEON Center), Moscow (a division of Spetzgeofisika at the time of data acquisition, now a division of Vniigeopfisika). In this cooperation, the records were digitized at GEON, who also provided tables of channel amplifications and other information. We performed the consultations with GEON, as well as the data transfer, all the primary data reduction, reformatting, and quality control. The digital records were later submitted to IRIS and incorporated into its global on-line databases.

Twelve DSS PNE projects were selected for this work as the most important and most recent (Figure 1, west to east): AGATE, BATHOLITH-2, RUBY-1 and 2, BAZALT-1, QUARTZ, CRATON, KIMBERLITE, RIFT, METEORITE, BATHOLITH-1, and BAZALT-2. Later in the project, it became apparent that the chemical-explosion recordings from project METEORITE suffered too many data gaps, and the chemical explosion part of data set SPAT was obtained in replacement of the obligations of this project.

This report is a shortened version of the final project report submitted to the Air Force Research Laboratory (AFRL) in June. In the following section, we give a brief summary of the DSS program in the former Soviet Union, followed by a summary of the data sets and data deliveries. In *Conclusions and Recommendations*, we recap the importance of the DSS data preservation work and also describe its perspectives.

RESEARCH ACCOMPLISHED

The Deep Seismic Sounding Program in the Former USSR and Recent Studies of its Data

The DSS program carried out by Soviet scientists from the 1960s to 1990s remains a unique source of seismic data sets, allowing a detailed study of the seismic structure of the upper mantle. Long-range seismic refraction/reflection profiles covered nearly the entire territory of the former USSR, amounting to about 1/6 of the whole continental lithosphere (Figure 1). This unique network of geophysical profiles with an overall length of 150,000 km utilized nearly 60 PNEs specially designed and set up for seismic purposes, along with hundreds of powerful chemical explosions (Figure 1). The power of explosions ranged from tens of kilograms to 4,000-15,000 kg for the chemical explosions (Solodilov, 1997; Egorkin et al., 1991; Kozlovsky, 1990) and to 7-20 kiloton for nuclear explosions (Fujita, 1995; Sultanov et al., 1999).

Large chemical explosions and PNEs were recorded by densely spaced (10-15 km), 3-component, short-period (1-2 Hz) portable analog recording systems. The recording ranges of the PNEs exceeded 3200 km, allowing observations of seismic phases diving down to 800 km into the mantle (Egorkin and Pavlenkova, 1981; Ryaboy, 1989; Kozlovsky, 1990).

Acquisition of DSS data sets was among the principal scientific priorities of the Soviet government. A special institution—the Special Regional Geophysical Expedition, or Spetzgeofisika, later known as the Center GEON (the Center for Regional Geophysical and Geoecological Research, and now a division of VniiGeofisika)—was established for this purpose. A comparable project using nearly 60 nuclear explosions and helicopter support across thousands of kilometers of extremely difficult sub-Arctic terrain would have cost billions of dollars in a Western economy. It is very unlikely that a seismological project of a similar scale will be undertaken in the near future (Fuchs and Wenzel, 1997). For these reasons alone, the preservation and the maximum use of the DSS data constituted one of the priorities in today's seismology. Since all of the recordings were performed on magnetic tape in analogue format, the danger of the loss of this invaluable data set was great. The seismological group lead by Professor Scott Smithson of the University of Wyoming was the first to start the cooperation with the GEON Center in Moscow to digitize the records from nuclear and chemical explosions from the profile QUARTZ to their full length. Also, the Geophysical Institute of Karlsruhe University and the GeoForschungsZentrum at Potsdam started a joint program with GEON to digitize data from other profiles (Fuchs and Wenzel, 1997).

The most important reason for applying every effort to the analysis of DSS data is that these data cover the intermediate range and provide the link between traditional wide-angle and regional and teleseismic seismology. The energy of the sources and the depths and distance coverage of 3-component recordings is far beyond the limits of any other branch of controlled-source seismology, whereas the linear geometry and density of the profiles is still far above the level provided by seismological networks. DSS interpretations provide practically the only source of information for high-resolution imaging of the upper mantle and are a major resource for demonstrating its profound heterogeneity. Most importantly, in most of the DSS profiles along with the PNE records, a very comprehensive crustal data set using large chemical explosions was acquired, providing images of the crust that are sufficiently detailed to allow a robust inversion for the deeper mantle structures.

DSS data are unique in the length of continuous profiling, in the strength of the explosions used, in the number of source points (the combination of nuclear and chemical shots along the whole profiles), and in the recording in two to four directions from each source point (Figure 1). Dense station spacing and known positions of the explosions allow us to resolve the velocity and attenuation structure of the upper mantle in unprecedented detail when compared with earthquake data.

Earlier publications in English of some of the DSS results obtained using various data processing techniques, including non-linear velocity filtering and travel time analysis, include Belyaevsky et al. (1976), Kats et al. (1978), Vinnik et al. (1978), Yegorkin et al. (1978), Yegorkin et al. (1979), Yegorkin and Yegorkina (1980), Vinnik and Yegorkin (1981), Yegorkin and Pavlenkova (1981), Yegorkin et al. (1981), Fuchs and Vinnik (1982), Pavlenkova and Yegorkin (1983), Koshubin et al. (1984), Burmakov et al. (1986, 1987), Alekseev et al. (1988), Egorkin and Sumerina (1988), Egorkin and Zyuganov (1988), Galdin et al. (1989), Ryaboy (1989), Egorkin and Mikhaltsev (1990), Yegorkin et al. (1991), Benz et al. (1992), Yegorkin (1992), Yegorkin et al. (1992). More recently, Schueller et al. (1997) used a travel-time, refraction-reflection tomography to invert for the *P*-wave velocity structure of the northwestern part of the profile QUARTZ; Ryberg et al. (1996) presented a 2-D interpretation based solely on the first arrivals from QUARTZ PNEs; Lorentz et al. (1997) applied tomographic inversion to the mantle arrivals from

QUARTZ PNEs; and Ryberg et al. (1998) stacked all available DSS records to derive a "generalized" one-dimensional (1-D) regional velocity model of Northern Eurasia. Mechie et al. (1997) compared the observations of the asthenospheric low-velocity zones (LVZ) in a number of DSS profiles. The progress in the understanding the heterogeneity of the upper mantle structure through controlled-source and passive seismology was summarized in the 1997 EUROPROBE conference (Fuchs, 1997). Recent work focused on integration of the results into 3-D pictures of the lithosphere analysis of the Siberian profiles and analysis of mantle and crustal scattering, receiver Functions, and coda properties (e.g., Ryberg et al., 1995; Morozov et al., 1998a; Morozov and Smithson, 2000; Morozov, 2001; Nielsen and Thybo, 2003). Several longer-offset PNEs (BATHOLITH-2, CRATON-1, QUARTZ-4; Figure 1) produced reflections from the core-mantle boundary.

Two fundamental general conclusions were drawn from DSS studies. First, a number of 1-D mantle models derived for the Northern Eurasia (Mechie et al., 1993; Priestley et al., 1994; Pavlenkova, 1996) exhibit a prominent LVZ below at about 200 km depth and probably reduced velocity contrast at the 660-km boundary compared to the iasp91 model (Ryberg et al., 1998). There is no general agreement about the sharpness of the mantle transition zone discontinuities, which is critical to understanding their cause in terms of mantle mineralogy and composition. Mechie et al. (1993) and Ryberg et al. (1998) modeled the 410-km discontinuity as a sharp transition consistent with the iasp1 model, but Priestley et al. (1994) argued that the 410-km discontinuity may actually be a 35-km thick transition zone.

Another important result of the DSS studies is the demonstration of a strongly heterogeneous, 2-D structure of the uppermost mantle within the regional scale and down to at least 400 km (Mechie et al., 1993; Priestley et al., 1994; Ryberg et al. 1995; Morozova et al., 1997). This heterogeneity manifests itself in the velocity and attenuation structure (Morozov et al., 1998b), as well as in the properties of regional and global mantle boundaries (Pavlenkova, 1996; Morozova et al., 1999). The variability of the uppermost mantle partly limits the significance of 1-D regional models and partly minimizes some of the controversies in interpretations; on the other hand, this variability demands (at least) 2-D interpretations, of which very few exist at the regional scale.

In the context of nuclear test monitoring research, our group at UW, and currently at the University of Saskatchewan, emphasized a variety of empirical mapping approaches. The following models were devalued in recent years from integrated interpretations of multiple profiles. These results were principally due to the DSS PNE data becoming available through the present project:

1) An empirical 3-D first-arrival travel-time model (Morozov et al., 2005) suitable for generation of reference Source-Specific Station Correction surfaces;

2) Phase amplitude ratio maps, including quantitative correlations with crustal properties (Li et al., 2007);

3) An empirical *Lg Q* model (Li et al., submitted to BSSA). As above, significant correlations with parameters of crustal structures were found, such as correlations of *Lg Q* variations with the presence of sedimentary basins and Moho depth gradients;

4) *P* and *Lg* coda *Q* models (Morozov et al., submitted to BSSA, a and b). Notably, in these studies, we propose a different description of frequency-dependent coda *Q* that is physically consistent, results in stable and transportable estimates, allows a direct correlation to the *Lg Q* studies above, and correlates well with regional tectonics;

5) Corner-frequency and magnitude-yield analysis of the PNEs (Li et al, in preparation for BSSA).

Digitization of the DSS PNE Profile Records

DSS data were recorded using specially designed three-component seismographs "Taiga" (the name means the Russian sub-Arctic coniferous forest) and "Cherepakha" (Turtle) that were specially designed for the program. The systems equipped with NSP-1 geophones (Figure 2) were deployed by helicopters at a nominal spacing of 10-15 km along the whole length of each profile and radio-controlled to simultaneously record the waves at distances of up to 1500-3000 km. Designed for 7 to 10 days of continuous recording of the ground motion velocity, the stations operated at 0.5-20 Hz frequencies within a dynamic range of 70 dB (Figure 3; Ryaboy, 1989).

Figure 2. Playback and digitizing system for CHEREPAKHA seismographs (GEON Center, Moscow, 2004).

From the early 1990s, GEON went through a number of turbulent reorganizations, lack of funding, retirements of the key personnel, and disputes about its building in downtown Moscow. All this certainly did not improve preservation of the historic Soviet-era PNE data sets (Figure 4). Fortunately, principally owing to the present project, GEON specialists had been able to survive this period and continue recovering and digitizing the data sets (Figure 2)

While preprocessing the PNE data, we encountered a number of difficult processing problems that were related to the unusual parameters and format of the records. In order to tackle these basic data manipulation tasks, we wrote a suite of tools for the CogniSeis® DISCO seismic processing system, which was the main seismic processing system running on the dedicated VAX 11/785 in the University of Wyoming Reflection Seismology group until 1997. Later, these tools were incorporated into a new processing system called SIA (http://seiswev.usask.ca/SIA), whose further development was in fact largely inspired by the needs of the DSS data projects.

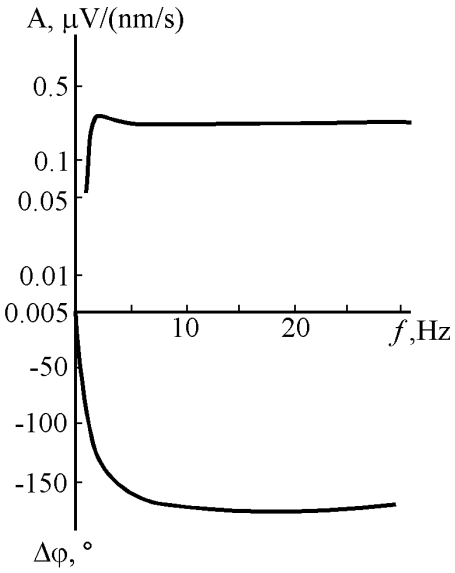

Figure 3. Amplitude and phase responses of "Taiga" recorders with NSP-1 seismometers used in DSS PNE recordings (after Ryaboy, 1989).

Figure 4. PNE analog magnetic tape data storage at the GEON Center (2004).

The PNE data sets were digitized from 1994-2005 at the GEON Center in Moscow. Digitization was performed to the full length of the analog records varying from about 100 sec for near-shot receivers to over 600 sec in far-offset PNE records. During the early stages of digitization, the digitizing equipment and software were not able to handle such long records, and so the records were split into several segments with 20-25 sec overlaps. Another complication of the initial data reduction was the shipment of the records to the University of Wyoming in four different Russian formats, none of which the existing software could read. The time starts, coordinates, gain factors, and other parameters of the records were provided in the form of hardcopy tables that we checked and loaded manually.

After the resulting records were delivered to UW, the parts of the records were concatenated using a cross-correlation technique that allowed locating the exact time starts of the record segments. At the same time, however, DISCO (a commercial seismic processing system designed for 2-D common midpoint [CMP] exploration data processing) was not able to handle the long (up to 30,000 samples per record) DSS records, and an interface had to be developed to allow splitting the records into smaller segments while allowing the processor to manipulate the long data traces in their integrity. These complications mostly affected the QUARTZ records; other data sets were provided by GEON in custom DSS formats.

Having loaded the data into DISCO, and later into SIA, we performed a tedious data editing procedure. This step involved plotting and inspecting all data records and selecting the channels with the best dynamic parameters. Typically, the DSS data were recorded into 6 channels at each recording point at 2 different gain levels. This allowed selection of the channels that were not overloaded and had better signal/noise ratios. This procedure was performed using manual editing, which took considerable time.

Many of the processing steps included in the data analysis required 3-component data. However, all three components of the recorded wavefield were not available for all stations; occasionally, some channels were missing. Given virtually no support for multicomponent data manipulation offered by the DISCO system, this irregularity (which is typical for wide-angle multicomponent data sets) of the data also caused a substantial difficulty for advanced signal analysis. This difficulty was overcome by the development of a series of special computer codes.

After the VAX 11/785 was taken out of operation in early 1997, all the tools for DSS data processing were transferred to the new seismic processing system recently developed at the UW seismology lab. This allowed us to efficiently handle DSS data and to add high performance of new UNIX-based computers (SGI Power Challenge L,

SGI Indigo, Sun Sparc, and HP workstations), more versatile data analysis, color PostScript and interactive plotting programs and an interface to PROMAX, to many Seismic UNIX programs, and currently 3-D visualization.

As a result of these efforts, the PNE data sets shown in Figure 1 were digitized, edited, and formatted in long-record (Program for the Array Seismic Studies of the Continental Lithosphere—PASSCAL—extension) SEG-Y formats, and delivered to IRIS for unrestricted dissemination (Table 1). We have also created tools for exporting the data sets in CSS3.0 or NNSA-schema databases. Upon a request, these data sets may be available in this format from our FTP site.

Table 1. Numbers of PNEs and chemical shots and final data delivery schedules

#	Data set	Acquisition year	PNEs	Chemical shots	Delivery dates to IRS and AFRL
1	QUARTZ	1984-87	3	51	12/2002
2	CRATON	19780-80	4	30	11/2002
3	KIMBERLITE	1979	3	36	11/2002, 10/2003 (chemical)
4	RIFT	1982-83	3	36	10/2003
5	RUBY-1 and 2	1988-89	2	27+26	02/2004
6	AGATE (5 profiles)	1985	1	36	06/2004
7	BATHOLITH-1 (3 profiles)	1980	1	52	12/2004
8	BATHOLITH-2 (4 profiles)	1987	1	89	12/2004
9	BAZALT-1 (3 profiles)	1989	0	88	07/2005
10	BAZALT-2 (2 profiles)	1990	0	87	07/2005
11	METEORITE*	1977	4	-*	06/2007
12	SPAT**	1981	1**	39	06/2007

*Due to loss of the original field material, chemical-shot data from project METEORITE are now deemed unrecoverable.
**Only chemical-shot records provided in replacement of METEORITE.

CONCLUSIONS AND RECOMMENDATIONS

As a result of this effort, the broad seismological and seismic monitoring communities have obtained a set of digital recordings of a large number of nuclear explosions recorded across a variety of propagation paths to distances of ~3000 km. The available PNE and chemical-explosion data sets from eleven major Russian seismic projects should make important contributions to the studies research of regional seismic phases, to seismic calibration of the region, and to helping develop transportable seismic discriminants in Northern Asia. Availability of the unique PNE recordings should foster research in nuclear test monitoring. In addition, from a broader scientific perspective, the digitized DSS recordings and models of the upper mantle could also provide ideal reference and calibration data sets for the detailed structure of the upper mantle targeted by the US Array.

Combination of the results based on the DSS PNE projects of this study (velocity; reflectivity; receiver functions; mantle attenuation; *Lg Q*, *P*- and *Lg* coda *Q*; scattering; phase amplitude ratios; and empirical first-arrival travel times) makes the area of PNE profiling one of the best-constrained seismically at short periods. This conclusion applies to both fundamental and applied (monitoring) research areas.

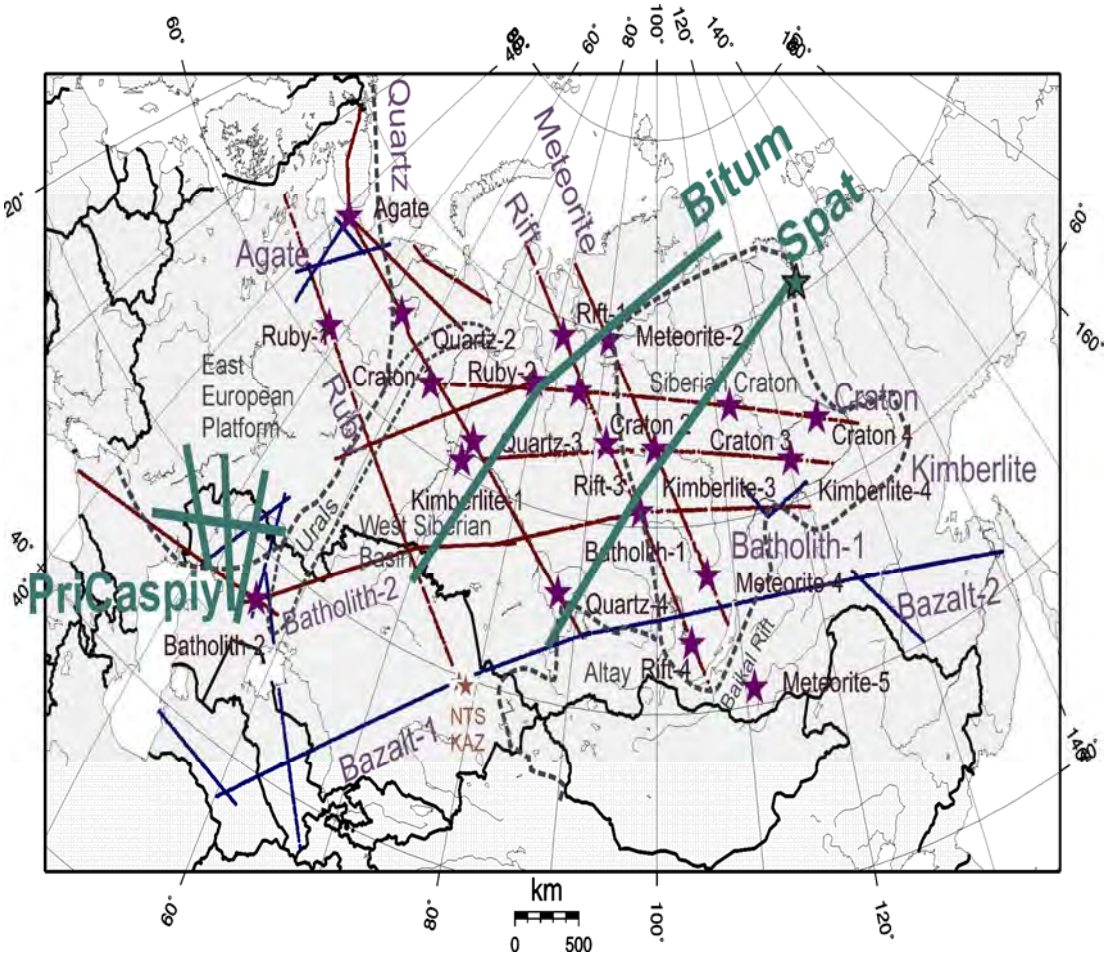

Figure 5. Map of DSS PNE profiling as in Figure 1 with the three remaining projects still available for digitization: BITUM, PRICASPIY, and SPAT (green lines). From profile SPAT, we have delivered the chemical-explosion data set as a part of the present project, and its PNE and earthquake data set still remain to be digitized.

The success of any geophysical investigation is determined by the data. In this project, we have preserved and made publicly available the complete seismic data sets from roughly 80% of the DSS PNE data that was still recoverable. Acquisition of such data, across similar distances at high latitudes, would be extremely expensive, and in the cases of PNEs, completely impossible today. Thus we strongly recommend that the remaining DSS PNE data be properly digitized and archived. The only remaining profiles that still could be digitized are SPAT (one PNE and earthquake data set), BITUM, and PRICASPIY (2 profiles; Figure 5). Digitization of these records would complete preservation of the historic DSS PNE data sets. Note that SPAT and BITUM lines are particularly important, as they cross the Siberian platform in NE-SW direction which is so far not represented in our data set (Figure 1). Multiple lines of project PRICASPIY also cover the Pre-Caspian Depression in different directions, in the vicinity of PNE BATOLITH-2 (Figure 5).

The depth of the potential analysis of the data sets is far from being exhausted. Only the QUARTZ data set has been studied thoroughly and from various standpoints and complemented by CRATON, KIMBERLITE, METEORITE, RIFT, and RUBY in only limited studies. Most of the critical (and also most tedious and difficult) work on detailed inversion of the crustal and mantle structure was done only by Russian groups (Pavlenkova and Yegorkin). Apart from QUARTZ, modern inversion techniques have been still insufficiently applied, and the very interesting fan lines from PNEs RUBY-1, RUBY-2, and AGATE have not been analyzed at all. Chemical explosion data sets are still underutilized, as well as PNEs AGATE, BATHOLITH, and SPAT. Integration of the results in a true 3-D model still remains to be performed, and this model should incorporate the various empirical attributes and be capable of numerical simulations. These are the directions in which, as we hope, the work will be continued in the future.

REFERENCES

Alekseev, A. S., A. V. Egorkin, and Pavlenkova N.I., (1988). Shear waves in lithosphere studies on the territory of the USSR, *Tectonophysics* 154: (3-4), 227–239.

Belyayevsky, N. A., B. S. Volvovsky, I. S. Volvovsky, A. V. Yegorkin, M. K. Polshkov, Ye. A. Popov, V. Z. Ryaboy, V. B. Sologub, N. M. Chernyshev, and Yurov Yu. G. (1976). Lithospheric structure along a profile from the Black Sea to the Polar Urals, Tectonophysics, 33: (3–4), 359–378.

Benz H. M., J. D. Unger, and Leith W. S. (1992). Deep seismic sounding in northern Eurasia: interpretation of the Murmansk-Kizil ultra-long-range profile, in: Proceedings of the 14th Annual Seismic Research Symposium, 16-18 September 1992, PL/DARPA, Arlington, Virginia, pp. 36-47.

Burmakov, Yu. A., L. P. Vinnik, A. V. Yegorkin, and N. M. Chernyshev (1986). Study of the lithosphere under the continental crust of Siberia using the seismic tomography method, Transactions (Doklady) of the USSR Academy of Sciences, *Earth Science Sections*, 287: (1), 78–82.

Burmakov, Yu. A., N. M. Chernyshev, L. P. Vinnik, and Yegorkin, A. V., (1987). Comparative characteristics of the lithospere of the Russian Platform, the West Siberian Platform and the Siberian Platform from seismic observations on long-range profiles, in: Kroener, A. (Ed.), Proterozoic lithospheric evolution, AGU Geodynamics Series, 17: AGU, 175–189.

Cipar, J., K. F. Priestley, A. V. Egorkin, and N. I. Pavlenkova (1993). The Yamal Peninsula-Lake Baikal deep seismic sounding profile, *Geophys. Res. Lett.* 20: (15), 1631–1634.

Egorkin A. V., Kosminskaya I. P, Pavlenkova, N. I., (1991). Multisided Seismic Investigations of Continental Lithosphere, Izvestiya, *Earth Physics* 27: 9 793-803.

Egorkin, A. V. and A. V. Mikhaltsev (1990). The Results of Seismic Investigations along Geotraverses, in Super-Deep Continental Drilling and Deep Geophysical Sounding, K. Fuchs, Y. A. Kozlovsky, A. I. Krivtsov and M. D. Zoback (Editors), Super-Deep Continental Drilling and Deep Geophysical Sounding, Springer, Berlin, 111–119.

Egorkin, A. V., and S. K. Zyuganov (1988). Results of investigations of the structure of the lithosphere on profiles in Siberia, *Soviet Geology and Geophysics* 29: (5), 107–114.

Egorkin, A. V., and Pavlenkova, N. I., (1981). Studies of mantle structure in the U.S.S.R. territory on long-range seismic profiles, *Phys. Earth Planet Inter*. 25: 12–26.

Egorkin, A. V., and Sumerina, E. P., (1988). Absorption of compressional waves in the consolidated crust of Siberia, *Soviet Geology and Geophysics* 29: (12), 100–107.

Fuchs K. and Vinnik, L.P., (1982). Investigation of the Subcrustal Lithosphere and Astenosphere by Controlled Source Seismic Experiments on Long-Rang Profiles; in: Palmason (ed.), Continental and Oceanic Rifts, AGU, *Geodynamics Ser*. 8: 81–98.

Fuchs, K., and Wenzel F., (1997). Conservation of lithospheric DSS data, in: Fuchs, K. (Ed.) Upper mantle heterogeneities from active and passive seismology, 11–32. Kluwer Academic Publ., Dordrecht.

Fujita, K., (1995). Peaceful nuclear explosions in the Sakha Republic (Yakutia), Russia, *Seismol. Res. Lett*. 66: (2), 20–24.

Galdin, N. E., A. V. Yegorkin, S. K. Zyuganov, L. I. Kagalova, and Chernyshev N. M., (1989). Deep structure of Earth's crust on the Kola Peninsula along the Pechenga-Umbozero-Pulon'ga-Ruch'l egion of VS-DSS profile, *Geotectonics* 22: (4), 308–318.

Kats, S. A., T. N. Yershova, K. G. Mikhailova, A. V. Yegorkin, Uteshev. V. N., (1978). Nonlinear interference analysis of seismic data on regional studies of the crust and upper mantle, Physics of the Solid Earth, 13 (6), 399-405.

Koshubin, S. I., N. I. Pavlenkova, and A. V. Yegorkin (1984). Crustal heterogeneity and velocity anisotropy from seismic studies in the USSR, *Geophysical Journal of the Royal Astronomical Society* 78; (1), 221–226.

Kozlovsky, Y. A. (1990). The USSR Integrated Program of Continental Crust Investigations and Studies of the Earth's Deep Structure under the Globus Project, in Super-Deep Continental Drilling and Deep Geophysical Sounding, Fuchs K., Kozlovsky Y. A., Krivtsov A. I. and Zoback M. D. (Editors), Springer, Berlin, 90–103.

Li, H., I. B. Morozov, and S. B. Smithson (2007). Characteristics of Lg phase propagation in northern Eurasia from PNE (Peaceful Nuclear Explosion) data, *Bull. Seism. Soc. Am.* 97: 426–439.

Li, H., I. B. Morozov, and Scott Smithson (submitted to BSSA) Mapping Lg Q at 1-3 Hz in Northern Eurasia using nuclear-explosion profiles.

Lorenz, F., F. Wenzel, and J. Mechie (1997). Lateral heterogeneity implications from 2-D nuclear-seismic travel-time inversion, in: Fuchs, K. (Ed.) Upper mantle heterogeneities from active and passive seismology, pp. 237–248, Kluwer Academic Publ., Dordrecht.

Mechie, J., A. V. Egorkin, K. Fuchs, T. Ryberg, L. Solodilov, and F. Wenzel (1993). P-wave velocity structure beneath northern Eurasia from long-range recordings along the profile Quartz, Phys. *Earth Planet Inter*. 79: 269–286.

Mechie, J., A. V. Egorkin, L. Solodilov, K. Fuchs, F. Lorenz, and F. Wenzel (1997). Major features of the mantle velocity structure beneath northern Eurasia from long-range seismic recordings of peaceful nuclear explosions, in: Fuchs, K. (Ed.) Upper mantle heterogeneities from active and passive seismology, pp. 33–50, Kluwer Academic Publ., Dordrecht.

Morozov I. B., V. I. Khalturin, L. N. Solodilov, E. A. Morozova, S. B. Smithson, and P. G. Richards (2005). 3-D first-arrival regional calibration model of northern Eurasia, *Bull. Seism. Soc. Am.* 95: 951–964.

Morozov, I. B. (2001). Comment on "High-frequency wave propagation in the uppermost mantl&equot; by T. Ryberg and F. Wenzel, *J. Geophys. Res*. 106: 30,715–30,718.

Morozov, I. B. and S. B. Smithson (2000). Coda of long-range arrivals from nuclear explosions, *Bull. Seismol. Soc. Amer*. 90: 929–939.

Morozov, I. B. and S. B. Smithson (2002). Imaging crustal structure along refraction profiles using multicomponent recordings of first-arrival coda, Bull. Seism. Soc. Am., 92, 3080-3086.

Morozov, I. B., C. Zhang, J. N. Duenow, E. A. Morozova, and S. B. Smithson (submitted to Bull Seism. Soc. Am. - a). Frequency dependence of regional coda Q: I. Numerical modeling and an example from Peaceful Nuclear Explosions.

Morozov, I. B., E. A. Morozova, and S. B. Smithson, (1998a). On the nature of the teleseismic Pn phase observed in the recordings from the ultra-long range profile “Quartz”, Russia, *Bull. Seismol. Soc. Am*. 88: (1), 62–73.

Morozov, I. B., E. A. Morozova, S. B. Smithson, and L. N. Solodilov. (1998b). 2-D image of seismic attenuation beneath the Deep Seismic Sounding profile “Quartz”, Russia, Pure and Applied Geoph. 153: 311–348.

Morozov, I. B., E. A. Morozova, S. B. Smithson, and L. N. Solodilov (1998b). On the nature of the teleseismic Pn phase observed on the ultralong-range profile 'Quartz,' Russia, *Bull. Seism. Soc. Am*. 88: 62–73.

Morozov, I. B., E. A. Morozova, S. B. Smithson, P. G. Richards, V. I. Khalturin, and L. N. Solodilov (2005). 3-D first-arrival regional calibration model of northern Eurasia, *Bull. Seismol. Soc. Am* 95: (3), 951–964, doi:10.1785/0120030173.

Morozov, I. B., H. Li, E. A. Morozova, and S. B. Smithson (submitted to Bull Seism. Soc. Am. - b), Frequency dependence of regional coda Q: II. Mapping in Northern Eurasia using nuclear-explosion profiles.

Morozova, E. A., I. B. Morozov, S. B. Smithson, and L. N Solodilov (1999). Heterogeneity of the uppermost mantle beneath the ultra-long range profile “Quartz,” Russian Eurasia, *J. Geophys. Res*. 104: (B9), 20: 329–20,348.

Nielsen, L., and H. Thybo (2003). The origin of teleseismic Pn waves: Multiple crustal scattering of upper mantle whispering gallery phases, *J. Geophys. Res*. 108: ESE 3-1 - ESE 3-13.

Pavlenkova, N. I., (1996). General features of the uppermost mantle stratification from long-range seismic profiles, *Tectonophysics* 264: 261–278.

Pavlenkova, N. I., and Yegorkin, A. V., (1983). Upper mantle heterogeneity in the northern part of Eurasia, Physics of the Earth and Planetary Interiors 33: (3), 180–193.

Priestley, K. F., J. Cipar, A. Egorkin, and N. I. Pavlenkova (1994). Upper-mantle velocity structure beneath the Siberian Platform, *Geophysical Journal International* 118: (2), 369–378.

Ryaboy, V. (1989). Upper mantle structure studies by explosion seismology in the USSR, Delphic Associates, 138 pp.

Ryberg, T., F. Wenzel, J. Mechie, A. Egorkin, K. Fuchs, and L. Solodilov (1996). Two-dimensional velocity structure beneath Northern Eurasia derived from the super long-range seismic profile Quartz, Bull. Seismol. Soc. Am. 86: 857–867.

Ryberg, T., K. Fuchs, A. V. Egorkin, and L. Solodilov (1995). Observations of high-frequency teleseismic Pn on the long-range Quartz profile across northern Eurasia, J. Geophys. Res. 100: 18151–18163.

Schueller, W., I. B. Morozov, and S. B. Smithson (1997). Crustal and uppermost mantle velocity structure of northern Eurasia along the profile Quartz, *Bull. Seismol. Soc. Am*. 87: 414–426.

Solodilov L. N., (1997). The GEON Center: 25 Years of Implementation of PNE in Studies of Earth's Deep structure; in Fuchs K (ed.), Upper Mantle Heterogeneity from Active and Passive Seismology, NATO ASI Series, 1-10.

Sultanov, D. D., J. R. Murphy, and Kh. D. Rubinstein (1999). A seismic source summary for Soviet Peaceful Nuclear Explosions, *Bull. Seism. Soc. Am*. 89: 640–647.

Vinnik, L. P., and Yegorkin, A. V., (1981). A low-velocity layer in the mantle of ancient platforms, based on data from seismic observations on long profiles, *Physics of the Solid Earth* 17: (12), 910–914, 1981.

Vinnik, L. P., V. Z. Ryaboy, L. N. Starobinets, A. V. Yegorkin, and Chernyshev, N. M., (1978). The velocity of P-waves in the upper mantle under the East European Platform, *Transactions (Doklady) of the USSR Academy of Sciences, Earth Science Section*, 242 (1–6), 1–4.

Yegorkin, A. V. (1992). Crustal structure along seismic geotraverses, *International Geology Review*, 34: (4), 345–362.

Yegorkin, A. V., and Yegorkina, G. V., (1980). Transverse waves in deep investigations, *Soviet Geology and Geophysics*: 22: (6), 95–104.

Yegorkin, A. V., I. P. Kosminskaya, and Pavlenkova, N. I., (1992). Multisided seismic investigations of continental lithosphere, *Physics of the Solid Earth* 27: (9), 793–803.

Yegorkin, A. V., S. L. Kostuchenko, Ye. Ye. Zolotov, S. K. Zyuganov, and Lutsenko, T. N., (1991). Deep structure of the convergence zone between the Kazakh fold belt and the West Siberian Plate, *Geotectonics*: 25: (3), 226–232.

Yegorkin, A. V., T. I. Danilova, and Rybatov, M. B., (1979). Method of identifying converted waves, *Soviet Geology and Geophysics* 20: (10), 91–101.

Yegorkin, A. V., V. V. Kun, and Chernyshev, N., M., (1981). Absorption of longitudinal and transverse waves in the crust and upper mantle of the West Siberian Plate and Siberian Platform, Physics of the Solid Earth, 17 (2), 105–115.

Yegorkin, A. V., V. Z. Ryaboy, L. P. Starobinets, and Druzhinin, V. S., (1978). Absorption of longitudinal waves in the crust and upper mantle, *Physics of the Solid Earth*, 13: (7), 467–477.

Yegorkin, A.V. and N. I. Pavlenkova (1981). Studies of mantle structure of USSR territory on long-range seismic profiles, *Phys. Earth Planet. Inter*. 25: 12–26.

NUMERICAL EXPERIMENTS INVESTIGATING THE SOURCE OF EXPLOSION S-WAVES

Stephen C. Myers, Jeffery L. Wagoner, and Shawn C. Larsen

Lawrence Livermore National Laboratory

Sponsored by National Nuclear Security Administration
Office of Nonproliferation Research and Development
Office of Defense Nuclear Nonproliferation

Contract No. W-7405-ENG-48/ROA02-08

ABSTRACT

In this study we use validated explosion simulations to investigate the locations at which explosion S-waves originate. Several mechanisms for generating S-waves from an explosion source have been put forward. These mechanisms include tectonic release, non-symmetrical source effects, non-linear source effects, conversion of P-waves to S-waves off the free surface, and scattering of near-source Rayleigh waves. Each of these mechanisms is physically sound, and each mechanism likely contributes to the observed S-wave field. Identifying where explosion S-waves originate provides an important constraint on the contribution of each S-wave mechanism. The simulations in this study are based on the well-recorded 1993 Nonproliferation experiment (NPE) (chemical kiloton). A regional 3-dimensional model surrounding the NPE is validated by first extracting vertical cross-sections cutting through the NPE source and stations at which the NPE was recorded. We then generate synthetic seismograms using a 2-dimensional finite difference calculation for each event-station path. Good agreement between synthetic and observed seismograms provides confidence that the model and simulations are reasonably accurate. The origin of S-waves is determined through both analysis of the simulated wavefield evolution and using the time-reversal method to refocus far-field S-waves back to their origin. Preliminary results suggest that the primary S-wave pulse originates near the free surface and at high-impedance geologic interfaces that are close to the explosion. These results suggest that scattering can account for much of the observed S-wave energy radiated from the NPE explosion.

OBJECTIVE

Regional monitoring relies heavily on comparisons of P- and S-phase amplitudes (Pomeroy et al., 1982; Walter et al., 1995). Further, widely used methods of determining magnitude make use of Lg and Lg coda amplitudes (e.g., Nuttli, 1986; Mayeda and Walter, 1996; Patton, 2001), and regional S-phases often add important arrival-time observations to limited, small-magnitude datasets used for location (PNE volume, 1994; Mayeda and Walter, 1996; Myers et al., 1999).

Most investigators agree that appreciable energy from the explosions is converted to S-waves near the source, but the dominant P-to-S transfer mechanism is not agreed upon. Several physically reasonable transfer mechanisms are proposed, including P-to-S conversion at the free surface, spall, scattering of short-period surface waves, tectonic release, and rock-damage (e.g., Vogfjord, 1997; Day and Mclaughlin, 1991; Gupta et al., 1992; Wallace et al., 1985; Johnson and Sammis, 2001). Each mechanism fits a subset of observations, and each mechanism, with the exception of surface-wave scattering, is understood from first principles. Currently the Rg-to-S mechanism is represented by an empirical transfer function (e.g., Gupta et al., 1992; Patton, 2001).

Most recent progress of this project has been to use the time-reversal technique with validated numerical simulations to identify the location at which S-waves originate.

RESEARCH ACCOMPLISHED

In previous years of this project we developed a detailed upper-crustal model centered on the 1993 NPE shot (Figure 1). The local model is 20 km on a side (including depth), and construction of the model leverages the extensive Lawrence Livermore National Laboratory (LLNL) database of geological and geophysical information that includes mapping, bore-hole logs, seismic surveys, and gravity surveys (e.g., Healey et al., 1963). While much of LLNL geological database is unpublished, it constitutes a wealth of knowledge that was accumulated over decades of study at the Nevada Test Site (NTS).

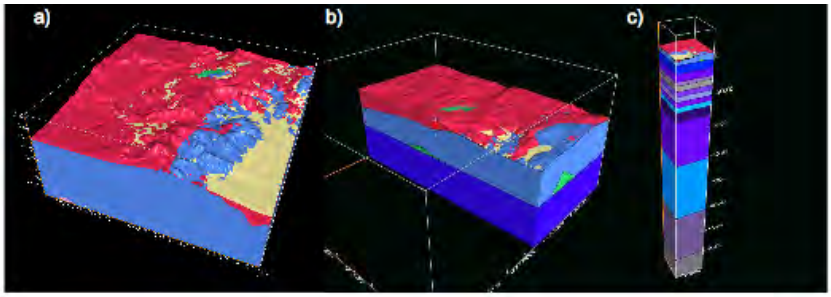

Figure 1. Local model around NPE shot determined from detailed geologic and geophysical studies. a) The entire local model. b) Cross section through the NPE shot. c) Local model merged into a lithospheric velocity stack.

The local model is imbedded in a regional model that extends to ~400km from the NPE source (Figure 2). The default velocity structure is a one-dimensional model based on work of Patton and Taylor (1984). Deviation from the default model is based on published studies in the region. The current version of the model includes variations in upper-crustal structure based on regional geologic maps of Nevada, Utah, California, and Arizona. We assume that crystalline rocks are continuous into the lower crust and that basin depths are proportional to the magnitude of local gravity anomalies (e.g., Blakely et al., 1997). The lower crustal velocities and Moho depth are modified based on the work of Zandt et al. (1994) and Mooney et al. (1998). Minor modifications to mantle velocities are based on refraction profiles summarized in Mooney et al. (1998). In specific areas we have incorporated tomographic studies, such as Biasi (2005) and Preston et al. (2005).

Considerable effort has been put into translating EarthVision models—as seen in Figures 1 and 2—into seismic models. We have developed a suite of codes that translate geologic units into either a constant P-wave, S-wave, and density or into a geologic unit may be translated into a specified portion of a

velocity/depth profile. Generally, the upper crust is modeled as constant velocity units, such as sedimentary units and granite bodies. The lower crust and upper mantle are modeled as smooth velocity vs. depth profiles, which are allowed to change laterally. Modeling the lower crust and upper mantle with smooth velocity profiles, as opposed to discrete layers, eliminates nuisance reflections and conversions from P to S energy.

.

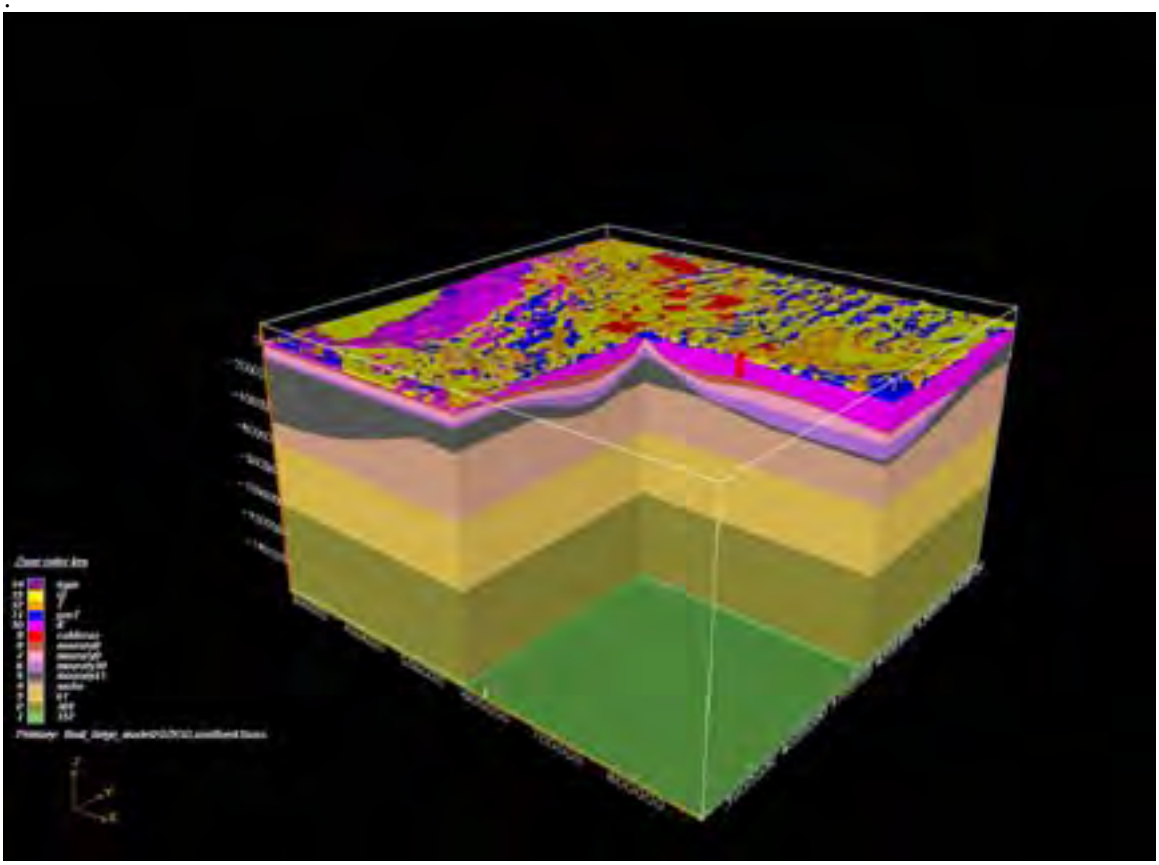

Figure 2. Regional geologic model centered on the Nevada Test Site. The model extends into California (to the left), Utah, and Arizona (to the right). The model is a compilation of geologic mapping; seismic profiles, receiver functions, and tomography; and gravity modeling for basin structure.

Model Validation Using NPE Observations

We use the E3D code of Larson and Grieger (1998) for seismic simulations. E3D is a full elastic code that allows the input of a general geologic structure, including the free surface. All of our simulations use a grid spacing of 60 meters, which enables interpretation to 3 or 4 Hz.

Our numerical simulations are based on the 1993 NPE. The NPE was a 1-kiloton chemical explosion at the NTS. NPE details and research reports can be found in Denny and Stull (1994). Figure 3 shows the extensive network of stations that recorded the NPE. We have compiled all these recordings to validate our model. We begin with the local recordings, which we used both to validate the near-source model and to estimate the NPE moment tensor.

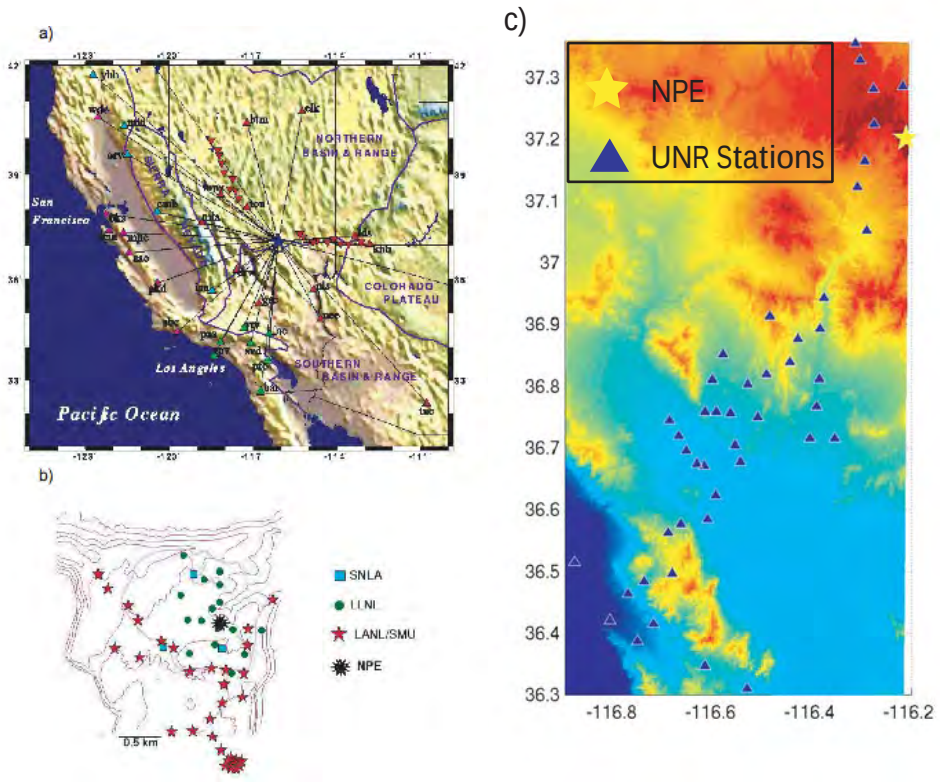

Figure 3: Stations with recordings of the NPE shot. We have compiled waveforms from all of these stations.

Figure 4 shows an example waveform (black) from a station that is approximately 2 km from the NPE. Simulations (red) with combinations of isotropic (Figure 4 a,b) and compensated linear vector dipoles (CLVD) (Figure 4 c,d) moment tensors and topographic free surface (Figure 4 a,c) and flat free surface (Figure 4 b,d) are compared with the data. It is clear that the isotropic source in a model that includes the topographic free surface is the best fit to the data. Comparisons with other local data (not shown) are similar, and we conclude that the NPE is best modeled as an isotropic source.

Figure 5 is an example of our regional validation effort. In this example we use the temporary, broadband (STS-2 sensor) deployment fielded by the University of Arizona. The cross section is color coded to P-wave velocity, which was taken from our regional 3-dimensional model. The upper crust is characterized by Paleozoic sedimentary rocks, which are interrupted by low-velocity basins. Velocity in the mid- and lower crust primarily increases with depth, but we include minor lateral variation in velocity as well has changes in Moho depth based on the work of Zandt et al. (1995). The interface between light and dark red in the lower quarter of the cross section is the Moho. We have superimposed a snapshot of the seismic wavefield on the cross section to demonstrate the complexity that results from this relatively simple model.

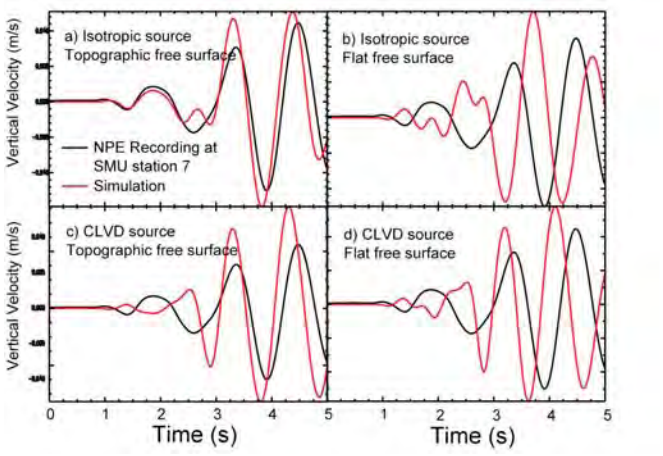

Figure 4. Recorded (black) and simulated (red) displacement seismograms for the NPE shot. These 3-dimensional simulations make use of the local NPE model (see above). Event-station distance is approximately 2 km. The NPE is best modeled as an isotropic source. Simulation with a realistic free surface is essential to match the data.
a) Simulation with isotropic moment tensor and free surface based on digital elevation model digital elevation model (DEM).
b) Simulation with isotropic source and flat free surface.
c) Simulation with CLVD moment tensor with DEM free surface.
d) Simulation with CLVD moment tensor and flat free surface.

The traces shown in Figure 5 compare recorded (black) and synthetic (red) velocity seismograms. Both velocity and synthetic records are band passed between 0.7 Hz and 3 Hz. Amplitudes are normalized because geometric spreading in the 2-dimensional synthetics is incorrect. In general, the comparison of observed and synthetic data is favorable. The degree of waveform complexity is nearly identical, and it would be difficult to tell which trace is real based on simple inspection. The relative amplitudes of the real and synthetic waveforms are also in good agreement (with the notable exception of station 8, where synthetic amplitudes after the first arrival are too large). Although the phase is matched in many instances (particularly the first arrival), we cannot claim to have simulated phase reliably. Nonetheless, the overall agreement between observed and synthetic data is very good, especially considering that the model was not directly derived from the data. Figure 5b shows cumulative energy for the 6 recordings and synthetics. In most cases the cumulative energy curves of data and synthetics are in good agreement. We also note that synthetic estimates are high in some case and low in others. i.e., there is not a consistent bias across all stations. We find that the overall model performance is good and that variability can be attributed to station site effects.

Observed and synthetic P/S ratios are in good (but not perfect) agreement (Table 1; Figure 6). In a band-pass of 0.5 Hz to 1.0 Hz the data are biased towards higher P/S ratios. We are currently working to understand the bias, but we note that the bias is only a couple tenths, which is well within the spread of most empirical P/S plots. In the 1.0 Hz to 3.0 Hz band P/S ratios for both data and synthetics increase, suggesting that our model is characterizing the wavefield at these frequencies.

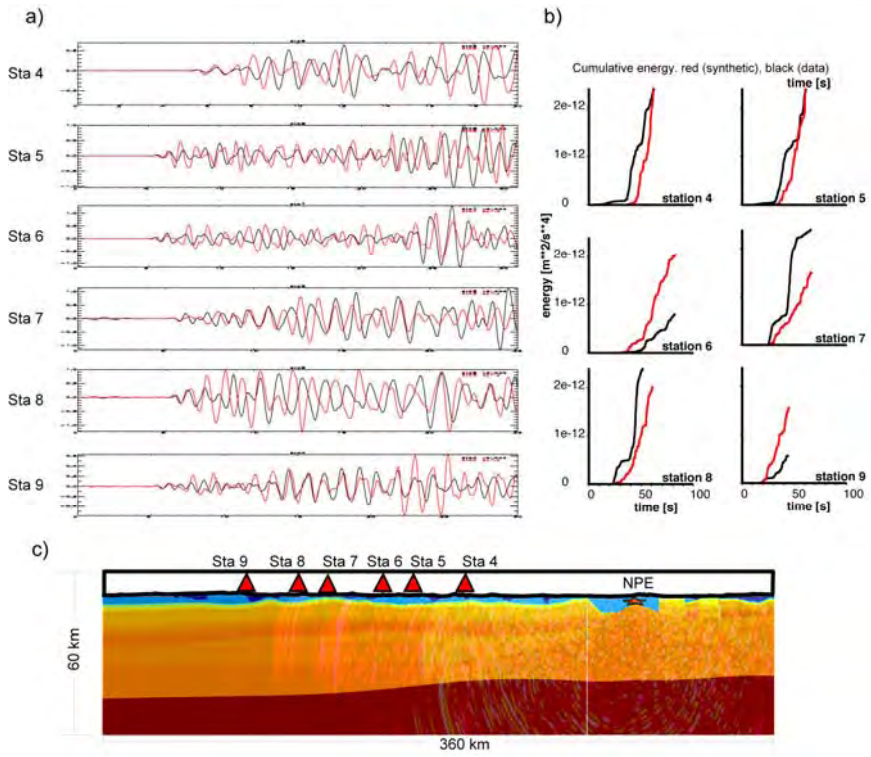

Figure 5. Model validation with regional seismic simulations of the University of Arizona broadband deployment (line extending east from NPE in Figure 2). a) Vertical velocity recordings of the NPE between 0.7 Hz and 3 Hz (black) with synthetics (red) for comparison. Amplitudes are normalized. A separate 2-dimensional simulation was made for each of the stations to account for slight azimuth variations in structure. The general character of the observed seismograms is matched by the synthetics, suggesting that the regional model is a good representation of true structure. b) Cumulative energy for observed and synthetic waveforms in a). c) Cross section shows a snapshot of the seismic wavefield overlain on a P-wave velocity for the station 9 simulation; west is to the right. The transition from red to near black in the lower quarter of the cross section is the Moho.

Table 1: P/S ratio for data and synthetics

	0.5 to 1.0 Hz		1.0 to 3.0 Hz	
	data	synth	data	synth
sta4	0.504	0.143	1.568	0.374
sta5	0.592	0.200	0.551	0.601
sta6	0.153	0.230	0.336	0.424
sta7	0.724	0.518	0.860	1.290
sta8	1.032	0.406	1.665	0.469
sta9	0.741	0.480	0.934	0.802

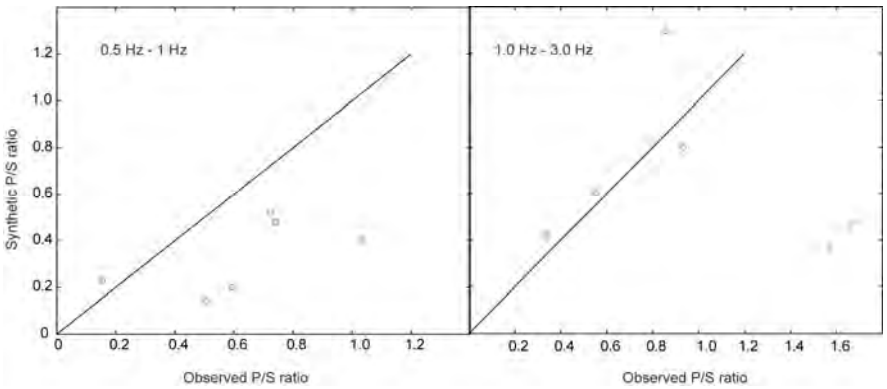

Figure 6. Comparison of observed and synthetic P/S ratios

Time Reversal to Locate S-Wave Origins

Using an isotropic source and our model that is based on geologic compilation, we reproduce the travel-times and first few swings of local and regional body phases. The amplitude characteristics of later portions of the regional phases (after the first swings) are generally in agreement with data, but the simulations are generally not in phase with data. These simulations use the simplest model that includes the known topography and geologic structure and uses the simplest explosion source (isotropic). Agreement between simulations and empirical data suggest that accounting for the known geologic structure can reproduce much of the waveform complexity and S-wave generation that is observed in the data.

Because the simulations use an isotropic source (pure P-wave source), the origin of the S-waves is in question. Visual examination of the wave field evolution over time shows that S-waves originate near the isotropic source, but the exact location(s) remains unclear.

We employ time-reversal techniques to better resolve the S-wave origin(s) (e.g., Larmat et al., 2006). As a first test of this approach we use 2-dimensional simulations (vertical cross-section) oriented approximately east-west through the NPE explosion (similar to Figure 5). The isotropic source is used, and the wave field is recorded at sensors approximately 20 km from the source. The sensors, which are not restricted to the free surface, are positioned at increments of 10° inclination in the vertical plane. Because the source is near the surface, 10° sampling results in 18 sensors. Using the divergence and curl operators on the simulated wave field, we isolate the P- and S-wave portions of the velocity seismograms (Figure 7). We then cut and time-reverse the initial P- and S-wave pulses and formulate the P- and S-wave moment tensors at each sensor. The P- and S-wave, time-reversed simulations are conducted separately to isolate the source of the two types of waves.

Figure 8 shows the results of the P- and S-wave time-reversal experiments. In both Figure 8a and 8b the peak particle velocity is normalized by node-specific material impedance to ascertain a node-by-node measurement of wave energy. In the case of P-wave time reversal (Figure 8a), the peak P-wave energy is—as expected—at the location of the simulated source (the source coincides with the red peak in energy in Figure 8a). Considerable energy in the first 1.5 seconds of the P-wave pulse is also seen to emanate from the free surface directly above the source.

In the case of S-wave time reversal (Figure 8b), the peak S-wave energy is along the sloping free surface to the east (right in Figure 8b) of the isotropic source (the eastern edge of Rainier Mesa). Some S-wave energy also emanates from the small basin to the west of the source. As expected, negligible S-wave energy originates at the isotropic source. We note that large velocity contrasts exist near the source, yet most of the S-wave energy originates at irregularities in the free surface near the source.

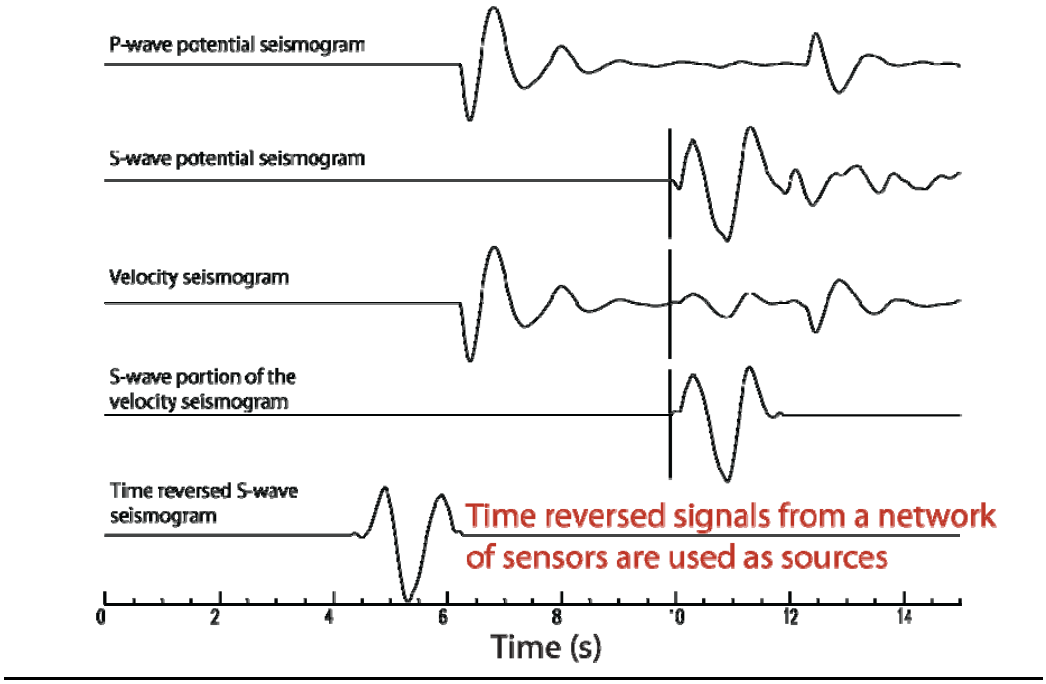

Figure 7. Time reversal procedure. Using the P- and S-potentials, we isolate the S-wave component of the velocity seismogram. We then reverse the S-wave component of the velocity seismogram and use it as a source in a simulation. Using many time-reversed sources we refocus S-wave energy back to its origin.

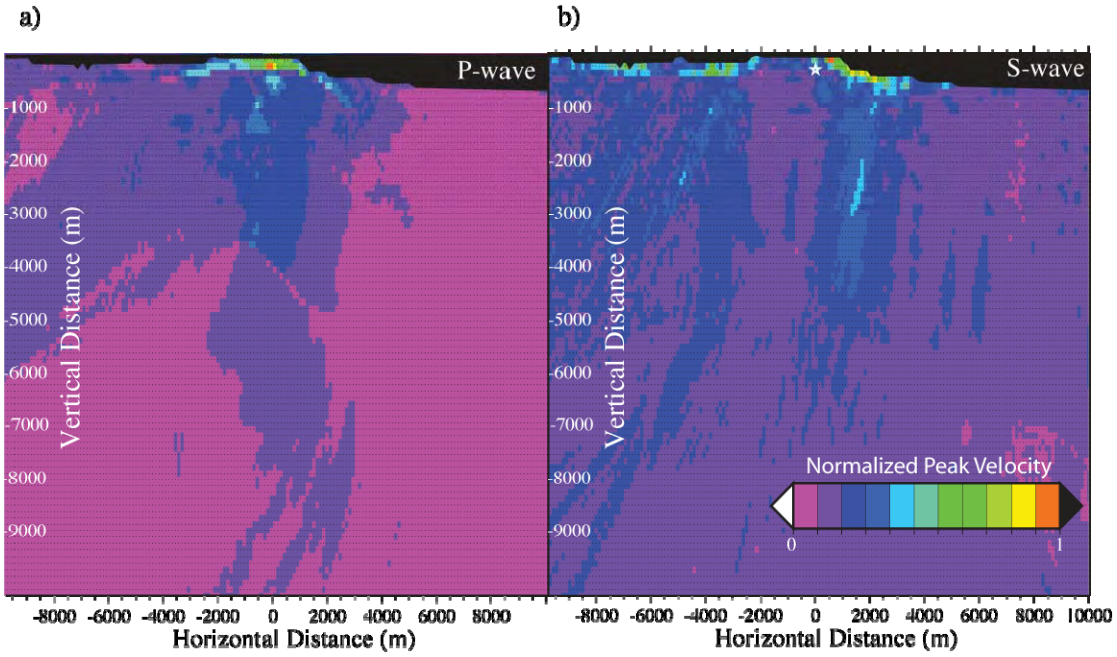

Figure 8. Peak, impedance-normalized velocity for time reversal of first 1.5 seconds of a) P-wave and b) S-waves. Peak(s) occur at the source of the waves. P-waves originate predominantly from the isotropic source and from reflection off the free surface. S-waves originate from the predominantly from the steep gradient in topography near the isotropic source.

CONCLUSIONS AND RECOMMENDATIONS

We have constructed a regional model centered on the NTS based on published and unpublished studies. The starting point of the regional model is a 1-dimensional model that is based on surface-wave studies. We include significant 3-dimensional modifications to the 1-dimensional model based on receiver function, refraction, reflection, and gravity studies. The regional model includes a detailed upper crustal model centered on the NPE explosion. This local model is constrained by geologic maps, borehole data, and geophysical studies at the NTS. The local model is seamlessly embedded into a regional model to enable realistic simulations of NTS sources to regional distance.

Validation of the model is based on recordings and simulations of the NPE shot, as well as phase travel-times from NTS explosions (Sweeney et al., 2006). Validation of the local model is complete and the model reliably predicts local NPE waveforms. Arrival times and relative amplitudes of regional phases are reliably predicted.

Local 3-dimensional simulations demonstrate that topographic scattering is an important source of S-wave generation for the NPE. We find that topographic scattering peaks S-wave amplitudes at approximately 1 Hz, which is in agreement with observations in many instances (at NTS and other locales). Topographic scattering produces a disordered wavefield and scatters energy in all directions. Simulations with a flat free surface produce S-waves, but little frequency dependence is observed.

The agreement between data and simulations is achieved with an isotropic (pure explosion) source. Therefore, we are not compelled to add complexity to the simple explosion source. Although simulated S-waves are qualitatively seen to originate near the isotropic source, the exact origin of the S-waves in these simulations is not entirely clear. We employ a time-reversal technique to better localize the origin of the initial P- and S-wave pulses. We find, as expected, that the initial P-pulse originates from the isotropic source and from the free surface directly above the source. S-waves originate from the steep topographic gradient to the east of the isotropic source (the edge of Rainier Mesa), but not symmetrically above the source, as analytical calculations would suggest.

ACKNOWLEDGEMENTS

We acknowledge the LLNL containment program for generous access to their extensive database of geologic and geophysical studies at the NTS. We also would like to thank Glenn Biasi and Walter Mooney for providing regional geophysical information. This work was also completed in cooperation with the University of Nevada, Reno (UNR), contract DE-FC03-02SF22656, and LLNL benefited from the structural information and tomographic studies conducted at UNR.

REFERENCES

Blakely, R. J., R. C. Jachens, J. P. Calzia, and V. E. Langenheim (1997). Cenozoic basins of the Death Valley extended terrane as reflected in regional-scale gravity anomalies, in Wright, L.A. and B.W. Troxel, eds., Cenozoic Basins of the Death Valley Region: Boudler, CO, *Geol. Soc. Am. Special Paper 333*.

Biasi, G. (2005). Mantle lithospheric clues to Walker Lane evolution, *Presented at the 2005 SSA meeting*, Incline, NV.

Day, S., and K. Mclaughlin (1991). Seismic source representations for spall, *Bull. Seismol. Soc. Am*. 81: 191–201.

Denny, M. D., S .P. Stull (1994). Proceedings of the Symposium on The Non-Proliferation Experiment (NPE): Results and Implications for Test Ban Treaties, Rockville Maryland; Lawrence Livermore National Laboratory.

Gupta, I. N., W. W. Chan, and R. A. Wagner (1992). A comparison of regional phases from underground nuclear explosions at East Kazakh and Nevada Test Sites, *Bull. Seismol. Soc. Am*. 82: 352–382.

Healey, D. L. and Miller, C. H., (1963). Gravity survey of the Gold Meadows Stock, Nevada Test Site, Nye County, Nevada. *USGS Technical Letter NTS-40*.

Johnson, L. R., and C. G. Sammis (2001). Effects of rock damage on seismic waves generated by explosions, *Pageoph*, 158: 1869–1908.

Larmat, C., J-P Montagner, M. Fink, Y Capdeville, A. Tourin, and E. Cevede (2006). Time-reversal imaging of seismic sources and application to the great Sumatra earthquake, *Geophys. Res. Lett*. 33: doi:10.1029/2006GL026336.

Larsen, S., and J. Grieger (1998). Elastic modeling initiative, Part III: 3-D computational modeling, *Soc. Expl. Geophys. Confer. Proceed*. 68:1803–1806.

Levander, A. R. (1988). Fourth-order finite-difference P-SV seismograms, *Geophysics* 53: 1425–1436.

Mayeda, K., and W. Walter (1996). Moment, energy, stress drop, and source spectra of western United States earthquakes from regional coda envelopes, *Jour. Geophys. Res*. 101: 11,195–11,208.

Myers, S.C., W.R. Walter, K. Mayeda, L. Glenn, (1999). Observations in support of Rg scattering as a source for explosion S waves: Regional and local recordings of the 1997 Kazakhstan depth of burial experiment, *Bull. Seismol. Soc. Am*. 89: 544–549.

Myers, S. C., D. B. Harris, M. L. Anderson, W. L. Rodi, W. R. Walter, M. P. Flanagan, and Flori Ryall (2003). Relative location accuracy and waveform subspace detector, in *Proceedings of the 25th Seismic Research Review—Nuclear Explosion Monitoring: Building the Knowledge Base*, LA-UR-03-6029, Vol. 1, pp. 259–268.

Mooney, W., G. Laske, G. Masters (1998). Crust 5.1: a global crustal model at 5x5 degrees, *Jour. Geophys. Res*. 103: 727–747.

Nuttli, O.W. (1986). Yield estimates of Nevada Test Site explosions obtained from seismic Lg waves, *J. Geophys. Res*. 91: 2137–2151.

Patton, H.J., and S.R. Taylor (1984). Q-structure of the basin and range from surface waves, *Jour. Geophys. Res*. 89: (NB8): 6929–6940.

Patton, H.J. (2001). Regional magnitude scaling, tranportability, and Ms:mb discrimination at small magnitudes, *Pageoph* 158: 1951–2015.

Pomeroy, P., W. Best, and T. McEvilly (1982). Test ban treaty verification with regional data – a review, *Bull. Seismol. Soc. Am*. 72: S89–S129.

Preston, L., K. Smith, and D. vonSeggern (2005). 3D velocity structure of the Yucca Mountain, *Seismo. Soc. Am. Spring Meeting, Presented at the 2005 SSA meeting*, Incline, NV.

Sweeney, J.J., S.C. Myers, and J.L. Wagoner (2006). Automated development of 3D local traveltime models, in *Proceedings of the 28th Seismic Research Review: Ground-Based Nuclear Explosion Monitoring Technologies*, LA-UR-06-5471, Vol. 1, pp. 530–537.

Vogfjord, K. (1997). Effect of explosion depth and earth structure on the excitation of Lg waves: S* revisited, *Bull. Seismol. Soc. Am*. 87: 1100–1114.

Wallace, T., D. Helmberger, and G. Engen (1985). Evidence for tectonic release from underground nuclear explosions in long period S waves, *Bull. Seismol. Soc. Am*. 75: 157–174.

Walter, W., K, Mayeda, and H. Patton (1995). Phase and spectral ratio discrimination between NTS earthquakes and explosions: Part I: empirical observations, *Bull. Seismol. Soc. Am*. 85: 1050–1067.

Zandt, G., S. C Myers, T. C Wallace (1995). Curst and mantle structure across the Basin and Range – Colorado plateau at 37° north latitude and implications for Cenozoic extension mechanism, *Jour. Geophys. Res*. 100: 10,592–10,548.

DEVELOPING AND EXPLOITING A UNIQUE SEISMIC DATA SET FROM SOUTH AFRICAN GOLD MINES FOR SOURCE CHARACTERIZATION AND WAVE PROPAGATION

Andrew A. Nyblade[1], William R. Walter[2], Rengin Gok[2], Lindsay Linzer[3], and Ray Durrheim[3]

Penn State University[1], Lawrence Livermore National Laboratory[2], and
Council for Scientific and Industrial Research[3]

Sponsored by National Nuclear Security Administration
Office of Nonproliferation Research and Development
Office of Defense Nuclear Nonproliferation

Contract No. DE-FC52-06NA27320[1] and W-7405-ENG-48[2]

ABSTRACT

In this project, we are developing and exploiting a unique seismic data set to address the characteristics of small seismic events and the associated seismic signals observed at local (< 200 km) and regional (< 2000 km) distances. The data set is being developed using mining-induced events from 3 deep gold mines in South Africa recorded on in-mine networks (< 1 km) comprised of hundreds of high-frequency sensors, a network of broadband seismic stations installed as part of this project at the surface around the mines (1–50 km), and a network of existing broadband seismic stations at local and regional distances (50–1000 km) from the mines. The final data set will contain:
(1) events spanning 5 orders of magnitude (M from approximately –1 to 3) well recorded at a wide range of local and regional distances, (2) events from a range of source depths (0–4 km), and (3) events from a variety of source types correlated with in-mine information such as pillar collapse and shear failure. Six months of data has been collected so far from the broadband seismic networks, and three months from the in-mine networks.

We are exploiting the data set to improve U.S. operational capabilities to monitor for low-yield nuclear tests by analyzing the mining-induced events in a number of ways. We are gathering and analyzing events with M > 2.5, as well as some selected smaller events, including point explosions (mine blasts), mine-related stress release, mining activities, and shallow earthquakes. We are creating cataloged information on origin times and locations ground truth 0 (GT0), source parameters, focal mechanisms, coda-derived source spectra, coda magnitudes, local-to-regional phase propagation characteristics, relative P and S excitation, source apparent stress variation, and local-to-regional body-wave amplitude ratios that can discriminate between the different source categories. We are systematically analyzing the direct body-wave and coda wave properties of these events in terms of variability with source type, depth, magnitude, distance and other characterization factors. These direct and coda wave amplitudes are of fundamental importance to yield estimation and source-type discrimination.

OBJECTIVES

In this project we are developing and exploiting a unique seismic data set for addressing the characteristics of small seismic events and the associated seismic signals observed at local (< 200 km) and regional (< 2000 km) distances. The data set is being developed using mining-induced events from three deep gold mines in South Africa recorded on in-mine networks comprised of numerous high-frequency sensors, a network of broadband seismic stations installed at the surface around the mines, and a network of broadband seismic stations at local and regional distances from the mines (Figure 1a, b). The in-mine data are providing high-fidelity recordings of the seismic wave field at distances of a few meters to a few kilometers from the source (Figure 1d). The surface mine network is providing broadband recordings of the wave field at distances of 1–2 km from the source out to distances of about 20 km, and the local and regional stations are providing broadband recordings from about 50 km out to distances of ~1000 km (Figure 1a, b, c).

The bulk of the effort in the first year of this project has gone into establishing the surface mine network and collecting data from the in-mine networks. The first stations in the surface mine network began recording in January 2007, at which time we also began assembling data from the in-mine networks. The surface mine network stations (Figure 1a) are comprised of RefTek 24-bit data loggers and Güralp CMG-3T broadband sensors. Four stations in the surface mine network are now operating, and a fifth station is under construction. Examples of the data quality are illustrated in Figures 1c and 1d.

The data set that we are assembling is unique in that it contains (1) events spanning 5 orders of magnitude (M from approximately –1 to 3) well recorded at a wide range of local and regional distances, (2) events from a range of source depths (0–4 km), and (3) events from a variety of source types (e.g., normal faulting, strike-slip faulting, mine blasts, pure double-couple events and isotropic events). In the coming year, we will add to the data set details of mine plans that will enable us to correlate certain mining events with mining activities, such as blasting and pillar collapse, and investigate the influence of mine cavities and lithology on wave propagation. We will exploit the data set by using the mining events in 10 related areas of research aimed at improving U.S. operational capabilities to monitor for low yield nuclear tests: (1) create an event catalog with accurate origin times and locations; (2) determine seismic moment, radiated energy, corner frequency, and stress drop; (3) obtain focal mechanisms from moment tensor inversion; (4) define several categories of event types (shear slip, tensile failure with volumetric component, explosions) using focal mechanisms and in-mine observations (e.g., pillar collapse); (5) define and calibrate a coda Mw scale for southern Africa; (6) using calibrated coda techniques, determine Mw for all cataloged events; (7) investigate the effects of depth and source mechanism on the coda-derived source spectra and evaluate the potential of using coda spectral peaking as a depth discriminant; (8) define and calibrate local-to-regional phase (direct P and S, Pn, Pg, Sn, and Lg) propagation characteristics, including the use of the magnitude and distance amplitude corrections (MDAC) technique to determine appropriate geometrical spreading and frequency dependent Q values for the region; (9) characterize relative P and S excitation and source apparent stress resulting from variations in source parameters, including magnitude, mechanism, depth, rock characteristics and source type; (10) define regional phase ratios that can discriminate between the different source categories, and compare these discriminants and their performance with ongoing work done for other types of mining events, such as in Scandinavia and the western U.S.

This project is being conducted by a team of researchers at Pennsylvania State University and Lawrence Livermore National Laboratory (LLNL), and in South Africa at the Council for Geoscience, the Council for Scientific and Industrial Research, and the University of the Witwatersrand.

RESEARCH ACCOMPLISHED

Three complimentary data sets are being assembled in this project: (1) high-frequency in-mine seismic data from three mines along the northwestern edge of the Witwatersrand basin, (2) seismograms from mine events recorded at distances of 1 to 20 km from the new broadband stations installed, and (3) broadband recordings of the mine events at local and regional distances recorded on 12 *AfricaArray* stations in South Africa that are part of the South African National Seismic Network (SANSN), International Monitoring System (IMS) stations BOSA (South Africa) and LBTB (Botswana), a global seisma-graphic network station (GSN) (SUR, South Africa), and an *AfricaArray* station in southern Mozambique.

Gold Mines and Mining Seismicity

The Witwatersrand basin is part of a granite-greenstone complex constituting the basement of the Kaapvaal craton. The basement evolved between 3.8 and 2.8 b.y. ago and has remained relatively stable except for the development of stratified basins. Subsidence of the Witwatersrand basin probably began before basement evolution was complete and resulted in the deposition of three major stratigraphic units, the Dominion Group, the Witwatersrand Supergroup, and the Ventersdorp Supergroup. Most of the gold is mined from the quartzites (commonly referred to as reefs) within the Witwatersrand Supergoup.

The mining activities of the Witwatersrand basin induce thousands of seismic events per day, many of which are larger than M = 2. The data are recorded at depth (1–5 km) by arrays of three-component geophones operated by AngloGold Ashanti, Ltd. and Integrated Seismic Systems International (ISSI). We are obtaining from three mines (Mponeng, Savuka, and TauTona) in the Far West Rand region (80 km southwest of Johannesburg; Figure 1a), waveforms from mining-induced events recorded on numerous high frequency geophones within the mines. Based on seismicity rates in these mines, the projected data set should contain between 20 to 35 M > 3 events per year, about 200 events per year between magnitude 2 and 3, and hundreds of mining blasts (mostly M < 0).

These mines are some of the deepest in the world and extract ore from two gold-bearing quartzites, the Ventersdorp Contact Reef and the Carbon Leader Reef (Figure 2). These two units are separated by 900 m vertically, extend 2–4 km below the surface, and dip to the south at 21 degrees (Figure 2). The mines contain faults and dykes with two major trends: N 5^{o} E and N 96^{0} E. Some of the faults have been reactivated by the mining, providing sources for many of the larger events.

Details of the geology within the mines have been determined by underground mapping, surface surveys, and well logs from deep boreholes. Densities of major lithologies present in the mines have been measured from rock samples, and the shear and bulk modulus of the lithologies have been determined using Vs and Vp measurements from test-blasting.

The geophones sample at frequencies of 400–10,000 Hz and are located at depth on the quartzite reefs. The station spacing underground is on the order of 100 m in the active mining zones. Because there are two horizons being mined simultaneously, event depth is well-constrained by the geophones at different depths, especially compared to other mining-induced data sets in which the seismometers are usually situated on a single plane.

In order to determine the locations of the mine events, ISSI technicians routinely pick P-wave and S-wave arrival times and run a ray-tracing algorithm. This method of locating events is successful (uncertainties are on the order of 10–20 m) because the geologic setting of the Far West Rand consists of layers without appreciable lateral heterogeneities. The layered velocity model used is based on geologic units that have been determined by underground surveying and mapping as well as surface-based refraction profiles and borehole data. The accuracy of the velocity model has been verified by test blasting used to determine wavespeeds through various strata.

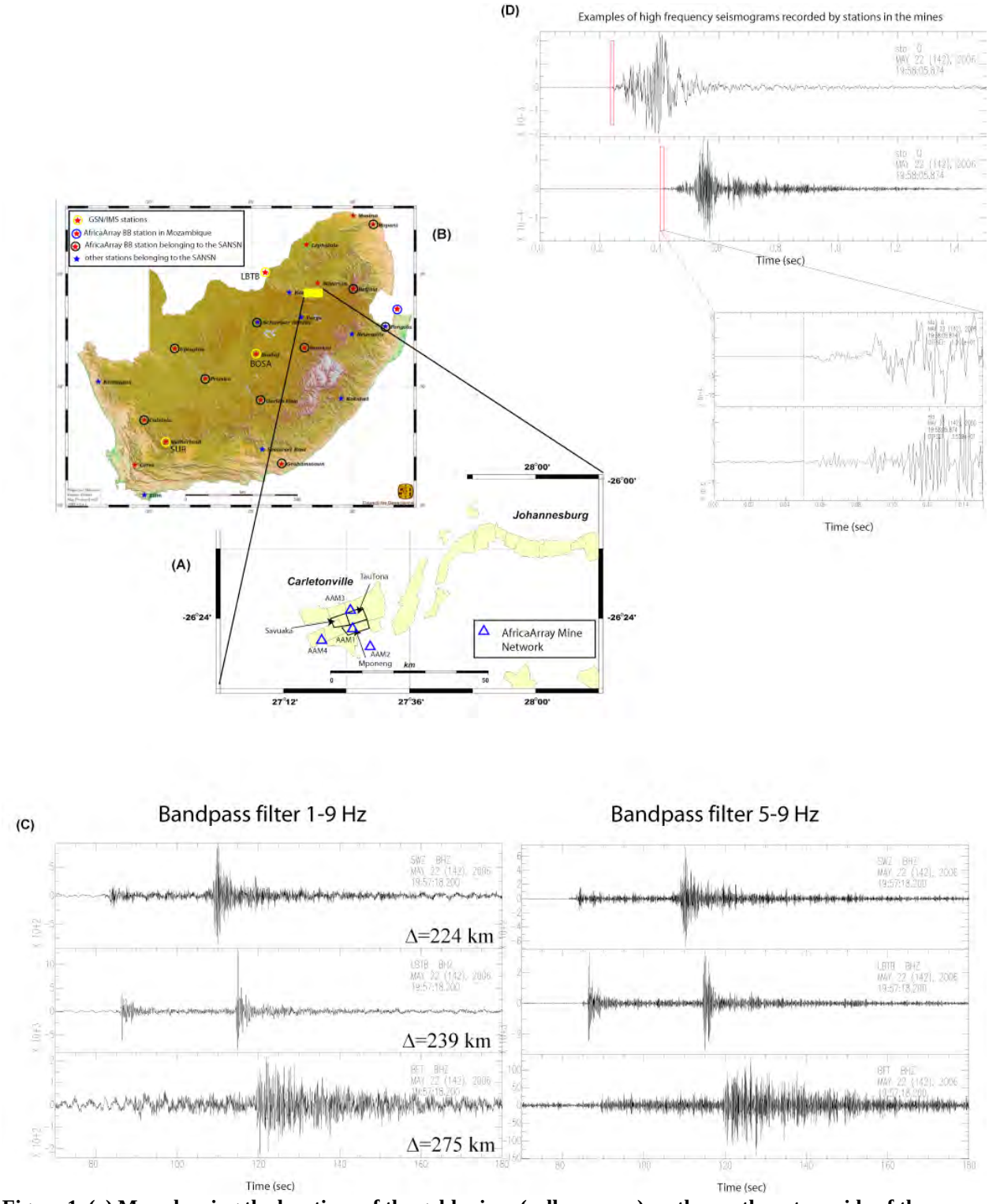

Figure 1. (a) Map showing the locations of the gold mines (yellow areas) on the northwestern side of the Witwatersrand basin (Far West Rand region). Data for this project come from the three mines labeled. The blue triangles show station locations of the surface mine network that has been constructed. (b) Map showing location of AfricaArray broadband stations at local and regional distances. (c) Vertical displacement seismograms from a M = 2.2 mining event recorded at near-regional distances. (d) The same event recorded on high-frequency in-mine seismic stations.

Surface Mine Network

Mining-induced events from the three mines described above are being recorded at distances of 1 to 20 km using a new, permanent, surface mine network comprised of broadband seismic stations. The surface mine network is also providing data from many events that occur in other deep mines around the Witwatersrand basin for which we will not obtain in-mine data, including many hundreds of events with M > 2.5. The locations of the stations so far installed with respect to the three mines are shown in Figure 1a.

Local and Regional Broadband Seismic Network

Sixteen permanent broadband seismic stations across southern Africa are providing high quality seismograms of the mining-induced events, data that is complimenting the data from the in-mine and mine surface networks. The locations of the local and regional stations are shown in Figure 1b. Twelve of the stations are part of the South African National Seismic Network, and data from these stations are being archived as *AfricaArray* data at the Incorporated Research Institutions for Seismology Data Management Center (IRIS DMC).

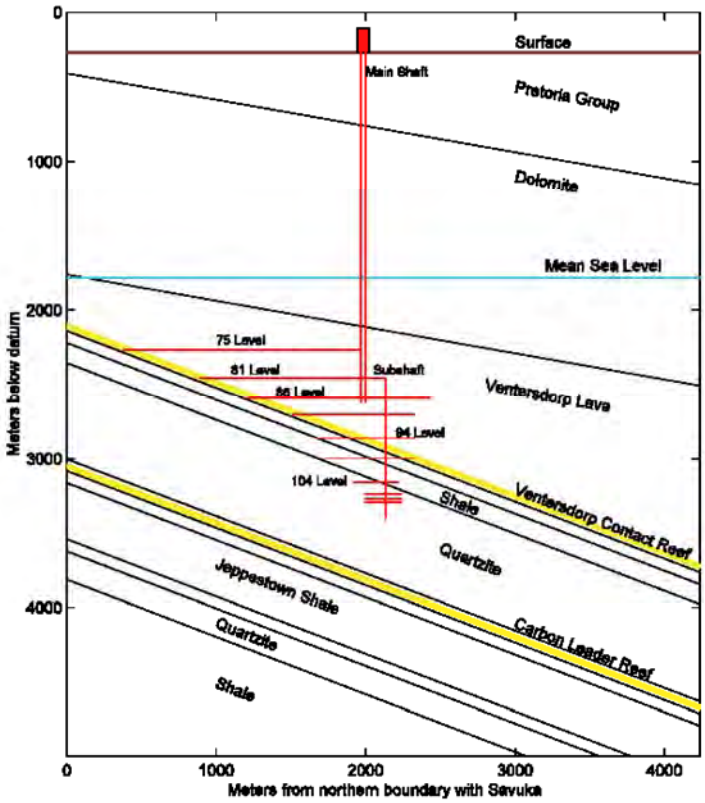

Figure 2. Cross-section through the main shaft of the Mponeng mine looking east. The two gold-bearing horizons are marked in yellow. The datum is measured from an elevation in Johannesburg, and so it is above the ground surface.

These stations are equipped with a 24 bit data loggers and broadband sensors (STS-2, Güralp 40T, KS 2000). Two of the sixteen stations are IMS stations (BOSA in South Africa and LBTB in Botswana) and one is an IRIS GSN station (SUR in South Africa). The final station is a new *AfricaArray* station in southern Mozambique at Changalane and equipped with a 24-bit digitizer and a Güralp CMG-3T sensor.

CONCLUSIONS ND RECOMMENDATIONS

In this section we provide details of how the seismic data is being used and will be used in the future to meet the objectives for each of the research areas identified in the Objectives section.

Create an Event Catalogue with Accurate Times and Locations

The in-mine network operators routinely locate and catalog events, and we are obtaining these catalogs and using them as a starting point to create an event catalog with accurate origin times and locations in universal coordinates. Each mine network is operated independently using a local coordinate system and a different timing system. We are transforming station and events locations into a universal coordinate system and using the surface mine network to calibrate the timing of each in-mine network by using larger, well-recorded events. An ML magnitude will also be included in the catalog based on the ML scale used routinely by the Council for Geoscience in their event bulletins. As the mining-induced event locations are typically constrained to within 10 to 20 meters by the mine network operators, we are not relocating any of the events.

Determine Source Parameters

In work recently completed (Richardson et al., 2004, 2005), we have determined for 27 M > 2.5 mine events in the Far West gold fields recorded between 1998 and 1999 seismic moment, radiated energy, corner frequency, and stress drop using the method of Richardson and Jordan (2002), which was adapted from the spectral method first developed by Andrews (1986). In order to determine source parameters, we median-stacked each event's spectra and integrated the results up to the Nyquist frequency to determine the integral of the displacement power spectra, the integral of the velocity power spectra, and the acceleration power spectral level. These parameters were then used to determine the source parameters radiated energy, seismic moment, and static stress drop using the equations provided in Richardson et al. (2004, 2005). We are using the in-mine data to determine seismic moment, radiated energy, corner frequency and stress drop using the same method.

Obtain Focal Mechanisms from Moment Tensor Inversion

We are determining focal mechanisms for events with M > 2.5 and a select number of smaller events using moment tensor inversion of the in-mine data. An example of a result for a magnitude 3.9 mine event is shown in Figure 3. One important difference between mine tremors and natural earthquakes is the effect of mining voids on the recorded waveforms. The voids can influence the frequency content of the seismograms, cause focusing and defocusing of the wave field, as well as cause unexpected amplifications. In addition, the moment tensor calculated for an event near the free surface of a stope, for example, can have a significant isotropic component related to the closure or convergence of the excavation. The mining geometry also can influence source parameters calculated for an event. For instance, the seismic moment calculated for a crushed pillar would have contributions from the failure of the pillar as well as from the convergence of the surrounding stope. (Gay et al., 1995, McGarr, 1992; Milev et al., 2005; Napier et al., 2005).

We have started to invert the in-mine data to determine moment tensor solutions for all events with M > 2.5, and a select number of smaller events. We anticipate that a number of the events will have non-double couple mechanisms, based on previous results from other researchers. To help characterize the non-double couple mechanisms, these mechanisms will be examined further using regional full waveform modeling following an approach that was developed for modeling other non-double couple sources, such as large mine collapses in Wyoming (Pechmann et al. 1995) and Germany (Bowers and Walter, 2002).

Define Several Categories Of Event Types

Using the focal mechanisms and in-mine observations, we will define several categories of event types, such as shear slip, tensile failure with volumetric component, and explosions. The mine plans will be very important for correlating with focal mechanisms to categorize event types, as will the records of blasting in the mines.

Defining and Calibrating A Coda Mw Scale For Southern Africa

Determining meaningful and accurate measures of the size of seismic events is a critical part of characterizing and cataloging the seismicity in a region. For the southern Africa region we want to define a useful scale that can cover the expected range of mining induced and natural events from about magnitude –1 to 4. Teleseismic magnitudes such as mb and Ms are limited mainly to events greater than magnitude 4. Local magnitudes scales such as ML are

valid for comparing relative sizes of events within the region but make it difficult to compare events across regions such as with other parts of the world. Local magnitude scales are also difficult to relate to fundamental physical properties of the source. For these reasons seismic moment magnitude has become the measure of choice for modern digital networks (e.g., Pasyanos et al. 1996, Kubo et al. 2002). However if waveform modeling were required to determine the moments it would be difficult to systematically determine moments for events less than about magnitude 3.0. Techniques based on regional coda envelopes (Mayeda and Walter, 1996; Mayeda et al., 2003) offer the potential to determine seismic moments for events over the entire range of interest down to magnitude –1 with local and in-mine data.

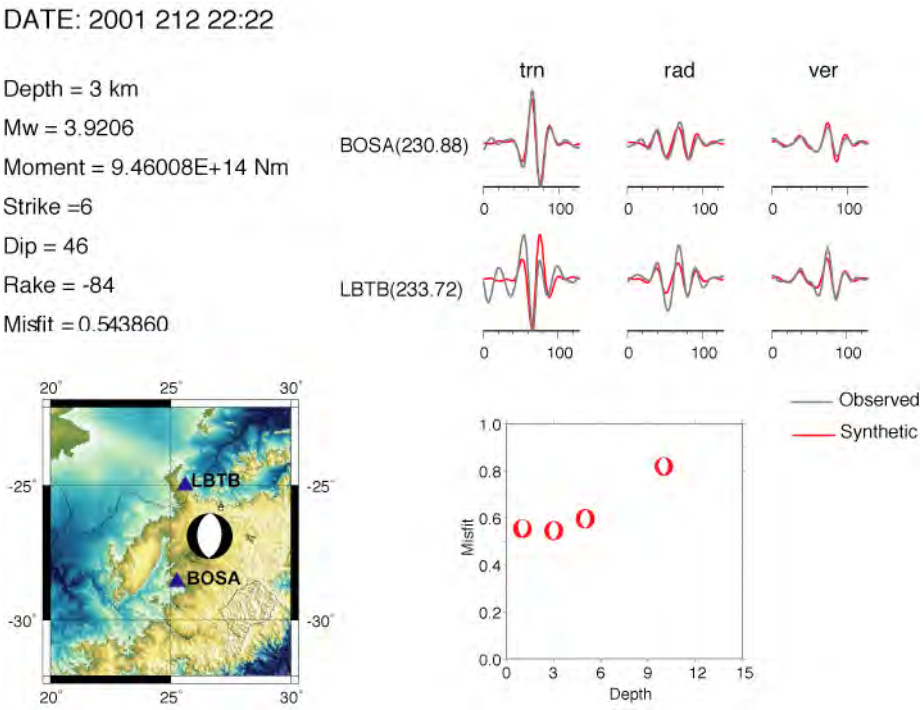

Figure 3. Body and surface waves from regional or near regional events were used to estimate the best fitting double-couple moment tensor. The technique minimizes the misfit between reflectivity generated complete synthetic seismograms and the three-component displacement data via a search over the strike, dip and rake of the source. An initial coarse grid-search to find the approximate minima is followed by a finer grid-search. For this event, we fitted the data over the period range of 20–50 sec. The displacements due to the six fundamental couples were calculated using Bowers (1997) velocity model. The best fit is obtained at 3-km depth.

Determining Coda-Source Spectra and Mw for Selected Catalogued Events

To determine coda-based source spectra and moments we will first calibrate magnitude for path and site effects in each narrow frequency band using a set of well-recorded events distributed in distance. Then we will tie the lower frequencies to moments determined from waveform modeled events in the region. For southern Africa there are a few larger events that have previously been modeled (e.g., Bowers, 1997) as well as some of the smaller mine events (Richardson et al., 2004, 2005). As part of this project we will perform additional moment tensor inversions of mining events as well as a few of the largest events using regional waveform modeling techniques to improve our calibrations. Finally a number of very small events will be used as empirical Green functions to determine the high frequency corrections. These events are chosen such that their corner frequencies are higher than the calibration frequencies, and we can assume their spectra is flat.

Once the regional stations are calibrated we will use existing LLNL scripts to calculate coda-derived source spectra and Mw. Processing will be done for the subset of cataloged events selected for detailed analysis as part of this project.

Analyzing Depth Effects on Coda-derived Source Spectra

The displacement source spectra of normal tectonic depth earthquakes (e.g 5–20 km) determined from local and regional coda envelopes have typical Brune (1970) style shapes: flat at long periods and then falling off at frequencies above a corner frequency. In contrast very shallow events (< 1 km) produce unusual "peaked" source spectra when the coda method is calibrated using normal depth earthquakes (e.g., Mayeda and Walter, 1996; Myers et al., 1999).

The coda-derived source spectral shape differences appear to depend on the differences in the excitation of coda as a function of depth. It has been hypothesized that this peaking is related to the stronger excitation with shallower depth of the fundamental Rayleigh wave Rg that is then scattered into the coda (e.g., Myers et al., 1999). If quantified, these shape differences could be exploited to flag very shallow events for nuclear monitoring purposes. The mine-induced seismicity completely covers the depth range of interest of 0- to 4-km depth. The in-mine network provides very good control on the source depth so this effect can be investigated. In addition we will use the moment tensor results to explore the effect of focal mechanism on the coda spectra as well. In particular, we want to see if the coda spectral shapes differ for events with isotropic components when compared with double-couple events.

Local-to-Regional Phase Propagation Characteristics

In southern Africa the local P and S phases as well as all four major regional phases Pn, Pg, Sn and Lg propagate and can be identified in seismograms. In order to be able to compare events of different distances or sizes with each other we need to be able to correct for source and path effects. Walter and Taylor (2002) developed a procedure to do this called Magnitude Distance Amplitude Correction (MDAC). The MDAC method includes path corrections due to geometrical spreading, frequency dependent attenuation, and site effects. The MDAC process also simultaneously corrects for source effects by removing a generalized Brune (1970) style spectra. It corrects both local P and S as well as the four regional phases in all frequencies allowing the researcher the freedom to explore any possible ratio of body wave amplitudes. In this project we will use a much larger data set to determine optimal MDAC parameters for the broadband stations in the region. We will explore the variability of the body wave amplitudes as a function of local to regional distance. These MDAC corrections will allow us to investigate both source parameter and discriminant behavior for the southern Africa events.

Source Parameters And Scaling

The regional amplitudes and their ratios show very large variation in southern Africa. We want to try to understand this scatter in terms of variations in source parameters such as relative P and S excitation and apparent stress with mechanism, depth, rock type, and other source region properties. We will take advantage of the in-mine data to look for correlations of seismic properties observed regionally with what is known to have happened near the source.

Regional Phase Amplitude Ratio Discriminants

It is well established that amplitude ratios of regional body-wave phases at frequencies of 1 Hz and higher can discriminate explosions from earthquakes (e.g., Bennett and Murphy, 1986; Taylor et al., 1988; Baumgardt and Young, 1990; Dysart and Pulli, 1990; Kim et al., 1993; Walter et al., 1995; Taylor, 1996; Fisk et al., 1996; Hartse et al., 1997; Rodgers and Walter, 2002; Taylor et al., 2002, and many others). Such ratios include ratios of P phases to S phases (phase ratios), low frequencies to high frequencies within a phase (spectral ratios), and ratios of high frequency in one phase to low frequencies in another (cross-spectral ratios). We will explore how well some of these ratios can discriminate between the different source categories of mine region events. These may include shear slip, tensile failure with volumetric component, and explosions. We will compare these discriminants and their performance with ongoing work done for other types of mining events and other major mining regions, such as in Scandinavia (e.g., Bungum et al., 2004) and the western U.S. (e.g., Leidig et al. 2004).

REFERENCES

Andrews, D. J. (1986). Objective determination of source parameters and similarity of earthquakes of different size, in *Earthquake Source Mechanics*, S. Das, J. Boatwright, C. H. Scholz, eds, vol. 6 of *Geophysical Monograph* 37: pp. 259–267, Am. Geophys. Union.

Baumgardt, D. R. and G. B. Young (1990). Regional seimsic waveform discriminants and case-based event identification using regional arrays, *Bull. Seism. Soc. Am.* 80: 1874–1892.

Bennett, T. J. and J. R. Murphy, Analysis of seismic discrimination capabilities using regional data from western United States events, *Bull. Seism. Soc. Am.* 76*:* 1069–1086, 1986.

Bowers, D. (1997). The October 30, 1994 seismic disturbance in South Africa: Earthquake or large rockburst? *J. Geophys. Res.* 102: 9843–9857.

Bowers. D., and W. Walter, Discriminating between large mine collpases and explosions using teleseismic P waves, *PAGEOPH,* 159: 803–830, 2002.

Brune, J., Tectonic stress and the spectra from seismic shear waves earthquakes, *J. Geophys. Res.* 75: 4997–5009., 1970.

Bungum H., T. Kverna, S. Mykkeltveit, M. Roth, V. Oye, K. Aastebol, D. B. Harris, and S. C. Larsen (2004). Energy portioning for seismic events in Fennoscandia and NW Russia, in *Proceedings of the 26th Seismic Research Review: Trends in Nuclear Explosion Monitoring*, LA-UR-04-5801, Vol. 1. pp. 387–396.

Dysart, P. S. and J. J. Pulli (1990). Regional seismic event classification at the NORESS array: seismological measurements and the use of trained neural networks, *Bull. Seism. Soc. Am.* 80: 1910–1933.

Fisk, M. D., H. L. Gray, and G. D. McCartor (1996). Regional event discrimination without transporting thresholds,:*Bull. Seism. Soc. Am.* 86, 1545–1558.

Gay, N.C., R. J. Durrheim, S. M. Spottiswoode, and A. J. van der Merwe (1995). Effect of Geology, in-situ stress, and mining methods on seismicity in Southern African gold and platinum Mines, 8th Intl. Congress on Rock Mechanics, Tokyo, Japan, Balkema, pp 1321–1325.

Hartse, H., S. R. Taylor, W. S. Phillips, and G. E. Randall (1997). A preliminary study of regional seismic discrimination in Central Asia with an emphasis on Western China, *Bull. Seism. Soc. Am.* 87*:* 551–568, 1997.

Kim, W.-Y., D. W. Simpson, and P. G. Richards (1993). Discrimination of earthquakes and explosions in eastern United States using regional high-frequency data, *Geophys. Res. Lett.* 20: 1507–1510.

Kubo, A., E. Fukuyama, H. Kawai, K. Nonomura (2002). NIED seismic moment tensor catalogue for regional earthquakes around Japan: quality test and application, *Tectonophysics*, 356: 23–48.

Leidig, M. R., B. W. Stump, J. L. Bonner, C. T. Hayward, A. A. Velasco, Diane F. Baker, H. Hooper, W. R. Walter, X. Yang, R. Zhou, C. L. Edwards, M. D. Renwald, and J. F. Lewkowicz (2004). Source phenomenology experiments in Arizona in *Proceedings of the 26th Seismic Research Review: Trends in Nuclear Explosion Monitoring,* LA-UR-04-5801, Vol. 1, pp. 427–438.

Mayeda, K. and W. R. Walter, Moment, energy, stress drop and source spectra of western United States earthquakes–from regional coda envelopes, *J. Geophys. Res.* 101: 11,195–11,208.

Mayeda, K., A. Hofstetter, J. L. O'Boyle, and W. R. Walter (2003). Stable and transportable regional coda magnitudes based on coda-derived moment rate spectra, *Bull. Seism. Soc. Am.* 93: 224–239.

McGarr, A. (1992). Moment tensors of ten Witwatersrand mine tremors, *Pure Appl. Geophys.* 139: 781–800.

Milev, A.M., M. W. Hildyard, L. M. Linzer, and S. M. Spottiswoode (2005). Underground Micro-seismic Monitoring of Pillar Systems to Evaluate Mechanism of Failure, 6th Intl Symposium on Rockbursts and Seismicity in mines, Perth, Australia, pp 239–246.

Myers, S. C., W. R. Walter, K. Mayeda and L. Glenn (1999). Observations in support of Rg scattering as a source for explosion S waves: regional and local recordings of the Kazakhstan depth of burial experiment, *Bull. Seism. Soc. Am.* 89: 544–549.

Napier J. A. L., S. M. Spottiswoode, E. Sellers, M. W. Hildyard, L. M. Linzer, and M. O. Kataka (2005). New criteria for rockmass stability and control using integration of seismicity and numerical modeling. SIM 02 03 01. Final SIMRAC Project Report. 141p..

Pasyanos, M.E., D.S. Dreger, and B. Romanowicz (1996). Toward real-time estimation of regional moment tensors, *Bull. Seism. Soc. Amer.* 86: 1255–1269.

Pechmann, J. C., W. R. Walter, S. J. Nava, and W. J. Arabasz (1995). The February 3, 1995 M_L 5.1 seismic event in the trona mining district of southwestern Wyoming, *Seism. Res. Lett.,* 66, 25–34.

Richardson, E., and T. H. Jordan (2002). Seismicity in deep gold mines of South Africa: Implications for tectonic earthquakes, *Bull. Seism. Soc. Am*, 2002.

Richardson, E., A. A. Nyblade, W. R. Walter, and A. J. Rodgers (2004). Seismic source characterization and energy partitioning from in-mine and regional broadband data in South Africa, in *Proceedings of the 26th Seismic Research Review: Trends in Nuclear Explosion Monitoring*, LA-UR-04-5801, Vol. 1, pp. 467–474.

Richardson, E., A. A. Nyblade, W. R. Walter, and A. J. Rodgers (2005) Seismic source characterization and energy partitioning from in-mine and regional broadband data in South Africa, in *Proceedings of the 27th Seismic Research Review: Ground-Based Nuclear Explosion Monitoring Technologies*, LA-UR-05-6407, Vol. 1, pp. 622–631.

Rodgers, A. J. and W. R. Walter (2002). Seismic Discrimination of the May 11, 1998 Indian Nuclear Test with Short-Period Regional Data From Station NIL (Nilore, Pakistan), *Pure Appl. Geophys.* 159: 679–700.

Taylor, S. R., N. W. Sherman and M. D. Denny (1988). Spectral discrimination between NTS explosions and western United States earthquakes at regional distances, *Bull. Seism. Soc. Am.* 78: 1563–1579.

Taylor, S. (1996). Analysis of high-frequency Pg/Lg ratios from NTS explosions and Western U.S. earthquakes, *Bull. Seism. Soc. Am.* 86: 1042–1053.

Taylor, S., A. Velasco, H. Hartse, W. S. Philips, W. R. Walter, and A. Rodgers (2002) Amplitude corrections for regional discrimination, *Pure. App. Geophys*. 159: 623–650.

Walter, W. R., K. Mayeda, and H. J. Patton (1995). Phase and spectral ratio discrimination between NTS earthquakes and explosions Part 1: Empirical observations, *Bull. Seism. Soc. Am.* 85: 1050–1067.

Walter, W. R. and S. R. Taylor, A revised magnitude and distance amplitude correction (MDAC2) procedure for regional seismic discriminants: theory and testing at NTS, Lawrence Livermore National Laboratory Report, UCRL-ID-146882, 2002.

ENHANCEMENTS OF GEOPHYSICAL MODELS FOR MONITORING

Michael E. Pasyanos, William R. Walter, Megan P. Flanagan
Rengin Gok, Stephen C. Myers, Kathleen M. Dyer

Lawrence Livermore National Laboratory

Sponsored by National Nuclear Security Administration
Office of Nonproliferation Research and Development
Office of Defense Nuclear Nonproliferation

Contract No. W-7405-ENG-48

ABSTRACT

Geophysical models constitute an important component of calibration for nuclear explosion monitoring. In order to keep them relevant to current monitoring problems, we have enhanced the models in several different ways. We will focus on discussing several of the enhancements here. We have significantly improved upon our surface wave model by expanding the region of the existing model of Eurasia and North Africa, south to cover all of Africa and north to cover the polar region into Alaska and Canada. We have also improved on our coverage in existing regions by including station-station dispersion paths based on ambient seismic noise. Surface waves are also being used to derive the crust and upper mantle velocity structure of these regions, including important parameters such as crustal thickness, upper mantle velocity, and lithospheric thickness. We will be comparing some of these results to other estimates of these parameters. We demonstrate some of the latest enhancements that we have made regarding stochastic models. For instance, we have been using the Markov Chain Monte Carlo (MCMC) technique to produce stochastic models in the Yellow Sea – Korean Peninsula (YSKP) region. By including more data sets (Love wave dispersion curves, gravity) and more data from the existing data sets (more travel times, more receiver functions, more Rayleigh wave dispersion curves), we have improved the lateral resolution of the model from 2 degrees to 1 degree. We will discuss some details of the methodology as well as features of the model. Finally, we will focus the last section on research to move beyond past and current 1-D, 2-D, and 2½-D methods and discuss some of the ongoing efforts to transition to fully 3-D models.

OBJECTIVE

Geophysical models constitute an important component of calibration for nuclear explosion monitoring. The objective of any geophysical model is to improve prediction of travel times, amplitudes, and other observables of local, regional, and teleseismic phases, in order to improve location, detection, association, identification and (in the event of an explosion) yield determination. In this paper, we will focus on recent enhancements to many of the models, which have kept them up to date and relevant for current monitoring problems. We first discuss improvements to the surface wave models which have expanded to cover over half of the globe and have increased in resolution due to the increase in measurements and available seismic data, as well as techniques such as ambient noise correlation that allow us to sample new paths. Tomographic images over a wide period range are robust and reliable enough to allow the inversion of highly developed models that cover both shallow sediment structure and deep lithospheric models, even in aseismic regions. The results can also be focused on regional or station-specific applications. Geophysical models such as the Western Eurasia and North Africa (WENA) model can be updated to reflect our increased understanding of regions. They continue to both be useful in their own right, and also serve as critical starting models for more data driven models, such as the Seismic Location Baseline Model (SLBM) (Myers et al., these Proceedings). Finally, stochastic models, which require the most sophisticated inversion technique and computational power, are increasingly becoming easier to implement, allowing broader applications of the method. Future enhancements to geophysical models will increasingly focus on improving resolution and combining individual data sets to produce a fully 3-D model which is predictive of a range of observables.

RESEARCH ACCOMPLISHED

Surface Wave Models

Over the past several years, Lawrence Livermore National Laboratory (LLNL) has been developing surface wave models for nuclear explosion monitoring (Pasyanos et al., 2001; Pasyanos, 2005). Dispersion measurements are made using multiple narrow-band filters on deconvolved displacement data from the LLNL Seismic Research Knowledge Base (SRKB). We continue to improve upon our surface wave model by adding more paths by taking advantage of new data sets and also by revisiting stations with more recent events. Most recently, we have added measurements from stations in Alaska and Canada, Siberia, southern and central Africa, and southeast Asia. To date, over 120,000 seismograms have been analyzed to determine the individual group velocities of 7-150 second Rayleigh and Love waves. Overall, we have made good quality dispersion measurements for 41,000 Rayleigh and 30,000 Love wave paths. Using a conjugate gradient method, we then tomographically invert these measurements to produce group velocity maps for Love and Rayleigh waves.

The group velocity models have been enhanced in several ways. First, with more measurements, we have been able to expand the region of coverage from Eurasia and North Africa both south to include all of Africa and north (over the pole) to include the northern parts of North America (Figure 1 and Figure 2). In these extended regions, path coverage (in particular crossing ray paths) is sufficient for intermediate periods where we have many measurements, but we currently do not have sufficient coverage for high resolution at shorter periods where some features are smeared. We anticipate improvement at these periods with additional dispersion measurements. Path coverage throughout the broad region has been further improved by the use of cross-correlation of ambient seismic noise to derive the Green function between two stations, and from which the dispersion characteristics can be derived (Ritzwoller et al., these Proceedings). The benefits of this method in seismology have been dramatically demonstrated for southern California in Shapiro et al. (2005). Path maps for Europe (from Yang et al., 2007) are illustrated in Figure 3.

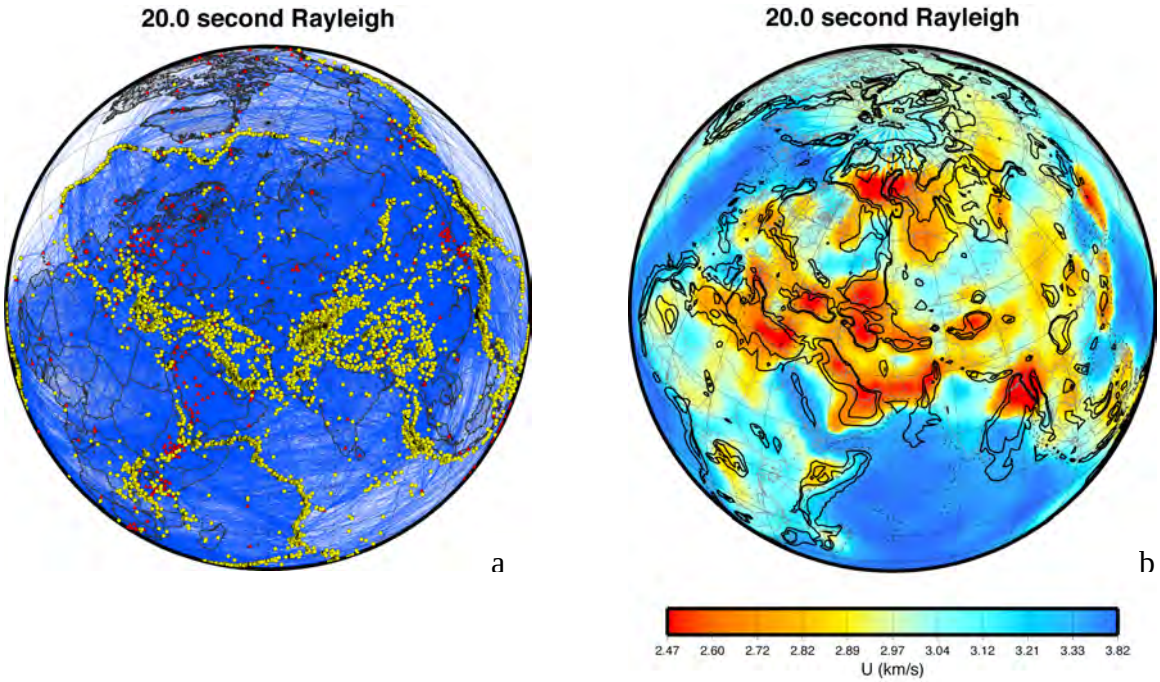

LLNL Seismic Research Knowledge Base (SRKB).

Figure 1. Surface wave dispersion maps for 20 second Rayleigh waves. (a) Path map showing coverage of the Eurasian and African continents. (b) Group velocity map of the same region (Pasyanos, 2005).

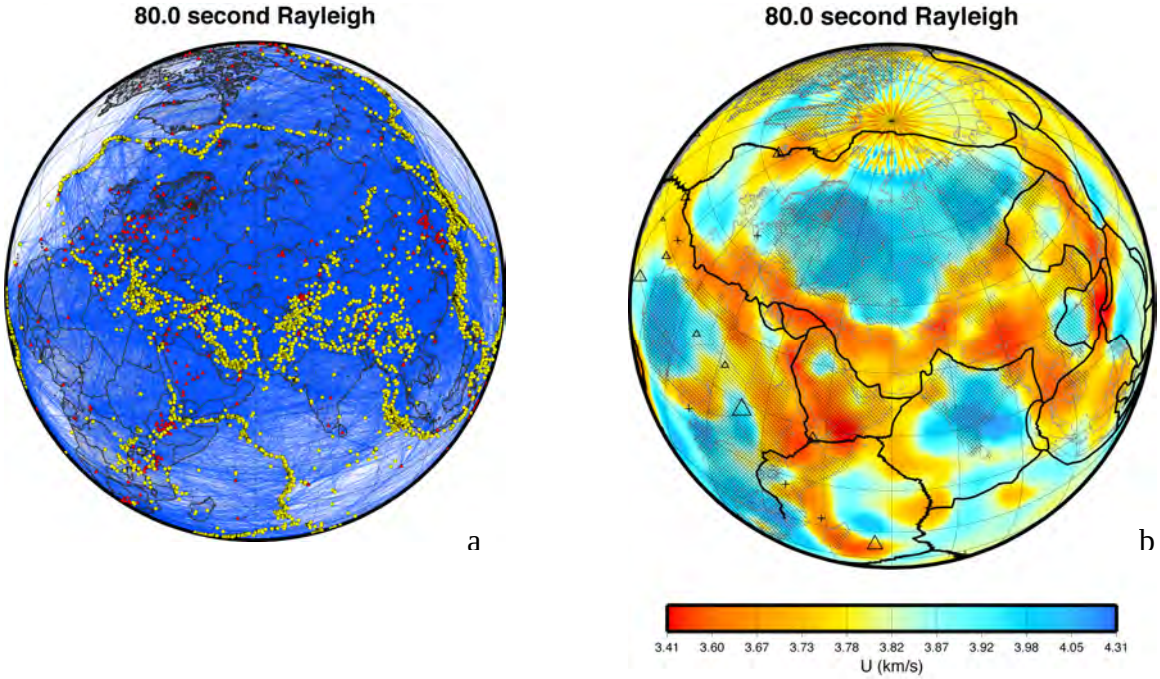

Figure 2. Surface wave dispersion maps for 80 second Rayleigh waves. (a) Path map showing coverage of the Eurasian and African continents. (b) Group velocity map of the same region (Pasyanos, 2005).

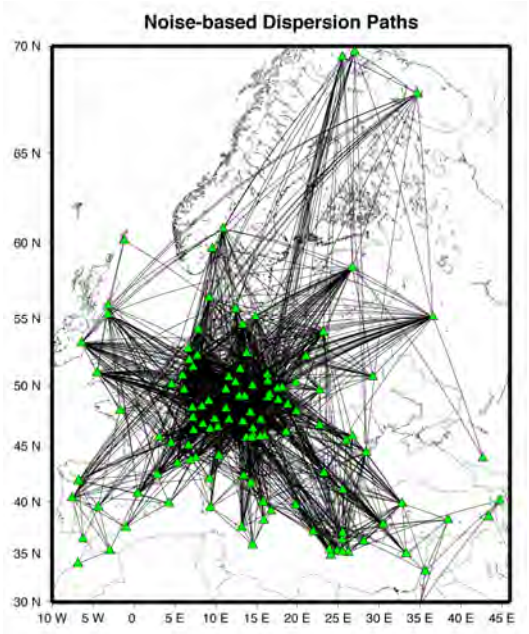

Figure 3. Cross-correlation path map for Europe. Stations are indicated by green triangles (measurements from Yang et al., 2007).

Velocity Models

One application of the surface wave models is to invert the dispersion results to derive models of the crust and upper mantle structure. This is particularly useful in aseismic regions that are poorly sampled by other data sets. Recently, we have used surface wave dispersion maps to construct a 3-D lithospheric velocity model of Africa and Arabia (Pasyanos and Nyblade, 2007), most of which is aseismic and not well-sampled by body waves. A crustal thickness map of the region is shown in Figure 4a. In North Africa, there is a crustal thickness contrast between the West Africa Craton and the East Saharan Shield. There is crustal thinning along the African Rift Systems (West and Central, as well as the East African Rift). In central and southern Africa, crust is consistently thick, although it appears to be thickest under the Congo Craton. Figure 4b shows a slice through the model at 200 km showing the faster velocities under the West African, Congo, and Kalahari Cratons in northern, central, and southern Africa, respectively.

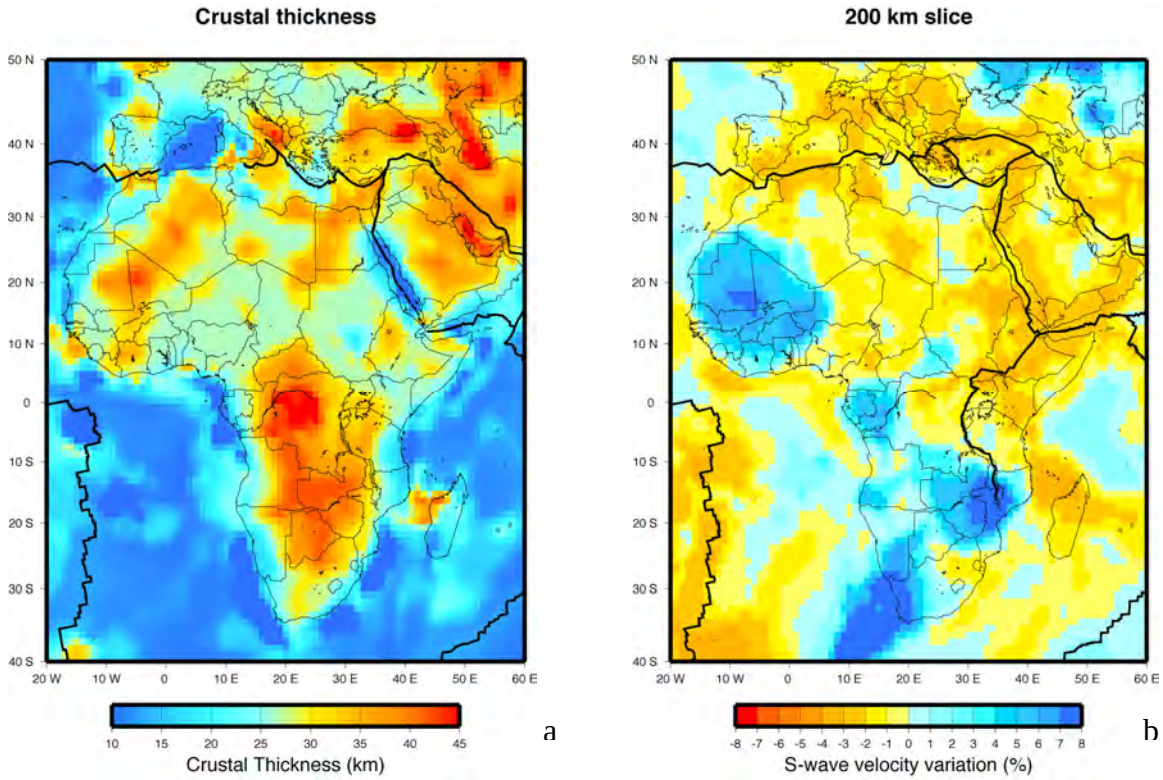

Figure 4. a) Crustal thickness map of Africa. b) S-wave velocity variation in the mantle under Africa at 200 km depth (from Pasyanos and Nyblade, 2007).

By applying the inversion of surface waves for structure to broad regions we can start to map out important tectonic features. For example, the velocities of long period surface waves are sensitive to the thickness of the lithosphere, which have been inverted for in Figure 5. Slower group velocities at short periods indicate the lack of a thick lithospheric lid and the presence of a slower, asthenospheric mantle not far below the crust. These are found at plate boundaries whether subducting convergent (Mediterranean, Japan), orogenic convergent (Turkish-Iranian Plateau, Himalayas), or divergent (Red Sea, oceanic rifts). Fast velocities at long periods indicate the presence of a thick lithospheric lid, as well illustrated by the lithospheric keels found under platforms and shields such as the West African Craton, Congo Craton, Indian Shield, South China Craton, Baltic Shield, Ukrainian Shield, and Russian Platform.

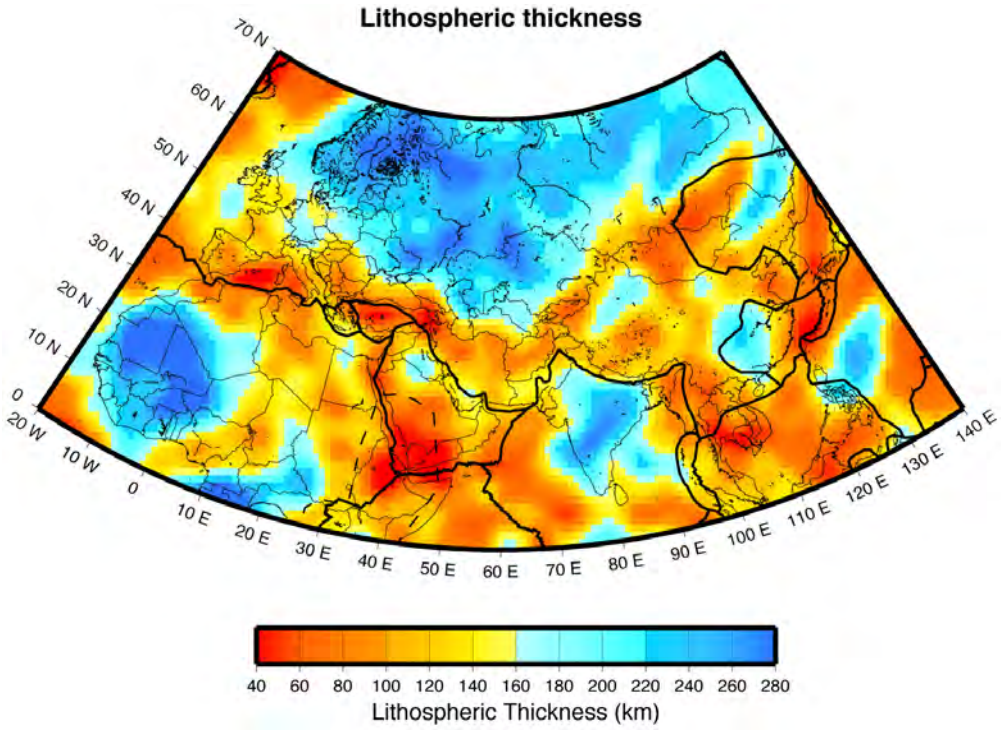

Figure 5. Lithospheric thickness map of Eurasia and North Africa. Plate boundaries are indicated by the solid black lines.

Regional Applications

We have used the surface wave models, mostly in conjunction with other data sets such as receiver functions, to produce regional velocity models. Recent studies have covered Arabia (Tkalcic et al., 2006), Kenya (Benoit et al., 2006), Kuwait (Pasyanos et al., 2007), eastern Turkey (Gok et al., 2007a), eastern Mediterranean (DiLuccio and Pasyanos, 2007), Iraq (Gok et al., 2007b), India and South Africa.

As an example, the KUW1 model was derived from the joint inversion of receiver functions and surface wave group velocities at station KUW in Kuwait. It is a 45 km thick crust with 8 km of sediments and very slow upper mantle velocities. Figure 6 shows how the KUW1 model (indicated by the solid blue line) compares to other models. In particular, we compare this velocity model to models determined from the simultaneous relocation of local seismic events using VELEST. These VELEST models do not have sensitivity in the shallow sediments and deep crust, but the resulting velocity profiles (shown by the red, brown, and black colored dashed lines) are very similar to the KUW1 model in the middle crust, regardless of various starting models, indicating that the KUW1 is also applicable for locating regional events. The preferred VELEST model (where the sedimentary column and deep crust are set to KUW1) is indicated by the solid purple line. The resulting models have significantly thicker crust than the current model used by the Kuwait National Seismic Network (KNSN), shown in green.

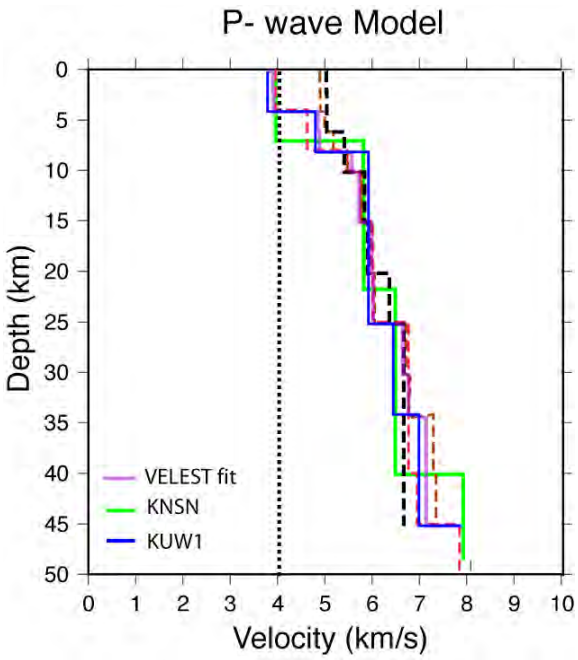

Figure 6. P-wave velocity profiles for Kuwait. See text for details (Pasyanos et al., 2007).

While the model can simultaneously fit surface waves, receiver functions, and local travel times, the model does not appear appropriate for regions not too distant from the station. Figure 7 shows the travel times of local Kuwaiti events and regional phases (Pn, Pg, Sn, Lg) from events in Iran recorded at station KUW, paths which primarily sample the Zagros Mts. The model fits reasonably well the local events (<1° distance) and the near regional events (3-4°), but the far regional events which have longer paths through the Zagros require faster upper mantle P-wave velocities and slower crustal P-wave and S-wave velocities.

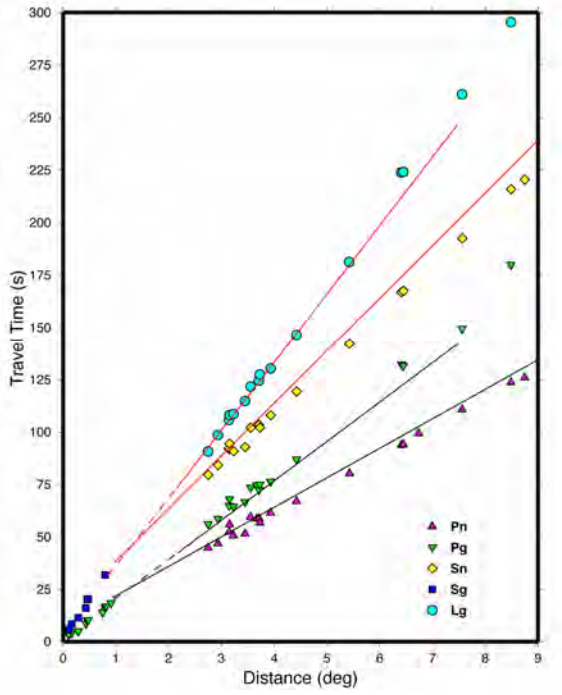

Figure 7. Travel times from local events and regional events in the Zagros recorded at station KUW in Kuwait (Pasyanos et al., 2007).

A Priori Models

The WENA model is an a priori three-dimensional model for Western Eurasia and North Africa (Pasyanos et al., 2004). Models like WENA can serve as background values for travel time correction surfaces and other derived parameters. In the original publication, we demonstrated our ability of the WENA model to predict a variety of data sets, including surface wave dispersion maps and matching crustal thickness estimates from receiver functions. In a followup paper, it was also demonstrated that it is also possible to improve regional travel-time prediction and seismic event location accuracy using this model (Flanagan et al., 2006). The authors conclude that a priori models are directly applicable where data coverage limits tomographic and empirical approaches, and the development of the uncertainty model enables merging of a priori and data-driven approaches using Bayesian techniques.

This model continues to evolve in several ways. First, the WENA model was joined with a Los Alamos model for Eastern Eurasia to produce a single model for Eurasia and North Africa (dubbed the Unified model). Secondly, crustal thicknesses in the model have been replaced by a 1-degree crustal thickness model derived from kriging thousands of individual crustal thickness estimates. The model continues to be tested and validated, recently to provide the best 1-D velocity profiles for waveform modeling.

Most recently, the attenuation structure of the model is being updated to replace the original placeholder values that were provided for crystalline crust and uppermost mantle layers. These updates will better reflect the tectonic history of the geophysical province (e.g., orogenic zone vs. shield) and allow the attenuation predictions of the model to more closely match those from empirical attenuation studies, such as those derived from Lg coda (e.g., Mitchell et al., 1997).

Stochastic Geophysical Models

In recent years, LLNL has been developing and refining the use of the Markov Chain Monte Carlo (MCMC) method to generate three-dimensional, data-driven stochastic earth models. We use MCMC to sample models from a prior distribution, test them against multiple data types in a staged approach, and develop a posterior distribution of seismic models that are most consistent with multiple seismic data sets (Pasyanos et al., 2006). This approach has several advantages over a single deterministic model. First, we are able to easily incorporate prior information on the model, such as the a priori geophysical models that were discussed earlier. Secondly, with this technique, we are able to reconcile different data types (such as body waves and surface waves) that can be used to constrain the model. We can also estimate the uncertainties of model parameters, properly migrating data uncertainties into model uncertainties. Finally, we can estimate uncertainties on predicted observable signals, such as would be required to apply this model as a correction surface.

While this approach has several advantages over deterministic models, the application of the method can be computationally expensive, allowing model development only in high-performance computing environments. For example, the application of this method to determine the crust and upper mantle structure of the Yellow Sea and Korean Peninsula (YSKP) region using surface wave dispersion data, body wave travel time data, gravity, and receiver functions has necessitated the use of Livermore Computing (LC) machines like Thunder, a 23 tflops peak-performance 1024 Node cluster where all nodes are 4-CPU, 1.4 GHz Itanium 2 "Madison Tiger4" nodes (see Figure 8). As we wish to apply this methodology to even broader regions with significantly larger data sets, one key objective has been to increase the efficiency of our runs. Over the past six months, we have solved some of the technical problems with increasingly larger data sets and have sped up the calculations significantly, allowing us to apply this to bigger problems.

Figure 8. Livermore Computing (LC) cluster Thunder.

Stochastic models represent one way of transitioning to 3D models, although there are a number of different approaches. Methods that developed separately are starting to converge. Surface wave models are increasing in resolution, allowing detailed shallow structure models. Body wave models have increasingly sophisticated modeling of the ray path, allowing more data to constrain the model. Data sets and computational power are both growing rapidly. On June 6-7, 2007, in Berkeley, CA, LLNL hosted the "Workshop on Multi-Resolution 3D Earth Models to Predict Key Observables in Seismic Monitoring and Related Fields" (Harris et al., these Proceedings). Questions raised during the workshop, such as model representation, data used to construct the model, operational constraints, uncertainties, etc., all have a significant effect on the best approach.

CONCLUSIONS AND RECOMMENDATIONS

Geophysical models play an important role in nuclear explosion monitoring, allowing us to capture the effect of the earth on seismic signals in a compact and self-consistent manner. As the availability of seismic data continues to expand and computational power rapidly grows, we have increasing power to truly image the high-resolution features of the earth that are necessary to support nuclear explosion monitoring operations. We have presented a variety of models currently being developed at LLNL. As data availability and computational power increase the models can be enhanced and combined in an effort to produce fully 3-D models.

REFERENCES

Benoit, M. H., A. A. Nyblade, and M. E. Pasyanos (2006). Crustal thinning between the Ethiopian and East African Plateaus from modeling Rayleigh wave dispersion, *Geophys. Res. Lett.* 33: L13301, doi:10.1029/2006GL025687.

Di Luccio, F. and M. E. Pasyanos (2007). Crustal and upper-mantle structure in the Eastern Mediterranean from the analysis of surface wave dispersion curves, *Geophys. J. Int.* 169: (3), 1139–1152.

Flanagan, M. P., S. C. Myers, and K. D. Koper (2006). Regional travel-time uncertainty and seismic location improvement using a 3-dimensional a priori velocity model, *Bull. Seism. Soc. Amer*. 97: 3, 804–825, doi:10.1785/0120060079.

Gök, R., M. E. Pasyanos, and E. Zor (2007a). Lithospheric structure of the continent-continent collision zone: Eastern Turkey, *Geophys. J. Int.* doi: 10.1111/j.1365–246X.2006.03288.x.

Gök, R., H. Mahdi, H. Al-Shukri, and A. Rodgers (2007b). Crustal structure of Iraq from receiver functions and surface wave dispersion, submitted to *Geophys. J. Int.*

Harris, D., J. Zucca, D. McCallen, M. Pasyanos, M. Flanagan, S. Myers, W. Walter, A. Rodgers, and P. Harben (2007). Considerations of the use of 3-D geophysical models to predict test ban monitoring observables, in current Proceedings.

Mitchell, B. J., Y. Pan, J. Xie, and L. Cong (1997). Lg coda Q variation across Eurasia and its relation to crustal evolution, *J. Geophys. Res*. 102: B10, 22,767–22,779.

Myers, S., S. Ballard, C. Rowe, G. Wagner, M. Antolik, W. Phillips, A. Ramirez, M. Begnaud, M. Pasyanos, D. Dodge, M. Flanagan, K. Hutchenson, G. Barker, J. Dwyer, and D. Russel (2007). Tomography and methods of travel-time calculation for regional seismic location, in these Proceedings.

Pasyanos, M. E., W. R. Walter, S. E. Hazler (2001). A surface wave dispersion study of the Middle East and North Africa for monitoring the Comprehensive Nuclear Test Ban Treaty, *Pure and Applied Geophysics*, 158: 1445–1474.

Pasyanos, M. E., W. R. Walter, M. P. Flanagan, P. Goldstein, and J. Bhattacharyya (2004). Building and testing an a priori geophysical model for western Eurasia and North Africa, *Pure and Applied Geophysics*, 161: 235–281.

Pasyanos, M. E. (2005). A variable-resolution surface wave dispersion study of Eurasia, North Africa, and surrounding regions, *J. Geophys. Res*. 110: B12301, doi:10.1029/2005JB003749.

Pasyanos, M. E., G. A. Franz, and A. L. Ramirez (2006). Reconciling data using Markov Chain Monte Carlo: An application to the Yellow Sea—Korean Peninsula region, *J. Geophys. Res*. 111: B03313, doi:10.1029/2005JB003851.

Pasyanos, M. E. and A. A. Nyblade (2007). A top to bottom lithospheric study of Africa and Arabia, submitted to *Tectonophysics.*

Pasyanos, M. E., H. Tkalcic, R. Gok, A. Al-Enezi, and A. J. Rodgers, (2007). Seismic structure of Kuwait, *Geophys. J. Int.* doi:10.1111/j.1365-246X. 2007–03398.

Ritzwoller, M., Y. Yang, R. Richmond, M. Pasyanos, A. Villasenor, V. Levin, A. Hofstetter, V. Pinsky, N. Kraeva, and A. Lerner-Lam (2007). Short period surface wave dispersion across the Mediterranean Region: improvements using regional seismic networks, in current Proceedings.

Shapiro, N. M., M. Campillo, L. Stehly, and M. H. Ritzwoller (2005). High resolution surface wave tomography from ambient seismic noise, *Science* 307(5715): 1615–1618.

Tkalcic, H., M. Pasyanos, A. Rodgers, R. Gok, W. Walter, and A. Al-Amri, (2006). A multi-step approach in joint modeling of surface wave dispersion and teleseismic receiver functions: Implications for lithospheric structure of the Arabian peninsula, *J. Geophys Res.* 111: B11311, doi:10.1029/2005JB004130.

Yang, Y., M. H. Ritzwoller, A. L. Levshin, and N. M. Shapiro (2007). Ambient noise Rayleigh wave tomography across Europe, *Geophys. J. Int.* 168: 1, 259–274, doi:10.1111/j. 1365–246X.2006.03203.x.

ANALYSIS AND SIMULATION OF THREE-DIMENSIONAL SCATTERING DUE TO HETEROGENEOUS CRUSTAL STRUCTURE AND SURFACE TOPOGRAPHY ON REGIONAL PHASES; MAGNITUDE AND DISCRIMINATION

Arben Pitarka[1], Don V. Helmberger[2], and Sidao Ni[1]

URS Group, Inc.[1] and California Institute of Technology[2]

Sponsored by Air Force Research Laboratory

Contract No. FA8718-07-C-0003[1,2]

ABSTRACT

The main purpose of this study is the basic understanding of scattering and its effects through step-by-step numerical experiments and waveform modeling, with the goal of providing useful insights into ongoing research for development of simple empirical models of scattering that can be used in reducing the scatter in measures of Lg and coda wave magnitude and for discrimination purpose as well. We are performing anelastic three-dimensional (3-D) finite-difference simulations of wave propagation in highly heterogeneous media for a range of source depths, receiver distances, and source types. Using a highly efficient and parallelized computer code and models with flat surface topography we have produced synthetic seismograms up to 3.5 Hz at regional distances up to 300 km. In future works we plan to extend the upper frequency limit to 6-8 Hz and model surface topography scattering effects by using a larger number of computer nodes. Our numerical experiments with 3-D velocity models that include random velocity perturbations and microbasins, designed to produce wave scattering in the upper 5 km of the crust, clearly show that wave-path scattering alone can produce Lg, P, and S coda waves with significant energy even for explosion sources. The energy of Lg coda waves depends on the source depth. P/Lg ratios estimated at different frequencies indicate that this ratio could be a good discriminant between explosions and earthquakes when calculated at high frequencies. P/Lg ratios below 1 Hz are very similar for shallow explosions and deep earthquakes.

OBJECTIVES

Our objective is to analyze and evaluate the effect of scattering on the amplitude and frequency content of Pg and Lg waves due to small-scale crustal heterogeneities and surface topography by 3-D finite-difference simulations and modeling of recorded waveform data. The research program will focus on the following topics:

1. Influence of scattering due to complex structure and surface topography on the variability observed in amplitude estimates of regional phases. We will analyze simulation results of regional wave propagation scattering, obtained with efficient two-dimensional (2-D) and 3-D finite-difference computer programs that can also treat surface topography, including mini-basins.
2. Influence of scattering effects due to rough topography near the source and station on the amplitude of observed regional phases involving explosion source. Topography analysis will be concentrated in small areas, mostly in Korean Peninsula, India, and Pakistan, where we have sufficient data on earthquakes and explosions.

RESEARCH ACCOMPLISHED

The influence of random heterogeneities and rough surface on Lg amplitude and Lg coda formation are shown to be significant. This very important phenomena needs to be investigated by both observational and numerical techniques. While analyses of recorded seismograms can reveal the degree of complexities in the crust and the effect of small-scale and large-scale perturbation on different wave phases, the numerical experiments can be used for isolating effects caused by the wave path, seismic source, and local structures. They can also be used to verify hypothesis that are at the foundation of several discrimination methodologies.

The regional discriminants and magnitude methods rely mainly on the general feature of decreased s-phase amplitude and increase of p-phase amplitudes for explosion sources. However explosions produce anomalous large s-phase amplitudes that confound regional methods. It is therefore important to understand the factors that are at the origin of such behavior. Several valid hypothesis dealing with the source process and crustal complexities have been proposed. In this study we investigate one of them—the effect of scattering due to random heterogeneities in the upper crust on the local and regional wavefield from explosion and earthquake sources.

Parameterization of Scattering Model

The wave scattering effects in our 3-D simulations are modeled by random perturbations of the velocity. The perturbations expressed in percentage of unperturbed shear-wave velocity are intercorrelated using a spatial correlation length. Results of sensitivity analyses with different velocity perturbations and correlation lengths, not shown here, confirm the importance of such modeling parameters in generating realistic wave-path effects in a broad frequency range. One way of deriving realistic scattering model parameters is to simulate observed broadband waveforms from small and moderate regional earthquakes using random perturbations of well calibrated velocity models. The objective of such modeling is to derive scattering parameterization of the velocity model by reproducing the gradual disappearance of the observed radiation pattern of P and S waves with increasing frequency. This is known to be caused by near-source and wave-path scattering. The use of both P and S waves as well as their respective coda decay provides excellent empirical constraints on deriving realistic random velocity perturbations with correct correlation lengths. The effect of wave scattering on P and S waves and their coda amplitude is illustrated in Figure 1.

Figure 1 shows the amplitude variation of the ground velocity envelope as a function of frequency from the Mw4.5 070120 earthquake in South Korea. We used broadband recordings at station CHC, CHJ, ULJ, and SES. The station and the earthquake locations are shown in Figure 2. The earthquake was located at a depth of 11 km. Its focal mechanism (strike=209^o, dip=90^o, rake=180^o) was determined using a cut and paste (CAP) inversion technique that is based on different weights for relatively high frequency waveform modeling of Pnl and relatively long period surface waves (Tan et al., 2006). And Pnl and surface waves are also allowed to shift in time to take account of uncertainties in velocity structure. Inversion of Pnl and surface waves provides better constraints on focal depth as well as source mechanisms. The pure strike-slip mechanism of the earthquake and its recording at stations near the P wave nodal planes are ideal for analyzing regional scattered waves. Stations CHJ and CHC are close to P-wave nodal planes.

Two general observations relevant to the wave scattering can be made. First, the P-wave scattering, expressed as the relative increase of amplitude of the P wave and its coda in the tangential component of motion at P-wave nodal stations, becomes significant at frequencies higher than 4 Hz. Note the relatively large amplitude of P coda waves on the tangential component at such frequencies. This indicates that high-frequency P to S-wave conversions are significant. It is important to note that scattering effects due to small-scale perturbation in the shallow crust cause the increase in amplitude of high frequency P-wave coda in all three components. P waves also could be very helpful in constraining the basic parameters of the scattering model. Second, because of their shorter wavelength S waves are more susceptible to wave propagation scattering effects. As shown in Figure 1, for such waves the amplitude difference between the three components that is controlled by the source radiation pattern is observed only at frequencies lower than 2 Hz. In general, at higher frequencies the amplitude of the S wave coda is mainly controlled by scattering. Consequently it is the same for all three components. The relatively low frequency random behavior of S waves can be used in deriving random variations in the crustal velocity model. This observed feature of P and S phases can help constraining scattering parameterization. In our ongoing effort for deriving scattering parameterization for the Korean Peninsula we will model several shallow earthquakes recorded at regional broadband stations.

The ratio between Pn and Pg seems to be stable over different frequencies. For strike-slip events such as the 070120 Korean earthquake, Pn should be much smaller than Pg because of its steeper takeoff angle. But for explosions, Pn and Pg seem to have similar amplitudes (Kim and Richards, 2007). For the Korean earthquake, Pn is indeed much weaker than Pg for all the frequency bands, arguing that the ratio between Pn and Pg can be used to constrain source mechanisms of events at high frequencies and should be very useful for discrimination purposes.

Modeling 3-D Scattering Effects

The origin of the high frequency scattering affecting mainly the P and Lg coda waves (above 1 Hz) could be due to either deep or shallow crustal structure complexities along the wave path or in the source region (e.g., Dainty 1996; Wu et al., 2000). The Lg wave shows evidence of scattering from small-scale structures. Other causes of scattering could also be large-scale structural complexities such as crustal thinning or multipathing (e.g., Ni and Barazangi, 1983; Phillips et al., 2000).

During this first phase of our study we have examined effects of wave propagation scattering due to complexities in the shallow crust. We have calculated synthetic seismograms for point sources buried at different shallow depths using a parallelized anelastic 3-D finite-difference code (Pitarka, 1999). Our finite difference code solves the stress-velocity wave equations in a heterogeneous medium using staggered grids. The technique for generating the 3-D velocity model on a regular grid with variable spacing allows for inclusion of small-scale complexities and surface topography as well. The technique we use to model free surface topography is an extension of the formalism that we have applied to modeling wave propagation in media with curved free surface (Pitarka and Irikura, 1996). The performance of our free-surface boundary condition technique at handling Lg coda waves for flat free surface and very long distances was compared with that of the FK method of Saikia (1994) for a shallow source. Also the technique has been validated against other standard and accurate techniques for modeling surface topography such as 2-D-Boundary Element Method (BEM) and the 2-D-Discrete Wavenumber-Boundary Integral Equation method of Takenaka et al. (1996).

We looked at the relative contribution of wave-field scattering on different frequency bands of P and Lg coda waves due to localized and highly heterogeneous small-scale bodies embedded in a reference planar layered velocity model that was used in modeling regional wave propagation in the South Korea region. The small-scale variations of the velocity are randomly distributed along the top 5 km of the crust. In addition to the small-scale fluctuations our velocity model includes several microbasins with sizes varying between 10-25 km and depth up to 2 km. The velocity fluctuations are in the range of 2-8% and their correlation length is 5 km. The selected minimum grid spacing of 200 m ensures accurate wave propagation modeling up to 3.5 Hz. The 3-D model occupies a volume of 400x200x60 km. The ground motion velocity was computed on a 2-D rectangular array of stations located on the free surface. The stations spacing is 20 km, and the maximum epicentral distance is 300 km. Several stations are located in the microbasins.

Aiming at understanding scattering effects in relation with the source type and source depth we performed simulations for an explosion point source located at a depth of 500 m, and for earthquake double-couple point sources located at 50 m and 8 km depths, respectively. Since we are looking at indirect mechanisms of S wave generation, mainly wave-path scattering, in our simulations we used the isotropic representation of the explosion source.

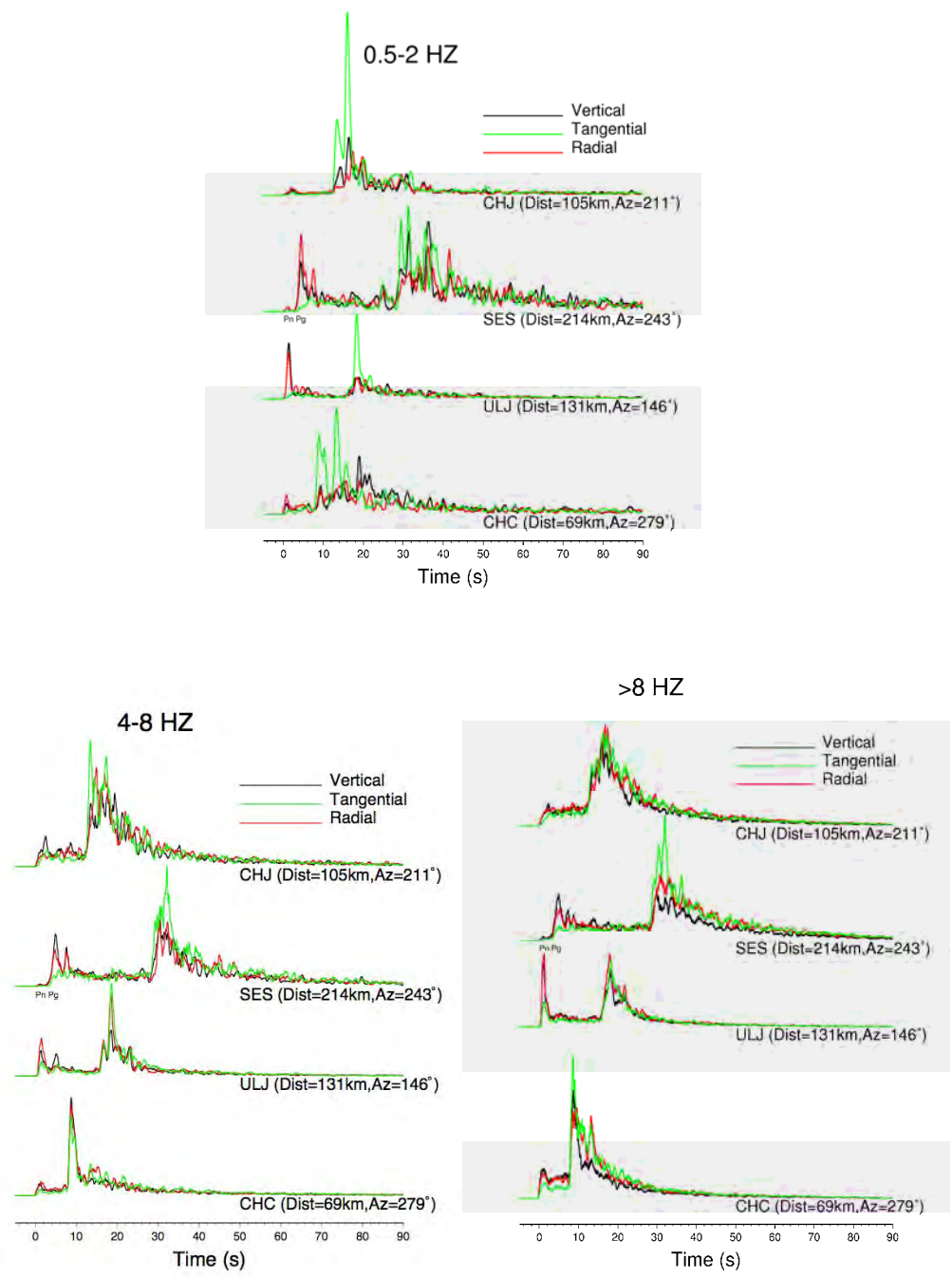

Figure 1. Smoothed envelopes of broadband velocity seismograms recorded at station CHJ, SES, ULJ, and CHC from the Mw 4.5 070120 earthquake in South Korea. The envelopes are calculated at four frequency bands indicated on top of each panel. Color traces show different components. The epicentral distance and azimuth are indicated at each trace. Note the large amplitude of the P wave on the vertical and radial components at stations CHJ, SES, and ULJ that are located near the nodal planes. The difference in the P wave seen between the three components is caused by the source radiation. It is preserved only at frequencies up to 4 Hz. In general, at frequencies higher than 4 Hz, the amplitude of P wave coda becomes the same at all components. This is a clear indication of scattering effects in the shallow crust.

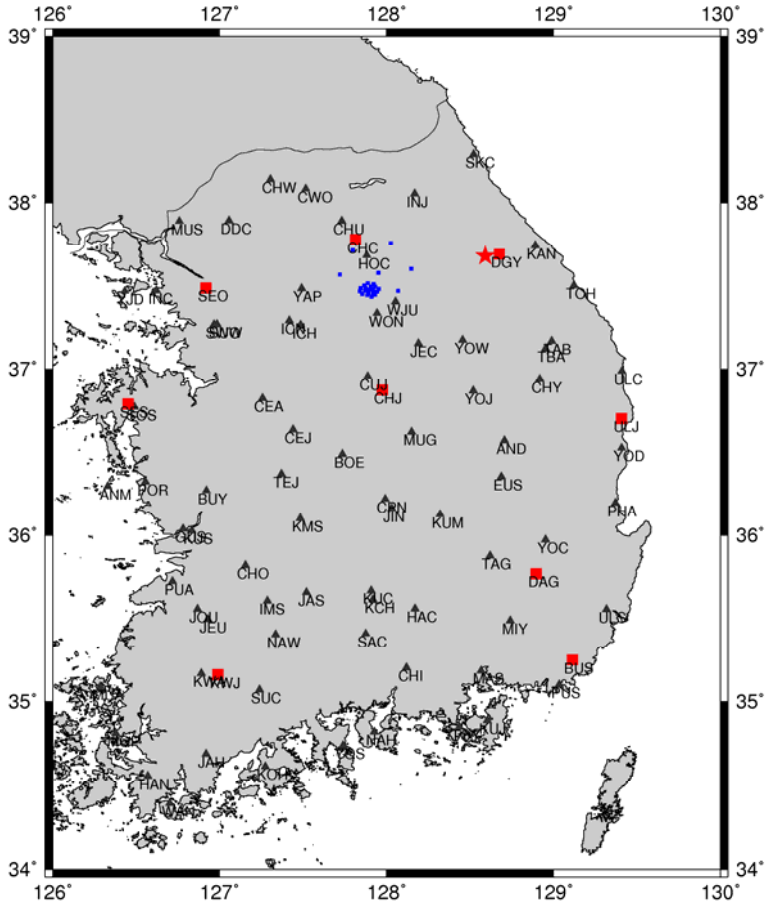

Figure 2. Map showing broadband (red square) and short-period strong motion (black triangle) stations in South Korea. Blue squares show International Monitoring System Korean Seismic Research Station (KSRS) stations, and the red star indicates the epicenter of the earthquake analyzes in this study.

The source time function is a modified Haskell type:

$$\psi(\tau) = \psi_{\infty}\left[1 - e^{-K\tau}\left[1 + K\tau + \frac{(K\tau)^2}{2} - B(K\tau)^3\right]\right] \quad (1)$$

where τ is the reduced time. The study by Mueller and Murphy (1971) established the basic scaling laws relating the constant K and ψ_{∞} to yield. The parameter K is directly related to the corner frequency, and depends on source strength such that the larger the event, the longer is the source duration, or

$$K = C_1 \frac{h^{0.42}}{W^{0.33}}, \quad (2)$$

where W is the yield in kt, h is the depth in meters, and C_1 is a constant determined by near-field modeling.

Simulation Results

Figure 3 shows the difference in wave propagation characteristics between the reference flat-layered model and the 3-D model with shallow crustal scattering. We compared the E-W component of synthetic velocity seismograms calculated at a linear array of receivers for a strike-slip earthquake located at a depth of 8 km. The strike angle of the fault is 90^o and the rake angle is 50^o. It is obvious that shallow random complexities create coda waves with long duration. The S and Lg coda waves are very energetic even at short distances.

Figure 4 compares the synthetic waveforms from a shallow isotropic explosion source buried at a depth of 0.5 km and a double couple point source with an arbitrary focal mechanism located at a depth of 8 km. Again the effects of the shallow heterogeneities expressed as P to S and S to P conversions as well as surface waves are very impressive, especially for the explosion source that does not emit S waves. Our numerical experiment clearly shows that wave-path scattering alone can produce Lg, P, and S coda waves with significant energy even for shallow explosion sources. Other simulations performed with the same scattering model confirm that the energy of Lg coda waves increases when the source depth decreases. An even more drastic effect can be expected for rough topography.

Using the waveforms from the shallow explosion source and deep earthquake source using the 3-D scattering model we estimated the P/Lg ratio at 0.5 Hz, 1 Hz, and 2 Hz. The P/Lg ratio was estimated at 95 receivers. The time window used for the P wave includes the direct P and P coda waves. The ratio at each frequency was obtained by averaging over a 0.5 Hz long frequency window centered at the required frequency. The comparison of P/Lg ratio between the explosion and earthquake is shown in Figure 5. Our result shows that for structures with shallow wave-path scattering P/Lg ratio at 2 Hz could be a good discriminant between explosions and earthquakes. P/Lg ratios below 1 Hz are very similar for shallow explosions and deeper earthquakes.

The difference of P/Lg ratio between the explosion and the deep earthquake at high frequency is controlled by the P rather than Lg waves. As demonstrated by our simulation the energy of Lg coda waves for both shallow explosion and deep earthquake sources is very similar. At longer distances P waves generated by the shallow explosion become richer in high frequency energy compared with the P waves coming from the earthquake source (see Figure 6). This is probably because for shallow sources P and converted P to S waves remain trapped within the scattering structure of the shallow crust. In contrast P waves coming from a deeper source, besides being attenuated, do not develop much coda waves as some of their energy reflected at the free surface leaks back to the deeper crust.

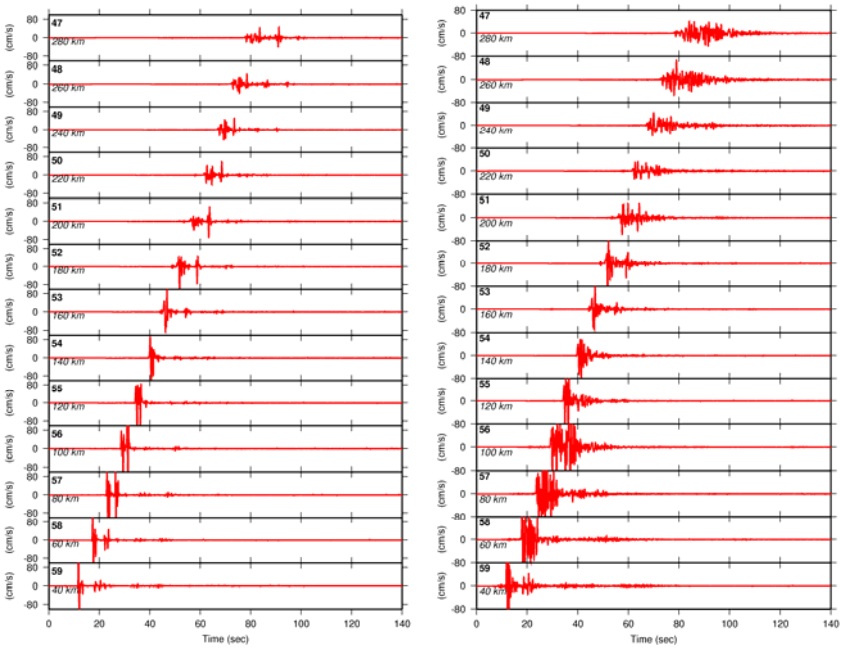

Figure 3. Comparison of the E-W component of synthetic velocity seismograms calculated at a linear array of receivers, for a strike-slip earthquake located at a depth of 8 km. The receiver number and distance is indicated on each panel. The synthetics shown on the left panel are calculated with a reference flat-layered model, and the ones on the right panel are calculated with a 3-D model that includes shallow crustal scattering effects.

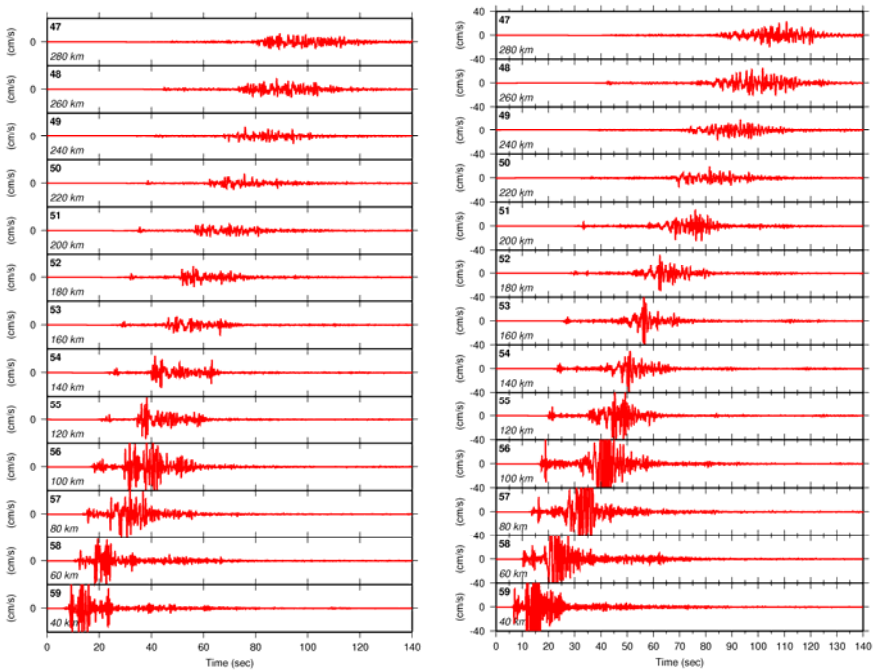

Figure 4. Vertical component of synthetic velocity for an earthquake with arbitrary focal mechanism and source depth of 8 km (left panel) and isotropic explosion source at a depth of 0.5 km (right panel). The synthetic seismograms are calculated with a 3-D model that includes shallow crustal scattering effects. Note the impressive energy of S and Lg coda waves developed for an explosion source.

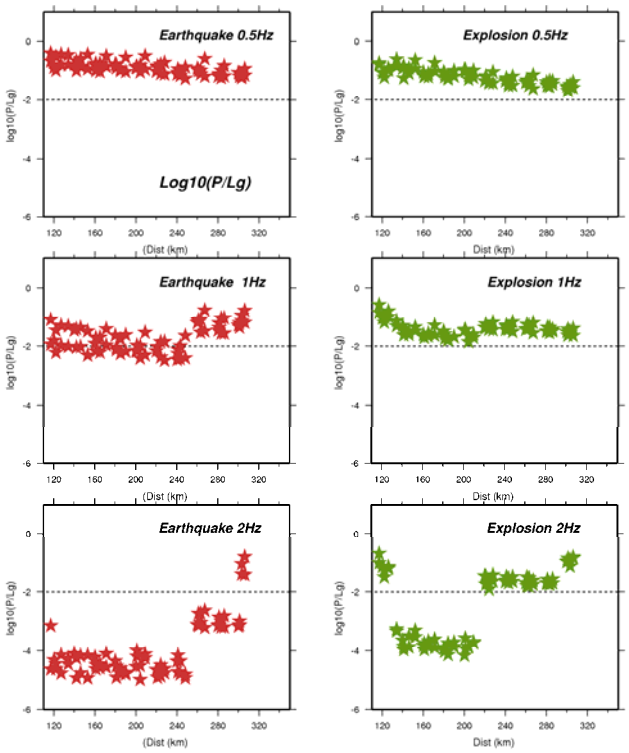

Figure 5. P/Lg ratios calculated at different frequencies for an earthquake at a depth of 8 km (left panels) and an isotropic explosion source at a depth of 0.5 km (right panels). For this case P/Lg calculated at the 2 Hz ratio can be considered as a discriminant at distances longer than 200 km.

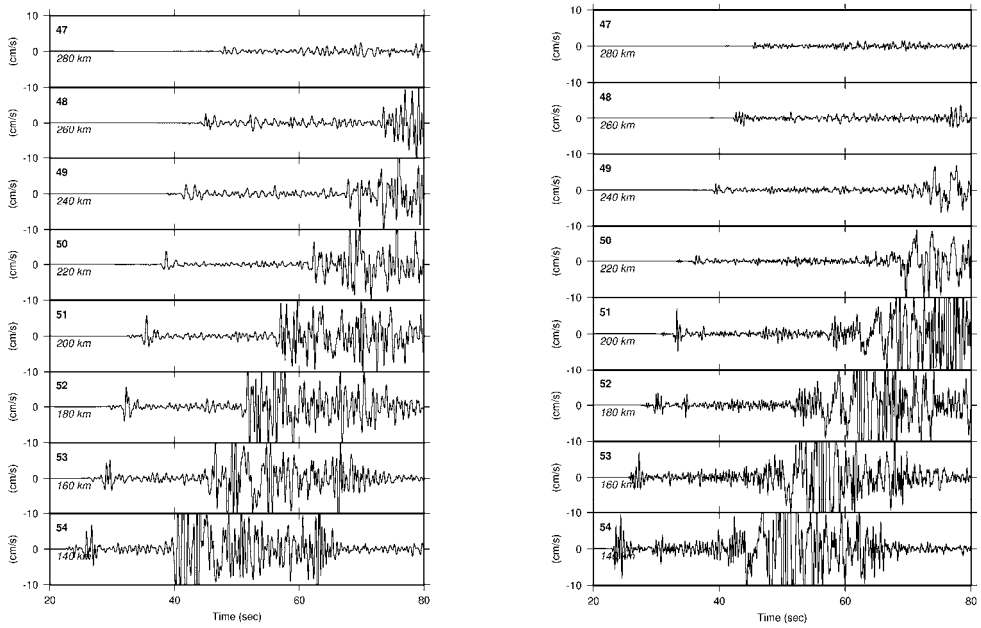

Figure 6. Vertical component of the P wave part of synthetic seismograms calculated for the earthquake (left panel) and shallow explosion (right panel). Note the explosion contains higher-frequency P coda waves.

CONCLUSIONS AND RECOMMENDATIONS

Our numerical experiments with 3-D velocity models that include random velocity perturbations and microbasins, representing wave scattering in the upper 5 km of the crust, clearly show that wave-path scattering is a major contributor to S and Lg coda waves from explosions. The energy of Lg coda waves depends on the source depth. P/Lg ratios estimated at different frequencies indicate that this ratio could be a good discriminant between explosions and earthquakes when calculated at high frequencies. P/Lg ratios below 1 Hz are very similar for shallow explosions and deeper earthquakes.

REFERENCES

Dainty, A. (1996). The influence of seismic scattering on monitoring. *Monitoring a Comprehensive Test Ban Treaty.* E. S. Husebye and A.M. Dainty, 663–688.

Goff, J. A., and T. H. Jordan (1988). Stochastic modeling of seafloor morphology: Inversion of sea beam data for second-order statistics, *J. Geophys. Res*. 93: 13589–13608.

Kim, W. and P.G. Richards (2007). North Korean Nuclear Test: Seismic Discrimination at Low Yield, *Eos Trans. Am. Geophys. Union*, Volume 88, Issue 14, p. 158–161.

Mayeda, K. M., A. Hofstetter, J. L. O'Boyle, and W. R. Walter (2003). Stable and transportable regional magnitudes based on coda-derived moment rate spectra, *Bull. Seism. Soc. Am*. 93: 224–239.

Mueller, A., and J. R. Murphy (1971). Siesmic characteristics of underground nuclear detonations, *Bull. Seism. Soc. Am.* 6: 1675–1692.

Myers, C. S., J. Wagoner, L. Preston, K. Smith, H. Tkalcic, and S. Larsen (2006). The effect of realistic geologic heterogeneity on local and regional P/S amplitude ratios based on numerical simulations, in *Proceedings of the 28th Seismic Research Review: Ground-Based Nuclear Explosion Monitoring Technologies,* LA-UR-06-5471, Vol. 1, pp. 146–155.

Ni, J. and Barazangi, M. (1983). High frequency seismic wave propagation beneath the Indian shield, Himalayan Arc, Tibetan Plateau, and surrounding regions: high uppermost mantle velocities and efficient Sn propagation beneath Tibet, *Geophys. J our. Roy. Astron. Soc*. 72: 655–689.

Phillips, W.S. and K. Aki (1986). Site amplification of coda waves from local earthquakes in central California, *Bull. Seism. Soc. Am*. 76: 627–648.

Phillips, W. S., H. E. Hartse, S. R. Taylor, and G. E. Randall (2000). 1 Hz Lg Q tomography in central Asia, *Geophys. Res. Lett*. 27: 3425–3428.

Pitarka, A. (1999). 3D elastic finite-difference modeling of seismic motion using staggered grid with nonuniform spacing, *Bull. Seism. Soc. Am*. 89: 54–68.

Pitarka, A. and K. Irikura (1996). Modeling 3D surface topography by finite-difference method: Kobe-JMA station site, Japan case study. *GRL* 20: 2729–2732.

Saikia, C.K. (1994). Modified frequency-wave-number algorithm for regional seismograms using Filon's quadrature-modeling of L(g) waves in eastern North America, *Geophys. J. Int*. 118: 142–158.

Takenaka, H., B.L. Kennett and H. Fujiwara (1996). Effect of 2-D topography and 3-D seismic wave field using a 2.5-D discrete wavenumber-boundary integral equation method, *Geophys. J. Int*., 124(3), 741-755.

Wu, Ru-Shan, S. Jin, and Xiao-Bi Xie (2000). Seismic wave propagation and scattering in heterogeneous crustal waveguides using screen propagators: I SH-waves, *Bull. Seism. Soc. Am*. 90: 401–413.

Tan, Y., L. Zhu, D.V. Helmberger and C.K. Saikia (2006). Locating and modeling regional earthquakes with two stations, *J. Geophys. Res.* 111: B01306, doi:10.1029/2005JB003775.

Xie, X., T. Lay and R. Wu (2005). Near-source energy partitioning for regional waves in 2D and 3D models, contributions of S^{*}-to-Lg and P-to-Lg scattering, in *Proceedings of the 27th Seismic Research Review*: *Ground-Based Nuclear Explosion Technologies,* LA-UR-05-6407, Vol. 1, 249–258.

WAVEFORM MODELING OF TELESEISMIC S, Sp, SsPmP, AND SHEAR-COUPLED PL WAVES FOR CRUST AND UPPER MANTLE VELOCITY STRUCTURE

Jay Pulliam, Mrinal K. Sen, and Abhijit Gangopadhyay

University of Texas at Austin

Sponsored by Air Force Research Laboratory

Contract No. FA8718-04-C-0014

ABSTRACT

We developed a waveform modeling code that computes synthetic seismograms with a parallelized reflectivity method and fits the observed waveforms by global optimization. Assuming a one-dimensional, isotropic, layered Earth, our code computes the synthetic seismograms independently for all layers, frequencies, and ray parameters. The code implements a global optimization algorithm using very fast simulated annealing (VFSA) that allows for searching within a broad spectrum of models in order to find the global minimum and hence minimizes dependency on the starting model. Our method also computes the posterior probability density (PPD) function and correlation matrix to evaluate the uniqueness of the resulting models and the trade-offs between the individual model parameters. We applied the code to determine the crust and upper mantle structure beneath permanent broadband seismic stations in Africa using teleseismic earthquakes (M 5.5-7.0 and 200-800 km focal depth) recorded at these stations. We modeled the S, SP, SsPmP, and shear-coupled PL waves from these earthquakes and our P- and S-wave velocity models compare well with, and in some cases improve upon, the models obtained from other existing methods. We obtained P- and S-wave velocities simultaneously and our use of the shear-coupled PL phase wherever available improved constraints on the models of the lower crust and upper mantle. Work is now in progress to apply this technique to data from permanent broadband seismic stations in China and Canada.

In China, based on our selection criteria, the number of earthquakes recorded at each station range between 3 and 31. The stations encompass tectonic provinces such as the north and south China blocks, Tibetan plateau, and Tien Shan Mountains. Results from the application of our technique are consistent with regional tectonics and models obtained from earlier studies using receiver functions and seismic tomography. The crustal thicknesses beneath stations in the north China block range between ~35-42 km with the crust in the central part of the block near station BJT being thicker. However, within the north China block towards its western edge, the crust appears anomalously thick (~55 km) beneath station LZH. This region also coincides with the border of the north China block and Tibetan plateau. The south China block consists of widely varying crustal thicknesses: ~37 km beneath station ENH in the northern part of the block and ~52 km beneath station KMI in the southern part, for example. The southern part of the south China block near station KMI also coincides with its border with the Tibetan plateau, where the Moho is significantly deeper than elsewhere in China, implying a deep crustal root. Station LSA, in Lhasa, Tibet, has a crustal thickness of ~53 km. In the Tien Shan Mountains in northwestern China, the crust is thicker than average (~42 km) but not as thick as that beneath the Tibetan plateau.

The seismic stations in Canada each recorded between 3 and 26 earthquakes suitable for analysis. The chosen stations span major tectonic provinces within the Canadian landmass such as the Cordilleran orogen, western plains and Slave province in western Canada, Grenville province and Appalachian orogen in eastern Canada, and the Canadian Arctic. Initial results from the application of our technique are consistent with earlier studies and regional tectonics. Crustal thicknesses beneath stations in the northern Cordilleran orogen, western plains, and Slave province range between 35-37 km. The Moho appears to be slightly shallower (31-35 km) beneath stations in the southern Cordilleran orogen. In eastern Canada, the crust beneath stations of the Grenville province and Appalachian orogen is generally thick (~44 km) with the exception of that beneath station DRLN, in the northeast, where it is ~33 km. Moho depths beneath stations in the Canadian Arctic range between ~35-42 km. We also observe low-velocity zones in the crust and uppermost mantle at some stations; however, the constraints on them are not strong. Taken together, the results provide a comprehensive snapshot of the velocity structure beneath Canada.

OBJECTIVES

In this project we developed a technique based on seismic waveform fitting by synthetic seismograms and demonstrated its usefulness with application to determine the crust and upper mantle velocity structure beneath Africa, China, and Canada. Our technique utilizes the reflectivity method (Kennett, 1983) to compute synthetic seismograms for an earthquake recorded at a seismic station and implements a global optimization algorithm using VFSA (Ingber, 1989; Sen and Stoffa, 1995) to determine the crust and upper mantle velocity structure beneath the station. Our technique is complementary to existing receiver function analysis method (e.g., Owens et al., 1987; Ammon, 1991) in that it retains the advantages of receiver functions but uses a different part of the seismogram, is sensitive to both P- and S-wave velocities directly, and obtains helpful constraints on model parameters in the vicinity of the Moho.

RESEARCH ACCOMPLISHED

Modeling Method

Earlier, Pulliam and Sen (2005) reported on the development of the waveform modeling technique during the first year (October 1, 2004 – September 30, 2005) of this project. This was followed by reporting of preliminary results of application of the technique to determine the crust and upper mantle velocity structure beneath Africa (Pulliam et al., 2006). Subsequently, final results of the structure beneath Africa were peer-reviewed and published earlier this year (Gangopadhyay et al., 2007). Therefore, in this paper we briefly outline the important aspects of the modeling technique and emphasize the results of its application to determine the crust and upper mantle structure beneath China and Canada. Work is currently ongoing to fine tune these results and to interpret the tectonics of these regions.

To improve upon the sampling area beneath a seismic station relative to receiver function inversions, when determining crustal velocity structure, and to obtain direct estimates of P- and S-wave velocities, we model the S, Sp, SsPmP, and shear-coupled PL (SPL) phases in the waveforms of selected earthquakes. Details of the propagation characteristics of these phases are provided in Pulliam and Sen (2005) and Gangopadhyay et al. (2007). Our waveform modeling technique combines a novel implementation of the reflectivity method (Kennett, 1983) with a global optimization algorithm (Sen and Stoffa, 1991; 1995). We compute the combined response of all layers of a candidate one-dimensional Earth model using the reflectivity method. The reflectivity calculation involves computation of reflectivity matrices for a stack of layers as a function of ray parameter and angular frequency and produces all phases possible for the specified stack of layers, source depth, and epicentral distance. The computations of the reflectivity responses for different ray parameters and frequencies are completely independent of each other. We use this independence to adapt the reflectivity program to parallel computer architectures, thereby decreasing the computation time nearly linearly with the number of processors used (Pulliam and Sen, 2005). Message passing therein is carried out using the Message Passage Interface (MPI) Standard (Gropp and Lusk, 1995). The computation is distributed over the ray parameters, and finally the partial responses are assembled, and the inverse transformation from ray parameter to offset (a plane wave transformation) is applied to generate synthetic seismograms at the required azimuths and distances.

Following the development of the forward problem, we perform an optimization procedure to determine, for a given source-receiver pair, the model that produces synthetic waveforms that "best fit" the data. The criterion we use to determine the best fit is the combined cross-correlation between the vertical component of the data and synthetics, and radial component of the same, in a specified time window. In this application, we define the error as the negative of a correlation function (Sen and Stoffa, 1991) given by $E(m) = -2[(\mathbf{d}_v \cdot \mathbf{s}_v)/\{|\mathbf{d}_v| + |\mathbf{s}_v|\} + (\mathbf{d}_r \cdot \mathbf{s}_r)/\{|\mathbf{d}_r| + |\mathbf{s}_r|\}]$, where $\mathbf{d}_v$, $\mathbf{d}_r$, and $\mathbf{s}_v$, $\mathbf{s}_r$ represent the vertical and radial components of the data and synthetics respectively, and $|.|$ indicates the L2 norm.

Traditionally, when the forward problem is linear or a weak non-linearity exists, derivative-based methods such as least squares are used to solve the inverse problem and estimate the model and its uncertainties (Tarantola, 1994; Sen and Stoffa, 1995). However, in the case of a non-linear problem such as is common in geophysics, these solution methods are generally not very successful. Therefore, in this analysis we employ a "global optimization algorithm," which is only weakly dependent on the choice of the initial model. In particular, we use a method called VFSA, which is a variant of simulated annealing (SA) aimed at making the computations more efficient (Ingber, 1989; Sen and Stoffa, 1995). SA is widely used to attain a global, rather than local, minimum while solving geophysical inverse problems (Sen and Stoffa, 1991; 1995 and references therein). The basic concepts of SA are

derived from statistical mechanics, where an analogy is drawn between the optimization problem and a physical system. SA is analogous to the natural process of crystal annealing, in which a solid in a heat bath is initially heated by increasing the temperature such that all the particles are randomly distributed in a liquid phase, which then gradually cools. The optimization process involves simulating the evolution of the physical system as it cools and anneals into a state of minimum energy. At each temperature, the solid is allowed to reach thermal equilibrium where the probability of it being in that state is given by the Gibbs or Boltzmann probability density function (Sen and Stoffa, 1995). VFSA is a variant of SA, developed to make it computationally more efficient. In particular, its salient features include the requirement of a temperature for each model parameter that can be different for different model parameters and the use of a temperature in the acceptance criterion that may be different from the model parameter temperatures (Sen and Stoffa, 1995). To further illustrate the VFSA technique, a simplified flow chart is shown in Figure 1. The method starts with an initial model (m^0) with an associated error or energy, $E(m^0)$. It then draws a new model, m^{new}, among a distribution of models from a temperature (T) dependent Cauchy-like distribution, r(T), centered on the current model (Figure 1). The associated error or energy, $E(m^{new})$, is then computed and compared with $E(m^0)$ (Figure 1). If the change in energy (δE) is less than or equal to zero, the new model is accepted and replaces the initial model. However, if the above condition is not satisfied, m^{new} is accepted with a probability of $[e^{\delta E/T}]$ (Figure 1). This rule of probabilistic acceptance in SA allows it to escape a local minimum. The processes of model generation and acceptance are repeated a large number of times with the annealing temperature gradually decreasing according to a predefined cooling schedule (Figure 1). VFSA is more efficient than the traditional SA because it allows for larger sampling of the model space during the early stages of the waveform fitting and much narrower sampling in the model space as the procedure converges and the temperature decreases, while still allowing the search to escape from the local minima. Additionally, the ability to perform different perturbations for different model parameters allows for individual control of each parameter and the incorporation of *a priori* information (Sen and Stoffa, 1995).

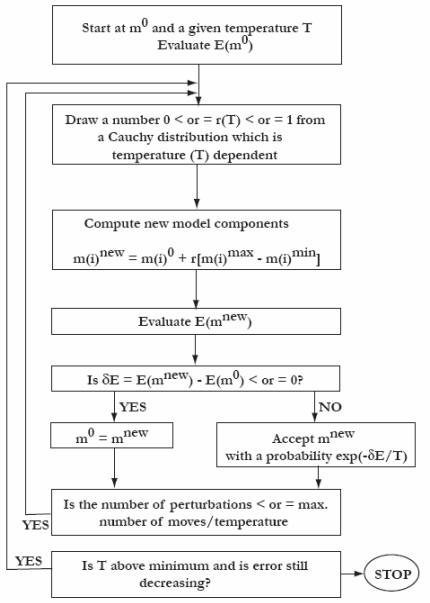

Figure 1. Flow chart elaborating the VFSA algorithm used in this study for the waveform inversion by global optimization (modified from Sen and Stoffa, 1995). $E(m^0)$-error function for the initial model m^0, $E(m^{new})$-error function for the new model m^{new}, T-temperature, r(T)-temperature dependent Cauchy-like distribution.

It is widely known that solutions to geophysical inverse problems are often non-unique. That is, their error functions either have broad minima or are multi-valued, indicating that models that are slightly different from the best-fitting model satisfy the data nearly as well, in the first case, or that one or more very different models also satisfy the data, in the second case. It is therefore necessary to explore the model space and thus identify the range of models that fit the data, and perhaps to identify characteristics of the models that are required by the data, rather than which simply are allowed by the data. VFSA conducts such a search efficiently, and the products of multiple such searches enable us to evaluate the uncertainty in a single, best-fitting solution. This evaluation is particularly necessary in seismic in waveform modeling because more than one model can often explain the observed data equally well, and trade-offs between different model parameters are common (Pulliam and Sen, 2005). The waveform modeling method we use in this study incorporates important statistical tools that allow the user to evaluate the uniqueness, and physical feasibility of the resulting model. The most useful of these tools in evaluating the results' reliability are the PPD function, and the parameter correlation matrix. To estimate these statistical parameters we cast the inverse problem in a Bayesian framework (e.g., Tarantola, 1994; Sen and Stoffa, 1995) and employ "importance sampling" based on a Gibbs' sampler (GS) (Sen and Stoffa, 1995; Pulliam and Sen, 2005). The goal of "importance sampling" is to concentrate sample points in the regions that are the most "significant" in some sense (perhaps, for example, where the error function is rapidly varying or many acceptable solutions lie). Because this concentration is achieved using a Gibbs' probability distribution, it has been named the "Gibbs' sampler" (Sen and Stoffa, 1995). The PPD function [$\sigma(\mathbf{m}|\mathbf{d}_{obs})$] is defined as a product of a likelihood function [$e^{-E(\mathbf{m})}$] and prior probability density function, $p(\mathbf{m})$. The prior probability density function, $p(\mathbf{m})$, describes the available information on the model without the knowledge of the data and defines the probability of the model $\mathbf{m}$ independent of the data. In our application here, we use a uniform prior within a minimum and maximum bound for each model parameter. The likelihood function defines the data misfit, and its choice depends on the distribution of error in the data (Sen and Stoffa, 1995 and references therein). Sen and Stoffa (1996) examined several different approaches to sampling models from the PPD and concluded that a multiple-VFSA based approach, though theoretically approximate, is the most efficient. In a multiple-VFSA approach we make several VFSA runs (20 in this study) with different random starting models and use all the models sampled along to characterize uncertainty in the model. We use all these sampled models to compute approximate marginal PPD and posterior correlation matrices to characterize uncertainties in the derived results. The posterior correlation matrix measures the relative trade-off between individual model parameters and is computed by normalizing the covariance between two model parameters (Sen and Stoffa, 1996). Computationally, the correlation between i^{th} and j^{th} model parameters is given by their covariances divided by the square root of the product of the covariances of each parameter with itself. In a later section during discussion of the application of the technique to seismological data recorded in China and Canada, we provide descriptions of interpretations of the resulting computations of the PPD and correlation matrix.

Application of the Method

We apply our modeling method to data from large-magnitude, deep-focus earthquakes recorded teleseismically at permanent broadband seismic stations spanning China and Canada during 1976-2005. The focal depths of these earthquakes range between 200 km – 600 km, and their magnitudes lie between 5.5 and 7.0. Since the goal of this study is to also model the SPL phase that is generated close to the seismic station (within an area of ~100 km × 100 km) (Frazer, 1977), we choose such a focal depth range to eliminate the SPL phase generated at the earthquake source. Epicentral distances from the seismic stations of the selected earthquakes are between 30° and 80° so as to avoid possible incorporation of phases that interacted with Earth's core. Initially, we filter the raw data obtained from the global database for the selected events, using a six-pole Butterworth bandpass filter with corner frequencies of 0.005 and 0.25 Hertz respectively. The data are then decimated such that the sample interval is 0.5 seconds. The data window we analyze includes 30 seconds before the arrival of the direct S phase and 180 seconds following it. The choice of the beginning time for our data window follows from a study by Jordan and Frazer (1975) who showed that for a deep focus event (~600 km) of intermediate magnitude (~6.1), at teleseismic distances, the SP phase resulting from a single conversion at the Moho (~35 km-40 km), precedes the S phase by about 5-6 seconds. Since the events we model in this study also lie in that category, and the only phase arriving before the S phase that we model is the Sp, we do not expect to observe any Moho-converted Sp phase before ~15 seconds from the S phase. Therefore, the start time of our data window (30 seconds before the S arrival) provides ample lead time for us to never miss the observation of the Sp phase if any. For each station, the initial model we choose is one obtained from a previous published study, wherever available, or from the Preliminary Reference Earth Model (PREM) (Dziewonski and Anderson, 1981) where an earlier study has not been published. We also experimented with an initial model consisting of crustal layers of equal thickness and increasing velocities, superimposed on PREM.

However, the final models obtained using our method were similar within one standard error, thereby emphasizing minimal dependence of our method on the starting model. For use in reflectivity computations, we also incorporate the source mechanism of each earthquake from the Harvard centroid moment tensor (CMT) catalog and use a Gaussian source-time function. Following similar forward calculations for each source – receiver pair, we carry out the waveform fitting procedure for each using 200 iterations. Before our choice of the number of iterations, we experimented with 200, 400, 600, and 800 iterations and have consistently observed that after ~165 iterations the error reaches an optimal value and does not change with subsequent iterations. This feature is a diagnosis in our method to confirm that the process has converged. Therefore, we chose 200 iterations as a threshold for all our computations. Additionally, earlier studies (Sen and Stoffa, 1995, and references therein) have shown that VFSA typically converges significantly faster than other methods in the category, hence the name. Based on examples documented by Sen and Stoffa (1995), we chose an initial temperature of 10^{-3} units at the start of our waveform fitting process for each model parameter and allowed it to cool down to 10^{-10} units throughout the process. In our method, we allow each model parameter (velocity of the P-wave, V_p; velocity of the S-wave, V_s; thickness of the layer; and density) to vary within ±10% of initial values. We conducted trial runs with the model parameters varied within ±10%, ±15%, ±20%, and ±30%. Our results produced similar final models that were within one standard error. Additionally, a significant variation in model parameters is not realistic given the tectonic and geologic setting of the regions. Therefore, to maintain reasonable computational time and to allow variations that are more realistic, we vary the model parameters ±10%.

Below, we report results of waveform fitting for selected teleseismic earthquakes recorded in China and Canada. For the seismic stations that recorded better quality data overall, we show the waveform correlations for events recorded at that station, and also describe the interpretations of the uncertainty computations as an example. A comment on amplitude matches: The most successful match between synthetics and data would be one in which the synthetic waveform matched the data exactly – wiggle for wiggle. This is unrealistic for several reasons, including the fact that models used to compute synthetics are layered, isotropic, limited to ten to sixteen layers, and have fixed attenuation (Q) values. Further, the source time function is assumed to be Gaussian, and its focal mechanism is assumed to be correctly represented by Harvard's CMT solution. To minimize complexities in the source time function we avoid very large earthquakes. Given the uncertainties in model Q and focal mechanisms, which will largely control relative amplitudes of various phases, we focus our fitting criteria on matching each phase's arrival time, polarity, and pulse character. Fitting the amplitude of each phase, while desirable, is deemed to be of lesser importance.

Waveform Modeling Results

China

Based on our selection criteria, we analyze 129 earthquakes recorded at eleven permanent broadband seismic stations in China. The number of earthquakes recorded at each station range between 3 and 31. Figure 2 shows the locations of these seismic stations and the geographical distribution of the earthquakes analyzed. The stations encompass tectonic provinces such as the north and south China blocks, Tibetan plateau, and Tien Shan Mountains.

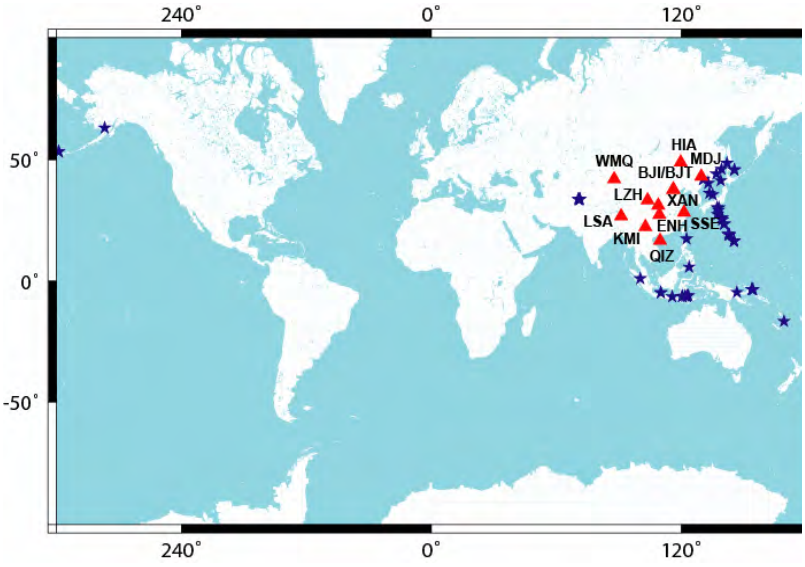

Figure 2. Map showing earthquakes analyzed in this study (blue stars) and the permanent broadband seismic stations in China (red triangles) that recorded them. The respective station codes are shown adjacent to location of each station.

Although all the events recorded at every station have been analyzed, work is ongoing to improve some of the modeling results. Therefore in this paper, we only present examples from those stations that show good waveform matches. Figure 3 shows examples of waveform fits of data from earthquakes recorded at seismic stations LSA, WMQ, and BJT. At all the seismic stations we observe and obtain good matches between data and synthetics generated by our modeling method for the direct S, Sp, and SsPmP phases. Except the direct S phase that we observe on both the components at all the stations, we note that the Sp phase is prominent on the vertical and radial components at LSA and WMQ but not on the radial component at BJT. Similarly, we observe the SsPmP phase on both components at LSA and WMQ but not on the vertical component at BJT. However, the SPL phase is only noted and well matched on the radial component at LSA. We confirm the presence of the SPL phase by analyzing the particle motion within the corresponding time window which turns out to be prograde elliptical.

Based on waveform fits obtained for each source-receiver pair we generate velocity models for each seismic station. However, the models generated for the same station using waveform fits from different earthquakes recorded at that

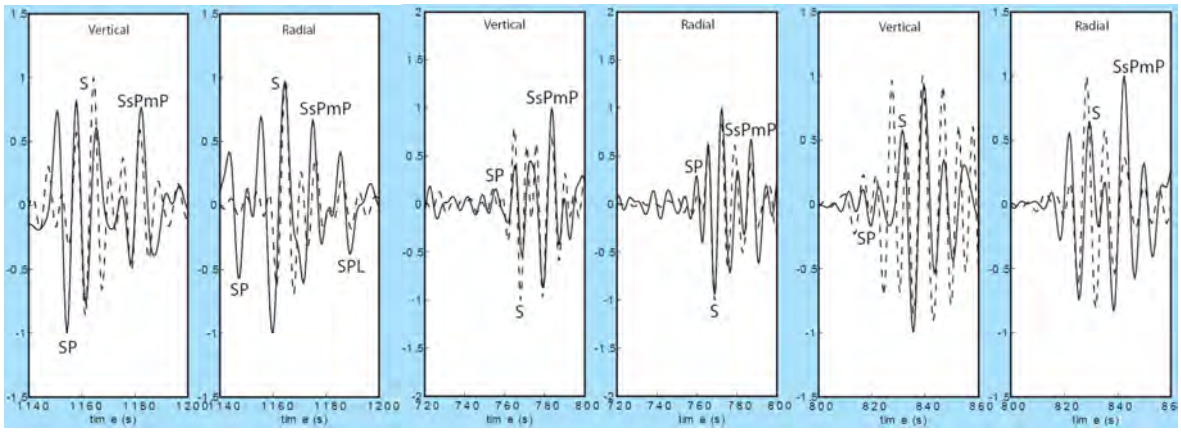

Figure 3. Vertical and radial component seismograms for example events recorded at LSA, WMQ, and BJT showing the observed (solid line) and synthetic (dashed line) waveforms. The correlated waveforms are indicated on the panels.

station, although similar, are not identical. To analyze which velocity model is more reliable we calculate the PPD and correlation matrices for the modeling results of each source-receiver pair. Here, we show examples of these statistical calculations from an event recorded at LSA (Figures 4a and b) and WMQ (Figures 4c and d).

Finally, in Figure 5 we show the velocity models for each seismic station in China that we have obtained from our modeling exercises so far. Wherever available we also show the models from an earlier study for comparison. Our models are consistent with regional tectonics and models obtained from earlier studies using receiver functions and seismic tomography. The crustal thicknesses beneath stations in north China block range between ~35 and 42 km with the crust in central part of the block near station BJT being thicker. However, within the north China block towards its western edge, the crust appears anomalously thick (~55 km) beneath station LZH. This region also coincides with the border of north China block and Tibetan plateau. The south China block consists of widely varying crustal thicknesses: ~37 km beneath station ENH in the northern part of the block and ~52 km beneath station KMI in the southern part, for example. The southern part of south China block near station KMI also coincides with its border with the Tibetan plateau, where the Moho is significantly deeper than elsewhere in China, implying a deep crustal root. Station LSA, in Lhasa, Tibet, has a crustal thickness of ~53 km. In Tien Shan Mountains in northwestern China, the crust is thicker than average (~42 km) but not as thick as that beneath the Tibetan plateau.

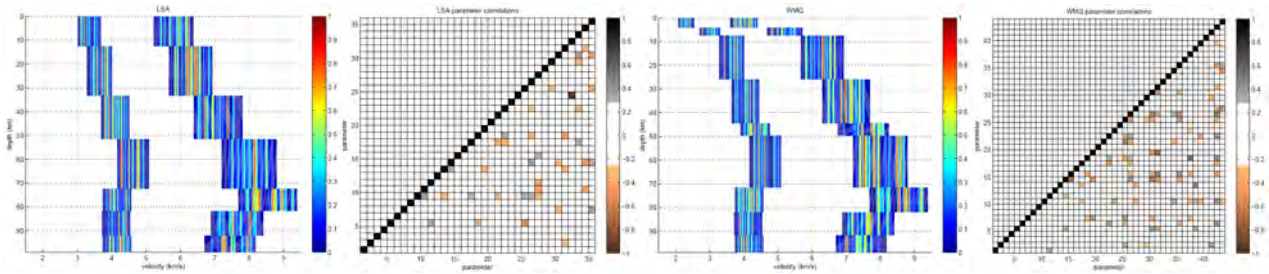

(a) (b) (c) (d)

Figure 4. PPD for example events recorded at (a) LSA and (c) WMQ. More peaked distributions indicate more uniqueness among different models and fewer trade-offs among model parameters. Model parameter correlation matrices for the same event at (b) LSA and (d) WMQ are also shown. Each small square represents a model parameter (Vp, Vs, thickness of layer, and density) on both axes. The correlations range between -1 and 1. Sparse colored squares off-diagonal indicate better constraints and greater confidence (fewer trade-offs) in those parts of the models. Note that LSA, where we observe and match the SPL phase, has fewer colored squares in the correlation matrix in the lower crust-upper mantle (b) compared to that at WMQ (d), suggesting that SPL improves constraints in those parts of the models.

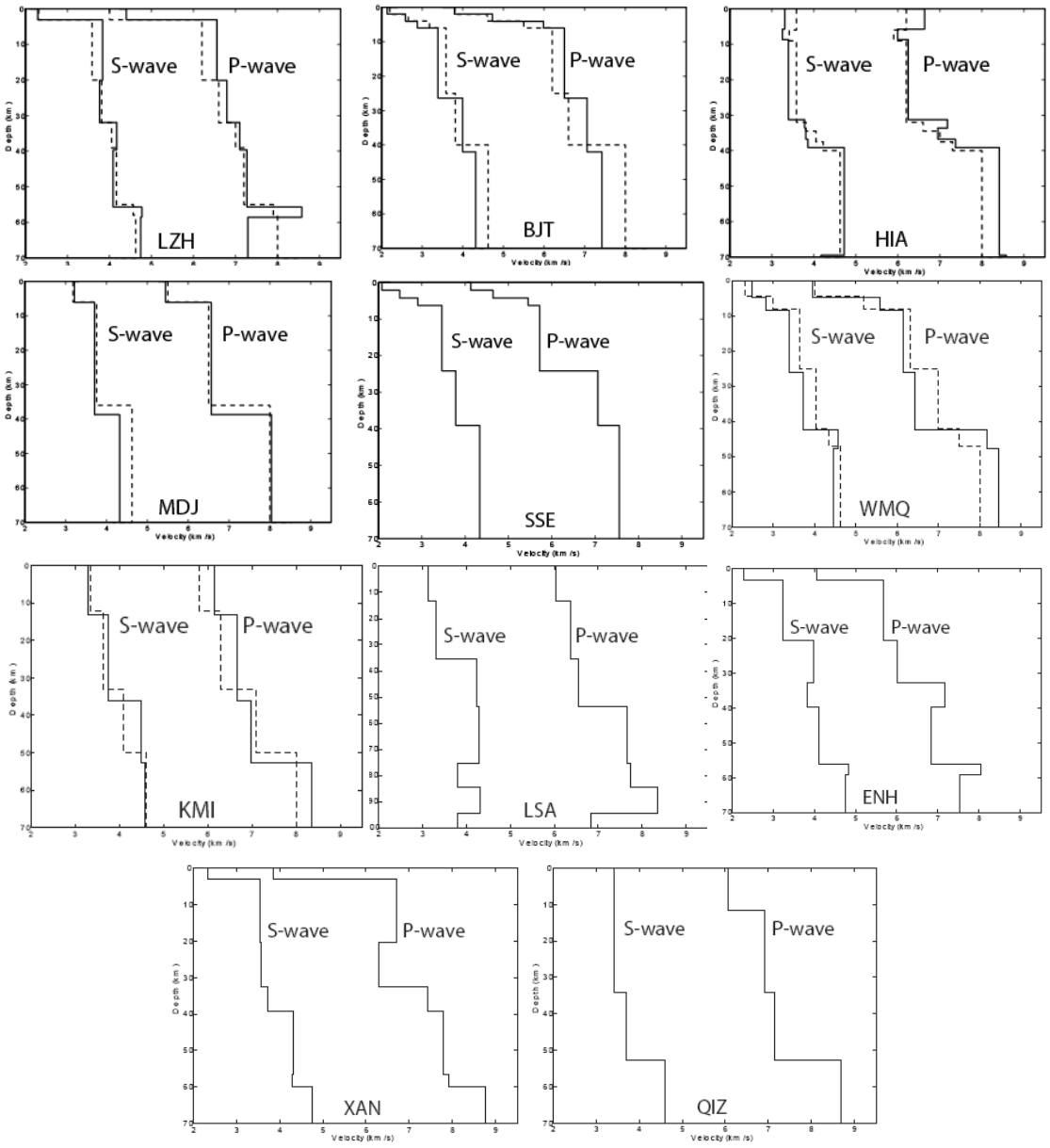

Figure 5. Obtained P- and S-wave velocity models (solid lines) for the eleven permanent broadband seismic stations in China. Station codes are indicated in each panel. The models (broken lines) in LZH, BJT, HIA, MDJ, WMQ, and KMI are from receiver function studies by Mangino et al. (1999).

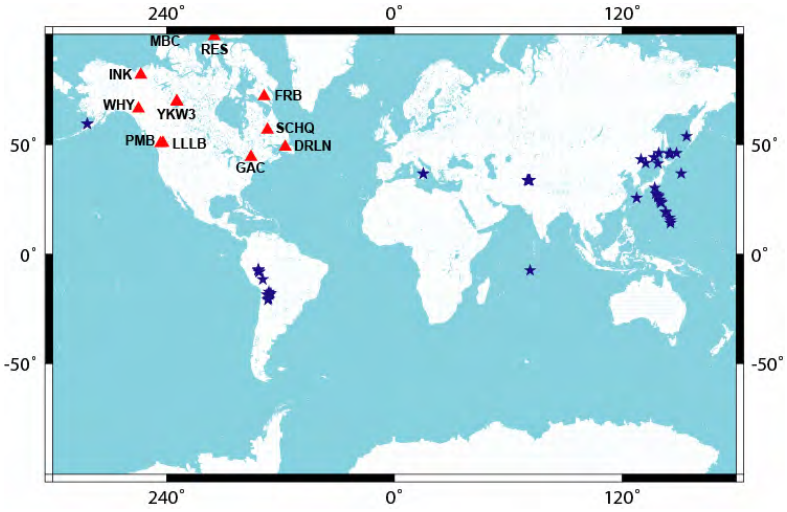

Figure 6. Map showing earthquakes analyzed in this study (blue stars) and the permanent broadband seismic stations in Canada (red triangles) that recorded them. The respective station codes are shown adjacent to location of each station.

Canada

In Canada we analyzed 137 earthquakes recorded at eleven permanent broadband seismic stations. Figure 6 shows the locations of these seismic stations and the geographical distribution of the earthquakes analyzed. The stations encompass tectonic provinces such as Cordilleran orogen, western plains and Slave province in western Canada, Grenville province and Appalachian orogen in eastern Canada, and the Canadian Arctic. In Figure 7 we show examples of waveform fits of data from earthquakes recorded at seismic stations INK, LLLB, and GAC. At all the seismic stations we observed and obtained good matches between data and synthetics of the direct S and SsPmP phases.

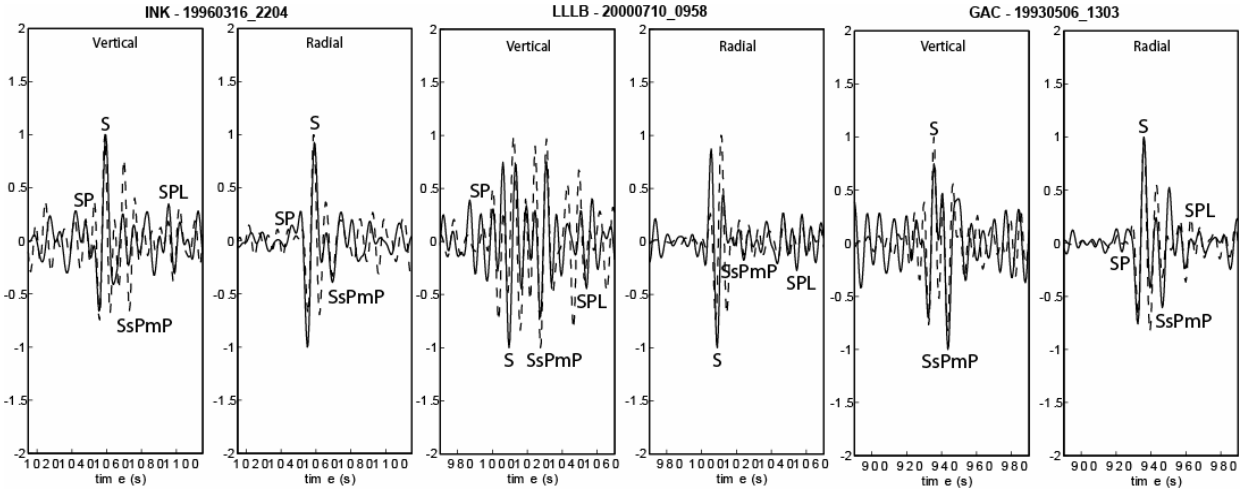

Figure 7. Vertical and radial component seismograms for example events recorded at INK, LLLB, and GAC showing the observed (solid line) and synthetic (dashed line) waveforms. The correlated waveforms are indicated on the panels.

We observed and matched the SP phase on both the components at INK but only on the vertical component at LLLB and the radial component at GAC. The SPL phase appears abundantly at the Canadian seismic stations, and we observed and obtained good matches on the vertical component at INK, both components at LLLB, and radial component at GAC. We confirmed our observation of the SPL phase by obtaining prograde elliptical particle motion diagrams that we show in Figure 8. As explained earlier, we also calculate the PPD and correlation matrix for each source-receiver pair. We show examples of these computations in Figure 9. In Figure 10 we present the final velocity models for each seismic station in Canada. Wherever available, we also show the earlier velocity models (Cassidy, 1995; Darbyshire, 2003) for comparison.

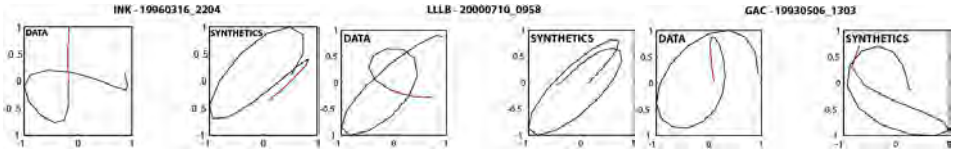

Figure 8. Particle motion diagrams for a time window of 8 seconds around the SPL phase on the data and synthetics for an event recorded at INK and 10 seconds at LLLB and GAC showing prograde elliptical motion diagnostic of the SPL phase. The red portions of the diagrams indicate beginning of the motion.

Our models beneath the Canadian seismic stations are consistent with earlier studies and regional tectonics (Figure 10). Crustal thicknesses beneath stations in the northern Cordilleran orogen, western plains, and Slave province range between 35 and 37 km. The Moho appears to be slightly shallower (31-35 km) beneath stations in the southern Cordilleran orogen. In eastern Canada, the crust beneath stations of the Grenville province and Appalachian orogen is generally thick (~44 km) with the exception of that beneath station DRLN, in the northeast, where it is ~33 km. Moho depths beneath stations in the Canadian Arctic range between ~35 and 42 km. We also observe low-velocity zones in the crust and uppermost mantle at some stations; however, the constraints on them are not strong. Taken together, the results provide a comprehensive snapshot of the velocity structure beneath Canada.

CONCLUSIONS

In this paper, we discuss a waveform fitting technique and demonstrate its application to determine 1-D, azimuthally dependent, crust and upper mantle P- and S-wave velocity structure beneath broadband seismic stations across China and Canada. Our models for both these regions are consistent with earlier models wherever available. Our method depends minimally on the initial model; we are able to compute synthetic seismograms that contain all possible phases for a prescribed source–receiver path and obtain direct estimates of the P- and S-wave velocities beneath the stations. Statistical tools incorporated in the technique allow us to assess uncertainties associated with our models and estimate trade-offs between model parameters in different layers. The use of the SPL phase as shown in the study, enhances our constraints for lower crust and upper mantle structure beneath the seismic stations.

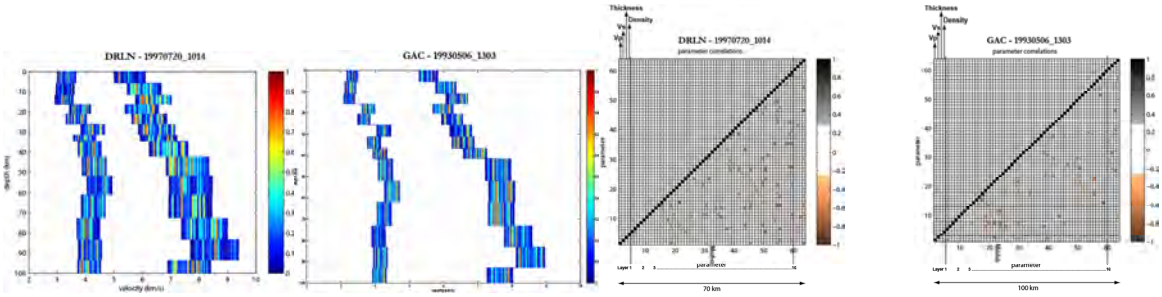

(a) (b) (c) (d)

Figure 9. PPD example events recorded at seismic stations (a) DRLN and (b) GAC. More peaked distributions indicate more uniqueness among different models and fewer trade-offs among model parameters. Model parameter correlation matrices for the same events at (c) DRLN and (d) GAC. Each small square represents a model parameter on both axes. The correlations range between -1 and 1. Sparse colored squares off-diagonal in the lower crust-upper mantle at GAC compared to that at DRLN indicate better constraints and fewer trade-offs in this part of the models. The examples again emphasize that the SPL phase when observed and well-matched better constrains the upper mantle.

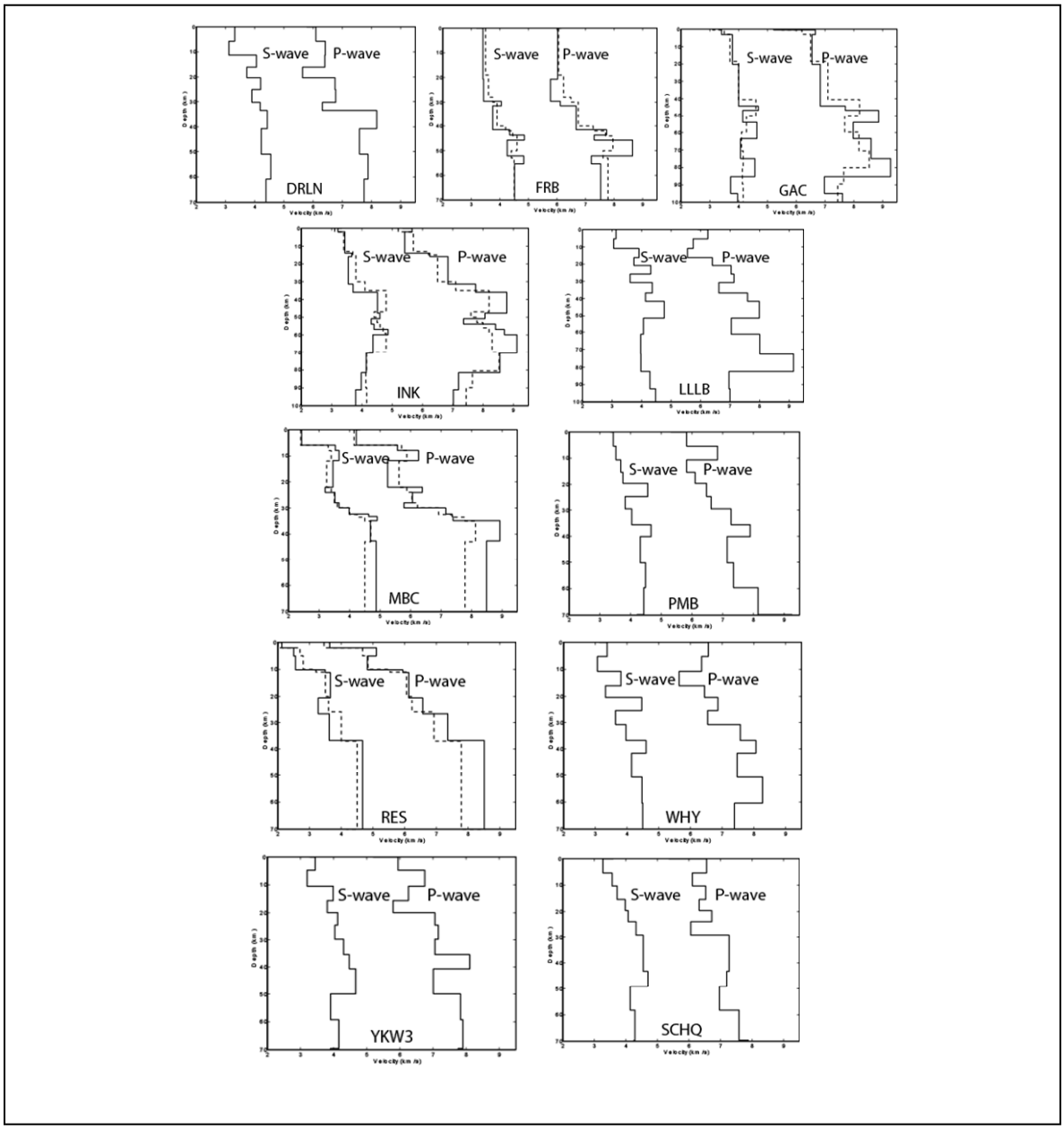

Figure 10. P- and S-wave velocity models (solid lines) for seismic stations in Canada. The P- and S-wave velocity models in FRB, MBC, and RES are from receiver function studies by Darbyshire (2003) and in GAC and INK are those from Cassidy (1995).

ACKNOWLEDGEMENTS

The archives of the Incorporated Research Institutions for Seismology (IRIS) provided data for this work.

REFERENCES

Ammon, C. J. (1991). The isolation of receiver effects from teleseismic P wave fronts, *Bull. Seismol. Soc. Am.* 81: 2,504–2,510.

Cassidy, J. F. (1995). A comparison of the receiver structure beneath stations of the Canadian National Seismic Network, *Can, J. Earth Sc.* 32: 938–951.

Darbyshire, F. A. (2003). Crustal structure across the Canadian High Arctic region from teleseismic receiver function analysis, *Geophys. J. Int.* 152: 372–391.

Dziewonski, A. M. and D. L. Anderson, D. (1981). Preliminary reference Earth model, *Phys. Earth Planet. Int.* 25: 297–356.

Frazer, L. N. (1977). Synthesis of shear coupled PL, Ph.D Thesis, Princeton Univ., Princeton, New Jersey, 54 pp.

Gangopadhyay, A., J. Pulliam, and M. K. Sen (2007). Waveform modeling of teleseismic S, Sp, SsPmP, and shear-coupled PL waves for crust- and upper mantle velocity structure beneath Africa, *Geophys. J. Int.*, doi:10.1111/j.1365-246X.2007.03470.x (in press).

Gropp, W. and E. Lusk (1995). Dynamic process management in an MPI setting, *7th IEEE Symposium on Parallel and Distributeed Processing,* p. 530.

Ingber, L. (1989). Very fast simulated reannealing, *Mathl. Comput. Modeling*, 12: 967–993.

Jordan, T. H. and L. N. Frazer (1975). Crustal and upper mantle structure from SP phases, *J. Geophys. Res.* 80: 1,504–1,518.

Kennett, B. L. N. (1983). Seismic wave propagation in stratified media, Cambridge University Press, 338 pp. Mangino, S., Priestley, K. & Ebel, J., 1999. The Receiver structure beneath the China Digital Seismograph stations, *Bull. Seis. Soc. Am.* 89: 1,053–1,076.

Owens, T. J., S. R. Taylor, and G. Zandt (1987). Crustal structure at regional seismic test network stations determined from inversion of broadband teleseismic P waveforms, *Bull. Seismol. Soc. Am.* 77: 631–662.

Pulliam, J. and M. K. Sen (2005). Assessing Uncertainties in Waveform Modeling of the Crust and Upper Mantle, in *Proceedings of the 27th Seismic Research Review:Ground-Based Nuclear Explosion Monitoring Technologies*, LA-UR-05-6407, Vol. 1, pp. 152–160.

Pulliam, J., M. K. Sen, and A. Gangopadhyay (2006). Determination of crust and upper mantle structure beneath Africa using a global optimization based waveform modeling technique, in *Proceedings of the 28th Seismic Research Review: Ground-Based Nuclear Explosion Technologies,* LA-UR-06-5471,Vol. 1, pp. 196–208.

Sen, M. K. and P. L. Stoffa, (1991). Non-linear one-dimensional seismic waveform inversion using simulated annealing, *Geophysics* 56: 1624–1638.

Sen, M. K. and P. L. Stoffa (1995). Global Optimization Methods in Geophysical Inversion, Elsevier Science Publishing Company, the Netherlands, 281 pp.

Sen, M. K. and P. L. Stoffa, (1996). Bayesian inference, Gibbs' sampler and uncertainty estimation in geophysical inversion, *Geophysical Prospecting* 44: 313–350.

Tarantola, A. (1994). *Inverse Problem Theory: Methods for Data Fitting and Model Parameter Estimation*, Elsevier, Amsterdam, the Netherlands, 600 pp.

SHORT PERIOD SURFACE WAVE DISPERSION ACROSS THE MEDITERRANEAN REGION: IMPROVEMENTS USING REGIONAL SEISMIC NETWORKS

Michael H. Ritzwoller[1], Yingjie Yang[1], Rachelle M. Richmond[1], Michael E. Pasyanos[2], Antonio Villaseñor[3], Vadim Levin[4], Rami Hofstetter[5], Vladimir I. Pinsky[5], Nadezda V. Kraeva[5], and Arthur Lerner-Lam[6]

University of Colorado at Boulder[1], Lawrence Livermore National Laboratory[2], Institute of Earth Sciences "Jaume Almera"—Barcelona[3], Rutgers University[4], Geophysical Institute of Israel[5], and Lamont-Doherty Earth Observatory[6]

Sponsored by National Nuclear Security Administration
Office of Nonproliferation Research and Development
Office of Defense Nuclear Nonproliferation

Contract Nos. DE-FC52-05NA26607[1] and W-7405-ENG-48[2]

ABSTRACT

We have begun to apply ambient noise surface wave tomography to broad-band seismic data obtained in Europe, North Africa, the Middle East, and Central Asia. The goal is to improve the calibration of surface wave propagation in aseismic areas. Ambient noise tomography (ANT) generates surface wave dispersion maps to periods as short as 6 across large areas and, therefore, provides new, high resolution constraints on crustal structures homogeneously over extended regions. Current work concentrates on the application of ANT in Europe where station coverage is highest, which allows improvements in the method to be made rapidly and transported elsewhere later.

In earlier work, we applied ambient noise tomography across Europe to one year of data from approximately 125 stations composing the Virtual European Seismic Network (VEBSN) (available from the ORFEUS Data Center) to produce Rayleigh wave group velocity maps from an 8–40 sec period. Current work builds on these results by using longer time series (to improve signal quality and provide measurement uncertainties) and assimilating data from temporary or emerging regional networks in the Mediterranean region to generate Rayleigh wave phase and group speed maps across Europe with better resolution and reliability. The study concentrates on improvements in three focus areas where regional array data are available: (1) the western Mediterranean, particularly the Iberian Peninsula, (2) the central Mediterranean, notably Italy and Switzerland, and (3) the eastern Mediterranean, including Israel, Syria, and Turkey. The western Mediterranean results are based on the Spanish National Network data, which provides much tighter constraints on the crustal structures of the Iberian Peninsula. In the Central Mediterranean, the RETREAT and CAT-SCAN Program for the Array Seismic Studies of the Continental Lithosphere (PASSCAL) experiments yield data that improve resolution in this area considerably. In the eastern Mediterranean, the Israeli DESERT2000 experiment and the Eastern Turkey PASSCAL experiment were performed simultaneously for an extended time period and, together with other regional stations, greatly improve ray coverage in the region.

We present Rayleigh wave group and phase speed measurements with associated uncertainties (where time series are sufficiently long) and dispersion maps in two of the three focus regions. Resolution and the retrieval of geologically correlated features on the dispersion maps are significantly improved using the regional data.

OBJECTIVE

The goal of this research is to develop a new method to obtain surface wave dispersion measurements based on ambient seismic noise and to produce a new data set of inter-station group and phase velocity measurements. These new data are used to produce group and phase velocity dispersion maps, particularly at periods below about 25 sec.

RESEARCH ACCOMPLISHED

Introduction

Surface wave empirical Green functions (EGFs) can be determined from cross-correlations between long time sequences of ambient seismic noise observed at different stations. The feasibility of the method was first established by experimental (e.g., Weaver and Lobkis, 2001; Lobkis and Weaver , 2001; Derode et al., 2003; Larose et al., 2004, 2005) and theoretical (e.g., Snieder, 2004; Wapenaar, 2004) studies. Shapiro and Campillo (2004) demonstrated that Rayleigh wave EGFs estimated from ambient noise possess dispersion characteristics similar to earthquake derived measurements and model predictions. Bensen et al. (2007a) describe the ambient noise data processing procedure in detail. The dispersion characteristics of surface wave EGFs derived from ambient noise have been measured and inverted to produce surface wave tomography maps in several regions, such as Southern California (Shapiro et al., 2005; Sabra et al., 2005; Gerstoft et al., 2006), the western US (Moschetti et al., 2007; Lin et al., 2007b), Europe (Yang et al., 2007), Tibet (Yao et al., 2006), New Zealand (Lin et al., 2007a), Korea (Cho et al., 2007), Spain (Villaseñor et al., 2007) and elsewhere. Ambient noise tomography has also been employed on a continental scale in Europe (Yang et al., 2007) and the US (Bensen et al., 2007b). Most of these studies obtained Rayleigh wave group velocity maps at periods below a 20 sec period, but longer period maps at periods of up to 70 sec (e.g., Yang et al., 2007; Bensen et al., 2007b), phase velocity maps (e.g., Yao et al., 2006; Lin et al., 2007b), and Love wave maps (e.g., Lin et al., 2007b) have also been developed.

Three publications have resulted from the research supported by this contract: Bensen et al. (2007a), Yang et al. (2007), and Villasenor et al., (2007). Bensen et al. (2007a) describes the data processing procedure that has been developed under this contract. The first ambient noise tomography of the Mediterranean region and Europe was performed by Yang et al. (2007) using one year of continuous seismic data taken predominantly from the VEBSN obtained from the Orfeus Data Center in Europe. Attempts to refine the maps of Yang et al. (2007) are based on utilizing regional and national network data that tend not to be available from the major international data centers such as the Incorporated Research Institutions for Seismology's Data Management Center (IRIS-DMC) or the Orfeus Data Center. A proof-of-concept study was performed using four months of data from the Spanish National Network and results appear in Villaseñor et al. (2007).

The focus of this paper is to report on further attempts to improve upon the first tomographic images provided by Yang et al. (2007) by extending results to phase velocities, improving resolution by introducing more seismic stations predominantly from regional networks and temporary installations, and improving the reliability of the measurements and uncertainty estimates by using longer time series. Because the available stations change over time, optimal improvements depend on using data from several years. We currently are working to process data from European seismic stations acquired from various sources recorded during the years 2000–2006. Differences in stations operating in 2000–2001 and 2005–2006 are shown in Figure 1. Regional networks such as the Spanish National Network and PASSCAL experiments are important resources. The earlier time periods are important for resolution in the eastern Mediterranean and parts of the Middle East.

State of Ambient Noise Data Processing

The ambient noise data processing procedure is described by Bensen et al. (2007a) in detail, but is summarized here briefly. All data are processed on a daily basis and then are stacked (superposed and added together) later to achieve cross-correlations over arbitrarily long time series currently ranging up to two years. The mean, trend, and instrument response of the daily three-component (E, N, Z) seismograms are removed and the resulting waveforms are band-pass filtered between periods of 5 sec and 100 sec. We now compute the full cross-correlation tensor and

not just vertical-vertical cross-correlations. To speed up the process, we do not rotate the components into the radial (R) and transverse (T) directions for each station-pair until the component cross-correlations (E-E, E-N, N-N, N-E) are performed. Earthquake signals and instrumental irregularities are then removed by temporal normalization. In order to postpone the component rotation until after cross-correlation, the East and North components are temporally normalized together. To achieve this, both components are band-pass filtered between 15 sec and 50 sec, a band that contains the most energetic surface wave signals from earthquakes. For each time point, the mean of the absolute value of each seismogram is computed in the 128 sec window centered on that point. The values of the East and North components are compared, and the larger is used to define the inverse weight for that time point. That weight is then applied to both the North and East component time-series, band-passed between 5 sec to 100 sec. This process effectively suppresses earthquake signals and maintains the linearity of the rotation operator. After temporal normalization, the signals are whitened in frequency. Before whitening, ambient noise is most energetic in the microseism bands below 20 sec period. Frequency whitening is carried out to broaden the period band of the dispersion measurement. Again, to maintain the linearity of the rotation operator, the East and North signals are whitened together. Because the spectra of both components are similar, on average, we do this by simply weighting the East and North signals in the frequency domain by the inverse of the smoothed East spectrum. Other methods, such as weighting by the mean of the two spectra or their product, produce similar results. We then stack all available daily cross-correlations for each component and station-pair in order to enhance the signal-to-noise ratio (SNR). Because all of these processes are linear in the rotation operator, the transverse-transverse, transverse-radial, radial-radial, and radial-transverse cross-correlations between each station-pair can be calculated by a linear combination of those four components. The resulting cross-correlations can be converted to Empirical Green's functions by introducing an additive phase factor (Lin et al., 2007b).

Examples of vertical component cross-correlation record sections are shown in Figure 2. Figure 2a is based on four months of ambient noise data from the Spanish National Network. Figure 2b is from 12-month time series centered on a station in central Italy. The arrivals near zero cross-correlation lag are not interpreted in this study, and their origin remains unknown. We believe that they result from the conversion of ocean waves to mantle propagating P-waves in the European Arctic. They are observed elsewhere across Eurasia, and understanding their generation and nature requires further effort. They do not, however, interfere with the fidelity of the surface wave dispersion measurements.

Yang et al. (2007) processed one year of data from 2004 taken from about 120 stations available from the Orfeus Data Center in Europe. Station coverage was similar to the red symbols shown in Figure 1a.

Improvements over the results of Yang et al. (2007) derive from three factors. First, we will use longer time series, two years of data, which will allow the computation of better measurement uncertainties. Uncertainties are computed from repeating the measurements in different seasons. Second, there are data resources in Europe, North Africa, and the Middle East that were not used by Yang et al. These include national networks such as the Spanish National Network and the Israeli DESERT2000 experiment, PASSCAL experiments such as the RETREAT and CAT-SCAN experiments in Italy and Eastern Turkey and Northern Anatolian Fault (ANF) experiments in Turkey, as well as other temporary deployments such as the Mid-Sea Experiment and the Carpathian Basin Project (CBP) in Austria and Hungary. We are now in the process of acquiring and beginning to process these data. Focus is being placed on three regions: (1) the western Mediterranean, (2) the central Mediterranean, and (3) the eastern Mediterranean. Third, we have extended the measurements to include phase velocities. Lin et al. (2007b) show that phase velocity measurements are more repeatable than group velocities and, thus, have lower uncertainties.

Western Mediterranean: Villaseñor et al. (2007) computed cross-correlations between stations within the Spanish National Network (SNN) during July, August, September, and October of 2005. Initially, only group velocity tomography maps were obtained, but we have subsequently measured phase velocities from these data. Additionally, group and phase speed measurements were obtained from cross-correlations between VEBSN and GEOFON stations on the Iberian Peninsula (available from Orfeus and IRIS, respectively) operating from April 2004 to March 2005.

Central Mediterranean: We have augmented the data processing performed by Yang et al. (2007) by computing cross-correlations and obtaining group and phase velocities from one year of continuous data (April 2004–March 2005) using the RETREAT and CAT/SCAN PASSCAL experiments in Northern and Southern Italy, the VEBSN,

and MEDNET station data available from IRIS. The addition of data from the two PASSCAL experiments in Italy significantly improves upon the initial results found by Yang et al. (2007).

The Eastern Mediterranean/Middle East: We are currently processing data from stations that operated during 2000 and 2001. This data set includes stations from the Eastern Turkey (PASSCAL) Seismic Experiment, the DESERT2000 experiment in Israel, and stations available from IRIS in Western Turkey and Crete.

Current Status: Example Group and Phase Velocity Maps

Figures 3 and 4 present examples of the current state of the group and phase velocity maps across the region of study. The tomographic method of Barmin et al. (2001) has been used. One aspect of this method is that outside the region of high path coverage, the maps revert to the average of the measurements. Thus, the periphery of all of the maps are white because in these regions there are few ray paths. Tomography is performed on a 1 deg $\times$ 1 deg grid over the region of study. Figure 5 is a map of sedimentary and crustal thicknesses taken from CRUST2.0, for comparison.

In Figure 3, low velocities on the 10 sec maps reveal the location of major sedimentary basins. The Po Basin in Italy, the North Sea Basin, the Silesian Basin in northern Germany and Poland, the Tyrrhenian and Adriatic Basins surrounding Italy, and the Valencia Trough east of Spain are some examples. The Valencia Trough and the Sub-Pyrenees Basin are seen better in Figure 4. At a 25 sec period, the maps reveal information about vertically integrated crustal shear velocities and crustal thickness (the latter particularly in phase velocities that sample deeper than group velocities). Low velocities are associated with thicker crust. Thus, there are low velocities beneath the Betic Mountains in southern Spain, the Alps, the Carpathians, the Dinarides in the Balkans, and the Apennines along the spine of Italy. The Hellenic Arc also appears as low velocities, but probably not because of particularly thick crust there.

Expected Continued Improvements

Figure 6 shows how path coverage has improved with the addition of measurements obtained in Spain using the Spanish National Seismic Network and data from two PASSCAL experiments in Italy (RETREAT, CAT/SCAN). Nevertheless, the high-resolution (non-white) regions of the maps in Figures 3 and 4 are mainly within continental Europe. Our goal is to improve data coverage in the Mediterranean Sea, North Africa, and parts of the Middle East.We plan to continue to improve the data set in each of the three regions by increasing the number of stations, and increasing the time duration of ambient noise analysis.

(1) We will improve upon the initial results of Villaseñor et al. (2007) by increasing the time duration of analysis of the Spanish National Network from four months to two years (2005 and 2006). Additionally, we will include in our analysis data from VEBSN, IRIS, MEDNET and other stations operating in Europe during this time period. By tying the Spanish National Network data to VEBSN and other stations, resolution in the western Mediterranean will be improved dramatically.

(2) To improve ray path coverage and resolution in the central Mediterranean we will compute cross-correlations between stations operating during 2005 and 2006, which includes the RETREAT and CAT/SCAN PASSCAL experiments in Italy and the Spanish National Network, as well as VEBSN and other stations located in this region (Fig 1b). These data will result in additional ray coverage across the Mediterranean Sea between Italy and the Iberian Peninsula and between Italy and the Hellenic Arc.

(3) Cross-correlations between stations operating during the years 2000 and 2001 from the Eastern Turkey Seismic Experiment, the DESERT2000 experiment in Israel, and stations available from IRIS in Western Turkey and Crete will yield improved resolution across Turkey, Syria, Israel, and the Eastern Mediterranean.

CONCLUSIONS

Three studies supported by this contract have already been published. Bensen et al. (2007a) described ambient noise data processing in detail and Yang et al. (2007) performed ambient noise tomography for Rayleigh wave group velocities using observatory data in Europe that was performed between 10 sec and 40 sec. In addition, assimilation of regional data by Villaseñor et al. (2007), notably using the Spanish National Network, established the ability of such data to improve resolution at short periods (6–20 sec) when used in concert with observatory data. Further data processing using PASSCAL experimental data in Italy has established similar results in the central Mediterranean region, and the data processing methodology has been extended to include phase velocities. In the near future, more regional data will be assimilated into the inversion to improve data coverage and resolution across much of the Mediterrean Sea, in particular in the eastern Mediterrean, including parts of the Middle East and North Africa.

ACKNOWLEDGMENTS

Most of the data used in this research were downloaded either from the IRIS DMC or the Orfeus Data Center. In addition to observatory data, data were obtained from the Spanish National Seismic Network and from two PASSCAL experiments, RETREAT and CAT/SCAN.

REFERENCES

Barmin, M., M. Ritzwoller, and A. Levshin (2001). A fast and reliable method for surface wave tomography, *Pure Appl. Geophys.* 158: 1351–1375.

Bensen, G. D., M. H. Ritzwoller, M. P. Barmin, A. L. Levshin, F. Lin, M. P. Moschetti, N. M. Shapiro, and Y. Yang (2007a). Processing seismic ambient noise data to obtain reliable broad-band surface wave dispersion measurements, *Geophys. J. Int.* 169: 1239–1260.

Bensen, G. D., M. H. Ritzwoller, and N. M. Shapiro (2007b). Broad-band ambient noise surface wave tomography across the United States, *J. Geophys. Res.* (submitted).

Cho, K., R. Herrmann, C. Ammon, and K. Lee (2007). Imaging the upper crust of the Korean Peninsula by surface-wave tomography, *Bull. Seism. Soc. Am.* 97(1B): 198–207.

Derode, A., E. Larose, M. Campillo, and M. Fink (2003). How to estimate the Green's function of a heterogeneous medium between two passive sensors? Application to acoustic waves, *Appl. Phys. Lett.* 83: 3054–3056.

Gerstoft, P., K. Sabra, P. Roux, W. Kuperman, and M. Fehler (2006). Green's functions extraction and surface-wave tomography from microseisms in southern California, *Geophys.* 71: 123–131.

Larose, E., A. Derode, M. Campillo, and M. Fink (2004). Imaging from one-bit correlations of wideband diffuse wave fields, *J. Appl. Phys.* 95: 8393–8399.

Larose, E., A. Derode, D. Clorennec, L. Margerin, and M. Campillo (2005). Passive retrieval of Rayleigh waves in disordered elastic media, *Phys. Rev. E.* 72: 46,607.

Lin, F., M. H. Ritzwoller, J. Townend, M. Savage, and S. Bannister (2007a). Ambient noise Rayleigh wave tomography of New Zealand, *Geophys. J. Int.* doi:10.1111/j.1365-705 246X.2007.03414.

Lin, F., M. P. Moschetti, and M. H. Ritzwoller (2007b). Surface wave tomography of the western United States from ambient seismic noise: Rayleigh and Love wave phase velocity maps, *Geophys. J. Int.* (submitted).

Lobkis, O. I. and R. L. Weaver (2001). On the emergence of the Green's function in the correlations of a diffuse field, *J. Acous. Soc. Am.* 110: 3011–3017.

Moschetti, M. P., M. H. Ritzwoller, and N. M. Shapiro (2007). Surface wave tomography of the western United States from ambient seismic noise: Rayleigh wave group velocity maps, *Geochem. Geophys. Geosys.* (in press).

Sabra, K. G., P. Gerstoft, P. Roux, W. Kuperman, and M. C. Fehler (2005). Surface wave tomography from microseisms in Southern California, *Geophys. Res. Lett.* 32: 717, 14,311–14,314.

Shapiro, N. and M. Campillo (2004). Emergence of broadband Rayleigh waves from correlations of the ambient seismic noise, *Geophys. Res. Lett.* 31: 1615–1619.

Shapiro, N. M., M. Campillo, L. Stehly, and M. H. Ritzwoller (2005). High-resolution surface-wave tomography from ambient seismic noise, *Science* 307: 1615–1618,

Snieder, R. (2004). Extracting the Green's function from the correlation of coda waves: A derivation based on stationary phase, *Phys. Rev. E.* 69: 46,610–46,624.

Villaseñor, A., Y. Yang, M. H. Ritzwoller, and J. Gallart (2007). Ambient noise surface wave tomography of the Iberian Peninsula: Implications for shallow seismic structure, *Geophys. Res. Lett.* 34: doi:10.1029/2007GL030164.

Wapenaar, K. (2004). Retrieving the elastodynamic Green's function of an arbitrary in-homogeneous medium by cross correlation, *Phys. Rev. Lett.* 93: 254, 301.

Weaver, R. L., and O. I. Lobkis (2001). On the emergence of the Green's function in the correlations of a diffuse field, *J. Acoust. Soc. Am.*110: 2011–3017.

Yang, Y., M. Ritzwoller, A. Levshin, and N. Shapiro (2007). Ambient noise Rayleigh wave tomography across Europe, *Geophys. J. Int.* 168: 259–274.

Yao, H., R .D. van der Hilst, and M. V. De Hoop (2006). Surface wave array tomography in SE Tibet from ambient seismic noise and two-station analysis: I-Phase velocity maps, *Geophys. J. Int.* 166: 732–744.

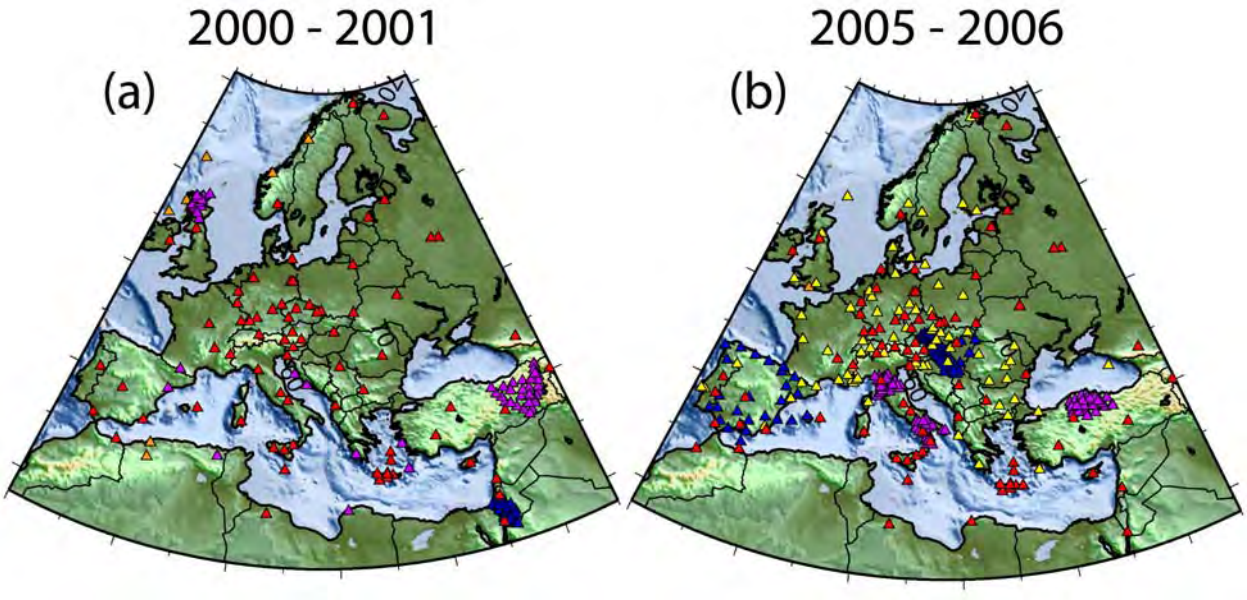

Figure 1. Contrast in station coverage in the years 2000–2001 versus 2005–2006. The station color code is as follows: BLUE—regional networks (e.g., Spanish National Network, the Israeli DESERT2000 experiment); RED—other data available through IRIS; YELLOW—VEBSN data available from the Orfeus Data Center in Europe; PURPLE—PASSCAL experiments or other European PASSCAL-like deployments (such as the MIDSEA experiment); ORANGE—SeisUK stations.

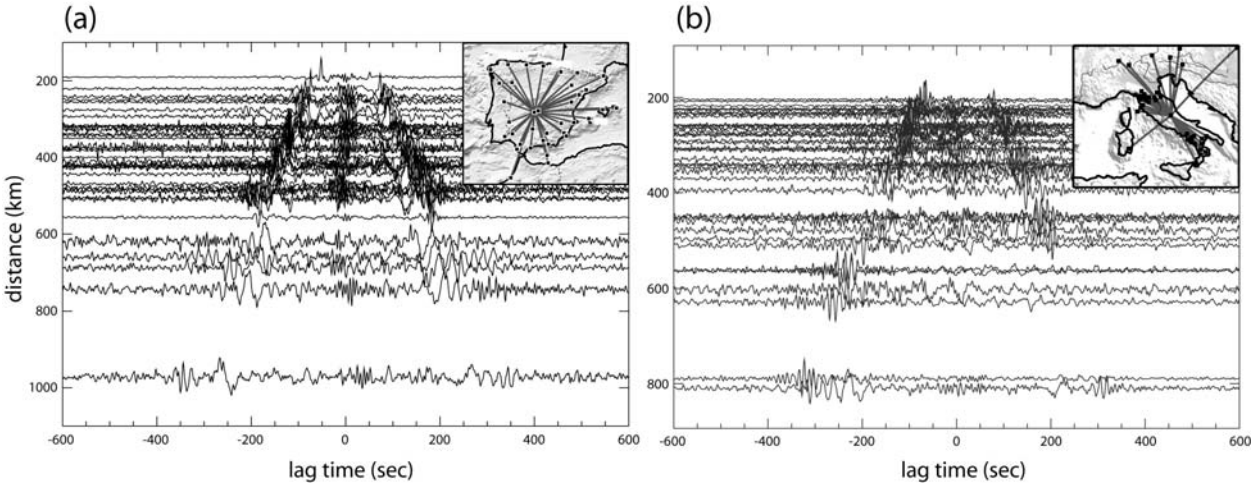

Figure 2. Record sections. (a) From the Spanish National Network. Cross-correlations are from 4 months of data. (b) From stations around Italy. Cross-correlations are from one year of data.

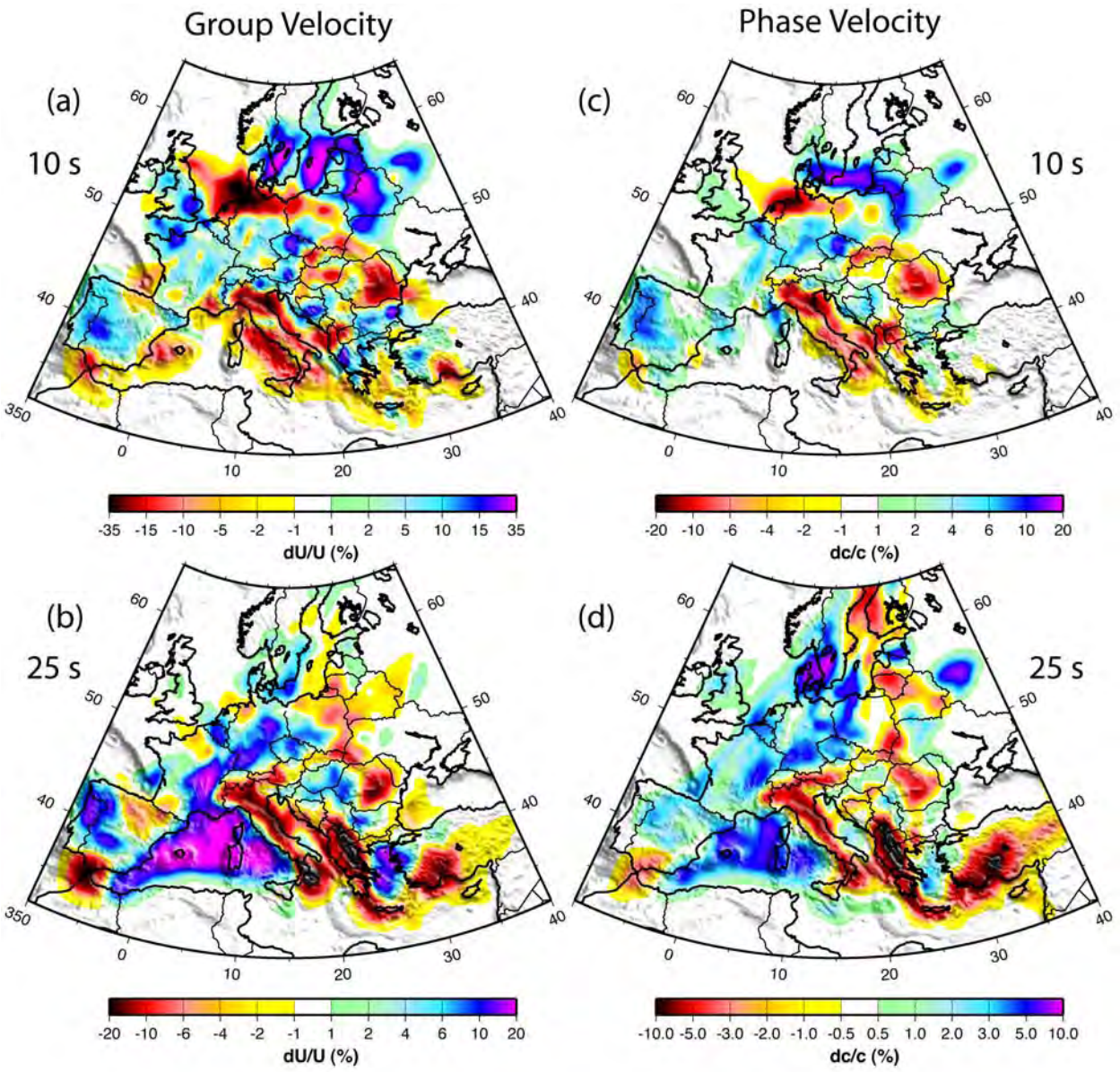

Figure 3. Examples of the current status of Rayleigh wave group and phase velocity maps across Europe. Phase velocities appear in the left column and group velocities in the right column. Maps at a 10 sec period are in the top row and at a 25 sec period in the bottom row.

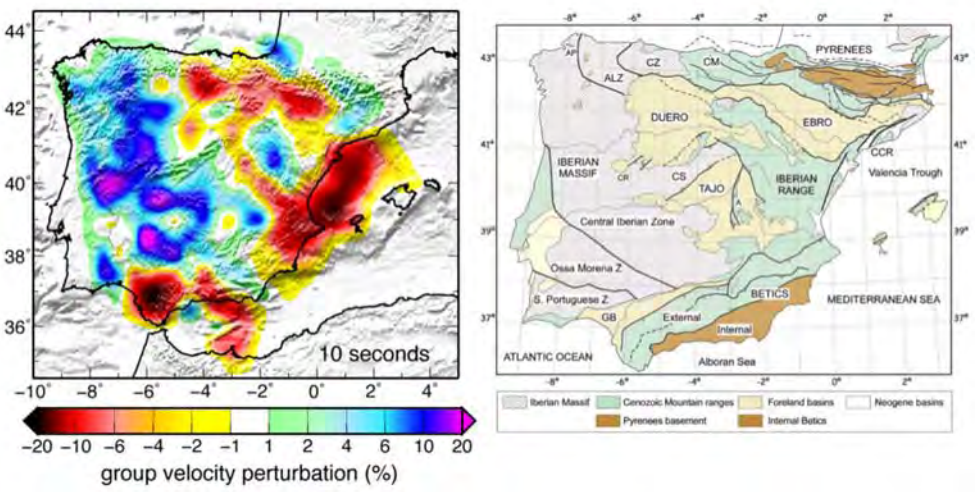

Figure 4. Rayeigh wave 10 sec group velocity map across Spain presented with a tectonic map for comparison. Low velocities are associated with the sub-Pyrenees Basin and the Valencia Trough off-shore. High velocities in the west are associated with the Paleozoic Iberian Massif and the Iberian Range is also correlated with high velocities at this period.

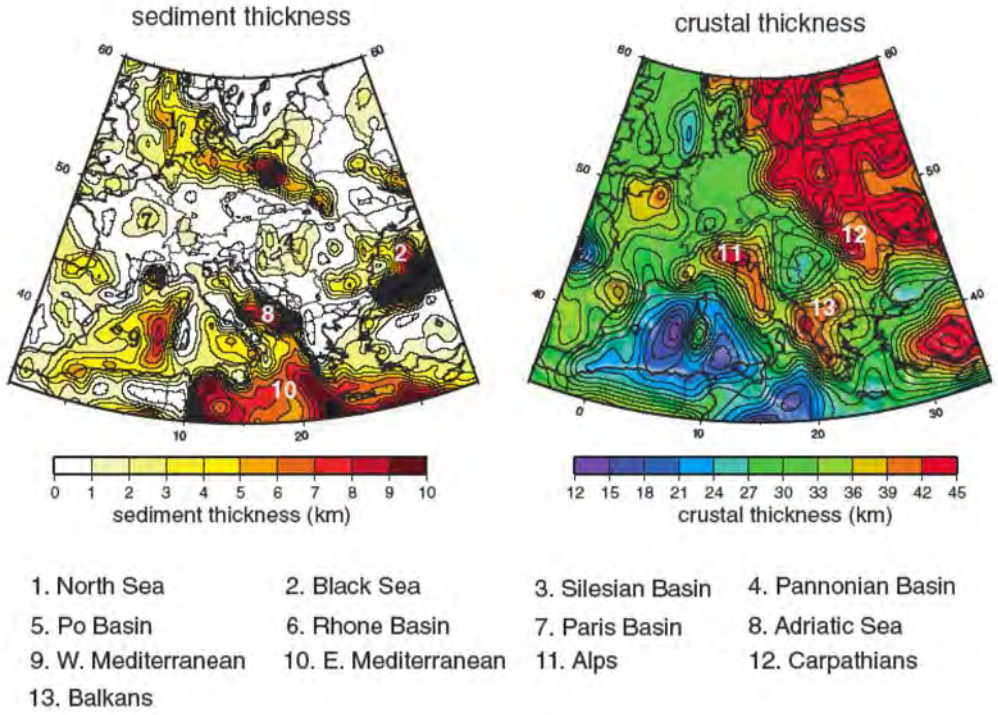

Figure 5. Sediment thickness and crustal thickness presented for comparison with Figure 4. Values taken from CRUST2.0.

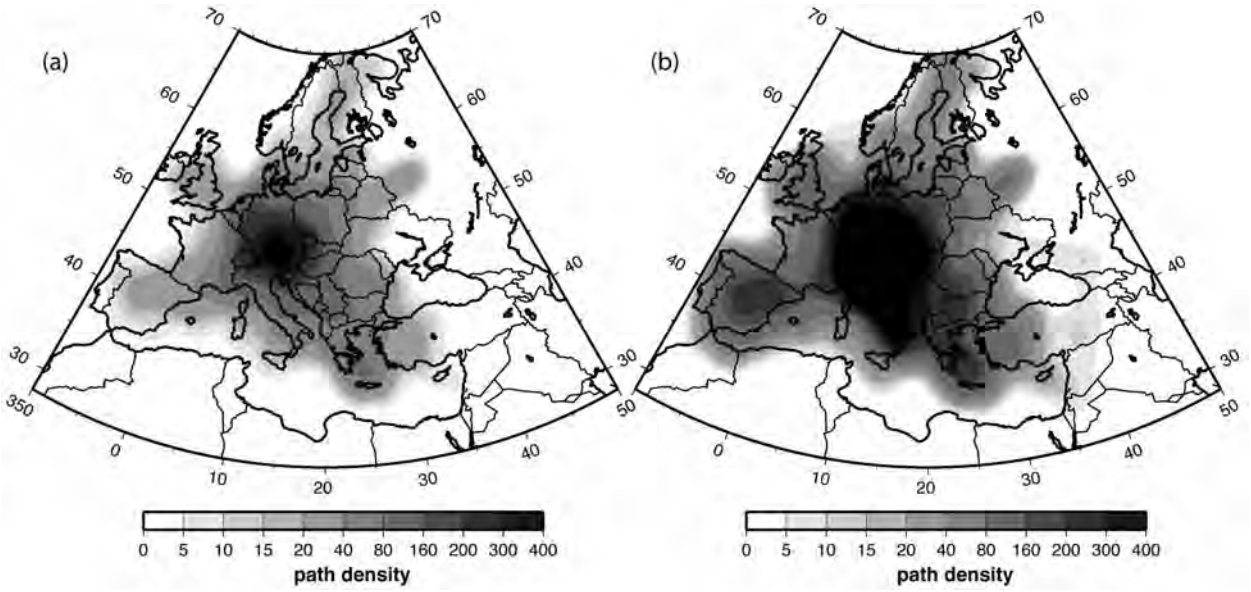

Figure 6. Path density. (a) From the study of Yang et al. (2007). (b) Current state of path density, showing improvements in Spain, central Europe, Italy and the central Mediterranean from recent data processing. Path density is defined as the number of paths intersecting a local 2 deg × 2 deg cell. Addition of more data from other regional networks will improve path density across the entire Mediterranean, particularly in the eastern Mediterranean and parts of the Middle East.

SASIA3D: A 3-D CRUST AND UPPER-MANTLE VELOCITY MODEL OF SOUTH ASIA DERIVED FROM JOINT INVERSION OF P-WAVE TRAVEL TIMES AND SURFACE-WAVE DISPERSION DATA

William L. Rodi[1] and Delaine T. Reiter[2]

Massachusetts Institute of Technology, Earth Resources Laboratory[1] and Weston Geophysical Corp.[2]

Sponsored by Air Force Research Laboratory

Contract No. FA8718-04-C-0027

ABSTRACT

Accurate travel-time predictions for regional seismic phases are essential for locating small seismic events with the accuracy needed for nuclear monitoring decisions. Travel times calculated through a three-dimensional (3-D) Earth model have the best chance of achieving acceptable prediction errors, if the model is constrained by sufficient data. With this motivation, we have developed a self-consistent 3-D *P* and *S* velocity model of the crust and upper mantle in a large region of southern and central Asia to a depth of approximately 400 km. The new model, which we are calling *SAsia3D*, is the result of a nonlinear, joint body-wave/surface-wave inversion method applied to *Pn* travel times collected from the Engdahl, van der Hilst and Buland (EHB) bulletin and group-velocity measurements provided by groups at the University of Colorado and Lawrence Livermore National Laboratory. Consistency between the *P* and *S* velocities is achieved by imposing bounds on Poisson's ratio and by invoking a regularization constraint that correlates variations in *P* and *S* velocity from an initial model. We have begun validating *SAsia3D* through relocation of ground-truth events in the study area using regional phase arrivals. The location validation exercises indicate that in many cases our 3-D model achieves excellent epicentral accuracy. Most notably, *SAsia3D* performs well when both regional *P* and *S* phase arrivals are included in the location. The regional *P/S* locations obtained with *SAsia3D* are frequently superior to the locations obtained with a large set of teleseismic and regional *P* arrivals and the AK135 reference model.

OBJECTIVES

The development and validation of accurate 3-D velocity models of the crust and upper mantle for regions of nuclear monitoring interest remain important goals for nuclear monitoring organizations. Systematic biases caused by inadequately modeled Earth structures cause errors in the estimation of geophysical parameters such as the travel times and amplitudes of regional seismic phases. More accurate and reliable estimates of these quantities (especially in aseismic regions) will improve nuclear monitoring efforts to detect, locate and discriminate regional events. Therefore, we have developed a joint 3-D inversion technique that incorporates both compressional-wave travel times and Rayleigh-wave group velocity measurements to determine the full *P* and *S* velocity structure of the crust and upper mantle.

In this paper we report on the development of a new model, *SAsia3D*, derived from data observed in the broad region shown in Figure 1. This region, extending from 10°–50° N and 40°–110° E, covers some of the most tectonically complex areas on Earth.

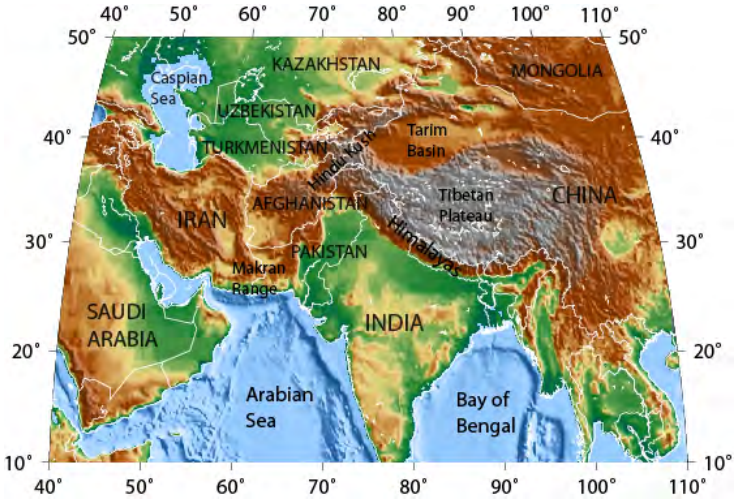

Figure 1. Topographic map of study region, which encompasses most of central and southern Asia, as well as portions of the Middle East.

RESEARCH ACCOMPLISHED

Body-wave (Travel-Time) and Surface-Wave (Rayleigh Dispersion) Data Sets

Compressional-wave travel-time database

The travel times we use in the *P*-wave tomography are taken from the EHB bulletin (Engdahl et al., 1998). We extracted arrivals from 1988–2004 having event and station locations within 0°–60°N, 30°–120°N and event depths between 0 and 200 km, including only first-arriving phases denoted *Pg*, *Pb* or *Pn* and which were defining phases for the EHB locations. To ensure small epicentral mislocations in the events, we required the secondary azimuth gap for a given event to be less than or equal to 130º (Bondár et al., 2004) and the number of teleseismic arrivals to be at least 15. The data set satisfying these criteria comprised 124,080 arrivals from 6,079 events and 735 stations.

We compressed this data set by forming summary events on a regular grid having 0.5° spacing in latitude and longitude and containing 13 nodes in depth between 0 and 200 km, with the depth spacing per node increasing from 5 to 20 km. For each summary-event node and each station/phase type, a summary travel-time residual (relative to the AK135 Earth model) was formed by averaging the individual residuals for the events near that node. Following this compression, stations containing fewer than 25 arrivals were dropped from the data set. The use of summary events acknowledges the redundant sensitivity of individual data to the Earth model (which is on 1° grid) and, combined with the station-dropping rule, reduces the ray-tracing requirements for the inversion substantially.

The final database used in the body-wave tomography contained 76,355 arrivals for 2,998 summary events and 438 stations. The data spanned epicentral distances to 18.7 degrees, and the travel-time residuals (relative to AK135) ranged from –8.0 to 8.8 s with a root-mean-square (RMS) residual error of 2.5 s. The path coverage for the travel-time database is shown on the left in Figure 2; it demonstrates that we have excellent coverage for nearly our entire study region, with the exception of the eastern tip of Saudi Arabia, where there is low seismicity and a lack of station coverage.

Surface-wave dispersion database

The surface-wave dispersion database was collected from several sources, but primarily consists of measurements made by the University of Colorado at Boulder (CUB) group (Ritzwoller and Levshin, 1998) and the Lawrence Livermore National Laboratory (Pasyanos, personal communication). Some measurements in the region were also made by the Weston Geophysical internal group. To eliminate potential outliers in the data set, we performed a period-by-period grooming of the data, in which we retained a group velocity measurement if it was within two standard deviations of the mean group velocity for that period. This exercise resulted in a database of 97,548 fundamental-mode Rayleigh group velocity picks from 3,847 events, 170 stations and 23 periods: T = 10–16, 18, 20, 25, 30, 35, 40, 50, 60, 70, 80, 90, 100, 120, 125, and 150 s. A depiction of the great-circle path coverage over our study region is shown on the right in Figure 2.

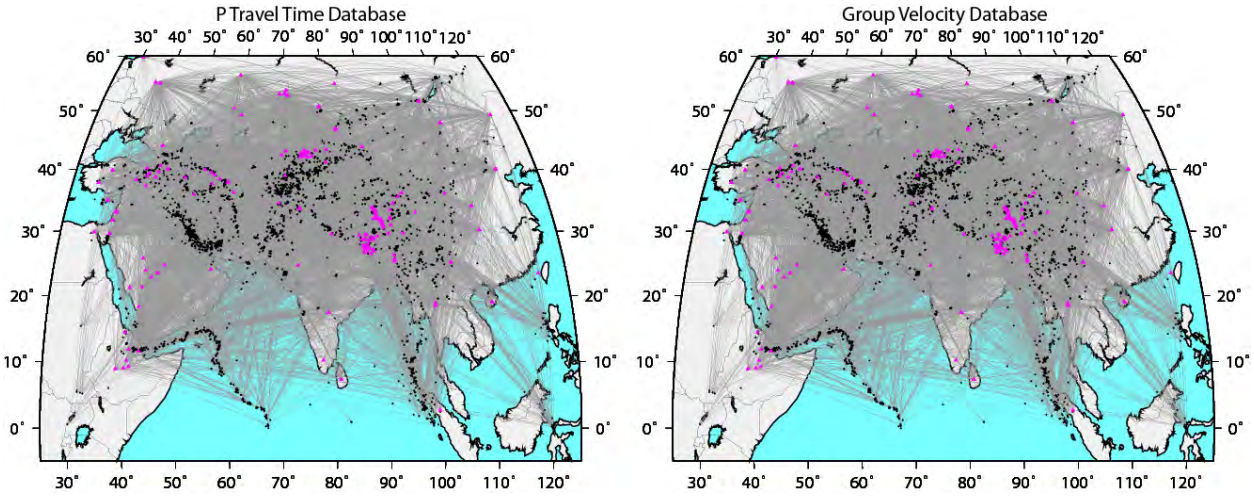

Figure 2. Path coverage for the summary-event *P*-wave travel-time (left) and surface-wave dispersion (right) data sets, displayed with great-circle rays between event and station locations. Purple triangles represent stations, and black dots are the summary-event (travel times) or event (group velocity) locations.

Model Parameterization and Initial Model

We parameterize a 3-D Earth model as a geographic grid of independent 1-D models, each comprising a *P* and *S* velocity (and density, for purposes of dispersion modeling) function versus depth. A 1-D model is specified by the velocities and depths of a fixed number of vertical nodes. Linear interpolation of velocities between nodes vertically, and of velocities and depths laterally, defines a complete spatial 3-D model.

The vertical nodes of the model are segregated into distinct "units" separated by velocity discontinuities. We selected these units based on the CRUST2.0 (Bassin et al., 2000) and AK135 (Kennett et al., 1995) models. The crust thus has seven units with each taken as a vertically homogeneous layer (sometimes of zero thickness): ice, water, soft sediment and hard sediment overlying three deeper crustal layers (nominally granitic, intermediate, and basaltic). The mantle has a single upper mantle unit between the Moho and 410 kilometers, underlain by a transition zone unit (410–660 km) and a single lower mantle unit (660–2891.5 km).

The free parameters in our joint inversion are the *P* and *S* velocities of the main crustal units (granitic through

basaltic) and of the mantle to a depth of 410 km. The mantle velocities are sampled at nine vertical nodes. An additional free parameter of the model is the Moho depth, which we adjust in the surface-wave inversion part of our inversion procedure. Moho adjustments are accommodated by proportionate thickening or thinning of the main crustal units.

The initial model for our joint inversion is a composite 3-D model consisting of the CRUST2.0 model for the crust and the 1-D AK1355 reference model for the mantle. The CRUST2.0 *Pn* velocities were ignored in favor of the AK135 velocities (V_P = 8.04 km/s, V_S = 4.48 km/s at the top of the mantle). However, the CRUST2.0 variable Moho depth was retained and accommodated by vertical compression or extension of the AK135 mantle thickness to a depth of 210 km.

Inversion Method

We have developed an algorithm that performs a joint, nonlinear inversion of body-wave travel times and surface-wave group delays to obtain fully 3-D regional models of the crust and upper mantle. Problem nonlinearity is handled by iterating over linearized inversion steps, with the aid of finite-difference ray tracing techniques to perform the necessary forward modeling in the updated Earth model at each iteration step.

At each step of the iteration, we perform linearized body-wave and surface-wave inversion as separate procedures. The body-wave data, comprising only first-arrival *P*-wave times, are used to update the *P* velocity model (V_P). The surface-wave dispersion data are used to update the *S*-wave model (V_S) in a two-step procedure, ignoring the small dependence of Rayleigh wave dispersion on *P* velocity. This sequential approach allows us to avoid some of the pitfalls associated with large simultaneous inverse problems. However, the separate inversions are coupled through the prior information applied to their respective velocity models.

The prior information used in each linearized inversion is of two types. First, we apply constraints on the size and spatial smoothness of velocity perturbations using a Tikhonov regularization approach (Tikhonov and Arsenin, 1977). The Tikhonov stabilizing functional in our case is based on a geostatistical formulation, whereby a prior variance and horizontal and vertical correlation distances are used in lieu of a simple regularization parameter (see Rodi et al., 2005). The second form of prior information consists of upper and lower bounds on the *P* and *S* velocities, which are allowed to vary with depth and tectonic regime. The velocity bounds are determined in part from bounds on Poisson's ratio. We describe some key aspects of the body-wave and surface-wave linearized inversion algorithms in the paragraphs below and refer the reader to Reiter and Rodi (2006) for additional details.

Body-Wave Inversion: At each step of the nonlinear iteration, the linearized travel-time tomography problem is solved using travel-time sensitivities calculated from the *P* velocity model of the previous step (beginning with the initial model). An updated 3-D *P* velocity model is fit to the current travel-time residuals, in a least-squares sense, subject to velocity bounds and geostatistical constraints. The velocity bounds combine a priori bounds on *P* velocity and on Poisson's ratio. The latter are used to map the current *S* velocity model, point by point, to an acceptable range of *P* velocities.

The *P* velocity update minimizes an objective function that sums data misfit and stabilizing functions, the latter embodying the geostatistical constraints. Velocity bounds are implemented with the use of a parameter mapping technique that solves directly for an unconstrained variable that is mapped onto a finite range of velocity values. This mapping technique changes the damped least-squares problem from a linear to a nonlinear one, even though the forward problem is linearized. We use a nonlinear conjugate gradients technique to obtain the solution.

The body-wave tomography results shown in this paper were obtained with the following choices of geostatistical parameters. The prior standard deviation of V_P, at each point in the model, was set to 1% of the initial model velocity at that point. The correlation distances for the mantle velocity were 300 km and 60 km in the horizontal and vertical directions, respectively. In the crust, the horizontal correlation distance was also 300 km, but the vertical correlation distance was set to half the crustal thickness. Velocities in the crust and upper mantle were de-correlated, i.e., no smoothing was applied across the Moho discontinuity.

Surface-wave inversion

We solve the linearized surface-wave inversion problem using a two-part solution. The first part entails fitting group velocity maps, one for each period, to the observed group delays over source-receiver paths. This tomography problem uses sensitivities obtained by applying 2-D finite-difference ray tracing to the *phase* velocity maps predicted by the V_P/V_S model of the previous iteration step. To produce an updated set of group velocity maps we employ the same tomography technique that is used to invert the body-wave travel times. The data are now the observed group delays and the 3-D model parameter is now group velocity as a function of latitude, longitude and period. The depth coordinate used in the body-wave tomography is replaced with logarithmic period, with an appropriate correlation "distance" assigned to accomplish some degree of smoothing over period (10% of the period in the results presented here). With regard to the other geostatistical parameters, the results presented here used a horizontal correlation distance of 300 km, as in the body-wave tomography, while the prior standard deviation of group velocity was set to 2% of the initial model values. A departure from the body-wave tomography technique is that group-velocity bounds were set very wide so as to have minimal effect on the solution; we did not derive the bounds that are implied by the shear-velocity bounds for the Earth.

Following the tomographic inversion of the group delays to retrieve a set of group-velocity maps at the set of twenty-three observation periods, we can extract an individual dispersion curve as a function of period from the maps, appropriate for any latitude/longitude point in our model grid. Applying a 1-D inversion method to the dispersion curve yields a V_S profile as a function of depth for the geographic point, and repeating this process for the whole model grid results in a 3-D *S*-wave velocity model. We solve the 1-D inversion problem by minimizing an objective function similar to that used in the *P*-wave travel-time tomography. The stabilizing function term imposes geostatistical smoothing, and minimization is subject to upper and lower *S* velocity bounds, including bounds inferred from Poisson's ratio bounds and the current V_P model. We also restrict the model to allow changes only in certain "depth zones," depending on the confidence we have in the resolving power of the dispersion data. As with the travel-time tomography, we employ the previously described parameter mapping technique to enforce the velocity bounds, but this time we use Gauss-Newton iteration to deal with the ensuing nonlinearity.

The shear-wave inversion results shown here were obtained with the following choices for smoothing parameters. The prior standard deviation of V_S was set to 3% of the average reference model velocity in the crustal layers and 2% in the mantle layers. As in the P-wave tomography, the vertical correlation distance was one-half of the crustal thickness and 60 km in the upper mantle. No smoothing was applied across the Moho discontinuity.

The biggest departure of our S-wave inversion technique from our *P*-wave tomography technique is that Moho depth is a free parameter in the former, acknowledging the sensitivity of group velocities at the observed periods to this parameter. The inversion for Moho depth is accomplished via grid search, with the *S*-wave inversion performed for each trial depth and the value achieving the smallest objective function taken as the solution. The Moho-depth grid spanned crustal thickness changes of –10% to +15% in steps of 5%.

In the next sections we present some results of performing four iterations of the joint inversion technique.

Joint Inversion Results

Vp *and* Vs *models*

In Figure 3 we show horizontal slices in the upper mantle through the *SAsia3D* model as a percent deviation from the AK135 model velocity at depths of 120, 210, 260, and 310 km. There is spatial correlation between the V_P and V_S models, but not as much in the upper mantle as in the crust (not shown). The primary observation to note in Figure 3 is the progressive slowing of the model as the depth increases, in both V_P and V_S. This suggests that the positive velocity gradient in the AK135 upper mantle is not consistent with our travel-time or dispersion data sets.

Figure 4 shows two vertical slices through the *SAsia3D* model along great-circle paths. The results are again shown as percent deviation from the initial model (i.e., CRUST2.0 over the AK135 mantle). We note that the percent deviation of the crust from its 3-D initial model is calculated with respect to an average 1-D model at a particular latitude-longitude point. On the left is a slice across the Saudi Arabian Peninsula to the northeast across southeastern Iran and into eastern Kazakhstan. The slice on the right has endpoints at 30° N latitude, stretching from western Iran

into central China. The predominant feature in the slices are the high velocity (with respect to the background model) areas beneath known areas of orogeny, such as the Makran in southern Iran and the Hindu Kush/Pamir in northern Afghanistan and western China. The V_P model shows these subsurface features most clearly, while the V_S model only hints at their outlines. There is also an interesting low velocity feature in both the V_P and V_S models beneath central Iran, which may have interesting implications for the active subduction processes occurring beneath the Eurasian continental collision zone.

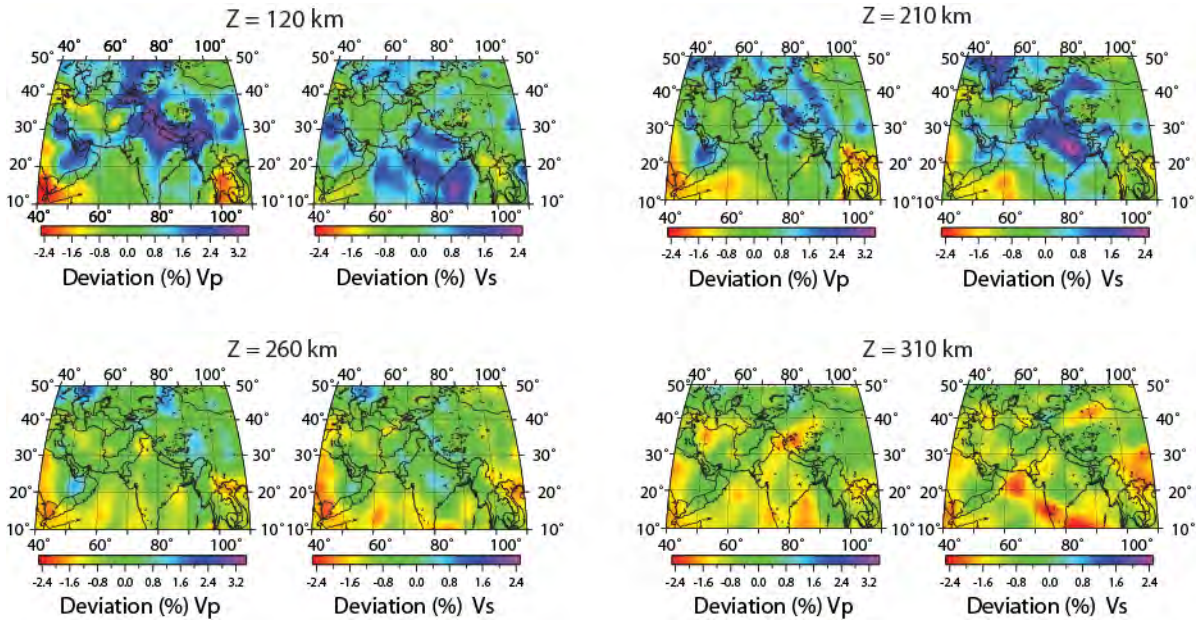

Figure 3. Results from the *SAsia3D* joint inversion model. Each subplot shows a slice at a given upper-mantle depth of V_P and V_S. The results are given as percent deviation from the AK135 velocity model at the slice's depth. The *SAsia3D* model tends toward lower velocities as the depth increases (e.g., 260- and 310-km depth slices).

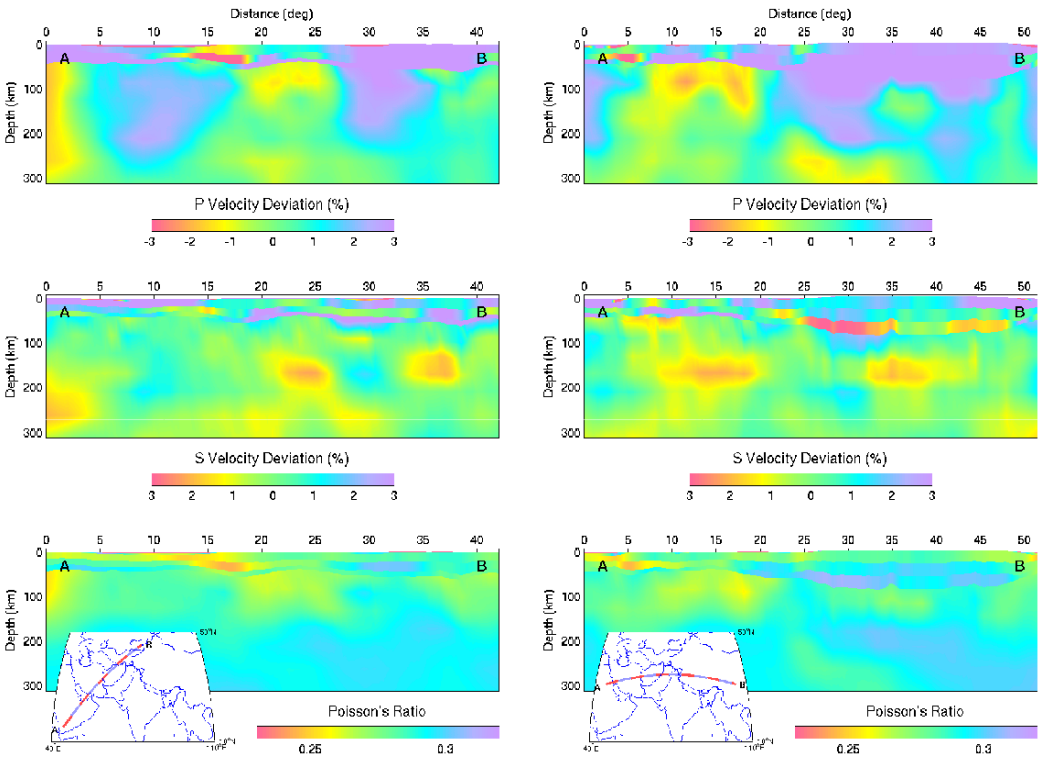

Figure 4. Two vertical slices for V_P (top), V_S (middle) and Poisson's ratio (bottom) through the *SAsia3D* joint model along great-circle paths. The results are shown as a percent deviation from the initial model (i.e., CRUST2.0 over an AK135 mantle).

Group velocity maps

One of the important corollary products of the inversion is a predicted set of group-velocity maps. Group velocities can be used to construct phase-matched filters in combination with regional surface-wave magnitude formulas to improve the m_b:Ms discriminant and extend it to smaller magnitudes (Pasyanos et al., 2004). We show the group velocity results at a period of 30 s predicted through the *SAsia3D* model in Figure 5 for the inversion region of 10°–50° N and 40°–110° E. We also show two zoomed views comparing *SAsia3D* with other recently published group-velocity maps. The two models for which we have results include those published by Pasyanos and Walter, 2002, and Mitra et al., 2005.

In general, comparison of our group velocity maps with those of the other authors indicates good agreement on most long-wavelength features, with differences restricted to smaller-scale features and specific velocity variations. We do note that at higher periods (not shown) the *SAsia3D* group velocities tend to be lower than those in the other models. It is not clear yet what is causing this phenomenon.

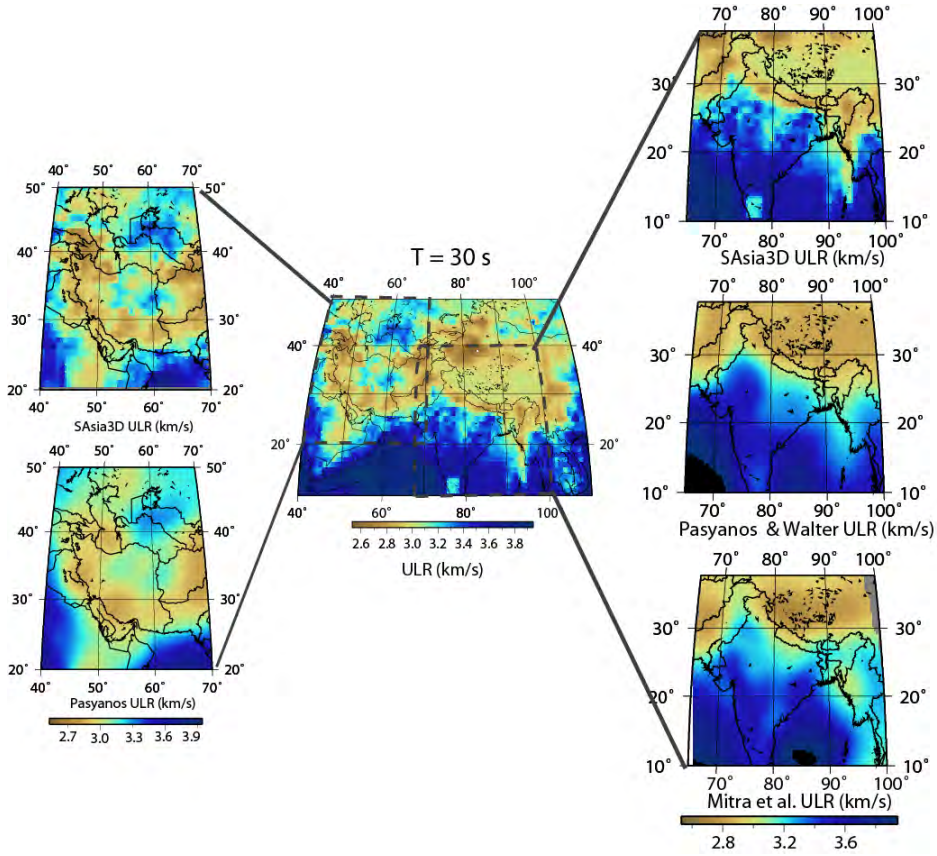

Figure 5. Predicted group velocities from SAsia3D at a period of 30 s. The middle plot shows the group-velocity map across our entire study region. The zoomed views on the left and right compare SAsia3D to models from Pasyanos and Walter (2002) and Mitra (2005). SAsia3D exhibits a slight shift to lower velocities, but overall the spatial patterns across the models are similar.

Validation Exercises

We have begun to validate the new *SAsia3D* model by relocating a ground-truth (GT) database of explosions and shallow earthquakes in the region (Bondár et al., 2004), and by comparing the travel-time predictions for the arrivals in the database within the boundaries of our region. Our initial location validation has been done using the event list published by Engdahl (2006) for the ISC Location Workshop held at the International Association of Seismology and Physics of the Earth's Interior (IASPEI) General Assembly in Santiago, Chile, in 2005. A filtering of that event database results in 10 explosions and 13 earthquakes within our region, with 833 *Pn* or *P* arrivals and 145 *Sn* or *S* arrivals. Figure 6 shows the locations of our initial validation events, color-coded according to the secondary azimuth gap of the regional arrivals.

We use the Grid-search Multiple-Event Location (GMEL) algorithm (Rodi, 2006) to perform our validation experiments. The goal of these experiments is to compare epicentral mislocations and travel-time residuals achieved with the new 3-D velocity model to the mislocations and residuals achieved with either our initial 3-D model or a standard 1-D reference model (in this case, AK135). The results are compiled in Figure 7, which is divided into mislocation comparisons in Figure 7a and the travel-time prediction results in Figure 7b. The event relocation experiments were run with event depths fixed to their reported values.

Each plot in Figure 7a tells a specific story about the ability of the *SAsia3D* model to improve the locations of the ground-truth (GT) events over the AK135 reference model and our starting model. The top left plot in Figure 7a shows that, in comparison to AK135, *SAsia3D* does a significantly better job of locating the GT events. There are more events on the "3-D Wins" side of the plot because the 3-D mislocations are closer to the zero axis. In contrast,

the top right subplot illustrates that the starting model (CRUST2.0 over AK135 mantle) does not decrease the GT mislocations over AK135 in any significant way.

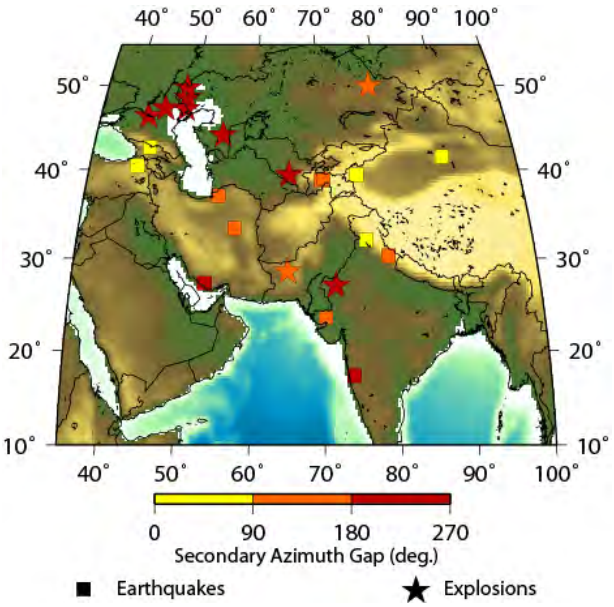

Figure 6. Reference-event (GT0–GT5) database from Engdahl (2006) within the confines of our study region. The events are color-coded by their secondary azimuth gap for the regional phases we used for relocation, which provides a measure of the network coverage bias.

The bottom two plots in Figure 7a should also be compared to the top left subplot. In the bottom left plot, we show the effect of changing from an L2 norm to an L1 norm in the location misfit criterion. We included this plot to illustrate that switching the norms from L2 to L1 (which should help to decrease the effect of a bad model in a location) does not compensate for the use of AK135 in the relocations. In other words, *SAsia3D* still produces lower mislocations than the 1-D model, even when the L1 norm is used. Lastly, the bottom right plot in Figure 7a shows the results of including the additional 145 *Sn* and *S* arrivals in the GT database, compared to the results from the 1-D model with all arrivals. In this case the results indicate that the addition of *S* arrivals helps AK135 more than *SAsia3D*, particularly for two poorly located earthquakes, but *SAsia3D* overall has systematically smaller mislocations than AK135, as when only *P* arrivals were used.

Figure 7b shows the travel-time residuals for the 833 *Pn* or *P* residuals (top) and the 145 *Sn* or *S* residuals (bottom) in our GT bulletin with respect to the AK135 (purple) and *SAsia3D* (green) models. The results show that *SAsia3D* produces a better fit for the *P*-wave residuals, shifting the mean closer to zero and decreasing the spread of residuals at most distances (there is still a slight negative bias at approximately 13°–15°). The *S*-wave residuals also exhibit a reduced bias, but only out to ~6°, past which there is a strong negative shift from the AK135 residuals. We are investigating the cause of this behavior, which may have a number of explanations.

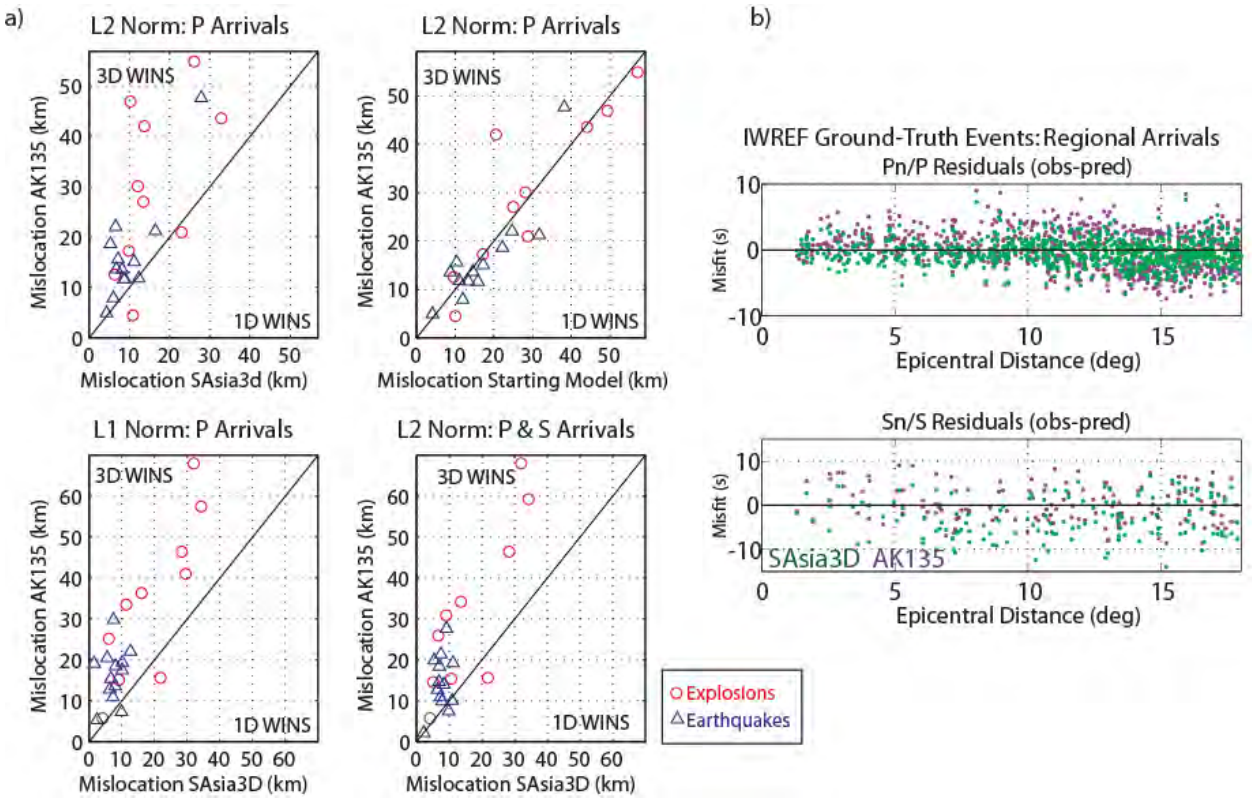

Figure 7. (a) Location validation results, shown as explosion (red triangles) or earthquake (blue circles) epicentral mislocation for the 1-D AK135 reference model versus the starting inversion model or *SAsia3D*. The details about the four subpanels are in the text. (b) The *P* and *S* regional travel-time residuals from the GT data set for the AK135 model (purple dots) and the *SAsia3D* model (green dots).

CONCLUSIONS AND RECOMMENDATIONS

We have completed the development of a new V_P and V_S model for central and southern Asia called *SAsia3D* using a new joint inversion technique that incorporates *P*-wave travel times and Rayleigh-wave group velocity data. The model has, in initial location validation exercises, proved to be very successful at locating ground-truth events with regional observations compared to both the AK135 reference model and the starting 3-D model.

The remaining tasks in this effort will include further location validation exercises using a larger set of ground-truth events. We will also test the accuracy of the group-velocity maps for predicting the observations used in m_b:Ms calculations, and perform a limited amount of full-waveform modeling to check the ability of *SAsia3D* to predict the kinetic behavior of both body waves and surface waves.

REFERENCES

Bassin, C., G. Laske and G. Masters (2000). The current limits of resolution for surface wave tomography in North America, *EOS Trans AGU* 81: F897.

Bondár, I., E. R. Engdahl, X. Yang, H. A. A. Ghalib, A. Hofstetter, V. Kirichenko, R. Wagner, I. Gupta, G. Ekström, E. Bergman, H. Israelsson, and K. McLaughlin (2004). Collection of a reference event set for regional and teleseismic location calibration, *Bull. Seis. Soc. Am.* 94: 1528–1545.

Bondár, I., S. C. Myers, E. R. Engdahl, and E. A. Bergman (2004). Epicentre accuracy based on seismic network criteria, *Geophys. J. Int.* 156: 483–496.

Engdahl, E. R. (2006). Application of an improved algorithm to high precision relocation of ISC test events, *Phys. Earth Planet. Interiors* 158: 14–18.

Engdahl E. R., R. van der Hilst, and R. Buland (1998). Global teleseismic earthquake relocation with improved travel times and procedures for depth determination, *Bull. Seis. Soc. Am.* 88: 722–743.

Kennett, B. L .N., E. R. Engdahl, and R. Buland (1995). Constraints on seismic velocities in the Earth from travel times, *Geophys. J. Int.* 122: 108–124.

Mitra, S., K Priestley, A. J. K. Bhattacharyya, and V. K. Gaur (2005). Crustal structure and earthquake focal depths beneath northeastern India and southern Tibet, *Geophys. J. Int.* 160: 227–248.

Pasyanos, M. E. and W. R. Walter (2002). Crust and upper-mantle structure of North Africa, Europe and the Middle East from inversion of surface waves, *Geophys. J. Int*. 149: 463–481.

Pasyanos, M. E., W. R. Walter, and S. E. Hazler (2004). A surface wave dispersion study of the Middle East and North Africa for monitoring the Comprehensive Nuclear-Test-Ban Treaty, *Pure Appl. Geophys*. 158: 1445–1474.

Ritzwoller, M. H. and A. L. Levshin (1998). Eurasian surface wave tomography: Group velocities, *J. Geophys. Res.*, 103: 4839–4878.

Reiter, D. and W. Rodi (2006). Crustal and upper-mantle P- and S-velocity structure in central and southern Asia from joint body-and surface-wave inversion, in Proceedings of the 28th Seismic Research Review: Ground-Based Nuclear Explosion Monitoring Technologies, LA-UR-06-5471, Vol. 1, pp. 209–218.

Rodi. W. (2006). Grid-search event location with non-Gaussian error models, *Phys. Earth. Planet. Int.* 158: 55–66.

Rodi, W., C. A. Schultz, G. Johannessen, and S. C. Myers (2005). Grid-search location methods for ground-truth collection from local and regional seismic networks, *Final Technical Report* to National Nuclear Security Administration, Dept. of Energy, Contract Nos. DE-FC03-01SF22397 and W-7405-ENG-48.

Tikhonov, A. N. and V. Y. Arsenin (1977). *Solutions of Ill-Posed Problems*. Washington, D.C.: V. H. Winston and Sons.

CALIBRATION OF THREE-DIMENSIONAL UPPER MANTLE STRUCTURE IN EURASIA USING REGIONAL AND TELESEISMIC FULL WAVEFORM SEISMIC DATA

Barbara Romanowicz[1], Aimin Cao[1], Ahyi Kim[1], Mark Panning[2], Michael E. Pasyanos[3], and Douglas S. Dreger[1]

Berkeley Seismological Laboratory[1], Princeton University[2], and Lawrence Livermore National Laboratory[3]

Sponsored by National Nuclear Security Administration
Office of Nonproliferation Research and Development
Office of Defense Nuclear Nonproliferation

Contract No. DE-FC52-04NA25543/BAA04-41

ABSTRACT

We present progress in the development of a new approach to develop and evaluate earth models at the regional scale that utilizes full waveform seismograms.

We have recently implemented a non-linear three-dimensional (3-D) Born approximation and constructed a 3-D shear velocity model of a subregion of Southeast Asia (longitude 75 to 150 degrees and latitude 0 to 45 degrees) based on this approach for the forward modeling part of the problem and linear Born kernels for the inverse part. Our initial model in the large region (longitude 30 to 150 and latitude -10 to 60 degrees) is derived from a large data set of teleseismic surface waveforms (fundamental mode and overtones in the period range 60-300 s) using the Nonlinear Asymptotic Coupling Theory (NACT), an approach used successfully for global and regional mantle tomography at Berkeley since 1995. In the subregion of study, our "N-Born" model is parameterized at relatively short wavelengths on the order of 200 km.

The NACT approach assumes two-dimensional (2-D) sensitivity kernels, confined to the vertical plane containing the source and the receiver, and is adequate for the development of a smooth velocity model. We first developed a model for Southeast Asia using NACT. Using this model as a starting model, we performed one iteration using the N-Born approach. This approach computes synthetic seismograms including the effects of single scattering (linear) as well as a non-linear part, as in the standard "path average approximation," that accounts for large accumulated phase delays on paths that sample large scale smooth anomalies. The inversion kernels are complete 3-D Born kernels.

A regional version of the Spectral Element Method (SEM) code, RegSEM.1, has been completed. This version of the code accepts a non-conformal grid, uses PML (Perfectly Matched Layers) at the borders of the region, and includes general 3-D anisotropy, Moho and surface topography, ocean bathymetry, attenuation, and ellipticity. We are computing synthetics in our N-Born model and will perform one iteration of inversion using 3-D Born sensitivity kernels to produce the next generation 3-D model of upper mantle structure in the subregion defined above.

In order to obtain finer velocity structures beneath the region of our study, we are performing forward modeling at shorter periods using the method of frequency-wave number integration (FKI). Using our N-Born 3-D model, we add sedimentary layers in the crust and change their thickness to improve the fit to the observed seismograms, and then, based on the refined velocity structures, we conduct our own moment tensor inversions, as intermediate steps.

OBJECTIVES

The primary objective of this research is to develop and apply an approach to utilize increasingly advanced theoretical frameworks and numerical methods to obtain improved regional seismic structure calibration. Specifically, a large-scale regional Eurasian model has been developed from a large data set of seismic waveforms using the path-average approximation (PAVA) and NACT (Li and Romanowicz, 1995), which are well-developed normal-mode based approaches that consider one-dimensional (1-D) and 2-D waveform sensitivity respectively along the great-circle path between source and receiver. We refine this model in a smaller region using a linear implementation of Born single-scattering theory (Capdeville, 2005), which more accurately represents the 3-D sensitivity of the seismic wavefield, for the inverse part of the problem and using a non-linear modified 3-D Born approximation for the forward part of the problem (Panning et al., 2006). Additionally, we have developed and implemented a regional version of SEM, a numerical approach that accurately models wave propagation in a complex 3-D Earth (e.g., Faccioli et al., 1996; Komatitsch and Vilotte, 1998; Komatitsch and Tromp, 1999). Finally, we plan to utilize a novel approach with stacked sources (Capdeville et al., 2003) to further speed computation.

A further objective of this research is to perform validation and improved calibration of the model described above using a variety of approaches and data sets, including ground-truth data sets from the Knowledge Base. Specifically, we plan to apply teleseismic receiver function modeling, regional broadband data forward modeling, and surface wave group velocity measurements to test and improve the model using data not included in the original inversion. While these additional data sets can help improve all aspects of the model, we anticipate the greatest improvement in the shallow structure, particularly the crust, which is not as well constrained by the longer-period data used in the initial model development.

This research can then serve as a proof of concept for applying a similar approach to the calibration of seismic structure in other regions of Earth.

RESEARCH ACCOMPLISHED

Our NACT shear wave model (Figure 1) has been developed from a global data set of surface wave waveforms crossing the region of interest (longitude 30 to 150 degrees and latitude -10 to 60 degrees). This region is highly heterogeneous, presenting a challenge for calibration, but it is well surrounded by earthquake sources, and a significant number of high quality broadband digital stations exist. We started from the existing waveform database that was collected at Berkeley over the last 10 years for the construction of global mantle tomographic models (Li and Romanowicz, 1996; Megnin and Romanowicz, 2000; Gung et al., 2003; Panning and Romanowicz, 2004) and added data from ~20 new events in the period up to 2005. We now have 38826 3-component waveforms from 393 events recorded at 169 stations. The data has been processed using an automated algorithm, which removes glitches and checks for many common problems related to timing, poor instrument response, and excessively noisy windows. A weighting scheme has been applied to insure even distribution of data across the region. This model is parameterized laterally in spherical spline level 6, which correspond to lateral resolution of ~200 km. The corresponding radially anisotropic model is parameterized in the spline level 5, which corresponds to a lateral resolution of ~400 km.

The next step in our study has been to perform an iteration of our 3-D model using the “non-linear” Born approximation (N-Born), which is modified from the more standard 3-D “linear” Born approximation by including a “Path Average” term. This term allows the accurate inclusion of accumulated phase shifts that arise in the case when the wavepath crosses a spatially extended region with a smooth anomaly of constant sign. The linear Born terms account for single scattering effects outside of the great circle path and are modeled according to the expressions of Capdeville (2005). Accounting for scattering outside of the great-circle path is the one difference with our initial NACT approach. We demonstrate the importance of the non-linear effect in Figure 2 by comparing 3-D Born and 3-D N-Born synthetics with those of SEM. This particular case illustrates the importance of including the non-linear “path average” phase shift for paths that accumulate large phase delays.

Because the calculation of the 3-D Born sensitivity kernels is very expensive computationally, we have to select a subregion (longitude 75 to 150 degrees and latitude 0 to 45 degrees), where the lateral heterogeneities are more significant than the surrounding regions. In order to further reduce the intensity of the computation, we require that both events and stations must be in the large region (longitude 30 to 150^{o} E and latitude -10 to 60^{o} N) and only the ray paths along the minor arcs are selected. We calculated 3-D Born sensitivity kernels for 162 events using the

computing facilities (Jacquard) of the National Energy Research Scientific Computing Center (NERSC—www.nersc.gov). When we generate synthetics for the N-Born inversion, we use PAVA (Woodhouse and Dziewonski, 1984) in the subregion to obtain the non-linear phase term and NACT outside the subregion. The adopted damping scheme for isotropic and radially anisotropic models is the same as that used in the NACT inversion.

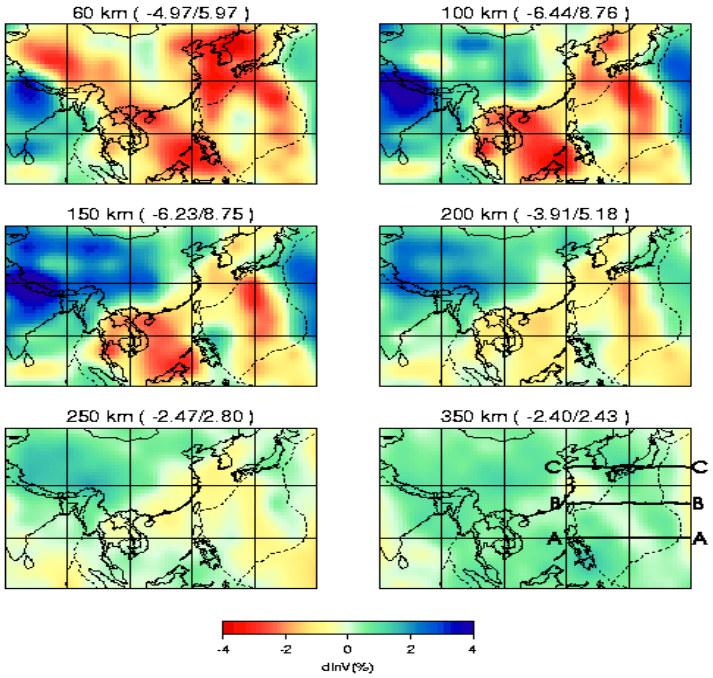

Figure 1. Starting isotropic shear velocity model derived using NACT, shown here only in the subregion (lon 75 to 150 degrees and lat 0 to 45 degrees) with map grid interval of 15 degrees. The lateral parameterization is in level 6 spherical splines, which give a resolution of ~200 km. Values are shown as percent perturbations from the isotropic velocity of the Preliminary Reference Earth Model (PREM).

Our N-Born shear velocity model is shown in Figure 3. Both N-Born and NACT derived models can fit waveforms very well, with up to ~83% variance reduction (depending on the choice of damping), and the N-Born residual variance is even lower than that of NACT (Figure 4). While the models agree in general, there are some notable differences between them in detail. For example, beneath the Tibetan plateau, the N-Born model shows a stronger fast velocity anomaly in the depth range 150 km to 250 km, which disappears at greater depth. This indicates that there is no delamination of lithosphere beneath the plateau, as has been suggested by some authors.

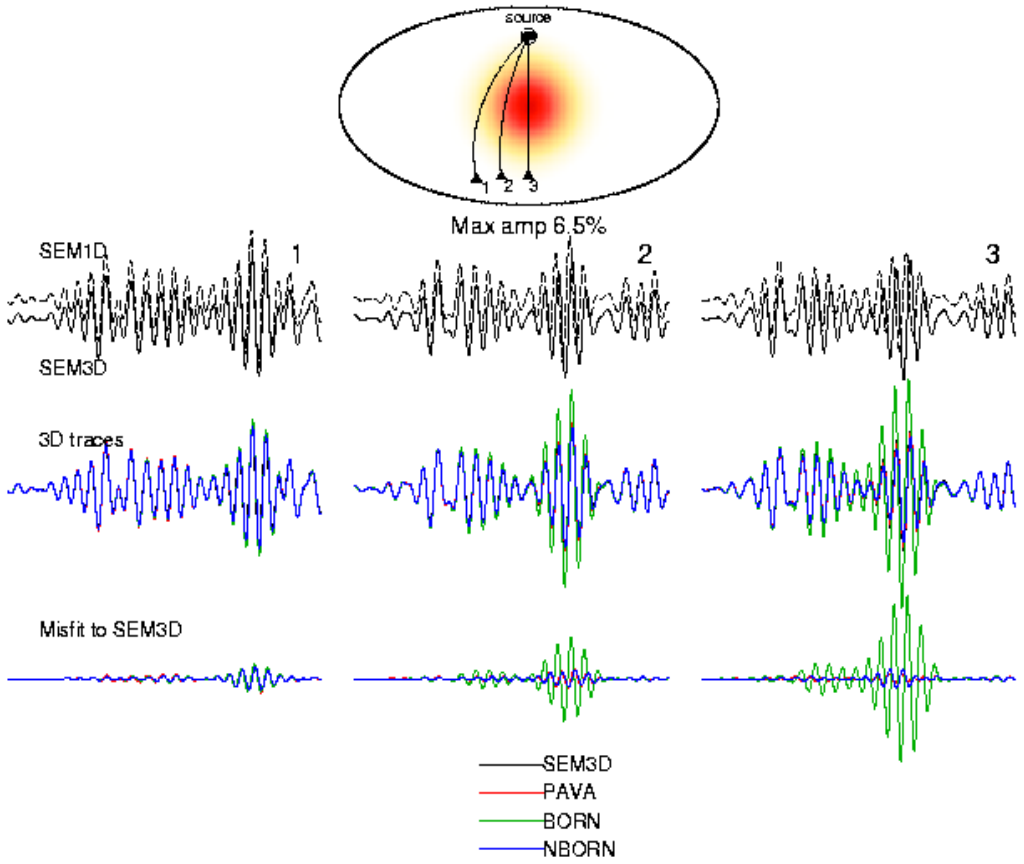

Figure 2. A comparison of synthetic seismograms using different approximations for paths through a large slow anomaly. The paths (numbered 1-3) projected on a slice of the model at 220 km depth are shown at top. The top row shows SEM synthetics through the 1-D background model (SEM1D; dashed) and through the 3-D model (SEM3D; solid) paths 1 (left), 2 (middle), and 3 (right). The middle row shows the predicted 3-D synthetics plotted on top of the SEM3D trace (black) for the path-average approximation (PAVA; red), linear Born approximation (BORN; green), and non-linearly modified Born (NBORN; blue). The bottom row shows the misfits for PAVA, BORN, and NBORN to the SEM3D trace. The amplitude is scaled to the maximum of the SEM3D trace in each column. While the Born approach is important to represent the 3-D effects in many configurations, this figure illustrates the case of a path sampling the center of a large anomaly. In this case, the non-linear, path average contribution to the seismogram dominates, and the linear Born approximation does a poor job at predicting the waveforms.

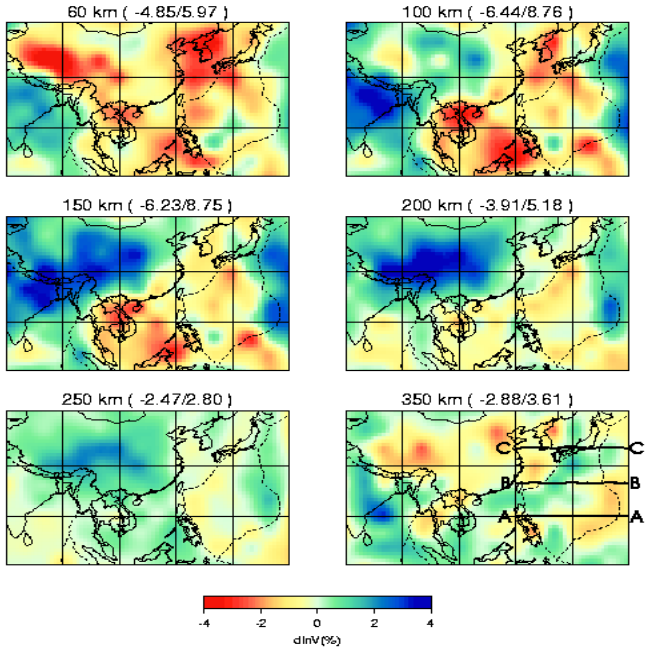

Figure 3. N-Born isotropic shear velocity model derived using the "non-linear" 3-D Born approximation in the same subregion as in Figure 1.

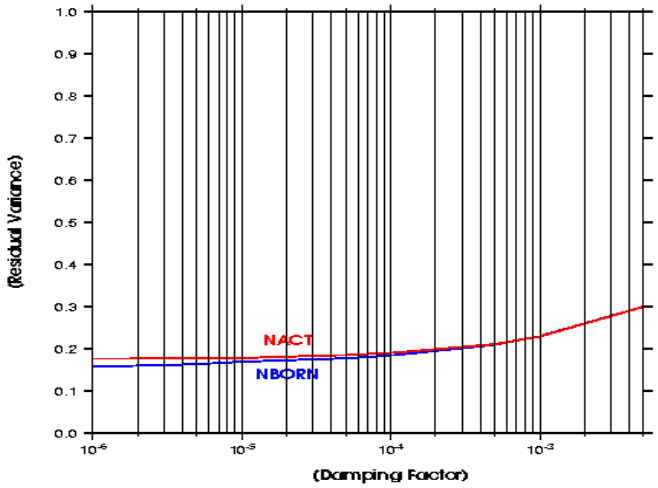

Figure 4. Residual variance as a function of the damping factor. In both N-Born and NACT models, the chosen damping factor for the models shown respectively in Figure 3 and Figure 1 is 5.0E-5.

In collaboration with researchers at Institut de Physique du Globe de Paris (IPGP), we have completed a regional version of the Spectral Element code (RegSEM.1). The regional SEM incorporates PML boundary conditions on the lateral borders of the region, which effectively eliminate spurious reflections from the borders, and a non-conforming mesh. Compared with previous versions, first of all, both Moho topography and surface topography have been included into the process of building the mesh. With reference to a Moho model, every element in the simulation domain is assigned an integer (1 for elements just above the Moho, -1 for those just below, and 0 for the others), and we are able to provide realistic velocity contrasts at the Moho discontinuity while introducing any 3-D elastic mantle model. Second, anisotropy has been included in this new version of regional SEM (any anisotropic structure can be considered). Third, we do not need to rotate events, stations, and models to be centered at the North

Pole before the simulation, as required in the previous versions. All the rotations can be done automatically, and all the input information related to the event focal mechanism and station coordinates are straightforward. Thus, it is now very convenient to add more stations into the station list. Finally, this new version of regional SEM has been fully optimized. The same computation now takes only one-third of the previous cluster hours. This will be very helpful for our future waveform inversion using the regional SEM method. For demonstration, we examine the effect of the Moho topography (CRUST2.0) on the synthetic waveforms computed in our NACT velocity model (Figure 5). Inclusion of the Moho topography can significantly change the fundamental Rayleigh waveforms in not only travel time but also amplitude. For the ray paths with significant oceanic portion (DAV), the shape of the waveform is also changed (Figure 6).

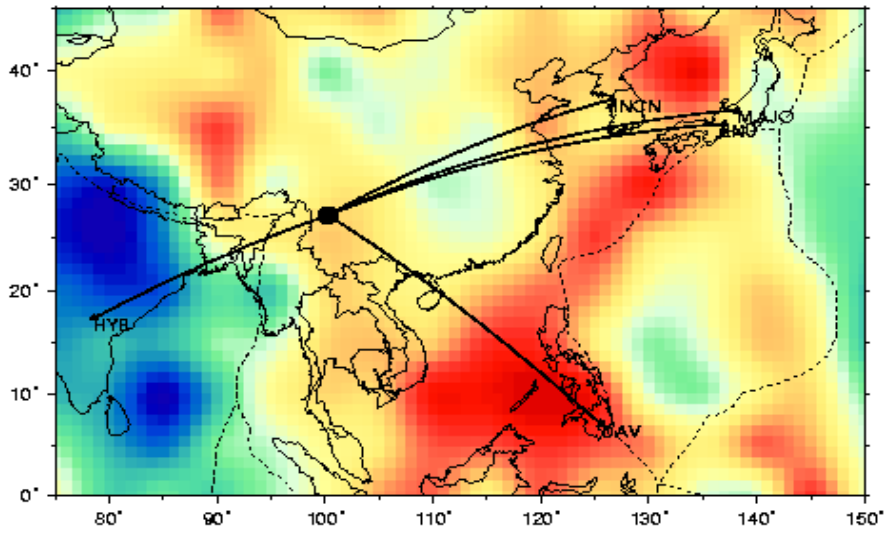

Figure 5. Map showing event and station locations for the SEM simulation shown in Figure 6. The background is our most recent model derived using NACT, shown at a depth of 60 km.

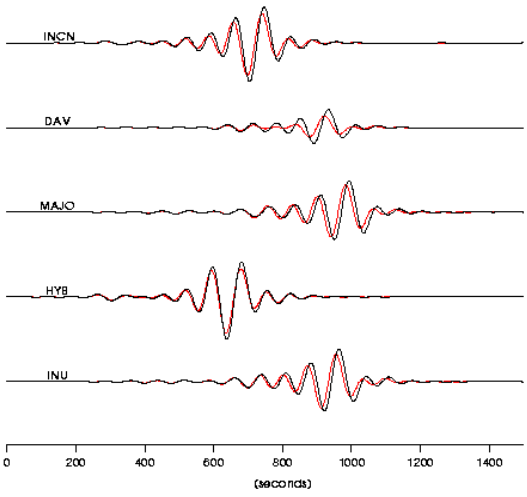

Figure 6. Comparison of vertical component SEM synthetics in our NACT derived model (Figure 1) with (red) and without (black) consideration of the Moho topography. Synthetics have been low-pass filtered with a corner at 60 sec.

In order to refine the velocity structure beneath the region of our study, we perform forward waveform modeling with the FKI method. Broadband seismograms are downloaded from the Incorporated Research Institutions for Seismology (IRIS) and corrected to absolute ground velocity (cm/sec). We show 2 event locations of events 2000256 (9/12/2000, Mw6.1) and 2003107 (4/17/2003, Mw6.3) and the IRIS station distributions (Figure 7). We start with the 2000256 event, for which the continental ray paths are dominant, to obtain the 1-D velocity structure between the source and each receiver. Broadband data are bandpass filtered at 0.005-0.05 Hz. We used the Harvard centroid moment tensor (CMT) solution for the source parameters, and the starting model is a 1-D layered average crustal velocity structure derived from CRUST2.0. Using the best velocity model we can obtain (Figure 8), we compute Green's functions and perform the moment tensor analysis for two ranges of frequency (0.01-0.05 Hz and 0.005-0.03 Hz). Then, we select the event 2003107, for which we have ray paths similar to event 2000256, to perform the moment tensor analysis using Green's function obtained from our 1-D simulation (Figure 9). We find a moment tensor solution in good agreement with the CMT solution, whereas the solution obtained using the PREM reference model is very poor. While this example was chosen because we expect that we can use Harvard CMT solutions for M>6 events as good references, this indicates that the additional regional modeling effort is worthwhile and will lead to better moment tensor solutions for smaller events in the area, when we extend the modeling to higher frequencies (0.02-0.05 Hz).

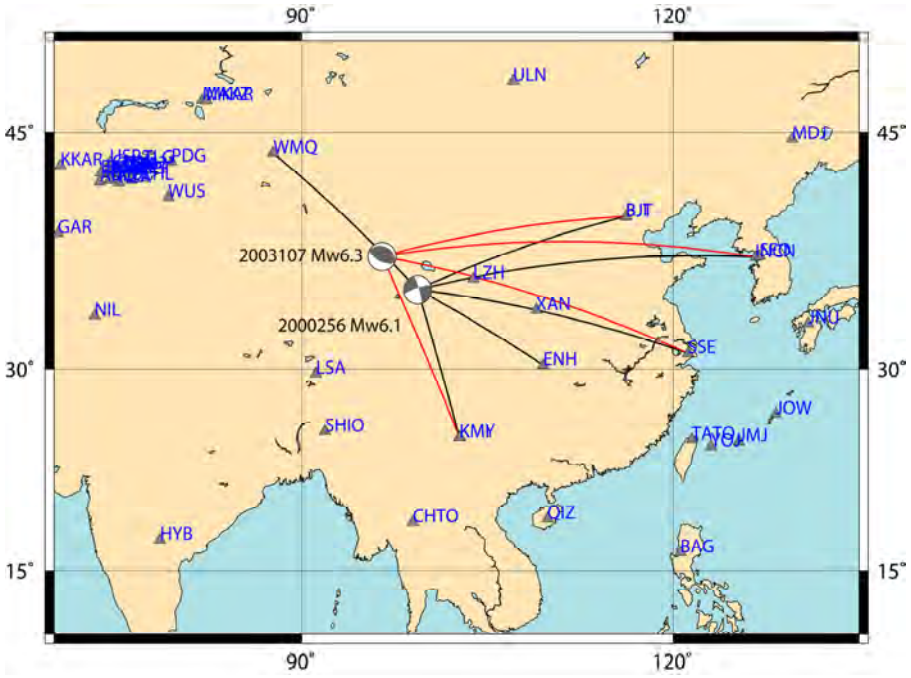

Figure 7. Event 2000256 (9/12/2000, Mw6.1), 2003107 (4/17/2003, Mw6.3), and IRIS station distributions. Source 2000256 (9/12/2000, Mw6.1) is used to obtain the velocity structures.

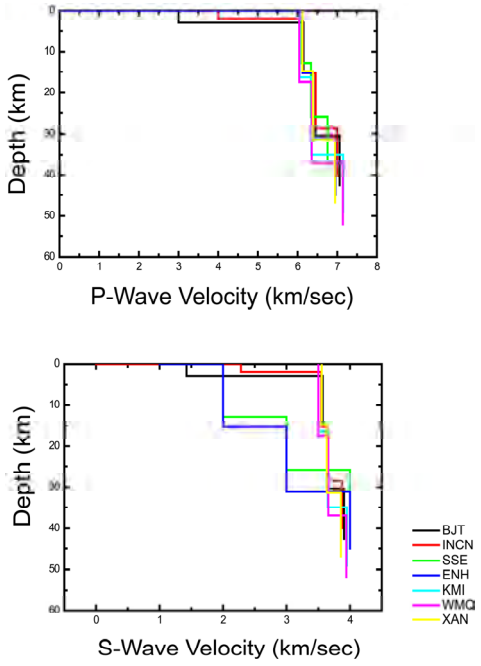

Figure 8. Best P-wave and S-wave velocity structures for the paths between event 2000256 and IRIS stations obtained from 1-D forward modeling.

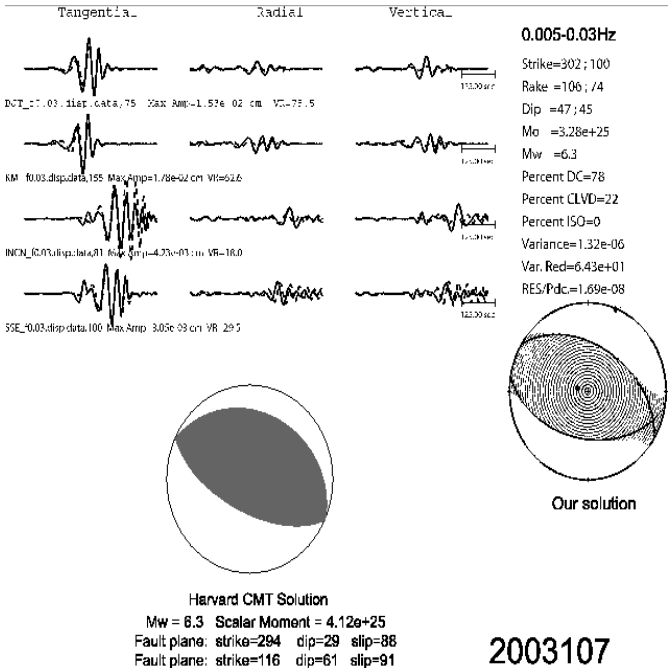

Figure 9. Top: Moment tensor solution for event 2003107 in the 0.005-0.03 Hz range using Green's function computed from the velocity model obtained using the 2000256 event (Figure 9). Bottom: Global CMT solution from Harvard University.

CONCLUSIONS AND RECOMMENDATIONS

A 3-D non-Linear Born implementation is shown to be promising to accurately model large scale lateral structures. This approach includes relatively rapid calculation of partial derivatives for use in the next inversion step where the forward modeling will be performed using the recently completed regional SEM numerical code.

Further work on the regional SEM synthetics and 3-D Born sensitivity kernels should offer continued improvement of the model. We are in the process of implementing an iteration of our model using the regional SEM code. Additionally, other approaches and data sets, including ground-truth data sets from the Knowledge Base, teleseismic receiver functions, broadband waveform forward modeling at shorter periods, and surface wave group velocities will allow for validation and improvement of the model and, in particular, for improved moment tensor solutions.

ACKNOWLEDGEMENTS

We would like to acknowledge the contributions of Yann Capdeville and Paul Cupillard at IPGP, who did extensive work on both the Born and SEM codes. Many computations were performed using computing resources obtained through a time allocation at NERSC from the Department of Energy (DOE) Office of Science, Geosciences Division, for which we thank Dr. Nick Woodward of DOE.

REFERENCES

Capdeville, Y., B. Romanowicz, and Y. Gung (2003). Global seismic waveform tomography based on the spectral element method, abstract, joint AGU/EGS/EUG Meeting, Nice, April 2003.

Capdeville, Y. (2005). An efficient Born normal mode method to compute sensitivity kernels and synthetic seismograms in the Earth, *Geophys. J. Int.* 163: 639–646.

Faccioli, E., F. Maggio, A. Quarteroni, and A. Tagliani (1996). Spectral-domain decomposition methods for the solution of acoustic and elastic wave equations, *Geophysics* 61: 1160–1174.

Gung, Y., B. Romanowicz, and M. Panning (2003). Anisotropy and lithospheric thickness, *Nature* 422: 707–711.

Komatitsch, D. and J. P. Vilotte (1998). The spectral element method: an effective tool to simulate the seismic response of 2D and 3D geological structures, *Bull. Seism. Soc. Am*. 88: 368–392.

Komatitsch, D. and J. Tromp (1999). Introduction to the spectral-element method for 3-D seismic wave propagation, *Geophys. J. Int.* 139: 806–822.

Li, X. D. and B. Romanowicz (1995). Comparison of global waveform inversions with and without considering cross branch coupling, *Geophys. J. Int.* 121: 695–709.

Li, X. D. and B. Romanowicz (1996). Global mantle shear velocity model developed using nonlinear asymptotic coupling theory, *J. Geophys. Res.* 101: 22,245–22,273.

Megnin, C. and B. Romanowicz (2000). The 3D shear velocity structure of the mantle from the inversion of body, surface and higher mode waveforms, *Geophys. J. Int.* 143: 709–728.

Panning, M. and B. Romanowicz (2004). Inferences on flow at the base of Earth's mantle based on seismic anisotropy, *Science* 303: 351–353.

Panning, M., F. Marone, A. Kim, Y. Capdeville, P. Cupillard, Y. Gung, and B. Romanowicz (2006). Improvements in mode-based waveform modeling and application to Eurasian velocity structure, *Eos. Trans.* AGU, 87(52). Fall Meet. Suppl.

Woodhouse, J.H. and A.M. Dziewonski (1984). Mapping the upper mantle: Three dimensional modeling of Earth's structure by inversion of seismic waveforms, *J. Geophys. Res.* 89: 5953–5986.

GEOPHYSICAL IMAGING OF ASIA AND SIBERIA: TOMOGRAPHY FOR SEISMIC VELOCITY, UPPER MANTLE GRADIENT, Lg ATTENUATION, AND JOINT INVERSION OF SURFACE WAVE DISPERSION, RECEIVER FUNCTIONS AND SATELLITE GRAVITY DATA

Charlotte A. Rowe[1], William S. Phillips[1], Monica Maceira[1], Michael L. Begnaud, Lee K. Steck[1], Xiaoning (David) Yang[1], Christian L. Lucero[1], Hans E. Hartse[1], Richard J. Stead[1], Kevin G. Mackey[2], Kazuya Fujita[2], and Charles J. Ammon[3]

Los Alamos National Laboratory[1], Michigan State University[2], and Pennsylvania State University[3]

Sponsored by National Nuclear Security Administration
Office of Nonproliferation Research and Development
Office of Defense Nuclear Nonproliferation

Contract No. DE-AC52-06NA25396

ABSTRACT

Our geophysical modeling efforts have focused on a variety of special studies. We continue to develop models for Eastern Russia using the Michigan State Siberia database, for which we have expanded over previous Pn velocity tomography by also inverting Lg amplitudes for a regional attenuation study, and a preliminary tomographic image of Pg travel times in Eurasia, including the Siberia region. Both Lg attenuation and Pg velocity tomographic studies illuminate features consistent with known aspects of Siberian and Russian Far East tectonics and are consistent with features derived in our earlier Pn study. Lg attenuation studies will help to improve our understanding of phase amplitudes for calibration across eastern Russia, and an improved Pg model will allow us to better calibrate travel times in the area when secondary phase arrivals are needed for event location.

We are exploring the effects of upper mantle velocity gradients on the two-dimensional (2-D) tomographic image for P-waves that travel through the upper mantle for regional-distance source-receiver pairs (2.5 to 18 degrees). By adding an upper mantle gradient term to the inversion for 2-D varying Pn velocity and crustal time terms, we are able to map a 2-D varying upper mantle gradient, based on travel times from high-quality event locations. Lateral gradients in the upper mantle across central and eastern Eurasia vary from -0.001 s^{-1} to 0.003 s^{-1}. High gradients appear to be associated with regions of tectonic convergence, both continental and oceanic, as well as stable cratonic regions. Variance reduction is 63% with respect to Pn tomography without gradients. An improved mapping not only of Pn velocities but also of the upper mantle gradients that influence the travel times for this phase is important for ongoing efforts to improve event location throughout central and eastern Asia.

We have recently developed a new joint inversion method using gravity and surface-wave group velocity data, which has been applied to the Tarim and Junggar sedimentary basins in central Asia. The resulting model has been tested and shows a 73% improvement on Rayleigh-wave detection at short periods. Encouraged by these findings, we now present a new three-dimensional (3-D) shear-velocity/density model for the Asian continent constructed through joint inversion of three different geophysical datasets. In addition to the surface wave dispersion values in the period range from 8 to 100 s obtained from the Colorado University Boulder (CUB) Earth model, and gravity observations that were derived from data obtained from the GRACE satellite mission, we also include receiver functions for 45 seismic stations across Asia. Our goal is to investigate the crustal and upper mantle structure beneath the region with increased resolution of shallow geological structures via joint inversion of these three data sets.

OBJECTIVES

To improve calibration capabilities in eastern Eurasia through development of geophysical models and through the acquisition and incorporation of new seismic data for poorly characterized regions.

RESEARCH ACCOMPLISHED

Eastern Russia—Lg Attenuation

We have inverted catalog amplitude parameters to derive a 2D function that maps laterally varying attenuation features for eastern Siberia and the Russian Far East. Data are from the Michigan State University (MSU) Siberia database, compiled through cooperative efforts of MSU, Russian network operators and Los Alamos researchers. In this preliminary analysis we use approximately 280,000 S and Sg amplitude readings from the combined MSU Siberia database. Each independent network (Figure 1) reports corrected amplitude readings for its stations (Mackey et al., 2003). These measurements are in theory frequency-independent, as station response has been removed. We have employed a differential tomographic method, in which each event used must have at least two reporting stations with corrected amplitude readings. Inversion results must be viewed as relative attenuation, rather than absolute.

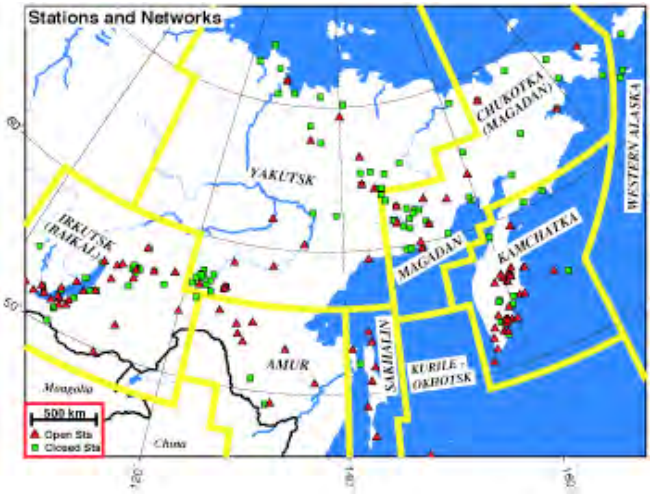

Figure 1. Independent seismic networks contributing to the Siberia database (Mackey et al., 2006).

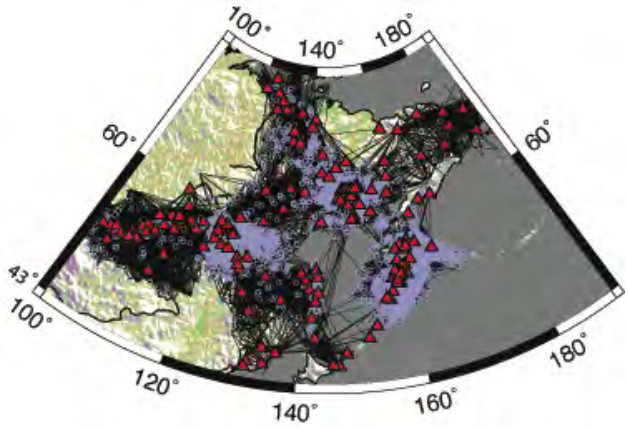

Figure 2. Ray paths used for Lg attenuation tomography.

Figure 2 shows ray paths for data used in the inversion. Events are shown in blue and stations are red triangles. For this preliminary analysis we have not merged the network amplitude data with additional data from our global database, so the coverage is not uniform; for the most part we will be able only to image areas within the individual networks. Tying the Russian network amplitudes in to absolute ground motions will be needed to merge the data sets.

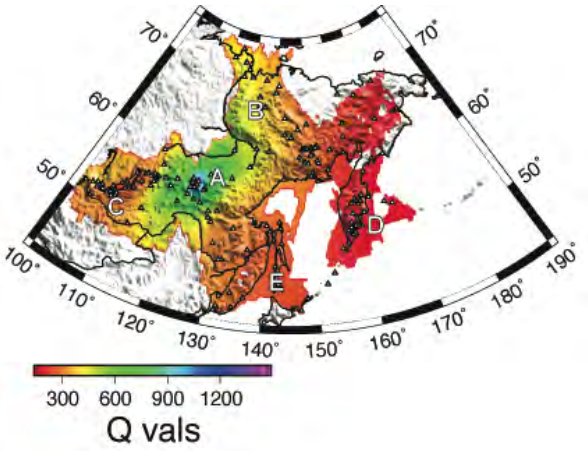

Figure 3. Preliminary Lg Q results.

We performed the tomography using a modification of the Lg-Q tomographic algorithm of Phillips et al. (2000). Since we assume the catalog readings (reported variously as Sg or Lg) were applied to Lg amplitudes, a spreading constant of .83 was used, which is appropriate for surface waves. Signal-to-noise was not constrained due to the lack of reported noise levels, but we assumed that reported amplitudes were adequately large for reliable measurement. The model grid step is ½ degree in both latitude and longitude. We applied a one-sigma data rejection constraint prior to final inversion.

Attenuation variability across northeastern Russia is consistent with expectations for some of the larger tectonic features of the region. Figure 3 shows preliminary results for this analysis. The central high lies within the stable Siberian Platform (A). A rather abrupt drop in Q is observed along the transition to the Verkhoyansk fold belt (B). This is also observed in Pg velocities discussed below. We see a more subtle change in the vicinity of the Baikal Rift (C), where attenuation values are slightly higher to the north and lower to the south. The landward side of the Kamchatka Peninsula (D) exhibits lower Q (higher attenuation) than the seaward side, consistent with differences we would expect between the cold Pacific slab on the east and back-arc materials to the west. Sakhalin Island (E) also exhibits low Q, which corresponds to markedly lower P velocities noted in other studies.

Eastern Russia—Pg Velocity Perturbations

We are undertaking Pg tomography for central and eastern Asia, with a special emphasis on northeastern Russia, to improve travel-time calibration for seismic event locations when secondary phases are used. The data set for this study is comprised of Pg arrivals from 498 seismic stations and over 63,000 events for a total of 266,352 arrivals. We restrict our analysis to crustal earthquakes ($z < 35$ km) and for epicentral distances between 0.6 and 14 degrees. In Figure 4 we show path coverage for this analysis. Data quality control for these arrivals consisted of examining a standard time-distance plot (Figure 5) and excluding any data that falls outside our ad hoc upper and lower bounds (blue and red lines in Figure 5) or if the travel times were negative. Pn contamination in the data is clearly seen in Figure 5, as are timing errors of 30 and 60 s. Larger errors observed are not shown.

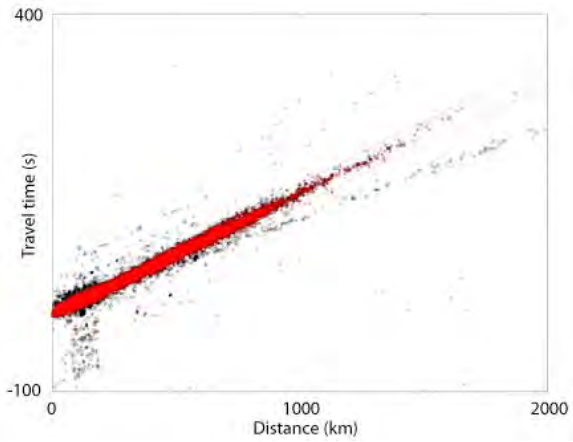

Figure 5. Time-distance plot showing data rejection/inclusion (Steck et al., 2006a).

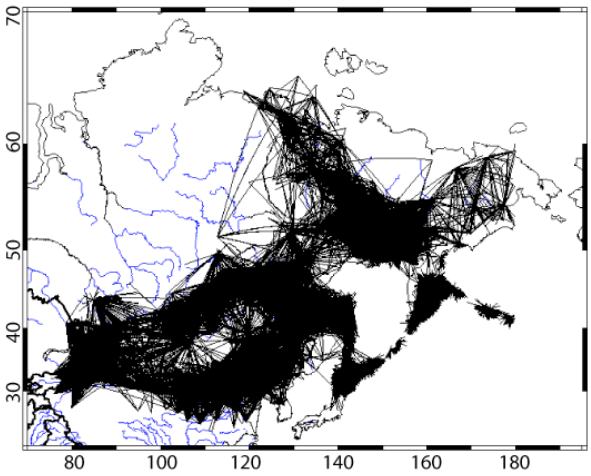

Figure 4. Pg Path coverage (Steck et al., 2006a).

Our method is a first-difference, regularized least-squares inversion, similar to Pn tomography. Travel-time residuals are calculated with respect to the iasp91 Pg travel-time model. The inversion is performed using an LSQR conjugate gradient method, and we solve for slowness perturbations as well as site and event terms. The station term sum is damped to zero while event terms are unconstrained. We assume a great circle path between source and receiver and for this preliminary analysis we do not include event depth, although data selection restricts sources to 35 km or shallower.

In Figure 6 we show the slowness perturbations for the region, with truncation of the color scale for the highest velocity regions: the forearcs of Pacific subduction zones (A and B). Actual slowness perturbations for these two regions exceeded –0.03 s/km. A pronounced velocity low is observed for Sakhalin Island (C), and the Baikal rift shows a velocity low (D), with higher values in the Siberian Platform (E) and Aldan Shield (F).

Site and event terms in this study were relatively small, with minor differences in event terms due largely to the unaccommoded hypocentral depth variations, and large site terms observed primarily in western China and northernmost Japan, where significant crustal thickness and subduction zone complexities, respectively, are likely to cause significant perturbations to average arrival time estimates compared to the iasp91 model.

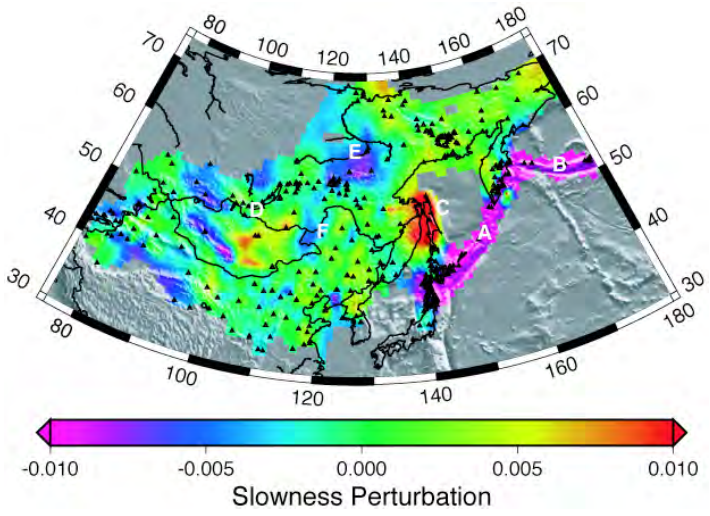

Figure 6. Pg Slowness perturbations (Steck et al., 2006a).

Upper Mantle Pn and Gradient in Eurasia

We explore the effect of laterally varying upper mantle P-wave velocity gradient on our models of Pn perturbations across Eurasia, in an extension of the Zhao (1993) and Zhao and Xie (1993) method. A sharp velocity contrast at the base of the crust and top of the underlying mantle results in a concentration of ray paths for a large variety of source-receiver offsets for crustal earthquakes, which significantly enhances seismologists' ability to image variations in the upper mantle velocity. Regional P-waves are not, however, critically refracted at the crust/mantle interface; rather, due to a combination of upper mantle velocity gradient and earth curvature, they penetrate to varying depths within the mantle, with longer paths sampling deeper regions (e.g., Hearn et al., 2004).

Zhao (1993) and Zhao and Xie (1993) explored the effects of an upper mantle gradient and demonstrated an improved Pn fit through the application of a uniform gradient in some regions. We have extended their method to a 2-D mapping of the gradient (Phillips et al., 2007) and show that these lateral variations in upper mantle gradient are easily obtained along with laterally varying Pn mapping, and the fit to the data is thus improved significantly.

Calculations show that approximate and analytic travel times can be matched with this method to within 1.0 s for a high-gradient mantle ($0.003 s^{-1}$) at 18 degrees offset; moreover, travel times that were ray traced through a laterally varying gradient model similarly matched approximate travel times based on path-averaged gradients. We allow the gradient term to vary in two dimensions by discretizing it in the same manner as for upper mantle velocity, and taking a path average, for inclusion in the tomographic inversion. This gradient term is weakly nonlinear because it requires multiplying gradient and slowness; however, we can address this by setting the average slowness to be constant and adjusting until the regional average slowness is matched. Mantle pierce points are set at 50-degree incidence angles, and model values at each ray segment center are obtained using bilinear interpolation from the surrounding four nodes (e.g., Thurber, 1983). Source and site terms are obtained along with grid-interpolated model parameters for each arrival datum; a linear system of equations is solved via LSQR conjugate gradient (Paige and Saunders, 1982) after applying first-difference constraints.

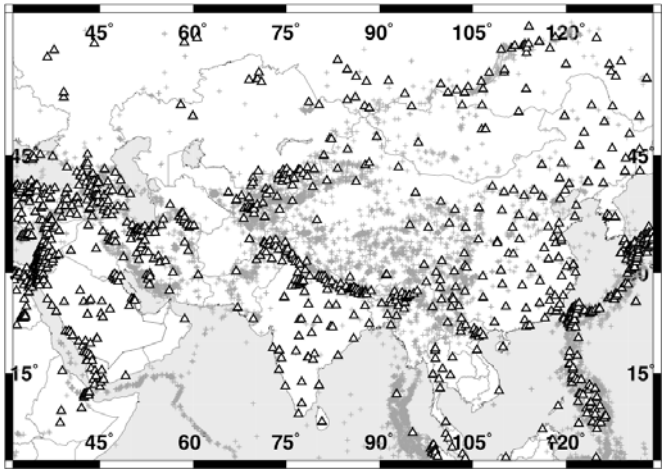

Figure 7.Events and stations contributing travel times for Pn inversion (Phillips et al., 2007).

Data used in this inversion are GT-25 (Bondar et al., 2004) or better. We used 10,396 events and 186,822 arrivals recorded at 1287 stations (Begnaud et al., 2006) within latitude 0–60 degrees north and longitude 30–135 degrees east. Figure 7 shows events (gray dots) and stations (triangles) employed in this study.

We inverted both with and without the gradient, to compare our technique with a standard method, obtaining residual RMS of 2.57 s and 1.57 s for non-gradient and gradient calculations, respectively. Including the gradient provided a variance reduction of 63%, demonstrating significant improvement over non-gradient inversion. These residuals are high compared to some reported in other work: McNamara et al. (1997), Hearn et al.. (2004), Liang et al. (2004), Sun et al. (2004) and Pei et al. (2007) report residual standard deviations of 0.55, 1.3, 1.33, 0.65 and 1.9 s, respectively, while a

differential tomography study (Phillips et al., 2005) reports residuals of 0.96 s. The higher values in our analysis can be attributed to minimal data culling as well as longer distance ranges in this study.

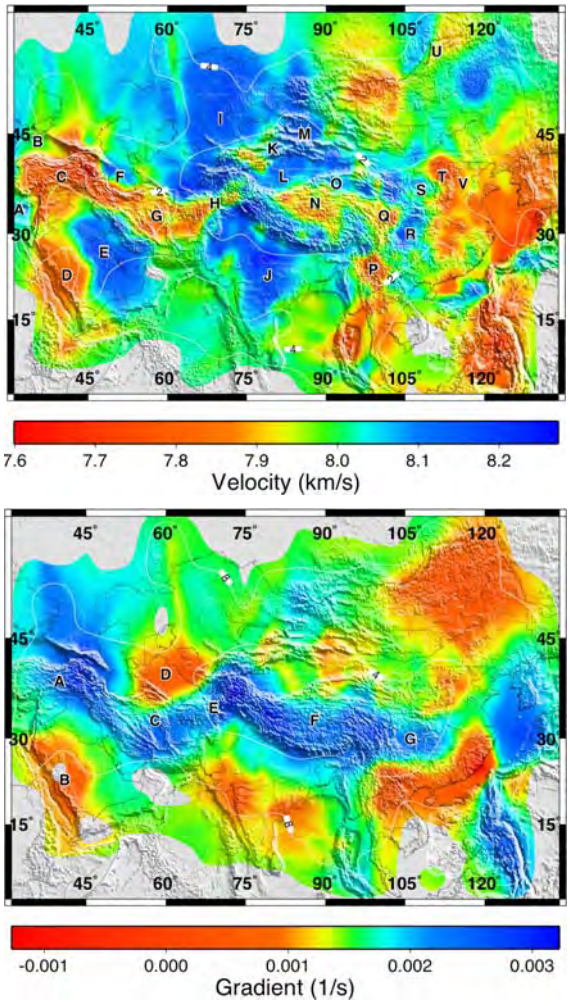

Figure 8. (top) Upper mantle Pn velocities; (bottom) Mantle gradient. Philips et al., 2007).

Our results from the gradient analysis (Figure 8, top) show dramatic differences in magnitude and extent of low velocity anomalies in high gradient areas; for instance, the two adjacent low velocity zones in north-central Tibet (N) and in the Songpan-Ganzi terrane (Q) are much more well-defined than in previous studies. Labels (Figure 8, top) correspond to the following regions: A) East Mediterranean, B) Black Sea, C) Anatolian Plateau, D) Arabian Shield, E) Arabian Platform, F) Caspian Sea, G) Iranian Plateau, H) Hindu Kush, I) Kazakh Shield, J) Indian Shield, K) Tian Shan, L) Tarim Basin, M) Junggar Basin, N) Tibetan Plateau, O) Qaidam Basin, P) Panxi Rift, Q) Songpan-Ganzi, R) Sichuan Basin, S) Ordos Basin, T) Shanxi Graben, U) Baikal Rift, V) North China Basin.

We also see increased definition in the southeastern areas of the low velocity Iranian Plateau (G).

Using longer, thus deeper and faster, paths in these areas degrades our ability to image low-velocity zones when gradients are not accommodated. Note, for instance the sparsely instrumented Tibetan area (N), which requires the use of longer raypaths. Incorporating gradient improves the imaging of low velocity areas that are of tectonic importance.

We observe vertical gradients of upper mantle P velocity from -0.001 to 0.003 s^{-1} in Asia, with an average across Tibet of 0.0025 s^{-1}. The gradient image (Figure 8, bottom) appears to correlate best with known crustal thickness; highs are expected to indicate low thermal gradients in the mantle lid. Labels (Figure 8, bottom) correspond to: A) Anatolian Plateau, B) Arabian shield, C) Iranian Plateau, D) Tajik Basin, D) Hindu Kush, F) Tibetan Plateau, G) Sichuan Basin.

By solving not only for two-dimensional Pn slowness, but also for 2-D upper mantle gradient, we obtain a significant improvement in fit to the data. The inclusion of upper mantle gradient in the inversion allows us in particular to improve the imaging of shallow low-velocity regions, whose slowness estimates are skewed by longer rays sampling deeper paths in an ordinary Pn analysis. The gradients we have obtained appear to be correlated with crustal thickness. The central high in the Tibetan Plateau, of about 0.0025 s^{-1}, is in accordance with the one-dimensional (1-D) gradient found by Zhao and Xie (1993) of 0.003 s^{-1}. Our slightly lower value arises from the damping we have used in the tomographic process, which tends to mute the extrema of a function; we expect somewhat lower values here than in a more focused study.

Joint Tomographic Inversion of Surface Wave Dispersion, Receiver Functions and Satellite Gravity Data

We have recently developed a new joint inversion method using gravity and surface-wave group velocity data, which has been applied to the Tarim and Junggar sedimentary basins in central Asia (Maceira and Ammon, 2007; Steck et al., 2006b). The resulting model has been tested and shows a 73% improvement on Rayleigh-wave detection at short periods (Randall et al., 2006). Encouraged by these findings, we present a new 3-D shear-velocity/density model for the Asian continent constructed through joint inversion of different geophysical datasets. Our goal is to investigate the crustal and upper mantle structure beneath the region with increased

resolution of shallow geological structures via joint inversion of surface-wave group velocities, receiver functions and satellite gravity observations.

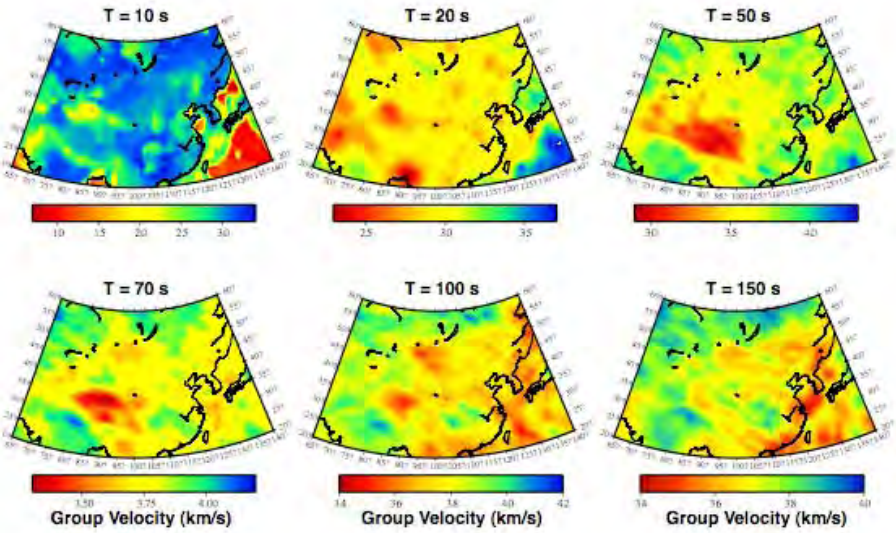

Figure 9. Fundamental mode Rayleigh wave group-velocity maps.

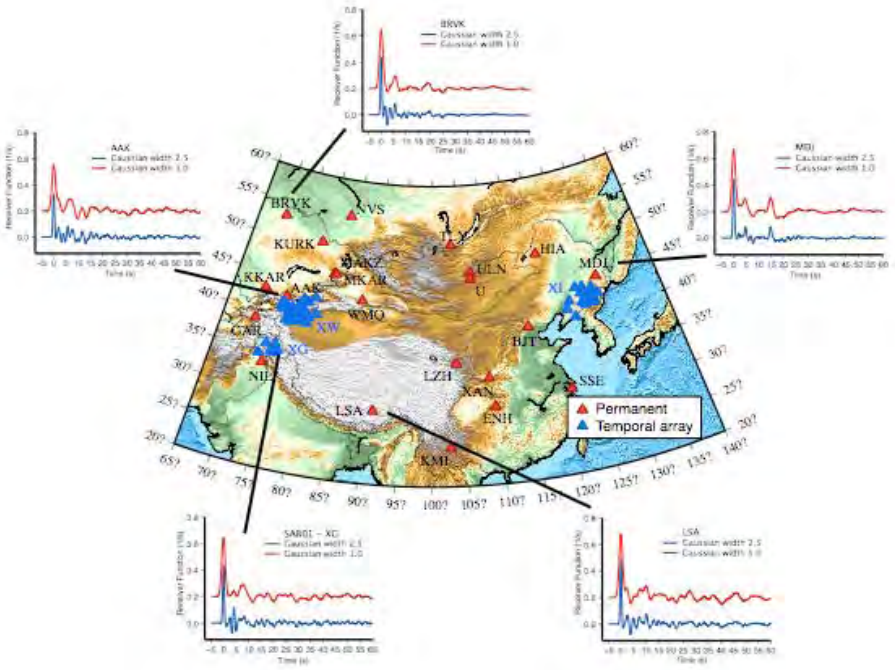

Figure 10. Topographic map of the study region with receiver functions for selected stations.

We parameterize the shear-wave velocity in terms of 1-D depth-dependent velocity profiles determined at the center of each cell in a grid of 1 degree by 1 degree. In each cell we consider three sets of data points: fundamental-mode group velocities, teleseismic P-wave receiver functions and free-air gravity anomalies. Surface wave dispersion measurements are primarily sensitive to vertical shear wave velocity averages, and receiver functions are sensitive to shear wave velocity contrasts and vertical travel-times; hence, shear velocity variations are usually the model parameters in this type of inversion studies. At shallow depths it is difficult to obtain high-resolution dispersion values and constrain the structure because the longer periods are less sensitive to upper crustal structures. Short periods are difficult to measure in tectonically and geologically complex areas. Alternatively, gravity inversions have the greatest resolving power at shallow depths. The gravity measurements supply constraints between seismic velocities and density. Thus by jointly inverting the three data sets, we expect to obtain a self-consistent 3-D shear velocity/density model with increased resolution of shallow geologic structures. Our approach to joint inversion follows the scheme described by Julià et al. (2000), with added gravity anomaly contributions.

Our dispersion velocity data set consists of fundamental mode Rayleigh-wave group velocities. We used the CUB (Colorado University at Boulder) Eurasian tomography model (Ritzwoller and Levshin, 1998; Levshin et al., 2001, 2002) in the period range between 8 and 150 s.

In general, the tomographic patterns in the CUB model show a very good correlation with known geologic and tectonic features in the area. Figure 9 shows fundamental mode Rayleigh wave group-velocity maps extracted from the CUB model that are used in the preliminary, simultaneous inversions of dispersion, receiver function and gravity, outlined below. Note that the color scale varies to preserve the details in each image.

We used teleseismic P-wave receiver functions (Ammon et al., 2004) for 45 stations across eastern Asia. Figure 10 shows a topographic map of the region under study; triangles represent stations analyzed in the receiver function analysis of Ammon et al. (2004). Sample receiver functions (in 2 bandwidths) are shown for selected stations. Initial peak on the receiver functions is generated by incident P arrival; subsequent arrivals are P-S converted waves from the structure beneath the recording station.

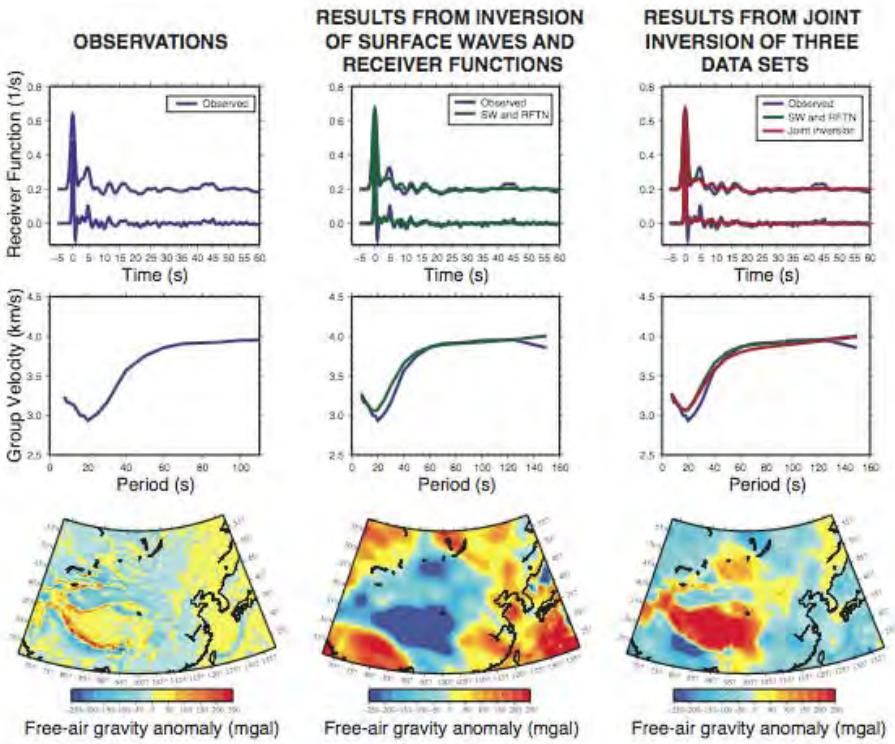

Figure 11. Observations, fit using surface wave dispersion and receiver functions, and fit using these plus satellite gravity.

Gravity observations were obtained from the Gravity Recovery and Climate Experiment (GRACE) satellite mission (Tapley et al., 2005).

An iterative, conjugate gradient-based least squares inversion is used to jointly model the three different data sets, using shear-velocity variations as the primary model parameters.

Figure 11 provides a comparison of the results of inversions of surface-wave dispersion observations and receiver functions, and gravity, surface wave dispersion and receiver functions. Top panels from left to right: receiver function (RFTN) data for a specific cell in our model (blue line); fit to the RFTN data from jointly inverting surface wave dispersion (SWD) and RFTN (green line); fit to the RFTN data from the joint inversion of the three data sets (red line). Middle panels from left to right: SWD data for the same typical cell (blue line); fit to the SWD from only inverting SWD and RFTN data (green line); fit to the SWD from the joint inversion of the three data sets (red line). Bottom panels from left to right: GRACE data for the region under study; predicted free-air gravity anomalies from the model resulting from inverting SWD and RFTN observations; predicted free-air gravity anomalies from the model resulting from the joint inversion of SWD, RFTN, and gravity observations.

The underlying philosophy of this effort is that the combination of the three types of data produces a more consistent Earth model. These results are preliminary and are primarily shown to illustrate the basic concepts in the analysis. Additional work is needed to improve and correctly predict the free-air gravity over such a large region.

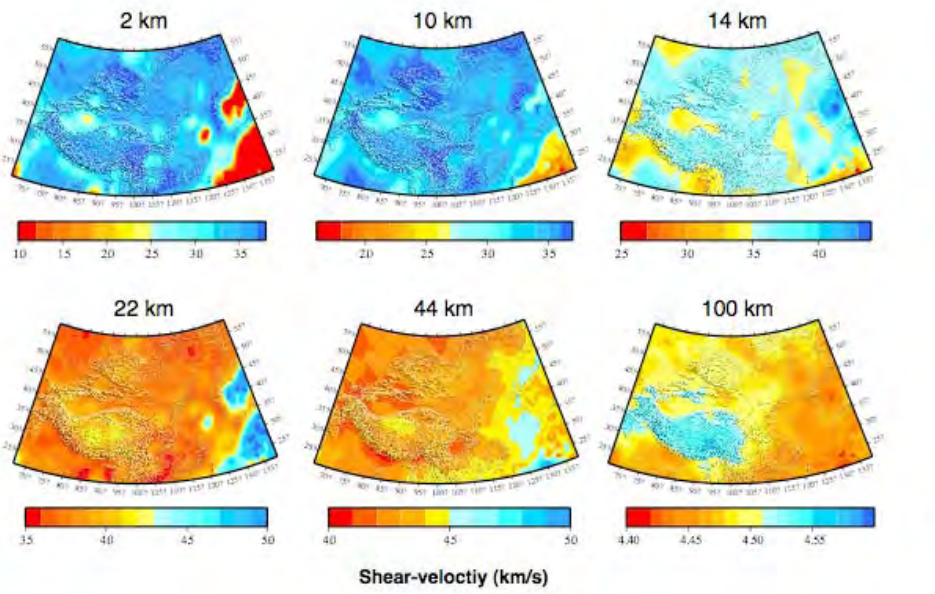

Figure 12. Preliminary shear velocity model for study area, determined through joint inversion of the three data sets.

Figure 12 shows the preliminary shear velocity model for Asia based on joint inversion of receiver function, dispersion curves and gravity; depth slices from six levels in the model are shown. Over a smaller region, Maceira and Ammon (2007) show that the addition of gravity observations can help sharpen structures blurred in surface-wave tomography. Here, high wave number signals in the deep parts of the model (where none of the data have the sensitivity or coverage to constrain such structures) suggest the mapping of shallow structure artifacts into the deeper parts of the shear-velocity model. More work is needed and planned on the integration of gravity and seismic signals over this large region.

CONCLUSIONS AND RECOMMENDATIONS

Results presented here confirm that innovative directions of research and important new data are improving the accuracy and applicability of our geophysical models for eastern Eurasia. The tremendous volume of new data at our disposal via the Siberian catalog is allowing us to undertake detailed modeling of this region that previously was poorly characterized in terms of its geophysical parameters. As new ways of addressing the complexities within the Earth are devised, we are able to incorporate a better understanding of their influence on our data products—such as the upper mantle gradient innovation in 2-D Pn mapping. Incorporating multi-parameter data sets, such as the satellite gravity in combination with seismic parameters, helps us to constrain inversions that previously were subject to ambiguity when only one type of data is used.

REFERENCES

Ammon, C. J., W. Sevilla, R. B. Herrmann, and G. E. Randall (2004). Systematic inversion of receiver functions and surface wave dispersion for crustal structure in central Asia, in *Proceedings of the 26th Seismic Research Review: Trends in Nuclear Explosion Monitoring*, LA-UR-04-5801, Vol.1, pp. 29–38.

Begnaud, M .L., L. K. Steck, and C. A. Rowe (2006). Improving seismic event locations in Asia by using catalog-scale empirical travel time correction surfaces, *EOS, Trans. AGU* 87: Fall Meet. Suppl. Abstract T51D-1550.

Bondar, L .S., C. Myers, F. R. Engdahl, and F.A. Bergman (2004), Epicentre accuracy based on seismic network criteria, *Geophys. J. Int.* 156: 483–496.

Hearn, T. M., S. Wang, J. F. Ni, Z. Xu, Y. Yu, and X. Zhang (2004). Uppermost mantle velocities beneath China and surrounding regions, *J. Geophys. Res.* 109: B11301, doi:10.1029/2003JB002847.

Julià, J., C. J. Ammon, R. B. Herrmann, and A. M. Correig (2000). Joint inversion of receiver function and surface wave dispersion observations, *Geophys. J. Int.* 143: 99–112.

Levshin, A. L., M. H. Ritzwoller, M. P. Barmin, and J. L. Stevens (2001). Short period group velocity measurements and maps in central Asia, in *Proceedings of the 23rd Seismic Research Review: Worldwide Monitoring of Nuclear Explosions*, LA-UR-01-4454, Vol. 1, pp. 258–269.

Levshin, A. L., J. L. Stevens, M. H. Ritzwoller, and D. A. Adams (2002). Short-period (7-s to 15-s) group velocity measurements and maps in central Asia, in *Proceedings of the 24th Seismic Research Review—Nuclear Explosion Monitoring: Innovation and Integration*, LA-UR-02-5048, Vol. 1, pp. 97–106.

Liang, C., X. Song, and J. Huang (2004). Tomographic inversion of Pn travel times in China, *J. Geophys. Res.* 109: B11301, doi:10.1029/2003JB002789.

Maceira, M. and C. J. Ammon (2007). Joint inversion of surface wave velocity and gravity observations and its application to Central Asian basins shear velocity structure, *J. Geophys. Res.* (submitted).

Mackey, K. G., K. Fujita, L. K. Steck, and H. E. Hartse (2003). Seismic regionalization in eastern Russia, in *Proceedings of the 25th Seismic Research Review—Nuclear Explosion Monitoring: Building the Knowledge Base*, LA-UR-03-6029, Vol. 1, pp. 73–82.

Mackey, K., H. E. Hartse, K. Fujita, L. Linkimer, L. Steck, R. Stead, and C. Rowe (2006). Seismic characterization of northeast Asia, in *Proceedings of the 28th Seismic Research Review: Ground-Based Nuclear Explosion Monitoring Technologies*, LA-UR-06-5471, Vol. 1, pp. 93–102.

McNamara, D. E., W. R. Walter, T. J. Owens, and C. J. Ammon (1997). Upper mantle velocity structure beneath the Tibetan Plateau from Pn travel time tomography, *J. Geophys. Res*. 102: 493–505.

Paige, C. C. and M. A. Saunders (1982). Algorithm 583, LSQR: Sparse linear equations and least-squares problems, *ACM Trans. Math Software* 8: 195–209.

Pei, S., J. Zhao, Y. Sun, Z. Xu, S. Wang, H. Liu, C. A. Rowe, M. N. Toksoz, and X. Gao (2007). Upper mantle seismic velocities and anisotropy in China determined through Pn and Sn tomography, *J. Geophys. Res*. 122: B05312, doi:10.1029/2006JB004409.

Phillips, W. S., H. E. Hartse, S. T. Taylor, and G. R. Randall (2000). 1 Hz Lg tomography in central Asia, *Geophys. Res. Lett*. 22: 3425–428.

Phillips, W. S., C. A. Rowe, and L. K. Steck (2005). The use of interstation arrival time differences to account for regional path variability, *Geophys. Res. Lett*. 32: L11301, doi:10.1029/2005GL022558.

Phillips, W. S., M. L. Begnaud, C. A. Rowe, L .K. Steck, S. C. Meyers, M. E. Pasyanos and S. Ballard (2007). Accounting for lateral variations of the upper mantle gradient in Pn tomography studies, *Geophys. Res. Lett*. (in press).

Ritzwoller, M. H. and A. L. Levshin (1998), Eurasian surface wave tomography: group velocities, *J. Geophys. Res*. 103: 4839–4878.

Steck, L. K., M. L. Begnaud, C. A. Rowe, and H. E. Hartse (2006a). Improved seismic event locations in Siberia using empirical and model-based travel-time corrections. *EOS, Trans, AGU*. 87: Fall Meeting Suppl., Abstract T51D-1549.

Sun, Y., X. Li, S. Kueli, F.D. Morgan, and M. N. Toksoz (2004). Adaptive moving window method for 3D P-velocity tomography and its application in China, *Bull. Seismol. Soc. Am*. 94: 740–746.

Thurber, C. H. (1983). Earthquake location and three-dimensioal crustal structure in the Coyote Lake area, central California, *J. Geophys. Res*. 88: 8226–8236.

Zhao, L.-S. (1993). Lateral variations and azimuthal isotropy of Pn velocities beneath Basin and Range Province, *J. Geophys. Res*. 98: 22109–22122.

Zhao, L-S. and J. Xie (1993). Lateral variations in compressional velocities beneath the Tibetan Plateau from Pn travel time tomography, *Geophys. J. Int.* 115: 1070–1084.

LG AND PG ATTENUATION IN THE MIDDLE EAST

Eric A. Sandvol[1], Bao Xueyang[1], Ekrem Zor[2], Jiakang Xie[3], Brian J. Mitchell[4], and David P. Schaff[5]

University of Missouri[1], TUBITAK Marmara Research Center—Earth Science Institute[2], AFRL/VSBYE[3], St. Louis University[4], and Lamont Doherty Earth Observatory, Columbia University[5]

Sponsored by National Nuclear Security Administration
Office of Nonproliferation Research and Development
Office of Defense Nuclear Nonproliferation

Contract Nos. DE-FC52-03NA99518[1,2], DE-FC52-03NA99519[3,5], and DE-FC52-03NA99520[4]

ABSTRACT

In order to construct reliable frequency-dependent Q models for both Lg and Pg, we have used approximately 8000 waveforms from approximately 500 events recorded by 11 permanent and temporary networks throughout the Middle East. Using these waveforms, we have developed a tomographic model with frequency-dependent Q using direct Lg waves in this region. We have also measured Pg across the Middle East including the Arabian platform and the Arabian shield. In general, we found lower Pg Q within the Arabian platform and less Pg attenuation for much of the Arabian Shield. Not surprisingly we found that the Pg Q does not vary as much as Lg Q; however, the general trend is the same: low Q within the plateau and high Q within the stable Arabian plate. The frequency dependence, however, is different from what we have found for Lg. We have found a higher average eta (~0.4) for Pg as compared with Lg. Resolution tests of 2x2 cell size for our Pg Q tomography indicate that we have very good resolution throughout much of the Anatolian Plateau and resolution of anomalies larger than 200 km in much of the northern Arabian plate.

We have begun work on validating our Lg and Pg attenuation models. We are developing a catalog of "amplitude ground truth" seismic events. We will use these events to test whether path corrections from our attenuation models can successfully predict the source spectra (i.e., moment and corner frequency). In order to develop a catalog of events with reliable event spectra, a search was performed on 373 events at 89 stations in the Middle East to look for doublets or repeating earthquakes. Exactly the same procedures and parameters were employed as those by Schaff and Richards (2004) who found 9% of the events in and near China. Only two events or one pair met the same criteria for repeating events as were used in China. This is 1% of the seismicity, as compared to 9% from all the currently available waveforms in China (1,301 events out of ~14,000). This difference may be due to the absence of magnitude 3.0s from the Middle East data set; these events would probably have a greater chance of having similar waveforms due to simpler rupture areas and closer proximity to one another. This catalog of similar waveforms will also allow us to calibrate and adjust our model to better predict a reliable source spectra.

OBJECTIVES

The objective of this study is to obtain laterally varying Q models for multiple regional waves, including Sn, Lg and Pg for the Middle East. We are developing Q models that have the highest possible lateral resolution. For some waves such as Lg and Pg, the resulting Q model will be in the form of a tomographic Q map; for other waves such as Sn, the resulting models will consist of blockage maps. Blockage effects will be represented by low effective Q values in the models.

Challenges Associated with Regional Phase Q Measurements

It is well known that the attenuation rate of regional waves, including the high-frequency Lg, Pg, Sn and Pn and the lower-frequency surface waves, is highly variable over major continents. Reliable knowledge of the lateral variation in regional wave attenuation rate, or its inverse, Q, is extremely important for event detection and identification in the nuclear monitoring program. The preferred way to acquire this knowledge is to conduct tomographic mapping of regional wave Q. However, in contrast to the wide success in seismic velocity tomography since the 1970s, there has been relatively little progress in Q tomography. The main obstacle is the difficulty in obtaining reliable measurements of Q: the observed amplitude of high-frequency waveforms is affected by a number of factors, including (1) possible non-isotropic source radiation patterns, (2) source spectra that may be only grossly described by a seismic moment and a corner frequency; (3) geometrical spreading terms caused by the wave front expansion which, in complex 3D Earth structures, may cause focusing and defocusing; and (4) potential site responses caused by local structural complications under the seismic stations. Effects of these factors are difficult to correct, causing biases in Q measurement. We have assembled a unique waveform database of waveforms with reliable instrument response information for both short period and broadband stations.

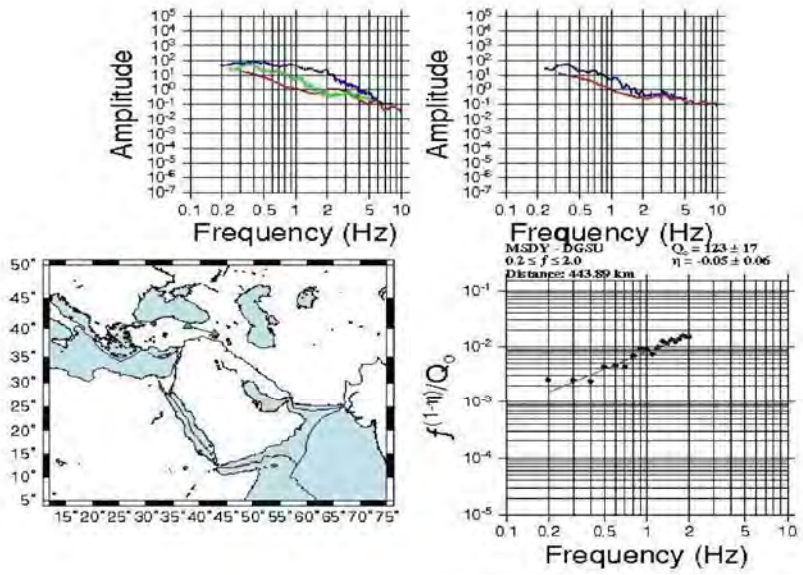

Figure 1. **Examples of Lg spectra analysis and calculation for Q via the 2-station method. We used a group velocity window length of 1 km/s and calculated smoothed spectra.**

RESEARCH ACCOMPLISHED

Using a two station approach we have determined the direct wave Q for both Pg and Lg phases traveling across a large portion of the Middle East. An example of the processing we used to determine the two-station Q for Lg is shown in Figure 1. To define the alignment we use an angle $\delta\theta$, which is the difference between the azimuths from the source and the two stations. Q_o and η values may contain errors because of the effects of Pg and *Lg* attenuation outside the path and a non-isotropic source radiation pattern using non-zero $\delta\theta$. In order to minimize this error, we chose to set $\delta\theta_{max}$ to 15° for both phases as explained by Xie et al. (2004) based on results of Der et al. (1984). The second important parameter in this method is the inter-station distance. The potential error caused by inter-station

distance is strongly related to the estimated Q_o value for the corresponding path and can be estimated by using the method given by Xie et al. (2004).

In order to keep our errors lower than 35% with a given modeling error value (δx=0.2), the inter-station ratio between Q_o (Q at 1 Hz) and Δ_{ij} (the inter-station distance) should not be greater than 1.6. By applying the criterion of $\delta\theta_{max}$= ±15º and the inter-station ratio = 1.6 to the ~2300 Lg spectra, we have found 1,383 two-station paths from approximately 140 regional events (Figure 1). When calculating Lg Q_o and η, we did not fix the Lg window on the waveform because Lg velocity typically varies by 20% from one region to another as emphasized by Nuttli (1973).

We have compared our results for Lg with coda methods and found that at the longer wavelengths, the relative attenuation structures agree quite well (Figure 2). The excellent ray path coverage and the nature of our tomography accounts for smaller scale fluctuations in the direct wave Q model (e.g., Figure 2b) that is not present in the coda Q maps (Figure 2a). In general, the smallest Q values are found throughout western and central Anatolia, with much higher Q values in the Saudi Arabian shield. In terms of the frequency dependence of the coda and direct Lg Q measurements, the coda measurements of η are consistently larger. This has been true not just for the Middle East but also for measurements throughout Eurasia. However, we do observe consistent spatial variations of η. This includes the finding of smaller values for the Arabian Shield (-0.1 for the direct phase and 0.4 for the coda measurements) and larger values for the Anatolian Plateau (0.5 for direct phase and 1.0 for coda).

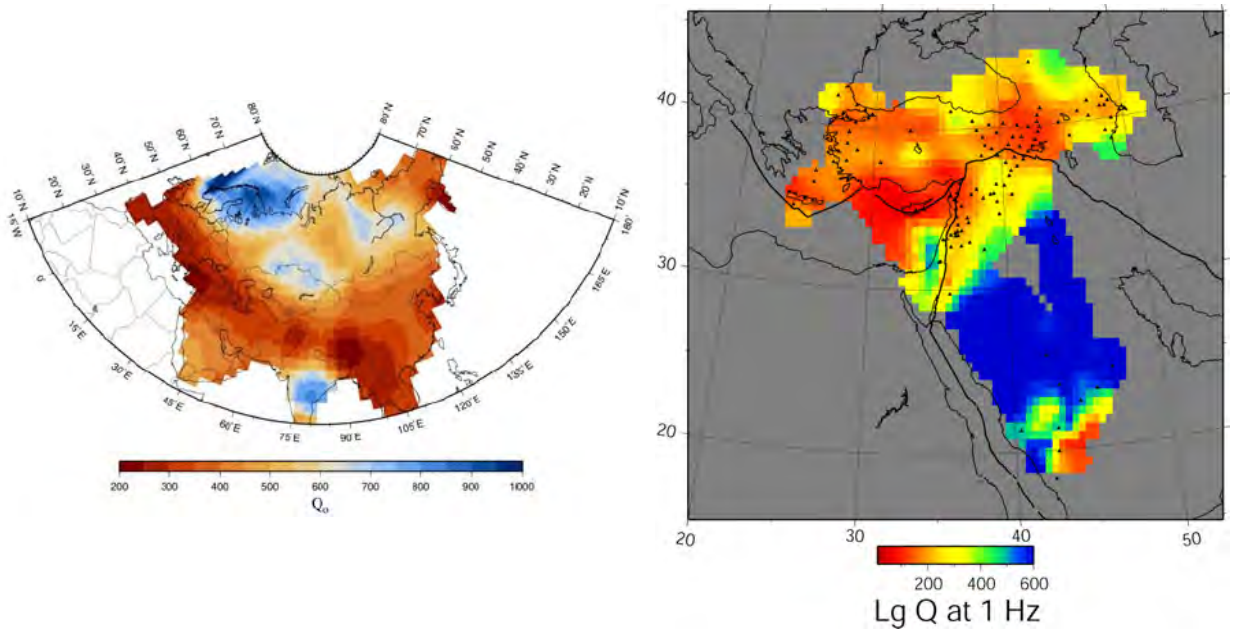

(a) **(b)**

Figure 2. A comparison of Lg Q_0 using the (a) direct wave two station methods and (b) coda (Cong and Mitchell, 2005).

Mapping Variations in η

We also finalized our model for the frequency dependence for both Pg and Lg frequency dependent Q. Figure 3 shows our map of η for the northern Middle East for both Pg and Lg. We found an anomalously low average η for the Middle East (0.22) for Lg including large regions of negative η. We found a correlation between large Q-values and small η values that is consistent with frequency dependent coda-Q measurements. The spatial variation in η also suggests that these anomalously low Q measurements might be, to some extent, a function of Sn-to-Lg converted energy. Not surprisingly, we found that the Pg Q does not vary as much as Lg Q; however, the general trend is the same: low Q within the plateau and high Q within the stable Arabian plate. Our estimated η value, however, is higher (~0.4) for Pg than for Lg (Figure 3). This observation is consistent with the idea that some of the anomalously low-frequency

dependence for Lg is caused by high-frequency energy leaking into the crust because this effect might be different for Pn-to-Pg converted energy.

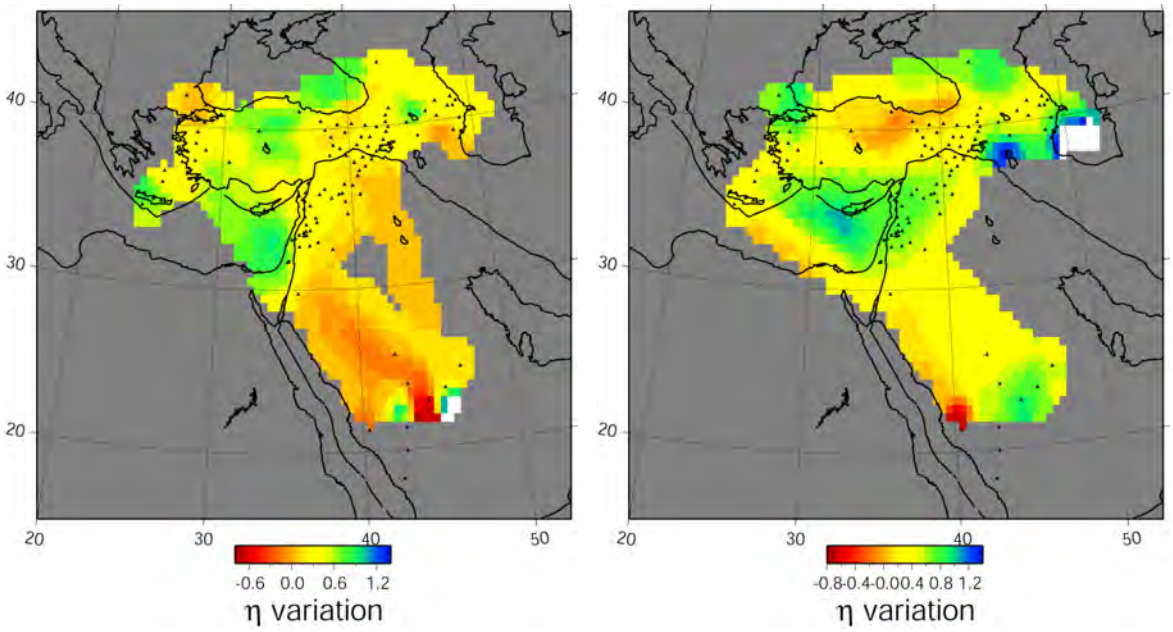

(a) **(b)**

Figure 3. A comparison of η values for (a) direct wave Lg model and (b) direct wave Pg model. The mean η values for Pg is substantially larger (0.4) than for Lg (0.2).

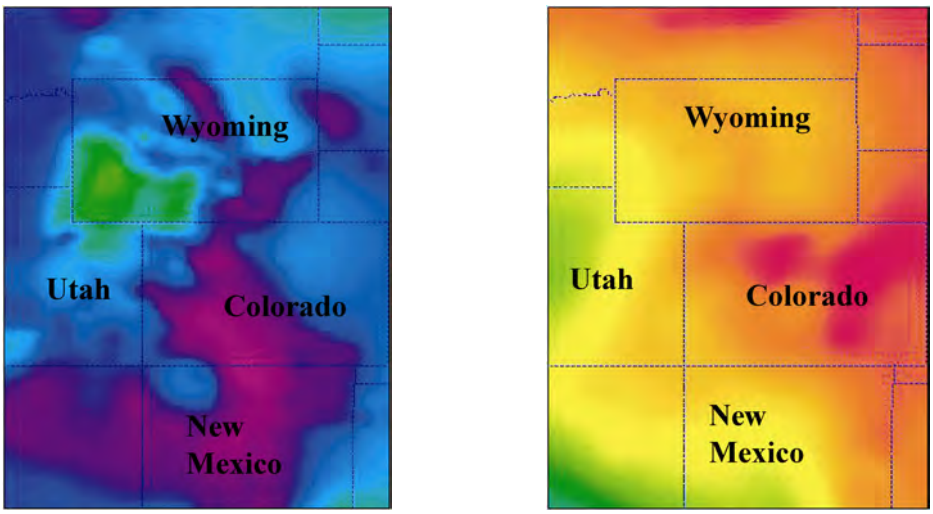

(a) **(b)**

Figure 4. (a) A map of the depth of sediments for the Rocky Mountains and surrounding regions. Colder colors indicate less sediment thickness. (b) A Moho map used for the calculation of synthetic regional seismograms. Hotter colors indicate thicker crust.

Investigating Pg Behavior using Synthetic Seismograms

In order to better understand the behavior of Pg propagation we calculated a fairly large number of synthetic waveforms to neglect the influence of instrument response and intrinsic attenuation terms by initialization of Q. We calculated these synthetic regional waveforms using the GEON-SYNSEIS tool that utilizes the E3D finite difference codes for a series of source receiver geometries. The model is from the GEON database for crustal and sediment thickness data for North America (Figure 4). Using this model and the SYNSEIS module we calculated

approximately 100 synthetic waveforms to investigate the behavior of Pg waveforms in a complex two-dimensional velocity model. In order to isolate the effects of scattering attenuation, we created a model with a uniform Qp and Qs (Figure 5). We found some correspondence between changes in sedimentary cover and Pg Q, which agrees with some of our observations that we have made for Pg propagation in the Middle East.

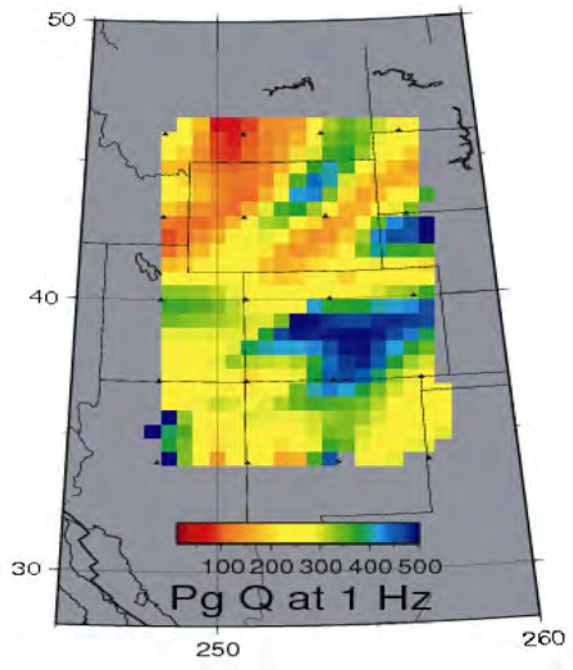

Figure 5. Pg Q estimates for a tomographic model using finite difference synthetics created from a model with a uniform intrinsic attenuation for the entire crust. We are using these synthetics to investigate the sensitivity of Pg waveforms to crustal structure.

In order to solve for the Pg Q values we assumed a geometric spreading term very similar to that of Lg. Because this is not necessarily a good assumption, we have begun to work on determining a reliable geometrical spreading term for Pg propagation in the Middle East. In order to measure the Pg geometric spreading, we estimated the Pg amplitudes at 1 Hz and then normalized the Pg amplitudes in order to determine the average distance relationship. We have found evidence of Pg propagation well beyond 12 degrees. Much of the scatter in Figure 1 can be attributed to lateral variations in the Pg attenuation structure.

Validation of Q Models

We have also begun work on validating our Lg and Pg attenuation models. We have developed a catalog of "amplitude ground truth" seismic events. We will use these events to test whether path corrections from our attenuation models can successfully predict the source spectra (i.e., moment and corner frequency). In order to develop a catalog of events with reliable event spectra, a search was performed on 373 events at 89 stations in the Middle East to look for doublets or repeating earthquakes. Exactly the same procedures and parameters were employed as were used by Schaff and Richards (2004) that found 9% of the events in and near China were repeating with cross-correlation coefficients (CC) above 0.8 and separation distances of no more than 1 km. Windows started 5 s before the P-wave and ended 40 s after the Lg-wave. The waveforms were filtered from 0.5 to 5 Hz. Only two events or one pair met the same criteria for repeating events as were used in China. This is 1% of the seismicity as compared to 9% in China (1,301 events out of ~14,000). However, the correlations are intended to find similar events that are close enough to use as empirical Greens functions for Q tomography.

Figure 6d shows the separation distance of the pairs that met the CC > 0.5 criteria, revealing that most of them indeed are close to each other within location errors. One explanation of why there is a smaller percentage of similar events in the Middle East as compared to China is the separation distance. 110 out of 373 total events (29%) have at

least one other event occurring within 10 km based on the catalog locations in the Middle East, whereas in China, 5,152 out of 14,214 events (36%) have at least one other event within 10 km based on the locations in the Annual Bulletin of Chinese Earthquakes (ABCE). The magnitude distributions for the two regions are similar (Figures 6a and 6b) for magnitude 4 and larger, so greater source complexity for larger magnitudes doesn't seem to be the reason for the smaller percentage of high correlations. Although magnitude 3.0s are missing from the Middle East dataset which in general probably have a greater chance of having similar waveforms. This is because these smaller events have simpler rupture areas and are very often in close proximity to one another. The other reason that the waveforms could be less similar in the Middle East would be if there were greater variability in focal mechanisms between nearby events. We are attempting to solve this problem by extracting many more waveforms with smaller magnitudes than we previously used in our two-station approach. The catalog of events for which we have collected waveforms is shown in Figure 7. We expanded our two-station waveform database by a factor of 10 in order to find more highly correlative waveforms from which we can create a reliable catalog of known source spectra.

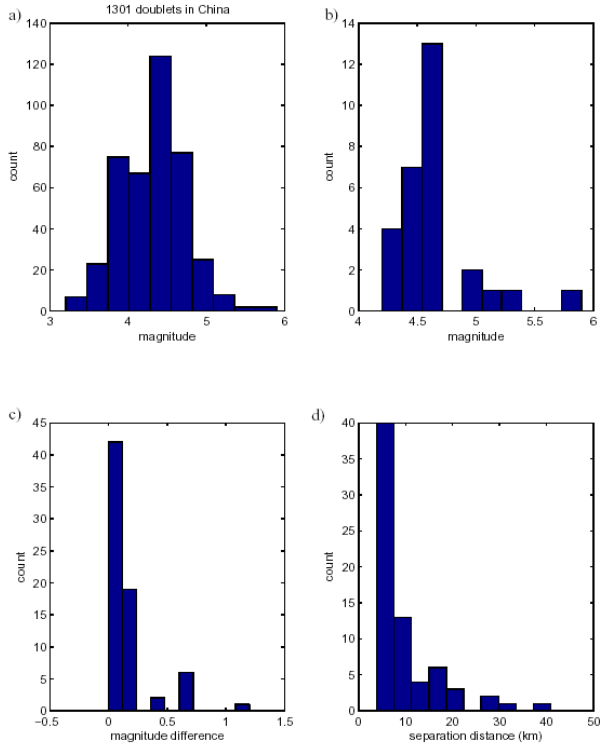

Figure 6. Comparison of magnitude distribution for doublets in China (a) and the Middle East (b). Distribution of magnitude difference (c) and separation distance (d) for pairs meeting the CC > 0.5 criteria.

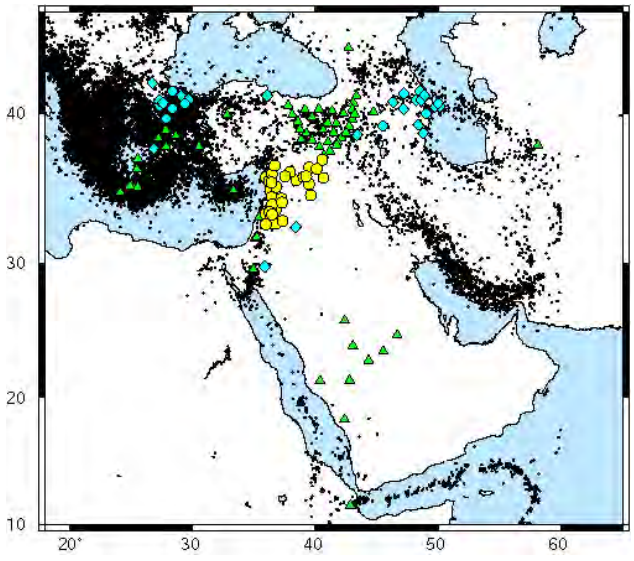

Figure 7. A map showing all seismic stations (colored symbols grouped by network) and seismic events from which we have collected seismic waveforms. We are in the process of searching this database to find event pairs with large cross-correlation coefficients.

CONCLUSIONS AND RECOMMENDATIONS

In this study, we processed a large set of new broadband waveform data to obtain both a Pg and Lg Q model for much of the Middle East. The resulting tomographic model in Figure 2b clearly shows the variation in Lg Q across the boundary between the Arabian Plate and the Turkish Plateau portion of the Eurasian Plate. The Lg Q_o values are generally higher within the Arabian Plate than beneath the Turkish Plateau. Other studies have similarly concluded that Lg propagation in the Turkish-Iranian Plateau is usually blocked or highly attenuated (Sandvol et al., 2001; Al-Damegh et al., 2004, Cong and Mitchell, 2005). We also observe substantial variation in Pg and Lg Q_o values within the Arabian Plate itself; we observe higher values beneath the Arabian shield than beneath the Arabian and northern Arabian Platform.

High Pg and Lg attenuation values within the Anatolian plateau (Q_o ~100–200) may be caused by a combination of scattering and intrinsic attenuation. Scattering attenuation is due to the tectonic complexity and the intrinsic attenuation could be due to the widespread crustal melting. However, the low Q_o values in eastern Anatolian plateau (~70–100) and portions of western Turkey (~60 to150) are probably due to the widespread Quaternary volcanism. In western Turkey, there is a correlation with the location of the young volcanism and the geothermal activity (İlkışık, 1995; Göktürkler et al., 2003). Zhu et al. (2006) have shown that the crustal thickness of western Turkey probably does not change rapidly enough to reduce or block the Lg phases and or affect Pg propagation. Beneath the western Taurus Mountains in southern Anatolia, relatively normal Pg and Lg Q_o values (~200–300) have been found. These relatively higher values may be related to the root of the mountain that would comprise a stable continental crustal waveguide like that in southernmost Tibet in the general region of the high Himalayas (>300) (Xie et al., 2004). Furthermore, the sedimentary cover is limited in this region, which might also improve the efficiency of Lg propagation in this region and attenuate the Pg waveforms. This would help to explain the very high Lg/Pg ratios that were found by Sandvol et al., (2001). For northeastern Turkey, the Caucasus and Azerbaijan, we also found some low to normal Lg Q_o values (~170–180) as well as some blocked two-station paths.

We found large variations in Pg and Lg Q_o for paths crossing the Arabian Peninsula (~300-800). The northern Arabian platform crust has low to normal Lg Q_o values (~300–350). In addition, we observe high Q_o values (~670–800) for the southern Arabian Plate where previous Lg/Pg studies show little attenuation. This is probably due to the lack of any substantial sedimentary cover in the Arabian shield. We also observe lower Q values (~550) for paths crossing the northern and southern Arabian platform where the sedimentary layer is thicker than the western Arabian plate. Additionally, we have found a dramatic decrease in Lg Q_o across the Arabian-Eurasian plate boundary. This is mostly due to a fundamental difference in the rheology of the Anatolian crust compared with the Arabian crust. Paths to the south of the Bitlis suture have Lg Q_o values of ~350–550 but the paths crossing the Bitlis suture have an Lg Q_o of ~200. This decrease may be related to the higher intrinsic attenuation due to partial melt in the eastern Anatolian Plateau. In contrast, the Pg Q values are uniformly low throughout the northernmost Arabian plate and into the Anatolian plateau.

Our primary focus for the remainder of our project is to attempt to validate both our final Pg and Lg Q models. We have finalized these models; however, it is important to verify that they can be used to extract information about the source spectra before they can be helpful in extracting reliable source spectra information (i.e., corner frequency and stress drop). Thus we are continuing our work on developing a method to validate our Lg and Pg attenuation models. In order to accomplish this validation we must create a catalog of calibration seismic events in which we have reliable earthquake source spectra. In order to obtain these events we are going to use earthquake event pairs with from which we can obtain the earthquake source spectra parameters. The resulting catalog can be used to both validate and to calibrate our existing Pg and Lg models. We are planning to adjust our tomographic models to successfully extract the source spectra in order to help create transportable discriminants for the Middle East.

ACKNOWLEDGEMENTS

We would like to thank Randa Mohamad and Dr. Niyazi Turkelli for providing data from the Syrian National Seismic Network and the Kandilli Observatory and Earthquake Engineering Institute network, respectively, and for assisting in the analysis of portions of the data. We would also like to thank Dr. Rob Mellors for providing data from the Azerbaijan Seismic Network.

REFERENCES

Al-Damegh, K., E. Sandvol, A. Al-Lazki, and M. Barazangi (2004). Regional seismic wave propagation (Lg and Sn) and Pn attenuation in the Arabian Plate and surrounding regions, *Geophys. J. Int.* 157: 775–795.

Cong, L. and B. Mitchell (2005). Regional variation in Rayleigh wave attenuation in southern asia predicted by new maps of Lg coda Q and its frequency dependence at 1 Hz, in *Proceedings of the* 27th *Seismic Research Review: Ground-Based Nuclear Explosion Monitoring Technologies*, LA-UR-05-6407, Vol. 1, pp. 23–30.

Der, Z., M.E. Marshal, A. O'Donnell, and T.W. McElfresh (1984). Spatial coherence structure attenuation the Lg phase, site effects, and interpretation of the Lg coda, *Bull. Seismol. Soc. Am.* 74: 1125–1148.

Göktürkler, G., M. Salk, and C. Sari (2003). The numerical modelling of the conductive heat flow in western Anatolia, *The Journal of the Balkan Geophysical Society* 6: 1–15.

İlkişik, O. M., (1995). Regional heat flow in western Anatolia using silica temperature estimates from thermal springs, *Tectonophysics.* 244: 175–184.

Nuttli, O. W. (1973). Seismic wave attenuation and magnitude relations for eastern North America, *J. Geophys. Res.* 78: 5212–5218.

Sandvol, E., K. Al-Damegh, A. Calvert, D. Seber, M. Barazangi, R. Mohamad, R. Gok, N. Turkelli, and C. Gurbuz (2001). Tomographic imaging of observed regional wave propagation in the Middle East, *Pure Appl. Geophys.* 158: 1121–1163.

Schaff, D.P. and P.G. Richards (2004). Repeating seismic events in China, *Science* 303: 1176–1178.

Xie, J., R. Gok, J. Ni, and Y. Aoki (2004). Lateral variations of crustal seismic attenuation along the INDEPTH profiles in Tibet from Lg Q inversion, *J. Geophys. Res.* 109: B10308, doi:10.1029/2004JB002988.

Zhu, L., B. Mitchell, N. Akyol, I. Çemen, and K. Kekovalı (2006). Crustal Thickness Variation in the Aegean Region and its implications for the Extension of Continental Crust, *J. Geophys. Res.* 111: doi:10.1029/2005JB003770.

TRANSITION ZONE WAVE PROPAGATION: CHARACTERIZING TRAVEL-TIME AND AMPLITUDE INFORMATION

Peter M. Shearer and Jesse F. Lawrence

University of California San Diego, Institute of Geophysics and Planetary Physics

Sponsored by Air Force Research Laboratory

Contract No. FA8718-06-C-0005

ABSTRACT

We characterize transition-zone seismic wave propagation by mapping and calibrating the travel-time and amplitude behavior of *P* waves traveling through the transition zone at epicentral distances from 13 to 30 degrees and modeling the triplications resulting from the 410- and 660-km discontinuities. We have built an online database of waveforms from the Incorporated Research Institutions for Seismology (IRIS) Fast Archive Recovery Method (FARM) archive from 1990 to 2005, which consists of broadband data from the global seismic networks as well as portable seismic arrays deployed in Program for Array Seismic Studies of the Continental Lithosphere (PASSCAL) experiments. We process the data in order to compute source and station amplitude terms to correct for different magnitude sources and near-receiver site effects as well as errors in the instrument response functions. We use records from the full teleseismic *P* distance interval to estimate source-time-function envelopes and deconvolve them from the traces, discarding data from sources that last longer than 60 s and signals with low signal-to-noise ratios (snr < 3). The deconvolved traces are stacked into bins according to distance, providing an initial distance (or Earth-structure) wavefield term. We also stack the deconvolved traces into bins for each station, providing an initial station wavefield term. Through several iterations we converge upon solutions for the event, station, and structure wavefield terms. This deconvolution technique is necessary to combine data from many different sources. We then compute both global and regional Earth-structure terms to obtain the average time-versus-distance amplitude of the wavefield, focusing on the 13 to 30 degree interval that is most sensitive to transition-zone structure. Because the timing of the secondary branches is quite variable, we implement an envelope-function stacking method in order to obtain robust results. We model our data stacks using WKBJ synthetic seismograms and a niching genetic algorithm to explore the model space of different transition-zone velocity structures. We compare these results with long-wavelength models of 410- and 660-km discontinuity topography obtained from *SS* precursors and more detailed images beneath individual seismic stations derived from receiver functions. Our goal is to produce integrated transition-zone models of seismic velocity and discontinuity topography that will improve our ability to locate and estimate magnitudes of events recorded at regional distances.

OBJECTIVES

This project studies the effects of heterogeneous transition-zone structure on seismic travel times and amplitudes. Accurate predictions of *P*- and *S*-wave travel times and amplitudes at distances between 13 and 30 degrees are hindered by the sensitivity of the multiple travel-time branches at these distances to variable structure in the mantle transition zone. Both discontinuity topography and bulk seismic velocity anomalies perturb seismic ray paths, which causes focusing and defocusing effects on wave amplitudes as well as travel-time anomalies. However, travel-time and amplitude information is critical for locating and estimating magnitudes of target events. By comparing regional variations of triplication amplitudes and travel times with predictions of 3D seismic velocity models, we will obtain improvements in mantle transition-zone models, as well as in the estimated locations and magnitudes of recorded events.

The effect of the mantle discontinuities at 410- and 660-km depth is shown in Figure 1, which depicts a series of *P*-wave ray paths between 13 and 35 degrees. Retrograde branches result from the velocity jump at each of the discontinuities, causing the familiar double triplication centered at about 20 degrees. However, the positions of these branches are very sensitive to the discontinuity depths, which typically vary by 30 km or more (e.g., Shearer, 1990, 1991, 1993; Shearer and Masters, 1992; Flanagan and Shearer, 1998a,b; Gu et al., 1998), and to the size of the velocity jumps at the discontinuities, which also exhibit considerable variation (e.g., Melbourne and Helmberger, 1998; Shearer and Flanagan, 1999; Chambers et al., 2005). In addition, there is some sensitivity to 3D velocity variations in the transition zone.

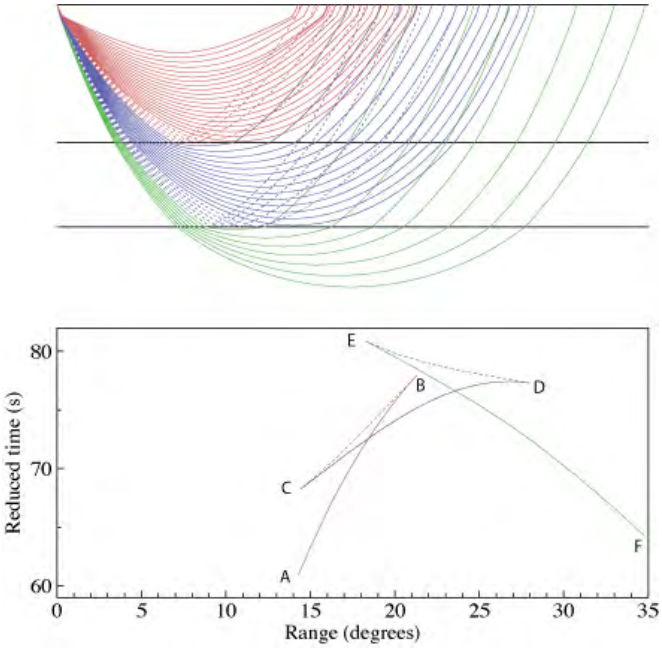

Figure 1. Discontinuities in the mantle transition zone at 410- and 660-km depths cause a pair of triplications in *P*- and *S*-wave arrivals between about 15 and 30 degrees. The ray paths (top) are color-coded, and correspond to the different branches in the travel-time curve plotted below (reduced at 10 s/degree). The AB branch consists of direct waves that bottom above the 410-km discontinuity (red solid). The BC branch reflects at 410 km (red dashed). The CD and DE branches bottom above and reflect off the 660-km discontinuity (blue solid and dashed). The EF branch bottoms in the lower mantle. This figure is adopted from Shearer (2000).

We compare observed *P*-wave travel times and amplitudes with predictions based on the best current models. These tests illuminate the strengths and weaknesses of these models, from which we determine if the models are sufficient to explain anomalous travel times and amplitudes at these distances (and consequently check to see how robust our current event locations and amplitude predictions are). This project compares times and amplitudes recorded at both temporary and permanent seismic stations for all triplication phases, not just the first arrivals. The triplications cause

difficulties for traditional methods of source location, magnitude estimation, and inversions for 3D velocity structure. Therefore, triplication data are typically avoided for seismic tomography and source location. However, details of the triplications can be useful for characterizing heterogeneity and calculating better source locations. With sufficient data the secondary branches can be used to model variations in discontinuity topography and seismic velocity. Once the structural properties are determined, the high sensitivity of triplication travel-time and amplitude fluctuations to source location and magnitude make triplications ideal for determining source characteristics. However, without an appropriate transition zone model, these times cannot yield accurate times or amplitudes.

The relevance of our results for nuclear test monitoring is that better structural models of transition-zone structure will reduce source location and magnitude uncertainties. The anomalous arrival times and amplitudes between 13 and 30 degrees currently limit the usefulness of regional phase data in calculating accurate source locations and event magnitudes. However, records from closer distances are not likely to be available in many parts of the world and small magnitude events are often not well recorded at longer distances because of the sharp drop in *P* and *S* amplitudes that occurs just beyond 30 degrees. Thus unraveling the complexities of the travel-time triplications and improving our models of the transition zone are likely to be critical for accurate monitoring of a significant number of target events.

RESEARCH ACCOMPLISHED

FARM Database

Our initial efforts have concentrated on assembling a database of waveforms from the IRIS FARM archive, which consists of broadband data from the global seismic networks as well as portable seismic arrays deployed in PASSCAL experiments. This involves transferring the data from the IRIS DMC and converting waveforms to seismic analysis code (SAC). We then run programs for quality assurance, redundancy checks, instrument response correction, meta-data archiving, and signal rotation to tangential and radial. The SAC files are currently stored on a RAID system, with backup for redundancy in the event of hardware failures.

We have also completed computing index files and signal-to-noise estimates for the *P* and *S* arrivals, which facilitates later processing and also provides a check on the timing integrity of the SAC waveforms. Our basic approach is to measure the signal-to-noise as the ratio between the maximum amplitude (peak to trough) in a time window that contains the phase of interest and a pre-event noise window of equal length. Because the raw data are broadband, we perform this operation separately for different frequency bands.

Amplitude Analysis

Triplicated phases are difficult to distinguish from each other, overlapping in time, and having varying amplitudes. This is further compounded by unconstrained source-time functions of the earthquake, and heterogeneous structure beneath seismic stations causing waveform variability. Here, we attempt to remove the source and station terms from all measured amplitudes for high signal-to-noise *P* waves, to constrain the amplitude variation that results from seismic structure. Initially we assume that the maximum peak-to-peak log amplitude (max-min), a_i, of the i^{th} *P*-wave is the sum of a source term, s_j, a receiver term, r_k, and an Earth response term, e_l,

$$a_i = s_j + r_k + e_l. \qquad (1)$$

Given N_a *P*-wave amplitudes, from any N_s sources, recorded at N_r sources, it is possible to solve for N_e Earth-response terms as a function of distance. The initial source term for each event is the mean of all a_i values for that event. The initial receiver terms are the means of all log amplitude measurements for that receiver minus the corresponding source terms ($r_k = a_i - s_j$). The distance-dependant Earth-response term is the mean of all log amplitude measurements for each distance minus the corresponding source and receiver terms ($e_l = a_i - s_j - r_k$). We can then iteratively solve for more accurate source, receiver, and Earth response terms, with

$$s_j = a_i - r_k - e_l \qquad (2)$$

$$r_k = a_i - s_j - e_l \qquad (3)$$

$$e_l = a_i - s_j - r_k. \quad (4)$$

When applied to all *P*-wave data in the FARM database, this method provides an estimate of amplitude as a function of distance, as shown in Figure 2. The overall amplitude versus distance behavior is very similar to that obtained by Veith and Clawson (1972) for magnitude calibration. The 13 to 33 degree distance range stands out as anomalous compared to the trend of decreasing amplitude with distance.

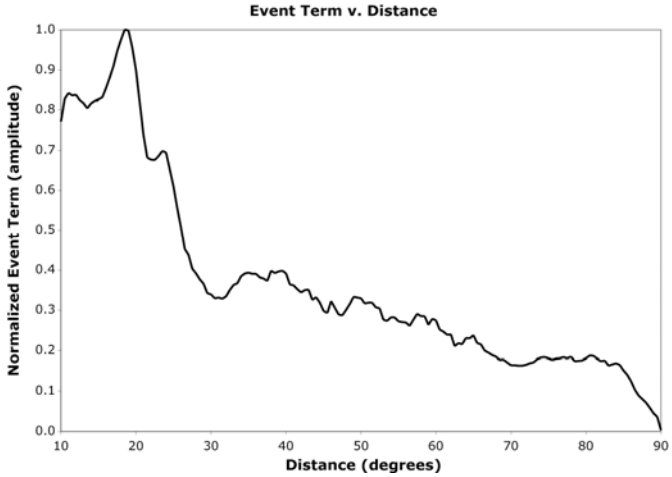

Figure 2. Distance-dependant Earth-response terms for amplitude from 10 to 90 degrees.

We have adapted a WKBJ synthetic seismogram code (Chapman, 1978) to generate suites of model predictions for comparisons to the data. Our analyses have concentrated on characterizing the globally averaged wavefield as a starting reference point for studies of regional variations. By comparing the Earth-response amplitude terms to WKBJ synthetic waveform amplitudes, it is possible to determine which seismic models are most probable. The amplitudes in the 13 to 33 degree range are sensitive to the seismic velocity structure of the transition zone. Amplitudes are highly sensitive to interface depth, sharpness, and velocity contrast for each of the discontinuities (*410*, *520*, and *660*). Figure 3 shows how amplitude can vary with small changes in seismic velocity structure. While not modeled here, the amplitudes are also strongly dependant upon quality factor, or attenuation, structure.

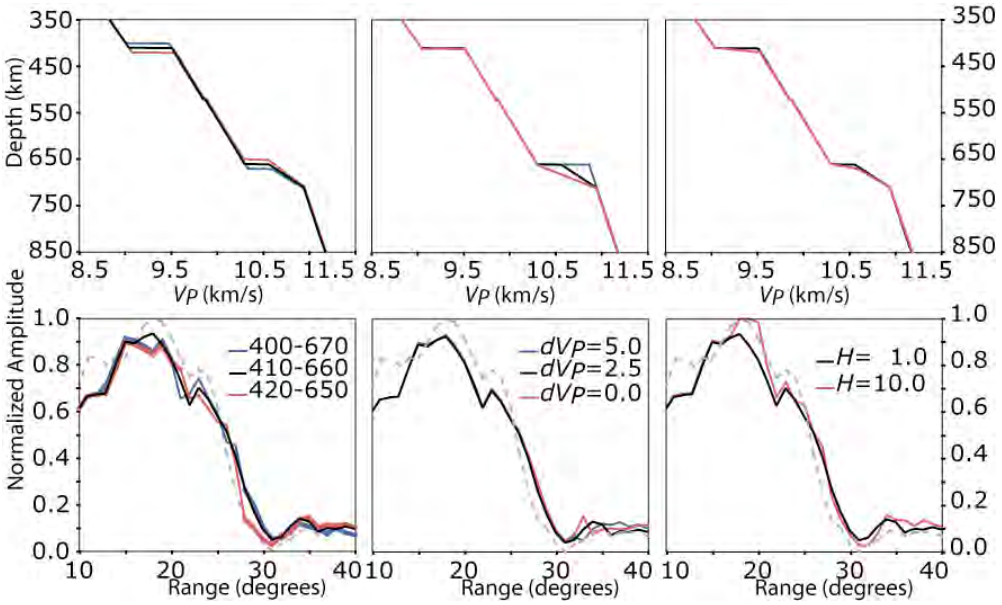

Figure 3. Examples of three different types of perturbations to transition zone structure: a) transition zone thickness, b) velocity contrast, and c) interface thickness. The corresponding WKBJ maximum amplitudes for *P* waves (d-f) change as a function of distance. The models are shown as black, blue, and red lines. The data are the dashed line.

Here, we model these data with a mass-forward modeling algorithm called the Niching Genetic Algorithm (NGA) (Koper et al., 1999). The NGA uses an evolutionary paradigm to create, mutate, and breed a population of velocity structure models such that those with poor fits to the data are eliminated, and those with good fits survive to continue the search of the model space for the best solution. Using this paradigm, we find the optimal solution to the *P*-wave data (Figure 4). This model is similar to the *P*-wave velocity structure found by Lawrence and Shearer (2006) using NGA waveform modeling of reflected energy from the transition zone (*PdP*, *SdS*, *Pds*, and *Ppdp*).

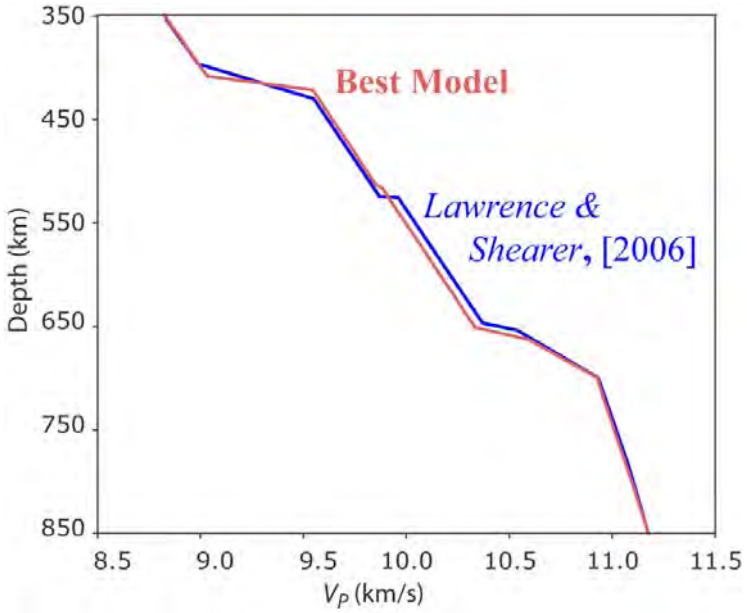

Figure 4. The (red) best fit model after 100 generations of an NGA simulated inversion yields a similar result to a similar parameter search based on (blue) *PdP*, *SdS*, *Pds*, and *Ppdp* reflected phases (Lawrence and Shearer, 2006).

Wavefield Analysis

In the amplitude section, we neglected time other than to ensure that we have windowed the appropriate phase. Here, we introduce a similar analysis that iteratively solves for time-dependent source, station, and Earth-response terms. Mathematically, one can conceptualize a waveform, $a(t)$, as the convolution of the source term, $s(t)$, the receiver term, $r(t)$, and the distance-dependant Earth-response term, $e(\Delta,t)$, plus noise, $n(t)$,

$$a(t) = s(t) * r(t) * e(\Delta, t) + n(t). \qquad (5)$$

Here, we assume that the source term, *s*, is a combination of the earthquake rupture and the near-source Earth response function. Furthermore, the receiver term is idealized as the convolution of the instrument response and the near-receiver Earth response.

Ideally, one could estimate the deep-Earth response by stacking waveforms with the source and receiver terms ($s(t)$ and $r(t)$) deconvolved. Unfortunately, the source and receiver terms are poorly constrained, the waveforms are not easily stackable because of dissimilarity and polarity issues, and noise is typically problematic. Therefore we develop and employ an automated stepwise stacking and deconvolution technique to boost the signal-to-noise ratio and to solve for the time-dependant source and receiver terms. We improve waveform similarity by examining the instantaneous amplitude or envelope function of the wavefield, $a_E(t)$, rather than the raw waveform. We initially estimate the source, receiver, and Earth-response functions as delta functions with amplitudes provided by the amplitude analysis above.

With preliminary estimates of *s*, *r*, and *e*, we can iteratively solve for each term from the envelope function,

$$
\begin{aligned}
s(t) &= a_E(t)^{*-1}\, r(t)^{*-1}\, e(\Delta,t) \\
r(t) &= a_E(t)^{*-1}\, s(t)^{*-1}\, e(\Delta,t). \\
e(\Delta,t) &= a_E(t)^{*-1}\, s(t)^{*-1}\, r(t)
\end{aligned}
\qquad (6)
$$

With this analysis, we obtain a time- and distance-dependant Earth-response term. For all data in the FARM database, the Earth-response term is shown in Figure 5.

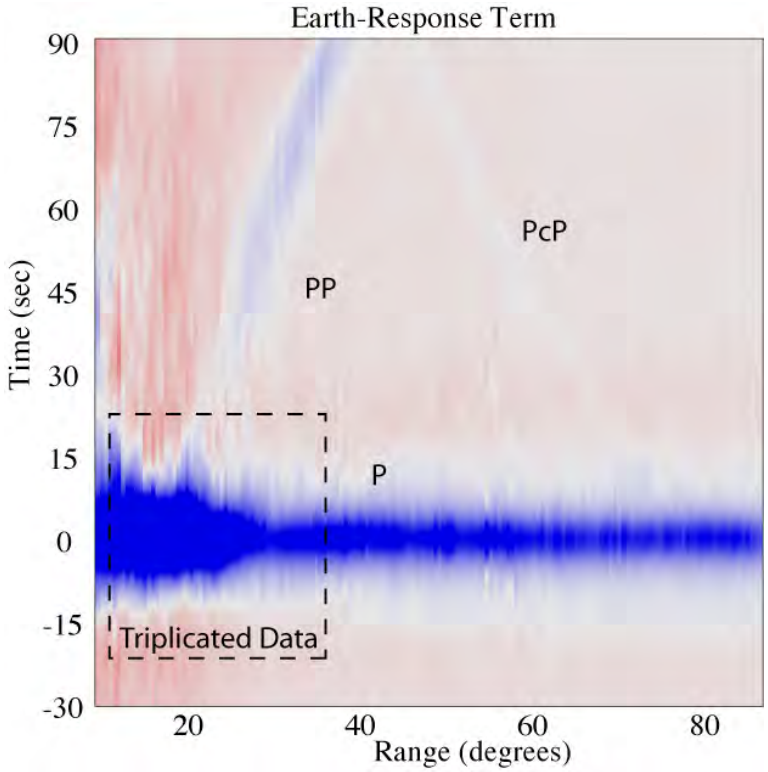

Figure 5. The time- and distance-dependant Earth-response function calculated from all FARM *P*-wave data. The box outlines the region of triplicated data. Blue is positive amplitude, red is negative. Various phases are indicated as *P*, *PP*, and *PcP*.

We can calculate synthetic time- and distance-dependant Earth-response functions using WKBJ. To estimate the appropriate frequency content and heterogeneity, we deconvolve the *P*-wave slant-stacked synthetic waveforms from 45 to 80 degrees and convolve the stacked observed waveforms for the same distance range. Synthetics using the model of Lawrence and Shearer, (2006) (LS06) are similar, but not identical to the observed Earth-response functions (Figure 6.a). Variants from LS06 demonstrate how the Earth-response function changes as a result of structure (Figure 6.b-d).

The optimal *P*-wave model found with a niching genetic algorithm simulated inversion for the wavefield is remarkably similar to the most optimal model found in Figure 4. Note that the most optimal model is merely representative as we assume that 3D heterogeneity has a broadening effect, and that we do not know precisely the scale of this heterogeneity. The primary difference between the optimal model found with wavefield analysis and that from amplitude analysis, is that the estimated depths for the global model are slightly different, which accounts for the timing. Recall that timing is inherently included in the wavefield analysis and not in the amplitude analysis. We expect that this method will also work with shear waves, although so far we have only examined *P* waves.

Once the station terms are well defined with the global analysis, it is possible to perform regional amplitude or wavefield analysis for high-quality individual events or sets of events. With less data it is critical to use only high-quality events and well-calibrated stations.

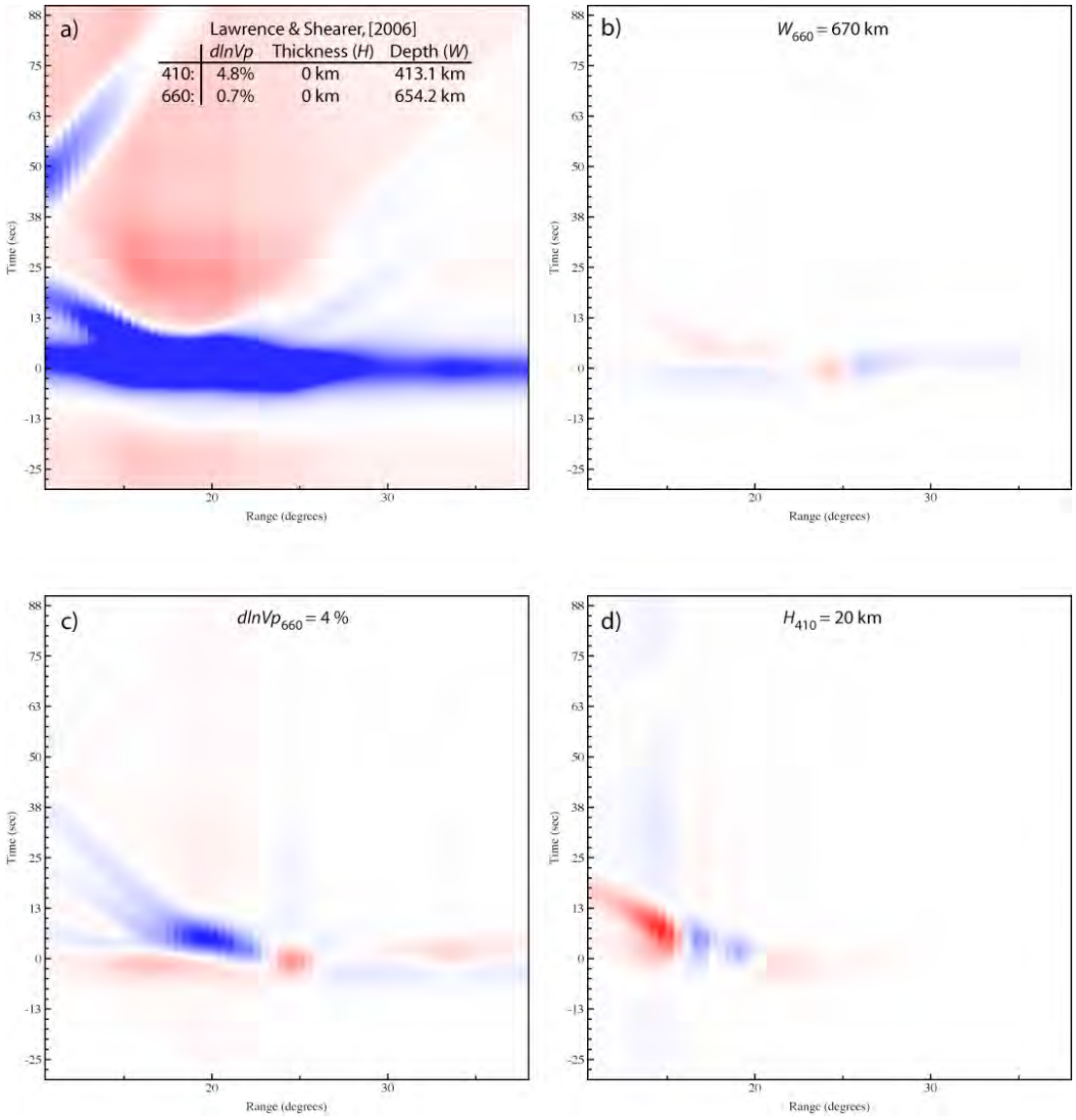

Figure 6. This figure shows a) the synthetic Earth-response function for the seismic velocity model found by Lawrence and Shearer (2006) (LS06), and deviations in Earth-response functions relative to LS06 as a result of b) a deeper 660 interface, c) a larger Vp_{660} contrast, and d) a thick 410 interface. Blue is positive, red is negative.

CONCLUSIONS AND RECOMMENDATIONS

This analysis has shown that it is possible to divide amplitude terms from digital seismic records into source, receiver, and Earth-response terms that account for the complicated wavefield variations in the 13 and 33 degree distance range. Through a multi-dimensional component analysis, each term is obtained iteratively. With well-resolved receiver terms and Earth-structure, it may be possible to estimate source functions with data at these regional distances. Note that the method requires large numbers of seismograms from many stations to achieve reliable results. It is only in the past few years that global data and station coverage have increased to a sufficient level that such an analysis can be roughly conducted. In the future, improved results are likely as more data are collected from regions of increased station coverage.

ACKNOWLEDGEMENTS

The data used here were supplied by IRIS DMC. We thank Kris Walker for his efforts with the FARM database.

REFERENCES

Chambers, K., A. Deuss and J.H. Woodhouse (2005). Reflectivity of the 410-km discontinuity from PP and SS precursors, *J. Geophys. Res*. 110: B02301, doi:10.1029/2004JB003345.

Chapman, C. H., (1978) A new method for computing synthetic seismograms, *Geophys. J. Astro*. *Soc*. 54: 481–518.

Flanagan, M.P. and P.M. Shearer (1998a). Global mapping of topography on transition zone velocity discontinuities by stacking SS precursors, *J. Geophys Res.* 102: 2673–2692.

Flanagan, M.P. and P.M. Shearer (1998b). Topography on the 410-km seismic velocity discontinuity near subduction zones from stacking of sS, sP, and pP precursors, *J. Geophys. Res*. 103: 21,165–21,182.

Gu, Y., A.M. Dziewonski and C.B. Agee (1998). Global decorrelation of the topography of transition zone discontinuities, *Earth Planet. Sci. Lett*. 157: 57–76.

Koper, D. K., M. E. Wysession, and D. A. Wiens (1999). Multimodal function optimization with a niching genetic algorithm: a seismological example, *Bull. Seism. Soc. Am.* 89: 978–988.

Lawrence, J.F., and P.M. Shearer (2006). Constraining seismic velocity and density for the mantle transition zone with reflected and transmitted waveforms, G^3, doi:10.1029/2006/GC001339.

Melbourne, T. and D. Helmberger (1998). Fine structure of the 410-km discontinuity, *J. Geophys. Res*. 103: 10,091–10,102.

Shearer, P.M. (1990). Seismic imaging of upper-mantle structure with new evidence for a 520-km discontinuity, *Nature*, 344**,** 121–126.

Shearer, P.M. (1991). Constraints on upper-mantle discontinuities from observations of long-period reflected and converted phases, *J. Geophys. Res*., 96, 18147–18182.

Shearer, P.M. (1993). Global mapping of upper mantle reflectors from long-period SS precursors, *Geophys. J. Int.*, 115**,** 878–904.

Shearer, P.M. (2000). Upper mantle seismic discontinuities, *in Earth's Deep Interior: Mineral Physics and Tomography from the Atomic to the Global Scale, AGU Geophysical Monograph* 117: 115–131.

Shearer, P.M. and M.P. Flanagan (1999). Seismic velocity and density jumps across the 410- and 660-kilometer discontinuities, *Science* 285: 1545–1548.

Shearer, P.M. and T.G. Masters (1992). Global mapping of topography on the 660 km discontinuity, *Nature* 355: 791–796.

Veith, K.F. and G.E. Clawson (1972). Magnitude from short-period P-wave data, *Bull. Seismol. Soc. Am.* 62: 435–452.

DEVELOPMENT OF SURFACE WAVE DISPERSION AND ATTENUATION MAPS AND IMPROVED METHODS FOR MEASURING SURFACE WAVES

Jeffry L. Stevens, Jeffrey W. Given, Heming Xu, and G. Eli Baker

Science Applications International Corporation

Sponsored by Air Force Research Laboratory

Contract No. FA8718-05-C-0023

ABSTRACT

The objective of this project is to optimize the measurement of surface waves, particularly at regional and local distances and at periods of 8–15 seconds. One goal of this project is the development of global regionalized dispersion and attenuation maps, with a particular focus on determining attenuation maps for Eurasia in the 8–15 second period band. Both the dispersion and attenuation maps are corrected for scattering and diffraction from heterogeneous earth structure. Successful application of these corrections requires an understanding of the characteristics of surface wave propagation in regions of variability high enough that common correction methods may fail. We implemented the algorithm of Zhou et al. (2004) for calculating finite frequency sensitivity kernels for dispersion and amplitude variations, and have been testing the algorithms using the one-degree dispersion maps of Stevens et al. (2005). Amplitude corrections predicted by the Born approximation are unreasonably large for long paths. In order to determine under what conditions the Born approximation gives valid results, we performed a 3D finite difference calculation using an earth model for the Tarim Basin embedded in a uniform structure typical of the Eurasian shield regions, and then compared the results with variations predicted by the Born approximation. The predicted wavefields were compared out to a distance of several hundred km. The Born approximation is generally consistent with the finite-difference results, but there are localized, strong interference effects in the finite-difference results not apparent in the Born calculation. The approximation is less accurate at a 10-s period than at a 20-s period.

We are also developing a "path corrected surface wave magnitude," which combines the time domain narrow-band surface wave magnitude procedure of Russell (2006) with the path corrected spectral magnitude of Stevens and McLaughlin (2001). This allows the magnitude to be regionalized to account for variations in amplitude due to differences in earth structure and attenuation. We perform a detailed comparison of these magnitude types and then apply them to data from the North Korean nuclear test. We calculate frequency dependent amplitude corrections using the Born approximation for surface waves along paths that recorded the North Korean explosion. The path corrected spectra for these data are flat to the north and south, and much more frequency dependent and larger in amplitude at stations to the west. The Born corrections are also flat to the north and south and much more variable along the other paths; however, they do not match the observations very well. This is probably either because the resolution of the models is insufficient or because the variability exceeds the limits of the Born approximation. The amplitude variations are too large to be explained by attenuation differences on these short paths, and they are also too large to be explained by tectonic release given the lack of observed Love waves, so structural effects are the most likely cause of the variations.

We are in the process of analyzing data for a large Eurasian data set and are attempting to separate amplitude variations due to attenuation from amplitude variations due to structure. We have collected data from Eurasian explosions at the Lop Nor and Balapan test sites, and from more recent earthquakes recorded at a high station density within the Eurasian continent. We are measuring amplitude variations, and then identifying the components of the amplitude variation, which are: 1) radiation pattern; 2) attenuation; 3) variations due to path structure; 4) variations due to off-path structure; and 5) unmodeled variations. After the analysis is completed, this attenuation data set will be used to invert for Q structure, which will then be used to generate maps that predict surface wave amplitudes due to earth structure and attenuation.

OBJECTIVES

The objective of this project is to optimize the measurement of surface waves, particularly at regional and local distances and at periods of 8–15 seconds. One goal of the project is the development of global regionalized dispersion and attenuation maps, with a particular focus on determining attenuation maps for Eurasia in the 8–15 second period band. Both the dispersion and attenuation maps are being corrected for scattering and diffraction from heterogeneous earth structure. We also implement a path corrected surface wave magnitude, which combines the time domain narrow-band surface wave magnitude procedure of Russell (2006) with the path corrected spectral magnitude of Stevens and McLaughlin (2001).

RESEARCH ACCOMPLISHED

Overview

Surface wave amplitudes are affected by both attenuation and earth structure. The effect on surface wave amplitudes of propagation normal to variations in earth structure is predicted fairly well by conservation of energy. Propagation along paths at grazing incidence to large structure variations, however, are much more difficult to predict. Our main interest in this project is on understanding amplitude variations in 8–15 second surface waves. In this frequency band, surface waves may be affected as strongly or more strongly by earth structure than by intrinsic attenuation, particularly along shorter paths. Our goal is therefore to be able to model and correct for both of these effects. Our approach is illustrated in Figure 1.

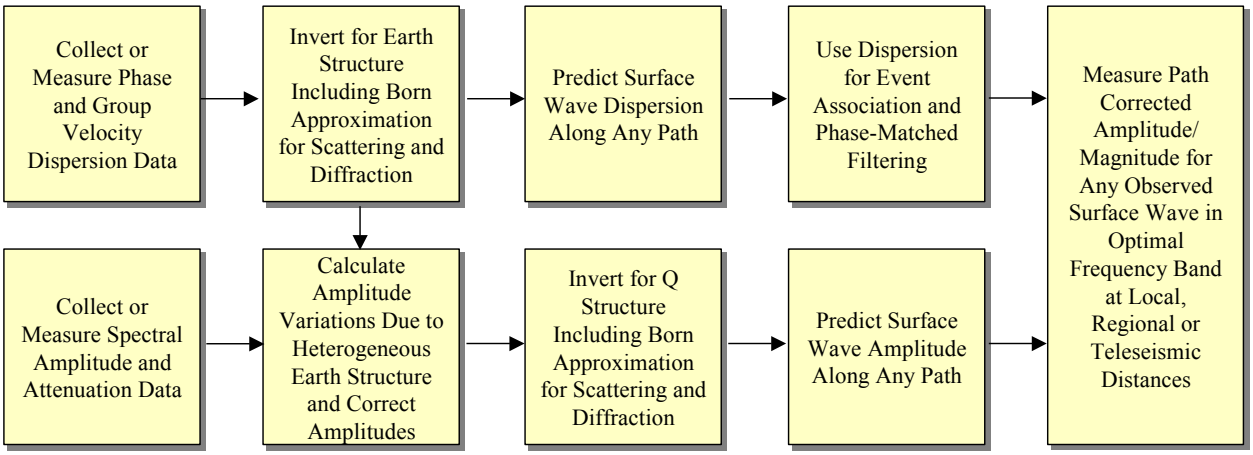

Figure 1. Overview of the surface wave dispersion and attenuation project.

In an earlier project (Stevens et al., 2005) we developed global, regionalized dispersion models that allow the phase and group velocity to be calculated between any two points on the earth. We did this by accumulating a large data set consisting of more than 1 million dispersion measurements derived by a number of researchers, and then inverting this data set to determine earth structure, which in turn was used to generate dispersion maps at all frequencies. In that project, we modeled surface waves in a heterogeneous earth using the following approximations: 1) surface waves propagate along great circle paths, 2) surface wave phase and group velocities and anelastic attenuation can be modeled using a path integral between source and receiver, and 3) energy is conserved with no mode conversion across material boundaries. This approximation is quite good for large parts of the world, particularly at lower frequencies, but the unmodeled variations become important in regions of structural complexity.

Separating amplitude variations due to attenuation from amplitude variations due to structure is difficult, so we have been performing experiments using events with well-constrained source mechanisms, using explosions from known test sites and Eurasian earthquakes with centroid moment tensor (CMT) solutions, and looking at pure continental paths. Since we have reasonably good earth models for these paths, we can predict the amplitudes along each path for each event, and then examine the differences between predictions and observations. Because of the large increase in the number of stations over the past couple of decades, there is now a great deal of redundancy for each event, so we can remove the source and predictable path effects with some confidence.

Surface wave magnitudes play an important role in earthquake/explosion discrimination. Three main problems exist with traditional surface wave magnitudes: 1) surface wave dispersion causes amplitude variations unrelated to the source; 2) it is not possible to reliably measure a traditional 20 second surface wave magnitude at local and regional distances because the surface wave is not dispersed enough; and 3) differences in earth structure and attenuation cause variations in surface wave amplitudes that are unrelated to the source. Several surface wave magnitude measurements have been proposed to address these limitations, and we propose some further improvements in the form of a regionalized path corrected surface wave magnitude. In the following section we compare these magnitude types in detail, and then apply them to the North Korean nuclear test. We also use this as an example of separating the surface waves into their component source, receiver and path parts, and examine the residual to show the effect of structural variations.

Comparison of Butterworth Filtered and Regionalized Surface Wave Magnitudes

Russell (2006) proposed a new type of surface wave magnitude $M_{s(b)}$ that uses a Butterworth filter to measure a time domain amplitude in a narrow band around any desired frequency, and then applies a correction for the frequency dependence of an explosion source function. The main purpose of $M_{s(b)}$ is to allow surface waves to be measured at regional distances at higher frequencies than traditional 20 second M_s. The magnitude is defined by

$$M_{s(b)} = \log\ A_b\ + \frac{1}{2}\log\ \sin\Delta\ + 0.0031\left(\frac{20}{T}\right)^{1.8}\Delta - 0.66\log\left(\frac{20}{T}\right) - \log\ f_c\ - 0.43 \qquad (1)$$

where A_b is the filtered amplitude, T is the measured period, and f_c is the Butterworth filter width. This magnitude also requires that the frequency band be less than a minimum value defined by $f_c \le \frac{G_{\min}}{T\sqrt{\Delta}}$. Russell (2006) finds G_{min}=0.6 for continental structures between 8 and 40 seconds, with smaller values required for deep sediment structures. Russell (2006) also shows that $A_b = \frac{f_c T\sqrt{\Delta}}{G} A$ where G is a constant which for typical continental paths is approximately 0.93, and A is the equivalent time domain amplitude. Note that if G_{min} is fixed, then the filter correction corresponds to a distance correction for a normally dispersed (non-Airy phase) surface wave of $\frac{1}{2}\log\Delta$.

Stevens and McLaughlin (2001) defined a path corrected spectral magnitude, which similarly was intended to allow surface waves to be measured at all distances and frequencies, and in addition is regionalizeable since it is derived from earth models. The path corrected spectral magnitude, $\log M_0'$, is calculated by dividing the observed surface wave spectrum by the Green's function for an explosion of unit moment and taking the logarithm of this ratio, averaged over any desired frequency band. The path corrected spectral magnitude is defined as the logarithm of:

$$M_0^{'} = \left| U_z(\omega, r, \theta) \middle/ \left(\frac{S_1^x(\omega, h_x) S_2(\omega) \exp[-\gamma_p(\omega) r]}{\sqrt{a_e \sin(r/a_e)}} \right) \right| \qquad (2)$$

where U_z is the observed vertical component surface wave spectrum, S_1^x depends on the source region elastic structure and the explosion source depth, S_2 depends on the receiver region elastic structure, and γ_p is the attenuation coefficient that depends on the attenuation integrated over the path between the source and receiver. All of the functions in equation 2 can be derived from plane-layered earth models (see Stevens and McLaughlin, 2001), and allow the measurement to be regionalized to account for differences in earth structure at the source and receiver, and due to attenuation along the path. Since M_0' is a physical quantity, equation 2 is assumed to be in SI units and $\log M_0'$ is in log(nt-m); however, in the following comparison we express U_z in nm-s for consistency with the other amplitude measurements. This adds a constant value of -9 to the normalization constant for $\log M_0'$.

Since equations 1 and 2 are both intended to flatten the surface wave spectrum, in principle they can be measured over any desired frequency band. In practice, the path corrected spectral magnitude (equation 2) has been calculated by averaging over a frequency band designed to avoid noise contamination, and has implemented an outlier rejection scheme to minimize bias from spectral dips and noise (Stevens et al., 2005). The implementation of the Butterworth

filtered magnitude (equation 1) by Bonner et al. (2006) has instead used the maximum value over a period band of 8–25 seconds, defined as M_s(VMAX), with analyst rejection of outliers.

A path corrected time domain magnitude can be derived by combining the path corrected spectral magnitude with $M_{s(b)}$, using the source and path corrections from earth models to replace the empirical corrections. We define the path corrected time domain magnitude $M_{s(bp)}$ as:

$$M_{s(bp)} = \log A_b + \frac{1}{2}\log \sin\Delta + \gamma_p \Delta \log e - \log S_1 - \log S_2 - \log f_c + C_{bp} \quad (3)$$

where C_{bp} is a constant chosen to make $M_{s(bp)}$ consistent with historical magnitudes. By defining $M_{s(bp)}$ to be equal to Rezapour and Pearce (1998) M_s at 50º, and simultaneously using the Rezapour and Pearce attenuation rate, and using the mean 20 second value of S_1 and S_2 for Central Asian continental structures ($\log(S_1)+\log(S_2)$=-17.41), we find C_{bp}=-17.96. We can also define a spectral magnitude directly from equation 2, using the relation (again from Russell, 2006) $A_b = \frac{4\pi}{3} f_c U_z$. This gives $\log M_0' - M_{s(bp)} = 11.74$, which is identical to the mean difference between $\log M_0'$ and Rezapour and Pearce M_s found through measurement of a large data set by Stevens and McLaughlin (2001). We can therefore define an equivalent spectral M_s, which we define as $M_{s(sp)}=\log M_0'-11.74$, which by adding the $\log M_0'$ normalization constant ½log(a_e)-9 gives an $M_{s(sp)}$ normalization constant of -17.34. Table 1 shows a comparison of the terms in each of these magnitudes, and in the Rezapour and Pearce M_s.

Table 1. Comparison of time domain and spectral magnitude measurement and correction terms

Magnitude Type	Amplitude Measure	Source	Receiver	Geometric Spreading	Attenuation	Dispersion	Filter	Norm
M_s	log(A/T)			$\frac{1}{2}\log \sin\Delta$	0.0046Δ	$\frac{1}{3}\log\Delta$		2.37
$M_{s(b)}$	log(A_b)	$-0.66\log\left(\frac{20}{T}\right)$		$\frac{1}{2}\log \sin\Delta$	$.0031\left(\frac{20}{T}\right)^{1.8}\Delta$		$-\log f_c$	-0.43
$\log M_0'$	log(U_z)	-log(S_1)	-log(S_2)	$\frac{1}{2}\log \sin\Delta$	$\gamma_p \Delta \log e$			$\frac{1}{2}\log a_e - 9$
$M_{s(sp)}$	log(U_z)	-log(S_1)	-log(S_2)	$\frac{1}{2}\log \sin\Delta$	$\gamma_p \Delta \log e$			-17.34
$M_{s(bp)}$	log(A_b)	-log(S_1)	-log(S_2)	$\frac{1}{2}\log \sin\Delta$	$\gamma_p \Delta \log e$		$-\log f_c$	-17.96

In this table A is the traditional time domain 20 second amplitude in nm, A_b is the Butterworth filtered magnitude (using a 3 pole two pass phaseless filter) in nm, and U_z is the Fourier spectral amplitude in nm-s. Figure 2 (left) shows a comparison of Russell's approximation to the explosion excitation function with $\log(S_1)+\log(S_2)$ (plus a constant to normalize to zero at 20 seconds). As the figure shows, this is a good approximation to the average excitation function across the frequency band; however, there is substantial regional variation in the function that is accounted for in the path corrected magnitudes.

Figure 2 (right) shows that attenuation calculated from earth models is somewhat higher than the Rezapour and Pearce attenuation, and both are higher than the Russell attenuation, which is based on the earlier model of von Seggern (1977). The model-based attenuation corresponds to a Rayleigh wave Q of about 400, while the Rezapour/Pearce and von Seggern/Russell attenuation correspond to Rayleigh wave Q of about 550 and 800, respectively. The Q models are still relatively generic, and are being improved as part of a task in this project; however, the Q value of 400 is more consistent with empirical Rayleigh wave Q studies than the higher values of the other magnitudes. This may be because those magnitudes were based on Rayleigh wave amplitudes covering a large distance range, and Rayleigh waves along lower Q paths may have attenuated away at the larger distances, biasing the attenuation estimates to higher Q values.

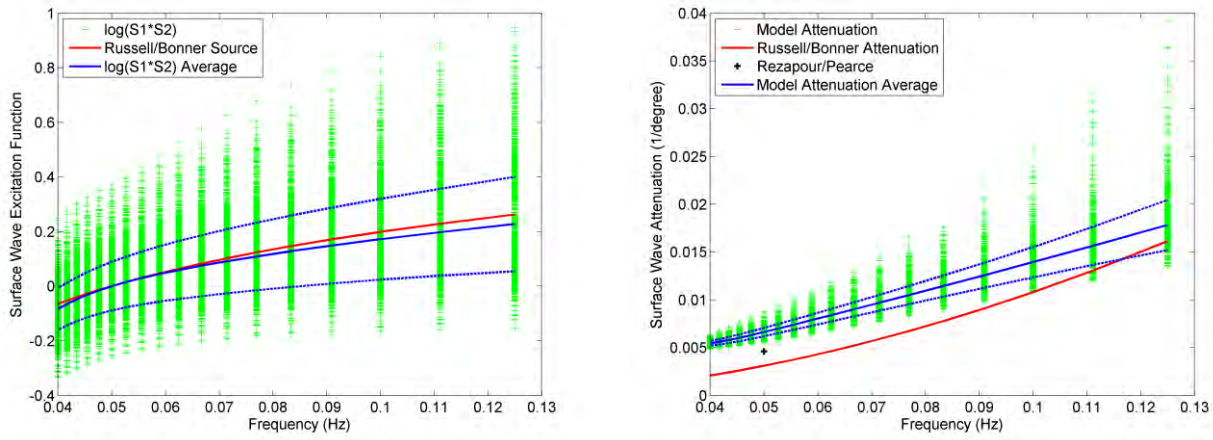

Figure 2. Left: Mean log(S1*S2) and ±1 standard deviation (blue). Red line shows the Russell approximation for the source function. Right: Mean attenuation and ±1 standard deviation (blue) derived from earth models, Russell approximation for attenuation (red), and Rezapour and Pearce global estimate at 20 seconds (black). In both, green marks show values for individual Eurasian structures.

Figure 3 compares the magnitude distance corrections, which are the equations listed in Table 1 calculated with A=1, G_{min}=0.6, $f_c = \frac{G_{\min}}{T\sqrt{\Delta}}$ and $A_b = \frac{f_c T\sqrt{\Delta}}{G} A$, for periods of 20 and 10 seconds, respectively.

Differences between the distance corrections are generally small. The main differences are the larger correction at close distances for the Rezapour and Pearce magnitude, and the larger correction for the path corrected magnitude with model-based attenuation at large distances. $M_{s(bp)}$ will, of course, vary for each source and receiver location corresponding to the particular earth structure and path attenuation. The magnitude correction at close distances is also larger for $M_{s(b)}$ than for $M_{s(bp)}$ because the difference in attenuation causes a small difference in the normalization constant which is calculated at 50 degrees.

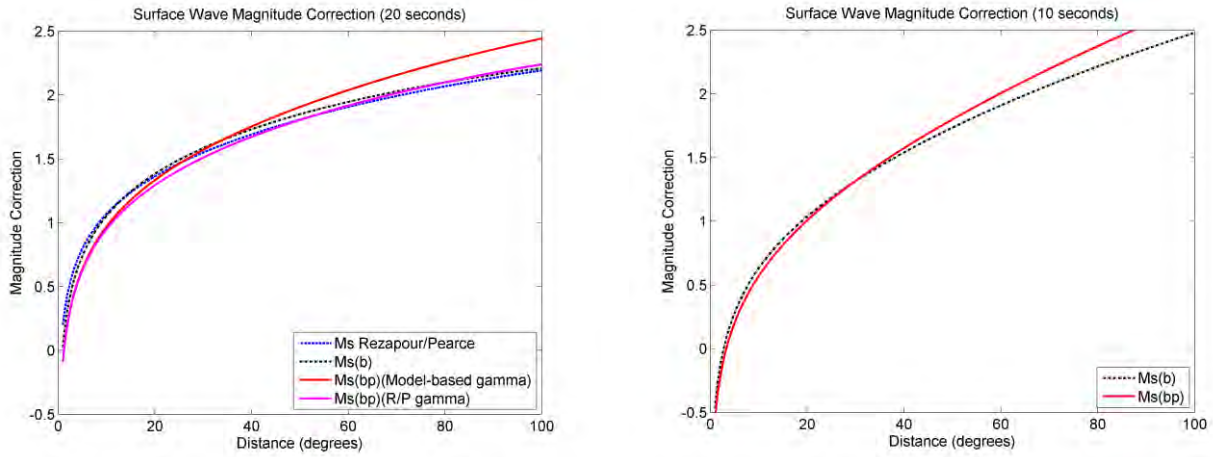

Figure 3. Twenty-second magnitude correction vs distance for Rezapour/Pearce (dashed blue), $M_{s(b)}$ (dot-dash black), $M_{s(bp)}$ with model-based gamma (solid red), and $M_{s(bp)}$ with Rezapour and Pearce gamma (solid maroon) (left). 10 second magnitude correction vs distance $M_{s(b)}$ (dot-dash black), and $M_{s(bp)}$ with model-based gamma (solid red) (right).

Analysis of Surface Waves from the North Korean Nuclear Test

To examine the differences between magnitudes in more detail and illustrate some potential problems, we apply the magnitude methods to surface waves from the North Korean nuclear test of October 9, 2006. This is a good test case because the surface waves are small—above noise level at only 7 of the closest stations (Figure 4), difficult to see at all in the unfiltered records, but visible at these stations when low pass filtered (Figure 5).

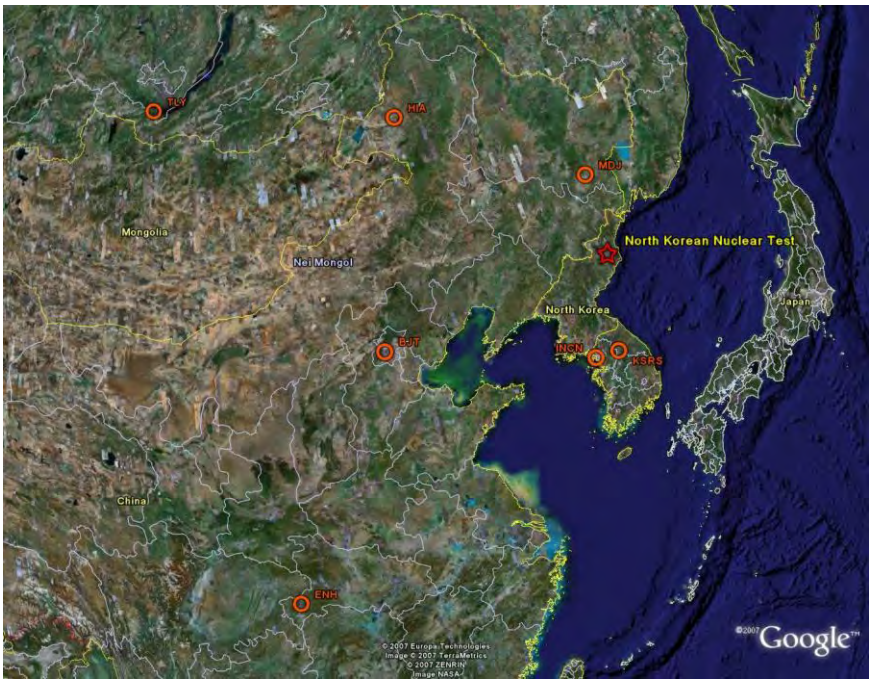

Figure 4. Location of the North Korean nuclear test and recording stations.

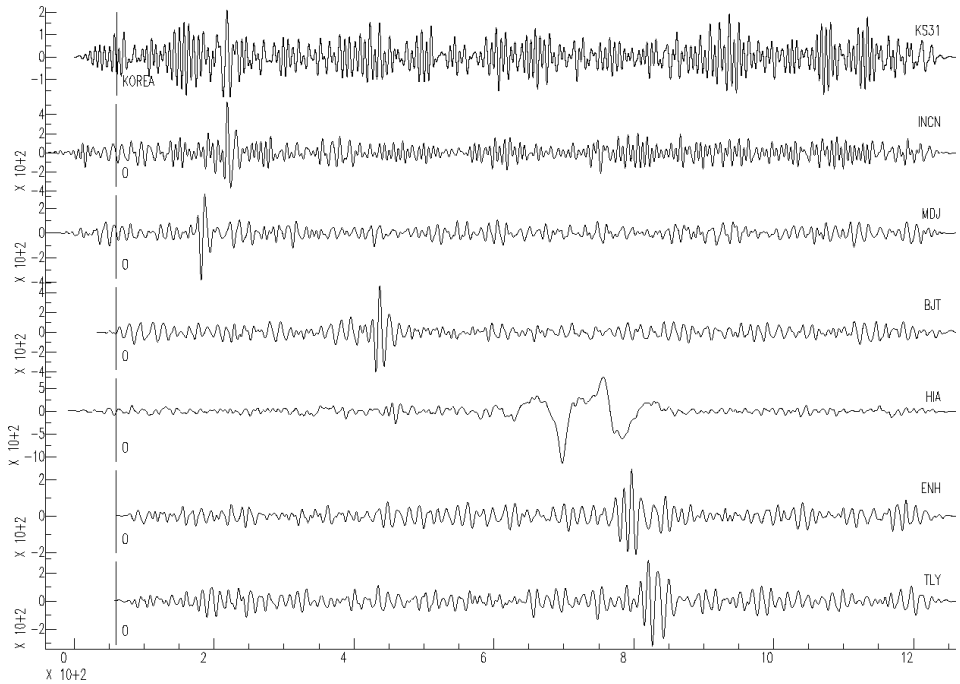

Figure 5. Data from the North Korean explosion filtered from 0.01–0.1 Hz. Surface waves are clearly visible at all stations. HIA has a glitch or interfering arrival after the explosion arrival. The explosion arrival is visible just after the BJT arrival.

Figure 6 shows the predicted spectra at each of the 7 stations based on the model based source and path corrections—these are the negative of the sum of corrections in row 5 of Table 1, and are equivalent to predicted, normalized explosion-generated surface wave spectra at each location. Differences between the model-based and Russell sets of corrections (Figure 6, right) range from -0.15 to 0.05 magnitude units.

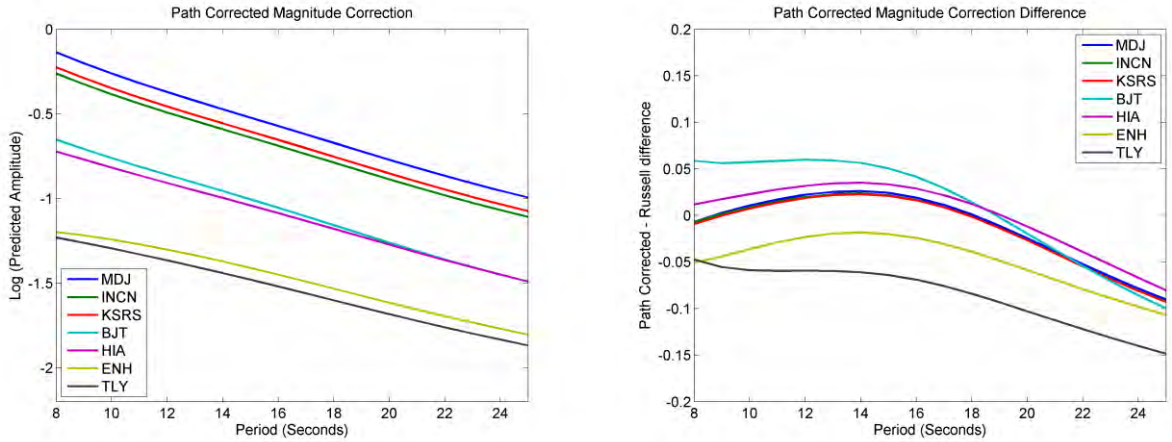

Figure 6. Path corrections for the 7 stations that recorded surface waves from the North Korean nuclear test using model based corrections (left) and differences between the model-based and Russell path corrections for the 7 stations recording the North Korean event.

Figure 7 (left) shows the calculated Butterworth filtered and path corrected spectral magnitudes for station BJT for 6 values of filter width, as specified by G_{min} ranging from 0.1 to 0.6. The higher values correspond to wider filter widths which have the effect of smoothing the spectrum and giving more consistent values between frequencies. A disadvantage of the larger values, however, is that the frequency band extends farther outside of the band of interest, possibly allowing contamination by noise or other phases. Figure 7 (right) shows the Butterworth filtered magnitude, the path corrected magnitude, the path corrected spectral magnitude, and the best value of the path corrected spectral magnitude calculated using a robust mean (Stevens et al., 2005). Figure 8 shows a comparison of Butterworth filtered magnitudes with and without path corrections. If the procedure were working perfectly and the surface wave spectra were just like synthetics, then all of the curves in Figures 7 and 8 would be flat lines. The path corrected spectra are slightly flatter than the Butterworth filtered spectra, but it is clear that unmodeled variations are significantly larger than the differences between the individual magnitude curves.

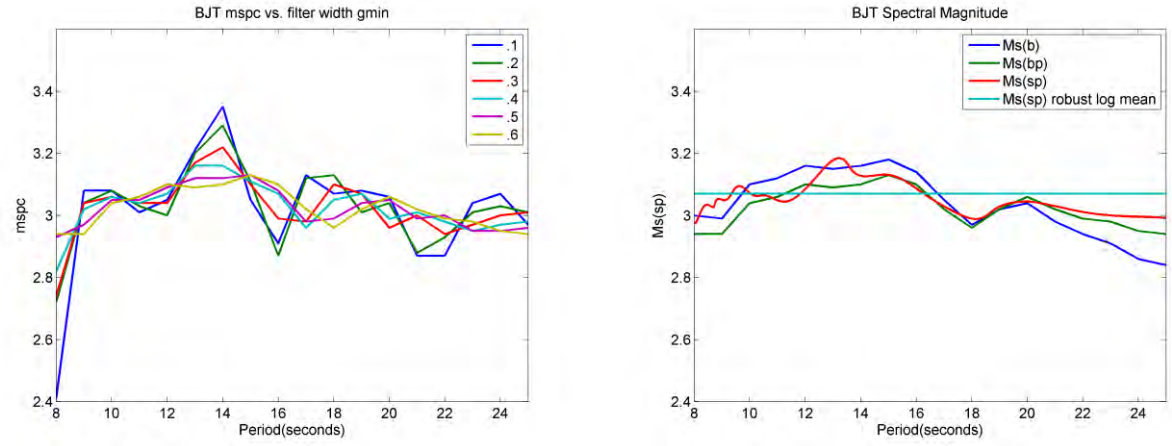

Figure 7. Calculation of path-corrected Butterworth filtered magnitude for 6 filter widths (left) at station BJT. Butterworth filtered, path corrected, and spectral magnitudes at BJT (right).

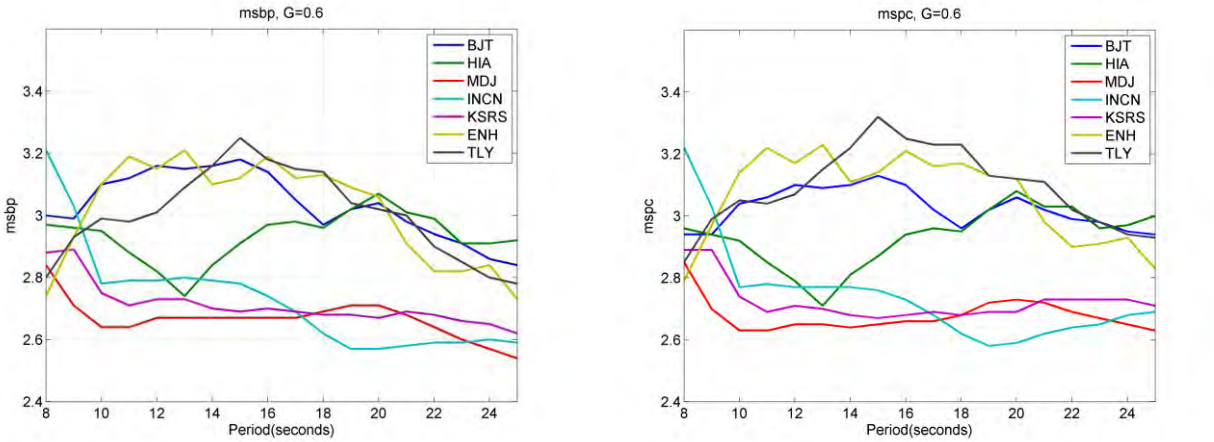

Figure 8. Butterworth filtered (left) and path corrected (right) magnitudes for the North Korean nuclear test with varying filter widths.

The spectra divide into two distinct groups—lower values at INCN, KSRS, and MDJ, and higher values at BJT, ENH, and TLY. Station HIA is more complicated, but generally higher. Furthermore, the three lower amplitude stations, which are also the closest stations, have much flatter corrected spectra than the three higher amplitude stations, suggesting a possible frequency dependent amplification of these surface waves. Also, the lower amplitude stations are located due north and south of the event, while the other stations are located to the west (and northwest/southwest) Since we have corrected for source and receiver structure, and attenuation differences could not be responsible for differences this large on paths this short, there are two remaining likely causes for the amplitude variations: tectonic release (or other azimuth dependent source components), and focusing due to path structure.

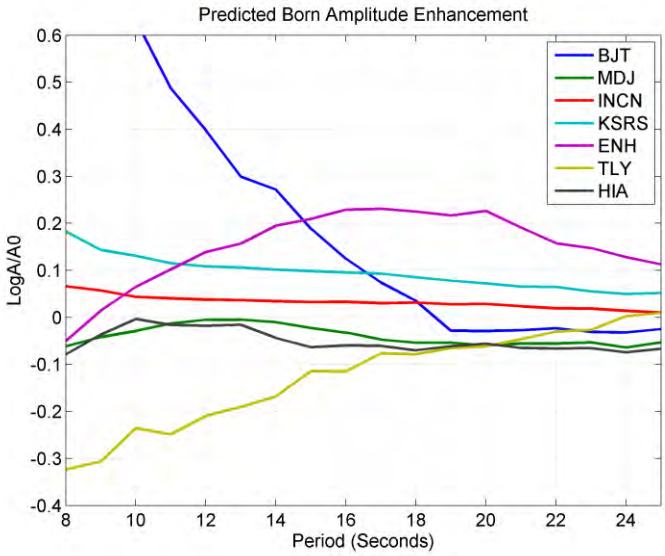

Figure 9. Amplitude corrections due to structure predicted using the Born approximation.

The effect of path structure calculated using the Born approximation (Zhou et al., 2004) and the earth models of Stevens et al. (2005) is shown in Figure 9. Although there are clearly some big differences between the predictions and observations, there are also some interesting similarities. First, the corrections for the three closest stations are almost flat and separated by approximately the same amount as the observations. Second, the amplitude correction for ENH is similar to what is observed for ENH and also similar to the observations at TLY and BJT. That is, the data show a peak in the spectrum in the middle periods, dropping back close to the level of the closer stations at the longest and shortest periods. On the other hand a very large amplification, which is not observed, is predicted for

BJT due to a grazing path along the north end of the Yellow Sea, and a big decrease, also not observed, is predicted for TLY. There are two likely explanations for this: 1) the one degree structural resolution is not sufficient for these short paths; and/or 2) the structural complexity exceeds the limits of the Born approximation. The amplification predicted for BJT by the Born approximation, for example, is very strongly dependent on exactly where the station is with respect to the low velocity zone. Also, the Born approximation is known to overpredict amplification at higher frequencies in such cases. Figure 10 shows a comparison of predictions from the Born approximation and a finite difference calculation for waves propagating near the Tarim Basin, another low velocity zone. The red band to the upper left of the Tarim Basin is the same amplification effect that is occurring in Figure 9 for station BJT. As shown in the finite difference calculation figure, this type of amplification stretches the limits of the Born approximation, and the actual amplification is smaller and more complicated. The comparison between the Born approximation and finite difference is much better at 20 seconds (see Stevens et al., 2006), so it is possible that in regions of structural complexity the Born approximation is adequate at 20 seconds but inadequate at 10 seconds.

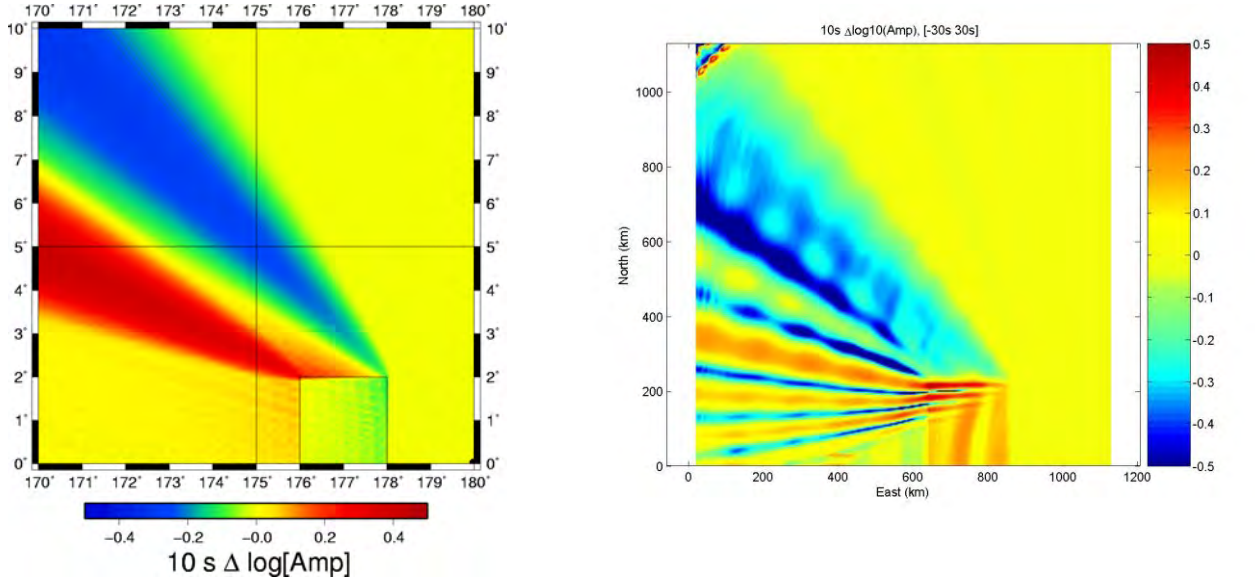

Figure 10. Comparison of Born approximation (left) with finite difference calculation (right) of amplitude perturbations at 10 seconds. The rectangular inclusion is modeled after the Tarim Basin structure, and the external structure after a Eurasian shield earth structure. The source is on the horizontal axis at the right edge of the plot. The amplitude is increased in a band above and to the left of the inclusion in both cases, and decreased above that. However, there are some interference effects in the finite difference calculation that are not reproduced in the Born calculation.

Tectonic release could cause the observed ~factor of 2 offset between the two station sets. If, for example, tectonic release had the mechanism of a normal fault with tension in the east-west direction, it would amplify stations to the west more than to the north. However, to cause a factor of 2 difference would require a secondary source large enough that large Love waves would also be expected. No Love waves are apparent in any of the data. In any case, path structure seems a more likely cause of the variability, and it is possible that the variations would be predictable with higher resolution earth models, and/or a more accurate method for accounting for structural variations.

One final issue is the most appropriate measurement of Ms derived from spectra. In our previous work, and in the discussion above of the path corrected spectral magnitude, we have used a robust mean value as the best estimate. Bonner et al., 2006, however, have instead used the maximum value of the Butterworth filtered Ms. This has some advantage in discrimination, because although the corrections flatten explosion spectra, they do not quite flatten earthquake spectra, which tend to be larger at lower frequencies. So in principle the Ms value for explosions is frequency independent, while the earthquake Ms can choose a higher value, improving the Ms:mb discriminant. As the explosion spectra above demonstrate, however, there are variations in the explosion spectra also, and choosing the maximum point can lead to an Ms that is too high, degrading discrimination. We made one modification to Bonner et al.'s Ms(VMAX) procedure by implementing a simple outlier rejection test—we calculate the mean and standard deviation of the magnitudes and reject outliers greater than two standard deviations from the mean. We

then recalculate the mean and repeat the outlier rejection, using the remaining points to calculate either the mean or maximum magnitude. Table 2 shows a comparison of magnitudes for this event using the different methods. The results show that the mean value estimates are more consistent than the peak value estimates.

Table 2. Station and network mean values for Ms as calculated using the methods described in the text.

Station	Distance (km)	Ms(b) Mean	Ms(b) Peak	Ms(bp) Mean	Ms(bp) Peak	Ms(sp) Mean
MDJ	369	2.65	2.71	2.67	2.73	2.69
KSRS	440	2.69	2.75	2.70	2.74	2.76
INCN	476	2.68	2.80	2.69	2.78	2.81
BJT	1103	3.03	3.18	3.02	3.13	3.07
HIA	1148	2.93	3.07	2.93	3.08	3.00
ENH	2147	3.01	3.21	3.06	3.23	3.20
TLY	2252	3.00	3.25	3.09	3.32	3.16
Mean (SD)		2.86 (0.18)	3.00 (0.23)	2.88 (0.19)	3.00 (0.25)	2.96 (0.20)

CONCLUSIONS AND RECOMMENDATIONS

We are attempting to understand and model the generation and propagation of surface waves in the 8–15 second period band in Eurasia. We model source excitation, receiver amplification and path dispersion and attenuation using earth models derived from a large global dispersion data set and relatively generic attenuation models. We then examine the residual and try to separate remaining path attenuation and variations due to path structure. We model the effect of heterogeneous structure using the Born approximation; however, the structural complexity and high frequencies required appear to push the Born approximation beyond its limits. We develop a path corrected surface wave magnitude which combines the time domain narrow-band surface wave magnitude procedure of Russell (2006) with the path corrected spectral magnitude of Stevens and McLaughlin (2001). We find that the Russell magnitude is a good match to the average value of the path corrected magnitude; however, there are substantial path and site specific variations that can be accounted for with the path corrected magnitude.

REFERENCES

Bonner, J. L., D. R. Russell, D. G. Harkrider, D. T. Reiter, and R. B. Herrmann (2006). Development of a time-domain, variable period surface-wave magnitude measurement procedure for application at regional and teleseismic distances—Part II: Application and M_s-m_b performance, *Bull. Seism. Soc. Am*., 96: 678–696, doi: 10.1785/0120050056.

Rezapour, M. and R. G. Pearce (1998). Bias in surface-wave magnitude Ms due to inadequate distance corrections," *Bull. Seism. Soc. Am*. 88: 43–61.

Russell, D. R. (2006). Development of a time-domain, variable period surface-wave magnitude measurement procedure for application at regional and teleseismic distances—Part I: Theory, *Bull. Seism. Soc. Am*. 96: 665–677, doi: 10.1785/0120050055.

Stevens, J. L. and K. L. McLaughlin (2001). Optimization of surface wave identification and measurement, *Pure Appl. Geophys.* 158: 1,547–1,582.

Stevens, Jeffry L., Jeffrey W. Given, G. Eli Baker, and Heming Xu (2006). Development of surface wave dispersion and attenuation maps and improved methods for measuring surface waves, in *Proceedings of the 28th Annual Seismic Research Review: Ground-Based Nuclear Explosion Monitoring Technologies*, LA-UR-06-5471, Vol. 1, pp. 273–282.

Stevens, J. L., D. A. Adams, G. E. Baker, M. G. Eneva, and H. Xu (2005). Improved surface wave dispersion models, amplitude measurements and azimuth estimates, SAIC final report submitted to AFRL under contract DTRA01-01-C-0082, March.

von Seggern, D. H. (1977). Amplitude-distance relation for 20-second Rayleigh waves*, Bull. Seism. Soc. Am.* 67: 405–411.

Zhou, Y., F. A. Dahlen and G. Nolet (2004), Three-dimensional sensitivity kernels for surface wave observables, *Geophys. J. Int*. 158: 142–168.

SEISMIC TOMOGRAPHY OF THE ARABIAN-EURASIAN COLLISION ZONE AND SURROUNDING AREAS

M. Nafi Toksöz[1], Robert D. Van der Hilst[1], Margaret H. Benoit[1], Levent Gülen[1], Dogan Kalafat[2], Huseyin S. Kuleli[1], Chang Li[1], and Youshun Sun[1]

Massachusetts Institute of Technology[1]
Kandilli Observatory & Earthquake Research Institute, Bogaziçi University[2]

Sponsored by Air Force Research Laboratory

Contract No. FA8718-07-C-0001

ABSTRACT

The objectives of this study are to determine P and S wave velocity structures in the crust and upper mantle, and to characterize seismic wave propagation in the Arabian-Eurasian collision zone and surrounding areas, including Iran, Arabia, eastern Turkey, and the Caucasus. The motivation for the proposed study is threefold. First, the Arabian-Eurasian plate boundary is an excellent place for the study of continent-continent collision processes. It is geologically younger and smaller than the much-studied India-Asian collision zone. Second, in the past several years the number of high quality seismic stations has increased significantly because of new and expanded networks in Oman, Kuwait, Saudi Arabia, Iran, Azerbaijan, and others. These provide high-quality P and S wave travel-time data. Third, observations show that wave propagation varies significantly with small changes in path across the suture zone, indicating rapid spatial changes in the crust and mantle properties. To obtain an accurate structural model of the region, high-resolution tomographic studies are required.

The tomography is done in two steps. First, 3-D P and S velocity structures are determined by regional travel-time tomography. Next, teleseismic body-wave tomography is carried out for upper mantle and transition zone structure. Preliminary tomographic results show a complex crust and upper mantle structures and evidence of subduction both in the north (South Caspian Sea) and the Makran zone in the south.

OBJECTIVES

The objectives of this study are to determine P and S wave velocity structures in the crust and upper mantle, and to characterize seismic wave propagation in the Arabian-Eurasian collision zone and surrounding areas, including Iran, Arabia, Eastern Turkey, and the Caucasus. The area of the study, shown in Figure 1, extends east-west from the Mediterranean to Central Asia, and north-south from the Caspian to the Gulf of Aden and the Indian Ocean. The area covers all of the Arabian plate, the collision zone, and the areas in the Eurasian plate whose structure and tectonics are affected by the collision. The project will include data from countries whose seismic networks have expanded significantly in recent years, such as Turkey, Azerbaijan, Iran, Kuwait, United Arab Emirates (UAE), Oman, and Saudi Arabia. These locations provide data for high resolution P and S wave travel-time tomography. Recent observations show that wave propagation and attenuation vary significantly even with small changes across the suture zone, indicating rapid spatial changes in the crust and mantle properties.

The 3-D velocity structure from this study will improve event location accuracy in the region. While several individual countries in the area prepare their own earthquake bulletins, no single comprehensive catalog of well-located earthquakes exists for the whole region. This study would utilize these individual event bulletins to provide an extensive database of relocated events. Additionally, the high resolution body wave travel-time tomographic models will aid in the calculation of model-based station corrections.

A number of unanswered questions remain about the structure and processes in the upper mantle beneath the collision zone. The fate of the Neo-Tethys plate subducted prior to the continental collision remains largely unknown. There are no intermediate and deep earthquakes under the Zagros-Bitlis suture zone, yet the subduction is too recent for the slab to reach thermal equilibrium and be assimilated. Some studies have suggested that the slab has recently broken off beneath the suture zone (Bird, 1978; Molinaro et al., 2005b). In the Makran subduction zone in the south, seismicity and structure have been studied with the deployment of dense seismic networks (Yamini-Fard and Hatzfeld, 2006), yet the nature of the transition from the subduction zone to the Zagros suture zone has not been fully resolved. High-resolution travel-time tomography would be a major step towards defining the present day crustal and mantle structure of the Middle East region.

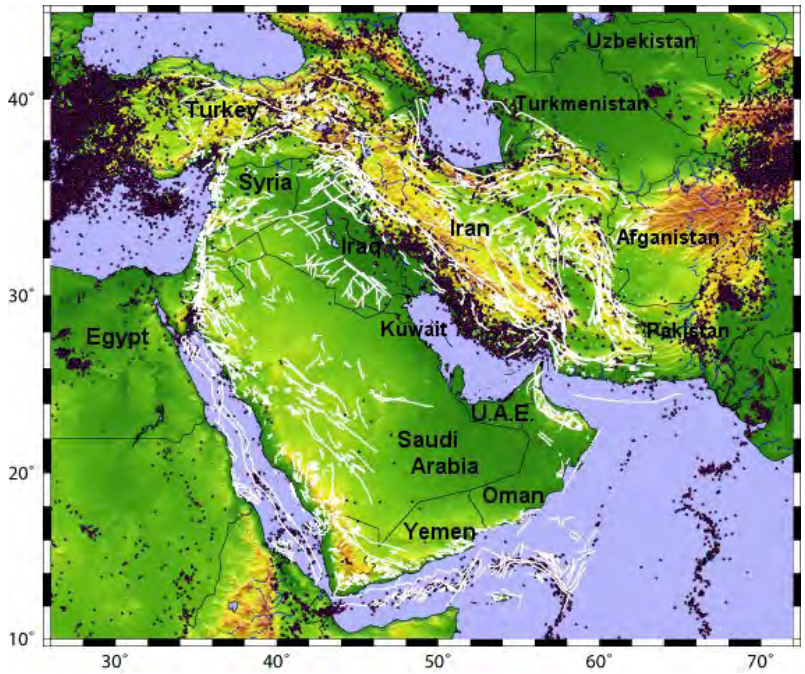

Figure 1. Topographic map of the Middle East and surrounding regions. White lines denote the location of known faults, while the black dots represent the epicenter locations of earthquakes in the region.

RESEARCH ACCOMPLISHED

Tectonic Setting

The Arabian-Eurasian plate boundary is extremely complex, and it is an ideal region to study a young (geologically) continent-continent collision belt. The current tectonics of the region are controlled by the collision and continuing convergence of the Arabian and Eurasian plates. The Arabian and Eurasian plates collided in the early Miocene, after the Neo-Tethys Sea was subducted beneath Eurasia (Bird, 1978; Şengör and Yılmaz, 1981; Jackson and McKenzie, 1984; Dewey et al., 1986). Several tectonic features were formed as a result of the deformation associated with the collision, such as the Bitlis Suture Zone, the Zagros fold and thrust belt, and the strike-slip East Anatolian fault that mark the Arabian-Eurasian plate boundary. Other tectonic features, such as the Caucasus Mountains and the Iranian and Anatolian Plateau, also formed as a result of the plate collision. Additionally, extensive basaltic volcanism occurred in Anatolia beginning around 8 Ma, though most of the volcanics are younger than 3 Ma (Pearce et al., 1990). The deformation and the seismicity surrounding the Arabian-Eurasian collision zone are similar to, but less intense than that of the Indian-Eurasian collision zone (Gülen, 1989). The Arabian-Eurasian convergence deformation patterns are shown in a simplified map in Figure 1.

Pre-, syn-, and post-collision tectonics have produced very complex structures in the region. The complex structure extends far beyond the collision zone into Iran, the Caucasus, and Anatolia. The Arabian Plate consists of a Late Proterozoic shield in the southwest, and a Phanerozoic platform in the north and northeast (Bird, 1978; Seber and Mitchell, 1992; Rodgers et al., 1999; Al-Damegh et al., 2005). Structural complexity in the Arabian Plate increases to the north and along the western boundary along the Red Sea and the Dead Sea Fault Zone. The geological features are obscured by the thick sediment cover on the Arabian plate to the southwest of the Zagros fold and thrust belt under the Caspian Sea.

Over the last decade, a number of seismic studies have examined the crust and upper mantle structure beneath the Middle East to constrain the nature of the Arabian-Eurasian collision zone. Large-scale surface wave tomography studies have shown variable crustal thickness and upper mantle velocities. Seismic velocities in the uppermost mantle are low beneath Arabia, Turkey, Iran, and the western part of the Arabian plate and are faster than those beneath the Eastern Arabian Platform and Caspian Sea regions (Pasyanos and Walter, 2002; Shapiro and Ritzwoller, 2002; Pasyanos et al., 2001; Villasenor et al., 2001; Ritzwoller and Levshin, 1998). Regional scale surface wave tomographic studies further highlight the complexity of the collision zone (Maggi and Priestley, 2005; Mohktar et al., 2001; Rodgers et al., 1999; Mindevalli and Mitchell, 1989) showing a thickened crust under the Caucasus and Zagros, and low shear velocity beneath the Turkish and Iranian plateaus.

Ritzwoller et al. (1998), Hearn and Ni (1994), and Al-Lazki et al. (2003; 2004), found slow Pn velocities ($\leq$ 8 km/s) beneath the Anatolian plateau, northwestern Iran, the Greater Caucasus, and northwestern Arabia. The Pn velocities beneath northern Arabia and the Caspian region are faster than average (Al Lazki et al., 2004; Ritzwoller et al., 2002). This high degree of variability suggests that the Earth structure may be extremely complicated in the region.

Studies of the propagation and attenuation characteristics of regional waves (e.g., Pn, Sn, and Lg) provide additional evidence for strong heterogeneities. Surface wave studies show high shear wave attenuation beneath Iran, Anatolia and the western part of the Arabian Plate and relatively low attenuation in central and eastern Arabia (Seber and Mitchell, 1992; Sandvol et al., 2001; Cong and Mitchell, 1998; Jamberie and Mitchell, 2004). The Lg wave propagation is attenuated through much of the collision zone between the Arabian and Eurasian plates (Kadinsky-Cade et al., 1981; Rodgers et al., 1987; Mitchell et al., 1997; Cong and Mitchell, 1998; Gök et al., 2000; Sandvol et al., 2001; Al-Damegh et al., 2004). An Lg blockage exists across the Bitlis suture zone and across the Zagros fold and thrust belt; however, Lg propagates efficiently across the Arabian Plate.

The Sn wave, which propagates in the uppermost mantle, is sensitive to mantle lid rheology. Sn is strongly attenuated in Anatolia and northwest Iran (Rodgers et al., 1987; Gök et al., 2000; 2003; Sandvol et al., 2001; Ritzwoller et al., 2002; Al-Damegh et al., 2004).

The conclusions that can be derived from these examples are that the seismic properties of the Zagros-Bitlis suture

zone and surrounding areas are extremely heterogeneous and require high resolution studies to elucidate. Data from the high density of seismic stations that have become available provide opportunity for such a study.

Pn Tomography in the Middle East Region

Pn travel time residuals are inverted for the lateral velocity variation and anisotropy within the mantle lid following Hearn's approach and computation method (Hearn, 1996). The preliminary results are shown in Figure 2 and they indicate significant lateral variations in Pn velocity, especially in the Caucasus and surrounding regions. Generally areas of thicker continental crust show lower velocities, while oceanic crust under the Black Sea, Southern Caspian Sea, and Azerbaijan show high velocities with respect to the reference uppermost mantle Pn velocity of 7.9 km/s.

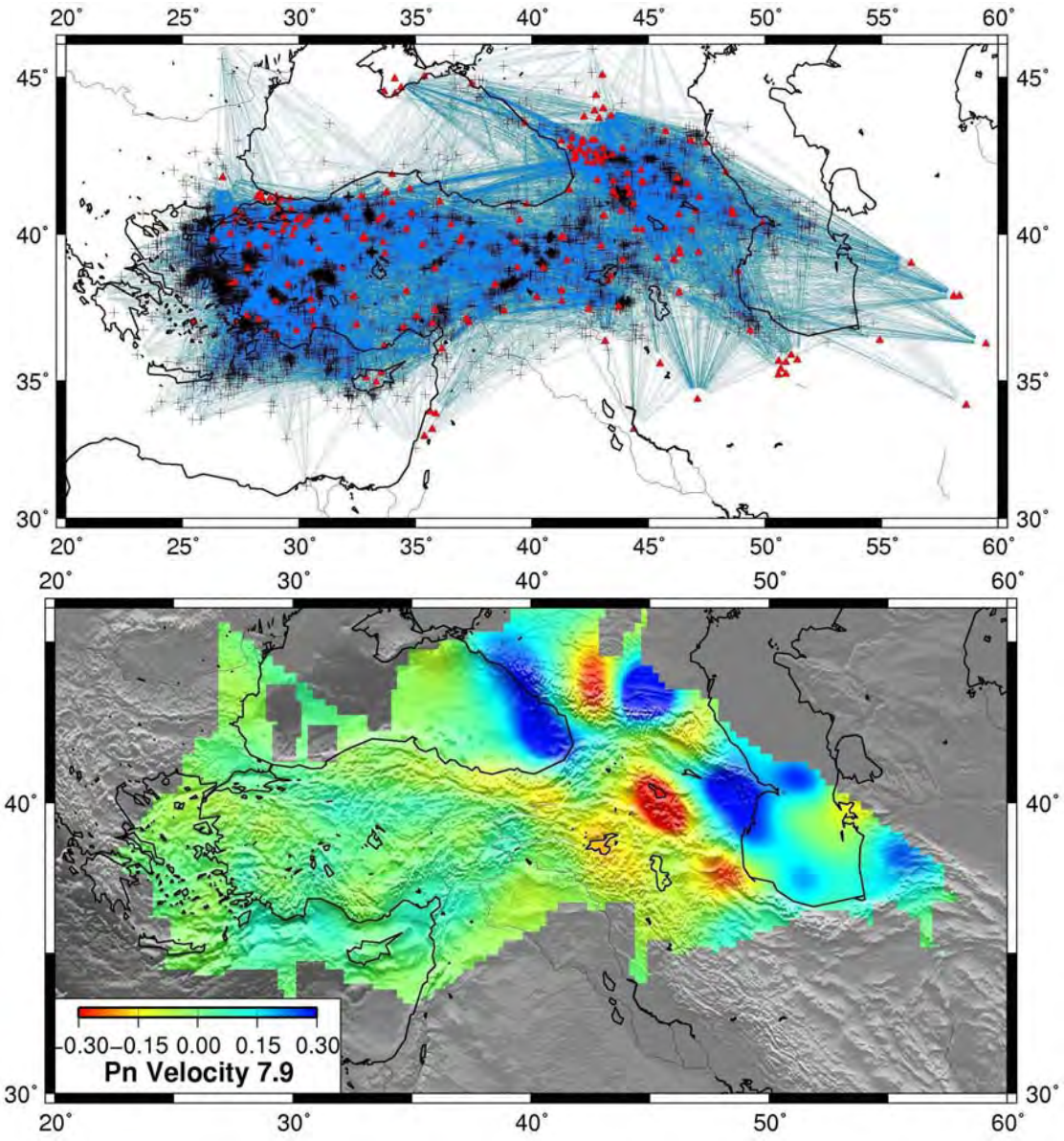

Figure 2. (a) Ray paths for Pn travel times. From 5465 events recorded by 245 stations (red triangles), 41,682 Pn rays were obtained (black crosses). (b) Pn velocity lateral variations. Average Pn velocity is 7.9 km/s. Lower velocities are shown in red, and higher velocities are shown in blue.

P-Wave Travel-time Tomography of the Middle East Region

Data and method

The data most relevant to this study for P-wave teleseismic travel-time tomography come from three sources: (1) picked arrival times from regional (temporary) seismic arrays; (2) the EHB (**E**ngdahl, van der **H**ilst, and **B**uland, 1998) datasets, reprocessed from the International Seismological Center (ISC) between 1964 and 2004; and (3) the global PP-P differential travel-time dataset.

Array data: We manually picked P-wave arrivals from local, regional, and teleseismic earthquake recorded at ~50 seismometers in Ethiopia and Saudi Arabia (yellow triangles in Figure 3). Travel time residuals are then computed by subtracting travel time calculated based on the *ak135* reference model (Kennett et al., 1995). The database will be continually expanded by obtaining data from networks in Oman, Kuwait, Saudi Arabia, and others.

Global EHB catalog: The second part of our data comes from the global EHB catalog. We use about 10 million P, Pg, pP, Pn, and PKP phases from 1964 to 2004. About 750 stations of the EHB are located within the Middle East region (red triangles in Figure 3) and they provide key constraints on the subduction along the Zagros-Bitlis suture zone.

Global PP-P data: We use the differential times of PP-P, accurately measured by waveform cross-correlation from digital seismogram (Woodward and Masters, 1991), to resolve structures in the upper mantle region with few earthquakes and stations.

To mitigate effects of uneven data coverage we use an adaptive parameterization, in which the size of grid block is based on the sampling density of the high frequency data (Li et al., 2006). To reduce the crustal anomaly smearing due to strong crustal heterogeneity along P-wave paths with small incidence angle, we use an a priori crustal model for the crustal correction by means of regularization (Li et al., 2006). We invert the whole mantle structure to avoid the errors caused by the anomalies elsewhere and the results presented here are a subset of the P-wave global model.

Upper mantle structure beneath the Middle East

In Figure 4 we present P-wave velocity variations beneath the Middle East in map view with the coast lines and plate boundary. In Figure 5 we illustrate the subduction along the Zagros and Makran by means of vertical cross sections.

Our model reveals an intriguing low velocity anomaly beneath Ethiopia from 100 km down to 500 km depth (Figure 4). Also, another low velocity anomaly is located beneath the northwestern part of the Arabian plate from 100 km to 300 km depth (Figure 4). These low velocity anomalies spread out at the lower mantle, suggesting that the hotspot may be the surface manifestation of a broad mantle upwelling connected to the African Super Plume in the lower mantle beneath southern Africa (Benoit et al., 2006).

High velocity anomaly is visible down to ~100 km depth beneath Azerbaijan. This result is consistent with our Pn tomography and indicates that the oceanic lithosphere beneath the Southern Caspian extends westward beneath Azerbaijan.

The subduction along the Zagros suture zone is well imaged (Figure 4; section A in Figure 5). Pronounced high velocity anomalies with a southward dip angle are detected in the upper mantle (above 410 km discontinuity) and earthquakes are confined above 150 km depth in the fast structures. The south-dipping slabs in the upper mantle (section A in Figure 5) may a result that Arabian plate has overridden itself during the post-collision between Arabian and Eurasian plates, like what we have observed at the Indian and Eurasian collision (Li et al., 2006). Slabs in the upper mantle seem to disconnect with the fast structures in the lower mantle, which can be interpreted at Mesozoic Neo-Tethys plate (section A in Figure 5). This is evidence for the brake-off of the slabs during the continental collision (Molinaro et al., 2005).

No slabs are observed along the Makran suture zone at the shallow depth (Figure 4; section B in Figure 5). Sparse earthquakes are confined in the crust beneath the Makran suture (section B in Figure 5). Slabs are detected from 410 km discontinuity down to the lower mantle, which are a part of the subducted Neo-Tethys oceanic slabs. These observations suggest that after the cessation of the Mesozoic Neo-Tethys subduction there is no significant collision between Arabian and Eurasian plates along the Makran suture.

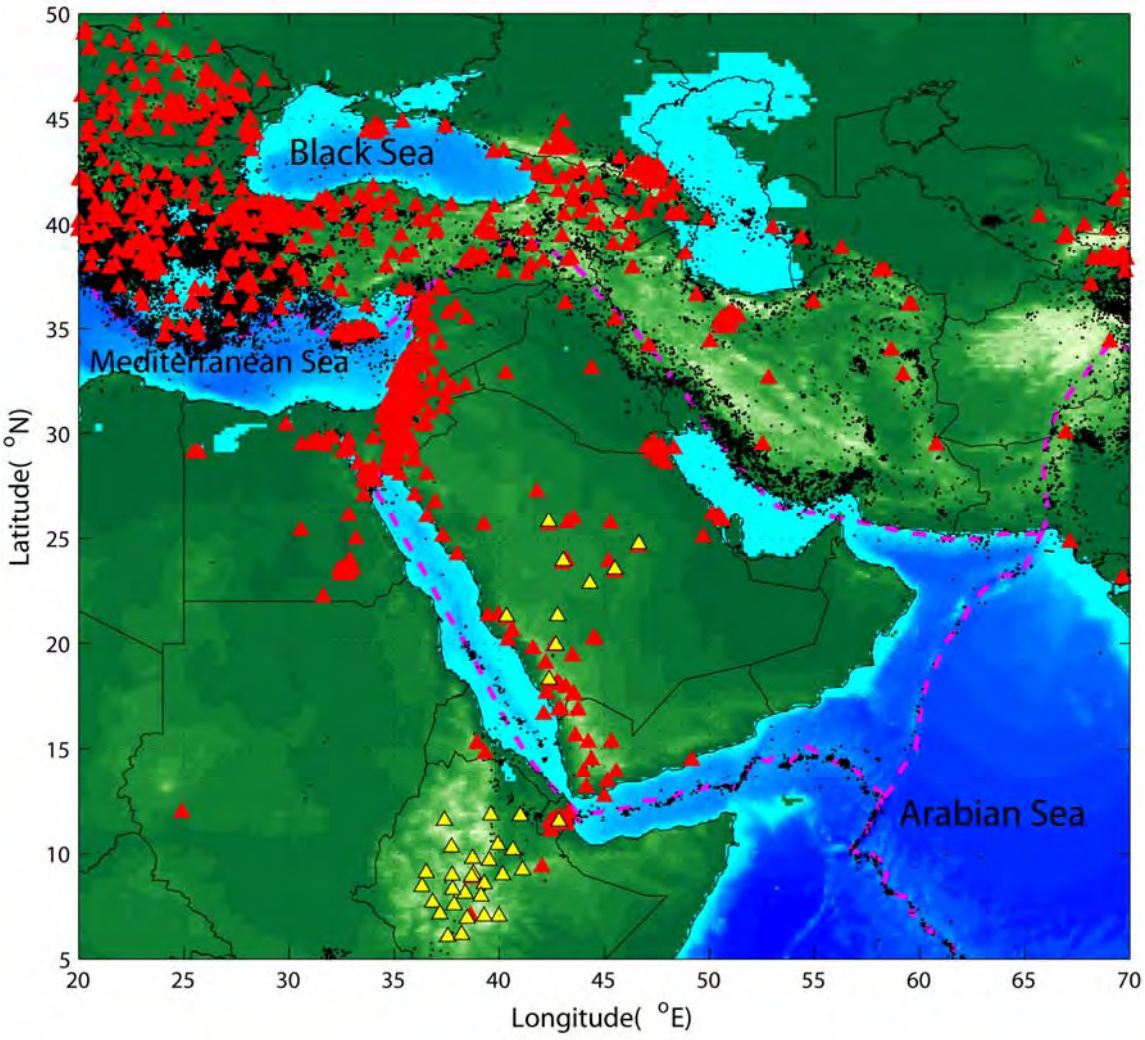

Figure 3. The distribution of seismic stations and earthquakes (black dots) in the Middle East region. The earthquake data are from the updated EHB catalog (Engdahl et al., 1998). The red triangles indicate the stations that are included in the ISC catalog. The yellow triangles are the stations from a temporay seismic network in Africa (Benoit et al., 2006) and the Saudi Arabian stations.

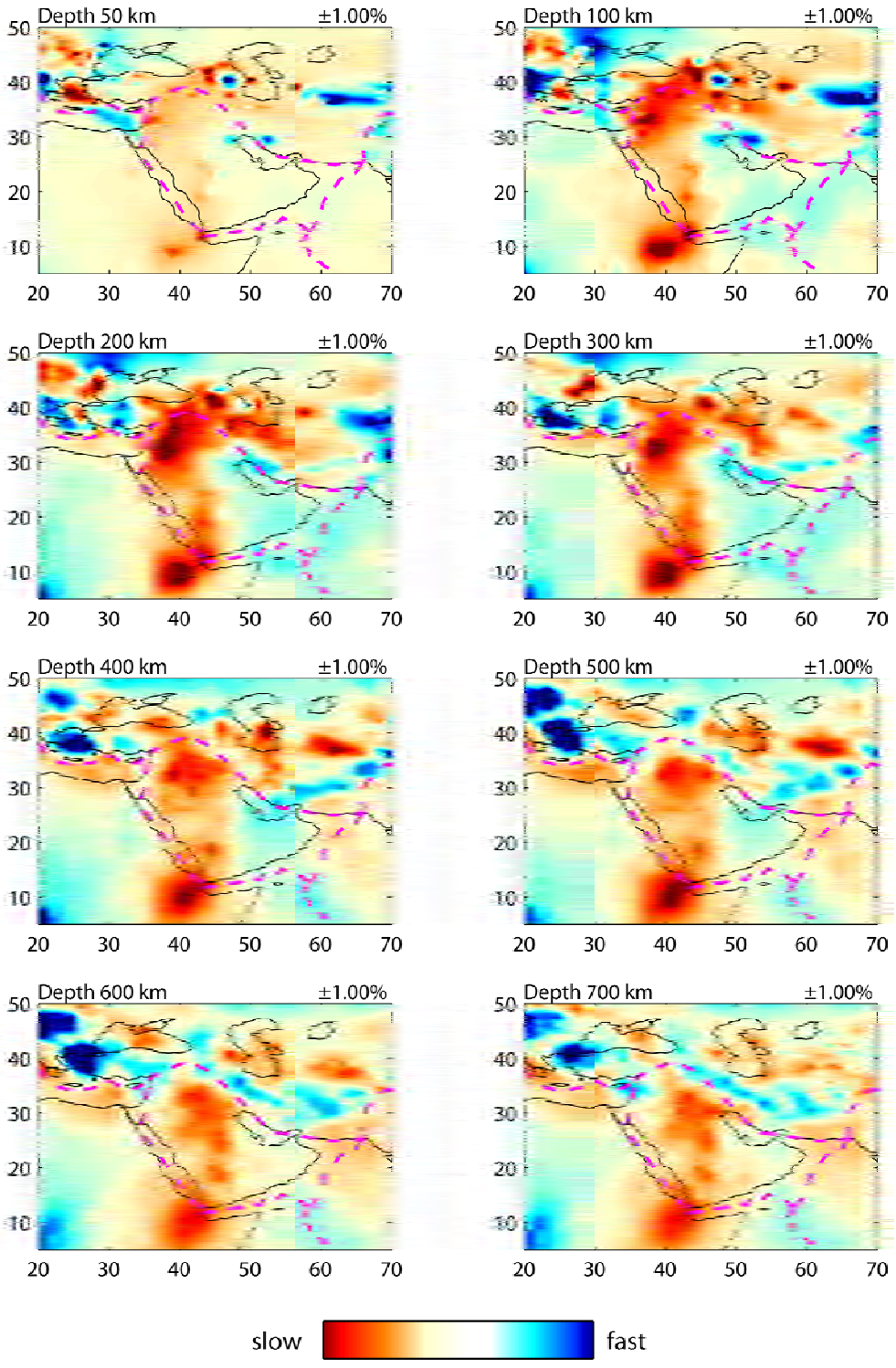

Figure 4. P-wave anomalies beneath the Middle East at different depths as indicated on the left upper corner in each subplot. The blue and red represent high and low velocity anomalies respectively. The dashed purple lines are the plate boundaries, and the black lines are the coastlines.

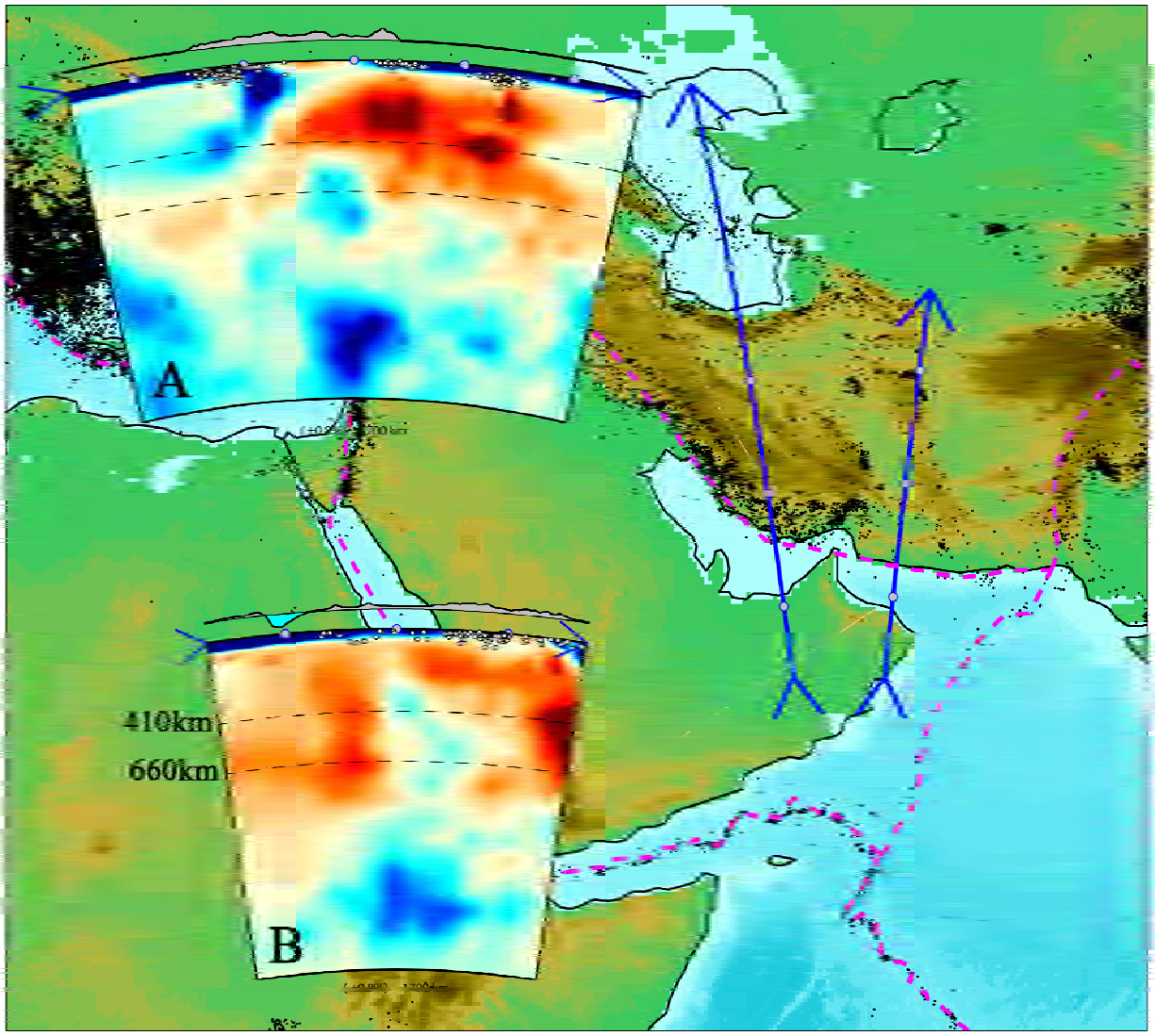

Figure 5. Vertical cross-sections showing the P-wave velocity anomalies down to 1700 km depth. As in Figure 4, the color scale indicates 0.8% deviations with respect to the 1-D *ak135* model. The dashed lines indicate the 410 km and 660 km mantle discontinuities. The topography is shown on the top of the cross-section.

CONCLUSIONS AND RECOMMENDATIONS

The preliminary tomographic results obtained in the Middle East region show a complex crust and upper mantle structure. Pronounced low velocity anomalies have been delineated beneath Ethiopia and northwestern part of the Arabian plate. These anomalies appear to emanate from the African Super Plume in the lower mantle beneath southern Africa. A high velocity anomaly is visible down to ~100 km depth beneath Azerbaijan which is consistent with our Pn tomography results that indicate the presence of oceanic lithosphere beneath Southern Caspian Sea and Azerbaijan. Pronounced high velocity anomalies with southward dip angles are detected beneath the Zagros and the Makran Suture Zones indicating that the Arabian plate has overridden itself during the post-collision between the Arabian and the Eurasian Plates. The tomographic models will be refined by applying crustal corrections and with the inclusion of local network data from Oman, Kuwait, Saudi Arabia, Turkey and others.

REFERENCES

Al-Damegh, K., E. Sandvol, A. Al-Lazki, and M. Barazangi (2004). Regional seismic wave propagation (Lg and Sn) and Pn attenuation in the Arabian Plate and surrounding regions, *Geophys. J. Int*. 157: 775–795.

Al-Damegh, K., E. Sandvol, and M. Barazangi (2005). Crustal structure of the Arabian plate: New constraint from the analysis of teleseismic receiver functions, *Earth & Planet. Sci. Lett*., 231, 177-196.

Al-Lazki, A., E. Sandvol, D. Seber, M. Barazangi, and N. Turkelli (2003). Pn tomographic imaging of mantle lid velocity and anisotropy at the junction of the Arabian, Eurasian, and African plates, *Geophys. Res. Lett.* 30: doi:10.1029/2003GL017391.

Al-Lazki, A. I., E. Sandvol, D. Seber, M. Barazangi, N. Turkelli, and R. Mohamad (2004). Pn tomographic imaging of mantle lid velocity and anisotropy at the junction of the Arabian, Eurasian and African plates, *Geophys. J. Int*. 158*:* 1024–1040.

Benoit, M. H., A. A. Nyblade, and J. C. Van Decar (2006). Upper mantle P wave speed variations beneath Ethiopia and the origin of the Afar Hotspot, *Geology* 34: 329–332.

Bird, P. (1978). Finite-element modeling of lithosphere deformation: The Zagros collision orogeny, *Tectonophysics* 50: 307–336.

Cong, L. and B. J. Mitchell (1998). Seismic velocity and Q structure of the Middle Eastern crust and upper mantle from surface wave dispersion and attenuation, *Pure Appl. Geophys.* 153: 503–538.

Dewey, J. F., M. R. Hempton, W. S. F. Kidd, F. Saroglu, and A. M. C. Şengör (1986). Shortening of continental lithosphere: The neotectonics of eastern Anatolia—A young collision zone, in *Collision Tectonics*, M. P. Coward and A. C. Ries (eds.) London: Geol. Soc. London, pp. 3–36.

Engdahl, E. R., R. D. van der Hilst, and R. Buland (1998). Global teleseismic earthquake relocation with improved travel times and procedures for depth determination, *Bull. Seism. Soc. Am*. 88: 722–743.

Gök, R., N. Turkelli, E. Sandvol, D. Seber, and M. Barazangi (2000). Regional wave propagation in Turkey and surrounding regions, *Geophys. Res. Lett.* 27: 429–432.

Gök, R., E. Sandvol., N. Turkelli, D. Seber, and M. Barazangi (2003). Sn attenuation in the Anatolian and Iranian plateau and surrounding regions, *Geophys. Res. Lett.* 30: doi:10.1029/2003GL018020.

Gülen L. (1989). From plate tectonics to global domain tectonics, in *Crust/Mantle Recycling at Convergence Zones*, S. R. Hart and L. Gülen (eds.), NATO ASI Series, C258. Boston: Kluwer Academic Publishers, pp. 173–179.

Hearn, T. M. and J. Ni (1994). Pn velocities beneath continental collision zones: The Turkish-Iranian plateau, *Geophys. J. Int*. 117: 273–283.

Hearn, T. M. (1996). Anisotropic Pn tomography in the western United States, *J. Geophys. Res*. 101: 8403–8414.

Jackson, J. and D. McKenzie (1984). The active tectonics of the Alpine-Himalayan belt between western Turkey and Pakistan, *Geophys. J. R. Astron. Soc*. *77*: 185–265.

Jamberie, A. L. and B. J. Mitchell (2004). Shear wave Q structure and its lateral variation in the crust of China and surrounding regions, *Geophys. J. Int*. 157: 363–380.

Kadinsky-Cade, J., M. Barazangi, J. Oliver, and V. Isacks (1981). Lateral variation in high-frequency seismic wave propagation at regional distances across the Turkish and Iranian plateaus, *J. Geophys. Res*. 86: 9377–9396.

Kennett, B. L. N., E .R. Engdahl, and R. Buland (1995). Constrains on seismic velocities in the Earth from travel times, *Geophys. J. Int.* 122: 108–124.

Li, C., R.van der Hilst, and M. N. Toksöz (2006). Constraining P-wave velocity variation in the upper mantle beneath SE Asia, *Phys. Earth Planet. Int*. 154: 180–195.

Maggi, A. and K. Priestley (2005). Surface waveform tomography of the Turkish-Iranian plateau, *Geophys. J. Int.* 160: 1068–1080.

Mindevalli, O. Y. and B. J. Mitchell (1989). Crustal structure and possible anisotropy in Turkey from seismic surface wave dispersion, *Geophys. J. R. Astron. Soc*. 98: 93–106.

Mitchell, B. J., Y. Pan, J. Xie, and L. Cong (1997). Lg code Q variation across Eurasia and its relation to crustal evolution, *J. Geophys. Res*. 102: 22,767–22,779.

Mokhtar, T. H., C. A. Ammon, R. B. Herrmann, and A. A. Ghalib (2001). Surface wave velocity across Arabia, *Pure Appl. Geophys.* 158: 144–1425.

Molinaro, M., P. Leturmy, J. C. Guezou, D. Frizon de Lamotte, and S. A. Eshraghi (2005a). The structure and kinematics of the southeastern Zagros fold-thrust belt, Iran: From thin-skinned to thick-skinned tectonics, *Tectonics* 24: TC3007.

Molinaro, M., H. Zeyen, and X. Laurencin (2005b). Lithospheric structure beneath the southeastern Zagros Mountains, Iran: Recent slab break-off? *Terra Nova*, doi: 10.1111/j.1365-3121.2004.00575.

Pasyanos, M. E., W. R. Walter, and S. E. Hazler (2001). A surface wave dispersion study of the Middle East and North Africa for monitoring the comprehensive Nuclear-Test-Ban Treaty, *Pure Appl. Geophys.* 158: 1445–1474.

Pasyanos, M. E. and W. R. Walter (2002). Crust and upper mantle structure of North Africa, Europe, and the Middle East from inversion of surface waves, *J. Geophys. Int*. 149: 463–481.

Pearce, J. A., J. F. Bender, S. E. DeLong, W. S. F. Kidd, P. J. Low, Y. Güner, F. Şaroğlu, Y. Yılmaz, S. Maarbeth, and J. G. Mitchell (1990). Genesis of collision volcanism in eastern Anatolia, Turkey, *J. Volcanol. Geotherm. Res*. 44: 189–229.

Ritzwoller, M. and A. Levshin (1998). Eurasian surface wave tomography: Group velocities, *J. Geophys. Res*. 103: 4839–4878.

Ritzwoller, M., A. Levshin, L. Ratnikova, and A. Egorkin (1998). Intermediate-period group-velocity maps across Central Asia, western China, and parts of the Middle East, *Geophys. J. Int*. 134: 315–328.

Ritzwoller, M. H., M. P. Barmin, A. Villasenor, A. L. Levshin, and E. R. Engdahl (2002). Pn and Sn tomography across Eurasia to improve regional seismic event locations, *Tectonophysics* 358: 39–55.

Rodgers, A. J., J. F. Ni, and T. N. Hearn (1987). Propagation characteristics of short-period Sn and Lg in the Middle East, *Bull. Seism. Soc. Am*. 87: 396–413.

Rodgers, A. J., W. R. Walter, R. J. Mellors, A. M. S. Al-Amri, and Y-S. Zhang (1999). Lithospheric structure of the Arabian Shield and Platform from complete regional waveform modeling and surface wave group velocities, *Geophys. J. Int.* 138: 871–878.

Sandvol, E., K. Al-Damegh, A. Calvert, D. Seber, M. Barazangi, R. Mohamad, R. Gok, N. Turkelli, and C. Gurbuz (2001). Tomographic omaging of Lg and Sn propagation in the Middle East, *Pure and Appl.Geophys*. 158: 1121–1163.

Seber, D. and B. Mitchell (1992). Attenuation of surface waves across the Arabian Peninsula, *Tectonophysics* 204: 137–170.

Şengör, A. M. C. and Y. Yılmaz (1981). Tethyan evolution of Turkey: A plate tectonic approach, *Tectonophysics 75*: 181–241.

Shapiro, N. M. and M. H. Ritzwoller (2002). Monte-Carlo inversion for a global shear velocity model of the crust and upper mantle, *Geophys. J. Int*. 152: 88–105.

Villasenor, A., M. H. Ritzwoller, A. L. Levshin, M. P. Barmin, E. R. Engdahl, W. Spakman, and J. Trampert (2001). Shear velocity structure of central Eurasia from inversion of surface wave velocities, *Physics of the Earth and Planetary Interiors* 123: 169–184.

Woodward, R. L. and G. Masters (1991). Global upper mantle structure from long-period differential travel-times, *J. Geophys. Res.* 96: 6351–6377

Yamini-Fard, F. and D. Hatzfeld (2006). Microseismicity and crustal structure of the Zagros-Makran Transition Zone (Iran): Evidence for a progressive transition from continental collision to oceanic subduction, in *Proceedings of the 2006 Gulf Seismic Forum*.

P- AND S-WAVE VELOCITY STRUCTURE OF THE CRUST AND UPPER MANTLE UNDER CHINA AND SURROUNDING AREAS FROM BODY AND SURFACE WAVE TOMOGRAPHY

M. Nafi Toksöz, Robert D. van der Hilst, Youshun Sun, Chang Li, and Huajian Yao

Massachusetts Institute of Technology

Sponsored by Air Force Research Laboratory

Contract No. FA8718-04-C-0018

ABSTRACT

The objective of this project is to use a combination of travel-time and surface wave tomography to obtain compressional and shear wave velocity distributions in the crust and upper mantle under China and surrounding areas.

For travel-time tomography, we took a two-step approach. First, we determined three-dimensional (3-D) P- and S-wave velocity structures for the crust and uppermost mantle using local and regional arrival time data. Travel data from the Annual Bulletin of Chinese Earthquakes (ABCE) and the International Seismological Centre (ISC/EHB) are used. A total of 345,000 P-wave, and a similar number of S-wave, arrival times are used for the tomographies. Tomographic inversions provide 3-D P- and S-wave velocities in the crust, Pn and Sn velocities, and Moho depths under China.

To extend the model deeper into the mantle through the upper mantle transition zone, ISC/EHB data for P and PP phases are combined with the ABCE data. To counteract the "smearing effect," the crust and upper mantle velocity structures, derived from regional travel times, are used. An adaptive grid method based on ray density is used in the inversion. A P-wave velocity model extending down to a depth of 1700 km is obtained. The combined regional-teleseismic tomography provides a high-resolution, 3-D P-wave velocity model for the crust, upper mantle, and the transition zone. The crustal models correlate well with geologic and tectonic features. The mantle models show the images of current and past subduction zones. A surprising result is that the "roots" of some geologic features, such as the Sichuan Basin and Ordos Plateau, extend deep into the upper mantle.

Using surface wave data from broadband stations, the S-velocity structure was determined. Multi-mode surface wave tomography was employed for the whole region of China and surrounding areas. In Tibet, where data from dense networks deployed by Massachusetts Institute of Technology (MIT) and Lehigh University arrays are available, 3-D S-wave velocity structures for the crust and uppermost mantle were obtained using ambient noise interferometry.

OBJECTIVES

The primary goal of this project is to obtain compressional and shear wave velocity distributions in the crust and upper mantle under China and surrounding areas using a combination of travel-time and surface wave tomography.

RESEARCH ACCOMPLISHED

Introduction

China and the surrounding area is a seismically active and geologically complex region (Figure 1). More than 500 earthquakes with magnitudes (M) greater than 6.0 occurred in this region between January 1978 and May 2004 (Sun and Toksöz, 2006). In this paper we present a 3-D compressional and shear wave velocity structure for the crust and upper mantle under China and surrounding regions, obtained using local and regional travel times and surface waves.

The available P- and S-wave velocity models of the crust and upper mantle in China and the surrounding area have been obtained using different approaches. Global models such as CUB 1.0 (Shapiro and Ritzwoller, 2002) and the SAIC 1° x 1° model (Stevens et al., 2001) were constructed from group and phase velocity dispersion measurements of surface waves. The global model CRUST 2.0 (Laske et al., 2001) was constructed from seismic refraction data and developed from the CRUST 5.1 model (Mooney, 1998) and a 1° x 1° sediment map (Laske and Masters, 1997). Only P-wave velocities are inverted by travel-time tomography. The S-wave velocities in the model are obtained by empirical Vp/Vs ratios or compiled from other sources. For East Asia, mantle S-velocity models were obtained from shear and surface waveforms (Friederich, 2003). Lateral spatial resolution of the models is larger than 200 km.

Regional models were constructed by Sn and/or Pn tomography (Ritzwoller et al., 2002; Hearn and Ni, 2001; Pei et al., 2007), and from surface waves (e.g., Wu et al., 1997; Lebedev and Nolet, 2003; Huang et al., 2003). P- and S-wave tomographies have been performed in several local regions in China (e.g., Huang and Zhao, 2004). All these models provide detailed crustal structures in specific regions. A detailed map for the whole China area remains to be developed.

In this study, using both travel-time body and surface wave tomography, we produce multi-scale, 3-D P- and S-wave velocity models for the crust, upper mantle, and transition zone. In the following sections we describe the data, P- and S-wave travel-time tomography, long wavelength surface wave tomography, and array tomography, respectively.

Data for Travel-Time Tomography

The P- and S-wave arrival times from local, regional, and global stations come from four sources: (1) ABCE Phase readings from about 220 stations of the Chinese Seismograph Network (CSN) during the period 1990-2004 (IG-CSB [Institute of Geology, Chinese Seismological Bureau], 1990-2004) (Figure 1); (2) EHB (Engdahl , van der Hilst, and Buland, 1998) data reprocessed from the International Seismological Centre (ISC) bulletins (1964–2004); (3) PP-P differential times, used to image the upper mantle beneath regions with few earthquakes and stations; and (4) broadband waveform data, used for surface wave tomography and for model validation using synthetic seismograms.

Combining the global, regional, and local seismic network data from various sources requires careful processing in order to avoid internal inconsistencies. The travel time picks from source 1 above have been integrated and processed along with data from source 2 (i.e., the existing EHB data) using a non-linear process of earthquake relocation and phase re-identification (Engdahl et al., 1998). Most baseline inconsistencies can simply be removed by recalculating all new picks relative to EHB hypocenters using ak135 travel time.

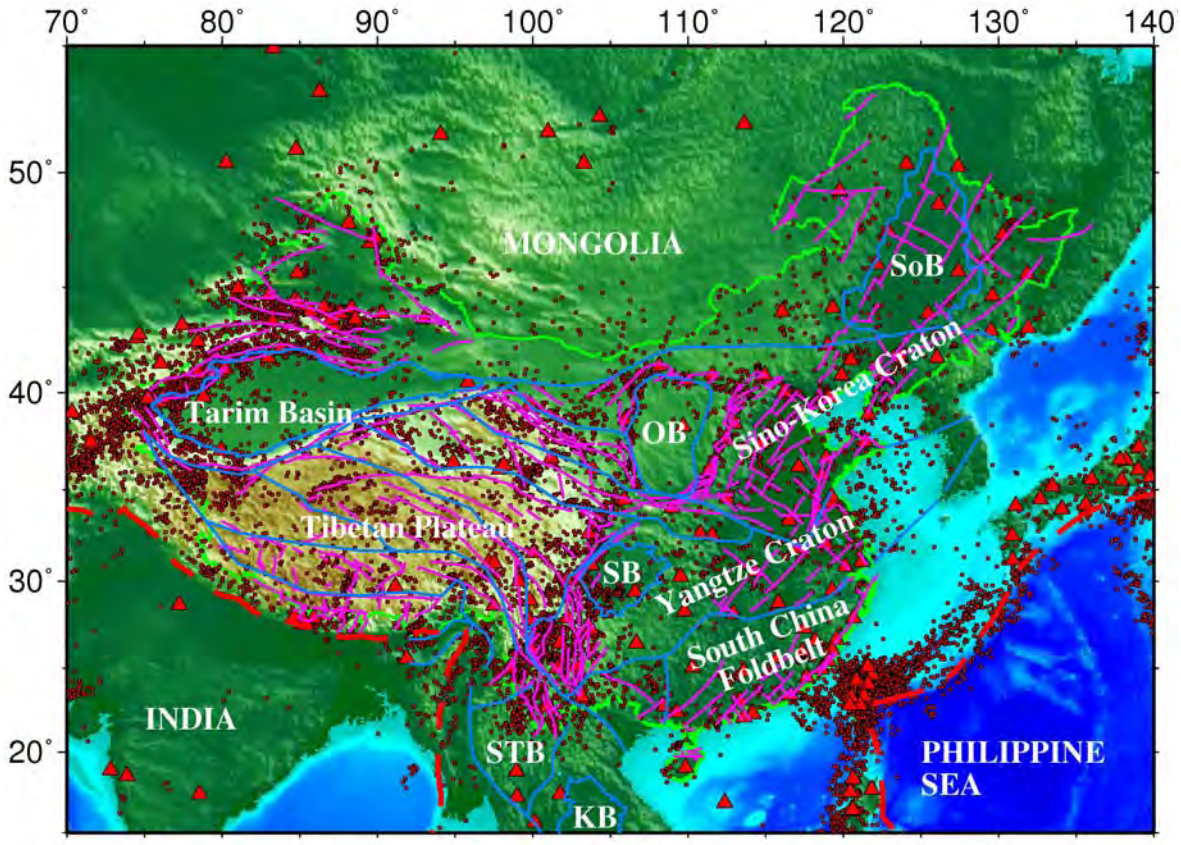

Figure 1. Shown are 25,000 earthquakes (M > 3.0 from 1990 to 2004), 220 stations, active faults, and major tectonic boundaries in China and the surrounding area. Earthquake epicenters are shown in red dots, and stations are shown in red triangles. The yellow line shows the boundary of China. Active faults in the China area are shown in purple lines, and tectonic sutures are shown in blue lines, where SoB is Songliao Basin; OB is Ordos Basin; SB is Sichuan Basin; KB is Khorat Basin; STB is Shan Thai Block; and IB is Indochina Block.

P- and S-Wave 3-D Velocity Models from Travel-Time Tomography

The tomography research used here builds on our team's extensive experience in travel-time tomography for the crust and mantle (van der Hilst et al., 1991; Kárason and van der Hilst, 2001; Sun et al., 2004; Li et al., 2006; Sun and Toksöz, 2006; Li, 2007; Sun et al., 2007). We took a two-step approach. First, we determined 3-D velocity structures for the crust and uppermost mantle (Pn, Sn). Second, we conducted the mantle tomography with the travel-times calculated from crustal models used as inputs, in order to reduce the "smearing" effect of shallow velocity structure on steep rays. In the proposed project we will follow a similar approach.

Crust and uppermost mantle P- and S-wave velocities

A high-resolution tomographic model for the heterogeneous crust is constructed by iterative, non-linear tomography. To generate adequate starting models for the non-linear inversion we combine pertinent information from global (Mooney, 1998; Bassin et al., 2000; Stevens et al., 2001; Ritzwoller et al., 2002), regional and local crust, and uppermost mantle models (Wang et al., 2003; Sun et al., 2004; Huang and Zhao, 2006; Li et al., 2006; Reiter and Rodi, 2006; Sun and Toksöz, 2006; Yao et al., 2006), in addition to Pn or Sn studies (Hearn and Ni, 2001; Hearn et al., 2004; Liang et al., 2004; Phillips et al., 2005; Rowe et al., 2005) and seismic refraction profiles (Morozov et al., 2005; Li, Mooney, and Fan, 2006). Next, we use the adaptive moving window (AMW) approach (Sun et al., 2004) to obtain crustal velocities and Pn and Sn models from a one-dimensional (1-D) Monte Carlo inversion of local ($\leq 20°$) arrival time data in the whole region, building these into the next model (Model #2).

The third step is a tomographic inversion of the local and regional arrival time data for 3-D variations in the P- and S-wave speed, using Model #2 as the initial input model.

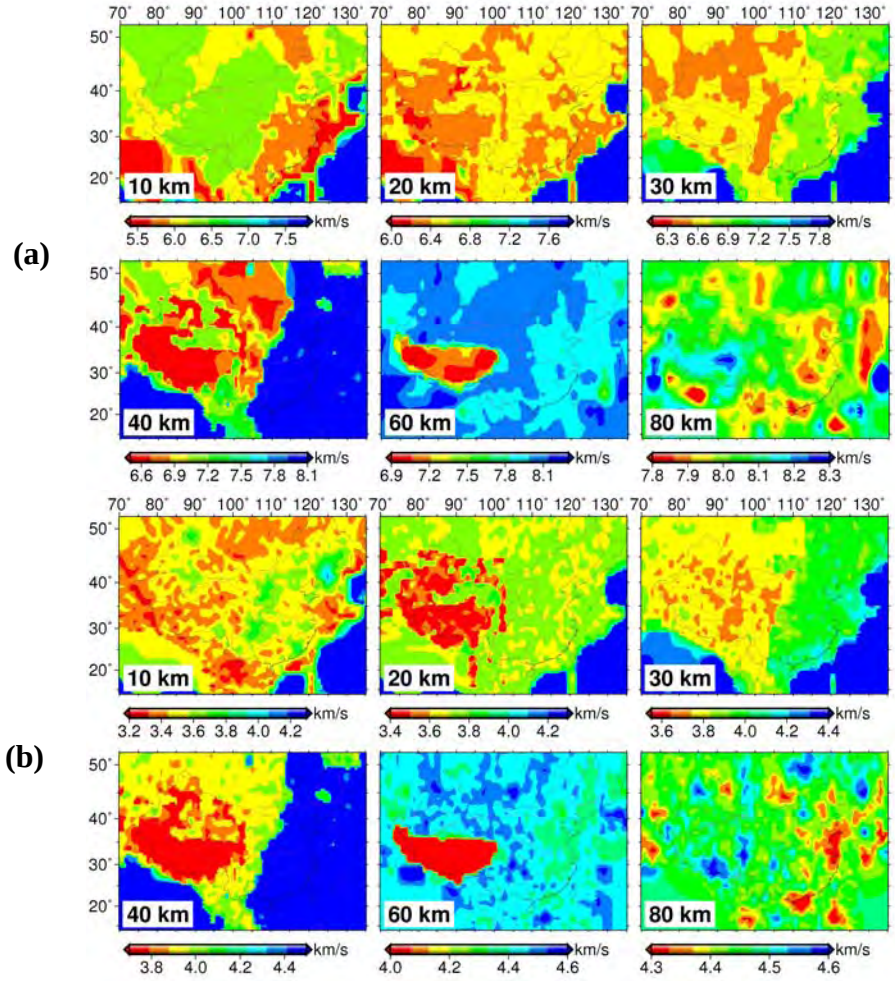

Figure 2. Horizontal slices of three-dimensional (a) Vp and (b) Vs models for China and surrounding regions at 10, 20, 30, 40, 60, and 80 km depths.

For this purpose we use a modified version of Zhao's tomographic method (Zhao et al., 1992; Sun and Toksöz, 2006), which allows for 3-D velocity variations everywhere in the model and can accommodate velocity discontinuities. The velocity structure is discretized using a 3-D grid. The velocity perturbation at each point is calculated by linear interpolation of the velocity perturbations at surrounding (adjacent) grid nodes. The velocity perturbations at grid nodes are the unknown parameters for the inversion procedure. To calculate travel-times and ray paths accurately and rapidly, the pseudo-bending technique (Um and Thurber, 1987) and Snell's law are used iteratively. We correct for station elevations by including station correction terms in the inversion. The LSQR algorithm (Paige and Saunders, 1982), with regularization, is used to solve the large and sparse system of equations. The non-linear tomographic problem is solved by repeated linear inversions. At each iteration, perturbations to hypocentral parameters and velocity structure are determined simultaneously.

P- and S-wave velocity tomograms obtained for China and surrounding areas, using this method, are shown in Figures 2 and 3. The 3-D velocity model reduces the residuals and event location errors. For example, for 11 explosions at the Lop Nor site, relocation with our 3-D models reduced hypocenter errors to 1 km or less (Sun and Toksöz, 2006, Table 2).

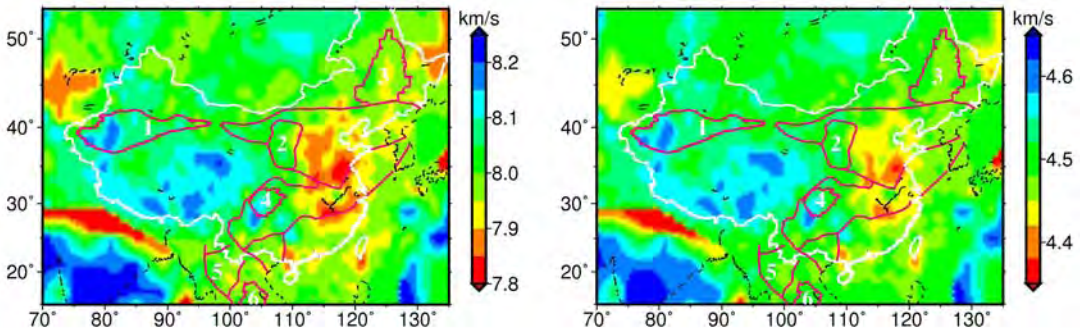

Figure 3. Pn (left) and Sn (right) velocities in China and surrounding regions. 1. Tarim Basin; 2. Ordos Basin; 3. Songliao Basin; 4. Sichuan Basin; 5. Shan Thai Block; and 6. Khorat Basin.

Mantle tomography

For the upper mantle tomography, we use the multi-scale travel-time methodology we developed and improved over 15 years (e.g., van der Hilst et al., 1991; Kárason and van der Hilst, 2001; Li et al., 2006). Even though we focus on accurate imaging of mantle structure beneath East Asia, we perform global inversions in order to avoid artifacts created by wave propagation through the structure outside the mantle volume that is of interest here. To mitigate effects of uneven data coverage, we adapt the size of the grid block to the sampling density of the high frequency data (Kárason and van der Hilst, 2000). The size of the blocks is a multiple of 45 km x 0.35° x 0.35° (in depth, latitude, and longitude) beneath the study region (down to 800 km depth) and 45 km x 0.7° x 0.7° elsewhere. To reduce artifacts created by strong crust heterogeneity that cannot be resolved upon linearized inversion for mantle structure, we apply a crust correction using the crust models resulting from the non-linear tomography described in the previous section.

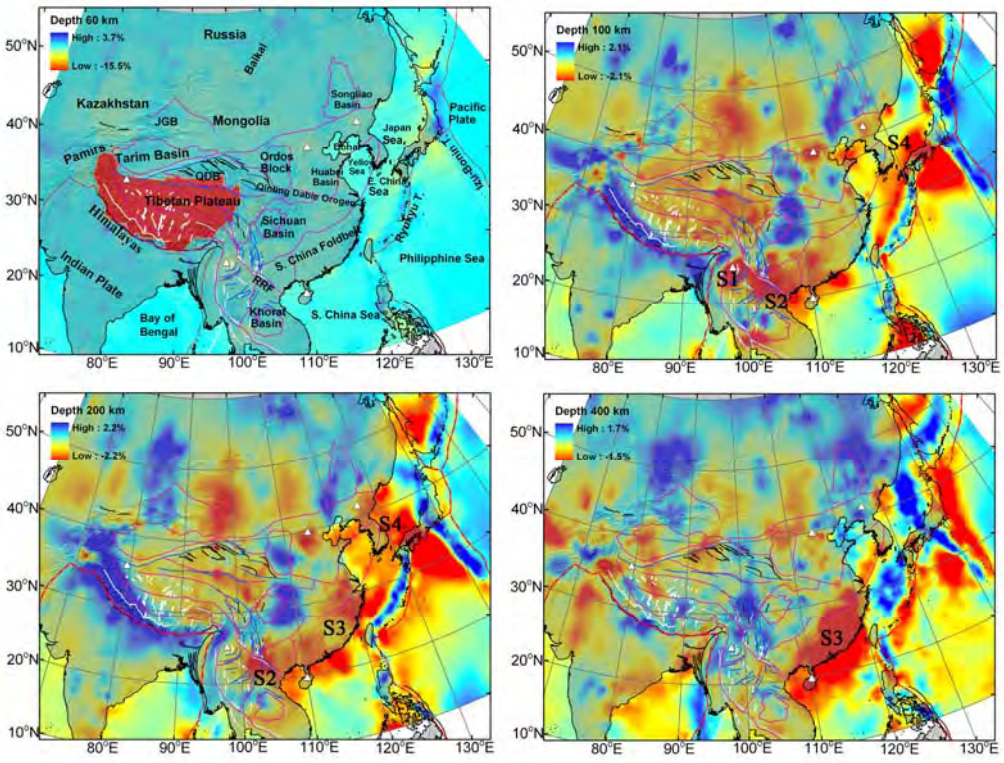

Figure 4. Lateral P-wave speed perturbations at 60, 100, 200, and 400 km depths.

We use, again, the iterative LSQR algorithm to minimize an objective function combining a measure of data misfit and regularization terms:

$$\varepsilon = \left\|\mathbf{Gm}-\mathbf{d}\right\|^2 + \lambda_1\left\|\mathbf{m}\right\|^2 + \lambda_2\left\|\mathbf{Lm}\right\|^2 + \lambda_3\left\|\mathbf{C}-\mathbf{m_c}\right\|^2. \quad (1)$$

In the first term, **m** represents the model vector, including the constant slowness perturbation in each grid cell as well as hypocenter perturbation terms. **G** is the sensitivity matrix, calculated using ray theory for the short period data and 3-D finite frequency kernels estimated from single scattering for long period data measured by waveform cross-correlation (Kárason, 2002). The data vector **d** represents the travel-time residuals. The second and third terms are traditional Tikhonov regularizations that produce "minimum structure" models consistent with the data. The second term represents "norm damping" and favors a result that is close to the reference model (it minimizes the amplitude of the model). The third term reduces the difference between adjacent cells and thus produces smooth variations; L is a first order differential operator. λ_1 and λ_2 are the weights of Tikhonov regularization.

The last term in (1) is used to prevent time delays accrued in highly heterogeneous crust from producing artifacts in the mantle model (Li et al., 2006), with **C** representing a best *a priori* estimate of the crust model and $\mathbf{m_c}$ representing the crustal part in the model vector **m**. The weight λ_3 is determined through synthetic tests (Li et al., 2006). P-wave velocity models obtained for China and surrounding areas by applying this method to a preliminarily assembled data set are shown in Figures 4 and 5.

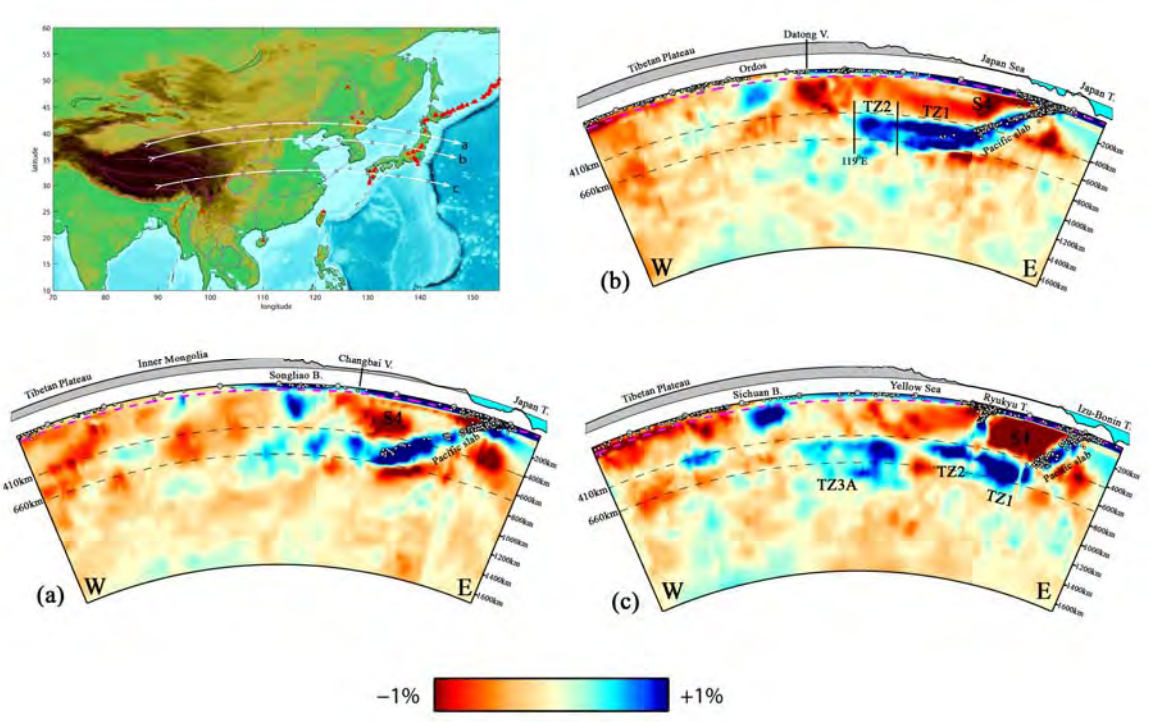

Figure 5. West-east vertical cross-sections (a), (b), and (c) through the 3-D P-wave velocity model (indicated as white lines in the upper left hand image).

Surface Wave Tomography

In addition to estimating S-wave velocities beneath East Asia from tomographic inversion of S-wave travel time data, we use surface waves to further constrain the S-wave velocity models.

Automated multi-mode Surface Wave Tomography

Using multi-mode inversion technology we resolve long wavelength structures in the upper mantle (Lebedev and van der Hilst, 2007). To enable application to the massive volumes of earthquake data now available through international data repositories, Lebedev's multi-mode inversion procedure is almost fully automated. The velocity model for East Asia is shown in Lebedev and van der Hilst (2007). The dense data coverage in China would enable the construction of shear wave velocity models at a substantially higher resolution.

Array Tomography Based on Ambient Noise Interferometry

Where we have dense station coverage we use cross-correlation and ambient noise tomography to obtain shear wave velocity (Campillo and Paul, 2003). We have developed a surface wave array tomography technique that uses phase velocity measurements from the empirical Green's functions (EGF) estimated from the ambient noise interferometry (Yao et al., 2006). Yao et al. (2006) shows, for broadband arrays in southeastern Tibet, the dense path coverage that can be achieved with this technique and the phase velocity at the period of 30 seconds from EGF analysis. Resolution tests suggest that with this data coverage one can resolve shallow mantle structure on length scales as small as ~100 km. Figure 6 shows the dense path coverage and lateral variations in S-wave velocity along several cross sections beneath the arrays.

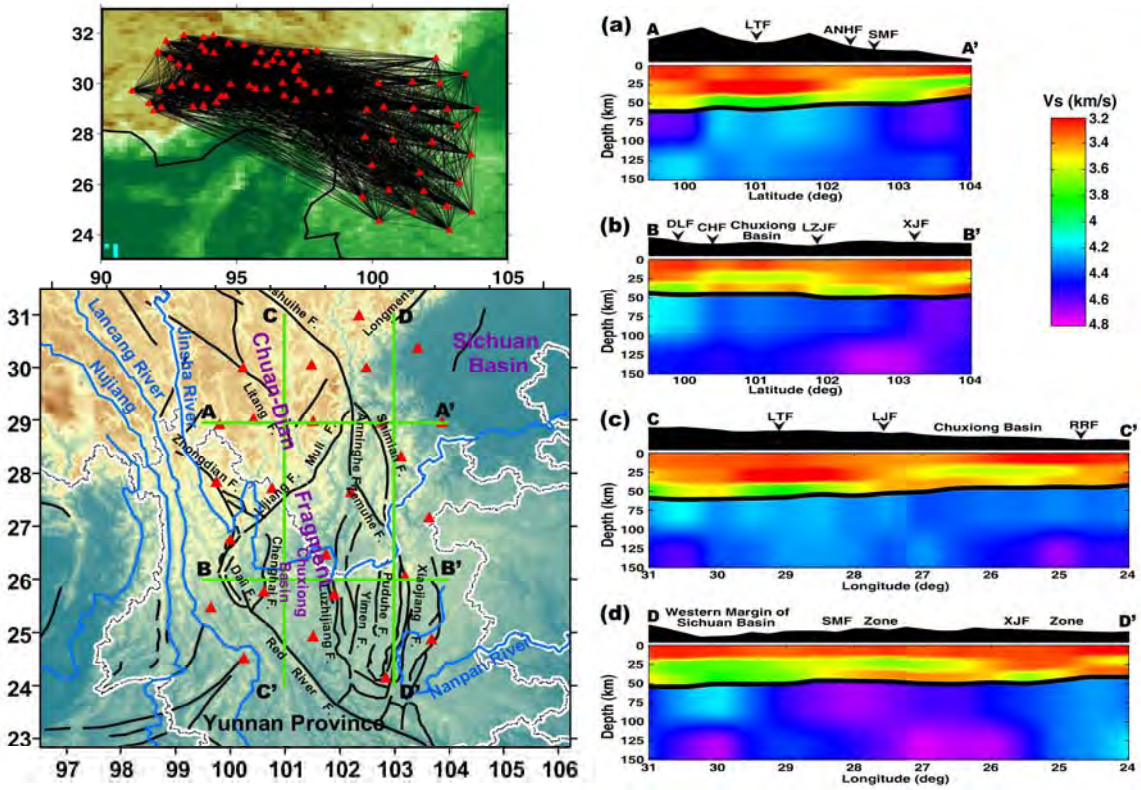

Figure 6. Interstation ray paths (upper left corner) from ambient noise interferometry study for MIT and Lehigh University arrays in southeastern Tibet. Shear wave speeds at four cross-sections through the Sichuan and Yunnan provinces of China from the combined results of ambient noise interferometry study and two-station dispersion analysis.

Because of the relatively short periods involved, using data from ambient noise interferometry alone would only constrain structure in the top half of the continental lithosphere. Therefore, we combine dispersion analysis of the empirical Green's functions from interferometry with constraints from traditional interstation dispersion analysis; together they allow spectral analysis over a wide frequency band (8–100 mHz), which allows resolution of structure between ~10 to 150 km depth (Yao et al., 2006, 2007).

CONCLUSIONS AND RECOMMENDATIONS

The 3-D compressional and shear-wave velocity models of the crust and upper mantle, obtained by travel-time and surface wave tomography, reveals pronounced lateral heterogeneities under China and surrounding regions. The velocity models exhibit the following features.

1. At the upper crust, down to 20 km depth, velocity variations strongly correlate with the major geological features.

2. There is a strong contrast between the regions to the east of 110°E longitude and the west. In eastern China, where crustal thickness is about 35 km or less, velocity variations are relatively small. Lower velocities delineate the rift structure of northeastern China. In the region to the west of 110°E longitude, the crustal velocities are much more variable. Crustal thickness varies between 35 km and 78 km. The roots of prominent features such as the Tibet, Tarim, Sichuan, and Ordos basins, dominate the subsurface velocity structures.

3. There is a prominent low velocity zone in the middle crust (around 40 km depth) under central Tibet. Shear velocity decreases by as much as 6% relative to the values north of Tibet and Tarim basin.

4. In general, there is good correlation between the P-wave and S-wave velocity variations. However, relative magnitudes of the variations (i.e., percentage velocity changes) are different in different regions. For example, the shear velocity decrease in the mid-crust under Tibet is twice as large as that of the P-wave velocity, percentage wise.

5. In the upper mantle, the percentage variation of shear velocities is greater than those of P-wave velocities.

Picking of shear wave arrivals is more prone to error than the picking of first arriving P waves, but previous studies have demonstrated the value of the reprocessed (EHB) S travel time residuals for seismic tomography (e.g., Kennett et al., 1998; Widiyantoro et al., 1998). Encouraged by those results, we will attempt travel time tomography for S-wave velocity beneath East Asia. For this purpose we will augment the EHB data with S picks from the 1200 stations of the Chinese Seismograph Network and the networks in Russia.

REFERENCES

Bassin, C., G. Laske, and G. Masters (2000). The Current Limits of Resolution for Surface Wave Tomography in North America. *EOS Trans AGU* 81: F897.

Campillo, M. and A. Paul (2003). Long-range correlations in the diffuse seismic coda, *Science*, 299: 547–549.

Engdahl, E.R., R.D. van der Hilst, and R. Buland (1998). Global teleseismic earthquake relocation with improved travel times and procedures for depth determination. *Bull. Seism. Soc. Am.* 88: 722–743.

Friederich, W. (2003). The S-velocity structure of the East Asian mantle from inversion of shear and surface waveforms, *Geophys. J. Int.* 153: 88–102.

Hearn, T.M. and J.F. Ni (2001). Tomography and location problems in China using regional travel-time data, in *Proceedings of 23rd Seismic Research Review: Worldwide Monitoring of Nuclear Explosions*, LA-UR-01-4454, Vol. 1, pp. 27–45.

Hearn, T. M., S. Wang, J. F. Ni, Z. Xu, Y. Yu, and X. Zhang (2004). Uppermost mantle velocities beneath China and surrounding regions, *J. Geophys. Res. 109*: doi:10.1029/2003JB002874.

Huang, J., and D. Zhao (2004). Crustal heterogeneity and seismotectonics of the Chinese capital region. *Tectonophysics* 385: 159–180.

Huang, J. and D. Zhao (2006). High-resolution mantle tomography of China and surrounding regions, *J. Geophys. Res*. 111: B09305, doi:10.1029/2005JB004066.

Huang, Z., W. Su, Y. Peng, Y. Zheng, and H. Li (2003). Rayleigh wave tomography of China and adjacent regions, *J. Geophys. Res*. 108: (B2), 2073, doi:10.1029/2001JB001696.

Kárason, H., and R.D. van der Hilst (2000). Constraints on mantle convection from seismic tomography. In M.A. Richards, R. Gordon and R.D. van der Hilst (Editors), *History and Dynamics of Plate Motion. Am. Geophys. Union, Geophys. Monogr. Ser.* 121: 277–288.

Kárason, H., and R.D. van der Hilst (2001). Tomographic imaging of the lowermost mantle with differential times of refracted and diffracted core phases (PKP, Pdiff), *J. Geophys. Res.* 106: 6569–6587.

Kárason, H. (2002). Constraints on mantle convection from seismic tomography and flow modeling, Ph.D. thesis, Massachusetts Institute of Technology, Cambridge, MA.

Kennett, B.L.N., S. Widiyantoro, and R.D. van der Hilst (1998). Joint seismic tomography for bulk-sound and shear wavespeed, *J. Geophys. Res*. 103: 12469–12493.

Laske, G., and G. Masters (1997). A global digital map of sediments thickness (abstract), *EOS 78*, F483.

Laske, G., G. Masters, and C. Reif (2001). CRUST 2.0: a new global crustal model at 2x2 degrees, http://mahi.ucsd.edu/Gabi/rem.dir/crust/crust2.html (last accessed July 2005).

Lebedev, S., and G. Nolet (2003). Upper mantle beneath southeast Asia from S velocity tomography. *J. Geophys. Res.* 108; doi 10.1029/2000JB000073.

Lebedev, S., and R.D. van der Hilst (2007). Global upper-mantle tomography with the automated multi-mode surface and S waveforms, *Geophys. J. Int*. (under review).

Li, C. (2007). Evolution of upper mantle beneath East Asia and the Tibetan Plateau from P-wave tomography, Ph.D. thesis, Massachusetts Institute of Technology, Cambridge, MA.

Li, C., R.D. van der Hilst, and M. N. Toksoz (2006). Constraining P-wave velocity variations in the upper mantle beneath Southeast Asia, *Phys. Earth Planet. Inter.* 154: 180–195.

Li, S.L., W.D. Mooney, and J. Fa, (2006). Crustal structure of mainland China from deep seismic sounding data, *Tectonophysics* 420: 239–252.

Liang, C., X. Song, and J. Huang (2004). Tomographic inversion of Pn traveltimes in China, *J. Geophys. Res*. 109: B11304, doi:10.1029/2003JB002789.

Mooney, W. D. (1998). CRUST 5.1: a global crustal model at 5° x 5°. *J. Geophys. Res.* 103: 727–747.

Morozov, I.B., E.A. Morozova, S.B. Smithson, P.G. Richards, V.I. Khalturin, and L.N. Solodilov (2005). 3D first-arrival regional calibration model of northern Eurasia, *Bull. Seism. Soc. Am*. 95: 951–964.

Paige, C., and M. Saunders (1982). LSQR: An algorithm for sparse linear equations and sparse least squares. ACM Trans. *Math. Software* 8: 471.

Pei, S., J. Zhao, Y. Sun, Z. Xu, S. Wang, H. Liu, C. A. Rowe, M. N. Toksöz, and X. Gao (2007). Upper mantle seismic velocities and anisotropy in China determined through Pn and Sn tomography. *J. Geophys. Res*. 112: B05312, doi:10.1029/2006JB004409.

Phillips, W. S., C. A. Rowe, and L. K. Steck (2005). The Use of interstation arrival time differences to account for regional path variability, *Geophys. Res. Letts*. 32; L11301, doi:10.1029/2005GL022558.

Reiter D. and Rodi W. (2006). Crustal and Upper-mantle P- and S- velocity structure in central and southern Asia form joint body -and surface- wave inversion, in *Proceedings of the 28th Seismic Research Review: Ground-Based Nuclear Explosion Monitoring Technologies*, LA-UR-06_5471, Vol. 1, pp. 209–218.

Ritzwoller, M. H., M. P. Barmin, A. Villasenor, A. L. Levshin, and E. R. Engdahl (2002). Pn and Sn tomography across Eurasia to improve regional seismic event locations. *Tectonophysics* 358; 39–55.

Rowe, C, Steck, L. K., W. S. Phillips, M. Begnaud, R. Stead, and H. Hartse (2005). Pn tomography and location in Eurasia, 2005 IASPEI Meeting, Santiago, Chile.

Shapiro, N. M., and M. H. Ritzwoller (2002). Monte Carlo inversion for a global shear velocity model of the crust and upper mantle. *Geophys. J. Int.* 151: 88–105.

Stevens, J. L., D. A. Adams, and G. E. Baker (2001). Improved surface wave detection and measurement using phase-matched filtering with a global one-degree dispersion model, in *Proceedings of the 23rd Seismic Research Review: Worldwide Monitoring of Nuclear Explosions*, LA-UR-01-4454, Vol. 1, pp. 420–430.

Sun, Y. and M.N. Toksöz(2006). Crustal structure of China and surrounding regions from P wave traveltime tomography, *J. Geophys Res*. 111: B03310, doi:10.1029/2005JB003962.

Sun, Y., X. Li, S. Kuleli, F. D. Morgan, and M. N. Toksöz (2004). Adaptive moving window method for 3-D P-velocity tomography and its application in China. *Bull. Seism. Soc. Am.* 94: 740–746.

Sun, Y., M.N. Toksöz, S. Pei, and D. Zhao (2007). S-wave Tomography of the Crust and uppermost mantle in China. In preparation for submission to J. *Geophys. Res.*

Um, J., and C. Thurber (1987). A fast algorithm for two-point seismic ray tracing. *Bull. Seism. Soc. Am.* 77: 972–986.

Van der Hilst, R.D., E.R. Engdahl, W. Spakman, and G. Nolet (1991 Tomographic imaging of subducted lithosphere below northwest Pacific island arcs, *Nature* 353: 37–42.

Wang, C.-Y., W. W. Chan, and W. D. Mooney (2003). Three-dimensional velocity structure of crust and upper mantle in southwestern China and its tectonic implications, *J. Geophys. Res.* 108: (B9), 2442, doi:10.1029/2002JB00.

Widiyantoro, S., B.L.N. Kennett, and R.D. van der Hilst (1998). Extending shear-wave tomography for the lower mantle using S and SKS arrival-time data, *Earth, Planets, and Space* 50: 999–1012.

Wu, F. T., A. L. Levshin, and V. M. Kozhevnikov (1997). Rayleigh wave group velocity tomography of Siberia, China, and vicinity. *Pure Appl. Geophys.* 149*:* 447–473.

Yao, H., R.D. van der Hilst, and M.V. De Hoop (2006). Surface-wave array tomography in SE Tibet from ambient seismic noise and two-station analysis: I - Phase velocity maps, *Geophys. J. Int*. 166: 732–744, doi: 10.1111/j.1365-246X.2006.03028.x.

Yao, H., C. Beghein, and R.D. van der Hilst (2007). Surface-wave array tomography in SE Tibet from ambient seismic noise and two-station analysis: II –crustal and upper mantle structure, submitted to *Geophys. J. Int.*

Zhao, D., A. Hasegawa, and S. Horiuchi (1992). Tomographic imaging of P and S wave velocity structure beneath northeastern Japan. *J. Geophys. Res.* 97 19909–19928.

JOINT INVERSION FOR 3-DIMENSIONAL S-VELOCITY MANTLE STRUCTURE ALONG THE TETHYAN MARGIN

Suzan van der Lee[1], Sung-Joon Chang[1], Megan P. Flanagan[2], Heather Bedle[1], Federica Marone[3], Eric M. Matzel[2], Michael E. Pasyanos[2], Arthur Rodgers[2], Barbara Romanowicz[3], and Christian Schmid[4]

Northwestern University[1], Lawrence Livermore National Laboratory[2], UC Berkeley[3], and ETH Zurich[4]

Sponsored by National Nuclear Security Administration
Office of Nonproliferation Research and Development
Office of Defense Nuclear Nonproliferation

Contract Nos. DE-FC52-04NA25541[1], W-7405-ENG-48[2], and DE-FC52-04NA25542[3]

ABSTRACT

For purposes of studying the lateral heterogeneity as well as for ultimately predicting seismograms for this region, we construct a new 3-D S-velocity model by jointly inverting a variety of different seismic data. We jointly invert regional waveforms, surface wave group velocity measurements, teleseismic *S* arrival times, and crustal thickness estimates from receiver functions, refraction lines, and gravity surveys. These data types have complementary resolving power for crust and mantle structures, vertical and lateral variations, shallow and deep mantle features, local and global structure. Therefore, a joint inversion of these data sets might help unravel the complexity of this tectonically diverse area. These measurements are made from a combination of mantle investigation of the deep suture between Europe and Africa (MIDSEA), Program for Array Seismic Studies of the Continental Lithosphere (PASSCAL), GeoScope, Geofon, Global Seismographic Network (GSN), International Deployment of Accelerometeres (IDA), MedNet, national networks, and local deployments throughout the study region which extends from the western Mediterranean region to the Hindu Kush and encompasses northeastern Africa, the Arabian peninsula, the Middle East, and part of the Atlantic Ocean for reference. We have fitted the waveforms of regional S and Rayleigh waves from over 3800 seismograms using Partitioned Waveform Inversion. We include over 3000 crustal thickness estimates from receiver functions, gravity measurements, and refraction profiles. We include Rayleigh wave group velocities for hundred thousands of paths transecting the region. We have over 3000 teleseismic S arrival times measured through cross correlation and over 170000 from picks originally reported to the International Seismological Centre (ISC). We demonstrate our inversion methodology and discuss results from combining these new measurements in a joint inversion for a three-dimensional S-velocity model. Finally, we will compute synthetic seismograms and travel-time surfaces through the new model.

OBJECTIVES

Our primary objective is developing a new 3-D *S*-velocity model for the Middle East and Mediterranean region, including North Africa, southern Europe, and Arabia that

1) is resolved in aseismic regions,
2) is resolved throughout the upper mantle (to 660 km),
3) resolves laterally varying crustal thickness,
4) contains laterally varying vertical velocity gradients,
5) is simultaneously compatible with multiple data sets,
6) utilizes several recent, unique waveform data sets, and
7) includes uncertainties of the model parameters.

These features would increase the model's ability to predict and calibrate regional travel times and waveforms, thereby providing improved event locations, focal mechanisms, and other event discriminants.

Secondly, we aim to convert the 3-D *S*-velocity model to a 3-D *P*-velocity model, using both literature on elastic properties (and their partial derivatives with temperature and pressure) of mantle rocks and empirical information provided by measured arrival times of teleseismic *P* and *P*ms waves.

Our third objective is to test both the *S*-and *P*-wave models' ability to predict regional *P* and *S* travel times, deflect wave paths and deform waveforms, and assess their effects first on the studied seismograms (travel times and amplitudes) and subsequently on the 3-D models derived from these data.

This report focuses on the primary objective, a new 3-D *S* velocity model.

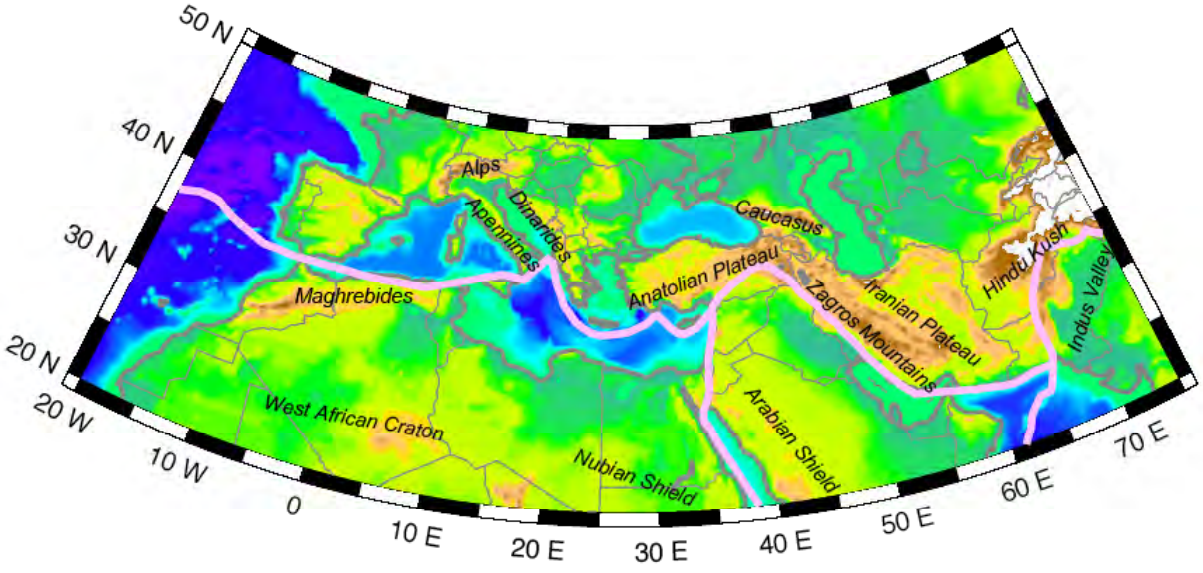

Figure 1. Topographic map of the study region. The pink line is the NUVEL1-A (DeMets et al., 1990) representation of the Eurasia-Africa-Arabia plate boundary. The study region is one of most tectonically complex in the world and is characterized by strong lateral variations.

The study region is centered around the Africa-Arabia-Eurasia triple junction (Figure 1), and extends west to the Africa-Eurasia-North America junction at the Azores, just off the map, and east to the Arabia-Eurasia-Indian Plate junction. The NUVEL1-A (DeMets et al., 1990) representation of these plate boundaries is shown by the pink line in Figure 1. The interaction of these six major tectonic plates with each other and with several microplates within an area of one quarter of the Earth's circumference yields this region rich with tectonic complexity. The three-dimensional structure of the upper mantle and crust are correspondingly complex. For example, while our region comprises only a few percent of the Earth's surface, it is home to more than half of all crustal types defined by

Mooney et al. (1998) to describe the Earth's crust globally. At the same time, the region is home to one of the most pervasive, though laterally varying low-velocity layers found beneath continental regions, which is interspersed with high-velocity bodies, related to Tethyan subduction, that extend hundreds of km vertically through the upper mantle and into the lower mantle (Van der Lee, 1990; Bijwaard et al., 1998; Marone et al., 2004; Schmid et al., 2007). We plan to capture various renditions of this structurally complicated part of the world in one *S*-velocity model through the joint inversion of several different types of seismic data simultaneously; the new model will refine our understanding of the structure and tectonics in this region of the Earth. The data types we combine are constraints from independent studies on the depth to the Moho, fundamental-mode Rayleigh-wave group velocity measurements, waveform fits of regional S and Rayleigh waves, and arrival times of teleseismic *S* waves.

RESEARCH ACCOMPLISHED

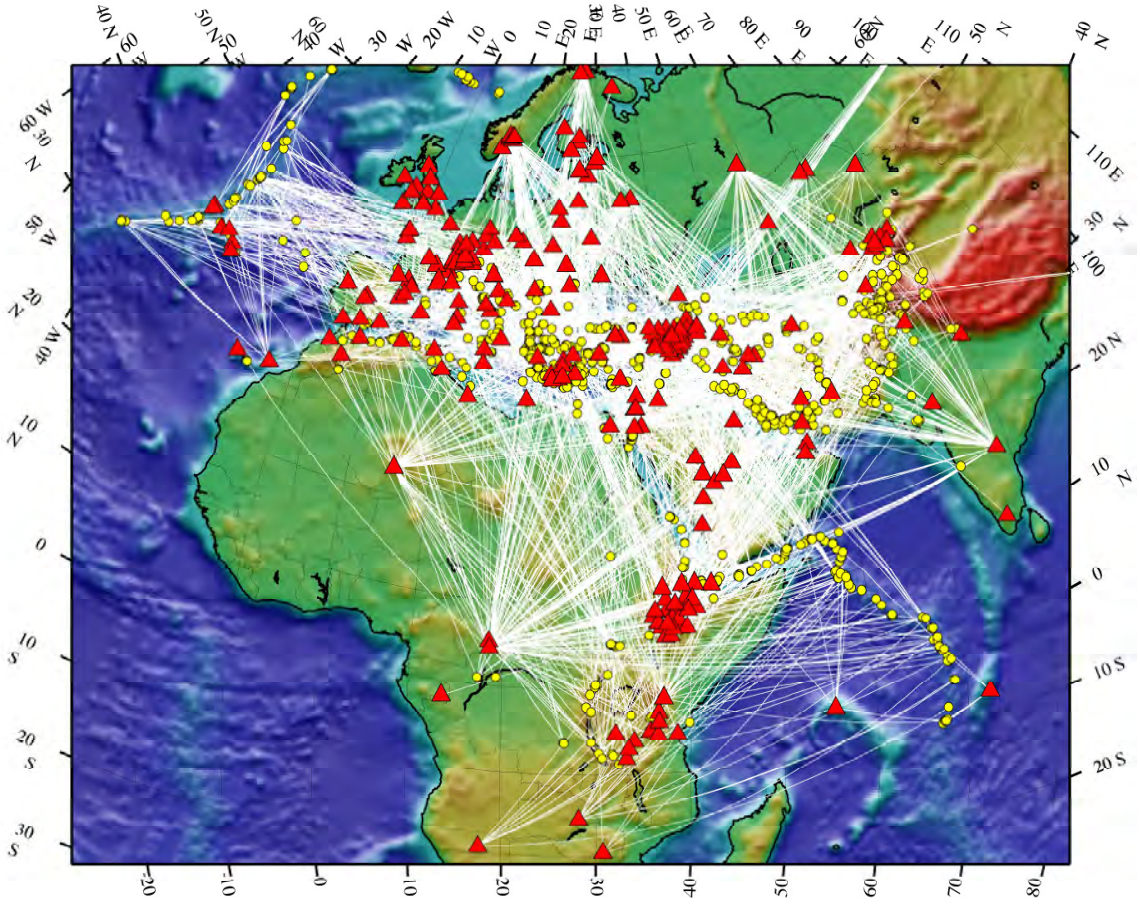

Figure 2. Map of raypath coverage showing all source-receiver paths for the region combining events (yellow circles) with Mb > 5.0 to all recording broadband stations (red triangles) at offsets between 5 and 50 degrees. This represents approximately 3,800 paths from both MIDSEA and LLNL databases.

Regional Waveform Fits

We have examined over 13,000 available waveforms from the Lawrence Livermore National Laboratory (LLNL) database which sample North Africa and the Middle East and successfully fit about 3800 of them using the non-linear inversion procedure employed by previous partitioned waveform inversion studies (Van der Lee and Nolet, 1997; Marone et al., 2004). The great-circle wave paths for these seismograms are shown in Figure 2. We have estimated path-averaged S-velocity structures for these paths using the same starting S-velocity model but a different crustal thickness (in 5 km increments) for each path, based on a priori reported estimates (Van der Lee and Nolet,

1997; Marone et al., 2004). The starting model often predicts significant phase differences relative to the data for both the S- and Rayleigh waves. The inversion procedure estimates the perturbations to the starting model by non-linear optimization (Nolet, 1990; van der Lee and Nolet, 1997). For the computation of synthetic waveforms we also need to know the source mechanisms of the events. We typically use the centroid moment tensors (CMT) from the Harvard or Global CMT project, and hypocenters from Engdahl's reprocessed ISC database. The frequency content of the data and synthetic is different for each fit and generally falls within the band 0.006 to 0.1 Hz.

The optimal shear-velocity models for some of the paths in Figure 2 have shown: 1) faster crustal velocities and slightly faster mantle velocities for the Nubian shield, which is consistent with work by Mokhtar and Al-Saeed (1994), Sandvol et al. (1998), Rodgers et al. (1999), and Julia et al. (2003); 2) lower velocities in the crust and upper mantle for path crossing the East African Rift; 3) faster crustal and low sub-Moho velocities path from the Gulf of Aden across the Arabian Shield; and 4) faster velocities for paths traversing the Russian Platform to the north. It is worth noting that the Red Sea broke up the Nubian-Arabian Shield and these provinces could have similar crustal petrology. Both provinces have volcanics and it has been speculated that mafic intrusion may explain the higher crustal velocities. The inferred mantle velocities beneath the Nubian Shield are slightly faster than the starting model. However, reported mantle velocities beneath the Arabian Shield are lower than average (e.g., Mokhtar and Al-Saeed, 1994; Rodgers et al., 1999, Maggi and Priestley, 2005).

The total ray path coverage is extensive from both the original MIDSEA dataset (Marone et al., 2004) and from data in the LLNL database (shown in Figure 2). We are able to extend the model area significantly to the east and achieve dense sampling of the Arabian Shield, Iran, Afghanistan, and Pakistan. We also have good coverage of northeast Africa, the Red Sea, and parts of the Russian Platform. We combine the 1-D, path-averaged, constraints obtained from these ~3,800 waveform fits with other data sets in the joint inversion for shear velocity structure.

Surface Wave Group Velocities

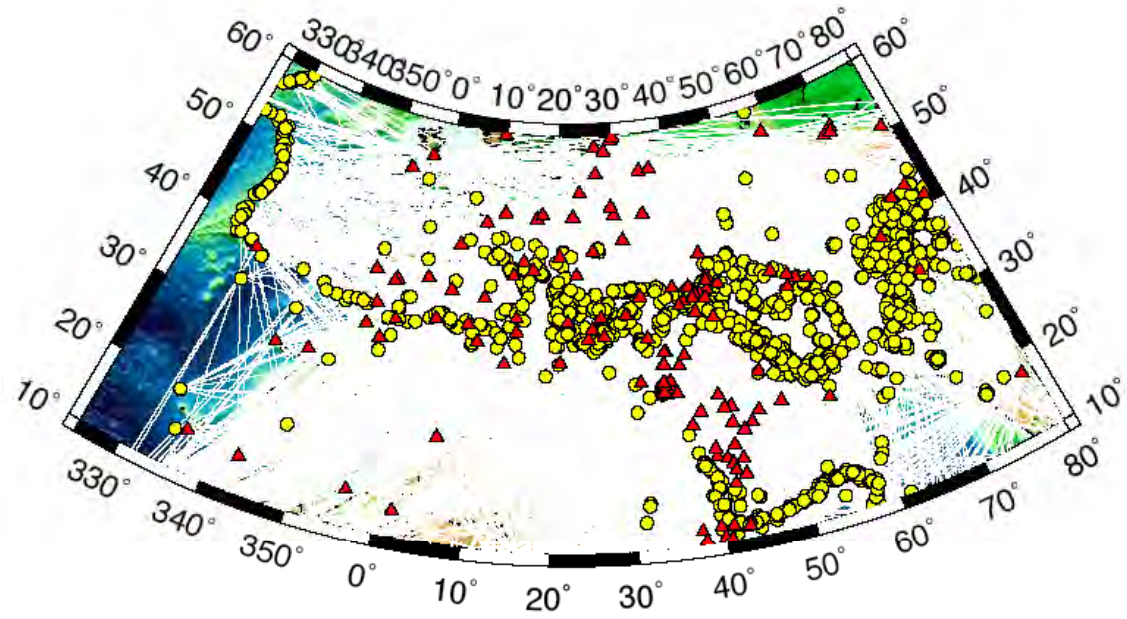

Figure 3. Total wave path coverage for the Rayleigh-wave group velocity data set. Yellow dots are earthquakes, and red triangles are seismic stations. White lines are great-circle wave paths.

We have measured group velocities of fundamental-mode Rayleigh waves recorded at MIDSEA and other stations in the region and used them to update previous group velocity maps (e.g., Pasyanos, 2005). Figure 3 shows the

great-circle wave paths for which we included fundamental-mode Rayleigh wave group velocities in our joint inversion. Compared to other data types we include, lateral coverage is best for this group velocity data set, though vertical coverage is provided mainly by the teleseismic arrival times (Figure 5) and regional *S* and Rayleigh waveforms (Figure 2).

Pasyanos (2005), for example, used these group velocities in a typical two-step inversion process, first inverting for lateral variations in group velocity for a given frequency of the Raleigh wave and then inverting the group velocities for different frequencies at a given locality for a local shear-velocity model. To allow a self-consistent treatment of all data in our joint inversion we modified these steps such that first we express the measured group velocities as path-averages and integrals over the *S*-velocity distribution with depth. For each path we thus obtain as many constraints on the laterally averaged *S*-velocity as we have measurements at different periods. Typically these equations have a high degree of redundancy with respect to describing the S-velocity distribution with depth and are far from independent. We distill the most powerful constraints out of each such set of equations using a singular value decomposition to recombine the equations into independent ones and discarding constraints associated with small singular values. This process also provides meaningful error estimates that we later use to weight the constraints with smaller error estimates more strongly during the joint inversion. We then solve these subsets of equations for the 3-D S-velocity distribution by combining all of them, with or without constraints from our other data sets, in a single, linear, least-squares, joint inversion. We benchmarked this new 2-step procedure against S-velocity models obtained with the traditional 2-step procedure and find that it performs well and efficiently. The added advantage is that we can jointly and self-consistently invert the group velocity data together with our other data.

Crustal Thickness Constraints

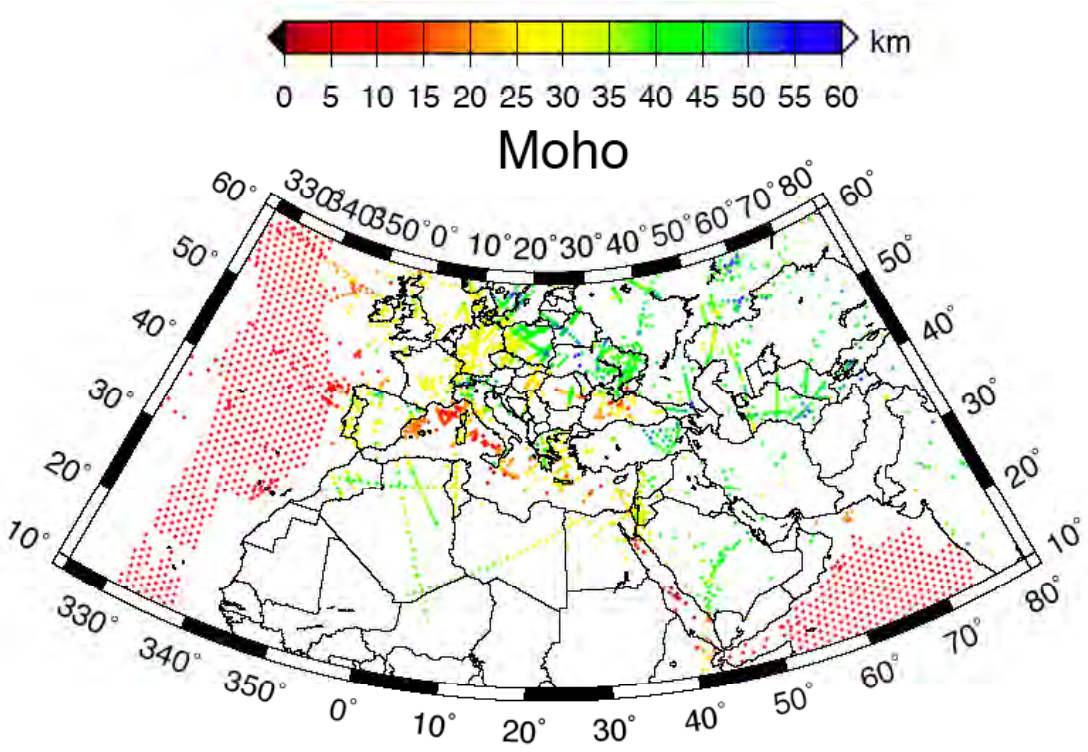

Figure 4. Total point coverage for independent constraints on Moho depth used in our joint inversion. The points are color-coded with respect to a priori determined Moho depths.

While the fundamental-mode Rayleigh-wave group velocities and regional S and Rayleigh waveforms have significant sensitivity to Moho depth, they cannot uniquely resolve Moho depth. We therefore include independent estimates of crustal thickness as point constraints in the joint inversion and thus compile such measurements from a

large number of published studies. A partial list of these studies is provided in Marone et al. (2003), and part of these points stem from the database used for CRUST5.1. We have added new estimates of Moho depth from more recent studies and interactively resolved or removed conflicting data and outliers from the data set. The majority of this data set is from receiver function studies. Remaining points are from active-source studies and some are from gravity surveys. The active-source constraints were assigned the lowest error and the Moho-depth estimates from gravity were assigned the largest errors. For the oceans we use a constraint of 10 km for Moho depth, but only for points also covered by data from our other data sets.

Teleseismic *S*-wave Arrival Times

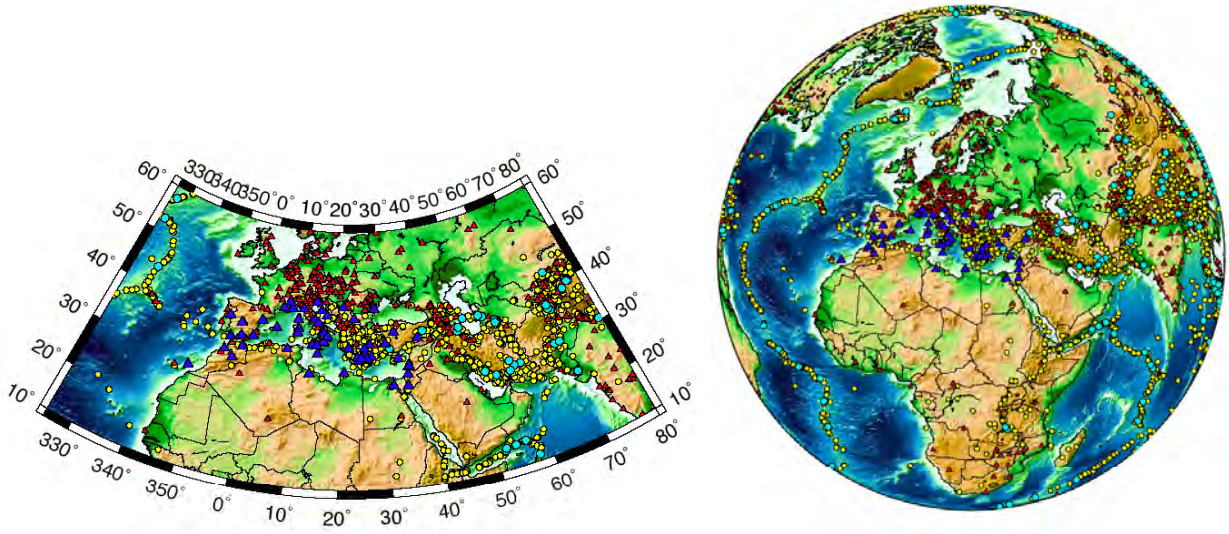

Figure 5. Earthquakes (circles) and stations (triangles) for which we have teleseismic S-wave travel-times in our joint inversion. Blue stations and cyan events are used for cross-correlation measurements and red stations and yellow events are from Engdahl's (Engdahl et al., 1998) database of arrival picks.

Figure 5 shows a map of all stations and earthquakes that produced S-wave arrival times that we use in our joint inversion. The majority of these are from Engdahl's reprocessed ISC data set spanning 38 years of recording. Nevertheless, because of their heterogeneity, these arrival times were assigned a higher error than those we measured through cross-correlation. The waveforms of teleseismic S recorded at MIDSEA and other stations in the study region were cross-correlated with the method of VanDecar and Crosson (1990), yielding high-accuracy relative S-wave arrival times. Figure 6 shows those portions of the teleseismic S-wave paths in our data set that lie within a half degree from the cross section. Both cross sections show large data gaps in the upper mantle beneath Arabia and North Africa, illustrating the rationale for jointly inverting these data with surface wave data, which are sensitive to upper-mantle structure all along their way from event to station. The cross sections in Figure 6 show that the top of the lower mantle is well covered by these data and that the ray paths are near-vertical in the uppermost mantle, providing excellent lateral resolving power. This lateral resolving power excellently complements the vertical resolving power of the regional S and Rayleigh waveform fits. Resolving Moho depth from uppermost mantle and crust velocities is aided by the independent constraints on the Moho and the fundamental-mode group velocity measurements.

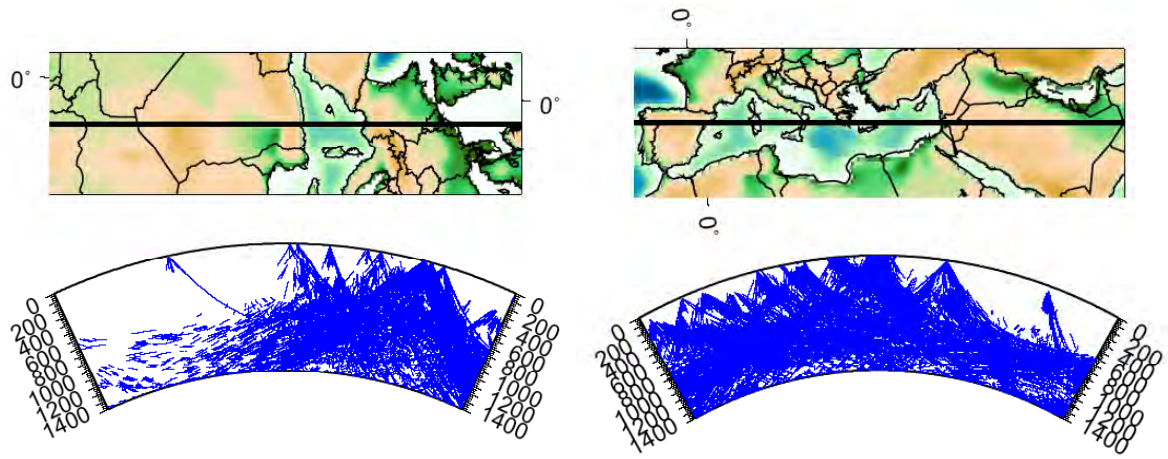

Figure 6. A NS and EW cross section through the study region showing segments of ray paths of teleseismic S waves used in our joint inversion that lie within half a degree from the cross section.

Inversion Results

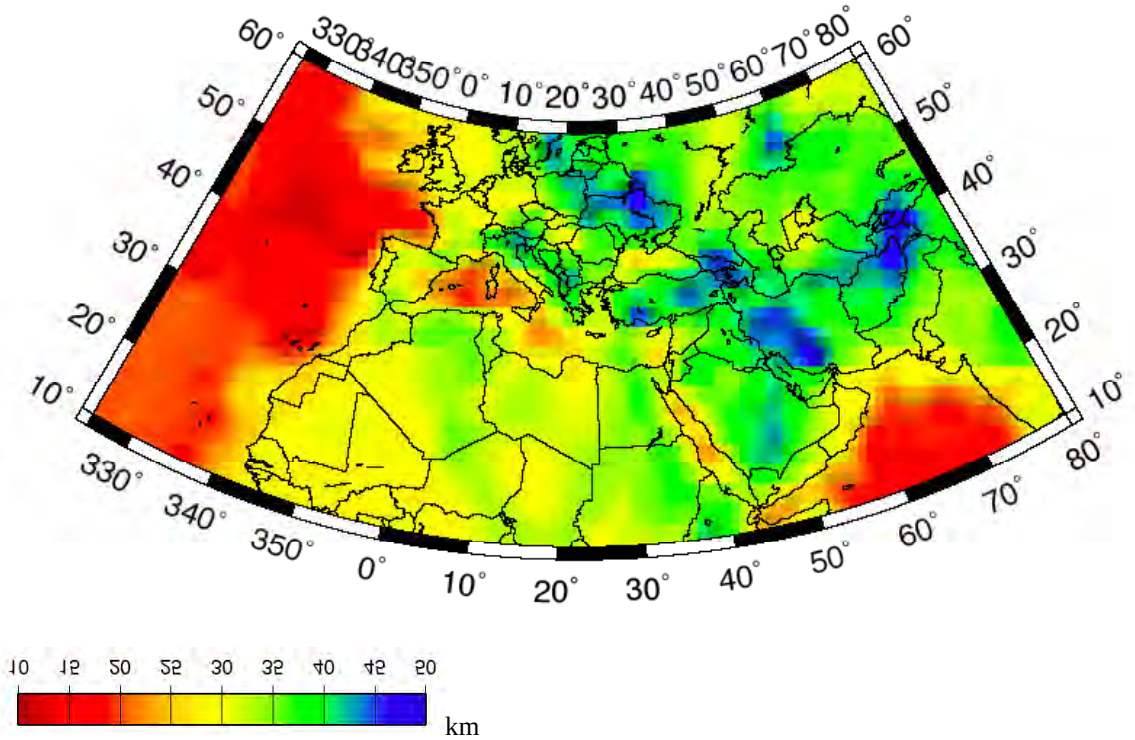

Figure 7. Moho map from joint inversion of Moho constraints (Figure 4), regional waveform fits (Figure 2), Rayleigh wave group velocities (Figure 3), and teleseismic arrival times (Figure 5).

The benefit of our joint inversion lies in the fact that the different types of data sets we use cover the same general volume of the mantle and crust along the Tethys suture but cover the volume in very different, but complementary ways; our data sets are both redundant and complementary. The redundancy is needed to increase accuracy and to ensure that all data sets measure the same structural phenomena. The data sets need to be complementary to increase resolving power over a larger volume of mantle and crust and thereby reduce trade-offs inherent in each type of

seismic data set. Combining the data sets therefore not only enhances resolving power where the region is covered by more than one data sets, but resolution is also enhanced in the regions covered by only one data set (such as the lower mantle or the upper crust) because of the reduced trade-offs with other regions of the model.

We have developed software that handles the joint inversion of constraints from regional waveform fits, crustal estimates, group velocities, and teleseismic arrival times. An early version of the joint inversion code has been tested on the teleseismic *S* arrival time data set of Schmid et al. (2006) and the data derived from regional waveform fitting from Marone et al. (2004). The results show only a percent or two increase in the variance reduction obtained in the linear inversion of both data sets compared to their individual inversions (Schmid et al., 2006). The resolving power of the joint data sets, however, has increased dramatically: the teleseismic data add more lateral resolution to the regional waveform data, while the regional waveform data add more depth resolution to the teleseismic data. The resolved depth range of the combined data sets has doubled with respect to their individual depth ranges. The regional waveform data resolve the upper mantle more strongly while the teleseismic arrival times resolve the lower mantle more strongly. The resolving power of the combined data is superior to that of each of the data sets alone. The joint inversion reduces the variance in the data sets by 40 % for the teleseismic delay times, 50 % for the Rayleigh-wave group velocities, 75 % for the Moho point constraints, and 90 % for the regional waveform fits.

Figure 7 shows the joint inversion result for Moho depth. The map shows a good resemblance with the point constraints in Figure 4, but is much smoother because the regional waveforms and group velocity data, as well as regularization constraints in the joint inversion provide a smooth interpolation between the point constraints. The map is also broadly consistent with CRUST2.0, except in northern Africa, where the crust from our joint inversion is about 5 km thinner. Resolution tests indicate that our combined data sets can resolve the crustal thicknesses of CRUST2.0.

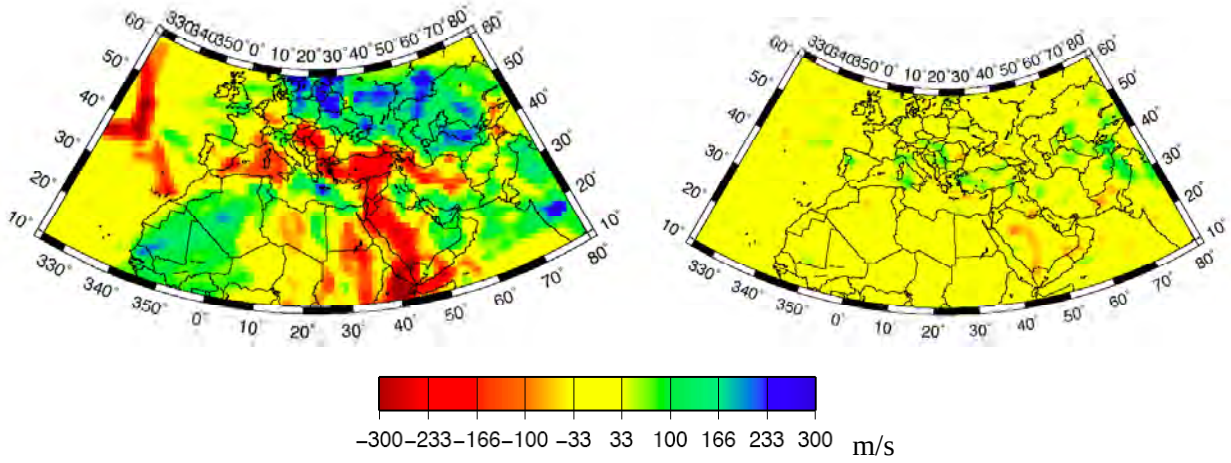

Figure 8. S-velocity perturbations relative to 1-D model MEAN (Marone et al., 2004) at a depth of 100 km (left) and 700 km (right) from our joint inversion.

The left panel of Figure 8 shows upper mantle shear velocity anomalies from the joint inversion at a depth of 100 km. The Mid-Atlantic Ridge, Algero-Provencal and Pannonian Basins, Tyrrhenian and Aegean Seas, Arabian and Nubian shields, and the Anatolian and Iranian Plateaus are underlain by significant low velocities. High velocities are imaged beneath the West-African Craton, to the northeast of the Tornquist-Tesseire Zone, beneath the Hellenic and Calabrian Arcs, and beneath the Arabian Platform and Zagros Fold Belt. The right panel of Figure 8 shows that the anomalies get weaker below the upper mantle and are dominated by high-velocity anomalies in the top of the lower mantle. These high-velocity anomalies appear to form an EW belt, roughly parallel to the Tethys suture.

CONCLUSIONS AND RECOMMENDATIONS

The broad consistency between seismic velocity anomalies inferred from teleseismic arrival times, Rayleigh wave group velocities, and regional waveforms shown here implies that these different types of data sets have recorded the same structural phenomena, despite differences in size and character between typical sensitivity kernels for each data set. This conclusion is further supported by an analysis of how teleseismic delay times depend on frequency (Schmid et al., 2006) and that the teleseismic arrival times and the regional waveforms are highly complementary. The shared sensitivity, though different in character, of receiver functions and Rayleigh wave group velocities to crustal structure helps to separate crustal effects on the observed data from mantle effects, when included in the joint inversion.

Through a joint inversion of teleseismic S-wave arrival time delays, waveform fits of regional S- and Rayleigh waves, group velocity measurements of fundamental-mode Rayleigh waves, and independent constraints on Moho depth, we have achieved considerable variance reduction in each data set simultaneously. The 3-D S-velocity model resulting from this joint inversion shows high and low-velocity anomalies that are broadly consistent with previous studies, restricted to a smaller region or a more limited data set. Our new model may be converted to a P-velocity model and used for locating events.

Our final steps in this project are to carry out this conversion to P-velocities and computing arrival time surfaces and synthetic seismograms for the purpose of potentially improving event location procedures.

ACKNOWLEDGEMENTS

Rick Benson of the Incorporated Research Institutions for Seismology guided the conversion of the MIDSEA data to Standard for Exchange of Earthquake Data (SEED) format, and Terri Hauk loaded it into the LLNL database.

REFERENCES

Bijwaard, H., W. Spakman, and E.R. Engdahl (1998), Closing the gap between regional and global travel time tomography, *J. Geophys. Res.* 103: 30055–30078.

DeMets, C. R.G. Gordon, D.F. Argus, and S. Stein (1990). Current plate motions, *Geophys. J. Int.* 101: 425–478.

Engdahl, E.R., van der Hilst, R. and Buland, R. (1998). Global teleseismic earthquake relocation with improved travel times and procedures for depth determination, *Bull. Seis. Soc. Am.* 88: 722–743.

Julia, J., C. Ammon and R. Herrmann (2003). Lithospheric structure of the Arabian Shield from the joint inversion of receiver functions and surface wave group velocities, *Tectonophysics* 371: 1–21.

Maggi, A. and K. Priestley (2005). Surface waveform tomography of the Turkish-Iranian Plateau, *Geophys. J. Int.* 160: 1068–1080.

Marone, F. S. van der Lee, and D. Giardini (2003). Joint inversion of local, regional, and teleseismic data for crustal thickness in the Eurasia-Africa plate boundary region, *Geophys. J. Int.* 154: 499–514.

Marone, F., S. Van der Lee, and D. Giardini (2004). 3-D upper mantle *S*-velocity model for the Eurasia-Africa plate boundary region, *Geophys. J. Int.* 158: 109–130.

Mokhtar, T. and M. Al-Saeed (1994). Shear wave velocity structures of the Arabian Peninsula, *Tectonophysics* 230: 105–125.

Mooney, W.D., G. Laske, and T.G. Masters (1998). CRUST 5.1: A global crustal model at 5° x 5°, *J. Geophys. Res.* 103: 727–747.

Nolet, G. (1990). Partitioned waveform inversion and 2-dimensional structure under the network of autonomously recording seismographs, *J. Geophys. Res.* 95: 8499–8512.

Pasyanos, M. E. (2005). A varible-resolution surface wave dispersion study of Eurasia, North Africa, and surrounding regions, *J. Geophys. Res*. 110: B12301, doi:10.1029/2005JB003749.

Rodgers, A., W. Walter, R. Mellors, A. M. S. Al-Amri and Y. S. Zhang (1999). Lithospheric structure of the Arabian Shield and Platform from complete regional waveform modeling and surface wave group velocities, *Geophys. J. Int.* 138: 871–878.

Schmid, C., S. van der Lee, and D. Giardini (2006). Correlated shear and bulk moduli to 1400 km beneath the Mediterranean region, *Phys. Earth Planet. Sci. Lett.* 159: 213–224.

Schmid, C., S. van der Lee, J. C. Vandecar, E. R. Engdahl, and D. Giardini (2007). 3-dimensional S-velocity of the mantle in the African-Eurasia plate boundary region from phase arrival times and regional waveforms, *J. Geophys. Res*., in press.

Sandvol, E., D. Seber, M. Barazangi, F. Vernon, R. Mellors, and A. Al-Amri (1998). Lithospheric seismic velocity discontinuities beneath the Arabian Shield, *Geophys. Res. Lett*. 25: 2873–2876.

VanDecar, J.C., and R.S. Crosson (1990). Determination of teleseismic relative phase arrival times using multi-channel cross-correlation and least-squares, *Bull. Seism. Soc. Am*. 80: 150–169.

Van der Lee, S. (1990), Tomographic inversion of delay times for P-velocities beneath Europe, *Master's thesis*, Utrecht University, 97 pp.

Van der Lee, S. and G. Nolet (1997). Upper-mantle S-velocity structure of North America, *J. Geophys. Res*. 102: 22,815–22,838.

Van der Lee, S., F. Marone, M. van der Meijde, D. Giardini, A. Deschamps, L. Margheriti, P. Burkett, S. C. Soloman, P. M. Alves, M. Chouliaras, A. Eshwehdi, A. Suleiman, H. Gashut, M. Herak, R. Oritz, J. M. Davila, A. Ugalde, J. Vila, and K. Yelles (2001), Eurasia-Africa plate boundary region yields new seismographic data, Eos Trans. AGU, 82: (51), 637–646.

NEAR SOURCE ENERGY PARTITIONING FOR REGIONAL WAVES IN 2D AND 3D MODELS: EFFECTS FROM RANDOM FREE SURFACE SCATTERING

Xiao-Bi Xie, Thorne Lay, Ru-Shan Wu, and Yaofeng He

University of California, Santa Cruz

Sponsored by Air Force Research Laboratory

Contract No. FA8718-05-C-0021

ABSTRACT

Regional seismic phases (e.g., Pn, Sn, Pg, Lg) play an important role in global monitoring of low-yield underground nuclear tests. Numerous empirical observations have shown that regional phases hold the keys to small-event magnitude and yield estimation and to discrimination between small explosions and earthquakes. However, building a sound physical basis for the application of the empirical relationships requires detailed knowledge of the regional phases (e.g., relative intensity and frequency dependence of different phases excited by earthquakes and explosions) and relationships linking the wave characteristics with a range of source and structure parameters. The complex excitation and energy-partitioning mechanisms yielding regional phases are difficult to empirically separate by data analysis. Thus, numerical modeling approaches are valuable for investigating excitation and propagation of regional seismic phases.

We use the 2D P-SV boundary-element simulation and the embedded array local slowness analysis method to investigate the effect of topographic scattering on the near-source energy partitioning for an explosion source. Random topographic models with different statistical properties, variable source depth, and different Q models are investigated using numerical simulations. With this method, the responses of different phases as functions of frequency and source/model parameters are calculated and their energy budget evaluated. The results reveal that free surface scattering has a strong effect on near-source energy partitioning. The scattering process can excite the Rg-wave for a moderately rugged topography but prevents the formation and propagation of short-period Rg-waves when the surface becomes too rugged. For models with a high-velocity shallow crust, the free surface scattering provides an important mechanism that transfers energy for an explosion source into the Lg-wave in the near-source region. At lower frequencies and for a moderately rugged free surface, the Rg-to-Lg transfer is relatively efficient. At higher frequencies and for a very rugged free surface, the body-to-Lg transfer may dominate the process. The correlation length of the random free surface fluctuation provides specific frequency dependence to the transfer function, with maximum coupling near $ka = 1$. Intrinsic attenuation within the uppermost crust has a strong effect on the energy transfer through surface scattering, with high-frequency content losing energy faster than do the lower-frequency waves.

To extend our analysis to the 3D case, we use a 3D finite-difference method that can handle both volumetric heterogeneity and irregular topography. This finite-difference method is ideal for simulating the near-source energy partitioning process. We calculate synthetic seismograms using 3D crust models with different random heterogeneity and random rough-surface parameters. The local slowness analysis method similar to that used in the 2D case is applied to the 3D simulation. We qualitatively investigate the effect of topographic scattering on explosion source energy partitioning in the near-source environment. As preliminary results, the 3D rough free surface causes strong attenuation for the Rg wave. The scattering modifies the energy distribution in the slowness domain and shifts part of the wave energy from small slowness to larger slowness. Apparent SH waves can be seen in scattered waves.

OBJECTIVE

Regional seismic phases (e.g., Pn, Sn, Pg, Lg) play an important role in global monitoring of low-yield underground nuclear tests. Numerous empirical observations have shown that regional phases hold the keys to small-event magnitude and yield estimation and to discrimination between small explosions and earthquakes (e.g., Nuttli, 1986, Taylor et al., 1989; Kim et al., 1993, 1997; Walter et al., 1995; Fisk et al., 1996; Taylor, 1996; Taylor and Hartse, 1997; Hartse et al., 1997; Fan and Lay, 1998a-c; Patton, 2001; Xie, 2002; Bottone et al., 2002). However, building a sound physical basis for the application of the empirical relationships requires detailed knowledge of the regional phases (e.g., relative intensity and frequency dependence of different phases excited by earthquakes and explosions) and relationships linking the wave characteristics with a range of source and structure parameters. The complex excitation and energy partitioning mechanisms yielding regional phases are difficult to empirically separate by data analysis. Thus, numerical modeling approaches are valuable for investigating excitation and propagation of regional seismic phases (e.g., McLaughlin and Jih, 1988; Xie and Lay, 1994; Bradley and Jones, 1998, 1999; Wu, et al. 2000a, b; Bonner, et al., 2003; Stevens et al., 2003; Myers, et al., 2005; Xie, et al., 2005a, b).

Although there are continuing controversies over the relative importance of various energy partitioning mechanisms affecting regional phases, most investigators agree that appreciable S-wave excitation for explosion sources occurs in the near-source region, reducing the performance of event discrimination approaches. Several possible near-source S-wave energy excitation mechanisms have been proposed to explain the generation of explosion Lg-waves. Among these, near-source coupling between P-, S-, and Rg-waves due to scattering at a rugged free surface may play an important role in Lg-wave excitation. This has been investigated by different authors from both observational and theoretical perspectives. From data analysis, Gupta et al. (1992, 2005) suggested that near-source scattering of explosion-generated Rg into S makes a significant contribution to low-frequency Lg signals. With Rg being strongly excited for very shallow explosions relative to deeper earthquakes, efficient Rg-to-Lg scattering often causes the low-frequency P/Lg ratio to fail to discriminate source type. Patton and Taylor (1995) analyzed the Lg spectral ratios from Nevada Test Site (NTS) explosions and suggested that the Lg-wave is generated by near-source scattering of Rg-waves into body waves, which become trapped in the crust. Myers et al. (1999) investigated the 1997 Depth of Burial Experiment at the former Soviet test site at Balapan, Kazakhstan. By comparing the regional and local recordings from explosions at different depths, they suggested that the data support Rg scattering as a major source of explosion S-waves.

Patton and Taylor (1995) introduced theoretical models of the explosion spall source to explain the observed similarity between Rg and Lg spectra. McLaughlin and Jih (1988) used finite-difference simulation to investigate topography influences on teleseismic P-waveforms and indicated possible Rg-to-P scattering due to the near-source topography. More recently, Bonner et al. (2003) and Wu et al. (2003) provided strong evidence in favor of the Rg-to-S scattering mechanism for the generation of the low-frequency S and Lg for explosions. Xie et al. (2005a, b; 2006) investigated the contribution of shallow volumetric scattering and surface scattering to explosion source energy partitioning and calculated the frequency dependent Lg excitation functions. They found that the high-frequency Lg energy is mainly from P-pS-to-Lg and P-to-Lg scattering, while the low-frequency energy is mainly from Rg-to-Lg scattering. Myers et al. (2005), using numerical simulation, investigated the effect of surface topography on the P-to-S conversion. They concluded that near-source topography and geologic complexity in the upper crust strongly contribute to the generation of S-waves.

Given the existence of a rugged free surface, the actual formation and coupling between waves in the near-source region is expected to be rather complex, so it is important to study this phenomenon with the source excitation as part of the model, not simply as a remote propagation effect. Scattering at the rough free surface can change the propagation direction of pP- and pS-waves, causing more of their energy to become trapped in the crustal waveguide and contribute to the Lg-wave than would occur for a flat surface. A rugged free surface and/or shallow heterogeneity also provides coupling between surface waves and body waves. Both body-wave to surface-wave and surface-wave to body-wave scattering can occur. Multiple scattering, variable source depth, and attenuation in the shallow layers are all factors that may affect the frequency-dependent regional wave energy partitioning and these effects need to be quantified.

We report results from both 2D and 3D numerical simulations. For the 2D case, we use a P-SV boundary-element simulation (Ge et al., 2005) and an embedded array slowness analysis method (Xie et al. 2005a) to investigate the effect of topographic scattering on explosion source energy partitioning. Following our last report (Xie, et al. 2006), which covers the effect of rms free surface fluctuation and the intrinsic attenuation on the Lg wave excitation, this report covers the effect of source depth and the correlation length of the rough surface on the energy partitioning. In

the 3D case, we use a 3D finite-difference method developed by Zhang and Chen (2006) and the slowness analysis method (Xie et al. 2005a) to investigate the problem. The 3D finite-difference method we adopted can accurately and efficiently implement the traction-free boundary conditions in the presence of an irregular topography. Both the volumetric heterogeneity and the rough free surface can be included in a model. Our preliminary results show that surface and volumetric scattering do cause coupling between the body and surface waves and significantly influence the overall partitioning of explosion energy in the regional wavefield.

RESEARCH ACCOMPLISHED

Energy Partitioning Formalism

For convenience, we symbolically write the near-source energy partitioning process for an explosion source as

$$E^K(p,f) = S(f)R^K(p,f), \tag{1}$$

where $E^K(p,f)$ is the near-source energy partitioned to the type *K* wave (*K* can be *P*, *S*, *Lg*, *Rg*, or other wave types), p is the slowness, f is the frequency, $S(f)$ is the spectrum of an isotropic explosion source. $R^K(p,f)$ is the energy response function of the near source structure for exciting type *K* wave and can be expressed as

$$R^K(p,f) = R_F^K(p,f) + \sum_J R_F^J(p,f)T^{J\to K}(p,f) - \sum_J R_F^K(p,f)T^{K\to J}(p,f). \tag{2}$$

On the right-hand side of this equation, $R_F^K(p,f)$ is the response of a flat, homogeneous layered earth model, partitioning the source energy into different phases. The transfer function $T^{J\to K}$ provides the *J*-to-*K* coupling that modifies the original partitioning by moving energy from one phase to another. The second term on the right-hand side denotes energy being imparted into the *K* wave through coupling, and the third term denotes energy lost from the *K* wave to other phases. The combined effect gives the total partitioning of the energy radiated from an isotropic source into the *K* wave energy distributed in slowness and frequency domains. This energy will develop into different regional phases that propagate to remote distances. Having a complete description of the slowness distribution allows us to accurately predict energy imparted to the distant regional phases based on the near-source energy budget.

The 2D Boundary Element Simulation

Because primary energy partitioning for an explosion source occurs within the near-source region, Xie et al., (2005a) developed a slowness analysis method that can be applied for full wavefield computations to separate the problem into consideration of near-source energy partitioning effects apart from long-range propagation effects. A localized slowness analysis for an array embedded in the numerical calculation tracks the energy partitioning occurring close to the source, replacing an expensive long-distance propagation calculation. Xie et al. (2005a) demonstrated that the energy partitioning from the near-source slowness analysis accurately predicts the energy distribution for surface observations at large range. The method has two major advantages. First, it allows analysis of the near-source processes in multiple domains, including space, time, slowness, and frequency. This allows isolation of different excitation and partitioning mechanisms within the complex near-source environment. Second, the embedded array slowness analysis method can be applied at a close range, well before the Lg-wave is actually formed. This allows numerous simulations for a relatively small-scale velocity model with very fine near-source structures. We use a 2D P-SV wave boundary-element method (Ge et al., 2005) to generate synthetics seismograms for an explosion source. The boundary element method has been proved to be an accurate wave propagation approach when the earth model includes irregular surfaces.

Space domain representation of surface scattering

Illustrated in Figure 1 are boundary element generated snapshots for wavefields in a model with free surface scattering. A random fluctuation with a correlation length of 0.5 km and an rms fluctuation of 0.15 km is used for the free surface and extends between distances 30 and 50 km. The source is located at distance of 20 km and a depth of 0.5 km. Figures 1a and 1b are horizontal and vertical displacements. In addition to familiar major phases (e.g., *P*, *pS*, *Rg*) expected for a shallow explosion in a flat earth model, scattered body and surface waves from the rough free surface are present in the wavefield. The surface-to-body and body-to-body wave scattering is distributed through

the entire medium following the primary waves, and the body-to-surface and surface-to-surface wave scattering is concentrated at very shallow depths following primary waves as they graze the surface.

To isolate the scattered phases, we subtract the wavefield generated for a flat surface from the wavefield for the model having a rough surface, yielding the results presented in Figures 1c and 1d. Most of the scattered body waves are shear waves. Due to the coupling between different wave numbers, the scattered body waves have a very broad range of propagation directions.

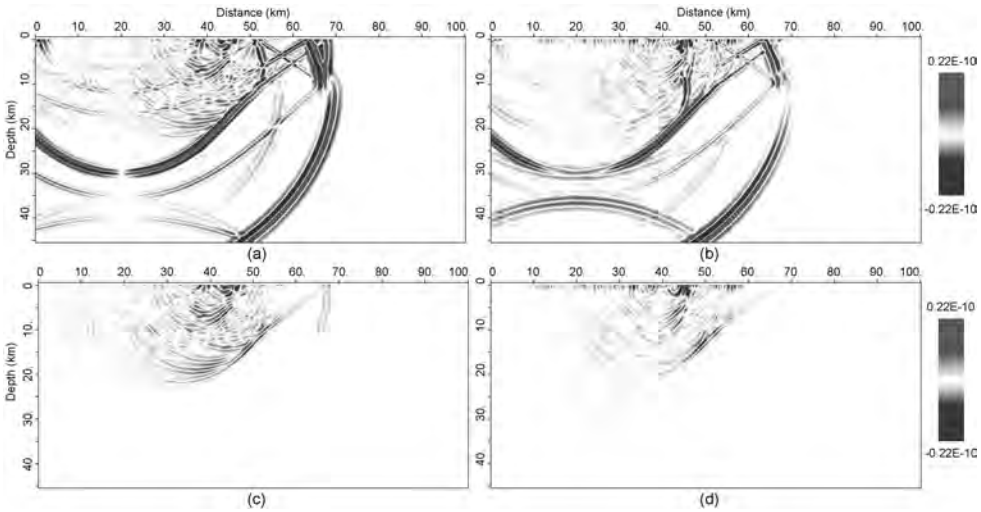

Figure 1. Wavefield snapshot at t = 10.0 s for a model with random free surface fluctuation, where (a) and (b) are horizontal and vertical components of the wavefield and (c) and (d) are horizontal and vertical components of the scattered wavefield obtained by subtracting the flat model wavefield from the random surface wavefield. The source is at 20 km horizontal position and 0.5 km depth.

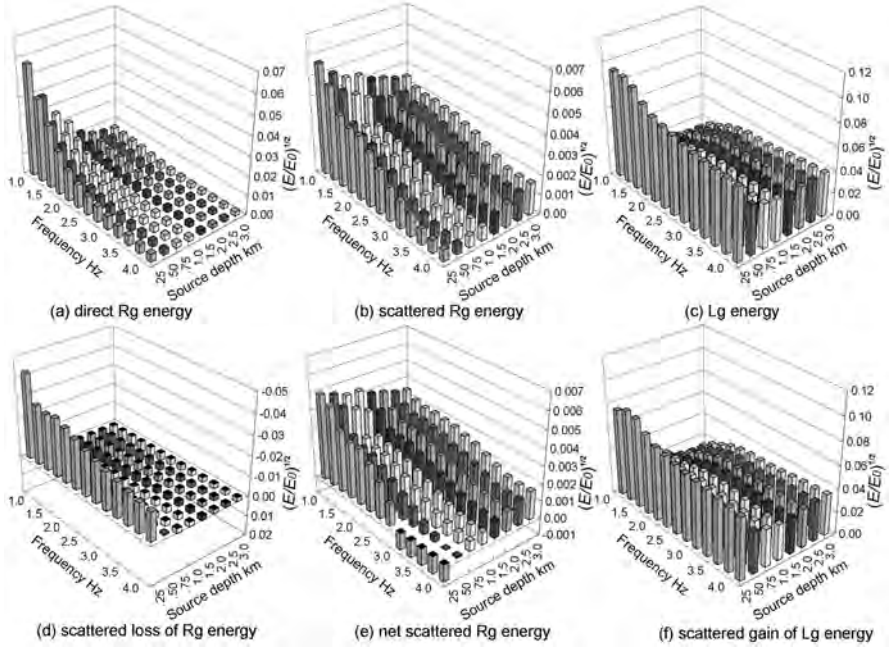

Figure 2. Responses as functions of frequencies and source depths. Top row: the near-source responses of direct *Rg* , scattered *R,g* and the *Lg*-waves, with (a) R^{Rg_direct} , (b) R^{Rg_scatt} and (c) R^{Lg} . Bottom row: the contributions of surface scattering to these responses, with (d) $R^{Rg_direct} - R_F^{Rg_direct}$, (e) $R^{Rg_scatt} - R_F^{Rg_scatt}$ and (f) $R^{Lg} - R_F^{Lg}$. Note, a negative vertical coordinate is used in (d).

The effect of source depth

We adopt a three-layer crust as our basic velocity model and add random free surface fluctuations with different statistical parameters to this basic model. The random topography has an exponential power spectrum. It is located above the source and extends in both directions for 20 km. To characterize the results statistically, we generate 10 realizations for each model. Synthetic seismograms are calculated for each realization and processed separately. We then average the measurements from individual realizations and use their mean value as the final result for a particular case.

To investigate the effect of source depth on the energy partitioning, we fix the rms free surface fluctuation at 0.15 km and the correlation length as 0.5 km and vary the source depth between 0.25 km and 3.0 km. Figures 2a to 2c present the response functions of direct *Rg*- , scattered *Rg*-, and *Lg*-waves with respect to frequencies and source depths. With increasing source depth, the *Rg* energy falls quickly. Shown in Figures 2d to 2f are separated net contributions from the free surface scattering obtained by subtracting the energy of the flat earth model from that for a random free surface. For direct *Rg* from a shallow source, a large amount of energy is lost due to scattering. However, for deeper sources, the scattering adds a small amount of energy to the *Rg*-wave. The scattered *Lg*-wave shows an apparent increase for sources shallower than about 0.5 km, which suggests a surface wave origin. The energy budget between Figures 2d and 2f is also comparable at lower frequencies. For *Lg*-wave with frequencies of 3 Hz or higher, the energy should come from body wave surface scattering. For deeper sources, the lower-frequency *Lg*-wave is very weak, indicating that both *Rg*-to-*Lg* and body-to-*Lg* conversions are weak within this frequency-depth range.

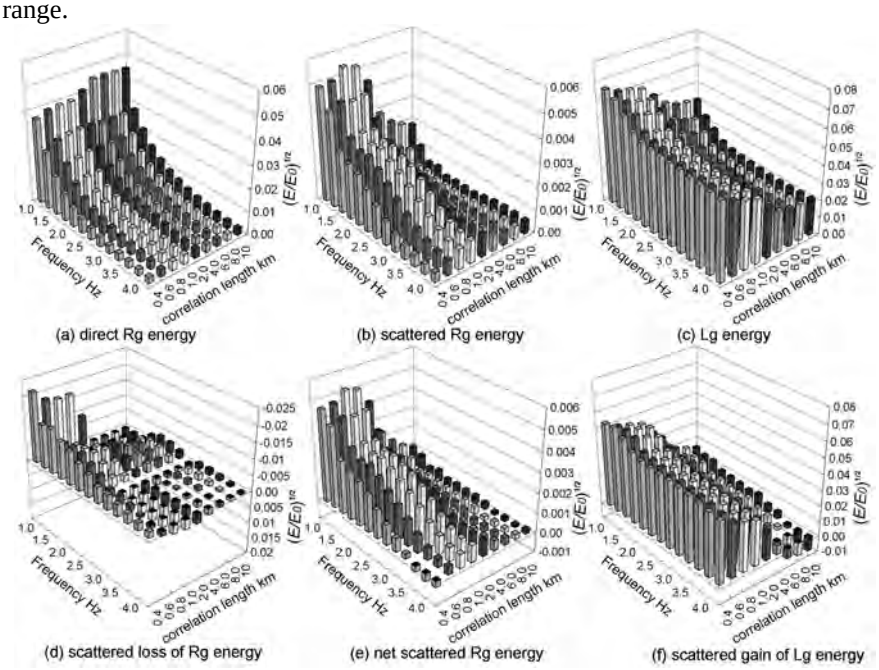

Figure 3. Similar to Figure 2, except responses are functions of frequencies and correlation lengths.

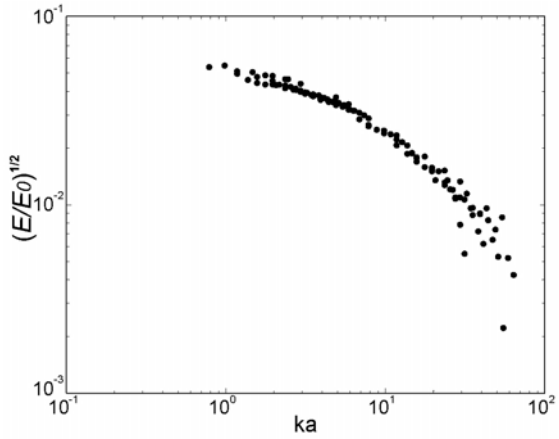

Figure 4. Net scattered Lg-energy as a function of normalized scale factor *ka*.

The effect of correlation length

To investigate the effect of correlation length on the energy partitioning, we fix the rms free surface fluctuation as 0.15 km and the source depth at 0.5 km and vary the correlation length between 0.4 km and 10 km. The response functions of *Rg*-, scattered *Rg*- and *Lg*-waves are shown in Figures 3a to 3c. The horizontal coordinate is frequency, and different rows are for different correlation lengths. From these response functions, we see that the last row (for a correlation length of 10 km) is almost the same as that for a flat earth model. This indicates that a very smooth long wavelength free surface fluctuation has almost no effect on these waves.

In Figure 3f, the net scattered contribution to the *Lg*-wave, the response function falls with increases of the correlation length at all frequencies. For frequencies used in the simulation (1 to 4 Hz) and *S*-wave velocity in the top layer (3.2 km/sec), the wavelengths are between 0.8 and 3.2 km. We calculate the response as a function of normalized scale length, ka, where $k = 2\pi/\lambda$, λ is the wave length and *a* is the correlation length, and present the behavior in Figure 4. The maximum scattering happens around $ka = 1$ and decreases for larger ka. Extension of the calculation to smaller ka is limited by the grid size used in the boundary element calculation and the dimension of the receiver array.

The 3D Finite-Difference Simulation

To include both volumetric heterogeneity and irregular topography in a 3D simulation and investigate their effects on near-source energy partitioning, we use the 3D finite-difference method developed by Zhang and Chen (2006). In this finite-difference algorithm, the physical domain is discretized by boundary-conforming grids. The irregular surface is transformed into a "flat" surface in computational space, thus avoiding the artifact usually caused by using the staircase approximation. To satisfy the free surface boundary conditions, the method uses the stress image method on the irregular topography. With this method, approximately 10 grid points per shortest wavelength are usually enough to maintain the global accuracy of the simulation. Shown in Figure 5 is the velocity model geometry used in near-source simulations throughout this report. The size of the model is $60\,\text{km} \times 60\,\text{km} \times 30\,\text{km}$, with a grid size of $600 \times 600 \times 300$. An explosion source is located at the center of the model with a depth of 0.5 km. The rough topography is located between epicenter distances 5 and 15 km. The volumetric heterogeneity is located between horizontal distances 5 and 15 km and between depths 1 km and 5 km. A $N_x \times N_y \times N_z = 10 \times 10 \times 16$ ($4\,\text{km} \times 4\,\text{km} \times 30\,\text{km}$) receiver array located at epicenter distance 28 km is used to collect the synthetic seismograms.

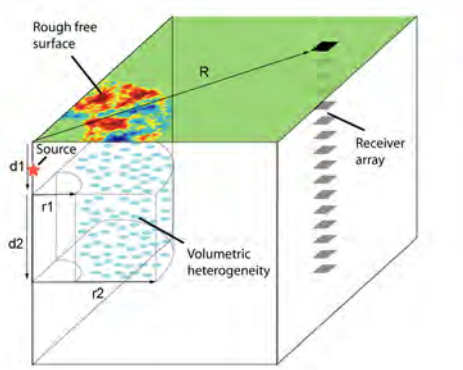

Figure 5. The 3D velocity model, including both irregular free surface and volumetric heterogeneity. The rough topography is located between distances 5 km and 15 km. The volumetric heterogeneity is located between distances 5 km and 15 km and between depths 1 km and 5 km. The synthetic seismograms are collected from a 3D array. Shown in the figure is one quarter of the model.

Shown in Figure 6 are snapshots for an explosion source in different velocity models. Rows (a) to (d) are for a layered model, a layered model with volumetric random velocity fluctuation, a layered model with irregular topography, and a layered model with both volumetric heterogeneity and random topography. The three columns are for x-, y- and z-components. The model geometry is shown in Figure 5. The rough surface has an exponential power spectrum, an rms fluctuation of 0.2 km, and a correlation distance of 2.0 km. The volumetric heterogeneity has an exponential power spectrum, an rms perturbation of 5%, and a correlation length of 2.0 km. For a layered model [row (a)], an explosion source generates P, pS, Rg, and some interface reflections, which are all P-SV waves. As examples, we see the x-component is zero in plane *yOz*, and y-component is zero in plane *xOz*. For models with volumetric and/or rough topography [rows (b) to (d)], there are appearent scattered waves following the primary phases. Particularly, SH-waves appear in the tangential component, e.g., the non-zero x-component in *yOz* plane and the non-zero y-component in *xOz* plane.

Shown in Figure 7 are synthetic seismograms for models with different free surfaces. The model geometry is shown in Figure 5. The top, middle, and bottom rows are for radius, tangential, and vertical components, respectively. Column (a) is for a layered crust model with a flat free surface. Column (b) is for a layered model with a rough topography that has a Gaussian power spectrum, an rms fluctuation of 0.1 km, and a correlation length of 2.0 km. The column (c) is similar to (b), except the random power spectrum is exponential. The results show that the rough topography strongly attenuates the surface wave and generates scattered SH waves.

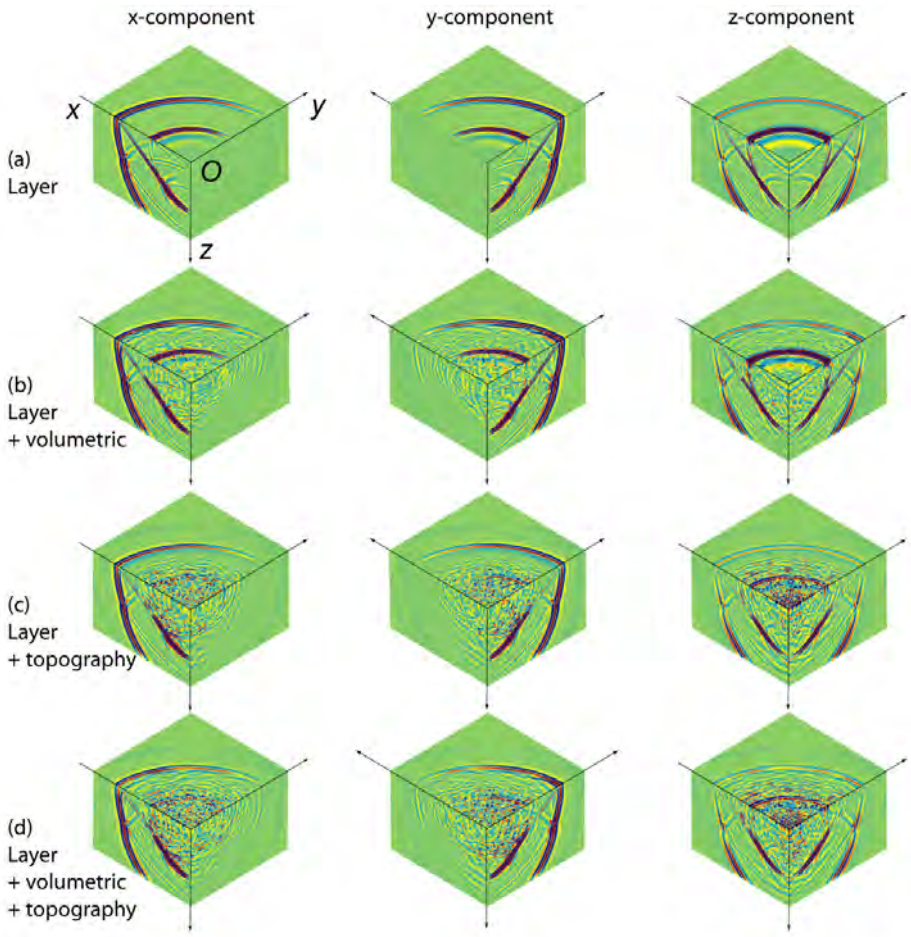

Figure 6. Snap shots for an explosion source in different velocity models. Rows (a) to (d) are for a layered model, a layered model with volumetric random velocity fluctuation, a layered model with irregular topography, and a layered model with both volumetric heterogeneity and random topography. The three columns are for x-, y- and z-components.

Shown in Figure 8 are synthetic seismograms and slowness analysis for (a) a layered crustal model and (b) a layered model with both rough free surface and volumetric heterogeneity. The model geometry is shown in Figure 5. The top, middle, and bottom rows are for radius, tangential, and vertical components, respectively. The rough surface has an exponential power spectrum, an rms fluctuation of 0.2 km and a correlation distance of 2.0 km. The volume heterogeneity has a 5% velocity perturbation, an exponential power spectrum, and a correlation length of 2 km. The synthetic seismograms are filtered between 0.5 and 5.0 Hz, and normalized using the same scale. The horizontal distance from the source to the center of the receiver array is about 28 km. The 2D slowness analyses are conducted in horizontal plane (the map view) with these panels roughly correspond to P, PP, PS, Rg, and coda waves. The results show that for an explosion source in a layered model, there is no SH wave and the energy is distributed within the upper mantle S-wave slowness (the dashed circle). For a model with rough free surface and the volumetric heterogeneity, the primary P and Rg waves are strongly attenuated due to the scattering. From slowness analysis, there are both SV and SH energy with their slowness distributed outside of the upper mantle S-wave slowness, indicating part of their energy to become trapped in the crustal waveguide to contribute to the *Lg*-wave.

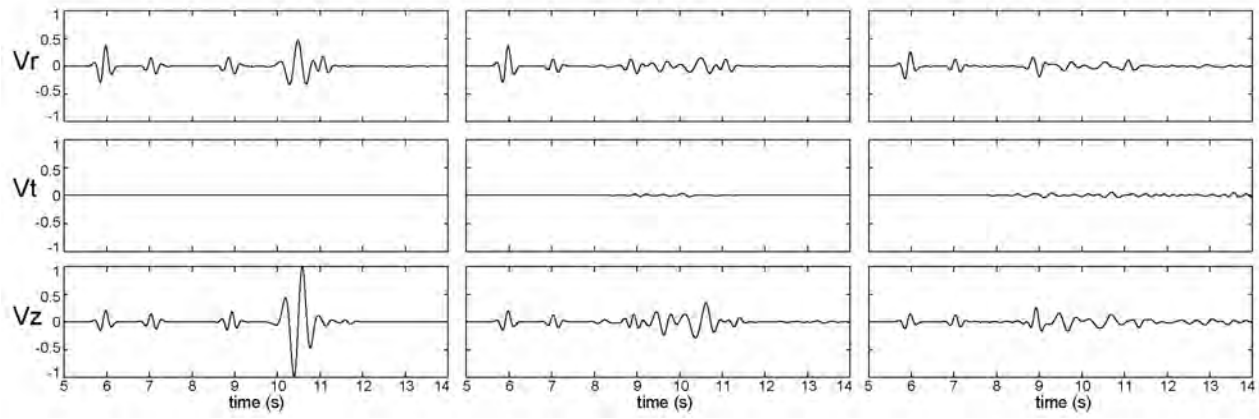

(a) (b) (c)

Figure 7. Synthetic seismograms for (a) a layered crust model with flat free surface, (b) a layered model with Gaussian rough free surface, and (c) a layered model with exponential rough free surface. All seismograms are normalized with the same scale.

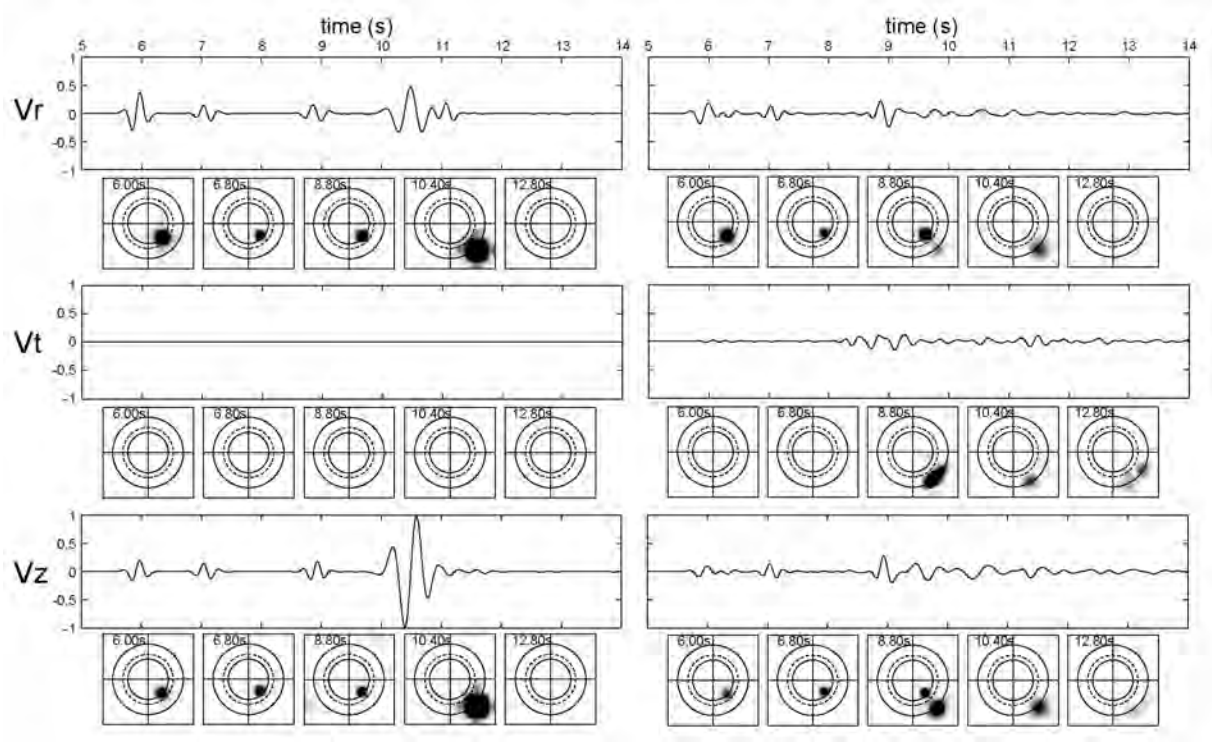

(a) (b)

Figure 8. Synthetic seismograms and slowness analysis for a layered crustal model [column (a)] and a layered model with both rough free surface and volumetric heterogeneity [column (b)]. The model geometry is shown in Figure 5.

CONCLUSIONS AND RECOMMENDATIONS

We use the 2D P-SV boundary-element simulation and the embedded array local slowness analysis method to investigate the effect of topographic scattering on the near-source energy partitioning for an explosion source. Random topographic models with different statistical properties, variable source depth, and different Q models are investigated using numerical simulations. The responses of different phases as functions of frequency and source/model parameters are calculated and their energy budget evaluated. The results reveal that free surface

scattering has a strong effect on near-source energy partitioning. However, in many cases, the scattering in 2D geometry may not be the same as in the real 3D world. We expand our analysis to fully 3D models with both volumetric heterogeneity and rough free surface. The preliminary result included in this report is promising. A series of analyses similar to what we applied to the 2D model will be conducted to the 3D model. Both the volume scattering and the free surface scattering will be judged for their roles in the near-source energy partitioning.

ACKNOWLEDEGMENT

The authors wish to thank Dr. Wei Zhang for kindly providing us with his 3D finite-difference code.

REFERENCES

Bonner, J. B., H. J. Patton, A. C. Rosca, H. Hooper, J. Orrey, M. Leidig and I. Gupta (2003). Aspects of *Rg* and *Lg* generation from the Shagan depth of burial explosions, in *Proceedings of the 25th Seismic Research Review—Nuclear Explosion Monitoring: Building the Knowledge Base*, LA-UR-03-6029, Vol. 1, pp. 384–394.

Bottone, S., M. D. Fisk, and G. D. McCartor (2002). Regional seismic event characterization using a Bayesian formulation of simple kriging, *Bull. Seism. Soc. Am*. 92: 2277–2296.

Bradley, C. R., and E. M. Jones (1998). Modeling propagation effects from explosion in Western China and India, in *Proceedings of the 20th Annual Seismic Research Symposium on Monitoring a Comprehensive Nuclear-Test-Ban Treaty*, Santa Fe, New Mexico, September 21–23.1998, pp. 173–181.

Bradley, C. R., and L. E. Jones (1999). Full waveform modeling of the effects of Q and structure over sub-regional paths, in western China, in *Proceedings of the 21st Annual Seismic Research Symposium on Monitoring a Comprehensive Nuclear-Test-Ban Treaty*, Las Vegas, Nevada, 21-24 September 1999, 28-38.

Fan, G. W., and T. Lay (1998a). Statistical analysis of irregular waveguide influences on regional seismic discriminants in China, *Bull. Seism. Soc. Am*. 88: 74–88.

Fan, G. W., and T. Lay (1998b). Regionalized versus single-station wave-guide effects on seismic discriminants in western China, *Bull. Seism. Soc. Am*. 88: 1260–1274.

Fan, G. W., and T. Lay (1998c). Statistical analysis of irregular waveguide influences on regional seismic discriminants in China: additional results for *Pn*/*Sn*, *Pn*/*Lg* and *Pg*/*Sn*, *Bull. Seism. Soc. Am*. 88: 1504–1510.

Fisk, M. D., H. L. Gray, and G. D. McCartor (1996). Regional discrimination without transporting thresholds, *Bull. Seism. Soc. Am*. 86: 1545–1558.

Ge, Z., L. Y. Fu and R. S. Wu (2005). *P-SV* Wavefield connection technique for regional wave propagation simulation, *Bull. Seism. Soc. Am.* 95 1375–1386.

Gupta, I. N., W. W. Chan, and R. A. Wagner (1992). A comparison of regional phases from underground nuclear explosions at East Kazakh and Nevada Test Sites, *Bull. Seism. Soc. Am*. 82, 352-382.

Gupta, I. N., W. W. Chan, and R. A. Wagner (2005). Regional source discrimination of small events based on the use of *Lg* wavetrain, *Bull. Seism. Soc. Am*. 95: 341–346.

Hartse, H. E., S. R. Taylor, W. S. Phillips, and G. E. Randall (1997). A preliminary study of regional seismic discrimination in central Asia with emphasis on western China, *Bull. Seism. Soc. Am*. 87: 551–568.

Kim, W. Y., V. Aharonian, A. L. Lerner-Lam, and P. G. Richards (1997). Discrimination of earthquakes and explosions in southern Russia using regional high-frequency three-component data from IRIS/JSP Caucasus Network, *Bull. Seism. Soc. Am*. 87: 569–588.

Kim, W. Y., D. W. Simpson, and P. G. Richards (1993). Discrimination of earthquakes and explosions in the eastern United States using regional high-frequency data, *Geophys. Res. Lett*. 20: 1507–1510.

McLaughlin, K. L., and R. S. Jih (1988). Scattering from near-source topography: Teleseismic observations and numerical simulations, *Bull. Seism. Soc. Am*. 78: 1399–1414.

Myers, S. C., W. R. Walter, K. Mayeda, and L. Glenn (1999). Observations in support of *Rg* scattering as a source for explosion *S* waves: Regional and local recordings of the 1997 Kazakhstan depth of burial experiment, *Bull. Seism. Soc. Am*. 89: 544–549.

Myers, S. C., J. Wagoner, L. Preston, K. Smith, and S. Larsen (2005). The effect of realistic geologic heterogeneity on local and regional *P*/*S* amplitude ratios based on numerical simulations, in *Proceedings of the 27th Seismic Research Review: Ground-Based Nuclear Explosion Monitoring Technologies*, LA-UR-05-6407, Vol. 1, pp. 123–132.

Nuttli, O. W. (1986). Yield estimates of Nevada Test Site explosions obtained from *Lg* waves, *J. Geophys. Res*. 91: 2137–2151.

Patton, H. J. (2001). Regional magnitude scaling, transportability, and Ms:mb discrimination at small magnitudes, *Pure appl. Geophys*. 158: 1951–2015.

Patton, H. J., and S. R. Taylor (1995). Analysis of *Lg* spectral ratios from NTS explosions: implications for the source mechanisms of spall and the generation of *Lg* waves, *Bull. Seism. Soc. Am*. 85: 220–236.

Stevens, J. L., G. E. Baker, H. Xu, T. J. Bennett, N. Rimer, and S. M. Day (2003). The physical basis of *Lg* generation by explosion sources, in *Proceedings of the 25th Seismic Research Review, Nuclear Explosion Monitoring: Building the Knowledge Base*, LA-UR-03-6029, Vol. 1, pp. 456–465.

Taylor, S. R. (1996). Analysis of high frequency *Pn*/*Lg* ratios from NTS explosions and western U.S. earthquakes, *Bull. Seism. Soc. Am*. 86, 1042–1053.

Taylor, S. R., M. D. Denny, E. S. Vergino, and R. E. Glaser (1989). Regional discrimination between NTS explosions and western U.S. earthquakes, *Bull. Seism. Soc. Am.* 79: 1142–1176.

Taylor, S. R. and H. E. Hartse (1997). An evaluation of generalized likelihood ratio outlier detection to identification of seismic events in Western China, *Bull. Seism. Soc. Am*. 87: 824–831.

Walter, W. R., K. M. Mayeda, and H. Patton (1995). Phase and spectral ratio discrimination between NTS earthquakes and explosions, Part I: Empirical observations, *Bull. Seism. Soc. Am.* 85: 1050–1067.

Wu, R. S., S. Jin and X. B. Xie (2000a). Seismic wave propagation and scattering in heterogeneous crustal waveguides using screen propagators: I *SH* waves, *Bull. Seism. Soc. Am*. 90: 401–413.

Wu, R. S., S. Jin and X. B. Xie (2000b). Energy partition and attenuation of *Lg* waves by numerical simulations using screen propagators, *Phys. Earth and Planet. Inter*. 120: 227–243.

Wu, R. S., X. B. Xie, Z. Ge, X. Wu, and T. Lay (2003). Quantifying source excitation and path effects for high-frequency regional waves, in *Proceedings of the 25th Seismic Research Review, Nuclear Explosion Monitoring: Building the Knowledge Base*, LA-UR-03-6029, Vol. 1, pp. 172–181.

Xie, J. (2002). Source scaling of *Pn* and *Lg* spectra and their ratios from explosions in central Asia: Implications for the identification of small seismic events at regional distances, *J. Geophys. Res.* 107: B7, 10.1029/2001JB000509.

Xie, X. B. and T. Lay (1994). The excitation of *Lg* waves by explosions: A finite-difference investigation, *Bull. Seism. Soc. Am*. 84: 324–342.

Xie, X. B., Z. Ge and T. Lay (2005a). Investigating explosion source energy partitioning and *Lg*-wave excitation using a finite-Difference plus slowness analysis method, *Bull. Seism. Soc. Am*. 95: 2412–2427.

Xie, X. B., T. Lay, and R. S. Wu (2005b). Near source energy partitioning for regional waves in 2D and 3D models, contributions of *S**-to-*Lg* and *P*-to-*Lg* scattering, in *Proceedings of the 27th Seismic Research Review: Ground-based Nuclear Explosion Monitoring Technologies*, LA-UR-05-6407, Vol. 1, pp. 249–258.

Xie, X. B., T. Lay, R. S. Wu and Y. He (2006). Near source energy partitioning for regional waves in 2D and 3D models, contributions of free surface scattering, in *Proceedings of the 28th Seismic Research Review: Ground-based Nuclear Explosion Monitoring Technologies*, LA-UR-06-5471, Vol. 1, pp. 304–314.

Zhang, W., and X. Chen (2006). Traction image method for irregular free surface boundaries in finite difference seismic wave simulation, Geophys. J. Int. 167: 337–353.

HIGH-RESOLUTION THREE-DIMENSIONAL SEISMIC IMAGING OF THE BAIKAL AND AMUR REGIONS OF EASTERN RUSSIA

Haijiang Zhang[1, 2], Kevin G. Mackey[3], Kazuya Fujita[3], Lee K. Steck[4], Charlotte A. Rowe[4], Clifford H. Thurber[1], and Steven Roecker[5]

University of Wisconsin-Madison[1], Massachusetts Institute of Technology[2], Michigan State University[3], Los Alamos National Laboratory[4], and Rensselaer Polytechnic Institute[5]

Sponsored by National Nuclear Security Administration
Office of Nonproliferation Research and Development
Office of Defense Nuclear Nonproliferation

Contract No. DE-FC52-06NA27325[1–4]

ABSTRACT

Eastern Russia is composed of a series of allochthonous terranes which have accreted to the Precambrian Siberian (North Asian) craton. This study is focused on the southern part (Baikal and Amur regions), where accretionary terranes form a suture zone between the Siberian and North China cratons, which is being exploited by the present-day boundary between the Eurasian plate and the Amur block. The complexities of accretion and subsequent intracontinental deformation likely result in a highly heterogeneous crust, a broad zone of deformation, and the formation of small blocks within the ancient suture and present-day plate boundary zones. We assembled catalog picks from ~13000 events and ~100 stations for the Baikal and Amur regions in the period of 1970 to 2005. Using the double-difference tomography method (Zhang and Thurber, 2003, 2006), our study for the first time provides a detailed seismic velocity model of the crust and upper mantle for this complicated area.

The original sources for the Siberia database vary from published Siberia-wide Russian earthquake bulletins to unpublished bulletins of regional network operators. It is very likely that there still exist some arrival time pick outliers in the assembled data. Quality assessment of picks and event-pair differential times is a critical aspect for achieving a high-quality velocity model for the Baikal and Amur regions. In our study we identify and remove outliers in catalog picks using event-pair differential times based on the fact that travel times from two nearby events should be consistent. In our data set, many arrivals at larger distances are identified in the catalog as Pg or Sg phases, which are often observable because of their relatively large amplitudes. To use the double-difference tomography method that is based on first arrivals, we adopt a simple strategy to remove secondary Pg and Sg picks. When the epicentral distance is greater than the estimated crossover distance of 130 km, only Pn and Sn phases are selected.

In our tomography algorithm, we use a spherical-Earth finite-difference (SEFD) travel time method to calculate travel times and trace rays. The basic concept is the extension of a standard Cartesian FD travel time algorithm (Vidale, 1990) to the spherical case through development of a mesh in radius, co-latitude, and longitude, expression of the finite difference (FD) derivatives in a form appropriate to the spherical mesh, and the construction of "stencils" to calculate extrapolated travel times. We benchmark the SEFD method against the "sphere-in-a-box" Cartesian FD travel time algorithm (Flanagan et al., 2007). To improve the accuracy and efficiency of the ray tracing, we adopt a hybrid approach. First, we utilize the FD method with a coarser grid interval to calculate an approximate ray path. Next we start bending this approximate ray path with the spherical pseudo-bending approach of Koketsu and Sekine (1998) until it converges to the desired accuracy.

Our preliminary Vp and Vs models show that at shallow depths (5–10 km), some model anomalies correlate relatively well with local geologic features. For example, the Upper Angara (northeast of Baikal) and Tunka (southwest of Baikal) basins show as strong low-velocity regions. At a depth of 110 km, the low velocities follow the active rift zone in the west and the presumed region of the present-day plate boundary in the east, possibly due to transtensional segments along the Amur-Eurasia boundary.

OBJECTIVES

The objectives of this project are to investigate and develop new and improved methodologies for regional-scale three-dimensional (3D) seismic tomography using a combination of event- and station-pair arrival time differences, and to apply the new methods to the Michigan State University (MSU) and Los Alamos National Laboratory (LANL) Siberia database. The tomographic work proposed here will provide a more reliable velocity model for both the crust and upper mantle of the accretionary regions to the south and east of the Siberian craton. There are four main tasks in this project: (1) an extension of our development of double-difference (DD) seismic tomography to the use of station-pair residual differences, including incorporation of a new method for resolution matrix calculation; (2) testing, refinement, and adaptation of a method for SEFD travel time calculations for use in DD tomography; (3) an extension of our Cartesian adaptive-grid DD tomography algorithm to spherical coordinates; and (4) collaborative work among the UW-Madison, LANL, and MSU groups to apply these analysis tools to the Siberia data set. In the 1st year of this project, our focus is to assemble a data set for the Baikal and Amur regions, incorporate a new resolution estimation method based on an approximate singular value decomposition (SVD) (Zhang and Thurber, 2007), refine and incorporate the SEFD travel time calculation method in our existing DD tomography code, and determine 3D P- and S-wave velocity models for the Baikal and Amur regions.

Figure 1 shows a schematic map of the study area showing primary tectonic features. The study area lies at the southern edge of the Siberian platform (North Asian Craton) and incorporates the suture between it and the terranes that form northern China (Figure 1). This suture closed in roughly mid-Mesozoic time. The present-day boundary between the Eurasia plate and the Amur block (or microplate) is exploiting this older zone of weakness and is represented by the extensional Baikal rift system (west of 120°E) and the Stanovoi fold belt (primarily strike-slip, east of 120°E). It is generally thought that the Baikal rift system is a far field effect of the India collision, although this is contentious.

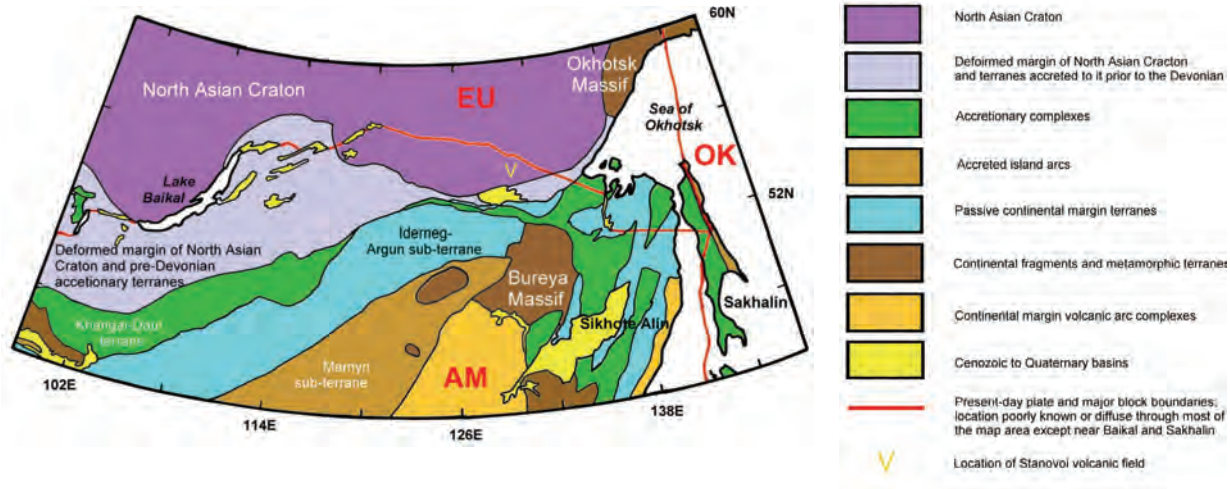

Figure 1. Tectonic map showing terranes and present-day plate boundaries in the study area. Terranes are grouped by tectonic origin. Red lines show approximate present-day plate and major block boundaries. EU = Eurasian plate, OK = Okhotsk block, AM = Amur block. V denotes location of Stanovoi Volcanic field. Simplified and modified after Parfenov et al. (1999, 2003).

RESEARCH ACCOMPLISHED

Data Collection and Quality Control

We have assembled a data set for the Baikal and Amur regions in the area of 45^o to 60^o latitude and 100^o to 145^o longitude from the MSU Siberia database. There are ~49000 P (Pg+Pn) and ~82000 S (Sg+Sn) phases corresponding to ~13000 events and ~100 stations. For each event, there are at least 4 observations. Figure 2 shows composite travel curve for Pg, Pn, Sg, and Sn phases using the original catalog locations. We found that many arrivals at larger distances are actually Pg or Sg phases because of their relatively large amplitudes. To use the DD

tomography method that is based on first arrivals, we adopted a simple strategy to remove secondary Pg and Sg picks. When the epicentral distance is greater than the estimated crossover distance of 130 km, only Pn and Sn phases are selected. At the first phase of simultaneous determination of event locations and velocity models, we also require there to be at least 8 observations available for each event. After this process, ~9300 P and ~7200 S phases are selected for ~1250 events (Figure 3).

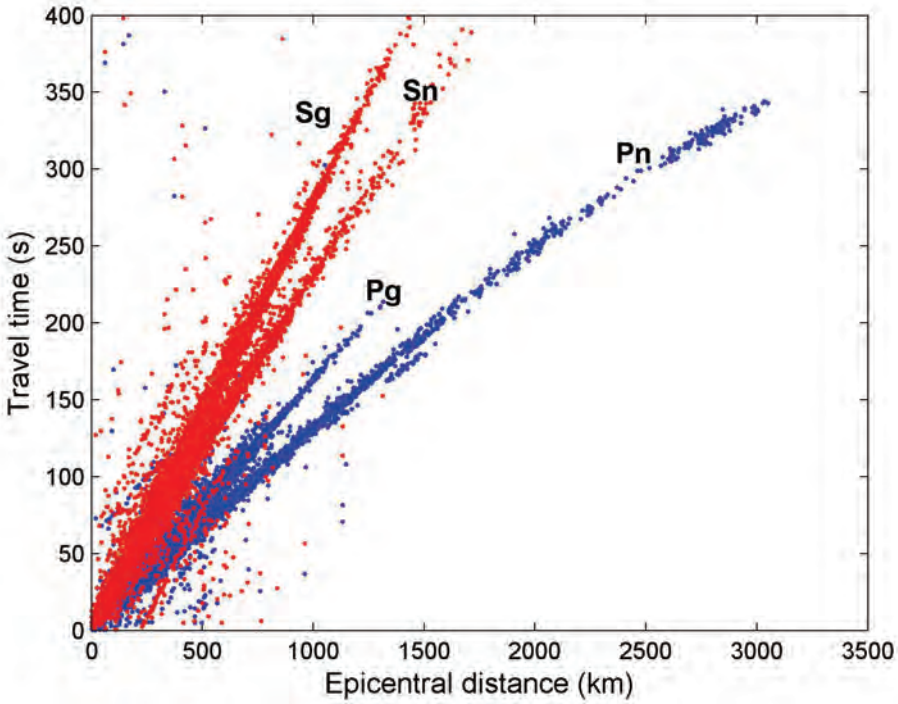

Figure 2. Composite travel time curve for Baikal and Amur regions. The epicentral distance is calculated using original Russian catalog locations.

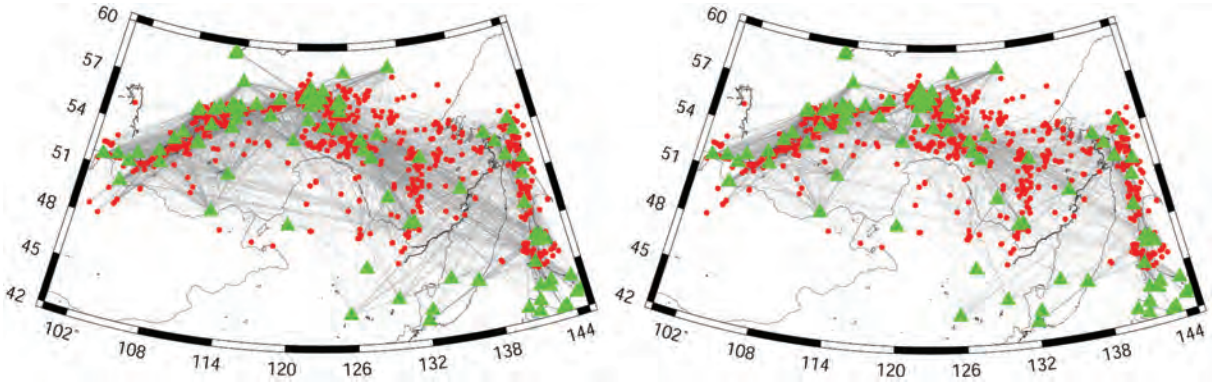

Figure 3. Event-station path coverage for P-waves (left) and S-waves (right). There are ~16500 paths from ~1250 events (red dots) and ~100 stations (green triangles).

The original sources for the MSU Siberia database vary from published Siberia-wide Russian earthquake bulletins to unpublished bulletins of regional network operators. As shown in Figure 2, it is very likely that there still exist some arrival time pick outliers in the assembled data. Quality assessment of picks and event-pair differential times is obviously a critical aspect for achieving a high-quality velocity model of the Siberia region. Here we report our strategy to identify outliers in catalog picks using event-pair differential times.

For each event pair, we calculate the absolute values of catalog differential P (or S) travel times at available stations and then calculate their average values (*ave*) and standard deviations (δ). At each station, we check to see if the absolute value of the differential time is within a specified range that is determined by *ave* + *C*δ. Because of different distances and azimuths from different stations to the event pair, the differential times may vary significantly due to strong source region heterogeneity. For this reason, we intentionally set the scale parameter *C* to be relatively large in order to simultaneously identify outliers and keep useful information. If the differential time is out of range at one station, then we flag the picks from these two events at this station as likely outliers. We then continue this process for all pairings of events and count the number of outlier flags for each pick. If it is greater than a specified threshold (*thr*), this pick will be removed from the data set. Both the scale parameter *C* and the threshold *thr* need to be tested to find appropriate values. For this data set, we select C to be 4 for P arrivals and 3 for S arrivals and *thr* to be 5. As a result, ~210 P and ~140 S phases are removed.

SEFD Travel Time Calculation

We tested the SEFD code developed by S. Roecker based on an analytical velocity model $V=V_0 (r_0/r)$, where V_0=4.0 km/s, r_0 is the Earth's radius and r is the distance between the source and receivers on the Earth's surface. Figure 4a shows the analytical travel times for a source located at latitude 21.2° and longitude 121.75°. We found that the travel-time errors for the SEFD method could be large near the source region when the grid interval is coarse. To deal with this inaccuracy problem near the source region, we test a multiple-grid strategy, in which a fine grid is used near the source region and a coarse one is used outside the source region. The travel-time field files for different grids are saved and loaded up appropriately if required. The tests show that this strategy improves the travel-time accuracy near the source region and can also potentially decrease the travel-time error accumulation away from the source region (Figure 4b).

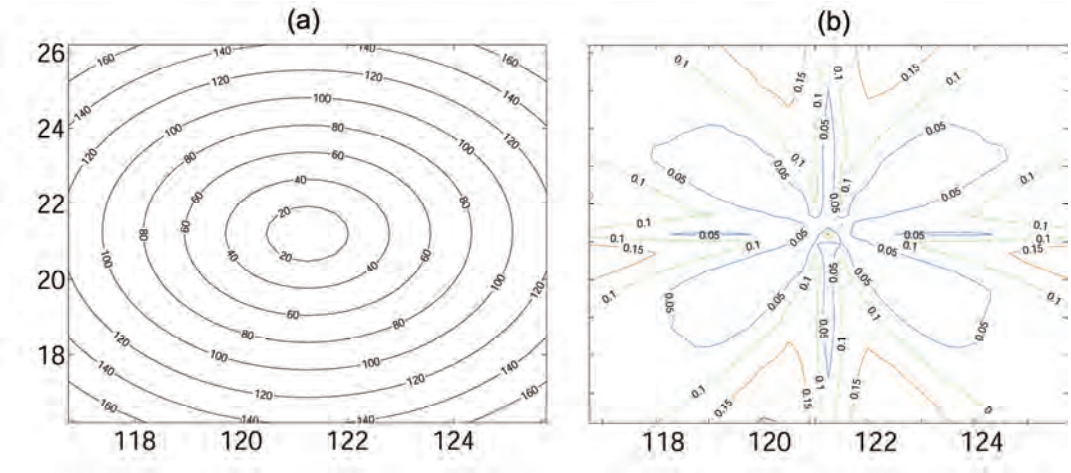

Figure 4. (a) Analytical travel-time contours for a source located at latitude 21.2° and longitude 121.75° based on the velocity model $V=V_0 (r_0/r)$. (b) Travel-time error contours between the SEFD method and analytical solutions. Here a multigrid approach is used to improve the accuracy near the source region (within 30 km). Grid interval is 10 km outside the source region and 1 km in the source region.

Hybrid Ray Tracer

During the reporting period, we successfully developed and tested a hybrid ray tracer combining the spherical pseudo-bending ray tracer of Koketsu and Sekine (1998) and the finite-difference travel time calculation method (Vidale, 1988; Hole and Zelt, 1995; Podvin and Lecomte, 1991) to calculate travel times and ray paths. It is known that in the case of strong heterogeneity, the pseudo-bending algorithm may fail to find the true two-point ray path because of non-linearity of the two-point problem. For this reason, we combine the finite-difference travel time calculation method with the pseudo-bending method in a way that the former provides an approximate ray path for the latter to start with and improve upon. The finite-difference travel time calculation method is capable of computing travel times to all points in the model and can locate diffractions in ray shadow zones. Therefore, it is stable and can find the correct solution even in a strongly heterogeneous medium. However, its accuracy depends on

the grid spacing size, and computation time may be unacceptable if accurate travel times are required. By combining the two methods, however, we can calculate ray paths accurately and efficiently.

Velocity Models of Baikal and Amur Regions

We directly constructed ~53700 P and ~40000 S event-pair differential times using the catalog times. For each event pair, there are at least 4 common observations and the average value is 9. Based on catalog locations, the inter-event distance for each event pair is required to be less than 200 km with an average value of 42 km. Because this is a rather complicated and large area, we tried using 4 different initial 1D models (Figure 5). Model 1 is based on the Quartz DSS line in the west Siberian basin (Morozov et al., 2005) and may not be applicable to the Siberian Platform proper. Model 2 is a mean "Eastern Siberian Platform" model that is based on data from both the Craton and Rift DSS lines (e.g., Egorkin et al., 1988; Cipar et al., 1993), as well as more local work (e.g., Kuznetsov and Titarenko, 1988). The DSS lines are the only ones that are long enough to sample the sub-lithospheric mantle. Compared to Model 1, Model 2 has a higher crustal velocity, a much sharper discontinuity at the Moho, and a smaller gradient through the upper mantle. Model 3 is a "Baikal Rift" model that represents the area under the active rift (Gao et al., 1994; Mishen'kin et al., 1999; and others). Model 4 is a "Southern Baikal" model that averages Primoria, Amur, and parts of eastern Baikal (e.g., Argentov et al., 1976; Mishen'kin et al., 1987; Song et al., 1996). The velocities below 70 km in Models 3 and 4 are the same as used in Model 2 as there have been no long-range profiles south and east of Baikal. The inversion grid intervals are 1 and 2 degrees in latitude and longitude, respectively. The grid nodes are located at depths of 0, 5, 10, 15, 20, 25, 30, 35, 40, 50, 60, 70, 80, 90, 100, 110, 120, 130, and 150 km. Because of potentially significant errors in the catalog arrivals, we applied a large smoothing weight of 200 to the double-difference tomographic system. The initial RMS arrival time residuals for the 4 starting models are 1.612, 1.617, 1.725, and 1.611 s, respectively. The final RMS arrival time residuals are 375, 380, 372, and 365 ms, respectively. The 4 final velocity models show very similar features, as also indicated by comparable final RMS arrival time residuals. Based on both initial and final RMS residuals, however, the velocity models calculated using Model 4 ("Southern Baikal"), which is presumed to represent a large portion of the sampled study area, is the best. Since Vp and Vs models share many similar features, we only present Vp models in the following sections.

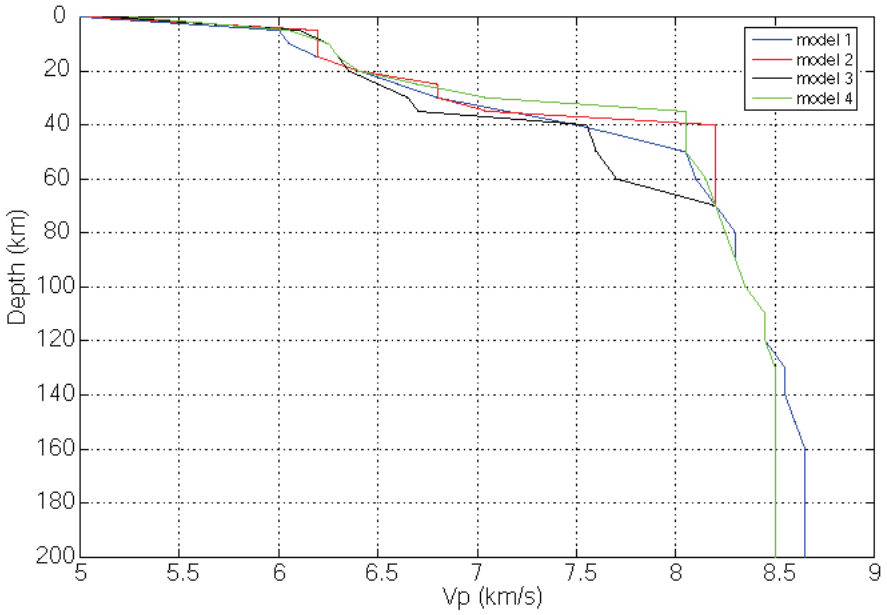

Figure 5. Four different 1D starting models for seismic tomography.

During inversion, we simultaneously determine earthquake locations and velocity models. Figure 6 shows the depth-frequency distribution for ~1250 relocated earthquakes. The number of earthquakes gradually increases at shallow depths and peaks around 10 km and then starts to decrease until at the depth of ~32 km. Most of

earthquakes are located at depths of 5 km to 25 km. Deverchere et al. (2001) also reported a similar depth range of earthquake locations in the Baikal rift, but with a peak distribution around 18 km. They also found some earthquakes occurring as deep as ~50 km. We argue that their earthquake locations are based on 1D Vp and Vs models and large errors could be caused by strong velocity heterogeneities in the Baikal rift. The depth distribution of earthquakes along longitude is similar across different geological features from west to east (Figure 6). Based on more accurate 3D velocity models our study provides more accurate depth estimation for earthquakes, which is very useful to infer the rheological state of the seismogenic layer and the brittle/ductile transition zone.

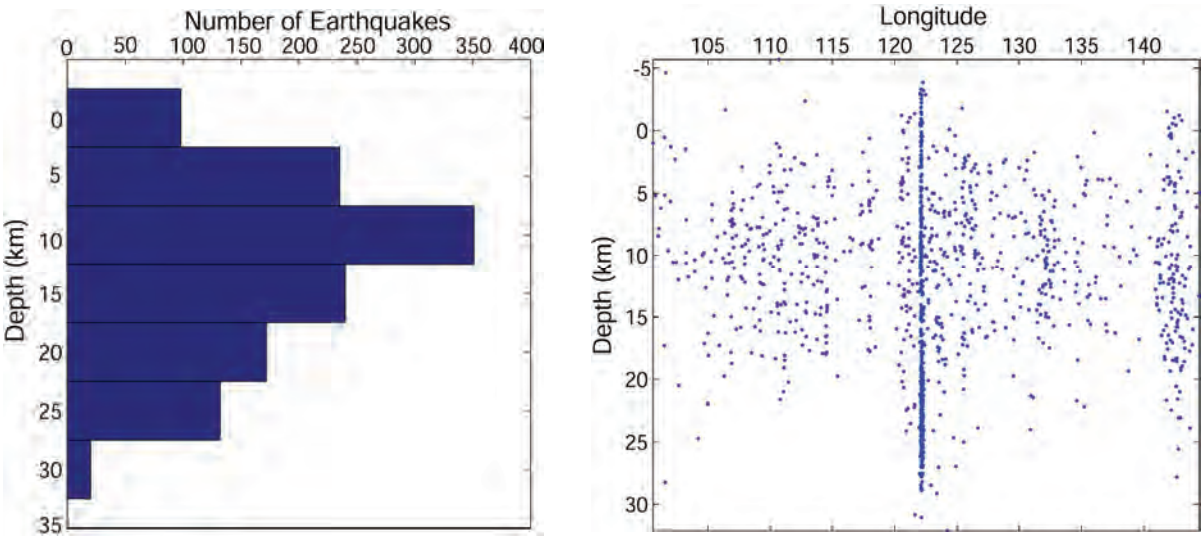

Figure 6. (Left) Depth-frequency distribution of relocated earthquakes from double-difference tomography. (Right) Earthquake depth distribution along longitude. The large cluster at 122°E represents the South Yakutian earthquake sequence of 1989.

Figure 7 shows horizontal slices of the 3D Vp model (using starting model 4) at depths of 5, 10, 20, 30, 40 50, 90, and 110 km, respectively. At shallow depths (5–10 km), some model anomalies correlate relatively well with local geology features. The Upper Angara (northeast of Baikal, indicated by 2 in the 5-km depth slice) and Tunka (southwest of Baikal, indicated by 1 in the 5-km depth slice) basins show as strong low-velocity regions. However, in the northern part of Baikal the velocity is very fast. Other models have also indicated that velocities are normal or slightly elevated at shallow depths beneath Lake Baikal proper (Mackey, 1999; Mishen'kin et al., 1999). A gradient from slow (north) to faster (south) velocities seems to mark the edge of the Siberian platform between longitude 126 and 135. To the north of latitude 54, there are finger-like high-velocity anomalies between longitude 117 and 130, which are similar to those shown in the Pg velocity model by Steck et al. (2007). A low-velocity anomaly lies below Sakhalin Island, as found by Mackey (1999) and Steck et al. (2007); although its cause is unclear, it may be associated with residual elevated temperatures from the Early Cenozoic accretionary phase. At the depth of 20 km, we noticed there are many low-velocity anomalies. Analysis of deep seismic sounding lines, as well as of teleseismic receiver functions, have shown low-velocity layers in the crust beneath the Baikal rift zone, early Mesozoic Mongolia-Okhotsk fold areas, and the Siberian platform (e.g., Mishen'kin et al., 1999; Zorin et al., 2002), as well as in the upper mantle (e.g., Egorkin et al., 1988). These low-velocity layers may reflect inhomogeneities in Earth's crust caused by different geological processes.

In general, the shallower sections of the model show greater heterogeneities, as expected from the variable nature of the crust (c.f., Fig. 1); however, no clear relationship is noted between surficial geology and the crustal velocities. In general lower velocities are concentrated in seismically active regions. Some of the low-velocity anomalies at 30–40 km depth in the southeastern part of the study area appear to be elongate in a northeast-southwest orientation, consistent with the strike of major structures and the late Mesozoic–Early Cenonoic subduction in the region.

Compared to the Pn slowness perturbation model from differential Pn tomography (Rowe et al., 2005), overall the depth slice of 40 km shows similar high/low anomaly patterns. For example, both models have a low velocity

anomaly around Sakhalin Island, and they have a band of high-velocity anomalies running from longitude 135/latitude 50 northwestward.

At the depth slices of 90 and 110 km, the low velocities very clearly follow the present-day plate (block) boundaries; the rift in the west and the presumed strike-slip segment to the east. Given that there may be (or have been) transtensional segments of the North China–Eurasia boundary (such as possibly near the Stanovoi volcanics), the low velocities along the plate (block) boundary are reasonable (Gao et al., 1994). The offset of the low-velocity zone at the northeast end of Lake Baikal to the east is associated with the Barguzin and other depressions.

As shown in the cross-section along 53^{o} latitude, there is clearly a low-velocity anomaly under the Baikal rift zone to depths of > 80 km, as proposed by Mishen'kin et al. (1999), although offset to the northwest. P-wave velocity images determined using teleseismic tomography shows that the low-velocity anomaly zone extends down to the mantle transition zone (Zhao et al., 2006; Lebedev et al., 2006). Crustal thickness, as represented by the 7.5 km/s contour, appears relatively constant throughout the entire study area and no sharp transition to velocities above 8.5 km/s is noted.

CONCLUSIONS AND RECOMMENDATIONS

In this study, we assembled a data set comprising first P- and S-wave arrivals for the Baikal and Amur regions of eastern Russia and applied the DD tomography method to obtain 3D Vp and Vs models for this complicated region. A hybrid ray tracer combining the SEFD travel-time calculation algorithm and the spherical pseudo-bending ray tracing is used to efficiently and accurately calculate travel times and find ray paths between events and stations. Outliers in catalog picks are identified and removed using event-pair differential times based on the fact that travel times from two nearby events should be consistent.

Overall, the model shows greater heterogeneities at shallow depths, as expected from the variable and complicated nature of the crust. Some Cenozoic and Quaternary basins such as the Upper Angara (northeast of Baikal) and Tunka (southwest of Baikal) basins around Lake Baikal correlate very well to strong low-velocity anomalies. Low-velocity anomalies in the mantle beneath the Baikal rift zone are clearly imaged in our model. The low velocities in the depth sections of 90 and 110 km follow the active rift zone in the west and the presumed region of the present-day plate boundary in the east, possibly due to transtensional segments along the Amur-Eurasia boundary.

Our current tomographic algorithm only uses first P- and S-wave arrivals. For this reason, many secondary Pg and Sg arrivals cannot be directly used in our seismic tomography. We are modifying the code so that the secondary Pg and Sg phases are also allowed, and as a result, the crust can be better imaged with better ray coverage. The current tomographic model is solved using a regular inversion grid in latitude, longitude, and depth. Next, we will use the adaptive-mesh tomography method based on tetrahedral diagrams to adapt the inverse mesh according to the data coverage.

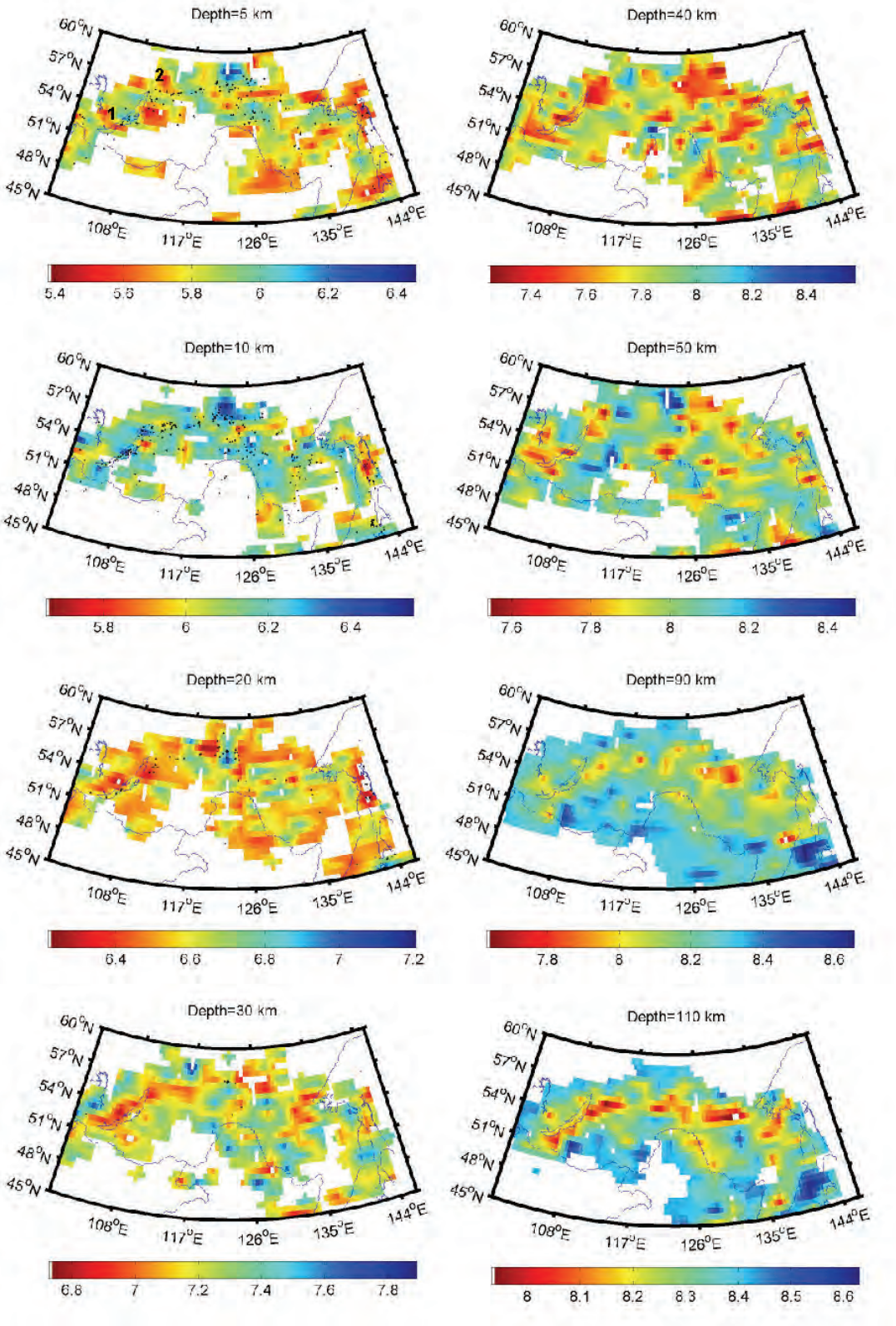

Figure 7. Horizontal slices of the 3D Vp models at depths of 5, 10, 20, 30, 40, 50, 90, and 110 km. In the 5-km slice, 1 denotes Tunka depression; 2 denotes the Upper Angara basin.

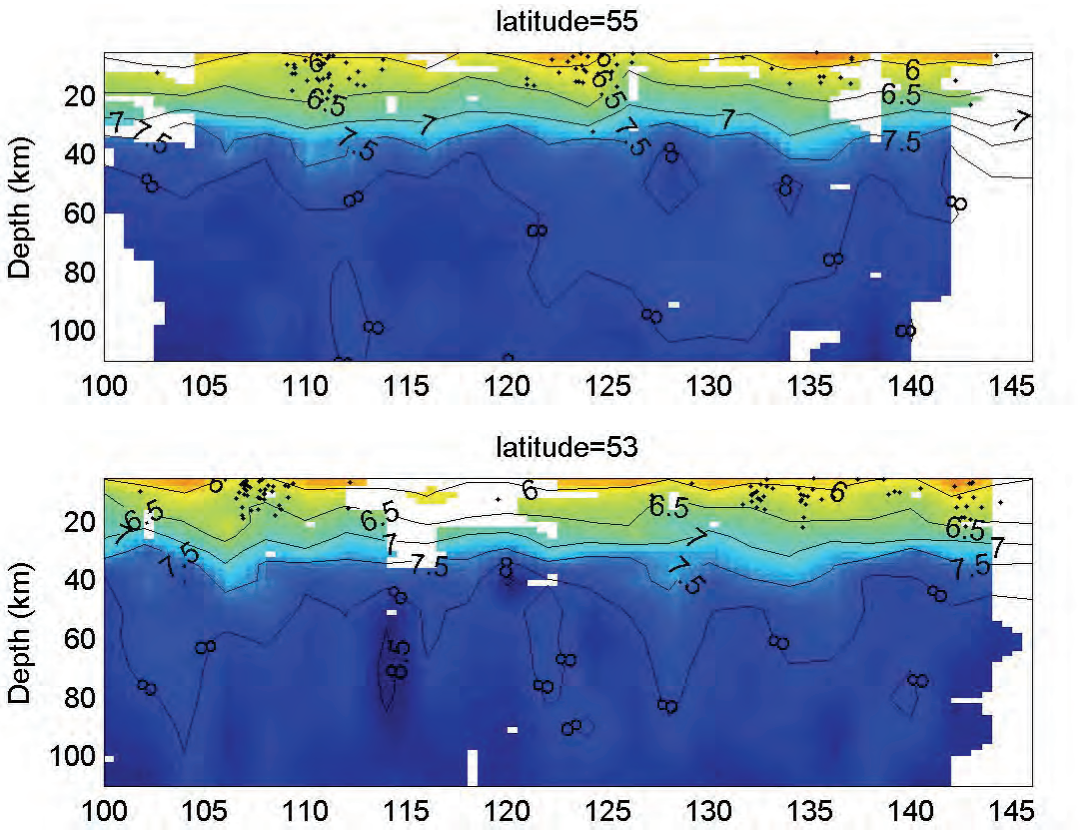

Figure 8. **Cross sections of the 3D Vp model along latitudes of 55° and 53°.**

REFERENCES

Argentov, V. V., G. S. Gnibidenko, A. A. Popov, and S. V. Potap'ev (1976). *Deep structure of Primoria.* Moskow: Nauka (in Russian).

Cipar, J. J., K. Priestley, A. V. Egorkin, and N. I. Pavlenkova (1993). The Yamal Peninsula-Lake Baikal deep seismic sounding profile, *Geophys. Res. Lett.* 20: 1631–1634.

Deverchere, J., C. Petit, N. Gileva, N. Radziminovitch, V. Melnikova, and V. San'kov (2001). Depth distribution of earthquakes in the Baikal rift system and its implications for the rheology of the lithosphere, *Geophys. J. Int.* 146: 714–730.

Egorkin, A. V., S. K. Zyuganov, and N. A. Pavlenkova (1988). Results of investigations of the structure of the lithosphere on profiles in Siberia, *Sov. Geol. Geophys.* 29: 107–114.

Flanagan, M. P., S. C. Myers, and K. D. Koper (2007). Regional travel-time uncertainty and seismic location improvement using a three-dimensional *a priori* velocity model, *Bull. Seism. Soc. Am.* 97: 804–825.

Koketsu, K., and S. Sekine (1998). Pseudo-bending method for three-dimensional seismic ray tracing in a spherical earth with discontinuities, *Geophys. J. Int.* 132: 339–346.

Gao, S., P. Davis, K. Liu, P. Slack, Y. Zorin, N. Logatchev, M. Kogan, P. Burkholder, and R. Meyer (1994). Asymmetric upwarp of the asthenosphere beneath the Baikal rift zone, Siberia, *J.Geophy. Res.* 99: 15319–15330.

Gao, S., K. H. Liu, P. M. Davis, P. D. Slack, Y. A. Zorin, V. Mordvinova, and V. M. Kozhevnikov (2003). Evidence for small-scale mantle convection in the upper mantle beneath the Baikal rift zone, *J. Geophys. Res.* 108: 2194, doi:10.1029/2002JB002039.

Kuznetsov, V. L., and Titarenko, V. V. (1988). Seismic model of the consolidated crust for the western part of the Siberian platform and its articulation zone with the West Siberian plate, *Geol. Geofiz.* 29: 128–135 (in Russian.)

Lebedev, S., T. Meier, and R. D. van der Hilst (2006). Asthenospheric flow and origin of volcanism in the Baikal Rift area, *Earth Planet. Sci. Lett.* 249: 415–424.

Mackey, K. G. (1999). *Seismological Studies in Northeast Russia*, Ph.D. dissertation, Michigan State University, xxiii + 346 pp.

Mishen'kin, B. P., Z. R. Mishen'kina, and V. V. Annenkov (1987). Deep seismic sounding on the Bureya massif, *Geol. Geofiz.* 28: 98–107 (in Russian).

Mishen'kin, B. P., Z .R. Mishen'kina, G. V. Petrik, I. F. Shelud'ko, M. M. Mandel'baum, V. S. Seleznev, and V. M. Solov'ev (1999). Deep seismic sounding of the Earth's crust and upper mantle in the Baikal rift zone, *Izvestiya, Phys. Solid Earth*, 35: 594–611.

Morozov, I. B., E. A. Morozova, S. B. Smithson, P. G. Richards, V. I. Khalturin, and L.N. Solodilov (2005). 3D first-arrival regional calibration model of northern Eurasia, *Bull. Seismol. Soc. Amer.* 95: 951–964.

Parfenov, L .M., L. I, Popeko, and O. Tomurtogoo (1999). The problem of tectonics of the Mongol-Okhotsk region, *Tikhookeans. Geol.* 18: 24–43 (in Russian).

Parfenov, L. M., A. I. Khanchuk, G. Badarch, R. J. Miller, V. V. Naumova, W. J. Nokleberg, M. Ogasawara, A. V. Prokopiev, and H. Yan (2003). Preliminary Northeast Asia geodynamics map, U.S. Geological Survey, Open File Rep. 03-205. Scale 1:5,000,000 (2 sheets).

Podvin, P. and I. Lecomte (1991). Finite difference computation of travel times in very contrasted velocity models: a massively parallel approach and its associated tools, *Geophys. J. Int.* 105: 271–284.

Rowe, C., L. K. Steck, W. S. Phillips, M. Begnaud, R. Stead, and H. Hartse (2005). Pn tomography and location in Eurasia, *2005 IASPEI Meeting* (Santiago, Chile).

Song, Y., S. V. Krylov, B. Yang, L. Cai, S. Dong, T. Liang, J. Li, X. Xu, Z. R. Mishen'kina, G. V. Petrik, I .F. Shelud'ko, V. S. Seleznev, and V. M. Solov'ev (1996). Deep seismic sounding of the lithosphere on the Baikal-northeastern China international transect, *Russ. Geol. Geophys.* 37: 1–13.

Steck, L. K., W. S. Phillips, C. A. Rowe, H. E. Hartse, M. L. Begnaud, R. J. Stead, K. Mackey, and K. Fujita (2007). Pg travel time tomography in Eastern Asia, *Seismol. Res. Lett.* 78: 306.

Vidale, J. (1988). Finite-difference calculation of travel times, *Bull. Seis. Soc. Am.* 78: 2062–2076.

Zhang, H. and C. H. Thurber (2007). Estimating the model resolution matrix for large-seismic tomography problems based on Lanczos bidiagonalization with partial reorthogonalization, *Geophys. J. Int.* 170: 337–345.

Zhang, H. and C. H. Thurber (2003). Double-difference tomography: The method and its application to the Hayward Fault, California, *Bull. Seism. Soc. Am.* 93: 1875–1889.

Zhang, H. and C. Thurber (2006). Development and applications of double-difference tomography, *Pure and Applied Geophys.* 163: 373–403, doi:10.1007/s00024-005-0021-y.

Zhao, D., J. Lei, T. Inoue, A. Yamada, and S. S. Gao (2006). Deep structure and origin of the Baikal rift zone, *Earth Planet. Sci. Lett.* 243: 681–691.

Zorin, Y. A., V. V.Mordvinova, E. Kh. Turutanov, B. G. Belichenko, A. A. Artemyev, G. L. Kosarev, and S. S. Gao (2002). Low seismic velocity layers in the Earth's crust beneath Eastern Siberia (Russia) and Central Mongolia: Receiver function data and their possible geological implication, *Tectonophysics* 359: 307–327.

REFINED LOCAL AND REGIONAL SEISMIC VELOCITY AND ATTENUATION MODELS FROM FINITE-FREQUENCY WAVEFORMS

Zhigang Zhang[2], Yang Shen[2], Li Zhao[3], Po Chen[4], and Xiaoping Yang[1]

Science Applications International Corporation[1] , University of Rhode Island[2], Institute of Earth Sciences, Academia Sinica, Taiwan[3], and Columbia University[4]

Sponsored by Air Force Research Laboratory

Contract No. FA8718-06-C-0014

ABSTRACT

Banana-doughnut sensitivity kernels of travel-time and amplitude variations account for wavefront healing and other diffraction effects that are ignored in the conventional Fermat ray theory. At continental scales one-dimensional (1D) reference models are often adequate and practical to be used in constructing the three-dimensional (3D) kernels. However, at local (e.g., crustal) scales 3D reference models are necessary for further improvement in imaging local and regional velocity structures. Our fully 3D tomography approach addresses this issue and eliminates both the high-frequency (ray) and structural-averaging (1D or 2D reference) approximations.

In previous numerical experiments we have shown the complexity in the sensitivity of finite-frequency head waves to 3D velocity perturbations compared to those predicted by ray theory. The frequency- and distance-dependence of the kernel sampling depth may provide a powerful tool to constrain the vertical velocity gradient in the mantle lithosphere and extend Pn/Sn tomography from presently two dimensions to three dimensions. In the second year of this three-year project we continue to develop and validate the theory and apply the fully 3D finite-frequency sensitivity kernels to synthetic and observed data sets. The systematic tests result in major corrections and ensure the accuracy of the calculation of the kernels. One important finding is that S-velocity anomalies have significant effects on P arrivals. The effects of P-velocity anomalies on S arrivals are much less. This suggests that when waveform-derived travel-time and amplitude anomalies are used in tomographic inversions, P-wave data should be related to not only P velocity but also S velocity. Neglecting this cross-coupling between the waveforms and velocities, as commonly assumed in practice, distorts the forward relation between the model and the data and may cause systematic biases in inversion results. We are carrying out a synthetic tomographic study to explore the power and limitation of the fully 3D finite-frequency kernels.

We are applying this fully 3D method to the eastern Turkey region where there are local and regional broadband waveform records, ground truth (GT) data, and models from previous studies. We use the Program for the Array Seismic Studies of the Continental Lithosphere (PASSCAL) data from the Eastern Turkey Seismic Experiment (ETSE) in 1999-2001. The 29-station network also recorded the Agri Dam explosions. Frequency-dependent travel-time and amplitude anomalies are measured at periods between 3 and 20 s based on narrow-band cross-correlagrams between records and synthetic seismograms calculated by the finite-difference method. These anomalies are used to invert for the perturbations in P- and S-wave speeds using finite-frequency sensitivity kernels. We have also developed the full-wave approach for computing the sensitivity kernels of the travel-time and amplitude anomalies to the perturbations in the Q values. A joint inversion of the same set of frequency-dependent travel-time and amplitude anomalies using the finite-frequency kernels for elastic wave speeds along with those for Q values enables us to account for the effect of both heterogeneity scattering and intrinsic attenuation on the amplitudes of waveforms. We are performing the joint inversions for the regional lithospheric anelastic structure in eastern Turkey and incorporating the calculation of sensitivity kernels for Q values in our fully 3D approach in order to invert for local anelastic structures using the ETSE dataset.

Our objective of this work is to develop refined local and regional velocity and attenuation models for selected areas of interest (AOIs) in Eurasia. We have compiled event and station lists for Korea and the eastern Turkey and northern Iran areas, and continue collecting GT data for model validation.

OBJECTIVES

In this work we obtain Finite-Frequency Seismic Tomography (FFST) velocity models for Eurasia and use them as 3D reference models to refine crustal and shallow upper mantle velocity and attenuation models for focused areas of interest (AOIs) by applying the fully 3D tomography approach.

RESEARCH ACCOMPLISHED

Finite-Frequency Sensitivity Kernels for Head Waves

In the studies of the crust and uppermost mantle, Pn and Sn are often attributed to be the compressional and shear head waves propagating in the uppermost mantle, though strictly a pure head wave is defined in models of uniform plane layers. Because the Pn phase is the first arrival at regional epicentral distances, it has been widely used in detecting and locating seismic events as well as inferring the velocity and attenuation structure of the uppermost mantle. In conventional Pn/Sn travel-time tomography, travel-time variations in Pn or Sn waves are usually attributed to velocity changes right beneath the Moho and in the crust near the source and receiver under ray approximation. Consequently conventional Pn/Sn tomographic inversions solve only the 2D problems of lateral variations in the uppermost mantle and provide no constraints on the vertical structure beneath the Moho. The simplification of horizontal Pn/Sn propagation introduces a bias in the predicted travel times since real waves dive beneath the Moho to depths that depend on the vertical velocity gradient and epicentral distance (Ritzwoller et al., 2002; Hearn et al., 2004). Since tomographic inversions are only as good as the forward problem that describes wave propagation, a practical theory providing a more accurate representation of realistic head waves is needed. The recent development of the finite-frequency seismic theory has made it possible to extract more information from broadband seismograms. Analogues of head waves in a continuous velocity structure, the finite-frequency effects of head waves, which have features distinctly different from turning waves (Aki and Richards, 2002), are yet to be carefully examined.

We obtain the Fréchet kernels of the head waves using the scattering-integral method of Zhao et al. (2005), which applies the principle of reciprocity for the Green's tensors between the points in the 3D model and the receiver. We define the travel-time delay measured by waveform cross correlation between the reference and perturbed waveforms as in Dahlen et al. (2000) and Zhao et al. (2000) and amplitude anomaly as in Zhao et al. (2006). Figure 1a shows the travel time sensitivity kernels for the vertical component Pn for a low velocity layer over half space model. Since the travel-time delay is the volume integration of the product of the kernels and the velocity perturbation, a low-velocity anomaly (negative velocity perturbation) in the negative kernel (red) region, for example, leads to a travel-time delay. Similarly, a low-velocity anomaly in the positive kernel (blue) region results in an earlier arrival. The asymmetry in the kernel is attributed to the difference in the distances from the interface to the source and receiver. At each depth below the source, the intensity of the kernels (the absolute magnitude) is larger on the source side. Right beneath the layer interface and along the ray path, the sensitivity kernels have weak negative values. The kernels become stronger (larger absolute values) horizontally away from the ray path before changing to positive values. A local minimum is clearly visible at the piercing point on the receiver side. All these features are consistent with the results of direct waveform simulation and cross correlation (Zhang et al., 2007). On the vertical profile half way between the source and receiver and perpendicular to the ray path (Figure 1b), the sensitivity decreases with depth from the interface to a minimum (zero) below the ray path. The local minimum is surrounded by strong negative sensitivities in an approximately half circle. The negative-sensitivity half ring is in turn surrounded by bands of positive and negative kernels in approximately half circles, which become narrower and weaker away from the ray path. On the vertical profile containing the source and receiver (Figure 1c), the kernels resemble those of tuning waves in the upper layer but differ significantly in the lower layer. Again the kernels are weak but non-zero along the ray path below the interface. The absolute magnitude of the kernels decreases with depth from the interface to a minimum (zero) before increasing to a maximum, the depth of which increases with the distance to the piercing points on the source or receiver side, whichever is smaller. The downward bending of the sensitivity kernels can be understood as the broadening of the Fresnel zones. The hollow region surrounding the ray path in the upper layer on the receiver side appears to be an upward extension of the local minimum in the lower layer. Unlike the "banana-doughnut" sensitivity kernels for turning waves, the travel-time kernels for the head wave are located on only one side of the ray path below the interface and thus may be characterized as the "split banana-doughnut" sensitivity kernels.

The amplitude sensitivity kernels of the head wave for the same model provide us a different perspective of the head wave behaviors (Figure 2). Comparing the travel-time and amplitude kernels, we note the strong amplitude sensitivity at the location of the local minimum (zero) in the travel-time sensitivity below the interface. We also note

that the travel-time and amplitude kernels change their positive or negative values at different depths, thus providing independent and complementary constraints on the velocity structure.

Layer interfaces in the real Earth are rarely exact flat, and the regions that are of geological interest usually have complex layer interfaces as well as vertical velocity variations. Additional numerical studies show that the interface topography has significant effects on the sensitivity kernels (Zhang et al., 2007). The depression or shoaling of the interface compresses or stretches, respectively, the travel-time sensitivity kernels, resulting in increased or decreased sensitivities beneath the interface topography. Because the distribution of the Fréchet kernels is a function of wavelength, head waves are dispersive if the velocity structure in the lower layer has a gradient with depth. Thus the finite-frequency head wave kernels, which account for the possible frequency dependence of the Pn/Sn travel time and amplitude and the deepening of the maximum sensitivity region with the propagation distance due to the broadening of the Fresnel zones, may provide a powerful tool to constrain the vertical velocity gradient in the mantle lithosphere and extend the Pn/Sn tomography from presently two dimensional to three dimensional.

Cross-Coupling of Waveform and Velocity Anomalies

In order to quantitatively assess the numerical accuracy in the calculations of waveforms and further validate finite-frequency kernels, we have carried out a series of numerical tests. We use a uniform medium with a Vp of 6.5 km/s and Vs of 3.5 km/s as the reference model. An explosive or a double-couple source is used to generate synthetic P and/or S waves, which are recorded by a receiver at the same depth (24 km) 53.4 km from the source. The dominant period of the synthetic waveform is 1.2 s. A cylindrically shaped velocity perturbation of 3% Vp or Vs, or both with a height of 6 km and the radius of 3 km is introduced to the reference model in the middle between the source and receiver. The waveforms from the perturbed and unperturbed models are cross-correlated to measure the travel-time and amplitude anomalies caused by the velocity perturbation. The results are compared to the predictions from the finite-frequency kernels. Figure 3 shows the case for the P arrival in a model with an explosive source and both Vp and Vs velocity perturbations. The kernel predictions match the measurements from direct waveform cross-correlation very well in all cases, validating the accuracy of the finite-frequency sensitivity kernels. One important finding of these numerical tests is that the P arrival is affected by both the P- and S-velocity perturbations. The effects of the S-velocity perturbation on the P arrival time and amplitude are roughly 10% of the effects of the P-velocity perturbation of the same magnitude. Since S-velocity anomalies are usually much larger than P-velocity anomalies in the real Earth (e.g., Karato, 1993), the effects of S-velocity perturbations can contribute as much as 20% of the P-wave travel-time and amplitude anomalies. Neglecting this cross-coupling between the waveforms and velocities, as commonly assumed in practice, distorts the forward relation between the model and the data and may cause systematic biases in tomographic inversion results. In contrast, the effects of the P-velocity perturbation on the S arrival are negligible.

Development of Full-Wave Approach to Q Tomography

In our full-wave tomography approach, we quantify the information carried by the recorded waveforms on the 3D structural variations using the so-called frequency-dependent phase and amplitude anomalies. These anomalies are measured from the cross-correlations between the recorded waveforms and the synthetics calculated in a 3D reference model by a fourth-order staggered-grid finite-difference algorithm (Olsen 1994):

$$C(t) = u^0(\mathbf{r}_\mathrm{R}, t; \mathbf{r}_\mathrm{S}) \otimes u(\mathbf{r}_\mathrm{R}, t; \mathbf{r}_\mathrm{S}) = \int_{-\infty}^{\infty} u^0(\mathbf{r}_\mathrm{R}, \tau; \mathbf{r}_\mathrm{S}) u(\mathbf{r}_\mathrm{R}, t+\tau; \mathbf{r}_\mathrm{S}) d\tau. \quad (1)$$

Here u^0 and u are synthetic and recorded seismograms, respectively, and $\mathbf{r}_\mathrm{S}$ and $\mathbf{r}_\mathrm{R}$ are locations of the source and the receiver, respectively. The maximum of the cross-correlagram can be used to define the phase delay δT and amplitude increase δA of the recorded seismogram relative to the synthetic:

$$\delta T = -\int_{-\infty}^{\infty} \dot{u}^0(\mathbf{r}_\mathrm{R}, t; \mathbf{r}_\mathrm{S}) \delta u(\mathbf{r}_\mathrm{R}, t; \mathbf{r}_\mathrm{S}) dt \Big/ \int_{-\infty}^{\infty} [\dot{u}^0(\mathbf{r}_\mathrm{R}, t; \mathbf{r}_\mathrm{S})]^2 dt\,, \quad (2)$$

$$\delta A = \frac{C_M - \tilde{C}_M}{\tilde{C}_M}, \quad (3)$$

where we define the amplitude anomaly in terms of the maximum amplitudes $C_M = C(\delta T)$ of the cross-correlagram and $\tilde{C}_M = \tilde{C}(0)$ of the auto-correlagram of the synthetic seismogram:

$$\widetilde{C}(t) = u^0(\mathbf{r}_\mathrm{R}, t; \mathbf{r}_\mathrm{S}) \otimes u^0(\mathbf{r}_\mathrm{R}, t; \mathbf{r}_\mathrm{S}) = \int_{-\infty}^{\infty} u^0(\mathbf{r}_\mathrm{R}, \tau; \mathbf{r}_\mathrm{S}) u^0(\mathbf{r}_\mathrm{R}, t+\tau; \mathbf{r}_\mathrm{S}) d\tau. \quad (4)$$

Frequency-dependent measurements are achieved by narrow-band filtering the cross-correlations around a number of discrete frequencies across the frequency range of interest. Upon applying the representation theorem (e.g., Aki and Richards, 2002) and the Born approximation, the waveform perturbation δu can be expressed as (e.g., Zhao et al., 2005)

$$\delta\mathbf{u}(\mathbf{r}_\mathrm{R}, t; \mathbf{r}_\mathrm{S}) = \int_\oplus \int_0^t [\nabla \mathbf{G}^0(\mathbf{r}_\mathrm{R}, t-\tau; \mathbf{r})]^{213} : [\delta\rho(\mathbf{r})\mathbf{I}\partial_{\tau\tau} - \delta\mathbf{C}(\mathbf{r})] : [\nabla \mathbf{u}^0(\mathbf{r}, \tau; \mathbf{r}_\mathrm{S})] d\tau \, d^3\mathbf{r}\,, \quad (5)$$

where $\delta\rho(\mathbf{r})$ and $\delta\mathbf{C}(\mathbf{r})$ are the model perturbations in density and the fourth-order elasticity tensor, respectively, $\mathbf{I}$ is the fourth-order identity tensor, and the symbol $[\cdot]^{213}$ indicates the transposition of a third-order tensor between its first and second indices (Ben-Menahem and Singh, 1981), i.e., $[\cdot]^{213}_{ijk} = [\cdot]_{jik}$. For the perturbation of any specific structural parameter such as the *S*-wave speed β, the expression for its phase-delay or amplitude increase Fréchet kernel can be derived by selecting the elements of $\delta\mathbf{C}(\mathbf{r})$ in eq.(5) corresponding to β, substituting the resulting equation for $\delta\mathbf{u}(\mathbf{r}_\mathrm{R}; \mathbf{r}_\mathrm{S})$ into eq.(2) or (3), and identifying the kernel for the spatial integral. For example, the Fréchet kernel for the amplitude increase due to the perturbation in shear-wave speed β is

$$K_A^\beta(\mathbf{r}_\mathrm{R}; \mathbf{r}; \mathbf{r}_\mathrm{S}) = \int_{t_1}^{t_2} 2\rho\beta\mathbf{u}(\mathbf{r}_\mathrm{R}, t; \mathbf{r}_\mathrm{S}) \cdot \mathbf{K}_u^\beta(\mathbf{r}_\mathrm{R}; \mathbf{r}, t; \mathbf{r}_\mathrm{S}) dt \,/ \int_{t_1}^{t_2} |\,\mathbf{u}(\mathbf{r}_\mathrm{R}, t; \mathbf{r}_\mathrm{S})\,|^2 \, dt, \quad (6)$$

where the waveform kernel for shear-wave speed β is

$$\mathbf{K}_u^\beta(\mathbf{r}_\mathrm{R}; \mathbf{r}, t; \mathbf{r}_\mathrm{S}) = \int_{-\infty}^{\infty} \{[\nabla \mathbf{G}(\mathbf{r}_\mathrm{R}, t-\tau; \mathbf{r})]^{213} : [(\nabla\mathbf{u}) + (\nabla\mathbf{u})^\mathrm{T}] - 2(\nabla\cdot\mathbf{G}^\mathrm{T})[\nabla\cdot\mathbf{u}(\mathbf{r}, \tau; \mathbf{r}_\mathrm{S})]\} \, d\tau. \quad (7)$$

When anelastic attenuation is considered, the bulk and shear moduli in the elasticity tensor $\delta\mathbf{C}(\mathbf{r})$ are analytically extended into frequency-dependent complex-valued quantities with the introduction of quality factors Q_κ and Q_μ:

$$\kappa = \kappa(\omega)[1 + iQ_\kappa^{-1}(\omega)], \quad \mu = \mu(\omega)[1 + iQ_\mu^{-1}(\omega)]. \quad (8)$$

For convenience in seismology, Q_κ and Q_μ can be related to the quality factors for the compressional and shear waves Q_α and Q_β. Perturbing eq.(8)

$$\delta\kappa = \delta\kappa(\omega)[1 + iQ_\kappa^{-1}(\omega)] + i\kappa(\omega)\delta[Q_\kappa^{-1}(\omega)], \quad \delta\mu = \delta\mu(\omega)[1 + iQ_\mu^{-1}(\omega)] + i\mu(\omega)\delta[Q_\mu^{-1}(\omega)]. \quad (9)$$

and substituting the perturbations in the new complex bulk and shear moduli into eq.(5), we can derive the expressions of the Fréchet kernels for Q_α and Q_β in the same way as we derive the expressions for the kernels in eqs.(6) and (7). Assuming that the quality factors are frequency-independent, the

$$K_A^\beta(\mathbf{r}_\mathrm{R}; \mathbf{r}; \mathbf{r}_\mathrm{S}) = \int_{t_1}^{t_2} 2\rho\beta\mathbf{u}(\mathbf{r}_\mathrm{R}, t; \mathbf{r}_\mathrm{S}) \cdot \mathbf{K}_u^{Q_\beta}(\mathbf{r}_\mathrm{R}; \mathbf{r}, t; \mathbf{r}_\mathrm{S}) dt \,/ \int_{t_1}^{t_2} |\,\mathbf{u}(\mathbf{r}_\mathrm{R}, t; \mathbf{r}_\mathrm{S})\,|^2 \, dt, \quad (10)$$

$$\mathbf{K}_u^{Q_\beta}(\mathbf{r}_\mathrm{R}; \mathbf{r}, t; \mathbf{r}_\mathrm{S}) = -Q_\beta^{-1} H[\mathbf{K}_u^\beta(\mathbf{r}_\mathrm{R}; \mathbf{r}, t; \mathbf{r}_\mathrm{S})], \quad (11)$$

where $H[f(t)]$ denotes the Hilbert transformation of the function $f(t)$. We have implemented the Fréchet kernel calculations for the quality factors using coupled normal-mode summations and are in the process of implementing these calculations using finite-difference method to invert for the anelastic crustal structures in selected AOIs.

We have carried out preliminary tomography inversions for shear-wave speed β and quality factor Q_β for East Asia using regional Rayleigh wave phase and amplitude anomalies (Zhao and Chen, 2006). Our dataset consists of broadband Rayleigh waves that traverse Eastern Eurasia. The seismic records were recorded on instruments from the Incorporated Research Institutions for Seismology (IRIS) global seismographic Network (GSN), cooperating networks such as the Chinese Digital Seismic Network (CDSN), and several IRIS PASSCAL experiments from Asia. All data were collected from IRIS DMC. The stations used are distributed in the region from 10ºN to 60ºN and 80ºE to 140ºE. We used stations recording either an LHZ or BHZ components, with a total of 72 stations. Events occurred in the region between 10ºN to 60ºN and 70ºE to 140ºE in the time period between 2000 and 2006. The magnitudes are greater than Mw 6. The total number of events collected was 151. The initial dataset was cleaned to remove data with a signal-to-noise level of less than approximately 2 in the central portion of the frequency band

(0.02-0.1 Hz), as well as data clearly contaminated by glitches or other problems. The final number of records used is 3160 from 146 events.

Full-Wave Tomography for Eastern Turkey

Northern Iran and eastern Turkey are tectonically active regions with abundant and relatively diffused seismicity. The Eastern Turkey Seismic Experiment, along with several other seismic stations in the area, provides an excellent waveform data set to develop and test the fully 3D tomography approach. We have implemented the full-wave tomography approach to an area in Eastern Turkey using the waveform dataset from the Eastern Turkey Seismic Experiment (ETSE) (Sandvol et al., 2003a,b; Al-Lazki et al., 2003; Gok et al., 2003; Turkelli et al., 2003; Zor et al., 2003). Figure 4 shows the distribution of the 29 ETSE stations and the epicenters of the 124 regional events located by the ETSE records (Turkelli et al., 2003). As a first iteration of our iterative full-wave anelastic tomography, we selected 19 ETSE stations within a study area of roughly 350 km x 300 km (down to 55-km depth) and 24 earthquakes for which the focal mechanisms are available (Turkelli et al., 2003). The study area and the locations of stations and earthquakes are shown in Figure 5.

In our first 3D tomography attempt, we used the layered crustal model MENA 1.1 (Walter et al., 2000) as the reference model. In order to model the wave interactions with the highly variable Moho interface in this region, we modified the bottom part of MENA 1.1 to allow for lateral variations in the Moho depth based on the results from the receiver function study of Zor et al. (2003). In the study area, the Moho depth changes from 38 km in the southern part to 50 km in the north.

We used a fourth-order staggered-grid finite-difference algorithm (Olsen 1994) to compute the synthetic seismograms in the layered crustal model with variable Moho depth. The crustal model has a minimum shear-wave speed of 1.1 km/s. In our finite-difference simulations, we used a grid spacing of 300 km, resulting in reliable waveforms up to a nominal frequency of about 0.5 Hz. Then the frequency-dependent phase and amplitude anomalies between the synthetic and recorded seismograms are measured for the 69 source-receiver paths shown in Figure 5 at 0.1 Hz, 0.15 Hz, 0.2 Hz, 0.25 Hz, 0.3 Hz, 0.35 Hz and 0.4 Hz. Measurements along several source-receiver paths are shown in Figure 6. Note that in our definitions for the phase and amplitude anomalies, positive measurements indicate phase delays and amplitude increases in the records relative to corresponding synthetics.

In order to compute the Fréchet kernels of the measurements with respect to the elastic and anelastic mode parameters, we have also calculated the receiver strain Green tensors (RSGTs) for all 19 stations as well as the source strain Green tensors (SSGTs) for the 24 events; see Zhao et al. (2006) for details of the Fréchet kernels using the RSGTs and SSGTs. The numerical calculations were carried out using 32 processors on a Linux cluster. The calculations took about two weeks of wall-clock time. The resulting SGT database occupies a disk space of about 13 Terabytes. These SGTs will be used to compute the Fréchet kernels for all the measurements from the 69 paths in the first step of an iterative full-wave 3D tomography.

CONCLUSIONS AND RECOMMENDATIONS

Significant progress has been made in developing and validating finite-frequency sensitivity kernels for 3D velocity and attenuation reference models. The finite-frequency head wave kernels will allow us to extend Pn/Sn tomography from presently 2D to 3D. The cross coupling between S-velocity perturbations and P waveforms provides a more accurate account of the forward problem. Together with the velocity models, the finite-frequency solutions of attenuation yield a self-consistent structure required by observed waveforms. We are applying the fully 3D kernels to synthetic tomography as well as real data in selected regions. In general, the scale of the study area to which we can apply the fully 3D finite-frequency tomography is linearly proportional to the available computational power. Finally, substantial efforts are needed to develop the method for large-scale 3D models and models with anisotropy.

REFERENCES

Aki, K., and P.G. Richards (2002). *Quantitative Seismology*, University Science Books.

Al-Lazki, A., D. Seber, E. Sandvol, N. Turkelli, R. Mohamad, and M. Barazangi (2003). Tomographic Pn velocity and anisotropy structure beneath the Anatolian plateau (eastern Turkey) and the surrounding regions, *Geophys. Res. Lett*., 30(24), doi:10.1029/2003GL017391.

Ben-Menahem, A. and S. J. Singh (1981). *Seismic Waves and Sources*, Springer-Verlag, New York.

Dahlen, F.A., S.-H. Hung, and G. Nolet (2000). Fréchet kernels for finite frequency traveltimes-I. Theory, *Geophys. J. Int.* 141: 157–174.

Gok, R., E. Sandvol, N. Turkelli, D. Seber, and M. Barazangi (2003). Sn attenuation in the Anatolian and Iranian plateau and surrounding regions, *Geophys. Res. Lett*. 30(24): 8042, doi:10.1029/2003GL018020.

Hearn, T.M., S. Wang, J.F. Ni, Z. Xu, Y. Yu, and X. Zhang (2004). Uppermost mantle velocities beneath China and surrounding regions, *J. Geophys. Res.* 109: doi:10.1029/2003JB002874.

Karato, S. (1993). Importance of anelasticity in the interpretation of seismic tomography, *Geophys. Res. Lett.* 20: 1623–1626.

Olsen, K.B. (1994). Simulation of three-dimensional wave propagation in the Salt Lake Basin, Ph.D. Thesis, University of Utah, Salt Lake City, Utah, 157p.

Ritzwoller, M.H., M.P. Barmin, A. Villasenor, A.L. Levshin, and E.R. Engdahl (2002). Pn and Sn tomography across Eurasia to improve regional seismic event locations, *Tectonophysics* 358: 39–55.

Sandvol, E., N. Turkelli, E. Zor, R. Gok, T. Bekler, C. Gurbuz, D. Seber, and M. Barazangi (2003a). Shear wave splitting in a young continent-continent collision: An example from Eastern Turkey, *Geophys. Res. Lett*. 30: (24), 8041, doi:10.1029/2003GL017390.

Sandvol, E., N. Turkelli, and M. Barazangi (2003b). The eastern Turkey seismic experiment: The study of a young continent-continent collision, *Geophys. Res. Lett*. 30: (24), 8038, doi:10.1029/2003GL018912.

Turkelli, N., E. Sandvol, E. Zor, R. Gok, T. Bekler, A. Al-Lazki, H. Karabulut, S. Kuleli, T. Eken, C. Gurbuz, S. Bayraktutan, D. Seber, and M. Barazangi (2003). Seismogenic zones in Eastern Turkey, *Geophys. Res. Lett*. 30: 8039, doi:10.1029/2003GL018023.

Walter, W.R., M.E. Pasayanos, J. Bhattacharyya, and J. O'Boyle (2000). MENA 1.1 – An updated Geophysical regionalization of the Middle East and North Africa, UCRL-ID-138079, Lawrence Livermore National Laboratory Report.

Zhang, Z., Y. Shen, and L. Zhao (2007). Finite-frequency sensitivity kernels for head waves, *Geophys. J. Int*, accepted for publication.

Zhao, L. and P. Chen (2006). A full-wave approach to elastic and Q tomography, *EOS Trans. AGU* 87: (52), Fall Meet. Suppl., Abstract S53C-04.

Zhao, L., T.H. Jordan, and C.H. Chapman (2000). Three-dimensional Fréchet differential kernels for seismic delay times, *Geophys, J. Int.* 141,:558–576.

Zhao, L., P. Chen, and T.H. Jordan (2006). Strain Green tensor, reciprocity, and their applications to seismic source and structure studies, *Bull. Seism. Soc. Am*. 96: 1753–1763, doi:10.1785/0120050253.

Zhao, L., T.H. Jordan, K.B. Olsen, and P. Chen (2005). Fréchet kernels for imaging regional earth structure based on three-dimensional reference models, *Bull. Seism. Soc. Am.* 95: 2066–2080.

Zor, E., E. Sandvol, C. Gurbuz, N. Turkelli, D. Seber, and M. Barazangi (2003). The crustal structure of the East Anatolian plateau (Turkey) from receiver functions, *Geophys. Res. Lett*. 30: 8044, doi:10.1029/2003GL018192.

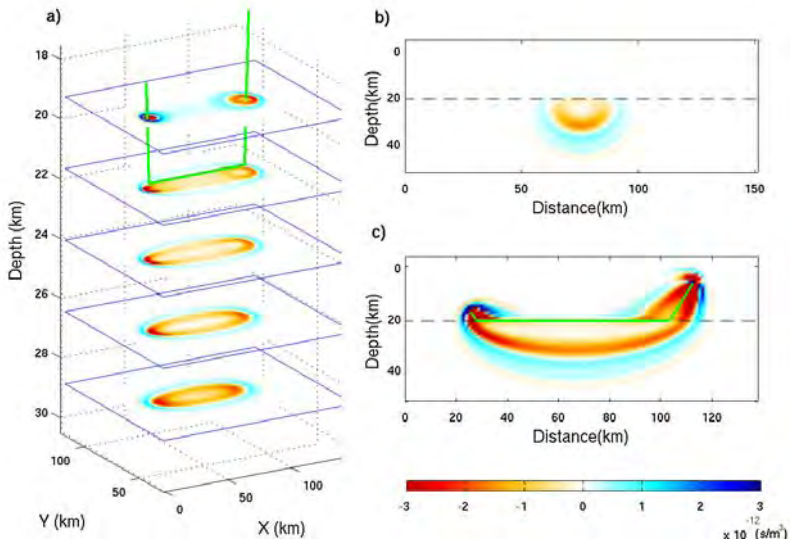

Figure 1. (a) The travel-time sensitivity kernels for the head wave recorded on the vertical component on the horizontal planes at depths below (21.6 km, 24 km, 26.4 km, 28.8 km) and above (19.2 km) the interface that separates the low and high velocity layers. The interface, source and receiver are at 21.4, 18, and 6.4 km depth, respectively. The P, S velocities and the density of the first layer are 5207 m/s, 3189 m/s and 2950 kg/m^3 respectively; those of the half space 9058 m/s, 5307 m/s and 3992 kg/m^3. The finite-difference model for simulating wave propagation has a regular grid of 280 x 301 x 126 in the source-receiver, transverse, and vertical directions, with a grid spacing of 400 m. The source time function has a dominant period of about 1.2 second. The green line marks the head wave ray path. The source is located on the left side of this figure. The negative (red colors) and positive (blue colors) values are so defined that a low-velocity anomaly located in the region of the negative kernels results in a travel-time delay and the same velocity perturbation in the region of positive kernels leads to an earlier head wave arrival. (b) The travel-time sensitivity kernel for the head wave on a vertical profile half way between the source and receiver and perpendicular to the ray path. The dashed line is the layer interface. (c) The travel-time sensitivity kernels for the head wave on the vertical profile containing the source and receiver.

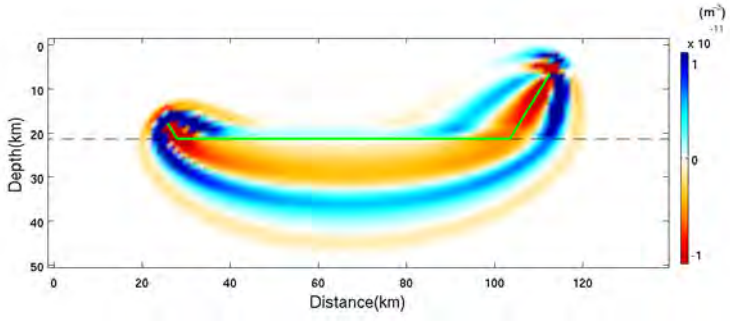

Figure 2. Amplitude sensitivity kernels for the vertical component of the head wave on the vertical profile containing the source and receiver. The dashed line indicates the layer interface and the green line highlights the ray path. The negative (red colors) and positive (blue colors) values are so defined that a low-velocity anomaly in the red region causes an amplitude increase and the same velocity anomaly in the blue region leads to a reduction in the amplitude of the head wave.

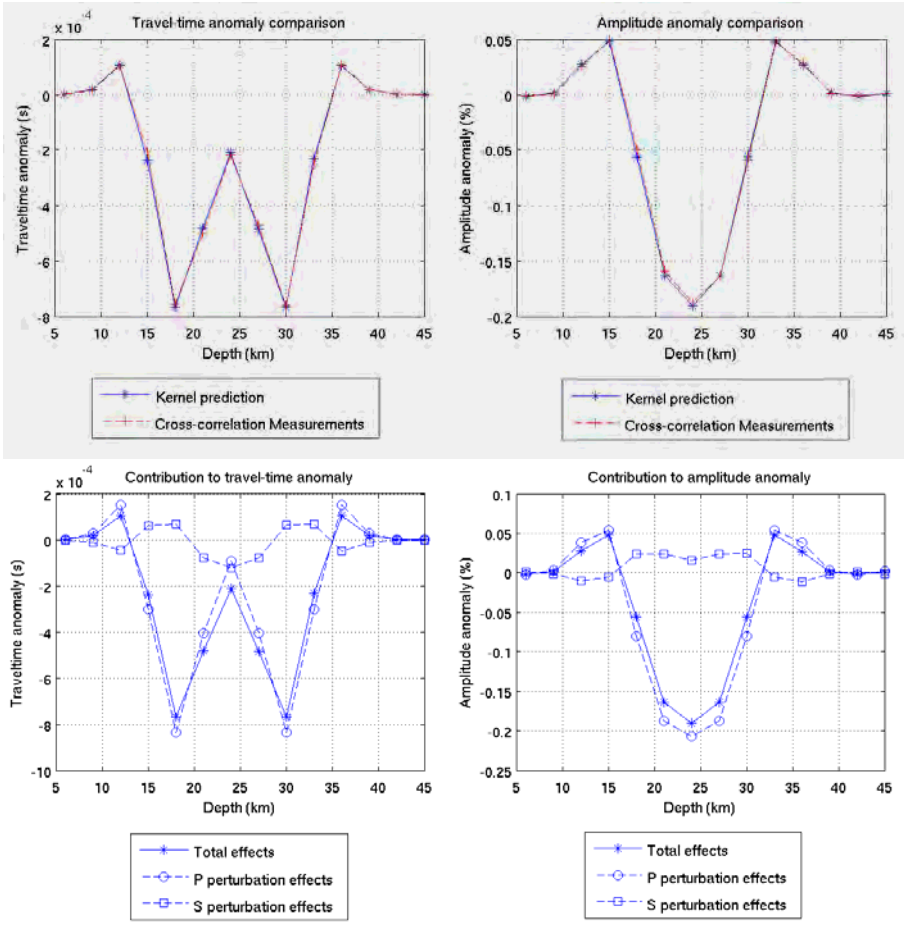

Figure 3. (upper panels) A comparison of the kernel predictions (stars) and waveform cross-correlation measurements (crosses) of travel-time and amplitude anomalies of a P wave from an explosive source. A cylindrical-shaped velocity perturbation of 3% Vp and Vs with a height of 6 km and the radius of 3 km is placed along a vertical profile in the middle between the source and receiver. Each symbol represents one simulation with the perturbation centered at a particular depth. See the text for additional information about the numerical experiments. Both travel-time and amplitude predictions match the direct waveform cross-correlation measurements well. (lower panels) The contributions of the travel-time and amplitude anomalies from the P-velocity perturbation (circles) and the S-velocity perturbation (crosses). Neglecting the S-velocity contribution, as in common practice, causes significant misfits.

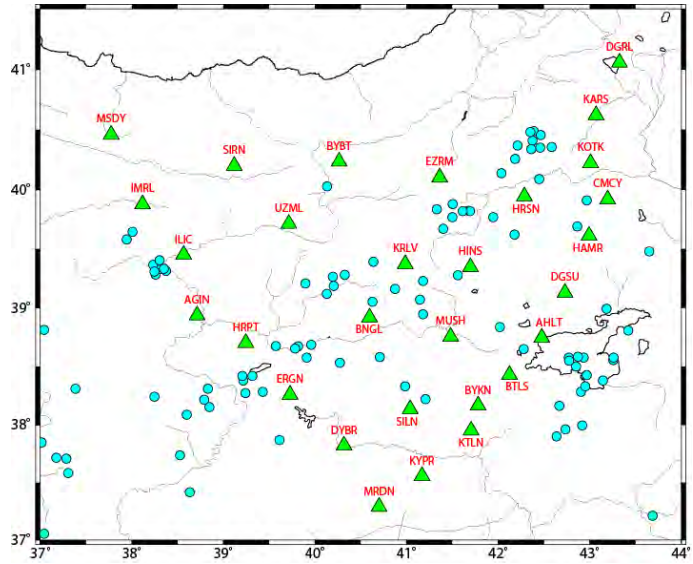

Figure 4. Data collection from the Eastern Turkey Seismic Experiment (ETSE). Triangles indicate the locations of the 29 ETSE stations, and circles show the epicenters of the 124 events located by ETSE (Turkelli et al. 2003).

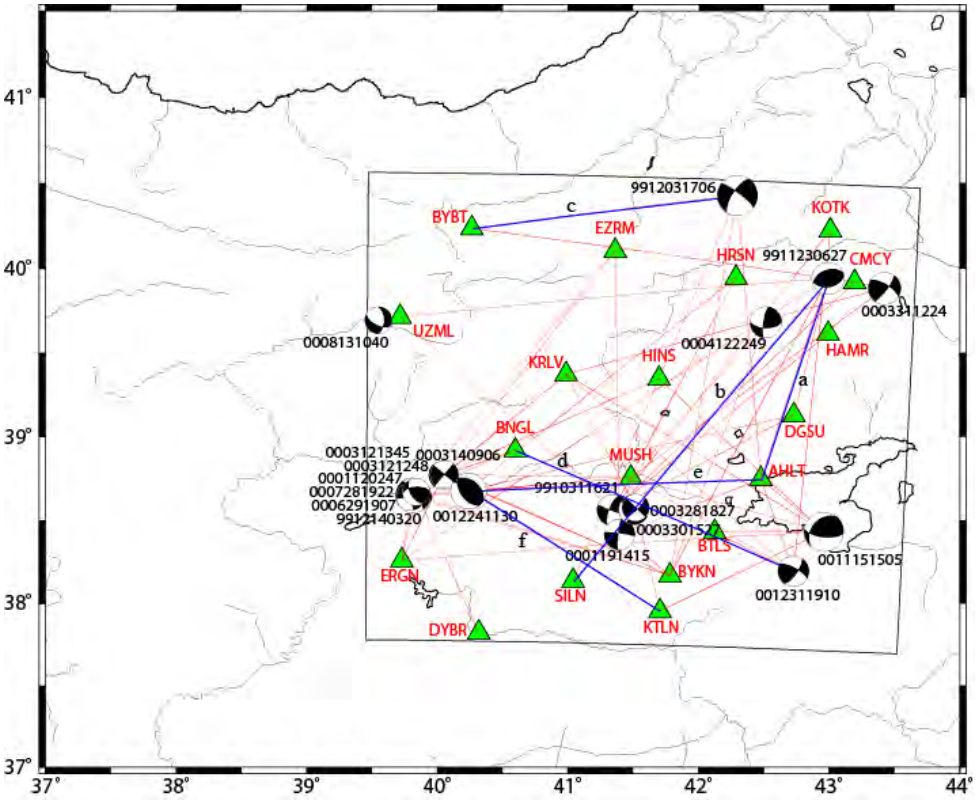

Figure 5. Full-wave tomography using the ETSE dataset. Boxed region shows the current study area. Triangles and beachballs show the locations of the 19 stations and 24 events with focal mechanism solutions (Turkelli et al. 2003) used so far in our tomography study, resulting in 69 source-receiver paths (red lines). Blue lines indicate the source-receiver paths whose frequency-dependent phase and amplitude anomaly measurements are shown in Figure 6.

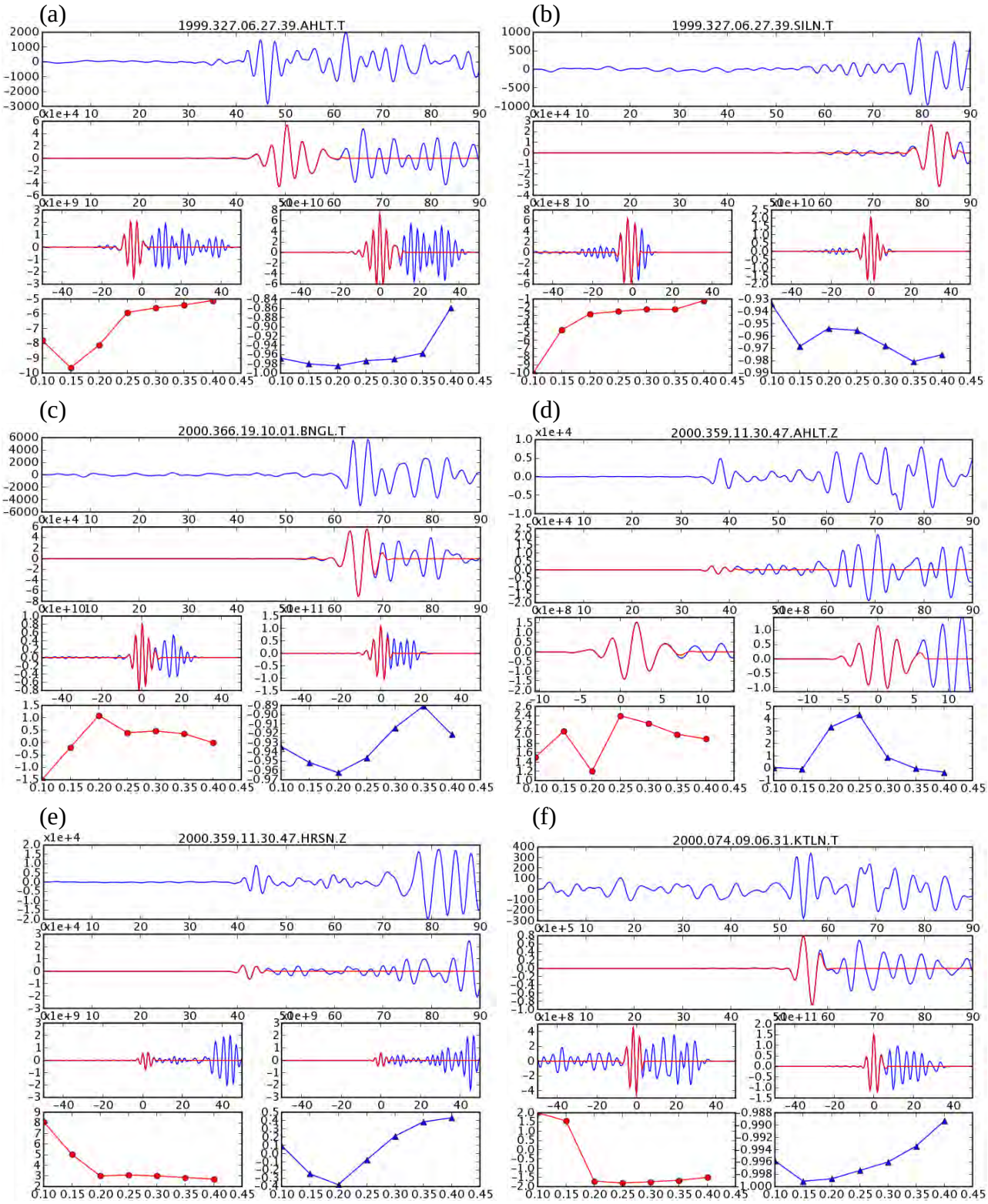

Figure 6. Frequency-dependent phase and amplitude anomaly measurements obtained from the paths (a)-(f) shown in Figure 5. In each panel, the top two traces are recorded and synthetic seismograms (Z for vertical and T for transverse) with the red line showing the synthetic in the time window of interest. In the third row are the cross-correlation (left) and auto-correlation (right) defined in eqs.(1) and (4), respectively. The bottom row shows the phase (left) and amplitude (right) anomalies at seven frequencies between 0.1 Hz and 0.4 Hz.

BROADBAND NETWORK OPERATION AND SHEAR VELOCITY STRUCTURE BENEATH THE XIUYAN AREA, NE CHINA

Rong-Mao Zhou[1,2], Brian W. Stump[2], Zhi-Xian Yang[3],Yun-Tai Chen[3], Robert B. Herrmann[4], Relu Burlacu[5], Christopher T. Hayward[2], and Kristine Pankow[5]

Los Alamos National Laboratory [1], Southern Methodist University[2], Institute of Geophysics, China Earthquake Administration[3], Saint Louis University[4], and University of Utah Seismograph Stations[5]

Sponsored by Air Force Research Laboratory

Contract No. FA8718-05-C-0020

ABSTRACT

We continue the operation of the Southern Methodist University (SMU)-Institute of Geophysics, China Earthquake Administration (IGPCEA) broadband seismic network. The current operating network includes three stations NW of Beijing and ten stations in Xiuyan, Liaoning Province, NE China.

On November 29, 1999, an earthquake of M_S 5.9 occurred in Xiuyan, Liaoning of China. This earthquake was followed by a number of aftershocks. To study the characteristics of this fault system and the structure beneath this area, 10 portable broadband seismometers were deployed around this region beginning August 2004. Instrumentation consists of STS-2 seismometers connected to Quanterra Q-330 digitizers and Baler recording systems located in hard rock vaults. The high-quality data set recorded by these 10 regional stations provides the opportunity to study the detailed velocity structure beneath this region using both teleseismic and regional signals.

Short-period surface wave dispersion curves from ambient noise were obtained using four months of data. Receiver functions and surface wave phase velocities from 42 teleseismic events that occurred between August 2004 and March 2006 have been determined. The combination of passive noise data and active earthquake data is being used to invert for crustal shear velocity structure beneath the Xiuyan area, NE China. This analysis is the first step in a more detailed source study of local and regional events.

Infrasound gauges originally destined for China have been installed in two arrays in Utah, with a third planned for summer of 2007. The array at station NOQ was installed May 2006 and the array at BGU May 2007. Data from these arrays are telemetered in real-time to the University of Utah and are archived at the Incorporated Research Institutions for Seismology (IRIS) Data Mangement Center DMC. The arrays consist of four infrasound sensors with approximate 200-m separation sampled at 100 samples per second. NOQ is located close to the Bingham open-pit copper mine, one source of infrasound signals. BGU is located near the Utah Test and Training Range (UTTR) of the Hill AFB, which routinely detonates large surface explosions from 40,000 to 80,000 lb. Cooperation with the group at Hill AFB has been initiated and resulted in initial attempts to model time varying atmospheric effects using data from the NOQ array. We plan to utilize these stations in combination with an experimental deployment of seismic and infrasound sensors to better characterize local and regional infrasound propagation from explosive sources (see, Seismic and Infrasound Energy Generation and Propagation at Local and Regional Distances, Stump et al., these Proceedings).

OBJECTIVES

The goals of the collaborative study between the SMU and the IGPCEA (formerly IGCSB) are to develop a database of earthquakes and human-induced events; to refine event locations in the Yanqing-Huailai Basin and the Haicheng area; to understand source characterization of natural and human-induced events; and to separate source and propagation path effects at regional distance.

The deployment of the broadband seismic network operated by SMU and IGPCEA has been completed. The current operating network includes three stations around the Yanqing-Huailai Basin, NW of Beijing and 10 stations in the Haicheng, NE China (Figure 1). The seismic data have been archived into the IRIS DMC Portable Data Collection Center database.

Beijing and Haicheng are two regions of historical natural and human-induced seismicity as well as a seismic hazard. The region includes the site of the first successful earthquake prediction in 1975 near Haicheng and the great Tangshan earthquake in 1976. The broadband seismic network provides near-source and regional coverage for the study area. Data from this network have been used to constrain the preliminary velocity structure around Beijing (Zhou, 2004) from surface wave study and investigate event discrimination for mining explosions (Zhou et al., 2006) as well as joint inversion of receiver functions and surface-wave dispersion for the detail structure beneath the Yanqing-Huailai Basin, NE of Beijing (Zhou et al., 2007).

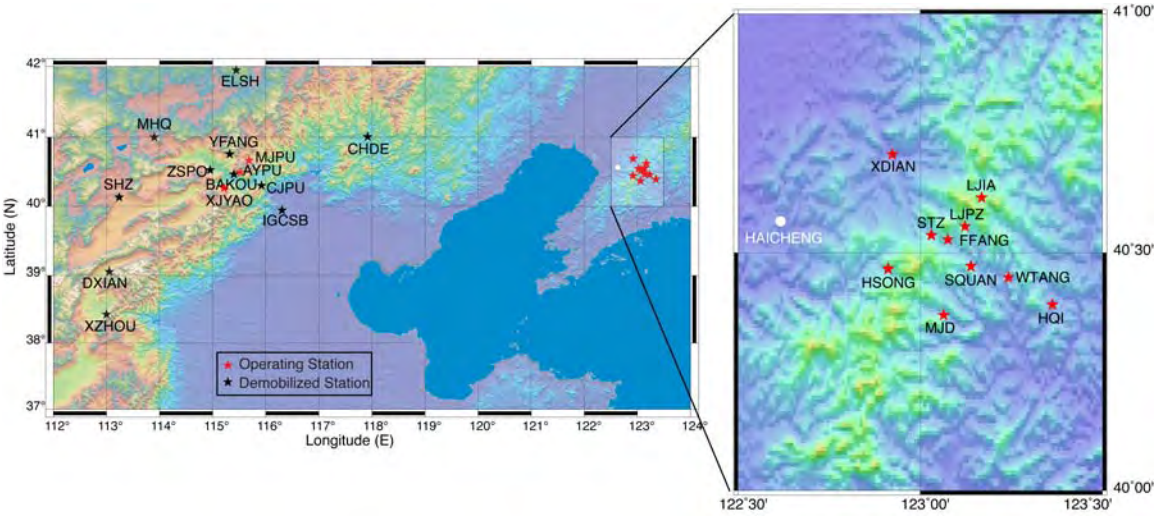

Figure 1. Map of the SMU-IGPCEA Broadband Seismic Network (operating stations: red stars; demobilized stations: black stars).

A final objective in this research is the instrumental quantification of seismic and infrasound signals observed at regional distances. The goal in this case is an investigation of man-made and natural sources of both infrasound and seismic waves. Initially, infrasound gauges were to be co-located with the seismometers deployed. After acquisition of the infrasound gauges, the deployment was made in the US at two (and soon three) seismic stations that are part of the University of Utah Seismic Stations.

RESEARCH ACCOMPLISHED

Study Area

In summer 2004, we demobilized five stations from Beijing area and installed them around the Haicheng area (Figures 1 and 2), the second focus area of this cooperative project and focus region of this study. To date, 13 broadband seismic stations have been installed and operated in the two regions (Figure 1).

The 1975 Haicheng Earthquake, the first predicted earthquake in China, occurred in this region and motivated an interest to understand seismicity for hazard reduction. The Haicheng area is also rich in natural resources such as iron, zinc, coal, oil and natural gas. Mining activities related to resource recovery provide additional sources of

seismic waves. Historically, a few larger earthquakes in addition to the 1975 event have occurred in the Haicheng-Xiuyan seismogenic zone (Haichenghe-Dayanghe fault) and surrounding area. Three earthquakes with magnitude 5.25, 5.5, and 5.9 occurred around Yinkou on September 19, 1859; April 7, 1885; and May 18, 1978, respectively (Wang et al., 2002). According to the bulletin from the Liaoning Digital Telemetry Network, the Haicheng-Xiuyan earthquake swarm started from two earthquakes, M_L 4.1 and M_L 4.2 on November 9, 1999. By the time the mainshock, M_S 5.9, occurred on November 29, 1999, 205 earthquakes had been recorded, including 28 M_L 2.0 ~ 2.9 earthquakes, 10 M_L 3.0 ~ 3.9 earthquakes and five earthquakes with M_L 4.0 ~ 4.9. The largest foreshocks were two M_L 4.4 events that occurred on November 25 and 26. These events reflect the seismic activity in this region. Figure 2 is a map of major faults and historical earthquakes around the Haicheng and Xiuyan area with the first 5 SMU-IGPCEA broadband seismic stations superimposed on the image.

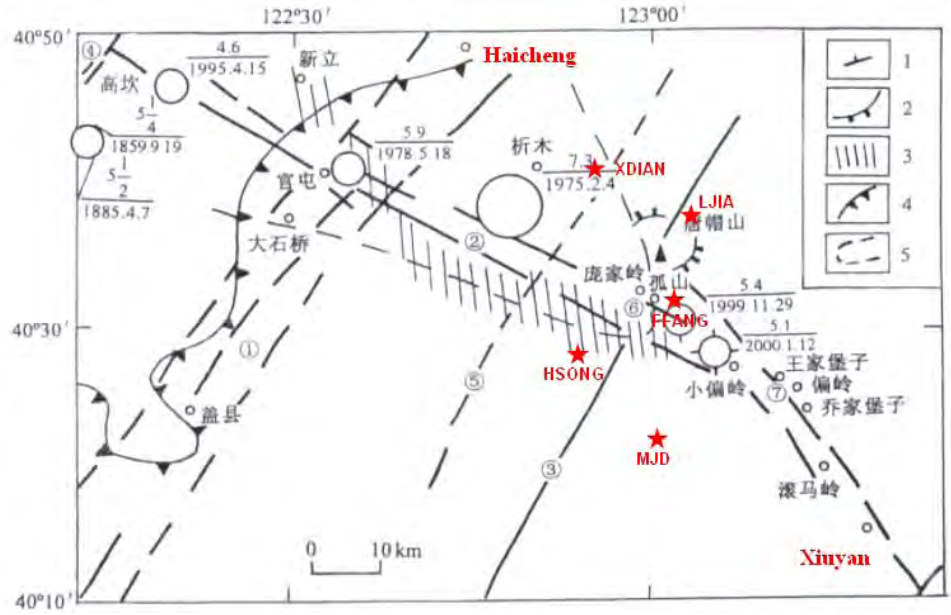

Figure 2. Map of major faults and historical earthquakes around Haicheng and Xiuyan area (Wang et al., 2002) superposing with SMU-IGPCEA stations (red stars). Major faults: (1) Jinzhou Fault; (2) Haichenghe-Dayanghe Fault; (3)Tanghe-gushan Fault; (4) Niuju-Youyangou Fault; (5) Ximu Fault; (6) Kangjialing Fault; and (7) Wangjiabuzi Fault.

Noise Correlation and Extraction of Intermediate Period Surface Waves

Using ambient noise and correlation techniques to extract surface waves between pairs of stations has evolved significantly since the first work by Shapiro et al. (2005). These techniques have proven to provide useful constraints on shallow crust and upper mantle structure in regions with few regional events that generate intermediate period surface waves. Continuous vertical-component seismic data from the initial five stations deployed in the Haicheng-Xiuyan region (FFANG, HSONG, LJIA, MJD and XDIAN, Figure 2) recorded during the first five months of 2004 provide an opportunity to apply this analysis approach. Stacked cross-correlation functions between pairs of these five stations are illustrated in Figure 3. Fundamental Rayleigh waves were extracted using Multiple Filter Analysis and Phase Matched Filter techniques and are reproduced in Figure 4.

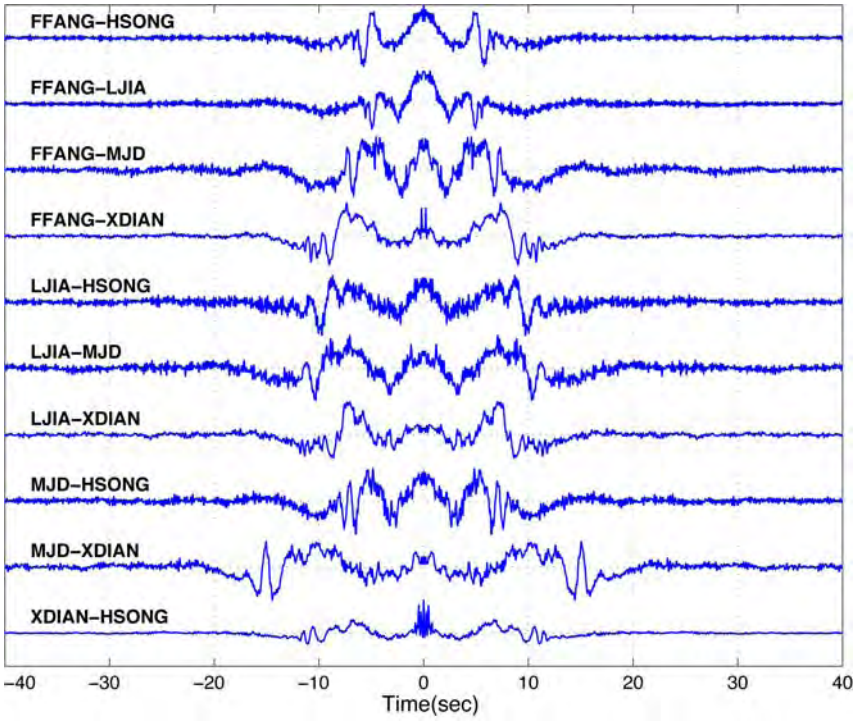

Figure 3. Cross-correlation functions between station pairs from continuous vertical-component seismic data from the five stations (FFANG, HSONG, LJIA, MJD and XDIAN) deployed in the Haicheng-Xiuyan region over the first five months of 2004.

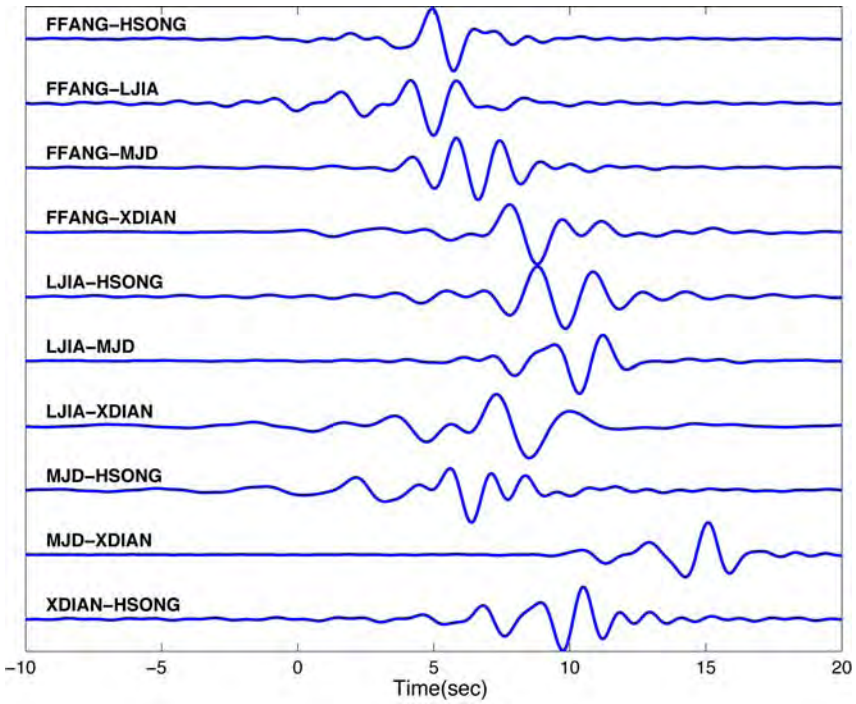

Figure 4. Fundamental Rayleigh waves extracted from cross-correlations in Figure 3 and station pairs illustrated in Figure 2.

Receiver Functions

Forty-two, high signal-to-noise ratio, teleseismic events with great circle epicentral distances in the range of 30-80 degrees from 2004 to 2006 have been chosen for receiver function analysis. This approach follows an earlier study in the Huailai Basin (Zhou *et al.*, 2007) and provides an opportunity to document variations in crust and upper mantle structure in NE China. Source parameters of these events were obtained from the Preliminary Determination of Epicenters (PDE) bulletins provided by the United States Geology Survey (USGS) National Earthquake Information Center (NEIC) and are listed in Table 1 with the distance ranges and back-azimuth of the events to station FFANG.

Receiver functions were computed using the iterative, time-domain deconvolution of Ligorría and Ammon (1999), an implementation of the Kikuchi and Kanamori (1982) technique. The receiver functions were extracted from all 42 events in Table 1. The radial component receiver functions at station FFANG with Gaussian window parameter α of 1.0, and 2.5 for Event 2004314 are plotted in Figure 5. Figure 6 is a plot of all receiver functions as a function of azimuth for the 41 events recorded at station FFANG. The radial component receiver functions are simple and demonstrate little azimuthal variation. The similarity of these receiver functions motivates the simple one dimensional receiver function analysis that follows.

Table 1. Event Parameters in the Receiver Function Study

Event Code	Date (Y-M-D)	hhmmss.mm	Latitude (°N)	Longitude (°E)	Magnitude	Depth (km)	Distance to FFANG (degree)	FFANG BackAzimuth (degree)
2004263	2004-09-19	202604.10	52.21	174.03	6.2	25	36.2030	53.6813
2004278	2004-10-04	192034.98	14.55	146.99	6	7	33.3010	134.3848
2004282	2004-10-08	082753.54	-10.95	162.16	6.9	36	62.8830	135.9383
2004314	2004-11-09	235823.65	-11.15	163.71	6.9	13	63.8796	134.6334
2004331	2004-11-26	022503.31	-3.61	135.4	7.2	10	45.5589	162.6404
2004366	2004-12-31	022400.52	7.12	92.53	6.3	14	43.1053	227.5609
2005001-E1	2005-01-01	062544.82	5.1	92.3	6.7	11	44.9091	226.2114
2005001-E2	2005-01-01	190807.80	7.34	94.46	6.1	55	41.8587	225.3843
2005002	2005-01-02	153556.72	6.36	92.79	6.4	30	43.5898	226.6287
2005004	2005-01-04	091312.25	10.67	92.36	6.1	23	40.3174	230.8754
2005016	2005-01-16	201752.76	10.93	140.84	6.7	24	33.4962	147.1242
2005017	2005-01-17	105032.56	10.99	140.68	6.1	12	33.3759	147.3374
2005022	2005-01-22	203017.35	-7.73	159.48	6.5	29	58.7492	136.5358
2005023	2005-01-23	201012.15	-1.2	119.93	6.3	11	41.8271	184.7185
2005024	2005-01-24	041647.44	7.33	92.48	6.3	30	42.9603	227.7951
2005036	2005-02-05	122318.94	5.29	123.34	7.1	525	35.2394	179.5434
2005039	2005-02-08	144821.97	-14.25	167.26	6.7	206	68.3876	133.3971
2005046	2005-02-15	144225.85	4.76	126.42	6.5	39	35.8949	174.3090
2005050	2005-02-19	000443.59	-5.56	122.13	6.5	10	46.0968	181.3060
2005053	2005-02-22	022522.92	30.75	56.82	6.5	14	53.4676	281.7589
2005057	2005-02-26	125652.62	2.91	95.59	6.8	36	45.0564	220.6328
2005061	2005-03-02	104212.23	-6.53	129.93	7.1	201	47.4796	170.7419
2005089	2005-03-30	161941.10	2.99	95.41	6.3	22	45.0763	220.9094
2005100	2005-04-10	102911.28	-1.64	99.61	6.7	19	47.2859	212.8012
2005101	2005-04-11	170853.94	-21.98	170.61	6.7	68	76.5471	135.3024
2005118	2005-04-28	140733.70	2.13	96.8	6.2	22	45.1520	218.6064
2005130	2005-05-10	010905.10	-6.23	103.14	6.4	17	50.2233	206.1693
2005134	2005-05-14	050518.48	0.59	98.46	6.8	34	45.7602	215.5464
2005139	2005-05-19	015452.85	1.99	97.04	6.9	30	45.1620	218.2150
2005165	2005-06-14	171012.28	51.24	179.31	6.8	17	39.5385	54.8414
2005186	2005-07-05	015202.95	1.82	97.08	6.8	21	45.2933	218.0528
2005205	2005-07-24	154206.21	7.92	92.19	7.5	16	42.6406	228.6387
2005309	2005-11-05	104821.28	-3.16	148.14	6.4	25	49.3349	146.1065
2005323	2005-11-19	141013.03	2.16	96.79	6.5	21	45.1303	218.6389
2005331	2005-11-27	102219.19	26.77	55.86	6.1	10	56.2551	278.1349
2005345	2005-12-11	142043.79	-6.57	152.2	6.6	10	54.1781	143.3937
2005347	2005-12-13	031606.38	-15.27	-178.57	6.8	10	77.6688	122.7911
2006002	2006-01-02	221340.49	-19.93	-178.18	7.2	582	81.4169	125.6328
2006008	2006-01-08	113455.64	36.31	23.21	6.7	66	73.7483	304.2130
2006027	2006-01-27	165853.67	-5.47	128.13	7.6	397	46.2325	173.0243
2006073	2006-03-14	065733.86	-3.6	127.21	6.7	30	44.2908	174.0854
2006090	2006-03-31	211447.24	3.79	126.37	6.2	54	36.8585	174.5142

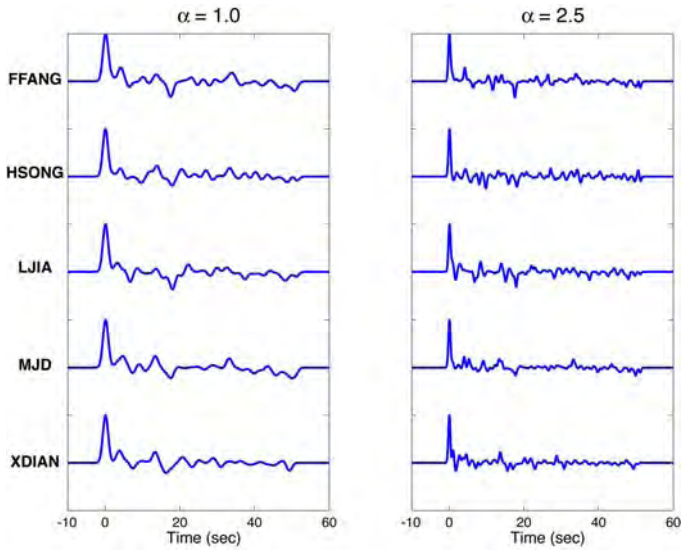

Figure 5. Receiver functions from Event 2004314 on November 09, 2004 with Gaussian window parameters α of 1.0 (left), and 2.5 (right).

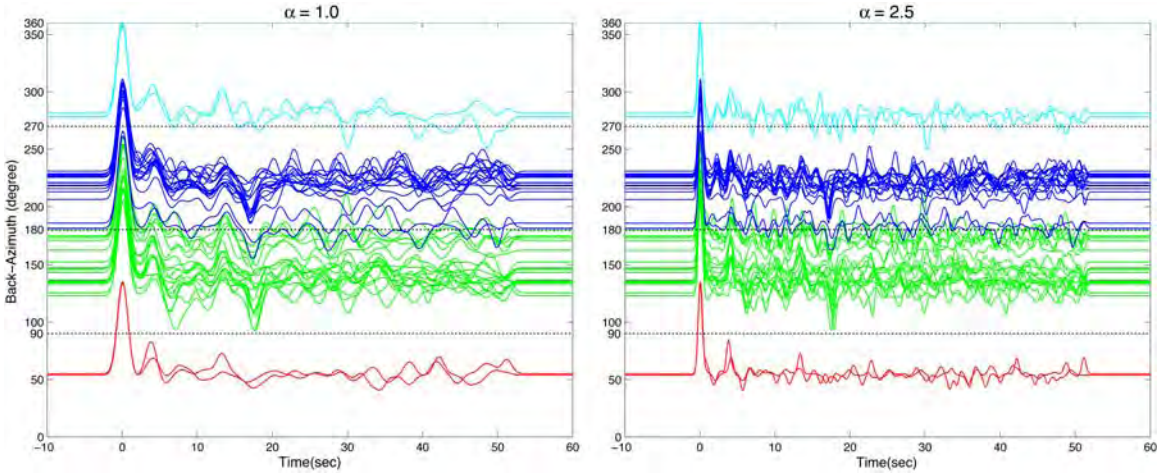

Figure 6. Receiver functions versus back-azimuth for all events recorded at stations FFANG (41 events) with Gaussian window parameters α of 1.0 (left), and 2.5 (right).

Joint Inversion

For the 42 events analyzed, the numbers of receiver functions obtained at each station vary: FFANG has 41, HSONG 14, LJIA 18, MJD and XDIAN 5 and 8, respectively. Based on this variability and the similarity of the FFANG receiver functions with azimuth, a joint inversion using all of the receiver functions at the five stations and group velocities from the ambient noise analysis has been conducted in order to estimate an averaged velocity model for this region. The starting model is given in Figure 7 in black with the final velocity model resulting from the joint inversion in blue.

A number of studies of crustal and upper mantle structure have been conducted in the area of northeast China after the 1975 Haicheng Earthquake (Lu, 1985; Lu et al., 1987; Lu et al., 1990; Niu et al., 2000; Pan, et al., 2001; and Lu et al., 2005). Their results indicated that the depth of Moho discontinuity is 31–34 km under Haicheng-Xiuyan area and a low velocity layer exists at the depth range around 21–28 km. Our averaged velocity model for this region is consistent with these earlier studies.

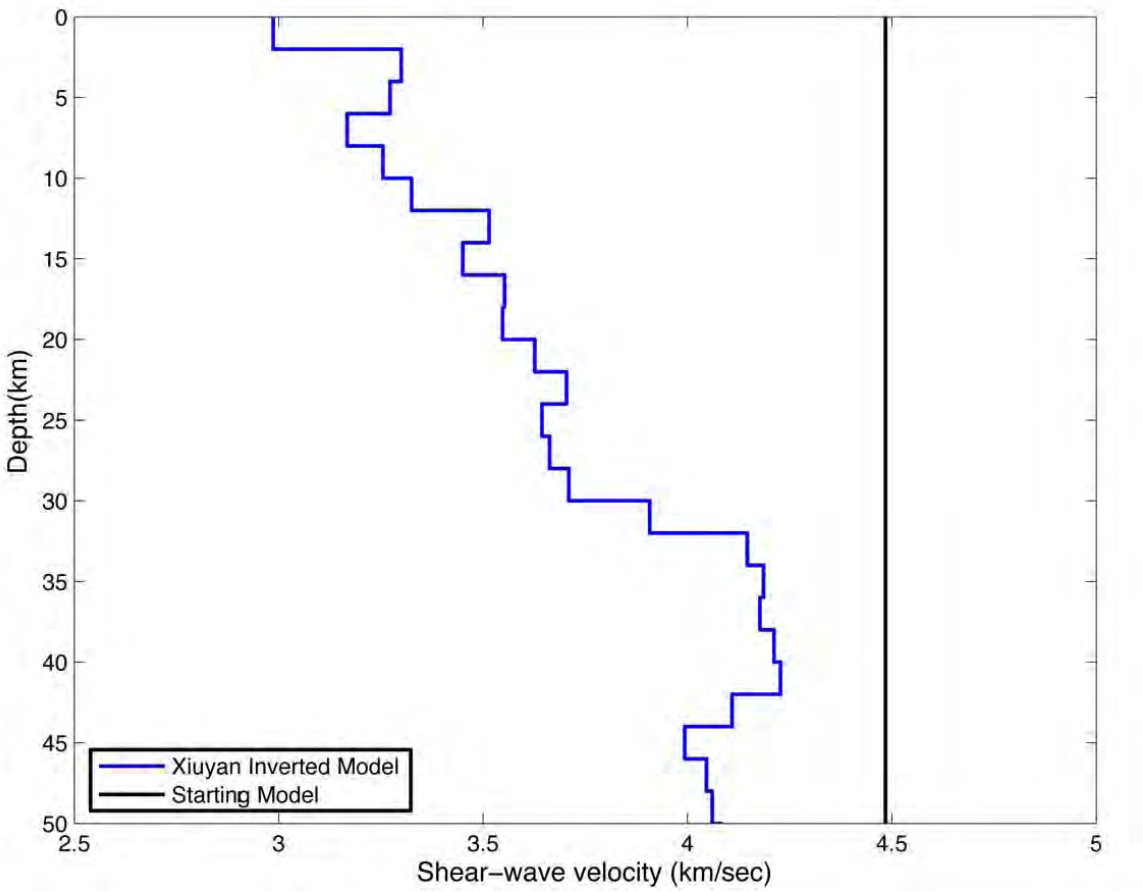

Figure 7. The starting shear wave velocity model (black) and the velocity model from the joint inversion (blue).

CONCLUSIONS AND RECOMMENDATIONS

The operation of the SMU-IGPCEA broadband seismic network is continuing. The data through June 2006 has been archived at the IRIS DMC.

A joint inversion of teleseismic receiver functions and surface wave group velocities from ambient noise analysis has been conducted and the shallow crustal shear velocity structure around Xiuyan area estimated. Crustal thickness beneath the Xiuyan area is about 34 km, which is consistent with the results from other geophysical studies in this region.

These new results can be compared to similar analysis in the Huailai Basin to the west (Figure 1). The estimated crustal thickness in the Haicheng-Xiuyan area appears to be slightly thinner than that previously estimated for the Huailai Basin (Zhou et al., 2007) as illustrated in Figure 8. Estimates of upper mantle velocity are also slightly larger in the region around the Huailai Basin.

Infrasound gauges were deployed in two (soon to be three) four and five element arrays in Utah for the purposes of assessing the utility of combined seismic and infrasound data for event characterization. The sites in Utah were co-located with existing University of Utah Seismograph Stations, providing both infrasound and seismic recordings in a region rich in explosive sources as well as earthquakes. These three arrays have become part of a larger field deployment planned for the summer of 2007 for the purpose of documenting large and frequent surface detonations of rocket motors at the UTTR. During the past year, over 21 rocket motor explosions have been observed acoustically and have provided the foundation for the planning of the larger experiment to document range and azimuth variations in infrasound propagation. The details of this database are discussed in the companion paper in

these proceedings, Seismic and Infrasound Energy Generation and Propagation at Local and Regional Distances, Stump et al.,2007.

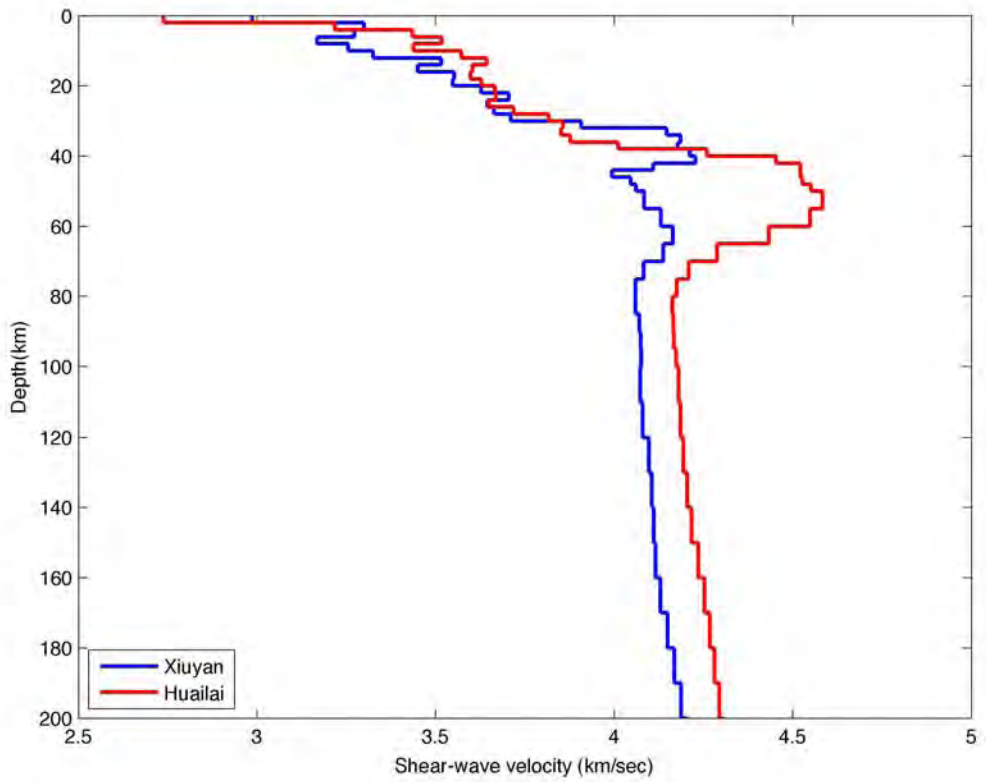

Figure 8: Comparison of shear wave velocity models developed for the Huailai Basin and the Haicheng-Xiuyan region illustrating variations in crustal thickness and upper mantle velocity in NE China.

ACKNOWLEDGEMENTS

The authors would like to thank Mary Templeton, Eliana Arias, Xiang-Wei Yu, Xiang-Tong Xu and Shi-Yu Bai for their help with network installation, data collection, and archiving. A large portion of the success of this experiment is due to the outstanding help and support of the seismological bureaus and seismic station operators in these regions. IRIS PASSCAL Instrument Center provided the STS-2 seismometers, Quanterra Q-330 and Baler systems.

REFERENCES

Ligorria, J. P. and C. J. Ammon (1999). Iterative deconvolution of teleseismic seismograms and receiver function estimation, *Bull. Seism. Soc. Am.* 89**:** 1395–1400.

Lu, Z.-X. (1985). Progress of geophysical prospecting study on the deep structure of Haicheng earthquake area, *Earthquake Research in China* 1**,** 56–65 (in Chinese with English abstract).

Lu, Z.-X., G.-C. Zhang, J.-Z. Li, L.-Z. Wang, and J.-M. Zhao (1987). Research on tectonic characteristics of the crust and upper mantle in Haicheng seismic area, *Journal of Changchun College of Geology* 17 (1): 99–108 (in Chinese with English abstract).

Lu, Z.-X., G.-D. Liu, M.-H. Wei, B.-Z. Meng, and J.-M. Zhao (1990). Lateral inhomogeneity of crust and upper mantle in South Liaoning, China and its relationship with the *M* 7.3 Haicheng earthquake, *ACTA Seismological Sinica* 12**:** 367–378 (in Chinese with English abstract).

Lu, Z.-X., D.-L. Jiang, Y. Bai, X. Niu, and B.-Z. Meng (2005). Exploration and research on the structure of the crust and upper mantle in Northeast China, *Seismological Research of Northeast China* 21(1): 1–8 (in Chinese with English abstract).

Kikuchi, M. and H. Kanamori (1982). Inversion of complex body waves, *Bull. Seism. Soc. Am.* 72**:** 491–506.

Pan, K., X.-Q. Jiang, Z.-Z. Lu, and P. Zhang (2001). Three dimension velocity image of the crust and upper mantle in Liaoning and its neighbor regions, *Seismological and Geomagnetic Observation and Research* 22**:** 92–98 (in Chinese with English abstract).

Shapiro, N. M., M. Campillo, L. Stehly, and M. H. Ritzwoller (2005). High resolution surface wave tomography from ambient seismic noise, *Science* 307: 1615–1618.

Stump, B., R. Burlacu, C. Hayward, J. Bonner, K. Pankow, A. Fisher and S. Nava (2007). Seismic and infrasound energy generation and propagation at local and regional distances, in current Proceedings.

Wang, A.-D., G.-Y. Gu, H. Huang and Y. Zhang (2002). Haicheng-Xiuyan 5.4 and 5.1 earthquakes on November 29, 1999, and January 12, 2000, in Liaoning Province, *Earthquake Cases in China (1997-1999)*, edited by Q.-F. Chen. Seismological Press, Beijing, China (in Chinese with English abstract).

Niu, X., Z.-X. Lu, D.-L. Jiang, Q.-Q. Lei, and S.-C. Shi (2000). Crust-mantle structure feature and the seismic activity of the main tectonic units in the North Tanlu fault zone, *ACTA Seismologica Sinica* 13**:** 159–165.

Zhou, R.-M. (2004). Intermediate period surface waves from mining explosions for crustal structure and source studies: application in the Western USA and Northeast China. *Ph. D. Dissertation*, Southern Methodist University, pp 240.

Zhou, R.-M., B. W. Stump, and C. T. Hayward (2006). M_s:m_b discrimination study of mining explosions in Wyoming, USA and Qianan, China. *Bull. Seismo. Soc. Am.* 96**:** 1742–1752, doi: 10.1785 / 0120050178.

Zhou, R., M., B. W. Stump, R. B. Herrmann, Y.-T. Chen, and Z.-X. Yang (2007). Teleseismic receiver function and surface wave study of velocity structure beneath the Yanqing-Huailai Basin, NW of Beijing, *Bull. Seismo. Soc. Am.*, in review.

Seismic Event Detection and Location

IMPROVING LOCATION/DETECTION METHODS FOR MONITORING RESEARCH USING LARGE-SCALE CORRECTION SURFACES, CROSS-CORRELATION TECHNIQUES AND GENETIC ALGORITHMS

Michael L. Begnaud[1], Charlotte A. Rowe[1], Lee K. Steck[1], and Woohan Kim[2]

Los Alamos National Laboratory[1] and Gyeongsang National University, Korea[2]

Sponsored by National Nuclear Security Administration
Office of Nonproliferation Research and Development
Office of Defense Nuclear Nonproliferation

Contract No. DE-AC52-06NA25396

ABSTRACT

The availability of seismic bulletin sources presents a problem when preparing data sets for studies. With so many choices, which catalog should be used? We have developed a method of merging data from all available seismic bulletins into a single database of non-redundant phases for each event. With this new database, additional ground truth (GT) events are readily identified due to the merging of all possible arrivals for each event. The compilation of over 8500 GT25 or better events in Asia allows the generation of large-scale travel time correction surfaces. We have created Pg, Pn, P, Sg/Lg, Sn, and S surfaces for the 1382 current and historic stations that detected a GT event. The availability of correction surfaces for any and all stations in a large region permit relocations that result in greater accuracy and increased event clustering for entire seismic catalogs.

We have adapted a retroactive cross-correlation pick adjustment algorithm to function as a cross-correlation scanning detector. Application of this tool demonstrates the benefits of such procedures in areas having numerous, repeating events that give rise to highly similar waveforms. The adaptive, cross-coherency filtering method in our correlation detector enhances correlation success by comparing only the portions of waveform spectra exhibiting high cross-spectral coherency; this boosts the successful correlation of similar signals while eliminating the unintentional discarding of potentially useful parts of the spectrum which can occur when a priori filters are relied upon. In a recent application we applied the method to a swarm of earthquakes occurring in the middle Rio Grande Rift near Socorro, New Mexico, during October 2005. Initial analyst review of the data stream identified ~300 earthquakes in this seismic swarm, while application of our coherency-based cross-correlation scanner identified over 1600 repeating events.

Location of events under conditions of poorly understood seismic velocity models with non-optimal station distribution is an ongoing problem for monitoring efforts. To improve event locations, particularly for increased robustness in depth estimation, we are working with colleagues at Gyeongsang National University, Korea, on a genetic algorithm that simultaneously finds an optimal average one-dimensional (1D) velocity structure and then relocates hypocenters in this model. The genetic-algorithm method for hypocentral parameters (GA-MHYPO) searches for a best-fit model within prescribed limits to minimize theoretical and observed travel time differences, using a two-point ray-tracing method. Once the optimal model has been found for the input data, these and other nearby events are relocated using the model. We are testing the algorithm, using the best-quality events from the Himalayan Nepal Tibet Seismic Experiment (HIMNT) PASSCAL Instrument Center deployment in Nepal and southern Tibet and have obtained improved location statistics for the shallowest events, as well as minor improvements for deeper earthquakes.

OBJECTIVES

We have been investigating new and improved methods for seismic location and detection related to explosion monitoring. The objectives for these investigations are to improve methods of GT collection, data mining, and accuracy for event arrival picking, and to develop new genetic location and detection methods.

RESEARCH ACCOMPLISHED

Large-Scale Travel Time Correction Surfaces for Asia

We have developed a method of merging data from all available seismic bulletins into a single database of non-redundant phases for each event. With this new database, additional GT events are readily identified due to the merging of all possible arrivals for each event.

Many seismic location studies utilize catalog arrival information to produce travel time correction surfaces, but for a particular subset of stations and phases. In order to take full advantage of the improved locations that correction surfaces can produce for any area, it is necessary to create these surfaces for any and all current or historical stations within the region. We have been able to merge arrival information for over 150,000 events in the Asia region (Lon: 40°–125°, Lat: 10°–85°) from 1964 to present. Using this merged arrival set, we used the Bondár et al. (2004) ground truth criteria to find over 8500 existing and relocated events that pass GT25 or better (epicentral errors less than 25 km). We have created Pg, Pn, P, Sg/Lg, Sn, and S travel time correction surfaces in the Asia region for the 1382 stations that detected a GT event. Using the resulting correction surfaces, we have relocated all Asia events on a catalog scale. This included testing the effect of the corrected secondary phases on the relocations versus using first-P phases alone. The resulting locations are more consistent in their locations and errors, are more accurate, and display increased clustering around tectonic features in Asia. In addition, the resulting locations provide a catalog-scale base of improved locations for other types of regional studies.

Merging seismic catalogs

The abundance of local, regional, and global seismic catalogs presents a problem for location and GT event determination. Which catalog arrivals are best to use? The main global catalogs are: International Seismological Centre (ISC), Reviewed Event Bulletin (REB) from the International Data Center (IDC), and Earthquake Data Report (EDR) from the United States Geological Survey (USGS). Regional catalogs for Asia include the Kazahkstan National Data Center (KNDC) and the Annual Bulletin of Chinese Earthquakes (ABCE). In addition, there are many local bulletins and special studies available. Each catalog can have common stations/networks for the same event, but also with many stations/networks that are not common. By merging the catalog arrivals into a consistent, non-redundant set, we are able to test more events against the GT criteria and have all available arrivals for locating any given event (Figure 1).

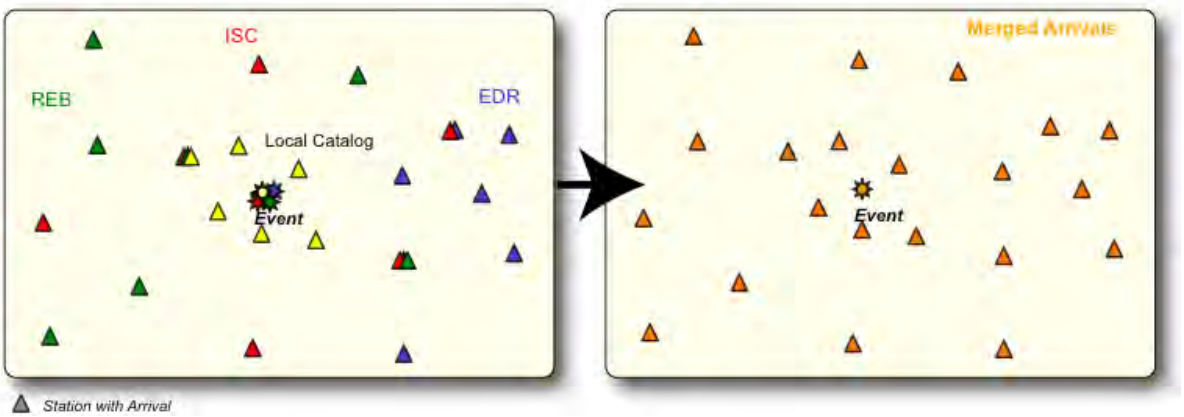

Figure 1. Cartoon example of catalog arrival merging for a single phase. Each local, regional, or global catalog is identified with a different color. Multiple triangles at a position indicate multiple catalogs listing an arrival for the same station. After merging based on an a priori ranking, each station has one arrival listed for a given phase.

Data mining for ground truth testing

After catalog arrivals have been merged and associated with an event, we process the events to mine for additional GT events, following the GT criteria of Bondár et al. (2004):

- Local networks (0–2.5°)—GT5, 95% confidence
  - At least 10 stations, all within 250 km, azimuthal gap <110°
  - At least 1 station within 30 km
  - Secondary azimuthal gap <160°
- Near-regional networks (2.5°–10°)—GT20, 90% confidence
  - Secondary azimuthal gap <120°
- Regional networks (2.5°–20°)—GT25, 90% confidence
  - Secondary azimuthal gap <120°
- Teleseismic networks (28°–91°)—GT25, 90% confidence
  - Secondary azimuthal gap <120°

A Perl script (*ARsorter)* searches through an event list and merges arrivals from ranked arrival sources together for the same event. Phases can be remapped to a consistent set. Option flags for only first-P or first-S phases can be specified. Arrivals from arrays are handled, keeping only one pick per phase per array as time defining (used for location). Travel-time tables are used to remap labeled first-P and first-S to regional name (i.e., Pg, Pn, etc.) and to look for major outliers.

We then process all events through the Bondár distance ranges, relocating with first-P arrivals only in those ranges. Events that then pass the criteria become GT events (Figure 2). Events with known/manually-set GT levels are not relocated; arrival associations are updated only.

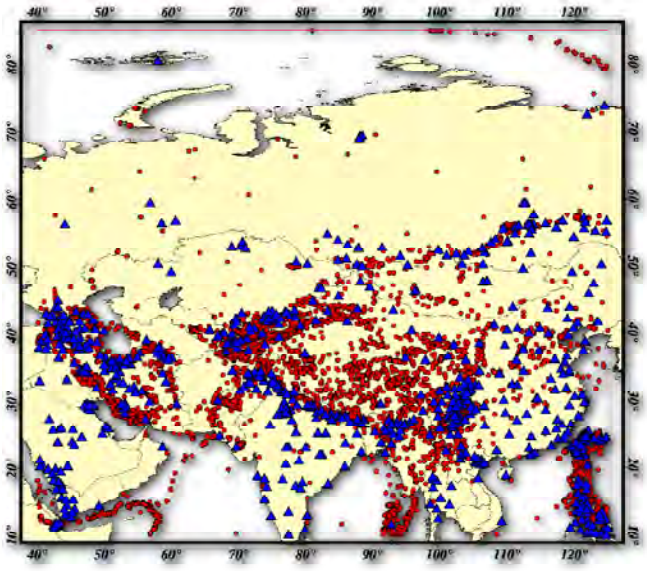

Figure 2. Stations (blue triangles) and ground truth events (red circles) for the Asia study region. A total of 1382 current and historical stations had GT event data from over 8500 possible GT25 and better events.

We select all current and historical single stations and arrays (1382 with GT data) from the Asia study region (Lon: 40°–125°, Lat: 10°–85°) (0). Array elements are not necessary as the reference stations provide the travel time correction. We have processed various global and regional catalogs for the entire globe in order to maximize the number of available GT25 and better events (over 8500) and their associated arrivals.

Correction surface generation

For the generation of correction surfaces, we use *Kbcit*, developed by Sandia National Laboratories (Ballard et al., 2004). We created two-dimensional travel time correction surfaces for P, S, Pn, Sn, Pg, and Sg/Lg phases for any available station in the region, producing 3666 individual surfaces. Phases are limited to beyond 2° because origin

depth will greatly affect points within 2°. For first-P and first-S surfaces, boundaries are placed at the change from Pn to P to limit "bleeding" of corrections across. Each phase uses the iasp91 model error surface (Kennett and Engdahl, 1991) for kriging the points, binned at 0.5°. Pg, Lg, S and Sn phases display far more scatter than Pn and P, most likely due to pick error.

Relocations and cluster analysis

To test the effects of the correction surfaces, we relocated any non-GT event in the study region having at least 4 Pn or P arrivals (first-P). No arrivals within 2° of a station were allowed because the correction surfaces were restricted to phases beyond 2°. Events were relocated using station elevation and ellipticity corrections. We performed three sets of relocations (first-P, first-P/S, all phases: first-P/S, Pg, Sg/Lg), limiting the defining phases for each set. The iasp91 model was used for relocations, with and without correction surfaces applied to determine how the surfaces affected origin clustering and phase residuals.

The resulting relocations (using *LocOO* from Sandia National Laboratories, [Ballard et al., 2004]) were binned into origin density grids using 0.05° cells having 25 km radii. The density grids, with and without correction surfaces, were differenced to help show areas of increased/decreased clustering, particularly around tectonic areas. Positive values (green) indicate shifts of iasp91 locations into those areas when using the correction surfaces. Note the areas on the northwest edge of Mongolia, west of the Tarim Basin, western India, and along the Himalayas where significant shifting of locations occurs when using the correction surfaces (Figure 3).

We plotted phase residual histograms for iasp91 locations and locations using correction surfaces for all P/S-type phases (Figure 4). The phase residual plots indicate a general reduction in residuals when using correction surfaces over iasp91 alone. Residual plots with distance (Figure 5) show dramatic bias removal for Sn and Lg phases. Residuals for Pg and teleseismic S, however, do not show any real improvement using the correction surfaces.

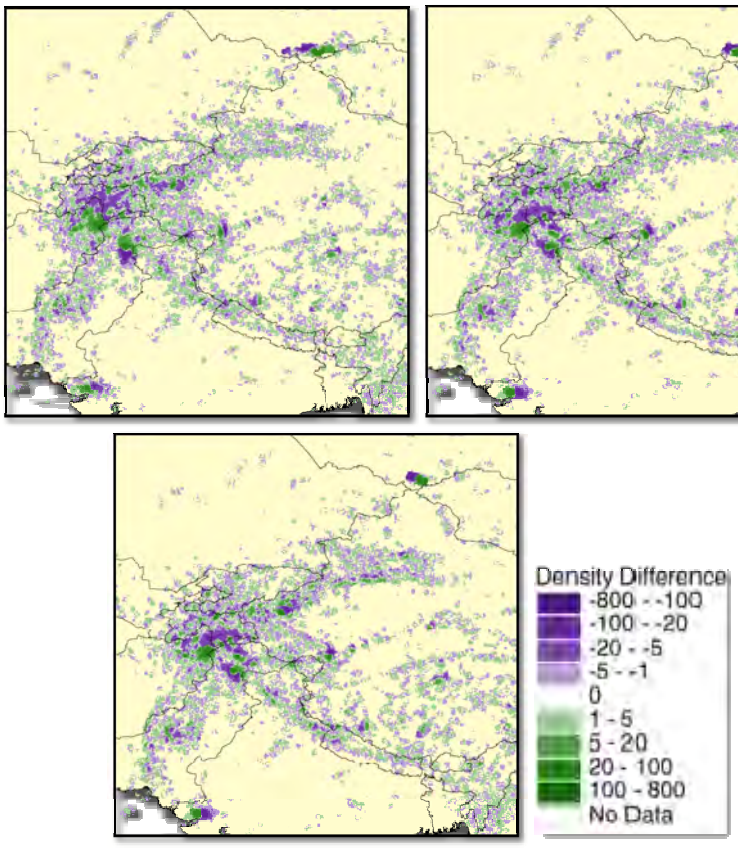

Figure 3. Origin density difference plots (density using corrections—iasp91 only) using different sets of defining phases for the western China region where the majority of events occurred: first-P (upper left), first-P/S (upper right), and all P/S (Pg, Pn, P, Sg/Lg, Sn, S). Purple indicates a reduction in origin density, green an increase in origin density. Note the shifting of linear patterns and large cluster shifts. The pattern of the shift for the prominent northeast cluster changes dramatically from first-P to using first-P/S or all P/S.

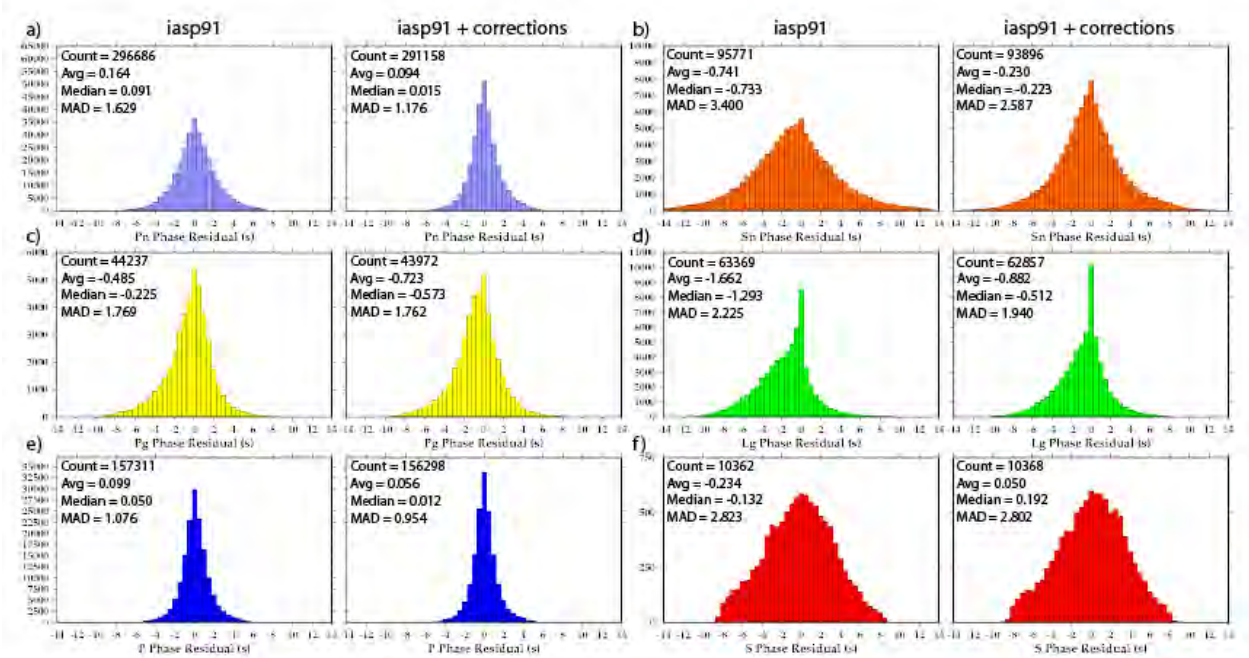

Figure 4. Phase residual histograms for relocations using iasp91 and iasp91 plus corrections for relocations using all P/S phases. a) Pn, b) Sn, c) Pg, d) Sg/Lg, e) teleseismic P, f) teleseismic S. All phases reduced average residual with decreased median and mean absolute deviation (MAD) values except for Pg and teleseismic S. These phases show virtually no change in the MAD values and slight degradation of the average/median values when using correction surfaces. Residuals for Sn show the most significant reduction in residuals when using corrections (69% for average, 24% MAD).

Cross-correlation scanning detector

Waveform cross-correlation (WCC) has been shown to significantly improve the relative hypocenter locations for events exhibiting similar waveforms (e.g., Aster and Rowe, 2000; Phillips, 2000; Rowe et al., 2002; Waldhauser and Ellsworth, 2000). Although relative event relocation has been shown to improve via WCC, it has also been shown that absolute event locations, which may be biased through overall pick bias at a given station, can be improved significantly through WCC-based phase repicking (e.g., Rowe et al., 2004).

We illustrate in Figure 6 the impact of pick bias. Shown are waveforms recorded at one station on the island of Montserrat, for a seismic swarm that occurred in 2005. The upper four panels illustrate initial phase pick scatter caused by emergent arrivals on a very noisy trace, and the improvement possible using WCC. Panels A) show waveform alignments (left) and resulting stack (right) aligned on preliminary picks. Panels B) show the realigned waveforms following WCC (left) and their associated stack (right). The lower panels show C) the Akaike Information Criterion (AIC) (Akaike, 1973) autopicker function (e.g., Leonard, 2000) applied to D) the realigned stack. Note on panel D the mean correlation pick (green line), which would be used for travel-time adjustments in all relative location schemes, is significantly later than the actual first arrival on the stack. The adjusted pick (red) based on the AIC autopicker, is closer to the correct P-wave arrival for this stack, and its contributing traces. Adjustment of all relative pick values by this offset will correct location bias in the event cluster, whose centroid may be significantly in error in terms of absolute location. This is particularly problematic for event families recorded by only a few stations; picking bias at one station can exert significant influence over the location.

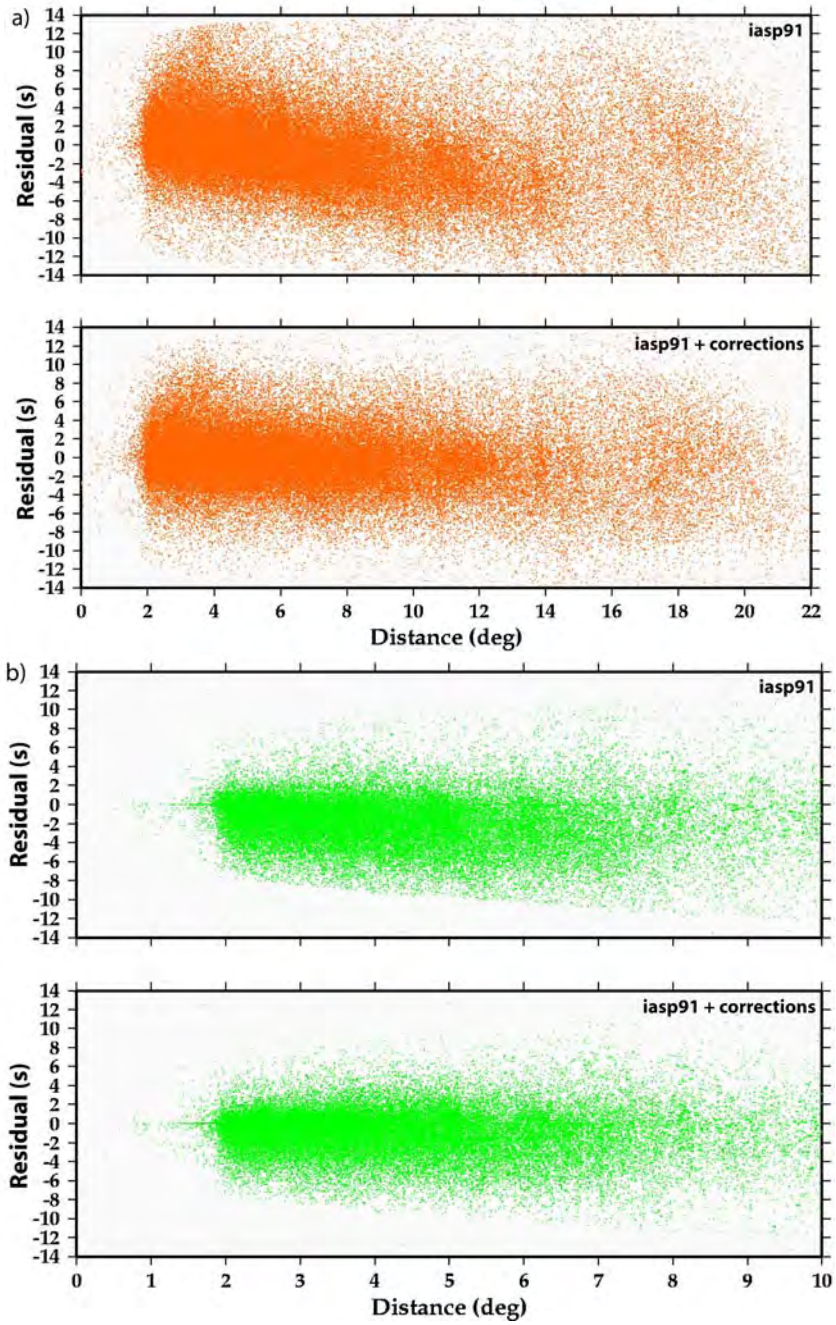

Figure 5. Examples of residuals with distance for (a) Sn and (b) Sg/Lg phases in relocations using all P/S phases, with and without corrections for iasp91. The residuals for these phases show a significant reduction in the trend with distance when using corrections.

The method of correlation detection (e.g., Harris, 2001; MacCarthy and Rowe, 2005; Rowe et al., 2005; Stankova et al., 2007) allows us to detect repeating seismic events within a waveform catalog by "scanning" the catalog with a master event or suite of basis events against which time-windowed segments of waveform data are correlated. In an application of this method to a seismic sequence that occurred in central New Mexico in 2005, the seismic cluster was identified by the data analyst as including ~300 earthquakes. Applying the WCC scanning detector (MacCarthy and Rowe, 2005) to the continuous digital waveform archive identified over 1600 events belonging to the cluster. At the same time, the WCC detector has applied a phase pick to the detected events, based on the pick for the master event. Waveforms (A) for the ~1600 detected events in the series, and the master waveform (B) used to scan the archive, are shown in Figure 7.

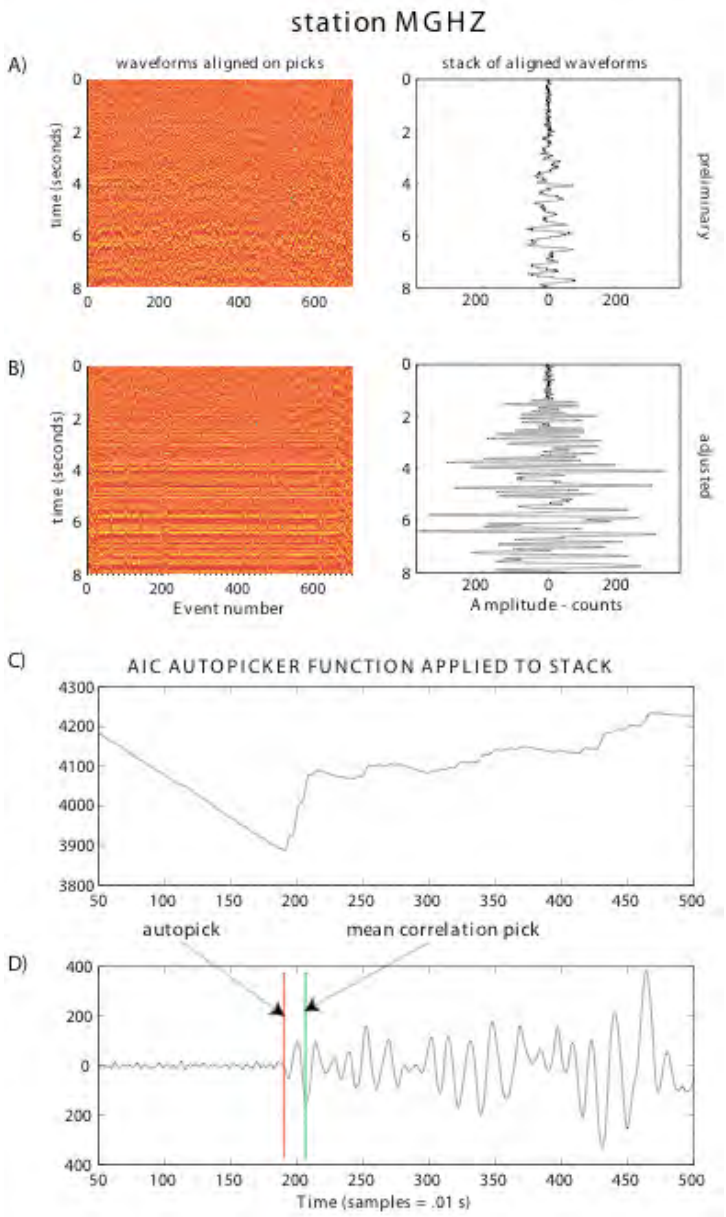

Figure 6. Illustration of correlation repicking and pick bias correction for absolute repacks. (A) 700 waveforms from a seismic event cluster aligned on preliminary picks (left) and stacked based on this alignment (right). (B) Traces re-aligned on WCC-adjusted picks (left) and stacked (right). (C) AIC autopicker function applied to the stack from B. (D) Stack from B, with mean correlation pick (vertical green line) and AIC pick (vertical red line) showing degree of pick bias at this station for these events.

Genetic Location Algorithm

The reliability of many seismic studies depends on the accuracy of hypocentral parameters. The hypocentral parameters determined by the conventional methods have errors although the P and S phase arrival time data may have no picking errors, if the true velocity structure is not used as the initial model. Unfortunately, the true velocity structure is not known for the most regions of Earth.

Using a genetic algorithm (GA) in earthquake location and velocity optimization problems, GA-MHYPO (Kim et al., 2006), searches for a global solution of the 1D velocity structure among the numerous models that are

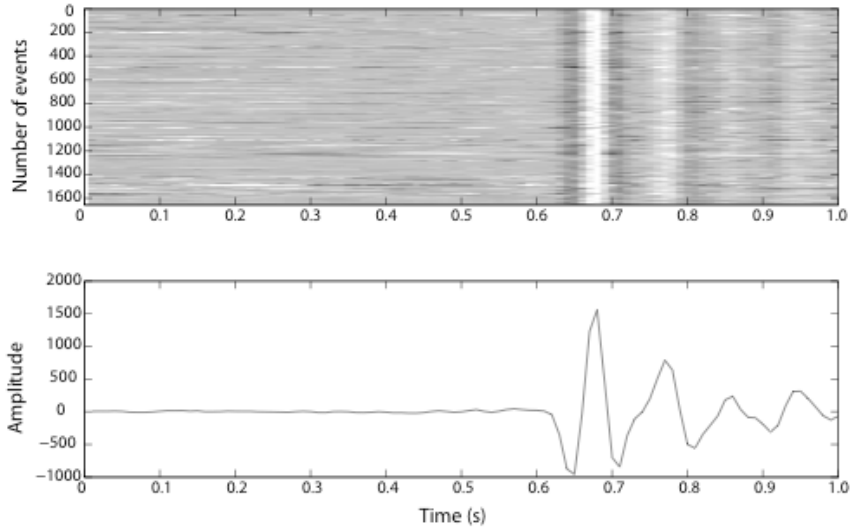

Figure 7. Earthquakes belonging to a seismic sequence occurring near Socorro, New Mexico, in October 2005. Top panel shows over 1600 waveforms recorded at station WTX, which were identified and picked using WCC detection scanning. Bottom panel shows master waveform used to scan the waveform archive. Only 300 of these earthquakes were identified during preliminary, manual analysis.

generated randomly within prescribed ranges. GA-MHYPO uses the velocity structure that provides the minimum travel-time difference between observed and calculated travel times for phases. The algorithm employs a two-point ray tracing method (Kim and Baag, 2002) to reduce error caused by ray paths between the source and receiver, and a weighting factor (Hahm et al., 2007) with respect to the take-off angle at a source to increase the accuracy of focal depth. Theoretically, GA-MHYPO can find the average true velocity structure between a source and receiver if the average true velocity structure was within the prescribed range and the phase data used has no picking error. Genetic algorithms in GA-MHYPO determine a global solution of 1D velocity structure to determine hypocentral parameters, while most existing methods use generally local solutions as the initial velocity model, which may differ from the true velocity. Therefore, the conventional methods have non-uniqueness problems depending on the basis of initial velocity models.

GA-MHYPO determines the hypocentral parameters accurately under ill conditions, because this method searches and uses the true or closer to average true velocity, and reduces computational error caused by ray path and focal depth. The ill conditions include limited number of phase data, large azimuthal gap, and noisy data with large picking error due to poor signal-to-noise ratios. We tested GA-MHYPO in a comparison with HYPOINVERSE (an example of conventional location methods) to investigate the relative location improvement for synthetic data both without, and with, picking error under a variety of situations, varying number of arrivals, azimuthal gap, and focal depth. The computational results show that the focal depth and horizontal errors determined by GA-MHYPO are less than 0.1 km for the error-free picks, and 1 km for the data with moderate picking error. Under ill conditions, the accuracy of hypocentral parameters obtained from GA-MHYPO in our test is improved by more than a factor of twenty for error-free data or a factor of five for the data with pick error, compared with those obtained by HYPOINVERSE.

The GA-MHYPO algorithm was applied to the Himalayan Nepal Tibet Seismic Experiment (HIMNT) data where 1D models have been previously calculated (Monsalve et al., 2006). Events were grouped by sites in order to process co-located events together (Figure 8). The genetic algorithm in GA-MHYPO searches for a best-fit 1D velocity profile within a prescribed range for the number of layers assigned. Dividing the depth profile into relatively small layers (5 km each for HIMNT data) permits the algorithm to search for an optimal velocity profile by perturbing each of these layers. We can see that the resulting velocity model for Group A and B (Figure 9) displays significantly more detail than the model arrived at by Monsalve et al. (2006). In the absence of additional information, the simpler model is generally best, but because of the concentration of events below 45 km, as well as from 0 km to 20 km, both the shallowest and deepest part of the velocity structure can be better characterized through use of GA-MHYPO. Between 25 and 45 km depth there are few hypocenters available to constrain the layers; hence, the values at these depths are less robust. Note in particular the significant velocity inversions found at

about 55 and about 75 km by GA-MHYPO. The large number of hypocenters contributing to these layers provides some confidence that the inversions are real, rather than an artifact arising from high-pick uncertainty for a few events. These velocity lows suggest lower crust and/or upper mantle complexity in this region of significant tectonic convergence, and may indicate the superposition of crust/mantle transition zones for the Indian and Eurasian plates.

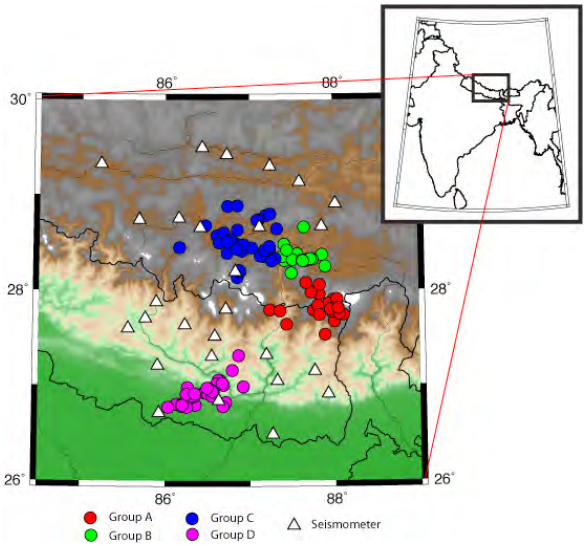

Figure 8. Events and stations from the HIMNT, with events subdivided into groups for testing with the GA-MHYPO algorithm.

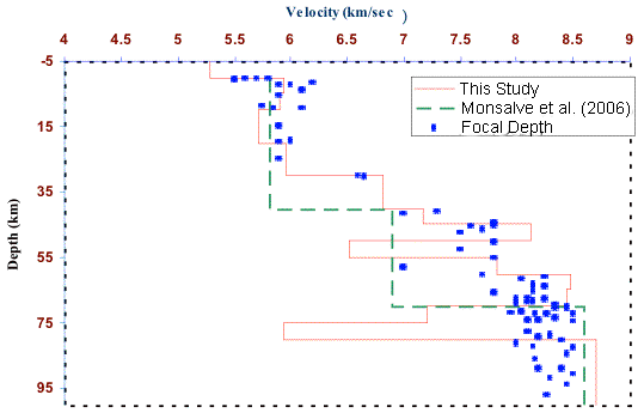

Figure 9. Velocity/depth profile using results from GA-MHYPO for event Groups A and B together. Events are plotted to show concentrations with depth. The velocity profile from GA-MHYPO has similarities to the previous Tibet profile (Monsalve et al., 2006) but is able to resolve low-velocity zones at depth.

CONCLUSIONS AND RECOMMENDATIONS

Merging seismic catalogs allows for more arrivals for relocation procedures and increases the number of GT events that can be mined from the database. The use of empirical travel time correction surfaces can be applied to ALL stations in an area, whether currently operational or historical, and permits the relocation of events across any time boundary. Relocating events in Asia using the catalog-scale correction surfaces results in significant translation and clustering of events, especially in the western China/Mongolia region. Analysis of phase residuals suggests the correction surfaces affect P, Pn, Sn, and Lg the most noticeably and that secondary phases “need” corrections if used for location.

WCC has been shown to significantly improve the relative hypocenter locations for events exhibiting similar waveforms. Although relative event relocation has been shown to improve via WCC, it has also been shown that

absolute event locations, which may be biased through overall pick bias at a given station, can be improved significantly through WCC-based phase repicking.

GA-MHYPO, a genetic earthquake location algorithm, searches for a global solution of the 1D velocity structure among the numerous models that are generated randomly within prescribed ranges. The algorithm uses the velocity structure that provides the minimum travel-time difference between observed and calculated travel times for phases and determines the hypocentral parameters accurately under ill conditions. Our models for the HIMNT region suggest the existence of two high velocity anomalies that may represent two Mohorovicic discontinuities in the India/Asia continental collision zone, each deriving from one of the two converging plates.

REFERENCES

Akaike, H. (1973). Information theory and an extension of the maximum likelihood principle, in *2nd International Symposium on Information Theory*, B. Petrov and F. Csaki (Eds.), pp. 267–281.

Aster, R. C. and C. A. Rowe (2000). Automatic phase pick refinement and similar event association in large seismic datasets, in *Advances in Seismic Event Location*, C. H. Thurber and N. Rabinowitz (Eds.). Amsterdam: Kluwer, pp. 231–263.

Ballard, S., M. Chang, J. Hipp, L. Jensen, R. Simons, and L. Wilkening (2004). The 2004 Knowledge Base parametric grid software suite, in *Proceedings of the 26th Seismic Research Review: Trends in Nuclear Explosion Monitoring*, LA-UR-04-5801, Vol. 1, pp. 211–220.

Bondár, I., S. C. Myers, E. R. Engdahl, and E. A. Bergman (2004). Epicentre accuracy based on seismic network criteria, *Geophys. J. Int.* 156: 483–496.

Hahm, I. K., W. Kim, J. M. Lee, and J. S. Jeon (2007). Determining the hypocentral parameters of local earthquakes using take-off angle as weighting factor, *Geosciences Journal* 11: 39–49.

Harris, D. B. (2001). Subspace techniques for detecting repeating events (abstract), *Seis. Res. Lett.* 72: 245.

Kennett, B. L. N. and E. R. Engdahl (1991). Traveltimes for global earthquake location and phase identification, *Geophys. J. Int.* 105: 429–465.

Kim, W. and C.-E. Baag (2002). Rapid and accurate two-point ray tracing based on a quadratic equation of takeoff angle in layer media with constant or linearly varying velocity functions, *Bull. Seism. Soc. Am.* 92: 2251–2263.

Kim, W., I. K. Hahm, S. J. Ahn, and D. H. Lim (2006). Determining the hypocentral parameters for local earthquakes in 1-D using genetic algorithms, *J. Geophys. Res.* 166: 590–600.

Leonard, M. (2000). Comparison of manual and automatic onset time picking, *Bull. Seism. Soc. Am.* 90: 1384–1390.

MacCarthy, J. K. and C. A. Rowe (2005). Automatic scanning detection for characterization of dome-related seismic swarms at Mount St. Helens, and their evolution through time (abstract), *Eos Trans. AGU*, AGU Fall Meeting.

Monsalve, G., A. Sheehan, V. Schulte-Pelkum, S. Rajaure, M. R. Pandey, and F. Wu (2006). Seismicity and one-dimensional velocity structure of the Himalayan collision zone: Earthquakes in the crust and upper mantle, *J. Geophys. Res.* 111: B10301, doi:10.1029/2005JB004062.

Phillips, W. S. (2000). Precise microearthquake locations and fluid flow in the geothermal reservoir at Soultz-sous-Forets, France, *Bull. Seism. Soc. Am.* 90: 212–228.

Rowe, C. A., R. C. Aster, B. Borchers, and C. J. Young (2002). An automatic, adaptive algorithm for refining phase picks in large seismic data sets, *Bull. Seism. Soc. Am.* 92: 1660–1674.

Rowe, C. A., J. K. MacCarthy, F. Giudicepietro, S. Scarpetta, and S. R. Taylor (2005). Seismic event identification using scanning detection: a comparison of denoising and classification methods (abstract), *Eos Trans. AGU*, AGU Fall Meeting.

Rowe, C. A., C. H. Thurber, and R. A. White (2004). Dome growth behavior at Soufriere Hills Volcano, Montserrat, revealed by relocation of volcanic event swarms, *Jour. Volc. Geotherm. Res.* **134**, 199-221.

Stankova, J., S. Bilek, C. A. Rowe, and R. C. Aster (2007). Characteristics of the October 2005 microearthquake swarm and reactivation of seismic swarms over decade-scale time periods near Socorro, New Mexico, *Bull. Seism. Soc. Am.*, in review.

Waldhauser, F., and W. L. Ellsworth (2000). A double-difference earthquake location algorithm: Method and application to the Northern Hayward Fault, California, *Bull. Seism. Soc. Am.* **90**, 6, 1353-1368.

GLOBAL GROUND TRUTH DATA SET WITH WAVEFORM AND IMPROVED ARRIVAL DATA

István Bondár[1], Ben Kohl[1], Eric Bergman[2], Keith McLaughlin[1], Yu-Long Kung[1], and Bob Engdahl[3]

Science Applications International Corporation[1], Global Seismological Services[2],
and University of Colorado at Boulder[3]

Sponsored by Air Force Research Laboratory

Contract No. FA8718-04-C-0020

ABSTRACT

We present the final results of our three-year research project to produce a high-confidence global ground truth (GT) 5 data set. During the course of this project we have developed, tested, and validated the hybrid HDC-RCA (Hypocentroidal Decomposition and Reciprocal Cluster Analysis) methodology to produce new GT5 or better event locations from event clusters. The HDC algorithm uses regional and teleseismic data to estimate precise relative event locations with respect to the cluster centroid. The RCA algorithm uses local data to precisely locate the cluster centroid. We have demonstrated that the HDC-RCA multiple event location methodology is able to produce high-confidence GT5 (epicenter and depth) or better event locations using only a few local stations, without reliance on independent GT information. A posteriori assessment procedures and a priori applicability criteria have been developed and tested to assure the quality and high-confidence of the resulting GT5 events.

We have developed a novel, adaptive approach to waveform cross-correlation for improved differential arrival time measurements. The method finds the optimal time-bandwidth product to perform waveform cross-correlation, thus maximizing the similarity between waveforms for a wide range of seismic phases. Correlations are accepted or rejected based on their significance level derived from the estimated time-bandwidth product. We have further developed an error model to estimate the a priori uncertainties in differential time measurements in order to facilitate their inclusion with bulletin arrival time picks in the HDC algorithm. We demonstrated that differential times contribute to significant improvements in resolving the relative event locations in the HDC analysis and validated the cross-correlation differential time measurement model.

We have processed some 90 event clusters from all over the world, producing over 2,200 GT5 or better event locations at a high confidence level. The data set provides GT5 clusters in areas of the world previously devoid of GT5 reference events.

OBJECTIVE

The three year project has concluded. The objective of the research project was to produce new high-confidence ground-truth events of GT5 from an updated EHB (Engdahl et al., 1998) bulletin on a global scale. To accomplish this goal we developed a novel hybrid method, the HDC-RCA analysis, which identified new ground truth event locations without reliance on dense local networks or prior GT information.

RESEARCH ACCOMPLISHED

During the course of this project we developed, tested, and validated the hybrid HDC-RCA methodology to produce new GT5 or better locations from event clusters. We developed a novel, adaptive approach to waveform cross-correlation for improved differential arrival time measurements. Correlations are accepted or rejected based on their significance level derived from the estimated time-bandwidth product. Even a fraction of differential times can lead to significant improvements in resolving the relative event locations in the HDC analysis. Over 3,000 differential times improved the HDC event patterns of 15 clusters.

We processed 86 event clusters from around the world, producing over 2,200 GT5 or better locations at a high confidence level. The data set provides clusters of GT5 events in areas of the world previously devoid of GT5 reference events. Furthermore, by exploiting the GT5 event locations, we produced some 5,000 empirical path corrections relative to the iasp91 (Kennett and Engdahl, 1991) model, which may be used to validate 3D global velocity models.

HDC-RCA Analysis

To generate new GT5 events we developed the two-step HDC-RCA methodology. Hypocentroidal decomposition (Jordan and Sverdrup, 1981; Bergman and Engdahl, 2007) determines accurate event location patterns relative to a provisional hypocentroid using regional and teleseismic phases. Reciprocal cluster analysis (Bondár et al., 2005, 2006, 2007), using local phases only, determines the accurate location of the cluster centroid by keeping the event and station patterns fixed. Since regional and teleseismic data usually lack the resolution to resolve the full depth pattern in a cluster, event depths are typically fixed in the HDC analysis to a best educated guess, based on analysis of individual events with depth phases, waveform analyses, or prior local data. The HDC analysis produces accurate relative locations, and updates the phase identifications so that they are consistent with the fixed depth and ak135 (Kennett et al., 1995) predictions. In the RCA analysis we propagate the relative location uncertainties from the HDC results to the RCA error budget so that events with large relative errors (location and origin time) are down weighted. We assume 0.5 root mean square (RMS) second reading error for local P phases (P, Pb, Pg, Pn), and 0.9 second RMS reading error for local S (S, Sb, Sg, Sn) phases. If there are no close-in stations to the centroid, we only solve for the horizontal shift of the cluster centroid (2 unknowns) by keeping the depths and origin times fixed to the HDC results; otherwise we solve for all model parameters (horizontal, vertical, and origin time shifts, 4 unknowns). The RCA step is generally over determined (only 2 to 4 unknowns). It is imperative to use local velocity models, especially for the depth inversion. We then shift the entire cluster to eliminate the bias in the HDC cluster centroid location. Finally, in order to obtain absolute location uncertainties, the uncertainties in the hypocentroid are combined with the relative location uncertainties of individual events and scaled to the 95% confidence level.

We developed applicability criteria for RCA, which serves as an a priori test to decide if it is worth trying RCA at all. We found that the combined secondary azimuthal gap (defined as the largest secondary azimuthal gap when considering the azimuths of all event-station pairs) provides a robust metric that predicts the location accuracy of the cluster centroid. The necessary conditions below provide GT5 applicability criteria for the cluster centroid, analogous to the GT5 criteria of Bondár et al. (2004) for single-event locations.

- The combined secondary azimuthal gap is less than 140°.
- There are at least 25 station-event pairs.

The hypocentroid depth can only be resolved at a high confidence level if there are close-in stations in the cluster. If a cluster fails to satisfy the above criteria, we reject the entire cluster. We consider these criteria necessary (but not sufficient) conditions to generate GT5 events. Once the absolute location of the cluster centroid is pinned down with high accuracy, we promote events to GT5 category if the semi-major axis of their combined absolute error ellipses (HDC+RCA), scaled to the 95% confidence level, is less than 5 km. It should be noted that failing the GT5 applicability criteria does not mean that the locations are wrong; it only means that the cluster centroid cannot

be recovered with GT5 accuracy at high confidence. In many cases the cluster centroid (and thus many of the events in the cluster) could still qualify for GT10.

Since we promote locations to GT5 status based on the size of their absolute error ellipses, it is important that both the HDC relative error ellipses and the RCA absolute error ellipse on the centroid are reliable and provide the actual coverage claimed by their confidence level.

One of the fundamental assumptions in the RCA algorithm is that HDC accurately recovers the event pattern. To validate this assumption we performed HDC on the Pahute Mesa, Nevada Test Site (NTS) cluster of 52 GT0 events. HDC, using regional and teleseismic phases with ak135 (Kennett et al., 1995) travel-time tables, mislocated the event centroid by 12 km. Figure 1 illustrates that when the HDC bias is removed, the HDC event pattern (blue dots) matches the true event pattern (green dots) quite well, and the HDC relative 90% confidence error ellipses provide almost 90% coverage as expected.

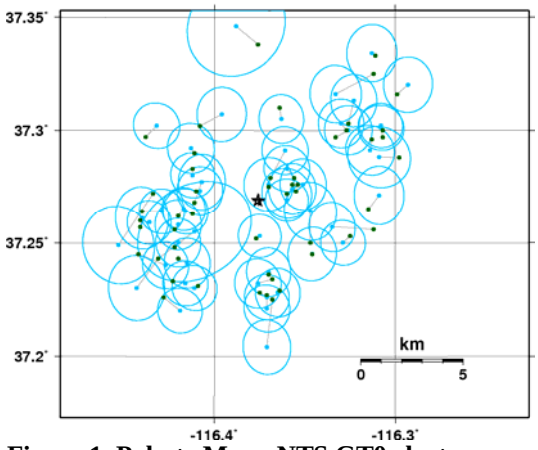

Figure 1. Pahute Mesa, NTS GT0 cluster. When the HDC location bias is removed, the HDC (blue) relative error ellipses cover 90% of the true (green) locations.

As we noted earlier, RCA eliminates the regional/teleseismic bias in the HDC hypocentroid. However, RCA is still prone to local bias due to unmodeled local velocity structure. We account for travel-time prediction errors inherent in a local velocity model by introducing generic, distance-dependent model errors, as plotted in Figure 2a. To validate that 1) the true event centroid is located within 5 km of the event centroid recovered by RCA, and 2) the RCA error ellipse covers the true centroid 95% of the time we again used the Pahute Mesa GT0 cluster. Since this time we are only interested in RCA performance and the effect of the local velocity model, we start from the true event pattern with no relative errors at all (i.e., we used the GT0 locations as the initial locations for RCA). We used the Western US velocity model by Ritsema and Lay (1995) and performed a bootstrapping RCA experiment by selecting near-optimal subnetworks with an increasing number of stations from the local network shown in Figure 2b.

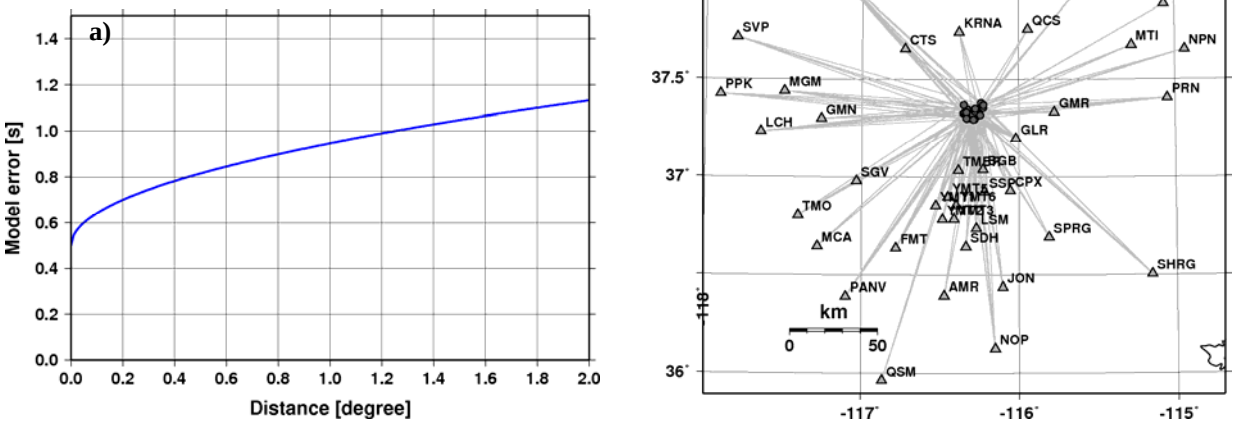

Figure 2. a) Distance dependent model error curve employed in RCA to account for local unmodeled travel-time prediction errors. b) Local network for the GT0 Pahute Mesa cluster used in subnetwork boostrap exercise.

The results are summarized in Figure 3. The local velocity model introduces a bias of about 2 km. While the event centroid mislocations are all less than 5 km (Figure 3b), the introduction of local model errors is necessary to

achieve 95% coverage. For the four cases where the centroid mislocation is larger than 5 km (orange dots in Figure 3a) the semi-major axes of the 95% error ellipses is also larger than 5 km, thus the semi-major axes of the absolute error ellipses of the individual events would also be too large to promote any events to GT5 status. Green triangles denote the bootstrap realizations for which events would be promoted to GT5 status. Blue dots represent the cases of missed GT for which the location is well within 5km, but the error ellipse is too large to be identified as GT5. This is consistent with our conservative approach to minimize the number of false alarms. In other words, we would rather loose some GT5 events than promote non-GT events to GT5 status.

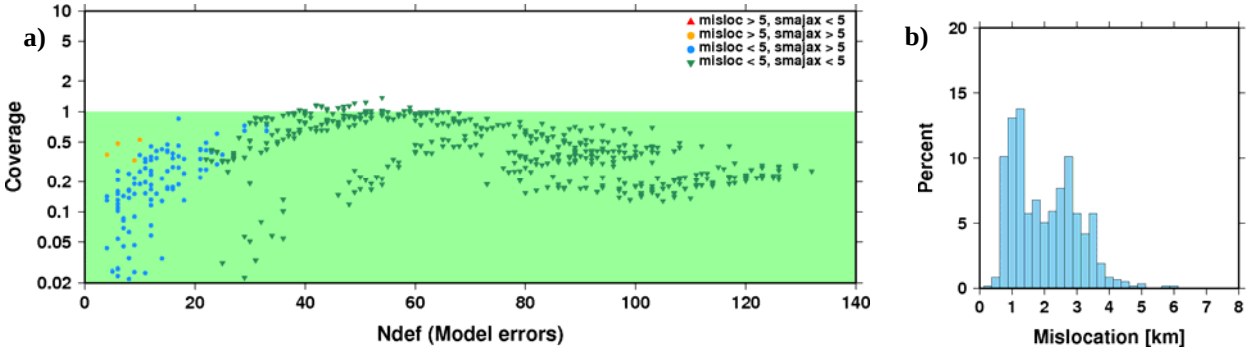

Figure 3. Results of subnetwork bootstrap exercise. a) The RCA error ellipses provide 95% coverage when local model errors are included. b) Except for 4 cases, the event centroid recovered by RCA is within 5 km of the true location.

Another assumption the RCA algorithm depends upon is that the observations are independent. With dense local networks, such as the one in Figure 2b, there is always a chance that similar ray paths produce similar travel-time prediction errors due to unaccounted local velocity heterogeneities. Thus, by ignoring the correlated error structure, the location uncertainties are underestimated. Indeed, when using the entire network (Figure 2b), the stations south of the cluster conspire to pull the RCA centroid slightly to the southeast, and the 95% absolute error ellipses (combined HDC and RCA location uncertainties) do not cover 95% of the true locations. However, when we use a subnetwork (Figure 4c) with a still acceptable combined secondary azimuthal gap, the 95% error ellipses do cover GT0 locations (Figure 4b) because the network now better satisfies the assumption of independent errors.

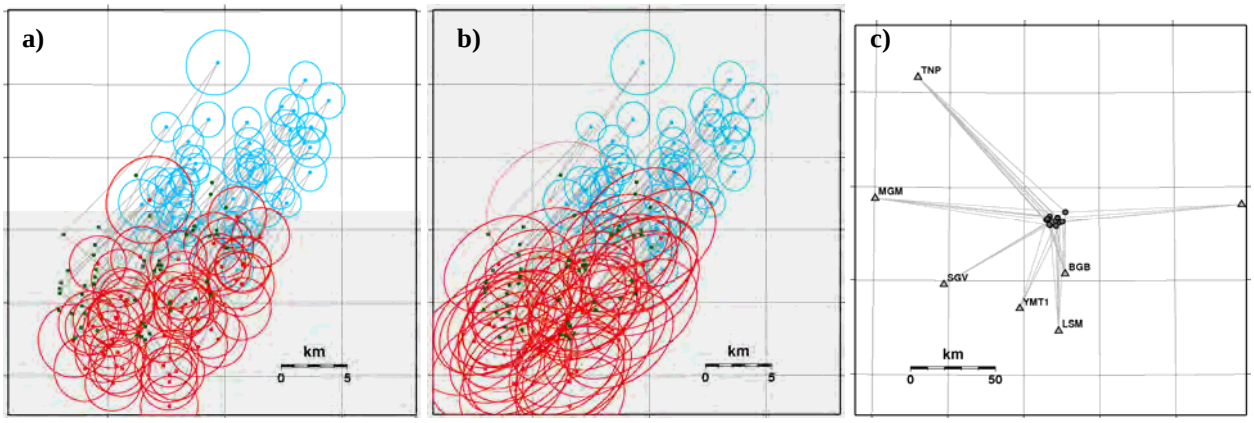

Figure 4. a) RCA results when using all stations in the local network shown in Figure 2b. Blue – HDC, red – RCA, green – GT0 locations. While the RCA event mislocations are about 3 km, the 95% error ellipses do not cover the GT0 locations. b) RCA results using the subnetwork in 4c. The error ellipses now cover the true locations, and 50 out of 52 events are identified as GT5.

Figure 4 conveniently allows us to make another important point. Since not every station recorded every event, had we had only the sparse seven-station network in Figure 4c, we could have only located four events with a conventional single event location algorithm. RCA, on the other hand, used 7 stations and 13 events to determine the HDC location bias which located all events within 5 km of GT0 and identifies 50 (out of 52) locations as GT5. Thus, in favorable conditions RCA may produce GT5 or better locations with sparse local networks.

Waveform Correlation

Significant sources of uncertainty in HDC relative locations are arrival-time measurement errors. Improvements in the HDC results may be obtained by using precise and accurate differential times from cross-correlations, either by picking the lag of the maximum from a time-domain correlation or by measuring the phase when using a cross-spectral approach (see Schaff et al., 2004 for a comparison of the techniques).

To apply the waveform cross-correlation methodology that has been very successful at local distances to regional and teleseismic data sets, we had to address several challenges. Central to exploiting the results of waveform cross-correlation is the selection of a correlation threshold. In most local applications (e.g., Schaff et al., 2004; Shearer, 1997) a heuristic approach is used to select an operational correlation threshold that was then demonstrated to be fairly robust at screening out the less reliable differential measurements. The relative uniformity of these data sets (all simple local P arrivals, typically only involving single or three-component short period data) allowed for the selection of a single uniform correlation threshold without adversely affecting the results. In our automated application, the regional and teleseismic recordings consisted of very diverse sets of stations, including single- and three-component stations as well as regional and teleseismic arrays. Data were collected from short period and broadband sensors with various responses and noise characteristics. Furthermore, regional and teleseismic recordings include a wide range of time-defining phase types (P, Pg, Pb, Pn, Sg, Sn) with varying signal bandwidths, durations and signal-to-noise ratios. Given the wide variety of time-bandwidths applicable to our data set, no single applicable correlation threshold was found.

In order to apply waveform correlation processing to a wide variety of signal bandwidths, durations, and instrument types, we developed several novel solutions. First, instead of setting an arbitrary threshold for the correlation coefficient, we measure the strength of correlation by its statistical significance. The significance of a correlation is defined as the significance level at which we can reject the hypothesis that we are correlating noise with noise in the measured time-bandwidth product (Bondár et al, 2006). This allows us to retain differential time measurements from correlation runs where the absolute correlation level might otherwise fall below the correlation threshold. In other words, a relatively low correlation may still be highly significant if the time-bandwidth product is large.

Instead of a single a priori filter and time-window we compute correlations from a suite of time-windows and a filter bank. Following Harris (1991), we measure the empirical time-bandwidth product and renormalize the maximum correlation to a value corresponding to a reference fixed time-bandwidth product. The renormalization allows us to bring all cross-correlation results into a common frame and thus set a single significance threshold. We set the reference target time-bandwidth product at 240, in which the 99.5% significance level corresponds to a correlation of 0.15. This time-bandwidth product is typical for regional arrays. Note that in a much narrower time-bandwidth of 15, which refers to parameters typically used in local cross-correlation analysis, the correlation at the same significance level would be 0.7. To optimize the significance, we compute cross-correlations over a suite of multiple filter bands and durations and then estimate the time-bandwidth for each. From the suite of cross-correlations (with different time-bandwidth products) we select the trace with the most significant renormalized correlation to measure the differential time. Alternatively, we stack the correlation suite using inverse-variance weighting, renormalize the stacked trace, calculate the significance of the maximum renormalized correlation, and if it is above the significance threshold we measure the differential time on the stacked, renormalized trace. In practice we find using the “best” correlation trace provides measurements of the differential time (less cycle skipping) as reliable as using the stack.

Figure 5 shows the distribution of “best” correlations for teleseismic P and regional Pn arrivals, i.e., those filter-band and duration combinations that yielded the highest maximum renormalized correlation above the significance threshold. As expected, the peak in the P distribution is for a short window (2.5 seconds) and the 0.8–4.5Hz filter bands. However, a large proportion (> 85%) of the correlations were optimal for a wide variety of other filter band and duration combinations, indicating that there is no single optimal filter-duration combination for all teleseismic P arrivals. The same is true for regional Pn phases.

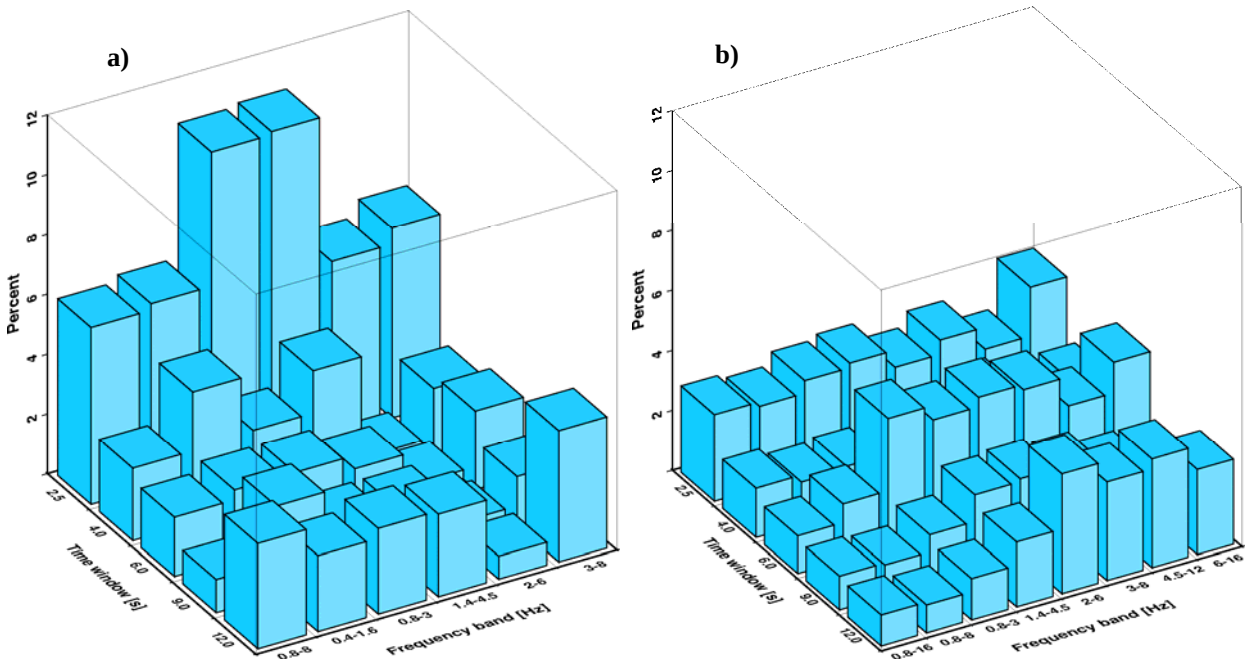

Figure 5. Histograms of best correlations in various time windows and frequency bands that yielded the highest maximum correlations above the significance threshold for teleseismic P (a) and regional Pn (b). There is no single a priori preferable filter and time window for either teleseismic P or regional Pn.

The HDC algorithm was modified to use differential time measurements along with arrival times. Because HDC now mixes the arrival and differential times, it is important to define the proper relative weighting between the arrival and differential data. This is achieved by assigning realistic measurement uncertainties to both the absolute arrival and differential times obtained from the correlation processing. Our measurement error model for differential times was empirically derived and has a power-law dependency on the renormalized Fisher Z-statistic.

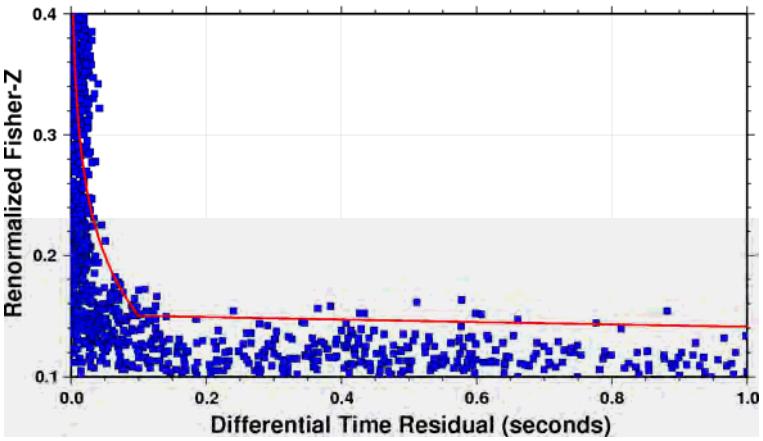

Figure 6. Differential time error model for renormalized correlations corresponding to the time-bandwidth product of 240 (typical for regional arrays). Data were re-sampled to 200 Hz prior to cross-correlation. Correlations below 0.15 (a significance level of 99.5%) are rejected.

A major challenge to quantitatively assessing a measurement error model is the lack of very accurate ground truth information, particularly for earthquake clusters, which form the bulk of the data considered in this project. To address this, we conducted a reciprocal experiment where we used clusters of seismic events (Kola Peninsula, Lop Nor and two Asian earthquake clusters) recorded at regional and teleseismic distances at arrays. We treated each cluster of events as a pseudo-array and treated the array elements as GT0 events. Figure 6 shows the distribution of maximum correlations (presented as the renormalized Fisher-Z value, corresponding to a time-bandwidth product of 240) as a function of the differential time residual. The curve in red is our derived measurement error model for $Z \geq 0.15$:

$\sigma_{\delta\tau} = \max\left(0.1 * 2^{-(z-0.15)/0.05}, 0.005\right)$. Note that differential time errors cannot be smaller than the sampling interval (as we perform cross-correlation processing in the time domain, we resample the waveforms at 200 Hz).

Figure 7 demonstrates the utility of using differential times in HDC processing. The figure shows the HDC locations for the Scotty's Junction, Nevada cluster without (Figure 7a) and with (Figure 7b) 396 differential P, Pn and Sn times. Note that the number of differential times is small compared to the 4199 bulletin picks. Even though less than 10% of the data are differential time measurements, due to their preferential weighting they yield tighter clustering of event locations and sizeable reductions in relative location uncertainties.

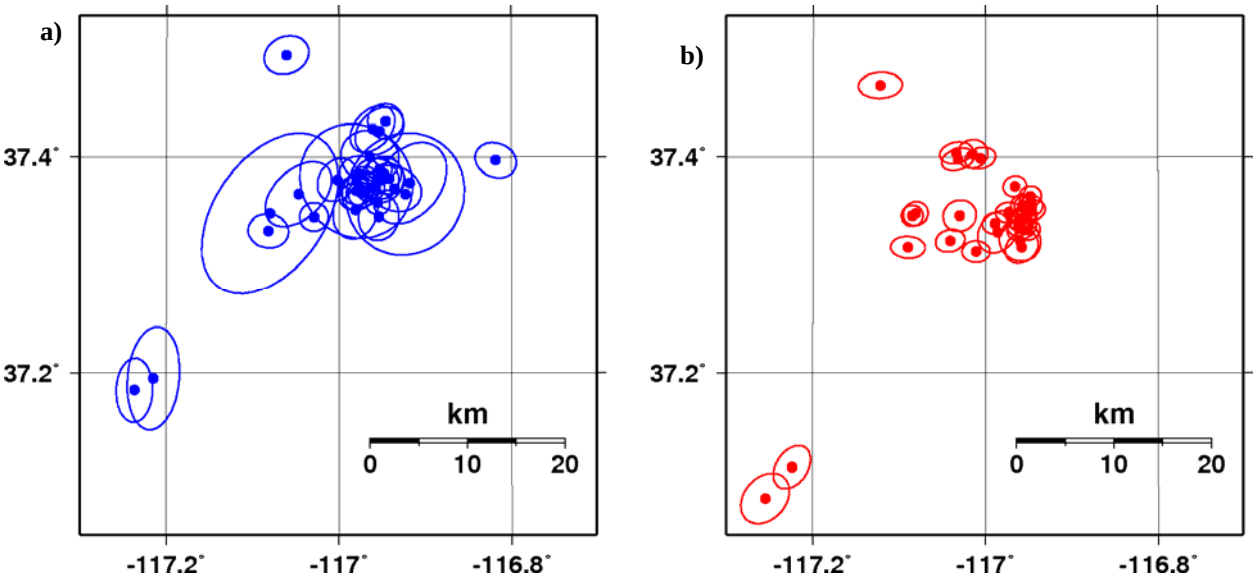

Figure 7. HDC locations for Scotty's Junction, Nevada, cluster when using a) bulletin picks only and b) both bulletin data and differential times. Even a small proportion of differential times improves the event pattern and reduces relative location uncertainties.

Figure 8 shows the distribution of *a posteriori* differential time residuals for both the bulletin picks (blue) and differential times obtained from cross-correlation processing (red). When cross-correlation differential times are used in the HDC analysis (Figure 8b), HDC obtains a much tighter fit to the cross-correlation differential times, without distorting the distribution of bulletin differential residuals.

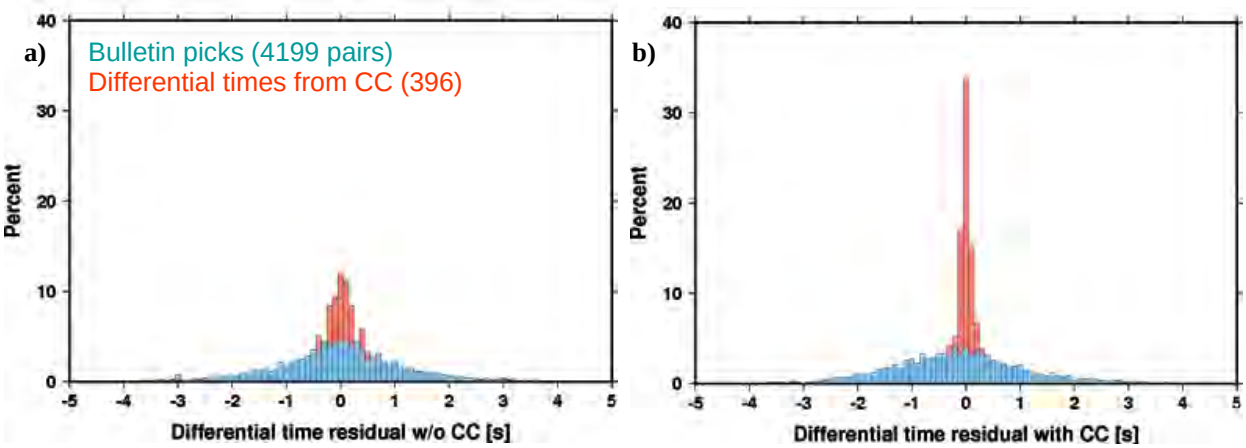

Figure 8. *A posteriori* distributions of differential time residuals of bulletin picks (blue) and those from waveform correlation (red) when using a) bulletin picks only and b) both bulletin data and differential times from cross-correlation analysis. The distribution of differential residuals derived from bulletin picks is nearly identical for both cases.

HDC-RCA Example

The Rogun, Tajikistan, cluster is located between the South Tien Shan and the Northern Pamir mountains. This region is characterized by the shallow seismicity along the Vaksh and Darvaz faults (Pegler and Das, 1998). The

HDC cluster (Figure 9a) consisted of 24 events with 376 regional/teleseismic stations. Altogether 13 events recorded by only 3 stations passed the RCA connectivity tests (Figure 9b). Even though we had only 3 stations, the geometry is so favorable that the combined secondary azimuthal gap was 110°. We used a local velocity model by Hamburger et al. (1993) to predict travel-times for the 44 Pg and Sg readings. Since we had no close-in stations, we ran RCA with a fixed depth solution (hypocentroid depth at 12 km). RCA shifted the entire cluster to the Vaksh river valley (Figure 7c) which is the surface expression of the Vaksh fault. The HDC-RCA analysis resulted in 17 GT5 events.

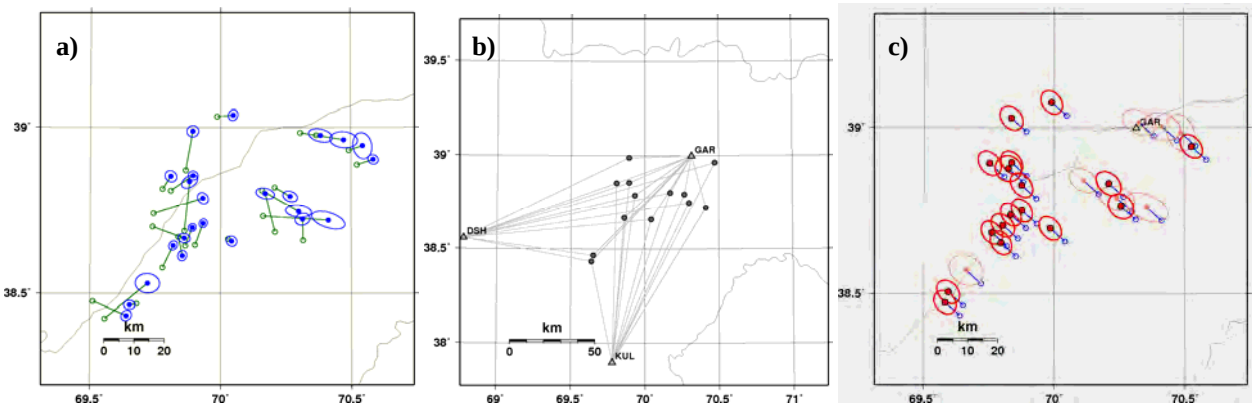

Figure 9. Rogun cluster, Pamir Mountains. a) HDC (blue) improves the event pattern with respect to the EHB single-event (green) locations. b) RCA geometry. c) RCA aligns the cluster with the Vaksh river valley.

The real strength of the HDC-RCA methodology is manifested when only a few local stations are available. Richards et al. (2006) point out that in order to achieve improved locations for more than 25% of the events in a cluster using the double-difference algorithm with differential times from waveform cross-correlation, a high local station density (one station per 100 km^2 and about 12-km distance between stations) is required. Because of the natural separation of tasks in the HDC-RCA methodology (HDC resolves the event pattern using regional and teleseismic stations, RCA reduces the bias in the hypocentroid using local data), the applicability of RCA is not restricted by such strong conditions on station density. As long as the RCA geometry is favorable, HDC-RCA is capable of producing GT events even with very sparse local station coverage.

CONCLUSIONS AND RECOMMENDATIONS

During the course of the project, we have developed a novel multiple event location method, the hybrid HDC-RCA algorithm. We have shown that HDC-RCA neither relies upon the existence of dense local networks, nor upon the existence of prior GT information. GT5 events identified by HDC-RCA are consistent with previously determined GT information. The methodology is capable of producing GT5 or better events from event clusters where other methods would not.

We applied our cross-correlation methodology to all clusters for which waveform data could be obtained at regional and teleseismic distances. We collected waveforms from both International Monitoring Station network stations and from the Incorporated Research Institutions for Seismology waveform repository for as many event-station pairs as possible. Altogether we processed about 870,000 pairs of arrivals from 47 clusters yielding about 9,200 significant correlations. We used the differential time measurements in HDC analysis for 15 clusters. For these 15 clusters, the large scale correlation processing produced 4,709 significant correlations, and thus accurate differential time measurements, of which 3,624 were used in the HDC analysis after outlier rejection.

We processed 86 clusters with the hybrid HDC-RCA analysis. Most of the clusters were extracted from an updated EHB (Engdahl et al., 1998) bulletin while in a few cases we added local data (e.g., aftershock deployments) not reported to the International Seismological Centre. We primarily focused on areas with sparse local networks. These are regions where the HDC-RCA methodology shows its real strength compared to other multiple event location methods. Our objective was to achieve a balanced global coverage of GT5 events. We also re-analyzed several classic clusters for additional cross-validation with past work (e.g., Racha). Figure 10 shows the geographic distribution of event clusters. From the 86 event clusters, 66 clusters produced altogether 2,279 GT5 or better events. We delivered the complete catalog (CSS tables) of over 3,000 event HDC and RCA locations, phase arrivals, selected path corrections, and waveforms.

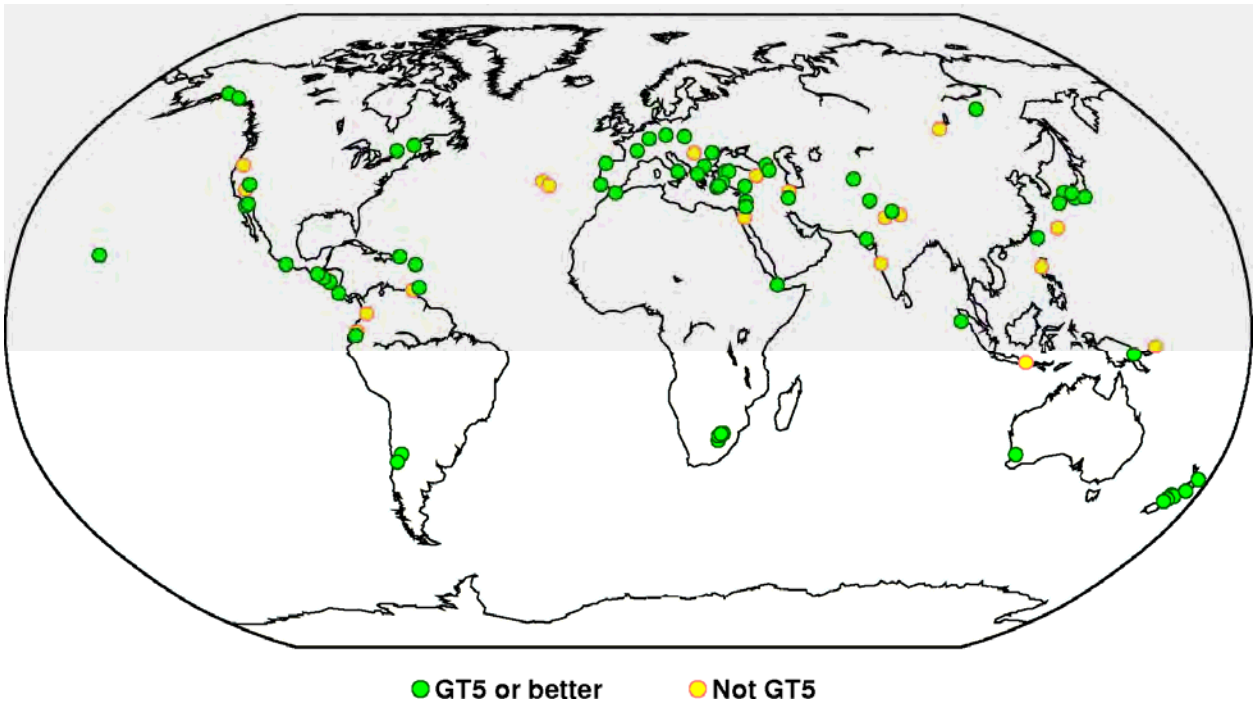

Figure 10. 86 event clusters processed during the course of the HDC-RCA GT5 project. 66 green dots represent clusters that produced GT5 or better event locations, yellow dots denote clusters that either failed the RCA applicability criteria or the 95% error ellipses were too large to promote any event locations to GT5.

REFERENCES

Bergman, E.A. and E.R. Engdahl (2007). Multiple event relocation for reference seismic events, in preparation.

Bondár, I., S.C. Myers, E.R. Engdahl, and E.A. Bergman (2004). Epicentre accuracy based on seismic network criteria, *Geophys. J. Int.* 156: 1–14, doi: 10.1046/j.1365-246X.2004.02070.x.

Bondár, I., B. Kohl, E. Bergman, K. McLaughlin, H. Israelsson, Y-L. Kung, P. Piraino, and E.R. Engdahl (2005). Global ground truth data set with waveform and improved arrival data, in *Proceedings of the 27th Seismic Research Review: Trends in Nuclear Explosion Monitoring*, LA-UR-05-6407, Vol. 1, pp.289–298.

Bondár, I., B. Kohl, E. Bergman, K. McLaughlin, H. Israelsson, Y-L. Kung, J. Given, and E. R. Engdahl (2006). Global ground truth data set with waveform and improved arrival data, in *Proceedings of the 28th Seismic Research Review: Ground-Base Nuclear Explosion Monitoring Technologies*, LA-UR-06-5471, Vol. 1, pp. 359–367.

Bondár, I., E. Bergman, E.R. Engdahl, B. Kohl, Y-L. Kung, and K. McLaughlin, (2007). A hybrid multiple event location technique to obtain ground truth event locations, submitted to *Geophys. J. Int.*

Engdahl, E. R., R. D. van der Hilst, and R.P. Buland (1998). Global teleseismic earthquake relocation with improved travel times and procedures for depth determination, *Bull. Seism. Soc. Am.* 88: 722–743.

Hamburger, M. W., W.A. Swanson II, and G.A. Popandopulo (1993). Velocity structure and seismicity of the Garm region, Central Asia, *Geophys. J. Int.* 115: 497–511.

Harris, D.B. (1991). A waveform correlation method for identifying quarry explosions, *Bull. Seism. Soc. Am.* 81: 2395–2418.

Jordan, T.H. and K.A. Sverdrup (1981). Teleseismic location techniques and their application to earthquake clusters in the south-central Pacific, *Bull. Seism. Soc. Am.* 71: 1105–1130.

Kennett, B. L. N. and E. R. Engdahl (1991). Travel times for global earthquake location and phase identification, *Geophys. J. Int*., 105, 429–465.

Kennett, B. L. N., E. R. Engdahl and R. P. Buland (1995). Constraints on seismic velocities in the Earth from travel times, *Geophys. J. Int*. 122: 108–124.

Pegler, G. and S. Das (1998). An enhanced image of the Pamir-Hindu Kush seismic zone from relocated earthquake hypocentres, *Geophys. J. Int.* 134: 573–595.

Richards, P. G., F. Waldhauser, D. Schaff, and W-Y Kim (2006). The applicability of modern methods of earthquake location, *Pure appl. geophys*. 163: 2–3, 351–372, doi: 10.1007/s00024-005-0019-5.

Ritsema, J. and T. Lay (1995). Long-period regional wave moment tensor inversion for earthquakes in the western United States, *J. Geophys. Res.* 100: 9853–9864.

Schaff, D., G. H. R. Bokelmann, W. L. Ellsworth, E. Zanzerkia, F. Waldhauser and G. C. Beroza (2004). Optimizing correlation techniques for improved earthquake location, *Bull. Seism. Soc. Am.* 94: 705–721.

Shearer, P. (1997). Improving local earthquake locations using the L1 norm and waveform cross correlation: Application to the Whittier Narrows, California, aftershock sequence, *J. Geophys. Res.* 102: 8269–8283.

IMPROVED EVENT LOCATION UNCERTAINTY ESTIMATES

István Bondár, Keith McLaughlin, and Hans Israelsson

Science Applications International Corporation

Sponsored by Air Force Research Laboratory

Contract No. FA8718-05-C-0018

ABSTRACT

The objectives of this project are to develop, test, and validate methodologies that improve location uncertainties in the presence of correlated, systematic model errors and non-Gaussian measurement errors. Un-modeled lateral heterogeneity in the Earth introduces systematic correlated travel-time errors that bias locations derived from unbalanced networks. Furthermore, emergent arrivals, noise bursts, and other blunders introduce non-Gaussian errors not properly modeled by standard least-squares location procedures.

In the previous year we presented a method based on copula theory to estimate the spatial correlation structure in arrival-time data. Based on these models, we have incorporated the full covariance matrix weighting into a standard linearized least-squares location algorithm. We have developed and validated generic variogram models (regional and teleseismic) using globally distributed clusters of GT5 events identified by the Global Ground Truth project (FA8718-4-C-0020). These models may be used as conservative correlation estimators to generate the full data covariance matrix for regions where there are insufficient data to estimate a variogram. We have demonstrated improvements in both locations and uncertainty estimates by accounting for correlated, Gaussian errors. While un-modeled location biases remain, location estimates are less sensitive to unbalanced network configurations. Coverage statistics are significantly improved for a wide range of number of defining phases with the improved error ellipses.

We have refined and tested our signal-to-noise ratio (SNR)-based measurement error model and developed a measurement error model using body wave magnitude (mb) as a substitute for SNR. We have incorporated both measurement error models into our standard linearized iterative least-squares algorithm. The increased variance and bias (late pick) for small events is quantified as a family of distributions dependent upon observed or expected SNR. Since the measurement errors now describe a non-Gaussian model, the standard least-squares location algorithm may no longer be optimal.

Our research now focuses on exploring alternative objective functions (l_p-norms) and regression algorithms that exploit both the spatial correlation models and the new non-Gaussian error models for improved location uncertainties. We show Monte Carlo comparisons contrasting Gaussian and non-Gaussian skewed distributions. A preliminary network geometry stability or quality criteria is proposed that predicts the sensitivity to non-Gaussian errors.

OBJECTIVES

The objectives of this project are to develop methodologies to estimate location uncertainties in the presence of correlated, systematic model errors and to characterize non-Gaussian measurement errors as a function of signal parameters such as SNR or network magnitude, a surrogate for SNR. The improved understanding of a correlated Gaussian error budget described by a full covariance matrix is now incorporated into a linearized location algorithm leading to more robust estimates of location uncertainty. The ultimate goal of this project is to develop transportable Gaussian and non-Gaussian error models that will provide reliable location uncertainty estimates for small events recorded by sparse or dense, balanced or imbalanced networks.

RESEARCH ACCOMPLISHED

The motivation for this project is the observation that location uncertainty estimates are often underestimated; error ellipses scaled to the 90% confidence level do not contain 90% of the true locations. This is due to violation of the assumptions of normally distributed independent observations commonly made by standard linearized location algorithms. Due to unaccounted velocity heterogeneities, similar ray paths produce systematic travel-time prediction errors and lead to correlated error structures. Furthermore, picking residuals are non-Gaussian and better described by skewed, heavy-tailed distributions. Phase picks suffer from systematic errors as onset times along the same ray paths are systematically picked late with decreasing event size, or more precisely, with decreasing SNR (e.g., Douglas et al., 1997, 2005a, 2005b). Douglas et al. (2005a) point out that automatic detections are more likely affected by the systematic errors than are manual picks made by experienced analysts. These systematic reading errors introduce location biases for smaller events.

In this project we focus on the treatment of correlated errors combined with non-Gaussian, non-zero-mean, heavy-tailed, skewed distributions of reading errors. Figure 1 illustrates our research strategy. During the first year of the project (Bondár et al., 2006a), we developed a new, copula-based methodology to estimate variograms. The variogram models were used to construct the network covariance matrix, which describes the correlated travel-time structure due to un-modeled path effects along similar ray paths. We incorporated the full data covariance matrix into an existing linearized iterative least-squares (ILS) algorithm and demonstrated improvements both in location and coverage with increasing numbers of defining phases or imbalanced networks. This year we concentrated our efforts on developing improved models of picking error bias and variance as a function of SNR and network magnitude. By exploiting new ground truth events produced by our related GT project (Bondár et al., 2007), we have developed generic, transportable variogram models for regional Pn and teleseismic P phases that can be used to construct network covariance matrices anywhere on the globe.

Baseline		*Year 1*		*Year 2*		*Year 3*	
Pick Error	*Model Error*	*Pick Error*	*Model Error*	*Pick Error*	*Model Error*	*Pick Error*	*Model Error*
Normal IID	Normal IID	Normal IID	Correlated Normal Specific variogram models	Non-Normal SNR/mb dependent bias and variance	Correlated Normal Generic variogram models	Non-Normal SNR/mb dependent bias and variance	Correlated Normal Generic variogram models
Linearized ILS inversion (diagonal covariance matrix)		**Linearized ILS inversion with full covariance matrix**		**Linearized ILS inversion with correlated errors with full covariance matrix and pick bias as travel-time correction**		**Monte Carlo-based hypothesis tests with correlated errors–validity of coverage ellipse given linearized approach–alternative Lp norms**	

Figure 1. Progress and strategy of research. Gray indicates existing state of the art, Green completed work, and Yellow future work. Year 1 culminated in an ILS algorithm that utilized a full covariance matrix based on new variogram models for improved location uncertainty. Year 2 completed validation tests for implementation of new picking error models and new generic variogram models.

Measurement Error Models

It has long been noted that arrival time errors depend on SNR (Freedman, 1966; Lomnitz, 1995). Low SNR arrival times tend to be read late and have increasing variance (Douglas et al., 2005b). Lateness in low SNR readings is not accounted for in standard locations of seismic events. However, arrival times for a given event read at stations with varying SNRs may, as Douglas et al. (2005b) point out, contribute to bias in the epicenter estimate. Delays in arrival readings have not been accounted for simply due to lack of reported SNR. Indeed, as Douglas et al. (2005b) observe, few actual estimates of reading error characteristics—delay, variance, distributions - have been published. Digital recording with associated automatic processing affords opportunities to characterize reading errors as a function of SNR as well as other signal attributes. For example, the International Data Centre (IDC) employs *a priori* variances for arrival time variance as a function of SNR—for both automatic and analyst picks; the SNR is defined as the ratio of the short-term average/long-term average of the detecting beam. The IDC makes, however, no assumption about lateness or bias in arrival times. Figure 2 illustrates that once path effects are removed, a trend of increasingly late picks with decreasing event size emerges.

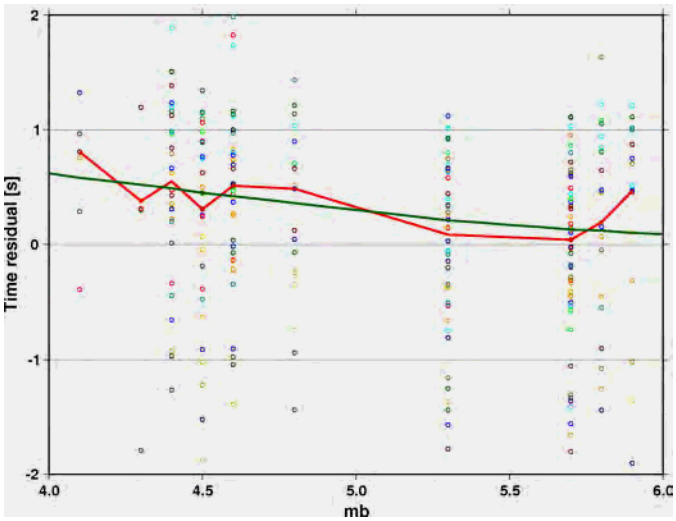

Figure 2. Median Pn station residuals with regard to GT0 locations of Yucca Flat explosions from CUB2 model predictions. Picks are systematically late with decreasing event size.

SNR-based picking error model

Our goal is to develop improved models of both bias and variance in reading errors as a function of SNR. To accomplish this goal, we follow a double-difference approach. We assume that arrival times with corresponding SNR estimates from a network of stations are available from an event cluster of GT events. We write the arrival time at station *i* from event *x* as $t_{ix} = OT_x + t_{ix}^{pred} + t_i^{path} + t_{ix}^{delay} + \varepsilon_{ix}$, where OT_x is the origin time of event x, t_{ix}^{pred} is the predicted (IASPEI91) travel time, t_i^{path}, is the path effect (station term), t_{ix}^{delay} is the pick delay and ε_{ix} is a random picking error. We assume only t_{ix}^{delay} and ε_{ix} are functions of SNR_{ix}. By forming selected double differences, the origin times and systematic station terms may be canceled:

$$(t_{ix} - t_{iy}) - (t_{jx} - t_{jy}) - (t_{ix}^{pred} - t_{iy}^{pred}) + (t_{jx}^{pred} - t_{jy}^{pred}) = (t_{ix}^{delay} - t_{iy}^{delay}) - (t_{jx}^{delay} - t_{jy}^{delay}) + (\varepsilon_{ix} - \varepsilon_{iy}) - (\varepsilon_{jx} - \varepsilon_{jy})$$

The right hand side of the equation can be calculated from the observed arrival times and the predicted travel times. The mean delay and the total variance (assuming that the travel-time prediction errors are more or less the same) are written as $\mu^{delay}(SNR) = (t_{ix}^{delay} - t_{iy}^{delay}) - (t_{jx}^{delay} - t_{jy}^{delay})$, and

$Var^{total} = 4Var_{hypo} + Var(SNR_{ix}) + Var(SNR_{iy}) + Var(SNR_{jx}) + Var(SNR_{jy})$.

For sufficiently large SNR values we assume the pick delay and its variance approach zero. Thus, if all four readings have large SNR, the total variance gives us an estimate of the model error variance. This allows us to get an estimate of the variance of reading errors when all four readings have small SNR:
$Var(SNR) \to (Var^{total} - 4Var_{hypo}^{large SNR})/4$. Now let us presume that three of the readings have large SNR, and one has a small SNR. Then the mean delay simply becomes $\mu^{delay}(SNR) \to t^{delay(SNRsmall)}$. Hence, the double-difference (DD) approach, with proper data selection, provides a methodology to derive models of bias and variance in picking errors.

To establish SNR-dependent models of delay and variance, we used first-arriving P from 12 HDC-RCA clusters (see Bondár et al., 2006b, 2007) with SNR ≥ 3 reported in the PIDC/IDC REB. We calculated all possible DDs in

each cluster and selected two subsets for each cluster. One subset consisted of the DD residuals for which the SNRs of all four arrivals were within a factor of 2. Figure 3a shows the DD residuals for this subset as a function of median SNR, as well as the scaled median absolute deviation (SMAD) of residuals along moving SNR windows. The other subset included DD residuals with the three largest SNR ≥ 40. The DD residuals are plotted as a function of minimum SNR in Figure 3b. The running median (dashed curve) is the estimate of reading error bias as a function of SNR.

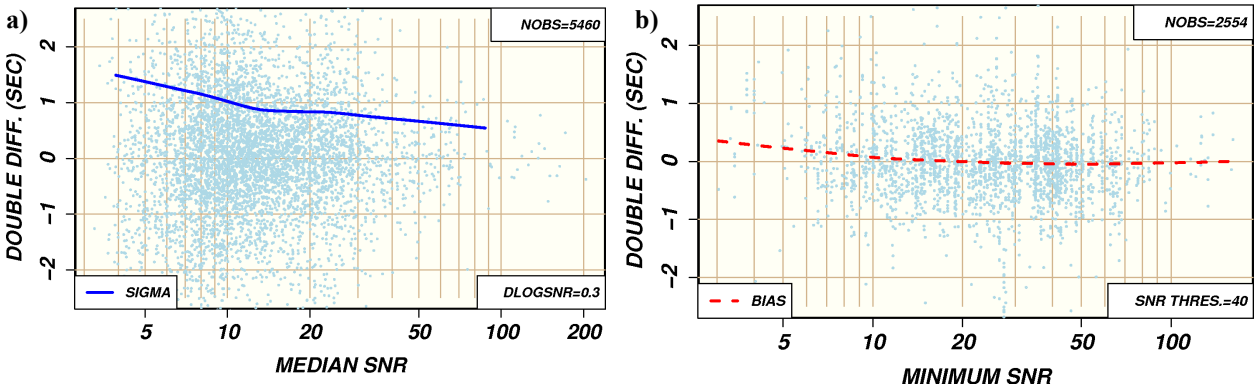

Figure 3. a) DD residuals where all four SNR are similar. The running SMAD (blue curve) represents the estimate of total variance. b) DD residuals where the SNR of three arrivals is large and the SNR of one arrival is small. The running median (red) provides an estimate of the reading error bias.

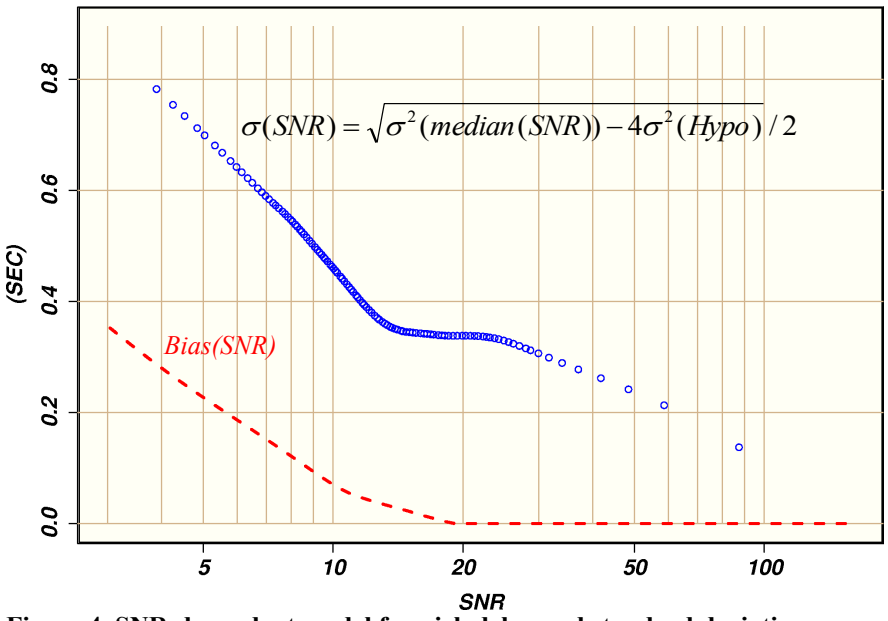

Figure 4. SNR-dependent model for pick delay and standard deviation.

Recall that the running SMAD in Figure 3a is an estimate of the total variance in the DD residuals which includes the background variance of travel-time prediction errors. We estimate Var_{hypo} from the second subset as the variance of DD residuals where the minimum SNR is larger than 40. This gives us an estimate σ_{Hypo} = 0.24s which has to be removed from the total variance estimates in order to get an estimate of the reading error variance. Our resulting model for reading error bias and variance is shown in Figure 4.

In the linearized ILS location algorithm the bias is implemented as a travel-time correction, while the variance is added to the main diagonal of the network covariance matrix.

Note that the International Monitoring Station (IMS) being a sparse, teleseismic network, the SNR-based measurement error model is dominated by teleseismic P phases, which explains the relatively small delays even at very low SNR values. As Figure 2 suggests, delays are expected to be much larger for regional phases.

The mb-based picking error model

Currently only the IDC Reviewed Event Bulletin reports SNR estimates for arrival picks, and as we indicated above, there is insufficient data to derive SNR-based error models for phases other than teleseismic P. Thus, the SNR-based error model has a very limited scope for practical application. To develop a measurement error model that can be

used for the vast majority of events with no reported SNR estimates of phase arrivals, we decided to use network magnitude as a surrogate for SNR. Network magnitude is admittedly a crude surrogate for mb, but at least it is reported for most events.

We used events from Yucca Flat and Pahute Mesa with network magnitudes (4< mb < 6) reported in the International Seismological Centre (ISC) bulletin to derive mb-based models of reading error bias and variance. We fit the measurement error model for first-arriving P phases as a smooth function of epicentral distance and mb. Figure 5 shows our mb distance based model. Not surprisingly, the picking delay is largest at far regional distances. For teleseismic distances, the bias estimates are smaller and show good agreement with those predicted by the SNR-based model.

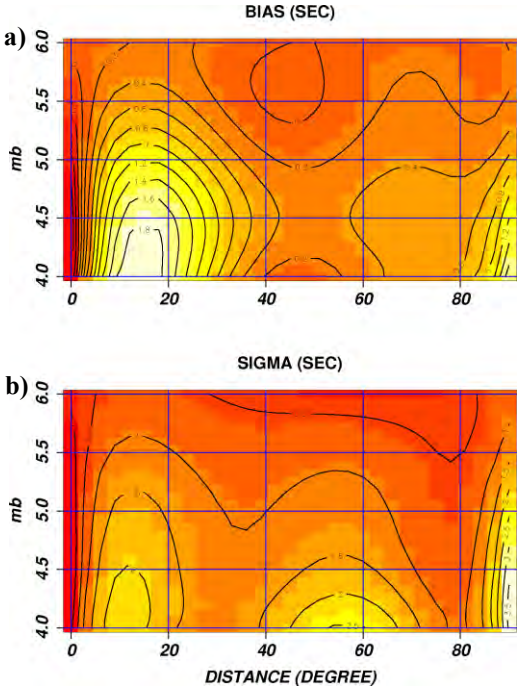

Figure 5. An mb-based model of bias (a) and variance (b) for reading errors.

Figure 5 suggests that the effect of phase pick delays on event locations with decreasing magnitude may be negligible for teleseismic networks, but cannot be ignored for local and regional stations. Note that the mb-based measurement error model assumes that path effects are largely accounted for; therefore they should properly be used in conjunction with source-specific station corrections (SSSCs) or other path corrections.

Figure 6 shows relocations of GT0-2 explosions from various event clusters with and without SSSCs and mb-delay corrections using regional Pn only. The SSSCs were calculated from CUB2 (Shapiro and Ritzwoller, 2004) travel-time predictions relative to IASPEI91 (Kennett and Engdahl, 1991) predictions. The calibrated travel times are primarily responsible for location improvements, although they suffer from some remaining regional biases. The effect of mb-delay corrections is less obvious, but nonetheless significant. The amplitude of the mb-delay corrections is much smaller than those from the SSSCs; therefore, they only move events by 1 or 2 kilometers maximum which is typically less than the accuracy of the GT0-2 event locations. However, they do tend to tighten event clusters, by moving smaller events closer to larger ones.

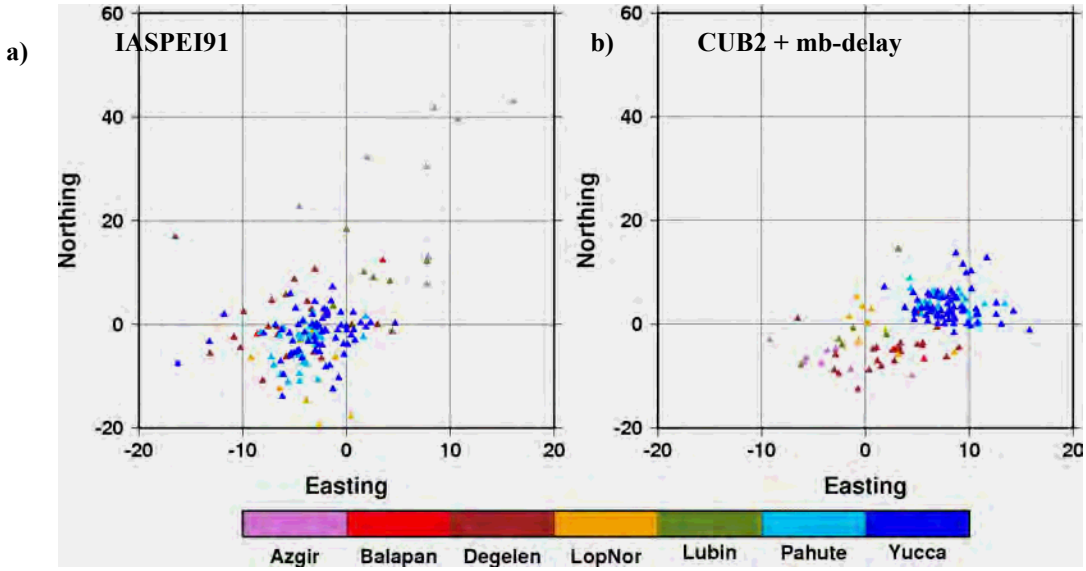

Figure 6. Relocation of GT0-2 event clusters using a) IASPEI91 baseline travel times and b) CUB2 travel-time predictions with mb-based delay and variance model. Events are colored according to

their cluster. Individual clusters tend to individually coalesce with application of the CUB2 and mb-delay corrections.

Generic Variogram Models

Last year we demonstrated utility of source region specific teleseismic P and Pn correlation structures. Nearly all source region specific teleseismic P variograms were similar and could generally be interchanged. Pn variograms demonstrated more diversity with source region and could not be interchanged. We additionally showed that once the bulk of the path effects are removed by calibration, it is possible to develop generic, transportable variogram models for both teleseismic P and Pn that may work well anywhere on the globe. We calculated Pn and P variogram models using our copula methodology (Bondár et al., 2006a) for all GT5 clusters from the global GT project (Bondár et al., 2007). For Pn and P calibration we used CUB2 (Shapiro and Ritzwoller, 2004) and Harvard (Antolik et al., 2003) SSSCs, respectively. Figure 7 shows the Pn and P variogram models obtained from GT residuals after calibration. The fact that the variograms look quite similar indicates that the CUB2 and Harvard global 3D models indeed account for major 3D heterogeneities. Consistent with previous results the calibrations reduced the overall variance (the sill) by just under 50%. Nevertheless, un-modeled velocity structures remain that generate correlated travel-time residuals. Because the calibrated travel times now account for the bulk of 3D Earth structure, it allows us to derive an isotropic variogram model not just from the individual clusters, but from the entire data set of globally distributed GT5 or better events. These models, shown as red lines on Figure 7, define generic Pn and P variograms that can be used to construct network covariance matrices for calibrated regions.

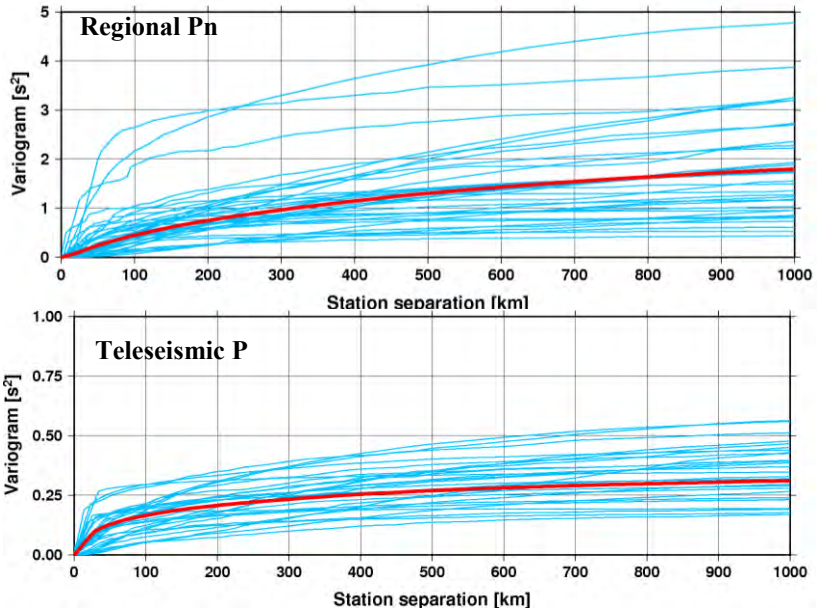

Figure 7. Variogram models for all GT clusters from the Global GT project (Bondár et al., 2007). The generic variogram model derived from all data is shown in red.

Validation Tests

To validate the generic calibrated error models (described by the network covariance matrix we generate from the transportable variogram models) as well as the mb/SNR-dependent delay correction and measurement error models we used over 2,000 globally distributed GT5 or better events produced under the Global GT project (Bondár et al., 2007). The regional and teleseismic ISC station coverage varies from sparse to dense networks for these clusters. To locate events we used our ILS location algorithm (Bondár et al., 2006a) developed in Year 1 that uses the full data covariance matrix to take into account the correlated structure in the travel times. Calibrated travel-time corrections, i.e., SSSCs, were generated from the CUB2 (Shapiro and Ritzwoller, 2004) and Harvard (Antolik et al., 2003) global 3D models for Pn and P, respectively. Figure 8 shows the mislocations relative to the GT5 locations for four test cases. Figure 9 shows cumulatives of mislocation, 90% error ellipse area, and coverage for three test cases. And, Figure 10 compares results at two clusters for two test cases. Calibrated travel-times, i.e., SSSCs, provide the first-order effect in location improvements for events mislocated significantly more than their GT level (visually in Figure 8 and bottom panel Figure 9). Taking into account the residual correlated data structure improves coverage (top panel Figure 9) with incremental improvements in locations. The mb-based picking error model tightens some of the clusters with a large range of magnitudes (Figure 10).

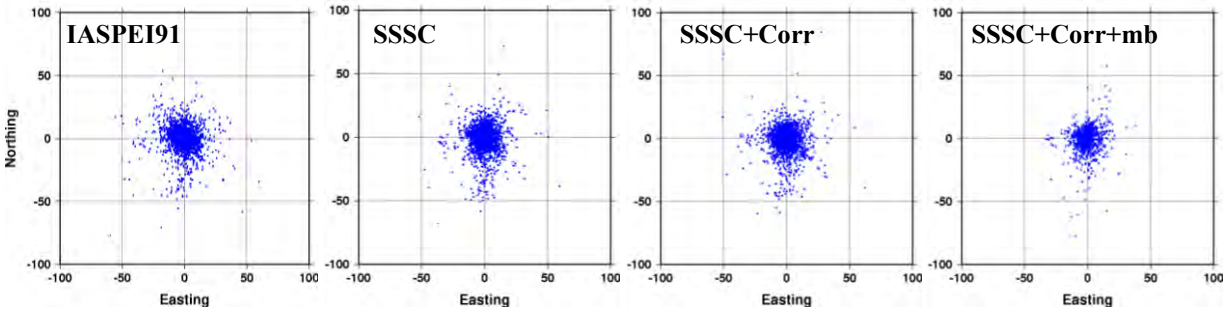

Figure 8. Relocations of over 2,000 globally distributed GT5 or better events with a) IASPEI91, b) SSSCs, c) SSSCs and full data covariance matrix, and d) SSSCs and full data covariance matrix and mb-based delay corrections and variances (a subset of events from a, b and c with 4 ≤ mb ≤ 6).

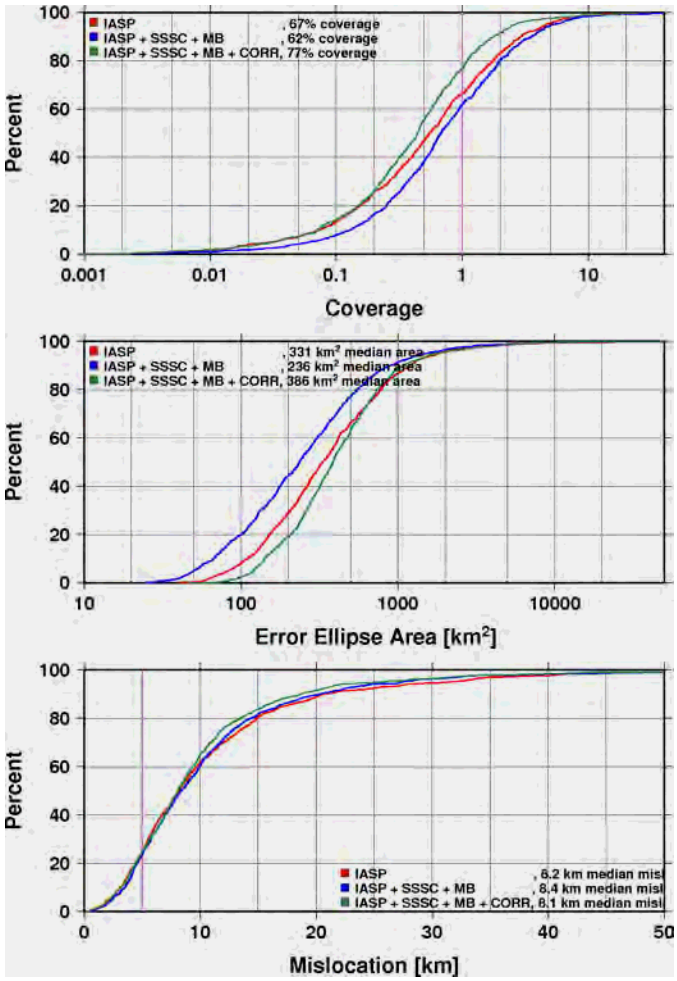

Figure 9. Cumulative distributions of mislocation (bottom panel), error ellipse area (middle panel) and coverage (top panel) for events with 4 ≤ mb ≤ 6 with IASPEI91 (red), SSSCs and mb-based delay corrections and variances (blue) and with correlated error structure (green).

Figure 9 shows cumulative distributions for mislocation, error ellipse area and coverage for 945 events with 4 ≤ mb ≤ 6 (the magnitude range where the mb-delay corrections and mb-variances are currently defined). Recall that the mb-based error models (blue) of bias and variance were derived from an explosion data set. These mb-dependent measurement error estimates may be too optimistic for earthquakes, which may explain why the area of the error ellipses is underestimated and insufficient coverage. While the median mislocations remain more or less the same, the generic correlated error model (shown in green) provides systematic location improvements above the 60th percentile (or mislocations exceeding 10 km). More important, taking into account the correlated structure, using the transportable Pn and P correlated error models increases the coverage from about 60% to 80% without significant inflation of the error ellipses. A small increase in the variogram sill would assure 90% coverage.

Figure 10 shows relocations for the Racha, Caucaus and the Kileaua, Hawaii GT5 clusters. Events are colored by their network magnitude and show internal clustering of large and small events. The new models appear to tighten the clusters by reducing the systematic location discrepancy between the small and large events. The net centroid bias is also reduced for both these clusters.

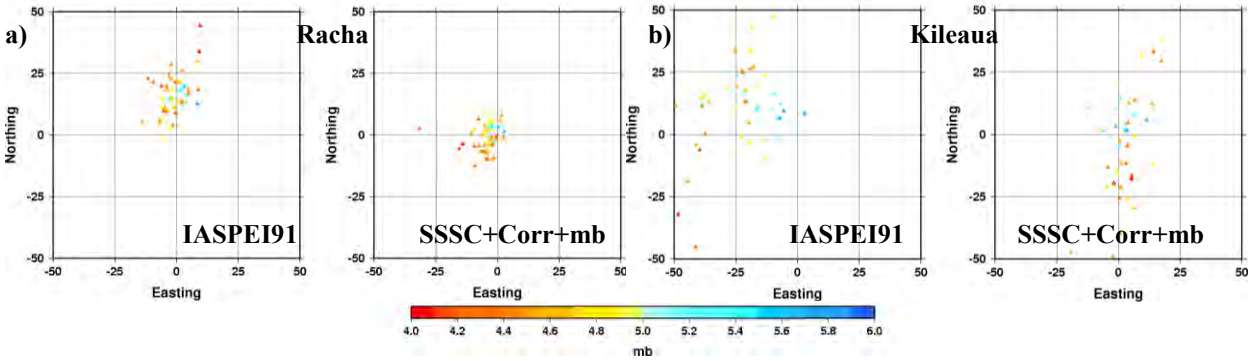

Figure 10. Location errors (eastings and northings in km) relative to GT5 locations without (IASPEI91) and with calibrated travel-times, mb-delay corrections and correlated errors for a) Racha, Caucasus cluster and b) Kileaua, Hawaii cluster. Events are colored according to their mb (4 < mb < 6). Disparities between large (redish) and small (blueish) events are reduced.

To test the SNR-based measurement error model, we used only those arrivals with reported SNR estimates. This basically restricted our globally distributed GT5 events to those that appear in the prototype IDC/IDC REB. As we mentioned earlier, the SNR-based delay and variance estimates are largely limited to teleseismic P, for which the delay correction is quite modest. There are indications that the SNR-based delay corrections make the clusters slightly tighter but the relocation tests are largely inconclusive and do not demonstrate significant improvements (or degradation). The transportable generic variogram models achieve the same coverage level (about 80%) for the sparse IMS network, indicating the same small sill adjustment to the variogram model is in order.

CONCLUSIONS AND RECOMMENDATIONS

We have developed generic transportable variogram models for Pn and P phases. By relocating a data set of globally distributed GT5 or better events, we demonstrated that the transportable variogram models used to construct network covariance matrices account for correlated structure in travel-time predictions and achieve 80% coverage for both sparse and dense networks. While we are still a bit shy of the nominal 90% coverage expected from the error ellipses scaled to the 90% confidence level, the models require only minor fine tuning to achieve actual 90% coverage.

We have developed a DD-based methodology to derive SNR-dependent models of bias and variance for reading errors. Since SNR estimates are rarely reported, we prototyped measurement error models of phase pick delay and variance using network magnitude. Admittedly, mb is a rudimentary surrogate for SNR but it is reported for most events. While the phenomenon that arrivals picked increasingly late with decreasing event size is well established (especially for automatic picks), so far little effort has been made to account for the systematic lateness of picks in a standard location algorithm. We implemented the SNR/mb-dependent bias estimates as travel-time corrections in our location algorithm. Application of the delay correction assumes that calibrated travel times are used. The SNR/mb-dependent phase pick variances are added to the diagonals of the network covariance matrix. The validation tests have shown that the effect of phase pick delay corrections is second order relative to calibrated travel-times. The phase pick delay corrections typically move locations less than the accuracy of our GT test events. Nevertheless, the error model improves some event patterns by reducing the systematic location discrepancy between small and large events, thus making the event clusters tighter.

As indicated in Table 1, our research now focuses on exploring alternative objective functions (l_p-norms), regression algorithms, and hypothesis tests to account for input travel-time errors with un-modeled spatial correlation and non-Gaussian picking errors. For example, the results of a simple Monte Carlo experiment are shown in Figure 11. Random local networks (10 stations with epicentral distances < 150 km) were chosen and assigned random errors drawn from Gaussian, Weibull, and Gumbel distributions (all with zero mean and standard deviation 1 s). The resulting distribution of mislocations from the input non-Gaussian errors are well described by the Normal model below the 80th percentile. However at the higher percentiles, the Gumbel and Weibull input skewed tails are poorly modeled by the Gaussian distribution. We found that deviations from a Normal model could be predicted by a simple Location Quality metric defined as QL = (1-azgap/360)(1-sazgap/360) where azgap and sazgap are the primary and secondary azimuthal gaps of the network. Figure 12 shows median and 95th percentiles location errors as a function of QL and it is clear that when QL exceeds 1/2 the network deviates from Normal. Simulations such as

these suggest the utility of stability tests based on network geometry for judging the validity of the Normal model for location uncertainty estimation.

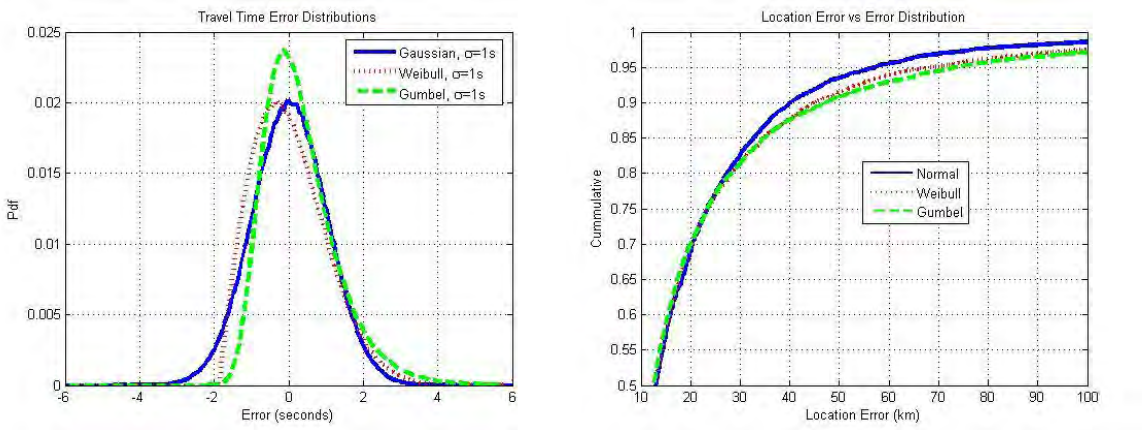

Figure 11. Gaussian, Weibull, and Gumbel input error distributions (each zero mean and 1 s standard deviation) were used in a Monte Carlo location experiment. Mislocations resulting from non-Gaussian input errors are under predicted by the Normal model above the 80th percentile.

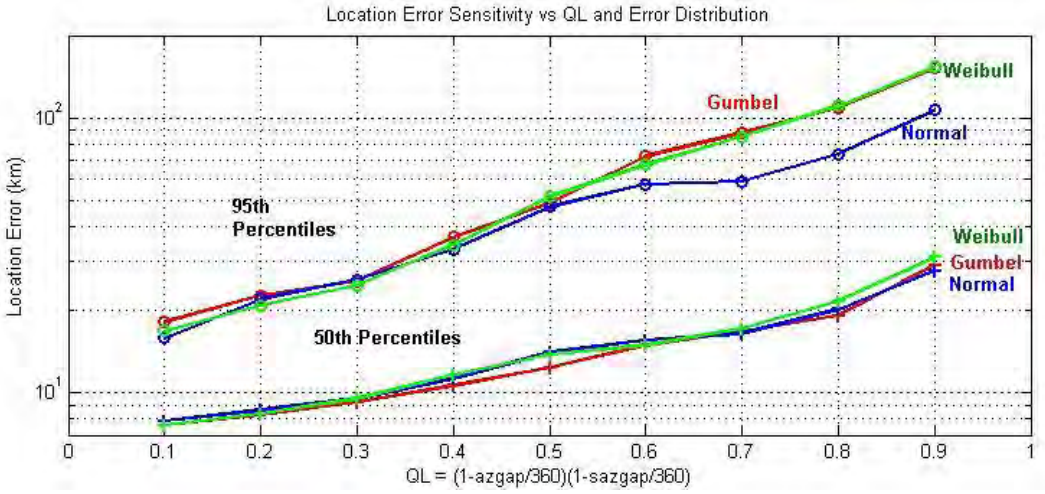

Figure 12. Deviations from the Normal model are greatest for poor network configurations described by QL. Small QL is good, while networks with large QL are potentially unstable.

REFERENCES

Antolik, M., Y.J. Gu, G. Ekström, and A. Dziewonski (2003). J362D28: A new joint model of compressional and shear velocities in the earth's mantle, *Geophys. J. Int.* 153: 443–466.

Bondár, I., K. McLaughlin, and H. Israelsson (2006a). Improved event location uncertainty estimates, in *Proceedings of the 28th Seismic Research Review: Ground-Based Nuclear Explosion Monitoring Technologies*, LA-UR-06-5471, Vol. 1, pp. 368–376.

Bondár, I., B. Kohl, E. Bergman, K. McLaughlin, H. Israelsson, Y-L. Kung, J. Given and E.R. Engdahl (2006b). Global ground truth data set with waveform and improved arrival data, in *Proceedings of the 28th Seismic Research Review: Ground-Based Nuclear Explosion Monitoring Technologies*, LA-UR-06-5471, Vol. 1, pp. 359–367.

Bondár, I., B. Kohl, E. Bergman, K. McLaughlin, Y-L. Kung, and E. R. Engdahl (2007). Global ground truth data set with waveform and improved arrival data, in current Proceedings.

Douglas, A., D. Bowers and J. B. Young (1997). On the onset of P seismograms, *Geophys. J. Int.* 129: 681–690.

Douglas, A., J.B. Young, D. Bowers and M. Lewis (2005a). Variation in reading error in P times for explosions with body-wave magnitude, *Phys. Earth Planet. Int*. 152: 1–6.

Douglas, A., J. B. Young, D. Bowers and P. D. Marshall (2005b). An analysis of P travel times for Nevada Test Site explosions recorded at regional distances, *Bull. Seism. Soc. Am*. 95: 941–950.

Freedman, H. W. (1966). A statistical discussion of Pn residuals from explosions, *Bull. Seism. Soc. Am*. 56: 677–695.

Lomnitz, C. (1995). Comment on "Errors in hypocenter location: Picking, model, and magnitude dependence," by S. D. Billings, M. S. Sambridge, and B. L. N. Kennett, *Bull. Seism. Soc. Am*. 85: 1527–1528.

Kennett, B. L. N. and E. R. Engdahl (1991). Travel times for global earthquake location and phase identification, *Geophys. J. Int*. 105: 429–465.

Shapiro, N. M. and M. H. Ritzwoller (2004). Thermodynamic constraints on seismic inversions, *Geophys. J. Int*. 157: 1175–1188, doi:10.1111/j.1365-246X.2004.02254.x.

IMPROVED GROUND TRUTH IN SOUTHERN ASIA USING IN-COUNTRY DATA, ANALYST WAVEFORM REVIEW, AND ADVANCED ALGORITHMS

Eric R. Engdahl[1], Eric A. Bergman[1], Stephen C. Myers[2], and Floriana Ryall[2]

University of Colorado[1] and Lawrence Livermore National Laboratory[2]

Sponsored by National Nuclear Security Administration
Office of Nonproliferation Research and Development
Office of Defense Nuclear Nonproliferation

Contract Nos. DE-FC52-03NA99516[1] and W-7405-ENG-48[2]

ABSTRACT

This research has the goal of developing in-country data sets that can be used to improve ground-based monitoring capabilities in southern Asia, in particular the region bounded by 20-44°N and 41-67°E, by providing information needed to develop and test more accurate travel time models for seismic phases that propagate in the crust and upper mantle. We have also incorporated phase picks from an experienced analyst who reviewed waveforms of particular interest for specific events. These in-country arrival times and analyst-reviewed picks have been associated with known earthquakes reported by international agencies, combined with existing bulletin readings, and relocated using the catalog EHB (Engdahl et al., 1998) methodology. Using in-country data we have formed new events, mostly at lower magnitudes that were not previously included in standard global earthquake catalogs. This has resulted in a catalog of earthquakes in the region for the period 1918-2006 for events larger than about magnitude 2.5. Catalog events larger than about magnitude 4.0 and well-constrained teleseismically have been highly reviewed. Events at lower magnitudes have been relocated with a standard procedure similar to the EHB procedure, but not all systematically reviewed.

The new catalog has been used to conduct detailed analysis of historic and recently occurring event clusters (often mainshock-aftershock sequences) using a multiple-event relocation technique and data sets of phase arrival times at distances from near-source to teleseismic. Absolute locations of such clusters are constrained using reference event information for one or more of the cluster events provided by local networks, aftershock deployments, or from non-seismic information such as interferomic synthetic aperture radar (InSAR) or geological mapping. We have also developed a method for direct calibration of a cluster by using arrival time data only from local stations, with an appropriate crustal model, to locate the hypocentroid of the cluster. These studies have produced numerous events with epicenter absolute accuracy of 5 km and better (GT5). When both location and origin time can be calibrated for a cluster, we are able to estimate the unbiased travel times to all reporting stations. These estimates are the basis for improved models of the crust and upper mantle, which in the future will permit more accurate routine earthquake locations using regional seismic data.

To date we have performed hypocentral decomposition (HDC) calibration analyses on 27 earthquake clusters in the region. We present a synopsis of 8 new clusters that have been calibrated at GT5 or better, including information on the method of calibration and GT-level of calibration achieved. We also present several representations of absolute travel time information derived from the calibrated clusters, showing distance-dependence of different phases and map views to show the regional coherency of travel-time variations.

OBJECTIVES

This research seeks to improve the database of ground truth information and velocity models useful for calibration in southern Asia with the following objectives: (1) Aggressive pursuit of in-country data acquisition, especially the collection of ground truth at GT5 level or better for events of magnitude 2.5 and larger recorded by dense local networks, including associated velocity models; (2) Expanded analyst review of relevant regional waveforms for ground truth events by the comprehensive re-picking of phase arrival times from all available waveforms, with special attention to the regional phases Pg, Pb, Pn, Sg, Sb and Sn; and (3) Application of advanced algorithms, specifically multiple event relocation, to refine and validate all available ground truth data, to achieve the optimal selection of data for analysis, to better understand the uncertainties of the results, and to handle the error budget as realistically as possible.

RESEARCH ACCOMPLISHED

Compilation of Arrival-Time Data and Relocation of Seismicity

The aim of the present study is to produce a comprehensive catalog of all instrumentally recorded events, magnitude 2.5 and greater, that have occurred during the period 1918–2006 for the region bounded by 20-44°N and 41-67°E. Available bulletin arrival-time data from in-country seismic networks in the region, as well as phase picks from an experienced analyst who reviewed waveforms of particular interest for specific events, have been compiled and, where possible, associated with known earthquakes reported by international agencies. However, with the in-country data we have also formed many new events, mostly at lower magnitudes that were not previously included in standard global earthquake catalogs. This combined catalog of more than 22,000 events has been relocated using the EHB (Engdahl et al., 1998) methodology. Epicenters from the resulting catalog are plotted in Figure 1a. Significant scatter is evident in Figure 1a since events at lower magnitudes have not all been systematically reviewed, whereas most events that are well-recorded teleseismically (Figure 1b) have been highly reviewed.

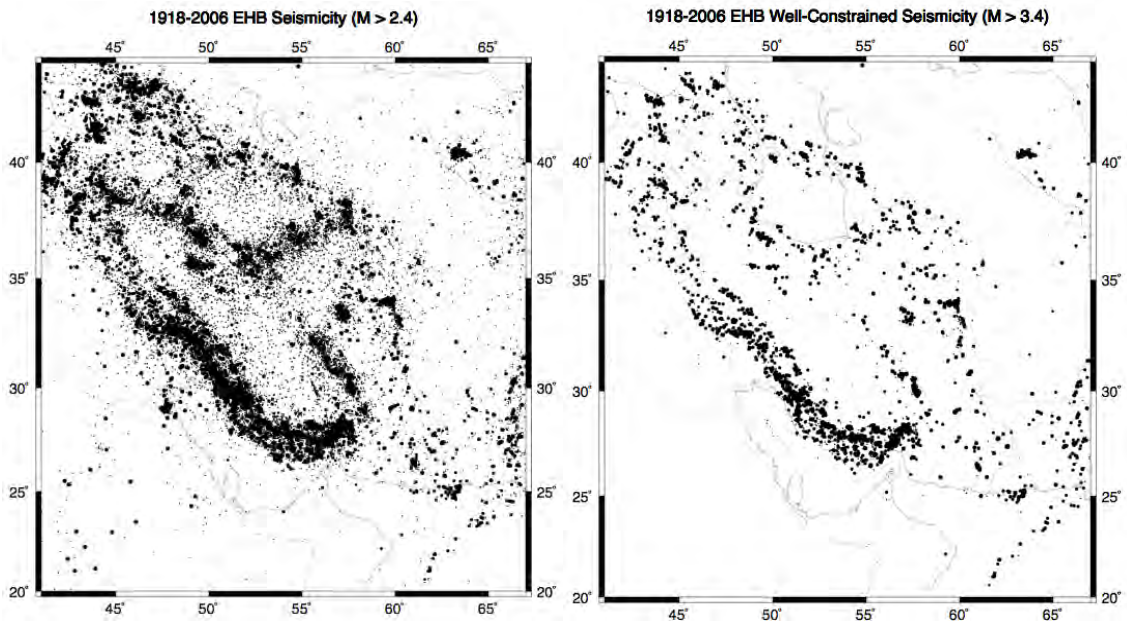

Figure 1. Seismicity maps of the study region, based on the new catalog assembled in this project, using in-country phase arrival time data that has been integrated with standard global bulletin readings. a) Over 22,000 earthquakes from 1918-2006 with magnitude 2.5 and greater, relocated using EHB methodology but most of the smaller events are unreviewed. b) Subset of events that are well-constrained with teleseismic readings, most of which have been reviewed.

Ground Truth Data

Critical to our ground truth data discovery and acquisition process are collaborative arrangements that have been made with key organizations in southern Asia. These arrangements are built on exchanges that are mutually beneficial to the parties involved, usually based on our applying advanced techniques to refine locations of the host country's natural seismicity in return for access to in-country ground truth information. These arrangements provide a forum for gathering and assessing potential ground truth data, and collecting waveform and phase reading data for events of interest from local and regional stations.

We are also in contact with several research groups developing ground truth locations from InSAR-detected ground displacement and other satellite-based location methods, as well as geological field work, that provide important constraints on earthquake location that are independent of seismic observations. Much new ground truth information is now being obtained from these sources as an ongoing activity.

Location Calibration of Earthquake Clusters through Multiple Event Relocation

The HDC (Jordan and Sverdrup, 1981) method for location calibration yields improved accuracy for both the relative and absolute locations of clustered earthquakes. The gist of the method is to use a multiple event relocation method with regional and teleseismic phase arrival times to constrain relative locations of clustered earthquakes and then to calibrate the absolute location of the cluster by obtaining independent information on the absolute location of one or more members of the cluster. The HDC analysis includes further refinement of the data set by making empirical estimates of reading errors and using these estimates to help identify outliers. These steps yield significant improvements in accuracy and resolution for the relocations. Of course, the main benefit of HDC analysis is to largely remove the biasing effects (path anomalies) of lateral heterogeneity in the Earth, which permits much better resolution of the relative locations of cluster earthquakes.

We have recently extended the calibration process to take into account the uncertainties in calibration data in estimating an optimal calibration shift for the cluster. We also estimate a term to account for the inconsistency between multiple calibration events. Our final estimate of local accuracy for events in calibrated clusters includes all these sources of uncertainty, as well as the uncertainty in relative locations derived from the HDC analysis.

We have also developed a method for direct calibration of a cluster by using arrival time data only from local stations, with an appropriate crustal model, to locate the hypocentroid of the cluster. We have found a number of cases in which no individual earthquake in the cluster is well-recorded enough to be treated as a calibration event, but the cumulative local-distance readings of all events do provide sufficient location accuracy to calibrate the hypocentroid directly at GT5 or better. Many of the clusters presented below have been calibrated in this manner.

Regional Path Anomalies

When both location and origin time can be calibrated for a cluster, we are able to estimate the unbiased travel times to all reporting stations. These estimates are the basis for improved models of the crust and upper mantle, which in the future will permit more accurate routine earthquake locations using regional seismic data.

We use the calibrated cluster arrival time data to infer empirical path anomalies (relative to the global model ak135) from each cluster source region to surrounding seismic stations. The path anomalies can be the result both of variations in bulk velocity and differences in ray path geometry caused by lateral heterogeneity.

Cluster Studies Revisited

The influx of new data from in-country sources has required us to revisit all earthquake clusters that had previously been considered finished. The new data, when combined with existing ground truth datasets, is providing very useful constraints on true travel times through the crust and upper mantle of the region. Hence, we have performed further detailed analysis of historic and recently occurring event clusters using our standard multiple-event relocation technique and data sets of phase arrival times at distances from near-source to teleseismic.

Synopses of New Calibrated Clusters

To date we have performed HDC calibration analyses on 27 earthquake clusters in the region (Figure 2). Not all clusters can be calibrated at GT5 levels of accuracy.

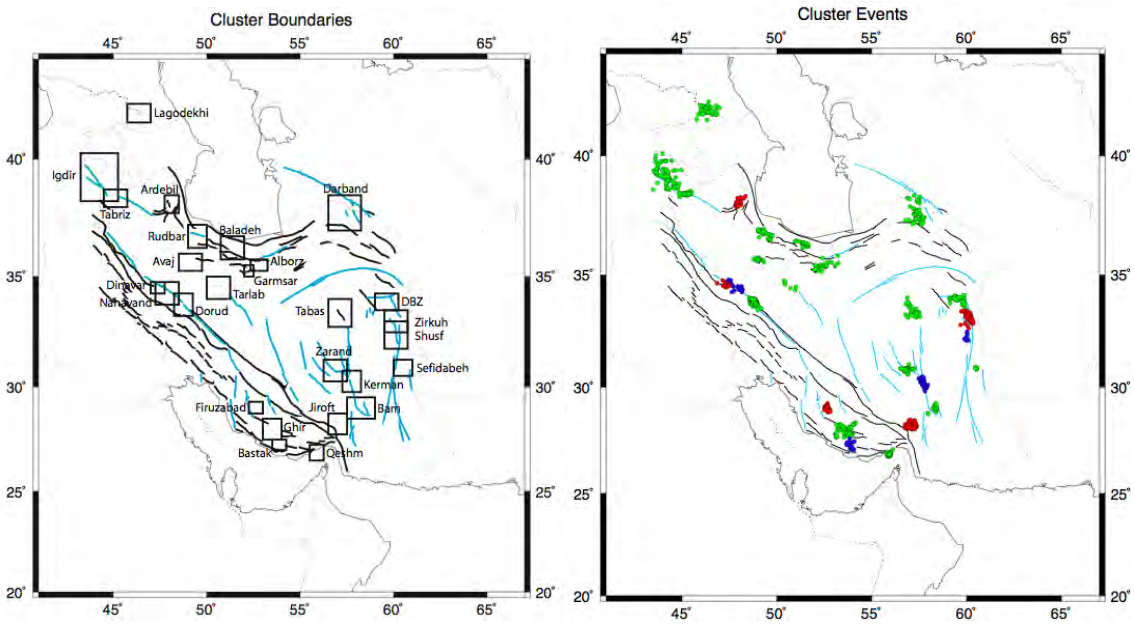

Figure 2. Earthquake clusters studied for ground truth calibration. a) Boxes show the region of each cluster, with the name we have assigned. Major strike-slip faults (blue) and thrust faults (black) are shown. b) The earthquakes of each cluster are shown. Events in each cluster are color coded according those clusters that are calibrated (not necessarily at GT5 or better) in both location and origin time (green), clusters that are calibrated in location but not origin time (blue), and clusters for which we have as yet been unable to achieve any calibration (red).

We present synopses of 8 clusters that have not been presented in previous Research Reviews and that have been calibrated in both location and origin time to GT5 or better, including information on the method of calibration and GT-level of calibration achieved. We also present several representations of absolute travel time information derived from the calibrated clusters, showing distance-dependence of different phases and map views to show the regional coherency of travel time variations.

Alborz

The Alborz cluster (Figure 3) is a small (11 events) cluster of relatively small ($2.5 \leq M \leq 4.5$) earthquakes. Most of the arrival time data is from nearby stations, and we used 81 P arrivals out to 1.5° epicentral distance to locate the hypocentroid of the cluster (direct calibration), with an uncertainty of about 2 km. When this is combined with the cluster vector uncertainties shown in Figure 2b, most of the events will be calibrated at GT5 or better.

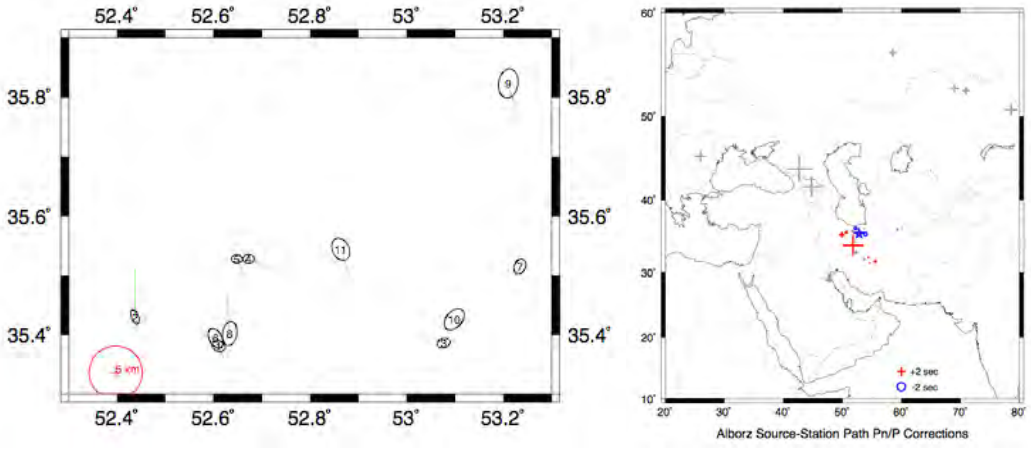

Figure 3. Alborz cluster. a) Results of the HDC analysis. Confidence ellipses are 90% level for relative locations. A circle of 5-km radius is shown in red for reference in the lower left corner. Green lines show change in relative locations from starting locations (EHB single event locations). b) Map of empirical path anomalies, relative to ak135. The blue star is the location of the cluster hypocentroid. Anomalies are calculated when there are two or more readings of the same phase at a given station. If there are 5 or more readings the sympol is in color (red for positive anomalies, blue for negative); otherwise the symbol is plotted in gray. Crosses indicate positive (late arrival) anomalies, circles indicate negative (early arrival) anomalies. The scale of path anomalies is shown at the bottom right of the figure.

Darband

The Darband cluster (Figure 4) contains 45 events scattered over a fairly large area. There are many readings at local distances and the hypocentroid was located with 144 P readings at distances less than 2.5 degrees (direct calibration), with an uncertainty of about 3 km. It was necessary to go out further than is desirable in epicentral distance in order to achieve adequate azimuthal coverage. Many events in the cluster will qualify as GT5 locations.

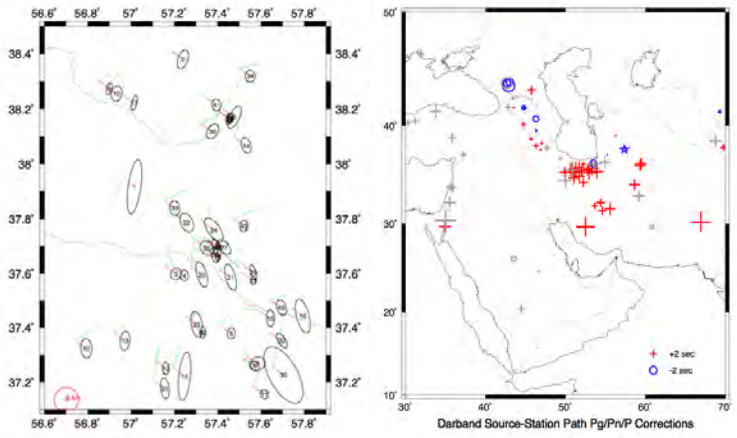

Figure 4. Darband cluster. See Figure 3 for explanation.

Dasht-e-Bayaz-Zirkuh

The Dasht-e-Bayaz-Zirkuh cluster (Figure 5) is composed of 42 events near the intersection of two major strike-slip fault systems, shown in blue in Figure 5a. The cluster contains several very large events and their aftershocks. To calibrate this cluster we used two calibration events that were very well located by a temporary seismic network studying aftershocks of a large earthquake in November 1979. Thus, we located the hypocentroid of this cluster using teleseismic P readings and shifted the cluster to best match the calibration

locations of these two events, with an uncertainty of the calibration of about 3 km. When the cluster vector uncertainty is added, over half of the events in the cluster qualify as GT5.

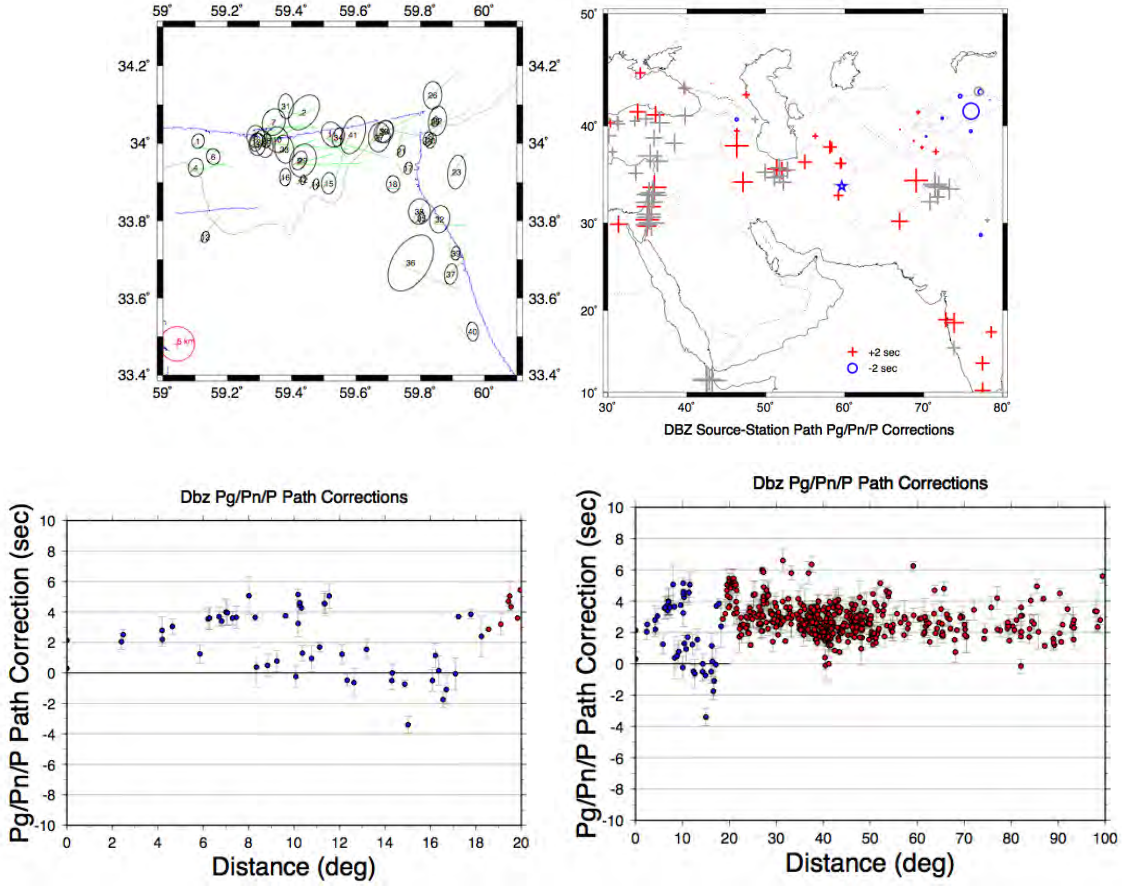

Figure 5. Dasht-e-Bayaz-Zirkuh cluster. See Figure 3 for explanation of a and b. c) Empirical path anomalies and spread of each measurement, over the regional distance range. d) Empirical path anomalies and spread of each measurement, over the regional and teleseismic distance range.

For this cluster we show the empirical path anomalies both in map view (Figure 5b) and as a function of distance (Figures 5c and 5d). Figure 5d shows empirical path anomalies over the regional distance range, while Figure 5d shows the anomalies over the regional and teleseismic range.

Dorud

The Dorud cluster (Figure 6) is based on a mainshock-aftershock sequence that began in March 2006 and a few events prior to that.

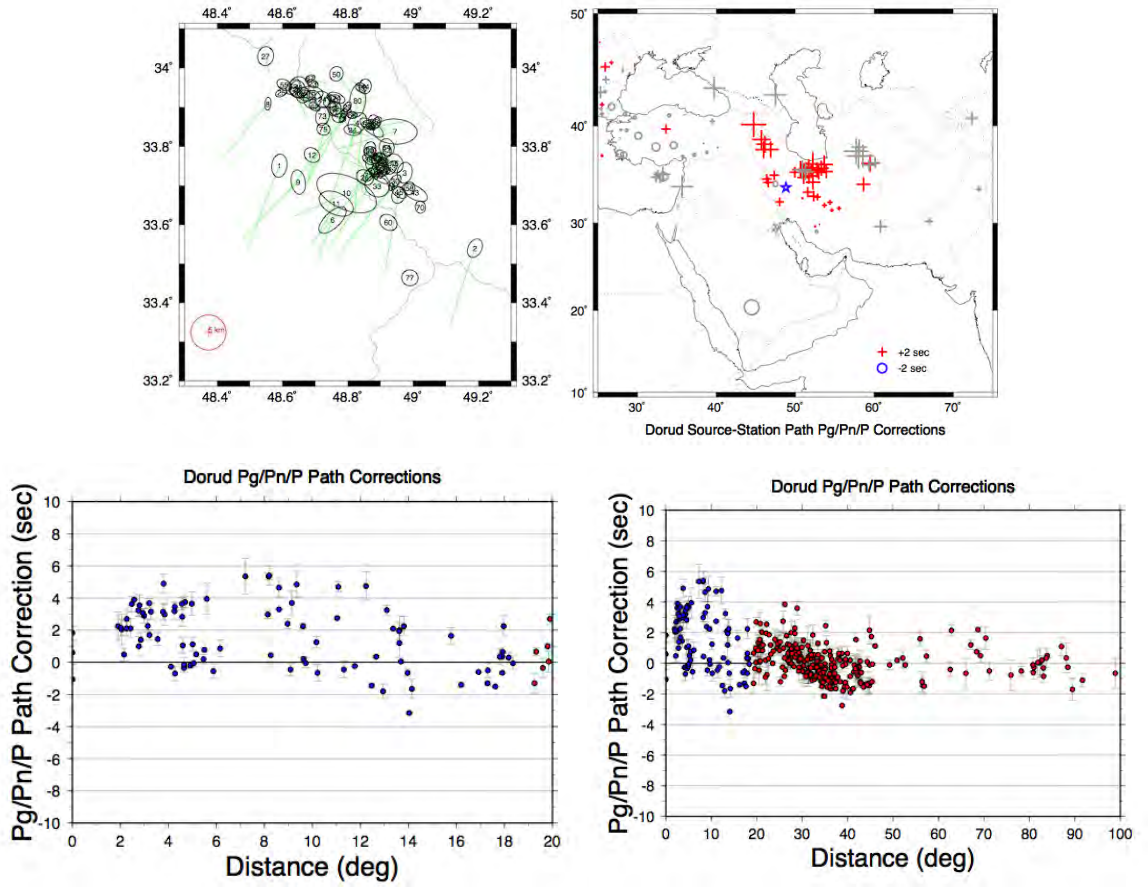

Figure 6. Dorud cluster. See Figure 3 for explanation of a and b, Figure 5 for explanation of c and d.

Our ability to analyze this cluster is strongly dependent on the availability of a large number of readings from local stations that were carefully repicked by one of our colleagues. The cluster contains 80 events, most of which are very well-constrained in relative location. We used direct calibration for this cluster because none of the individual events was well-recorded enough by local stations to be treated as a calibration event. Cumulatively, however, we had 344 P readings at distances of less than 2.0 degrees to locate the hypocentroid, which gave us a calibration with about 3 km uncertainty. When the uncertainty of the cluster vectors is added, many of the events in the cluster qualify as GT5.

Garmsar

The Garmsar cluster (Figure 7) is composed of 17 small events, maximum magnitude 3.9, for which there is little arrival time data beyond about 5.0 degrees. In-country data was vital in being able to analyze this cluster. We used direct calibration with 105 P readings at distance no more than 1.3 degrees, achieving an uncertainty in calibration of about 2 km. 15 of the events qualify as GT5.

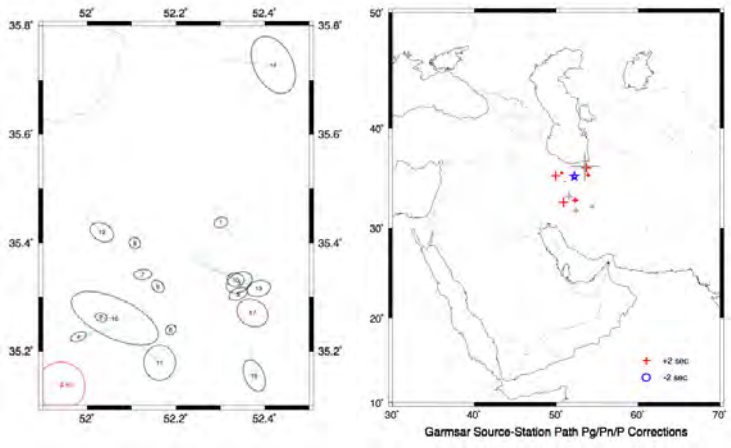

Figure 7. Garmsar cluster. See Figure 3 for explanation.

Lagodekhi

The Lagodekhi cluster (Figure 8) contains 44 events in a somewhat diffuse pattern, but not so large as Igdir. We used direct calibration because none of the individual events were suitable as calibration events. With 158 P arrivals at distances less than 1.3 degrees we achieved an uncertainty in the calibration of 3 km and about half the events in the cluster would qualify as GT5.

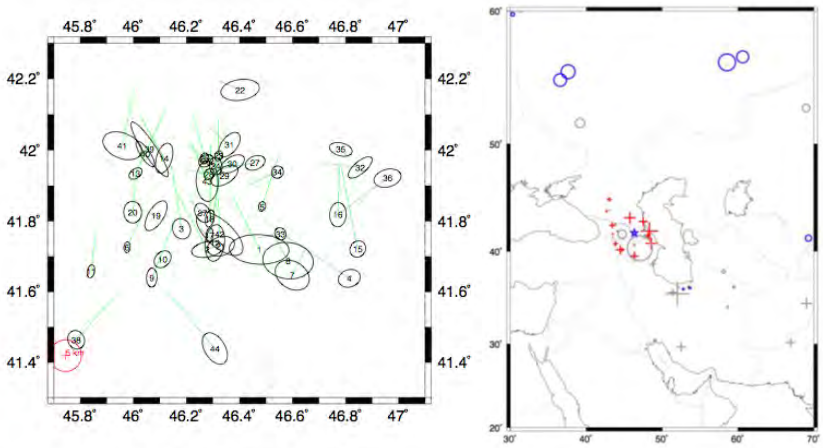

Figure 8. Lagodekhi cluster. See Figure 3 for explanation.

Qeshm

The Qeshm cluster (Figure 9) is based on a mainshock in November 2005 and an extended aftershock sequence.

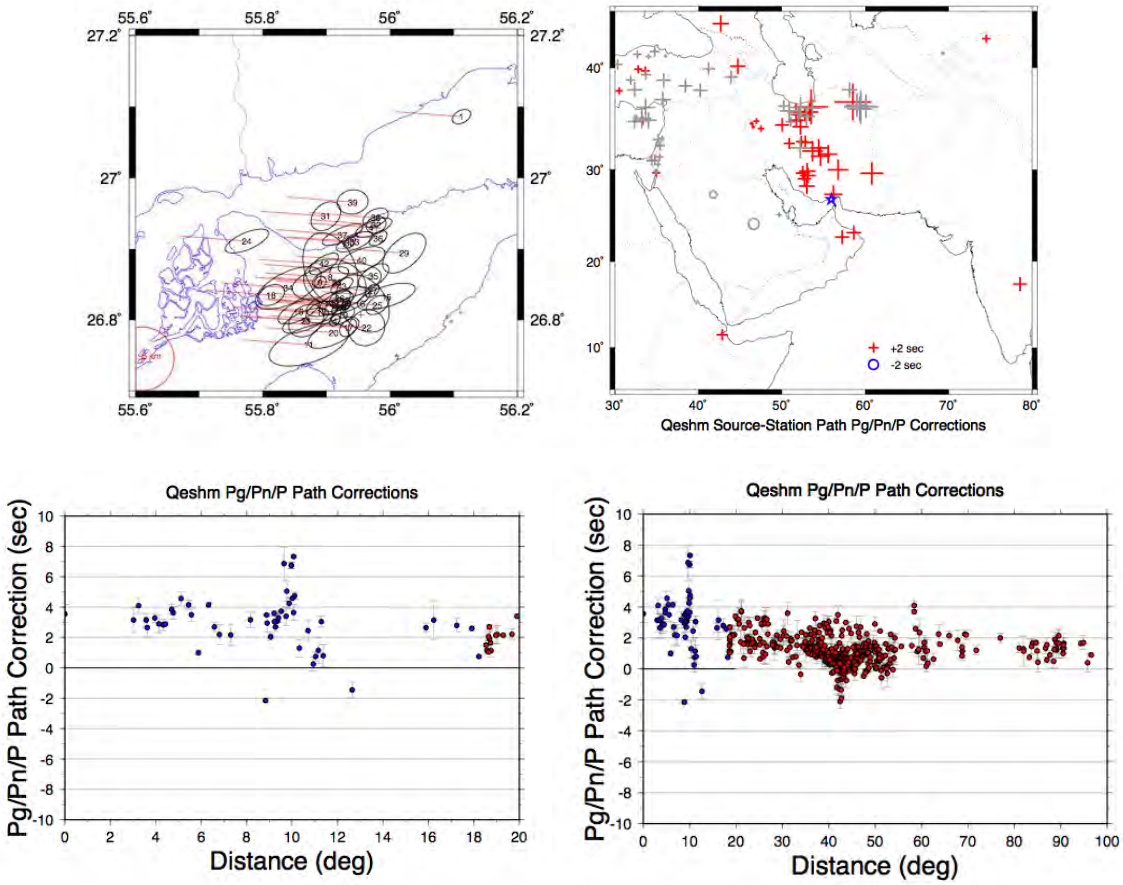

Figure 9. Qeshm cluster. See Figure 3 for explanation for a and b. See Figure 5 for explanation of c and d. The red lines in 9a indicate the shift needed to bring the cluster into alignment with the calibration data. The starting locations for this run were taken from the prior run to aid convergence, so there is almost no change in relative location (green lines).

The relative locations of the 43 events are well-constrained by in-country data and also by readings at a critical azimuth from a neighboring country, which we were able to obtain through colleagues. Calibration of this cluster is based on a combination of InSAR and seismic data. The InSAR study provides strong constraint on the location of the mainshock and our local colleagues provided us with two calibration events based on an aftershock survey, which confirms the InSAR location and also provides calibration for the origin times. The uncertainty of the calibration is about 2 km, and when cluster vector uncertainties are added, 36 of the events qualify as GT5.

Sefidabeh

The Sefidabeh cluster (Figure 10) is a quite unusual episode of seismic activity, a series of moderate-sized earthquakes over a few days in early 1994 in a place with no prior or subsequent seismic activity. The tectonic significance of the seismicity is discussed in Parsons et al., 2006. The cluster contains 7 events that are all well-recorded, and the cluster vectors uncertainties are quite small (Figure 10a). Calibration is done with a combination of InSAR and seismic data. InSAR analysis (Parsons et al., 2006) places strong constraints on the locations of the cluster events, with about GT3 calibration uncertainty. Through the help of one of our colleagues we obtained P and S readings from two stations at very short epicentral distance, a few tens of km. Although these readings were insufficient to locate the events, we could use them to calibrate the origin time of the cluster. six of the events in the cluster qualify as GT5.

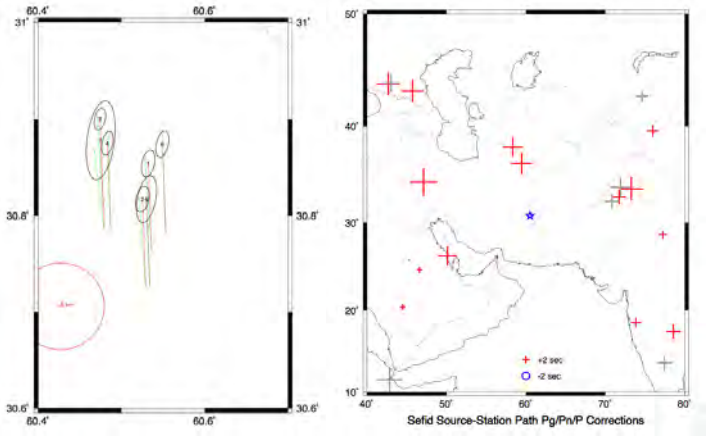

Figure 10. Sefidabeh cluster. See Figure 3 for explanation. The red lines in 10a indicate the shift needed to bring the cluster into alignment with the calibration data. The starting locations for this run were taken from the prior run to aid convergence, so there is almost no change in relative location (green lines).

Summary of Travel-Time Anomalies

We have combined the empirical path anomalies of all the clusters that are calibrated in both location and origin time to produce a summary plot of P arrivals as a function of epicentral distance (Figure 11).

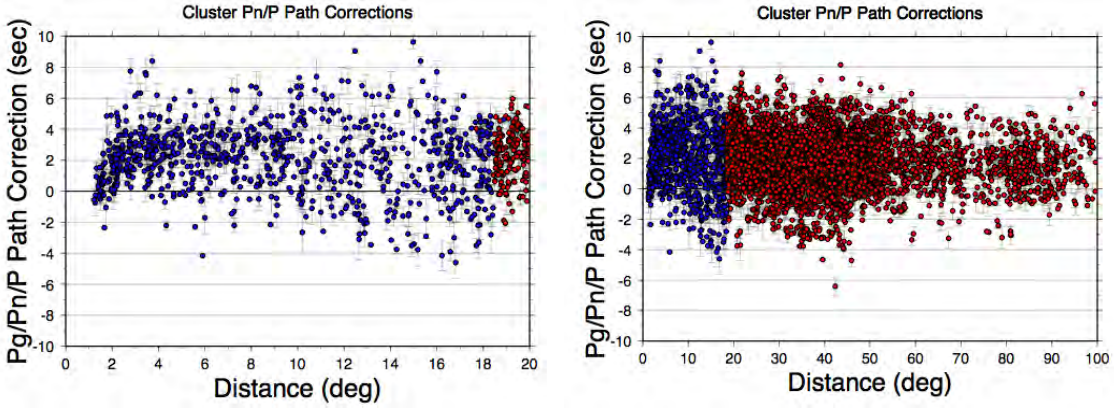

Figure 11. Empirical path anomalies, relative to ak135, and spread for P phases from 12 earthquake clusters that are calibrated both in location and origin time. a) Regional distance. b) Regional and teleseismic distance.

The empirical path anomalies for individual clusters (e.g., Figures 5, 6, and 9) show evidence both for departures from the average earth model used for reference (ak135), and for lateral heterogeneity. When the path anomalies are combined however, most structure is lost in a cloud of impresive width, a range of 10–12 seconds for P phases over the regional and teleseismic distance range (Figure 11). Even here there is a suggestion of about 2–3 seconds baseline offset from ak135 in the study region. This can be accounted for with a crustal structure that is both thicker (40–45 Km Moho depth, vs. 35 km for ak135) and slower in bulk velocities. It is clear, however, that accurate earthquake location in this region will require the use of crustal models that are more specific to the source regions.

CONCLUSIONS AND RECOMMENDATIONS

We have relocated more than 22,000 earthquakes of magnitude 2.5 and greater, occurring between 1918 and 2006, in the region bounded by 20-44°N and 41-67°E. From this catalog we have acquired new or improved ground truth events and calibrated earthquake locations in the region, based on detailed multiple event relocation and use of calibration data, both from local seismic network data and from InSAR and geological data. We have been able to include substantial numbers of phase readings at in-country seismograph stations

that have improved the quality and quantity of calibrated earthquake locations in this region. We are continuing to develop resources for local network data and expect these efforts to lead to new ground truth events and resulting data on empirical path anomalies that will substantially improve location capabilities in this region.

REFERENCES

Engdahl, E. R., R. D. Van der Hilst, and R. P. Buland (1998). Global teleseismic earthquake relocation with improved travel times and procedures for depth determination, *Bull. Seism. Soc. Amer*. 88: 722–743.

Jordan, T. H. and K. A. Sverdrup (1981). Teleseismic location techniques and their application to earthquake clusters in the south-central Pacific, Bull. Seis. Soc. Amer. 71: 1105–1130.

B. Parsons, T. Wright, P. Rowe, J. Andrews, J. Jackson, R. Walker, M. Khatib, M. Talebian, E. Bergman, and E. R. Engdahl. (2006). The 1994 Sefidabeh (eastern Iran) earthquakes revisited: new evidence from satellite radar interferometry and carbonate dating about the growth of an active fold above a blind thrust fault, *Geophys. J. Int.* 164: 202–217.

GROUND TRUTH LOCATIONS USING SYNERGY BETWEEN REMOTE SENSING AND SEISMIC METHODS

Gene A. Ichinose[1], Hong Kie Thio[2], and Don V. Helmberger[3]

AFTAC/TTR/MTC[1], URS Group Inc.[2], and California Institute of Technology[3]

Sponsored by National Nuclear Security Administration
Office of Nonproliferation Research and Development
Office of Defense Nuclear Nonproliferation

Contract No. DE-AC52-03NA99505/BAA03-72

ABSTRACT

In this study, we have relocated a set of 50 ground truth (GT) earthquakes as determined from regional modeling, to estimate the performance of the station correction methodology. We constructed station-specific source correction or "station correction" surface from 760 station corrections (global distribution) based on a small set of five well and closely located earthquakes in the central Tibetan Plateau. The station corrections were interpolated to develop a global surface for P-wave travel time corrections. As a test, we relocated a set of 50 GT earthquakes, with some seismic events located about 800 km from the center of the PASSCAL array across the Tibetan Plateau and surrounding regions. When the corrections were applied to the iasp91 velocity model, the mislocations decreased by an average by 37% for 37 out of the 50 GT events. This indicates significant improvement in seismic event locations relative to using the iasp91 model without P-wave travel-time corrections. Surprisingly, the distribution of mislocations did not vary or correlate with distance and some of the farthest events from the center of the Tibetan Plateau were improved more than the locations in the center where the travel time corrections are more relevant. Myers and Schultz (2000) noted that correction surfaces for nearby stations are similar, suggesting coherent variations between the one-dimensional (1D) velocity model and the true velocity structure. Based on the assessment of the results, corrections could be developed from a small cluster of earthquakes and transported for use with seismic events outside of this area out to a radius of 800 km. Additional tests should be performed to further validate these claims especially when crossing tectonic boundaries. This type of calibration and predicted transportability of the P-wave travel-time station corrections will make it more useful for regions of little to no tectonic activity or areas where detailed three-dimensional (3D) velocity model calibration has not yet been performed because of the ease of use in the application of the station correction methodology.

OBJECTIVES

The development of the International Monitoring System (IMS) is intended to meet the monitoring requirements of the Comprehensive Nuclear-Test-Ban Treaty (CTBT). One requirement is the location of seismic events with an uncertainty of less than 1000 km^2 for earthquakes with a magnitude smaller than 4. This has motivated a number of recent studies to develop methods for improving the accuracy and precision of seismic event locations, especially with sparse datasets. These studies can be divided into two categories: calibration-based and model-based. The focus of the calibration-based method is the determination of station or source specific corrections using 1D velocity models, whereas the focus of the model-based method is the development and use of 3D velocity models. Examples of calibration-based studies include Bondar and North (1999), Yang et al. (2001), Richards-Dinger and Shearer (2000), Myers and Schultz (2000), Thurber et al. (2001), and Trabant and Thurber (2001). The former two studies are also examples of the use of spatially varying path corrections for location calibration over large regions. Examples of model-based studies include Smith and Ekstrom (1996) global-scale 3D model tests, Firbas (2000) regional-scale 3D model tests, and Thurber et al. (2001) local-scale 3D model tests. We note that station corrections, which are constant correction values common to a cluster of seismic events are also often included in 3D model solutions at all scales.

Our focus of this paper is on testing the range of applicability of the calibration-based station correction methodology. The correction uncertainties are greatly dependent on the accuracy of the origin time and hypocentral location of seismic events used both in the calibration stage of the corrections and in the testing stage. Since calibration-based station corrections or station-specific source corrections are constructed from GT events that are rare or often difficult to estimate accurately, then testing for transportability will provide information on its applicability in the location of seismic events in sparsely monitored and seismically inactive regions. This information can also be useful for generally improving the earthquake locations for tectonic interpretations using global earthquake catalogs.

We will reduce the uncertainties in testing the station corrections by using 50 GT earthquakes defined by Bondar and North (1999) with epicenter uncertainties on the order of 5 to 10 km (i.e., GT5 to GT10). Each station can have a P-wave travel time correction for a specific source region and that correction will be applied to other earthquakes expanding out to distance offsets on the order of 100s km. The station corrections can be composed from a single or multiple GT events. We do not use source specific station corrections (SSSC) because the event coverage for any particular station is not well distributed and the focus is to evaluate the correction methodology for a cluster of events with a set of station corrections. When using multiple seismic events, stations that did not record at least two of the seismic events within a cluster are set to zero, a background value or a value that is interpolated between stations.

RESEARCH ACOMPLISHED

All ground truth locations and origin times used in this study are taken from the catalog developed by Zhu et al. (2006). They developed a regional 1D P-wave velocity model starting with the International Seismological Centre (ISC) locations and phase arrival data. Using additional phase arrivals and waveform data from the Sino-U.S. PASSCAL seismic recording experiment on the Tibetan Plateau (Owens et al., 1993), Zhu et al. (2006) computed Green's functions from their calibrated model. They then improved the estimates of the focal mechanisms and source depths using the Cut and Paste (CAP) waveform inversion methodology (e.g., Zhu and Helmberger, 1996) with the calibrated Green's functions. They applied a non-linear approach that does not depend on an initial model, which iteratively and simultaneously estimates the velocity model and relocates the hypocenters. They relocated about 50 seismic events recorded by the PASSCAL array between 1991 and 1992 (e.g., Zhu et al., 2006; Tan et al., 2006). These locations are shown in Figure 1 and all events are located within 7 degrees (~800 km) of the center of the PASSCAL array. Based on the analysis of the waveform data and calibration of velocity model, the locations of these events are likely to be uncertain by about 5 to 10 km, (D. Helmberger, Personal Communication).

We use the iasp91 velocity model as a 1D global reference velocity model commonly used as the default in most operational settings. Since the GT catalog of earthquakes by Zhu et al. (2006) has been calibrated to a unique local Tibetan Plateau velocity model, we therefore remove any shifts or biases in origin times due to the difference between the local and global velocity models. We fix the location latitude, longitude, and depth and redetermine the origin time using the global iasp91 model to remove any bias.

We selected five seismic events located near the center of the PASSCAL array that were well recorded globally. These five events were used to calibrate the P-wave travel-time corrections. They ranged in size from M_w 4.1 to 4.7 with 26 to 96 ISC recording stations. If there were 2 or more P-wave recordings for a station between the five events, the average P-wave residual was used in the P-wave travel-time correction surface; otherwise, it was either set to zero or interpolated from 2 or more nearby stations with more data. The average residual was used in the P-wave travel-time corrections if it was larger than one standard deviation. We assume that the average residual is the correction so that it can be added to the travel time for a particular station in future relocations as a correction term. The station corrections were then gridded to develop a global surface by interpolation between data points. The interpolation was performed using the nearest neighbor algorithm (e.g., Wessel and Smith, 1998). We assume that the P-wave travel-time correction surface goes to zero when no data are present. The grid node interval was set to 1 by 1 degree. A circular area with a 15 km search radius is centered on each node with only 1 sector. The average value is computed as a weighted mean of the nearest point from each sector inside the search radius. The weighting function used is $w(r) = \frac{1}{1+d^2}$, where $d = 3\left(\frac{r}{R}\right)$, R is the search radius and r is distance from the node. This weight is modulated by the observation points' weights. We compared the multi-event P-wave travel-time correction surface by comparison with a surface constructed using just one of the largest events (Julian day 222) that was an M_w 4.7 with 92 phase arrivals. The resulting surface was very similar in amplitude but slightly different is fine details within 30 degrees due to the increased number of events used in the multi-event correction surface.

We checked the location, depth, and focal mechanism for 10 of the largest earthquakes in the Zhu et al (2006) GT catalog using the regional, long period full waveform moment tensor inversion method (e.g., Ichinose et al., 2003). We performed an inversion on the PASSCAL data recorded by very broadbanded instruments to estimate the centroid origin time, location, and depth, as well as the 5-degrees-of-freedom moment tensor using an a priori velocity model appropriate for the region. The inversion results suggest that all 10 events had double couple mechanism. The differences in depth and locations were within good agreement and only a few km different. The mechanisms were all similar within 10 degrees in strike, dip, and rake and within 0.1 in scalar moment magnitude. The largest differences in location and origin time were for events that had poor station coverage along the outer edges of the PASSCAL array.

Earthquake locations and residual calculations were performed using a grid search routine that used iasp91 travel time tables calculated for discrete distances and depths optimally selected and commonly used in LocSAT (IDC, 1999). The program TauP (Crotwell et al., 1998) was used to calculate the travel-time tables. The appropriate travel-time table is loaded given a source and receiver distance, source depth, and appropriate phase type. A cubic spline is fit to the table values, and the approximate travel-time value is estimated for the source-receiver pair.

Figure 2 shows the global P-wave travel-time correction surface constructed from 760 station correction estimates ranging from –4.0 to +2.5 seconds with average and median values at approximately zero. The largest negative corrections were distributed in India, Southeast Asia, and Australia, but there were no strong positive corrections mapped for this source region.

We located the 50 earthquakes in the GT catalog (Table 1), first without and then with the corrections and computed the mislocation vectors relative to GT locations. The relocations are performed using the previously described grid search algorithm, and the residuals are not weighted by the distance or residual size typically employed in location programs to improve locations in the presence of poor quality data due to bad picks and high noise. The average mislocation was 19.5 km ($\pm 1\sigma$ = 10.4 km) without the correction and 15.4 ($\pm 1\sigma$ = 8.9 km) with the correction. The median mislocation also decreased to 13.8 km with the correction down from 19.3 km without the correction indicating the distributions of mislocations changed from a Gaussian "normal" distribution to one more skewed toward smaller mislocation distances. Figure 3 shows the improvement in locations after the corrections relative to the uncorrected locations. The larger the symbol, the closer in distance the relocation is to the GT location before using the correction. These improvements in relocations do not show any spatial pattern when corrections are applied to seismic events far outside the original source region used in the correction calibration. They are not correlated with distance from the center of the array. Some of the GT test events were out farther than 5 degrees (~500 km) from the source area where corrections are calculated. The events farthest from the center of the array show the largest improvement in location. Overall, 37 of the 50 earthquakes examined improved by an average of 37% (Figure 4; Table 1). The column in Table 1 showing Γ represents the percent improvement using station corrections (SC) between (1) and (2).

CONCLUSIONS AND RECOMMENDATIONS

In this study, we have relocated a set of 50 GT earthquakes as determined from regional modeling, to estimate the performance of the station correction methodology. We constructed station-specific source correction or "station correction" surface from 760 station corrections (global distribution) based on a small set of five well and closely located earthquakes in the central Tibetan Plateau. The station corrections were interpolated to develop a global surface for P-wave travel time corrections. As a test, we relocated a set of 50 GT earthquakes, with some seismic events located about 800 km from the center of the PASSCAL array across the Tibetan Plateau and surrounding regions. When the corrections were applied to the iasp91 velocity model, the mislocations decreased by an average by 37% for 37 out of the 50 GT events. This indicates significant improvement in seismic event locations relative to using the iasp91 model without P-wave travel-time corrections. Surprisingly, the distribution of mislocations did not vary or correlate with distance, and some of the farthest events from the center of the Tibetan Plateau were improved more than the locations in the center where the travel time corrections are more relevant. Myers and Schultz (2000) noted that correction surfaces for nearby stations are similar, suggesting coherent variations between the one-dimensional velocity model and the true velocity structure. Based on the assessment of the results, corrections could be developed from a small cluster of earthquakes and transported for use with seismic events outside of this area out to a radius of 800 km. Additional tests should be performed to further validate these claims, especially when crossing tectonic boundaries. This type of calibration and predicted transportability of the P-wave travel-time station corrections will make it more useful for regions of little to no tectonic activity or areas where detailed 3D velocity model calibration has not yet been performed, because of the ease of use in the application of the station correction methodology.

REFERENCES

Bondar, I. and R. G. North (1999). Development of calibration techniques for the Comprehensive Nuclear-Test-Ban Treaty (CTBT) international monitoring system, *Phys. Earth Planet. Int*. 113: 11–24.

Crotwell, H. P., T. J. Owens, and J. Ritsema (1999). The TauP ToolKit: Flexible seismic travel-time and ray-path utilities, *Seism. Res. Lett.* 70: 154–160.

Ichinose, G. A., J. G. Anderson, K. D. Smith, and Y. Zeng (2003). Source parameters of eastern California and western Nevada earthquakes from regional moment tensor inversion, *Bull. Seism. Soc. Am.* 93: 61–84.

IDC (1999), IDC processing of seismic, hydroacoustic, and infrasonic data, *IDC Documentation 5.2.1*, 302.

Myers, S. C. and S. C. Schultz (2000). Improving sparse network seismic location with Bayesian kriging and teleseismically constrained calibration events, *Bull. Seism. Soc.* Am. 90: 199–211.

Owens, T. J., G .E. Randall, F. T. Wu, and R. S. Zeng (1993). PASSCAL instrument performance during the Tibetan plateau passive seismic experiment, *Bull. Seism. Soc. Am*. 83: 1959–1970.

Richards-Dinger, K. B. and P. M. Shearer, P.M. (2000). Earthquake locations in southern California obtained using source-specific station terms, *J. Geophys. Res.* 105: 10,930–10,960.

Smith, G. P. and G. Ekstrom (1996). Improving teleseismic earthquake locations using a three-dimensional Earth model, *Bull. Seism. Soc. Am.* 86: 788–796.

Thurber, C. H., C. M. Trabant, F. Haslinger, and R. Hartog (2001). Nuclear explosion locations at the Balapan, Kazakhstan, nuclear test site: the effects of high-precision arrival times and three-dimensional structure, *Phys. Earth Planet. Int.* 123: 283–301.

Trabant, C. and C. Thurber (2001). Ground truth events and location capability at Degelen Mountain, Kazakhstan, *Phys. Earth Planet. Int.* (submitted).

Tan, Y., L. Zhu, D. V. Helmberger, and C. Saikia (2006). Locating and modeling regional earthquakes with two stations, *J. Geophys. Res*. 111: (B01306), doi:10.1029/2005JB003775.

Wessel, P. and W. H. F. Smith (1998). New improved version of GMT released, *EOS Trans., AGU*, 79: 574.

Zhu, L., Y. Tan, D. V. Helmberger, and C. Saikia (2006). Calibration of the Tibetan Plateau using regional seismic waveforms, *Pageoh* (in press).

Zhu, L. and D. V. Helmberger (1996). Advancement in source estimation techniques using broadband regional seismograms, *Bull. Seism. Soc. Am*. 86: 1634–1641.

Table 1. The CAP origin times, locations and mislocation vectors calculated from relocations using iasp91 without "station corrections" SC(1), iasp91 with SC(2), and published ISC(3) location.

ID	Date (y/m/d)	Time (h:m)	Lat	Lon	Δr(1) (km)	Φ(1) (°)	Δr(2) (km)	Φ(2) (°)	Δr(3) (km)	Φ(3) (°)	Γ̣ (%)
199	07/18/91	13:24	30.42	94.71	19.7	295	13.2	284	2.9	31	33%
201	07/20/91	19:02	30.42	94.81	6.1	343	2.0	295	2.9	31	67%
204	07/23/91	16:51	30.41	94.78	9.0	314	1.9	309	8.3	335	79%
205	07/24/91	06:06	30.44	94.69	13.9	310	10.7	264	7.7	11	23%
206	07/25/91	01:52	30.38	94.64	14.7	294	14.0	254	2.9	31	5%
209	07/28/91	23:58	30.40	94.74	12.5	267	19.6	8	15.2	215	0%
210	07/29/91	15:48	30.42	94.69	11.2	307	9.1	281	8.3	335	19%
211	07/30/91	22:22	30.43	94.74	8.8	295	3.1	246	8.3	335	64%
222	08/10/91	20:21	33.97	92.18	13.5	348	4.2	319	7.7	13	69%
239	08/27/91	05:14	34.37	91.84	33.4	314	26.3	314	3.1	35	21%
242	08/30/91	14:32	34.60	97.56	24.5	64	27.7	78	7.3	110	0%
245	09/02/91	11:05	37.77	95.57	48.6	11	43.7	12	7.5	110	10%
251	09/08/91	23:54	36.71	98.66	12.2	21	11.4	56	8.1	337	6%
252	09/09/91	21:54	28.69	94.94	15.4	206	28.9	183	13.0	344	0%
255	09/12/91	23:06	29.68	95.62	11.4	302	1.1	22	9.0	254	90%
263	09/20/91	11:16	36.24	100.16	20.8	20	16.2	27	7.7	166	22%
270a	09/27/91	07:39	34.77	99.02	19.3	34	17.0	70	8.2	336	12%
270b	09/27/91	11:56	29.82	90.36	58.0	187	27.7	183	8.3	335	52%
270c	09/27/91	23:31	30.91	95.63	266.6	129	273.7	129	3.0	33	0%
283	10/10/91	00:39	34.50	89.60	23.8	294	8.1	306	3.1	35	66%
323	11/19/91	01:04	32.49	93.82	43.1	359	23.5	11	25.4	152	45%
325	11/21/91	13:37	34.02	90.14	28.7	327	28.7	327	10.1	42	0%
328	11/24/91	07:35	34.04	88.94	11.8	19	15.2	66	7.3	110	0%
329	11/25/91	10:08	34.02	88.89	10.5	35	11.6	72	4.2	233	0%
330a	11/26/91	15:31	33.99	88.92	19.7	10	21.2	24	8.2	204	0%
330b	11/26/91	21:16	34.14	94.27	5.2	54	5.2	54	4.2	307	0%
336	12/02/91	19:45	32.10	94.56	10.6	247	14.9	198	15.5	299	0%
343	12/09/91	05:56	33.59	94.00	15.6	246	12.0	200	22.6	4	23%
348	12/14/91	08:20	34.04	88.83	15.5	349	10.7	345	3.0	35	31%
349	12/15/91	15:59	30.14	93.88	23.2	329	16.4	335	7.0	111	29%
351	12/17/91	20:27	34.04	88.83	15.9	318	12.6	302	4.2	307	20%
357a	12/23/91	01:58	34.05	88.84	25.1	346	14.4	356	4.2	307	43%
357b	12/23/91	02:14	34.01	88.86	18.9	323	8.1	309	8.2	336	57%
358	12/24/91	21:27	29.98	92.41	20.8	234	20.8	215	2.9	31	0%
360	12/26/91	13:24	30.92	99.50	13.8	306	11.3	260	2.9	148	18%
365	12/31/91	21:14	30.91	99.67	24.3	8	14.4	13	7.1	111	41%
2	01/02/92	02:35	34.09	88.76	29.0	329	17.8	326	3.0	35	39%
8	01/08/92	17:41	30.00	92.32	19.9	228	28.8	189	11.4	311	0%
23	01/23/92	10:26	34.52	93.21	2.1	256	6.3	151	3.1	35	0%
34	02/03/92	15:44	34.60	93.23	19.5	347	9.0	3	8.2	336	54%
37	02/06/92	03:35	29.71	95.66	19.4	347	13.8	2	2.9	150	28%
40	02/09/92	12:44	29.74	95.68	19.5	339	10.8	320	7.0	69	45%
76	03/16/92	01:18	34.50	86.33	24.6	358	21.7	25	4.1	307	12%
90	03/30/92	18:29	32.53	93.82	657.0	332	637.0	331	20.9	33	3%
104	04/13/92	03:47	31.75	88.22	20.7	226	26.4	202	3.0	33	0%
109	04/18/92	18:19	36.07	92.76	16.8	106	11.0	89	7.4	110	34%
137	05/16/92	20:19	36.31	100.27	25.4	35	25.2	51	4.0	232	1%
139	05/18/92	19:55	34.79	86.53	11.3	148	23.3	114	4.1	307	0%
143	05/22/92	05:47	30.89	99.70	26.5	0	8.3	38	12.6	7	69%
155	06/03/92	02:42	33.96	88.94	20.0	315	10.0	336	7.2	110	50%

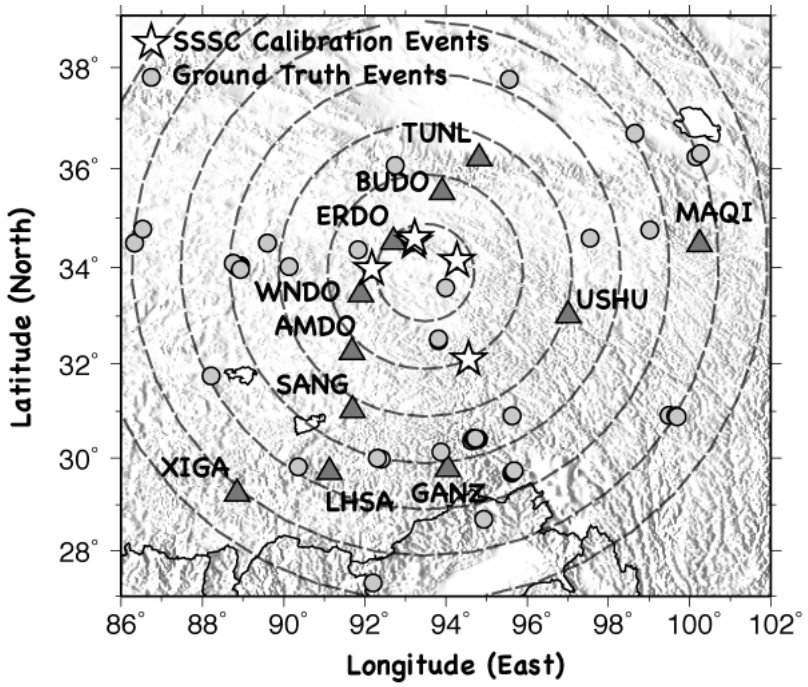

Figure 1. Location map of the 5 station correction calibration events and other GT5-GT10 events used in this study. The distance rings are at 1 degree increments centered on the centroid location of the 5 calibration events.

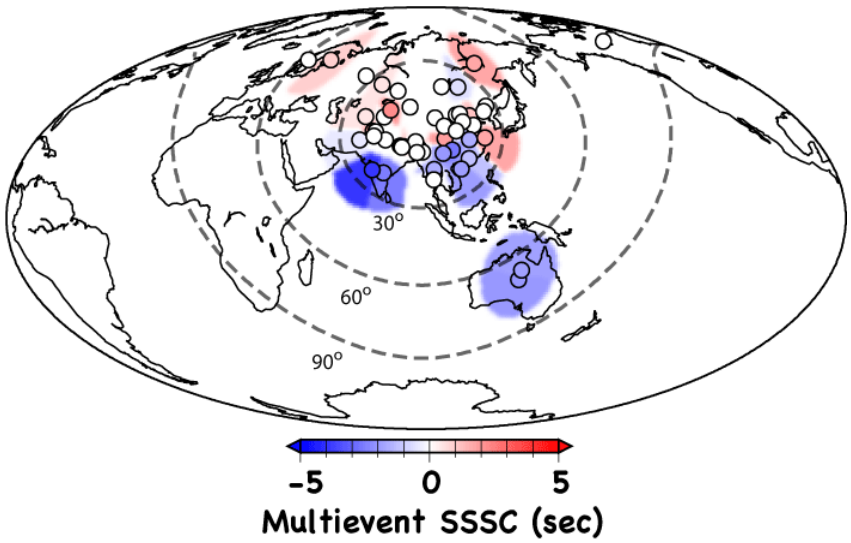

Figure 2. Global P-wave travel-time correction surface constructed using station residuals from 5 of the best-located seismic events within central Tibetan Plateau region from the GT catalog. The average station residuals from 2 or more events were used only if the value was below 1 standard deviation. The surface was constructed using the nearest neighbor algorithm. The 3 distance rings are centered at the centroid of the 5 GT event locations (33.87N, 93.49E) and are spaced in 30-degree increments.

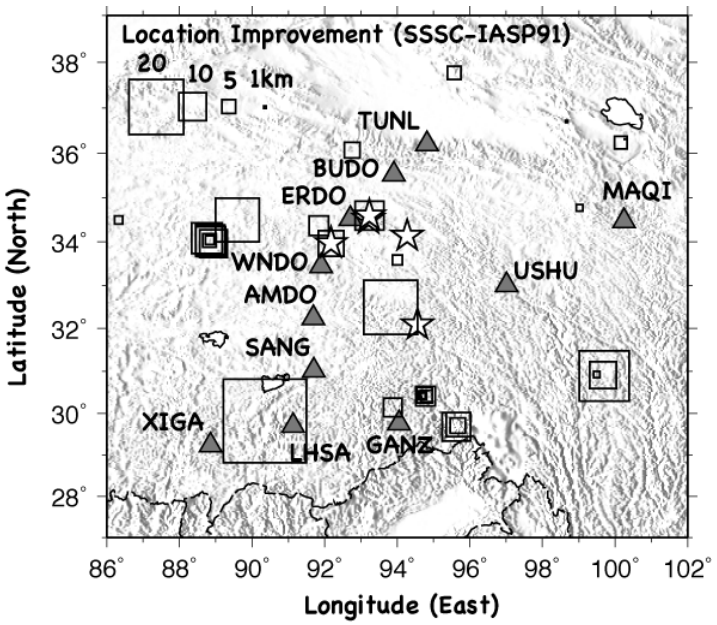

Figure 3. Location improvement in km, that is the difference between the mislocations with and without the P-wave travel-time corrections relative to the iasp91 model.

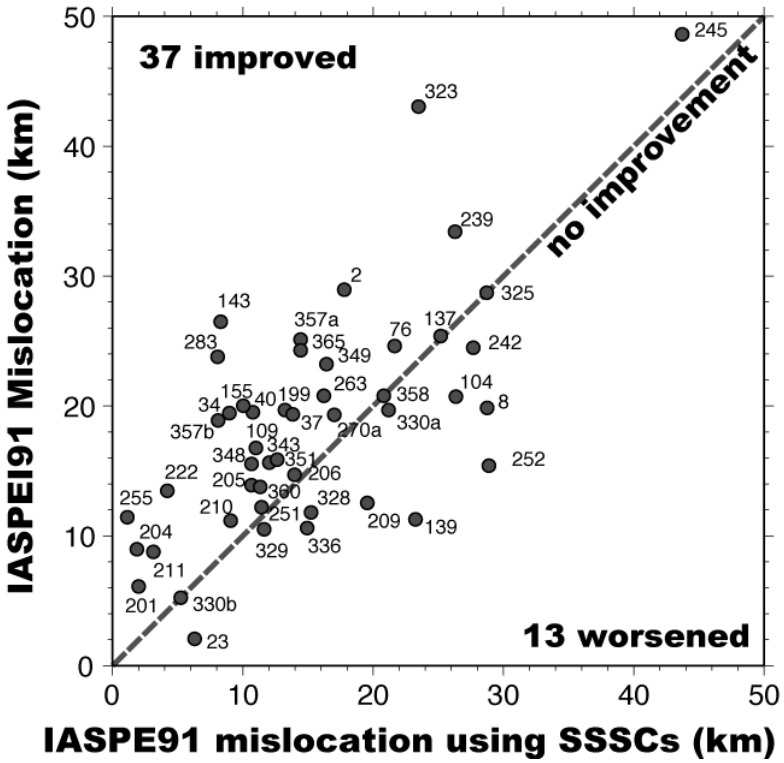

Figure 4. Mislocation plot for the 50 GT5-10 events with and without the multievent P-wave travel-time corrections. A total of 37 events improved in location while 13 events worsened in location relative to the GT catalog location.

TOMOGRAPHY AND METHODS OF TRAVEL-TIME CALCULATION FOR REGIONAL SEISMIC LOCATION

Stephen C. Myers[1], Sanford Ballard[2], Charlotte A. Rowe[3], Gregory S. Wagner[4], Michael S. Antolik[5], W. Scott Phillips[2], Abe L. Ramirez[1], Mike L. Begnaud[2], Mike E. Pasyanos[1], Doug A. Dodge[1], Megan P. Flanagan[1], Kevin D. Hutchenson[5], Glenn T. Barker[2], John J. Dwyer[4], and David R. Russell[4]

Lawrence Livermore National Laboratory[1], Sandia National Laboratory[2], Los Alamos National Laboratory[3], Air Force Technical Applications Center[4], Quantum Technology Sciences, Inc.[5]

Sponsored by National Nuclear Security Administration
Office of Nonproliferation Research and Development
Office of Defense Nuclear Nonproliferation

Contract Nos. W-7405-ENG-48[1], DE-AC04-94AL8500[2], DE-AC52-06NA25396[3], and FA8620-05-C-4301[5]

ABSTRACT

We are developing a laterally variable velocity model of the crust and upper mantle across Eurasia and North Africa to reduce event location error by improving regional travel time prediction accuracy. The model includes both P and S velocities, and we describe methods to compute travel times for Pn, Sn, Pg, and Lg phases. For crustal phases Pg and Lg we assume that the waves travel laterally at mid-crustal depth, with added ray segments from the station/event to the mid crustal layer. Our work on Pn and Sn travel times extends the methods described by Zhao and Xie (1993). With consideration for a continent-scale model and application to seismic location, we extend the model parameterization of Zhao and Xie (1993) by allowing the upper-mantle velocity gradient to vary laterally. This extension is needed to accommodate the large variation in gradient that is known to exist across Eurasia and North Africa. Further, we extend the linear travel-time calculation method to mantle-depth events, which is needed for seismic locators that test many epicenters and depths. Using these methods, Sandia National Laboratory has developed a code to compute regional travel times on-the-fly from the velocity model in milliseconds, forming the basis of a flexible travel-time facility that may be implemented in an interactive locator.

We use a tomographic technique to improve upon a laterally variable starting velocity model that is based on Lawrence Livermore and Los Alamos National Laboratory model compilation efforts. Our tomographic data set consists of approximately 20 million regional arrivals from events that meet the ground truth (GT) criteria of Bondar et al. (2004) and other non-seismic constraints. Each datum is tested to meet strict quality control standards that include comparison with established distance-dependent travel time residual populations relative to the model iasp91. In addition to bulletin measurements, nearly 50 thousand arrival measurements were made at the national laboratories. The tomographic method adjusts Pn velocity, mantle gradient, and a node-specific crustal slowness correction for optimized travel-time prediction.

OBJECTIVES

This project produces a laterally variable velocity model of the crust and upper mantle that is specifically designed for use in routine seismic location. At this time the Seismic Location Baseline Model (SLBM) is focused on travel-time prediction at local and regional distances. Therefore, ray paths are wholly within the crust and upper mantle. Like any travel-time prediction method used in a location algorithm the SLMB must return

1. An accurate travel-time prediction and
2. An uncertainty estimate of the travel-time prediction error

Because the SLBM is meant for use in routine location algorithms where networks can be dynamic and pre-computation of travel times for all available data may not be possible, the SLBM must also

3. Compute the travel time on-the-fly given regional- or local-distance station/event coordinates and
4. Return the travel time in milliseconds, thus enabling the estimation of a location in a few seconds

Further, we aim to improve a starting model that is based on a geophysical compilation. The improvement will be achieved using a ground-truth data set and a tomographic technique that is tailored to optimize model parameters important to seismic location.

RESEARCH ACCOMPLISHED

We meet the objectives outlined above by adapting several approaches for model parameterization and travel-time calculation into one package for computation of regional- and local-distance travel times for Pn, Sn, Pg, and Lg phases.

A challenge for this project is developing a model parameterization that enables fast and accurate prediction of each local/regional phase at all applicable distances. Well-established methods can be used to compute regional Pn and Sn travel times (e.g., Hearn, 1984), but the accuracy of these methods degrades at far regional (>1000 km) distance (e.g., Hearn et al., 2004). To more accurately predict Pn and Sn at far-regional distances, Zhao (1993) and Zhao and Xie (1993) approximate upper-mantle structure with a linear gradient, resulting in a simple expression for calculating travel time. For Pn and Sn, we adapt the Zhao and Xie (1993) approach for application to seismic location. For Pg and Lg (Sg) at local distances, we extract a vertical cross section from the model and use 2-dimensional ray tracing to compute the travel time. At regional distance, we approximate the crustal waveguide (Pg and Lg phases) with a laterally variable velocity layer, while accounting for propagation to/from the station/event using ray tracing.

In each instance we use tomographic methods to improve travel-time prediction of the model. Lawrence Livermore and Los Alamos National Laboratories (LLNL and LANL, respectively) are developing a joint ground truth data set for tomography that includes stringent quality control measures for arrival-time measurements. We adapt Pn tomographic methods (e.g., Hearn 2004; Zhao and Xie, 1993, Phillips et al., 2007) to improve travel-time predictions of each regional phase.

Model Parameterization

We combine the laterally variable layer approach of Pasyanos et al. (2004) with the linear mantle gradient of Zhao and Xie (1993). Layer definitions are specified in Table 1. Note that the thickness of some layers may be zero. For instance, on the continents the depth of the water layer coincides with the depth of the model layer exposed at the surface. Velocity vs. depth profiles are defined at nodes, and the profiles at the nodes are interpolated using an efficient code developed at Sandia National Laboratory (SNL) to determine velocity at any arbitrary location (lat,lon,depth). SNL has also developed a tessellation node structure on a spheroid with node spacing of approximately 1° (Figure 1). At present, the model development domain is Eurasia and North Africa, and nodes inside that domain capture the effects of 3-dimensional structure on travel times. Outside of the development domain nodes are set to a default velocity profile based on iasp91 (Kennett and Engdahl, 1991). This parameterization provides a seamless and extensible model. Expansion beyond Eurasia and North Africa does not require a change in the model parameterization itself, only modification of the velocity structure at previously defined nodes. Further, SNL has incorporated the GRS80 ellipsoid in to the model, eliminating the need for the conventional ellipticity correction to travel-time predictions.

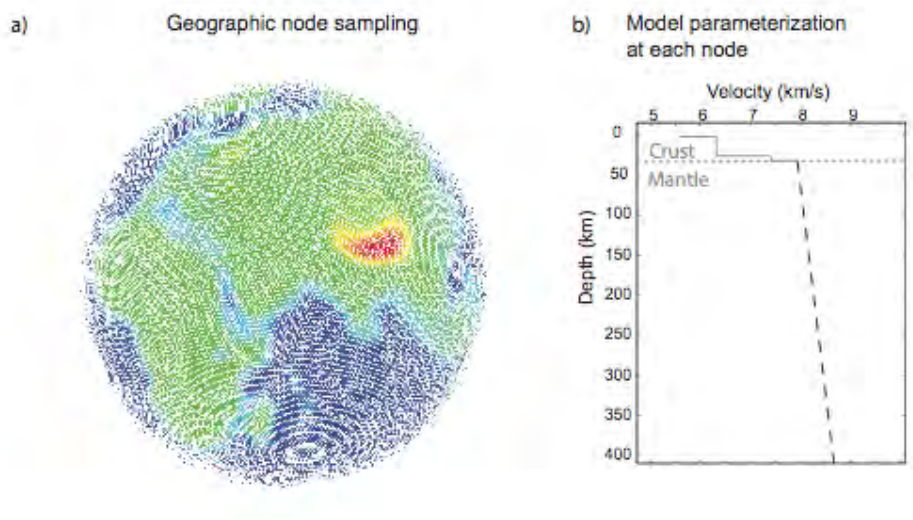

Figure 1. SLBM global parameterization. a) An example tessellation with approximately 1° grid spacing. Color is based on approximate Moho depth. b) An example velocity/depth profile as defined at each node. The mantle portion of the profile is specified by the velocity at the crust/mantle interface and a linear gradient.

Table 1. Model entities and associated parameters. Depths and velocities at each node are interpolated to define a 3-dimensional crustal model that overlies a laterally variable model in the shallow mantle. Note that the mid-crustal layer is distinct, in that the velocities are specified individually for each phase. For Pn and Sn the mid-crustal layer is used in conjunction with all other crustal layers to compute travel times for rays that travel steeply through the crust. For Pg and Lg distinct middle crust velocities are used to model the horizontal slowness of the regional phases that are trapped in the crust.

Model entity	Layer Depth	P-wave velocity	S-wave velocity	P-wave gradient	S-wave gradient
Water	Yes	Yes	Yes		
Sediment 1	Yes	Yes	Yes		
Sediment 2	Yes	Yes	Yes		
Sediment 3	Yes	Yes	Yes		
Upper Crust	Yes	Yes	Yes		
Middle Crust	Yes	Independent for Pn, Pg	Independent for Sn, Lg		
Lower Crust	Yes	Yes	Yes		
Moho	Yes	Yes	Yes		
Mantle Gradient				Yes	Yes

Travel-Time Calculation, Pn and Sn

The travel-time calculation is based on the method described in Zhao (1993) and Zhao and Xie (1993). This calculation is similar to the widely used approach of Hearn (1984), with an additional term (γ) introduced to account for diving rays that may occur due to a positive velocity gradient with depth and Earth sphericity.

The travel-time calculation is

$$TT = \sum_{i=1}^{N} d_i s_i + \alpha + \beta + \gamma \qquad [1]$$

where *d* and *s* are the distance and slowness (taken as 1/MohoVelocity) in each of the *i* segments comprising the great-circle path between Moho pierce points near the station/event, α and β are the crustal travel times at the source and receiver, and γ is a term that accounts for the effect of both mantle velocity gradient and earth sphericity.

We define α as

$$\alpha = \sum_{j=1}^{M} \left[\sqrt{r_j^2 / v_j^2 - p^2} - \sqrt{r_{j+1}^2 / v_j^2 - p^2} \right] \qquad [2]$$

where *v* and *r* are the velocity and layer radius of the *M* crustal layers from the event to the Moho, and *p* is the ray parameter (*p=1/v*, *v* evaluated at the ray bottoming depth).

We similarly define β as

$$\beta = \sum_{k=1}^{N} \left[\sqrt{r_k^2 / v_k^2 - p^2} - \sqrt{r_{k+1}^2 / v_k^2 - p^2} \right] \qquad [3]$$

where *v* and *r* are defined as above for the *L* crustal layers from the station to the Moho. The same *p* is used in both Eqns [2] and [3]. Because the ray bottoming depth is a function of the pierce point, *p* is determined through an efficient, iterative process.

Per Zhao and Xie (1993),

$$\gamma = -\frac{c^2 Xm^3}{24 V_0} \qquad [4]$$

where X_m is the horizontal distance traveled in the mantle, c is a velocity gradient in the mantle that is normalized by the velocity at the crust mantle boundary plus an additional term to account for Earth sphericity (Helmberger, 1973), and V_0 is a regional average of Pn velocity over the entire study area.

We introduce spatially varying *c* into the model (Phillips et al., 2007), and we calculate γ by averaging c along each ray. V_0 remains an average Pn velocity over the whole model, which allows us to take advantage of linear tomographic inversion methods (see below). Tests suggest that the approximation to V_0 introduces negligible travel-time error given Pn velocities ranging from 7.5 km/s to 8.3 km/s.

The Zhao (1993) method is applicable to events in the crust, making the approach well suited to nuclear explosion monitoring. However, seismic location algorithms may explore the possibility that an event occurred in the mantle, necessitating a consistent method of travel-time predictions for mantle events. The following extends the travel-time method to events in the shallow mantle, with the condition that $c^2h^2 << 1$ (h is the bottoming depth of the ray)

$$TT = \alpha + t_m \qquad [5]$$

where α is the crustal travel time from the Moho to the station (as defined in [2]), and t_m is the travel time in the mantle. Figure 2 shows the geometry and defines many of the variables used in the following equation.

$$t_m = \frac{\left[t_{Moho} \frac{x_m}{d} - \left(\frac{c^2 x_m^2}{24 V_0} \right) \right] \pm \left[t_{Moho} \left(\frac{x_z}{d(1 + c_m z_m)} \right) - \left(\frac{c^2 x_z^2}{24 V_{0z}} \right) \right]}{2} \qquad [6]$$

If the ray leaves the event upwards, then the second term is subtracted. If the ray leaves the event downwards, then the second term is added. t_{Moho} is the travel time for a ray traversing the Moho from the event to the point where the ray enters the crust and propagates to the station. x_m is the horizontal distance as measured at Moho radius by a ray that starts at the Moho then travels downward passing through the event and continuing to the station. x_z is similar to x_m, but the horizontal distance is measured at the radius of the event. *d* is the horizontal distance traveled in the mantle from the event to the Moho pierce point below the station, as measured at Moho radius. c_m is the mantle velocity gradient normalized by average Moho velocity, with the addition of a term to account for earth sphericity

(Helmberger, 1973). z_m is the depth of the event below the Moho. V_{oz} is the average model velocity at the depth of the event.

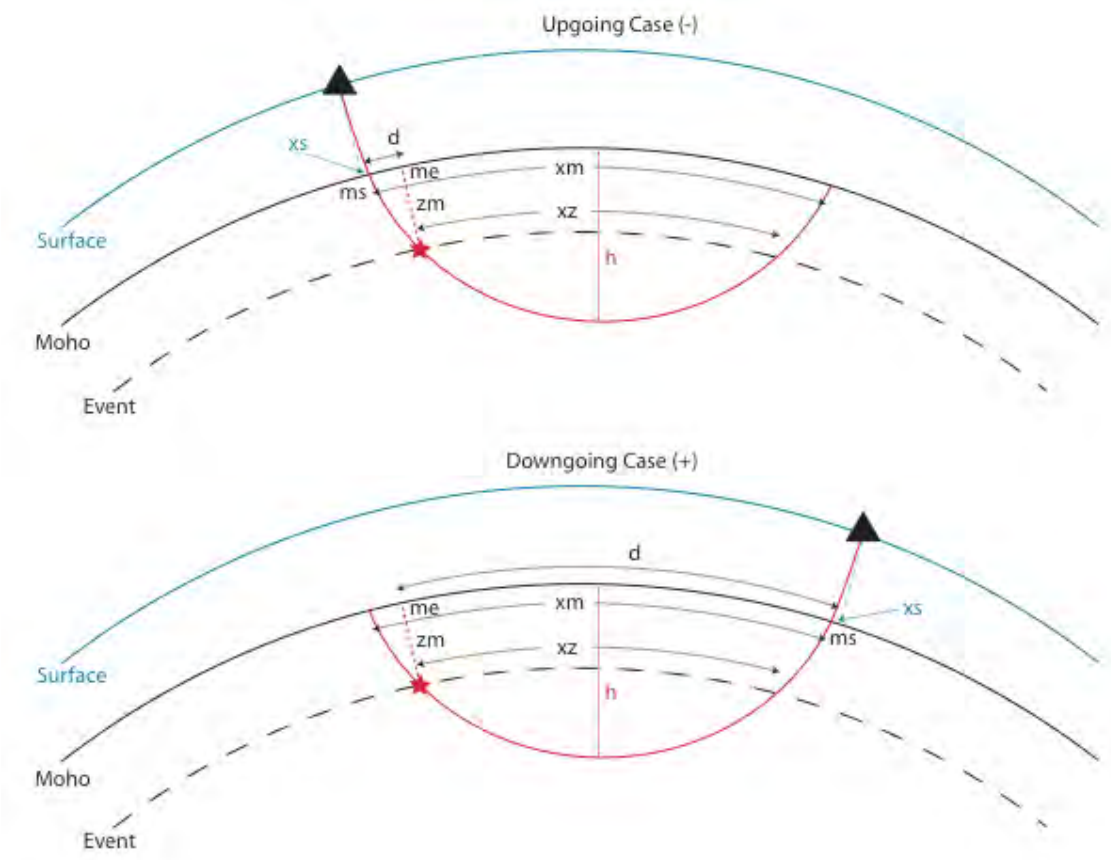

Figure 2. Geometry and variable definition extending the Zhao and Xie (1993) formulation to events in the shallow mantle. The red star is the event location and the triangle is the station location.

Travel-Time Calculation, Pg and Lg

Both Pg and Lg phases are trapped in the crust, and both phases exhibit complex waveforms that require hundreds or thousands of rays to model. Further, the first arriving ray with sufficient energy to be observed is dependent on geologic structure and station/event distance. Therefore, it is difficult to physically model the observed travel time using conventional ray techniques. Empirically, Pg and Lg travel at horizontal velocities of approximately 6.0 km/s and 3.2 km/s (respectively), which is suggestive of propagation in the middle crust. Further, event depth can impart a static travel-time delay, suggesting a component of propagation from the event to the middle crust then up to the station. We capture this travel-time behavior with a simple approximation whereby:

$$TT = \sum_{i=1}^{N} d_i s_i + \alpha + \beta \qquad [7]$$

where d_i is the distance traveled in the middle crust in each of N ray segments and α and β propagate the phase to and from the middle crust, respectively. When the source is above the middle crust, then the calculation is almost the same as [1], but the correction for a diving ray is not used. When the source is below the mid-crustal layer, we assume that the ray travels horizontally until Earth sphericity causes the ray to intersect the mid-crustal layer. While this approach by no means captures the physical complexity of Pg and Lg wave propagation, we find that it is suitable for estimating travel time.

Computational Efficiency

Travel-time facilities used in routine location algorithms must be computationally efficient. Analysts often iterate on arrival-time measurements, first locating the event with clear arrivals, then adding additional arrivals (or adjusting previous measurements) based on a preliminary location. The demands of routine seismic analysis preclude waiting more than a second or two for the calculation of a location before continuing work. Considering that a location requires the computation of travel times for many phases, over many iterations, often with numerical calculation of derivatives (at least 4 travel-time calculations per observation per iteration), the time to compute an individual travel time must be negligible (milliseconds).

The algebraic form of the travel-time formulas that are specified above consume negligible computer time. The primary challenge is fast extraction of the cross sectional profile needed for the travel-time calculation from the laterally variable model. The tessellation model parameterization developed at SNL takes advantage of mature algorithms to determine which triangle any given point lies within, which nodes comprise the triangle, and node weights used for interpolation. Figure 3 shows an example of a cross section and the Pn ray that is used to compute the travel time.

Test results show a linear increase in computer time as a function of station/event distance. In the distance range from ~200 km to ~2200 km, Pn/Sn travel times require ~1 milliseconds to 2 milliseconds to compute on a desktop computer with ~1.5Ghz clock speed. Pg/Lg times are faster.

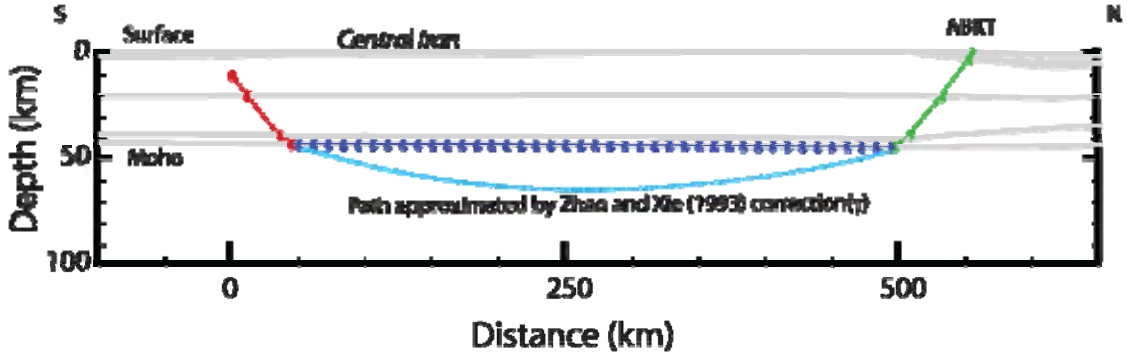

Figure 3. Cross section extracted from the laterally variable SLBM model. The components of the Pn/Sn travel-time calculation are also shown. The blue, red, green, and cyan colors correspond to the first, second, third, and fourth terms of Eqn 1.

Travel-Time Accuracy

We make use of many approximations to meet the challenge of fast, on-the-fly travel-time calculation. We test the accuracy of these calculations by comparing travel times computed using the methods described above (SLBM) with travel times computed using a fully 3-dimensional calculation described in Flanagan et al. (2007). The Flanagan et al. (2007) study uses the WENA1.0, 3-dimensional model of Pasyanos et al. (2004). For testing purposes, we use the WENA1.0 crustal model and mantle velocity at the Moho discontinuity. We then compute the linear mantle gradient using the velocity at the Moho and the velocity at 130 km depth.

Figure 4 shows representative results of our tests. Figure 4a,b shows the difference in Pn travel times computed using the SLBM method and using 3-dimensional finite difference, respectively. In both cases the comparisons are relative to the iasp91 model, and Pn travel times are computed using the TauP toolkit of Crotwell et al. (1999). The general features of Figure 4a and 4b are similar, with deviations from iasp91 travel times ranging from approximately 2 seconds late to 6 seconds early. Figure 4c shows the difference between the SLBM and finite-difference calculations, with deviations between the two methods generally between plus and minus 1 second. Errors in the finite difference calculations themselves are reported to be approximately plus and minus 0.5 seconds (Flanagan et al., 2007). These tests suggest that the efficient SLBM computational errors are slightly larger than the computationally demanding finite-differences calculations, and SLBM errors are relatively small compared to iasp91 travel-time anomalies.

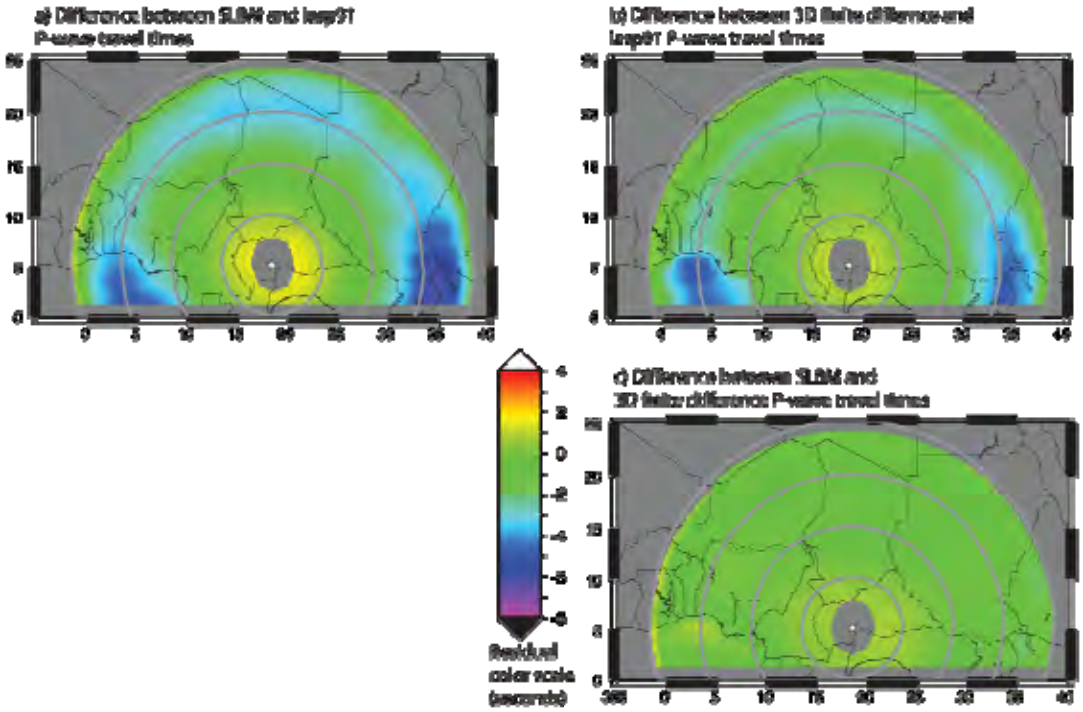

Figure 4. Comparision of Pn travel times using SLBM and 3D finite difference calculations for station BGCA in central Africa. For SLBM and 3D finite-difference calculations the WENA1.0 model of Pasyanos et al. (2004) is used. Circles around the station are 5° increments. See text details.

Tomography

Test results presented above suggest that the SLBM travel-time method is in good agreement with 3-dimensional calculations. The WENA1.0 model used in the tests above is shown to improve travel-time prediction and location accuracy relative to the iasp91 default model (Flanagan et al., 2007). We will further improve SLBM travel-time accuracy using tomographic methods.

A data set with small errors in event location and arrival-time measurements is critical to tomographic studies. Data coverage is also critically important. LLNL and LANL have combined ground-truth data sets for this study. Both national laboratories contribute global, regional, and local bulletins (some not widely available), as well as tens of thousands of arrival-time measurements made at the national laboratories. All event locations are evaluated against Bondar et al. (2004) epicenter accuracy criteria, and all picks are evaluated against an error budget that accounts for event mislocation, iasp91 prediction error, and arrival-time measurement error. Observations outside of the 99% confidence bounds for total error are removed. Figure 5 shows the extensive data coverage for Pn, Sn, Pg, and Lg throughout Eurasia.

We are using the SLBM travel-time calculator in tomographic inversion programs. The general form of the tomographic inversion for Pn/Sn is as follows:

$$T^k = \sum_{i=1}^{N} s_i^k x_i^k + \frac{\left(c^k\right)^2 \left(X_m^k\right)^3}{24 V_0} + \sum_{j=1}^{N} a_j^k \sum_{p=1}^{Q} \frac{l_p^k}{v_p^k} \qquad [8]$$

A significant difference between the formulation presented here and more typical Pn-tomography formulations is the introduction of a scalar value that adjusts the slowness of the crustal stack, as opposed to a static time-term to

account for crustal travel-time delays. Adjusting the crustal slowness produces a model that is better suited to account for the effects of event depth on predicted travel times and therefore better for estimating event depth.

The tomographic free parameters are more easily identified in matrix form:

$$\begin{bmatrix} x_1^1 & \cdots & x_N^1 & -\frac{x_1^1 (X_m)^3}{24 V_O X_m} & \cdots & -\frac{x_N^1 (X_m)^3}{24 V_O X_m} & \sum_{p=1}^{Q} \frac{l_{1p}^1}{v_{1p}} & \cdots & \sum_{p=1}^{Q} \frac{l_{Np}^1}{v_{Np}} \\ \vdots & & & & \ddots & & & & \vdots \\ x_1^K & \cdots & x_N^K & -\frac{x_1^K (X_m)^3}{24 V_O X_m} & \cdots & -\frac{x_N^K (X_m)^3}{24 V_O X_m} & \sum_{p=1}^{Q} \frac{l_{1p}^K}{v_{1p}} & \cdots & \sum_{p=1}^{Q} \frac{l_{Np}^K}{v_{Np}} \\ & & & & & \text{Regularization} & & & \end{bmatrix} * \begin{bmatrix} s_1 \\ \vdots \\ s_N \\ c_1^2 \\ \vdots \\ c_N^2 \\ a_1 \\ \vdots \\ a_N \end{bmatrix} = \begin{bmatrix} T^1 \\ \vdots \\ T^K \\ \text{Regularization} \end{bmatrix} \quad [9]$$

where

T = *travel time,*
s = *Pn slowness,*
x = *Pn distance (or weight),*
c = *normalized velocity gradient v=vo(1+cz),*
Xm = *length of Pn path,*
Vo = *average Pn velocity,*
v = *velocity of a crustal layer,*
k = *index on K paths (travel-time observations),*
i = *index on N model nodes (mantle path),*
j = *index on N model nodes (crustal path),*
p = *index on Q crustal layers, and*
a = *scalar adjustment to the crustal slowness stack at each node.*

CONCLUSIONS AND RECOMMENDATIONS

We describe the progress of the SLBM project to date. This project is distinct because it tailors the travel-time prediction algorithm and tomography results for use in routine seismic location algorithms. Emphasis is placed on travel-time prediction accuracy and computational efficiency of regional phases.

The tessellation model parameterization provides seamless global coverage. The use of a tessellation approach also allows fast interpolation of model parameters to extract the great-circle cross section of velocity structure that is needed to compute regional travel times. The current focus of the SLBM effort is Eurasia and North Africa, and model nodes outside of that area are set to a default velocity structure based on the iasp91 model (Kennett and Engdahl, 1991). We note that the model is extensible, and a global calibration effort would entail updating node-centered velocity profiles (by whatever means), which does not require updates to the model tessellation or travel-time codes.

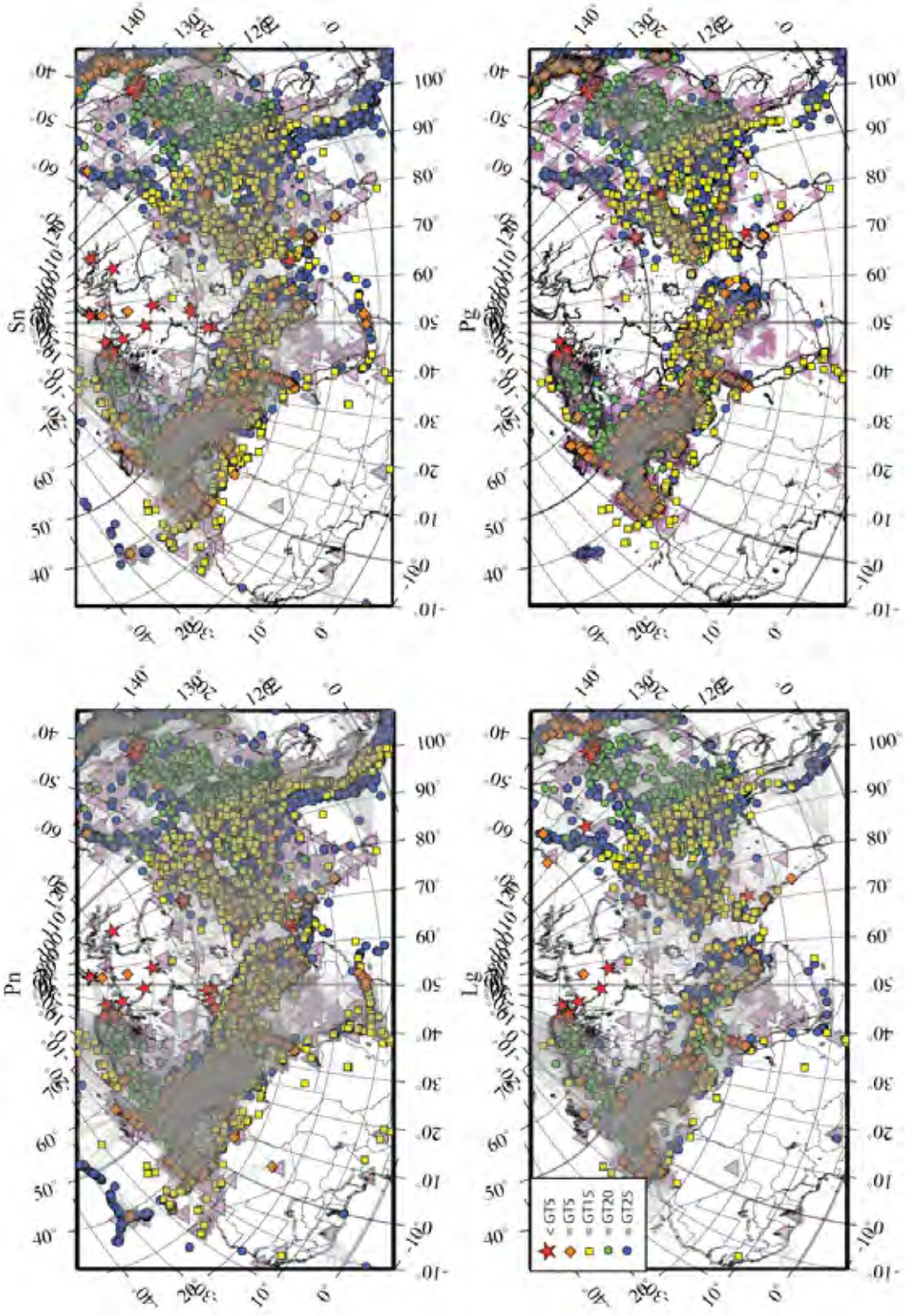

Figure 5. Tomographic data set. Purple triangles are stations with at least 1 regional-distance arrival-time measurement. Ground-truth location and accuracy (as defined in Bondar et al., 2004) are shown in the legend in the lower left. Regional ray coverage (shown by gray lines) is excellent throughout the study area, with the exception of North Africa.

We make use of several approximations that result in a relatively simple algebraic form for travel-time calculations. We have tested the accuracy of the approximate methods against full, 3-dimensional finite-difference calculations. The differences between the approximate methods and full, 3-dimensional finite-difference methods are estimated to be less than 10% of errors observed by using a simple iasp91 background model. Therefore, we conclude that the approach developed here is a significant improvement in routine location practice.

We have developed an extensive, quality-controlled, ground-truth data set across Eurasia and North Africa. This data set will be used in tomographic codes that employ the SLBM travel-time calculator to further optimize the model parameters that are most important to seismic location.

ACKNOWLEDGEMENTS

This project would not be possible without the enthusiastic support of Leslie Casey in the Department of Energy office of NNSA/NA-22. Steve Myers also wishes to thank Dave Harris for daily interactions and general technical discussions.

REFERENCES

Bondar, I., S. Myers, E. R. Engdahl, and E. Bergman, (2004). Epicenter accuracy based on seismic network criteria, *Geophys. J. Int.* 156: no. 3, 483–496.

Flanagan, M. P., S. C. Myers, and K. D. Koper (2007). Regional travel time uncertainty and seismic location improvement using a three-dimensional a priori velocity model, *Bull. Seismolog. Soc. Am*. 97: 804–825.

Crotwell, H. P., T. J. Owens, and J. Ritsema (1999). The TauP ToolKit: flexible seismic travel-time and raypath utilities, *Seism. Res. Lett.* 70: 154–160.

Hearn, T. M. (1984). Pn travel times in southern California, *Jour. Geophys. Res*. 89: 1843–1855.

Hearn, T. M., S. Wang, J. F. Ni, Z. Xu, Y. Yu, and X. Zhang (2004). Uppermost mantle velocities beneath China and surrounding regions, *J. Geophys. Res.* 109: B11301, doi:10.1029/2003JB002874.

Helmberger, D.V. (1973). Numerical seismograms of long-period body waves from seventeen to forty degrees, *Bull. Seismol. Soc. Am*. 63: 633–646.

Kennett, B. L. N. and E. R. Engdahl, (1991). Traveltimes for global earthquake reference location and phase identification, *Geophys. J. Int*, 105: 429–465.

Pasyanos, M. E., W. R. Walter, M. P. Flanagan, P. Goldstein, and J. Bhattacharyya (2004). Building and testing an a priori geophysical model for western Eurasia and North Africa, *Pure. And Applied Geophys*. 161: 235–281.

Phillips, W. S., M. L. Begaud, C. A. Rowe, L. K. Steck, S. C. Myers, M. E. Pasyanos, and S. Ballard (2007). Accounting for lateral variations of the upper mantle gradient in Pn tomography studies, *Geophys. Res. Lett*., Revised.

Zhao, L.-S. (1993). Lateral variations and azimuthal isotropy of Pn velocities beneath Basin and Range province, *Jour. Geophys. Res*. 98: 22:109–22.

Zhao and Xie (1993). Lateral variations in compressional velocities beneath the Tibetan Plateau from Pn traveltime tomography, *Geophys. J. Int*. 115: 1070–1084.

GROUND TRUTH, MAGNITUDE CALIBRATION AND REGIONAL PHASE PROPAGATION AND DETECTION IN THE MIDDLE EAST AND HORN OF AFRICA

Andrew A. Nyblade[1], Richard A. Brazier[1], Aubreya Adams[1], Yongcheol Park[1], Arthur J. Rodgers,[2] and Abdullah Al-Amri[3]

Penn State University[1], Lawrence Livermore National Laboratory[2], and King Saud University[3]

Sponsored by National Nuclear Security Administration
Office of Nonproliferation Research and Development
Office of Defense Nuclear Nonproliferation

Contract Nos. DE-FC52-05NA26602[1] and W-7405-ENG-48[2]

ABSTRACT

In this project, we are exploiting several seismic data sets to improve U.S. operational capabilities to monitor for low yield nuclear tests across the Middle East (including the Iranian Plateau, Zagros Mountains, Arabian Peninsula, Turkish Plateau, Gulf of Aqaba, Dead Sea Rift) and the Horn of Africa (including the northern part of the East African Rift, Afar Depression, southern Red Sea and Gulf of Aden). The data sets are being used to perform three related tasks. (1) We are determining moment tensors, moment magnitudes and source depths for regional events in the magnitude 3.0 to 6.0 range. (2) These events are being used to characterize high-frequency (0.5–16 Hz) regional phase attenuation and detection thresholds, especially from events in Iran recorded at stations across the Arabian Peninsula. (3) We are collecting location ground truth at GT5 (local) and GT20 (regional) levels for seismic events with M > 2.5, including source geometry information and source depths.

Towards meeting these objectives, seismograms from earthquakes in the Zagros Mountains recorded at regional distances have been inverted for moment tensors, which have then been used to create synthetic seismograms to determine the source depths of the earthquakes via waveform matching. The source depths have been confirmed by modeling teleseismic depth phases recorded on Global Seismographic Network (GSN) and International Monitoring System (IMS) stations. Early studies of the distribution of seismicity in the Zagros region found evidence for earthquakes in the upper mantle. But subsequent relocations of teleseismic earthquakes suggest that source depths are generally much shallower, lying mainly within the upper crust. All of the regional events studied so far nucleated within the upper crust, and most of the events have thrust mechanisms. The source mechanisms for these events are being used to characterize high-frequency (0.5–16 Hz) regional phase attenuation and detection thresholds for broadband seismic stations in the Arabian Peninsula, including IMS stations and stations belonging to the Saudi Arabian National Digital Seismic Network.

To improve event locations, source mechanisms and attenuation estimates, new regional P and S wave velocity models of the upper mantle under the Arabian Peninsula have also been developed using data from teleseismic events recorded at stations within the Arabian Peninsula and Horn of Africa. These models show slower-than-average velocities within the lithsopheric mantle under the entire Arabian Shield. However, at sublithospheric mantle depths, the low velocity region appears to be localized beneath the western side of the Arabian Shield.

OBJECTIVE

The objective of this effort is to determine ground truth source parameters (depth, moment, focal mechanism) for earthquakes in the Middle East. For this reporting period we focused on events in the Zagros Mountains of Iran and used unique broadband waveforms from regional stations. Source moments are being used to calibrate coda wave moment magnitudes (Mayeda et al., 2003) and to model high-frequency regional body-wave amplitude spectra with the magnitude-distance amplitude correction (MDAC) methodology (Walter and Taylor, 2002). In subsequent periods, we will determine models of the propagation characteristics, including attenuation, of high-frequency regional phases. These models will then be used to estimate detection thresholds by comparing model-based predictions of signal amplitudes to background noise levels. To help in this effort, we have also developed new velocity models of the upper mantle beneath the Arabian Peninsula.

RESEARCH ACCOMPLISHED

Introduction

In this project, we are exploiting unique and open source seismic data sets to improve seismic monitoring for the Middle East (including the Iranian Plateau, Zagros Mountains, Arabian Peninsula, Turkish Plateau, Gulf of Aqaba, Dead Sea Rift) and the Horn of Africa (including the northern part of the East African Rift, Afar Depression, southern Red Sea and Gulf of Aden). Broadband waveform data sets are being used to perform three related tasks. (1) We are determining moment tensors, moment magnitudes and source depths for regional events in the magnitude 3.0 to 6.0 range.(2) These events are being used to characterize high-frequency (0.5–16 Hz) regional phase attenuation and detection thresholds, especially from events in Iran recorded at stations across the Arabian Peninsula. (3) We are collecting location ground truth at GT5 (local) and GT20 (regional) levels for seismic events with M >2.5, including source geometry information and source depths.

The results of this research will enhance monitoring capabilities within the study region by improving our understanding of high frequency regional phase attenuation and how this attenuation affects detection thresholds. Accurate hypocentral locations of M >2.5 seismic events are needed to construct travel time correction surfaces, which are of fundamental importance to ground-based nuclear explosion monitoring.

Towards meeting these objectives, seismograms from earthquakes in the Zagros Mountains recorded at regional distances have been inverted for moment tensors, which have then been used to create synthetic seismograms to determine the source depths of the earthquakes via waveform matching. The source depths have been confirmed by modeling teleseismic depth phases recorded on GSN and IMS stations. Early studies of the distribution of seismicity in the Zagros region found evidence for earthquakes in the upper mantle. But subsequent relocations of teleseismic earthquakes suggest that source depths are generally much shallower, lying mainly within the upper crust. All of the regional events studied so far nucleated within the upper crust, and most of the events have thrust mechanisms. The source mechanisms for these events are being used to characterize high-frequency (0.5–16 Hz) regional phase attenuation and detection thresholds for broadband seismic stations in the Arabian Peninsula, including IMS stations and stations belonging to the Saudi Arabian National Digital Seismic Network.

To improve event locations, source mechanisms and attenuation estimates, new regional P- and S-wave velocity models of the upper mantle under the Arabian Peninsula have also been developed using data from teleseismic events recorded at stations within the Arabian Peninsula and Horn of Africa. These models show slower-than-average velocities within the lithsopheric mantle under the entire Arabian Shield. However, at sublithospheric mantle depths, the low velocity region appears to be localized beneath the western side of the Arabian Shield.

Background

The Arabian Shield consists of late Proterozoic crystalline basement overlain by Tertiary and Quaternary volcanic rocks in some places. The breakup of the Arabian Plate from Africa initiated at about 30–35 Ma,

with the formation of the Red Sea-Gulf of Aden rift system (Coleman and McGuire, 1988). Volcanism was widespread between 30 and 12 Ma, and uplift of the Arabian Shield occurred at about 13 Ma (Coleman and McGuire, 1988). The volcanism and uplift are thought to be related to the presence of hot upper mantle (Camp and Roobol, 1992). The uplifted Arabian Shield contains two major features: one is the Makkah-Madinah-Nafud (MMN) volcanic line in the south and the other is the Ha'il-Rutbah Arch in the north (Figure 1). The MMN volcanic line, extending north-south, has been the major site of volcanism in Saudi Arabia over the past 10 Ma and the Ha'il-Rutbah Arch has been the site of several periods of uplift (Camp and Roobol, 1992).

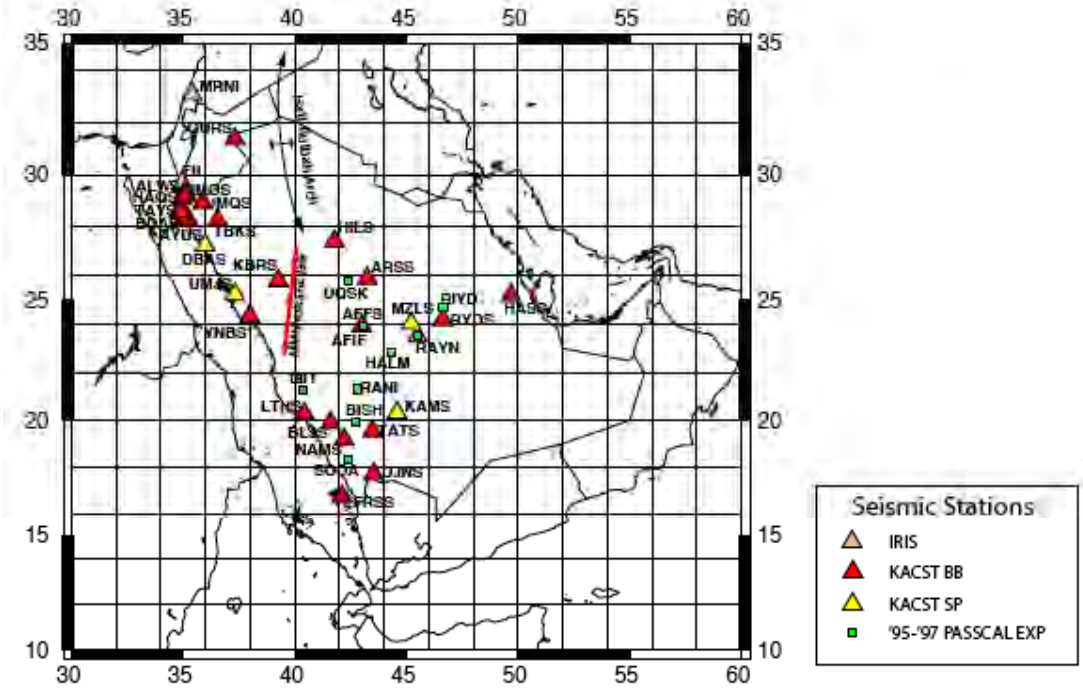

Figure 1. Map showing seismic stations in the Arabian Peninsula used in this study. KACST stations belong to the Saudi Arabia Digital National Seismic network.

The Zagros Mountain Belt, one of the world's most seismically active mountain ranges, marks the convergent boundary between the Arabian and Eurasian plates in southwestern Iran (Figure 2). The upper 11 km of the crust consists of folded sedimentary layers, while the lower 36 km of the crust are composed of faulted crystalline basement rock. The most prominent fault exposed at the surface is the Zagros Main Thrust, which marks the northern extent of seismicity associated with the Zagros Mountains and separates the Zagros Mountains from the Central Iranian Plateau. The Moho dips to the northeast from a depth of 40 km beneath the Persian Gulf to a maximum depth of approximately 65–70 km beneath the Zagros Main Thrust (Paul et al., 2006). Early studies of the distribution of seismicity in the Zagros region found evidence for earthquakes in the upper mantle (Nowroozi, 1971; Bird et al., 1975). Subsequent recalculations of teleseismic earthquakes indicated that source depths were much shallower, lying within the upper crust (Maggi et al., 2000, 2002).

Zagros Earthquakes

Source depths and focal mechanisms for six well-studied events have been obtained (Table 1). A grid search method was used to determine the source parameters of each event. First, regional waveforms for each event were inverted for a moment tensor over a range of potential source depths. Synthetic seismograms were then computed using a reflectivity code for each source mechanism and compared to observed waveforms. In addition to the KACST and Program for the Array Siesmic Studies of the continental Lithosphere (PASSCAL) stations, data recorded at regional distances on open stations to the north and east were used, providing fairly good azimuth ray coverage for each event. The quality of the

visual fit between the synthetic and observed waveforms, along with the root mean square error, was used to determine the best-fitting focal mechanism and associated source depth.

In addition, to help constrain focal depths, teleseismic depth phases from open stations in the 30 to 90 degree distance range have been modeled using the focal mechanism obtained from the grid search at a particular depth.

Figure 2. Colored topography map of the Middle East showing the location of the main plates and the Zagros Mountains.

The locations of the events are shown in Figure 3. Most of the events studied occurred within the central portion of the Zagros Mountains where there are the best constraints on crustal structure provided by receiver function and gravity studies. Figures 4a and 4b summarize graphically the results for two of the events, and serve to illustrate the quality of the waveform fits that we have obtained. Source depths for the events are within the upper crust.

Table 1a. Source parameters for well-studied events in the Zagros Mountains. Event letters are the same as in Figure 3.

Event Letter	Event ID Number	Date MM/DD/YYYY	Time	M0	Mw	Mw CMT	Strike/Dip/Rake (Plane 1)	Strike/Dip/Rake (plane 2)
A	9962	11/13/1998	13:01:10	1.35E+24	5.4	5.4	144.21/65.33/120.95	269.05/38.80/41.76
B	1320614	10/31/1999	15:09:40	7.13E+23	5.2	5.2	158.09/69.17/102.39	306.38/24.10/60.58
C	4070289	03/01/2000	20:06:29	1.93E+23	4.8	5.0	298.57/49.98/134.73	61.56/57.04/50.03
D	1582024	02/17/2002	13:03:53	1.01E+24	5.3	5.5	109.24/10.24/76.99	302.46/80.03/92.33
E	4357281	07/10/2003	17:40:16	4.64E+24	5.7	5.6	343.19/6.42/35.13	218.22/86.31/95.26
F	1559906	04/13/2001	01:04:27	3.93E+23	5	5.1	96.81/14.85/134.62	231.21/79.49/79.45

Table 1b. Moment tensors and source depth for well-studied events in the Zagros Mountains. Event letters are the same as in Figure 3.

Event Letter	Mxx	Mxy	Mxz	Myy	Myz	Mzz	Depth
A	8.67E+10	3.73E+10	-4.49E+09	5.16E+09	-9.42E+10	-9.19E+10	12 (+-2)
B	2.35E+10	1.97E+10	-1.13E+10	2.72E+10	-5.13E+10	-5.08E+10	12 (+-2)
C	1.79E+10	2.01E+08	-1.97E+09	-4.28E+09	1.04E+10	-1.36E+10	9 (+-3)
D	2.85E+10	1.84E+10	7.94E+10	2.29E+09	5.09E+10	-3.08E+10	4 (+-2)
E	4.01E+08	1.31E+10	2.90E+11	8.04E+10	-3.54E+11	-8.08E+10	39 (+10/- 15)
F	1.52E+10	5.69E+08	2.55E+10	2.08E+09	-2.50E+10	-1.73E+10	8 (+-3)

In addition to the six well-studied events in the region of the Zagros where crustal structure is best known, we also have preliminary moment tensor solutions for several other events spread throughout the Zagros Mountains. Teleseismic depth phases for these events have been identified on short-period data from the Norwegian Seismic Array (NORSAR), but they have not yet been modeled to determine source depth. The preliminary results for these events are provided in Table 2.

Table 2a. Source parameters for other events in the Zagros Mountains

Event Num.	Event ID Number	Date MM/DD/YYYY	Time	M0	Mw	Mw CMT	Strike/Dip/Rake (Plane 1)	Strike/Dip/Rake (plane 2)
1	6307	04/19/1997	05:53:14	1.36E+24	5.4	5.5	177.91/9.16/251.53	16.60/81.31/87.08
2	6758	10/20/1997	06:09:04	9.64E+23	5.3	5.6	129.15 /0.60/120.46	278.68/ 89.49/89.7
3	8893	07/10/2003	19:40:27			5.9	315.51/5.86/-4.29	49.77/89.56/264.16
4	4357280	02/17/2002	17:06:37	7.52E+24	5.9	5.9	67.7/1.83/142.71	194.97/88.89/88.54

Table 2b. Moment tensors and source depth for other events in the Zagros Mountains

Event Num.	Mxx	Mxy	Mxz	Myy	Myz	Mzz	Depth
1	1.89E+10	1.64E+10	7.23E+10	-5.18E+10	-1.81E+11	3.29E+10	4 (+-2)
2	5.58E+09	2.69E+09	9.5E+10	-8.20E+09	1.46E+10	2.62E+09	4 (+-2)
3	-2.32E+10	-8.2E+08	1.53E+09	-1.60E+09	-1.32E+10	7.27E+10	5 (+-2)
4	9.23E+10	1.00E+10	1.89E+11	-1.84E+10	-7.23E+11	-7.39E+10	5 (+-2)

The focal depth of earthquakes can affect the excitation of regional phases, particularly the guided Lg phase, which is composed of higher mode surfaces waves whose amplitudes are strongly depth dependent. The source parameters determined above can be used to infer how focal mechanism and depth might impact regional phase S-wave generation and this might in turn impact P/S discriminants. Two nearby events (A and H) were recorded at station HILS on the northern Arabian Shield. Event A is the same event as in Table 1 and Figure 3. Event H was reported in Nyblade et al. (2006) for this project. These events had similar magnitudes (5.4 versus 5.7) and although are both thrust mechanisms their strikes are slightly different. The high-frequency (0.5–5 Hz) response of these events are shown in Figure 5. Note that Lg is weaker with respect to the Pn for the deeper event (H), making the Pn/Lg ratio discriminant more explosion-like for this event. This suggests a possible depth-dependence of the Lg amplitude (and Pn/Lg ratio discriminant). Alternatively, the further event (H) may be located in a region of thicker crust, which leads to disruption of the crustal waveguide along the path to HILS. Both explanations would cause additional scatter in body-wave discriminants, compounding discrimination strategies. These observations will be explored in further work on this project.

Body Wave Tomography

Upper mantle structure strongly impacts the propagation of regional Pn and Sn phases. We report velocity structure of the upper mantle reported from teleseismic P and S body waves. While this study resolves deep upper mantle structure, there are likely relationships with structure directly below the crust. To investigate upper mantle structure under the Arabian Shield, measured and inverted relative travel times from stations in Arabia. We augmented the KACST data with delay times measured from permanent stations in the region (RAYN, EIL and MRNI) and the 1995-7 Saudi Arabian PASSCAL Experiment data set. Figure 1 shows the locations of seismic network used in this study. We computed travel time differences for two nearly co-located stations (AFFS and AFIF in Figure 1) between KACST and the PASSCAL networks in order to investigate possible biases between these data sets before combining all delay times from different seismic networks. We sorted events recorded on the common stations by back azimuth and distance and measured P-wave travel time residuals from arrival times subtracted from a theoretical travel time. The trends of the residuals with back-azimuth and distance are very similar and indicate no bias between the travel time residuals for the common stations.

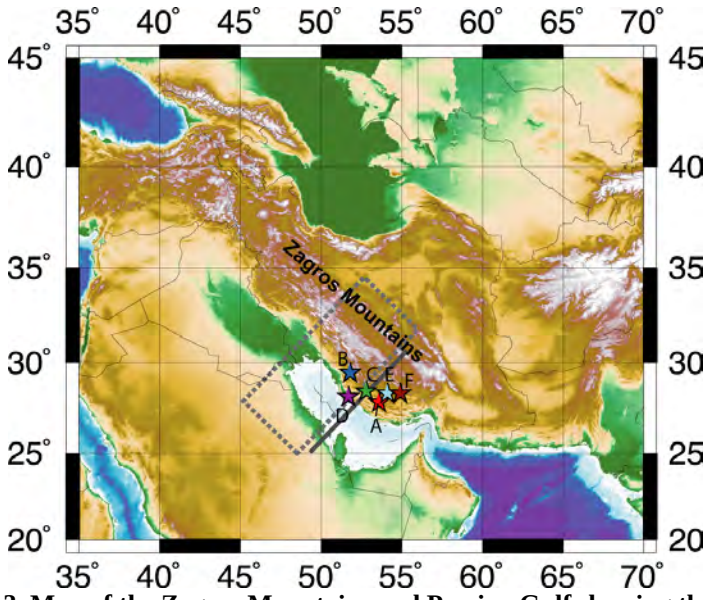

Figure 3. Map of the Zagros Mountains and Persian Gulf showing the locations of earthquakes studied. Letters correspond to the events in Table 1. The grey box shows area where crustal thickness has been constrained using gravity data and the white line shows were crustal thickness has been imaged using receiver functions.

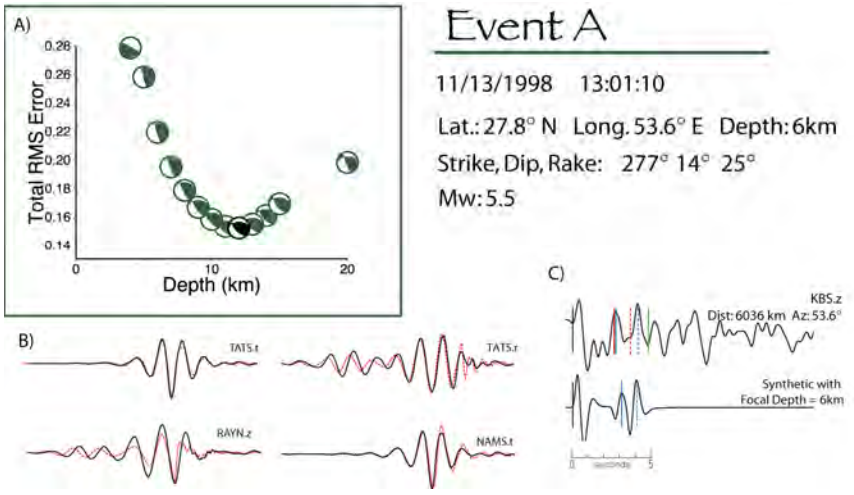

Figure 4a. Example result for one of the well-studied earthquakes illustrating the method used for obtaining source parameters and the quality of the waveform fits. A) Plot of focal depth vs. error showing a source depth of about 12 km. B) Long period regional displacement waveforms (black line) and synthetics (red dotted line) for a number of stations. C) Short period teleseismic waveforms showing depth phases. The top trace is the data and the bottom one is a synthetic. Solid blue line is our pP pick and the dotted blue line is our sP pick. The other colored lines show pP and sP picks from various catalogs. The short period depth phases give a source depth of 6 km, which is not inconsistent with the source depth obtained from the grid search, indicating a broad minimum in the RMS error (see A) between about 6 and 15 km depth.

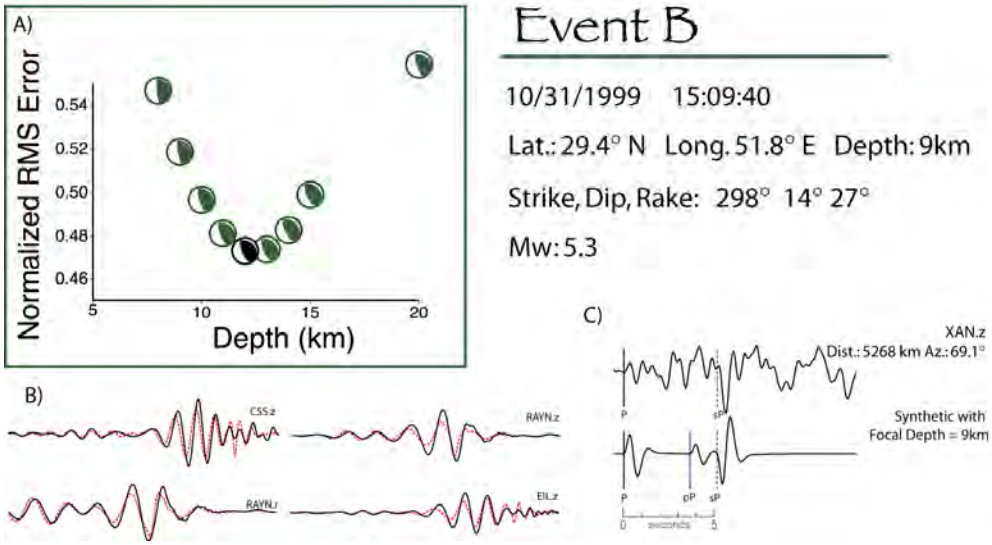

Figure 4b. Example result for one on the well-studied earthquakes illustrating the method used for obtaining source parameters and the quality of the waveform fits. A) Plot of focal depth vs. error showing a source depth of about 12 km. B) Long period regional displacement waveforms (black line) and synthetics (red dotted line) for a number of stations. C) Short period teleseismic waveforms showing depth phases. The top trace is the data and the bottom one is a synthetic. Solid blue line is our pP pick and the dotted blue line is our sP pick. The short period depth phases give a source depth of 9 km, which in not inconsistent with the source depth obtained from the grid search, indicating a broad minima in the RMS error (see A) between about 9 and 15 km depth.

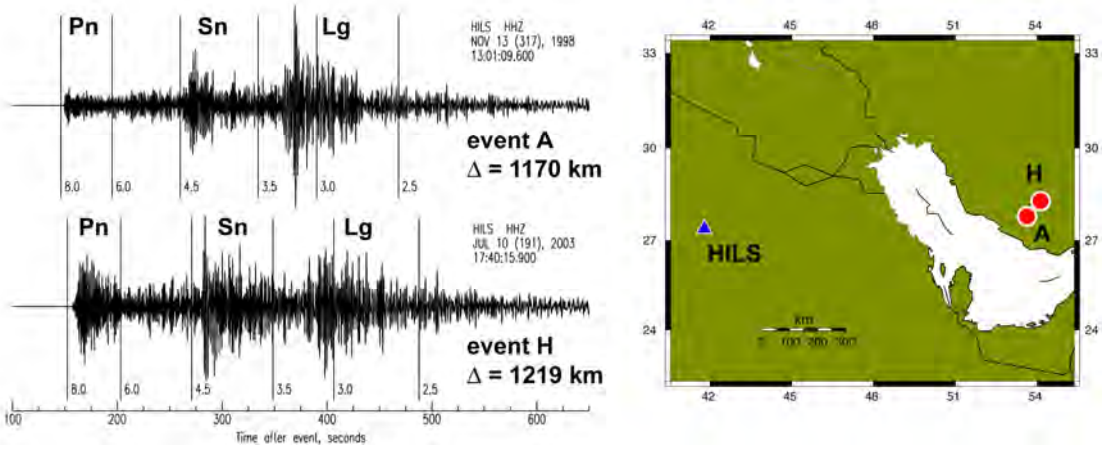

Figure 5. (left) Vertical component waveforms (filtered 0.5–5 Hz) for events A (top) and H (bottom) at station HILS (Al Hail, Saudi Arabia). (right) These events are closely located with event H slightly further away.

For the data sets, we computed relative arrival time residuals using a multi-channel cross-correlation method (VanDecar and Crosson, 1990) and inverted for a three dimensional velocity model using the method of VanDecar (1991). For the inversion, we parameterized travel time slowness using a grid of knots comprised of 34 knots in depth, 56 knots latitude between 12.0° N and 37.0° N and 56 knots in longitude between 29.5° E and 55.0° E. The horizontal knot spacing is one third of a degree, and the vertical knot spacing is 25 km in the inner region of the seismic array (17.4° N-30.7° N, 35.5° E-48.5° E, and 0–200 km depth). We used the IASP91 model (Kennett and Engdahl, 1991) as the initial model for the inversion.

Results for the P-wave Tomography

We used 401 earthquakes resulting in 3,416 ray paths with P- and PKP-wave arrivals. The majority of the events are located in the western Pacific Rim between back azimuths of 15 and 150 degrees, but the events are distributed over a wide range of back azimuths. The waveforms were filtered with a zero-phase two-pole Butterworth filter between 0.5 to 2 Hz before the relative travel time residuals were computed. The multi-channel cross-correlation (MCCC) procedure was performed over a three-second window on the filtered data. A final model was selected by investigating the way in which changes in regularization levels (flattening and smoothing values) affect the reduction in travel time residuals. To determine a preferred model, 2,000 iterations of the conjugate gradient procedure are performed with several different pairs of flattening and smoothing values. For our preferred model, we have chosen a model with the values of 1,600 for flattening and 3200 for smoothing.

Figure 6 shows depth slices (a–d) and vertical cross-sections (e and f) through the model. A preliminary interpretation of these features would suggest that low velocities beneath the Gulf of Aqaba and southern Arabian Shield and Red Sea are related to mantle upwelling and seafloor spreading. Low velocities beneath the northern Arabian Shield may be related to volcanic centers. The origins of the low velocity features near the eastern edge of the Arabian Shield and western edge of Arabian Platform are unknown.

Results from the S-Wave Tomography

For the S-wave model, we used 201 earthquakes resulting in 1,602 ray paths with S and SKS-wave arrivals. Although the total number of rays for the S-wave model is half of the rays for the P-wave model, the event distribution shows better coverage of back azimuth. The signal processing procedures for the S-wave data are exactly the same as for the P-wave data, but traces were filtered over a lower frequency band (0.04 to 0.1 Hz), and relative arrival time residuals were computed by the MCCC method using fifteen-second window. As a result we could use the short-period stations for the P-wave analysis, but were limited to data from the broadband stations for the S-wave model. The first order velocity variations seen in the S model are similar to the P model, and therefore we do not show the S-wave model here.

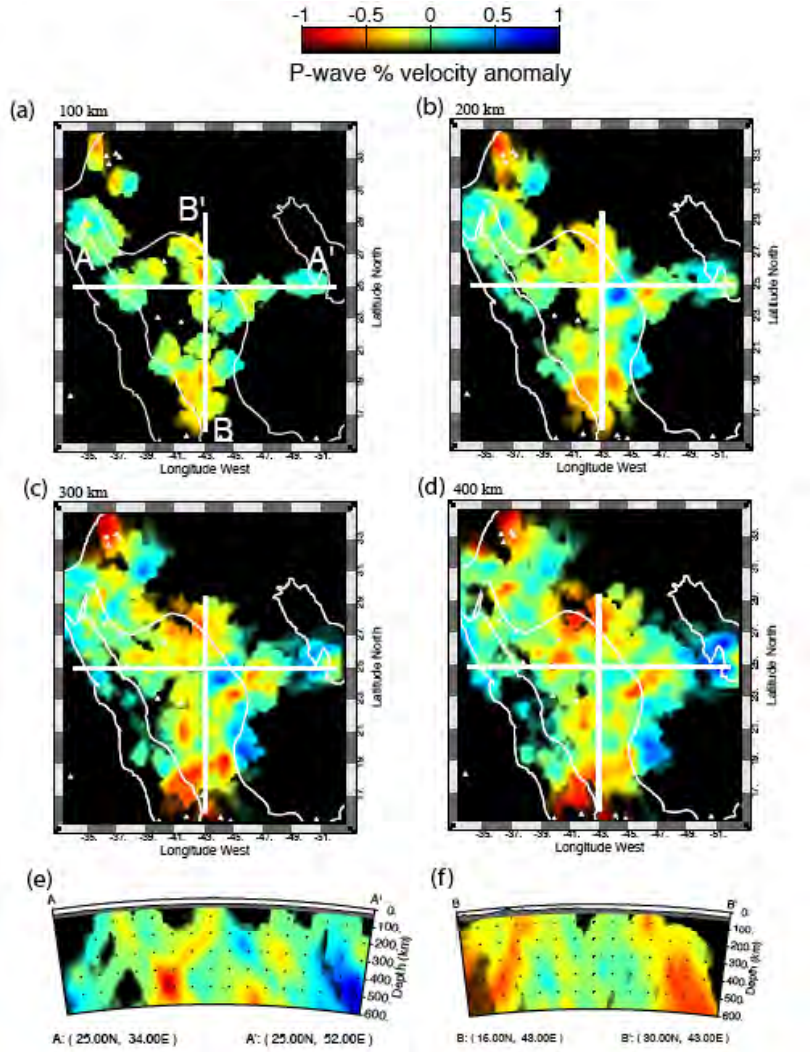

Figure 6. Results of P-wave tomography. (a–d) Depth slices through the model at depths of 100, 200, 300, and 400 km. (e–f) Vertical slices through the model along E-W (e) and N-S (f) profiles denoted with white lines in a–d.

CONCLUSIONS AND RECOMMENDATIONS

We reported progress on the determination of ground truth source parameters (focal depths and mechanisms, seismic moments) for earthquakes in the Zagros Mountains. These moments can be used to calibrate coda wave magnitudes and to model high frequency regional phase amplitude spectra with the MDAC methodology. We will explore the effect of location and focal depth on regional phase amplitudes and discriminants and estimate propagation properties (including attenuation, quality factors). Regional phase propagation models (derived from the MDAC methodology) will be developed to improve understanding of high frequency body-wave discriminants and amplitude detection thresholds in the Middle East.

ACKNOWLEDGEMENTS

The facilities of the IRIS Data Management System, and specifically the IRIS Data Management Center, were used for access to waveform and metadata required in this study.

REFERENCES

Bird, P., M. N. Toksoz, and N. H. Sleep (1975). Thermal and mechanical models of continent-continent convergence zones, *J. Geophys. Res*. 80: 4405–4416.

Camp, V. E. and M. J. Roobol (1992). Upwelling asthenosphere beneath western Arabia and its regional implications, *J. Geophys. Res.* 97: 15255–15271.

Coleman, R. G. and A. V. McGuire (1988). Magma systems related to the Red-Sea opening, *Tectonophysics* 150: 77–100.

Kennett, B. and E. R. Engdahl (1991). Travel times for global earthquake location and phase identification, *Geophys. J. Int.* 105: 429–465.

Maggi, A., J. Jackson, K. Priestley, and C. Baker (2000). A re-assessment of focal depth distributions in southern Iran, the Tien Sha and northern India: Do earthquakes really occur in the continental mantle?, *Geophys. J. Int.* 143: 629–661.

Maggi, A., K. Priestley, and J. Jackson (2002). Focal depths of moderate to large earthquakes in Iran. *Journal of Seismology and Earthquake Engineering* 4: 1–10.

Mayeda, K., A. Hofstetter, J. O'Boyle, and W. Walter (2003). Stable and transportable regional magnitudes based on coda-derived moment-rate spectra, *Bull. Seism. Soc. Am*. 93: 224–239.

Nowroozi, A. A. (1971). Seismotectonics of the Persian Plateau eastern Turkey, Caucasus, and Hindu-Kush Regions, *Bull. Seism. Soc. Am*. 61: 317–342.

Nyblade, A., A. Adams, R. Brazier, Y. Park, and A. Rodgers (2006). Ground truth, magnitude calibration and regional Phase propagation and detection in the Middle East and Horn of Africa, in *Proceedings of the 28th Seismic Research Review: Ground-Based Nuclear Explosion Monitoring Technologies*, LA-UR-06-5471, Vol. 1, pp. 156–165.

Paul, A., A. Kaviani, D. Hatzfeld, J. Vergne, and Mohammad Moktari (2006). Seismological evidence for crustal scale thrusting in the Zagros mountain belt, *Geophys. J. Int.*(submitted).

VanDecar, J. C. (1991). Upper mantle structure of the Cascadia subduction zone from non-linear teleseismic travel time inversion, Ph. D. thesis, Univ. of Washington, Seattle, WA.

VanDecar, J. C. and R. S. Crosson (1990). Determination of teleseismic relative phase arrival times using multi-channel, cross-correlation and least squares, *Bull. Seism. Soc. Am.* 80: 150–169.

Walter, W. and S. Taylor (2002). A revised magnitude and distance amplitude correction (MDAC2) procedure for regional seismic discriminants, Lawrence Livermore National Laboratory technical report, UCRL-ID-146882.

CRUSTAL AND MANTLE STRUCTURE BENEATH EASTERN EURASIA FROM INVERSIONS OF FINITE-FREQUENCY BODY AND SURFACE WAVES

Yong Ren[2], Ting Yang[3], Wei Zhang[2], Yang Shen[2], Brian Covellone[2], and Xiaoping Yang[1]

Science Applications International Corporation[1] , University of Rhode Island[2], and University of Texas at Austin [3]

Sponsored by Air Force Research Laboratory

Contract No. FA8718-05-C-0017

ABSTRACT

In this project we use 3D sensitivity kernels of finite-frequency body and surface waves to develop the crustal and mantle velocity structure beneath eastern Eurasia. We have processed available broadband waveforms from both permanent and Program for the Array Seismic Studies of the Continental Lithosphere (PASSCAL) stations. Delay times are measured by waveform cross-correlation in three frequency bands for P (0.5-2.0 Hz, 0.1-0.5 Hz and 0.03-0.1Hz) and S-waves (0.1-0.2 Hz, 0.05-0.1 Hz and 0.02-0.05 Hz). The measurements from these frequency bands for P are inverted jointly to obtain P velocity models, and similarly for S. The travel times are corrected for crustal effects using frequency-dependent crustal corrections. In areas with dense stations such as Tibet, we obtain high-resolution images of the crust and upper mantle structure that lead to unexpected geological findings. A prominent low-velocity anomaly is imaged in the crust and upper mantle to at least 300 km depth beneath a north-south trending rift zone in southeast Tibet. This anomaly is above a high-angle, southeastward dipping, high-velocity anomaly that extends into the upper mantle transition zone. Previous studies have suggested that the north-south rift zones in the Tibetan plateau are shallow features formed by the eastward motion of the shallow crust that are decoupled from the mantle lithosphere by a low-viscosity lower crust. Our new tomographic images provide strong evidence for the upper mantle origin of the north-south rift zones in the Tibetan plateau and the delamination of a thickened mantle lithosphere.

To improve data sampling at shallow depths, we are developing a new method to utilize the estimated Green's functions derived from cross-correlation of ambient noise at pairs of stations. Unlike previous studies that use the estimated Green's functions to solve for phase or group velocity maps and then a point-wise S velocity structure under a one-dimensional (1D) assumption, we construct three-dimensional (3D) sensitivity kernels for the finite-frequency Green's functions. A joint inversion of finite-frequency S-waves and estimated Green's functions, which are dominated by surface waves, will be carried out to resolve both the crust and upper mantle structure. These two data sets are easily integrated since the sensitivity kernels for body waves and estimated Green's functions relate the velocity and waveform perturbations (phase delay and/or amplitude reduction) in a similar way.

In the final year of this three-year project, we will complete the P and S velocity models and use them in forward modeling and event relocation. Travel-time corrections will be computed for selected stations in relocating the ground truth (GT) events collected in eastern Eurasia, and the location results will be evaluated.

OBJECTIVES

The goal of this work is to use 3D sensitivity kernels of finite-frequency body and surface waves to develop the crustal and mantle velocity structure beneath eastern Eurasia to improve seismic calibration for nuclear explosion monitoring.

RESEARCH ACCOMPLISHED

Data

We have collected and utilized a large data set of broadband waveforms to construct the finite-frequency velocity model beneath eastern Eurasia. Figure 1 shows the distribution of the stations, including the Global Seismographic Network (GSN), Japanese F-net and JISNET, Taiwan Broadband Seismic Network, other regional seismic networks available at the Data Management Center (DMC) of the Incorporated Research Institutions for Seismology (IRIS) and elsewhere (e.g. part of the Chinese Digital Seismic Network), and available stations from PASSCAL.

We select global earthquakes in the updated Engdahl-van der Hilst-Buland (EHB) bulletins prior to 2004 and the National Earthquake Information Center (NEIC) bulletins for recent events with magnitude greater than 5.5 recorded by the seismic stations in eastern Eurasia. We use event-station paths with epicentral distances between 30° and 85°. Delay times are measured by an automated waveform cross-correlation routine based on VanDecar and Crosson (1990) in three frequency bands for P waves (0.5–2.0 Hz, 0.1–0.5 Hz and 0.03–0.1Hz) and S waves (0.1–0.2 Hz, 0.05–0.1 Hz and 0.02–0.05 Hz). The signal-to-noise-ratio threshold is set as 20 for quality control in each frequency band and the selected records are visually inspected for consistency. The signal-to-noise ratio is defined as the ratio of the peak-to-peak amplitude of the main arrival to the standard deviation of the time series in an 80-s window before the main arrival. Figure 2 shows examples of the measurements of P and S differential travel times.

To reduce the tradeoff between crustal and mantle velocity heterogeneities in seismic tomography, we remove the frequency dependent crustal correction from the teleseismic travel times by cross-correlating the impulse responses of a crust model filtered in a narrow frequency band (Yang and Shen, 2006). We use a crustal model from Sun et al. (2004) for stations in China, and CRUST2.0 (Bassin et al., 2000) for stations elsewhere to calculate the travel-time difference with respect to IASPEI91 for the three frequency bands, and apply those frequency dependent adjustments to teleseismic travel times.

High-Resolution P- and S-Velocity Models in Selected Areas

The distribution of the seismic stations in eastern Eurasia is uneven (Figure 1). In places where the stations are dense, we carry out detailed data analyses to obtain high-resolution P- and S-velocity models. In addition to collecting data needed for the continental-scale inversion, these detailed studies allow us to analyze seismic data further and obtain high resolution images of the crust and mantle structure. As an example, southeastern Tibet is such a region with several PASSCAL experiments (Figure 1) for high-resolution images of the crustal and mantle structure to provide constraints on the continental collision and plateau building processes. We processed data from the Namche Barwa Seismic Experiment (Sol et al., 2007), which deployed a 50-station broadband array and a 20-element short-period array in southeastern Tibet during 2003–2004. Data from the GSN station LSA, which is located close to this temporary network, are also included in this study. Following the data processing method outlined above, we obtained 44,000 P and 19,500 S delay times, which are then utilized to invert for spatial variations in P- and S-wave velocity perturbations according to the 3-D finite frequency kernel formulation (Dahlen et al., 2000; Hung et al., 2004; Yang et al., 2006).

The model space is parameterized with a regular 3D grid of 33×33×33 centered at (93° E, 30° N), and has a dimension of 18° in longitude, 14° in latitude, and 1200 km in depth. The grid spacing is approximately 53 km in longitude, 46 km in latitude, and 40 km vertically. The inverse problem is resolved using a standard damped least square algorithm (Paige and Saunders, 1982) and the damping parameter is determined through a trade-off analysis of model norm versus variance reduction as shown in Figure 3 (Menke, 1989). We use checkerboard resolution tests with the same damping parameter as in the real data inversion to evaluate the ability of a given data coverage and inversion technique to recover crustal and mantle structures. These tests showed that structures are well recovered beneath the stations at a depth of between ~50 km and ~450 km. The minimal size of the laterally and vertically resolved structure is ~100 km.

Our results show a prominent N-S trending low-velocity anomaly at ~92°E down to at least 300 km depth (Figure 4). These structures are observed on both V_p and V_s models. We associate the high-velocity anomalies southwest and east of the north-south trending low velocity anomaly to the Indian lithosphere, which extends to ~250 km depth. We observe no evidence for a subducted Indian lithosphere at depth of 300 km or more beneath the study area. The north-south low velocity anomaly across Indus-Yarlung Suture coincides strikingly with a rift on the surface at southeastern Tibet (e.g., Tapponnier and Molnar, 1977; Armijo et al., 1986; Yin, 2000) and is above a high-angle, southeastward dipping, high-velocity anomaly that extends into the upper mantle transition zone, as shown on the cross-sections (Figure 4c). We associate the high-angle dipping, high-velocity anomaly to a sunken delaminated mantle lithosphere since its post-collisional thickening and the detachment of the mantle lithosphere can give way to asthenospheric upwelling that we associate to the north-south trending low velocity structure in our tomographic models. This mantle upwelling can thus weaken the overlying crust, localize and initiate the rifts observed on the surface in the Tibetan Plateau, at least in the region near the Eastern Himalayan Syntaxis. The observations suggest an upper mantle origin of the rift zones and that delamination plays a key role in the process (Yong and Shen, 2007), contrary to previous studies which argued that the north-south rift zones in the Tibetan plateau are shallow features, formed by the eastward motion of the shallow crust decoupled from the mantle lithosphere by a low-viscosity lower crust (e.g., Shen et al., 2001; Jiménez-Munt and Platt, 2006).

P-Velocity Model of Eastern Eurasia

The tomographic model for eastern Eurasia extends to 2500 km deep and is parameterized by a 81x81x51 grid with spacing of 1.0°, 1.25°, and 58 km in latitude, longitude and depth, respectively. As in the detailed studies, the inversion is carried out using the finite-frequency tomography methodology (Hung et al., 2004; Yang et al. 2006). We also utilize a convolutional quelling technique (Meyerholtz et al., 1989) to improve imaging in this continental-scale study.

Figure 5 shows the P-velocity anomalies at 232 km, 406 km, 580 km and 754 km depth. An inspection of the sampling of the structure beneath eastern Eurasia by the finite-frequency data finds that there is good data coverage in the depth range of 350–1500 km in most parts of the study area, but gaps exist in the shallow upper mantle and crust, except in regions with dense stations (e.g., southeast Tibet, Japan). Finite frequency surface wave tomography is necessary to obtain higher resolution in the shallow structure.

Sensitivity Kernels for Green's Functions from Ambient Noise Cross-Correlation

We utilize Green's functions derived from the cross-correlation of ambient noise at pairs of stations to image the crust and shallow mantle. Previous studies have demonstrated the efficacy of extracting information on crustal and shallow mantle structure from seismic noise to improve path coverage and spatial resolution (e.g., Shapiro and Campillo, 2004; Sabra et al., 2005; Shapiro et al., 2005; Yao et al., 2006; Yang et al., 2007; Cho et al., 2007). The fact that the estimated Green's function is based on cross-correlation makes it straightforward to adapt this type of measurement to the frequency-dependent phase-delay anomalies. Unlike previous studies that use the estimated Green's functions to solve for phase or group velocity maps and then a point-wise S velocity structure under a 1D assumption (e.g., Yao et al., 2006; Yang et al., 2007; Cho et al., 2007), we construct 3D sensitivity kernels for the finite-frequency Green's functions. Figure 6 shows the travel-time (phase-delay) sensitivity kernels for a Green's function corresponding to the estimate from the cross-correlation of vertical records at two stations separated by ~900 km. The dominant period of the seismic wave is ~10 s. The kernels are calculated using the scattering integral method (Zhao et al., 2005; Zhang et al., 2007). The reference velocity model in this figure is AK135, but any 3D heterogeneous model can be used since synthetic waveforms are computed by finite-difference full-waveform simulation. The kernel shows an approximately 200 km wide elliptical area of strong sensitivity on the horizontal slice at 18 km depth. Along the ray path the sensitivity is a local minimum, but non-zero. This general pattern of sensitivity is similar to that of Rayleigh waves from earthquakes in previous studies using semi-analytical solutions or normal modes (Zhou et al., 2005; Zhao and Jordan, 2006). A joint inversion of finite-frequency S-waves and estimated Green's functions will be carried out to resolve both the crust and upper mantle structure.

Model Validation by Ground-Truth Event Relocation

Our database also consists of a large number of GT events with location uncertainties better than 5 km (GT0-GT5) for model validation. Stations are selected to compute travel time corrections from the finite-frequency model for GT event relocation to assess location improvements. The final P and S velocity models will be used in calculating relative travel-time corrections from the kernels, and the GT events will be relocated and compared with and without the corrections.

CONCLUSIONS AND RECOMMENDATIONS

We have created a large data set of broadband waveforms and used cross-correlation to measure P- and S-wave travel-time delays at several frequency bands, which are then utilized to invert for spatial variations in P and S-wave-speed perturbations according to the 3-D finite frequency kernel formulation. We have carried out both detailed and large-scale tomographic studies and have obtained velocity models that provide new insights into geological processes. We have calculated the 3D sensitivity kernels for Green's functions derived from the cross-correlation of ambient noise at pairs of stations. A joint inversion of finite-frequency S-waves and estimated Green's functions will be carried out to resolve the crust and shallow mantle structure and reduce the tradeoff between shallow and deep velocity anomalies. The independent 3D P and S velocity models will be used in improving seismic calibration in Eurasia.

REFERENCES

Armijo, R., P. Tapponnier, J. P. Mercier, and T. Han (1986). Quaternary extension in southern Tibet, *J. Geophys. Res.* 91: 13,803–13,872.

Bassin, C., G. Laske, and G. Masters (2000). The current limits of resolution for surface wave tomography in North America, *EOS, Trans. Am. Geophys. Un.* 81: F897.

Cho, K. H., R. B. Herrmann, C. J. Ammon, K. Lee (2007). Imaging the upper crust of the Korea Peninsula by surface-wave tomography, *Bull. Seism. Soc. Am*. 97 (1B): 198–207, doi: 10.1785/0120060096.

Dahlen, F.A., Hung, S.-H., & Nolet, G. (2000). Fréchet kernels for finite frequency traveltimes-I. Theory, *Geophys. J. Int*, 141: 157–174.

Hung, S-H ,Y. Shen, and L.-Y. Chiao (2004). Imaging seismic velocity structure beneath the Iceland hot spot: A finite frequency approach, *J. Geophy. Res.* 109: doi: 10.1029/2003JB002889.

Jimenez-Munt, I., and J.P. Platt (2006). Influence of mantle dynamics on the topographic evolution of the Tibetan plateau: Results from numerical modeling, *Tectonics* 25: TC6002, doi:10.1029/2006TC001963.

Menke, W. (1989), *Geophysical data analysis: Discrete Inverse Theory*, Academic, San Diego, Calif.

Meyerholtz, K. A., G. L. Pavlis, and S. A Szpakowski (1989). Convolutional quelling in seismic tomography, *Geophysics* 54: 570–580.

Paige, C. C., and M. A. Saunders (1982). LSQR: An algorithm for sparse linear-equations and sparse least-squares, *Trans. Math. Software* 8: 43–71.

Sabra, K. G., P. Gerstoft, P. Roux, and W. A. Kuperman (2005). Extracting time-domain Green's function estimates from ambient seismic noise, *Geophys. Res. Lett*. 32: L03310, doi: 10.1029/2004GL021862.

Shapiro, N. M. and M. Campillo (2004). Emergence of broadband Rayleigh waves from correlations of the ambient seismic noise, *Geophys. Res. Lett.* 31: L07614, doi: 10.1029/2004GLL019491.

Shapiro, N. M., M. Campillo, L. Stehly, and M. H. Ritzwoller (2005). High-resolution surface-wave tomography from ambient seismic noise, *Science* 207: 1615–1618.

Shen, F., L. Royden, and B. C. Burchfiel (2001). Large-scale crustal deformation of the Tibetan plateau, *J. Geophys. Res*. 106 (B4): 6793–6816.

Sol, S., A. Meltzer, R. Burgmann, R. D. van der Hilst, R. King, Z. Chen, P. O. Koons, E. Lev, Y. P. Liu, P. K. Zeitler, X. Zhang, J. Zhang, and B. Zurek (2007). Geodynamics of the southeastern Tibetan Plateau from seismic anisotropy and geodesy, *Geology* 35: 563–566, doi:10.1130/G23408A.1.

Sun, Y., L. Xu, S. Kuleli, F. D. Morgan, and M. N. Toksoz (2004) Adaptive moving window method for 3-D P-velocity tomography and its application in China. *Bull. Seism. Soc. Am.* 94: (2) 740–746.

Tapponnier, P. and P. Molnar (1977). Active faulting and tectonics of China, *J. Geophys. Res.* 82: 2905–2930.

VanDecar, J. C., and R. S. Crosson (1990), Determination of teleseismic relative phase arrival times using multi-channel cross-correlation and least squares, *Bull. Seismol. Soc. Am.* 80: 150–169.

Yang, T. and Y. Shen (2006), Frequency dependent crustal correction for finite frequency seismic tomography, *Bull. Seism. Soc. Am.* 96: (6), 2441–2448, doi:10.1785/0120060038.

Yang, T., Y. Shen, S. van der Lee, S. C. Solomon, and S. H. Hung (2006). Upper mantle structure beneath the Azores hotspot from finite-frequency seismic tomography, *Earth Planet. Sci. Lett.* 250: 11–26.

Yang, Y., M. H. Ritzwoller, A.L. Levshi, and N.M. Shapiro (2007). Ambient noise Rayleigh wave tomography across Europe, *Geophys. J. Int.* 168: 259–274.

Yao, H., R. D. van der Hilst, and M. V. de Hoop (2006). Surface-wave array tomography in SE Tibet from ambient seismic noise and two-station analysis –I. Phase velocity maps, *Geophys. J. Int.* 166: 732–744, doi: 10.1111/j.1365-246X.2006.03028.x.

Yin, A. (2000). Mode of Cenozoic east-west extension in Tibet suggesting a common origin of rifts in Asia during the Indo-Asian collision, *J. Geophys. Res.* 105: 21,745–21,759.

Yong, R., and Y. Shen (2007). Tomographic evidence for a possible link between lithosphere delamination and the north-south trending rifts in Tibet, in preparation.

Zhang, Z., Y. Shen, and L. Zhao (2007), Finite-frequency sensitivity kernels for head waves, *Geophys. J. Int.,* accepted for publication.

Zhao, L., T. H. Jordan, K. B. Olsen, and P. Chen (2005). Frechet kernels for imaging regional earth structure based on three-dimensional reference models, *Bull. Seism. Soc. Am*. 95: 2066–2080.

Zhao, L. and T. H. Jordan (2006). Structural sensitivities of finite-frequency seismic waves: a full-wave approach, *Geophys. J. Int.* 165: 981–990, doi:10.1111/j.1365-246X.2006.02993.x.

Zhou, Y., F. A. Dahlen, G. Nolet, and G. Laske (2005), Finite-frequency effects in global surface-wave tomography, *Geophys. J. Int.,* 153, 1087–1111, doi:10.1111/j.1365-264X.2005.02780.x.

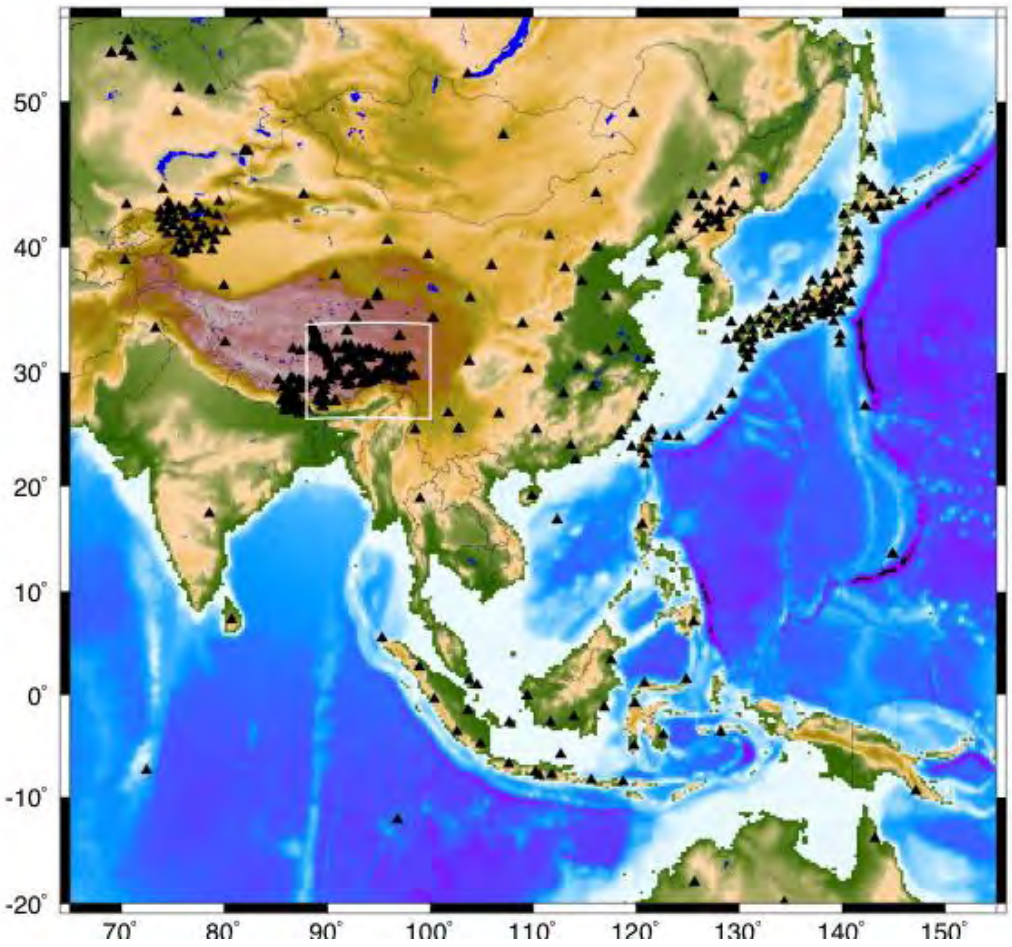

Figure 1. Topography of Eastern Eurasia and the distribution of broadband seismic stations used in this study (triangles). The box outlines a detailed study in southeastern Tibet.

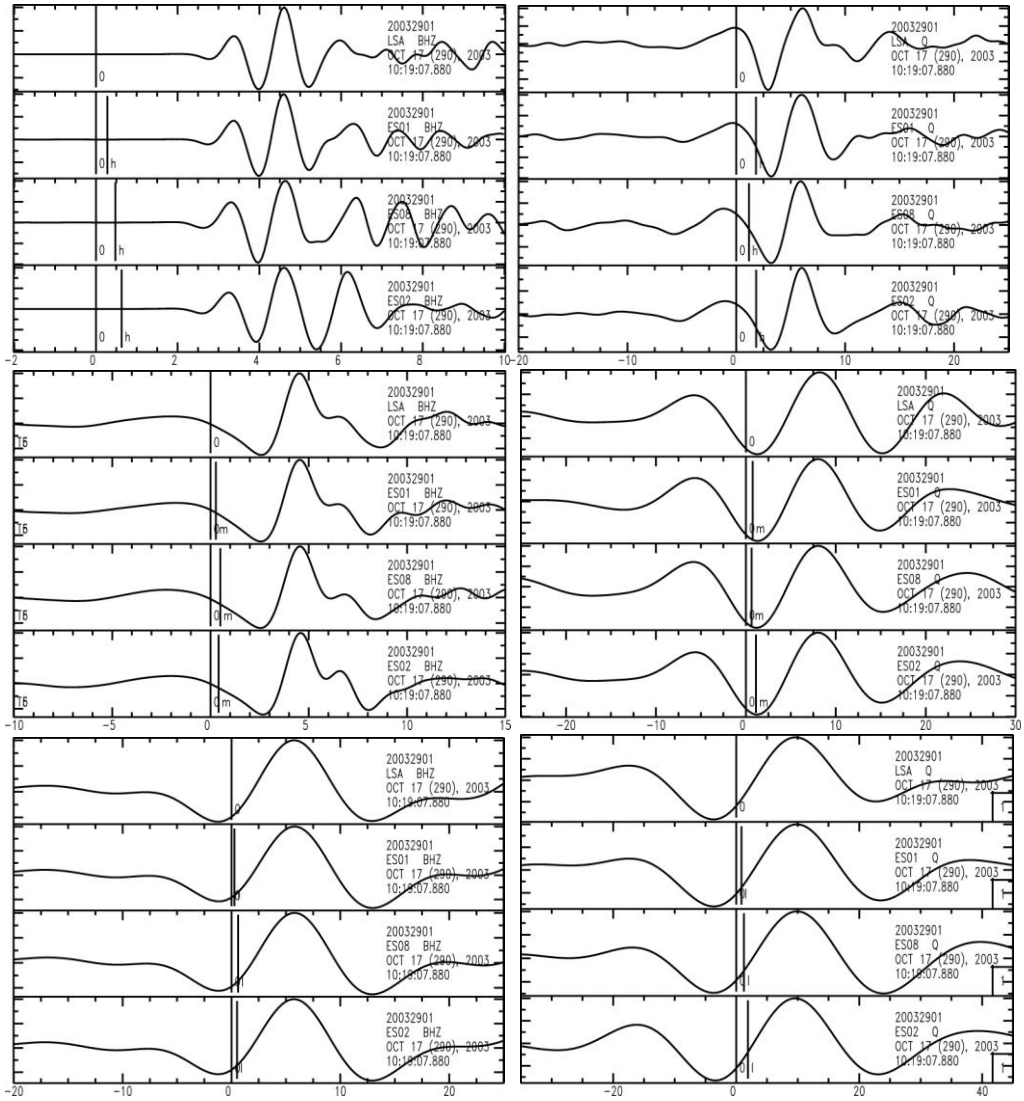

Figure 2. Examples of measurements. (left) P differential travel times in three frequency ranges: 0.5-2.0Hz, 0.1-0.5 Hz, and 0.03-0.1 Hz. (right) S differential times in three frequency ranges: 0.1-0.2 Hz, 0.05-0.1 Hz, and 0.02-0.05 Hz. The waveforms have been shifted by the delay times determined from cross-correlation (short vertical lines).

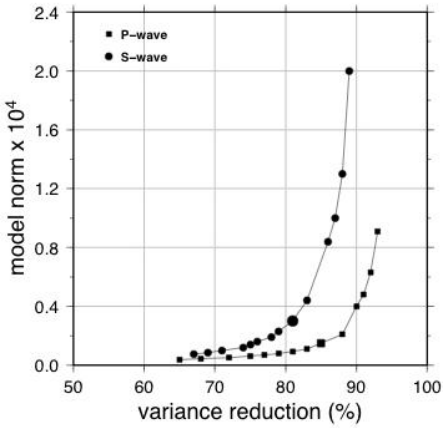

Figure 3. Trade-off between model norm and variance reduction with different damping factors for P and S velocity models. Larger symbols represent the models presented in this study. Only the high and intermediate frequencies are used here.

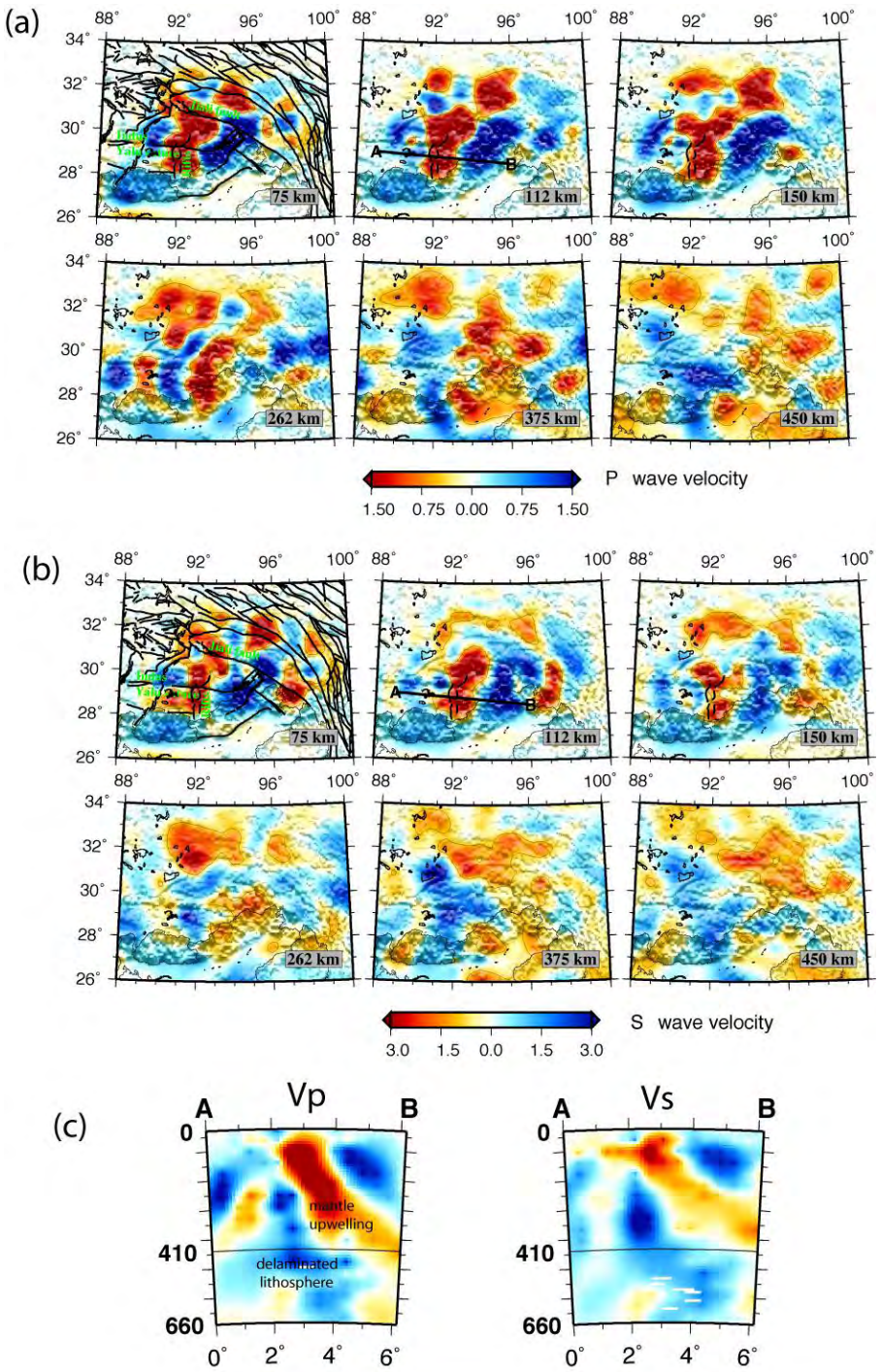

Figure 4 (a) P-velocity perturbations at several depths beneath southeastern Tibet: 75 km, 112 km, 150 km, 262 km, 375 km, and 450 km. Black lines in the 75-km horizontal slice represent the known faults. Notice the north-south trending faults (rift) coincide with a prominent north-south trending low-velocity anomaly. Line AB on the 112-km-depth image marks the location of the vertical profile in (c). (b) S-velocity perturbations at the same depths. (c) Cross-section A-B through P and S-wave tomographic models, along the Indus-Yarlung suture and across a rift in southeastern Tibet. We attribute the high-dipping-angle, high-velocity anomaly as a delaminated mantle lithosphere and the low-velocity anomaly that extends downwards beneath the rift as the upwelling of the asthenosphere to fill the gap caused by mantle delamination. The color scales for Vp and Vs are the same as in (a) and (b), respectively.

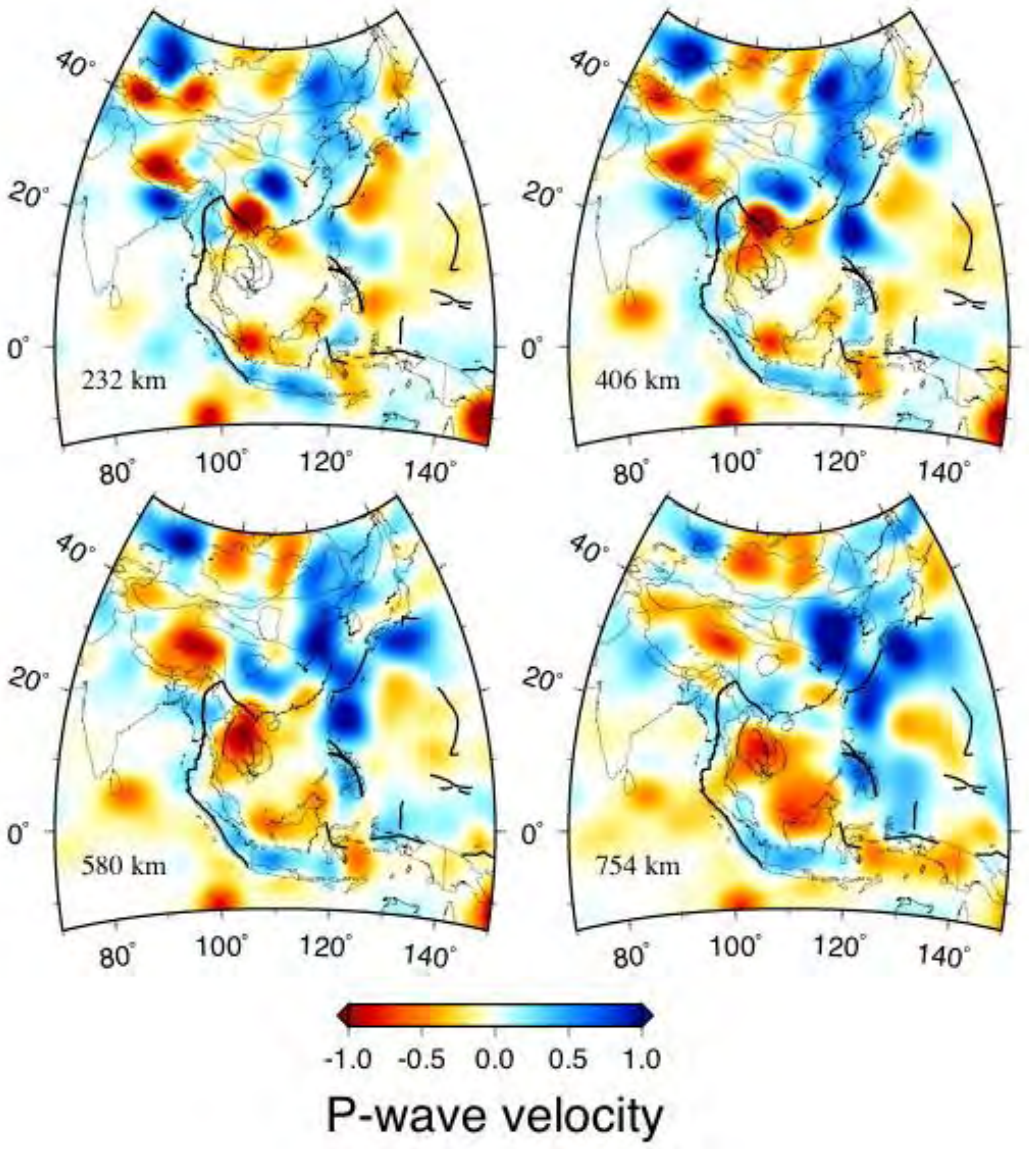

Figure 5. Horizontal slices of the tomographic model at 232 km, 406 km, 580 km and 754 km depth showing the velocity perturbation distribution in the mantle beneath Eastern Eurasia.

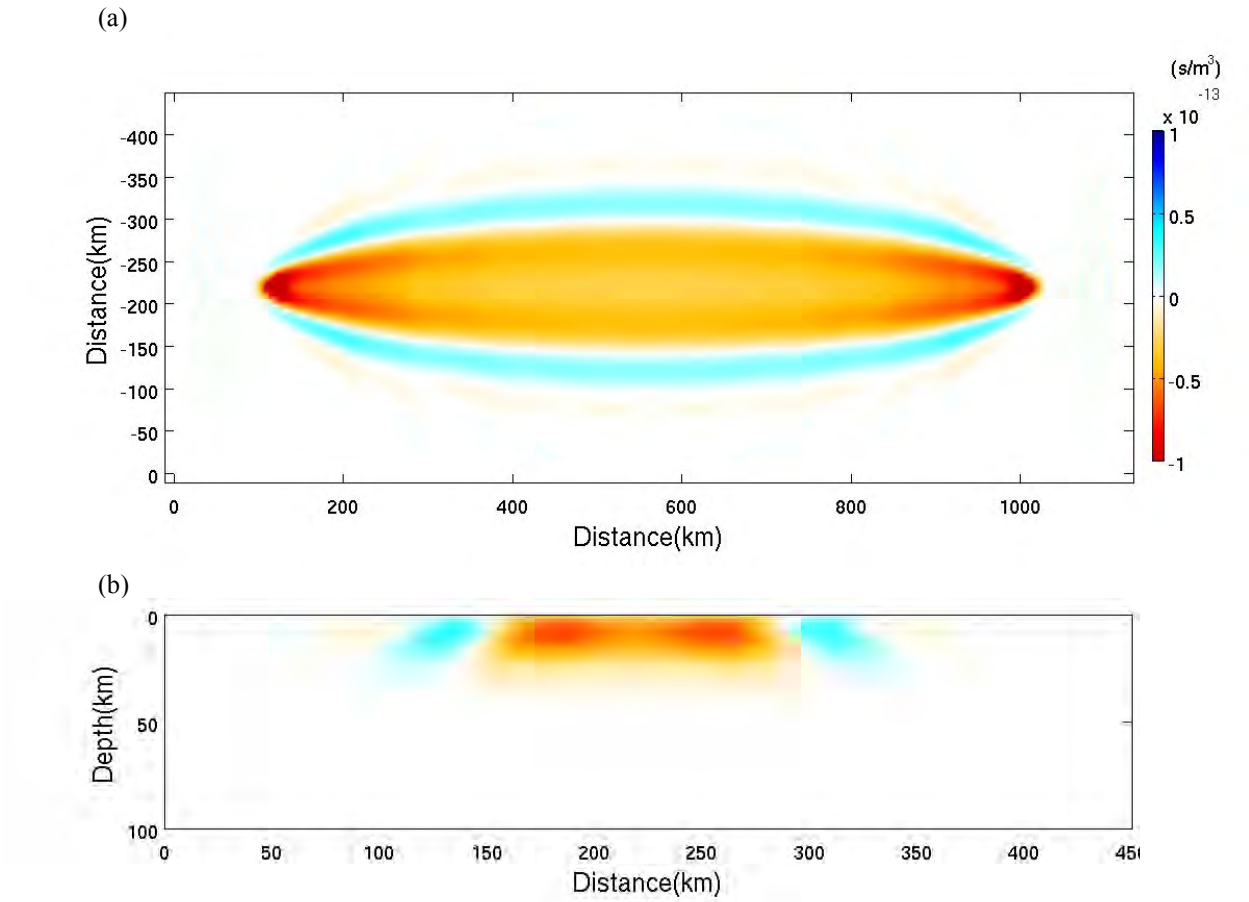

Figure 6. Travel-time (phase) sensitivity kernel to S-velocity perturbation for a 10-s Green's function for the vertical components of a pair of stations separated by ~900 km. (a) The horizontal slice of the kernel at 18 km depth. (b) The vertical slice of the kernel perpendicular to and in the middle of the station-station path. The kernel reflects primarily the finite-frequency effects of the fundamental Rayleigh waves. It is so defined that a low S-velocity perturbation in the negative (red) region results in a phase delay measured by waveform cross-correlation, while the same perturbation in the positive (blue) region results in an earlier arrival. The sensitivity is strongest near the stations and decreases toward the middle. Along the path between the two stations, the sensitivity is a local minimum but non-zero. Notice the width of the sensitivity (~200 km) is much greater than the wavelength of the 10-s surface wave (~30 km), indicating the importance of the finite-frequency effects in tomographic inversion.

ADAPTIVE WAVEFORM CORRELATION DETECTORS FOR ARRAYS: ALGORITHMS FOR AUTONOMOUS CALIBRATION

Frode Ringdal[1], Steven J. Gibbons[1], and David B. Harris[2]

NORSAR[1] and Lawrence Livermore National Laboratory[2]

Sponsored by National Nuclear Security Administration
Office of Nonproliferation Research and Development
Office of Defense Nuclear Nonproliferation

Contract Nos. DE-FC52-05NA26604[1] and W-7405-ENG-48[2]

ABSTRACT

Waveform correlation detectors compare a signal template with successive windows of a continuous data stream and report a detection when the correlation coefficient, or some comparable detection statistic, exceeds a given threshold. Since these methods exploit characteristic details of the full waveform, they provide exquisitely sensitive detectors with far lower detection thresholds than typical short-term average/long-term average (STA/LTA) algorithms. The drawback is that the form of the sought-after signal needs to be known quite accurately a priori, which limits such methods to instances of seismicity whereby a very similar signal has already been observed by every station used. Such instances include earthquake swarms, aftershock sequences, repeating industrial seismicity, and many other forms of controlled explosions. The reduction in the detection threshold is even greater when the techniques are applied to multiple channels since stacking can be performed on the correlation coefficient traces with a significant array-gain. A detected event that is co-located with the master event will record the same time-difference at every site in an arbitrarily spaced network which means that the correlation coefficient traces can be stacked coherently even when there is little or no similarity between the actual signals at the different sites.

In the first year of this three-year investigation, the emphasis was upon estimating the detection threshold reduction for a range of highly repeating seismic sources using arrays of different configurations and at different distances from the events examined. In the case studies pursued (induced seismicity in a coal mine, aftershock sequences in Fennoscandia, and the 2002 Coso sequence in Southern California) the master events were all of magnitude less than 4.5 and, in many cases, nearby instruments were able to confirm the similarity of waveforms at local distances which increased the likelihood of successful detection at regional distances. In the second year, we examined case studies aimed at investigating the applicability of matched filter detectors to more difficult sources. The first case is a sequence of military explosions on the Kola Peninsula in Russia at approximately 200 km from the ARCES seismic array. The difficulty here is the lack of waveform similarity from event to event, presumably due to large variation in the detonation procedure and source-time function, which results in quite low correlation coefficients. However, the alignment and coherence of the correlation coefficient traces between the different sites of the small-aperture array provides additional selection criteria which eliminate the vast majority of spurious event hypotheses. The second case study is the extensive aftershock sequence from the M=7.7 event 8 October 2005 in Pakistan. Many of these events were well in excess of magnitude 5 with correspondingly larger rupture sizes than had been considered previously. Driving multichannel correlation detectors at teleseismic distances using many of the larger events as master signals classifies rapidly subsequent events which are likely to be associated with the various templates. Many additional events were then successfully identified by correlating high-frequency regional waveforms over the large aperture K-NET network at distances of over 900 km.

The relative location of detected events is an important part of the event categorization process and we demonstrate how the horizontal double-difference relocation procedure of Schaff and Richards (2004) can be applied to events of smaller magnitude when the correlation trace stacking is applied over small to medium sized arrays at a range of different directions from the source. We also demonstrate cases of erroneous timing on International Monitoring System (IMS) arrays that have been measured accurately as a result of the correlation procedure for repeating seismic events.

OBJECTIVE

The overall objective of this proposed three-year study is to develop and test a new advanced, automatic approach to seismic detection using waveform correlation, with special application to seismic arrays. The principal goal is to develop an adaptive processing algorithm. By this we mean that the detector is initiated using a basic set of reference ("master") events to be used in the correlation process, and then an automatic algorithm is applied successively to provide improved performance by extending the set of master events selectively and strategically. These additional master events are generated by an independent, conventional detection system. A periodic analyst review will then be applied to verify the performance and, if necessary, adjust and consolidate the master event set.

RESEARCH ACCOMPLISHED

In the first year of this project, the emphasis was on two major aspects of array-based waveform correlation detectors. Firstly was the issue of the reduction in detection thresholds possible using seismic arrays of different spatial configurations and at different epicentral distances. Secondly was the construction of subspace detectors (a generalization of the matched filter detector which accommodates a greater variation in the permissible waveforms) and a comparison between the success rate and false alarm rate of 1-dimensional and multidimensional subspace detectors.

In this second year, a number of case-studies have explored situations that are less than ideal for correlation detectors—primarily due to a demonstrable variation in the waveforms. We report on two such cases here. The first is a series of presumed multiple ammunition explosions which are challenging due to very heterogeneous source-time functions. The second is an extensive aftershock sequence from a large earthquake. Although all the scenarios studied in the first year were limited to small magnitudes (all less than 4.5 and mostly less than 3.5), this earthquake sequence consisted of events up to magnitude 7.7 covering a very large geographical area. Two further topics which are covered briefly: firstly, the rapid identification of erroneous instrumental timing over arrays through correlating long data segments from repeating seismic events and, secondly, relative relocation of seismic events.

Application of a Waveform Correlation Detector to a Sequence of Explosions with Differing Source-Time Functions

In March 2005, Norwegian authorities alerted NORSAR to concerns of citizens living in the far north of Norway who had experienced loud noise from an unknown source. From an association of reported times with seismic signals, it was concluded that numerous events had occurred on the Kola Peninsula of NW Russia (Figure 1); sound waves coming from the appropriate directions were also observed on the seismic sensors of the ARCES array and on the Apatity seismic array and microbarograph subarray (Ringdal et al., 2005). The automatic location estimates from generalized beamforming (GBF) (Ringdal and Kværna, 1989) showed considerable variation (Figure 1, left panel) but analyst reviewed solutions (including some which applied direction estimates from the infrasound phases) appeared to result in quite consistent location estimates close to the circle in Figure 1. The primary reason for the large spread in automatic event locations is that multiple detections are made for both P-type and S-type regional phases in each signal with highly differing patterns of occurrence. This indicates multiple firing sequences. The automatic phase association algorithm is unable to identify which bursts of energy correspond to which shots and different hypothetical source locations will provide arbitrarily better or worse fits to phase detection sequences. The heterogeneity of the waveforms from this particular event sequence is clear from the traces in the right panel of Figure 1.

Our aim is to identify similar and subsequent events. The fully automatic event lists are clearly little help in this aim without the introduction of much manual analysis. The Zapoljarni mines on the Kola Peninsula frequently result in seismic signals whose automatic event location estimates overlap with the presumed explosion site. Waveform correlation is an appealing method, but low values of the correlation coefficients resulting from comparing the seven traces in Figure 1 make it clear that a detection threshold for a correlation detector would have to be very low and that we might have to accept a very high false alarm rate. One observation from the mutual correlations between these seven events is that despite relatively low values of the Array Correlation Coefficient Beam (ACCB), performing f-k analysis on the single channel correlation coefficient traces (e.g., Gibbons and Ringdal, 2006) resulted in very well defined slowness vectors (i.e., indicating good alignment of the correlation coefficient traces).

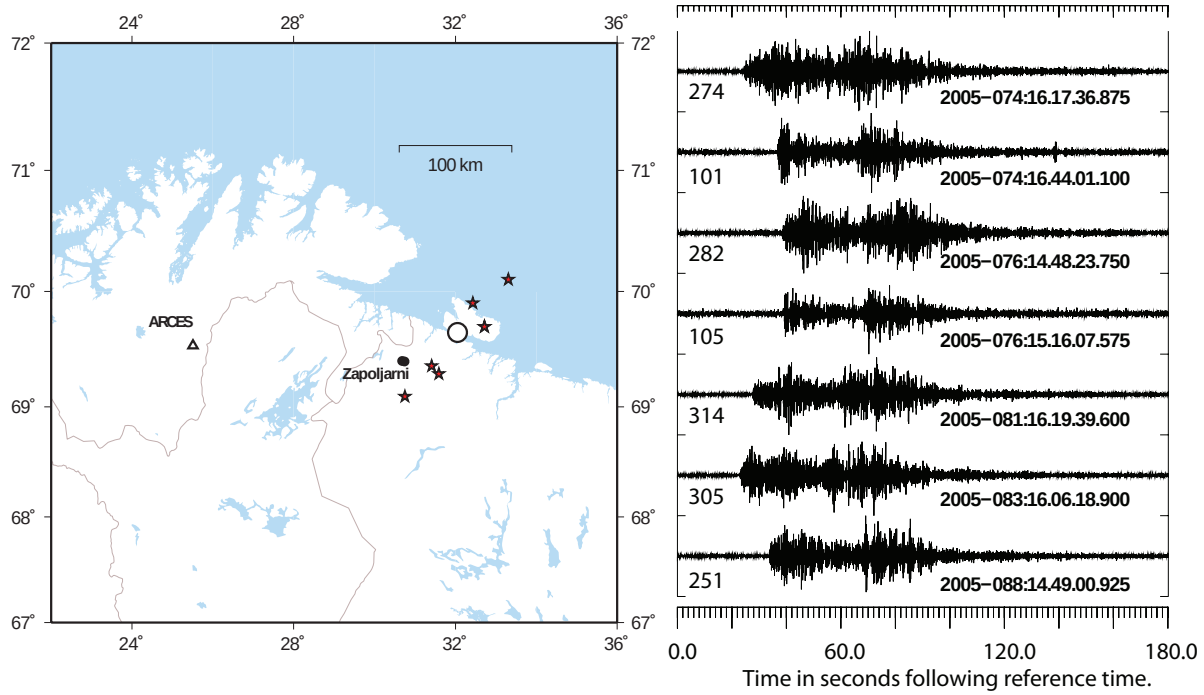

Figure 1. (left) Estimated location of the Kola Peninsula explosion site (open circle) in relation to the ARCES seismic array and the Zapoljarni mines (closed circles). The stars indicate fully automatic location estimates (GBF: Ringdal and Kværna, 1989) for seven events (two co-located) which NORSAR were made aware of due to reports of loud noises from residents in northern Norway. (right) ARA0_sz seismograms (bandpass filtered 3–8 hz) for these events, each trace starting at the GBF origin time estimate as indicated. The number displayed is the maximum amplitude of the trace.

With the detection threshold set necessarily low, between January 1, 2002, and December 31, 2005, a total of 17,485 detections were made based upon the ACCB value alone. The vast majority of these were demonstrably false alarms by inspection and other selection criteria were deemed necessary: the ratio of ACCB maximum to the standard deviation, the apparent slowness of the correlation coefficient traces, and the coherence of the correlation coefficient traces. This multi-variate selection condition reduced the number of detections to 243. Of these detections, 220 corresponded to the times detected events on the GBF which appeared to originate from a similar source region and which often showed similar properties. Of special interest is the appearance of sound waves on the ARCES array some 12 to 14 minutes after the explosions, which supports the hypothesis that the events are of a similar nature. An example of such a detected event is displayed in Figure 2, displaying the somewhat dissimilar waveforms and the ACCB with no clearly defined maximum. Three of the 243 detections did not correspond to automatic GBF event hypotheses, although careful manual VESPAgram analysis indicated evidence of weak P- and S- type regional phases coming from the appropriate direction. The remaining events were clearly false alarms and resulted from the occurrence of very high amplitude, short-duration, Rg-type phases arriving from approximately the same backazimuth.

Whilst the actual events are somewhat poorly constrained (i.e., there is no Ground Truth, and no independent confirmation of the location of the explosion site or sites) the method we have applied has demonstrated that correlation detectors which apply additional constraints (primarily on the alignment of the single channel correlation coefficient traces) have been able to produce an extensive list of very likely candidate events with very few obvious false alarms. It is worth noting that there are no coincidental correlation detections with signals from Zapoljarni mining events. Any other existing procedure to identify that number of candidate events would almost certainly also result in many false alarms and much additional analyst time.

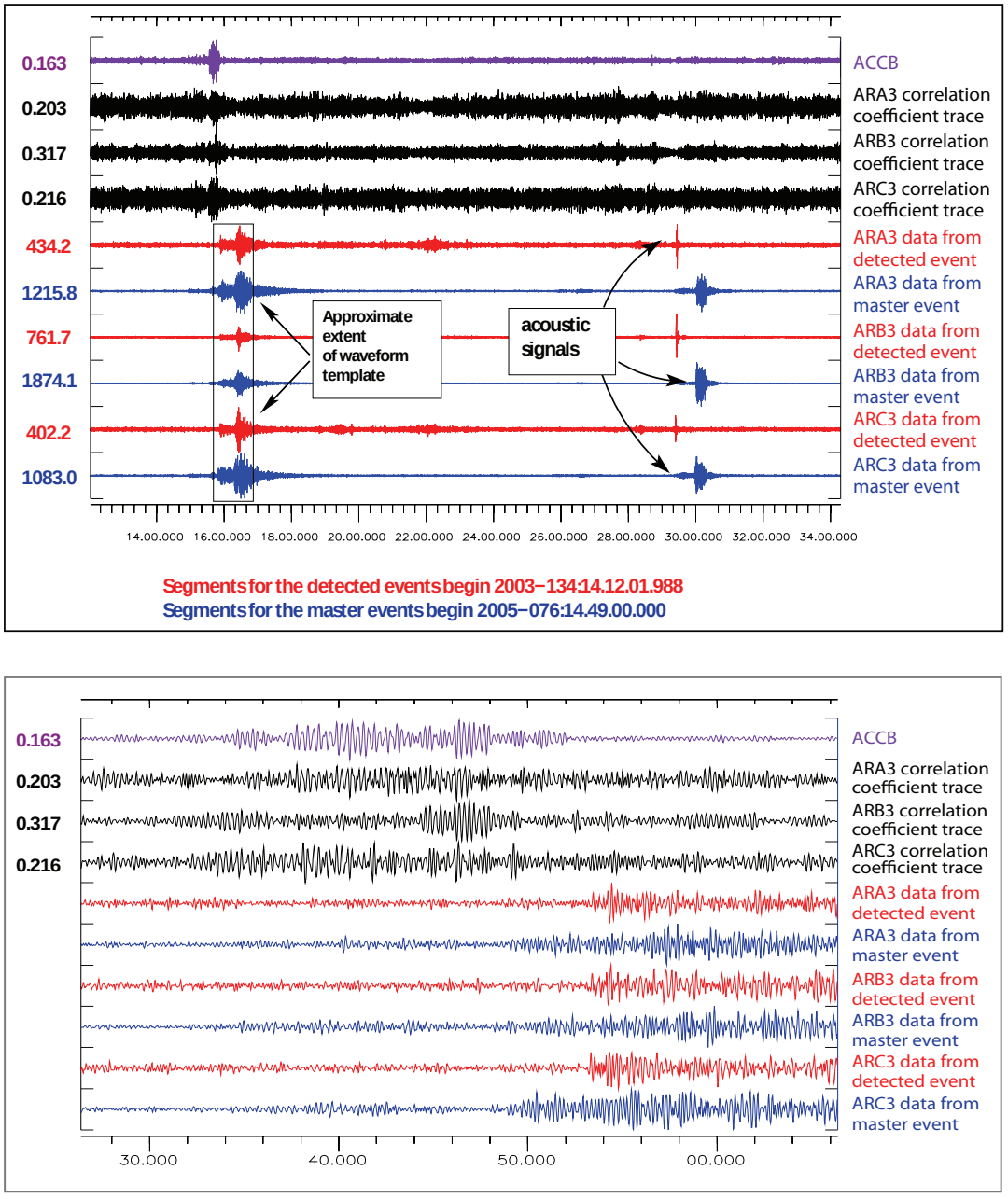

Figure 2. A typical correlation detection on the ARCES array using a template from a Kola Peninsula event on March 17, 2005. The seismic signals from both master and detected events are followed by infrasound arrivals. Note the long duration of the semblance of the correlation coefficient traces and the absence of well-defined peak in the ACCB.

Application of a Waveform Correlation Detector to an Extensive Aftershock Sequence using a Sparse Network

One kind of scenario in nuclear explosion monitoring where a large number of detection templates may be required to cover a wide source region is an active mine. The extent of the mine is likely to be larger than the "correlation footprint" of the event (Geller and Mueller, 1980), and a different template is likely to be required for many distinct regions of the mine. Autonomous calibration may be necessary given that as excavation continues into previously untouched rock masses, the distance of the new seismic sources from previously observed sources will increase and the correlation between the corresponding signals will decrease. The autonomous calibration algorithm will need to decide in which circumstances a new template should be added to (or removed from) the event pool.

A very different scenario is the occurrence of a large earthquake followed by an extensive series of aftershocks. In contrast to the gradual change to the continual low magnitude seismicity in the mine, a large earthquake is likely to occur in a region of a main fault zone where seismicity has not been observed for many years, if ever, and is likely to be followed by large numbers of seismic events covering a very large range of the magnitude spectrum, which warrant rapid and exhaustive categorization. The problems involved in applying correlation detectors are obvious. The main shock is likely to be in excess of magnitude 7 with a corresponding rupture length many times larger than the fundamental wavelengths of the aftershocks which are sought. The spectral content of the resulting waveform will also differ significantly from smaller aftershocks.

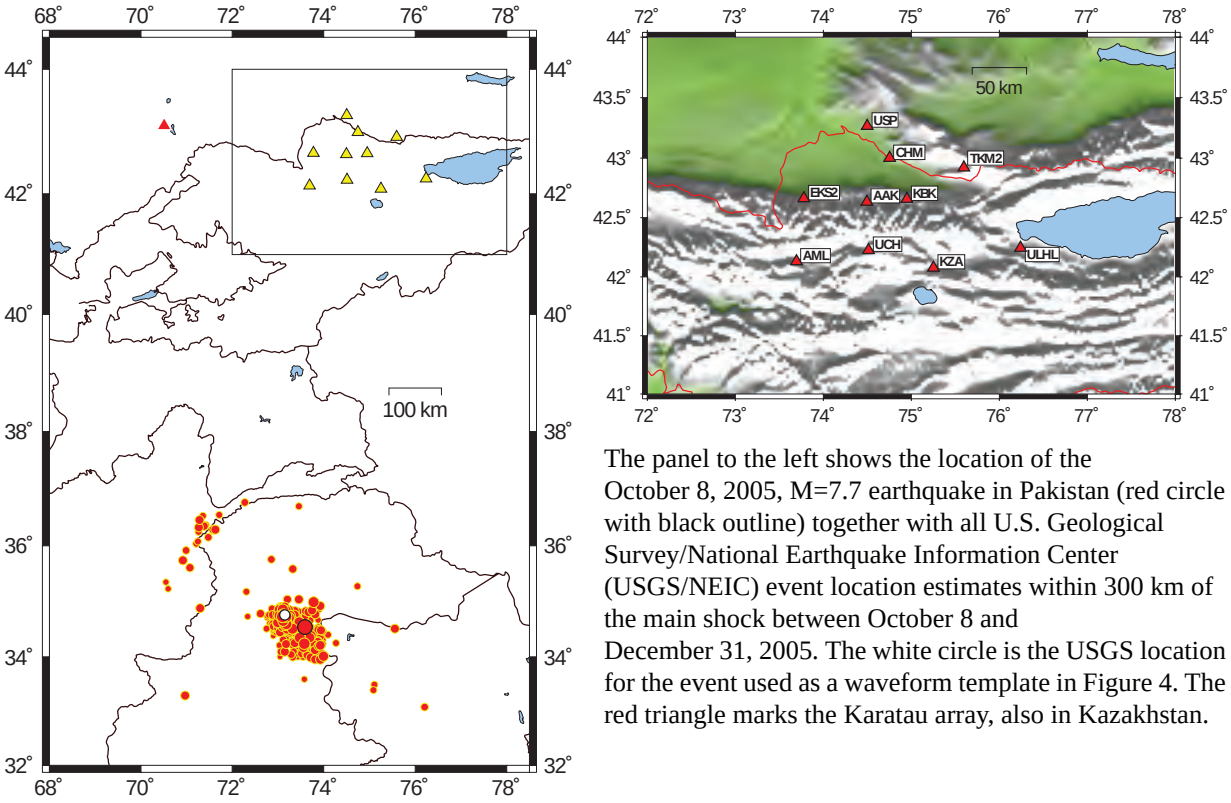

The panel to the left shows the location of the October 8, 2005, M=7.7 earthquake in Pakistan (red circle with black outline) together with all U.S. Geological Survey/National Earthquake Information Center (USGS/NEIC) event location estimates within 300 km of the main shock between October 8 and December 31, 2005. The white circle is the USGS location for the event used as a waveform template in Figure 4. The red triangle marks the Karatau array, also in Kazakhstan.

Figure 3. Locations of the October 8, 2005, Pakistan earthquake and related events together with stations of the K-NET network in Kyrgyzstan/Kazakhstan.

One such example is the M=7.7 earthquake which caused devastation in Pakistan on October 8, 2005. A template from the master event was extracted for the NORSAR and ARCES arrays at teleseismic distances and correlated experimentally against subsequent data. Not surprisingly, this resulted in few convincing detections (as characterized by sudden significant maxima on the ACCB) but rather a similarity of correlation traces over extended time segments. This is probably due to the fact that the wavefronts from subsequent events at these distances appears to the array to come from a similar direction, but that the actual waveforms (which are considerably more limited in frequency content than the regional signals displayed in Figure 2) do not show a convincing degree of similarity.

Data from the KNET stations (Figure 3) was obtained from the Incorporated Research Institutions for Seismology (IRIS) and similar correlation detectors were initiated. The master signal deriving from the main event was not useful for detecting aftershocks at these regional distances. However, waveform templates obtained from smaller aftershocks did result in many quite convincing detections on the KNET data. An example is shown in Figure 4. This is a larger aperture network than any that we have previously attempted the correlation coefficient beamforming on and the array gain is excellent with marginal peaks on the single channel traces summing to one well defined maximum and cancelling at other points in time. While the master event displayed in Figure 4 is significantly smaller than the main shock, it is also significantly larger than master events considered so far in this project. The recordings of these two events at teleseismic distances also show a degree of likeness but, as with the Russian explosions at ARCES in the previous section, are likely to require additional constraints (primarily regarding correlation trace alignment) in order to produce useful (low false-alarm-rate) detection lists.

.

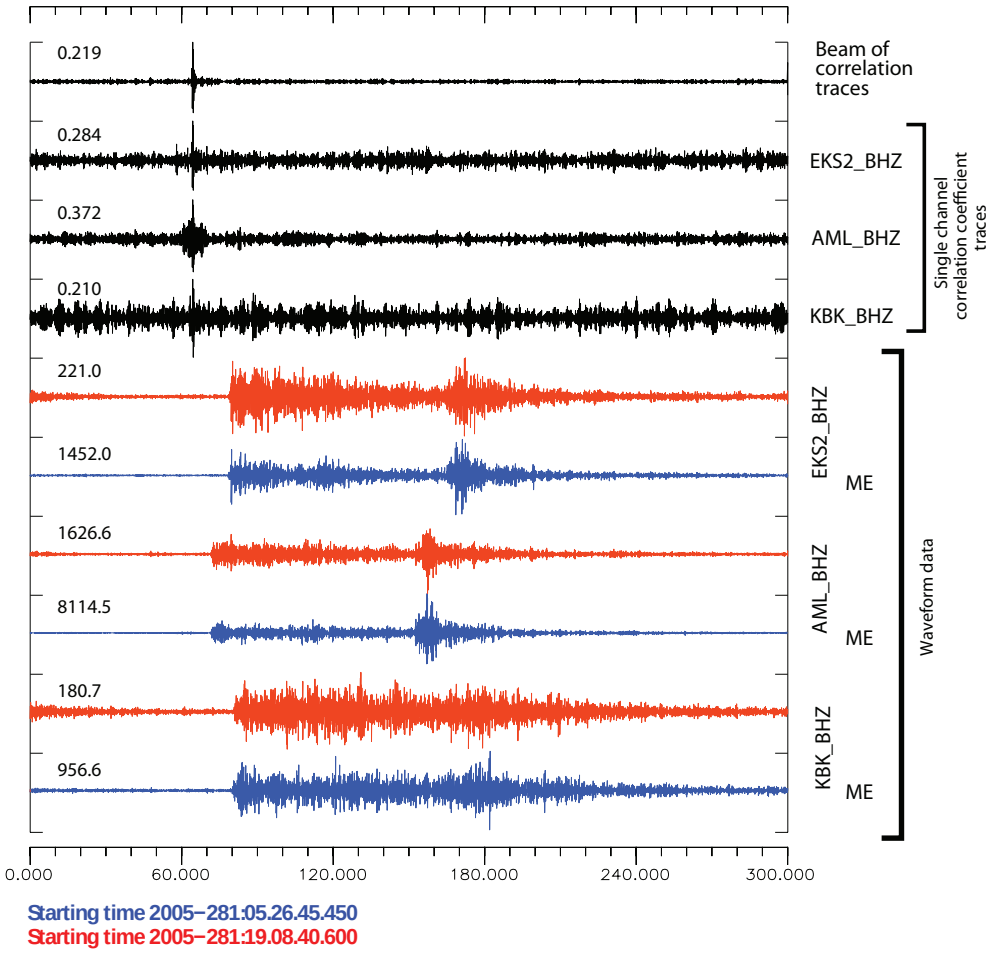

Figure 4. A positive correlation detection made over the KN-network. All waveforms are filtered between 2.5 and 8.0 Hz and the waveform template has a length of 180.0 seconds beginning at a time 2005-281:05.27.50.000. The USGS/NEIC event bulletin lists the master event as origin time 2005-281:05.26.05.120, latitude 34.760^{o}N, longitude 73.150^{o}E, depth 10.0 km and magnitude 5.5. The same bulletin lists the detected event with origin time 2005-281:19.08.00.490, latitude 34.800^{o}N, longitude 73.170^{o}E, depth 10.0 km and magnitude 4.9.

If a correlation-based rapid categorization scheme for major earthquakes and aftershock sequences is to be successful it is likely to have to consider a large number of events at a large range of magnitudes and using stations at different epicentral distances. The regional stations are likely to be necessary for identification and clustering analysis, and teleseismic stations at different azimuths might be useful in making preliminary, automatic judgments about whether events are likely to belong to the source region of interest.

The Identification of Erroneous Timing over Arrays from Correlation Detections

Rubin (2002) demonstrated how inconsistency between small errors inferred from high-accuracy cross-correlation delay-time measurements and large errors in relative event location estimates can be indicative of erroneous instrumental timing on one or more stations in a network. Given a single source of repeating seismic events, and two stations which record waveforms independently from all events, a misalignment of cross-correlation traces provides an immediate indication of an instrumental timing error at one, or both, of the stations. If such events occur sufficiently frequently over an extended period, well-determined time-dependent station corrections can be calculated using a limited number of "snapshot" measurements (Gibbons, 2006). Such methods are especially useful for sparse networks and 3-component stations since methods which exploit the coherence of microseismic noise (Koch and Stammler, 2003) are not applicable. However, even on small-aperture arrays, the alignment information for each channel can and should be applied at each opportunity to test consistency of timing across the network. An example of erroneous timing on the FINES array is displayed in Figure 5.

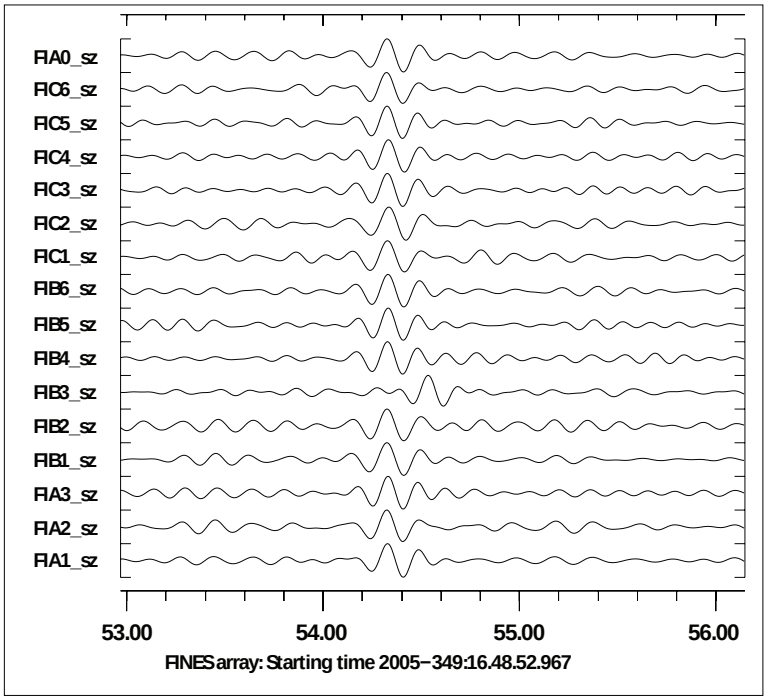

The panel to the left shows correlation coefficient traces for the 16 short-period vertical channels of the FINES array over a short time-window where the master signal template is a 20-second-long data segment beginning at a time 2005-175:04.27.22.35000 (bandpass filtered between 2.5 and 8.0 hz). The maximum of the correlation beam occurs at a time 2005-349:16.48.54.32750. Details of the events are provided in Gibbons et al. (2007). The multi-channel cross-correlation method of VanDecar and Crosson (1990) allows a very accurate measurement of the relative timing anomaly on the channel FIB3_sz. However, since GPS-lock for this site was on for neither the master event nor the detected signals, it is impossible to calculate a correction from this data alone. The FIB3 element has been non-operational since January 2006.

Figure 5. Rapid identification of a timing anomaly on the IMS primary array FINES from the misalignment of correlation coefficient traces.

Diagnostics regarding the alignment of the correlation coefficient traces are as meaningful and easy to implement over a sparse network (e.g., Figure 4) as over a small aperture array (e.g., Figure 5).

Horizontal Relative Event Locations using Stacked Cross-Correlation Traces

Central to the theme of detection through waveform similarity, is the question of spatial separation of events and the ability to provide accurate relative locations (Richards et al., 2006). The stacking of correlation coefficient traces over a seismic array lowers the detection threshold and, for the same reasons, provides improved cross-correlation time estimates, especially in cases where a single station observation would be insufficient. If an event cluster is recorded by a network of seismic arrays, there may be a possibility that events of lower magnitude may be included in inversions for relative location estimates using double-difference (DD) type algorithms. The events described in Gibbons et al. (2007) were recorded by both array stations at regional distances and 3-component stations at local distances. The local network recordings were unfortunately too incomplete for a full double-difference relative relocation. However, a stacking of correlation coefficient traces for the Lg-phase over each of the seismic arrays, together with an application of the Schaff and Richards (2004) DD-algorithm, allowed for a stable solution (Figure 6) - consistent with the existing local recordings - despite the low signal-to-noise ratio of the events at regional distances.

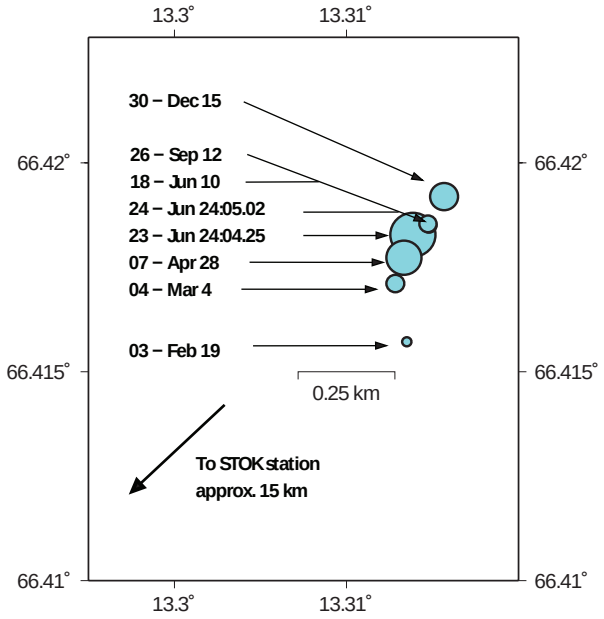

Figure 6. Relative location estimates obtained for 8 events in the Rana region of northern Norway using the Lg double-difference formulation of Schaff and Richards (2004) based upon delay times indicated by correlation coefficient beams at 4 seismic arrays at distances over 600 km. Details provided in Gibbons et al. (2007).

Gibbons et al. (2007) describe a sequence of events in the north of Norway between March and December 2005, ranging from magnitudes 0.5 to 3.5, which were all detected by correlation with a waveform template from the largest of the events on the large aperture NORSAR array at a distance of approximately 600 km. Observations from a local station (STOK at Stokkvågen) aligned by correlation of the large amplitude S-arrival indicate a small difference in S-P times (~0.05 secs) but with uncertainty due to the emergent and low-amplitude P-arrivals. However, a number of the events were also recorded by three other seismic arrays at regional distances at which the largest amplitude part of the wavetrain is the Lg-phase. Schaff and Richards (2004) observed that the Lg phase from many events in China was remarkably consistent in facilitating a double-difference horizontal relative location based upon differential delays for this phase from a number of regional stations. This procedure could be applied in this case to quite low magnitude events using time delays on the correlation stacks.

CONCLUSIONS AND RECOMMENDATIONS

We have explored the use of multi-channel waveform correlation detectors in a number of situations that present a number of challenges primarily due to waveform dissimilarity. Two case studies have been introduced in the current paper. The first case study is a sequence of presumed military explosions in northwestern Russia. Whilst the source location for these is poorly constrained, it is assumed that they take place within a reasonably compact region and that the primary reason for the waveform dissimilarity is differences in the source-time functions. This is supported by the sequence of multiple phase arrivals recorded by the ARCES array, which result in a characteristic large spread in automatic event location estimates determined by spurious phase associations. A template extracted from the simplest waveform was correlated against several years of ARCES data. Typical low correlation coefficient values between events that were evidently related resulted in an aggressively low detection threshold. Accepting triggers based upon the correlation beam value alone resulted in an excessive number of detections of which the vast majority were clearly spurious. Applying multi-variate selection criteria, with emphasis upon the alignment of the correlation coefficient traces at distinct sites, reduced this number dramatically. In a four year period, 243 detections passed the specified tests of which 220 corresponded with events which could be located manually close to the assumed

explosion site. All of the evident false alarms from this particular case-study were the result of high-amplitude local Rg phases from a similar direction.

The second case study is the extensive aftershock sequence from the magnitude 7.7 earthquake in Pakistan on October 8, 2005. Such sequences present a huge challenge to the nuclear explosion monitoring effort, due both to the increased noise level the global network is subjected to and the increased demand on analyst resources in locating and categorizing all events. A fully automatic event categorization based upon waveform similarity is therefore highly desirable, but is difficult due to the large magnitude of the main shock (large rupture length, source spectrum which will vary significantly from that of small aftershocks) and the wide geographical distribution of aftershocks (will clearly require a very large number of waveform templates to have a hope of covering with a correlation or subspace detector). A number of very clear correlation detections were made using data at teleseismic distances (the NORSAR and ARCES seismic arrays) and at regional distances (the KNET stations at a distance of approximately 900 km). In an example displayed, the master event has estimated magnitude of 5.5, substantially higher than any considered so far in this project (e.g., Gibbons and Ringdal, 2006; Stevens et al., 2006; Gibbons et al., 2007). It may be that a sequence of master events covering a cascade of different magnitudes may be necessary to bridge the spectral differences and geographical coverage involved. Application of the correlation trace beamforming method over the KNET stations represents a large increase in the array aperture that has been applied in the current project, and its success has been mirrored in recent work by other authors (e.g., Shelly et al., 2007).

Repeating seismic events facilitate “spot-checks” on instrumental timing, which can be applied to an array or network of arbitrary dimensions since coherence between sensors is not required. On small aperture arrays, where timing verification using coherent low-frequency microseisms is possible, correlation trace alignment testing can be used to validate and confirm results obtained using alternative methods. In many cases, the accuracy obtained measuring a moveout in a sharp correlation peak calculated from a long wavetrain might be higher than that possible by correlating transient coherent wavelets over pairs of channels. This is additional motivation for the identification of repeating seismic sources. In the current paper and in Gibbons et al. (2007) we demonstrate erroneous instrumental timing on three different IMS array stations.

The presence of networks of seismic arrays may facilitate the accurate relative relocation of seismic events of smaller magnitude than would be possible with networks of single stations. Provided that the interstation distance is short compared with the epicentral distance, the cross-correlation traces from several sensors can be stacked to measure a more stable time difference between two corresponding phases in a given direction from the source. If such measurements are available at enough sites, we can apply double-difference type techniques (Waldhauser and Ellsworth, 2000) to event relocation. We measured time-differences for the Lg-phase for earthquakes in the Rana region of northern Norway at four IMS seismic arrays and applied the horizontal DD-relocation procedure of Schaff and Richards (2004) to obtain a stable relative event location solution that is consistent with limited recordings at local distances.

ACKNOWLEDGEMENTS

We are grateful to the operators of the KN network (Kyrgyz Seismic Telemetry Network: Kyrgyz Institute of Seismology, IVTAN/KIS) and the IRIS data exchange center for making this data available.

REFERENCES

Geller, R. J. and Mueller, C. S. (1980). Four Similar Earthquakes in Central California, in *Geophys. Res. Lett*. 7: 821–824.

Gibbons, S. J. (2006), On the Identification and Documentation of Timing Errors: An Example at the KBS station, Spitsbergen, *Seism. Res. Lett*. 77: 559–571.

Gibbons, S. J., Bøttger Sørensen, M., Harris, D. B. and Ringdal, F. (2007). The detection and location of low magnitude earthquakes in northern Norway using multichannel waveform correlation at regional distances, in *Phys. Earth Planet. Int*. 160: 285–309.

Gibbons, S. J. and Ringdal, F. (2006). The detection of low magnitude seismic events using array-based waveform correlation, in *Geophys. J. Int*. 165: 149–166.

Koch, K. and Stammler, K. (2003). Detection and Elimination of Time Synchronization Problems for the GERESS Array by Correlating Microseismic Noise, *Seism. Res. Lett.* 74: 803–816.

Ringdal, F. and Kværna, T. (1989). A multi-channel processing approach to real time network detection, phase association, and threshold monitoring, in *Bull. Seism. Soc. Am.* 79: 1927–1940.

Ringdal, F., Gibbons, S. J., Kværna, T., Kremenetskaya, E., Asming, V., Vinogradov, V., Mykkeltveit, S. and Schweitzer, J. (2005). Research in regional seismic monitoring, in *Proceedings of the 27th Seismic Research Review*: *Ground-based Nuclear Explosion Monitoring Technologies*, LA-UR-05-6407, Vol. 1, pp 423–432.

Richards, P. G., Waldhauser, F., Schaff, D. P., and Kim, W.-Y. (2006). The Applicability of Modern Methods of Earthquake Location, in *Pure. Appl. Geophys.* 163: 351–372.

Rubin, A. M. (2002). Using Repeating Earthquakes to Correct High-Precision Earthquake Catalogs for Time-Dependent Station Delays, in *Bull. Seism. Soc. Am.* 92: 1647–1659.

Schaff, D. P. and Richards, P. G. (2004). Lg-wave cross correlation and double-difference location: application to the 1999 Xiuyan, China, sequence, in *Bull. Seism. Soc. Am.* 94: 867–879.

Shelly, D. R., Beroza, G. C., and Ide, S. (2007). Non-volcanic tremor and low-frequency earthquake swarms. *Nature* 446: 305–307.

Stevens, J. L., Gibbons, S., Rimer, N., Xu, H., Lindholm, C., Ringdal, F., Kværna, T., Murphy, J. R. (2006). Analysis and simulation of chemical explosions in nonspherical cavities in granite, in *J. Geophys. Res.* 111: B04306, doi:10.1029/2005JB003768.

VanDecar, J. C. and Crosson, R. S. (1990). Determination of teleseismic relative phase arrival times using multi-channel cross-correlation and least squares, in *Bull. Seism. Soc. Am.* 80: 150–169.

Waldhauser, F. and Ellsworth, W. L. (2000). A double-difference earthquake location algorithm: method and application to the Northern Hayward Fault, California, in *Bull. Seism. Soc. Am.* 90: 1353–1368.

ERROR ANALYSIS IN THE JOINT EVENT LOCATION/SEISMIC CALIBRATION INVERSE PROBLEM

William L. Rodi

Massachusetts Institute of Technology

Sponsored by Air Force Research Laboratory

Contract No. F19628-03-C-0109

ABSTRACT

In previous years of this project we have formulated an approach to analyzing seismic event location uncertainty that considers the effects of both observational errors in arrival-time data and prediction errors incurred in travel-time forward modeling. The analysis takes place in the setting of the multiple-event location problem, whereby arrival-time data from a set of events are used to simultaneously solve for the locations of the events and travel-time corrections associated with the observed event-station paths. One of the events is taken as the target of the uncertainty analysis while the remaining events are treated as calibration events whose data constrain the path corrections within some level of uncertainty. Based on this joint inversion formulation, we developed a numerical scheme for computing a confidence region on the target event location that implicitly accounts for the calibration errors in the path-corrections, including the effects of uncertainty in the calibration event locations, nonlinearity of the travel-time forward problem, and non-Gaussian pick errors in observed arrival times. The confidence region is found by mapping a likelihood function, as defined for the multiple-event problem, on a hypocenter grid for the target event. The previous work focused on the basic multiple-event location problem, in which travel-time corrections comprise a simple time term for each observed station/phase combination.

This paper describes our recent efforts to adapt our location uncertainty approach to the more general, and more difficult, problem in which travel-time corrections are linked to errors in the velocity model used for travel-time prediction. The resulting multiple-event location problem identifies travel-time calibration with 3D tomography. Replacing time-term corrections with tomographic corrections in our formulation is straightforward conceptually, but not computationally. The likelihood-mapping scheme is computationally intensive and, in the tomographic case, would require performing 3D travel-time tomography hundreds or thousands of times to obtain one confidence region. To address tomographic corrections in a practical manner, we must separate the location and calibration aspects of the problem, as in customary treatments of event location uncertainty, while seeking a computational scheme that retains the generality of our joint inversion formulation as much as possible. Therefore, we have designed a two-stage approach that relies on a Gaussian description of the errors in the travel-time corrections involved with the target event, as inferred from a tomographic analysis of the calibration data (the first stage). This defines a Gaussian prior distribution on travel-time prediction errors for the second stage, the location of the target event. The computation of the target event confidence region via likelihood mapping otherwise retains the full generality of our formulation, allowing for non-Gaussian pick errors and nonlinearity of the forward problem. This paper describes the theoretical basis for our location uncertainty approach, presenting the two-stage formulation as an approximation to the complete joint location/calibration formulation. It also describes numerical algorithms under development for implementing the two-stage approach.

OBJECTIVE

This project is developing new mathematical and computational techniques for quantifying the errors in seismic event locations, including the effects of observational errors and errors in the forward model for travel-time prediction. Our approach associates the latter, or *model errors*, with the uncertainty in path travel-time corrections that have been inferred from a calibration analysis. The problems of event location and calibration (with arrival-time data from calibration events) are coupled through the travel-time corrections, and the objective of this project has been to analyze the two problems as a joint inversion problem. In so doing, one avoids making some of the simplifying, and ad hoc, assumptions that are often made when calibration results are exported to an event locator. In previous years we have applied the joint inversion framework to a simple situation (corrections as station time terms) to compute confidence regions on event locations that account for many complexities that are typically ignored or approximated: nonlinearity of the forward problem, non-Gaussian observational errors, and uncertainty in calibration-event locations.

The current year of the project has focused on the problem of applying our joint location/calibration uncertainty framework to more realistic parameterizations of travel-time corrections, in particular, corrections based on a 3D velocity model. Calibration analysis then becomes the task of 3D travel-time tomography. It was clear from the start that the joint approach, which is computationally intensive even for the time-term problem, could not be practically applied to this situation without some sort of approximation. The project goal became to discover a way to separate the calculations along traditional lines, i.e. a calibration stage providing inputs to a follow-up location stage. A key part of this goal was to retain the completeness and generality of the joint approach as much as possible. This paper describes our location uncertainty framework in general and its approximate formulation as a two-stage process, including some specific algorithms under development for implementing this prioress.

RESEARCH ACCOMPLISHED

Single-Event Location

First, we consider the single-event location problem in which the hypocenter **x** and origin time t of an event are to be determined from n arrival-time data, d_i, $i = 1,\ldots n$, observed for various seismic phases at a network stations. We can write this inverse problem as

$$d_i = T_i(\mathbf{x}) + t + c_i + e_i, \tag{1}$$

where T_i is a travel-time function for the ith station/phase, determined by a reference Earth velocity model; c_i is an unknown correction to this function; and e_i is an observational (pick) error. Since each correction c_i is not known, it can be considered a travel-time prediction error, or *model* error.

To solve this problem we have adopted a maximum-likelihood framework. The likelihood function is the product of two factors: one based on an assumed probability distribution for the pick errors, and one based on a prior distribution of the travel-time corrections. The latter is needed because we are treating the c_i as explicit, unknown variables. We assume a generalized Gaussian distribution for pick errors (Billings et al., 1994). The negative logarithm of the likelihood function, ignoring constant terms, is then given by

$$\Lambda_{tar}(\mathbf{x}, t, \mathbf{c}) = \Psi_{\text{tar}}(\mathbf{x}, t, \mathbf{c}), + \Phi_c(\mathbf{c}; \mathbf{x}), \tag{2}$$

where Φ_c is the prior (negative) log likelihood on **c**, which we have allowed to depend on the event hypocenter (but not its origin time), and where the *data misfit* function Ψ_{tar} is given by

$$\Psi_{\text{tar}}(\mathbf{x}, t, \mathbf{c}) = \frac{1}{p}\sum_{i=1}^{n} \left| d_i - T_i(\mathbf{x}) - t - c_i \right|^p / \sigma_i^p. \tag{3}$$

The σ_i are standard errors assigned to the data; this paper will assume these are known *a priori*.

The maximum-likelihood estimate of the event location parameters are those values $(\hat{\mathbf{x}}, \hat{t})$ that, together with $\mathbf{c} = \hat{\mathbf{c}}$, minimize Λ_{tar}:

$$\Lambda_{\text{tar}}(\hat{\mathbf{x}}, \hat{t}, \hat{\mathbf{c}}) = \min_{\mathbf{x},t,\mathbf{c}} \Lambda_{\text{tar}}(\mathbf{x}, t, \mathbf{c}). \quad (4)$$

We note that in this equation, and others to follow, minimization with respect to a set of parameters is the equivalent of solving an inverse problem for those parameters.

Location confidence regions

Our approach to uncertainty analysis in single-event location derives a confidence region on a subset of the unknown problem parameters based on a "reduced" log-likelihood function that is minimized with respect to the remaining parameters. We will explain our uncertainty approach by considering confidence regions on the target event hypocenter, **x**, which considers the function

$$\Lambda_x(\mathbf{x}) = \min_{t,\mathbf{c}} \Lambda_{\text{tar}}(\mathbf{x}, t, \mathbf{c}). \quad (5)$$

A confidence region on the epicenter, for example, would involve an additional minimization over focal depth.

Stated simply, a confidence region on **x** is a region in **x**-space that encompasses the smallest values of Λ_x, which of course includes the maximum-likelihood estimate $\hat{\mathbf{x}}$. The confidence region is defined by the inequality

$$\tau(\mathbf{x}) \equiv \Lambda_x(\mathbf{x}) - \Lambda_x(\hat{\mathbf{x}}) \le \tau_\beta \quad (6)$$

where $\tau(\mathbf{x})$ defines a test statistic and τ_β is a critical value of the test statistic selected for a given confidence level β (e.g. $\beta = 0.95$ for a 95% confidence region). Rodi (2006) discusses different ways of defining τ_β, in either a Neyman-Pearson or Bayesian framework, and for computing τ_β numerically. Amongst these choices, the preferred approach we have settled on is as follows.

We base the definition of τ_β on a Bayesian framework, which treats $\tau(\mathbf{x})$ as the exponent of a posterior distribution on **x**. Then τ_β is the solution to

$$\int_{\tau(\mathbf{x}) \le \tau_\beta} d\mathbf{x}\, e^{-\tau(\mathbf{x})} = \beta \int_{\text{all } \mathbf{x}} d\mathbf{x}\, e^{-\tau(\mathbf{x})}. \quad (7)$$

Rodi (2006) refers to this definition as "quasi-Bayesian" because the implied posterior distribution of **x** is not derived from a posterior joint distribution on all the parameters by integrating out *t* and **c**. The minimization over *t* and **c** in equation (5) is used instead.

The numerical algorithm we have developed consists of two steps. The first step, likelihood *mapping*, computes τ on a grid in **x** -space. The second step, likelihood *integration*, estimates the integral on the right-hand side of equation (7) with numerical integration of the grid values of τ. From this integral, and a histogram of the grid-sampled τ values, it is straightforward to calculate τ_β as a function of β and then identify the grid points that belong to the confidence region for any given β.

Figure 1 shows an example of our numerical confidence region algorithm applied to a Nevada Test Site (NTS) explosion at the Pahute Mesa testing area. The center panel shows the log-likelihood function mapped on an epicenter grid. The right panel shows the confidence regions, at three confidence levels, that result after performing the likelihood integration step to find τ_β. This example did not account for model errors: the travel-time corrections, c_i, were fixed to zero. Additionally, the event depth was fixed to its known value.

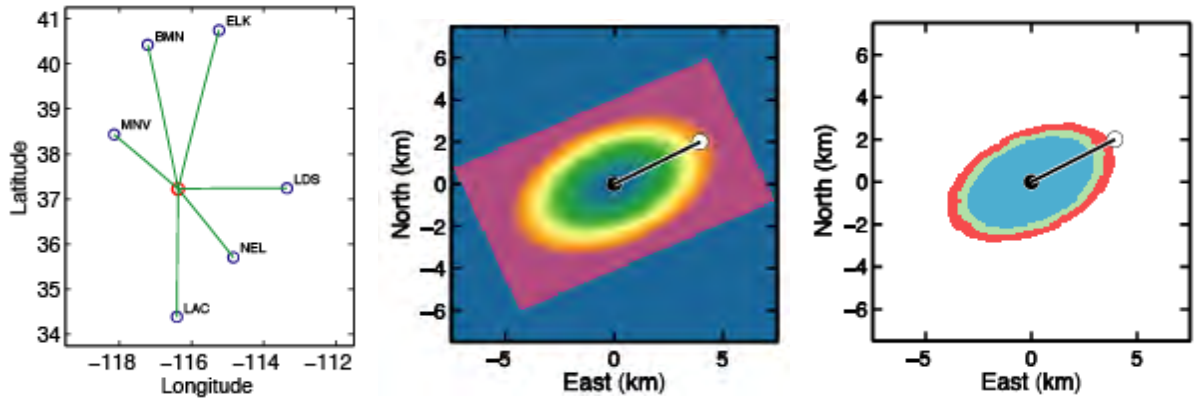

Figure 1. Likelihood function and confidence regions for a Pahute Mesa explosion, derived from 6 Pn arrivals, with the pick error distribution assumed to be Gaussian (p = 2). *Left*: The station geometry. *Center*: Log-likelihood function mapped on an epicenter grid. *Right*: Epicenter confidence regions determined from the likelihood function. Confidence regions are shown for 90, 95 and 98% confidence (blue, green and red, respectively). In the right two panels, the black circle marks the maximum-likelihood estimate for the event location, and the white circle is its GT0 location (from Walter et al., 2003).

The computational efficiency of our numerical confidence region algorithm depends on how much CPU time it takes to evaluate $\Lambda_x(\mathbf{x})$, involving the minimization in equation (5), for each grid point $\mathbf{x}$. When model errors are allowed, this is controlled largely by the nature of the prior misfit function for corrections, $\Phi_c(\mathbf{c};\mathbf{x})$, appearing in equation (2).

Prior Likelihood on Corrections and Calibration

It is common in seismic event location algorithms to treat the travel-time corrections c_i as independent Gaussian random variables (model errors) with known means and variances. Later in our development we will do the same (but including covariances). First, let us consider the formal relationship between Φ_c, the prior log-likelihood function on $\mathbf{c}$, and the problem of seismic calibration.

We assume that calibration is performed with seismic arrival-time data observed from m calibration events. Following our single-event formulation, we can write the calibration problem then as

$$d_{i,j} = T_i(\mathbf{x}_j) + t_j + c_{i,j} + e_{ij}, \tag{8}$$

where i indexes station/phase pairs and j indexes the events. Equation (8) holds for the subset of (i, j) paths for which data are available. The unknowns in this problem are the path travel-time corrections c_{ij} and, to the extent that the calibration events do not have GT0 locations, $(\mathbf{x}_j, t_j)$, $j = 1, \ldots, m$.

The set of station/phase combinations indexed by i may be the same as those for the single-event location problem of equation (1), but we do not require this to be true. Henceforth, the n station/phases under discussion may be considered a master set, with equations (1) and (8) holding for appropriate subsets for which observations are available.

To link the target-event location problem, (1), and the calibration problem, (8), we need to link the path travel-time corrections c_i and c_{ij} through some underlying parameterization. In previous years, the project has focused on the "basic" multiple-event location problem (e.g., Pavlis and Booker, 1983), which equates the corrections to a set of

time terms common to the events but different between station/phase combinations. Letting a_i be the time term for the *i*th station/phase, we then have

$$c_i = a_i \tag{9}$$
$$c_{ij} = a_i . \tag{10}$$

In the current year, we have considered the more complex situation of *tomographic* travel-time corrections. Under the linear approximation to the velocity dependence of travel times, these corrections can be expressed as

$$c_{i,j} = \int d\mathbf{x}' k_i(\mathbf{x}';\mathbf{x}_j)\delta u(\mathbf{x}'), \tag{11}$$

where $k_i(\mathbf{x}';\mathbf{x}_j)$ is a travel-time sensitivity kernel and $\delta u(\mathbf{x}')$ is the slowness difference between the real Earth and the reference Earth model used for evaluating the travel-time function T_i. In this case, the slowness perturbation $\delta u(\mathbf{x}')$ serves as the underlying parameterization of travel-time corrections and c_i in the single-event problem is defined by integrating this perturbation with an appropriate sensitivity kernel for the target event, $k_i(\mathbf{x}',\mathbf{x})$.

We can generalize these specific parameterizations and others as

$$c_i = \mathbf{a}_i(\mathbf{x})^T \mathbf{q} \tag{12}$$
$$c_{ij} = \mathbf{a}_i(\mathbf{x}_j)^T \mathbf{q}, \tag{13}$$

where the vector **q** contains an underlying, discrete set of parameters for generating travel-time corrections. It will be convenient to write equation (12) alternatively as

$$\mathbf{c} = \mathbf{A}(\mathbf{x})\mathbf{q}, \tag{14}$$

where the vectors $\mathbf{a}_i(\mathbf{x})$ (transposed) occupy the rows of the *sensitivity* matrix $\mathbf{A}(\mathbf{x})$.

Being consistent with our maximum-likelihood formation for single-event location, we define a (minus) log-likelihood function for the calibration problem as

$$\begin{aligned}\Lambda_{\text{cal}}(\mathbf{x}_1,t_1,\ldots,\mathbf{x}_m,t_m,\mathbf{q}) = \Psi_{\text{cal}}(\mathbf{x}_1,t_1,\ldots,\mathbf{x}_m,t_m,\mathbf{q}) \\ + \Phi_{\text{gt}}(\mathbf{x}_1,t_1,\ldots,\mathbf{x}_m,t_m) + \Phi_q(\mathbf{q}).\end{aligned} \tag{15}$$

Ψ_{cal} is the misfit function for the calibration data:

$$\Psi_{\text{cal}}(\mathbf{x}_1,t_1\ldots.,\mathbf{x}_m,t_m,\mathbf{q}) = \frac{1}{p}\sum_{ij}\left| d_{ij} - T_i(\mathbf{x}_j) - t_j - \mathbf{a}_i(\mathbf{x}_j)^T\mathbf{q}\right|^p . \tag{16}$$

Φ_{gt} and Φ_q express prior information on the calibration event locations and calibration parameters, respectively. We can now state a formal relationship between calibration and a prior likelihood function for model errors in the single-event location problem:

$$\Phi_{\text{cal}}(\mathbf{c};\mathbf{x}) = \min_{\mathbf{q}:\mathbf{A}(\mathbf{x})\mathbf{q}=\mathbf{c}} \min_{\mathbf{x}_2,t_1\ldots,\mathbf{x}_m,t_m} \Lambda_{\text{cal}}(\mathbf{x}_1,t_1\ldots,\mathbf{x}_m,t_m,\mathbf{q}). \tag{17}$$

The two minimizations embody an inversion of the calibration data for the calibration parameters **q** in conjunction with a relocation of the non-GT0 calibration events. The minimization constrains **q** to match the given correction vector: $\mathbf{A}(\mathbf{x})\mathbf{q} = \mathbf{c}$. Equation (17) defines an implicit transformation of the posterior distribution on the calibration parameters **q**, as implied by an inversion of calibration data, into a prior distribution on $\mathbf{A}(\mathbf{x})\mathbf{q}$.

Joint Location/Calibration Analysis

A confidence region on the target event hypocenter **x** requires mapping the function $\Lambda_x(\mathbf{x})$ in hypocenter space, which in turn requires the evaluation of $\Phi_c(\mathbf{c};\mathbf{x})$ for each grid point **x** (see equations (2) and (5)). If one could evaluate equation (17) in some closed form, it would be possible to separate the computations involved in calibration and target event location. In general, however, this is not possible without invoking some approximation.

The main goal of this project was to investigate an approach that bypassed the computation of Φ_c by combining the location and calibration problems into a joint inverse problem. In the development here, this means substituting equation (17) into (2) so that (5) becomes (with some rearranging)

$$\Lambda_x(\mathbf{x}) = \min_{\mathbf{q}} \left\{ \min_{t} \Psi_{\text{tar}}\left(\mathbf{x}, t, \mathbf{A}(\mathbf{x})\mathbf{q}\right) + \min_{\mathbf{x}_1, t_1 \ldots, \mathbf{x}_m, t_m} \Lambda_{\text{cal}}\left(\mathbf{x}_1, t_1 \ldots, \mathbf{x}_m, t_m, \mathbf{q}\right) \right\} \tag{18}$$

The computational burden resulting from doing this is apparent. To evaluate $\Lambda_x(\mathbf{x})$ for each grid-point **x** requires performing a minimization over all the remaining parameters of the joint inverse problem, including calibration parameters (**q**) and calibration event locations ($\mathbf{x}_1,t_1,\ldots,\mathbf{x}_m,t_m$). Therefore, a large inverse problem is solved repeatedly in order to calculate Λ_x on a grid.

These calculations are feasible for the basic multiple-event location problem, and we have implemented a joint inversion uncertainty analysis for this problem as part of a location program (GMEL) developed under this and previous projects. Figure 2 shows confidence regions for the same Pahute Mesa event as in Figure 1, derived using 32 other explosions at Pahute Mesa and Rainier Mesa as calibration events. Only one of the calibration events, a relatively well-recorded event at Rainier Mesa (16 Pn arrivals), was assigned a finite ground-truth level. The three panels show the resulting confidence regions, which now take model errors into account, under three assumptions about the GT level of that calibration event: GT0, GT2 or GT5 (at 90% confidence). We see that the confidence regions are larger than when model errors are assumed to be zero (Figure 1), and grow as the uncertainty in the GT calibration event location is increased. Figure 3 repeats the GT0 case with various non-Gaussian pick error distribution: p = 1.5, 1.25 and 1 (left, center, right, respectively).

The confidence regions shown in Figures 2 and 3 took between 5 and 30 CPU minutes each to compute, the ones for smaller p taking the longest. In at least one case (right panel in Figure 3) the likelihood function was not mapped sufficiently well to compute accurate values of τ_β, meaning even more computation was needed. To apply the joint inversion approach with tomographic corrections, thus, would be prohibitive since each point on a likelihood grid would require performing a full 3D tomography in conjunction with calibration event relocation.

The remainder of this paper outlines a two-stage approach to event location uncertainty which, following conventional practice, isolates the bulk of the calculations in a calibration stage, whose results can be used efficiently for calculating confidence regions for target events as they arise. The two-stage approach depends on approximating the distribution of model errors, Φ_c, as Gaussian.

Gaussian Approximation

To simplify notation in this and the next section, we will not show the dependence of Φ_c on **x**. This dependence derives from the dependence of **A**, the sensitivity matrix for the target event, on **x**.

Let $\mathbf{c} = \mathbf{c}_0$ minimize Φ_c (**c**). Since the gradient of Φ_c is zero at $\mathbf{c}_0$, a quadratic approximation is given by

$$\Phi_c(\mathbf{c}) \approx \Phi_c(\mathbf{c}_0) + \frac{1}{2}(\mathbf{c}-\mathbf{c}_0)^T \mathbf{V}_c^{-1}(\mathbf{c}-\mathbf{c}_0) \tag{19}$$

where $\mathbf{V}_c$ is a symmetric matrix. This approximation is equivalent to assuming that **c** has a Gaussian prior probability distribution with moments

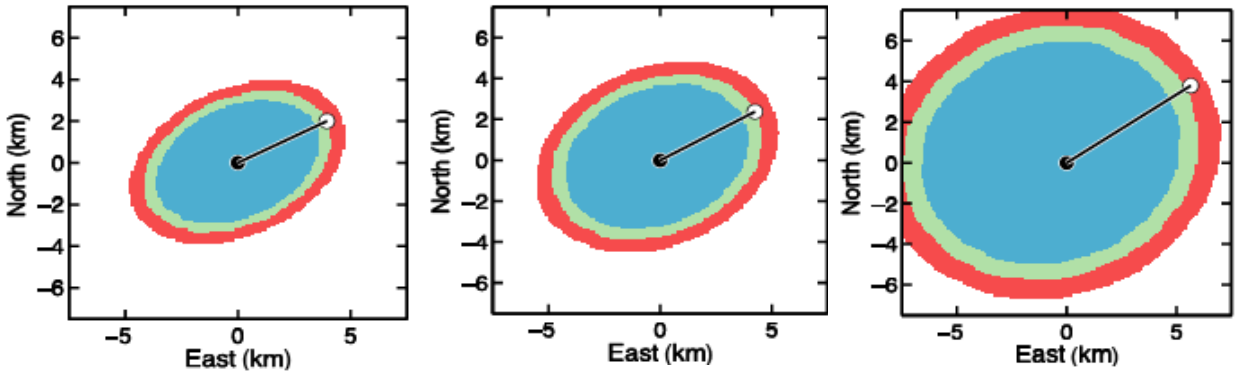

Figure 2. Confidence regions for the same Pahute Mesa event as in Figure 1, but accounting for uncertainty in travel-time corrections (model errors). The corrections were constrained by 32 calibration events (other NTS explosions) with one of them assigned a finite GT level: GT0 (left), GT2 (center), or GT5 (right). The pick error distribution was assumed to be Gaussian (p = 2).

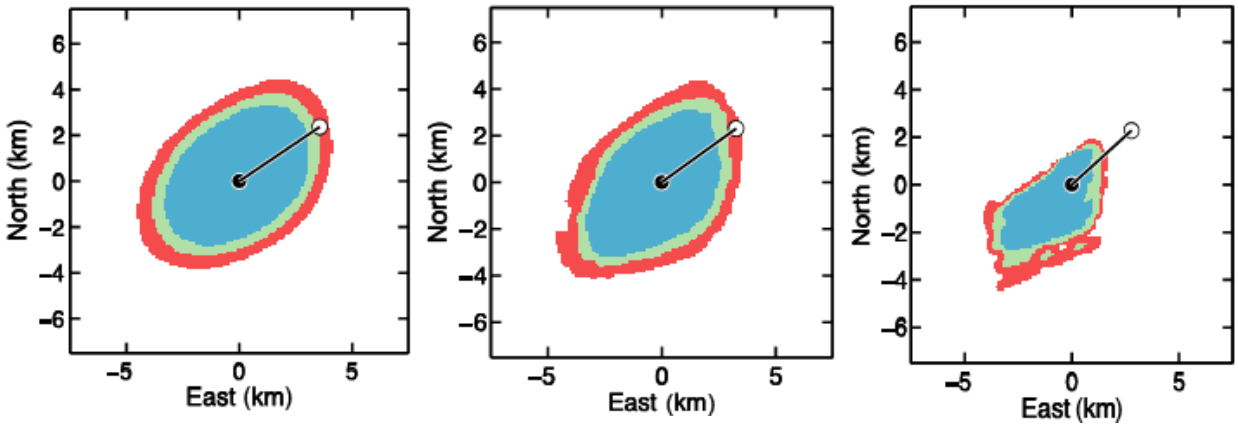

Figure 3: Confidence regions for the same Pahute Mesa event, accounting for model errors as constrained by 32 calibration events (see Figure 2). The GT calibration event is assumed to be GT0 and the pick error distribution is non-Gaussian: p = 1.5 (left), p = 1.25 (center), and p = 1 (right).

$$\mathrm{E}[\mathbf{c}] = \mathbf{c}_0 \tag{20}$$

$$\mathrm{Var}[\mathbf{c}] = \mathbf{V}_c . \tag{21}$$

The quadratic approximation makes it possible to separate the calculations of the joint location/calibration problem into two stages. The next two sections show how the mean and variance of **c** can be derived from the calibration analysis (stage one) and used in locating the target event (stage two).

Stage 1: Calibration

The calibration problem involves minimizing Λ_{cal} in equation (15) with respect to both the correction parameter vector **q** and the calibration event locations $(\mathbf{x}_j, t_j)$. We assume here that an algorithm is available to solve this problem, e.g. GMEL for basic multiple-event location.

Letting $\hat{\mathbf{q}}$ be the maximum-likelihood estimate of **q** obtained from solving the calibration problem, we can take the mean of **c** to be

$$c_0 = \mathbf{A}\hat{\mathbf{q}}. \tag{22}$$

To obtain the variance of **c** we can use a perturbation method described by Rodi and Myers (2007) for computing covariance matrices (their "implicit" method). Applied to the task at hand, the method solves a sequence of perturbed calibration problems, one for each row of **A**, in which the calibration log-likelihood function is augmented with an additional term. For the *i*th row, the augmented function is

$$\Lambda'_{\text{cal}}(\ldots,\mathbf{q}) = \Lambda_{\text{cal}}(\ldots,\mathbf{q}) + \frac{1}{2\sigma^2}\left(\mathbf{c}_0 + \rho\mathbf{n}_i - \mathbf{A}\mathbf{q}\right)^T\left(\mathbf{c}_0 + \rho\mathbf{n}_i - \mathbf{A}\mathbf{q}\right), \tag{23}$$

where $\mathbf{n}_i$ is the *i*th column of the identity matrix. The residual vectors yielded by the perturbed solutions $\left(\mathbf{c}_0 + \rho\mathbf{n}_i - \mathbf{A}\mathbf{q}\right)$ can be used to construct $\mathbf{V}_c$. As presented by Rodi and Myers (2007), this is an exact method applicable when Λ_{cal} is a quadratic function of **q**. Here, Λ_{cal} might not be quadratic owing to trade-offs between **q** and the calibration event locations or, more blatantly, the assumption of non-Gaussian pick errors ($p \neq 2$). For our purposes then, it is a method for fitting a quadratic function to $\Phi_c(\mathbf{c})$. The choice of the constants ρ and σ might then be crucial; ρ should anticipate the standard deviation of c_i and σ should be somewhat smaller than ρ.

The quantities $\mathbf{c}_0$ and $\mathbf{V}_c$ will depend on the target event hypocenter, **x**, exactly when **A** does. If this dependence cannot be neglected, then our two-stage approach would require that that $\mathbf{c}_0$ and $\mathbf{V}_c$ be calculated on an appropriate grid in **x**-space suitable for interpolation to an arbitrary **x**.

Stage 2: Location of a Target Event

We now restore the dependence of $\mathbf{c}_0$ and $\mathbf{V}_c$ on **x**.

Using the Gaussian (quadratic) approximation to Φ_c, the maximum-likelihood estimates of the target event location and travel-time correction vector, $\left(\hat{\mathbf{x}}, \hat{t}, \hat{\mathbf{c}}\right)$, will minimize

$$\Lambda_{\text{tar}}(\mathbf{x}, t, \mathbf{c}) = \Psi_{\text{tar}}(\mathbf{x}, t, \mathbf{c}) + \frac{1}{2}\left(\mathbf{c} - \mathbf{c}_0(\mathbf{x})\right)^T \mathbf{V}_c^{-1}(\mathbf{x})\left(\mathbf{c} - \mathbf{c}_0(\mathbf{x})\right), \tag{24}$$

where Ψ_{tar} is given by equation (3).

First, we point out that when the data errors are Gaussian ($p = 2$) one can minimize Λ_{tar} analytically with respect to **c** for fixed **x** and *t*. Substituting the solution for **c** into equation (24) yields a quadratic data misfit function with the data d_i, corrected by $(c_0)_i$ and with the diagonal covariance matrix for pick errors, diag$\{\sigma_1^2, \ldots, \sigma_n^2\}$, augmented by the full matrix $\mathbf{V}_c$. Some location programs (e.g., LocOO, Ballard, 2002) can accommodate such misfit functions. However, this analytic elimination of **c** cannot be done for non-Gaussian pick errors.

The event location scheme we are developing treats **c** as an explicit unknown, and performs minimization in a hierarchy. We are currently implementing the scheme in GMEL under the assumption that **A** does not depend on **x** (such as in basic multiple-event location). We describe the algorithm for this situation first.

The inner loop of the algorithm minimizes Ψ_{tar} (the data misfit) with respect to (**x**,*t*), using grid search, with **c** fixed to some current value. Denote the grid-search solution as ($\mathbf{x}^*(\mathbf{c})$, $t^*(\mathbf{c})$). We can then define an objective function for **c** as

$$\Lambda_c(\mathbf{c}) = \Psi_{\text{tar}}\left(\mathbf{x}^*(\mathbf{c}), t^*(\mathbf{c}), \mathbf{c}\right) + \frac{1}{2}\left(\mathbf{c} - \mathbf{c}_0\right)^T V_c^{-1}\left(\mathbf{c} - \mathbf{c}_0\right). \tag{25}$$

The outer loop of the location algorithm minimizes $\Lambda_c(\mathbf{c})$ using a nonlinear conjugate gradients (NLCG) technique. Each step of the NLCG loop updates **c** and performs a grid search to update $\mathbf{x}^*(\mathbf{c})$ and $t^*(\mathbf{c})$. When the NLCG iteration converges, we have $\mathbf{x}^*(\mathbf{c}) = \hat{\mathbf{x}}$ and $t^*(\mathbf{c}) = \hat{t}$.

When $\mathbf{c}_0$ and $\mathbf{V}_c$ *do* depend on $\mathbf{x}$, such as for tomographic corrections, the scheme could be modified to perform the grid-search on the complete function Λ_{tar} in (24) rather than just its first term. However, this might incur a high computational cost. If the dependence of $\mathbf{c}_0$ and $\mathbf{V}_c$ on $\mathbf{x}$ is not too strong, it might suffice to update $\mathbf{c}_0$ and $\mathbf{V}_c$ only once per NLCG iteration. Rodi and Myers (2007) show evidence that $\mathbf{V}_c$, for tomographic corrections, *does* depend strongly on $\mathbf{x}$, however.

CONCLUSIONS AND RECOMMENDATIONS

This project has developed a rigorous theoretical framework for uncertainty analysis in seismic event location, linking travel-time prediction errors (model errors) to uncertainty in travel-time calibration. This link, and the fact that calibration events themselves have location errors, recognizes event location and seismic calibration as coupled inverse problems of similar structure. Our framework thus formulates the task of characterizing the location uncertainty in an event of interest as the focus of an uncertainty analysis in the larger joint location/calibration inverse problem.

In previous years we implemented this framework for a relatively simple calibration scenario (basic multiple-event location with time-term corrections) to demonstrate the validity and generality of the approach. A pessimistic, but tentative, conclusion of Rodi (2006) was that a joint location/calibration approach might not be computationally feasible for more complex scenarios as when calibration is done by 3D travel-time tomography. Aside from computational issues, we add the logistical reality that event location and, certainly, seismic calibration are not fully automated processes that can be embedded in a computer algorithm of the type we developed. These tasks are performed by different groups of people, often with different sources of data, and on different time frames.

Our recent work has attempted to reformulate our uncertainty method as a two-stage process, calibration followed by the location of new events, in a way that preserves the rigor and generality of the joint inversion approach. This task requires that calibration uncertainty be captured and exported to an event locator. We developed one such formulation that makes the new assumption that calibration uncertainty can be characterized by a Gaussian distribution on model errors, allowing for covariances between the errors. The formulation retains the accommodation of forward problem nonlinearity, non-Gaussian errors in arrival-time observations, and uncertainty in calibration event locations. Further, we have designed new algorithms to implement our two-stage formulation that place the bulk of the computations in the calibration stage and, in principle, are applicable to a wide variety of calibration scenarios including 3D tomographic calibration. We are in the process of implementing the new algorithms for basic multiple-event location in order to corroborate the computational advantages and test the Gaussian approximation for model errors in this problem.

REFERENCES

Ballard, S. (2002). Seismic event location using Levenberg-Marquardt least squares inversion, Sandia Report, SAND2002-3083.

Billings, S.D., M.S. Sambridge and B.L.N. Kennett (1994). Errors in hypocenter location: picking, model and magnitude dependence, *Bull. Seism. Soc. Am.* 84: 1978–1990.

Pavlis, G.L, and J.R. Booker (1983). Progressive multiple event location (PMEL), *Bull. Seism. Soc. Am.* 73: 1753–1777.

Rodi, W. (2006). Error analysis in the joint event location/seismic calibration inverse problem, in *Proceedings of the 28th Seismic Research Review*: *Ground-Based Nuclear Explosion Monitoring Technologies*, LA-UR-06-5471, Vol. 1, pp. 465–474.

Rodi, W. and S. C. Myers (2007). Modeling travel-time correlations based on sensitivity kernels and correlated velocity anomalies, *Proceedings of the 29th Monitoring Research Review*, these Proceedings.

Walter, W.R., K.D. Smith, J. L. O'Boyle, T.F. Hauk, F. Ryall, S.D. Ruppert, S.C. Myers, M. Anderson, and D.A. Dodge (2003), Improving the fundamental understanding of regional seismic signal processing with a unique western United States dataset, *Proceedings of the 25th Seismic Research Review—Nuclear Explosion Monitoring: Building the Knowledge Base*, LA-UR-03-6029, Vol. 1, pp. 486–494.

MODELING TRAVEL-TIME CORRELATIONS BASED ON SENSITIVITY KERNELS AND CORRELATED VELOCITY ANOMALIES

William L. Rodi[1] and Stephen C. Myers[2]

Massachusetts Institute of Technology[1] and Lawrence Livermore National Laboratory[2]

Sponsored by National Nuclear Security Administration
Office of Nonproliferation Research and Development
Office of Defense Nuclear Nonproliferation

Contract No. DE-FC52-05NA26603[1] and W-7405-ENG-48[2]

ABSTRACT

A major contributor to the error in regional and teleseismic event locations is travel-time prediction error, attributable to velocity anomalies in the real Earth that are not represented in the reference Earth model an event locator uses for travel-time calculation. The prediction errors at two stations will, in general, be correlated depending on the spatial coherency of the velocity anomalies compared to the distance between the stations. The motivation for this project is the observation by previous workers that large event location errors can be induced when prediction error correlations are ignored and the observing network of stations is far from uniform. Recently, event location algorithms have been generalized to accept a non-diagonal covariance matrix for data errors as a mechanism for accommodating correlated errors in travel-time predictions. Our project is addressing what to input for the covariance matrix, based on considerations of seismic wave propagation and the statistical characterization of the Earth's velocity heterogeneity. Specifically, we are developing numerical algorithms that generate a travel-time covariance matrix for a network of stations, as a function of the event location, by integrating a velocity covariance function, as defined in geostatistical analysis, with the travel-time sensitivity kernels appropriate for the event-station paths. This paper describes two alternative techniques for performing this calculation, which are compared in a numerical example. A second example of our approach investigates the variation of travel-time variances and correlations over regional and near-teleseismic distances, computed using ray sensitivities for a 1D reference Earth model. This example demonstrates a strong dependence on ray parameter that agrees qualitatively with empirical observations.

OBJECTIVE

To achieve accurate event locations and estimates of location uncertainty, seismic event location algorithms must account for two types of errors: *pick* errors in the measured arrival times of the seismic phases observed at various stations, and *model* errors incurred in predicting travel time for the observed station/phase combinations as a function of the event location. Model errors are attributable to velocity anomalies in the Earth that are not rendered in the velocity model used for travel-time prediction. When the observing stations are sufficiently close to one another, their model errors are expected to be correlated. While it is now standard practice for event location algorithms used in nuclear monitoring to assign error *variances* that include the contribution from model prediction errors, the algorithms generally set the error *covariances* to zero; correlations are ignored. Doing so can seriously degrade location accuracy when the distribution of seismic stations is far from uniform (e.g. Chang et al., 1983; Yang et al. 2004).

This project is investigating the phenomenon of correlated travel-time prediction errors from a physical point of view, making use of the principles of wave propagation through heterogeneous media and our knowledge of the statistical properties of the Earth's heterogeneity. Specifically, we are developing techniques to calculate covariance matrices of travel-time model errors by integrating travel-time sensitivity kernels with plausible correlation functions describing the Earth's velocity heterogeneity. Our preliminary efforts in this development were reported by Rodi and Myers (2006). Here we summarize our approach and report on our recent efforts.

RESEARCH ACCOMPLISHED

Formulation of Approach

Given a set of n arrival time data from an event, one can decompose the data errors as (for $i = 1,\ldots,n$)

$$\mathrm{e}_i = e_{\mathrm{p},i} + \mathrm{e}_{\mathrm{m},i}, \tag{1}$$

where the first term is the *pick*, or measurement, error and the second term is the *model* error, or error in the travel-time prediction from a reference Earth velocity model. Typically, event location algorithms assume that the variances assigned to the arrival time data, σ_i^2, include a contribution for each type of error:

$$\sigma_i^2 = \sigma_{\mathrm{p},i}^2 + \sigma_{\mathrm{m},i}^2. \tag{2}$$

However, the errors for different i are assumed uncorrelated. We are addressing the problem of calculating a full covariance matrix for model errors, having components $\sigma_{\mathrm{m},ij}$ defined by

$$\sigma_{\mathrm{m},ij} = \mathrm{E}[e_{\mathrm{m},i}\, e_{\mathrm{m},j}]. \tag{3}$$

E[ ] denotes the expectation operator.

To explain our approach to covariance modeling, we consider only P-wave arrivals. Let $v_0(\mathbf{x})$ denote the P velocity function for the reference model, and $v_E(\mathbf{x})$ denote the Earth's true (and unknown) velocity function. Then, model errors can be linked to the slowness difference, which we denote $m(\mathbf{x})$:

$$m(\mathbf{x}) = v_E^{-1}(\mathbf{x}) - v_0^{-1}(\mathbf{x}). \tag{4}$$

We assume that the travel-time dependence on slowness can be adequately approximated as linear, allowing us to express the model error in the ith datum as

$$e_{\mathrm{m},i} = \int a_i(\mathbf{x})\, m(\mathbf{x})\, d\mathbf{x}\,, \tag{5}$$

where $a_i(\mathbf{x})$ is the first-order sensitivity kernel of the ith travel-time functional, as evaluated at v_0. In the high-frequency limit, this kernel is concentrated along the geometrical ray connecting the event and station

locations. For finite frequency, it is spatially distributed around this ray. In either case, we point out that the model error is a function of the event *and* station locations.

We consider $m(\mathbf{x})$ to be a Gaussian random field, having zero mean and a specified covariance between any two points, described by a covariance operator $C(\mathbf{x},\mathbf{x}')$:

$$\mathrm{E}\left[m(\mathbf{x})\right] = 0 \tag{6}$$

$$E\left[m(\mathbf{x})m(\mathbf{x}')\right] = C(\mathbf{x},\mathbf{x}'). \tag{7}$$

The covariance between two model errors is then given by

$$\sigma_{\mathrm{m},ij} = \int d\mathbf{x}\, a_i(\mathbf{x}) \int d\mathbf{x}'\, C(\mathbf{x},\mathbf{x}')\, a_j(\mathbf{x}'). \tag{8}$$

Equation (8) implies that the extent to which two model errors are correlated depends on the spatial relationship between their sensitivity kernels in relation to the correlation structure of the velocity field.

Velocity Model Covariance Operators

When $m(\mathbf{x})$ is a stationary random field, $C(\mathbf{x},\mathbf{x}')$ depends only on the difference between the points $\mathbf{x}$ and $\mathbf{x}'$. For example, if $m(\mathbf{x})$ is isotropic with a *correlation function* of the exponential type (Deutsch and Journel, 1998), then

$$C(\mathbf{x},\mathbf{x}') = \sigma^2 \exp\left[-\frac{|\mathbf{x}-\mathbf{x}'|}{\lambda}\right], \tag{9}$$

where σ^2 is the variance of the slowness field and λ is a correlation length. However, the Earth's velocity heterogeneity is not well-approximated as stationary over the spatial scales affecting regional and teleseismic waves. It is difficult to generalize an operator such as the exponential form above to allow for nonstationarity while preserving the essential properties of $C(\mathbf{x},\mathbf{x}')$, in particular its being a positive-definite operator.

A flexible approach to characterizing nonstationary random fields is to specify the covariance operator indirectly through its operator inverse, which we denote *D*, such that

$$DC(\mathbf{x},\mathbf{x}') = \delta(\mathbf{x}-\mathbf{x}'). \tag{10}$$

If we take *D* to be a differential operator, then $C(\mathbf{x},\mathbf{x}')$ is its Green's function. Rodi et al. (2003) implemented this approach with *D* as

$$D = \frac{\mathrm{const}}{\lambda_1^2\lambda_2\sigma^2}\left[\delta(\mathbf{x}) - \frac{1}{(2l-3)}\left(\frac{\lambda_1^2}{r^2}\nabla_1^2 + \lambda_2^2\frac{\partial^2}{\partial z^2}\right)\right]^l, \quad l \geq 2. \tag{11}$$

Here, *l* is an integer specifying the order of the operator; ∇_1^2 is the horizontal Laplacian operator; λ_1 and λ_2 are horizontal and vertical correlation lengths, respectively; and σ^2 is the variance. The exponential-type covariance operator of equation (9) is given by $l = 2$, ignoring boundaries.

In previous work (Rodi and Myers, 2006) we have implemented our numerical algorithms for covariance modeling with *D* being nonstationary only by virtue of the boundary at the Earth's surface and velocity discontinuities (e.g., the Moho), across which $C(\mathbf{x},\mathbf{x}')$ is allowed to "de-correlate", i.e. $C(\mathbf{x},\mathbf{x}') = 0$ when $\mathbf{x}$ and $\mathbf{x}'$ are on opposing sides of the discontinuity. One of the accomplishments of the current year has been to implement a more general form of nonstationarity whereby σ and λ_2 (vertical correlation distance) are allowed to vary with depth.

Covariance Modeling Algorithms

The numerical techniques we have developed apply to a discrete model parameterization. We thus replace the model function $m(\mathbf{x})$ with a $k \times 1$ vector $\mathbf{m}$; the sensitivity kernels $a_i(\mathbf{x})$ with $k \times 1$ vectors $\mathbf{a}_i$; and the operators C and D with $k \times k$ matrices $\mathbf{C}$ and $\mathbf{D}$. We require that

$$\mathbf{DC} = \mathbf{I}, \tag{12}$$

where $\mathbf{I}$ is the $k \times k$ identity matrix.

In the discrete formulation, the double integral of equation (8) becomes the quadratic matrix expression

$$\sigma_{\mathrm{m},ij} = \mathbf{a}_i^T \mathbf{C} \mathbf{a}_j . \tag{13}$$

It is also useful to express the full $n \times n$ model-error covariance matrix, which we denote $\mathbf{V}_\mathrm{m}$ and whose elements are the $\sigma_{\mathrm{m},ij}$. To do this, we first define the $n \times k$ sensitivity matrix having the sensitivity vectors as its rows:

$$\mathbf{A}^T = \left(\mathbf{a}_1 \;\; \mathbf{a}_2 \;\; \cdots \;\; \mathbf{a}_n \right). \tag{14}$$

We can then write

$$\mathbf{V}_\mathrm{m} = \mathbf{ACA}^T . \tag{15}$$

We now outline two numerical methods we have developed for computing $\mathbf{V}_\mathrm{m}$. Both assume that $\mathbf{D}$ is specified directly, with $\mathbf{C}$ then being given implicitly as the inverse of $\mathbf{D}$. Both methods require that the sensitivity vectors, $\mathbf{a}_i$, be given explicitly.

Explicit Method

This method entails solving a linear system for each j, given by

$$\mathbf{Du}_j = \mathbf{a}_j. \tag{16}$$

Given the solution vector $\mathbf{u}_j$, the elements of one column of the model-error covariance matrix can be found as

$$\sigma_{\mathrm{m},ij} = \mathbf{a}_i^T u_j , \qquad i = 1, \ldots, n \tag{17}$$

since, analytically, $\mathbf{u}_j = \mathbf{Ca}_j$. Repeating for each $j = 1,\ldots,n$, the full matrix $\mathbf{V}_\mathrm{m}$ is generated.

Being an approximation to a differential operator, the matrix $\mathbf{D}$ is highly sparse. Therefore, our implementation of this method solves (16) with a conjugate gradients technique.

Theoretically, the matrix obtained with the explicit method will be symmetric since $\mathbf{u}_i^T \mathbf{a}_j = \mathbf{u}_j^T \mathbf{a}_i$ if the solution vectors $\mathbf{u}_j$ are exact. Numerically, however, this will not be the case exactly. Therefore, we average the two numerical estimates of $\sigma_{\mathrm{m}ij}$ $(i \neq j)$ to generate a symmetric approximation to $\mathbf{V}_\mathrm{m}$.

Implicit Method

This method was described by Rodi and Myers (2006) and we summarize it here for completeness.

For each j we solve a *minimization* problem for a vector in the model space, $\mathbf{w}_j$:

$$\left(\mathbf{n}_j - \mathbf{A}\mathbf{w}_j \right)^T \mathbf{V}_\mathrm{p}^{-1} \left(\mathbf{n}_j - \mathbf{A}\mathbf{w}_j \right) + \mathbf{w}_j^T \mathbf{D} \mathbf{w}_j = \text{minimum} \tag{18}$$

where $\mathbf{V}_P$ is some assumed, *diagonal* covariance matrix for pick errors, and $\mathbf{n}_j$ is the jth column of the $n \times n$ identity matrix. Again, we compute the solution $\mathbf{w}_j$ with a conjugate gradients technique. Given the solution, we form the residual vector

$$\mathbf{r}_j = \mathbf{n}_j - \mathbf{A}w_j . \tag{19}$$

Repeating this process for each j = 1, …, n, we generate a residual matrix column-by-column:

$$\mathbf{R} = \begin{pmatrix} \mathbf{r}_1 & \mathbf{r}_2 & \cdots & \mathbf{r}_n \end{pmatrix}. \tag{20}$$

Rodi and Myers (2006) showed that

$$\mathbf{R} = \mathbf{V}_p \left(\mathbf{A}\mathbf{C}\mathbf{A}^T + V_p \right)^{-1}. \tag{21}$$

Therefore, two useful quantities can be generated from **R**. The first is the inverse of the *total* covariance matrix:

$$\left(\mathbf{V}_m + V_p \right)^{-1} = V_p^{-1}\mathbf{R}. \tag{22}$$

This matrix can be used by an event location algorithm in the calculation of a misfit function, assuming $\mathbf{V}_P$ is appropriate. Second, we have the object of this project, the model-error covariance matrix:

$$\mathbf{V}_m = \left(\mathbf{V}_p^{-1}\mathbf{R} \right)^{-1} - \mathbf{V}_p . \tag{23}$$

As before, the numerically generated $\mathbf{V}_m$ obtained from this formula is not guaranteed to be symmetric, but we can average it with its transpose to make it so.

For the purpose of calculating $\mathbf{V}_m$ by the implicit method, the matrix $\mathbf{V}_P$ is arbitrary. We have found that setting it to a fraction of the identity yields accurate results. If $\mathbf{V}_P$ is sufficiently small, we can ignore it and directly obtain a third quantity which can be useful in a location algorithm:

$$\mathbf{V}_m^{-1} \approx \mathbf{V}_p^{-1}\mathbf{R}. \tag{24}$$

Comparison of Explicit and Implicit Methods

Rodi and Myers (2006) presented an example of a travel-time (model-error) covariance matrix for a network of 12 regional stations observing a shallow earthquake in northeastern Iran. Figure 1 displays the station geometry for this example. The event comes from the EHB (Engdahl et al., 1998) data base and is one of the events used by Reiter and Rodi (2006) in their body-wave tomography study of southern Asia. The covariance calculations were performed using sensitivity vectors (discretized kernels) generated by Reiter and Rodi (2006) for their initial 3D velocity model, calculated with a finite-difference raytracing technique. The results we show here have been updated using a more recent tomographic model (Rodi and Reiter, 2007) and revised values of geostatistical parameters for the Earth's velocity. Velocity variations were assigned a standard deviation (σ) of 3% in the crust and 1.5% in the upper mantle. The vertical correlation distance (λ_2) in the crust was set to half the crustal thickness, while λ_2 = 60 km was used throughout the upper mantle. The horizontal correlation distance was 300 km in the crust and upper mantle.

We display two aspects of the 12×12 model-error covariance matrices ($\mathbf{V}_m$) resulting from our calculations. Figure 2 displays the 12 standard deviations (square-root of the diagonal elements) as a function of epicentral distance. The 66 independent off-diagonal elements, normalized as correlation coefficients, are plotted as a function of inter-station azimuth in Figure 3. The distance and azimuth dependence of the covariances behave as expected, qualitatively at least validating our modeling approach (see Rodi and Myers, 2006, for a more detailed discussion of the results). For our purposes here, we point out that the two numerical techniques we applied, which are compared in each figure, produce very similar results, although some small difference can be seen.

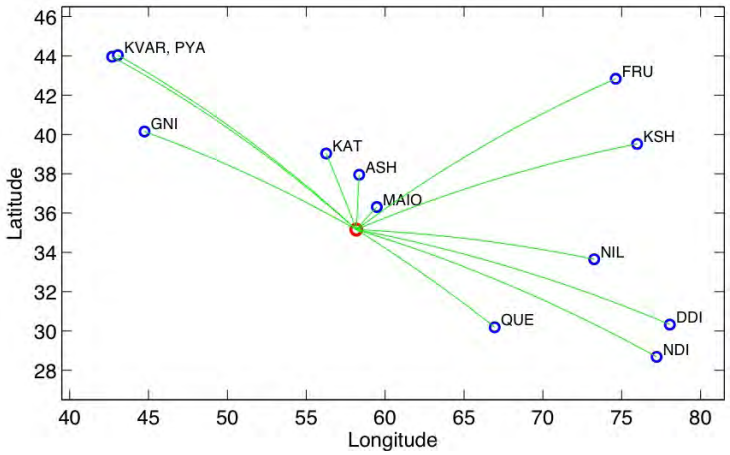

Figure 1. Event/station geometry used for testing our travel-time covariance modeling algorithms. The event epicenter is marked as the red circle. The event had Pn arrivals for 12 stations, marked as blue circles.

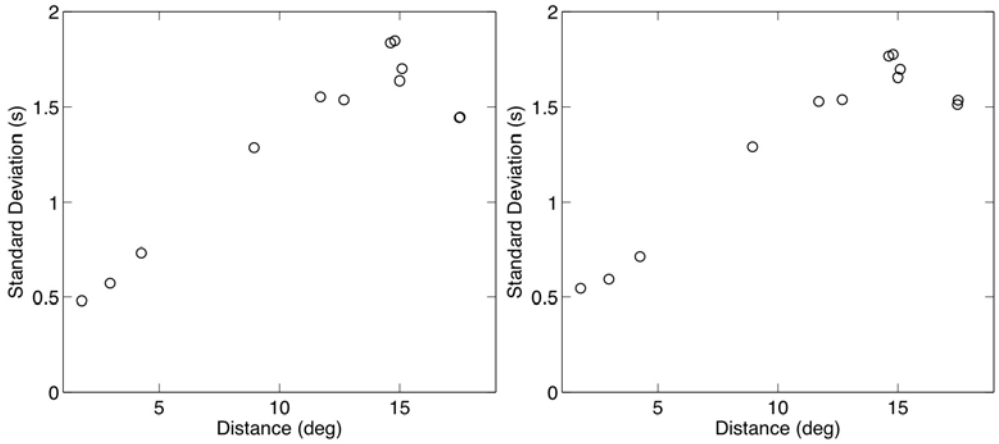

Figure 2. Standard deviation of model error as a function of epicentral distance computed with the explicit method (left) and implicit method (right). The event-station geometry is shown in Figure 1.

Distance Dependence of Travel-Time Covariance

Our second example uses a linear array of 70 stations equally spaced from 0.5° to 35° in epicentral distance from a nominal event location at a common azimuth. The resulting 70 × 70 covariance matrix then reveals the dependence of travel-time variance on distance and of travel-time correlation on distance and distance separation between stations. The calculations were done using travel-time sensitivities for the *ak135* 1D Earth model (Kennett et al., 1995), obtained with analytical solutions for geometrical rays (e.g., Buland and Chapman, 1983) and transformed to discrete sensitivities for a 3D model parameterization. The covariance matrix computations were performed with our explicit method.

We performed the calculations under two assumptions about the geostatistical parameters of velocity heterogeneity. In each, the correlation distances were the same as in the previous example (λ_1 = 300 km, λ_2 = 17.5 km in the crust and 60 km in the mantle). The standard deviation of velocity variations in the crust was also common to both cases: σ = 3% as before. The two geostatistical models differed in the velocity standard deviation assigned to the mantle. The first case used σ =1.5% throughout the mantle. The second case had σ = 2% in the upper mantle (above the

410-km discontinuity) and σ = 1% below 410 km. These parameters were chosen to illustrate the parameter dependence and are not necessarily indicative of the actual geostatistical properties of the Earth.

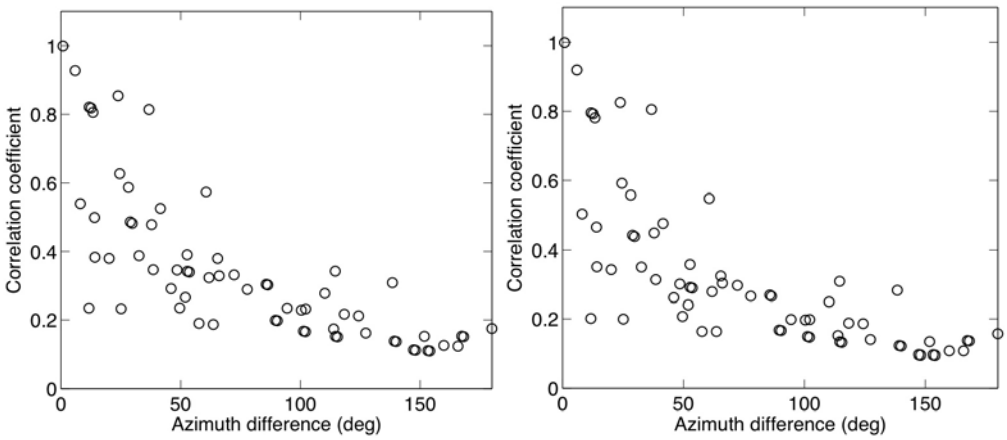

Figure 3. Correlation coefficient between model-errors as a function of azimuth difference between stations, computed with the explicit (left) and implicit (right) methods. The event-station geometry is shown in Figure 1.

Figure 4 shows the standard deviation of travel-time model errors for the two geostatistical models, each plotted versus epicentral distance. Distance-dependent discontinuities in the travel-time standard deviation are evident at the same distances in both models. These discontinuities are directly attributed to discontinuities in ray parameter, which are controlled by the *ak135* model. From approximately 2° to 15° travel-time error increases consistently, but not strictly linearly. The rate of increase in the error diminishes with distances, as rays begin to average over several correlation lengths of velocity variations. At approximately 15°, rays begin to dive deeper into the upper mantle and travel more vertically, resulting in more averaging over the shorter correlation-length anomalies in the vertical dimension. Several breaks in the error structure are evident as rays dive below the 410-km velocity discontinuity and then the 660-km discontinuity. Error structure stabilizes at teleseismic distances ($\geq$ 24°) when rays bottom in the lower mantle and the ray parameter remains continuous. Travel-time error is lower at teleseismic distance because vertically traveling rays in the more strongly heterogeneous upper mantle average over more wavelengths of geologic heterogeneity, recalling that we assumed the vertical scale of heterogeneity to be much smaller than the horizontal scale.

The travel-time error structure shown in Figure 4 is similar to that derived empirically (e.g., Flanagan et al., 2007). The similarity between empirical and our model-based predictions of travel-time error as a function of distance is encouraging. Further, these results provide insight into the non-intuitive but robust observation that teleseismic travel-time errors with long ray paths are smaller than regional travel-time errors with shorter ray paths.

Figure 5 shows the correlation matrix corresponding to the standard deviations shown in Figure 4. Analogous to the breaks in travel-time standard deviation, Figure 5 shows a roughly block-diagonal structure, with the blocks delimited by the same crossover distances and associated jumps in ray parameter. These results demonstrate that simple estimates of travel-time correlation based on the distance between stations do not adequately account for correlations between travel-times near crossover distances. If two stations straddle a break in ray parameter, then travel-time residuals are likely to be uncorrelated. This result has profound implications for both location algorithms and empirical methods (e.g., kriging) that make use of the travel-time residual covariance matrix.

CONCLUSIONS AND RECOMMENDATIONS

Our efforts to date confirm the feasibility of using a model-based approach to compute travel-time residual covariances. The numerical techniques we have developed are quite flexible in the station geometries and types of

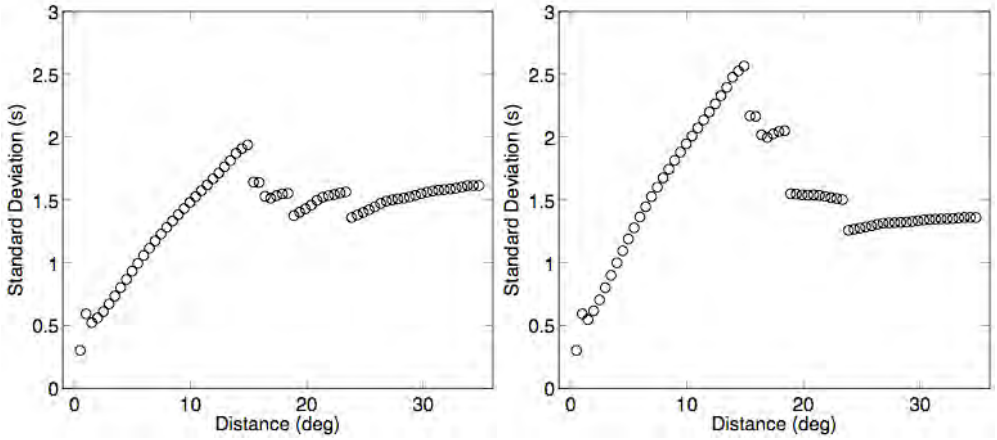

Figure 4. Standard deviation of travel-time model error as a function of epicentral distance computed with different geostatistical parameters for velocity heterogeneity. Both have a 3% velocity standard deviation (σ) in the crust. The results on the left correspond to σ = 1.5% everywhere in the mantle, while those on the right assign σ = 2% in the upper mantle above a depth of 410 km, and σ = 1% below 410 km. The same correlation lengths of heterogeneity were used in both cases (see text).

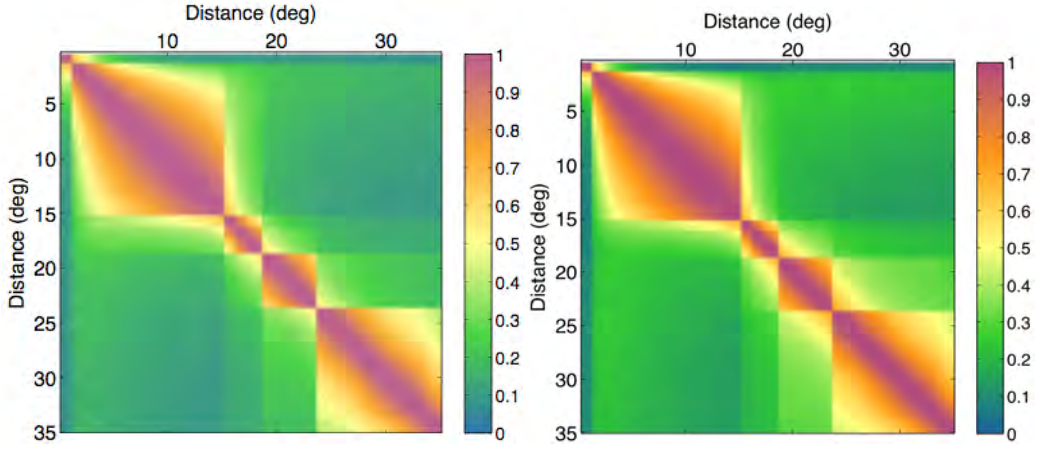

Figure 5. Correlation coefficient between model errors at different epicentral distances and a common azimuth, computed with the same two geostatistical models compared in Figure 4; σ = 1.5% throughout the mantle (left) and σ = 2% above 410 km and 1% below 410 km (right).

Earth models they can accommodate (1D and 3D), providing a useful tool for the theoretical investigation of how travel-time covariances behave in a variety of situations. Applying the techniques under even simple assumptions about the statistical properties of velocity anomalies in the Earth has already yielded important insights into previous empirical studies of travel-time residual structure as a function of epicentral distance (e.g. Myers and Schultz, 2000). Our approach goes beyond such studies by predicting details of the nonstationary correlations, which are difficult to resolve with empirical data but which are important to a seismic event locator. A crucial test of our approach will be location-validation experiments that quantify the location improvement one can achieve by using realistic travel-time covariance models.

REFERENCES

Buland, R., and C. H. Chapman (1983). The computation of seismic travel times, *Bull. Seism. Soc. Am.* 73: 1271–1302.

Chang, A. C., R. H. Shumway, R. R. Blandford and B. W. Barker (1983). Two methods to improve location estimates—preliminary results, *Bull. Seism. Soc. Am.* 73: 281–295.

Deutsch, C. V. and A. G. Journel (1998). *GSLIB: Geostatistical Software Library and User's Guide*, 2nd ed., Oxford University Press, Inc., New York, 369 pp.

Engdahl E. R., R. van der Hilst, and R. Buland (1998). Global teleseismic earthquake relocation with improved travel times and procedures for depth determination, *Bull. Seism. Soc. Am.* 88: 722–743.

Flanagan, M. P., S. C. Myers, and K. D. Koper (2007). Regional travel-time uncertainty and seismic location improvement using a three-dimensional a priori velocity model, *Bull. Seism. Soc. Am.* 97: 804–825.

Kennett, B. L. N., E. R. Engdahl, and R. Buland (1995). Constraints on the velocity structure in the Earth from travel times, *Geophys. J. Int.* 122: 108–124.

Myers, S. C., and C. A. Schultz (2000). Improving sparse network seismic locations with Bayesian kriging and teleseismically constrained calibration events, *Bull. Seism. Soc. Am.* 90: 199–211.

Reiter, D. and W. Rodi (2006). Crustal and upper-mantle P- and S-velocity structure in central and southern Asia from joint body- and surface-wave inversion, in *Proceedings of the 28th Seismic Research Review: Ground-Based Nuclear Explosion Monitoring Technologies*, LA-UR-06-5471, Vol. 1, pp. 209–218.

Rodi, W. L. and D. T. Reiter (2007). SAsia3d: A 3-D crust and upper-mantle velocity model of south Asia derived from joint inversion of P-wave travel times and surface-wave dispersion data, these Proceedings.

Rodi, W. and S. C. Myers (2006). Modeling travel-time correlations based on sensitivity kernels and correlated velocity anomalies, in *Proceedings of the 28th Seismic Research Review: Ground-Based Nuclear Explosion Monitoring Technologies*, LA-UR-06-5471, Vol. 1, pp. 475–483.

Rodi, W., S. C. Myers and C. A. Schultz (2003). Grid-search location methods for ground-truth collection from local and regional seismic networks, in *Proceedings of the 25th Seismic Research Review—Nuclear Explosion Monitoring: Building the Knowledge Base*, LA-UR-03-6029, Vol. 1, pp. 311–319.

Yang, X., I. Bondar, J. Bhattacharyya, M. Ritzwoller, N. Shapiro, M. Antolik, G. Ekstrm, H. Israelsson, and K. McLaughlin (2004). Validation of regional and teleseismic travel-time models by relocating ground-truth events, *Bull. Seism. Soc. Am.* 94: 897–919.

SEISMIC SOURCE LOCATIONS AND PARAMETERS FOR SPARSE NETWORKS BY MATCHING OBSERVED SEISMOGRAMS TO SEMI-EMPIRICAL SYNTHETIC SEISMOGRAMS: APPLICATIONS TO LOP NOR AND NORTH KOREA

David Salzberg and Margaret Marshall

Science Applications International Corporation

Sponsored by Air Force Research Laboratory

Contract No. FA8718-05-C-0019

ABSTRACT

The purpose of this study is to demonstrate the feasibility of a full-waveform earthquake location using semi-empirical synthetic waveforms and received data from as few as two regional stations. We previously demonstrated the ability to locate both natural and man made events using events from Central California (natural events) and the Nevada Test Site (NTS) (natural and man-made events). We were able to locate most events to within GT 5 (based on a comparison with the reference (GT, ground truth) catalog and our estimates of the precision of the error ellipses. This precision includes events with varying depths, mechanisms, location, and size. Of particular interest is the ability to simulate and locate an earthquake waveform (Little Skull Mountain, LSM) using an explosion reference event (NTS explosion JUNCTION). Reciprocity suggests that the earthquake could be used to simulate the waveforms from explosions.

In this presentation, the focus is two-fold: first, we present the results of the location study as applied to a Lop Nor, China data set; second, we present parameter extract (yield) of a nuclear explosion (North Korea) based on a distant reference event using records from one station. The Lop Nor example demonstrates (1) the portability of the approach, and (2) the ability to apply it to regions of interest for nuclear monitoring. Unlike the US datasets, general high quality ground truth is only available for a few events: the explosions at Lop Nor (GT from Fisk, 2002). Locations of the nearby earthquakes are not known with enough precision to assess our ability to obtain GT 5 or better location; indeed, it is possible that our locations are the best.

In comparison, the North Korea Nuclear explosion of October 9, 2006, occurred in a seismically isolated region (no nearby earthquakes). However, an active source experiment for wide-angle reflection and refraction near the border in China (Wu, personal communications) provides some sort of calibration. While the yield from the China experiment was small (1.2–1.5 tons, according to Wu), a good signal was recorded at the station MDJ for one particular explosion. This event, roughly ½ way between the North Korean Nuclear Explosion and MDJ, provides our reference event for our yield estimate of the North Korean Nuclear Explosion, which is about 450 tons.

OBJECTIVES

The objective of the research is to provide a method that gives accurate locations (GT5) and source mechanisms using a sparse regional network when two or more seismic stations record the event. Tests using synthetic waveforms indicate that location accuracy on the order of 300–500 km^2 and depth uncertainty of less than 5 km can be obtained with recordings from only two stations low pass-filtered at 0.5 Hz using hold waveforms or 0.1 Hz when using just the Rayleigh waves.

The objective of this paper is two-fold:

- Demonstrate the applicability of our semi-empirical approach outside of the United States by applying it to events in the region around the Lop Nor Test Site.
- Apply the semi-empirical methodology to determine the Yield and characteristics of the October 9, 2006, North Korean Nuclear Test.

RESEARCH ACCOMPLISHED

Portability of the Semi-Empirical Method

We previously derived our semi-empirical methodology from the following equation:

$$u_e(\omega, r) = \frac{s(\omega)}{u(\omega, r_o)} \cdot e^{i\Delta k(r - r_o)} \cdot u(\omega, r) \ , \qquad (1)$$

where u is the synthetic seismogram, s is the observed seismogram, r_o is the range to the reference event, r is the range to the new event, and Δk is the wave number corresponding the phase mismatch reference data and synthetic (Salzberg et al., 2005, 2006).

This approach has been demonstrated by applying it to regional waveforms from both Central California earthquakes and NTS explosions; the results are shown in Figures 1 and 2. We have begun analysis of events around the Chinese Lop Nor test site, particularly those assigned GT1 by Fisk (2002). Preliminary results based on one station show that we are able to resolve the correct range (Figure 3), even with a nearest station at about 1150 km.

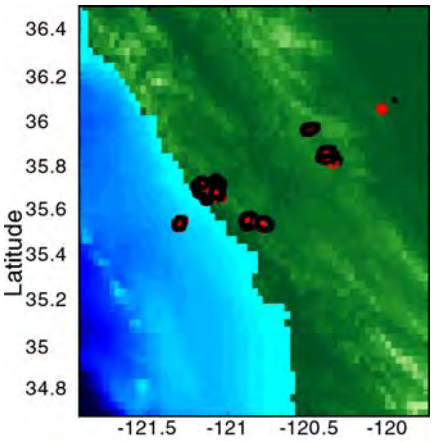

Figure 1. The error ellipses for our relocated earthquakes relative to an aftershock of the Parkfield earthquake. The lines represent the error in our location compared with GT (red circles).

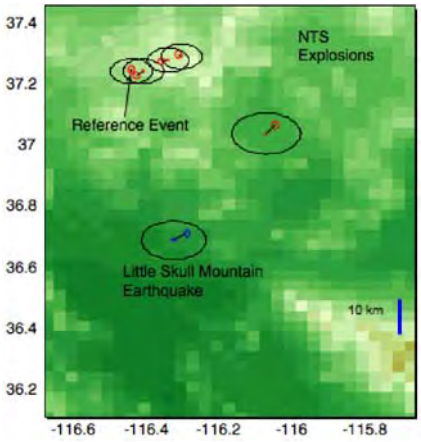

Figure 2. The error ellipses for our relocated explosions and the LSM earthquake. The lines represent the error in our location compared with GT (red circles). The blue vertical line on the right is 10 km long. In all cases, the mislocation is less than 5 km, though for the LSM earthquake, the mean axis of the error ellipse approaches 5 km.

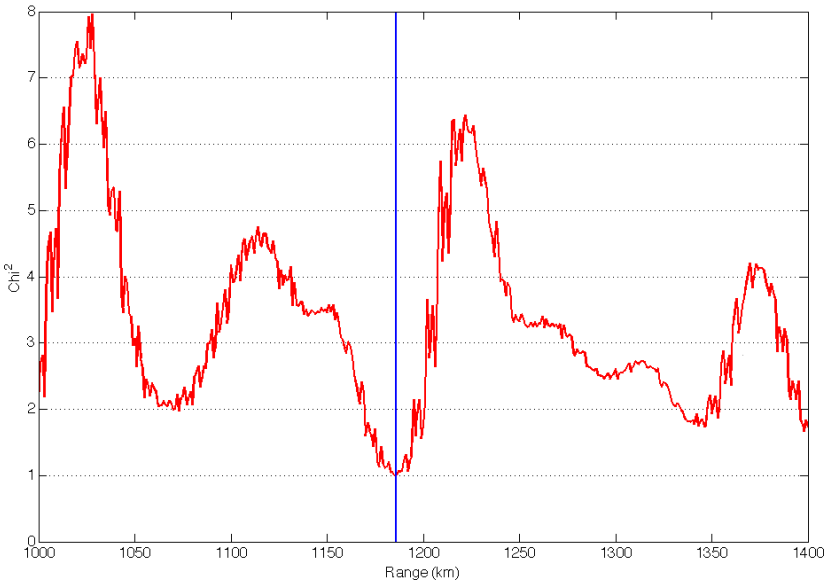

Figure 3. χ^2 vs. range for the May 1992 nuclear explosion recorded at station AAK. The minimum in χ^2 is at the correct GT range, indicating that the range was successfully estimated.

Analysis of the North Korean Nuclear Test

Introduction

We have used a slight modification of our semi-empirical synthetic seismogram method of Salzberg (2005, 2006) to estimate the yield of the North Korea Nuclear test of October 09, 2006. The data used for the processing is from the seismic station,MDJ, which is located in northeastern China, as shown in Figure 4. The reference data, used for calibration, was from a wide-angle refraction experiment. The 1.2- to 1.5-t shot was set off 190 km south of MDJ, or about ½ way between the North Korean test and MDJ. While the data for the Chinese reference event is noisy (Figure 5), at higher frequency bands, (> 1 Hz), the signal is clear. The signal for the North Korea Nuclear test has significant signal at all frequencies (Figure 6).

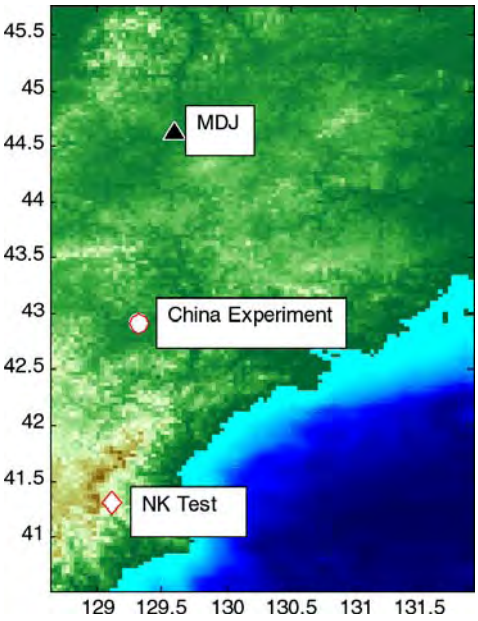

Figure 4. A map showing the relative locations of the North Korean test, the China experiment, and the seismic station MDJ.

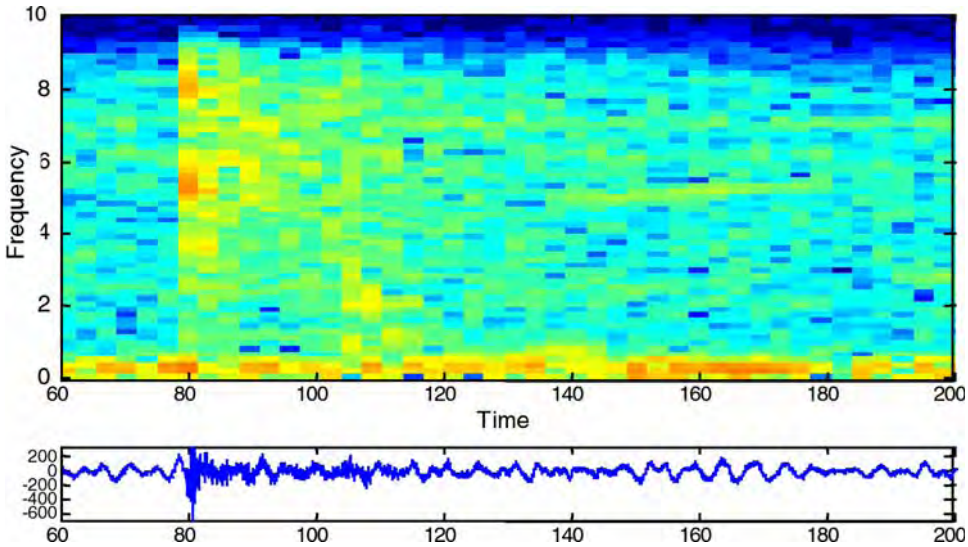

Figure 5. Unprocessed waveform and spectrogram for the waveform from a wide-angle refraction/reflection experiment in northeastern China (1.2–1.5 t). This event is used as a reference event.

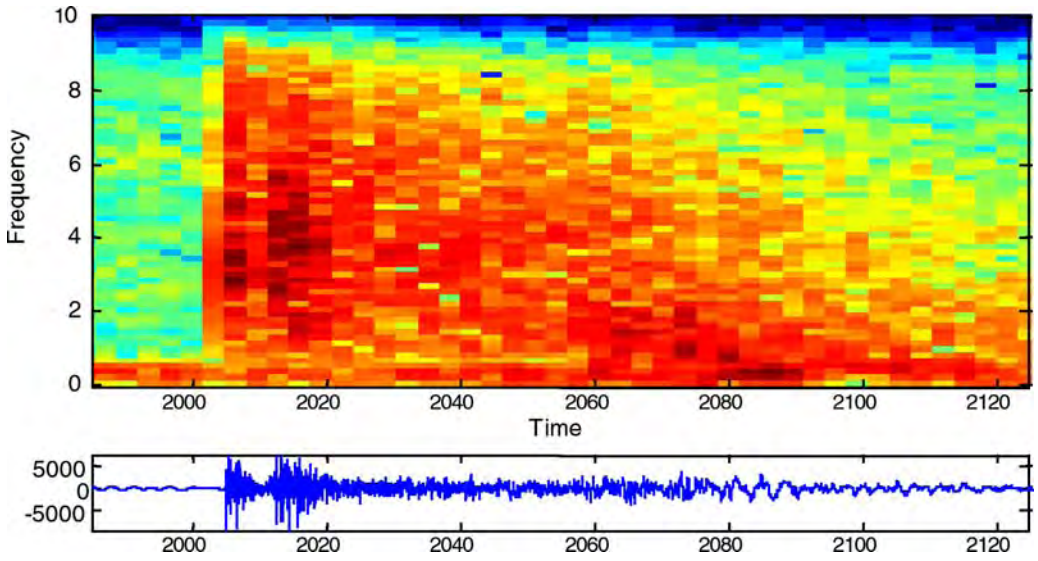

Figure 6. Unprocessed waveform and spectrogram for the North Korean nuclear test.

Method

The approach is to compute a semi-empirical synthetic, which is expressed as

$$new(\omega) = \frac{reference(\omega)}{synthetic_{reference}(\omega)} \cdot synthetic_{new}(\omega),$$

where *reference* and *new* refer to the observed waveforms, and *synthetic* refers to the synthetic waveform computed for a specific event range, depth, and mechanism. Thus, as we know the location of the nuclear and chemical explosions, the mechanism (assumed to be isotropic explosion), and the yield for the chemical shot, formulation can be rewritten to

$$new(\omega) = \frac{reference(\omega)}{synthetic_{reference}(\omega) \cdot yield_{reference}} \cdot synthetic_{new}(\omega) \cdot yield_{new},$$

where the synthetics are computed for the same yield.

Application

As the separation between the reference event (Chinese experiment) and the North Korean explosion was significant (190 km, or ½ of the propagation distance, shown in Figure 4), and the frequency content of the data required high-frequency (>5 Hz) analysis, a coherent comparison was not feasible. Instead, the yield will be estimated by integrating (or summing) the energy envelopes. The data (high-pass filtered at 2 Hz) for the two events are shown in Figure 7. Conceptually, this approach can be viewed as comparing the integrated energy envelopes of the data (Figure 8) and synthetics (Figure 9). This is represented as

$$Yield_{NK} = Yeild_{CN} \cdot \frac{\sum O_{NK}}{\sum O_{CN}} \cdot \frac{\sum S_{CN}}{\sum S_{NK}} ,$$

where *O* is the energy envelope for the observations of the two events, *S* is the energy envelope of the synthetics for the two events, the subscript *NK* refers to the North Korean test, and *CN* refers to the China experiment. The yield results are shown in Table 1 are obtained by multiplying the synthetic fact (3.7) by the observation difference (50) by the yield (1.2–1.5 t), which gives 222 to 277 t.

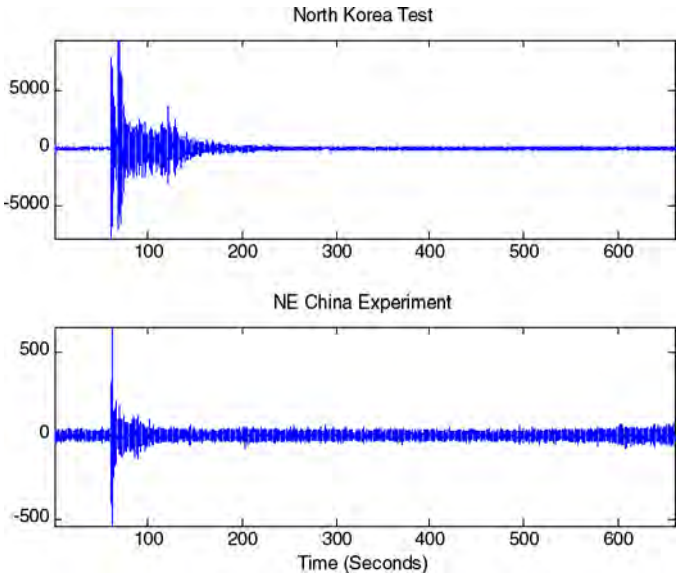

Figure 7. High-pass filtered waveforms at 2 Hz for the North Korean test and the Chinese experiment. The high-pass filtering significantly enhances the signal-to-noise ratio.

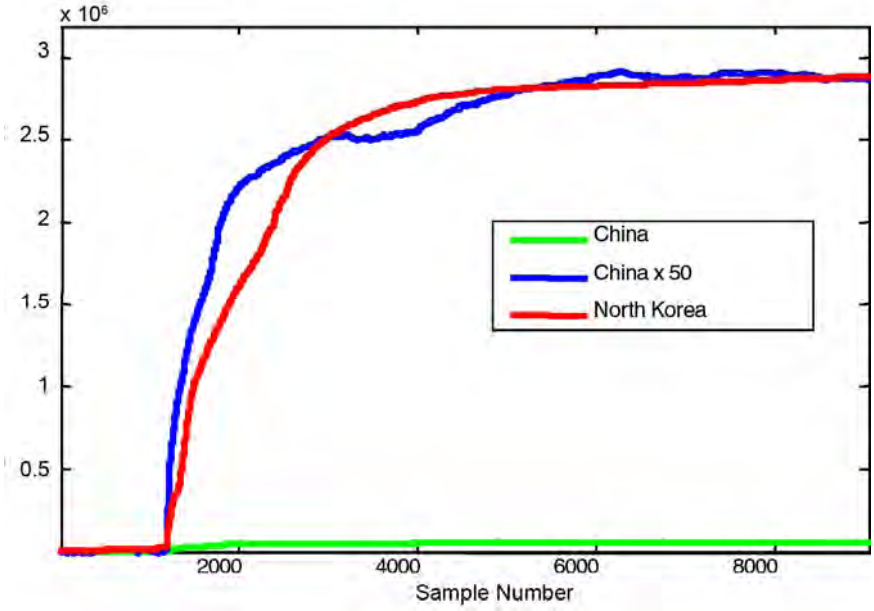

Figure 8. The integrated energy envelope for the waveform data from the North Korean test (red), the China experiment (green), and the scaled China experiment (blue). A scaling factor of 50 was used.

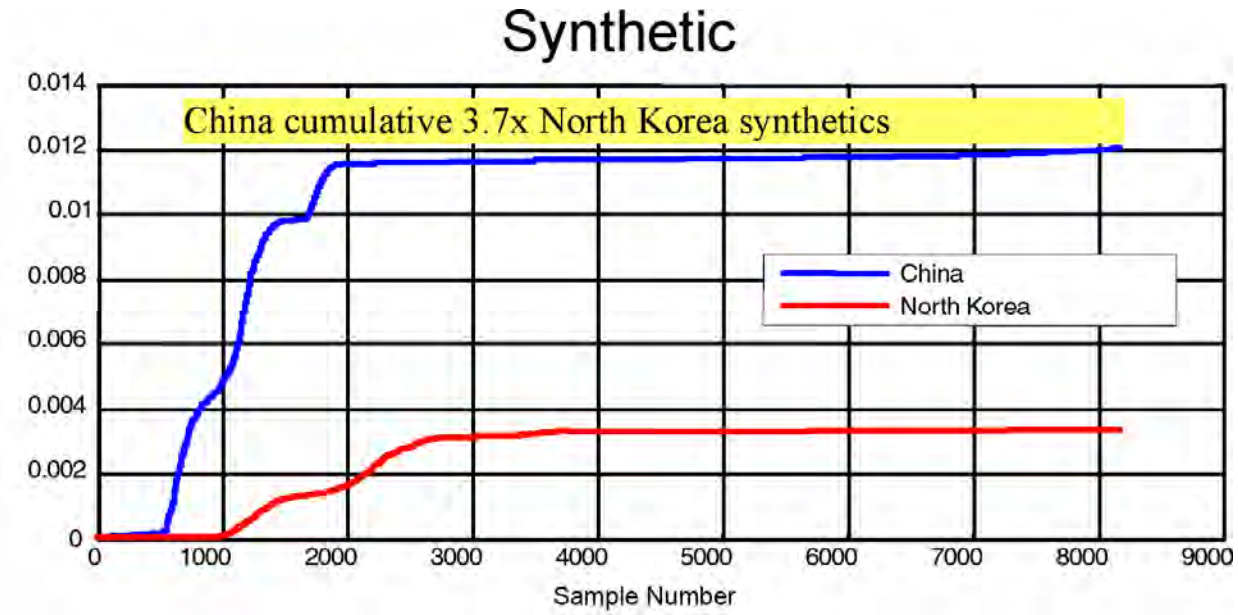

Figure 9. The integrated energy envelope for the synthetic waveforms from the North Korean test (red) and the China experiment (blue). The curve differences result from the differing event-station distances (390 vs. 190 km).

Applying the empirical approach, and using synthetic seismograms that were computed using the IASPEI velocity model (Kennett and Engdahl, 1991) and Herrmann's (2002) wave number integration software for source depths of 0.5 km at ranges of 190.5 m (China) and 369.5 km (North Korea). The empirical filtering was then used to transform the synthetic for China, and a scaling factor was determined by (1) windowing both the empirically filtered synthetic and the observed data using a window based on the signal to noise levels, and(2) summing the windowed envelopes.

Noise reduction

As an alternative to using the high-pass filtering to improve the signal-to-noise ratio of the China test, we investigated using a Savitzky-Golay smoothing filter (Orfanidis, 1996) to characterize the noise. The noise is then subtracted from the observed waveform for further processing. The results, shown in Figure 10, indicate that this approach can be used to minimize the longer period noise. The reduced long-period noise will allow for the processing at longer periods. These results are shown in Figure 11, and listed in Table 1.

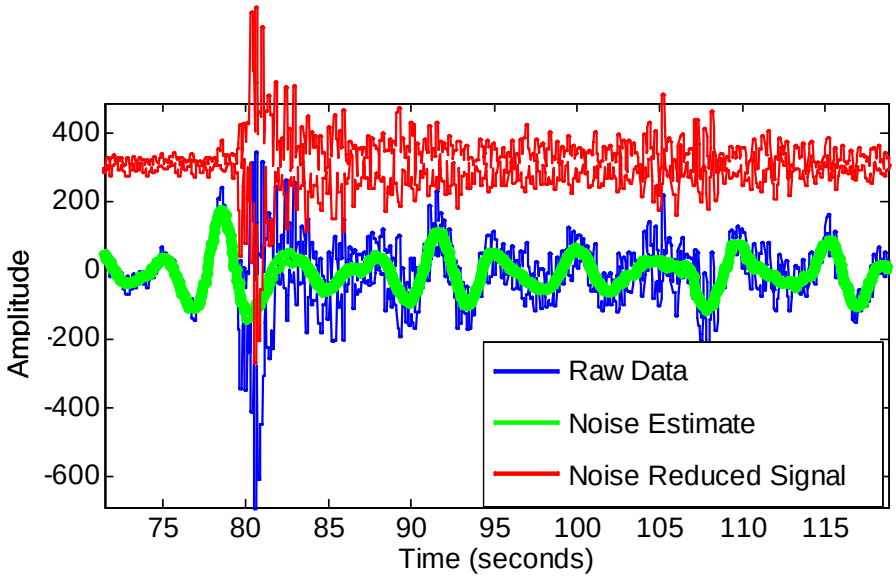

Figure 10. The raw data (blue), the noise estimate (green), and the residual (red) indicates that the Savitzky-Golay smoothing filter is successful in modeling the noise, allowing us to remove the noise from the data.

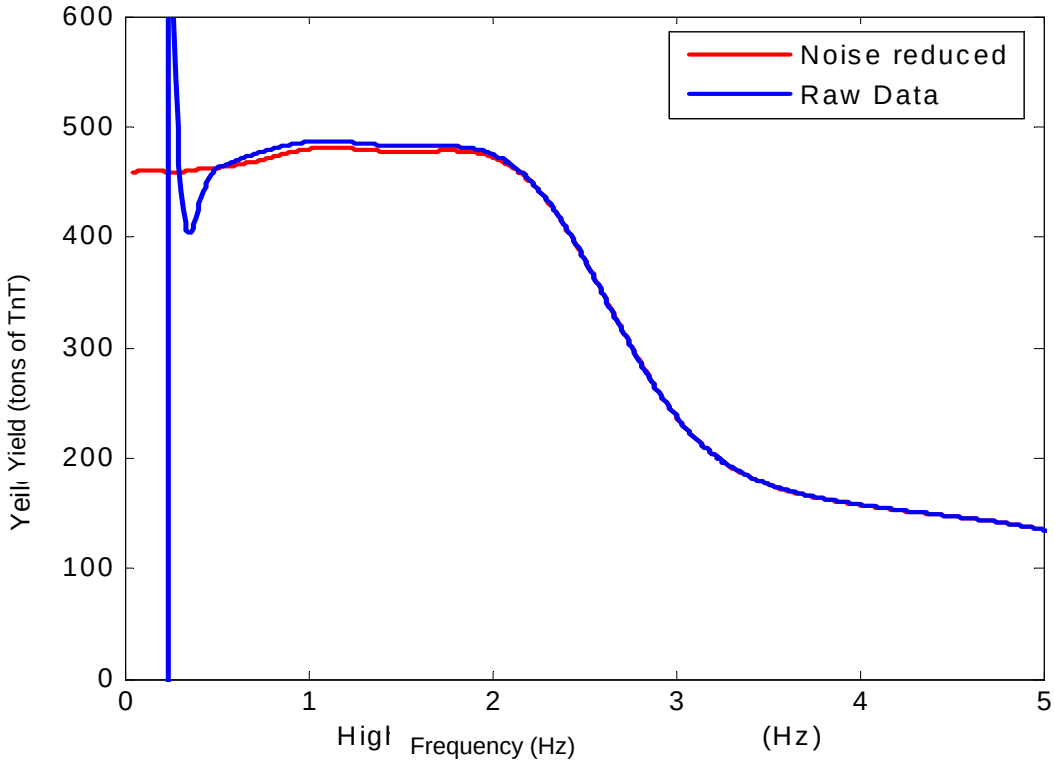

Figure 11. Yield estimates (in tons, vertical axis) based on the noise-corrected data as a function of high-pass filtered corner frequency. This shows, that at higher frequencies, the yield estimates are lower than a more broadband solution.

Table 1: Yields with the different approaches.

Approach	Yield (1.2 t ref)	Yield (1.5 t ref)
Integrated Energy Envelopes	222	277
Semi-empirical, high-passed at 2 Hz, non-corrected.	213	267
Noise-corrected semi-empirical approach, broad band	372	465

CONCLUSIONS AND RECOMMENDATIONS

In this and prior publications, we have demonstrated the utility of semi-empirical Green's functions for both source locations and source parameter extraction. In particular, we have showed that when a reference event and new event are nearly co-located, we can use a high frequency whole waveform approach to determine location to within ½ km. Once the two events are separated by more than a few kilometers, the differential propagation velocities of the various seismic phases requires a phase-by-phase (wave number based) approach. With such an approach, we are able to locate events to within GT5 even when the events have different mechanisms and are separated by more than 50 km. Furthermore, we demonstrated the ability to use the approach in a variety of regions: Central California, NTS, and Lop Nor, China. We also demonstrated the ability to use the semi-empirical approach to determine source parameters (Yield) for the 2006 North Korean Explosion, even though the reference event was 180 km away.

The technique is promising. As is, it could provide the capability to enhance locations to GT5 levels in regions of interest. With additional focused research, it is likely that the approach would allow for accurate (GT2 or better) locations in many regions of interest. In addition, the ability of this approach to allow for varying mechanisms could be combined with subspace detection technology (Harris, 2006) to provide a subspace detector whose basis functions are moment tensor elements. Finally, it would be worthwhile to apply the yield estimate approach to areas with known yields, such as NTS, to provide increased confidence in the approach.

ACKNOWLEDGEMENTS

The data used in the study was obtained from the IRIS Data Management Center.

REFERENCES

Fisk, M. (2002). Accurate locations of nuclear explosions at the Lop Nor Test Site using alignment of seismograms and IKONOS satellite imagery, *Bull. Seism. Soc. Am.* 92: 2911–2922.

Harris, D. (2006). Subspace detectors: Theory, Lawrence Livermore National Laboratory report #UCRL-TR-222758.

Herrmann, R. H. (2002). *Computer Programs in Seismology*, http://www.eas.slu.edu/People/RBHerrmann/CPS330.html

Kennett, B. and Engdahl, E. (1991). Travel times for global earthquake location and phase identification, *Geophys. J. Int.* 105: 429–465.

Orfanidis, S. J. (1996). *Introduction to Signal Processing*. (Englewood Cliffs, NJ: Prentice-Hall).

Salzberg, David H., Simultaneous inversion of moderate earthquakes using body and surface waves: Methodology and applications to the study of the tectonics of Taiwan, Ph.D. thesis, State University of New York at Binghamton, Binghamton, NY.

Salzberg, David H., Karen E. Votaw, and Margaret E. Marshall (2005). Seismic source locations and parameters for sparse networks by matching observed seismograms to semi-empirical synthetic seismograms, in *Proceedings of the 27th Seismic Research Review: Ground-Based Nuclear Explosion Monitoring Technologies*, LA-UR-05-6407, Vol. 1, pp. 454–462.

Salzberg, David H. and Margaret E. Marshall (2006). Seismic source locations and parameters for sparse networks by matching observed seismograms to semi-empirical synthetic seismograms, in *Proceedings of the 28th Seismic Research Review: Ground-Based Nuclear Explosion Monitoring Technologies*, LA-UR-06-5471, Vo 1, pp. 484–492.

IMPROVING MAGNITUDE DETECTION THRESHOLDS USING MULTI-STATION, MULTI-EVENT, AND MULTI-PHASE METHODS

David Schaff and Felix Waldhauser

Lamont-Doherty Earth Observatory, Columbia University

Sponsored by Air Force Research Laboratory

Contract No. FA8718-05-C-0022

ABSTRACT

Last year we reported on the results of both a semi-empirical analysis and a case study in Xiuyan, China, that demonstrated that a correlation detector can lower magnitude detection thresholds by over one full unit for similar events as compared to a standard STA/LTA detector. Ninety out of 90 events (100%) were detected by cross correlation for the case study whereas a procedure like the pIDC employs detected only 11%. We found that less than perfect matches still provided useful detections due to location, focal mechanism, and magnitude differences. Events with magnitude differences as large as 2.3 and 3.3 were shown to produce detection spikes on the correlation traces. Work is continuing applying the correlation techniques on a larger scale to 1,000 events at Parkfield, California, and 19,000 events in and near China. We are attempting to see how broadly applicable correlation methods can be applied to different tectonic settings and for what percentage of the seismicity. One hundred eleven million correlations were performed on Lg-waves for the events in China at 363 stations. Preliminary results suggest two thirds of the 19,000 events can be detected by cross correlation using this relatively sparse regional network. For Parkfield 82% of the events studied can be detected by cross correlation. Correlation detection is able to find additional events beyond what standard processing detects for China (70% increase) and for Parkfield (225% increase). Most event separation distances for events that correlate at Parkfield are less than 1 km. The distribution of magnitude differences for events that correlate at Parkfield is not distinguishable from the input magnitude distribution.

OBJECTIVES

Research will be conducted on techniques for generating a multiphase detection bulletin derived by two means: station array processing (multi-station) and source array processing (multi-event). Comparison and quantification of improvement over standard P-wave, single-event, single-station procession will be evaluated.

RESEARCH ACCOMPLISHED

Introduction

The second year of this project has focused on a correlation detector or multi-event technique applied to larger regions of seismicity. Waveform cross correlation has a long history of improving locations and identifying events (e.g., Poupinet et al. (1984); Harris (1991)). Recently it appears that large percentages of events may be similar enough to enable correlation detectors to be applied on a broad scale (Schaff and Richards (2004); Schaff and Waldhauser (2005)). The first year of the project demonstrated a full magnitude unit improvement in detection thresholds compared to a short-term average/long-term average (STA/LTA) type detector for similar events for both semi-empirical synthetic runs and a case study of 90 events in the 1999 Xiuyan earthquake sequence in China. The synthetic runs showed that this improvement is obtained with acceptable false alarm rates of about one per day. Gibbons and Ringdal (2006) also have shown order of magnitude improvement using a correlation detector for the Norwegian Seismic Array (NORSAR) array. The second year has applied these techniques to 18,886 events in and near China and to 539 events in Parkfield California.

Application to China

The left plot of Figure 1 shows the 18,886 events in and near China and 363 stations used for this study. The events come from the Annual Bulletin of Chinese Earthquakes (ABCE) from 1985 to 2005. The stations are those for which waveforms are available at the Incorporated Research Institutions for Seismology (IRIS) Data Management Center (DMC). Several of the stations are only temporary deployments. There are only a few long-running stations in China, which correlation techniques work best for, so the actual network of stations for most of the events is quite sparse with large inter-station distances. A total of 111 million cross correlations were performed taking about 2 weeks of continuous processing time on a four-CPU computer. All events with separation distances of less than 150 km were correlated. In other words, every event is a master event to see the maximum possible number of correlations possible. So far only Lg-phases have been processed. 50-s windows were used searching forward and 30-s windows searching backwards using time-domain cross correlation. The seismograms

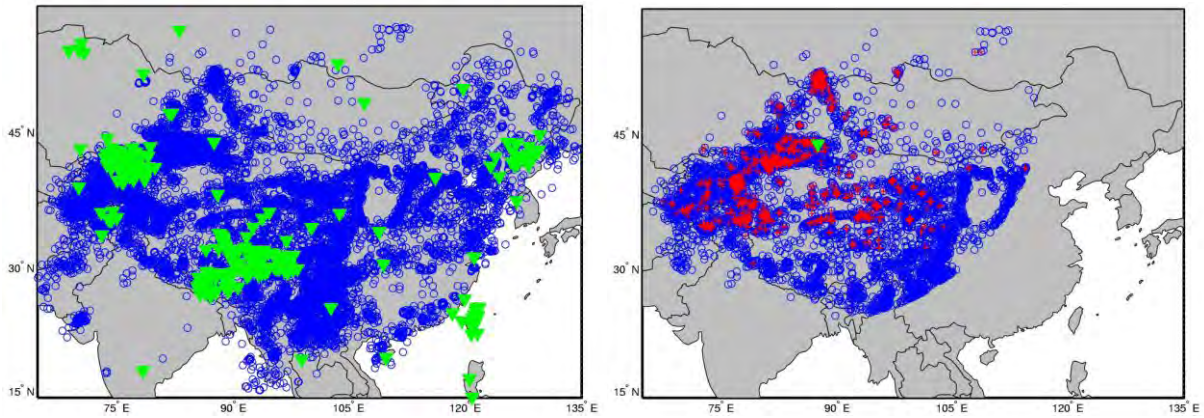

Figure 1. (left) 18,886 events (blue circles) recorded at 363 stations (green triangles) in and near China. (right) events in blue recorded at station WMQ (green triangle). 17% of the events (red) have CC > 0.5 with at least one other event at this station.

were filtered from 0.5 to 5 Hz. The cross correlation traces for the three components are averaged together to constructively enhance the detection spikes when present. A "scaled cross correlation coefficient" (SCC) was used to initially sift the data. All correlations with SCC > 4.5 were saved.

A study was made to estimate false alarms using real data for selected stations. It is assumed that randomly selected time windows should not contain events that correlate. From this it is possible to determine curves of the false alarms per day as a function of cross correlation coefficient (CC) and SCC. For traces that are already sifted with an SCC 6, a CC of 0.24 corresponds to approximately one false alarm per day. A CC of 0.5 corresponds to 0.0022 false alarms per day. An SCC of 6.65 corresponds to a little over one false alarm per day. Based on the pair-wise distance matrix for the correlations and the number of samples in the lags searched over, we can estimate the percent of the 18,886 events for which detections are processed that would be expected to be false alarms. Because a CC of 0.5 appears to be so robust for these long 50 s windows we assume that a trigger at a single station provides a reliable detection. The right plot of Figure 1 shows the events within 20 degrees recorded at station WMQ. The events in red are 17% of the total that have CC > 0.5. Notice how the Tibetan Plateau blocks the Lg-wave propagation for this station. For the other thresholds of one false alarm per day, it is necessary to require at least two stations observing that pair to count as a detection. Using a combination of these criteria (CC > 0.5 at 1+ stations, CC > 0.24 at
2+ stations, or SCC > 6.65 at 2+ stations) we estimate the percent of events that would be false alarms to be approximately 3%. Applying these criteria to the time windows corresponding to where the theoretical travel times would arrive for the 18,886 events results in 12,902 events that are detected or 68%. Therefore it is estimated that 65% represent true detections.

Figure 2 shows the magnitude distribution for the 18,886 events and the 12,902 events detected by cross correlation. Eight thousand, three hundred fifty-eight events found by a "pIDC" type detector are also shown (44%). The pIDC employed an STA/LTA detector on the vertical component for P-waves in overlapping narrow pass bands. Three stations triggered are necessary to be counted as a detection. The number in parentheses in the legend is the 95% confidence lower limit of the magnitudes detected. Overall it can be seen there is a 0.2 unit reduction in magnitude detection threshold for correlation compared to the "pIDC". However 2.8 is also the 95% lower limit of all the magnitudes in the catalog. Therefore the range of magnitudes is not low enough to test if correlation improves detection thresholds more than 0.2 units overall.

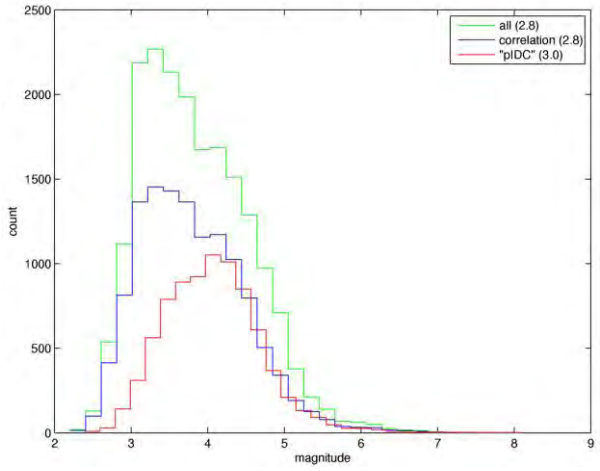

Figure 2. Histograms of the magnitude distribution for all 18,886 events and the 12,902 events detected by correlation and 8,358 found with pIDC type procedures. Correlation finds more events and lower magnitude thresholds restricted by the lower limit of the catalog magnitude of completeness. The number in parenthesis in the legend gives the 95% confidence lower limit for the magnitude distribution.

More insight can be gained by plotting magnitude as a function of station distance. The left plot of Figure 3 shows the detections for the "pIDC". The red line is the 95% lower limit of the magnitudes in 50 km bins of station distance. The trend is seen to increase from about 2.9 at zero to 3.5 for 2,200 km station distances. The right plot of Figure 3 shows that the number of observations that are detected steadily decreases after about 500 km. Figure 4 shows similar plots for the correlation detector. The red line is the 95% lower limit of the magnitudes in 50 km bins. The green line is the 95% trend from Figure 3. It is seen that the two lines diverge for greater station distances. The right plot of Figure 4 shows that correlation detection observations drop off faster with station distance. The difference between the two 95% trends is plotted in Figure 5. At zero the difference is 0.2 units and then increases to a maximum of 0.9 units at greater station distances. The interpretation of these results is that for longer station distances the magnitudes in the catalog are sufficiently complete to observe nearly an order of magnitude improvement in threshold reduction between the two techniques. For closer station distances lower magnitude events are not available in this catalog to test if the full unit reduction still holds.

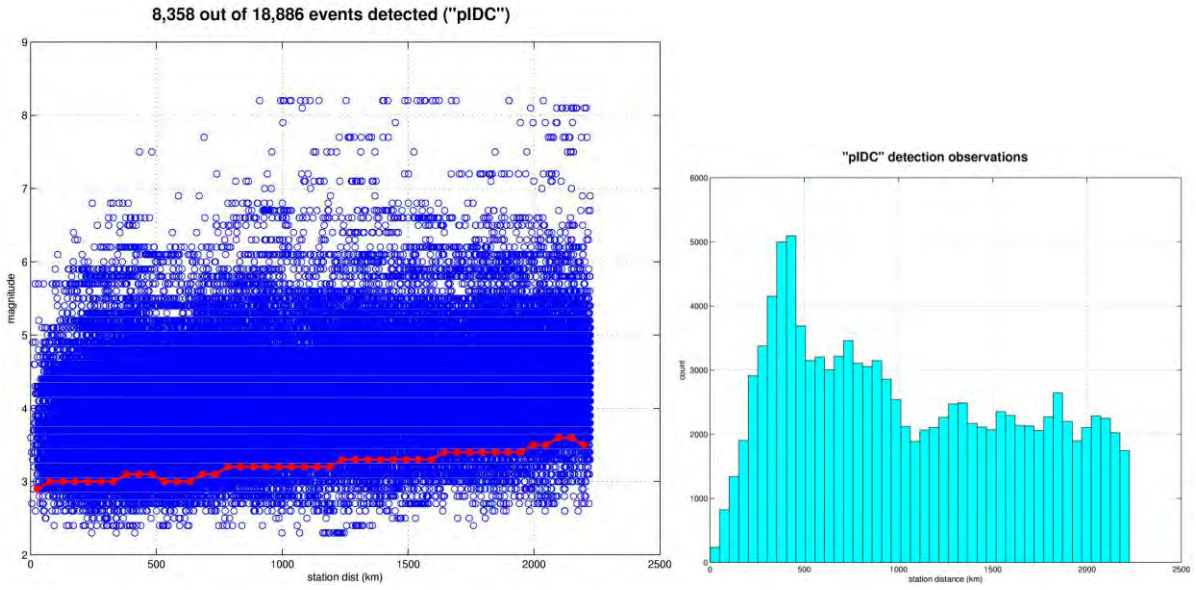

Figure 3. (left) Plot of magnitude vs station distance for all triggers for "pIDC". Red line shows 95% confidence lower limit of magnitude in 50 km bins. (right) Histogram of number of observations as a function of station distance.

We see that approximately two thirds of the events in the catalog are detected by cross correlation (12,902), a sizeable fraction indicating that these methods can be applied on a broad scale across diverse tectonic regions. However, this catalog was based on a much denser network of stations than the one that we have waveforms available for. To get an idea of how applying correlation methods to an existing network would improve things it is instructive to see how many events are detected by correlation and an STA/LTA detector on the same network. Seven thousand, sicty-three events were detected by correlation out of the 8,358 found by a "pIDC" procedure or 85%. For comparison Schaff and Waldhauser (2005) determined that 95% of the 225,000 events in northern California correlated at four or more stations with CC > 0.7 with at least one other event. Therefore correlation is able to detect the great majority of the seismicity for these large regions of seismicity. This can be an important independent confirmation of the existence of new events and help to weed out false alarms. Besides lowering magnitude detection thresholds correlation also detects more events that the "pIDC" procedure missed due to a variety of reasons (Figure 1, right plot). The correlation detector finds 5,839 additional events over the 8,358 events from the "pIDC" detector or a 70% increase. Therefore we might expect catalogs for existing networks to also increase with the complementary benefits of correlation detector techniques.

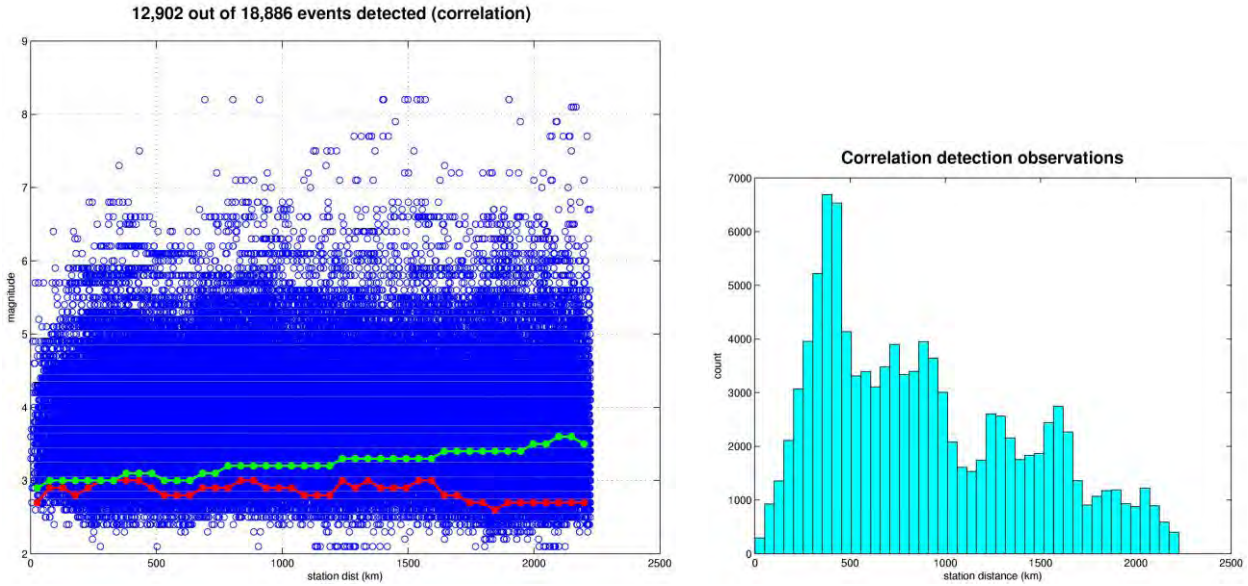

Figure 4. (left) Plot of magnitude vs. station distance for all triggers for correlation detector. Red line shows a95% confidence lower limit of magnitude in 50 km bins. Green line is the curve for the "pIDC" from Figure 3. (right) Histogram of number of observations as a function of station distance.

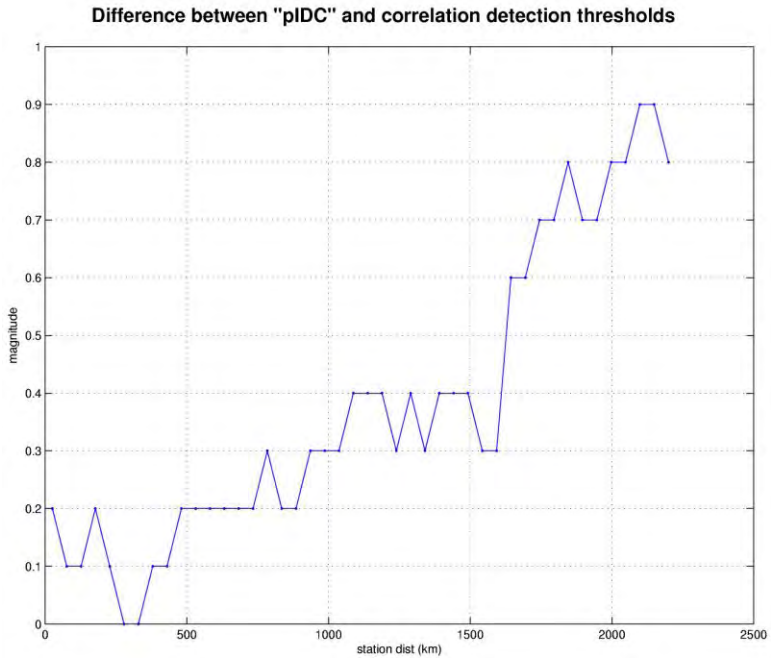

Figure 5. Difference between "pIDC" (green) and correlation (red) lines on Figure 4 as a function of station distance.

Application to Parkfield, California

Results are preliminary for Parkfield. Five hundred thirty-nine events with waveforms available and magnitudes of 2 or greater are analyzed at five continuous stations archived at IRIS (Figure 6). The first arriving P-wave, S-wave, and Lg-wave are processed. The window lengths are 15 s, 20 s, and 50 s respectively. The lags searched over are 10 s, 15 s, and 30 s respectively. The filter bands are 0.75 to 2 Hz, 0.5 to 3 Hz, and 0.5 to 5 Hz respectively.

In this case because of the limited number of stations we are able to estimate false alarms directly for each station. The codes are run as normal except the windows selected are 120 s before the first arriving P-wave which is assumed to contain only noise. The window lengths, lags, and filter bands are kept the same for each "phase". Based on these results we are able to determine that only 8 out of the 539 events or 1.5% would be expected to trigger as false alarms using a criteria of SCC > 6.3 at two or more stations or phases. Applying this same criteria to the normal processing for windows centered on the theoretical arrival times of the phases for the 539 events yields 444 events that are detected by cross correlation or 82% of the M 2 or larger events in the study area. A cross section of these 444 events is shown in Figure 7.

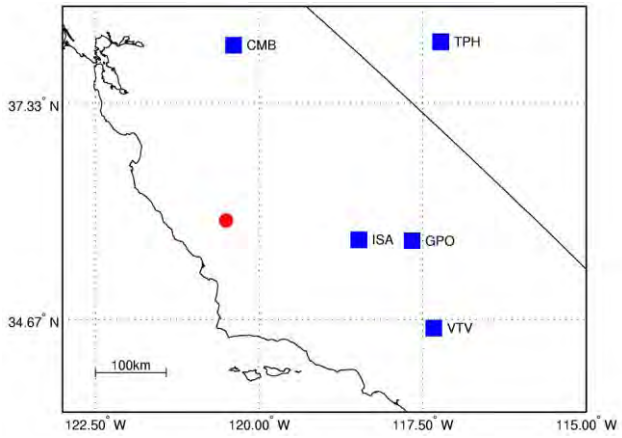

Figure 6. Map of California showing location of Parkfield study area (red dot) and five continuous stations used (blue squares).

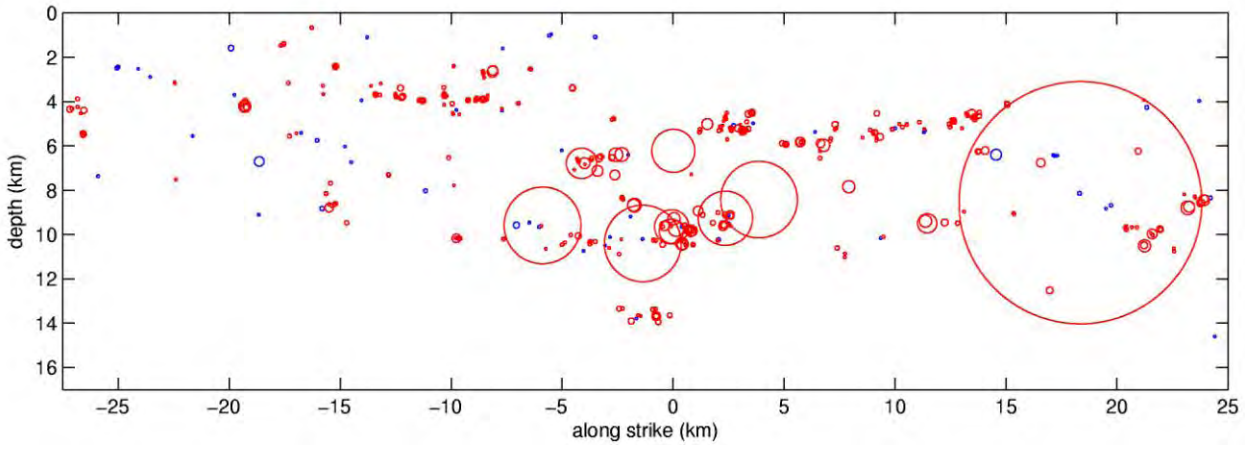

Figure 7. Along fault cross section from NW to SE for 539 events studied that have M greater than or equal to 2. Four hundred forty-four events (82%) in red are detected by cross correlation. Blue events are missed detections. Source areas for events are estimated based on a circular crack model and a 3 MPa stress drop.

The distribution of magnitudes for the correlation detections and "pIDC" is plotted in Figure 8. Because of the limited number of stations considered for the "pIDC" detector we require only 2 stations to trigger to count as a detection instead of 3. It is seen that the correlation detector finds 311 additional events over the 138 found from the "pIDC" or a 225% increase. In this case for these station distances both detectors are able to find M 2 events at the 95% confidence limit so no reduction in magnitude threshold is observed. Fortunately the catalog in this region extends to magnitudes of 1 and 0 so we can most likely test if similar order of magnitude improvements are observed as seen for China and at NORSAR. If the increase in number of events detected is an indication we might expect this general rule to also hold. Out of the 138 events that are found by the "pIDC" detector 133 events are detected by cross correlation or 96%.

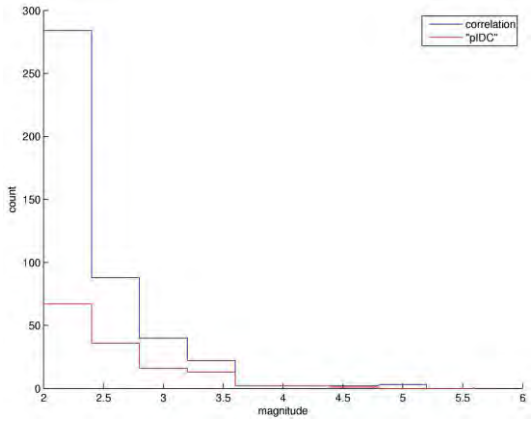

Figure 8. Histogram of the distribution of magnitudes detected by correlation and "pIDC" for Parkfield.

The left plot of Figure 9 shows the distribution of event separation distances for detections that met the criteria of SCC > 6.3 at two or more stations or phases. It is observed that they strongly cluster less than one kilometer with a median of 0.8 km. The pair-wise input correlations considered were all events separated by 20 km or less. A distribution of that observation matrix is shown in the right panel of Figure 9 with a median of 9 km. The difference between the two distributions is striking confirming the expectation that closely separated events correlate the best and that there are few false alarms in the results as estimated (1.5%).

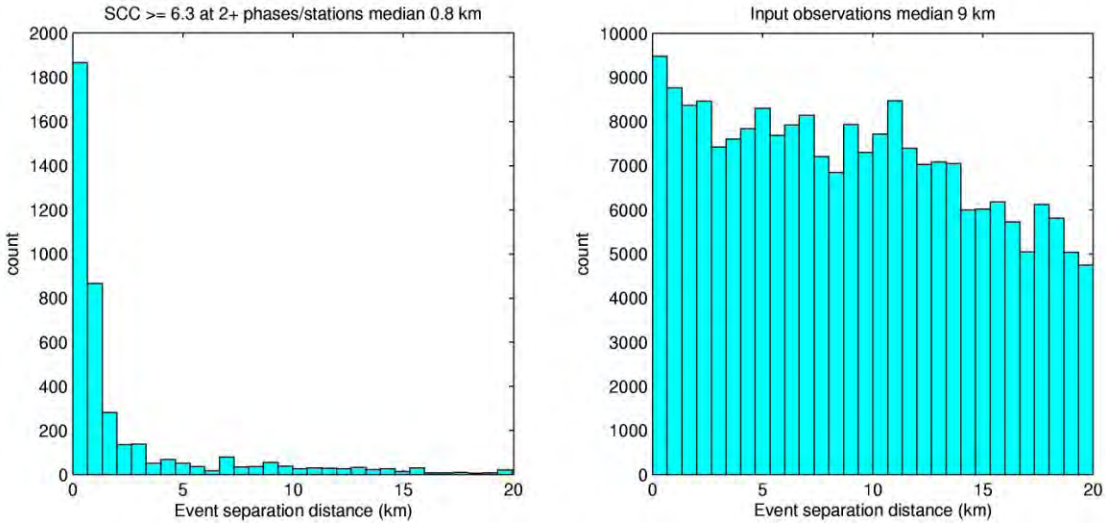

Figure 9. Histograms of event separation distance of correlation detections (left) and input matrix (right).

Similar plots are shown in Figure 10 except for the magnitude difference between the pairs. It is interesting to note that this time the median magnitude difference and distribution is similar for the two comparisons suggesting that events with greater difference in magnitude can correlate well enough to provide useful detections. This is helpful to know because one of the applications we would like a correlation detector to be able to do is to use a larger magnitude event to hopefully detect a smaller magnitude event that is buried in the noise. These results are consistent for a large set of events with examples shown for the Xiuyan case study of event pairs with 2.3 and 3.3 magnitude unit differences that correlated well enough to be detected.

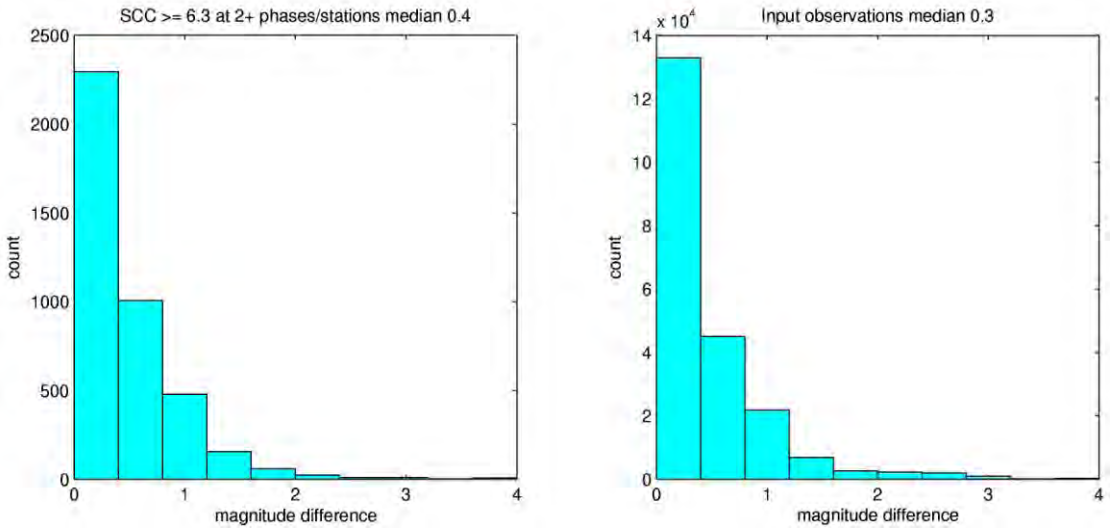

Figure 10. Histograms of magnitude difference of correlation detections (left) and input matrix (right).

CONCLUSIONS AND RECOMMENDATIONS

- Correlation detects a sizeable fraction of the seismicity for China (about two thirds) and for Parkfield (82%) with false alarm rates of a few percent.
- When correlation detectors and STA/LTA filters are applied to the same network, correlation finds the significant majority of detections that standard processing detects for China (85%), for Parkfield (96%), and for northern California (95%).
- Correlation provides an independent and complementary means to confirm detections to STA/LTA and can help to weed out false alarms.
- Correlation detects additional events beyond standard processing for China (70% increase) and for Parkfield (225% increase).
- Overall for China a reduction in magnitude detection threshold of 0.2 units is observed for correlation compared to "pIDC" procedures. Closer examination reveals that this difference increases to 0.9 units with increasing station distance. It is assumed that magnitude completeness of the catalog is the reason a larger improvement is not seen for closer station distances. Lower magnitudes and further station distances need to be examined for Parkfield to see if there is any reduction in magnitude detection threshold.
- Most event separations that correlate well enough to trigger a detection at Parkfield are less than 1 km even though all event separations out to 20 km were searched.

- Magnitude differences between the pairs of events that correlate have a distribution that is virtually indistinguishable from the input distribution indicating that less than perfect waveform matches still provide useful detections.

ACKNOWLEDGEMENTS

We are grateful to the operators of the Chinese Digital Seismic Network and to the IRIS data management center for archiving the waveforms used in this project. We thank Paul Richards, Won-Young Kim, and Bill Menke for helpful discussions. We thank Bob Bookbinder and Dave Lentrichia for computer support.

REFERENCES

Gibbons, S. J., and F. Ringdal (2006). The detection of low magnitude seismic events using array-based waveform correlation, *Geophys. J. Int.* 165: 149–166.

Harris, D. B. (1991). A waveform correlation method for identifying quarry explosions, *Bull. Seism. Soc. Am.* 81: 2395–2418.

Poupinet, G., W. L. Ellsworth, and J. Frechet (1984). Monitoring velocity variations in the crust using earthquake doublets: an application to the Calaveras Fault, California, *J. Geophys. Res.* 89: 5719–5731.

Schaff, D. P., and P. G. Richards (2004). Repeating seismic events in China, *Science* 303: 1176–1178.

Schaff, D. P., and F. Waldhauser (2005). Waveform cross-correlation-based differential travel-time measurements at the Northern California Seismic Network, *Bull. Seism. Soc. Am.* 95: 2446–2461.

PROGRESS IN THE DEVELOPMENT OF RUGGED LOW POWER COMPACT SILICON MEMS SENSORS FOR USE IN NUCLEAR EXPLOSION MONITORING

Ian M. Standley[1] and W. Thomas Pike[2]

Kinemetrics Inc.[1] and Imperial College London[2]

Sponsored by Air Force Research Laboratory

Contract No. FA8718-06-C-0011

ABSTRACT

In this paper we present the results of our ongoing development of a family of high Q-factor in-plane microelectromechanical systems (MEMS) seismic sensors. We discuss the trade-offs in optimizing the performance for nuclear explosion monitoring. Three different geometries are presented with different optimizations of size versus predicted performance, shock, and vibration resistance. Two of these devices require a vacuum cavity within the device to obtain high Q-factors of the order of ~20,000, while the other device can work with a Q of ~500 that can be obtained in an unsealed cavity. Results of our initial evaluations of the Q obtainable under vacuum are presented showing that Q-factors in excess of 20,000 are obtainable. We also discuss the design and operation of the displacement transducers required for these devices. The transfer of the MEMS fabrication technology from a university to a commercial facility is discussed along with initial fabrication results from a 150mm wafer commercial process, including the formation of vacuum sealed cavities.

OBJECTIVES

The objective of this research program is to develop a silicon MEMS sensor suitable for use in Nuclear Explosion Monitoring Systems (NEMS). In Phase A we are developing a triaxial sensor model that we will fabricate and evaluate. This design would then be further optimized in Phase B of the development.

RESEARCH ACCOMPLISHED

Introduction

Our goal in Phase A of the project has been to complete the design and fabrication of the MEMS component of the sensor optimized for NEMS applications. The MEMS sensor integrates the proof mass and its suspension, a displacement transducer, and a set of electromagnetic transducer coils.

To produce a working microseismometer (μSeis) this MEMS element is coupled with electronic circuitry that excites the displacement transducer, amplifies and demodulates the displacement signal and then feeds back the correct signal to the coils to cause the device to operate as a force-balance acceleration or velocity sensor. Finally, both the MEMs elements and the associated electronics have to be held in a suitable mechanical package to allow the device to operate under field conditions.

Requirements for NEMs Devices

For sensing Nuclear Explosions it has been suggested that the noise performance in the band from 10 Hz to 40 Hz is of considerable interest. This band has normally been ignored by broad band sensors which tend to cross the low noise model at approximately 10 Hz. In fact, even the New Low Noise Model (NLNM) is not specified at higher frequencies and in the graph below we have just extrapolated the value from those at ~10Hz. At most sites cultural noise is a significant problem at these frequencies. This is discussed in detail in McNamara et al., 2004 and the figure below shows that at higher frequency the noise is above the NLNM and has degraded at even the best sites in the Continental U.S. due to increased cultural activity.

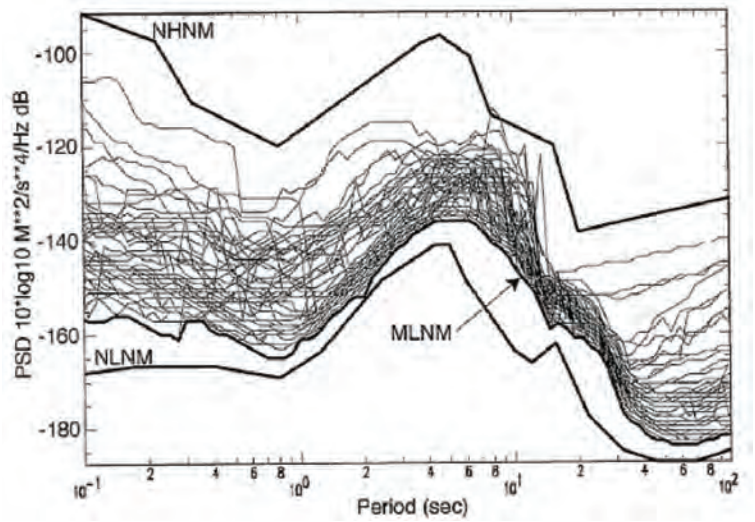

Figure 1. PDF mode low noise model (MLNM) from McNamara (2004)

From this figure, we can see that a noise floor of -160dB would resolve the lowest signal level at the vast majority of low noise sites. This level corresponds to ~1 nano-g/√Hz in the band of interest. This is the design level that we will use for the microseismometer. Given this requirement our goal was to optimize the design of the MEMS element consistent with the limitations of micro-fabricated devices. A fundamental limit to the performance of a seismometer is given by the Brownian motion of the proof mass itself. The level of this noise is proportional to the square root of the so called "*MTQ*" product of the proof mass and its suspension. Here, *M* refers to the mass of the proof mass, *T* is the period of the natural frequency of the spring mass system, while *Q* is the quality factor of the resonance. For a typical classical broadband sensor using standard mechanics the mass is typically in the order of 200 grams, the

period is several seconds, and Q-factors are of the order of ~10. These values result in an *MTQ* product of the order of about unity. For the NEMS application an *MTQ* product of ~0.01 is required, but with MEMS devices which are batch fabricated from a circular wafer of silicon we are limited to a greatly reduced mass as our die size needs to be limited to about two centimeters square to ensure a reasonable number of devices on a wafer and a reasonable yield of functional parts from those wafers. This results in practical proof masses of the order of 0.25g or almost one thousand times less than a classical broadband instrument.

It would seem that the ideal way to increase the *MTQ* product is to just make a very weak suspension with a very large *T*. However, while this would work for a horizontal sensor, for a vertical sensor the spring has to balance the earth's gravity and a weak spring would just collapse. Furthermore, in many classical seismometers all the three-axis sensors are tilted: in the so-called Galperin orientation the three sensors are identical and are orientated to lie along the corners of a cube mounted on its corner and each sensor sees about 60% of the earth's gravity. The three axes are recombined electrically to get the vertical and two horizontal components. This Galperin orientation is optimal for a MEMS device as only a single device design is required, rather than separate horizontal and vertical geometries. Thus we need to balance about 0.6 g requiring a spring mass system with a resonance of greater than 10Hz to allow the spring deflection to be accommodated within the dimensions of the device .

Thus, we have lost a factor of 1000 for the mass and an additional factor of >10 for the frequency. For our ~1 nano-g/√Hz target noise level we are more than a factor of one hundred too low if we were limited to the Q-factor of ~10 of mechanical sensors. However, with a MEMS device we can achieve Q-factors of the order of ~500 in gas at atmospheric pressure, and over 20,000 in a device sealed in a vacuum allowing us to achieve our required MTQ product. This explains our interest in MEMS devices for a NEMS sensor as by engineering the Q-factor of the device we can theoretically achieve our required noise floor from a device weighing less than ¼ g in about the area of a postage stamp.

Device Geometries

After our discussions on the requirements for NEMS devices we altered our original plan and decided to produce three different device geometries. This change was driven by four factors:

1. There is less interest in signals with periods greater than 40 seconds in NEMS sensing, but more interest in extending the high frequency band to 40 Hz.

2. The silicon suspensions had proven fragile and smaller high frequency devices promise to be more robust.

3. Overall package size is an important concern for the final product.

4. The MEMS fabrication house we had selected, IMT, has considerable experience in packaging NEMS devices in sub mtorr vacuum.

The first device is based on our original design with a 20mm x 20mm die size and a natural frequency of 12.5Hz sealed at ambient pressure with a Q-factor of approximately 500. This device includes the changes we had made to improve the shock resistance of the device and the same device is being fabricated at both Imperial College and IMT. This device uses a 200 micron period for the displacement transducer and assumes a spacing of the DT wafer of ~ 38 microns when sealed at ambient pressure.

The second device still utilizes a 20mm x 20mm dies size but increases the natural frequency to a nominal value of 30 Hz, and is designed for vacuum packaging. The higher natural frequency due to the flexure design should further improve the shock and vibration resistance of this device. The design Q-factor is 20,000 which we believe should be obtainable is a vacuum level of ~0.1 mTorr and would be dominated by the combination of the intrinsic "Q" of the silicon and the additional damping of the metal interconnects running on the silicon flexures. This device uses a 100-micron period for the displacement transducer and assumes a spacing of the DT wafer of ~ 20 microns when vacuum sealed.

The third device is an experiment to see if a smaller die of 10mm x10mm that would be configured as an accelerometer could achieve the desired noise floor at higher frequencies using vacuum packaging. The resonant frequency is designed to be 75Hz and the design Q-factor is 20,000. This device uses a 100 micron period for the

displacement transducer and assumes a spacing of the DT wafer of ~ 20 microns when vacuum sealed. The relatively high resonant frequency should result in a rugged and small device.

The design parameters are shown in Table 1, while Figure 2 shows the theoretical suspension noise predicted for each of these devices.

Table 1. Device Parameters.

	Die Dimensions	Resonant Frequency /Hz	Design Q-factor	Environment	DT Period /µm	Shock Resistance
12.5Hz Device	20mm x 20mm x 0.5mm	12.5Hz	500	Ambient Pressure	200	Moderate
30 Hz Device	20mm x 20mm x 0.5mm	30Hz	20,000	Vacuum ~0.1mTorr	100	High
75 Hz Device	10mm x 10mm x 0.5mm	75Hz	20,000	Vacuum ~0.1mTorr	100	Very High

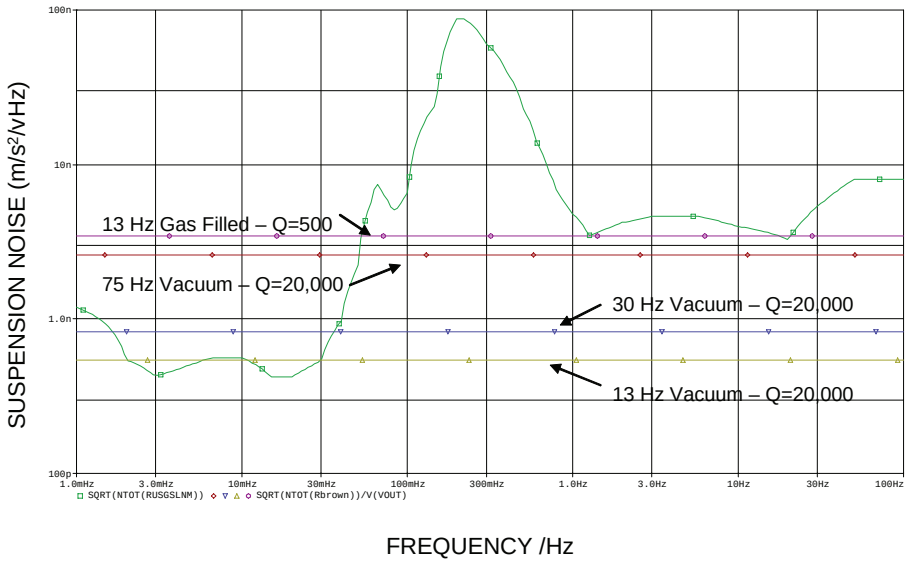

Figure 2. Predicted suspension noise performance of the various µSeis geometries related to the NLNM.

These suspension noise values represent a lower limit to the noise floor of the devices, in reality the actual sensor noise will be determined by other design elements in the electronics. Currently the electronic noise is predicted to be a little lower than the level of the 13Hz gas filled device so the electronics is expected to be the performance limiter for the vacuum sealed devices.

Quality factor of Micro-Machined Suspensions

As previously discussed the thermal noise of the microseismometer increases with the damping of the suspension. Damping in these suspensions is a sum of materials damping in the spring itself and gas damping, which at atmospheric pressures is dominated by viscous forces and is independent of pressure. The materials damping, which will dominate at very low pressures, will consist of damping in the silicon itself, expected to be very small, and losses in the surface layers resulting from the deep reactive-ion etching (DRIE) process together with losses in the

metallization of traces along the springs, potentially a much larger contribution (Figure 3). In between the high and low pressure regimes the damping will be pressure dependent, varying in proportion to the viscosity and as the root of pressure.

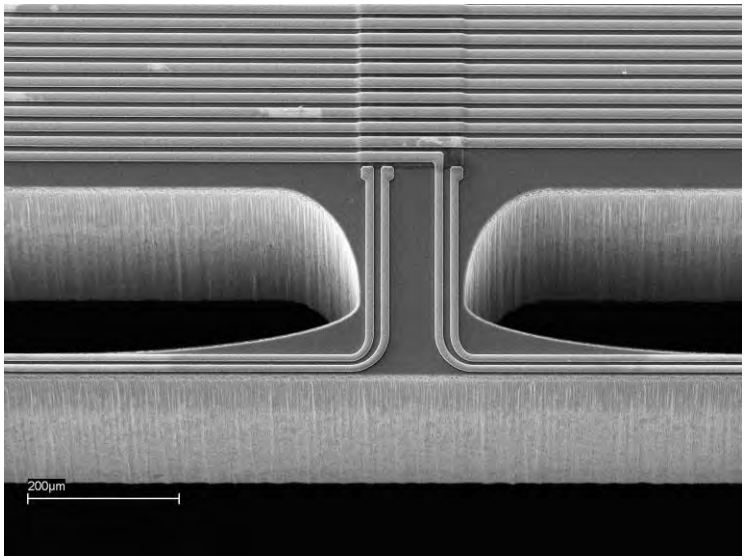

Figure 3. Part of the micromachined suspension showing sidewall damage and trace metallization that will both contribute to the overall damping.

The Q factor of the suspensions for the microseismometer has been investigated as a function of pressure, metallization and geometry to quantify the relative contributions of the energy-loss mechanisms (Pike and Standley, 2005). Figure 4 shows a plot of the variation of Q-factor with pressure, as determined by ring-down experiments in air using an optical microscope, or at reduced pressure in an environmental scanning electron microscope. The three regimes are evident and show that low-pressure packaging has the potential of increasing the Q by 500, which would reduce the suspension noise by a little over twenty times.

At the low-pressure limit the Q-factor was found to vary by a factor of two within nominally identical unmetallized suspensions, with the difference attributed to the position of the suspension die within the wafer – it is well known in DRIE that the quality of etching does vary both as a function of distance from the centre of the wafer, and across the wafer with orientation with respect to the gas flow (Chen et al., 2002). In comparison the presence of metallization did not produce a discernible drop ion the Q factor. This is most likely due to the very low relative cross section of the metal traces, just 2×10^{-3} of the silicon beam.

In our initial work, the suspension geometry had a more marked effect. Q-factors of the order of about 100,000 were regularly seen in 15 Hz suspensions micro-machined in 20-mm dies, while 75-Hz suspensions on 10-mm dies had a Q-factor more than ten times lower (<10,000). This was a concern that vacuum encapsulation would only provide a significant improvement in lower resonant-frequency suspensions. However, some recent results where we used a special process to clean the wafers after DRIE resulted in Q-factors of greater than 50,000 for the 75 Hz suspensions on the 10mm square dies leading us to believe that we can get high Q-factors in the smaller devices which was very encouraging.

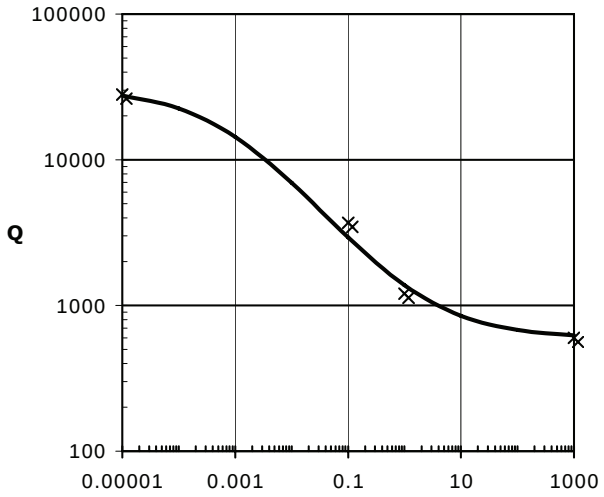

Figure 4. Q factor as a function of pressure

Displacement Transducer

The displacement sensor for the microseismometer is a linear capacitive array transducer (LCAT). The LCAT concept is based on displacement transducer techniques originally developed for conventionally scaled instrumentation, for instance, calipers and linear motion sensors (Baxter and Buehler, 1986; Zhu et al., 1991). The transducer consists of two parallel planes of periodic electrode arrays for drive and pickup (Figure 5). The spacing between the two sets of plates is *d*, and the period of the LCAT *p*. The strength of the capacitive coupling due to the overlap between drive and pickup electrodes varies periodically with the lateral offset between the two planes. In the μSeis transducer the drive electrodes are driven with out-of-phase voltages, and two sets of pick-up electrodes provide a differential output signal. The capacitive coupling from the positive and negative drives to the corresponding pickup electrodes is given by C_{pos} and C_{neg}. At the operating point the displacement sensitivity is a maximum and $C_{pos} \simeq C_{neg}$. Stray cross-couplings, summing to C_{int} will attenuate the output due to the resulting capacitive divider with the transducer capacitance. External capacitance C_{ext} will provide further attenuation. Optimization of the LCAT consists of determining the transducer geometry that produces maximum displacement sensitivity.

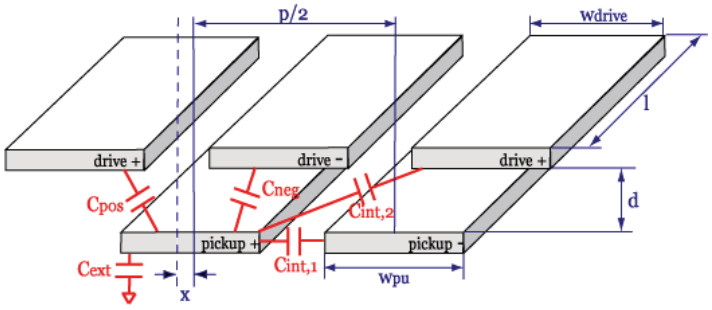

Figure 5. Diagram of a portion of the differential LCAT geometry.

This optimization is demonstrated for a mechanical prototype of the microseismomter. There is an optimal *d/p* that decreases as the C_{ext}/C_{tran} decreases. The mechanical microseimometer's calculated optimal sensitivity (normalized to a 1V drive) is 294 V/m at w_{pu}/p = 0.45, w_{drive}/p = 0.5. The experimental sensitivity is 276 V/m and a comparison between the calculated and measured periodic responses is shown in Figure 7. Looking at Figure 6, we see that the sensitivity is well maintained for small deviations from the optimum. For very large strays ($C_{ext}/C_{tran,}$>10), the

optimum *d*/*p* asymptotically approaches 0.3. This method of optimization allows designs to be visualized intuitively with respect to the optimization domains and has been successfully applied to the microseismometer design.

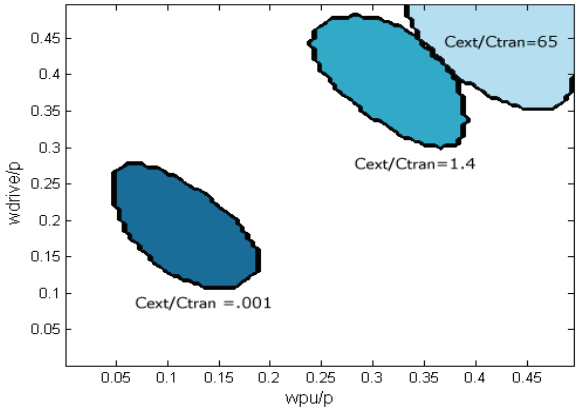

Figure 6. Domains delineating the electrode geometries producing sensitivities within 3% of optimum for scaled large (as observed), medium and small external capacitances

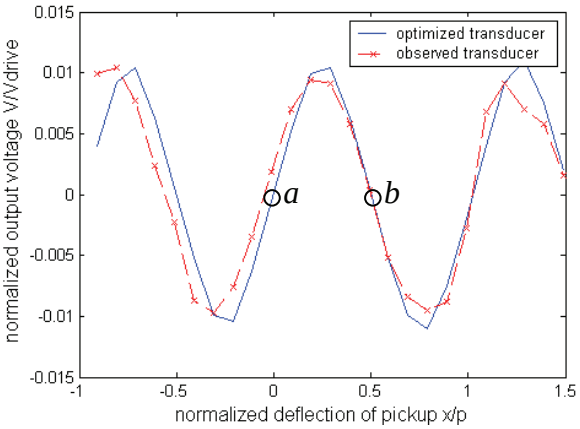

Figure 7. LCAT output voltage as a function of displacement for the optimized and observed transducers. The feedback points selected for the transfer functions of Figure 8 are indicated.

Feedback Control

In order to linearize the output, maximize the range and produce the required velocity output the microseismometer, incorporates feedback to an actuator stabilize the proof mass, with this actuator signal providing the output to the sensor. As the transducer, the LCAT, has multiple null points it is possible to operate the microseismometer with the proof mass positioned at one of a series of positions separated by half the LCAT period. Adjacent null points require a change in sign of the feedback to maintain stability. Figures 8 and 9 show the transfer function of the μSeis mechanical prototype at two adjacent null points. The differences in the closed-loop resonances are due to the non-linearity of the prototype suspension.

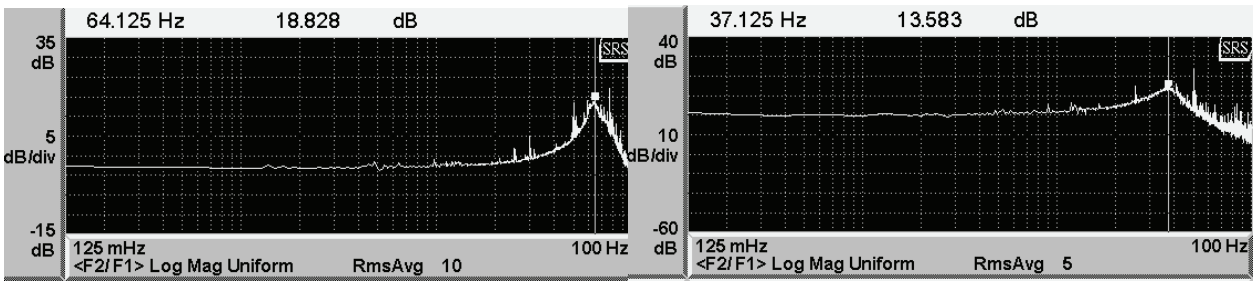

(a) **(b)**

Figure 8. Closed loop transfer functions of the prototype microseismometer suspension taken at the adjacent operating points of Figure 5. The feedback gain is inverted between the points.

Operation of the microseismometer is normally closed loop, but the feedback actuation force is limited to displacements just a little larger than one period of the LCAT. As the force limit is reached, a comparator resets the feedback, opening the loop for at least one period of the suspension during which the proof mass re-centers at the new operating position. To assess the feasibility of the scheme, a simulation (Simulink, Mathworks Inc.) was constructed incorporating the dynamics of the μSeis. The results for a stepped input are shown in Figure 9. The proof mass displaces only slightly for input steps less than the actuator range, the shifts a result of the finite gain of the feedback loop. As the actuation limit is reached, the loop is opened and the motion of the proof mass can be seen as it moves to the next null point. Resets are possible of multiple LCAT periods if a sudden change in the signal occurs.

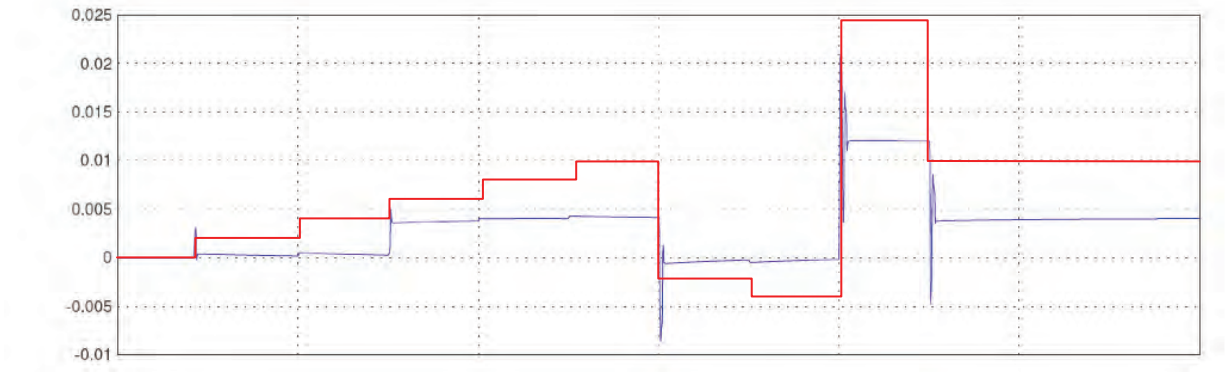

Figure 9. Simulation of combined closed and open loop operation of the μSeis in response to a stepped input over a 30s period. The input is in red, the position of the proof mass is in blue, showing operation at displacements of 0, 1 and 3 multiples of the LCAT period.

The final output of the microseismometer under this operation can therefore be constrained to match the range of the digitizer, maximizing the range of the instrument while minimizing the actuation force, and hence noise re-injected back into the feedback loop.

Transferring Technology to a Commercial MEMS Facility

The silicon microstructure used in the development has been produced in the fabrication facilities at Imperial College on a 100mm fabrication line designed for prototyping experimental MEMS technology, but not dedicated to being able to produce wafers with the high yield required for successful utilization of a device in a product serving the NEMS community. A large part of our development work in the last 8 months has been taking the process developed at Imperial and translating it to work on a commercial MEMS fabrication line. The company we selected to work with was IMT of Santa Barbara California. IMT was selected as they had experience of DRIE and had the same equipment as Imperial College; they had successfully sealed MEMS devices in a high vacuum, and had experience of producing high conductivity electroplated conductors for use in electromagnetic actuators.

The commercialization of a MEMS device and the transfer of the process developed in a University environment to a commercial facility present some unique challenges. MEMS technology is not standardized, unlike the processes used for integrated circuits, so each university and company has their own suite of developed processes. The net result of this is a process redesign to transition from the research to the commercial environment. Such process redesigns tend to have a cascade effect as changes in one process require other changes to maintain compatibility with the metallurgy or etchants required in later stages. From our experience with this transition it certainly needs to be attempted earlier rather than later in the development program and in future programs we would want to involve the commercial facility as soon as the initial design concepts had been proven. One could ask why not do the whole development in a commercial facility? We believe that the answer is that some tasks are more suited both in development time and expense to a university environment. In particular universities expect to be able to fabricate a broad range of designs in parallel, while commercial companies concentrate on high-yield batch fabrication of a single design. An example of this can be seen in increasing the shock resistance of the design of the microseismometer; at Imperial we tried many different spring configurations on the same wafer iterating our mask designs after testing and using low cost masks to solve this problem. This would have been time consuming and more expensive in a commercial facility with the more expensive and longer lead-time photo-masks and with a workflow dedicated to producing batches of identical wafers.

IMT has run a number of short tests to validate each part of the process before attempting to produce the device wafers. This technique has been very valuable as it highlights areas of difficulty and allows them to be resolved on wafers with minimal processing rather than sacrificing wafers with many layers of processing on untested processes.

One of the major challenges was not expected. The DRIE equipment used at both Imperial and IMT is the same model and hence we expected a fairly easy transition of this process that had taken considerable initial development time at Imperial. Although the equipment was the same model the wafer hold down mechanism for the 100mm wafers used at Imperial was different to the 150mm wafer used at IMT. As the DRIE stage releases the proof mass we were finding at IMT that the proof mass and springs would release from the carrier stage and be subject to footing damage. This took considerable process development to overcome. Initially the Q-factors obtained at IMT were variable and lower than obtained at Imperial, but by developing a special cleaning process we have now demonstrated Q-factors of ~100,000 in vacuum for the μSeis 12.5Hz device. This is very encouraging, as it exceeds our design goal. Our previous experience suggests that the metal traces will not degrade this number significantly.

At IMT we have also demonstrated that we can seal a silicon wafer to a glass wafer with the required spacing and maintain a vacuum within the device cavity. Figure 10 shows a vacuum sealed wafer and several other electron micrographs of the DRIE and the wafer metallization. Note in the vacuum sealed wafers the black dot in the center and the interference fringes where the wafers have been pushed together by atmospheric pressure and are touching in the center. The DRIE wafer shows a quadrant of the device with the proof mass visible at the top and the three flexure supports and intermediate frames visible below. The final electron micrograph shows two electroplated conductors passing over the edge of the insulating layer.

We are now processing the production wafers at IMT using the processes developed in the short tests discussed above; the wafers are currently waiting for the final metallization before the DRIE etch.

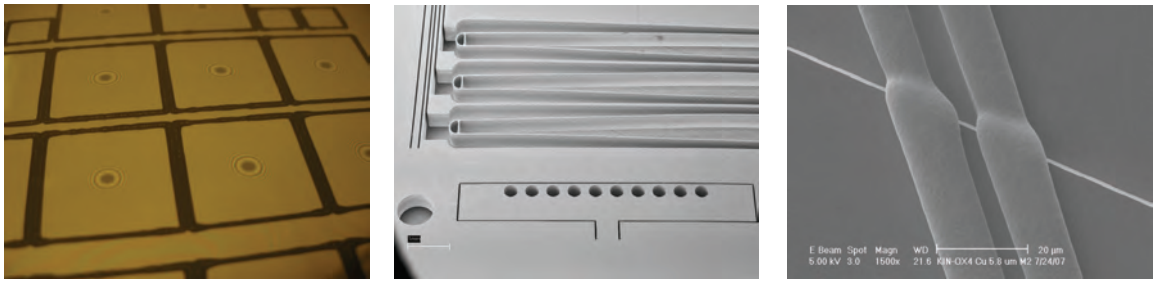

(a) (b) (c)

Figure 10. (a) A sealed test wafer showing the deflection of the areas in the center of the die by the pressure differential. (b) A test wafer after DRIE showing the springs and proof mass. (c) A test wafer showing the conductors passing over the insulator step.

CONCLUSIONS AND RECOMMENDATIONS

In our work to date we have demonstrated that we can produce MEMS devices with relatively low natural frequencies compared with previous accelerometers and with very high Q-factors especially when we utilize vacuum sealing. The *MTQ* product of these devices would ensure a suspension noise floor suitable for use in a NEMS sensor. We have also developed a displacement transducer (LCAT) that offers very good performance and coupled with the electro-magnetic coils on the device forms the elements required for a velocity feedback seismometer. We have transferred the majority of the processes required for the fabrication of the microseismometer sensors to a commercial fabrication facility and have shown we can vacuum seal devices. We are now in the process of fabricating completed devices. We will then test the performance of the individual components and then integrate the devices with the mechanics and circuitry to test as a seismometer.

If this testing is successful we would recommend additional work on optimizing both the MEMS element and the electronics to both increase performance and reduce size. Future work aimed at integrating a digitizer into this package may result in a very useful device for NEMS use.

ACKNOWLEDGEMENTS

We would like to thank the teams at Imperial and Kinemetrics who aided the authors in the design, fabrication and testing of the devices: Sunil Kumar, Sanjay Vijendran, Werner Karl Trevor Semple, John Stagg, and Ireck Briones. The team at IMT Inc, of Santa Barbara, California, led by Ian Johnston modified the process and performed the fabrication of the commercial devices.

REFERENCES

Baxter, L. K., and R.J. Buehler (1986). United States Patent, No. 4,486,250.

Chen, K. S., A. A. Ayon, X. Zhang X, and S. M. Spearing (2002) Effect of process parameters on the surface morphology and mechanical performance of silicon structures after deep reactive ion etching (DRIE) *J. Microelectromechanical Systems* 11: 264, 275

Pike, W. T. and I. M. Standley (2005) Determination of the dynamics of micromachined lateral suspensions in the scanning electron microscope, *J. Micromechanics and Microengineering* 15: S82, S88

Zhu, F., J. W. Spronck a, and W. C. Heerens (1991). A Simple Capacitive Displacement Sensor *Sensors And Actuators A-Physical* 26: 265, 269.

REGIONAL SEISMIC FOCAL DEPTH ESTIMATION IN COMPLEX TECTONIC ENVIRONMENTS

Anastasia Stroujkova[1], Delaine T. Reiter[1], and Robert H. Shumway[2]

Weston Geophysical Corporation[1] and University of California, Davis[2]

Sponsored by National Nuclear Security Administration
Office of Nonproliferation Research and Development
Office of Defense Nuclear Nonproliferation

Contract No. DE-FG02-03ER83820

ABSTRACT

The accurate estimation of the depth of small, regionally recorded events continues to be an important and difficult monitoring research problem. In our previous work we developed a combined regional depth estimate, which represents a weighted average of multiple independent measurements of event depths. Our combined measurement includes focal depths found through assisted array processing of early *P*-wave coda, surface-wave amplitude inversions, and hypocenters estimated from regional travel times. We performed an initial validation of our methodology by applying it to moderate-sized events located within regional distances of the KSAR (Wonju, South Korea) teleseismic array. Our study in Korea showed that the new method produced accurate and consistent depth estimates using regional data. We also found that the IASPEI91 global reference velocity model was appropriate for the relatively simple tectonic region within regional distances of the KSAR array.

In this study we further investigate the validity of our regional depth estimator in a more tectonically complex area, specifically in the region around the array in Turkey (Keskin; BRAR/BRTR). The region surrounding the BRAR/BRTR array is dominated by the continental collision between the Eurasian, African and Arabian plates. In a complicated tectonic zone such as this, a global reference velocity model may not adequately predict the regional travel times and amplitudes of observed regional phases, which can potentially lead to poor focal depth estimates. To address this issue we have examined the sensitivity of the depth estimator to the velocity model used in the analyses. We have applied the depth estimator to regional data from well-located events in the Middle East for the IASPEI91 reference and two regional velocity models. Our results indicate that a poorly chosen velocity model can produce inconsistencies between the individual technique depth estimates. However, the depth estimator is less sensitive to the velocity model than might be expected; i.e., in many cases we show good correlation between our regional depth estimator results obtained using different velocity models.

OBJECTIVE

We have developed a technique that statistically combines measurements from regional data into a single focal depth estimator. Our continuing research objective is to validate the technique in a variety of tectonic environments by systematically testing the behavior and robustness of our regional depth estimator with well-recorded, moderate sized events from different regions of nuclear monitoring concern. In this study we report on results calculated from events in the region surrounding the regional array in Keskin, Turkey (BRAR/BRTR).

RESEARCH ACCOMPLISHED

The study area surrounding the Keskin (BRAR/BRTR) array in Turkey represents a 1000-km-wide zone of continental collision between the Eurasian, African and Arabian plates. The region east of the Keskin array (Turkey and Western Iran) is composed of several distinct seismotectonic areas, shown in Figure 1.

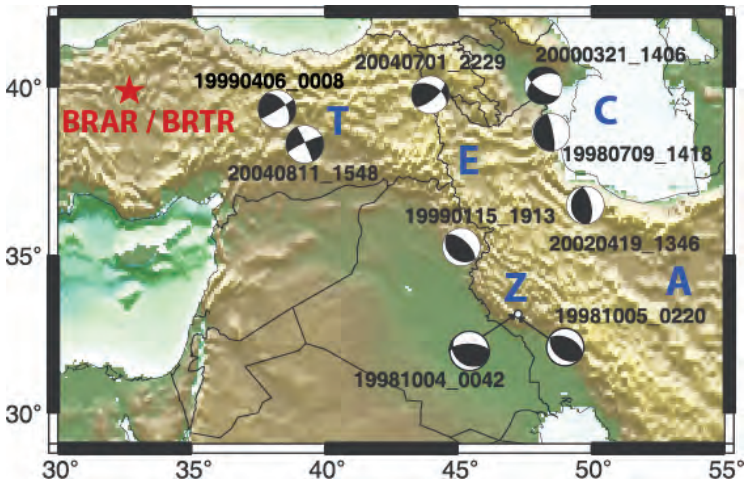

Figure 1. Map showing tectonic features (blue letters), locations and focal mechanisms of study events, and the BRAR/BRTR array in Turkey (red star). The geographic and tectonic features indicated with blue letters include Turkey (T), Eastern Iran (E), Alborz mountains (A), Central Caspian (C), and Zagros mountains (Z).

Each tectonic region shown in Figure 1 exhibits a characteristic pattern of focal depth distribution. In a recent study Engdahl et al. (2006) described several general patterns of earthquake focal depths using a revised version of the Engdahl, van der Hilst and Buland (EHB) location database (Engdahl et al., 1998). The patterns they observed can be described as follows:

1. **Region T**: Seismicity in Turkey is dominated by strike-slip focal mechanisms, which are concentrated between depths of 10–20 km.
2. **Region E:** Seismicity in Eastern Iran is in the upper crust, shallower than ~20 km, with a median depth of 12±5 km.
3. **Region Z**: In the Zagros fold-and-thrust region, most of the earthquakes are shallower than 30 km, with median depth of 15±7 km.
4. **Region C**: Central Caspian seismicity follows the Apsheron-Balkhan Sill, resulting in a depth range of 30–100 km that deepens toward the north.
5. **Region A**: Seismicity in the Alborz region in Northern Iran is distributed through the crust, with a median depth of 20±8 km.

According to Engdahl et al. (2006), the uncertainty of the focal depth estimates reported in the revised EHB database is ~10 km, which is sufficiently accurate to allow differentiation between the various tectonic subregions. In our validation study we have taken advantage of the seismic focal depth distributions described by Engdahl et al. (2006) to provide additional constraints on depths predicted by the estimator. In Figure 1 we also show the sample

subset of events we have studied thus far in the region to the east of the BRAR/BRTR array. We have applied our depth estimator technique to nine events that fall into each of the tectonic categories described above. The selected events sample most of the subregions described above. The main criteria for an event's selection were: 1) proximity to the Keskin array; and 2) high-quality bulletin locations and moment-tensor solutions from the Harvard Centroid Moment Tensor (CMT) catalog (Dziewonski et al., 1981). Table 1 lists the International Seismic Centre (ISC) coordinates and Harvard CMT magnitudes of the events in our study. We note that the ISC depths are in many cases significantly deeper than the regional lower depth limits predicted from other studies, including the database in Engdahl et al. (2006).

Table 1. Location parameters from our Turkey regional earthquake study database. A designation of 'd' in the ISC depth column indicates that the hypocenter solution was allowed to range freely in depth, while 'f' indicates that the depth was fixed in the hypocenter estimate. The column labeled 'pP_DEPTH' is the ISC composite depth from teleseismic pP-P phase observations.

Event ID (Origin Date)	Lat. ºN	Long. ºE	ISC Location Depth (km)	pP_DEPTH (km)	Tectonic Region	Mw	Distance to BRAR, º
19980709_1418	38.60	48.48	55.4 d	39 ± 3	C	5.9	12.18
19981004_0042	33.23	47.20	24.9 d	22 ± 4	Z	5.3	13.35
19981005_0220	33.24	47.24	18.1 d	30 ± 3	Z	5.4	13.37
19990115_1913	35.25	45.13	59.2 d	55 ± 3	Z	5.1	10.80
19990406_0008	39.37	38.21	30.7 d	11 ± 2	T	5.4	4.23
20000321_1406	40.05	48.20	77.6 d	60 ± 1	C	5.1	11.13
20020419_1346	36.52	49.77	38.8 d	32 ± 6	C	5.2	13.1
20040701_2229	39.78	43.97	5.0 f	18 ± 2	E	5.1	7.98
20040811_1548	38.34	39.25	7.4 f	14 ± 1	T	5.6	4.57

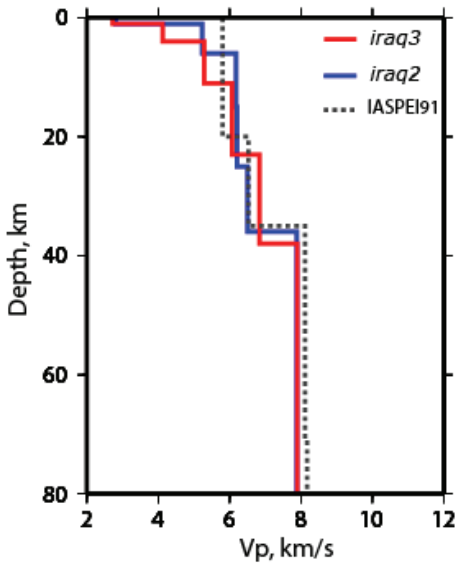

Zagros mountains (*iraq2*)

Thickness km	V_p, km/s	V_s, km/s	ρ gm/cm3
1.00	2.80	1.62	2.05
5.00	5.23	3.02	2.50
9.00	6.18	3.57	2.70
10.00	6.20	3.58	2.70
11.00	6.50	3.75	2.70
50.00	7.88	4.55	3.14
Half-space	7.88	4.55	3.14

Mesopotamia Foredeep (*iraq3*)

Thickness km	V_p, km/s	V_s, km/s	ρ gm/cm3
1.00	2.73	1.58	2.05
3.00	4.12	2.38	2.32
7.00	5.29	3.05	2.50
12.00	6.07	3.50	2.70
15.00	6.84	3.95	2.85
50.00	7.89	4.56	3.14
Half-space	7.89	4.56	3.14

Figure 2. Left: velocity versus depth plots for the models used in the study, including the IASPEI91 reference model, Zagros Mountains (*iraq2*) and Mesopotamia Foredeep (*iraq3*). Right: velocity and density values versus layer thickness for the *iraq2* and *iraq3* models.

The region to the east of the BRAR/BRTR array is suitable for our goal of studying the behavior of our depth estimator in various observational settings, because the velocity structure to the east of the BRTR array is highly heterogeneous and poorly constrained. For our subset of events to the east of the BRTR array, we compared the results of the estimator using the IASPEI91 reference model (Kennett and Engdahl, 1991) and two 1-D regional

velocity models developed for Iraq (Figure 2). The *iraq2* model was developed by Al-Eqabi (2007) for the Zagros mountains in Northern Iraq, and the *iraq3* model (Al-Eqabi, 2007) was developed for Mesopotamia Foredeep from South Turkey to Baghdad. The *iraq2* and *iraq3* models have slightly lower velocities below the Moho than IASPEI91, which contradicts some velocity studies in the area (e.g., Hatzfeld et al., 2003). In another study (Doloei and Roberts, 2003), receiver functions predicted the presence of a low-velocity layer below the Moho. However, travel-time tables that include a low-velocity layer lead to shadow zones in some distance ranges. The lowering of the upper-mantle velocity in the *iraq2* and *iraq3* models is a simple way to avoid ray-tracing complications.

The Regional Depth Estimator

To develop a regional depth estimator, we combine several measures related to depth d_i; (i = 1, 2, …, n) and their standard errors σ_i into an overall estimator for the depth of an event (Draper and Smith, 1998). The estimator is constructed by a statistical averaging of the *n independent* observations of depth:

$$\hat{D} = \left(\sum_{i=1}^{n} \frac{1}{\sigma_i^2} \right)^{-1} \sum_{i=1}^{n} \frac{d_i}{\sigma_i^2}, \qquad (1)$$

with an estimated standard deviation given by

$$\sigma_{\hat{D}} = \sqrt{\left(\sum_{i=1}^{n} (1/\sigma_i^2) \right)^{-1}} \; . \qquad (2)$$

The simplification in Equation 1 implies that $\hat{D}$, which combines a variety of individual measurements, requires knowledge of the standard errors associated with each measurement method. We emphasize that this type of statistical averaging is only valid for *independent* depth estimates; i.e., measurements that are not shared between the methods.

In our current formulation of the estimator, we incorporate three independent depth measurement methods. The first depth measurement is directly estimated from regional depth-phase delays (*pPn-Pn* and *sPn-Pn*) determined using an Enhanced Cepstral F-Statistic Method (ECFSM; Stroujkova and Reiter, 2006). We derive our second independent depth measurement from the hypocenter found in a sparse-network location of catalog *Pn* and *Sn* arrivals supplemented by analyst-derived *pPn* and/or *sPn* arrival times. Our third depth measurement is derived from the inversion of regional surface-wave spectral amplitudes (SWA). In the following sections we provide details on the application of the individual methods to the events in our study database.

Depth Measurement 1: Enhanced Cepstral Processing

The travel-time delay between a primary arrival and its reflection from the Earth's surface (e.g., *pPn-Pn* or *sPn-Pn*) can be directly converted to a source depth using a velocity profile near the source position. Cepstral methods can be used to find these time delays through analysis of the periodicity in log spectra (Bogert et al., 1963, Oppenheim and Schafer, 1975). However, cepstral methods, including the Cepstral F-Statistic Method (CFSM, Bonner et al., 2002), are not a reliable way to identify depth-phase delays at regional distances, because they produce multiple false detections. Additional evidence must therefore be used to verify whether phases detected by the CFSM are actual depth phases. We currently estimate the apparent velocities, amplitudes and frequency content of both the direct arrival and suspected surface reflections to help confirm (or decisively eliminate) the cepstral detections of regional depth-phase arrivals. These phase characteristics can be found using multiple methods such as MUltiple SIgnal Classification (MUSIC) (e.g., Schmidt, 1979; Schissele et al., 2004), and cross-correlation analysis (e.g., Cansi, 1995), both of which produce phase characteristic estimates with sufficient accuracy and resolution. We are calling this revised method of analysis the ECFSM.

To calculate the standard error needed by our depth estimator for the ECFSM, we use an *ad hoc* method (Stroujkova and Reiter, 2006) to examine up to six of the largest peaks above the 99% confidence level found in the cepstral F statistic. If a peak is determined to be a phase arrival with a velocity and back azimuth similar to the *Pn* arrival, it is

retained for further analysis. To be defined as similar, an arrival's velocity estimate using the MUSIC estimator must be within 0.5 km/s of the *Pn* estimate and the back azimuth within 10° for high signal-to-noise ratio (SNR) data (1.0 km/s and 15° for poor SNR). Then we assume the delay time at a particular peak can be either a *sPn* or a *pPn* arrival, and compute the *sPn* and *pPn* depths associated with the delay time using the background velocity model. The final depth and standard error are computed as the average and standard deviation of all the viable *sPn* and *pPn* depths. This method provides a worst-case estimate of the depth and standard error, but eliminates the requirement that the analyst decide which arrival among many possibilities is a particular depth phase.

Using the above approach, we applied the ECFSM (using cross-correlation to determine the confirming phase characteristics) to calculate the event depths and standard errors of the events in Table 1. Figure 3 shows two examples of the ECFSM and cross-correlation results applied to the BRAR/BRTR short-period data. In the left set of panels, we show the results from Event 20040811_1548, which is a strike-slip event in Region T. There is one peak in the cepstra (2^{nd} subplot from the top) that is reflected in the F statistic (it is important that both the cepstra and the F statistic are peaked at the same time), which is confirmed by the cross-correlation analysis in the bottom three subpanels. We confirm a phase arrival in the cross-correlation analysis by identifying a stable velocity and back-azimuth occurring over a 2-3 second time window, accompanied by a low value of root-mean-square (RMS) residuals. In order to maintain a fairly smooth appearance of the cross-correlation results, the processing window is 2.3 seconds in length. The final results for Event 20040811_1548 indicate a *pPn* arrival at an approximately 9-second delay.

In the right set of subpanels of Figure 3, we show the ECFSM results from Event 20020419_1346, which occurred in the south portion of Region C (Caspian). Waveforms from this region are notoriously difficult to analyze (e.g., Mangino and Priestley, 1998), but the results we found with ECFSM are fairly straightforward to interpret for this particular event. The cepstra and F statistic reveal two significant peaks that are consistent with *pPn* and *sPn* arrival characteristics in the cross-correlation results.

There is no velocity model involved in the initial portion of the cepstral analysis: it is a signal processing technique that produces only the travel-time delays and statistical likelihood of the presence of a phase echo. In the enhanced portion of the cepstral analysis we convert the estimated time delays to a depth plus associated standard error using each of the three velocity models we compared in our study. The results of these calculations can be found in Table 3 for the events in Table 1.

Depth Measurement 2: Sparse-Network Regional Hypocenter Estimation

To determine our second independent depth measurement, we compute event hypocenters using the GMEL software package (Rodi, 2006). GMEL (an acronym for Grid-search Multiple-Event Location) finds solutions to the multiple-event location problem using a grid search to find the best-fitting location parameters (origin times, hypocenters, and travel-time corrections) and associated error estimates from a set of arrival time data measured from multiple events, stations and seismic phases. In this study we ran GMEL in single-event mode; that is, the case in which the event locations and the origin times are the only unknowns. While the events in our study were all observed teleseismically, we limited the arrival-time data in our relocations to travel times from stations within 17º from each event.

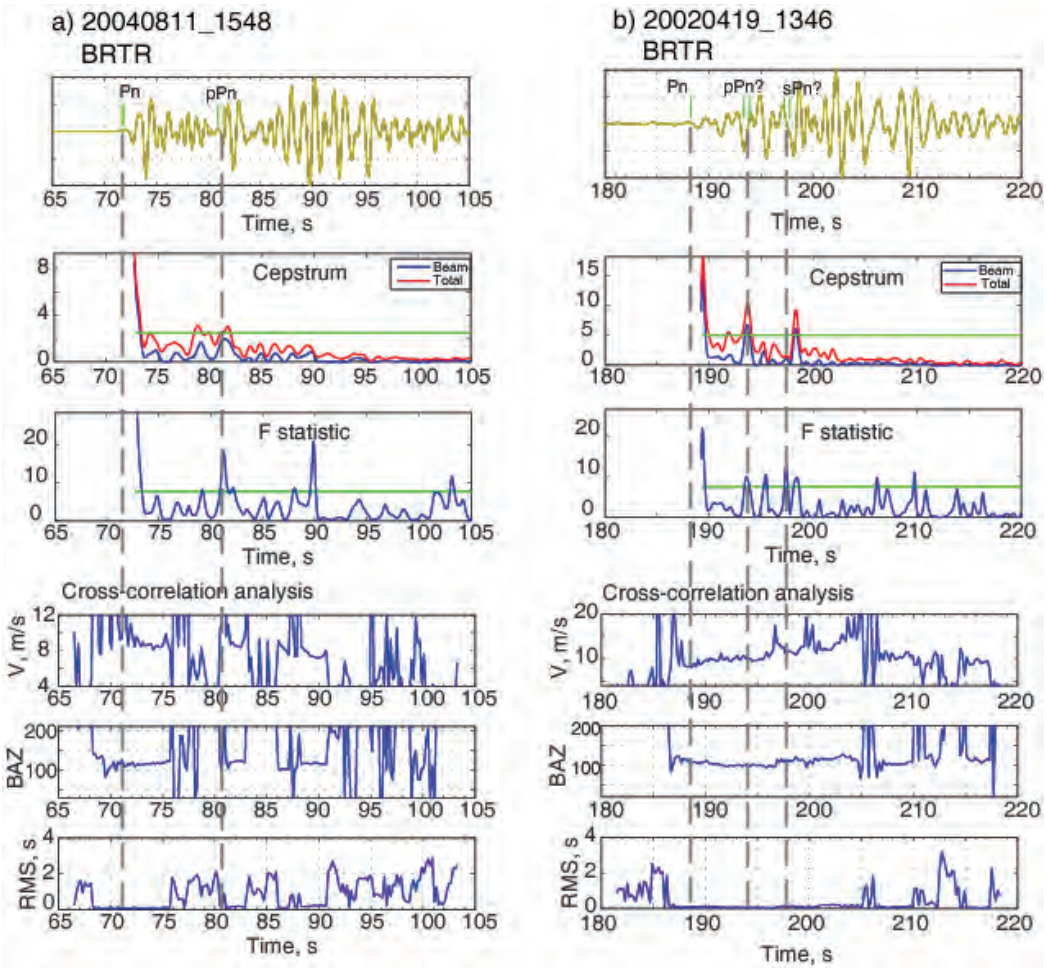

Figure 3. Examples of ECFSM and cross-correlation array processing applied to study events: a) Event 20040811_1548 and b) Event 20020419_1346. The top subplot shows array beam; second subpanel shows the beam and total cepstra from the CFSM; and the third subpanel shows cepstral F Statistic with a green line at the 99% significance level. The bottom three subpanels show the results of the cross-correlation analysis, including apparent horizontal velocity, back azimuth and the RMS error.

The majority of the arrival data included in the GMEL runs came from the ISC catalog. However, to constrain the GMEL hypocenter depths we supplemented catalog *Pn* and *Sn* arrival times with analyst picks of regional depth-phase arrival times. We picked candidate depth-phase arrivals at the available regional three-component (3-C) broadband stations and confirmed those picks using polarization analysis. To ensure the independence of focal depths estimated using GMEL from those estimated via the enhanced CSFM, we did not include any arrivals observed at BRTR in the GMEL runs.

Table 2 shows the summary of the GMEL relocation results, which indicate that the choice of velocity model did not significantly affect the depths retrieved by the GMEL hypocenter relocation. In every case but one for which the ISC allowed a free-depth solution, the GMEL depth was shallower. In both of the fixed-depth cases, the GMEL depth was slightly deeper.

Table 2. Results obtained by GMEL for events in Table 1 using different velocity models.

Event ID	Number of Phase Arrivals		Network Secondary Azim. Gap (°)	*iasp91*		*iraq2*		*iraq3*	
	Pn	*pPn* & *sPn*		Epicenter shift, km	Depth shift, km	Epicenter shift, km	Depth shift, km	Epicenter shift, km	Depth shift, km
19980709_1418	85	3	119	26.1	-22.1	18.6	-22.1	18.7	-22.1
19981004_0042	74	0	113	8.9	-24.9	11.5	-24.8	10.4	-24.9
19981005_0220	64	4	114	17.5	-1.1	18.1	-0.7	18.1	-7.0
19990115_1913	53	0	80	0.9	-59.2	4.9	-26.2	4.7	-36.7
19990406_0008	93	1	64	9.0	-27.0	12.8	-19.6	12.4	-19.6
20000321_1406	38	10	107	27.3	-45.1	32.5	-44.3	32.0	-54.5
20020419_1346	28	3	135	31.8	-35.1	27.4	-35.1	28.1	-35.1
20040701_2229	92	1	105	17.8	22.9	8.0	25.9	7.9	12.5
20040811_1548	85	5	118	7.8	0.5	9.1	3.7	8.0	3.7

Depth Measurement 3: Inversion of SWA

For the third independent depth measurement included in the depth estimator, we invert the spectral amplitudes of Rayleigh and Love waves for event depth and focal mechanism using source inversion codes (Herrmann and Ammon, 2002). The software performs a grid search over a model space of moment M_0, focal depth h, and mechanism (strike ϕ, dip δ, and rake λ) to minimize the misfit between observed and predicted surface-wave amplitude spectra. The input required for the inversion consists of the spectral amplitudes of the fundamental Rayleigh and Love waves from a set of regional stations and a 1-D regional Earth model.

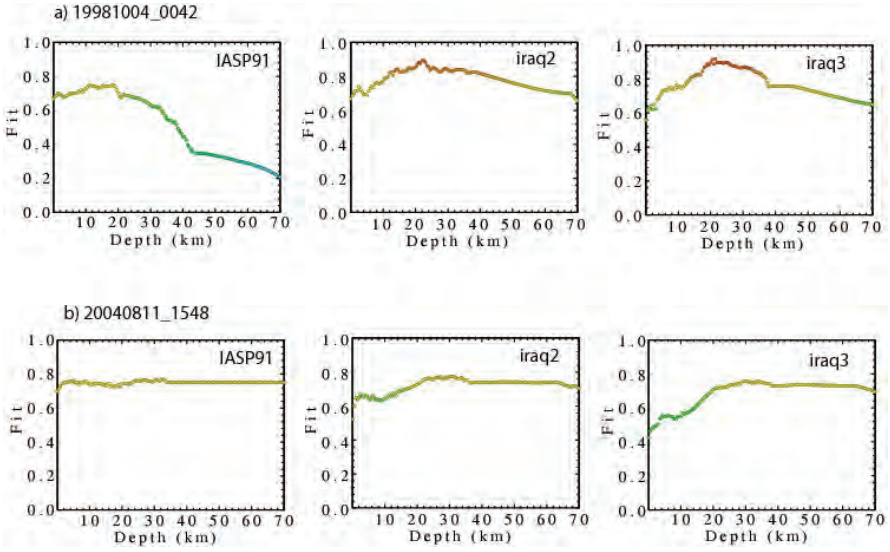

Figure 4. Examples of depth confidence levels calculated from surface-wave amplitude inversion for a) Event 19981004_0042 and b) Event 20040811_1548. Results are shown for the three velocity models described earlier: IASPEI91 (left panels), *iraq2* (middle panels) and *iraq3* (right panels). The best depth estimate corresponds to the maximum value of the fit function.

To derive the surface-wave amplitude spectra for the inversion, we applied multiple-filter analysis (Herrmann, 1973; Bhattacharya, 1983) to surface waves observed at regional distances from our study events. We then ran the inversion method to estimate the depths and focal mechanisms for the nine events listed in Table 1 using the IASPEI91 reference model and the processed spectral-amplitude data. We estimate the standard error on depths

from the surface-wave spectral amplitude inversions using a jack-knife method. This involves repeating the inversion *N*-1 (where *N* equals the number of stations) times, leaving one of the stations out during each calculation. Table 3 shows the average depth and its standard deviation that were calculated from all the inversion results.

Figure 4 shows an example of the inversion fit with respect to depth for Events 19981004_0042 and 20040811_1548 using the different velocity models. The fit functions for Events 19981004_0042 show well-defined maxima for all of the velocity models. In contrast, the fit functions for Event 20040811_1548 have broader maxima, with the IASPEI91 model producing the least defined peak. This broader fit function is reflected in the higher value of depth uncertainty (σ_{swa} = 9.8 km) computed for Event 20040811_1548 using the IASPEI91 model.

Summary of Regional Depth Estimator Results

Table 3 summarizes the results of the application of our depth estimator approach to the study events in Table 1. For each event we include the results comparing the three velocity models: IASPEI91, *iraq2* and *iraq3*. There are several observations that can be made regarding the correlation between the different individual estimates. First, we note that the new estimator depths correlate quite well with depths expected for each event's tectonic region (as described in Engdahl et al., 2006). We also find that all of the ISC free-depth solutions and composite pP_DEPTH estimates are much deeper than the depths found with our new estimator .

Secondly, there is a high degree of correlation between the depths estimated with ECFSM and SWA. Correlation coefficients calculated between the ECFSM and SWA methods are high for all velocity models (0.80, 0.89 and 0.94 for IASPEI91, *iraq2* and *iraq3* respectively). This is consistent with a high correlation between the ECFSM and SWA methods we found in our previous study of events in the Korean Peninsula and eastern China.

We also observe that in some cases the three individual methods produce significantly different estimates with tightly constrained standard errors (small σ_i's), resulting in a weighted combination (estimator) that is not meaningful (c.f. Events 19981004_0042 and 19990115_1913). We have observed this undesirable feature of the depth estimator in prior studies and plan to improve the statistical estimator to eliminate this type of occurrence. For the current data set the largest number of these inconsistencies occurred with the *iraq3* velocity model.

The results in Table 3 indicate significant variability between the individual depth estimates for a given event, depending on the velocity model used, particularly for the GMEL and SWA methods. However, the estimator depth values are very similar across the various velocity models. The correlation coefficients between the results obtained using different velocity models are: $C_{\text{IASPEI91-}iraq2}$ = 0.96, $C_{\text{IASPEI91-}iraq3}$ = 0.91, and $C_{iraq2\text{-}\,iraq3}$ = 0.90. These values are quite high, which indicates that the new estimator is not strongly sensitive to the velocity model. Of course this observation may not hold true in regions where there is strong regional variation in velocity-sensitive parameters such as crustal thickness, which for the current study remained fairly constant across the three velocity models studied.

Table 3. Summary of depth estimator results. Results for the individual depth-estimation methods as well as the new combined estimator (bolded columns) are shown for the three velocity models IASPEI91, *iraq2* and *iraq3*.

									29.2	**1.8**
19980709_1418	55.4 d	IASPEI91	29	1.9	22.3	8.3	33.3	5.4	**28.3**	**1.8**
		iraq2	28	1.9	23.1	9.1	33.3	6	**33.7**	**1.7**
		iraq3	36.5	1.9	13.9	5.1	33.3	6.5	**14.3**	**1.5**
19981004_0042	24.9 d	IASPEI91	18.5	1.9	7.8	2.6	0	8.6	**16.2**	**1.8**
		iraq2	22.5	2.3	7	2.8	0	26.3	**4.9**	**1.1**
		iraq3	21.5	7.1	4.5	1.1	0	38.3	**9.3**	**0.4**
19981005_0220	18.1 d	IASPEI91	11	1.1	8.7	0.5	17	4	**14**	**1.5**
		iraq2	22.5	2.3	7	2.8	17.4	2.9	**6.1**	**0.9**
		iraq3	13	5.6	5.1	0.9	16.8	3.2	**15.5**	**0.4**
19990115_1913	59.2 d	IASPEI91	16.5	1.8	15.4	0.4	0	54.8	**15.4**	**0.4**
		iraq2	16.5	2.9	15.4	0.4	33	104.9	**9.9**	**0.6**
		iraq3	22	3.8	9.6	0.6	22.5	91.7	**13.3**	**1**
19990406_0008	30.7 d	IASPEI91	17	1.7	11.9	1.3	3.7	4.4	**12**	**1.3**
		iraq2	24	6.1	11.5	1.4	11.1	7.5	**8.1**	**1.3**
		iraq3	24	6.1	7	1.4	11.1	5	**35**	**1**
20000321_1406	77.6 d	IASPEI91	34.5	1.3	43	2.9	32.5	1.9	**37**	**1.6**
		iraq2	68.5	6.2	38	2.9	33.3	2	**26.8**	**1.5**
		iraq3	62	6.9	30	3	23.2	1.8	**10.2**	**0.6**
20020419_1346	38.8 d	IASPEI91	3.5	2.2	10.9	0.6	3.7	3.2	**10**	**0.6**
		iraq2	6	3	10.5	0.6	3.7	2.7	**6.8**	**0.4**
		iraq3	10.5	4.1	6.9	0.4	3.7	1.9	**5.8**	**0.6**
20040701_2229	5.0 f	IASPEI91	16	4.6	5.4	0.6	27.9	5.6	**4.9**	**0.5**
		iraq2	11.5	2.8	4.6	0.5	30.9	8.2	**4**	**0.3**
		iraq3	19	1.4	3.2	0.3	17.5	3.5	**14.7**	**1.6**
20040811_1548	7.4 f	IASPEI91	30.5	9.8	24	2.6	7.9	2.1	**24.1**	**1.2**
		iraq2	31	1.9	24.8	2	11.1	2.5	**16.8**	**1.3**
		iraq3	30	2.6	15.4	2.8	11.1	1.8		

CONCLUSIONS AND RECOMMENDATIONS

In our previous validation experiment of the regional depth estimator approach in the region of eastern China and South Korea (Stroujkova and Reiter, 2006), we demonstrated excellent success in producing correlated and consistent depths between the individual methods included in the combined estimator. As a consequence, the estimator produced tightly constrained estimates of the depths of earthquakes in our data set. One potential reason for the successful application of our approach in Korea was the fairly homogeneous nature of the tectonic features within regional distances of the events in our study. This allowed us to use a simple 1-D reference model for all of our calculations, rather than incorporating more complex velocity models to produce better data fits in each estimation method.

In this study we examined the validity of the estimator in another, more complex regional setting. Our goal was to determine how robust the method is when the tectonic complexity (and potential lack of data fit to a single reference velocity model) increases. Based on our initial results we conclude that various individual depth-estimation methods have different degrees of sensitivity to the velocity model used in computations. A good correlation observed between the estimates obtained with different velocity models is a promising result. In addition, our depth estimate is in a good agreement with the pattern of focal depth distribution in the region (Engdahl et al., 2006). We find that the depths reported in the ISC catalog tend to be significantly overestimated (e.g., Table 1).

While we acknowledge the limited size of the database we have examined to date in the region around Turkey, we have found that the new estimator can provide robust depth estimates from regional data in a tectonically complex

region. In future work we will continue to apply the new estimator in different tectonic settings. We will also address some of the short-comings of the method, such as the need for improvement in the statistical behavior of the estimator, which is currently a fairly simple weighted average.

REFERENCES

Al-equabi, G. I. Personal Correspondence. 2007.

Bhattacharya, S. N. (1983). Higher order accuracy in multiple filter technique, *Bull. Seism. Soc. Am*. 73: 1395–1406.

Bogert, B. P., M. J. R. Healy and J. W. Tukey (1963), The quefrency analysis of time series for echoes: cepstrum, pseudo-autocovariance, cross-cepstrum and saphe cracking, in *Proceedings of a Symposium on Time Series Analysis*, ed. M. Rosenblatt, John Wiley and Sons, Inc., New York.

Bonner, J. L, D. T. Reiter, and R. H. Shumway (2002), Application of a cepstral F statistic for improved depth estimation, *Bull. Seism. Soc. Am* 92: 1675–1693.

Cansi, Y. (1995). Earthquake location applied to a mini-array: K-spectrum versus correlation method, *Geophys. Res. Lett.* 20: (17), 1819–1822.

Crotwell, H.P., T.J. Owens, and J. Ritsema (1999). The TauP Toolkit: Flexible seismic travel-time and ray-path utilities. *Seism. Res. Ltrs.*, 70, 154–160.

Doloei, J. and R. Roberts (2003). Crust and uppermost mantle structure of Tehran region from analysis of teleseismic P-waveform receiver functions, *Tectonophysics* 364: 115–133.

Draper N. R. and H. Smith (1998). *Applied Regression Analysis* (3rd edition). New York: Wiley.

Dziewonski, A. M., T.-A. Chou, and J .H. Woodhouse (1981). Determination of earthquake source parameters from waveform data for studies of global and regional seismicity, *J. Geophys. Res.* 86: 2825–2852.

Engdahl, E.R., R.D. van der Hilst, and R.P. Buland, 1998, Global teleseismic earthquake relocation with improved travel times and procedures for depth determination, *Bull. Seism. Soc. Am.* 88: 722–743.

Engdahl, E.R., J. Jackson, S. Myers, E. Bergman, and K. Priestley (2006). Relocation and assessment of seismicity in Iran region, *Geophys. J. Int.* 167: 761–778.

Hatzfeld, D., M. Tatar, K. Priestley, and M. Ghafory-Ashtiany (2003). Seismological constraints on the crustal structure beneath the Zagros Mountain belt (Iran), *Geophys. J. Int.* 155: 403–410.

Herrmann, R., and C. Ammon, (2002). Surface waves, receiver functions and crustal structure. In *Computer programs in seismolo*gy.

Kennett B. L. N., and E. R. Engdahl (1991), Travel times for global earthquake location and phase identification, *Geophys. J. Int.* 105: 429–465.

Mangino, S., and K Priestley (1998). The crustal structure of the southern Caspian region, *Geophys. J. Intl*. 133 (3): 630–648.

Oppenheim, A. V., and R. W. Schafer (1975). *Digital Signal Processing*. New York: Prentice Hall.

Rodi, W. (2006). Grid-search event location with non-Gaussian errors, *Phys. Earth & Planet. Int.* 158 (1): 55–66.

Schisselé, E., J. Guilbert, S. Gaffet, and Y. Cansi (2004). Accurate time-frequency-wavenumber analysis to study coda waves, *Geophys. J. Intl*. 158: (2), 577–591.

Schmidt, R.O. (1979). Multiple emitter location and signal parameter estimation. *Proc. RADC Spectral Estimation Workshop*, 243–258, Rome, Italy.

Stroujkova, A. and D. Reiter (2006). Regional Depth Phase Detection and Focal Depth Estimation: Application to Events in Southeast Asia, in *Proceedings of the 28th Seismic Research Review: Ground-Based Nuclear Explosion Montoring Technologies,* LA-UR-06-5471, Vol. 1, pp. 520–529.

Seismic Identification and Source Characterization

SEISMIC SOURCE SCALING AND DISCRIMINATION IN DIVERSE TECTONIC ENVIRONMENTS

Rachel E. Abercrombie[1], Kevin M. Mayeda[2], William R. Walter[3], Gisela M. Viegas[1], and Katherine Murphy[2]

Boston University[1], Weston Geophysical Corporation[2], and Lawrence Livermore National Laboratories[3]

Sponsored by Air Force Research Laboratory

Contract No. FA8718-06-C-0024.

ABSTRACT

The objectives of this study are to improve low-magnitude regional seismic discrimination by performing a thorough investigation of earthquake source scaling using diverse, high-quality datasets from varied tectonic regions. Local-to-regional high-frequency discrimination requires an estimate of how earthquakes scale with size. Walter and Taylor (2002) developed the Magnitude and Distance Amplitude Corrections (MDAC) method to empirically account for these effects through regional calibration. The accuracy of these corrections has a direct impact on our ability to identify clandestine explosions in the broad regional areas characterized by low seismicity. Unfortunately our knowledge of source scaling at small magnitudes (i.e., $m_b < \sim 4.0$) is poorly resolved. It is not clear whether different studies obtain contradictory results because they analyse different earthquakes, or because they use different methods. Even in regions that are well studied, such as test sites or areas of high seismicity, we still rely on empirical scaling relations derived from studies taken from half-way around the world at inter-plate regions.

We investigate earthquake sources and scaling from different tectonic settings, comparing direct and coda wave analysis methods. We begin by developing and improving the two different methods, and then in future years we will apply them both to each set of earthquakes. Analysis of locally recorded, direct waves from events is intuitively the simplest way of obtaining accurate source parameters, as these waves have been least affected by travel through the earth. But there are only a limited number of earthquakes that are recorded locally, by sufficient stations to give good azimuthal coverage, and have very closely located smaller earthquakes that can be used as an empirical Green's function (EGF) to remove path effects. In contrast, coda waves average radiation from all directions so single-station records should be adequate, and previous work suggests that the requirements for the EGF event are much less stringent. We can study more earthquakes using the coda-wave methods, while using direct wave methods for the best recorded subset of events so as to investigate any differences between the results of the two approaches.

Finding "perfect" EGF events for direct wave analysis is difficult, as is ascertaining the quality of a particular EGF event. We develop a multi-taper method to obtain time-domain source-time-functions by frequency division. If an earthquake and EGF event pair are able to produce a clear, time-domain source pulse then we accept the EGF event. We then model the spectral (amplitude) ratio to determine source parameters from both direct P and S waves. We use the well-recorded sequence of aftershocks of the M5 Au Sable Forks, NY, earthquake to test the method and also to obtain some of the first accurate source parameters for small earthquakes in eastern North America. We find that the stress drops are high, confirming previous work suggesting that intraplate continental earthquakes have higher stress drops than events at plate boundaries.

We simplify and improve the coda wave analysis method by calculating spectral ratios between different sized earthquakes. We first compare spectral ratio performance between local and near-regional *S* and coda waves in the San Francisco Bay region for moderate-sized events. The average spectral ratio standard deviations using coda are ~0.05 to 0.12, roughly a factor of 3 smaller than direct *S*-waves for $0.2 < f < 15.0$ Hz. Also, direct wave analysis requires collocated pairs of earthquakes whereas the event-pairs (Green's function and target events) can be separated by ~25 km for coda amplitudes without any appreciable degradation. We then apply coda spectral ratio method to the 1999 Hector Mine mainshock (M_w 7.0, Mojave Desert) and its larger aftershocks. We observe a clear departure from self-similarity, consistent with previous studies using similar regional datasets.

OBJECTIVES

The objectives of this study are to improve low-magnitude regional seismic discrimination by performing a thorough investigation of earthquake source scaling using diverse, high-quality datasets from varied tectonic regions. Local-to-regional high-frequency discrimination requires an estimate of how earthquakes scale with size. Walter and Taylor (2002) developed the MDAC method to empirically account for these effects through regional calibration. The accuracy of these corrections has a direct impact on our ability to identify clandestine explosions in the broad regional areas characterized by low seismicity. Unfortunately our knowledge at small magnitudes (i.e., $m_b < \sim 4.0$) is poorly resolved, and source scaling remains a subject of on-going debate in the earthquake seismology community. Recently there have been a number of empirical studies suggesting scaling of micro-earthquakes is non-self-similar (e.g. Kanamori et al.,1993; Abercrombie, 1995; Mayeda and Walter; 1996, Mori et al., 2003; Stork and Ito, 2004; Izutani and Kanamori, 2001, yet there are an equal number of compelling studies that would suggest otherwise (e.g., McGarr, 1999, Ide and Beroza, 2001, Imanishi et al., 2004, Prieto et al., 2004. It is not clear whether different studies reach different conclusions because they use different datasets and scaling varies with location, or because they use different methods. Sonley and Abercrombie (2006) show that small variations in the commonly used methods can lead to significant differences in results. Even in regions that are well studied, such as test sites or areas of high seismicity, we still rely on empirical scaling relations derived from studies taken from half-way around the world at inter-plate regions.

In summary, we address the following problems.

1. Do different studies obtain different results because they use different methods, or because they analyse different data sets? We will investigate whether coda and direct wave methods applied to the same datasets provide the same scaling.
2. Is scaling dependent upon the tectonic setting? We will investigate earthquakes from different tectonic settings and depth ranges, using the same coda and direct wave methods.
3. There have been few studies in intra-plate areas where seismicity is low and/or in regions where a clandestine test might occur. The MDAC method currently assumes earthquake source scaling that was derived exclusively from the western United States. Can we extrapolate or transport results from one region to others, or must we calibrate to each specific region? We will analyse earthquakes from both interplate (e.g., California) and intraplate (e.g., Eastern North America) regions to specifically address this question.

RESEARCH ACCOMPLISHED

Our approach to obtaining improved source parameters for small earthquakes focuses on the direct and coda wave methods: to improve and investigate them both, and then to apply them to diverse data sets.
Locally recorded, direct waves from events have been least affected by travel through the earth, and so are thought to be the best candidate for obtaining accurate source parameters. But there are only a limited number of earthquakes that are recorded locally, by sufficient stations to give good azimuthal coverage. Even fewer of these have an equivalently well recorded, very closely located smaller earthquake that meets the stringent criteria required to be a good EGF to remove path effects. This EGF method is the preferred one for isolating the source, but concern about the quality of the EGFs is a major source of uncertainty in studies that use these methods. In contrast, coda waves average radiation from all directions so single-station records should be adequate, and previous work suggests that the requirements for the EGF event are much less stringent. Our approach is to:

1. Develop an easy to apply coda wave spectral ratio method to obtain source parameters for large groups of earthquakes
2. Identify the mainshock – EGF earthquake pairs that meet stringent criteria for selecting the EGF, and obtain source parameters from the direct waves for this subset of events.
3. Use the direct wave results to confirm, and if necessary correct, the coda wave results
4. Apply these methods to data sets from a range of tectonic environments.
5. Determine the implications of the determined source scaling results for both coda calibration and regional discrimination using MDAC and other similar means of source and path-corrected discriminants.

So far we have worked to develop and improve both the coda wave and direct wave methods we will apply consistently to all the data sets. The coda wave approach is now published (Mayeda et al., 2007).

Development of Coda Spectral Ratio Method: the San Francisco Bay Area

We chose 10 stations operated by the Berkeley Digital Seismic Network (BDSN) along with 62 events between $3.5 < M_L < 5.2$ spanning ~1 to 220 km epicentral distance. All stations are three-component high-frequency (80 sps) channels and the events are all located to within 2 km in absolute location by the Northern California Data Center (NCDC) in conjunction with the University of California, Berkeley Seismological Laboratory (BSL).

Each waveform was corrected for instrument response, then visually inspected and clipped data were not processed. Since the aim of this part of the study was to look at amplitude ratio variability with event separation and azimuth, we selected event pairs without consideration of magnitude. In total, we found 259 possible event pairs that ranged between ~0 and 25 km distance in absolute separation. For both the coda and direct waves we chose 14 narrow frequency bands ranging between 0.2 and 25.0 Hz. For the coda, we formed averaged narrowband time-domain envelopes using the two horizontal components following the method of Mayeda et al. (2003)]. For the direct S-waves, log RMS amplitudes from the amplitude spectra were obtained for a 5 second window starting at the S-wave onset for each component. To further screen the data, we required a minimum of 5 stations recording the event pairs per frequency band, and ended up with as many as 184 pairs at 4.0-6.0 Hz and as few as 35 pairs at 15.0-20.0 Hz. Virtually all events have source mechanisms derived from moment-tensor inversion and, as expected, strikes and dips are consistent with the orientation of the regional faults in the greater San Francisco Bay region.

Based on prior work on local and regional coda, we hypothesize that amplitude ratios of the same event-pair will be much more stable for coda than for direct *S*-waves. We tested this hypothesis by forming narrowband amplitude ratios for both wave types and compared their standard deviations for many event pairs. In practice, direct wave empirical Green's function studies have limited their data to co-located events with the same source mechanism (e.g., Mori et al., 2003; Izutani and Kanamori, 2001; Venkataraman et al., 2002). This, however, severely limits the useable amount of data, and if proven feasible, the coda's stability and minimal move-out will allow inclusion of more events that are separated in distance and not necessarily of the same focal mechanism. This will allow for redundancy and lower variance estimates, a point thoroughly discussed recently by Prieto et al. (2007).

For both the coda and direct *S*-waves, we formed amplitude ratios for event pairs by simply subtracting the $\log_{10}$ amplitudes for each station that recorded the event pair. Since the site and path are the same for both events, the ratio should reflect the source differences in the frequency band. Figure 1a shows an example of direct wave amplitude ratios (top) and coda wave ratios (bottom) for an event pair that has the same depth of 7 km, with an epicentral location difference of 15.7 km. In general, for a magnitude 4 event, the measurement window for the coda envelope was ~300 seconds for 0.2-0.3 Hz, and ~100 seconds at 2-3 Hz. We note that for the direct waves, there was no difference if we used horizontal or vertical elements. Both events are roughly the same size and, as expected, the $\log_{10}$ average of the ratios is close to 0; however, the direct wave results are significantly more scattered.

Using all available ratios, such as the example shown in Figure 1a, we plot the amplitude ratio standard deviation as a function of event-pair offset for each frequency band (Figure 1b). We see that the coda amplitude ratios are roughly a factor of 3 smaller and do not show any appreciable increase with event separation, in sharp contrast to the direct waves. This means that the use of the coda will allow for the inclusion of many more events in spectral ratios studies, whereas in direct wave studies, only those events that are virtually co-located are used. Equally important, the coda spectral ratios are significantly less scattered and thus source parameters, such as corner frequency, will be better constrained when we fit the observed data with theoretical source models, such as the commonly used omega-square model (Aki, 1967; Brune, 1970).

We also investigated whether any of the pairs of earthquakes used in the coda wave study met the criteria for use in direct-wave analysis. Unfortunately, we found only one pair of events that were able to produce a source pulse. This is inadequate to perform any sort of rigorous comparison so we did not pursue this work further. The comparison does demonstrate how useful the coda methods should be when we have closely compared and calibrated them to some high-quality direct wave analyses. They will enable the study of many earthquakes which do not meet the criteria needed for high-quality direct wave EGF analysis.

Initial Application of the Coda Spectral Ratio Method to the M_w 7.0 Hector Mine Sequence

Next, we turn our attention to local and regional recordings of the M_w 7.0 Hector Mine mainshock and 6 aftershocks ranging between M_w 3.7 and 5.4. In this case we consider 6 broadband stations ranging between ~60 and 700 km: GSC, PFO, MNV, CMB, TUC, and ELK.

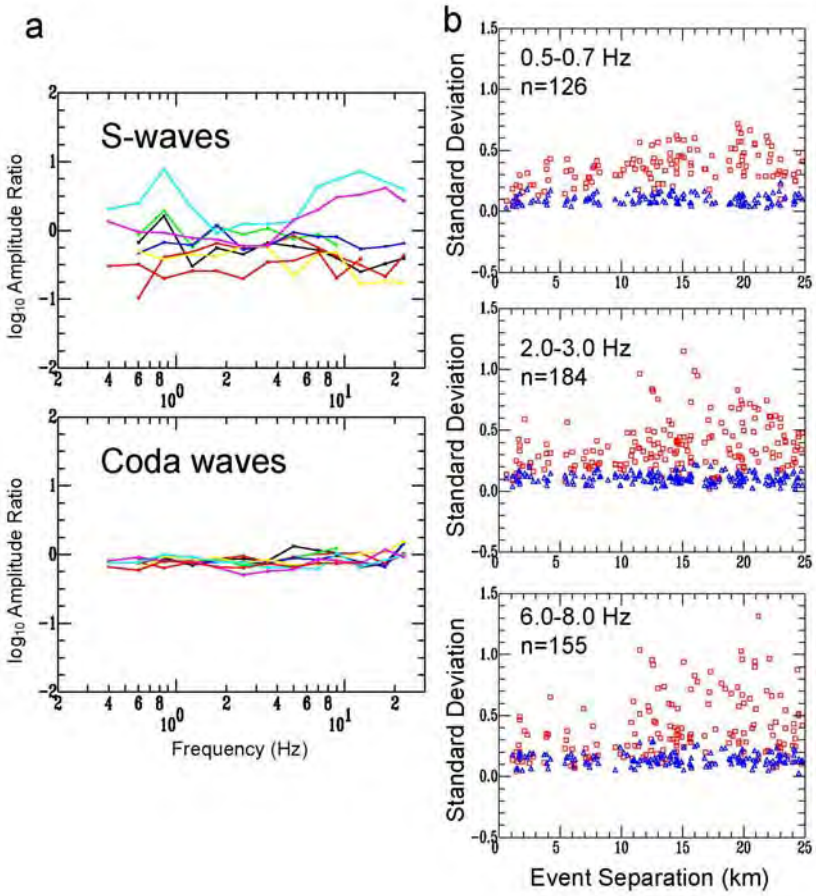

Figure1. (a) An example of amplitude ratio pairs for a pair of events (M3.6 and 3.7) separated by 16 km epicentral distance. (Top) direct S-wave ratios for 8 color-coded stations show significant scatter over the entire frequency range, whereas (bottom) the coda wave amplitude ratios are very stable from station to station. (b) amplitude ratio standard deviation versus event separation for coda (blue triangles) and direct waves (red squares) for all ratios that had at least 5 stations recording. Three frequency bands are shown: top 0.5-0.7 Hz, middle 2.0-3.0 Hz, and bottom 6.0-8.0 Hz. Note that the coda scatter shows almost no dependence on distance, in contrast to the direct waves, and is roughly a factor of 3 smaller.

All the events have independent regional seismic moment estimates from full waveform inversion by G. Ichinose using the methodology outlined in Ichinose et al., [2003]. For consistency, we used the regional estimates of M_w to avoid any biases since they were all computed using the same method, velocity model, and station distribution. For the mainshock, we use an M_w of 7.0 following the results of G. Ichinose .

Assuming a simple single corner frequency source model (Aki, 1967; Brune, 1970), the ratio of the moment-rate functions for two events (1 and 2) is given by,

$$\frac{\dot{M}_1(\omega)}{\dot{M}_2(\omega)} = \frac{M_{0_1}\left[1+\left(\omega/\omega_{c_2}\right)^2\right]^{p/2}}{M_{0_2}\left[1+\left(\omega/\omega_{c1}\right)^2\right]^{p/2}} \qquad (1)$$

where M_0 is the seismic moment and w_c is the angular corner frequency ($2\pi f_c$) and p is the high frequency decay rate. At the low frequency limit the source ratio shown in equation 1 is proportional to the ratio of the seismic moments $\left[M_{0_1}/M_{0_2}\right]$, whereas at the high frequency limit, equation 1 is asymptotic to $\left[M_{0_1}/M_{0_2}\right]^{\left(1-\frac{p}{3}\right)}$ under self-similarity. If we follow the usual *Brune* [1970] omega-square model and set p=2, the exponent of the high-frequency ratio becomes 1/3. However, it has been proposed by Kanamori and Rivera (2004) that the scaling between moment and corner frequency could take on the form,

$$M_o \sim \omega_c^{-(3+\varepsilon)} \qquad (2)$$

where *e* represents the deviation from self-similarity and is usually thought to be a small positive number. For example, Walter et al. (2006) and Mayeda et al. (2005) found *e* to be close to 0.5 for the Hector Mine mainshock and its aftershocks using independent spectral methods. For the current study we use the source spectrum portion of the MDAC methodology of Walter and Taylor (2001), which allows for the variation of the corner frequency that does not have to be self-similar. For example,

$$\omega_c = \left(\frac{k\sigma_a}{M_0}\right)^{1/3} \quad \text{and} \quad \sigma_a = \sigma'_a\left(\frac{M_0}{M'_0}\right)^{\psi} \quad \text{and} \quad \psi = \frac{\varepsilon}{\varepsilon+3} \qquad (3)$$

where σ_a is the apparent stress [*Wyss*, 1970], σ'_a and M'_0 are the apparent stress and seismic moment of the reference event, and ψ is a scaling parameter. For constant apparent stress, ψ = 0 and *e* =0, however, *Mayeda and*

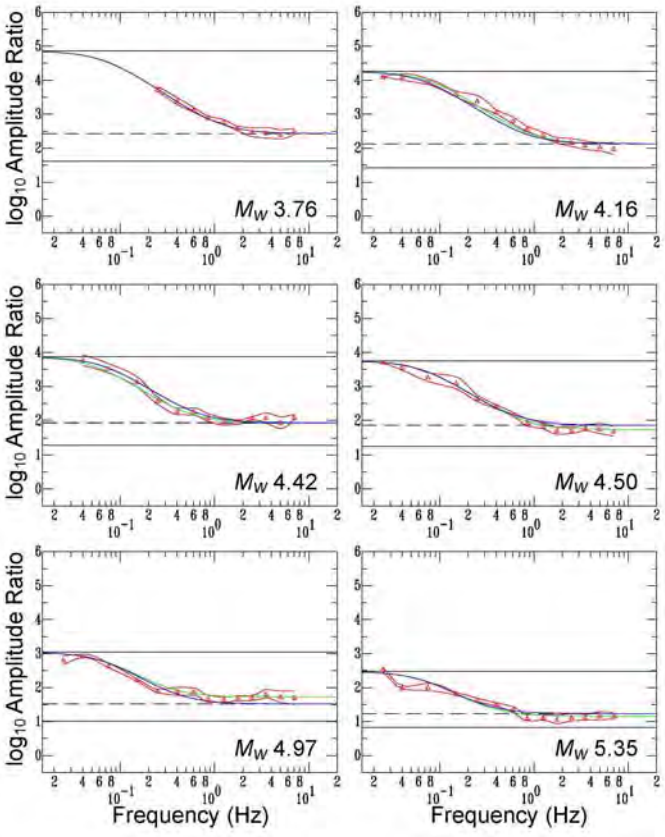

Figure 2. Spectral ratios for the Hector Mine mainshock relative to 6 aftershocks. In each figure, we show the low and high frequency asymptotes from equation 1 as solid black horizontal lines and dashed lines represent the case when *p* = 1.5. The average for each band is shown by red triangles and red lines represent ±1σ . Blue lines represent the best fitting MDAC spectral ratios that fit all 6 ratios simultaneously, whereas the green lines represent the case when each ratio was fit individually. We find that the best fitting model corresponds to a reference event of M_w 5.0 with an apparent stress of 0.1 MPa and a scaling parameter (ψ), of 0.25, in good agreement with previous studies using independent methods.

Walter [1996] found ψ=0.25 for moderate to large earthquakes in the western United States. By using the corner frequency defined in (3) into equation 1, we can apply a grid search to find the parameters that best fit the spectral ratio data.

Using all 6 stations, we formed the average spectral ratio between the mainshock and each of the aftershocks, then grid-searched using equation 1 and 3 assuming that the reference moment corresponded to an M_w 5.0 event and the reference apparent stress was varied between 0.5 and 10 bars. As observed for San Francisco Bay Area events, the coda spectral ratios for Hector Mine events were very stable, with average standard deviations less than 0.1 for all frequencies. Figure 2 shows all 6 ratios along with the high and low frequency asymptotes for equation 1 assuming both simultaneous model fits (blue lines) and individual ratio fits (green lines). Given the variance of the individual fits, it is preferable to use the simultaneous fit results. In all cases the high frequency asymptote is significantly above the theoretically predicted value. This is consistent with a break in self-similarity where *e* is between 0.5 and 1.0, and it is inconsistent with a standard self-similar *Brune* [1970] style omega-square model. The only way to keep the self-similar assumption and match the data is to have a less than omega-squared spectral decay at high frequencies. The decay parameter *p* must be greater than 1.5 to keep the energy finite (e.g., Walter and Brune,

1993). If the high-frequency decay value *p* were close to 1.5 it would be possible to nearly match the spectral ratios shown as dashed lines in Figure 2. However, given that such shallow falloff is not consistent with most earthquake observations (e.g., Hough, 2001) and independent methods (e.g., Mayeda et al., 2005; Walter et al., 2006), our preferred interpretation is that the apparent stresses are systematically lower for the aftershocks than the mainshock. If all events have Brune-style spectra with an f^{-2} fall-off at high frequencies, this implies the corner frequency scaling is steeper than f^{-3} for self-similar, constant apparent stress scaling. Finally, we compare our estimate of the corner frequency of the mainshock with the teleseismic estimate of 0.059 Hz from Venkataraman et al. (2002). Our estimate of 0.069 Hz from simultaneous fitting of the ratios is in good agreement, supporting the validity our approach.

Development of direct wave EGF Method, and application to eastern North America:

Analysis of earthquakes in stable, intraplate, low seismicity regions is important to characterize these regions, but it is hard because of the sparcity of earthquakes and stations, and hence useful data. Relatively little is known about earthquake sources in intraplate regions, and often relationships based on minimal data, or simply extrapolated from interplate regions are assumed due to lack of local information. For example, Somerville et al. (2002) use the recordings of only 3 moderate-sized earthquakes to propose source scaling relationships for earthquakes in the Northeastern USA and other stable continental regions. Their results imply that earthquakes in the Northeastern USA have relatively high stress drops. This result was confirmed by Shi et al. (1998) who analysed almost 50 small earthquakes from the region. Their study included 8 empirical Green's function pairs (Shi et al., 1996), but mostly individual earthquakes. They also found a decrease in stress drop with seismic moment, at small magnitudes (< M~3). This may indicate that earthquake source scaling is different in this intraplate region, or else may represent a limit to the resolution as was found earlier in the San Andreas Fault plate boundary region (e.g., Abercrombie and Leary, 1993). Shi et al. (1998) were mostly limited by data availability to using regional recordings at single stations, and so to frequencies less than about 25 Hz.

In the last decade there has been a significant increase in the number of broadband seismic stations deployed in eastern North America, leading to growing number of well-recorded earthquakes (M2-5). On April 20, 2002 an earthquake of magnitude M_L 5.3 occurred in the northeastern Adirondack Mountains, Seeber et al. (2002). Following the mainshock, Lamont-Doherty Earth Observatory (LDEO) deployed digital portable seismographs to monitor aftershocks. The portable network spanned an area about 24 by 20 km with an average inter-station spacing of 4 – 6 km, smaller than the average source depth. Between April 22 and November, 2002, 74 small aftershocks were detected and located in the epicental area of the mainshock. These data (200 samples/s) represent the best recorded earthquakes in the region to date, and so provide an unprecedented opportunity to investigate source parameters in this intraplate setting.

We calculate the source parameters using two methods commonly applied to direct waves recorded at local stations: spectral modeling of the individual three-component P and S waves (e.g., Abercrombie, 1995), and the EGF method (e.g. Mori and Frankel, 1990, Abercrombie and Rice, 2005). Both methods require high frequency content data to work well. Many studies consider the EGF method superior as it corrects for all path and site effects by using a smaller, collocated earthquake as an EGF. The EGF method cannot be used to calculate the seismic moment of the earthquakes, but this is the most reliable information that can be obtained from the individual spectral analysis. Using cross-correlation we identify two clusters of earthquakes with very similar waveforms, that include the largest aftershocks recorded by the portable network. Both clusters include an M≥3, an M≥2, and a number of M1-2 earthquakes. We model the spectra obtained by dividing the spectrum of the large earthquake by the smaller one.

It is not clear in many studies how close the EGF events are to a perfect Green's function. They are typically too small to obtain focal mechanisms, and the location uncertainties are larger than the preferred separation between events. We select only events that are located within the uncertainties of the large event, and have a high degree of waveform similarity, determined by cross-correlation. As a further test, we transform all the spectral ratios back to the time domain, and we only use pairs where we are able to resolve a clear source pulse. If a source time function is observable in this way, then it demonstrates that the phase components of the spectra are also very similar. This test is similar to the investigation performed by Mori and Frankel (1990) to determine how closely located earthquakes pairs must be for the EGF method to work well. To calculate the source time functions, we worked with Dr. German Prieto to develop a multitaper approach to calculate the source time function. Multitaper methods have long been preferred to calculate source spectra and spectral ratios as they better represent the frequency content of the waveforms than do cosine and other tapers (e.g., Park et al., 1987). Unfortunately, existing multitaper codes only worked with amplitude spectra and so could not be used to perform the complex deconvolution and retrieve the

source time functions. Dr. Prieto adapted his code to enable it to perform the full complex deconvolution so that we could use the same frequency analysis to obtain both the best spectra, and the source time functions. The method is similar to that developed by Park and Levin (2000) to obtain receiver functions.

We correct the velocity seismograms for the instrument response, and then selected time windows of 0.75 seconds that start 0.1 seconds before the P or S wave onset. We use the multitaper method (Park et al., 1987; Prieto et al., 2007) to calculate the Fourier displacement amplitude spectra. We use 7 weighted tapers and a time-bandwidth-product of 4. The algorithm also removes a noise line centered at 60 Hz, if present. Figure 3 shows an example of the seismograms, spectra, and EGF analysis for 3 events in one cluster.

We first calculate source parameters using the individual spectra, to determine the seismic moments, and also to compare the results of this standard method with that of the preferred EGF method. Before modeling the individual amplitude spectra, we re-sample them on a logarithmic scale, so that the fits were not biased to the high frequencies. We use samples at intervals of $10^{0.02}$, and the amplitude value was the average of all the points in a neighborhood of $\pm 10^{0.01}$. We fit the displacement amplitude spectra with an omega square source model (Boatwright, 1980; Abercrombie 1995),

$$\Omega(f) = \frac{\Omega_0 \, \mathrm{e}^{-\pi f t/Q}}{\left[1+\left(f/f_c\right)^{\gamma n}\right]^{\frac{1}{\gamma}}}, \qquad (4)$$

where $\Omega(f)$ is the displacement amplitude spectrum, f is the frequency, Ω_0 is the long period level of the spectrum, f_c is the corner frequency, t is the travel time of the seismic waves (P or S), Q is the attenuation quality factor and γ and n are constants ($\gamma = n = 2$) that control the shape of the spectrum curvature around the corner frequency. We use the Nelder-Mead simplex method (multidimensional unconstrained nonlinear minimization method) to fit the spectra with eq. (4) using Ω_0, f_c and Q as variables. The travel time was calculated dividing the epicentral distance (S minus P) by the P or S wave velocity (6.500 km/s or 3.7528 km/s). The displacement spectra are fitted at bandwidths with signal to noise ratio above 3.

We calculate the seismic moment for each component i at each station, M_{0i}, using Brune's (1970) relationship,

$$M_{0i} = \frac{4\pi\rho \, c^3 R \, \Omega_{0i}}{\phi U_{\phi\theta}}, \qquad (5)$$

where ρ is the density(ρ = 2900 kg/m^3), c is the wave of interest velocity (P, α = 6500 m/s; or S, β = 3752.8 m/s), R is the hypocentral distance (determined from S minus P arrival times), ϕ is the free-surface parameter ($\phi = 2$), and $U_{\phi\theta}$ is the mean radiation pattern ($U_{\phi\theta} = 0.52$ for P waves and $U_{\phi\theta} = 0.63$ for S waves). We take the mean of all available components to calculate a final value for each station.

We assume the circular fault model of Madariaga (1976) to calculate source radius (r) and stress drop ($\Delta\sigma$) from M_{0i} and f_{ci},

$$r_i = \frac{k\beta}{f_{ci}}, \qquad (6)$$

where β is the S wave velocity and k is a constant ($k = 0.32$ for P waves and $k = 0.21$ for S waves), and then take the mean of all available components. Following Eshelby (1957) the stress drop on a circular crack is

$$\Delta\sigma = \frac{7}{16}\frac{M_0}{r^3}. \qquad (7)$$

We then apply the EGF method to the earthquakes in the clusters we identified. We use the same amplitude spectra to calculate spectral ratios between the different events, and we also use the extension of the multitaper method to the complex spectra to deconvolve the spectral ratios back to the time domain and so obtain estimates of the source time functions. We only continued the analysis if we obtained a clear source pulse, justifying our choice of EGF event. We resample the spectral ratios on a logarithmic scale (in the same way as the individual spectra). We model the spectra ratios using

$$\Omega_r(f) = \Omega_{0r}\left[\left.1+\left(f/fc_2\right)^m \right/ 1+\left(f/fc_1\right)^m\right]^{\frac{1}{\gamma}}, \qquad (8)$$

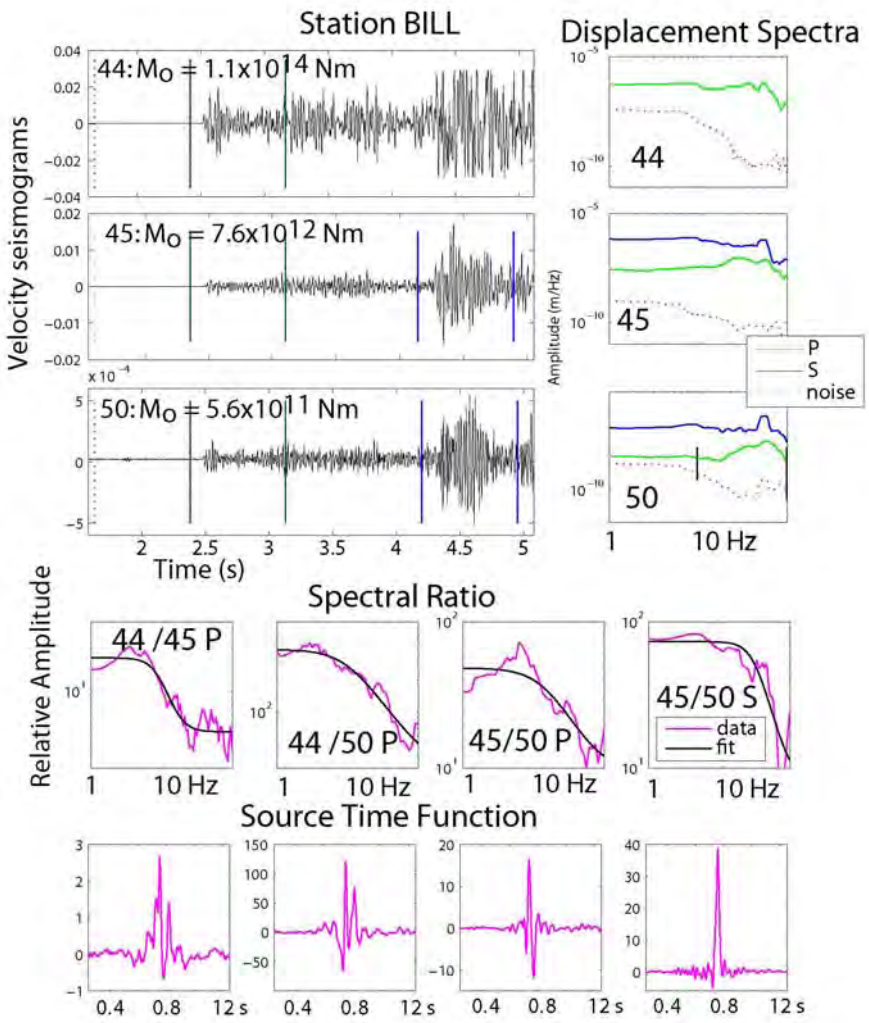

Figure 3. Example of the direct wave analysis for 3 earthquakes in one cluster of Au Sable Forks aftershocks. We show the vertical component, velocity seismograms, with the noise, P and S windows marked. The corresponding displacement spectra are shown using the same color coding. The spectral ratios and source time functions obtained by transforming the ratios back to the time domain are shown at the bottom. Earthquake 44 appears to have a complex source time function with at least 2 subevents.

where $\Omega_r(f)$ is the displacement amplitude spectral ratio, Ω_{0r} is the relative long period level of the spectrum, f_{c1} is the corner frequency of the large earthquake, f_{c2} is the corner frequency of the small earthquake. We use the same method as for the individual spectra, with variables Ω_{0r}, f_{c1} and f_{c2}, and fit the spectral ratios in the bandwidth where the signal to noise ratio of both earthquakes is above 3. We then calculate source parameters from the spectral fitting as for the individual spectra.

We obtain preliminary stress drops in the range of 10-100 MPa for ten aftershocks of the Au Sable Forks earthquake with moments in the range 10^{10} to 10^{15} Nm. These values are consistent with the previous studies which find relatively high stress drops for intraplate regions such as eastern North America. They are consistent with the results of Shi et al. (1998) for their EGF events, but we do not see a breakdown in constant stress drop scaling at lower magnitudes, suggesting that this may have been an artifact of the limited bandwidth available to Shi et al.

CONCLUSIONS AND RECOMMENDATIONS

In summary, we have developed and performed initial testing of our preferred analysis methods for the direct and coda waves. The next step is to use these to obtain source parameters so as to compare the methods.

The initial analysis of the aftershocks of the Au Sable Forks earthquake confirms that earthquakes in eastern North America have relatively high stress drops (10-100 MPa). They also suggest that the decrease in stress drop with decreasing moment reported by Shi et al. (1998) may be an artifact of the limitations of their data. The next stage of this analysis is to calculate the radiated seismic energy from the spectra, and then to obtain source parameters using locally recorded direct waves for further aftershocks, and other recent earthquakes in the eastern North America region that have good EGF events that meet our stringent criteria.

The averaging nature of coda waves has been shown to provide significantly lower amplitude variance than any traditional direct phase method. It is thus ideal in regions with sparse stations and events so that most events are only well-recorded by a single station. The new spectral-ratio method developed in this study makes the coda method much easier and simpler to apply, greatly extended the number of earthquakes that can be studied. We demonstrate that coda envelope amplitude ratios are an effective tool at isolating the average source effect, with average scatter that is roughly 3 times less than direct phase ratios. Moreover, the minimal move-out for coda allows event pairs to be selected that have significant lateral separation and/or focal mechanism differences, in sharp contrast to direct phase EGF and spectral ratios studies which require co-located events, and ideally, identical focal mechanisms. For the Hector Mine mainshock and selected aftershocks, there are basic conclusions that can be drawn: 1) Inferred mainshock corner frequency is similar to teleseismic estimate; 2) The observed source ratios at low frequency are in good agreement with independent moment estimates; 3) At high frequency, none of the spectral ratios is asymptotic to $\left[M_{0_1}/M_{0_{i1}}\right]^{1/3}$, similar to *Izutani's* [2005] finding for the mid Niigata sequence;

4) The best fitting scaling parameter, ψ, is 0.25 and e =1, consistent with previous studies on the same dataset using different methodologies; 5) The scaling of seismic moment and corner frequency does not follow an f^{-3} dependence and seems consistent with an f^{-4} dependence.

The next stage is to compare the results of the coda wave method with those from the direct-wave analysis using EGF pairs of events that are similar enough to produce source time functions from the direct wave deconvolution. We will perform direct wave analyses on the subset of Hector Mine aftershocks that have high quality EGFs, and apply the coda wave analysis to earthquakes from eastern North America including those used for the direct wave analysis. In this way we will determine whether the results of the coda-wave ratio method really do represent average source parameters, or whether any corrections or systematic biases need to be considered.

ACKNOWLEDGEMENTS

We thank Luca Malagnini for his contribution to the work on coda spectral ratios, German Prieto for developing the multi-taper code to obtain time-domain source time functions, and Won-Young Kim for providing the portable aftershock recordings of earthquakes in eastern North America, and information about his regional wave analysis. We also would like to thank G. Ichinose for invaluable waveform inversion information.

REFERENCES

Abercrombie, R. E. (1995). Earthquake source scaling relationships from -1 to 5 M_L using seismograms recorded at 2.5 km depth, *J. Geophys. Res.* 100: 24,015–24,036.

Abercrombie, R. E., and Leary P. C., 1993, Source parameters of small earthquakes recorded at 2.5 km depth, Cajon Pass, southern California: implications for earthquake scaling, *Geophys. Res. Lett*. 20: 1511–1514.

Abercrombie, R.E., and J.R. Rice (2005), Can observations of earthquake scaling constrain slip weakening?, *Geophys. J. Int.* 162: 406–424.

Aki, K. (1967), Scaling law of seismic spectrum. *J. Geophys. Res.* 72, 1217–1231.

Boatwright, J., (1980), A spectral theory for circular seismic sources: simple estimates of source duration, dynamic stress drop, and radiated energy, *Bull. Seismol. Soc. Am.* 70**:** 1–28.

Brune, J. N. (1970), Tectonic stress and spectra of seismic shear waves from earthquakes, *J. Geophys. Res.* 75: 4997–5009.

Eshelby, J. D.,1957, The determination of the elastic field of an ellipsoidal inclusion and related problems, Proc. *Roy. Soc. Lond., A,* 241: 376–396.

Hough, S. E. (2001), Empirical Green's function analysis of recent moderate events in California, *Bull. Seism Soc. Am.* 91: 456–467.

Ichinose G.A., J.G. Anderson, K.D. Smith, and Y. Zeng (2003), Source parameters of eastern California and western Nevada earthquakes from regional moment tensor inversion, *Bull. Seism. Soc. Am* 93: 61–84.

Ide, S. & Beroza, G. C., 2001. Does apparent stress vary with earthquake size, *Geophys. Res. Lett.* 28*:* 3349–3352.

Imanishi, K., W.L. Ellsworth, and S.G. Prejean (2004), Earthquake source parameters determined by the SAFOD Pilot Hole seismic array, *Geophys. Res. Lett.* 31: L12S09, doi:10.1029/2004GL019420.

Izutani Y. and Kanamori, H. (2001), Scale-dependence of seismic energy-to-moment ratio for strike-slip earthquakes in Japan, *Geophys. Res. Lett.* 28, 20, 4007–4010.

Izutani, Y. (2005), Radiated energy from the mid Niigata, Japan, earthquake of October 23, 2004 and its aftershocks, *Geophys. Res. Lett.* 32: L21313, doi:10.1029/2005GL024116.

Kanamori, H., Mori, J., Hauksson, E., Heaton, T. H., Hutton, L. K., & Jones, L. M., 1993. Determination of of earthquake energy release and M_L using TERRAscope, *Bull. Seismol. Soc. Am.* 83**:** 330–346.

Kanamori H. and L. Rivera (2004). Static and dynamic scaling relations for earthquake and their implications for rupture speed and stress drop, *Bull. Seism. Soc. Am.* 94: 314–319.

McGarr, A., 1999. On relating apparent stress to the stress causing earthquake slip, *J. Geophys. Res.* 104: 3003–3011.

Madariaga, R., 1976. Dynamics of an expanding circular fault, *Bull. Seismol. Soc. Am.* 66:, 639–666.

Mayeda, K., L. Malagnini, and W. R. Walter (2007), A new spectral ratio method using narrow band coda envelopes: Evidence for non-self-similarity in the Hector Mine sequence, *Geophys. Res. Lett.* 34: L11303, doi:10.1029/2007GL030041.

Mayeda, K. M. and W. R. Walter, (1996). Moment, energy, stress drop and source spectra of Western U.S. earthquakes from regional coda envelopes, *J. Geophys. Res.* 101: 11,195–11,208.

Mayeda, K., Hofstetter A., O'Boyle J. L., Walter, W. R. (2003), Stable and transportable regional magnitudes based on coda-derived moment-rate spectra. *Bull. Seismol. Soc. Am.* 93: 224-239.

Mayeda, K., R. Gok, W. R. Walter, and A. Hofstetter (2005). Evidence for non-constant energy/moment scaling from coda derived source spectra, *Geophys. Res. Lett.*, 32: L10306, doi:10.1029/2005GL022405.

Mori, J. and A. Frankel, 1990, Source parameters for small events associated with the 1986 North Palm Springs, California, earthquake determined using empirical Green functions, *Bull. Seism. Soc. Am.* 80: 278–295.

Mori, J., R.E. Abercrombie, and H. Kanamori (2003). Stress drops and radiated energies of aftershocks of the 1994 Northridge, California, earthquake, *J. Geophys. Res.* 108: No. B11, 2545, doi:10.1029/2001JB000474.

Park, J., and V. Levin, 2000, Receiver functions from multiple-taper spectral correlation estimates, *Bull. Seism. Soc Am.*, 90: 1507–1520.

Park, J., C. R. Lindberg, and F. L. Vernon (1987), Multitaper spectral analysis of high frequency seismograms, *J. Geophys. Res.* 92: 12,675–12,648.

Prieto, G. A., Shearer, P. M., Vernon, F. L., and Kilb, D. (2004), Earthquake source scaling and self-similarity estimation from stacking P and S spectra, *J. Geophys. Res.* 109: B08310, doi 10.1029/2004JB003084.

Prieto, G. A., D. J. Thomson, F. L. Vernon, P. M. Shearer and R. L. Parker (2007), Confidence intervals of earthquake source parameters, *Geophys. J. Int.* 168: 1227–1234. doi: 10.1111/j.1365-246X.2006.03257.x,

Seeber, L., W-Y. Kim, J. G. Armbruster, W-X. Du, A. Lerner-Lam and P. Friberg (2002). The 20 April 2002 M_w5.0 earthquake near Au Sable Forks, Adirondacks, New York: A first glance at a new sequence, *Seism. Res. Lett.* 73: 480–489.

Shi, J., W. Y. Kim and P. G. Richards (1996). Variability of crustal attenuation in the northeastern United States from Lg waves, *J. Geophys. Res*. 101: 25231–25242.

Shi, J., W. Y. Kim and P. G. Richards (1998). The corner frequencies and stress drops of intraplate earthquakes in the northeastern United States, *Bull. Seism. Soc. Am.* 88**:** 531–542.

Somerville, P., N. Collins, N. Abrahamson, R. Graves, and C. Saikia (2002) Ground motion attenuation relation for the central and eastern Unites States. Final Report to NEHRP, U.S. Geological Survey.

Sonley, E., and R. E. Abercrombie, (2006). Effects of methods of attenuation correction on source parameter determination, American Geophysical Union Monograph, EARTHQUAKES Radiated energy and physics of faulting, Abercrombie, McGarr, DiToro, and Kanamori. eds.

Stork, A. L., and H. Ito, 2004, Source Parameter Scaling for Small Earthquakes Observed at the Western Nagano 800-m-Deep Borehole, Central Japan , *Bull. Seismo. Soc. Am.* 94,1781-1794, DOI: 10.1785/012002214

Venkataraman, A., L. Rivera, and H. Kanamori, (2002). Radiated energy from the 16 October 1999 Hector Mine earthquake: regional and teleseismic estimates, *Bull. Seism. Soc. Am*, 92, 1256–1265.

Walter, W. R., and J. N. Brune, (1993). Spectra of seismic radiation from a tensile crack, *J. Geophys. Res*, 98, 4449–4459.

Walter, W. R. and S. R. Taylor (2000). A revised magnitude and distance amplitude correction (MDAC2) procedure for regional seismic discriminants: theory and testing at NTS, Lawrence Livermore National Laboratory Report, UCRL-ID-146882, http://www.llnl.gov/tid/lof/documents/pdf/240563.pdf

Walter, W. R., K. Mayeda, R. Gök, A. Hofstetter (2006). The scaling of seismic energy with moment: Simple models compared with observations, *Earthquakes: Radiated Energy and the Physics of Faulting, AGU Geophysical Monograph Series*, 170.

Wyss, M. (1970), Stress estimates of South American shallow and deep earthquakes, *J. Geophys. Res.*, 75, 1529–1544.

A MATHEMATICAL STATISTICS FORMULATION OF THE TELESEISMIC EXPLOSION IDENTIFCATION PROBLEM WITH MULTIPLE DISCRIMINANTS

Dale N. Anderson[1], Deborah K. Fagan[1], Mark A. Tinker[2], Gordon D. Kraft[2], and Kevin D. Hutchenson[2]

Pacific Northwest National Laboratory[1] and Quantum Technology Sciences, Incorporated[2]

Sponsored by Air Force Technical Applications Center

and

National Nuclear Security Administration
Office of Nonproliferation Research and Development
Office of Defense Nuclear Nonproliferation

Contract Nos. DE-AC05-RLO1830/PL07-ECM-NEM02[1] and FA8620-05-C-4301[2]

ABSTRACT

Seismic monitoring for underground nuclear explosions answers three questions for all global seismic activity: Where is the seismic event located? What is the event source type (event identification)? If the event is an explosion, what is the yield? The answers to these questions involve processing seismometer waveforms with propagation paths predominately in the mantle. Four discriminants commonly used to identify teleseismic events are depth from travel time, presence of long-period surface energy (mb versus Ms), depth from reflective phases, and polarity of first motion. The seismic theory for these discriminants is well established in the literature (see for example Pomeroy et al. [1982] and Blandford [1982]). However the physical basis of each has not been formally integrated into probability models to account for statistical error and provide discriminant calculations generally appropriate for multi-dimensional event identification. This paper develops a mathematical statistics formulation of these discriminants and offers a novel approach to multi-dimensional discrimination that is readily extensible to other discriminants. For each discriminant a probability model is formulated under a general null hypothesis of H0: Explosion Characteristics. The veracity of the hypothesized model is measured with a p-value calculation (see Stuart et al. [1994] and Freedman et al. [1991]) that is filtered to be approximately normally distributed and is in the range [0, 1]. A value near zero rejects H0, and a moderate to large value indicates consistency with H0. The hypothesis test formulation ensures that seismic phenomenology is tied to the interpretation of the p-value. These p-values are then embedded into a multi-discriminant algorithm that is developed from regularized discrimination methods proposed by Smidt and McDonald (1976), DiPillo (1976) and Friedman (1989). Performance of the methods is demonstrated with 102 teleseismic events with magnitudes (mb) ranging from 5 to 6.5 in Anderson et al. (2007). Example p-value calculations are also given for two of these events. Preliminary studies on the statistical properties of p-values are presented here.

OBJECTIVES

Anderson et al. (2007) propose a unifying framework for seismic event identification that can be populated with a diversity of seismic discriminants. For inclusion in the framework, a discriminant's physical theory must be mathematically embedded into a probability model designed to capture significant sources of error. This is accomplished by formulating each discriminant as a statistical hypothesis test under a general null hypothesis of H0: Explosion Characteristics. For example, a depth null hypothesis under Explosion Characteristics might be H0: event depth ≤ 10 km with the logical alternative hypothesis HA: event depth > 10 km. The veracity of the null hypothesis for each discriminant is measured with a p-value calculation, which is used as the discriminant. The p-value ranges between zero and one, with a value near zero indicating inconsistency with Explosion Characteristics and a moderate to large value indicating consistency with Explosion Characteristics. With this approach to discriminant construction, the p-value carries information about source type fully adjusted for natural and measurement variability. This places a high standard on the construction of the discriminants—seismic phenomenology and path corrections must be integrated into an appropriate probability model, and a seismic-based hypothesis test must be constructed. The p-values under this formulation can be viewed as standardized discriminants with common interpretation across geographical regions and different discriminants.

For continuous discriminants such as depth from travel time, spectral ratios, or mb versus Ms, when the null hypothesis is true (e.g., explosion), the p-value will have a uniform probability distribution, and when the null hypothesis is false (earthquake), the p-value will have a probability distribution with most of its mass near zero. Here, the concentration of probability mass at zero is determined by the degree of disagreement between the true probability model of the data and the null hypothesis model.

The hypothesis test p-values can be mildly transformed to become standardized discriminants *Y* that also possess predictable statistical properties. They also range between zero and one, their interpretation is completely analogous to that of p-values, and they are approximately Gaussian. Therefore, established Gaussian discrimination methods can be used to formulate a unified decision from standardized discriminants. Specifically, the equation

$$Y = \frac{2}{\pi}\arcsin(\sqrt{p - value})$$

is well established in statistical theory as a transformation to achieve Gaussian behavior in data bounded between zero and one. Figure 1 illustrates the effect of standardizing the hypothesis test p-values. Precedence for interpreting p-values as discriminants can be found in Maharaj (2000), and Dumbgen and Homke (2000).

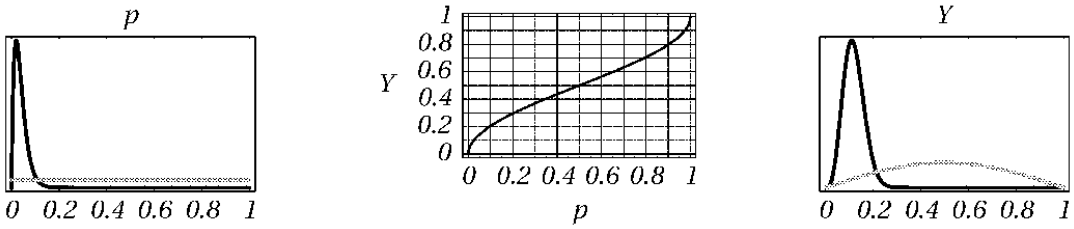

Figure 1. Transformation to induce an approximate Gaussian distribution on individual p-values (denoted *p* in the graphs) to derive standardized discriminants. The H0 probability distribution is gray, and the HA probability distribution is black.

In the framework proposed in Anderson et al. (2007), standardized discriminants *Y* are mathematically combined for source identification. This is accomplished with a *typicality index* calculation (see McLachlan [1992]) that measures the degree of agreement a suite of observed discriminants have with the earthquake and explosion populations. With the typicality index calculation, an event can be declared

- consistent with historical explosions,
- not consistent with historical earthquakes,
- consistent with explosions and earthquakes (indeterminate), or
- not consistent with either earthquakes or explosions (unidentified).

These declarations are technically defensible.

In the framework, a second source identification calculation is made that assumes only two possible decisions – earthquake or explosion (indeterminate and unidentified are not possible). Bayesian statistical methods can be used to calculate the P(earthquake | event data) and P(explosion | event data). Note again that these probabilities sum to one. One possible rule is to simply take the higher of the two probabilities as the source identification. The objective of this research was to determine some of the statistical properties Bayesian source identification calculations with simulated teleseismic discriminants *X* versus the corresponding standardized discriminants *Y*.

RESEARCH ACCOMPLISHED

A simulation was performed that emulates the first-order properties of teleseismic discriminants for earthquakes and explosions. The simulation represents the potential source populations for two discriminants e.g., mb versus Ms (denoted X_1), and a teleseismic spectral ratio discriminant (denoted X_2) (see Taylor and Marshall [1991]). A subset of the simulation is reported here. The explosion model used to simulate X_1 and X_2 had the centroid (0,0) and a covariance matrix $\begin{pmatrix} 1 & 0.6 \\ 0.6 & 1 \end{pmatrix}$. The earthquake model had the centroid (-2,-2) with a suite of covariance matrices $\begin{pmatrix} 1 & 0.2 \\ 0.2 & 1 \end{pmatrix}$, $\begin{pmatrix} 1 & 0.4 \\ 0.4 & 1 \end{pmatrix}$, $\begin{pmatrix} 1 & 0.6 \\ 0.6 & 1 \end{pmatrix}$ and $\begin{pmatrix} 1 & 0.8 \\ 0.8 & 1 \end{pmatrix}$.

First, using one of the earthquake/explosion model combinations above (the true explosion/earthquake models), 30 explosions and 300 earthquakes were simulated emulating the acquisition of teleseismic discriminant calibration data (X_1 and X_2). These calibration data were used to calculate the centroids (calibrated centroids) and a pooled covariance (calibrated covariance) for the explosion and earthquake models for data X_1 and X_2. The simulated calibration data were then converted to p-values from a Z-score. The Z-scores for the X_1 data are gotten by subtracting the calibrated explosion mean from the X_1 data and dividing by the standard deviation of X_1 from the calibrated covariance matrix. The p-value calculation for each data point X_1 is then the left tail probability of the standard Gaussian distribution (see Figure 2). Calculations are analogous for the X_2 data. With the p-value calculations, the explosion data for both X_1 and X_2 will have a histogram that is uniformly distributed and the earthquake data will have a distribution that is tightly packed near zero (see the left graphic in Figure 1). The calibration p-values are then transformed to standardized discriminants Y_1 and Y_2. These data are then used to calculate the centroids (calibrated centroids) and a pooled covariance (calibrated covariance) for the explosion and earthquake models for data Y_1 and Y_2. On completion of the calibration step, we have the models for source event identification with either teleseismic discriminants X_1 and X_2 or standardized discriminants Y_1 and Y_2.

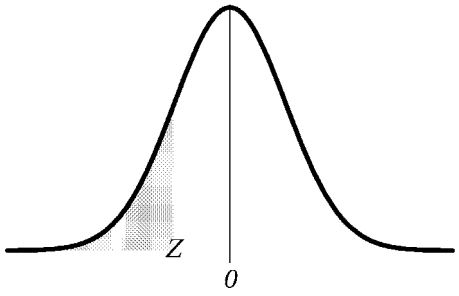

Figure 2. Graphical representation of p-value calculations from Z-scores for X_1 and X_2.

In the next step, 5000 explosions and 5000 earthquakes are simulated using the true earthquake/explosion models. These data emulate new events with associated teleseismic discriminants (X_1 and X_2). The standardized discriminants Y_1 and Y_2 are calculated from these data using the calibrated explosion means and the standard deviations from the calibrated covariance matrix – the calculations are exactly as those made with the calibration data step. It is these 5000 simulated explosions and 5000 simulated earthquakes that are used to compare the properties of X_1 and X_2 versus Y_1 and Y_2 in the Bayesian source identification calculation. For this simulation study, the larger of P(earthquake | event data) and P(explosion | event data) is taken as the source identification with both

the teleseismic discriminant data X_1 and X_2, and the standardized discriminants. With these simulated event data the probability of correctly identify an explosion (PD [=] probability of detection) and the probability of a false-alarm (FA [=] false-alarm probability) can be calculated, that is, the number of times an explosion is correctly identified divided by 5000 and the number of times an explosion is identified as an earthquake divided by 5000. *To compare the properties of Bayesian source identification with the two discriminants, we use the ratio FA/PD. In other words, this ratio is the false-alarms per detection, and the smaller this ratio the better.* The ratios FA/PD are reported in Table 1 for Bayesian source identification with simulated teleseismic discriminants and standardized discriminants. The true models used in the simulation are graphically represented in the top row. In all cases, using the standardized discriminants gives better false-alarm performance relative to explosion identification probability. This is consistent with the results observed in the full simulation.

Table 1. False-alarms per detection for simulated teleseismic discriminants and standardized discriminants. True models used to simulate teleseismic discriminants X_1 and X_2 are presented graphically in the first row. Ellipses for the models are 95% probability regions.

	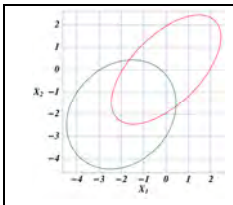	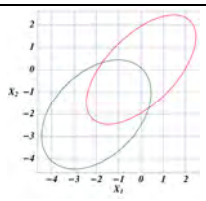	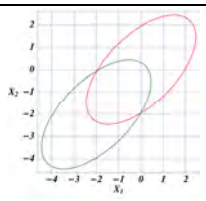	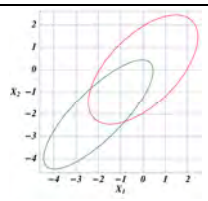
Simulated teleseismic discriminants	0.093	0.186	0.164	0.147
Standardized discriminants	0.040	0.121	0.090	0.073

CONCLUSIONS AND RECOMMENDATIONS

Conclusions are preliminary – theorems are not proven with simulations. However, we can conclude, based on simulations of statistical population behavior typical of some teleseismic discriminants, that standardized discriminants give improved operational performance over teleseismic discriminants, as measured by false-alarms per detection (FA/PD). Using p-values as discriminants has the advantage of unifying physical and statistical corrections into a single measurement. Therefore, in principle, p-values represent pure information about a seismic event source type. This is a compelling reason for using p-values as discriminants on its merits. The preliminary performance properties of p-values further supports p-values as seismic discriminants. Further research includes comprehensive simulations and potentially the development of mathematical arguments (theorems) that generalize this property of standardized discriminants.

REFERENCES

Anderson, D. N., D. K. Fagan, M. A. Tinker, G. D. Kraft and K. D. Hutchenson (2007). A Mathematical Statistics Formulation of the Teleseismic Explosion Identification Problem with Multiple Discriminants. to appear in *Bull. Seism. Soc. Am.*

Blandford, R. (1982). Seismic event discrimination. *Bull. Seism. Soc. Am.* 72: 69–87. DiPillo, P. (1976). The application of bias to discriminant analysis. *Communications in Statistics (Theory and Methods)* 5: 843–854.

Dumbgen, L. and L. Homke (2000). P-values for discriminant analysis. Preprint series A-00-14, Schriftenreihe der Institute fuer Informatik/Mathematik, University of Lubeck, Germany.

Freedman, R., R. Pisani, R. Purves, and A. Adhikari (1991). *Statistics*, Second Edition, W.W. Norton & Company Inc., New York.

Friedman, J. (1989). Regularized discriminant analysis. *Journal of the American Statistical Association*, 84:165–175.

Maharaj, E. (2000). Clusters of time series. *Journal of Classification*, 17:297–314.

McLachlan, G.J. (1992). *Discriminant Analysis and Statistical Pattern Recognition*. John Wiley & Sons, New York.

Pomeroy, P.W., W.J. Best, and T.V. McEvilly (1982). Test ban treaty verification with regional data–A review. *Bull. Seism. Soc. Am.* 72: S89–S129.

Smidt, R. and L. McDonald (1976). Ridge discriminant analysis. Technical Report 108, University of Wyoming, Department of Statistics, Laramie, Wyoming.

Stuart, A., K. Ord and S. Arnold (1994). *Kendall's Advanced Theory of Statistics: Volume 2A, Classical Inference and the Linear Model*, 6th Edition Arnold Publishers, London.

Taylor, S. and P. Marshall (1991). Spectral discrimination between Soviet explosions and earthquakes using short-period array data. *Geophys. J. Int.* 106:265–273.

DISCRIMINATION CAPABILITY FOR MINING EVENTS IN THE ALTAI-SAYAN REGION OF RUSSIA AND THE WESTERN UNITED STATES

Marie D. Arrowsmith[1], Stephen J. Arrowsmith[2*], Brian Stump[1], and Michael A. H. Hedlin[2]

Southern Methodist University[1] and University of California San Diego[2]

Sponsored by National Nuclear Security Administration
Office of Nonproliferation Research and Development
Office of Defense Nuclear Nonproliferation

Contract Nos. DE-FC52-03NA99510[1] and DE-FC52-03NA99511[2]

ABSTRACT

As more seismic and infrasound stations and arrays are deployed for nuclear explosion monitoring, catalogs of seismic events contain not only earthquakes, but many types of anthropogenic sources. Mining events are commonly recorded at regional distances by these stations, with the possibility of misidentification, (e.g., a legitimate mining explosion mistaken as nuclear). Additionally, a nuclear explosion could potentially be embedded in a mining explosion and be missed. Different discriminants have been utilized to separate mining events from natural seismicity with varying degrees of success. In this paper we present results of ongoing efforts to test several discriminants (amplitude ratios, time varying spectral analysis, time-of-day analysis, and infrasound) for two active mining regions: the Powder River Basin (PRB) in the western United States and the Altai-Sayan (AS) in Russia. The first phase of work on this contract has focused on using seismic and infrasound data in the PRB as a test bed for developing and assessing different mining explosion discriminants. This work is outlined in detail by Arrowsmith et al. (2006a, 2007). The results obtained indicate that phase amplitude discriminants, which have been found to be successful in separating earthquakes from nuclear explosions, do not separate earthquakes and mining explosions in this region, probably due to a combination of source and path effects. However, a time-varying spectral discriminant developed as part of this project was very successful at identifying the largest types of mining explosions (cast blasts). We also identified infrasound signals from large mining explosions in this region, suggesting good potential for the use of infrasound as an additional discriminant in this region when winds are favorable.

The AS region is the largest Russian exporter of coal, with over 26 surface coal mines in operation and events ranging from 60 to 700 tons in size. In cooperation with scientists at the Siberian Geophysical Survey, we compiled a catalog of 263 earthquakes and 843 probable mining events. Despite efforts to gather ground truth information on the mining events in the catalog, little is known about the blasting practices utilized for any of the assumed mining events in the database. Therefore, the criteria used in identifying events as either natural or manmade remain poorly defined. Based on the results of our analysis in the PRB, we applied similar techniques to the AS database to compare discrimination capability for purportedly comparable events. We selected two stations for our analysis: the International Monitoring System (IMS) station ZAL and Incorporated Research Institutions for Seismology (IRIS) station KURK. We selected 69 earthquakes and 260 mining events at ZAL and 41 earthquakes and 68 mining events at KURK for detailed analysis based on signal quality and first arrival picks. We performed a time-of-day analysis with respect to location by investigating daytime events versus nighttime events as a function of geographic location based on work by McCarthy et al. (2007). Daytime events clearly correlate with known mining locations, and earthquakes show a mix of both daytime and nighttime activity within the whole AS. Using the subset of data, we computed various amplitude ratios. There were no amplitude ratio discriminants at either station that clearly separated mining events from earthquakes, regardless of whether a distance correction (such as magnitude and distance amplitude corrections [MDAC]) was applied. Finally, we utilized time-varying spectral analysis. We applied multiple combinations of training parameters, but no combination of parameters successfully separated the two event classes in this region. Although these results are disappointing, they do not necessarily indicate that these two discriminants are ineffective for this region because the ground-truth information is insufficient to fully assess this capability. Based on experience in the PRB we review these findings and outline types of ground-truth information that would be required to fully assess discriminant capability for future studies of this type.

* Currently at Los Alamos National Laboratory

OBJECTIVES

This paper delineates research progress toward the following two objectives:

I. Continued Development of Discriminants and Application to the Testing Dataset in Wyoming

The first objective for this phase of our project was to continue the development of mining explosion discriminants, in particular the infrasound and amplitude discriminants, in conjunction with testing using the subset of data in Wyoming (see Arrowsmith et al., 2006, for more details on the dataset).

II. Application of Discriminants to a New Region: Altai-Sayan in Russia

The second objective for this phase of our project was to apply the seismic discriminants (time-frequency and amplitude ratios) to data from a different region with a different tectonic structure and different blasting practices. The purpose of this is to assess the portability of these discriminants to different regions.

RESEARCH ACCOMPLISHED

I. Powder River Basin in Wyoming, USA

In this paper we build on our previous paper (Arrowsmith et al., 2006c) with regard to the continued development of discriminants. There we described a time-frequency discriminant, which is applicable to either single stations or arrays, and applied it to the subset of data from Wyoming (Figure 1). The results showed that the time-frequency discriminant was very effective at distinguishing large open-pit mining explosions ("cast blasts") from earthquakes, but less successful at distinguishing smaller explosions. The method was found to successfully identify 97% of events in a blind test (comprising earthquakes and cast blasts). We also tested traditionally well-performing amplitude discriminants, such as high-frequency Pg/Lg, on regional phase amplitudes from both mining events and earthquakes near the PDAR seismic array. Initial results indicated that this is a poorly performing discriminant, evidenced by variability in Pg and Lg amplitudes for similar event types at high frequencies.

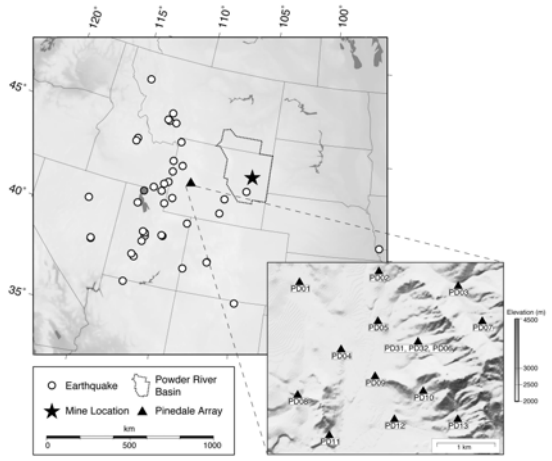

Figure 1. The PDAR seismic array (triangles) located in western Wyoming, USA. Circles represent the subset of earthquakes used in the 2006 study; the star represents locations of mining events that were analyzed.

Amplitude ratio discriminant

We have extended our investigation of the amplitude ratio discriminant in this region by considering additional earthquakes that lie along the path between the mine location and the PDAR array and by integrating a set of single-fired explosions detonated at the same mine in 1995 and 1997 (Stump et al., 2003), to ascertain whether or not path effects are affecting discrimination capability or whether the source types at this mine simply do not discriminate against background population. Figure 2 shows Pg/Lg (6–8 Hz) discriminant values for earthquakes and for different types of mining events (see Arrowsmith et al., 2006c, for a description of these types of events).

None of the event types discriminate from the earthquake population, which is particularly surprising for the single-fired events, which would be expected to be more explosion-like in terms of discrimination capability.

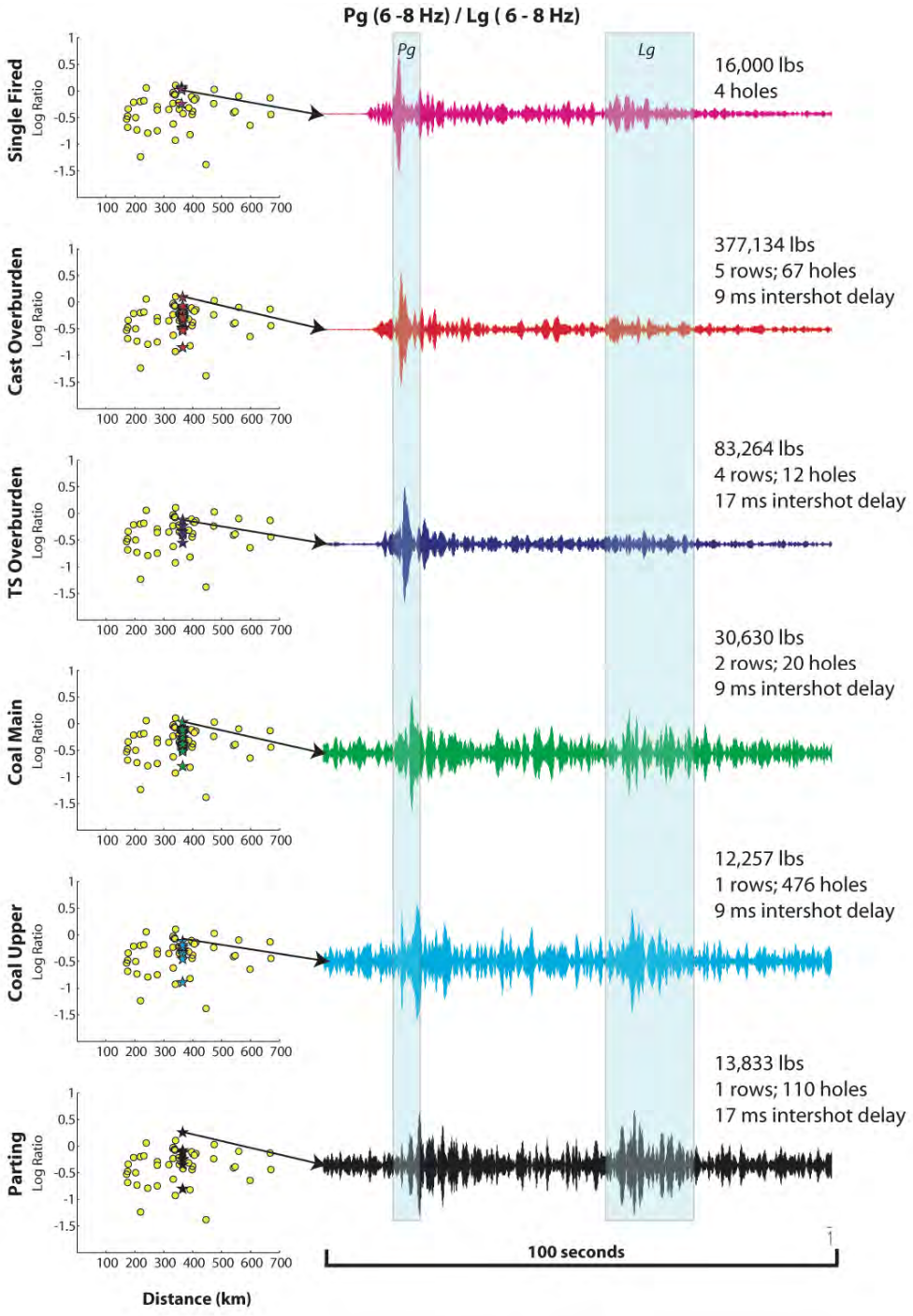

Figure 2. MDAC-corrected discriminant values at PDAR station PD31 (broadband vertical component) for six different types of mining events, as a function of distance. Waveforms for selected events are shown at the right, bandpass filtered in the 6–8 Hz band, with the Pg and Lg phase highlighted. Detonation information about the event is given as well.

In addition to investigating different mining event types, we have also looked at the uncorrected discriminant values for the earthquake population to determine if any regional trends emerged. Figure 3 shows earthquake Pg/Lg (6–8 Hz) Hz values as a function of location. Hotter colors indicate more explosion-like events, while cool colors show earthquake-like events. Those events on the path from the mine location (red square) and PDAR (yellow square) generally discriminate better from the explosions that traverse the same path—a promising conclusion. We are continuing to evaluate this problem by looking at additional regional stations that surround the mine at a variety of azimuths.

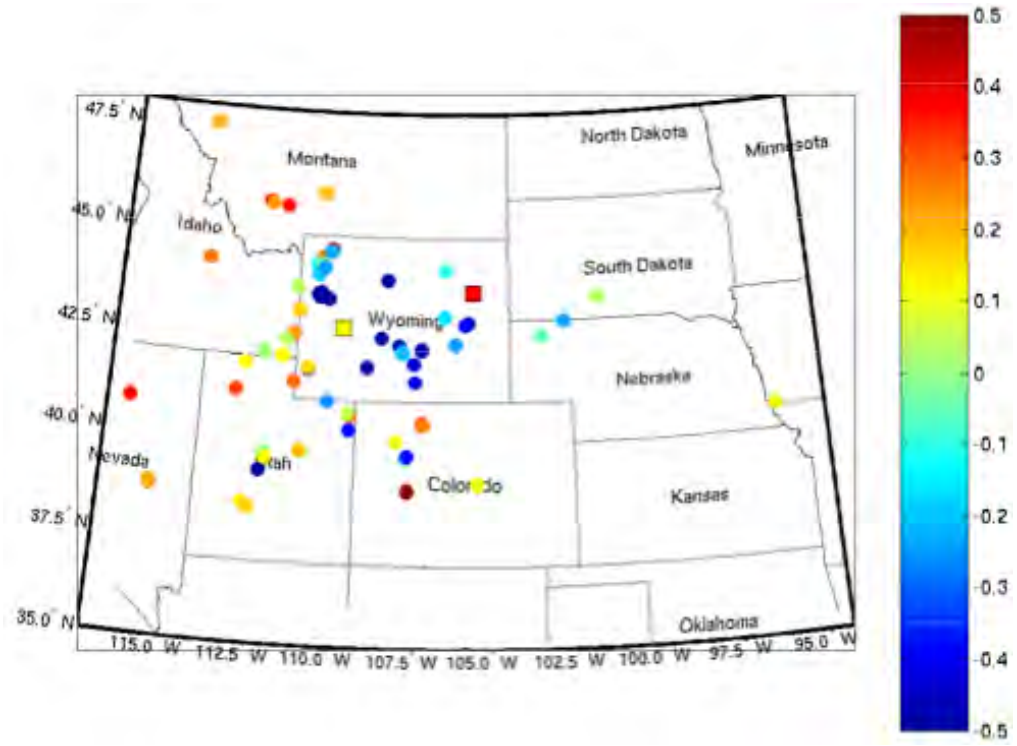

Figure 3. Uncorrected earthquake discriminant values (Pg/Lg (6–8 Hz)) at PDAR (yellow square) as a function of location. The mine location is indicated by the red square.

Infrasound discriminant

We have assessed the use of infrasound as a discriminant for mining explosions by studying the ability to detect infrasound signals from large ground-truth cast blasts at the PDIAR infrasonic array in Wyoming (Figure 4). We have also assessed the factors that influence the ability to detect mining explosions through a detailed noise analysis and propagation modeling. Unfortunately, we have found that PDIAR is a very noisy array (Figure 4) compared with typical levels of ambient infrasonic noise (Bowman et al., 2005). This implies that the potential for infrasound as a mining explosion discriminant must be reassessed for typical noise-level sites. However, we have developed a robust scheme for associating infrasound signals with known events (either through acquired ground-truth or seismically derived event bulletins). We have also observed four high-quality signals at PDIAR from mining explosions (out of a total of 32 events). The signals (Figure 5) are typically observed during summer months, when the wind directions are favorable and ambient noise levels are relatively low. The ray-tracing modeling backs up these observations by demonstrating that variations in atmospheric properties play an important role in whether or not we observe detections. However, although ambient noise levels and propagation modeling can explain most of the observations, they do not completely satisfy the observations. A further variable that we do not have any constraint on is the source size, and we speculate that this may explain the outlying observations, although un-modeled variations in atmospheric properties may also play a role.

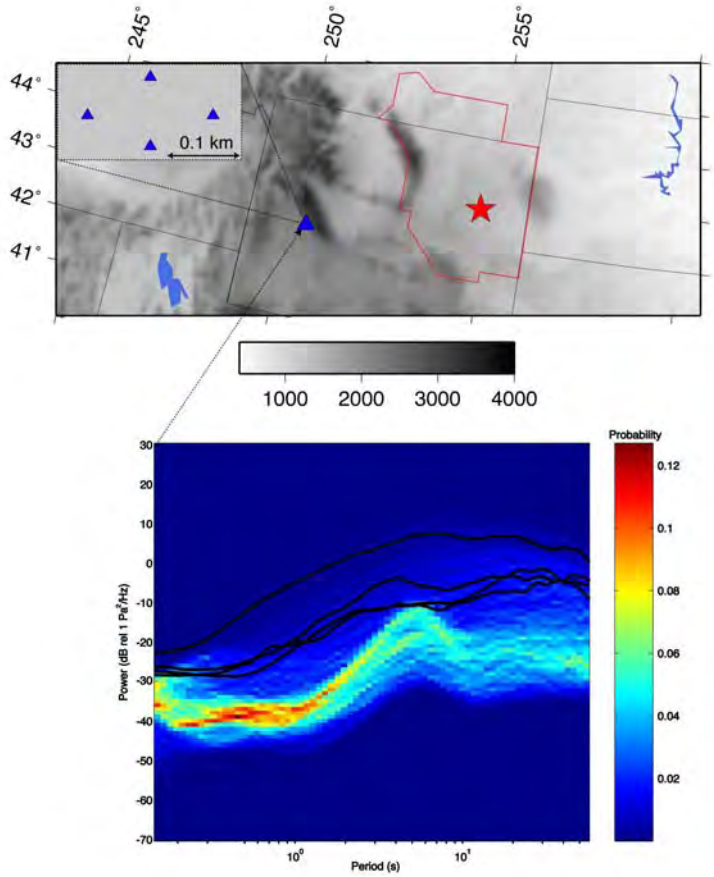

Figure 4. The PDIAR infrasound array. Top panel: Location of the PDIAR array (blue triangle) in relation to the location of the mine (red star) in the Powder River Basin (shown by the red line). The distance from the mine to the array is approximately 368 km. Bottom panel: Probability density function of the ambient noise power spectral density at PDIAR. The black lines show spectra of signals that were detected in the 1–5 Hz band.

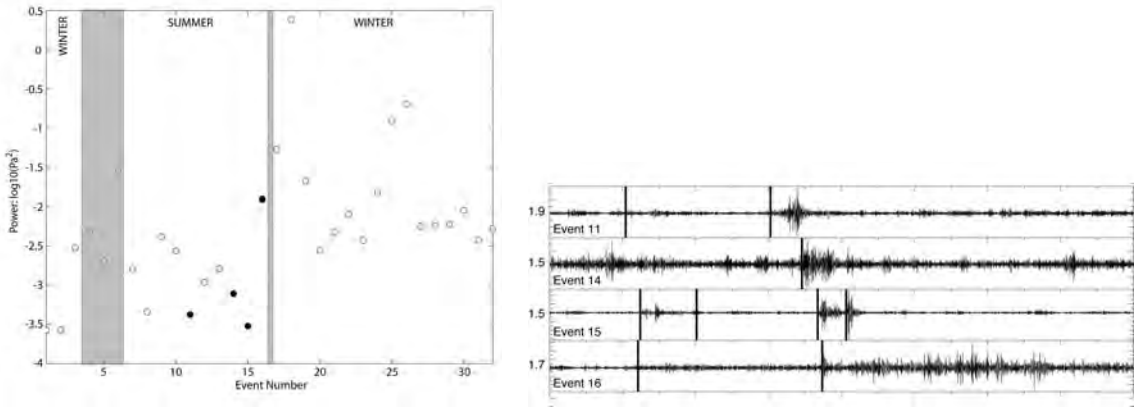

Figure 5. Infrasonic detections from cast blasts in Wyoming. Left panel: Detected shots (solid circles) and undetected shots (open circles) as a function of event number, which increases in relation to time. Gray regions indicate transitional months for stratospheric winds. Right panel: Beam-formed waveforms for the four high-quality detections (individual phase arrivals are denoted by solid vertical lines). The pre-event noise power is plotted on the vertical axis in both panels.

II. Altai-Sayan in Siberia, Russia

The AS (Figure 6) is an active mining region with numerous types of mines and quarries, including iron ore, zinc, copper, lead, molybdenum, bauxite, gold, and silver; this region is also Russia's top producer of coal. Approximately 40% of active surface coal-mines in Russia are in the AS. The region also has prevalence of natural seismicity due to the Asia-India collision zone to the south and the Baikal rift zone to the east. These factors make the region an ideal test bed for discrimination techniques designed to separate signals from earthquakes and mining explosions, including time-of-day analysis, amplitude ratios, and time-frequency analysis.

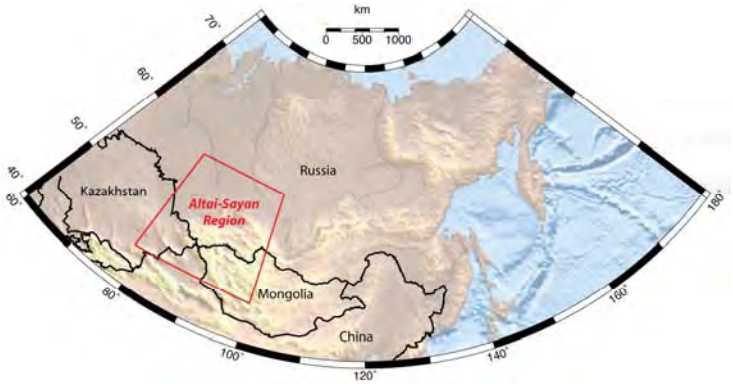

Figure 6. The Altai-Sayan region (red) is located in western Siberia and encompasses portions of Kazakhstan, Mongolia, and China. Subsequent figures of the Altai-Sayan region mirror the outlined area in this figure.

In order to assemble a database containing natural and mining-related events, we collaborated with scientists from the Altai-Sayans Seismological Expedition (ASSE), who provided us event lists (location, origin time, and m_b converted from Russian K class) of 263 probable earthquakes and 843 probable mining explosions. We were not provided the criteria for how ASSE seismologists classified event types. Literature reviews (e.g., Rautian and Leith, 2002) suggest that time-of-day criteria are most commonly used, but ASSE scientist Albina Filena (1999) notes that other methods are sometimes used, including surface wave analysis and comparison of the ratios of transverse to longitudinal waves.

The ASSE maintains a dense network of stations in the AS region, but due to various issues, we were unable to gain access to this data, and instead requested data from five seismic stations (ZAL, KURK, MAKZ, TLY, and BRVK) using the event catalogs provided to us by the ASSE. From these five stations, we gathered approximately 24,000 waveforms. For the study presented here, we discuss results from IMS station ZAL and IRIS station KURK. Station ZAL is a short-period three-component station that has known instrument response problems (see Acknowledgements section), so measurements relying on instrument-corrected data (such as amplitudes) should be given scrutiny. KURK is a three-component broadband station that has undergone various instrument response changes in the past ten years. A noise study (Arrowsmith, 2006b) at this station shows that noise amplitudes vary as a function of time, indicating there may be problems with the available instrument responses at this station as well.

Of the 263 earthquakes and 843 mining explosions for which we requested data from ZAL and KURK, we selected 329 events at ZAL (69 earthquakes and 260 mining events) and 109 events at KURK (41 earthquakes and 68 mining events) for further analysis. These waveforms were selected based on signal quality (no glitches or data dropouts, single event per waveform) as well as on the ability to pick a first arrival (i.e. signal-to-noise quality). Figure 7 shows distance distributions of the events, as well as event locations with respect to station location for this subset of events. All events are at regional or near-regional distances. The signal-to-noise ratio (SNR) of the data subset indicates that at ZAL, the SNR is greatest between frequencies of 1 and 8 Hz. At KURK, where event-station distances are greater, SNR quality is much lower. For the earthquake population, the best SNR is found between 1 and 4 Hz for all phases. For the mining events, the optimal frequency bands for analysis are between 1 and 8 Hz for all phases.

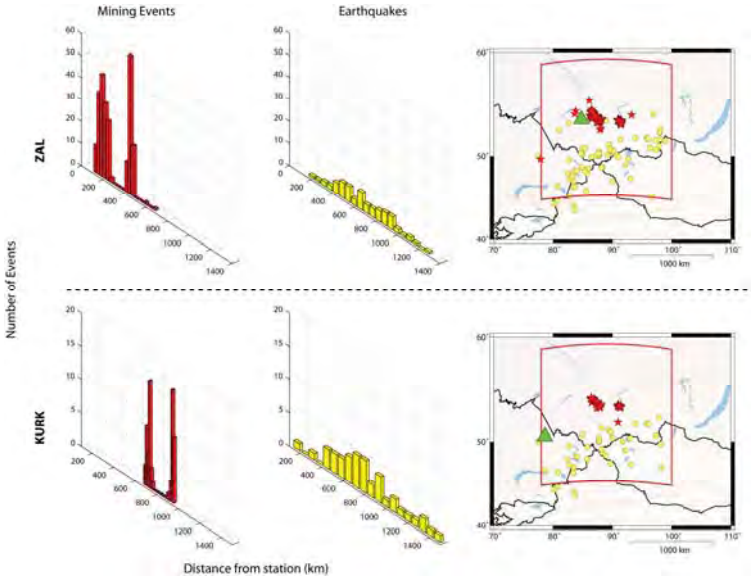

Figure 7. Distance and location distributions for selected events at ZAL (top panels) and KURK (bottom panels). Red events are probable mining events and yellow events are probable earthquakes. Station locations (right column) are noted as green triangles.

Time-of-day discriminant

In a region where we have limited ground truth, an important discriminant is the time-of-day information. While time-of-day information is not based on waveform metrics, it is a valuable criterion for providing information on the broad types of events that occur in specific regions. Analysis of time-of-day as a function of event location effectively outlines regions of mining activity (where the dominant percentage of daytime events occur in regions of known mine locations). Figure 8 shows the distribution of events with respect to month and hour for both mining explosions and earthquakes at ZAL and KURK. Mining events clearly occur during working hours, while the earthquakes exhibit no clear time-of-day dependence, providing confidence in the event bulletins supplied to us by the ASSE. These results also illustrate that time-of-day is not the sole criterion used by the ASSE in constructing the event bulletins, since the earthquakes also occur during working hours. A study such as that of MacCarthy et al. (2007), which utilizes time-of-day information in conjunction with satellite imagery and waveform cross correlation, could further provide constraints on anomalously timed events (e.g., several probable mining events in the total database, as classified by the ASSE, which occur at non-traditional working hours).

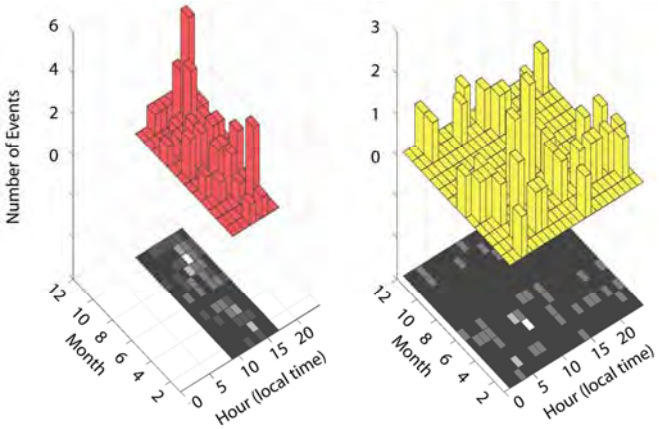

Figure 8. Time-of-day distribution with respect to month and hour of day for the ZAL/KURK data subset for both probable mining events (left) and earthquakes (right). Surface reflections of the histograms show trends, where lighter colors indicate larger numbers of events.

Amplitude ratio discriminant

In order to process the data for amplitude measurement, we measured the identified regional phases (Pn, Pg, Sn, and Lg) on the vertical components of both ZAL (short-period) and KURK (broadband) as well as on the radial and tangential components. We used a regional 1D velocity model of the AS as guidance for predicted phase arrival times. Picks were made on events where event signals could confidently be delineated above background noise levels after high passing the data at 1 Hz. The picked waveforms were instrument corrected to displacement (meters), demeaned, tapered (5% or 5-second taper, whichever is shorter) and bandpass filtered into six frequency bands commonly used for discrimination (0.5–1.0 Hz, 1.0 –2.0 Hz, 2.0–4.0 Hz, 4.0–6.0 Hz, 6.0–8.0 Hz, and 8.0–10.0 Hz). Root mean square and peak-to-peak amplitude measurements were made in velocity windows defined using the phase pick time as well as fast and slow group velocities for each phase.

We calculated amplitude ratios at both ZAL and KURK for various different discriminants (high frequency P to high frequency S and high frequency P to low frequency S). Figure 9 shows the result for two of these discriminants at ZAL and KURK. The two distinct mining trends, which are evident in Figure 7, can be seen prominently on each figure. The ratios for the mining explosions vary from between –2 to 2 for all discriminants; this trend overlaps with the earthquake populations. Although there are a few events that separate from the earthquakes, the majority of events do not discriminate well. At KURK, there seem to be more events that plot outside the earthquake trend, although with the limited number of earthquakes, it is difficult to assess whether the performance of the discriminant is truly better than the ZAL case.

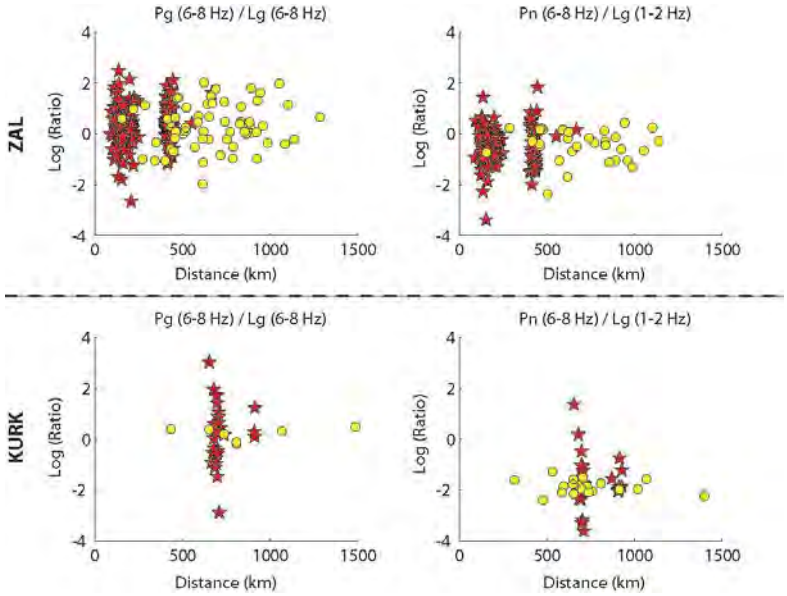

Figure 9. Uncorrected amplitude ratios measured at ZAL (top) and KURK (bottom) for probable mining explosions (red stars) and probable earthquakes (yellow circles). Data have been plotted as a function of distance for two different discriminants. Only data points with a SNR ratio of 2 have been plotted.

Time-frequency discriminant

We have applied the time-frequency discriminant to this region using data at both ZAL and KURK. The input parameters used in the method were trained to the dataset at each station using 1350 different input parameter combinations (see Arrowsmith et al., 2006c, for more details). The results indicate that the discriminant is successful for separating certain mining explosions from the general earthquake population at ZAL (Figure 10). However, the majority of mining explosions do not separate from the earthquake population at ZAL, and the discriminant is not successful at KURK. However, we note that the time-frequency discriminant only worked in the PRB for the largest event class, the cast blasts (Arrowsmith et al., 2006a). Without detailed ground truth on blast size, type and details of the timing sequence, it is difficult to fully assess the effectiveness of this discriminant in this region.

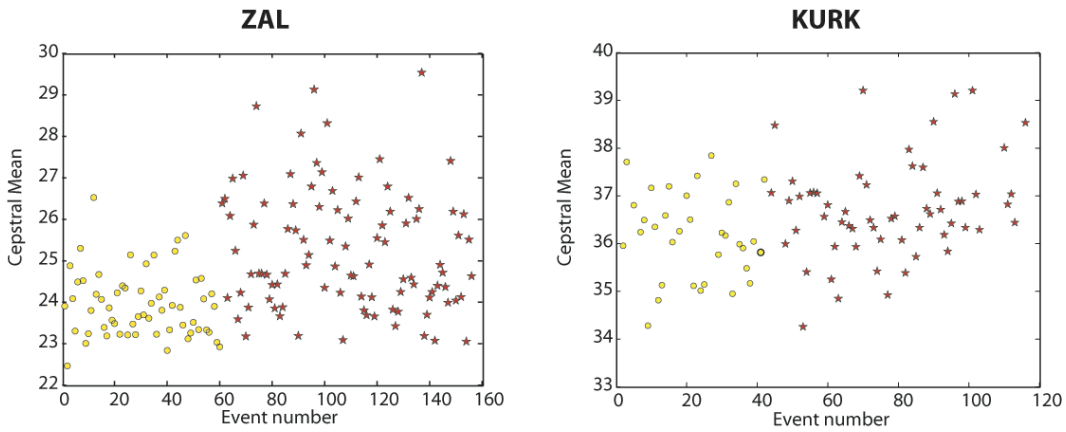

Figure 10. Time-frequency discriminant (cepstral mean) for ZAL (left) and KURK (right). Earthquakes are plotted as yellow circles and probable mining explosions as red stars.

CONCLUSIONS AND RECOMMENDATIONS

One of the main goals of this paper is to assess the effectiveness of existing mining explosion discrimination algorithms in the PRB and the AS region of Russia. Furthermore, we are interested in the comparison between the results obtained in these two regions, using a similar set of techniques. This comparison relates to the general problem of discriminant portability, whereby some discriminants are effective in certain regions but not in other regions.

The findings presented in the AS region are similar to those obtained in the PRB. Firstly, we observe that the amplitude ratio discriminants are not successful in separating mining explosion waveforms from those generated by earthquakes. These findings are also consistent with work by Jenkins and Sereno (2001) and Koch and Fah (2002), who found that the amplitude ratio discriminant was either ineffective, or ineffective for certain types of shots and/or certain stations. However, despite these findings, there is evidence that the amplitude ratio discriminant may be applicable to mining explosions in some regions (e.g., Kim et al., 1994). However, it is clear that the amplitude ratio discriminant is not as useful as it is for separating nuclear explosions from the earthquake population. In the PRB study, spectral ratios for the earthquakes showed a regional pattern with those earthquakes propagating along the same path as the observed explosions indicating some separation from the explosion data set.

We've concluded a preliminary study of infrasound generated by mine blasts in the PRB and found that given favorable winds and low station noise, an infrasound signal is often detected from large mining events, even though our monitoring station—PDIAR—was not optimally located for such a study. Given the limitations posed by the event-station geometry in our small study, we cannot draw firm conclusions regarding the utility of infrasound for ruling out a surface mine blast if a signal has not been detected under favorable conditions. Such a conclusion, perhaps employing more data collected in other areas and further research into wave propagation through our unsteady atmosphere, is needed.

Secondly, we observe that the time-frequency discriminant successfully separates some of the mining explosions from the earthquake population in both the AS and the PRB. In the PRB, we were able to show that the time-frequency discriminant separated 97.4% of a certain type of mining explosions (cast blasts) from the earthquake population (Arrowsmith et al., 2007). The cast blasts are much longer in time duration than the other mining explosions that might contribute to the success of time-frequency discriminant. However, in the AS we do not have detailed ground-truth information on the types of mining explosion. It is possible that the mining explosions that separate from the earthquake population in this region correspond to a particular blast type, but we do not have sufficient ground-truth information to check this.

During the course of this study we have encountered difficulties in obtaining detailed ground-truth information on mining explosions (as described above). This problem is common in certain countries and highlights the need to rely on secondary ground-truth information (e.g., time-of-day information and satellite imagery [MacCarthy et al., 2007]). However, for the purposes of fully assessing mining explosion discriminants, we have found that it is

necessary to obtain at least some minimal information directly from the mining operators, such as shot type and origin time. For more detailed studies, further information on shot properties, such as shot grid patterns, inter-shot and inter-row delay times, and yields are also useful. Despite the limitations of the ground truth acquired in the Russian component of the study, we have been able to provide some confidence in the bulletins through a detailed time-of-day analysis, and have been able to provide a preliminary assessment of discriminants that largely matches the results obtained in the PRB (Arrowsmith et al., 2006a).

ACKNOWLEDGEMENTS

We would like to thank Hans Hartse, who provided his scripts for plotting the time-of-day maps. Jonathan MacCarthy provided a draft of his Kazakhstan mining identification work, which was quite useful in validating our own results. The IRIS Data Management Center supplied data from KURK and PD31. Steve Beil of Arch Coal provided ground-truth data at the Wyoming mine and Michele Kelley at AFTAC graciously helped with providing us with PDIAR data. Finally, thanks to George Randall for invaluable station information.

REFERENCES

Arrowsmith, S. J., M. A. H. Hedlin, M. D. Arrowsmith, and B. W. Stump (2007). Identification of delay-fired mining events using seismic arrays: Application to the PDAR array in Wyoming, USA, *Bull. Seism. Soc. Am*. 97: 989-1001.

Arrowsmith, M. D. (2006b). A report on the quality of seismic amplitudes measured using broadband and short-period vertical component waveforms requested from the IRIS data archives, Los Alamos National Laboratory, LA-UR-06-6649.

Arrowsmith, S. J., M. D. Arrowsmith, M. A. H. Hedlin, and B. W. Stump (2006a). Discrimination of delay-fired mining events in Wyoming using an automatic time-frequency discriminant, *Bull. Seism. Soc. Am.* 96: 2368–2382.

Arrowsmith, S. J., M. D. Arrowsmith, M. D., M. A. H. Hedlin, and B. W. Stump (2006c). Discrimination of mining events using regional seismic and infrasound waveforms: Application to the US and Russia, in *Proceedings of the 28th Seismic Research Review: Ground-Based Nuclear Explosion Monitoring Technologies*, LA-UR-06-5471, Vol. 1, pp. 549–559.

Bowman, J.-R., G. E. Baker, and M. Bahavar (2005). Ambient infrasound noise, *Geophys. Res. Lett.* 32: doi:10.1029/2005GL022486.

Filina, A. G. (1999). Recognition of records from industrial explosions in the Altai-Sayan region, *Izvestiya*, *Physics of the Solid Earth* 35: 461–468.

Jenkins, R. D. and T. J. Sereno, Jr. (2001). Calibration of regional S/P amplitude-ratio discriminants, *Pure and Applied Geophysics,* 158: 1279–1300.

Kim, W. Y., D. W. Simpson, and P. G. Richards (1994). High-frequency spectra of regional phases from earthquakes and chemical explosions, *Bull. Seism. Soc. Am.* 84: 1365–1386.

Koch, K. and D. Fäh (2002), Identification of earthquakes and explosions using amplitude ratios; the Vogtland area revisited, *Pure and Applied Geophysics* 159: 735–757.

MacCarthy, J. K., H. E. Hartse, and C. A. Rowe (2007). Identifying repeating mine blasts in a sparse network using waveform cross-correlation and satellite imagery (in preparation).

Rautian, T. and W. Leith (2002). Composite regional catalogs of earthquakes in the Former Soviet Union, United States Geological Survey Open File Report 02-500.

Stump, B. W., D .C. Pearson, and V. Hsu (2003). Source scaling of contained chemical explosions as constrained by regional seismograms, *Bull. Seism. Soc. Am.* 93: 1212–1225.

CALIBRATION OF THE M_s(VMAX) TECHNIQUE IN EURASIA

Jessie L. Bonner[1], Michael E. Pasyanos[2], Michelle Johnson[1], and David G. Harkrider[1]

Weston Geophysical Corp.[1] and Lawrence Livermore National Laboratory[2]

Sponsored by National Nuclear Security Administration
Office of Nonproliferation Research and Development
Office of Defense Nuclear Nonproliferation

Contract Nos. DE-AC52-04NA25547[1] and W-7405-ENG-48[2]

ABSTRACT

We continue to develop and test the Matlab program EVALSURF, which estimates variable-period ($8 < T < 25$ sec) Rayleigh-wave magnitudes using the Russell (2006) and M_s(VMAX) measurement technique (Bonner et al., 2006a) for comparison to the historical formulas of Marshall and Basham (1972) and Rezapour and Pearce (1998). The program uses the updated Lawrence Livermore National Laboratory (LLNL) group velocity models (Pasyanos, 2005) to identify, phase match filter, and extract the fundamental mode Rayleigh waves for analysis. During the past year, we have used EVALSURF to 1) estimate the surface wave magnitudes for the 9 October 2006 North Korean event, 2) examine the effects of large sedimentary basins on surface wave magnitudes, and 3) estimate surface wave magnitudes to periods as great as 40 seconds.

We applied the EVALSURF (Bonner et al., 2006b) technique to the surface waves generated by the reported nuclear explosion detonated in North Korea on 9 October 2006. We feel confident that Rayleigh waves were observed at 12 stations at distance up to 40 degrees. The M_s (VMAX) technique estimates a surface wave magnitude of 2.94 with interstation standard deviation of 0.17 magnitude units (m.u.). We found this estimate to be slightly above the Murphy et al (1997) event screening value (which is M_s=2.90) for an International Data Center (IDC) m_b of 4.1. If the m_b is indeed accurate, this could suggest a convergence of the populations at small magnitudes (Stevens and Day, 1985); however, Bonner et al. (2006a) saw no evidence of the convergence at the Nevada Test Site for events of similar and smaller m_b. We examined the three-component records at each station and found no conclusive evidence that Love waves were generated and recorded.

When Russell (2006) developed the surface wave magnitude formula used in EVALSURF, he used a single attenuation relationship derived from a North American dataset (Herrmann and Mitchell, 1975). Questions arose as to whether this formula would be valid for paths through large sedimentary basins where short-period ($T < 20$ sec) attenuation was much higher than the model used to develop the magnitude formula. We have applied EVALSURF to Rayleigh waves recorded at stations just before and immediately after propagating through the thick sediments of the South Caspian Basin. There is less than 0.1 m.u. difference between the M_s(VMAX) estimates before and after the basin. These results do not support large differences in the M_s(VMAX) magnitudes due to propagation through thick basins.

We have also increased the upper limit of periods used in the EVALSURF technique from 25 to 40 sec. The results of a pilot study using the extended period range suggest that the longer-period surface wave analysis improved earthquake screening for deep (>35 km) events. We used the Murphy et al. (1997) criterion and screened 96%, 80%, and 78% of the earthquakes using extended-period EVALSURF, Marshall and Basham, and Rezapour and Pearce formulas, respectively.

OBJECTIVES

Developing a methodology for calculating surface wave magnitudes that is valid at both regional and teleseismic distances, applicable to events of variable sizes and signal-to-noise ratios, calibrated for variable structure and propagation, and easy to automate in an operational setting, is an important monitoring goal. Our objectives are to create such a methodology, and to use it to lower M_s estimation and detection thresholds. We hope that the method will provide a seamless tie between M_s estimation at regional and teleseismic distances.

We continue to develop and test the Matlab program EVALSURF (Bonner et al., 2006b), which estimates variable-period ($8 < T < 25$ sec) Rayleigh-wave magnitudes using the Russell (2006) and M_s(VMAX) measurement technique (Bonner et al., 2006a) for comparison to the historical formulas of Marshall and Basham (1972) and Rezapour and Pearce (1998). The program uses the updated LLNL group velocity models for Eurasia (Pasyanos, 2005) to identify, phase match filter, and extract the fundamental-mode Rayleigh waves for analysis. During the past year, we have used EVALSURF to 1) estimate the surface wave magnitudes for the 9 October 2006 North Korean event, 2) examine the effects of large sedimentary basins on surface wave magnitudes, and 3) estimate surface wave magnitudes to periods as great as 40 sec.

RESEARCH ACCOMPLISHED

Updates to Group Velocity Models

We have updated LLNL group velocity maps (Pasyanos, 2005) for southern Asia using new data recorded at several stations in the region. Rayleigh-wave dispersion curves (at periods of 10 sec and greater) were generated and included in a new tomographic inversion. The tomographic inversions for southern Asia at T=15 and T=30 seconds are shown in Figure 1. The results highlight the Indian shield region as relatively fast compared to the slower regions associated with the Himalayas and Bay of Bengal.

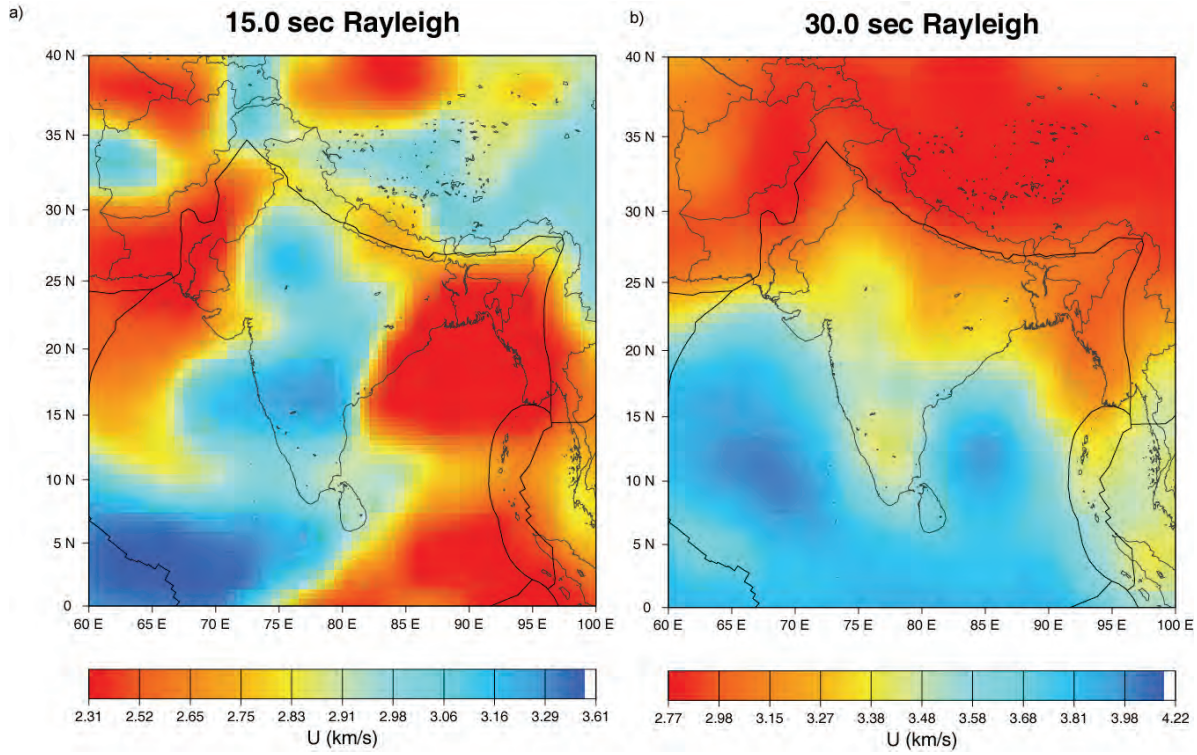

Figure 1. Tomographic inversion of Rayleigh wave group velocity in southern Asia for a) T=15 and b) T=30 seconds.

9 October 2006 North Korean Event

We applied the EVALSURF technique to the short-to-intermediate period surface waves generated by the reported nuclear explosion detonated in North Korea on 9 October 2006.

Data. The Incorporated Research Institutions in Seismology (IRIS) dedicated a data download page to this event. We requested the SEED format data for stations within 40 degrees of the reported epicenter from the dedicated IRIS web page. After we downloaded the data, we converted it to seismic analysis code (SAC) format. We then used the SAC "transfer from evalresp" option to correct for the instrument response and convert to displacement in nanometers. Data from KSRS were obtained from the US National Data Center and were corrected to displacement using the frequency/amplitude/response file. All horizontal components were rotated to the great circle azimuth. Examples of the data for the closest station (MDJ) are shown in Figure 2. At this distance (~370 km), there is a large amplitude Rayleigh wave arrival observed on the radial and vertical components. There was no significant Love wave energy in the surface wave analysis window.

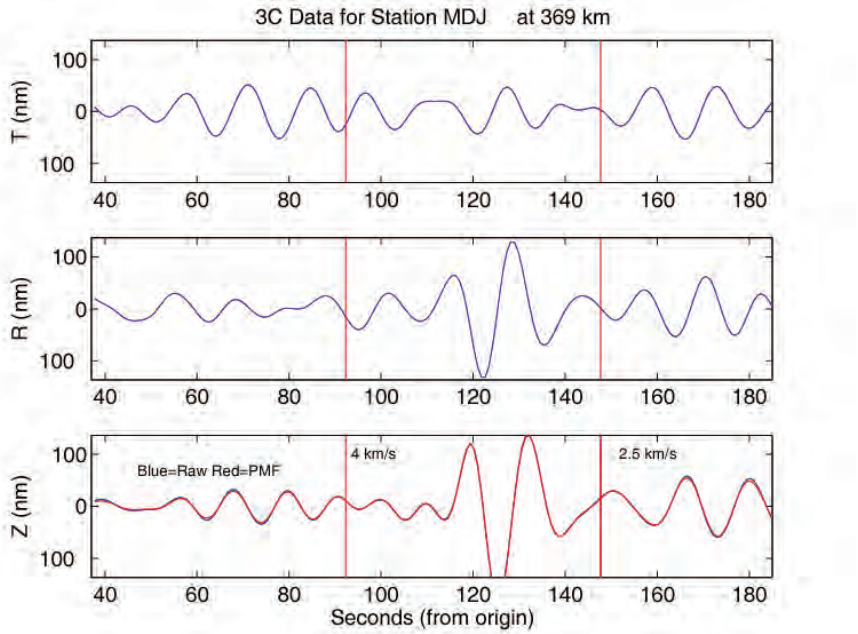

Figure 2. Three component seismograms, rotated to the true back azimuth, from the North Korean event recorded at MDJ. Both the phase match filtering (red) and raw (blue) seismograms are shown in the lower subplot.

***M*$_s$(VMAX) Analysis.** Russell (2006) developed a time-domain method for measuring surface waves with minimum digital processing, using zero-phase Butterworth filters. The method can effectively measure surface-wave magnitudes at both regional and teleseismic distances, at variable periods between 8 and 25 sec.
For applications over typical continental crusts, the magnitude equation is:

$$M_{s(b)} = \log(a_b) + \frac{1}{2}\log(\sin(\Delta)) + 0.0031\left(\frac{20}{T}\right)^{1.8}\Delta - 0.66\log\left(\frac{20}{T}\right) - \log(f_c) - 0.43, \qquad (1)$$

where a_b is the amplitude of the Butterworth-filtered surface waves (zero-to-peak in nanometers) and $f_c \le \frac{0.6}{T\sqrt{\Delta}}$ is the filter frequency of a third-order Butterworth band-pass filter with corner frequencies $1/T$-f_c and $1/T$+f_c. Examples of the filters for the surface waves at MDJ are shown in Figure 3. At the reference period T=20 seconds, the equation is equivalent to Von Seggern's formula (1977) scaled to Vaněk et al. (1962) at 50 degrees. For periods $8 \le T \le 25$, the equation is corrected to T=20 seconds, accounting for source effects, attenuation, and dispersion.

We refer to this technique as M_s(VMAX) for Variable-period, MAXimum amplitude magnitude estimates. The method has been extensively tested in the western United States and Eurasia (Bonner et al., 2006a). The magnitudes estimated for MDJ are shown in Figure 4 as a function of the evaluation period. Note how the excitation corrections in the Russell (2006) formula work well to flatten the Rayleigh-wave spectra at this particular station. The magnitude at the period of largest amplitude is recorded—in this case 2.77—for further use. EVALSURF also calculates Marshall and Basham (1972) and Rezapour and Pearce (1998) magnitude estimates at each station.

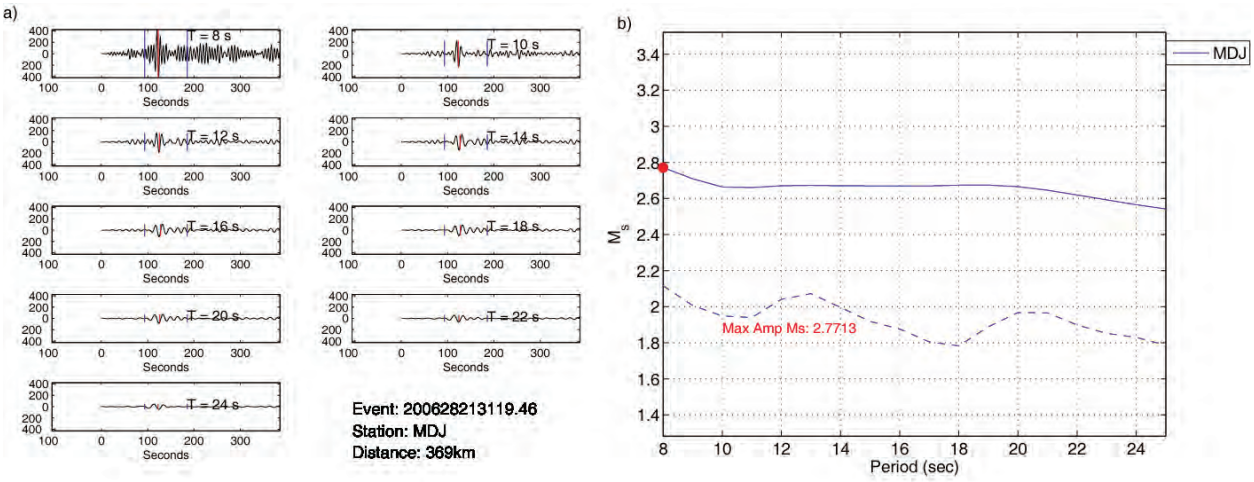

Figure 3. EVALSURF processing of the MDJ seismograms from the North Korean event. a) Narrow-band filtering for the North Korean event recorded at MDJ. b) Magnitude "spectra" estimated using M_s(VMAX) for the MDJ vertical component.

Magnitude Estimates. The results of the EVALSURF analysis for IRIS stations within 40 degrees of the North Korean event are summarized in Table 1 and Figure 4. We feel confident that Rayleigh waves were observed at INCN, ENH, TLY, HIA, BJT, MDJ, ERM, MAJO, and KS31. We also believe we observe longer period (>20 sec) surface waves at MKAR, LSA, and CHTO. We were unable to identify Rayleigh waves at NACB, YULB, YAK, MA2, YSS, and PET; however, we did calculate a noise-based M_s(VMAX) at each of these stations (Figure 4). A few other stations were available from IRIS in the regional distance range; however, there were instrument response problems that could not be resolved.

Table 1. M_s(VMAX) Results for the 09 October 2006 North Korean event.

Station	Distance (deg)	Period	*Ms*(VMAX)
MDJ	3.32	8	2.77
KS31	3.98	10	2.71
INCN	4.28	10	2.85
MAJO	8.53	20	2.82
BJT	9.92	12	3.16
HIA	10.33	8	2.97
ERM	10.53	11	2.93
ENH	19.31	13	3.2
TLY	20.26	15	3.23
LSA	32.76	23	2.91
MKAR	33.67	23	2.81
CHTO	34.14	20	2.89

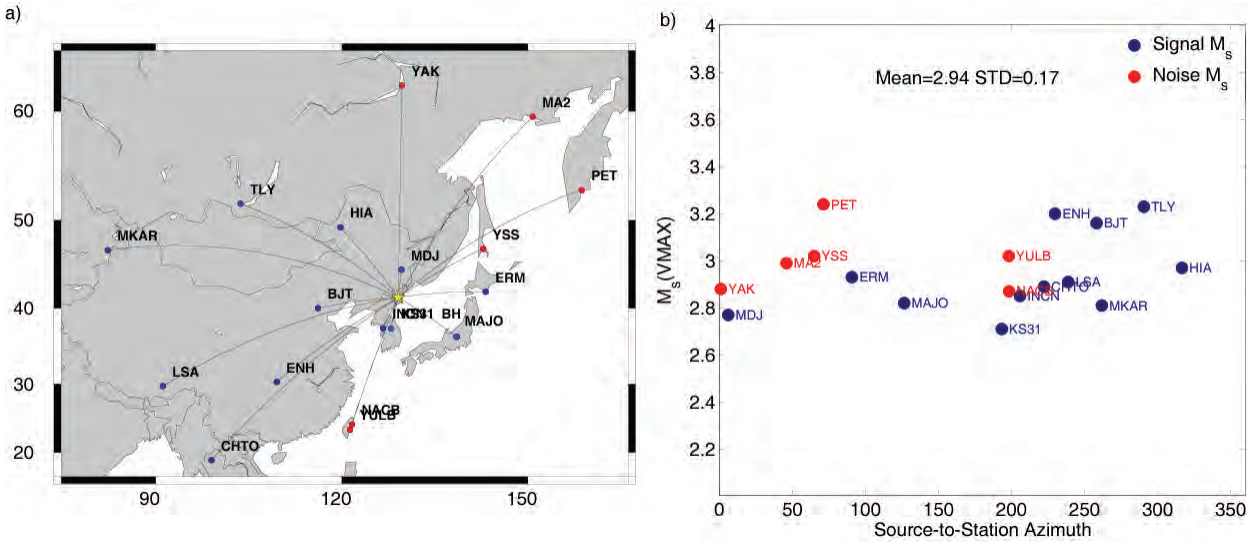

Figure 4. Signal- and noise-based M_s(VMAX) estimates for the 9 October 2006 North Korean event. a) Map of stations showing where noise-based (red circles) and signal-based (blue circles) surface wave magnitudes were estimated. b) Station magnitudes show a network average of 2.94, which considers only signal-based (blue) measurements.

The United States Geological Survey (USGS) and International Data Center (IDC) reported body wave magnitudes (m_b) of 4.2 and 4.1 respectively. The M_s(VMAX) estimates a network surface wave magnitude of 2.94 with interstation standard deviation of 0.17 m.u. We compared these data to our previous research (Figure 5) and found this estimate is slightly above the Murphy et al (1997) event screening value (which is M_s=2.90) for an IDC m_b of 4.1. If the m_b is indeed accurate, this could suggest a convergence of the populations at small magnitudes (Stevens and Day, 1985); however, Bonner et al. (2006a) saw no evidence of the convergence at the Nevada Test Site for events of similar and smaller m_bs. We note that three large magnitude estimates, at stations EHN, BJT, and TLY, are from similar back azimuths and are clearly separated from the other stations' estimates (see Figure 5). Future work must determine whether these larger estimates are due to source processes, un-modeled attenuation effects in Eq. 1, or instrument response problems.

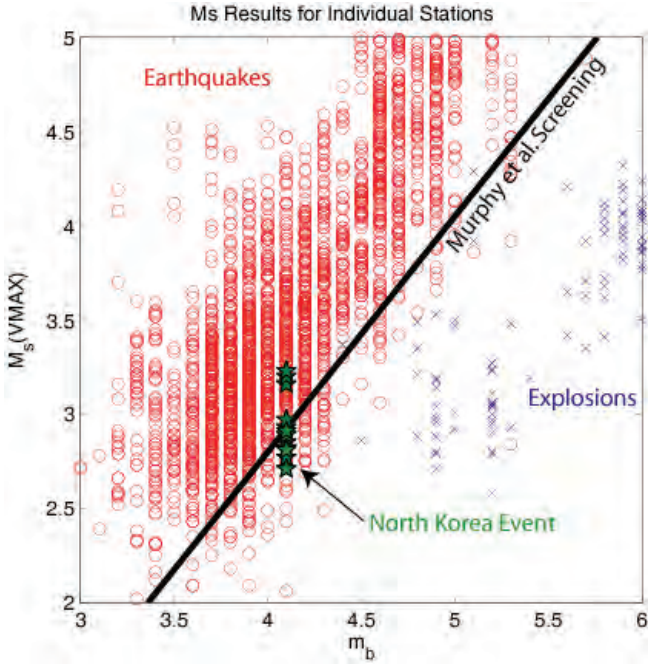

Figure 5. The North Korean event has an average M_s(VMAX) that falls slightly above the Murphy et al. (1997) screening line. The m_bs are from the IDC.

M_s(VMAX) Evaluation in the Caspian Basin

When Russell (2006) developed the surface wave magnitude formula (Eq. 1) used in EVALSURF, he used a single attenuation relationship derived from a North American dataset (Herrmann and Mitchell, 1975). Questions arose as to whether this formula would be valid for paths through large sedimentary basins where short-period (T <20 sec) attenuation was much higher than the model used to develop the magnitude formula. To address this possible problem, we have quantified the M_s(VMAX) performance in a thick sedimentary basin using a dataset recorded in the mid-1990s around the Caspian Sea (Priestley and Mangino, 1995). Two of their stations, KAT and LNK (Figure 6), were on the same great circle paths for several large earthquakes recorded during the deployment. The stations were uniquely positioned on the edges of the South Caspian Basin, which is one of the thickest sedimentary basins on earth with 15–25 km of unconsolidated sediments that overlie 10–15 km of oceanic crust (Neprechnov 1968; Rezanov and Chamo, 1969).

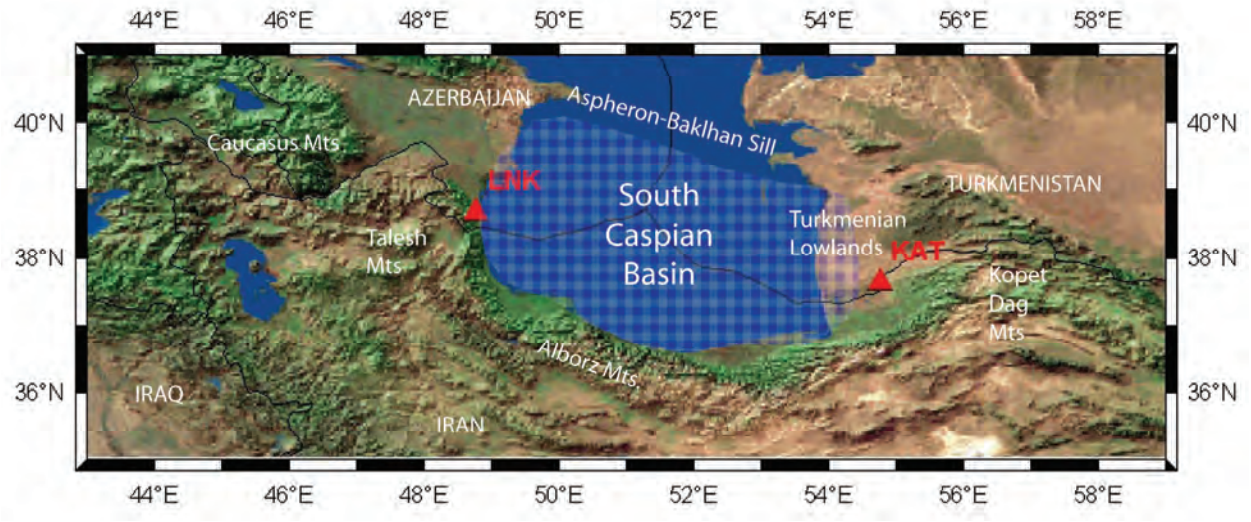

Figure 6. Map showing the South Caspian Basin and the locations of temporary seismic stations LNK and KAT. The checkered region shows where suspected "oceanic" crust underlies the South Caspian Basin based on previous deep seismic sounding data.

Figures 7a and b show vertical component seismograms for two earthquakes whose epicenters lie on the same great circle path as KAT and LNK. The data have been filtered between 0.01 and 0.1 Hz to highlight the surface waves. The pair of seismograms on the left show surface waves propagating from the west to the east from an m_b=5.6 earthquake along the Central Mid-Atlantic Ridge over 8900 km from station LNK. The pair on the right shows surface waves that are traversing from east to west from an m_b=5.6 epicenter in the Java Sea over 7700 km from station KAT. Each subplot has the same amplitude scale and shows data between group velocities of approximately 5 km/sec and 2 km/sec.

We estimated M_s(VMAX) for our dataset of earthquakes recorded at both KAT and LNK along the same great circle path (Figures 7c and d). The difference between the M_s(VMAX) estimates measured before and after propagating through the basin is less than 0.1 magnitude unit (m.u.) for four different earthquakes. For three of four events, the magnitude estimated for surface waves exiting the basin are ~0.1 m.u. smaller than the before-basin magnitude.

These results do not support large differences in the M_s(VMAX) magnitudes due to propagation through this basin. The observed differences of < 0.1 m.u. are smaller than the typical standard deviation from a network analysis, which is generally >0.2 m.u. (Bonner et al., 2006b). Note that the differences in the magnitudes for the two stations do not increase significantly at shorter-periods in the analysis. The small differences in the magnitudes are significant because the Q model in this basin (Priestley et al., 2001) is very different from the period-dependent Q models (Herrmann and Mitchell, 1975) used to develop the Russell (2006) equation.

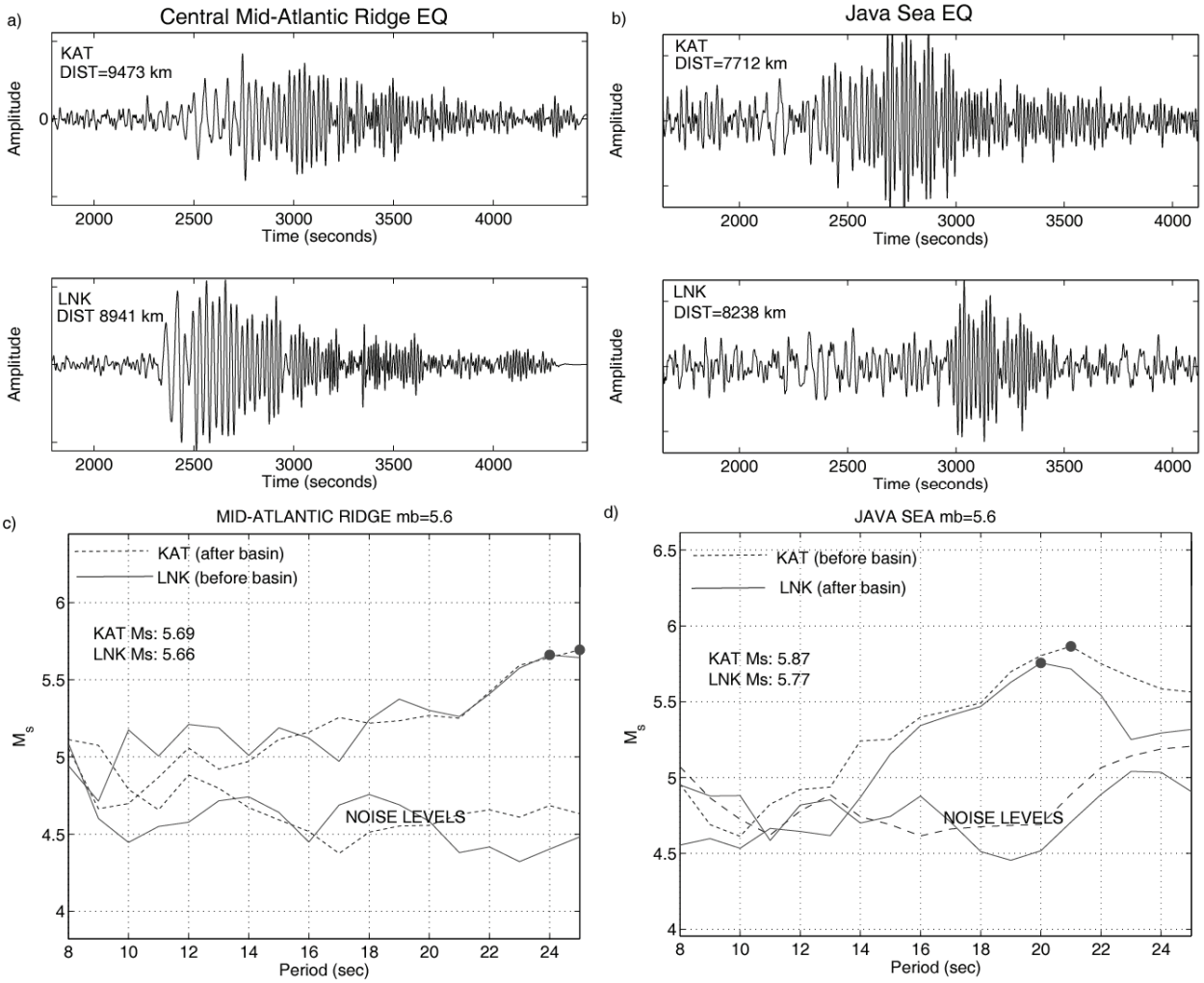

Figure 7. Examples of earthquakes recorded at stations KAT and LNK before and after propagating through the South Caspian Basin for events along the Mid-Atlantic Ridge (a) and Java Sea (b). The data have been filtered between 0.01 and 0.1 Hz to highlight the fundamental-mode Rayleigh waves. M_s(VMAX) "spectra" for the Mid-Atlantic Ridge (c) and Java Sea (d) earthquakes as recorded at KAT and LNK. The magnitudes estimated using the maximum amplitude surface waves before and after traversing the South Caspian Basin agree within 0.1 m.u. despite the anomalously thick sedimentary section in the basin.

Extending M_s(VMAX) to 40 Seconds Period

We observed an edge effect associated with ending the surface-wave magnitude analysis at 25 sec (Bonner et al., 2006a). There are two explanations for this behavior. The Rayleigh wave spectral shape from earthquakes tends to favor longer periods when the events are deeper than the crust. In addition, we expect to observe a general trend of longer period measurements with increasing distances due to the nature of surface wave propagation. This trend is related to the rapid attenuation of shorter-period amplitudes compared to the longer periods at larger epicentral distances.

We are currently working to calibrate the Russell (2006) formula and M_s(VMAX) technique to periods up to 40 sec in order to determine whether the variance can be further reduced and event screening improved. To complete this task, we have determined that the terms in Eq. 1 are valid up to 40 sec including the source excitation dependence on period (-0.66 log (20/T)). To examine the performance at these periods, we compiled a dataset of

surface wave recordings from events with a wide range of focal depths. Figure 8 shows our pilot study dataset, which so far includes 26 earthquakes in a small region of the Philippine subduction zone with depths ranging from 10 to 155 km as recorded on seven far-regional to near-teleseismic stations. Data from these stations and events were obtained from IRIS, corrected for the instrument response, converted to displacement in nm, and analyzed with EVALSURF extended to 40 seconds period.

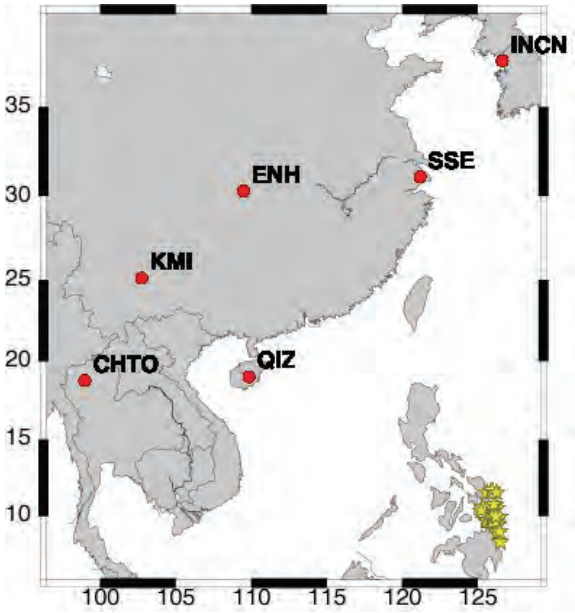

Figure 8. Pilot study database used for extending M_s(VMAX) to 40 seconds period. Thus far, we have analyzed 26 events with depths ranging from 10 to 155 km on seven stations at near-teleseismic distances.

We plotted m_b-M_s(VMAX) in Figure 9 to show how the discriminant is affected by focal depth. Increased depth causes the surface wave magnitudes to decrease faster than the m_b resulting in greater separation between the two magnitudes. This leads to possible contamination with the explosion population.

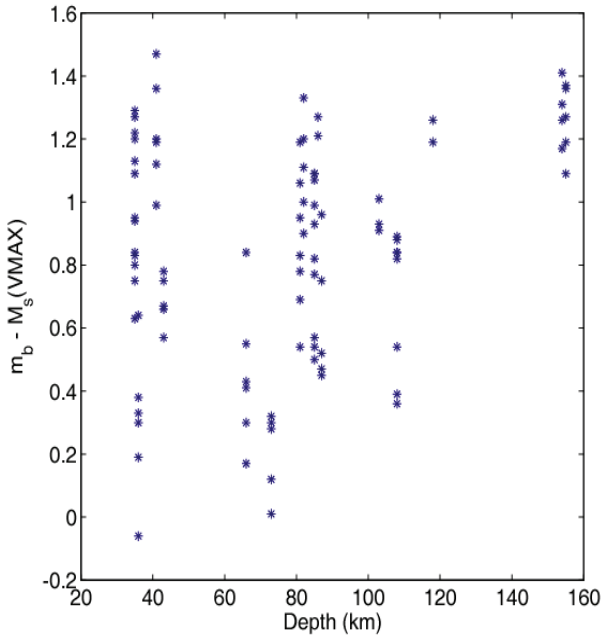

Figure 9. Depth effects on the m_b-M_s(VMAX) discriminant for the events shown in Figure 8.

In addition to M_s(VMAX), we estimated Marshall and Basham (1972) and Rezapour and Pearce (1998) magnitudes for each station-event pair (Figure 10). The data were plotted versus IDC m_b and evaluated against the Murphy et al. (1997) screening criterion. We calculated the number of earthquake M_s estimates that fell below the screening line,

which were labeled as improperly screened, and tabulated them in each subplot. The results show that the M_s(VMAX) method has the fewest earthquakes that could not be screened. Only 4% of the individual station measurements fell below the Murphy et al. (1997) screening line, and after the network magnitudes were formed, none were incorrectly screened. This is in contrast to the Marshall and Basham (1972) and Rezapour and Pearce (1998) magnitudes which did not perform earthquake screening as well as M_s(VMAX), particularly on these deeper events.

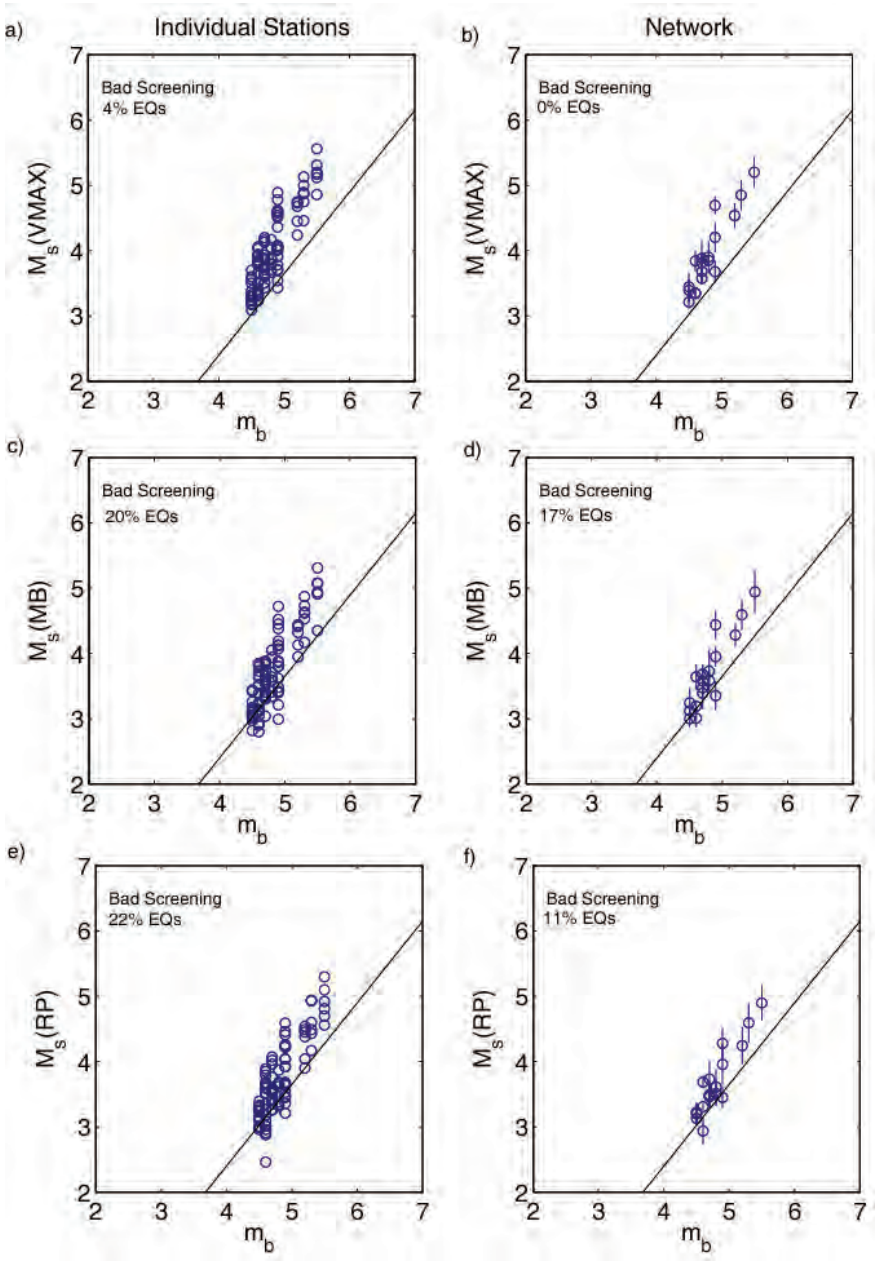

Figure 10. M_s versus m_b for a set of earthquakes in the Philippine subduction zone (10-155 km depth). Individual station M_s estimates are shown in a) M_s (VMAX) c) Marshall and Basham and e) Rezapour and Pearce. Network magnitudes are shown in b) M_s (VMAX) d) Marshall and Basham and f) Rezapour and Pearce. The solid black line is the Murphy et al. (1997) screening line.

CONCLUSIONS AND RECOMMENDATIONS

The variable-period surface wave magnitude M_s(VMAX) continues to provide a better and more consistent estimate of source size, particularly for smaller events and at shorter distances. During the past year, we estimated the 9 October 2006 North Korea event's surface wave magnitude as 2.94 with interstation standard deviation of 0.17 m.u. This magnitude was high relative to the reported m_b, resulting in the only explosion we have analyzed with network M_s(VMAX) that does not fall below the Murphy et al. (1997) screening line. Also during the past year, we have shown that estimates of M_s(VMAX) do not vary considerably (<~0.1 m.u) on opposite sides of the thick, highly attenuative sediments of the South Caspian Basin. Finally, preliminary results of extending the M_s(VMAX) method to 40 seconds shows improved event screening for deeper events. We do note that application of the M_s(VMAX) method to 40 seconds is limited. For small deep events, the longer period surface waves are difficult to observe above the background noise, and will most likely be screened based on depth phases or hypocentral location techniques.

ACKNOWLEDGEMENTS

We thank David Russell and Jon Creasey for insightful contributions to EVALSURF and this research. We also wish to thank IRIS for some of the data used in this research project.

REFERENCES

Bonner, J. L., D. Russell, D. Harkrider, D. Reiter, and R. Herrmann (2006a). Development of a Time-Domain, Variable-Period Surface Wave Magnitude Measurement Procedure for Application at Regional and Teleseismic Distances, Part II: Application and Ms-mb Performance, *Bull. Seism. Soc. Am.* 96: 678–696.

Bonner, J. L., M. Pasyanos, M. Leidig, H. Hooper, and D. Harkrider, (2006b). A comparison of different surface wave magnitude measurement procedures on a Eurasian dataset, in *Proceedings of the 28th Seismic Research Review*: Ground-Based Nuclear Explosion Monitoring Technologies, LA-UR-06-5471, Vol. 1, pp. 560–569.

Herrmann, R. B., and B. J. Mitchell (1975). Statistical analysis and interpretation of surface wave anelastic attenuation data for the stable interior of North America, *Bull. Seism. Soc. Am.* 65: 1115–1128.

Neprochnov, Y. P. (1968). Structure of the earth's crust in epi-continental seas: Caspian, Black, and Mediterranean, *Can. J. Earth. Sci.* 5: 1037-1043.

Marshall, P. D. and P. W. Basham (1972). Discrimination between earthquakes and underground explosions employing an improved Ms scale, *Geophys. J. R. Astr. Soc.* 29: 431–458.

Murphy, J. R., B. W. Barker, and M. E. Marshall, (1997). Event screening at the IDC using the *Ms/mb* discriminant. *Maxwell Technologies Final Report.* 23 p.

Priestley, K. and S. Mangino (1995). Seismic studies of the Caspian Basin and surrounding regions. *Final Report. PL-TR-95-2154.* 73 p.

Priestley, K. H. J. Patton, and C. A. Schultz (2001). Modeling anomalolus surface wave propagation across the Southern Caspian Basin. *Bull. Seism. Soc. Am*. 91: 1924–2001.

Pasyanos, M. E. (2005). A variable-resolution surface wave dispersion study of Eurasia, North Africa, and Surrounding Regions, *J. Geophys. Res.* 110: B12301.

Rezanov, I. A. and S. S. Chamo, (1969). Reasons for absence of a granitic layer in the basins of the South Caspian and Black Sea type. *Can. J. Earth Sci*. 6: 671–678.

Rezapour, M., and R. G. Pearce (1998). Bias in surface-wave magnitude Ms due to inadequate distance correction, *Bull. Seism. Soc. Am.* 88: 43–61.

Russell, D. R. (2006). Development of a Time-Domain, Variable-Period Surface Wave Magnitude Measurement Procedure for Application at Regional and Teleseismic Distances, Part I: Theory, *Bull. Seism. Soc. Am.* 96: 665–677.

Stevens, J. L. and S. M. Day (1985). The physical basis of the m_b:M_s and variable frequency magnitude methods for earthquake/explosion discrimination, *J. Geophys. Res*. 90: 3009–3020.

Vanek, J., A. Zatopek, V. Karnik, Y. V. Riznichenko, E. F. Saverensky, S. L. Solov'ev, and N. V. Shebalin, (1962). Standardization of magnitude scales. *Bull. (Izvest.) Acad. Sci. U.S.S.R., Geophys. Ser.* 2: 108.

von Seggern, D. (1977). Amplitude distance relation for 20-Second Rayleigh waves. *Bull. Seism. Soc. Am.* 67: 405–411.

NEXT-GENERATION MDAC DISCRIMINATION PROCEDURE USING MULTI-DIMENSIONAL SPECTRAL ANALYSES

Mark D. Fisk[1], Steven R. Taylor[2], Howard J. Patton[3], and William R. Walter[4]

ATK Mission Research[1], Rocky Mountain Geophysics, LLC[2], Los Alamos National Laboratory[3], and Lawrence Livermore National Laboratory[4]

Sponsored by National Nuclear Security Administration
Office of Nonproliferation Research and Development
Office of Defense Nuclear Nonproliferation

Contract No. DE-AC52-07NA28116

ABSTRACT

Theoretical understanding of regional P/S discriminants and their frequency dependence has been an important, long-standing research topic. Following Xie and Patton (1999), Fisk et al. (2005) and Fisk (2006) used modified Brune (1970) and Mueller and Murphy (1971) [MM71] models to explain the frequency dependence of Pn/Lg and Pn/Sn discrimination performance for earthquakes and underground nuclear explosions (UNEs) near the Lop Nor, Semipalatinsk, and Novaya Zemlya test sites as mainly due to differences in explosion P and S corner frequencies. Fisk (2007) used source model fits to estimate Pn, Pg, and Lg corner frequencies for Nevada Test Site (NTS) explosions and found that Lg corner frequencies exhibit similar scaling with source size as for Pn and Pg, but shifted lower, analogous to observations by Fisk (2006) for other test sites. A key result is that increasing separation of regional P/S at higher frequencies between earthquakes and explosions at all of these test sites has a consistent model-based explanation mainly in terms of the difference between explosion P and S corner frequencies. Discrimination begins to improve at the explosion S-wave corner frequency and saturates at the explosion P-wave corner frequency, in agreement with empirical experience obtained over decades. We describe how grids of P/S spectral ratios for all combinations of frequencies for P and S wave spectra, which exhibit far greater differences in relative spectral amplitudes and shapes between explosions and earthquakes than considered before, and source models can be used to significantly enhance discrimination performance and confirm the physical basis of the results. We have just started a three-year project to develop and test an innovative processing and discrimination procedure, based on robust features of multi-dimensional spectral ratios for regional seismic phases, and using comparisons to source models, that builds naturally upon the existing Magnitude and Distance Amplitude Correction (MDAC) technique (e.g., Taylor et al., 2002). Key aspects of this work will be to (1) compute two-dimensional (2D) spectral ratios for earthquakes and explosions at various nuclear test sites, using corrected spectra that will be available to us from an existing contract; (2) compare and correct empirical spectra using model predictions, based on a Brune earthquake model and new parametrizations of MM71 for explosion P and S waves; (3) assess features of the spectral ratios that capture spectral differences for various event types and enhance discrimination; (4) quantify uncertainties of the corrected spectral measurements for various regions, stations, and event types; (5) develop a discrimination procedure and test its performance on diverse sets of data, including applications to nuclear test sites and the Korean Peninsula; and (6) develop visualization techniques that allow the discrimination results and model comparisons to be assessed by a human analyst.

OBJECTIVES

We have just started a project to develop and test an enhanced discrimination procedure, based on robust features of multi-dimensional spectral ratios for regional seismic phases, and utilizing source models. The objective is to develop a discrimination methodology and software tools that build upon the existing MDAC procedure by exploiting differences of relative spectral amplitudes and shapes due to source type that are currently not used, but are visually apparent (shown below). Another objective is to provide direct comparison of the empirical results to model calculations to confirm the physical basis of the discrimination results and, in turn, to better understand source mechanisms that affect regional discriminants. Below we motivate our approach and describe planned tasks.

Background and Motivation

Numerous independent empirical studies (Bennett et al., 1989; Taylor et al., 1989; Baumgardt et al., 1992; Kim et al., 1993, 1997; Walter et al., 1995; Fisk et al., 1996; Taylor, 1996; Taylor and Hartse, 1997; Hartse et al., 1997; and many others) have demonstrated that high-frequency (typically above 3-4 Hz) regional P/S ratios (e.g., Pn/Lg, Pn/Sn, Pg/Lg) provide useful separation of earthquakes and explosions. Fisk et al. (2001) provided a systematic comparison of regional waveforms and P/S ratios for explosions and earthquakes near all known nuclear test sites, which showed that regional P/S discriminants at frequencies above about 4 Hz provide useful discrimination in all site-by-site comparisons. (Note that valid application of P/S discriminants to broad areas requires treatment of significant variations due to distance, path, and station effects that must be properly calibrated on a region/station-specific basis.) While there is now a substantial body of empirical evidence that regional P/S ratios provide good discrimination at higher frequencies (e.g., above about 3–4 Hz) and poor discrimination at lower frequencies, we are just beginning to gain theoretical understanding of this phenomenon.

As observed by Xie and Patton (1999), frequency-dependent discrimination performance of Pn/Lg for earthquakes and explosions near the Lop Nor Test Site (LNTS) in China appears to be mainly due to differences in corner frequencies of P and S waves and spectral overshoot for explosions. Fisk et al. (2005) and Fisk (2006) confirmed this behavior of Pn/Sn and/or Pn/Lg spectral ratios for events near LNTS, STS, and NZTS. Figure 1 depicts locations of LNTS and STS nuclear explosions and earthquakes. Many STS UNEs up to 1989 were recorded digitally by BRV (Borovoye, Kazakhstan) and WMQ (Ulumuchi, China). More recent events, including LNTS explosions since mid 1994, were recorded digitally by up to 19 regional stations in Kazakhstan, Kyrgyzstan, Pakistan, Russia, Mongolia, and China.

Figure 2 shows Pn/Sn spectral ratios for nine LNTS nuclear explosions since 1992 with regional data (magenta curves), two explosions in 1996 (red curves), and two earthquakes in January 1999 (green curves). Preliminary attenuation and station corrections were applied to the individual phase spectra at the various stations; the Pn/Sn ratios were then formed and network averaged. Figure 2 also shows theoretical relative spectra predicted for the two 1999 earthquakes and the two 1996 nuclear explosions (gray and black curves, respectively), using a modified Brune (1970) model for earthquakes and an MM71 model for explosions in granite, including a conjecture by Fisk (2006) that the explosion S waves may be modeled by the same functional form as for P waves, but with corner frequency reduced by the ratio of near-source S and P velocities, $v_s(S)/v_s(P)$. The models adequately represent the empirical Pn/Sn spectral ratios and indicate that the frequency dependence of P/S discrimination performance is mainly due to different explosion P and S corner frequencies and stronger frequency-dependent spectral shapes (including overshoot) for explosions. Fisk (2006) used the same Brune and MM71 models at Lop Nor, Degelen, Balapan, and Novaya Zemlya, and showed similar results for Pn/Sn and/or Pn/Lg at all hard rock nuclear test sites. Namely, P/S discrimination emerges at the explosion S-wave corner frequency and saturates at the P-wave corner frequency. This result is in agreement with empirical experience obtained over several decades.

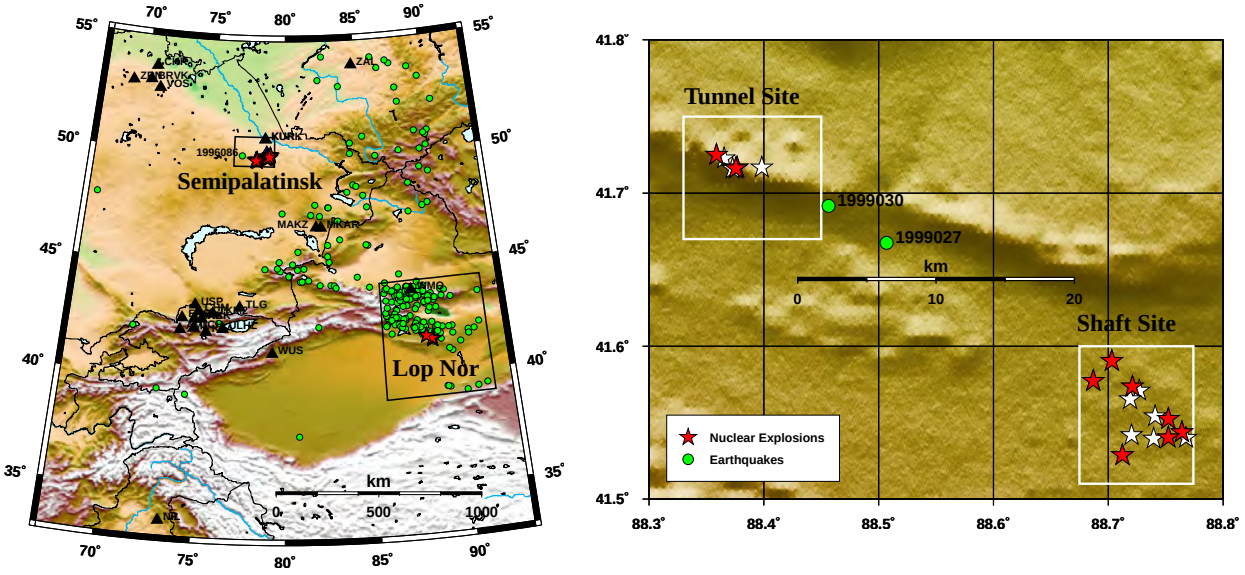

Figure 1. (Left) Locations of nuclear explosions and regional earthquakes considered by Fisk (2006). (Right) Enlarged view of LNTS, including 9 UNEs with regional data (red stars) and two nearby earthquakes in 1999.

Figure 2 not only illustrates a model-based explanation of why P/S discrimination performance is typically better at higher frequencies (i.e., above the Pn corner frequency for explosions, which depends on source size), but also that the earthquakes and explosions have fundamentally different spectral shapes, which should be exploited to improve discrimination. For example, the top and middle plots in Figure 3 shows the result of forming Pn/Sn spectral ratios for all combinations of frequencies for the Pn and Sn spectra of the 1999/01/27 (mb 4.0) and 1999/01/30 (mb 5.4) earthquakes and the 1996/07/29 (mb 4.7) and 1996/06/08 (mb 5.8) nuclear explosions. The spectra were limited to signal-to-noise ratio (SNR) greater than 2.5, which is why the grids for the smaller events have less extent. The spectral ratios for the events, which were corrected for attenuation and station effects, are now also all corrected by a modified Brune model, analogous to the MDAC approach (Taylor et al., 2002). (Alternatively, the spectral ratios could all be corrected by an explosion source model.) The 2D spectral plots for the earthquakes in Figure 3 have values close to zero and little variability over the usable bandwidth of Pn and Sn, as they should, if properly corrected for source, attenuation, and station terms. Alternatively, the plots for the explosions exhibit significant departures from zero and striking spectral structure, including spectral modulations due to overshoot and surface interference effects (Fisk et al., 2005). The bottom plots in Figure 3 show model predictions of the 2D spectral ratios for mb 4.7 and 5.8 explosions in granite. These grids were corrected by the same Brune model used for the empirical grids, so that a direct comparison may be made. It can be seen that these model results exhibit similar qualitative behavior as the corresponding empirical grids for the explosions (middle plots). Plots of Pn/Lg 2D spectral ratios for these events (not shown here) are very similar.

These 2D grids (convenient for plots) may be regarded as slices in a higher-dimensional discriminant space. The small squares in each plot of Figure 3 represent a typical frequency band used to measure P/S, which provides useful discrimination at LNTS, but is not optimal. Figure 3 indicates that cross-spectral ratios (e.g., Pn[3-8 Hz]/Sn[0.5 Hz]), advocated by Taylor et al. (2002), improve discrimination for LNTS events, now with a model-based interpretation. Also, multivariate methods that use combinations of P/S discriminants in high- and low-frequency (HF and LF) bands also tend to separate explosions and earthquakes better than just using the “best” single HF band because the correlations capture information regarding differences in spectral shapes between explosions and earthquakes;

however, not as effectively as could be done by characterizing the broader spectral structure shown in Figure 3.

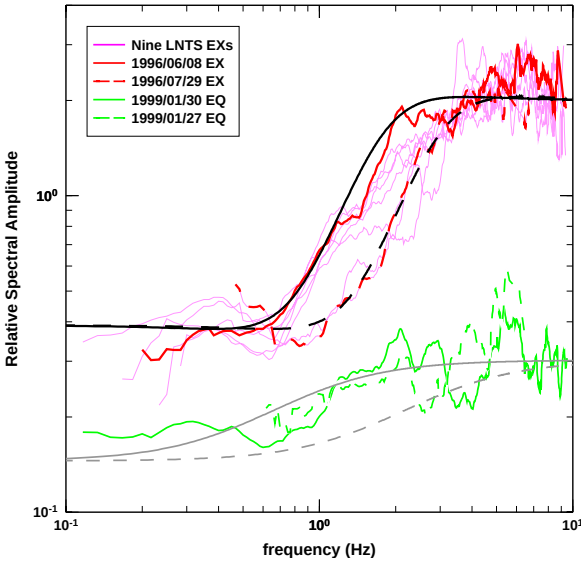

Figure 2. Network-averaged Pn/Sn spectral ratios, corrected for attenuation and station effects, for nine LNTS explosions and two nearby earthquakes. Model predictions are shown for two 1996 explosions and two 1999 earthquakes (black and gray curves).

Our objective is to improve regional discrimination by utilizing this much richer spectral content. Ultimately, we wish to compare features of empirical 2D spectral ratios to model calculations to provide confident event identifications with statistical and physical meaning. However, it is not necessary to match empirical 2D spectral ratios to explosion model calculations in order to successfully enhance regional discrimination. Just using the spectral content, as in the upper four plots of Figure 3, which do not utilize any explosion model information, can improve discrimination performance. This would be a natural extension of the MDAC procedure, using similar methods to correct amplitudes of regional phases for magnitude and distance effects, but then utilizing far more spectral information than currently used. Direct comparison to model predictions for explosions would be an added benefit.

Note that the empirical results for LNTS were averaged over 5 to 18 stations. In practical monitoring situations, events are typically recorded by only one or a few, at most, regional stations. Thus, path and station-specific variability is very important. The raw spectra of regional phases at various stations for LNTS events exhibit considerable variability, requiring different attenuation and station corrections. However, the qualitative frequency dependence of the network-averaged spectral ratios is also observed at the individual stations. As an example, the magenta curves in Figure 2 for nine UNEs, recorded by very different numbers (5 to 18) and subsets of stations, exhibit remarkable consistency in spectral behavior, after applying station-specific corrections. A necessary task will also be to quantify the variances associated with explosion and earthquake spectra over various stations, events, and source regions.

To illustrate applicability using only one station and to other test sites, Figure 4 shows Pn/Lg spectral ratios at WMQ, corrected for attenuation and station terms, for small and large UNEs (red curves) at Degelen and Balapan, and a nearby M_W 4 earthquake on 1996/03/26 using WMQ data only (cyan) and averaging over 17 stations (green). Fisk (2006) shows more results for 51 STS UNEs recorded by WMQ and/or BRV, and for NZTS UNEs. The gray curve in each plot is the Brune model prediction for the earthquake. The black curves are the MM71 model results for each explosion. The model and empirical Pn/Lg spectral ratios compare quite well, given that only one station is used for the UNEs. Figure 5 compares empirical (left) and model (right) Pn/Lg 2D spectral ratios for the earthquake (top), the 1988/09/14 JVE at Balapan (middle), and the 1987/07/17 UNE at Degelen (bottom). Despite the variability using only a single station, the model results exhibit similar behavior as the empirical grids for the UNEs.

As a final example, Figure 6 compares model and empirical 1D and 2D Pn/Sn spectral ratios for the 1998/05/11 UNE in India, using data from station NIL (Nilore, Pakistan). More work is needed to examine the behavior of P/S discriminants for other geological region types and more events, but a consistent model-based understanding of frequency-dependent P/S discrimination seems to be emerging, at least for all existing nuclear test sites on hard rock (Lop Nor, Balapan, Degelen, Novaya Zemlya, Indian).

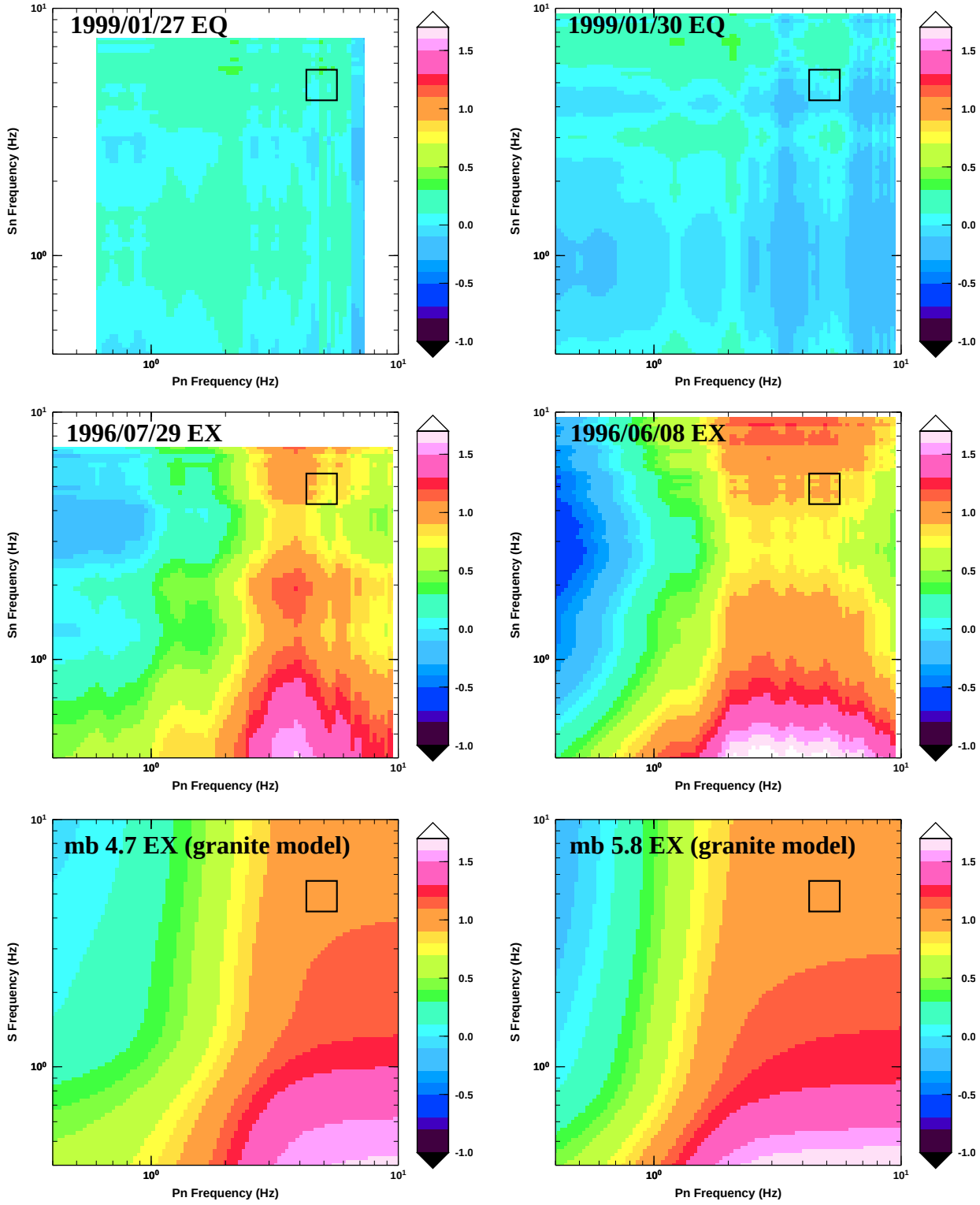

Figure 3. Contours of Pn/Sn 2D spectral ratios as functions of Pn and Sn frequencies for two earthquakes (top), two LNTS nuclear explosions (middle), and corresponding explosion model predictions (bottom). All spectra were corrected for attenuation and station effects, network averaged, and corrected for source size using a Brune model. The squares in each plot show typical frequency bands used to measure Pn/Sn.

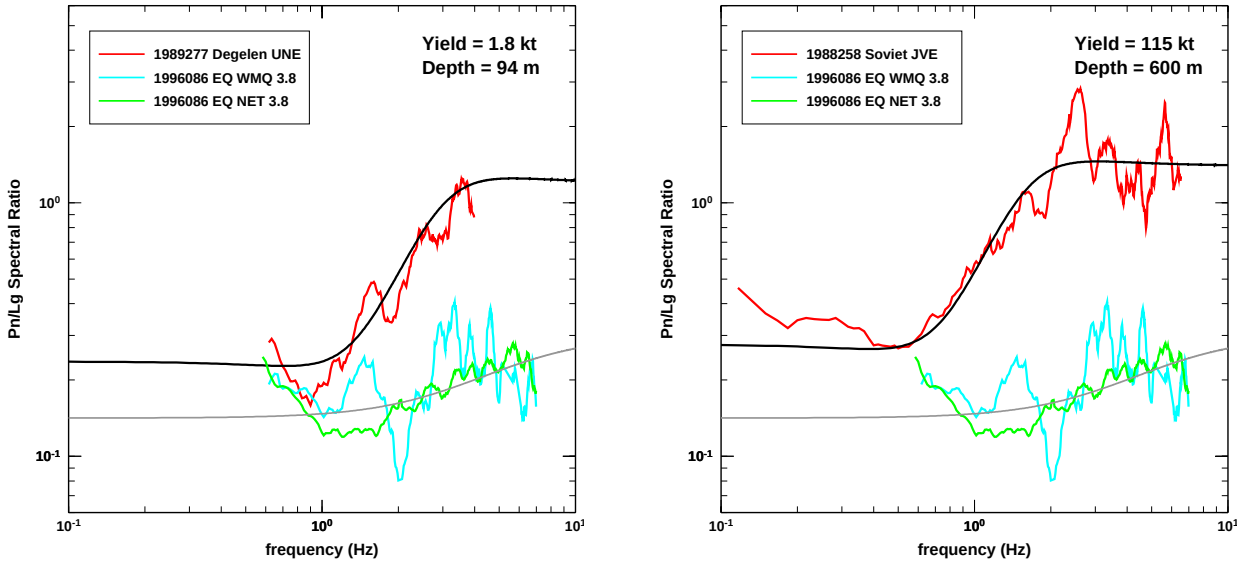

Figure 4. Examples of empirical and model Pn/Lg spectral ratios at WMQ for a Degelen explosion (left) and the 1988/09/14 Soviet JVE at Balapan (right). Pn/Lg spectral ratios, using WMQ only and network averaged over 17 regional stations, are shown for the nearby 1996/03/26 earthquake.

There are several caveats worth noting. First, theoretical understanding of explosion S waves is relatively limited at present. Although the MM71 source function, with S corner frequency scaling relative to the P corner frequency by $v_s(S)/v_s(P)$, provides reasonable interpretation of Pn/Sn and Pn/Lg ratios for explosions at hard rock (granite and shale) nuclear test sites (Fisk, 2006), further work is needed to model explosion S-waves in other types of media. In more recent work, Fisk (2007) processed regional seismograms for 68 NTS explosions above and below the water table in tuff, rhyolite, and alluvium and for 38 nearby earthquakes that were provided by Bill Walter of Lawrence Livermore National Laboratory (LLNL). Fisk (2007) corrected the spectra and computed model fits, using geological information of emplacement conditions from Springer et al. (2002). He found that Lg corner frequencies exhibit similar scaling with source size as for Pn and Pg, but shifted lower, analogous to observations by Fisk (2006) for other test sites. A key result is that increasing separation of regional P/S at higher frequencies between earthquakes and explosions at all of these test sites has a consistent model-based explanation mainly in terms of the difference between explosion P and S corner frequencies.

Existing work by other contractors, directed at quantifying explosion S wave models for diverse media and emplacement conditions, may also be directly applicable to our work. We expect that there will be considerable information compiled on explosion S-wave models for other types of media for this project and we reiterate that it is not necessary to model explosion S waves in order to successfully enhance regional discrimination capabilities.

Explosions in other types of media may not exhibit such dramatic spectral structure as in Figure 3. For example, MM71 predicts lower overshoot in tuff than granite, which would lead to different spectral behavior. Similar to the bottom two plots in Figure 3, Figure 7 shows model predictions for mb 4.7 and 5.8 explosions in tuff. In limited frequency bands (e.g., 4-6 Hz), the model results for tuff and granite are similar (cf. Figure 3), but the full spectral content provides more information regarding the differences in P/S explosion signatures due to different media properties. Despite some differences in spectral content for shots in tuff versus granite, both cases indicate very interesting spectral behavior that can be exploited to enhance regional discrimination.

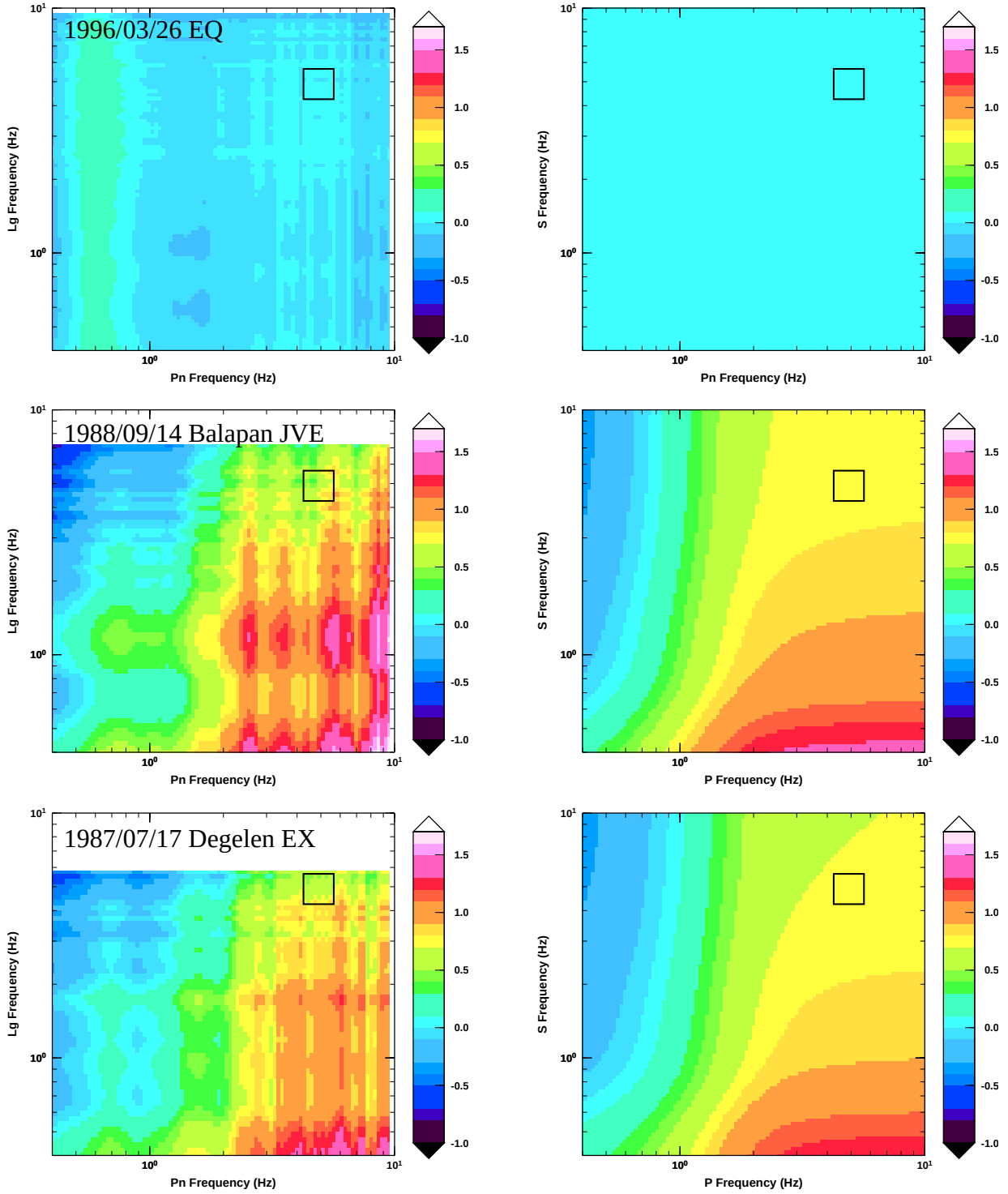

Figure 5. Comparison of empirical (left) and model (right) Pn/Lg 2D spectral ratios for the 1996/03/26 earthquake (top), the 1988/09/14 JVE at Balapan (middle), and the 1987/07/17 UNE at Degelen Mountain (bottom). The empirical grids for the explosions were computed using only a single station (WMQ).

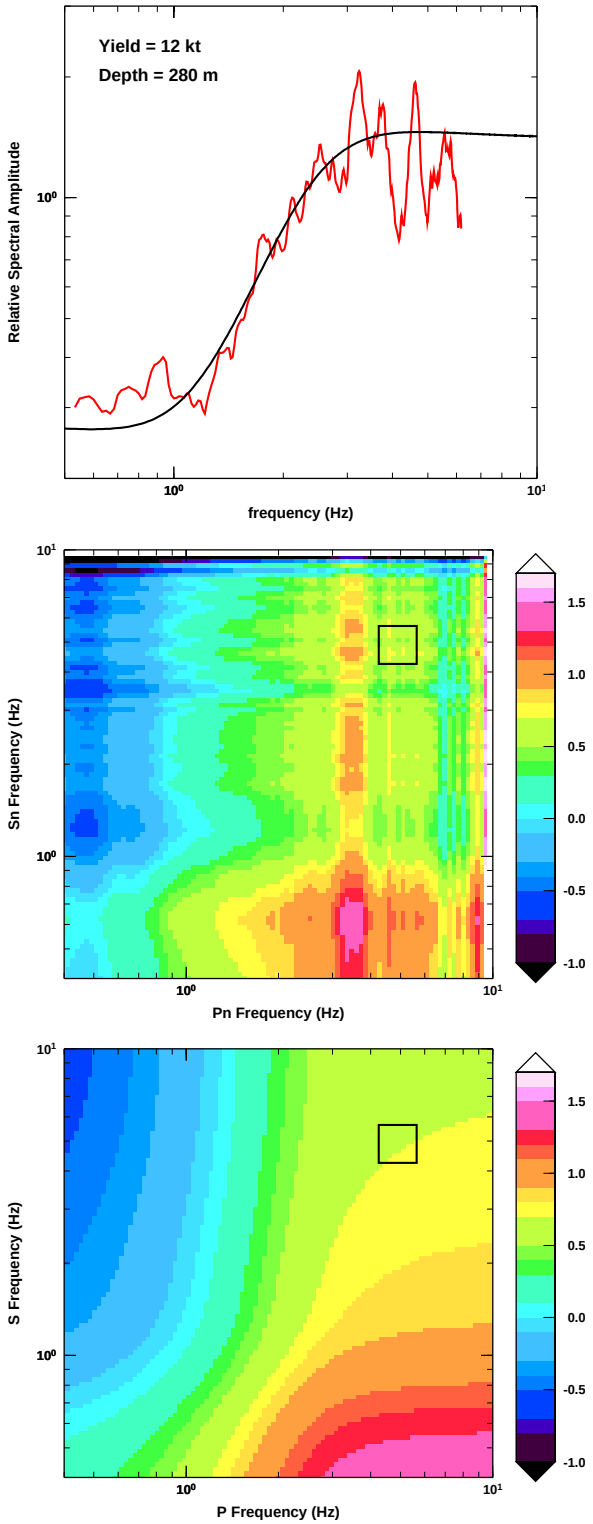

Figure 6. Comparison of model and empirical 1D (top) and 2D (lower two plots) Pn/Sn spectral ratios for the 1998/05/11 UNE in India, using data from station NIL (Nilore, Pakistan).

Second, a discrimination procedure should be developed and tested on a large, representative sets of explosions and earthquakes. Under past and existing contracts, we have assembled fairly comprehensive data sets of earthquakes and explosions near the Lop Nor, Novaya Zemlya, Semipalatinsk, Nevada, and Indian test sites. We have computed regional phase spectra and are correcting them for magnitude, distance, and station effects. Thus, most of the corrected spectra, necessary to develop and evaluate our proposed discrimination procedure, are available to us.

Third, SNR is expected to be lower for smaller events and for those at far regional distances. The effective bandwidth of 2D spectral ratios for many typical events will be more limited than some of the cases shown above. Blockage of regional phases and other strong attenuation effects must be considered and treated for any regional seismic discrimination approach. These issues will require robust procedures to handle the effective bandwidth of regional seismic phase spectra.

Although the focus of this effort is on P/S 2D spectral discriminants, we also plan to examine 2D spectral ratios for the same phase type. For example, use of Lg spectral ratios (Lg[HF]/Lg[LF]) has been an appealing idea for many years now (e.g., Murphy and Bennett, 1982; Taylor et al., 1988; Walter et al., 1995; Patton and Taylor, 1995) because Lg often has the highest SNR of regional phases and problems measuring weak Pn or Pg, or near their cross-over distance, are avoided. Whether information from Lg 2D spectral ratios can be used to improve discrimination on a consistent basis remains to be investigated. Even if the intrinsic discrimination performance, based on Lg 2D spectral ratios, is lower than for P/S, the overall monitoring performance may be enhanced significantly because of many more available Lg measurements for smaller events.

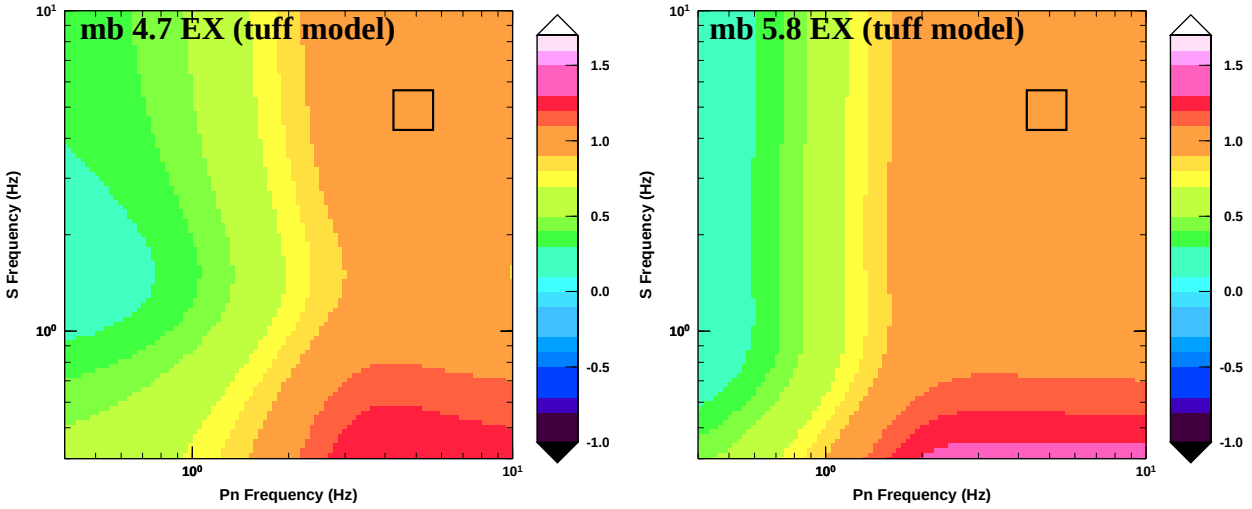

Figure 7. Model results for explosions in tuff, corrected by the same Brune model predictions as in Figure 3.

RESEARCH ACCOMPLISHED

Key tasks of this project will be to (1) compute 2D spectral ratios (Pn/Sn, Pn/Lg, Lg/Lg, etc.) for earthquakes and explosions at nuclear test sites, using corrected spectra that are available to us from past work; (2) compare and correct the empirical spectra using model predictions based on a modified Brune (1970) model for earthquakes and modifications of MM71 for explosion P and S waves, that are being compiled under an existing contract; (3) evaluate distinctive features of the 2D spectral ratios that robustly capture model-based spectral differences of various event types and enhance discrimination performance; (4) quantify uncertainties of the corrected spectra for various regions, stations, and event types, as well as misfits of empirical and model 2D spectral ratio comparisons; (5) develop a robust discrimination procedure and evaluate its performance on broad sets of data; and (6) develop visualization techniques that allow the discrimination results and model comparisons to be assessed by a human analyst. We will also tune and apply these techniques to events on the Korean Peninsula. The start date for this contract was too late to obtain results for this paper, but we are working on the first milestone of assembling and processing the data sets.

CONCLUSIONS AND RECOMMENDATIONS

We expect to develop enhanced processing and discrimination methods that provide significant improvements in seismic event discrimination performance using regional data. We believe that the planned efforts will lead to the next generation of regional discriminants and will provide LANL and LLNL with enhanced discrimination capabilities that could be incorporated straightforwardly into an existing event-identification framework. We further expect that the proposed methods, utilizing model-based comparisons and graphical display capabilities for earthquakes and explosions, will enhance the physical interpretation and visualization of the discrimination results and will, in turn, also provide better understanding of earthquake and explosion source processes that influence regional discriminants.

REFERENCES

Baumgardt, D. R., J. Carney, M. Maxson, and S. Carter (1992). Evaluation of Regional Discriminants using the Intelligent Seismic Event Identification System, Semi-Annual Technical Report SAS-TR-93-38, ENSCO, Inc., Springfield, VA.

Bennett, T. J., B. W. Barker, K. L. McLaughlin, and J. R. Murphy (1989). Regional Discrimination of Quarry Blasts, Earthquakes, and Underground Nuclear Explosions, GL-TR-89-0114, Hanscom AFB, MA.

Brune, J. N. (1970). Tectonic stress and the spectra of seismic shear waves from earthquakes, *J. Geophys. Res.* 75: 4997–5009.

Fisk, M. D. (2007). Corner Frequency Scaling of Regional Seismic Phases for Underground Nuclear Explosions at the Nevada Test Site, *Bull. Seism. Soc. Am*. 97: 977–988.

Fisk, M. D. (2006). Source spectral modeling of regional P/S discriminants at nuclear test sites in China and the Former Soviet Union, *Bull. Seism. Soc. Am*. 96: 2348–2367.

Fisk, M. D., S. Bottone, and G. D. McCartor (2001). Regional Seismic Event Characterization Using Bayesian Calibration, MRC-R-1621, Mission Research Corp., Santa Barbara, CA.

Fisk, M. D., S. R. Taylor, and T. Lay (2005). Modeling and empirical research on energy partitioning of regional seismic phases used for explosion monitoring, in *Proceedings of the 27th Seismic Research Review: Ground-Based Nuclear Explosion Monitoring Technologies,* LA-UR-05-6407, Vol. 1, pp. 539–549.

Fisk, M. D., H. L. Gray, and G. D. McCartor (1996). Regional discrimination without transporting thresholds, *Bull. Seism. Soc. Am.* 86: 1545–1558.

Hartse, H.E., S.R. Taylor, W.S. Phillips, and G.E. Randall (1997). Regional seismic discrimination in central Asia with emphasis on western China, *Bull. Seism. Soc. Am.* 87: 551–568.

Kim, W. Y., V. Aharonian, A. L. Lerner-Lam, and P. G. Richards (1997). Discrimination of earthquakes and explosions in southern Russia using regional high-frequency three-component data from IRIS/JSP Caucasus Network, *Bull. Seism. Soc. Am.* 87: 569–588.

Kim, W. Y., D. W. Simpson and P. G. Richards (1993). Discrimination of earthquakes and explosions in the eastern United States using regional high-frequency data, *Geophys. Res. Lett.* 20: 1507–1510.

Mueller, C. S. and J. R. Murphy (1971). Seismic characteristics of underground nuclear detonations Part I: seismic spectrum scaling, *Bull. Seism. Soc. Am.* 61: 1675–1692.

Murphy J. R. and T. J. Bennett (1982). A discrimination analysis of short-period regional seismic data recorded at Tonto Forest Observatory, *Bull. Seism. Soc. Am.* 72: 1351–1366.

Patton, H. J., and S. R. Taylor (1995). Analysis of Lg spectral ratios from NTS explosions: Implications for the source mechanisms of spall and the generation of Lg waves, *Bull. Seis. Soc. Am.* 85: 220–236.

Springer, D. L., G. A. Pawloski, J. L. Ricca, R. F. Rohrer, and D. K. Smith (2002). Seismic source summary for all U.S. below-surface nuclear explosions, *Bull. Seism. Soc. Am.* 92: 1806–1840.

Taylor, S. R., A. A. Velasco, H. E. Hartse, W. S. Phillips, W. R. Walter, and A. J. Rodgers (2002). Amplitude corrections for regional seismic discriminants, in *Pure and Appl. Geophys., Special Edition on Monitoring the Comprehensive Nuclear-Test-Ban Treaty: Seismic Event Discrimination and Identification* 159: 623–650.

Taylor, S. R., and H. E. Hartse (1997). An evaluation of generalized likelihood ratio outlier detection to identification of seismic events in western China, *Bull. Seism. Soc. Am.* 87: 824–831.

Taylor, S. R. (1996). Analysis of high-frequency Pg/Lg ratios from NTS explosions and western U.S. earthquakes, *Bull. Seism. Soc. Am.* 86: 1042–1053.

Taylor, S. R., M. D. Denny, E. S. Vergino, and R. E. Glaser (1989). Regional discrimination between NTS explosions and western U.S. earthquakes, *Bull. Seism. Soc. Am.* 79: 1142–1176.

Taylor, S. R., N. W. Sherman, and M. D. Denny (1988). Spectral discrimination between NTS explosions and western United States earthquakes at regional distances, *Bull. Seism. Soc. Am.* 78: 1563–1579.

Walter, W. R., K. M. Mayeda, and H. J. Patton (1995). Phase and spectral ratio discrimination between NTS earthquakes and explosions. Part I: Empirical observations, *Bull. Seism. Soc. Am.* 85: 1050–1067.

Xie, J. and H. J. Patton (1999). Regional phase excitation and propagation in the Lop Nor region of central Asia and implications for P/Lg discriminants, *J. Geophys. Res.* 104: 941–954.

IDENTIFYING ISOTROPIC EVENTS USING AN IMPROVED REGIONAL MOMENT TENSOR INVERSION TECHNIQUE

Sean R. Ford[1], Douglas S. Dreger[1], and William R. Walter[2]

University of California, Berkeley[1] and Lawrence Livermore National Laboratory[2]

Sponsored by National Nuclear Security Administration
Office of Nonproliferation Research and Development
Office of Defense Nuclear Nonproliferation

Contract No. DE-FC52-06NA27324/BAA06-42

ABSTRACT

Using a regional time-domain waveform inversion for the complete moment tensor we calculate the deviatoric and isotropic source components for several explosions at the Nevada Test Site (NTS) as well as earthquakes, and collapses in the surrounding region of the western U.S. The events separate into specific populations according to their deviation from a pure double-couple and ratio of isotropic to deviatoric energy. The separation allows for anomalous event identification and discrimination between explosions, earthquakes, and collapses. Error in the moment tensor solutions and source parameters is also calculated.

We investigate the sensitivity of the moment tensor solutions to Green's functions calculated with imperfect Earth models, inaccurate event locations, and data with a low signal-to-noise ratio. We also test the performance of the method under a range of recording conditions from excellent azimuthal coverage to cases of sparse station availability, as might be expected for smaller events. Finally, we assess the depth and frequency dependence upon event size. This analysis will be used to determine the range where well-constrained solutions can be obtained.

OBJECTIVES

This research seeks to apply a regional distance complete moment tensor approach to tectonic, volcanic and man-made seismic events in order to document performance in the ability to identify and characterize anomalous (non-double-couple) seismic radiation. Identification of events with demonstrably significant non-double-couple components can aid in discrimination and possibly yield determination (Given and Mellman, 1986; Patton, 1988; Dreger and Woods, 2002). As an initial application we calculate the full moment tensors of 15 nuclear tests at the NTS, three collapses (two mine collapses and one explosion cavity collapse), and 12 earthquakes near the NTS (Figure 1).

RESEARCH ACCOMPLISHED

We implement the time-domain full regional waveform inversion for the complete moment tensor (2nd rank tensor, M_{ij}) devised by Minson and Dreger (2007) after Herrmann and Hutchensen (1993) based on the work of Langston (1981). The complete moment tensor allows for a characterization of the relative amounts of deviatoric (M_{ij} where $i \neq j$) and isotropic (M_{ij} where $i=j$) source components, the similarity of those components with prior events in the source region, and a constraint on the source depth. The isotropic component is related to the volume change associated with a source (Muller, 1973), and in the case of an explosion this volume change is expected to be significant.

In general, synthetic seismograms are represented as the linear combination of fundamental Green's functions where the weights on these Green's functions are the individual moment tensor elements. The Green's functions for a one-dimensional (1-D) velocity model of eastern California and western Nevada (Song et al., 1996) are calculated as synthetic displacement seismograms using a frequency-wavenumber integration method (Saikia, 1994). The synthetic data is filtered with a 4-pole acausal Butterworth filter with a low-corner of 0.02 Hz and a high-corner of 0.05 Hz and 0.1 Hz for events with $M_W \geq 4$ and $M_W < 4$, respectively. At these frequencies, where the dominant wavelengths are approximately 100 km, we assume a point source for the low-magnitude regional events investigated in this study. The point source assumption allows for linearization in the time-domain, which is where we carry out the least-squares inversion. Data are collected for a total of 55 stations from the U.S. National Seismic Network, IRIS/USGS, Berkeley Digital Seismic Network, Trinet, and the Lawrence Livermore National Laboratory (LLNL) network (Figure 1). We remove the instrument response, rotate to the great-circle frame, integrate to obtain displacement, and filter similarly to the synthetic seismograms.

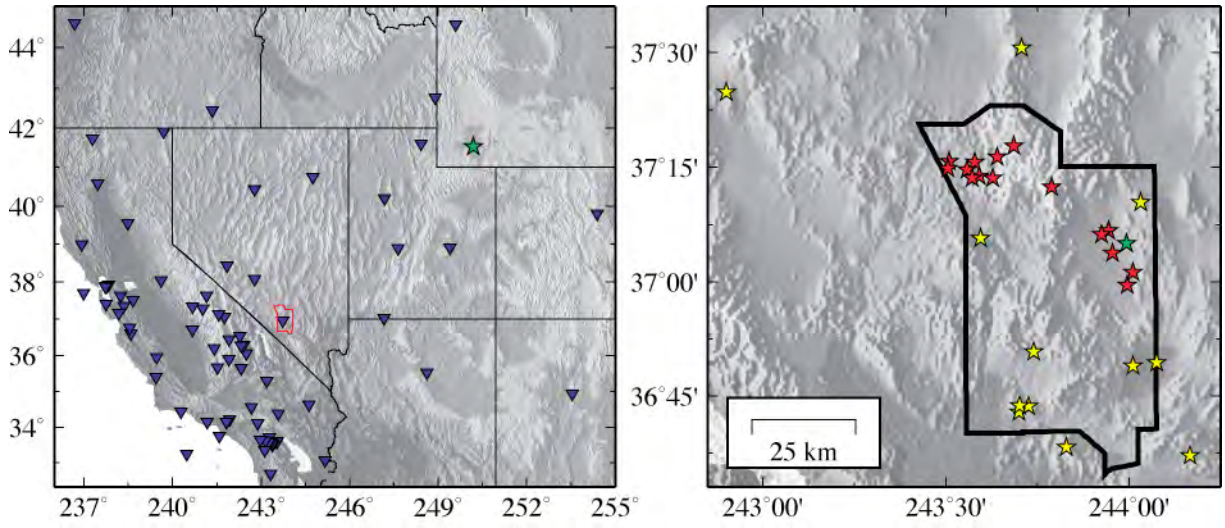

Figure 1. Maps of the western U.S. with stations (blue inverted triangles), earthquakes (yellow stars), explosions (red stars), and collapses (green stars) used in this study. The right panel shows a blow-up of the NTS region, where the NTS is outlined in black. The NTS is also plotted in the left panel in red.

We calibrated the algorithm by calculating the full and deviatoric moment tensor for the 1992 Little Skull Mountain event. The deviatoric solution is obtained by constraining the trace of the moment tensor to be zero ($M_{33} = -(M_{11}+M_{22})$). Our result fits the data very well and is highly similar to the double-couple solution of Walter (1993), the deviatoric solution of Ichinose et al. (2003), and the full solution of Dreger and Woods (2002). We calculate the full moment tensor of 12 earthquakes in the region near the Nevada Test Site (NTS, Figure 1). An example of the fit to the data for an aftershock of the 1992 Little Skull Mountain event is given in Figure 2a, where the moment tensor solution (Full) is decomposed to an isotropic (ISO) and deviatoric component ($M'_{ij} = M_{ij} - \delta_{ij}$ $(M_{11}+M_{22}+M_{33})/3$). The deviatoric component is separated into a double-couple (DC) and compensated linear vector dipole (CLVD; Knopoff and Randall, 1970) that share the orientation of the major axis. The total scalar moment (M_0) is 2.23×10^{22} dyne-cm ($M_W = 4.17$). M_0 is equal to the sum of the isotropic moment ($M_{ISO} = (M_{11}+M_{22}+M_{33})/3$) and deviatoric moment (M_{DEV}), where all quantities are defined according to Bowers and Hudson (1999). The solution has a very small isotropic moment ($M_{ISO} = 1.39 \times 10^{21}$ dyne-cm) and there is little change between the Full and DC solutions. With the same algorithm we calculate the full moment tensors of 15 nuclear test explosions at the NTS (Figure 1). An example of the analysis is given by the solution for the 1991 HOYA test in Figure 2b. The largest component in the decomposition is isotropic and it contributes 59% of the total scalar moment.

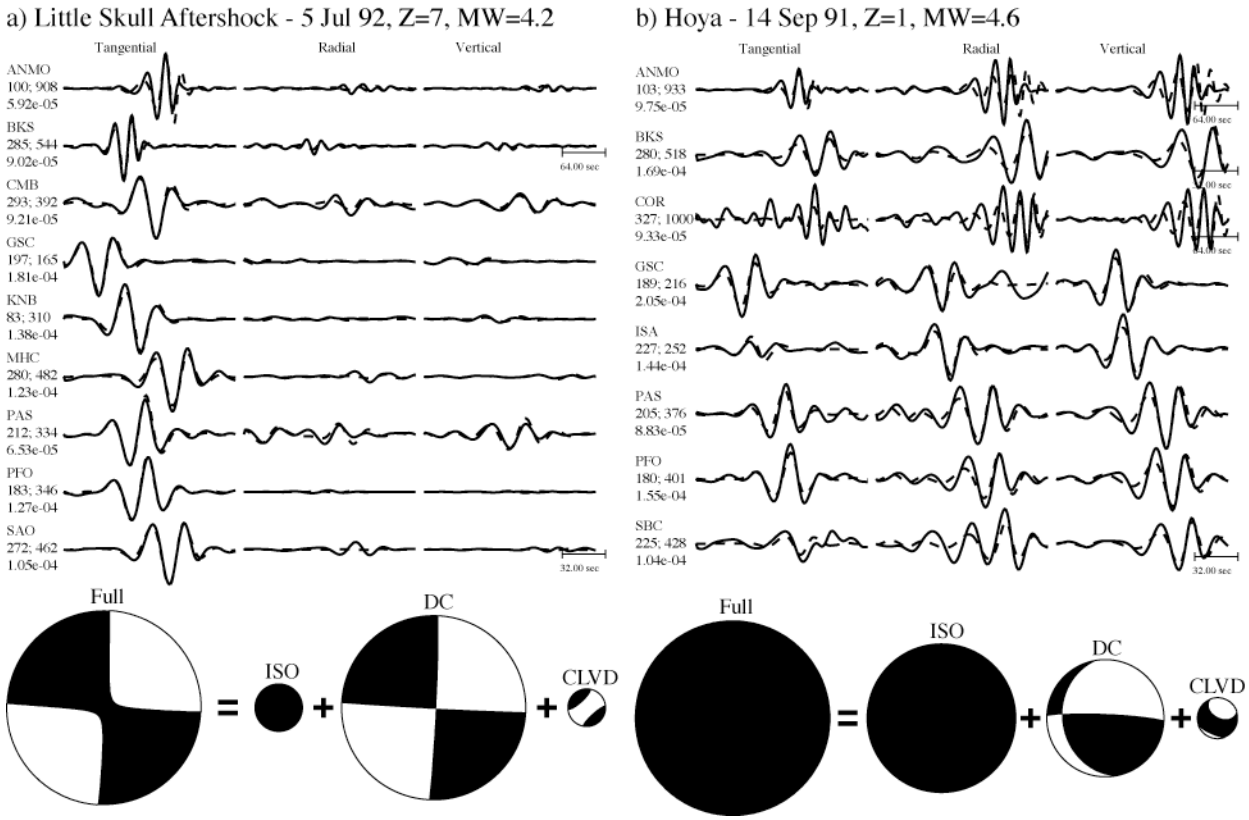

Figure 2. Moment tensor analysis of (a) aftershock of the 1992 Little Skull Mt. event and (b) the 1991 nuclear test, HOYA. The station name with azimuth, distance and maximum displacement (cm) is to the left of the data (solid line) and fit (dashed line) produced by inversion in the 20–50 s passband. Below the data is the full (Full) focal mechanism (lower hemisphere projection), which is decomposed to the isotropic (ISO) and deviatoric components, where the deviatoric component is separated into a double-couple (DC) and compensated linear vector dipole (CLVD) that share the orientation of the major axis. The area of the circles are relative to their scalar moment contribution. The largest component in the aftershock decomposition is the DC. The Full solution of the nuclear test is entirely compressive (black), which is due to the isotropic component contributing more than 50% of the total scalar moment.

Error in the moment tensor solutions is analyzed by plotting the best-fit and 95% confidence ellipses of the axes of minimum compression (**T**), maximum compression (**P**) and null (**N**), which are the eigenvectors of the symmetric moment tensor (Figure 3). The confidence ellipses are obtained from the model covariance matrix, where the variance is estimated by the residuals. In an effort to better characterize the source and confidence in the isotropic solution, we adopt the source vector convention described in Riedesel and Jordan (1989). Vectors are defined describing the general,

$$\mathbf{MT} = m_1\mathbf{T} + m_2\mathbf{N} + m_3\mathbf{P} ,$$

double-couple,

$$\mathbf{DC} = \mathbf{T} - \mathbf{P} ,$$

isotropic,

$$\mathbf{ISO} = \mathbf{T} + \mathbf{N} + \mathbf{P} ,$$

and CLVD sources,

$$\mathbf{CLVD1} = \mathbf{T} - \mathbf{N}/2 - \mathbf{P}/2 ;$$
$$\mathbf{CLVD2} = \mathbf{T}/2 + \mathbf{N}/2 - \mathbf{P} ,$$

where m_1, m_2, and m_3 are the principal moments for the T, N, and P axes. Therefore, the source vectors are subspaces of the space defined by the eigenvectors of the moment tensor. The vectors are plotted on the focal sphere (similar to **T**, **N**, **P**) for the Little Skull Mountain aftershock and NTS explosion, HOYA in Figure 3b. The general source vector, **MT**, for the Little Skull Mountain event lies very near the

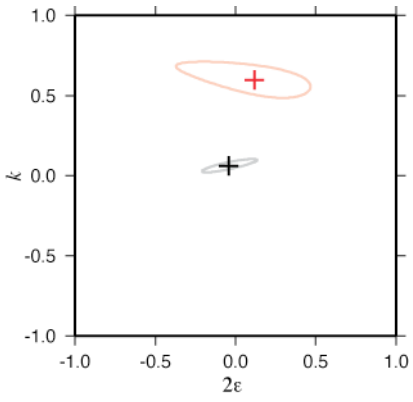

Figure 4. Source-type plot for the Skull Mt. aftershock (black) and NTS test HOYA (red) and the associated 95% confidence regions.

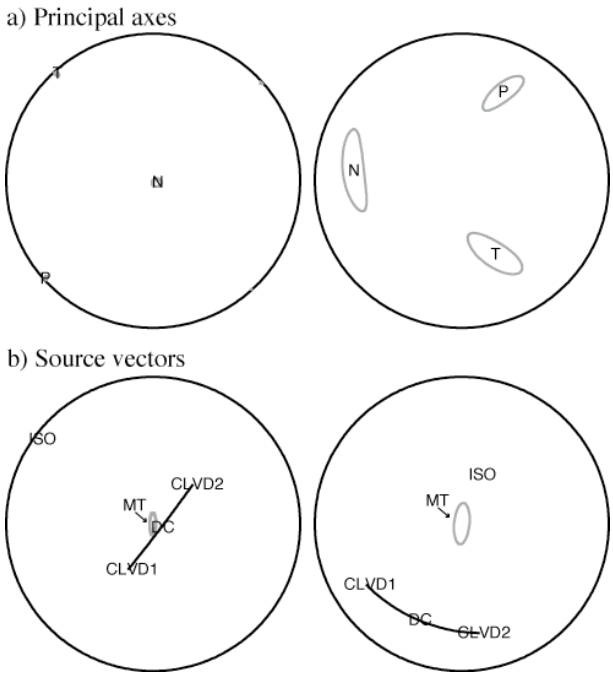

Figure 3. Principal axes analysis of the solutions for the Little Skull aftershock (left column) and NTS test HOYA (right column). (a) Principal axes in the lower hemisphere projection and the associated 95% confidence region. (b) Source vectors where the 95% confidence region of the MT vector is plotted in grey. The confidence region contacts the deviatoric subspace (defined as a line in the lower hemisphere projection between CLVD1 and CLVD2) for the earthquake solution but not for the explosion.

great-circle connecting the DC and CLVD vectors. This great-circle defines the subspace on which **MT** will lie if the source is purely deviatoric. The MT vector is also collinear with the DC vector, which is to say that the source is almost purely double-couple. The MT vector for the HOYA test lies well off the line defining the deviatoric solution space. The 95% confidence ellipse of **MT** is also plotted and it does not intersect the deviatoric solution space, which is to say that the solution has a significant isotropic component at the 95% confidence level. However, Riedesel and Jordan (1989) only consider perturbations to the principal moments and not the principal axes to construct confidence regions, which may be an inaccurate assumption if variance in the model parameters is great (Vasco, 1990). The proposed Monte Carlo approach described later is able to account for large variance.

It is difficult to grasp the source-type from the standard focal mechanism plot. For example, one cannot discern the relative contributions of the isotropic and deviatoric components from the Full focal mechanism in Figure 2b. Furthermore, decompositions of the deviatoric component are non-unique, where the DC and CLVD decomposition followed here could be replaced by two DCs (Julian et al., 1998). Following the source-type analysis described in Hudson et al. (1989) we calculate -2ε and k, which are given by

$$\varepsilon = \frac{-m'_1}{|m'_3|},$$

and

$$k = \frac{M_{ISO}}{|M_{ISO}| + |m'_3|},$$

where m'_1, m'_2 and m'_3 are the deviatoric principal moments for the T, N, and P axes, respectively. ε is a measure of the departure of the deviatoric component from a pure double-couple mechanism, and is 0 for a pure double-couple and ± 0.5 for a pure CLVD. k is a measure of the volume change, where +1 would be a full explosion and −1 a full implosion. -2ε and k for the Little Skull Mountain aftershock and NTS explosion HOYA are given in Figure 4, where error in the values is derived as before. The earthquake is almost at the origin, which defines a pure DC, whereas the explosion is far from this point due to the large value of k.

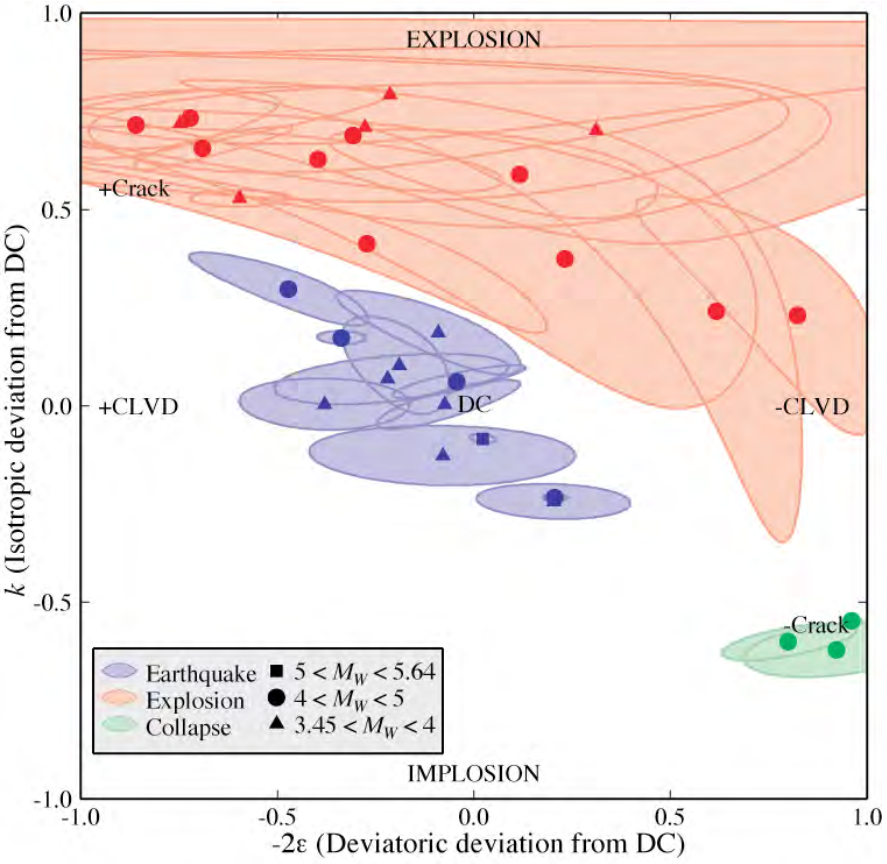

Figure 5. Source-type plot of the 12 earthquakes (blue), 15 explosions (red), and 3 collapses (green) and their associated 95% confidence regions (shaded) analyzed in this study. The magnitude of the event is given by the symbol. The abscissa measures the amount of volume change for the source and the ordinate measures the departure from a pure DC.

We carry out similar analyses for three collapses (one cavity and two mine) and produce the source-type plot (Figure 5). The nuclear tests occupy the region where $k > 0.25$, the earthquakes cluster near the origin (with some interesting deviations), the collapses plot almost exactly at (1,-5/9), which is the location for a closing crack in a Poisson solid. The populations of earthquakes, explosions, and collapses separate in the source-type plot. These initial results are very encouraging and suggest a discriminant that employs the k, -2ε parameters. However, some of the 95% confidence regions for the explosions are very large and the solution is not well constrained. These events will be investigated further as described below. We also note that we limit explosions to those recorded by more than two stations at a broadband channel, thereby limiting the data set to tests after Hornitos near the end of 1989. We hope to expand the dataset by making use of earlier digital data from the LLNL network.

The error analysis presented above is due to misfit of the data by the least-squares inversion. Part of the misfit may be due to nonstationary noise and we test the sensitivity of the inversion to increased noise with a series of synthetic sources with varied signal-to-noise ratios (SNR). We find that a full explosion returns $k < 0.5$ only when SNR < 2 (Figure 6a). Typically, we use data with an SNR greater than 10. Another source of error not incorporated into the formal error analysis employed above is incorrectly calculated Green's functions due to ignorance of the true event depth and Earth structure.

The method that produces the results presented above attempts to find an optimal depth for the earthquakes by perturbing the reported depth a few kilometers, performing the inversion, and finding the best-fit solution. For all explosions and collapses the depth is fixed at 1 km. If this method were to be used for an event with an unknown source type, the depth could be an important source of error, as well as an important parameter for identification. We perform another synthetic test in which an explosion at 1 km is inverted with Green's functions calculated at varying depths. We find that for an optimal station distribution k is greater than 0.5 for depths up to 8 km (Figure 6b), which is a demonstration of the fact that an isotropic radiation pattern has no sensitivity to takeoff angle, which depends on depth. As shown by Dreger and Woods (2002) there is limited resolution of the shallow depth of explosions using regional distance data. Although an explosive radiation pattern alone does not have depth sensitivity the relative excitation of low frequency body waves (*Pnl*) and Rayleigh waves does enable the method to discern the relatively shallower depths of explosions compared to earthquakes. Finally, we test how error in the Earth structure is mapped through the Green's functions to error in the solution. We use a simple 3-layer velocity model and vary the depth and velocities of those layers. We find that only for large variation in the layer velocity (>50%) can $k < 0.2$ be retrieved. We present the difference between the given model and the theoretical one by calculating a correlation coefficient for the Green's functions from the two models (CC; Figure 6c). The solution is especially sensitive to the

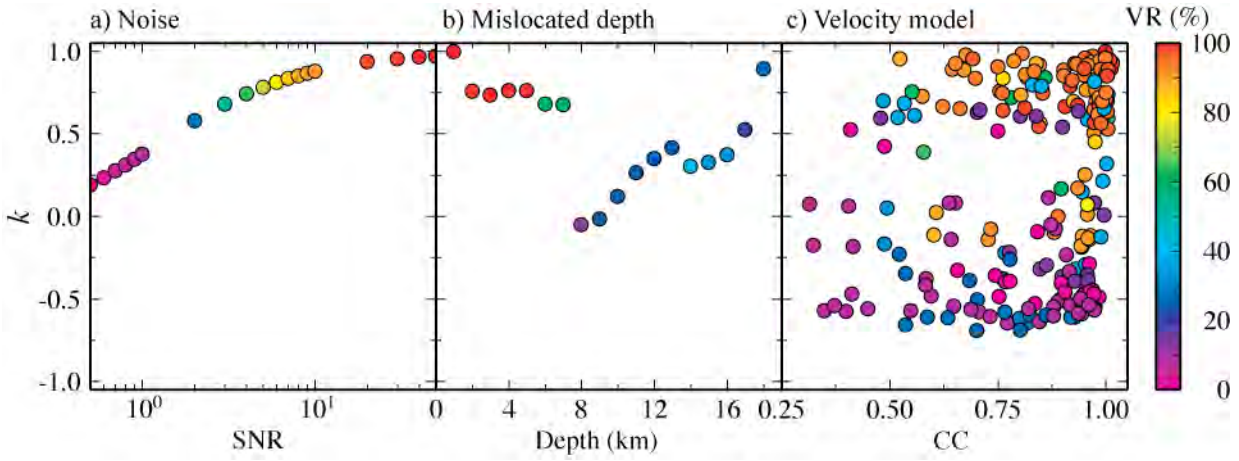

Figure 6. Sensitivity analysis for a synthetic explosion at a depth of 1 km in a three-layer 1D velocity model. (a) Noise is added in the inversion. (b) The inversion is carried out assuming an incorrect depth. (c) The inversion is carried out for different three-layer velocity models where CC is the normalized correlation coefficient between the Green's functions for the correct velocity model and those of the incorrect velocity model used in the inversion. The symbols are colored as a function of variance reduction (VR).

uppermost layer. Sileny (2004) had a similar conclusion when investigating the deviatoric solution, where velocity perturbation of more than 30% and event depths mislocated by two times the actual depth return a well-resolved solution. Future work will identify what perturbations in the velocity model are the most significant given a station distribution and realistic noise considerations. A further consideration is the assumption of an isotropic Earth structure in the presence of anisotropic data, which may produce a spurious CLVD component (Sileny and Vavrycuk, 2002). Fortunately, the 1-D velocity model seems to be a good approximation in the presence of smoothly varying 3-D heterogeneity (Panning et al., 2001).

Another consideration is the ability to resolve displacements for explosions near the surface. Since tractions normal to the vertical vanish at the free surface, the excitation coefficients associated with those tractions must vanish (Julian et al., 1998). Therefore at the free surface the moments of M_{13}, M_{23}, and the isotropic part of the M_{ij} cannot be resolved. Given and Mellman (1986) showed that at a source depth of 1 km the fundamental mode excitation functions associated with the moments listed previously effectively go to zero. We investigate the potential problems associated with traction vanishing at the free surface by inverting noisy data from a synthetic source composed of 60% explosion, 20% 45° dip-slip, and 20% vertical CLVD (as is commonly resolved for several NTS events) at a depth of 400 m in a three-layer 1-D velocity model using Green's functions calculated with the same velocity model at a mislocated depth of 1 km. Figure 7 shows that an explosive component can be resolved under favorable noise conditions, though with error in the magnitudes of the moment tensor elements listed previously and M_{ISO} by almost 50%. This behavior would affect yield estimation, though event discrimination would still be reliable at high SNR. At SNR < 10 considerable moment goes into M_{23} producing a significant vertical dip-slip component in the deviatoric source where there should be none. This provides a diagnostic for unresolved components in solutions, which can be seen in three of the most poorly resolved full moment tensors. This behavior is similar for events deeper than 300 m. At less than 200 m depth, the synthetic displacements become too small and the solution using these particular Green's functions is unreliable.

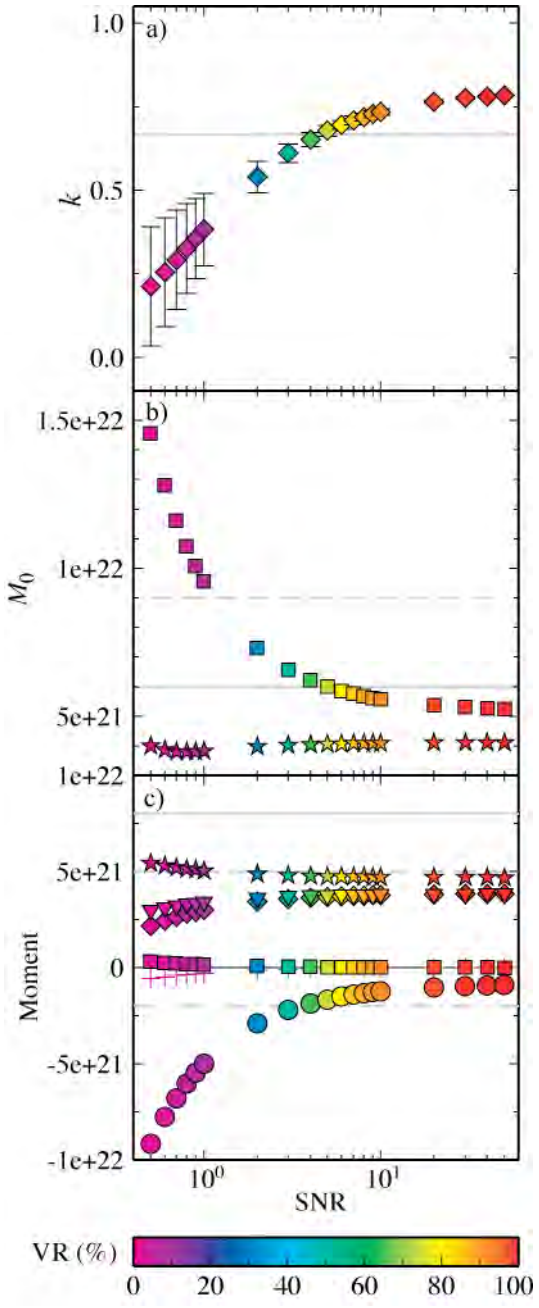

Figure 7. A noisy synthetic composite event at a depth of 400 m is inverted using Green's functions for an event at 1 km. (a) Source-type parameter *k*, where the theoretical value is given by the grey line. (b) M_0 (square) and M_{ISO} (star), where the theoretical values are given by the dashed and solid grey lines, respectively. (c) M_{33} (star), M_{13} (cross), M_{23} (circle), M_{11} (diamond), M_{22} (triangle) and M_{12} (square) where theoretical values are given by the grey lines. Symbol color is the variance reduction (VR) of the solution.

CONCLUSIONS AND RECOMMENDATIONS

Nuclear test explosions from NTS and earthquakes from the surrounding region separate into specific populations according to source-type parameters, which are based on relative magnitudes of isotropic and deviatoric moments. The separation allows for anomalous event identification

and discrimination between explosions, earthquakes, and collapses. Synthetic tests show that mislocation in depth on the order of a few kilometers and small deviations in a simple 1-D velocity model still recovers a significant isotropic component, though Earth complexity is inadequately represented by a three-layer structure. We also assess error due to vanishing traction at the free surface and are able to resolve a reliable solution at depths greater than 300 m, where error is expressed as an increasing vertical dip-slip component in the deviatoric solution, which is a diagnostic indicating that vanishing traction could be a problem in poorly resolved low SNR applications. Of the 15 explosions we studied only 3 of the poorest resolved solutions showed this behavior.

A more complete treatment of the error introduced by ignorance of the event location and Earth structure can be given by a Monte Carlo approach, where several solutions are computed for a priori distributions of the hypocentral location and Earth model obtained from independent analyses. For example, confidence regions for a given hypocentral location as published by the NEIC can act as the a priori location distribution and the hundreds of 1-D velocity models for a given region produced from a Markov Chain Monte Carlo method as in Pasyanos et al. (2006) can act as the velocity model distribution. Each of the moment tensor solutions could then be plotted producing a scatter density, which would aid in the understanding of how parameterization choice nonlinearly affects the moment tensor solutions, and help map the solution space of best-fit moment tensors. We will also search for solution dependence on individual measurements via Jackknife resampling of the data for specific stations and channels (Ichinose et al., 2003; Templeton and Dreger, 2006). Patton (1991) showed a correlation between yield and scalar moment for a given NTS region with events below the water table. Following this we hope to search for correlations based on the geophysical parameters given by Springer et al. (2002) for all NTS tests. We can also look at the principal axes of the explosions to see if they are responding to the regional stress environment, which may have important ramifications for understanding tectonic release coincident with nuclear tests. We will probe the tectonic contribution further in the context of the F-value, $F = \alpha^2/2\beta^2 \, M_{DEV}/M_{ISO}$, where α and β are the compressional and shear speeds of the medium, respectively. Toksoz and Kehrer (1972) showed that certain F-values can produce recordings of explosions with non-isotropic components similar to some observations. The explosions analyzed here do not have as much non-isotropic energy as has historically been observed at NTS and in other regions (Walter and Patton, 1990; Ekstrom and Richards, 1994). This may be due to the "wearing out" of the test site over time (Aki and Tsai, 1972), so we will expand the data set of explosions to encompass other regions exhibiting exotic records like the "reversed" Rayleigh waves observed for the 1998 Indian tests (Walter and Rodgers, 1999).

ACKNOWLEDGEMENTS

We thank Jeff Stevens for discussions regarding vanishing tractions at the free surface and Howard Patton for insights on the CLVD contribution to the explosion source. Figures were made with Generic Mapping Tools (Wessel and Smith, 1998).

REFERENCES

Aki, K. and Y.-B. Tsai (1972). Mechanism of love-wave excitation by explosive sources, *J. Geophys. Res.* 7 7: 1452–1475.

Bowers, D. and J. A. Hudson (1999). Defining the scalar moment of a seismic source with a general moment tensor, *Bull. Seis. Soc. Amer.* 89: 1390–1394.

Dreger, D. and B. Woods (2002). Regional distance seismic moment tensors of nuclear explosions: Seismic source mechanism through moment tensors, *Tectonophysics* 356: 139–156.

Ekstrom, G. and P.G. Richards (1994). Empirical measurements of tectonic moment release in nuclear-explosions from teleseismic surface-waves and body waves, *Geophys. J. Int.* 117: 120–140.

Given, J. W. and G. R. Mellman (1986). Estimating explosion and tectonic release source parameters of underground nuclear explosions from Rayleigh and Love wave observations, Sierra Geophysics report SGI-R-86-126.

Herrmann, R. B. and K. Hutchensen (1993). Quantification of M_{Lg} for small explosion, Phillips Laboratory report PL-TR-93-2070.

Hudson, J. A., R. G. Pearce, R. G., and R. M. Rogers (1989). Source type plot for inversion of the moment tensor, *J. Geophys. Res.* 9: 765–774.

Ichinose, G. A., J. G. Anderson, K. D. Smith, and Y. Zeng (2003). Source parameters of eastern California and western Nevada earthquakes from regional moment tensor inversion, *Bull. Seis. Soc. Amer.* 93: 61–84.

Julian, B. R., A. D. Miller and G. R. Foulger (1998). Non-double-couple earthquakes: Part 1. Theory, *Rev. Geophysics,* 36: 525–549.

Knopoff, L. and M. J. Randall (1970). The compensated linear-vector dipole; a possible mechanism for deep earthquakes, *J. Geophys. Res.* 75: 4957–4963.

Langston, C. A. (1981). Source inversion of seismic waveforms; the Koyna, India, earthquakes of 13 September 1967, *Bull. Seis. Soc. Amer.* 71: 1–24.

Minson, S. and D. Dreger (2007). Improved seismic moment tensor inversion, *Geophys J. Int.* (submitted).

Muller, G. (1973). Seismic moment and long-period radiation of underground nuclear explosions, *Bull. Seis. Soc. Amer.* 63: 847–857.

Panning, M., D. Dreger, and H. Tkalcic (2001). Near-source velocity structure and isotropic moment tensors: A case study of the long valley caldera, *Geophys. Res. Lett.* 28: 1815–1818.

Pasyanos, M. E., G. A. Franz, and A. L. Ramirez (2006). Reconciling a geophysical model to data using a Markov Chain Monte Carlo algorithm: An application to the Yellow Sea-Korean Peninsula region, *J. Geophys. Res.* 111: B03313.

Patton, H. J. (1988). Source models of the Harzer explosion from regional observations of fundamental-mode and higher mode surface waves, *Bull. Seis. Soc. Amer.* 78: 1133–1157.

Patton, H. J. (1991). Seismic moment estimation and the scaling of the long-period explosion source spectrum, in *Explosion Source Phenomenology,* P. G. Richards (Ed.). American Geophysical Union.

Riedesel, M. and T. H. Jordan (1989). Display and assessment of seismic moment tensors, *Bull. Seis. Soc. Amer.* 79: 85–100.

Saikia, C. K. (1994). Modified frequency-wavenumber algorithm for regional seismograms using Filon's quadrature: Modelling of Lg waves in eastern North America, *Geophys. J. Int.* 118: 142–158.

Sileny, J. (2004). Regional moment tensor uncertainty due to mismodeling of the crust, *Tectonophysics* 383: 133–147.

Sileny, J. and V. Vavrycuk (2002). Can unbiased source be retrieved from anisotropic waveforms by using an isotropic model of the medium?; Seismic source mechanism through moment tensors, *Tectonophysics* 356: 125–138.

Song, X. J., D. V. Helmberger, and L. Zhao (1996). Broad-band modelling of regional seismograms: The basin and range crustal structure, *Geophys. J. Int.* 125: 15–29.

Springer, D. L., G. A. Pawloski, J. L. Ricca, R. F. Rohrer, and D. K. Smith (2002). Seismic source summary for all U.S. below-surface nuclear explosions, *Bull. Seis. Soc. Amer.* 92: 1806–1840.

Templeton, D. C. and D. S. Dreger (2006). Non-Double-Couple Earthquakes in the Long Valley Volcanic Region, *Bull. Seism. Soc. Am*. 96: 69–79.

Toksoz, M. N. and H. H. Kehrer (1972). Tectonic strain release by underground nuclear explosions and its effect on seismic discrimination, *Geophys. J. Roy. Aston. Soc.* 31: 141–161.

Vasco, D. W. (1990). Moment-tensor invariants; searching for non-double-couple earthquakes, *Bull. Seis. Soc. Amer*. 80: 354–371.

Walter, W. R. (1993). Source parameters of the June 29, 1992, Little Skull Mountain earthquake from complete regional waveforms at a single station, *Geophys. Res. Lett.* 20: 403–406.

Walter, W. R. and H. J. Patton (1990). Tectonic release from the soviet joint verification experiment, *Geophys. Res. Lett.* 17: 1517–1520.

Walter, W. R. and A. J. Rodgers (1999). Regional waveform modeling in Southwestern Asia: Tectonic release from the May 11, 1998, Indian nuclear tests, SSA-99 94th annual meeting; Meeting abstracts, *Seis. Res. Lett.* 70: 228.

Wessel, P. and W. H. F. Smith (1998). New, improved version of generic mapping tools released, *Eos Transactions of AGU* 79: 579.

DEPTH-OF-BURIAL AND DECOUPLING EXPLOSION EXPERIMENTS IN ISRAEL: NEAR-SOURCE AND NEAR-REGIONAL SEISMIC ENERGY GENERATION

Yefim Gitterman, Rami Hofstetter, and Vladimir Pinsky

Geophysical Institute of Israel

Sponsored by Air Force Research Laboratory

Contract F19628-03-C-0124

ABSTRACT

During the third year of the project, two source phenomenology experiments were conducted at Oron phosphate quarry in Northern Negev. A special complicated technology was used for the creation of large cavities (up to 3.5 m) at different depths (up to 63 m), and accommodation of large near-spherical charges of ANFO explosives.

A series of decoupled and fully coupled (reference) explosions with charges of 1240 kg in the cavities was conducted on July 17, 2006. Extensive observations in near-source zone and remote area demonstrated peculiar signal characteristics and energy generation features related to these specific decoupled seismic sources. S/P energy ratios and decoupling factors were estimated at local distances, matching roughly to theoretical conceptions.

The project central Depth-of-Burial (DOB) experimental series was conducted on January 2, 2007, and included three equal near-spherical charges of 4,200 kg at depths 26 m, 45 m and 59 m. The main objective of the experiment was to investigate relations between explosion depth and spectral/energetic/magnitude parameters of regional seismic phases. The design and configuration of the Oron DOB experiment were preferable in purity of conditions compared to the previous Balapan DOB experiment (1997): media homogeneity (all charges were placed in similar consolidated sediments), full containment and small separation (~200 m) of the explosions, charge scaled depths in the range of Nevada Test Site (NTS) nuclear tests. An important goal of our experiment was to get rid of the asymmetry effect caused by the difference of lithostatic pressures above and below the vertical lengthy cylinder explosive source, typical for borehole chemical explosions, and to study the generation of shear waves for about spherically symmetric sources, typical for nuclear tests.

Numerous good recordings of signals from all shots were obtained at portable near-source accelerometers and close-in 3C seismic stations, permanent local short period (SP) and broad band (BB) stations, and International Monitoring System (IMS) stations EIL and MMAI in Israel, and ASF in Jordan. An important effect observed for near-source accelerometer records was a clear trend of the signal peak amplitude and energy enhancement with the charge depth increase. This effect was accompanied by a significant signal frequency raise, providing empirical verification and estimation of decreasing seismic source size due to increase of overburden lithostatic pressure. Evidently, high frequencies of the radiated signal resulted in rapid attenuation of seismic energy with distance, a drastic drop of amplitude for deeper shots is clearly manifested already at distance of several km, and consequently a clear expected tendency of signal energy and magnitude reduction with depth is observed at regional distances. Analysis of seismic waveforms (in the broad band 1–20 Hz) at close local and regional distances (3.5–240 km) demonstrated a clear decrease of peak amplitude and energy for S-phase and corresponding S/P ratios for deeper shots. The frequency dependence of spectral amplitudes on shot depth was observed at most stations for the both phases: a decrease of amplitudes with increasing shot depth between about 1 and 10 Hz is converted to the opposite trend at higher frequencies ~10–20 Hz.

A special feature of Oron DOB experiment - the placement of the charges in boreholes, separated by only a few hundred meters, in order to eliminate variations in waveforms and travel times due to different propagation conditions—provided a good opportunity for a comparative location study. Using measured P onsets at the observation range and a local 1D velocity model, the three explosions were located by two procedures: the standard grid-search least square procedure (LSQR), and a new model-free robust “Grid-Sign” (GS) algorithm with essential advantage shown by the latter due to eliminating error of the unknown velocity model misfit.

OBJECTIVES

1) conducting of near-spherical explosions of special design at different depth, in homogeneous media, excluding all factors affecting radiated signals except of the DOB; and also partially decoupled shots;
2) quantifying the decoupling factor for these specific seismic sources, analysis of energy generation and partitioning into various regional phases (P and S).
3) estimation and analysis of relationship between explosion depth and spectral/energetic (magnitude) parameters of regional seismic signals.

RESEARCH ACCOMPLISHED

During the third year of the project, two source phenomenology explosion experiments were conducted at Oron phosphate quarry in Northern Negev (Figure 1). A special complicated blast design and technology were utilized, developed by Rotem Amfert Negev, Ltd., and Tamar Advanced Quarrying, Ltd., to provide near-spherical explosion sources. ANFO explosives were accommodated in large cavities (up to 3.5 m) at different depths (up to 63 m), created beforehand by a series of small shots in boreholes of a small diameter (6.5"), thus forming large near-spherical charges. This technique was used for the calibration Rotem 25-ton explosion in 2002 (Gitterman et al., 2002), where cavities of ~1 m size were created in holes at the depth ~15 m.

Decoupling Experiment

A series of decoupled and fully coupled (reference) explosions with charges of 1,240 kg in the cavities was conducted on July 17, 2006 (Figure 2a). The spacing between the shots was 30–120 m. The idea and design of this experiment were initiated by special circumstances in preparations of the planned DOB experiment (Gitterman et al., 2006). Note that this "Decoupling" experiment was not quite pure, because all 3 shots were placed at different depths, and the cavity volume could be estimated rather approximately.

The site geology was presented by near-surface alluvium, and underlying consolidated marls and phosphates with similar mechanical properties and elastic velocities (Figure 2b), providing rock media homogeneity for all the sources. Different 3C observation systems were deployed at near-source distances: 9 accelerometers ETNA, range 100–700 m; 3 sensors BlastMateIII, 500–1000 m; 5 SP seismic stations L4C, 4–23 km.

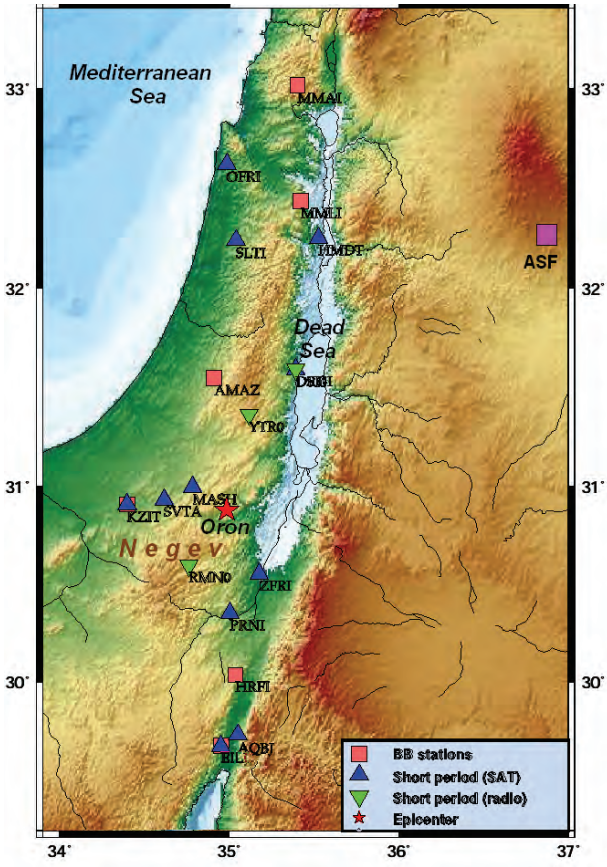

Figure 1. Explosion site and regional seismic stations that recorded signals.

Extensive good-quality datasets obtained for all shots in near-source zone and remote area demonstrated peculiar signal characteristics and energy generation features related to these specific decoupled seismic sources. Very high signal frequencies accompanied by the highest peak accelerations were observed at all near-source distances for the decoupled Ex.2 (Figure 3). Possibly a smaller volume size of the seismic source, due to a larger depth (63 m) can contribute to this effect. However, it is problematic to explain a sharp rise of the radiated signal frequencies from 3–15 Hz to 30–40 Hz only by the doubled depth increase (as in the DOB experiment data, see below). A more reasonable guess (A. Dainty, pers. comm.) explains this effect by air-shock wave reverberations in the air-filled cavity. Considering the cavity maximal vertical dimension l_v~4 m, and the average shock wave velocity V~400 m/s, a rough estimation of the dominant reverberation frequency is $f_r = V/2l_r$ ~50 Hz, i.e., comparable to the observations. This phenomenon was modeled for cavity decoupled nuclear explosions in salt and tuff (Stevens et al., 1991); however, much higher reverberation frequencies (>100 Hz) were obtained.

Rapid attenuation of high-frequency seismic energy for Ex.2 resulted in minimal signal amplitudes already at the closest portable station at 4 km (Figure 4a) and at all regional stations (Figure 4b), and appropriate small local (duration) magnitude M_L=1.5, estimated by the Israel Seismic Network, compared to M_L=2.4 for the reference coupled Ex.3. Note very weak S-waves for Ex.2, compared to Ex.3.

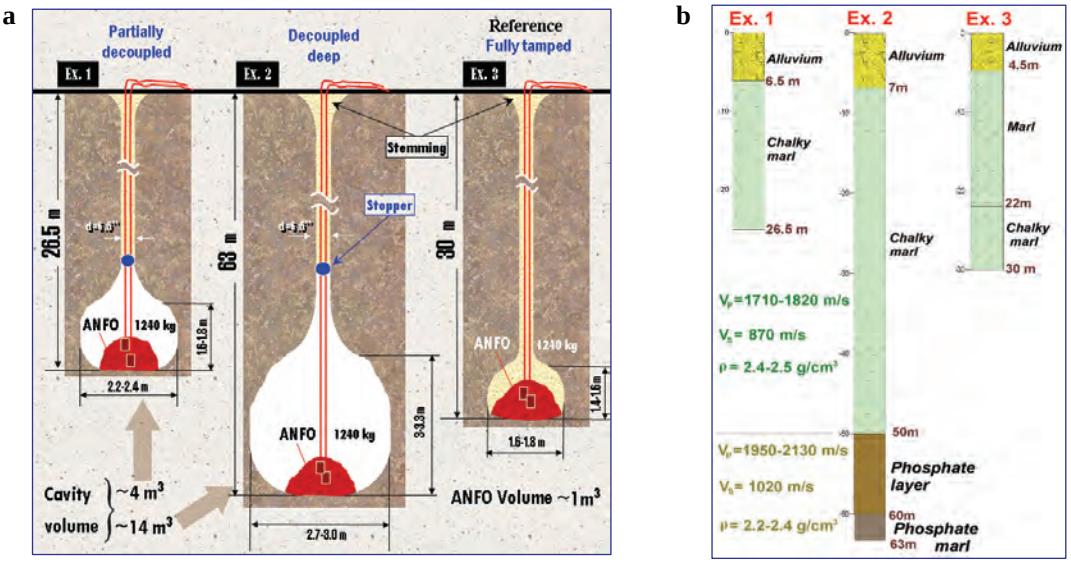

Figure 2. Design of the Decoupling experiment (a) and the site geology from the shot borehole drilling logs (b).

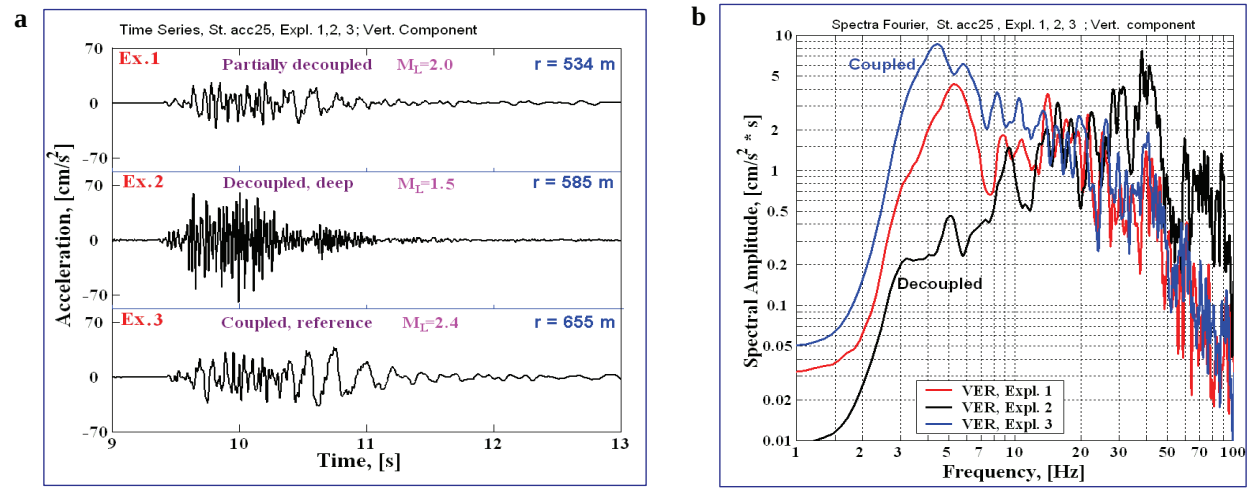

Figure 3. Vertical signal records (a) and spectra (b) at ~0.6 km (accelerometer ETNA). Local (duration) magnitudes M_L and epicentral distances are also shown.

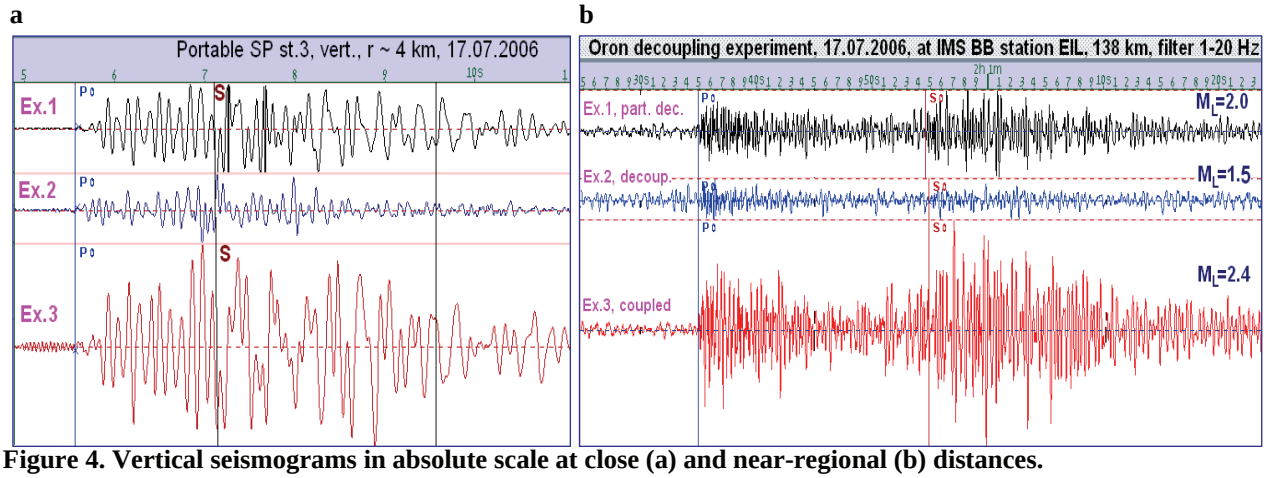

Figure 4. Vertical seismograms in absolute scale at close (a) and near-regional (b) distances.

We tried to estimate a Decoupling Factor (DF) as the ratio of peak (vertical) amplitude for the coupled (reference) shot (Ex.3) to the amplitude for a partially decoupled shot (Ex.1, Ex.2). We used vertical records of two SP (ZFRI, PRNI) and two BB (HRFI, EIL) stations in the distance range 40–140 km (Figure 5). We roughly estimated the cavity volume V as ~4 m^3 for Ex.1 and ~14 m^3 for Ex2 (see Figure 2a), and the TNT equivalent charge as W_{eq}~1000 kg (1,240 kg ANFO), then the Charge/Volume ratio W_{eq}/V (kg/m^3) was calculated as ~250 for Ex.1 and ~70 for Ex.2. The average DF values obtained (Figure 5b) fit predicted factors; however, they were calculated for granite (Stevens et al., 2003).

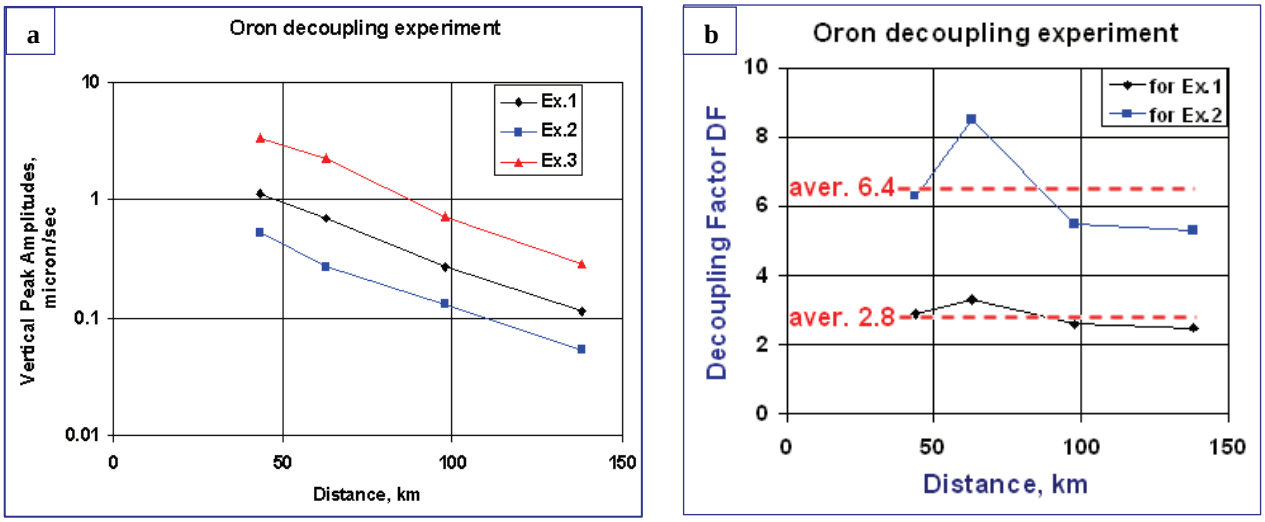

Figure 5. Signal peak amplitude (a) and Decoupling Factor (b) in a broad distance range for the partially decoupled explosions in soft sediment media.

We estimated seismic energy partition for the three explosions. For the selected five stations (a portable SP station at ~4 km was added) we calculated seismic energy for regional phases P, S (vertical component) in time windows T different for each station, but under condition Ts/Tp~1.5, and then S/P energy ratios (Figure 6). Obtained estimation results show that at all distances maximal S/P ratios are found for the coupled Ex.3, minimal S/P ratios—for the deep decoupled Ex.2.

Note that the twice larger shot depth for Ex.2 (compared to Ex.3) could result in smaller S-wave energy radiation (see below), and thus contribute together with the decoupling effect to the observed difference in S/P ratios.

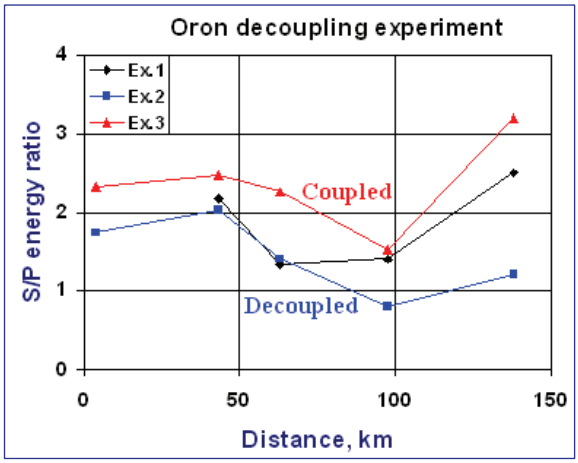

Figure 6. Energy partition estimation: S/P energy ratio for the Decoupling series shots.

Depth-of-Burial Experiment

The project central DOB series was conducted on Jan 2, 2007, and included three equal near-spherical charges of 4200 kg ANFO at depths 26 m, 45 m and 59 m, spacing between the shots was 200–300 m (Figure 7, Table 1). The main objective of the experiment was to investigate relations between explosion depth and spectral/energetic/magnitude parameters of regional seismic phases, especially S/P ratio. The site geology was presented by the same soft sediments with similar mechanical properties as for the nearby (~2.5 km away)

Decoupling explosion site (Figures 2b, 7), therefore rock media was homogeneous for all the sources. The charge weight was utmost maximal which provided full containment for all 3 shots: we observed a small ground surface uplifting on the video-record and thin cracks around the hole for the shallowest Ex.1, but no craters were found.

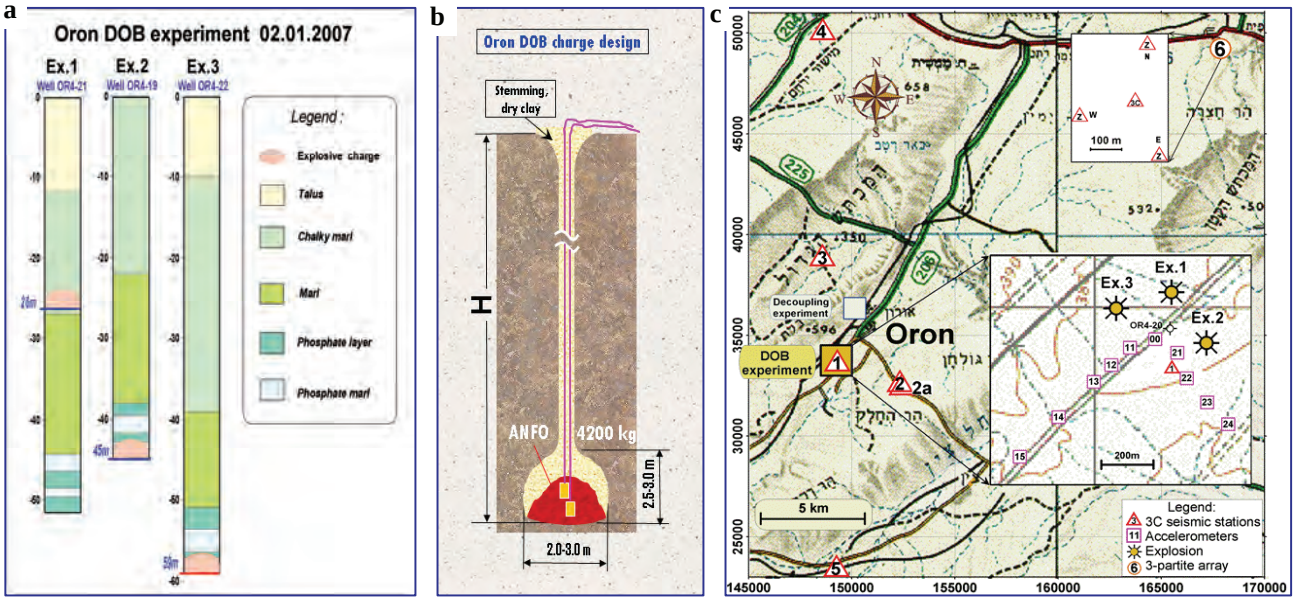

Figure 7. Geology of explosion boreholes from drilling logs (a); specific charge design providing large near-spherical seismic sources (b); location of the two experiment sites and portable stations, two insertions show detailed location of the tripartite array elements (st.6) and configuration of the explosion boreholes and accelerometers (c).

Tabel 1. Parameters of DOB Explosions

Ex. No.	Hole ID	Hole depth H, m	O.T. GMT	Local duration magnitude	Coord. (local)		Lat.	Long.
					X, km	Y, km		
1	OR4-21	26	09:31:12.317	2.7	149.294	34.058	30.89714	34.99353
2	OR4-19	45	10:01:13.442	2.6	149.428	33.858	30.89530	34.99498
3	OR4-22	59	10:30:31.276	2.5	149.082	33.994	30.89656	34.99133

Different 3C observation systems were deployed at near-source distances: 10 accelerometers ETNA, range 120–870 m; 4 SP seismic stations L4C, 3.5-16 km; a tripartite SP array (st.6) at 24 km deployed by Israel National Data Center (NDC) (Figure 7c). Extensive good quality datasets were obtained for all explosions from portable and permanent regional seismic stations, including IMS BB stations EIL, MMAI array, ASF, Jordan (Figure 1), in broad distance range 0.15–238 km. The records demonstrated peculiar signal characteristics and energy generation features related to these specific near-spherical seismic sources at different depths.

At near-source accelerograms, highest amplitudes are observed for the deepest Ex.3, though it was the weakest event with the minimal magnitude, estimated at regional distances (Table 1). A clear trend of peak amplitude and energy enhancement with the charge depth are found, with a simultaneous rise of signal frequencies. Sample vertical accelerograms for the closest (equidistant ACC00) and remotest (ACC15) stations and the whole signal amplitude spectra (Figure 8) show that the largest peak ground acceleration values for the Ex.3 are accompanied by high frequencies: maximal energy at 10-20 Hz and significant spectral peaks at higher frequencies up to 40–50 Hz, unlike the "shallow" Ex.1, with maximal energy at 3–14 Hz and a sharp drop at higher frequencies.

As early as r~3.5 km, the attenuation of high-frequency seismic energy results in minimal peak amplitudes and spectra for Ex.3 in the range 0.5-10 Hz, yet keeping maximal energy at higher frequencies (Figure 9). A drastic drop of amplitude for the deepest Ex.3 (compared to Ex.1) is clearly manifested at a continuous 1-hour record of closely

located 3-component SP st.6 in the portable tripartite array (Figure 10). The well known reduction of signal energy and event magnitude with the source depth (e.g., Richards and Kim, 2005) is observed at all local and near-regional distances (Figure 11). Decrease of spectral amplitudes with increasing shot depth between about 1 and 10 Hz is converted to the opposite trend at higher frequencies ~10–20 Hz (Figures 9-11,b). Local (duration) magnitude M_L values for 3 DOB shots, averaged over several stations of Israel Seismic Network and plotted versus source depth, demonstrate linear relationship (Figure 12a). A similar correlation for analogous Balapan DOB experiment is plotted by utilizing energy class K values estimated from regional stations (Mikhailova et al., 2001) (Figure 12b).

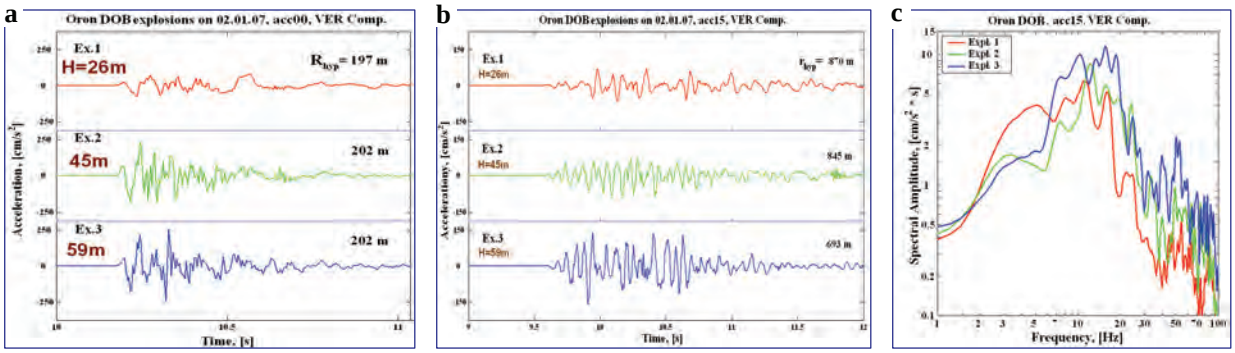

Figure 8. Vertical accelerograms at close station ACC00 equidistant from 3 DOB shots (a), and the remotest station ACC15 (b) and amplitude spectra (c). Hypocentral distances to the shots are shown.

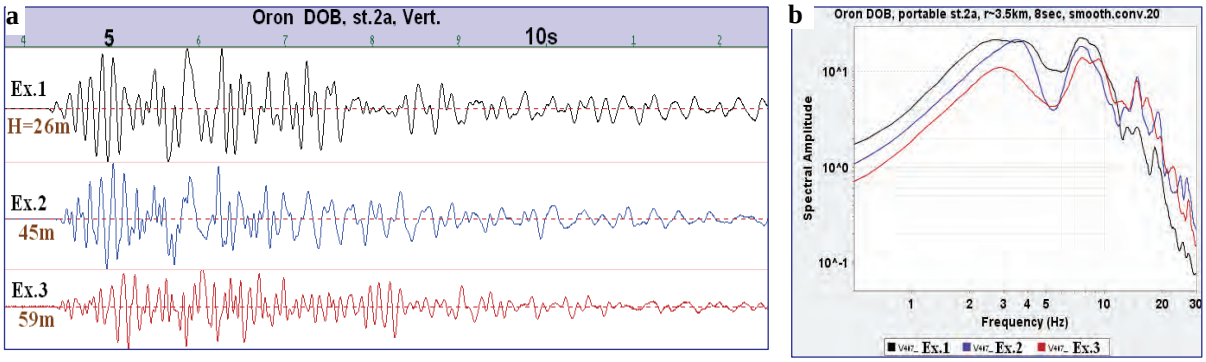

Figure 9. Vertical seismograms in absolute scale (a) and spectra of the whole signal (8 sec) (b) at the closest SP station at r~3.5 km. Note dominant energy for the deepest Ex.3 at high frequencies f >10 Hz.

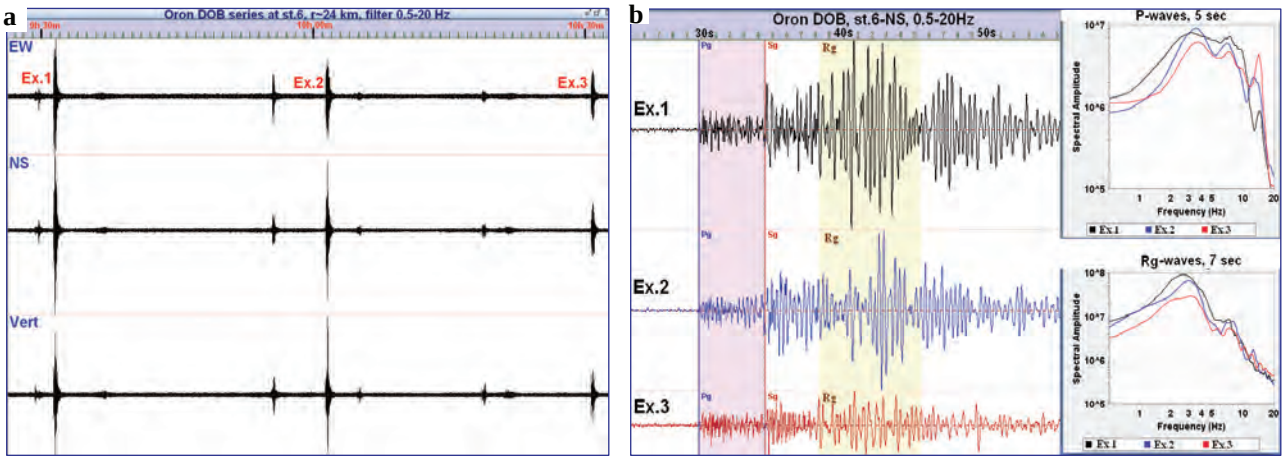

Figure 10. Close local recordings (in absolute scale) at the central 3C station of the SP tripartite array (St.6) at r~24 km: continuous 3C recording section of all 3 shots (a), NS records and spectra of P and Rg phases (b). A clear Rg onset is observed at vertical records (velocity ~2 km/s). Note a dominant spectral peak for Ex.3 at 13-15 Hz in P-phase which is not observed in Rg-phase.

To characterize better seismic energy generation for Oron DOB explosions we calculated the whole signal energy in the time domain recorded at 3C stations in the broad distance range (24–238 km), for different components – Vertical, Horizontal (the sum of energies for NS and EW components) and Vector (Figure 13). The Vertical energy shows a rather weak decrease with the source depth, while the Horizontal and Vector values drop more sharply.

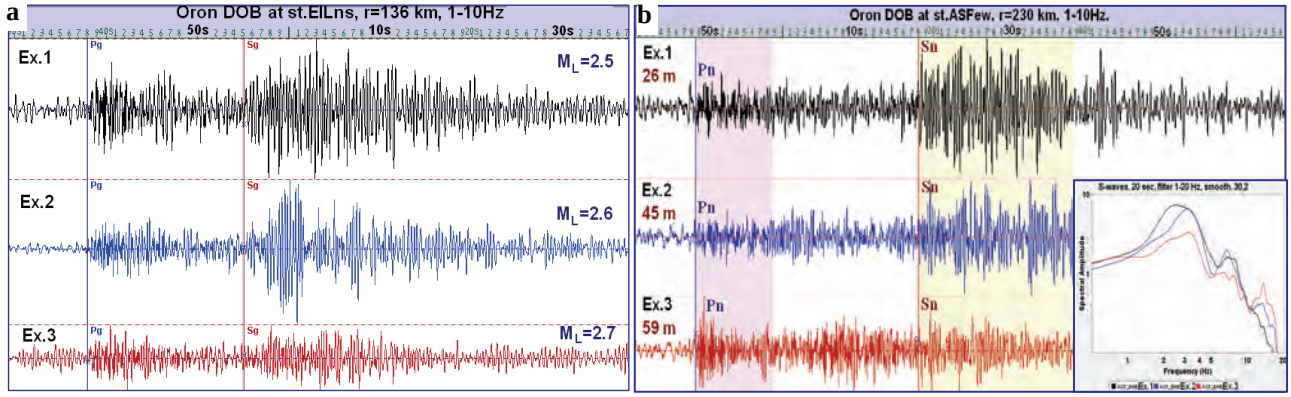

Figure 11. Horizontal seismograms (in absolute scale) at two IMS BB stations: EIL-NS (Radial) component (a), ASF-EW (~Transversal) component, windows for calculation spectra and spectral ratio are shown; conversion of spectra dominance for different shots at ~10 Hz is observed (b).

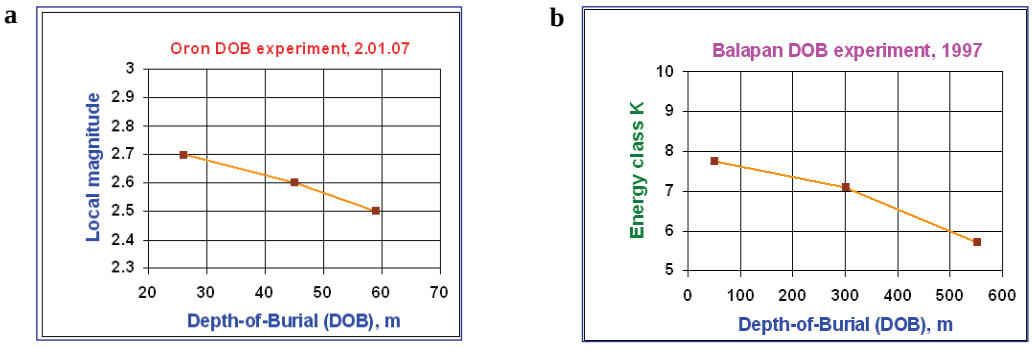

Figure 12. Magnitude versus source depth for two DOB experiments: local (duration) magnitude M_L at Oron (a) and Energy class K at Balapan (b).

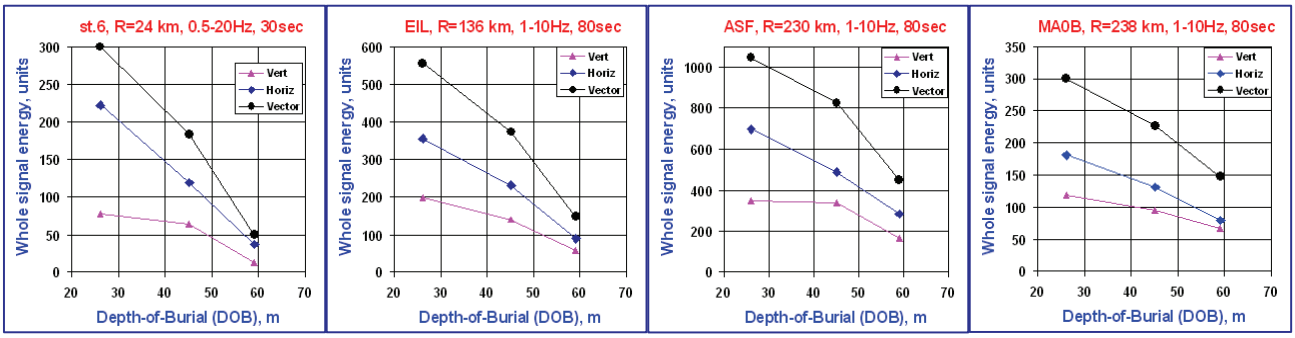

Figure 13. Seismic energy of the whole signal recorded at different components of several SP and BB stations versus source depth. Note different frequency range (filtering used) and signal duration.

Energy partition. As expected, at close local and near-regional distances observed amplitudes and energy of S-waves show significant and monotonous decrease with depth; while P-waves remain about constant or even increase (Figures 10b, 11). We evaluated relative excitation of P and S energy using 3C stations, based on identical propagation paths in the experiment, for differing depth sources. We calculated P/S spectral ratios for smoothed amplitude spectra of P and S phases and S/P energy ratios for different regional phases (Figures 14, 15). Different time windows were used depending on distance and reliable phase identification: equal short duration for clear phases Pg and Sg (4 sec), and Rg (7 sec) at the close SP st.6 (24 km) (see Figure 10b), and larger diverse windows for P-group (10 sec) and S-group (20 sec) at remote BB stations EIL, ASF and MMA0B (Figures 11, 14a), which include (Pn, Pg) and (Sn, Sg, Lg), because different P and S phases are not well separated at this distance range. Filtering was applied to close (0.5–20 Hz) and remote (1–10 Hz) records.

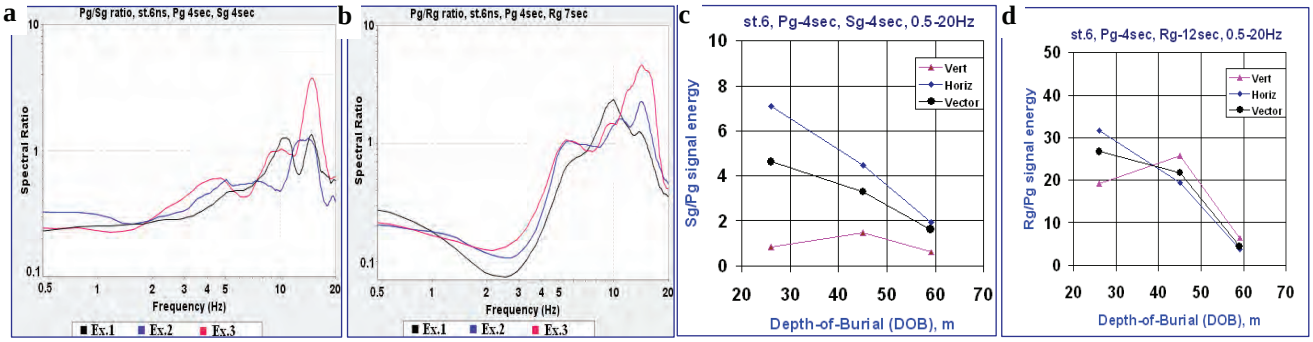

Figure 14. Energy partition at close local station st.6 (24 km): spectral ratios Pg/Sg (a) and Pg/Rg (b) suppose a weak dependence on source depth at 2–5 Hz; signal energy ratios Sg/Pg (c) and Rg/Pg (d) show an obvious decrease for deeper shots, especially for the Horizontal (EW+NS) component.

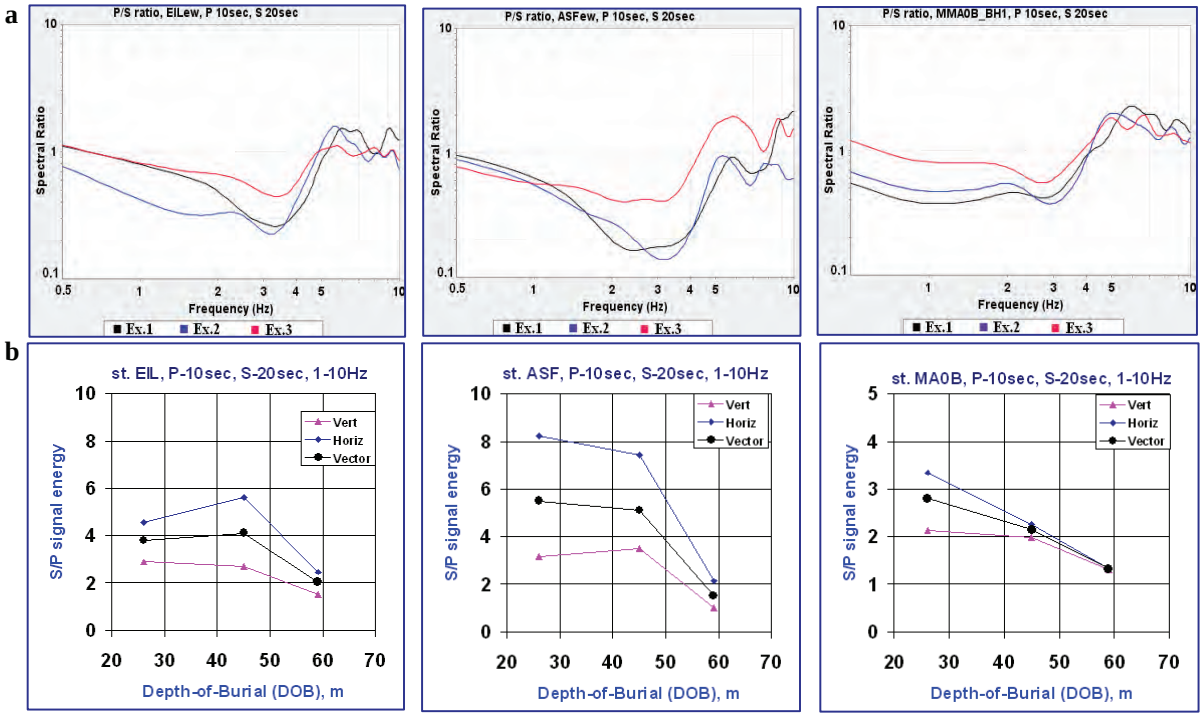

Figure 15. Energy partition at near-regional distances: spectral ratios P/S show decreased S-wave excitation for deeper shots in the range ~(0.5–8) Hz (a); signal energy ratios S/P decrease, in general, monotonous with depth (b).

Spectral ratios of Pg/Sg and Pg/Rg at close st.6 (24 km) (Figure 14a,b) show a weak dependence on DOB in a narrow band 2–5 Hz, whereas at near-regional distances a clear strong raise in the ratios is observed with increasing explosion depth, in the broader range about (0.5-8 Hz) (Figure 15a), as similar to results obtained for the Balapan DOB experiment (Mayers et al., 1999). Another characteristic of the radiated energy partition, the signal energy ratio S/P shows an obvious, monotonous (in-average) decrease for deeper shots, especially for the horizontal component.

Location analysis

A special feature of the Oron DOB experiment—the placement of the charges in holes, separated by only a few hundred meters, in order to eliminate variations in waveforms and travel times due to different propagation conditions—provided a good chance for a comparative location study. Using measured P onsets at the observation range and a local 1D velocity model, the three explosions were located by two procedures: the standard grid-search LSQR, and a new model-free robust GS algorithm (Pinsky, 2007) with the essential advantage shown by the latter due to eliminating the error of the unknown velocity model misfit (Figure 16, Table 2).

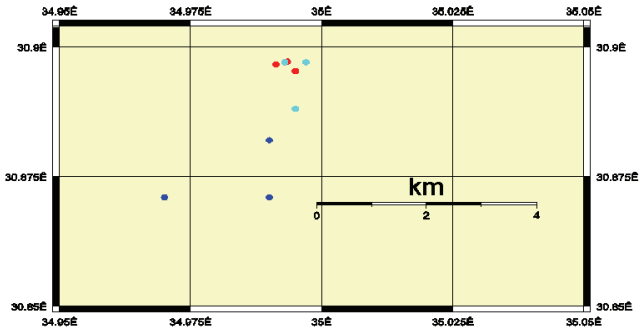

Table 2. Location error for three DOB explosions by different algorithms

#	Number of stations	GS	LSQR
		Error, km	Error, km
Ex.1	17	0.5	2.2
Ex.2	22	1.2	3.1
Ex.3	14	0.6	3.1

Figure 16. Location of the three DOB shots (● - Ground Truth) by the LSQR (●) and the GS (●) algorithms.

Discussion

The Oron Decoupling experiment was not pure, because the series shots were not placed at the same depth. However main features of the decoupling effect were observed and estimated, matching roughly to theoretical conceptions. The high frequencies (40–50 Hz), which we observed for near-source accelerograms of the decoupled shot, are lower than modeled for shock-wave reverberation (100–600 Hz) from nuclear sources (Stevens et al., 1991). It is explained by the fact that air-shock wave velocities for small chemical charges are much lower than for nuclear detonations with extremely high temperatures and pressures. The results also show that the utilized unique design of near-spherical sources can be used for the preparation of the full-scale, pure and cost-effective Decoupling Experiment.

The design and configuration of Oron DOB series were preferable in some conditions compared to the previous Balapan DOB experiment (Table 3). Initially we planned much deeper and afterwards—little smaller depths than realized, but after discussions (A. Dainty, pers. communication) we decided on the final charge depths in order to provide: 1) scaled depths in the range of NTS nuclear tests h=95-425 m/kT$^{1/3}$ (Springer et al., 2002); 2) full containment of all series shots.

Table 3. Comparison of design for two DOB experiments.

Parameter	1997 Balapan DOB	Oron DOB
Charge shape, aspect ratio (AR)	cylinder, L~34 m, AR~34	near-spherical, R~1-1.5m, AR~1
Scaled depth h=Hc/W$^{1/3}$, m/kT$^{1/3}$	113, 968, 1,823	167, 294, 387
Rock homogeneity	50-m shot—in sediments (shales), two others—in granites	Consolidated sediments: marls, chalky marls, phosphate marls
Explosion containment	50-m shot created a 40-m crater, for deeper shots the casing was ejected	all shots contained, 26-m shot created surface thin cracks
Spacing of the series shots	2.5–8.2 km	220–360 m (the same propagation even for close stations)

The increase of overburden lithostatic pressure with depth opposes to the opening and propagating of cracks and prevents non-linear deformations, thus squeezing the inelastic zone and decreasing seismic source size and volume in the model by Sharpe (1942), together with the volume expansion δV (Richards and Kim, 2005). Appropriate increased dominant frequencies of a radiated signal that we observed jointly with the near-source largest signal amplitudes, resulted in rapid attenuation of seismic energy with distance and minimal local magnitude.

For a long vertical source the decrease in pressure at shallow depth causes much stronger non-linear deformation above the explosion than below it, and this asymmetry results in the direct generation of shear waves, which would not be generated by spherical sources (Stevens, 2006). An important goal of our experiment was to get rid of the asymmetry effect caused by the difference of lithostatic pressures above and below the vertical lengthy cylinder explosive source, typical for borehole chemical explosions, and to study the generation of shear waves for about spherically symmetric sources, typical for nuclear tests. Nevertheless, we note that the observed on video-record small-amplitude surface uplifting for the shallowest Ex.1, H=26 m, may indicate an asymmetry effect caused by closeness to the surface, contributing to the generation of larger S-wave energy.

CONCLUSIONS AND RECOMMENDATIONS

- Oron experimental explosion series were conducted for the empirical modeling of decoupling effects and the relation between nuclear test depth and spectral/energetic parameters of regional seismic signals.
- A clear magnitude/energy reduction with depth was observed at regional distances, complemented by near-source observations of higher frequencies (and larger amplitude/energy) for deeper charges.
- S/P energy and spectral ratios and decoupling factors were estimated at close local and near-regional distances, roughly matching theoretical conceptions and known observations.
- The Oron DOB experiment with the original and adequate configuration and charge design was preferable in some conditions than the previous Balapan DOB (where detrimental factors affecting signals could not be excluded).
- Oron experiments demonstrated the feasibility of the utilized method of seismic source design for construction of near-spherical charges of different size (up to 10 tons) and at different depths (up to 70–80 m) and conducting broad-scale, low-cost experimental series: decoupling, DOB, variable charge weight.

ACKNOWLEDGEMENTS

Many individuals and organizations contributed to the success of the explosion experiments. We appreciate help of A. Dainty for useful discussions and information before and after the experiments. Special thanks to B. Hayoun of Tamar Ltd., Y. Levi and U. Yassur of Rotem Amfert Negev Ltd. for crucial a role in the preparation and conducting the special design explosions. Y. Ben-Horin of Israel NDC provided excellent records of the DOB experiment with a portable tripartite array. The GII staff performed technical support throughout the experiment, data processing and analysis; special thanks to U. Peled, M. Kalmanovich, N. Perelman, and A. Polozov.

REFERENCES

Gitterman, Y., V. Pinsky, A. Shapira, M. Ergin, D. Kalafat, G. Gurbuz, and K. Solomi (2002). Improvement in detection, location and identification of small events through joint data analysis by seismic stations in the Middle East/Eastern Mediterranean region, in *Proceedings of the 24th Seismic Research Review Nuclear Explosion Monitoring: Innovation and Integration,* LA-UR-02-5048, Vol. 1, pp. 271–282.

Gitterman, Y., R. Hofstetter, and V. Pinsky (2006). Source features and scaling of buried and surface experimental explosions in Israel, in *Proceedings of the 28th Seismic Research Review: Ground-Based Nuclear* Explosion Monitoring Technologies, LA-UR-06-5471, Vol. 1, pp. 597–606.

Mayers, S. C., W.R. Walter, K. Mayeda and L. Glenn (1999). Observations in support of Rg scatterieng as a source for explosion S waves: regional and local recordings of the 1997 Kazakhstan Depth of Burial Experiment, *Bull. Seism. Soc. Am.*.89: (2), 544–549.

Mikhailova, N., Germanova, T., Aristova, I. (2001). Estimation of energy and magnitude characteristics based on seismic records of chemical explosions in 1997-2000 on the former Semipalatinsk Test Site, in: *Geophysics and Non-Proliferation problems, 2001, Kazakhstan*, V.2, NNC RK, 93–98 (in Russian).

Pinsky V. (2007). Accurate location of seismic sources with and without travel time model, in: *Earthquake monitoring and seismic hazard mitigation in Balkan countries, NATO ARW series*, edited by E. Husebye and C. Christova, Springer.

Richards, P. G. and W.-Y. Kim (2005). Equivalent volume sources for explosions at depth: theory and observations, *Bull. Seism. Soc. Am.*, Vol.95, No.2, 401–407.

Sharpe, J. A. (1942). The production of elastic waves by explosion pressure: part I, theory and empirical field observations, *Geophysics* 7: 144–154.

Springer, D.L., G. A. Pawloski, J. L. Ricca, R. F. Rohrer and D. K. Smith (2002). Seismic Source Summary for All U.S. Below-Surface Nuclear Explosions, *Bull. Seism. Soc. Am.*92: (5), 1806–1840.

Stevens, J., J. Murphy and N. Rimer (1991). Seismic source characteristics of cavity decoupled explosions in salt and tuff. *Bull. Seism. Soc. Am.*, Vol.81, No.4, 1272–1291

Stevens, J., N. Rimer, H. Xu, J. Murphy, B. Barker, S. Gibbons, C. Lindholm, F. Ringdal, T. Kvaerna, and I. Kitov (2003). Analysis and simulation of cavity-decoupled chemical explosions, in *Proceedings of the 25th Seismic Research Review—Nuclear Explosion Monitoring: Building the Knowledge Base*, LA-UR-03-6029, Vol. 1, pp. 466–475.

Stevens, J. (2006). Development and Future of Explosion Source Theory, *Abstracts of the 2006 Annual SSA meeting*, San Francisco, California, 18–22 April.

REGIONAL EVENT IDENTIFICATION RESEARCH IN ASIA

Hans E. Hartse, George E. Randall, Xiaoning (David) Yang, and Charlotte A. Rowe

Los Alamos National Laboratory

Sponsored by National Nuclear Security Administration
Office of Nonproliferation Research and Development
Office of Defense Nuclear Nonproliferation

Contract No. DE-AC52-06NA25396

ABSTRACT

Recent event identification efforts at Los Alamos National Laboratory (LANL) include mining event ground-truth data collection in central Asia, and efforts to improve the magnitude and distance amplitude correction (MDAC) discrimination methodology through derivation of Eurasian two-dimensional, regional-phase attenuation models and frequency-dependent Pn and Sn geometric-spreading models for a spherical Earth.

Our mining event efforts have identified mines around the former Soviet nuclear test site in eastern Kazakhstan. Using the Kazakh National Data Centre (KNDC) bulletin from 2002 to 2005, and waveforms recorded at station KURK and array MKAR, we combined time-of-day seismic event analysis, waveform cross correlations, seismic event location methods, image analysis, and seismic discrimination methods to identify active mines. Our goal was to tie event clusters with similar waveforms to specific mine sites, and thereby establish ground truth location and event type (earthquake or explosion) information. We found 13 event clusters that are probable mine sites, accounting for 277 individual seismic events. At least 4 of our event cluster locations are within 15 km of open pit mines, clearly visible on low-resolution imagery. All individual members of these clusters occur between 8am and 8pm local time. We presumed 75 local night-time events were earthquakes, and we found that none of these night time events had similar waveforms.

Using these probable mining events and the 75 unclustered night events as presumed earthquakes, we tested traditional body-wave discriminants in bands between 0.5 and 12 Hz, and find Lg spectral ratios and Pg/Lg high-frequency ratios show some ability to separate the event populations, but the separation is poor compared with the case of contained, single-charge explosions and earthquakes. The Pg spectral ratio, which has been shown to separate earthquakes and nuclear explosions in central Asia, does not separate mining explosions from earthquakes in eastern Kazakhstan. We will continue to investigate discriminant measurement and correction methods in an attempt to improve performance in separating mining events from both earthquakes and single-charge underground nuclear events.

In parallel with a project between the University of California, Santa Cruz (UCSC) and LANL to develop 1-Hz, two-dimensional, regional-phase attenuation models for Eurasia to improve the magnitude and distance amplitude correction (MDAC) discrimination methodology, we are working on developing regional-phase attenuation models for Eurasia for a broad range of frequencies between 0.5 and 10 Hz. We have finished an initial phase of data collection and amplitude measurement for around 100 stations in the region. Based on the data coverage, we collected a dataset of Pn picks from the LANL location database to be used in further data collection. We have also conducted synthetic simulations to investigate the geometric spreading of Pn and Sn in a spherical earth. From the modeling results, we propose new, frequency-dependent Pn and Sn geometric-spreading models for a spherical Earth.

While measuring phase and noise amplitudes using 20 sample per second (SPS) data obtained at Global Seismographic Network (GSN) stations operated through the Incorporated Research Institutions for Seismology (IRIS) International Deployment of Accelerometers (IDA) (II) group in Asia, we found that a combination of relatively early anti-alias filter roll-off and operations at relatively low gains, typically result in inaccurate registration of seismic noise and signals (from all but large events) in 6 to 8 Hz bands. Known II stations with this problem include AAK, BRVK, KURK, NIL, and TLY. This contrasts with other GSN stations in Asia where accurate 6 to 8 Hz measurements can be obtained from 20 SPS data streams.

OBJECTIVES

Over the past year we have continued studies to collect mining-event ground-truth data in central Asia, and we have continued efforts to derive Eurasian two-dimensional, regional-phase attenuation models and frequency-dependent Pn and Sn geometric-spreading models for a spherical Earth. The results of these efforts are all directed toward improved discrimination between earthquakes and explosions using regional and local seismic data.

RESEARCH ACCOMPLISHED

Kazakh Mining Ground Truth Study

We have been expanding our seismic ground truth data collection efforts for central Asia by identifying mines and mining explosion seismograms. Working with KNDC1 bulletins (2002–2005), we combine time-of-day seismic event analysis, waveform cross correlations, seismic event location methods, image analysis, and seismic discrimination methods to identify active mines in the area between International Monitoring System (IMS) array MKAR and Global Seismic Network (GSN) station KURK. Most of the events within this area occur during daytime (Figure 1), are usually small (often recorded at only one or two stations or arrays), and therefore tend to be poorly located. Our goal is to tie event clusters to specific mine sites, and thereby establish ground truth location and event type (earthquake or explosion) information.

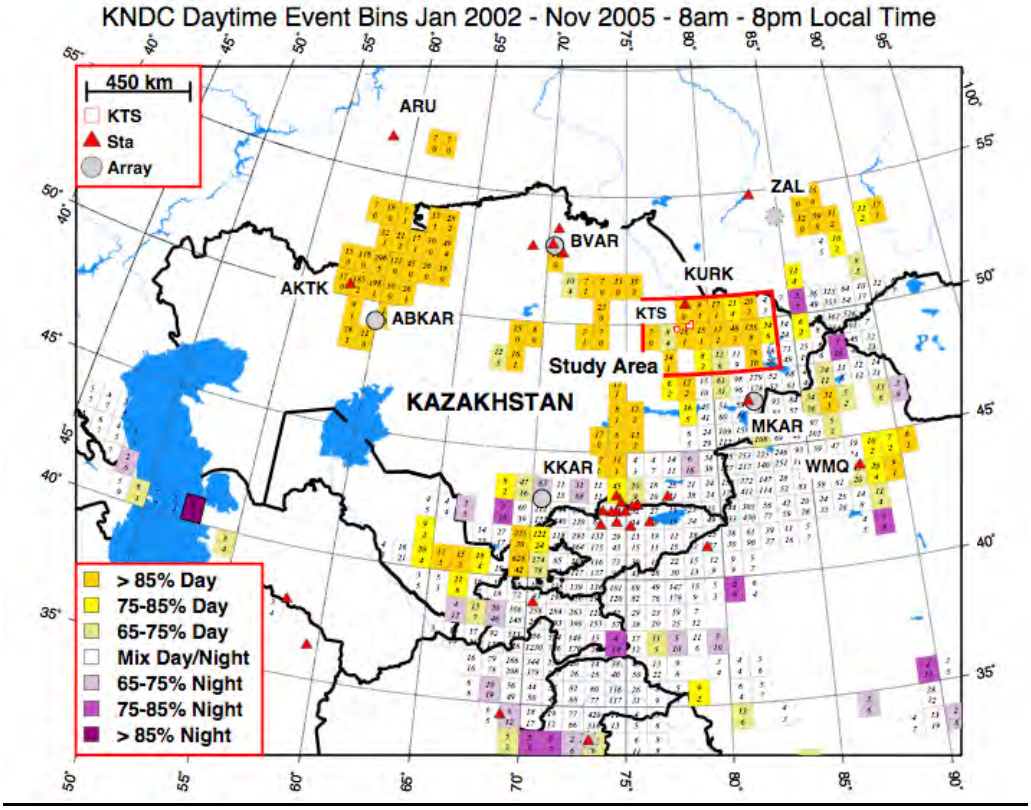

Figure 1. Time-of-day seismicity for Kazakhstan and surrounding regions. Primary event information source is the KNDC web-published bulletin. Gold and yellow regions are dominated by daytime mining explosions. Within each bin upper number is the daytime event count and the lower number is the nighttime event count. We focused on the area within the red box between array MKAR and station KURK in eastern Kazakhstan, which includes the former Soviet nuclear test site (KTS).

Using KNDC locations as a guide, we assembled about 450 three-component, event-segmented waveforms from MKAR array-element MK31. After bandpass filtering between 1.5 and 5.5 Hz, we then cross-correlated the first 20 seconds of each component's event-record with every other event record from the same component (that is, BHZ was correlated with other BHZ records, etc.). After stacking and normalizing the individual component correlations

into three-component correlations, we assembled similar-event clusters based on peak correlation coefficients exceeding 0.4. From the relative timing offsets within a given cluster's correlation peaks, we time-shifted, aligned, and stacked the individual event waveforms to create a single, three-component record at stations MK31 and KURK, and we stacked MKAR SHZ array elements. These waveform sums become the reference waves of each event cluster. Figure 2 shows the stacked BHZ wave and several aligned individual waves at station MK31 for event cluster A (see Figure 3 for event cluster locations).

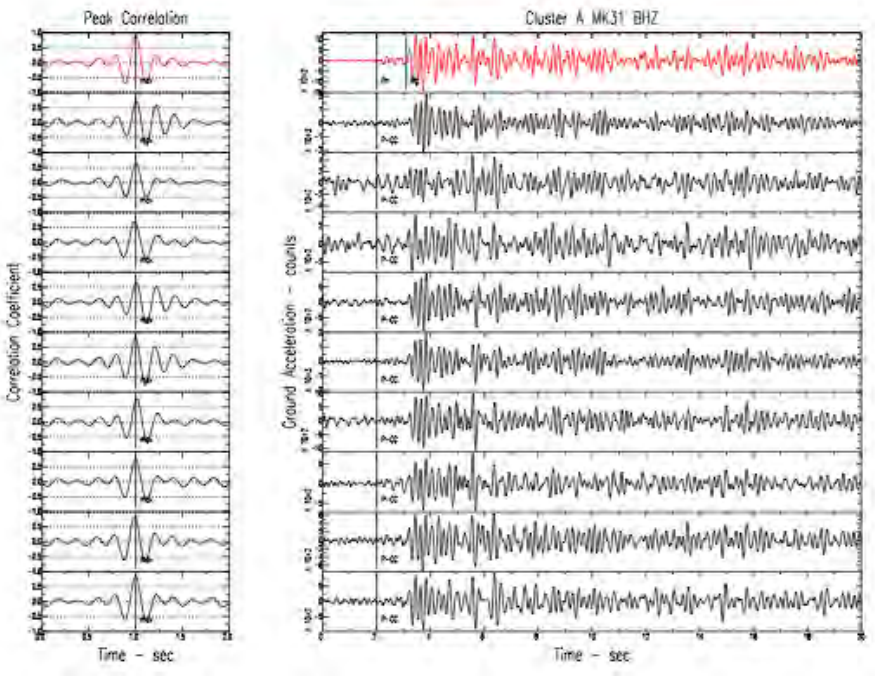

Figure 2. Event cluster A sample waveform stack (in red) and individual, vertical-component, time-aligned P-waves (in black) at MK31 BHZ. The three-component cross-correlation results are shown at left. Note improved signal-to-noise ratio on the stacked wave for Pn (first break). See Figure 3 for cluster locations.

We found 13 daytime clusters, each with 5 or more individual events, that are probable mine sites, accounting for 280 of the 450 KNDC events composing our original data set. We picked times of regional phases (Pn, Pg, Sn, and Lg) from each cluster's stacked waves at array MKAR and station KURK. We also estimated back-azimuths from MKAR by applying frequency wavenumber methods to the short-period, stacked array elements, and we estimated back-azimuths from the stacked, three-component waves at KURK when signal-to-noise was favorable. Using the picks and back-azimuth estimates we re-located each mining-event cluster, thus reducing the 280 individual KNDC locations to 13 cluster locations (Figure 3). Event-station distances for the clusters are between about 75 and 550 km and most individual event magnitudes are between about 1.25 and 2.5 mb.

We found that nearly every clustered event occurred between hours 02 and 14 GMT, or between 8 am and 8 pm local time (Figure 4). We assume the unclustered night events are earthquakes (solid blue circles, Figure 3), and thus have been able to test body-wave discriminants following standard processing methods outlined in Hartse et al. (1997). The Pg/Lg high-frequency discriminant shows some event separation (Figure 5), but not the separation seen between earthquakes and single-charge, contained explosions (Hartse et al., 1997). The Lg spectral ratio does not appear to separate the mining explosions from the earthquakes (Figure 5). We will continue to investigate discriminant measurement and correction methods in an attempt to improve performance in separating mining events from earthquakes and from single-charge, contained explosions.

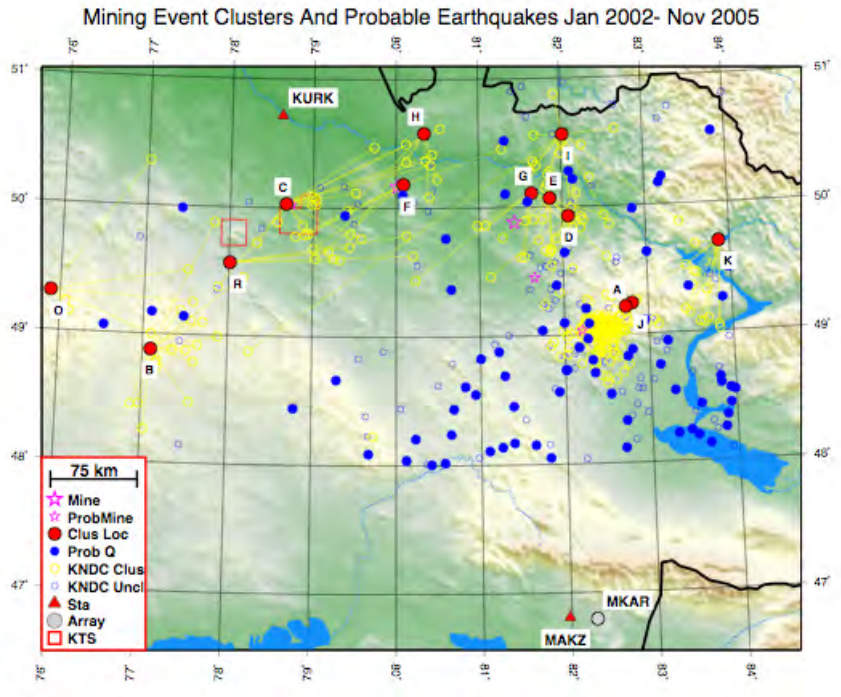

Figure 3. Study area showing individual KNDC locations (open yellow circles), which we formed into 13 event clusters (follow yellow lines to solid red circles). Solid blue circles show presumed earthquakes (unclustered night events), and open blue circles are remaining unclustered day events, which could be earthquakes or explosions.

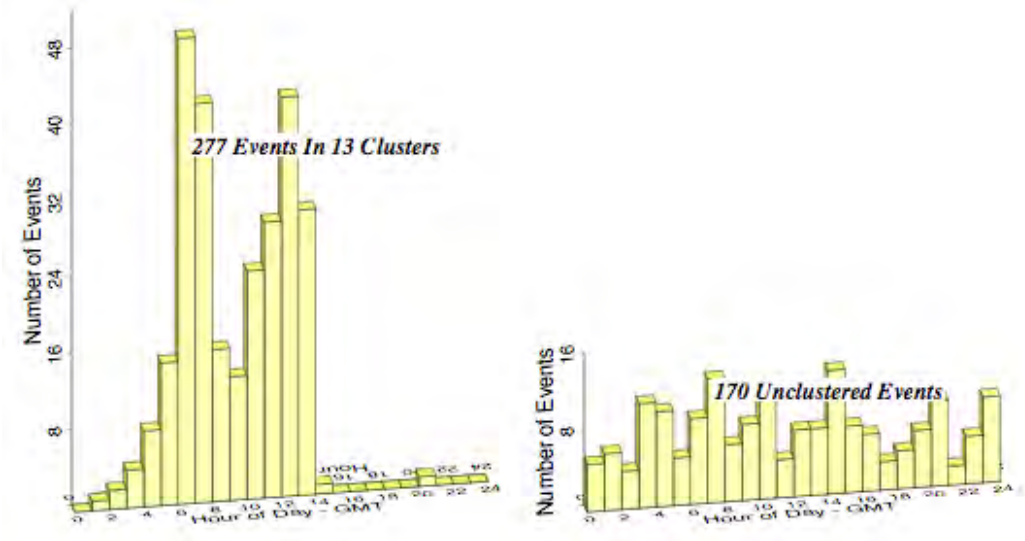

Figure 4. Time-of-day histograms for seismic events in study area. Left shows events associated with the 13 clusters. Local noon is 6 GMT. Note nearly all event activity abruptly ends at 1400 GMT, or 8 pm local time, another indication of mining activity. Histogram on right shows the 170 unclustered seismic events from within the study area. Only slightly more events are occurring during local day compared with local night, suggesting most day-time mining events have been successfully clustered.

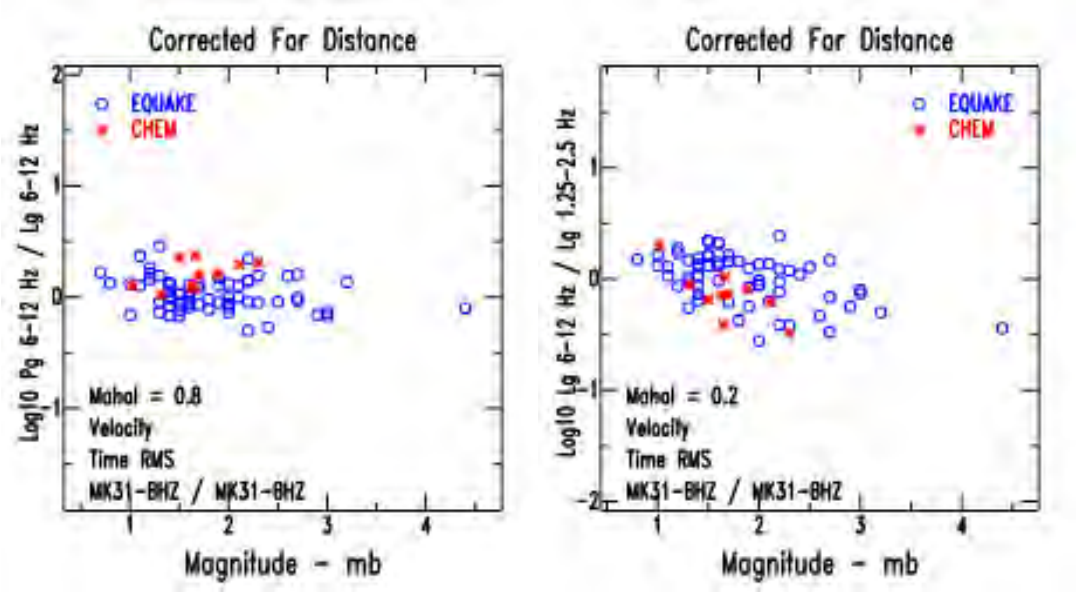

Figure 5. Sample discriminants. Only simple distance corrections have been applied. The high-frequency Pg/Lg shows some separation (left). The Lg spectral ratio shows little separation (right).

Based on seismic locations we have identified some mines on Google Earth and other images (Figure 6). Despite using only two stations at distances of up to 550 km, we have found at least four mine images that are within 14 km of our seismic locations. Improved seismic locations will allow for better ties between the seismicity and the mines in this area.

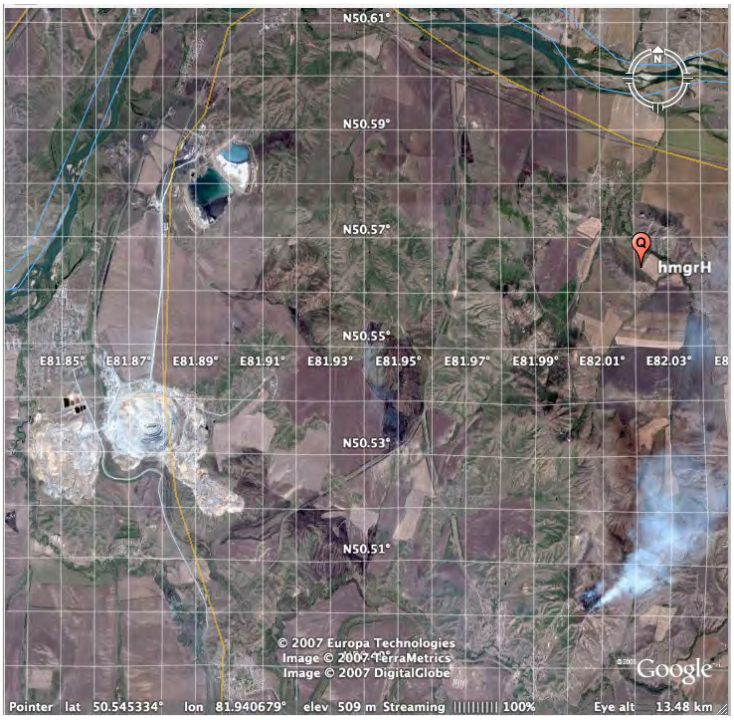

Figure 6. Google Earth image showing open-pit mine (on left) and seismic location of event cluster H with label "hmgrH" (on right). Separation distance between mine and seismic location is about 12 km.

Pn Attenuation Tomography between 0.5 and 8 Hz and Development of a New Pn Geometric-Spreading Model

Two-dimensional regional-phase (Pn, Pg, Sn and Lg) attenuation models improve the performance of MDAC methodology by providing better path corrections. Since regional-phase amplitudes in different frequency bands are used in MDAC corrections to form discriminants, regional-phase attenuation models for corresponding bands are needed. One method of obtaining the models at different frequencies is to derive the model at 1 Hz and use an assumed relationship between frequency and attenuation coefficient to deduct attenuation models at other frequencies. A second approach is to develop attenuation models at multiple frequency bands directly from observed data. Based on the second approach, we are developing regional-phase attenuation models for Eurasia for a broad range of frequencies between 0.5 and 8 Hz. Our focus has been on developing Pn attenuation models. This effort is in parallel to a project between UCSC and LANL to develop 1-Hz, 2D regional-phase attenuation models for the same region (Lay, et al., 2006).

We have finished two rounds of data collection and amplitude measurement. We collected waveform data from the Data Management Center (DMC) of the IRIS and from the LANL GNEMRE database. Using these waveform data, we made regional-phase amplitude measurements at frequencies of 0.5, 0.75, 1.0, 1.25, 1.5, 2.0, 2.5, 3.0, 4.0, 6.0, and 8.0 Hz. We used a semi-automatic procedure based on analyst picks and/or nominal regional-phase travel times to window different phases for amplitude measurement. Figure 7 shows the path coverage of 1-Hz Pn amplitudes that have signal-to-noise ratio of 2 or larger and a source-receiver distance of 2,000 km or shorter. We are currently collecting more amplitude data based on Pn picks stored in the LANL GNEMRE location database in order to improve coverage in certain areas. Figure 8 shows the path coverage of Pn picks from the database. Using this dataset, we hope to improve Pn path coverage, especially in northern Eurasia and India to some extent.

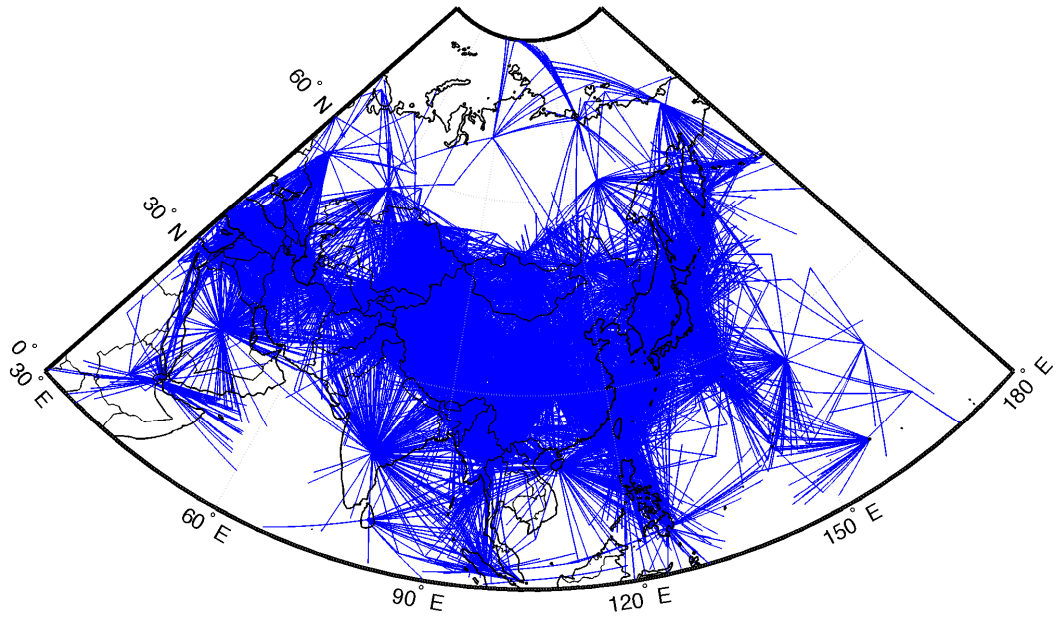

Figure 7. Path coverage of 1-Hz Pn amplitude measurements with signal-to-noise rates of 2 or larger and path lengths of 2,000 km or less.

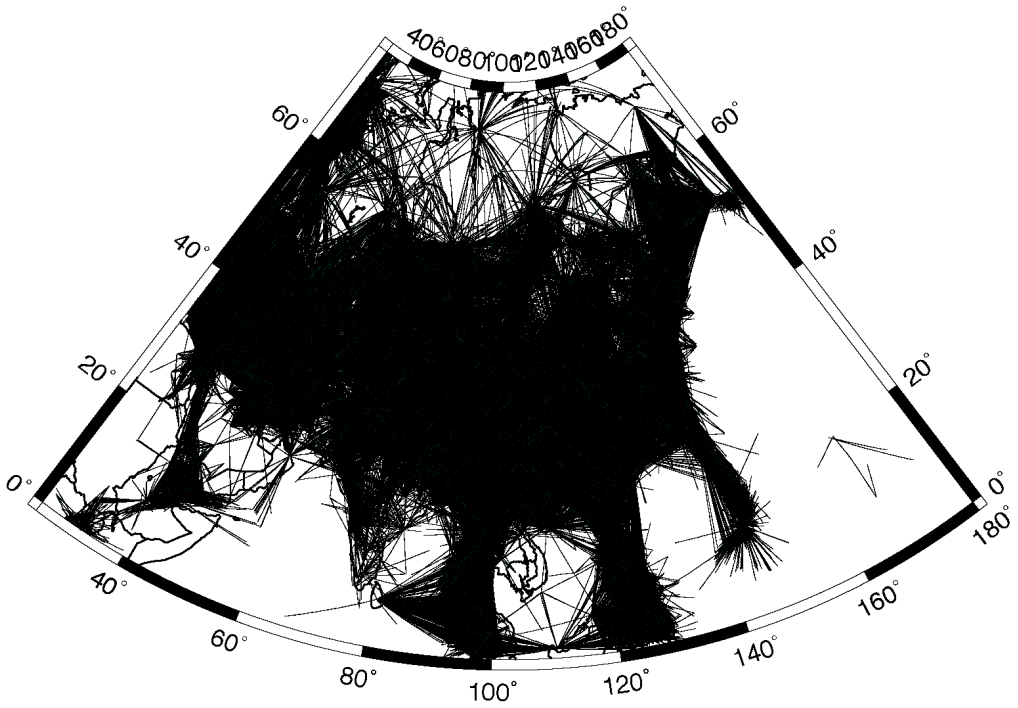

Figure 8. Path coverage Pn picks from the LANL GNEMRE location database.

Because of the tradeoff between geometric spreading and attenuation, it is necessary to accurately constrain the geometric spreading of the regional phases in order to develop reliable regional-phase attenuation models. Whereas the geometric spreading of crustal phases Pg and Lg may be relatively simple (Yang, 2002), the geometric spreading of upper-mantle phases Pn and Sn is more complex due to the sensitivity of these phases to the upper-mantle velocity structure and the Earth's sphericity.

In collaboration with researchers at UCSC, we conducted detailed simulation of Pn geometric spreading in a spherical Earth model. In order to quantify the first-order effects of the Earth's sphericity on Pn geometric spreading, we used a simple one-layer-crust over a constant-velocity-mantle spherical elastic Earth model in our simulations. We specified a crustal thickness of 40 km, representative of continental crusts. A reflectivity method was used to calculate synthetic Pn seismograms after the spherical Earth model was transformed into a plane-layered model through the Earth flattening transformation.

Figure 9 gives an illustration of Pn propagation in a spherical Earth from the simulation. On the left is the record section of synthetic Pn seismograms. Pn amplitudes as a function of epicentral distance and frequency are plotted on the right. The figure reveals several interesting characteristics of Pn traveling in a spherical Earth. Due to the Earth's sphericity, the apparent Pn velocity is not constant, but varies with epicentral distance. As is predicted by theory (e.g., Červený and Ravindra, 1971), the pulse shape of Pn evolves from that of the source, which is an impulse, at distances close to the critical distance (about 0.8°) to the shape of a far-field body wave, which is the time derivative of the source pulse, at farther distances. At about 10° to 12°, the wave that has no reflection at the Moho separates from the rest of the Pn wave packet and, somewhere between 16° and 19°, the wave that reflected once at the Moho separates.

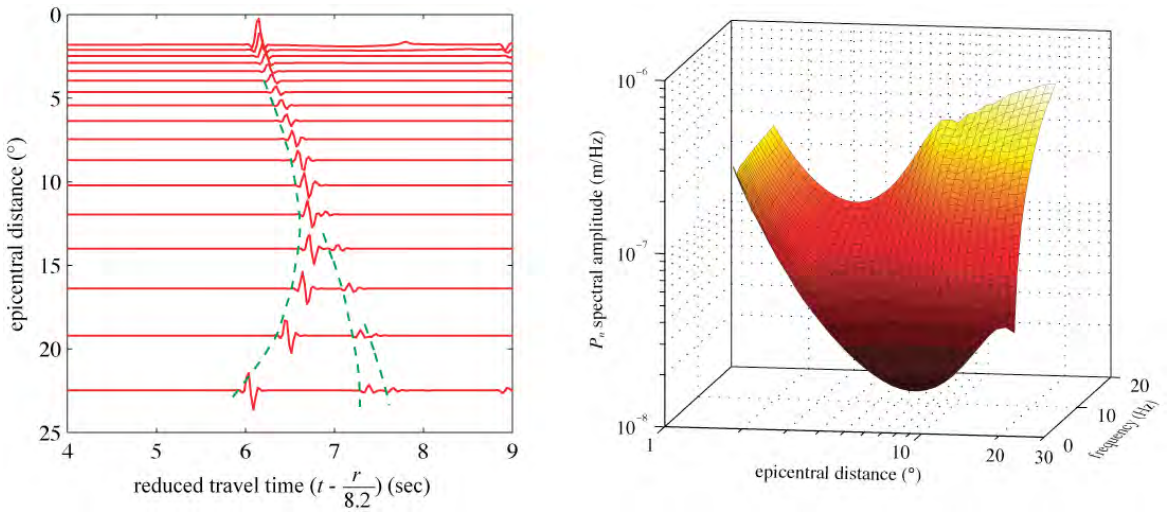

Figure 9. Record section of synthetic Pn seismograms in a spherical Earth model and Pn amplitudes as a function of epicentral distance and frequency. Green lines in the record section mark the first wave pulse (no reflection at Moho), the second wave pulse (one reflection) and the rest of the interference wave packet.

The behavior of Pn geometric spreading in a spherical Earth apparently cannot be accurately represented by a power-law model, which is commonly used. Based on the simulation results, we propose a new, frequency-dependent Pn geometric-spreading model that accounts for the effects of the Earth's sphericity. The new model is formulated as:

$$G(R,f)=\frac{10^{n_3(f)}}{R_0}\left(\frac{R_0}{R}\right)^{n_1(f)\log\left(\frac{R_0}{R}\right)+n_2(f)} \qquad (R_0 = 1 \text{ km}) \quad (1)$$

And

$$n_i(f)=n_{i1}\left[\log\left(\frac{f}{f_0}\right)\right]^2+n_{i2}\log\left(\frac{f}{f_0}\right)+n_{i3} \qquad (i = 1, 2, 3;\ f_0 = 1 \text{ Hz}). \quad (2)$$

The main differences between the new geometric-spreading model and the standard frequency-independent power-law model are the addition of the first term in the exponent and the frequency dependence of parameters n_i. In the logarithm domain, the new model is a quadratic function of log-distance, whereas the power-law model is linear. Values of model coefficients n_{ij} obtained by fitting the model to synthetics are listed in Table 1.

Using a set of observed Pn amplitude data from Eurasia, we estimated average Pn attenuation after correcting the amplitudes for geometric spreading with both the new spreading model and power-law models. Results show that the new spreading model yields reasonable Q values, whereas the power-law model results in Q values that are either too large or negative.

Table 1 Coefficients of the new Pn geometric-spreading model

n_{11}	n_{12}	n_{13}	n_{21}	n_{22}	n_{23}	n_{31}	n_{32}	n_{33}
-0.217	1.79	3.16	-1.94	8.43	18.6	-3.39	9.94	20.7

Data Issue For Some 20 SPS BH Asian Seismic Stations

While collecting and measuring amplitudes of Asian seismic events, we have found that some 20 SPS broadband data cannot be reliably measured in the 6 to8 HZ band. This occurs at Project IDA stations AAK, BRVK, KURK, NIL, and TLY. Essentially, at these stations the anti-alias filter begins to roll-off near 5 Hz (Figure 10), and somewhere between 6 and 8 Hz the data stream has been attenuated to below an integer value of one. Thus, velocity spectra of small events flatten near a value of 1, and any attempt to correct these data into displacement artificially boosts the 6 to 8 Hz measurements. When working with displacement amplitudes, this creates a noise floor higher than it should be. Figure 11 shows 20 SPS and 40 SPS displacement amplitudes versus time (in years) from IDA station KURK. For the 4 to 6 Hz measurements, the 20 and 40 SPS instruments are nearly in agreement, but for the 6 to 8 Hz measurements, many of the 20 SPS measurements are high relative to the 40 SPS measurements. This situation does not occur for IC and IU 20 SPS data because the anti-alias roll-off does not begin until 8 Hz (Figure 10, green curve). We recommend that II 20 SPS be measured up to 6 Hz, but not beyond that limit.

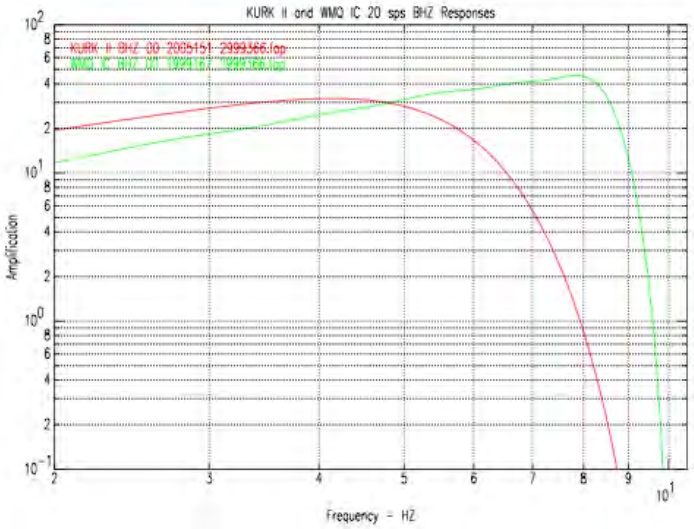

Figure 10. Response curves for 20 SPS II station KURK (in red), and IC station WMQ (in green).

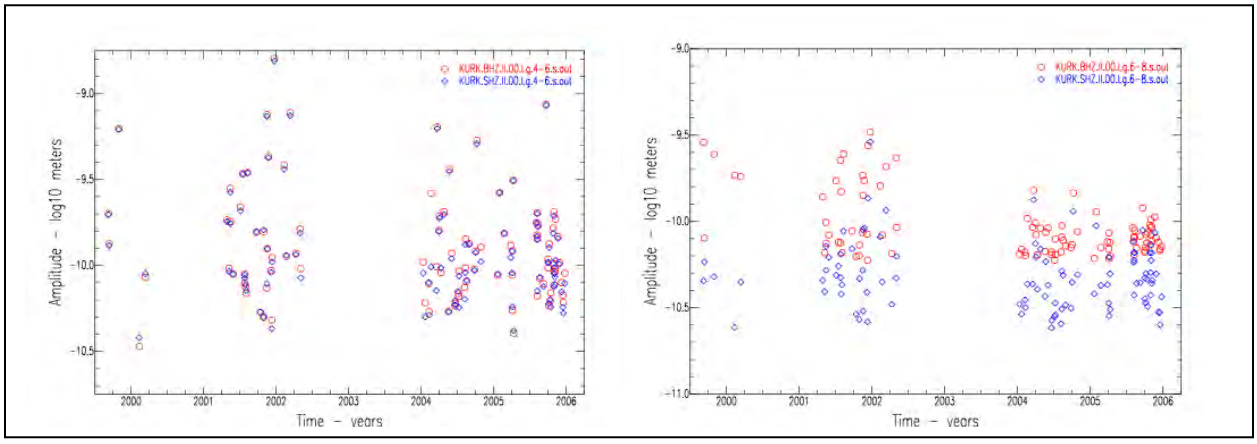

Figure 11. Comparison between KURK II displacement measurements at 20 SPS (red) and 40 SPS (blue) in the 4- 6-Hz (left) and the 6- 8-Hz (right) bands. The 20 SPS 6- 8-Hz measurements are boosted artificially due to early (5 Hz) roll-off of the anti-alias filter. The same situation applies to 20 other SPS II stations in central Asia.

CONCLUSIONS AND RECOMMENDATIONS

We have an ongoing program to identify mining seismicity clusters from waveform correlation and to tie these to overhead imagery for ground truth. For our eastern Kazakhstan study area, we tied 277 out of a total 447 events to 13 distinct mining-event clusters. We have identified features on at least 4 images that clearly show mines within 10 km of our seismic event-cluster locations. By assuming night events are earthquakes, we have been able to test body-wave discriminants. Only the Pg/Lg high-frequency discriminant shows some event separation. The Pg spectral ratio, which does separate earthquakes and nuclear explosions in Asia, does not separate mining explosions from earthquakes in eastern Kazakhstan. We will continue to investigate discriminant measurement and correction methods in an attempt to improve performance in separating mining events from both earthquakes and single-charge underground nuclear events.

In parallel with a project between UCSC and LANL to develop 1-Hz, two-dimensional, regional-phase attenuation models for Eurasia to improve the MDAC discrimination methodology, we are working on developing regional-phase attenuation models for Eurasia for a broad range of frequencies between 0.5 and 10 Hz. We have finished an initial phase of data collection and amplitude measurement for around 100 stations in the region. Based on the data coverage, we collected a dataset of Pn picks from the LANL location database to be used in further data collection. We have also conducted synthetic simulations to investigate the geometric spreading of Pn and Sn in a spherical earth. From the modeling results, we propose new, frequency-dependent Pn and Sn geometric-spreading models for a spherical Earth.

While measuring phase and noise amplitudes using 20 SPS data obtained at IRIS IDA stations operated in Asia, we found that a combination of relatively early anti-alias filter roll-off and operations at relatively low gains, typically results in inaccurate registration of seismic noise and signals (from all but large events) in 6 to 8 Hz bands. Known II stations with this problem include AAK, BRVK, KURK, NIL, and TLY. We recommend measuring amplitudes at frequencies no higher than 6 Hz at these stations and sample rates.

ACKNOWLEDGEMENTS

We thank the entire LANL GNEMRE team for supporting efforts that make this work possible, and we especially thank Richard Stead, Julio Aguilar-Chang, and Diane Baker for their database assembly and maintenance efforts. We thank the IRIS DMC for rapidly filling data requests. We used data from operators and host institutions affiliated with IC, IU, II, KZ, and KN networks. Figure 6 was provided by Cliff Thurber of the University of Wisconsin.

REFERENCES

Červený, V., and R. Ravindra (1971). *Theory of Seismic Head Waves*, University of Toronto Press, Toronto.

Hartse, H. E., S. R. Taylor, W. S. Phillips, and G. E. Randall (1997). A preliminary study of regional seismic discrimination in central Asia with emphasis on western China, *Bull. Seismol. Soc. Am.* 87: 551–568.

Lay, T., X. Yang, X. B. Xie, and M. D. Arrowsmith (2006). Development of regional tomographic attenuation models for Eurasia, in *Proceedings of the 28th Seismic Research Review: Ground-Based Nuclear Explosion Monitoring Technologies*, LA-UR-06-5471, 71-81.

Yang, X. (2002). A numerical investigation of Lg geometrical spreading, *Bull. Seismo. Soc. Am.* 92: 3,067–3,079.

SEISMIC SOURCE AND PATH CALIBRATION IN THE KOREAN PENINSULA, YELLOW SEA AND NORTHEAST CHINA

Robert B. Herrmann[1], William R. Walter[2], and Michael E. Pasyanos[2]

Saint Louis University[1] and Lawrence Livermore National Laboratory[2]

Sponsored by National Nuclear Security Administration
Office of Nonproliferation Research and Development
Office of Defense Nuclear Nonproliferation

Contract Nos. DE-FC52-04NA25539[1] and W-7405-ENG-48[2]

ABSTRACT

Two significant seismic events were analyzed using the crustal velocity model developed under this contract. The M_W = 4.55 Korean earthquake of January 20, 2007, occurred in the Republic of Korea on land and within the dense digital seismic network. Using P-wave arrivals from 60 broadband, short-period and acceleration stations, the event occurred at 37.68N, 128.58E at a depth of 7.5 km at 20070120115653.8. Source inversion was performed using the accelerometer recordings in the 0.05–0.20 Hz band and the broadband data in the 0.02–0.10 Hz band, with identical focal mechanisms and source depths of 9 and 11 km, respectively. This is the largest event on land in South Korea since the Mw 4.7 event on December 13, 1996. Forward modeling of the waveforms at INCN and MDJ indicates the ability of the current model to match observations on the Korean Peninsula and the effect of significant pulse shape modification for paths that partially cross the Sea of Japan. The results of using the local network data provide a ground truth point for other studies analyzing seismic events on the peninsula.

The isotropic seismic moment of the October 9, 2006, North Korean explosion was estimated from the Rayleigh-wave spectral amplitudes observed at MDJ and INCN. Very little Love wave signal was observed, indicating weak tectonic release. The explosion yield was investigated using the Denny and Johnson (1991) model relating yield to the observed isotropic moment as a function of depth of burial and material properties. Sensitivity analysis highlights the strong effect of the assumed velocity and density structure in the upper kilometer of the Earth and the assumed depth of burial on the estimated yield. The crustal velocity model developed under this contract provides strong constraints on the expected shear-wave velocities in the shallow parts of the crust. Issues to be investigated include the effect of wave propagation through the Eastern Sea (Sea of Japan) to stations in South Korea, and the effect of attenuation on isotropic moment estimates over longer paths, e.g., to the station BJT in Beijing.

OBJECTIVES

The primary focus is the determination of moment magnitudes for earthquakes in the Korean Peninsula, Yellow Sea and Northeast China region for use in the calibration of coda based seismic moment determination. The source parameters are to be determined from the inversion of broadband waveforms of earthquakes in the region. To address the lack of large earthquakes, inversion of small earthquakes requires calibration of the shear-wave velocities in the upper crust in order to use the predominant signal in the higher frequency band of 0.05–0.2 Hz.

RESEARCH ACCOMPLISHED

In spite of the reduced level of effort during the past year, significant results include the initial use of the Korean Meteorological Administration (KMA) accelerometer network for broadband source inversion and travel time studies. In addition the surface waves generated by the October 9, 2006, North Korean explosion were used in combination with the Korean crustal structure developed under this effort to estimate source yield.

Moment Tensor Solutions for Korea Earthquakes

At the end of 2006, KMA changed their web site for access to digital seismograms. The positive aspect of this change is that digital waveforms for the velocity and acceleration sensors are available for all local earthquakes from 2001 to the present, and for many teleseisms from 2005 to the present. The waveforms data are in miniSEED, so that access is required to the station coordinate file. No station response information is provided though. The web page is designed in Javascript and works solely through the CGI interface, so that it is no longer possible to use the command *wget* to directly access the waveforms. The web site leading to the waveforms is http://www.kma.go.kr/neis/neis_01_02_01.jsp.

During the past twelve months only one earthquake, that of January 20, 2007, was large enough for source inversion. This was the largest earthquake on land since the Mw 4.7 event on December 13, 1996. Figure 1 shows the distribution of accelerometer and broadband stations used in the analysis. The locations given by different groups are as follows:

The St. Louis University (SLU) location uses the velocity model derived from the joint inversion of receiver functions and surface-wave dispersion developed under this contract for waveform studies (Herrmann et al., 2005). The SLU solution used 81 arrival times of P, S and Lg from 8 to 507 km.

The striking feature of the data set was the usefulness of the accelerometer channels for source inversion. We obtained separate source estimates using the broadband waveforms, the accelerometer waveforms and the surface-wave amplitude spectra from the broadband waveforms (Table 2). Figures 2 and 3 show representative fits to the low-pass filtered ground velocity for selected broadband and accelerometer waveforms. The large number of observations also provide a test of the velocity model. Figure 4 compares the P-wave first arrival picks to the model prediction. This is a valid comparison since our location is very close to the independent teleseismic USGS location.

Table 3 shows the earthquake source parameters determined for this and other events in the region under this contract.

Yield Estimation of the October 9, 2006, North Korean Explosion

The recent North Korean event of October 9, 2006, highlights both the opportunities of regional monitoring and the difficulties of working with a smaller than expected event. Seismic signals were observed regionally and teleseismically by open networks, permitting accurate location and determination of magnitude. The test was not automatically detected and located by the current NEIC system (Koper et al., 2007) although NEIC analysts were able to use P waves in the 3.3–81.0 degree distance range once they knew where to look. Subsequent studies demonstrated that large research arrays discerned the P wave and that signal stacking can be used to enhance the signal (Ammon and Lay, 2007).

Yield estimates are typically performed using a stable monitoring network and carefully constructed source-station corrections to estimate m_b, together with a regionally calibrated magnitude-yield relationship. Yield estimation is not trivial because the magnitude-yield relation depends upon source medium properties, depth of burial and the

teleseismic propagation parameters, especially anelastic attenuation parameter t*.The final yield estimate is couched in terms of being valid for a normal depth of burial. Presumably an under-buried explosion is not a problem since it might blow out. An over-buried shot is problematic since it would have a lower than expected signal for a given yield and can be misinterpreted if assumed to be at a normal depth.

Koper et al. (2007) approached yield estimation for this test from the regional surface-wave signals at the stations MDJ (370 km) and INCN (475 km) to determine the isotropic moment. This was done using a Korea-specific crustal model developed for earthquake source inversion from surface-wave and receiver function observations (Herrmann et al., 2005) to create synthetic seismograms for a point explosion source. Spectral amplitudes of the observed and synthetic seismograms at periods between 10 and 30 seconds were obtained through multiple filter analysis (program *do_mft* of the Computer Programs in Seismology package). A simple regression determined the isotropic moment to be

$$M_I = 3.10\ (\pm 0.62)\ x10^{21}\ \text{dyne-cm.} \qquad (1)$$

These two stations were used since the paths from the test to the station did not significantly cross the Sea of Japan (Figure 5). The BJT station (1,103 km) at Beijing, China, was not used because of the greater distance, lack of knowledge of anelastic attenuation coefficients for the surface wave, and concern about path dependent effects for propagation through the sedimentary basins near Beijing. The paths are shown in Figure 5. Walter et al. (2007, these Proceedings) found a very similar isotopic moment using a slightly different velocity model and stations MDJ, TJN, INCN and BJT.

To estimate yield, the relations developed by Denny and Johnson (1991) were programmed in a general way in an Excel spreadsheet to permit an easy investigation of the relationship of changes in the material properties, yield, and depth of burial upon the seismological seismic moment estimate. Figure 6 shows the result of asking the question "What are the combinations of yield and emplacement depth compatible with the observed isotropic moment?" Two velocity models were considered for the upper kilometer—a generic Nevada Test Site (NTS) model characterized by a density of 2,000 kg/m^3 and S-velocity of 1,000 m/s, and a Korean model with a density of 2500 kg/m^3 and an S-velocity of 3,000 m/s. The NTS model was included since the Denny and Johnson data set included many events from NTS and since NTS is a well used reference model for explosions. The Korean model is based on the upper kilometer of the Herrmann et al (2005) model, and is thought to be representative of the mountainous shot region in North Korea.

Figure 6 serves several purposes. First, the importance of shot media is obvious because of the difference between the NTS and Korean curves. Since shots are typically within one kilometer of the surface, this highlights the importance of knowing near-surface velocity structure when studying buried explosions. A second aspect is more forensic in nature. If the yield is known independently, such as from a magnitude-yield relation, then Figure 6 can be used to estimate the depth of the shot. This is actually an important consideration for the North Korea shot since it is presumed to be smaller than expected for a first-time shot. If it were designed for a larger yield and buried at a normal scaled depth, then this event would be overburied with implications on the use of regional phase corner frequency to constrain yield.

There are many seismic stations that have observed this event. South Korea has roughly 20 broadband and 80–100 digital accelerometer recordings that have not been released. There is an International Monitoring System array in Wanju (roughly halfway across the peninsula, east of Inchon). As these data become available, there will be new challenges, specifically the effect of the mixed ocean-continent path across the Sea of Japan to most stations in South Korea. This will affect not only the low frequency surface-waves but also the high frequency regional signals.

Interestingly the high frequency signals at MDJ, TJN, and INCN were very impulsive. Richards and Kim (2007) compared MDJ recordings of explosions in and near North Korea to similarly located earthquakes and chemical explosions from the point of view of discrimination. The impulsive nature of the North Korean explosion P-wave at MDJ was obvious. Walter et al. (2007, these Proceedings) compared P to S amplitudes at several different high frequencies for stations MDJ and TJN and find good discrimination of the test from earthquakes in the region. Figure 7 presents the filtered vertical components at MDJ and INCN. The MDJ background noise was very low. Because of the higher noise level at INCN, the bandpass of 0.5–3.0 Hz was used for this comparison. The MDJ trace has a very strong Pn followed by a crustal P-wave arrival or Moho reflection. The INCN record has a sharp P_n. Since the P_n spectra can be used to estimate the source corner frequency, which is related to yield, source material, and

depth of emplacement (Denny and Johnson, 1991). There should be concerns about the effect of crustal and upper mantle structure on the P_n spectra, especially given the very impulsive nature of these regional arrivals since synthetic seismograms would never give such sharp P_n arrivals for a simple layer-cake velocity model.

As mentioned, the surface-wave signal at BJT (1,100 km) was not used. There was a good surface-wave at longer periods; however, without correction for Q-effects, the estimated moment was significantly smaller than those from MDJ and INCN. This path effect must be understood for completeness.

CONCLUSIONS AND RECOMMENDATIONS

Because the path from the North Korea explosion to the INCN station was partially through the Eastern Sea (Sea of Japan), the question of the specific path effect on the surface-wave amplitude spectrum is important for yield estimation. The effects might be estimated by considering the reverse path from the January 20, 2007, earthquake north to the station MDJ. The general issue of source depth might be resolved by including the accelerometer waveforms in the location of larger events in the southern half of the peninsula in order to provide more ground truth events in the region. These same data may provide constraints on the crustal velocity model that produces such impulsive high frequency P waves for the explosion.

ACKNOWLEDGEMENTS

Maps were created using GMT (Wessel and Smith, 1995).

REFERENCES

Ammon, C. J. and T. Lay (2007). US Array records of the 9 October 2006 North Korea nuclear test, *EOS Trans. AGU* 88: 37–38.

Denny, M. D., and L. R. Johnson (1991). The explosion seismic source function: model and scaling laws reviewed, in Explosion Source Phenomenology, Geophysics Monograph 65, edited by H. J. Patton and P. G. Richards, pp 1-24, American Geophysical Union, Washington.

Herrmann, R. B.,Y. -S. Jeon and H.-J. Yoo, (2005). Broadband source inversion using digital data from Korea seismic networks, in *Proceedings: 4th International Seminar on Seismic Tomography of Far-East Asia and Related works, December 2, 2005,* Korea Institute of Geoscience and Mineral Resources, Daejeon, Korea.

Koper, K. D., R. B. Herrmann and H. M. Benz (2007). Overview of open seismic data form the North Korea event of 9 October 2006, *Seism. Res. Letters* (submitted).

Richards, P. G., and W. Y. Kim (2007). Seismic signature, *Nature Physics* 3: 4–6.

Walter, W., E. Matzel, M. Pasyanos, D. Harris, R. Gok, and S. Ford (2007). Empirical observations of earthquake-explosion discrimination using P/S ratios and implications for the sources of explosion S-waves, in *Proceedings of the 29th Monitoring Research Review: Ground-Based Nuclear Explosion Monitoring Technoloigies,* in current Proceedings.

Wessel, P. and Smith, W. (1995). New version of the generic mapping tools released. *EOS Trans. AGU* 76: 329.

Table 1. Location estimates of the January 20, 2007 earthquake.

Year	Month	Day	Hour	Min	Sec	Lat	Lon	Depth	Mag	Auth
2007	01	20	11	56	54.3	37.64	128.47	10	4.4	USGS
2007	01	20	11	56	51	37.75	128.69		4.8	KNEIC
2007	01	20	11	56	53.9	37.68	128.59	7.4	4.55	SLU

Table 2. Source parameters of the January 20, 2007 earthquake

Date set	H (km)	Strike (deg)	Dip (deg)	Rake (deg)	Mw
Accelerometer Waveform	9	115	85	-5	4.55
Broadband Waveform	11	115	85	-5	4.56
Surface-wave spectra	10	115	90	0	4.61

Table 3. Source parameters for earthquakes in the Yellow Sea Korea Peninsula region.

Date	Time(UT)	Lat(N)	Lon(E)	Depth	Mw	Strike	Dip	Rake	Source
		37.2	128.8	8	4.63	30	80	160	Walter
12/13/1996	04:10			6	4.67	211	61	163	Herrmann
06/25/1997	18:50	35.8	129.2	11	4.34	130	55	35	Herrmann
03/05/1999	14:41	40.3	127.5	0	3.69	32	58	164	Walter
04/07/1999	14:32	37.2	128.8	2	3.70	110	75	-10	Herrmann
		40.5	123.0	10	4.84	36	84	-176	Walter
01/11/2000	23:43			15	5.06	27	43	-178	HRV
12/09/2000	09:51	36.6	130.0	12	4.06	10	25	75	Herrmann
11/21/2001	01:49	36.7	128.3	7	3.39	115	55	35	Herrmann
11/24/2001	07:10	36.7	130.0	12	3.81	220	71	164	Herrmann
03/17/2002	00:26	37.0	124.5	7	3.71	30	65	-120	Herrmann
		40.7	128.4	10	4.0	330	80	-30	Walter
04/16/2002	22:52	40.7	128.7	7.0	3.98	340	85	35	Herrmann
07/08/2002	01:49	35.9	129.7	19	3.75	130	70	25	Herrmann
07/23/2002	12:48	35.6	122.2	19	4.83	120	70	25	Herrmann
12/09/2002	22:42	38.9	127.3	6	3.62	25	65	-180	Herrmann
01/09/2003	08:33	37.4	124.2	5	3.83	355	65	-170	Herrmann
03/22/2003	20:38	35.0	124.4	14	4.80	30	80	-170	Herrmann
03/30/2003	11:10	37.6	123.8	13	4.57	25	80	-155	Herrmann
04/15/2003	17:55	36.4	126.2	9	3.21	300	35	50	Herrmann
06/09/2003	01:14	36.0	123.6	15	3.89	35	85	20	Herrmann
		43.8	119.6	25	5.27	220	78	166	Walter
				26	5.39	202	56	174	GS
08/16/2003	10:58			30	5.39	317	57	10	HRV

Date	Time(UT)	Lat(N)	Lon(E)	Depth	Mw	Strike	Dip	Rake	Source
10/13/2003	09:12	37.0	126.5	9	3.77	25	75	-175	Herrmann
01/05/2004	16:49	38.7	125.1	7	3.30	135	60	25	Herrmann
		45.4	118.3	8	5.46	158	29	80	GS
03/24/2004	01:53			13	5.35	167	28	86	HRV
04/26/2004	04:29	35.8	128.2	10	3.59	150	60	50	Herrmann
05/29/2004	10:14	36.7	129.9	11	5.08	350	30	70	Herrmann
06/01/2004	11:22	36.7	129.3	11	5.08	350	30	70	Herrmann
08/05/2004	20:32	35.9	127.4	8	3.18	206	85	-165	Herrmann
		41.9	127.9	10	3.84	30	85	-170	Walter
12/16/2004	18:59			8	3.94	48	75	-170	Herrmann
06/14/2005	22:07	33.2	126.1	8	3.78	270	80	-5	Herrmann
06/29/2005	14:18	34.5	129.0	11	4.13	145	45	30	Herrmann
10/09/2005	23:51	37.9	124.9	6	3.55	175	73	148	Herrmann
01/19/2006	03:25	37.2	128.8	8	3.50	200	75	-180	Herrmann
03/31/2006	12:23	44.6	124.2	5	4.71	334	44	52	Walter
04/29/2006	02:01	37.1	129.9	6	3.63	100	70	-10	Herrmann
01/20/2007	11:56	37.7	128.6	9	4.55	205	85	-175	Herrmann

Herrmann: http://www.eas.slu.edu/Earthquake_Center/MECH.KR/

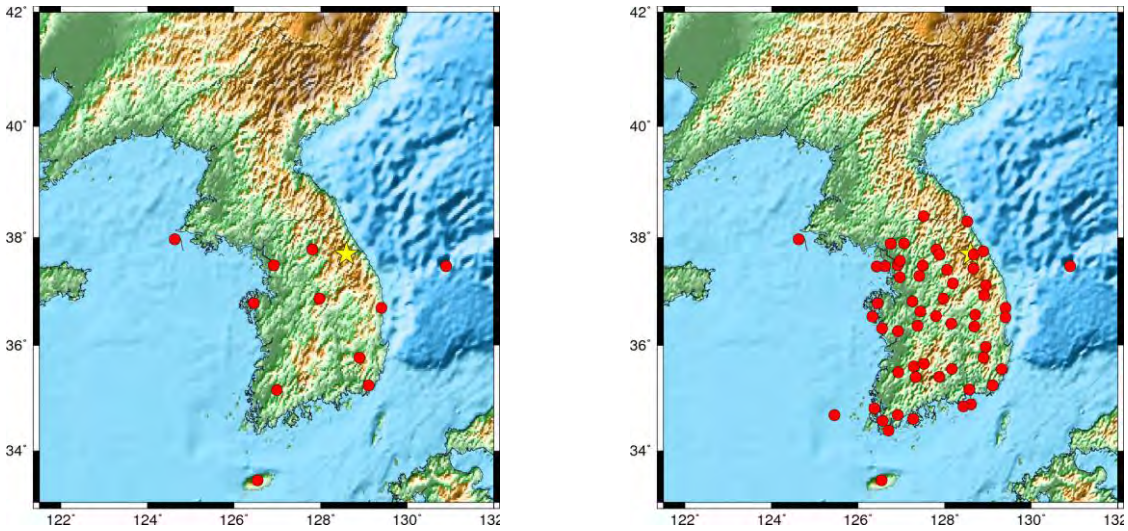

Figure 1. Location of the January 20, 2007 Korea earthquake (star) and the station locations for waveform analysis. Left: locations of KMA broadband sensors; right: locations of digital accelerometers.

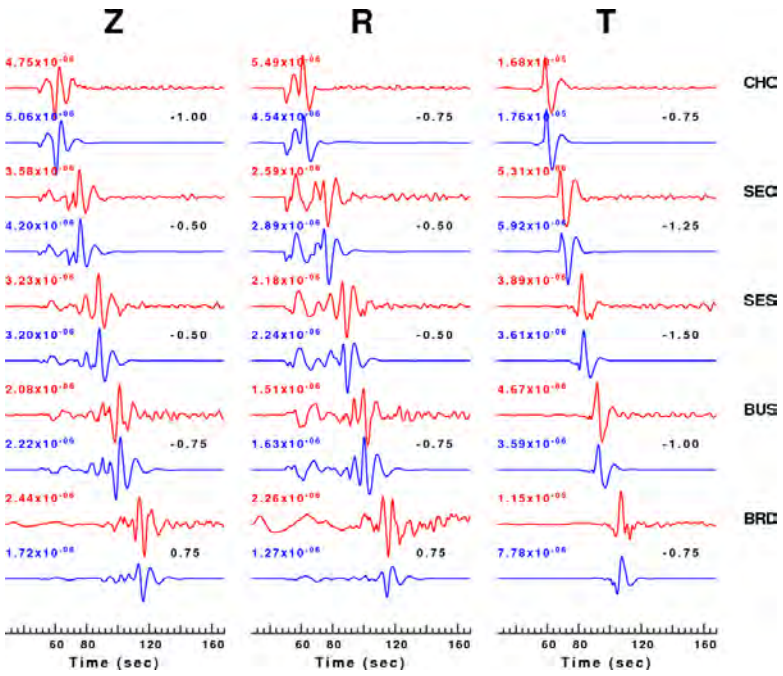

Figure 2. Selected broadband sensor recordings and model fit in order of increasing epicentral distance. All waveforms are ground velocity filtered with the sac/gsac commands *hp c 0.02 n 3* and *lp c 0.01 n 3*. For station/component pair (red is observed and blue is predicted) the same plot scale is used. The peak filtered velocity value is indicated adjacent to above the trace on the left. The number on the right indicates the time shift used for maximum correlation. Note that the time shift is with respect to the selected P-wave arrival and also that the Green's functions are computed with *DELTA=0.25* sec. The epicentral distances in *km* to the stations are CHC (70), SEO (150), SES (215), BUS (275) and BRD (350).

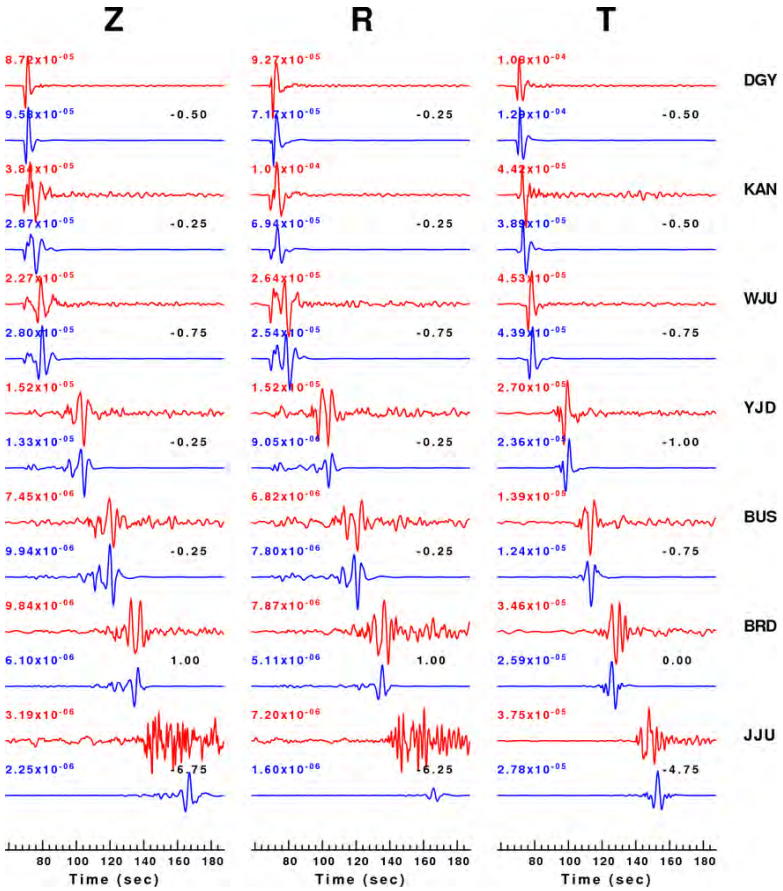

Figure 3. Selected accelerometer recordings integrated to round velocity (*m/s*) and filtered with the sac/gsac commands *hp c 0.05 n 3* and *lp c 0.20 n 3*. The epicentral distances in *km* to the stations are DGY (7), KAN (27), WJU (58), YJD (192), BUS (275), BRD (350) amd JJU (506). The trace display is discussed in Figure 2.

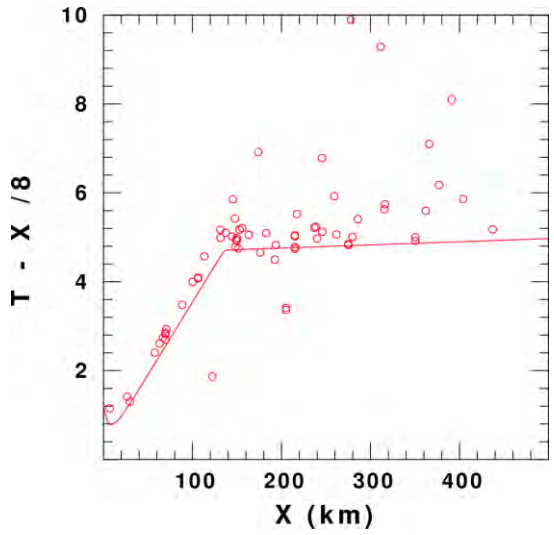

Figure 4. Observed and model predicted P-wave first arrival times for the relocated event.

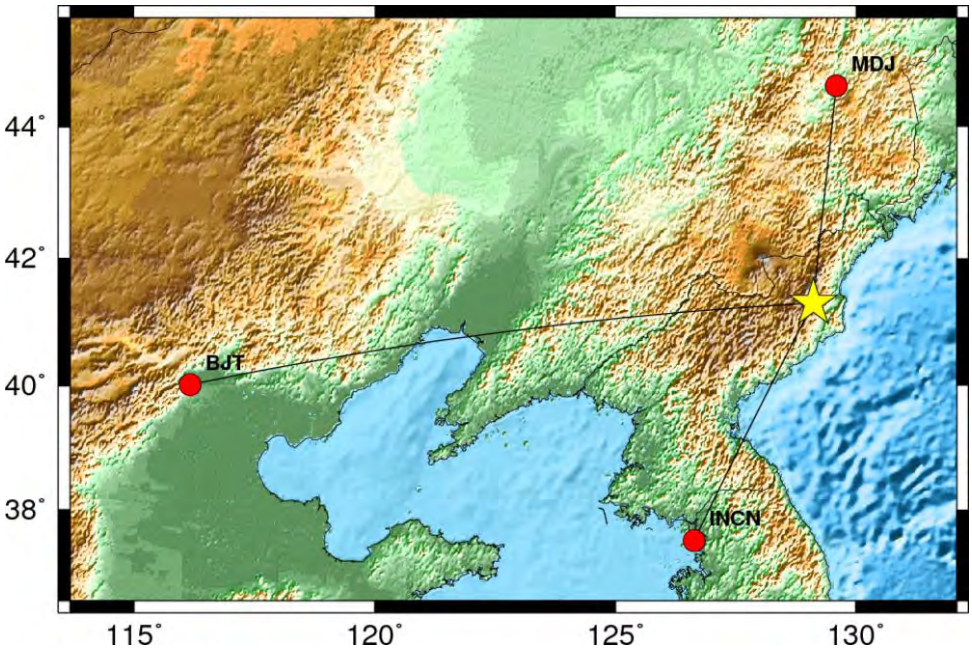

Figure 5. Paths to stations from the North Korean test.

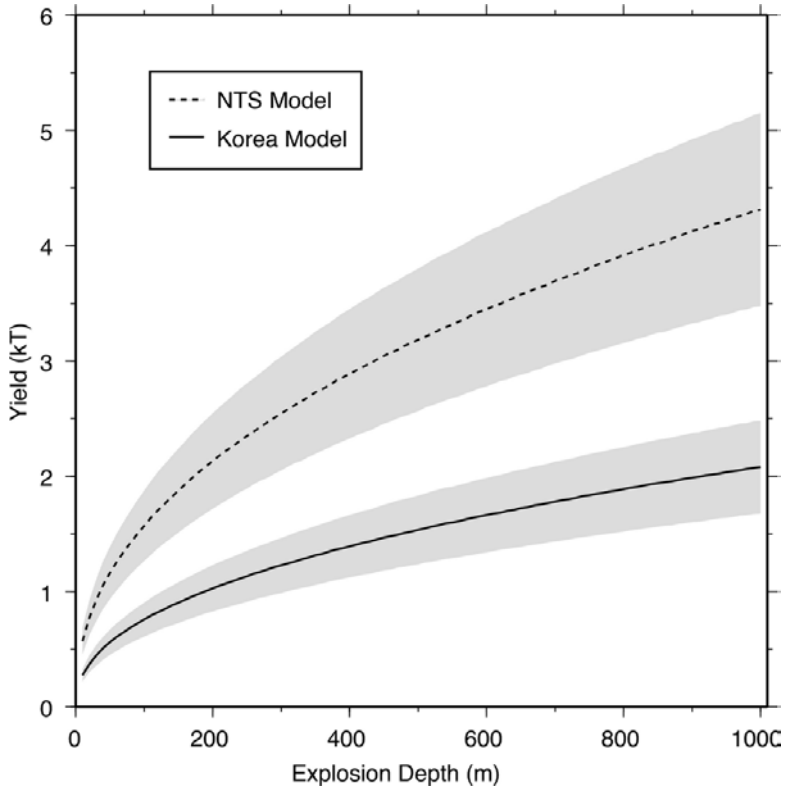

Figure 6. Yield estimates as a function of depth for the observed isotropic moment for two velocity models. The shaded regions reflect the variability due to the ± bounds of the observed moment (Koper et al., 2007).

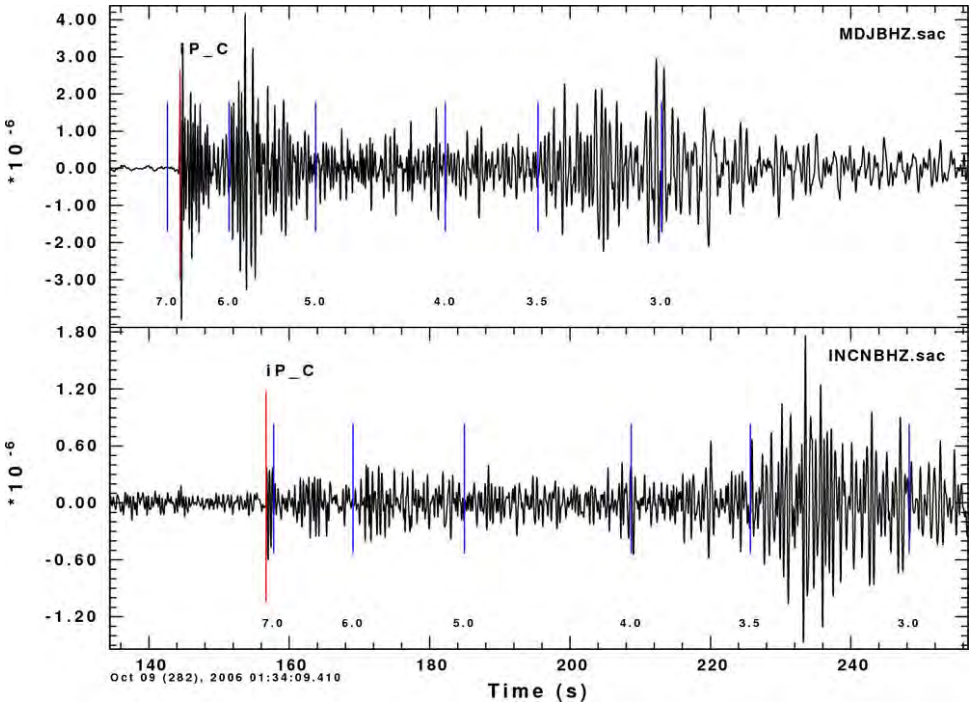

Figure 7. Comparison of bandpass filtered vertical component recordings at MDH (369 km) and INCN (475 km). These ground velocity traces (m/sec) had been filter using the sac/gsac commands: *hp c 0.5 n 2 p 2* and *lp c 3 n 2 p 2*. The *markt* command is used to show the group velocities of the signal.

INCLUSION OF A BODY WAVE SEISMIC MOMENT TENSOR ESTIMATOR IN THE CTBTO/IDC PROCESSING SUITE

Ronan J. Le Bras and Tim Hampton

Provisional Technical Secretariat of the Preparatory Commission for the
Comprehensive Nuclear-Test-Ban Treaty Organization (CTBTO)

ABSTRACT

The experimental SEL0 system of the CTBTO's Preparatory Commission (Le Bras et al., 2006) now includes a moment tensor (MT) and moment magnitude estimate. The SEL0 system rapidly detects and locates events. The effort to include further processing of large natural events, and get a better size estimate for large natural events than the *mb* magnitude was started in the summer of 2005. The basic scientific software that performs the MT inversion was acquired from Y. Yagi from Tsukuba University, Japan. It performs a time-domain, long-period body-waves MT inversion soon after an event is automatically detected and located, within about 20 minutes after its occurrence. We wrote signal processing scripts to prepare the broad-band International Monitoring System (IMS) vertical seismic data for MT inversion, including deconvolution of the complete instrument responses. We included the scientific software into the Commission's environment and have now achieved its seamless integration through the web page displaying the results of the SEL0 bulletin.

The addition of the moment tensor inversion module allows us to estimate the size and focal mechanism of the detected events, which is of interest for better characterization of the event in a limited time frame. This is important since the only available measure of the size of the earthquake for SEL0 events was the *mb* scale, which saturates for larger events. We have been able to interactively run a number of inversions and we present case examples and statistics from selected events since December 2006.

OBJECTIVES

The objective of this project is to integrate an MT and moment magnitude M_w (Hanks and Kanamori, 1979) measurement in the International Data Centre (IDC) processing system to take advantage of the broadband data sent to the CTBTO IDC. For the following reasons, this additional processing item will be of use to the IDC and the monitoring community in general:

- The additional module will be of use in the prototype processing pipeline using the IMS network that can produce a timely bulletin useful as input for agencies charged with warning the general public about impending disasters such as tsunamis.

- The IDC automatic bulletins measure the size of events using the *mb* magnitude which is known to saturate for events larger than about magnitude 6.5 (e.g., Abe, K, 1995). It is therefore necessary to develop other methods of assessing the size of large events in a timely manner. For large events, the focal mechanism also provides additional information for the tsunamigenic potential of the event.

- The focal mechanism for seismic events is mentioned in Annex 2 of the Protocol to the CTBT as a potentially useful attribute for event screening.

- The method may be applied to data archived at the IDC and used to calibrate the IMS network at low frequencies for large events whose seismic moments have been estimated by other agencies such as the Harvard University centroid moment tensor (CMT) or the National Earthquake Information Center (NEIC) of the U.S. Geological Survey (USGS).

RESEARCH ACCOMPLISHED

Interactive Inversion from the SEL0 Web Page

The IDC operates an experimental processing pipeline to obtain a global bulletin within about 20 minutes of the occurrence of the event (Le Bras et al., 2006). This bulletin, and therefore, the processing pipeline have been named SEL0 in line with the naming convention for the other three automatic bulletins (SEL1, SEL2, and SEL3) published by the IDC for distribution to the member states of the preparatory commission for the CTBTO. These later bulletins are available in a database visible to authorized users 1 hour 50 minutes, 6 hours, and 12 hours, respectively, after the occurrence of the events.

The SEL0 bulletin has proven useful for locating events over magnitude 6 worldwide in a very timely fashion. A drawback, however, has been that the estimates of the size of the events were based on the *ML* and *mb* magnitudes, which saturate rapidly for large events. The *mb* saturation threshold is particularly low for the specific *mb* calculation used at the IDC (Kebede and Koch, 2003). The amplitudes are measured on vertical channels in a relatively narrow 5.5-second window around the first arrival picks, which leaves out larger amplitudes that may occur later in the coda for large events. The frequency band for *mb* is also limited to 0.8 to 4.5 Hz. Since one of the main purposes of the IDC *mb* magnitude is to screen out natural events using the *mb/Ms* ratio, this does not cause any severe problems for the mission of the IDC. To better estimate the size of larger events it is desirable to measure the moment magnitude (Hanks and Kanamori, 1979). The moment magnitude samples lower frequencies and is correspondingly measured in larger time windows. This can be achieved through several means, including modeling the low frequency body waves for the event. To obtain the moment tensor (MT) solution from body waveform (P-wave), we assumed a simple triangle source time function and 5 elementary moment tensor components (Kikuchi and Kanamori 1982), and varied the duration of source time and the centroid depth. The Green's function is calculated by the method of Kikuchi and Kanamori (1991). To remove the effects of detailed source process and detailed 3D structure, we apply a low-frequency band-pass filter on the waveforms before the moment tensor inversion. The estimated magnitude range of the event determines the bounds on the band-pass filter.

The web interface for the SEL0 bulletin has been upgraded to allow MT inversion for any event once it is visible on the web page. Another, more general web interface is also in development to allow access to the IDC archive

database. The back-end processing called through both these interfaces involve an experimental program, called *gparse*, a command-line system with an expandable set of alphanumerical and graphical I/O as well as signal processing commands, which can also be used in batch mode.

An example of inversion for a SEL0 event with comparison to other sources, the Celebes Sea event of December12, 2006

Figure 1 shows the waveform fit obtained for this event. The fit was obtained semi-automatically from the SEL0 web page, with the user selecting a magnitude range, a depth range and identifying the event as an offshore event. The fit is quite acceptable (variance of 0.37) given that no editing was done on the station list and that the quick automatic epicenter was used as input to the process. This solution was available a few minutes after the event was written to the SEL0 bulletin. The geographical distribution of the stations is shown on Figure 2, a global map centered on the event. Note that more IMS stations would be available to refine the solution if non-associated stations were used in the inversion. Table 1 shows a comparison of this quick solution with two other published solutions (USGS and Harvard.)

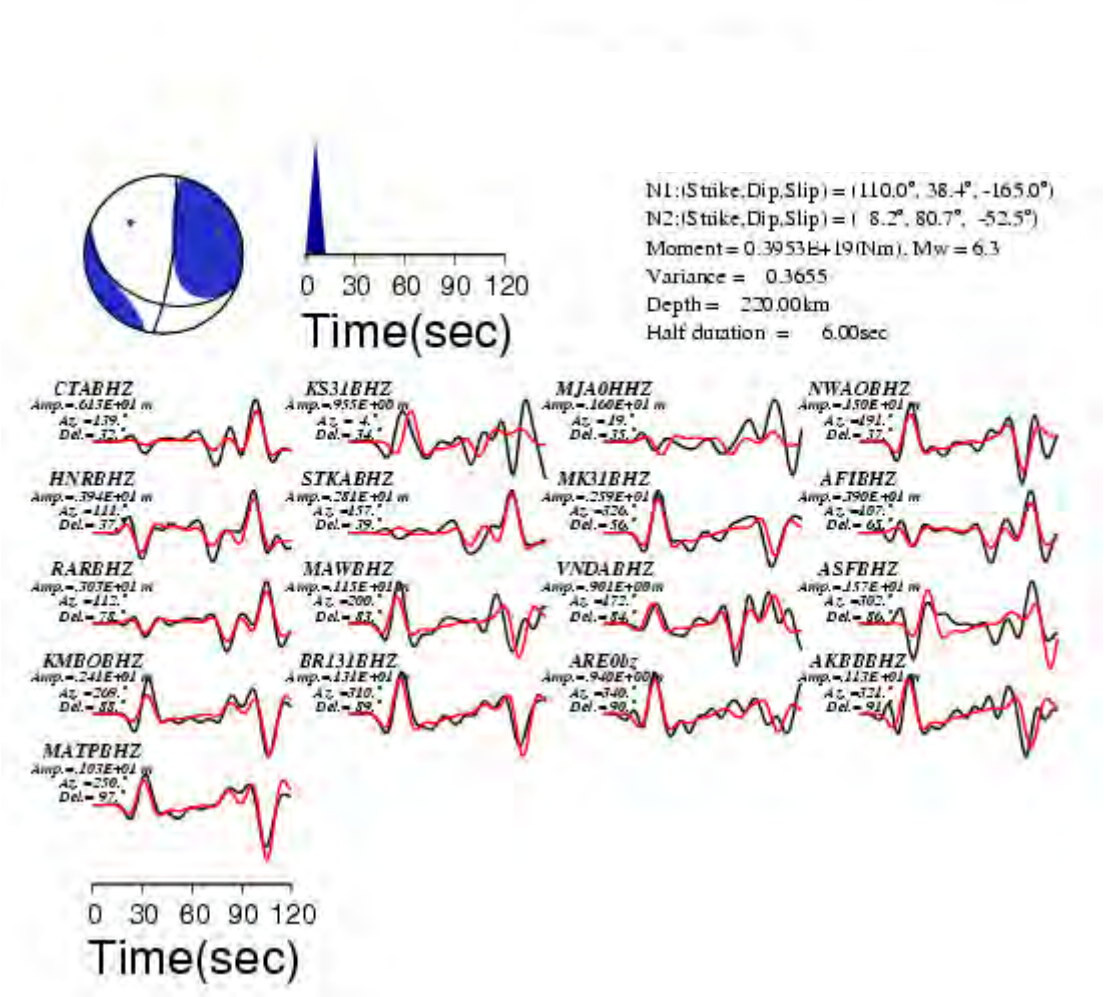

Figure 1. Example of waveform fit for an event in the Celebes Sea on December 12, 2006. The data (black line) and synthetic waveforms (red line) are filtered in the band (0.008–0.095) Hz. The fit is acceptable with a variance of about 0.37. Note the very clear depth phases for this event, whose hypocenter is estimated to be at 220 km depth.

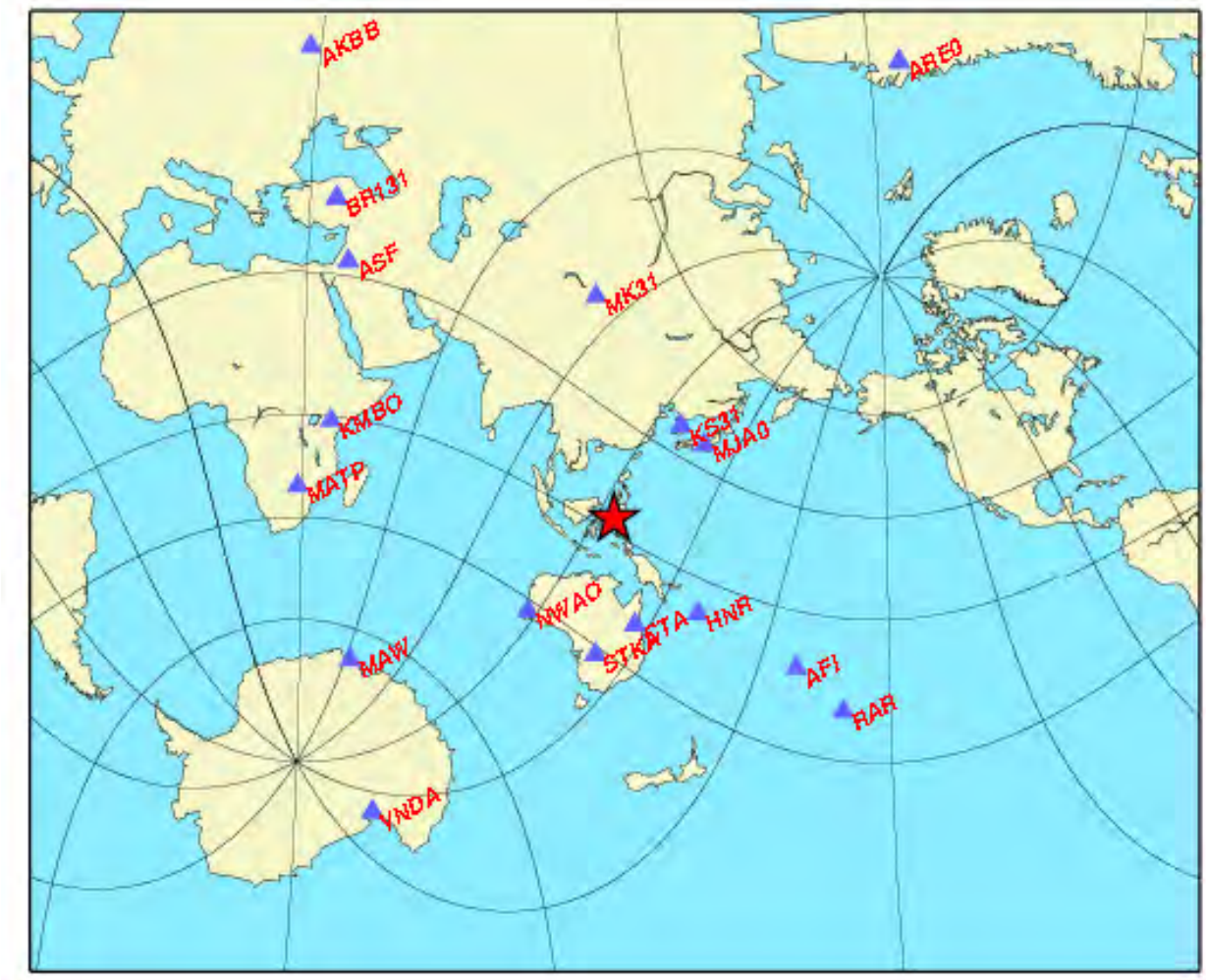

Figure 2. Map centered on the Celebes Sea event (red star) showing the location of the broadband stations (blue triangles) used in the MT inversion. Only associated SEL0 stations were used in this case. This result was obtained shortly after the event was written to the SEL0 database table.

Table 1. This table shows the comparison of the CTBTO MT inversion results for the Celebes Sea event with two other sources (USGS and Harvard.) Note that the agreement is good with both sources, bearing in mind that no editing of the stations list has taken place and that only stations associated by SEL0 have been used in the inversion.

Celebes Sea event of December 12, 2006 (MT components in units of 10^{19} N-m)				
CTBTO (Mw 6.3)				
Epicenter	[3.72, 124.82]	**Mrr**	**-1.04**	
Depth	220 km	**Mtt**	**-1.13**	
		Mpp	**2.17**	
		Mrt	**-0.06**	
Time	15:48:04.58	**Mrp**	**-2.90**	
		Mtp	**-2.12**	
USGS (Mw 6.3)				
Epicenter	[3.72, 124.72]	**Mrr**	**-1.27**	
Depth	208 km	**Mtt**	**-0.04**	
		Mpp	**1.32**	
		Mrt	**-0.16**	
Time	15:48:03.42	**Mrp**	**-3.32**	
		Mtp	**-1.12**	
Harvard (Mw 6.3)				
Epicenter	[3.90, 125.01]	**Mrr**	**-0.91**	
Depth	212 km	**Mtt**	**0.38**	
		Mpp	**0.53**	
		Mrt	**-0.16**	
Time	15:48:06.20	**Mrp**	**-3.19**	
		Mtp	**-1.25**	

Interactive Inversion Generalized to Other Bulletins and Additional Inversion Options

A new web interface has been developed which allows additional options to be used in the inversion process and most importantly allows inversion on the analyst-generated reviewed bulletin (REB). The additional options added when compared to the SEL0 web page are the ability to choose the bulletin from which the event is selected and choose whether the inversion should use the associated stations or all stations in the broad-band vertical seismic network.

The Mozambique event of February 22, 2006

Figure 3 shows the waveform fit obtained using this interface where all stations are selected rather than only associated stations and the noisy stations are eliminated through a manual process. Figure 4 shows the distribution of the stations used in the inversion on a map centered close to the epicenter, and Table 2 shows a comparison with the USGS and Harvard solutions. Note that our solution is slightly closer to the Harvard solution for this event.

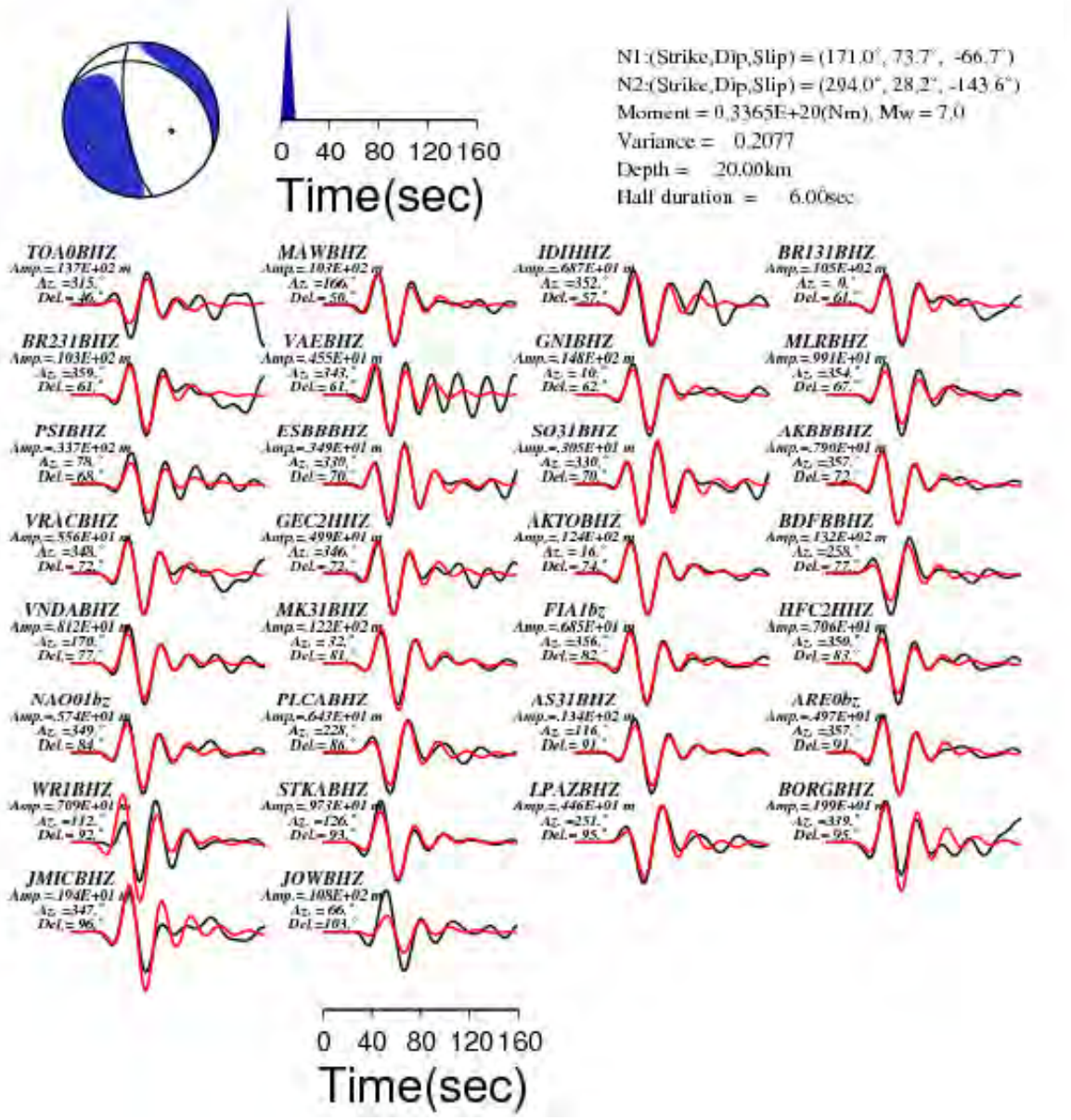

Figure 3. Example of waveform fit for the normal rift-style event of February 22, 2006, in Mozambique. The data (black line) and synthetic waveforms (red line) are filtered in the band (0.005–0.05) Hz. The fit is good with a variance of about 0.21.

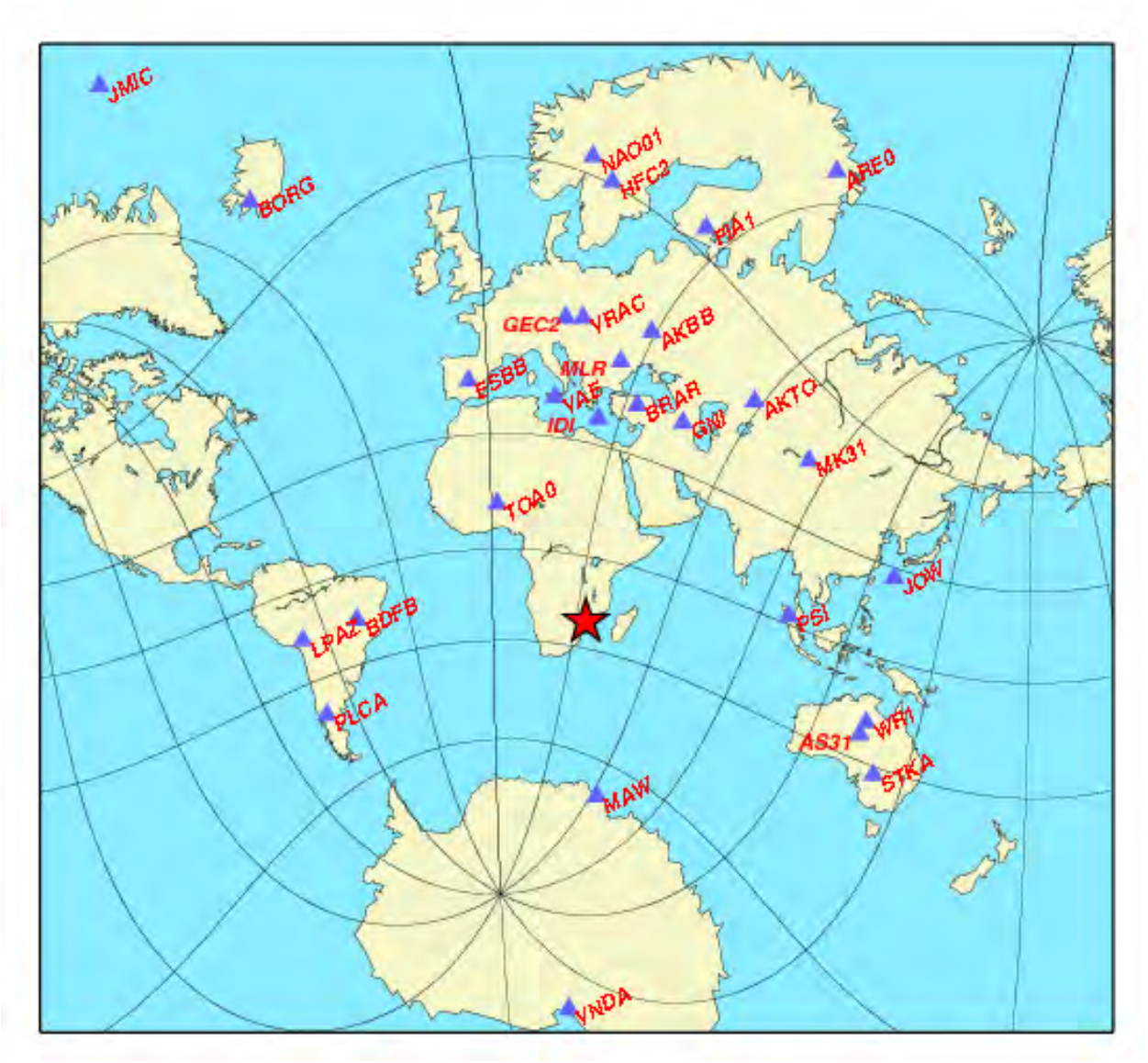

Figure 4. Map centered on the Mozambique event (red star), showing the location of the broadband stations (blue triangles) used in the MT inversion. Note that the map shows only one of the broadband elements for arrays BRAR (BR231 shown as BRAR, BR131 not shown) and ESBB (ESBB shown, SO31 not shown.)

Table 2. This table shows the comparison of the CTBTO MT inversion results for the Mozambique event with two other sources (USGS and Harvard.) Note that the agreement is quite good with both sources, with a slightly better proximity to the Harvard solution for the focal mechanism.

Mozambique event of February 22, 2006 (MT components in units of 10^{19} N-m)				
CTBTO (Mw 7.0)				
Epicenter	[-21.18, 33.51]	**Mrr**	**-1.53**	
Depth	20 km	**Mtt**	**0.11**	
		Mpp	**1.42**	
		Mrt	**-0.28**	
Time	22:19:05.06	**Mrp**	**2.56**	
		Mtp	**-1.53**	
USGS (Mw 7.0)				
Epicenter	[-21.22, 33.32]	**Mrr**	**-3.62**	
Depth	23 km	**Mtt**	**-0.63**	
		Mpp	**4.25**	
		Mrt	**0.75**	
Time	22:19:08.11	**Mrp**	**2.11**	
		Mtp	**-0.92**	
Harvard (Mw 7.0)				
Epicenter	[-22.20, 33.33]	**Mrr**	**-2.88**	
Depth	12 km	**Mtt**	**-0.14**	
		Mpp	**3.02**	
		Mrt	**-0.49**	
Time	22:19:15.00	**Mrp**	**3.10**	
		Mtp	**-1.46**	

Statistics on the variance of the semi-automatic solutions as a function of the magnitude of the events

We have collected statistics on the variance of the waveform fit as a function of the moment magnitude. It is clear that for events of moment magnitude with approximately Mw > 6.0, the variance is usually below 0.4, which constitutes an acceptable fit. Figure 5 shows the scatter plot for a few events processed semi-automatically through SEL0. It is likely that the reason for the generally bad performance at lower magnitudes is due to an insufficient signal to noise ratio in the low frequency ranges used in the inversion. It may be possible to refine the definition of the frequency ranges to be used for these lower magnitude events.

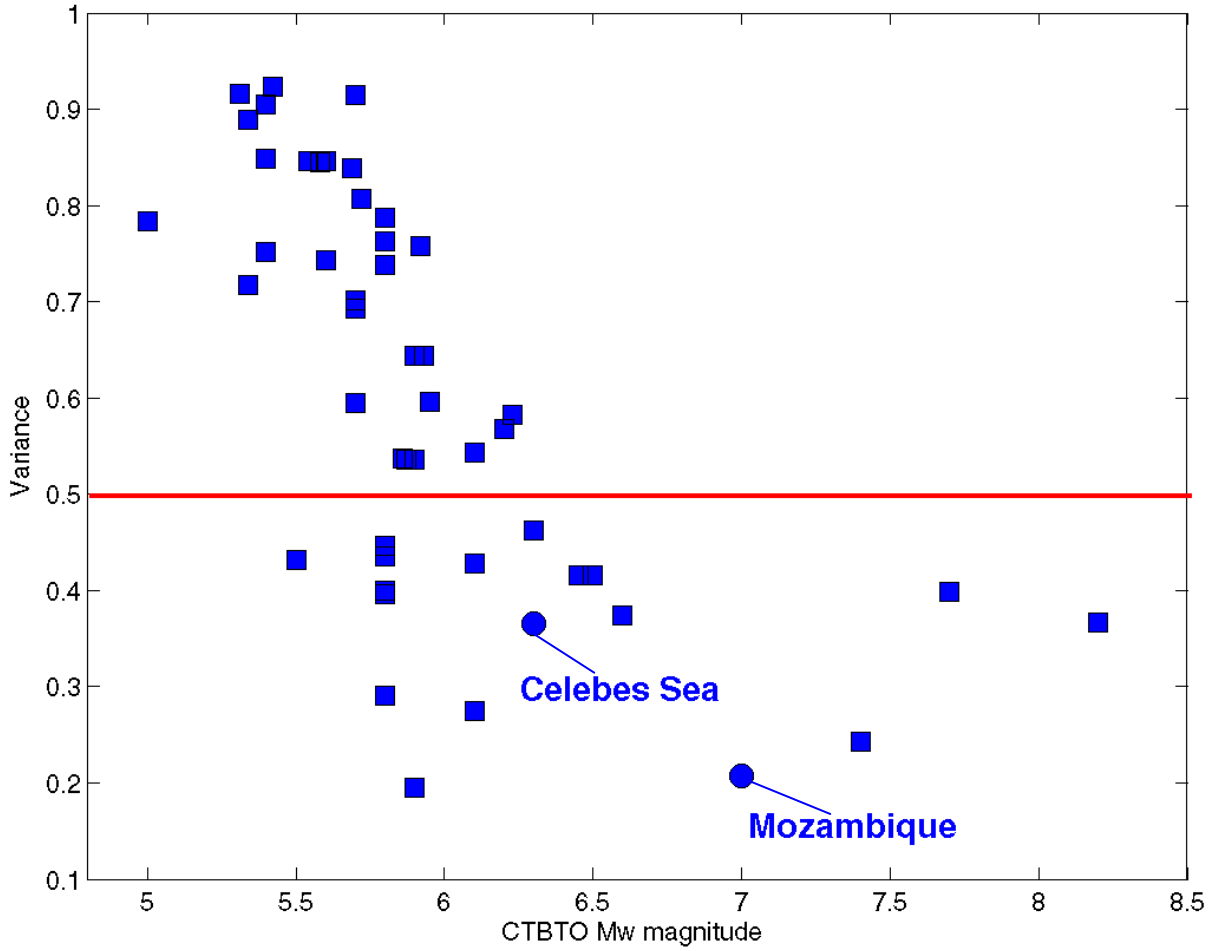

Figure 5. Scatter plot showing the relationship between the variance obtained from the MT inversion and the magnitude of the event for a sample of the SEL0 events processed semi-automatically. For comparison, the circles show the values for the two events (Celebes Sea and Mozambique) detailed in this paper. It is clear that, on this sample, we obtain consistently better results at the higher end of the magnitude spectrum (above about M_w = 6.5).

CONCLUSIONS AND RECOMMENDATIONS

We have integrated body-wave MT inversion software into the IDC processing environment on an experimental basis. The inversion is integrated with the SEL0 (Le Bras et al., 2006) web page. At present, an experienced user can obtain a fast and accurate MT with a few mouse clicks and within a few minutes.

Several challenges lie ahead to make the MT inversion process more automated, faster and robust for smaller magnitude events. To fully automate the MT process, good automatic estimates of the following inputs are required:

- Automatic determination of water depth at epicenter, if the event is offshore.
- Reliable initial depth range for the event.
- Reliable magnitude estimate to choose the appropriate frequency range for the inversion.

- Beam forming at stations where several broad-band stations are available.

Some criteria are being developed in terms of the minimum number of associated/non-associated stations that need to be included into the inversion process, as well as the quality of the waveform fit as measured by the total variance. A pre-processing of the amplitude data between the P and PP phases using newly developed methods to obtain fast order of magnitude for the event should be useful as input to the process in terms of assigning a magnitude range to the event. We are currently experimenting along these lines (Bormann and Wylegalla, 2005; Lomax, 2005; Guilbert et al., 2005). These criteria could be implemented and integrated into our signal processing environment, *gparse*.

To refine the solution after analyst review, an interactive tool to select the best channels would be useful to replace a tedious manual preparation as is the case currently, especially for smaller magnitude events where low frequency waveforms are often contaminated by noise.

ACKNOWLEDGEMENTS

We thank Drs. Lassina Zerbo, IDC Director, and Florence Rivière, IDC Coordinator, for allowing us to publish this research and for their support; Dr. Yuji Yagi, Tsukuba University, Japan, for allowing the IDC to use his waveform inversion software in its processing suite and for reviewing the manuscript; and Dr. Jeffrey Given, SAIC, for reviewing an early manuscript.

Disclaimer

The views expressed in this paper are those of the authors and do not necessarily reflect the views of the CTBTO Preparatory Commission.

REFERENCES

Abe, K. (1995). Magnitudes and Moments of Earthquakes, in *Global Earth Physics, A Handbook of Physical Constants*, AGU Reference Shelf 1:206, 213.

Bormann, P. and K. Wylegalla (2005). Quick estimator of the size of great earthquakes, *Eos Trans. AGU* 86: 464.

Guilbert J., J. Vergoz, E. Schisselé, A. Roueff, and Y. Cansi (2005). Use of hydroacoustic and seismic arrays to observe rupture propagation and source extent of the M_w= 9.0 Sumatra earthquake, *Goephys. Res. Lett.* 32: L15310, doi:10,1029/2005GL022966.

Hanks, T. C. and H. Kanamori (1979). A moment magnitude scale. *J. Geophys. Res.* 84: 2348–2350.

Kebede, F. and K. Koch (2003). Comparison of IDC and ISC bulletins for the year 2000, IDC Internal technical report CTBT/IDC/SR/2003-1.

Kikuchi, M. and H. Kanamori (1982). Inversion of body waves, *Bull. Seismol. Soc. Am*. 72: 491–506.

Kikuchi, M. and H. Kanamori (1991). Inversion of complex body waves—III, *Bull. Seismol. Soc. Am*. 81: 2335–2350.

Le Bras, R., T. Hampton, J. Coyne, and A. Boresch (2006). SEL0: A fast prototype bulletin production pipeline at the CTBTO in *Proceedings of the 28th Annual Seismic Research Review: Ground-Based Nuclear Explosion Monitoring Technologies*, LA-UR-06-5471, Vol. 2, pp. 1007–1015.

Lomax, A. (2005). Rapid estimation of rupture extent for large earthquakes: Application to the 2004, M9 Sumatra-Andaman mega-thrust, *Geophys. Res. Lett.* 32: L10314, doi:10.1029/2005GL022437.

EFFECTS OF FROZEN ROCK ON EXPLOSIVE COUPLING

Mark Leidig[1], Jessie Bonner[1], Randy Martin[2], Sara Dougherty[1] and Katherine Murphy[1]

Weston Geophysical Corp.[1], New England Research, Inc.[2]

Sponsored by Air Force Research Laboratory

Contract No. FA8718-04-C-0026

ABSTRACT

Laboratory studies have demonstrated that frozen rock is significantly stronger than unfrozen rock, and it has been hypothesized that this increased strength can significantly alter seismically estimated yield. Weston Geophysical Corporation conducted the Frozen Rock Experiment (FRE) in central Alaska in August 2006 to provide empirical data in order to test the hypothesis. This region of Alaska has abrupt lateral boundaries in discontinuous permafrost, and we detonated 3 shots in frozen rock and 3 shots nearby in unfrozen rock ranging in size from 200 to 350 lbs. Nearly 125 accelerometers and seismometers were deployed specifically for this experiment at distances of 10 m to over 20 km. Videographic and velocity of detonation data were also collected. The data from this experiment are being analyzed to aid in determining actual yield for explosions in permafrost regions.

We developed a 1-D velocity model for the test site region using refraction analyses and inversion of surface wave dispersion and receiver functions. During development of this model, we found evidence of seismic anisotropy in the shallow crust. This model, with inclusion of the anisotropy, fit the observed *P*- and *S*-wave arrivals well, but predicted a later arrival for the surface waves than was observed. Therefore, we initiated development of a 3-D velocity model for the region that could account for lateral velocity changes. Laboratory analysis of test site rock samples document the rheologic differences of the test site medium when both frozen and unfrozen. Velocities increased ~12% for V*p* and V*s* when the sample was frozen to below -10 °C. Elastic moduli also showed significant increases in the frozen samples. These results are in agreement with prior studies and are indicative of the increased strength of frozen rock.

The explosive source is being defined in various ways. Theoretical Mueller-Murphy (MM) source spectra were generated using the test site seismic velocities determined *in-situ*. Ratios of the unfrozen/frozen spectra were computed. Although there are no calibrated MM rock properties for gneiss or schist, which are found in the test site, modeling indicates that MM spectra generated from a rhyolite model fits the observed data well when the differences in the test site velocities are considered. In addition, recordings on close-in accelerometers and seismometers provide data for moment tensor inversions, which help define the symmetry and phenomenology of the explosions. Dr. Charlie Sammis has performed extensive analysis modeling the damage around an explosive source. His model involves multiple zones of rock pulverization and fracturing. It is hypothesized that displacement along small fractures, integrated over the entire damage volume, can produce the large shear waves observed from explosions. The model is dependant on the rock strength, which has been shown to increase in frozen rock. We are collaborating to provide him with data to validate his model.

Spectral analyses were conducted to determine the differences in seismic phases generated by the explosions. Spectral ratios of the full waveform for equal yield detonations show that frozen shots produced larger vertical spectral amplitudes at all frequencies, except between approximately 4 and 9 Hz. In this frequency range, the unfrozen shots were up to 1.4 times larger, while above 10 Hz, the frozen shots were 4 times larger.

Large shear waves are observed in the FRE data. Broadband transverse components, as close as 3 km, show a large amplitude arrival just prior to the Rayleigh wave, which could be a Love or SH wave. Record sections of the Texan recordings clearly show an arrival we determined to be a shear wave. The *P*/*S* ratio appears to vary depending on the shot type and may therefore provide important information on the mechanics of shear wave generation from an explosive source.

OBJECTIVES

Weston Geophysical Corporation conducted the Frozen Rock Experiments (FRE) in central Alaska to characterize the variations in ground motion scaling and coupling for explosions in frozen and unfrozen rock. We recorded the explosions on a large array of near-source and local stations deployed specifically for the experiment. The data are currently being analyzed to quantify the variations observed. The results will be interpreted to help understand possible biases in the estimation of seismic yield from explosions in frozen rock.

RESEARCH ACCOMPLISHED

Experiment Background

A critically important aspect of nuclear test monitoring is yield estimation. United States monitoring agencies must be able to accurately estimate yields for nuclear explosions detonated in regions of monitoring concern. If frozen-rock emplacement conditions create a circumstance favorable for biased yields, data must be available such that any bias can be accounted for when the yield is estimated. Prior studies (Mellor, 1971) have established that frozen-rock properties are considerably different from unfrozen-rock properties. Moreover, it has been hypothesized that these altered properties may be sufficient to cause significant variations in seismic coupling, which in turn, significantly alters seismic yield estimates.

Sammis and Biegel (2004) noted that an increase in low-temperature uniaxial strength is related to the ice in the initial pores and cracks. The ice increases the apparent coefficient of sliding friction on these initial cracks. Since the strengthening is strain-rate dependent, for nuclear explosions the full strengthening should occur in a small range near 0 °C. Increasing the seismic velocity and/or rock strength would cause reduced seismic amplitudes in the far-field for explosions in frozen rock, which would result in an underestimated yield.

Experiment Location and Design

We conducted the experiment just north of Fairbanks, AK because that region contains discontinuous permafrost, with frozen and unfrozen rock in close proximity. Farther north, it is difficult to find unfrozen rock and farther south, it is difficult to find frozen rock. Figure 1 shows the location of the FRE test sites and locations of some of the seismic sensors deployed specifically for this project. The diagram in Figure 2 shows a cross-section of the FRE test site. Explosions of 200 and 350 lb of ammonium nitrate fuel oil (ANFO) were conducted in a gneiss/schist at the frozen test site in Goldstream Valley. A third frozen rock explosion of 350 lb was conducted in frozen gravels. The hill overlooking the valley is composed of unfrozen, dry schist and is where we detonated three shots of 100, 200, and 350 lb. In general, the centroid depth of the shots was between 6 and 8 m. All tests detonated as planned with the exception of shot 5 (350 lbs unfrozen), which cratered.

High-g accelerometers and short-period seismometers were deployed at near-source distances to record the shot time and source phenomenology of the explosions. The data are being analyzed to ascertain spall effects and compute moment tensors. Broadband and vertical component (“Texan”) seismometers were deployed at local distances to help quantify phase generation and propagation. High-resolution videographic data were recorded to verify the explosions detonated as planned and to analyze surface phenomenology.

Laboratory Analysis

Rock samples from the test sites were sent to New England Research, Inc. for analysis. The physical rock properties of each sample were measured both saturated and dry at room temperature, and then the measurements were performed again when the samples were chilled to below -10 °C. Seismic velocities and elastic moduli are shown in Figure 3. Both the compressional and shear velocities increased ~12% when frozen. In addition to the velocity increases, the bulk modulus, Poisson’s ratio, and uniaxial strain increased 36%, 26%, and 28%, respectively when the samples were frozen. These findings are in agreement with previous studies of frozen rock properties and indicate a much stronger rock at the frozen test site than the unfrozen site.

The increased strength is caused by freezing the water in a rock’s pores and cracks and was observed in the field with velocity of detonation recorders (VODRs), which showed an increase in explosive performance for the frozen

shots. A stronger rock better confines the explosion and causes a faster explosive burn rate. This also results in a smaller explosive cavity radius and reduced sliding along pre-existing fractures.

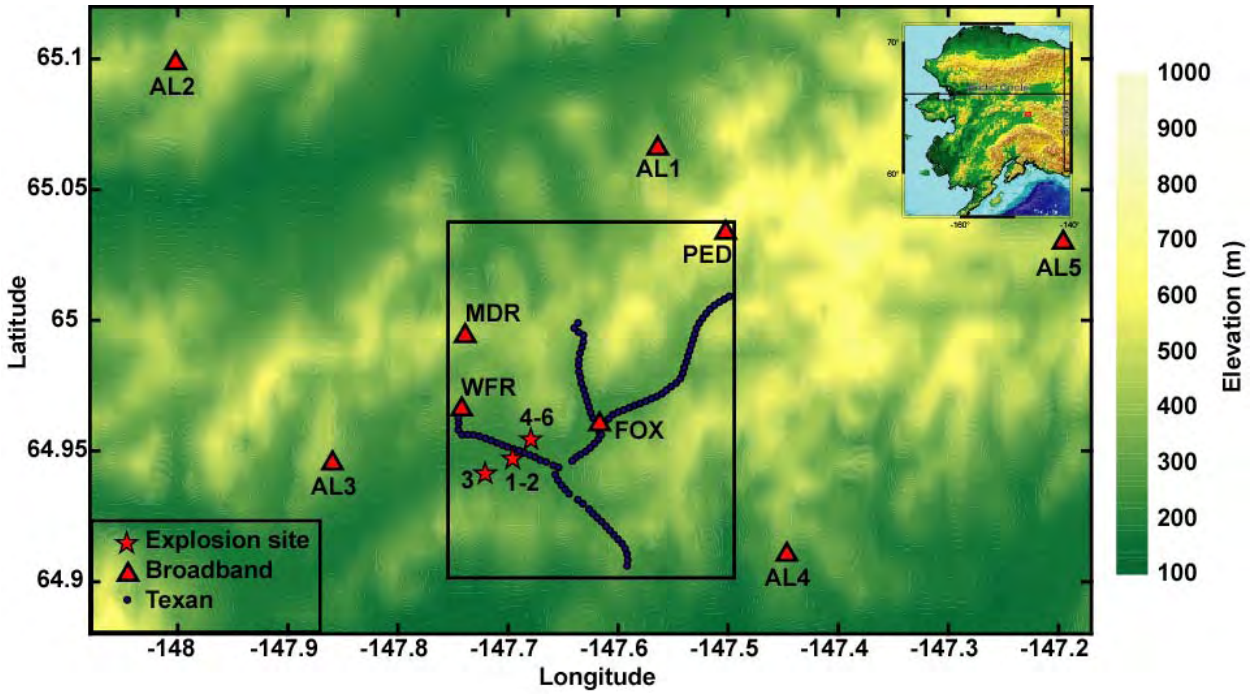

Figure 1. Location map of the test site region. Shot locations (stars) and deployed seismic stations (triangles and dots) are shown. Close-in accelerometers and seismometers are not shown.

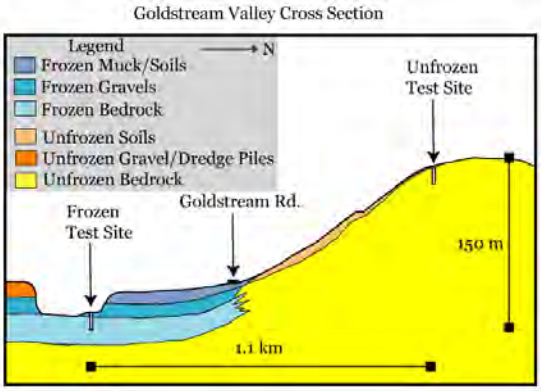

Figure 2. Cross-section of the test site. The frozen shots were located in a valley and the unfrozen shots were detonated on a hill overlooking the valley.

Velocity Model

To determine the in-situ velocity model for the test site, we combined shallow test site refraction data with Texan recordings of the shots and teleseismic earthquake receiver functions to develop a 1-D velocity model. The shallow refraction profiles were collected prior to detonation of the shots with a hammer source and a 60-channel recorder. An analyst picked the first breaks, which were combined with standard refraction equations to determine the *P*-wave velocity, while the ground roll was inverted to calculate the shear wave velocity. We then used the Texan shot recordings to perform similar analyses at deeper depths. It was observed on the Texans that the *P*-wave arrival times were azimuth dependent (Figure 4). A velocity anisotropy of ±10% and a fast direction of ~70° best removed the azimuthal dependence. The corrected Texan travel times can be observed on the right side of Figure 4.

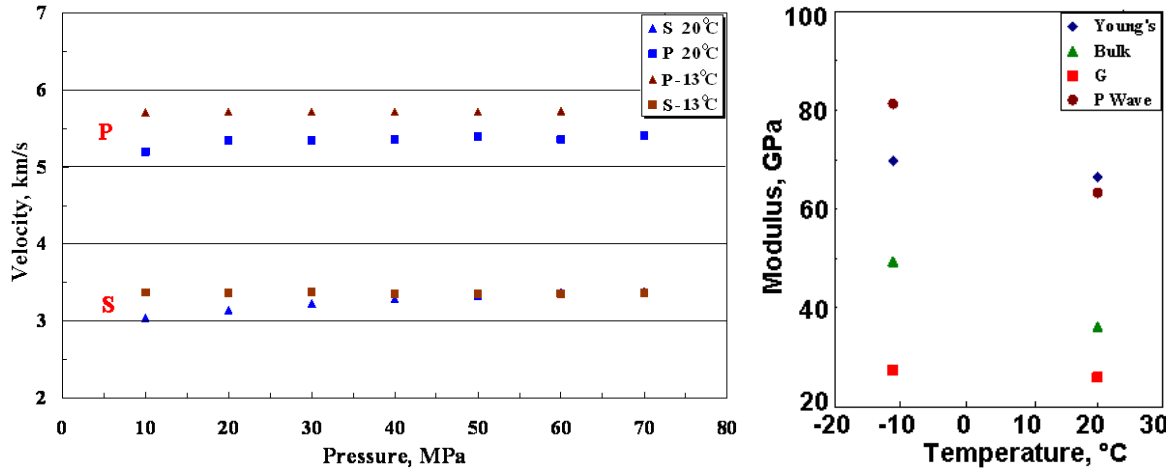

Figure 3. Ultrasonic *P*- and *S*-wave velocities (left) and elastic moduli (right) for a test site rock sample at room temperature and frozen.

To determine the velocity in the remainder of the crust, receiver functions from teleseismic earthquakes were jointly inverted with surface wave dispersion from the FRE shots recorded on nearby broadband seismometers (Figure 5). A niching genetic algorithm (Koper et al., 1999) was used to search the parameter space for the best fitting model. Figure 6 plots this (red) and the range of models that adequately fit the observed data.

This 1-D model fit the observed *P* and *S* arrivals very well, but the surface waves arrived earlier than predicted by the model at some stations. We are developing a 3-D model to better fit the surface wave arrivals. The final velocity model will be used in moment tensor inversions to examine the source phenomenology of the explosions.

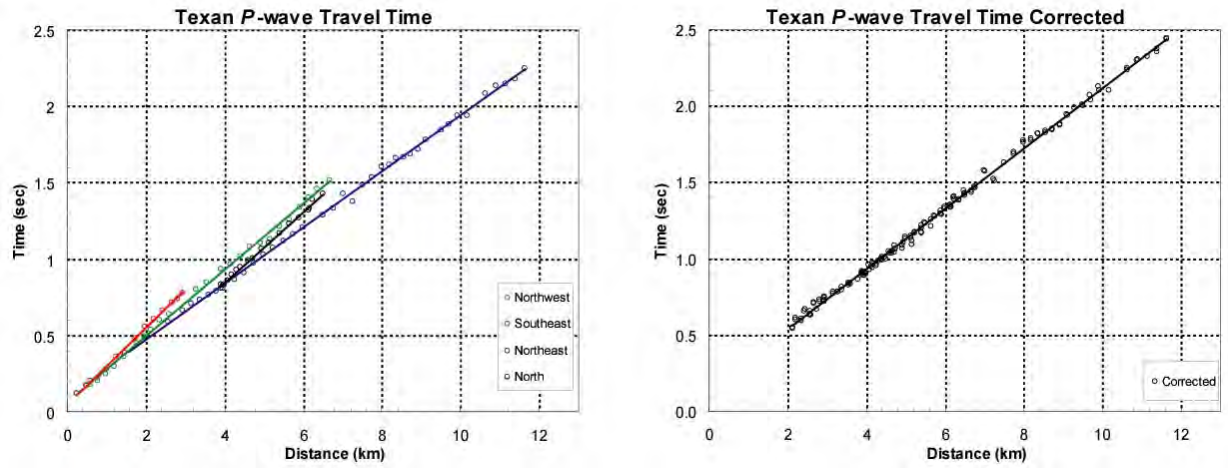

Figure 4. *P*-wave travel time plot of an FRE shot (left) recorded by the Texan network. Note the varying travel times based on station location (colored trend lines). On the right are the travel times at distances greater than 2 km for the same data after the anisotropic correction has been applied. All data can now be fit by a single velocity trend line.

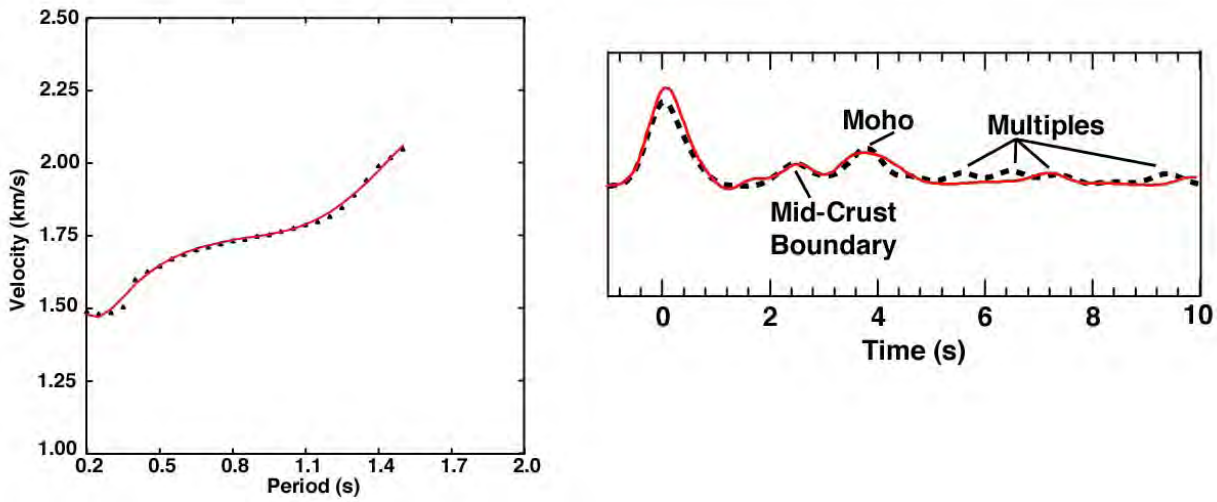

Figure 5. Plot of the best fit to a joint inversion of surface wave dispersion (left) and a receiver function (right). Black dashed lines are the observed data and red lines are the modeled data.

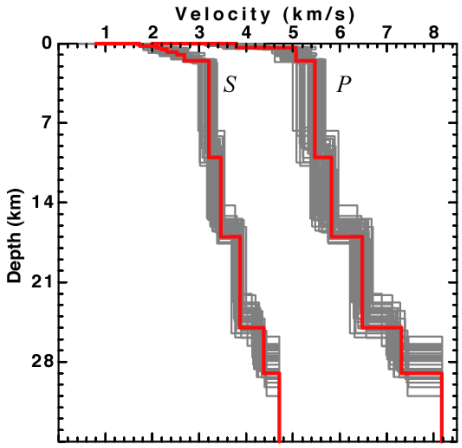

Figure 6. Best fitting 1-D velocity model (red) for the FRE test site and the range of models that satisfactorily fit the observed data (grey).

Shear Wave Generation

In theory, spherical explosion sources do not directly generate shear waves. They can indirectly generate shear energy through *P*-to-*S* reflections, *Rg* scattering, tectonic release, spall, and fracturing of the surrounding medium. Broadband transverse components show arrivals at a similar time and size as the Rayleigh wave for the FRE shots (Figure 7). This energy is interpreted to be a Love or SH wave arriving slightly prior to the Rayleigh wave. The shear energy does not seem to be affected by varying amounts of topography along the travel path, as paths completely in Goldstream Valley have large shear arrivals.

The shear arrival on Texan record sections (Figure 8) does not appear to be generated at the same time as the *P* phase. It is very difficult to pick the shear arrival at close-in stations so we cannot precisely determine the time delay or exactly where it is being generated. Examination of spall and calculations of *P*-to-*S* conversions from the free surface found that these two sources may be contributing to the shear energy, but neither were likely the primary source. Dr. Charlie Sammis has theorized that the summation of fracturing around the explosion could generate significant shear energy from an explosive source. We are providing him with data from this experiment to test this theory.

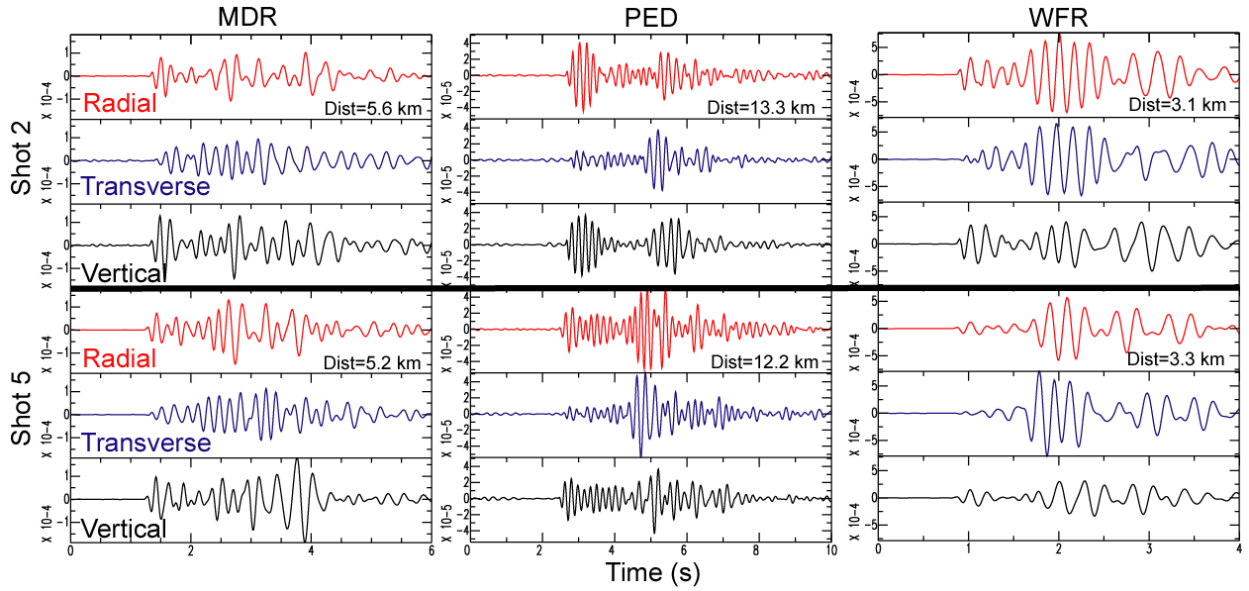

Figure 7. Three-component broadband data bandpass filtered from 3-6 Hz showing large transverse arrivals slightly earlier than the Rayleigh-wave arrival.

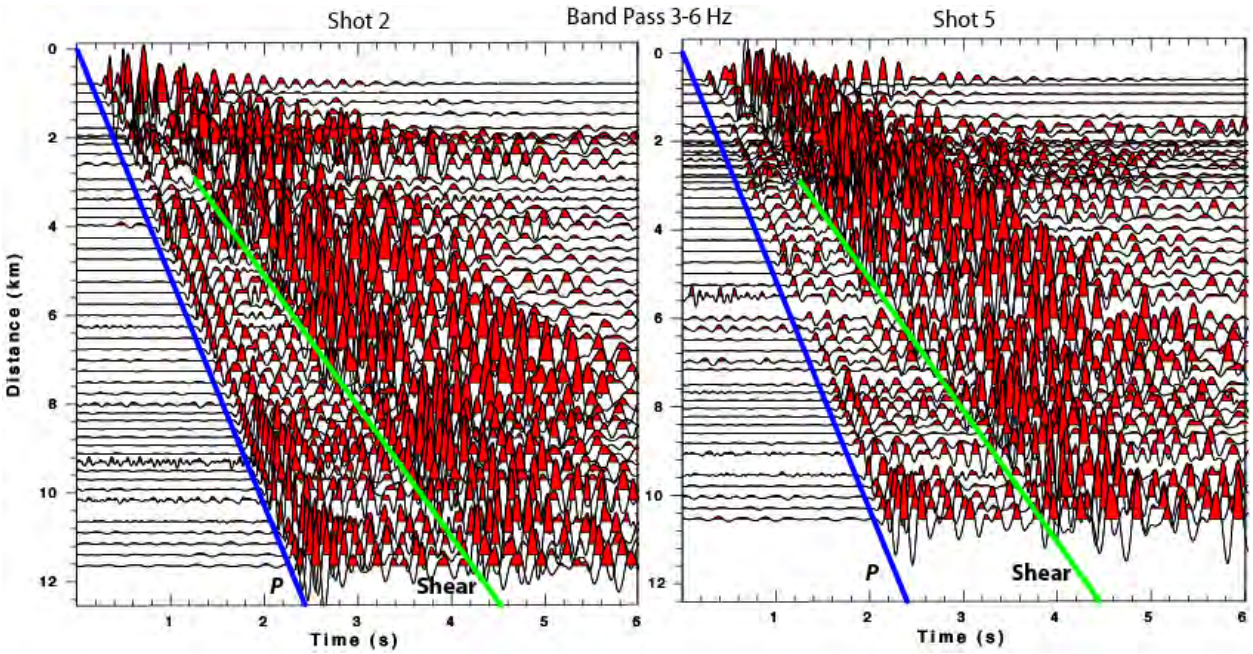

Figure 8. Texan data band passed from 3-6 Hz highlighting the *P* (blue) and shear (green) arrivals from both the frozen (shot 2) and unfrozen (shot 5) 350 lb shots.

Spectral Analysis

We calculated ratios of the full waveform FRE shot spectra to examine differences in the frozen and unfrozen explosion frequency content. In Figure 9, the Texan frozen/unfrozen spectral ratios are plotted for the 200 and 350 lb explosions. Median ratios for both size shots are very similar as are the individual ratios at each station. Below 4 Hz, the frozen shot amplitudes are ~2 times larger than the unfrozen shot amplitudes. From 4-9 Hz, the ratio drops below one suggesting that the unfrozen shots are larger in this range. The spectral ratio quickly rises to almost five above 10 Hz. This dramatic increase is likely related to the higher corner frequency for the frozen shots.

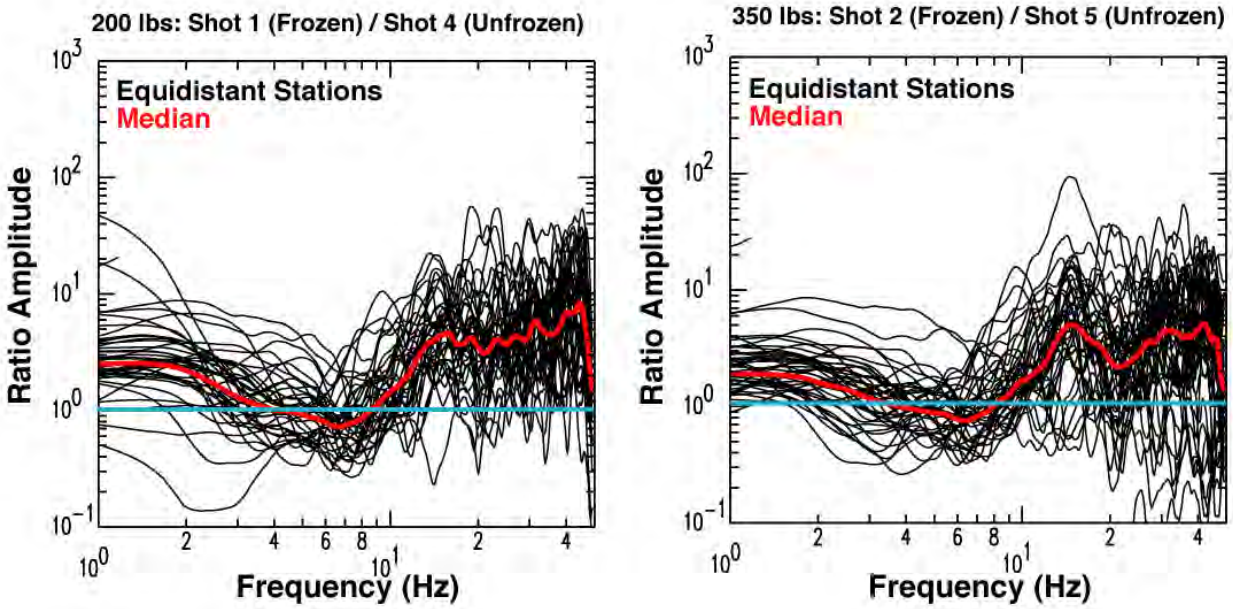

Figure 9. Spectral ratios for shot 1/shot 4 and shot 2/shot 5. Individual ratios are shown in black and the median is shown in red. A ratio greater than one indicates the frozen shot is larger than the unfrozen shot.

Mueller-Murphy Modeling

Seismic refraction studies at the two test sites suggest that the *in situ P*-wave velocity for the frozen rock medium was 28% faster than the unfrozen medium, while the *S*-wave velocity was 40% faster. These differences cannot be attributed only to the slight variations in the lithology between the two metamorphic assemblages and must also be related to strengthening when ice fills the cracks. When the differences in the velocities are incorporated into the Mueller-Murphy (1971) source with medium-dependent properties similar to rhyolite, we observe a good fit between observed and theoretical spectral ratios (Figure 10). The MM source with the *in situ* velocities predicts the different corner frequencies for the two media. When the laboratory-determined velocities were input into the MM source, there was considerable mismatch between the observed and theoretical ratios. The fracture networks at the two test sites, either filled with ice or air, contribute significantly to the differences in the observed seismograms.

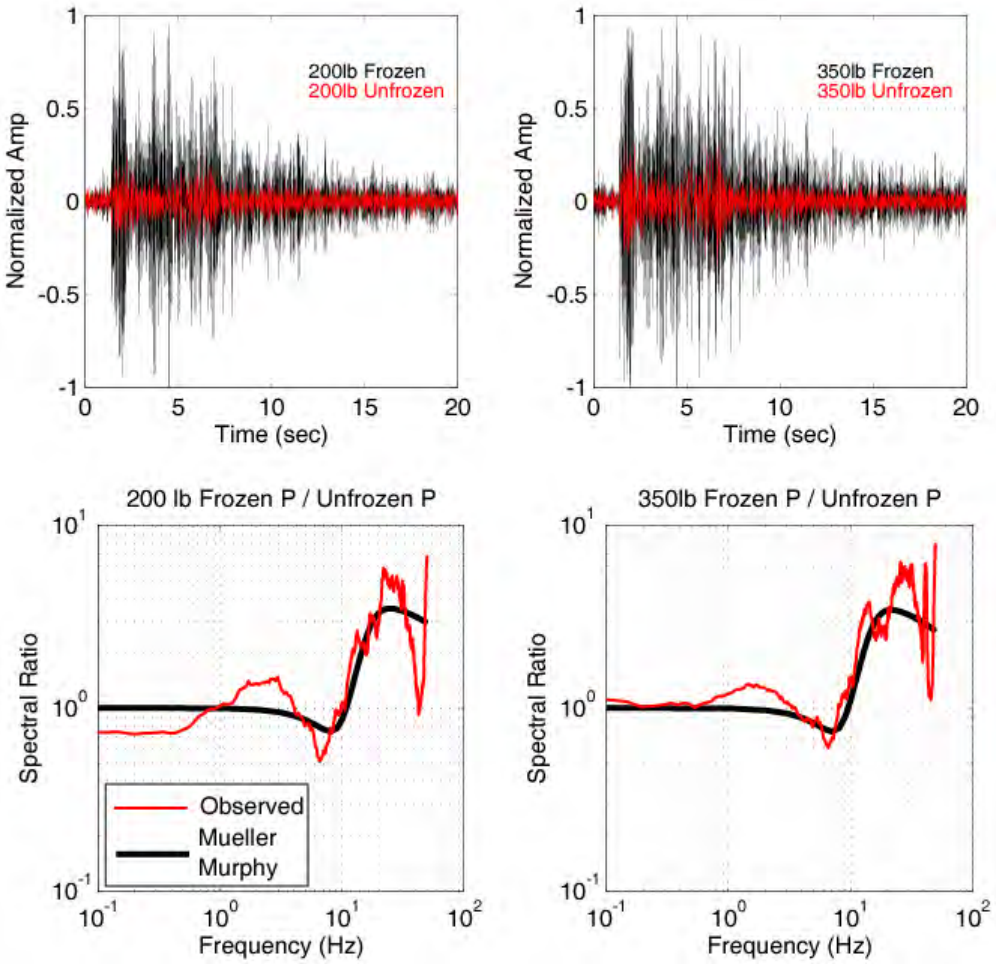

Figure 10. Amplitude differences between explosions in frozen and unfrozen rocks and the MM source. The upper plots show the waveforms recorded at 22 km from the explosions. The lower plots show the *P*-wave spectral ratios for these waveforms (red) compared to theoretical spectral ratios (black) from the MM source based on *in situ* velocity differences between the two test sites.

Phase Amplitudes

To further examine the frozen vs. unfrozen differences, the maximum amplitude of the *P*, *S*, and surface wave phases were measured on the Texan data. The Texans were deployed in a wide range of soils and gravels that caused the stations to have large amplitude variations. To avoid the site and distance effects, only stations that were equidistant to both test sites were used. In Figure 11, we plot the individual phase amplitudes and the *P*/*S* ratios for these stations.

The *P* amplitudes for shots 2 and 5 are very similar, and the same is true for shots 1 and 4, except at distances greater than 6 km where shot 1 is smaller. The unfrozen shots have significantly larger *S* amplitudes between 4 and 8 Hz. At many stations, the 200 lb unfrozen *S* amplitude is larger than the 350 lb frozen amplitude. The site effects can be observed by large scatter as a function of distance, but consistency in amplitude between shots. The unfrozen shots have larger *S* amplitudes from 2–4 Hz as well (not shown), but in the 8–16 Hz window, the frozen amplitudes are larger. Examination of the *P*/*S* ratios in Figure 11 shows larger values for the frozen shots, particularly for distances greater than 5 km. Interestingly, unfrozen shot 4 (200 lb) has larger ratios than unfrozen shot 5 (350 lb). Based on the *P* and *S* amplitude plots, it appears that this ratio difference is caused by shot 4 generating almost as much *P* energy as shot 5. A possible explanation is that shot 5 cratered while shot 4 had retarc. Surface wave amplitudes of the frozen shots are 2–3 times larger than the unfrozen shots in the 0.5–2 Hz pass band

(Figure 11). This is a surprising result and needs further study. Our future plans are to try and model the difference in the *P/S* ratios using the Mueller-Murphy source with the corner frequency scaled proportionally to the *S*-wave velocity following the methods of Fisk (2007).

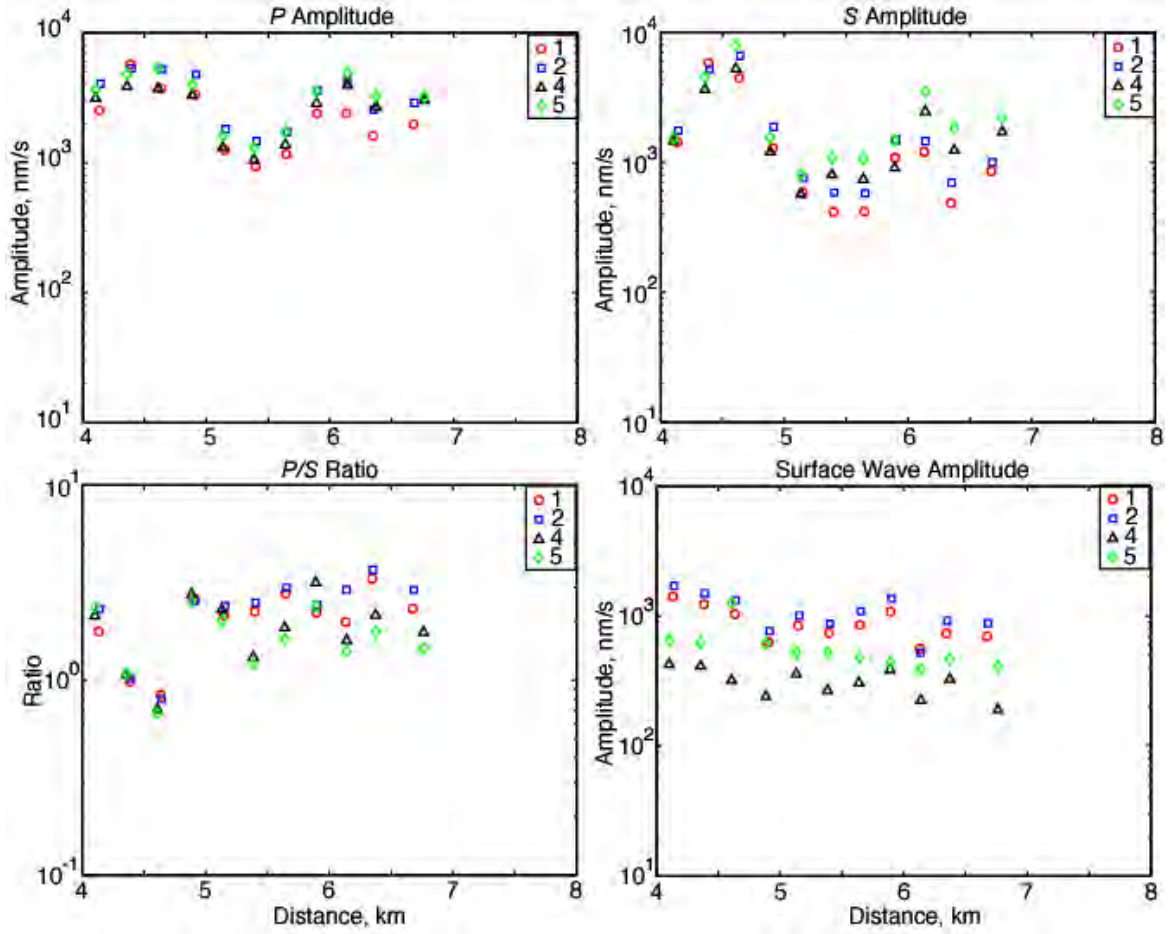

Figure 11. Phase amplitudes from equal size explosions. *P* amplitudes (upper left) are similar for the frozen and unfrozen shots. The unfrozen shots have larger *S* amplitudes though (upper right) and therefore, the *P/S* ratios are larger for frozen shots (bottom left). The frozen shots generated significantly more surface wave energy in the 0.5–2 Hz pass band (bottom right).

CONCLUSIONS AND RECOMMENDATIONS

The data collected from the Frozen Rock Experiment show that differences in amplitudes between our explosions at the frozen and unfrozen rock test sites are frequency dependent. The frozen rock medium was stronger and resulted in a smaller cavity radius, which increases the corner frequency when compared to the unfrozen rock medium. Above 10 Hz, the frozen explosions had significantly larger amplitudes, but between 4 and 9 Hz, the unfrozen shots produced larger amplitudes. It is expected that the amplitudes from the explosions in the unfrozen rock would have been larger had we been able to conduct them in water-saturated unfrozen rock. We are currently negotiating with landowners near the test site region to conduct another set of explosions in wet and unfrozen rock.

We have shown that the observed amplitude differences can be effectively modeled using the Mueller-Murphy (1971) source for rhyolite and the observed test site *P*- and *S*-wave velocities. The differences in the velocities for the two test site media can be attributed to two factors: a) slight lithology variations (gneiss/schist vs. schist) between the two test sites and b) strengthening caused by the ice-filled cracks in the frozen medium. Laboratory samples show 12% difference in the *P*-wave velocity between samples of the unfrozen schist and frozen

gneiss/schist. In situ velocities measured from refraction studies at each test site indicate a much larger 28% difference in the *P*-wave velocities, which results in a very good fit between the observed spectral ratios and the MM source.

Larger shear wave arrivals were recorded from the shots in unfrozen schist, while larger surface waves were observed for the shots in frozen rock. There are several explanations for these phenomena that we are currently studying. First, the increased strength of the frozen rock may inhibit sliding along fractures thus reducing shear wave generation at the source. Another explanation could be that the unfrozen rock shots were detonated near the summit of a hill leading to possible *Rg*-*S* scattering, thus reducing the surface wave amplitudes while increasing the *S*-waves. A third explanation could be differences in the tensile strength between the frozen and unfrozen overburden, which could greatly change the properties of secondary sources such as spall and block motions.

Future research will include using ongoing moment tensor calculations to generate regional and teleseismic distance synthetic waveforms. We will then hopefully be able to determine whether explosions in frozen rock produce biased yields at the frequencies typically observed in nuclear monitoring operations. We will also continue work to document the *S*-waves generated by the FRE explosions to aid the understanding of shear wave generation from explosions.

REFERENCES

Fisk, M. (2007). Corner frequency scaling of regional seismic phases for underground nuclear explosions at the Nevada Test Site. *Bull. Seism. Soc. Am*. 97: 977–988.

Koper, K. D. M. E. Wysession, and D. A. Wiens (1999). Multimodal function optimization with a niching genetic algorithm: A seismological example, *Bull. Seism. Soc. Am*. 89: 978–988.

Mellor, M. (1971). Strength and deformability of rocks at low temperatures, Hanover, NH, Cold Regions Research and Engineering Laboratory (CRREL), U. S. Army Corps of Engineers, Research Report 294.

Mueller, R. A., and J. R. Murphy (1971). Seismic characteristics of underground nuclear detonations: Part I, Seismic scaling law of underground detonations, *Bull Seism. Soc. Am*. 61: 1675.

Sammis, C. and R. Biegel (2004). Mechanics of strengthening in crystalline rock at low temperatures: a preliminary assessment, in *Proceedings of the 26th Seismic Research Review: Trends in Nuclear Explosion Monitoring*, LA-UR-04-5801, Vol. 2, pp. 475–484.

REGIONAL *P* CODA FOR STABLE ESTIMATES OF BODY WAVE MAGNITUDE: EXTENDING THE M_S:m_b DISCRIMINANT TO SMALLER EVENTS

Kevin Mayeda and Jessie Bonner

Weston Geophysical Corporation

Sponsored by the Air Force Research Laboratory

Contract No. FA8718-06-C-0027

ABSTRACT

The most successful teleseismic discriminant is M_s:m_b, and many studies are underway to try to extend surface wave magnitude (M_s) estimation to regional distances. A problem that is encountered at regional distances and small magnitudes is how to estimate m_b so that the M_s:m_b discriminant is meaningful and consistent with teleseismic measures.

Over the past several years, a regional *S*-coda wave methodology has been developed that provides for the lowest variance estimate of the seismic source spectrum. Thus, regional M_W and m_b estimates derived from *Sn* and *Lg* coda are very stable, even when only a single station is used. However, these m_b's are inherently biased for earthquakes because they are an *S*-based measurement, and explosions are relatively depleted in *S*-waves. Previous research projects have used region-specific m_b scales based on direct measurements of *Pn* and *Pg* to improve the M_s:m_b discrimination, even though the m_b estimates often had a large variance.

In our preliminary research, we have found that *P*-coda envelopes for both explosions and earthquakes can be obtained for events from both the Nevada Test Site (NTS) and Novaya Zemlya (NZ) regions without bias. Our next step at NTS will be to derive path corrections, similar to the approach of Mayeda et al. (2003) for *Lg*-coda. We will compare inter-station scatter of distance-corrected amplitudes as a function of window length. This will provide an empirical measure of error based on window length for each frequency band. For each frequency band, we will regress our coda envelope amplitudes against regional and teleseismic estimates of m_b (e.g., m_b(*Pn*), m_b(*P*)) to determine which band provides the lowest variance. This will yield slope and intercept values for each frequency band. We will then derive m_b(*Pn*) and m_b(*P*) (following Denny et al., 1989) to compare against m_b(*P*-coda) to assess performance at the network and single-station level. Most of the nuclear explosions already have an m_b(*Pn*) compiled by Vergino and Mensing (1989). Patton (2001) has estimated m_b(*Pn*) for many historic NTS earthquakes. For recently recorded earthquakes, we will need to estimate m_b(*Pn*) and m_b(*P*). Finally, we will compute M_s(VMAX) from the regional stations and form an M_s(VMAX)*:*m_b(*P*-coda) discriminant to compare against teleseismic values and trends.

OBJECTIVE

An important aspect of nuclear explosion monitoring is discrimination and yield estimation. U.S. monitoring scientists must be able to both discriminate explosions from earthquakes as well as assign an accurate lower bound to the yields for nuclear explosions detonated in regions of monitoring concern. Seismic monitoring has historically been performed on large (> ~1 kt) nuclear explosions, which typically have dozens of teleseismic *P*-wave recordings (e.g., Murphy et al., 2001). The large number of measurements can be used to effectively average over the three-dimensional (3D) Earth structure and any azimuth-dependent effects from the source. In some special cases t* corrections have been performed to account for potential upper mantle structure (e.g., $m_b(P)$ bias for NZ explosions).

Over the past several years, the Department of Energy (DOE) labs, have developed a regional coda wave methodology to obtain the lowest variance estimate of the seismic source spectrum. Thus, regional M_W and m_b estimates derived from *Sn* and *Lg* coda are very stable, even when only a single station is used. However, these m_b*'s* are inherently biased for earthquakes because they are an *S*-based measurement, and explosions are relatively depleted in *S*-waves. Previous research projects have used region-specific m_b scales based on direct measurements of *Pn* and *Pg* to improve the M_s:m_b discrimination, even though the m_b estimates often had a large variance.

This project addresses a number of questions. Can we reduce the variance in regional m_b estimates using a sparse-station *P*-coda methodology, as opposed to using multitudes of direct *Pn* and *Pg* measurements? How will the stability of these m_b(*P*-coda) estimates compare to the highly successful and stable (but unfortunately biased) methods involving *Lg* and *Sn* coda? How many stations will be needed? Will the use of m_b(*P*-coda) improve M_S:m_b discrimination at regional distances? Research conducted during the past year has answered several of these questions as described in the following sections of this paper.

RESEARCH ACCOMPLISHED

Underground nuclear explosion monitoring requires the discrimination of small nuclear explosions and earthquakes. The most successful teleseismic discriminant compares the 20-second period surface wave magnitude (M_s) with the ~1-Hz body wave magnitude (m_b). This discriminant is referred to as M_s:m_b, and many studies are underway to try to extend surface wave magnitude (M_s) estimation to regional distances. A problem that is encountered at regional distances (<~2000 km) and small magnitudes is how to estimate m_b so that the M_s:m_b discriminant is meaningful and consistent with teleseismic measures.

Novya Zemlya. We measured relative *P*-coda envelope amplitudes using the October 24, 1990, NZ explosion as a reference event. By scaling narrowband envelopes between our reference event and the other explosions and earthquakes, we were able to tabulate relative coda amplitudes. Figure 1 shows coda envelopes at the Norwegian Seismic Array along with derived body wave magnitudes made from the *P*-coda. These preliminary results are very promising in that earthquake m_b's are also in good agreement with the maximum likelihood magnitude, m_b(ML). This is in sharp contrast to results from regional m_b(*Lg*) and m_b(*Lg* coda) (e.g., Patton, 1988; Mayeda 1993). In those studies, m_b was tied to explosions at the NTS; however, applying the same formulas to earthquakes results in an overestimation of ~1 magnitude unit. For example the 1992 M_W 5.5 Little Skull Mountain earthquake at NTS would have an m_b(*Lg*) of ~6.6.

Paths from NZ to the Norwegian Seismic Array are still at regional distance and one might expect the *P*-wave and its coda to be comprised of waves that sample the crust and upper mantle over a range of take-off angles from the source. At teleseismic distances however, we might expect that the averaging nature observed for local and regional coda waves to breakdown. At these distances, first arriving *P*-waves are likely emanating from a limited range of take-off angles near the bottom of the focal sphere. To investigate this, we processed roughly 30 NZ explosions recorded at the U.K. arrays Eskdalmuir in Scotland (EKA) and Yellowknife in Canada (YKA), located at ~30 and 44 degrees from NZ, respectively.

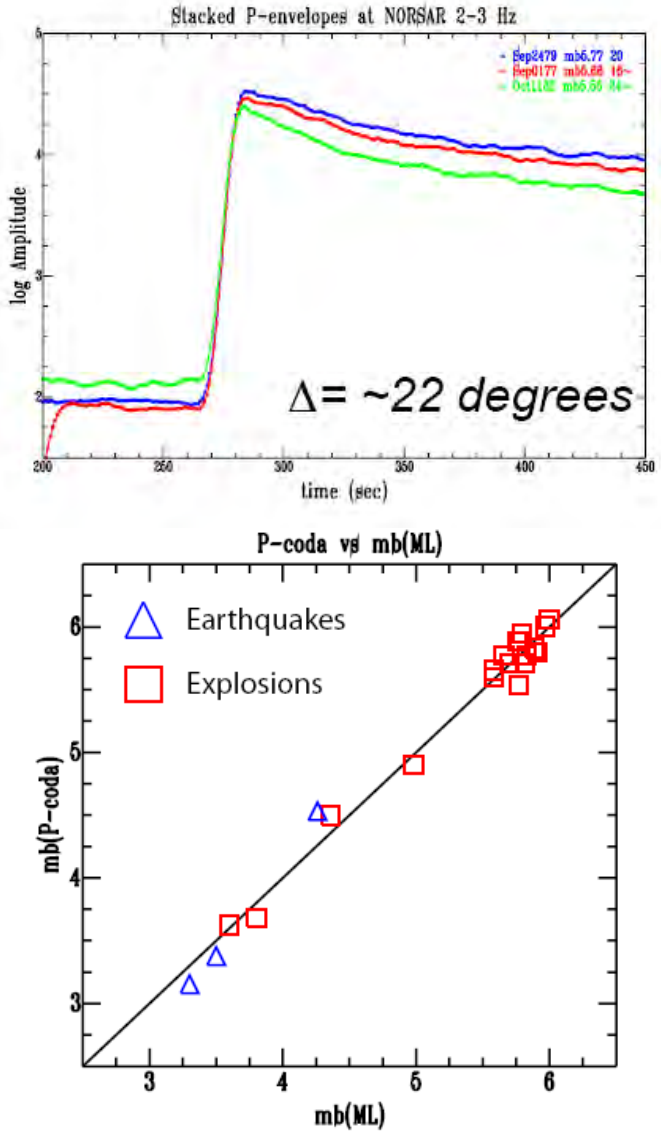

Figure 1. *P*-coda envelopes (2–3 Hz) stacked over the Norwegian Seismic Array for three NZ (top). The m_b(*P*-coda) for both explosions and earthquakes (bottom) do not exhibit a bias, in contrast to m_b(Lg) and m_b(Lg coda).

Figure 2 shows envelopes at EKA for 4 NZ explosions with roughly the same magnitude that were located within a few kilometers of each other (see Figure 1 in Lilwall and Marshall, 1986). We see an immediate discrepancy for the September 24, 1979, event. Though it has the largest m_b(ML) it is roughly a factor of 3 smaller in amplitude (0.5 in $\log_{10}$) at EKA relative to the other three events. The direct *P*-wave, coda, and *PcP* phase (not shown) are all small. In fact, the EKA station magnitude for this event is also low relative to the global m_b(ML) estimate. The closest event is the September 27, 1978, event, but this does not appear to be anomalous. Careful inspection of the raw data shows nothing unusual for the September 24th event. (Note: The pre-event noise is lower for the October 11, 1982, event because of improvements to the electronics in late 1979). We note that this event at the Norgwegian Seismic Array is in good agreement with the m_b(ML) as well as at YKA. Assuming this is real, then this suggests a near-source process such as focusing directly beneath this event. Moreover, the scale-length must be small since a nearby event is not affected. This supports the notion that teleseismic *P*-codas will not have the same averaging properties that local and regional codas exhibit.

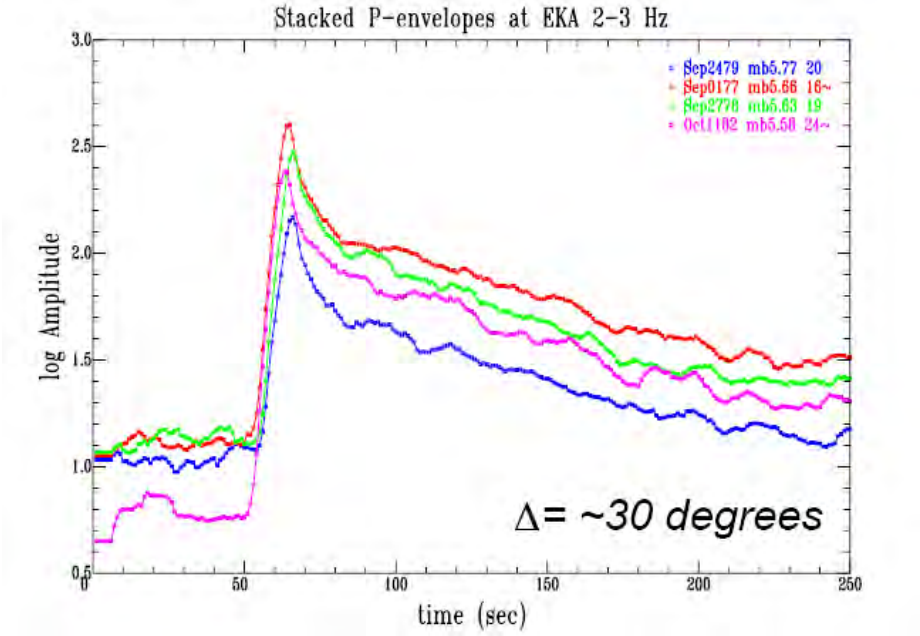

Figure 2. We show 4 NZ explosion *P*-coda envelopes at station EKA for events with roughly the same magnitude; however, we observe a large discrepancy with the September 24, 1979, event. Though it has the largest magnitude, it is a factor of 3 smaller in amplitude.

Nevada Test Site. Next, we applied the same methodology to explosions and earthquakes at NTS. Using the April 18, 1983, explosion as a reference, we computed m_b(*P*-coda) at the Berkeley seismic station, BKS, located ~5.5 degrees away. This amounted to roughly 60 seconds of *Pg* coda that we were able to measure. As found for NZ events, we also did not find any bias between m_b(*P*-coda) for explosions and earthquakes relative to the teleseismic m_b(*P*).

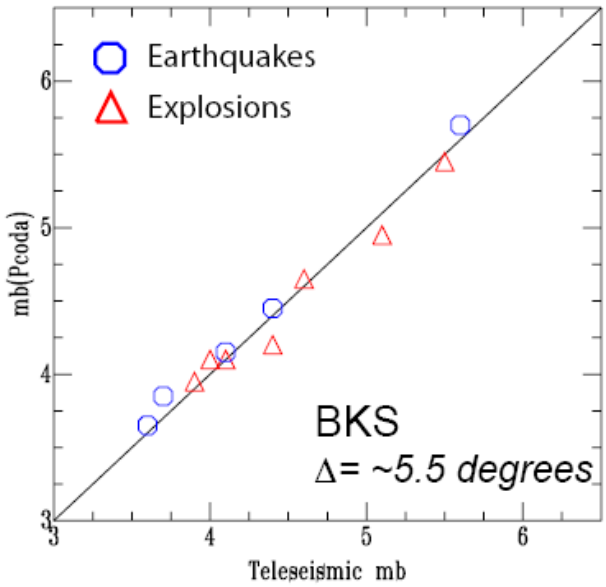

Figure 3. Relative *P*-coda envelope amplitudes were made using the August 18, 1983, explosion as a reference. m_b(*P*-coda) for NTS explosions and earthquakes agree with teleseismic m_b(*P*), in good agreement with Norwegian Seismic Station results for NZ events. At 5.5° degrees, we had ~60 seconds of *P*-coda to form the measurements on multiple narrow frequency bands that were regressed separately.

CONCLUSIONS AND RECOMMENDATIONS

Our preliminary findings suggest that at regional distances the *P*-coda can be used as a surrogate for teleseismic m_b for both earthquakes and explosions, based on the findings at the Norwegian Seismic Station for NZ events as well as those at NTS (e.g., Figures 1 and 3). At teleseismic distances, the *P*-coda appears to share the same radiation pattern as the direct *P*-wave and does not appear to average over the focal sphere as is observed for local and regional shear waves (e.g., Figure 2). Nonetheless, the derived body wave magnitude m_b(*P*-coda) at EKA and YKA for NZ explosions is in good agreement with the globally averaged results using direct teleseismic *P*. Furthermore, m_b(*P*-coda) can be computed on clipped data which is quite common for the larger NZ explosions recorded at EKA and YKA.

In addition to computing m_b(*P-coda*) vs M_s(VMAX) for both datasets, our plans are to process many regional and near-teleseismic stations that recorded NTS events at a range of azimuths. We will process many regional and near-teleseismic stations that recorded TS events at a range of azimuths. Specifically, we will

1. document the inter-station stability and compare the direct *P* results,
2. document the magnitude variance as a function of the coda measurement window,
3. develop magnitude-yield curves,
4. derive detection threshold curves,
5. evaluate the transportability of foreign test sties, and
6. generalize the method to broad area monitoring as is done with the regional shear-wave coda methodology.

REFERENCES

Denny, M. D., S. R. Taylor, and E. S. Vergino (1989). Erratum: Investigation of m_b and M_s formulas for the western United States and their impact on the M_s/m_b discriminant, *Bull. Seism. Soc. Am.* 79: 230.

Lilwall, R. C. and P. D. Marshall (1986), Body wave magnitudesf and locations of Soviet underground explosions at the Novaya Zemlya test site, AWRE report no. 0 17/86, HMSO, London.

Mayeda, K. (1993). m_b(*Lg*Coda): A stable single station estimator of magnitude, *BSSA* 83: 851–861.

Mayeda, K., A. Hofstetter, J. L. O'Boyle, and W. R. Walter (2003). Stable and transportable regional magnitudes based on coda-derived moment-rate spectra, *Bull. Seism. Soc. Am.* 93: 224–239.

Murphy, J. R., I. O. Kitov, B. W. Barker, and D. D.Sultanov (2001). Seismic source characteristics of Soviet peaceful nuclear explosions, monitoring the TBT: Source processes and explosion yield estimation, *Pure Appl. Geophys.* 158: 2077–2101.

Patton, H. J. (1988). Application of Nuttli's method to estimate the yield of the Nevada Test Site explosions recorded on Lawrence Livermore National Laboratory's seismic system, *Bull. Seism. Soc. Am.* 78: 1759–1772.

Patton, H. (2001). Regional magnitude scaling, transportability, Ms:mb discrimination at small magnitudes, *Pure and Appl Geophys*. 158: 1951–2015.

Vergino, E. S. and R. W. Mensing (1989). Yield estimation using regional m_b(*Pn*), Lawrence Livermore National Laboratory report UCID-101600.

SMALL-EVENT YIELD AND SOURCE CHARACTERIZATION USING LOCAL P- AND S-WAVE CODA SOURCE SPECTRA

Kevin M. Mayeda[1] and W. Scott Phillips[2]

Weston Geophysical Corporation[1] and Los Alamos National Laboratory[2]

Sponsored by Air Force Research Laboratory

Contract No. FA8718-07-C-0010

ABSTRACT

The mission of the Air Force Tactical Applications Center (AFTAC) requires accurate yield estimation for nuclear explosions. Historically, the focus has been on larger yield events (m_b > ~4.5) using teleseismic body wave magnitudes and applying test-site-specific corrections for yield estimates. Recently, the Department of Energy (DOE) labs in conjunction with the AFTAC Seismic Review Panel have developed a regional coda methodology which, to date, provides unprecedented stability and avoids test site bias because it is based upon absolute source spectra. Increasingly, however, there is interest in monitoring smaller events both for yield and source characterization. Unfortunately, these events may only be recorded with adequate signal-to-noise ratio at local distances from one station.

This project outlines steps to extend the well-established regional coda methodology to local distances using *S*- and *P*-wave codas in regions of little to no calibration data and/or regions of high attenuation and lateral complexity. Previous studies show that local coda has a unique property of homogenizing its energy over a volume of Earth's crust such that path corrections for distances less than ~200 km are not necessary, or minimal at worst. This special feature may make it easier to define an a priori set of coda calibration parameters that can be transported to new but geophysically similar regions. For example, we will focus on coda path, envelope shape, and peak envelope velocity functions from various local coda studies and derive average "local background" models then apply them to other regions for testing and evaluation, including cases to mimic an un-calibrated, single-station deployment. We will use existing data sets from a variety of active tectonic settings and source types with the aim of assessing performance under the assumption of little to no calibration data. We will also blend the models with regional calibrations that lack local data.

OBJECTIVES

The following outlines many of the questions and objectives that we will address in this study:

1) To what extent can an average local background coda model (e.g., path corrections, envelope shape, velocity, etc.) be developed and transported to a new area with no prior calibration? Specifically, can we transport these averaged parameters to a new, tectonically similar region? What are the associated errors?
2) For regional coda calibrations that lack local data and are unconstrained at these distances (e.g., central Asia, north Africa), can we seamlessly blend in the appropriate local background model?
3) Can local coda measurements in a heterogeneous region provide a stable yield estimate relative to direct wave measures?
4) Due to its inherent shorter window length, to what extent can the local *P*-wave coda be used and how do results compare with *S*-coda? How does this compare with results from an on-going regional *P*-wave coda study?
5) How much is gained by additional stations, or is one station enough?
6) For low seismicity regions, how can we obtain higher confidence estimates of site-response corrections? For example, can we use a single ground-truth source spectrum or calibration event? If so, what are the errors?
7) For highly attenuative regions, what is the minimum coda window length needed to maintain a stable amplitude estimate? What is the minimum magnitude threshold where we can still maintain stable estimates? Can we derive average detection threshold curves?
8) Can our local coda spectra be used for high-frequency seismic discrimination, for example, coda spectral ratios?
9) Can the spectral shape of the local, coda-derived source spectra provide depth-of-burial information?

RESEARCH TO BE ACCOMPLISHED

As work on this project has yet to commence, the following outlines the motivation and research plan for the next two years. In this project we plan to demonstrate the capability of providing significantly lower uncertainties in yield estimation by extending the well-established regional narrowband coda methodology to local distances in regions of little to no calibration data using both *P* and *S*-wave codas. Furthermore, because of its stable nature, local coda-derived source spectra will be used to characterize a range of different event types (e.g., shallow and normal-depth earthquakes, mining-related explosions and their associated events, nuclear tests, rock bursts, and volcanic-related events). The motivation for using the coda comes from the fact that it has unique properties that, if exploited fully, can significantly improve our ability to monitor small events at local distances. For example, local high-frequency (>~0.5 Hz) *S*-wave coda has the unique property of homogenizing its energy over a volume of Earth's crust such that path corrections for distances less than ~200 km are not necessary or minimal. Furthermore, the local coda averages over the focal sphere as well as the source-time function of the event, thus eliminating the need for dense seismic networks. Even in regions of strong lateral complexity, the local coda has been shown to be very stable, usually a factor of 4 to 5 times less variable than direct *S*-phases. This means that to achieve the same level of precision with the traditional direct phases, one would need a local network composed of ~16 to 25 stations surrounding the source, which in most cases would be unrealistic, especially in clandestine monitoring. Because the coda averages over the 3-D crustal heterogeneity as well as the source radiation pattern, it is ideal for small-event local monitoring with as few as one station. To demonstrate this, Figure 1 shows inter-station magnitude results for NTS explosions recorded at near-regional distances (e.g., 200 to 300 km away). Here we compare the inter-station performance between $m_b(L_g)$, $m_b(Pn)$, and $m_b(L_g\text{coda})$ from Mayeda (1993). We observe that the coda-based m_b's have the lowest standard deviation by roughly a factor of 4 to 5. This property makes it ideal for monitoring situations where station coverage is sparse.

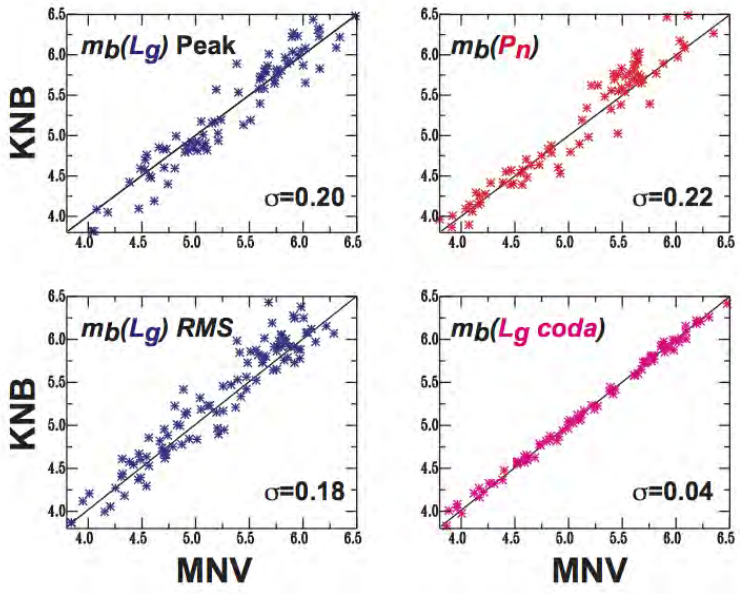

Figure 1. Interstation comparisons of magnitude at two near-regional stations, KNB (Δ ~250 km) and MNV (Δ ~200 km) (from Mayeda, 1993). Note that the scatter in the coda-derived m_b's (lower right) is a factor of 4 to 5 times smaller than the conventional regional magnitude measures using direct *P* and L_g.

For regional applications of the coda methodology, path corrections can be significant and the DOE labs have a large effort in calibrating broad regions. However for local monitoring, path effects on the coda are not as important. For example, Figure 2 illustrates a unique property of coda waves that has been the basis of numerous studies over the past several decades, namely that the coda approaches a homogeneous distribution in space and time behind the expanding direct-wave front (e.g., Aki, 1969; Aki and Chouet, 1975; Phillips and Aki, 1986). In this example we show three panels of three events that are recorded at station BKS and another station, SAO, located ~140 km to the southeast. The three events were chosen such that one was relatively close to BKS, the other roughly in between, and the last event was close to SAO. In all panels we see that the coda envelope levels are approximately the same, independent of the source-station distance. This is in sharp contrast to the direct waves (*P*, *S*, and L_g), which differ significantly in amplitude because of attenuation, geometrical spreading, and radiation pattern. A way to help visualize this is to imagine the direct *S*-wave moving radially away from the source. Behind the *S*-wave front, there is a pool of scattered energy in its wake that decays at the same rate, irrespective of distance from the source. As stated to the PI years ago by the late Kei Aki, "It's like a kind of magic!" Whether one believes in single or multiple scattering, isotropic or non-isotropic scattering (e.g., see review by Sato and Fehler, 1998), the observational evidence clearly shows that the crust tends to homogenize the coda energy at local-to-near-regional distances (e.g., Aki, 1969). This means that *any* seismic station within this region would provide a stable amplitude measure irrespective of its location relative to the source origin.

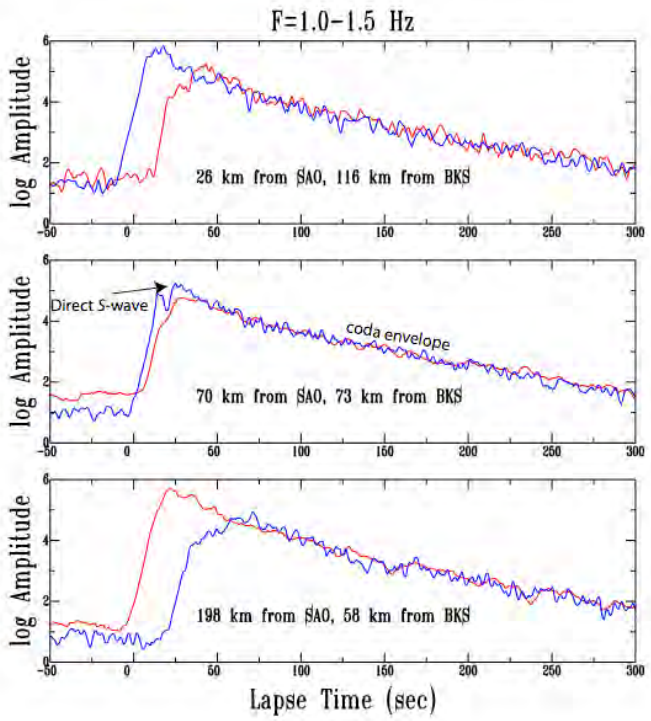

Figure 2: Example envelopes (*f* = 1.0–1.5 Hz) for three local earthquakes located in the San Francisco Bay region recorded at stations SAO (blue) and BKS (red), part of the Berkeley Digital Seismic Network (BDSN). At this range of distances, the scattered *S*-waves or "coda" are homogeneously distributed in the crust (from Mayeda et al., 2005).

As mentioned earlier, the motivation behind this proposal comes from the desire to estimate yield accurately and characterize the source, especially those that are small, clandestinely tested, or in regions of high regional attenuation. Ground-based nuclear explosion monitoring relies heavily on teleseismic and regional sensors that are sparsely distributed around the world, usually with station spacing on the order of ~1000 km or more. Station distribution and regional attenuation will determine what size event can be reasonably recorded and processed. However, if local assets could be obtained, this would allow for much higher signal-to-noise ratio measurements. The size of the event, the emplacement conditions, and regional attenuation structure will dictate what calibration steps one would have to undertake. For example, in a highly attenuative region such as Iran, high frequency waves (f > ~2 Hz) would likely be missing from regional seismograms even at M ~4. A local determination of the source spectra would provide a yield estimate and potentially depth-of-burial based on the location of the spectral peak in the coda-derived source spectrum. Likewise, if local monitoring were used in an on-site inspection, the background seismicity and duration of deployment will influence which calibration steps to follow.

Unlike yield estimates from magnitudes based on relative amplitudes from direct waves, estimating explosion yield from the coda has been developed around absolute source spectra (Figure 3).

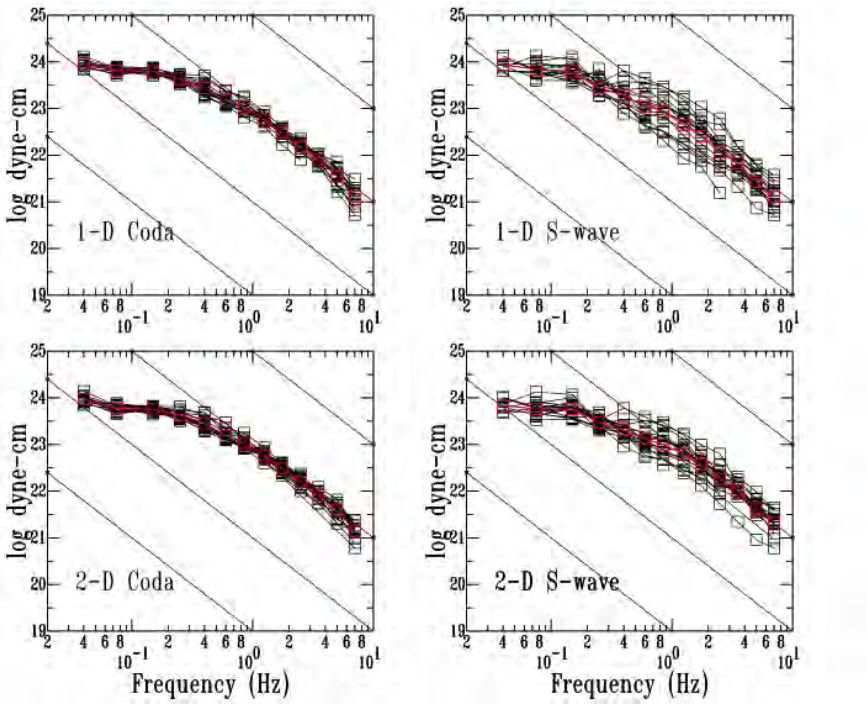

Figure 3: Absolute source spectra (moment-rate spectra) for the M_W 5.0 Napa earthquake of September 3, 2000. Top two panels show results assuming 1-D, radially symmetric path corrections for coda and direct waves. Bottom panels show results using spatially varying 2-D *Q*. Black lines represent individual station spectra and red lines represent the average. Stations are situated at a variety of azimuths and range between a few tens of kilometers to over 400 kilometers (from Mayeda et al., 2005). Notice that the coda-derived source spectra are remarkably stable in comparison with direct *S* and L_g spectra.

By using absolute spectra, we avoid potential regional biases, for example, those related to upper mantle and crustal differences (Sykes and Cifuentes, 1984). Currently, regional coda-derived amplitude-yield curves have been developed for different emplacement conditions. Local crustal structure can adversely affect the radiated energy and introduces large amplitude variability over short distances and azimuth ranges, especially at high frequency (f > ~1-Hz). In sharp contrast, the path effects on coda are negligible for local distances and in fact benefit from the crustal heterogeneity because it provides the homogenization (e.g., see Figure 2). We anticipate that local coda data from a variety of regions behave similarly thus facilitating construction of average local background models.

For classic yield estimation using direct waves such as teleseismic m_b, regional biases can be imprinted on the estimated yield due to low upper mantle Q (e.g., t^* corrections for Central Asia and Novaya Zemlya). For the coda, the DOE national labs have developed a regional coda yield methodology that obviates the problem of regional bias by correcting the coda amplitudes all the way back to the absolute moment-rate spectra. The only corrections required are for the *S*-to-coda transfer function and site response, both of which are frequency dependent and could be obtained through geophysical analogy or with a single ground-truth event. To date, the coda methodology has been applied in numerous geophysically complex regions. We plan to expand upon the well-established coda methodology outlined in Mayeda et al. (2003) to test the feasibility of using well-studied, or "ground truth," regional and local source spectra as calibration events for local stations in regions of interest. This "first of its kind" calibration procedure will be validated with data from a number of different local networks by leveraging existing data and calibration results.

The monitoring situation and region of study will dictate the calibration steps. For example, in an aseismic region we are often faced with using geophysical analogy and transporting calibration results (e.g., velocity

and attenuation structure) from a well-studied region to the new region of interest. The same might be true for an active region, but with no prior seismic data or calibration. On the other hand, monitoring could be done clandestinely or peripherally (e.g., North Korea, Pakistan, etc.), and depending on the situation, a few or many sensors could be deployed in advance for calibration. This proposal is an initial "first-step" or scoping study that will outline our steps to test local monitoring situations using both *P* and *S*-wave codas. Future plans would involve characterizing a range of event types (e.g., shallow and normal-depth earthquakes, mining-related explosions and their associated events, nuclear tests, and volcanic-related events) and deriving a suite of local background models for a range of tectonic settings. For this pilot study, we will focus on active regions and test the transportability to another "active" region under the assumption of no a priori calibration data or information.

Since coda yield estimation for explosions is based upon calibration to the regional earthquake source spectrum, we will remain consistent and calibrate to earthquakes in each of our study regions. We point out that our proposed local *P*-wave coda research is not duplicative and in fact complements our on-going regional-to-near-teleseismic *P*-coda research. One issue for the local *P*-wave coda is the short duration; however, as shown by Mayeda et al., (2003), *any* length of coda outperforms the direct arrival.

We plan to test the performance of the local background methodology using narrowband coda envelopes in regions where calibration data may not be available from as few as one seismic sensor, perhaps clandestinely deployed within ~200 km of a monitoring region of interest. Specifically, we will compare amplitude variability between local *P* and *S* waves and their associated coda waves in a number of different regions (e.g., local data from the San Francisco Bay Area, Nevada Test Site, northern and central Italy, Yellow-Sea Korean Peninsula, central Asia, and others as needed; see Figure 4). Though most areas have ample data, we will mimic conditions where we have little to no ground truth and/or as few as one monitoring station. In doing so, we can compare against well-calibrated results and assess our performance.

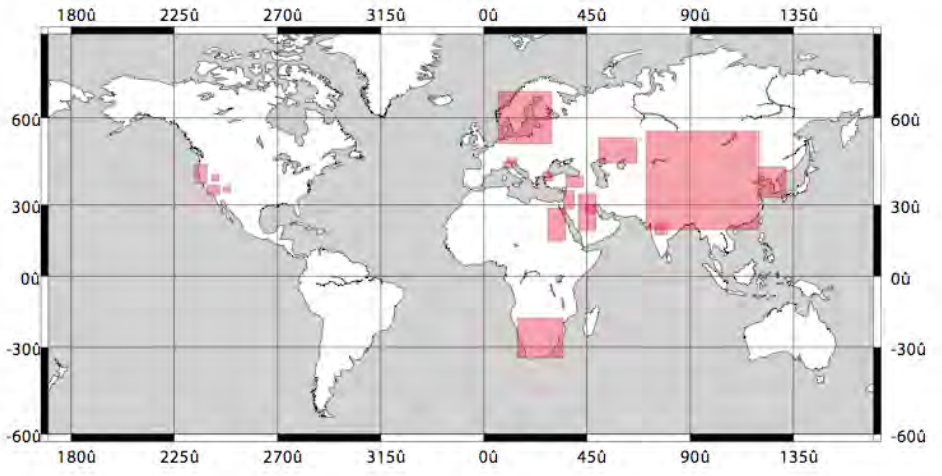

Figure 4: Map of local and near-regional coda studies for which we have preliminary coda calibrations. In addition to these waveform and calibration data, we will leverage existing in-house seismic data from Los Alamos National Laboratory and Lawrence Livermore National Laboratory databases to facilitate the construction of local coda background models for various tectonic provinces.

CONCLUSIONS AND RECOMMENDATIONS

For this project, we will be focusing on applying the coda methodology outlined by Mayeda et al. (2003) to local data with emphasis on transporting local background models to similar geophysical regions. Of course if a monitoring situation provides for ample seismic data, then we would opt for a complete calibration, but our first assumption will be that data may be sparse or nonexistent. At these shorter distances, we have

every reason to believe that the calibration will be easier because path corrections become much less important (e.g., Figure 2). Mayeda et al., (2003) started with the following empirical equation to describe the regional coda envelope,

$$A_c(f,t,r) = W_o(f)\cdot S(f)\cdot T(f)\cdot P(r,f)\cdot H\left(t-\frac{r}{v(r,f)}\right)\cdot\left(t-\frac{r}{v(r,f)}\right)^{-\gamma(r,f)}\cdot exp\left[b(r,f)\cdot\left(t-\frac{r}{v(r,f)}\right)\right]$$

where $W_o(f)$ is the *S*-wave source amplitude, $S(f)$ is the site response, $T(f)$ is the *S*-to-coda transfer function resulting from scattering conversion, $P(r, f)$ includes the effects of geometrical spreading and attenuation (both scattering and absorption), H is the Heaviside step function, $v(r,f)$ is the peak velocity of the *S*-wave arrival and $\gamma(r,f)$ and $b(r,f)$ control the coda envelope shape, and t is the time in seconds from the origin time. The following figures show results of empirical results for coda path corrections, peak envelope velocity, and coda shape parameter. As stated earlier, we plan to construct average background models then test them in geophysically similar regions and assess performance.

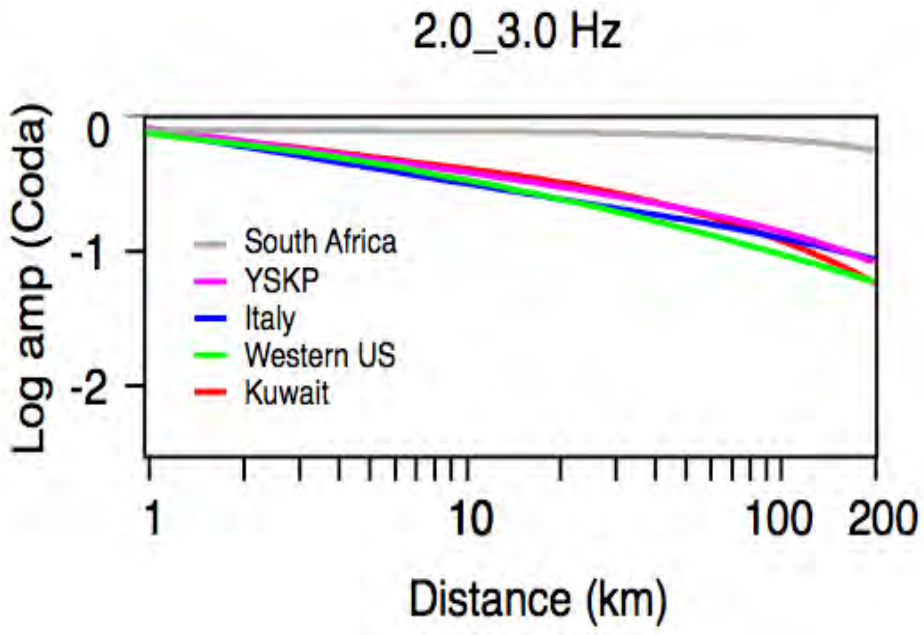

Figure 5: Preliminary coda path corrections are shown for 5 regions at 2–3 Hz. Notice that to first order, attenuation functions, *P(r, f)*, are very similar for the active regions, whereas data from the South African craton behaves completely differently.

This preliminary result shown in Figure 5 is very promising because it suggests that "local background" path corrections can be constructed, and then applied to new, local regions of monitoring interest without prior path calibration. We should point out that the coda path correction, $P(r, f)$, has been modified since the Mayeda et al., (2003) study which adopted a functional form that looks like the Brune source spectrum (Brune, 1970) (i.e., flat at short distances, then decreasing beyond a critical distance). The new formulation (curves shown in Figure 5) is being tested by the DOE labs and appears to significantly improve local-distance data. The formulation is modified from the Street et al. (1975) equation for geometrical spreading that transitions smoothly from spherical spreading of direct *S*-waves to cylindrical spreading for L_g waves beginning at a chosen critical distance. In the new formulation, (S. Phillips, personal communication, 2006) the function is modified to allow for different spreading before the cross-over distance and also provides for control on the curvature near the cross-over. This was critical. In addition to background path parameters shown in Figure 5, we will derive average coda shape parameters, $b(r,f)$, and peak velocity, $v(r,f)$, as function of distance and test the extent to which average values can be applied to

other geophysically similar regions. Again, we will assess the performance of the average background models by comparing directly with our "ground-truth" estimates using region-specific calibrations using the entire local dataset.

REFERENCES

Aki, K. (1969). Analysis of the seismic coda of local earthquakes as scattered waves, *J. Geophys. Res*. 74: 615–631.

Aki, K. and B. Chouet (1975). Origin of coda waves: source, attenuation and scattering effects, *J. Geophys. Res*. 80: 3322–3342.

Brune, J. N. (1970). Tectonic stress and spectra of seismic shear waves from earthquakes, *J. Geophys. Res.* 75: 4997–5009.

Mayeda, K. (1993). m_b(*Lg*Coda): A stable single station estimator of magnitude, *BSSA* 83: 851–861.

Mayeda, K., A. Hofstetter, J. L. O'Boyle, and W. R. Walter (2003). Stable and transportable regional magnitudes based on coda-derived moment-rate spectra, *BSSA* 93: 224–239.

Mayeda, K., L. Malagnini, W. S. Phillips, W. R. Walter, and D. Dreger (2005). 2-D or not 2-D, that is the question: A northern California test, *Geophys. Res. Lett*. 32: doi:10.1029/2005GL022882.

Myers, S. C., W. R. Walter, K. Mayeda, and L. Glenn (1999). Observations in support of Rg scattering as a source for explosion S waves: Regional and local recordings of the 1997 Kazakhstan depth of burial experiment, *Bull. Seismol. Soc. Am*. 89: 544–549.

Phillips, W. S. and K. Aki (1986). Site amplification of coda waves from local earthquakes in central California, *Bull. Seism. Soc. Am*. 76: 627–648.

Sato, H. and Fehler, M. (1998). *Seismic Wave Propagation and Scattering in the Heterogeneous Earth*, AIP Modern Acoustics and Signal Processing series. New York: Springer Verlag.

Street, R. L., R. Herrmann, and O. Nuttli (1975). Spectral characteristics of the Lg wave generated by central United States earthquakes, *Geophys. J. R. Astr. Soc.* 41: 51–63.

Sykes, L. R. and I. L. Cifuentes (1984).Yields of Soviet underground nuclear explosions from seismic surface waves: Compliance with the Threshold Test Ban Treaty, *Proc. Natl. Acad. Sci*. 81: 1922–1925.

REGIONAL MAGNITUDE RESEARCH SUPPORTING BROAD-AREA MONITORING OF SMALL SEISMIC EVENTS

W. Scott Phillips, Howard J. Patton, Richard J. Stead, George E. Randall, and Hans E. Hartse

Los Alamos National Laboratory

Sponsored by National Nuclear Security Administration
Office of Nonproliferation Research and Development
Office of Defense Nuclear Nonproliferation

Contract No. DE-AC52-06NA25396

ABSTRACT

The Los Alamos National Laboratory's Ground-Based Nuclear Explosion Monitoring Research and Engineering (GNEMRE) Program has a long-standing magnitude research project in support of regional yield estimation and source discrimination. This project has developed magnitude-yield scaling relationships based on regional P, S phases and coda waves to improve our capabilities to monitor nuclear explosions over broad areas and at low yields. Due to the great variability of regional seismograms, the methods developed for broad-area monitoring must be adaptable to different phases and frequency bands. These requirements, along with an understanding of the transportability of scaling relationships, pose a significant challenge from both practical and theoretical standpoints since any broad-area method needs a sound physical basis to be ultimately successful.

Coda wave efforts have recently focused on practical aspects such as schema design for the exchange of calibration parameters and details of signal processing coding to match measurements between institutions, as well as advanced aspects of extending near-regional coda techniques to broad area and far-regional distances. We have developed the MagYield 0.10 schema, which ties to National Nuclear Security Administration (NNSA) Knowledge Base (KB) core schema for the exchange of envelope recipes, coda calibration parameters, and yield regression parameters. Exacting tests of signal processing methods between institutions uncovered issues with a widely used deconvolution code and code-dependent effects of non-ideal bandwidth/Nyquist ratios. Extension of the coda method to broad area far-regional distances showed the importance of 2-D path effects, as well as 2-D phase type (P vs. Sn vs. Lg coda) and 2-D transfer function effects. A detailed investigation of a near- regional data set from the Korean Peninsula showed that large numbers of small, low stress events can cause bias in the empirical Green's function (EGF) phase of coda calibration, leading to slight spectral peaking near 1 Hz and coda moments that do not scale one-to-one with independent estimates. This is mitigated by weighting EGF data by low frequency spectral slope, leading to an automatic method that can be applied uniformly to different regions.

We continue to study multi-frequency relative scaling observations of Pn and Lg-coda waves for explosions detonated at the Nevada Test Site (NTS) and the Semipalatinsk Test Site (STS). Observations for both test sites show that Pn amplitudes yield scale 10-30% higher than coda amplitudes for high frequencies between 2-8 Hz. The contrast in scaling shows strong frequency dependence at NTS for lower frequencies, with Pn scaling as much as 50% higher than Lg coda waves for frequencies near 0.6 Hz. On the other hand, Pn and coda amplitudes for STS explosions do not scale differently for any frequency band less than 2 Hz. These observations have implications for yield estimation and seismic discrimination, among them being that high-frequency phase ratios should display yield dependence. We have developed a model that predicts the observed scaling differences at high frequencies. Two essential elements of the model are (1) Rg generation by a compensated linear vector dipole (CLVD) and (2) near-source scattering of Rg as the source of S waves making up Lg and Lg coda. The CLVD is a kinematic representation for tensile failure related to non-linear interactions of explosion shock waves with the free surface. Work on this model continues with the goal to explain the strong frequency dependence of NTS observations and the reason(s) for differences in relative scaling between NTS and STS.

OBJECTIVES

We seek to improve yield estimation and seismic discrimination capabilities for broad areas and small events through the development of regional magnitude methodologies and data sets of direct phases and coda waves. Our research advances the state of the art in nuclear monitoring though (1) characterization of the scaling behavior and transportability of regional magnitudes based on path-corrected amplitudes using advanced calibration techniques and (2) development of physical models to interpret the observations and to lay a physical basis supporting operational techniques.

RESEARCH ACCOMPLISHED

Broad area coda calibration. We calibrate coda amplitudes for purposes of determining Mw, which is used in event identification procedures, and yield, via direct comparison to test site results for high frequencies (>1 Hz). Coda techniques are known to be effective over near-regional distances (Mayeda et al., 2003), and for comparing events in the same source region at far regional distances. Our challenge is to extend the coda technique to broad areas and far regional distances over our central and eastern Asia study region (Figure 1). This requires two-dimensional (2-D) calibration. Phillips et al. (2001) have demonstrated the effectiveness of 2-D path calibration. 2-D calibration is especially critical for events for which both continental and oceanic paths are observed, due to varying levels of blockage of the Lg, and Lg coda, and we have begun to include oceanic paths in our data set to investigate techniques to account for this.

Full 2-D, broad area calibration begins with differentiating between various coda types. Figure 2 shows group velocities of the beginning of the coda, which often, but not always, correspond to the envelope peak, for three frequency bands. We observe Lg, Sn and P coda over regional distances, with Lg dominant at short distances and lower bands. Figure 3 shows the distribution of coda types for station WMQ in western China and also indicates 2-D variations within the Lg type. We see that Sn coda are observed at shorter distances across regions of low crustal Q, such as Tibet. Thus, both coda type and the group velocity variations within a given type vary laterally and this must be accounted for using station centric lookup tables or tomographic models. Strategies for doing so remain to be tested.

We use a spectral EGF technique to extend absolute measures of spectra, based on ground truth moments, to the higher bands (> 1 Hz) that are important for yield estimation. Thus, the calculation of the transfer function terms, via EGF, is a critical calibration step. We solve for the frequency dependent transfer terms by requiring spectra from a large group of events to fit a Brune model for bands well below individual estimates of corner frequency. Corner frequency is estimated crudely based on magnitude (e.g., Walter and Taylor, 2001). Effects of the crude estimate are mitigated by limiting to a factor of 4 below the corner. In a focused study of events from the Korean Peninsula, we found that low frequency spectral slopes are not flat, in a relative sense, but can vary by a few tenths from event to event, with some dependence on source region. This may be due to regional variation in apparent stress. Without investigating the root cause further, we weighted the higher slope (higher stress) events more heavily in the EGF procedures and obtained more realistic spectra (slight spectral peaks at 1 Hz disappeared), and ground truth moments scaled one-to-one with coda moments (a slight deviation for small events due to the aforementioned 1 Hz peaks disappeared).

Furthermore, we developed a 2-D, EGF technique to account for variation of the transfer function across our study region. Results show a regional variation (Figure 4) that primarily reflects differences in the dominant coda types. This variation is best accounted for at an earlier stage of calibration by splitting into Lg and Sn coda, applying corrections for different path effects and a differential transfer term before combining results together. Tests of such methods remain to be performed and rely on data sets from low Q crustal regions to estimate Sn coda path effects at the shortest possible distances. Results of comparing ground truth and coda moments after applying the 2-D transfer function shows good agreement, especially for continental events evaluated using regional techniques (Figure 5).

Observations of Pn, Lg-Coda scaling differences. We continue to study multi-frequency relative scaling observations of Pn and Lg-coda waves for explosions detonated at the NTS and the STS. Relative scaling slopes

were estimated using two methods. Briefly, the first method determines the relative scaling slope (Pn relative to Lg coda) from regressions on log-log plots of coda versus Pn amplitudes, passed through identical narrow-band filters (see Patton and Phillips, 2005). If the explosions are located in small enough test area, the path effects to a given station should be the same. The second method utilizes ground-truth yields to perform separate amplitude-yield regressions on Pn and coda amplitudes; relative scaling slopes were obtained by taking the ratio of the estimated yield slopes. In carrying out the yield regressions, the effect of gas porosity was accounted for. All amplitudes were subjected to signal-to-noise (SNR) checks: SNR for Lg-coda waves decrease rapidly above ~6 Hz for Livermore NTS Network recordings. Nevertheless, it is clear that the codas are those of Lg waves for all bands, as *Sn* is not as well recorded on this network compared to Lg. On the other hand, Lg amplitudes recorded at Borovoye for STS explosions can drop below the level of Sn-coda waves for frequency bands above the 2–3 Hz passband. Thus, even though many recordings of the Borovoye archive (Kim et al., 2001) are well above the noise levels at high frequencies, our measurement windows contain a superposition of Sn and Lg codas.

Figure 6 is a summary of scaling results for NTS explosions. Narrow frequency passbands used for filtering the amplitudes are denoted with horizontal lines on the abscissa. The results for both methods are in reasonably good agreement for stations Elko (ELK) and Kanab (KNB). Both stations have similar frequency dependence, showing rapid change at low frequencies, going from no scaling differences in the lowest band to 50%–60% faster scaling for Pn relative to Lg coda in the next band, 0.5–0.7 Hz. With the exception of the lowest band, the results of all bands indicate that Pn amplitudes scale at a higher rate than Lg coda amplitudes, and the close agreement between results of both methods strengthen the reliability of these findings. Plotted with the observations is the prediction based on the Fisk conjecture (Fisk, 2006; 2007) using NTS parameters specified in Figure 3 of Mueller and Murphy (1971). P and S slopes used for the model calculations are means for a yield range between 0.1 and 1000 kt. An important question to answer is why are there significant departures in the observations at low and high frequencies from the prediction, which is based on the Mueller-Murphy model and on differences in the P and S corner frequencies according to the Fisk conjecture.

Near-source scattering mechanisms for S wave generation. A key tenet of near-source scattering mechanisms proposed for regional phase generation is that the amplitude-frequency dependence of the input wave should be imprinted onto the scattered waves. This tenet traces its roots to early studies using coda waves to extract source spectra (e.g., Aki, 1969), and can be justified if the scattering transfer function is linear and varies smoothly across the frequency band of interest. In the case of near-field scattering of P waves into S, the P-wave source spectrum is imprinted on the scattered S waves (e.g., P-wave imprinting). Gupta et al. (1992) were the first to suggest that near-source scattering of Rg waves makes a significant contribution to low-frequency (< 2 Hz) Lg. Under this hypothesis, the frequency dependence of Rg amplitudes is imprinted onto subsequently scattered P and S waves and is called Rg imprinting.

The first studies to support Rg imprinting used spectra of Lg waves for Yucca Flats, NTS, and Semipalatinsk explosions (Patton and Taylor, 1995, referred to as PT95; Gupta et al., 1997). PT95 studied spectral ratios for nearby Yucca Flats shots, one at normal containment depth (normal buried, NB) and the other an overburied (OB) shot serving as an empirical Green's function. A prominent null was observed in the spectral ratios near 0.55 Hz. According to PT95, an explosion is comprised of an initial burst, represented by a monopole force system, plus a source of tensile failure, represented by a compensated linear vector dipole (CLVD). In their model, the CLVD excites Rg waves much stronger than the monopole does for NB explosions, and the spectral null is caused by an effect of CLVD source depth on Rg excitation and is imprinted onto the scattered S waves making up Lg.

Recent modeling work has revealed that a CLVD source as strong as that proposed by PT95 violates long-period Rayleigh wave phase observations (Patton and Phillips, 2006). A new source model was developed to fit Lg spectral ratios without violating the long periods and over a broader frequency range than PT95 modeled. The interested reader is referred to Patton and Phillips for details about the new model. Even though the model uses simple analytic solutions for a half-space medium and is still under development, it makes two very interesting predictions: (1) at low frequencies (< ~2Hz), the ratios should be characterized by spectral modulations resulting from interference of Rg waves emitted by the CLVD and monopole sources and (2) at high frequencies, the Rg excitation is dominated by the CLVD. The first prediction is consistent with the general characteristics of Lg spectral ratios for NTS explosions, while the second has interesting implications for observed yield scaling differences between P and Lg.

Before discussing the effects on regional phase scaling observations, we briefly summarize the evidence for Rg imprinting utilizing a new integrative analysis approach involving difference spectrograms (Gupta et al., 2007).

Difference spectrograms. A spectrogram may be considered a two-dimensional matrix of numbers providing amplitude and frequency information for each point of a time series. The new method of Gupta et al. takes the point-by-point difference of log amplitudes between spectrograms of two nearby explosions recorded at a common station. As with the spectral ratio approach, if one of the explosions is overburied, the source characteristics of the NB explosion can be isolated in the resultant difference spectrogram since the OB shot acts as an empirical Green's function.

Figure 7a, taken from Gupta et al. (2007), shows the difference spectrogram of Rousanne (NB) and Techado (OB) on Yucca Flats for station ELK. The difference spectrogram was obtained by (1) aligning the Pn onsets, (2) obtaining noise-corrected log amplitude spectrograms using a moving time window of 12.8 s with a time shift of 0.5 s, (3) subtracting three-dimensional matrices of log amplitudes (Rousanne-Techado), and (4) contour plotting the resulting values after converting to linear amplitude and smoothing. Amplitude modulations can be seen on the difference spectrogram with spectral nulls at ~0.55 Hz and 1.1 Hz. The null at 0.55 Hz seems to start in the Pg coda and is expressed at several different times within the Lg wavetrain and coda.

Figures 7b–d show spectral ratios for time windows corresponding to Pg coda, Lg, and Lg coda. The ELK results in all three windows are good general agreement with the results for the four-station Livermore-network average. Vertical dash lines correspond to the frequencies where the spectrogram shows persistent nulls. The null at 0.55 Hz is most clearly expressed for Lg coda and is weakly expressed for Pg coda. Figure 7e shows a summary of spectral ratios for Pg coda, Lg, and Lg coda plus for a window corresponding to the arrival of Pn and its coda. Note that the Pn spectral ratio shows no evidence of modulation for frequencies below 1 Hz, consistent with the difference spectrogram. Gupta et al. interpret amplitude modulations at low frequencies (< ~2 Hz) observed for Pg coda, Lg, and Lg coda as a consequence of Rg imprinting.

Rg imprinting and implications for regional phase scaling. It has not escaped our attention that the most serious discrepancy between the Fisk prediction and the relative scaling observations presented above corresponds to the frequency band 0.5–0.7 Hz, where a strong amplitude null exists in the spectral ratios and difference spectrograms for Lg and Lg coda, but not for Pn waves. Furthermore, the high frequency discrepancies in Figure 6 occur in the frequency range where the model of Patton and Phillips predicts that the CLVD should be controlling the excitation of Rg waves. Patton and Phillips (2006) provide a "back-of-the-envelope" calculation assuming some scaling relationships for the CLVD source. This calculation supports the notion that Rg waves might yield scale at a lower rate than P waves for the Mueller-Murphy model at high frequencies, consistent with the observations for Pn and Lg coda waves. Hence, Rg imprinting could be the cause of scaling differences between Pn waves and regional shear phases, like Lg and its coda.

CONCLUSIONS AND RECOMMENDATIONS

In order to calibrate coda amplitudes over broad areas and to far regional distances we must work to extend 2-D coda calibration to coda type, shape, and transfer function steps, accounting for superposed Lg and Sn coda. This requires analysis of data from regions of low crustal Q in order to measure Sn coda over the widest range of distances. Further, interest in monitoring source regions near coastlines requires similar efforts to account for partial and full blockage of Lg and Lg coda over oceanic paths.

Because of the potential importance of near-field scattering in the generation of regional phases by underground explosions, we are starting the groundwork on a new scaling model for asymmetric explosion sources involving the superposition of monopole and CLVD force systems. This model will be applied to the problem of Rg excitation to investigate whether or not variations in Rg scaling with respect to Mueller-Murphy scaling for P can mimic the relative scaling observations in Figure 6 across the entire frequency range. There is much work to be done to develop a CLVD source model and associated scaling relationships.

ACKNOWLEDGEMENTS

We thank the LANL GNEMRE team for bulletin integration, event location, waveform acquisition, and database support.

REFERENCES

Aki, K. (1969). Analysis of the seismic coda of local earthquakes as scattered waves, *J. Geophys. Res.* 74: 615–631.

Fisk, M. D. (2006). Source spectral modeling of regional P/S discriminants at nuclear test sites in China and the former Soviet Union, *Bull. Seismol. Soc. Am.* 96: 2348–2367.

Fisk, M. D. (2007). Corner frequency scaling of regional seismic phases for underground nuclear explosions at the Nevada Test Site, *Bull. Seismol. Soc. Am.* 97: 977–988.

Gupta, I. N., W. Chan, and R. Wagner (1992). A comparison of regional phases from underground nuclear explosions at East Kazakh and Nevada Test Sites, *Bull. Seismol. Soc. Am.* 82: 352–382.

Gupta, I. N., T. Zhang, and R. Wagner (1997). Low-frequency Lg from NTS and Kazakh nuclear explosions—Observations and interpretation, *Bull. Seismol. Soc. Am.* 87: 1115-1125.

Gupta, I. N., H. J. Patton, W. W. Chan, H. A. A. Ghalib, and R. A. Wagner (2007). Difference spectrograms: A new method for studying S-wave generation from explosions, *Bull. Seismol. Soc. Am.* (submitted).

Kim, W.-Y., P. G. Richards, V. Adushkin, and V. Ovtchinnikov (2001). Borovoye digital archive for underground nuclear tests during 1966–1996, Data report on the web at http://www.ldeo.columbia.edu/res/pi/Monitoring/Data/brv_exp_archive.html, Borovoye Archive for UNT (information product in PDF).

Mayeda, K., A. Hofstetter, J. L. O'Boyle, and W. R. Walter (2003). Stable and transportable regional magnitudes based on coda-derived moment-rate spectra, *Bull. Seism. Soc. Am.* 93: 224–239.

Mueller, R. A. and J. R. Murphy (1971). Seismic characteristics of underground nuclear detonations, Part I: Seismic spectrum scaling, *Bull. Seismol. Soc. Am.* 61: 1675–1692.

Patton, H. J. and S. R. Taylor (1995). Analysis of Lg spectral ratios from NTS explosions: Implications for the source mechanisms of spall and the generation of Lg waves, *Bull. Seismol. Soc. Am.* 85: 220–236.

Patton, H. J. and W. S. Phillips (2005). Regional magnitude research supporting broad-area monitoring of small seismic events, in *Proceedings of the 27th Seismic Research Review: Ground-Based Nuclear Explosion Monitoring Technologies*, LA-UR-05-6407, Vol. I, pp. 606–611.

Patton, H. J. and W. S. Phillips (2006). Regional magnitude research supporting broad-area monitoring of small seismic events, in *Proceedings of the 28th Seismic Research Review: Ground-Based Nuclear Explosion Monitoring Technologies*, LA-UR-06-5471, Vol. 1, pp. 646–653.

Phillips, W. S., H. J. Patton, H. E. Hartse, and K. M. Mayeda (2001). Regional coda magnitudes in Central Asia and mb(Lg) transportability, in *Proceedings of the 23rd Seismic Research Review: Worldwide Monitoring of Nuclear Explosions*, LA-UR-01-4454, Vol.1, pp. 580–589.

Walter, W. R and S. R. Taylor (2001). A revised magnitude and distance amplitude correction (MDAC2) procedure for regional seismic discriminants: Theory and testing at NTS, Lawrence Livermore National Laboratory report UCRL-ID-146882, http://www.llnl.gov/tid/lof/documents/pdf/240563.pdf.

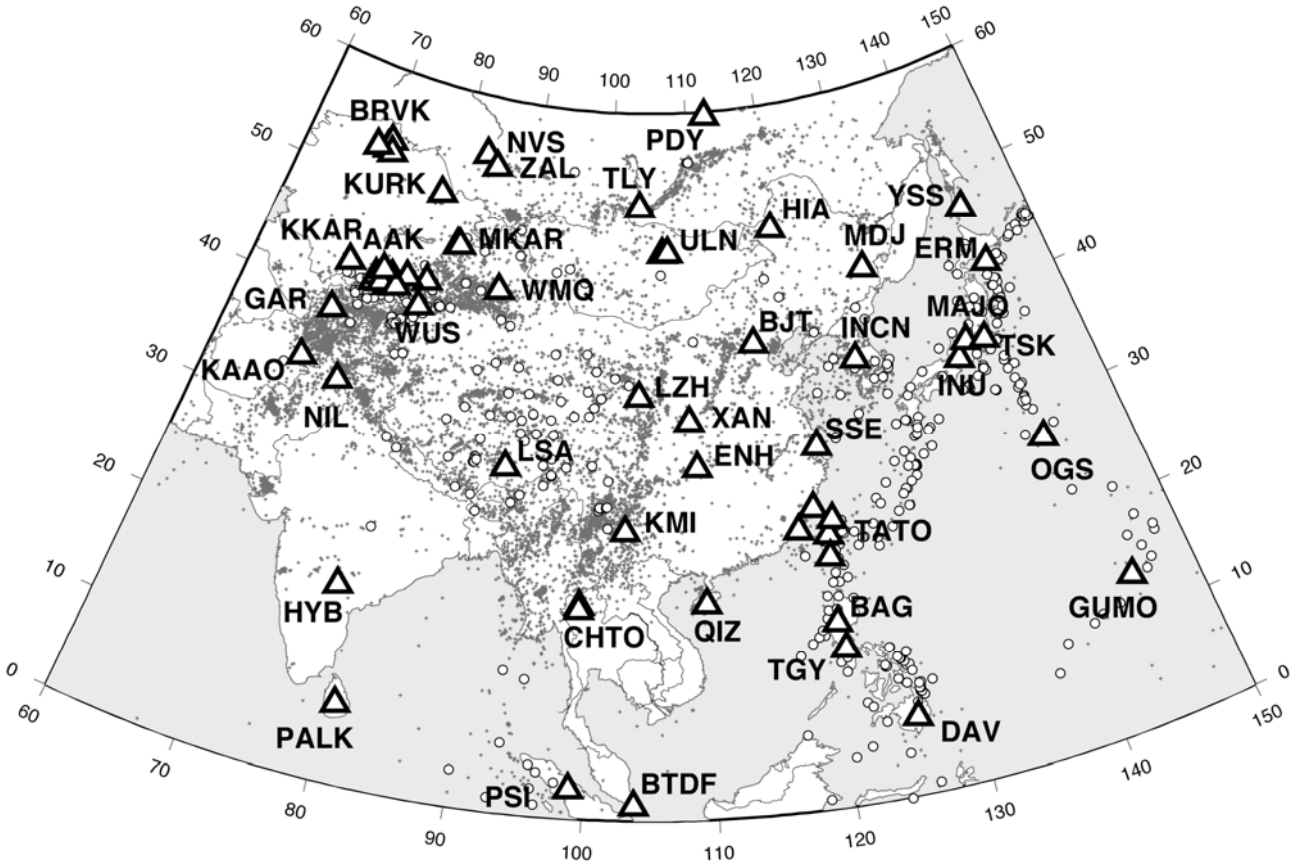

Figure 1. Stations (triangles) and events (dots) used in the broad area coda study. Open circles indicate ground truth moment events.

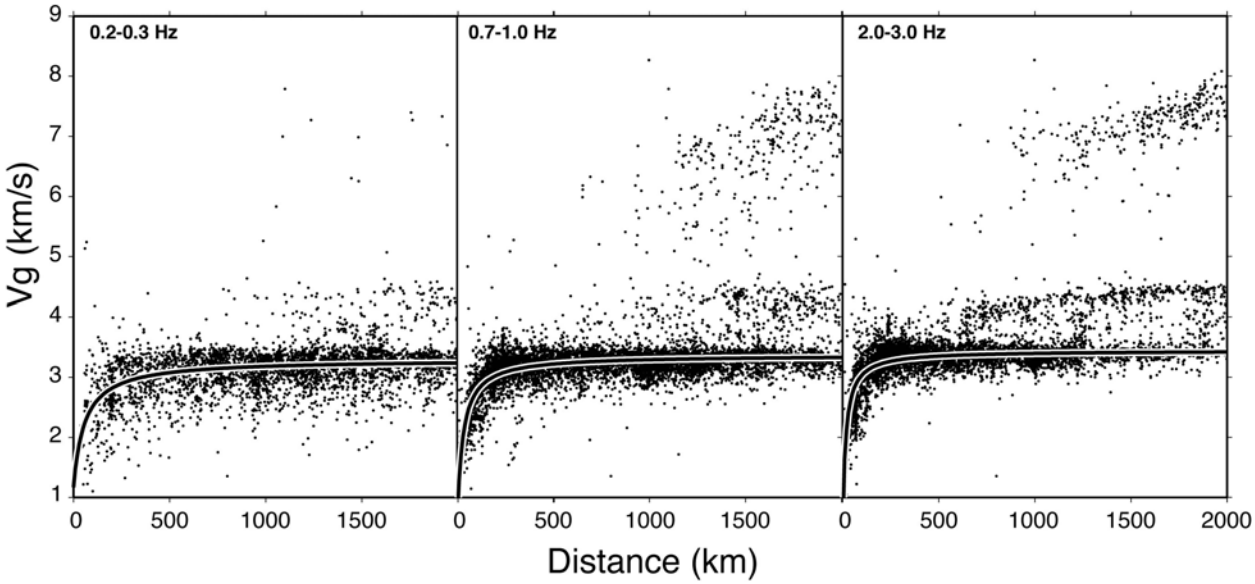

Figure 2. Group velocity of the beginning of the coda (manually picked) versus distance for three bands. The fitted curve represents the Lg branch.

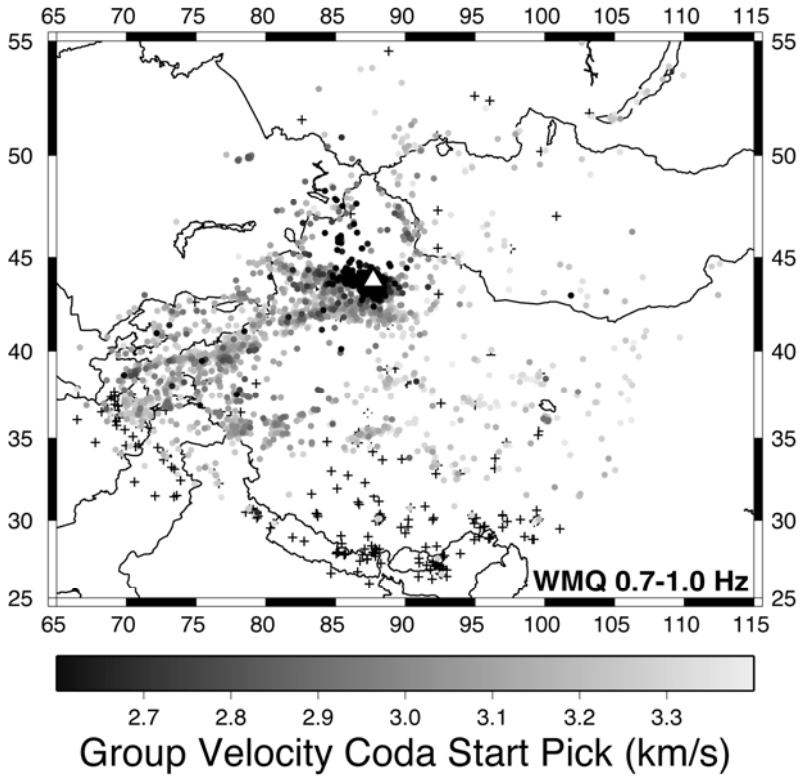

Figure 3. Geographical distribution of the group velocity of the beginning of the coda for station WMQ, band 0.7–1.0 Hz. Group velocities between 2.6 and 3.4 km/s are represented by the gray scale. Group velocities greater than 3.4 km/s are indicated by crosses. The low velocities near the station are due to the standard distance effect. Additional low velocities for events under the Junggar Basin and at the western end of the Tarim basin are 2-D effects. Group velocities are generally slower from western and faster from eastern azimuths.

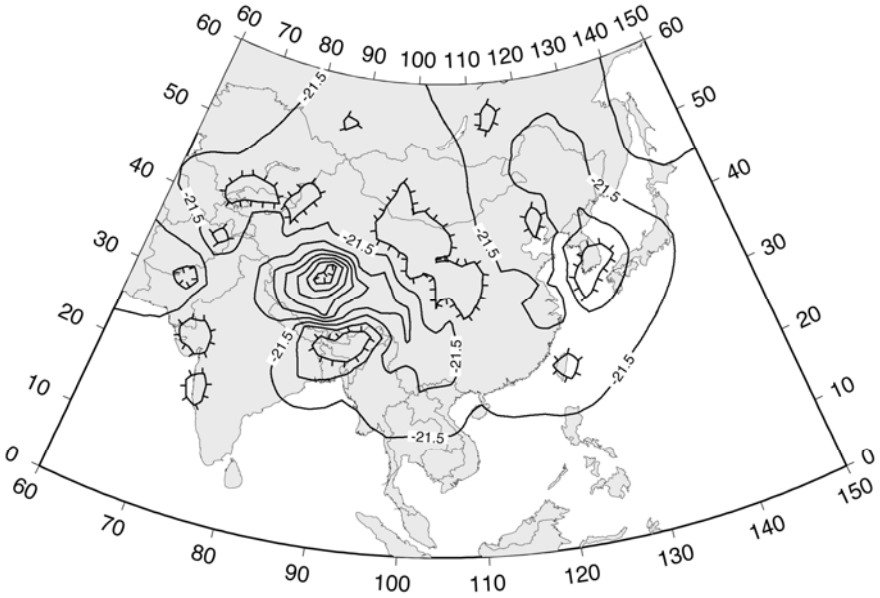

Figure 4. Transfer function (log10 N-s) obtained using a 2-D EGF technique. Contour intervals are 0.1 N-s; the –21.5 N-s contour is annotated. Contour ticks point in downhill directions.

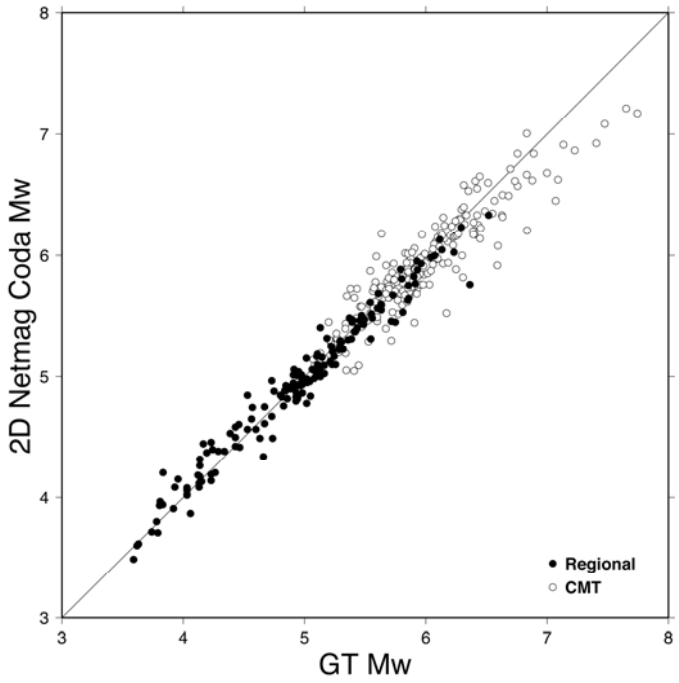

Figure 5. Ground truth (GT) versus coda network Mw. Closed circles indicate regionally derived ground truth Mw for continental events. Open circles indicate Harvard centroid moment tensor (CMT) Mw for oceanic events.

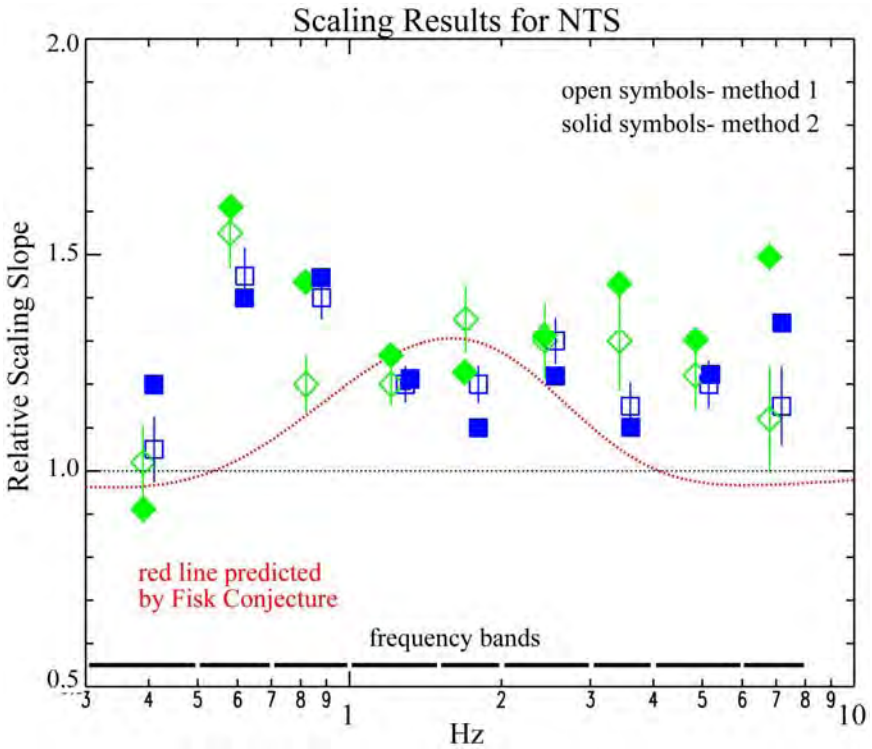

Figure 6. Relative yield scaling slope of Pn with respect to Lg coda waves for NTS explosions. Open symbols with error bars (two sigma on relative slope estimate) are results for method 1, while solid symbols are results for method 2 obtained by taking the ratio of the slopes from yield regressions, Pn/LgCoda. For example, the results of the 0.5–0.7 frequency band show that Pn slope is ~1.5 times larger than the slope for Lg coda waves. The red dotted line is a prediction of the relative scaling slopes based on the Fisk conjecture and the Mueller and Murphy explosion source model.

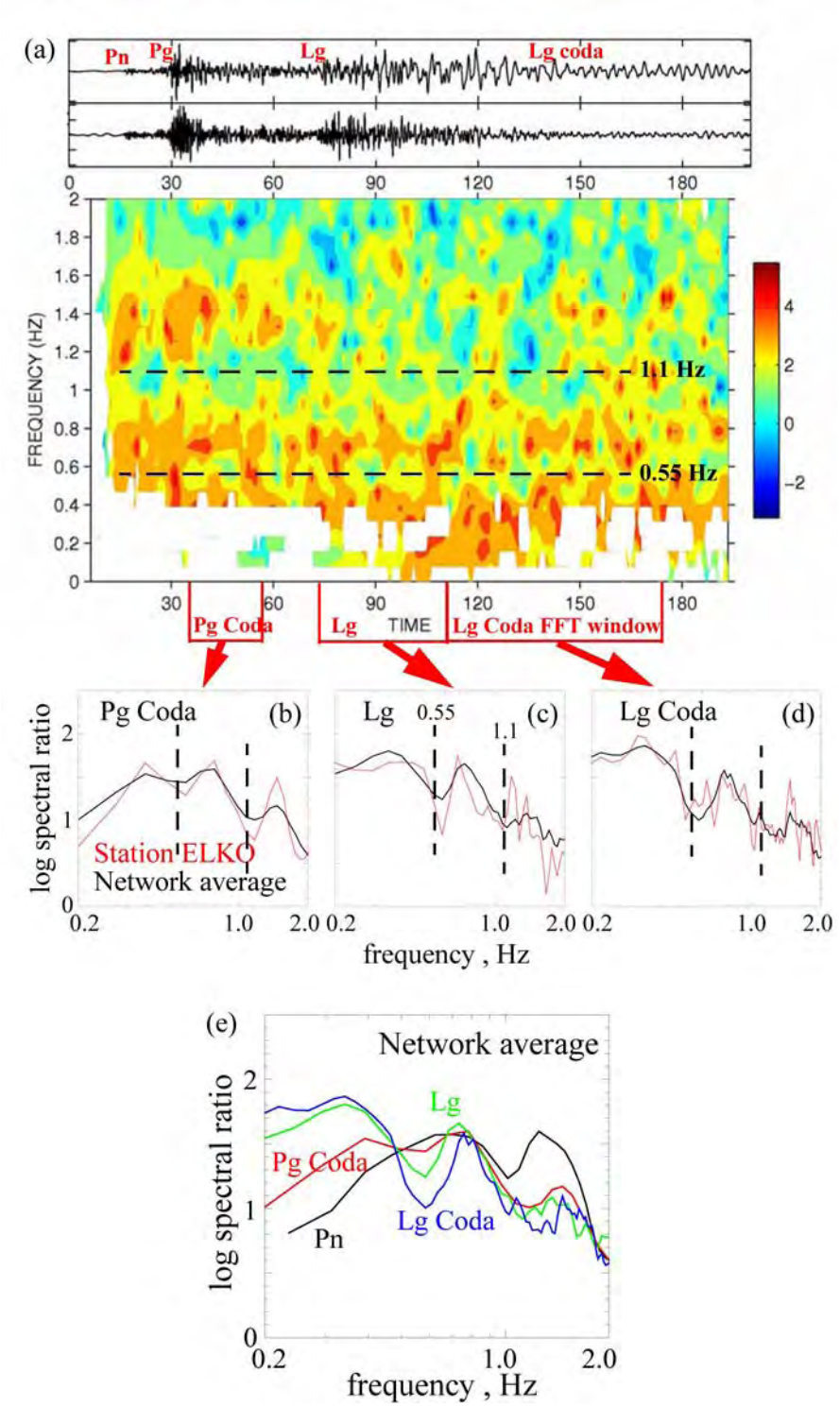

Figure 7. (a) Rousanne-Techado difference spectrogram for ELK (seismograms plotted at the top). Dash lines are positioned over nulls at 0.55 and 1.1 Hz. The null at 0.55 Hz is observed in Pg coda, Sn, Lg, and Lg coda. The null at 1.1 Hz is also observed in the Pn phase. (b)–(d) Spectral ratios for the time windows shown on the abscissa of the spectrogram plot corresponding to Pg coda, Lg, and Lg coda. (e) Summary of the spectral ratios for Pn, Pg coda, Lg, and Lg coda. Signal-to-noise ratio is marginal below 0.3–0.4 Hz.

DEVELOPING MULTIPLE-FREQUENCY DISCRIMINANTS FOR USE WITH REGIONAL CODA-AMPLITUDE MEASUREMENTS

Arben Pitarka[1], Kevin M. Mayeda[2], and Nancy R. Collins[1]

URS Group, Inc.[1] and University of California, Berkeley[2]

Sponsored by National Nuclear Security Administration
Office of Nonproliferation Research and Development
Office of Defense Nuclear Nonproliferation

Contract No. DE-AC52-04NA25545[1,2]

ABSTRACT

This paper investigates the feasibility of employing local to near-regional coda-wave amplitude measurements, in multiple, narrow bands, for the purpose of discriminating small seismic events. The motivation comes from previous studies that have shown that regional, single-station coda-magnitude estimates are more stable and accurate than any direct phase measure to date (e.g., Mayeda et al., 2003). Typically, the source amplitude estimates derived from the coda have interstation variances on the order of 0.07 log amplitude units; hence, the method is excellent for regions with sparse station coverage. The method has been thoroughly tested over large geographic regions spanning both local and regional distances for the purpose of magnitude estimation. In terms of discrimination, only a preliminary study using coda waves was performed on Nevada Test Site (NTS) explosions and earthquakes in the study by Walter et al., (1995). Since this time, however, no additional studies have been conducted, in spite of the coda's successful application for moment magnitude (M_W) estimates in the broad areas of Eurasia and the Middle East. Due to the nature of the scattered energy comprising the coda, path and azimuthal source-radiation effects are averaged over, making coda amplitudes insensitive to local structure, in sharp contrast to direct regional phases such as *Pn*, *Pg*, and *Lg*. Calibrated with respect to seismic moment (M_0) or M_W, coda-derived source spectra provide a means to obtain moment estimates from seismograms of smaller or more distant events that cannot be analyzed with conventional waveform or spectral source-inversion techniques because of signal-to-noise limitations. Tying coda magnitude to *Mw* also provides a physical measure of event size that is unbiased and therefore transportable. We have completed a new path and site calibration for frequencies ranging between 0.3 and 8.0 Hz using openly available Incorporated Research Institutions for Seismology (IRIS) and Korea Meteorological Administration (KMA) stations for small to moderate-sized regional events within the Korean Peninsula. This involved tying the coda measurements to independently determined seismic moments for earthquakes in the region (R. Herrmann, pers. comm., 2007). Our next step will be to test seismic discrimination performance using coda spectral ratios and comparing their stability with those derived from direct Lg.

OBJECTIVE

The objective of this proposal is to test the performance of a high-frequency spectral ratio discriminant that uses regional Lg coda from explosions and earthquakes in the Korean peninsula. Over the past decade, significant advances have been made in regional monitoring that take advantage of stable amplitude measurements derived from narrowband coda envelopes. For example the Department of Energy (DOE) laboratories, with guidance from the Air Force Technical Applications Center (AFTAC) Seismic Review Panel, have developed a regional coda wave methodology to obtain the lowest variance estimate of the seismic source spectrum (e.g., Mayeda et al., 2003). Thus, regional M_W derived from Sn and Lg coda are very stable, even when only a single station is used. For the case of the current study region, we have performed a preliminary one-dimensional (1-D) calibration for Korean peninsula earthquakes using openly available stations from IRIS and KMA and then have formed spectral ratios. Our plan is to apply the same path and site corrections to explosions in the region and compare the spectral ratio performance against direct Lg.

RESEARCH ACCOMPLISHED

Currently within the explosion monitoring research community, there is interest in identifying and locating small underground nuclear explosions from sparsely instrumented networks. The most successful teleseismic discriminant compares the 20-second period surface wave magnitude (M_S) with the ~1-Hz body wave magnitude (m_b). However for smaller events that are deficient in long-period surface wave energy, the only alternative is to use high-frequency discriminants from the regional phases such as Pn, Pg, Sn, and Lg. However, because of strong lateral heterogeneity in the crust at short length scales, single-station direct phase measurements have high variance.

First, we have collected waveform data from both IRIS and KMA Web sites (Figure 1). Of these, a large fraction have been waveform modeled (*R. Herrmann*, pers. comm., 2007, http://www.eas.slu.edu/Earthquake_Center/MECH.KR/) and estimates of *Mw* were used to calibrate the coda-derived source spectra using the methodology outlined in Mayeda et al. (2003).

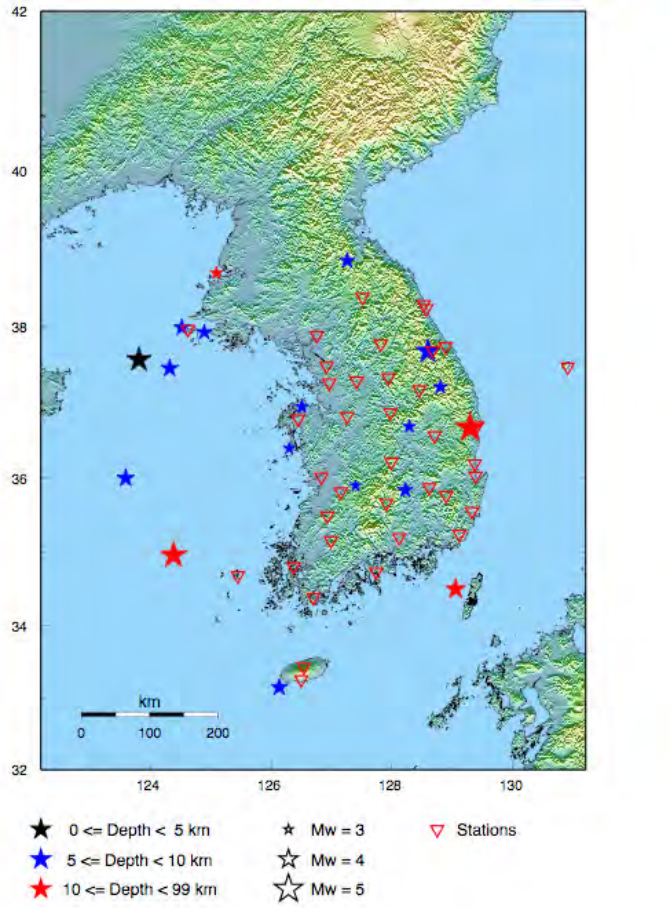

Figure 1. Map of calibration events and stations available in the current study.

We formed $\log_{10}$ averaged envelopes from the two horizontal components for consecutive narrow frequency bands ranging between 0.5 Hz to 8.0 Hz. The coda envelopes for each frequency band can be idealized with the following equation,

$$A_C(f,t,r) = W_o(f)\cdot S(f)\cdot T(f)\cdot P(r,f)\cdot H(t-t_S)\cdot (t-t_S)^{-\gamma(r)}\exp\left[-b(r)\cdot(t-t_S)\right], \qquad (1)$$

where f is the center frequency, r is the epicentral distance in kilometers, t is the time in seconds from the origin time, t_s is the *S*-wave travel time in seconds, W_o represents the *S*-wave source, T represents the *S*-to-coda transfer function, S is the site effect, P includes the effects of geometrical spreading and attenuation, H is the Heaviside step function, $\gamma(r)$ and $b(r)$ are the distance-dependent coda shape factors that control the coda envelope shape. However for the purpose of generating synthetics we set W, T, S, and P to unity. Following the methodology outlined in Mayeda et al. (2003), the coda shape parameters and velocity of the peak S/L_g-wave arrival were fit using the form of a hyperbola.

Unlike direct waves, the local to near-regional coda appears to be homogeneously distributed in the crust behind the expanding direct wave front and thus requires a different formulation for the attenuation (see Figure 2).

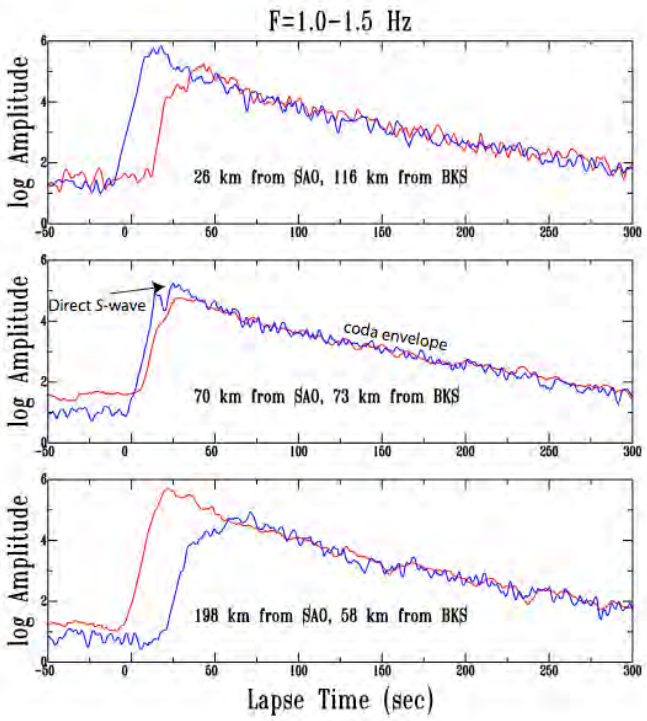

Figure 2. Example envelopes (*f*=1.0-1.5 Hz) for three local earthquakes located in the San Francisco Bay region recorded at stations SAO (blue) and BKS (red), part of the Berkeley Digital Seismic Network (BDSN). These two stations are separated by roughly 140 km. Irrespective of the events' distance to each station, the coda envelopes attain the same amplitude level, in sharp contrast with the direct arrivals. At this range of distances, the scattered *S*-waves or 'coda' are homogeneously distributed in the crust (figure taken from Mayeda et al., 2005).

For each narrowband envelope in our data set, raw coda amplitudes were determined by generating synthetics at the appropriate distance and using a source of unity then DC shifting using an L-1 norm to fit the observed envelope. The amount of the DC shift is the nondimensional raw coda amplitude. Next, we use the following empirical equation for coda path correction of Mayeda et al. (2003).

$$P(r, f) = \left[1 + \left(\frac{r}{p_2} \right)^{p_1} \right]^{-1} \qquad (2)$$

Using common recordings at each station pair, we then grid searched over p_1 and p_2 and tabulated the interstation scatter for each frequency band. The choice of frequency-dependent path correction for the entire region was based upon the path parameters p_1 and p_2, which gave the lowest average interstation standard deviation between station pairs. In general, the interstation standard deviation ranged between 0.07 and 0.15, whereas the scatter for distance-corrected Lg and surface waves resulted in an interstation scatter of 0.27-0.45, roughly a factor of 3 to 4 times larger. These results confirm our initial hypothesis that the coda can effectively average over the effects of both source and path heterogeneity.

Next, we use the independent *Mw* estimates to calibrate the coda-derived source spectra. (See Mayeda et al. [2003] for calibration details.) Figure 3 shows example source spectra for a range of stations after all frequency-dependent path and site corrections were applied to each station. In general, the coda-derived spectra are very stable, in good agreement with previous published applications of the coda methodology.

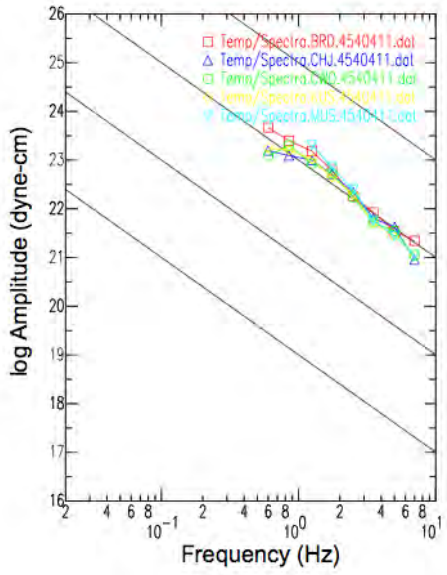

Figure 3. Example coda-derived source spectra for a range of stations. In general, the coda spectra are stable; however, our path calibration is preliminary, and we expect further improvement by reducing the amplitude scatter.

To validate the results, Figure 4 shows coda-derived *Mw* estimates (y-axis) are in good agreement with independent estimates (x-axis). We use roughly 10 events to perform the moment-rate calibration, then apply the same site-transfer corrections to all the events in our data set.

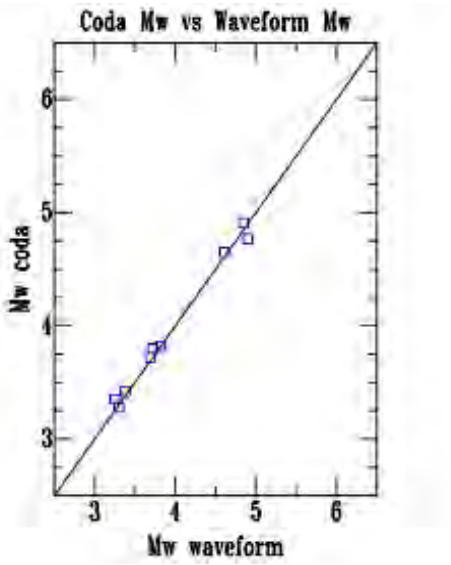

Figure 4. *Mw* derived from the low-frequency level of the coda spectra plotted against independent *Mw* from waveform modeling.

Next, using the spectra like the one shown in Figure 3, we form amplitude ratios for all earthquakes in our calibration data set (Figure 5). For each range of pass bands, a consistent trend is observed that is expected due to corner-frequency changing as a function of magnitude. In general the data scatter is small and suggests that the coda spectral ratios are reducing the variance associated with source radiation pattern and path heterogeneity. The next

part of the project will be to process a training explosion data set that will consist of mining-related explosions, single-fired explosions, and the recent North Korean nuclear test.

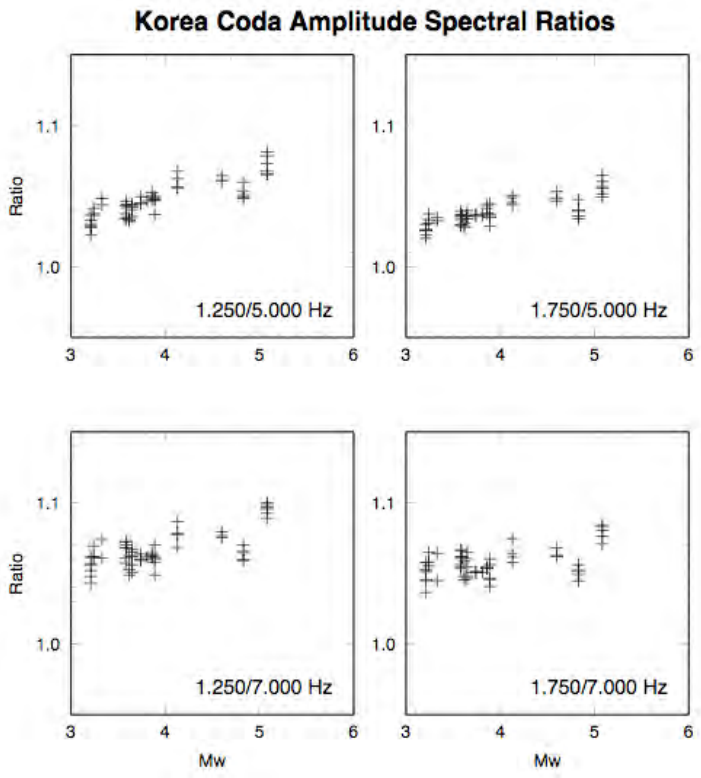

Figure 5. Single-station coda spectral ratios for the 15 calibration earthquakes distributed in and around the Korean peninsula for a range of different pass bands.

CONCLUSIONS AND RECOMMENDATIONS

We have performed a preliminary coda calibration for openly available stations in and around the Korean peninsula for 15 earthquakes ranging between *Mw* 3.2 and 5.1. In general, the 1-D coda calibration is performing well, and we expect future refinements to further reduce the data variance. The coda path and site calibrations will be improved in the next phase of the project, and we will begin processing of explosion data. At that point, we will also compute direct Lg spectral ratios to compare the discriminant performance against the coda spectral ratios.

REFERENCES

Mayeda, K., A. Hofstetter, J.L. O'Boyle, and W.R. Walter (2003). Stable and transportable regional magnitudes based on coda-derived moment-rate spectra, *Bull. Seism. Soc. Am.* 93: 224–239.

Mayeda, K. L. Malagnini, W.S. Phillips, W. R. Walter, and D. Dreger (2005). 2-D or not 2-D, that is the question: A northern California test, *Geophys. Res. Lett*. February, Doi:10.1029/2005GL022882.

Walter, W., K. Mayeda, and H. Patton (1995). Phase and spectral ratio discrimination between NTS earthquakes and explosions, Part I: Empirical Observations, *BSSA* 85: 1050–1067.

CHARACTERIZING FRACTURE DAMAGE AT FROZEN AND UNFROZEN SITES IN THE ALASKA FROZEN ROCK EXPERIMENT AND ITS EFFECT ON SEISMIC RADIATION

Charles G. Sammis

University of Southern California

Sponsored by Air Force Research Laboratory

Contract No. FA8718-04-C-0012.

ABSTRACT

In order to assess the effect of ice on seismic coupling of explosions in frozen rock, a consortium of Weston Geophysical, New England Research, and the University of Southern California planned and executed a field experiment near Fairbanks, Alaska. Chemical explosions between 200 and 350 lbs were detonated at two sites: one in a dry schist above the water table and the other in a saturated frozen gneiss. The most significant difference between the seismic radiation from the two sites was the generation of more high frequency energy at the frozen site resulting in a higher corner frequency and, therefore, a smaller elastic radius. Explosions at the two sites were modeled using the Johnson-Sammis (2001) non-linear model that includes the Ashby-Sammis (1990) damage mechanic. This damage mechanics requires an estimate of the initial damage at each site, which we obtain by combining the seismic velocities measured by Weston Geophysical with the laboratory ultrasonic velocities measured in samples of the two source rocks by New England research. Using the self-consistent theory developed by O'Connell and Budiansky (1974), the ultrasonic data were used to find the undamaged moduli. These undamaged moduli were then used together with the seismic data to estimate the initial damage at the frozen and at the unfrozen sites. The lower value of initial damage found for at the frozen rock site, when used in the source model, predicted a smaller elastic radius and higher frequency seismic radiation than did an equivalent calculation using the higher value of initial damage found at the unfrozen site, in agreement with the field observations. The lower value of initial damage found at the frozen rock site is also consistent with the field observation that explosions at the frozen rock site produced larger fragments.

OBJECTIVE

In order to assess the effect of ice on seismic coupling of explosions in frozen rock, a consortium of Weston Geophysical, New England Research, and the University of Southern California planned and executed a field experiment near Fairbanks, Alaska. Chemical explosions between 200 and 350 lbs were detonated at two sites: one in a dry schist above the water table and the other in a saturated frozen gneiss. The objective of the work described here is to combine the seismic P and S wave velocities measured in the field with ultrasonic velocities measured in the laboratory to estimate the initial fracture damage at each site. We wish to test the hypothesis that the dry schist above the water table has a higher value of initial damage than does the saturated frozen gneiss, and that this higher value of initial damage results in a larger elastic radius and lower corner frequency as observed in the field experiment.

RESEARCH ACCOMPLISHED

During the past year, we have collaborated with Weston Geophysical and New England Research in the interpretation of data from the Alaska frozen rock experiment conducted by Weston Geophysical during the summer of 2006. Our working hypothesis has been that ice in the cracks of the source rock produced significant stiffening and strengthening that affected the seismic coupling, which led to the smaller apparent size.

In the Alaska experiment, seismic radiation from chemical explosions in dry schist (above the water table) was compared with explosions having the same yield, but set off in a frozen gneiss. The primary result, shown in Figure 1, was that the spectral levels of radiation from both sites were comparable, but the corner frequency of radiation from the frozen rock site was higher. This higher corner frequency would lead to the erroneous conclusion that the explosion in frozen-rock was smaller.

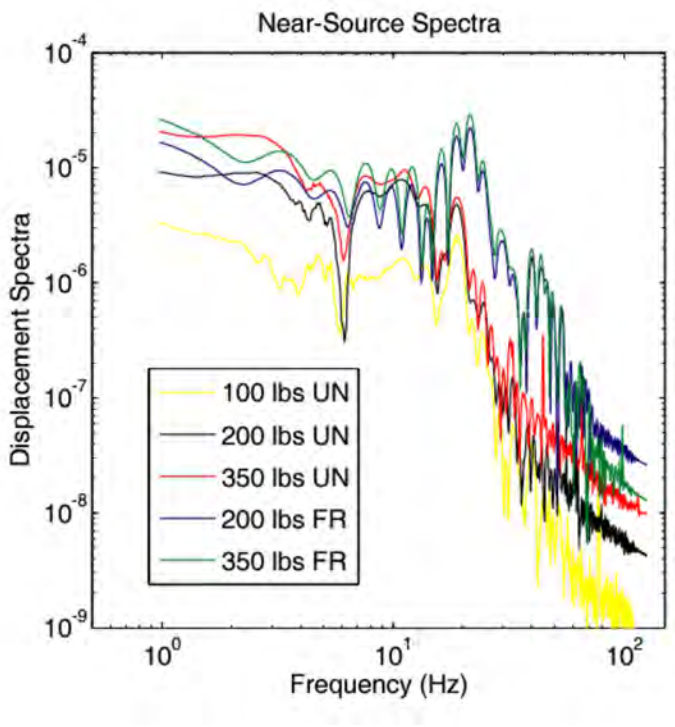

Figure 1. Displacement spectra for explosions in unfrozen dry schist (UN) and frozen gneiss (FR). Note the spectral peak and higher corner frequency for shots at the frozen site. (Figure courtesy of Jessie Bonner at Weston Geophysical).

In order to make a quantitative interpretation of this result, we wish to model the Alaska explosions using the Johnson and Sammis (2001) source model. This model incorporates the Ashby and Sammis (1990) micromechanical damage mechanics, which we have previously shown gives a good description experimental data for the temperature dependence of strength in frozen crystalline rock (Sammis and Biegel, 2004, 2005). The basic idea is that ice in the cracks strengthens the rock and increases its elastic stiffness by reducing the initial damage D_o.

In the Ashby and Sammis (1990) formulation, the initial damage D_o is defined as

$$D_o = \frac{4}{3}\pi N_V \langle a \rangle^3 \tag{1}$$

where N_V is the number of cracks per unit volume and $\langle a \rangle$ is the average radius of these cracks which comprise the initial damage. When water in the cracks freezes, it immobilizes some of them, reducing N_V thereby lowering D_o. Ice bridges in longer cracks reduce their effective radius a, also reducing D_o.

Our hypothesis is that frozen rock has a smaller D_o than does unfrozen rock. In our source model, this results in less explosion-induced damage in the frozen rock, and a higher corner frequency – as observed.

We use the theory developed by O'Connell and Budiansky (1974) to estimate D_o from the seismic velocities measured by Weston Geophysical at each field site. Figure 2 from their paper shows the ratios $\bar{v}_P / v_P$ and $\bar{v}_S / v_S$ as functions of a crack density parameter, which they define as $\varepsilon = N_V \langle a \rangle^3$ and which is simply related to D_o in equation (1) as

$$D_o = \frac{4}{3}\pi\varepsilon \tag{2}$$

The quantities $\bar{v}_P$ and $\bar{v}_S$ are velocities in the fractured rock, while v_P and v_S are velocities in the unfractured rock.

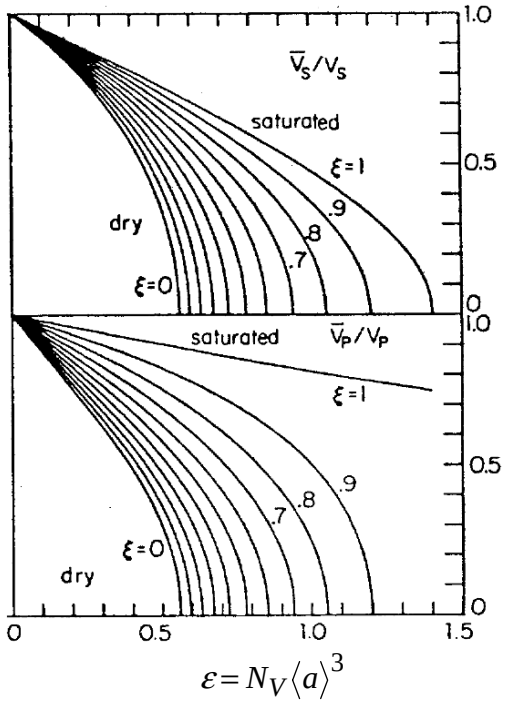

Figure 2. Decrease in velocity with increasing fracture parameter ε. Velocities in the damaged rock, $\bar{V}$, are scaled by the velocities in undamaged rock V. (From O'Connell and Budiansky, 1974).

In order to use Figure 2 to find the crack density parameter ε (and hence the initial damage D_o) from the seismic velocities ($\bar{v}_P$ and $\bar{v}_S$) at each test site, we need to know the un-fractured velocities (v_P and v_S) for the source rock at each site (the schist and the gneiss). These we estimate using the ultrasonic velocities measured in laboratory samples of each rock type by New England Research (NER).

For the schist source rock from the dry (un-frozen) site, NER measured P and S wave velocities under dry, saturated, and frozen conditions, at confining pressures ranging from 5 to 70 MPa. Table 1 summarizes the values at 5 and at 70 MPa - values at intermediate pressures vary monotonically between these limits.

Table 1. Ultrasonic data for schist source rock from the dry unfrozen site.

	P (MPa)	$\bar{v}_P$ (m/s)	$\bar{v}_S$ (m/s)	ν	v_P* (m/s)	v_S* (m/s)
Dry	5	4150	2800	0.082	5253	3294
	70	4750	3200	0.085	5723	3556
Saturated	5	5200	3000	0.25	5306	3261
	70	5450	3400	0.18	5561	3579
Frozen (-8C)	5	5800	3700	0.16		
	70	5700	3700	0.14		

*Unfractured reference velocities v_P and v_S found using ε_P and ε_S from Table 2.

The last two columns of Table 1 contain estimates of the un-fractured P and S wave velocities that were made using the calculations summarized in Table 2. In Table 2, values of $\frac{\bar{v}_P(sat.)}{\bar{v}_P(dry)}$ and $\frac{\bar{v}_S(sat.)}{\bar{v}_S(dry)}$ are calculated from the data in Table 1. Note that $\frac{\bar{v}_P(sat.)}{\bar{v}_P(dry)} = \frac{\bar{v}_P(sat.)/v_P}{\bar{v}_P(dry)/v_P}$ and that $\frac{\bar{v}_S(sat.)}{\bar{v}_S(dry)} = \frac{\bar{v}_S(sat.)/v_S}{\bar{v}_S(dry)/v_S}$ and that the ratios on the right hand side of these equations can be found as a function of ε in Figure 2 and are plotted explicitly in Figure 3. The values of ε in Table 2 were found using Figure 3 as indicated on the figure. Once ε was determined, the ratios $\bar{v}/v$ were found from Figure 2 and appear in the last four columns of Table 2. These ratios were used together with the measured seismic velocities to calculate the un-fractured velocities in the gneiss samples, which are give in the last two columns of Table 1. Note that the un-fractured velocities found by this method are very similar to the velocities measure in the frozen samples. This observation supports our assumption that ice immobilizes the fractures.

Table 2. Ultrasonic velocity ratios used to find fracture parameter ε in gneiss lab samples.

P (MPa)	$\frac{\bar{v}_P(sat.)}{\bar{v}_P(dry)}$	$\frac{\bar{v}_S(sat.)}{\bar{v}_S(dry)}$	ε_P	ε_S	$\frac{\bar{v}_P}{v_P}$ (dry)	$\frac{\bar{v}_P}{v_P}$ (sat.)	$\frac{\bar{v}_S}{v_S}$ (dry)	$\frac{\bar{v}_S}{v_S}$ (sat.)
5	1.25	1.07	0.18	0.16	0.79	0.98	0.85	0.92
70	1.15	1.06	0.13	0.15	0.83	0.98	0.90	0.95

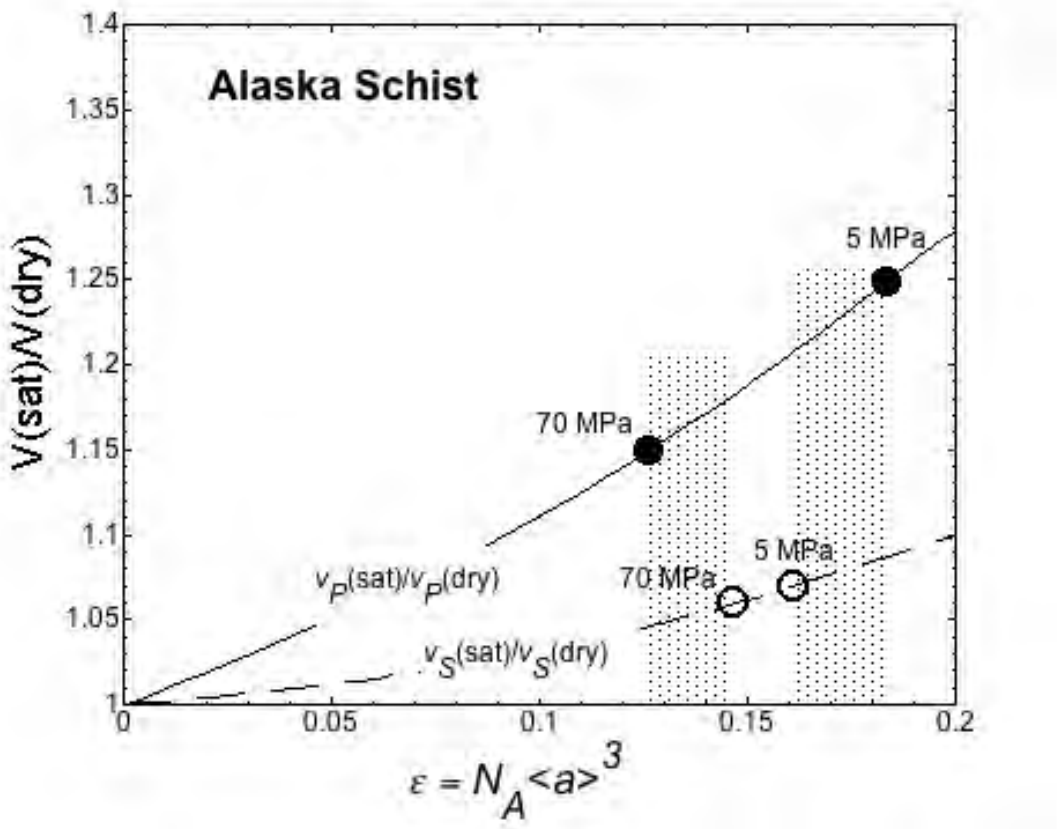

Figure 3. The ratio of saturated to dry velocities as a function of the crack parameter e. The curves were calculated from Figure 2. The points are ratios of the ultrasonic data for schist from Table 1. Note the decrease in crack parameter as confining pressure closes cracks.

For the gneiss source rock from the frozen site, NER measured P and S wave velocities under saturated and frozen conditions, also at confining pressures ranging from 5 to 70 MPa. Table 3 summarizes the values at 5 and at 70 MPa - values at intermediate pressures vary monotonically between these limits.

Table 3. Ultrasonic velocities for gneiss source rock from the frozen site.

	P (MPa)	$\bar{v}_P$ (m/s)	$\bar{v}_S$ (m/s)	ν
Saturated	5	5450	3050	0.27
	70	5550	3200	0.25
Frozen (-8C)	5	5800	3400	0.24
	70	5800	3450	0.23

Since no measurements were made under dry conditions, we can not use the same method we used to estimate the un-fractured velocities in the schist. However, based on the results for the schist, we can assume that the frozen velocities are a reasonable approximation to the un-fractured velocities.

Having estimated the un-fractured velocities v_P and v_S for both source rocks, it is now possible to estimated the fracture parameter at each test site. The seismic field velocities and implied fracture parameters at each site are summarized in Table 4.

Table 4. Ultrasonic velocities for schist source rock from the dry unfrozen site.

	$\bar{v}_P$ (m/s)	$\bar{v}_S$ (m/s)	ν	$\frac{\bar{v}_P}{v_P}$	$\frac{\bar{v}_S}{v_S}$	ε_P	ε_S	$\langle\varepsilon\rangle$	$\langle D_o\rangle$
Unfrozed Site	2700	1700	0.17	0.47	0.46	0.41	0.45	0.43	1.80
Frozen Site	3800	2400	0.17	0.66	0.65	0.28	0.35	0.31	1.30

Note that for both P and S waves, the fracture parameter ε, and the equivalent initial damage D_o, is larger at the unfrozen site, consistent with the hypothesis that ice reduces the fracture density in the source rock. When these values of D_o are used in the Johnson and Sammis (2001) source model, the unfrozen site has a larger elastic radius and lower corner frequency than the frozen site, as observed in the Alaska frozen rock experiment.

CONCLUSIONS AND RECOMMENDATIONS

The hypothesis that ice in cracks decreases the fracture damage is supported by a joint quantitative analysis of the seismic velocities at the frozen and dry un-frozen test sites in the Alaska frozen rock experiment and ultrasonic velocity measurements on lab samples from the two sites. The lower initial damage at the frozen site results in a smaller elastic radius and higher corner frequency as observed.

ACKNOWLEDGEMENTS

This paper is the result of close collaboration with Weston Geophysical, New England research, and Lane Johnson at U.C. Berkeley.

REFERENCES

Ashby, M. F. and C. G. Sammis (1990). The Damage Mechanics of Brittle Solids in Compression, *Pure appl. Geophys*: 133: 489–521.

Johnson, L. R. and C. G. Sammis (2001). Effects of rock damage on seismic waves generated by explosions, *Pure Appl. Geophys.*: 158: 1869–1908.

O'Connell, R. J. and B. Budiansky (1974). Seismic velocities in dry and saturated cracked solids, *J. Geophys. Res.:* 79: 5412–5426.

Sammis, C. G. and R .L. Biegel (2004). Mechanics of strengthening in crystalline rock at low temperatures: a preliminary assessment, in *Proceedings of the 26th Seismic Research Review: Trends in Nuclear Explosion Monitoring*, LA-UR-04-5801, Vol. 1, pp. 475–484.

Sammis, C. G. and R. L. Biegel (2005). Seismic radiation from explosions in frozen crystalline rock, in *Proceedings of the 27th Seismic Research Review***:** *Ground-Based Nuclear Explosion Monitoring Technologies*, LA-UR-05-6407, Vol. 1, pp. 642–652.

SPECTRAL STUDIES OF SHALLOW EARTHQUAKES AND EXPLOSIONS IN SOUTHERN CALIFORNIA

Peter M. Shearer and Bettina P. Allmann

Institute of Geophysics and Planetary Physics, University of California San Diego

Sponsored by Air Force Research Laboratory

Contract No. FA8718-06-C-0004

ABSTRACT

We compute and analyze *P*-wave spectra from 18,101 earthquakes and 1770 explosions recorded by 196 broadband seismic stations in southern California at epicentral distances of up to 200 km. We use an online waveform database stored on a RAID system at Caltech, which provides complete access to the Southern California Seismic Network (SCSN) seismogram archive. We compute spectra using 1.28 s noise and signal windows, positioned immediately before and after the *P* arrivals. After applying a signal-to-noise cutoff, we process the spectra using an iterative robust least-squares method to isolate source, receiver, and propagation path contributions. This corrects for first-order attenuation structure, as well as near-receiver site effects and any errors in the instrument response functions. Using the earthquake spectra and a simple source model, we compute an empirical Green's function to remove the tradeoff between the source terms and other terms in our model. Our observed earthquake spectra fit reasonably well with a constant stress drop model over a wide range of moment. However, the explosion spectra show significant differences from the earthquake spectra and have generally steeper falloffs at high frequencies. We also compare *P* and *S*-wave amplitudes and find modestly smaller average *S* amplitudes for the explosions compared to the earthquakes. The best earthquake/explosion discriminant is the RMS misfit to an ω^{-2} source model, which works for ~90% of the events.

OBJECTIVES

Routine seismic discrimination between earthquakes and explosions has been a long-standing goal in nuclear test ban treaty research (for a recent review, see Stump et al., 2002). A variety of methods have been employed, including amplitude ratios among regional phases (e.g., Bennett and Murphy, 1986; Wuster, 1993; Plafcan et al., 1997; McLaughlin et al., 2004), spectral studies (e.g., Taylor et al., 1988; Gitterman and van Eck, 1993; Kim et al., 1994; Walter et al., 1995; Gitterman et al., 1998), coda studies (e.g., Su et al., 1991; Hartse et al., 1995), ripple-fire detection schemes (e.g., Hedlin et al., 1990; Smith, 1993; Carr and Garbin, 1998; Hedlin, 1998; Arrowsmith et al., 2006), and other methods (e.g., Musil and Plesinger, 1996; Parolai et al., 2002; Leidig et al., 2004; Tibuleac et al., 2004).

The goal of this project is to systematically analyze and compare source spectra from locally recorded earthquakes and explosions in Southern California (Figure 1) in order to develop new insights into discrimination methods. Advances in data storage and computer capabilities make possible much more extensive analyses than have been performed in the past, which will provide a better picture of the distribution of source spectral properties and amplitudes. By examining tens of thousands of events, we will quantitatively characterize differences between earthquakes and explosions in terms of their spectral content and their *P/S* energy ratios. We also plan to identify and examine anomalous events, in particular earthquakes that may appear like explosions in spectral discrimination methods in order to determine how common they are and whether alternate discrimination techniques can be applied.

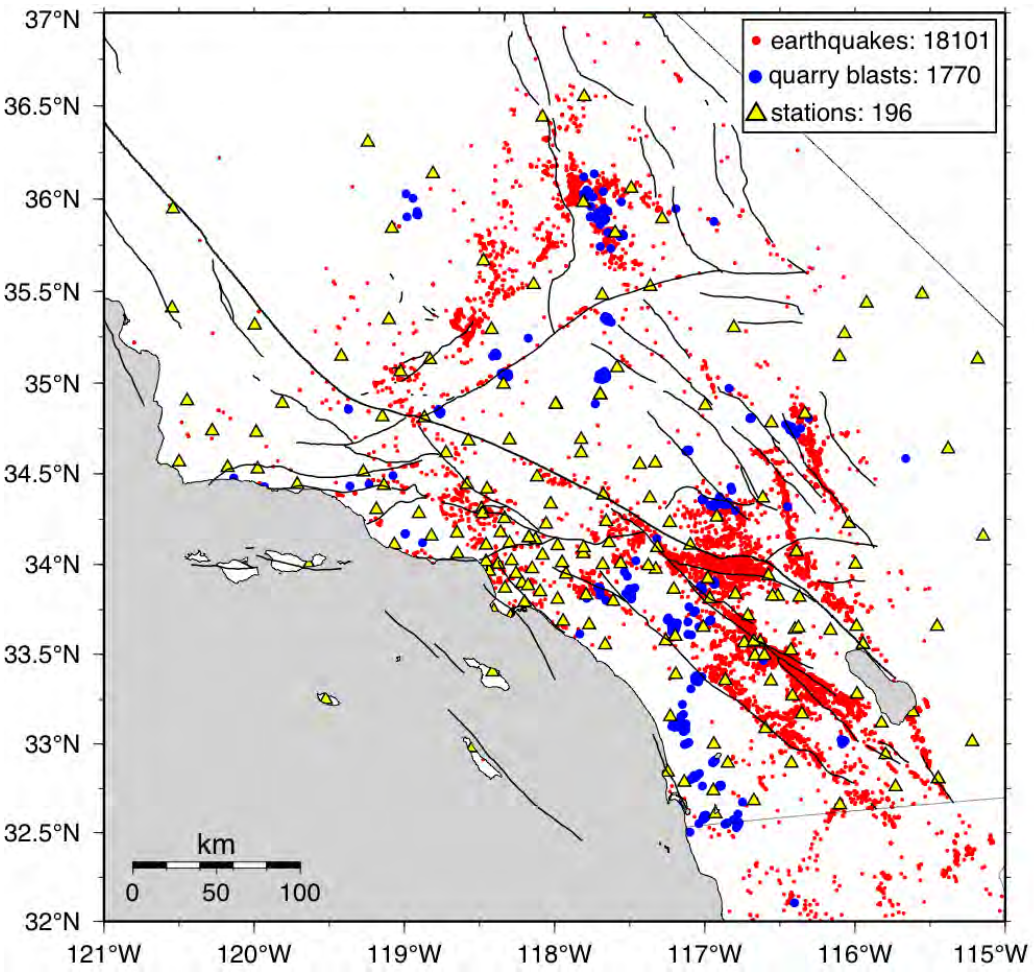

Figure 1. Locations of 18,101 earthquakes (red) and 1770 explosions (blue) in southern California from 2000 to 2005 as recorded by broadband stations (yellow) of the SCSN.

The project builds upon a recently completed large-scale analysis of southern California earthquake spectra (Shearer et al., 2006), to include a set of 1770 mining and other explosions between 2000 and 2005. The Shearer et al. earthquake study has already provided the largest set of earthquake spectra and stress drops computed to date, showing that individual event stress drops range between 0.2 and 20 MPa. The large number of stations and events available in southern California allows applying empirical calibration methods to remove receiver response and path propagation effects. Our efforts focus on southern California because of the unmatched size and quality of the available data, but we expect the results and insights will be applicable to other regions of more direct interest to nuclear monitoring programs. While the Shearer et al. (2006) study analyzed 1989–2001 data from short-period vertical-component stations, we examine 2000–2005 data from three-component, broadband stations. The newer data have the advantage of the horizontal components and a larger dynamic range (i.e., the older data clip on earthquakes above ~M3.5).

RESEARCH ACCOMPLISHED

The SCSN has several hundred stations and records about 12,000 to 35,000 earthquakes each year. Recently we began storing seismograms from all archived events in an online RAID system that provides rapid and random access to the data (Hauksson and Shearer, 2005). Spectra are computed as follows: For each seismogram we pick the *P* and *S* arrivals and estimate their amplitudes. This is done using the operator pick, if available, or using the output of an automatic picking algorithm for a window around the predicted arrival time (based on the catalog event location and a 1-D velocity model). Traces are resampled to a uniform 100 Hz sample rate. Spectra are computed for 1.28 s noise and signal windows, immediately before and after the pick time. We compute results for all available channels and components for both *P* and *S*, including rotation of the horizontals (if present) into transverse and radial records. Both signal and pre-event noise spectra are corrected to displacement and stored in a special binary format.

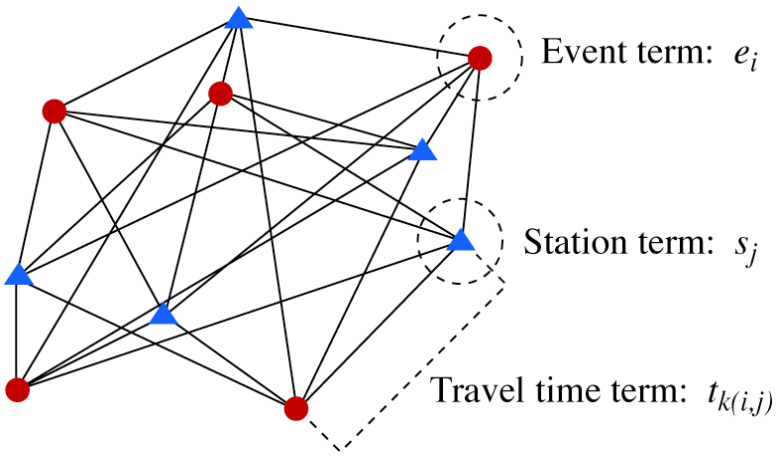

Figure 2. A cartoon showing how measured spectra can be modeled as a product of event, station, and travel-time dependent terms.

We apply a signal-to-noise (STN) cutoff to the spectra, requiring that the STN amplitude ratio be at least 3 for three separate bands of 5 to 10 Hz, 10 to 15 Hz and 15 to 20 Hz. Next, we process the spectra in order to isolate source, receiver and propagation path effects. This is an important step because individual spectra tend to be irregular in shape and difficult to fit robustly with theoretical models. However, by stacking and analyzing thousands of spectra it is possible to obtain more consistent results. The basic approach is illustrated in Figure 2 and is similar to that used by Warren and Shearer (2000, 2002) and Prieto et al. (2004). Each observed displacement spectrum $d_{ij}(f)$ from source i and receiver j is a product of a source term e_i (which includes the source spectrum and near-source attenuation), a near-receiver term s_j (which includes any uncorrected part of the instrument response, the site response and the near-receiver attenuation), and a travel-time dependent term $t_{k(i,j)}$ (which includes the effects of geometrical spreading and attenuation along the ray path). In the log domain, this product becomes a sum:

$$d_{ij} = e_i + s_j + t_{k(i,j)} + r_{ij} \ ,$$

where r_{ij} is the residual for path ij. We parameterize t in terms of the predicted P travel time between the source and receiver, using the event locations and velocity model from Lin et al. (2007). This accounts for both the event depth and the source-receiver distance. The travel-time term $t_{k(i,j)}$ is discretized by its index k at 1 s increments in travel time. Because each station records multiple events and each event is recorded by multiple stations, this is an over-determined problem. We solve this equation using a robust, iterative, least-squares method in which we sequentially solve for the terms t_k, s_j, and e_i, while keeping the other terms fixed at each stage. We suppress outliers by assigning L1-norm weights to misfit residuals greater than 0.2 s (or less than –0.2 s). This weighting scheme is necessary to ensure robustness with respect to a small number of spectra with large excursions compared to the bulk of the data. In practice we found that the method converged rapidly to a stable solution after a few iterations.

Radiation pattern differences are not included in equation (1) and would be difficult to include in our processing because they are not generally available for the smaller magnitude events. By using multiple stations for each source, however, radiation pattern effects will tend to average out. Note that this method resolves only differences in the relative shapes of the spectra. Without additional modeling assumptions, it cannot, for example, resolve how much of the spectral falloff is due to source effects and how much is due to attenuation common to all paths. The advantage of the method, however, is that it identifies and removes anomalies that are specific to certain sources or receivers. Because there may be difficulties in obtaining reliable and accurate instrument response functions for many of the stations in the archive, this is an important processing step that provides a way to correct for some of these problems.

Our focus has been on the stacked source spectra, e_i, which we ultimately use to estimate the moment and corner frequency of each event. At this stage, however, the source spectra only contain relative information among the different events. In order to estimate absolute spectra from our source stacks, we use the local magnitude M_L to obtain the scaling factor necessary to convert our relative moment estimates to absolute moment and we use an empirical Green's function approach to correct the spectral shapes for attenuation and other path effects (for details, see Shearer et al., 2006). To study the average shape of the spectra, we stack our results within equally spaced bins in the estimated seismic moment (obtained from the low-frequency part of the spectrum). Figure 3 shows these stacked spectra for both earthquakes and quarry blasts. The dashed lines show the best-fitting predictions of the ω^{-2} source model of Madariaga (1976), assuming a constant stress drop.

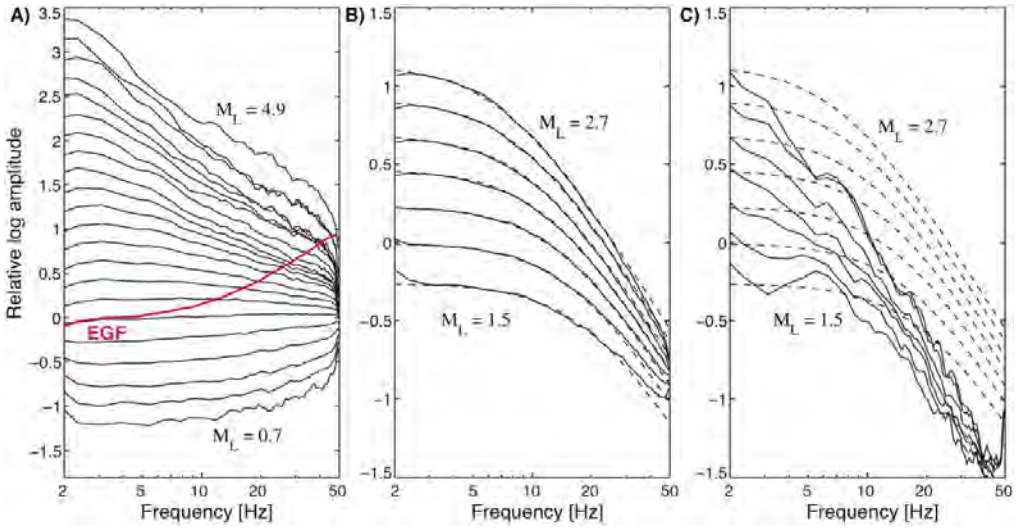

Figure 3. Stacked *P*-wave source displacement spectra from 2000 to 2005 within bins of estimated seismic moment for 17810 earthquakes and 1744 quarry blasts. (A) Stacked earthquake source terms obtained from the iterative inversion. Red line shows the empirical Green's function (EGF) used to correct these spectra for attenuation and other path effects assuming a constant stress drop model. (B) EGF corrected earthquake source terms compared to predictions of the Madariaga (1976) source model (dashed lines). (C) Stacked source terms for quarries.

Figure 3 shows that averaged earthquake spectra in southern California are well fit by a standard source model. However, the averaged quarry spectra appear anomalous in at least two respects: (1) they exhibit large misfit compared to the source model predictions, and (2) they have generally steeper falloffs at high frequencies than ω^{-2}, which will lead to lower corner frequencies and stress drop estimates. The lack of high frequency radiation from the quarries is somewhat surprising and may reflect ripple firing and/or strong near-surface attenuation. In any case, we attempt to use these two differences to discriminate between earthquakes and quarry blasts in southern California. We do this by computing the best-fitting ω^{-2} source model to the individual EGF-corrected source spectra. For each event, we obtain an estimate of the moment, the corner frequency and a measure of the root mean square (RMS) misfit to the source model. Various combinations of these parameters are plotted against each other in Figure 4. Note that the quarry blasts have generally higher misfits and smaller corner frequencies than the earthquakes. However, the two populations are not completely separated and there is some degree of overlap (see Figure 5), particularly in the corner frequency estimates.

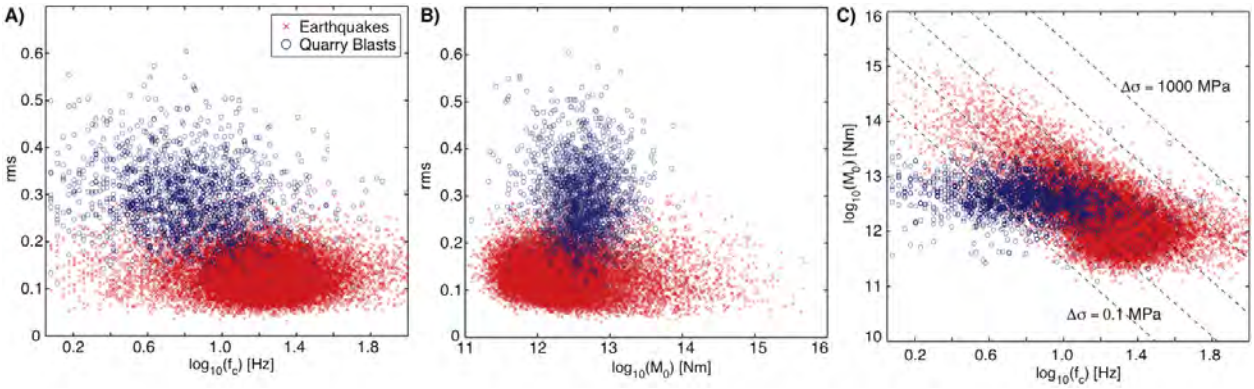

Figure 4. Earthquakes (red) and quarry blasts (blue) as a function of parameters derived from fitting their EGF-corrected spectra to an ω^{-2} source model. (A) Misfit vs. corner frequency. (B) Misfit vs. moment. (C) Moment vs. corner frequency. Stress drop estimates in (C) are from the Madariaga (1976) model.

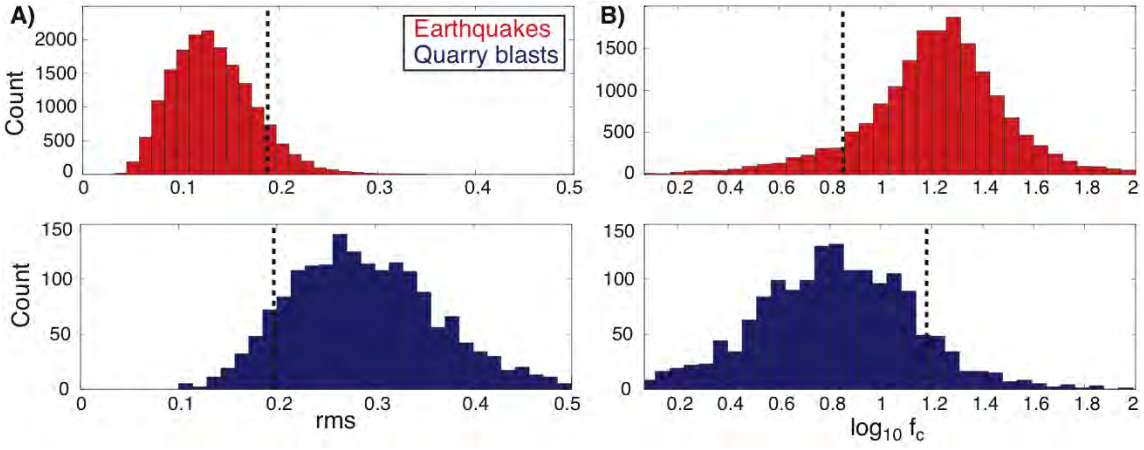

Figure 5. Histograms comparing the distribution of RMS misfit to an ω^{-2} source model (left) and corner frequency (right) for both earthquakes (red) and quarry blasts (blue). The dashed vertical lines divide the distributions into 10% and 90% parts. Note that 90% of the quarries have model misfits greater than that of 90% of the earthquakes, but that there is much more overlap in the corner frequency distributions.

In practical applications, the main interest is to discriminate between shallow earthquakes and explosions. We therefore compare the quarry blast results to earthquakes shallower than 5 km only. Although a much smaller number of events is now being used (~ 3000), the overall results of Figure 4 and 5 do not change.

Our results from analysis of *S*-wave spectra from transverse-component records have so far been inconclusive, in part because of the generally lower signal-to-noise ratios at high frequencies for the *S* waves compared to the *P* waves. However, we do observe lower average *S/P* amplitude ratios for the quarries using simple peak amplitudes in the unfiltered seismograms (Figure 6), although there is a large amount of overlap in the distributions.

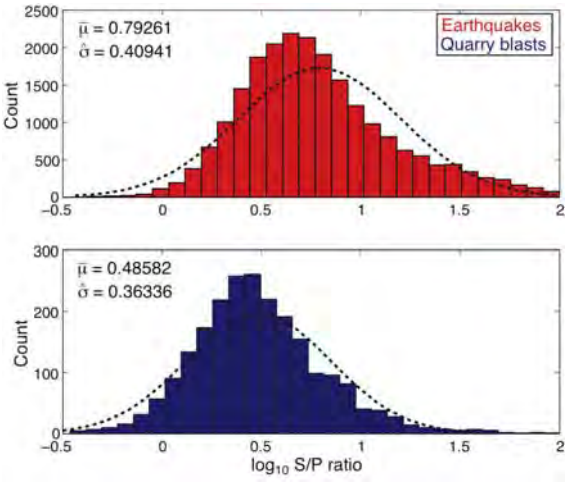

Figure 6. Histograms comparing the distributions of *S/P* amplitude ratios between earthquakes (top) and quarry blasts (bottom).

CONCLUSIONS AND RECOMMENDATIONS

Earthquakes and explosions in Southern California exhibit significant differences in their average *P*-wave spectral properties. Quarry blast spectra are not well fit by standard source models and typically have lower corner frequencies and anomalously steep falloffs at high frequencies compared to earthquakes of the same estimated moment. However, spectra from individual events have large variations and do not always permit an unambiguous identification of event type. Future results from analysis of *S*-wave spectra may provide additional discriminants.

ACKNOWLEDGEMENTS

We thank Egill Hauksson for his help in maintaining the waveform database and computing the spectra.

REFERENCES

Arrowsmith, S. J., M. D. Arrowsmith, M. A. H. Hedlin, and B. Stump (2006). Discrimination of delay-fired mine blasts in Wyoming using an automatic time-frequency discriminant, *Bull. Seismol. Soc. Am.* 96: 2368–2382, doi: 10.1785/0120060039.

Bennett, T. J. and J. R. Murphy (1986). Analysis of seismic discrimination capabilities using regional data from western United States events, *Bull. Seismol. Soc. Am*. 76: 1069–1086.

Carr, D. B. and H. D. Garbin (1998). Discriminating ripple-fired explosions with high-frequency (>16 Hz) data, *Bull. Seismol. Soc. Am*. 88: 963–972.

Gitterman, Y., V. Pinsky, and A. Shapira (1998). Spectral classification methods in monitoring small local events by the Israel seismic network, *J. Seismol*. 2: 237–256.

Gitterman, Y. and R. van Eck (1993). Spectral of quarry blasts and microearthquakes recorded at local distances in Israel, *Bull. Seismol. Soc. Am*. 83: 1799–1812.

Hartse, S. E., W. S. Phillips, M. C. Fehler, and L. S. House (1995). Single-station spectral discrimination using coda waves, *Bull. Seismol. Soc. Am.* 85: 1464–1474.

Hauksson, E. and P. Shearer (2005). Southern California hypocenter relocation with waveform cross-correlation, part 1: Results using the double-difference method, *Bull. Seismol. Soc. Am.* 95: 896–903, doi:10.1785/0120040167.

Hedlin, M. A. H. (1998). A global test of a time-frequency small-event discriminant, *Bull. Seismol. Soc. Am*. 88: 973–988.

Hedlin, M. A. H., J.-B. Minster, and J. A. O. Orcutt (1990). An automatic means to discriminate between earthquakes and quarry blasts, *Bull. Seismol. Soc. Am*. 80: 2143–2160.

Kim, W. Y., D. W. Simpson, and P. G. Richards (1994). High-frequency spectra of regional phases from earthquakes and chemical explosions, *Bull. Seismol. Soc. Am*. 84: 1365–1386.

Leidig, M.R., B.W. Stump, J.L. Bonner, C. T. Hayward, A. A. Velazco, D. F. Baker, H. Hooper, W. R. Walter, X. Yang, R. Zhou, C. L. Edwards, M. D. Renwald, and J. F. Lewkowicz (2004). Source phenomenology experiments in Arizona, in *Proceedings of the 26th Seismic Research Review: Trends in Nuclear Explosion Monitoring*, LA-UR-04-5801, Vol. 1, pp. 366–374.

Lin., G., P. M. Shearer, and E. Hauksson (2007). Applying a 3D velocity model, waveform cross-correlation, and cluster analysis to locate Southern California seismicity from 1981 to 2005, *J. Geophys. Res*. (submitted).

Madariaga, R. (1976). Dynamics of an expanding circular fault, *Bull. Seismol. Soc. Am*. 66: 639–666.

McLaughlin, K. L., J. L. Bonner, and R. Barker (2004). Seismic source mechanisms for quarry blasts: Modelling observed Rayleigh and Love wave radiation patterns from a Texas quarry, *Geophys. J. Int*. 156: 79–93.

Musil, M. and A. Plesinger (1996). Discrimination between local microearthquakes and quarry blasts by multi-layer perceptrons and Kohonen maps, *Bull. Seismol. Soc. Am*. 86: 1077–1090.

Parolai, S., L. Trojani, M. Frapiccini, and G. Monachesi (2002). Seismic source classification by means of a sonogram-correlation approach: Application to data of the RSM Seismic Network (central Italy), *Pure Appl. Geophys.* 159: 2763–2788.

Plafcan, D., E. Sandvol, D. Seber, M. Barazangi, A. Ibenbrahim, and T.-E. Cherkaoui (1997). Regional discrimination of chemical explosions and earthquakes: a case study in Morocco, *Bull. Seismol. Soc. Am*. 87: 1126–1139.

Prieto, G. A., P. M. Shearer, F. L. Vernon, and D. Kilb (2004). Earthquake source scaling and self-similarity estimation from stacking P and S spectra, *J. Geophys. Res*. 109: doi:10.1029/2004JB003084.

Shearer, P. M., G. Prieto ,and E. Hauksson (2006). Comprehensive analysis of earthquake source spectra in Southern California, *J. Geophys. Res*. 111: B06303, doi:10.1029/2005JB003979.

Smith, A. T. (1993). Discrimination of explosions from simultaneous mining blasts, *Bull. Seismol. Soc. Am.* 83: 160–179.

Stump, B., M. A. H. Hedlin, D. C. Pearson, and V. Hsu (2002). Characterization of mining explosions at regional distances, *Reviews of Geophysics* 40: 1011, doi:10.1029/1998RG000048.

Su, F., K. Aki, and N. N. Biswas (1991). Discriminating quarry blasts from earthquakes using coda waves, *Bull. Seismol. Soc. Am*. 81: 162–178.

Taylor, S. R., N. W. Sherman ,and M. D. Denny (1988). Spectral discrimination between NTS explosions and western United States earthquakes at regional distances, *Bull. Seismol. Soc. Am*. 78: 1563–1579.

Tibuleac, I. M., J. Britton, D. B. Harris, T. Hauk, H. Hooper, and J. L. Bonner (2004). Detection methods for mining explosions in southern Asia, in *Proceedings of the 26th Seismic Research Review: Trends in Nuclear Explosion Monitoring*, LA-UR-04-5801, Vol. 1, pp. 427–438.

Walter, W. R., K. M. Mayeda, and H. J. Patton (1995). Phase and spectral ratio discrimination between NTS earthquakes and explosions, part I: Empirical observations, *Bull. Seism. Soc. Am.* 85: 1050–1067.

Warren, L. M. and P. M. Shearer (2000). Investigating the frequency dependence of mantle Q by stacking P and PP spectra, *J. Geophys. Res*. 105: 25,391–25,402.

Warren, L. M. and P. M. Shearer (2002). Mapping lateral variations in upper mantle attenuation by stacking P and PP spectra, *J. Geophys. Res*. 107: B12, 2342, doi:10.1029/2001JB001195.

Wuster, J. (1993). Discrimination of chemical explosions and earthquakes in central Europe—A case study, *Bull. Seismol. Soc. Am*. 83: 1184–1212.

ANALYSIS OF SHEAR WAVE GENERATION BY DECOUPLED AND PARTIALLY COUPLED EXPLOSIONS

Jeffry L. Stevens, Heming Xu, and G. Eli Baker

Science Applications International Corporation

Sponsored by Air Force Research Laboratory

Contract No. FA8718-06-C-0007

ABSTRACT

The objective of this project is to investigate the sources of shear wave generation by decoupled and partially coupled explosions, and the differences in shear wave generation between tamped and decoupled explosions, using data analysis and numerical modeling of decoupled and partially coupled explosions.

A perfectly spherical explosion at the center of a perfectly spherical cavity large enough to fully decouple the explosion would generate no shear waves, so all shear waves from decoupled explosions are due to asymmetries in and near the cavity, and to scattering and conversions. We explicitly model the shear waves generated by an explosion offset from the center of a spherical cavity, which causes the shock wave to vary in amplitude and arrival time around the cavity surface. We present a general solution to this problem and calculations of an airshock propagating in the cavity and impacting the cavity wall. The offset explosion has a dipole component and can generate significant shear waves with a modest offset from the center.

We model the Sterling decoupled explosion and show that the near field shear waves observed from that event are likely caused by the cavity shape. The Sterling cavity was approximately spherical except for a flat cavity floor due to melted and recrystallized salt. We model the impact of the shock wave from the explosion on the cavity walls using a 2D Eulerian finite difference code that simulates the evolution of the air shock in the cavity coupled with a 2D Lagrangian finite difference code that simulates the nonlinear region outside the cavity. Calculated shear waves generated by the impact of the shock wave with the cavity floor are in good agreement with the near field observations. The rock adjacent to Salmon was intensely fractured by the explosion, so it is possible that some of these cracks were opened by Sterling. Propagation of the hydrofractures driven by the Sterling explosion is modeled by coupling stress wave dynamics in rock with fluid mechanics in the fractures. The results show that the cavity pressure is insufficient to overcome the overburden to propagate fractures into rock, except for the area immediately below the explosion on the cavity floor. The simulations match the first arrivals of both P and S waves quite well, however the observations also have substantial P and S coda, which are not reproduced by the calculations.

Records at a common set of local stations of a tamped and subsequent water filled cavity explosions provide an opportunity to distinguish between shear wave generation mechanisms. The P and S spectra of the tamped and decoupled explosions are similar, except for a 9 Hz bubble pulse in the P, but not the S spectra of the decoupled explosions. This is inconsistent with shear wave generation by P-wave scattering. The high frequencies and 600 m depth are inconsistent with generation by Rg scattering. Synthetic modeling demonstrates that a spherical explosion source is insufficient to generate the observed shear waves, but they are predicted by compensated linear vector dipole (CLVD) synthetics. Finally, the observed P and S travel times from 1 to 5 km are consistent with CLVD synthetics, that is, with generation at the source. While not inconsistent with scattering to S, such scattering would have to be nearly instantaneous, occur very close to the source, and not occur at greater distance from the source, as the S arrivals are impulsive, temporally compact, and move out smoothly with distance.

OBJECTIVES

The objective of this project is to investigate the sources of shear wave generation by decoupled and partially coupled explosions, and the differences in shear wave generation between tamped and decoupled explosions. This is being accomplished through a program of data analysis and numerical modeling of decoupled and partially coupled explosions.

RESEARCH ACCOMPLISHED

Introduction

This project investigates shear waves from decoupled and partially coupled explosions, focusing on source mechanisms for shear waves, constrained by observations and numerical simulations. Although a nuclear explosion detonated at the center of a perfect spherical cavity large enough to decouple the explosion would generate no shear waves (other than conversions due to the earth's surface and scattering), in fact no cavity has perfect spherical symmetry, nor is the explosion exactly at the center, and shear waves have been observed from all decoupled explosions, even quite close to the source.

In this paper, we examine the following:

1. We present a general solution to the problem of shear waves generated by an explosion offset from the center of a spherical cavity, which causes the shock wave to vary in amplitude and arrival time around the cavity surface, followed by calculations of an airshock propagating in the cavity and impacting the cavity wall.
2. We present a detailed numerical model of the Sterling experiment.
3. We perform data analysis and numerical modeling of shear waves from Russian nuclear explosions in water-filled cavities.

Shear Waves from a Non-Isotropic Explosion Source

We model the seismic waves from a non-isotropic explosion source, specifically an explosion offset from the center of a spherical cavity, using a modification of the method developed by Stevens (1980) to solve the problem of seismic waves generated by an explosion in a prestressed elastic medium. The general solution for the seismic wave field from a set of tractions applied to the inside of a spherical cavity is given by

$$u = -\int_{\Sigma} u \cdot T(G) \cdot \hat{n} dA + \int_{\Sigma} G \cdot T(u) \cdot \hat{n} dA \,, \tag{1}$$

where Σ is the cavity surface, u on the left side of the equation is the displacement at any location outside the cavity, and u inside the integral is the displacement on the cavity wall. G is the elastic Green's tensor in spherical coordinates, and T is the stress operator. The second term represents the response of the medium to the applied stress from the explosion, and the first term represents the additional motion due to the response of the cavity wall Equation 1 can be solved by expanding the displacement, traction and Green's tensor in vector spherical harmonics. The case of interest here is shown in Figure 1 (left), where the explosion source is initially offset from the center of an air-filled cavity of radius R by a distance d. The right side of Figure 1 shows the calculated P and S waves from the explosion. The offset from the center causes the shock wave to impact the side of the cavity closest to the explosion earlier and with greater force than the opposite side of a cavity. This is equivalent to a dipole source acting in the direction of the offset, and as illustrated, can generate S waves comparable in amplitude to the initial P wave. Note that the offset in origin breaks the symmetry of the problem except for axisymmetry about the offset axis. If the offset is oriented horizontally relative to the surface, strong SH waves will be generated. Zhou and Harkrider (1992) similarly found that a point explosion offset from the center in a solid-filled spherical region embedded in a whole space acts primarily as a dipole source.

Figure 2 shows the results of a full nonlinear calculation of a 0.38 kt explosion offset by 5 meters from the center of a 9 meter radius air-filled cavity in strong granite. Overburden pressure is 130 bars. The explosion is almost fully decoupled, but there is some nonlinear deformation within a few meters of the cavity. The results show strongly asymmetric P waves as a function of angle around the cavity, and substantial S wave generation on the transverse component.

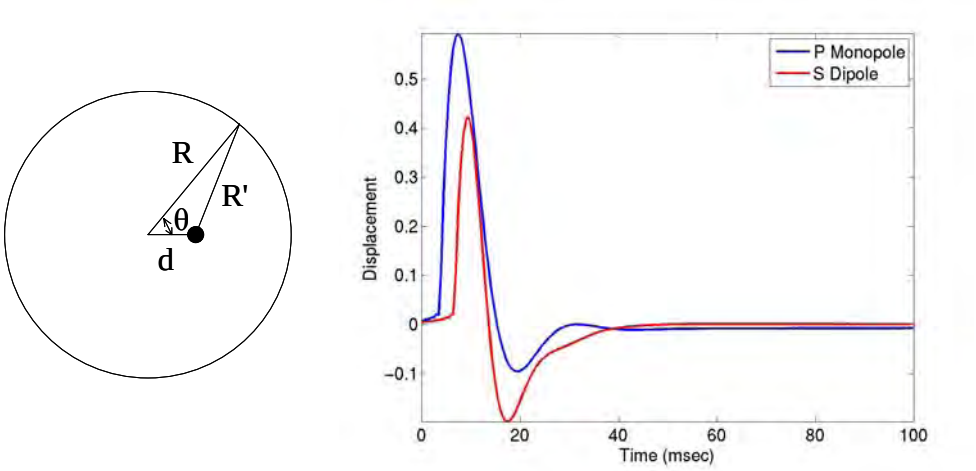

Figure 1. Calculated P and S waves (right) for an explosion in an air-filled cavity with the origin of the explosion offset from the center (left). In this example the cavity radius is 17 m and the offset from the center is 8.5 m.

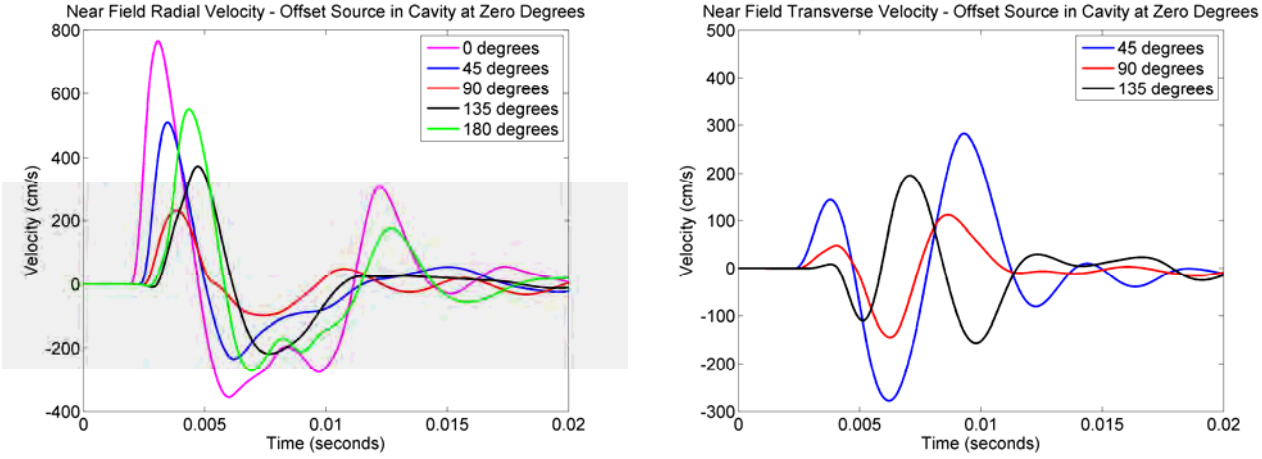

Figure 2. Nonlinear calculation of near field radial and transverse velocity at a distance of 20 meters from an explosion in a 9 meter radius cavity in granite, offset from the center by 5 meters. The left figure shows radial velocity, which is mostly P wave, and the right shows transverse velocity, which is mostly S wave, at angles of 0, 45, 90, 135, and 180 degrees as illustrated in Figure 1. Transverse motion is zero by symmetry at 0 and 180 degrees, but is strong at 45, 90, and 135 degrees. Waveforms are low-pass filtered at 200 Hz.

Sterling Axisymmetric Calculations

The 0.38 kt nuclear Sterling experiment was detonated at the center of the cavity excavated by the 5.3 kt Salmon test. The post-Salmon cavity was found to be approximately spherical with a 17-m radius, except that a pool of molten salt recrystalized in the bottom of the cavity with the pool floor approximately 10 m from the center (Langston, 1983). In this configuration, the explosive pressure waves reached the floor pool and spherical wall at different times and strength, resulting in asymmetric effects including SV wave generation. Langston (1983) constructed kinematic source models to simulate the observations, and his results suggested that the SV waves were radiated primarily by induced normal faulting occurring beneath the cavity. In this study, we simulate the Sterling explosion using the actual cavity geometry and salt properties obtained from the Salmon explosion modeling.

Methodology

We model the Sterling event using the two-dimensional axisymmetric Lagrangian finite difference code CRAM, coupled with the Eulerian code STELLAR. The grid setup is similar to that for the Salmon event calculation

(Stevens et al., 2006). To successfully simulate waves due to the cavity explosion, the initial grid must be in equilibrium so that the motions due to the empty cavity under overburden pressure are close to zero. The equilibrium solution is obtained by running CRAM in an overdamped mode with an initial approximate solution until motions become negligible throughout the CRAM computational grid. The early time interactions between the air shock due to an explosion and the surrounding salt interaction are simulated with STELLAR and then the results at 2.627 ms are overlaid onto the CRAM grid for calculating wave propagation at later times.

Comparisons between observations and simulations

Figure 3 shows the STELLAR results at 2.6 msec. The velocity, pressure and plastic work distribution are consistent with the non-spherical cavity geometry. The highest plastic work is found below the salt floor and indicates salt hardening. Figure 4 shows the horizontal-radial and vertical velocity data along with the numerical calculations. The observed P wave amplitudes and pulse widths are predicted quite well using the Rimer/Cherry salt model (Rimer and Cherry, 1982) at all 8 near cavity stations although our calculations show less complex P wave coda prior to SV arrivals than observed. SV are well predicted at the shot level stations (middle 3 figures) and below (bottom 2 figures). Most striking is the comparison at the two deeper stations (bottom 2 figures) where the predicted polarity and amplitudes of the SV waves are in excellent agreement with the observations. The calculated SV coda is also less complex than observed. The calculated SV waves at the stations above the shot level are smaller than observed, which could be due to some additional asymmetry in the shock arrival time on the upper cavity wall not modeled in the calculations. The good agreement between data and simulations implies that, not only does the shape of the cavity explain the observations, but that the empirical salt model used in the calculation is adequate to describe the salt's properties even at lower stress.

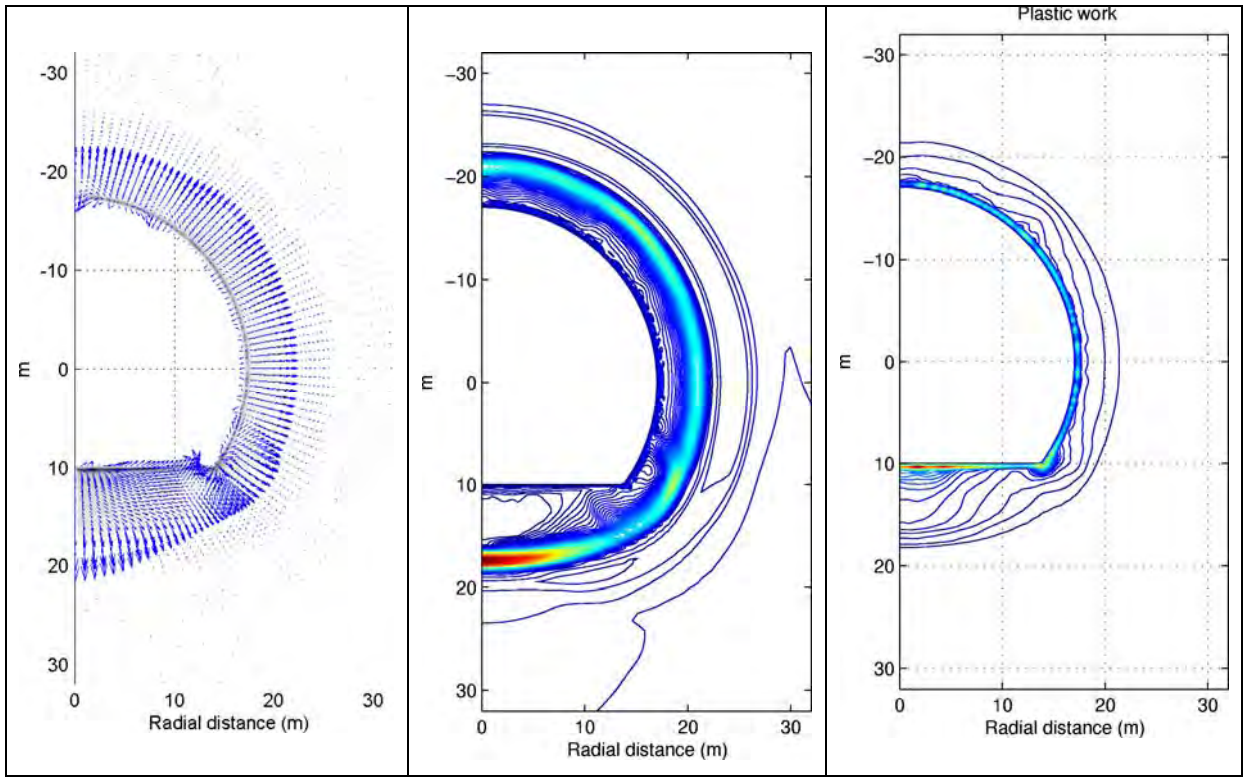

Figure 3. Interaction between the air shock and the salt calculated from STELLAR at a time of 2.627 msec. Left: particle velocity vectors. Middle: pressure contours. The maximum pressure is 2.8 kbar at 7m below the salt floor. Right: plastic work distribution. The maximum plastic work incurred is about $5x10^6$ ergs/cm^3at the pool floor, corresponding to the yield surface of 680 bars. The higher plastic work indicates the higher yield surface (material hardening).

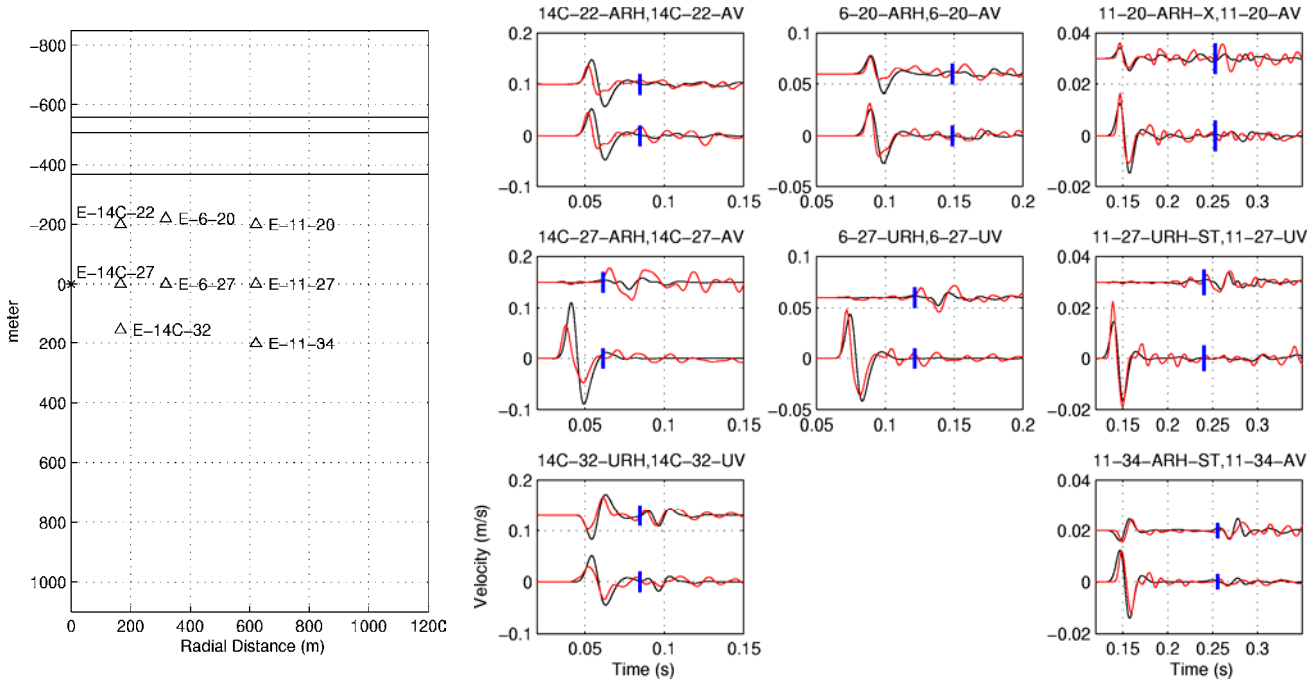

Figure 4. Left: stations for comparison of Sterling data and calculations. Right: Observed (red lines) and synthetic (black) waveforms at near-cavity locations in salt. The top curve in each plot represents the vertical component (positive up) and the bottom curve represents the horizontal radial component. The bold vertical bars denote the theoretical SV arrival time (vs=2540 m/s). The agreement on P wave arrivals and amplitudes is striking, and the agreement on S wave arrivals and amplitudes is better for the shot-level locations and below than for above shot-level stations.

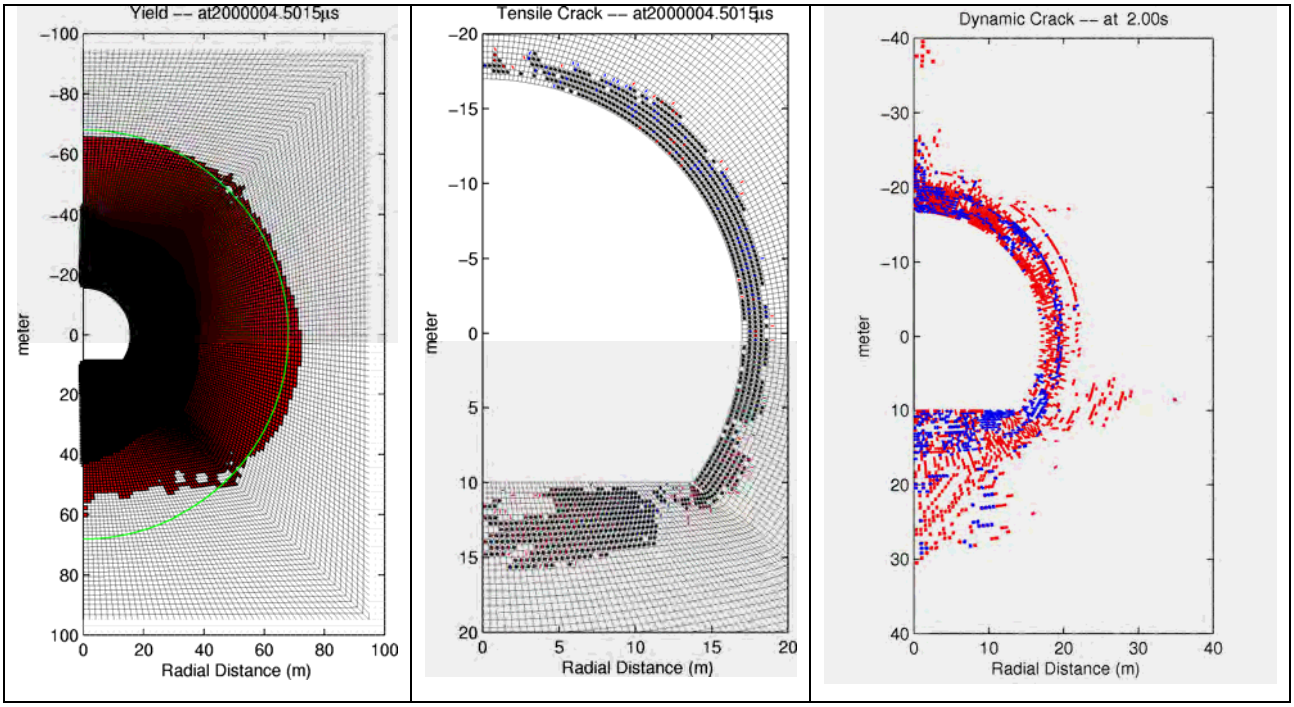

Figure 5. Left: nonlinear deformation distribution due to the Sterling explosion. The green circle is drawn to highlight, by contrast, the nonsphericity of the yield region. Middle: tensile crack distribution due to the Sterling explosion. Tensile cracks open only near the cavity wall. No spall is observed in the calculation. Right: locations where dynamic fractures could occur.

Nonlinear deformation and cracking

Figure 5 shows the nonlinear deformation and tensile cracks from the Sterling calculation. This is an overburied cavity explosion and so the high overburden pressure limits the yield region to about 65 m above and to the right of the cavity, and to less than 60 m below. The Rimer/Cherry salt model hardens after accumulating plastic work, and so the region below the cavity, which experienced the highest shock pressure, also hardened the most, limiting the extent of the nonlinear zone below the cavity. This causes additional asymmetry in the outgoing waves, adding to SV generation.

We also performed two sets of tests to see where hydrofractures could occur (see Nilson et al., 1991; Stevens et al., 2006). The right panel of Figure 5 shows the fracture locations if the entire surrounding salt is pressurized by the cavity. This calculation depicts the preferred pathway for the possible fractures driven open by the cavity pressure. It shows that the vertical fracture near the axis of symmetry below the cavity floor is more likely to propagate due to higher shock impact than at other locations but its extension is limited to 20 meters into the salt. To test Langston's conjecture on the kinematic fault geometry, we also modeled a single preexisting conical crack connecting to the outer bottom edge of the cavity. The results indicate that the crack at that location could not be driven open in tension by the cavity pressure because the overburden pressure is too high to allow it to open, as implied by the right panel of Figure 5.

Incidence dependence of initial S and S-coda waveforms indicates multiple S-wave sources

We observe variations in SV polarity with incidence, not just for the initial arrival, but also in the later S coda. Besides polarity, timing and similarity of waveforms throughout the coda can provide insight into the mechanism that generates it. If coda S-waves are generated at or very near the cavity, they will have the same delay as direct S at all stations along similar ray paths from the cavity. If the coda is generated by scattering at some distance from the cavity, or even by nonlinear deformation at 40 to 50 m from the cavity, the arrivals will move out with distance at a different rate than direct S and so the coda waveforms will not be similar along a given radius out from the cavity. We use recordings at three distances, at, above, and below the shot point to assess the dependence of different parts of the S-wave record on incidence and to assess whether the coda is similar.

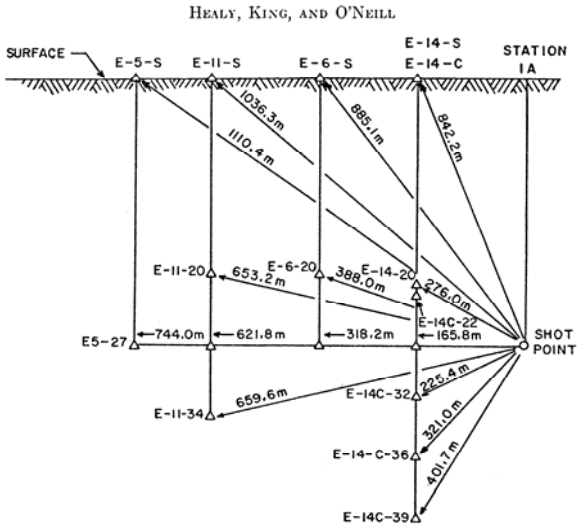

Figure 6. (from Healy, et al., 1971). Locations of near field strong motion instruments.

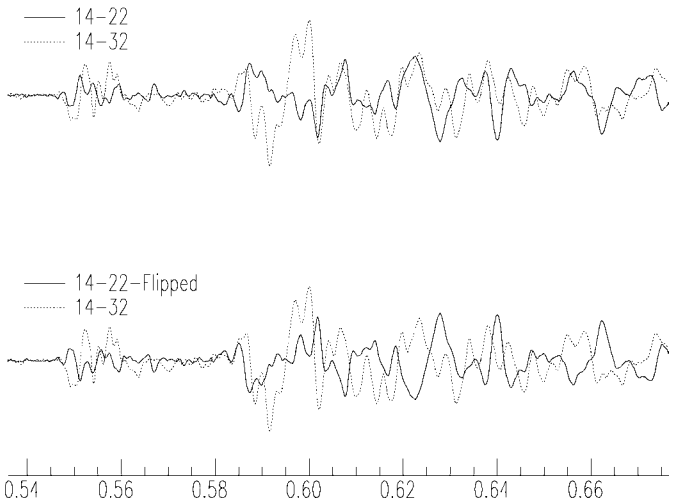

Figure 7. VT component records from 14–22 (solid, above shot level) and 14–32 (dotted, same distance below shot level) aligned on the predicted S time of 0.581 seconds. The top set of traces are normal polarity. The polarity of the above-shot-level record is flipped in the bottom pair of traces.

Figure 6 shows the locations of the instruments. To illustrate the nature of the Sterling S-waves, we first compare records at the same distance, 225 m from the source, so all similar phases should be aligned, but from stations 153 m above and below shot level respectively (Figure 7). The records are rotated in the SV plane normal to the radial, to minimize P and maximize SV. We refer to that as the vertical-tangential (VT) component, to distinguish it from the

component normal to the radial, but in the horizontal plane. The above-shot-level trace is plotted solid, and the below-shot-level trace is dotted. The traces are overlain, both with normal polarity (above) and with reversed polarity (below) for the above shot record. The large S-coda traces overlay very well beginning ~0.02 seconds after the predicted S-wave time of 0.58 seconds. The lower two traces, with the above shot record flipped, show that the initial S-waves (0.58 to 0.585 seconds) have opposite polarity above and below shot level. This suggests two mechanisms may be operating. The first has a radiation pattern with incidence. No radiation pattern in the coda can be discerned from these data.

Figure 8 shows multiple above, at, and below shot records aligned on the predicted S-wave time, given a velocity of 2.53 km/s, filtered from 30–200 Hz to eliminate differences due to attenuation at the more distant stations, and overlain. Records at the same or similar incidence have similar waveforms from the initial S throughout the coda, indicating that the bulk of the energy is coming directly from the source.

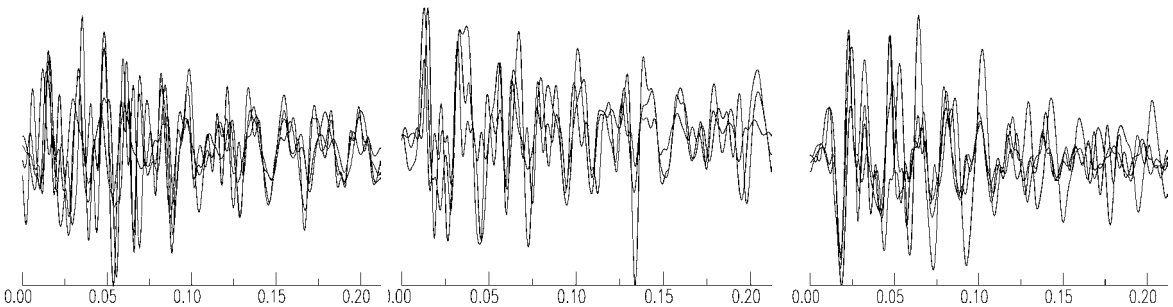

Figure 8. Overlain above (left), at (middle), and below (right) shot point VT component records aligned by the predicted S-wave time at 2.53 km/s, and filtered from 30 to 200 Hz. Above shot point records are from stations 11-20, 14-20, 14-22, and 6-20; at shot point records are from 166, 318, and 622 m distance; and below shot point records are from stations 14-32, 14-36, 14-39, and 11-34.

We next stack each of these sets of records. Figure 9 illustrates the differences between the stacks of waveforms recorded at different take-off angles. The stacks at and above shot level have the same first arrival polarity, opposite that of the below shot level records. The at and below shot level records, however, become similar after 50 ms, indicating a change in radiation pattern with time. Finally we note the strong periodicity of the coda, at approximately 60 Hz, which could suggest oscillations of the cavity itself or the volume of nonlinear deformation immediately around the cavity. There are some differences between observations in Figures 7 and 9, due to frequency content. Further analysis may allow us to distinguish frequency dependence of the source location and radiation with time.

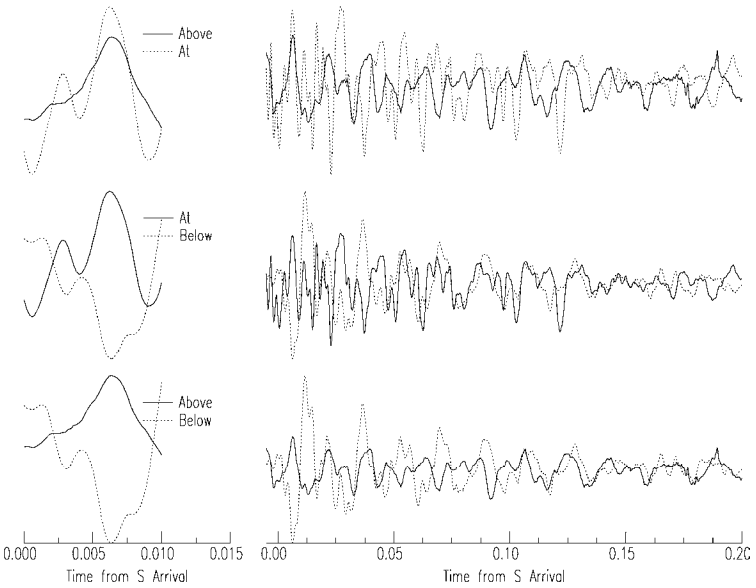

Figure 9. Overlain stacks of above and at (top), at and below (middle), and above and below (bottom) shot point records shown in Figure 8. The initial 0.01 seconds of S are shown to the left, and the waveforms from initial S through the coda are shown on the right.

To recap the observations and implications of Sterling S-waves, stacks of coda from at, above, and below shot level records show that the coda are similar at similar incidence. This implies that the S-wave coda source is located at or very near the cavity, and has a radiation pattern with incidence. The radiation pattern differs from that of the initial S-wave, suggesting a different mechanism from that of the initial S.

Explosions in Water-Filled Cavities

We are examining records from a unique series of explosion, a tamped 27 Kt explosion at 597 m depth in salt at Azgir, followed by four very small explosions (yields 0.35, 0.10, 0.01 and 0.08 kt) in the water-filled, 32.5 m radius, cavity of the original explosion. These are effectively decoupled, in that the small explosions do not cause significant nonlinear deformation of the cavity, but provide large signals as the pressure is much greater in water than it would be in an air-filled cavity. Local radial and vertical component records are available at common stations for multiple events, and 3-component records are generally available from stations at 20 km or more distance, and from several closer stations. All of the explosions generated shear waves. We present time and frequency domain observations that bear on their source, specifically, alignment of the S minus P-wave times, and the presence or absence of a bubble-pulse peak in S- and P-wave spectra.

Figure 10 shows the overlain Hilbert transformed radial and the vertical records at 7.8 km from the 0.01 Kt explosion (bottom), and corresponding explosion (top) and CLVD synthetics (middle), which help us to identify the shear waves. Records are filtered from 5 to 15 Hz, as the data are noisy below 5 Hz. Times are relative to initial P, as absolute times are unknown. Synthetic seismograms use the structure described in Murphy et al. (2001), overlain on a more general Azgir structure (Table 1). The initial P is somewhat complex in both data and synthetics. The secondary arrival 0.4 seconds after P could admit a number of explanations, including P-to-S conversion from the sediment-rock interface beneath the station. Finding a unique explanation is unlikely, but the arrival is too early to be anything but scattered P and so can be used to represent the P source spectrum. The latter part of the next arrival, at ~1.4 seconds after P in the data, is retrograde elliptical, and there are similar arrivals in both sets of synthetics. We typically observe near source explosion shear waves to have retrograde elliptical particle motion consistent with their identification as higher mode Rg. The large S arrival at 3.5 seconds after P in the CLVD synthetics is consistent with an S group velocity of 1.5 km/s, with a P-wave velocity of 4 km/s, so the large S arrival appears to have been trapped in the low velocity surface layer. The amplitude in the data increases before that synthetic arrival, although it only becomes retrograde elliptical again at the approximate time of the synthetic arrival. That's consistent with the earlier part of that large arrival being multiple higher Rg modes (which make up S), with a single isolated higher mode at the end. Identification as S is also consistent with large S arrivals at 1.5 km/s in other records. To compare spectra of these records, we use initial P to 1.1 seconds after to isolate just P, and from 1.9 to 3.1 seconds after P to isolate S.

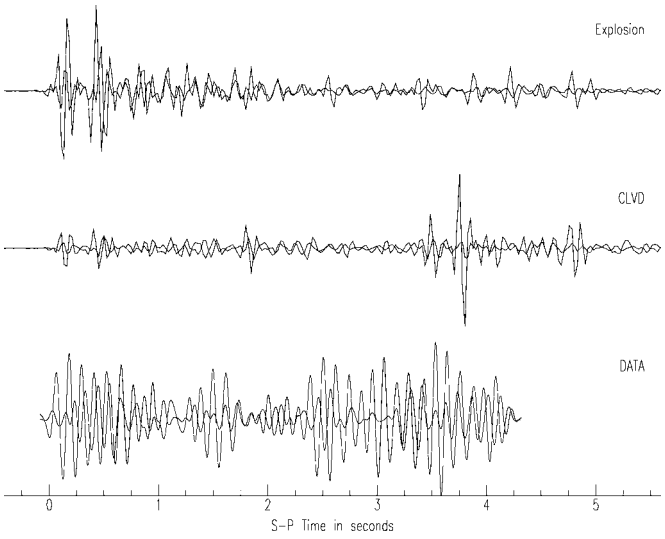

Figure 10. Overlain Hilbert transformed radial and vertical component spherical explosion (top) and CLVD (middle) synthetics at 7.8 km, for 597 m depth, and corresponding records from AZ24, the 0.01 Kt explosion (bottom).

Table 1. Azgir velocity model. Second layer represents anhydrite cap on massive salt dome.

Thickness (m)	Vp	Vs	Density	Qp	Qs
0.240	1.50	0.60	2.00	40	25
0.056	2.20	0.95	2.00	60	35
5.0	4.25	2.40	2.2	200	150
2.0	5.2	2.95	2.30	600	500
2.0	5.889	3.306	2.549	300	0
19.97	5.935	3.332	2.566	333	0
10.00	6.284	3.527	2.693	352	0
12.00	8.357	4.691	3.449	394	0
115.00	7.980	4.479	3.312	403	0

Bubble pulse signature in P- but not S-wave spectra

Murphy et al. (2001) showed that peaks in the decoupled explosions' spectra could be explained by bubble pulse resonances near 8 to 10 Hz, where the extent of the pulse is damped differently depending on the amplitude of the reflected shock wave. A bubble pulse resonance peak is clear in each of the decoupled explosions' P spectra (red) at 7.8 km, but is absent from the tamped explosion's P-spectra (Figure 11). If the shear waves are dominated by pS (as predicted for a low velocity structure), they should be similar to the P-wave spectra and should have the same resonance peak. The peak is absent, however, from the S spectra, indicating that the S is not simply scattered from P.

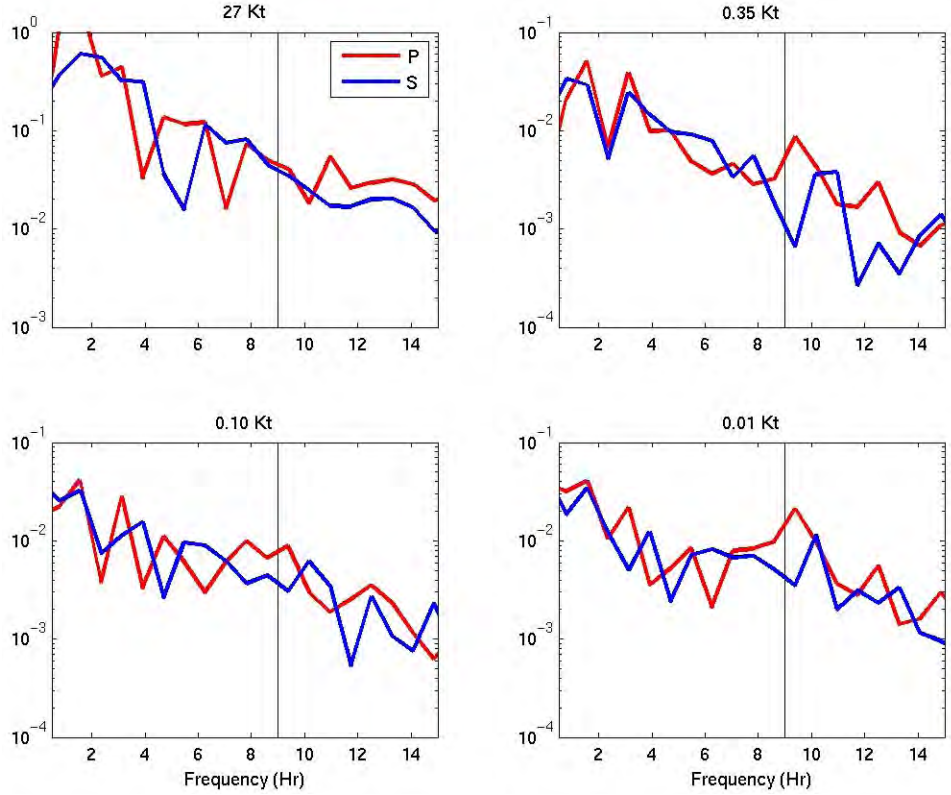

Figure 11: P and S spectra of the tamped and the three decoupled explosions recorded at 7.8 km

If the S-wave comes directly from the source, then the data S-P times plotted vs distance should be similar. Event AZ25, the 0.08 Kt explosion, was recorded at 6 stations, at 0.82 to 4.6 km from the source. Figure 12 shows the data and CLVD synthetic record sections and the P and S picks. The data S-P times are very similar to those of the CLVD synthetics (the explosion synthetics do not reproduce the S-phase). A fit to just the measured S-P times from data intersects zero distance at 0.36 seconds. The same fit for synthetics intersects at 0.30 seconds. Consistent S-P times for data and synthetics suggests that the shear waves must either be generated at the source or scattered from very near the source.

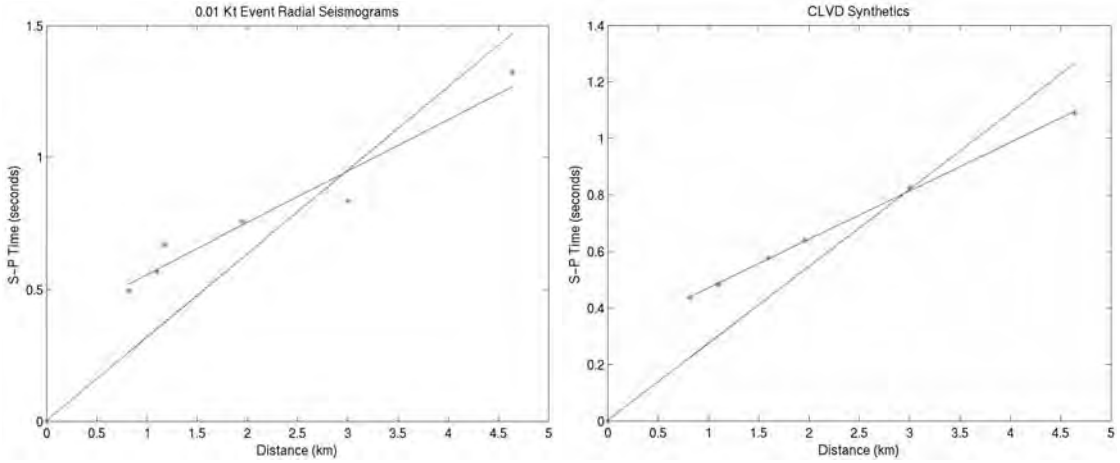

Figure 12. S-P arrival times from event AZ25 (left) and CLVD synthetics (right). Lines are fits to S-P times vs. distance.

CONCLUSIONS AND RECOMMENDATIONS

We find that source asymmetry including, for example, an explosion offset from the source of a spherical cavity can lead to significant asymmetry in seismic waves and generation of S waves. We performed a detailed numerical model of the Sterling decoupled explosion and find that the near field waveforms including near field shear waves can be explained by the cavity shape and the asymmetry caused by varying impact of the explosion shock across different parts of the cavity. However, the S coda continues much longer and at higher amplitude than predicted by the simulations. Analysis of observations from explosions in water-filled cavities shows that S waves are always present, and that they are generated at or very close to the source.

REFERENCES

Healy, J., C. King, and M. O'Neill (1971). Source parameters of the Salmon and Sterling nuclear explosions from seismic measurements, *J. Geophys. Res*. 76: 3344–3355

Langston, C.A. (1983). Kinematic analysis of strong motion P and SV waves from the Sterling event. *J. Geophys. Res.* 88: 3486–3497

Murphy, J. R., D. D. Sultanov, N. Rimer, and B. W. Barker (2001). Seismic source characteristics of nuclear explosions in water-filled cavities, *Pure Appl. Geophys.* 158: 2,105–2,121.

Nilson, R., N. Rimer, and E. Halda (1991). Dynamic modeling of explosively driven hydrofractures, *J. Geophys. Res.*, 96: B11, 18,081–18,100.

Rimer, N. and J. T. Cherry (1982). Ground motion predictions for the Grand Saline experiments, S-CUBED VSC-TR-82-25.

Stevens, J. L. (1980). Seismic radiation from the sudden creation of a spherical cavity in an arbitrarily prestressed elastic medium, *Geophys. J. R. Astr. Soc.* 61: 303–328.

Stevens, Jeffry L., Heming Xu, and G. Eli Baker (2006), Analysis of shear wave generation by decoupled and partially coupled explosions, in *Proceedings of the 28th Annual Seismic Research Review: Ground-Based Nuclear Explosion Monitoring Technologies*, Vol. 1, pp. 693–703.

Zhou, L. and D. G. Harkrider (1992). Wave fields from an off-center explosion in an embedded solid sphere, *Bull. Seism. Soc. Am.* 82: 1,927–1,955.

SEISMIC AND INFRASOUND ENERGY GENERATION AND PROPAGATION AT LOCAL AND REGIONAL DISTANCES: PHASE 1 – DIVINE STRAKE EXPERIMENT

Brian Stump[1], Relu Burlacu[3], Chris Hayward[1], Jessie Bonner[2], Kristine Pankow[3], Aileen Fisher[1], and Sue Nava[4]

Southern Methodist University[1]
Weston Geophysical Corporation[2]
University of Utah Seismograph Stations [3]
ENSCO, Inc.[4]

Sponsored by Air Force Research Laboratory

Contract No. FA8718-06-C-0028

ABSTRACT

There are unanswered critical questions on the phenomenology surrounding the generation and local-to-regional distance propagation of seismic and low frequency acoustic energy from shallow sources (industrial and mining explosions, chemical test explosions, underground mine related stress release, and earthquakes) that impact the use of observations for source identification, location and characterization in areas with little ground truth. While there have been extensive seismic and acoustic observations of shallow sources (McKenna, 2005; Mutschlecner and Whitaker, 2005; ReVelle, 2004; Patton et al*.,* 2003; Yang et al*.,* 1999, and Dighe et al*.,* 1998) these have been limited in most cases to a moderate number of short-term stations for a single group of events or have focused on signals from one location into one possibly augmented array. Therefore, there is a need to extend the previous observational and theoretical studies using dense networks of simultaneous seismic and infrasound observations of a wide variety of sources at local and regional distances. The acquisition of a dense profile of observations along one or more profiles that characterize the wavefield transition from local to regional distances is a critical component needed to understand seismic and infrasound propagation. Ground truth provides source constraints that are necessary for unique interpretations.

The Defense Threat Reduction Agency (DTRA) planned detonation of approximately 700 tons of explosives in Area-16 of the Nevada Test Site (NTS) was to provide the opportunity to gather such a dataset. On February 22, 2007, DTRA announced the cancellation of the Divine Strake explosion. During the preparation for the Divine Strake experiment and as a result of a single infrasound array and seismic network across Utah, a number of large and consistent infrasound sources have been identified and characterized. These preliminary efforts have resulted in the identification of regular (21 recorded to date) and large (40,000–80,000 lb) surface explosions at the Utah Test and Training Range (UTTR) of the Hill AFB. These sources are producing excellent near-regional seismic and infrasound signals that are currently being stored at the Incorporated Research Institutions for Seismology (IRIS) Data Management Centre (DMC). Our group has cooperated with the group at Hill AFB and begun modeling these events and has used atmospheric profiles that are regularly taken by the Air Force in this modeling exercise (documented in our annual report). Additional sources of infrasound such as mining explosions are also documented in the report, and the regional earthquake database is being compiled.

Based upon this unexpected source of large, surface explosions and close cooperation between the Air Force and our group, the initial goals of our project can be reached by shifting our focus to these new sources now that Divine Strake has been canceled. The rocket motor explosions, unlike the single Divine Strake explosion, occur about every week providing an opportunity to develop seismic and infrasound recordings under a wide range of atmospheric conditions. Cooperation with the Air Force will provide the necessary atmospheric data needed for modeling. Our consortium is redesigning the regional experimental deployment to take advantage of the regular rocket motor explosions at UTTR and plans to implement the experiment in the summer of 2007.

OBJECTIVES

The initial objective of this project was to record regional seismic and infrasound signals from the planned Divine Strake explosion. On February 22, 2007, DTRA announced the cancellation of the Divine Strake explosion. During the preparation for the Divine Strake experiment and as a result of the infrasound array and seismic network across Utah (Figure 1), a number of large and consistent infrasound sources have been identified and characterized. These sources included large (40,000–80,000 lbs) surface explosions at the UTTR of the Hill AFB. These sources are producing excellent regional seismic and infrasound signals that are currently being stored at the IRIS DMC. Our group has cooperated with the group at Hill AFB and has begun modeling these events and has used atmospheric profiles that are regularly taken by the Air Force in this modeling exercise. Additional sources of infrasound such as mining explosions are also documented in the report and the regional earthquake database is being compiled.

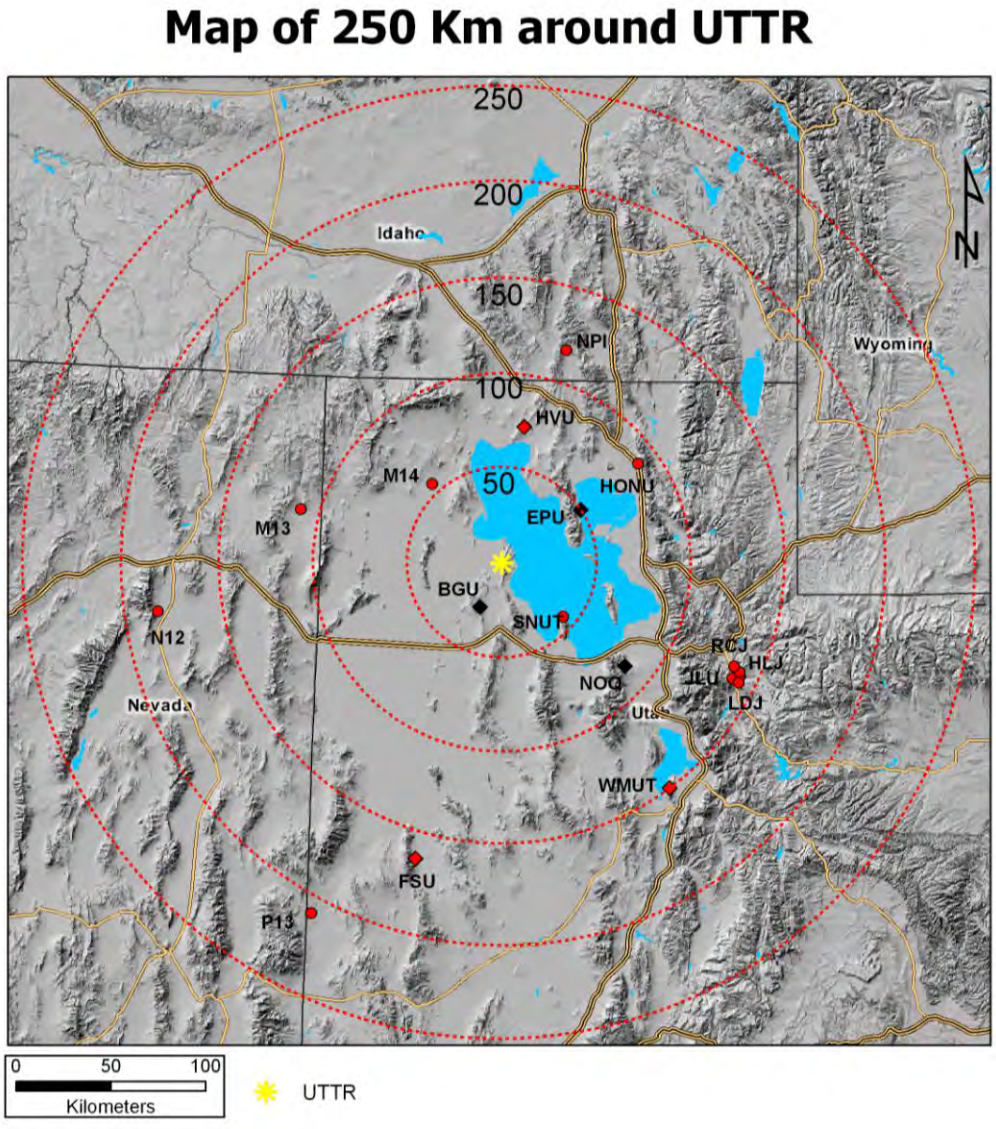

Figure 1: Existing and planned seismo-acoustic stations in Utah. The yellow star is UTTR, the site of the explosion. Solid black diamonds are permanent infrasound arrays, red diamonds are temporary infrasound arrays, and red circles are locations of single infrasound gauges.

Based upon this unexpected source of large surface explosions and close cooperation between the AF and our group, the initial goals of our project are being addressed by focusing our experimental work on these new sources. Preliminary data collected and analyzed in this report illustrate that both seismic and infrasound signals are observed at the distances of interest to our proposal as it was funded. The rocket motor explosions, unlike the single Divine Strake explosion, occur about every week providing an opportunity to develop seismic and infrasound recordings with a range of atmospheric conditions. Cooperation with the AF together with our own planned atmospheric profiling will provide the necessary atmospheric data needed for modeling.

As a result of preparations for Divine Strake two, four-element infrasound arrays are deployed at seismic sites BGU and NOQ both part of the University of Utah Seismograph Stations (UUSS) regional network (Figure 1). One additional array is planned at a third site, EPU. These three arrays are all telemetered in real-time to the University of Utah. NOQ has operated for over one year and regularly records seismic and infrasound signals from UTTR rocket motor detonations as well as numerous explosions from nearby mining operations.

UTTR explosions are planned weekly during the summer of 2007, and so a four-week equipment deployment to supplement the two current and one planned infrasound arrays has been planned. The planned four-week campaign will provide the opportunity to record 3 to 4 UTTR explosions as well as numerous other events that occur during the time period. The experiment has the following components as illustrated in Figure 1:

- 3 close-in acoustic plus seismic stations to document the source in the 100–1000 m range.
- Supplementation of the existing three-infrasound arrays to bring the total number to six. The three additional arrays will be deployed at distances beyond 100 km and may be expanded to five elements each.
- Addition of a single infrasound sensor at 4 Earthscope US Array and 7 UUSS sites in order to quantify infrasound to seismic coupling as well as to expand the number of azimuths and ranges recorded.

In preparation for the planned experiment a visit was made to UTTR on 4 June 2007 to observe the detonation of a rocket motor. The explosion was observed from a distance of about 1 mile as illustrated in Figure 2.

Figure 2: Images documenting the rocket motor detonation (explosive weight 39,000 lb) on June 4, 2007, at UTTR.

RESEARCH ACCOMPLISHED

Research in the last year has focused on three areas. In order to deploy a substantial number of infrasound gauges to document the regional propagation path effects, it was necessary to acquire and characterize a new and cost effective acoustic gauge. Second, while waiting for the Divine Strake experiment to occur two (soon to be three) infrasound arrays were deployed in Utah. Preliminary analysis and modeling of data recorded at one of these arrays identified a number of interesting infrasound sources. Finally, as a result of the cancellation of Divine Strake and the identification of the large surface explosions at UTTR, an experiment was designed to document UTTR detonations in the summer of 2007. A visit to UTTR for the June 4, 2007, rocket motor explosion (Figure 2) provided preliminary data used to complete the planning for the experiment.

New Infrasound Gauges

Twenty-five, new cost-effective infrasound gauges were ordered and received from Inter Mountain Laboratory (IML) (Figure 3). The lower cost of these gauges provided the opportunity to purchase enough gauges (25) to instrument a number of infrasound sites. These gauges, as illustrated in Figure 3, are composed of 20 individual microphones whose output is summed to improve the instrument signal to noise. The instruments were designed for the purpose of avalanche monitoring. However, no data sheets or instrument response tests were published for the gauges. As our application is different, we needed to quantify the gauge response.

The electronics pictured in Figure 3 include a variety of filtering and signal conditioning components. Each gauge has eight ports for connection to porous hoses for noise reduction purposes. As a result of the filtering and signal conditioning capabilities built into each gauge, two different outputs, with different frequency responses, are available from each gauge.

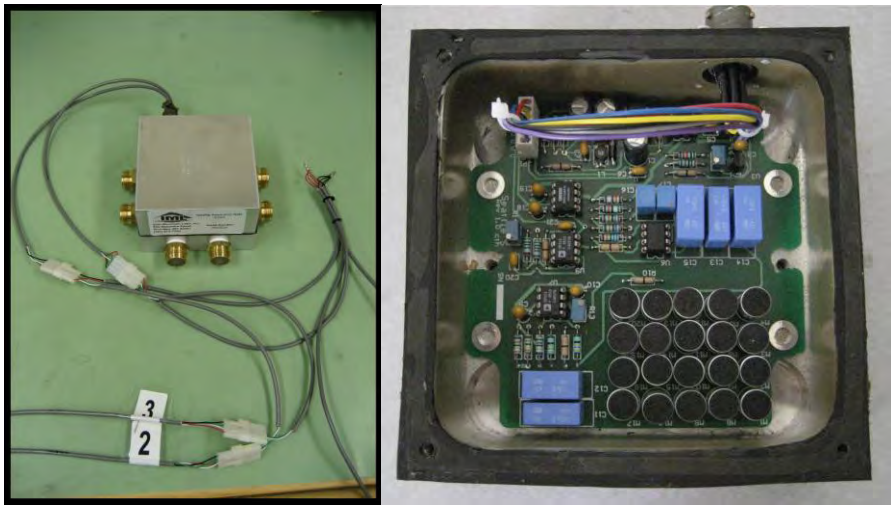

Figure 3: The IML infrasound gauge is pictured above. The exterior view is illustrated to the left with six of the eight ports for hose connections. The interior view of the gauge is illustrated to the right with the 20 microphone cartridges in the lower right and the accompanying signal conditioning and filtering electronics.

Laboratory tests were conducted on all 25 IML gauges. For calibration purposes, each IML gauge was run along side a reference gauge, a Chaparral 2. Three-hour data segments were recorded and used to determine the frequency response of the filtered and unfiltered output of the IML gauge as well as the response of the Chaparral 2 for comparison (Figure 4, left). The data were also used to compute the coherence of the IML filtered and unfiltered outputs with the reference Chaparral 2 output (Figure 4, right). The Chaparral 2 has a broader band response (Figure 4) but there is great similarity between the IML and the Chaparral 2 in the important band of 1–10 Hz. The high coherence between the Chaparral 2 and the unfiltered IML to nearly

50 s and to below 10 s with the filtered IML output suggests that, despite the difference in responses, the IML gauge can be utilized to retrieve signals below 1 Hz.

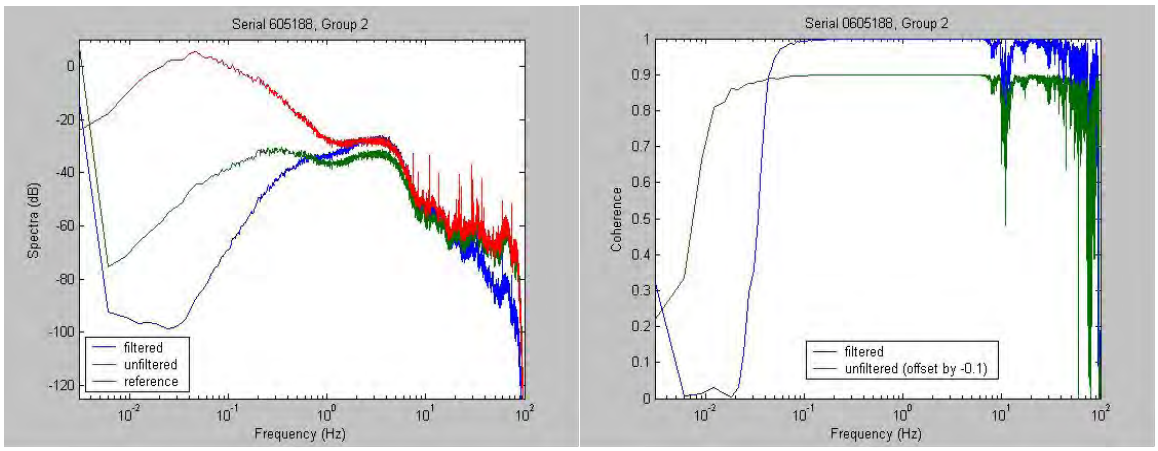

Figure 4: Response of the Chaparral 2 (red), unfiltered IML (green), and filtered IML (blue) from the calibration tests (left). Coherence between the Chaparral 2 and the filtered IML output (blue) and the Chaparral 2 and the unfiltered IML output (green, offset by 0.1 units for display) is displayed to the right.

Similar tests were conducted on all 25 gauges. Results from these tests indicate that the response and coherence estimates for the one gauge in Figure 4 are similar for all 25 gauges. A theoretical transfer function for the IML gauge was developed as part of the analysis. The IML response was removed from the data taken during the laboratory tests and the resulting output convolved with the known Chaparral response. As illustrated in Figure 5, the observed Chaparral data (high pass filtered at 10 s) are reproduced by this deconvolution followed by convolution procedure.

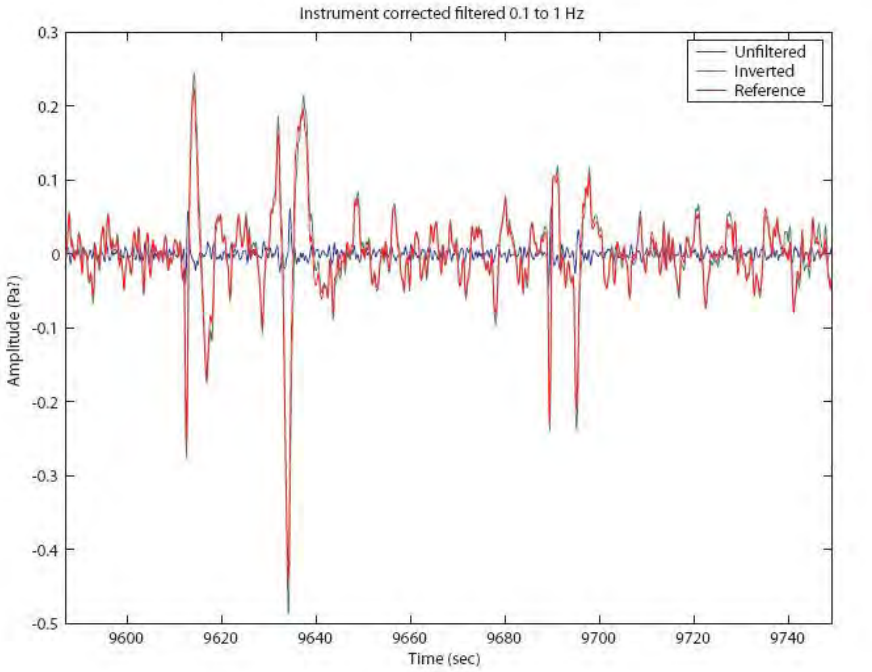

Figure 5: Comparison of IML output (unfiltered), Chaparral output (reference, high pass filtered at 10 s) and IML output corrected for IML response and convolved with known Chaparral response (inverted, high pass filtered at 10 s). The instrument corrected IML data closely match the Chaparral output for the same time window.

Preliminary Seismo-Acoustic Observations and Modeling

The infrasound array deployed at NOQ has regularly recorded signals from two locations since its installation in May 2006. The first source is mining explosions from the Bingham Canyon Mine operated by Kennecott Utah Copper. The mine is located to the south of the station (Figure 6) and blasts almost daily.

Figure 6: Location of two sources of infrasound signal observed at the NOQ. Bingham Canyon Mine is to the south of the station and the Utah Test and Training Range is to the northwest. Image generated by Google Earth.

Figure 7 shows a seismic and infrasound signals recorded from a Bingham blast on May 5, 2006, at NOQ. This event had an M_L of 1.8 and was observed at 15 stations of the UUSS regional network. Clear infrasound signals accompany this event.

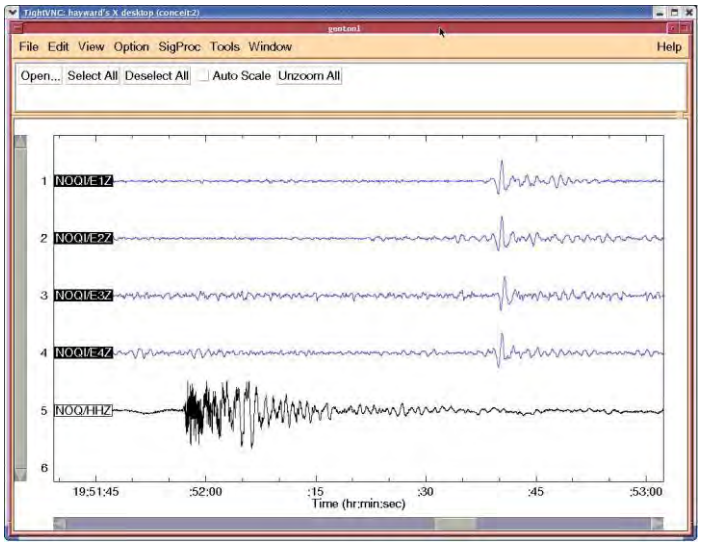

Figure 7: This signal is from a mining blast detonated at Bingham open-pit copper mine on May 5, 2006. The event had an M_L=1.8 and was observed by 15 stations of the UUSS regional network.

The second set of sources that have been recorded on a regular basis at NOQ are a result of the explosive disposal of Trident rocket motors to the northwest of the station (Figure 6). These detonations are

conducted at the Thermal Treatment Unit (TTU) of the UTTR of the Hill AFB. Two events recorded to date at NOQ from these detonations are illustrated in Figure 8. These figures illustrate the signal coherence, phase velocity and azimuth estimates for events on May 9 and August 21 using the InfraTool (Hart and Young, 2005). Coherence across the array is good for both events and produced stable azimuth estimates. One interesting thing to note in this example is the marked difference in both amplitude and signal duration for these two signals. The signal from the May 9 detonation is nearly 40 times larger in amplitude than that from August 21 and much shorter in duration.

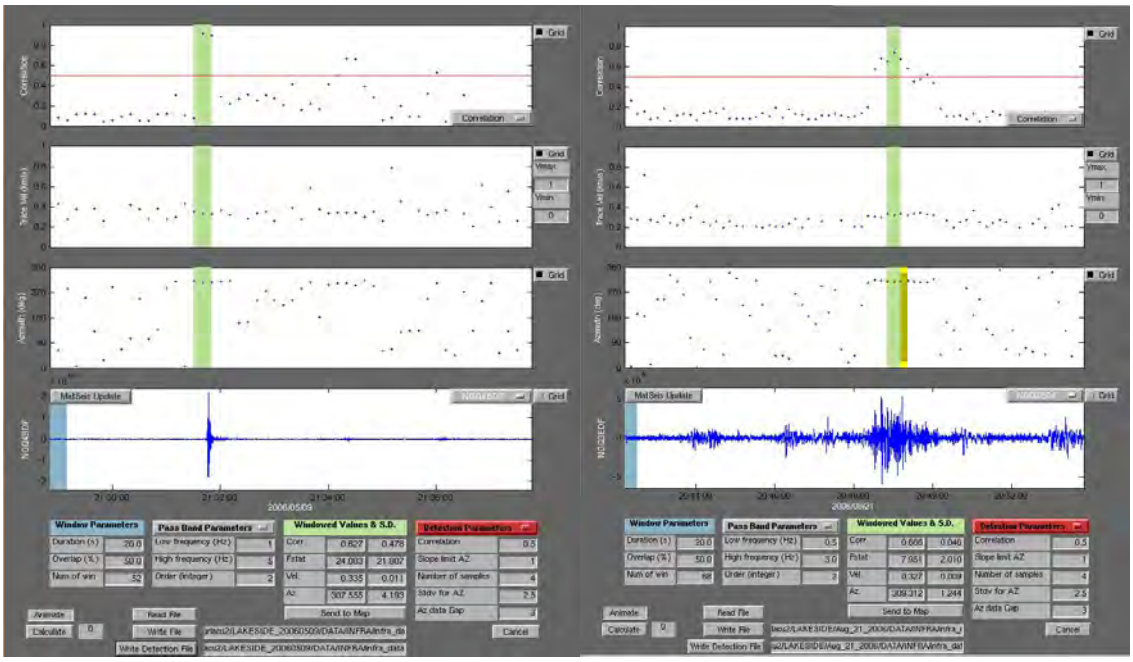

Figure 8: Infrasound signals recorded at NOQ from Trident rocket motor disposal explosions conducted at the UTTR. Processing results using InfraTool for a detonation on May 9 (left) and August 21 (right) are displayed.

It is interesting to note that infrasound signals from these rocket motor detonations are observed on some of the seismic stations of the UUSS regional network (Figure 9). These additional data, possibly calibrated for seismic to acoustic coupling, may prove useful in our infrasound studies.

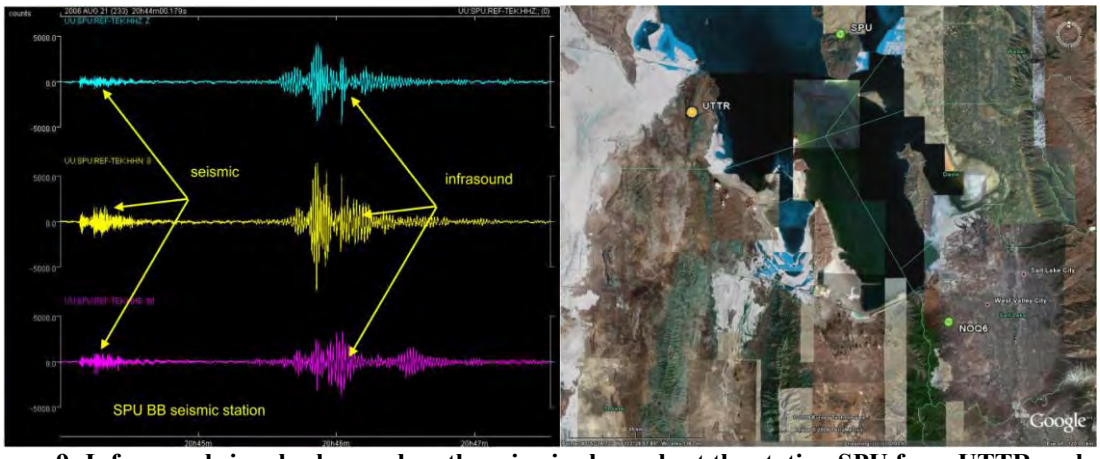

Figure 9: Infrasound signals observed on the seismic channels at the station SPU from UTTR rocket motor detonation (left) on August 21. The location of SPU relative to the source at UTTR and the infrasound array at NOQ is illustrated to the right. Overhead image generated by Google Earth.

The relatively large number of infrasound signals recorded at NOQ from repeated sources such as the rocket motor detonations at UTTR motivated a preliminary look at some simple modeling of the signals. As noted in Figure 8, large variations in amplitudes and wave characteristics have been observed. The explosions from UTTR are in the zone of silence and so some understanding of the path effects was of interest as well. The modeling package InfraMap written and maintained by BBN (Gibson and Norris, 2006) was utilized in this preliminary work. Figure 10 illustrates some early results comparing ray tracing using the MSIS/HWM model to a local model based on actual tropospheric soundings taken prior to the rocket motor detonation. The MSIS/HWM model predicts no ray arrivals inside of 300 km while the data based model predicts rays that turn in the troposphere and arrive at distances comparable to where we have infrasonic observations of the explosions.

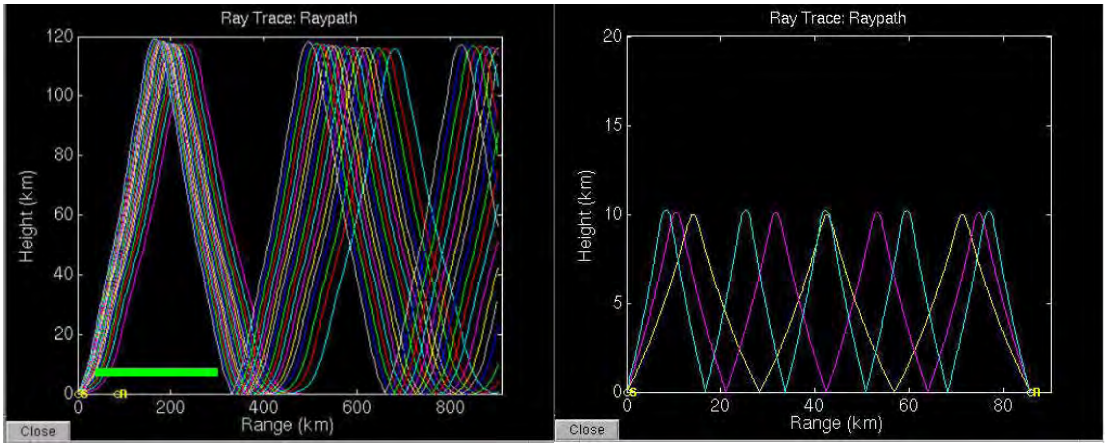

Figure 10: Ray tracing results using the MSIS/HWM (left) and local model based on low altitude sounding data (right) at the time of one of the UTTR rocket motor explosions.

June 4, 2007, UTTR Rocket Motor Detonation

As part of the planning exercise for the summer of 2007 experiment a visit was made to UTTR and one of the rocket motor detonations was observed. The visit included discussions with UTTR personnel concerning atmospheric monitoring during the detonations. At the time of the detonation two of the infrasound arrays, BGU (Figure 11) and NOQ (Figure 12), were operating. Data from these two arrays as well as seismic observations across the UUSS seismic network (Figure 13) provided the basis for the experiment plan as illustrated in Figure 1. The June 4, 2007, detonation was recorded both by the UUSS seismic network and by the 2 infrasound arrays (NOQ and BGU).

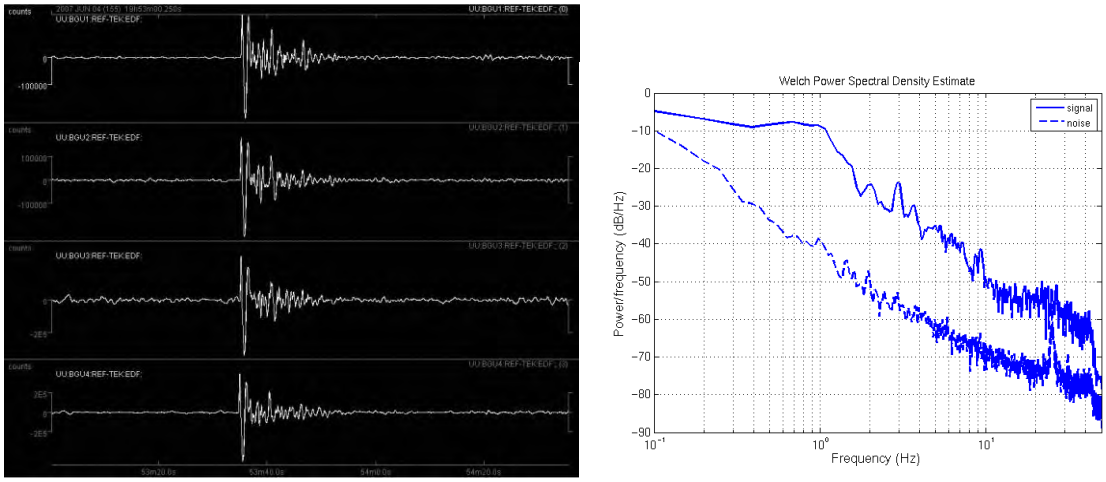

Figure 11. Observation of the June 4, 2007, UTTR explosion at the array BGU (Figure 1), Noise and signal spectra for the BGU1 element of the BGU infra array are displayed to the right.

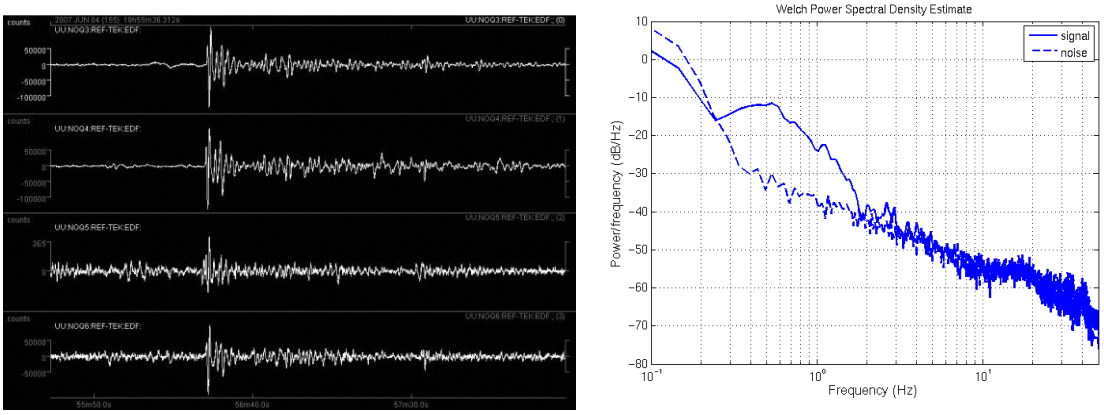

Figure 12. Observation of the June 4, 2007, UTTR explosion at the array NOQ (Figure 1). Noise and signal spectra for the NOQ3 element of the NOQ infra array are displayed to the right.

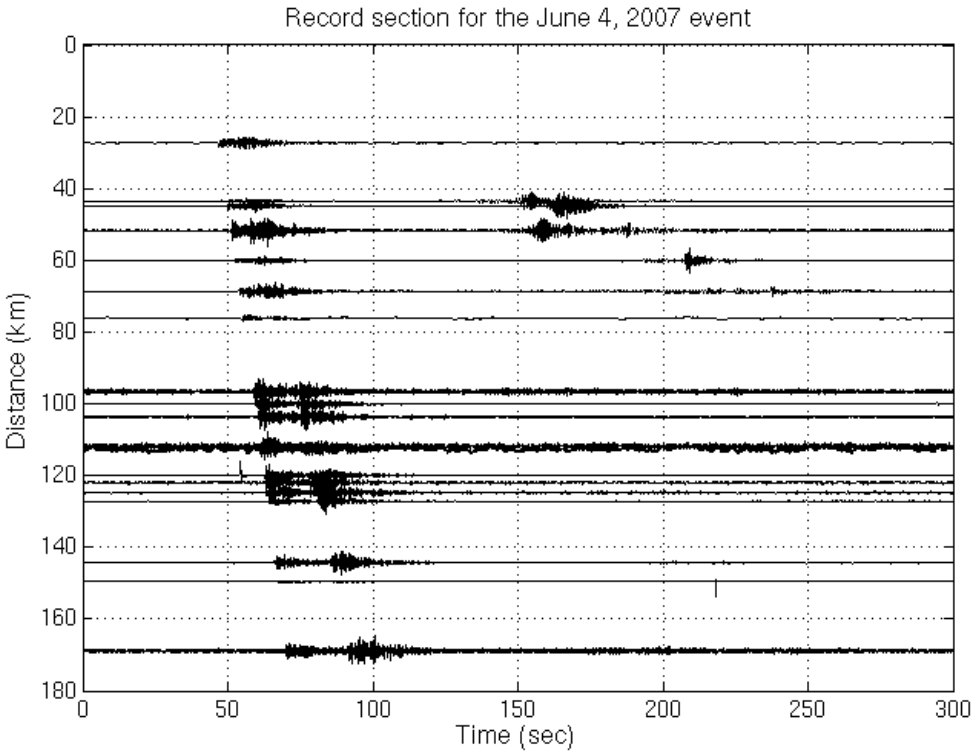

Figure 13. Record section of seismic stations from the UUSS regional network illustrating the seismo-acoustic signals from the June 4, 2007, UTTR detonation.

CONCLUSIONS AND RECOMMENDATIONS

A new type of infrasound gauge manufactured by Inter Mountain Laboratory has been acquired for the experiment. These gauges designed for avalanche monitoring are modest in cost and so provide the opportunity to use a larger number of sensors when compared to the cost of conventional gauges. Twenty-five of these gauges were acquired and tested and compared to a conventional infrasound gauge in our laboratory. This comparison indicates that these gauges will be useful in recording signals in the

1–10 Hz band and can be pushed to lower frequencies based on good coherence with signals from conventional gauges to periods as long as 50 seconds.

Two infrasound arrays have been installed at UUSS seismic sites in Utah. The infrasound array at NOQ, installed in May 2006, is regularly recording infrasound signals including repeated sources from mining explosions at Bingham Canyon Mine and Trident rocket motor detonation at UTTR. The variability of these signals and the ability to make infrasound observations on some of the seismic stations as part of the UUSS regional network has motivated a preliminary modeling study. This study suggests that short-term variations in the troposphere may greatly affect not only the amplitude but also the wave characteristics in the so-called zone of silence.

An experimental plan has been developed for deploying seismic and infrasound gauges to record UTTR near-surface explosions over a month time period. A total of six infrasound arrays, three close-in infrasound and seismic stations and 11 single infrasound gauges co-located with existing seismometers will be deployed. An approximate one-month deployment spanning August 2007 is planned during which several UTTR detonations are anticipated.

ACKNOWLEDGEMENTS

Instruments for the planned portable deployment described in Figure 1 are being provided by PASSCAL. Contract FA8718-05-C-0020, Air Force Research Laboratory, has supported the array deployments at NOQ and BGU separately.

REFERENCES

Dighe, K., R. Whitaker, W. Armstrong. (1998). Modeling Study of Infrasonic Detection of a 1-kt Atmospheric Blast. *20th Annual Seismic Research Symposium on Monitoring a Comprehensive Test Ban Treaty (CTBT),* Santa Fe, New Mexico

Gibson, R. and D. Norris (2006). *User's Guide for InfraMAP, Version 5.1*. DTRA01-01-C-0084.

Hart, D. and C. Young (2005). MatSeis, User's manual, version 1.10, *Sandia National Laboratories*.

McKenna, S. M. H. (2005). Infrasound Wave Propagation at Near-Regional and Tele-Infrasonic Distances, *Ph.D. Thesis,* Southern Methodist University.

Mutschlecner, J. P. and R.W. Whitaker (2005). Infrasound from earthquakes, *J. Geophy. Res.* 110: D01108.

Patton, H. J., J. L. Bonner, and I. Gupta (2003). Modeling a CLVD + monopole explosion source for the Shagan depth of burial explosions, poster presentation at the *25th Annual Seismic Research Review—Nuclear Explosion Monitoring: Building the Knowledge Base,* LA-UR-03-6029.

ReVelle, D. O. (2004). Discrimination between earthquakes and mining blasts using infrasound, *Knowledge Base Report*, Los Alamos National Laboratory, 34pp.

Yang, X., B. W. Stump, and D. C. Pearson (1999). Moment tensor inversion of single-hole mining cast blasts, *Geophys. J. Int*. 139: 679–690.

EMPIRICAL OBSERVATIONS OF EARTHQUAKE-EXPLOSION DISCRIMINATION USING P/S RATIOS AND IMPLICATIONS FOR THE SOURCES OF EXPLOSION S-WAVES

William R. Walter, Eric Matzel, Michael E. Pasyanos, David B. Harris, Rengin Gok, and Sean R. Ford

Lawrence Livermore National Laboratory

Sponsored by National Nuclear Security Administration
Office of Nonproliferation Research and Development
Office of Defense Nuclear Nonproliferation

Contract No. W-7405-ENG-48

ABSTRACT

We continue exploring methodologies to improve earthquake-explosion discrimination using regional amplitude ratios such as *P/S* (ratio of P- and/or S-wave energy). The earliest simple source models predicted *P/S* wave amplitudes for explosions should be much larger than for earthquakes across the body wave spectrum. However empirical observations show the separation of explosions from earthquakes using regional *P/S* amplitudes is strongly frequency dependent, with relatively poor separation at low frequencies (~1 Hz) and relatively good separation at high frequencies (> ~3 Hz). We demonstrate this using closely located pairs of earthquakes and explosions recorded on common, publicly available stations at test sites around the world (e.g., Nevada, Lop Nor, Novaya Zemlya, Semipalatinsk, India, Pakistan, and North Korea). We show this pattern appears to have little dependence on the point source variability revealed by longer period surface wave modeling. For example regional waveform modeling shows strong tectonic release from the May 1998 India test in contrast with very little tectonic release in the recent North Korea test, but the *P/S* discrimination behavior is similar in both events, using the limited regional data available.

While accepted explosion *P*-wave models have been available for many years, the frequency behavior of the *P/S* discriminant has inspired a variety of competing models to explain how explosions generate *S*-waves. We briefly review some of these models in the context of the *P/S* discriminant observations. One hypothesis is that *S*-waves are generated mainly from conversion of *P*-waves and surface waves, so *S*-waves from explosions can be predicted from the *P*-wave models via a frequency dependent transfer function. A different hypothesis is that significant generation of S-waves comes from the CLVD (compensated linear vector dipole) component created by spall above the explosion. A recent model by Fisk (2006) shows the explosion *S*-wave spectra can be modeled using the *P*-wave spectra with the corner frequency reduced by the ratio of the wave velocities, which seems to imply a direct generation of *S*-waves in the source region. We examine a number of nuclear tests from around the world in light of these models. Given the importance of depth on some of the model predictions we reexamine some of the overburied explosions in Nevada. We also look at chemical explosions, including dedicated single shots at different depths and mining shots at adjacent open pit and underground mines to look at depth effects. Finally we examine a subset of Nevada data with signal above noise up to 16 Hz to determine if discrimination performance saturates at frequencies around 6 Hz as some models predict, or continues to improve at higher frequencies.

OBJECTIVES

Monitoring the world for potential nuclear explosions requires characterizing seismic events and discriminating between natural and man-made seismic events, such as earthquakes and mining activities, and nuclear weapons testing. We continue developing, testing, and refining size-, distance-, and location-based regional seismic amplitude corrections to facilitate the comparison of all events that are recorded at a particular seismic station. These corrections, calibrated for each station, reduce amplitude measurement scatter and improve discrimination performance. We test the methods on well-known (ground truth) datasets in the U.S. and then apply them to the uncalibrated stations in Eurasia, Africa, and other regions of interest to improve underground nuclear test monitoring capability.

RESEARCH ACCOMPLISHED

As part of the overall National Nuclear Security Administration Ground-based Nuclear Explosion Monitoring Research and Engineering program (GNEMRE), we continue to pursue a comprehensive research effort to improve our capabilities to seismically characterize and discriminate underground nuclear tests from other natural and man-made sources of seismicity. To reduce the monitoring magnitude threshold, we make use of regional body and surface wave data to calibrate each seismic station. Our goals are to reduce the variance and improve the separation between earthquakes and explosion populations by accounting for the effects of propagation and differential source size, and by optimizing the types and combinations of amplitude measurements used.

Regional Phase Amplitude P/S Observations

In the early days of underground nuclear testing the expectation, as shown in Figure 1, was that explosions would generate little S-wave energy and relative P/S wave amplitudes could be used as one technique to distinguish them from earthquakes. Prior to the advent of widespread digital seismometry in the 1990's observations of regional P/S amplitudes tended to be dominated by frequencies around 1 Hz. As shown in Figure 2 at a number of major nuclear test sites, these observations did not show clear separation between event types. Here we focus on closely spaced pairs of events to minimize any path effects.

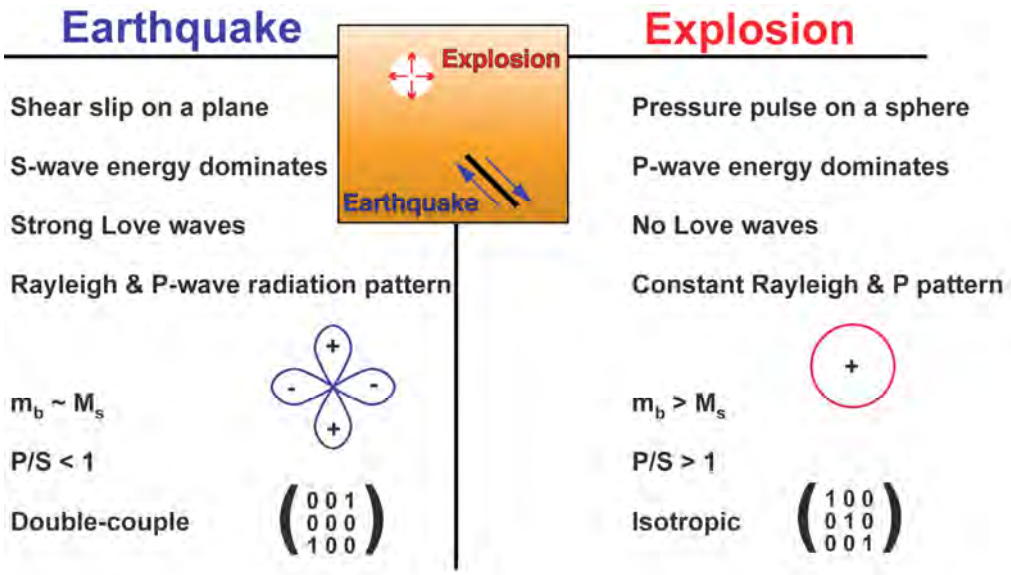

Figure 1. An overview of the theoretical differences between a pure explosion and a pure earthquake leading to expected observational differences. Actual underground nuclear explosions are often more complex.

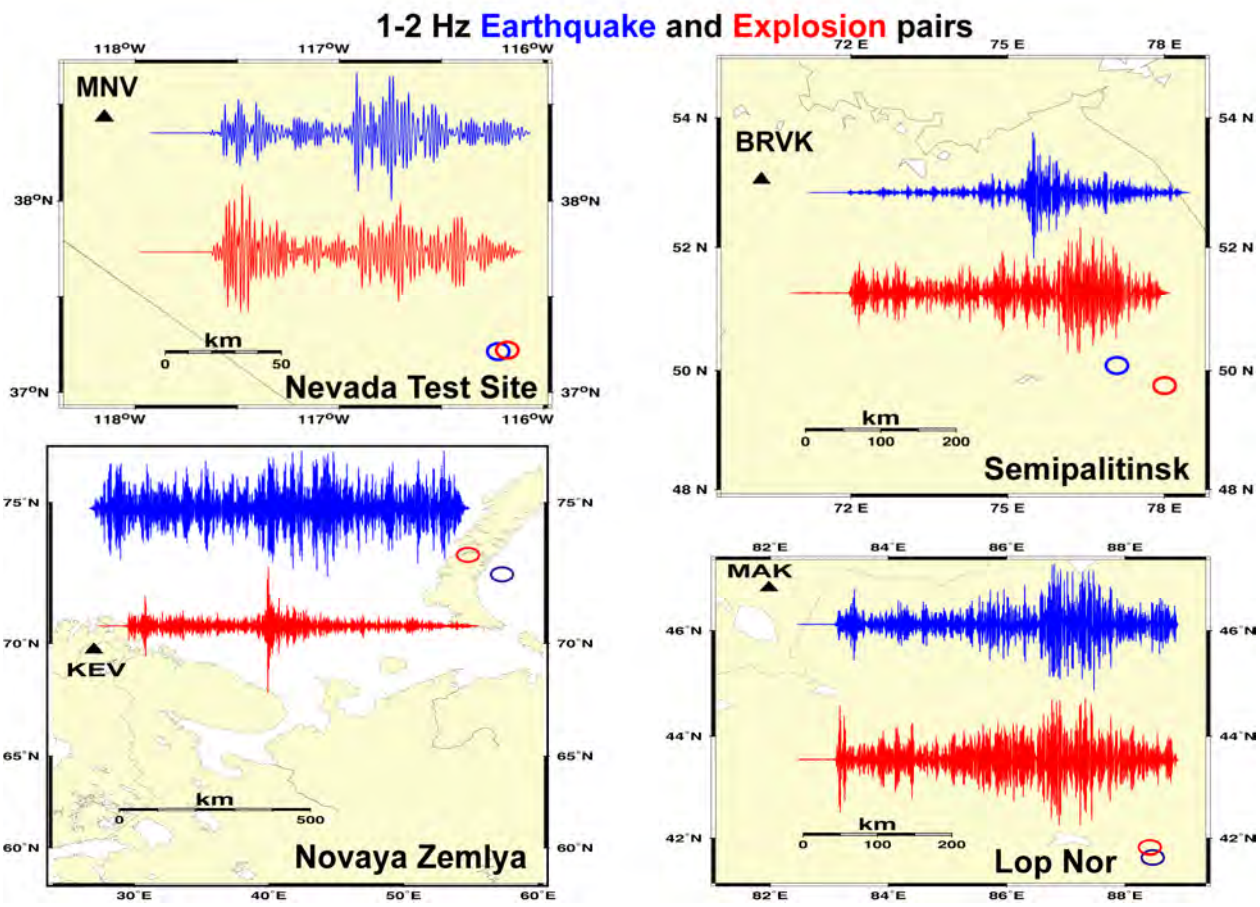

Figure 2. Bandpass filtered 1-2 Hz seismograms of earthquake (red) and explosion (blue) pairs at nuclear test sites show little consistent relative P to S wave amplitude differences between the two source types. Low-Frequency P/S does not discriminate closely located events recorded on the same station at nuclear test sites.

With the advent of widespread digital seismometry in the late 1980's and early 1990's a large number of different researchers found that at high frequencies, greater than around 2-4 Hz, the regional P/S amplitude ratios did discriminate explosions from earthquakes (e.g., Dysart and Pulli, 1987; Baumgardt and Young, 1990; Kim et al., 1993; Walter et al., 1995; Taylor, 1996; Hartse et al., 1997; Battone et al., 2002). For example in Figure 3 we show the same events in Figure 2, except they are filtered at a higher frequency, 6-8 Hz. In this case the explosions clearly show larger P/S amplitude ratios than the earthquakes for all cases.

Examination of P/S ratios at high frequencies has now been done all over the world. As we show in Figure 4, the characteristic pattern of explosions have larger relative P-wave amplitudes than S-wave amplitudes appears to hold everywhere, provided that we filter the data at a high enough frequency and that we compare events with very similar paths. This is true even for the recently announced nuclear test by North Korea on October 9, 2006, as shown in Figure 4. In this case the nearest earthquakes for comparison are around 100 km away, but we can bracket the test with earthquakes and clearly see that it is deficient in high frequency S-wave energy.

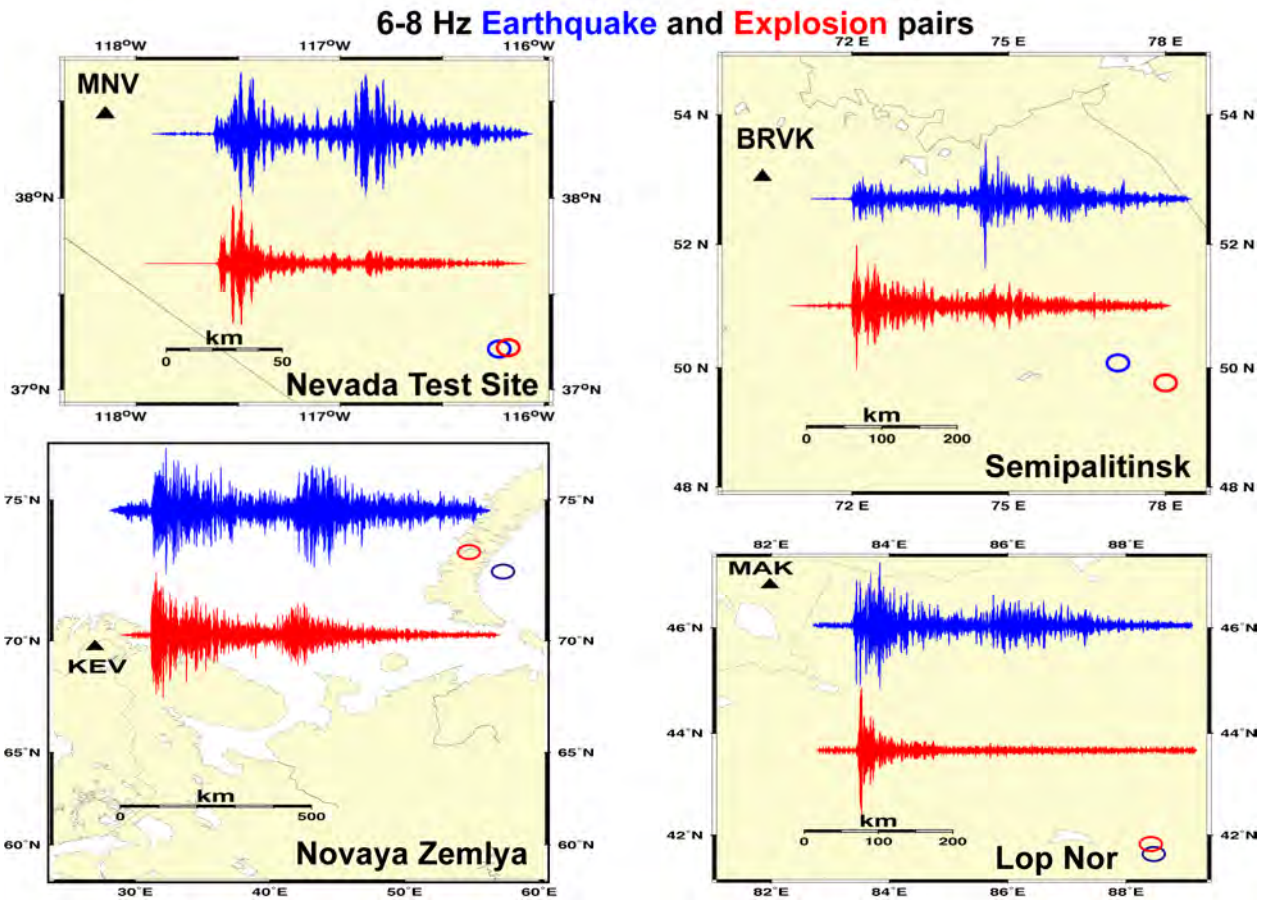

Figure 3. 6-8 Hz bandpass seismograms of the same events in Figure 2 show significant and consistent relative P to S wave amplitude differences between the two source types. High-frequency P/S appears to discriminate closely located, similarly sized events recorded on the same station globally.

This North Korean test example shows the importance of accounting for path, as the S-wave energy in this case is partitioned into both Sn and Lg phases. The path of the recorded seismic energy crosses the Sea of Japan, a region of oceanic crust where Lg does not efficiently propagate. One can see that the earthquake with a greater proportion of its path in the Sea of Japan has stronger Sn than the other. In such cases it is important to correct for path effects and to consider P/S ratios for all the observable regional phases; in case one S-wave phase is attenuated to below the level of the noise.

When similarly sized earthquakes and explosions are nearly co-located, we can understand the observed seismic contrasts, such as the relative P-to-S wave excitation, in terms of depth, material property, focal mechanism and source time function differences. However, it is well known that path propagation effects (e.g., attenuation, blockage) and source scaling effects (e.g., corner frequency scaling with magnitude) can make earthquakes look like explosions and vice versa. We developed a technique called magnitude and distance amplitude corrections (MDAC) (Walter and Taylor, 2001) that can account for these effects with proper calibration. We use the earthquakes alone to determine the MDAC parameters such as geometrical spreading, frequency dependent Q and the average apparent stress. After calibration the MDAC formulation provides expected spectral amplitudes as a function of phase, frequency, magnitude and distance. These can then be subtracted from the actual observations. For earthquakes the corrected data should exhibit a close to zero mean, and no significant trends with magnitude and distance. Explosions should have significant non-zero mean residuals, leading to improved discrimination.

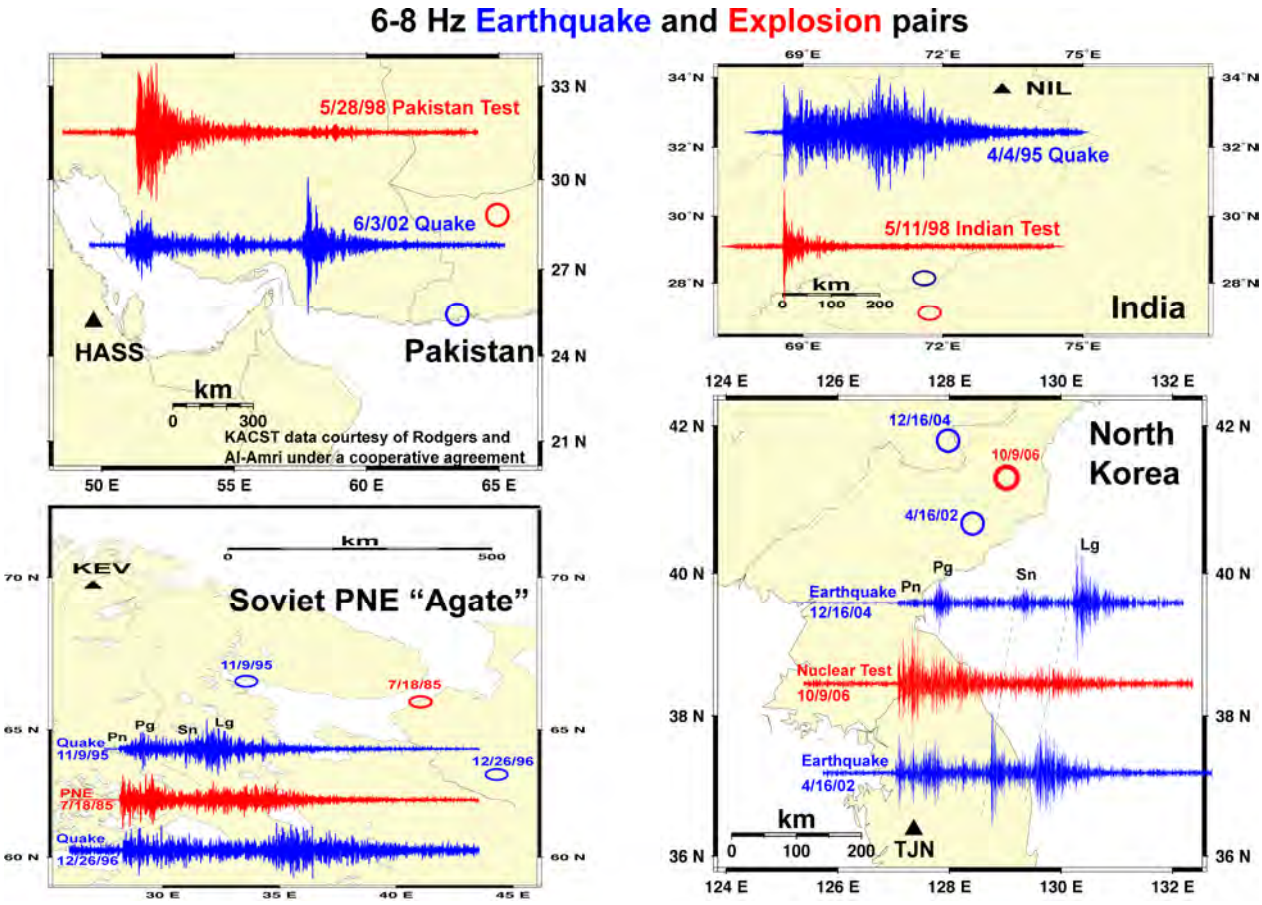

Figure 4. Examination of high frequency filtered seismograms of closely spaced groups of earthquakes and underground nuclear explosions at many different locations around the world show a characteristic difference: explosions have relatively larger P/S amplitude values. High-frequency P/S appears to work everywhere.

As shown in Figure 5, we applied MDAC to correct for path effects for earthquakes all around the Korean Peninsula, Yellow Sea and Northeastern China region recorded at stations MDJ and TJN, which are publicly available through data centers such as the Incorporated Research Institutions for Seismology (IRIS) and the Ocean Hemisphere Project Data Management Center (OHPDMC). While the North Korean test is easily discriminated at both stations at high frequencies such 6-8 Hz, the two stations show slightly different frequency behavior, with MDJ discriminating well at all frequencies above 2 Hz, while TJN appears to keep improving as the frequency increases all the way to 8 Hz. We are analyzing the frequency dependence of the P/S ratios for a variety of regions in order to better quantify the effect.

A remarkable feature of the high frequency P/S ratios for discriminating underground nuclear tests is that they seem to work even in cases where the long period signals indicate that the explosions are complex. A case in point is the May 11, 1998 Indian test shown in Figure 4. That test shows significant Love waves and reversed Rayleigh waves (Walter et al, unpublished data, Selby et al., unpublished data) indicating a large amount of tectonic release and significant non-isotropic components of the moment tensor source. Despite the complexities in the source the S-waves disappear at frequencies of 1 Hz and higher and the test easily discriminates from nearby earthquakes as shown in Figure 4 and by Rogers and Walter (2002). In fact it looks very similar to the North Korean case, which as we show in the next section has almost no tectonic release. These two characteristics:
1) S-waves from explosions are strong at lower frequencies and diminish at frequencies greater than about 2–4 Hz,
2) S-waves from explosions at higher frequencies are independent of tectonic release and long-period character,

are important constraints on any model that tries to explain how nuclear tests generate S-waves.

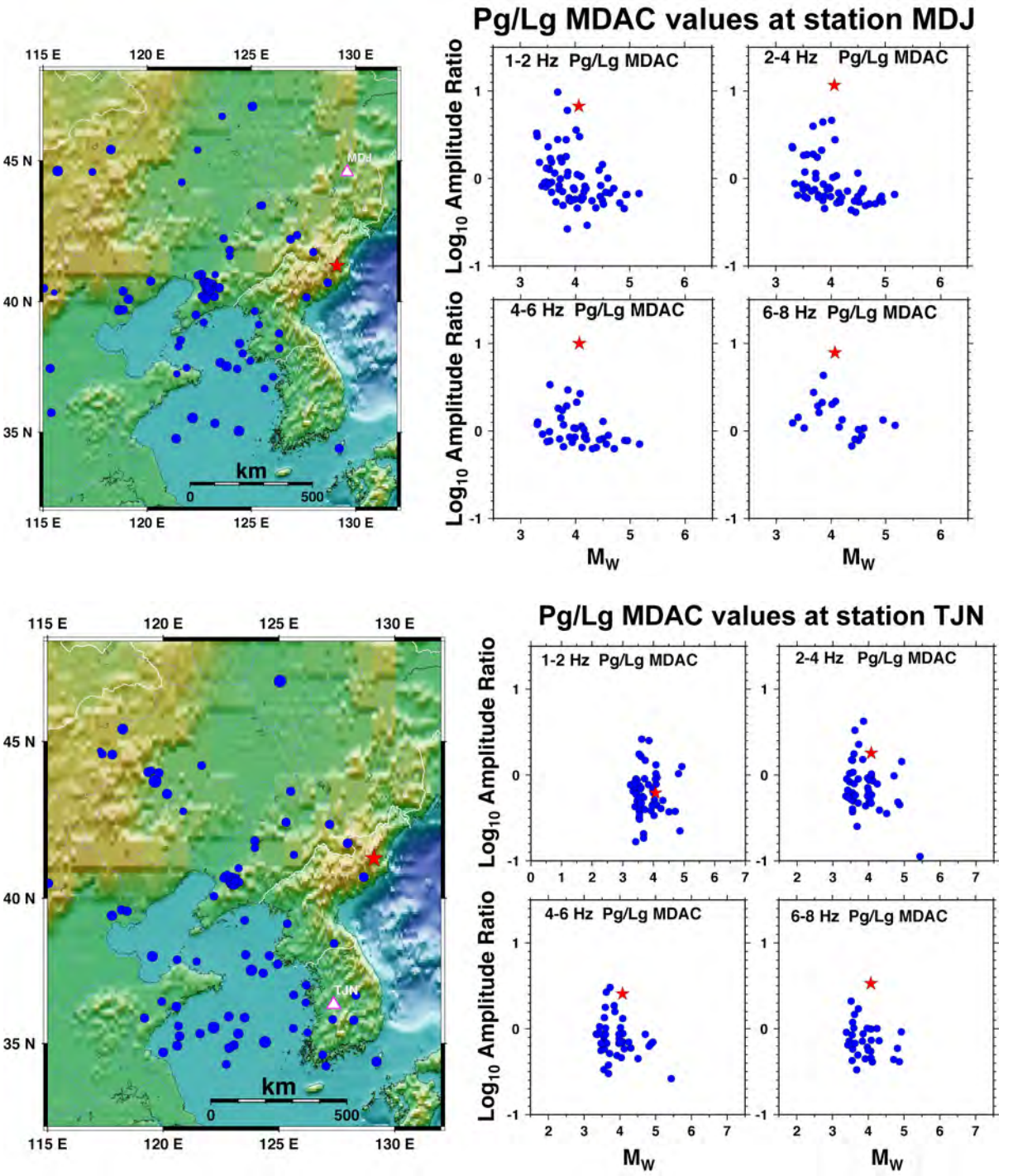

Figure 5. The maps show the earthquakes (blue circles) and the October 9, 2006, North Korean nuclear test (red star) observed at seismic stations MDJ and TJN. The scatter plots show the MDAC path corrected P/S ratios in four different frequency bands. For station MDJ discrimination improves as you move from 1–2 to 2–4 Hz but seems more or less constant at higher frequencies. In contrast for TJN the P/S discriminant seems to continue to improve as frequency increases up to 6-8 Hz.

In Figure 6 we show long-period waveform fits of the North Korean nuclear test compared with a nearby earthquake. This test shows little tectonic release and appears reasonably well fit at long-periods by a purely isotropic moment tensor.

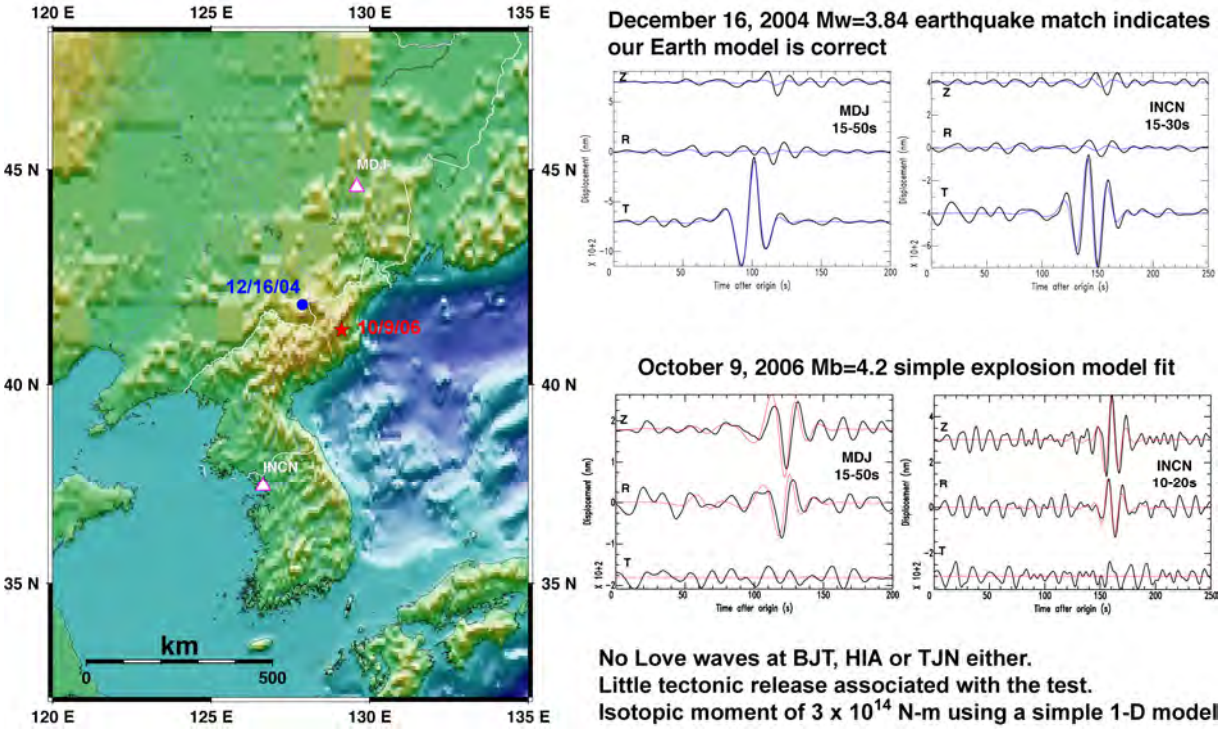

Figure 6. Long-period waveform modeling for point source moment tensor parameters of the October 9, 2006, North Korean nuclear test and a nearby earthquake on December 16, 2004. Top plots show good waveform fits mainly to Love waves for the earthquake, which indicates we have a good earth model for synthetic seismogram generation. The bottom plots show that a pure isotropic explosion source provides a very good fit for the mainly Rayleigh waves observed for the nuclear test. The long-period waveforms are fit by a simple explosion without Love waves indicating minimal tectonic release.

Explosion S-waves Models

While there are long-standing explosion P-wave models that have been used for many years, there is still no widely accepted model to predict S-waves from nuclear tests. Here we show two different ideas about how S-waves are generated from nuclear explosions and in each case we are able to match some S-wave observations from the North Korean declared nuclear test of October 9, 2006.

We show in Figure 7 some very preliminary comparisons of parametric models with source spectra inferred from path corrected observations at station TJN. On the left we compare the Mueller-Murphy (1971) granite P-wave model with inferred P source observations. Note that we can have a variety of models with the same spectral level at low frequencies (< 2 Hz) depending upon depth and source size. As of this writing the North Koreans have not announced any information on yield and emplacement conditions. For this particular station subject to the assumptions (e.g., path correction is right, radiation is isotropic, Mueller-Murphy granite model is applicable, etc.), we are able to match the P waves reasonably well using the 100-m depth model, however the long period level is a bit high compared to the waveform modeling moment.

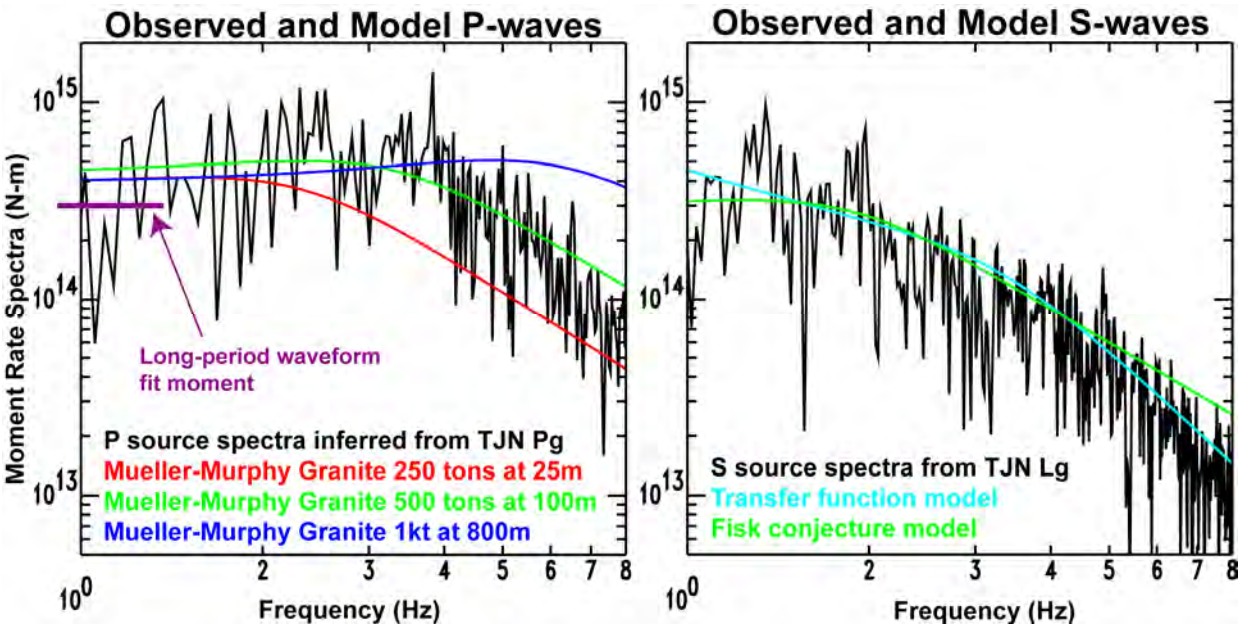

Figure 7. We infer P- and S-wave source spectra from observed station TJN Pg and Lg spectra after correcting for path effects. On the left we compare the P-wave spectra with Mueller-Murphy granite models for yields from 250 to 1000 tons and depths from 25 m to 800 m. On the right we compare two models for S-waves with data. See text for discussion.

The S-wave case is shown on the right hand side of Figure 7. We follow the Walter et al. (1994) idea that the S-waves come mainly from conversion and can be matched by modifying the P-spectra, using a P to S transfer function. Here we simply assume a transfer function of similar form to that shown in Figure 6 of Walter et al. (1994) is applicable, that is strong conversion near 1 Hz and weaker conversion at higher frequencies. We used a simple linear relationship in log-amplitude versus log-frequency space, which decays about a factor of ten in amplitude from 1 Hz to 10 Hz. Multiplying by the assumed P-wave source model, in this case the Mueller-Murphy granite function for 500 tons at 100 meters depth, we get the light blue line shown in Figure 7. The result is a reasonable match to the observed data. This simply illustrates it is possible to predict explosion S-waves using simple parametric P-wave models and transfer functions, but it is not the only way to do so.

For comparison we can also apply the Fisk (2006) conjecture that the S-waves are matched by lowering the Mueller-Murphy corner frequency by the ratio of the P to S wave velocity. The implication of this model is that S-waves are generated close to the source and are tied to the elastic radius similarly to P-waves. The Fisk (2006) conjecture does not specify the absolute level so here we scaled it to match the data as shown in green in Figure 7. This is also a reasonably good match to the observed data. Within this frequency band and allowing arbitrary absolute scaling, both models are similar. However at higher and lower frequencies (or much larger or smaller, or much deeper explosions) there are significant differences between these two models. In particular the Fisk (2006) conjecture would say that P/S discrimination at these same frequencies (e.g., 4-8 Hz) would not work well for much smaller (or much deeper) explosions. Fisk (2006) states the frequency band must be above the S-wave corner for discrimination to be effective.

Future Work

To better address differences in predictions between the various models of S-wave generation we need to study events with very different source size, depth and emplacement conditions. For nuclear tests the few very overburied events offer a chance to examine effects that might be related to corner frequency effects. Similarly chemical explosions, to the extent they are similar to nuclear explosions offer a much wider range of source conditions. We are using both of these types of data to test and develop better understanding and better models for predicting nuclear explosion S-waves.

To better address practical explosion identification we are improving our MDAC source and path corrections and looking at optimal combinations of normalized regional amplitude measurements. For example given that there is often discrimination power in all of the frequency bands where P/S is observed, we are testing and quantifying the improvement provided by using multiband P/S ratios to discriminate explosions from earthquakes.

CONCLUSIONS AND RECOMMENDATIONS

Regional discrimination algorithms require calibration at each seismic station to be used for nuclear explosion monitoring. We apply a magnitude and distance amplitude correction (MDAC) procedure to remove source size and path effects from regional body-wave phases. This allows the comparison of any new regional events recorded at a calibrated station with all available reference data and models. This also facilitates the combination of individual measures at multiple stations to form multivariate discriminants that can significantly improve performance over single station individual measures. We are working to quantify the performance of P/S ratio discriminants as a function of frequency and number of stations. We are using the Arizona Source Phenomenology Experiment (AZSPE) data to explore the use of industrial chemical explosions to help calibrate regional discriminants in areas where nuclear explosion data is not available.

ACKNOWLEDGEMENTS

We thank Stan Ruppert and Terri Hauk for loading and maintaining the LLNL database. We thank Doug Dodge and Mike Ganzberger for developing and maintaining the LLNL software code RBAP, which was used to make the regional measurements.

REFERENCES

Battone, S., M. D. Fisk, and G. D. McCarter (2002). Regional seismic-event characterization using a Bayesian formulation of simple Kriging, *Bull. Seism. Soc. Am*. 92: 2277–2296.

Baumgardt, D. R. and G. B. Young (1990). Regional seismic waveform discriminants and case-based identification using regional arrays, *Bull. Seism. Soc. Am.* 80: 1874–1892.

Dysart, P. S. and J. J. Pulli (1987). Spectral study of regional earthquakes and chemical explosions recorded at the NORES array. SAIC technical report C87–03.

Fisk, M. D. (2006). Source spectral modeling of regional P/S discriminants at nuclear test sites in China and the Former Soviet Union, *Bull. Seism. Soc. Am*. 96: 2348–2367.

Hartse, H., S. R. Taylor, W. S. Phillips, and G. E. Randall (1997). A preliminary study of regional seismic discrimination in Central Asia with an emphasis on Western China, *Bull. Seism. Soc. Am*. 87: 551–568.

Kim, W. –Y., D. W. Simpson, and P. G. Richards (1993). Discrimination of earthquakes and explosions in the Eastern United States using regional high frequency data, *Geophys. Res. Lett.* 20: 1507–1510.

Kim, W. -Y., V. Aharonian, A. L. Lerner-Lam, and P. G. Richards (1997). Discrimination of earthquakes and explosions in Southern Russia using regional high frequency three-component data from the IRIS/JSP Caucasus network, *Bull. Seism. Soc. Am.* 87: 569–588.

Mayeda, K., L. Malagnini, W. S. Phillips, W. R. Walter, and D. Dreger (2005). 2-D or not 2-D, that is the question: A Northern California test, *Geophys. Res. Lett.* 32: doi:10.1029/2005GL022882.

Mueller R.A. and J. R. Murphy (1971). Seismic characteristics of underground nuclear detonations. Part I. Seismic scaling law of underground detonations, *Bull. Seismol. Soc. Am.* 61: 1675–1692.

Rodgers, A. J. and W. R. Walter (2002). Seismic discrimination of the May 11, 1998 Indian Nuclear Test with short-period regional data from Station NIL (Nilore, Pakistan). *Pure Appl. Geophys.* 159: 679–700.

Springer, D. L., G. A. Pawlowski, J. L. Ricca, R. F. Rohrer, and D. K. Smith (2002). Seismic source summary for all U.S. below-surface nuclear explosions, *Bull. Seism. Soc. Am.* 92: pp. 1806–1840.

Taylor, S. (1996). Analysis of high-frequency Pg/Lg ratios from NTS explosions and Western U.S. earthquakes, *Bull. Seism. Soc. Am.* 86: 1042–1053.

Taylor, S., A. Velasco, H. Hartse, W. S. Philips, W. R. Walter, and A. Rodgers (2002). Amplitude corrections for regional discrimination, *Pure. App. Geophys*. 159: 623–650.

W.R. Walter, K. Mayeda, and H. J. Patton (1994). Regional seismic observations of the Non-Proliferation Experiment at the Livermore NTS network, in *Proceedings of the Symposium on the Non-Proliferation Experiment (NPE): Results and Implications for Test Ban Treaties*, M. Denny and S. Stull Eds., 6.193–6.201.

Walter, W. R., K. Mayeda, and H. J. Patton (1995). Phase and spectral ratio discrimination between NTS earthquakes and explosions Part 1: Empirical observations, *Bull. Seism. Soc. Am.* 85: 1050–1067.

Walter, W. R. and S. R. Taylor (2001). A revised Magnitude and Distance Amplitude Correction (MDAC2) procedure for regional seismic discriminants, Lawrence Livermore National Laboratory UCRL-ID-146882: http://www.llnl.gov/tid/lof/documents/pdf/240563.pdf

Walter, W. R., K. D. Smith, J. L. O'Boyle, T. F. Hauk, F. Ryall, S. D. Ruppert, S. C. Myers, M. Anderson, and D. A. Dodge (2003). Improving the fundamental understanding of regional seismic signals with a unique western United States dataset, in *Proceedings of the 25th Seismic Research Review—Nuclear Explosion Monitoring: Building the Knowledge Base*, LA-UR-03-6029, Vol. 1, pp. 486–494.

2007

Proceedings of the 29th Monitoring Research Review: Ground-Based Nuclear Explosion Monitoring Technol

To view these Proceedings online, visit
https://www.nemre.nnsa.doe.gov/review2007

Vol. II

Proceedings of the 29th Monitoring Research Review: Ground-Based Nuclear Explosion Monitoring Technologies

September 25–27, 2007

Denver, Colorado

Volume II

Hydroacoustic Monitoring
Radionuclide Monitoring
Infrasound Monitoring
Data Processing and Analysis

Approved for Public Release; further dissemination unlimited.

National Nuclear Security Administration

AIR FORCE RESEARCH LABORATORY

LA-UR-07-5613

Table of Contents - Volume II

4. Hydroacoustic Monitoring 695

4-01 **de Groot-Hedlin, C., D. Blackman, and C. Jenkins**
Hydroacoustic Propagation Through the Antarctic Convergence Zone: Study of Errors in Yield and Location Estimates for Explosive Charges 697

4-02 **Hanson, J., C. Reasoner, and J. Bowman**
Hydroacoustic Propagation and Reflection Loss Using Explosions Found in the Indian Ocean 707

5. Radionuclide Monitoring 717

5-01 **Biegalski, S., C. Weaver, S. Waye, O. Ezekoye, and P. Hopke**
Testing of Aerosol Sampler to Remove Radon and Thoron Progeny Interference from Aerosol Samples for Nuclear Explosion Monitoring 719

5-02 **Biegalski, S., K. Biegalski, and D. Haas**
Testing the Spectral Deconvolution Algorithm Tool (SDAT) with Xe Spectra 729

5-03 **Cooper, M., J. Hayes, T. Heimbigner, C. Hubbard, J. McIntyre, M. Ripplinger, and B. Schrom**
Automated QA/QC Check for β-γ Coincidence Detector 739

5-04 **Farsoni, A., D. Hamby, K. Ropon, and S. Jones**
A Two-Channel Phoswich Detector for Dual and Triple Coincidence Measurements of Radioxenon Isotopes 747

5-05 **Hennig, W., H. Tan, W. Warburton, A. Fallu-Labruyere, K. Sabourov, J. McIntyre, M. Cooper, and A. Gleyzer**
Characterization of Phoswich Well Detectors for Radioxenon Monitoring 757

5-06 **Hull, E., R. Pehl, J. Lathrop, P. Mann, R. Mashburn, B. Suttle, H. Miley, C. Aalseth, and T. Hossbach**
Segmentation of the Outer Contact on P-Type Coaxial Germanium Detectors 764

5-07 **Hull, E., R. Pehl, J. Lathrop, P. Mann, R. Mashburn, B. Suttle, H. Miley, C. Aalseth, T. Bowyer, and T. Hossbach**
Mechanically Cooled Large-Volume Germanium Detector Systems for Nuclear Explosion Monitoring 770

5-08 **Milbrath, B., M. Cooper, L. Lidey, T. Bowyer, J. Hayes, J. McIntyre, L. Karr, D. Shafer, and J. Tappen**
Radioxenon Atmospheric Measurements in North Las Vegas, NV 779

5-09 **Walker, D., A. Beyerle, G. Miller, and R. Arthur**
Characterization and Performance Evaluation of an HPXe Detector for Nuclear Explosion Monitoring Applications 787

5-10 **Williams, R., J. Hayes, and R. Kirkham**
Improved Calibration and Operation of a Stable-Gas Quantification Manifold as Part of a Radioxenon Collection System 798

5-11 **Wotawa, G. and A. Becker**
Atmospheric Transport Modeling and Data Fusion in Support of Comprehensive Nuclear-Test-Ban Treaty Verification 806

6. Infrasound Monitoring 813

6-01 **Arrowsmith, S. and D. ReVelle**
Infrasound Monitoring of Local, Regional and Global Events 815

6-02 **Christie, D., B. Kennett, and C. Tarlowski**
Advances in Infrasound Technology with Application to Nuclear Explosion Monitoring 825

6-03 **de Groot-Hedlin, C.**
Finite Difference Modeling of Infrasound Propagation to Local and Regional Distances 836

6-04 **Gibson, R., D. Drob, and D. Norris**
Advancement of Infrasound Propagation Calculation Techniques Using Mesoscale Atmospheric and Terrain Specifications 845

6-05 **Herrin, E., P. Golden, P. Negraru, and M. McKenna**
Infrasound in the "Zone of Silence" 855

6-06 **Norris, D., J. Bhattacharyya, and R. Whitaker**
Development of Advanced Propagation Models and Application to the Study of Impulsive Infrasonic Events 864

6-07 **O'Brien, M., D. Drob, and J. Bowman**
Improved Infrasound Event Location 874

6-08 **Walker, K., M. Zumberge, and M. Dzieciuch**
OFIS Experiments at Camp Elliott: Paving the Way to Infrasonic Radar and a Portable Infrasonic Sensor Calibrator 884

6-09 **Walker, K., M. Zumberge, J. Berger, M. Hedlin, and P. Shearer**
An Improved Method of Back Azimuth Determination with a Multi-Arm OFIS 894

6-10 **Whitaker, R.**
Infrasound Signals as Basis for Event Discriminants 905

7. Data Processing and Analysis 915

7-01 **Bahavar, M., B. Barker, T. Bennett, J. Bowman, H. Israelsson, B. Kohl, Y. Kung, J. Murphy, R. North, V. Oancea, M. O'Brien, and G. Shields**
Enhanced Resources of the SMDC Monitoring Research Program for Source Information and Data Acquisition 917

7-02 **Carr, D., J. Lewis, S. Ballard, E. Martinez, J. Hampton, B. Merchant, R. Stead, M. Crown, J. Roman-Nieves, and J. Dwyer**
Advances in the Integration of Large Data Sets for Seismic Monitoring of Nuclear Explosions 927

7-03 **Hart, D., B. Merchant, and E. Chael**
Seismic and Infrasound Sensor Testing Using Three-Channel Coherence Analysis 935

7-04 **Hipp, J. and C. Young**
Clustering of Large Event Sets Using Delaunay Tessellations and K-Medoid Optimization 945

7-05 **Ringdal, F., T. Kvaerna, S. Mykkeltveit, S. Gibbons, and J. Schweitzer**
Basic Research on Seismic and Infrasonic Monitoring of the European Arctic 955

7-06 **Ruppert, S., D. Dodge, M. Ganzberger, T. Hauk, and E. Matzel**
Enhancing Seismic Calibration Research Through Software Automation and Scientific Information Management 965

975

Appendices

Acronyms, etc. 977

Guide to Seismic Phases 980

Hydroacoustic Monitoring

HYDROACOUSTIC PROPAGATION THROUGH THE ANTARCTIC CONVERGENCE ZONE: STUDY OF ERRORS IN YIELD AND LOCATION ESTIMATES FOR EXPLOSIVE CHARGES

C. de Groot-Hedlin[1], Donna K. Blackman[1], and C. Scott Jenkins[2]

Scripps Institution of Oceanography (SIO), University of California at San Diego[1]
Naval Surface Warfare Center, Indian Head Division (IHDIV)[2]

Sponsored by Army Space and Missile Defense Command

Contract No. W9113M-05-1-0019

ABSTRACT

A series of small calibration shots was conducted in late December 2006, along a transect from New Zealand to Antarctica in order to document the differences in spectral characteristics, transmission loss, travel-time, and azimuth both observed and predicted using propagation models typical for nuclear monitoring. The high gradients in ocean temperature and salinity that characterize the Antarctic Convergence Zone (ACZ) are expected to alter the propagation path, and the commonly rough sea surface is likely to scatter significant energy from sources south of ~53°S, where the sound channel breaches the surface. Seasonal variability in the ACZ makes it difficult to model such effects accurately at all times, so our experiment was designed to determine the scale of error introduced by such uncertainty in structure. Depth charges, set to trigger at 300, 460, and 600 m, were deployed at 6 stations between 54°S and 63°S. The International Monitoring System (IMS) hydroacoustic station off Cape Leeuwin, Australia, recorded shots from all but one site. Macquarie Ridge probably blocked that source area. Several shots were also recorded at the Diego Garcia and Juan Fernandez IMS stations. This new data set will be characterized in terms of source-receiver transmission loss and spectral characteristics, used to infer source yield, as well as source location errors. Preliminary analysis of arrivals at IMS hydroacoustic stations in the Indian Ocean indicates that the time duration of each arrival depends on source location, and not on source depth or size. Conversely, the spectral content of the signals depends on source depth and charge size, but not on the source location.

OBJECTIVES

Our objectives were to conduct a series of calibration shots within and to the south of the ACZ that would generate acoustic signals at frequencies f>30 Hz and to analyze the signals recorded at hydrophone stations operated by the IMS. The overall goal was to compare observed source-receiver travel times to the IMS hydrophone stations to those predicted by numerical models for paths crossing the Antarctic convergence zone and to use results to determine the accuracy to which sources may be located within the ACZ. A second objective was to determine the accuracy of source yield estimates for explosive sources within the ACZ. A calibration experiment was needed because ocean temperature and salinity gradients within the southern ocean are not sufficiently well characterized to predict how travel times may be affected by seasonal and climactic variations.

Acoustic travel times vary seasonally because the upper ocean is warmed during summer and cools in winter, and sound travels faster in warmer water than in cold water. This seasonal variation in travel times has been observed in the Acoustic Thermometry of Ocean Climate (ATOC) experiment (Dushaw et al., 1999). Variability in travel times is particularly pronounced at high northern latitudes, where seasonal temperature changes may extend to the sound channel axis (Dushaw et al., 1999), and is expected to be significant in the southern ocean as well. The relevance for nuclear test monitoring is that acoustic signal travel-time errors translate directly into source location uncertainty, so it is necessary to determine how well travel times can be predicted from the Levitus database (Levitus, 1994), which is based on long-term averages. The ability of the IMS to estimate source locations within the Comprehensive Nuclear Test-Ban Treaty (CTBT) limit has been assessed for most of the world's oceans. To date, however, there had not been sufficient ground-truth data available to assess IMS location capabilities for the southern ocean.

The calibration shots were conducted over a period of three days in December 2006, so we obtained essentially a snapshot of propagation through the ACZ. Analysis of our signals will allow us to document the travel-times and transmission losses for the corresponding structure, to quantify travel-time errors associated with limited accuracy in ACZ models, and to characterize how well an unknown event in the southern ocean could be located. Other objectives are to determine how propagation through the ACZ affects signal strength and how source depth affects the transmission loss and travel times for source within the ACZ

RESEARCH ACCOMPLISHED

The Research Cruise

Research Vessel Ice Breaker (RVIB) Nathanial B. Palmer departed Lyttleton, New Zealand, on 22 December 2006 (local time) and began a transit line toward the Adare Basin, the research area in the NW Ross Sea, for the main project on which our experiment piggybacked. The hydroacoustic project was conducted along the transit line during the first week of the cruise. Permission had been granted to conduct calibration shots in New Zealand waters, but no unblocked acoustic paths to the operational IMS stations were available during daylight hours, the latter being a requirement of our marine mammal mitigation procedure. From the southern edge of Campbell Plateau to ~63°S, hydroacoustic stations were occupied twice a day, approximately 120 nm apart.

Each station comprised a series of activities: The first to begin was the marine mammal watch (1 hr before expected shot time). After half an hour a sonobuoy was launched to allow mammal sound monitoring. An Expendable Bathy-Thermograph (XBT) was launched and ship speed slowed (to 1-2 kts) just before station occupation. An over-the-side hydrophone was deployed, and recording started. Signal underwater sound (SUS) charges were dropped at about 5 minute intervals at each station. When shots were completed, ship transit at full speed was resumed.

Marine Mammal Watch.
Before and throughout each acoustic station, marine mammal observers did visual checks in all directions for any animals that might be in the vicinity, particularly within the safety zone for the calibration shots. A safety zone size of 1 km was used for all 4-lb charges (~160 dB re μPa energy density at this range from the shot). A marine mammal observer participated in the watch for each station. About 30 minutes before the planned shots, a surplus US Navy sonobuoy was launched, and a marine mammal observer listened for marine mammals on the headphones. Two scientists participated in the marine mammal watch (~1.5 hours total).

SUS Depth Charges.
The SUS charges employed were MK59-mod1a with a 4-lb main charge. These were manufactured at the Indian Head Division (IHDIV) with firing depths of 1000', 1500', and 2000'. Transport from Yorktown, VA, to Christchurch was arranged by the US Navy via a military training flight from McChord Air Force Base. Transshipment approval from New Zealand Environmental Risk Management Authority was obtained, and temporary storage of the SUS was arranged at a local quarry storage facility.

At each hydroacoustic station, multiple SUS charges were hand-dropped one at a time from the helo deck. A single drop was done for each depth setting, starting from shallowest and working to deepest. The shot locations are listed in Table 1; their basic paths to the IMS hydrophones are shown in Figure 1. At stations A1-A4, a single charge was dropped for each trigger depth. The intent at A1 was to deploy one 1000' charge and two 1500' charges, since water depth was only 800 m. Interestingly the signal from the 3rd drop has charge-seafloor range and bubble pulse frequency closer to what would be expected for a 2000' firing. This suggests, contrary to the SUS manual, that occasionally firing depth can be off the trigger setting by up to 150 m. For the 1000' charge at A1, the seafloor reverberation and bubble frequency was within 25 m of expected trigger depths. The period of the bubble pulse for all subsequent stations was within the range expected for each nominal trigger depth and an uncertainty of ~35 m, as the SUS manual reports.

At stations A2-A4 and A6, drops were done for each depth setting (1000', 1500', and 2000'). At station A5 only 2 drops were done with the 2nd having two 1500'-triggered charges taped together, for an 8-lb total charge. The larger charge was chosen after onshore monitoring of IMS recordings by Catherine de Groot-Hedlin indicated that none of the signals from A2 had been detected at the Cape Leeuwin hydrophones. As later became clear, topographic blockage, not insufficient signal strength. was the culprit. At station A6, four drops were done with 2 being set for 1500' detonation. A combination of 4-lb, 8-lb, and 12-lb total charges were deployed at this last station.

Table 1: Shot locations and times

Station SUS (ft-lb)	jday	shot time (Z)	shot depth [m]	latitude (S)	longitude (E)
A1					
S1000-4	359	4:06:01.79	330	53.850	171.7252
S1500-4	359	4:12:34.18	523	53.853	171.7258
S1500-4	359	4:18:43.70	614	53.856	171.7262
A2					
S1000-4	359	17:39:48.73	300	55.9788	171.7180
S1500-4	359	17:46:21.52	460	55.9794	171.7204
S2000-4	359	17:52:45.04	600	55.9798	171.7232
A3					
S1000-4	360	4:03:36.43	300	57.5648	171.7184
S1500-4	360	4:09:52.01	460	57.5674	171.7208
S2000-4	360	4:15:39.35	600	57.5698	171.7228
A4					
S1000-4	360	17:35:30	300	59.448	172.5763
S1500-4	360	17:41:40	460	59.449	172.5780
S2000-4	360	17:47:34	600	59.450	172.5804
A5					
S1000-4	361	4:01:32.95	300	60.9068	174.9546
S1500-8	361	4:08:33.52	460	60.9102	174.0356
A6					
S1000-4	361	17:31:03.03	300	62.7006	176.2032
S1500-8	361	17:39:10.25	460	62.7030	176.2038
S1500-12	361	17:47:43.37	460	62.7044	176.2062
S2000-12	361	17:56:06.04	600	62.7058	176.2090

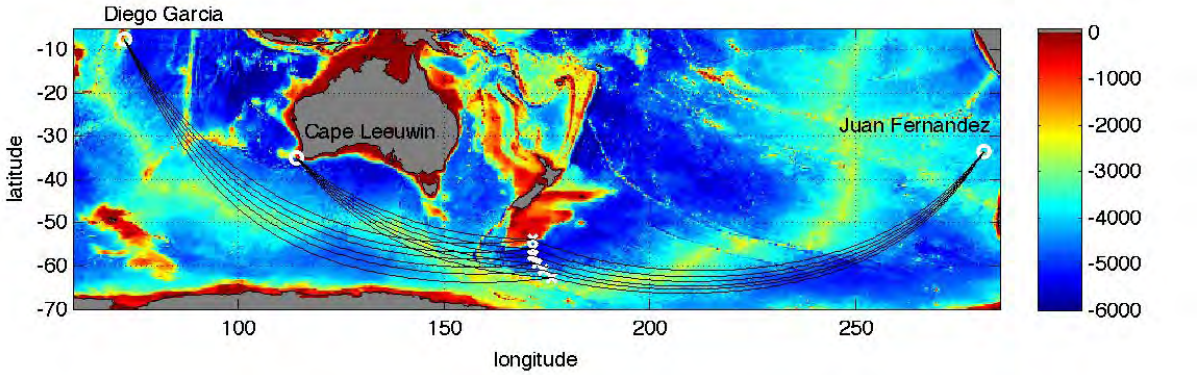

Figure 1. Map showing shot locations (x'es), IMS hydrophone station locations (circles), bathymetry, and geodesic paths from source to receiver. Stations are numbered A1 to A6 from north to south.

Near-Source Hydrophone.
A near-source hydrophone recording system was put together by Scripps Institution of Oceanography's (SIO's) Ocean Bottom Seismograph Instrument Pool personnel. This consisted of a data logger, a new 100 ft cable by Impulse, and a new HiTech HTI-90U hydrophone. A sample rate of 1000 Hz was used for single channel recording at the near-source hydrophone. The GPS time sync from the ship's system was fed into the data logger. Ship speed during the 20-30 minute station varied from ~1-2 kts. Signal-to-noise ratio (SNR) of the SUS shots on the near-source hydrophone was very good. Seafloor reverberation was recorded only at the shallowest station (A1, ~810 m); it was not evident in unfiltered data from the 3800-5400 m depths at the other stations.

Hydrophone depth was consistently shallower than hoped for (4-6 m instead of 10-15 m) due to the ship's forward motion and the relatively small weight (~4 kg) used to sink the hydrophone. Thus the recorded signal consists of a direct arrival plus an amplitude-reversed reflection from the air-sea interface. Destructive interference occurs at low frequencies, i.e., those for which the wavelength is greater than the hydrophone depth or an odd multiple of the hydrophone depth, since the wavefield at the hydrophone is the sum of the arrival plus its amplitude-reversed image. In retrospect, it was just as well that the hydrophone did not sink to greater depth, as that would have resulted in destructive interference at higher frequencies. As it was, destructive interference was significant mainly at f>150 Hz, i.e., beyond the passband at the IMS stations and at f<15 Hz, where SNRs of the signals recorded at the IMS stations were low anyway. The sea surface reflection cannot be completely separated from the source signature since only one hydrophone was used rather than a vertical array, as would have been optimal. The effect of the sea surface reflection is to introduce an error in the source spectrum estimates of about 4 dB, as discussed in the Data Analysis section.

IMS Hydrophone Station Recordings.

Before the cruise, we arranged to have IMS data from relevant hydroacoustic stations copied by the Air Force Technical Application Center (AFTAC) to an SIO workstation for the 10-day period that calibration shots were expected. There were 3 IMS stations with unblocked acoustic paths from the shots: Cape Leeuwin (H01), off SW Australia; Juan Fernandez (H03), off Chile; and Diego Garcia (H08). Crozet IMS hydrophones were all blocked by the Kerguelen plateau. Unfortunately, the southern Juan Fernandez station had not been operational since the end of 2005, and it was not fixed in time for this experiment. During the experiment Blackman alerted de Groot-Hedlin of upcoming shots and emailed approximate times/locations upon completion of each station. Time periods on either side of the predicted shot arrival times at the IMS stations were investigated at SIO, and a report on detections was e-mailed back to the ship.

Sonograms for shots recorded at the IMS hydrophone stations are shown in Figure 2. The transmission paths are not entirely free of topographic blockages; for most paths, there is some ridge or plateau that projects at least partway into the sound channel and strips off the highest order modes. None of the shots from A2 were recorded at Cape Leeuwin – apparently shallow features along the Macquarie Ridge that are not resolved in the current Sandwell and

Smith topography model scattered the energy; however, all other shots had good SNR in the 25-100 Hz band at Cape Leeuwin. Signals from A1 through A3 were detected at Juan Fernandez, at a distance of over 8000 km but were blocked by Juan Fernandez Island for shots further to the south. Conversely, signal transmission was poor to Diego Garcia for sites A1 and A2 and slightly better for subsequent shots to the south.

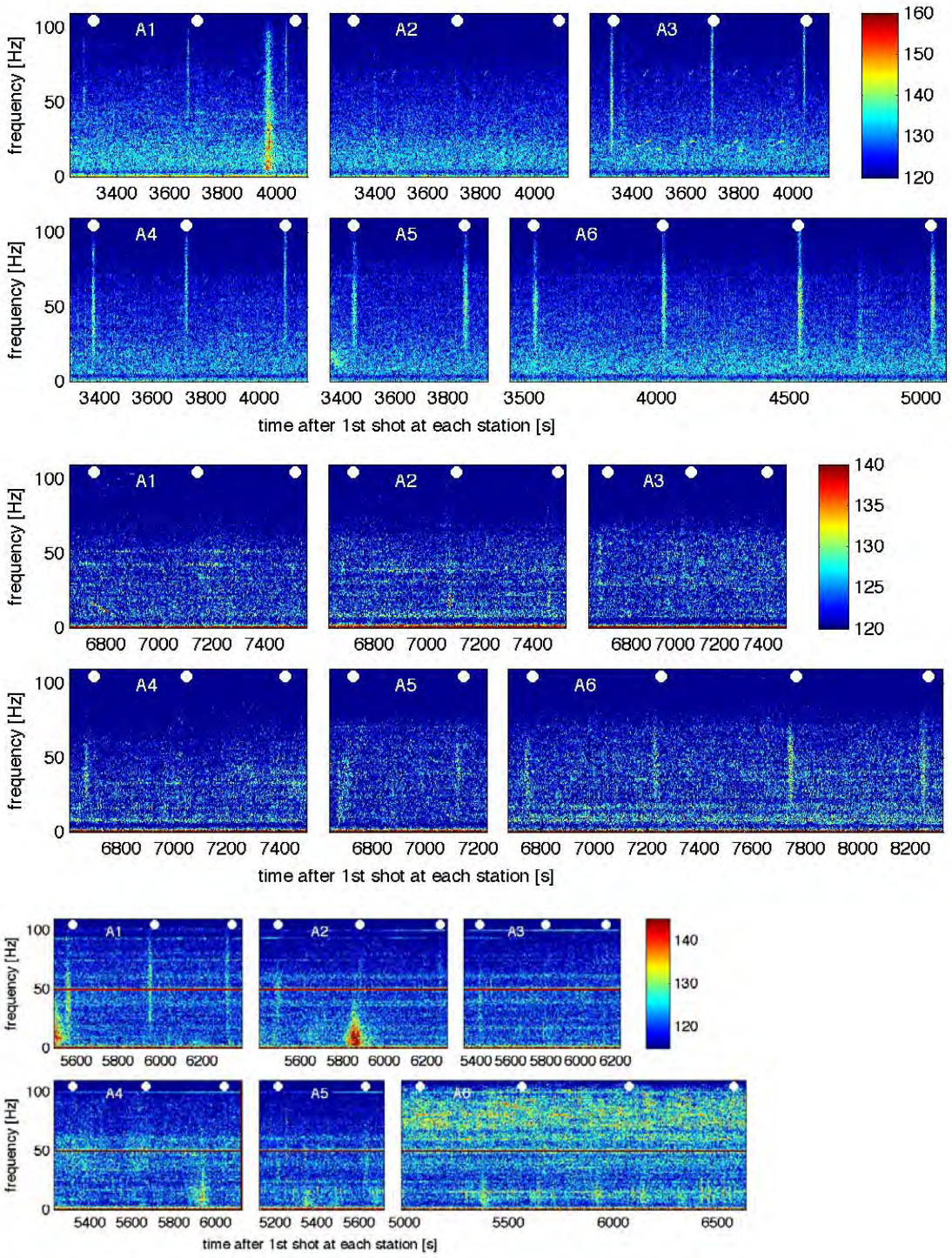

Figure 2. Sonograms for shot recordings at Cape Leeuwin (H01W, top), Diego Garcia South (H08S, middle), and Juan Fernandez (H03N, bottom). Station is labeled (A1-A6) in each subpanel. The time axis for each sonogram is with respect to the first shot in the sequence. White dots indicate a first-order estimate of expected travel time.

Data Analysis

We focus on two aspects of the analysis here: comparison of the observed and predicted travel times and estimation of the observed transmission losses as a function of frequency from source to receiver. The former relates to location estimates, the latter to yield estimates.

Transmission Losses

As previously discussed, a single near-source hydrophone at a depth of about 3-6 m was used to record the near-source pressure field. Thus, the recorded signal consists of a direct arrival plus a time-delayed, amplitude-reversed reflection from the air-sea interface, which may be represented in the time domain as

$$S_{rec}(t) = S_{true}(t) - R \times S_{true}\,(t\text{-}t_{echo}) = TF * S_{true}(t),$$

where TF is the transfer function representing the initial arrival and its echo and * denotes convolution. Convolution in the frequency domain is equivalent to multiplication in the time domain, so the power spectrum can be determined by dividing the power spectrum of the near-source recording by the power spectrum of the estimated transfer function. Fortunately, the zeros of the power spectrum of the transfer function lie either at very low frequencies for which the SNR was negligible and at f>125 Hz, i.e., at frequencies greater than the band of interest, since the instrument response of the IMS hydrophone stations drops off sharply at approximately f=100 Hz (Hanson and Bowman, 2005).

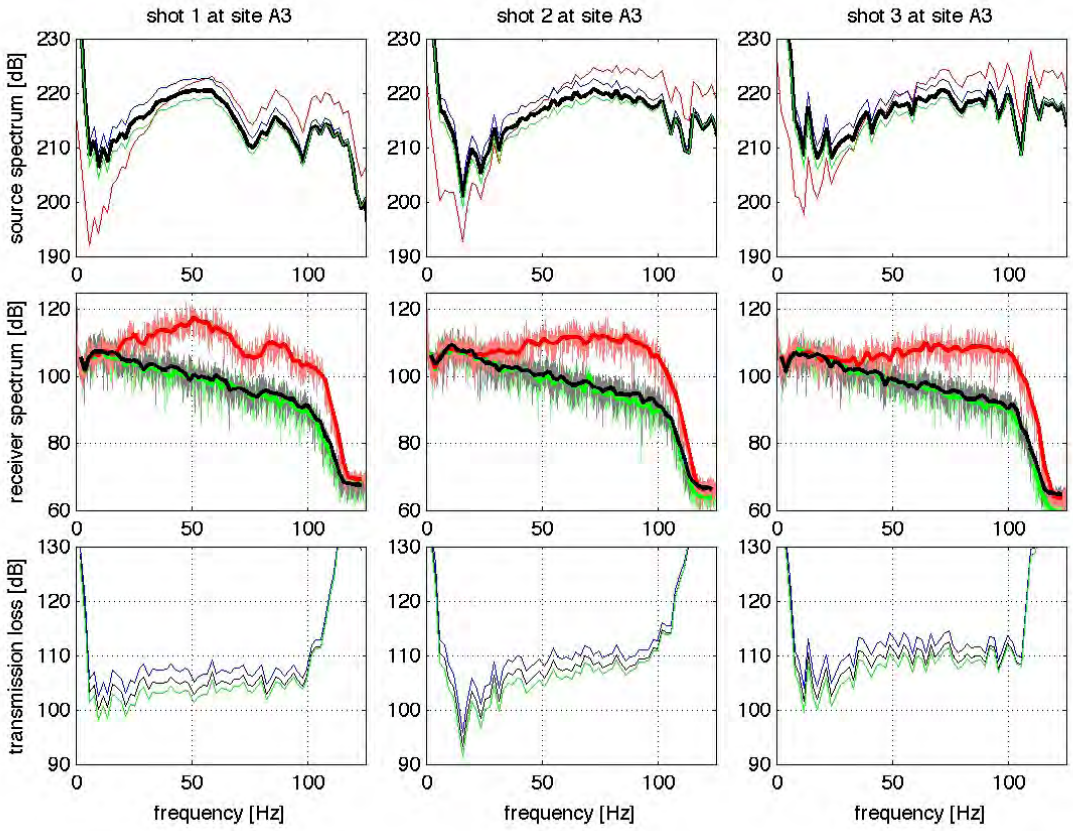

Figure 3. Source spectrum estimates (top row). raw (red) and corrected for echo from water surface, assuming time delays between initial pulse and reflected pulse of 4 ms (blue), 5 ms (black), and 6 ms (green). Power spectrum estimate for arrivals at Cape Leeuwin (middle row). Red lines are averaged signal spectrum, and green and black lines are power spectra for noise before and after the signal arrival, respectively. Heavy lines represent smoothed spectra. Transmission loss (bottom). Left to right – 4-lb shots at 300 m depth, 460 m depth, and 600 m depth. The blue, black, and green lines correspond to transmission losses derived from the source power spectral estimates of the same reflected-delay time assumption, keyed to color as in the top row panels.

However, deconvolution introduces some inaccuracy in the source spectrum estimate since one must know the precise delay time between the initial arrival and its echo, as well as the reflection coefficient off the surface—this is not exactly R = -1 for a rough sea surface. For these shots, cepstral analysis (not shown here) indicated a delay time of about 4-6 s. The source spectra for each shot conducted at site A3 (57.56°S, 171.72°E) are shown in the top row of Figure 3. All shots were 4-lb shots; shot 1 was detonated at 300 m, shot 2 at 460 m, and shot 3 at 600 m. The "zeros" in the source spectra are as predicted by bubble pulse theory; the first "zero" is at approximately 70 Hz for the 300 m shot, but for the deeper shots the first zeros are at frequencies greater than 100 Hz. The red lines indicate the uncorrected power spectra, while the blue, black, and green lines indicate the estimated power spectra corresponding to delays of 4 ms, 5 ms, and 6 ms, respectively. The difference between the source spectrum estimates – about 4 dB – is the error introduced by the necessity of having to deconvolve the sea surface reflection from the arrival.

Figure 3 also shows the power spectra for the waveforms recorded at Cape Leeuwin for the A3 shots, averaged over all three hydrophones (middle row), and the average source-receiver transmission losses for each shot. The results indicate that the transmissions are fairly uniform over the frequency range for which SNR>1. This is fortunate, as it means that the spectral scalloping associated with an explosive source may be observed at ocean basin scale distances. This result confirms computational predictions made using PE code modeling (Collins, 1993) indicating that transmission losses should be fairly uniform over the 30-100 Hz band for this source-receiver path. Also, note that the signal peak shifts toward lower frequencies for the shallower shots, with a peak at approximately 50 Hz for the 300 m shot. In addition, transmission losses are slightly lower for the shallower shots than for deeper shots.

Analysis of the remainder of the arrivals showed that the SNR was low at low frequencies for all source-receiver pairs; an unfortunate consequence is that the back azimuths cannot be computed accurately at the IMS hydrophone triplets. In theory, precise back azimuths can be computed by cross-correlating signals over narrow frequency bands and finding the best plane wave solution to the relative delay times. However, the degree of correlation decreases as the number of wavelengths between each hydrophone in the triplet increases. For the IMS stations, hydrophone separations are approximately 2 km within each triplet, thus the cross-correlations are most effective at frequencies of approximately 10 Hz or less. Thus the low SNR f < 20 Hz made this method infeasible. Determining back azimuths using travel time picks proved ineffective as well; the waveforms were emergent, thus travel times picks were accurate to only 0.5 seconds, which yielded very poor precision on computed azimuths.

Travel Times and Phase Duration

As a first approximation, travel times were computed assuming that hydroacoustic propagation follows geodesic paths from each source to receiver, i.e., the effects of lateral ray bending due to lateral variations in the sound speeds were ignored. The ocean sound speed profiles, derived from the Levitus database, were corrected for the effect of Earth curvature over these paths; this allows one to examine an arc path over the spherical Earth as a rectangular slice. Travel times and durations were then computed using group velocities corresponding to normal modes. Figure 4 shows an example of a travel time computation for mode 1 along a profile from site A1 to Juan Fernandez. As indicated, the axis of the sound channel shoals significantly toward the polar ocean and group velocities, especially for the lowest lower modes, vary significantly along the transmission path. The variation in group velocity along the path decreases at higher mode numbers. The effect of Earth curvature on total travel time is relatively insignificant: the travel time for the path shown in Figure 4 decreases by only about 0.3 seconds over a range of about 8200 km when Earth curvature is accounted for.

Our results also show that in most cases both the expected arrival time and duration can be predicted quite accurately using adiabatic normal mode theory. Figure 5 shows a sonogram and waveform of the recordings at Cape Leeuwin for the 12-lb shot at a depth of 460 m at station A6. Also shown are predicted arrival times for the first 20 modes at a source frequency of 40 Hz (white triangles). Travel times were computed as illustrated in Figure 4: a group velocity was computed for each of a number of points along a geodesic path from source to receiver, and the results were integrated to estimate the travel time. Higher order modes have higher average group velocities and thus arrive earlier than the mode 1 arrival – the one marked by the last triangle at the top of Figure 5. However, mode 1 is the most robust mode, i.e., the least susceptible to being stripped by bathymetry; this suggests that, for an underwater source, the time pick should be at the end of the waveform, rather than at the peak amplitude or peak frequency. The results shown in Figure 5 indicate that the duration of the arrival – about 18 seconds – agrees well with the degree of dispersion predicted using adiabatic mode theory for propagation along a geodesic path.

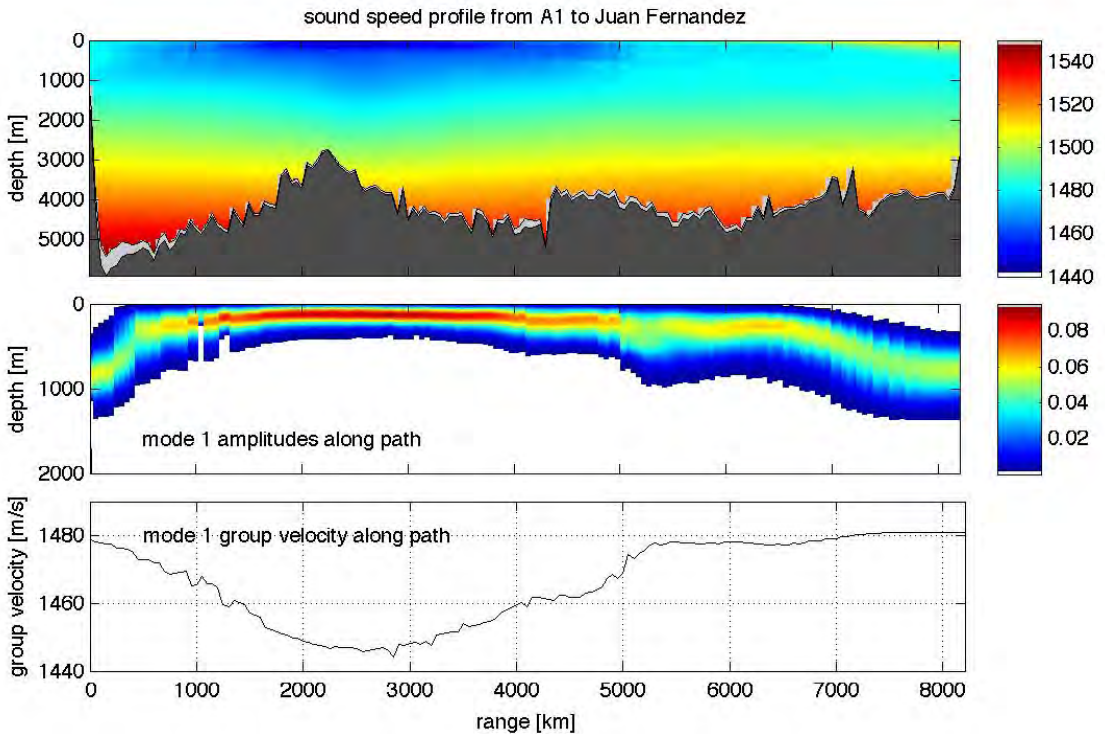

Figure 4. Top. Average winter sound speed profile along the source-receiver path, derived from the Levitus database, and corrected for Earth curvature. Sediment thickness (from Mooney et al., 1998) is indicated by the light gray zone. Center. Mode 1 amplitudes along the path for a source frequency of 40 Hz. Attenuation occurs where non-zero amplitudes intersect the bottom bathymetry, i.e., attenuation is negligible along this deep water path for mode 1. However, some scattering may take effect since transmission is surface limited over much of the path. Bottom. Group velocities along the travel path for mode 1 for a 40 Hz source. Group velocities are used to predict the acoustic travel time from source to receiver.

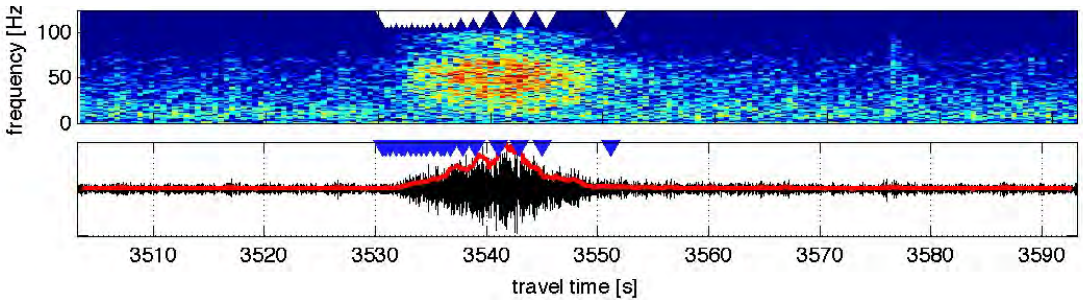

Figure 5. Sonogram and waveform for a recording at a single hydrophone at Cape Leeuwin for a 12-lb shot at a depth of 460 m at station A6. White (and blue) triangles show the expected arrival times for the first 20 modes, based on mean winter sound speed models and propagation along a geodesic travel path. Lateral ray-bending due to sharp velocity contrasts at the ACZ reduces the travel time by approximately 0.9 s for mode 1 - the last arrival.

Figure 6 shows the corresponding results for observations at Diego Garcia for the same shot. Predicted travel times for only 10 modes are shown here since the attenuation is predicted to be greater for this travel path. The waveform duration is again on the order of 18 seconds, as predicted by the computed mode arrival times. Arrivals for shots at stations A1 through A4 have durations on the order of 8-11 seconds, where observed, while stations A5 and A6 have

durations on the order of 18-20 s. That is, there is greater dispersion for sites further to the south within the polar ocean. The waveform durations at all stations were predictable using adiabatic normal mode theory and using winter sound speed profiles derived from the Levitus database.

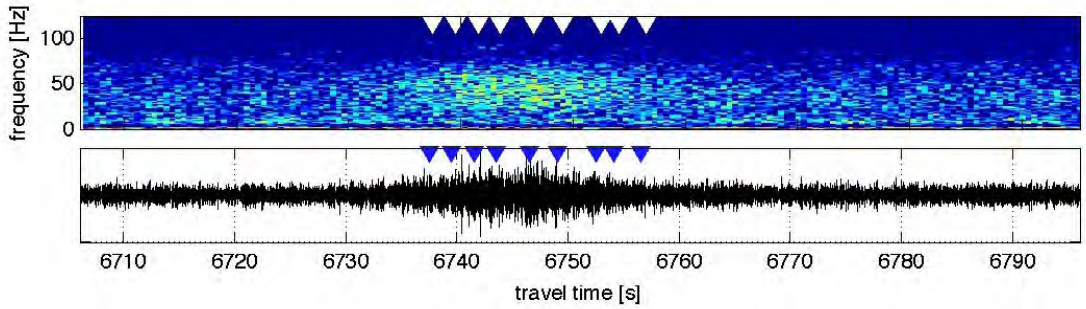

Figure 6. Sonogram and waveform for a recording at a single hydrophone at Diego Garcia South for a 12-lb shot at a depth of 460 m at station A6. White (and blue) triangles show the expected arrival times for the first 10 modes, based on mean winter sound speed models and propagation along a geodesic travel path. Lateral ray-bending due to sharp velocity contrasts at the ACZ reduces the travel time by approximately 0.9 s for mode 1.

Predicted arrival times for mode 1 agree with observations to within several seconds at these stations. Note these travel times are for propagation along the geodesic path; lateral ray-bending reduces the travel time by approximately 0.9 seconds for mode 1 at both Cape Leeuwin and Diego Garcia South. Figure 7 shows the lateral path deflections for paths from each shot site to each IMS hydrophone station, superimposed on a map of the group velocities. There is a significant increase in group velocities going from south to north across the Antarctic Convergence Zone for mode 1 as indicated, thus ray-bending is significant for mode 1. Ray-bending decreases the travel time to the Diego Garcia stations by as much as 5 seconds at station A3, by up to 3.9 s at Juan Fernandez, and by up to 2.2 s at Cape Leeuwin, as compared to propagation along a geodesic path. The contrast in group velocities across the ACZ decreases at higher modes; thus, ray-bending becomes less significant with increasing mode number.

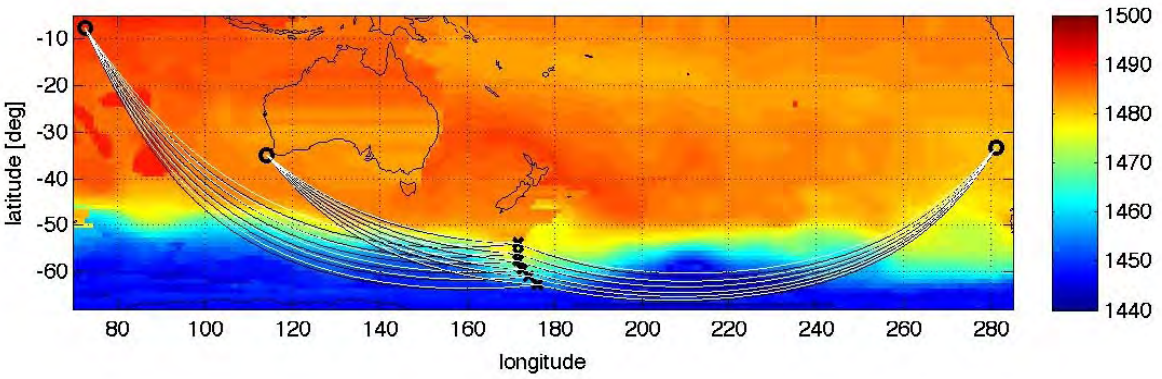

Figure 7. Lateral variation in group velocities causes a deflection of the propagation path from the geodesic; this effect was computed using the ray-bender code supplied in the hydrocam software (Farrell et al., 1996). Effect of lateral ray-bending from the December 2006 shots (labeled A1-A6) to the IMS hydrophone stations for mode 1 arrivals at a source frequency of 40 Hz. The black curves are geodesics; the white curves show the deflected ray paths corresponding to the minimum travel time paths. Group velocities were computed using average winter sound speed profiles and vary from approximately 1450 m/s (blue) to 1495 m/s (yellow). Lateral deflection has the effect of decreasing the travel time by several seconds for mode 1 and slightly less for higher order modes.

Both arrival times and waveform durations were predictable at all shot sites, to within 2 seconds —using adiabatic normal mode theory and using winter sound speed profiles derived from the Levitus database. This implies that location estimates should be accurate for sources observed at two or more stations. However, determinations of paths for shots near the boundary of the ACZ, between the colder waters to the south and warmer water to the north, are affected significantly by complexities in the shape of the time-varying boundary. Thus, temperature and sound speed profiles derived from the Levitus database, which is drawn from observations averaged over a long term, may produce somewhat less accurate predictions for near-boundary shot sites than for sites further to the south, well within the Antarctic circumpolar current, where discrepancies between local and mean velocities may average out.

CONCLUSIONS AND RECOMMENDATIONS

We have completed a relatively inexpensive experiment by piggybacking on a previously funded research cruise. We fired a series of test shots along a transit from Christchurch, New Zealand, to McMurdo station in the Antarctic, allowing us to test propagation characteristics across a range of polar front acoustic propagation paths. Most shots were detected at least one IMS station. Our main results to date are as follows:

- Highest SNR values were recorded for shots at 300 m depth, the shallowest depth tested.
- Observed transmission losses are fairly uniform as a function of frequency, in agreement with theoretical results provided by PE computations.
- There is significant variation in group velocities along the path, particularly at the lowest modes.
- Oceanographic gradients within the polar front alter the path of an acoustic wave, decreasing travel time by as much as 5 s, as compared to propagation along a geodesic path.
- Observed travel times and phase durations for sites well to the south of the ACZ boundary agree to within several seconds with theoretical results from adiabatic mode computations.
- Significant discrepancies in travel time are observed for sites nearest the ACZ boundary.

Comparison of observations with theoretical results suggests that further investigation of acoustic propagation for sites nearest the ACZ boundary is needed. We have thus proposed another research cruise to obtain more detailed measurements. Our new plan calls for several improvements to the previous experiment design. First, shots will be conducted at shallower depths than for our previous experiment to increase both the SNR and the width of the frequency band of the recorded signal. Second, we plan to deploy either a vertical hydrophone array or autonomous instruments near the source to more accurately estimate the source spectrum. Finally, we plan to do repeat SUS charges at a given depth at a single site; this would allow us to stack signals from a given depth, thereby increasing the SNR at the IMS stations and ensuring that marine mammals are not harmed.

REFERENCES

Collins, M.D. (1993). A split-step Padé solution for the parabolic equation method, *J. Acoust. Soc. Am*. 93: 1736–1742.

Dushaw, B. D. (1999). Inversion of multimegameter range acoustic data for ocean temperature. *IEEE J. Oceanic Engineering* 24: 215–223.

Farrell, T., K. LePage, and C. Barclay (1996). Users guide for the hydroacoustic coverage assessment model (hydroCAM), BBN Technical Memorandum W1273.

Hanson, J. A., and J. R. Bowman (2005). Dispersive and reflected tsunami signals from the 2004 Indian Ocean tsunami observed on hydrophones and seismic stations, *Geophys. Res. Lett.* 32: L17606, doi:10.1029/2005GL023783.

Levitus, S., *World Ocean Atlas* (1994). NOAA Atlas NESDIS 4, Washington D.C.

HYDROACOUSTIC PROPAGATION AND REFLECTION LOSS USING EXPLOSIONS FOUND IN THE INDIAN OCEAN

Jeffrey A. Hanson, Colin L. Reasoner, and J. Roger Bowman

Science Applications International Corporation

Sponsored by Army Space and Missile Defense Command

Contract No. W9113M-05-C-0138

ABSTRACT

We investigate propagation and reflection loss using hydroacoustic waves from explosion sources in the Indian Ocean recorded at the International Monitoring System's (IMS) hydrophone stations. We developed a discovery procedure that searches the automatic processing results from the International Data Centre (IDC) for signals that match explosive characteristics. Potential candidate explosions are confirmed by examination of the raw waveform data. Using this procedure, we have identified hundreds of explosions throughout the Indian Ocean Basin. The instigators of the explosions are not known, but the locations and characteristics of the explosions lend themselves to likely candidates. These include military exercises, construction, geophysical exploration, and local fishing practices.

We examined hydroacoustic data covering a 6-year period and identified 305 separate explosions. Of these, 25 were recorded at three hydrophone triads – Cape Leeuwin, Australia (H01W), Crozet Island (H04N) and Diego Garcia (H08S) – 79 were recorded at two triads – H04N and H08S – and 201 were recorded at a single triad. In addition, we have observed many airgun surveys, but they are not of interest here due to their local nature. We are able to locate explosions observed at three or two triads using direct arrivals. In some cases, we can locate explosions recorded at a single triad using observed reflections. Absolute arrival times can be estimated to less than 2 seconds, and relative times for closely spaced explosions can often be estimated to within a few samples (4 to 12 milliseconds). Back-azimuth uncertainty estimates range from a few tenths of a degree to several degrees depending on the frequency content of the signal and noise conditions at the triad.

The explosions are distributed in three general locations: the Arabian Sea off northwestern India, the Bay of Bengal, and along the islands of western Indonesia. The explosions in the Arabian Sea and the Bay of Bengal are likely of military origin, while the western Indonesian explosions are more likely from blast fishing. The Arabian Sea explosions occur near a test firing range off shore from Dwarka, India. The Indonesian explosions occur in clusters that correspond to the islands ranging from Simeulue Island in Aceh Province to the northwest tip of Java.

Received signals have energy distributed in frequency starting at 2 to 10 Hz and continuing up to the Nyquist frequency (125 Hz). Peak received levels from the explosions range from 105 to 150 dB rel. 1 μPa. Basic attenuation corrections indicate the yield sizes range from less than one to tens of kilograms. Bubble pulse estimates place a trade-off constraint on source size and depth. The bubble pulse delay time estimates range from 0.1 to 0.5 seconds. The explosions along Indonesia have bubble pulses clustered near 0.2 seconds suggesting that the explosions have similar sizes and depths. Bubble pulse estimates for the same explosion measured at different triads (H04N and H08S) agree to within a few milliseconds.

The explosions are located so that paths to different stations intersect different bathymetry. Most have direct deep water paths to at least one of the hydrophone triads. Attenuation estimates can be made by comparing amplitudes between stations. Relative amplitudes between triads for closely spaced explosions are stable (to within 3 dB) and demonstrate the robustness of attenuation estimates. Attenuation is observed to vary for paths that intersect specific bathymetric features, many of which do not reach the Sound Fixing and Ranging (SOFAR) channel axis. This is particularly evident for paths crossing near the Afanasiy-Nikitin Seamount south of Sri Lanka. Small changes in path (within 100 km) are observed to cause attenuation differences of as much as 20 dB.

OBJECTIVES

This project is designed to improve discrimination of underwater seismic events and improve location of hydroacoustic sources in or just above the water column. This is accomplished by analyzing hydroacoustic data from a multitude of explosion sources to assess high-frequency (>30-50 Hz) signal loss of hydroacoustic energy propagating in the SOFAR channel, from reflections off coastlines, and interaction with bathymetric obstacles along path. We use variations in the observed residual amplitudes to identify important environmental factors that influence high-frequency transmission loss. This allows for better prediction of the reflected wave field and better understanding of the robustness of explosion-characteristic measures from reflected or highly attenuated signals.

RESEARCH ACCOMPLISHED

Data Set of In-Water Explosions

We have discovered 438 explosion signals from 305 distinct in-water explosion sources detonated by other parties in the Indian Ocean and recorded on hydrophone stations of the International Monitoring System (IMS) (Figure 1, Table 1). To identify candidate explosions, we examined results of our automatic processing of Indian Ocean hydrophone stations for the period September 2004 to March 2005 (Hanson et al., 2007). We also examined automatic processing results by the IDC for the period November 2001 through May 2007. The IDC processed data separately from each of the triad hydrophones, whereas our processing treated the triads as arrays. Array processing allowed identification of signals with lower signal-to-noise ratio (SNR), due to array gain, and the estimation of arrival azimuth and slowness.

To find previously unknown in-water explosions, we developed search criteria based on our previous experiences studying long-range propagation of signals produced by small in-water explosions (e.g., Reasoner et al., 2005; Hanson et al., 2001; Brumbaugh and LeBras, 1998). These criteria exploit signal features routinely measured in our own automatic processing of transient hydroacoustic signals (Hanson and Bowman, 2006) or by automatic processing results from the IDC (see e.g., Hanson et al., 2001). The criteria included significant peaks in the estimated cepstrum, broadband energy content (significant energy to at least 80 Hz), short signal durations, and phase velocities consistent with horizontally propagating waves.

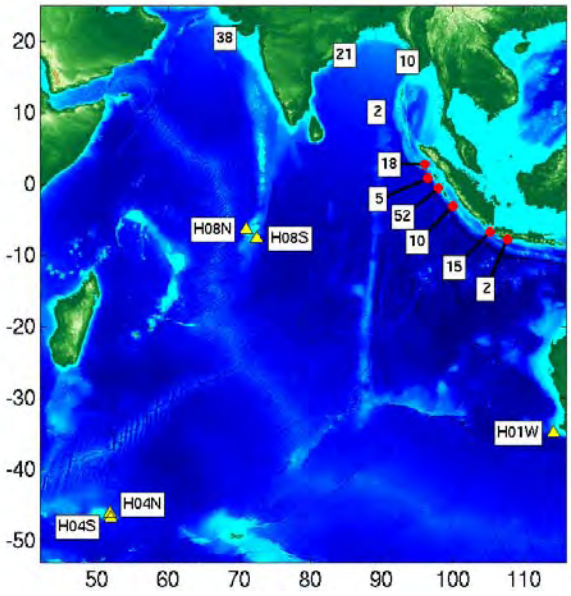

Figure 1. Locations of explosions (numbered squares) recorded at one or more IMS hydrophones (yellow triangles). Numbers indicate sets of explosions in close proximity to one-another.

We conducted an intensive search for in-water explosions in two parts. The first, more comprehensive, search covered a seven-month period of data that spanned from September 2004 through March 2005. These data were processed in-house using the algorithms described in Hanson and Bowman (2006). Signals matching our criteria were examined regardless of peak energy level. The second part of our search covered a six-year period from 2001 to 2007. For this search, we used the automatic processing results from the IDC and further constrained the search criteria to find only larger explosions with a peak received level > 140 dB rel. 1 μPa.

Our search criteria admit some ice events, shallow earthquakes and other unidentified transient signals. Signals from all candidate explosion signals were examined to confirm or refute explosion characteristics. Figure 2 shows spectrograms for three arrivals confirmed as explosions, owing to their high frequency content, scalloped spectra, and short durations. Because the explosions are generally low yield, they are often only detected at one hydrophone

triad by automatic processing. However, more detailed examination of data at other triads, assuming likely source areas, enabled us to find arrivals from the same explosions at multiple stations. In addition, reflected energy is observable for many explosions (Figure 2). We are able to locate many of the explosions based on the multiple arrivals.

Of the 305 explosions we discovered, 25 were recorded at three or more hydrophone triads, 79 were recorded at two triads (H04N and H08S), and 201 were recorded by a single triad. Explosion signals are observed most commonly at Crozet Island North (H04N) and Diego Garcia South (H08S). In addition to the explosions in Table 1, we observed many airgun surveys, but did not investigate them because their signals are generally recorded only by a single, nearby hydrophone triad and are not useful for studying long-range transmission loss. The 305 explosions found in this study dramatically increase the number of known in-water explosions in the Indian Ocean from the 17 explosions detonated on a 2003 traverse from Cape Town to Cocos-Keeling Island (Blackman et al., 2003) and two explosions in 2004 in the Bay of Bengal (Graeber and Firbas, 2005; Spiliopoulos and Jepsen, 2005; Reasoner et al., 2005; Bowman et al., 2005).

Table 1. Explosion arrivals in the Indian Ocean basin

Hydrophone Triad	Number
Cape Leeuwin (H01W)	60
Crozet Island North (H04N)	156
Crozet Island South (H04S)	4
Diego Garcia North (H08N)	42
Diego Garcia South (H08S)	176
Total	438

The explosions in the Indian Ocean basin are distributed in three general locations: the Arabian Sea off northwestern India, the Bay of Bengal, and along the islands of western Indonesia. Figure 1 shows the number of explosions observed in each source area. Explosions offshore of Indonesia are often observed at two or three triads. In contrast, because of signal blockage, explosions offshore of northwestern India are observed by a single triad, H08N, and offshore of Myanmar, only by H08S. Locations for some of these explosions are estimated using back-azimuths and differential arrival times of direct and reflected signals (Hanson and Bowman, 2006). The 38 explosions shown in the Arabian Sea offshore of Dwarka, India are those for which H08N arrivals had valid estimated back-azimuths.

The instigators of the explosions are not known, but the locations and characteristics of the explosions lend themselves to likely candidates. These include local fishing practices (particularly off Indonesia), military exercises (e.g., off India), construction and demolition, and geophysical exploration.

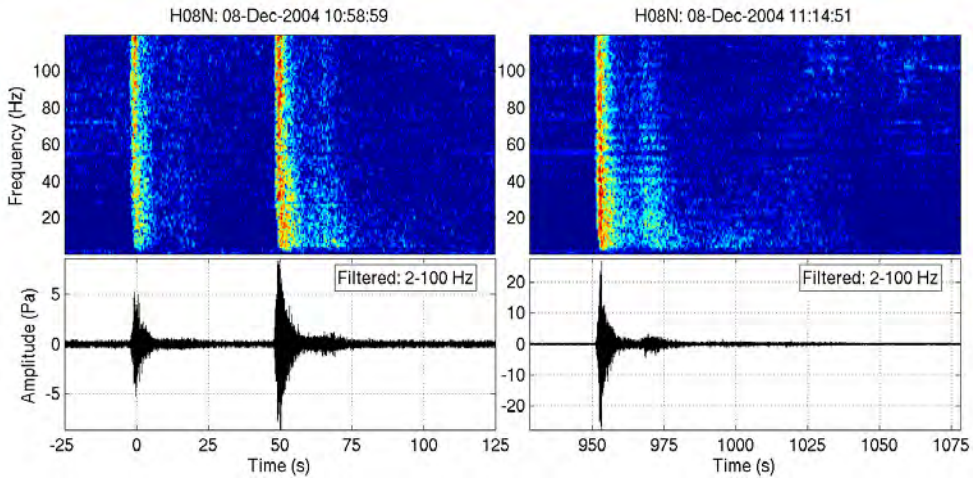

Figure 2. (Left) Spectrogram and waveform of two explosions recorded at Diego Garcia North (H08N). The direct arrivals are broadband signals with frequencies extending from 2 Hz to greater than 100 Hz and are followed by lower amplitude, lower frequency reflected arrivals. (Right) Spectrogram and waveform of an explosion recorded at H08N. The direct arrival and first reflected arrival show clear scalloping from the bubble pulse.

Characterization of Explosions

Explosion signals have energy distributed in frequency starting at 2 to 10 Hz and continuing up to the Nyquist frequency (125 Hz). Peak received levels from the explosions range from 105 to 150 dB rel. 1 µPa. Basic attenuation corrections indicate the yield sizes range from less than one kilogram to tens of kilograms. The explosion signals are concentrated during the daylight hours in the Indian Ocean (Figure 3). This is consistent with our interpretation that these events are man-made explosions.

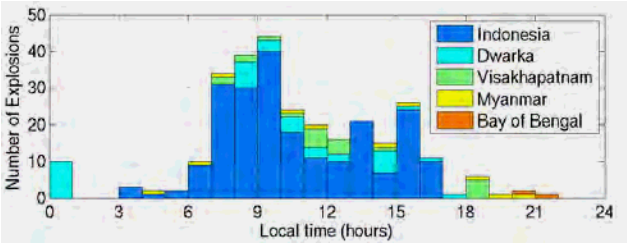

Figure 3. Time of day distribution of explosions color coded by location.

We initially estimated the locations of 102 Indonesian explosions using the measured arrival times and back-azimuths with a standard location algorithm that used the IDC's 2D, seasonal, travel-time tables. Although two arrival time estimates and two back-azimuth estimates are technically enough to uniquely locate events, the uncertainties in back-azimuth—a few tenths of a degree to several degrees depending on the frequency content of the signal and the noise conditions at the triad—projected over thousands of kilometers provide little constraint on locations. However, absolute arrival times can generally be estimated to within 2 s or less. Therefore, we used arrival times as the main data constraint and back-azimuth estimates to confirm associations.

Figure 4 shows how the different data constrain locations. The back azimuths are consistent with locations along Sumatra and Java, but do not put tight constraints on actual locations as seen in Figure 4a, which shows locations based on projected back-azimuth crossing points. Although the arrival time differences between two stations can be measured precisely and the model errors are likely small, a two station time difference does not constrain the location to a point but instead to a continuous curve such that the travel time difference between the two stations remains constant. Because there is no closed form solution on an ellipsoid, we determined these curves by iterative search. In Figure 4b, curves using the arrival time differences between H08S and H04N are shown for each explosion as they intersect Indonesia. The lines overlie one another such that the 102 explosions fall into tight clusters. The uncertainties from measurement error are no wider than the plotted lines. Different assumptions in travel time model can shift the curves by tens of kilometers, but all in the same direction. Although most explosions have only two observations, 23 explosions were observed at H01W in addition to H04N and H08S. These explosions can be located accurately (Figure 4c) and lie just off the coast of the western islands. Since we suspect that the explosions are used for fishing, it is reasonable to expect that the explosions are not far from the islands. Thus, the intersection of the two-station, time-difference curves with the coast is likely close to the actual location. To stabilize our final locations we chose to use the intersection with the 500 meter depth contour—intersections with shallower bathymetry contours are more ambiguous because of their high curvature. Since the bathymetry in the area is steep, the 500 meter contour is only 10 to 20 km from the coast, and thus our locations are likely only slightly biased to the west. Figure 4d shows our final explosion locations.

The explosions occur in clusters that correspond to the islands ranging from Simeulue Island in Aceh Province to western Java (Figure 4d). The events collect into six main groups (labeled A-F), but within each group there are several smaller clusters. Groups A through D appear associated to the islands off western Sumatra and roughly correspond with Simeulue, Nias, Batu and Mentawi Islands, respectively. There is a gap in the explosions between 3˚30'S and 6˚30'S which corresponds to a gap in the western islands with the exception of the lightly populated Enggano Island. If explosions have also been detonated offshore of Sumatra itself, then their signals have been blocked by the bathymetric ridge that extends south of the offshore islands. The explosions in Group E are near Panaitan island in the Ujung Kulon National Park, a world-renowned surf break, and Group F occurs off the coast of West Java Province.

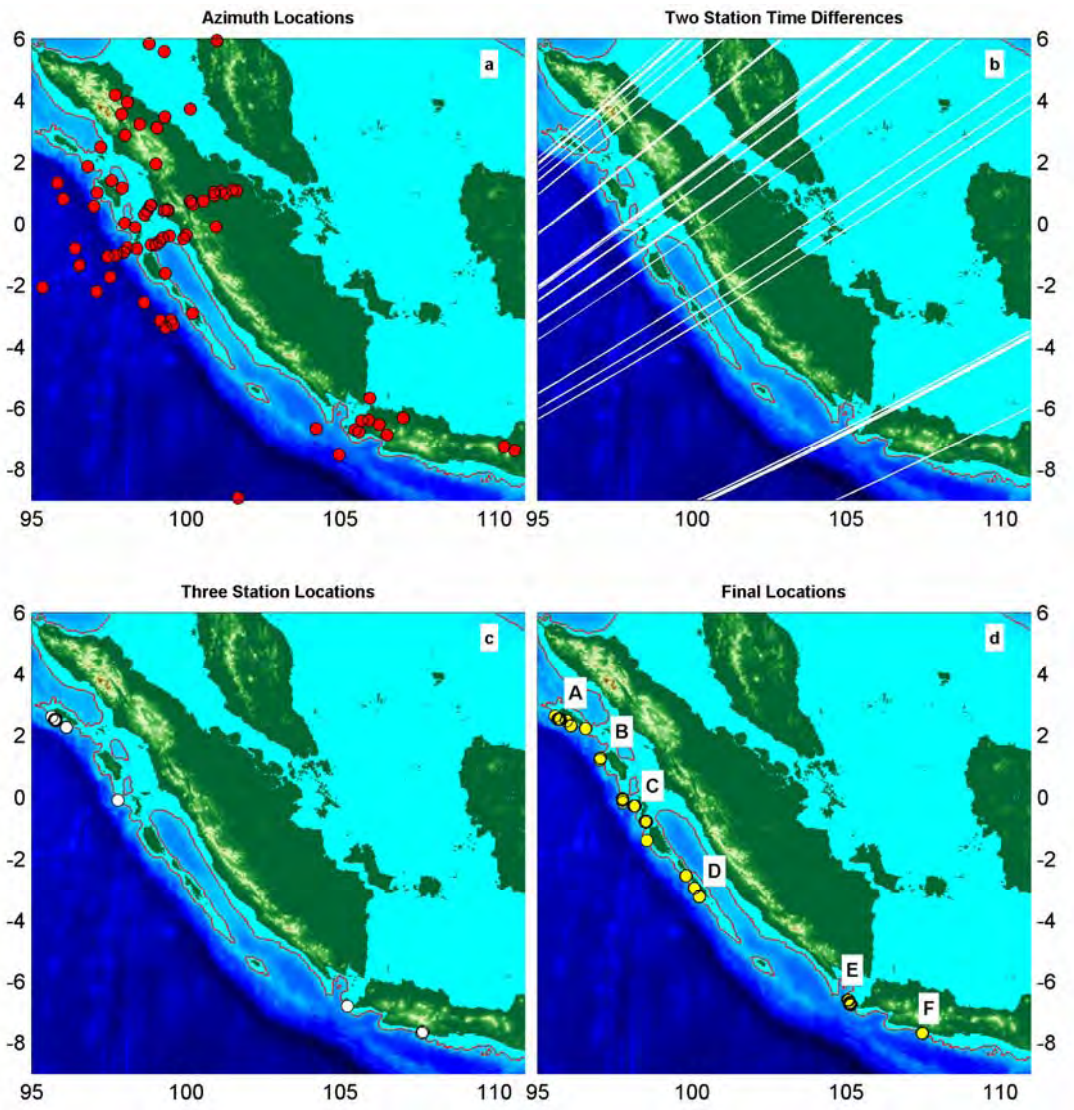

Figure 4. Location determination of 102 explosions west of Sumatra and Java. Seventy-nine explosions are observed at H08S and H04N, and 23 explosions are, in addition, observed at H01W. (a) Back-azimuth locations are consistent with Sumatra or Java sources, but with large uncertainty. (b) Constant arrival time difference curves for arrivals at H04N and H08S. (c) Three-station time-based locations for 23 explosions that lie along the western islands. (d) Locations based on location curves in (b) intersecting the 500 m bathymetry contour (red line).

The cepstral delays of the explosion arrivals are tightly clustered near 0.2 s at both H04N and H08S, suggesting that the explosions have similar sizes and depths. Bubble pulse estimates place a trade-off constraint on source size and depth. The bubble-pulse delay time estimates range from 0.1 to 0.5 s (Figure 5). The right panel of Figure 5 shows representative depth-yield tradeoff curves for cepstral delays from 0.10 to 0.25 s, which correspond to small or deep sources. Explosions with yields of 10 kg or less with a 0.2 s delay would have had to occur at depths less than 50 m.

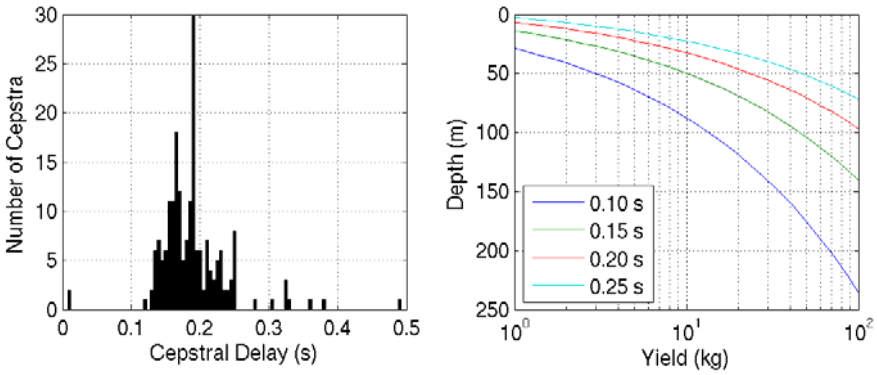

Figure 5. (a) Histogram of cepstral delays for all H01W, H04N and H08S arrivals associated to explosions offshore of Sumatra and Java. (b) Representative depth-yield tradeoff curves for selected cepstral delays.

The cepstral delay time values are useful in confirming the arrival associations. The cepstral delays estimate the bubble pulse periods of the explosions and, hence, should be independent of path and receiver effects. The mean difference in cepstral delay times estimated at H04N and H08S for 75 Sumatra and Java explosions is essentially zero with a standard deviation of less than 2 milliseconds. This is less than the sampling rate of the instruments (4 milliseconds between samples), which is possible because we interpolate the delay time.

The hypothesis that the Indonesian explosions are largely from blast fishing is somewhat surprising since we would expect these explosions to be small, shallow, and in shallow water, none of which are properties conducive to basin wide propagation. We conducted preliminary modeling to help determine how, or if, the signals from these explosions could make it into the sound channel. Figure 6 shows the sound speed profile for three depth ranges from the Generalized Digital Environmental Model (GDEM) offshore of equatorial Sumatra (blue line). The left panel shows the sound speed profile for the entire water column. The middle and right panels show the thermocline and mixed layer profiles, respectively. The red line is a simplified model for future sensitivity experiments that represents the surface duct as a single gradient defined by points at the surface and 75 meters, and the thermocline as a negative gradient defined by points at 100 and 200 meter depths. These two gradients are a good approximation to the GDEM data.

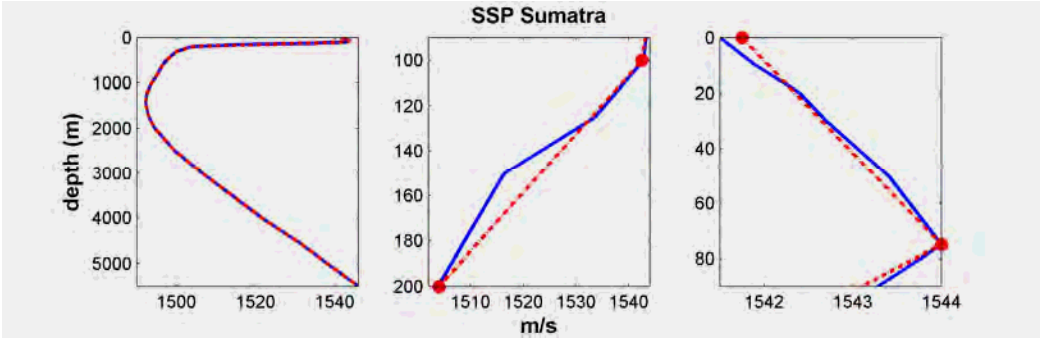

Figure 6. Sound speed profile from GDEM (blue) and simplified version (red) used in modeling hydroacoustic propagation in the equatorial Indian Ocean offshore of Sumatra.

We used the sound speed profile described above to model propagation with different source bathymetry to examine the possibility of getting energy from shallow explosions trapped and propagating horizontally in the sound channel. Figure 7 shows results from Gaussian beam ray tracing using BELLHOP (Porter and Bucker, 1987). The source frequency used for all models is 50 Hz, and the source depth is 25 meters. Rays were calculated for take-off angles ranging from -20 to +20 degrees. The first model (a) is for a range independent ocean (5,300 meters deep). It is clear that the sound bounces vertically with some energy trapped in the surface duct, but no energy is trapped in the deep sound channel. The next model (b) starts with a 6-degree wedge, which is a typical overall slope for the Sunda Trench. The wedge is effective at converting steep rays to horizontal rays, and then, because the ocean is deepening so quickly, the rays are trapped by the sound channel and do not interact with the seafloor. The third model (c) is the

same as (b) except the first 5 km is a 100-meter deep shelf. Energy still manages to enter the deep sound channel. The bottom model (d) uses an example of a more realistic trench bathymetry profile perpendicular to Sumatra (from ETOPO2). It is also effective at trapping energy into the deep sound channel. Bottom properties, including shear velocity, attenuation, and roughness, can diminish or enhance transmission into the sound channel, but it is clear that the bathymetry and sound speed profile near Sumatra conspire to allow small shallow explosions to be heard at basin-wide distances. Although shallow sources add complication to interpretation, they are probably more representative of realistic explosion monitoring type problems.

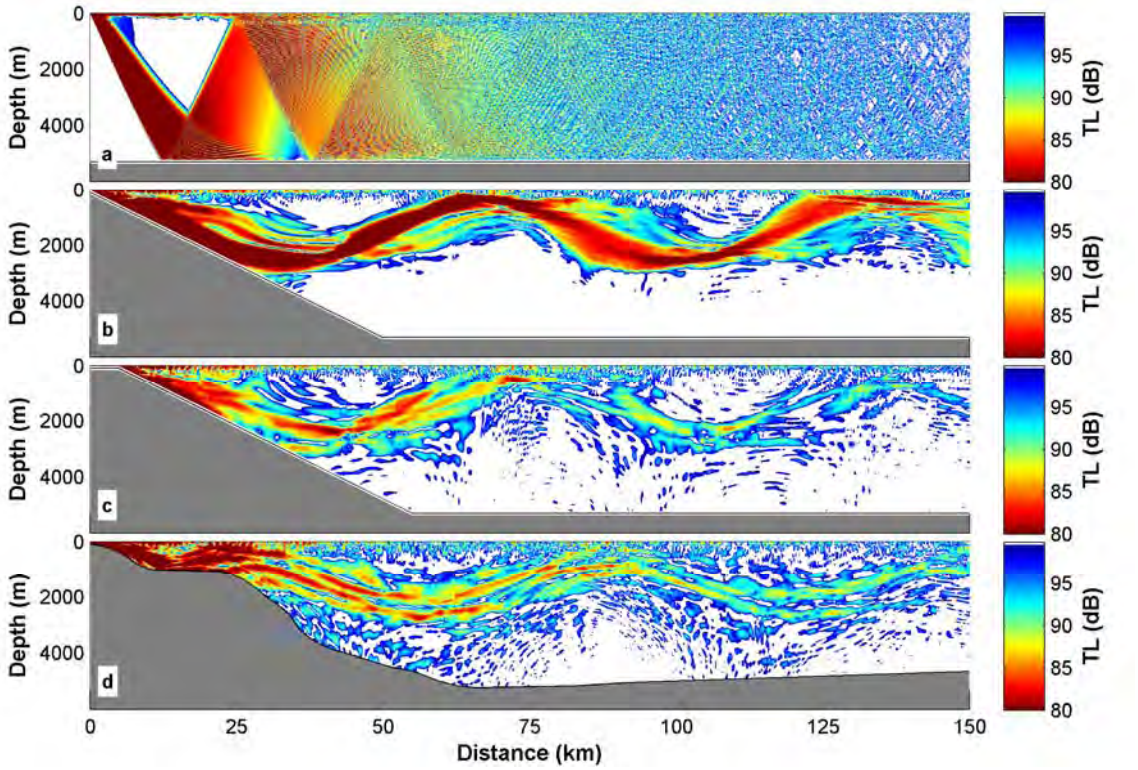

Figure 7. Transmission loss predicted from ray tracing for a source at 25 m depth and a frequency of 50 Hz for (a) open ocean, 5,300 m depth, (b) a 6º continental slope, (c) a 6º continental slope and a continental shelf 5 km wide, and (d) bathymetry from ETOPO2 (Smith and Sandwell, 1997).

Transmission Loss for Direct Arrivals

The explosions are located so that paths to different stations intersect different bathymetry. Most have direct deep water paths to at least one of the hydrophone triads. Attenuation estimates can be made by comparing amplitudes between stations. Explosions in Group A, near Simeulue Island, can be further divided into five sub-groups based on arrival time differences between H04N and H08S (Figure 4b). Figure 8 shows an example of observed variations in the relative received level for closely spaced events. Each panel shows the frequency dependent amplitude ratios between H04N and H08S relative to the expected loss based on distance traveled assuming cylindrical spreading and $0.5 \cdot 10^{-3}$ dB/km intrinsic attenuation (Urick, 1979). The explosions are separated by less than 100 km (small when compared to the 2,900 and 6,900 km paths to H08S and H04N, respectively). However, the relative amplitudes vary by more than 20 dB. Paths to both stations are generally deep and are rarely less than 2,000 m (except at the source). Conventional wisdom would expect little difference in attenuation among these paths. It is important to understand how these high frequency amplitude variations arise from such small differences in path.

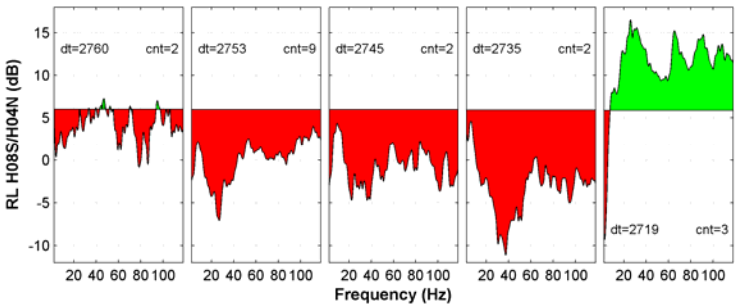

Figure 8. Frequency dependent received level (RL) differences between H08S and H04N for five slightly different paths in Group A. The arrival time differences (dt) and the number of events (cnt) are specified for each path. The water level is set to the expected RL difference assuming no obstacles (~6 dB). Red indicates that the signal is smaller than expected at H08S and green indicates that the signal is smaller than expected at H04N.

Paths from Group A explosions to H08S cross two potentially significant bathymetric features: The Ninety East Ridge and the Afanasiy-Nikitin Seamount (Box 1 and 2 in Figure 9). Paths to H04N only cross the Ninety East Ridge (Box 3). These sections of the Ninety East Ridge are relatively deep. The Afanasiy-Nikitin Seamount rises up to 1,800 m below sea level. Although this is deeper than the sound channel axis, it is still a significant impediment to sound propagation. The section of the Ninety East Ridge that these paths intersect is likely too deep to have much effect on transmission.

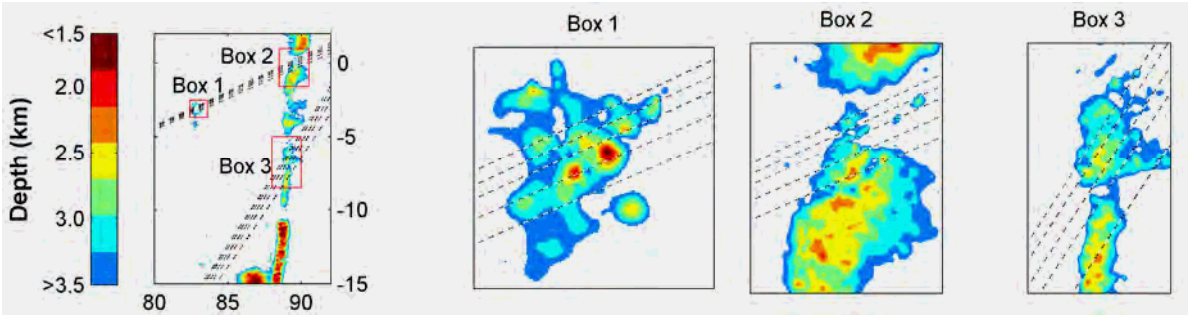

Figure 9. Significant bathymetry along Group A explosions paths to H08S (northern dashed lines) and H04N (southern dashed lines). The five paths are for the clusters within Group A (Figure 4)—the northern most path corresponds to the left most panel in Figure 8. Paths to H08S intersect the Afanasiy-Nikitin Seamount (Box 1) and the Ninety East Ridge (Box 2). Paths to H04N also intersect the Ninety East Ridge (Box 3). The bathymetry is from ETOPO2.

Modeling hydroacoustic transmission loss (TL) can be a difficult problem. Although there has been much success with TL modeling provided enough environmental constraints, general basin-wide TL modeling is not yet practical. Not only do global databases lack the necessary resolution in bathymetry and accuracy in seafloor properties, but also unknowns in source factors make highly precise, and not necessarily accurate, modeling of dubious value. We are taking a more statistical approach to the problem that if properly calibrated should be of use for understanding the uncertainties in hydroacoustic monitoring capabilities. At the distances and frequencies of most interest to nuclear-test monitoring (2 to 100 Hz) intrinsic attenuation is small, and most attenuation other than geometrical spreading is caused by interaction with the seafloor or sea-surface. The sound that propagates thousands of kilometers will consist of a narrow set of rays. The angles of the ray bundle as measured at the sound channel axis will generally be less than 10 degrees. Assuming the rays have constant horizontal slowness, the grazing angle at the seafloor will be less than 10 degrees, which is generally less than the critical grazing angle for typical compressional velocities. Thus, reflection loss will be due to intrinsic P-wave attenuation or due to the seafloor supporting shear waves.

Our approach is to approximate the seafloor interaction at any given point as a function of ray angle measured at the sound channel axis. Using a ray theoretical model, we define the signal loss per distance traveled as a function of ray parameter, p, for a given sound speed profile, $v(z)$, and sea bottom depth, z_b, as

$$\chi(p : v(z), z_b) = N(p) \cdot BL(\theta(p : z = z_b)) \text{ where } BL = -10 \cdot \log(R(\theta)) \qquad (1)$$

N is the number of ray interactions per distance traveled, and R is the reflection coefficient as a function of grazing angle, θ. We assume that the bottom loss is proportional to the vertical slowness, which at small angles is proportional to the grazing angle. The number of ray interactions per distance traveled can be calculated from the eikonal equation assuming constant ray parameter and integrating along path (e.g., Lay and Wallace, 1995):

$$N(p) = \left[2p \int_{z_b}^{z_0} \left[\gamma^2 + p^2 \right]^{-1/2} dz \right]^{-1} \tag{2}$$

where z_0 is the ray's turning point, and γ is slowness as a function of depth. We are most interested in estimating a reasonable variance on the signal loss along the path. We use the sensitivity of our modeled signal loss to grazing angle at the seafloor as a measure of uncertainty by assuming that the attenuation per reflection is proportional to the grazing angle. For shallow grazing angles (which rays at long distance must be), this is a reasonable first approximation. By taking partial derivatives with respect to the grazing angle at the seafloor, a variance in bottom loss with distance can be estimated:

$$\mathrm{var}(BL) = \alpha^2 \left(\frac{\partial N}{\partial \theta} \theta + N \right)^2 \delta\theta^2 \tag{3}$$

Figure 10 shows the function of seafloor interaction versus depth and take-off angle for two sound speed profiles. The first sound speed profile is the Munk Profile (1974), and the second is an equatorial Indian Ocean profile extracted from GDEM. The area in white indicates zero interaction (rays turn before hitting bottom), and the areas in red indicate strong seafloor interaction. The Indian Ocean sound speed profile has a broader sound channel as indicated by the width of blue in the figure. The ray interaction for a 2,500-meter deep seafloor in the equatorial Indian Ocean only begins for angles greater than 6 degrees, but a 1,750-meter deep seafloor has ray interaction starting at 2 degrees. This may seem like a small difference, but it is a large proportion of a ray packet that travels long distance.

In the case of shallow explosions, like those west of Indonesia, steeper ray angles between 2 and 6 degrees are critical, as can be seen from the ray tracing results in Figure 7. This helps explain the strong sensitivity of received levels to slight variations in the paths crossing the Afanasiy-Nikitin Seamount observed in Figure 8. If the seamount were in an area with a more typical sound speed profile, such as found at higher latitudes, it would probably cause little attenuation of the signal.

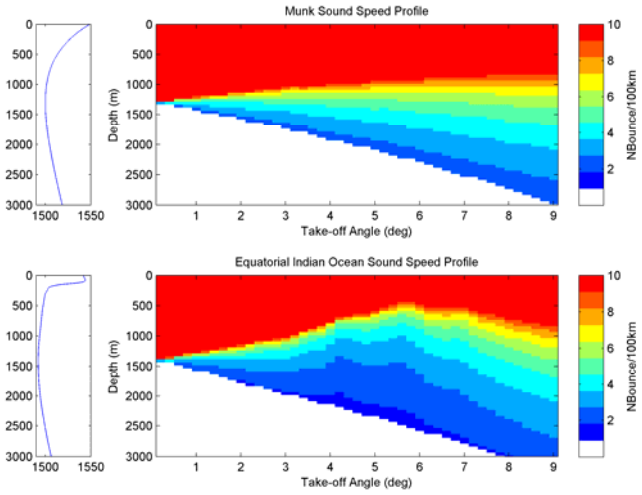

Figure 10. Contour plot of the number of bounces per 100 km as a function of take-off angle and water depth for (upper panel) the Munk (1974) sound speed profile (shown to left), and (lower panel) a GDEM profile for the equatorial Indian Ocean. The sound speed profile for the Indian Ocean increases the maximum bathymetric depth predicted to interact with explosion signals.

CONCLUSION AND RECOMMENDATION

We developed a discovery procedure that searches automatic processing results for explosion-like signals. From this procedure, we identified 305 previously unknown explosions located in three general areas of the Indian Ocean. The explosion signals are broadband and often contain reflected signals. We have shown that small shallow explosions can, given the right source geometry, propagate signals to basin-wide distances. Many of the direct arrivals are observed at multiple stations, which we have used to determine precise locations. The observed attenuation can be very sensitive to slight variations in bathymetry, which is probably enhanced due to the sound speed profiles of the equatorial Indian Ocean and the shallow nature of the sources.

ACKNOWLEDGEMENTS

We thank Manocher Bahavar and Paul Piraino for obtaining the hydrophone data used in this research.

REFERENCES

Blackman, D. K., J. A. Mercer, R. Andrew, C D. de Groot-Hedlin, and P. E. Harben (2003). Indian Ocean calibration tests: Cape Town-Cocos Keeling 2003, in *Proceedings of the 25th Seismic Research Review—Nuclear Explosion Monitoring: Building the Knowledge Base*, LA-UR-03-6029, Vol. 1, pp. 517–523.

Bowman, J. R., J. A. Hanson, and D. Jepsen (2005). An active-source experiment in the Indian Ocean, in *Proceedings of the 27th Seismic Research Review: Ground-Based Nuclear Explosion Monitoring Technologies*, LA-UR-05-6407, Vol. 2, pp. 722–732.

Brumbaugh, D. A. and R. J. Le Bras (1998). Hydroacoustic signals from a ground-truth data set of marine explosions, SAIC technical report, SAIC-98/3008.

Graeber, F. and P. Firbas (2005). Recent developments in hydroacoustic data processing at the IDC, *Hydroacoustic Workshop*, Victoria, British Columbia, May 1–5.

Hanson, J. A. and J. R. Bowman (2006). Methods for monitoring hydroacoustic events using direct and reflected T waves in the Indian Ocean, *J. Geophys. Res*. doi:10.1029/2004JB003609.

Hanson, J. A., C. L. Reasoner, and J. R. Bowman (2007). Investigations of natural events in the Indian Ocean using three hydrophone stations, SAIC Technical Report SAIC-07/3019.

Hanson, J., R. Le Bras, P. Dysart, D. Brumbaugh, A. Gault, and J. Guern (2001). Operational processing and special studies of hydroacoustics at the Prototype International Data Center, *Pure and Applied Geophysics*, 158 425–456.

Lay, T. and T. C. Wallace (1995). *Modern Global Seismology*, Academic Press, p78.

Munk, W.H. (1974). Sound channel in an exponentially stratified ocean with applications to SOFAR, *J. Acoust. Soc. Am.* 55: 220–226.

Porter, M. B. and H. P. Bucker (1987). Gaussian beam tracing for computing ocean acoustic fields, *J. Acoust. Soc. Amer.* 82: 1349–1359.

Reasoner, C.L., J.A. Hanson. and J. R. Bowman (2005). Characterization of two underwater explosions in the Bay of Bengal on May 5, 2004, SAIC Technical Report SAIC-05/3001.

Smith, W. H. F., and D. T. Sandwell, (1997). Global seafloor topography from satellite altimetry and ship depth soundings, *Science* 277: 1957–1962.

Spiliopoulos, S. and D. Jepsen (2005). Studies in the Indian Ocean: Preliminary phase identification and synergies with the seismic network, *Hydroacoustic Workshop*, Victoria, BC, May 1–5, 2005.

Urick, R.J. (1979). *Sound Propagation in the Sea*, Defense Advanced Research Projects Agency, Washington, D.C.

Radionuclide Monitoring

TESTING OF AEROSOL SAMPLER TO REMOVE RADON AND THORON PROGENY INTERFERENCE FROM AEROSOL SAMPLES FOR NUCLEAR EXPLOSION MONITORING

Steven R. Biegalski[1], Christopher J. Weaver[1], Scot Waye[1], Ofodike A. Ezekoye[1], and Phillip K. Hopke[2]

The University of Texas at Austin[1] and Clarkson University[2]

Sponsored by Army Space and Missile Defense Command

Contract No. W9113M-05-1-0016[1,2]

ABSTRACT

Studies show that aerosols with natural activity have an aerodynamics diameter in the range of 0.1 to 1.0 μm. In contrast, atmospheric nuclear explosions produce radioactive aerosols with aerodynamic diameters of less than 0.1 μm. Surface nuclear explosions produce a bimodal distribution of radioactive aerosol particles with aerodynamic particles greater than 1.0 μm and less than 0.1 μm. A high-volume (70 m^3h^{-1}), low-pressure aerosol impactor has been developed that separates the particles into the three size distributions: aerosols with aerodynamic diameters greater than 1.0 μm, between 0.1 and 1.0 μm, and smaller than 0.1 μm.

This sampler has been tested and compared to the performance of a micro-orifice uniform deposit impactor (MOUDI). Testing was completed by measuring natural aerosol samples as well as testing with a submicrometer monodisperse aerosol generation system. Additional pressure taps have been included in the system to improve system characterization. As a result of the testing and measurements, design modifications are being made for system optimization.

OBJECTIVES

This work seeks to develop an aerosol sampler that physically separates aerosols containing radioactivity from natural origin from aerosols containing radioactivity produced in a nuclear weapons explosion. Aerosols with natural radioactivity have been shown to have a size distribution predominantly between 0.1 and 1.0 μm. Grundela and Porstend (2004) showed this was the case for data collected in Göttingen, Germany for thoron and radon progenies. Similar studies, including Bondietti, et al. (1987) also found this size range for Thoron progeny. Aerosols with radioactivity from nuclear explosions were found to have a bimodal size distribution depending on the type of detonation. Aerosols were collected after a 20 kt nuclear explosion. For air explosions, the aerosol particles had a diameter of less than 0.1 μm and for surface explosions, the particle size was larger than 1.0 μm (Storebø, 1974). These data were consistent with aerosols collected in Sweden from a September 26, 1976, Chinese 20–200 kt nuclear explosion conducted above-ground (De Geer et al., 1978). It is therefore advantageous to separate aerosol particles into at least three size groups by particle diameter: greater than 1.0 μm, between 0.1 and 1.0 μm, and less than 0.1 μm.

There are many designs of aerosol samplers that separate the particles by size. Inertial impactors, especially cascade impactors, are ideal for this task. Particle inertia in a curved flow makes the particles deviate from the streamline, impacting a collection surface (Willeke and Baron, 1993). By controlling the fluid flow through the geometry of the sampler, particular sizes can be separated. When multiple single-stage impactors are placed in series, particle sizes of decreasing diameter may be collected. One difficulty with the current study is the small particle size of radioactive aerosols from aboveground nuclear explosions (particle size is less than 0.1 μm). Conventional impactors normally only have a particle diameter limit of 0.3–0.4 μm (Vanderpool et al., 1990). Two methods that have been used previously to obtain lower particle diameters are using a MOUDI or using a low-pressure impactor. The nozzles in a MOUDI are difficult to manufacture, especially for the case of a high volume flow since thousands of nozzles are needed for the lower stages. Lowering the pressure in a stage changes the mean free path between fluid particles and allows for smaller diameter particles to be collected. A critical stage is needed to create a pressure drop and a vacuum pump is needed in order to pull the desired pressures.

Once the aerosols containing radioactivity from natural sources are separated from those with radioactivity from nuclear explosions, the samples are analyzed. With the reduced background, gamma-ray spectroscopy of the aerosol filters will result in detection limit improvements. The filters will not need significant decay times between collection and gamma-ray spectrum acquisition. These improvements will be most notable where radon and thoron levels are high. The size distribution will also enable identification of a surface or atmospheric explosion.

The current focus of the study is the design and validation of the previously mentioned aerosol sampler. A generic impactor was modeled using a computational fluid dynamics program, FLUENT 6.1. Both circular and rectangular nozzles were modeled and benchmarked with previous studies. This provided insight into the physics of the fluid flow and particle behavior. By calculating the necessary geometries and pressures needed to obtain the desired aerosol particle sizes, the cascade impactor was manufactured and assembled. In order to verify the size distribution for each stage, fluorescent test aerosol particles of known size were produced and collected by the sampler onto the filters of each stage. The filters were then analyzed for size distribution for design validation.

RESEARCH ACCOMPLISHED

In the previous work, computer fluid modeling of round and rectangular nozzles was benchmarked against previous literature and the designs for critical orifice stages were developed to modify a commercial six-stage impactor (TE-230 high-volume cascade impactor with TE-5000 high-volume air sampling system made by Environmental Tisch). The TE-230 impactor has a variable motor that can vary the volumetric flow rate. At 20 cfm, the cutoff diameters are 10.2, 4.2, 2.1, 1.4, 0.73, 0.41, and 0 μm. At 40 cfm, the cutoff diameters are 7.2, 3.0, 1.5, 0.95, 0.49, and 0 μm (the 6^{th} stage is not used because the pump cannot handle the pressure drop). New plates were machined as mentioned above, and a new pump was obtained that would accommodate the high flow rate and large pressure drop. In order to attain the relatively high flow rate of 66 m^3/h (1100 L/min) with the low pressure of approximately 0.2 atm (absolute) after the last stage, a Rietschle Thomas Zephyr DLR60 dry compression claw compressor with a 5-HP motor was acquired.

To test the effect of the introduction of the critical stages into the Tisch impactor, a submicrometer monodisperse aerosol generator was procured and assembled to produce aerosols containing test particles with various diameters at the following values: 0.051, 0.10, 0.20, 0.92, 1.0, and 2.1 μm. A TSI Model 2076 constant output atomizer, seen in Figure 1, creates submicrometer aerosols from solutions or suspension. Compressed air expands through an orifice, forming a high-velocity jet, as shown in Figure 2a (TSI, 2005). As the liquid is drawn through the atomizing section, the large droplets impact on the wall opposite the jet and drain back. A fine spray leaves the atomizer and is dried by silica gel in an annular tube (TSI Model 3063 diffusion dryer), seen in Figure 2b.

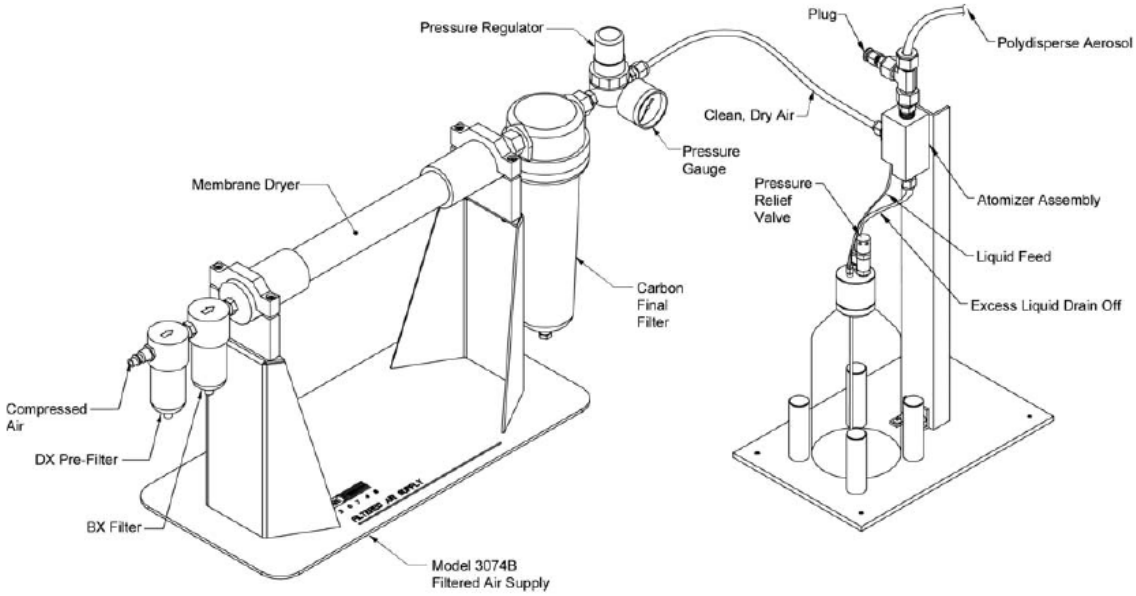

Figure 1. TSI Model 2076 Constant Output Atomizer.

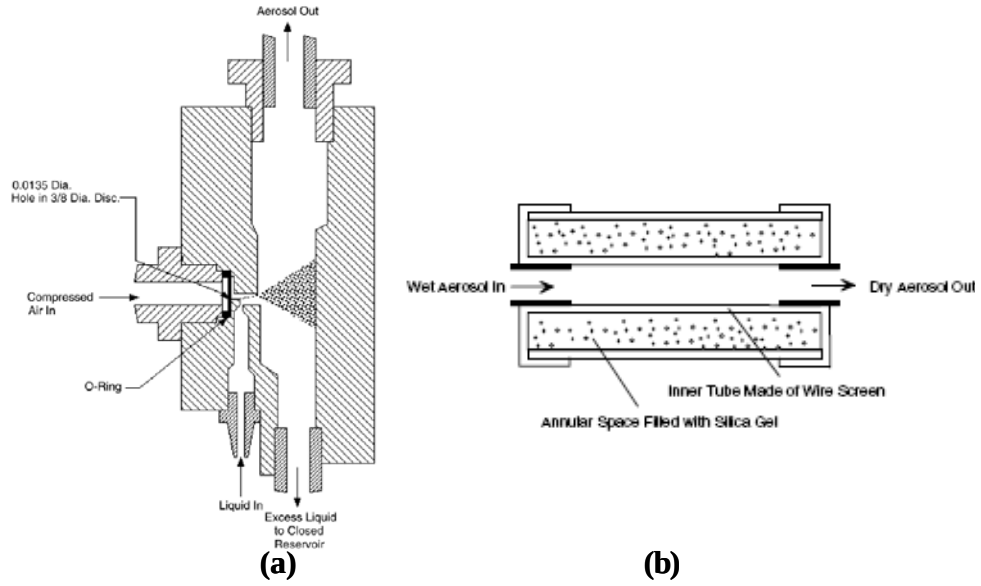

Figure 2. (a) TSI Model 2076 Constant Output Atomizer and (b) TSI Model 3063 Diffusion Dryer.

After the aerosols were conditioned by the diffusion dryer, they were run through a TSI Model 3012A Krypton-85 Neutralizer so that any charge on the particles can be removed. The actual aerosol generation system can be seen fully assembled in Figure 3. To verify that the system was correctly producing the desired aerosols, the assembly was calibrated using the MOUDI, which has twelve stages with cutoff diameters of 18, 10, 5.6, 3.2, 1.8, 1.0, 0.56, 0.32, 0.18, 0.1, 0.056, and 0 μm. Achieving quantitative results for the collection efficiency was not necessary as the particle collection could be verified visually as being almost completely collected in the appropriate stage, with only minimal collection on the adjacent stages. The time needed for sufficient test particle collection is on the order of 1 to 1.5 hours. The impaction on the adjacent stages is the result of the collection efficiency for each stage being less than 100%, allowing some particles to be collected too early as well as too late. To visually inspect the collection on each stage, the filters were exposed to ultraviolet light which allowed the fluorescent test particles to be easily seen. Each test particle size was verified and all proved to be generated as expected.

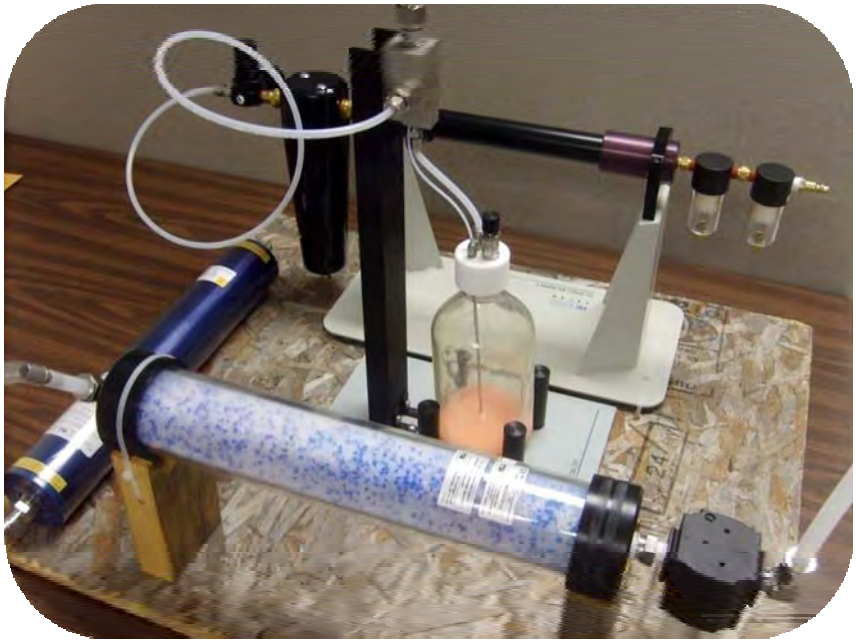

Figure 3. Assembled aerosol generation apparatus.

Further tests were conducted with the MOUDI to confirm that the size distribution of naturally occurring radionuclides lies within the diameter range of 0.1 to 1.0 μm (Grundela and Porstend, 2004). For these tests, the MOUDI was set up outside of the UT Nuclear Engineering Teaching Laboratory to collect for approximately four days to achieve a saturation activity for the radionuclides within the Radon and Thoron progeny that are to be investigated. The buildup of the activity on the filters due to one particular isotope will reach saturation at about 5 to 7 half-lives. For example, ^{212}Pb has a half-life of 10.64 hours and would reach saturation after about 3 days. Other isotopes that were analyzed were ^{214}Pb, ^{214}Bi, ^{212}Pb, and ^{208}Tl.

Once the MOUDI collection was stopped, the twelve stages were grouped into three stages that were representative of the three size regimes of interest. Stages that collected particles of size 1.0 μm and higher were referred to as the course region, size 0.1 to 1.0 μm were identified as the fine region and anything below 0.1 μm were referred to as the superfine region. To reduce the decay time for the samples, each of the groups were quickly prepared and their gamma spectrums were simultaneously counted on three Hyper-Pure Germanium detectors for a total of 12 hours each. At the end of the three counts, the spectra were analyzed to determine the initial activity on the filters at the time the MOUDI collection ended.

The various spectra were back-corrected to account for the decay in the time between ending sample collection and starting the gamma-ray spectrum acquisition, t_d, the decay during the spectrum collection, t_a, and losses due to the efficiency, ε, of the various detectors at a particular energy, as well as the probability, γ, for a particular gamma ray

to be emitted. This correction can be seen in the following equations that relate the number of counts a detector sees at a particular energy to the initial activity, where λ is the decay constant for the particular isotope:

$$\begin{aligned} &\#\text{ of counts} = \#\text{ of decays} * \varepsilon * \gamma \\ &= \int_{t_d}^{t_a+t_d} (Activity)dt * \varepsilon * \gamma \\ &= A_o \varepsilon\gamma \left[\frac{e^{-\lambda t}}{-\lambda} \right]_{t_d}^{t_a+t_d} \\ &\Rightarrow A_o = \frac{\text{counts} * \lambda}{\varepsilon\gamma\left(e^{-\lambda t_d}\right)\left(1-e^{-\lambda t_a}\right)} \end{aligned} \tag{1}$$

Once the data had been back-corrected to reflect the changes mentioned above, the initial activity, A_o, of each set of filters was compared to one another for the activity of a particular isotope. The activities were then represented in an activity per unit of volume using Equation 2 to see the size distribution within one cubic meter of air, where *Q* is the concentration of radionuclides in the air in atoms per m^{-3} and F is the volumetric flowrate in $m^3\ s^{-1}$.

$$\begin{aligned} &Q = \frac{\text{counts} * \lambda}{F\varepsilon\gamma\left(e^{-\lambda t_d}\right)\left(1-e^{-\lambda t_a}\right)\left(1-e^{-\lambda t_c}\right)} \\ &\text{where, } A\left(\frac{Bq}{m^3}\right) = Q\lambda \end{aligned} \tag{2}$$

In Table 1, the activity of each group for various isotopes is shown and the coarse group (0.1 to 1.0 μm) can be seen to have the most activity in all isotopes studied in this test. Figure 4 also shows the relative activity of ^{212}Pb found on each set of filters. These results provide further evidence that naturally occurring radionuclides in the radon and thoron progenies are found to be of sizes that can be filtered out to reduce the background activity in an aerosol sample.

Table 1. MOUDI results for naturally occurring activity from 4 day collection.

Isotope ($t_{1/2}$)	Superfine Activity	(+/-)	Fine Activity	(+/-)	Coarse Activity	(+/-)
^{212}Pb (10.64 hrs)	0.095	0.033	0.299	0.028	0.009	0.019
^{214}Pb (26.8 min)	-	-	0.593	1.403	-	-
^{214}Bi (19.9 min)	1.571	2.613	5.312	2.629	1.912	1.647
^{208}Tl (3.053 min)	22.569	43.943	299.777	119.666	-	-

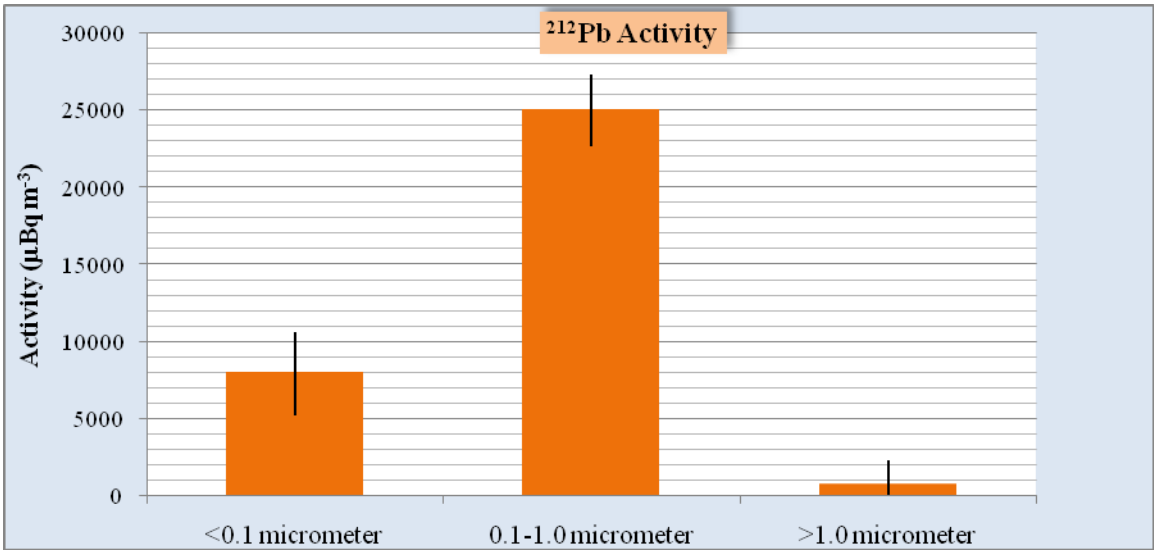

Figure 4. Activity due to Pb-212 after 4 day MOUDI collection.

The MOUDI results were also used to model the detection limits if a radionuclide aerosal sampler analyzer (RASA) configuration were used. The data used to determine the 140Ba concentration from the 212Pb was the USP075-Charlottesville, VA RASA data collected from November 19, 2000 to January 21, 2001. From Figure 5, the detection limits in the regions < 0.1 µm and > 1.0 µm have been greatly reduced using the aerosol separation method.

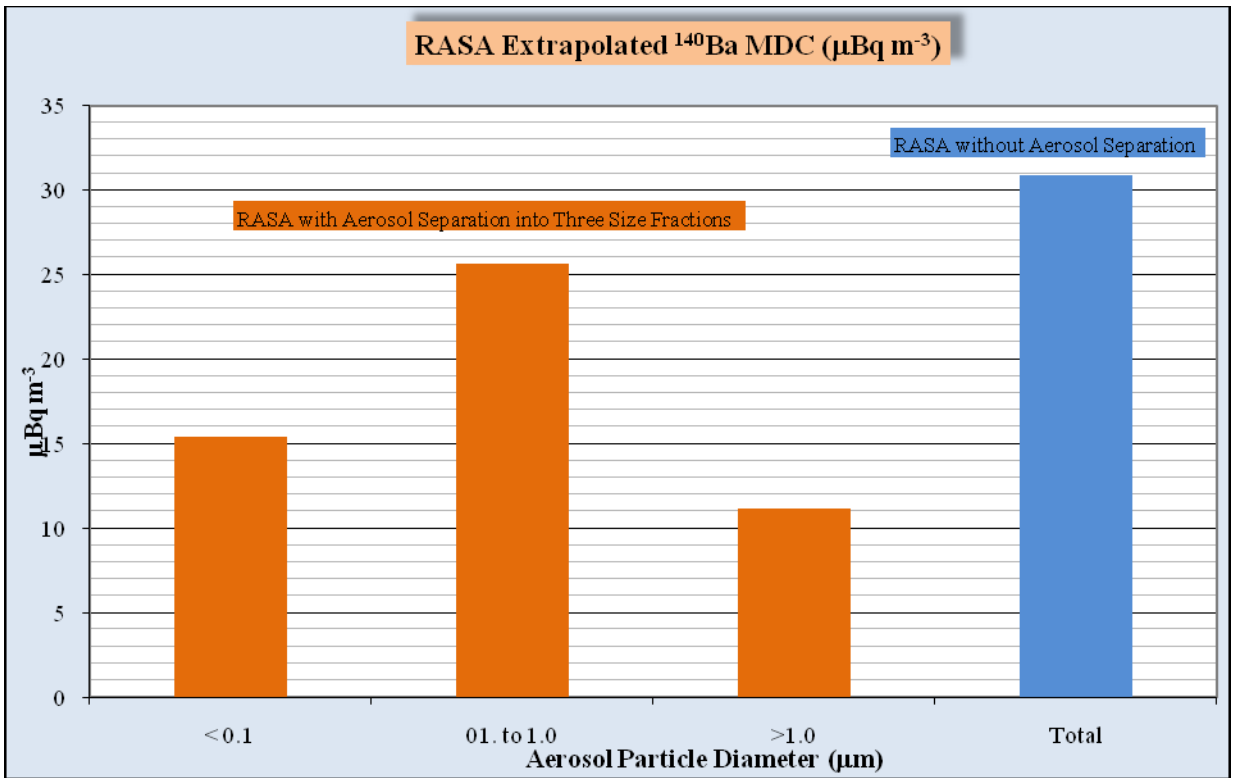

Figure 5. MOUDI data extrapolated to represent the detection limits with RASA using particle separation

To determine the abundance of longer-lived isotopes within the aerosol samples taken by the MOUDI, Neutron Activation Analysis (NAA) was performed on the sets of filters that resulted from a two-day collection outside of the University of Texas Nuclear Engineering Teaching Laboratory. To irradiate the samples and perform the analysis, the Mark II TRIGA Research Reactor was used to expose the samples to a neutron flux and the gamma-ray spectra were collected using the same labs as for the above analysis. The samples were irradiated for 8 hours and allowed to decay for approximately 4 weeks before starting the spectra acquisition. The long decay time was necessary as all of the elements investigated are characterized as relatively long-lived and the decay period reduces the background as well as lowers our detection limits. The results found for the masses of various isotopes are listed and shown in Figure 6.

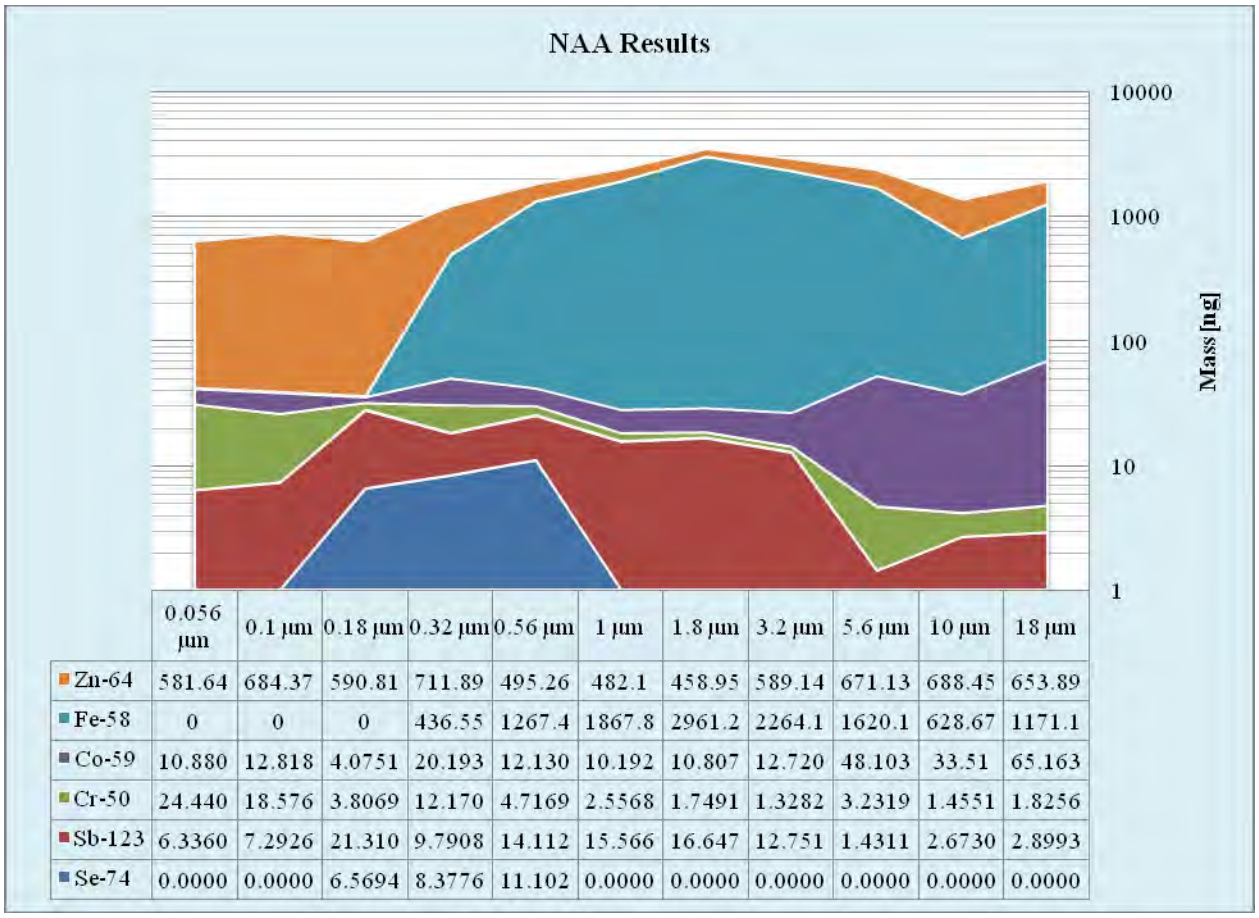

	0.056 µm	0.1 µm	0.18 µm	0.32 µm	0.56 µm	1 µm	1.8 µm	3.2 µm	5.6 µm	10 µm	18 µm
Zn-64	581.64	684.37	590.81	711.89	495.26	482.1	458.95	589.14	671.13	688.45	653.89
Fe-58	0	0	0	436.55	1267.4	1867.8	2961.2	2264.1	1620.1	628.67	1171.1
Co-59	10.880	12.818	4.0751	20.193	12.130	10.192	10.807	12.720	48.103	33.51	65.163
Cr-50	24.440	18.576	3.8069	12.170	4.7169	2.5568	1.7491	1.3282	3.2319	1.4551	1.8256
Sb-123	6.3360	7.2926	21.310	9.7908	14.112	15.566	16.647	12.751	1.4311	2.6730	2.8993
Se-74	0.0000	0.0000	6.5694	8.3776	11.102	0.0000	0.0000	0.0000	0.0000	0.0000	0.0000

Figure 6. The masses of various isotopes found in the MOUDI sample filters using Neutron Activation Analysis.

Using the Nuclear Explosion Monitoring Inertial Impactor (NEMII) system, initial tests were performed to determine the effectiveness of the modifications designed in the previous phase of the project. The system was tested using both the aerosol generation system mentioned earlier as well as taking prolonged (24+ hours) aerosol collections and using a Geiger-Müller Counter to compare the relative activity of each filter. The results from both of these tests showed that the system was not operating as expected concerning the 0.1 µm impaction stage. The test aerosols were not being collected at this stage and were being collected on the following filter which is the last filter stage of the system where only 0 to 0.1 µm sized particles should be collected. The GM counter results also show that most of the radioactivity from the aerosol collection was located on the last filter, again suggesting that the particles 0.1 to 1.0 µm were passing the appropriate filter. To better characterize the pressure levels within the critical stages, low-pressure gauges, which can be seen in Figure 6, were installed to give a real-time measurement of the behavior of the system in these important regions of the impactor. According to the calculations using the nozzle design tools developed in the previous phase of the project, the pressures after the first and second critical orifice stages should be 0.55 atm and 0.30 atm, respectively, corresponding to pressure drops of 0.45 and 0.70 from atmospheric pressure. The measurements taken showed that the actual pressures in these stages were 0.917 atm after the first stage and 0.883 after the second stage.

Figure 6. Installation of Low-Pressure Gauges at the critical orifice stages.

The pressures in these stages were lowered by restricting the nozzle flow using rubber gasket material in an attempt to achieve the desired pressure drops, thus allowing for correct particle separation. The pressures expected were eventually maintained, yet this change still had no effect on the particle separation. At this point, further investigation into the calculation of these stages was made and is currently ongoing in an effort to more accurately model the flow within the impactor stages.

Recent tests were done using the methods of impactor design that do not rely on achieving low-pressures within the impactor (Demokritou, 2002), and these have shown improved results for the 0.1 μm collection stage. The impactor design in previous work has shown that for high flow rates of 900 liters/minute or higher (NEMII: 1100 L/min) the impactor does not need to achieve low pressure to acquire a cutoff diameter size of 0.1 μm. The major difference between our current setup and this alternate method is that the Stokes number will not remain constant throughout the impactor but will be dependent on the fluid velocity as the Demokritou group has shown. Further characterization of the flow within the impactor will be calculated and new nozzle plates will be manufactured using this alternate model.

CONCLUSIONS AND RECOMMENDATIONS

Over the past year, tests have been conducted which verify the size distributions of naturally occurring radionuclides, especially those found within the Radon and Thoron decay chain. The tests were conducted using a MOUDI, which is a commercially available impactor with particle size separation as fine as 0.056 μm. The results agree with past experiments that found that there is a preferred size regime for these particles starting at 0.1 μm and extending to 1.0 μm. The MOUDI was also used to calibrate an aerosol generation system from TSI, Inc. which is able to disperse fluorescent polystyrene particles for collection. The aerosol generation system has been assembled and accurate particle size dispersion has been verified. Neutron Activation Analysis has been conducted on MOUDI collection filters from a 48-hour aerosol sampling and long-lived isotopes have been identified and masses have been found for each.

The NEMII system has been tested using both the TSI aerosol generation system and by measuring radioactivity amounts within aerosol samples taken at the UT Nuclear Engineering Teaching Laboratory. Each set of measurements has shown incorrect particle collection on the 0.1 μm cutoff stage. Low-pressure gauges were installed on the two critical orifice stages to monitor the pressures at these points. The pressures achieved did not agree with those calculated in the design of the stages. After a series of modifications to reach the target pressures were made, the collection at the 0.1 μm stage did not improve.

Further tests and calculations are currently being done to improve the particle separation based upon results from past experiments (Demokritou, 2002) that do not rely on critical orifices, but instead exploit the benefit of using a high-volume sampler and allow the Stokes number to vary accordingly. These tests have seen improved particle separation. Additional work will include Neutron Activation Analysis on the filters from the NEMII system in comparison to the NAA work done on the MOUDI samples once reasonable particle separations have been accomplished.

REFERENCES

Bondietti, E.A., C. Papastefanou, and C. Rangarajan (1987). Aerodynamic size associations of natural radioactivity with ambient aerosols, in *Radon and its Decay Products-Occurrence, Properties and Health Effects*, ed. P. K. Hopke. ASC-Symposium Series 3131, 377–397.

Demokritou, P., I. G. Kavouras, S. T. Ferguson, and P. Koutrakis (2002). Development of a High Volume Cascade Impactor for Toxicological and Chemical Characterization Studies, *Aerosol Science and Technology* 36: (9): 925–933

De Geer, L. E., R. Arntsing, I. Vintersved, J. Sisefsky, S. Jakobsson, and J. A.Engstrom (1978). Particulate radioactivity, mainly from nuclear explosions, in air and precipitation in Sweden mid-year 1975 to mid-year 1977, *FOA Report, FOA-C—40089*.

Grundela, M. and J. Porstend (2004). Differences between the activity size distributions of the different natural radionuclide aerosols in outdoor air, *Atmospheric Environment* 38: 3723–3728.

Storebø, P.B. (1974). Formation of radioactivity size distributions in nuclear bomb debris, *Aerosol Science* 5: 557–577.

TSI Model 3063 Diffusion Dryer Instruction Manual P/N 1933062, Revision G, 2003.

TSI Model 3076 Constant Output Atomizer Instruction Manual P/N 1933076, Revision J, 2005.

Vanderpool, R. W., D.A. Lundgren, and P.E. Kerch (1990). Design and Calibration of an In-Stack Low-Pressure Impactor, *Aerosol Science and Technology* 12: 215–224.

Willeke, K. and P.A. Baron (1993). *Aerosol Measurement: Principles Techniques and Applications*, Van Nostrand Reinhold, New York.

TESTING THE SPECTRAL DECONVOLUTION ALGORITHM TOOL (SDAT) WITH XE SPECTRA

Steven R. Biegalski, Kendra M. Foltz Biegalski, and Derek A. Haas

The University of Texas at Austin

Sponsored by Army Space and Missile Defense Command

Contract No. W9113M-05-1-0017

ABSTRACT

The Spectral Deconvolution Analysis Tool (SDAT) software was developed to improve counting statistics and detection limits for nuclear explosion radionuclide measurements. SDAT utilizes spectral deconvolution spectroscopy techniques and can analyze both β-γ coincidence spectra for radioxenon isotopes and high-resolution HPGe spectra from aerosol monitors.

The SDAT tool has been integrated into a standalone graphical user interface (GUI). This GUI may import spectra, analyze the data for Xe concentrations, and graphically display the results. This tool has been tested with data generated via MCNPX models as well as real data.

OBJECTIVES

Environmental xenon sampling and measurement units are used in nuclear weapons test monitoring networks because radioxenon isotopes may be all that is released from tests performed deep underground or underwater. Some environmental xenon sampling and measurement units, like the Automated Radioxenon Sampler-Analyzer (ARSA) developed by Pacific Northwest National Laboratory (PNNL) and the Swedish Automated Noble Gas Unit (SAUNA) developed by the Swedish National Defense Research Establishment (FOI), use β-γ coincidence detectors that are energy dispersive on both the β and γ energy axes. Signals from four radioxenon isotopes (^{131m}Xe, ^{133}Xe, ^{133m}Xe, ^{135}Xe) comprise a sample spectrum. Under poor operating conditions, a few radon daughters (^{214}Pb, ^{214}Bi) may interfere with the sample spectrum. Applying conventional region-of-interest (ROI) spectrum analysis algorithms to such 3-D spectra results in relatively high minimum detectable concentrations (MDCs) due to the subtractive process of determining net counts in the ROI.

To overcome this problem, a project team from The University of Texas in Austin is developing software to deconvolve the 3-D sample spectra into the most probable combination of signals using the non-negative least-squares method. This method can use the entire signal from each radionuclide and consequently may improve the signal to noise ratio. It has been postulated that the use of such an algorithm will result in a better ability to resolve spectral interferences and thus improve counting statistics and detection limits for nuclear explosion radionuclide measurements. The SDAT GUI, expands upon a previously developed algorithm, the Multiple Isotope Component Analysis (MICA) tool.

The SDAT tool was tested against the CORIANT code (Foltz Biegalski, 2001) on data produced from an automated radioxenon sampler/analyzer (ARSA) unit when it was stationed in Guangzhou, China. The CORIANT tool utilizes a region of interest approach to the spectral analysis while SDAT utilizes a spectral deconvolution approach. Samples were selected that contain clear radioxenon signals. While a true test of SDAT will be the analysis of samples with low count rates, this test was conducted as a first step to show that the two methods produce similar results.

RESEARCH ACCOMPLISHED

This occurred in three steps. The first step was the creation of the SDAT tool. The second step was the creation of standard library inputs for the SDAT code, which was accomplished via MCNP simulations. The third step was to analyze samples with SDAT and compare the results to those produced with CORIANT.

Step 1: Creation of SDAT GUI

The detector response for a sample consists of a 255x255 matrix of numbers. Each entry represents the number of counts registered in a certain E_γ, E_β bin. Each row represents a γ-channel bin and each column represents a β-channel bin. We will refer to this structure as a histogram. Other information contained in the sample file includes calibration information and other sample characteristics, e.g., the sample Xe gas volume from which the total sampled atmospheric volume is calculated.

The sample histogram will be deconvolved into individual isotopic responses using the SDAT concept to determine atmospheric activity concentrations for each radioxenon of interest. To do this, however, we must have calibrated histograms of all the possible individual signals that can make up a sample histogram. These histograms should have the same size and calibration characteristics as the sample histogram in addition to good counting statistics. Therefore, we need the following detector response matrices with their associated activities:

$$\left[^{131m}Xe\right]_{255x255},\ \left[^{133m}Xe\right]_{255x255},\ \left[^{133}Xe\right]_{255x255},\ \text{and}\ \left[^{135}Xe\right]_{255x255}$$

Each detector-response histogram can be generated using a detector modeling program like MCNP or acquired by counting a calibration source on the detector. Since the ARSA has four beta detector cells, the above detector response histograms would need to be generated or acquired for each beta cell. In addition, the energy, resolution, and efficiency calibrations have to be determined for each beta cell. With all of this information at hand, and knowing in which detector cell the sample was counted, the following algorithm can be applied to a sample for determining the atmospheric radioxenon concentrations.

The SDAT code was developed to input the library and sample files. These files are text files. The current version of SDAT just reads the sample spectrum and does not read any header information that may be associated with Sample Pulse Height Data (SPHD) formatted files. The open sample window is shown in Figure 1.

Once the proper files have been selected, SDAT analyzes the data and displays the results. Figure 2 shows the results display. The sample is displayed as a 2-D plot in the top left corner. Below the sample plot are three tables. The top left table is the Axis Parameters table which allows users to modify the minimum and maximum x and y intercepts of all the plots in the *SDAT* window. By default, they are set at 0 and 250. The Parameter/Value Table is situated to the right of the Axis Parameters table and contains a summary of the parameters specified in the *Open Single* window, i.e., the sensitivity number, the sample file name, and the library file names for each radioxenon of interest. This table is located in the bottom left corner of the *SDAT* window. It contains the concentration coefficients and errors of each radioxenon of interest calculated with and without the use of data weighting via the weighting matrix described earlier. The resulting multiplier coefficients can be used to determine the activity of each radioxenon using equation 1.

$$C_i = \frac{M_i A_i}{V} \tag{1}$$

where

C_i = Sample activity concentration of radioxenon isotope *I;*

M_i = Multiplier coefficient of radioxenon isotope *i* as determined by SDAT;

A_i = Activity represented by library file of radioxenon isotope *I*; and

V = Air volume sampled.

The activity concentration uncertainties of each radioxenon can be determined using equation 2.

$$\sigma_{C_i} = \frac{1}{V}\sqrt{\left(A_i\sigma_{M_i}\right)^2 + \left(M_i\sigma_{A_i}\right)^2 + \left(\frac{M_i A_i \sigma_V}{V}\right)^2} \tag{2}$$

where σ_x is the uncertainty of variable *x*. All other variables have been defined above.

The weighted result and unweighted result plots are located at the top middle and top right corner of the *SDAT* window. The plots are calculated as shown in equation 3.

$$\left(\sum_i C_i [lib]_i\right)\cdot[\xi], \tag{3}$$

where C_i are the concentration coefficients for radioxenon isotope *i*, $[lib]_i$ are the library files for radioxenon isotope *i*, and $[\xi]$ is the weighting matrix for the weighted result plot and the identity matrix for

the unweighted result plot. These plots may be compared with one another and the original sample plot to see how well the SDAT calculated results model the sample data.

The Weighted Residual and Unweighted Residual Plots are located directly below the Weighted Result and Unweighted Result Plots. The plots are calculated shown in equation 4.

$$\left| [Sample] - \left(\left(\sum_i C_i [lib]_i \right) \cdot [\xi] \right) \right|, \qquad (4)$$

where [*Sample*] is the original sample data and all other symbols have been previously defined. These plots show the differences between the original sample data and the calculated models of the sample as shown in the weighted result and unweighted result plots. SDAT also allows for sample re-analysis may with different input data. Results may also be saved.

Over time, the energy vs. channel calibration of both beta and gamma detectors can change. If the changes are significant, the SDAT program will return large errors because the sample signal will no longer match those in the library files. In such cases, the sample spectra should be rescaled to match the energy calibration properties of the original library files. Alternatively, the library files can be rescaled to match the sample calibration properties and saved. This program can also be used to compress or expand the data as desired. Figure 3 shows the SDAT rescaling window.

Step 2: Creation of Xe Library Files via MCNP

Library files were created for ^{131m}Xe, ^{133m}Xe, ^{133}Xe, and ^{135}Xe via a combination of MCNPX and MATLAB post processing. This is the same method as reported in Haas et al. (2007). The library files were created for each of the four cells in the β–γ coincidence detector system utilized in the ARSA system. The library files were then adjusted to match the energy calibration of the samples collected in the field. Figure 4 shows a comparison between the synthetically generated ^{133}Xe library file and a sample with ^{133}Xe collected by the ARSA in Guangzhou, China.

Step 3: Comparison of SDAT with CORIANT Results

As an initial quality control check, five spectra were analyzed wit SDAT. These samples collected with an ARSA unit in Guangzhou, China were initially analyzed by CORIANT at the Center for Monitoring Research in Arlington, VA. Figure 5 illustrates the comparison that was made between the SDAT results and the CORIANT results. The ^{133}Xe results compare very well. Since these results are from samples collected in the field, the correct quantity of ^{133}Xe in the sample is not known. This just serves as a check to make sure that the SDAT tool produces acceptable results for samples with strong Xe signals.

The analysis of ^{131m}Xe, ^{133m}Xe, and ^{135}Xe were also performed. These results did not compare as well as the ^{133}Xe results shown in figure 5. This issues with the ^{131m}Xe and ^{133m}Xe was primarily a detection issue. CORIANT reported ^{131m}Xe and ^{133m}Xe present in all of the samples analyzed. However, SDAT calculated ^{131m}Xe to be present in four out of the five samples and did not calculate ^{133m}Xe to be present in any of the samples. Discrepancies in these results are largely attributed to having correct β channel calibrations, which are questionable for both the CORIANT and the SDAT analysis. Visual inspection of the data does not show any clear ^{131m}Xe or ^{133m}Xe signals.

Another issue raised by this comparison is the error calculation performed in SDAT. The error bars produced for this comparison appear to be smaller than expected. While the error calculations may be correct, efforts should be made to review the error calculation in SDAT.

CONCLUSIONS AND RECOMMENDATIONS

The first version of the SDAT code was completed. Samples were analyzed with the code using MCNPX/MATLAB generated library files. Results from this comparison agreed with CORIANT results from the Center for Monitoring Research. Future work for the SDAT code will include an incorporation of activity calculations as well as an ability to read SPHD file headers.

The highest priority work will entail the creation of radioxenon isotopes via The University of Texas at Austin TRIGA reactor. These spectra will be important to use as library files for SDAT. They will also allow for advanced testing of SDAT with low counting statistics samples. Since the xenon concentrations may be experimentally controlled, the accuracy and precision of SDAT may be determined.

REFERENCES

K.M. Foltz Biegalski (2001). *J. Radioanalytical Nucl. Chem.* 248: (3), pp. 663–672.

D. A. Haas, S. R. Biegalski, and K. M. Foltz Biegalski (2007) Modeling β-γ coincidence spectra of ^{131m}Xe, ^{133}Xe, ^{133m}Xe, and ^{135}Xe Signals, *Journal of Radioanalytical and Nuclear Chemistry* (in press).

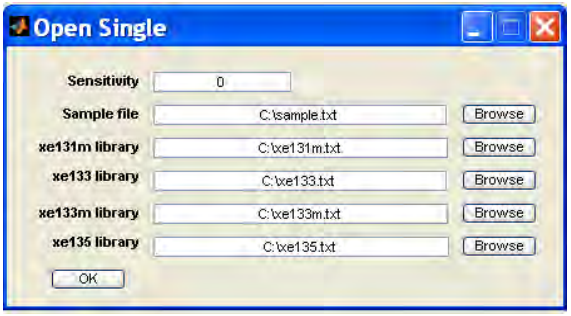

Figure 1. SDAT GUI open single window.

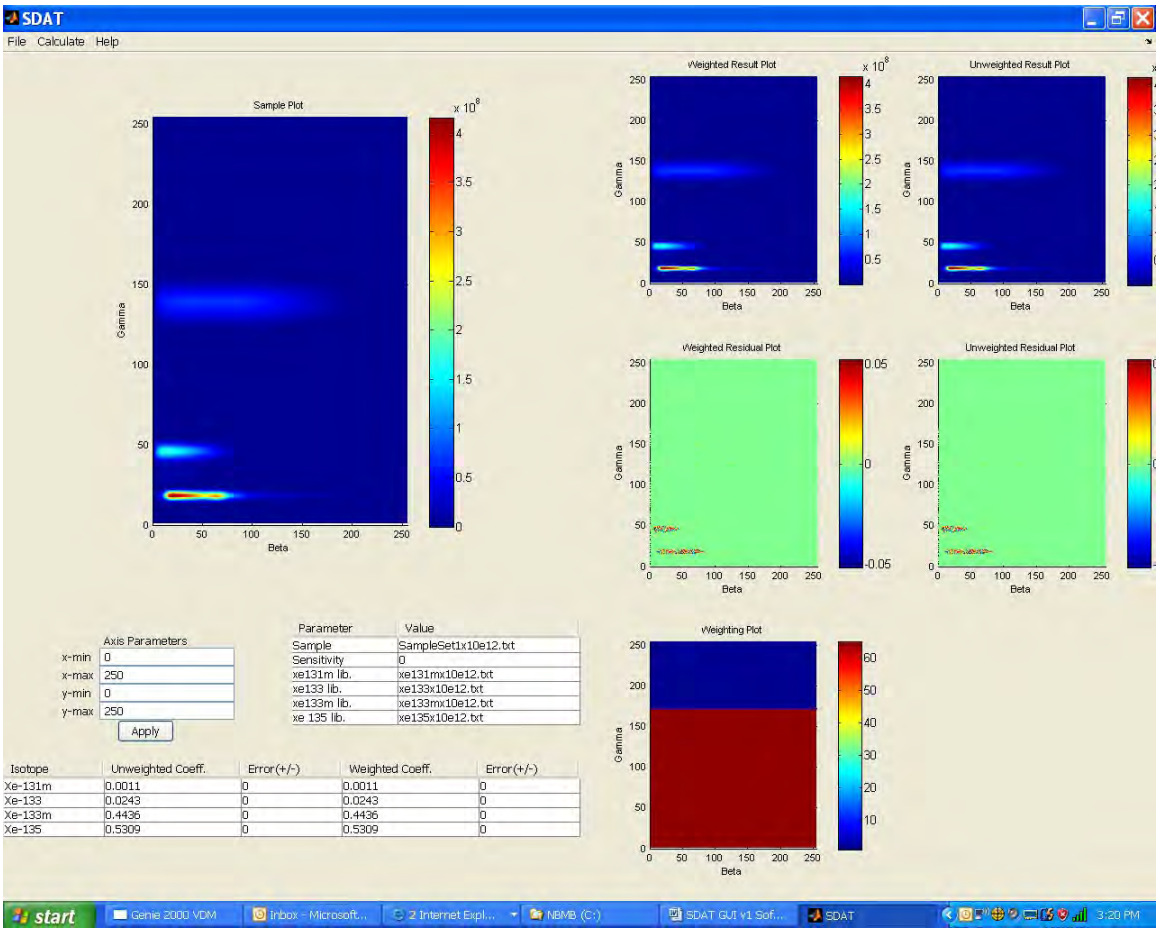

Figure 2. SDAT GUI sample analysis results display.

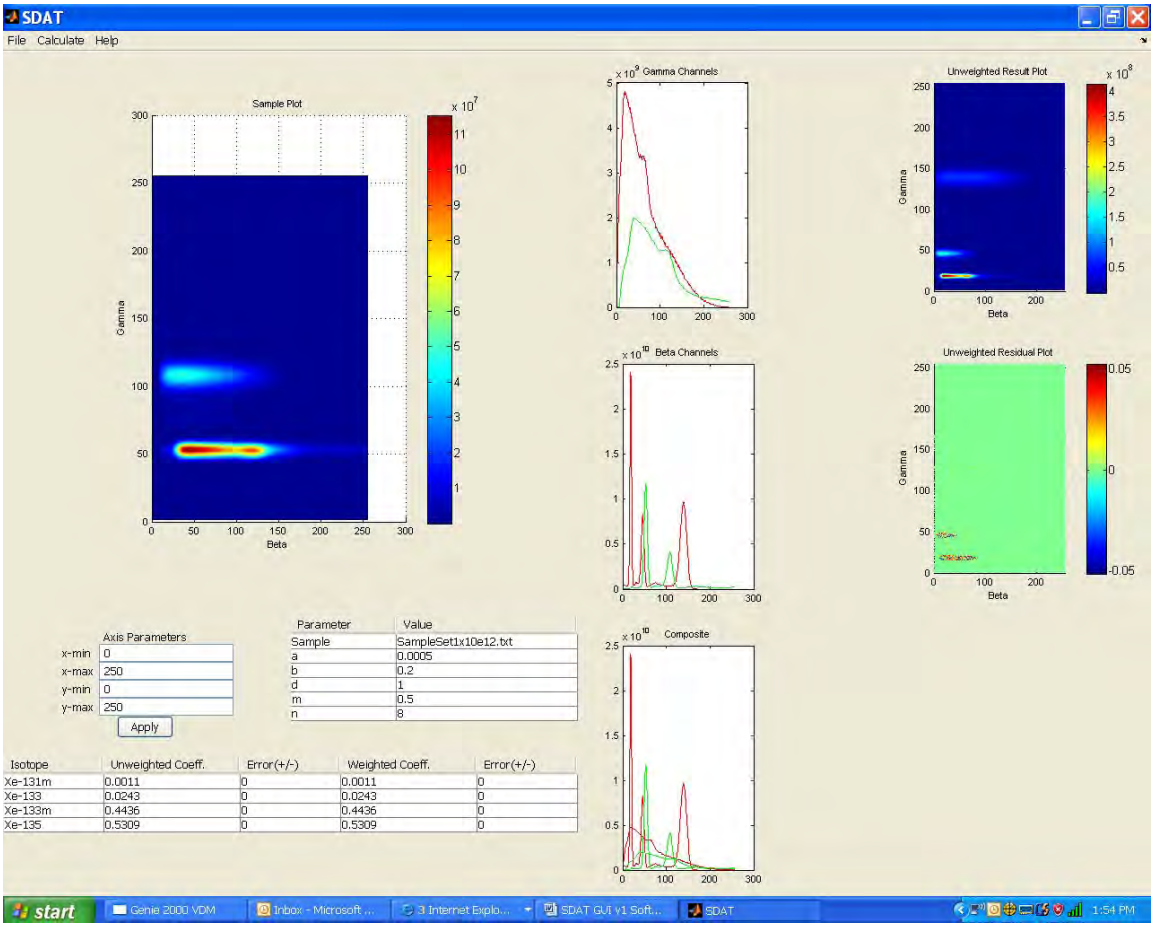

Figure 3. Display after rescaling a sample.

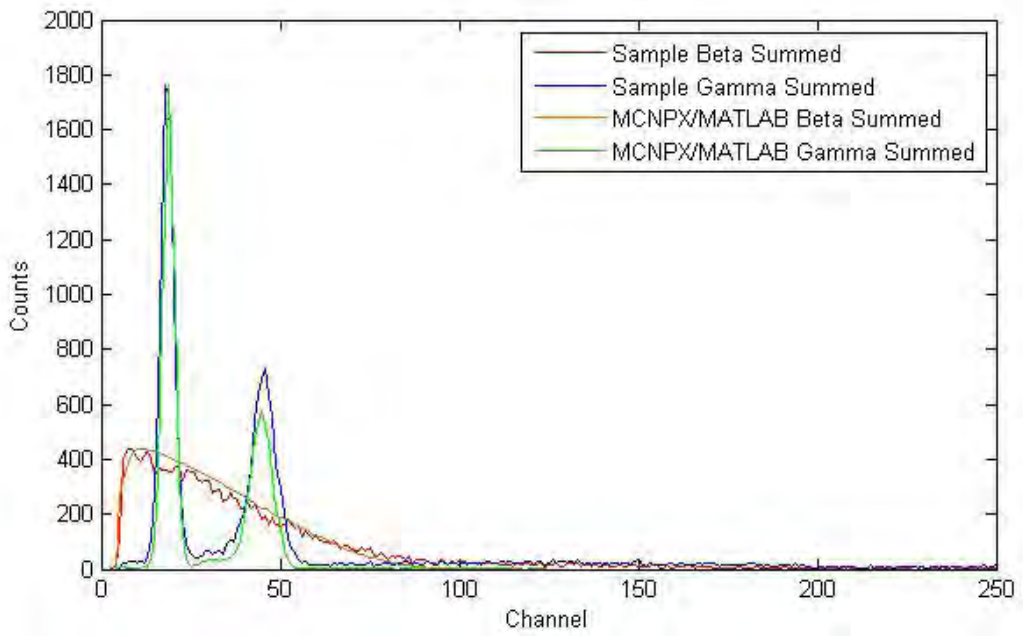

Figure 4. Comparison of β and γ compressed spectra from MCNPX/MATLAB generated ^{133}Xe library file and from sample collected in Guangzhou, China.

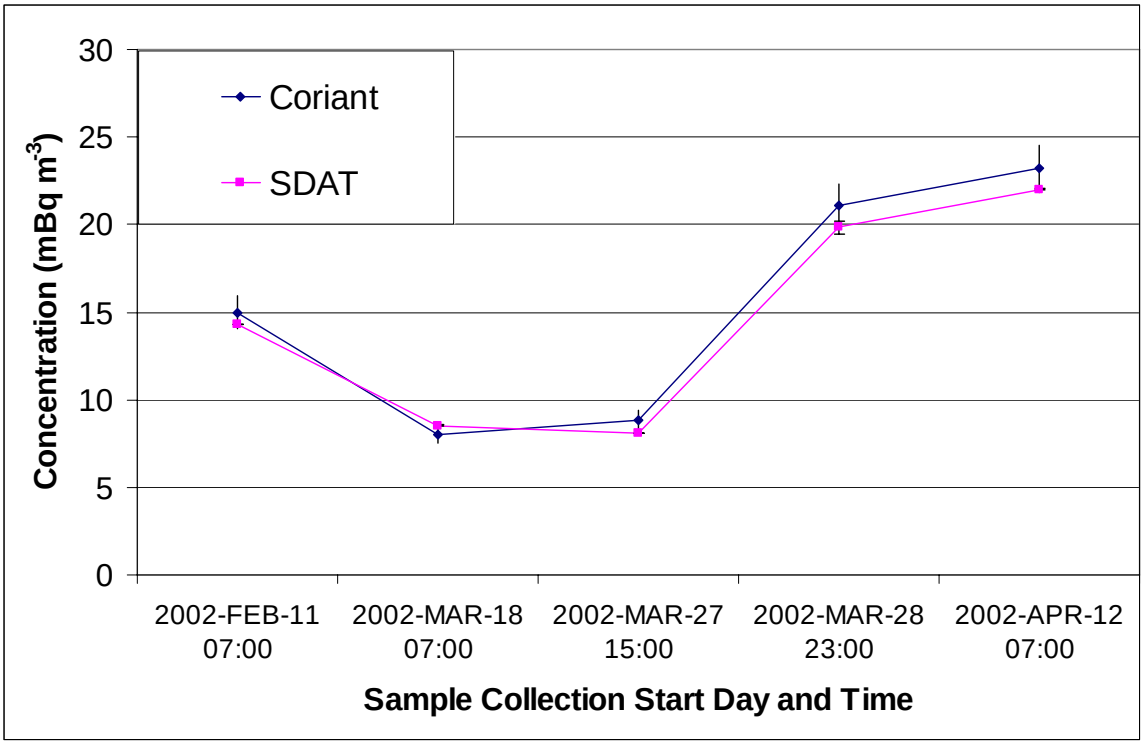

Figure 5. Comparison of results between SDAT and CORIANT for five samples from the ARSA in Guangzhou, China.

AUTOMATED QA/QC CHECK

FOR β-γ COINCIDENCE DETECTOR

Matthew W. Cooper, James C. Hayes, Tom R. Heimbigner, Charles W. Hubbard, Justin I. McIntyre, Michael D. Ripplinger, and Brian T. Schrom

Pacific Northwest National Laboratory

Sponsored by National Nuclear Security Administration

Contract No. DE-AC05-RLO1830/PL07-DAS-NEM02

ABSTRACT

The Automated Radioxenon Sampler/Analyzer (ARSA) (Hayes 1999), built by Pacific Northwest National Laboratory (PNNL), can collect and detect several radioxenon isotopes. The ARSA is very sensitive to ^{133}Xe, ^{131m}Xe, ^{133m}Xe, and ^{135}Xe due to the compact high-efficiency β–γ coincidence detector it uses. As detection technology improves and more emphasis is placed on system automation, QA/QC checks become of increasing importance. By automating the QA/QC checks, the reliability of the data sets is ensured without the necessity of monitoring. Often, the automated QA/QC checks will be done on site, where radio-xenon gas is not readily available so it is important to be able to use sealed point sources as an alternative. Immediately after the initial calibration of the detector, a ^{137}Cs source, which has a 661.7-keV γ-ray, is used to generate both γ and β spectra. The two spectra are saved to file, are called the template spectrum, and will be used as the template to perform on site QA/QC checks.

The QA/QC check will automatically find the start and end points of the β spectrum and compare them with those from the template spectrum. A similar method is used for the γ spectrum; however, in a γ spectrum the 661.7-keV peak can be used for the high energy end. If the points do not match, a gain and offset can be calculated to make the QA/QC spectra match the template spectra.

A second and more advanced method is to take a β–γ coincidence spectrum for the template spectrum. A comparison of the QA/QC β–γ coincidence spectrum to the template spectrum will be used to determine what if any adjustments need to be made on the gain and offset. A detailed discussion of the QA/QC checks will be included in the paper.

OBJECTIVES

Monitoring radioactive releases from nuclear explosions is a major component of the International Monitoring System (IMS) network (Hayes 1999). As part of the international effort to develop monitoring equipment, PNNL deployed the ARSA to Germany for an international demonstration of radionuclide equipment (Bowyer 1999). The ARSA measures radioxenon isotopes directly by first collecting and processing whole air samples that potentially contain a small amount of radioxenon (Bowyer 1999). After the samples are collected and processed and the xenon is isolated, it is counted in a nuclear detector. A critical component in the quantification of the radioxenon isotopes is the nuclear detector calibration. There are three major components to characterizing the ARSA nuclear detector: energy calibration, detection efficiency measurements, and spectral interference ratios. The nuclear detector is calibrated at the laboratory, but also requires monitoring in the field to ensure proper performance [to attain the lowest minimal detectable concentration (MDC) (McIntyre 2006)].

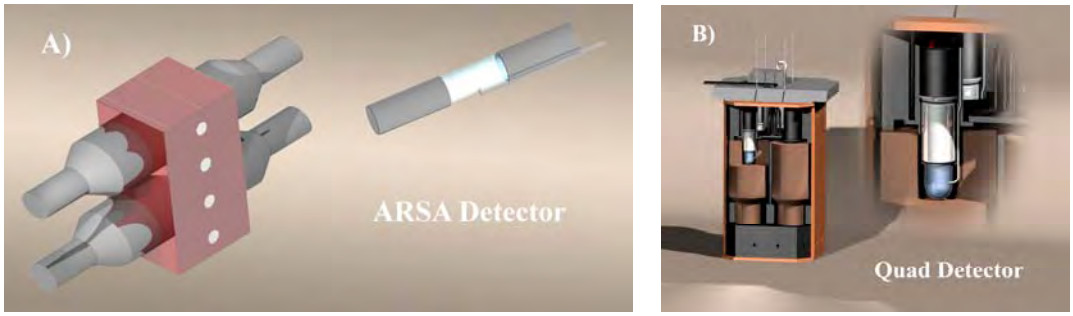

Figure 1. A: An ARSA type β-γ detector. The NaI(Tl) detector component is to the left and the gas-cell that slides into the NaI(Tl) is to the right. B: A Quad β-γ detector. The full detector is rendered on the left side and is comprised of 4 well-type CsI(Na) detectors and four gas-cells (β-cell). A magnified view of a single β-cell is given on the right.

Two similar styles of β-γ coincidence detectors are shown in figure 2. The detector on the left is the original ARSA detector and one on the right is an updated version called the Quad β-γ coincidence detector (Bowyer 1999 and Cooper 2005). Both nuclear detector types utilize an inorganic scintillator to detect x-rays and gammas and a gas-cell made of plastic scintillator to hold the gas sample and to detect outgoing charge particles, β, α, and conversion electrons (CE). In addition, both detectors are comprised of four gas-cells which individually measure one gas sample at a time. For the purposes of this paper the Quad detector was used to perform all test and measurements. The remainder of the paper will step through how The Quad β-γ coincidence detector is characterized and what steps can be taken to verify good performance while in the field.

RESEARCH ACCOMPLISHED

Laboratory calibration of a single β-γ detector involves use of ^{137}Cs as an initial check, followed by spiking the detector with radioactive gasses for precise determination of the nuclear detector characteristics. The three radioactive gases that PNNL uses are ^{133}Xe, ^{131m}Xe, and ^{222}Rn. Where possible, pure spikes are used; however, some contaminants are likely (e.g., ^{131m}Xe contaminant in a ^{133}Xe spike). These contributions are subtracted out during the calibration process to yield the correct parameters. All three spikes emit combinations of γ-rays and x-rays in coincidence with CE and β particles (see Table 1). Due to minor fluctuations in the gas processing system of the ARSA, ^{222}Rn gas can be introduced into the gas cell, along with the radioactive xenon isotopes. While this radon decays via alpha decay and is only detected in the beta spectrum, two of its subsequent daughter products, ^{214}Pb and ^{214}Bi, decay via β-γ coincidence. The dominant ^{214}Pb is shown in Table 1 as it is the primary decay product of ^{222}Rn that interferes with the radioxenon β-γ coincidence spectra.

Table 1. Energy and branching ratios for the three radioactive gas spikes.

	^{131m}Xe	^{133}Xe	^{214}Pb[a]
Half-life (days)	11.84	5.24	0.0186
Primary γ-ray Energy (keV)	163.9	81.0	351.87
γ-ray Abundance (%)	1.96	37	37.1
Primary X-ray Energy (keV)	30.0	31.0	77.1
X-ray Abundance (%)	54	48.9	11.0
β-particle End-point Energy (keV)		346	1023
β-particle Abundance (%)		100	100
Primary CE Energy (keV)	129	45	37
CE Abundance (%)	60.7	54.1	10.7

[a] ^{222}Rn Daughter

Detector Spike

The nuclear detector is first setup using a ^{137}Cs source to adjust the high voltage (HV) on both the β and the γ detectors using γ-singles to adjust the HV for the γ detector and β-γ coincidence to adjust the HV for the β detector. The high voltage adjustments set the range of energies displayed in the gamma and beta singles spectrum as well as the β-γ coincidence plane. Subsequent measurements using the radioactive gases calibrate the channel to energy scale for these spectra more accurately. As soon as the HV is set, a 3-day detector background is taken. The data collected during this background count, and for spike tests, includes three spectrum, γ-singles, β-singles and β-γ coincidence data. After all four well detectors have collected the background spectra, a series of spikes is put into each β-cell. The spikes are large enough (~30 Bq for ^{131m}Xe) to collect high statistics in a 1-hour count and begin with Rn. The second spike is ^{133}Xe and the final spike is ^{131m}Xe. After each set of data is collected, a pump and flush process is used for several days to remove the residual gas that adheres and penetrates the walls of the gas cell. Once the pump and flush cycle is complete the next set of radioactive gas is injected into the detector.

Detector Energy Calibration

The γ- and x-ray spectrum generated (Figure 2) from the radon daughters is used to calibrate the CsI(Na) or NaI(Tl) well detectors. This spectrum gives seven peaks (53.2 keV (γ-ray ^{214}Pb), 78.8 keV (x-rays ^{214}Pb), 241.9 keV (γ-ray ^{214}Pb), 295.1 keV (γ-ray ^{214}Pb), 351.9 keV (γ-ray ^{214}Pb), 609.3 keV (γ-ray ^{214}Bi), and 30 keV (CsI x-ray)). A linear fit to a plot of channel vs. energy gives the γ-ray energy calibration for the system.

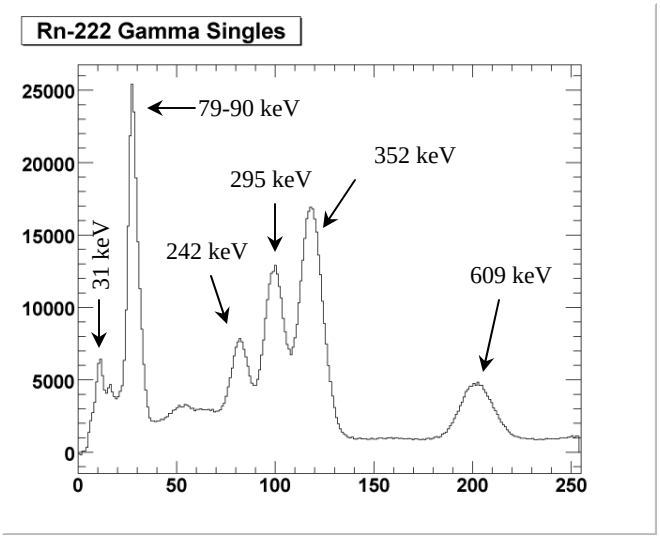

Figure 2. γ-singles spectrum from a ^{222}Rn spike. The peaks are primarily from the radon daughter ^{214}Pb with the highest peak being the 609-keV γ-ray from ^{214}Bi.

The CE and β end-point energies are used to calibrate the β-detector and entails using all three radioactive gas data sets. The ^{131m}Xe β-γ data give a peak at 129 keV for the β and 30 keV for the γ, which can be seen as a contaminant for ^{133}Xe in Figure 3. In Figure 3, the ^{131m}Xe peak is at roughly channel 32 on the abscissa. The remainder of the β energy calibration is done using end-point energies. To determine the end-point energy a region of interest (ROI) is made around a β-γ line. The ROI is then projected onto the x-axis to get a β spectrum. The channel at which the β continuum approaches zero is the end-point energy value.

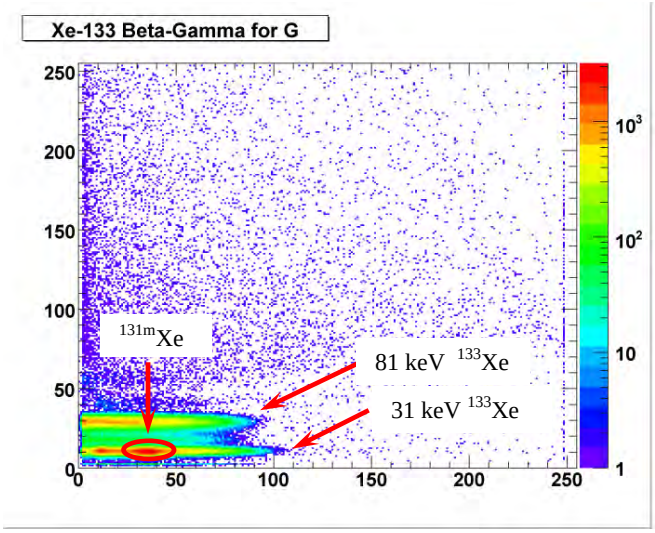

Figure 3. A β-γ spectrum from a ^{133}Xe spike with some ^{131m}Xe contamination.

Detector Efficiency

The β-γ efficiency measurement uses the same three data sets as are used to calibrate the β and γ energies: ^{131m}Xe, ^{133}Xe, and ^{214}Pb (^{222}Rn daughter). Due to the ~100% β and CE efficiencies, in general the number of counts in a β-singles spectrum, weighted by the branching ratio (BR) and efficiency (ε), will equal the number of counts in the

β-γ spectrum, weighted by its branching ratio and efficiency as shown in Equation 1. The BR is the percentage of particles, which decay by a particular decay mode with respect to the total number decays.

$$\frac{Counts_{\beta}}{Br_{\beta} * \varepsilon_{\beta}} = \frac{Counts_{\beta\gamma}}{Br_{\beta\gamma} * \varepsilon_{\beta\gamma}} \quad \textbf{(1)}$$

where,

$$\varepsilon_{\beta\gamma} = \varepsilon_{\gamma} * \varepsilon_{\beta} \quad \textbf{(2)}$$

And, in general, $Br_{\beta\gamma}$ equals Br_{γ} since there is an exact coincidence between the β and γ decay modes. In the case of ^{131m}Xe ε_{β} is assumed to be ~100% due to the 99.9% solid angle coverage for β's decays within the β-cell and the 129-keV CE that is a single line and not a beta continuum.

$$\varepsilon_{\beta\gamma} = \left(\frac{Counts_{\beta\gamma}}{Counts_{\beta}}\right)\left(\frac{Br_{\beta}}{Br_{\beta\gamma}}\right)\underbrace{\varepsilon_{\beta}}_{=1} \quad \textbf{(3)}$$

Since ^{133}Xe has a 31-keV x-ray in coincidence with a β continuum plus a 45-keV CE, it is possible to use the ^{131m}Xe γ efficiency to determine the ^{133}Xe-80 keV γ efficiency.

$$\varepsilon_{\gamma}^{(80keV)} = \left(\frac{Counts_{\gamma}^{Xe-133(80keV)}}{Counts_{\gamma}^{Xe-133(30keV)}}\right)\left(\frac{Br_{\gamma}^{Xe-133(30keV)}}{Br_{\gamma}^{Xe-133(80keV)}}\right)\varepsilon_{\gamma}^{(30keV)} \quad \textbf{(4)}$$

Equation 4 is possible due to the overlap in energies between ^{131m}Xe and ^{133}Xe at 30 keV (the detector will have the same γ efficiency for all γ-rays that occur at the same energy). By using the β–γ response from ^{214}Pb the γ efficiency at 80 keV is applied to determine the γ efficiency at 242, 295, and 352 keV. Once again this is due to overlapping γ energy, which in this case is at 80 keV.

$$\varepsilon_{\gamma}^{(X)} = \left(\frac{Counts_{\gamma}^{Pb-214(X)}}{Counts_{\gamma}^{Pb-214(80keV)}}\right)\left(\frac{Br_{\gamma}^{Pb-214(80keV)}}{Br_{\gamma}^{Pb-214(X)}}\right)\varepsilon_{\gamma}^{(80keV)} \quad \textbf{(5)}$$

Where, "X" can be 242, 295, or 352 keV.

As mentioned earlier, one complicating factor is any contaminants present in the spike. Figure 4 shows a ^{131m}Xe spectrum containing ^{133}Xe and ^{222}Rn contaminants. One method to remove the contaminants from the spectrum is to have a pure spectrum of ^{133}Xe and a pure spectrum of ^{222}Rn and subtract them from the ^{131m}Xe spectrum.

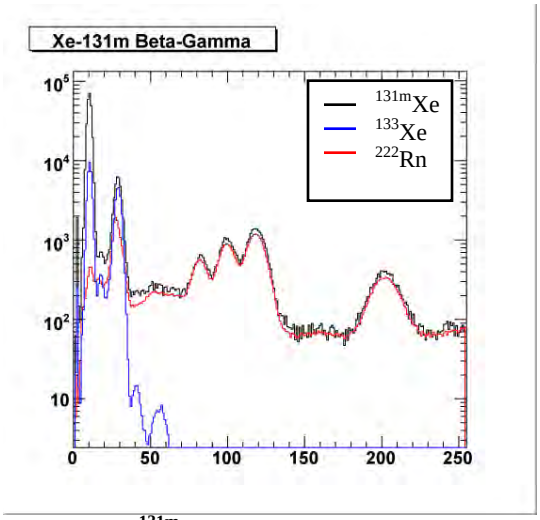

Figure 4. A ^{131m}Xe spectrum (black line) with both ^{133}Xe and ^{214}Pb contaminants present. The red spectrum is a pure ^{214}Pb spectrum that was normalized to the ^{131m}Xe contaminant level above 80 keV. Similarly, the blue spectrum is a pure ^{133}Xe spectrum also normalized to the ^{131m}Xe contaminant level above 30 keV.

The easiest way to do the subtraction is to first normalize the ^{222}Rn spectrum to the level of contaminant present using the 242-, 295-, and 352-keV peaks. After the spectrum is normalized, the ^{222}Rn is then subtracted from the ^{131m}Xe spectrum; this must be done before the ^{133}Xe contaminant level can be determined because ^{222}Rn contains an 80 keV peak from ^{214}Pb, which interferes with the 81-keV ^{133}Xe peak. After the ^{222}Rn is subtracted, the 80-0keV peak in the ^{131m}Xe spectrum should be solely produced by the ^{133}Xe contaminant, so normalization of the ^{133}Xe spectrum follows. The normalized ^{133}Xe (blue) and normalized ^{222}Rn (red) spectra are displayed in Figure 5.

β-γ Detector Auto-Calibration

As stated earlier it is important to have a well-calibrated detector during field operation. To accomplish this, an automated process has been developed that can track and adjust the energy calibration. ^{137}Cs is an easily obtained source that has a 661.7-keV γ-ray that will Compton scatter into the β detector. Figure 5 shows a typical β-γ spectrum taken using a ^{137}Cs source. The diagonal line in the spectrum is the constant energy line, where the β energy plus the γ energy is equal to 661.7 keV. The constant energy line ends well short of zero E_γ due to the maximum energies imparted to the Compton scattered electron, (reference Reeder 2004 describes the process in detail)

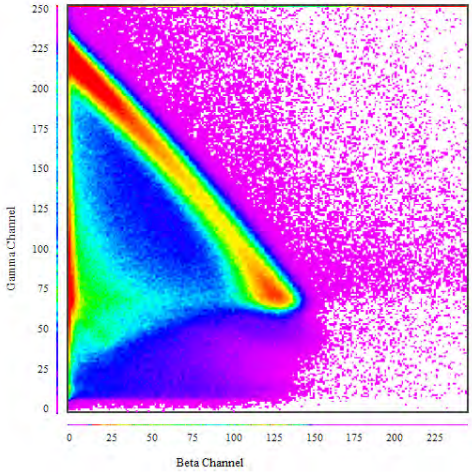

Figure 5. A β-γ spectrum taken using a ^{137}Cs source.

A method to verify and recalibrate a system in the field uses the β- and γ-singles spectra from a ^{137}Cs source to adjust gains and HV settings. The first step is to collect high-statistics β- and γ- singles from a fully calibrated detector, which will be referred to as a template spectrum (Figure 6). The template spectra will then be used as a comparison for what a calibrated detector should look like. When a detector is deployed, the first step is to acquire a β-singles and a γ-singles ^{137}Cs spectrum and compare the singles data with the template spectra. The comparison is done in two steps.

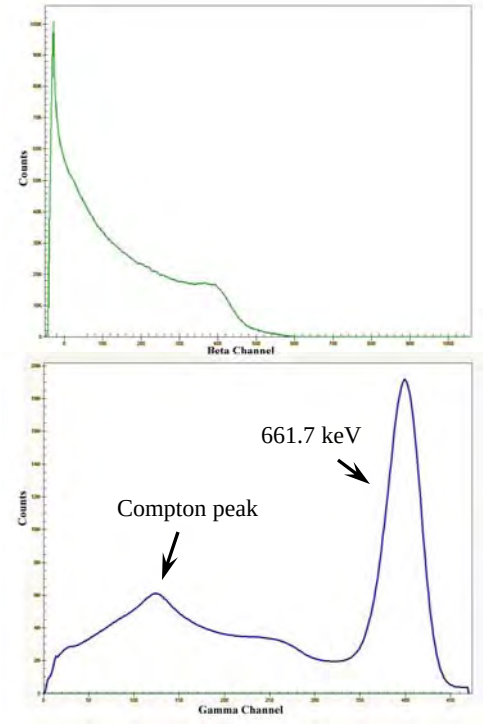

Figure 6. The top figure is a β-singles spectrum from Compton scattering using a ^{137}Cs source. The bottom spectrum is a γ-singles spectrum using a ^{137}Cs source.

First, the γ singles are analyzed to find the 661.7-keV peak and the Compton peak. The separation between the peaks represents the gain on the γ channel, which is then adjusted to match the template spectrum peak separation. Next, the 661.7-keV peak position is adjusted to the peak position in the template spectrum, giving the offset on the γ channel. Therefore, by adjusting the gain and offset the template spectrum, the γ spectrum and the calibration file should be aligned.

The second half of the processes is used to calibrate the β singles spectrum. This method finds the beginning and end-point of the spectrum. Using

$$\frac{\sqrt{\sum_{0}^{n} counts}}{\sum_{0}^{n} counts} = C, \qquad (6)$$

where C is 0.1 for finding the end-point. Similarly,

$$\frac{\sqrt{\sum_{n}^{250} counts}}{\sum_{n}^{250} counts} = C, \qquad (7)$$

where C is 0.05 for finding the beginning point. In both cases, *n* is the channel number. The value of C is determined empirically to give the best statistical results. The two points, beginning and end-point, are compared with those calculated from the β-template spectrum to determine the gain and offset for the β-cell.

CONCLUSIONS AND RECOMMENDATIONS

All detectors must be fully characterized before use, and this is especially important for fielded systems. For many detectors and for field calibration verification, this is a routine process using sealed sources. However, for detectors used in the ARSA and similar coincidence counting systems, sealed sources do not make the best choice for the initial energy calibration. Instead the use of radioactive gases gives a more accurate method of determining energy calibrations and interference ratios.

The initial characterization of a β-γ detector involves injecting multiple sources to cover the complete spectrum of energies. The three gases used are ^{131m}Xe, ^{133}Xe, and ^{222}Rn, which must be pure and high activity (30-60 Bq) to obtain high enough statistics to minimize the errors for a 1-hour acquisition. By carefully analyzing each data set the γ-ray efficiency, β-particle efficiency, γ-ray energy calibration, and β-particle energy calibration are determined.

Since a detector is only as good as its calibration the next step is to maintain the calibration of the detector system. This is most easily done in an automated fashion using a ^{137}Cs source. Through comparing new calibration files to template spectra it is possible to adjust the gain and offset to regain a good energy calibration on a detector system that otherwise would give misleading information.

Further development of the auto-calibration is in order. Some potential changes involve using a chi squared minimization of a β-γ calibration file with a β-γ template spectrum. Another direction involves using a comparison of principal components to determine the line of constant energy in a β-γ spectrum.

REFERENCES

Hayes J. C, K. H Abel, T. W Bowyer, T. R Heimbigner, M. E Panisko, P. L Reeder, J. I McIntyre, R. C Thompson, L. C Todd, and R. A Warner (1999). Operations of the automated radioxenon sampler/analyzer – ARSA, Chapter 6. Radionuclide Monitoring in *Proceedings of the 21st Seismic Research Symposium: Technologies for Monitoring the Comprehensive Nuclear-Test-Ban Treaty,* LA-UR-99-4700 Vol. 1, pp. 249–260.

Bowyer, T. W., J. I. McIntyre, and P. Reeder (1999). High sensitivity detection of Xe isotopes via β-γ coincidence counting, in Proceedings of the 21st Seismic Research Symposium: Technologies for Monitoring the Comprehensive Nuclear-Test-Ban Treaty, LA-UR-99-4700, Vol. 2, pp. 2321–241.

McIntyre J. I, T. W Bowyer, and P. L Reeder (2006). Calculation of minimum-detectable-concentration levels of radioxenon isotopes using the PNNL ARSA system . PNNL-13102, Pacific Northwest National Laboratory, Richland, WA.

Reeder P. L, T. W Bowyer, J. I McIntyre, WK Pitts, A Ringbom, and C Johansson (2004). Gain Calibration of a B/Γ Coincidence Spectrometer for Automated Radioxenon Analysis. *Nuclear Instruments and Methods in Physics Research. Section A, Accelerators, Spectrometers, Detectors and Associated Equipment* 521 (2-3): 586–599.

McIntyre J. I, A. J Carman, C. E Aalseth, J. C Hayes, T. R Heimbigner, T. W Hossbach, C. W Hubbard, K. E Litke, H. S Miley, S. J Morris, M. D Ripplinger, and R Suarez (2005). Enhanced B-Γ Coincidence Counting Gas Cell. In *2004 IEEE Nuclear Science Symposium Conference Record* , Vol. 2, pp. 884–888. IEEE, NY.

Cooper, M. W., A. J. Carman, J. C. Hayes, T. R. Heimbigner, C. W. Hubbard, K. E. Litke, J. I. McIntyre, S. J. Morris, M. D. Ripplinger, and R. Suarez (2005). Improved β-γ coincidence detector for radio-xenon detection, in Proceedings of *The 27th Seismic Research Review: Ground-Based Nuclear Explosion Monitoring Technologies*, LA-UR-05-6407, Vol. 2, pp. 779–787.

A TWO-CHANNEL PHOSWICH DETECTOR FOR DUAL AND TRIPLE COINCIDENCE MEASUREMENTS OF RADIOXENON ISOTOPES

Abi T. Farsoni, David M. Hamby, Kimberly D. Ropon, and Sean E. Jones

Oregon State University

Sponsored by National Nuclear Security Administration
Office of Nonproliferation Research and Development
Office of Defense Nuclear Nonproliferation

Contract No. DE-FC52-06NA27322

ABSTRACT

As part of the Comprehensive Nuclear Test Ban Treaty, the International Monitoring System (IMS) has been established for monitoring xenon radioisotopes in the atmosphere to detect atmospheric or underground nuclear explosions. Experimental results from the Automated Radioxenon Sampler/Analyzer (ARSA) system, developed at Pacific Northwest National Laboratory, show that the system is capable of detecting very low concentrations of the fission product radioxenon isotopes ^{133}Xe, ^{133m}Xe, ^{131m}Xe and ^{135}Xe. To build a more practical radioxenon detection system as sensitive as the ARSA system but with reduced cost, size, power consumption and complexity, several detection systems have been developed or are currently under development.

It has been shown (McIntyre et al. 2004) that triple coincidence measurements of beta, conversion electons (CE) and x-ray from the radioxenon gas provides a significant reduction of Compton scatter interference in the 30-keV line and therefore much lower (2–3 orders of magnitude) concentrations of ^{133}Xe can be detected even with a high radon background. The triple coincidence measurement eliminates the need for additional separation columns and traps (required for removing the background radon) and allows for reduced passive shielding as well, thus reducing the size and power consumption of the system.

In this paper, a two-channel phoswich detector is introduced and studied. The detector consists of a thin hollow disk (with 2 mm thickness and 76.2 mm diameter) as the xenon gas cell, surrounded by two identical planar triple-layer phoswich detectors. This design provides a solid angle of about 3.4 π for the gas cell, close to that of the ARSA system (~ 3.5 π). The planar shape of the detectors has several important advantages, among which are the reduced cost due to its simplicity, and because it has a minimum non-uniformity in light collection efficiency, will not unreasonably degrade the beta or gamma energy resolution. Moreover, utilizing digital signal processing for the proposed two-channel beta/gamma detection system, gamma-ray singles, beta singles, (β/γ) coincidence and (β/CE/x-ray) triple coincidence signals can be detected. Monte Carlo modeling of radiation transport and light collection were performed to study the phoswich detector response, and will be discussed in this paper.

OBJECTIVE

Several prototypic radioxenon detection systems have been developed to monitor atmospheric or underground nuclear explosions by measuring the concentration of the four xenon radioisotopes: ^{131m}Xe, ^{133m}Xe, ^{13g3}Xe, and ^{135g}Xe. To increase the sensitivity, these systems detect radioxenons via a beta-gamma coincidence counting. The ARSA system developed at the Pacific Northwest National Laboratory is one such system which is generally considered as a reference system since its sensitivity to detect ultra-low concentrations of radioxenons has been proven in several field tests (McIntyre et al. 2006). The ARSA system has four plastic (BC-404) gas cells, each coupled to a pair of PMTs, to hold the xenon gas and detect beta/CE particles as well. Gamma- and x-rays are detected by two optically isolated NaI(Tl) crystals, each viewed by two PMTs (McIntyre et al., 2001).

Despite its sensitivity, the ARSA system needs very careful gain matching and calibration, which is not always easy to achieve. Memory effect and radon interference are among other issues which the ARSA system faces. Previous tests of the ARSA system have shown that latent radioxenon and radon remains in the gas cells even after evacuation of the gases, leading to a memory effect which increases the background level for subsequent measurements. The current technology for separating ambient xenon from the air is also very efficient at collecting ambient radon. Additional separation columns and traps are required to remove the radon and consequently increase system size and power consumption.

Employing the phoswich technology with a beta-gamma coincidence counting capability accompanied by digital signal processing of PMT pulses can simplify radioxenon detection. In a phoswich detector, two or more scintillation layers are coupled to a single PMT. The energy deposition in each layer from incident beta and/or gamma, in coincidence or singles, are then determined via digital pulse shape analysis of the PMT's anode pulses (Ely et al., 2003; Hennig et al., 2006; and Farsoni and Hamby, 2007).

To enhance radioxenon detection, based on previous work (Farsoni and Hamby, 2006) and considering manufacturing limitations, a two-channel phoswich detector has been designed, modeled, and ordered. The detector consists of a thin hollow disk (2 mm thickness and 76.2 mm diameter) as the xenon gas cell, surrounded by two identical planar triple-layer phoswich detectors. In designing the detector, several priorities have been considered, including reducing the memory effect; improving the 30 keV x-ray/(CE + beta) coincidence region; increasing the system sensitivity by employing both dual and triple coincidence counting; improving light collecting uniformity; and decreasing the overall cost through simplifying the detector design. A two-channel digital pulse processor is under development and will be employed to detect and digitally process coincidence signal pulses.

RESEARCH ACCOMPLISHED

Two-Channel Phoswich Detector

Various geometries and phoswich designs were investigated to meet both the radioxenon detection requirements and current available manufacturing capabilities. Choosing the shape of the gas cell was the most important part of this study. To enhance the beta/CE detection and minimize the partial energy absorption in xenon gas itself, the average travel distance from the source to the beta layer must be minimized. Also, to reduce cost, the shape of the gas cell should be as simple as possible. In particular for multi-layer scintillation detectors, any irregular shape will increase the overall cost, and because of non-uniformity in light collection efficiency, irregularities degrade system energy resolution. Therefore, the simplest design was chosen: a thin hollow disk, 2-mm thick and 76.2-mm in diameter, which accommodates 9.12 cm^3 of sample gas (the ARSA's gas cell has a volume of 6.14 cm^3). The gas cell is surrounded by two identical planar phoswich detectors. An aluminum sleeve is used to join the two detectors and completes the gas cell. This design provides a solid angle of about 3.4 π for the gas cell, close to that of the ARSA system (~ 3.5 π).

Compared with a single-channel phoswich detector (i.e., phoswich well-type detector, Hennig et al., 2006), which is able to detect only dual coincidences (β/ γ and (CE + β)/x-ray), the proposed two-channel design is able to work in both dual and triple coincidence modes. Besides dual coincidences, ^{133}Xe and ^{135}Xe have a triple coincidence (β/CE/x-ray). The triple coincidence provides further reduction in the Compton background and the interference from radon daughters in a two-dimensional beta/gamma coincidence energy distribution (McIntyre et al., 2004). This eliminates the need for additional separation columns and traps (required for removing the background radon) and allows for reduced passive shielding as well, thus reducing system size and power consumption.

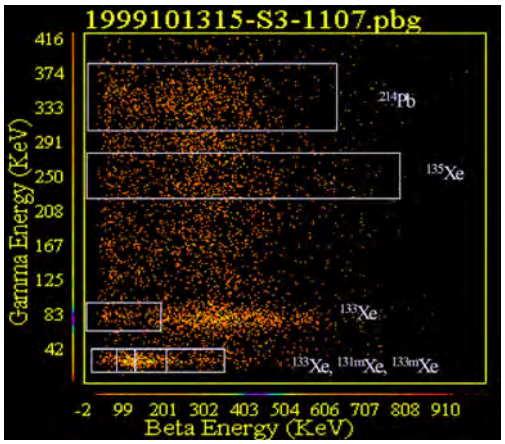

Figure 1. Two-dimensional beta/gamma spectrum (taken from McIntyre et al., 2006).

Generally, a two-dimensional beta/gamma spectrum is used to monitor xenon radioisotopes in the ARSA system (Figure 1). There are three boxed areas (in the absence of any radon daughters) from which the concentration of four radioxenons can be calculated. These areas are located at three gamma/x-ray energies; 30, 80, and 250 keV. The 30 keV x-ray area is the most complicated and needs more attention since it contains energy depositions from three xenon radioisotopes: ^{133}Xe, which emits beta (E_{max} 346 keV) and CE (45 keV); ^{131m}Xe, which emits CE (129 keV); and ^{133m}Xe, which emits CE (199 keV). As seen in Figure 1, and shown in more detail in Figure 2, this area is devided into three regions; Region I, II, and III for detecting ^{131m}Xe, ^{133m}Xe, and ^{133}Xe, respectively. Region III has two parts, the left and right extremes, of which their sum is used for ^{133}Xe concentration calculations (McIntyre et al., 2006).

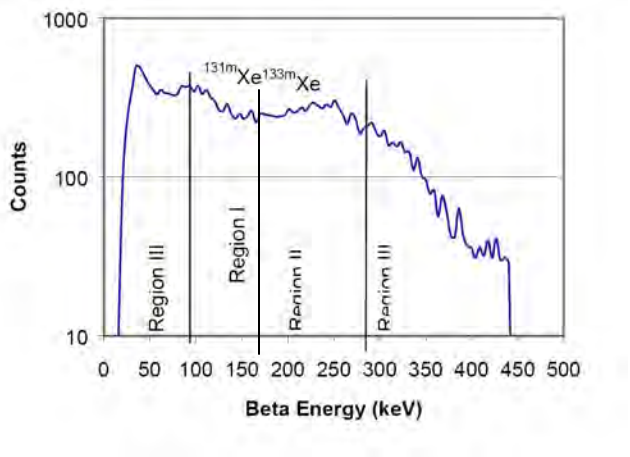

Figure 2. The 30 keV gamma-gated beta-spectrum for pure ^{133}Xe divided into three regions to discriminate two metastable radioxenons, ^{131m}Xe and ^{133m}Xe (taken from McIntyre et al., 2006).

The minimum detectable concentration (MDC) of ^{131m}Xe and ^{133m}Xe can be improved if the background in the corresponding regions (I and II) is reduced. There are two main sources of "background" in these regions in a dual coincidence counter: Compton scatter from gamma-rays with higher energies and beta particles from ^{133}Xe (E_{max} 346 keV). Employing the two-channel phoswich detector and a triple coincidence measurement, we introduce a new pulse processing method where the background under these regions due to ^{133}Xe can be reduced approximately by half (Figure 3). From this Figure, the eight possible triple-coincidence scenarios can be divided into two scenario groups: one group where the beta particle and conversion electron are detected in the same phoswich and the other group where the beta particle is detected by one phoswich and the conversion electron is detected by the other phoswich. In the first group, beta particles and conversion electrons (45 keV) are absorbed in a single phoswich and cannot be separated, thus the resulting pulse from the beta layer is recorded in the beta spectrum. This situation can be observed in the two-dimensional spectrum from the ARSA system as well (Figure 1), due to simultaneous absorption of conversion electrons and betas; the 30 keV-gated beta spectrum is shifted to higher energies, i.e., summed with CE, 45 keV. In the second group (scenarios 5 to 8), the beta particle and conversion electron are absorbed in opposite phoswich detectors; thus, they can be separated when a triple event is identified and confirmed by detecting a 30 keV x-ray in one of two phoswich detectors. Now, without losing any useful information, the beta event can be rejected while the CE event is recorded in the beta spectrum, resulting in reduction of the beta-background in Regions I and II. In fact, by using this technique, 50% of the triple-coincidence events previously recorded in Regions I, II, and III (right) from ^{133}Xe are now shifted and recorded in Region III (left), significantly improving in the MDC of ^{131m}Xe and ^{133m}Xe. In the ARSA system, only dual coincidence events in the 80 keV and some events in the 30 keV areas (Region III, left and right) are used for calculating the ^{133}Xe concentration. The MDC of ^{133}Xe itself, therefore, can be improved by this technique as well, since Region III (left) now contains some triple coincidence events which previously were lost in Regions I and II.

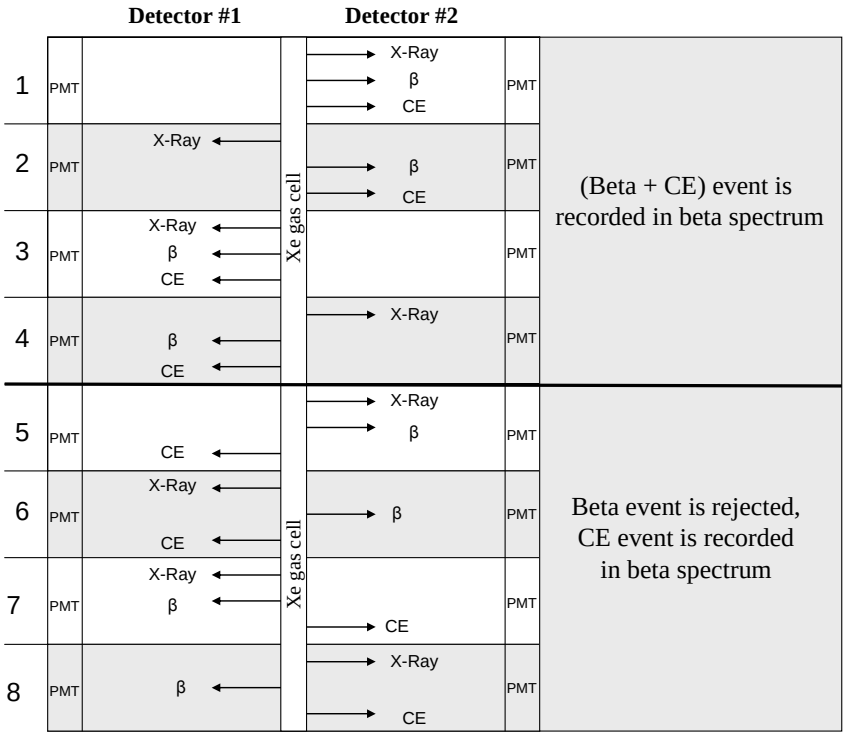

Figure 3. Employing two different pulse processing schemes for eight possible scenarios when a triple coincidence event in 30 keV x-ray area is detected.

Triple-Layer Phoswich Design

In the simplest design for a beta/gamma planar phoswich detector, two scintillation layers with sufficiently different decay times are used. Generally, the first layer from low-Z materials is intended for beta spectroscopy while the second layer from high-Z materials is assigned for gamma detection. A plastic scintillator might be the best choice for beta detection since it can be easily built in very thin layers, minimizes backscatter, and creates minimal bremstrulung radiation. Since most plastic scintillators possess very fast decay times (a few nsec), to facilitate the digital pulse-shape processing, a relatively slow and high-Z scintillator should be selected for gamma-ray detection. Among the inorganics, two scintillators are the most attractive ones: CsI(Tl) and NaI(Tl). Unfortunately both of these scintillators are hygroscopic and should be isolated from the plastic scintillator by a quartz optical window. The minimum quartz window offered by our detector manufacturer (Saint Gobain Crystals & Detectors), was 6.35 mm which was not acceptable for detecting 30 keV x-rays (see the simulated photon efficiency of NaI(Tl)* in Figure 5). Our MCNP simulations, however, show that adding a 2-mm CaF_2 layer between the plastic scintillator (1.5 mm of BC-400) and the quartz optical window will improve the detection efficiency of 30 keV x-rays by a factor of about 7, but will reduce the efficiency of 81 and 250 keV gamma-rays by 5% and 2%, respectively. Therefore, since the 30 keV x-ray regions carry vital spectral information for detecting the three radioxenons, it was decided to design the phoswich detector with three scintillation layers: BC-400 (2.4 nsec) for beta particle and CE detection, CaF_2 (900 nsec) for 30 keV x-ray detection and NaI (230 nsec) for gamma-ray detection.

Figure 4 shows the two-channel triple-layer phoswich detector design. The thickness of BC-400 is 1.5 mm and is sufficient to absorb most of the beta/CE particles emitted from radioxenons. The thicknesses of the CaF_2 and NaI(Tl) layers were chosen to be 2.0 and 25.4 mm, respectively.

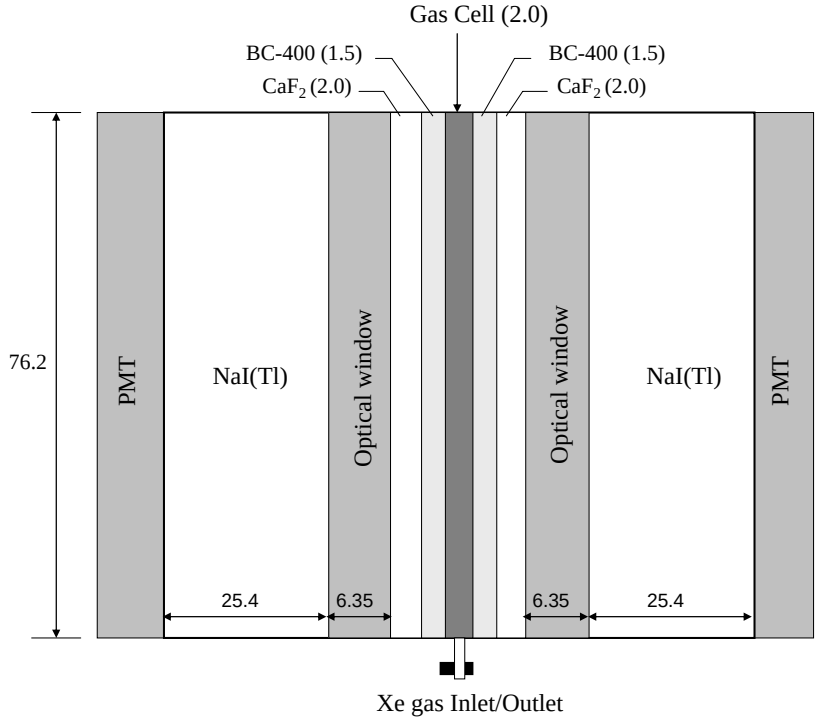

Figure 4. Schematic arrangement of the two-channel phoswich detector. All dimensions are in mm.

MCNP Analysis

A Monte Carlo analysis using the MCNP5 code was performed to study the response of the triple-layer phoswich detector to incident beta/CE and gamma/x-rays from xenon radioisotopes. Except for the simulations presented in Figure 9, for simplicity all simulations were performed in a single detector. Also in all simulations, the gas sample was a mixture of xenon and helium gas, a 10-keV threshold was applied for all simulated results and a very thin layer of aluminum (1 μm) was assumed to exist (deposited) on the surface of the BC-400 (facing the gas cell). Use of a 1-μm aluminum layer on plastic scintillators has clearly demonstrated a reduced memory effect from radioxenon gases remaining in the cells after evacuation (Seifert, 2005). Additionally, this layer will optically isolate the two halves of the detection system.

The simulated total interaction probability as a function of photon energy in sample gas, BC-400, CaF_2 and NaI(Tl) of the triple-layer phoswich detector is shown in Figure 5a. To investigate the effectiveness of using 2-mm CaF_2 for detecting low-energy photons, the simulation (indicated by NaI(Tl)*) was also executed for a dual-layer phoswich version consisting of BC-400/quartz optical window/Na(Tl) with the same thicknesses as used in previous simulations. As expected, in the dual-layer version, only a small fraction (~ 5%) of 30 keV photons reach and interact with the NaI(Tl)* layer due to the quartz optical window. In the triple-layer version, however, the 30 keV photons can be detected in the CaF_2 with a significantly increased efficiency of about 36% (a total efficiency of 72% for both sides of the detector). With an increase in the photon energy, the CaF_2 efficiency decreases rapidly and the efficiency of both the NaI(Tl) and NaI(Tl)* increases. The detection efficiencies for 81 and 250 keV photons in NaI(Tl)* are 27% and 25%, and are 22% and 24% respectively for NaI(Tl). The photoelectric efficiencies of the CaF_2 and NaI(Tl) for photons of different energies are depicted in Figure 5b. Although possessing a lower Z , the CaF_2 shows a photoelectric fraction (photoelectric/total probability ratio) of about 99% for 30 keV photons.

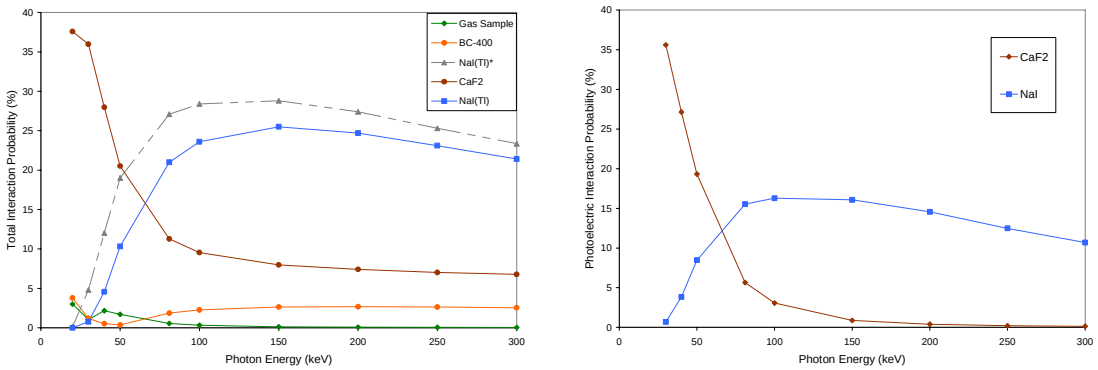

(a) **(b)**

Figure 5. (a) Total interaction probability of photons with xenon gas, BC-400, CaF_2 and NaI(Tl) in the triple-layer phoswich detector (NaI(Tl)* is from the 2-layer version and is given for reference, see the text) and (b) photoelectric interaction probability of photons with CaF_2 and NaI(Tl). The figure shows the simulations for one side of the detection system.

By re-executing the photon simulation for different thicknesses of the CaF_2 layer, changes in detection efficiency of the CaF_2 and NaI(Tl) were examined for photon energies of most interest (30, 81, and 250 keV)(Figure 6). We found that a 2.0 mm thickness of CaF_2 was a good choice since its 30 keV efficiency versus thickness follows a non-linear increase, while beyond this thickness it shows an approximate linear function. For the three photon energies, in the range of 1–3 mm of CaF_2, the detection efficiency of the NaI(Tl) layer decreases linearly, but at different rates.

The simulated interaction probabilities of monoenergetic electrons with layers of the phoswich detector are presented in Figure 7. The BC-400 shows almost a flat efficiency (~ 45%) for incident electrons with energies higher than about 100 keV. The figure also shows a threshold energy (around 500 keV) for absorption of incident electrons in the CaF_2; this is expected since the range of 480 keV electrons in the BC-400 is about 1.5 mm. Although this figure shows a relatively high probability for interacting incident electrons with the gas sample and aluminum window, on average only a very small fraction of electron energy is absorbed in these layers. Simulations show that an average energy of 3.8 keV and 1.8 keV is deposited in the sample gas from incident 50 keV and 900 keV electrons, respectively.

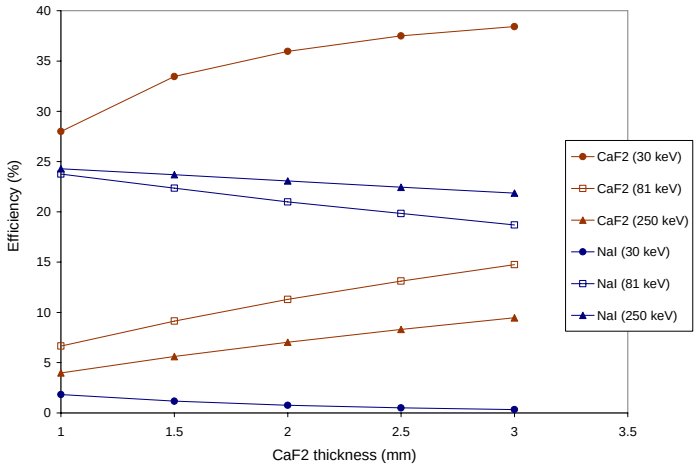

Figure 6. Total efficiencies for the three major photon energies from xenon radioisotopes with CaF_2 and NaI(Tl), as a function of CaF_2 thickness. For all simulations, the thickness of BC-400 and NaI(Tl) were 1.5 and 25.4 mm, respectively.

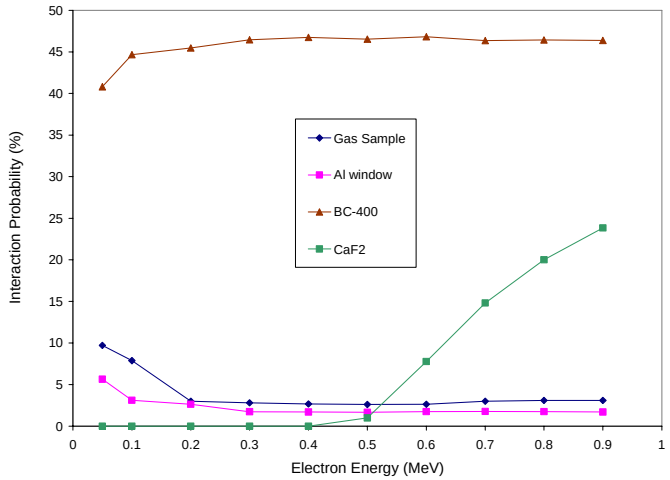

Figure 7. Simulated interaction probabilities as a function of incident electron energy.

The BC-400 layer does not fully stop all beta particles from ^{135}Xe (E_{max} 905 keV) and a small fraction of high energy betas, can penetrate into the CaF_2 layer and produce a false coincidence event. Also, any partial beta energy deposition in intermediate materials (i.e., sample gas and Al window) results in the energy distribution becoming softer. Although this effect is not important for measuring the beta events from ^{135}Xe, it needs more attention for beta particles emitted from ^{133}Xe since it may increase the beta-background in Region I and II (Figure 2; McIntyre, 2006), thus increasing the MDC of ^{131m}Xe and ^{133m}Xe. To examine these effects, the theoretical beta energy distributions of ^{133}Xe and ^{135}Xe were used to simulate the energy deposition distribution in different layers of the phoswich detector (Figure 8). In Figure 8a, since the BC-400 fully accommodates the highest energy betas (364 keV) from ^{133}Xe, no energy absorption is observed in the CaF_2 layer. For beta particles from ^{135}Xe (Figure 8b), the simulation shows a total efficiency of 1.4% in the CaF_2 layer. For ^{133}Xe, approximately 90% of energy deposition in the sample gas and aluminum window is occurring at energies below 10 keV; this value is 95% for ^{135}Xe. Therefore, by accounting for other effects such as photostatistics and light collection non-uniformity, this level of partial absorption is not expected to add a significant extra beta background to the Regions I and II of the 30 keV x-ray-gated beta spectrum (see Figure 2).

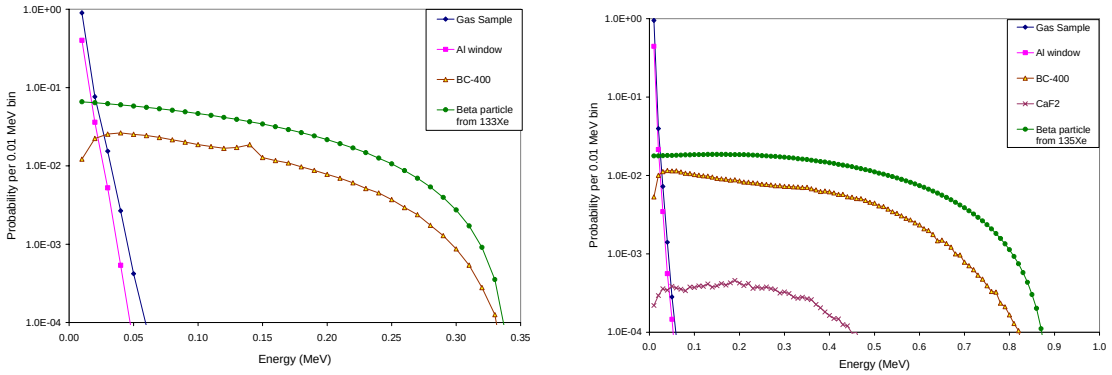

(a) **(b)**

Figure 8. Energy deposition distribution in Xe gas, Al window, BC-400 and CaF_2 from beta particles of (a) ^{133}Xe and (b) ^{135}Xe. Figure also shows the energy distribution of each beta source as reference.

Broadening of the CE peaks (129 and 199 keV), due to partial energy deposition of incident conversion electrons in the plastic scintillator, was studied for both the ARSA and our phoswich detectors. In Figure 9, three gas/beta-cell geometries were studied and compared: the original ARSA gas cell, the ARSA gas cell with interior aluminum coating, and our phoswich gas cell. Energy absorption in the sample gas for the ARSA's gas cell shows a harder distribution than that of the phoswich detector. This results in a higher average energy deposition in the ARSA's gas cell (5.9 keV from 129 keV CE) than in that of the phoswich detector (2.8 keV from 129 keV CE). At both CE energies, the BC-404 layer in the original ARSA system shows a more peaked energy distribution, while the ARSA's gas cell with an aluminum coating shows a broader peak. Therefore, compared with the ARSA system, our first estimate from Figure 9 shows that adding a 1-μm Al coating on the plastic scintillator will not significantly broaden the CE peaks in the x-ray-gated beta spectrum.

Light Collection Efficiency

The uniformity of light collection efficiency in our phoswich design was studied using the Monte Carlo optical simulation software, DETECT2000. In order to produce a continuous and high resolution data set, light was generated in three-hundred individual pixels, covering the entire cross section of the scintillators,

in a plane about the axis of symmetry. One million optical photons of a wavelength attributable to the peak output of its parent scintillator were generated in each pixel, yielding variances on the order of 0.005%. Figure 10-a presents the simulated distribution of light collection efficiency about the detector's line of symmetry, assuming a reflection coefficient of 0.95 on the outer surface of the phoswich detector. To estimate the contribution of non-uniformity of light collection efficiency in the energy resolution, the volume-weighted distribution of light collection efficiency in each scintillation layer of the phoswich detector is calculated and shown in Figure 10b. The peak broadening (resolution) in the volume-weighted distribution of light collection efficiency is about 1.2% and 1.6% for the first two layers and the NaI(Tl), respectively. This small variation in light collection efficiency is a result of the simple and planar shape of the phoswich design and will not add a significant uncertainty to the beta or gamma energy determination.

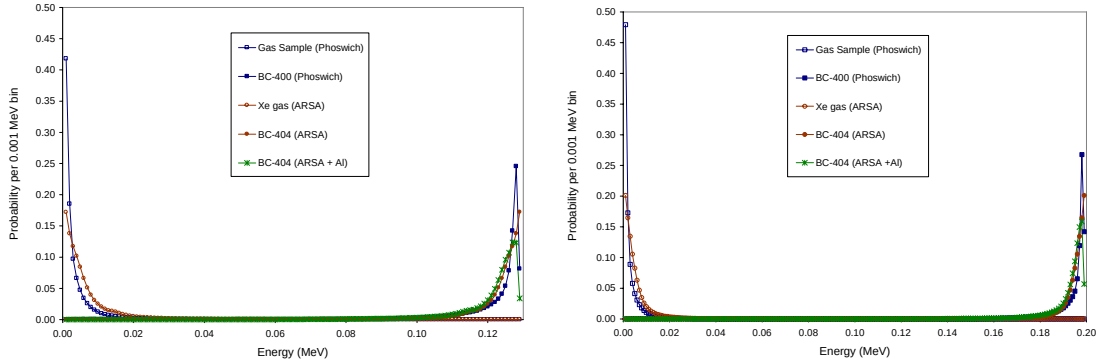

(a) **(b)**

Figure 9. Comparing the response of the ARSA and our phoswich detectors to conversion electrons from (a) ^{131m}Xe (129 keV) and (b) ^{133m}Xe (199 keV).

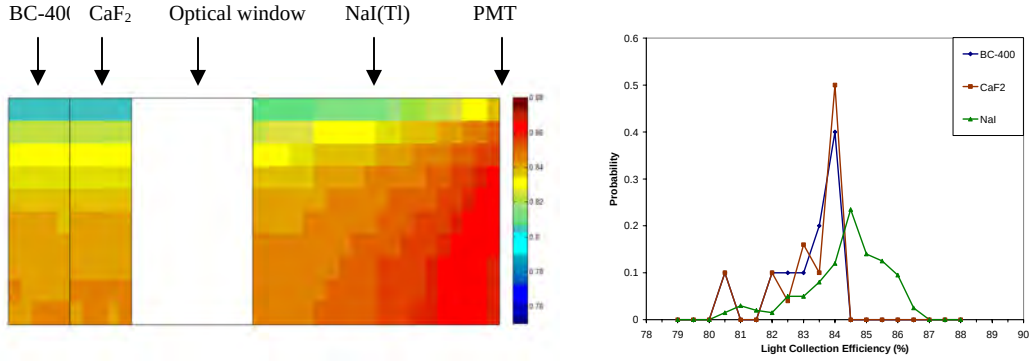

(a) **(b)**

Figure 10. Distribution of light collection efficiency (a) and volume-weighted light collection efficiency (b).

CONCLUSION

To enhance radioxenon detection, a prototypic two-channel phoswich detector has been designed, modeled and ordered. The detector features several advantages over the ARSA system: a reduced memory effect, detection of both dual and triple coincidence events, improved energy resolution due to a minimized non-uniformity in light collection, and a decreased overall cost, size and power consumption. By detecting triple coincidence events, we introduced a new novel technique to significantly improve the MDC of ^{133}Xe, ^{131m}Xe, and ^{133m}Xe. Likewise, the radiation transport modeling presented in this paper shows the advantages of triple-layer over dual-layer phoswich detectors to meet both the requirement for detecting low-energy photons and overcoming manufacturing limitations. As a result of the planar shape of the phoswich design, light collection modeling shows that the phoswich detector has a small non-uniformity in the light collection efficiency and therefore improves energy resolution over other current designs.

REFERENCES

Ely, J. H., C. E. Aalseth, J. C. Hayes, T. R. Heimbigner, J. I. McIntyre, H. S. Miley, M. E. Panisko, and M. Ripplinger (2003), Novel beta-gamma coincidence measurements using phoswich detectors, in *Proceedings of the 25th Seismic Research Review—Nuclear Explosion Monitoring: Building the Knowledge Base*, LA-UR-03-6029, Vol. 2, pp. 533–541.

Hennig, W., H. Tan, W. K. Warburton, and J. I. McIntyre (2005). Digital pulse shape analysis with phoswich detectors to simplify coincidence measurements of radioactive xenon, in *Proceedings of the 27th Seismic Research Review: Ground-Based Nuclear Explosion Monitoring Technologies*, LA-UR-05-6407, pp. 787–794.

Seifert, C. E., J. I. McIntyre, K. C. Antolick, A. J. Carman, M.W. Cooper, J. C. Hayes, T. R. Heimbigner, C. W. Hubbard, K. E. Litke, M. D. Ripplinger, and R. Suarez (2005). Mitigation of memory effects in beta scintillation cells for radioactive gas detection, in *Proceedings of the 27th Seismic Research Review: Ground-Based Nuclear Explosion Monitoring Technologies*, LA-UR-05-6407, pp. 804–814.

Farsoni, A. T. and D. M. Hamby (2006), Study of a triple-layer phoswich detector for beta and gamma spectroscopy with minimal crosstalk, in *Proceedings of the 28th Seismic Research Review: Ground-Based Nuclear Explosion Monitoring Technologies*, LA-UR-06-5471, pp. 794–792.

Farsoni, A. T. and D. M. Hamby (2007), A system for simultaneous beta & gamma spectroscopy, *Nuclear Instruments and Methods in Physics Research, Section A* 578: 528–536.

McIntyre, J. I., K. H. Able, T. W. Bowyer, J. C. Hayes, T. R. Heimbigner, M. E. Panisko, P. L. Reeder, and R. C. Thompson (2001). Measurements of ambient radioxenon levels using the automated radioxenon sampler/analyzer (ARSA), *J. of Radioanalytical and Nuclear Chemistry* 248: 629–635.

McIntyre, J. I., C. E. Aalseth, T. W. Bowyer, J. C. Hayes, T. R. Heimbigner, S. Morris, and P. L. Reeder (2004). Triple coincidence radioxenon detector, in *Proceedings of the 26th Seismic Research Review: Trends in Nuclear Explosion Monitoring*, LA-UR-04-5801, pp. 581–587.

McIntyre, J. I., T. W. Bowyer, and P. L. Reeder (2006). Calculation of minimum detectable concentration levels of radioxenon isotopes using the PNLL ARSA system, technical report PNNL-13102.

CHARACTERIZATION OF PHOSWICH WELL DETECTORS FOR RADIOXENON MONITORING

Wolfgang Hennig[1], Hui Tan[1], William K. Warburton[1], Anthony Fallu-Labruyere[1], Konstantin Sabourov[1], Justin I. McIntyre[2], Matthew W. Cooper[2], and Anshel Gleyzer[3]

XIA LLC[1], Pacific Northwest National Laboratory[2], and PhotoPeak, Inc[3]

Sponsored by National Nuclear Security Administration
Office of Nonproliferation Research and Development
Office of Defense Nuclear Nonproliferation

Contract No. DE-FG02-04ER84121

ABSTRACT

Devices to measure the amount of radioactive xenon in the atmosphere have been installed in several locations around the world as part of the International Monitoring System to detect nuclear weapons testing. These devices extract small samples of xenon from large volumes of air and look for characteristic radioxenon isotopes emitting beta and gamma radiation in coincidence. To detect these coincidences, they currently employ a complex system of separate beta and gamma detectors which is very sensitive, but which requires careful calibration and gain matching of several detectors and photomultiplier tubes to achieve desired detection limits.

An alternative to separate beta and gamma detectors is the use of a single phoswich detector in which beta-gamma coincidences are detected by pulse shape analysis. The phoswich detector consists of a plastic scintillator (absorbing betas) optically coupled to a CsI(Tl) scintillator (absorbing gammas) and thus requires only a single photomultiplier tube and electronics readout channel, greatly simplifying setup and calibration. In this paper, we present the results from an experimental evaluation of two phoswich well detector prototypes, including energy resolution,
2-D beta/gamma energy histograms from a variety of test sources, and background count rates. From these measurements, we derive detector properties such as coincidence detection efficiency, background rejection and the ability to separate beta only, gamma only, and coincidence events. We will further discuss setup and calibration procedures and compare them to those for existing detector systems.

OBJECTIVES

As part of the International Monitoring System established by the Comprehensive Nuclear-Test-Ban Treaty, devices to measure the amount of radioactive xenon in the atmosphere have been installed in several locations around the world to detect nuclear weapons testing. These devices, one example being the Automated Radioxenon Sampler and Analyzer (ARSA) instrument developed at Pacific Northwest National Laboratory (Reeder, 1998), extract Xe from large volumes of air and then measure its radioactivity in an extremely low background counter. Since the Xe isotopes of interest all emit one or more beta particles or conversion electrons simultaneously with one or more gamma rays or X-rays, beta-gamma coincidence can be used effectively to suppress the natural background.

Currently, the devices use time based coincidence detection with separate detectors for beta and gamma radiation, which requires several channels of photomultiplier tubes (PMTs) and readout electronics. This leads to complex systems that require careful gain matching and calibration. Phoswich detectors have been studied as a potential simpler solution (Ely, 2003; Hennig et al., 2006-1), using pulse shape analysis (PSA) to detect coincidences in the signal from a single PMT. Using Monte-Carlo simulations, we previously studied several possible designs of phoswich well detectors that could be used as drop-in replacements for the existing ARSA detector unit (Hennig et al., 2006-2). The objective of the work presented in this paper was to build prototypes of the more promising designs and characterize their performance, i.e. determine properties such as energy resolution, coincidence detection efficiency, background rejection and the ability to separate beta only, gamma only, and coincidence events.

RESEARCH ACCOMPLISHED

Measurements

Two detector prototypes, named PW2 and PW3, were built. They both consist of a 1" diameter BC-404 plastic cell (absorbing betas) enclosed in and optically coupled to a 3" CsI(Tl) crystal (absorbing gammas), but differ in detector geometry as shown in Figure 1. PW2 is easier to manufacture, but due to the cut in CsI parallel to the PMT window, the light collection and thus energy resolution are degraded (Hennig et al., 2006-2). The geometry of PW3 has the best light collection and resolution among all designs studied in the simulations, but is more difficult to manufacture. The detector as currently built has a PMT with low gain and relatively high noise. Thus any results presented here for PW3 represent a detector that has not yet been fully optimized.

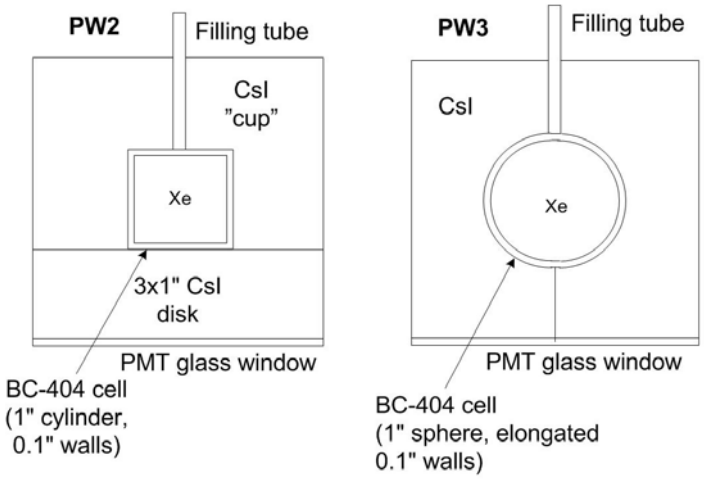

Figure 1. Geometries of phoswich well detectors studied. Left: 1st well prototype (PW2); right: 2nd well prototype (PW3).

Energy Resolution

For PW2, we obtain an overall resolution of ~12% full width at half maximum (FWHM) for 662keV gamma rays from a ^{137}Cs source outside the detector. Closer analysis shows that there are actually 2 overlapping peaks with resolutions of ~7% and ~9% FWHM, their relative intensity varying according to location of the source. We

attribute this to the different light collection efficiency in the two sections of the CsI crystal (Hennig et al., 2006-2). For PW3, the resolution is ~9%, a single peak independent of the location of the source. Resolutions for other sources and energies are given in Table 1. Note that for low energies, the resolution of PW2 becomes equal to PW3, because the fixed ~6% separation of the 2 peaks from the two CsI crystal segments becomes negligible when added in quadrature with other peak broadening effects, such as photostatistics. Due to the noisy, low gain PMT currently used with PW3, its resolution is *worse* than PW2 at very low energies. These measurements will be repeated soon with a replaced PMT.

Table 1. Energy resolution (FWHM) of PW2 and PW3. For external sources, no PSA to separate event types was applied. Values in () are preliminary results that need to be repeated with a replaced PMT.

	PW2	PW3	Notes	ARSA (Reeder, 2004)
Resolution at Ec = 662keV (external ^{137}Cs)	12%	9%	PW2: two peaks, ~7% and ~9%	12%
Resolution at Ec = 609keV (internal ^{222}Rn)	12%	10%	Coincidence events only	
Resolution at Ec = 120keV (external ^{57}Cs)	16%	17%		22%
Resolution at Ec = 60keV Ec = 29keV (external ^{241}Am)	18% 31%	(23%) (36%)	PW3: small signal close to noise with this PMT	
Resolution at Ec = 30keV Ep = 129keV (internal ^{131m}Xe)	(36%) 29%	(48%)	Coincidence events only PW3: small signal close to noise with this PMT	32% 37%

Energy Histograms

Using the fact that interactions in the plastic scintillator generate very fast pulses (< 100ns) while the CsI pulses are slow (several microseconds), each pulse from the phoswich detector is processed to extract the portion of energy deposited in CsI and plastic scintillators (Hennig et al., 2006-1). Figure 2 shows 2D histograms of CsI energy (Ec) vs. plastic energy (Ep) for measurements with a ^{222}Rn source (NIST SRM 4974). The 2D histograms show horizontal lines of coincidence events from beta particles (Ep varies) and photons (peaks at Ec = 80keV, 241keV, 295keV, 351keV and 609keV) from ^{222}Rn daughter products. The 80keV line is offset in Ep as a conversion electron with constant energy emitted at the same time as the variable energy beta particle. The energy resolution of Ec for the 609keV coincidence line is about 11.8% FWHM in PW2, with a noticeable shoulder or second peak towards higher energies (see Figure 3). For PW3, the resolution is about 10.2% with no shoulder.

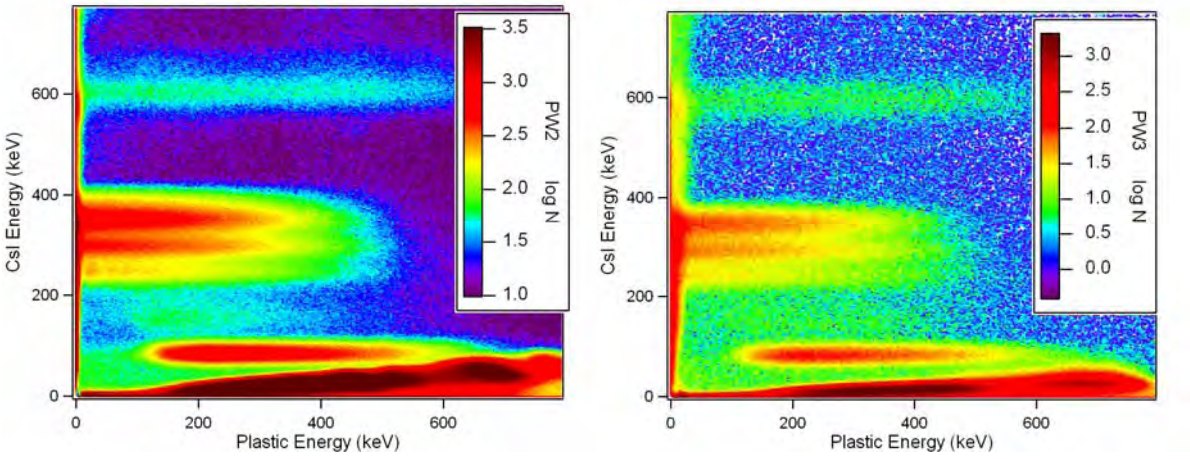

Figure 2. 2D energy histograms for PW2 (left) and PW3 (right) for measurements with a ^{222}Rn source. Note the color scales differ due to different number of counts in each measurement.

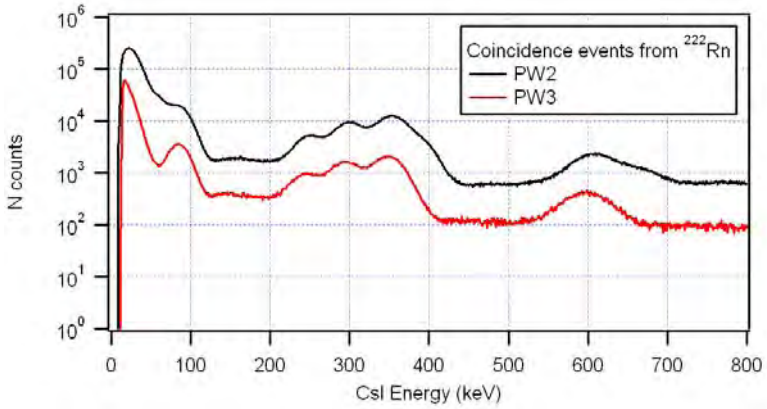

Figure 3. Histograms of energy deposited in CsI (in coincidence events only) for PW2 and PW3 in measurements with a ^{222}Rn source. The shoulders in the peaks of PW2 at 400 and 670 keV are due to the non-uniform light collection in different sections of the detector.

In both detectors, but less pronounced in PW3, there is also a rising diagonal line starting at Ec ~ 0keV, Ep ~ 150keV. The "peaks" along the line—allowing for a different energy scale and non-linearity at low energies for heavy charged particles (Knoll, 2000)—match the alpha energies in the ^{222}Rn decay chain. We thus conclude that these events are alpha particles, generating a slightly different pulse shape (slower decay) than electrons or photons when interacting with the plastic scintillator. The PSA algorithms, in their current form, interpret the slower decay as a contribution of a slow CsI pulse and thus compute a component in Ec proportional to the pulse height. Because Rn is removed from the sample to minimize interference in the 80keV line in Xe monitoring measurements, there should then be no significant interference from alpha particles either. On the other hand, it is also possible to modify the PSA algorithms to detect and remove alpha pulses from the recorded data, e.g., by shape-matching fits, measuring the fall time or additional sums over characteristic intervals in the pulse.

Figure 4 shows a 2D histogram of Ec vs. Ep for measurements with a ^{131m}Xe source. The 2D histogram has one coincidence peak due to 30keV X-rays in coincidence with 129keV conversion electrons and a plastic only peak at ~160keV from conversion electrons that are not in coincidence. The resolution for coincidence events for PW2 is ~29% at Ep = 129keV. In measurements with a mixture of ^{131m}Xe and ^{133g}Xe, the resolution at Ec = 30keV is ~ 36% for PW2 and ~48% for PW3.

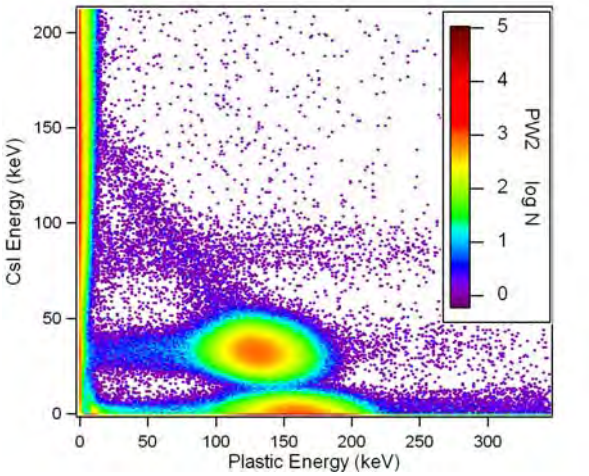

Figure 4. 2D energy histograms for PW2 for measurements with a ^{131m}Xe source. The 80keV line comes from traces of other sources (^{222}Rn or ^{133}Xe). Measurements for PW3 are still in progress.

Background: In monitoring applications, the samples of radioxenon collected are very small, so the background count rate of the detector has to be as small as possible. In a lead enclosure (lead wall thickness is 2" with an additional 0.5" inner lining with Oxygen-Free High Conductivity [OFHC] copper), we measure an overall rate of 4-5 counts/s for PW2, of which ~0.05 counts/s are coincidences. The overall rate for PW3 is 3-7 counts/s, of which ~0.04-0.09 counts/s are coincidences. The ARSA detector, consisting of two much bigger NaI crystals, has an overall background rate of ~30 counts/s of which 0.1 counts/s are coincident, i.e., the background in Xe regions of interest is can be up to a factor of 2 higher.

Characterization

Coincidence Detection Efficiency

The coincidence detection efficiency at a given energy is defined as the number of net coincidence counts in the peak, divided by the number of all net counts in the peak. From the ^{131m}Xe measurement for PW2, we obtain the coincidence detection efficiency for the 30keV peak as 97.6%. A small fraction (about 1.5%) of coincidence events fall outside the main peak, due to two processes: 1) Conversion electrons pass through the plastic and reach the CsI, i.e., a portion of the conversion electron's energy is deposited in the CsI and added to the measured X-ray energy. This creates the diagonal line to the upper left from the main peak in the histogram. 2) Conversion electrons lose some of their energy in passive parts of the detector, i.e., a portion of the conversion electron's energy is lost. This causes the horizontal line to the left from the main peak. For a given conversion electron energy, the fraction of such events depends primarily on the wall thickness of the plastic cell (Hennig et al., 2006–2).

Measurements with a mixture of ^{131m}Xe and ^{133g}Xe result in an estimated coincidence detection efficiency of 98.5% for PW2 and 98.9% for PW3. As expected, the values are very similar since the difference in detector design affects mostly the light collection, not the absorption of radiation.

Background Rejection

Adding an external ^{137}Cs source as "controlled background" in measurements with PW2 in the lead enclosure, we find an increase in overall count rate of 77 counts/s (with this particular source). Most of the ^{137}Cs photons interact only with the CsI; however a small fraction will Compton scatter from the CsI to the plastic or vice versa, generating coincidence events. The increase in the coincidence count rate is only 0.48 counts/s, i.e. 0.6% of the overall increase. Thus the background rejection rate (background represented by a ^{137}Cs source) is 99.4% for PW2. For PW3, we compute a background rejection rate of 99.2% from a measurement with a source adding 526 counts/s.

Ability to Separate Event Types

Events are processed one by one with PSA algorithms to categorize them as CsI only (gamma), plastic only (beta) or both (coincidence) based on user defined thresholds in energy and signal rise time. Close inspection of a subset of events indicate an error rate of ~1% in each category due to the automated pulse shape analysis, for example 1% of the events categorized as coincidence events are actually CsI only events or plastic only events. The most common reasons for mis-categorization are noise spikes in very low energy events and random coincidences (e.g., 2 plastic pulses following each other closely), and most of the mis-categorized events thus fall close to the origin in the 2D histogram, outside the region of interest for Xe isotopes.

From the resolution of the coincidence peak and the distribution of beta only and gamma only events along the axes in the 2D histogram, we estimate the minimum detectable coincidence energy for PW2 to be Ec ~ 13keV and Ep ~ 25keV in the plastic, which means that lower energies are not clearly distinguishable from CsI only or plastic only events, respectively. A setup using separate, optically isolated detectors with typical thresholds may have a minimum detectable coincidence energy of Ec ~ 14keV and Ep ~ 5keV, but no radioxenon coincidences of interest occur at such low energies.

Calibration

Quantitative isotope analysis for radioxenon monitoring relies on measuring the number of counts in specific regions of interest in the 2D histogram. Therefore, in repeated measurements and over long periods of time, the detector system has to deliver spectra with a fixed range in both beta energy and gamma energy (exact same scale keV/bin).

For a single detector (one scintillator with PMT), the deposited energy can be assumed to be proportional to the measured pulse height, and thus a single gain calibration constant is usually sufficient to histogram pulses into an energy spectrum. However, even when holding external environmental factors such as temperature and magnetic field constant, gains may drift over time. Therefore the calibration constant has to be verified periodically and either the constant or the PMT gain has to be adjusted to correct for any gain changes.

In the phoswich detector system, the plastic and CsI energies are derived by PSA algorithms from the measured pulse height (called E) and a sum accumulated over the initial portion of the pulse (called P). Both E and P depend on the gain of the detector as in a single detector. The algorithms rely on two processing constants, essentially the ratios P/E for plastic only and CsI only events. These ratios are detector constants depending on the pulse shape and relative light output of the plastic and CsI scintillators. They are easily determined in calibration measurements with beta/gamma emitting reference sources such as ^{222}Rn and ^{131m}Xe, but even an external ^{137}Cs source generates in a few minutes a sufficient number of plastic only pulses for the calibration. Most importantly, the P/E ratios *do not* depend on the gain of the detector, since both fast and slow components of the pulse are equally affected by any gain changes. This can be seen in Figure 5 (left), plotting the P/E ratios and the position of the 662keV peak from ^{137}Cs as a function of PMT bias (i.e., gain). While the peak position shifts to higher bins at higher gains, the P/E ratios remain constant (the standard deviation of measured P/E ratios is 0.5% for the plastic scintillator and 0.2% for CsI). Consequently, in measurements with different gains, the energy scales of Ep and Ec both change by the same factor. The slope fitted to the Compton scattered events in the 2D histogram—the light blue line in Figure 5 (right)—remains a constant within the precision of the measurement.

In practice this means that even though the PSA introduces additional processing constants to determine the individual energies, only the overall gain calibration has to be verified and adjusted periodically. The processing constants have to be determined only once, for example at the production or installation of the detector. In periodic adjustments for gain, only a single measurement with a ^{137}Cs reference source, as simple as determining the peak position of the 662keV peak, is required to calibrate the scales of both energy axes. Alternatively, if there are well-defined peaks in the naturally occurring singles background, they might also be used to monitor and stabilize the PMT's gain.

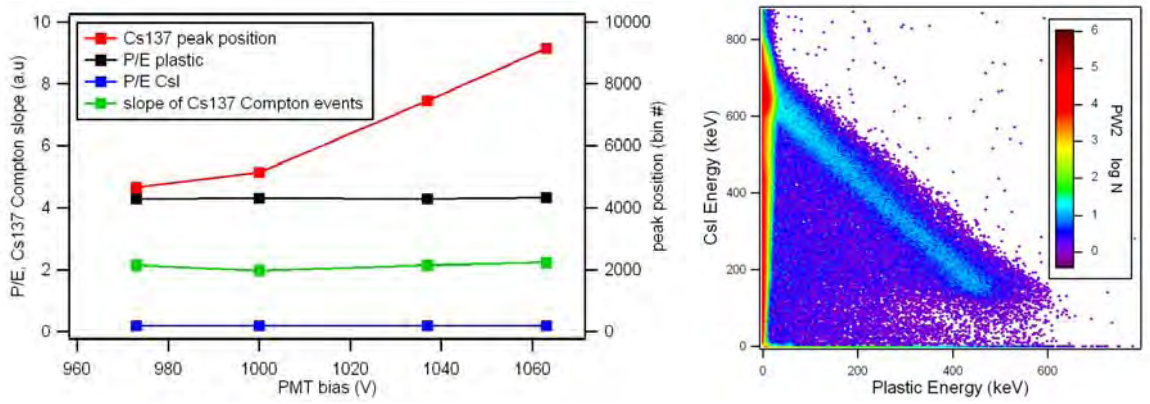

Figure 5. Left: Variation of peak position and processing constants with PMT bias (i.e., gain). Right: 2D energy histogram for a ^{137}Cs source. The slope of the full energy Compton events (line of light blue pixels) is plotted in green in the left graph for different values of PMT bias.

In contrast, the existing ARSA detector system has separate beta and gamma detectors and uses multiple PMTs to read out the same scintillator. Therefore, during calibration these shared PMTs first have to be adjusted to have the exact same gain, and then for each scintillator a gain calibration constant has to be determined. This amounts to 6 gain matches and 6 gain constants for 4 sample cells compared to only 1 gain dependent calibration constant per sample cell for the phoswich detector. The resulting simplifications in field operation that are expected to result from this reduction in necessary calibration measurements have, naturally, been a major driving force for the development of this phoswich technology.

CONCLUSIONS AND RECOMMENDATIONS

In summary, we have built and evaluated two phoswich well detector prototypes. Overall, their performance is comparable to that from the existing ARSA detector: the background is somewhat lower, the resolution slightly better or equal, and the energy thresholds for coincidence detection somewhat higher. PW3 has better energy resolution, as expected from previous simulations, but more tests are necessary with a better PMT to complete its evaluation. The key advantage of the phoswich detectors is their much simpler calibration, since the single PMT requires only periodic calibration of one gain dependent constant per sample cell instead of three, and the beta energy can be scaled from the peak position of the ^{137}Cs gamma peak. Future work will include the production and long term evaluation of two additional phoswich detectors made in the same geometry as PW3.

REFERENCES

Ely, J. H., C. E. Aalseth, J. C. Hayes, T. R. Heimbigner, J. I. McIntyre, H.S. Miley, M. E. Panisko, and M. Ripplinger (2003). Novel Beta-Gamma coincidence measurements using phoswich detectors, in *Proceedings of the 25th Seismic Research Review—Nuclear Explosion Monitoring: Building the Knowledge Base*, LA-UR-06-6029, Vol. 2, pp. 533–541.

Hennig, W., H.Tan, W. K. Warburton, and J. I. McIntyre (2006). Single channel beta-gamma coincidence detection of radioactive Xenon using digital pulse shape analysis of phoswich detector signals, *IEEE Transactions on Nuclear Science* 53: (2) p. 620.

Hennig, W., H.Tan, A. Fallu-Labruyere, W. K. Warburton, J. I. McIntyre and A. Gleyzer (2006). Design of a phoswich well detector for radioxenon monitoring, in *Proceedings of the 28th Seismic Research Review: Ground Based Nuclear Explosion Monitoring Technologies*, LA-UR-06-5471, Vol. 2, pp. 801–810.

Knoll, G. F. (2000) *Radiation Detection and Measurement*, J Wiley & Sons, Inc. Chapter 8.

Reeder, P. L., T.W. Bowyer, and R. W. Perkins, (1998). Beta-gamma counting system for Xe fission products, *Journal of Radioanalytical and Nuclear Chemistry* 235: (1–2), 89–94.

Reeder, P. L., T.W. Bowyer, J. I. McIntyre, W.K. Pitts, A. Ringbom, and C. Johansson (2004). Gain calibration of β/γ coincidence spectrometer for automated radioxenon analysis., *Nuclear Instruments and Methods in Physics Research* A 52, 586–599.

SEGMENTATION OF THE OUTER CONTACT ON P-TYPE COAXIAL GERMANIUM DETECTORS

Ethan L. Hull[1], Richard H. Pehl[1], James R. Lathrop[1], Peggy L. Mann[1], Ronnie B. Mashburn[1], Bruce E. Suttle[1], Harry S. Miley[2], Craig E. Aalseth[2], and Todd W. Hossbach[2]

PHDs Co.[1] and Pacific Northwest National Laboratory[2]

Sponsored by DOE Office of Science, Nuclear Physics SBIR Phase 2

Contract No. DE-FG-02-05ER84157

ABSTRACT

Germanium detector arrays are needed for low-level counting facilities. The applications of such user facilities include characterization of low-level radioactive samples. In addition, the same detector arrays can perform important fundamental physics measurements including the search for rare-events like neutrinoless double-beta decay. Germanium coaxial detectors having segmented outer contacts can provide sensitivity improvement in low-background measurements. The segmented outer detector contact allows pulse-shape analysis measurements that provide additional background reduction. Currently, n-type (reverse electrode) germanium coaxial detectors are used whenever a segmented coaxial detector is needed because the outer boron (electron barrier) contact is thin and can be relatively easily segmented. Coaxial detectors fabricated from p-type germanium cost less, usually have better energy resolution, and can be larger than n-type coaxial detectors. However, it is difficult to reliably segment p-type coaxial detectors because thick (~ 1 mm) lithium-diffused (hole barrier) contacts are the standard outside contact for p-type coaxial detectors. During this Phase II small business innovation research grant (SBIR), we are developing thinner, segmented, and stable lithium-diffused contacts. Many small planar test detectors have been fabricated with segmented lithium-diffused contacts. Center contact and guard-ring structures have been fabricated on the detectors to study the rectification and segmentation properties of lithium-diffused contacts. Fabrication techniques have been established that successfully produce repeatable rectification and segmentation. The rectification and segmentation appear to be stable with respect to modest temperature cycles. These results are fundamental steps toward developing segmented lithium-diffused contacts for p-type coaxial detectors. Large segmented p-type coaxial detectors based on this technology could serve as gamma-ray spectrometers on instruments such as the Radionuclide Aerosol Sampler / Analyzer (RASA). These detectors will provide more sensitive, lower background, measurements than currently available unsegmented p-type coaxial detectors.

OBJECTIVES

Germanium detector arrays are needed for low-level counting facilities. The practical applications of such user facilities include characterization of low-level radioactive samples. In addition, the same detector arrays can also perform important fundamental physics measurements including the search for rare events like neutrino-less double-beta decay (Miley et al., 1991; Miley, et al., 1990; Majorana Collaboration White Paper, 2003; and Goulding et al., 1984). Coaxial germanium detectors having segmented outer contacts could provide the next level of sensitivity improvement in low background measurements. The segmented outer contact allows performance of advanced pulse-shape analysis measurements. These techniques can be used to discriminate between multiple Compton-scattered gamma-ray events and single-point beta-decay events. Because of their complexity, segmented coaxial detectors are expensive and available only after relatively long lead times. Improved detector segmentation techniques would be both important and timely. Such technological advances will reduce fabrication costs and improve availability of these detectors for the low-level counting community.

Currently, n-type (reverse electrode) germanium coaxial detectors are used whenever a segmented coaxial detector is needed. To obtain reasonably accurate coaxial detector segmentation, the outer detector contact must be the segmented contact. The most conveniently segmented conventional outer contact is the boron-implanted outer contact of an n-type coaxial detector. The ability to segment the outer boron contact is the reason segmented n-type coaxial detectors are suggested for use in low background gamma-ray measurements. However, n-type coaxial detectors should only be used in environments where radiation damage is a concern and/or a thin outer detector

contact is desired. Segmented p-type (conventional electrode) coaxial detectors would have technical and financial advantages in low background counting experiments.

P-type coaxial detectors are significantly less expensive and have better gamma-ray energy resolution than n-type coaxial detectors. Fundamentally, this is due to the presence of electron-trapping sites found in even the best detector-quality germanium. A small percentage of the electrons arising from gamma-ray interactions in the detector are trapped before reaching the electron-collecting contact. The charge is trapped for a sufficient duration and is not included in the processed signal for that event. The resulting pulse-height deficits cause broadening of gamma-ray peaks. The magnitude of this energy-resolution degradation from electron trapping is strongly dependent on the geometry of the detector. In detectors of coaxial geometry, the charge carriers collected on the inner contact are responsible for inducing most of the total signal from gamma-ray interactions occurring in most of the volume of the detector. In n-type coaxial detectors, electrons are collected on the inner contact. Consequently, the gamma-ray energy resolution of n-type coaxial detectors is degraded by even small amounts of electron trapping. On the other hand, the spectroscopy of p-type detectors of coaxial geometry relies more heavily on the collection of holes on the inner contact. As a result, electron trapping causes much less resolution degradation in a p-type coaxial detector than in an n-type coaxial detector. The decreased sensitivity to electron trapping makes a greater fraction of the germanium crystals viable for fabrication into p-type coaxial detectors having excellent energy resolution. The lesser importance of electron trapping allows fabrication of larger diameter p-type coaxial detectors. Thus fewer detectors are needed to make an array having a given total volume. It is important to note that electron trapping is still not thoroughly understood and difficult to control in the growth of detector-quality germanium. Any large-scale low-level counting facility employing segmented coaxial detectors would greatly benefit, both technically and financially, from the use of p-type coaxial detectors.

Currently the segmentation of the outer lithium-diffused n+ contact of a p-type coaxial detector is a nontrivial operation. The outer contact of a p-type coaxial detector is conventionally made using a rather thick (as much as ~1 mm thick) lithium-diffused layer as the hole-barrier contact. Thick lithium-diffused contacts are very rugged and reliable but require rather drastic techniques for segmentation. Some techniques involve cutting through the lithium-diffused layer with a saw to segment the contact. Although it can work, such detector fabrication techniques are expensive, time consuming, and mechanically cumbersome. In the event that a saw-cut lithium contact does not successfully function, successive fabrication attempts may prove difficult. Accommodating the saw-cut grooves during the subsequent fabrication attempts may be sufficiently complicated to compel regrinding the crystal to a smaller diameter or even starting over again with a new crystal. In addition, such saw cuts can cause charge-collection and surface-channel problems in the vicinity of the grooves between the segments. Grooves often result in effectively “dead” germanium near the grooves. The initial saw cuts and electronically “dead” germanium consume valuable isotopically enriched germanium.
To make segmented p-type coaxial detectors viable, better outer contacts must be developed to replace saw-cut segmented thick lithium contacts. There are other contact technologies with the potential to provide hole-barrier contacts that are more easily segmented than thick-lithium n+ (hole barrier) contacts. This study seeks to determine the best solution for producing thin-segmented hole barrier contacts on p-type germanium detectors. This will make p-type coaxial detectors viable for large-scale low-level counting arrays. We have started investigating alternative techniques for making segmented hole-barrier contacts in lieu of conventional thick lithium-diffused n+ contacts. Amorphous germanium contacts represent one possible alternative. During Phase I of this SBIR we fabricated and tested many small planar test detectors (~2–4 mm thick, ~30-mm diameter) having segmented amorphous germanium contacts as the hole-barrier (+ biased) contacts. We focused on making the amorphous germanium hole barrier as high as possible. A larger hole barrier provides better rectification and a higher probability of successful fabrication of large diameter p-type coaxial detectors using the thin amorphous germanium contact over the entire outside area of the detector. Amorphous germanium contact technology naturally lends itself to the simple fabrication of finely segmented germanium detectors (Luke et al., 1992; Hull et al., 2002; and Hull et al., 2003). By making many planar test detectors, we studied the rectification and segmentation of amorphous germanium contacts with a focus on increasing the hole-barrier contact. We demonstrated the viability of our fabrication techniques by fabricating a small p-type coaxial detector (MJ1) having an amorphous germanium outer contact. The successful rectification of the amorphous germanium contact over the large curved outer contact of MJ1 serves as a first step toward a viable manufacturing process for segmented p-type coaxial detectors. This work was sufficient to provide a successful Phase 2 application (Hull, E. 2005, Hull, E. 2006).

During the first year of Phase 2, significant strides have been made to analyze the potential for the fabrication of segmented lithium-diffused contacts on germanium detectors. In principle, lithium-diffused contacts could be used to form rectifying hole barriers that are segmented. The goal of Phase 2 is the research of segmented lithium contacts by fabrication of planar and coaxial germanium detectors.

RESEARCH ACCOMPLISHED

Initially, effort was dedicated to building a lithium evaporation and diffusion station for evaluating the limitations of segmented lithium-diffused contacts on germanium detectors. A Veeco 7760 thermal vacuum evaporation system was converted into a system suitable for evaporation and thermal diffusion of lithium into germanium. A vacuum housing and shielding structure was designed and built. These shields prevent the outer vacuum vessel and vacuum sealing surfaces from becoming coated with lithium during the evaporation process. A manually actuated shutter was installed to control the duration of the thermal evaporation of lithium from the source onto the detectors. Figure 1 is a photograph of the lithiation station when closed. A current supply capable of producing .75 Amps at 100 V is used to drive current in a Zener diode on a heating plate in the vacuum system. The detectors are heated on this plate to diffuse the evaporated lithium into the germanium. The temperature of the plate was read out using a DT670 LakeShore diode. The temperature measurement requires reading the voltage drop on the diode when 10 microamps of current is supplied to the diode.

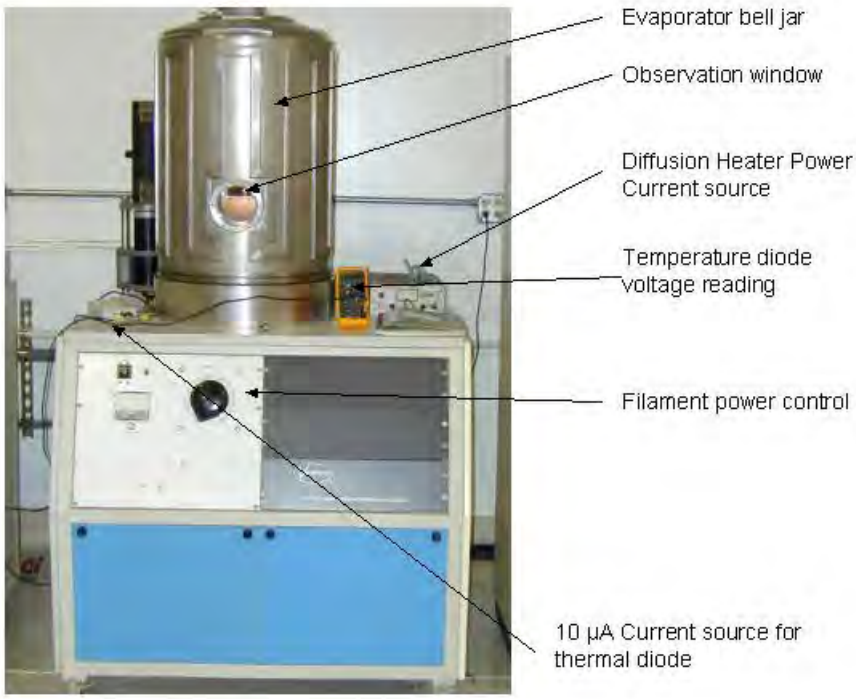

Figure 1. The lithiation system provides a high vacuum environment for the evaporation and diffusion of lithium into germanium.

A procedure for low temperature lithium diffusion was developed using small planar test detectors. The detectors were etched in a mixture of 3:1 HNO_3:HF and rinsed in methanol. The temperature of the plate was increased after the lithium was evaporated. The detectors were warmed to ~ 100º C for ~ 1hr. The detectors were then cooled to ~ 80º K in a vacuum test cryostat. The rectification and separation of the lithium contacts were tested the following morning. These detectors showed some signs of rectification, but the rectification was so poor that most of the

detectors would only withstand an electric field of ~ 200 V/cm before the diode broke down. This is not nearly enough electric field to operate a large coaxial detector. Even at electric fields less than breakdown, these detectors showed very poor looking gamma-ray signals characteristic of a non-rectifying semiconductor junction. These detectors also exhibited poor segmentation between the center and guard-ring contacts of the detector.

The temperature of the lithium diffusion was increased to ~125° C for ~ 1 hr, by sending more power to the Zener diode in the diffusion hot plate. This relatively small increase in temperature improved the rectification of the lithium contact tremendously. After the ~125º C diffusion, the detectors rectified well enough to tolerate electric fields of ~ 1000-4000 V/cm and showed much more reasonable looking gamma-ray signals when the center and guard ring segments were shorted together externally and sent to a single preamplifier. The signals were still very noisy, typically $FWHM_{noise}$ = 3-5 keV. In addition, the center and guard-ring segments of the detector were not separating well. That is why the leads connected to the segments were shorted together and sent to a single preamplifier. The first few detectors diffused at 125°C had an inter-electrode resistance of ~ 200 Ω between the center and guard-ring segments. With the preamplifiers typically having feedback resistor values of at least 1 GΩ and operating voltages of a ~ 0.1 V, there is no possibility to form a segmented germanium detector with such a low inter-electrode impendence.

To address the problem of segmentation, a brief (1 second) etch was attempted on the segmented surfaces of four of the working detectors with 3:1 HNO_3:HF. This completely ruined the rectification of all but one of the four detectors. The single functioning detector remained segmented with an inter-electrode impedance of ~ 200 Ω. Performing a following etch also has the disadvantage of making the segmentation lines on the detector completely disappear. The segmentation pattern left by the lithium shadow-mask evaporation is very faint immediately after the lithium diffusion. However, after a following 1-second 3:1 etch, the lithium-diffusion segmentation pattern is almost completely invisible. This is an extreme disadvantage when aligning contact pins for connection to a segmented detector.

More detectors were made using the lithium shadow evaporation technique. The masks were made wider and placed closer to the surface of the germanium during the evaporation. It was hypothesized that the lithium was somehow undershooting the shadow mask; although there was no visible evidence to support this explanation. Unfortunately, the same result was observed regardless of the shadow geometry. The lithium contacts would rectify well but would not segment beyond a few hundred ohms; at least 6 orders of magnitude too low. After many attempts, we became worried that stable segmentation was not possible with closely spaced lithium contacts. Several different shadow evaporation techniques were attempted using different mask configurations.

After several more attempts, a masking technique was finally identified that produced very high impedance between the detector segments. Using this “new technique,” inter electrode impedances of ~ 100 GΩ are routinely obtainable while the excellent rectification is maintained. The successful segmentation and rectification of lithium was dramatic and important for this project. In addition, this processing technique leaves a pattern that is also clearly visible on the surface of the detector. This is necessary for the positive alignment of connection pins to the electrodes on multi-segment detectors.

The photograph presented in Figure 2 shows one of the segmented-lithium planar detectors. The segmentation line between the center and guard ring is clearly visible on this 1-mm thick detector. The detector rectified, separated, and operated successfully up to ~ 400 V, providing an electric field of ~ 4000 V/cm.

Figure 2. A 1-mm thick planar test detector has a segmented lithium-diffused contact visible on the top surface. The contact withstood ~ 4000 V/cm electric field and segmented with several hundred GΩ.

To measure the degree of segmentation, the effective resistance between the center and guard-ring electrodes was measured. When the resistance is extremely high, a higher voltage resistance measurement technique must be used. The center segment is allowed to operate normally with a preamplifier having a 1 GΩ feedback resistor. Because of the 1 GΩ feedback resistor, the DC feedback voltage of this preamplifier will change in voltage by 1 mV when a current of 1 pA flows into (or out of) the gate of the JFET. The guard-ring electrode of the detector was then attached to a ~ 10 V DC voltage source to drive current between the guard ring and center contact. A voltage of ~ 10 V is enough to cause a swing in the DC level of the center contact preamplifier but not high enough to significantly affect the electric field inside the detector. This detector was biased at 400 V for these measurements. Using this measurement technique, the detectors made with the new segmentation technique showed an inter-electrode resistance of
~ 50×10^{12} Ω or 50 TΩ. This is a huge resistance. A resistance of several GΩ s is quite sufficient for detector operation. Achieving such a high resistance value means that the gap between the electrodes is fully depleted and there is little or no surface conductivity from surface channels. The 125°C 1-hr lithium diffusion should create a contact that is ~ 100 μm thick and wide. Because our gap is ~ 1 mm, there should be ~ .8 mm of depleted material in the gap region.

After more trials and work on the technique, more encouraging results were obtained. The detectors generally held ~ 3000 V/cm of electric field with no measurable leakage current, and had an interelectrode resistance of ~ 15 TΩ. These detectors were cycled to higher temperatures in the test cryostat to note any change in the interelectrode resistance. The detectors were cycled to 85°C for 5 hrs while the cryostat was pumped with a turbo molecular pump. After this temperature cycle, the detectors still had an interelectrode resistance of ~ 15 TΩ. A subsequent 2-hour temperature cycle to 100°C lowered the measured resistance to ~ 2.5 TΩ, still very high. The most dramatic change observed as a function of these temperature cycles was the point at which the voltage between the center and guard-ring electrodes was sufficient to break down the resistance and create a very large conductive channel current. When the detectors were originally fabricated, the gap could withstand 30 V before breaking down with the detector biased

at 300 V. After the 85° C cycle it took only 22 V and then after the 100° C cycle it took only 15 V to break down the gap. Normally, the only potential difference between the electrodes on a segmented germanium is ~ 0.1 V from the slight differences in the JFETs on the front end of each preamplifier.

CONCLUSIONS AND RECOMMENDATIONS

Segmented lithium-diffused contacts appear quite stable. These contacts should provide a viable segmented hole barrier contact on p-type coaxial germanium detectors for low-level counting and the search for neutrinoless double beta decay.

REFERENCES

Goulding, F. S., D. A. Landis, P. N. Luke, N. W. Madden, D. F. Malone, R. H. Pehl, and A. R. Smith (1984). Semiconductor detectors and double beta decay, *IEEE Trans Nucl. Sci*. NS-31: 285–299.

Hull, E. L., H. Miley, R. Pehl, C. Aalseth, and T. Hossbach (2005). Segmentation of the outer contact on p-type coaxial germanium detectors, in *Proceedings of the 27th Seismic Research Review: Ground-Based Nuclear Explosion Monitoring Technologies: Ground-Base Nuclear Explosion Monitoring Technologies*, LA-UR-05-6407, Vol. 2, pp. 795–804.

Hull, E. L., R. Pehl, J. Lathrop, G. Martin, R. Mashburn, H. Miley, C. Aalseth, and T. Hossbach (2006). Segmentation of the outer contact on p-type coaxial germanium detectors, in *Proceedings of the 28th Seismic Research Review: Ground-Based Nuclear Explosion Monitoring Technologies*, LA-UR-06-5471, Vol 2, pp. 811-821.

Hull, E. L. (2003). Germanium detectors for gamma-ray imaging, in *Radiation Detection Technologies Program, R&D Portfolio*, D. P. Spears and G. M. Alonzo (Eds.). NNSA Office of Nonproliferation Research and Engineering.

Hull, E. L., M. T. Burks, C. P. Cork, W. Craig, D. Eckels, L. Fabris, A. Lavietes, P. N. Luke, N. W. Madden, R. H. Pehl, and K. P Ziock (2002). A germanium orthogonal strip detector system for gamma-ray imaging, in *Proceedings of the AIP Conference 632: Unattended Radiation Sensor Systems for Remote Applications*, 118.

Luke, P. N., C. P. Cork, N. W. Madden, C. S. Rossington, and M. F. Wesela, (1992). Amorphous Ge bipolar blocking contacts on Ge detectors, *IEEE Trans. Nucl. Sci*. NS-39: 590.

Majorana Collaboration White Paper (2003). The Majorana zero-neutrino double-beta decay experiment, LA-UR-03-7709 and PNNL-14420, http://majorana.pnl.gov/MajoranaWhitePaper.pdf.

Miley, H. S., R. J. Arthur, R. L. Brodzinski, W. K. Hensley, J. H. Reeves, and F. T. Avignone (1991). Low background detectors for exotic physics experiments, in *Proceedings of the 4th International Workshop on Low Temperature Particle Detectors*.

Miley, H. S., F. T. Avignone, R. L. Brodzinski, J. I. Collar, and J. H. Reeves (1990). Suggestive evidence for the 2-neutrino double-beta decay of Ge-76, *Phys. Rev. Lett.* 65: 3092–95.

MECHANICALLY COOLED LARGE-VOLUME GERMANIUM DETECTOR SYSTEMS FOR NUCLEAR EXPLOSION MONITORING

Ethan L. Hull[1], Richard H. Pehl[1], James R. Lathrop[1], Peggy L. Mann[1], Ronnie B. Mashburn[1], Bruce E. Suttle[1], Harry S. Miley[2], Craig E. Aalseth[2], Theodore W. Bowyer[2], and Todd W. Hossbach[2]

PHDs Co.[1] and Pacific Northwest National Laboratory[2]

Sponsored by National Nuclear Security Administration
Office of Nonproliferation Research and Development
Office of Defense Nuclear Nonproliferation

Contract No. DE-FC52-06NA27323

ABSTRACT

Compact maintenance-free mechanical cooling systems are being developed to operate large volume (~ 570 cm^3, ~ 3 kg, 140 % or larger) germanium detectors for field applications. A new generation of domestically produced Stirling-cycle mechanical coolers provide the basis for this evolution. When properly instrumented, these systems can cool the very largest volume germanium detectors with no maintenance or liquid nitrogen requirements. The user can leave these systems unplugged on the shelf until needed. The maintenance-free operating lifetime of these detector systems will exceed 5 years. These features are necessary for remote long-duration liquid-nitrogen free deployment of large-volume germanium gamma-ray detector systems for nuclear explosion monitoring. The Radionuclide Aerosol Sampler/Analyzer (RASA) will greatly benefit from the availability of such detector systems by eliminating the need for liquid nitrogen at RASA sites while still allowing the very largest available germanium detectors to be utilized for the highest sensitivity measurements. To reliably provide such systems, the basic technical fundamentals are being investigated: temperature, vacuum, and vibration. A RASA cryostat and detector have been developed and fabricated. The cryostat has been tested and verified to cool a very large (as large as 10-cm long by 10-cm diameter) detector to temperatures as low as 50 K. The system is free of microphonic noise with the cooler operating at full power. The lower detector operating temperature, coupled with robust detector fabrication technology, provides a detector system that will operate reliably for a very long time (5+ years).

OBJECTIVES

PHDs Co. is developing mechanically cooled detector systems for large volume germanium detectors (~ 570 cm^3, ~ 3 kg, ~ 140 %, or larger) for field use in rugged conditions. A new generation of Stirling-cycle mechanical cooler is being used to reliably cool the very largest germanium detectors while requiring no maintenance. The detectors will be cooled to extremely low operating temperature, resulting in much more reliable detector operation. These new coolers have operating lifetimes that exceed five years. The coolers require no maintenance. Using these coolers, PHDs Co. is developing germanium detector systems that can be left unattended, running or not, for several years with no maintenance. The flip of a switch brings the system to life. The relatively large heat lift of these coolers can cool a detector to operating temperature for gamma-ray measurements in a few hours. These features will make liquid-nitrogen free operation of the largest (~200%) germanium gamma-ray detectors viable and convenient for nuclear explosion monitoring. The RASA will benefit from the availability of such detectors (Bowyer et al., 1997; Miley et al., 1998).

Mechanical cooling of germanium detectors has historically been a difficult endeavor. The success or failure of mechanically cooled germanium detectors stems from three main technical issues: temperature, vacuum, and vibration. These factors affect one another. A detailed analysis of these factors and their effects on detector performance was recorded last year (Hull et al., 2006). These factors are being studied in the laboratory at the most fundamental levels to insure a solid understanding. Based on this study, prototype detector-cooler systems are being designed and fabricated as prototypes for field tests.

RESEARCH ACCOMPLISHED

The first year of this project has seen several major accomplishments. A stable vacuum configuration has been realized for the RASA detector cryostat. A corresponding detector, cryostat, cooler system (called RASA1) has been designed, fabricated, and tested. After some fine tuning, the detector system shows no measurable microphonic noise with the cooler operating at full power. A detector operating temperature of 50 K was achieved with a cryostat capable of holding a 10-cm diameter x 10-cm long detector. A new preamplifier has been designed to accommodate the RASA1 detector. A system very similar to RASA1 was tested with a planar detector that shows excellent spectroscopy performance and a detector temperature of 45 K. A vacuum residual gas analyzer (RGA) system was placed in service to study vacuum accumulation of gases for the sake of making the most rugged, long lasting vacuum systems possible for RASA germanium detector systems.

The first prototype design for the RASA1 detector system is shown in Figure 1. RASA1 is specifically designed to fit into and operate with a RASA station in the field. The design provides centering of a coaxial germanium detector at the center point of the filter paper assembly in the RASA station. With a few simple internal part modifications, the design accommodates any detector size up to a diameter of 10 cm and a length of 10+ cm. As depicted in Figure 1, RASA1 is a relatively small overall assembly. The cooler, vacuum-cryostat body, and vacuum cap close together to accommodate all faculties essential to the operation of a germanium detector. A 7-cm diameter x 7-cm long coaxial germanium detector is being installed in the RASA1 as a demonstration of the system functionality. Emphasis was placed on the loading and holding the detector in a manner consistent with a rugged assembly. The detector is held in a specially designed capsule containing wave springs that can hold the detector with a force equivalent as high as 100 Gs if desired. Internal mechanical provisions shield the high voltage components from the signal gate lead to prevent microphonic noise. The design accommodates all metal vacuum seals to maintain the best possible vacuum for the longest possible duration. Emphasis was placed on cooling the detector to the very lowest temperature possible. The immediate design of such a RASA1 prototype system was a response to the urgent need for such a system as expressed to us by RASA users at Patrick Air Force base.

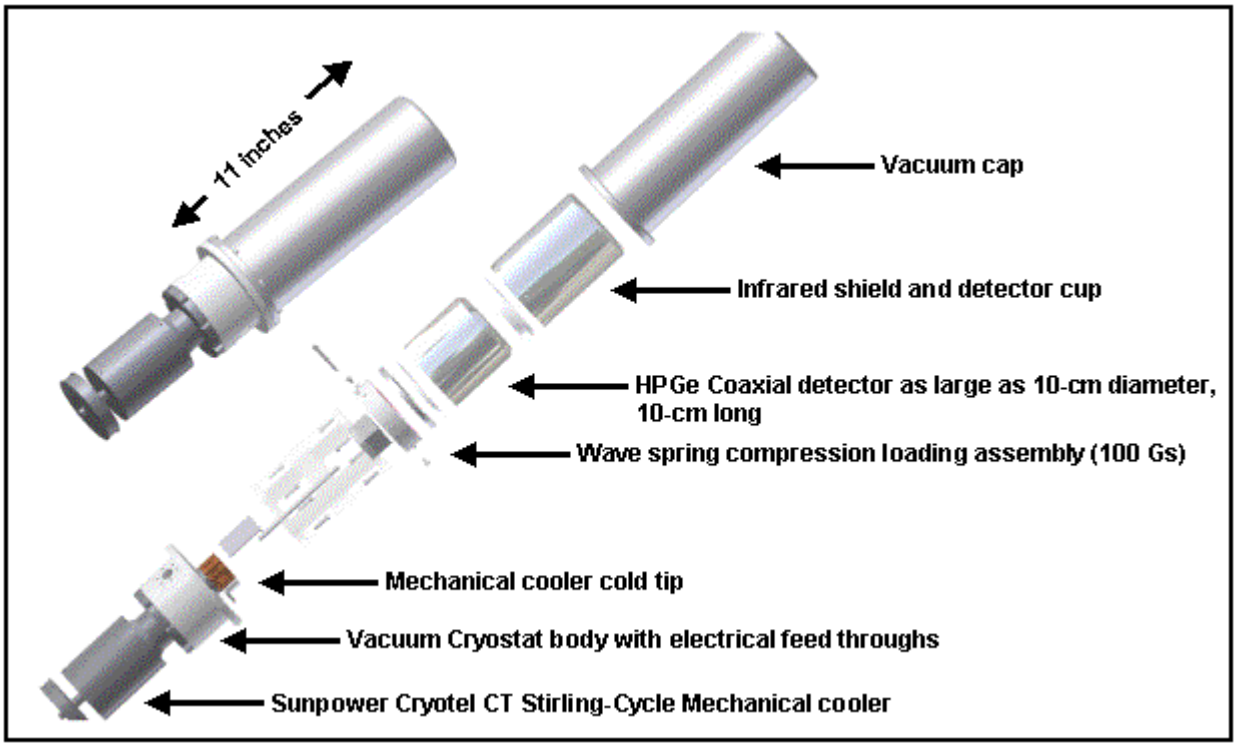

Figure 1. A drawing shows the assembled and unassembled RASA1 detector system design. The upper left view of the RASA1 shows that it is an integrated cooler-detector assembly.

Upon finishing the design, the mechanical parts for the RASA1 system were fabricated and assembled. The mechanical, electronic, and detector related parts were assembled and integrated with a Stirling-cycle mechanical cooler as shown in Figure 2. RASA1 was assembled with a brass dummy detector in place for thermal-vacuum-cryogenic testing. The vacuum integrity of the system was verified to be helium leak tight. The detector is extended a good distance away from the support structure. This assembly must be made in such a way to position the detector down the bore of the RASA system near the filter paper cylinder where the gamma rays are collected. Extending the detector outward in this manner was a challenging design requirement. Modifications were made to the detector support structure to insure solid holding of the detector during cooler operation. Although the detector cup is only 1.5 mm from the inside of the outer vacuum can, there appears to be no problem with the two surfaces contacting each other when the cooler is operated or when the system is shaken and moved in a normal manner. As described later, an early version of the detector support structure had the misfortune of resonating with a harmonic frequency of the vibrating mechanical cooler. This caused the end cap of the detector to literally "sing" with a very dramatic high-pitched tone. Replacing the support structure with a non-symmetric part eliminated the resonant vibration. In the present configuration shown in Figure 2, the system operates very quietly and has no measurable microphonic noise response in the detector spectroscopy channel at unipolar peaking times as long as $T_P = 8$ μs.

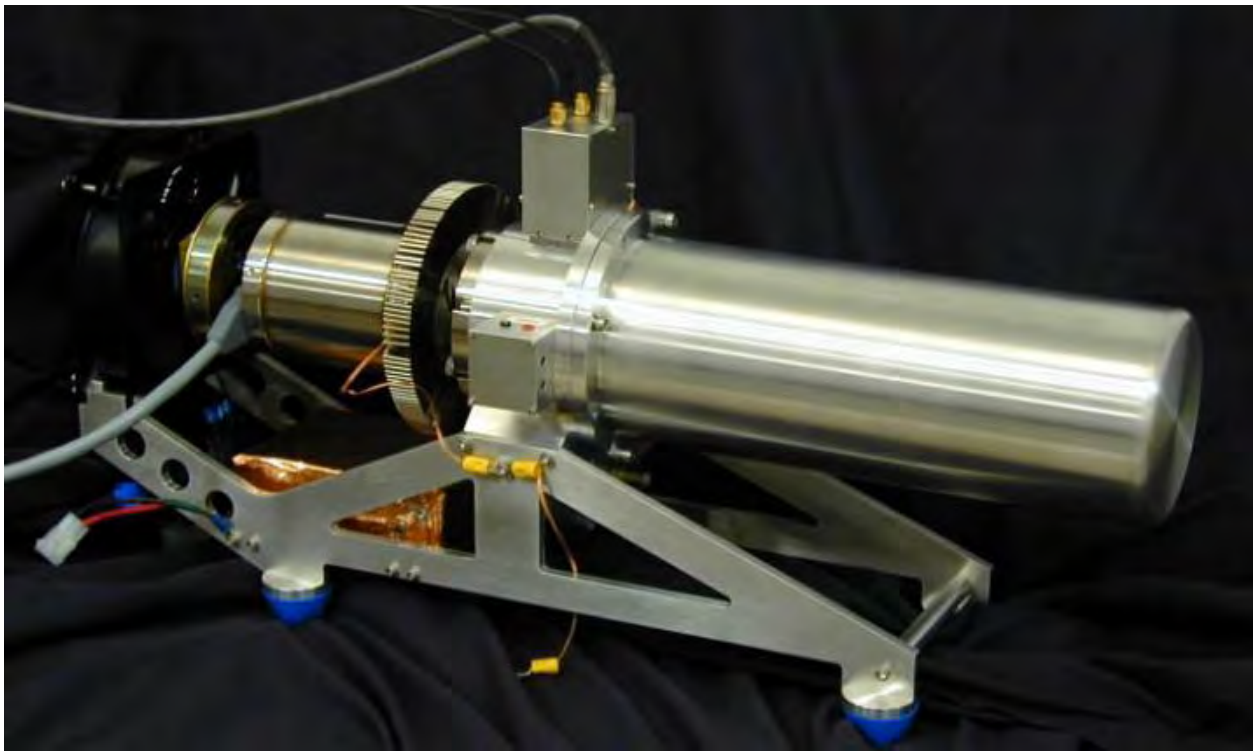

Figure 2 A photograph of the assembled RASA1 detector system.

After RASA1 was assembled as shown in Figure 2, several thermal vacuum cool-down tests were performed. Before each of these tests, the vacuum of the system was pumped to the $1x10^{-6}$ Torr level overnight and helium leak checked to insure vacuum integrity. For the first trial, the system was cooled with the cooler disconnected from the internal detector assembly to evaluate the cooler alone. As anticipated the cooler cold tip cooled to the lowest possible temperature (~ 35 K) in ~ 20 minutes. After the cooler performance was verified, the system was cooled with the internal detector assembly thermally connected to the cooler. The assembly held a 70 cm x 70 cm brass detector dummy. The cooler was switched on and the temperature of the detector assembly and the cooler cold tip were monitored as a function of time. The temperature of the detector and the cooler are shown in Figure 3 as a function of time. With the cooler operating at full (160 W) input power, the system reached equilibrium temperature of 43 K at the cold tip and 50 K at the detector. This is an excellent result. Maintaining the detector at an extremely low temperature, such as 50 K, will insure rugged and reliable detector operation. Nearly all of the problems with semiconductor detectors increase dramatically as a function of increasing temperature (Pehl et al., 1973). To show the operating temperature range of RASA1, the cooler was throttled back to the lowest input power setting (80 W). At this power setting, an equilibrium detector temperature of 73 K and cold tip temperature of 51 K were measured. Of course, higher detector temperatures can always be achieved by powering the Zener diode on the detector assembly. The Zener heater can place as much as 50 W of power on the detector assembly. This feature is useful to decrease the warm up time of the detector and for vacuum-baking the detector.

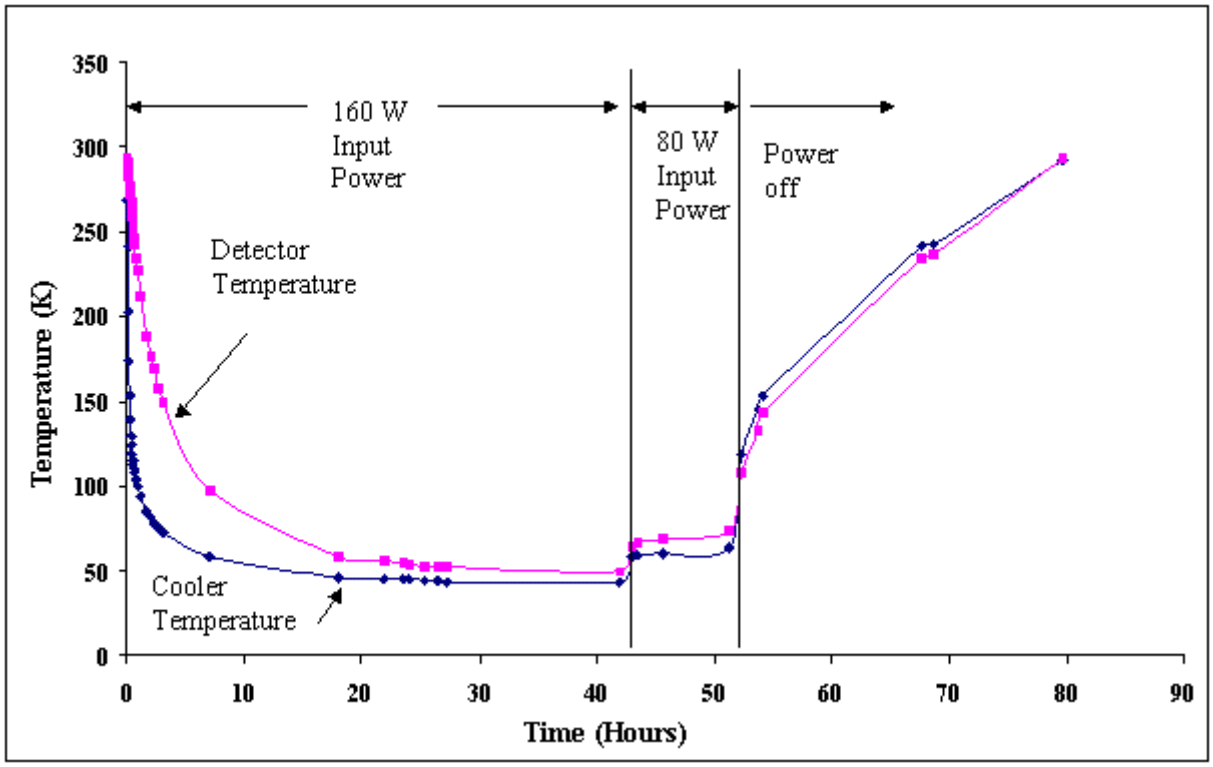

Figure 3 The cool-down curve for the RASA1 detector system with a thermal mass in place of the detector. The thermal mass has a heat capacity comparable to a 10-cm long, 10-cm diameter germanium detector.

Initially a problem was observed with the preamplifier used for RASA1. Standard PHDs Co. high bandwidth, low noise preamplifiers were initially used for RASA1. These preamplifiers were originally designed for gamma-ray imaging with germanium strip detectors. Consequently, the preamplifiers have relatively fast rise times to perform the high bandwidth measurements required for gamma-ray position location. The junction gate field effect transistor (JFET), feedback capacitor, and feedback resistors were removed from one of the preamplifiers and placed inside the cryostat on the detector assembly. The JFET was placed as close the detect detector signal contact as possible. The JFET is placed on a thermal standoff that allows the JFET to "self heat" to a temperature in the ~ 150 K region. This is done because JFETs have poor noise performance at or below liquid nitrogen temperature (77 K). The JFET, feedback capacitor, and feedback resistor installed inside the cryostat and while the rest of the preamplifier is outside the cryostat. Consequently, rather long (~ 9 inch) leads must connect the internal and external components. With these long leads in place, the preamplifier is unstable and oscillates uncontrollably with a 90-MHz sine wave from – 12 V to + 12 V. This situation is completely unacceptable for detector operation. Consequently, a new PHDs Co. preamplifier was designed that incorporates a stabilizing feature to eliminate the oscillation. The stability modification was required to successfully operate the back end of the preamplifier outside of the cryostat while operating the front end of the preamplifier inside the cryostat. The placement of three passive electronic components on the external preamplifier board provide more stable, lower bandwidth, low noise operation that is perfectly appropriate for RASA detector operation. On the other hand, if high bandwidth performance is desired for an imaging germanium strip detector, the components are not placed on the preamplifier board. A photograph shows the new preamplifier in Figure 4.

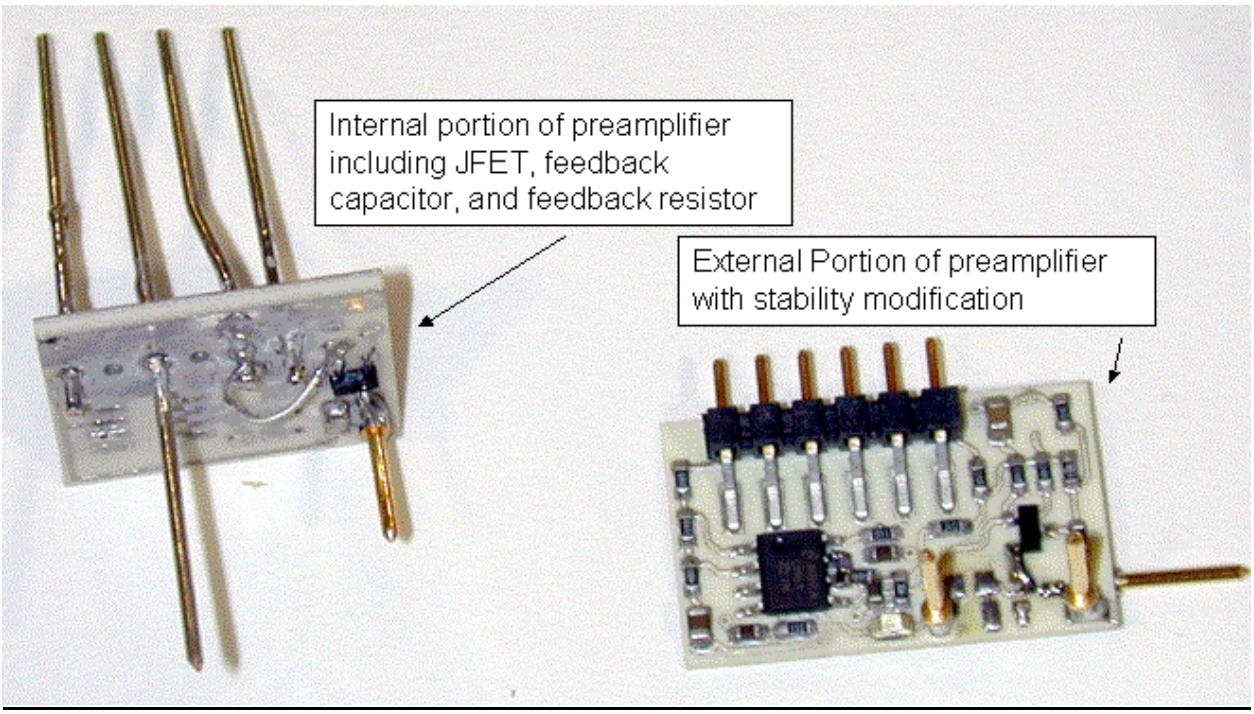

Figure 4 The RASA1 preamplifier accommodates low noise and the stability required for the RASA1 detector-cryostat geometry.

The most difficult part of the RASA1 system development was the battle against microphonic noise problems arising from the vibrating mechanical cooler. Microphonic noise from vibrating mechanical coolers has always been an Achilles heel for mechanically cooled germanium detector systems. We have developed a method for systematically testing the RASA1 cryostat with the preamplifier and cooler operating in the exact configuration of the final detector system. The cooler is operated and allowed to vibrate with the JFET gate lead connected to the beryllium-copper contact finger that makes connection to the inner bore of the detector in the final assembled prototype. We have found that this can be done at room temperature without pulling a vacuum on the cryostat. This enables us to move and feel vibrating parts inside and outside the cryostat while the cooler is operating to determine which components are causing problems. As described above, some of the originally designed mechanical vacuum parts in the cryostat have had to be discarded and replaced. Fortunately, after many trials and much machine work we have been able to completely eliminate any measurable microphonic noise at a unipolar peaking times as long as T_P = 8 μs. The thermal standoff that holds the detector assembly rigidly while allowing it to cool was found to be a problem. The part was made to be very sturdy and had a cylindrically symmetric design. Unfortunately, the part was found to resonate with the cooler frequency (60 Hz) or a harmonic thereof creating an audible ringing when the cooler was operating. By simply touching (and dampening) the vibrating part at almost any point on its surface, the ringing could be stopped. It seemed that breaking the symmetry of the part was enough to quell the vibration. We replaced the thermal standoff with a part purposely lacking cylindrical symmetry to eliminate this problem. In addition, the vacuum cap and infrared shield were both quite thin, only 0.030" thick. The ends of both thin parts also vibrated like drum heads in parallel to each other. These two parts were replaced with 0.060" thick parts to eliminate this problem. We also modified the fixture that holds the JFET, feedback capacitor, feedback resistor, and beryllium copper finger against the electrode(s) of the detector. The rigidity of this new internal assembly was required to eliminate the last measurable traces of microphonic noise. It is worth mentioning a note on the scale of the microphonic noise problem. The full width at half maximum (FWHM) of a 1332-keV gamma-ray peak from a good germanium detector should never exceed FWHM = 3 keV. At times during these battles against microphonic noise we measured a microphonic noise as high as FWHM = 15 keV. This would have been totally unacceptable for good detector performance. We reduced the microphonic noise to a level lower than the channel noise of the JFET with no capacitance on the gate, FWHM < 0.7 keV.

Using the same design prescriptions that will be used for RASA1, another detector system was fabricated for another of our projects. This system is called MG1. MG1 holds a planar germanium detector instrumented using the same configuration developed for RASA1. MG1 exhibits excellent noise performance using a unipolar peaking time of T_P = 6-8 μs. In Figure 5, the gamma-ray energy spectrum shown with MG1 demonstrates the viability of the technology. The RASA1 detector is being fabricated and integrated into RASA 1 using the same prescription and detector fabrication techniques used for the planar detector in MG1.

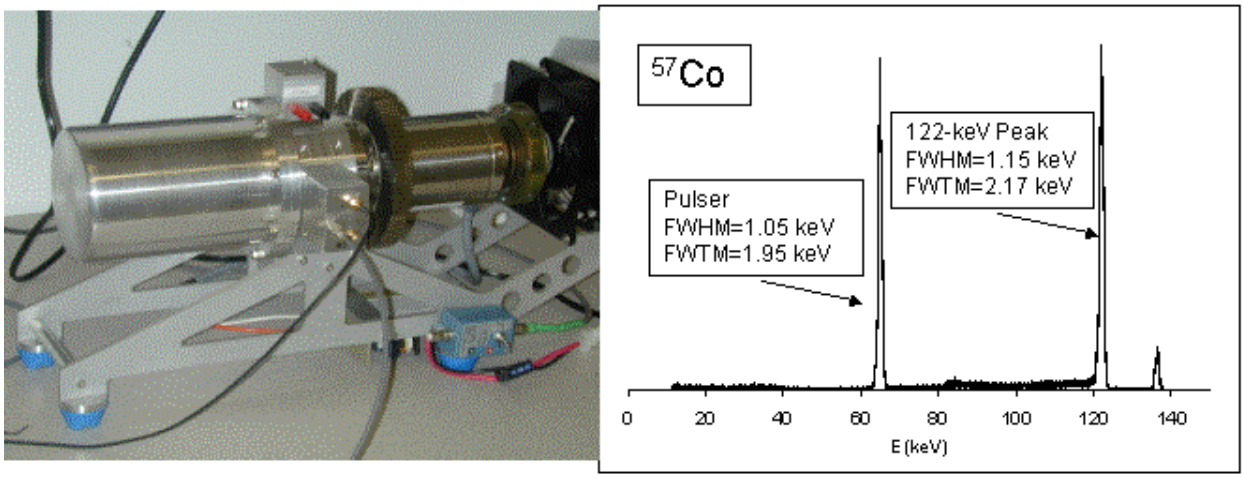

Figure 5 The leftmost view shows the planar detection system (MG1) mechanical cooled detector system. This system uses the same mechanical cooler and basic design to be used for RASA1. It has served as an excellent test bed for the electronic, cryostat, and detector combination to be used for RASA detectors. The energy spectrum on the right shows a noise FWHM = 1.05 keV with the cooler operating (and vibrating) at full power. A peaking time of T_P = 6 μs was used to make this measurement. The same energy resolution is measured with the cooler switched off. MG1 was built for radiation damage testing using a cryostat very similar to RASA1. The detector reaches a temperature of 45K.

In addition to all of the work specifically tied to the design and fabrication of the RASA1 prototype, a vacuum system has been placed in service for studying the accumulating gasses in vacuum. The foremost longevity problem for germanium detector systems is a gradual loss of vacuum integrity that occurs over year-long time periods. The system shown in Figure 6 has been assembled just to study the accumulation of gases in a metal cavity the size of a cryostat over long time periods. Metal-sealed cavities made of aluminum and stainless steel have been fabricated, pumped, and baked while on this vacuum system. The cavities are sealed off using an internal metal sealing valve. The cavities are allowed to evolve gasses over various time periods to study the accumulation over time. A residual gas analyzer shares the vacuum common to the cavities and the turbo molecular pump. The RGA determines the amount and species of gasses that accumulate in the metal cavities over time. This system has been brought up to operational status and demonstration measurements have been made that verify the intended operation of the system. Over the next year, long-term accumulation measurements will be made to determine the species and quantity of gases accumulating in germanium detector cryostats that cause the degradation of vacuum.

Figure 6 The turbo-molecular pumping station has a residual gas analyzer installed to perform gas accumulation studies pertinent to the fabrication of long-lasting cryogenic systems with excellent vacuum integrity.

CONCLUSIONS AND RECOMMENDATIONS

The RASA1 prototype has been designed and fabricated as a demonstration of a new integrated mechanical cooling system suitable for use with RASA stations. Good technical progress has been made to overcome the problems associated with a compact, mechanically cooled germanium detector system. These new systems will have extremely long operating lifetimes with no maintenance requirements. At the end of this project PHDs Co. will offer a new product line: the MCX mechanically cooled detector product line for use with RASA and similar remotely deployed detection systems.

REFERENCES

Bowyer, S. M., H. S. Miley, R. C. Thompson, and C. W. Hubbard (1997). Automated particulate sampler for Comprehensive Test Ban Treaty verification (the DOE radionuclide aerosol sampler/analyzer), *IEEE Transactions on Nuclear Science* 44 3 (1): 551–556

Miley, H. S. , S. M. Bowyer, C. W. Hubbard, A. D. Mckinnon, R. W. Perkins, R. C. Thompson, and R. A. Warner. (1998). A Description of the DOE Radionuclide Aerosol Sampler/Analyzer for the Comprehensive Test Ban Treaty. *Journal of Radioanalytical and Nuclear Chemistry* 235 (1–2): 83–87.

Hull, E. L., R. Pehl, J. Lathrop, R. Mashburn, H. Miley, C. Aalseth, and T. Hossbach (2006). Mechanically cooled large volume germanium detector system for nuclear explosion monitoring, in *Proceedings of the 28th Seismic Research Review: Ground-Based Nuclear Explosion Monitoring Technologies*, LA-UR-06-5471, Vol 2, pp. 821–830.

Pehl, R.H., E. E. Haller, and R.C. Cordi, (1973) Operational characteristics of germanium detectors at higher temperatures, *IEEE Trans. Nucl. Sci*. 20: 494.

RADIOXENON ATMOSPHERIC MEASUREMENTS IN NORTH LAS VEGAS, NV

Brian D. Milbrath[1], Matthew W. Cooper[1], Lance S. Lidey[1], Theodore W. Bowyer[1], James C. Hayes[1], Justin I. McIntyre[1], Lynn Karr[2], David Shafer[2], and Jeff Tappen[2]

Pacific Northwest National Laboratory[1] and Desert Research Institute[2]

Sponsored by National Nuclear Security Administration
Office of Nonproliferation Research and Development
Office of Defense Nuclear Nonproliferation

Contract No. NTL100/19144

ABSTRACT

Pacific Northwest National Laboratory (PNNL) deployed the Automated Radioxenon Sampler/Analyzer (ARSA) in North Las Vegas for two weeks in February and March 2006 for the purpose of measuring the radioxenon background at a level of sensitivity much higher than previously obtained in the vicinity of the Nevada Test Site (NTS). The measurements establish what might be expected if future measurements were ever taken at the NTS itself and investigate improved methods of environmental monitoring of NTS. A second detector, the Portable Environmental Monitoring Station (PEMS), built and operated by the Desert Research Institute (DRI), was deployed in conjunction with the ARSA and contained a pressure ion chamber, aerosol collection filters, and meteorological sensors.

Some of the radioxenon measurements detected ^{133}Xe at levels up to 3 mBq/m^3. This concentration of radioxenon is consistent with the observation of low levels of radioxenon emanating from distant nuclear reactors. Previous measurements in areas of high nuclear reactor concentration have shown similar results, but the western U.S., in general, does not have many nuclear reactors. Measurements of the wind direction indicate that the air carrying the radioxenon came from south of the detector and not from the NTS.

OBJECTIVES

Background

In the 1990s, PNNL developed the ARSA as a prototype sampling station for the International Monitoring System (IMS) (Bowyer et al., 2002). The IMS is a network of stations originally developed to monitor compliance with the Comprehensive Nuclear-Test-Ban Treaty (CTBT). Ultimately, the IMS will have at least 40 radioxenon sampling stations placed around the world (Protocol, 1996). Concurrent with ARSA's development, was the development of similar detectors by a few other countries: France, Russia, and Sweden. The automated nature of the detectors is crucial as several of the planned stations are to be at remote locations. The ARSA and its counterparts are much more sensitive than anything commercially available at the time of their development, with sensitivities as low as 0.1 mBq/m^3 (Bowyer et al., 2002).

Radioxenon is in the mass range where large fission yields occur from uranium- or plutonium-based nuclear weapons. In a nuclear explosion, several radioxenon isotopes are produced with half-lives convenient for detection (short enough for high radioactivity, but long enough for detection): ^{135}Xe (9.14 hr), ^{133}Xe (5.25 d), ^{133m}Xe (2.19 d), and ^{131m}Xe (11.93 d). As an inert noble gas, xenon doesn't combine chemically with other elements (in ground or atmosphere) and is likely to escape even from an underground explosion. Nuclear reactor operations also release radioxenon, and there are some medical and industrial sources (Bowyer et al., 1998). ^{133}Xe is detected much more frequently than the other three radioxenon isotopes during normal atmospheric monitoring (Auer et al., 2004) so seeing other radioxenon isotopes is important for nuclear explosion monitoring.

Radioactive noble gas detection is internationally accepted, can accommodate significant stand-off distances, and is quite sensitive without being overly intrusive (i.e., revealing detailed information relative to weapon design). Given its importance in international monitoring and the fact that such sensitive noble gas measurements have not previously been performed at the Nevada Test Site (NTS), it was decided that measurements should be performed using the ARSA to establish a baseline of comparison to possible future NTS background measurements. There was also interest in the measurements for improved environmental monitoring purposes. Thus, it was decided to perform a pair of measurements with the ARSA, first near Las Vegas, 65 miles away from the NTS, and then later at the NTS's Mercury townsite.

Detector Systems

Two detectors were deployed: the ARSA and the PEMS.

The ARSA is about the size of two soda machines and weighs approximately 3000 pounds (see Figure 1). It takes in air at the rate of 144 m^3/day (one 48 m^3 sample each eight hours) from the outside and separates and concentrates the 87 ppb Xe present. The air is first compressed, filtered, cooled, and moved through dryers to remove the H_2O and CO_2. A series of adsorption charcoal traps are used to remove first the radon, and then the xenon from gases of even lower boiling points. These traps must be regenerated (outgassed using heat) after each sample. Pre-purified nitrogen is used as a carrier gas. Additional traps are used for further removal of contaminant gasses, though some radon still gets through and is the chief source of background (Bowyer et al., 1999). Radioxenon counting is performed using a beta-gamma coincidence cell based on a NaI(Tl) and plastic scintillator, which is surrounded by a lead cave to reduce background (McIntyre et al., 2001). After counting, a thermal conductivity detector (TCD) is used to quantify the amount of Xe in the sample. Archive bottles may be filled for later retrieval and lab analysis.

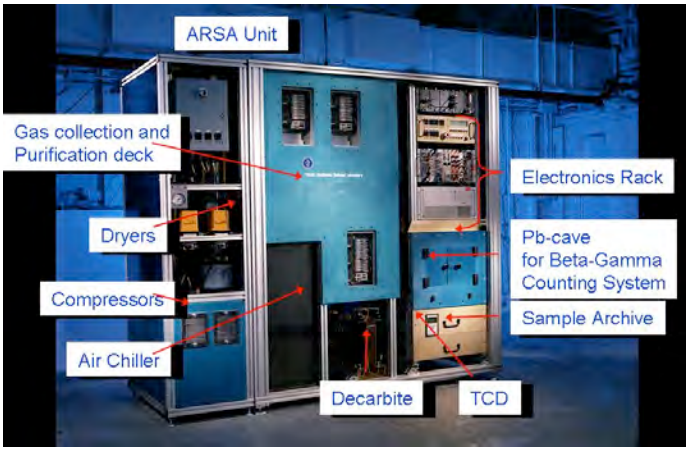

Figure 1. The ARSA system with various components labeled.

In order that ARSA be continuously monitoring the atmosphere, many of the above steps are performed with parallel subsystems. For example, there are four beta-gamma nuclear detector cells. Every 8 hours, a 24-hour count is completed for one sample. Before starting a new 24-hour sample count, an 8-hour "background" count is measured for a given cell for subsequent subtraction. This is necessary, in part, because some residual xenon and radon gas adheres to the cell walls, resulting in a "memory effect" (McIntyre et al., 2001). When operating properly, the ARSA has a sensitivity of approximately 0.1-0.2 mBq/m^3 for ^{133}Xe.

In tandem with the ARSA, measurements were also made using the PEMS constructed and operated by DRI. The PEMS is modeled after the Community Environmental Monitoring Program (CEMP) stations operated by DRI around the NTS (CEMP, 2007). Figure 2 shows the PEMS detector as deployed for this measurement. The weather "tower" (on the left side of the picture) measured wind speed and direction, air temperature, humidity, barometric pressure, and precipitation. To the right in the picture, on a triangular stand, is a Reuter-Stokes pressurized ion chamber (PIC), capable of measuring gamma exposures of 2–800 μR/hr. Rightmost on the PEMS trailer (shaped like a doghouse) is an air particulate sampler. The sampler collects particulate greater than 0.3 microns in size at a flow rate of 2.0 cubic feet per minute. Two samples of approximately one week each were taken, with the filters analyzed for gammas using well-shielded high-purity germanium (HPGe) detectors at PNNL.

Figure 2. The PEMS detector as deployed for this measurement.

RESEARCH ACCOMPLISHED

The detectors were deployed in the trailer parking lot south of the Rack Assembly Tower (bldg. A-14) at the Department of Energy's Nevada Site Office (DOE-NV) in North Las Vegas, NV, as pictured in Figure 3. The ARSA detector was transported from PNNL to North Las Vegas and deployed in a trailer (see Figure 4). In previous ARSA deployments, the detector was dismantled and shipped by container. Transport by road appeared to result in some minor damage to ARSA upon arrival, which PNNL staff were able to fix after some effort. Thus, the ARSA measurements reported are for March 1–7, 2006, when the ARSA was running successfully, while the PEMS measurements reported begin on February 22, 2006.

Figure 3. The PEMS (foreground) and ARSA detectors in front of the Rack Assembly Tower at DOE-NV.

Figure 4. The trailer ARSA was deployed in.

ARSA Measurements

Figure 5 shows the detected ^{133}Xe concentrations, including statistical errors for the time period. The times shown on the x-axis refer to the midpoint of the sample collection period in local time, which occurred at approximately 5 a.m., 1 p.m., and 9 p.m. each day. For example, the first measurement occurred at 5 a.m., March 1, and is plotted as 1.21 on the x-axis. There is a gap of four measurements between 9 p.m., March 1, and 1 p.m., March 3, due to an ARSA shutdown. The pink line shows the minimum detectable concentration (MDC) values, which are typically between 0.1 and 0.2 mBq/m^3. The MDC rises at the end due to the memory effect of xenon from the earlier spike remaining in the detection cells. The other three xenon radioisotopes (^{135}Xe, ^{133m}Xe, and ^{131m}Xe) were not observed during this measurement campaign, and are thus not shown. The average MDC value for ^{135}Xe was 2.1 mBq/m^3. Elevated levels of the other xenon radioisotopes in combination with ^{133}Xe are expected from nuclear explosions.

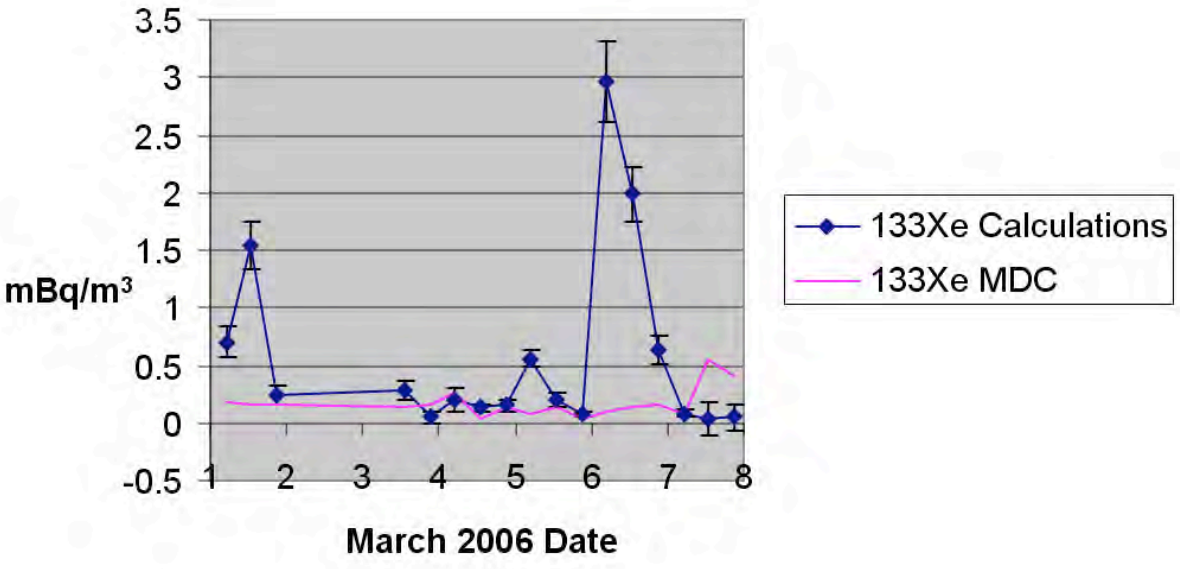

Figure 5. ^{133}Xe measurements by ARSA, beginning at 5:00 a.m., March 1, 2006.

^{133}Xe was clearly seen a few times at a relatively low level, with the largest spike (almost 3.0 mBq/m^3) occurring on March 6th. Previous, much-longer measurements at Freiburg, Germany (Auer et al., 2004), and Allentown, Pennsylvania (Bowyer et al., 1997), frequently measured values of 1–3 mBq/m^3. Those two locations were chosen for their proximity to many commercial nuclear reactors. Comparatively, the western United States has much fewer nuclear reactors. Measurements at PNNL, which is only 10 miles from the Columbia Nuclear Generating Station (though usually upwind), only observed radioxenon infrequently (McIntyre et al., 2001).

Nuclear reactors release radioxenon as a fission gas, either through cracks in fuel rods, or from neutron-induced fission in uranium on the outside of the fuel rods or in the cooling water (Auer et al., 2004). Especially large amounts may be released during core refueling (McIntyre et al., 2001), but the observed xenon in this measurement was not large (at Freiburg, ^{133}Xe concentrations up to 100 mBq/m^3 were observed [Auer et al., 2004]). Although reactors generally have some mechanism in place to trap released radioxenon (Bowyer et al., 1997), it is still the dominant source of released atmospheric radiation for nuclear reactors (Bowyer et al., 1998). Radioxenon is also used for some medical applications.

PEMS Measurements

Figure 6 displays the PIC data from the PEMS detector for the entire time deployment period. The values measured are consistent with those observed at the CEMP station located at DRI in Las Vegas, NV, approximately 10 miles away and available online (CEMP Station, 2007). Displayed are the ten-minute average measurements (in units of μR/hr) of the gamma activity made by the PIC. The measurements run from 8:30 a.m., February 22, through 8:30 a.m., March 9 (144 measurements per day, as shown on the x-axis). The diurnal variation is quite apparent. The chief source of this radiation is the natural radon background, and any xenon contribution is miniscule.

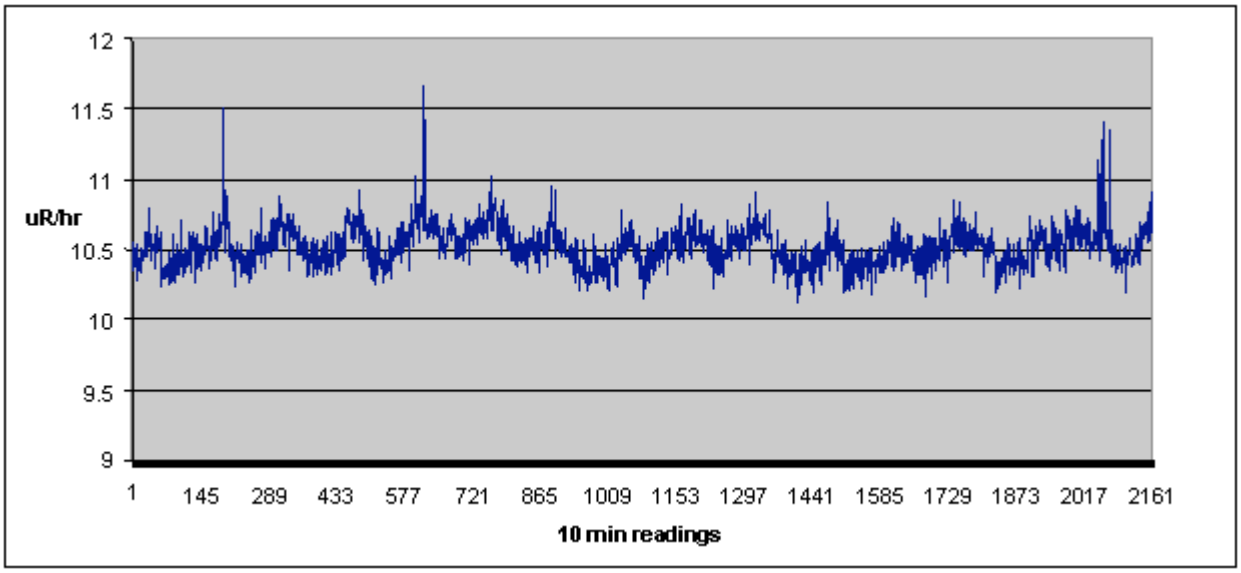

Figure 6. Ten-minute average PIC measurements by the PEMS, from 8:30 a.m., February 22, through 8:30 a.m., March 19, 2006, in north Las Vegas.

The filters collected by the PEMS were allowed to decay for one week (to reduce the radon contribution) and then measured for approximately two days using a well-shielded HPGe detector. Nothing out of the ordinary was observed. In particular, in the 2–10 pCi/sample level, ^{208}Tl, ^{212}Pb, ^{228}Ac, and ^{214}Pb were observed. ^{7}Be and ^{40}K were measured at approximately 200 pCi/sample. These radioistopes are naturally occurring and commonly detected in air samples.

The PEMS station also measured meteorological data. Figure 7 shows the wind rose from March 6, the day of the largest xenon spike observed. Winds were from the SSW. The NTS is NW of north Las Vegas and thus unlikely to be the source of the radioxenon.

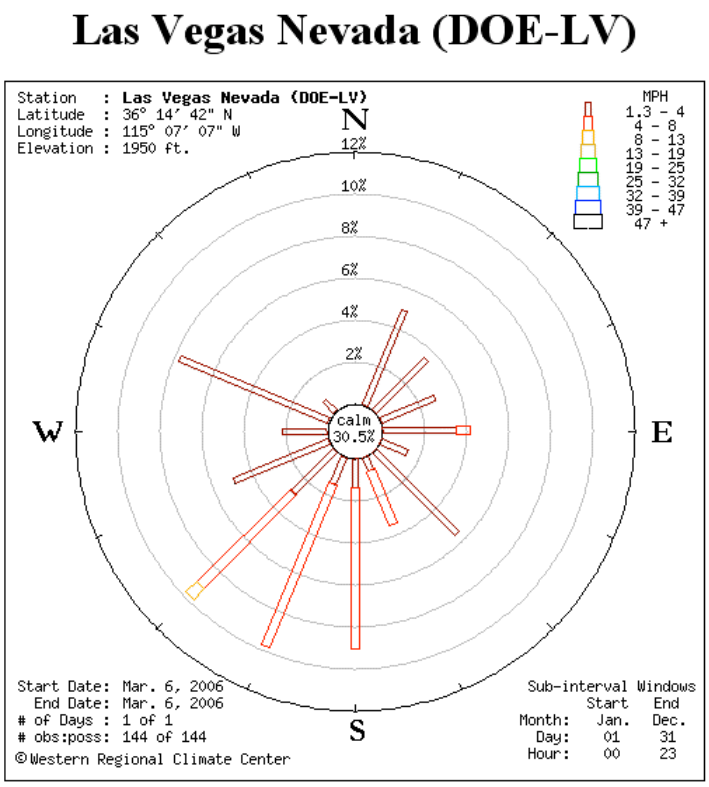

Figure 7. Wind rose for March 6, 2006.

CONCLUSIONS AND RECOMMENDATIONS

The ARSA detector was deployed in North Las Vegas for the purpose of measuring the radioxenon background at a level of sensitivity much higher than previously done in the vicinity of the NTS. Such measurements are relevant in case similar measurements were to be performed in the future at the NTS itself. A second detector, the PEMS, was deployed in conjunction with the ARSA and contained a PIC, aerosol collection filters, and meteorological sensors. Some ARSA measurements detected ^{133}Xe at levels up to 3 mBq/m^3. While this is certainly not a large concentration of Xe, it was somewhat of a surprise. Previous measurements in areas of high nuclear reactor concentrations have shown similar results, but the western U.S., in general, does not have many nuclear reactors. Wind directions at the time indicated that the radioxenon came from a location south of the detector, and not from the NTS.

The result that the radioxenon background levels in southern NV are generally quite low, but that radioxenon can occasionally be detected is important to any future measurements that might occur at the NTS. Follow-up measurements at the NTS and over a longer period (several months, including overlapping wind-direction seasons) would be beneficial to establish expected baseline background levels. This exercise also provided valuable experience to PNNL concerning the deployment of the ARSA in a more mobile setting than it had in the past, and several improvements would have to be made prior to a subsequent deployment at NTS.

ACKNOWLEDGEMENTS

The authors would like to express their appreciation to DOE-NV's Bob Day, Ed Forness, and Daryl Thome for their assistance in site selection and interfacing with the appropriate people at the North Las Vegas site. A special thanks goes to Kent Brooks (Bechtel-NV, now National Security Technologies) at the North Las Vegas location for his instrumental documentation work to allow this measurement to occur. PNNL's Tom Heimbigner and Rey Suarez provided computer support, and Elwood Lepel provided measurement analysis of the aerosol filters. DRI's Scott Campbell and Greg McCurdy supported the PEMS deployment.

REFERENCES

Auer, M., A. Axelsson, X. Blanchard, T. W. Bowyer, G. Brachet, I. Bulowski, Y. Dubasov, K. Elmgren, J. P. Fontaine, W. Harms, J. C. Hayes, T. R. Heimbigner, J. I. McIntyre, M. E. Panisko, Y. Popov, A. Ringbom, H. Sartorius, S. Schmid, J. Schulze, C. Schlosser, T. Taffary, W. Weiss, and W. Wernsperger (2004). Intercomparison experiments of systems for the measurement of xenon radionuclides in the atmosphere, *App. Rad. and Isotopes* 60: 863–877.

Bowyer, T. W., K. H. Abel, W. K. Hensley, M. E. Panisko, and R. W. Perkins (1997). Ambient ^{133}Xe levels in the northeast US, *J. Env. Rad.* 37: 143–153.

Bowyer, T. W., C. Schlosser, K. H. Abel, M. Auer, J. C. Hayes, T. R. Heimbigner, J. I. McIntyre, M. E. Panisko, P. L. Reeder, H. Sartorius, J. Schulze, and W. Weiss (2002). Detection and analysis of xenon isotopes for the Comprehensive Nuclear-Test-Ban Treaty international monitoring system, *J. Env. Rad.* 59: 139–151.

Bowyer, T. W., K. H. Abel, C. W. Hubbard, M. E. Panisko, P. L. Reeder, R. C. Thompson, and R. A. Warner (1999). Field testing of collection and measurement of radioxenon for the Comprehensive Nuclear-Test-Ban Treaty, *J. Radioanal. and Nuc. Chem*. 240: 109–122.

Bowyer, T. W., R. W. Perkins, K. H. Abel, W. K. Hensley, C. W. Hubbard, A. D. McKinnon, M. E. Panisko, P. L. Reeder, R. C. Thompson, and R. A. Warner (1998). Xenon radionuclides, atmospheric: Monitoring in *Encyclopedia of Environmental Analysis and Remediation*, R. Meyers (Ed.), pp. 5295–5314. New York City: John Wiley & Sons.

CEMP (2007). http://www.cemp.dri.edu/.

CEMP Station Summary (2007). http://www.cemp.dri.edu/cgi-bin/cemp_stations.pl?stn=lasv.

McIntyre, J. I., K. H. Abel, T. W. Bowyer, J. C. Hayes, T. R. Heimbigner, M. E. Panisko, P. L. Reeder, and R. C. Thompson (2001). Measurements of ambient radioxenon levels using the automated radioxenon sampler/analyzer (ARSA), *J. Radioanal. and Nuc. Chem*. 248: 629–635.

Protocol to the Comprehensive Nuclear-Test-Ban Treaty (1996). Part 1, Section C, Paragraph 10.

CHARACTERIZATION AND PERFORMANCE EVALUATION OF AN HPXe DETECTOR FOR NUCLEAR EXPLOSION MONITORING APPLICATIONS

David M. Walker[1], Albert G. Beyerle[2], George E. Miller[3], and Richard J. Arthur[4]

Quantum Technology, LLC[1], Mirmar Sensor, LLC[2],
University of California-Irvine[3], and Pacific Northwest National Laboratory[4]

Sponsored by National Nuclear Security Administration
Office of Nonproliferation Research and Development
Office of Defense Nuclear Nonproliferation

Contract No. DE-FG02-06ER84636

ABSTRACT

Expanding missions in nuclear explosion monitoring (NEM) and nuclear security have highlighted the need for high-resolution ambient-temperature gamma detectors that can provide radionuclide-specific monitoring under demanding field conditions. Recent improvements in high-pressure xenon (HPXe) detectors indicate that this technology has potential to provide rugged, large volume ambient temperature gamma detectors with adequate resolution for radionuclide analysis to meet needs in several mission areas.

The purpose of this Phase I study was to evaluate the feasibility of HPXe-based monitoring systems for meeting required detection sensitivity limits for ^{140}Ba for specified NEM sampling and counting conditions. An HPXe detector was selected and characterized for the NEM application. A series of experimental measurements with a custom NIST-traceable 9-radionuclide source were conducted to define the energy, efficiency and resolution performance of the detector, and to compare the performance with sodium iodide and germanium detectors.

Monte Carlo (MCNP) simulation was used to select optimum air filter geometries (concentric cylinder), to examine efficiency improvements for aluminum vs. steel detector wall material (aluminum ~50% more efficient), and to estimate optimum shield dimensions for an HPXe based nuclear explosion monitor.

MCNP modeling was also used to estimate the detection sensitivity of the HPXe detector for the nuclear explosion fission product indicator, ^{140}Ba. Background spectra for the HPXe detector were calculated with MCNP by using input activity levels as measured in routine NEM runs at Pacific Northwest National Laboratory (PNNL). Analysis of the composite spectra indicates that the required detection sensitivity for ^{140}Ba can likely be met using the 537 keV gamma peak in the composite spectrum of the HPXe detector. Based on the Phase I project results, a design concept was defined for a NEM Prototype to be developed in the Phase II program.

HPXe appears to be a candidate for applications requiring simple, high reliability ambient temperature radionuclide measurement systems with slightly less energy resolution capability than that of cooled germanium systems. Unfulfilled applications exist now for these performance capabilities in nuclear non-proliferation, homeland security, nuclear site cleanup, nuclear power, and portable instruments for health physics needs.

OBJECTIVES

The overall purpose of this R&D project is to evaluate potential performance benefits of ambient-temperature HPXe detectors for applications in the NEM program. The project is focused on matching the capabilities of HPXe detector systems with both the measurement requirements and operational considerations for specific NEM applications.

Specific objectives of Phase I project were as follows:

1. Identify a promising HPXe detector for NEM application; measure the basic detector parameters to provide data for calculations of performance and detection sensitivity limits for specific NEM applications.
2. Develop and verify an MCNP model for HPXe-based systems that can provide quantitative evaluation of the performance for HPXe-based systems and optimization of designs for specific NEM applications.
3. Define a conceptual design for an HPXe-based NEM prototype system for field testing.

RESEARCH ACCOMPLISHED

Background

Radioisotope identification for NEM by gamma spectroscopy requires extremely reliable high-resolution and high-efficiency gamma detectors. Although high purity germanium (HPGe) detectors now represent the energy resolution performance standard for laboratory gamma spectroscopy, their inherent reliability issues and requirement for cryogenic cooling present practical operational problems in applications for field or remote nuclear security monitoring. The final summary slide of a recent seminar (Aiken, 2007) with participation by eight federal government agencies with nuclear security missions listed the first priority item needed for improved nuclear detection and response capability as: “New detector materials to provide high resolution ambient temperature operation.”

A brief summary of the current status of germanium detectors and of candidates for non-cooled detectors for radionuclide specific nuclear security applications is shown in Table 1. The two alternate technologies that appear to hold the most immediate potential for higher resolution ambient temperature detectors for nuclear security are La-halide scintillation crystals and high-pressure xenon chambers.

Table 1: Candidate Detector Technologies for Nuclear Explosion Monitoring

Detector Type	Resolution at 662 keV	Active Volume	Stability	Reliability	Practical Limitations
HPGe	0.2-0.5 %	moderate	Excellent	Moderate	Need for cryogenic cooling & vacuum, mechanical ruggedness, size limit, cost
HPXe	1.7-2.4 %	Excellent	Excellent	Excellent	Low density, less high energy efficiency, cost, evolving technology
CdZnTe	2-3 %	Poor	Poor	Moderate	Very small size, poor long-term stability, cost, evolving technology
La-Halides	2.5-4 %	Moderate	Moderate	Unknown	Temperature dependent output, natural radioactivity, cost, evolving technology
NaI	7-9 %	Excellent	Moderate	Excellent	Insufficient resolution, drift, crystal fracture

The goals of this R&D project are to evaluate HPXe detector performance as applied to improvements in nuclear explosion monitoring, and to develop and test a prototype system that will allow prompt field evaluation of promising NEM applications. This paper describes the Phase I effort consisting of selection and characterization of HPXe detectors for NEM applications, and of conceptual design of a NEM system prototype unit to be developed in the Phase II project.

The first activity of the Phase I project was selection of an HPXe detector suited for NEM applications and characterization of the detector performance by experimental measurements and MCNP5 simulations. Detection sensitivity for an HPXe-based NEM system was then estimated by combining the performance characterization data with the reported background data from field operation of radionuclide aerosol sampler analyzer (RASA) systems. Design concepts for the NEM prototype unit to be built in the Phase II effort were then defined based on the Phase I results.

Detector Selection and Characterization

Detector Selection - The primary performance benchmarks for the HPXe-based NEM are the specifications of the National Aeronautics and Space Administration solicitation and of the International Monitoring System (IMS) requirements for certification. As reported in the literature, the IMS required detection sensitivity specification is met by both the PNNL RASA system with a 90% HPGe detector (Miley, 1998) and by the EML AUTORAMP system with a 30% HPGe detector (Lanner, 1977). The active volume of a germanium detector of 90% relative efficiency is about 350 cc.

The density of germanium (5.3 g/cc) is about 13 times greater that of xenon as compressed to 0.4 g/cc in the HPXe detector. However, the photopeak efficiency per unit volume is much closer for the two materials, since photoelectric cross section in the energy range below 600 keV is proportional to between Z^4 and Z^5. Thus, the photoelectric cross section of xenon (Z=54) is about 8–14 times greater than for germanium (Z=32) over the 100–600 keV energy range of interest for detection and quantification of ^{140}Ba.

In view of the atomic number and density differences between HPXe detectors and germanium detectors, a Frisch-grid HPXe detector of active dimensions 11.4 cm diameter by 20.3 cm length (4.5 in. diameter X 8 in. length) and 2.4% full width at half maximum (FWHM) resolution at 662 keV was selected for testing as a candidate to meet the IMS sensitivity spec. The test HPXe detector, shown in Figure 1, has an active volume of more than 1900 cc, or more than 5 times that of the 90% germanium detector. The increased diameter and length for this HPXe detector as compared to the 90% germanium detector also allows the use of a single filter of large area for NEM monitor applications.

Figure 1 HPXe Test Detector (Front) during Test Series at UC-Irvine

Detector Characterization - Authoritative energy and efficiency calibration data were obtained for the selected HPXe detector by obtaining measured spectra using a custom 9-radionuclide point source with NIST traceability.

All counting experiments were performed at the University of California -Irvine research reactor facility using commercial radionuclide sources and special sources prepared by reactor irradiations. The calibration parameter measurements were made with the point source positioned at 25 cm from the detector axis at the midpoint of the detector length.

The energy versus channel number measurements at ten energy points from 88 keV to 1836 keV were fitted with insignificant residual differences to a linear equation for energy versus channel number : E = -7.596 + 1.013. As expected, the energy response of the HPXe detector was very linear.

FWHM energy resolution measurements were also made for the HPXe detector at energies of the peaks of the 9-radionuclide calibration source. Energy resolution was calculated using the Gaussian fitting routine of the Genie 2000™ Gamma Acquisition and Analysis software. The resolution equation with coefficients fitted to the measured resolution of the HPXe detector (2.4% FWHM at 662 keV) is shown in Figure 2. An MCNP calculated case for a detector with the same dimensions as the test detector, but with 2.0% resolution at 662 keV is also shown.

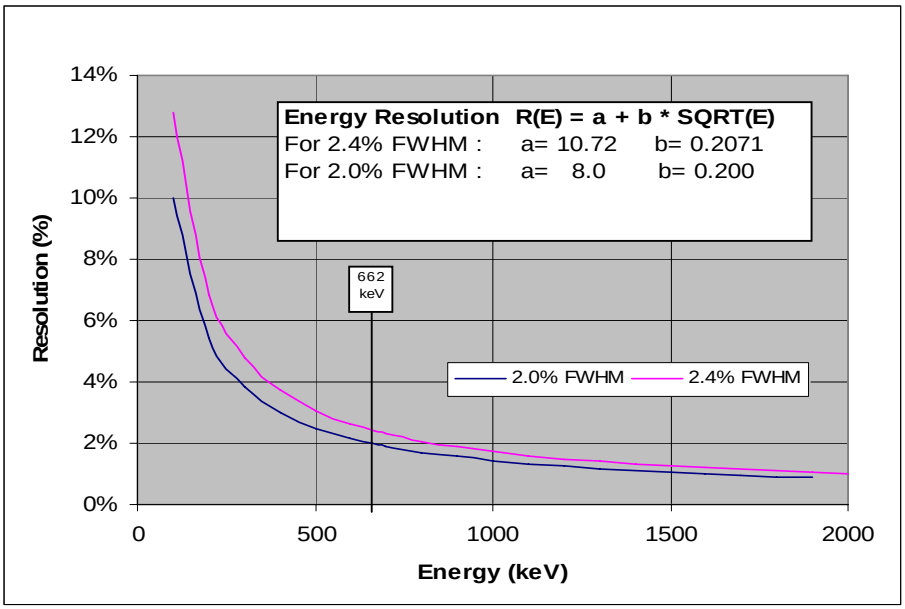

Figure 2 HPXe Test Detector Resolution Calibration

The 9-radionuclide source was then used to measure absolute photopeak efficiency over the 88-1836 keV range for the HPXe detector, as well as for a 30% germanium detector and a 3X3 NaI detector in the same geometry. Figure 3 shows that the photopeak efficiency of the selected HPXe detector (green line/yellow measured points) excels below about 400keV as compared to the 30% germanium detector, and offers similar efficiency as that of the germanium detector above 400 keV. As compared to a 3X3 NaI detector, the test HPXe detector efficiency is greater than that of a 3X3 NaI detector below 200keV, but significantly less at all energies above 200 keV.

Detector Stability

Detector stability with respect to time and temperature is a very important consideration for nuclear monitoring at remote stations and for field measurements with portable radionuclide measurement systems. Spectra with gain shift due to drift with time or temperature are much more likely to result in incorrect identification of radionuclides, particularly if the spectra are transmitted to central stations for analysis.

Measurements previously reported by one of the investigators confirmed that the gain and temperature stability of HPXe detectors is excellent (Beyerle, 2005). Time variance of the gain was measured to be less than $\pm$ 0.02% per week. The temperature stability of the HPXe detector was measured to be about $\pm$ 0.2% over the extended range of 25°C–80°C (77°F–176°F). Temperature stability is important for applications such as outdoor air monitoring or vehicle portal monitoring systems where the detector temperature may change significantly on a daily and seasonal basis.

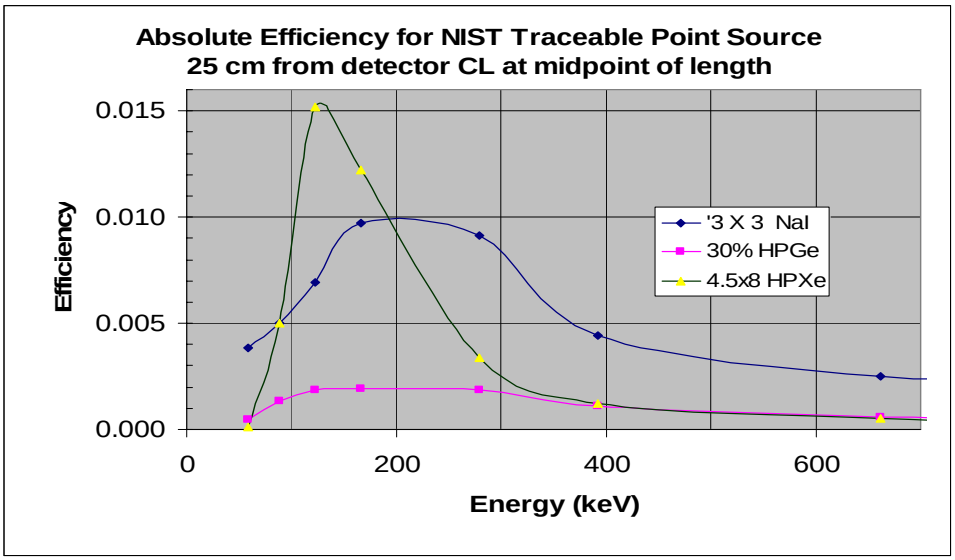

Figure 3 Efficiency Comparison of HPXe, NaI and HPGe

Monte Carlo Simulations

Because Monte Carlo simulations with MCNP5 were used to predict HPXe detector performance not conveniently confirmed by direct measurements in the Phase I project, the ability of the MCNP simulations to accurately predict HPXe performance was experimentally confirmed. Individual HPXe spectra were obtained with commercial sources of ^{57}Co (122.1 keV) and ^{137}Cs (662 keV), and with custom short lived sources of ^{128}I (442.9 keV), ^{64}Cu (511 keV), ^{41}Ar (1293.5 keV) and ^{28}Al (1779.0 keV) prepared and counted at the UC-Irvine research reactor.

Figure 4 shows comparisons over two energy ranges of experimentally measured spectra and MCNP spectra corrected to give the 2.4 % FWHM resolution of the test HPXe detector. Note that all basic features of the photopeak, Compton edge, back scatter edge, escape peaks, and x-ray emissions and edges that appear in the measured spectrum are also apparent in the MCNP simulation.

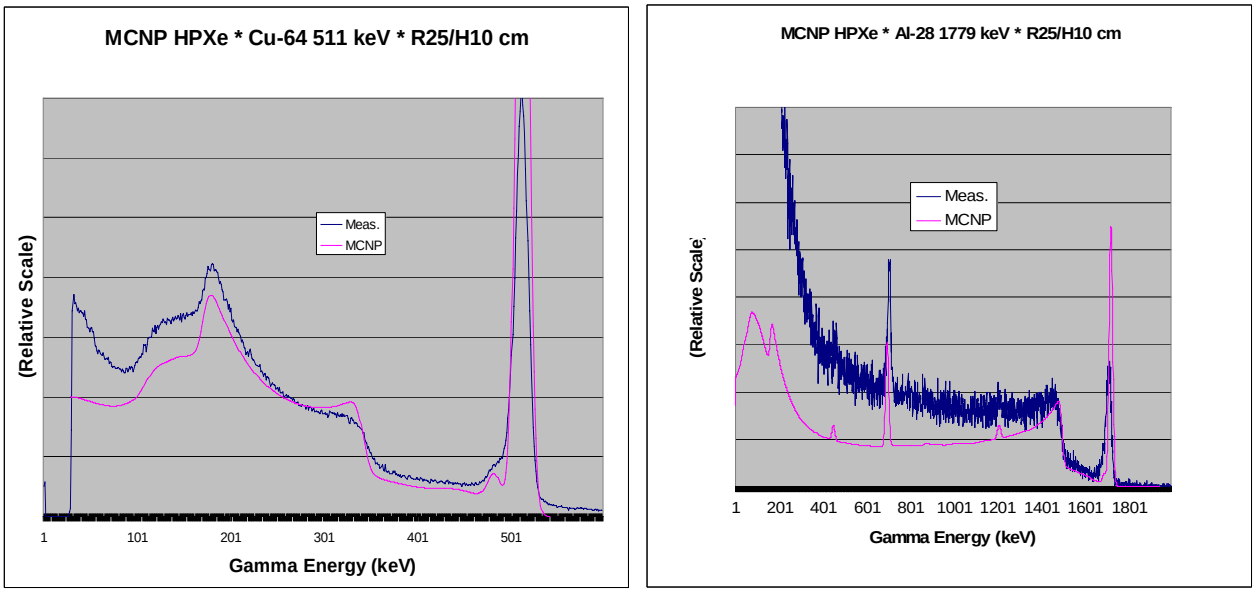

Figure 4 Comparison of Measured and MCNP5 Single Line Spectra for HPXe

The experimental detector runs were made with an unshielded detector, thus giving a much larger background continuum over the low energy range than did the MCNP simulated spectra that did not include background components. A rudimentary shield of lead pieces was constructed around the HPXe detector for an experimental background measurement. The integrated count of the background over the energy range of 100keV -1000 keV for shielded versus unshielded showed a reduction by a factor of more than 14 in gross background counts. The custom designed detector, electronics and shield of the Phase II program will significantly reduce the background, and are expected to bring the MCNP simulation and observed performance into close quantitative agreement.

Once the general credibility and bounds of applicability of the MCNP model were established during Phase I, the model was used to resolve questions and to guide the development effort in several areas:

- A source sample geometry of a concentric cylindrical filter was modeled in MCNP with a 9-radionuclide mix evenly distributed over the cylindrical shell to provide energy-dependent efficiency coefficients for the anticipated concentric cylindrical filter geometry of the NEM prototype system.
- MCNP simulated background spectra were generated for the HPXe detector and source geometry as expected from background components collected during a typical 24 hour NEM sampling period. The input source term for the MCNP runs was taken from concentration levels provided by PNNL from routine sampling runs with the RASA system.
- The effect of xenon gas pressure (xenon density) on detector performance was evaluated as a means to quantify the effect of xenon density on both the efficiency and peak-Compton ratio for a fixed detector volume.
- The effect of the thickness of the steel wall of the HPXe detector was evaluated, as was the improvement in efficiency by constructing the detector wall of aluminum rather than steel. The MCNP results predict that aluminum gives an efficiency improvement for this detector of about 50% at 122 keV, declining to about a 10% improvement at 1836 keV.
- An MCNP model of a 5 cm thick lead shield closely spaced around the cylindrical sample was used to predict the amount of backscatter and pair production in the shield volume from the known aerosol background components in the filter and to ensure that they would not cause interference at crucial points of the gamma spectrum. This model will be used to evaluate the benefit of a copper liner on the inside wall of the shield for the NEM Prototype system of Phase II.

Estimating HPXe Performance for NEM Applications

The second major objective of Phase 1 was to estimate the performance of HPXe detectors for the radionuclide mix of the Comprehensive Nuclear-Test-Ban Treaty-IMS application as defined by previous RASA/Automated Radioxenon Sampler/Analyzer (ARSA) work. In the absence of an air sample collection system and an effective shield for the HPXe test for the Phase I effort, field data from the RASA program provided by PNNL were used to estimate system background and interference under typical IMS sampling conditions.

Performance targets for NEM radionuclide measurement systems were taken from two sources: the NNSA specification of the solicitation, and the IMS specification for radionuclide monitoring systems for certified IMS monitoring stations. The nominal IMS collection/counting cycle is a 24 hour collection period, a 24-hour delay for decay of natural background components on the filter, and a 24 hour counting time.

For IMS certification, NEM radionuclide measurement systems are required to have a detection sensitivity of $\leq$ 30 $\mu Bq/m^3$ of ^{140}Ba for the nominal counting cycle with collection of a 12,000m^3 sample on the filter. The NNSA solicitation for this topic area stated a slightly different requirement of 20 $\mu Bq/m^3$ of ^{140}Ba in air for a 25,000 m^3 sample collected during the 24 hour sampling period. The two specifications are similar in the required detector performance, with the IMS specification requiring slightly better detector performance than the NNSA requirement.

Estimating counts were recorded in HPXe spectra for various concentrations of ^{140}Ba. The five gamma energy emissions from ^{140}Ba that have greater than 1% relative abundance are listed in Table 2. MCNP runs were made with input parameters corresponding to the selected HPXe detector with ^{140}Ba distributed randomly on a concentric cylindrical filter source of 15.2 cm diameter by 20.3 cm length (6 in. diameter by 8 in. length). The IMS cycle of 24-hour collection, 24-hour decay, and 24-hour count time was applied for four cases of airborne ^{140}Ba concentrations and total volumes of air sampled through a used filter. (A “used” filter is defined as a filter containing the airborne

particulates routinely collected by sampling the specified total volume of air at the required collection efficiency, but not containing fresh fission products from a nuclear explosion.)

Table 2 MCNP Calculated Net Counts for Four Test Cases

^{140}Ba Decay Data		Counts in ^{140}Ba peaks for 4 Sample Cases			
Eγ (keV) for ^{140}Ba Lines of < 1% Iγ	**Iγ (%)**	20uBq/m3 12,000 m3	30uBq/m3 12,000 m3	20uBq/m3 25,000 m3	30uBq/m3 25,000 m3
162.66	6.2	1498	2110	3340	5028
304.85	4.3	537	768	1154	1761
423.73	3.2	186	274	457	600
437.58	1.9	145	205	305	399
537.26	24.4	947	1379	2068	3065

Estimating Spectrum Baseline and Interference under NEM System Conditions - An analysis of data from the RASA and ARSA programs shows that the major contributors to the natural gamma spectrum baseline for a "used" filter are ^{7}Be, ^{40}K, ^{212}Pb / ^{212}Bi / ^{208}Tl from the thorium decay series, and ^{214}Pb / ^{214}Bi from the ^{238}U decay series (Arthur et al., 2001). During the Phase I project, PNNL provided used RASA filters for counting on the HPXe detector, but the delay caused by logistics of handling and shipping the sample caused the measurements to be unrepresentative because of the rapid decay of the major natural products on the filter.

An analysis of PNNL data from the RASA program indicates that most of the significant gamma peaks and continuum counts in a spectrum for IMS measurement conditions are produced by the gamma emissions from the filter as shown in Table 3. The gamma emission rates of Table 3 were used as input source terms for runs with the MCNP model for the concentric filter around the 2.4% HPXe detector.

Table 3 Gamma Emissions from Used Filter with 24 Hour delay

Gamma Energy (keV)	Intensity %	Gammas/ Second	Radionuclide Source	Gamma Energy (keV)	Intensity %	Gammas/ Second	Radionuclide Source
238.6	43.3	17.41	Pb-212	727.3	6.58	2.87	Bi-212
277.4	6.13	0.94	Tl-208	785.4	1.102	0.48	Bi-212
300.1	3.28	1.32	Pb-212	860.6	12.42	1.91	Tl-208
477.6	10.52	3.34	Be-7	1460.8	11.00	0.78	K-40
510.8	22.6	3.48	Tl-208	1620.5	1.49	0.65	Bi-212
583.2	84.5	13.01	Tl-208	2614.53	99.0	15.25	Tl-208

In order to simulate a NEM spectrum, a composite spectrum was generated by a channel-by-channel summing of counts in the MCNP generated ^{140}Ba spectrum with counts in the used filter spectrum from MCNP runs for an assumed HPXe resolution of 2.4%. Figure 5 shows both the baseline-only spectrum (blue line) from used filter

background activity, and the composite spectrum of the sum of used filter and ^{140}Ba counts (red line) for the NNSA and IMS specification for NEM systems. The ^{140}Ba peaks at 305, 424 and 438 keV have low intensity and interferences that would prevent their use for ^{140}Ba quantification. The 163 and 537 keV peaks appear to be viable candidates for ^{140}Ba analysis.

The 163 peak will generate the most counts because of the very high efficiency of the HPXe detector in the 100–200keV range. Although the MCNP calculated baseline is fairly low in this energy region, the actual baseline will be larger than shown because of counts from low energy background sources not included in the input source data for the MCNP model.

The 537 keV peak has very good potential to provide quantitative results for the stated ^{140}Ba concentrations and sampling conditions with the 2.4% FWHM HPXe detector. The 537 peak of ^{140}Ba overlaps the 511 peak and x-ray escape peak of the 583 line, but the multiplet resolution routines of commercial analysis software package could readily extract a quantitative number from the data shown. Since the energies of the ^{140}Ba and ^{208}Tl peaks are known, a deconvolution algorithm based on fitting the three Gaussian peaks to the known energies should give even better quantitative results for ^{140}Ba.

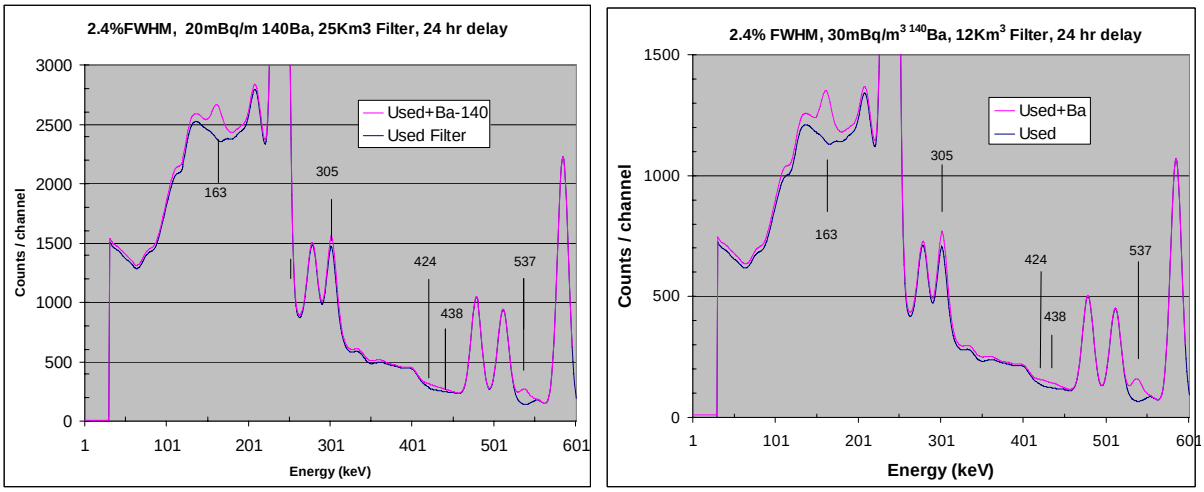

Figure 5 HPXe (2.4% FWHM) Spectra for NNSA and IMS Specifications

One of the first tasks of the Phase II program is to produce an HPXe detector with the same active volume dimensions as the test HPXe detector of Phase I, but with energy resolution of $\leq$ 2.0% FWHM at 662 keV. A smaller HPXe detector is routinely produced with $\leq$ 1.7% FWHM resolution, thus, production of the 2.0% detector for the NEM application is expected to be a straightforward engineering development effort. The theoretical resolution limit for HPXe detectors is less than 1%.

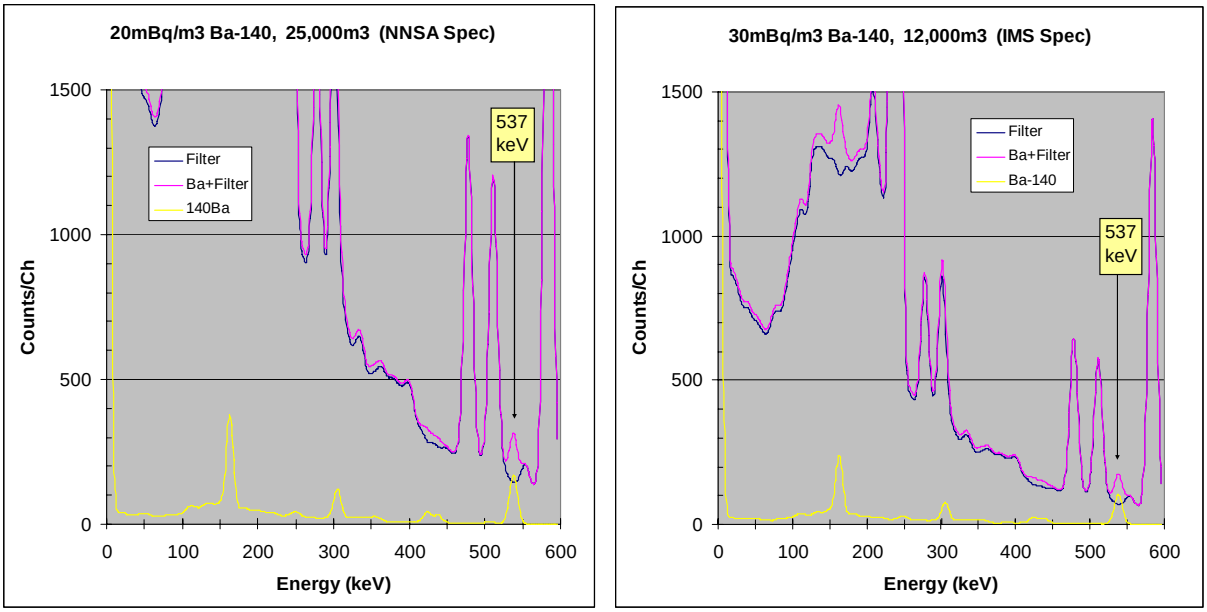

Figure 7 HPXe (2.0% FWHM) Spectra for NNSA and IMS Specifications

Figure 7 shows the calculated spectra for the NNSA and IMS standard conditions with an HPXe detector of 2.0% resolution. The 537 keV ^{140}Ba line is now clearly resolved from the ^{208}Tl peak at 511 keV and the x-ray escape peak of the 538 keV gamma emission of ^{208}Tl.

Estimating Detection Sensitivity - Because the background from the filter could not be experimentally measured on an HPXe detector during the Phase I program, the calculation of the lower detection limit for ^{140}Ba for a HPXe-based NEM system is subject to large uncertainties with the present information. However, a preliminary estimate of detection sensitivity was made using the Currie methods (Currie, 1984) for calculating concentration detection limits at 95% confidence levels for gamma spectra. Input parameters used were the calculated absolute efficiency of 0.015 at 537 keV for the concentric cylindrical filter, and baseline count data in a 13keV window under the 537 keV peak as shown in Figure 7. Using the IMS conditions of a 12,000m^3 sample, a 24 hour decay time and a 24-hour counting time, the calculated critical count level is 173 counts, and the concentration detection limit for ^{140}Ba is 11.2 μBq/m^3 for a 2.0% FWHM HPXe detector of the dimensions of the test detector. (The IMS spec is $\leq$ 30 μBq/m^3.)

Again, the MDC calculation has a very large uncertainty at this stage of the project for the reasons mentioned. A series of bench test measurements with shielded HPXe detectors and freshly collected filter samples will be performed early in the Phase II program to provide the data required to calculate an authoritative MDC for the HPXe NEM Prototype system.

Conceptual Design for the NEM Prototype System

A third goal of the Phase I program was to develop a conceptual design for a Phase II explosion monitor prototype that best meets the specifications and intent of the SBIR subtopic.

An extensive base of practical information was made available to investigators by the developers of the two U.S. HPGe-based NEM systems that have demonstrated the ability to meet the IMS specification. The Investigators were given hosted visits to PNNL in Richland Washington to review an operating RASA monitor, and to DHS-EML in New York City to review an operating AUTORAMP NEM monitor.

The preliminary concept for the NEM Prototype system to be designed and constructed during the Phase II effort is as follows:

Detector—For improved resolution and ruggedness, the NEM HPXe detector will be a gridless design which is expected to give a FWHM resolution of $\leq$ 2.0% at 662 keV. The dimensions and active detector volume of the NEM Prototype detector will be the same as for the Phase I test HPXe detector, but the detector package size will be

minimized by separating the high voltage power supply and a portion of the signal processing electronics from the detector package.

Filter—A cylindrical pleated filter cartridge of about 14 cm (5.5 in.) I.D. by 20.3 cm (8in.) length, with a nominal 2.5 cm (1.0 in.) thickness will be used in the HPXe-based prototype system. Based on the AUTORAMP pleated filter area multiplication factor of more than 2.5, the effective filter area for the cartridge is about 2430 cm^2 (377 in^2). The cartridge filter concept has proven to be both effective and highly reliable for automated sample changing during field operation of the AUTORAMP system.

Air Sampling System—Air flow for the air sampling system will be provided by a centrifugal blower unit that draws outside air through the filter chamber. A commercially available integral blower and motor unit with continuous duty cycle rating will be purchased that provides the 12,000 flow rate required by the IMS specification. A blower/motor unit similar to the units used in either the RASA or AUTORAMP systems would provide the required airflow performance.

Shield—A custom lead shield will be designed to provide a minimum of 2" thickness of lead. The shield will be a vertical cylindrical design with a split top lid that can be opened and closed under computer control for automated filter cartridge insertion and removal.

System Computer and Control Software—The NEM Prototype system will use an industrial grade PC with a master control program to control operations, provide data acquisition, analysis, archiving, reporting, diagnostics and communications. The master control program will be defined and developed internally as one of the major tasks of the Phase II program, and will integrate commercial off-the-shelf software for spectrum analysis and auxiliary functions where possible to minimize the extent of development of new computer code.

Automatic Filter Cartridge Sample Changer—Since an automatic sample changer is not required to evaluate the detection sensitivity performance of the prototype unit, a sample changer will not be incorporated into the initial NEM Prototype unit. Provisions for adding the sample changing mechanism and software at a later time will be designed into the initial unit based on the requirements of the first field application for the NEM Prototype unit. Commercial robotic XYZ systems of the type used in the AUTORAMP system are available with control software packages that are compatible with operation by the master control program software of the NEM Prototype.

CONCLUSIONS AND RECOMMENDATIONS

The Phase I experimental measurements and MCNP simulations based on previous RASA experiences indicate that a NEM system based on the selected 2.4 % resolution HPXe detector will likely meet IMS and NNSA specifications. Spectra generated and calculated using MCNP5 for ^{140}Ba and filter baseline show sufficient counts for the 537 keV peak to allow ^{140}Ba to be detected and quantified at meaningful levels for NEM applications.

The MCNP simulations also indicate that further improvements in detection sensitivity provided by changing to a gridless detector design with $\leq$ 2.0% energy resolution will further enhance the detection sensitivity for NEM applications. A Phase II proposal has been submitted with detailed goals, work plans and schedules for development and testing of a recommended HPXe-based NEM Prototype system.

During the review of activities in the nuclear non-proliferation area, it became apparent that the NEM program also has an active need for versatile field measurement systems for site inspection and follow up of suspect events. NNSA's need for high resolution ambient temperature portable and transportable nuclear measurement systems is shared by several other US agencies and international groups with nuclear security missions. The rugged, stable HPXe detector appears to have strong potential to provide practical solutions for many of these unfulfilled measurement needs.

ACKNOWLEDGEMENTS

The Investigators for the Phase I project received cooperation and technical assistance both from the DOE PNNL RASA/ARSA technical staff, and from the DHS Environmental Measurements Laboratory and retired EML staff member, Colin G. Sanderson.

REFERENCES

Aiken, S. C. (2007).Health Physics Aspects of Homeland Security, *Proceedings of the 11th Annual Savannah River Chapter HPS Technical Seminar*.

Arthur, R. J., T. Bowyer, J. Hayes, T. Heimbigner, J. McIntyre, H. Miley, and M. Panisko (2001). Radionuclide measurements for nuclear explosion monitoring, in *Proceedings of 23rd Seismic Research Review: Worldwide Monitoring of Nuclear Explosions*, LA-UR-01-4454, Vol. 2, pp. 57–63.

Beyerle, A. G. (2005). Stability of high-pressure xenon gamma-ray spectrometers, in *Proceedings of Hard X-ray and Gamma-Ray Detector Physics VII*, International Society for Optical Engineering. Vol. 5, pp. 922–928.

Currie, L. A. (1984). Lower Limit of Detection: Definition and Elaboration of a Proposed Position for Radiological Effluent and Environmental Measurements, USNRC NUREG/CR-4007, p.133.

Lanner, N., C.G. Sanderson, V.C. Negro, S.Wurms, and N.Shiu, (1997). AUTORAMP—An Automatic Unit for Unattended Aerosol Collection, Gamma-Ray Analysis and Data Transmission from Remote Locations, *Radioactivity and Radiochemistry* 8: (3), 25–30.

Miley, H. S., S. M. Bower, C. W. Hubbard, A. D. McKinnon, R. W. Perkins, R. C. Thompson, and R. A. Warner (1998). A description of the DOE Radionuclide Aerosol Sampler/Analyzer for the Comprehensive Test Ban Treaty, *J. Radioanal. Nucl. Chem*. 235: (1–2), 83–87.

IMPROVED CALIBRATION AND OPERATION OF A STABLE-GAS QUANTIFICATION MANIFOLD AS PART OF A RADIOXENON COLLECTION SYSTEM

Richard M. Williams, James C. Hayes, and Randy R. Kirkham

Pacific Northwest National Laboratory

Sponsored by National Nuclear Security Administration
Office of Nonproliferation Research and Development
Office of Defense Nuclear Nonproliferation

Contract No: DE-AC05-RLO1830/PL07-ZINC-NEM02

ABSTRACT

Radioxenon detection as part of the Nuclear Explosion Monitoring program involves measuring the ratio of the radioactive Xe isotopes (^{135}Xe, ^{133}Xe, ^{131m}Xe and ^{133m}Xe) to the stable (non-radioactive) isotopic abundance. Pacific Northwest National Laboratory currently uses a thermal conductivity detector (TCD) to measure the stable xenon gas composition immediately after the nuclear measurement is complete on their automated radionuclide samplers. When combined with absolute pressure, temperature and volume, the total volume of stable xenon (cubic centimeters of xenon at standard temperature and pressure) collected can be calculated and the quantity of radioxenon per volume of air is derived. A commercial TCD is a reliable device for measuring percent composition of binary mixtures provided the pressure of the sample is at or near atmospheric pressure; under these conditions the thermal conductivity of the sample is independent of pressure. However, at low sample pressures a pressure-dependent term begins to influence the thermal conductivity of the gas sample and needs to be accounted for if reliable results are to be obtained. To establish a means of correcting for the pressure effect, several blended gas mixtures (xenon in nitrogen) were analyzed over a wide range of pressures (10–760 Torr) on a test manifold fitted with a commercial TCD. These data were then analyzed and an automated calibration algorithm established and used to correct for the pressure effect in the raw TCD readings. The currently implemented routine uses the absolute pressure measurement to “look-up” the necessary calibration coefficients, which are used for TCD pressure normalization. It is estimated that this technique allows the use of TCD instruments to measure binary mixtures reliably down to a pressure of 10 Torr, much lower than is currently achievable with these devices. These results and an in-depth discussion of the pressure compensation approach will be reviewed in this paper.

OBJECTIVES

The objective of this work is to establish and demonstrate a technique for removing the pressure dependence from percent composition measurements of a binary gas taken with a commercial TCD. It is shown that this approach improves the accuracy of the measured percent xenon in nitrogen in low pressure gas samples compared with conventional approaches, positively impacting the error budget in radioxenon measurements.

A TCD is a simple device used for measuring the percent composition of a binary gas mixture. Such a measurement is an important part of the stable gas measurement (along with temperature, pressure and volume) and is usually performed after the activity of a xenon gas sample is determined by a nuclear counting measurement (Hayes et al., 1999). Binary gas mixtures are often encountered in radioxenon measurements due to the presence of a carrier gas (e.g., nitrogen or helium) used in the chromatographic isolation of the xenon sample. A typical TCD operates by measuring the power dissipated by a heated wire placed in the gas sample itself (Jitschin and Ruschitzka, 1993). Gas mixtures with a higher thermal conductivity remove more heat from the wire than gases with low thermal conductivity. Compositional analysis of the binary mixture is achieved by comparing the measured power dissipated against a 2-point calibration employing pure samples of the two gases.

The thermal conductivity of a gaseous mixture is a function of many parameters and is nontrivial to calculate. One very important aspect of the thermal conductivity of gases is its invariance to pressure at 1 atmosphere and above. Due to the gas dynamics that govern thermal conductivity, terms involving pressure cancel at these higher pressures. Therefore, all commercially available TCDs are specified for operation at or very near atmospheric pressure. A problem arises when these sensors are used at lower pressures because the thermal conductivity of the gas depends on both the intrinsic properties of the gas, as well as, the pressure of the gas. In many applications where compositional analysis is required, the pressure of the sample may be well below 1 atm (or 760 Torr) introducing significant accuracy errors. Because of this a study was performed to determine the feasibility of pressure compensating TCD readings from xenon/nitrogen gas mixtures over a range of pressures from 10 to 760 Torr.

RESEARCH ACCOMPLISHED

For this study a simple apparatus was assembled consisting of a commercially available TCD unit (HiTech Instruments, model K1550), an absolute pressure transducer (MKS Instruments, 1000-Torr capacitance manometer) and a secondary binary gas analyzer based on an acoustic measurement (Lorex Industries, Piezocon). These units were connected to a small leak tight manifold that could be evacuated to < 100 m Torr. Certified gas mixtures were purchased from 20%, 40%, 60%, 80%, and 95% xenon in nitrogen, in addition to standard purity nitrogen and xenon gases. The Piezocon sensor from Lorex industries was used to accurately and precisely measure the “true” composition of the purchased mixtures. The Piezocon has a rated accuracy of better than 0.1% for xenon/nitrogen mixtures. The HiTech TCD was calibrated using pure nitrogen and xenon carefully following the manufacturer’s instructions.

The procedure for a typical measurement involved evacuating the manifold to the base pressure and flushing with the gas mixture to be tested; this was repeated 3 times. The gas mixture was then added to the manifold to a pressure of 800 torr. The pressure, TCD value and Piezocon reading were all recorded. The pressure in the manifold was then reduced to the next target value by slightly opening a valve connected to the vacuum pump. The three readings were recorded and the pressure reduced again down to a lower limit of 2.5 Torr. This entire process was repeated 3 times to check for consistency and to provide for average sensor readings (with an estimate of error). Once the measurements for one mixture were complete, the cylinder was exchanged, the manifold flushed, and the series of 3 measurements were repeated. One additional mixture was created in the manifold by adding pure xenon to pure nitrogen already in the manifold and using their partial pressures to establish the percent composition (5.4% xenon in nitrogen) at a final pressure of 760 torr. Thorough mixing of this custom blend was verified by monitoring the Piezocon’s output over 24 hours. After approximately 16 hours the gases were sufficiently mixed for the measurement to begin. Only one series of measurements for this mixture was performed (instead of the 3 for the other gases). All measurements were performed near room temperature.

Pressure-dependent TCD data obtained for the 40% xenon in nitrogen mixture is shown in Figure 1. As mentioned previously, an accurate measurement of the percent composition is simultaneously obtained using a commercial acoustic sensor (Piezocon from Lorex Industries) for pressures > 75 Torr (the Piezocon stops responding below this

pressure). The acoustic sensor has much higher precision and accuracy compared with the TCD; however, it suffers from a larger internal volume and a minimum operating pressure of 75 Torr, making it unsuitable for many applications where a limited amount of sample is available for analysis. Two notable observations about the pressure dependence of the TCD can be made from Figure 1. A large offset between the TCD and the acoustic sensor is present at atmospheric pressure where the TCD instrument is specified to operate. Also shown in Figure 1 is the impact of pressure on the TCD reading itself, which is a minor effect at higher pressure but becomes significant at pressures below 200 Torr.

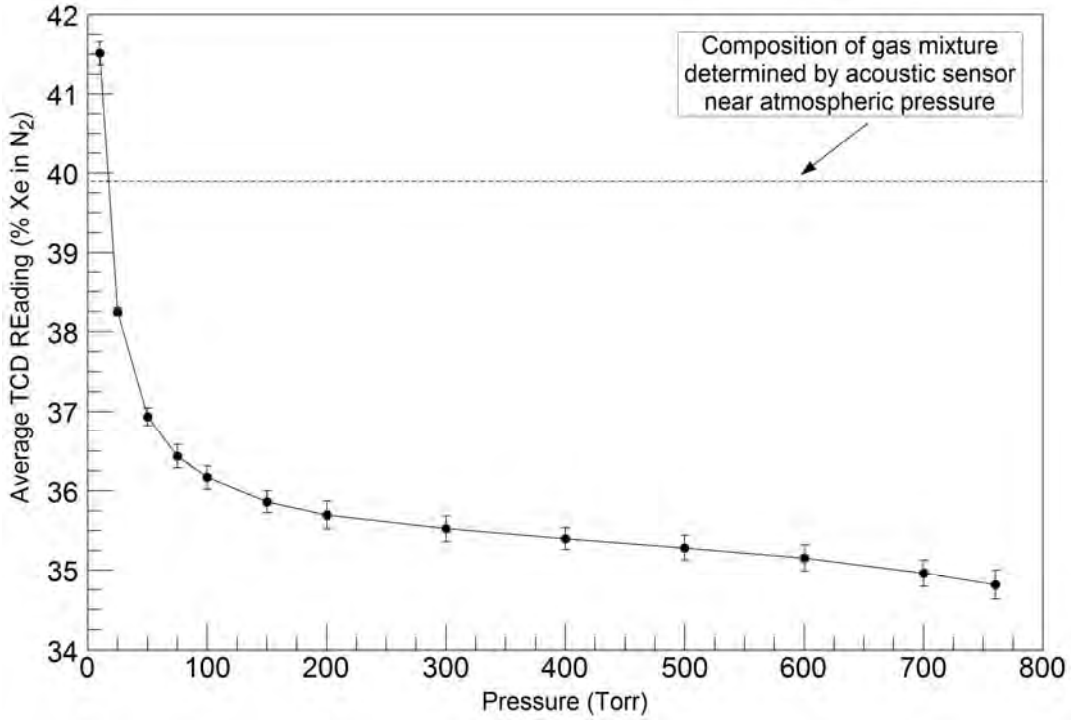

Figure 1. TCD readings as a function of pressure for a specific Xe/N_2 mixture (39.9%). The error bars represent 1 standard deviation of the 3 runs performed for this mixture.

Figure 2 shows the TCD reading as a function of pressure for all the gas mixtures used in this study. All traces show similar pressure dependence to that shown in Figure 1. The TCD readings for the low-pressure 100% xenon samples are artificially clamped or saturated at 100% since the instrument is not designed to output signals above 100%. The offset between the TCD instrument and the acoustic sensor at 760 Torr varies considerably and is largest for mid-range percent compositions.

Compensation Approach

The strategy for compensating the TCD reading involves determining an empirical relationship between "true" percent composition and measured percent composition for a wide range of mixtures and pressures. This is done by first interpolating the data in figure 2 along the pressure coordinate to yield a grid resolution of 1 Torr. The curves are all smoothly varying; therefore, the interpolation step is not likely to add significant error. Once the interpolation step is complete the "true" versus measured percent composition for each pressure is fit with a 5^{th} order polynomial. The coefficients from the fitting process for each pressure along the 1 Torr grid are stored. Three of these curves are plotted in Figure 3 along with their corresponding polynomial fit for 10, 200 and 760 Torr.

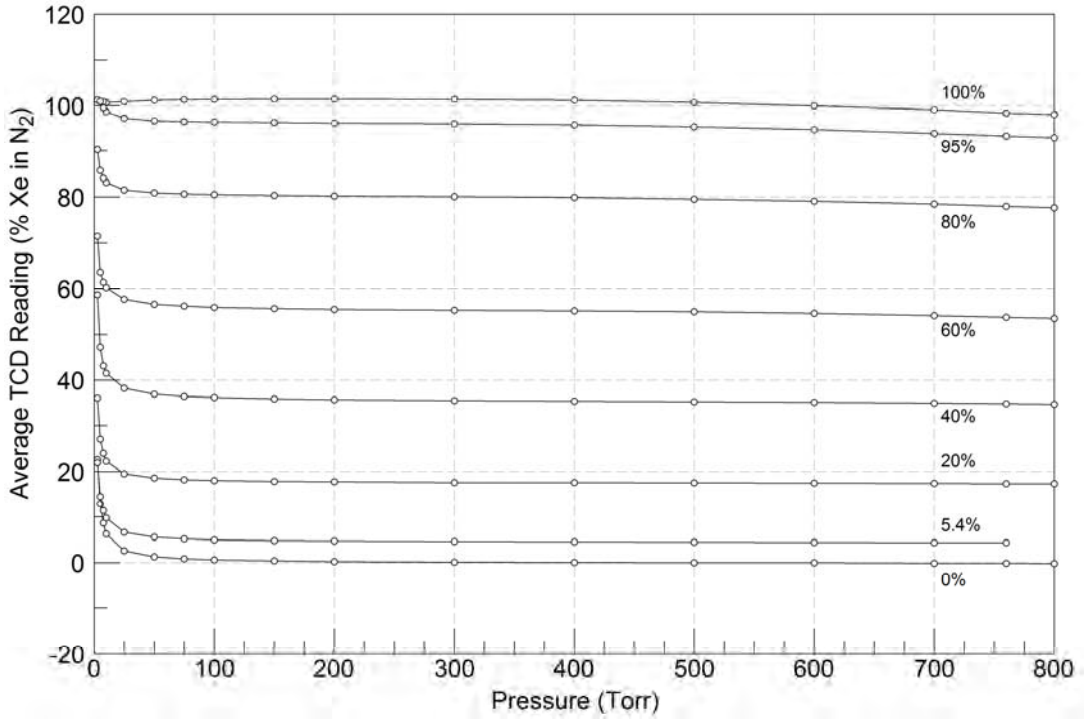

Figure 2. Pressure dependence of TCD compositional analysis as a function of sample pressure for all mixtures of xenon in nitrogen used in this study. Open circles are measured data, solid lines are interpolated data on a 1-Torr grid. Actual %Xe values are inserted for comparison.

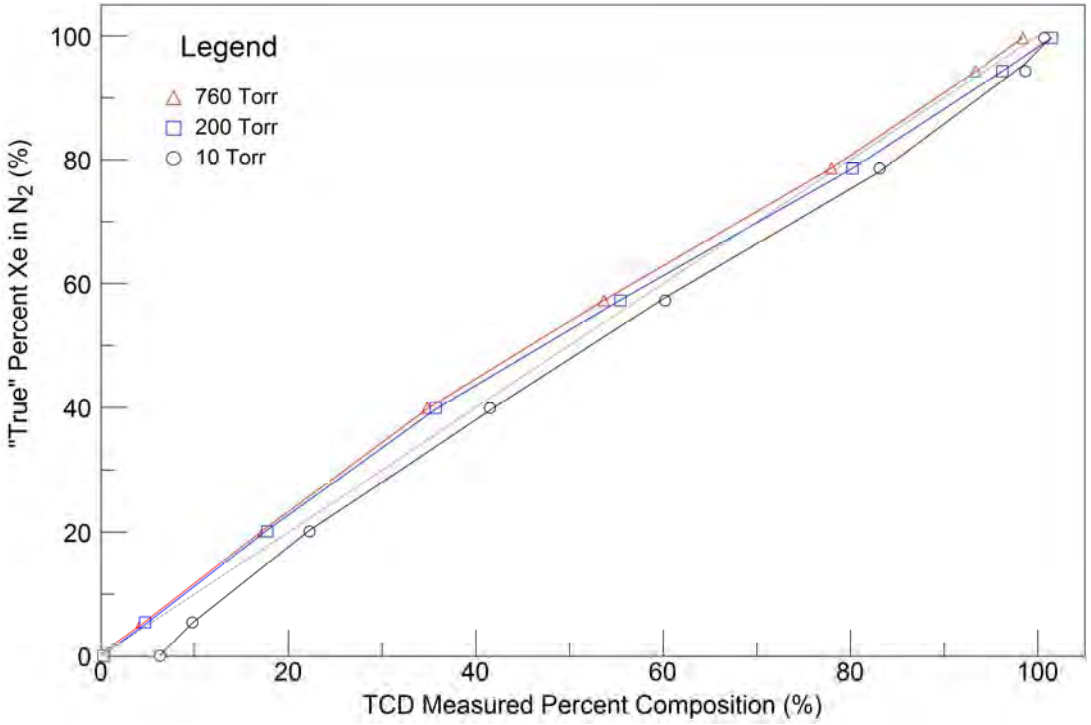

Figure 3. Actual versus measured percent composition for various xenon/nitrogen mixtures at three different pressures (760, 200, and 10 Torr), along with their corresponding 5th order polynomial fits. A dashed gray line with a slope of 1 is shown for reference.

Using this approach the previously measured TCD readings (shown in Figure 2) were used to generate a full set of coefficients for the 13 different pressures selected for this work. These polynomial coefficients are listed in Table 1. In the final form the matrix is much larger, with pressure resolution of 1 Torr.

Table 1: Polynomial values used in the compensation equation for the different pressures measured in this work.

	Polynomial Coefficients					
Pres. (Torr)	**a0**	**a1**	**a2**	**a3**	**a4**	**a5**
10	-11.72989	2.1644216	-0.0523550	0.0011240	-1.160E-05	4.479E-08
25	-3.426932	1.3785450	-0.0111410	0.0001835	-2.080E-06	9.966E-09
50	-1.355051	1.1667738	0.0026191	-0.0001701	1.767E-06	-4.985E-09
75	-0.785500	1.1193978	0.0062028	-0.0002692	2.889E-06	-9.469E-09
100	-0.480391	1.0955389	0.0080529	-0.0003210	3.483E-06	-1.188E-08
150	-0.227057	1.0760084	0.0098273	-0.0003729	4.091E-06	-1.436E-08
200	-0.061589	1.0536303	0.0114900	-0.0004161	4.554E-06	-1.613E-08
300	0.078753	1.0448359	0.0124288	-0.0004452	4.905E-06	-1.759E-08
400	0.150177	1.0419728	0.0127096	-0.0004522	4.980E-06	-1.787E-08
500	0.225328	1.0346178	0.0133195	-0.0004682	5.163E-06	-1.860E-08
600	0.282149	1.0385274	0.0128814	-0.0004497	4.908E-06	-1.743E-08
700	0.355955	1.0286183	0.0136278	-0.0004636	5.029E-06	-1.781E-08
760	0.358801	1.0425580	0.0124370	-0.0004211	4.470E-06	-1.530E-08

Implementation and Testing

When measuring an unknown mixture, the TCD reading and absolute pressure are recorded. The pressure value is used to "look-up" the correct coefficients for the polynomial expression, which also contains the raw TCD reading; for example at 200 Torr the expression is,

$$\%_{Xe/N2}(@200Torr) = -0.06158 + 1.0536(\%_{TCD}) + 0.01149(\%_{TCD})^2 - 4.1616\times10^{-4}(\%_{TCD})^3 + 4.5534\times10^{-6}(\%_{TCD})^4 - 1.6131\times10^{-8}(\%_{TCD})^5. \quad (1)$$

A software routine was written incorporating the polynomial coefficients and communication protocol for the TCD unit and the pressure transducer. The routine records the raw TCD reading and pressure and returns the compensated TCD value. To test the overall approach, the original raw TCD and pressure measurements were used as input to the software routine. The compensated TCD output data are plotted in Figure 4, along with the raw TCD measurements and indications of the actual mixture composition. As can be seen in Figure 4, the compensated TCD values are nearly independent of pressure (except at the lowest pressures measured) and the offsets are removed. A comparison of the relative accuracy errors between the raw and compensated TCD values is shown in Figure 5a and 5b, respectively. The relative accuracy error is defined as

$$rel.error(\%) = \left[\left(TCD(\%Xe) - Actual(\%Xe) \right) \Big/ Actual(\%Xe) \right] \times 100\% \quad (2)$$

where the Actual (%Xe) value is that value measured by the acoustic sensor at 760 Torr. The relative errors include the calibration offset error in addition to the pressure effect. The compensated errors are all within +/- 1.0% down to 10 Torr, with the exception of the 5.4% xenon sample. The relative errors on the 0% xenon sample are extremely large simply because of the way relative errors are calculated in Equation. 2 with the "true" value in the denominator (which in essentially zero) and therefore are not shown. For the lowest percent composition sample (5.4% xenon),

the absolute error in the compensated results is on the order of 0.1 – 0.3%. It is worth noting that for samples consisting of greater than 50% xenon in nitrogen, the total relative error (in the raw TCD readings) down to 10 Torr is typically less than +/- 5%.

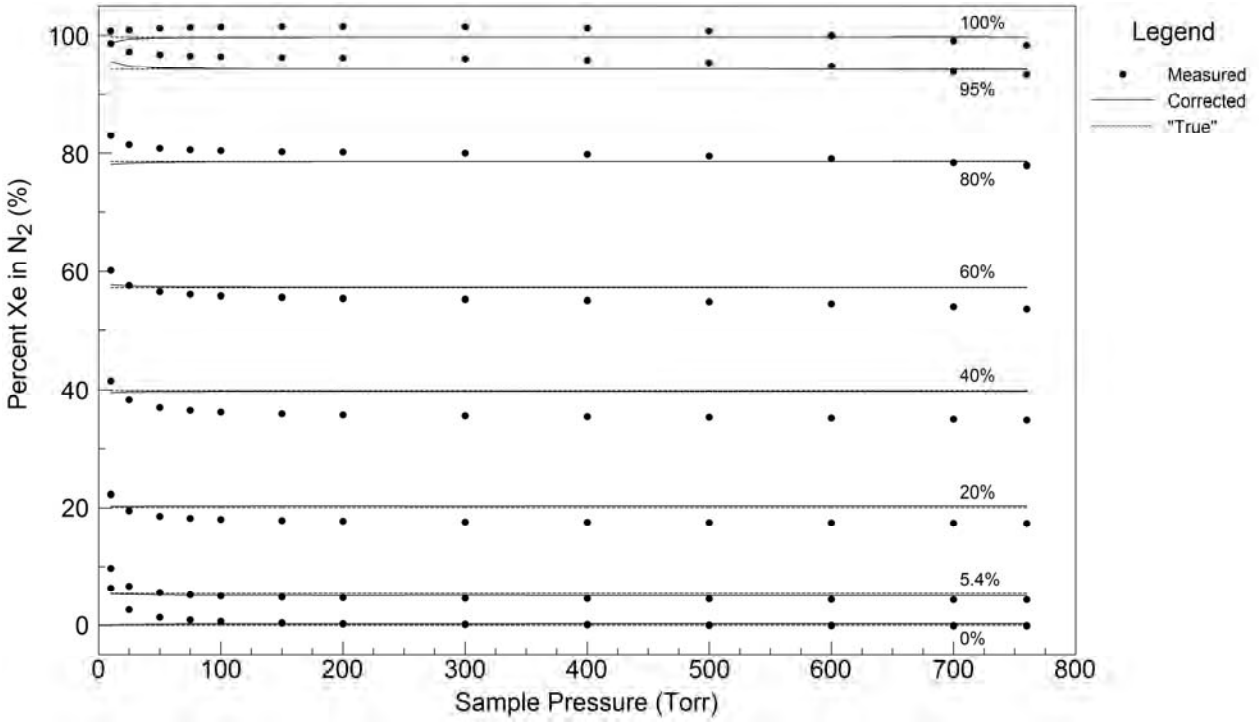

Figure 4: Comparison of raw TCD readings (dark circles), compensated readings (solid lines) and true values (dashed lines) for all the mixtures over the pressure range (10-760 Torr). The compensation removes both the pressure effect and the calibration offset error.

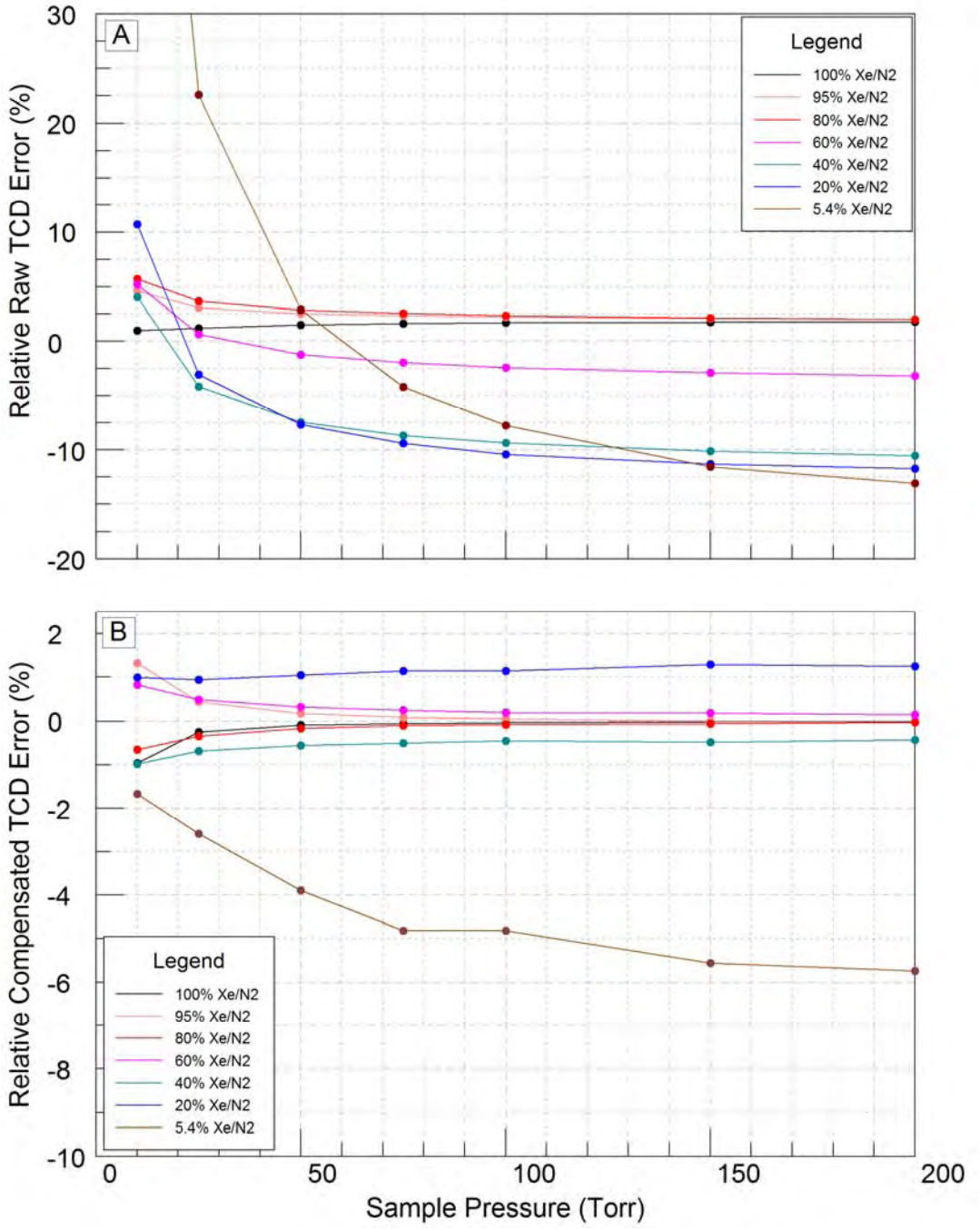

Figure 5. The relative accuracy error of the raw (uncompensated) TCD values as a function of pressure and composition is shown in the upper plot (5a). The relative accuracy error of the compensated TCD values is shown in 5b.

CONCLUSIONS AND RECOMMENDATIONS

It was shown that by carefully measuring the output of a thermal conductivity detector as a function of both percent composition of a binary mixture and absolute pressure, a calibration routine can be developed that extends the useful range of a standard TCD down to pressures of 10 Torr, with relative accuracy errors <1% for mixtures containing greater than 5-10% xenon in nitrogen. This approach allows for the use of standard TCD units in the accurate determination of % xenon in nitrogen in low-pressure gas samples, which have also been analyzed for radioxenon by nuclear methods.

REFERENCES

Hayes, J. C., K. H. Abel, T. W. Bowyer, T. R. Heimbigner, M. E. Panisko, P. L. Reeder, J. I. McIntyre, R. C. Thompson, L. C. Todd, and R. A. Warner (1999). Operations of the Automated Radioxenon Sampler/Analyzer—ARSA, in *Proceedings of the 21st Seismic Research Symposium: Technologies for Monitoring the Comprehensive Nuclear-Test-Ban Treaty*, LA UR-99-4700, Vol. 2, pp. 249–260.

Jitschin, W. and M. Ruschitzka (1993). Metrological properties of the thermal conductivity gauge, *Vacuum* 4: 607–609.

ATMOSPHERIC TRANSPORT MODELING AND DATA FUSION IN SUPPORT OF COMPREHENSIVE NUCLEAR-TEST-BAN TREATY VERIFICATION

Gerhard Wotawa and Andreas W. N. Becker

Provisional Technical Secretariat of the Preparatory Commission
for the Comprehensive Nuclear-Test-Ban Treaty Organization

ABSTRACT

Waveform signals can be processed to distinguish between explosions and natural events and can help locating explosion centers fast and with high accuracy. However, they cannot be used to demonstrate a possible nuclear nature for the event. This final proof can only be provided by detection of airborne radioactivity downwind of the event. To support the verification of the Comprehensive Nuclear-Test-Ban Treaty (CTBT) based on particulate radionuclide and noble gas monitoring in combination with seismic explosion location results, the Provisional Technical Secretariat (PTS) has developed the Atmospheric Transport Modeling (ATM) software.

The software receives as input weather analyses from two world-leading centers (European Centre for Medium-Range Weather Forecasts and US Center for Environmental Prediction) in near-real-time and with high resolution. The PTS then computes, 14 days backward in time, source-receptor sensitivity (SRS) fields for all radionuclide samples taken at its operating and non-operating (future) sites. The diagnostic Lagrangian particle diffusion model FLeXpaRT is utilized as transport code. The code simulates transport and diffusion in inverse (backtracking) mode. The simulated adjoint tracer is released at the exact location of the monitoring site from the end to the start time of the air sampling, and then re-sampled every three hours at the surface level (0–30 m) on a global grid up to 14 days backward. The resulting SRS fields (equivalent to concentration fields in forward simulations) are stored in a database and are available ahead of the measurement results. In case of qualified events, the PTS will have the opportunity to request SRS fields from all Regional Specialized Meteorological Centres (RSMCs) of the World Meteorological Organisation (WMO). The WMO has agreed to provide this support in near-real-time, and has included SRS fields as products in its global data processing and forecasting system (GDPFS), making it a world standard for backtracking computations beyond CTBT verification.

Based on the pre-computed SRS fields needed as input, the post-processing software WebGrape has been developed. If the user specifies a measurement scenario, WebGrape can correlate these measurements with resulting signals from all possible single grid-cell source scenarios ($1° \times 1°$, 3 hours) world-wide to identify consistent source locations of the detected radionuclides. Such results can easily be overlaid with information from seismic processing, for example seismic event locations and error ellipses, allowing fusion of, in space and time, the estimates from both technologies. If the user suspects a particular source scenario, WebGrape computes the world-wide measurement scenario that would result from his assumption. WebGrape does not require extensive computing resources, and results that would have required their own research project in the past are now available within minutes. The SRS concept allows for further post-processing efforts. SRS fields can easily be folded with gridded emission inventories available on the same grid. This provides an excellent method to verify, validate, and easily adapt emission inventories. Such methods may also be useful for the verifications of environmental agreements that ban or control the emission of certain trace gases.

OBJECTIVES

The major objective of the work presented was to create a fast, accurate, highly automated and standardized system that combines near-real-time weather and atmospheric transport information with monitoring results of radionuclides to allow (i) the assessment of consistent source locations based on anomalous measurements, (ii) the estimation of possible measurement signals caused by suspected events, and (iii) the fusion between events measured at radionuclide stations with seismic events. Regarding standardization, a key objective was to allow an easy integration of results from other centers. As far as user interaction is concerned, a key requirement was to integrate all results into a graphical tool to States Parties and PTS-internal users, where they could perform the analyses described in points (i)–(iii).

RESEARCH ACCOMPLISHED

Introduction

As discussed by Wotawa et al. (2003, 2006), Stohl et al. (2003), and Seibert and Frank (2004), the receptor-oriented concept of source-receptor sensitivity (SRS) is best suited to describe transport in relation to a fixed-location monitoring network, where the number of stations is much lower compared with the number of potential sources. To define SRS, let us consider the activity concentration, c, of one specific radionuclide measured within one sample taken during 24 hours at a radionuclide station. Then, c [Bqm^{-3}] can be expressed as the sum of the products of a spatial-temporal source field S [Bq] and a corresponding SRS field M [m^{-3}] at discrete locations (i,j) and time intervals n as follows:

$$c = \sum_{i,j,n} M_{ijn} S_{ijn} \tag{1}$$

SRS fields need to consider basic physical properties of the observed radionuclide(s) like dry and wet deposition. Radioactive decay does not need to be included; this can be done at the post-processing step (see below). Taking into account the uncertainty related to deposition, including but not limited to the uncertainty of precipitation analyses and computations, SRS fields are usually computed assuming passive tracer transport.

PTS Automated Atmospheric Transport Processing

The PTS routinely computes the SRS fields pertaining to all radionuclide (RN) samples by applying the Lagrangian transport model FLeXpaRT (Stohl et al, 1998, 2005) in backward (adjoint) mode using analyzed global meteorological data provided by the European Centre for Medium-Range Weather Forecasts (ECMWF) with a resolution of 1˚ × 1˚ and three hours, and by the U.S. National Centers for Environmental Prediction (NCEP) with a resolution of 1˚ × 1˚ and six hours. The SRS fields are pre-computed, i.e., available before the daily measurements have been analyzed. They are stored in a database. SRS fields are computed assuming passive tracer transport (no deposition, no decay). This implies that the fields are highly relevant for noble gas observations, but do not consider any removal in case of particulate RN observations.

Post-Processing of SRS Fields

Equation (1) can be easily generalized to a multi-measurement scenario c_k taking into account that the SRS fields M_{ijn} have to be computed for every sample k. SRS fields can be post-processed to predict all measurements based on an assumed (known) source scenario. This we call measurement scenario reconstruction. Or, alternatively, if we have a measurement scenario at hand, but no source scenario, we can go through all possible single-grid cell sources (same resolution as SRS grid) to compute $i \times j \times n$ possible measurement scenarios. These scenarios are then correlated with the real observations. Grid cells (in space and time) with high correlation values (r^2) are source locations that would be consistent with the measurements. The area with highest values of r^2 is therefore called the “Possible Source Region”. Due to the fact that SRS fields are pre-computed and readily available, post-processing results can be made available within minutes after a measurement scenario becomes known.

The concept has been extensively tested using available measurements outside the direct treaty verification domain. Among others, we utilized data from the European Tracer Experiment (ETEX). As part of the experiment, 340 kg of Perfluoromethylcyclohexane,C_7F_{14} (PMCH) were released from a stack in Monterfil, France between 23 October 1994 16:00 coordinated universal time (UTC) and 24 October 3:50 UTC (ETEX-1), and 490 kg of

Perfluoromethylcyclopentane, C_6F_{12} (PMCP) from November 14, 1994, 15:00 UTC to November 15, 2:45 UTC. PMCH and PMCP are passive tracers that were subsequently recorded at more than 150 sites all across Europe every three hours. To arrive at a spatial and temporal resolution comparable with the PTS monitoring system, PMCH/PMCP data were only used from a subset of five selected stations over Europe and were re-sampled to 12 hours. SRS fields were computed for the five selected locations and each re-sampled pseudo-sample. Source correlation analyses were done for ETEX-1 and ETEX-2 and yielded excellent (ETEX-1) and good results (ETEX-2) (see Figure 1). A measurement scenario reconstruction for ETEX-1 showed a good correspondence at all stations with the real measurements (Figure 2).

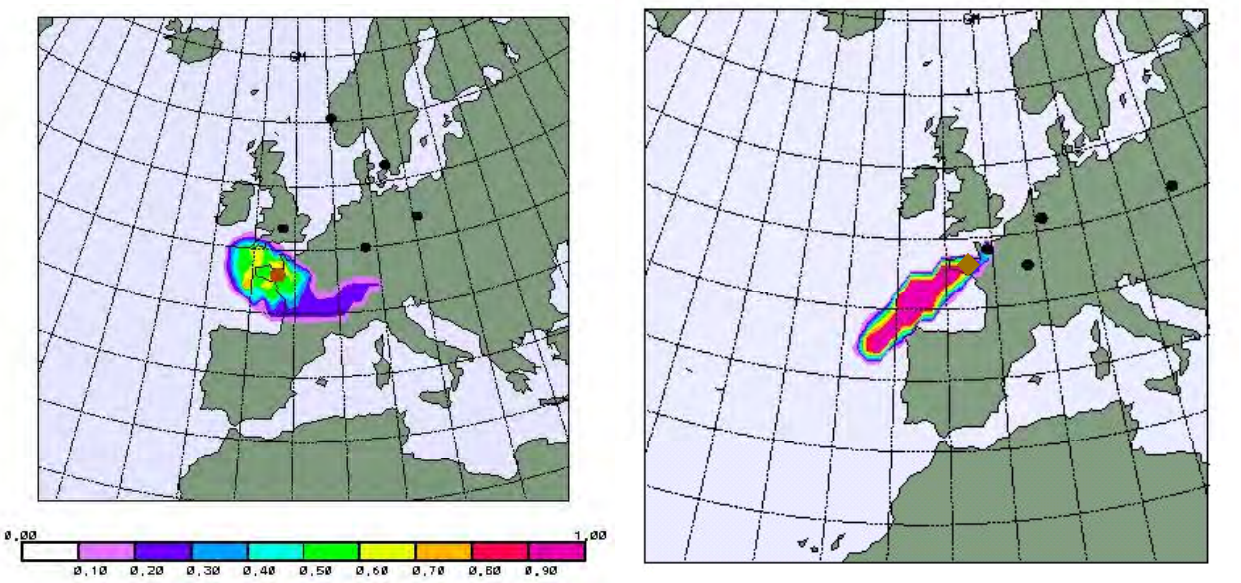

Figure 1. Source correlation results computed for the European Tracer Experiment (ETEX); Results for ETEX-1 (left; October 1994) have been compiled using PMCH data from five stations re-sampled to 12 hours, for ETEX-2 (right; November 1994) using PMCP data from four stations.

In April 1984, special measurements of radioactive cesium (^{137}Cs) were performed in Stockholm/Sweden immediately after the accident in the nuclear power plant (NPP) at Chernobyl, former Soviet Union, became known. We computed SRS fields for this monitoring site. A SRS-based measurement scenario reconstruction assuming a realistic source term showed strong correspondence in variance and level with the time-series of the measurements (Figure 3). A source correlation analysis yielded a possible source region that was confined around the NPP location (not shown here).

SRS fields can also be folded with gridded emission inventories that are available on the same grid to predict time series of measurements at one or more stations. This method has been applied to predict ^{137}Cs measured in Yellowknife based on an experimental emission inventory that was assumed to be proportional to the fire pixels in the boreal forest area recorded with the moderate-resolution imaging spectroradiometer (MODIS) instrument onboard the TERRA satellite. As a result, we found out that monthly averages of ^{137}Cs were predicted with impressive accuracy for two consecutive years, establishing the boreal forest as a significant source of the material through burning (see Wotawa et al., 2006). Furthermore, related bottom-up emission estimates based on these calculations confirmed and consolidated the emission values per area burnt as established in the literature for single cases during short time periods. As a second application, monthly averaged values of the radio-xenon isotope ^{133}Xe were predicted for Yellowknife and Spitsbergen. The emission inventory was estimated according to the geographical location of the NPP, and the emission terms were taken from a consolidated report. Differences in concentration levels at both sites could be explained, and it was shown that ^{133}Xe measured in the high latitudes is probably older than 14 days (see Saey et al., 2006).

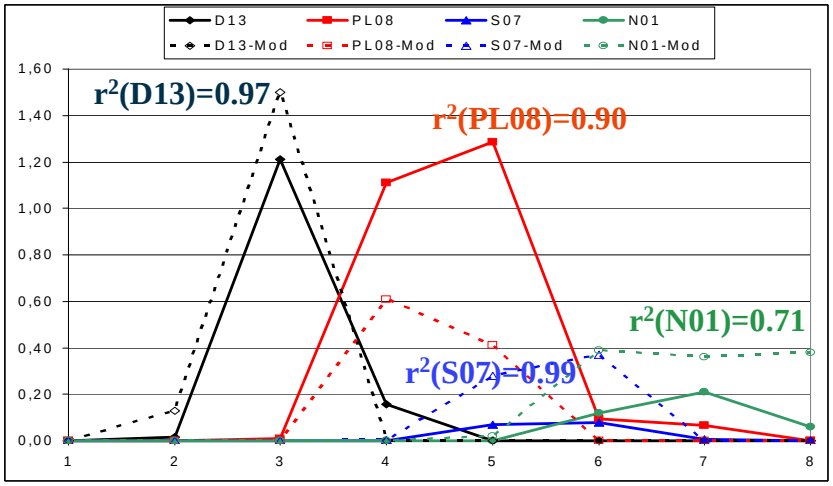

Figure 2. Reconstruction of PMCH measurements (ngm^{-3}) for the stations in Germany (D13), Poland (PL08), Sweden (S07) and Norway (N01) based on the SRS Fields and the known ETEX-1 release parameters (340 kg of PMCH released at Monterfil, France, 2.008˚ W, 48.058˚ N between October 23, 1994, 16:00 UTC and October 24, 3:50 UTC) and comparison with the real measurements. The time axis denotes the number of 12-hour intervals after October 24 0 UTC.

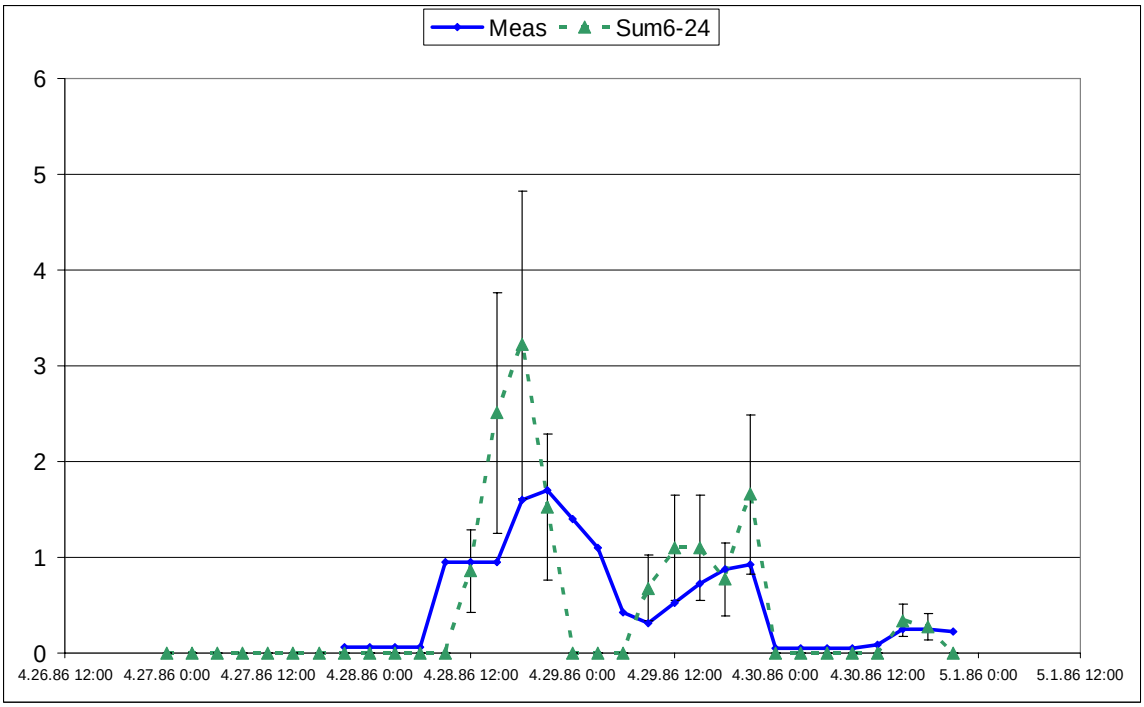

Figure 3. SRS-based reconstruction of ^{137}Cs measurements (Bqm^{-3}) for Stockholm, Sweden between April 26 and April 30, 1984, assuming a release of 1.5 10^{16} Bq of ^{137}Cs released at the Nuclear Power Station Chernobyl, former Soviet Union, on April 26, 1984, between 6 and 24 UTC; The reactor exploded on April 25 at about 21:23 UTC, releasing about 10^{17} Bq of ^{137}Cs in the following 2 weeks, with a delay of some 6-12 hours after the first explosion.

In October 2006, a SRS-based measurement scenario reconstruction was performed for Yellowknife, Canada, after the announced nuclear test in North Korea. We assumed a ^{133}Xe source term equivalent to a 1-kt underground nuclear explosion (1.3 10^{15} Bq) at the location of the seismic event within the closest 3-hour time window. The results predict a double-peak response in Yellowknife of about 0.5 mBqm^{-3} ^{133}Xe after 14–20 days. The

measurements in fact recorded a double-peak structure with a maximum of about 0.7 $mBqm^{-3}$, but two days earlier than predicted (Figure 4). After a transport of this distance, this is still a very interesting result.

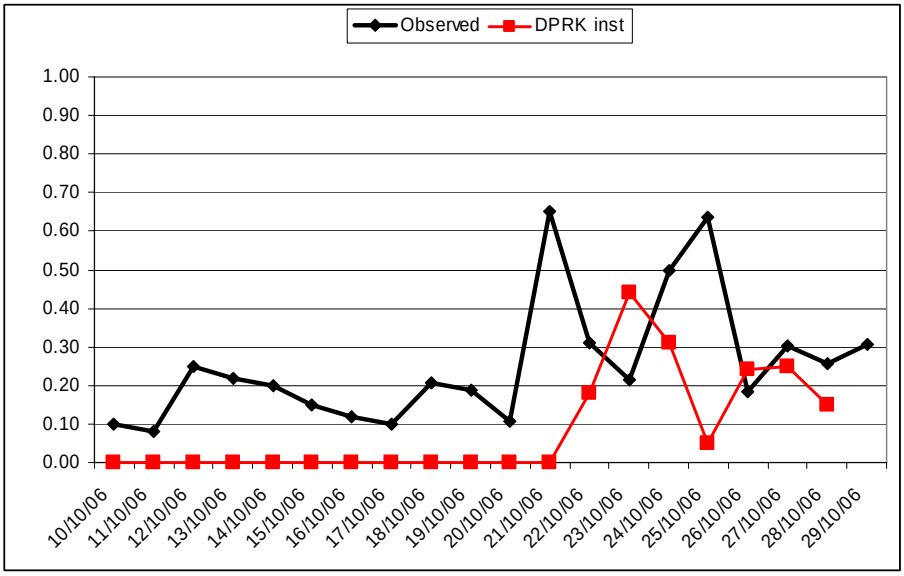

Figure 4. SRS-based reconstruction of ^{133}Xe measurements ($mBqm^{-3}$) for Yellowknife, Canada, between October 10 and 29, 2006, assuming a release of 1.3 10^{15} Bq of ^{133}Xe released at 129˚ E 41˚ N at October 9, 2006, between 0 and 3 UTC. At about 1:35 UTC an event on this location at the Korean Peninsula was recorded by the PTS seismic network.

To allow users from the PTS and all States Parties users (National Data Centers) to analyze and display Atmospheric Transport Modeling (ATM) results pertaining to the RN measurements, a graphical tool, WebGrape, has been developed. WebGrape reads in SRS fields from the internal database (in-house users) or from the PTS products web page (NDC users). The users can then display so-called “fields of regard” for a single measurement (the area of the globe where releases would influence the measurements; see Figure 5), they can define measurement values and perform source correlation computations, and they can also define a source scenario and get a list of affected measurements. All results can be overlaid with seismic locations and error ellipses from all available seismic bulletins, if these data are made available in a predefined format. The tool is still under development, and a beta version has been released to internal and external test users.

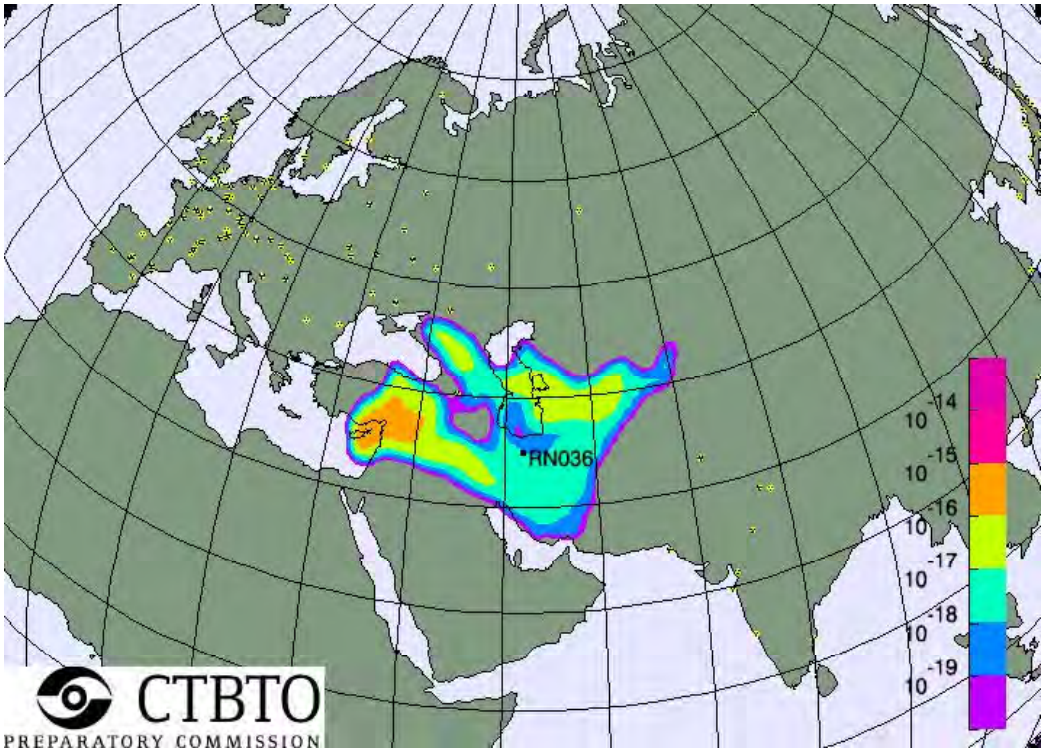

Figure 5. View from the graphical tool WebGrape (display of a so-called "field of regard" for the RN station RN036). This software helps users from the PTS and the National Data Centers to display and analyze atmospheric transport modeling results in connection with RN measurements. SRS-based source correlation analyses and measurement reconstructions can be performed, displayed and stored. The software works on every state of the art PC or Laptop.

International Backtracking Response System

Comprehensive Nuclear-Test-Ban Treaty Organization (CTBTO)/PTS and WMO have developed and tested a system where the PTS notifies WMO RSMCs in case of qualified RN events. The RSMCs then sends SRS fields calculated with their own models to the PTS. These SRS fields pertain to the RN samples under scrutiny (and typically also measurements from neighboring stations, depending on the PTS request) and. Details of the measurements are not exposed to RSMCs, only station coordinates and measurement times. WMO SRS fields supplement the PTS in-house computations, and can be imported into the WebGrape tool for further analysis.

The response system has been tested in two experiments (2003 and 2005). The experiments were based on a fictitious measurement scenario computed by means of a forward run with an ATM from an automatically chosen release location. The fictitious measurements served then as basis for the notification of the RSMCs. In both experiments, the multi-model average source correlation results were closer to the real release location compared with the source correlation results from all participating models. As in the emergency response field linked to forward modeling, this underpins once more the strength of the ensemble dispersion modelling (EDM) concept also in the backtracking domain (Becker et al., 2007).

At the meeting of the WMO Commission for Basic Systems in Seoul in November 2006, it was unanimously recommended that the CTBTO-WMO backtracking response system should be included in the WMO manual for the GDPFS. The recommendation stated that backtracking computations can be requested by the PTS related to the CTBT verification purposes, but also by any National Meteorological Service (NMS) for any other purpose. Format, communication, and procedures were taken as proposed by the PTS. A formal integration of the system into the PTS processing in case of a so-called Level-5 event in the particulate RN network (detection of more than one treaty-relevant RN) is expected later in 2007.

CONCLUSIONS AND RECOMMENDATIONS

The PTS successfully integrated the best available meteorological analysis data and state-of-the art ATMs in its automated processing to support the interpretation of RN monitoring results. Standardized SRS fields are computed and stored in near-real-time and before the related measurements are available. This allows to predict measurement scenarios based on release assumptions, and to perform source correlation calculations. A powerful post-processing tool is under beta-testing, which allows users to post-process and display the ATM results and to fuse ATM results with event locations and error ellipses from seismic bulletins. A CTBTO-WMO response system has been set up, that allows the PTS to request SRS fields from a number of WMO RSMCs spread all over the world to supplement its own computations. The related backtracking EDM system will greatly enhance the results from a technical viewpoint, but also increase the political acceptance due to the wide geographical spread of the contributors. It is recommended that this system be included in the standard processing as soon as possible, and also that the system be expanded to noble gas monitoring as soon as an appropriate noble gas event classification system is in place.

Further analyses are needed, especially in the noble gas area. Unlike in the particulate area, there is just limited experience with global monitoring of radio-xenon isotopes. The need for further studies includes the comparison of top-down with bottom-up emission estimates. Top-down estimates are based on reports from facilities and/or countries, while bottom-up estimates come from the measurements and the ATM computations. This is especially true for the isotope ^{133}Xe, where a hemispheric-scale background has been identified. To better interpret measurements and to develop a categorization scheme, the structure, frequency, and strength of the impact of known emitters to specific monitoring stations needs to be established and to be taken into consideration.

ACKNOWLEDGEMENTS

The ^{137}Cs data for Stockholm related to the Chernobyl accident have been made available by Lars-Erik De Geer, former PTS staff member, currently at the Swedish Defense Research Agency. The ETEX experiment has been conducted by the European Commission, and the data have been downloaded from the server of the Joint Research Centre Environment Institute.

REFERENCES

Becker, A., G. Wotawa, L.-E. De Geer, P. Seibert, R. R. Draxler, C. Sloan, R. D'Amours, M. Hort, H. Glaab, P. Heinrich, Y. Grillon, V. Shershakov, K. Katayama, Y. Zhang, P. Stewart, M. Hirtl, M. Jean, and P. Chen (2007). Global backtracking of anthropogenic radionuclides by means of a receptor oriented ensemble dispersion modeling system in support of Nuclear-Test-Ban treaty Verification, *Atmos. Environ.* 41: 4520, 4534.

Saey, P. R., G. Wotawa, L.-E. De Geer, A. Axelsson, M. Bean, R. D'Amours, K. Elmgren, J. Peterson, A. Ringbom, T.J. Stocki and R.K. Ungar (2006). Radioxenon background at high northern latitudes, *J. Geophys. Res.* 111: D17306, doi:10.1029/2005JD007038

Seibert, P. and A. Frank (2004). Source-receptor matrix calculation with a Lagrangian particle dispersion model in backward mode, *Atmos. Chem. Phys.* 4: 51, 63.

Stohl, A., M. Hittenberger, and G. Wotawa (1998). Validation of the Lagrangian particle dispersion model FLeXpaRT against large scale tracer experiment data, *Atmos. Environ.* 32: 4245, 4264.

Stohl, A., C. Forster, S. Eckhardt, N. Spichtinger, H. Huntrieser, J. Heland, H. Schlager, S. Wilhelm, F. Arnold, and O. Cooper (2003). A backward modeling study of intercontinental pollution transport using aircraft measurements, *J. Geophys. Res.* 108: 4370.

Stohl, A., C. Forster, A. Frank, P. Seibert, and G. Wotawa (2005). Technical note: The Lagrangian particle dispersion model FLeXpaRT version 6.2, *Atmos. Chem. Phys.* 5: 2461, 2474.

Wotawa, G., L.-E. De Geer, P. Denier, M. Kalinowski, H. Toivonen, R. D'Amours, F. Desiato, J.-P. Issartel, M. Langer, P. Seibert, A. Frank, C. Sloan, and H. Yamazawa (2003). Atmospheric transport modelling in support of CTBT verification—Overview and basic concepts, *Atmos. Environ.* 37: 2529, 2537.

Wotawa, G., L.-E. De Geer, A. Becker, R. D'Amours, M. Jean, R. Servranckx, and K. Ungar (2006). Inter- and intra-continental transport of radioactive cesium released by boreal forest fires, *Geophys. Res. Lett.* 33: L12806, doi:10.1029/2006GL026206.

Infrasound Monitoring

INFRASOUND MONITORING OF LOCAL, REGIONAL AND GLOBAL EVENTS

Stephen J. Arrowsmith and Douglas O. ReVelle

Los Alamos National Laboratory

Sponsored by National Nuclear Security Administration
Office of Nonproliferation Research and Development
Office of Defense Nuclear Nonproliferation

Contract No. DE-AC52-06NA25396

ABSTRACT

Methodologies for the detection, association, location and identification of infrasound sources at local, regional and global distances are discussed. In the first part of this paper we apply a new regional monitoring method to data from the Washington State seismo-acoustic network and identify 206 local and regional infrasonic events in a dataset comprising 28 days of data. We detect multiple signals from mining explosions at two sites in Washington State, including 5 events that were recorded in a regional seismic bulletin. We also automatically detect and associate signals from the March 9th 2005 eruption at Mount Saint Helens, and locate the event to be within 5 km of the caldera. The second part of this paper outlines a technique for identifying infrasound signals from large known events on a global scale. We apply the technique to data from International Monitoring System (IMS) infrasound arrays for three super-bolides occurring on September 3rd, 2004, over Antarctica; on October 7th, 2004, over the Indian Ocean; and on December 9th, 2006, over North Africa. For each bolide we observe signals at multiple infrasonic arrays, with observations at ranges from ~1,000 to ~13,000 km. We investigate the causes of the asymmetric distributions of observations and show that site-noise is a dominant effect up to a range of ~10,000 km. We discuss how the preliminary work outlined in this paper provides important constraints for the purpose of event identification at local, regional and global distances. For large events, we outline how the synthesis of local, regional and global infrasonic data would provide the optimum dataset for event location and identification.

OBJECTIVES

This research encompasses four objectives, as follows.

1–Development of Automatic Local and Regional Infrasound Monitoring Tools

The objective of the first part of this study is to develop a suite of automatic local and regional infrasound monitoring tools. The separate algorithms, which broadly comprise detection, association, location, and identification algorithms, will be integrated into a fully-automatic infrasound monitoring package.

2-Assessment of Infrasound Events in Washington State

The second objective is to apply the infrasound monitoring algorithms to data from the Washington State seismo-acoustic network, which is jointly operated by the University of California at San Diego and the Geological Survey of Canada.

3-Development of a Global Event-Based Infrasonic Association Tool

The third objective is to develop an event-based algorithm for associating infrasound detections at IMS infrasound arrays with known events on a global scale.

4-Assessment of the Global Infrasonic Detection of Three Superbolides

The final objective is to test the event-based global association tool by applying it to three superbolide events.

RESEARCH ACCOMPLISHED

1-Development of Automatic Local and Regional Infrasound Monitoring Tools

In this section we provide a broad summary of the development of regional infrasonic detection, association, location, and identification algorithms to date. Further details on each methodology will be provided in future publications.

The development of an automatic infrasonic detection algorithm is at an early stage. We are currently working on comparing existing detection algorithms (e.g., f-statistic and correlation-based methods) using real signals, and on developing a novel multivariate infrasonic detection algorithm.

To date, the bulk of work under this objective has been on developing a regional infrasound association tool. The input data to this tool are a set of infrasonic detections of arrivals at multiple spatially-separated arrays. The association algorithm is comprised of two main parts: (1) the association of separate phases from the same event at an individual array, and (2) the association of events at multiple spatially-separated arrays. We term these two components “phase association” and “event association” respectively. Due to the complexity associated with the explicit identification of an infrasonic phase based on the propagation path (Brown et al., 2002), we have developed an algorithm to identify two types of phases: first arrivals and later arrivals. A given event can then produce a single first arrival and N later arrivals at a particular infrasound array. There are three criteria used to determine if a given arrival is associated with an earlier arrival: (1) Arrival time (i.e., the difference in arrival time should be less than some threshold), (2) Backazimuth (i.e., the difference in backazimuth should be less than some threshold), and (3) Event duration (i.e., each event, which comprises a first arrival and N later arrivals ($N \geq 0$), should not exceed a threshold duration at an individual array). If an individual arrival is not associated with any preceding arrivals, it is automatically flagged as a first arrival (“I”), otherwise it is flagged as a later arrival (“Ix”). An obvious limitation of this technique is for highly repetitive sources where separate events will be associated, leading to an underestimation of the total number of events. However, a side benefit is the identification of highly-repetitive sources, which are associated with large numbers of later arrivals.

For event association we use a grid-search algorithm to identify events (i.e., groups of “I” arrivals at the different arrays that are associated). To this end, an irregularly spaced geographic grid is constructed that covers the region of interest (e.g., Figure 1 shows the grid that was constructed for monitoring the Washington State region). The spacing

between grid nodes is chosen based on the event localization resolution of the infrasound network. For each grid node location we compute a set of great-circle backazimuths (at each array) and maximum and minimum delay times (between each pair of arrays). We then apply a grid-search procedure, where we perform a for-loop over each grid node location and search for groups of "I" arrivals where the observed delay-times and backazimuths are consistent with the given grid node.

The event location method that we have developed to date assumes a uniform atmosphere. Further development will allow for the use of 3D atmospheric models. Event locations are obtained using a least squares strategy, where an initial guess of the event location (taken from the backazimuth intersection point for two arrays) is refined in an iterative fashion. We compute error ellipses following the procedure of Flinn (1965), where the partial derivative matrix relates an east-west or north-south deviation to a change in the backazimuth recorded at the array.

The development of a regional infrasonic discrimination/identification algorithm is in its early stages. At present, we are working on identifying common characteristics within clusters of events, and using this information as a preliminary constraint on event identification. However, we will focus more on this problem in the future, building on work by ReVelle (2006).

2-Assessment of Infrasound Events in Washington State

We have applied automatic infrasound detection, association, and location algorithms to data from the Washington State seismo-acoustic array (Figure 1). To date, we have utilized the PMCC infrasonic detector (Cansi, 1995) for automatic detection of events. The PMCC detector has been fully integrated into our automatic processing scheme. However, we plan to integrate the new multivariate detector into the processing scheme following further development and comparison with existing detectors.

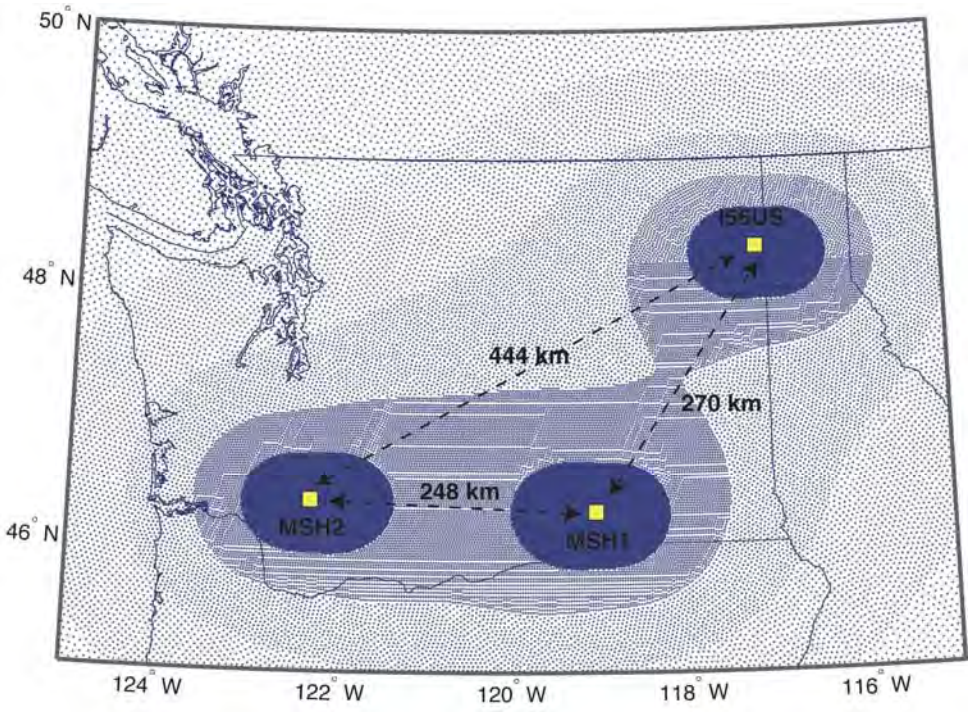

Figure 1. Map showing the locations of three seismo-acoustic arrays from the Washington State seismo-acoustic network. Great-circle distances between each array are displayed. Grid nodes used in the grid-search algorithm are denoted by pixels.

The detection and association algorithms were applied to 28 full days of data at MSH1, MSH2 and I56US. We selected days to study between November 1st 2004 and March 17th 2005, during which known events with the potential for generating infrasound occurred. The known events comprised 27 mining explosions (which were listed in the Pacific Northwest Seismic Network (PNSN) bulletin, with magnitudes from 2.0 to 3.1) and a large eruption of Mount Saint Helens on March 9th 2005, which is documented by Matoza et al. (2007). Figure 2 shows locations of

the 206 infrasound sources that were obtained after applying the detector and association algorithms to the data at two stations only: MSH1 and MSH2. Each grid node used in the association algorithm is color-coded by the number of events that it is associated with (with hot colors indicating larger numbers of events). This figure provides a useful indication of the locations of sources of infrasound in Washington State and the surrounding region. Since these data were obtained during winter months, most sources are located to the west of the network (downwind of the dominant stratospheric wind direction). The details of the figure are sensitive to two free parameters for matching predictions at each grid-node with observed detections: the allowed deviation in backazimuth, and the allowed range of group-velocities (or "celerities"). The choice of these parameters is made by tuning the algorithm using known events, but this is beyond the scope of this summary paper.

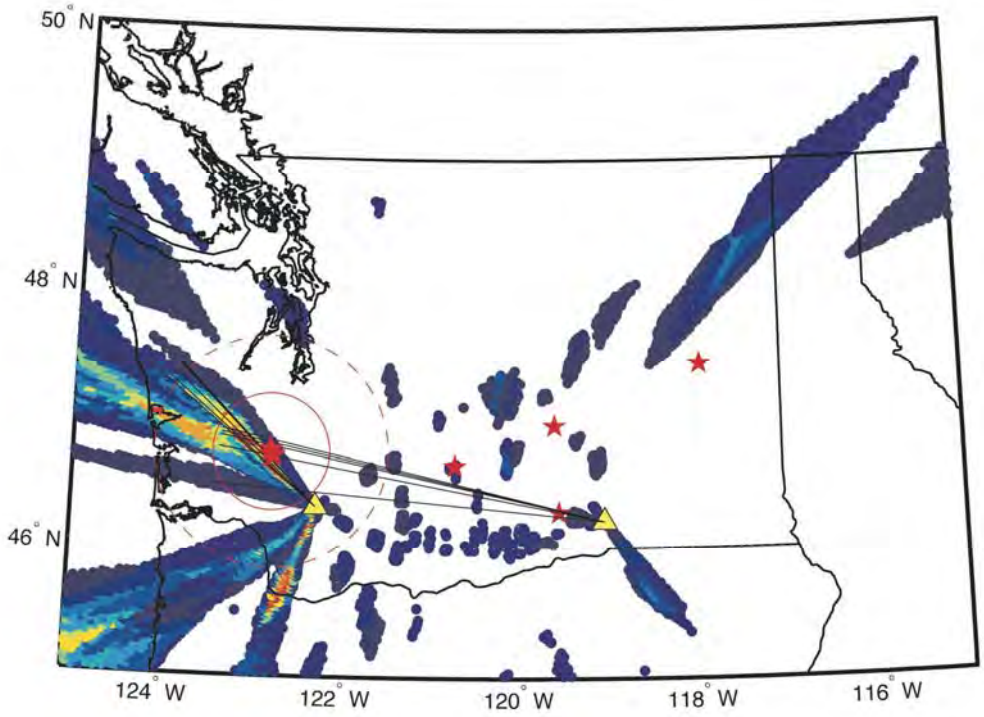

Figure 2. Map that shows the grid nodes that are associated with events recorded at two of the three infrasonic arrays (MSH1 and MSH2) shown in Figure 1. Each grid node is color coded by the number of events associated with that given location. Red stars denote the locations of mining explosions in the PNSN seismic catalog. The solid red circle denotes a range of 50 km from the most active mine (comprising > 20 events), while the dashed red circle denotes a range of 100 km. Solid black lines denote the backazimuths of signals at MSH1 and MSH2 that are associated with known mining explosions.

Figure 2 demonstrates that the automatic algorithm has successfully detected a number of signals from the active mine at ~ 46.7°N, 122.8°W. In total there are 13 events located within 50 km of the active mine (i.e., within the solid red circle), 5 of which can be directly tied to specific mining explosions in the seismic event bulletin. There are also some additional repeating sources that are picked up, for example there are several events that appear to come from the Portland area (located to the SSW of MSH2 near the state boundary). However, it is beyond the scope of this preliminary survey to discuss these signals in detail.

Figure 3 shows the infrasonic waveforms corresponding to the 5 mining explosions listed in the seismic bulletin that were detected at MSH1 and MSH2. Each signal is impulsive, clearly visible above the noise, and can be easily separated from the background "clutter" at each site.

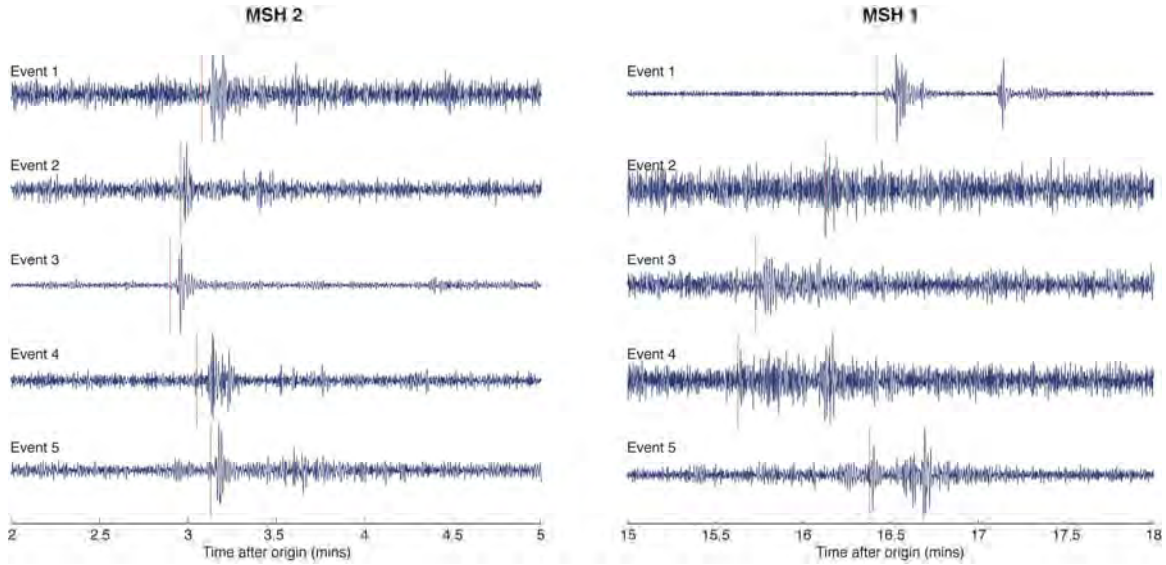

Figure 3. Infrasonic waveforms (band-pass filtered from 1 – 5 Hz) for each of the 5 ground-truth mining events that were automatically detected and associated at arrays MSH1 and MSH2. Red lines denote automatically picked arrival times.

None of the mining explosions that were detected at MSH1 and MSH2 (Figures 2 and 3) were also detected at I56US. Furthermore, despite a total of 206 events being detected at MSH1 and MSH2 ("two-station events"), there was only 1 three-station event that was detected at all three sites. However, the single event that was detected and associated automatically at all three sites was a known eruption of Mount Saint Helens. The infrasound signals from this event at MSH1 and MSH2 have been previously documented by Matoza et al. (2007), but the event was also recorded clearly at I56US. Figure 4 shows the locations of specific grid nodes that were associated with this event (un-associated nodes are not plotted). It is clear that the automatic procedure has been very successful in locating this event, as all three grid nodes are located within 5 km of the center of the caldera at Mount Saint Helens.

Figure 4. Locations of grid nodes that were automatically associated with detections at MSH1, MSH2 and I56US for the eruption of Mount Saint Helens on March 9th, 2005. The locations are superimposed on a satellite photograph, and are located within 5 km of the center of the caldera.

3-Development of a Global Event-Based Infrasonic Association Tool

Given the origin time and location for a large event, we have developed an automatic procedure for identifying associated infrasound signals at IMS stations on a global scale. The focus here is on "telesonic" events, rather than regional infrasonic events. The motivation for this portion of the study was provided by Wexler and Hass (1962) who documented the global detection of infrasonic signals from a nuclear explosion on October 30th 1961 as well as the detection of the Great Siberian bolide (Tunguska) that occurred on June 30, 1908. The first stage in the algorithm we have developed identifies signals at IMS stations that occur within a specified time of the event, and within a specified azimuthal-deviation from the great-circle path. The allowed times are calculated based on typical infrasonic group velocities (Ceplecha et al., 1998), and the allowed azimuthal-deviations are based on an empirical relation calculated for known explosions. Infrasound signals at each station are detected using the PMCC method (Cansi, 1995). The second stage removes signals at each station that are: (a) short-duration and narrow-band, and (b) occur at similar backazimuths to highly repetitive sources that also generate signals outside the range of possible arrival times for the given event. Test (b) utilizes backazimuth, frequency, trace velocity, arrival time, and the number of similar detections as criteria for rejecting detections. Such detections are typically either associated with small (local) events or repetitive sources near a given station.

4-Assessment of the Global Infrasonic Detection of Three Superbolides

We have applied the global infrasonic detection algorithm to three superbolide events, which occurred on September 3rd, 2004 over Antarctica, on October 7th, 2004 over the Indian Ocean, and on December 9th, 2006 over North Africa. Figure 5 shows the locations of stations that detected the Antarctic event (after applying the global event association method described above). Similar plots were obtained for the two other events but are not presented here. The most significant results are the large numbers of stations that detect each event (6 stations for Event 09/03/04, 6 stations for Event 10/07/04, and 6 stations for Event 12/09/06), and the strongly asymmetrical distributions of observations. To provide further confidence that the detections are correctly associated, we have reapplied the global event association method to the same three events, but using arbitrary origin times (i.e., simply changing the origin time by 24 hours). We find that in each case we observe *at least* 66% more associated detections for the real event origin time. This provides confidence that the majority of the detections are correctly associated. Table 1 provides a summary of the associated infrasonic detections for each of the three superbolides.

Whether or not a given station detects an event appears to be strongly governed by factors other than range. In particular, two factors that influence the detectability of infrasound from an event are: (1) ambient noise levels at a given station, and (2) propagation effects. In order to assess the importance of ambient noise levels on the signal detection, we have computed pre-event noise spectra for each station. Each power spectrum was computed for a beamformed waveform at each array using a time window of ~ 1 hour (i.e., 2^{16} data points), and smoothed by averaging the power spectrum over 1/8 octave intervals. The resultant power spectra for stations at ranges less than 10,000 km are plotted in Figure 6. The plot demonstrates that for two events (Events 09/03/04 and 10/07/04), there is a clear separation between noise-levels at stations that detected the event and stations that did not detect the events. In fact, for these two events the difference in noise levels between stations that detected the events, and stations that did not, is approximately 20 dB on average. This suggests that site-noise effects play a dominant role on the detectability of infrasound from such large events. We note that such a separation is not observed for more distant stations (>10,000 km), suggesting that propagation effects may dominate noise effects at larger ranges. This observation is somewhat surprising as we generally expect smaller amplitudes at greater ranges, which would be more sensitive to corruption by noise.

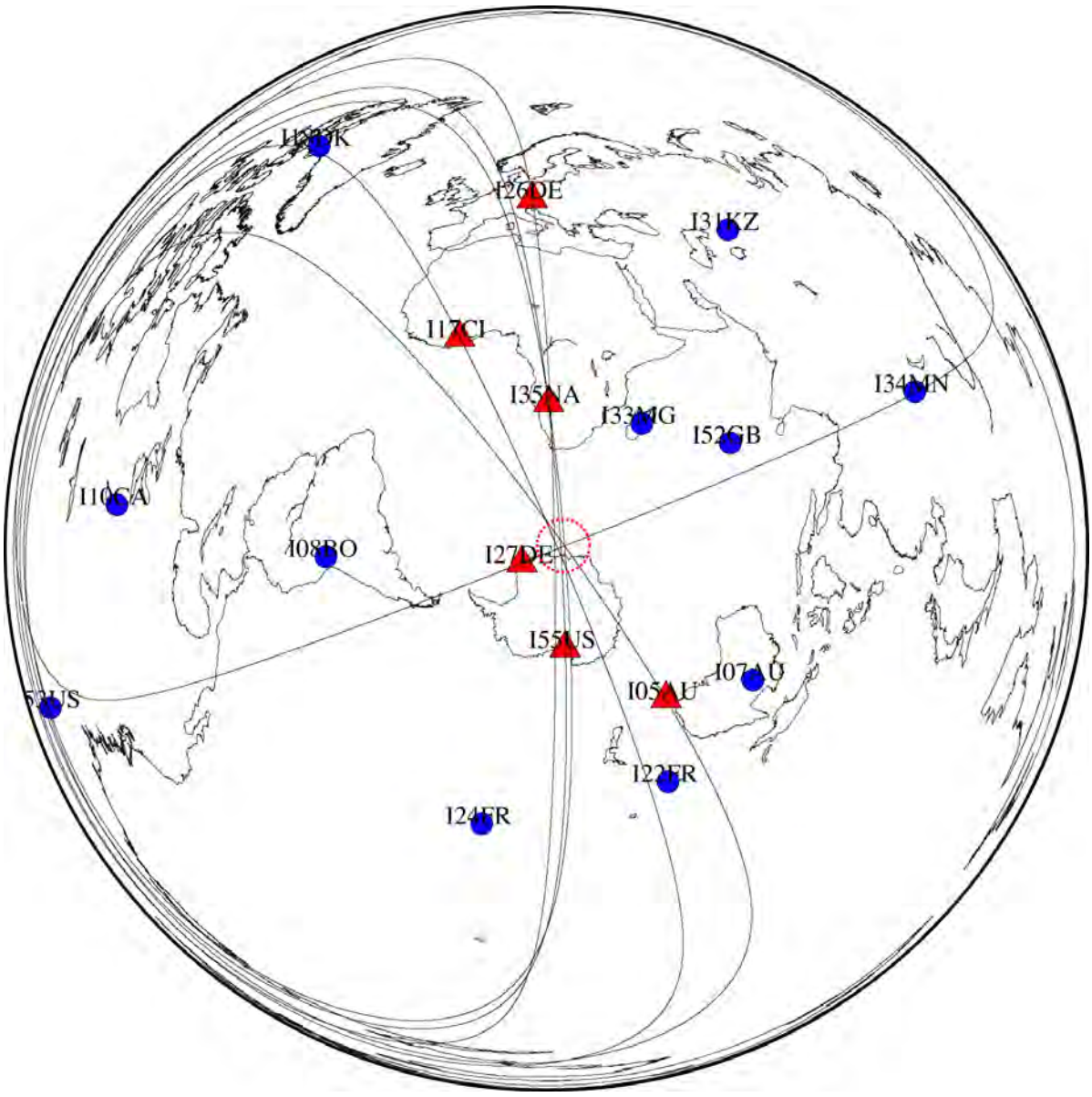

Figure 5. Azimuthal equidistant projection showing stations that detected the 09/03/04 Antarctic event (red triangles) and stations that did not (blue circles). The event was determined to be located in the center of the dashed red circle based on satellite observations. The plotted great-circle paths show the backazimuths of observed signals at each array projected back towards the source location.

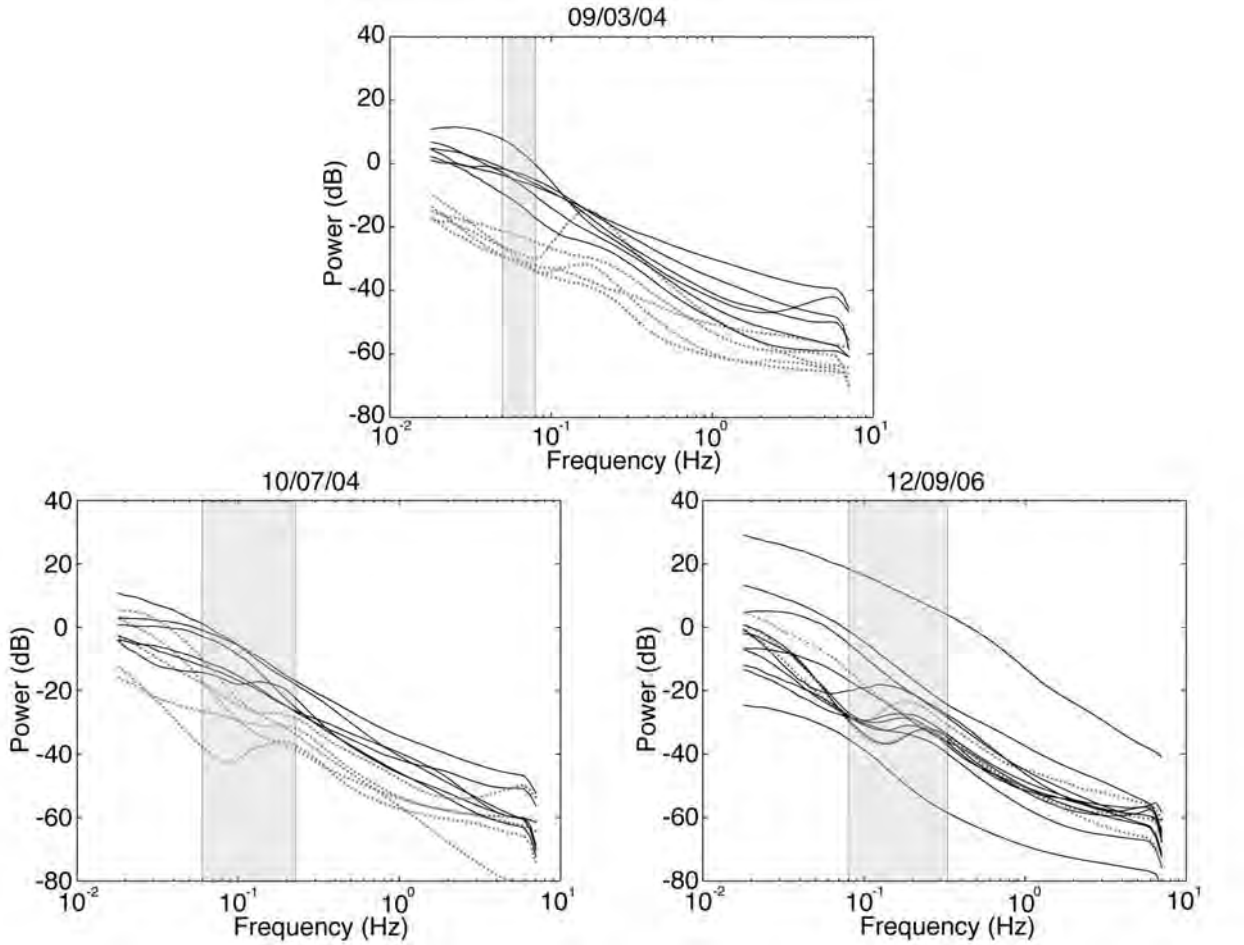

Figure 6. Noise spectra for each of the three bolides. Solid black lines denote spectra for stations that did not detect the events and gray dashed lines denote spectra for stations that did (for stations at ranges less than ~10,000 km). Regions shaded gray denote the frequency band over which detections were observed from each bolide.

CONCLUSIONS AND RECOMMENDATIONS

This paper comprises two main parts: The first part addresses local/regional infrasonic monitoring, and the second part addresses global infrasonic monitoring. In each case we outline new algorithms for detecting and associating infrasound signals from events of interest. We then apply the techniques to a regional dataset in Washington State and to global data from the IMS infrasound array. In the first case we detect, associate and locate 206 events in the Washington State region for a dataset comprising 28 days, and in the second case we identify multiple signals from large events at ranges of up to ~13,000 km, and comment on the factors that influence the detectability of these events. The two cases have slightly different applications: the local/regional monitoring algorithms are fully automatic and will be applicable to processing real-time data, while the global algorithms are event-based and focused on known events of interest. However, both cases will be complementary for the case of large events that are detected at a regional scale, which can provide a seed origin time and location for searching for global "telesonic" infrasound. In a nuclear monitoring regime, the use of both local/regional and global data will provide an optimum dataset for event location and identification, particularly where regional data is sparse.

ACKNOWLEDGEMENTS

We thank Rod Whitaker for his valuable insights and comments, Michael Hedlin for providing the Washington State data at very short notice, Brian Stump and Chris Hayward for their continuing help and contribution, George Randall for his moral support and scientific contributions, Steve Taylor for his statistical insights and Wayne Edwards and Peter Brown for their contribution to the global part of this study.

REFERENCES

Brown, D. J., C. N. Katz, R. Le Bras, M.P. Flanagan, J. Wang, and A. K. Gault (2002). Infrasonic Signal Detection and Source Location at the Prototype International Data Center, *Pure Appl. Geophys.* 159: 1081–1125.

Cansi, Y. (1995). An automated seismic event processing for detection and location: The P.M.C.C. method, *Geophys. Res. Lett.* 22: 1021–1024.

Ceplecha, Z., J. Borovicka, W.G. Elford, D.O. ReVelle, R.L. Hawkes, V. Porubcan, and M. Simel (1998). *Meteor Phenomena and Bodies*, Space Science Reviews 84: 327–471.

Flinn, E.A. (1965). Confidence Regions and Error Determinations for Seismic Event Location, *Reviews of Geophysics* 3: 157–185.

Matoza, R.S., M.A.H. Hedlin, and M.A. Garces (2007). An infrasound array study of Mount St. Helens, *Journal of Volcanology and Geothermal Research* 160: 249–262.

ReVelle, D.O. (2006). Earthquake depth predictions using infrasonic waves, these Proceedings.

Wexler, H. and W.A. Hass (1962). Global Atmospheric Pressure Effects of the October 30, 1961, Explosion, *J. of Geophysical Research* 67: 3875–3887.

Table 1. Summary of associated detections at IMS infrasound arrays for the three superbolide events.

Event	Array	Range (km)	Arrival time (UT)	Duration (s)
09/03/04	I27DE	1044	13:15:25	1300
09/03/04	I55US	3743	15:50:03	1565
09/03/04	I35NA	5390	17:20:45	1650
09/03/04	I05AU	7114	18:47:55	1900
09/03/04	I17CI	8423	20:26:15	2550
09/03/04	I26DE	12918	00:27:45 (on 09/04)	2000
10/07/04	I52GB	2201	15:50:50	540
10/07/04	I32KE	4679	17:38:50	80
10/07/04	I55US	7204	20:01:15	1250
10/07/04	I17CI	9001	21:45:50	100
10/07/04	I26DE	10182	23:02:55	6150
10/07/04	I10CA	17241	06:17:55 (on 10/08)	1700
12/09/06	I26DE	2727	06:08:43	750
12/09/06	I35NA	5094	11:40:30	1360
12/09/06	I30JP	10320	15:13:30	70
12/09/06	I41PY	10632	16:05:20	110
12/09/06	I56US	10979	20:11:20	70
12/09/06	I04AU	11629	16:57:50	150

Footnote: The signal durations observed for these three superbolides do not increase as a function of range, as would be predicted theoretically. We speculate that the reason for this discrepancy is due to site noise, which degrades the signal detectability at each site.

ADVANCES IN INFRASOUND TECHNOLOGY WITH APPLICATION TO NUCLEAR EXPLOSION MONITORING

Douglas R. Christie, Brian L. N. Kennett, and Chris Tarlowski

Australian National University

Sponsored by Air Force Research Laboratory

Contract No.: FA8718-04-C-0032

ABSTRACT

The principal goal of this investigation is to develop new techniques that will enhance the use of infrasound for the detection, location, and discrimination of atmospheric nuclear explosions at stations in the global infrasound monitoring network. This work is focused primarily on two important problems. The first is concerned with limitations imposed on array detection of explosion-generated infrasound by the loss of signal correlation between elements in large sparse arrays, and the second encompasses the long-standing problem in the field of infrasound monitoring of unacceptably high levels of background noise caused by wind-generated turbulence. This study is also concerned with the identification and classification of the fundamental physical processes that result in background noise at all frequencies at infrasound monitoring stations. The results of this study are based on a thorough analysis of a large infrasound database comprising six years of archived data from IS07 Warramunga in northern Australia, three years of archived data from IS05 Hobart in Tasmania, a one-year archive of data from IS04 Shannon in southwest Australia, shorter periods of selected data from other International Monitoring System (IMS) infrasound stations and data collected during a number of field experiments in Australia using a portable infrasonic array.

The study of the spatial correlation properties of infrasound signals has shown that a low degree of signal correlation can seriously limit the reliable detection of infrasound generated by distant explosions in the primary monitoring passband (0.4 to 1.5 Hz) at a number of sparse IMS arrays with widely separated array elements. We have, however, found that the currently accepted parameters that are used in the standard theoretical description of infrasound signal correlation lead to predictions for signal correlation that are less than the observed values. The model parameters have therefore been refined to give a theoretical description that is in better agreement with observations. We have also extended the calculations of the predicted variation of array-averaged signal correlation as a function of azimuth and frequency to a number of typical IMS array configurations with a large number of elements. A comparison of these results with observations suggests that the performance of some monitoring stations with non-standard array configurations may be limited at higher frequencies by signal correlation problems.

Considerable progress has been made on the development of a noise-reducing system that can strongly attenuate, and in some cases, effectively eliminate wind-generated background noise in the monitoring passband at infrasound monitoring stations. Wind-generated noise is a serious problem, especially during the daytime, at many infrasound stations. Work on wind-noise reduction in the past has been primarily concerned with the development of improved wind-noise-reducing pipe-array systems. It is clear that further refinements to these pipe-array systems will not lead to a significant improvement in wind-noise-reducing capability since the size of these arrays and the number of inlet ports have reached practical limitations. We have therefore developed a new type of wind-noise-reducing system that mechanically attenuates and transforms turbulent eddies that generate noise in the primary monitoring passband. The design and performance of a wide variety of these turbulence-reducing systems is given in this paper along with recommendations for the use of these systems. The latest version of this system has proven to be very effective. Indeed, tests of this system have shown that this system almost completely eliminates wind noise in the primary monitoring passband under typical daytime wind conditions at an unsheltered semi-desert site. In addition, we have found, in some circumstances, that these turbulence-reducing enclosures may be used with only a single inlet port as effective stand-alone wind-noise reducing systems that do not require a pipe array.

OBJECTIVES

The primary objectives of this research project are to identify problems with the detection of atmospheric nuclear explosions at infrasound monitoring stations and to develop techniques using infrasound technology that will enhance detection capability for regional and distant nuclear explosions in the atmosphere.

This project is concerned with an investigation of the monitoring capability of infrasound stations in the global network with special attention devoted to the detection of explosions that occur over the vast open ocean areas in the Pacific and Indian Oceans. The monitoring stations that surround these remote areas need to have good detection capability for explosions at distances of up to at least 4500 km in order to achieve reliable two-station detection capability for 1kiloton explosions.

RESEARCH ACCOMPLISHED

Introduction

Much of the research in this project is based on a survey of signal detection capability and background noise characteristics of certified Australian IMS monitoring stations (see Figure 1). This survey has highlighted three important problems that may limit the performance of stations in the global monitoring network:

a) Distant explosions may be detectable only as longer period signals (Christie et al., 2005a) when wave propagation is restricted to a thermospheric waveguide. It is therefore essential to ensure that routine data analysis procedures include a search for longer period signal components at frequencies below the microbarom passband. Problems associated with the decay of higher frequency signal components at a given station will depend on the location and distance to the source and the seasonal waveguide characteristics between the source and the monitoring array.

b) The optimum monitoring passband (Christie et al. 2005b; 2006) for stratospheric arrivals from regional and distant explosions is generally limited to a frequency range extending from about 0.4 Hz to slightly above 1.0 Hz. The lower frequency limit depends on the intensity of microbarom infrasonic signals and the high frequency limit is determined by both spatial aliasing of higher frequency signals and problems with signal coherence between array elements. The detection of higher frequency signals depends critically on the design of the array configuration. Spatial aliasing problems can be eliminated by using an eight- or nine-element array configured in the form of a logarithmic spiral or in the form of a larger aperture pentagon array with a smaller aperture triangular sub-array (or centered triangle sub-array) located at the center of the main array. Signal coherence between array elements at higher frequencies also depends on the array configuration. Results obtained to date have shown that detection capability for regional and distant explosions at existing monitoring stations with a small number of array elements and a large aperture will be marginal due to the low degree of signal coherence between array elements. The study of signal coherence is proving to be a fairly complex subject. The goal of this part of the project is to provide an accurate signal coherence model that can be used to optimize the array design at infrasound monitoring stations.

c) Wind-generated background noise is by far the most important technical issue in the field of infrasonic monitoring. More than half of the stations in the global monitoring network are subject at times to unacceptably high levels of wind-generated background noise. It is clear that the development of a system that will significantly reduce and possibly eliminate wind-generated noise at infrasound monitoring stations would greatly enhance the performance of the IMS infrasound monitoring network and would lower the global monitoring threshold. The use of an effective and reliable wind-noise suppressing system at IMS infrasound stations would probably result in three-station detection capability for 1 kiloton explosions at most stations in the global network. Global three-station detection capability is desirable since this would significantly improve the reliability of the network and would greatly enhance location capability. Results from the new type of wind-noise-reducing system described in this paper suggest that the use of this noise-reducing-system, either as a stand alone system or in conjunction with existing pipe arrays, can substantially reduce wind-noise levels in the primary monitoring passband. In view of the overall importance of the wind-noise problem to the field of infrasound monitoring, a major part of this paper will be devoted to a description of the design and evaluation of the new type of wind-noise-reducing system.

Spatial Correlation of Explosion-Generated Infrasonic Signals at IMS Infrasound Monitoring Stations

The array configuration at the three certified IMS infrasound stations on Australian territory, IS04 Shannon in the southwest corner of Australia, IS05 Hobart near the east coast of Tasmania and IS07 Warramunga in the Northern Territory, are compared in Figure 1. The aperture of each of the arrays illustrated in Figure 1 is approximately the same and the configuration at each array includes both a large aperture main array and a small aperture sub-array. However, the array configurations at these stations differ substantially. The small aperture sub-array at IS07 is located at the center of the larger aperture main array. In contrast, the small aperture sub-arrays at IS04 and IS05 are located outside the area of the larger aperture array. The unusual array configurations at IS04 and IS05 were determined by the available land area and problems with the supply of power to the array elements. The design of the array configurations at IS04 and IS05 is not ideal and signal correlation problems could lead to reduced detection capability at higher frequencies. This possibility is discussed briefly below. The array responses of all of the arrays shown in Figure 1 exhibit reasonably good side-lobe-suppression characteristics. Spatial aliasing of signals may be a problem at higher frequencies for low signal-to-noise ratios, but this problem can be minimized using the technique described by Kennett et al. (2003).

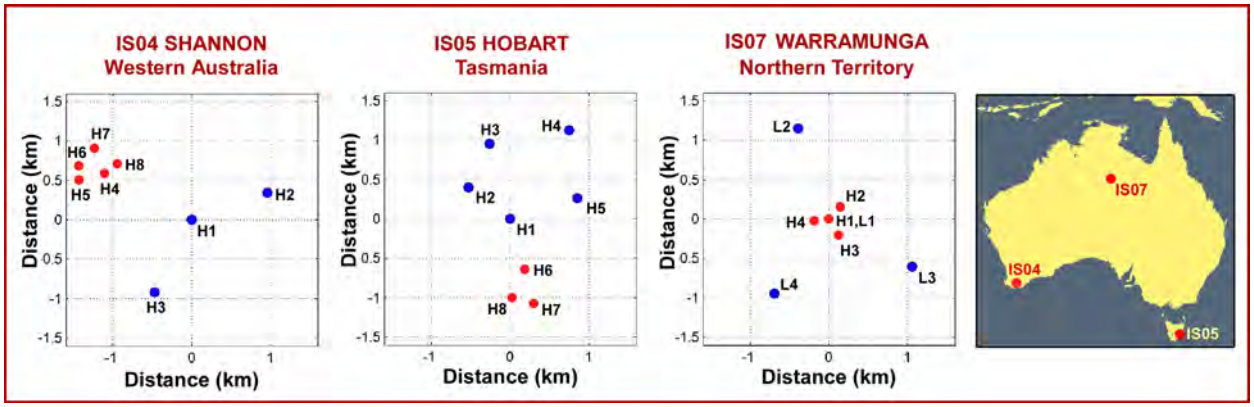

Figure 1. Comparison of the array configurations at IS04 Shannon, IS05 Hobart and IS07 Warramunga. Each array includes a small-aperture sub-array.

A large number of open-cut mines are located throughout the Australian mainland and in Papua New Guinea to the north of the Australian continent. Waveform data recorded at IS04, IS05, IS07 and temporary portable array stations from a large number of explosions at these mines have been assembled into a database for the investigation of the spatial coherence properties of explosion-generated infrasonic waves. This data set has been supplemented by waveform data from a number of volcanic eruptions, bolide explosions, and test chemical explosions. The data set includes signals generated by explosions located at distances ranging from a few hundred kilometers to more than 3000 kilometers. These signals have been detected at a wide range of azimuths and during all seasons of the year.

The technique that has been used to determine the coherence properties of infrasonic signals has been described in Christie et al. (2006). The basic theoretical framework for a signal coherence model is given in Gossard (1969), Gossard and Sailors (1970) and Mack and Flinn (1971) (see also Gossard and Hooke (1975). We have adopted the model proposed by Mack and Flinn since this simple model captures the essential physics of the problem and the model parameters can be easily determined from observations. Mack and Flinn (1971) derived an expression for signal coherence that provides a good fit to the observed coherence of long period infrasonic signals generated by large explosions detected at great distances at a large aperture infrasonic array. Since signal correlation, *C*, between two sensors separated by vector **r** at a specified frequency, is given by the square root of the squared coherency (Blandford, 2000), the expression for signal coherence in Mack and Flinn can be rewritten for convenience as:

$$C(\mathbf{r},T) = \sqrt{\gamma^2(\mathbf{r},T)} = \sqrt{\left|\frac{\sin\left(2\pi x \sin(\Delta\theta)/cT\right)}{2\pi x \sin(\Delta\theta)/cT}\right|^2 \cdot \left|\frac{\sin\left(2\pi y \Delta c/(cT(c+\Delta c))\right)}{2\pi y \Delta c/(cT(c+\Delta c)}\right|^2}, \qquad (1)$$

where *T* is period, *c* is the mean phase velocity, *x* and *y* are the components of the vector separation r, $\pm\Delta c$ represents the observed loss of signal coherence due to a small variation in wave velocity along the direction of wave propagation and $\pm\Delta\theta$ is a measure of the observed loss of coherence along the wavefront due to a small variation in wave azimuth. Blandford (1997) extrapolated the long-period results of Mack and Flinn to higher frequencies and found a new set of model parameters, Δc = 15 m/s and $\Delta\theta$ = 5º, that provides a fairly good fit to observations at frequencies above 0.1 Hz. Additional work on the subject has been reported by Armstrong (1998), Blandford (2000, 2004), McCormack (2002) and Christie et al. (2005a, b; 2006).

The comparison of signal correlation observations with theory is often made by attempting to find observed values of signal correlation for sensors aligned parallel and perpendicular to the wavefront and comparing these results with the curves described by expression (1) with y = 0 (sensors aligned parallel to the wavefront) and x = 0 (sensors aligned normal to the wavefront) for various frequencies and sensor separation distances. This procedure may be subject to error when the comparison is based on data from a fixed array with a small number of array elements where few, if any, array element pairs are aligned normal and perpendicular to the wave propagation direction. We have therefore adopted a new procedure in which we calculate the array-averaged correlation coefficient as defined by the Mack and Flinn model as a function of azimuth and frequency and compare this directly with observations. This procedure includes a contribution from all array element pairs and can be used with any array configuration and any source azimuth. A brief description of the calculation of the polar distribution of the array-averaged correlation coefficient is given in Christie et al. (2006). The calculation is carried out by computing the predicted angular variation of the signal correlation as defined by (1) for each sensor pair in an array in geographical coordinates and then averaging the results at each azimuth over all sensor pairs. The resulting polar distribution of the array-averaged correlation coefficient provides a unique characteristic of the array configuration that can be used to enhance array design. The azimuthal distribution of signal correlation given by expression (1) is highly anisotropic at higher frequencies. As a consequence, the polar distribution of the array-averaged correlation coefficient may also be anisotropic and this can have a detrimental influence on the detection capability at certain azimuths for higher frequency waves.

Preliminary results that illustrate problems with the deterioration of signal coherence when the distance between array elements is large and problems with an anisotropic array-averaged correlation coefficient at higher frequencies have been given in Christie et al. (2006). The investigation of the coherence properties of infrasound signals is an ongoing project. Here, we extend the results of the calculation of the array-averaged correlation coefficient to triangular arrays with various apertures and compare the results with further observations of explosion-generated infrasonic waves recorded at IS07 Warramunga at frequencies of 0.5, 1.0, and 2.0 Hz. Three tri-partite sub-arrays at IS07 (see Figure 1) are chosen to illustrate potential signal coherence problems:

(A) A small sub-array formed by array elements H1, H2 and H3 with an aperture of about 0.3 km,

(B) A medium size sub-array formed by array elements H2, L3 and L4 with an aperture of about 1.5 km, and

(C) A large aperture array defined by array elements L2, L3 and L4 with an aperture of about 2 km.

The predicted azimuthal variation of the array-averaged correlation coefficient for each of these sub-arrays at frequencies of 0.5, 1.0, and 2.0 Hz as computed from the Mack and Flinn model with Blandford's parameters (Δc = 15 m/s and $\Delta\theta$ = 5°) are presented in Figure 2. As can be seen from these results, the array-averaged correlation coefficient is highly anisotropic at higher frequencies in the case of the larger aperture arrays. The value of the array-averaged correlation coefficient predicted for these larger arrays is also too small to allow reliable detection of signals at frequencies of 1.0 Hz or higher. The predictions indicate that good detection capability at all azimuths at frequencies of up to 2.0 Hz will only be possible in the case of the small 0.3 km aperture tri-partite array. The azimuthal distribution of the array-averaged correlation coefficient for the large 2.0-km array is also anisotropic and attenuated at a frequency of 0.5 Hz, which suggests that detection capability will be marginal at all frequencies above 0.5 Hz for sparse arrays with apertures of 2 km or more.

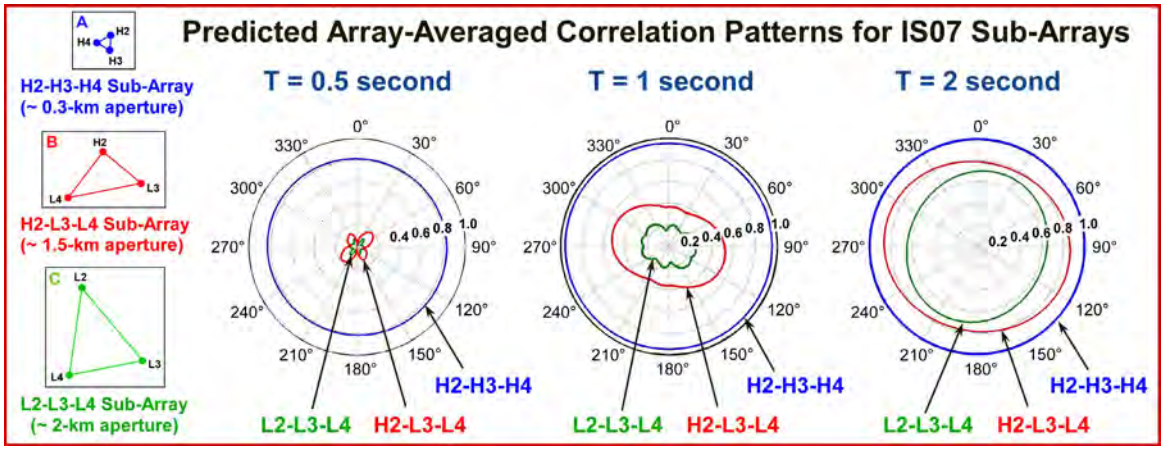

Figure 2. Predicted azimuthal variation of the array-averaged correlation coefficient for (A) a small aperture (~0.3 km) sub-array (in blue), (B) a medium aperture (~1.5 km) sub-array (in red) and (C) a large-aperture (~2 km) sub-array (in green) at IS07 Warramunga, Australia at periods of 0.5, 1.0, and 2.0 seconds. The azimuth is measured from north. The calculations are based on Δc = 15 m/s and Δθ = 5° as found by Blandford (1997).

Observations of array-averaged correlation coefficients obtained using the three tripartite sub-arrays at IS07 Warramunga for infrasonic waves from a variety of naturally occurring and man-made explosions are compared with the predictions of the Mack and Flinn model in Figure 3. These observations are in fairly good agreement with the model predictions. Observed signal correlation decreases rapidly with increasing frequency and with increasing array aperture in agreement with the Mack and Flinn model. The observations confirm that the degree of signal correlation of infrasound from regional and distant explosions is very low on sparse arrays with apertures of about 1 km or more at frequencies above 1 Hz. These results indicate that the detection capability of some existing IMS 4-element infrasound arrays with apertures of more than 2 km for regional and distant explosions will be marginal when automatic routine processing is carried out using detection algorithms that are based on signal correlation between array elements.

It is worth noting, however, that the theory of Mack and Flinn with model parameters Δc = 15 m/s and $\Delta\theta$ = 5º as found by Blandford (1997) predicts array-averaged correlation coefficients that are somewhat smaller than those observed, especially in the case of mining and other chemical explosions with frequencies of 0.5 and 1.0 Hz. It therefore appears that the present coherence model for infrasound signal correlation is too restrictive. The Mack and Flinn parameters, Δc and $\Delta\theta$, need to be adjusted to give a better fit to the observations. This process is underway and a preliminary estimate for a more accurate set of parameters is Δc = 14 m/s and $\Delta\theta$ = 4.5º. We emphasize that the relatively small changes to the current signal correlation model do not in any way change the essential conclusions. The monitoring capability of 4-element IMS arrays with apertures of more than 2 km for regional and distant nuclear explosions is, at best, marginal.

The results presented above for the array-averaged correlation coefficient suggest that there may be other fundamental problems with the design of an array configuration that could result in marginal detection capability. This can be illustrated by the unusual asymmetric array configurations at IS04 and IS05. An array configuration should be designed to maximize the number of array element pairs that contribute significantly to the array-averaged correlation coefficient and to ensure a symmetrical azimuthal distribution of the array-averaged correlation coefficient in the monitoring passband. In this regard, the array configurations at IS04 and IS05 are not optimum, even though they both exhibit a reasonable array response. In the case of the IS04 and IS05 arrays, the array-averaged correlation coefficient will be dominated at higher frequencies by contributions from the smaller aperture sub-array (shown in red in Figure 1). Contributions from most array element pairs formed by one element in the large array and one element in the small sub-array will be negligible. This means that the arrays at IS04 and IS05 will be dominated by a small sub-array and the overall array-averaged correlation coefficient at higher frequencies will be reduced. In addition, the asymmetry in the arrays at IS04 and IS05 will lead to anisotropy in the azimuthal distribution of the array-averaged correlation coefficient at frequencies in the primary monitoring passband.

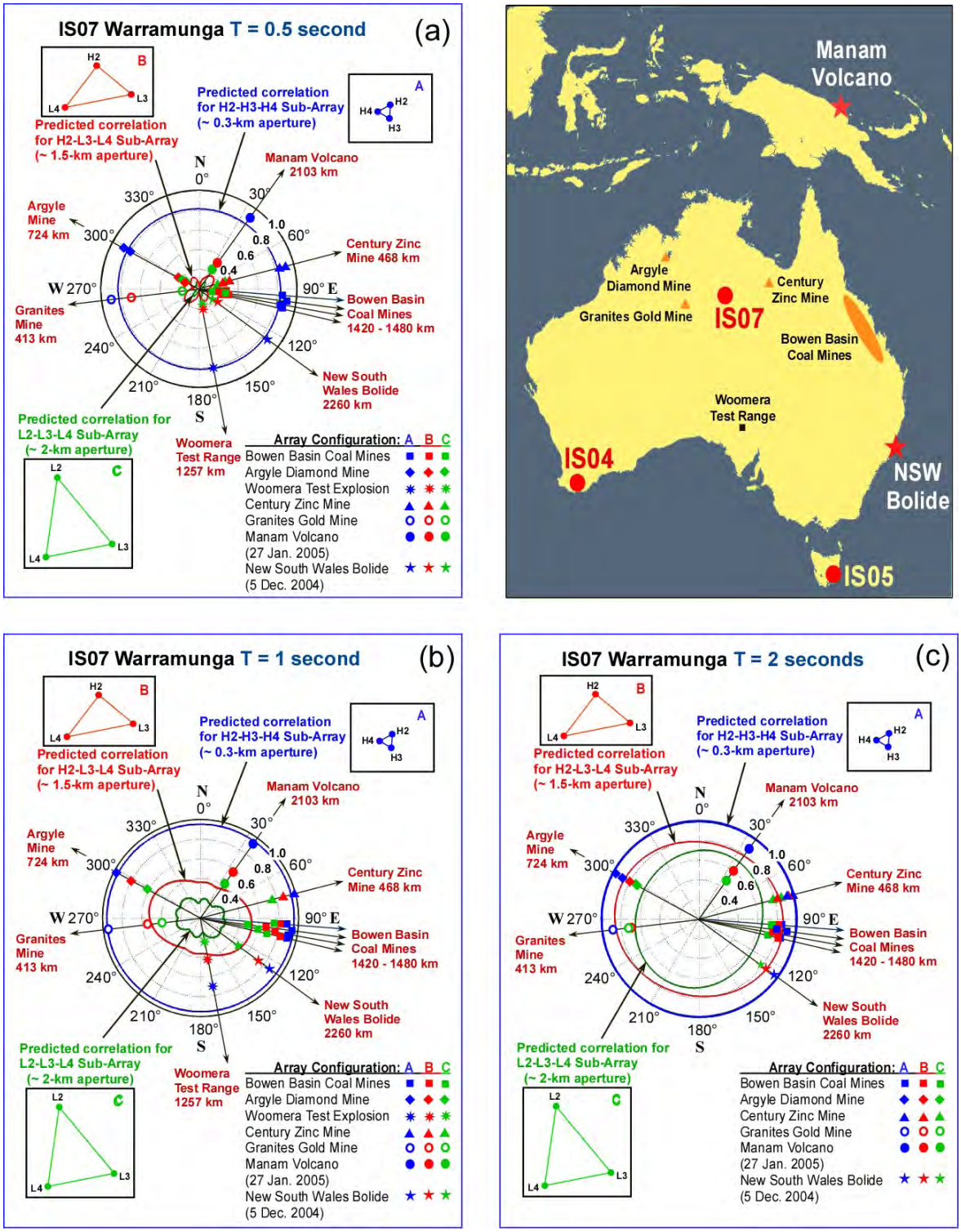

Figure 3. Comparison of theoretical and observed array-averaged correlation coefficients for infrasonic signals from regional and distant mine and other chemical explosions and distant volcanic and bolide explosions recorded on small, medium and large aperture sub-arrays at IS07 Warramunga. (A) 2.0 Hz infrasonic signals. (B) 1.0 Hz infrasonic signals. (C) 0.5 Hz infrasonic signals.

Development of a New Wind-Noise-Reducing System

Wind-generated background noise has been an exasperating problem in the field of infrasound monitoring for more than 50 years. While there has been some progress in the last 10 years in the development of improved noise-reducing systems, the improvements have been relatively small. Adaptive signal processing of data from a large number of distributed sensors at each array element has been proposed as an effective noise-reducing technique (Tamadgee et al., 2001; Bass and Shields, 2004; Shields, 2005). Tests of the small-scale wind barrier designed by L. Liszka at the Swedish Institute of Space Physics in 1972 for noise reduction at higher frequencies have been reported by ReVelle (private communication, 2000) and Hedlin and Berger, 2001. An important development has been the use described by Bedard et al. (2004) of a porous wind fence with corrugations as a means for wind noise reduction at higher frequencies in an infrasound tornado-warning system. Almost all noise-reducing systems in use at infrasound monitoring arrays are based on the spatial averaging of the micropressure fluctuations around an array element using a complex pipe array. It seems clear that further refinements to existing pipe array designs will not lead to significant improvements. Pipe arrays occupy a large area and are expensive to install. In addition, higher frequency signals are attenuated and distorted by pipe arrays and the transfer function may not be accurately known.

The infrasonic wind-noise problem can be illustrated by the noise levels at IS07 Warramunga (see Figure 4) which are similar to those found at many infrasonic monitoring stations installed in areas with relatively little protection from the ambient winds. All winds are measured at a height of 2.0 m. The ambient wind speed at IS07 is usually very low at night and high during the day. This invariably results in unacceptably high background noise levels during the daytime. The lower limit on the sensitivity of IS07 at frequencies above 1 Hz (red curve in Figure 4 for zero wind speed) is determined by the electronic noise floor of the MB2000 microbarometer (~$4x10^{-7}$ Pa^2/Hz). We have also included for comparison power spectral density estimates of background noise recorded simultaneously at H2 in zero wind conditions using a Chaparral Physics Model 5 microbarometer (blue curve). This microbarometer has a much lower electronic noise floor than the MB2000 microbarometer.

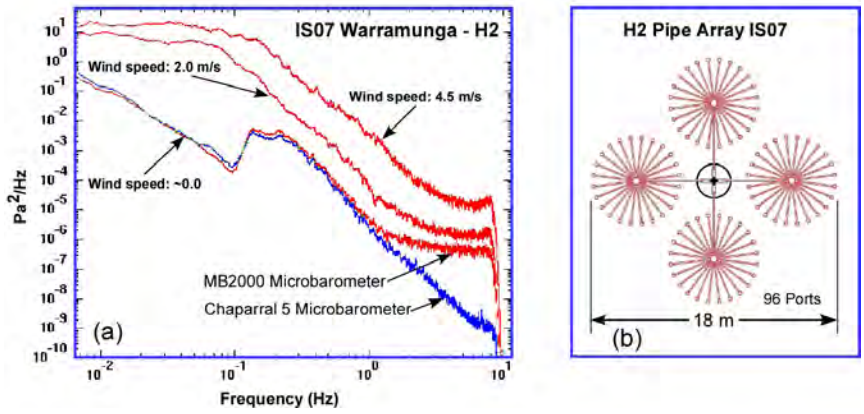

Figure 4. (a) Power spectral density of infrasonic background noise recorded at site H2 at IS07 Warramunga. Curves shown in red were recorded using the DASE MB2000 microbarometer installed at H2 with a standard CTBTO 18-m diameter rosette noise-reducing pipe array system on the input to the microbarometer. The 96-port pipe array is illustrated schematically in (b). The blue curve in (a) corresponds to data recorded simultaneously in zero wind using a Chaparral Physics Model 5 microbarometer.

The state-of-the-art pipe arrays at IS07 do not resolve the problem of high wind noise levels during the daytime. A new approach to the problem of wind-noise-reduction is required. We have therefore focused on techniques that result in the attenuation and transformation of wind-noise-generating turbulent eddies in the neighborhood of the inlet (or inlets) to the microbarometer infrasound sensor. This is achieved through the use of turbulence-reducing enclosures constructed from porous screens stretched over a rigid framework. We have constructed and tested a fairly large number of turbulence-reducing enclosures during the last nine months. All of these experiments have been carried out at IS07 Warramunga using Chaparral Physics Model 5 microbarometers for evaluation. The design of the turbulence reducing enclosures was originally based on open structures with two concentric porous walls with

outward-facing inclined deep serrations on the top, which help to prevent the blocked ambient flow from folding over the walls and generating unwanted turbulence near the surface inside the structure.

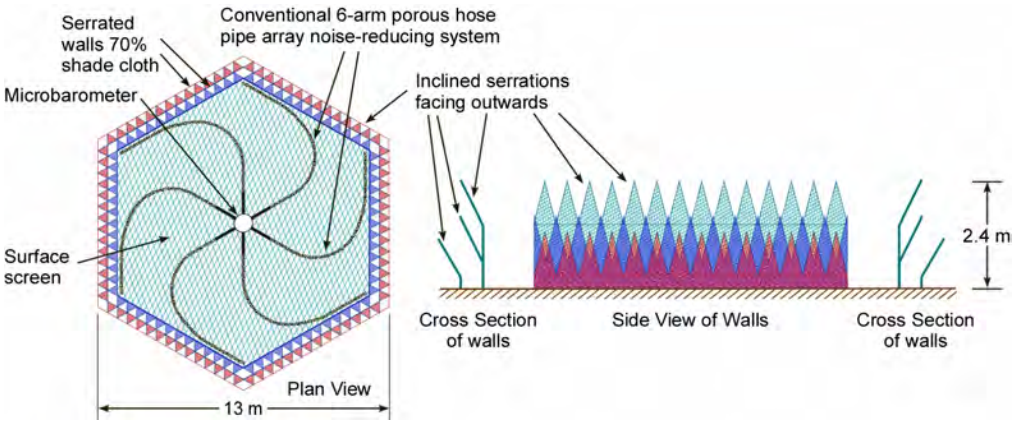

Figure 5. Schematic diagram illustrating Version 2 of the turbulence-reducing enclosure with three rows of inclined overlapping deep serrations arranged on two porous walls. The plan view also shows the layout of the conventional 6-arm porous hose pipe array system, which was used to test this noise-reducing system.

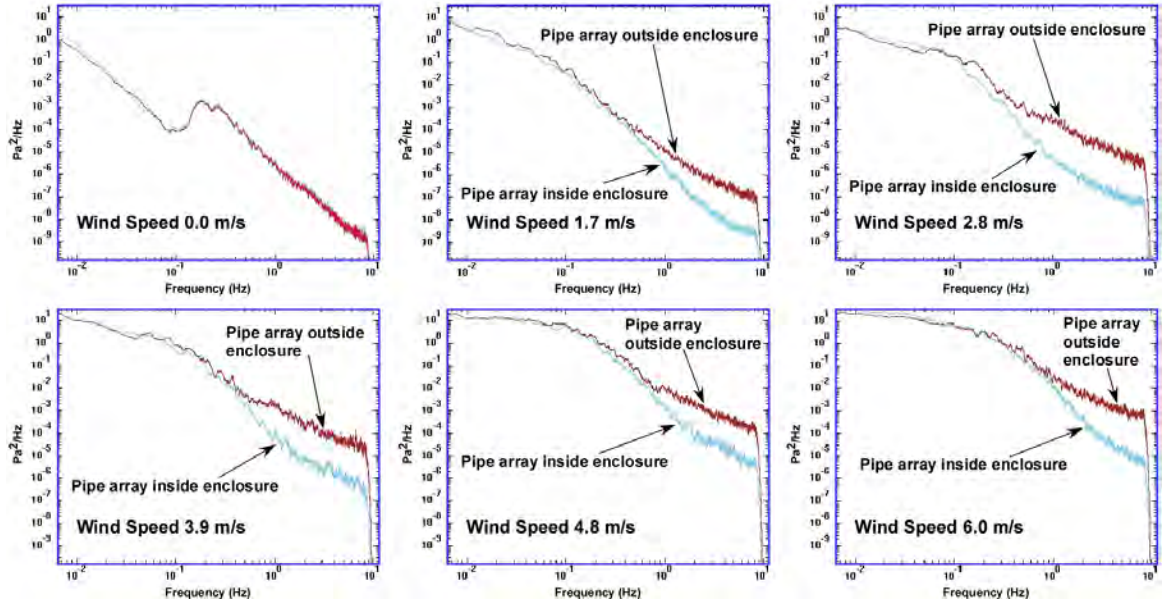

Figure 6. Comparison of power spectral density estimates of background noise for porous hose pipe array systems located inside and outside Version 2 of the turbulence-reducing enclosure for wind speeds up to 6.0 m/s.

The inner wall of the first version of the enclosure (Version 1) was 1.6-m high. The performance of this open enclosure was fairly good in modest winds, but the efficiency dropped rapidly as wind speeds increased above 3.2 m/s. A schematic diagram of the second turbulence-reducing enclosure (Version 2) with 2.4-m high inner walls is shown in Figure 5 and the results of the performance tests for this open enclosure are presented in Figure 6. These tests were carried out with identical conventional porous hose pipe arrays located inside and outside the enclosure. The performance of Version 2 of the enclosure is significantly better than the performance of Version 1. The higher walls in this case are clearly beneficial. However, the efficiency of Version 2 of the enclosure decreased rapidly in winds of more than 4.5 m/s. Versions 1 and 2 of the enclosure, when used with a conventional pipe array, provide good noise reduction in modest winds, but neither of these systems reduce wind noise to completely acceptable

levels at IS07 during average daytime wind conditions. Versions 3 and 4 were constructed to test the influence of increasing the height of the walls to 3.2 m. The increased wall height did not improve the performance of these open enclosures. Tests at this point indicated that the interaction of the higher serrations on the walls with the ambient winds at a height of 3 m was generating turbulence inside the structure. We then added radial baffles inside the structure along with an inner walled enclosure in an attempt to reduce the level of turbulence inside the structure. Both of these additions were effective, but the gains in performance were relatively small. However, we found that a roof over the inner structure resulted in a dramatic decrease in noise levels at the center of the enclosure. We then decided to remove all higher serrations and to transform the enclosure into a closed structure with a lower profile. Version 5 of the enclosure (see Figure 7) was constructed with a reduced height of 2.0 m, a second smaller roofed chamber at the center for use with a single port system, radial baffles, and a screened roof over the entire structure. *Horizontal* outward-facing serrations and *downward* -inclined, outward-facing larger-scale serrations, both attached at the outer edge of the roof, were introduced to minimize the generation of turbulence on the upper edges of the structure. Test results (see Figure 8) show that Version 5 of the enclosure is a very effective noise-reducing system.

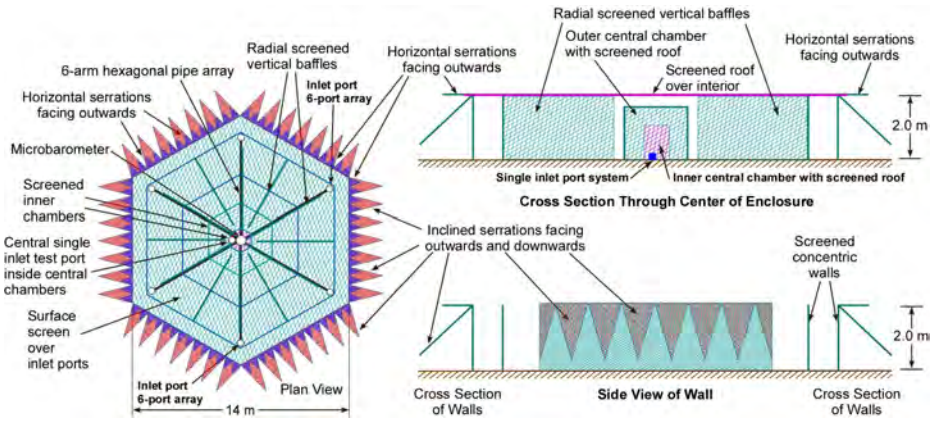

Figure 7. Schematic diagram illustrating Version 5 of the turbulence-reducing enclosure with vertical baffles, enclosed inner chambers and a screened roof over the entire interior of the structure. All higher serrations on the outer walls have been replaced by (a) horizontal outward-facing serrations and (b) larger scale outward-facing and downward-inclined serrations attached to the upper edge of the structure.

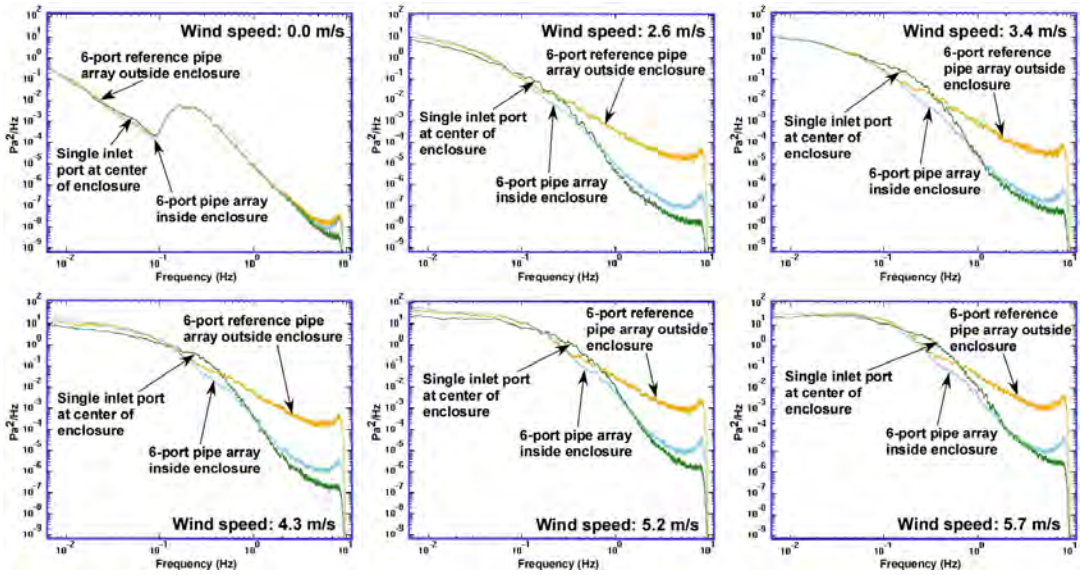

Figure 8. Comparison of power spectral density estimates of background noise recorded with identical 6-port pipe array systems located inside and outside Version 5 of the enclosure. The green curve corresponds to background noise recorded on a single inlet port system located at the center of the enclosure.

Note that the performance of Version 5 of the enclosure was evaluated using identical 12-m diameter 6-port pipe arrays located inside and outside the structure. Tests were also carried out with a single-port system located at the center of the enclosure. The results presented in Figure 8 show that Version 5 of the system reduces wind noise in the monitoring passband to acceptable levels for monitoring purposes in ambient winds of up to 4.3 m/s, even when the pipe array inside the structure is replaced by a single inlet port. It is also interesting to note that noise levels recorded on the single-port system inside the structure at high frequencies are less than the electronic noise floor of the MB2000 microbarometer ($4x10^{-7}$ Pa^2/Hz), which is used at IS07 (and many other monitoring stations), in winds of up to 4.3 m/s. The performance of the single-port system is usually better than the performance of the 6-port pipe array at frequencies above 1.0 Hz, but the 6-port pipe array is more effective at lower frequencies. We have examined infrasonic signals recorded both inside and outside the enclosure at all frequencies of interest to see if these signals are affected by the enclosure. In all cases, we have found that infrasonic signals are not attenuated or distorted. The enclosure is virtually transparent to infrasound. In summary, the use of Version 5 of the wind-noise-reducing system at all array elements at IS07 Warramunga would effectively resolve wind-noise problems in the monitoring passband at this unsheltered IMS infrasound station.

A further example of the high degree of wind-noise reduction that has been achieved in the monitoring passband is illustrated in Figure 9 by the background noise waveforms recorded using Version 5 of the noise-reducing system under typical daytime conditions at IS07. The waveforms shown in Figure 6 were recorded near noon on 4 May 2007. It is clear from the results presented in Figure 6 that wind-generated noise in the primary monitoring passband has been dramatically reduced by the turbulence-reducing enclosure.

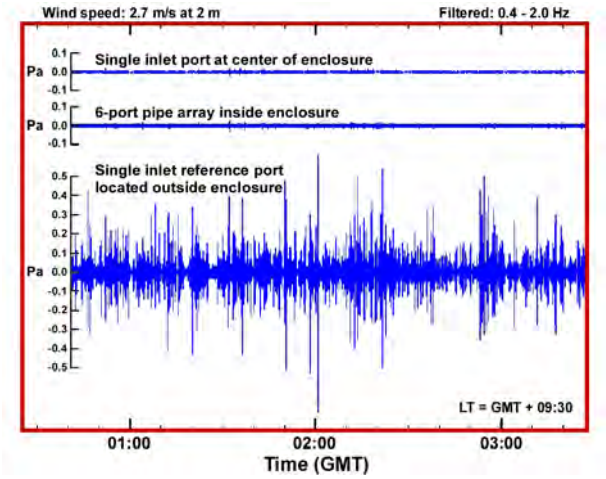

Figure 9. Comparison of background noise in the monitoring passband recorded on a single inlet port system and a 6-port pipe array system located inside Version 5 of the turbulence-reducing enclosure with background noise recorded simultaneously on a single inlet reference port located outside the enclosure. All traces have the same amplitude scale.

CONCLUSIONS AND RECOMMENDATIONS

The results of the detailed investigation of infrasound signal coherence properties presented here show that the monitoring performance of existing larger-aperture 4-element infrasound monitoring stations in the global network may be marginal for regional and distant explosions. The arrays at these stations should be upgraded to 8- or 9- element arrays.

The turbulence-reducing enclosure illustrated in Figure 7 provides a dramatic reduction in wind-generated noise in the infrasound monitoring passband. The use of this system can potentially resolve wind-noise problems at most infrasound monitoring stations. This system can be used to significantly enhance the performance of existing pipe arrays at established infrasound monitoring stations or, in some cases, as effective stand alone single-inlet port noise-reducing systems that do not require a pipe array. It is recommended that the use of this system should be considered in the design of all new infrasound monitoring stations

REFERENCES

Armstrong, W. T. (1998). Comparison of infrasound correlation over differing array baselines, *Proceedings of the 20th Annual Seismic Research Symposium on Monitoring a Comprehensive Test Ban Treaty*, Santa Fe, New Mexico, 543–554.

Bass, H. E. and F. D. Shields (2004). The use of arrays of electronic sensors to separate infrasound from wind noise, in *Proceedings of the 26th Seismic Research Review: Trends in Nuclear Explosion Monitoring*, LA-UR-04-5801, Vol. 1, pp. 601–607.

Bedard, Jr., A. J., B. W. Bartram, A. N. Keane, D. C. Welsh, and R. T. Nishiyama (2004). The infrasound Network (ISNET): Background, design details, and display capability as an 88D adjunct tornado detection tool, *Proceedings of the 22nd Conf. On Severe Local Storms*, Hyannis, MA, *Amer. Meteor. Soc*. Paper 1.1.

Blandford, R. R. (1997). Design of Infrasonic Arrays. Air Force Technical Applications Center Report, AFTAC-TR-97-013.

Blandford, R. R. (2000). Need for a small subarray at IMS infrasound stations—Implications of shuttle and S. Pacific nuclear signals, *Proceedings Infrasound Workshop*, Passau, Germany.

Blandford, R. R. (2004). Optimal infrasound array design for 1kt atmospheric explosions, *Proceedings of the Infrasound Technology Workshop*, Hobart, Australia.

Christie, D. R., B. L. N. Kennett and C. Tarlowski (2005a). Detection of distant atmospheric explosions: Implications for the design of IMS infrasound array stations, *Proceedings Infrasound Technology Workshop*, Papeete, Tahiti.Christie, D. R., B. L. N. Kennett and C. Tarlowski (2005b). Detection of regional and distant atmospheric explosions, in *Proceedings of the 27th Seismic Research Review: Ground-Based Nuclear Explosion Monitoring Technologies*, LA-UR-05-6407, Vol. 2, pp. 817–827.

Christie, D. R., B. L. N. Kennett and C. Tarlowski (2006). Detection of atmospheric explosions at IMS monitoring stations using infrasound techniques, in *Proceedings of the 28th Seismic Research Review*: Ground-Based Nuclear Explosion Monitoring Technologies, LA-UR-06-5471, Vol.2, pp. 882–892.

Gossard, E. E. (1969). The effect of bandwidth on the interpretation of the cross-spectra of wave recordings from spatially separated sites, *J. Geophys. Res.* 74: 325.

Gossard, E. E. and Sailors, D. B. (1970). Dispersion bandwidth deduced from coherency of wave recordings from spatially separated sites, *J. Geophys. Res.* 75: 1324–1329.

Gossard, E. E. and Hooke, W. H. (1975). Waves in the Atmosphere. Elsevier, New York. Chapter 9, Section 65.

Hedlin, M. A. E. and J. Berger (2001). Evaluation of infrasonic wind reduction filters, in *Proceedings of the 23rd Seismic Research Review: Worldwide Monitoring of Nuclear Explosions*, LA-UR-01-4454, Vol. 1, 121–130.

Kennett, B. L. N., D. J. Brown, M. Sambridge, and C. Tarlowski (2003). Signal parameter estimation for sparse arrays, *Bull. Seism. Soc. Am.* 93: 1765–1772.

Mack. H. and E. A. Flinn (1971). Analysis of the spatial coherence of short-period acoustic-gravity waves in the atmosphere, *Geophys. J. R. Astr. Soc.* 26: 255–269.McCormack, D. (2002). Towards characterization of infrasound signals, *Proceedings Infrasound Technology Workshop*, De Bilt, The NetherlandsShields, F. D. (2005). Low-frequency wind noise correlation in microphone arrays, J. Acoust. Soc. Am., 117, 3489-3496.

Talmadge, C. L., D. Shields and K. E. Gilbert (2001). Characterization and suppression of wind noise using a large-scale infrasound sensor array, *Proceedings Infrasound Technology Workshop*, Kailua-Kona, Hawaii.

FINITE DIFFERENCE MODELING OF INFRASOUND PROPAGATION TO LOCAL AND REGIONAL DISTANCES

Catherine de Groot-Hedlin

Scripps Institution of Oceanography, University of California at San Diego

Sponsored by Army Space and Missile Defense Command

Contract No. W9113M-06-1-0003

ABSTRACT

The finite difference (FD) method yields the solution to a discretized version of the full acoustic wave equation for arbitrarily complex media. It is a full spectrum approach and is thus reliable at all angles of propagation, including backscatter. This offers an advantage over other standard propagation methods in wide use, as it allows for accurate computation of acoustic energy levels in the case where significant scattering can occur near the source, such as may happen for an explosion near the surface, or underground. This fits in with nuclear monitoring goals, in that it allows for an improved understanding of the generation and propagation of infrasound energy from arbitrary sources, including underground and near-surface explosions.

Two types of FD methods of solving the acoustic wave equation are presented in this paper. The first is a finite difference frequency domain (FDFD) method, applied in cylindrical coordinates to simulate the effects of a point source in an azimuthally symmetric medium. The second is a finite difference time domain (FDTD) approach including the effects of both gravity and wind, applied in two-dimensional Cartesian coordinates. In this paper equations are developed for the FDTD approach where both wind and gravity effects are considered.

It is shown that the FD approach can be used to solve for sound intensities in arbitrarily complex models that may include high material contrasts and arbitrary topography. In this paper, results of FDTD and FDFD approaches are compared for the case of a shallow underground source, for a boundary with significant topography. The effects of wind and gravity on the solution are examined.

OBJECTIVES

An FDTD method of numerically synthesizing infrasound energy in a realistic environment is sought. The FDTD method yields the solution to a discretized version of the full acoustic wave equation for arbitrarily complex media. It is a full spectrum approach and is thus reliable at all angles of propagation, including backscatter. This offers an advantage over other standard propagation methods in wide use, as it allows for accurate computation in cases where significant scattering can occur near the source, such as may happen for an explosion near the surface or underground. The effects of wind or gravity on infrasound propagation may also be incorporated into the infrasound propagation problem with relative ease using finite difference techniques. This fits in with nuclear monitoring goals, in that successful completion of this project will allow for an improved understanding of the generation and propagation of infrasound energy in arbitrarily complex environments.

In this paper, both an FDFD approach and an FDTD approach are used to solve for the infrasound signals generated by an underground source. A method of incorporating wind and gravity are outlined for the FDFD approach.

RESEARCH ACCOMPLISHED

An FDTD method of numerically acousto-gravity waves in a windy environment has been developed. The equations governing infrasound propagation are derived below for the time domain; their incorporation into an FDTD method are explained in the next subsection. Examples are given in the final sub-section and compared to the frequency domain method.

Low frequency wave equations for a fluid in motion

In the absence of viscosity, the equations governing propagation of sound in the atmosphere are the conservation of momentum,

$$\rho \frac{D\mathbf{V}}{Dt} = -\nabla P + \mathbf{F}, \tag{1}$$

conservation of mass

$$\frac{D\rho}{Dt} + \rho \nabla \cdot \mathbf{V} = 0, \tag{2}$$

and the equation of state

$$\frac{DP}{Dt} = C^2 \frac{D\rho}{Dt}, \tag{3}$$

(Gill, 1982; Ostashev *et al.*, 2005). These equations relate the velocity $\mathbf{V}$, the pressure P, and the density ρ. The external forces acting upon the medium are denoted by $\mathbf{F}$, and C is related to the adiabatic sound speed. At low frequencies, the gravitational force $\mathbf{F} = -\rho\mathbf{g}$ must be included, where

$$\mathbf{g} = [0, 0, 9.8]\ m/s^2 \tag{4}$$

indicates gravitational acceleration; the negative sign on the force indicates that a downward force acts upon a positive density fluctuation caused by the propagating sound wave.

The convective derivative (also known as the Lagrangian derivative) $\frac{D}{Dt}$ is defined by

$$\frac{D}{Dt} = \frac{\partial}{\partial t} + (\mathbf{V} \cdot \nabla). \tag{5}$$

The derivative on the left represents the change with time in a reference frame moving with the fluid. The first term on the right side of Equation (5) represents the change at a point fixed in space. The second term represents the change as the observer moves with the fluid at the velocity $\mathbf{V}$, and is called the advective term. Generally, quantities are expressed in terms of a fixed point in space in order to compare computational results with observations made at stationary sensors.

The propagation of sound waves in the atmosphere introduce fluctuations in the pressure, density, and velocity fields. The standard procedure in solving Equations ~(1)–(3) is to consider a solution of the form

$$P = p_o + p_s; \quad \rho = \rho_o + \rho_s; \quad \mathbf{V} = \mathbf{w} + \mathbf{v}; \quad C^2 = c^2 + (c^2)'; \tag{6}$$

where p_o, ρ_o, and **w** are the ambient solutions in the absence of fluctuations p_s, ρ_s, and **v** due to the propagating sound wave. The adiabatic sound speed is given by *c*, and $(c^2)'$ is the perturbation in the squared sound speed caused by the passage of the sound wave (Ostashev et.al., 2005). In what follows, **w** denotes wind velocity profile, and **v** denotes the acoustic particle velocity associated with the sound wave. Waveforms are derived by computing the pressure perturbations, p_s, as a function of time.

To obtain first order linear equations feasible for implementation in an FDTD method, it is assumed that the ambient field is in equilibrium, and that the sound wave pressure is very small in comparison with the ambient pressure. The former assumption implies that Eqs. (1-3) are satisfied in the absence of a propagating sound wave so that zeroth order terms cancel when Eqs. (6) are substituted into Equations (1)-(3). The latter assumption means that second and higher order terms cancel. Retaining only linear terms, Equation (1) becomes

$$\rho_o\Big(\frac{\partial \mathbf{v}}{\partial t} + \mathbf{v}\cdot\nabla\mathbf{w} + \mathbf{w}\cdot\nabla\mathbf{v}\Big) + \rho_s\Big(\frac{\partial \mathbf{w}}{\partial t} + \mathbf{w}\cdot\nabla\mathbf{w}\Big) = -\nabla p_s - \rho_s\mathbf{g}, \tag{7}$$

where the external gravitational force has been included.

Under the assumption that winds are steady, *i.e.*, $\partial\mathbf{w}/\partial t = 0$, and there is no variation along the direction of the wind, *i.e.*, $\mathbf{w}\cdot\nabla\mathbf{w} = 0$, the equation governing acoustic particle velocity reduces to

$$\rho_o\Big(\frac{\partial \mathbf{v}}{\partial t} + \mathbf{v}\cdot\nabla\mathbf{w} + \mathbf{w}\cdot\nabla\mathbf{v}\Big) = -\nabla p_s - \rho_s\mathbf{g}. \tag{8}$$

Combining Eqs. (2) and (3), and inserting Eqs. (6) yields the following equation for the pressure fluctuations due to the propagating sound wave:

$$\frac{\partial p_s}{\partial t} + \mathbf{w}\cdot\nabla p_s + \mathbf{v}\cdot\nabla p_0 = -\rho c^2\nabla\cdot\mathbf{v} - \Big(\rho_o(c')^2 + \rho_s c^2\Big)\nabla\cdot\mathbf{w} \tag{9}$$

The hydrostatic equation $\nabla p_o = -\rho_o\mathbf{g}$ holds under the assumption of steady state and range-invariant winds. Furthermore, Ostashev *et al.*(2005) states that the divergence term $\nabla\cdot\mathbf{w}$ may be ignored to order $(w/c)^2$; under this assumption Eq. (9) becomes

$$\frac{\partial p_s}{\partial t} + \mathbf{w}\cdot\nabla p_s = \rho_o\mathbf{v}\cdot\mathbf{g} - \rho_0 c^2\nabla\cdot\mathbf{v}, \tag{10}$$

where the gravity vector is as defined in Eq. (4).

The equation for fluctuations in density may be derived from Eq. (3), the equation of state, as

$$\frac{\partial \rho_s}{\partial t} + \mathbf{v}\cdot\nabla\rho_o + \mathbf{w}\cdot\nabla\rho_s = \frac{1}{c^2}\Big(\frac{\partial p_s}{\partial t} + \mathbf{v}\cdot\nabla p_o + \mathbf{w}\cdot\nabla p_s\Big), \tag{11}$$

under the assumptions that the ambient pressure and density values do not vary with time, and that $(c')^2\mathbf{w}\cdot\nabla\rho_0 = 0$, which is satisfied by horizontal winds, and densities that vary weakly with range. This equation for density variations is similar in form to Eq. 6.14.3 of Gill (1982), with the exception that horizontal winds **w** are included in Eq. 11. Making use of the hydrostatic equation $\nabla p_o = -\rho g$, the above equation may be re-written as

$$\frac{d\rho_s}{dt} - v_z\rho_o N^2/g = c^{-2}\Big(\frac{dp_s}{dt}\Big), \tag{12}$$

where $g = 9.8m/s^2$ is the vertical component of gravity, v_z is the vertical particle velocity, d/dt represents the time derivative in a reference frame moving with the wind, and the Brunt-Vaisala frequency N - also called the buoyancy frequency - is defined as

$$N^2 = -g\big(\rho_0^{-1}d\rho_o/dz + g/c^2\big). \tag{13}$$

For a stable medium, N is a positive real number equal to the frequency of a parcel in vertical motion. Equation 13 indicates that, for a reference frame moving with the wind, the Brunt-Vaisala frequency is unaltered. However, measurements are made in a stationary reference frame, indicating that the winds control the measured velocity of the gravity waves. The buoyancy frequency depends on the vertical gradient of the ambient density. From the hydrostatic equation $p_o(z) = -\rho_o g$ and the ideal gas law $\delta p_o/\delta z = \rho_o R T$, where R is a gas constant and T is the temperature in degrees Kelvin, the ambient density is derived as $\rho_o(z) = \rho_o(0) \exp(-g z/RT)/RT$. The vertical derivative of the density may be derived from this relation.

Equations 8, 10, and 11 form a complete set of first order linear equations for the pressure, acoustic particle velocity and density fluctuations associated with a propagating infrasound wave in a windy medium, valid under the assumptions stated previously. To summarize, these equations are valid under the assumptions that the ambient pressure, density, and wind fields do not vary with time, the winds are horizontal, and vary only with altitude. That is, the wind must be range-invariant.

Finite difference modeling of infrasound in a windy environment

Here, an FDTD method is outlined for infrasound propagation in a windy, stratified medium. That is, it is assumed that the wind blows horizontally and is invariant along range. The densities, and sound velocities vary much more gradually in the horizontal direction than vertically. The method is applied to a 2-D model, that is, the source is assumed to be an infinite line source. The method resembles an FDTD method for sound waves in a windy atmosphere described in detail by Ostashev et.al. (2005), but with the addition of gravity.

For a 2-D model in the x-z plane with horizontal wind speed w_x, Eqs. (8) becomes

$$\frac{\partial v_x}{\partial t} = -w_x \frac{\partial v_x}{\partial x} - v_z \frac{\partial w_x}{\partial z} - \rho_o^{-1}\Big(\frac{\partial p_s}{\partial x}\Big) \tag{14a}$$

$$\frac{\partial v_z}{\partial t} = -w_x \frac{\partial v_z}{\partial x} - \rho_o^{-1}\Big(\frac{\partial p_s}{\partial z} + \rho_s g\Big). \tag{14b}$$

Eq. (10) becomes

$$\frac{\partial p_s}{\partial t} = -w_x \frac{\partial p_s}{\partial x} + \rho_o v_z g - \rho_o c^2 (\frac{\partial v_x}{\partial x} + \frac{\partial v_z}{\partial z}) \tag{15}$$

and Eq. (11) becomes

$$\frac{\partial \rho_s}{\partial t} = -v_z \frac{\partial \rho_o}{\partial z} - w_x \frac{\partial \rho_s}{\partial x} + \frac{1}{c^2}\Big(\frac{\partial p_s}{\partial t} - v_z \rho_o g \ + w_x \frac{\partial p_s}{\partial x}\Big), \tag{16}$$

The static sound speed c and ambient density ρ_o may vary with both altitude and range; the wind speed w_x varies only with altitude. Equations. 14–16 are in a form suitable to computation by FDTD techniques. Note that for $w_x = 0$, that is, zero wind velocity, and g=0, these equations reduce to the usual equations for acoustic propagation in a static medium (e.g., Botteldoren, 1994).

The finite difference (FD) method relies on replacing linear partial differential equations by a set of discrete equivalents. Field solutions are then computed over a discrete set of nodes that comprise the spatial grid. Figure 1 indicates how field variables are defined and how the medium is discretized for the staggered grid method, initially developed by Yee (1966). The model is decomposed into a set of discrete cells of dimension $\Delta x \times \Delta z$. The sound speed c and ambient density ρ_o are uniform over a given cell, but may vary from cell to cell. Pressure and gravity nodes are defined at the center of each cell and the velocity variables are located midway between the pressure nodes. The staggered grid formulation increases the accuracy of the FD solution, since central differences are used to compute the discrete derivatives (Taflove and Hagness, 2000). The locations of the vertical velocity nodes are defined in such a way as to allow a rigid surface (v_z=0) to be defined at the bottom of the model.

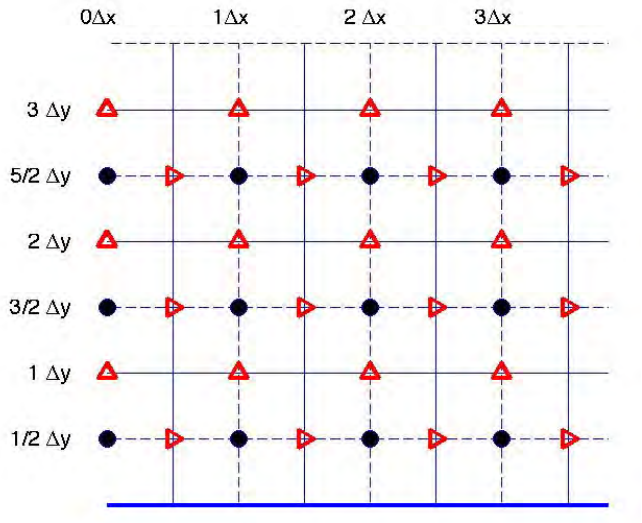

Figure 1. The finite difference model is decomposed into a set of discrete cells, indicated by the solid lines, each with uniform velocity c and ambient density ρ_o. The acoustic pressure and density perturbations are defined by the nodes at the center of each cell, indicated by the filled circles. The locations of the horizontal velocity v_r (triangles pointing right) and vertical velocity variables v_z (triangles pointing up) are defined on a spatially staggered grid, as shown.

Typically, in a nonmoving medium, the acoustic velocities and pressures are computed in a leap-frog manner (Yee, 1966), thus the velocities and pressures are computed at alternating time-steps, and the fields from the previous time step are overwritten. Without the wind terms, the governing equations (Equations 14–16) indicate that time derivatives in the acoustic particle velocities depend on the spatial derivatives of the pressure variables, and vice versa. However, with the inclusion of advection terms, first order derivatives in space and time must be computed simultaneously. Various numerical implementations have been suggested for the computation of the FDTD equations for sound propagation in windy environments (Blumrich and Heinmann, 2002; Van Renterghem and Botteldoren, 2003; Ostashev et.al., 2005). Here, the method of Ostashev et.al. (2005) is followed. That is, pressure and velocity fields are over saved over two time steps so that time derivatives may be computed using central differences. Refer to Ostashev et.al., (2005) for further detail.

A method of applying FD methods in the frequency domain, in cylindrical coordinates, for a point source in an azimuthally symmetric model was developed by de Groot-Hedlin (2006).

Comparison of FDFD and FDTD solutions in a model with topography

In this subsection, comparisons are made between FDFD and FDTD results for a shallow underground source in a medium with topography. The source is embedded within a medium with a sound speed 2 km/s and a density of 2000 k/m3. The sound speed within the air is shown in Figure 2.

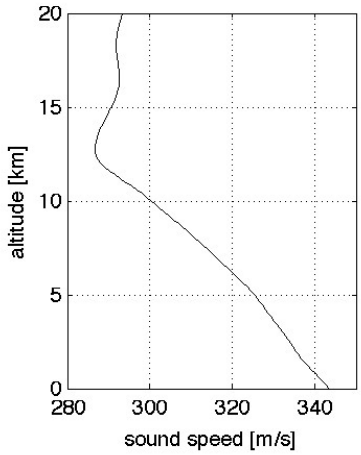

Figure 2. Sound velocity profile within the air. This sound velocity profile is taken from a G2S model for the Mt. St. Helens region for March 9, 2005. The density decreases with altitude by slightly over an order of magnitude over this altitude scale.

The sound velocity profile shows a decrease in sound speed with altitude for the first 10 km; this corresponds to a typical sound velocity profile in which the temperature decreases with altitude. The effect is to cause some deflection of sound upwards, away from the surface.

The finite difference time domain method is applied in Cartesian coordinates, thus the model is invariant along a direction perpendicular to the x-z plane. The source is thus a line source.

This model features a broad, symmetric peak, with a highest altitude of 2 km. The source was located directly beneath the peak at an altitude of 1.2 km, i.e., a distance of 0.9 km below the ground surface. The center frequency of the source was 0.5 Hz. “Receivers” were located at intervals of 5 km from each side of the peak at distances from 5 km to 30 km from the center of the model.

Several “snapshots” of the acoustic pressure are shown in Figure 3. As indicated, the pressure propagates quickly through the ground then couples to the air. A later arrival corresponds to acoustic energy that couples to the air near the source and propagates outward from there. Thus there should be two main arrivals at each receiver, a first one corresponding to acoustic energy propagating through the earth, coupling to the air near the receiver, and a second corresponding to coupling to the air near the source. The traces corresponding to this model are shown in Figure 4. For this model, ray-based propagation methods which rely on a high frequency approximation indicate that acoustic energy is refracted upward, away from the ground so that the more distant receivers lie in a shadow zone. These results thus indicate the extent to which synthesis of the whole waveform is required.

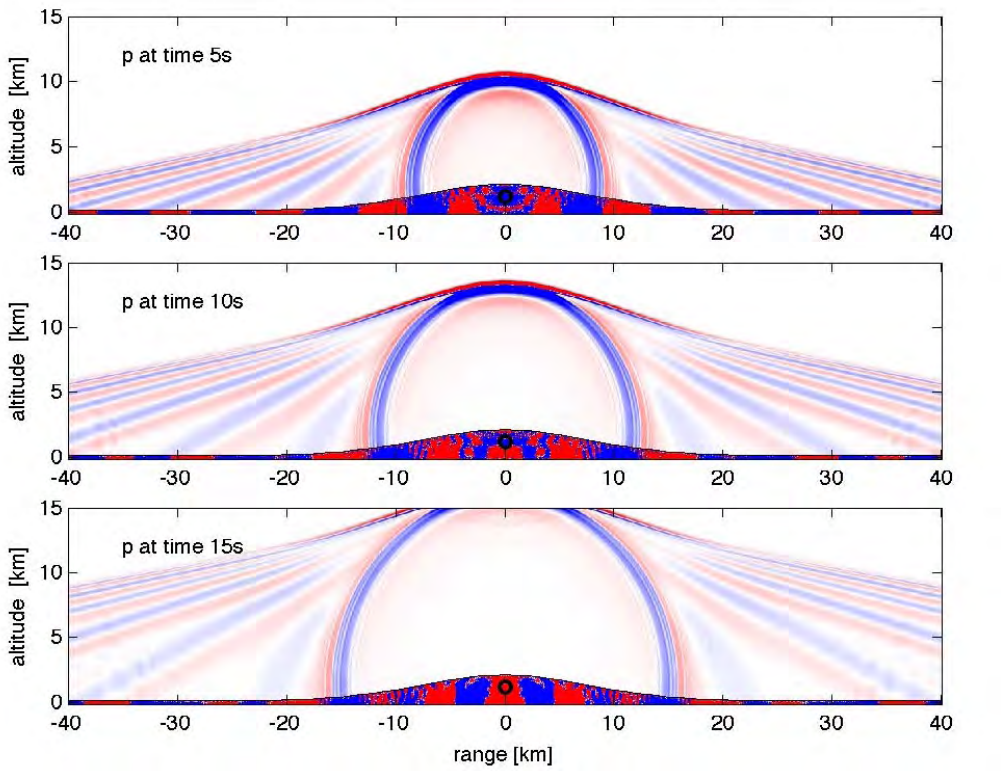

Figure 3. "Snapshots" of the acoustic pressure emanating from a 0.5 Hz source at 0.9km below the central peak at the time points 5 s, 10 s, and 15 s. An identical color scale is shown for each plot.

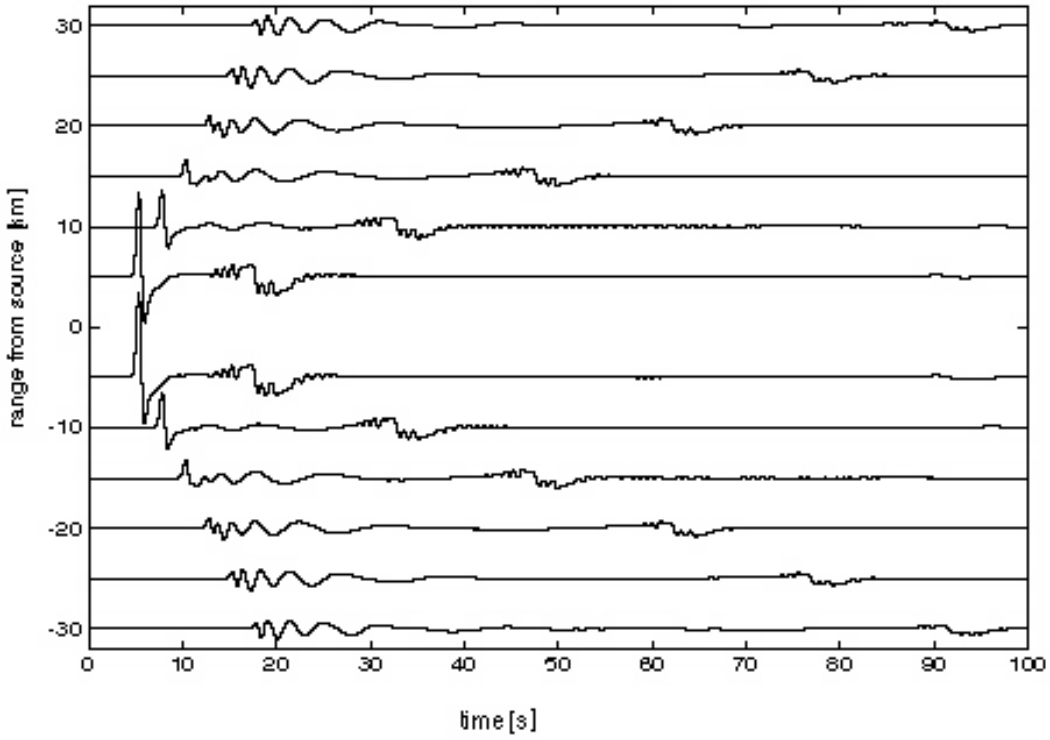

Figure 4. Waveforms at distances of 5 km to 30 km from the peak.

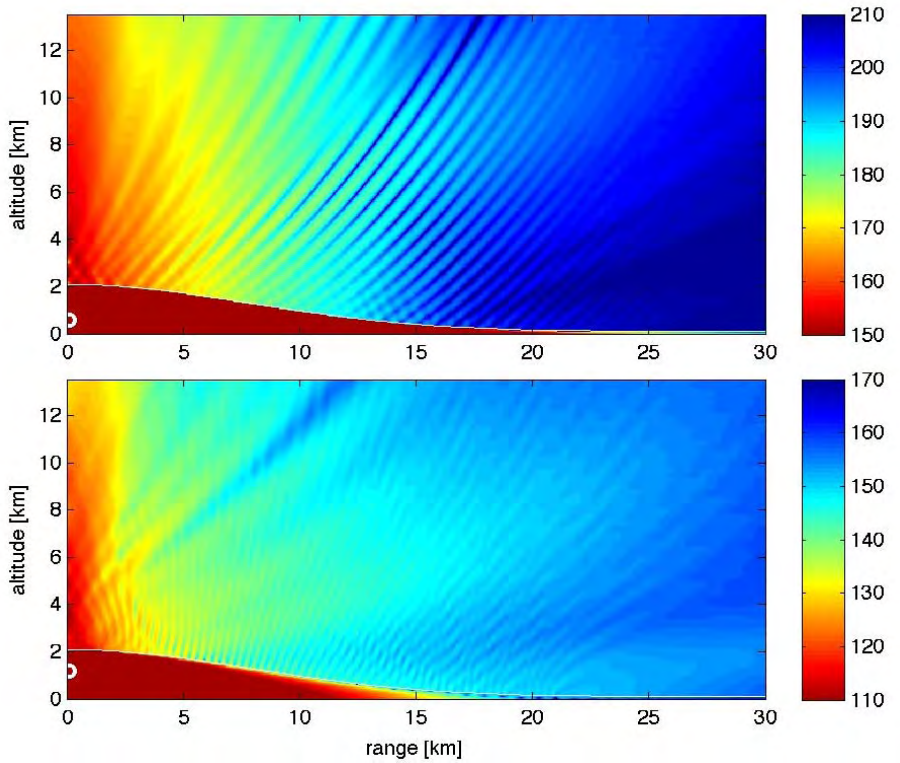

Figure 5. Transmission loss results derived from finite difference frequency domain modeling of (top) a 0.5Hz source at 0.6km, i.e., 1.5km below the surface and (bottom) for the same source at 1.2km. The second source is equivalent to the one shown for the FDTD simulation. Note the difference in colorscales for the two source depths.

For the finite difference time domain results, there was no discernable difference in the results with or without gravity, as gravitational results become significant at much lower frequencies. Incorporation of a realistic wind profile showed only minor asymmetry in the waveform results on either side of the peak. Wind and gravity have not yet been incorporated into finite difference frequency domain modeling.

CONCLUSIONS AND RECOMMENDATIONS

Equations have been developed to incorporate the effects of both wind and gravity into an FDTD modeling method. FDFD methods of incorporating these effects are less robust as they require the inversion of large matrices.

It has been demonstrated that a full waveform modeling technique is required to model infrasound generated by an underground source. Further verification of the FD method is needed for sources within a fraction of a wavelength from a boundary with a strong impedance contrast.

REFERENCES

R. Blumrich, and D. Heinmann (2002). A linearized Eulerian sound propagation model for studies of complex meteorological effects, *J. Acoust. Soc. Am.* 112: 446–455.

Botteldoren, D., 1994, Acoustical finite-difference time-domain simulation in a quasi-Cartesian grid, *J. Acoust. Soc. Am.* 95: 2204–2212.

de Groot-Hedlin, C., (2006). Finite difference methods for acoustic and acousto-gravity wavefields: application to low frequency infrasound propagation, in *Proceeding of the 28th Seismic Research Review: Ground-Based Nuclear Explosion Monitoring Technologies*, LA-UR-06-5471, Vol. 2, pp. 893–899.

Gill, A. E. (1982). *Atmosphere-Ocean Dynamics*, Academic Press, San Diego, CA.

Ostashev, V.E., D.K. Wilson, L. Liu, D.F. Aldridge, N.P. Symons, D. Marlin (2005). Equations for finite-difference, time-domain simulation of sound propagation in moving inhomogeneous media and numerical implementation, *J. Acoust. Soc. Am.*, 117, 503–517.

Van Renterghem, T., and D. Botteldoren, (2003). Numerical simulation of the effect of trees on downwind noise barrier performance, *Acust. Acta. Acust.* 89: 764–778.

Yee, K.S, 1966, Numerical solution of initial boundary value problems involving Maxwell's equations in isotropic media, *IEEE Trans. Antennas and Propagation* 14: 302–307.

ADVANCEMENT OF INFRASOUND PROPAGATION CALCULATION TECHNIQUES USING MESOSCALE ATMOSPHERIC AND TERRAIN SPECIFICATIONS

Robert G. Gibson[1], Douglas P. Drob[2] and David E. Norris[1]

BBN Technologies[1] and Naval Research Laboratory[2]

Sponsored by U.S. Army Space and Missile Defense Command

Contract No. W9113M-05-C-0132

ABSTRACT

Numerical calculation of infrasound propagation paths is necessary to support accurate infrasound event identification, phase association, and source location. Predicting the details of infrasound propagation relies both on propagation models that capture the fundamental physical processes and on characterization of the propagation medium, namely the global atmosphere from the ground to altitudes above 100 km. Therefore the accuracy of propagation modeling depends in part on the fidelity of the atmospheric characterization. Furthermore, for infrasound propagation at regional and local ranges, characterized by higher frequencies than propagation at global ranges, effects of the boundary conditions of the propagation domain, in particular the terrain elevation, become increasingly important.

The analysis tool kit *Infra*sound *M*odeling of *A*tmospheric *P*ropagation (InfraMAP) integrates infrasound propagation models and environmental representations, including synoptic updates of the atmospheric specification at low and middle altitude, such as the output from numerical weather prediction models that supplement climatological characterization of temperature, wind, and air composition at high altitude. The Naval Research Laboratory (NRL) Ground-to-Space (G2S) semi-empirical spectral model provides a global specification of the atmosphere that can be utilized in InfraMAP. These capabilities for propagation calculation and atmospheric specification allow infrasound researchers to investigate critical propagation phenomena, conduct sensitivity studies, and compare results of numerical modeling with observed signals.

Recent efforts develop techniques for utilizing accurate, high-resolution regional atmospheric specifications and terrain elevation databases with infrasound propagation modeling codes. Mesoscale atmospheric models, which focus on the meteorology of a specific region, can account for and resolve important wind and temperature phenomena relevant to regional and local infrasound propagation. Such models can also provide atmospheric profiles that are consistent with the variable terrain elevation in a region. By investigating realistic atmospheric models and terrain specifications at a range of resolutions, we seek insight into the appropriate spatial and temporal scales that are necessary for achieving improved infrasound predictions at the relevant frequencies. Ground truth events are studied in order to assess performance of techniques for incorporating mesoscale atmospheric models and terrain specifications with propagation models and to evaluate the benefits for infrasound monitoring.

RESEARCH OBJECTIVES

In order to advance the state of the art for high-fidelity infrasound predictions, it is necessary to develop both propagation calculation techniques and atmospheric characterizations that capture more of the fundamental physics that affect infrasound. The overall objective of this effort is to improve understanding of the effects of atmospheric dynamics on the propagation of infrasound, thus improving infrasonic event identification, phase association and source localization. This is being accomplished by developing and analyzing advanced high-resolution atmospheric specifications for use with propagation models and applying them in comparison studies using ground truth infrasound events. Specific objectives include the following:

- Comparing ground-truth observations to propagation predictions using existing atmospheric specifications and propagation models. This includes sensitivity studies using the NRL G2S specification at various resolutions and studies of atmospheric model biases and error budgets.
- Developing a multi-resolution, regional environmental specification capability, based on the NRL G2S framework, for use in propagation calculations. This includes assimilation of mesoscale atmospheric models that provide high-resolution meteorological information on local and regional scales.
- Comparing ground-truth observations to propagation predictions using the newly developed regional specifications that incorporate mesoscale atmospheric properties and terrain elevation.
- Investigating effects of including variable terrain elevation in ray-tracing propagation predictions.
- Developing research products that are useful for improving nuclear explosion monitoring capability.

This paper discusses recent progress in providing accurate atmospheric specifications for ground-based nuclear explosion monitoring via infrasound. Prior work by Drob et al. (2003) has provided a simple framework to account for atmospheric complexity over certain height ranges. The NRL G2S semi-empirical spectral model combines numerous sparse data sets using global spectral methods to specify the details of the entire atmosphere for use in infrasound propagation calculations. The infrasound analysis tool kit InfraMAP, developed by BBN Technologies, makes use of G2S and allows options for specifying the propagation environment by incorporating the output from global numerical weather prediction (NWP) models to supplement the baseline climatological characterization of temperature, wind and air composition (Gibson and Norris, 2003, 2004). These global synoptic specifications are used with infrasound propagation models in order to improve predictions compared to those based on climatology. The global G2S specification has been reasonably well validated and has been applied successfully in many infrasound event studies. However, observed infrasound phases have not been well predicted by state of the art propagation models for several ground-truth events over regional scales (e.g., Bhattacharyya et al., 2003). Therefore, further modeling advances that address the fundamental physical processes that affect infrasound are required. Also required, in parallel, are advances in specification of the propagation environment that address fundamental atmospheric physics at appropriate spatial and temporal scales and that can be utilized to improve the performance of advanced propagation models.

There is strong interest in the monitoring community in understanding the physics of regional-scale infrasound propagation. At various infrasound propagation ranges there remain a number of unanswered scientific questions, including: the effect and significance of terrain and internal wave scattering; meteorological reasons for losses of signal coherency; and the frequent infrasonic detection of events in the classical “zone of silence.” For infrasound propagation over regional scales it is clear that regional, or mesoscale, NWP analyses are required to investigate and account for these complex atmospheric effects. For example, mesoscale specifications can enable the resolution of tropospheric and marine inversion layers recently shown to be significant for regional infrasound propagation (e.g., Herrin et al., 2006). A key goal of this research project is therefore to improve the temporal, horizontal, and vertical resolution (i.e., information content) of the existing G2S specifications in the 0 to 35 km region by incorporating output from operational NWP models and thus provide improved regional atmospheric specifications for detailed infrasound propagation calculations. We seek to produce a mesoscale version of the G2S model that can be used with InfraMAP and other propagation calculation codes, and we are improving the capabilities of InfraMAP to support higher-resolution atmospheric specifications and more advanced calculation techniques. This paper discusses recent research that will result in improved accuracy and understanding of the underlying physics of infrasound propagation calculations for nuclear explosion monitoring, particularly at regional and local ranges.

RESEARCH ACCOMPLISHED

Improving NRL G2S with Mesoscale Atmospheric Specifications

The atmospheric structure responsible for the transport of infrasonic energy can change rapidly in both time and space. Below 55 km these structures are being resolved by NWP systems that assimilate vast amounts of data from a diverse network of operational satellite, ground-based, and in situ sensors. National and Department of Defense (DoD) weather centers can provide regional atmospheric specifications that have a very high spatiotemporal resolution and accuracy compared to comprehensive global specifications, including G2S. This improvement is achieved by focusing additional efforts on the meteorological observations and atmospheric physics specific to a given geographic region.

Mesoscale NWP codes typically are nested grid point models that interpolate global $1° \times 1°$ (or $0.5° \times 0.5°$) 6-h meteorological data sets and enhance them through applying additional physical constraints as well as auxiliary input data sets and observations over a particular region. Model output resolutions better than 10x10 km at 1-h time intervals are possible. Some mesoscale NWP codes even include nested grids within nested grids to help resolve significant features and areas of interest. Compared to global NWP models, the mesoscale NWP models include improved specification of atmospheric boundary layer effects, account for non-hydrostatic fluid dynamics, and can resolve large- to medium-scale stationary mountain waves, as well as some types of propagating gravity waves (for example, see Janjic et al., 2001, Janjic, 2003). Output from mesoscale NWP models are merged with global G2S specifications in the process of generating the new mesoscale-G2S specifications (Gibson et al., 2006).

In the prior year's research review, we discussed how prototype mesoscale-G2S specifications can be as accurate or more accurate than individual radiosonde profiles and better for use in infrasound propagation calculations for events of interest. This is because the assimilative NWP analysis products self-consistently combine many different data sets and types of information (e.g., radiosonde profiles, satellite temperature soundings, ground-based meteorological-station observations, and geophysical fluid dynamic constraints) to provide improved accuracy and spatiotemporal information content, while adding range dependence to the atmospheric specifications (Gibson et al., 2006). The primary difference between the existing global G2S specification and the improved mesoscale version is in the available spatiotemporal resolution (i.e., fine-scale structure). Figure 1 shows a comparison of the G2S (red) and mesoscale-G2S (blue) zonal wind profiles (east-west) at the source location during the first launch of the second White Sands Missile Range (WSMR) infrasound calibration experiment (WSMR-II).

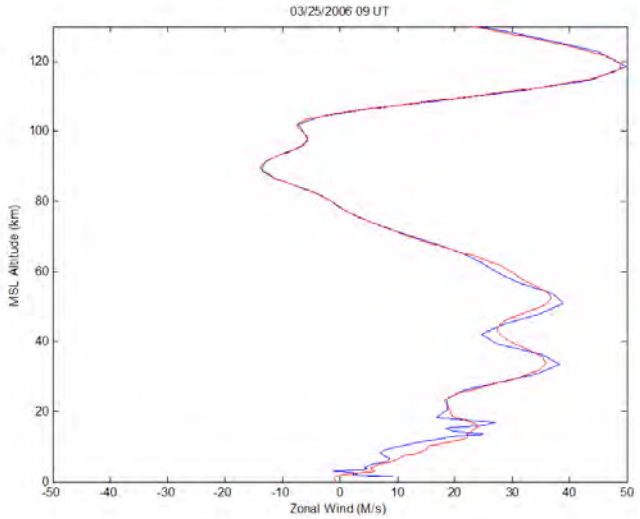

Figure 1. Comparison of G2S (red) and mesoscale-G2S (blue) zonal wind profiles (east-west) for the first launch of the WSMR-II experiment. The vertical coordinate is altitude above mean sea level.

In this example the mesoscale-G2S specifications qualitatively match the existing global G2S specifications. Note, however, the fine-scale wind structures below 20 km given by the mesoscale model, which are typically filtered out in the production of the global G2S specifications. These atmospheric structures (associated with internal gravity

waves and related phenomena) can affect infrasound propagation at regional and local ranges and may be responsible for anomalous infrasonic detections in the classical zone of silence. The increased vertical resolution and additional physics inherent in the mesoscale NWP models will enable the new mesoscale-G2S specifications to resolve the vertical temperature (and sound speed) gradients in the first 20 to 500 meters of the atmosphere that result from direct radiative/thermal coupling at the air/land/sea interface. These effects can be significant over major bodies of water or desert regions where day-night surface temperature differences are substantial. The ability to provide this information above an infrasound array (where locally only the 2-m meteorological-station temperatures measurements are available) will be a valuable resource in developing an understanding of infrasound signal coherency loss and related boundary layer coupling phenomena.

Mesoscale NWP specifications for the continental U.S. (CONUS), Alaska, Hawaii, and several U.S. territories are readily available from the National Oceanic and Atmospheric Administration's (NOAA) National Centers for Environmental Prediction (NCEP). Earlier in this effort we began autonomously downloading and archiving the NOAA Rapid Update Cycle (RUC) time series for the CONUS domain. The RUC system provides mesoscale atmospheric specifications hourly, from 0 to 25 km altitude, at both 20 km and 13 km horizontal resolution. We have assembled a database of 20×20 km RUC specifications at 3-h intervals, from 15-Oct-2005 to the present time.

More recently, our research has focused on using the Weather Research and Forecasting (WRF) Model, which is at the forefront of the US meteorology enterprise (http://wrf-model.org/index.php). The effort to develop WRF has involved collaboration among the National Center for Atmospheric Research (NCAR), NOAA's NCEP and Forecast Systems Laboratory (FSL), the Air Force Weather Agency (AFWA), the Naval Research Laboratory, Oklahoma University, and the Federal Aviation Administration (FAA). WRF allows researchers the ability to conduct simulations reflecting either real data or idealized configurations.

There are currently two main versions of the WRF model—a research version known as Advanced Research WRF Model (WRF-ARW) and the operational version known as the Nonhydrostatic Mesoscale Model (WRF-NMM). The WRF-NMM model is run operationally by NOAA/NCEP and employs a hybrid sigma-pressure vertical coordinate system and rotated latitude-longitude grid. For these reasons this version of WRF is believed to be the best one to provide reliable and accurate mesoscale specification for mesoscale-G2S. Current WRF-NMM model output includes the main atmospheric state variables needed to perform infrasound propagation calculations—pressure, temperature, and the horizontal wind velocity components. Additional atmospheric state variables include specific humidity, vertical wind, and turbulent kinetic energy. Surface level microphysics is also an important aspect of mesoscale NWP models. As a result, auxiliary meteorological quantities included are planetary boundary layer (PBL) height, subgrid scale roughness height, friction velocity, solar zenith angle, surface radiation fluxes, precipitation amounts (including breakdowns of water, snow, and ice), cloud fractions (including low, middle, and high), soil moisture, etc.

Model Domains and Example Implementations

In earlier stages of this effort, the mesoscale-G2S grid used for software integration and testing purposes, systems automation development, and ground-truth validation efforts was limited to the western half of CONUS. More recently, we have utilized the capabilities of the WRF model to generate WRF-NMM specifications for several domains around the world. Representative examples of these domains include the (a) Middle East, (b) Korean Peninsula, (c) southwest United States, and (d) Vanuatu Archipelago; these domains are shown in Figure 2. The Middle East domain can be used to generate specifications for ground-truth events such as the 18-Feb-2004 train car explosion in Iran, and the Korean Peninsula domain can be used to study events such as the reported 9-Oct-2006 underground nuclear weapon test. The southwest U.S. domain supports study of events such as the White Sands Missile Range (WSMR) infrasound calibration experiment, and the Vanuatu Archipelago domain can be used to study events such as infrasound observations from the Lopevi and Yasur volcanoes, e.g., at station I22FR.

Each of these mesoscale specifications is initialized with digital terrain and ground cover databases and the 6-h NOAA operational Global Forecast System (GFS) analysis fields; these same fields are also used by the current global version of G2S. The baseline WRF-NMM specifications produced have a total of 37 vertical levels extending up to approximately 20 km. The number of horizontal grid points provided for each of the domains shown above is 300×219, 240×161, 280×181, and 280×181, respectively. The effective horizontal model resolutions are 15×15 km, 12.5×12.5 km, 10×10 km, and 15×15 km, respectively.

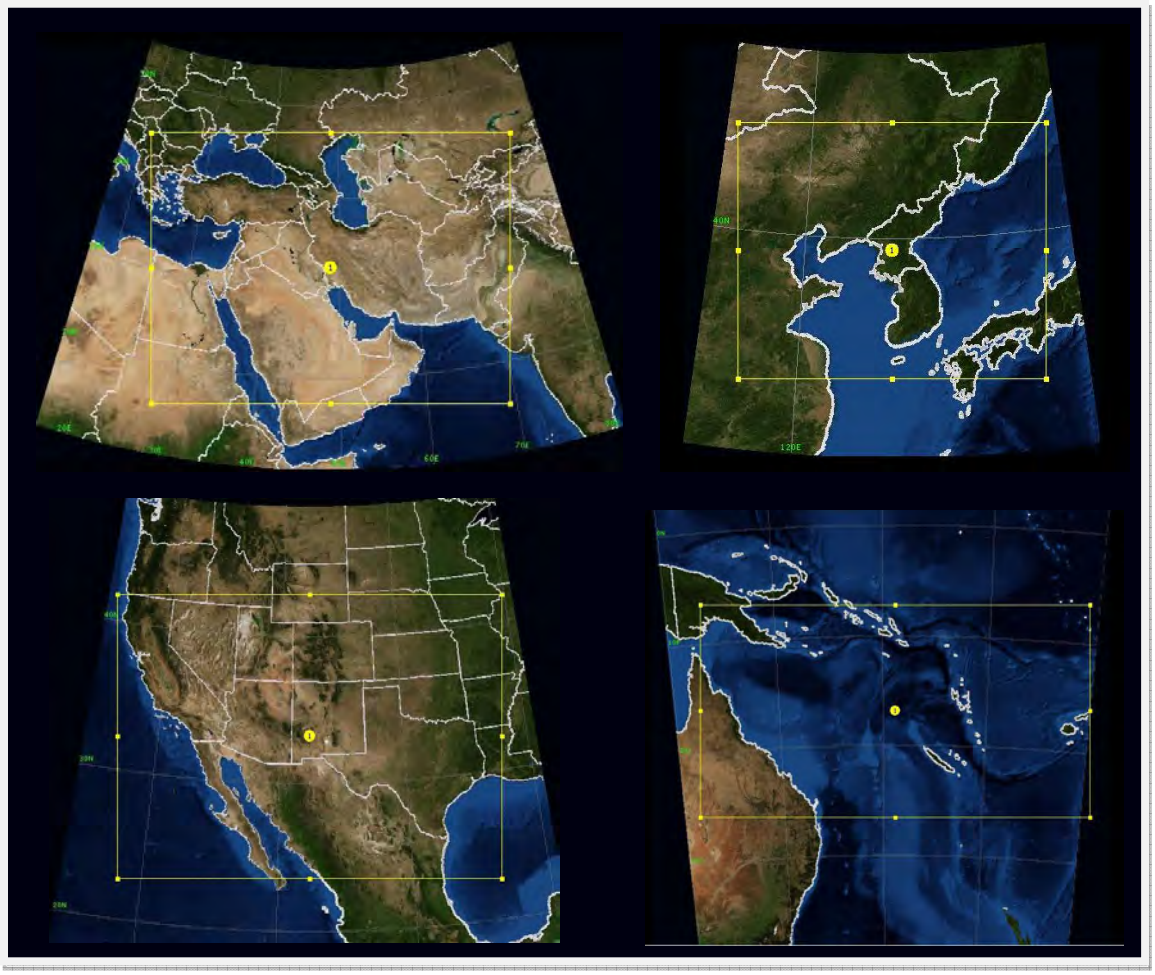

Figure 2. Example of several WRF model domains generated for infrasound event analysis.

A static digital terrain elevation model is required to combine mesoscale and global atmospheric specification fields with the background high-altitude empirical models in order to translate them into altitude coordinates so that they can be used in infrasound propagation calculations. Capabilities have been built into the G2S client software to provide terrain elevation estimates at 30′ resolution (1 km) for any location on the globe. The NOAA Global Land One-km Base Elevation (GLOBE) digital terrain model provides the underlying data (Hastings and Dunbar, 1998).

Recent and ongoing research work is toward development of the capability to generate custom specifications at resolutions similar to these shown above for any arbitrary domain. Effort is required to process the WRF model output fields and combine them with G2S specifications at higher altitudes for use in infrasound propagation calculations. It is reasonably straightforward to augment (or simply replace) the first 20 to 25 km of the existing G2S specifications with WRF specifications since G2S effectively reproduces the NOAA-GFS specifications used by the WRF model at the 20 km upper boundary to within observable accuracies. Additional computational challenges arise due to the staggered grid employed for horizontal output fields in the WRF model. In this system the scalar (mass) and vector (wind) fields are provided at different locations. The staggered gridding scheme simplifies computational aspects of the numerical integration of the WRF model's prognostic continuity, mass, momentum, and energy equations. The model also employs a projection that rotates Earth's latitude/longitude grid so that the intersection of the equator and prime meridian is at the center of the model domain. This minimizes the convergence of meridians over the domain, but results in uneven grid spacing. Therefore these grids must be subsequently interpolated to a regular latitude/longitude grid for utilization in the propagation models in InfraMAP.

Selected examples from the mesoscale atmospheric specifications for the Southwest U.S. domain shown in Figure 2 are presented below. Figure 3 shows the static sound velocity at an altitude 10 meters above the ground/sea surface. The date and time, September 09, 2005, 09:00 UT, correspond to the first WSMR infrasound calibration experiment. Note the high sound velocity areas over the deserts of the Southwest United States. Another notable meteorological feature is the warm surface air mass (high sound velocities) over the Gulf of California in contrast to the cold marine surface air layer over the Pacific Ocean.

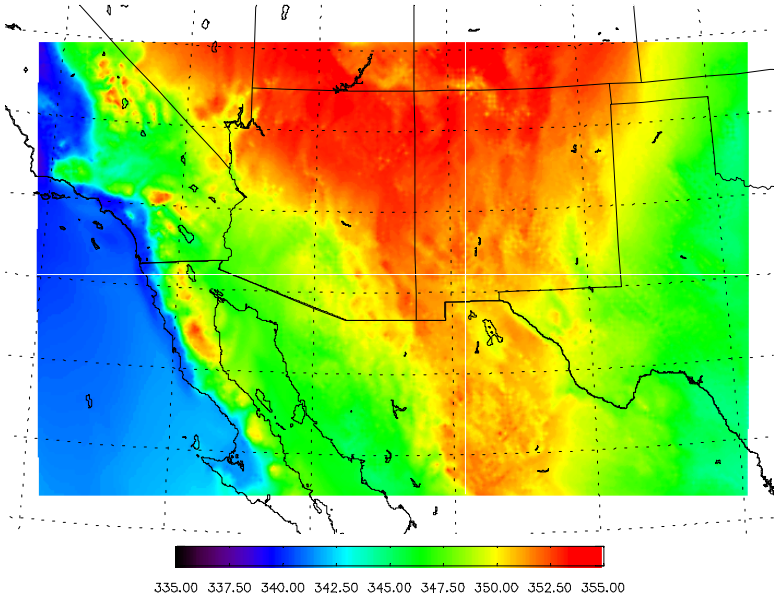

Figure 3. Example output of static sound velocity (m/s) at a height 10 m above the ground/ocean surface (September 09, 2005, 09:00 UT). Lines indicate the locations of vertical slices presented in subsequent figures.

Figure 4 shows an east-west cross section of the meridional (north-south) wind component. These fields are interpolated from the vertical hybrid sigma-pressure grid to an equally spaced vertical grid at 200 m intervals.

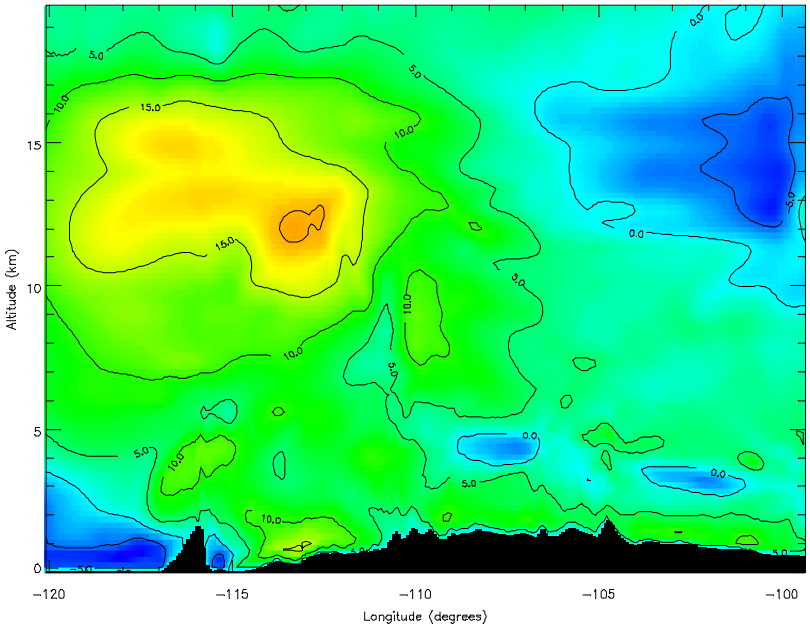

Figure 4. Illustrative east-west vertical slice of the meridional (north-south) wind fields (m/s) for the southwest U.S. mesoscale model domain, as shown above (September 09, 2005, 09:00 UT).

The horizontal and vertical extent of the topography can clearly be seen—for example, at the Baja Peninsula and the Gulf of California. Notable meteorological features include down-slope/drainage winds along the Gulf of California. Decreases in the horizontal winds at the surface, tending toward zero due to friction, are noticeable with the increased vertical resolution of the mesoscale NWP specifications. Figure 5 shows a north-south cross section of the zonal (east-west) wind component. Again the vertical and horizontal extent of the topography relative the vertical and horizontal gradients in the wind fields can be seen.

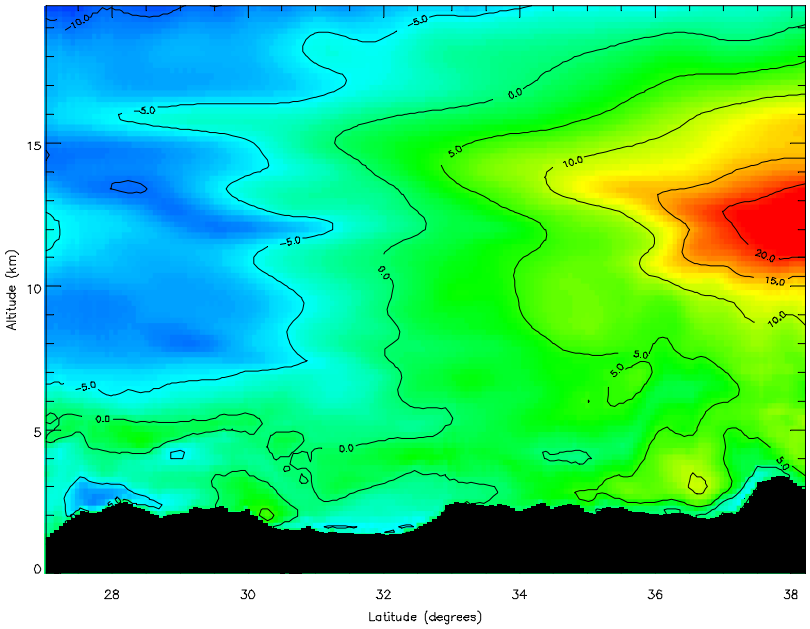

Figure 5. Illustrative north-south vertical slice of the zonal (east-west) wind field (m/s) for the southwest U.S. mesoscale model domain, as shown above (September 09, 2005, 09:00 UT).

Propagation Calculation Techniques Incorporating Mesoscale-G2S and Variable Terrain Elevation

Using the mesoscale fields described above we have begun to investigate the information content and consequences of mesoscale-G2S specifications for infrasound signal propagation for ground-truth events. Comparison studies to date have focused on the ground-truth data sets generated by the 2005/2006 WSMR series of rocket grenade tests. Model-to-measurement and model-to-model comparisons are intended to help identify the relevant physics affecting infrasound propagation and determine the level of confidence in existing and recently developed modeling capabilities. In support of this goal, we have continued development of calculation techniques and software routines for integration of new G2S specifications with propagation models. Environmental characterization fields (e.g., temperature, wind, sound speed) contained in mesoscale data blocks can currently be displayed and manipulated in InfraMAP. Various terrain databases have also been incorporated and can be displayed over both global and mesoscale domains. Propagation modeling techniques using ray-tracing over variable terrain elevation have been developed and integrated in prototype form in InfraMAP. Development of additional modeling capabilities (e.g., parabolic equation) incorporating variable terrain is in progress as a parallel effort.

Additional examples of mesoscale atmospheric fields suitable for use with infrasound propagation calculation techniques in InfraMAP are shown below. Figure 6 displays the height above mean sea level of the first (lowest) layer of a mesoscale-G2S atmospheric specification over the western U.S. Due to the terrain-following nature of the coordinate system, the available specification fields closest to Earth's surface can be seen to follow the major terrain features. At each layer of the specification, all fields necessary for propagation calculations are available. Figure 7 shows an example of one of these fields, horizontal wind velocity, both for the first (lowest) layer and also the 30th layer above the surface. Both zonal and meridional wind components are available; however, for illustration, the figures display the overall magnitude of the horizontal wind.

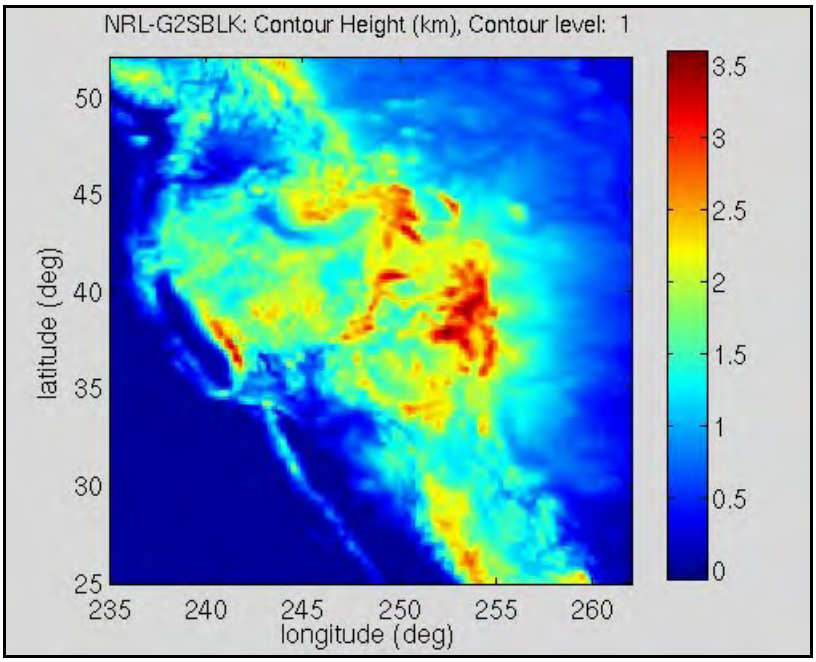

Figure 6. Height (km) above mean sea level of the first (lowest) layer of a mesoscale-G2S atmospheric specification over the western U.S.

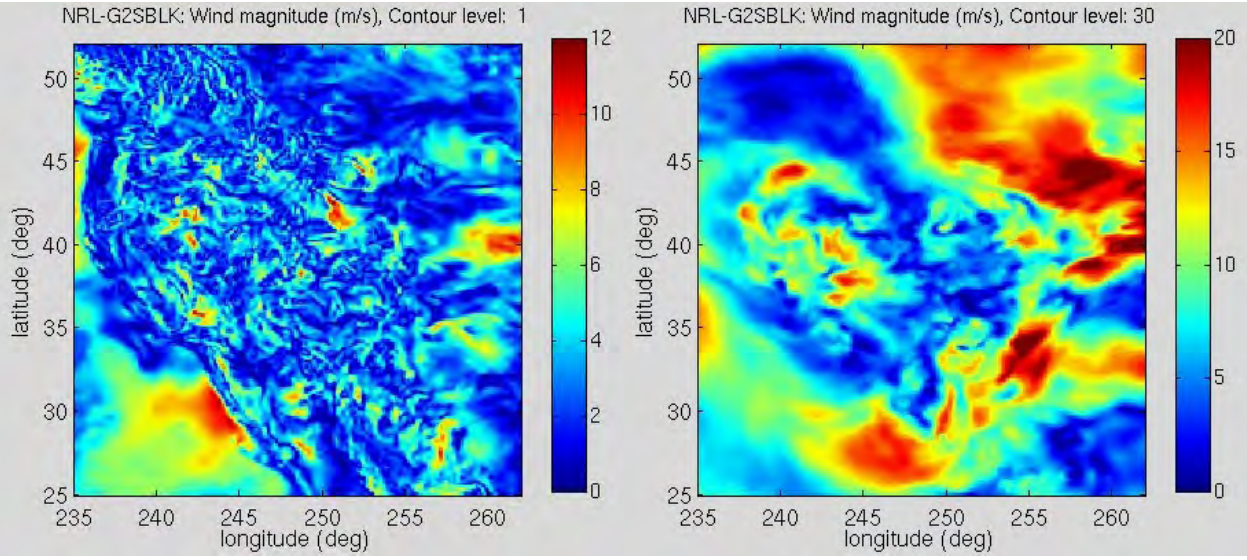

Figure 7. Horizontal wind magnitude (m/s) for the first or lowest layer (left) and for the 30th layer (right) of a mesoscale-G2S atmospheric specification over the western U.S.

The terrain-following nature of the specification layers can also be seen by viewing fields across a slice of the atmosphere. Figure 8 shows horizontal wind magnitude for an east-west vertical slice of the same mesoscale-G2S atmospheric specification shown in Figures 6 and 7. The vertical resolution of the mesoscale system is on the order of 10 to 50 m near the surface, increasing to larger, yet variable values with altitude.

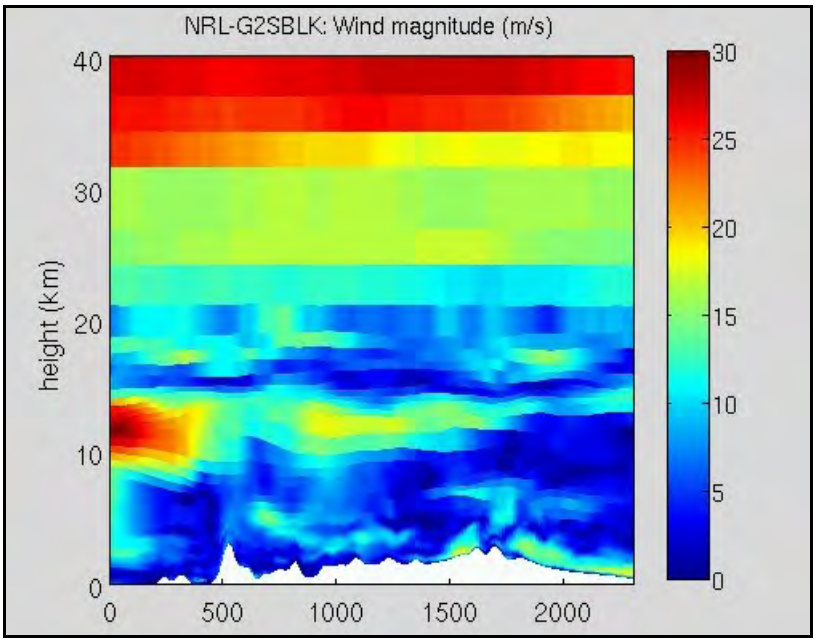

Figure 8. Illustrative east-west vertical slice of the horizontal wind field magnitude (m/s) for the mesoscale-G2S atmospheric specification over the western U.S., as shown in Figures 6 and 7. Horizontal axis is range in km.

In the prior year's research review, progress toward characterizing the interaction of infrasound with Earth's surface was addressed, in particular the effects of variable terrain elevation on propagation. Research in this area has continued, including efforts to identify the relevant spatial scales over which the variable terrain elevation needs to be resolved for infrasound propagation calculations. Figure 9 displays ray paths for propagation from one of the grenade events in the WSMR rocket test series, showing interaction with the high-resolution terrain database.

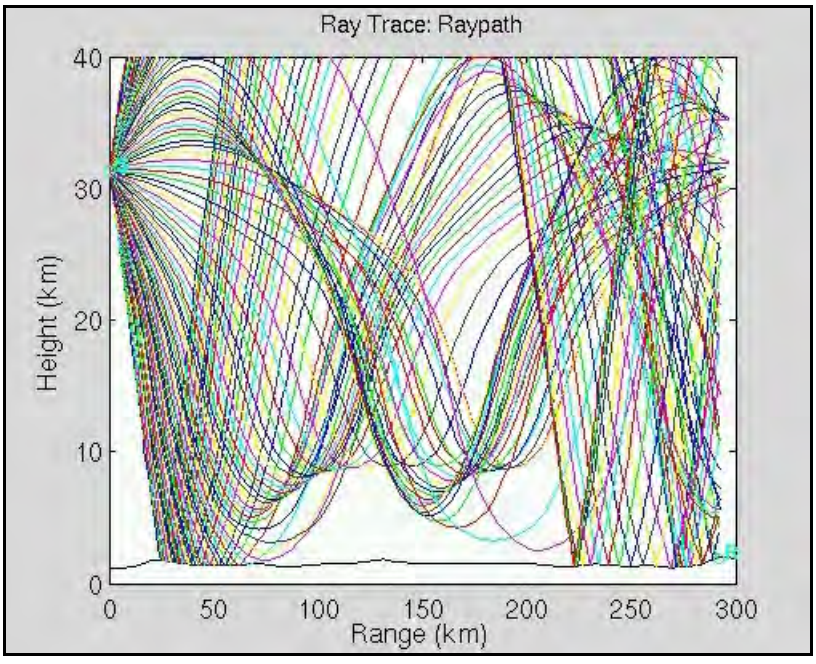

Figure 9. Modeled infrasound ray paths for an elevated explosive source during the WSMR rocket test series. Reflection of rays off complex terrain elevation is shown.

CONCLUSIONS AND RECOMMENDATIONS

Mesoscale atmospheric specifications improve the characterization of the lower regions of the atmosphere and are therefore used with infrasound propagation models in order to improve predictions compared to those based on global specifications. Significant progress has been made toward improved calculation techniques for infrasound propagation, particularly over regional and local ranges. The capability has been developed to supplement existing global G2S specifications with high-resolution mesoscale-G2S specifications for a variety of regional domains and a range of event times in the recent past.

Modeling advances that utilize mesoscale specifications while addressing the fundamental physical processes that affect infrasound are in progress. Also required, in parallel, are continued advances in specification of the propagation environment that address fundamental atmospheric physics at appropriate spatial and temporal scales and that can be utilized to improve the performance of advanced propagation models. As mesoscale-G2S models are applied to the analysis of infrasound ground-truth events, research will continue toward tuning the model resolutions in order to provide the most effective specifications for the analysis of infrasound signals. We also intend to explore how to improve accuracy of the WRF-NMM output (and thus mesoscale-G2S specification fields) by direct assimilation of raw measurements and other auxiliary high-resolution data sets (e.g., 5×5 km resolution sea surface temperatures).

Study of ground-truth events at long range will improve understanding of the strengths and weaknesses of both global and regional atmospheric specifications. Study of local and regional events will improve understanding of the importance of mesoscale atmospheric phenomena and terrain elevation effects.

REFERENCES

Bhattacharyya, J., H. Bass, D. P. Drob, R. Whitaker, D. Revelle, and T. Sandoval (2003). Description and analysis of infrasound and seismic signals recorded from the Watusi explosive experiment, on September 28, 2002, in *Proceedings of the 25th Seismic Research Review—Nuclear Explosion Monitoring: Building the Knowledge Base*, LA-UR-03-6029, Vol. 1, pp. 587–596.

Drob, D. P., J. M. Picone, and M. A. Garcés (2003). The global morphology of infrasound propagation, *J. Geophys. Res.* 108: doi: 10.1029/2002JD003307.

Drob, D. P. (2004). Atmospheric specifications for infrasound calculations, *InfraMatics Newsletter*, No. 5.

Gibson, R. and D. Norris (2003). Integration of InfraMAP with near-real-time atmospheric characterizations and applications to infrasound modeling, in *Proceedings of the 25th Seismic Research Review—Nuclear Explosion Monitoring: Building the Knowledge Base*, LA-UR-03-6029, Vol. 2, pp. 638–645.

Gibson, R. and D. Norris (2004). Integration of InfraMAP software with near-real-time atmospheric characterizations, BBN Technologies final report for Air Force Research Laboratory (AFRL/VSBYE) under Contract DTRA01-01-C-0084.

Gibson, R., D. Drob, and D. Norris (2006), Advancement of infrasound propagation calculation techniques using synoptic and mesoscale atmospheric specifications, in *Proceedings of the 28th Seismic Research Review: Ground-Based Nuclear Explosion Monitoring Technologies*, LA-UR-06-5471, Vol. 2, pp. 900–909.

Hastings, D. A. and P. K. Dunbar (1998). Development and assessment of the Global Land One-km Base Elevation digital elevation model (GLOBE), in *International Society of Photogrammetry and Remote Sensing | Commission IV | Symposium, ISPRS Archives*, Vol. 32: pp. 218–221.

Herrin E. T., T. S. Kim, and B. W. Stump (2006). Evidence for an infrasound waveguide, *Geophys. Res. Let.* 33: Art. No. L07815.

Janjic, Z. I., J. P. Gerrity, and S. Nickovic (2001). An alternative approach to nonhydrostatic modeling, *Month. Weather Rev.* 129: 1164–1178.

Janjic, Z. I. (2003). A nonhydrostatic model based on a new approach, *Meteorol. Atmos Phys.* 82: 271–285.

INFRASOUND IN THE "ZONE OF SILENCE"

Eugene T. Herrin[1], Paul W. Golden[1], Petru T. Negraru[1] and Mihan H. McKenna[2]

Southern Methodist University[1], and US Army Engineer Research and Development Center-GSL[2]

Sponsored by Army Space and Missile Defense Command

Contract No. W9113M-06-C-0028

ABSTRACT

Experiments designed to understand the propagation of infrasound signals at distances of less than 200 km were conducted in central Nevada, USA during the week of 11 September 2006. A controlled suite of explosions on the surface, designed to destroy surplus military ordnance, provided the source of the infrasound signals. Three temporary 4-element infrasound arrays were deployed in a line due north of the sources at distances from 76 to 157 km. In addition, seismo-acoustic data was provided by the permanent Nevada Infrasound Array (NVIAR) and collocated seismic array NVAR, located about 36 km east of the source.

The experiment was successful, and detections from all explosions were recorded at all arrays. Therefore, the assumption of the absence of signals in the "zone of silence" is incorrect in this case. At NVIAR the shorter distance and impulsive signals indicated the arrival of direct waves. However, other signals recorded at distances of 76 to 157 km were longer in duration, and initial travel time analysis indicated the rays were turning in the stratosphere. Simultaneous balloon launched rawinsonde weather recordings collected between the sources and the stations through the tropopause showed there were no conditions that would allow turning rays or reflections in the troposphere. Because the travel times were too short for turning rays above the stratosphere, we conclude that the energy was refracted in the stratosphere. Obviously improved atmospheric models through the stratosphere are needed to explain the occurrence of infrasound signals in the "zone of silence".

OBJECTIVES

Classic infrasound propagation theory describes a 'zone of silence' where no energy is predicted to reach sensors near the surface from the limit of the direct arrival out to 200–250 km from the infrasound source. However, recent studies (McKenna, 2005; Golden et. al., 2007) showed that under various wind and temperature conditions infrasound signals can be recorded within these distances. The purpose of this research study is to characterize the conditions under which atmospheric returns are recorded in the zone of silence. A better understanding of these types of signals could be helpful in characterizing the sources at these distances.

RESEARCH ACCOMPLISHED

Experiments were conducted near Hawthorne NV on September 11–13, 2006 (Julian days 254, 255, and 256) designed to collect infrasound and seismic data from well-controlled explosions on the ground surface. Carefully controlled ordnance disposal explosions are conducted by Hawthorne Army Ammunition Depot contractors on a regular basis. These well documented sources provided seismic and infrasound signals for studies of infrasound propagation in the traditional "zone of silence". Figure 1 shows the location of the International Monitoring System (IMS) Primary Seismic array PS-47 (NVAR) with the configuration of the experimental infrasound array (NVIAR) in the middle, as well as the Army Ammunition Depot and disposal pits.

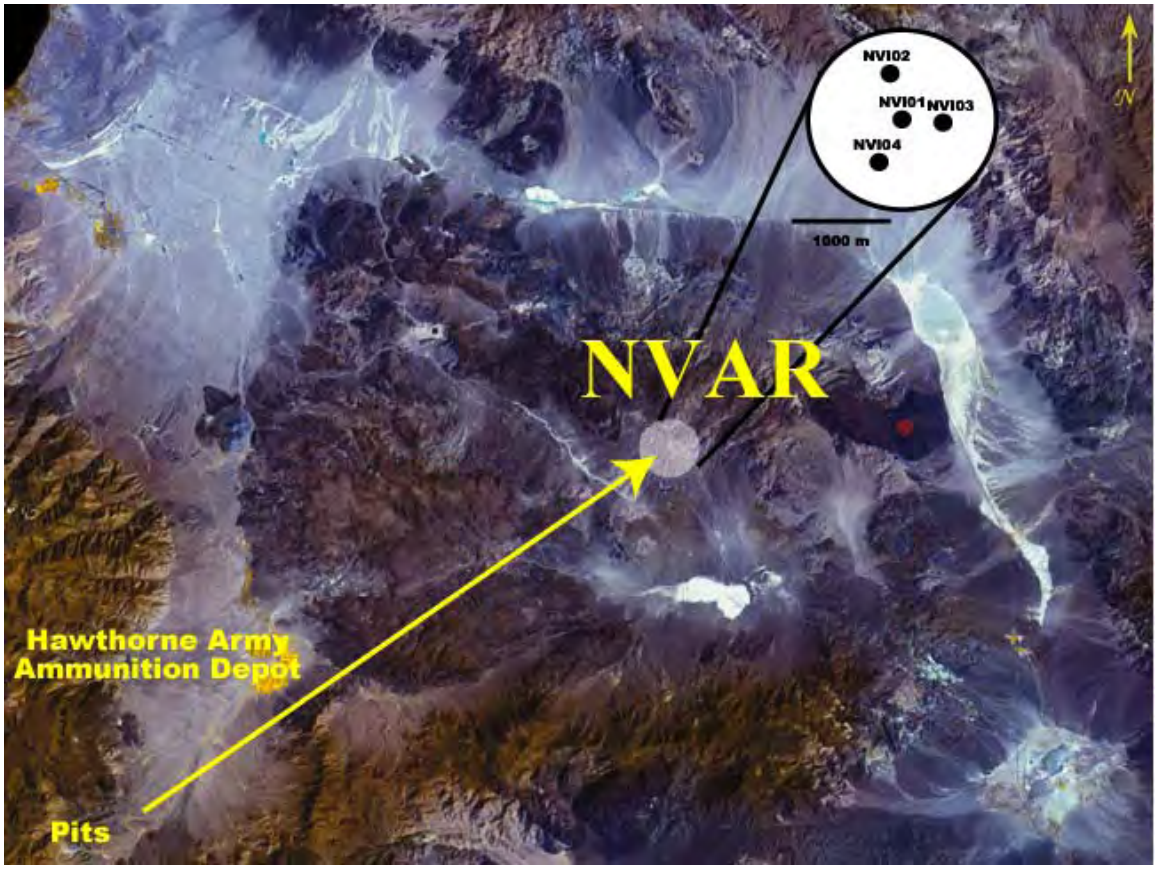

Figure 1. Location of NVAR and the Hawthorne Army Ammunition Depot. The configuration of NVIAR is also shown.

In addition to collecting data at NVIAR during our experiments, we deployed three 4-element portable infrasound arrays at distances of 76, 108, and 157 km north of the demolition location. The array at 76 km was located within the village of Shurz NV (SHURZ), while the other 2 arrays were north and south of the city of Fallon NV, designated Fallon north (FALN) and Fallon south (FALS), along State Highway 95. During the experiment FALS recorded a significant number of infrasound arrivals which were probably associated with activities at the nearby

Fallon Naval Air Station. Each of the three portable arrays consisted of 4 IML infrasound sensors located in line with the direction of propagation of the signals at separation distances of 50, 100, and 150 meters as shown in Figure 2. The linear configuration was chosen to maximize the time delays across the array.

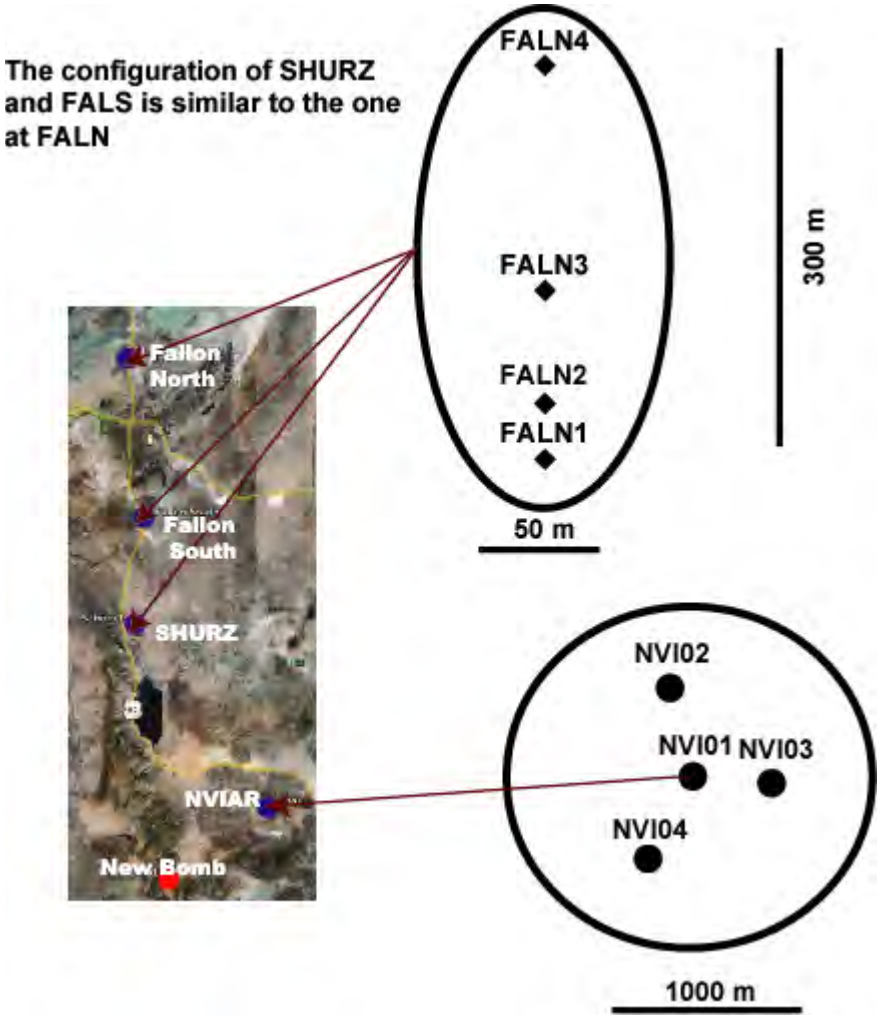

Figure 2. Satellite image of the area of temporary infrasound arrays deployed for the experiments with plan layouts of each array.

Thus, including the permanent array, we have observations at 36, 76, 108, and 157 km from the source. With the exception of NVIAR the stations are all in the traditional "zone of silence". Signals from the explosions recorded at NVIAR are direct arrivals, not turning rays. The presence of the array in the direct arrival distance range provides near source seismic and infrasound waveforms allowing us to calculate very accurate origin times for each explosion. With the exception of FALS, that experienced some cable problems, all the other channels of the arrays recorded data from the munitions explosions. Figures 3, 4, and 5 show the beam (delay and sum) of the arrays for the first day of the experiment.

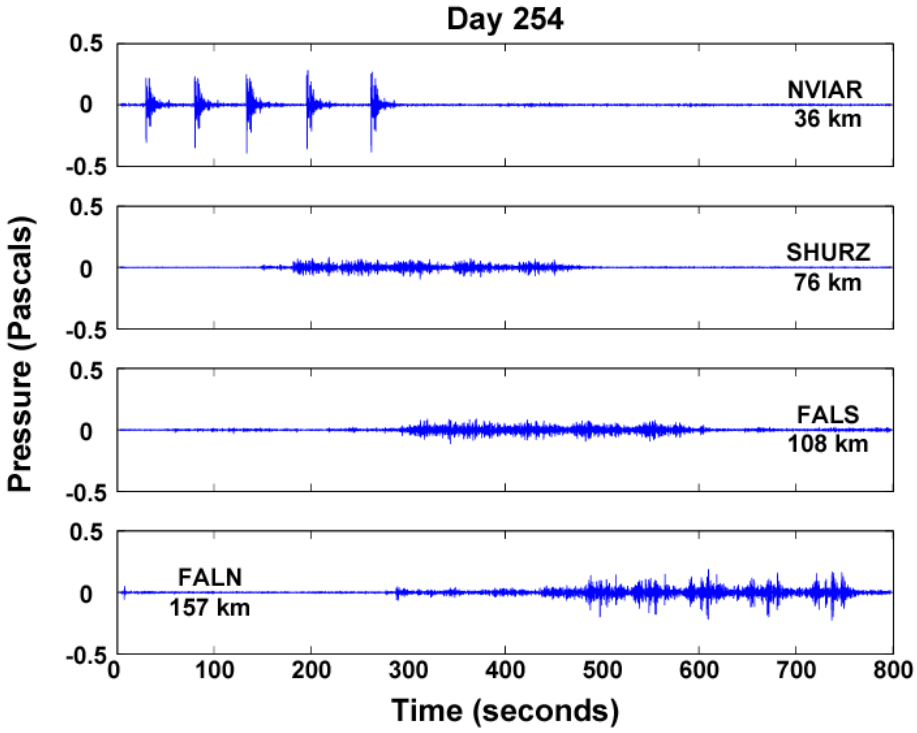

Figure 3. Filtered beam (0.5-3 Hz) for the first day of the experiment.

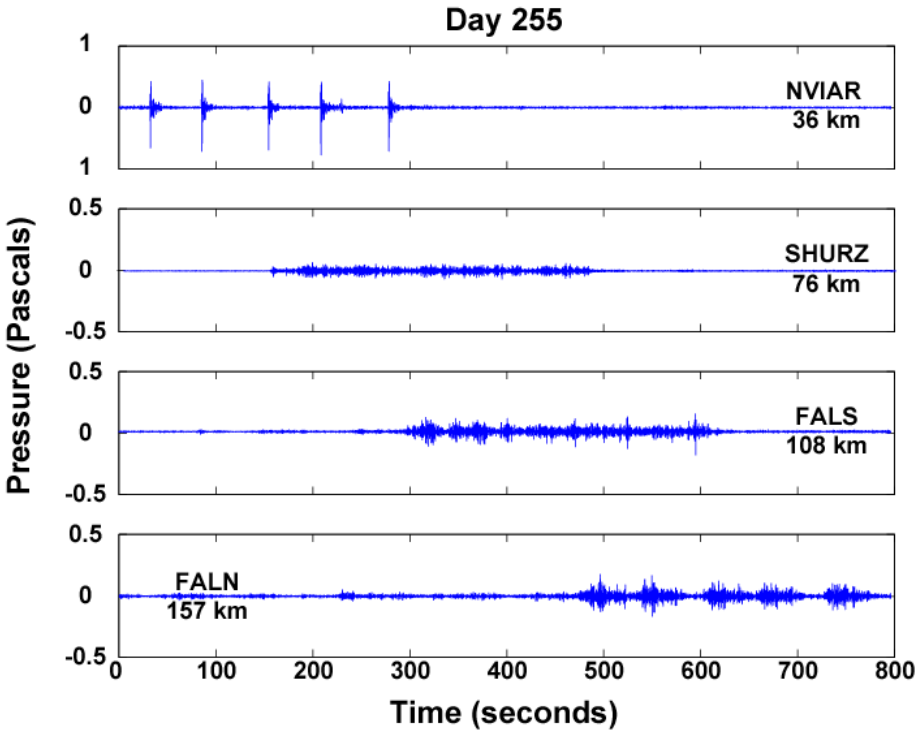

Figure 4. Filtered beam (0.5-3 Hz) for the second day of the experiment

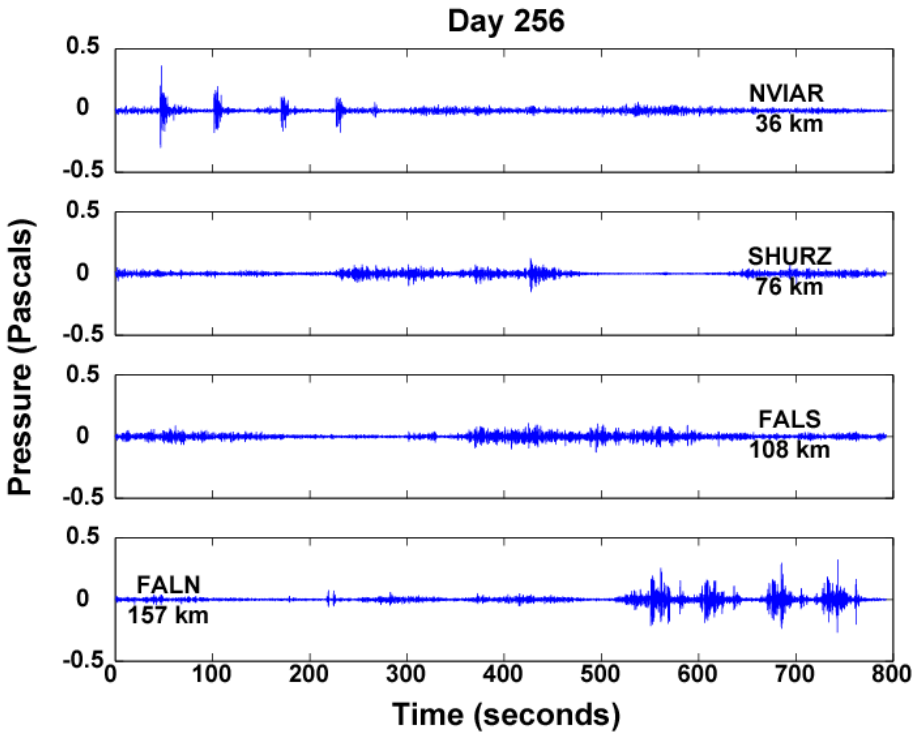

Figure 5. Filtered beam (0.5-3 Hz) for the last day of the experiment

In addition to the infrasound array data we collected meteorological data at the Hawthorne NV airport. We employed the National Severe Storms Laboratory (NSSL) to collect balloon launched rawinsonde meteorological data during our three experiment days. The rawinsondes were used to collect temperature, dewpoint, barometric pressure, GPS latitude, longitude, altitude, and wind speed and direction data.

Table 1 gives the arrival times, travel times and velocities for the first arrivals at each array for all three days while Figure 6 shows the velocities for each day at each of the four arrays.

Table 1. Arrival times, travel times and velocities of first arrivals at each array for all three days of the experiment.

Acoustic Arrival Times			
	DAY 254	DAY 255	DAY 256
NVAR	17:41:28.102	17:54:10.35	20:50:48.590
SHURZ	17:43:58.74	17:56:39.8	20:53:07.3
FALS	17:45:49.78	17:58:30.0	20:55:19.0
FALN	17:48:54.17	18:01:33.34	20:58:20.24
Acoustic Travel Times (seconds)			
NVAR	105	105	105
SHURZ	256	255	244
FALS	367	365	376
FALN	551.5	548.5	557
Average Travel Velocities (m/s)			
NVAR	343	343	343.8
SHURZ	296	297	310
FALS	294	295	286
FALN	284	285	281

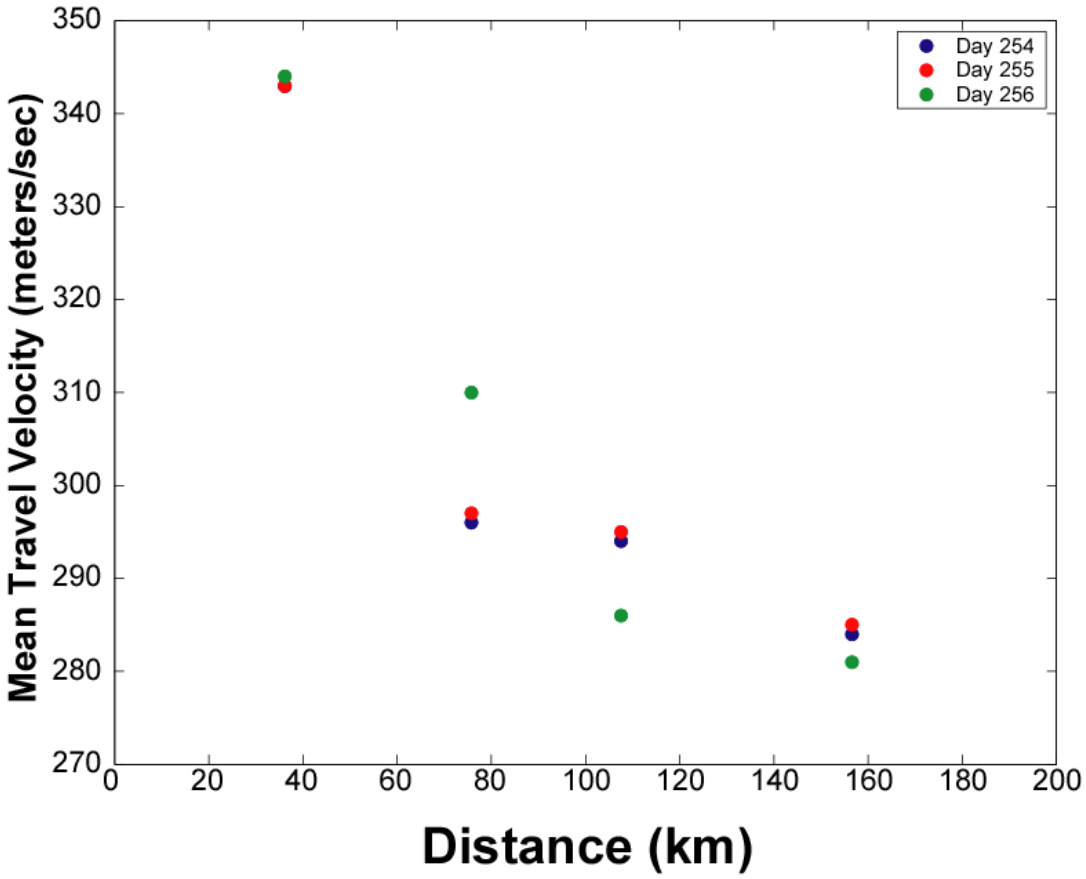

Figure 6. Infrasound travel velocity at each array for all three days of experiments.

At NVIAR travel velocities for all arrivals were about 343 m/s. At the other arrays velocities between 263 m/s and 297 m/s were determined. These velocities indicate that except for NVIAR all of the arrays recorded stratospheric returns. We would expect travel velocities between 200 and 240 m/s for thermospheric returns. There were no arrivals with velocities below about 263 m/s indicating that none of the arrivals were from thermospheric returns (Mutschlecner and Whitaker, 1999).

There is also an interesting observation at SHURZ for the first two days. An infrasound arrival is recorded approximately 30 seconds before the arrival of the main wavetrain. This arrival, shown in Figure 7 has the same back-azimuth as the main arrivals and a travel velocity of 341 m/s. We interpret this as being a direct arrival and 30 seconds later an arrival with a travel velocity of 296 m/s was recorded indicating a stratospheric return. Any other potential direct arrivals of the later shots are masked by the much larger amplitudes of the stratospheric returns. Therefore at a distance of 76 km from the source both direct and stratospheric arrivals are recorded. However on day 256 we could not observe the direct arrival due to higher local noise conditions. In addition, the yields of the explosions were all smaller than the previous two days.

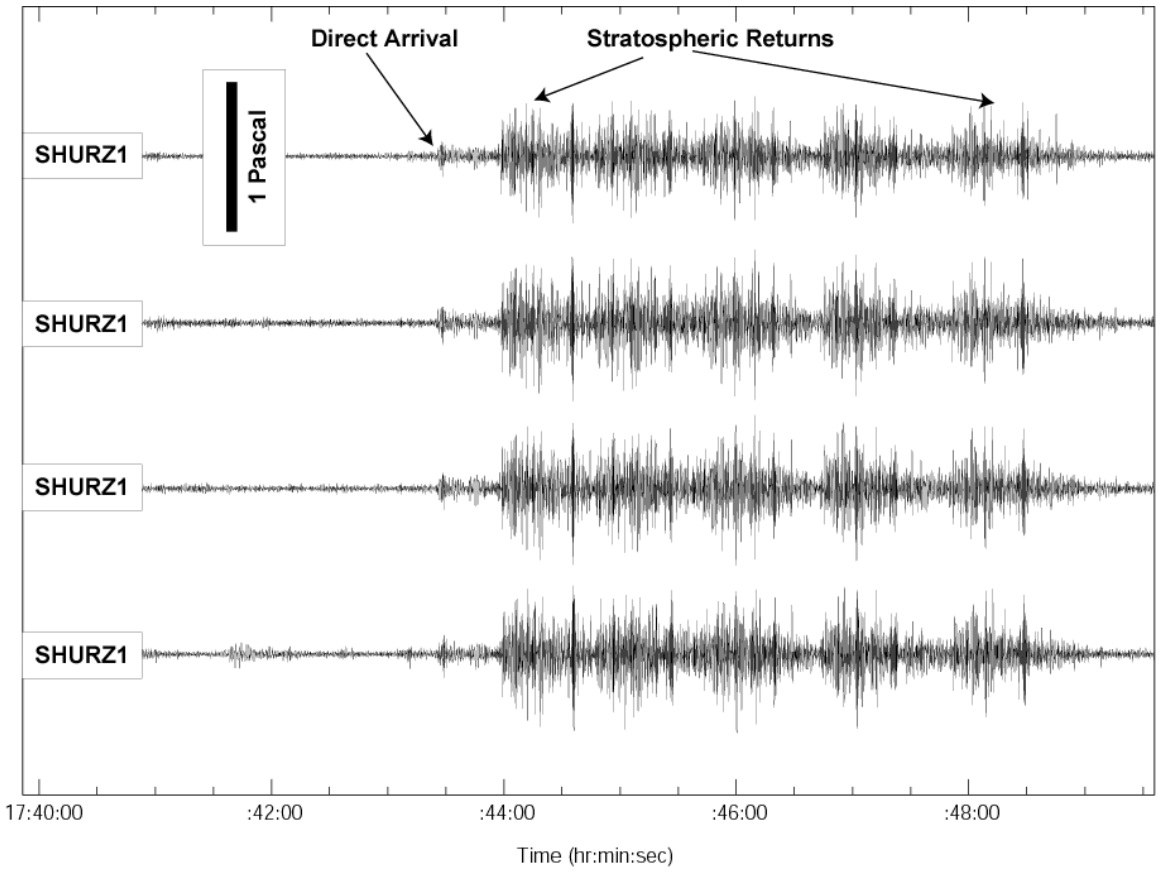

Figure 7. Infrasound data from day 254 recorded at SHURZ, showing both direct arrivals and stratospheric returns.

CONCLUSIONS AND RECOMMENDATIONS

This unique dataset provides us the opportunity to try to gain a better understanding of the dynamics of the atmosphere allowing infrasound propagation in the “zone of silence”. Initially it was believed that infrasound propagation in the classic “zone of silence” is controlled by short lived temperature inversions in the troposphere (Mckenna, 2005), and that the infrasound signals are propagating through those ephemeral ducts. Local meteorological data recorded in the source/receiver path during the time of the explosions show no inversions in the troposphere, yet signals are recorded at all arrays. In the case of NVIAR, these are direct arrivals and the other arrays are all located within the so called "zone of silence". With the exception of a direct arrival on one day of our experiment at SHURZ, all the recorded signals at stations SHURZ, FALS and FALN are stratospheric returns, based on average travel velocities. Clearly troposphere inversions are not the only mechanism that controls the “zone of silence”.

Preliminary modeling with InfraMap software using the Naval Research Laboratory Ground to Surface (NRL-G2S) coefficients for day 256 is not able to predict the stratospheric returns recorded at the temporary arrays. The atmospheric temperature profile derived from InfraMap is shown in Figure 8. The model agrees with our rawinsonde data up to balloon burst in the lower stratosphere around 24 km.

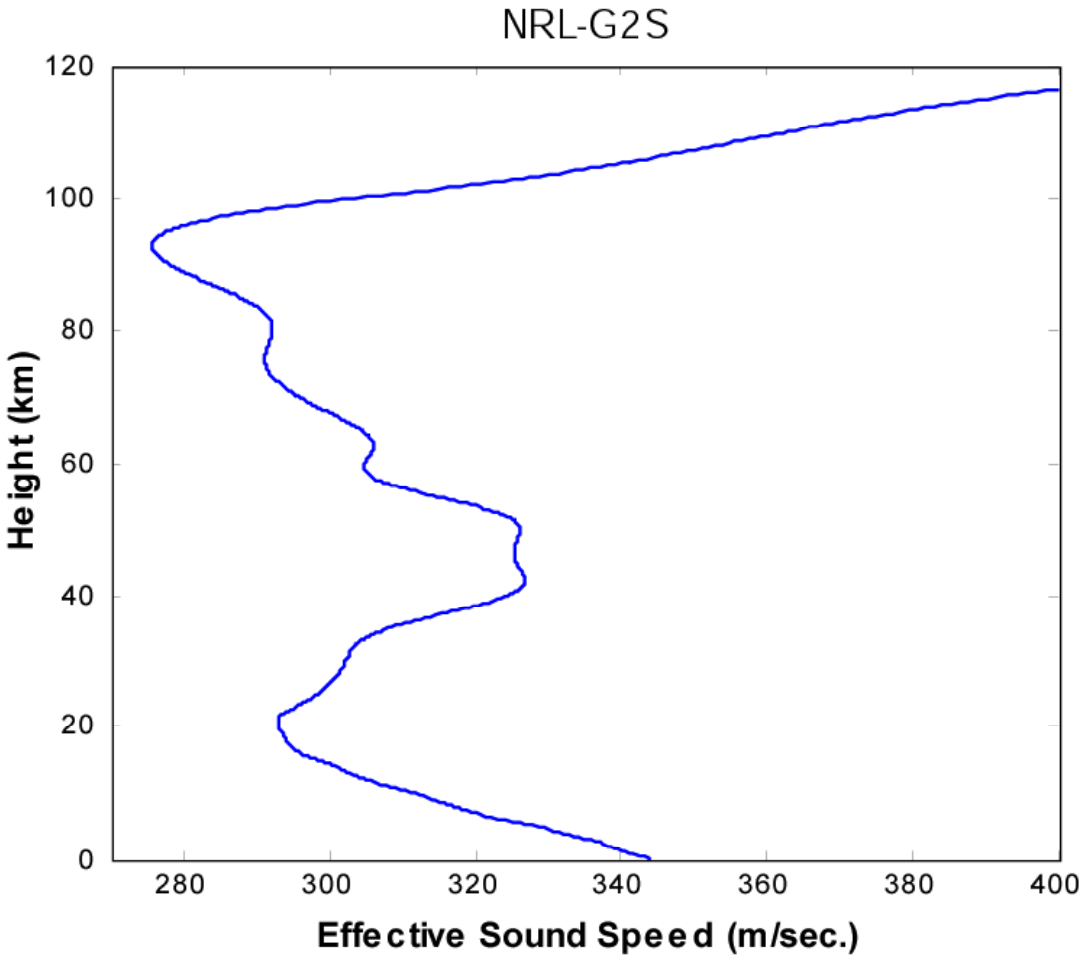

Figure 8. Temperature profile from InfraMap modeling.

A very low altitude inversion is common for desert environments due to ground heating from sunlight. This inversion was observed each day during our experiments and is seen in the actual rawinsonde temperature profile in Figure 10. Though hard to see in the model profile the inversion generates a rolling wave that attenuates at distances less than 100 km as is shown in Figure 9. This could explain the direct arrival recorded at SHURZ at a distance of 76 km from the source, while at FALS at a distance of 108 km it was attenuated. However, modeling indicates no energy should return to the surface at any of our stations. Obviously atmospheric models in the stratosphere need to be refined to successfully predict arrivals within the "zone of silence".

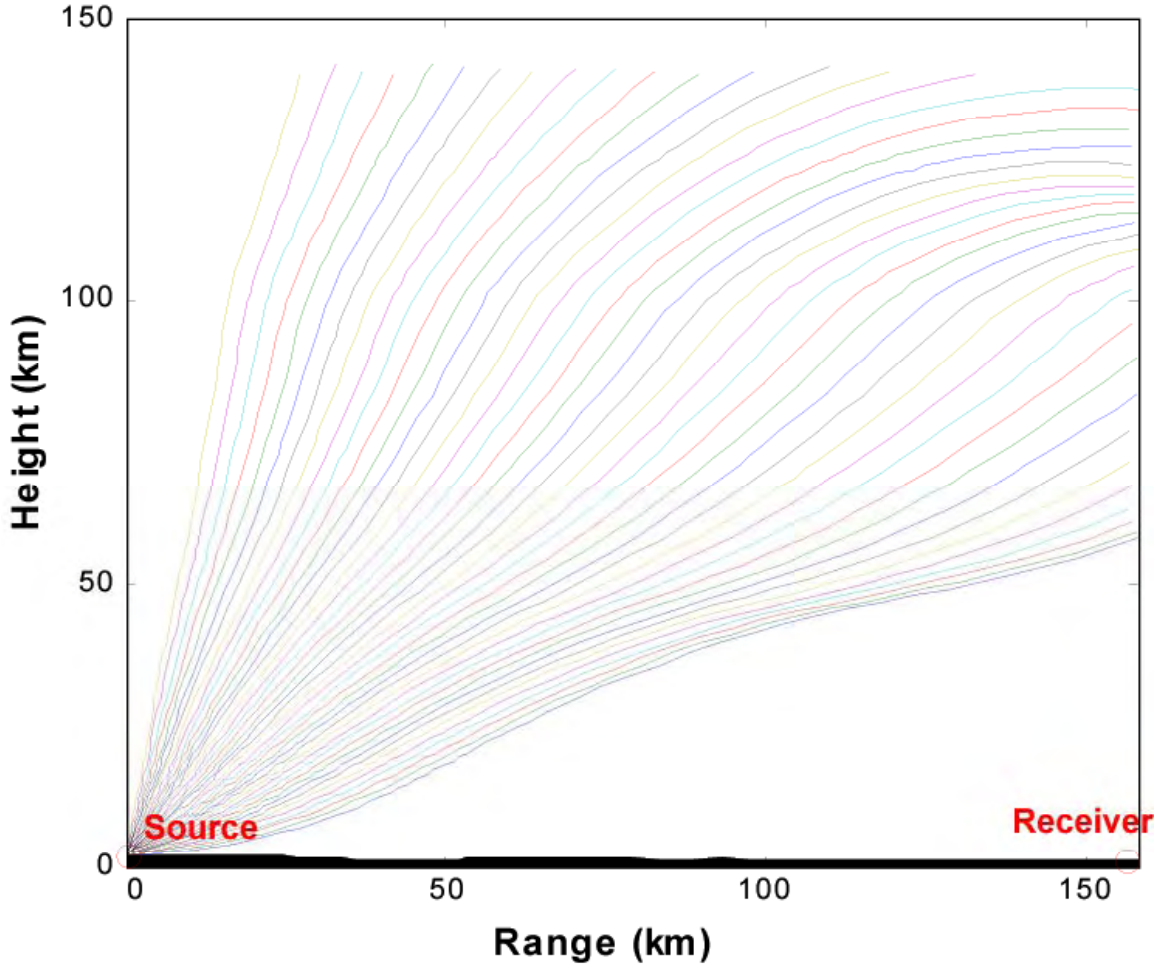

Figure 9. Rays traced through the atmospheric model, indicating that there should be no energy returned to the surface at distances of 76 to 157 km. A direct arrival could be recorded at distances up to 100 km.

REFERENCES

McKenna, S.H. (2005). Infrasound wave propgation over near regional and tele-infrasonic distances, Southern Methodist University, PhD Thesis.

Golden P., E. T. Herrin and P. T. Negraru (2007). Infrasound in the zone of silence, in *Proceedings of the European Geophysical Union*, Vienna, April 2007.

Muschlecner, J. P. and R. W. Whitaker (1999), Thermospheric Infrasound Signals, Proceedings of the 21st Seismic Research Symposium, Las Vegas NV. Pp. 151–158.

DEVELOPMENT OF ADVANCED PROPAGATION MODELS AND APPLICATION TO THE STUDY OF IMPULSIVE INFRASONIC EVENTS

David E. Norris[1], Joydeep Bhattacharyya[1], and Rodney W. Whitaker[2]

BBN Technologies[1] and Los Alamos National Laboratory[2]

Sponsored by Army Space and Missile Defense Command

Contract No. W9113M-05-C-0135

ABSTRACT

Research advances have been made in the areas of advanced model development, ground truth (GT) event studies, and model validation. They are focused on understanding the driving mechanisms that affect measured waveforms, and quantifying the prediction performance of new modeling capabilities. High fidelity predictions of infrasonic waveforms properties, including travel time and amplitude, improve source localization. These advances also support discrimination between various infrasonic impulsive events.

New additions have been made to the GT database. These additions mainly focus on events that are directly related to nuclear weapons testing: near-surface nuclear explosion (NE), underground nuclear explosion (UNE), and high-explosives (HE) events. They are well-calibrated GT events and significant domain knowledge resides with our Los Alamos National Laboratory (LANL) colleagues. Digital waveforms from the HE events at range of 1.5 to 60 km have been acquired and will be used to explore the boundaries between propagation regimes near the infrasound source.

New propagation modeling capabilities include a ray model that incorporates the effects of diffraction, PE/TDPE models that incorporate small-scale atmospheric variability, and PE/TDPE models that account for terrain. Detailed model comparisons studies have been complete for both the 1988 Henderson explosion and White Sands Missile Range (WSMR) I, II, and III rocket experiments.

OBJECTIVES

The objectives for this research contract are twofold. The first objective involves developing advancements in propagation modeling capabilities: a PE model accounting for ambient density gradients, a ray model that includes the effects of diffraction, and PE and TDPE models that account for variable terrain and fine-scale atmospheric structure. The second objective involves identifying and compiling ground truth data sets and using them for event analysis and model comparison studies.

Through these efforts, some of the driving mechanisms affecting the measured waveforms will be identified, and the prediction performance of the new models will be quantified. These advances will ultimately improve event localization capabilities. More robust prediction of infrasonic arrivals, for example, those that reach the ground through diffraction, more accurate travel-time predictions, and more robust amplitude predictions will improve localization. In addition, these advances will support discrimination between various infrasonic impulsive events.

RESEARCH ACCOMPLISHED

Ray Diffraction

A significant limitation to standard ray theory occurs when shadow zones are present. Shadow zones are regions where no rays penetrate and zero amplitude is predicted. They form between ground bounces and below elevated ducts. Despite ray theory predictions, acoustic energy can reach into shadow zones through diffraction and scattering (Gilbert and Raspet, 1990).

We have extended the capabilities of ray tracing by integrating a ray diffraction model for application to the boundary of elevated ducts. The modeling approach is based on identifying a diffraction region and propagating the diffracted ray from this point down to the receiver. The travel time is computed over the total ray path from the source to the diffraction region and from the diffraction region to the receiver.

As an example, consider the April 23, 2001, north pacific bolide that was observed at a multitude of stations, including IS57 in Pinon Flats, California. Figure 1 shows a fan of rays computed from the source region along the bearing to IS57. All these rays are trapped in an elevated stratospheric duct. However, observations suggest a signal velocity (range over travel time) more consistent with a stratospheric path than a thermospheric one. This arrival may result from energy leaking out of the elevated stratospheric duct.

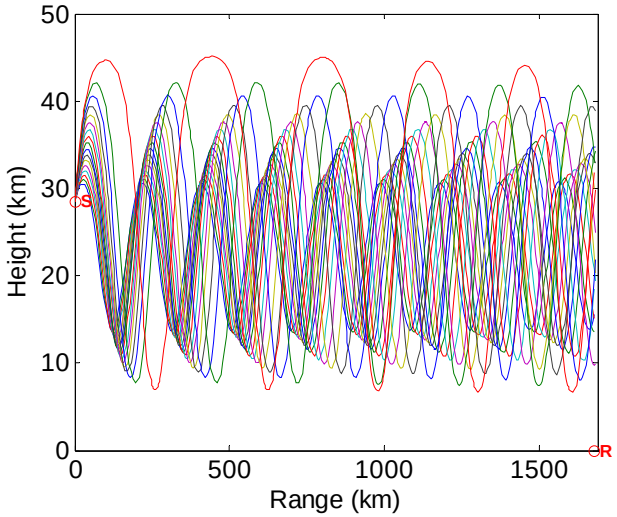

Figure 1. Stratospheric rays from the April 23, 2001, Pacific bolide to IS57.

To test this hypothesis, a diffracted ray is computed off of the lower turning height region for a representative ray. This region is approximately 50 km short in range from the receiver. The representative and diffracted rays are shown in Figure 2. The total travel time from source to receiver over this path is 5653 s. The observed arrival time spans a range from 5608 to 6298 s, with a peak energy at 5953 s. The predicted arrival time falls within this range and differs from the peak arrival by 5%. This comparison supports the hypothesis that IS57 observed diffracted stratospheric energy.

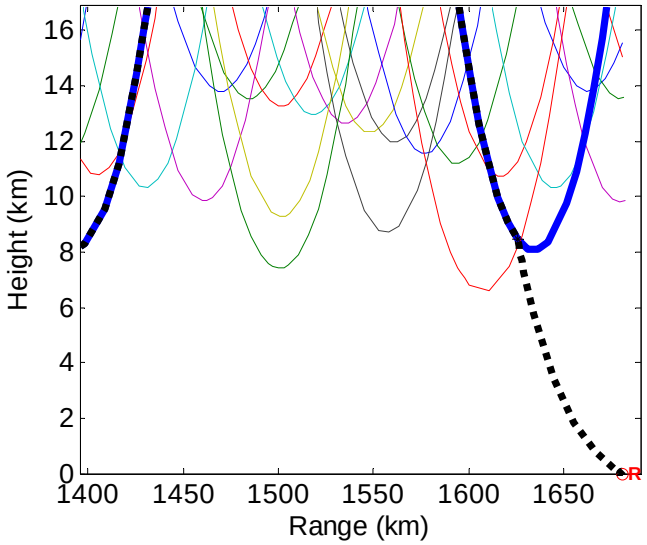

Figure 2. Stratospheric rays near the receiver, showing ray with lower turning height of 8 km (blue) and diffracted ray (dotted black).

Ground Truth Database

We have continued to expand our GT database by focusing on events that are directly related to the nuclear weapons testing, e.g., near-surface and underground nuclear explosions and HE events. These are well-calibrated, man-made events and significant domain knowledge resides with our LANL colleagues.

Underground nuclear explosions

Los Alamos National Laboratory has operated infrasound arrays in Nevada, New Mexico, and Utah since the early 1980s. These were mostly four-element arrays, with three sensors arranged in a triangle and the fourth at the center. In some cases, seismic data were also recorded at the same sites. Over the years, these arrays have recorded a variety of acoustic events, including UNEs at the Nevada Test Site (NTS) and subsequent cavity collapses, and conventional explosions both above and below ground.

Near-surface nuclear explosions

We have obtained digital waveform data for the near surface nuclear explosions from Operation Teapot carried out in the spring of 1955 from Eric Chael of Sandia National Laboratories (SNL) (Chael, 2004). This series includes several events with yields from 1 kt to 43 kt, all detonated a few hundred feet above ground. Table 1 lists the events for which we have digital records from these series of tests. Chael has extracted about 15 traces per test from the available stations, some of which used two sensors separated about 1 mile along the direction from NTS. For the larger events, detected signals are distinct at frequencies between 0.5–3.0 Hz; for the smaller events (<20 kt), higher frequencies are observed (Chael, 2004). We have separately contacted Jack Reed (currently retired) to obtain the station locations and have been successful in extracting accurate locations from his private archives.

Table 1. Near-surface nuclear explosions with available digital waveforms.

Event Name	Date	Time	Location	Latitude (°N)	Longitude (°E)	Height (km)	Size (kT)
Yankee	05/04/54	18:10:00	Bikini	11.6655	165.3869	N/A	13500
Wasp	02/18/55	19:59:59	NTS	37.0867	-116.0219	0.2	1
Turk	03/07/55	13:20:00	NTS	37.1383	-116.1175	0.2	43
Hornet	03/12/55	13:20:00	NTS	37.0403	116.0253	0.1	4
Bee	03/22/55	13:05:00	NTS	37.0947	-116.0239	0.2	4
Ess	03/23/55	20:30:00	NTS	37.1683	-116.0439	0	1
Wasp Prime	03/29/55	17:59:55	NTS	37.0867	-116.0578	0.2	3
HA	04/06/55	18:00:04	NTS	37.0286	-116.0578	11.2	3

Near-surface high-explosives events

Controlled HE field tests can be some of the best infrasonic sources for validating propagation models at local to near-regional distances. Much of our current knowledge of infrasound generated by explosions is a results of the HE tests made at the WSMR by the Defense Nuclear Agency (DNA). The DNA HE shots were a series of chemical explosions during the 1980s and early 1990s. Currently, we have obtained the source location, source size, event time, and station locations for several of the HE events. The times are accurate to milliseconds and the locations are accurate to about 10 m.

We have obtained digital waveform data files for Distant Image and Minor Uncle, and paper records for Miser's Gold. The digital data were recorded with 3-channel Terra Tech 12-bit tape recorders sampling at 200 Hz. Channels 1 and 2 for all these files are vertical and radial seismic and Channel 3 is pressure recorded with the Validyne gages in pascals. Though no hose arrays were used for wind noise reduction, just an open port about 16 inches off the ground, the data at distances less than 60 km have good signal-to-noise ratios (SNR). Figure 3 gives an example digital waveform recorded during the Minor Uncle test.

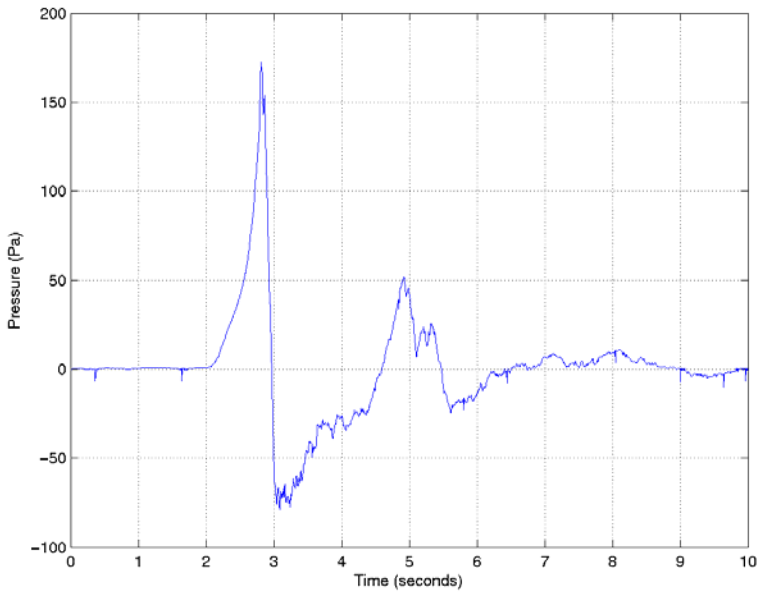

Figure 3. Minor Uncle infrasound signal measured at San Antonio, NM, at a range of approximately 50 km.

For each of the HE shots, we have access to infrasound recordings at a set of single component stations. Figure 4 shows some of the waveforms for the Distant Image event. Along with infrasound waveforms, our near-source HE data set includes seismic waveforms that might be used for seismo-acoustic studies critical to nuclear explosion monitoring. Figure 5 shows the digital recordings of co-located seismic and infrasound waveforms.

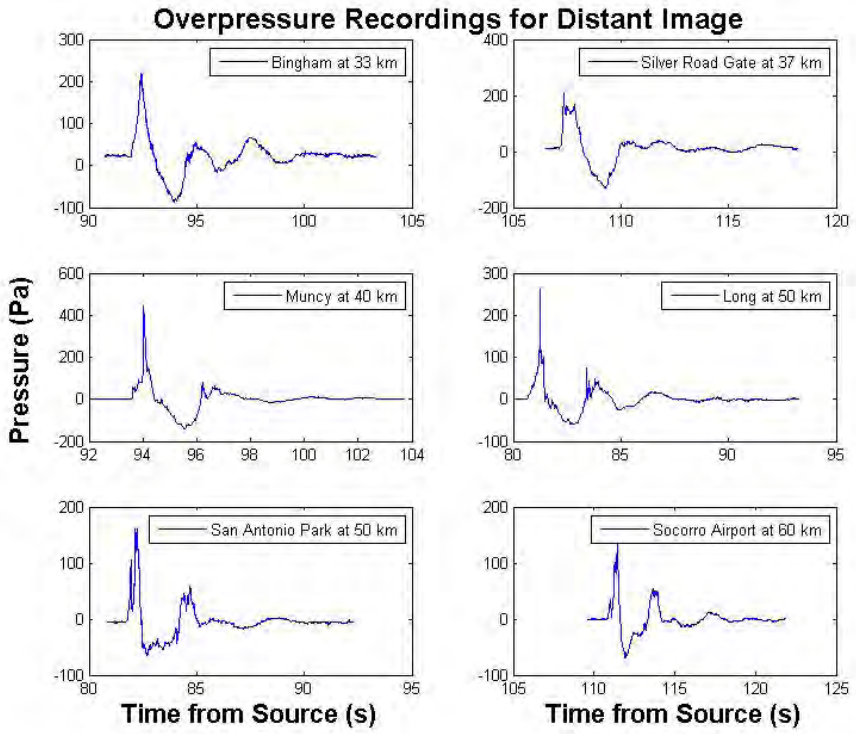

Figure 4. Infrasound waveforms at a set of stations for the Distant Image event.

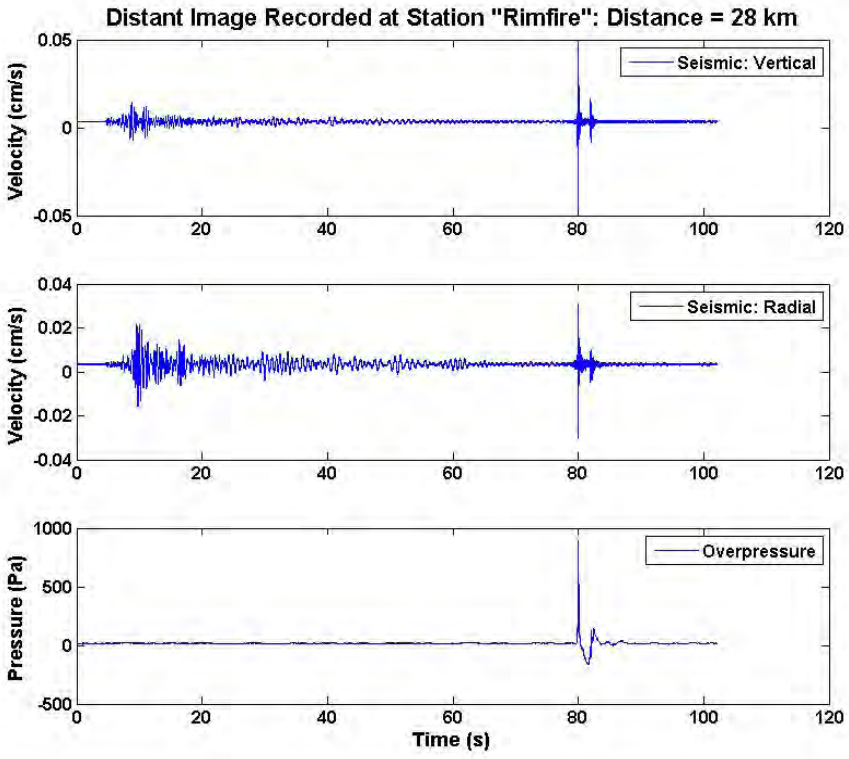

Figure 5. Seismic and infrasound waveforms from the Distant Image shot, recorded at co-located stations.

Special events from the LANL tape database

We have computer tapes at LANL that contain infrasound recordings of explosions during 1983 to 1991. We have developed MATLAB scripts that let us extract the digital waveforms and save them ASCII format. This data set includes data from the large accidental explosion that occurred at a chemical plant in Henderson, Nevada, on May 4, 1988. The tape data set also contains digital waveforms for a set of five UNEs carried out at NTS, Nevada. We are currently extracting these waveforms. Figure 6 shows the waveforms recorded at St. George, Utah, from the Texarkana event.

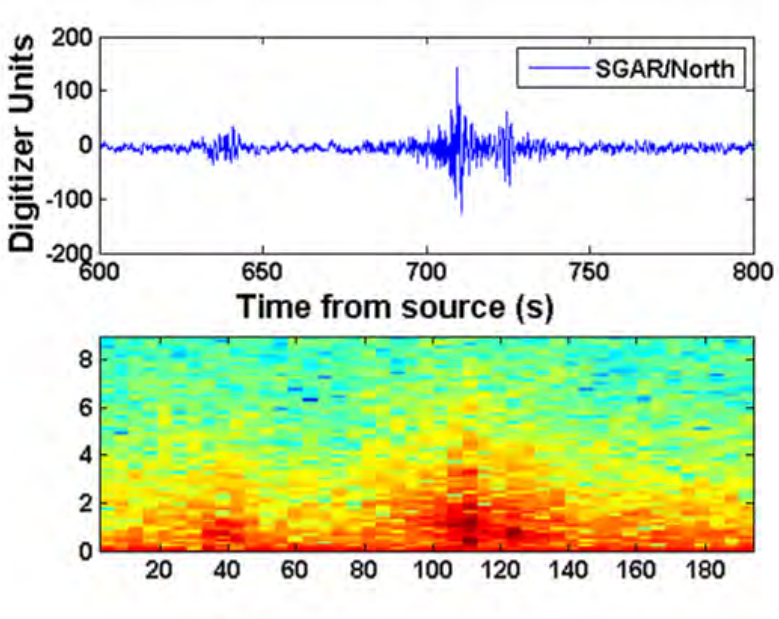

Figure 6. Recorded infrasound waveforms at one of the SGAR array elements, along with its spectrogram, from the Texarkana underground nuclear explosion of February 10, 1989.

Preliminary Analysis of Waveform Parameters Related to the WSMR Explosions

We have developed a time-domain parabolic equation (TDPE) technique to model the recorded waveforms from the WSMR explosions. Our broadband synthetic waveforms are computed for the GT source and the receiver locations published for the experiment and meteorological conditions obtained from the Naval Research Laboratory (NRL) G2S model. The TDPE synthetics are thus expected to capture realistic propagation conditions and can thus be compared to the recorded waveforms.

In this analysis, we carry out comparison studies for several parameters that define the signal from the WSMR shots recorded at several western U.S. infrasound array stations. These parameters are as follows:

- Travel time of the stratospheric propagation, using the GT source time
- The signal duration
- Dominant frequency of the signal
- RMS signal level
- Signal velocity, derived from source and receiver location and the travel time

We carry out an interactive analysis to estimate the aforementioned parameters from the data and model. This step is essential to assure quality of the measurements. We use the relationship of the signal with respect to the background noise to identify the start and end times of the waveforms, and thus the duration times can be somewhat under-predicted for low SNR signals. In our analysis, we focus on the signals between 0.5–3.0 Hz for both data and TDPE modeled waveforms.

We consider the data recorded at near-receiver ranges (nominally within 100 km) and those at regional distances along a particular profile toward the west from the explosions, namely, stations GILA, CHIR, and SAGU. This allows us to explore the propagations in the infrasound "shadow zone" and at distances close to the first bounce for stratospheric propagation. We focus on three separate explosions for this study: WSMR I Shot 1, WSMR I Shot 2, and WSMR III Shot 2. Signals from each of these events propagated well to the west, leading to clear detections to most of the stations considered in our study.

First we examine the variation of signal parameters between stations. Figure 7 shows the comparison between travel times for the three events. We note that the travel time misfits, generally, are significantly larger for stations at shorter distances. However, we do not detect a bias, positive or negative, for the travel time difference.

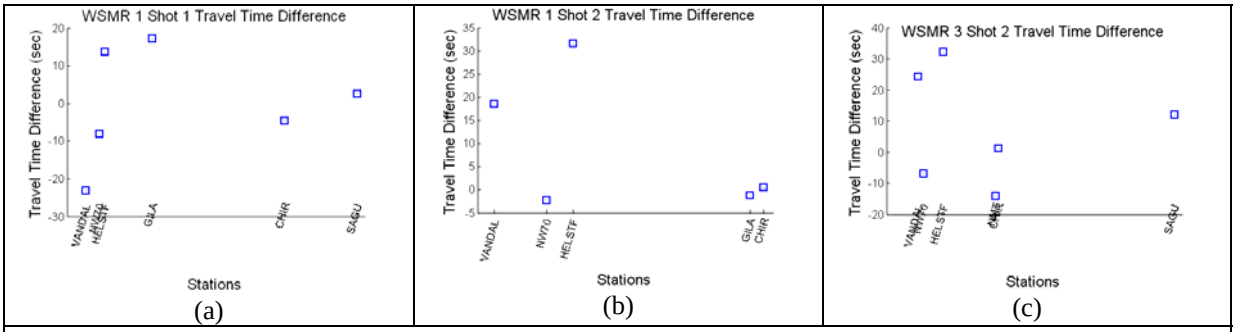

Figure 7. Difference in travel time between recorded and modeled data as a function of source-receiver distance.

Figure 8 shows a comparison between the RMS of the recorded and modeled signals. We note a consistent trend that the signal amplitudes are better predicted for the stations at farther distances. We note that the amplitude differences are comparable for most stations between the two explosions of WSMR I while they are in turn slightly larger than that of WSMR III. In nearly all of the paths, the amplitude of the recorded signal is larger than the synthetics, probably indicating that our modeling is overpredicting the signal attenuation.

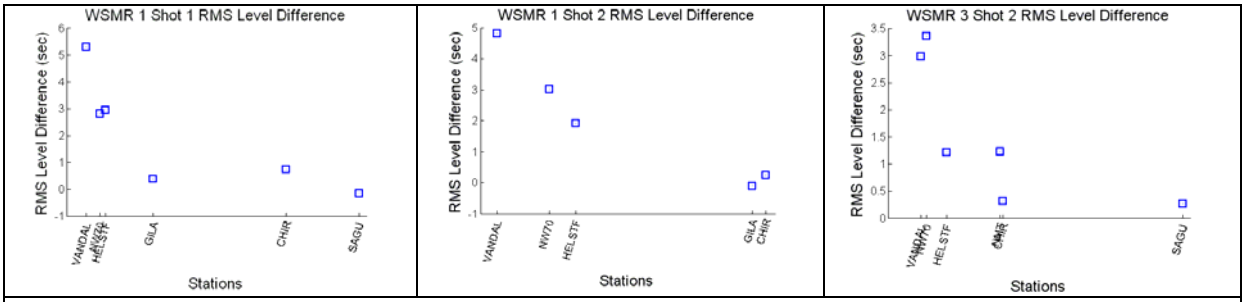

Figure 8. Comparison of RMS amplitudes of recorded and modeled signals (i.e., recorded-modeled) as a function of source-receiver distance.

Figure 9 shows a comparison of the durations between recorded and modeled signals. We note that the durations are well modeled for the close-in stations, but not for stations at further distances. As mentioned earlier, our durations are based on the visual inspection of SNR and not on array processing based detection analysis. This can lead to an under-prediction of the duration for recorded data, especially for stations at farther distances where we expect the SNR to be comparatively short. Moreover, at farther distances, there can be a significant "ringing" in our band-limited synthetics which in turn can lead to erroneous picks of signal start and end time. We are currently exploring these effects to resolve the misfits in signal duration.

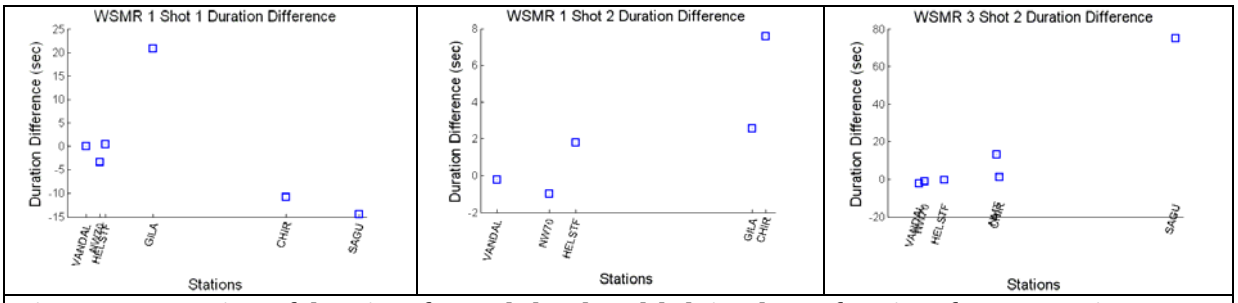

Figure 9. Comparison of duration of recorded and modeled signals as a function of source-receiver distance.

Figure 10 shows a comparison of the peak frequency of the signal. We note a trend that the peak frequencies are better modeled for stations at larger distances. Generally, we observe that the peak frequency of the data is slightly higher than that of the synthetic.

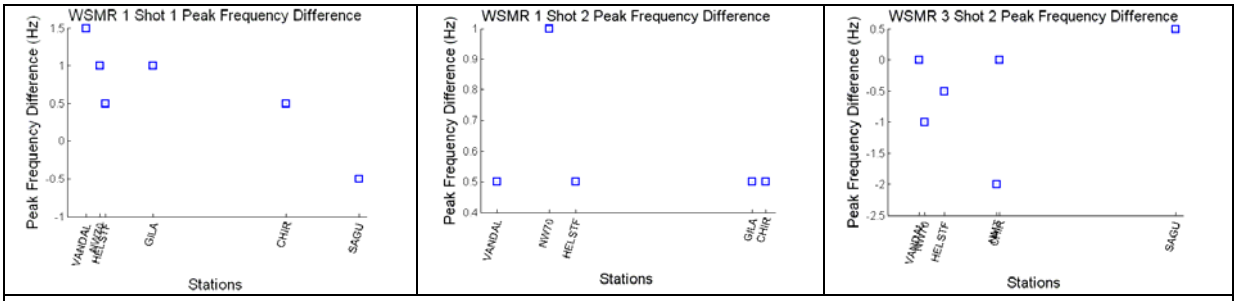

Figure 10. Comparison of peak frequencies of recorded and modeled signals as a function of source-receiver distance.

Figure 11 shows a comparison of the signal group velocity between recorded and modeled signals. Please note that we plot the actual velocity rather than the difference between those of recorded and modeled data. We note that the difference between the velocities decreases with increasing distance.

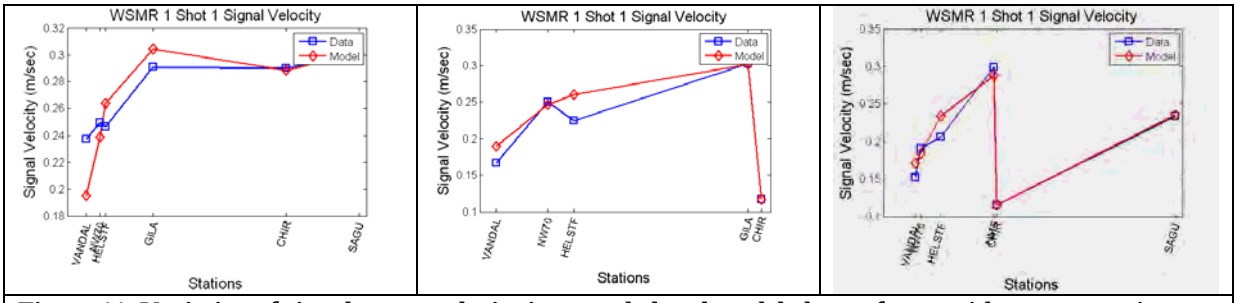

Figure 11. Variation of signal group velocity in recorded and modeled waveforms with source-receiver distance.

Now we examine the variation of signal parameter between shots. The WSMR experiments have been carried out over three separate days and covering the spring, summer and fall seasons. Moreover, there is a significant variation in altitude between the six shots involved in these experiments (Israelsson et al., 2007). Therefore, we can expect that the signal features described above can significantly differ for recordings at particular stations between the different shots. In this section, we explore the variation of some of these features, namely travel time, signal duration and amplitude, between shots and also in comparison with TDPE predictions. We focus on a subset of the stations for which the infrasonic arrivals have been clearly detected for all events and shots (Israelsson et al., 2007): VANDAL, HELSTF, and CHIR. These stations are nominally within 36 ± 10.1 km, 62 ± 10.2 km, and 292 ±1 .2 km from each of the shots, and thus represent a range of propagation environments.

Travel time

Figure 12 shows the travel times of the largest amplitude stratospheric arrival for the data and the TDPE model. Generally, we observe an increase in travel time with distance. However, we observe an anomalously large travel time, consistent between data and model, for WSMR II at CHIR. Importantly, the observed travel time can vary by up to 50 s (≈ 40% of the total travel time for WSMR I at VANDAL) for nearly identical paths propagating within several hours of each other. These results are consistent with those presented in Israelsson et al. (2007).

Figure 13 shows the difference between the observed and modeled travel times. We note that the observed waveforms for HELSTF are delayed compared to predictions. CHIR arrivals are usually early, compared to predictions, except the anomalous one for WSMR II mentioned above.

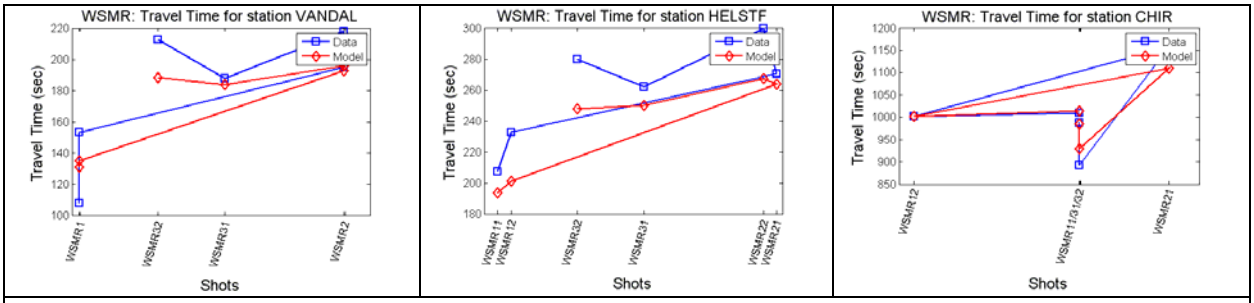

Figure 12. Observed and modeled travel times for stratospheric arrivals for all three WSMR events. The legend on the x-axis show the distance to the source and indicates both the event number (1/2/3) and shot number (1/2) within each event.

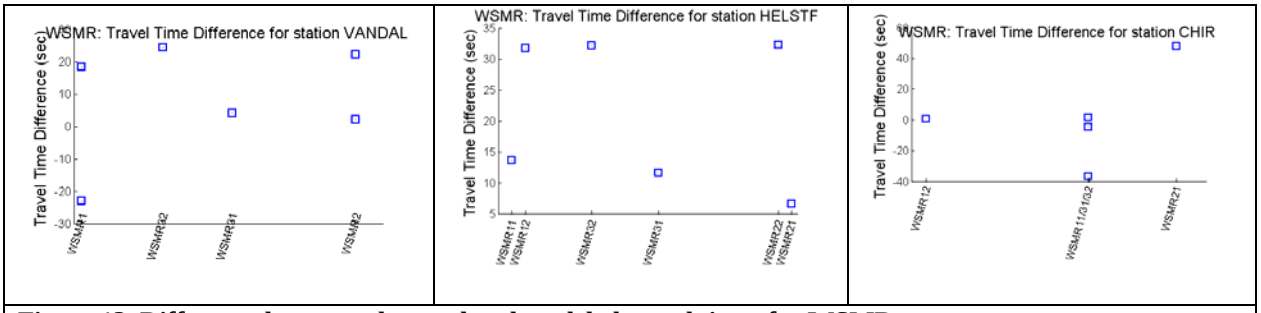

Figure 13. Difference between observed and modeled travel times for WSMR events.

Signal duration

Figure 14 shows the shot-by-shot comparison of signal duration (duration of data waveform – duration of model waveform) of the dominant stratospheric arrival. We do not observe a significant trend in our comparison of data with TDPE synthetics. However, we do note anomalously large modeled waveform duration at CHIR for WSMR II.

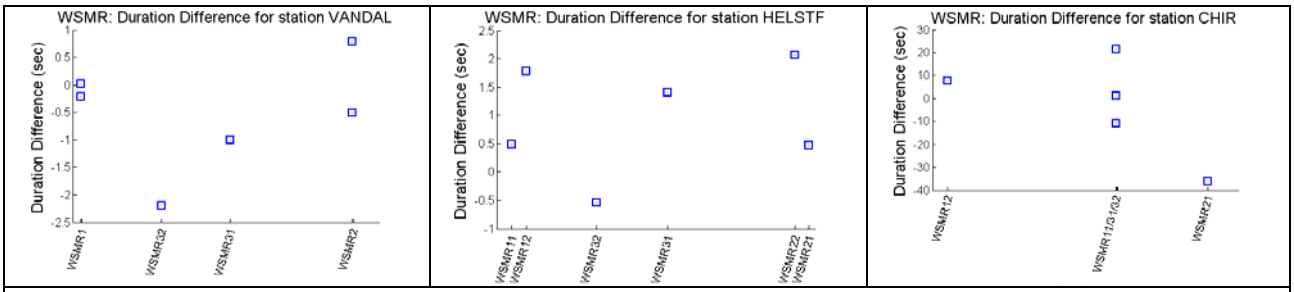

Figure 14. Observed-modeled signal duration of stratospheric arrivals for all six WSMR events.

Signal amplitude

Figure 15 shows the shot-by-shot comparison of signal amplitude, estimated using its RMS value (RMS_{data} – RMS_{model}), of the dominant stratospheric arrival. As mentioned before, the mismatch decreases with distance away from the source, and the observed amplitude is larger than the modeled one. For the closer in stations, the amplitude mismatch is largest for WSMR I and is probably related to the large source location uncertainty for these shots (Israelsson et al., 2007).

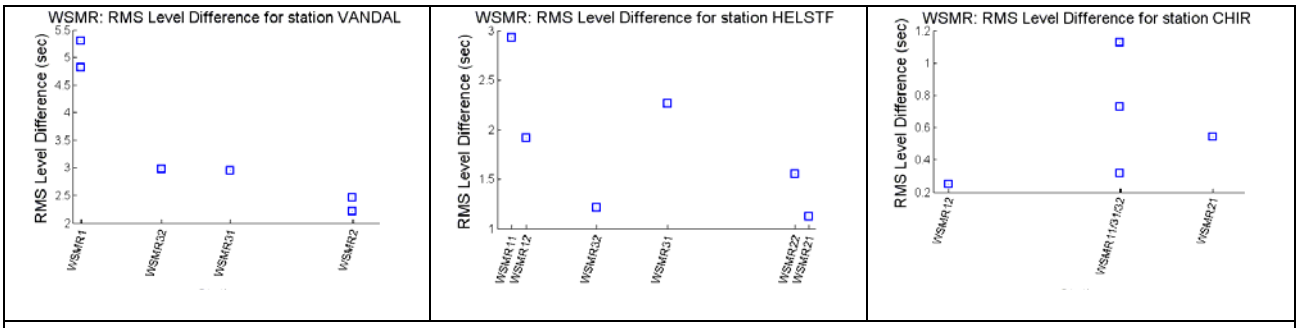

Figure 15. Observed-modeled RMS amplitude of stratospheric arrivals for all six WSMR events.

In summary we have carried out an analysis of infrasound signal parameters as recorded at a set of stations for three specific events related to the WSMR set of experiments and compare them to those predicted from infrasound propagation modeling. We note that the agreement between data and model is generally good. The misfits increases for stations lying closer to the source and indicates that possibly non-linear effects related to short-range propagation (< 100 km) might not be fully captured by our modeling technique. More realistic attenuation models will probably be required for improved waveform fits. We note significant differences in signal features misfits between different events. We are currently pursuing improvements in propagation modeling and signal picking to resolve these differences.

CONCLUSIONS AND RECOMMENDATIONS

The results of this research effort continue to advance our capabilities for accurately predicting infrasonic propagation parameters and assess the influence of fundamental physical processes. New propagation modeling capabilities include a ray diffraction model that addresses elevated ducts. Significant additions have been made to the GT database, including measurements from the DNA HE shots. In addition, preliminary comparison studies of the WSMR rocket tests are quantifying the modeling performance and areas of focus for future research.

REFERENCES

Chael, E. and R. Whitaker (2004). Infrasound signal library, in *Proceedings of the 26th Seismic Research Review: Trends in Nuclear Explosion Monitoring*, LA-UR-04-5801, Vol. 1, pp. 618–623.

Gilbert, K. and R. Raspet (1990). Calculation of turbulence effects in an upward-refracting atmosphere, *J. Acoust. Soc. Am.* 87: 2428–2437.

Israelsson, H., M. Bahavar, and R. North (2007). Source and signal summary for the WSMR infrasound experiments, SAIC report SAIC-07-2201.

IMPROVED INFRASOUND EVENT LOCATION

Michael S. O'Brien[1], Douglas P. Drob[2], and J. Roger Bowman[1]

Science Applications International Corporation[1] and Naval Research Laboratory[2]

Sponsored by Army Space and Missile Defense Command

Contract No. W9113M-06-C-0027

ABSTRACT

The purpose of this project is to improve the ability to locate infrasound events by improving the Horizontal Wind Model (HWM) used in the prediction of infrasound observables, in particular, travel time and back azimuth. Our general approach uses new wind data to develop a higher-resolution and more accurate HWM and tests the performance of Ground to Space (G2S) specifications based on the new HWM, relative to those based on HWM-93 using a large set of ground-truth events. We assembled a preliminary data set of 180 events with which to exercise our statistical framework for testing the effect of atmospheric wind models on the accuracy of infrasound event locations. We also assembled wind data representing a 100-fold increase compared to those used for HWM-93 and incorporated these wind data into the mechanism used to generate improved HWMs. We applied this mechanism to construct a preliminary version of HWM-07, and demonstrated that this preliminary model displays some important features that were missing from HWM-93, such as wind velocities of up to 70 m/s at an altitude of 110 km. We created an efficient mechanism to trace rays through atmospheric models for a large suite of infrasound source-station pairs. Initially, we have based our generation of travel-time and back-azimuth predictions on the HARPA 3-D ray-tracing programs. We refined the statistical framework for testing the effect of atmospheric wind models on predictions and applied it to first arrivals for a preliminary data set of 251 source-receiver pairs from 108 events to evaluate and compare predictions made against the existing, baseline atmospheric specifications for our study, G2S and HWM-93/MSISE-00, on which it is based, above 50 km. As expected, we find that G2S more often and more accurately predicts stratospheric first arrival times and back azimuths, whereas the two models are both equally poor at predicting thermospheric arrival times and back azimuths. It is for thermospheric arrivals that we expect the most improvement to result from the improvements of HWM-07.

OBJECTIVES

The primary purpose of this project is to improve our general ability to locate infrasound events by improving the HWM used in the prediction of infrasound observables. We do this using recent wind measurements and direct infrasound observations.

A second purpose of this project is to evaluate, statistically, the abilities of new and existing models to locate infrasound events and predict the principal infrasound observables, arrival time and back azimuth. We do this by comparing model predictions against a large set of infrasound observations.

RESEARCH ACCOMPLISHED

Background

The source location problem is a central element of nuclear explosion monitoring. In regional scenarios, it can provide important corroboration of explosive events but only if signals can be reliably attributed. Source location and, thus, location-related observables are central to source attribution. In remote regions that are not well monitored by other land-based technologies, such as the southern oceans, infrasound may provide the only information that constrains location.

The reliability of infrasound source locations depends on the reliability with which signal features can be predicted from source properties. This requires detailed knowledge of sound propagation in the atmosphere and the physical properties that control it, in particular, the static sound speed and wind field. The state of the art in representing the atmospheric properties pertinent to infrasound propagation is the Naval Research Laboratory (NRL) G2S model (Drob and Picone, 2000; Drob et al., 2003). This model combines climatological data captured in MSISE-00 and HWM-93 with numerical weather prediction (NWP) data, such as the Navy Operational Global Atmospheric Prediction System (NOGAPS) and the National Oceanic and Atmospheric Administration (NOAA) National Center for Environmental Prediction Global Forecast System (NCEP-GFS). Wind models that are based solely on climatology often substantially underestimate tropospheric and stratospheric wind jets, which leads to significant under prediction of the fraction of energy that is ducted through these layers (Drob and Picone, 2000; Drob et al., 2003). The utilization of the near-real-time NWP data in G2S significantly improves estimates of tropospheric and stratospheric wind jets that profoundly influence sound speed at lower altitudes (<50 km).

While the G2S models are the most comprehensive atmospheric representation available, significant infrasound residuals for thermospheric arrivals are still obtained using them. Le Pichon et al. (2005) found that back-azimuth residuals using G2S models averaged several degrees for repeated thermospheric propagation paths. Others (e.g., O'Brien and Shields, 2004) observe that, where only thermospheric arrivals are predicted, the predicted times systematically over-predict observed arrival times. The principal source of these discrepancies appears to be the wind model in the mesospheric/lower thermospheric (MLT) region, where weather data cannot assist. Recent direct measurements of winds at higher elevations indicate that HWM-93 significantly underestimates winds there. Stronger MLT winds imply larger azimuthal deflections, lower turning heights, and shorter travel times for predicted arrivals.

HWM-07 Prototype

The purpose of this task at this stage of the project is to demonstrate that we can successfully incorporate all the new atmospheric wind data into the mechanism to be used to generate HWMs. A new, unified HWM empirical model framework, applicable to *all* altitude regions and allowing for greater extensibility (e.g., future increases in resolution) has been developed and is in intermediate testing phases. The revamped HWM horizontal formulation now includes a complete linear and orthogonal spatiotemporal spectral basis set:

$$\begin{aligned} U(\tau,\lambda,\delta,\theta) = &\sum_{s=0}^{S}\sum_{l=0}^{L}\sum_{n=l}^{N} C^{r}_{s,l,n}\Psi_1(\tau,\delta,\theta) - C^{i}_{s,l,n}\Psi_2(\tau,\delta,\theta) + B^{r}_{s,l,n}\Psi_3(\tau,\delta,\theta) + B^{i}_{s,l,n}\Psi_4(\tau,\delta,\theta) \\ &+ \sum_{s=0}^{S}\sum_{m=0}^{M}\sum_{n=l}^{N} C^{r}_{s,m,n}\Psi_1(\tau,\lambda,\theta) - C^{i}_{s,m,n}\Psi_2(\tau,\lambda,\theta) + B^{r}_{s,m,n}\Psi_3(\tau,\lambda,\theta) + B^{i}_{s,m,n}\Psi_4(\tau,\lambda,\theta) \end{aligned} \quad (1)$$

In this equation $U(\tau,\lambda,\delta,\theta)$ represents the zonal wind field at a given model level as a function of day of the year, longitude, local solar time, and latitude, respectively. The vector spherical harmonics (VSH) are expressed in the complex spectral amplitudes coefficients, $C_{r,i},B_{r,i}$. A similar relationship for $V(\tau,\lambda,\delta,\theta)$ exists given the basis function parity/orthogonality relationship U: $\{C_r,C_i,B_r,B_i\}$ and V: $\{B_r,B_i,-C_r,-C_i\}$. The Fourier time modulated VSH basis functions are

$$\Psi_1^{s,m,n}(\theta,\lambda,\tau) = \frac{-1}{\sqrt{n(n+1)}}\frac{dP_n^m(\theta)}{d\theta}[\cos(m\lambda)\cos(s\tau)+\cos(m\lambda)\sin(s\tau)] \quad (2)$$

$$\Psi_2^{s,m,n}(\theta,\lambda,\tau) = \frac{1}{\sqrt{n(n+1)}}\frac{dP_n^m(\theta)}{d\theta}[\sin(m\lambda)\cos(s\tau)+\sin(m\lambda)\sin(s\tau)] \quad (3)$$

$$\Psi_3^{s,m,n}(\theta,\lambda,\tau) = \frac{-m}{\sqrt{n(n+1)}}\frac{P_n^m(\theta)}{\cos(\theta)}[\sin(m\lambda)\cos(s\tau)+\sin(m\lambda)\sin(s\tau)] \quad (4)$$

$$\Psi_4^{s,m,n}(\theta,\lambda,\tau) = \frac{-m}{\sqrt{n(n+1)}}\frac{P_n^m(\theta)}{\cos(\theta)}[\cos(m\lambda)\cos(s\tau)+\cos(m\lambda)\sin(s\tau)] \quad (5)$$

where $P_{n,m}(\theta)$ is the normalized associated Legendre polynomials and (s,l,m,n) are the seasonal, local time, longitudinal, and latitudinal spectral wave numbers, respectively. For maximum wave numbers of S = 2, L = 3, M = 2, and N = 8, there are 580 non-degenerate unknowns per model level.

The vertical variations in the HWM-07 model are represented by 5 km B-spline weighting kernels (e.g., De Boor, 1968), as illustrated in Figure 1. The HWM-07 empirical model specifications for the zonal and meridional wind components are thus given by the equation $[U,V] = \Sigma\alpha_i(z)U_i(\tau,\lambda,\delta,\theta)$, where $\alpha_i(z)$ is the amplitude of the respective weighting kernel in the altitude domain d_i.

The new model formulation and implementation also trivializes future increases in spectral resolution and input data set density for the foreseeable future. Linearization allows the replacement of the non-linear Levenberg-Marquard parameter estimation procedure with a straightforward linear least-squares estimation procedure (e.g., Rogers, 1996):

$$\hat{x} = x_a + (K^T S_\varepsilon^{-1} K + S_a^{-1})^{-1} K^T S_\varepsilon^{-1}(y - Kx_a) \quad (6)$$

$$\hat{S} = (K^T S_\varepsilon^{-1} K + S_a^{-1})^{-1} \ . \quad (7)$$

In this equation $\hat{x}$ is the model parameter estimates; x_a is an a priori estimate of the model spectral parameters [i.e., $\alpha(z)*C_r, C_i, B_r, B_i$], based on a previous iteration and data subset; variable K is the forward spectral matrix [i.e., the model basis functions $\Psi(\tau,\lambda,\delta,\theta)$]; S is the covariance matrix of the model parameter estimate; S_a is the covariance matrix of the a priori model parameter estimate; y is the observations; and S_ε is the covariance matrix or inverse uncertainty of the observations.

The data used to generate the new models are briefly summarized in O'Brien et al. (2006). The entire set of $O(10^9)$ data is far too large to be fit at once. Instead, we update the coefficients iteratively, at each step introducing a new random sub-sample of about 70,000 to 160,000 data from the entire set, depending on the altitude region. This limits working memory requirements to less than 10 GB yet allows all data to eventually influence the model coefficients. With each

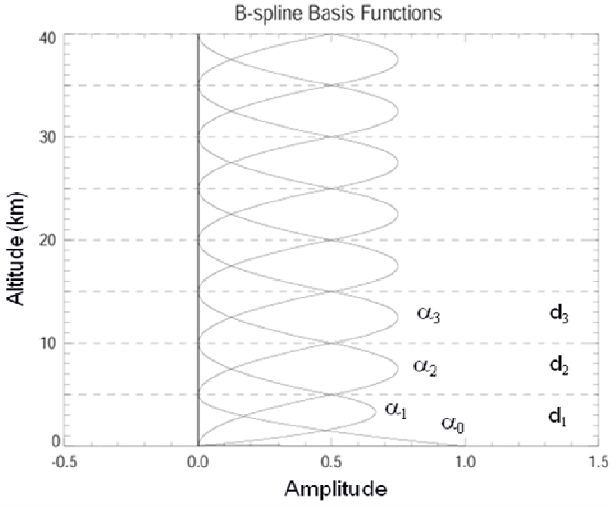

Figure 1. Example of B-spline weighting kernels.

iteration, the coefficient variances decrease; that is, the coefficients improve, so that their influence in the next iteration increases over that of the next data sub-sample. Iteration continues until the coefficients converge. The number of data sampled from each data set/type and altitude region is made roughly equal in each iteration. Data sets that span sparse regions, or are the only data set in a given domain, are weighted higher. Conversely, data sets that overlap with many other data sets are weighted lower.

Codes for the new model formulation, including a new client module that will be distributed to users when the model coefficients are more mature, are more compact, succinct, understandable, efficient, and extensible than the legacy HWM-93 code. The new client module also supports OpenMP parallelization of key subroutines and do loops, allowing for exploitation of recent advances in low-cost, multi-core processor architectures and supporting FORTRAN compilers. This will be important further into this project when large ensembles of infrasound propagation calculations for ground-truth events are required to refine and tune model parameters and performance.

Preliminary Model Comparisons—HWM-07 versus HWM-93

Although HWM-07 can be regarded as only preliminary at present, it already shows markedly improved agreement with the newer data over HWM-93. As anticipated, the preliminary HWM-07 has much higher amplitude tidal winds in the 85 to 135 km altitude regions, in part because the representation of the diurnal migrating tide is now in line with more-recent measurements and scientific understanding. It also includes the observed seasonal variations, phase quadratures, and hemispheric symmetries and asymmetries of the respective zonal and meridional wind components. Typical improvements are illustrated in the top and bottom rows of Figure 2, which shows WINDII wind measurements (Shepherd et al., 1993) averaged in overlapping 2-hour bins and 10 degree latitude bins (black lines), together with corresponding point-for-point averages from HWM-93 (blue lines) and the current preliminary HWM-07 (red lines). The top row illustrates the strong zonal winds observed on either side of the meridional wind maxima that are better captured in HWM-07 but are almost absent in HWM-93. At higher latitudes, some winds now captured exceed 70 m/s. However, there are fitting issues still to be resolved in HWM-07. The bottom row of plots illustrates the strong meridional winds observed at subtropical latitudes (±22.5º). These are clearly captured better by HWM-07 than by HWM-93, but not fully, thus motivating further model adjustments.

In addition, HWM-07 contains fewer features believed to be artifacts than does HWM-93. For example, the amplitude of semidiurnal tidal oscillations, in particular the zonal component near the equator above 115 km, is significantly weaker in HWM-07 than in HWM-93, as illustrated in Figure 3. HWM-07 much better matches the WINDII satellite data in the left panel, which show no evidence of the strong diurnal component.

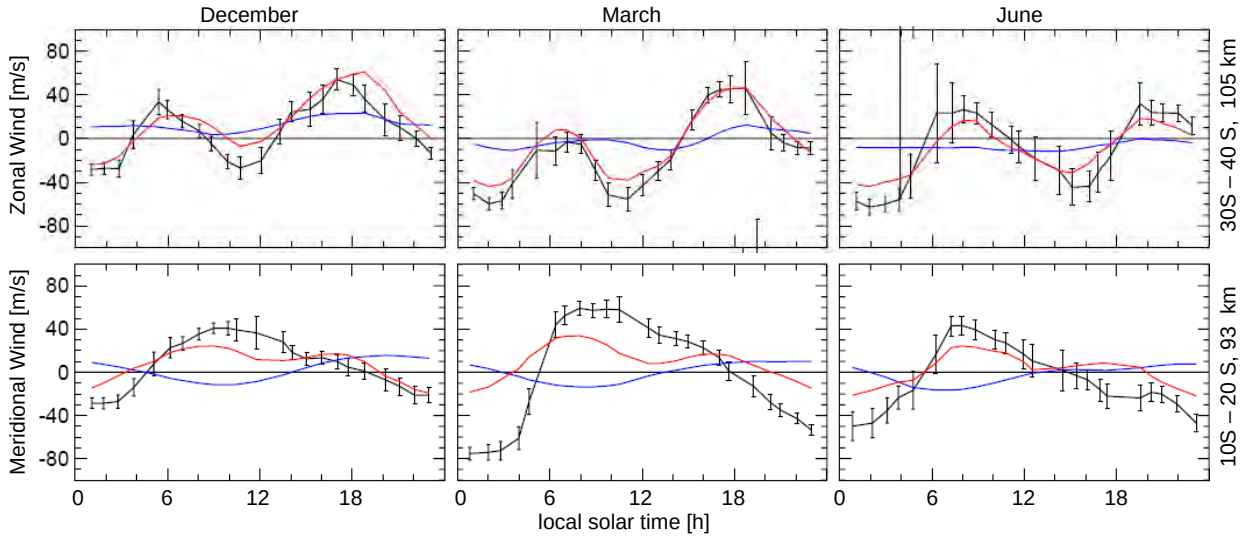

Figure 2. Examples of WINDI wind data (Shepherd et al., 1993—black lines) averaged in one-hour time-of-day bins showing significantly improved predictions of HWM-07 (red lines) over HWM-93 (blue lines). Top: HWM-07 captures most of zonal winds averaged between 30S and 40S at an altitude of 105 km, while HWM-93 captures little. Bottom: HWM-07 captures more of the meridional winds between 10S and 20S than HWM-93, but further improvement is still possible.

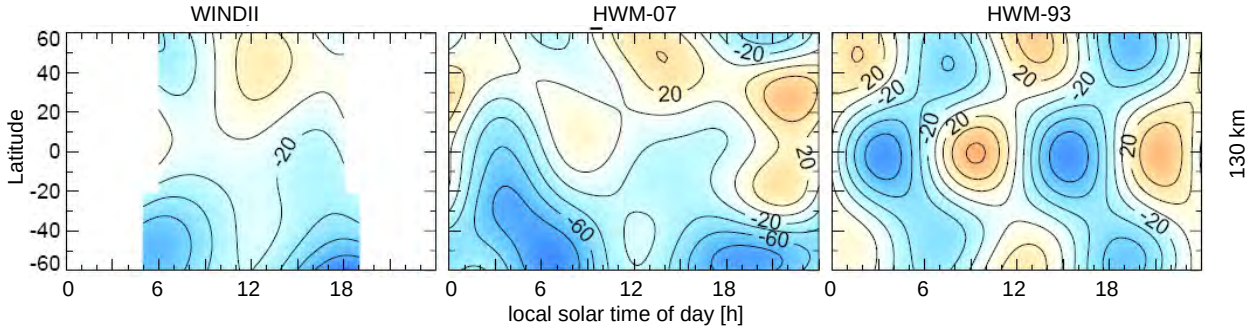

Figure 3. Comparison of December zonal winds [m/s] at 130 km altitude from WINDI wind data (Shepherd et al., 1993) with predictions of HWM-93 and HWM-07. Spurious tidal harmonic artifacts that are present in HWM-93 are eliminated in HWM-07.

Most importantly, more accurate wind specifications of greater magnitude in the 95 to 120 km altitude region will result in significantly lower thermospheric ducting heights for infrasound. This will lead to shorter predicted travel times and less molecular attenuation. Travel time calculations utilizing current HWM-93 specification generally over predict thermosphere wave guide travel times (e.g., O'Brien and Shields, 2004). For example, arrival times predicted by ray tracing though G2S for four of the five observed arrivals from the Watusi chemical test explosion on September 9, 2002, are over predicted by 200 to 700 seconds; the first ray predicted to land along the source-receiver azimuth of the fifth station does so about 60 km past the station. All of these rays are predicted to turn at heights of 105 to 140 km. In addition, given the current frequency-dependent infrasonic attenuation coefficients (e.g., Sutherland and Bass, 2005), current PE and ray-tracing calculations of many ground-truth events where thermosphere arrivals are observed predict too much attenuation. For the case of significant cross-track lower thermosphere wind conditions, the new wind specifications will result in the calculation of greater azimuthal deviations, again in line with infrasonic observations (e.g., Le Pichon et al., 2006).

Statistical Assessment Method

The virtues and shortcomings of any wind model must be evaluated with respect to the accuracy with which it predicts infrasound data. In this respect, the most reliable observables are arrival time and back azimuth. O'Brien et al. (2006) developed statistics for quantifying the overall abilities of models to predict these for an arbitrary set of source-receiver combinations. In particular, statistics comparing predictions from two models *p* and *q* have the form

$$F_{p-q} = \frac{\chi_p^2 / N_p}{\chi_q^2 / N_q} \sim F_{N_p, N_q}, \tag{8}$$

where χ_k^2 is a sum of squares of the N_k residuals from model *k*; F_{p-q} can be built from any subset of observations, such as travel times or back azimuths. Later, we compute $F_{\text{HWM-G2S}}$ for HWM93-MSISE00 and G2S using only travel times, only back azimuths, and both. If, as we believe, G2S better predicts the observations, *F* will be greater than 1. Our assertion is that F_{pq} is approximately distributed as F_{N_p, N_q}, against which we can test its statistical significance. This depends on having good estimates for the residual uncertainties. We estimate these for fractional travel time *T* and back azimuth deviation from the receiver-source azimuth *A* using the following error models:

$$\sigma_T^2 \approx \frac{\sigma_t^2}{T^2} + \frac{\sigma_r^2}{R^2} + \frac{\sigma_e^2}{R^2} + \frac{\sigma_\tau^2}{T^2} + \frac{\sigma_{MT}^2}{T^2} \tag{9}$$

$$\sigma_A^2 \approx \sigma_a^2 + \frac{\sigma_r^2}{R^2} \qquad \sigma_{MA}^2 \tag{10}$$

Here, σ_t, and σ_a are uncertainties in observed arrival time and back azimuth; σ_r, σ_e, and σ_t are the uncertainties in source time, location, and elevation. These are one of the subjects of the next section. The actual uncertainties introduced into A and T by the model are σ_{MT} and σ_{MA}, which we seek to quantify. We assume that uncertainty in station location is relatively insignificant.

Preliminary Infrasound Event Data Set

The meaningfulness of assessment statistics grows with the number of observations that can be compared to model-based predictions. Thus, a significant component of this project is devoted to collection and analysis of ground truth event data. In principle, any event is usable within our framework, as long we can reasonably estimate σ_r, σ_e, and σ_t, which strongly influence σ_A and σ_T and, hence, the statistical power of each datum and its weight in the assessment statistics. Without accurate uncertainties, we risk polluting statistics with erroneous data whose value is erroneously overestimated. Thus, a significant component of the ground-truth analysis is devoted to estimating the source parameter uncertainties. Typically, the less well we can estimate the source parameters themselves, the less well we can estimate their uncertainties, so we conservatively eliminate poorly constrained events, such as large earthquakes and rocket launches, having spatially and temporally extensive sources. Other events with large estimated uncertainties may be eliminated subsequently if they appear to degrade the statistics disproportionately.

The map in Figure 4 shows source-receiver paths for the 180 events for which we have estimated σ_r, σ_e, and σ_τ to be small enough to admit either travel time or back azimuth to the observation set. Of these, 108 are in western North America and 31 at the Zheleznogorsk mining site in Russia. The remaining events are distributed fairly randomly around the globe.

In the last year we have improved the ground-truth data for over 120 events. Source parameters for all the events are stored in the Monitoring Research Program infrasound database found on the web at http://www.rdss.info.

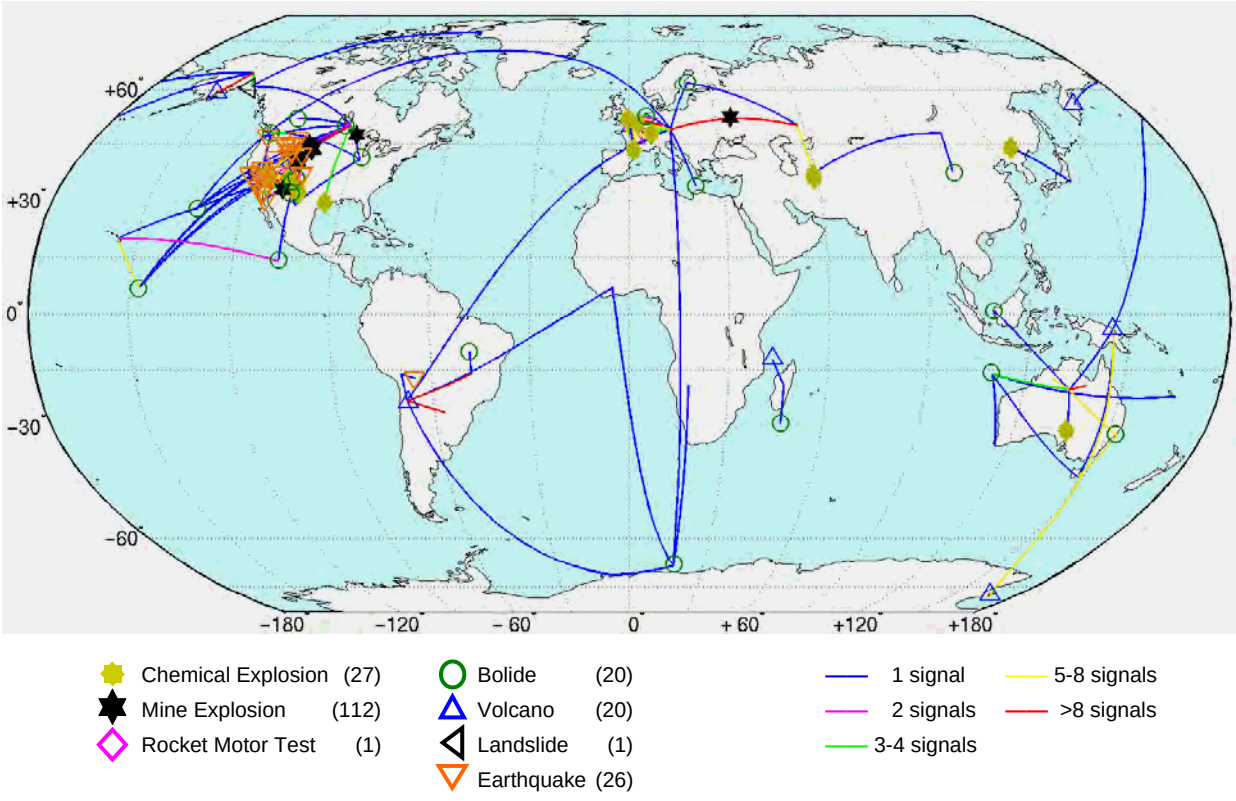

Figure 4. Map of events in the preliminary infrasound event data set.

Atmospheric Propagation Modeling

We have obtained model-based predictions by tracing rays through the candidate models using the HARPA 3-D ray-tracing programs packaged with InfraMAP (Norris and Gibson, 2006). We have not attempted here to account for terrain except by elevating the sources and receivers to their actual heights above sea level. Future computations will account for terrain using the NRL RAMPE ray tracer and the terrain-correcting versions of HARPA recently released in beta with InfraMAP.

We executed eigenray searches for 108 events for which we have already generated G2S models, including 640 arrivals from 251 source-receiver pairs. Even for this fraction of the anticipated final data set and only two atmospheric models, G2S and HWM93-MSISE00, the ray tracing represents a large computational task – it required about 160 hours of CPU time on an AMD Opteron 285 microprocessor, although instabilities with finding the intersections between rays and the ground may account for a significant portion of that time. The task also demands significant bookkeeping, since the ray-tracing programs must be executed separately for each source-receiver-model scenario, each producing multiple outputs. To facilitate the repeated task of computing eigenrays for an arbitrarily large set of source-station pairs, we have created efficient UNIX scripts for running the HARPA programs, extracting the prediction data from its outputs, and assimilating its results into an Oracle database, where the evaluation statistics are computed.

However, the process of mapping predictions to arrivals is more difficult to automate or even objectify. In some way this must be done by correlating the values of measured and predicted observables, such as arrival time, back azimuth, slowness, amplitude, and duration. Even some unobservable predicted ray properties such as turning height or number of ground reflections may influence the mapping. It is not always clear how much weight each predicted and observed datum should get in the process, creating a significant combinatorial problem, especially if there are multiple observed and predicted arrivals for a given source-receiver pair.

Ultimately, we will have to face these vagaries, but here we present statistical comparisons based on a more illustrative mapping that avoids them altogether. We map only first arrivals, each to the predicted arrival with the best fitting arrival time. The mapping does not guarantee or even purport to be the best mapping in the sense of all the observables—some mappings are certain to be incorrect—but it is unambiguous. We also consider separate statistics for arrivals predicted to have maximum turning heights in the troposphere/stratosphere (TS) region (<65 km) and the MLT region (> 65 km) because we expect predictions based on G2S to differ significantly from those based on HWM93-MSISE00 only where the rays spend most of their time at TS altitudes. Figure 5 (a) illustrates that, in fact, all the predicted turning height are easily separated into these height regions, all having maximum turning heights below 55 km (TS) or above 100 km (MLT).

As expected, using G2S leads to predictions of significantly more TS arrivals (about 1/3 more) and more arrivals overall than HWM93-MSISE00. This is illustrated in the Figure 5(b) histogram of the percentage of source-receiver pairs for which the models predicted any arrival, grouped by the ducting region predicted for the first arrival. The anticipated superiority of G2S is confirmed in Table 1, in which we have tabulated $F_{\mathrm{G2S/HWM}}$ and the corresponding significance levels for all combinations of travel-time and back-azimuth data in each of the TS and MLT ducting regions. From all perspectives G2S has outperformed HWM93-MSISE00 ($F_{\mathrm{G2S/HWM}} > 1$), mostly with high statistical significance. The histograms of travel-time residuals in Figure 6 illustrate that a major reason for the domination is the replacement of a number of highly erroneous MLT first-arrival predictions of HWM93-MSISE00 by much more accurate TS predictions of G2S. This leads to dramatically better predictions in both ducting regions, especially of travel times.

Table 1. $F_{\mathrm{G2S\text{-}HWM}}$ statistics for first arrival prediction residuals and associated significance levels in parentheses. Values greater than 1 indicate that G2S residuals are smaller.

Data Type	Maximum Turning Height		
	< 65 km	> 65 km	All
Travel times only	1.84 (99.7%)	1.20 (82.9%)	1.40 (98.9%)
Back azimuths only	1.13 (67.5%)	2.11 (99.9%)	1.66 (100%)
Travel time and back azimuths	1.34 (95.7%)	1.84 (100%)	1.70 (100%)

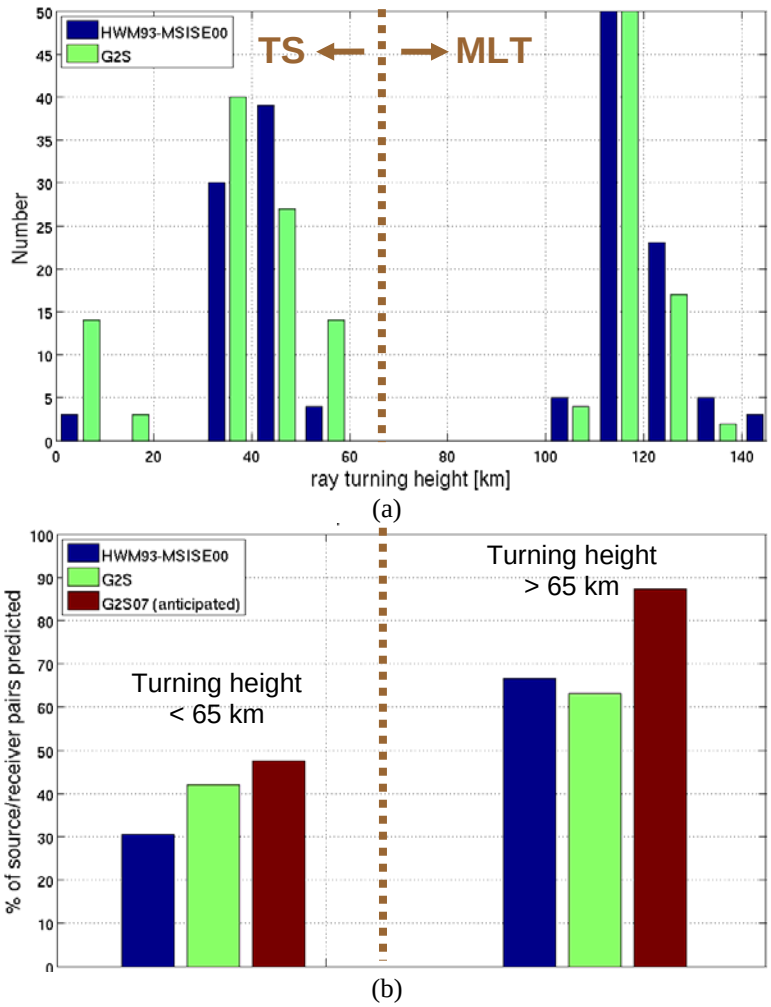

Figure 5. (a) Turning heights of predicted first -arrival predictions from G2S and HWM93-MSISE00 define well-separated troposphere/stratosphere (TS) and mesosphere/lower thermosphere (MLT) turning height domains. (b) Percentages of source-receiver pairs predicted by each model grouped by the turning heights of the predicted first arrivals. G2S predicts significantly more lower-atmospheric arrivals. We anticipate a similar increase in the number of predicted MLT arrivals from HWM-07.

We anticipate that HWM07-MSISE00 and G2S-07 will provide additional improvement to MLT predictions over their existing counterparts. Figure 6(b) shows the strong tendency of either HWM-93-based model to over predict travel times. Some of this is no doubt the result of failure to predict much faster TS arrivals. However, some is the simple result of over predicting the MLT travel times. With generally stronger MLT winds, HWM-07 will have higher overall effective sound speeds in the MLT region. This will have a two-fold effect to shorten MLT travel times by increasing the propagation speed and lowering predicted MLT turning heights, thereby shortening propagation paths. A less likely improvement is that increased mesospheric winds will effectively raise the top stratospheric duct in some cases, thereby increasing the number of faster stratospheric predictions.

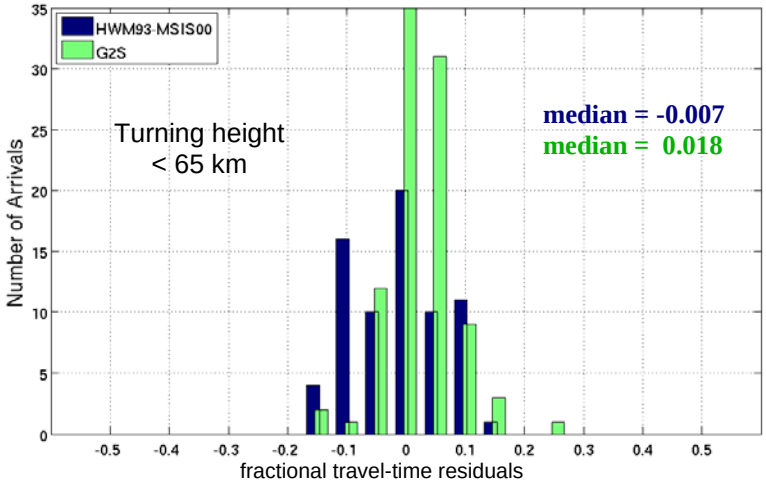

(a)

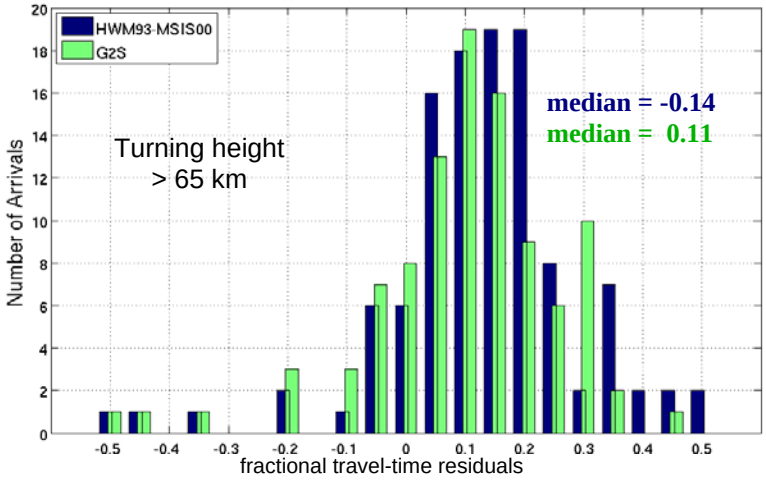

(b)

Figure 6. Fractional travel-time residuals for first arrivals predicted to turn at heights within (a) the TS region below 65 km and (b) the MLT region above 65 km. Travel times in both regions are better predicted by G2S. MLT residuals are strongly biased toward late prediction, which HWM-07 is intended to address.

CONCLUSIONS AND RECOMMENDATIONS

We have begun construction of the new atmospheric wind specification HWM-07. The new model is structurally and computationally superior to its predecessor HWM-93. Already, we have achieved significantly improved fit to many wind data sets gathered since HWM-93 was created and reduced model artifacts. Continued refinement of the model parameters is still required to fit all the salient features that are manifest in the wind data.

We have refined our data set of ground-truth events, carefully assessing source parameters and their accuracy. We have increased the number of constraining events to almost 200 and will continue to expand this set. We have developed statistical and computational machinery required to generate arrival predictions by ray tracing for a large set of source-receiver pairs to test against the observations. We have applied the machinery to first arrivals from HWM93-MSISE00 and G2S, clearly and quantitatively demonstrating the anecdotally accepted prediction superiority of G2S arrivals.

REFERENCES

De Boor, C. (1968). On uniform approximation by splines, *J. Approx. Theory* 1: 219–235.

Drob, D. P., J. M. Picone, and M. Garces (2003). Global morphology of infrasound propagation, *J. Geophys. Res*. 108 (D21): 4680, doi: 10.1029/2002JD003307.

Drob, D. P. and J. M. Picone (2000). Statistical performance measures of the HWM-93 and MSISE-90 empirical atmospheric models and the relation to infrasonic CTBT monitoring, in *Proceedings of the 22nd DoD/DOE Seismic Research Symposium: Planning for Verification of and Compliance with the Comprehensive Nuclear-Test-Ban Treaty (CTBT)*, Vol. 1, pp. 161–169.

Le Pichon, A., E. Blanc, D. P. Drob, S. Lambotte, J. X. Dessa, M. Lardy, P. Bani, and S. Vergniolle (2005). Infrasound monitoring of volcanoes to probe high-altitude winds, *J. Geophys. Res*. 110, D13106, doi: 10.1029/2004JD005587.

Le Pichon, A., K. Antier, and D. Drob (2006), Multi-year validation of the NRL-G2S wind fields using infrasound from Yasur, *InfraMatics* 16: 1–9.

Norris, D. and R. Gibson (2006). User's guide for InfraMAP (Infrasonic Modeling of Atmospheric Propagation): Version 5.1, BBN technical memorandum W2078, July.

O'Brien, M. and G. Shields (2004). Infrasound source locations using time-varying atmospheric models, in *Proceedings of the 26th Seismic Research Review: Trends in Nuclear Explosion Monitoring*, LA-UR-04-5801, Vol. 2, pp. 660-669.

O'Brien, M., J. Bowman, and D. Drob (2006). Improved infrasound locations through refining atmospheric models using wind data and ground-truth infrasound events, in *Proceedings of the 28th Annual Seismic Research Review: Ground-Based Nuclear Explosion Monitoring Technologies*, LA-UR-06-5471, Vol. 2, pp. 926-935.

Rogers C. D. (1996). *Inverse Methods for Atmospheric Sounding*. Singapore: World Scientific Pub. Co.

Shepherd, G. G., G. Thuillier, W. A. Gault, B. H. Solheim, C. Hersom, J. M. Alunni, J.-F. Brun, S. Brune, P. Charlot, D.-L. Desaulniers, W. F. J. Evans, F. Girod, D. Harvie, R. H. Hum, D. J. W. Kendall, E. J. Llewellyn, R. P. Lowe, J. Ohrt, F. Pasternak, O. Peillet, I. Powell, Y. Rochon, W. E. Ward, R. H. Wiens, and J. Wimperis (1993). WINDII—The wind imaging interferometer for the upper atmosphere research satellite, *J. Geophys. Res.* 98: 725–10, 750.

Sutherland, L. C. and H. E. Bass (2005). Atmospheric absorption in the atmosphere up to 160 km, *J. Acoust. Soc. Am*. 115: 1012–1032, doi: 10.1121/1.1631937.

OFIS EXPERIMENTS AT CAMP ELLIOTT: PAVING THE WAY TO INFRASONIC RADAR AND A PORTABLE INFRASONIC SENSOR CALIBRATOR

Kristoffer T. Walker, Mark Zumberge, and Matthew A. Dzieciuch

University of California, San Diego

Sponsored by Army Space and Missile Defense Command

Contract No. W9113M-06-1-0002

ABSTRACT

Optical fiber infrasound sensors (OFIS) are long compliant tubes wrapped with two optical fibers that integrate pressure variation along the length of the tubes via laser interferometry at the speed of light. We have previously shown that several OFIS arms can resolve the back azimuth and elevation angle of infrasound signals due to the spectral fingerprint of the instrument response in the recorded signal and the time separation provided by separating the centers of each OFIS arm. In this paper, we present the recent results of calibration, coherence, wind-noise reduction, and fine-tuning experiments that we accomplished in route to completing our grant objectives. Specifically, we show that the sensitivity of the OFIS is temperature dependent, and develop a real-time calibration system that allows us to compensate for this variation. We also show that M-sequences transmitted via subwoofers can be used as portable calibration tools in the low-frequency audible range and can test wind noise reduction technologies for some sensors. Comparison of a 60-m OFIS with a B&K microphone at a signal frequency of 50 Hz for a source ~300 m away shows that the OFIS reduces wind and other types of undesirable noise by 12 dB over the B&K microphone with an attached sponge wind filter. We also present the layout of a six-arm OFIS array at Camp Elliott (CEL) in north San Diego county where our investigations are continuing. This array has an aperture of 150 m, and is collocated with a digital video camera that will provide confirmation of the back azimuth and elevation angle of aircraft infrasound signals that are tracked by a passive infrasonic radar system.

OBJECTIVES

The overall objective of this research is to use the high precision provided by laser interferometry to reliably record minute infrasonic signals in the presence of detrimental wind noise. Specifically, we are further developing the OFIS, which is a silicone tube wrapped with two fibers that integrates the pressure variation along the length of the tube in an effort to stack the coherent signal while attenuating incoherent wind noise (Fig. 1). We have previously shown evidence that the OFIS has a lower noise floor than traditional pipe-arrays in low-wind conditions from 1-10 Hz (Zumberge et al., 2003). We are also developing techniques that take advantage of the averaging and tuning properties of the OFIS to measure signal orientation parameters (e.g., phase velocity direction). Because an OFIS array typically occupies less space than traditional mechanical wind filters (Fig. 2), we seek to find the optimum configuration of an OFIS array that minimizes the occupied space while maximizing the signal back azimuth resolution.

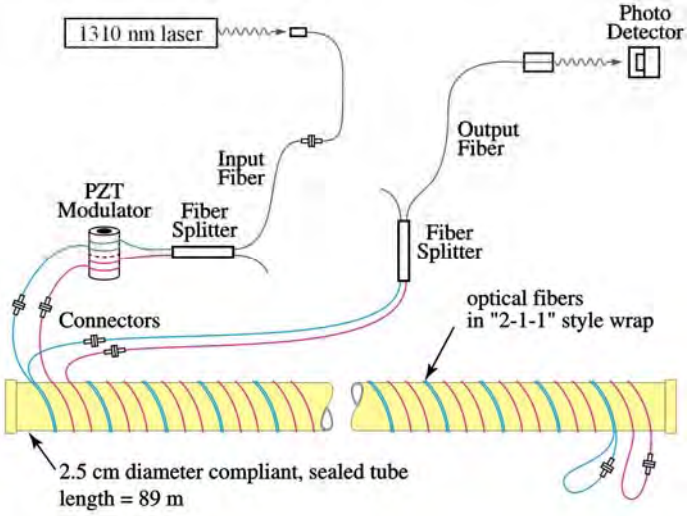

Fig. 1. Schematic of one of six Optical Fiber Infrasound Sensor (OFIS) arms that are operating at Camp Elliott (CEL) in north San Diego county.

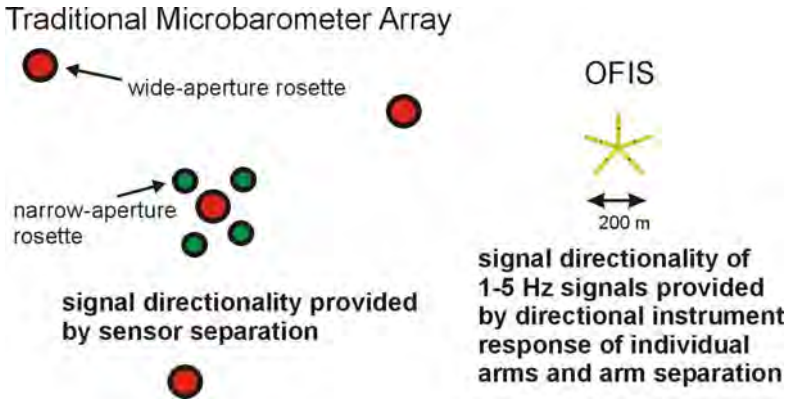

Fig. 2. A typical 8-element infrasound array (left) and a 5-arm OFIS on the right. Rosettes are spatial filters created by an array of inlets connected to underground pipes that all connect to a centrally located microbarometer.

The specific objective of this research that we report on here is to develop a new, generic infrasound calibration tool using M-sequence methodologies and to develop a real-time OFIS infrasonic radar system with which we can directly compare to real-time sky video in the tracking of certain aircraft.

RESEARCH ACCOMPLISHED

Camp Elliott OFIS Array

We deployed four parallel, 60-m OFIS at Camp Elliott (CEL), in north San Diego county near Miramar USMC Air Station in the late spring of 2006. During the summer of 2007, we installed a six-arm OFIS at CEL (Fig. 3). Each arm is 60 m long and located on the surface. The central element is a circular OFIS with a 7 m diameter. A weather station, a five megapixel video camera, and a B&K microphone with sponge wind filter were also installed. The OFIS arms may also be buried beneath about 4 in of coarse gravel during the autumn of 2007.

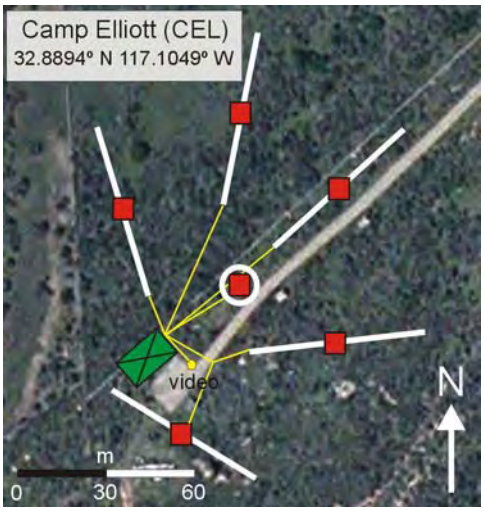

Fig. 3. 2007 Camp Elliott OFIS array collocated with an all-sky digital video camera to use as ground truth for the real-time infrasonic radar system.

Obstacles and Objective-Related Accomplishments

The OFIS performed well during the WSMR II experiment in the spring of 2006. The signal-to-noise ratio was comparable to most the collocated porous-hose Chaparral elements that did not have obvious noise problems (of an unknown origin). However, we observed some minor, but anomalous rocket signal amplitudes with four 60-m OFIS arms. At Camp Elliott (CEL) we laid out these OFIS arms within a few inches of each other parallel to the strain meter to further investigate this (Fig. 3). We also made similar anomalous amplitude observations when we investigated this at Pinion Flats Observatory (PFO) during a comparison between a short (30 m) and long (180 m) OFIS in November 2006. One of our findings resulted in a new feature to the OFIS—a real-time calibration system that is analogous to using predictable ubiquitous Earth tides in seismometer calibration.

Differential Optical Path Lengths

The laser beam is split into two fibers that are wrapped around the OFIS (Fig. 1). At the end of these two fibers, they are recombined to form a fringe signal (x) that is measured by a photo detector. A piezo-electric crystal that is wrapped by one of the two fibers, is driven by a 156 kHz oscillator. This oscillator also drives a lock-in amplifier that measures the derivative (y) of the fringe signal with respect to a change in the optical path length difference. A pressure change therefore traces out an ellipse of some geometry in x/y space (in Volts). A least-squares inversion is applied to the x/y data in real time to obtain the ellipse parameters, which are used to obtain the phase angle (and pressure change) along the ellipse for every x/y point in real-time. The time window that is used to obtain the ellipse parameters is typically the last 25 seconds of recorded data.

The two optical fibers comprising the Mach-Zender interferometer need to be about the same length for the type of laser used in order to establish a reliable ellipse for a given pressure signal. However, we did not know precisely how close their lengths needed to match before the interferometer was impacted detrimentally by optical noise. To quantify this, four different lengths of fiber were connected in various ways to the fibers wrapped around an OFIS to create about 20 different differential fiber lengths. For each case, we determined the best-fitting ellipse, then

calculated the ellipse-radius-normalized RMS distance between the ellipse and the data points (Fig. 4). We expect for a differential fiber length of 0 to be a nearly perfect match (RMS=0). We found that the ellipse begins to become detrimentally affected when the differential fiber length exceeds about 7 inches. Consequently, we trimmed all the fibers on our OFIS arms such that the differential fiber lengths are less than 2 inches.

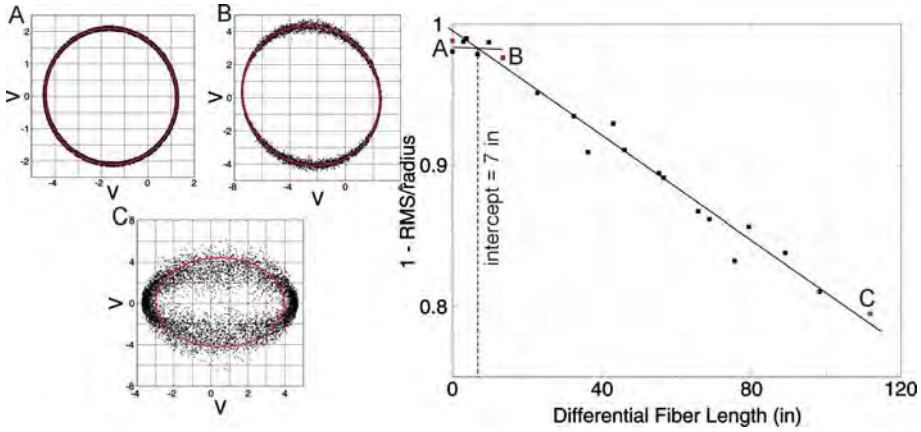

Fig. 4. Determining the relationship between optical noise and differential fiber length.

Polarization Change and White Socks

The ellipse size and geometry is one factor in the OFIS sensitivity. Ideally, we would like a circle that maximizes the range on the A/D converters (+/- 10 V in x/y space). A minor issue that affects uptime is polarization change in the fibers wrapped around the OFIS. Polarization change is strongly correlated with temperature variations of the sensor (due to silicone expansion/contraction and temperature change of the fiber itself). Although this can be circumvented easily by using a diversity detector, a more elegant solution is preferred since a diversity detector requires at least twice the amount of optical/electrical components in the data recording system. Ignoring polarization change can lead to down times of up to ~10% of the time (greatly depends on environmental conditions).

The silicone tube is wrapped with insulation and placed inside 4 inch diameter, perforated black drainage tube (Fig. 5a). This tube can absorb a lot heat from the sun, which can contribute to large internal temperature variations and polarization change. To minimize this, we performed an experiment by splitting PVC pipe along its length, and laying it on top of the OFIS. Our preliminary results suggested that the PVC does very well in reducing polarization change. However, it also seemed to reduce the amplitude of the infrasound signals observed, and they are difficult to keep stationary in wind (which can also lead to an increase in noise as the PVC repeatedly impacts the underlying OFIS).

We performed another experiment by installing a white exterior mesh shield over the OFIS (Fig. 5b). This also seems to have reduced the temperature/polarization change while at the same time eliminating the problems inherent in the PVC pipe approach. Figure 5c shows the x/y data for the leftmost OFIS (Fig. 5a w/o the white shield) in 4 minute time bins beginning at 8:00 AM local time. From 8:00 to noon the temperature increases gradually from 59º to 77º F (18º change) and the ellipse changes its geometry and almost collapses twice. Figure 5d shows the x/y data for the same OFIS but with the white shield (Fig. 5b) on a different day. The temperature ranges from 61º to 85º (24º change), and the ellipses do not change as much. We have adopted this shield as part of the OFIS fabrication routine. Although the shields do not eliminate polarization change, an OFIS buried under ~4 in of coarse gravel or a thermally controlled OFIS does not experience polarization change (100% uptime).

Fig. 5. White shields on the OFIS combat temperature-induced polarization change. The photos were taken on different days than when the ellipse data were recorded.

OFIS Calibration

The OFIS has been carefully calibrated many times in the laboratory and in the field using daytime rocket launch signals. This empirical calibration factor that converts the phase angle along the ellipse to pressure change is about

2.5 Pa-m/rad (Zumberge et al., 2003), where the length unit is the length of the OFIS (the longer OFIS the OFIS, the more sensitive it is).

We recently developed a real-time calibrator to investigate how the sensitivity of the OFIS behaves with respect to changes in outside temperature, inside temperature, when it is wet (raining), and atmospheric pressure (Fig. 6). The calibrator is comprised of a PVC ring that has a speaker sealed to one end, and a plate sealed to the other. A pipe connects the sealed chamber to all the OFIS arms. The speaker is driven by a sinusoid source with a 30 s period. Inside the silicone tube at each OFIS end, a *Setra* differential pressure sensor with a range of +/- 62 Pa records the sinusoid calibrator signal. We apply a narrow bandpass filter to both the Setra and OFIS recordings to obtain the calibration signal amplitude in Pa and radians, respectively. We then can calculate the optimum calibration factor, which we assume is valid at all frequencies based on a previous sweep calibration study that showed the OFIS impulse response was flat in the low-frequency audible sound range.

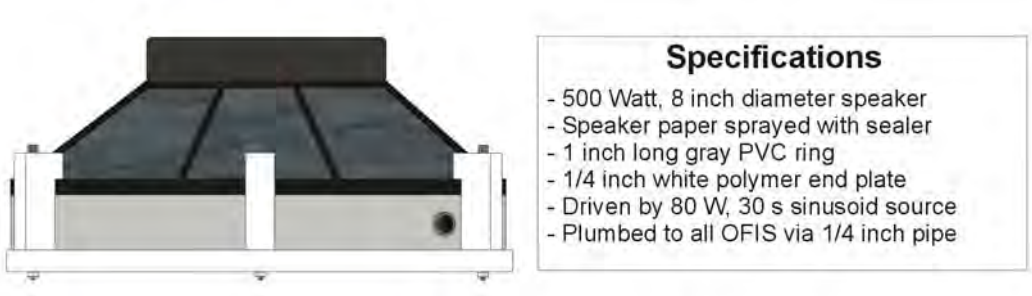

Fig. 6. OFIS real-time calibrator sketch.

Analyzing a day of data beginning at 18:00 UTC (hour 18, 11 AM local time) in 15-minute time bins for the four OFIS arms at CEL shows that the sensitivity of the OFIS is correlated with outside temperature change. Figure 7a shows the amplitude of the calibration signal as recorded by the OFIS arms and associated Setras. The OFIS amplitudes are converted to pressure using the constant, previously estimated OFIS calibration factors to facilitate ease of comparison. If the calibration factors were correct, the Setra and OFIS amplitudes would be identical. Instead, the OFIS amplitudes vary throughout the day with temperature (Fig. 7b) and get smaller at night beginning at hour 27 (7 PM local time). Viewed in another way, the corrected calibration factors for each OFIS (Fib. 7c) show that the OFIS is more sensitive than previously thought when the temperature is above 80º F, but less sensitive when the temperature dips at night. It is unclear why OFIS 3 and 4 respond differently to the temperature change than OFIS 1 and 2.

The sensitivity of the OFIS varies linearly with temperature between 60-80º F (Fig. 7d). In this figure, the calibration factor for OFIS 1 is plotted with respect to temperature. The factor lags the temperature change as expected due to the effect of the heat capacity and the insulation surrounding the silicone tube. However, another experiment spanning a larger temperature range showed that at temperatures below 60º F, the calibration factor rises much more rapidly. Above 80º F, all the factors appear to converge to ~2.0 Pa-m/rad. Therefore for the broader range of temperatures, the relationship is non-linear.

There is a rapid buildup of pressure inside the OFIS during periods of temperature change. Although we dissipate most of this buildup using peek tubes of certain lengths, we determined that pressure buildup inside the OFIS is not related to the sensitivity simply by venting one OFIS at night and not observing any change in the real-time acoustic noise amplitude. We also compressed one OFIS with 1 psi of air for a day and did not see any change in the difference in the amplitudes of the signals when compared with the other OFIS, suggesting that the variation in the calibration is not associated with a variation in the tension of the fiber around the silicone tube (which may occur due to thermal expansion/contraction of the silicone). Our working hypothesis is that the rigidity of the silicone (and sensitivity of the sensor) changes significantly with temperature. However, other observations suggest that there is another factor (possibly in combination with a changing rigidity) that is responsible.

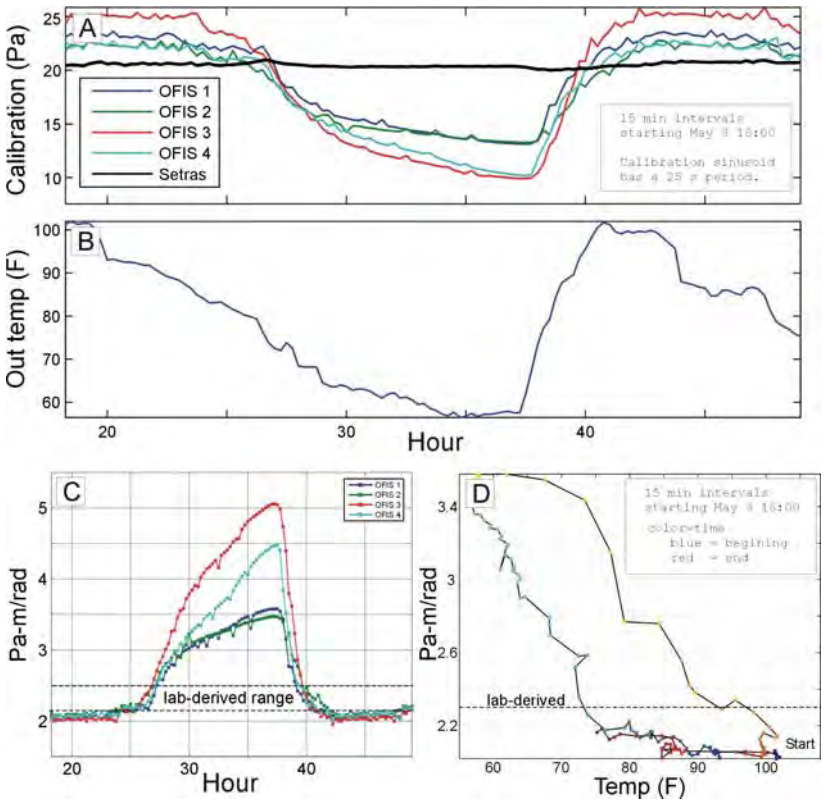

Fig. 7. Calibration results. The OFIS calibration factor (Pa-m/rad) reflects the sensitivity of the OFIS to pressure signals, with larger values indicating lesser sensitivity. The OFIS is most sensitive at temperatures above 85° F.

Coherence of Parallel OFIS

There are several ways to compare the impulse responses of two sensors in the infrasound frequency range. One technique is to put two sensors close together, then calculate and stack coherence functions for recorded background noise in time series X and Y. The coherence is a measure of the similarity (linear relationship) between two signals as a function of frequency. Specifically, it is defined in frequency space as the magnitude of the X/Y cross-correlation complex spectrum divided by the product of the X/Y autocorrelation complex spectra. The magnitude of the coherence is 1 for frequencies where there is a perfect linear relationship across the time window, and 0 at frequencies where there is no relationship. For signals that are identical, but time shifted, the coherence is 1 for all frequencies. Typically a coherence of less than 0.25 indicates that no significant relationship exists.

Three parallel OFIS at CEL were separated by about 4 inches and paired off to form three unique pairs. The magnitude of the coherence functions for these pairs was calculated and stacked in 15 minute bins (Fig. 8). Two sets of data were used. The first set was collected when the 3 parallel OFIS were interconnected via the calibrator plumbing (Fig. 6), which added an additional, shared 100 feet of pipe between the calibrator and the ball valves at the end of the OFIS arms. The second set of data was collected when the 3 OFIS were not interconnected. Because acoustic noise can rise with wind speed, we also stack only those coherence functions for which the median wind speed is greater than or equal to 3 m/s. We see that for most cases, the coherence is above about 0.40. Also, for each case, the coherence increases at frequencies >15-20 Hz for higher wind speeds. Conversely, for frequencies below 15 Hz, the coherence decreases for higher wind speeds. This decrease is especially pronounced for the case where the OFIS arms are interconnected. We speculate that a decrease in coherence in the presence of an increase in wind noise might be related to resonation or mechanical capacitance (for the interconnected case) in the OFIS arms, which vary in length by up to 8 m. In addition, between the calibrator and OFIS arms, there are several acoustic impedance contrasts. The acoustic impedance at the ball valves changes when we open them up, which may also be related to the differences in coherence between case (a) and (b). Finally, these data only span 1 day (Fig. 8b) and 2 days (Fig. 8a), which may not be enough data to be statistically significant. We will repeat this experiment by

truncating the OFIS to the same length, analyzing a week's worth of noise data and several individual signals, applying the corrected calibration factors, stacking the associated power spectral densities for each bin, and calculating the 95% confidence coherence level. If the repeated experiment also suggests an increase in noise from 1-20 Hz when wind speed increases, we will likely modify the calibration system such that it turns on for 30 seconds once every 15 minutes, while opening solenoid valves to each OFIS arm.

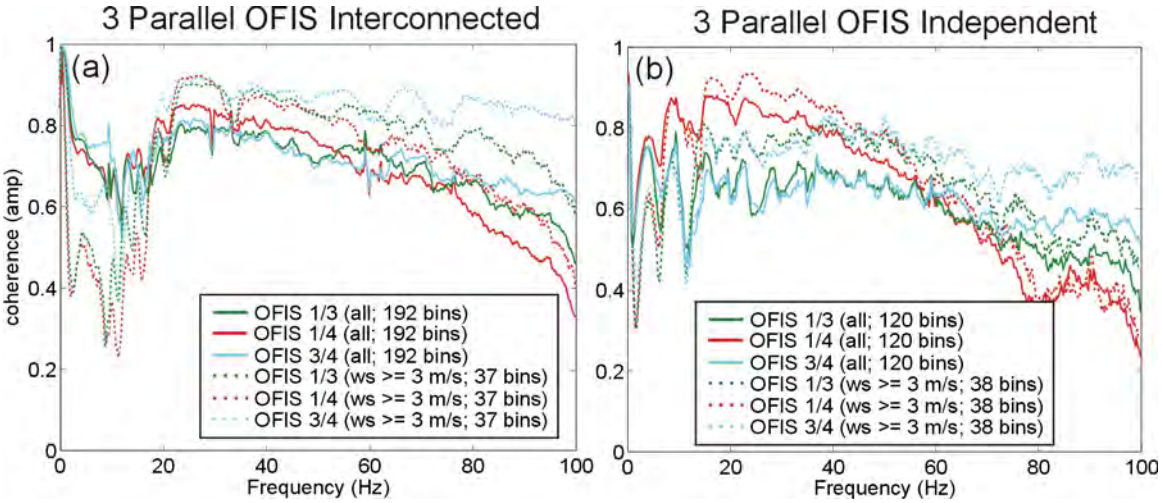

Fig. 8. Coherence of interconnected and independent parallel OFIS (OFIS 1, 3, and4) at CEL.

M-Sequence Calibration Technique

It is difficult to accurately calibrate infrasound sensors because of the difficulty in generating infrasound. Standard subwoofers are designed to have flat impulse responses down to ~20 Hz. Propane cannons or impulsive devices have difficulty generating infrasound in the 1-5 Hz range. We are in the process of experimenting with an array of 12-inch, 500 Watt subwoofers in an attempt to extend the array impulse response into the infrasound band. Since the source is peak power limited, we are using an M-sequence signal, which allows us to increase the SNR by coherent processing and thus to observe distant, low-source power signals recorded over many minutes. With this technique, one can measure the impulse response of each OFIS arm under various wind noise conditions.

An M-sequence is a pseudo-random series of binary digits that has been extensively used in communication and imaging systems during the last 50 years. M-sequences are periodic, and generated with the use of a bit register and feedback law (Golomb, 1967). The period of an M-sequence is $2^N - 1$, where N is the length of the bit register. We then phase modulate a sinusoid of a frequency f_c with the M-sequence digits contolling the phase. For example, we modulated a 50 Hz signal with 255 bit sequence at a chip rate of 2 carrier cycles per digit to get a 10.2 s long signal. We consecutively transmitted 24 of these coded signals to obtain a signal 244.8s long. We process the received signal by correlation with the original signal and then demodulating. We stack these together to enjoy a processing gain of 10*log10(24*255) = 37.9 dB.

This example was implemented at CEL using a single subwoofer placed 270 m from the four OFIS and a B&K microphone with a sponge wind filter. The azimuth from the subwoofer to the OFIS center was 4º from the OFIS perpendicular, which means the signal wavefronts were approximately plane waves that impacted the entire 60-m OFIS and microphone simultaneously. Both sensors were sampled at 200 Hz. The 4-minute long coded signal was impossible to observe by inspection in the 1 Hz high-passed B&K microphone time series, but is observed with a visual signal-to-noise ratio of 5 dB in the OFIS recording (Fig. 9a). The spectrograms for both sensors show that the signal was observed. The demodulated signal peak corresponding to the first arrival has a signal to noise ratio of 34 dB for the B&K, and 46 dB for the OFIS (Fig. 4d), which confirms that a 60-m OFIS is exceptionally sensitive to low-frequency sound and attenuates well wind noise and other sources of low-frequency sound that come from different directions that are not perpendicular to the length of the OFIS.

One application of this technique is to analyze each of the 24 coded signals separately and to measure the demodulated power and travel time of these signals. Since we hold the power input into the subwoofer constant

(~120 Watts), any demodulated power or travel time fluctuations result from a change in the impulse response of the medium. Therefore one can measure the coherence time of the atmosphere or changes in the velocity profile with time. We find a considerable degree of variability in the demodulated B&K signal power (Fig. 9e), and a more smooth variability for the OFIS recordings (Fig. 9f), suggesting that the array gain of the OFIS effectively averages fluctuations in the Green's function. We performed the same experiment at f_c = 20, 10, 5, and 1 Hz. We only observed the coded signal for the 50 and 20 Hz cases, running into the expected subwoofer roll-off at sub-audible frequencies.

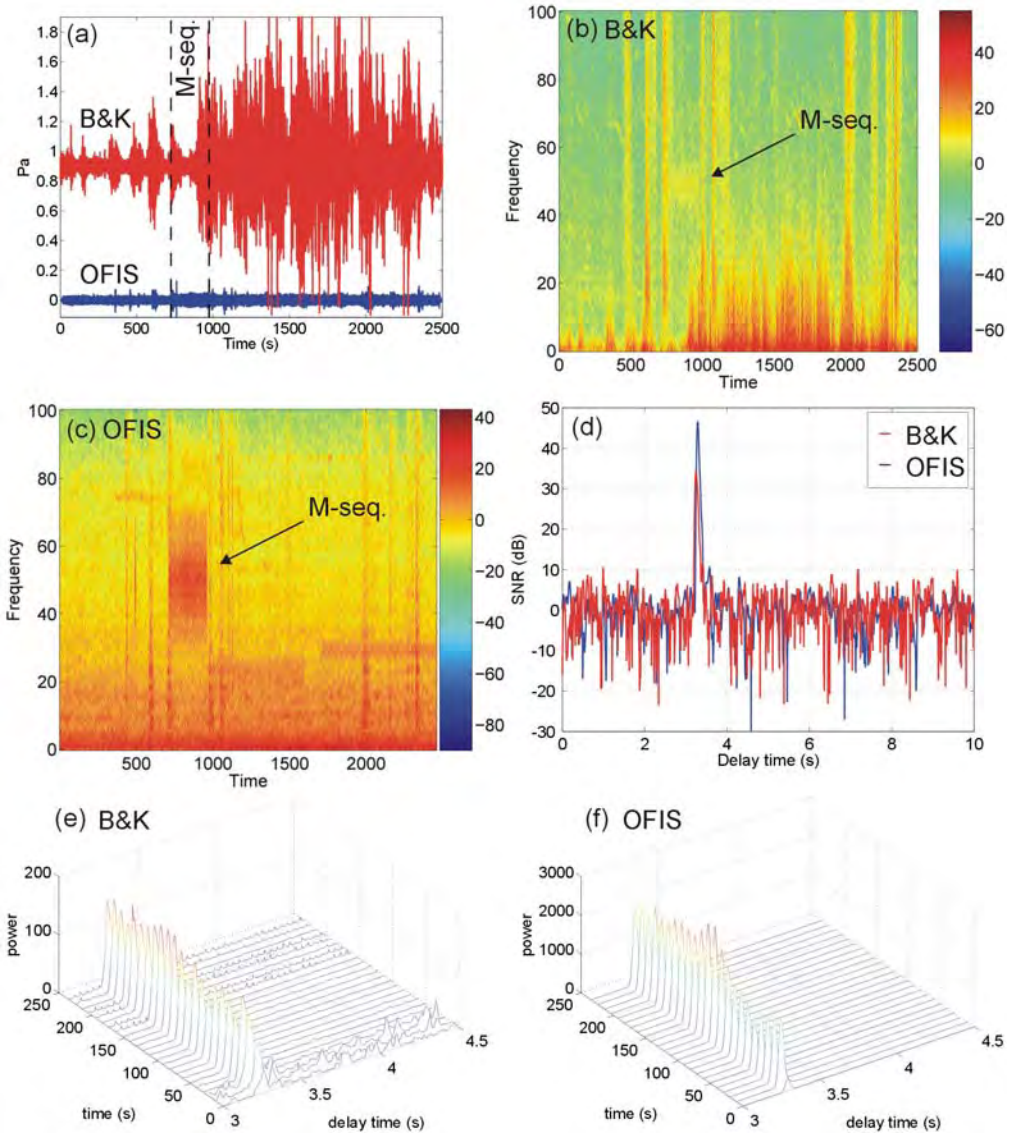

Fig. 9. M-sequence calibration technique using a 12-inch subwoofer at 270 m distance from a tuned OFIS and a Brüel & Kjær (B&K) microphone with sponge wind filter.

Real-Time Infrasonic Radar

Previous PFO OFIS studies showed significant deviations at times between the back azimuths determined by an OFIS and a microbarometer array. Although a 2006 WSMR II rocket explosion provided a good signal that proved the OFIS could be more accurate than the co-located Chaparral sensor array (presumably in this case because of handheld GPS inaccuracies in locating the array element positions or problems with moisture in the porous hoses connected to the Chaparrals or in the Chaparrals themselves), it is generally ambiguous as to the more accurate

technique since the true signal back azimuths are not usually known. The six-arm OFIS at CEL (Fig. 3) will test various OFIS configurations and phase velocity direction determination by exposing the OFIS array to a number of infrasound sources (slowly moving aircraft) that can be confirmed via video. This is expected to eliminate any ambiguities.

The obstacles in this research were the OFIS arm preparations (resulting in the findings reported above), the Camp Elliott site preparation, and the migration of the OFIS data logging software from an in-house format running on Windows XP to an industrial-strength streaming format (analogous to the CD1.1 format) running on a more secure and less problematic UNIX machine. We have installed a video camera and confirmed that we can easily make out moving sources across the sky (http://sail.ucsd.edu/~walker/c130_landing.mov). What remains to be done now is to route data from the video camera and OFIS DSP's into a program that analyzes the OFIS data and creates a radar plot in near real time, and compare between the video display and the OFIS radar display.

CONCLUSIONS AND RECOMMENDATIONS

The sensitivity of the OFIS is temperature dependent. Fortunately the first order sensitivity level of the OFIS is still far above the threshold such that it can accurately detect and accurately record infrasound signals throughout the normal daily temperature fluctuation. Therefore, the real-time speaker calibrator that we developed provides a means to compensate for this sensitivity variation assuming the recorded background noise is acoustic in nature.

Preliminary evidence suggests that the coherence of adjacent, parallel OFIS arms varies from 1.0 down to 0.4. In higher wind conditions, the coherence goes down significantly in the 1-20 Hz band if the newly developed speaker calibrator system is being implemented. More data processing is necessary to confirm this finding and understand why it happens.

White mesh shields provide a good level of protection against rapid temperature change of the sensor, which leads to polarization change that negatively impacts the size and geometry of the ellipse and can reduce uptime of the OFIS sensor by up to ~10%. In addition, trimming the differential fiber length of the two fibers wrapped around the OFIS to within 2 inches eliminates optical noise associated with the coherence time of the laser we use, which improves the definition of the ellipse.

M-sequences can be used to drive weak sources of infrasound to develop a calibration tool. The concept was demonstrated in the audible band with a 20 and 50 Hz signal, which showed that a 60-m OFIS attenuated wind and other undesirable noise by 12 dB more than that provided by a standard B&K microphone with attached sponge wind filter. It remains to be seen if an array of subwoofers can conspire with M-sequences to form such an infrasound sensor calibrator.

ACKNOWLEDGEMENTS

We wish to thank Pat Walsh, Mike Kirk, John Lyons, Skip Mikuls, Joel White, Matt Norenberg, Clint Coon, and Eric Blum for their lab and field assistance. We also wish to thank David Horwitt for developing the next generation of our data logging system, David Chavez for developing and maintaining the near-real time system that keeps our data streaming, and Jon Berger, Michael Hedlin, and Robin Matoza for useful discussions. Finally, we are indebted to the U.S. Army Space and Missile Defense Command for funding this work.

REFERENCES

Golomb, S.W. (1967). *Shift Register Sequences*. Holden-Day Inc., San Francisco, California.

Zumberge, M.A., J. Berger, M.A.H. Hedlin, E. Husmann, and S. Nooner (2003). An optical fiber infrasound sensor: A new lower limit on atmospheric pressure noise between 1 and 10 Hz, *J. Acoust. Soc. Am.* 113: 2474.

AN IMPROVED METHOD OF BACK AZIMUTH DETERMINATION WITH A MULTI-ARM OFIS

Kristoffer T. Walker, Mark Zumberge, Jonathan Berger, Michael A. Hedlin, and Peter M. Shearer

University of California, San Diego

Sponsored by U.S. Army Space and Missile Defense Command

Contract No. W9113M-05-1-0020

ABSTRACT

The detection of infrasound in the presence of wind is challenging. Increasing wind speeds lead to higher noise floors. While the exact nature of the noise is still a subject of investigation, several technologies and array configurations have been developed to maximize the signal to noise ratio and lower the detection threshold. Optical fiber infrasound sensors (OFIS) are long compliant tubes wrapped with two optical fibers that integrate pressure change along the length of the tube with laser interferometery. Spatially incoherent wind noise is naturally attenuated relative to spatially coherent infrasound. Because the signal pressure variation is integrated along the length of the tube, the instrument response is a function of the orientation of the OFIS arms relative to the orientation of the wavefront. We show with theory and real infrasound data recorded at Piñon Flat Observatory in southern California that this spectral property can be exploited with multiple OFIS arms in different ways to determine the phase velocity of infrasound signals. Based on these findings and unpublished results, we propose two OFIS configurations as alternatives to rosette pipe array infrasound stations.

OBJECTIVES

Infrasound is generated by a variety of natural and manmade sources, and can travel far distances under certain atmospheric conditions. Atmospheric explosions are particularly good at producing far-reaching infrasound in the 0.01-10 Hz band (Landau and Lifshitz, 1959). This has recently led to increased interest in infrasound for Comprehensive Nuclear Test-Ban Treaty (CTBT) compliance verification. The tool for this monitoring is the International Monitoring System (IMS), which is to include 60 globally distributed infrasound stations, about 20 of which are currently constructed.

Recording signals of interest is a challenge in the presence of wind. Increasing wind speeds correlate with increasing noise levels across the entire infrasound band (Kaimal and Finnigan, 1994). One source of wind-related noise is the advection of density anomalies across the sensor at the wind speed (<20 m/s; Taylor's hypothesis). Because infrasound travels at much faster acoustic speeds (~330-350 m/s) and propagates across the Earth's surface at subhorizontal angles (e.g., McKisic, 1997), large-aperture arrays of sensors and associated processing techniques are typically used to separate the rapidly moving signal from the more slowly moving turbulence, and determine the direction to the source.

Spatial wind filters also help reduce turbulence noise before it reaches the sensor. There are generally two types of spatial filters: pipe networks and hose networks. Pipe networks are often buried and centrally connected to a microbarometer or microphone. A common design is the "rosette" pipe filter, consisting of several clusters or rosettes of low-impedance pipe network inputs (Alcoverro, 1998; Hedlin and Raspet, 2003). These rosettes vary in aperture from 18 to 70 m depending on the frequency band of interest. Hedlin et al. (2003) and Hedlin and Alvocerro (2005) evaluated an array or "rosette" of underground pipes centrally connected to a microbarometer or microphone sensor. As the spatially coherent infrasound wavefront propagates across the ports of these wind filters, the signal diffuses into the pipe, and propagates toward the central sensor at the speed of sound where they constructively interfere. If wind noise originates from density anomalies that are advected across the array (Taylor hypothesis) with a spatial coherence that is shorter than the rosette aperture, the noise destructively interferes at the central sensor. This leads to a standard amplitude signal to noise gain of $n^{1/2}$, where n is the square root of the number of pipe array ports. The rosette response depends on the apparent speed and frequency of the signal that propagates across the array as well as the array size, in part because the signals travel through the pipe network to the sensor at the speed of sound. The disadvantages of rosette filters are that they are usually large and logistically challenging to build, the rosettes can strongly attenuate signal strength depending on their aperture, significant resonance occurs for frequencies about ~0.7 Hz, and the arrays are not suited for temporary deployments. However, this filter is fairly successful in attenuating wind noise, and is employed by many of the IMS infrasound arrays in arrays of up to 8 elements and apertures of up to 2 km across.

Another type of wind filter is a porous hose network. These porous hoses are inexpensive, and connect to a central microphone or microbarometer in a similar fashion as in the pipe arrays. However, the infrasound diffuses into the porous hose at all points of contact with the wavefront. This provides more points of sampling for the coherent wavefront, which could increase the signal to noise ratio more than that for a rosette pipe array. Although the arrays are relatively simple to deploy, the porous hoses kink easily and are not easy to manipulate. It is also not uncommon to have a high noise level that disappears when the hose is replaced or disconnected from the sensor.

A more recent technique is to create a massive array of inexpensive piezo-electric microphones, and to use array processing techniques to attenuate incoherent wind noise while preserving coherent signal. The success of this technique depends on the sensitivity of the microphones, the aperture of the array, and the number and spacing of the sensors used to form the beam. The disadvantage of this technique is that it can require extensive computational and data-storage resources. Shields (2005) used an array of 28 sensors that had ~0.02 V/Pa sensitivity to investigate the optimum sensor separation distance. He shows that wind turbulence has a consistent spatial coherence for wind speeds in the 4–7 m/s range, allowing one to select the optimum sensors in the array to use in the beam for a known wind speed and direction to achieve better than $n^{1/2}$ noise reduction (where $n < 28$).

Motivation for this Study

The optical fiber infrasound sensor is described by Zumberge et al. (2003) as a different approach to reducing wind noise. The OFIS is a long compliant tube that measures instantaneous pressure variation along the length of the tube with an effective sensitivity (for comparison purposes) of ~60-180 V/Pa depending on the OFIS length of 30-90 m

and the size and geometry of the interferometer ellipse. These tubes can be oriented in a circle or a line. A circle does not maximize the distance over which an OFIS can spatially average incoherent noise. Zumberge et al. (2003) and recent unpublished work shows that the noise floor of a 90-m linear OFIS is as much as 20 dB lower than that of a traditional 70-m rosette pipe filter for winds up to 3 m/s in the 1–10 Hz band. While the linear OFIS is efficient in attenuating wind noise, its feasibility as an operational solution to infrasound data collection also depends on the ability to use it to record the infrasound signal reliably and measure the signal propagation direction (back azimuth and elevation angle). In this paper, we demonstrate three fundamental techniques and their variations on how one can use an array of linear OFIS arms to determine the phase velocity direction. The theory is presented, along with applications to real data, and conclusions regarding the optimum array configuration.

RESEARCH ACCOMPLISHED

Sensor Directivity

The velocity vector of the propagating wavefront in free space is hereinafter referred to as the "phase velocity" *c*. Similarly, we refer to the "apparent velocity" as the velocity of the intersection of the wavefront with the Earth's surface. The instrument response, *R*, of a linear OFIS relative to a reference point at the end of the OFIS has the amplitude and phase response

$$R_a(f) = \mathrm{sinc}\left(\frac{L\pi f}{c}\cos(\theta)\right) \quad (1)$$

$$R_p(f) = L\pi f \cos(\theta)/c \quad (2)$$

where f is frequency, L is the length of the OFIS, and θ is the angle between the phase velocity direction and the OFIS

$$\theta = \cos^{-1}(\cos(\theta_H)\cos(\theta_V)) \quad (3)$$

where θ_H are θ_V are the horizontal and vertical and angles, respectively (Zumberge et al., 2003). The phase response is just a time shift from the center of the OFIS to reference point. For typical infrasound signals from distance sources, is θ_V = 0-30° (subhorizontal) and $\theta \cong \theta_H$. Figure 1a shows R_a as a function of θ for three typical infrasound signal frequencies. Figure 1b shows the variation of R_a with frequency for several angles. For low frequencies and long wavelengths (or orthogonal angles), the OFIS is effectively a point sensor and records the wavefront perfectly. For all other conditions, a frequency-dependent attenuated version of the signal is recorded. In other words, the fingerprint of the directionally-dependent instrument response is recorded in the amplitude spectrum of the signal.

The sinc form of this response can also be thought of as the Fourier transform of a boxcar time series function, which represents the averaging of an impulse function signal as it propagates across the OFIS. For rays perpendicular to the OFIS, the impulse signal is recorded perfectly (flat amplitude spectrum) since the wavefront is parallel to the OFIS. For rays at oblique angles to the OFIS, the impulse is smeared in time into a boxcar shape with lower amplitude, resulting in the narrower sinc function for the amplitude spectrum.

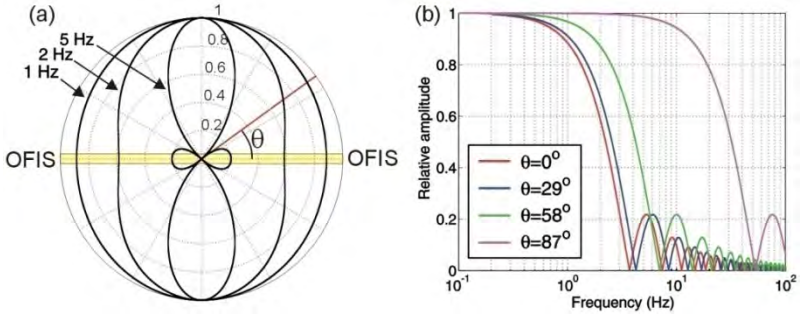

Fig. 1. Frequency response *R* for a 90-m long OFIS as a function of frequency and angle θ from the length of the OFIS (eqns. 1,3).

In the frequency domain, each recorded OFIS signal S_r is a convolution of the signal waveform with the instrument response $S_r = S_w R$. Conversely, if θ is known, one can deconvolve the instrument response to determine the signal spectrum $S_w = S_r / R$. Although the forward step is a stable, the inverse step is not in this case because the denominator R has near-zeros for certain frequencies (Fig. 1). To get around this problem, we use water-level deconvolution (e.g., Langston, 1979), which increases the amplitude of R in these troughs to 2% of the maximum.

Phase Velocity Determination Techniques

In this section, we describe the theory behind the different techniques used to derive the phase velocity direction. Most of these techniques are a type of directional instrument-response dependent beamforming. Figure 2 shows different OFIS configurations (a-d) that are appropriate to use with these techniques if the length of the OFIS arms are longer than 1/4 wavelength of the signal. Configuration (e) could be used in the same sense as pipe rosette filters or hose arrays with no azimuthal directionality.

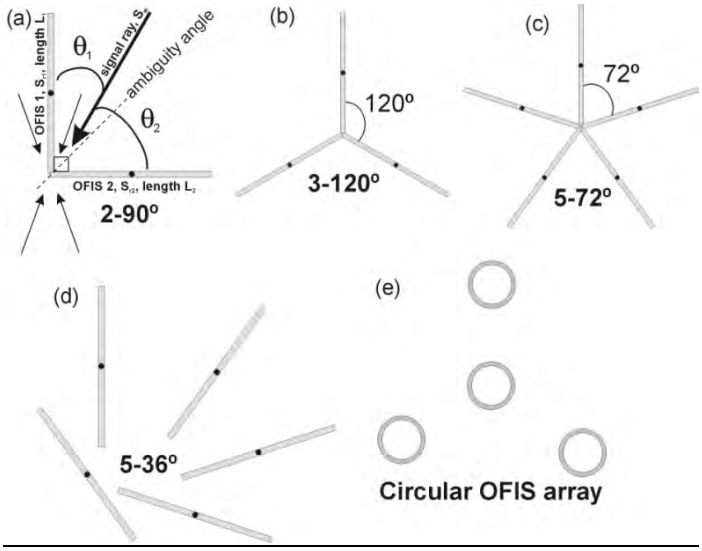

Fig. 2. Some possible OFIS array configurations.

Water-Level Deconvolution (WLD), Predicted OFIS Comparison Technique

One usually wants to obtain θ and the signal with the highest signal to noise ratio (SNR) possible. One approach is to have an array of several circular OFIS in a configuration with an aperture optimized for beamforming in the frequency band of interest. However, one can exploit the directionality property of a linear OFIS by forming an array of OFIS arms in different orientations. For each possible ray orientation, an $R(\theta)$ exists that relates S_w to what should be recorded by each OFIS. Because the recorded OFIS signal is $S_r = f(S_w, \theta, L, c)$, where only S_w and θ are the unknowns, one can estimate S_w and θ if one records the signal on two OFIS with different orientations $S_{r1} = f(S_w, \theta_1, L_1, c)$ and $S_{r2} = f(S_w, \theta_2, L_2, c)$, where θ_1 and θ_2 are related to the phase velocity direction by the array configuration (Fig. 2a). One can do this by substitution, i.e., using S_{r1} to predict ${S_w}^p$, and then ${S_{r2}}^p = {S_w}^p R_2 = S_{r1} R_2 / R_1$, and perform a grid search over trial θ to minimize the sum of squares of the misfit between the inverse Fourier transforms of S_{r2} and ${S_{r2}}^p$. The global minimum corresponds with the phase velocity direction. Knowledge of the misfit function allows us to calculate formal 2σ error bars by assuming the misfit function reflects a random chi-squared noise process (Jenkins and Watts, 1968). We determine the number of degrees of freedom based on the average recorded signal bandwidth (Silver and Chan, 1991), which frees us from the requirement that the observed signal samples are independent of each other (white spectrum).

The accuracy using this technique (which we call "WLD" even though that is technically the abbreviation for a type of deconvolution) is mostly dependent on the SNR and the orientation of the ray with respect to the OFIS arms that are being used to estimate the waveform signal (deconvolution step). For example, in Figure 2a the deconvolution of $R(\theta_1)$ from OFIS 1 (using OFIS 1 to predict OFIS 2) is more prone to noise amplification in the regional around the global minimum than the deconvolution of $R(\theta_2)$ from OFIS 2 (using OFIS 2 to predict OFIS 1) for the shown ray. There are three ways to compensate for this sensitivity. First, one can sum both misfit functions throughout the grid search. Another approach is to skip grid points for which the trial ray is within some angle of the reference OFIS orientations (this only works if you have an array of more than 2 OFIS arms). Finally, one can use only the OFIS arm that is most perpendicular to the trial ray as the reference OFIS.

The 2-90º OFIS configuration has a special property (Fig. 2a). The 90º separation offers identical spectral resolution for phase velocity directions in all of the quadrants. In addition, it is computationally the fastest in part because one only needs to do the grid search within one of those quadrants to get the spectral resolution for all possible phase velocity directions. For each trial, we can therefore obtain the spectral constrains, and then time shift the resulting inverse Fourier transformed waveform by $dt = (L_2 \cos\theta_{H2} - L_1 \cos\theta_{H1}) \cos\theta_V / 2c$ to calculate four separate quadrant misfit values (if we set R_p=0). The 2-90º configuration has been tested by analyzing recorded signals at the Piñon Flat Observatory with the WLD method (unpublished data). The configuration works fairly well for sub-horizontally propagating signals with a very good to excellent SNR (> 12 dB). However, it does not work well for signals with a low SNR. In addition, a fundamental limitation of any two-arm OFIS configuration is that it cannot be used to determine a phase velocity direction within the vertical plane defined by the azimuth in between the two OFIS (Fig. 2a). Only higher order OFIS configurations can resolve that ambiguity.

In general, the WLD technique can be applied to multiple OFIS arms in different configurations, but the computational time for the above method is proportional to $n(n\text{-}1)$ and there is an additional doubling of CPU time associated with going from a 2-90º configuration to a higher order configuration because quadrant symmetry is replaced by hemisphere symmetry.

Simultaneous Array Deconvolution (SAD) Technique

The WLD technique can amplify noise because of the deconvolution step. The simultaneous array deconvolution (SAD) is a more stable deconvolution technique. One estimates the unattenuated signal spectrum by weighting, as a function of frequency and trial phase velocity direction, the recorded spectra of the OFIS arms such that only those OFIS arms that are in a good position to estimate S_w at each frequency are effectively used in the deconvolution. For example, if OFIS 1, 2, 3, and 4 recorded a signal with a phase velocity direction that was 0º, 29º, 58º, and 87º from those OFIS arms, respectively (Fig. 1b), SAD would determine for a frequency of 7 Hz the signal spectrum from the OFIS spectra weighted from greatest to least: OFIS 4, 2, 1, and 3. In other words, the SAD technique is theoretically more stable than the water-level deconvolution approach because recorded spectra values, where troughs are predicted to exist by R, are effectively not used to estimate the signal spectrum. This approach is a least-squares inversion. Assume $\boldsymbol{D}$ is an m x n matrix containing the OFIS recorded complex spectra, where m is the number of OFIS and n is the length of the spectrum. The forward problem is represented in matrix notation as $\boldsymbol{D} = \boldsymbol{GW}$, where $\boldsymbol{W} = \boldsymbol{wI}$ contains S_w and $\boldsymbol{G}$ is an m x n matrix containing the m response functions of length n for the trial phase velocity direction. The least squares solution for $\boldsymbol{D}$ given $\boldsymbol{W}$ is $\boldsymbol{W} = [\boldsymbol{G}^T\boldsymbol{G}]^{-1}\boldsymbol{G}^T\boldsymbol{D}$. Expanding for the i[th] frequency component,

$$w_i = \frac{G_{1i}D_{1i} + G_{2i}D_{2i} + \cdots + G_{mi}D_{mi}}{G_{1i}^2 + G_{2i}^2 + \cdots + G_{mi}^2}$$

This equation represents the best technique for estimating S_w providing that each OFIS has the same intrinsic noise level. From here, one can calculated the predicted OFIS recordings in the same manner as discussed above, and derive a misfit function. Alternatively, another measure of the misfit is the residual function in frequency space. For the trial phase velocity direction θ_t

$$M(\theta_t) = \sum_{i=1}^{m}\sum_{j=1}^{n}\left(D_{ij} - G_{ij}w_j\right)^2$$

The advantage to using the time-domain misfit is that you can normalize each waveform before taking the misfit, which allows for compensation of calibration problems and can sometimes improve stability.

Array Response Comparison (ARC) Technique

The array response comparison (ARC) technique does not involve deconvolution. Recall that the observed signals for 2 OFIS are $S_{r1} = S_w R_1$ and $S_{r2} = S_w R_2$. One can multiply both sides of these equations by the opposite instrument response function $S_{r1} R_2 = S_w R_1 R_2$ and $S_{r2} R_1 = S_w R_2 R_1$. Because of the commutative property of multiplication in the frequency domain, the right hand side of these two equations are equal, and therefore $S_{r1} R_2 = S_{r2} R_1$. Each of these products can be thought of as the array response to the signal if the centers of the OFIS were collocated and the OFIS arms optically interconnected. Each OFIS can be used to estimate the array response for some trial phase velocity direction. For the correct direction, the array responses should be identical. Therefore, for *n* OFIS arms, one can perform the grid search within a hemisphere, where for each trial direction all OFIS recordings are convolved with their *n*-1 neighbor instrument responses and transformed back to the time domain where the misfit is evaluated for both hemispheres (although one could also analyze the misfit in the frequency domain). The ARC technique compares calculated waveforms that are more smoothed than any of the predicted individual OFIS recordings from the WLD or SAD methods.

Resolution and Signal to Noise Ratio

The above OFIS array methods rely on two types of phase velocity direction resolution: time separation and instrument response discrimination. Time separation is the property that is exploited in classical array processing, either in time or frequency space. Instrument response discrimination (spectral resolution) is a unique form of resolution enjoyed by any sensor that averages along a line. However, given the amplitude decay of the response function at higher frequencies, there is a balance between spectral resolution and SNR (Fig. 3). As the noise floor increases, the higher signal frequencies that are recorded by OFIS arms at oblique angles get buried in the noise. Alternatively, for signals that only have frequencies below 1 Hz, there is no spectral resolution for a 90-m OFIS. If the noise floor is above the water level used in the WLD technique, noise can be amplified, degrading the resolution by an amount dependent on the OFIS configuration. One must take care to pick the optimum value of the high cut frequency when using a bandpass filter to isolate the band of greatest spectral resolution (Fig. 3).

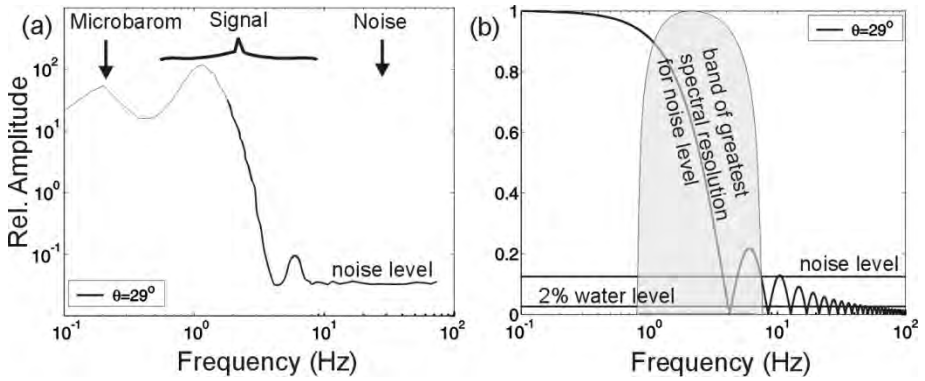

Fig. 3. Cartoon of the infrasound band of greatest spectral resolution, and how it relates to the length of the OFIS arms, a heuristic noise level, and phase velocity direction.

The SAD technique can be more stable for higher noise floors because it weighs the i^{th} frequency of all OFIS spectra by the amplitude of the associated predicted instrument response function, resulting in little contribution in the deconvolved signal from energy below noise floors that are significantly lower than the peak of the signal spectrum. However, if the noise floor is too high on one of several OFIS arms, this noise will be mapped into the deconvolved signal because SAD is a least squares technique that can weigh the spectrum of an uncharacteristically noisy OFIS greatly, which can quickly degrade the back azimuth resolution since all OFIS comparisons are made using the noisy deconvolved signal spectrum.

The ARC method may also be more stable for higher noise floors, since there is no potential to amplify noise. However, this multi-filter technique can potentially reduce the signal strength recorded on all the OFIS (including ones aligned perfectly to record the signal) to the point where lower frequency noise begins to dominate the spectrum. For fair to poor SNR, one must take particular care to isolate the signal energy with the optimum low-cut frequency. The choice of high-cut frequency is not as sensitive, since most of the higher frequency noise energy is beat down by the method.

Application to Real Data

During the summer of 2005, we recorded many infrasound signals with varying SNR with a 3-120º OFIS collocated with an IMS infrasound array at Piñon Flat Observatory (PFO), in the southern California high desert. Comprised of eight elements fitted with rosette pipe filters, the array served as a reference with which to compare signal phase velocity directions. Infrasound at PFO originates from quarry mines, bombing ranges, sonic booms, rocket launches, and aircraft flying out of Los Angeles. Most signals observed by the OFIS were in the 2–10 Hz range, and were recorded by the high frequency (HF) subnetwork (aperture of ~130 m). A known timing problem with one of the data loggers limited our analysis to only three HF elements. To facilitate data processing, we limited our analyses of the OFIS data to the 2–5 Hz band for the WLD and SAD techniques. For the ARC technique, we had the same low-cut frequency, but chose the high cut based solely on inspection of the data. For the pipe array, we chose the optimum bandpass filter, which usually was 2–5 Hz. We show results for signals with elevation angles of 0-60º as determined by the pipe array. The speed of sound was determined by the temperature during the time of the recording.

Figure 4 shows the waveforms for the optimum parameters (BAZ, ELE) for the WLD, SAD, and ARC methods as applied to one of the PFO events. The unattenuated signal waveforms are estimated for each OFIS (blue) and subsequently averaged (top, light blue) using the WLD method. The SAD method also estimates the signal waveform (top, green). The 0.92 correlation indicates a good match. The WLD estimate has higher amplitudes presumably due to noise amplification. The observed (black) and predicted (WLD/red, SAD/green) OFIS recordings from the WLD and SAD methods correlate well, but the SAD predictions are consistently better with an average correlation of 0.98 (versus 0.93). The three array responses (purple) correlate very well with their average.

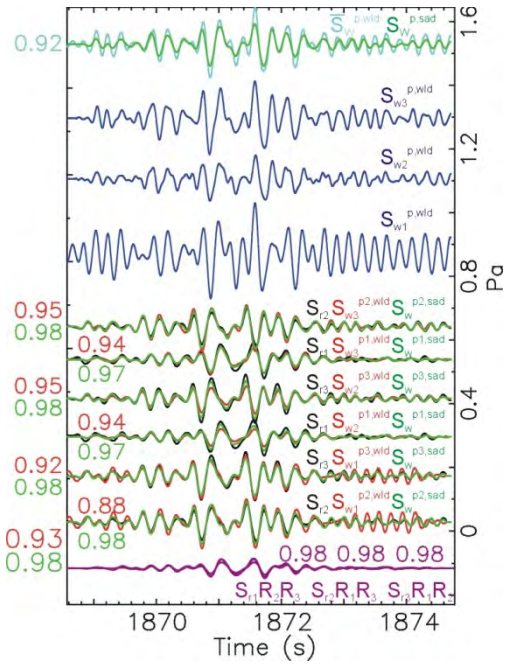

Fig. 4. Analysis of PFO OFIS signal 2005/09/20 (263) 02:31:09 UTC originating from BAZ=287º, ELE=43º.

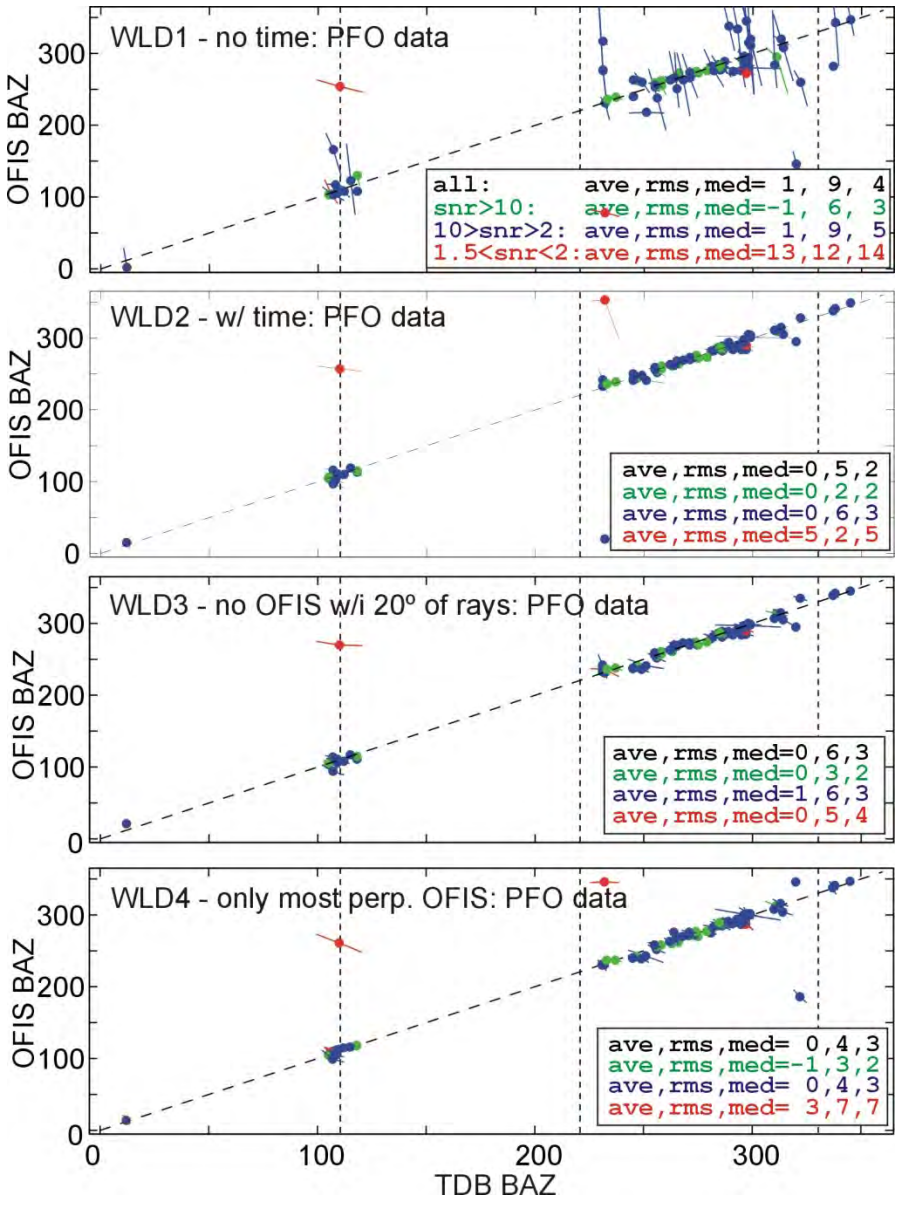
WLD1 - no time: PFO data
all: ave,rms,med= 1, 9, 4
snr>10: ave,rms,med=-1, 6, 3
10>snr>2: ave,rms,med= 1, 9, 5
1.5<snr<2:ave,rms,med=13,12,14
WLD2 - w/ time: PFO data
ave,rms,med=0,5,2
ave,rms,med=0,2,2
ave,rms,med=0,6,3
ave,rms,med=5,2,5
WLD3 - no OFIS w/i 20º of rays: PFO data
ave,rms,med=0,6,3
ave,rms,med=0,3,2
ave,rms,med=1,6,3
ave,rms,med=0,5,4
WLD4 - only most perp. OFIS: PFO data
ave,rms,med= 0,4,3
ave,rms,med=-1,3,2
ave,rms,med= 0,4,3
ave,rms,med= 3,7,7
OFIS BAZ
TDB BAZ
0
100
200
300

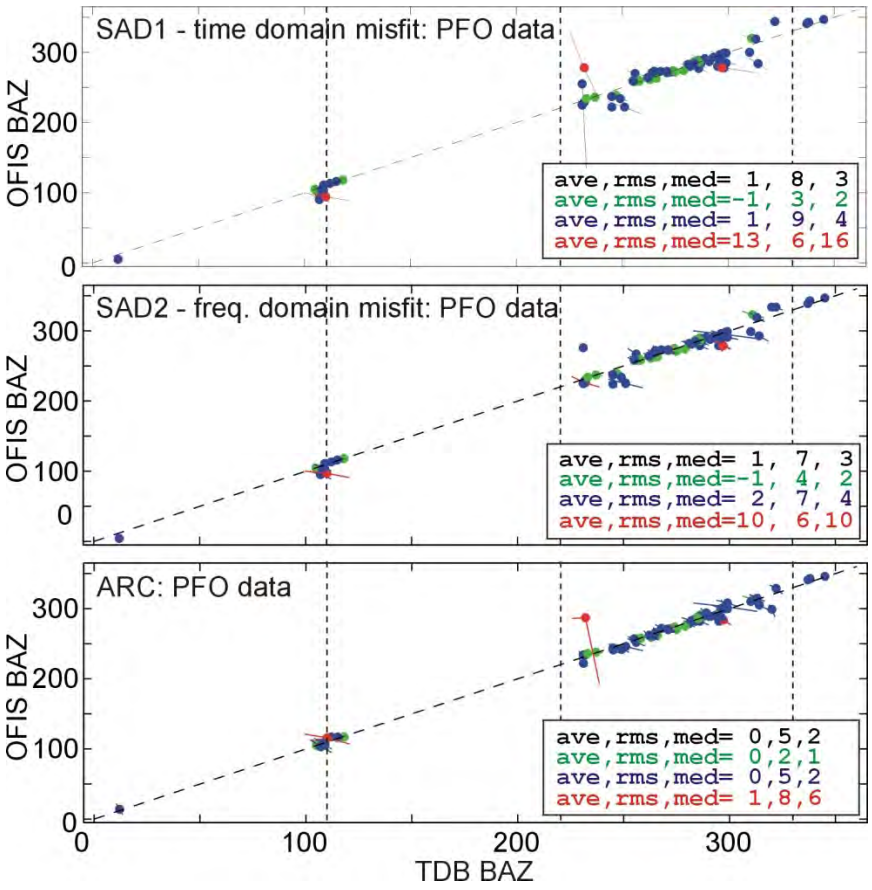

Fig. 5. Comparison of real signal back azimuths (recorded by a 3-120º OFIS and collocated pipe array at PFO) using several OFIS methods and time domain beamforming for the pipe array. SNR is the average amplitude signal-to-noise ratio of the OFIS-recorded signal.

The OFIS back azimuths from seven techniques are compared against those obtained with time-domain beamforming (TDB) using the pipe array (Fig. 5). The TDB uncertainty is obtained using the same technique as that for most of the OFIS methods, and is therefore directly comparable. The plotted error bars indicate the vector sum of the OFIS and TDB error bars, and should span the unity-slope dashed line. The vertical dashed lines indicate the azimuths of the OFIS arms, where one might expect to find difficulty for some OFIS methods for low SNR. The BAZ differences within +/-25º are used to estimate the average, RMS, and median absolute deviations.

The WLD1 results are one measure of the spectral resolution power for a 3-120º array with 90-m arms for signals in the 2-5 Hz band. Time separation is not used for these results (R_p is set to 0, and for each trial ray, a cross-correlation is applied between the predicted and observed waveforms and the optimum lag is used). Only for excellent SNR does the technique gives fair results. One can also observe inaccuracy for signals associated with rays that are subparallel to an OFIS arm. Spectral resolution would be better if the ratio of the OFIS arm length to signal wavelength was greater, or if the *effective* angular separation of the OFIS arms (60º for 3-120º configuration) was smaller (e.g., a 5-72º or 5-36º configuration, both of which have a 36º effective separation).

The WLD2 technique includes time separation resolution. It performs better than the WLD1 technique at all SNR levels with an RMS and median absolute difference of 5º and 2º. Not using OFIS arms that are within 20º of the trial rays (WLD3) reduces the problems observed near the OFIS arm azimuths, but is in general not as accurate as WLD2. Only using the most perpendicular OFIS in the deconvolution step (WLD4) does not seem to perform much better than the WLD2 method. However, this can be explained by the reduction in the number of compared waveforms used throughout the misfit function (2 pairs in WLD4 versus 6 pairs in WLD2 per trial ray).

The SAD techniques (SAD1 is the time-domain misfit whereas SAD2 is the frequency-based misfit) perform about as well as the WLD2 and WLD4 techniques for excellent SNR. However, for lower SNR, they are superior to the WLD techniques (the outliers are generally corrected). Comparing the RMS and median values are not very meaningful for this SNR because the other methods did not generate many results within the +/- 25º range used to calculate the deviation statistics.

In general, the ARC technique appears to provide the most accurate results over the widest SNR range. All of the outliers (>25º) associated with the OFIS azimuths have been corrected, and ARC has the same overall deviation statistics as WLD2 with RMS and median absolute deviations of 5º and 2º, respectively. However, upon detailed comparison between the deviations in the excellent, good, and poor SNR ranges, ARC is superior to the WLD2. In fact, a difference of 20º for a single ARC value is what gives rise to the 5º overall RMS. Without that one value, the RMS reduces to 4º (lowest of all methods). None of these techniques show evidence for a bias (significant non-zero average deviation for all SNR for any method).

CONCLUSIONS AND RECOMMENDATIONS

Our results suggest that SAD is the best method to remove the instrument response and recover the unattenuated infrasound signal. In addition, the ARC method yields estimated back azimuths that are the most similar to those obtained by classical array processing techniques like beamforming. However, most of the other techniques that use spectral and time separation resolution also perform fairly well, and also can lead to more precise estimates of back azimuth than a pipe array of comparable aperture and number of sensors.

The PFO phase velocity directions, determined by a three-OFIS array (3-120º) located on the surface with a 180-m aperture, are similar in accuracy and uncertainty to that provided by a collocated, three-element subnetwork of a certified IMS array with 18-m rosettes separated by roughly 300 m. An OFIS is more prone to instrument noise on the surface than when it is buried. A buried 90-m OFIS has a noise floor as much as 20 dB lower than the low-frequency rosette pipe array elements in the 1–10 Hz band (Zumberge et al., 2003). Based on our comparisons between different algorithms, and on synthetic data tests, we conclude that one attractive solution for determining phase velocity direction for all possible directions and frequencies down to 0.05 Hz is to have four OFIS elements in a triangular array with a ~1.5 km aperture (Fig. 6a). Each OFIS element would have two collocated 5–72º subarrays: one with 60 m arms and the other with 180 m arms. The two subarrays would be azimuthally offset by 36º. This would give adequate spectral and time resolution in the 0.5–12 Hz range *within each of the four elements* using the ARC technique. One obtains an even greater resolution when the 0.5–12 Hz results from each element are combined. Resolution for lower frequencies (0.05-0.5 Hz) would be obtained only by the time separation of the four triangular elements. The OFIS elements would be buried to insure that the noise floor would be significantly lower than that provided by rosette pipe arrays in wind speeds up to at least 3 m/s, and possibly 8 m/s based on recent observations.

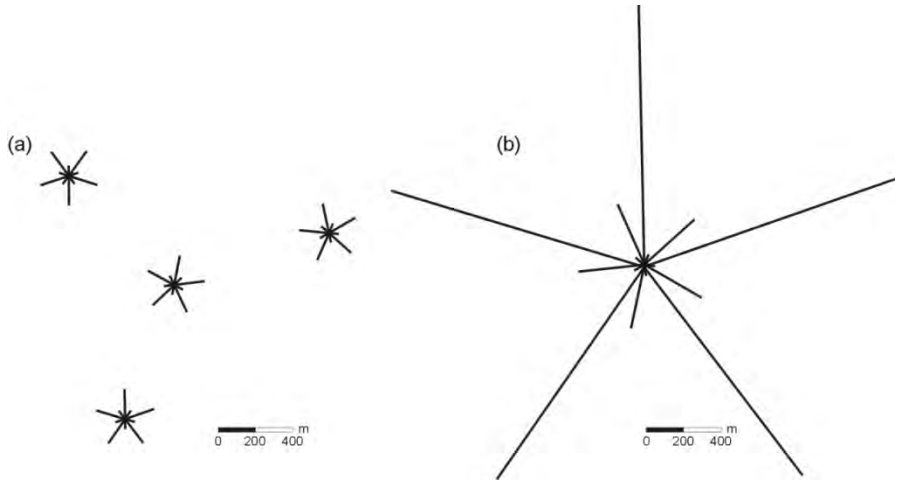

Fig. 6. Possible OFIS configurations as an alternative way to measure infrasound signals in the presence of wind noise.

Although the optical system for OFIS arms that are longer than 180 m has not been tested, another attractive solution for the same 0.05–12 Hz range would be to have just one OFIS rosette comprised of three 5–72º subarrays with different OFIS lengths: 1440 m, 360 m, and 60 m (Fig. 6b). This solution provides spatial averaging of the coherent signal over a much longer distance, which may provide better wind noise reduction than the first configuration. Both of these buried OFIS solutions only require a narrow trench of about a foot in depth, and disturb less surface area than a buried, rosette pipe array infrasound station. The OFIS configurations also have a lower profile because they do not have a surface expression other than the lines of gravel-filled trenches.

The ARC technique would be simple to implement on the second configuration because you could use this technique for all three 5–72º subarrays. For a broadband signal, one could combine the final misfit functions from the three 5–72º configurations to determine the phase velocity direction. The first configuration could also use the ARC method, and combine the misfits from all four triangular array elements, but only for the 0.5–12 Hz band. Analysis of the 0.05-0.5 Hz band would require using each of the 40 OFIS arms (or four elements if you stack the intra-element OFIS signals) with classical array processing software.

ACKNOWLEDGEMENTS

We thank P. Durdevic, P. Walsh, C. Coon, E. Blum, and R. Matoza for their assistance with field work.

REFERENCES

Alcoverro, B. (1998). Proposition d'un systeme de filtrage acoustique pour une station infrason IMS, *CEA-DASE Scientific Report No. 241*.

Alcoverro, B., and A. Le Pichon, A. (2004), Design and optimization of a noise reduction system for infrasound measurements using elements with low acoustic impedance, *J. Acoust. Soc. Am.* 117: 1717.

Hedlin, M.A., B. Alcoverro, and G. D'Spain (2003), Evaluation of rosette infrasonic noise reducing spatial filters, *J. Acoust. Soc. Am.* 114: 1807–1820.

Hedlin, M.A.H. and R. Raspet (2003). Infrasonic wind noise reduction by barriers and spatial filters, *J. Acoust. Soc. Am.* 114: 1379–1386.

Hedlin, M.A.H., and B. Alcoverro (2005). The use of impedance matching capillaries for reducing resonance in rosette infrasonic spatial filters, *J. Acoust. Soc. Am.* 117: 1880–1888.

Jenkins, G. M., and D.G. Watts (1968). *Spectral Analysis and its Applications*, Holden-Day, San Francisco.

Kaimal, J.C., and J.J. Finnigan (1994). *Atmospheric Boundary Layer Flows: Their Structure and Measurement*, Oxford Univ. Press, New York.

Landau, L. D., and E. -. Lifshitz, E. M. (1959). *Fluid Mechanics*, Pergamon, Oxford.

Langston, C. (1979), Structure under Mount Rainier, Washington, inferred from teleseismic body waves, *J. Geophys. Res.* 84: 4749–4762.

McKisic, J. M. (1997), Infrasound and the infrasonic monitoring of atmospheric nuclear explosions: A literature review, *Final report submitted to the DOE and Phillips Lab*, PL-TR-97-2123.

Shields, F.D. (2005), Low-frequency wind noise correlation in microphone arrays**,** *J. Acoust. Soc. Am.* 117: 3489–3496.

Silver, P.G., and W.W. Chan (1991), Shear wave splitting and subcontinental mantle deformation, *J. Geophys. Res.*, 96: 16429–16454.

Zumberge, M.A. et al. (2003), An optical fiber infrasound sensor: a new lower limit on atmospheric pressure noise between 1 Hz and 10 Hz, *J. Acoust. Soc. Am.* 113: 2474–2479.

INFRASOUND SIGNALS AS BASIS FOR EVENT DISCRIMINANTS

Rodney W. Whitaker

Los Alamos National Laboratory

Sponsored by National Nuclear Security Administration
Office of Nonproliferation Research and Development
Office of Defense Nuclear Nonproliferation

Contract No. DE-AC52-06NA25396

ABSTRACT

Herein we summarize the first several months' effort in this research project of calculating the near-field infrasound signals generated by ground motion sources such as underground tests and earthquakes. Our approach is a direct application of the Rayleigh integral to the ground motion acceleration as seen by an observer at altitude near the source. The numerical integration is straightforward; however, the specification of the acceleration time history may be more difficult. Results of such calculations can, with good ground motion models for underground tests and earthquakes, be used to look for differences in the near-field infrasound signals that would be the basis for discriminants. So far, the work has concentrated on getting basic codes in place and on modeling underground test signals, which will be the emphasis of this contribution. There are 34 events for which model ground motion parameters were derived, earlier by others, from the ground motion data. We now have access to the Nevada Test Site (NTS) ground motion database. This can help in improving ground motion models for underground tests. Another new development was the successful application of a two-dimensional time-domain finite-difference code to this problem. The code was run with a time dependent velocity boundary condition and to a problem time of 40 seconds showing the acoustic signal in the 12 km by 12 km domain. Results from this code can be used to benchmark other codes. Another planned use for this near-field modeling work is to provide realistic initial conditions for long-range acoustic propagation codes.

OBJECTIVES

Under the earlier Los Alamos National Laboratory (LANL) infrasound program measuring infrasound signals from underground nuclear tests (UGT) at the NTS, some work was done on finding discriminants between UGTs and earthquakes. Plots of wind-corrected infrasound pressure amplitude vs M_b and signal duration vs M_b showed promising separation of the two signal types. These results are shown in Figure 1 below. While the two groups were not perfectly separated in these variables, the results were encouraging in a search for possible discriminants. The result for duration is probably due to the longer duration of earthquake motion compared to the

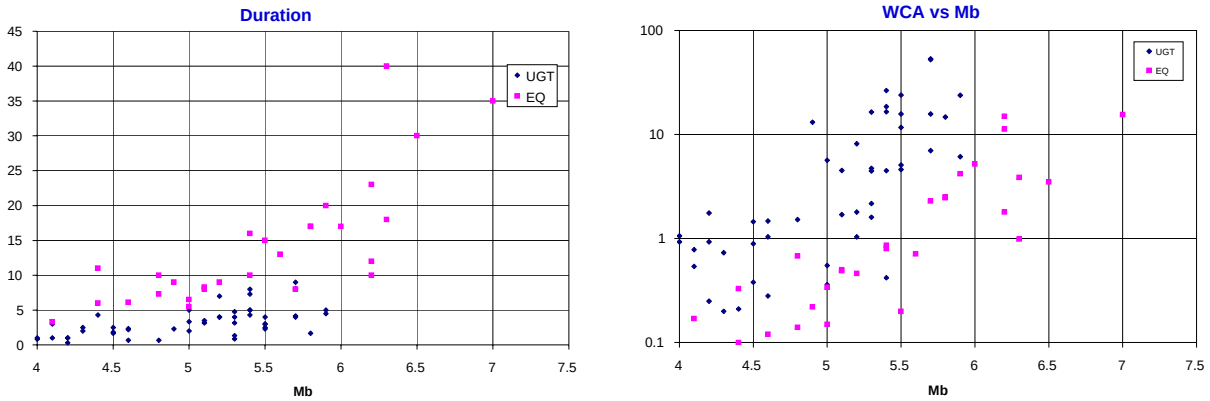

Figure 1. These figure illustrate the initial comparisons for UGTs and earthquakes for signal duration (left) and wind corrected amplitude (right) as functions of M_b.

relatively short duration for a UGT. On the other hand, UGT amplitudes would be larger due to the much larger ground motion at an UGT, although the larger area extent of the earthquake would be a competing factor.

The objective of this research is to find differences in the near-field infrasound signals of UGTs and earthquakes that can be the basis for establishing discriminants between the two sources. Such differences in the near-field would likely survive to longer range. Mutschlecner and Whitaker (2005) present an analysis of infrasound signals from earthquakes.

In this contribution we summarize a numerical technique to calculate the near-field infrasound signals generated by ground motion sources such as underground tests and earthquakes. Here we use a direct application of the Rayleigh integral to the ground motion acceleration as seen by an observer at an altitude near the source. The numerical integration is straightforward; however, the specification of the acceleration time history may be more difficult. For this contribution we emphasize results for UGTs.

RESEARCH ACCOMPLISHED

Background

In the early 1980s, LANL, under Department of Energy (DOE) funding, started a program to measure the ground motion induced acoustic signals from UGTs at the NTS. At the time, DOE was interested in technologies that could supplement seismic monitoring in the tasks of detection and yield estimation of UGTs. LANL infrasound arrays near St. George, UT, and at Los Alamos, NM, were in operation for almost every UGT from early 1983 until the end of US testing in September 1992.

Part of the LANL infrasound program included work on the propagation of infrasound signals to distances of 1000 km and sometimes farther. Because many of the NTS UGTs had some level of ground motion measurements in the form of acceleration records, it seemed that we could easily calculate the near-field infrasound signals from the UGTs. In addition, Sandia National Laboratories (SNL) fielded air-dropped pressure sensors over several tests (Banister et al., 1987) and had already started such calculations as a component of their program, Banister (1979). Around the same time, Lee and Walker (1980) developed another simple model for the parameterization of acceleration records from NTS tests, which highlighted some of the important parameters.

Rayleigh Integral

One can use the Rayleigh integral, Pierce (1989), to calculate the near-field pressure signal from a ground motion source with a specified acceleration history. The Rayleigh integral can be expressed as

$$p(R_0,t) = \frac{\rho}{2\pi}\int \frac{a(r,(t-R/c))}{R} dA_s \qquad (1)$$

where a is the acceleration of the ground, r is a location on the ground (referenced to a center position), dA_S is an element of area on the ground, R is the distance from the ground element to the observing point, t is time, ρ is the air density, c is the speed of sound in air, p is the air pressure, and R_0 is the observation location. The Rayleigh integral geometry is shown in Figure 2, for a circular region of ground motion.

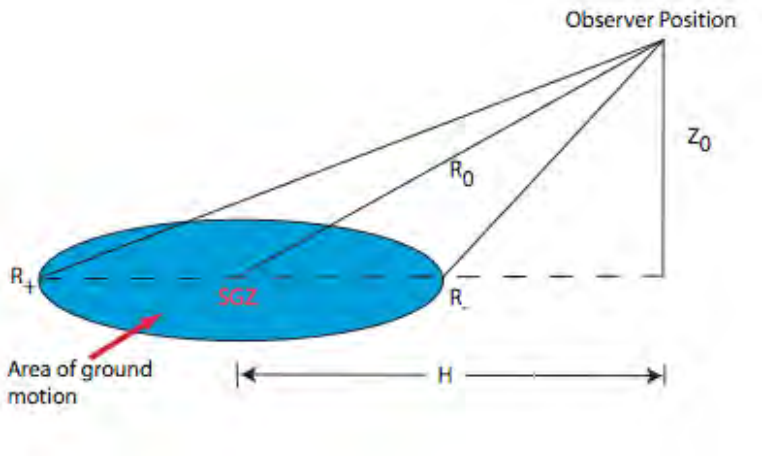

Figure 2: Illustration of the observer parameters in the Rayleigh intergral technique. SGZ is the surface ground zero at the center of the ground motion, and R_+ and R_- indicate the extent of motion. The observer is at a horizontal distance H from SGZ and vertical distance Z_0 above SGZ, at a slant range of R_0.

Real events can have departures from circular symmetry and this can be incorporated in the calculations. Specifying the acceleration as a function of position and time can be more difficult. A grid is set up on the ground dividing the area into a set of area elements as a function of range and angle from the center. The assumed acceleration model then gives the acceleration value as a function of time for each element.

Surface Ground Motion from UGTs

The surface ground motion from an UGT results from the propagation of the stress wave through the geology at the event to the surface. The simple model of ground motion acceleration from an UGT is that of a short impulse of acceleration, followed by deceleration to a minus one g phase due to spall (ballistic free fall) and concluding with the slap down impulse at spall closure. This is shown in Figure 3 (left figure). Spall is due to the reflection, at the free surface, of the upward elastic wave causing the ground to go into tensile failure and separate. The spall region free-falls briefly at -1 g, where g is the acceleration at the earth's surface. This model is quite oversimplified but is illustrative. The initial pulse can be complicated with plastic components. The slapdown pulse can show more detail as well. Small events may not enter into spall and therefore have no -1 g phase. Even large events could be buried deep enough to minimize the surface ground motion; however, that would be expensive. At NTS the depth of burial (DOB) was selected based on containment criteria, the need to contain all radioactive gases in the ground and spall was often present in the records. A more complicated and real acceleration record from a Yucca Flats test at NTS,

taken from Jones et al. (1993), is shown in Figure 3 (right figure), which illustrates the additional features that may be present.

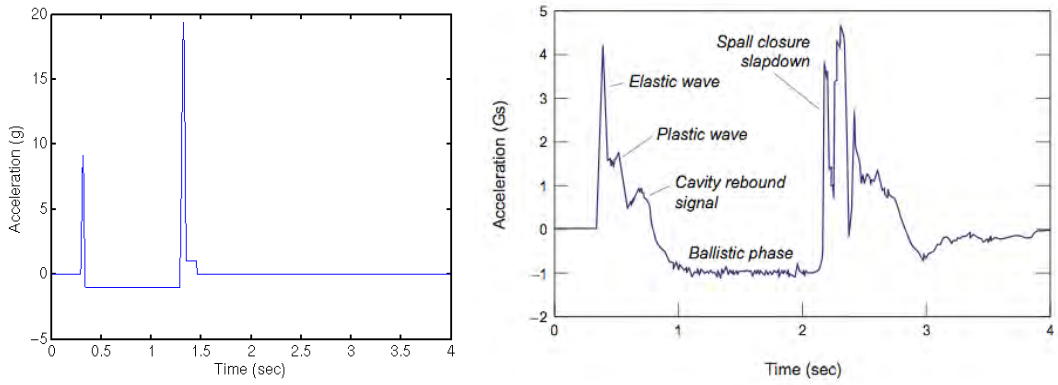

Figure 3: Simple model of ground motion from a UGT (left) showing acceleration (in g) vs time in seconds. A more complicated acceleration record is shown at the right.

In the case that the initial acceleration pulse is a short parabola with maximum acceleration A and width w, it is easy to show that the peak vertical velocity, V_{pk} is given by 2Aw/3 at the end of positive acceleration and the vertical displacement at this time is given by $Aw^2/3$. As the velocity drops from the peak during the -1 g phase, the peak displacement occurs at the time when the velocity crosses zero and is

$$d_{pk} = \frac{Aw^2}{3} + \frac{V_{pk}^2}{2g}. \qquad (2)$$

The analysis in Lee and Walker (1980) leads to a number of insights based on a simple model of the ground motion acceleration. They point out that, after the initial acceleration pulse, the ground motion is determined by the peak velocity alone.

In the present work we are building off some earlier efforts using the Rayleigh integral method. That work followed the development given in Banister (1979) but used different accelerations models for UGTs. The numerical codes for the basic computations have been restored, and cases in the Banister report were reproduced, which served as a useful check. Also recovered were acceleration parameters for 34 NTS events, shown in Table 1 (see the end of this article), for which peak acceleration values and pulse widths for the elastic wave were determined along with the same for the plastic component and rebound signal, if they were present for the event. A simple exponential decay with range is assumed. These were determined from measured data for NTS UGTs in the NTS ground motion database, App and Tunnell (1994). However, detailed documentation on how these final parameters were determined has been lost. Nevertheless, Figure 4 shows two results for NTS events relating the wind corrected infrasound pressure amplitude (wca) to SGZ peak vertical velocity (left) and the wca as a function of near-field amplitude, Jones et al (1993).

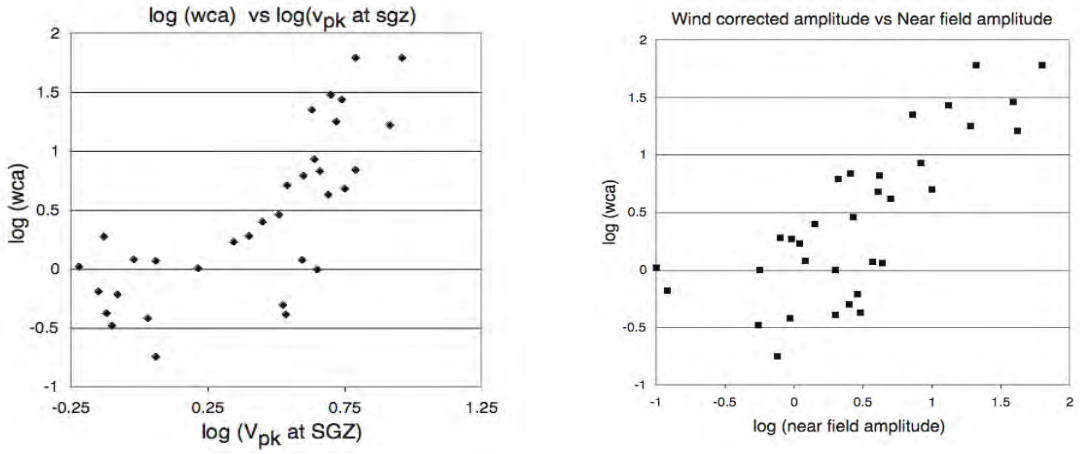

Figure 4: Wind corrected amplitudes (mbar) vs SGZ peak vertical velocity (m/s) on the left, and wind corrected amplitudes(mbar) vs computed near-field amplitudes (mbar). Wind corrected amplitudes are from the LANL, St. George, UT, infrasound array.

Other Ground Motion Models

In the current work we are working with surface accelerations, whether modeled or specified by actual measurements. Stump (1985) developed a momentum-conserving, equivalent body force model and included it in a normal moment tensor for use in synthetic seismograms. This reference summarizes much of the earlier work. Denny and Johnson (1991) review models for the seismic explosion source with comparisons to some data. Patton (1990) and Stump and Weaver (1992) examine data from NTS events on Pahute Mesa and examine relations for peak velocity and range decay behavior, among others.

Some Current Results

In Figure 6 we show some results of the current Rayleigh integral code for one of the 34 events with the modeled ground motion parameters. This case is for Towanda, U19ab, with a depth of burial of 660 m and the assumed elastic wave velocity was 2044 m//s, which determines the arrival time at a given slant range. One elastic arrival is assumed in this case. After slapdown, there is a damped oscillatory boundary condition applied to bring the final velocity to zero. Figure 5 shows the modeled acceleration record at SGZ for this event. For the pressure integration, the observer is at an altitude of 10km and the horizontal distances are 0 km, 1 km, 2 km, and then 3 km, and the results are shown in Figure 6. At 0 km range the looks similar to the velocity at SGZ exhibiting the on axis result for a uniform piston. In this case, the Rayleigh integral can be transformed, Pierce (1989), Lee and Walker (1980), so that the pressure is proportional to the difference in velocities at retarded times for the piston center and the retarded time at the piston edge. At the largest range, the large negative feature is due to nearly coherent arrivals from the spall region.

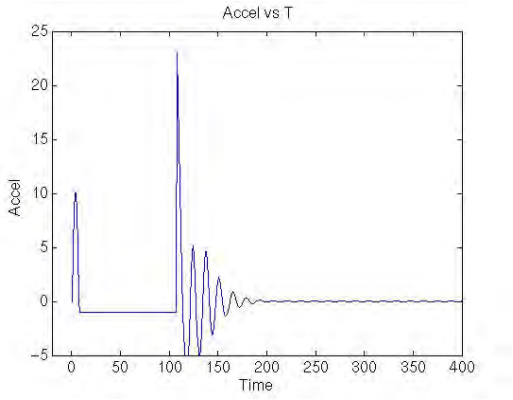

Figure 5: Modeled SGZ acceleration for U19ab, where accelerations are in g and time is in seconds.

For reference purposes we show in Figure 7 the locations of the 34 events on a map of NTS with the areas outlined in yellow.

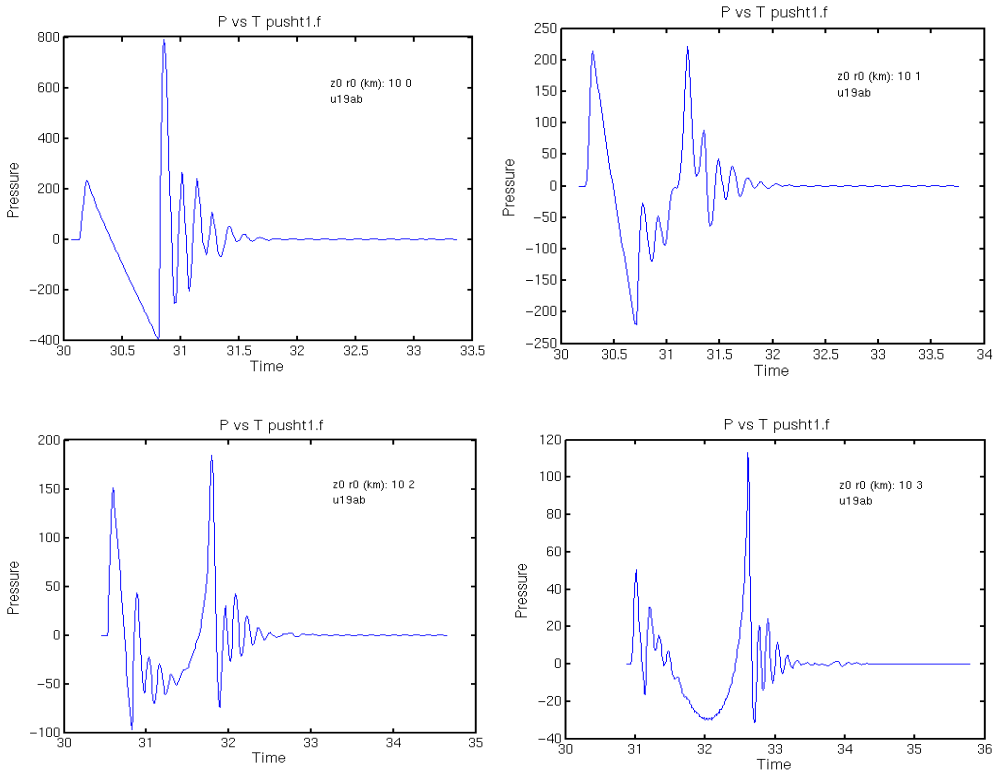

Figure 6: Near-field infrasound signals for ground motion modeled on U19ab. Pressures are in mbar and time in seconds. The observer altitude is 10 km and observer ranges are 0 km, upper left; 1 km, upper right; 2 km, lower left; and 3 km, lower right.

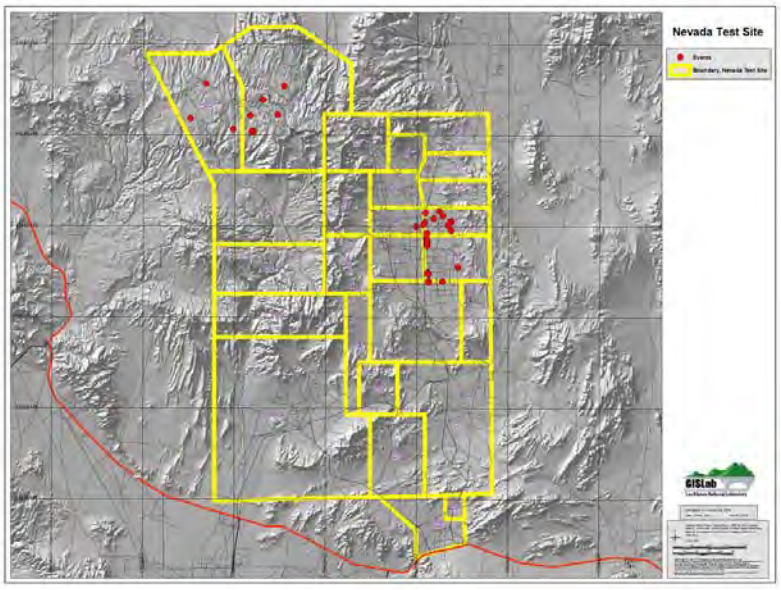

Figure 7: NTS map showing the locations of 34 events.

Two Unexpected but Useful Developments

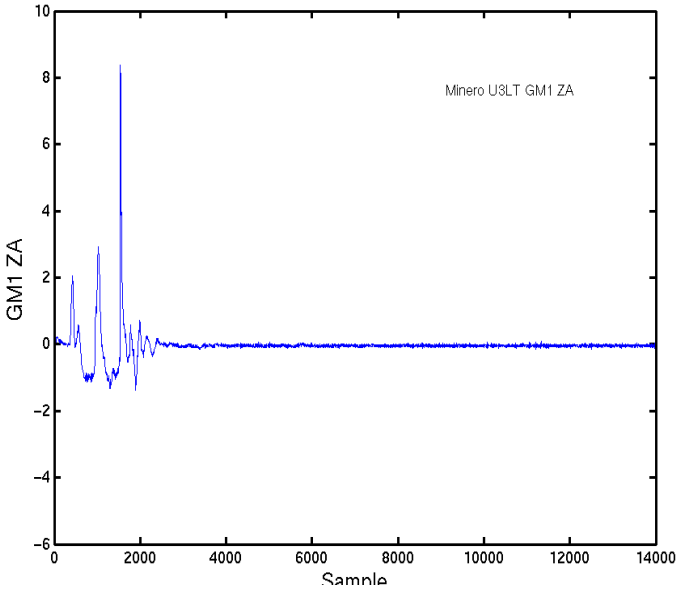

Figure 8: The SGZ acceleration record for the Minero event showing vertical acceleration vs sample number from the raw data file. Accelerations are in m/s^2.

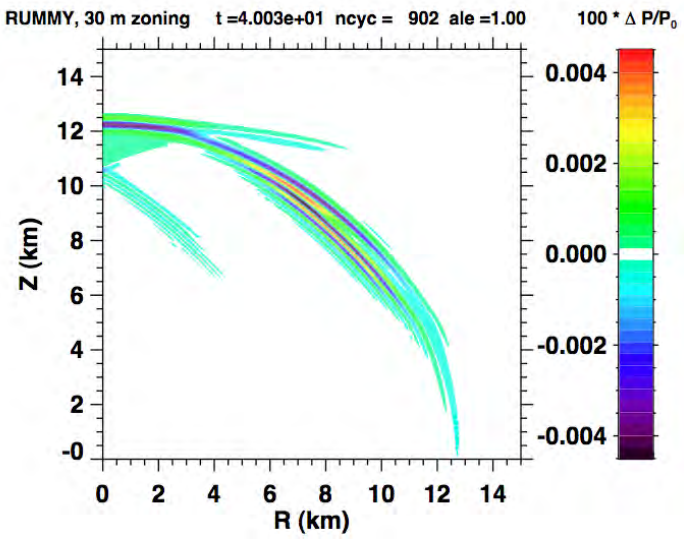

Figure 9: An acoustic signal as calculated by the CAVEAT code.

During this work, we obtained access to the data that had resided in the NTS ground motion database. This was the body of recorded ground motion data of accelerations and velocities for NTS UGTs. These seismic analysis code (SAC) files were provided by Allen Cogbill. Some events were well instrumented while others had a small number of stations. An example is shown in Figure 8, at left, for the Minero event at SGZ. These are raw data and some records contain noise spikes or other glitches that would need to be corrected before they could be directly used. Even so, they may provide verification of the Perak model parameters for the 34 events in Table 1. For events with sufficient ground motion stations, these could be used directly in the pressure integration.

Another unplanned development was a test application of the time-domain finite-difference numerical hydrodynamic code, CAVEAT (Addessio et al., 1992), to the calculation of the near-field infrasound signal from a ground motion source. In this two-dimensional, cylindrically symmetric (r, z) calculation, the mesh extends to just over 14 km in range and height. CAVEAT is used by the weapons phenomenology team at LANL and is a general computational fluid dynamics (CFD) program. For this test case, a time dependent velocity boundary condition was used at the surface and was somewhat based on ground motion data from event Rummy. Figure 9 shows contours of the pressure wave, $\Delta P/P_0$, in the calculation domain at 40 seconds. Variations of the signal with polar angle are easily seen. These calculations take longer than the Rayleigh integral but give results over the full domain. Inter-comparison of results from the two approaches may provide insight into the signal generation process.

CONCLUSIONS AND RECOMMENDATIONS

We have reviewed our recent work on calculating near-field infrasound signals from ground motion sources using acceleration records or parameterized modes. Our goal remains to look for discriminants between UGTs and earthquakes in the near-field as a basis for discriminants in the far-field signals observed by infrasound arrays. We summarized some results for work in the early 1990s related to the current work. The application of a time-domain, finite-difference fluid dynamics code will provide additional results for comparison.

While various runs are made for UGTs, we will begin to examine surface ground motion data and models for earthquake sources that can be incorporated into the current program. Characteristics of infrasound signals from a set of earthquakes are presented in Mutschlecner and Whitaker (2005), including some discussion of earthquake ground motions as they relate to the observed signals. Le Pichon et al. (2006) include an analysis of 12 earthquakes and plot their results for infrasound amplitude and duration vs M_S along with those in Mutschlecner and Whitaker (2005) with rather excellent agreement of the two data sets.

ACKNOWLEDGEMENTS

J. Paul Mutschlecner headed up the LANL infrasound effort during the period of underground testing and provided support and encouragement for many activities. This work benefited from and built upon earlier work by SNL researchers John Banister and Jack Reed and their co-workers. James J. Walker (LANL and later Amparo Corp) contributed to the analysis of UGT ground motion records. Eric Jones and Fred App used their knowledge of NTS UGT phenomenology to identify important characteristics of the surface ground motion as they related to test site area properties. Allen Cogbill provided a tar ball of SAC files of NTS ground motion measurements (acceleration, velocity and displacement) taken from the older ground motion database, App and Tunnell (1994). The CAVEAT calculation was performed by Eugene Symbalisty. Christy Flaming prepared two of the figures, and Thomas McTighe prepared the NTS map.

REFERENCES

Addessio, Frank L., John R. Baumgardner, John K. Dukowicz, Norman L. Johnson, Bryan A. Kashiwa, Rick M. Rauenzahn, and Charles Zemach (1992). CAVEAT: A computer code for fluid dynamics problems with large distortion and internal slip, Los Alamos National Laboratory technical report, LA-10613-MS, Rev. 1.

App, Frederick N. and Thomas Tunnell (1994). User manual for the NTS ground motion database retrieval program: ntsgm, Los Alamos National Laboratory technical report, LA-UR-94-1538.

Banister, J. R. (1979). A program for predicting ground motion induced air pressures, Sandia National Laboratories report SAND 78-2361.

Banister, John R., William V. Hereford, and Otis M. Solomon (1987). Preliminary results of MUNDO high altitude pressure measurements, Sandia National Laboratories report, SAND 86-2885.

Denney, Marvin D. and Lane R Johnson (1991). The explosion seismic source function: Models and scaling laws reviewed. *Explosion Source Phenomenology*, Geophysical Monograph 65. Washington, DC: American Geophysical Union.

Jones, Eric M., Frederick N. App, and Rodney W. Whitaker (1993). Ground motions and the infrasound signal: A new model and the discovery of a significant cavity rebound signal, Los Alamos National Laboratory technical report LA-UR-93-861.

Lee, Huan and James J. Walker (1980). Model for ground motion and atmospheric overpressure due to underground nuclear explosions, Los Alamos Scientific Laboratory Report LA-8554-MS.

Le Pichon, A., P. Mialle, J. Guilbert, and J. Vergoz (2006). Multistation infrasonic observations of the Chilean earthquake of 2005 June 13, *Geophys. J. Int.* 167: 838–844.

Mutschlecner, J. Paul and Rodney W. Whitaker (2005). Infrasound from earthquakes, *J. Geophys. Res.* 110: D01108, doi:10.1029/2004JD0050067.

Patton, Howard J. (1990). Characterization of spall from observed strong ground motions on Pahute Mesa, *Bull. Seism. Soc. Am*. 80: 1326.

Perret, William R. (1976). Surface motion Induced by nuclear explosions beneath Pahute Mesa, Parts I and II, Sandia National Laboratories report SLA-74-0348.

Pierce, Allan D. (1989). *Acoustic: An Introduction to Its Physical Principles and Applications.* New York: Acoustical Society of America.

Stump, Brian W. (1985). Constraints on explosive sources with spall from bear-source waveforms, *Bull. Seism. Soc. Am*. 75: 361.

Stump, Brian W. and Thomas A. Weaver (1992). Physical models of spall zone ground motions and the determination of decay rates, Los Alamos National Laboratory technical report LA-UR-92-451.

Wecksung, George W. (1985). Acoustic radiation patterns associated with the ground motion produced by a contained nuclear explosion, Amparo Corporation report (unpublished).

Table 1. Events with modeled ground motion parameters

Event Name	Hole	Longitude	Latitude	Date
ABILENE	U3MN	-116.04519	37.013115	4/7/88
ALAMO	U19AU	-116.377558	37.252395	7/7/88
AMARILLO	U19AY	-116.354441	37.275412	6/27/89
ATRISCO	U7BP	-116.007419	37.084155	8/5/82
BARNWELL	U20AZ	-116.410277	37.231037	12/8/89
BEXAR	U19BA	-116.313782	37.296033	4/4/91
CABRA	U20AJ	-116.460926	37.30063	3/26/83
CAPROCK	U4Q	-116.048917	37.103086	5/31/84
COALORA	U3LO	-116.04621	37.056108	2/11/83
DALHART	U4U	-116.050126	37.088955	10/31/88
DIVIDER	U3ML	-115.988778	37.020635	9/23/92
DOLCETTO	U7BI	-116.000232	37.089754	8/30/84
DUORO	U3LV	-116.043924	37.000333	6/20/84
GLENCOE	U4I	-116.066905	37.082962	3/22/86
HERMOSA	U7BS	-116.033208	37.094766	4/2/85
HOUSTON	U19AZ	-116.37212	37.22737	11/14/90
KINIBITO	U3ME	-116.046234	37.053224	12/5/85
LAREDO	U3MG	-116.043939	36.998551	5/21/88
LOCKNEY	U19AQ	-116.37559	37.227947	9/24/87
MINERO	U3LT	-116.04557	37.011903	12/20/84
MOGOLLON	U3LI	-116.046915	37.011614	4/20/86
MUNDO	U7BO	-116.023247	37.10618	5/1/84
PONIL	U7BV	-116.002632	37.089767	9/27/85
SALUT	U20AK	-116.489947	37.247799	6/12/85
TAHOKA	U3MF	-116.046171	37.060915	8/13/87
TAJO	U7BL	-116.016377	37.098248	6/5/86
TEXARKANA	U7CA	-116.001477	37.076741	2/10/89
TORNERO	U3LL	-116.045553	37.010645	2/11/87
TORTUGAS	U3GG	-116.04716	37.065727	3/1/84
TOWANDA	U19AB	-116.326088	37.253358	5/2/85
TURQUOISE	U7BU	-116.046822	37.072795	4/14/83
VAUGHN	U3LR	-116.046195	37.058031	3/15/85
VERMEJO	U4R	-116.053674	37.085186	10/2/84
VILLITA	U3LD	-116.018242	37.000059	11/10/84

Data Processing and Analysis

ENHANCED RESOURCES OF THE SMDC MONITORING RESEARCH PROGRAM FOR SOURCE INFORMATION AND DATA ACQUISITION

Manochehr Bahavar, Brian W. Barker, Theron J. Bennett, J. Roger Bowman, Hans Israelsson, Ben Kohl, Yu-Long Kung, Jack R. Murphy, Robert G. North, Victoria Oancea, Mike O'Brien, and Gordon Shields

Science Applications International Corporation

Sponsored by Army Space and Missile Defense Command

Contract No. DASG60-03-C-0009

ABSTRACT

The Research and Development Support Services (RDSS) project of the Space and Missile Defense Command (SMDC) provides a range of resources and services for use in nuclear explosion monitoring research and development. R&D. This presentation focuses on recent developments and enhancements to the infrasound, seismic, and hydroacoustic resources, most of which can be accessed from the RDSS website at www.rdss.info. In particular, on-going and recent developments and improvements are related to (1) the nuclear explosion database archive and (2) infrasound signals and associated source information.

The RDSS project has traditionally maintained an archive of information on source metadata and seismic waveforms from worldwide nuclear explosions. These resources were previously documented in the year 2000, and we are now completing a major revision and update which includes newly published or revised information about historical explosions, access to additional or corrected waveform data for some explosions, and new data from more recent nuclear tests (e.g., North Korea). In addition to maintaining these research data archives, we have been developing a number of web tools which enable visualization of and easier access to these explosion resources, including tabular-, map-, and imagery-based event selection and comparisons, station coverage and response information, as well as review of data quality and acquisition of the available seismic waveform data.

Identification of infrasound events for the RDSS infrasound database has continued. This is based on a search of the RDSS waveform archive for signals that can be associated with recent events from seismic bulletins, volcanic activity reports, and reports in the press of accidental explosions, bolides, etc. Signal processing with Infratool and simple modeling with InfraMap are also used in the association. During the last year waveform data have been added to the archive from new infrasound stations in Asia and North Africa. Many events were identified with signals recorded at these stations which provide several new repeated source-receiver paths, particularly in central Asia, for modeling atmospheric propagation. RDSS has also continued its responsibility for collecting, compiling, and distributing data and metadata for the three rocket experiments in 2005–2006 at White Sands Missile Range (WSMR), including a number of quality control checks on the waveform data.

OBJECTIVE

The RDSS project of the SMDC has the objective to support the nuclear explosion monitoring research and development community providing a range of data, state-of-the-art data access tools, and value-added datasets. This paper focuses on recent developments and enhancements to the seismic and infrasound resources, which can be accessed from the RDSS website. In particular, recent developments have been directed at (1) the nuclear explosion database archive and options for display and retrieval of the associated data resources, and (2) identification of infrasound events and association of the related signals.

RESEARCH ACCOMPLISHED

Nuclear Explosion Database

The SMDC Nuclear Explosion Database (NEDB) has historically provided access to source metadata and associated waveforms for worldwide nuclear explosions. This activity was documented in a series of reports (Yang et al., 1997, 1998, 1999, 2000) and in the online nuclear explosion research database provided at www.rdss.info. In recent years supplemental information has become available describing many of the explosion sources (e.g., Springer et al., 2002; Khalturin et al., 2001, 2005; DTRA, 2007; Bennett et al., 2004) from historical events plus source and waveform data from a new nuclear explosion—the October 2006 North Korea test (Bennett et al., 2006; Richards and Kim, 2007; Kim and Richards, 2007). These source data have now been added to the NEDB. In addition, we have performed a variety of QA/QC checks on both source data (including comparisons of published locations with satellite imagery) and station information to improve the database and ensure accuracy of the available waveforms. We have upgraded our station database to ensure that station names and station coordinates best match those contained in the official International Registry of Seismograph Stations. We have also been collecting additional station calibration and instrument response information that will be helpful for users who would like to do additional processing of the waveform data.

The prior version of the NEDB (Yang et al., 2000) included metadata from underground/underwater US nuclear explosion sources based on Springer and Kinnaman (1971, 1975) which only included events prior to October 1973. The corresponding complete listing describing all US underground/underwater explosions (Springer et al., 2002) has been digitized, checked for errors, and incorporated into the NEDB (Figure 1a). Errors in the Springer list include precision differences (e.g., Figure 1b)—related to location roundoff, which we have not yet attempted to correct, as well as some accuracy errors (e.g., Figure 1c)—mainly event names or in a few cases event locations, which we have corrected. In addition, we conducted a thorough and careful analysis of US atmospheric nuclear explosions, based on information from historical reports newly available from the Defence Threat Reduction Agency (DTRA) website (www.dtra.mil/rd/programs/nuclear_personnel/atr.cfm), and generated revised or more complete information on origin times, locations, and yields than those contained in the previous version of the NEDB.

We have also drawn upon a number of other published resources for nuclear tests from the former Soviet Union (FSU). For FSU events near Semipalatinsk (Figure 2a), we compared previously reported underground event locations (e.g., Leith., 1998, and Trabant et al., 2002, for the Degelen mountain area; or Thurber et al., 1993, 1994, and National Nuclear Center of Kazakhstan Republic (NNCKR), 1999, for the Balapan test area) with imagery analysis to ascertain the best location ground truth. Some systematic errors were identified (e.g., Figure 2b) and are now corrected in the revised NEDB, by sorting the previously reported event locations and using the one closer to features apparent on the available satellite imagery. The corrected explosion data, along with previously published location information (including ISC bulletin data) from the alternative references, are now provided in the NEDB and enable comparisons between the different source locations and related information. The NEDB also includes results from similar analyses of previously published event locations for peaceful Nuclear Explosions (PNEs) (Sultanov et al., 1999) and for Novaya Zemlya nuclear tests (Richards, 2000; Khalturin et al., 2005; Khristoforov, 1996).

Table 1 summarizes source reference information for the various countries and test areas included in the NEDB. After reviewing and comparing the source data from each of the events in the database, we formed the preferred source origin time, location (latitude and longitude), depth/height, yield/yield range, and type (e.g., underground, underwater, surface, tower, airdrop, balloon, high-altitude) for each event with an associated reference authority for each parameter. For most countries and test areas, one or two reference authorities (as indicated in the table) provide the bases for most of the preferred source solutions. It should also be noted that the preferred source origin time and location are in many cases independent of seismic information and for such cases may not agree with seismic location solutions. As noted above, to provide a relatively stable connection to the seismic source information for nuclear explosions, the NEDB includes International Seismological Centre (ISC)

seismic solutions (or for some of the older events, Preliminary Determination of Epicenters solutions) along with the corresponding network magnitudes and other complete bulletin information. It is anticipated that comparisons of the preferred solutions and seismic solutions will enable a number of interesting analyses. In addition, we include in the NEDB travel-time residuals measured from stations reporting in the ISC bulletin with respect to predicted times for the preferred nuclear explosion locations and origin times. Such measurements should provide additional opportunities to investigate some features of global and regional velocity models.

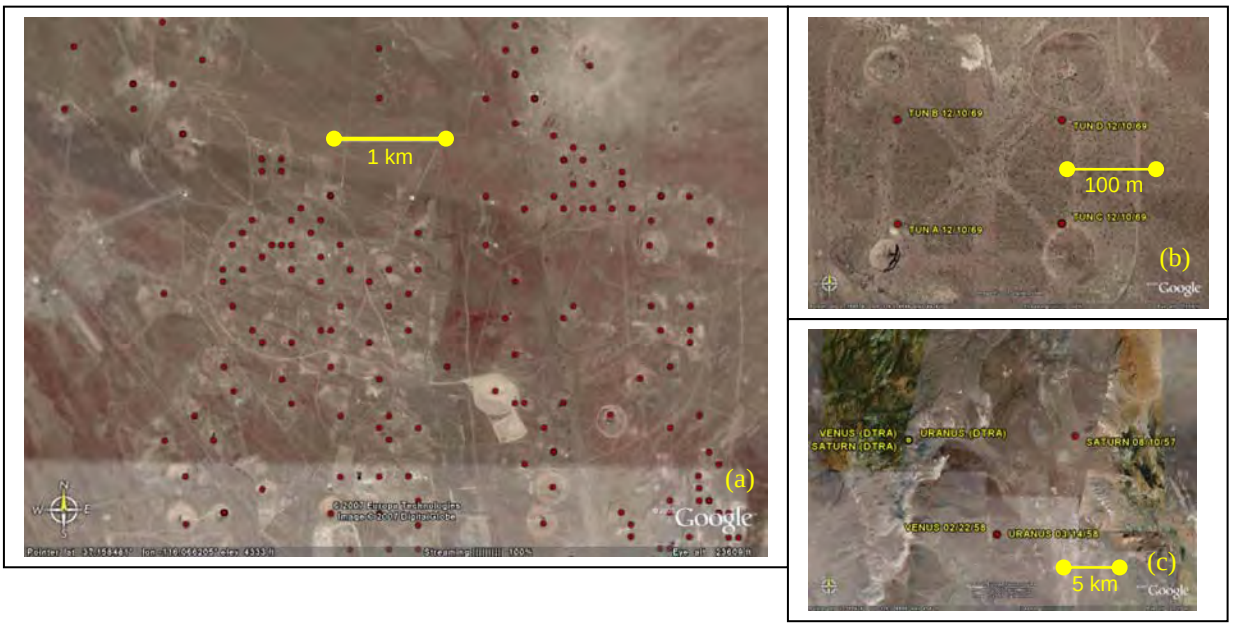

Figure 1. Springer et al. (2002) locations of US underground nuclear tests at the Nevada Test Site from the northern part of Yucca Flat (a). Comparison of the TUN series Springer locations (red) with satellite imagery illustrating roundoff error in Springer locations (b). Comparison of Rainier Mesa tunnel location of VENUS, SATURN, and URANUS tests (yellow) with locations reported by Springer (red) illustrating apparent location errors (c).

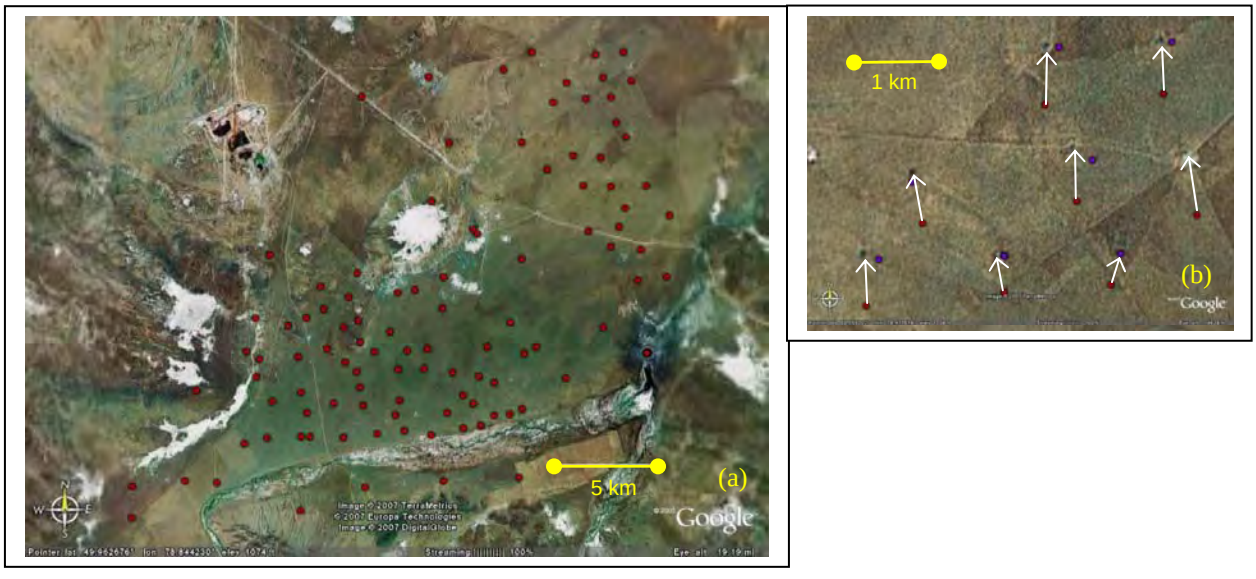

Figure 2. NNCKR locations of FSU underground explosions in the Balapan area of Semipalatinsk (a). Comparison of event locations reported by NNCKR (red) and Thurber et al., 1994 (purple), with satellite imagery from northeast Balapan (b) shows systematic location offsets relative to imagery features.

Table 1. Summary of principal nuclear explosion source reference information used in the NEDB.

Country	Region/Source	Reference/Authority*
China	Lop Nor	Gupta; Fisk; Bennett et al.; AWE
Former Soviet Union	Semipalatinsk	Mikhailov; Bocharov; NNCKR; Khalturin et al.; Leith;Thurber et al.; Trabant et al;Adushkin/Leith; Stevens et al.; AWE
	Novaya Zemlya	Mikhailov; Khristoforov; Richards; Khalturin et al.; Adushkin/Leith; Skorve; AWE; IAEA
	PNEs	Mikhailov; Sultanov et al.; Khalturin et al.; Adushkin/Leith
	Other	Mikhailov; Haave et al.; Zmuda et al.
France	Sahara	Burrows et al.; Bolt; IAEA
	South Pacific	Burrows et al.; Bolt; IAEA; AWE
India	Pokhran	Gupta/Pabian; Norris/Arkin
North Korea	Mount Mantap	Richards/Kim; Bennett et al.
Pakistan	Chagai	Norris/Arkin; Pabian
United Kingdom	Australia	Bolt; MARTAC; AWE
	Pacific	Bolt; AWE
	Nevada (US)	DOE; Springer et al.
United States	Nevada (Atmospheric)	DOE; DTRA; Griggs/Press
	Nevada (Underground)	DOE; DTRA; Springer et al.
	Pacific	DOE; DTRA; Griggs/Press
	South Atlantic	DOE; DTRA
	Other	DOE; Springer et al.
Unknown	Western Indian Ocean	GlobalSecurity; Sublette; Wikipedia

* Complete reference list available at the RDSS website.

Enhancement of the access to the NEDB is part of a more general upgrade of the SMDC RDSS website designed to provide more options and more intuitive interaction and connectivity to the data resources. Access to the NEDB is provided under the Research Databases menu option at the RDSS home page. Figure 3 illustrates the main NEDB menu with a variety of options for table-based or map-based selections to retrieve source and station information and the related waveforms from the data archive.

Imagery and map access to the NEDB is provided through GoogleMap. An imagery-based rendition illustrating the regions and subregions worldwide where nuclear explosions have occurred is shown in Figure 4. The GoogleMap interaction enables a range of comparisons between events, ties between events and surface features visible in the imagery, alternative ground truth information, and distribution of recording stations, similar to those illustrated above in Figures 1 and 2.

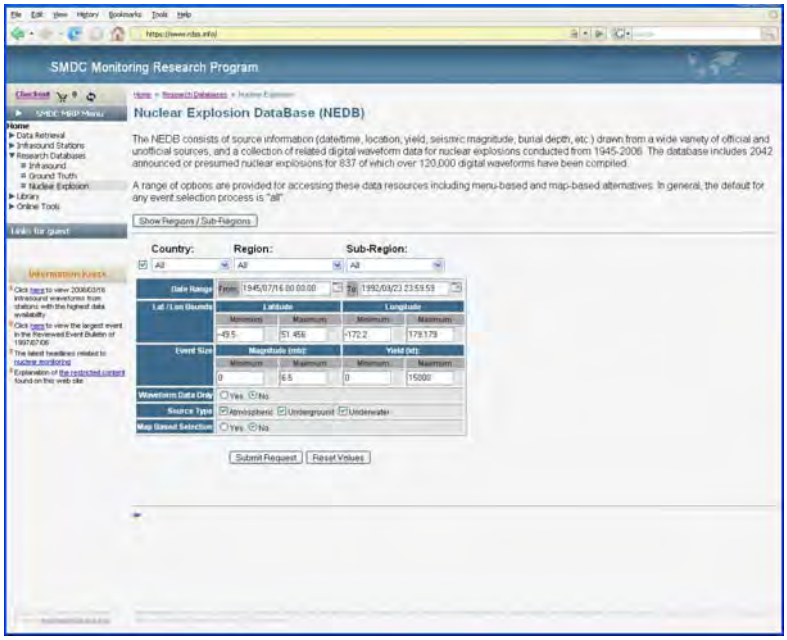

Figure 3. Homepage for the Nuclear Explosion Database at the RDSS website illustrating the menu options for refining nuclear explosion selections from the NEDB.

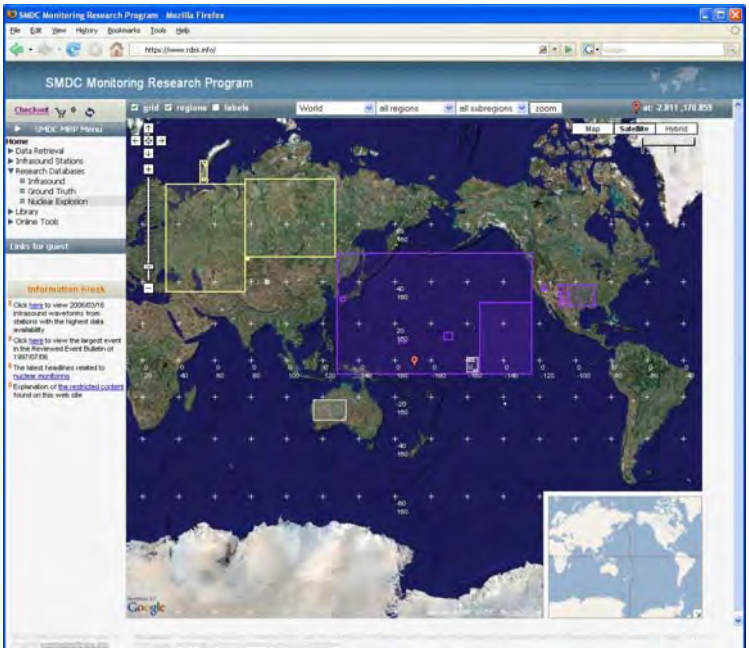

Figure 4. GoogleMap display of worldwide nuclear explosion region/subregions with boundaries color-coded by country; map and menus allow further drill-down to access source data and related waveforms.

The NEDB website provides an intuitive step-through process for accessing and retrieving the digital waveforms from the RDSS archive for nuclear explosions. The data retrieval options include selection based on individual explosions, groups of explosions, individual stations, groups of stations, and distance criteria. As summarized in Table 2, the NEDB archive is considered one of the most complete resources for digital waveforms from nuclear explosions. It currently includes more than 120,000 digital waveforms from 837 nuclear explosions recorded at the global network of seismic stations (Figure 5), covering distance ranges from near-regional to teleseismic. Available waveforms can be previewed and subjected to some basic processing (e.g., bandpass filtering) using the Waveform Viewer tool (illustrated in Figure 6) prior to actual selection and downloading.

Table 2. Summary description of NEDB data archive resources.

Events with Digital Waveform Data	Stations with Digital Waveforms	Total Waveforms	Total Data Volume
~ 840	~ 570	> 120,000	~ 6 GBytes

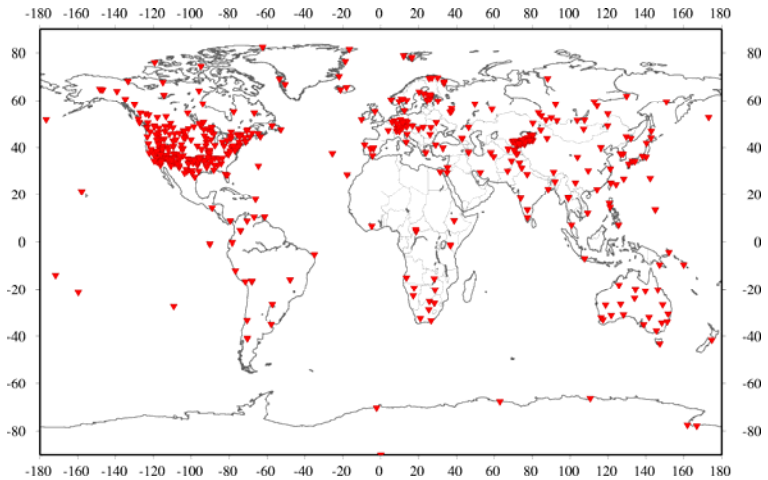

Figure 5. Map showing locations of seismic stations (N ≈ 570) for which there are digital waveform data in the NEDB archive.

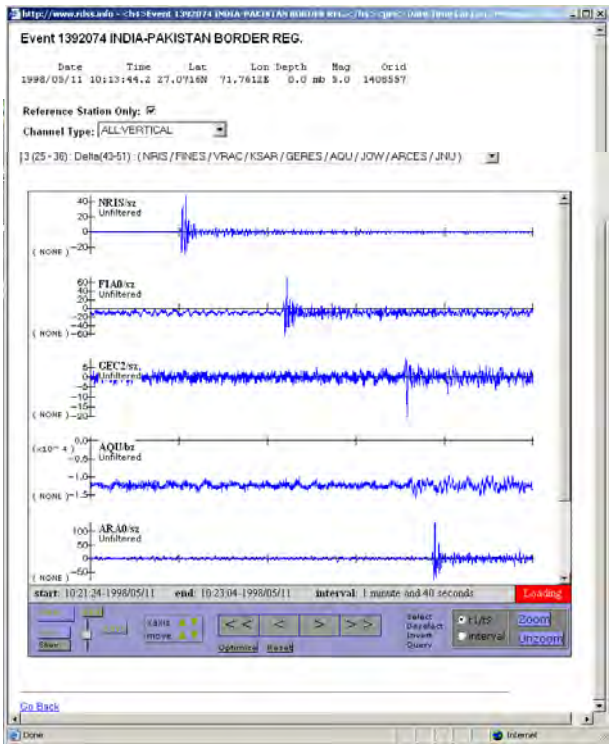

Figure 6. An example of available waveforms from a sample nuclear explosion displayed using the Waveform Viewer tool.

Infrasound Database

Identification of infrasound events for the RDSS infrasound database is based on a search of the RDSS waveform archive for signals that can be associated with recent events in seismic bulletins, volcanic activity reports, and media reports of events such as accidental explosions and bolides. Signal processing based on adaptations of Infratool and of the Maximum Cross-Correlation Method (MCCM) is used in this association. Modeling of atmospheric wave-propagation with InfraMap is also used in some cases. The search for candidate infrasound events has been focused on (1) mining events in Eurasia, (2) larger events with long paths and multi-station recordings of infrasound signals, and (3) cases with repeatable events during different times of the year for given source-station paths. Source data on infrasound events and their associated waveforms are also available to the nuclear explosion monitoring community in the research database provided at the SMDC RDSS website (www.rdss.info).

Mining events in Eurasia - Development of a database of presumed mining events in Eurasia to be included in the Infrasound Database (Bahavar et al., 2006) is based on a compilation of potential source areas by Kohl (2006) from analysis of satellite imagery and from reports in the literature such as Demin et al. (1996). Recent work on the Eurasian mining events has focused on recordings at the International Monitoring Station (IMS) four-element infrasound array at Zalesevo in Russia (I46RU), for which data became available in early 2007. So far, about 100 events have been identified in about 10 widely located areas with infrasound signals recorded at I46RU. Some of these events appeared in the International Data Centre (IDC) event bulletins (REB and SEL1), but most of the events were reported in the seismic bulletin of the Kazakhstan National Data Center (KNDC), which draws upon an extensive regional seismic station network. The map to the left in Figure 7 compares KNDC seismic locations of events, for which infrasound signals could be associated, with mining locations from Kohl (2006). There is a large concentration of events at ranges of 100–200 km in the vast Kuzbass mining district to the east of the station (Figure 7, panel to the right). There are also a number of mines located in a largely westerly direction from I46RU at varying distances up to about 3,000 km (Zaleznogorsk iron mine). Figure 8 compares infrasound signals recorded at I46RU and the Kazakhstan infrasound array (I31KZ) from an event at the Zaleznogorsk mine on April 4, 2007. Infrasound signals from two other Zalesnogorsk events during the winter and early spring were also recorded at I46RU.

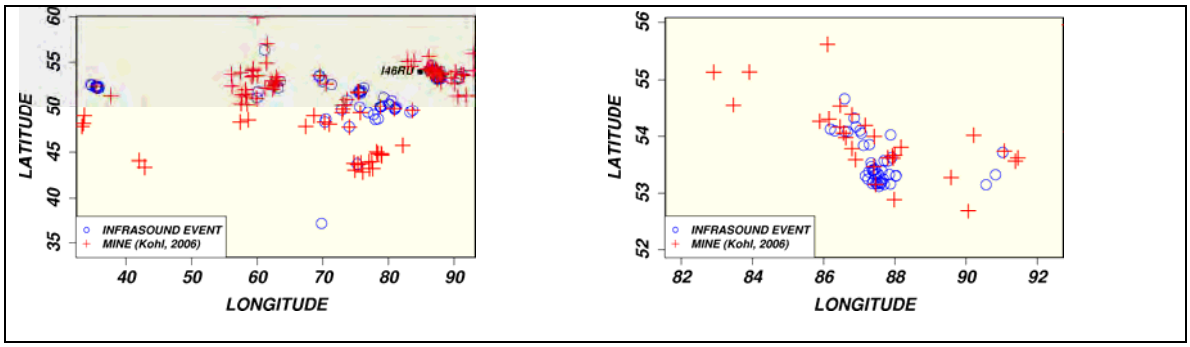

Figure 7. The left plot shows mines (red crosses) in Eurasia compiled by Kohl (2006) together with events (blue circles) with associated infrasound signals recorded at the IMS station Zalesevo (I46RU) indicated in upper right. The events occurred between January and June of 2007. The large number of mines just to the east of the station is in the Kuzbass mining district. The plot to the right shows mines and events with infrasound signals in the Kuzbass district and surrounding areas. Most of the Kuzbass events were located near two mines in the extreme southern part of the district.

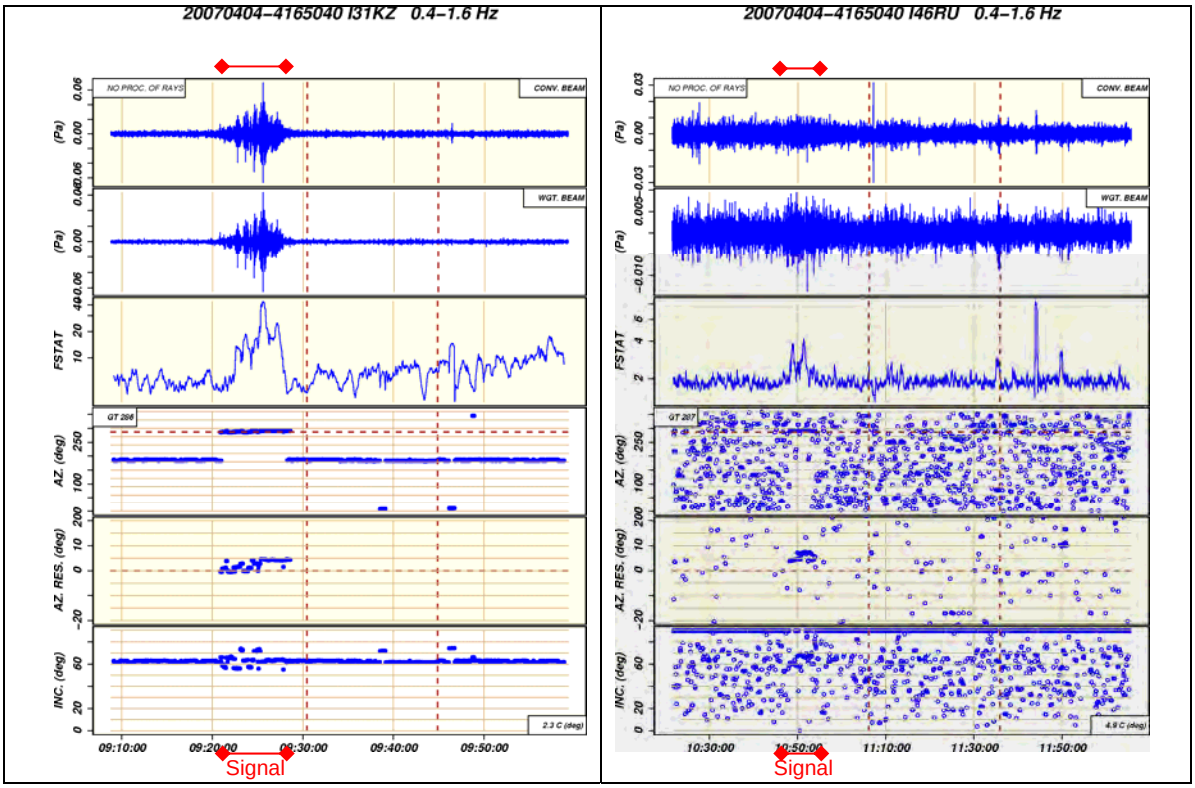

Figure 8. Example of signals recorded for an event from the Zalesnogorsk mine (IDC solution 2007 April 4 08:00:13 52.29 N 35.63 E) recorded at the two IMS stations Aktyubinsk (I31KZ, to the left) and Zalesevo (I46RU, to the right) at distances about 1,500 and 3,200 km respectively. The coherent signal energy (azimuth around 180 degrees) before and after the signal for the mining event on the I31KZ recording (left panel) originates most likely from gas flares at the Zhanazkol Oil and Gas field about 240 km to the south of the station (Smirnov, 2006). The signal at I46RU (right panel) is barely visible on the beams (top traces) but has a clear increase in the F-statistic with an azimuth around the expected back-azimuth. The red dashed vertical lines correspond to celerities of 0.29 and 0.25 km/s.

Multi-station and long path events—The addition of stations to the IMS network has broadened the coverage of infrasound signals recorded across longer paths (> 500 km) in various parts of the world. It has also increased the number of events for which signals were recorded at more than one station. Figure 9 shows great-circle event-station paths for infrasound signals during the last year recorded at large distances and/or at more than one station. There are paths on all continents except Antarctica.

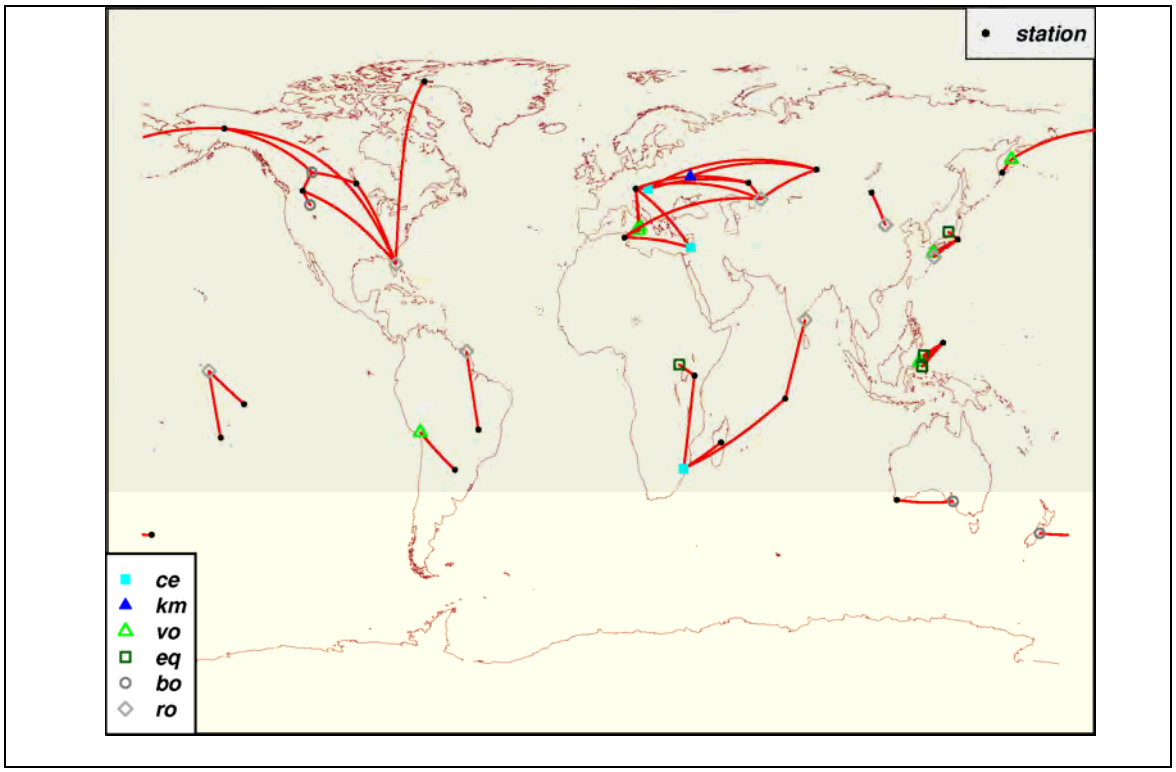

Figure 9. Great circle paths for selected events between June 2006 and June 2007 with associated infrasound signals recorded across long propagation paths and/or at multiple stations. Source types are chemical explosions (ce), known mines (km), volcanic eruptions (vo), large earthquakes (eq), bolides (bo), and rocket launches (ro).

Seasonal differences in repeatable events—A previous study (Israelsson and Kohl, 2006) showed reasonable agreement between observed and modeled seasonal patterns of detection and non-detection of infrasound signals from mining events in the Powder River Basin, WY at the IMS station I10CA (Lac Du Bonnett). I10CA is about 1,000 km to the NE from the mining area (see map in Figure 10). The IMS station I56US (Newport, OR), is also at a distance of about 1,000 km and similarly equipped as I10CA, but lies in a NW direction from the mining area. Due to the seasonal variation of the horizontal wind, the I56US station has a detection pattern almost opposite that of I10CA, with infrasound signals being detected at I56US primarily in the summer months. These opposite detection patterns for infrasound stations at similar distances are somewhat similar to those reported by Bahavar et al. (2006) for Zalesnogorsk at the two stations I31KZ and I26DE. The lower diagram in Figure 10 compares detections and non-detections of infrasound signals at the two stations from 126 mining events distributed fairly evenly throughout 2006 and located within an area with a diameter of about 25 km in the Powder River Basin. The ambient noise levels at expected arrival times or prior to observed arrival times of infrasound signals show no obvious correlation with these detection patterns (lower diagram Figure 10).

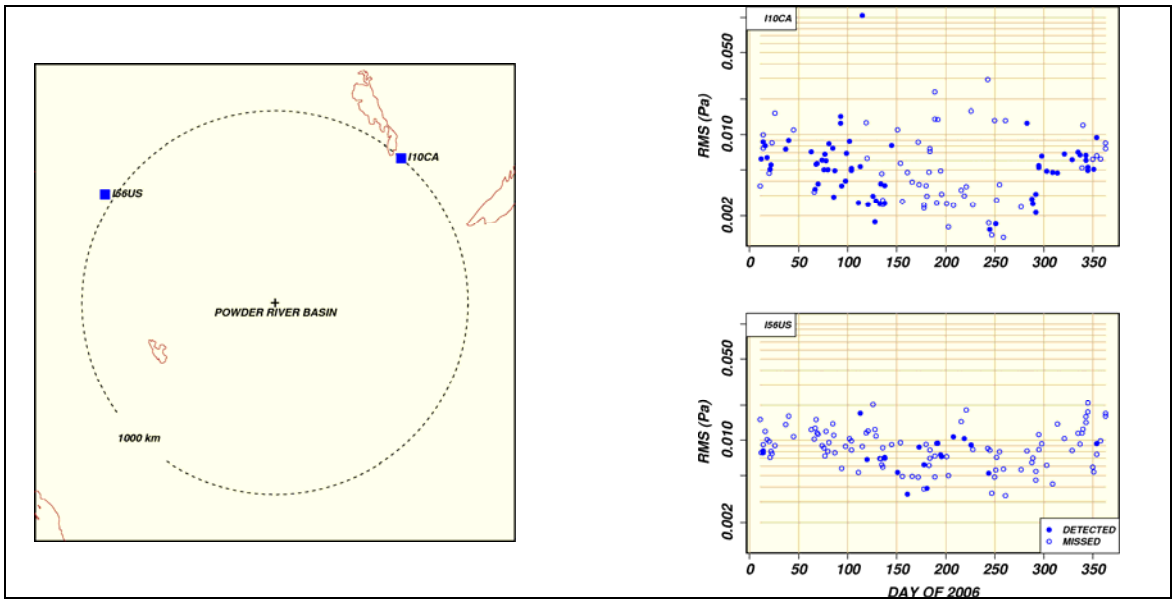

Figure 10. Map with relative locations of IMS stations I56US (Newport, OR) and I10CA (Lac du Bonnett, Canada) and the Powder River Basin mining district (left) and pattern of detection/non-detection (filled/open circles) of infrasound signals from 126 events during 2006 (right).

CONCLUSIONS AND RECOMMENDATIONS

The NEDB for the SMDC RDSS has been updated to include newly published or revised information about historical nuclear explosions, access to additional or corrected waveform data for some explosions, and new data from more recent nuclear tests. Access to the data archive for the NEDB has been upgraded to include options for table- and map-based searches and comparisons between events, alternative locations, and surface features visible in satellite imagery through an integrated GoogleMap tool. The website also provides an intuitive step-through process for accessing, displaying (using the Waveform Viewer tool), and retrieving nuclear explosion digital waveform data from the NEDB archive. For infrasound, comparisons of RDSS waveform archives with event bulletins (seismic and volcanic) and media reports have resulted in new infrasound events and their associated waveforms being added to the database. Mining events from Eurasia and the US include repeatable events and multiple-station recordings over several paths which can be used to analyze seasonal dependence in signal propagation and station noise and their effects on infrasound signal detection.

REFERENCES

Bahavar, M., J.R. Bowman, H. Israelsson, B. Kohl, R. North, M. O'Brien, and G. Shields (2006). Infrasound resources of the SMDC monitoring research program, in *Proceedings of the 28th Seismic Research Review: Ground-Based Nuclear Explosion Monitoring Technologies*, LA-UR-06-5471, Vol. 2, pp. 863–872.

Bennett, J. (editor), M. Bahavar, B. Barker, G. Beall, I. Bondar, D. Brumbaugh, M. Fisk, J. Hanson, H. Israelsson, B. Kohl, Y.-L. Kung, J. Murphy, R. North, V. Oancea, and J. Stevens (2004). Seismic Calibration of Lop Nor, China Test Site Region for Improved Regional Monitoring, SAIC Report SAIC-04/2208.

Bennett, J., R. North, B. Kohl, J. Murphy, J. Stevens, I. Bondar, M. Fisk, M. Bahavar, B. Barker, H. Israelsson, and V. Oancea (2006). Analysis of IMS Data from the North Korean (DPRK) Nuclear Test of October 9, 2006, SAIC Report SAIC-06/2203.

Defense Threat Reduction Agency (2007). Research and Development Enterprise, Nuclear Test Personnel Review Program, Related Historical Volumes from Atmospheric Nuclear Tests (http://www.dtra.mil/rd/programs/nuclear_personnel/atr.cfm).

Demin, V.N., M.N. Malahova, P.N. Martysevich, N.N. Mihaylova, A. Nurmagambetov, Yu.F. Kopnichev, V.I. Edomin (1996). Data Base of Chemical Explosions in Kazakhstan, Lawrence Livermore National Laboratory Report UCRC-CR-126765 S/C# B301622.

Israelsson, H. and B Kohl (2006). Infrasound from Suites of Mining Explosions at Large Distances – Observations and Modeling, Presentation at Infrasound Technical Workshop, Fairbanks, Alaska (http://www.gi.alaska.edu/infrasound/ITW2006).

Khalturin, V., T. Rautian, P. Richards (2001). A study of small magnitude seismic events during 1961–1989 on and near the Semipalatinsk Test Site, Kazakhstan, *PAGEOPH* 158: 143-171.

Khalturin, V., T. Rautian, P. Richards, and W. Leith (2005). A review of nuclear testing by the Soviet Union at Novaya Zemlya, 1955–1990, *Science and Global Security* 13: 1-42.

Khristoforov, B. (1996). About the Control of the Underwater and Above Water Nuclear Explosions by Hydroacoustic Methods, Institute for Dynamics of the Geospheres, Russian Academy of Sciences, Final Report for Project SPC-95-4049.

Kim, W.-Y., and P. Richards (2007). North Korean nuclear test: seismic discrimination at low yield, *Am. Geophys. Union EOS* 88: 160–161.

Kohl, B. (2006). Database of Features in Central Asia: Locations of Mines and Quarries that generate Infrasound recorded at I31KZ and I34MN, SAIC Report SAIC-06/2201.

Leith, W. (1998). Degelen Nuclear Test and Tunnel Data, U.S. Geological Survey Memorandum, 26 June 1998.

National Nuclear Center of Kazakhstan Republic (1999). Table of Locations of Balapan Nuclear Explosions Newly Mapped by NNCKR, in *Proceedings of First Workshop on IMS Location Calibration, 12-14 January 1999*, Oslo, Norway.

Richards, P. (2000). Accurate Estimates of the Absolute Location of Underground Nuclear Tests at the Northern Novaya Zemlya Test Site, in *Proceedings of Second Workshop on IMS Location Calibration, 10–24 March 2000*, Oslo, Norway.

Richards, P., and W.-Y. Kim (2007). Seismic Signature, *Nature Physics* 3: 4–6.

Smirnov, A. A. (2006). Identification of Flame bem lights groups as an unique infrasound source using I31KZ data, Presentation at Infrasound Technical Workshop, Fairbanks, Alaska (http://www.gi.alaska.edu/infrasound/ITW2006).

Springer, D. and R. Kinnaman (1971). Seismic source summary for U.S. underground nuclear explosions, 1961-1970, *Bull. Seism. Soc. Am.* 61: 1073–1098.

Springer, D. and R. Kinnaman (1975). Seismic source summary for U.S. underground nuclear explosions, 1971-1973, *Bull. Seism. Soc. Am.* 65: 343–349.

Springer, D., G. Pawloski, J. Ricca, R. Rohrer, and D. Smith (2002). Seismic source summary for all U.S. below-surface nuclear explosions, *Bull. Seism. Soc. Am*. 92: 1806–1840.

Sultanov, D., J. Murphy, Kh. Rubbibstein (1999). A seismic source summary for soviet peaceful nuclear explosions, *Bull. Seism. Soc. Am.* 89: 640–647.

Thurber, C., H. Quin, and P. Richards (1993). Accurate locations of nucelar explosions at Balapan, Kazakhstan, 1987 to 1989, *Geophys. Res. Letters* 20: 399–402.

Thurber, C., H. Quin, and R. Saleh (1994). Catalog of locations of nuclear explosions at Balapan, Kazakhstan, 1965 to 1985, *Bull. Seism. Soc. Am.* 84: 458–461.

Trabant, C., C. Thurber, and W. Leith (2002). Ground truth seismic events and location capability at Degelen Mountain, Kazakhstan, *Phys. Earth Plan. Int.* 131: 155–171.

Yang, X., R. North, and C. Romney (1997). CMR Nuclear Explosion Database, CMR Technical Report CMR-97/19.

Yang, X., R. North, and C. Romney (1998). CMR Nuclear Explosion Database (Revision 1), CMR Technical Report CMR-98/27.

Yang, X., R. North, and C. Romney (1999). CMR Nuclear Explosion Database (Revision 2), CMR Technical Report CMR-99/16.

Yang, X., R. North, and C. Romney (2000). CMR Nuclear Explosion Database (Revision 3), CMR Technical Report CMR-00/16.

ADVANCES IN THE INTEGRATION OF LARGE DATA SETS FOR SEISMIC MONITORING OF NUCLEAR EXPLOSIONS

Dorthe B. Carr[1], Jennifer E. Lewis[1], Sandy Ballard[1], Elaine M. Martinez[1], Jeff W. Hampton[1], Bion J. Merchant[1], Richard J. Stead[2], Michelle Crown[3], Jorge Roman-Nieves[3], and John J. Dwyer[3]

Sandia National Laboratories[1], Los Alamos National Laboratory[2], and Air Force Technical Applications Center[3]

Sponsored by National Nuclear Security Administration
Office of Nonproliferation Research and Development
Office of Defense Nuclear Nonproliferation

Contract Nos. DE-AC04-94AL8500[1] and DE-AC52-06NA-25396[2]

ABSTRACT

The National Nuclear Security Administration (NNSA) Ground-Based Nuclear Explosion Monitoring Research and Engineering (GNEMRE) program has been integrating large sets of seismic events and their associated measurements for almost a decade to support nuclear explosion monitoring. During that time the integration process has changed significantly, generally becoming more complex and more automated as the number of events and the range of associated measurements has steadily grown. In this paper, we explain the methodology for integrating database tables from different products that are part of a Knowledge Base (KB) release.

The major effort of KB integration is merging events and their associated information in Oracle database tables. We have developed a substantial foundation of structure and software to assure data integrity in the integration of diverse data sets. The structural part of this foundation utilizes Oracle data dictionary tables along with complementary custom database tables. These custom tables contain information specifically related to how KB database objects are built. Information such as descriptions and database types are stored in these custom tables so that the KB structure is easily modifiable making it more flexible than it would be following a traditional database design. This "metadata" of the supporting structures is called the "schema schema," and all the integration tools are based on this structure.

Los Alamos National Laboratory (LANL) has developed a tool to make sure the information in the product database tables is accurate and valid. Called the Quality Control Tool (QCTool), this tool checks that the database tables conform to the database structures found in the "schema schema" and that the values in the database tables are reasonable. Database tables are not merged together until the errors generated by QCTool are either corrected or explained.

Sandia National Laboratories (SNL) has developed a suite of merging tools that are part of a set of generalized database interface tools called DBTools. These tools are based on the concept of a "RowGraph," which builds a set of information for an event based on the specified relationships. Using RowGraphs the applications in DBTools can then easily read and write a complete set of information. There are four major DBTools that are used to integrate the database tables for the KB: EvLoader (Event Loader) merges events and their associated information from different KB products into one complete set of database tables without duplicating information and updating IDs so that there are no conflicts, WFMerge (Waveform Merge) merges flat file waveforms and their associated database information using correlation parameters to determine if waveforms are the same, DTX (DaTa eXchange) is used to merge the station parameter information, and Remap is used to create tables that remap IDs from one set of tables to another set of tables. For example, Remap is used to remap IDs from one version of the KB to another version and from the KB to other database accounts. Two other tools in DBTools that can be used in manipulating database tables in the KB are DBCompare and Unloader. DBCompare is used to compare tables for equality as defined by the tool user. Unloader deletes one or more specified rows from the database and also deletes all rows that are connected to the specified row(s) according to specified relationships. Rows are only deleted if doing so will not violate any foreign key relationships in the database, i.e., no rows are left orphaned. Using the QCTool and DBTools to check and merge information we are assured of a complete quality set of referenced database tables in the KB.

OBJECTIVES

One process for integrating a Knowledge Base (KB) is to take Oracle database tables with seismic event information and their associated measurements from different product integrators and merge the information into one set of complete tables. With each release of the KB, the process has become more complex as the number of tables and the size of the tables have both increased. We have developed a process to merge all the different database information into a complete set of quality referential database tables in the KB, using a number of tools designed at SNL and LANL.

RESEARCH ACCOMPLISHED

The NNSA Knowledge Base consists of Oracle database tables, flat-file information, and tools. The bulk of the KB is in the database tables. The core database tables hold seismic event information – origins, arrivals, associations, and magnitudes that come from various global, regional, and local bulletins. Other database tables include custom parameter information for location, event identification, and coda magnitudes that is generated from research. There are database tables that contain waveform metadata that point to flat-file waveforms on the system. Finally, there are database tables that contain information about the seismic stations – locations, channel names, instrument responses, etc. The major integration task for the KB is to combine database tables from different sources (product integrators) into one set of complete tables.

SNL needed to find a good way to merge the Oracle tables from the different sources without creating duplicate records. There needed to be proper links maintained between the related information, and SNL needed to make sure the information in the tables was accurate and correct. What evolved was a set of database integration tools. Richard Stead at LANL (Stead et al., 2006; Stead, 2007) developed the QCTool used for quality assurance and quality control. Sandy Ballard and Jennifer Lewis at SNL (Ballard and Lewis, 2004; Ballard and Lewis, 2007) developed DBTools to manipulate the information in the database. The six DBTools applications are used to compare and merge information in different database tables: EvLoader, WFMerge, DTX, Remap, DBCompare, and Unloader.

Schema Schema

Both the QCTool and DBTools depend on knowing the particulars of the database tables that are being QC'd and manipulated. This is accomplished with a database schema that holds table definition information for the KB schemas or what has been termed: "schema schema." The schema schema concept was deliberately designed by Richard Stead to have a close relationship to the Oracle data dictionary, to make the use and understanding of the schema schema simple and straightforward. However, it does go well beyond the Oracle data dictionary in various ways—in particular, because it exists apart from the tables it describes and it exists at all times regardless of which objects are currently defined or how they are defined. Any schemas can be described in the schema schema tables.

There are four tables in the "schema schema." The table **tabdescript** provides descriptions of the tables defined in each schema. Table descriptions are meant only to provide a text description of the table and its affiliation to a schema. The **coldescript** table provides descriptions of the columns defined in each schema. Column descriptions are meant to provide all data necessary to fully document the column and provide for quality control of the column. Only one column definition per column name per schema is permitted. The table **colassoc** links the columns described in the **coldescript** table to the tables described in the **tabdescript** table in such a way as to provide column ordering, roles, and information on keys within the context of a particular table. The **colassoc** table also says whether the table described is an "idowner" table, meaning that the primary key is an ID and the unique key defines the ID. The **glossary** table defines all abbreviations, acronyms, and other odd names used throughout the descriptions and also define the legal entries for columns with range types of defined and finite set. For the KB, there are two major defined schemas: NNSA KB Core and NNSA KB Custom. However, the CSS3.0, USNDC P2B2, and USNDC P3 schemas are also captured in the schema schema tables. The descriptions and definitions of the schema schema tables and columns can be found in the NNSA KB Database Guide (Carr, 2006).

QCTool

QCTool (Quality Control Tool) is an automated quality assurance and quality control tool for database tables. The tool executes three kinds of QC checks: single-table, multi-table, and complex joins. The single-table check verifies

that the table matches the documented table structure described in the schema schema tables and provides the QCTool access to a complete description of that table. The defined primary key for the table is validated, along with any unique keys that exist for that table. Then each column in the table is checked. The maximum and minimum values are found. If the values in the columns are strings, they are checked to make sure they match defined terms. If NA values are allowed, the number of rows that have the NA value is determined. If the values in the column are numeric, they are checked to make sure they fall within the defined range. None of the checks may yield errors, but they can indicate errors when subsequently reviewed.

The three kinds of multi-table checks are single-column cross reference between tables, two-column cross reference between tables, and indirect cross references. A single-column cross reference requires that every value in the specified column of the table being checked is also found in the specified column of the table that the first table is to be compared against. The two-column check is the same as the single-column check, except that each unique pair of values from the two specified columns in the table being checked must be found in the two columns specified for the comparison table. The indirect cross-reference check handles cases where the reference for a column in the table being checked is specified by a second column in the same table. The archetypical example of this is the **wftag** table, where the reference for the *tagid* column is specified by the *tagname* column; that is, if *tagname* equals "evid," then *tagid* contains an *evid* and should be compared to columns in other tables that are *evids* (like **event**.*evid*), but if *tagname* equals "arid," then the contents of *tagid* must be compared to *arids* (like **arrival**.*arid*).

The third and final checks are the complex joins. These are specified in an auxiliary table called **complexjoin**. The **complexjoin** table supports QC operations by providing a mechanism to specify any consistency requirements or expectations across as many as three generalized tables. There is always a target column for validation, and additional tables can be defined. The operation applied to the target column that is required to be true is specified in the *joinop* column, and it is a standard SQL operator. The *clause* column provides the portion of the where clause that follows *joinop* and will often include subqueries and the special strings '&t1,' '&t2,' and '&t3' for the three tables. Some simple examples for the KB include verifying that a date in a table corresponds to the time specified in the same table, verifying that the contents of a field in one table correspond to those in another when there is no direct link between the tables (such as **wfdisc**.*instype* versus **instrument**.*instype*), and verifying that a count in a field of one table equals the count of those objects in another table (such as **origin**.*ndef* versus the count of time-defining arrivals in **assoc**).

DBTools

DBTools is a suite of applications for manipulating information in a relational database in an intelligent way. This means that DBTools (1) does not duplicate information already in the database, (2) links new information to related information already in the database, and (3) remaps identification numbers on the input data to prevent conflict with identification numbers already in the database. All the applications depend on a library of utilities called DBUtilLib.

DBUtilLib is based on the concept of a RowGraph. A RowGraph manages a set of connected rows from a database. Mathematically, this set of rows forms a directed graph consisting of a set of vertexes (the rows) and edges (one-way connections between pairs of vertexes). Starting from any row, it is possible to access every other row that is connected to the starting row. The relationships that define how the rows are related are specified by the user. Once a set of database tables has been identified and the relationships between those tables defined, one may specify some initial row in the database and extract all other rows in all the other tables in the database that are related to the initial row by one or more defined relationships. DBUtilLib is written in a completely generic manner. No information is hard-coded about any particular set of tables. Instead DBUtilLib uses the schema schema as the way to determine the objects and their structure at run time. This approach makes the tools that use DBUtilLib immune to most schema changes such as addition/deletion of columns from a table or changes in the size of a particular data element, such as going from i8 to i9.

DBTools has six major applications: EvLoader, WFMerge, DTX, Remap, DBCompare, and Unloader.

EvLoader (Event Loader) merges one or more rows from a source event table into a target event table. All information in the database that is linked to the source event row(s) (such as origins, arrivals, etc.) is also merged based on how the user specifies what information is related to the source event in the parameter file. The code operates in two modes. In the first, origins in the source event are merged with origins in the target event based on *evid* number. In the second mode of operations, source events are merged with target events based on

spatial/temporal correlation. Origins that are members of the same event in the source tables will remain members of the same event in the target tables.

WFMerge (WaveForm Merge) is a waveform merging application. This application handles the merging of binary waveform files and their associated **wfdisc** database table information. The **wfdisc** table contains metadata about the waveforms, while the waveforms themselves are stored on disc. WFMerge can also handle **wftag** table information associated with the **wfdisc** table by keeping **wftag** rows in synch with their corresponding **wfdisc** rows and by using a remap table to remap the tagids in the **wftag** table.

DTX (DaTa eXchange) merges data from one data source into another data source. DTX recognizes three information storage formats: a set of database tables, a set of ASCII flat files, and XML file that has many tables and their associated data within one file. These three formats correspond directly to the three different data access types recognized by DBUtilLib. DTX can convert information from any one of these formats into any of the others. Both formats can be the same, as might be the case if DTX is moving data from one set of database tables to another set of database tables.

Given two sets of database tables, the Remap application will generate a remap table that will relate the identification numbers in the source tables to the identification numbers in the target tables of the same type. When researchers at the NNSA laboratories send database information to other labs, the identification numbers are generally renumbered when the information is merged into the other laboratory's database. This utility will allow the researchers to discover the identification numbers in the other lab's database that equate to their original identification numbers.

Unloader deletes one or more specific rows from the database and also deletes all rows that are connected to the specified rows(s) according to relationships either specified in the parameter file or deduced from the table definition table information (schema schema). Rows are only deleted if doing so will not violate any foreign key relationships in the database, i.e., nothing else is still pointing to them.

DBCompare is an application for comparing tables for equality. The user defines the equality. There are four types of table comparisons that DBCompare can handle: (1) idowner tables, (2) non-idowner tables, (3) remap tables, and (4) all tables. DBCompare compares the data in all of the tables in the source schema with tables of the same type in the target schema. It then does the reverse of that and compares the data in all of the tables in the target schema with tables of the same type in the source schema. It is also possible to compare only the source to the target, but not the target to the source. If all of these comparisons succeed, then all of the tables in both schemas are the same.

KB Integration Process

The major part of KB Integration is to merge database tables from individual product integrators into one set of tables. The product integrators send their database tables to the KB Integrator. The tables are checked to make sure they comply with established standards by using QCTool. Then the tables are merged into the target tables using EvLoader, WFMerge, DTX, and Remap (Figure 1). The following text goes into details about the process.

Check Data with the QCTool

The first step in the process is to check the data in the database tables with the QCTool. There is a master KB QCTool parameter file that has all the multi-table checks that are necessary to determine that the tables in the KB have clean consistent data. That parameter file is copied and edited to work with the specific tables in the dataset. Because a standard parameter file is used, the editing is minor. Some of the potential changes are to define the prefixes and suffixes for the table names, to add the correct username and password to access the database, and to define the output file names. The **complexjoin** table is also standardized, so unless the product integrator sends new rows for the table, it is considered to be correct. The QCTool does check against the **glossary** table when it does the single-table checks. Most errors found when checking against the **glossary** table are missing definitions. The column *auth* is usually the problem. The product integrator sends the **glossary** table as part of the delivery, and any new information must be inserted into the **glossary** table used by the KB Integrator before running the QCTool. The final step is to set all the primary and unique keys on the tables that will be checked.

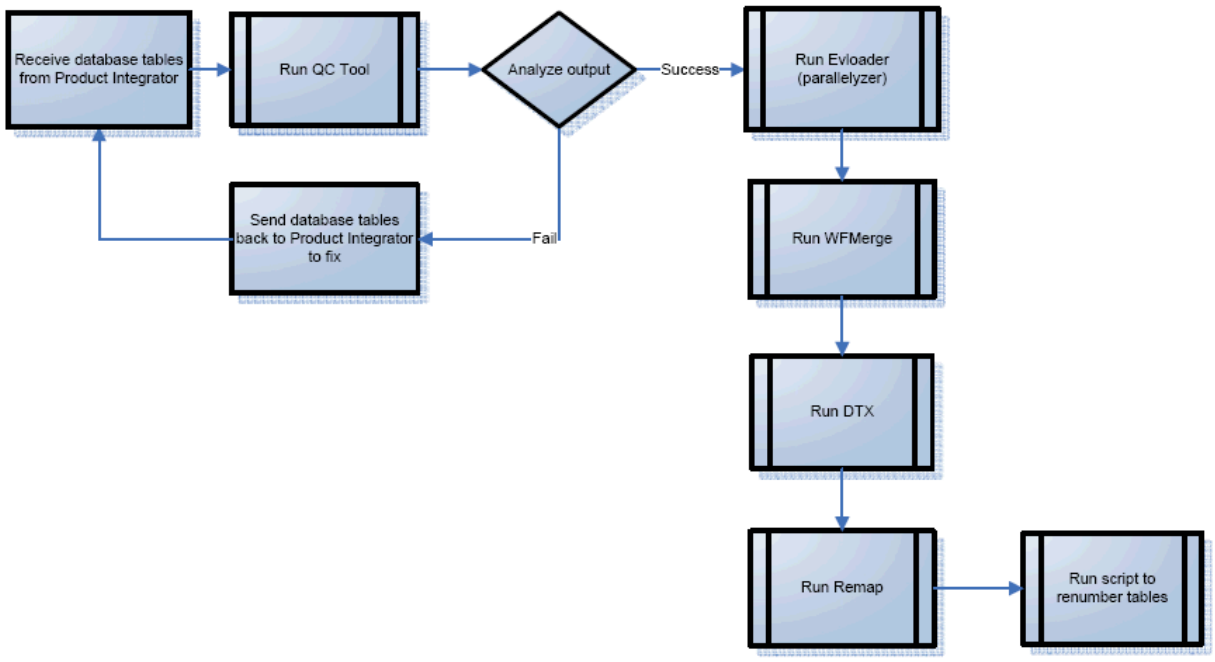

Figure 1. KB integration process.

The QCTool is run using a simple command – "qctool parfilename.par." The first check that is done is to make sure that the tables follow the NNSA KB Core or NNSA KB Custom schemas as defined in the schema schema tables. If they do not, QCTool immediately exits without doing any other checks. If the tables match the schemas, the QCTool continues by first doing the single-table checks. It writes the information from these checks into a file "single-table.out." The structure of the output file is very easy to navigate. The tables are checked in alphabetical order. First the primary and unique keys for the table are confirmed. If they cannot be set, this is the first error message for that table in the "single-table.out" file. Then each column in the table is listed. The NA value for the column is printed, and there is a statement about whether the column is allowed to have the NA value. Then the max and min values are listed to give the user a range, and the top two most common repeated values are listed. If the QCTool finds a problem, such as a value that does not match the range defined in the schema schema tables, that error is listed out, along with the SQL query that was used to discover the error.

The second checks that are done are the multi-table checks that are documented in the parameter file. The output from these checks is in the file "reference.out." Only errors are written to the output file. Again, the query that was used when the errors were found is provided. Any of the checks that are skipped, usually because one of the tables being checked does not exist, are noted. The complexjoin checks are last, and they are recorded in the output file "complexjoin.out." This file lists all the joins that are run from the **complexjoin** table. If there is an error, the error is noted along with the query used to generate the error.

The KB Integrator looks at the output files from the QCTool run and notes any errors. If the QCTool was run at the product integrator's site (and the KB Integrator encourages this), then the KB Integrator compares the errors found running QC Tool to errors noted by the product integrator. Many errors, especially those concerning the range of values in a column, can be noted and listed as caveats. If the tables have errors not described or explained by the product integrator, the tables go back to the product integrator to fix. It is only when the QCTool has been run successfully, i.e., all errors noted by the QCTool are either fixed or explained and documented, that the information in the tables can be merged into the KB target tables.

Merge catalog and parameter data

The bulk of the database information is seismic event information (origin, arrivals, magnitudes) that comes from various earthquake catalogs, and parameter data developed by the product integrator to help detect, locate, and identify events. This information is merged using EvLoader.

As with QCTool, there is a master KB parameter file for EvLoader. The most important part of the parameter file for EvLoader, and any of the other DBTools, is the defined relationships between the tables in the schema. A relationship is how tables relate to one another within the schema. A relationship can exist between two, and only two, tables. If a table is related to more than one other table, it must have one relationship defined for each table it is related to. To define a relationship, a *relationship id*, *source table*, *target table*, *relationship where clause*, and *constraint identifier* are required. The *relationship id* is a string that identifies the relationship, and the applications are not concerned with its actual value; it is mostly used to display useful information about the relationship. The *source table* is where the relationship between two tables originates. The *target table* is where the relationship between two tables ends. The *relationship where clause* is a SQL where clause that defines what columns in the two tables involved in the relationship must be equal for two rows from the tables to be related. The *constraint identifier* identifies the number of rows required and/or allowed to be returned as the result of executing a SQL SELECT statement that uses the *relationship where clause* on the *target table* for the relationship to be valid. All the relationships that can be defined between tables in the NNSA KB Core and NNSA KB Custom schemas that hold seismic event information and their associated parameters are in the master KB parameter file for EvLoader.

The master KB parameter file is copied and edited to work with the tables in the data set. Again, because a standard parameter file is used, the editing is minor. The source tables, target tables, and origin ranking table need to be defined. The origin ranking table is used by EvLoader to determine the preferred origin in the **event** table. When merging events into the KB, we use the spatial/temporal correlation mode of EvLoader. The way EvLoader works is that target events are selected as potential recipients of source origins if their preferred origin falls within defined spatial and temporal ranges. The spatial and temporal ranges are defined by setting a maximum correlation distance and a maximum correlation time. The maximum correlation distance and maximum correlation time can be different for different catalogs. EvLoader is set up so that there can be one set of spatial and temporal defined ranges for global catalogs and another for regional catalogs. These values are defined in the parameter file, along with a list of the catalog authors considered to be regional catalogs.

Once the parameter file is finalized, constraints and indexes are set on all the source and target tables. EvLoader will run faster if the correct indexes are on the table. Then sequences are created for all the IDs in the tables that will be remapped. As IDs need to be remapped in the merge process, EvLoader will use the next number in the sequence for that particular ID. The number at which the sequence starts is determined by looking at the maximum values of the IDs in the target tables.

EvLoader can be run in two ways. The first runs the program sequentially through the events in the source table. The command to use is – "evloader parfilename.par." Each event is merged sequentially, and it takes anywhere from 100ths of a second to a few seconds to merge an event, depending on how many arrivals and amplitudes are attached to the event. If you have small tables, this is a reasonable way to use EvLoader. However, if you have large tables, it can take many hours for EvLoader to finish. The way to speed up the time it takes for EvLoader to merge large database tables is to run it in parallel. The command to use is – "parallelyzeevloader parfilename.par #", where # is the number of processes to initiate. When using the parallelyze option, a temporary table is created that counts the number of arrivals and amplitudes for each event. The total number of events is then divided into groups that have a similar number of arrivals/amplitudes. The number of groups is the number of processes that are to be initiated. The program copies the parfilename.par file so that there is one parameter file for each process. Each parameter file will merge one specific group of events. EvLoader is then started using each parameter file simultaneously.

For example: The source data set has 10,000 events with a total of 350,000 arrivals and 100,000 amplitudes. The parfile evloaderA.par is created to merge the data set with EvLoader. If the events are merged sequentially, it can take many hours, if not days, to merge the entire data set. To merge the events in parallel, use the command "parallelyzeevloader evloaderA.par 10." A temporary table is created that counts up the arrivals/amplitudes for each event and then breaks the events into 10 groups that each have approximately 45,000 arrivals and amplitudes [(350,000 + 100,00)/10]. Ten parameter files are created from evloaderA.par, one for each group, and then are

started simultaneously. Because there are 10 roughly equal groups, the merge should take place in a much shorter time period, and all the groups should finish around the same time.

EvLoader merges one event at a time. Using the distance and time correlation parameters defined in the parameter file, EvLoader either inserts the event and its associated information as a new event in the target table or adds it to an existing event in the target table. Once the merge using EvLoader is completed, there are a number of tests to determine how well the merge went. The first is to compare the number of rows in the source tables to the number of new rows in the target tables. It is expected that, in most cases, all the rows from most of the source tables will be added to the target tables. The number of rows in the event table is dependent on how EvLoader decided to merge the source events into the target events, so it may not be a one-to-one match. Also, if events/origins in the source tables being merged into the target tables are already in the target tables, they will not be merged again. If there are discrepancies seen when looking at the number of rows in the tables, then DBCompare and Remap are used to compare the information in the target tables to the information in the source tables. If it is determined that events were merged incorrectly, then Unloader can be used to remove information from the target tables. If the EvLoader merge is successful, then the next step is to merge the waveforms and their associated metadata.

Merge waveforms

Once the catalog and event parameter tables are merged, the next step is to merge the waveforms and their metadata found in the **wfdisc** and **wftag** tables using WFMerge. There is a master KB parameter file for WFMerge that defines the relationships between the **wfdisc** and **wftag** tables. This file is copied and edited to work with the **wfdisc** and **wftag** tables and waveforms in the data set. As with EvLoader, edits include defining the source and target tables. Three additional tables, **source_remap** table, **idgaps** table, and **backup_wfdisc** table are also defined. The **source_remap** table is used to remap *tagids* in the **wftag** table. The **idgaps** table is used by WFMerge to get new IDs when the source tables are merged into the target tables. When a row in the target **wfdisc** table is modified or deleted, it will be saved to the **backup_wfdisc** table. If no **backup_wfdisc** table is specified, no backups will be made. WFMerge merges database information, but also merges waveform files. The copy of the parameter file is edited to define the source and target waveform directories and the waveform name format. Correlation, timeshift, samprate tolerance, and calper tolerance parameters used for merging the actual waveforms on disk are specified. Finally, the **source_remap** table is created by using information from the EvLoader merge.

WFMerge is run using the command – "wfmerge parfilename.par." Each waveform is merged one at a time. If there is no overlap between the source **wfdisc** row/waveform and the target **wfdisc** row/waveform, then the *wfid* in the source **wfdisc** row is updated and the row is inserted into the target **wfdisc** table. The source waveform is copied to the target waveform directory. If the source **wfdisc** row/waveform overlaps with some target **wfdisc** row/waveform, then first, the information in the source **wfdisc** row and target **wfdisc** row are merged into a single **wfdisc** row and written to the **target** wfdisc table. The old wfdisc rows from both the source and target are written to the **backup_wfdisc** table. Then, several checks are performed on the source and target waveforms to make sure they are consistent with one another before the waveforms are merged. If any of the checks are violated the waveforms will not be merged.

After WFMerge is completed, checks are run to make sure the merge was successful. Again, the first test is to compare the number of new rows in the target table to the number of rows in the source table. There will not be a one-to-one match if any of the source waveforms overlapped with target waveforms, but the comparison does provide useful information. If there appears to be a problem when comparing the number of rows in the tables, then DBCompare and/or Remap can be used to figure out what happened during the merge. If WFMerge successfully merged the waveforms and their metadata, the next step is to merge the station parameter information.

Merge station information

DTX is used to merge the station parameter information. The major problem in merging these tables is that only two of the six station parameter tables defined in the NNSA KB Core schema are "idowner" tables. What is meant by this is that there are no numeric ID primary keys for the **affiliation**, **network**, **sensor,** and **site** tables. Therefore, the first step in the station parameter merge is to create custom source and target station parameter tables that look like the original tables, but contain numeric IDs that are primary keys and foreign keys. The script

create_idowner_station_tables.sql is used to do this. The custom station parameter tables created by the script are the tables used to merge the station parameter information.

The master KB parameter file for DTX contains the defined relationships between the custom station parameter tables. This parameter file is copied and edited to work with the tables in the data set. The only edits that are really needed are to define the source and target tables. The command – "dtx parfilename.par" is used to start DTX. The information is merged by creating RowGraphs containing the source data and adding new information to the target tables that does not duplicate information in the target tables. Once the merge is completed, the first test is to compare the number of rows added to the target tables to the number of rows in the source tables. It is expected that the numbers should be very close, if not the same. If the numbers are not the same, then DBCompare and Remap can be used to compare the information in the target tables to the information in the source tables. Once the DTX merge is considered to be successful, the station parameter target tables are changed back to the structures defined in the NNSA KB Core schema. The script *change_original_station_tables.sql* is used to change the tables back. At this point, all the database tables have been successfully merged.

Remap IDs

The final step in the integration process is to remap the IDs in the new KB target tables to the IDs in the prior release of the KB. This is done so that the user of the KB doesn't have to deal with changing IDs every time a KB release is made. The program Remap compares a source table to a target table and generates a remap table of IDs based on a user defined equality. For example, the *orids* in a source and target **origin** table are remapped based on *lat*, *lon*, *depth*, *time*, and *auth*. As stated earlier, idowner tables are tables where an ID is the primary key. There are master KB Remap parameter files for remapping each of the idowner tables in the KB database. Using the command – "remap parfilename.par," with each idowner master remap parameter file, each idowner source table (prior KB release) is remapped to the idowner target table (new KB release). Scripts are then used to change the IDs in the new KB release tables to the IDs for that information in the prior release.

Once the IDs have been remapped, the Oracle database tables are ready to be tested with the other information in the KB to make sure that the integration process was successful and the products in the KB work as expected.

CONCLUSIONS AND RECOMMENDATIONS

We have developed a process to integrate large Oracle database tables that contain seismic data and produce clean, consistent, and useful information. To do this process effectively, we have developed a suite of tools that make it easy to QC and manipulate the data in the database tables. We also have tools that can be used to check that the merge process was successful. The tools are written in a generic manner and use the schema schema tables to define the schema of the database tables that are being accessed by the tools. So while we are using the tools to QC and merge seismic data, they can be used for any kind of data that has a schema defined in the schema schema tables.

ACKNOWLEDGEMENTS

The authors wish to acknowledge Chris Young and Mark Harris for their encouragement on documenting this process.

REFERENCES

Ballard, S., and J. Lewis (2004). DBTools: A Suite of Tools for Manipulating Information in a Relational Database, in *Proceedings of the 26th Seismic Research Review: Trends in Nuclear Explosion Monitoring*, LA-UR-04-5801, Vol. 2, pp 700–709.

Ballard, S. and J. Lewis (2007). DBTools Help Document, Sandia National Laboratories, in preparation

Carr, D. (2006). National Nuclear Security Administration Knowledge Base Database Guide (2006). Sandia National Laboratories, SAND2004-0961P.

Stead, R., M. Begnaud, and J. Aquilar-Chang (2006). Advances in Data Integration and Quality Control in Support of the NNSA Knowledge Base, in *Proceedings of the 28th Seismic Research Review: Ground-Based Nuclear Explosion Monitoring Technologies*, LA-UR-06-5471, Vol.2, p. 1028–1037.

Stead, R. (2007). QCTool User's Manual, Los Alamos National Laboratory, in preparation.

SEISMIC AND INFRASOUND SENSOR TESTING USING THREE-CHANNEL COHERENCE ANALYSIS

Darren Hart, John Merchant, and Eric P. Chael

Sandia National Laboratories

Sponsored by National Nuclear Security Administration
Office of Nonproliferation Research and Development
Office of Defense Nuclear Nonproliferation

Contract No. DE-AC04-94AL85000

ABSTRACT

Sleeman, van Wettum, and Trampert (2006) recently introduced a method for measuring the intrinsic noise spectra of seismic sensors which relies on determining the mutual signal coherence among three similar, collocated instruments. Unlike standard two-channel coherence tests, the available comparisons among three sensors allow the total incoherent noise power to be uniquely distributed among the individual sensors. We are looking to add this technique to the suite of tests we use for evaluating sensors at Sandia National Laboratories' Facility for Acceptance, Calibration, and Testing (FACT) site. In this paper, we briefly describe the method and demonstrate its effectiveness using synthetic signals with known amounts of coherent and incoherent power. Next we apply the procedure to characterize broadband STS2 low-gain seismometers set up in a vault at the Albuquerque Seismological Laboratory (ASL) of the United States Geological Survey (USGS). In addition, we have tested some Chaparral 2.5 infrasound sensors, first exposed to ambient atmospheric background and then isolated inside a sealed test chamber for recording a controllable broadband pressure source. We also looked at determining digitizer self-noise with this technique by feeding a single seismometer component (vertical) into three channels of a common digitizer electronics board. These test configurations allowed us to investigate two primary aspects of the input signal character, i.e., signal-to-noise ratio (SNR) and background vs. generated signals. They also allow us to investigate the linearity aspects of the sensor and digitizer in the presence of large background signals. Besides permitting the proper allocation of the incoherent noise among the three sensors, the technique also produces more stable sensor noise estimates in high signal-to-noise situations than the two-channel approach, as long as the participating sensors have reasonably similar performance over the analysis band.

OBJECTIVES

The Air Force Technical Applications Center (AFTAC) is tasked with monitoring compliance of existing and future nuclear test treaties. To perform this mission, AFTAC uses several different monitoring techniques to sense and monitor nuclear explosions, each designed to monitor a specific domain (e.g., space, atmosphere, underground, oceans, etc.) Together these monitoring systems, equipment and methods form the United States Atomic Energy Detection System (USAEDS). Some USAEDS seismic stations may be included in the International Monitoring System (IMS). Each agency involved in the monitoring community has requirements which the system and components (sensors and data loggers) must pass before deployment and later certification. Historically, Sandia National Laboratories has been involved in the testing of seismic systems to monitor for compliance with the terms of nuclear weapon test ban treaties. More recently, a complete set of tests have been designed for characterization of infrasound sensors. Two important aspects of component evaluation are determining the sensors self-noise and verifying an instrument's frequency amplitude phase response.

The new technique described by Sleeman, van Wettum, and Trampert (2006) for measuring the intrinsic noise spectra of seismic sensors relies on determining the mutual signal coherence among three similar, collocated instruments. Unlike standard two-channel coherence tests for calculating instrument noise as described by Holcomb (1989), which only has two possible noise models, either the two sensors have the same noise model (i.e,. N = N1 = N2) or the noise is lumped to one sensor (i.e., N = N1 and N2 0). Using three sensors, no assumptions are made about individual sensor noise models. The available comparisons among three sensors allow the total incoherent noise power to be uniquely distributed among the individual sensors. First, synthetic data was generated and various transforms were applied to investigate SNR, and relative response differences using this technique. We then use this technique to investigate the combined self-noise in three test configurations. The first test was three STS-2 low gain (~1500 V/m/s) seismometers recorded on a Q330 digitizer with its preamp enabled. The second test was to feed a single seismometer component into six data acquisition channels on two A/D boards of a Q330HR digitizer in order to determine the individual digitizer channels self noise. The third, and final, test was to determine the self-noise of three Chaparral Physics model 2.5 low-gain (~0.4 V/Pa) infrasound sensors recorded on a Geotech Smart24D datalogger.

The method of results comparison was to compute the dynamic range using the convention, $20*\log10(N_{rms}/FS_{RMS})$, where N_{rms} is the root mean square (RMS) of the noise spectra (band limited) and FS_{rms} is the sensor's full-scale RMS value. All raw data first has the bit-weight applied to convert from counts to volts. Once processing was complete, theoretical responses are removed and the spectra are converted from units of volts to earth units of velocity (m/s) for seismic and DWR application tests and Pascal (Pa) for infrasound. For both seismic and infrasound sensors the full-scale peak-to-peak voltage is 40, this translates to a 14.14 volts RMS. Using the standard STS2 generator constant of 0.002 g/mA, 14.14 volts RMS converts to a full-scale RMS velocity of 0.001274 m/s.

RESEARCH ACCOMPLISHED

Synthetic Tests

To evaluate the performance and behavior of the three-channel correlation method, we conducted a number of tests using synthetic computer-generated waveforms with known amounts of coherent and incoherent signal. For the first test, we generated three sequences of independent Gaussian random samples, to represent the unknown internal sensor noise that we intend to measure. Next we added a common series of random samples with the same variance to the three independent series, to represent an environmental signal such as microseismic or acoustic noise that would be the same on collocated sensors. For this case, the power spectral density (PSD) of the independent noise on each channel should comprise one-half the total signal power, therefore each channel's estimated noise spectrum should fall 3 dB below the power spectrum of the composite trace. The top row of Figure 1 demonstrates that the correlation analysis among the three signals does indeed yield the correct result, with the internal noise estimate for each signal lying 3 dB below the total PSD.

Next we tested the effectiveness of the method at higher SNR, by adding a common signal with a RMS amplitude four times that of the noise. In this case, the independent noise constitutes only 1/17 of each trace's total power, so the noise spectra should fall 12 dB (-10*log(17)) below each trace's total PSD. The middle row of Figure 1 shows that the correlation analysis again provides accurate estimates of the incoherent noise spectra, even at high SNR. The

variances of the noise spectra along the middle row are essentially the same as those in the low-SNR test in the row above. We conclude that this technique can reliably estimate the internal noise spectra of similar sensors even in the presence of relatively high ambient background signals.

A third test illustrates the behavior when applied to dissimilar sensors, with differing levels of intrinsic noise. This time, independent noise series with relative RMS amplitudes of 1, 1/2, and 1/4 of the common signal were used to form the three traces. The estimated noise spectra should now be 3, 7, and 12 dB down from the total PSD curves of the three channels, since the noise contributes, respectively, 1/2, 1/5, and 1/17 of the total power of the traces. The results of the analysis (bottom row of Figure 1) are approximately as expected. However, the noise estimate for the trace with high SNR, or low internal noise, now has substantial variance about its predicted level. So it seems that for sensors with significantly different levels of intrinsic noise, the three-channel correlations will yield the most stable noise estimate for the one with the lowest SNR, and unbiased but less stable results for the others. For all of the tests, we note that the variance of the noise spectra could be reduced by using longer traces.

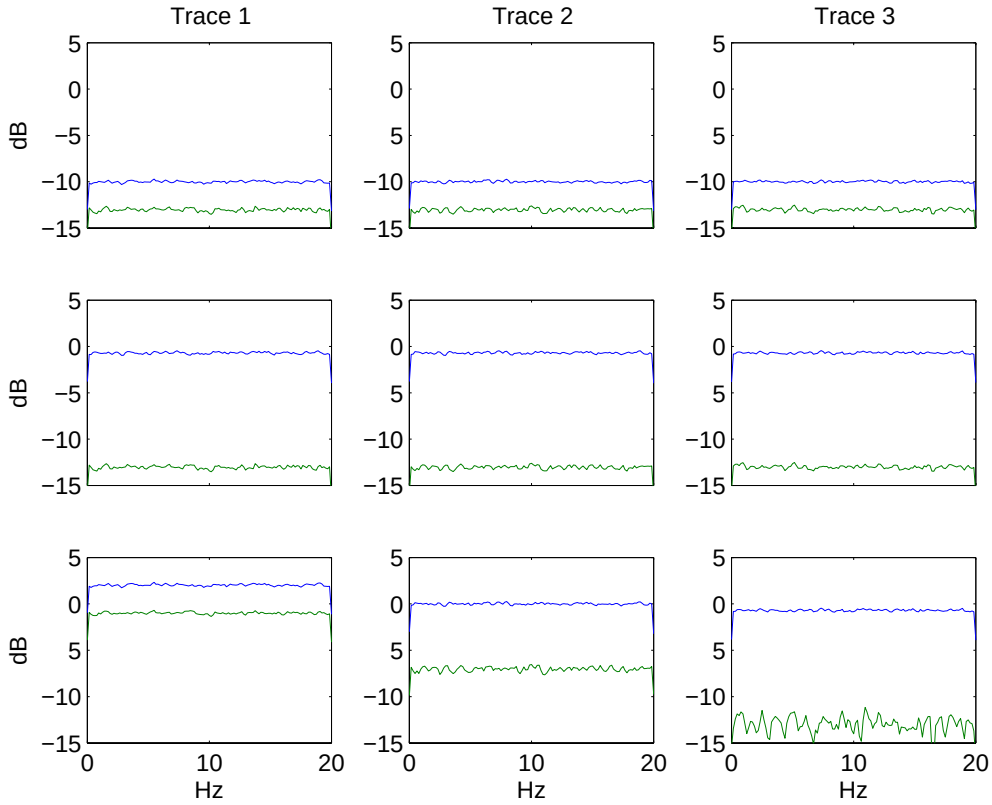

Figure 1. Tests of correlation method using synthetic data. First row, PSD of the 3 traces (total power in blue, incoherent noise in green) with the noise 3 dB below the signal. Second row, PSD of the 3 traces with the noise 12 dB below the signal. Third row, PSD of the 3 traces with the noise at variable levels below the signal.

Seismic Application Test

Using the three sensor coherence technique, we hope to determine the self-noise of three STS2 low-gain seismometers and compare these sensor noise estimates to the standard STS2 low-gain seismometer noise model by C. R. Hutt of USGS/ASL (see acknowledgments), which from here on we will refer to as STS2 NM. This experiment was conducted in the USGS ASL's west tunnel between May and June 2007. The sensors were installed and sand packed to allow for sensor temperature stabilization, which can reduce sensor noise and improve coherence below 0.05 Hz. The test required the Q330's digitizer to have the preamp enabled with a gain of 30. This allowed the noise floor of the digitizer channels to be reduced by roughly 26 dB. Data were acquired at 40 and 100 samples

per second (sps). Twelve and six hour windows of seismic background data were analyzed at 40 and 100 sps data, respectively.

Estimated sensitivities and digitizer channel bit-weights are listed in Table 1. Using a background signal for this analysis allowed us to examine the sensor's response to the local non-uniform coherent-signal spectrum.

Table 1. Seismic application test configuration

Model/Serial Number	Sensitivity of Vertical Component at 1 Hz	Sample Rate(s)	Analysis Window Length (hours)	Data logger/Serial Number	Bit-Weight (V/count)
STS2 low-gain / 120619	1508 V/m/s	40/100	12/6	Q330 – preamp enabled/1010	7.947e-8
STS2 low-gain / 120621	1496 V/m/s	40/100	12/6	Q330 – preamp enabled/1010	7.947e-8
STS2 low-gain / 80655	1507 V/m/s	40	12	Q330HR Port B – preamp enabled/1551	7.947e-8

Results:
From the three-sensor correlation technique the PSD and self-noise spectra were further processed to remove a common STS2 response model. The instrument response model gain, poles and zeros are listed in Table 2.

Table 2. Seismic application STS2 sensor response model

Gain (V/m/s)	1500		
Zeros	+/– 0.0		
Poles (radian)	–2.513e + 2	–3.656e-2 +/– j 3.688e –2	–1.131e + 2 +/– j 4.673e + 2

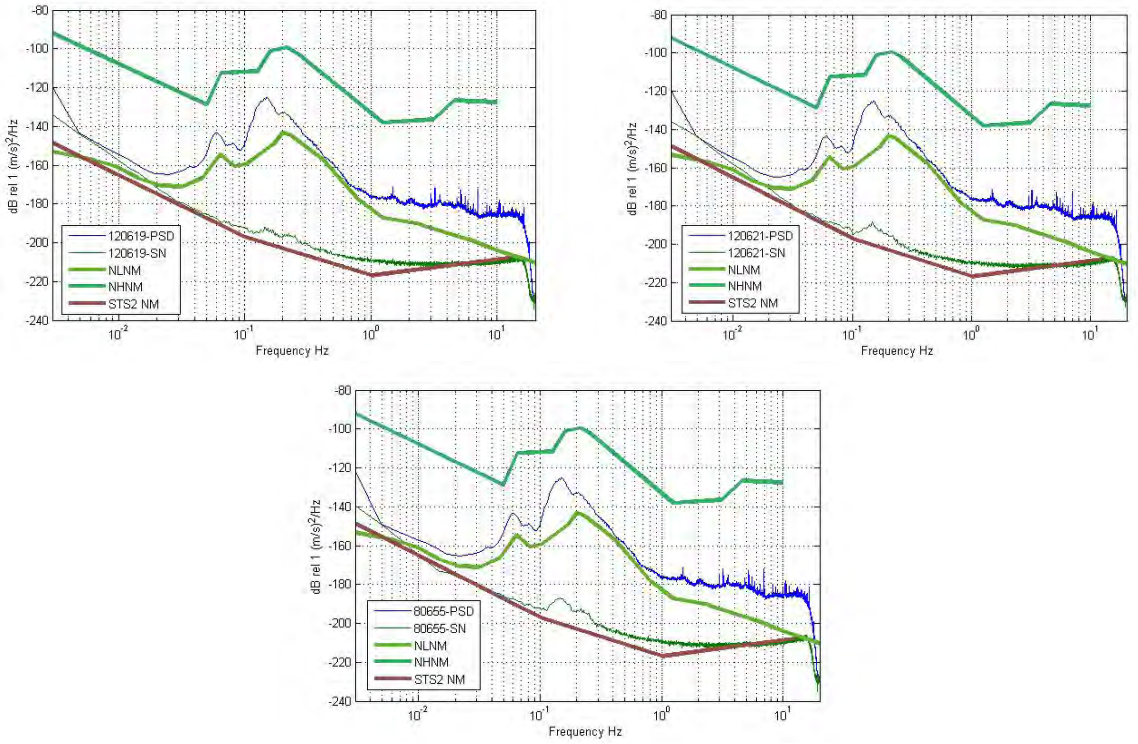

Figure 2a, b, c. Illustrations of vertical component PSD and self-noise estimates for three sensors tested (SN 120619, 120621, and 80655). A nominal instrument response was removed from each spectrum, plotted against the Peterson high and low noise models and STS2 NM.

Figures 2a, -b, and -c show vertical component instrument corrected PSD and self-noise spectra plotted against the Peterson New High-Noise Model (NHNM) and New Low-Noise Model (NLNM) and STS2 NM. These figures illustrate the uneven nature of the background signal to the sensor self-noise estimates.

Figure 3 gives the ratio of PSD to self-noise, or SNR, for the three sensors. At low frequencies, below 0.01 Hz, the SNR approaches zero. The peak SNR, 80 dB, is observed at 0.16 Hz, and decreases to 30 dB near 1 Hz. The SNR stays above 20 db out to 16.2 Hz.

From 0.01 to 0.1 Hz the noise estimates are in agreement with the STS2 NM, but approaching 0.1 Hz they start to increase in noise relative to the STS2 NM. In the sensor noise spectra we observe a rise in each around the same frequencies that we observe the largest SNR. This may be attributed to off-axis sensor design of UVW to XYZ transform, slight misalignment of sensors, or non-linear behavior of sensors at large SNR conditions. The self-noise spectra band of 0.5 Hz to 4 Hz is stable and decreasing in value but above the STS2 NM. Above 4 Hz the STS2 NM and self-noise spectra are again in agreement.

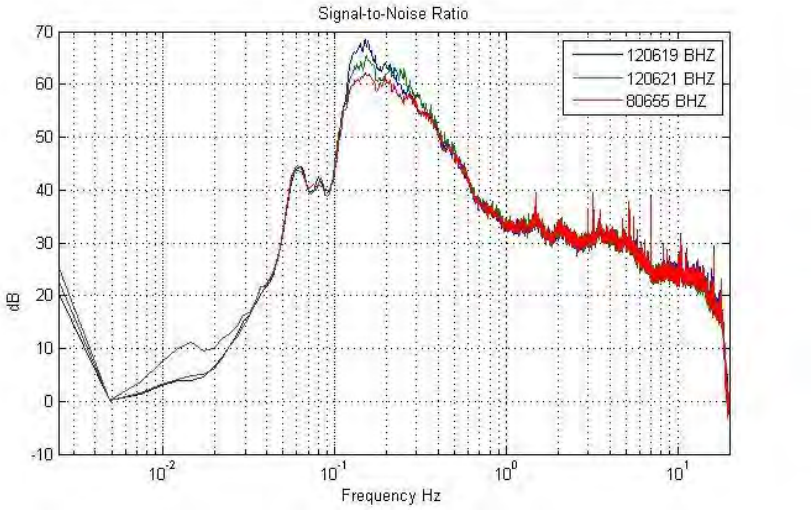

Figure 3. SNR estimates for three sensors tested.

The RMS noise estimates, RMS full-scale and dynamic range of the three STS2 low gain seismometers are listed in Table 3. Using the STS2 low-gain noise model the maximum potential dynamic range (MPDR) was estimated to be –143.46 dB rel 1 $(m/s)^2/Hz$. Comparing the dynamic range of the test sensors to the MPDR of the STS2 NM shows the test sensors are 8.7 to 3.8 dB noisier than the STS2 low-gain theoretical noise model. We believe this is due to the combined effect of sensor and digitizer noise (i.e., N = Ns + Nd). Specifically, the digitizer noise floor is above the sensor noise floor between 0.3 and 3 Hz.

Table 3. Results of seismic application test. RMS noise was computed between 0.01 and 16 Hz.

Serial Number	Sample Rate	RMS Noise (m/s)	RMS Full Scale (m/s)	Dynamic Range	Difference from MPDR of STS2 NM
120619	40	1.5493e-10	0.001274	–138.3	5.2
120621	40	1.4968e-10	0.001274	–138.6	4.9
80655	40	8.7064e-11	0.001274	–143.3	0.2
120619	100	2.2373e-10	0.001274	–135.1	8.4
120621	100	2.3296e-10	0.001274	–134.8	8.7

Digitial Waveform Recorder (DWR) Test

The goal of testing the DWR was to determine the self-noise of the six channels of a Q330HR digitizer. In addition, the testing should, determine if the non-linear behavior observed in the seismic application test results could be attributed to non-linear behavior of the digitizer. This experiment was conducted in the USGS ASL's west tunnel between May and June 2007. The output from a single seismometer component was split and fed into three input channels on the digitizer. The test was run twice: once with the seismometer inputting to the standard resolution 24 bit channels and once with the seismometer inputting to the high-resolution 26 bit channels. The digitizer was installed and allowed to run for several weeks in an isolated environment for temperature stabilization. To match the

test configuration of the seismic application test the preamps were enabled. This allowed the noise floor of the Q330HR to be reduced by roughly 29 dB for the standard channels (i.e., 24 bit) and 26 dB for the high-resolution channels. Data was acquired at both 40 and 100 samples per second (sps). Twelve and six hour windows of seismic background data were analyzed for the 40 and 100 sps data, respectively. Estimated sensor sensitivities and digitizer channel bit-weights are listed in Table 4.

Table 4. Digitizer test configuration

Model/Serial Number	Sensitivity at 1 Hz	Sample Rate	Analysis Window Length (hours)	Data logger/Serial Number	Bit-Weight (V/count)
STS2 LG / 120657 (Z)	1506 V/m/s	40/100	12/6	Q330HR portA/1551 Preamp enabled	2.980e-8
STS2 LG / 120657 (Z)	1506 V/m/s	40/100	12/6	Q330HR portA/1551 Preamp enabled	2.980e-8
STS2 LG / 120657 (Z)	1506 V/m/s	40/100	12/6	Q330HR port A/1551 Preamp enabled	2.98e-8
STS2 LG / 120619 (Z)	1508 V/m/s	40/100	12/6	Q330HR port B/1551 Preamp enabled	7.947e-8
STS2 LG / 120619 (Z)	1508 V/m/s	40/100	12/6	Q330HR port B/1551 Preamp enabled	7.947e-8
STS2 LG / 120619 (Z)	1508 V/m/s	40/100	12/6	Q330HR port B/1551 Preamp enabled	7.947e-8

Results

From the three-channel correlation technique, the PSD and self-noise spectra were further processed to remove a common STS2 response model. The instrument response model parameters are listed in Table 2.

Figure 4 shows the instrument corrected self-noise spectra of channels 4–6 for Port B of Q330HR (SN:1551). The self-noise spectra are plotted against the NLNM and STS2 NM. We see that using the standard resolution (i.e., 24-bit) port B with its preamp enabled, we will not fully resolve the noise of the STS2 LG seismometer. We also do not observe a rise in the digitizer noise spectra at or around the peak SNR frequency of 0.2 Hz.

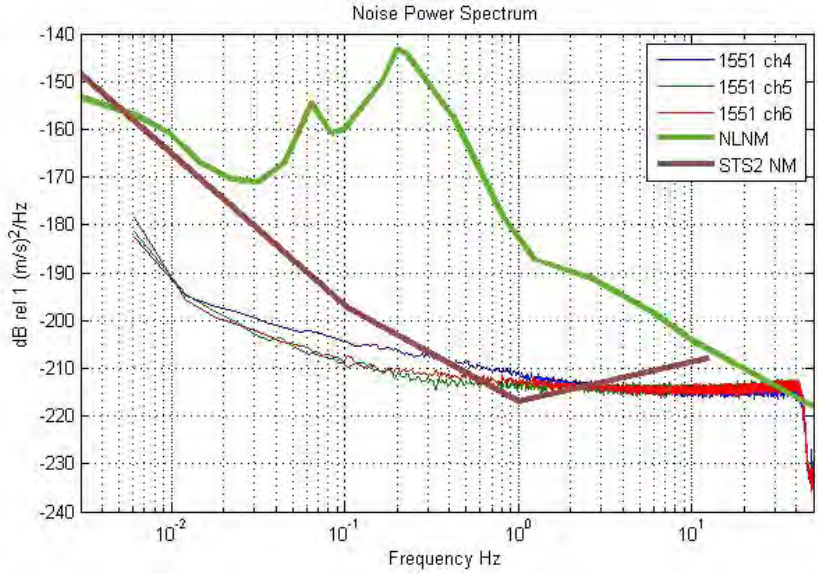

Figure 4. Self-noise spectra for Q330HR (SN: 1551) channels 4, 5 and 6.

Figure 5 shows the instrument corrected self-noise spectra of channels 1–3 for Port A of Q330HR (SN:1551). The self-noise spectra are plotted against the NLNM and STS2 NM. We see that using the high resolution (i.e., 26 bit) port A with its preamp enabled, we can resolve the noise of the STS2 LG seismometer. Again, we do not observe a rise in the noise spectrum at or around the peak SNR frequency.

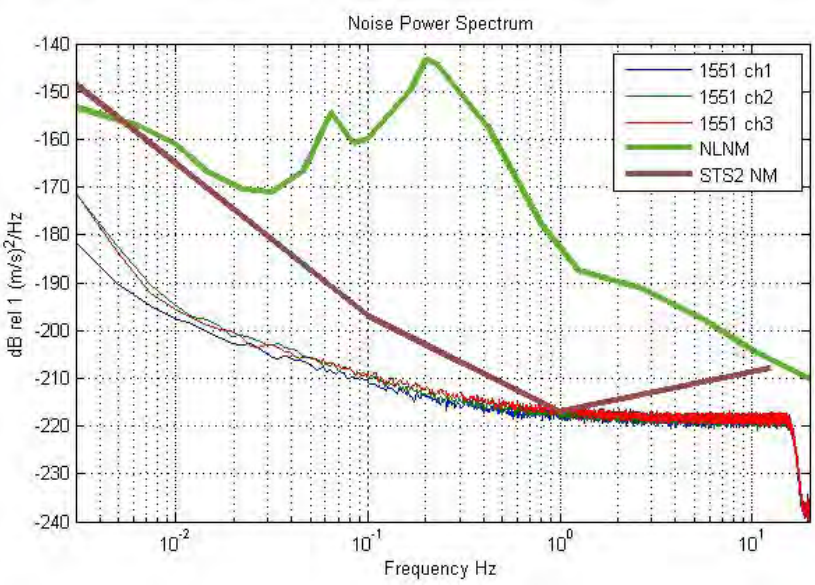

Figure 5. Self-noise spectra for Q330HR (SN: 1551) channels 1, 2, and 3.

The RMS noise estimates, RMS full-scale and dynamic range of the six Q300HR channels tested are listed in Table 5. Using the STS2 low-gain noise model developed by Bob Hutt of the ASL, the MPDR was estimated to be –143.46 dB rel 1 $(m/s)^2$/Hz. Comparing the dynamic range of the test sensors to the MPDR of the Hutt noise model shows the digitizer channels are –16.6 to–11.9 dB quieter than the STS2 low-gain theoretical noise model.

Table 5. Results of DWR application test. RMS noise was computed between 0.01 and 16 Hz.

Serial Number	Sample Rate	RMS Noise (m/s)	RMS Full Scale (m/s)	Dynamic Range	Difference from MPDR of STS2 NM
120657-Z/1551 ch1	40	1.2618e-11	0.001274	–160.1	–16.6
120657-Z/1551 ch2	40	1.3035e-11	0.001274	–159.8	–16.3
120657-Z/1551 ch3	40	1.3381e-11	0.001274	–159.6	–16.1
120619-Z/1551 ch4	40/100	2.1774e-11 / 2.1880e-11	0.001274	–155.3	–11.9
120619-Z/1551 ch5	40/100	2.0389e-11 / 2.0434e-11	0.001274	–155.9	–12.5
120619-Z/1551 ch6	40/100	2.0489e-11 / 2.0490e-11	0.001274	–155.9	–12.4

Infrasound Application Test

The goal of the infrasound application test was to determine the self-noise of three Chaparral Physics 2.5 (CP2.5) low-gain infrasound sensors and compare these noise estimates with an existing CP2.5 noise model developed by Whitaker and Kromer, 2003 and obtained through personal communication. One noteworthy point to make is the Whitaker and Kromer CP2.5 noise model may not be representative of the current Chaparral Physics product model 2.5, due to a change in manufacture location since 2003.

This experiment was conducted in an underground testing vault at the Sandia FACT site, located near Albuquerque, NM. The data were acquired between 5/7/2007 and 5/8/2007 on a Geotech Smart24D data logger. Data were acquired at both 40 and 200 sps. Twelve and six hour windows were analyzed for the 40 and 200 sps data, respectively. More test configuration parameters are listed in Table 6.

Two types of data were processed: white noise and acoustic background. A Wavetech 132-S817 signal generator was used to generate the white noise at approximately 40% of full-scale amplitude voltage. The white signal was input to a piston-phone, which converts the voltage signal to an acoustic signal. The generated acoustic signal has an equally distributed SNR, ~25–30 dB, across the application band of 0.1 to 8 Hz. The acoustic background data because of its variability were segmented into three groups based on increasing SNR levels low, medium, and high. The 12 hour total window was divided into three 3 hour windows for this comparison. By analysis of the data in this manner we can investigate sensor linearity in the presence of differing background signals.

Table 6. Infrasound application test configuration

Model/Serial Number	Sensitivity at 1 Hz	Sample Rate	Analysis Window Length (hours)	Datalogger/Serial Number	RMS Full Scale (Pa)	Bit-Weight (V/count)
CP 2.5 – 061843	0.414 V/Pa	40/200	12/6	Smart24D/s1036	17.1	3.27e-7
CP 2.5 – 061845	0.409 V/Pa	40/200	12/6	Smart24D/s1036	17.3	3.27e-7
CP 2.5 - 061855	0.426 V/Pa	40/200	12/6	Smart24D/s1036	16.6	3.27e-7

Acoustic Background Test Results

The three-sensor correlation technique was applied to acoustic background data of three differing levels. The resulting PSD and self-noise spectra were further processed to remove a common Chaparral 2.5 response model. The instrument response model parameters are listed in Table 7.

Table 7. Infrasound application Chaparral 2.5 sensor response model

Gain (V/Pa)	0.400
Zeros	+/– 0.0
Poles (radian)	–0.25 + j0.0

Figures 6a, b and c show the instrument corrected self-noise spectra of the three sensors tested for progressively increasing levels of acoustic background signal. For reference, the self-noise spectra are plotted against the Acoustic Low-Noise Model (ALNM), produced by Bowman et al, 2004 and the Chaparral 2.5 noise model of Whitaker and Kromer (personal communication). Figure 6a represents the low signal level, 6b the medium signal level, and 6c the high input signal level. The most notable feature between these results is the observation of an overall bias of the new Chaparral 2.5 sensors noise estimates versus the existing sensor noise model. The new sensor noise estimate appears to be 12–16 dB noisier than the existing model. The other notable observation is the sensor self-noise increases with increasing background signal level. Is this a non-linear effect of the sensor, or poor test design?

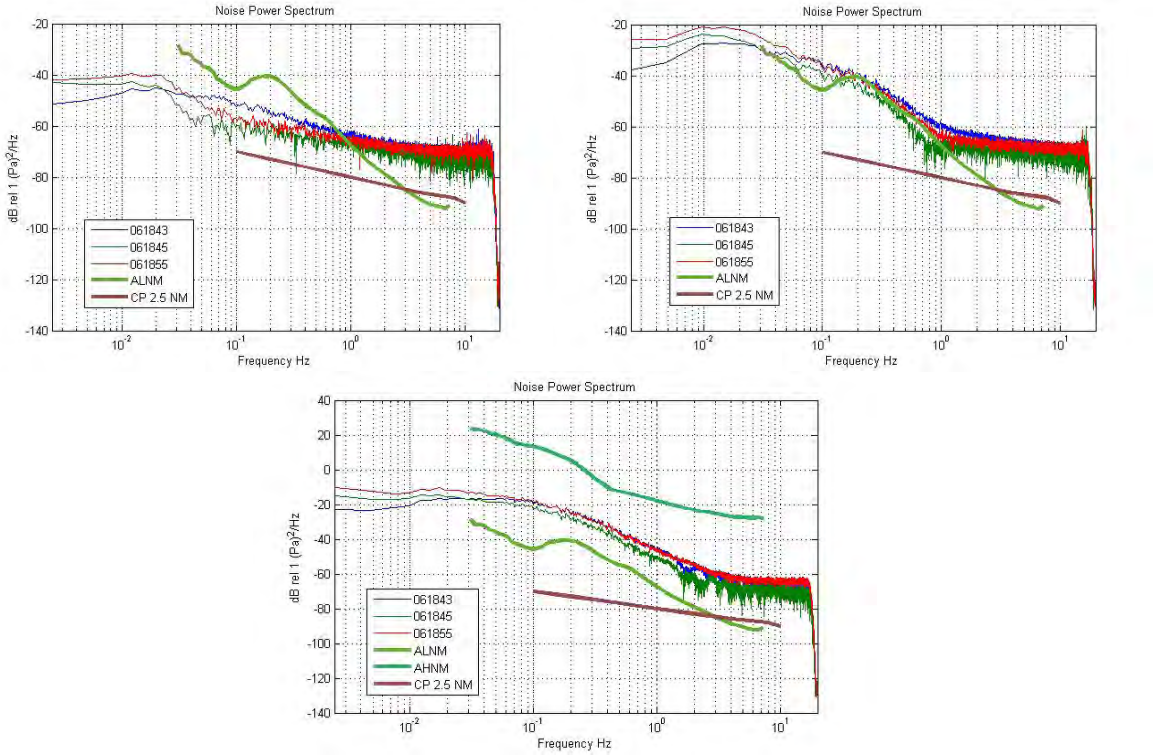

Figure 6a, b, c. Illustrations of infrasound sensors self-noise estimates with differing input signal levels for the three sensors tested: SN 120619, 120621, and 80655. A nominal instrument response was removed from each spectrum, plotted against the SAIC ALNM and Chaparral 2.5 noise model of Whitaker and Kromer, 2003.

Using approximations of sensor sensitivities we compute the RMS full-scale pressure for each sensor. The RMS noise estimates were made for the frequency band of 0.1–8 Hz and the dynamic range was computed for each sensor and background signal level. The compiled results are in Table 8. For the three sensors tested the largest dynamic ranges were observed during low signal level background conditions.

Table 8. Results of infrasound application test using acoustic background data. RMS noise was computed between 0.1 and 8 Hz

Serial Number	Sample Rate	RMS noise (Pa)	RMS Full Scale (Pa)	Dynamic Range
061843 – Low Noise	40	5.602e-4	17.1	-89.7
061843 – Med Noise	40	0.0020	17.1	-78.6
061843 – High Noise	40	0.0121	17.1	-63.0
061845 – Low Noise	40	3.406e-4	17.3	-94.1
061845 – Med Noise	40	0.0012	17.3	-83.2
061845 – High Noise	40	0.008	17.3	-66.7
061855 – Low Noise	40	4.409e-4	16.6	-91.5
061855 – Med Noise	40	0.0017	16.6	-79.8
061855 – High Noise	40	0.0120	16.6	-62.8

White Noise Test Results

The three-sensor correlation technique was applied to acoustic white noise data. The resulting PSD and self-noise spectra were further processed to remove a common Chaparral 2.5 response model. The instrument response model parameters are listed in Table 6.

Figure 7 shows the instrument corrected self-noise spectra of the three sensors tested using the white noise input signal. We again plot the self-noise spectra against the ALNM and the Chaparral 2.5 noise model of Whitaker and Kromer. We again observe an overall bias of the new Chaparral 2.5 sensor noise estimates versus the existing Chaparral 2.5 noise model. The sensor noise estimates appear to be 8–12 dB noisier than the existing model. Thus, we believe there might be a physical design change within the Chaparral 2.5 that warrants defining a new noise model for this specific sensor model.

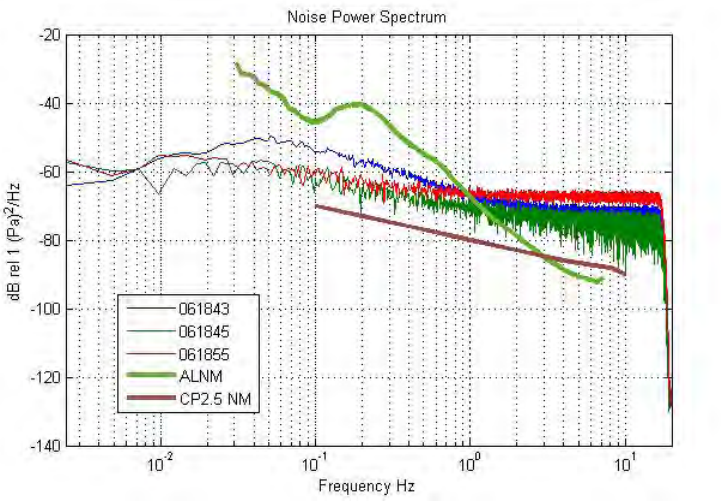

Figure 7. Infrasound sensor self-noise spectra for white input signal.

Again, RMS noise estimates were made for the frequency band of 0.1–8 Hz and the dynamic range was computed for each sensor. The compiled results are in Table 9. For the three sensors tested the dynamic ranges were approximately the same as those observed for the low input signal level.

Table 9. Results of infrasound application test using white noise data. RMS noise was computed between 0.1 and 8 Hz

Serial Number	Sample Rate	RMS Noise (Pa)	RMS Full Scale (m/s)	Dynamic Range
061843	40	4.130e-4	17.1	–92.3
061845	40	2.496e-4	17.3	–96.9
061855	40	4.607e-4	16.6	–91.1

CONCLUSIONS AND RECOMMENDATIONS

The new technique described by Sleeman, van Wettum, and Trampert (2006) for measuring the intrinsic noise spectra of seismic sensors relies on determining the mutual signal coherence among three similar, collocated instruments. Using this three sensor scheme, no assumptions must be made about individual sensor noise models. Testing this technique with synthetic data allowed us to explore several aspects of performance, most notably, correct extraction of coherent and incoherent noise levels. Secondly, this technique provides the ability to reliably estimate the internal noise spectra of similar sensors even in the presence of relatively high ambient background signals.

Proceeding into seismometer application testing, we noted close agreement with test sensor internal noise estimates and the STS2 NM, below 0.05 Hz and above 3 Hz. Between 0.05 and 3 Hz we believe that digitizer noise and non-linear sensor effects cause the differences observed between the STS2 NM and the internal seismometer noise estimates. Because of the observed microseism feature on the seismometer internal noise spectra, we explored using this technique to determine if the added noise was being added by the digitizer. Processing a common signal input recorded by three different digitizer channels allowed us to determine the digitizer self-noise for three channels. The results of this testing ruled out the digitizer as the cause of the microseism noise feature. Additional testing should allow us to fully resolve the STS2 low-gain noise model. We also recommend comparing these DWR channel noise estimates with Input Terminated Noise (ITN) Test data for these digitizers.

The technique was applied to three acoustic sensors, Chaparral model 2.5. Two types of acoustic data were processed: acoustic background and signal generated white noise. The acoustic background data allowed us to see how the sensors performed in the presence of differing input signal levels. We observed that the estimated internal sensor noise increased as the input signal level increased. Hence, the sensor's dynamic range decreased as the input signal level increased. As a second point of comparison, white noise data produced RMS noise and dynamic range estimates that best matched those values obtained from the acoustic background test set with the lowest input signal level. We also observed that the existing Chaparral 2.5 noise model is 8–12 dB higher than current noise estimates and propose developing a new Chaparral 2.5 noise model based on current production line product. Further investigation should also be done to see if different input signal levels of white noise yield consistent noise estimates for sensors under test.

The other important results of the three-sensor correlation technique are the relative gain and phase estimates. Further work should also be done to explore the usefulness of the relative gain and phase for sensor response characterization or in basic sensor acceptance testing.

ACKNOWLEDGEMENTS

We would like to thank our colleagues at the USGS ASL for their cooperation in providing access to their test facility, and to C. R. Hutt at USGS ASL for the standard STS2 low-gain seismometer noise model.

REFERENCES

Bowman, R. J., G. E. Baker, and M. Bahavar (2004). Infrasound station ambient noise estimates, in *Proceedings of the 26th Seismic Research Review: Trends in Nuclear Explosion Monitoring*, LA-UR-04-5801, Vol. 1, pp. 608–617.

Holcomb, L.G. (1989). A direct method for calculating instrument noise levels in side-by-side seismometer evaluation, USGS Open-File Report 89-214.

Sleeman, R., A. van Wettum, and J. Trampert (2006). Three-channel correlation analysis: A new technique to measure instrumental noise of digitizers and seismic sensors, *Bull. Seism. Soc Am.* 96: 258–271.

CLUSTERING OF LARGE EVENT SETS USING DELAUNAY TESSELLATIONS AND K-MEDIOD OPTIMIZATION

James R. Hipp and Christopher J. Young

Sandia National Laboratories

Sponsored by National Nuclear Security Administration
Office of Nonproliferation Research and Development
Office of Defense Nuclear Nonproliferation

Contract No. DE-AC04-94AL8500

ABSTRACT

This paper introduces a new fully-automated method for identifying clusters in large event sets. The method uses a Delaunay tessellation to determine the clusters and initial membership, then applies an iterative K-medoid optimization to refine membership in the clusters until stability is achieved. The method is robust and computationally efficient, with performance improvement over standard K-medoid optimization from $O(n^2)$ to $O(n \log n)$, which is achieved by making use of the Delaunay tessellation neighbor connectivity information. It produces clusters that meet three key criteria: 1) for each cluster, each event is closer to the representative event for that cluster (the medoid) than to the representative events for nearby clusters, 2) for each member event in a cluster, there is a closest neighbor that is no further away than D_{max}, 3) no event in a cluster is further than D_{max} from any other event in the cluster. D_{max} is a user-defined parameter that can be used to control the number and size of clusters. The basic algorithm consists of three steps. First, initial clusters are identified by forming a Delaunay tessellation for the entire set, then removing all edges longer than $D_{max.}$ Second, the initial clusters are sub-divided using a medial-axis subdivision algorithm until no cluster has a maximum event-to-event span greater than $D_{max..}$ Third, given these groups, membership in the groups and K-medoid representatives for each are optimized in a hill-climbing iterative process. In most cases, this sequence produces excellent results, but we have found rare cases where the method can form poor clusters or event-to-cluster assignments. Hence we have added an additional clean up step that can break up clusters with a main body of members and a few outliers to merge the main body with a nearby cluster (if one is available), and that can re-assign an outlier member to another cluster if that cluster has nearby events to the outlier.

The technique is demonstrated with a large set of ISC catalog events and results for various regions are examined. The number of clusters and cluster membership change with different values of Dmax are shown and results with and without the final clean up step are compared.

OBJECTIVES

A standard method for clustering sets of seismic events is a fixed grid approach. While technically simple the approach has some undesired drawbacks. Among these the most notable are the complete disregard of spatial proximity and density information in choosing neighbors and the occasional occurrence of cluster representatives that lie extremely close to one another across their shared cluster boundary.

Past indifference toward utilization of more traditional clustering techniques for use in identifying clusters of seismic events is most likely due to a perceived lack of necessity for such an approach; the perceived additional complexity involved with implementing the method; and possible performance degradation issues related to using a complex approach over a simple and fast method. The perceived lack of necessity for a different approach stems from the fact that the simple fixed grid method generally works even with the undesirable effects mentioned in the first paragraph above. If, however, a new approach could eliminate the drawbacks while both preserving performance and design simplicity, then perhaps the new method would be considered an acceptable replacement for the fixed grid approach.

The remainder of this paper describes the proposed method and shows that leveraging capabilities already developed by SNL for the GNEMRE program will ensure that desired performance goals are easily met with very little additional complexity.

RESEARCH ACCOMPLISHED

Introduction

Many technical fields such as spatial data mining and operations research are interested in the problem of clustering arbitrary unstructured geo-referenced data sets. Most of these spatial clustering techniques make use of data proximity. In these methods proximity is based on a selected Euclidean metric which attempts to capture the spatial autocorrelation and near association of neighboring spatial data. Two general approaches are typically followed to form the clusters: a) a bottom-up approach which agglomerates spatial points to form clusters based on their relative nearness to one another; and b) a top-down approach which attempts to partition a heterogeneous data set into smaller more similar groups.

Of particular interest for clustering seismic events are top-down medoid-based clustering methods. In these methods the point representing an arbitrary cluster must be chosen from the set of events forming the cluster. Other methods include those based on discovering a mean, or average, location within the cluster to use as a cluster representative. Mean-based methods are generally more popular and possess fast solution algorithms of order $O(n)$ time. However, the calculated mean representative locations are not necessarily near the cluster center when outliers are involved in the calculation and suffer many other statistical bias and consistency problems. A good description of the advantages and disadvantages of mean- and medoid-based methods can be found in Estivill-Castro et al. (2001).

The medoid (or K-Medoid where K refers to the number of clusters) approach suffers two primary drawbacks. The first, which it shares with mean-based methods, is that the number of clusters must be defined in advance. The second is that for large data sets containing up to n points the solution times are of order $O(n^2)$.

In this paper we shall show a method that reliably calculates the number of required clusters and that utilizes spatial based proximity information embedded within the Delaunay tessellation (Delaunay, 1934) of the event set to improve performance to $O(n \log n)$. Since code to construct a spherical Delaunay tessellator had already been developed for the GNEMRE program, only the K-Medoid clustering algorithm needed to be developed.

Approach

To proceed with the discussion of the clustering approach we shall assume an initial distribution of geo-referenced events located in an unstructured fashion anywhere on the surface (or near surface) of the Earth. Our goal shall be to find clustered sets of those events that share close spatial proximity and are no more distant from one another (in a cluster) than some user prescribed distance $\boldsymbol{D_{max}}$. We shall call $\boldsymbol{D_{max}}$ the desired cluster size parameter. The set of discovered clusters shall be returned as an array of cluster objects each containing a list of one or more events,

which defines the cluster's event set, and a single event, the cluster representative, which signifies the best characterization of the cluster.

Before proceeding further we shall define the concepts of an event group, the maximum span of a cluster, and a consistent cluster which will be used repeatedly in the discussion that follows:

a) A group of events (or event group) shall be defined such that for any event contained in the group there is a closest neighbor event, also contained in the group that is never further away than some distance $\boldsymbol{D_{max}}$. Or conversely, two event groups are distinct if all events in the first group are further away than $\boldsymbol{D_{max}}$ from all events in the second group.
b) The maximum span of a cluster is defined such that no event in any arbitrary cluster is further away than $\boldsymbol{D_{max}}$ from any other event in the same cluster.
c) A cluster is said to be consistent if all events contained by an arbitrary cluster are closer to the clusters representative event than to any other representative in the remaining set of adjacent clusters of the event group.

The clustering approach defined in this paper begins by identifying isolated event groups from the initial set of globally distributed events. Next, each event group is processed sequentially by sub-dividing the group into an initial "best" guess of consistent clusters where the number of clusters is chosen in a minimalist way while still guaranteeing that the maximum span of each cluster is not violated. Finally, the group is processed using a top-down k-medoid algorithm to find the best set of cluster representatives for the group.

The remaining pages of this paper shall describe the process in reverse order. First we will describe the k-medoid optimization assuming an event group has been found and an initial set of clusters and representatives have been assigned. Next we will describe small fix-ups to handle the rare cases where poor quality clusters are formed and events are assigned to inappropriate clusters. Then we will return to describe the method for forming the initial best guess of clusters and their representatives given an arbitrary event group. Finally, we will describe the process for forming event groups given the initial distribution of globally geo-referenced events.

The K-Medoid Optimization

The K-Medoid clustering optimization algorithm attempts to improve an initial clustering definition for an event group that has been decomposed into a consistent set of initial "best" guess clusters. Figure 1 illustrates an example event group composed of 4 initial clusters whose initial representatives are outlined in red circles. The sequence of optimization steps for this example are shown in Figure 2a-d. The optimization heuristic operates by iteratively discovering a new set of representatives for the clusters that globally minimizes

$$M(C) = \sum_{i=0}^{N_p - 1} w_i d_{ki} \qquad (1)$$

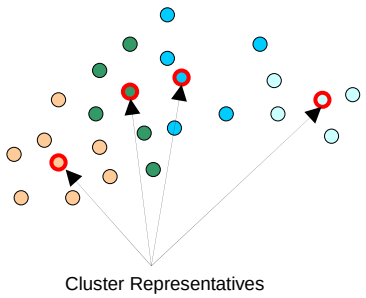

Figure 1. Event groups initial cluster definition.

where the sum is taken over all events (N_p) in the event group. The value d_{ki} represents the distance between the i^{th} event and the k^{th} cluster representative. The weights can be used to influence the minimization by defining a criterion that represents something other than proximity. For purposes of the remainder of this paper the weights will be assumed to be one for all events such that *M(C)* is strictly proximity based.

We intend to find the global minimum subject to two constraints:

a) No event-to-event distance span in the cluster shall exceed the pre-defined maximum distance, $\boldsymbol{D_{max}}$, and
b) No two clusters from the group can be combined to form a new cluster whose maximum span is also < $\boldsymbol{D_{max}}$.

The first of these constraints is simply the definition, previously given, for the maximum allowable span of any cluster. The second definition is a similar attempt to control the minimum size of a cluster so that is not significantly

smaller than D_{max}. The first constraint is used during the optimization to prohibit new representatives from being formed that will cause an excessive span even if the value of *M(C)* is smaller given the new representative for some cluster. The second constraint ensures that adjacent clusters that can be represented by a single cluster, assuming the first constraint is not violated, are merged into a single cluster reducing the total number of clusters in the group by one.

With the aforementioned constraints and definitions we define the K-Medoid optimization as follows:

> Given an initial set of representative clusters, fixed in number, from an arbitrary event group, exchange non-representative events with representatives until a reduced value for *M(C)* is discovered. When a more optimum event is discovered swap the old representative with the new event and continue with the next event in the group repeating the test. Continue until none of the non-representative events reduces the value of *M(C)* more than the current set of representatives subject to the previously defined constraints.

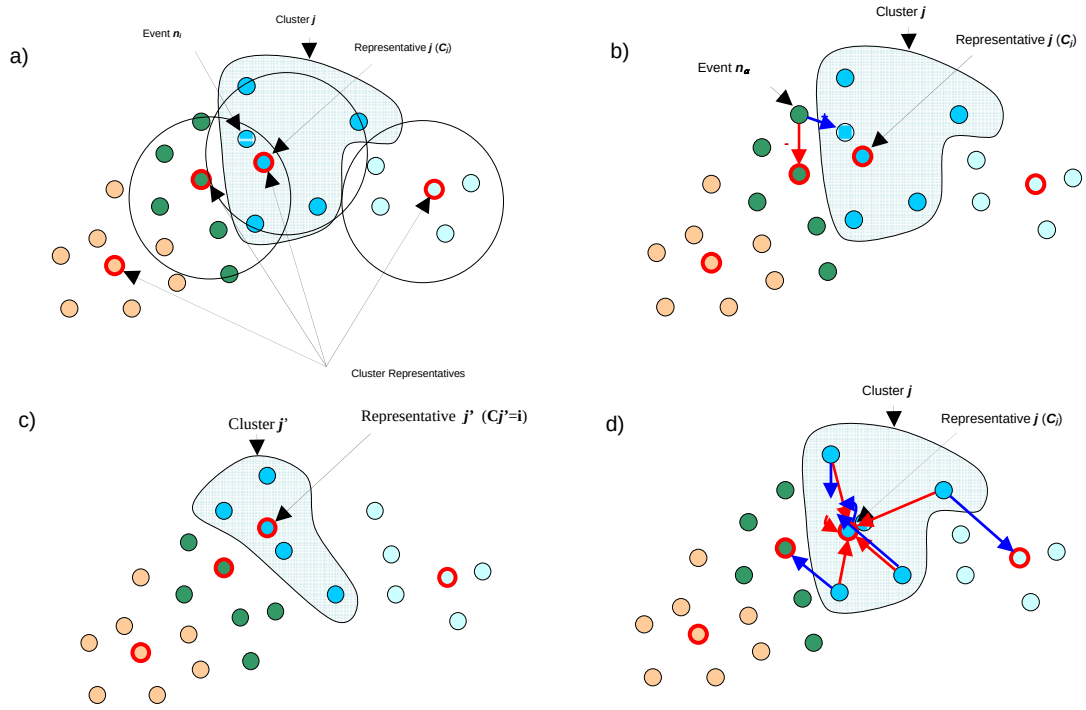

Figure 2 An example of the K-medoid optimization process.

Figure 2a shows an arbitrary iteration of the algorithm where event n_i is to be tested to see if it is a better representative for cluster *j* than its current representative. The change in *M(C)* caused by replacing the current representative of cluster *j* with event n_i is composed of two components. These components include:

a) Those events that currently belong to clusters other than *j* but are transferred to cluster *j'* when event n_i becomes its representative (let *j'* be the j^{th} cluster when event n_i is made its representative); and
b) The original events of cluster *j* which may remain in cluster *j'* or may be transferred to other clusters when event n_i becomes the new representative.

Let's examine events of type a) first. For our example only one event, n_α, is transferred from a non-*j* cluster to cluster *j'* when n_i becomes the representative of cluster *j'*. The net change in *M(C)* as a result of the transfer of n_α into cluster *j'* is composed of the additional contribution of assigning n_α into cluster *j'* minus the removal of the contribution from the cluster that currently contains n_α. We'll let $r(\alpha)$ be the index of the cluster containing n_α before the swap. This net change in *M(C)* is shown in Figure 2b. Because event n_α lies closer to n_i than its old

representative (that is why it is being transferred) the net result is always negative. For this reason, events of type a) that occur in a k-medoid swap tests always produce a reduction in *M(C)*.

For events of type b) we need to examine the contributions to the change in *M(C)* from all of the events that reside in the current cluster *j*. In our example problem shown in Figure 2c, four of the original cluster *j* events will remain in cluster *j'*, while two of the original events will be moved to nearby adjacent clusters. The net change in the value of *M(C)* is caused by the loss of all contributions of cluster *j* events with the cluster *j* representative (red arrows) and a gain due to the reattachment of cluster *j* events with the cluster *j'* representative or other representatives other than *j'* (blue arrows). We can write these contributions over all cluster *j* events as

$$\sum_{\beta} w_{\beta}\left(d'_{m(\beta)\beta} - d_{j\beta}\right) = \sum_{\beta} w_{\beta}\left(\left|n_{\beta} - n_{C'_{m(\beta)}}\right| - \left|n_{\beta} - n_{C_j}\right|\right) \tag{2}$$

where β is taken over all original events of cluster *j*. The new reassignment cluster indices are contained in $m(\beta)$ for each event in cluster *j*.

The total change in *M(C)* is given by summing changes from both case a) and case b) which gives

$$\delta M(C) = \sum_{\beta} w_{\beta}\left(d'_{m(\beta)\beta} - d_{j\beta}\right) + \sum_{\alpha} w_{\alpha}\left(d'_{j\alpha} - d_{l(\alpha)\alpha}\right) \tag{3}$$

If the change in $\delta M(C)$ is < 0.0 then event n_i represents a more optimum cluster representative than does the original cluster representative C_j and a swap is performed. This case is illustrated in Figure 2d. If, however, $\delta M(C)$ is > 0.0 then representative C_j is better and the swap is not performed. In either case the algorithm advances to the next event n_i for further testing. The algorithm halts when no further swapping occurs after a complete pass through all events in the group.

K-Medoid Optimization Constraint Satisfaction

As previously discussed the k-medoid optimization is constrained to avoid clusters with spans that exceed D_{max} or spans that are unnecessarily small (much less than D_{max} / 2). In the first case we enforce the constraint by ensuring that representative swaps are not performed during optimization if the swap results in a cluster whose span exceeds D_{max}. Figure 3 illustrates a case of two clusters before testing an event as a replacement representative for the topmost cluster. Notice that both clusters have a span that is less than D_{max} before the test.

Following the test the event is found to reduce *M(C)* (assume for the sake of the example) which results in the migration of an event from the cluster containing the test event to the lowermost cluster in order to ensure cluster consistency requirements (events must reside in the cluster for which they are closest to the clusters representative). However, as shown in Figure 4 the event migration results in a span that exceeds D_{max}. For this case the swap is disallowed and the original configuration before the test is restored.

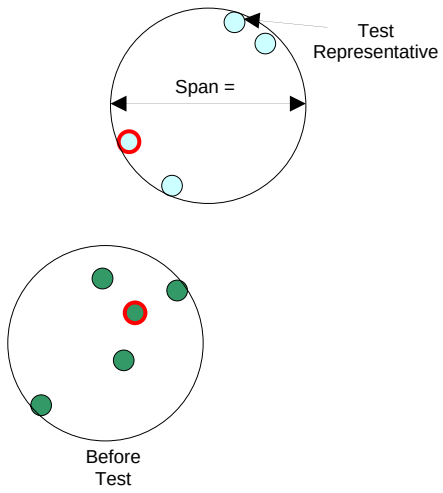

Figure 3. Adjacent cluster pairs before a test representative swap.

The second constraint is satisfied by attempting to merge adjacent clusters with one-another during the optimization process. If two clusters can be merged, as shown in Figure 5, where the resulting merger produces a new cluster whose span is still less than D_{max} then the merger is processed. The net result reduces the cluster count by one which generally increases the intra-cluster spacing.

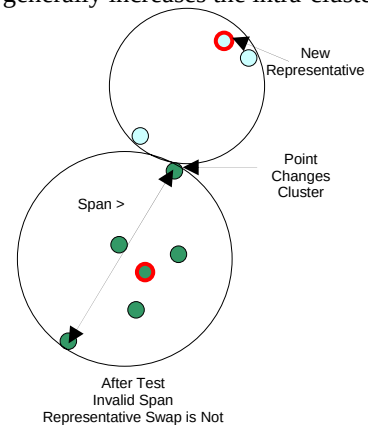

Figure 4. Adjacent cluster pairs following a representative swap resulting in an excessive span.

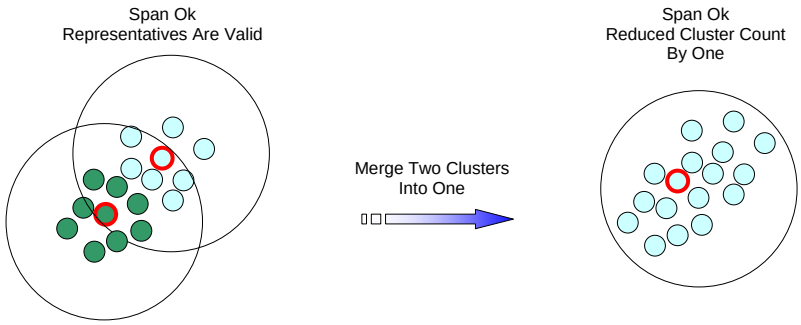

Figure 5. Adjacent cluster merge reducing the cluster count by one.

Poor Quality Cluster and Event Assignment Corrections

Given the imposition of the constraints on the k-medoid optimization, accompanied by sometimes poorly correlated local spatial distributions, we find that the algorithm will, in rare circumstances, form poor clusters or event-to-cluster assignments. Sometimes it is better to have a slightly larger value for *M(C)* if the result leads to a more favorable assignment of events to their respective clusters. Two different types of quality issues can arise. The first occurs when a poor quality cluster is formed. The other occurs when an event assignment is constructed with a cluster with which it is poorly correlated and a better choice is available. We have developed and implemented algorithms to deal with both, but do not have space to provide details in this paper.

Event Group Initial Cluster Definition

In the previous sections we examined the k-medoid clustering algorithm, some of the constraints under which it operates, and some quality correction issues that can occur under rare circumstances. In this section we shall go back to the beginning to answer the question of how to form an initial set of clusters from a given event group. It is this initial cluster definition upon which the k-medoid algorithm operates. In the next section we will answer the question of how to form event groups given a set of events distributed in an arbitrary unstructured fashion around the globe.

As mentioned earlier, part of the problem with medoid- and mean-based clustering algorithms is how to define the number and configuration of the clusters given an arbitrary point set. Although the k-medoid algorithm can find the best set of *N* clusters in a group of events it has no way to ascertain what *N* should be. It must be provided.

For our specific problem we are interested in determining the number of clusters necessary to represent the events in a group given some desired size, D_{max}, for each cluster. Here we shall define a method of approximating the cluster count and initial distribution using a medial axis sub-division scheme. As before, let the span of a cluster be the largest distance between any two events in the cluster. If the span of a cluster exceeds D_{max} then sub-divide the cluster into two new sub-clusters. In turn, evaluate each of the new sub-cluster spans. If one or both still exceed D_{max} then one or both are also split into two new sub-clusters. This process is repeated recursively until the newly formed sub-cluster pairs are defined by a set of events whose span is less than or equal to D_{max}.

The best way to sub-divide the events into sub-cluster pairs is to simply split the clusters event set along a line (or plane in 3-space) that is orthogonal to the line (or plane) that defines the clusters span and positioned so that it contains the spans mid-point. This new splitting axis is called the medial axis of the span. The sub-division process is illustrated in Figures 6a through 6c.

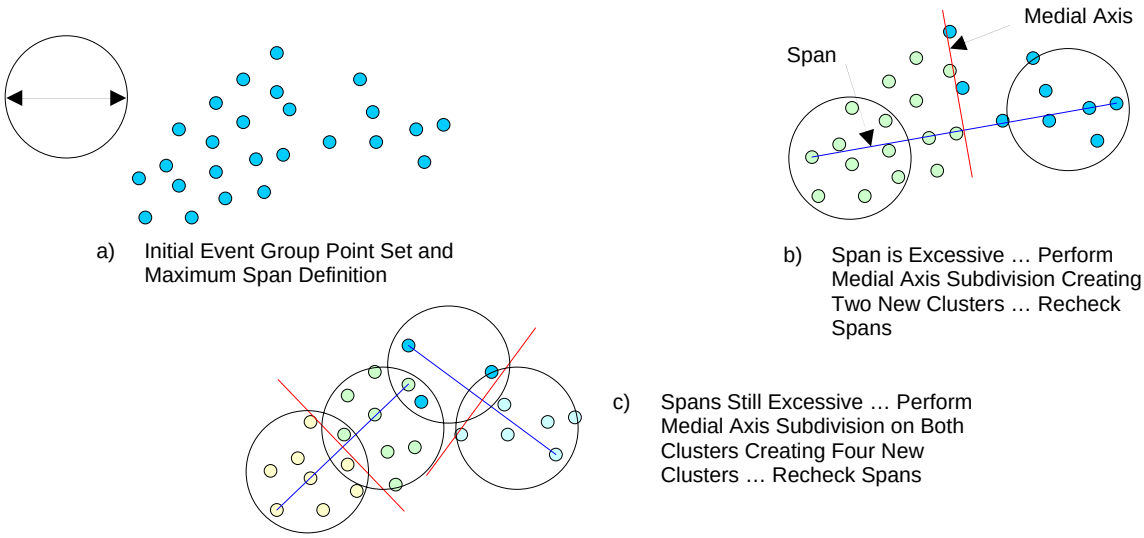

Figure 6. Medial-axis sub-division of an initial event group into 4 sub-clusters all of whose spans are < D_{max}.

The span axes are denoted in blue while the medial axes are shown in red. Notice that the medial axis effectively sub-divides the cluster into two new clusters that lie on opposite sides of the medial axis. A simple test (scalar triple product in 3-space) can be used to determine which side of the medial axis an event lies. Events lying on either side of the medial axis are inserted into two new sub-clusters and the original cluster is removed (deleted). In the example above the original set of events in the group are subdivided into 4 sub-clusters whose spans are all less than D_{max}.

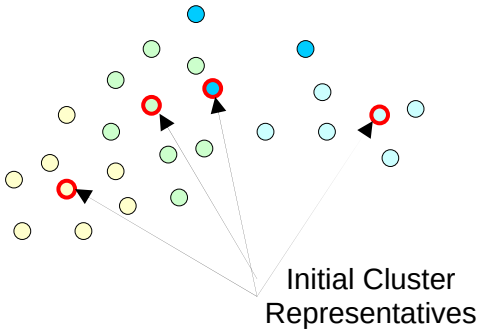

Figure 7. Event group initial cluster representative formations.

The previously described decomposition of the original event group into a set of clusters whose spans are all less than D_{max} determines the initial number of clusters that will be provided to the k-medoid clustering algorithm. However, it has not defined the best characteristic representative for each cluster which must be accomplished before performing the k-medoid optimization. This is done by simply performing a local optimization test for $M(C)$ on each event in each cluster. The one that minimizes $M(C)$ for each cluster is chosen as its representative. Figure 7 shows the result given the final clusters shown in Figure 6 above.

The final step before entering the k-medoid optimization algorithm is to ensure that the initial clusters are all consistent. This means that we must check each cluster to ensure that all events owned by the cluster are closest to that cluster's representative than to any other representative in the remaining clusters. For our example three events are found to be erroneously assigned within other clusters and must be reassigned. These reassigned events are shown in Figure 8.

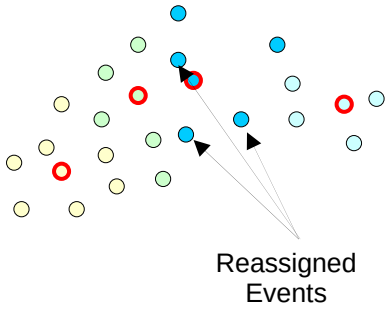

Figure 8. Event reassignment required to preserve cluster consistency.

Once the reassignment operation is complete we have a consistent set of clusters whose spans are all less than D_{max}. This set of clusters is provided to the k-medoid algorithm to find the best set of representatives for the entire group.

Event Group Discovery

We can now answer the final question of how to efficiently construct event groups given the raw event data distributed in an unstructured manner over the entire Earth's surface (near). Here we shall make direct use of the nearest neighbor information contained in a Delaunay tessellation of the raw event positions.

Since we already have code to construct a spherical Delaunay tessellator we need only input the event positions and build the tessellation. Figure 9 below shows the resultant edge connectivity between ISC catalog events for the year 2000 with depth <= 33 km and mb >=3.0. The input set contains 22,766 events. The small white square near Greece will be shown in the remaining figures to illustrate the process steps.

Event groups are defined by finding connected sets of events where the distance between neighboring events in the connected set is less than D_{max}. This can be accomplished in order $O(n)$ time using the topology of the Delaunay tessellation. The algorithm simply picks the first unmarked node (event) in the tessellation. By marking we are simply setting a flag to indicate that the node has been visited. If the node is already marked we proceed to the next node. This continues until no unmarked nodes remain.
Any unmarked nodes are processed by first marking the node as having been visited and adding it into a new event group. We then add the node to a stack. Next the algorithm enters a loop processing all nodes in the stack until it is empty. The stack processing begins by first popping the next node off of the stack which is taken as the current process node. Then we loop over each edge of the node (the tessellation topology stores this information) and check the edge length to see if it is less than or equal to D_{max}. If it is and the node opposite the current process node on the edge has not been flagged as visited we mark it as such and add that opposite node to the stack and to the current event group (a cluster). This continues for each edge of the current process node. Finally the algorithm checks to see if any nodes remain in the stack and loops to obtain the next current process node if the stack is not empty.

When the stack is empty the algorithm returns to the outer loop over all tessellation nodes to find the next unmarked node. When no unmarked nodes remain the event groups have all been discovered. Each group consists of one or more events. We can best visualize these by turning off all edges that exceed D_{max}. This is shown in Figure 10 for a D_{max} value of ½ degree. The groups are highlighted with an outlined yellow curve to aid in their visualization.

Event groups whose total span is less than D_{max} form completed clusters. Groups whose span exceeds D_{max} must be

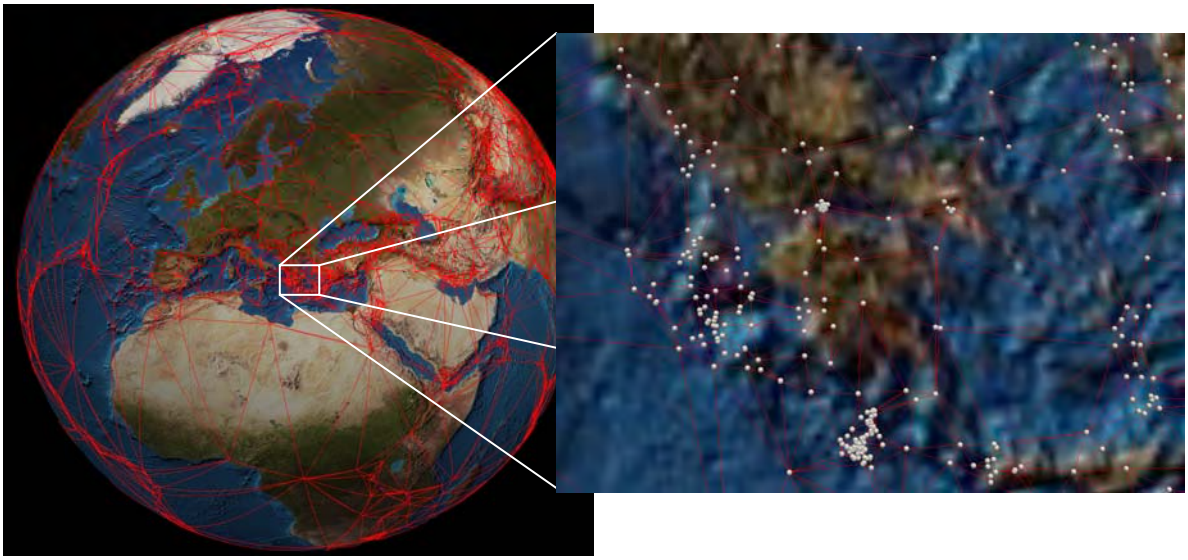

Figure 9. 22,766 spherically tessellated events from the ISC catalog.

processed by the medial-axis sub-division algorithm to form initial consistent clusters which are further processed by the k-medoid clustering algorithm to find the best set of representatives in the group.

In Figure 10 all isolated events and groups of 2 events are immediately considered as completed. The remaining groups must be processed by the medial-axis subdivision and k-medoid algorithms. The result of that processing is shown in Figure 11. The cluster representatives are outlined in white while the clusters are signified by the red circles centered on the maximum span of each cluster.

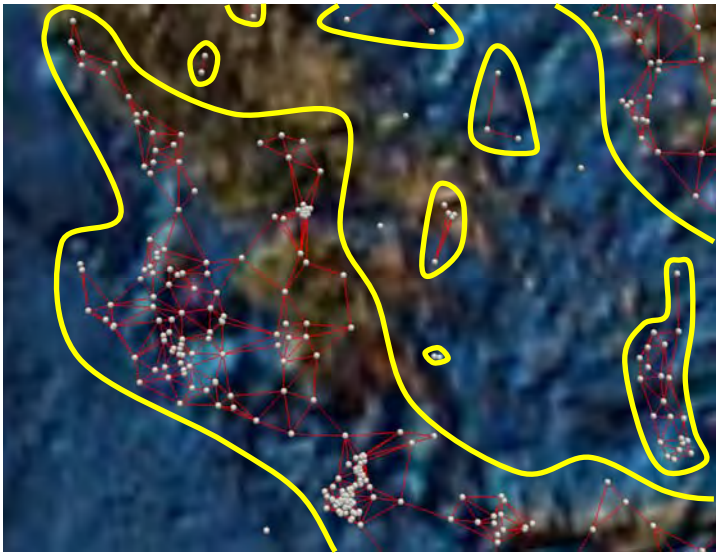

Figure 10. Local event groups and isolated events in the magnified region.

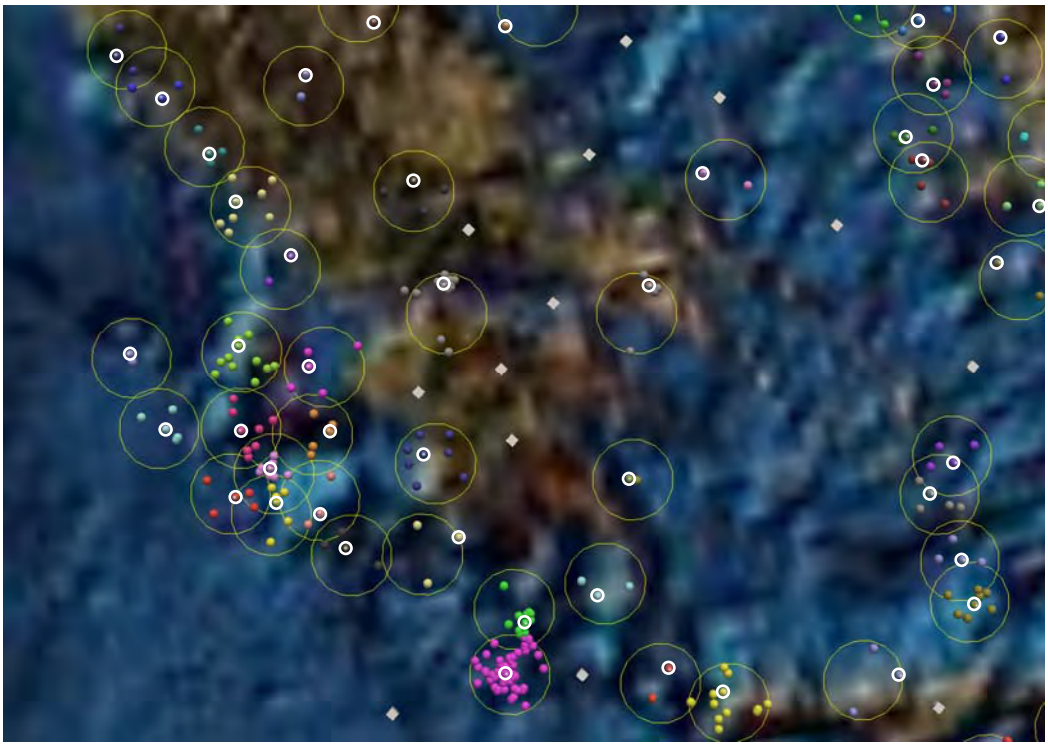

Figure 11. Magnified region depicting final cluster formation following group formation, initial cluster definition, and k-medoid optimization. White circles represent cluster representatives. Red circles are D_{max} in diameter centered on cluster maximum spans. For clarity, single event groups are shown as white diamonds.

The final total clustering algorithm can be summarized in pseudo-code as follows:

a) Tessellate raw event globally on a sphere
b) Decompose events into groups whose neighbor separation is < Dmax
c) Move groups whose span is < Dmax into a completed cluster list (includes isolated events)
d) For each remaining incomplete event group:

- Decompose group into a set of sub-clusters using the medial-axis sub-division algorithm
- Peform k-medoid representative optimization on entire group
- Fix poor quality clusters and event assignments
- Add each optimized sub-cluster to the completed cluster list

CONCLUSIONS AND RECOMMENDATIONS

We have described a proposed alternative to the standard fixed grid algorithm for clustering seismic events which eliminates the primary drawbacks of that methodology. The new approach uses a well known k-medoid optimization algorithm for finding optimized clusters in unstructured data. Additionally, our approach takes advantage of the Delaunay tessellation capability already developed for the GNEMRE program, and it has performance capabilities that are more than acceptable for the largest problems currently under consideration.

REFERENCES

Estivill-Castro, V., M. E. Houle (2001). Robust Distance-Based Clustering with Applications to Spatial Data Mining, Algorithmica, 30 (2):216–242.

Delaunay, B.N. (1934). Sur la Sphere Vide, *Bull. Acad. Science USSR VII*: Class. Sci. Math., 793–800.

BASIC RESEARCH ON SEISMIC AND INFRASONIC MONITORING OF THE EUROPEAN ARCTIC

Frode Ringdal, Tormod Kværna, Svein Mykkeltveit, Steven J. Gibbons, and Johannes Schweitzer

NORSAR

Sponsored by Army Space and Missile Defense Command

Contract No. W9113M-05-C-0224

ABSTRACT

This project represents a three-year research effort aimed at improving seismic and infrasonic monitoring tools at regional distances, with emphasis on the European Arctic region, which includes the former Novaya Zemlya test site. The project has three main components: a) to improve seismic processing in this region using the regional seismic arrays installed in northern Europe, b) to investigate the potential of using combined seismic/infrasonic processing to characterize events in this region and c) to carry out experimental operation, evaluation and tuning of the seismic threshold monitoring technique, with application to various regions of monitoring interest.

We have begun exploiting the data from the Swedish infrasound array network, which provides a useful supplement to the seismic and infrasonic arrays in Norway and NW Russia. We continue our work towards developing and evaluating a joint seismic/infrasonic bulletin for northern Fennoscandia and adjacent regions. This bulletin would be similar to the automatic seismic bulletin that we are currently providing on the NORSAR Web pages, but it would also contain infrasonic phase associations. Furthermore, we plan to generate an infrasonic event bulletin using only the estimated azimuths and detection times of infrasound phases recorded by stations in the Nordic network.

We have continued our studies of seismic and infrasonic recordings of a set of more than 100 surface explosions in northern Finland, carried out for the purpose of destroying old ammunition. Waveform correlation analysis indicates that these explosions were very closely spaced, and occurred at most within a few hundred meters of each other. This is a unique set of events given the repeatable nature of the source. Very similar waveforms and amplitudes are observed for the seismic phase arrivals, indicating a similar explosion yield and source function for each event. In contrast, the infrasonic recordings show great variation between events, both with regard to the number and amplitudes of detected infrasonic phases, as well as their travel times. A variation of several tens of seconds in travel times for corresponding phases for different events is observed at a distance of about 175 km.

The recent upgrade of the Spitsbergen seismic array, which has included installation of five new three-component seismometers, as well as an increase in the sampling rate from 40 to 80 Hz, has resulted in significant improvements in high frequency signal characterization as well as S-phase detection. We demonstrate some results from analysis of recent small seismic events near Novaya Zemlya and in the Barents Sea.

We have analyzed the recorded waveforms from the 9 October 2006 North Korean nuclear explosion in order to investigate the capability of the Seismic International Monitoring System (IMS) network to monitor the North Korean test site for possible future explosions. Our analysis is based upon the so-called Site-Specific Threshold Monitoring (SSTM) approach. Using actual seismic data recorded by a given network, SSTM calculates a continuous “threshold trace,” which provides, at any instant in time, a probabilistic upper magnitude bound on any seismic event that could have occurred at the target site at that time. We find that the current IMS primary network has a typical “threshold monitoring capability” of between mb 2.3 and 2.5 for the North Korean test site. Not unexpectedly, it turns out that the Korean array (KSRS) is of essential importance in obtaining such low thresholds. Non-IMS stations could also make important contributions, and we find that by adding the nearby Incorporated Institutions for Seismology (IRIS) station MDJ in China, the threshold monitoring capability is improved to between magnitude 2.1 and 2.3. For comparison, the three-station network detection threshold is found to be typically one magnitude higher than these numbers. We note, however, that the SSTM approach is not aimed at detecting events, but rather to supplement traditional detection processing by enabling the analyst to focus on and analyze extensively instances where a possibly undetected event of monitoring interest could have occurred.

OBJECTIVE

The objective of the project is to carry out research to improve the current capabilities for monitoring small seismic events in the European Arctic, which includes the former Russian test site at Novaya Zemlya. The project has three main components: a) to improve seismic processing in this region using the regional seismic arrays installed in northern Europe, b) to investigate the potential of using combined seismic/infrasonic processing to characterize events in this region and c) to carry out experimental operation, evaluation and tuning of the seismic threshold monitoring technique, with application to various regions of monitoring interest.

RESEARCH ACCOMPLISHED

Establishing a Nordic Network of Infrasound Arrays

An important aspect of the infrasonic studies is the availability of data from a distributed network of arrays. The Swedish infrasound array network provides a useful supplement to the seismic and infrasonic arrays in Norway and NW Russia. We have begun exploiting the data from this combined network, which will allow a much improved joint seismic/infrasonic regional processing at NORSAR. The Apatity infrasound array is a three-element array co-located with the nine-element Apatity short-period regional seismic array, which was installed in 1992 on the Kola Peninsula, Russia by the Kola Regional Seismological Centre (KRSC). The 25 element ARCES array is a short-period regional seismic array, located in northern Norway. ARCES has no infrasound sensors, but because of the near surface installation conditions, many of its seismic sensors are also sensitive to infrasound signals (e.g., Ringdal and Gibbons, 2006). Current plans are to install an infrasound array near the ARCES site in 2007/2008. The Swedish Infrasound Network (Liszka, 2007) has been in operation since the beginning of the 1970s. Operated by the Swedish Institute of Space Physics, the network has until recently comprised four infrasound stations: Kiruna, Jämtön, Lycksele and Uppsala. The station in Uppsala was moved to Sodankylä, Finland, during the summer of 2006. The currently available network of arrays for infrasound processing in the Nordic region is shown in Figure 1.

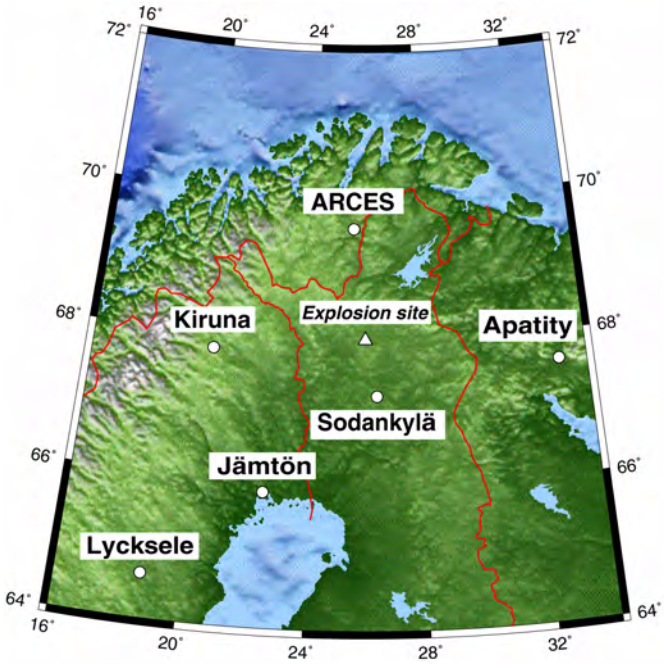

Figure 1. Locations of the arrays used for infrasonic processing in the Nordic countries. The site of the explosions in northern Finland discussed in this paper is marked on the map.

Case study of explosions in northern Finland

Each year between mid-August and mid-September, a series of explosions in the north of Finland has been recorded by the stations of the Finnish national seismograph network and also by the seismic arrays in northern Fennoscandia and NW Russia. Based upon event locations given in the seismic bulletin of the University of Helsinki, the geographical coordinates of the explosion site are assumed to be approximately 68.00^{o}N and 25.96^{o}E. The explosions are carried out by the Finnish military in order to destroy outdated ammunition and are easily identified from the automatic seismic bulletins at NORSAR for several reasons. Firstly, they are always detected with a high signal-to-noise ratio (SNR) on the ARCES array; secondly they register very stable azimuth estimates on the detection lists; and thirdly they take place at very characteristic times of day (the origin time indicated by the seismic observations almost invariably falls within a few seconds of, typically, a full hour or half-hour in the middle of the day).

Between 2001 and 2006, a total of 141 events were found that appeared to fit the general attributes of explosions from this site. The fully automatic location estimates displayed a rather large geographical spread and, assuming that these events are in fact essentially co-located, the origin times would be correspondingly spurious. However, by applying a waveform correlation procedure we could confirm that the explosions were indeed closely spaced, probably within an area of some hundred meters in diameter (Ringdal and Gibbons, 2006).

The signals recorded by the ARCES seismic array provide an excellent perspective of the differences in seismic and infrasonic recordings of the explosions, as illustrated in Figure 2 for the year 2005. A large amplitude infrasonic signal approximately 600 seconds after the origin time is observed for almost all of these events but, unlike the seismic signals which are almost identical for each explosion, the temporal characteristics and the amplitudes of the infrasonic arrivals differ greatly among events. There is also significant variability in the travel time of the infrasonic phases from event to event, and there is evidence of multiple infrasonic arrivals as well. The similarity of the seismic waveforms for these explosions not only constrains the events to be almost co-located but rule out the possibility of multiple explosions as is common for ripple-fired mining blasts (Gibbons et al., 2005). We conclude that differences in the occurrence and appearance of infrasonic arrivals from event to event are the result of atmospheric conditions alone. The seismic data also indicate very similar waveform amplitudes for the events from which we conclude very similar explosion yields. This will provide a useful measure of the variability in yield estimation from the sound waves.

To obtain a better overview of the occurrence of signals with typical sound velocities, we calculated a detection statistic, C(t), which is essentially identical to that defined in Equation (15) of Brown et al. (2002). Figure 3 displays a color-scaled indication of C(t) for the ARCES array for a five-minute long time-window following each of the events subject to C(t) exceeding a threshold of 0.01 and the estimated slowness and azimuth falling in the indicated ranges. The vast majority of the events register a candidate acoustic phase between approximately 620 and 660 seconds after the event. A smaller number of events also indicate an earlier arrival from approximately 500 seconds. This figure confirms that evidence of one or more atmospheric sound arrivals was observed for almost every explosion, even in cases where the signal amplitude was smaller than the ambient noise level. The most common arrivals occur approximately 600 seconds after the event with a superimposed variation which appears to vary quite smoothly over a several day time-scale.

There are many interesting questions which need further investigation. For the recordings at ARCES, the infrasonic arrivals after approximately 650 seconds are quite consistent despite showing far greater variation than the corresponding seismic signals. On the other hand, the arrivals at approximately 550 seconds occur relatively seldom and, when they occur, they appear to produce a larger amplitude seismic response than the later signals (see, for example, the waveforms from Aug. 27, Sep. 3, and Sep. 14 on Figure 2). More detailed information about the atmospheric conditions along the path from the explosion site to the ARCES array would be useful in order to address these questions.

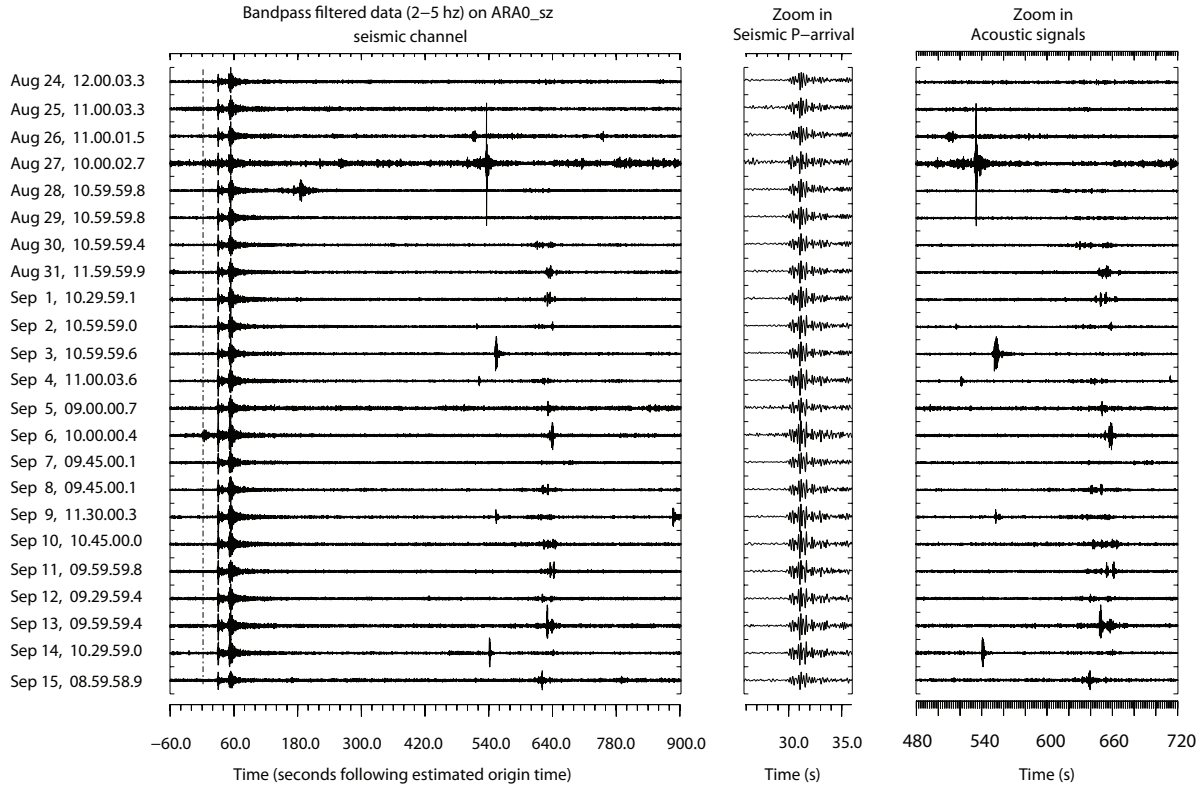

Figure 2. Recordings on the ARCES seismic array (channel ARA0_sz) of 23 events at the Finnish explosion site in August and September 2005. The time provided to the left is the estimated event UTC origin time. All waveforms are aligned to the maximum correlation coefficient and have identical vertical scaling. Signals arriving between 450 and 700 seconds after origin time are demonstrated by array analysis to propagate with sound velocity from an approximate 173 degrees backazimuth. All arrivals between 200 and 450 seconds correspond to unrelated seismic events.

Detection of Small Seismic Events near Novaya Zemlya

The recent upgrade of the Spitsbergen seismic array, which has included installation of five new three-component seismometers as well as an upgrading of the sampling rate from 40 to 80 Hz, has resulted in large improvements in the processing of seismic events at regional distances. As shown by Ringdal et al. (2006), S-phase detection at the array has been significantly improved. Furthermore, the increased sample rate has made possible more detailed studies of high-frequency propagation in the vicinity of the array. Since January 2006 four small seismic events near Novaya Zemlya have been detected (Table 1).

Table 1. Seismic events near Novaya Zemlya detected during 01/2006-06/2007.

Date	Origin time	Latitude (N)	Longitude (E)	Magnitude (mb)
05/03/2006	23.17.35.7	76.80	66.04	2.65
14/03/2006	20.57.02.4	75.07	53.05	2.23
30/03/2006	10.46.02.8	70.79	51.50	2.30
26/06/2007	03.19.05.0	73.45	53.43	2.75

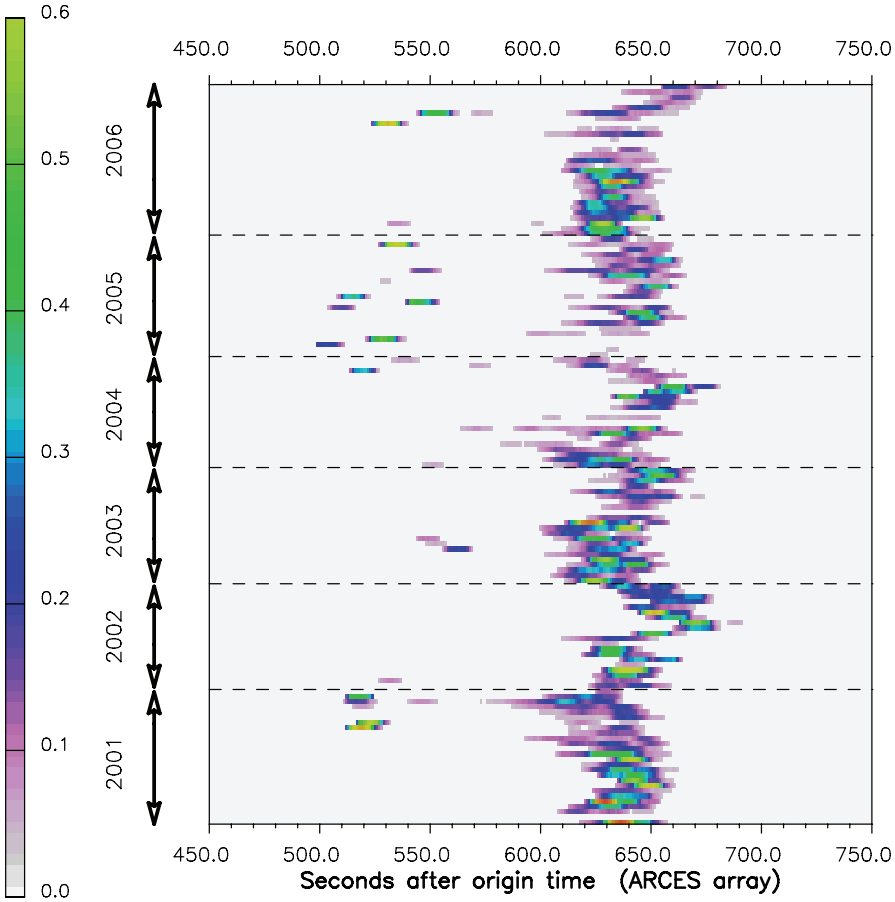

Figure 3. Detection statistics over the full ARCES seismic array within the time windows as indicated following each of the 141 identified explosions in northern Finland between 2001 and 2006. A pixel is drawn every second, at time t, for each event provided that the preferred slowness and backazimuth evaluated over the 10.0 second long window beginning at time t fall within an acceptable range for acoustic waves from the given source. The color indicates the value of the detection statistic.

Figure 4 shows spectrograms of the Spitsbergen B1 seismometer (vertical component) for the Novaya Zemlya event on 5 March 2006. The top part is the original spectrogram using 80 Hz sampling, the bottom part is converted to the response of the previous Spitsbergen system, with 40 Hz sampling. The most noticeable feature of the original spectrogram is the remarkable amount of high-frequency energy, taking into account the large epicentral distance (more than 1000 km). We note that there is significant P-wave energy even above 20 Hz. A similar observation can be made for the other events in Table 1. All of them have high SNR in the filter band 20 to 36 Hz, although the high-frequency energy is not quite as pronounced as for the event shown in Figure 4.

It is interesting to compare this original spectrogram to the bottom spectrogram in Figure 4, which shows how the same event would have been recorded with the previous array configuration (40 Hz sampling rate). It is not surprising that the high frequency information would have been lost for previous events, and we will never know whether the interesting Novaya Zemlya events in the past several years would have shown similar characteristics. It might be considered to upgrade other seismic systems located in areas of good high-frequency propagation and low noise (e.g. the ARCES array) to a higher sampling rate in the future.

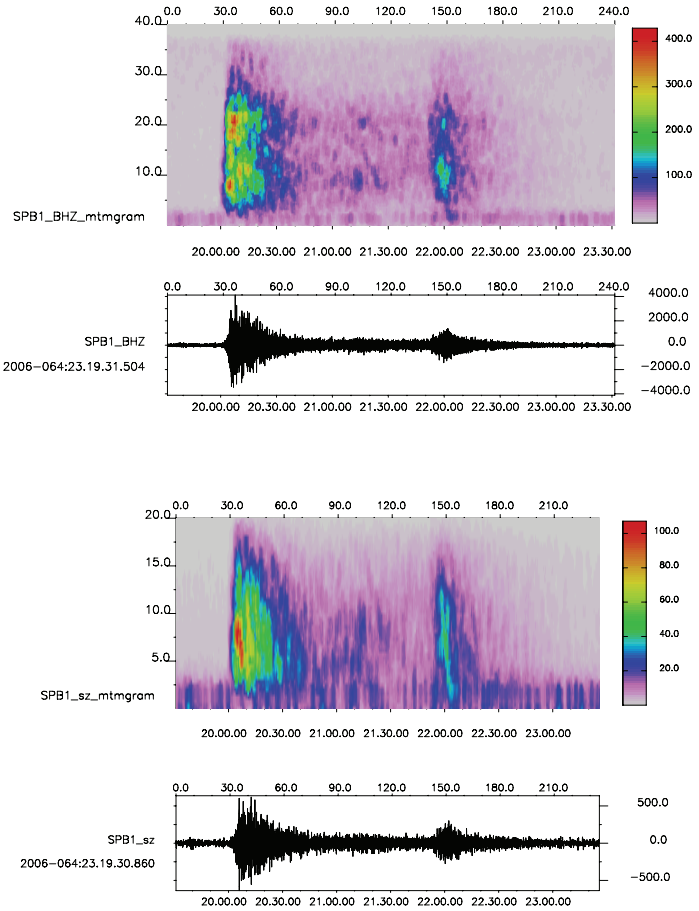

Figure 4. Spectrograms for the Spitsbergen B1 seismometer (vertical component) for the Novaya Zemlya event on 5 March 2006. The top part is the original spectrogram using 80 Hz sampling, the bottom part is converted to the response of the previous Spitsbergen system, with 40 Hz sampling.

Threshold Monitoring of the North Korean Nuclear Test Site

On 9 October 2006 the Democratic Peoples Republic of Korea (DPRK) conducted an underground nuclear explosion at a test site near Kimchaek. The explosion was detected by several seismic stations in the IMS, and was also reported by the United States Geological Survey (USGS). We have analyzed the recorded waveforms at selected seismic stations in order to investigate the capability of the global seismic network to monitor the DPRK test site for possible future explosions. Our analysis is based upon the so-called SSTM approach. Using actual seismic data recorded by a given network, SSTM calculates a continuous threshold trace, which provides, at any instance in time, an upper magnitude bound on any seismic event that could have occurred at the target site at that time.

Let us first emphasize that a large number of seismic stations world-wide recorded this event, and that many of these stations were not analyzed as part of this study. Our main reason for not including such stations is that in a site-specific capability study of the type discussed here, the resulting threshold is dominated by a few stations of exceptionally high detection capability. We have focused our analysis on these exceptional stations. In fact, as will be shown later in this study, the monitoring capability of our selected network (9 stations) for the North Korean test site is essentially defined by the best three stations in that network. Additional stations would be useful for resolving instances of excessive noise at one or more of these three stations, and would also be helpful during interfering earthquakes, but will generally have only a modest contribution to an overall lowering of the monitoring threshold.

The network selected for this study comprises in general those IMS stations which had the best signal-to-noise ratio (SNR) for the 9 October explosion plus the Chinese station at Mudanjiang (MDJ), located about 370 km north of the test site. MDJ data is openly available through the IRIS data management center. We note that data from the Korean Seismic array (KSRS) in South Korea was not operationally available from the IDC for the time period of the test. We are grateful to KIGAM for providing us with the KSRS data for our analysis.

Using the nuclear test for calibrating the signal propagation characteristics at the various stations, we carried out a site-specific tuning of the network stations. The details are described in Kværna et al. (2007). We then applied the methodology described in Kværna and Ringdal (1999) to obtain the threshold processing results. We will show two different types of threshold traces for the North Korea nuclear test site:

- The *detection threshold traces*, which estimate, (at the 90% probability level) the smallest seismic event that can be detected by 3 or more stations in the network (SNR>4).
- The *monitoring threshold traces*, which estimate (at the 90% probability level) the largest seismic event that could possibly have occurred.

In each of the following figures, the *detection threshold traces* are marked in red, the *monitoring threshold traces* are marked in blue.

Figure 5 shows the results for the day of the nuclear test (9 October 2006), using only those stations that were operational at the IDC during that day. We note that the detection threshold is typically around 4.0 or slightly below. At the time of the test, the detection threshold is around 3.75. The monitoring threshold averages about one magnitude unit lower than the detection threshold, i.e. close to magnitude 3.0.

Figure 6 shows a one-day plot of detection traces (red) and monitoring traces (blue) for 15 November 2006, when a large earthquake occurred in the Kurile Islands. By that time, the KSRS array was operational in the IDC, and we also extracted a full day's data from the MDJ station in China. The top panel uses the IMS network (including KSRS); the middle panel shows the effect of adding the MDJ station and the bottom panel shows results from using only the three stations KSRS, MDJ and MJAR. We can make the following observations:

- The operational IMS network (now with KSRS available) shown in red on the top panel of Figure 6 has a detection threshold of about magnitude 3.8, which is almost unchanged from the threshold observed in Figure 5 when KSRS was not available.
- In contrast, the monitoring trace (blue) on the top panel is lower by more than half a magnitude unit compared to the corresponding trace in Figure 5 where KSRS was not available.
- When adding MDJ to the IMS network (middle panel) we obtain a modest decrease (to about 3.5) for the detection trace (red), whereas the monitoring trace (blue) is now as low as 2.0 on the average. (Here we assume that detection processing is carried out for MDJ).

Finally Figure 6 gives an indication of how a regional network, comprising only the best stations, would compare to a global network. This is illustrated in the bottom panel of the figure, which shows that using the network of MJAR, KSRS and MDJ appears to perform almost as well as the "full" network. However, this does not mean that the remaining stations are unimportant. In fact, during interfering events these additional (teleseismic) stations may help lower the thresholds. This is particularly evident for the detection traces (red). Also, if one of these three stations should have abnormally high noise conditions, or (worse) being out of operation, it is important to have additional stations that can contribute to reducing the resulting decline in capabilities.

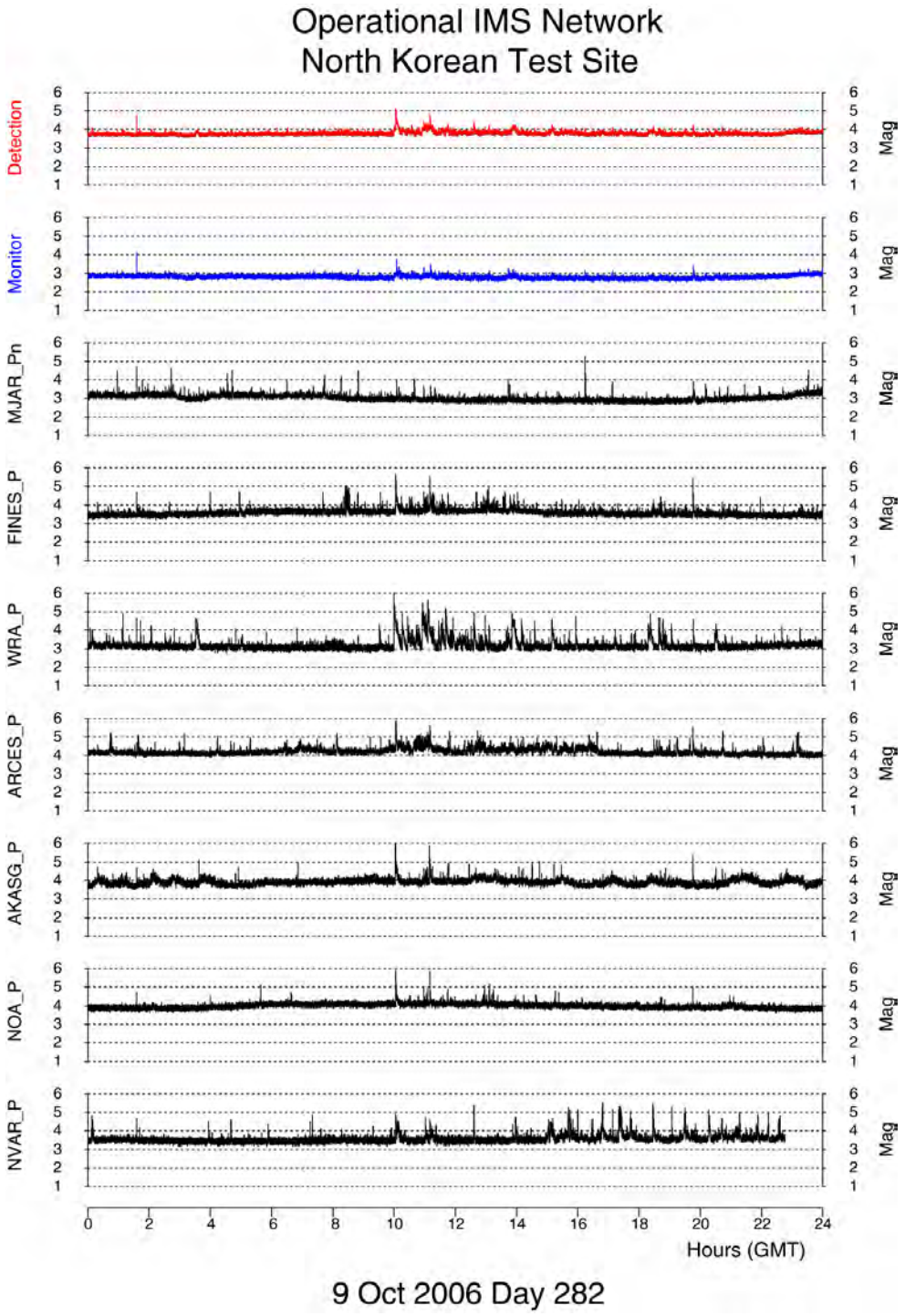

Figure 5. Threshold monitoring results for the day of the nuclear test (9 October 2006). In this figure we have used only those of our selected stations that were operational at the IDC during that day. Detection thresholds (red) are close to magnitude 4.0 or slightly below, except for occasional increases during the nuclear test (at 01.35) and during some interfering events later in the day. The monitoring thresholds (blue) average about magnitude 3.0. The individual station P-thresholds (black) are also shown.

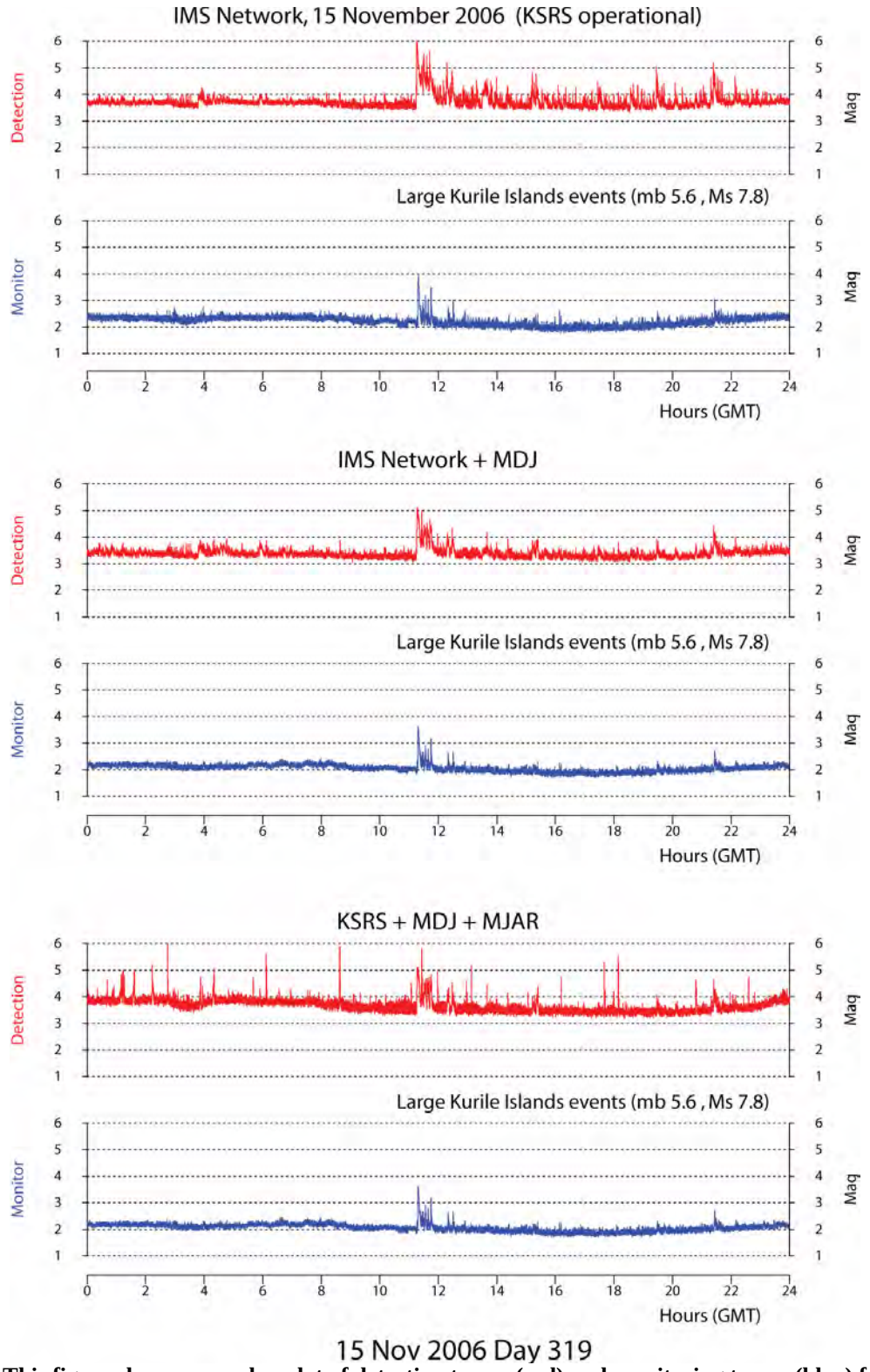

Figure 6. This figure shows a one-day plot of detection traces (red) and monitoring traces (blue) for 15 November 2006. The top panel uses IMS stations (including KSRS); the middle panel shows the effect of adding the MDJ station and the bottom panel shows results from using only KSRS, MDJ and MJAR.

CONCLUSIONS AND RECOMMENDATIONS

The Swedish infrasound array network provides a useful supplement to the seismic and infrasonic arrays in Norway and NW Russia. We have begun exploiting the data from this network, which will allow a much improved joint seismic/infrasonic regional processing at NORSAR. We continue our work towards developing and evaluating a joint seismic/infrasonic bulletin for northern Fennoscandia and adjacent regions. This bulletin would be similar to the automatic seismic bulletin that we are currently providing on the NORSAR Web pages, but it would also contain infrasonic phase associations. Furthermore, we will experimentally attempt to generate an infrasonic event bulletin using only the estimated azimuths and detection times of infrasound phases recorded by stations in the Nordic network.

The data set of more than 100 surface explosions in northern Finland in almost exactly the same place recorded by the ARCES and Apatity arrays has provided an excellent opportunity for studying infrasonic versus seismic phase propagation characteristics. Very similar waveforms and amplitudes are observed for the seismic phase arrivals, indicating a similar explosion yield and source function for each event. In contrast, the infrasonic recordings show great variation between events, both with regard to the number and amplitudes of detected infrasonic phases, as well as their travel times. A variation of several tens of seconds in travel times for corresponding phases for different events is observed at a distance of about 175 km.

The recent upgrade of the Spitsbergen seismic array, which has included installation of five new three-component seismometers, as well as an increase in the sampling rate from 40 to 80 Hz, has resulted in significant improvements in high frequency signal characterization as well as S-phase detection.

We have analyzed the recorded waveforms from the 9 October 2006 North Korean nuclear explosion in order to investigate the capability of the seismic IMS network to monitor the North Korean test site for possible future explosions. We find that the current IMS primary network has a typical “threshold monitoring capability” of between mb 2.3 and 2.5 for the North Korean test site. Not unexpectedly, it turns out that the Korean array (KSRS) is of essential importance in obtaining such low thresholds. Non-IMS stations could also make important contributions, and we find that by adding the nearby IRIS station MDJ in China, the threshold monitoring capability is improved to between magnitude 2.1 and 2.3. For comparison, the three-station network detection threshold is found to be typically one magnitude higher than these numbers.

REFERENCES

Brown, D. J., Katz, C. N., Le Bras, R., Flanagan, M. P., Wang, J., and Gault, A. K. (2002). Infrasonic Signal Detection and Source Location at the Prototype International Data Centre, *Pure appl. geophys.* 159: pp. 1081–1125.

Gibbons, S. J., Kværna, T. and Ringdal, F. (2005). Monitoring of seismic events from a specific source region using a single regional array: a case study, *J. Seismology* 9: 277–294.

Kværna, T., Ringdal, F. and Baadshaug, U. (2007). The capability for seismic monitoring of the North Korean test site. Semiannual Technical Summary, 1 July – 31 December 2006, NORSAR Sci. Rep. 1-2007, 41–72.

Kværna, T. and Ringdal, F. (1999). Seismic threshold monitoring for continuous assessment of global detection capability, *Bull. Seism. Soc. Am.* 89: 946–959.

Liszka, L. (2007): Infrasound - A summary of 35 years of infrasound research, Manuscript submitted for printing, 150 pp.

Ringdal, F. and S.J. Gibbons (2006). Seismic/Infrasonic Processing: Case study of explosions in north Finland. Semiannual Technical Summary, 1 July – 31 December 2005, NORSAR Sci. Rep. 1-2006, 54–68.

Ringdal, F., and Kværna, T.,Gibbons, S.J., Mykkeltveit, S. and Schweitzer, J. (2006). Basic research on seismic and infrasonic monitoring of the European Arctic, in *Proceedings of the 28th Seismic Research Review*: *Ground-Based Nuclear Explosion Monitoring Technologies,* LA-UR-06-5471, Vol.2, pp. 1017–1027.

ENHANCING SEISMIC CALIBRATION RESEARCH THROUGH SOFTWARE AUTOMATION AND SCIENTIFIC INFORMATION MANAGEMENT

Stanley D. Ruppert, Douglas A. Dodge, Michael D. Ganzberger, Teresa F. Hauk, and Eric M. Matzel

Lawrence Livermore National Laboratory

Sponsored by National Nuclear Security Administration
Office of Nonproliferation Research and Development
Office of Defense Nuclear Nonproliferation

Contract No. W-7405-ENG-48

ABSTRACT

The National Nuclear Security Administration (NNSA) Ground-Based Nuclear Explosion Monitoring Research and Engineering (GNEMRE) Program at Lawrence Livermore National Laboratory (LLNL) has made significant progress enhancing the process of deriving seismic calibrations and performing scientific integration, analysis, and information management with software automation tools. Several achievements in schema design, data visualization, synthesis, and analysis were completed this year. Our tool efforts address the problematic issues of very large datasets and varied formats encountered during seismic calibration research. As data volumes have increased, scientific information management issues such as data quality assessment, ontology mapping, and metadata collection that are essential for production and validation of derived calibrations have negatively impacted researchers' abilities to produce products. New information management and analysis tools have resulted in demonstrated gains in efficiency of producing scientific data products and improved accuracy of derived seismic calibrations.

Significant software engineering and development efforts have produced an object-oriented framework that provides database centric coordination between scientific tools, users, and data. Nearly a half billion parameters, signals, measurements, and metadata entries are all stored in a relational database accessed by an extensive object-oriented multi-technology software framework that includes elements of stored procedures, real-time transactional database triggers and constraints, as well as coupled Java and C++ software libraries to handle the information interchange and validation requirements. Significant resources were applied to schema design to enable recording of processing flow and metadata. A core capability is the ability to rapidly select and present subsets of related signals and measurements to the researchers for analysis and distillation both visually (JAVA GUI client applications) and in batch mode (instantiation of multi-threaded applications on clusters of processors). Development of efficient data exploitation methods has become increasingly important throughout academic and government seismic research communities to address multi-disciplinary large scale initiatives.

Effective frameworks must also simultaneously provide the researcher with robust measurement and analysis tools that can handle and extract groups of events effectively and isolate the researcher from the now onerous task of database management and metadata collection necessary for validation and error analysis. Sufficient information management robustness is required to avoid the loss of metadata that would lead to incorrect calibration results in addition to increasing the data management burden. Our specific automation methodology and tools improve the researchers ability to assemble quality-controlled research products for delivery into the NNSA Knowledge Base (KB). The GNEMRE Program software and scientific automation tasks also provide the robust foundation upon which synergistic and efficient development of seismic calibration research may be built.

OBJECTIVE

The NNSA GNEMRE Program has made significant progress enhancing the process of deriving seismic calibrations and performing scientific integration with automation tools. We present an overview of our software automation efforts and framework to address the problematic issues of improving the workflow and processing pipeline for seismic calibration products, including the design and use of state-of-the-art interfaces and database centric collaborative infrastructures. These tools must be robust, intuitive, and reduce errors in the research process. This scientific automation engineering and research will provide the robust hardware, software, and data infrastructure foundation for synergistic GNEMRE Program calibration efforts. The current task of constructing many seismic calibration products is labor intensive, complex, expensive and error prone. The volume of data as well as calibration research requirements has increased by several orders of magnitude over the past decade. The increase in quantity of data available for seismic research over the last two years has created new problems in seismic research; data quality issues are hard to track given the vast quantities of data, and this quality information is readily lost if not properly tracked in a manner that supports collaborative research. We have succeeded in automating many of the collection, parsing, reconciliation and extraction tasks individually. Several software automation tools have also been produced and have resulted in demonstrated gains in efficiency of producing derived scientific data products. In order to fully exploit voluminous real-time data sources and support new requirements for time-critical modeling, simulation, and analysis, continued expanded efforts to provide scalable and extensible computational framework will be required.

RESEARCH ACCOMPLISHED

The primary objective of the Scientific Automation Software Framework (SASF) efforts is to facilitate the development of information products for the GNEMRE regionalization program. The SASF provides efficient access to, and organization of, large volumes of raw and derived parameters, while also providing the framework to store, organize, integrate and disseminate derived information products for delivery into the NNSA KB.

These next generation information management and scientific automation tools are used together within specific seismic calibration processes to support production of tuning parameters for the United States Atomic Energy Detection System (USAEDS) run by the Air Force. The automation tools create synergy and synthesis between complex modeling processes and very large data sets by leveraging a scalable and extensible database centric framework. The requirements of handling large datasets in diverse formats, and facilitating interaction and data exchange between tools supporting different calibration technologies, has led to an extensive scientific automation software engineering effort to develop an object oriented database-centric framework using proven research-driven workflows and excellent graphics technologies as a unifying foundation.

The current framework supports integration, synthesis, and validation of the various different information types and formats required by each of the seismic calibration technologies. For example, the seismic location technology requires parameter data (site locations, bulletins), time-series data (waveforms), and produces parameter measurements in the form of arrivals, gridded geospatially registered correction surfaces and uncertainty surfaces. Our automation efforts have been largely focused on research support tools, RBAP (Regional Body-wave Amplitude Processor) and KBALAP (Knowledge Base Automated Location Assessment and Prioritization). Further, increased data availability and research requirements have driven the need for multiple researchers to work together on a broad area, asynchronously.

Database Centric Coordination Framework

As part of our effort to improve our efficiency we have realized the need to allow researchers to easily share their results with one another. For example, as the location group produces ground truth (GT) information, that information should become available for other researchers to use. Similarly, phase arrival picks made by any qualified user should also become immediately available for others to use. This concept extends to sharing of information about data quality. It should not be necessary for multiple researchers to have to repeatedly reject the same bad data, or worse, miss rejecting bad data. Rather, once data are rejected because of quality reasons they

should automatically be excluded from processing by all tools. We are implementing this system behavior using database tables, triggers, stored procedures and application logic. Although we are at the beginning of this implementation, we have made significant progress over the last year with several kinds of information sharing using the new database centric coordination framework. These are discussed below.

Significant software engineering and development efforts have been applied successfully to construct an object oriented database framework that provides database centric coordination between scientific tools, users, and data. A core capability this new framework provides is information exchange and management between different specific calibration technologies, and their associated automation tools, such as seismic location (e.g,. KBALAP), seismic identification (e.g., RBAP), and data acquisition and validation (e.g., KBITS). A relational database (ORACLE) provides the current framework for organizing parameters key to the calibration process from both Tier 1 (raw parameters such as waveforms, station metadata, bulletins, etc.) and Tier 2 products (e.g., derived measurements such as GT, amplitude measurements, calibration and uncertainty surfaces). Seismic calibration technologies (location, identification, etc.) are connected to parameters stored in the relational database by an extensive object-oriented multi-technology software framework that includes elements of schema design, PL/SQL, real-time transactional database triggers, and constraints, as well as coupled Java and C++ software libraries to handle the information interchange and validation requirements. This software framework provides the foundation upon which current and future seismic calibration tools may be based. Interim results and a complete set of working parameters must be available to all research teams throughout the entire processing pipeline. Finally, our development staff has continually and efficiently leveraged our java code library, achieving 45% code reuse (in lines of code) throughout several thousand java classes. Source code control is managed by CVS (source code) and ER Studio (schema designs).

Sharing of Derived Event Parameters

In order to calibrate seismic monitoring stations, the LLNL Seismic Research Database (SRDB) must incorporate and organize the following categories of primary and derived measurements, data, and metadata:

Tier 1: Contextual and raw data
- Station parameters and instrument responses
- Global and regional earthquake catalogs
- Selected calibration events
- Event waveform data
- Geologic/geophysical data sets
- Geophysical background model

Tier 2: Measurements and research results
- Phase picks
- Travel time and velocity models
- Rayleigh and Love surface wave group velocity measurements
- Phase amplitude measurements and magnitude calibrations
- Detection and discrimination parameters
- Integrated/merged GT data sets

Automating Tier 1

Corrections and parameters distilled from the calibration database provide needed contributions to the NNSA KB for the ME/NA/WE region and will improve capabilities for underground nuclear explosion monitoring. The contributions support critical functions in detection, location, feature extraction, discrimination, and analyst review. Within the major process categories (data acquisition, reconciliation and integration, calibration research, product distillation) are many labor intensive and complex steps. The previous bottleneck in the calibration process was in the reconciliation and integration step. This bottleneck became acute in 1998 and the KBITS suite of automated parsing, reconciliation, and integration tools for both waveforms and bulletins (ORLOADER, DDLOAD, UpdateMrg) were developed. The KBITS suite provided the additional capability required to integrate data from many data sources and external collaborations. Data volumes grew from the 11,400 events with 1 million

waveforms in 1998 to over half a billion raw parameters, measurements and associated 100 terabytes of continuous data today (e.g., Ruppert et al., 1999; Elliott et al., 2006).

Continuous seismic data automation

We receive enormous amounts of seismic data daily that must be properly processed. Previously, the movement and management of data were performed manually by our IT staff and were extremely time intensive and inefficient. In response, we designed and implemented a distributed (multi-machine), multi-process solution to help automate the collection, movement, cataloging, reporting, viewing and error processing of waveform segmentation data from multiple academic and government sources. The distributed processes are being written in Java, using encrypted data transfers, logging, an embedded Java relational database (Derby) for maintaining transfer metadata, and a monitoring interface for reporting and quality control. Also, the ability to easily query and view available continuous data was added to improve the efficiency of quality control and recording of metadata.

Automating Tier 2

As the data sources required for calibration have increased in number and source location, it has become clear that the manual, labor intensive process of humans transferring thousands of files and unmanageable metadata cannot keep the KBITS software fed with data to integrate, nor could the seismic researcher efficiently and consistently find, retrieve, validate, or analyze the raw parameters necessary to effectively produce seismic calibrations in an efficient manner. Significant software engineering and development efforts were applied to address this critical need to produce software aids for the seismic researcher. Thus, the main focus of our development efforts is on the development of two scientific automation tools, RBAP and KBALAP, for seismic location and seismic identification calibration tasks, respectively.

The RBAP Program

The RBAP is a station-centric Tier 2 automation tool; it is an interactive, graphical and highly specifiable software program that acts as a picker and an MDAC calculator (Elliott et al., 2006). RBAP helps to automate the process of making amplitude measurements of regional seismic phases for the purpose of calibrating seismic discriminants at each station. RBAP generates station centric raw, and Magnitude Distance Amplitude Correction (MDAC) corrected Pn, Pg, Sn and Lg amplitudes along with their associated calibration parameters (e.g. phase windows, MDAC values, reference events, etc.) in database tables. It strictly follows Working Group (WG) 2 standardized MDAC processing, and it replaces the original collection of LLNL scripts. RBAP has a number of advantages over the previous scripts. It is much faster, significantly easier to use, allows for collaboration, scales more easily to a larger number of events and permits efficient project revision and updating through the database.

RBAP projects are station centric; stations can be either single stations or arrays, where arrays focus on a reference element. Each project also specifies one or more regions, which can be simple rings or user-defined polygons; each region may be assigned its own velocity model. Once defined, concepts such as geographic regions are available to all researchers and all projects; interfaces include extensive use of modern mapping technologies and data tables. Table schema are driven by research workflows. RBAP makes use of the data type manager concept extensively, and includes separate managers for velocity models, regions and events. Events are shown color-coded on a map for ease of use. RBAP also includes a graphical phase picker that generates windows automatically for the Pn, Pg, Sn and Lg phases using times predicted by the velocity model. The picker is geared towards using signal-to-noise ratios for regional body wave amplitude measurements, and picks are automatically advanced according to applied velocity models. A new GIS and picking subsystem is now in place. The new GIS package will replace the MapObjects system currently in use.

Some key features of RBAP are listed below:

- Based on WG 2 standardized algorithm
- Fast and efficient calibration
- Project management
- Utilizes database for up-to-date results
- Batch processing
- Engenders collaboration, consistency and efficiency

Support for tiered projects—new in FY07

Users can now create a parent "calibration" project which would define the velocity model and MDAC parameters for a specific station and region. Typically this would be done using earthquake only data. Subsequent "child" projects could then be created for the same station and region, and MDAC corrected amplitudes would be calculated using the parent's calibrated parameters. This will allow us to explore different source types in understanding discrimination.

Adding MDAC and Coda Magnitude processing module to RBAP—new in FY07

MDAC calibration in RBAP has been enhanced with the addition of a DiscrimTool utility. The DiscrimTool is a Java based GUI program that allows a user to retrieve large blocks of raw and MDAC corrected amplitude measurements from the database based on a user defined discriminant
(e.g., Pg (6–8 Hz)/Lg (6–8 Hz)). Multiple data sets can be selected and plotted so that users can investigate different discriminants on the fly. The tool is currently being modified to allow an inversion for optimal discriminant combinations.

To supplement RBAP in source identification we are developing a waveform processing tool (WFT) with the capability of measuring amplitudes and coda magnitudes. WFT was originally written as part of the Hydroacoustic Blockage Assessment Tool (HABAT) code, but has been enhanced to work generally with seismic data and has since been used in combination with seismic inversion projects (Flanagan et al., 2006). We have recently added two programs to the WFT: the Amplitude Measurement Tool (AMT) calculates spectral amplitudes, while the Coda Tool calculates coda magnitudes for calibrated regions. The AMT (Figure 1) was designed to allow basic amplitude measurements and MDAC processing for flatfile data—specifically for cases when the LLNL database in inaccessible, or when investigating phases that are not normally dealt with (such as the hydroacoustic T phase). It performs all the basic RBAP amplitude calculation using the same MDAC parameter setup developed in RBAP, allows creation of DiscrimData tables and can plot the results. The Coda Tool (Figure 2) will allow an investigator with a basic background in coda theory to read either database or flat file seismic data and calculate source magnitudes given a regional calibration. Once data are read in, the user can calculate seismic data envelopes, calculate synthetics based on published theory (Mayeda et al., 2003), compute the spectral amplitudes, add site and path corrections and compute the final coda Mw.

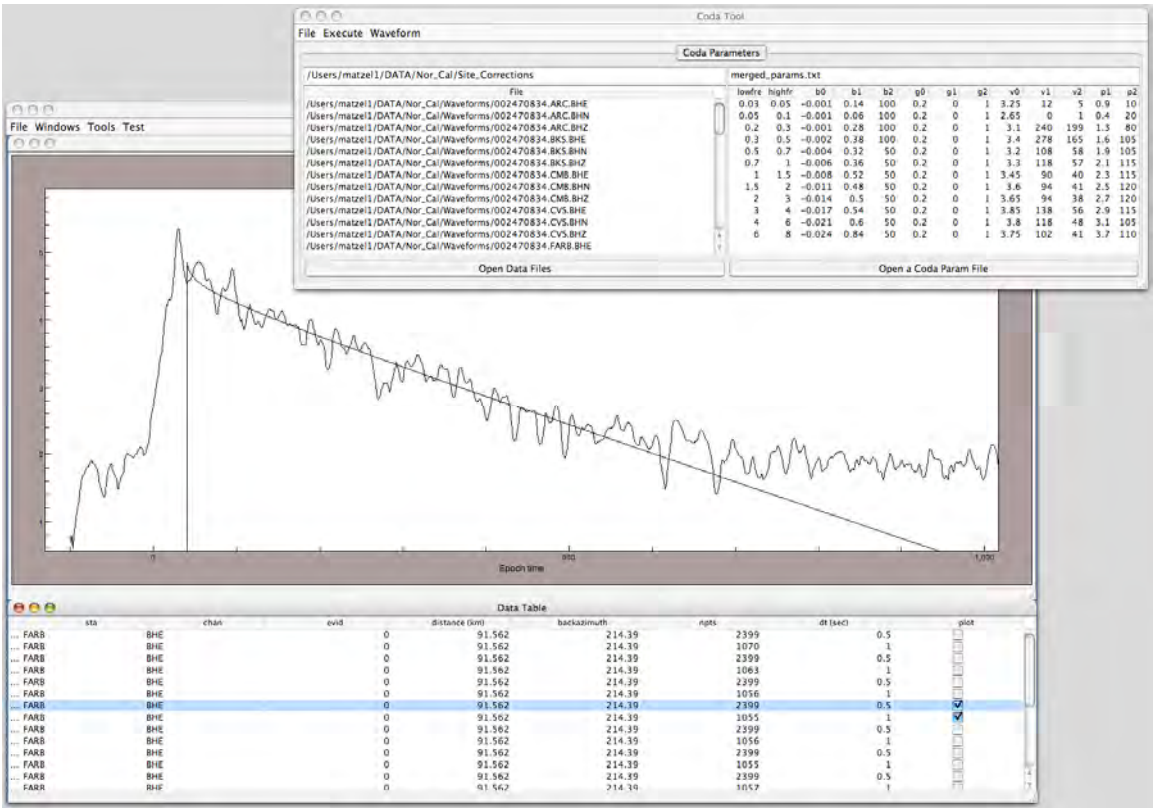

Figure 1. A screenshot of the Coda Mw measurement tool, illustrating the measured data envelopes compared with synthetic envelopes.

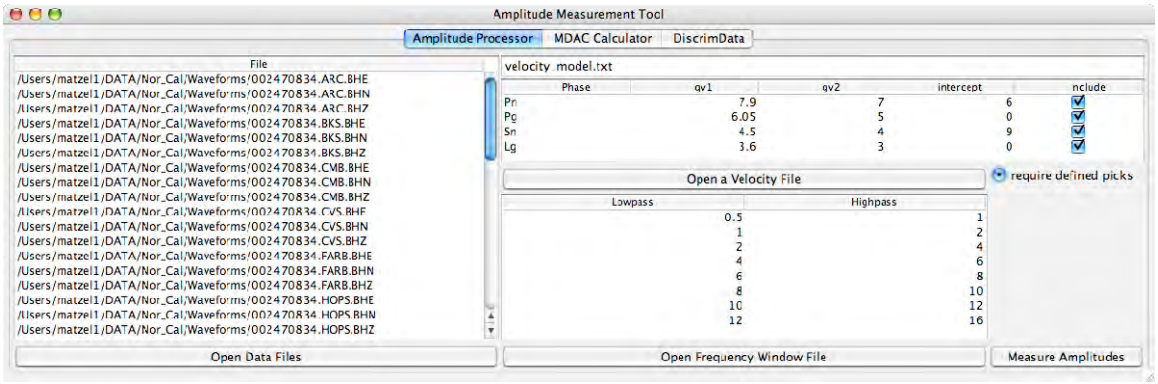

Figure 2. A screenshot of the Amplitude measurement tool, which calculates spectral amplitudes for the seismic analysis code (SAC) and CSS flatfiles and applies MDAC corrections to the results.

The KBALAP Program

The Knowledge Base Automated Location Assessment and Prioritization (KBALAP) program is another Tier 2, event centric automation effort in the GNEMRE program (Elliott et al., 2006). It is a highly interactive, graphical tool which uses a set of database services and a client application based on data selection profiles that combine to efficiently produce location ground truth data which can be used in the production of travel time correction surfaces, and as part of the preferred event parameters used by other tools in our processing framework.

KBALAP's database services are responsible for evaluating bulletin and pick information as it enters the system to identify origin solutions that meet pre-defined GT criteria with no further processing, and for identifying events that would likely meet a pre-defined GT level if a new origin solution were produced using available arrivals. The

database service is also responsible for identifying events that should have a high priority for picking based on their existing arrival distribution, and the availability of waveform data for stations at critical azimuths and distances.

The interactive portion of KBALAP has the following principal functions:

- Production of GT origins through prioritized picking and location,
- Specification of GT-levels for epicenter, depth, origin time, etype
- Batch-mode location of externally produced GT information
- Production of array azimuth-slowness calibration data
- Easy review and modification of event parameters used by all GNEM researchers

Some key KBALAP features are listed below:
- Fast and efficient location
- Project management and collaboration
- Batch processing

The Site Merge Effort—New in FY07

Information about seismic station position and installed instrumentation is to a greater or lesser extent, fundamental to all the processing done within the GNEM Program. However, despite the importance of accurate information about seismic stations, in practice it is difficult to obtain a compilation of station information that does not include errors. There are many sources for these errors, including the following:
- Imprecise surveying/reporting by station operators
- Transcription errors
- Unrecorded station movements or equipment modifications.

The situation is complicated even more by the fact that many different compilations have been produced using different sources and different assumptions, and these compilations are inconsistent with one another.

In the past, we have dealt with inconsistencies on a case by case basis. When a problem was identified, we would "fix" the offending data in our SITE table and go on. While this approach was problematic in a number of ways, given the limitations of the CSS SITE table and our need to build out other parts of our infrastructure, it was judged to be the best we could do. As the labs coordinate more in the process of producing calibration products for monitoring purposes, the need for a unified, consistent SITE table has become more apparent. Producing and maintaining such a table by integrating and reconciling our individual SITE tables is an even more difficult undertaking than simply maintaining an internal-use-only SITE table. Mainly this is because of the need to resolve conflicts in a way that is trackable, reproducible, and with documented decisions/assumptions.

We were tasked this year with performing the location ground truth merge (GT merge) between contributing laboratories. This effort depends critically on having a unified SITE table of the highest possible quality. This has accelerated our work on producing a SITE merge, and we now have a system that while still in need of further development, is adequate for purposes of the GT merge. Our merge process is implemented in Java and in PL/SQL and uses a number of tables to track metadata about the merge process. The codes allow for repeated contributions by the same author allowing, for example, updating of the merged SITE as new versions of the NEIC station book become available. The results and documentation will be provided to the relevant NNSA GNEM working groups for coordination and consideration.

Our approach to merging SITE data is to handle the position, elevation, operating epochs, station movements, array membership and possible code aliasing separately. We take this approach because there is no guarantee that a particular contributor's information about a SITE will be uniformly better or worse than information from another source.

When SITE data come into the system, they are placed into a multi-author site table (and supporting tables) that hold all the unmerged data. Before a new merge is executed, a process is run that identifies unresolved discrepancies (over a threshold value) in position and elevation. Any stations with unresolved discrepancies are added to

appropriate discrepancy tables. Although the merge can continue without resolving the discrepancies, these stations will not become part of the merged SITE table.

Discrepancies can be resolved in one of two ways; either by making entries in a preferred position (or preferred elevation) table or by making entries in a rejected position (elevation) table. The reason column in each of these tables allows up to a 2000 character discussion of the reason for the decision. With this system, it is relatively easy to find out why a particular position or elevation was or was not used, and if better information becomes available it is easy to change the first decision and re-do the merge. The software also helps resolve position discrepancies by producing KML files that allow display in Google Earth of clusters of discrepant station position estimates.

Handling of alternate station codes is still somewhat rudimentary in this system. The NEIC station book lists over 500 such alternate codes. These are stored in a table and our NEIC and ISC parsers do not create entries in the multi-author SITE table for these codes. However, many of the contributing SITE tables have many alternate codes that are not specifically called out as such. Currently, our system identifies candidate alternate codes by doing a pair-wise comparison of positions for stations in the multi-author SITE table. Candidates not already in the alternate code table are placed in a candidate table where they can be inspected manually. Alternate codes are not included in the final merged SITE table. The current system does not yet handle temporary alternate codes.

We have used our SITE merging system to combine SITE information from the most recent NEIC and ISC station books, the current NNSA GNEMRE SITE tables, and the Incorporated Research Institutions for Seismology (IRIS) SITE table (derived from data-less SEED volumes minus temporary deployments and California stations). There are nearly 36,000 entries in the multi-author site table which produce nearly 14,000 merged SITE entries. There are 166 preferred positions, 41 preferred elevations, 55 rejected positions, and 514 rejected elevations. The position overrides were determined mostly through a combination of inspection in Google Earth and residual analysis using GT events. Most of the elevation overrides were arrived at by comparison of reported elevations with elevations computed using the gtopo30 elevation model.

The GT Merge Effort

It has become necessary to merge the GT25 and better datasets between contributing laboratories for use in both a tomographic inversion for *Pn* velocity of Eurasia and for computing first-*P* correction surfaces using the KBCIT software. The merge is intended both to resolve GT common between labs (choosing the better GT estimate when possible) and to perform an extensive set of quality control steps to the origin and phase data. We have developed a software system implemented in Java, Oracle relational database, and PL/SQL to perform this merge process (Flanagan et al., 2007).

The software brings together into a GTMERGE schema the GT data from both labs along with all supporting ORIGIN, ORIGERR, ASSOC and ARRIVAL data. All data are given new IDs unique within the GTMERGE schema, and events in common between labs are identified by spatial-temporal correlation. The Bondar-Myers-Engdahl-Bergman (BMEB) Epicenter accuracy criteria are used (Bondar et al., 2004). For those events in common, a set of ranking rules is applied to select the best non-BMEB GT. A small subset of the input GT that cannot be ranked is placed in a manual resolution table.

The quality check (QC) steps performed by the software include the following:
- Enforcing common phase naming conventions
- Removing arrivals that are too early or too late to be of interest
- Removing phases not of interest
- Identifying and removing arrivals that are too discrepant to be useful
- Enforcing distance-dependent phase name conventions
- Choosing a “best” arrival for each EVID-STA-PHASE table

After QC is complete, the system evaluates all the BMEB GT for strict adherence to their criteria. All events that fail this check have a new origin solution computed using phase gathers appropriate to the GT level. If the new solution meets its criterion, then it is included in the final merge results. Otherwise, the event is rejected. When all GT have been re-evaluated, a new set of constrained origin solutions is computed using teleseismic P-arrivals. These

"baselined" origins are the final product of the merge effort. The data set produced by the merge effort includes about 97,000 distinct events with nearly 20,000,000 arrivals.

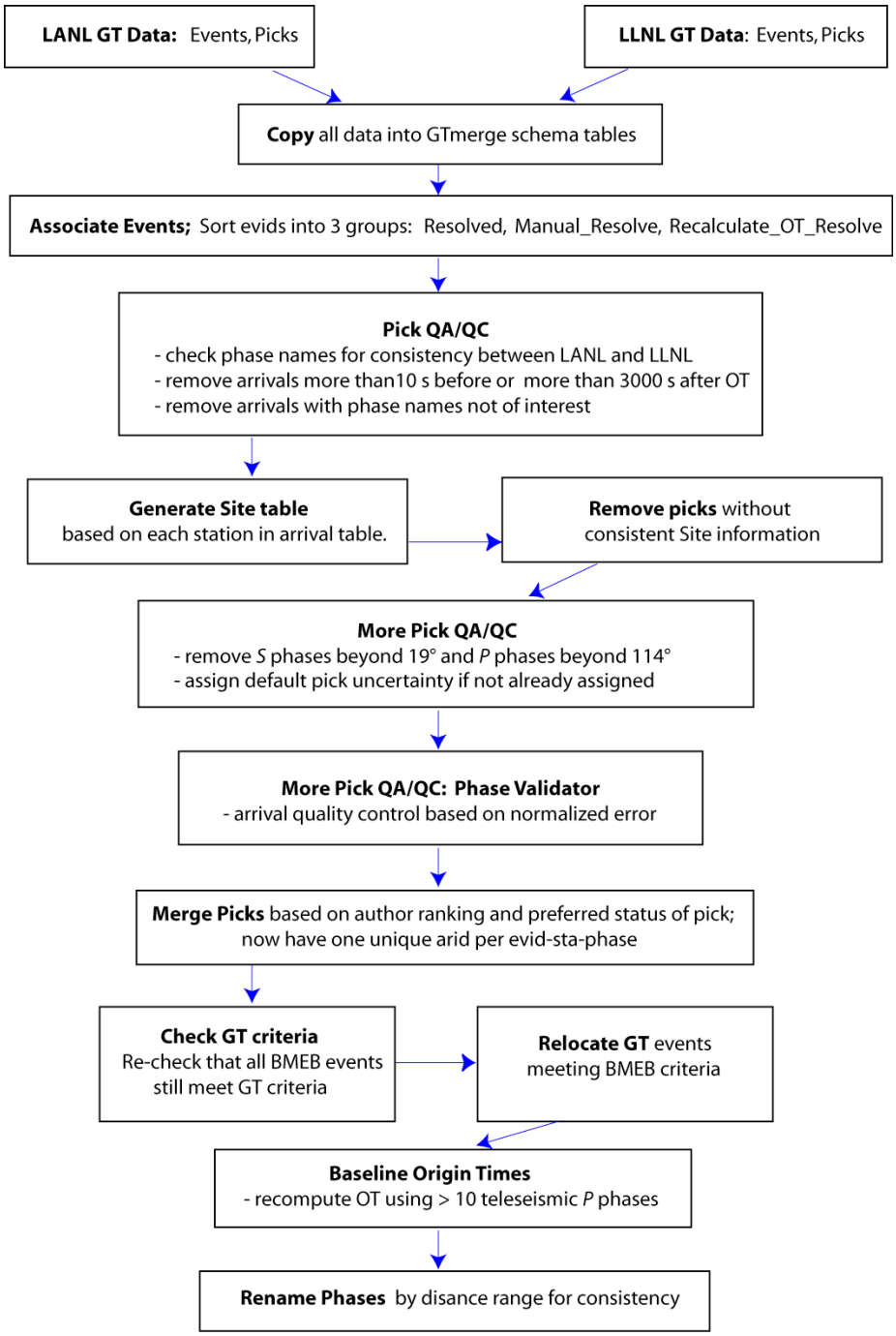

Figure 3. Overview of the GT merge process.

CONCLUSIONS AND RECOMMENDATIONS

We present an overview of our software automation efforts and framework to address the problematic issues of consistent handling of the increasing volume of data, collaborative research efforts and researcher efficiency, and overall reduction of potential errors in the research process. By combining research driven interfaces and workflows

with graphics technologies and a database centric information management system coupled with scalable and extensible cluster based computing, we have begun to leverage a high performance computational framework to provide increased calibration capability. These new software and scientific automation initiatives will directly support our current mission including rapid collection of raw and contextual seismic data used in research, provide efficient interfaces for researchers to measure and analyze data, and provide a framework for research dataset integration. The initiatives will improve time-critical data assimilation and coupled modeling and simulation capabilities necessary to efficiently complete seismic calibration tasks. This GNEMRE Program's scientific automation, engineering and research, will provide the robust hardware, software, and data infrastructure foundation for synergistic calibration efforts.

ACKNOWLEDGEMENTS

We acknowledge the assistance of the LLNL computer support unit in implementing and managing our computational infrastructure. We thank Jennifer Aquilino, Laura Long, and John Hernandez for their assistance in configuration and installation of our Linux cluster and workstations.

REFERENCES

Bondar, I., S. Myers, E. Engdahl, and E. Bergman (2004). Epicenter accuracy based on seismic network criteria, *Geophys. J. Int.* 156: 483–496.

Elliott. A. , D. Dodge, M. Ganzberger, T. Hauk, E. Matzel, and S. Ruppert (2006). Enhancing seismic calibration research through software automation and scientific information management, in *Proceedings of the 28th Seismic Research Review: Ground-Based Nuclear Explosion Monitoring Technologies*, LA-UR-06-5471, Vol. 2, pp. 967–975.

Flanagan, M, D. Dodge, and S. Myers (2007), GT Merge Processing Documentation—Beta Version, in University of California, Radiation Laboratory, 1–15 (in review).

Flanagan, M., E. Matzel, S. van der Lee, H. Bedle, M. Pasyanos, F. Marone, B. Romanowicz, C. Schmid, and A. Rodgers (2006), Joint inversion for three-dimensional velocity structure of the broader Africa-Eurasia collision region, in *Proceedings of the 28th Seismic Research Review: Ground-Based Nuclear Explosion Monitoring Technologies*, LA-UR-06-5471, Vol. 1, pp. 397–406.

Mayeda, K., A. Hofstetter, J. L. O'Boyle, and W. Walter (2003). Stable and transportable regional magnitudes based on coda-derived moment-rate spectra, *BSSA* 93: 224–239.

Ruppert, S., T. Hauk, J. O'Boyle, D. Dodge, and M. Moore (1999). Lawrence Livermore National Laboratory's Middle East and North Africa Research Database, in *Proceedings of the 21st Seismic Research Symposium: Technologies for Monitoring the Comprehensive Nuclear-Test-Ban Treaty*, Vol. 1, pp. 243.

Appendices

Acronyms, etc.

Acronym	Definition
AEDS	Atomic Energy Detection System
AFRL	Air Force Research Laboratory
AFTAC	Air Force Technical Applications Center
AIC	Akaike Information Criterion
AK135	seismic travel time model
ANFO	ammonium nitrate fuel oil
ANOVA	analysis of variance code
ArcView	commercial GIS software
ARSA	Automated Radioxenon Sampler/Analyzer
BDSN	Berkeley Digital Seismic Network
BEM	boundary element method
Be-7	beryllium-7
CDSN	Chinese Digital Seismic Network
CEA	Commissariat l'Energie Atomique (French bulletin)
ChISS	Russian abbreviation for multichannel spectral seismometer
CLVD	compensated linear vector dipole
CMT	Harvard centroid moment tensor
CodaMag	tool to implement magnitude calculations (Mayeda, 1993; Mayeda and Walter, 1996)
CRUST2.0	crustal model (Bassin et al., 2000)
CTBT	Comprehensive Nuclear-Test-Ban Treaty
CTBTO	Comprehensive Nuclear-Test-Ban Treaty Organization
CU	University of Colorado
CUB2.0	3D global models (Shapiro et al., 2002)
CU-Boulder	University of Colorado, Boulder
DEM	digital elevation model
DMC	Data Management Center (IRIS)
DOB	depth of burial
DoD	Department of Defense
DOE	Department of Energy
DOS	Department of State
DSS	deep seismic sounding
EDR	Earthquake Data Reports - a USGS publication
EHB	Engdahl, E.R., van der Hilst, R. & Buland, R., 1998. Global teleseismic earthquake relocation with improved travel times and procedures for depth determination, Bull. Seismol. Soc. Amer., 88, 722-743
ERL	Earth Resources Laboratory (MIT)
ERS	European Remote Sensing (satellites)
ETOPO	earth topographic (database)
ETOPO5	terrain model
EventID	tool to implement event discrimination (Hartse et al., 1997; Walter et al., 1999)
EvLoc	location software
FDSN	Federation of Digital Seismic Networks
FD	finite difference
FE	finite element
F-K	frequency wavenumber
Fstat, F-stat	F-statistic
FSU	Former Soviet Union
GBF	generalized beamforming
GEON	Geosciences Network

Acronym	Definition
GII	Geophysical Institute of Israel
GIS	geographical information system
GMT	generic mapping tool
GNEMRE	Ground-Based Nuclear Explosion Monitoring Research and Engineering Program
GSN	global seismographic network
GT	ground truth
GTx	ground truth information of accuracy x km
HDC	hypocentroidal (or hypocentral) decomposition
HE	high explosive
HPGe	high purity germanium
HPXe	high-pressure xenon
HydroCAM	Hydroacoustic Coverage Assessment Model
Hz	hertz
IAEA	International Atomic Energy Agency
IASPEI	International Association of Seismology and Physics of the Earth's Interior
iasp91	standard earth model
IDA	International Deployment of Accelerometers
IDC	International Data Centre
IDG	Russian Institute for the Dynamics of the Geospheres
ILS	iterative least squares
IMS	International Monitoring System
InfraMAP	Infrasound Modeling of Atmospheric Propagation
InSAR	Interferometric Synthetic Aperture Radar
IRIS	Incorporated Research Institutions for Seismology
IRP	integrated research product
ISC	International Seismological Centre
ISTC	International Science and Technology Center
JHD	joint hypocenter determination
KB	Knowledge Base
KBCIT	Knowledge Base Calibration Integration Tool
KMA	Korean Meteorological Administration
KNDC	Kazakhstan National Data Center
LANL	Los Alamos National Laboratory
LBNL	Lawrence Berkeley National Laboratory
LDA	linear discriminant analysis
LDEO	Lamont-Doherty Earth Observatory
LLNL	Lawrence Livermore National Laboratory
LVZ	low velocity zones
Matlab	commercial software application
MatSeis	seismic analysis package developed by SNL using Matlab
mb	body wave magnitude
Md	duration magnitude
MDAC	magnitude and distance amplitude corrections
MEMS	microelectromechanical systems
MIT	Massachusetts Institute of Technology
Ms	surface wave magnitude
MSE	mean squared error
MSU	Michigan State University
MUSIC	MULtiple Signal Classification
Mw	moment magnitude
NA-22	Office of Nonproliferation Research and Development

Acronym	Definition
NASA	National Aeronautics and Space Administration
NCEDC	Northern California Earthquake Data Center
NEIC	National Earthquake Information Center
NEM R&E	Nuclear Explosion Monitoring Research and Engineering
Nm	newton-meters
NNSA	National Nuclear Security Administration
NOAA	National Oceanic and Atmospheric Administration
NORSAR	Norwegian Seismic Array
NPE	Nonproliferation Experiment
NRL	Naval Research Laboratory
NTS	Nevada Test Site
PASSCAL	Program for the Array Seismic Studies of the Continental Lithosphere
PDF	portable document format
PNE	peaceful nuclear explosions
PNNL	Pacific Northwest National Laboratory
PrepCom	Preparatory Commission
PSD	power spectral density
PSU	Penn State University
Q	Seismic Q factor (reciprocal of attenuation)
RASA	Radionuclide Aerosol Sampler Analyzer
RCA	reciprocal cluster analysis
REB	Reviewed Event Bulletin - an IDC report
RF	receiver functions
RGA	residual gas analyzer
RMS	root mean square (errors)
ROC	receiver operating characteristic
RSS	residual sum of squares
SAC	seismic analysis code
SBIR	Small Business Innovation Research
SCSN	Southern California Seismic Network
SEM	spectral element method
SLU	Saint Louis University
SMDC	Space Missile Defense Command (Army)
SNL	Sandia National Laboratories
SNR	signal-to-noise ratio
SOFAR Channel	SOund Fixing And Ranging - primary sound channel in the ocean
SP	short period
STA/LTA	short-term average/long-term average
SVD	singular value decomposition
T* (t-star)	A measure of the "damping" or attenuation along a path. T* is the ratio of the travel time along a ray path to the average Q (seismic "quality" factor) along it.
T-phase	hydroacoustic phase
UCB	University of California, Berkeley
UCSD	University of California, San Diego
UNE	underground nuclear explosions
UNR	University of Nevada, Reno
USAEDS	United States Atomic Energy Detection System
USGS	United States Geological Survey
USNDC	United States National Data Center
WSMR	White Sands Missile Range

Guide to Seismic Phases

The change of seismic velocities within Earth, as well as the possibility of conversions between compressional (P) waves and shear (S) waves, results in many possible wave paths. Each path produces a separate seismic phase on seismograms. Seismic phases are described with one or more letters, each of which describes a part of the wave path. Upper case letters denote travel through a part of the earth (e.g. P or S), and lower case letters denote reflections from boundaries. A complete, standardized nomenclature for seismic wave paths is available at the web site: http://www.isc.ac.uk/Documents/IASPEI/sspl.html. This information has also been published [Storchak, D.A., J. Schweitzer, P. Bormann (2003), "The IASPEI Standard Seismic Phase List", Seismol. Res. Lett. 74, 6, 761-772], and a pdf file of this publication is available from the same web site.

In the verification context, wave propagation in Earth is divided into *teleseismic* (distances greater than 2000 kilometers) paths and *regional* (distances less than 2000 kilometers) paths.

Teleseismic Phases

In these plots, the seismic event is at the left, and seismic ray paths are shown to possible stations at several angular distances from the event.

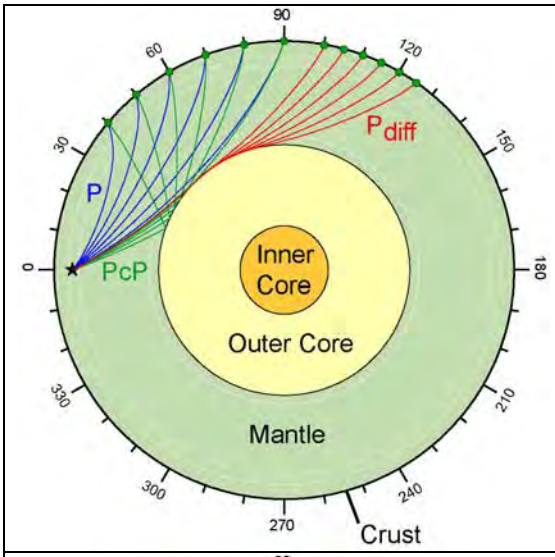

P A primary (compressional) wave that follows a simple path from event source to the station.

PcP A P wave that goes downward through the mantle (the first "P"), is reflected from the top of the outer core ("c") and goes upward through the mantle to the station (second "P").

P_{diff} A P wave that has been bent (diffracted) around the outer core boundary and arrives at a station in the ray "shadow" of the outer core.

S A secondary (shear) wave that follows a path similar to the P wave (not shown).

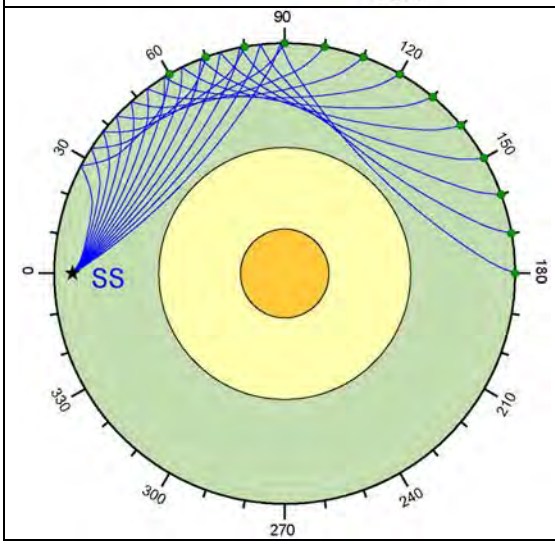

SS A shear wave that has traveled through the mantle ("S"), undergone one reflection from the underside of Earth's surface and traveled again through the mantle (second "S"). Unlike with most other reflected waves, there is no separate letter to denote the reflection at the surface; it is implicit.

PP A compressional wave that follows paths similar to those of SS (not shown).

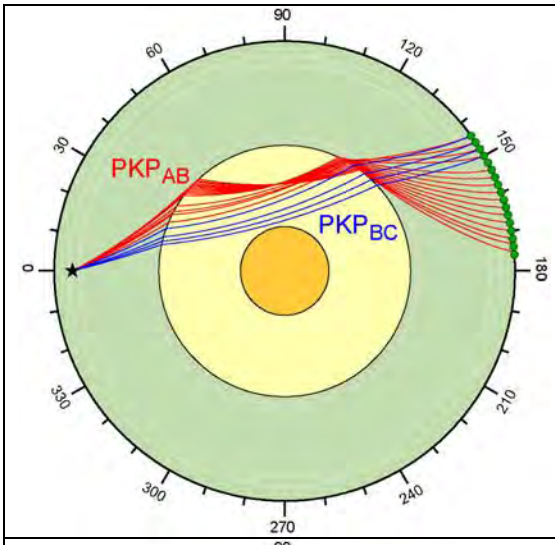	**PKP**	A P wave that has traveled through the mantle ("P"), been transmitted across the mantle-outer core boundary and traveled through the outer core ("K"), transmitted back across the outer core-mantle boundary and traveled as a P wave to the station ("P"). Because of the large difference between the P wave velocity in the mantle and the outer core, this wave is bent (refracted) strongly at the boundary. Seismic waves can follow slightly different paths (labeled PKP_{AB}, PKP_{BC}) and still arrive at about the same time.
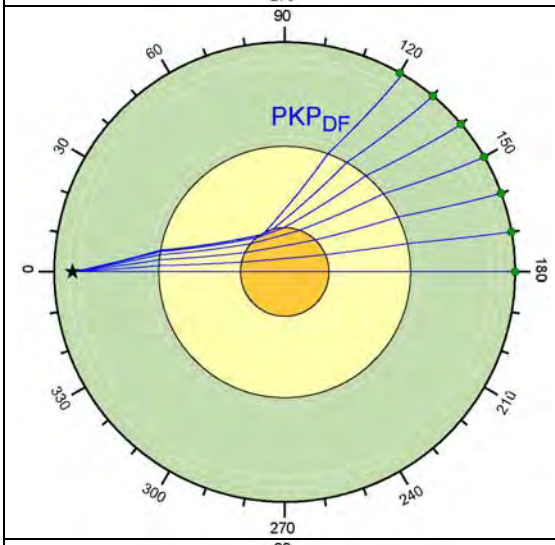	**PKIKP**	A P wave that has traveled through the mantle ("P"), been transmitted across the mantle-outer core boundary ("K"), crossed the outer-core inner-core boundary and traveled through the inner core as a P wave ("I"), then followed a similar path in reverse to get from the inner core to the station (the second "KP"). An alternate name for this phase is PKP_{DF} (shown in the path illustration).
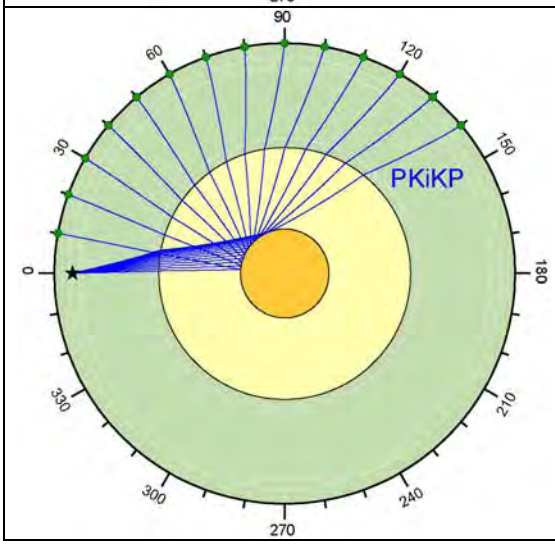	**PKiKP**	This phase has followed a series of paths similar to the PKIKP phase, except it was reflected off the top of the inner core-outer core boundary (this is the "i" part of the path), rather than being transmitted through the inner core.

Figures courtesy of Ed Garnero, Arizona State University (http://garnero.asu.edu/research_images/index.html)

Depth Phases

A number of "depth" phases are referred to in the proceedings. The paths of these phases are nearly the same as P waves. The depth phases all result from a reflection from the Earth's surface near the epicenter of the event. The time delay between the P wave and the depth phase is proportional to the depth of the event (hence the term "depth" phase).

pP A P wave that started out upward from the source ("p"), reflected off the Earth's surface, and traveled to the station as a P wave ("P").

sP An S wave that started out upward from the source ("s"), reflected off the earth's surface and also converted to a P wave, which then traveled to the station as a P wave ("P").

pwP Similar to the pP phase. A P wave that started out upward from the source ("p"), reflected off the ocean surface ("w" - water) and traveled to the station as a P wave ("P").

Regional Phases

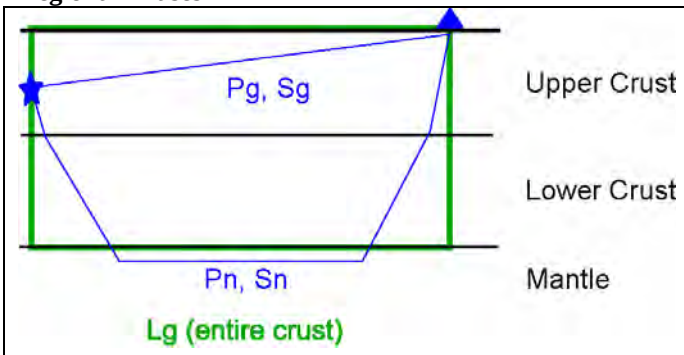

A highly simplified representation of the crust of Earth, which is seldom so simple and flat. Changes of crustal thickness and velocities can disrupt crustal phases, notably Lg.

Pg (Sg) At short event-station distances, an upgoing P (S) wave from a source in the upper crust (depicted here) or a P (S) wave bottoming in the upper crust. At larger distances the Pg phase includes arrivals resulting from multiple P-wave reverberations within the entire crust that propagate at a group velocity around 5.8 km/s.

Pn (Sn) A P (S) wave bottoming in the uppermost mantle or an upgoing P wave from a source in the uppermost mantle

Lg A wave group observed at larger regional distances and caused by superposition of multiple S-wave reverberations and S to P and/or P to S conversions inside the whole crust. The maximum energy travels with a group velocity around 3.5 km/s